IFMBE Proceedings

César A. González Díaz · Christian Chapa González · Eric Laciar Leber · Hugo A. Vélez · Norma P. Puente · Dora-Luz Flores · Adriano O. Andrade · Héctor A. Galván · Fabiola Martínez · Renato García · Citlalli J. Trujillo · Aldo R. Mejía (Eds.)

Volume 75

VIII Latin American Conference on Biomedical Engineering and XLII National Conference on Biomedical Engineering

Proceedings of CLAIB-CNIB 2019, October 2–5, 2019, Cancún, México

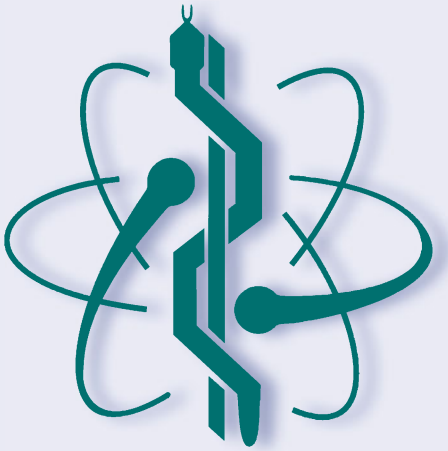

Springer

IFMBE Proceedings

Volume 75

Series Editor

Ratko Magjarevic, Faculty of Electrical Engineering and Computing, ZESOI, University of Zagreb, Zagreb, Croatia

Associate Editors

Piotr Ładyżyński, Warsaw, Poland
Fatimah Ibrahim, Department of Biomedical Engineering, Faculty of Engineering, University of Malaya, Kuala Lumpur, Malaysia
Igor Lackovic, Faculty of Electrical Engineering and Computing, University of Zagreb, Zagreb, Croatia
Emilio Sacristan Rock, Mexico DF, Mexico

The IFMBE Proceedings Book Series is an official publication of *the International Federation for Medical and Biological Engineering* (IFMBE). The series gathers the proceedings of various international conferences, which are either organized or endorsed by the Federation. Books published in this series report on cutting-edge findings and provide an informative survey on the most challenging topics and advances in the fields of medicine, biology, clinical engineering, and biophysics.

The series aims at disseminating high quality scientific information, encouraging both basic and applied research, and promoting world-wide collaboration between researchers and practitioners in the field of Medical and Biological Engineering.

Topics include, but are not limited to:

- Diagnostic Imaging, Image Processing, Biomedical Signal Processing
- Modeling and Simulation, Biomechanics
- Biomaterials, Cellular and Tissue Engineering
- Information and Communication in Medicine, Telemedicine and e-Health
- Instrumentation and Clinical Engineering
- Surgery, Minimal Invasive Interventions, Endoscopy and Image Guided Therapy
- Audiology, Ophthalmology, Emergency and Dental Medicine Applications
- Radiology, Radiation Oncology and Biological Effects of Radiation

IFMBE proceedings are indexed by SCOPUS and EI Compendex. They are also submitted for ISI proceedings indexing.

Proposals can be submitted by contacting the Springer responsible editor shown on the series webpage (see "Contacts"), or by getting in touch with the series editor Ratko Magjarevic.

More information about this series at http://www.springer.com/series/7403

César A. González Díaz ·
Christian Chapa González ·
Eric Laciar Leber · Hugo A. Vélez ·
Norma P. Puente · Dora-Luz Flores ·
Adriano O. Andrade · Héctor A. Galván ·
Fabiola Martínez · Renato García ·
Citlalli J. Trujillo · Aldo R. Mejía
Editors

VIII Latin American Conference on Biomedical Engineering and XLII National Conference on Biomedical Engineering

Proceedings of CLAIB-CNIB 2019, October 2–5, 2019, Cancún, México

Springer

Editors
César A. González Díaz
Instituto Politécnico Nacional
Mexico City, Mexico

Eric Laciar Leber
Universidad Nacional de San Juan
San Juan, Argentina

Norma P. Puente
Universidad Autónoma de Nuevo León
Nuevo León, Mexico

Adriano O. Andrade
Universidade Federal de Uberlândia
Uberlândia, Brazil

Fabiola Martínez
Universidad Autónoma Metropolitana
Mexico City, Mexico

Citlalli J. Trujillo
Instituto Nacional de Rehabilitación
Mexico City, Mexico

Christian Chapa González
Departamento de Ingeniería
Electrica y Computación
Universidad Autónoma de Ciudad Juárez
Chihuahua, Mexico

Hugo A. Vélez
Universidad de Guadalajara
Guadalajara, Mexico

Dora-Luz Flores
Universidad Autónoma de Baja California
Ensenada, Baja California, Mexico

Héctor A. Galván
Instituto Nacional de Cancerología
Mexico City, Mexico

Renato García
Universidad Federal de Santa Catarina
Florianópolis, Brazil

Aldo R. Mejía
Universidad Autónoma de San Luis Potos
San Luis, Mexico

ISSN 1680-0737 ISSN 1433-9277 (electronic)
IFMBE Proceedings
ISBN 978-3-030-30647-2 ISBN 978-3-030-30648-9 (eBook)
https://doi.org/10.1007/978-3-030-30648-9

© Springer Nature Switzerland AG 2020
This work is subject to copyright. All rights are reserved by the Publisher, whether the whole or part of the material is concerned, specifically the rights of translation, reprinting, reuse of illustrations, recitation, broadcasting, reproduction on microfilms or in any other physical way, and transmission or information storage and retrieval, electronic adaptation, computer software, or by similar or dissimilar methodology now known or hereafter developed.
The use of general descriptive names, registered names, trademarks, service marks, etc. in this publication does not imply, even in the absence of a specific statement, that such names are exempt from the relevant protective laws and regulations and therefore free for general use.
The publisher, the authors and the editors are safe to assume that the advice and information in this book are believed to be true and accurate at the date of publication. Neither the publisher nor the authors or the editors give a warranty, expressed or implied, with respect to the material contained herein or for any errors or omissions that may have been made. The publisher remains neutral with regard to jurisdictional claims in published maps and institutional affiliations.

This Springer imprint is published by the registered company Springer Nature Switzerland AG
The registered company address is: Gewerbestrasse 11, 6330 Cham, Switzerland

Preface

The VIII Latin American Conference on Biomedical Engineering and the XLII National Conference on Biomedical Engineering (CLAIB-CNIB 2019) were carried out together by the Regional Council of Biomedical Engineering for Latin America (CORAL) and the Mexican Biomedical Engineering Society (SOMIB) in October 2–5, 2019, in Cancún, México. We are proud to present in this book a selection of papers from all over the world, reporting on the latest findings and technological outcomes in the biomedical engineering field. The content is organized into fifteen parts to reflect outstanding scientific research lines in biomedical engineering. Innovative topics tissue and molecular engineering, as well as bioimpedance sensors and micro-nano devices are discussed in this book. Content innovation and academic quality have been warranted by a careful peer-reviewing, which was coordinated by an expert Scientific Committee and involved academic reviewers from all continents. With a final acceptance rate of 50%, this book is the result of a great effort involving more than 1000 scientists, both professors and students, participating as authors, reviewers, and scientific committee members. We are sure that the contributions presented in this book will give you a deep overview of the leading edge in your expertise and other areas. On behalf of Scientific and Organizing Committees, we thank authors, academic reviewers as well as sponsoring societies such as CORAL, SOMIB, and the National Council for Science and Technology (CONACYT), México, for their contribution. Moreover, we encourage readers to enjoy this amazing piece of scientific literature as a breadth of knowledge in the biomedical engineering field.

Christian Chapa González
Co-chair Program CLAIB-CNIB 2019

César A. González Díaz
Chair Program CLAIB-CNIB 2019

Distinguished Lecturer Message

It is my great pleasure and honor to welcome you all in reading the IFMBE proceedings of CLAIB-CNIB 2019. This international conference that was held in Cancun, Mexico, gave a unique occasion for us, to host all our colleagues from all over the world with an outstanding spectrum of over 200 research papers from 25 countries, to focus on the challenges of developing future technologies in medicine and biology. The real purpose of conferences like this is the chance to socialize with those share your interest and expertise, and the chance to pick up new ideas or share the trending ideas on some critical aspects of health care. This is a great opportunity that this conference represents a chance for you to not only keep abreast of your own area of expertise, but also to find out what is the leading edge in other areas. May be your specialty is other than medical and biological engineering, but this compilation of works just might provide you with some nugget of information that transforms your approach to a bigger challenge. I hope that all of you had enjoyed the larger opportunity we had during CLAIB-CNIB 2019—a tremendous experience and expertise throughout the length and breadth of wide range of fields under one roof—generating a wave of motivation and diversity spreading across the Americas to the world.

Ricardo L. Armentano
Distinguished Lecturer CLAIB-CNIB 2019

Organization

CLAIB-CNIB 2019 is organized by the Regional Council of Biomedical Engineering for Latin America (CORAL) and the Mexican Biomedical Engineering Society (SOMIB) in cooperation with National Council for Science and Technology (CONACYT), México.

Executive Committee

Conference Chair

Herberth Bravo Hernández	President of the Mexican Biomedical Engineering Society (SOMIB), México

Program Chair

César A. González Díaz	Instituto Politécnico Nacional, México

Organizing Chair

Francisco Javier Aceves Aldrete	Universidad de Guadalajara, México

Scientific Committee

Program Chair

César A. González Díaz	Instituto Politécnico Nacional, Mexico

Program Co-chair

Christian Chapa González	Universidad Autónoma de Ciudad Juárez, Mexico

Session Coordinators

Renato García	Universidad Federal de Santa Catarina, Brazil

Eric Laciar Leber	Universidad Nacional de San Juan, Argentina
Hugo A. Vélez	Universidad de Guadalajara, Mexico
Norma P. Puente	Universidad Autónoma de Nuevo León, Mexico
Dora-Luz Flores	Universidad Autónoma de Baja California, Mexico
Adriano O. Andrade	Universidade Federal de Uberlândia, Brasil
Héctor A. Galván	Instituto Nacional de Cancerología, Mexico
Fabiola Martínez	Universidad Autónoma Metropolitana, Mexico
Pedro Berthemes Filho	Universidad de Santa Catarina, Brasil
Alexander Golberg	University of Tel Aviv, Israel
Citlalli J. Trujillo	Instituto Nacional de Rehabilitación, Mexico
Aldo R. Mejía	Universidad Autónoma de San Luis Potosí, Mexico
Amanda Ortiz Zitle	Universidad Autónoma de Baja California, Mexico

Awards Committee

Student Competition

Citlalli J. Trujillo	Instituto Nacional de Rehabilitación, Mexico

Scientific Challenge

Aldo R. Mejía	Universidad Autónoma San Luis Potosí, Mexico
Guadalupe Dorantes Méndez	Universidad Autónoma San Luis Potosí, Mexico
Bersain Alexander Reyes	Universidad Autónoma San Luis Potosí, Mexico

Innovahealth Challenge

Amanda Ortiz Zitle	Universidad Autónoma de Baja California, Mexico

Organizing Committee

Organizing Chair

Francisco Javier Aceves Aldrete

Organizing Co-chairs

Ana Luz Portillo Hernández
Dora-Luz Flores

International Guests

Elliot Vernet Saavedra

Workshops

Carlos Graniel Tamayo

Exposition Chair

Herberth Bravo Hernández

Exposition Co-chairs

Herberth Bravo Hernández
Ivette Patrón Villegas

Education Committee

Chair

Lilian Beatriz Paredes Cardenas

Co-chairs

Janetthe Mariana Tarín León
Gerardo Ames

Logistics Committee

Chair

Zaynic Inc. Mexico

Graphic Design

Judith González

Administrative Support

Alexa Ruano

Referees

Adriana Santos Martel	Universidad Autónoma de Ciudad Juárez, Mexico
Adriano Alves Pereira	Universidade Federal de Uberlândia, Brazil
Adriano O. Andrade	Universidade Federal de Uberlândia, Brazil
Adson Ferreira da Rocha	Universidade de Brasília, Brazil
Agustina Garcés	Universidad Nacional de San Juan, Argentina
Alberto Cavazos Gonzalez	Universidad Autonoma de Nuevo Leon, Mexico
Alcimar Barbosa Soares	Universidade Federal de Uberlândia, Brazil

Aldo R. Mejía	Universidad Autónoma de San Luis Potosí, Mexico
Alejandra López	Universidad de Sonora, Mexico
Alejandro Galaviz	Centro de investigacion Cientifica y Educacion Superior de Ensenada, Mexico
Alessandra Cavalcanti de Albuquerque e Souza	Universidade Federal do Triângulo Mineiro, Brazil
Alexandra La Cruz	Universidade de Brasília, Brazil
Alfredo Corniali	Diretoria de Vigilância Sanitária Secretaria de Saúde do Estado da Bahia, Brazil
Alher Mauricio Hernandez	Universidad de Antioquia, Colombia
Alma Edith Martínez Licona	UAM Iztapalapa, Mexico
Alvaro Gabriel Pizá	Universidad Nacional de Tucumán, Argentina
Amanda Gomes Rabelo	Universidade Federal de Uberlândia, Brazil
Ana Beatriz Ramírez Silva	Universidad Industrial de Santander, Colombia
Ana Lía Albarracin	INSIBIO-CONICET, Argentina
Ana Paula Bittar Britto Arantes	University of New Brunswick, USA
Ana Paula Perini	Universidade Federal de Uberlândia, Brazil
André Candido Porto	Universidade Federal de São Carlos, Brazil
Andrés Antonio González Garrido	Universidad de Guadalajara, Mexico
Anselmo Frizera Neto	Universidade Federal do Espírito Santo, Brazil
Antonio Hernandez	American College of Clinical Engineering—ACCE, USA
Antonio Padilha Lanari Bo	Universidade de Brasília, Brazil
Antonio Rienzo	Universidad de Valparaíso, Chile
Antonio Sanchez Uresti	Universidad Autonoma de Nuevo Leon, Mexico
Aurelio Horacio Heredia Jimenez	Universidad Popular Autónoma del Estado de Puebla, Mexico
Aurora Espinoza Valdez	Universidad de Guadalajara, Mexico
Beatriz Janeth Galeano Upegui	Universidad Pontificia Bolivariana, Colombia
Bersaín Alexander Reyes	Universidad Autónoma de San Luis Potosí, Mexico
Carelia G. Gaxiola Pacheco	Universidad Autónoma de Baja California, Mexico
Carlos Dell'Aquila	Universidad Nacional de San Juan, Argentina
Carlos Ferrer-Riesgo	Universidad Central "Marta Abreu" de Las Villas, Cuba

Carolina Tabernig	Universidad Nacional de Entre Ríos, Argentina
César A. González Díaz	Instituto Politécnico Nacional, Mexico
César Covantes Osuna	Universidad de Guadalajara, Mexico
César Javier Ortiz Echeverri	Universidad Autónoma de Querétaro, Mexico
Christian Chapa González	Universidad Autónoma de Ciudad Juárez, Mexico
Citlalli J. Trujillo	Instituto Nacional de Rehabilitación, Mexico
Claudia Edith Bonell	Universidad Nacional Entre Rios, Argentina
Cornelio Posadas Castillo	Universidad Autonoma de Nuevo Leon, Mexico
Dania Gutierrez	Instituto Politecnico Nacional, Mexico
Daniel Campos Delgado	Universidad Autónoma de San Luis Potosí, Mexico
David Cervantes Vásquez	Universidad Autónoma de Baja California, Mexico
Diego Sebastián Comas	Universidad Nacional de Mar del Plata, Argentina
Dora-Luz Flores	Universidad Autónoma de Baja California, Mexico
Edgar Román Arce Santana	Universidad Autónoma de San Luis Potosí, Mexico
Edgard Lamounier	Universidade Federal de Uberlândia, Brazil
Edgard Morya	Instituto Santos Dumont, Brazil
Eduardo Gerardo Mendizabal Ruíz	Universidad de Guadalajara, Mexico
Eduardo Lázaro Martins Naves	Universidade Federal de Uberlândia, Brazil
Eduardo Martinez Montes	Centro de Neurociencias de Cuba, Cuba
Eduardo Rocon	Centro de Automática y Robótica CSIC-UPM, Spain
Emilce Preisz	Universidad Nacional de Entre Rios, Argentina
Enrique Mario Avila Perona	Universidad Nacional de San Juan, Argentina
Eric Laciar Leber	Universidad Nacional de San Juan, Argentina
Erick Eduardo Guzmán Quezada	Universidad Autónoma de Guadalajara, Mexico
Ernesto Suaste Gómez	CINVESTAV Sección Biolectrónica, Mexico
Esmeralda S. Zúñiga	Universidad Autónoma de Ciudad Juárez, Mexico

Eunice Vargas Viveros	Universidad Autónoma de Baja California, Mexico
Evelio González Dalmau	Centro de Ingeniería Genética y Biotecnología, Cuba
Everardo Gutiérrez López	Universidad Autónoma de Baja California, Mexico
Fabiola Martínez	UAM Iztapalapa, Mexico
Fabricio Brasil	Instituto Santos Dumont, Brazil
Fernando Alarid	CIDE- Aguascalientes, Mexico
Fernando Daniel Farfán	Universidad Nacional de Tucumán, Argentina
Fernando Pérez Escamirosa	Universidad Nacional Autónoma de Mexico, Mexico
Flavio Enersto Trujillo Zamudio	Hospital Regional de Alta Especialidad de Oaxaca, Mexico
Francisco Berumen Murillo	Université Laval, Canada, Canada
Francisco Javier Alvarado	Universidad de Guadalajara, Mexico
Francisco Javier Alvarado Rodríguez	Universidad de Guadalajara, Mexico
Francisco Javier Buchelly Imbachí	Universidad Nacional de Mar del Plata, Argentina
Gabriel Alfredo Ruiz	Universidad Nacional de Tucumán, Argentina
Gabriel Cañadas	Universidad Nacional de San Juan, Argentina
Gabriella Lelis Silva	Universidade Federal de Uberlândia, Brazil
Gilberto Ochoa Ruíz	Universidad Autónoma de Guadalajara, Mexico
Griselda Quiroz Compean	Universidad Autonoma de Nuevo Leon, Mexico
Guadalupe Dorantes Mendez	Universidad Autónoma de San Luis Potosí, Mexico
Gustavo Abraham	INTEMA (UNMdP-CONICET), Argentina
Gustavo Bizai	Universidad Nacional Entre Ríos, Argentina
Gustavo Meschino	Universidad Nacional de Mar del Plata, Argentina
Héctor A. Galván	Instituto Nacional de Cancerología, Mexico
Hougelle Simplício	Instituto Santos Dumont, Brazil
Hugo A. Vélez	Universidad de Guadalajara, Mexico
Imelda Olivas Armendáriz	Universidad de Sonora, Mexico
Isela Bonilla Gutiérrez	Universidad Autónoma de San Luis Potosí, Mexico
Isnardo Torres	ABIOIN, Colombia

Israel A. Flores	Universidad Autónoma de Nuevo León, Mexico
Izabela Lopes Mendes	Universidade do Vale do Paraíba, Brazil
Javier E. Camacho	Universidade EIA, Colombia
Javier Fernando Adur	Universidad Nacional Entre Rios, Argentina
Jesus Emmanuel Gomez Correa	Centro de investigacion Cientifica y Educacion Superior de Ensenada, Mexico
Joaquín Azpiroz Leehan	UAM Iztapalapa, Mexico
John Jairo Villarejo Mayor	Universidade Federal do Paraná, Brazil
Johnny Rodriguez Maldonado	Universidad Autonoma de Nuevo Leon, Mexico
José Manuel Ferrer Villena	Pontificia Universidad Católica del Perú, Perú
Jose Maria Flores	Universidad Nacional de Entre Rios, Argentina
José Mejía	Universidad Autónoma de Ciudad Juárez, Mexico
Jose Ramon Rodriguez Cruz	Universidad Autonoma de Nuevo Leon, Mexico
Juan Angel Rodriguez Liñan	Universidad Autonoma de Nuevo Leon, Mexico
Juan Carlos Perfetto	Universidad de Buenos Aires, Argentina
Juan Manuel Fontana	Universidad Nacional de Río Cuarto, Argentina
Juan Manuel Olivera	Universidad Nacional Tucumán, Argentina
Juan Pablo Graffigna	Universidad Nacional de San Juan, Argentina
Juan Pastore	Universidad Nacional de Mar del Plata, Argentina
Juan Valentín Lorenzo Ginori	Universidad Central “Marta Abreu” de Las Villas, Cuba
Julián Villamarin	Universidad Antonio Nariño, Colombia
Karen Yael Castrejón	Universidad Autónoma de Ciudad Juárez, Mexico
Leandro Ariza Jimenez	Universidad EAFIT, Colombia
Lidia H. Rascón	Universidad Autónoma de Ciudad Juárez, Mexico
Lígia Reis Nóbrega	Universidade Federal de Uberlândia, Brazil
Lilibeth Ortega-Pineda	Universidad EIA, Colombia
Lorena Correa	Universidad Nacional de San Juan, Argentina
Lorena Orosco	Universidad Nacional de San Juan, Argentina

Luciane Aparecida Pascucci Sande de Souza	Universidade Federal do Triângulo Mineiro, Brazil
Lucio Pereira Neves	Universidade Federal de Uberlândia, Brazil
Luis Alfredo Rocha	Universidad Nacional de Tucumán, Argentina
Luis Enrique Bergues Cabrales	University of Oriente, Cuba
Luis Felipe Devia Cru	Centro de investigacion Cientifica y Educacion Superior de Ensenada, Mexico
Luis Fernando Mercado	Universidad Autonoma de Nuevo Leon, Mexico
Luis Harnán Danyau Izarnótegui	Universidad de Valparaiso, Chile
Luis Mercado	Universidad Autonoma de Nuevo Leon, Mexico
Luis Rocha	Universidade Nacional de Tucuman, Argentina
Luis Vilcahuaman	Pontificia Universidad Catolica del Peru, Peru
Luiza Maire David Luiz	Universidade Federal de Uberlândia, Brazil
Luz Maria Alonso Velardi	Instituto Tecnologico de Estudios Superiores de Monterrey, Mexico
Marco Octavio Mendoza Gutiérrez	Universidad Autónoma de San Luis Potosí, Mexico
Marcus Fraga Vieira	Universidade Federal de Goiás, Brazil
María Agustina Bouchet	Universidad Nacional de Mar del Plata, Argentina
Maria Elizete Kunkel	Universidade Federal de São Paulo, Brazil
Maria Isabel Veras Orselli	Universidade Franciscana, Brazil
María Virginia Walz	Universidad Nacional Entre Ríos, Argentina
Mariana Cardoso Melo	Universidade Federal de São Paulo, Brazil
Mariela Azul Gonzalez	Universidad Nacional de Mar del Plata, Argentina
Martha Elena Londoño López	Universidad EIA, Colombia, Colombia
Martha Ortiz Posadas	UAM Iztapalapa, Mexico
Martín Oswaldo Méndez García	Universidad Autónoma de San Luis Potosí, Mexico
Mauricio Corredor Rodríguez	Universidad de Antioquia, Colombia
Mauro Conti Pereira	Universidade Católica Dom Bosco, Brazil
Maycon Crispim de Oliveira Carvalho	Universidade Anhembi Morumbi, Brazil
Mayra Deyanira Flores	Universidad Autonoma de Nuevo Leon, Mexico
Miguel Cadena Méndez	Universidad Autonoma de Mexico, Mexico
Mónica Huerta	Universidad Simón Bolíver, Venezuela

Myriam Cristina Herrera	Universidad Nacional de Tucuman, Argentina
Nelly Gordillo	Universidad Autónoma de Ciudad Juárez, Mexico
Noemi Lizarraga Osuna	Universidad Autonoma de Baja California, Mexico
Norma Alicia Barboza Tello	Universidad Autonoma de Baja California, Mexico
Norma P. Puente	Universidad Autonoma de Nuevo Leon, Mexico
Nydia Paola Rondon Villarreal	Universidad Industrial de Santander, Colombia
Odín Ramírez	Instituto Tecnológico de Tlalnepantla, Mexico
Omar Paredes	Universidad de Guadalajara, Mexico
Oscar Eduardo Cervantes García	Universidad Autonoma de Nuevo Leon, Mexico
Pablo Daniel Cruces	Universidad de Buenos Aires, Argentina
Pablo Diez	Universidad Nacional de San Juan, Argentina
Patricia Juárez Camacho	Centro de Investigación Científica y Educación Superior de Ensenada, Mexico
Paula Bonomini	Universidad de Buenos Aires, Argentina
Paulo Eduardo Ambrosio	Universidade Estadual de Santa Cruz, Brazil
Paulo Eigi Miyagi	University of Sao Paulo, Brazil
Pedro Arini	Universidad de Buenos Aires, Argentina
Pedro Bertmes Filho	Universidade do Estado de Santa Catarina, Brazil
Percy Nohama	Pontifícia Universidade Católica do Paraná, Brazil
Priscila Sousa de Avelar	IEB-UFSC, Brazil
Rafael Torres Amarís	Universidad Industrial de Santander, Colombia
Raúl Correa	Universidad Nacional de San Juan, Argentina
Raúl Molina Salazar	Universidad Autónoma Metropolitana-Iztapalapa, Mexico
Raul Rangel Rojo	Centro de investigacion Cientifica y Educacion Superior de Ensenada, Mexico
Raúl Romo Doña	Universidad Nacional de San Juan, Argentina
Rebeca del Carmen Romo Vázquez	Universidad de Guadalajara, Mexico

Renan Moioli	Instituto Santos Dumont, Brazil
Renato García	IEB-UFSC, Brazil
Renato Zaniboni	IEB-UFSC Brasil, Brazil
Ricardo Salido Ruiz	Universidad de Guadalajara, Mexico
Ricardo Silva	Penn State University, USA
Ricardo Taborda	Universidad Nacional de Cordoba, Argentina
Roberto Carrillo	Universidad de Sonora, Mexico
Rocío Ortiz Pedroza	UAM Iztapalapa, Mexico
Roger Clotet	Universidad Simón Bolíver, Venezuela
Rosa María Weisz	Universidad Nacional de Entre Rios, Argentina
Rossana Rivas Tarazona	Pontificia Universidad Catolica del Peru, Peru
Ruben Acevedo	Universidad Nacional de Entre Ríos, Argentina
Rubiel Vargas Cañas	Universidad del Cauca, Colombia
Said David Pertuz Arroyo	Universidad Industrial de Santander, Colombia
Selma Terezinha Milagre	Universidade Federal de Uberlândia, Brazil
Sergio Muhlen	Universidade Estadual de Campinas, Brazil
Sérgio Ricardo de Jesus Oliveira	Universidade Federal de Uberlândia, Brazil
Teodiano Freire Bastos Filho	Universidade Federal do Espírito Santo, Brazil
Valdeci Dionisio	Universidade Federal de Uberlândia, Brazil
Veronica Medina	Universidad Autónoma Metropolitana-Iztapalapa, Mexico
Victor Eduardo Martínez Abaunza	Universidade Federal do Rio Grande do Sul, Brazil
Victor Hugo Casco	Universidad Nacional Entre Rios, Argentina
Virginia Ballarin	Universidad Nacional de Mar del Plata, Argentina
Wisley Falco Sales	Universidade Federal de Uberlândia, Brazil
Yolanda Torres Pérez	Universidad San Thomas, Colombia

Sponsoring Institutions

Regional Council of Biomedical Engineering for Latin America (CORAL)
Mexican Biomedical Engineering Society (SOMIB)
National Council for Science and Technology (CONACYT), Mexico

SOMIB
Sociedad Mexicana de
Ingeniería Biomédica

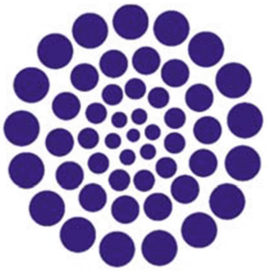

CONACYT

Contents

Processing of Biomedical Signals

EEG-PML: A Software for Processing and Machine Learning Analysis of EEG Signals 3
Lluvia Gwendolyn Alvarado-Robles, Carlos Miguel Munguia-Nava, Israel Román-Godínez, Ricardo Antonio Salido-Ruiz, and Sulema Torres-Ramos

Performance Evaluation of Average Methods in the Time Domain Using Quality Measures for Automatic Detection of Evoked Potentials 12
Idileisy Torres-Rodríguez, Carlos Ariel Ferrer-Riesgo, Martha Madyuri Pérez de Morales Artiles, and Alberto Taboada-Crispi

Analysis of the Maternal Cardio-Electrohysterographic Coupling During Labor by Bivariate Phase-Rectified Signal Averaging 21
Cinthia Gabriela Esquivel-Arizmendi, Claudia Ivette Ledesma-Ramírez, Adriana Cristina Pliego-Carillo, Juan Carlos Echeverría, Miguel Ángel Peña-Castillo, Gustavo Pacheco-López, and José Javier Reyes-Lagos

Capture of the Voluntary Motor Intention from the Electromyography Signal 28
Leandro Alexis Hidalgo Torres, Yanexy San Martín Reyes, and Juan David Chailloux Peguero

Early Prediction of Weight at Birth Using Support Vector Regression 37
Oliver Campos Trujillo, Jorge Perez-Gonzalez, and Verónica Medina-Bañuelos

Algorithm to Quantify Maximum Isometric Voluntary Contraction in Subjects with Osteoporosis 42
Angel Gallegos Ledezma, Ivett Quiñones Uriostegui, Virginia Bueyes-Roiz, and Rafael Zepeda Mora

Prediction of Breast Cancer Diagnosis by Blood Biomarkers Using Artificial Neural Networks 47
Balam Benítez-Mata, Carlos Castro, Rubén Castañeda, Eunice Vargas, and Dora-Luz Flores

Measuring Periodicity Perturbations in Pathological Voice: General-Purpose Software vs. Custom-Tailored Methods 56
Reinier Rodríguez-Guillén and Carlos A. Ferrer-Riesgo

Estimation of Heart Rate and Respiratory Rate via Blind Estimation from Smartphone-Based Contact Image Photoplethysmography 63
Rodrigo García-López, Javier Benítez-Benítez, Daniel Ulises Campos-Delgado, and Bersaín A. Reyes

Characterization of Forearm Electromyographic Signals for Automatic Classification of Wrist Movements 71
Milagros G. Salazar-Medrano, Bersaín A. Reyes, Marco Mendoza, and Isela Bonilla

Correlation of EEG Brain Waves in a Time Perception Task 79
Sergio Rivera-Tello, Rebeca Romo-Vázquez, and Julieta Ramos-Loyo

Estimation of Beta Burst Durations from Subthalamic Nucleus Local Field Potentials in Parkinson's Disease Through Hilbert and Continuous Wavelets Transforms 85
Arnaldo Fim Neto, Julia Baldi De Luccas, Bruno Leonardo Bianquenti, Tiago Paggi Almeida, Maria Sheila Rocha, Takashi Yoneyama, Fabio Luiz Franceschi Godinho, and Diogo Coutinho Soriano

A Comparative Study of Time and Frequency Features for EEG Classification 91
Cesar Ortiz-Echeverri, Omar Paredes, J. Sebastian Salazar-Colores, Juvenal Rodríguez-Reséndiz, and Rebeca Romo-Vázquez

Cortical Auditory Evoked Potentials Elicited by Spanish Words: An Equivalent Current Dipoles Clustering Study 98
Norma Castañeda-Villa, Pilar Granados-Trejo, and Juan Manuel Cornejo-Cruz

Classification of Heart Health by LPC and MFCC Coefficients and Statistical Features 104
Manuel A. Soto-Murillo, Karen E. Villagrana Bañuelos, Julieta G. Rodriguez-Ruiz, Jared D. Salinas-González, Carlos E. Galván-Tejada, Hamurabi Gamboa-Rosales, and Jorge I. Galván-Tejada

Nonlinear, Time-Varying and Frequency-Selective Analysis During the Orthostatic Challenge in Patients with Vasovagal Syncope 113
Laura E. Méndez-Magdaleno, Guadalupe Dorantes-Méndez, Sonia Charleston-Villalobos, and Tomás Aljama-Corrales

Feature Selection and Machine Learning Applied for Alzheimer's Disease Classification 121
Ana Gabriela Sánchez-Reyna, Carlos H. Espino-Salinas, Pablo C. Rodríguez-Aguayo, Jared D. Salinas-Gonzalez, Laura A. Zanella-Calzada, Elda Y. Martínez-Escobar, José M. Celaya-Padilla, Jorge I. Galván-Tejada, Carlos E. Galván-Tejada, and for the Alzheimer's Disease Neuroimaging Initiative

Fuzzy Logic as a Control Strategy to Command a Deep Brain Stimulator in Patients with Parkinson Disease 129
Gabriel Martín Bellino, Carlos Rodolfo Ramirez, Alejandro Miguel Massafra, and Luciano Schiaffino

Cerebral Cortex Atlas of Emotional States Through EEG Processing 138
Alejandro Gómez, O. Lucia Quintero, Natalia Lopez-Celani, and Luisa Fernanda Villa

Estimation of the Very Low Frequency Components in Heart Rate Variability During Hemodiafiltration 145
Raul Martínez-Memije, Brayans Becerra-Luna, Raul Cartas-Rosado, Oscar Infante-Vázquez, Claudia Lerma, Hector Pérez-Grovas, and Jóse Manuel Rodríguez-Chagolla

NeuroMoTIC: An Smart Tool to Support Pediatric Epilepsy Diagnosis 151
Rubiel Vargas-Canas, Maria Eugenia Mino-Arango, and Diego Mauricio Lopez-Gutierrez

Comparative Analysis of Alpha Power Spectral Density in Real and Virtual Environments 156
Fabian O. Romero-Soto, David I. Ibarra-Zárate, and Luz Maria Alonso-Valerdi

Analysis of Cardiorespiratory Variations During Sleep in Shift Workers by Univariate and Multivariate Detrended Fluctuation Analysis 164
Raquel Delgado-Aranda, Guadalupe Dorantes-Méndez, and Martín Oswaldo Méndez

Morphological and Temporal ECG Features for Myocardial Infarction Detection Using Support Vector Machines 172
Wilson J. Arenas, Silvia A. Sotelo, Martha L. Zequera, and Miguel Altuve

Window Functions Analysis in Filters for EEG Movement Intention Signals 182
C. Covantes-Osuna, O. Paredes, H. Vélez-Pérez, and R. Romo-Vázquez

Algorithm for Presumptive Diagnosis of Cardiac Murmurs over Auscultated Heart Signals 191
Andrea García-Cedeño, Eduardo Pinos, and Mónica Huerta

Recurrence Analysis of EEG Power and HRV Time Series for Asynchronous BCI Control 202
Claudia Ivette Ledesma-Ramírez, Erik Bojorges-Valdez, Oscar Yanez-Suarez, and Omar Piña-Ramírez

Joint Exploitation of Hemodynamic and Electrocardiographic Signals by Hidden Markov Models for Heartbeat Detection 208
Nelson F. Monroy and Miguel Altuve

Hand Movement Detection from Surface Electromyography Signals by Machine Learning Techniques 218
Jose Alejandro Amezquita-Garcia, Miguel Enrique Bravo-Zanoguera, Felix Fernando González-Navarro, and Roberto Lopez-Avitia

Characterization of Intrinsic Mode Functions of the Electrical Cochlear Response 228
Norma Castañeda-Villa, Pilar Granados-Trejo, and Juan Manuel Cornejo-Cruz

Remote Optical Estimation of Respiratory Rate Based on a Deep Learning Human Pose Detector 234
Isaac René Aguilar Figueroa, Jesús Vladimir Martínez Nuño, and Eduardo Gerardo Mendizabal-Ruiz

Respiratory Rate Estimation by a Non-invasive Optical Method Based on Video Image Processing 242
C. A. Hurtado-Otalora, J. D. Pulgarin-Giraldo, and A. M. Gonzalez-Vargas

Computer Vision-Based Estimation of Respiration Signals 252
Maria Eugenia Paz Reyes, Jasiel Dorta_Palmero, Jessica Leon Diaz, Efren Aragon, and Alberto Taboada-Crispi

Processing of Biomedical Images

Computer-Aided Detection Systems for Digital Mammography 265
Marlen Perez-Diaz, Ruben Orozco-Morales, Eduardo Suarez-Aday, and Rosana Pirchio

Time Estimation of Topotecan Penetration in Retinoblastoma Cells Through Image Sequence Analysis 272
Debora Chan, Ursula Winter, Paula Schaiquevich, Rodrigo Ramele, and Juliana Gambini

A Comparative Study of Reinforcement Learning Algorithms Applied to Medical Image Registration 281
Ramiro F. Isa-Jara, Gustavo J. Meschino, and Virginia L. Ballarin

Measurement of the Degradation Rate of Anodized AZ91 Magnesium Temporary Implants Using Digital Image Processing Techniques 290
Francisco Javier Buchelly, Martina Gomez, Silvia M. Cere, Josefina Ballarre, Virginia L. Ballarin, and Juan I. Pastore

Development of Eclipse Scripting API for Automatic Delineation of Femoral Head 298
Bruno Assumpção Gomes da Silva, Rodrigo Souza Dias, Antonio Cassio de Assis Pellizzon, Álvaro Luiz Fazenda, and Fabiano Carlos Paixão

Comparative Evaluation of Anisotropic Filters Used to Reduce Speckle in Ultrasound Images 304
Lucas Gonçalves Santos, Carlos Marcelo Gurjão de Godoy, Leopoldo de Jesus Prates, and Regina Célia Coelho

A System for High-Speed Synchronized Acquisition of Video Recording of Rodents During Locomotion 309
Cesar Ascencio-Piña, Marco Pérez-Cisneros, Sergio Dueñaz-Jimenez, and Gerardo Mendizabal-Ruiz

An Entropy-Based Graph Construction Method for Representing and Clustering Biological Data 315
Leandro Ariza-Jiménez, Nicolás Pinel, Luisa F. Villa, and Olga Lucía Quintero

Automatic Lid Segmentation in Meibography Images 322
Luis DelaO-Arévalo, Erik Bojorges-Valdez, Everardo Hernández-Quintela, Nallely Ramos-Betancourt, and Jesus H. Davila-Alquisiras

Brain Tortuosity as Biomarker to Classify Mild Cognitive Impairment and Control Subjects 327
Eduardo Barbará Morales, Karla C. Rojas Saavedra, Luis Jiménez Ángeles, and Verónica Medina Bañuelos

Classification of Handwritten Drawings of People with Parkinson's Disease by Using Histograms of Oriented Gradients and the Random Forest Classifier 334
João Paulo Folador, Adrian Rosebrock, Adriano Alves Pereira, Marcus Fraga Vieira, and Adriano de Oliveira Andrade

Improving Myoelectric Pattern Recognition Robustness to Electrode Shift Using Image Processing Techniques and HD-EMG 344
Roberto Díaz-Amador, Miguel Arturo Mendoza-Reyes, and Carlos A. Ferrer-Riesgo

Classification of Plasmodium-Infected Erythrocytes Through Digital Image Processing 351
Juan Valentín Lorenzo-Ginori, Lyanett Chinea-Valdés, Yanela Izquierdo-Torres, Rubén Orozco-Morales, Niurka Mollineda-Diogo, Sergio Sifontes-Rodríguez, and Alfredo Meneses-Marcel

Noise Reduction in Phase-Contrast Mammography Images with Synchrotron Radiation 361
Yusely Ruiz-Gonzalez, Javier D. Brizuela-Cardoso, and Marlen Pérez-Díaz

Interface for Contour Extraction and Determination of Morphologic Parameters in Digital Images of Footprints Based on Hernandez-Corvo Protocol 367
H. A. Miranda C., Luz Alejandra Flores Cu, Santiago Camacho López, Horacio Rostro González, and Miroslava Cano Lara

Cervix Type Classification Using Convolutional Neural Networks 377
Daniel A. Cruz, Carmen Villar-Patiño, Elizabeth Guevara, and Marisol Martinez-Alanis

Comparative Analysis of Different Techniques to Determine Motility Parameters in Video Sequences of Ram and Buck Sperm 385
Francisco Javier Buchelly, Ramiro Fernando Isa Jara, Lucía Zalazar, Andreina Cesari, Juan I. Pastore, and Virginia L. Ballarin

3D Kidney Reconstruction from 2D Ultrasound Images 393
Mariana Teresa Alvarez-Gutiérrez, Aldo Rodrigo Mejía-Rodríguez, Ines Alejandro Cruz-Guerrero, and Edgar Román Arce-Santana

Mask R-CNN to Classify Chemical Compounds in Nanostructured Materials 401
Carlos Cabrera, David Cervantes, Franklin Muñoz, Gustavo Hirata, Patricia Juárez, and Dora-Luz Flores

Follow-up of Cutaneous Leishmaniasis by Three-Dimensional Reconstruction Based on Photogrammetry: Proof of Concept 412
Caren Garzón-Márquez, Manuela Gómez-Ramírez, Javier D. Murillo, Sara Robledo, A. Hernandez, Benjamín Castañeda, and Sandra Pérez-Buitrago

Image-Based Analysis of Human Tissue Regeneration During Therapy Based on Photobiostimulation and Natural Latex Biomembranes 421
Mayla dos Santos Silva, Lorena de Sousa Moreira, Franciéle de Matos da Silva, Wellington Rodrigues, Breno Amadeus Sales Marinho de Sousa, Luiz José Lucas Barbosa, Cristiano Jacques Miosso, and Suélia de Siqueira Rodrigues Fleury Rosa

Semantic Segmentation of Lung Tissues in HRCT Images by Means of a U-Net Convolutional Network 426
Sarahí Hernández-Juárez, Aldo R. Mejía-Rodríguez, Edgar R. Arce-Santana, S. Charleston-Villalobos, A. T. Aljama-Corrales, R. González-Camarena, and M. Mejía-Ávila

Fast Optic Disc Localization Using Viola-Jones Algorithm 435
Yainet García García, Reinier Rodríguez Guillén, Y. García, and Alberto Taboada-Crispi

Biosensors

Recording and Analysis of the Vestibulo-Ocular Reflex with Pendular Movement in the Vertical Plane 445
Geovanny Palomino Roldán and Ernesto Suaste Gómez

Fabrication of PPy/PVC Electrodes for ECG Monitoring 449
Ernesto Suaste-Gómez, Ilian Pérez-Solís, and Grissel Rodríguez-Roldán

Implementation of the NEURONIC INFANTIX Newborn Hearing Screening System 453
José Carlos Santos-Ceballos, Jorge German Pérez-Blanco, Yosvani Pantoja-Gómez, Francisco Martín-González, Alejandro Torres-Fortuny, Eduardo Eimil-Suarez, and Ernesto Velarde-Reyes

Prototype Sensor with Optical Principle for Measuring Strength of the Fingers 460
Jessica Ferreira, Catherine Moreno, A. Ramírez, and Ricardo Espinosa

A Rapid and Low-Cost Lung Function Testing Method Based on an Optical Flow Sensor 469
Markus Höglinger, Bianca Wiesmayr, Werner Baumgartner, and Anna T. Stadler

A New Approach to Cardiovascular Screening in Newborn 478
Rene Gonzalez-Fernandez, Luis Reyes-Morales, Alejandro Torres-Fortuny, and Hany Pazos-Espinosa

Graphene Nanosensor for NO Metabolites Detection 486
Andrés Fuentes-Aranda, Carlos Maya-Escamilla, Columba Rentería-Montoya, Mercedes Teresita Oropeza-Guzmán, Oscar Vázquez-Mena, and Viviana Sarmiento

Bioinstrumentation and Micro-Nanotechnologies

Heart Rate Monitor for Athletes in Activity 497
Gisella Borja, Evert De Los Ríos, José Ledesma, and Glayder Viloria

Instrumented Footwear for Diabetic Foot Monitoring: Foot Sole Temperature Measurement 501
Sofía D. Rodríguez-Sáenz, Sarahí S. Franco-Pérez, Aurora Espinoza-Valdez, Ricardo A. Salido-Ruiz, and Fátima B. Curiel-López

Analysis of the Thermal Distribution Generated by a Thermal Patch to Evaluate Its Feasibility to Treat Patient's Pain Relief 508
Luis A. Castellanos-Rivera, Edgar A. Mandujano-García, Antonio Ruiz-Morán, Melany Barrón-Salazar, Benjamín A. Morales-Ruiz, and Citlalli J. Trujillo-Romero

Prototype of a Multivariable Measurement System 519
Israel Sánchez-Domínguez, Paul Erick Méndez Monroy, and Ernesto Pérez-Rueda

Development and Pilot Testing of a New Electromyography Device 524
Douglas Crochi, Tiago R. S. Silva, André Silva, Marcello F. Santos, Natasha H. Ota, Paulo Daudt, Silvia C. Martini, Silvia R. M. S. Boschi, Terigi A. Scardovelli, and Alessandro P. Silva

Initial Approaches for Manipulation of Human Lens for Irradiation in a Solar Simulator: A Study for Cataract 530
Fernanda Oliveira Duarte, Andre Fragalli, Mauro Masili, Sidney Julio de Faria e Sousa, and Liliane Ventura

Wearable Spine Postural Monitoring Embedded System for Occupational Health in Sitting Position 538
Edisson Pugo-Méndez, Juan Cabrera-Zeas, Luis Serpa-Andrade, Eduardo Pinos-Vélez, and Freddy Bueno-Palomeque

Non-invasive Ultrasonic Stimulator Applied in the Treatment of Urinary Incontinence in Women 543
Aurelio H. Heredia J., Karim Tapia Q., María del R. L. Cabrera L., Germán Barrientos C., Roberto C. Ambrosio L., and Mario Moreno M.

SpO_2 Alarm: A Tool for Health Care 548
Nancy Lisset Domínguez-Hernández, Lady María Murrieta-Brígido, and Pablo Samuel Luna-Lozano

Development of a Device Based on Oscillometry and Photoplethysmography for Measuring Blood Pressure 560
Haydeé Alicia Yáñez-Ocampo, Brayans Becerra-Luna, Raúl Cartas-Rosado, Raúl Martínez-Memije, and Oscar Infante-Vázquez

Treatment of Abdominal Hypertension: Development of an Original Non-invasive Device ABDOPRE 567
Alicia Schandy, Francisco Pracca, and Franco Simini

Portable Wireless Monitoring Center Designed in LabVIEW and myRIO 1900 575
Héctor García-Estrada, Karen Jazmín Mendoza-Bautista, María Guadalupe Ramírez-Sotelo, and Agustín Ignacio Cabrera-Llanos

Design of a Suitable NIR System for Monitoring Hemodynamic Changes in the Brain Prefrontal Cortex 582
Miguel Angel Santiago Gorostieta-Esperon and Luis Jiménez-Ángeles

A Prototype for Automatically Blood Pressure Measurement with Wireless Communication to a Graphical User Interface in MATLAB 588
Alicia Sofía Virueña-Vázquez, Haydeé Alicia Yáñez-Ocampo, Sebastián Aguiñaga-González, Juan Pablo Matadamaz-Castro, María del Carmen Arquer-Ruiz, María Guadalupe Flores-Sánchez, and José Israel Hernández-Oropeza

Development of Auricular Transcutaneous Vagal Stimulation Device Integrated with Signal Monitoring 593
Eugênia Gonzales Lopes, Eleonora Tobaldini, Nicola Montano, Karina Rabello Casali, and Henrique Alves de Amorim

Development of a Bimodal Electronic Resuscitator Prototype for Adult Patients 601
Andrea Paola Pineda-Espinosa, Ana Paulina Barba-Muñoz, Rodrigo Antonio Sánchez-Mateos, María del Carmen Arquer-Ruiz, and José Israel Hernández-Oropeza

System to Continuous Differential Acquisition of Arterial Blood Pressure During Tilt Test 606
Carmenchu Regueiro-Busoch, Carmen Busoch-Morlán, René Joaquín Díaz-Martínez, and Angel Regueiro-Gómez

Assessment of AMR-ACB System Using Maghemite Nanoparticles in Theranostic Concentration 611
Leopoldo de Jesus Prates, Fabiano Carlos Paixão, Marli Leite de Moraes, Regina Célia Coelho, Robson Rosa da Silva, and Carlos Marcelo Gurjão de Godoy

Fabrication and Study of Organic Nanomaterials as Photosensitizers for Photodynamic Therapy 616
Nelly Monjaraz-Carrillo, Alejandro Valdez-Calderón, Yunuén D. Solorio-Cendejas, Gabriel Ramos-Ortiz, and Mario Rodríguez

Biomaterials, Molecular, Cellular and Tissue Engineering

Evaluation of Titanium-Niobium Alloy as a Possible Material to Manufacture Endodontic Files 627
Javier Nino-Barrera, Oscar Rodriguez-Montano, and Carlos Cortes-Rodriguez

Formation of Tumor Spheroids by Spontaneous Cellular Aggregation in Incubation: Effect of Agarose as a Compaction Agent 637
Christian Chapa-González, Marcos Bryan Valenzuela-Reyes, Lizbeth Lucero Alemán-Miranda, Laura Elizabeth Valencia-Gómez, Adeodato Israel Botello-Arredondo, and Esmeralda Saraí Zúñiga-Aguilar

Synthesis and Characterization of Hydrogels Cross-Linked with Gamma Radiation for Use as Wound Dressings 643
Paola Bustamante, Carolina Anessi, Natalia Santoro, Nazarena Ciavaro, and Celina Horak

Morphology and Viability of Nerve Cells Cultured on Plasma Polymerized Polypyrrole-Coated Scaffolds 652
Diana Osorio-Londoño, J. Rafael Godínez-Fernández, Ma. Cristina Acosta-García, Juan Morales-Corona, and Roberto Olayo-González

Analysis and Quantification of Bone Tissue Around Anodized Zirconium Implants 656
Guillermo Abras, Maria Rosa Katunar, Josefina Ballarre, Virginia L. Ballarin, and Juan Ignacio Pastore

In Situ Mechanical Characterization of Skin: Participation in the Program Nodos Binacionales de Salud 663
Michelín Alvarez-Camacho, Ana Laura Pérez-Medina, Paris Joaquín Velasco-Acosta, Andreas Schoetz, and Citlalli Jessica Trujillo-Romero

Residual SDS Reducing Methods in the Process of Decellularization of Muscle Tissue 670
Christian Chapa-González, Miguel Ángel Alfaro-Zapata, Joseph Kinsella, Adeodato Israel Botello-Arredondo, and Esmeralda Saraí Zúñiga-Aguilar

Modeling and Simulation

Animation of Atrial and Ventricular External Walls of a Virtual 3D Heart Based on Echocardiogram Images 681
Gabriela Colares Ali Ganem, Regina Célia Coelho, and Carlos Marcelo Gurjão de Godoy

Mathematical Model of the Oculomotor System 685
Jesica Talero, Karen Leiva, and Ricardo Espinosa

Route to Chaos in a Nonlinear Model of HIV Dynamics with Antiretroviral Treatment 694
Lorena de Sousa Moreira, Rodrigo Andres Miranda Cerda, and Ronni Geraldo Gomes de Amorim

Automatic Control Applied to Servosystems. Influence of the State Transition Matrix in Functional Variables of DC Motors Used in Myoelectric Prostheses 699
Carlos Alvarez Picaza, C. R. Ferrari, J. I. Veglia, and M. A. Ulibarrie

SCHSim: A Simulator of Elastic Arterial Vessels Using Windkessel Models 709
Andrew Guimarães Silva, Daniel G. Goroso, and Robson Rodrigues Silva

Effects of Astaxanthin on Pulse Rate Variability of Mice Under Chronic Stress 718
Daniel Escutia-Reyes, Rigoberto Oros-Pantoja, José Javier Reyes-Lagos, Adriana Cristina Pliego-Carrillo, Claudia Ivette Ledesma-Ramírez, Daniela Rodríguez-Muñoz, and Eugenio Torres-García

Criticism of Baroreflex Estimation Methods in Time Domain 724
Juan Carlos Perfetto and Aurora Graciela Ruiz

Bioinformatics and Computational Biology

A Preliminary Comparison of P-Tool Consistency 731
Javier Murillo, Flavio Spetale, Elizabeth Tapia, Flavia Krsticevic, Olivier Cailloux, Serge Guillaume, Gustavo Vazquez, Tamara Fernandez, Sebastien Destercke, Sergio Ponce, and Pilar Bulacio

DNA-MC: Tool for Mapping and Clustering DNA Sequences 736
Valeria Ramírez, Israel Román-Godínez, and Sulema Torres-Ramos

Using Convolutional Neural Networks with Direct Acyclic Graph Architecture in Segmentation of Breast Lesions in US Images 743
Marly Guimaraes Fernandes Costa, João Paulo Campos Mendes, Wagner C. A Pereira, and Cicero F. F. Costa Filho

Spatial Visual Perceptions by Means of Simulated Prosthetic Vision . . . 752
Diego Lujan Villarreal and Wolfgang H. Krautschneider

Standardized Approaches for Assessing Metagenomic Contig Binning Performance from Barnes-Hut *t*-Stochastic Neighbor Embeddings 761
Julian Ceballos, Leandro Ariza-Jiménez, and Nicolás Pinel

Understanding Ventricular Tachyarrhythmias Related to Acute Myocardial Ischemia: A Computational Modeling Approach 769
Andrés Mena, José Felix Rodríguez-Matas, Ana González-Ascaso, and José M. Ferrero

Evaluation of Linked Determinants Between Diabetes and Caries 777
Nubia M. Chavez-Lamas, Laura A. Zanella-Calzada, Carlos Eric Galván-Tejada, Hamurabi Gamboa-Rosales, Jorge I. Galván-Tejada, José M. Celaya-Padilla, and Huizilopoztli Luna-García

Evaluation of Kernels Applied in Support Vector Machines in the Data Analysis of Organochlorines Exposure in Study of Biomarkers 784
Jorge Alejandro Lopera-Rodríguez, Martha Zuluaga, and Jorge A. Jaramillo-Garzón

Diagnosis of Type 2 Diabetes and Pre-diabetes Using Machine Learning 792
Erika Severeyn, Sara Wong, Jesús Velásquez, Gilberto Perpiñán, Héctor Herrera, Miguel Altuve, and José Díaz

Biomechanics

Development of a Protocol for the Evaluation of the Mechanical Behavior of a Transtibial Prosthesis by Infrared Thermography 805
Natali Olaya Mira and Carolina Viloria Barragán

Assessment of Changes in the Pressure Distribution While Sitting in an Instrumented Cushion During an Undergraduate Class 812
Freddy L. Bueno-Palomeque, Carlos A. Tamay-Crespo, and Richard M. Ramos-Tituana

Assessment of the Ground Reaction Forces on Metatarsal Foot Bones Due to Changes on Pinball Region Contact 822
Roberto González-Navarrete, Natali Mancera-Campos, Agustin Vidal-Lesso, and Elías Ledesma-Orozco

Biomechanical Evaluation of Hemiarthroplasty in First Metatarsal Bone 831
Mario Alberto Madrid, Ricardo Becerro de Bengoa Vallejo, and Javier Bayod López

Comparative Study of Biomechanical Model of the L4-L5 Lumbar Section with Mechanical Fixation 841
Eduardo Osquel Pérez-Rivero, Raide Alfonso González-Carbonell, Armando Ortiz-Prado, and Victor Hugo Jacobo-Armendáriz

Biomechanical Analysis of Weeding Labor in Mexican Farmers Through the Simultaneous Use of Photogrammetry and Accelerometry 850
Lázaro Morales-Acosta, Armando Ortiz-Prado, Victor Hugo Jacobo-Armendáriz, and Raide Alfonso González-Carbonell

Virtual Training System for Mechanical Transhumeral Prostheses 858
Andrea Montero, Andrea Gutiérrez, and Carlos Galván Duque

Energy Harvesting from Fingers Motions Using a Wearable System: An Experimental Analysis 866
Omar Méndez-Lira, Ernesto Sifuentes, and Rafael González-Landaeta

Assessment of Plantar Pressure in a Foot Finite Element Model Considering a Sliding Contact Between Soft Tissues 874
Marco A. Martínez Bocanegra, Javier Bayod, Agustín Vidal-Lesso, Ricardo Becerro de Bengoa Vallejo, and Andrés Mena Tobar

Boccia Assistant Biomechanics: A Case Study 884
Juan Pablo Angel-Lopez, Julialba Castellanos-Ruiz, Leidy Tatiana Rojas-Lopez, Daniela Ramirez-Restrepo, Andrea Gomez-Alzate, Yenny Marcela Orozco-Ocampo, Carlos Andres Aguirre-Ospina, and Maria Camila Hoyos-Restrepo

Validation of the Foot Base for Measuring the Control of Ankle Movements 894
Juan M. Gomez-Gonzalez, Molina Cecilia, and Braidot Ariel

Protocol for the Functional Evaluation of Patients with Knee Injury Treated in a Local Rehabilitation Centre 907
Camila Ileana Duré, Julio Savio, Bruno Marengo, Germán Perotti, Paola Catalfamo Formento, and Claudia Edith Bonell

Biomark: A Toolbox for Visualization and Kinematic Gait Analysis . . . 913
Francisco J. Alvarado-Rodríguez, Cesar Covantes-Osuna, Erick Guzmán-Quezada, Rebeca Romo-Vázquez, Sandra Guevara-Vega, Paola Ruiz-Padilla, and Hugo Vélez-Pérez

Results of the Use of Personalized Insoles for the Treatment of Cavus Foot and Comorbidities 921
Paola Hernández-Gandarillas, Sergio Luis Orozco-Villaseñor, José de Jesús Mayagoitia-Vázquez, Israel Miguel-Andrés, José Pablo Herrera-Rangel, and Karla Daniela de la Cruz-Alvarado

Implementation of Novel Technologies and CAD Software to the Improve and Reduce of Costs in Orthotics Adaptation 933
Isaac F. Nava-Vázquez, Eduardo de Avila-Armenta, Lorena Espinoza-Bermúdez, Estefani Esquivel-Cordero, Viviana Chora-López, Jorge I. Galván-Tejada, Carlos E. Galván-Tejada, and Hamurabi Gamboa-Rosales

Biomechanical Model to Evaluate Movement Characteristics in Infants 939
Virginia Bueyes-Roiz, Ivett Quiñones-Uriostegui, Karen L. Cortés-García, and Yannick Quijano

Surface Representation of the Urinary Bladder and Bio-mechanical Analysis by Linear Dynamic Model 945
Keith Guzman-Diaz, Aurora Alvarado-Gonzalez, Daniela Herrera, Ana Hernandez-Reynoso, Sergio Rodríguez-Reynoso, and Alejandro Garcia-Gonzalez

Classification of Lower Limb Amputees Gait Using Machine Learning Algorithms 950
Eduardo de Mendonça Mesquita, Adriano Pericles Rodrigues, Adriano de Oliveira Andrade, and Marcus Fraga Vieira

Musculoskeletal Modeling as a Tool for Biomechanical Analysis of Normal and Pathological Gait 955
Manuel Cardona and Cecilia García Cena

Quantification of Coordination Variability During Gait in Fallers and Non-fallers Older Adults at Different Speeds 964
Guilherme Augusto Gomes De Villa, Adriano de Oliveira Andrade, and Marcus Fraga Vieira

Center of Pressure Periodic Displacement with Alternate Current Unilateral Vestibular Stimulation 970
Pliego Adriana, Vega Rosario, and Soto Enrique

Leonardo Da Vinci, the Great Innovator in Cardiovascular Biomechanics 975
Ricardo Armentano

Biorobotics

Design and Development of 3D Printed Electromyographic Upper Limb Prosthesis 985
Osmar Vazquez, Mariel Alfaro-Ponce, Isaac Chairez, and Barbara Arteaga-Ballesteros

Prototype of a Surgical Robot with Contact Force Feedback 993
Misael Sánchez-Magos, Caridad Mireles-Pérez, Kenny Pérez, Francisco Medina, Mariana Ballesteros, David Cruz-Ortiz, Ivan Salgado, and Isaac Chairez

Proportional and Simultaneous Control Strategy for 3 DoF of Hand 1002
J. Cuadros-Acosta, J. Perez-Guerra, V. Herrera-Ruiz, M. Garcia-Florez, and J. Murillo-Escobar

Biopsy Robot Design for Breast Cancer Identification 1012
Joav Madrid, Tatiana Álvarez, and Ángel Luis Rodriguez

Development of a Lower-Limb Exoskeleton for Assistance of Movements in the Sagittal Plane 1023
Itzel García, Lourdes Luna, Marco Mendoza, Aldo Mejía-Rodríguez, Isela Bonilla, and Guadalupe Dorantes-Méndez

Design for Additive Manufacturing of a Robotic Hand with Two Thumbs 1031
Horacio León

Neural Engineering

Automatic Recognition and Feature Extraction of Motor-Evoked Potentials Elicited by Transcranial Magnetic Stimulation 1037
Jose E. Tecuapetla-Trejo, Jessica Cantillo-Negrete, Raquel Valdés-Cristerna, Paul Carrillo-Mora, Oscar Arias-Carrion, Emmanuel Ortega-Robles, and Ruben I. Carino-Escobar

Preliminary Design of a Regions-Based BCI Speller for Locked-in Patients 1043
Lucas Baldezzari and Gerardo Gabriel Gentiletti

Real-Time Home-Devices Control Based on Pupil Position 1051
Cristian E. Ordoñez, Eduardo L. Blotta, and Juan Pastore

Parkinson's Disease Classification Using Artificial Neural Networks . . . 1060
Carlos Castro, Eunice Vargas-Viveros, Alejandro Sánchez, Everardo Gutiérrez-López, and Dora-Luz Flores

Design and Implementation of a Multifunctional Myoelectric Control for Upper Limb Prostheses 1066
Gonzalo Oviedo, Mariano Sosa, Juan Manuel Fontana, Eric Laciar, and Leonardo Molisani

Post-stroke Injured Cerebral Cortex: Frequency Analysis of the Desynchronization of Its Sensorimotor Rhythms During Motor Intent 1073
Carolina B. Tabernig, L. Carolina Carrere, Gerardo G. Gentiletti, and Erika G. Spaich

Evaluating Strategies for Improving the Detection of Auditory Steady-State Responses in the AUDIX System 1079
Isabel Arnaiz, Eduardo Martínez-Montes, and Alejandro Torres-Fortuny

Reusable, Cased and Mechanically Held Graphite-Based Dry ECG Electrodes 1085
Rodrigo Soto Domínguez, Uriel Anguiano Piña, and Bersaín A. Reyes

Bio-Signal Acquisition Analysis for Stress Level Determination 1093
Sergio Alfonso Sánchez-Manzo, Ricardo Antonio Salido-Ruiz, O. Rocío Manzo-Palomera, Ángel Alfredo Sánchez-Michel, and Guillermo Alonso Cervantes-Cardona

***Therapainting*: Interactive Art-Therapy Tool Based on Head Movements and Eye Blinks** 1101
Fernando González-Martínez, Luz María Alonso-Valerdi, and David I. Ibarra-Zárate

Analysis of Alternating Hand Movement in Parkinson's Disease Patients 1107
Williams Saraguro, Boris Barzallo, Andrea García-Cedeño, Juan Carlos Guillermo, Catalina Punín, Ángel Soto, David Rivas, Roger Clotet, and Mónica Huerta

BCI for Meal Assistance Device 1117
Brayan Camilo Castro Sánchez, Laura Camila Loaiza Carvajal, Fitzgerald Leonard Gerardo Toro Quitian, and Juan Manuel López López

Rehabilitation

A Setup for Lower-Limb Post-stroke Rehabilitation Based on Motor Imagery and Motorized Pedal 1125
Teodiano Bastos-Filho, M. A. Romero, V. Cardoso, A. Pomer, B. Longo, and D. Delisle

A Robotic Lower-Limb Exoskeleton for Rehabilitation 1130
Arlindo Elias-Neto, Ana Cecilia Villa-Parra, Thomaz Botelho, A. Frizera-Neto, and Teodiano Bastos-Filho

Development of a Sip-and-Puff Interface for Communication and Control of Devices 1137
José Cláudio da Silva Junior and Walter Germanovix

Development of a Feeding Device for Patients with Motor Impairment in Upper Limbs 1147
Natacha H. Ota, Tiago R. S. Silva, Douglas Crochi, Cecilia P. Muffo, Silvia C. Martini, Alessandro P. Silva, Terigi A. Scardovelli, and Silvia R. M. S. Boschi

Comparison of Assessment Methods Using Virtual Games for Balance Rehabilitation 1153
Fabiana R. S. de M. Cavalcanti, Silvia R. M. da S. Boschi, Cecilia Muffo, Alessandro P. da Silva, Terigi A. Scardovelli, and Silvia C. Martini

A Wireless BCI-FES Based on Motor Intent for Lower Limb Rehabilitation 1162
L. Carolina Carrere, Leandro Escher, and Carolina Tabernig

Development of a Serious Game Controlled by Myoelectric Signals 1171
Mariano Sosa, Gonzalo Oviedo, Juan Manuel Fontana, Ronald O'Brien, Eric Laciar, and Leonardo Molisani

Design of a Portable Electric-Stimulation System to Reduce the Essential Tremor on the Hand 1178
Reynol García-Guadarrama and Rigoberto Martínez-Méndez

Mechanomyography Spasticity Assessment of Flexor and Extensor Wrist Muscles for the Classification of Boccia Athletes in Para Sports: A Pilot Study 1184
Elgison da Luz dos Santos, Maria de Fátima Fernandes Vara, Maira Ranciaro, Gustavo Tanaka Zelaga, Amanda Mayara Pereira Gomes, Isabel Cristina Bini, Guilherme Nunes Nogueira Neto, Eddy Krueger, and Percy Nohama

Postural Tremor Reduction System Design for Parkinson's Disease Patients 1191
María José Enciso Lopez and Ángel Luis Rodríguez Morales

Contribution of Virtual Environments to the Perception of Balance Rehabilitation Tasks: A Psychophysiological Study 1200
Oscar I. Caldas, Juan D. Abril, Oswaldo Rivera, Carlos Rodriguez-Guerrero, and Oscar F. Avilés

Medical Physics and Nuclear Medicine

Retinal Illuminance and the Relationship with Color 1211
Nataly A. Garcia-Morales and Ernesto Suaste-Gómez

Application of Structured Light Illumination and Compressed Sensing to High Speed Laminar Optical Fluorescence Tomography 1216
Ichiro Sakuma, Toshiki Kobayashi, Hiroshi Seno, Yuki Akagi, Keiichi Nakagawa, Masatoshi Yamazaki, and Naoki Tomii

A Method to Automate the Metabolite Postprocessing and Quantification on Magnetic Resonance Spectroscopy Signals 1220
Francisco López-Caracheo, Carlos Andres Perez-Ramírez, Arturo Hernández-Medina, Roberto E. Mercadillo-Caballero, and Erick H. Pasaye-Alcaraz

Effects of Poor Junctions on the Effectiveness of Electromagnetic Shields of MRI Rooms 1226
Rafael Navet de Souza and Sérgio Santos Muhlen

Thermography as a Diagnostic Tool for Early Detection of Diabetic Foot Ulceration Risk: A Review 1233
Cesar A. Salazar and Martha L. Zequera Díaz

Frequency Parametric Study for a HIFU Transducer Intended for Bone Tumor Treatment 1253
Juan Carlos García-López, Raquel Martínez-Valdez, Citlalli J. Trujillo-Romero, Arturo Vera, and Lorenzo Leija

Photothermal Signature Characterization of Breast Microcalcifications Ex-Vivo by Photoacoustic Method 1261
Lizbeth Anahí Serrano-Aguilar, Rosa María Quispe-Siccha, Argelia Pérez-Pacheco, Roberto Mosiñoz-Montes, Gregorio Quintero-Beuló, Azcary Vázquez-Tinajero, Fernando Lara-González, Mercedes Hernández-González, Joselín Hernández-Ruíz, and Juan C. López-Alvarenga

Innovation of Technologies for Health

HOMA-IR Assessment for Impaired Glucose Tolerance, Impaired Fasting Glucose and Insulin Resistance Diagnosis 1275
Erika Severeyn, Jesús Velásquez, Gilberto Perpiñán, Héctor Herrera, Sara Wong, José Díaz, and Miguel Altuve

System for Monitoring Environmental Variables in a Pharmacy Area Using an Alternative IoT Architecture (a Pilot Study) 1284
Jefferson Sarmiento-Rojas, John-Sebastian Sanchez-González, Pedro-Antonio Aya-Parra, and Daniel-Alejandro Quiroga-Torres

Development a Virtual Game to Stimulate Grip and Pinch Movements 1292
Domingo L. Cancela, Douglas Crochi, Fabiana R. S. M. Cavalcante, Alessandro P. Silva, Silvia C. Martini, Terigi A. Scardovelli, and Silvia R. M. S. Boschi

Methodology for Defining Ubiquitous Management Indicators in Primary Health Care 1298
Reginaldo Dias Soares Filho, Juliano Martins, and Renato Garcia

Home and Physiological Remote Monitoring System for Elderlies and People with Chronic Diseases 1306
Sergio Ponce, Sofia Avetta, Alexis Sparapani, Camilo Garcia, David Piccinini, and Natalia López

A Medical IoT-Based Remote Monitoring System: Application on Diabetic Foot 1313
Luis Fernando Moncada-Sánchez, Ricardo Antonio Salido-Ruiz, and Aurora Espinoza-Valdez

Device Validation to Monitor Speed in High Performance Roller Skaters Through the Internet of Things (IoT) 1320
Paula-Andrea Wilches-Castellanos, Daniel-Alejandro Quiroga-Torres, Pedro-Antonio Aya-Parra, and Jefferson Sarmiento-Rojas

Monitoring of Critical Variables in the Imaging Service from the Internet of Things (IoT) 1326
Oscar Pinzón Cadena, Cesar Garcia Preciado, Oscar Julián Perdomo Charry, Angelmiro Nuñez Cruz, Nidia Patricia Córdoba Hernández, Alexandra Beltran, Jefferson Sarmiento-Rojas, Daniel-Alejandro Quiroga-Torres, and Pedro-Antonio Aya-Parra

Differences in Heart Rate Variability Between Diabetic and Non-diabetic Intradialytic Hypotensive Patients 1333
Francisco Arturo López del Angel, Joaquín Azpiroz Leehan, and Gerardo Daniel Rosas Andreu

Clinical Engineering and Education

A Prioritization System for Timely HIV/AIDS Patient Care 1341
Alexis Cruz-Escudero, Laura Angelica Hernandez-Lopez, Daniel Ernesto Sanchez-Baqueiro, and Fabiola M. Martinez-Licona

Stakeholders Studies in HTA: A Theoretical Approach 1349
Fabiola M. Martinez-Licona, Raul Enrique Molina-Salazar, and Pedro Constantino Solis-Perez

Comparative Analysis of Two Indicators of Technical Evaluation for the Replacement of Medical Equipment 1357
Tlazohtzin R. Mora-García, L. Angélica Hernández-López, M. Fernanda Piña-Quintero, Ana B. Pimentel-Aguilar, and Martha R. Ortiz-Posadas

An Indicator to Determine the Surplus or Deficit of the Medical Equipment in Critical Care Units 1365
Tlazohtzin R. Mora-García, M. Fernanda Piña-Quintero, and Martha R. Ortiz-Posadas

Clinical Engineering Performance Benchmarking – A Practical Guide 1373
Binseng Wang

Medical Equipment for Breast Clinics A View of Biomedical Engineering from Practice 1380
Gustavo Adolfo Martinez Chavez

Web Software for Technology and Medical Infrastructure Management of a Clinical Engineering Department 1386
Carlos Augusto Centeno, Javier Alfredo Voos, Guillermo Riva, and Carlos Zerbini

Characterization of Medical Equipment Acquisition Processes by Considering the Evaluation of Technology, Pilot Case: POCT Blood Gas Analyzers 1398
Laura Valentina Bocanegra Villegas, Juan Camilo Osorio Salgado, Sandra Patricia Usaquén Perilla, and José Isidro García Melo

Evaluation of a Protocol to Measure the Total Heart Beat Index in Research and Clinical Environments 1403
Ramiro Muñoz, Catalfamo Formento Paola, Cesar Ignacio Dutto, Camila Ileana Dure, and Bonell Claudia

Correlation Between Sterilized Prongs and Nasal Injury in Newborns Subjected to Non-invasive Ventilation 1410
Débora F. Camillo Ribeiro, Beatriz L. Fernandes, and Percy Nohama

Economic Impact of Remote Monitoring System of the Obesity in Children: Costs of Monitoring and Conventional Practices 1417
Walter Saraiva Lopes, Diego Pereira da Silva, William Tsutomu Watanabe, Henrique da Costa Rodrigues, Silvia Helena Bastos de Paula, Robson Rodrigues da Silva, and Daniel Gustavo Goroso

A Review of the Literature on Virtual Learning Environments for Professionals in Primary Health Care 1428
Francisco Douglas Lima Abreu, Márcia A. S. Bissaco, Alessandro Pereira da Silva, Terigi Augusto Scardovelli, Silvia Regina Matos S. Boschi, Camila Cristina Martini Rodrigues, and Silvia C. Martini

Analysis and Validation of Electrical Safety Procedures for Biomedical Devices 1434
Débora Rubio, Nicolas Lescoulié, Débora Arce, Martín Roberti, and Sergio Ponce

Maintenance Management Requirements in Medical Technology 1441
Gustavo Adolfo Barrera-Saavedra and Andrés Mauricio González-Vargas

Fault Prioritization System for a Vital Signs Monitor Based on Fuzzy Logic 1449
Karen Jazmin Mendoza Bautista, Héctor García Estrada, María Guadalupe Ramírez Sotelo, and Agustín Ignacio Cabrera Llanos

Evaluation of Algorithms for the Elaboration of the Preventive Maintenance Program of Medical Devices in the Medical Center ISSEMyM Toluca 1458
Angélica C. López-Carranza and Edgar G. Del Hierro-Gutiérrez

How to Improve Learning in Biomedical Engineering Students from an Integrated and Formative Evaluation 1472
William Ricardo Rodríguez Dueñas

Bioimpedance

Gel Impedance Used as a Pressure Sensor: Preliminary Results 1481
Simon Brunnquell, Vinicius Sirtoli, and Pedro Bertemes-Filho

Biosensor of Inflammation Biomarker *NLRP3* Based on Electrical Bioimpedance 1488
Modesto Gómez-López, Ángel Miliar-García, Nadia Mabel Pérez-Vielma, G. Ames-Lastra, Eleazar Lara-Padilla, Katia Verónica Chávez, Arianne Ruby García, Josemaría Delgado, Ernesto Cortés, and César Antonio González Díaz

EMG-Based Kinematic Impedance Control of a Lower-Limb Exoskeleton 1494
Lourdes Luna, Itzel García, Marco Mendoza, Guadalupe Dorantes-Méndez, Aldo Mejía-Rodríguez, and Isela Bonilla

Evaluation of Respiratory Signal Record Based on Impedance Pneumography and Textile Electrodes 1502
Carlos Rubén Dell'Aquila, Gabriel Eduardo Cañadas, and Eric Laciar

Author Index 1511

Processing of Biomedical Signals

EEG-PML: A Software for Processing and Machine Learning Analysis of EEG Signals

Lluvia Gwendolyn Alvarado-Robles(✉),
Carlos Miguel Munguia-Nava, Israel Román-Godínez,
Ricardo Antonio Salido-Ruiz, and Sulema Torres-Ramos

Department of Computer Sciences, Universidad de Guadalajara, Centro Universitario de Ciencias Exactas e Ingenierías, Guadalajara, Mexico
lluvia.alvarado@alumnos.udg.mx,
sulema.torres@cucei.udg.mx

Abstract. Studies on EEG involve great amount of data to be processed and analyzed, requiring valuable time that the researchers could spend on more important tasks. On this work we developed a software that incorporates pre-processing algorithms like visualization and windowing tools, band pass filter and artifact removal tools, along with the machine learning algorithms: K-Means to group the data and Decision Trees to classify it. We expect that EEG-PML facilitates researchers work and, with the help of the machine learning algorithms, the studies over the EEG data can advance over new areas of research.

Keywords: EEG signal processing · Signal characterization · Classification · Machine learning

1 Introduction

Electrical brain activity is acquired using the Electroencephalogram (EEG) recording device due to this being a non-invasive and inexpensive technique [1].

EEG clinic and research studies produce a great amount of data which needs to be processed and analyzed. Nowadays, there are many software that implement traditional signal processing and analysis like EEGLAB [2], LabChart [3], and BrainVision Analyzer 2 [4]. Yet, some of those tools require the installation of additional toolboxes that could generate an extra expense, and some other toolboxes need the users to have certain programming skills to processes raw signals. In addition, in the era of artificial intelligence, the lack of integrated machine learning tools on this type of software could be slowing down the search for new subjacent information on the EEG data. In this regard, even though there are many signal processing and analysis algorithms that use machine learning, most of them are available through libraries or application user interfaces (APIs) like scikit-learn's (K-Means [5] and Decision Tree [6] algorithms), which turns out to be a problem for non-programmers or non-computational skilled users.

© Springer Nature Switzerland AG 2020
C. A. González Díaz et al. (Eds.): CLAIB 2019, IFMBE Proceedings 75, pp. 3–11, 2020.
https://doi.org/10.1007/978-3-030-30648-9_1

On the other hand, visual programming languages has become a great tool to easily programming algorithms or data processing sequences by dragging and dropping, connecting and configuring components; improving the user experience and reducing the learning curve [7], some examples of these are LabView [8], Matlab/Simulink, Orange Data Mining [9] among others.

Therefore, in this paper we propose a software that integrates pre-processing, visualization and machine learning algorithms, specifically for EEG, which will facilitate researchers work, letting them focus on the analysis of the processed data, rather than on its implementation.

2 Materials and Methods

EEG – Processing and Machine Learning Analysis (EEG-PML) is presented as a scalable tool, therefore, the modular architecture was chosen. The graphical interface of the software presents its tools in a tree-like arrangement, the root being always the data input module. The nodes represent the different tools to process and classify EEG signals. The data passes from the parent module to its child modules letting the processes stack upon each other, allowing the researcher to customize their analysis. Each module has its proper tool for data visualization and provides the option to export the results. The included modules will be further explained in the following sections.

2.1 Data Input and Windowing

The data input module is the core module of the software, here EEGs are stored, visualized and divided into windows if necessary. The module accepts the following formats of EEG recordings: EDF, EDF+, GDF, ACQ and MAT. Once an EEG is loaded, the researcher can open it in the module's visualization tool in which the signals can be zoomed in and out, and moved over time once they are zoomed.

This module also allows the researcher the selection of windows from an EEG to mark important stimulus. On the visualization tool mention earlier, the user can also visualize and create the windows to analyze, either manually or by uploading a CSV file containing the millisecond of the stimulus and the window length for each window in each EEG.

This module also provides the option to export the manually created windows into a CSV file for future use, as well as the EEGs divided into the corresponding windows.

2.2 Artifact Removal

Artifacts are non-desired signals that can appear in an EEG recording, disturbing the important data, and thus affecting the EEG interpretation. Artifacts most of the time come from muscular and eye movement, blinks and the heartbeat [1]. For better results in the analysis of the data, these artifacts need to be removed.

EEG-PML removes artifacts from EEG by using the Blind Source Separation method: Fast Independent Component Analysis (ICA) [10]. This method will obtain

the Independent Components (IC) in which the EEG can be decomposed by finding an un-mixing matrix **w**, following the next steps:

Choosing an initial random weight matrix w.
Letting $w^+ = E\{xg(w^T x)\} - E\{w^T x\}w$.
Letting $w = w^+ / \|w^+\|$
If it has not converged, repeat from step 2.

Considering that convergence happens when the values of **w** do not change from one iteration to the next one.

Even though there has been research on automatic methods to select and eliminate the artifactual IC, these are still not completely effective and can even remove important data of the EEG recording. For that reason, in EEG-PML we provide the IC directly to the researcher through an easy-to-use graphic interface, containing the necessary tools to analyze them and decide which IC are artifactual and effectively remove them, leaving the EEG data clean and ready for further processing. The cleaned EEG can be visualized and explored through the included visualization tool, in which the user can view the signals before and after artifact removal. This module also can export the cleaned EEG in EDF+ format.

2.3 Bandpass Filter

In EEG, some events are more noticeable on certain frequency bands [11], hence researchers may want to analyze the data in just this range of frequencies called "Frequency Bands". EEG-PML provides an easy-to-use tool for this purpose, providing by default the most common frequency bands for filtering of EEG signals: Gamma (40–100 Hz), Beta (12–40 Hz), Alpha (8–12 Hz), Theta (4–8 Hz) and Delta (0–4 Hz). Also, the module provides the researcher with the option to create customized frequency bands.

The filtering of the EEG is applied through a Bandpass filter using the Fast Fourier Transform (FFT) [12] that decomposes the signal from the N point time domain into N time domain signals composed of a single point, then the frequency spectra of this points is calculated and synthesized into a single frequency spectrum. From this calculated spectrum, the points that fall out of the selected frequency band are turned to 0. After this, the inverse FFT is applied to the frequency spectrum and the EEG signals are reconstructed with only the desired frequencies.

The module counts with its own tool for visualization that shows the original EEG and the new EEGs created by each bandpass filter. The filtered EEGs can also be exported to EDF+ format.

2.4 Characterization

Once the EEG are properly pre-processed and the windows for the analysis have been selected, it is necessary the extraction of the important features of the signals, in order to perform a machine learning analysis. EEG-PML allows the researcher to use the characterization tool, which extracts these features from the EEG. The data generated

by this tool can then be utilized by the machine learning modules or exported into CSV format to be processed on other software. The software allows extracting four different features from the signals: the magnitude (EM) (Eq. (1)) and phase spectrum (EF) (Eq. (2)) along with their frequency (F) [13], area under the curve (Eq. (3)) [14], maximum voltage (Eq. (4)), and minimum voltage (Eq. (5)). These features are extracted from each EEG selected channel.

$$EM = \sqrt{(real[FFT(x(t))])^2 + (imag[FFT(x(t))])^2} \tag{1}$$

$$EF = tan^{-1}\left(\frac{imag[FFT(x(t))]}{real[FFT(x(t))]}\right) \tag{2}$$

$$A = \int_0^T x(t)dt \tag{3}$$

$$MaxV = \max(x(t)) \tag{4}$$

$$MinV = \min(x(t)) \tag{5}$$

Where x represents the signal of a single channel of the EEG, t represents the millisecond of the recording, FFT is the Fast Fourier Transform and T is the length of x in milliseconds.

For each EEG feature representation, the researcher has the option to assign a class label to each feature vector to be processed with a supervised classification algorithm, like decision trees, on the other hand, the feature vectors could be leaved without class label to be processed with an unsupervised algorithm like K-Means.

2.5 Machine Learning

EEG-PML has the implementation of a supervised learning algorithm, a Decision Tree model and an unsupervised learning algorithm, K-Means. The above-mentioned algorithms grant the user a variety of options to interpret the data and a visual interface for easy use of the tool.

K-Means. EEG-PML offers the researcher the option to use K-Means, one of the most popular and effective clustering algorithms [15]. This algorithm was selected with the purpose of making clusters of EEG recordings to facilitate finding similar data patterns in the signals.

The module has customizable settings that include the type of initialization, number of clusters, number of iterations and the number of epochs.

K-Means algorithm uses a method that divides data into mutually exclusive clusters [16]. In this way, it treats each instance (represented by the set of features proposed here) in the data as an object having a location in space and finds a partition in which objects within each cluster are as close to each other as possible, and as far from objects in other clusters. Each cluster in the partition is defined by the data and by its centroid. The centroid for each cluster is the point with the minimum distance from all objects in

that cluster. The module counts with its own tool to visualize the data and the resulting clusters.

When using K-Means it is important to get the optimal clusters, this is why silhouette can be used as an index to measure the quality of the final clustering.

The silhouette value for each point is a measure of how similar a given point is respect to other points in its own cluster compared to points in other clusters. It is defined as [16, 17]:

$$s(i) = \frac{b(i) - a(i)}{\max\{a(i), b(i)\}} \tag{6}$$

And b(i) as:

$$b'(i) = \min\{d'(i, C)\} \tag{7}$$

where s is the silhouette value and takes values from −1 to 1, A, B and C are clusters, i is any object i in the data set, a(i) is average dissimilarity of i to all other objects of A, d (i, C) is average dissimilarity of i to all objects of C, b(i) is the minimum d(i, C).

In (Eq. (6)), $s < 0$ values indicate points that are assigned to the wrong cluster, $s = 0$ indicates points that are not distinctly of other clusters and $s > 0$ values indicates points that are very distant from their neighboring clusters.

The module counts with its own tool for visualization of the clusters and the resulting silhouette value.

Decision Tree. To provide the researcher with a classification tool to visualize the most relevant features in the set of EEGs, the supervised algorithm of decision tree is used to facilitate the decision making. It only requires the researcher to assign labels to each EEG in the module of characterization. The tree has three types of nodes, a root node that has no incoming edges and zero or more outgoing edges, internal nodes, each of which has one incoming edge and two or more outgoing edges and a leaf that has one incoming edge and zero outgoing edges. In a decision tree, each leaf is assigned a class label.

The process of creating a decision tree starts by calculating the Gini coefficient [18] that measures the inequality among values, a zero expresses equality and one expresses inequality. Once the Gini value is calculated, the feature that comes closest to 1 is selected to be the root of the tree, after this the remaining samples are separated to repeat the process in the following levels of the tree until there are no samples left [6].

The module has customizable settings that include the name of the tree, number of leaves, and the number of splits for cross-validation. After the tree is generated, the researcher can visualize the resulting tree, the score of the cross-validation and can export the tree into a PNG file [19].

3 Results

Each tool from EEG-PML was tested for proper operation, all of the tools proved correct execution. Below, part of the results of the test can be observed.

For the tests, a database of 57 EEGs was used [20]. These set of EEGs come from a study realized on kids with ages between 8 and 11 years old. The study consisted on testing the mathematical abilities of these kids by letting them solve a series of numerical comparison problems. The length of the recordings used to test this software was of 11 s. The set of EEGs was divided into 3 groups according to the final performance of each kid obtained on the WRAT-4 [21]. The groups where labeled as "High", "Medium" and "Low". To test our software, only the EEGs from the groups High and Low were selected, resulting in a set of 36.

The Artifact Removal module was tested loading the mentioned set of EEGs onto the software, then we added the module to the tree's root and selected the IC to be removed. After the module effectively removed the artifactual IC, the module's visualization tool was opened to observe the resulting EEGs. Figure 1 depicts the previous state of the EEG marked in red and the resulting signals in black.

After the artifacts on the signals were removed, each EEG was filtered on the band pass filter module using the bands of: Gamma, Beta, Alpha, Theta, Delta and a custom band (0.5–30 Hz). The resulting signals where saved onto new EEGs grouping them by band with the purpose to realize a comparison of the results on the machine learning algorithms.

The Characterization module was tested selecting a window of 1 s length from each EEG, which marks the important stimulus to analyze. All of the features and all of the channels were selected, the EEGs were labeled according to their groups as A for "High" and B for "Low". In Fig. 2, part of the resulting table of features and classes is shown.

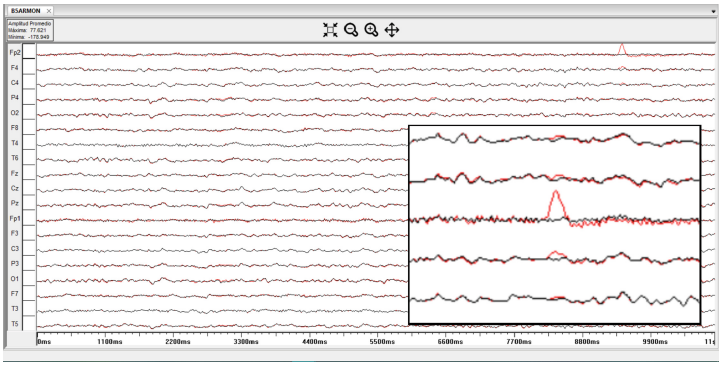

Fig. 1. Resulting EEG after artifact removal.

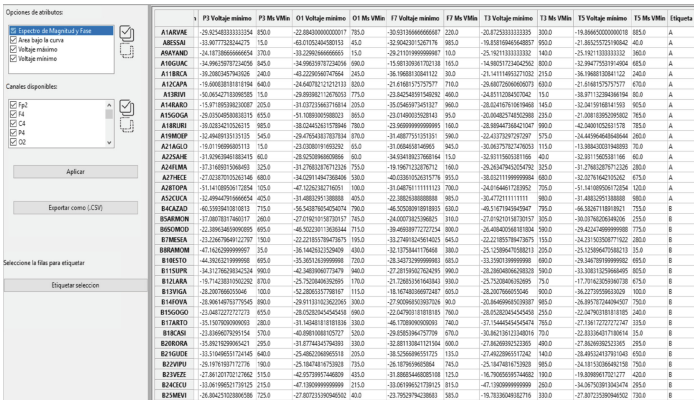

Fig. 2. Characterization of the EEG signals.

The Decision Tree module was tested using the results obtained from the Characterization module's test. The maximum levels for the tree was set to 100 and the number of folds for cross validation to 10. As mentioned before, a comparison was made between the filtered bands and the results can be observed in Table 1.

Table 1. Performance of the decision tree algorithm classifying the selected set of EEGs filtered by different bands.

Band	Accuracy (%)
Custom (0.5–30 Hz)	72
Gamma (40–100 Hz)	52
Beta (12–40 Hz)	44
Alpha (8–12 Hz)	47
Theta (4–8 Hz)	55
Delta (0–4 Hz)	75

Figure 3 shows the Decision Tree for the Delta band, which corresponds to the best accuracy (75%).

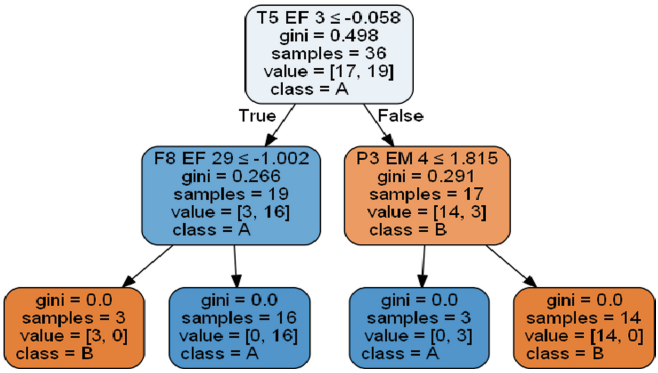

Fig. 3. Resulting decision tree for delta band with a 75% of accuracy.

The tree model classifies the EEG according to the next rules:

1. $((T5EF3 \leq -0.058) \wedge (F8EF29 > -1.002)) \vee ((T5EF3 > -0.058) \wedge (P3EM4 \leq 1.815)) \rightarrow class = A$
2. $((T5EF3 \leq -0.058) \wedge (F8F29 \leq -1.002)) \vee ((T5EF3 > -0.058) \wedge (P3EM4 > 1.815)) \rightarrow class = B$

4 Conclusions

It was possible to develop a software that integrates different tools for pre-processing of EEG signals like windowing, bandpass filter and artifact removal, along with tools for the analysis of this signals using machine learning algorithms like K-Means and Decision Trees. The integration of the mentioned tools onto our software solves the need of different toolboxes to realize analysis on EEG, making this work more fluid and easier for the researchers. Moreover, the software is based on components so it can be expanded easily, and counts with a friendly interface for the user.

Aside from this, the implemented metrics to characterize the EEG signals, allowed us to obtain a satisfactory classification of the data.

As a future work, more modules could be included in the software to allow the extraction of different signal's features, metrics to obtain relations between channels, and other machine learning tools.

Acknowledgment. The authors of this paper would like to acknowledge the EEG database provided by Andrés Antonio González Garrido and Fabiola Reveca Gómez Velázquez.

Conflict of Interest. The authors declare that they have no conflict of interest.

References

1. Islam, M.K., Rastegarnia, A., Yang, Z.: Methods for artifact detection and removal from scalp EEG: A review. Neurophysiol. Clin. Clin. Neurophysiol. **46**(4–5), 287–305 (2016)
2. SCCN EEGLAB [Computer Software]. https://sccn.ucsd.edu/eeglab/index.php. Accessed 18 May 2018
3. ADInstruments LabChart [Computer Software]. https://www.adinstruments.com/products/labchart. Accessed 18 May 2018
4. BrainProducts BrainVision Analyzer 2 [Computer Software]. https://www.brainproducts.com/productdetails.php?id=17. Accessed 18 May 2018
5. Sklearn.cluster.kmeans Scikit-learn: Machine Learning in Python. https://scikit-learn.org/stable/modules/generated/sklearn.cluster.KMeans.html. Accessed 21 Jul 2018
6. Decision Trees Scikit-learn: Machine Learning in Python. https://scikit-learn.org/stable/modules/tree.html. Accessed 25 Jul 2018
7. Ray, P.P.: A survey on visual programming languages in internet of things. Sci. Prog. **2017**, 6 (2017)

8. Elliott, C., Vijayakumar, V., Zink, W., Hansen, R.: National instruments LabVIEW: a programming environment for laboratory automation and measurement. JALA: J. Assoc. Lab. Autom. **12**(1), 17–24 (2007)
9. Demsar, J., Curk, T., Erjavec, A., Gorup, C., Hocevar, T., Milutinovic, M., Mozina, M., Polajnar, M., Toplak, M., Staric, A., Stajdohar, M., Umek, L., Zagar, L., Zbontar, J., Zitnik, M., Zupan, B.: Orange: data mining toolbox in Python. J. Mach. Learn. Res. **14**, 2349–2353 (2013)
10. Hyvärinen, A., Oja, E.: Independent component analysis: algorithms and applications. Neural Networks **13**(4–5), 411–430 (2000)
11. Roach, B.J., Mathalon, D.H.: Event-related EEG time-frequency analysis: an overview of measures and an analysis of early gamma band phase locking in schizophrenia. Schizophr. Bull. **34**(5), 907–926 (2008)
12. Smith, S.W.: The scientist and engineer's guide to digital signal processing (1997)
13. Cerna, M., Harvey, A.F.: The fundamentals of FFT-based signal analysis and measurement. National Instruments, Junho, 54 (2000)
14. Yeh, S.T.: Using trapezoidal rule for the area under a curve calculation. In: Proceedings of the 27th Annual SAS® User Group International (SUGI 2002) (2002)
15. MacQueen, J.B.: Some methods for classification and analysis of multivariate observations. In: Proceedings Fifth Berkeley Symposium on Mathematical Statistics and Probability, vol. 1, pp. 281–297. University of California Press (1967)
16. Rousseeuw, P.J.: Silhouettes: a graphic aid to the interpretation and validation of cluster analysis. J. Comput. Appl. Math. **20**, 53–65 (1987)
17. sklearn.metrics.silhouette_score Scikit-learn: Machine Learning in Python. https://scikit-learn.org/stable/modules/generated/sklearn.metrics.silhouette_score.html. Accessed 22 Jul 2018
18. Gini, C.: Variabilità e Mutabilità, Harvard University (1912)
19. Gansner, E., Ellson, J., North, S. Graphviz (Version 2.38) [Computer software]. https://graphviz.gitlab.io/download/. Accessed 28 Jul 2018
20. González, A.A., Gómez, F.R.: The analysis of EEG coherence reflects middle childhood differences in mathematical achievement. Brain Cogn. **2018**(124), 57–63 (2018)
21. Wilkinson, G.S., Robertson, G.J.: Wide Range Achievement Test (WRAT4). Psychological Assessment Resources, Lutz (2006)

Performance Evaluation of Average Methods in the Time Domain Using Quality Measures for Automatic Detection of Evoked Potentials

Idileisy Torres-Rodríguez[1(✉)], Carlos Ariel Ferrer-Riesgo[1], Martha Madyuri Pérez de Morales Artiles[2], and Alberto Taboada-Crispi[1]

[1] Informatics Research Center, Universidad Central "Marta Abreu" de Las Villas, UCLV, 54830 Santa Clara, Cuba
{itrodriguez, cferrer, ataboada}@uclv.edu.cu
[2] Cardiocentro "Ernesto Che Guevara" de Villa Clara, 50200 Santa Clara, Cuba
mmadyuri88@gmail.com

Abstract. For the reduction of noise and extraction of the evoked potentials several methods have been reported in the literature based on the average of signals, which try to counteract the limitations of the classical technique used for the signal enhancement, which is the coherent average. The quality of the resulting signal can be evaluated using measurements in the time domain or the frequency domain. The objective of this work is to evaluate the performance of different average methods using quality measures in the time domain to determine which combination of an average method with quality measurement is better adjusted to the detection of transient auditory evoked potentials. To fulfill this objective, the classic coherent average, the median, the weighted average and four other versions of the robust average based on the median are tested. The quality measures used to compare the different average methods are the correlation coefficient, the standard deviation ratio and the variance of the single point. It was obtained as a result that the robust method Tanh mean, together with the measure of the variance of single point offers the best results.

Keywords: Auditory Evoked Potentials · Evoked potentials · Average methods · Trimmed estimators · CCR · SDR · Fsp

1 Introduction

The evoked potentials are bioelectrical signals that respond to an external stimulation [1]. Auditory Evoked Potentials (AEP) are especially found in the screening of auditory deficits in neonates, in diagnoses for certain brain diagnoses and intraoperative monitoring, among others [2, 3]. The techniques of noise reduction for the extraction of Evoked Potentials are mostly based on the average of signals [1, 4–7]. The classic signal average is not the best option when the signal has an impulsive noise and artifacts are found in it. In the literature, several average methods are reported that try to counteract the limitations of the arithmetic mean or average of the classical ensemble [5, 8–10]. To evaluate the quality of the potentials found and the adequate noise

© Springer Nature Switzerland AG 2020
C. A. González Díaz et al. (Eds.): CLAIB 2019, IFMBE Proceedings 75, pp. 12–20, 2020.
https://doi.org/10.1007/978-3-030-30648-9_2

reduction, several measures have been used, mainly based on the estimation of the resulting signal-to-noise ratio and the calculation of residual noise. Specifically, to evaluate the quality in the extraction of AEP, there is a group of statistical measurements in the time domain that has been proposed, these measurements are generally used in the automatic detection of responses [3]. Most of the reported work evaluates the performance of the measures using only the classical average for the extraction of the signals or compare the performance of several average methods using only one measure of quality. The objective of this work is to evaluate the performance of several average methods using several quality measures in the extraction of transient auditory evoked potentials. The average methods selected for comparison are the classical average, this is the best unbiased estimator when the number of times to average tends to infinity. Another method used is the weighted average, this method is a possible solution when there are variations in the noise level of potential to potential. But the weighted average considers that the variance within the potential is fixed and, sometimes, it can overestimate the allocation of the weights, besides the allocation of the weights, depends on the noise model that is assumed. One solution is to use robust averaging methods, capable of handling those outliers [1]. In [8] several robust methods are compared and a new one is proposed, these methods are chosen to analyze their performance in AEP.

2 Methods

2.1 Average Methods

The coherent average or arithmetic mean (M_Mean, for its identification in the work) as it is also known, can be calculated from the ensemble matrix that is formed with the M evoked answers. Where the response p_i to the i-th stimulus is assumed as the sum of the deterministic component of the signal or response evoked s plus a random noise r which is asynchronous with the stimulus. The model for each of the M responses is given by Eq. (1).

$$p_i = s + r_i, \quad 1 \leq i \leq M \tag{1}$$

The deterministic component of the signal, $\hat{s}$, can be estimated using Eq. (2), where N is the number of samples that compose each answer [1].

$$\hat{s} = \frac{1}{M} \sum_{i=1}^{M} p_i(n), \quad 1 \leq n \leq N \tag{2}$$

The fundamental premise for applying the average of signals is that the current noise is stationary and normal, with zero mean. Consequently, the variance of the noise must be fixed and equal in all the potentials. This condition is not always met and the result of a coherent average is affected. In the literature several methods have been proposed to try to counteract the limitations of the coherent average, among them is the

weighted average and the robust average [1]. The deterministic component of the signal is estimated using a weighted average according to the Eq. (3).

$$\hat{s}_w(n) = \sum_{i=1}^{M} w_i p_i(n) \tag{3}$$

In the weighted average (Weighth_mean) each evoked response is weighted according to certain criteria, one of the most used criteria is to assign weights depending on the variance of the estimated noise in each response. At a potential with a high noise level, a smaller weight is assigned [5, 9, 11, 12]. The Eq. (4) correspond to these criteria.

$$w_i = \frac{1}{\sigma_i^2}\left(\sum_{j=1}^{M}\frac{1}{\sigma_j^2}\right)^{-1} \quad i = 1, \cdots, M \tag{4}$$

In Eq. (4), σ_i^2 is the noise variance in the *i-th* potential. If the noise variance were constant in all records, the optimum value of w_i would be *1/M* and would be in the presence of the traditional average. The coherent average and the weighted average represent linear techniques and consequently perform very well when the noise is of Gaussian type [1, 8]. However, in the case that artifacts appear occasionally, with large amplitude values (outliers), these techniques are limited. In the literature, a family estimators, commonly referred to as trimmed mean has been proposed to reduce contamination by possible outliers [1, 5, 8]. The trimmed estimators are based on the median (Median), where the median constitutes the Maximum Likelihood (ML) estimator of *s* when the noise is considered Laplacian [1]. Computation of median includes ordering of samples in the ensemble matrix according to their amplitudes of all epochs for each time point relative to stimulus, independently from other time points. Due to this independence, median averaging cannot be affected by the nonstationarity of noise within an epoch. In the trimmed mean methods the coherent average is combined with the median for obtaining the final response, the ensemble matrix is ordered and a part of extreme values is discarded or modified, but all other values are used for averaging in the same way as in conventional mean averaging. The rejection of extreme values is different from the artifact rejection concept. In [8], Leonowicz and *et al.* compare different estimators based on the median to improve the signal-to-noise ratio and to the extraction of evoked responses (α-trimmed mean, Winsorized mean, Trimmed L–mean), and they propose a new method named tanh mean. The Eq. (5) is to estimate the deterministic signal using α- trimmed mean.

$$\hat{s}_\alpha(n) = \frac{1}{M - 2K}\sum_{i=K+1}^{M-K} p_i(n) \tag{5}$$

If the Eq. (5) is compared concerning the Eq. (3) is easy to note that the weights can be assigned using the following equation:

$$w_i = \begin{cases} \frac{1}{M-2K}, & K+1 \le i \le M-K \\ 0, & \textit{en otro caso} \end{cases}, \tag{6}$$

where α is the percent of trimming and M is the number of responses and K = αM, is the number of observations that they are eliminated of each extreme of the ordered matrix. The weights for to estimate the deterministic signal using Winsorized mean can be seen in the Eq. (7), for the Trimmed L-mean [13] in the Eq. (8) and Tanh mean in the Eq. (9).

$$w_i = \begin{cases} 0, & i \le K \quad \acute{o} \quad i \ge M-(K-1) \\ \frac{K+1}{M}, & i = K+1 \quad \acute{o} \quad i = M-K \\ \frac{1}{M}, & K+2 \le i \le M-(K+1) \end{cases} \tag{7}$$

$$w_i = \begin{cases} \dfrac{\binom{i-1}{K}\binom{M-i}{K}}{\binom{M}{2K+1}}, & K+1 \le i \le M-K \\ 0, & \textit{en otro caso} \end{cases}, \tag{8}$$

where $\binom{i}{K} = \frac{i!}{K!(i-K)!}$.

For the case of the Tanh mean, the weights are calculated using the hyperbolic tangent functions as is showed in the Eq. (9).

$$w_i = \begin{cases} \tanh(k*i) - vs, & i < \frac{M}{2} \\ -\tanh(k*i-M) + vs, & i \ge \frac{M}{2} \end{cases} \tag{9}$$

In Eq. (9), k is the factor controlling the slope of the weights for extreme values in data and vs determines the vertical shift [8]. The classical ensemble average and the ensemble median can both be viewed as special cases of trimmed estimators [1, 5, 8]. In this work, the mentioned methods are compared.

2.2 Quality Measures in the Time Domain

Conventionally, the presence or absence of an evoked response is determined by visual inspection, which requires expertise to detect specific wave patterns. Several techniques have been used for the automatic detection of auditory-evoked potentials, some of the most used are: the correlation coefficient ratio (CCR), this measures is a statistic that reflects the replicability between two sub-averages [14, 15] is computed according to Eq. (10).

$$CCR = \frac{\sum_{i=1}^{NM} (\hat{s}_1 \hat{s}_2)}{\sqrt{\sum_{i=1}^{NM} (\hat{s}_1) \sum_{i=1}^{NM} (\hat{s}_2)}}, \tag{10}$$

where $\hat{s}_1$ and $\hat{s}_2$ are the estimated signals for each sub-average, N is the number of samples in the epoch and M is the total epochs in the ensemble, another measure is standard deviation rate (SDR) [14, 15]. The SDR is a signal-to-noise ratio within the variance of the estimated signal (var($\hat{s}$)) and the residual noise variance (var(θ)) as shown in the Eq. (11).

$$SDR = \frac{\text{var}(\hat{s})}{\text{var}(\theta)} \tag{11}$$

The residual noise is estimated as the difference between the even sub-average and the odd sub-average.

$$\theta = (\hat{s}_1 - \hat{s}_2) \tag{12}$$

The distribution based on the signal-to-noise ratio (SNR) using a single point of the response (Fsp) is another measure [2, 16, 17]. Fsp provides an estimate of the response SNR, according to Eq. (13) the power of the signal is estimated from the averaged response equal to previous equations, while the power of noise is estimated using the single point (*sp*) variance divided by the number of epochs in the ensemble matrix.

$$Fsp = M * \text{var}(\hat{s})/\text{var}(sp) \tag{13}$$

2.3 Data

The database used in this study consists of transient auditory evoked potentials registered in 34 neonatal patients between 1–3 months of age born in the Hospital Materno Ramón González Coro, in the capital of our country. The signals were recorded using a click stimulation with duration 0.1 ms at different intensities 100, 80, 70, 60, 30 dB NHL and 0 dBpSPL with hearing aids (EarTone3A) [54, 55]. Ag/AgCl dry electrodes were used that were fixed with electrolytic paste on the forehead (positive), ipsilateral mastoids (negative) and contralateral mastoids (earth). The impedance values were kept below 5 kΩ. The bioelectric activity was amplified with a gain of 120,000 and filtered between 20 and 2,000 Hz. The sampling frequency used was 13.3 kHz, and the analysis windows to form the seat matrix was approximately 15 ms, this is around 200 samples per window (N = 200).

2.4 Experiment Description

The database original was pre-processed with professional software (EEGLAB) to reduce artifacts present in the records and obtain a clean version of the original data. All epochs with values outside the threshold of ±5 μV were eliminated. Only the records of 100 dBnHL ware used to guaranty the maximum values of the quality measures, for a total of two datasets, each with 68 records correspondents in 34 patients by two ears. The quality measures were calculated for each response average obtained using the different average methods in the original and pre-processed data. This experiment allows comparing the performance of the different average methods in the presence of different noise levels. To experiment, a Monte Carlo experiment of 300 realizations was designed, where 250 epochs were randomly chosen in each one to obtain the estimated signal and calculate the measurements. This experiment allows us to evaluate the robustness of the methods and to determine which one gives better with less amount of epochs to average. The values obtained for each measure were standardized within 0 and 1 to facilitate the comparison.

3 Results

First, for evaluated the robustness of methods, the Wilcoxon test was performed. Each standardized measure was compared within the original data and the pre-processed data. The *p* values obtained from a Wilcoxon test are presented in Table 1. Values below 0.05 show that there are differences between the result obtained with the original data and the pre-processed data. Average methods based on the median behave similarly when the records have epochs with values more or less than ±5 μV, while the classical average and weighted average have differences between the two databases.

Table 1. Results of the Wilcoxon test in the comparison of the methods between original signals and preprocessed signals (*p values*).

Average methods	CCR	Fsp	SDR
M_Mean	0.0233	0.0356	0.0482
Median	0.9447	0.3341	0.1457
Weighth_mean	0.0428	0.0429	0.0457
Trim_mean	0.2621	0.2024	0.2130
Win_mean	0.1687	0.3178	0.2789
TL_mean	0.1982	0.1385	0.1682
Tanh_mean	0.0850	0.1905	0.1385

The average standardized values of the CCR, the SDR, and the Fsp for each of the methods in each database are shown in Fig. 1. On the abscissa axis are the methods of averaging and in the axis of the ordinates the normalized values of the quality measures. In the Fig. 1 can be seen how to exist differences within the results obtained with the original data and the pre-processed data for the M_Mean and Weight_mean. For the case of the trimmed estimators, these differences are not appreciable. This result corroborates that the trimmed estimators have major performance when existing outliers in the records.

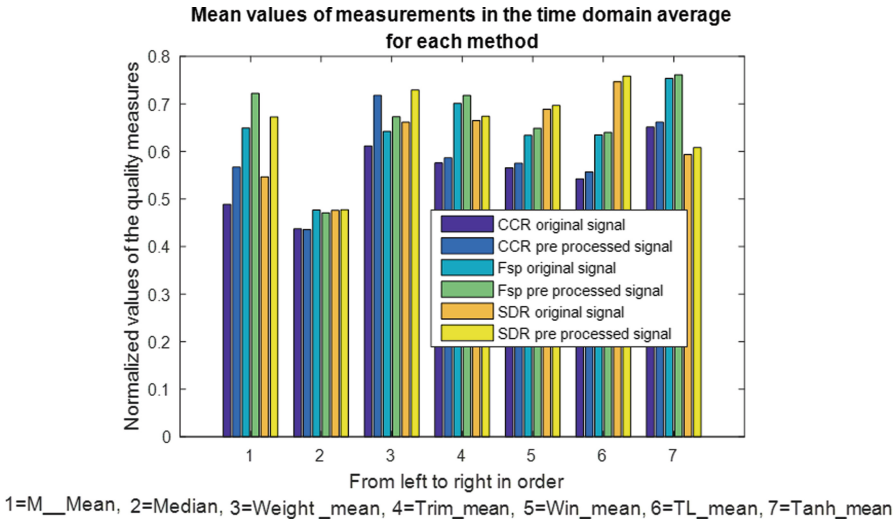

Fig. 1. Average values of the measurements for all methods

To identify in a general way which method offered the best results, a Friedman test was carried out, providing a p-value of less than 0.05, suggesting that there are significant differences in at least two methods. The Friedman test was developed using the results normalized obtained only in the original database. The test resulted in a value of $p < 0.05$, which suggests that there are significant differences between at least two methods. To identify the methods in which the differences existed, a post-hoc test was developed using the Bonferroni method.

Figure 2 shows the results obtained in the post-hoc test. Non-overlapping segments are those that show significant differences. It can be seen how the Median has the worst total performance, differing significantly from the Weight_mean, the Trim_mean and the Tanh_mean. In general, the best performance was obtained by the Tanh_mean.

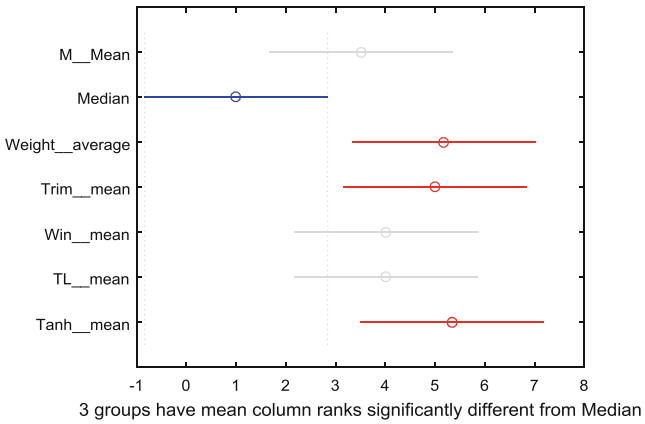

Fig. 2. Differences between the average ranks of the different measures using the different methods

4 Conclusions

Different average methods have different performances in obtaining Auditory Evoked Potentials. Both the coherent and weighted averaging present differences when there are outliers in the record of the answers. Although the post-hoc test shows that the weighted average does not present significant differences regarding the Trim_mean and Tanh_mean in the original data, it was verified that this can be affected when the information contains outliers. In general, using the three measures, Tanh_mean presented the best results. According to the Fig. 1 the best results of Tanh_mean were using Fsp measures.

References

1. Sörnmo, L., Laguna, P.: Bioelectrical Signal Processing in Cardiac and Neurological Applications. Elsevier (2005)
2. Weerathunge, W.A.H.R., Bandara, D.M.S.L., Amaratunga, M.G.B., De Silva, A.C.: Robust algorithm for objective hearing screening of newborns using Automated Auditory Brainstem Response. In: 2016 Moratuwa Engineering Research Conference (MERCon), pp. 149–155 (2016). https://doi.org/10.1109/MERCon.2016.7480131
3. Rajkumar, C., Augustine, A., Lepcha, A., Balraj, A.: Automated auditory brainstem response: Its efficacy as a screening tool for neonatal hearing screening in the postnatal ward. Indian J. Otol. **22**(4), 237 (2016). https://doi.org/10.4103/0971-7749.192134
4. Andrew P.B., Wayne, J.W.: Automated analysis of the auditory brainstem response. In: Proceedings of the 2004 Intelligent Sensors, Sensor Networks and Information Processing Conference 2004, pp. 541–546 (2004). https://doi.org/10.1109/issnip.2004.1417519
5. Pander, T.: A new approach to robust, weighted signal averaging. Biocybern. Biomed. Eng. **35**(4), 317–327 (2015). https://doi.org/10.1016/j.bbe.2015.06.002

6. Kim, K., Lim, S.-H., Lee, J., Kang, W.-S., Moon, C., Choi, J.-W.: Joint maximum likelihood time delay estimation of unknown event-related potential signals for EEG sensor signal quality enhancement. Sensors **16**(6), 891 (2016). https://doi.org/10.3390/s16060891
7. Pander, T., Przybyła, T., Czabański, R.: An application of the Lp-norm in robust weighted averaging of biomedical signals, J. Med. Informatics Technol., 22(2) (2013)
8. Leonowicz, Z., Karvanen, J., Shishkin, S.L.: Trimmed estimators for robust averaging of event-related potentials. J. Neurosci. Methods **142**(1), 17–26 (2005). https://doi.org/10.1016/j.jneumeth.2004.07.008
9. Leski, J.M.: Robust weighted averaging [of biomedical signals]. IEEE Trans. Biomed. Eng. **49**(8), 796–804 (2002). https://doi.org/10.1109/tbme.2002.800757
10. Pander, T., Pietraszek, S., Przybyła, T.: A Novel Approach to Robust Weighted Averaging of Auditory Evoked Potentials, pp. 321–332. Springer, Cham (2014). https://doi.org/10.1007/978-3-319-06596-0_30
11. Davila, C., Mobin, M.S.: Weighted averaging of evoked potentials. IEEE Trans. Biomed. Eng. **39**(4), 338–345 (1992). https://doi.org/10.1109/10.126606
12. Silva, I.: Estimation of postaverage SNR from evoked responses under nonstationary noise. IEEE Trans. Biomed. Eng. **56**(8), 2123–2130 (2009). https://doi.org/10.1109/tbme.2009.2021400
13. Elamir, E.A.H., Seheult, A.H.: Trimmed L-moments. Comput. Stat. Data Anal. **43**(3), 299–314 (2003). https://doi.org/10.1016/s0167-9473(02)00250-5
14. Mijares, E., Pérez Abalo, M.C., Herrera, D., Lage, A., Vega, M.: Comparing statistics for objective detection of transient and steady-state evoked responses in newborns. Int. J. Audiol. **52**(1), 44–49 (2013). https://doi.org/10.3109/14992027.2012.736030
15. Savio López, G., Mijares Nodarse, E., Pérez Abalo, M.C., Vega Hernandez, M., Lage Castellanos, A., Hernández Barros, D.: Eficiencia de la detección automática de potenciales evocados auditivos de estado estable a múltiples frecuencias evaluada mediante la metodología ROC. Rev. Logop. Foniatría y Audiol. **27**(1), 12–23 (2007). https://doi.org/10.1016/s0214-4603(07)70067-0
16. Valderrama, J.T., et al.: Automatic quality assessment and peak identification of auditory brainstem responses with fitted parametric peaks. Comput. Methods Programs Biomed. **14**(3), 262–275 (2014). https://doi.org/10.1016/j.cmpb.2014.02.015
17. Chesnaye, M.A., Bell, S.L., Harte, J.M., Simpson, D.M.: Objective measures for detecting the auditory brainstem response: comparisons of specificity, sensitivity and detection time. Int. J. Audiol. **57**(6), 468–478 (2018). https://doi.org/10.1080/14992027.2018.1447697

Analysis of the Maternal Cardio-Electrohysterographic Coupling During Labor by Bivariate Phase-Rectified Signal Averaging

Cinthia Gabriela Esquivel-Arizmendi[1], Claudia Ivette Ledesma-Ramírez[1], Adriana Cristina Pliego-Carillo[1], Juan Carlos Echeverría[2], Miguel Ángel Peña-Castillo[2], Gustavo Pacheco-López[3,4], and José Javier Reyes-Lagos[1(✉)]

[1] Faculty of Medicine, Autonomous University of the State of Mexico (UAEMex), Toluca 50180, Mexico
jjreyesl@uaemex.mx
[2] Basic Sciences and Engineering Division, Metropolitan Autonomous University (UAM), Campus Iztapalapa, Mexico City 09340, Mexico
[3] Biological and Health Sciences Division, Metropolitan Autonomous University (UAM), Campus Lerma, Lerma 52005, Mexico
[4] Department of Health, Science, and Technology, Swiss Federal Institute of Technology (ETH) Zurich, 8092 Zurich, Switzerland

Abstract. Maternal cardio-electrohysterographic coupling (MCEC), which is defined as the interaction of uterine electrical activity and maternal heart rate, is a physiological phenomenon poorly explored in the obstetric field. In this work, we evaluated the mechanism of MCEC before and during labor based on the Bivariate Phase-Rectified Signal Averaging Analysis (BPRSA).

A group of women in the third trimester of pregnancy (TT = 44) and another group during active labor (AL = 51) were studied at the Maternal and Childbirth Research Centre (CIMIGen, Mexico City). We extracted 20 min of maternal heart-rate time series as well as the envelopes of the uterine electrical activity signals (electrohysterogram) obtained from a high-frequency recorded electrocardiogram. The coupling between uterine electrical activity and maternal heart rate was analyzed by BPRSA. Significant differences were found between TT vs. AL for cross-correlation of BPRSA signals (0.93 vs. 0.97, $p < 0.01$), respectively. These results suggest that during active labor, a higher MCEC is observed in comparison to the third trimester of pregnancy. The presence of increased MCEC could be involved in the physiological manifestation of labor.

Keywords: Cardio-electrohysterographic coupling · EHG · Maternal heart rate

© Springer Nature Switzerland AG 2020
C. A. González Díaz et al. (Eds.): CLAIB 2019, IFMBE Proceedings 75, pp. 21–27, 2020.
https://doi.org/10.1007/978-3-030-30648-9_3

1 Introduction

Despite human parturition being such a fundamental event in women's life, the exact mechanisms involved in the initiation and maintenance are not entirely elucidated. It is well known that during parturition, significant hemodynamic changes occur owing to pain, anxiety, and uterine contractions. Specifically, uterine contractions induce effects on maternal heart rate, systolic, and diastolic blood pressure [1]. It is well known that the maternal hemodynamic activity increases at different stages of labor; for example, the cardiac output rises by 12% in the first stage and by 34% in the second stage. This elevation continues with each contraction, augmenting as well the stroke volume [2].

Few studies have evaluated the influence of uterine contractions on maternal cardiac dynamics during labor at term. Previous evidence indicates that the autonomic nervous system seems to regulate the hemodynamic changes that occur during labor, which suggests the actual mechanisms of how cardiac activity increases during periods of uterine contractions [3]. Our previous studies indicate that some nonlinear properties of maternal R-R intervals were influenced by the presence or absence of uterine contractions [4]. Recent findings have shown that sinusoidal patterns arise on maternal R-R series and electrohysterogram (or uterine electromyogram) data streams in correspondence with uterine contractions during labor [5]. This evidence supports the interaction of uterine electrical activity and maternal heart rate, which could be defined as the "maternal cardio-electrohysterographic coupling" or MCEC. By this interaction, the uterine activity triggers maternal heart rate. Thus, the relationship between uterine electrical activity and maternal heart rate might provide valuable information about the maternal autonomous nervous system during labor.

Casati *et al.* presented a new methodology for studying the coupling between the fetal heart rate and uterine electrical activity during the first stage of labor, demonstrating that in labor most women and fetuses have an interdependence between uterine electrical activity and fetal heart rate [6]. However, the MCEC was not explored in that study. The algorithm implemented by Casati *et al.* is known as the Averaged Rectified Signal in Bivariate Phase (BPRSA). This method overcomes the limitation of nonstationary signals and background noise [7].

This study aimed to assess the MCEC before and during labor by BPRSA in healthy women. We hypothesize that the MCEC quantifies the physiological interaction between maternal heart rate and uterine contractions during labor.

2 Methods

In a cross-sectional study design, healthy women, without complications, at the third trimester of pregnancy (TT = 44) and during low-risk active labor at term (AL = 51) were monitored with a trans-abdominal electrocardiogram/electrohysterogram high-frequency recording device (Monica AN24, Monica Healthcare, Nottingham, UK). Women were recruited at the Maternal and Child Research Center (CIMIGen, Mexico City) from 2014 to 2016. The age range of the participants was 20–33 years.

Maternal heart-rate time series (mHR) and the envelopes of EHG (eEHG) were extracted using the Monica DK Software (Monica Healthcare, Nottingham, UK). The eEHG and the mHR were averaged every two seconds to obtain the profile of the uterine activity following the methodology conducted by Casati *et al.* [6].

In the first step of the analysis, twenty minutes of the EHG-mHR time series were used for the BPRSA analysis obtained from recordings of the active stage of labor (AL) and at the third trimester of pregnancy (TT). All participants in the AL group presented 4 cm of dilation, cervical effacement of at least 50% and an adequate number of contractions, i.e., 3 to 4 within ten minutes. No clinical signs or symptoms of labor were reported in any of the participants of the TT group. For the analysis of this step, the only criteria for selection was the presence of 20 min, with 50% of signal loss.

In each trace, the inter-relations between eEHG (as trigger signal), as detected by increasing values of uterine activity, and synchronous values of mHR (as target signal) were analyzed using the BPRSA algorithm.

Modulations of the BPRSA signal can be attributed to periodicities in the trigger signal. If there are no interrelationships between the trigger and target signal, the BPRSA signal shows no periodic patterns. For further information, refer to Bauer [8].

For the calculation of the monovariate PRSA method, the anchors are derived from the target signal itself (here: the eEHG signal). The monovariate PRSA signal contains all periodicities of the target signal, and its noise and nonstationarities are removed. Anchors points are obtained by comparing averages of T values of eEHG as follows:

$$\frac{1}{T}\sum_{j=0}^{T-1} eEHG(i+j) > \frac{1}{T}\sum_{j=1}^{T-1} eEHG(i-j) \tag{1}$$

We set T = 18 in order to include the upper physiological frequency of uterine activity, and a window equal to 200 s was delimited around the anchor points [6]. Figure 1 summarizes the steps of BPRSA analysis for the mHR and eEHG signals. The second step was the quantification of coupling between the trigger and target signals by the normalized cross-correlation coefficient (CC_{BPRSA}). These calculations were done using Matlab® software (the MathWorks, Inc. Natick, Massachusetts, USA).

The differences between CCBPRSA values of TT and AL groups were tested by a Mann-Whitney test because the data did not satisfy the normality criterion (Shapiro-Wilk test). Two-tailed, p-values lower than 0.05 were considered statistically significant. GraphPad software (Prism 7.0) was used to assess the statistical analyses.

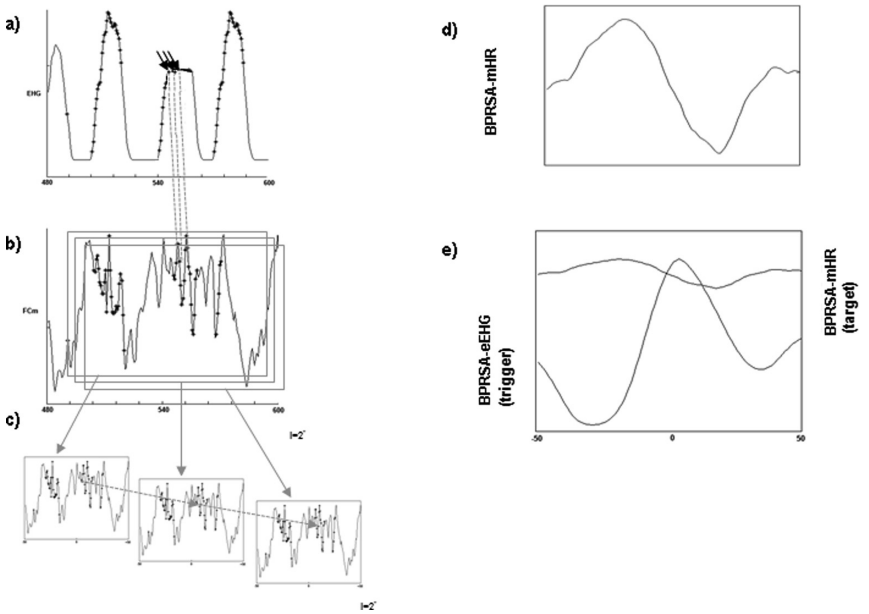

Fig. 1. Description of the Bivariate Phase Rectified Signal Averaging (BPRSA) method. (a) Uterine Activity by the envelope of the EHG (trigger signal): each data point is the average of raw signal every 2 s. Each black dot represents an anchor point (eEHG increases). (b) Maternal heart rate or mHR (target signal). The circles represent anchor points derived from the eEHG signal; (c) segments of maternal heart rate, centered around the anchor point (time windows of 200 s, each data point (i) is the average of mHR every 2 s); (d) phase rectification at the anchor points and signal averaging and (e) BPRSA graph representing PRSA transformation of Uterine Activity and BPRSA transformation of mHR.

3 Results

The BPRSA analysis was applied on 95 mHR-eEHG traces recorded during the third trimester of pregnancy (TT = 44) and active labor (AL = 51). Figure 2 shows a box plot depicting the mean values of the CC_{BPRSA} between TT (median gestational age of 36[36–37] weeks) and AL (median gestational age of 39.5[39–40] weeks). Significant differences (p = 0.001) were found (0.97 vs. 0.93, respectively).

Figure 3 shows representative signals from the AL and TT groups, where the presence or absence of the MCEC is observed. The signals obtained by using the BPRSA technique and its corresponding C_{BPRSA} analysis are also shown.

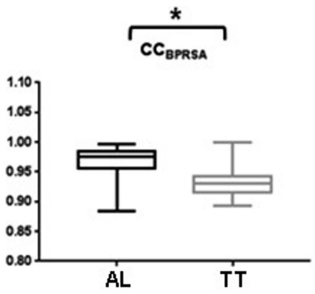

Fig. 2. Comparison between the mean values of the cross-correlation coefficients of the Bivariate Phase-Rectified Signals (BPRSA) for active labor (AL) and third trimester of pregnancy (TT). *p < 0.01

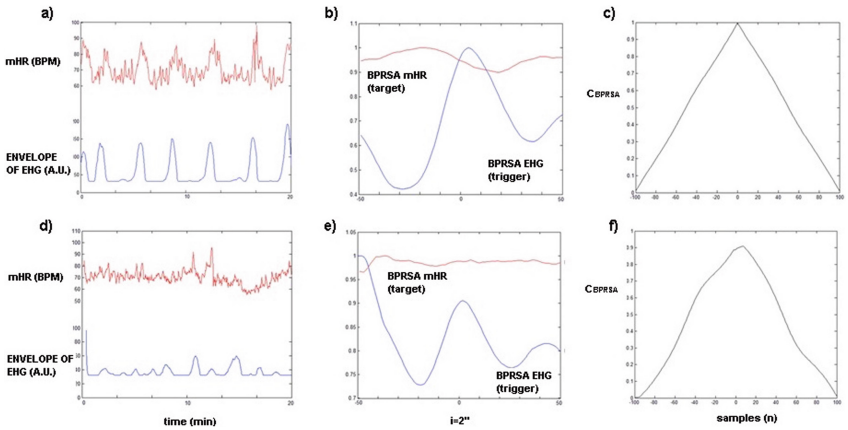

Fig. 3. Active labor (AL) panels: a, b, & c. Third trimester of pregnancy panels: d, e, & f. (a) 20 min recordings of the envelope of the electrohysterogram (eEHG, blue line) with arbitrary units (A.U.) and maternal heart rate (mHR, red line) at AL; (b) bivariate phase-rectified averaged signal (BPRSA) graphs showing maternal cardio-electrohysterographic coupled periodicities (red line oscillation) for AL. The time axis centered around time 0 (aligned anchors) allows to observe the oscillation of the signals before and after the triggering event (time windows of 200 s, each data point (i) is the average of BPRSA-signals every 2 s); (c) cross-correlation analysis (C_{BPRSA}) of BPRSA signals for AL; (d) 20 min recording of the eEHG and mHR at the third trimester of pregnancy (TT); (e) BPRSA graphs showing absence of coupling (flat red line) and (f) cross-correlation analysis of BPRSA signals for TT.

4 Discussion

The BPRSA method has been introduced in previous studies to describe the coupling between the uterine activity and fetal heart rate during labor [6], which presents the advantage of not being affected by non-stationary effects. To our best knowledge, this is the first study that quantifies the MCEC during low-risk active labor at term in comparison with the third trimester of pregnancy.

We found that during active labor, higher MCEC is manifested in comparison with the third trimester of pregnancy (Fig. 2). Specifically, the uterine activity seems to trigger maternal heart rate or eEHG → mHR at active labor, and also in smaller terms at the third trimester of pregnancy. As it is observed in the representative signals (Fig. 3b), the resulting signal BPRSA-mHR (target) exhibits a central oscillation, which is indicative of the presence of coupling between the eEHG and the mHR during labor [6, 7]. On the other hand, the BPRSA-mHR (target) exhibits a flat line (Fig. 3e), which is indicative of a lower uterine activity but also a reduced coupling between the eEHG and the mHR at the third trimester of pregnancy. These results were quantified by the cross-correlation between both BPRSA signals (Fig. 3c and f). Our results are consistent with studies that have observed the influence of uterine contractions on maternal cardiac dynamics during labor at term [5]. Thus, the MCEC appears to be manifested during labor to satisfy the autonomic, hemodynamic, and energetic demands of human parturition [9].

Uterine contraction-associated accelerations of the maternal heart rate are considered to reflect both a transient contraction-related increase in cardiac output and endogenous catecholamine secretion [10]. According to the literature, the uterine activity during labor can result in the autotransfusion of approximately 300–500 ml of blood into the central circulation [11], which leads to increased maternal heart rate. Our results are also in line with other reports showing that the accelerations seen in the second stage of labor coincide with the uterine contractions and have a steeper ascent and descent pattern [12]. Other relevant findings indicate that mHR patterns during the second stage of labor correlate with the active pushing efforts [13].

Future work will involve the evaluation of MCEC in pathological conditions such as preterm labor, gestational diabetes, and preeclampsia.

5 Conclusion

Overall, based on the bi-directional analysis of the cardiac and uterine systems using the BPRSA method, our results confirm higher cardio-electrohysterographic coupling during low-risk term labor in comparison with the third trimester of pregnancy. We identified that the uterine contractions seem to trigger maternal heart rate at low-risk active labor at term. Thus, the MCEC appears to be manifested during labor to satisfy the autonomic, hemodynamic, and energetic demands of human parturition. The presence of this coupling could be considered as a non-invasive and representative indication related to the physiological onset of labor. Finally, BPRSA metrics could be useful for translational studies and to understand the physiological mechanism involved in human parturition.

References

1. Domènech, A.P., Gatzoulis, M.A.: Embarazo y cardiopatía. Rev Esp Cardiol. **59**(9), 971–984 (2006)
2. Cunningham, F.G., Leveno, K.J., Bloom, S.L., Hauth, J.C., Rouse, D.J., Spong, C.Y.: Williams Obstetrics, 23rd edn, pp. 374–410. Williams Obstetrics, Dans (2001)
3. Suzuki, N., Sugawara, J., Kimura, Y., Nagase, S., Okamura, K., Yaegashi, N.: Assessment of maternal heart-rate variability during labor using wavelet-based power spectral analysis. Gynecol. Obstet. Invest. **74**(1), 35–40 (2012)
4. Reyes-Lagos, J.J., Echeverría-Arjonilla, J.C., Peña-Castillo, M.Á., García-González, M.T., Ortiz-Pedroza, M.D.R., Pacheco-López, G., et al.: A comparison of heart rate variability in women at the third trimester of pregnancy and during low-risk labour. Physiol Behav. **149**, 255–261 (2015)
5. Altini, M., Rossetti, E., Rooijakkers, M., Penders, J., Lanssens, D., Grieten, L., et al.: Combining electrohysterography and heart rate data to detect labour. In: DANS: 2017 IEEE EMBS International Conference on Biomedical and Health Informatics, BHI 2017, pp. 149–152 (2017)
6. Casati, D., Stampalija, T., Rizas, K., Ferrazzi, E., Mastroianni, C., Rosti, E., et al.: Assessment of coupling between trans-abdominally acquired fetal ECG and uterine activity by bivariate phase-rectified signal averaging analysis. PLoS One **9**(4), 94557 (2014)
7. Schumann, A.Y., Kantelhardt, J.W., Bauer, A., Schmidt, G.: Bivariate phase-rectified signal averaging. Phys. A. Stat. Mech. Appl. **387**(21), 5091–5100 (2008)
8. Bauer, A., Barthel, P., Müller, A., Kantelhardt, J., Schmidt, G.: Bivariate phase-rectified signal averaging-a novel technique for cross-correlation analysis in noisy nonstationary signals. J. Electrocardiol. **42**(6), 602–606 (2009)
9. Reyes-Lagos, J.J., Echeverría-Arjonilla, J.C., Peña-Castillo, M.Á., Montiel-Castro, A.J., Pacheco-López, G.: Physiological, immunological and evolutionary perspectives of labor as an inflammatory process. Adv. Neuroimmune Biol. **5**(2), 75–89 (2014)
10. Sherer, D.M., Dalloul, M., Pierre, N., Abulafia, O.: Intrapartum repetitive maternal heart rate deceleration pattern simulating nonreassuring fetal status. Am. J. Perinatol. **22**(03), 165–167 (2005)
11. Lee, W., Rokey, R., Miller, J., Cotton, D.B.: Maternal hemodynamic effects of uterine contractions by M-mode and pulsed-Doppler echocardiography. Am. J. Obstet. Gynecol. **161**(4), 974–977 (1989)
12. Van Veen, T.R., Belfort, M.A., Kofford, S.: Maternal heart rate patterns in the first and second stages of labor. Acta Obstet. Gynecol. Scand. **91**(5), 598–604 (2012)
13. Söhnchen, N., Melzer, K., De, Tejada B.M., Jastrow-Meyer, N., Othenin-Girard, V., Irion, O., et al.: Maternal heart rate changes during labour. Eur. J. Obstet. Gynecol. Reprod. Biol. **158**(2), 173–178 (2011)

Capture of the Voluntary Motor Intention from the Electromyography Signal

Leandro Alexis Hidalgo Torres, Yanexy San Martín Reyes, and Juan David Chailloux Peguero(✉)

Department of Bioengineering (CEBIO), Havana Technological University (CUJAE), 14 St. b/ Ciclovía and Rotonda, #11901 Havana, Cuba
juandavid@automatica.cujae.edu.cu

Abstract. The objective of this work is to automatically identify basic hand movements: Opening, Closing, Bending, Extension, Pronation and Supination, including the Resting condition. Feature extraction was implemented making use of three approaches: time, frequency and time-frequency domains, obtaining the characteristics Mean Absolute Value (MAV), Root Mean Square (RMS), Wave Length (WL), Autoregressive Coefficients (AR) and Discrete Wavelet Transform (DWT). Principal Component Analysis (PCA) was applied for dimensionality reduction and classification was performed using Linear Discriminant Analysis (LDA). As a result it was possible to identify the movements with success rates that reached 92% with the hybrid vectors conformed by the coefficients MAV, RMS and AR.

Keywords: EMG signal · Principal Component Analysis · Linear Discriminant Analysis

1 Introduction

Electromyography constitutes a useful tool in the diagnosis of neuromuscular diseases and disorders affecting motor control. It have been also used as feedback signal in the control of upper limb robotic prosthesis [1] and even estimating finger movements [9]. Another application in recent years has been the use as a complementary signal for electroencephalography (EEG) information in the design of hybrid Brain-Computer Interfaces (hBCI), to support the recovery of patients with motor disabilities caused by pathologies and/or traumatisms [2,8]. An approach to fulfill this objective deal with the acquisition and processing of EMG signal which is qualitatively associated with the type of movement produced [4].

Our research aims to develop a methodology that allows the classification of movements of the upper limbs of healthy subjects. With this objective in mind, an appropriate selection of characteristics and reduction of the dimensionality of the electromyographic signal must be carried out. The future application of this study will be to constitute one of the components of an hBCI system that will

© Springer Nature Switzerland AG 2020
C. A. González Díaz et al. (Eds.): CLAIB 2019, IFMBE Proceedings 75, pp. 28–36, 2020.
https://doi.org/10.1007/978-3-030-30648-9_4

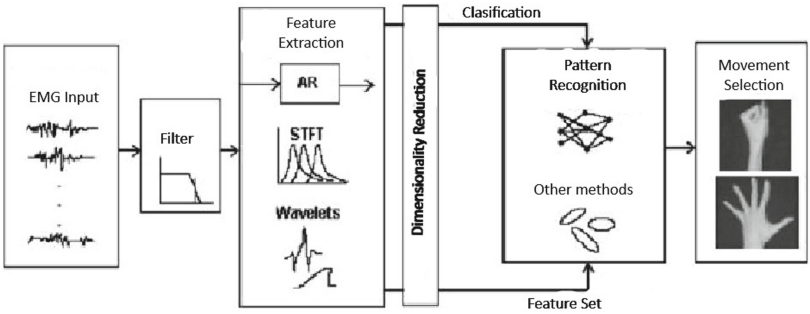

Fig. 1. Classic stages for pattern identification of motor intention of upper limbs by means of the digital processing of electromyographic signal.

have the purpose of supporting neuro-rehabilitation therapies, thus contributing to the reduction of the recovery period and integration of patients into daily living activities.

2 Materials and Methods

In this section it is described the methodology followed in the different stages represented in Fig. 1 pursuing the motor intention inference from the application of pattern recognition of the electromyographic signal.

2.1 Surface EMG Database

A publicly accessible database of surface electromyographic records, recorded from thirty (30) healthy subjects was used [3] in order to test the effectiveness of the digital processing methods applied to the biosignals. Electromyographic signals were recorded from seven different locations in the right upper limb of each subject and an additional point located in the biceps by means of *Duo-Trode* Ag-AgCl electrodes (Myotronics, 6140). A *Red-Dot* Ag-AgCl electrode was applied on the wrist with the objective to supply a common ground reference. Location of the electrodes can be observed at Fig. 2(a).

The signals were amplified (Model 15, Grass Telefactor) by a factor of 1000 with a frequency bandwidth ranging from 1 Hz to 1 kHz. A 3 kHz of sampling frequency was applied by the analog to digital converter inside the *National Instruments*'s PCI-6071E acquisition card. Signals were filtered by a bandpass Butterworth approximation with specifications of frequencies between 20 Hz to 400 Hz and also a Notch filter was implemented to suppress the main power-line frequency component. Subsequently sEMG signals were re-sampled at 1 kHz for the classification stage. Data was collected for the different types of movements executed by the volunteers: Flexion, Extension, Opening, Closing, Pronation, Supination and Rest condition (Fig. 2(b)). Gestures were repeated four times

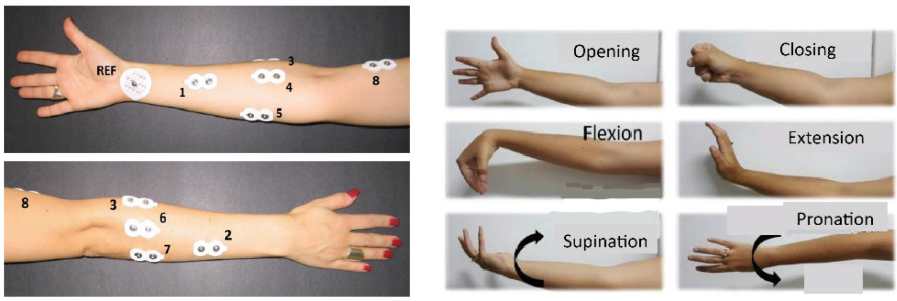

(a) Location of surface electrodes. (b) Gestures or movements to classify.

Fig. 2. Electrode location on the upper limbs and types of movements to classify. *Pictures taken and modified from:* http://www.sce.carleton.ca/faculty/chan/download/mec1.zip

during three seconds, selecting each type of movement to be executed in a random way, obtaining 84 s of duration in each trial. Rest periods of five seconds were introduced at the beginning and the end of each trial to avoid data loss during the signal acquisition process, leading to trials of 94 s. A total of six trials were completed in a session and the whole process was developed in four sessions.

Current work made use of session four of the recordings from ten (10) randomly selected volunteers out of a global population of thirty (30), where the first two trials were used as training data and the remaining four trials as test data. Matlab software (*Mathworks*), version R2016a was the processing tool of the digitalized electromyographic signals.

2.2 Feature Extraction

Several feature subsets, labeled Sc1, Sc2... to Sc6 were implemented. These subsets were divided the following way: the two first subsets (Sc1 and Sc2) correspond with temporal analysis, subset Sc3 correspond with frequency analysis. Subsets Sc4 and Sc5 were associated with time-frequency analysis of EMG signals by means of the Discrete Wavelet Transform (DWT). Lastly, Sc6 subset, was conformed as a hybrid vector integrated by temporal and frequency characteristics. Table 1 shows the described subsets, where: WL: *Waveform Length*, MAV: *Mean Absolute Value*, AR: *Autoregressive Coefficients* and RMS: *Root Mean Square Value*.

The non-stationary property attributed to the EMG signal is a problem for its analysis, however this aspect can be partially mitigated if frames of short duration of the signal are chosen. It is for this reason that in order to obtain each of the features an analysis of sliding windows of 256 ms of length was made, spaced 128 ms for training, thus giving a 50% of overlapping in the first 2 trials and 32 ms for tests [5], obtaining a 87.5% of overlapping in the remaining 4 trials, just as explained before.

Table 1. Subset of features selected for the feature extraction stage.

Subset (Sc)	Features	Characteristic × Channel (8)
Sc1	WL-MAV	16
Sc2	MAV-RMS	16
Sc3	AR	32
Sc4	MAV (D1, D3, D5)	24
Sc5	RMS (D2, D4, A5)	24
Sc6	MAV-RMS-AR	48

2.3 Dimensionality Reduction

For the reduction of dimensionality, the unsupervised PCA method [10] was used due to its usefulness for the compression of information and in the identification of patterns on a sample of data. In the research carried out by Canadian scientists [6], it is concluded that the reduction of dimensionality with PCA yields better results in the classification. In this case the feature matrix is mapped, this allows "mapping", in a non-linear way, the feature space towards a new space of smaller dimensions. In order to automate the process of selection the proper principal components, a criterion was followed in which components were kept if their eigenvalues were greater or equal to the 2% of the maximum of them. In this case, a new space was obtained where the variance of the data was at least 95%.

2.4 Classification

The Linear Discriminant Analysis (LDA) [7], due to its simplicity of application, training and statistical strategy, was the one selected in the current investigation to evaluate the behavior of the subsets of certain features. This is achieved at the output of the classifier, where a membership index of EMG signal to a given class is obtained. The classes defined in the study are established according to the Table 2.

Table 2. Class assignment to each type of movement.

Gesture	Class
Opening	1
Closing	2
Flexion	3
Extension	4
Supination	5
Pronation	6
Rest	7

The evaluation of the classifier was carried out with respect to its performance, this evaluation was based on two aspects: Correct Classification Rate (CCR) and Active Error Rate (AER), both are defined mathematically in the following equations:

$$CCR = 100\% * \frac{Number\ of\ Right\ Decisions}{Total\ Decisions} \tag{1}$$

$$AER = 100\% * \frac{Number\ of\ Incorrect\ Active\ Decisions}{Total\ Active\ Decisions} \tag{2}$$

3 Results and Discussion

An analysis was made for each of the feature subsets, where the classification percentage score for the 10 subjects under study and the 7 classes is shown in Fig. 3.

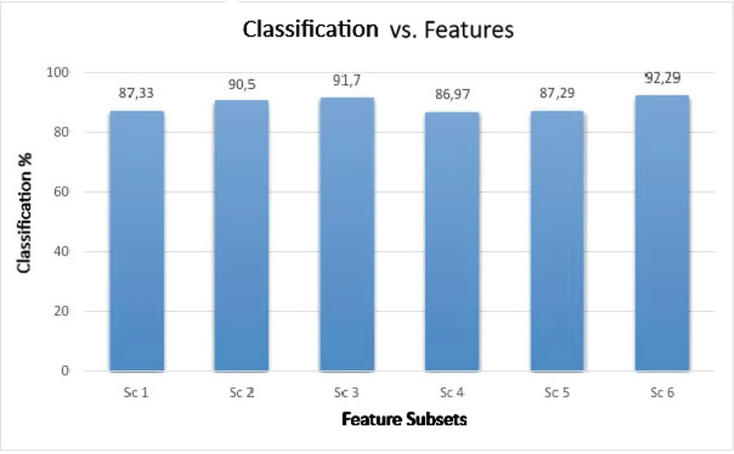

Fig. 3. Classification scores achieved for each subset of features.

Making an analysis of the graphic shown in Fig. 3, it is concluded that the subsets Sc2, Sc3 and Sc6, conformed by the features MAV, RMS and AR (autoregressive coefficients), contribute in more than 90% to the classification and the hybrid subset Sc6 highlights as the most accurate in the classification. That is, they could be features that define more accurately the behavior of the classes under study. However, the same does not apply to the subsets Sc1, Sc4 and Sc5, because its contribution is below 88%.

Figure 4(a) and (b) shows the classification rate per class corresponding to the best (Sc6) and worst (Sc4) feature subsets.

As can be seen in Fig. 4(a), the subset Sc6, formed by the coefficients of the autoregressive model designed by the parameters MAV and RMS, is the one that characterizes with higher success rates each of the classes under study. It can be clearly observed that each of the gestures made by the subjects were classified with accuracy values above 90%, which is an excellent result for the desired application. The classes identified with greater accuracy were the "Opening", "Extension" and "Closing".

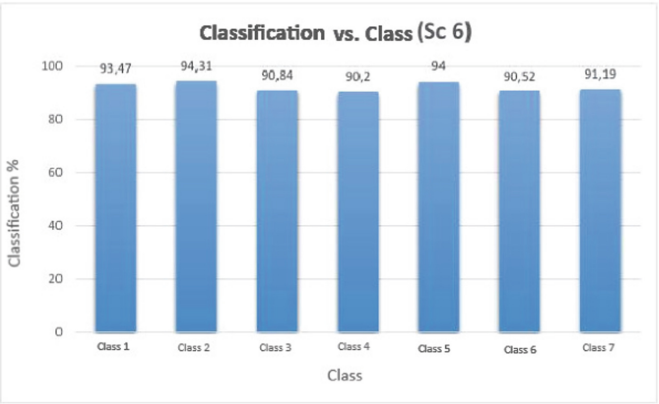

(a) Classification levels achieved with the Sc6 subset.

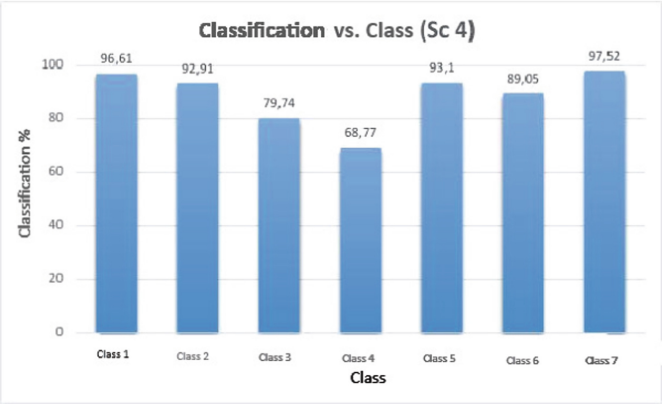

(b) Classification levels achieved with the Sc4 subset.

Fig. 4. Classification values reached by each class through the use of the subsets Sc6 and Sc4.

Similarly, the percentages of classification obtained by using the Sc4 subset are presented in the Fig. 4(b). This subset, formed by the absolute average values of the details D1, D3 and D5, resulting from the decomposition of the signals by using the mother *Wavelet Daubechies* 4, was the one that least characterized the classes under study. As can be seen in the Fig. 4(b), the critical values

are presented by classes 3 and 4, these were classified with very low success rates, with lot of errors in the classification. However, some types of movements were successfully classified by this subset, such was the case of the "Opening", "Supination" and the "Resting" state.

Figure 5(a) and (b) allow a clearer analysis of the results of the classification process of the subsets Sc6 and Sc4, respectively, from the graphic of confusion matrix.

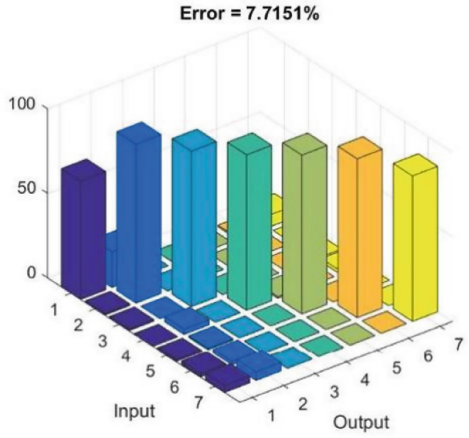

(a) Sc6 confusion matrix.

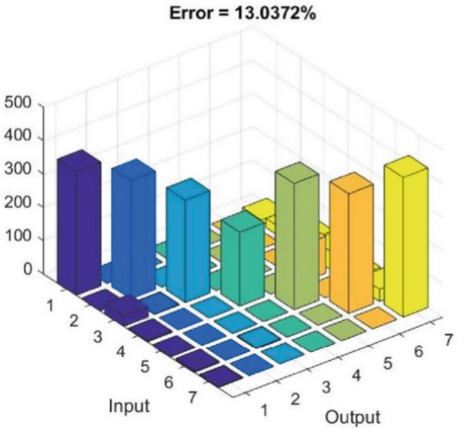

(b) Sc4 confusion matrix.

Fig. 5. Classification sequence graph using the subsets Sc6 and Sc4.

This resource allows to evaluate the precision in addition to indicating the errors and successes committed in the classification process. In this matrix the rows represent the class to which the signal belongs and the columns refer to

the class in which said signal was classified. Thus, in the main diagonal of said matrix the number of correctly classified samples is located and in the other positions the samples classified incorrectly.

4 Conclusions

From the analysis of the results of this research it was possible to conclude that the use of hybrid vectors generates good results in the classification process, since they provide more information about the characteristics that together highlight more the differences between the signals belonging to different types of movements.

The efficiency and good performance of EMG signal classifiers depend to a large extent on the stages of feature extraction and dimensionality reduction, as these are phases that simplify the process by extracting the most relevant information from the signal.

Considering the previous points, the main objective of this work was achieved, which allowed to obtain high success rates in the classification of motion patterns in EMG signals from techniques of feature extraction, dimensionality reduction and classification, which require little computational capacity in order to implement a portable hybrid BCI system in a future research. Combining this structure in parallel with a motor imagery BCI would allow us to have a platform that takes into account the patient's voluntary motor intention, generated at the level of the cerebral cortex, to support the process of neuro-rehabilitation of subjects with impairment of volitive mobility of their upper limbs, by incorporating a functional electrical stimulation device at the output of the classification stage. The fusion of neurophysiological signals (EEG and EMG) would intuitively produce a more stable and robust signal control compared to independent modalities. With the advancement of current technologies, this system can be synthesized into hardware (for example an FPGA) with promising results.

References

1. Blana, D., Krasoulis, A., Nazarpour, K., Chadwick, E.: Control of a robotic hand with an EMG-driven, real-time biomechanical computer model. In: 8th World Congress of Biomechanics. Newcastle University (2018)
2. Bulea, T.C., Kilicarslan, A., Ozdemir, R., Paloski, W.H., Contreras-Vidal, J.L.: Simultaneous scalp electroencephalography (EEG), electromyography(EMG), and whole-body segmental inertial recording for multi-modal neural decoding. J. Vis. Exp. **26**, e50602 (2013). https://doi.org/10.3791/50602. http://www.jove.com/video/50602
3. Chan, A.D.C., Green, G.C.: Myoelectric control development toolbox. In: 30th Conference on Canadian Medical Biological Engineering Society, Toronto, Canada, pp. 1–4 (2007). http://www.sce.carleton.ca/faculty/chan/matlab/myoelectriccontroldevelopmenttoolbox.pdf

4. Chowdhury, R.H., Bin, M., Reaz, I., Alauddin, M., Ali, M., Bakar, A.A.A.: Surface electromyography signal processing and classification techniques. Sensors **13**, 12431–12466 (2013). https://doi.org/10.3390/s130912431. http://www.mdpi.com/journal/sensors
5. Graupe, D., Magnussen, J., Beex, A.: A microprocessor system for multifunctional control of upper-limb prostheses via myoelectric signal identification. IEEE Trans. Autom. Control **23**(4), 538–544 (1978). https://doi.org/10.1109/TAC.1978.1101783
6. Hargrove, L.J., Li, G., Englehart, K.B., Hudgins, B.S.: Principal components analysis preprocessing for improved classification accuracies in pattern-recognition-based myoelectric control. IEEE Trans. Biomed. Eng. **56**(5), 1407–1414 (2009). https://doi.org/10.1109/TBME.2008.2008171. http://ieeexplore.ieee.org
7. Phinyomark, A., Hu, H., Phukpattaranont, P., Limsakul, C.: Application of linear discriminant analysis in dimensionality reduction for hand motion classification. Meas. Sci. Rev. **12**(3), 82–89 (2012)
8. Rouillard, J., Duprès, A., Cabestaing, F., Leclercq, S., Bekaert, M.H., Piau, C., Vannobel, J.M., Lecocq, C.: Hybrid BCI coupling EEG and EMG for severe motor disabilities. Procedia Manuf. **3**(Ahfe), 29–36 (2015). https://doi.org/10.1016/j.promfg.2015.07.104. http://dx.doi.org/10.1016/j.promfg.2015.07.104
9. Saikia, A., Kakoty, N.M., Phukan, N., Balakrishnan, M., Sahai, N., Paul, S., Bhatia, D.: Combination of EMG features and stability index for finger movements recognition. Procedia Comput. Sci. **133**, 92–98 (2018)
10. Wold, S., Esbensen, K., Geladi, P.: Principal component analysis. Chemometr. Intell. Lab. Syst. **2**(1), 37–52 (1987). https://doi.org/10.1016/0169-7439(87)80084-9. http://www.sciencedirect.com/science/article/pii/0169743987800849. Proceedings of the Multivariate Statistical Workshop for Geologists and Geochemists

Early Prediction of Weight at Birth Using Support Vector Regression

Oliver Campos Trujillo[1(✉)], Jorge Perez-Gonzalez[2], and Verónica Medina-Bañuelos[1]

[1] Neuroimaging Laboratory, Electrical Engineering Department, Universidad Autónoma Metropolitana, 09340 Iztapalapa, Mexico
olivergtc@gmail.com, vera@xanum.uam.mx
[2] Instituto de Investigaciones en Matemáticas Aplicadas y en Sistemas, Universidad Nacional Autónoma de México, 97302 Mérida, Yucatán, Mexico
jorge.perez@iimas.unam.mx

Abstract. Birth weight (BW) is an important indicator of neonatal well–being associated with multiple adverse conditions and thus its early estimation may be crucial for timely treatment. In this paper we propose a BW estimation strategy based on Support Vector Regression of a set of multimodal maternal–fetal features obtained in pregnancy's first trimester. The obtained results show an average difference of 250 g between the estimated and the real BW, with percentage errors below 3% in all cases. These results contrast with other reported studies, that estimate BW very close to delivery.

Keywords: Birth weight prediction · Machine learning · Regression

1 Introduction

Early estimation of birth weight (BW) is a key factor in antenatal assessment and obstetric care during pregnancy, because this parameter has been shown to be closely associated to neonatal and infant mortality. Low birth weight (LBW) babies present significantly higher mortality rates and therefore this condition has been identified as a major public health problem around the world [1]. Predicting BW remains a challenge because several maternal factors interact with its evolution, such as eating habits, anthropometry, physical activity and treatment during pregnancy. Other risk factors related to LBW include drug abuse, smoking, infections, etc. BW is obtained after delivery in an objective, accurate and simple way, but it is necessary to estimate fetal weight during pregnancy for monitoring and surveillance purposes. The estimated fetal weight (EFW) can be obtained from anthropomorphic measurements taken directly at Ultrasound (US) images but it is also necessary to measure BW in order to validate EFW linear regression curves. Milner et al. [2] present a review comparing different clinically used formulas for EFW. They conclude that most methods overestimate FW, due to the difficulty of measuring fetal parameters at late stages of pregnancy. Nonetheless, they found

© Springer Nature Switzerland AG 2020
C. A. González Díaz et al. (Eds.): CLAIB 2019, IFMBE Proceedings 75, pp. 37–41, 2020.
https://doi.org/10.1007/978-3-030-30648-9_5

that the best results were provided by Hadlock's formula, with a random error of 9.2% and a mean percentage error of −1.5%.

Several projects to predict an adverse outcome of pregnancy using machine learning (ML) techniques have been reported. Models based on ML require careful design, an adequate selection of hyperparameters and suitable data pre–processing. Sereno et al. [3] estimated BW using support vector regression (SVR) accompanied by a previous cleaning of anomalous samples and outliers. Their BW estimations resulted in an average error of 2.2% and a concordance of all samples below a threshold of 5% error. Jinhua [4] combined fuzzy logic with SVR to obtain the model's optimal parameters and to increase robustness in the presence of noisy data. They attained a mean absolute percentage error of 6.6% between EFW and BW. These research projects were designed to predict BW close to delivery, and therefore estimations are compared with formulas applied at this late phase. The works by Kang et al. [5] and O'Connor et al. [6] attempted to estimate BW using parameters taken during pregnancy's first trimester. The former makes an association between crown–rump length (CRL) and BW finding an optimal relationship ($R = 0.362$) at 67 days of gestation. Nahum et al. [7] reports that FW estimation made from US–extracted parameters presents limitations and suggest that they must be combined with other metrics, such as fetal gender or maternal demographics. The formulas that integrate those parameters seem to establish new standards for FW estimation and its comparison with BW. O'Connor et al. examined the relationship between BW and maternal arterial elasticity. Combining this parameter with maternal demographics such as height, weight and parity to the lineal model regression provided a predictive correlation of $R = 0.21$ with respect to the real BW.

These studies present several drawbacks: most algorithms are designed to predict BW at a pregnancy stage close to delivery; ML models are designed considering mostly image extracted fetometry parameters; these studies were carried out in non-Latin-American populations thereby making them less suitable for clinical application in Mexico. To contribute to the solution of these limitations, a method to predict BW as early as the first trimester of pregnancy is presented in this work. The proposed regressor receives multimodal inputs and was trained and tested in a Mexican population.

2 Materials and Methods

2.1 Data Set Description

A total of 23 maternal–fetal variables were acquired at the National Institute of Perinatology of Mexico by obstetric experts. These variables include fetal sex; anthropometric data of the mother such as: height, weight, body mass index; placental thickness (PT), placental length (PL) and PT/PL and PL/PT ratios; ultrasound fetometries including: CRL, biparietal diameter, cranial circumference, femur length and abdominal circumference and their corresponding estimated gestational ages; pulsatility indexes of the left and right uterine arteries

(maximum, minimum and mean values). All variables were acquired in pregnancy's first trimester (between 9 and 14 weeks); BW was obtained after delivery. As a pre–processing step, incomplete or poorly captured data were eliminated, with a total population of 250 women.

2.2 Support Vector Regression

Support Vector Machines are a ML algorithm widely used for classification (SVC) and regression (SVR) of biological data due to their great capability of adaptation to non–parametric multimodal data [8]. In order to test different prediction schemes, four variants of the SVR were implemented: Linear, Polynomial (Poly), Radial Basis Function (RBF), and Nu. Their respective hyperparameters were optimized by a grid. Each SVR variant maps the input data to another separation hyperspace by means of an assigned transformation kernel. The SVRs were fed with the 23 described variables with the task of properly predicting BW. A 10–fold cross validation was carried out with 200 cases during the training step and with 50 cases for the final validation.

2.3 Algorithms' Performance

Algorithms' performances were measured with Mean Absolute Error (MAE) and Mean Percentage Error (MPE) defined as:

$$MAE = \frac{1}{N}\sum_{i=1}^{N} \mid y_i - \widehat{y}_i \mid, \quad MPE = \frac{100}{N}\sum_{i=1}^{N} \frac{y_i - \widehat{y}_i}{y_i}, \tag{1}$$

where y_i is the real BW and $\widehat{y}_i$ is the estimated value.

A concordance analysis was carried out by defining absolute and percentage error thresholds. The bounds were set at 100, 200 and 300 g for MAE measure and at 5%, 10% and 20% for MPE. Results are reported as the percentage of cases that fell below this threshold.

3 Results and Discussion

MAE and MPE metrics are reported in Table 1 for the training (left) and test (right) data sets. A mean error of around 255 g for MAE was obtained during training, which increased by approximately 50 g for the testing step, as expected, due to a certain degree of overfitting, and because unseen data are not represented by the SVR model.

It can be observed that SVR RBF yields the lowest MAE for training as well as for test data. Also, its MPE value was the lowest for test performance. This may be due to the non–linear separability of the data and suggests that this regressor may be suitable for BW estimation. Compared to other approaches [3,4] the obtained errors are competitive, attaining percentual errors below 3%.

Table 1. Performance parameters

	Cross–validation		Final test	
Regressor	MAE (g)	MPE (%)	MAE (g)	MPE (%)
SVR Linear	259.19 ± 209.72	2.65 ± 13.19	300.16 ± 218.30	-0.426 ± 12.81
SVR Poly	261.2 ± 203.34	2.23 ± 12.59	304.97 ± 208.43	0.897 ± 12.94
SVR RBF	249.74 ± 196.75	2.75 ± 12.40	287.60 ± 195.86	0.364 ± 11.95
NuSVR	254.03 ± 188.31	0.68 ± 12.17	302.74 ± 184.25	2.3935 ± 12.19

It must be remarked that our method considers information acquired in very early gestational age.

The concordance analysis is shown in Table 2 where it can be observed that a high percentage of the studied populations (more than 85%) present errors inferior than 30% in BW estimation. The NuSVR method performed slightly better than the others with 92% of the populations in this rank. These results are far below than those obtained by Sereno et al. [3] whose method estimated BW of all the studied populations below the 5% error threshold. Again, these authors estimated BW some hours before delivery and therefore input data was highly reliable. In terms of absolute errors, around 60% of the test population fall below the 300 g threshold, and this result must be improved in order to be useful for clinical application, for instance by looking for the optimal exploration gestational age window, as [6] reported in their researches.

Table 2. Concordance analysis.

	Cross–validation						Final test					
	AE (%)			PE (%)			AE (%)			PE (%)		
Regressor	**100 g**	**200 g**	**300 g**	**5%**	**10%**	**30%**	**100 g**	**200 g**	**300 g**	**5%**	**10%**	**30%**
SVR Linear	23	47.5	66.5	34.5	65.5	91	20	48	60	32	60	86
SVR Poly	25.5	47	67	36	64.5	88	16	44	60	28	56	88
SVR RBF	23.5	50.5	68.5	35	67.5	90	26	38	54	32	50	88
NuSVR	25	45.5	64.5	33	63	92	18	38	50	24	46	92

*All values are expressed as cumulative percentages. **AE:** Absolute Error, **PE:** Percentage Error.

4 Conclusions

In this research several SVR–based methods were tested for early prediction of weight at birth. Fetal and maternal parameters were obtained during the first trimester of pregnancy and included not only US image–extracted, but also vascular, demographic and anthropometric information. Our results show that SVRs are useful tools for this application, especially SVR RBF that presented slightly better results. Because all methods were tested in a Mexican population they seem promising for clinical application. These results can be improved by exploring different gestation windows or by incorporating other parameters such as CRL.

Acknowledgements. This work was supported by CONACyT (Consejo Nacional de la Ciencia y Tecnologiá) with scholarship number 41178 for Oliver Campos.

Conflict of Interest. The authors declare that they have no conflict of interest.

References

1. World Health Organization Maternal Health and Safe Motherhood Programme: Low birth weight: a tabulation of available information. Technical report, Geneva (1992)
2. Milner, J., Arezina, J.: The accuracy of ultrasound estimation of fetal weight in comparison to birth weight: a systematic review. Ultrasound **26**(1), 32–41 (2018)
3. Sereno, F., Marques, P., Matos, A., Bernardes, J.: Support vector regression applied to foetal weight estimation. In: International Conference on Neural Networks, vol. 2, pp. 1455–1458 (2001)
4. Yu, J., Wang, Y., Chen, P.: Fetal weight estimation using the evolutionary fuzzy support vector regression for low-birth-weight fetuses. IEEE Trans. Inf. Technol. Biomed. **13**(1), 57–66 (2009)
5. Kang, J., Park, E., Yang, Y.: Crown-rump length measured in the early first trimester as a predictor of low birth weigh. Yonsei Med. J. **54**(4), 1049–1052 (2013)
6. O'Connor, C., O'Higgins, A., Segurado, R., Turner, J., Stuart, B., Kennelly, M.: Maternal arterial elasticity in the first trimester as a predictor of birthweight. J. Obstet. Gynaecol. **36**(5), 602–607 (2016)
7. Nahum, G.G., Stanislaw, H.: Ultrasound alone is inferior to combination methods for predicting fetal weight. Ultrasound Obstet. Gynecol. **30**(6), 913–914 (2007)
8. Chang, C.C., Lin, C.J.: Training v-support vector regression: theory and algorithms. Neural Comput. **14**(8), 1959–1977 (2002)

Algorithm to Quantify Maximum Isometric Voluntary Contraction in Subjects with Osteoporosis

Angel Gallegos Ledezma[1(✉)], Ivett Quiñones Uriostegui[2], Virginia Bueyes-Roiz[2], and Rafael Zepeda Mora[2]

[1] Universidad Iberoamericana, Prol. Paseo de la Reforma 880, 01219 Mexico City, Mexico
angel1906_15@hotmail.com
[2] Instituto Nacional de Rehabilitación LGII, Calz. México-Xochimilco 289, 14389 Mexico City, Mexico

Abstract. Osteoporosis is a systemic disease characterized by low bone mass that enhance bone fragility and increases fracture risk. Just in 2005, a total of 21,000 hip fractures were registered in Mexico and it is expected to rise within the next thirty years. In order to reduce fractures, physicians at INR-LGII are implementing exercise programs focused on the improvement of muscle strength to have a better bone quality. This program has electromyography and strength as output variables which need to be processed for interpretation; this signal processing is performed by an algorithm that delivers the voluntary maximum isometric strength, as well as mean and length in seconds of the electromyography envelope.

Keywords: Electromyography · Muscle contraction · Osteoporosis · Software · Voluntary maximum isometric strength

1 Introduction

Osteoporosis is a systemic disease characterized by low bone mass that makes bones more fragile and susceptible to fractures [5]. This fractures are cause of disability. In Mexico, the prevalence of osteoporosis in 50 years old general population is 17% of women and 9% of men in lumbar spine; 16% and 6% respectively in hip. Approximately 21,000 hip fracture cases were reported in 2005, and it expects to reach 110,055 in 2050; producing high costs for the health system [2].

The progressive loss of bone mass, balance and muscular strength are associated with ageing. The amount of skeletal muscle and the muscle circumference decrease in 40% from 30 to 60 years old and in 25% to 40% per decade after 60 years old. Reduced muscle strength and power have been identify systematically as risk factors for injuries and falls related, and it is possible that these associations are due to central role of strength and muscle power performance in the recovery of deficient balance. Moreover, muscle strength and power are

© Springer Nature Switzerland AG 2020
C. A. González Díaz et al. (Eds.): CLAIB 2019, IFMBE Proceedings 75, pp. 42–46, 2020.
https://doi.org/10.1007/978-3-030-30648-9_6

involved with protective responses that reduce the lesion risk if a fall is produced [1]. Osteoporosis and sarcopenia have many risk factors in common, and cause a higher risk of mobility limitations, falls, fractures and disability. Ageing is rising, and the morbidity of osteoporosis is increasing too, which makes this disease an important public health problem worldwide [9].

Muscle strength have been measured traditionally through grip dynamometry or isokinetic peak torque for knee extension in the dominant leg, both with a good clinic correlation [6,7]. Simple evaluation of the strength in lower extremities have demonstrated to be as effective to predict the balance, functional mobility and falls in elderly people, as measures based on muscle mass that are more expensive and slow [7]. Despite the good correlation of grip dynamometry with outcomes like falls, the determining muscles of maintaining the bipedal position are the antigravitatory ones, from which the gluteus medius and rectus femoris play a key role, that is why evaluation of these muscles could correlate better with the incidence in falls. It is not recommended to conduct studies of isokinetic dynamometry in population with osteoporosis due to potential fracture risk, hence it is important to find alternatives in measurement and determination of maximum isometric voluntary force (MIVF). At Instituto Nacional de Rehabilitación Luis Guillermo Ibarra Ibarra (INR-LGII), a training program for patients older than sixty years old with osteoporosis is investigated in order to reduce falls and fractures using MIVF and muscle activation measure with surface electromyography (sEMG) as output variables. With the aim of analysing and processing these signals an algorithm was developed to get the MIVF, as well as the average and length of the sEMG envelope segment that corresponds to sustained contraction produced by the MIVF.

2 Materials and Methods

2.1 Acquisition of sEMG Signals

Force and sEMG signals were acquired using a DataLOG capture equipment (Fig. 1) with surface electromyography amplifiers SX230FW (Biometrics, LTD, Newport, UK), and silver/silver chloride electrodes that were placed in gluteus medius and rectus femoris muscles in both legs, following recommendations from SENIAM project (Surface ElectroMyoGraphy for the Non-Invasive Assessment of Muscles) [3], that is, electrodes were placed parallel to the muscle fibres and with an inter electrode distance of 20 mm. The reference electrode was placed in the lateral condyle of the right knee. MIVF of each muscle was measure using a MyoMeter (Biometrics, LTD, Newport, UK) and following the techniques of manual muscle examination [4] at maximum resistance with the knee in extension and hip in abduction. The signals were acquire and pre-processed by DataLOG software system and after exported in format .txt. Force was saved in kilograms (kg) and sEMG in Volts (V).

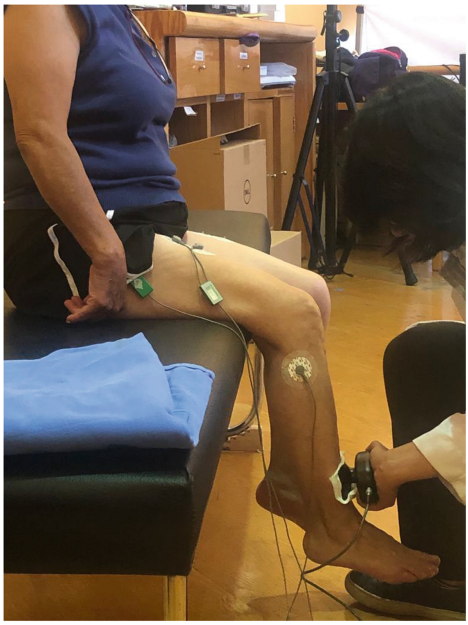

Fig. 1. Assembly for acquisition of force and sEMG signals in subjects with osteoporosis.

2.2 Software Development

The graphic interface for signal processing of sEMG and force was developed on a MacBook Pro computer (beginning of 2015) with Linux Operating System and written in Python version 3.6. Geany was the text editor used for this purpose. The sEMG and force signals were read from a .txt file which comes from the acquisition system Biometrics Ltd. This file contains headings that generate the same system and data of signals sampled at 1kHz into three columns: force, rectus femoris sEMG and gluteus medius sEMG, in that order. Electromyography data is extracted based on the muscle of interest.

The processing begins by obtaining the envelope of sEMG signal in order to identify the moment of sustained contraction produced by MIVF. To get the envelope, the sEMG signal was rectified first [8] and after a fourth order low pass Butterworth infinite impulse response filter [10] was implemented with a cut-off frequency of 1 Hz in continuous time. These features allow to highlight the sustain contraction by showing it as a plateau. In order to get the average (in Volts) of sustained contraction, a threshold of 30% from MIVF was established to approach the beginning and the end of muscular contraction in the electromyography envelope. Coming up next, the bounded fragment of sEMG envelope was isolated to set up another threshold of 80% from the maximum value of that fragment and then get the average of the upper 20% signal that actually represents the sustained contraction. Finally, duration in seconds of last segment was calculated dividing the number of samples by the sampling frequency.

3 Results

Fifty-four women with osteoporosis were recruited. The participant's age was between 59–82 years old (mean 69 years, S.D. 5.7 years). Twenty-six of the subjects that participated received conventional physical activity indications for osteoporosis, while twenty-eight received an experimental exercise program based on force, three times a week during one year. When the evaluation of force and sEMG was being carried out the observer was blind to the participants group. The data obtained was processed in the developed software; this was able to identify the MIVF of the signal obtained from the myometer. From the maximum value of force we identified a plateau in the envelope of sEMG corresponding to the sustained contraction of the muscle. This allows to obtain the average of the electromyographic processed signal during the contraction and the duration of it. In Fig. 2 a graph with the processed data can be observed, where the raw signal of sEMG is shaded in light grey, in blue is represented the force signal indicating the place where the MIVF is located and finally, in red the electromyography envelope is represented. From the envelope, it is possible to appreciate the plateau in each contraction; however, only the plateau located just below the MIVF is taken into account. Until now, only 34 patients concluded 6 months and 13 had concluded 12 months of therapy. Table 1 shows the results obtained from force in each group where it is possible to notice that so far experimental therapy has better results than conventional therapy because it is improving strength in patients over time.

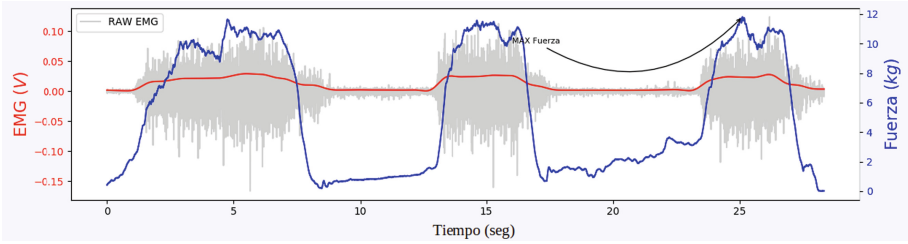

Fig. 2. Graphic representation of the processing output in the left gluteus medius.

Table 1. Mean force of patients through therapy.

Type of therapy	Muscle	Initial (kg)	6 months (kg)	12 months (kg)
Conventional therapy	Rectus Femoris	19.07	17.68	17.93
	Gluteus Medius	15.12	12.66	13.29
Experimental therapy	Rectus Femoris	17.96	21.28	21.70
	Gluteus Medius	12.67	14.63	15.96

4 Conclusion

The software meets with the processing objectives, that is, identify and quantify MIVF as well as the plateau of sustained contraction in the envelope of sEMG. Thus, maximum force value in kg, average of the electromyography plateau in Volts and its duration in seconds are obtained. In addition to this, the software allows to identify visually whether the technique to obtain MIVF was correct or not. If the envelope of sEMG shows a plateau during the contraction, then the technique was implemented properly, otherwise, something went wrong. Therefore, this tool suggest an alternative of muscular evaluation for patients with osteoporosis since isokinetic techniques are not recommended. As future work, full data analysis will be performed when all patients finish therapy.

Conflict of Interest. There is no conflict of interest that apply to this work.

References

1. Benichou, O., Lord, S.: Rationale for strengthening muscle to prevent falls and fractures: a review of the evidence. Calcif. Tissue Int. **98**(6), 531–545 (2016)
2. Clark, P., Carlos, F., Martínez, J.L.V.: Epidemiology, costs and burden of osteoporosis in Mexico. Arch. Osteoporos. **5**(1–2), 9–17 (2010)
3. Hermens, H.J., Freriks, B.: The SENIAM project (2006). http://www.seniam.org
4. Hislop, H., Montgomery, J., Connolly, B.: Daniels and Worthingham's Muscle Testing: Techniques Of Manual Examination, 6th edn. Marbán (2002)
5. Kanis, J.A., Melton, L.J., Christiansen, C., Johnston, C.C., Khaltaev, N.: The diagnosis of osteoporosis. J. Bone Miner. Res. **9**(8), 1137–1141 (1994). https://doi.org/10.1002/jbmr.5650090802
6. Lauretani, F., Russo, C., Bandinelli, S., Bartali, B., Cavazzini, C., Iorio, A.D., et al.: Age-associated changes in skeletal muscles and their effect on mobility: an operational diagnosis of sarcopenia. J. Appl. Physiol. **93**(5), 1851–1860 (2003)
7. Menant, J., Weber, F., Lo, J., Sturnieks, D., Close, J., Sachdev, P., et al.: Strength measures are better than muscle mass measures in predicting health-related outcomes in older people: time to abandon the term sarcopenia? Osteoporos. Int. **28**(1), 59–70 (2017)
8. Merletti, R.: Standards for reporting EMG data. J. Electromyogr. Kinesiol. **24**(2), 1–2 (2014). https://doi.org/10.1016/S1050-6411(14)00042-X
9. Sinaki, M., et al.: The role of exercise in the treatment of osteoporosis. Curr. Osteoporos. Rep. **8**(3), 138–144 (2010)
10. Zschorlich, V.R.: Digital filtering of EMG-signals. Electromyogr. Clin. Neurophysiol. **29**(2), 81–86 (1989)

Prediction of Breast Cancer Diagnosis by Blood Biomarkers Using Artificial Neural Networks

Balam Benítez-Mata[1(✉)], Carlos Castro[1], Rubén Castañeda[2], Eunice Vargas[1], and Dora-Luz Flores[1]

[1] Facultad de Ingeniería, Arquitectura y Diseño, Universidad Autónoma de Baja California, 22860 Ensenada, Baja California, Mexico
angel.benitez@uabc.edu.mx

[2] Ensenada, Baja California, Mexico

Abstract. The use of artificial neural networks (ANNs) has been very helpful in carrying out prediction, classification and data optimization tasks. In this work, ANNs were used to predict the diagnosis for breast cancer in a women population with overweight or obese and possible diabetes, coupled with a pre or postmenopausal stage and compared against other machine learning techniques reported in literature. The algorithms used to train the ANNs models were Scaled Conjugate Gradient, Resilient Backpropagation and Conjugate Gradient Backpropagation with Powell Beale Restarts. The algorithms results were compared with the original dataset creator's work, as well as other authors using the same dataset for classification task, a better classification was accomplished using this work ANNs. With four predictors the next values were obtained, AUC = 0.96, sensitivity = 0.96, specificity = 0.96 and Youden index = 0.92. With nine predictors the next values were obtained, AUC = 0.96, sensitivity = 0.95, specificity = 0.97 and Youden index = 0.92. Different strategies are suggested to improve the results, exploring more hidden layers and a different validation method.

Keywords: Artificial neural networks · Breast cancer · Classification · Machine learning

1 Background

According to World Health Organization, in 2014, 422 million people had diabetes [1]; in 2016 more than 1,900 million adults over 18 years old were overweight or obese [2]; and in 2018, breast cancer (BC) was the most common type of cancer in women, causing approximately 15% of annual deaths related to cancer, that is an estimate of 627,000 women, affecting a total of almost 2.1 million [3]. Obtained data from the Global Observatory of Cancer, showed that just in 2018

R. Castañeda—Independent researcher.

© Springer Nature Switzerland AG 2020
C. A. González Díaz et al. (Eds.): CLAIB 2019, IFMBE Proceedings 75, pp. 47–55, 2020.
https://doi.org/10.1007/978-3-030-30648-9_7

there were slightly more than 2 million new BC cases in women of all ages in the world, representing 24.2% of the total incidence and the most frequent type of cancer in women [4].

Several studies have concluded that there is a relationship between overweight and obesity, which increases the chances for developing diabetes, and BC. Identifying also some molecules presenting abnormal concentrations [5–9]. These abnormal concentrations can be used as biomarkers, helping to differentiate accurately a BC-patient from a control patient [10,11]. Blood based biomarkers are a non-invasive alternative for cancer detection, e.g., proteins, antibodies against proteins associated to tumor antigens, miRNAs (ribonucleic micro-acids, sequences of 20–25 nucleotides) which regulate the expression of genes, nucleic acid methylations, etc. These biomarkers allow detection of metabolites and lipids from preinvasive stages or early development of the disease [12–14].

Machine learning (ML) techniques have been used to demonstrate their ability in prediction [15,16], classification [17,18] and prognosis [19,20], of BC using biomarkers or medical images. Artificial neural networks (ANNs), one of the many ML techniques, are a tool for modeling data with the ability to capture and represent complex relationships between inputs and outputs in a specific model. The goal is to create a model with the ability to relate an input with its respective output, in such a way that when enter an input, the model presents an output, being the latter unknown.

The main goal using ML in medical data is to find alternatives which improve the diagnosis and detection of BC in early development stages as imaging techniques are unable to provide enough information [21,22]. It is the case for BC detection through mammography, which presents a disadvantage when applied to population with high tissue density, which estimate population under 45–50 years, mammography's sensitivity decreases from 67% to approximately 45%, and up to 25% for women undergoing hormonal treatment [23,24].

2 Methodology

The Breast Cancer Coimbra Data Set was used, obtained from the Machine Learning Repository Center for Machine Learning and Intelligent Systems of the University of California in Irvine [25], is a dataset with 116 entries, no blank spaces, nine predictors, all of them quantitative variables, and one classification dependent variable, indicating either absence or presence of disease. In total 1,116 data make up the dataset.

The MATLAB R2016b software was used to build the models (MathWorks Inc., Natick, MA, E.U.A.). The data set was separated into 10 vectors, nine of them predictors and one target. For all vectors, a unit-based normalization was performed, the local minimum and maximum were identified in each vector, and vector values were scaled into the range 0 to 1. According to an analysis carried out by Patricio et al. [26], the relative importance of the predictors is, from greater to lesser: Glucose (V1), Resistin (V2), Age (V3), BMI (V4), HOMA (V5), Leptin (V6), Insulin (V7), Adiponectin (V8), MCP -1 (V9).

The experimentation methodology is summarized in Fig. 1. The model has two experimental groups, the first group uses the variables V1 to V4, the four most important predictors, while the second group consist of variables V1 to V9, the whole data set. Before training, the inputs were normalized so that they will have zero mean and unity standard deviation. The processing by hidden layers is done by means of a hyperbolic tangent activation function and the output data is normalized into a centralized way into the range 0 to 1.

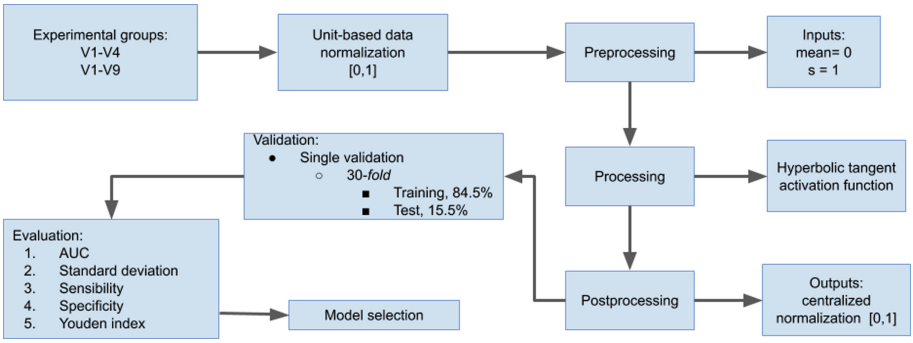

Fig. 1. Experimental methodology for generating diagnostic prediction models.

Multilayer perceptron (MLP) was the topology adopted for the ANNs, Fig. 2. Capable of distinguishing complex patterns in the input data once new information is presented to the network associated with its respective output [27]. The networks were configured to contain the minimum number of hidden layers starting from one and stopped the increment when surpassing the performance metrics obtained by Patricio et al. [26]. For the output layer a sigmoidal hyperbolic tangent transfer function was used, reported to obtain better results in classification problems [28,29].

For training ANNs, different backpropagation algorithms were used due to its effectiveness in biomedical approaches [30–32], which propagates the output errors backwards to all nodes so all weights are updated in each hidden layer [32,33]. The training algorithms used in this work are: Scaled Conjugate Gradient (SCG), Conjugate Gradient Backpropagation with Powell-Beale Restarts (CGB) and Resilient Backpropagation (RP).

A simple 30-*fold* validation with random sub sampling was carried out, randomly dividing data in each iteration into a training subset with 84.5% of data and a test group with 15.5% of data.

The models evaluation was performed through the area under (AUC) the Receiver Operating Characteristic (ROC) curve, standard deviation, sensitivity, specificity and Youden index (J) [36–39]. A classification test was carried out to evaluate the accuracy of the models diagnosis, introducing each data input of the data set to the built model; the predicted classifications were compared against the real value. Due to the binary classification nature for this problem, the test

results are rounded to the nearest integer, when an element has a fractional part of exactly 0.5, it is rounded up to the integer with a greater magnitude [35].

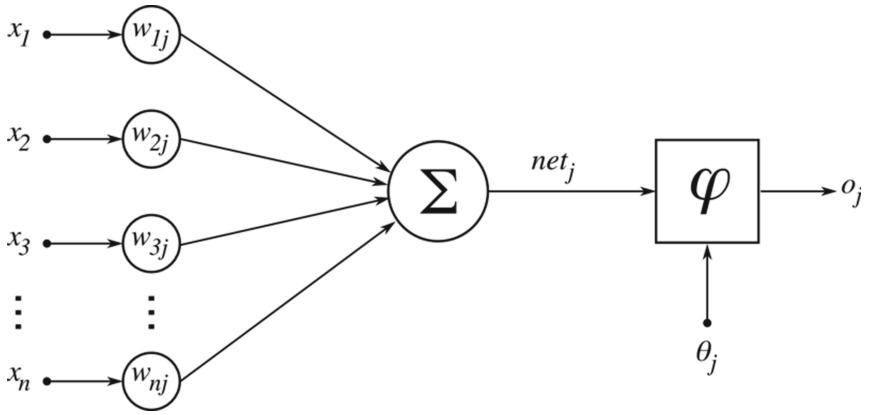

Fig. 2. Multilayer perceptron topology for ANNs. x_n are the inputs to the network, w_{nj} represents the hidden layers which update weights in each new iteration. Followed by an output layer, perceptron unit, $\sum$, which sums all the results to obtain a probability ϕ, with its associated cutoff value θ_j, and resulting in a prediction o_j [34].

For the models selection, evaluation by metric importance is done in the next order: value obtained for the AUC, standard deviation, AUC range and Youden index. An average, result of the 30-fold validation, was obtained for each of the parameters mentioned above for all built configurations in order to obtain a generalized result for each configuration group sharing the exact same conditions, the above was carried out with software R version 3.5.1 (2018-07-02) [40]. The configuration had to comply with the highest average value for the AUC, the lowest average value for the standard deviation, the narrowest range of AUC for whole configuration and the highest average value for the Youden index. For comparison between ML models the average value for sensibility and specificity were taken into account. The above was done for all experimental groups without exception and the best configurations were identified for each of the trained algorithms.

3 Results

A total of 123 different configurations were obtained, each with 30 iterations resulting from the *k-fold* validation.

After identifying the best configuration for each training algorithm SCG, CGB, RP, for both experimental groups, V1 - V4 and V1 - V9, a comparison against the results obtained by [26] was performed. The Table 1 presents a comparison for the best algorithms obtained by [26] against the algorithms obtained

in this work, using the four most relevant predictors. The best algorithms correspond to: an SCG algorithm, with a single hidden layer configuration and 28 nodes; a CGB algorithm, with one hidden layer configuration and 28 nodes; an RP algorithm, with one hidden layer configuration, 4 - 24 - 1.

Table 1. Comparison against ANNs with four predictors, Glucose, Resistin, Age, BMI.

	Patricio et al. [26]			Proposed method		
	LR	RF	SVM	SCG	RP	CGB
AUC	0.81	0.86	0.89	0.91	0.91	0.93
Sensibility	0.75	0.83	0.85	0.91	0.90	0.92
Specificity	0.84	0.84	0.87	0.92	0.92	0.93
J	0.59	0.67	0.72	0.83	0.82	0.85

LR = Logistic Regression, RF = Random Forest, SVM = Support Vector Machine, SCG = Scaled Conjugate Gradient, RP = Resilient Backpropagation, CGB = Conjugate Gradient Backpropagation with Powell-Beale Restarts, AUC = area under the curve, J = Youden index.

In Table 2 is presented a comparison between the best algorithms obtained by [26] against the two hidden layer algorithms obtained in this work, using the nine dataset predictors. The best algorithms correspond to: an SCG algorithm, with a two hidden layers configuration, 24 and 20 nodes in each layer, respectively; a CGB algorithm, with nodes configuration 9 - 24 - 22 - 1 in two hidden layers; an RP algorithm, with configuration 9 - 24 - 20 - 1 in two hidden layers.

Table 2. Comparison against ANNs with nine predictors Glucose, Resistin, Age, BMI, HOMA, Leptin, Insulin, Adiponectin, MCP-1.

	Patricio et al. [26]			Proposed method		
	LR	RF	SVM	SCG	RP	CGB
AUC	0.79	0.81	0.83	0.94	0.93	0.95
Sensibility	0.73	0.82	0.78	0.93	0.92	0.94
Specificity	0.83	0.74	0.81	0.96	0.93	0.96
J	0.56	0.55	0.59	0.89	0.85	0.90

LR = Logistic Regression, RF = Random Forest, SVM = Support Vector Machine, SCG = Scaled Conjugate Gradient, RP = Resilient Backpropagation, CGB = Conjugate Gradient Backpropagation with Powell-Beale Restarts, AUC = area under the curve, J = Youden index.

4 Discussion

Several ANNs configurations were identified in this work to be superior to the algorithms presented by other authors and projects.

Specifically talking about ANN training algorithm, CGB algorithms surpassed the rest of the RP and SCG algorithms, for both experimental groups. The best algorithm for each group is, with four predictors an ANN with configuration, 4 - 28 - 1, obtaining an AUC = 0.93, sensitivity = 0.92, specificity = 0.93 and Youden index = 0.85. And with nine predictors, an ANN with one hidden layer, 9 - 24 - 22 - 1, values for AUC = 0.95, sensitivity = 0.94, specificity = 0.96 and Youden index = 0.90.

The results shown above demonstrate the ability of this work ANNs to predict an accurate and precise diagnosis of the disease better to those reported in [26], as the original creators of the used dataset, obtaining an AUC average value of 0.89 (using SVM), and by [41,42], who used the same dataset obtaining the highest AUC value of 0.81 (using RF) and 0.75 (using ANNs), respectively.

The variation in the number of hidden layers and neurons in each one of the algorithms imply a certain degree of complexity. A greater quantity of the mentioned ones, the greater complexity of the model and more computational resources will be required to carry out the task, the optimization must be kept in mind when improving these prediction models, computational time and memory usage are some examples to assess in further research.

The attractiveness of these models is the ability to involve them in the health sector in order to support the decision making of medical personnel, in this way, a diagnosis can be carried out quickly, timely and with reliable results.

As future work is proposed to carry out a different validation process, this could improve the results to make the prediction. Explore the performance behavior when increasing the number of hidden layers and nodes can give a better insight on the prediction capability for these models.

Conflict of Interest. The authors declare that they have no conflict of interest.

References

1. World Health Organization: Diabetes (2018). https://www.who.int/es/news-room/fact-sheets/detail/diabetes
2. World Health Organization: Obesity and overweight (2018). https://www.who.int/es/news-room/fact-sheets/detail/obesity-and-overweight
3. World Health Organization: Cancer: Breast cancer (2019). https://www.who.int/cancer/prevention/diagnosis-screening/breast-cancer/en/
4. International Agency for Research on Cancer: World cancer statistics (2019). http://gco.iarc.fr/today/data/factsheets/populations/900-world-fact-sheets.pdf
5. Crisóstomo, J., Matafome, P., Santos-Silva, D., Gomes, A.L., Gomes, M., Patírcio, M., Letra, L., Sarmento-Ribeiro, A.B., Santos, L., Seiça, R.: Hyperresistinemia and metabolic dysregulation: a risky crosstalk in obese breast cancer. Endocrine **53**(2), 433–442 (2016). https://doi.org/10.1007/s12020-016-0893-x

6. Georgiou, G.P., Provatopoulou, X., Kalogera, E., Siasos, G., Menenakos, E., Zografos, G.C., Gounaris, A.: Serum resistin is inversely related to breast cancer risk in premenopausal women. The Breast, vol. 29, pp. 163–169. (2016). https://doi.org/10.1016/j.breast.2016.07.025
7. Dalamaga, M.: Resistin as a biomarker linking obesity and inflammation to cancer: potential clinical perspectives. Biomarkers Med. **8**, 107–118 (2014)
8. Santillán-Benítez, J.G., Mendieta-Zerón, H., Gómez-Oliván, L.M., Torres-Juárez, J.J., González-Bañales, J.M., Hernández-Peña, L.V., Ordóñez-Quiroz, A.: The tetrad BMI, leptin, leptin/adiponectin (L/A) ratio and CA 15–3 are reliable biomarkers of breast cancer. J. Clin. Lab. Anal. **27**(1), 12–20 (2013). https://doi.org/10.1002/jcla.21555
9. Dalamaga, M., Sotiropoulos, G., Karmaniolas, K., Pelekanos, N., Papadavid, E., Lekka, A.: Serum resistin: a biomarker of breast cancer in postmenopausal women? association with clinicopathological characteristics, tumor markers, in flammatory and metabolic parameters. Clin. Biochem. **46**(7–8), 584–590 (2013). https://doi.org/10.1016/j.clinbiochem.2013.01.001
10. Henry, N.L., Hayes, D.F.: Cancer biomarkers. Mol. Oncol. **6**(2), 140–146 (2012). https://doi.org/10.1016/j.molonc.2012.01.010
11. Vaughan, L.: Biomarkers in acute medicine key points. Medicine **45**(3), 150–156 (2016). https://doi.org/10.1016/j.mpmed.2016.12.005
12. Loke, S.Y., Lee, A.S.G.: The future of blood-based biomarkers for the early detection of breast cancer (2018)
13. Duffy, M.J., McDermott, E.W., Crown, J.: Blood-based biomarkers in breast cancer: from proteins to circulating tumor cells to circulating tumor DNA. Tumor Biol. **40**(5), 1–11 (2018). https://doi.org/10.1177/1010428318776169
14. Uttley, L., Whiteman, B.L., Woods, H.B., Harnan, S., Philips, S.T., Cree, I.A.: Building the evidence base of blood-based biomarkers for early detection of cancer: a rapid systematic mapping review. EBioMedicine **10**, 164–173 (2016). https://doi.org/10.1016/j.ebiom.2016.07.004
15. Wang, H., Zheng, B., Yoon, S.W., Ko, H.S.: A support vector machine-based ensemble algorithm for breast cancer diagnosis. Eur. J. Oper. Res. **267**(2), 687–699 (2018). https://doi.org/10.1016/j.ejor.2017.12.001
16. Tapak, L., Shirmohammadi-Khorram, N., Amini, P., Alafchi, B., Hamidi, O., Poorolajal, J.: Prediction of survival and metastasis in breast cancer patients using machine learning classifiers. Clin. Epidemiol. Glob. Health, 1–7 (2018). https://doi.org/10.1016/j.cegh.2018.10.003
17. Guo, Y., Shang, X., Li, Z.: Identification of cancer subtypes by integrating multiple types of transcriptomics data with deep learning in breast cancer. Neurocomputing **324**, 20–30 (2019). https://doi.org/10.1016/j.neucom.2018.03.072
18. Xu, Y., Wang, Y., Yuan, J., Cheng, Q., Wang, X., Carson, P.L.: Medical breast ultrasound image segmentation by machine learning. Ultrasonics **91**(July), 1–9 (2019). https://doi.org/10.1016/j.ultras.2018.07.006
19. Kourou, K., Exarchos, T.P., Exarchos, K.P., Karamouzis, M.V., Fotiadis, D.I.: Machine learning applications in cancer prognosis and prediction. Comput. Struct. Biotech. J. **13**, 8–17 (2015). https://doi.org/10.1016/j.csbj.2014.11.005
20. Kalinli, A., Sarikoc, F., Akgun, H., Ozturk, F.: Performance comparison of machine learning methods for prognosis of hormone receptor status in breast cancer tissue samples. Comput. Methods Programs Biomed. **110**(3), 298–307 (2013). https://doi.org/10.1016/j.cmpb.2012.12.005

21. Núñez, C.: Clinica chimica acta blood-based protein biomarkers in breast cancer. Clin. Chim. Acta **490**(December), 113–127 (2019). https://doi.org/10.1016/j.cca.2018.12.028
22. Sumbal, S., Javed, A., Afroze, B., Zulfiqar, H.F., Javed, F., Noreen, S., Ijaz, B.: Circulating tumor DNA in blood: future genomic biomarkers for cancer detection. Exp. Hematol. **65**, 17–28 (2018). https://doi.org/10.1016/j.exphem.2018.06.003
23. Lourenco, A.P., Benson, K.L., Henderson, M.C., Silver, M., Letsios, E., Tran, Q., Gordon, K.J., Borman, S., Corn, C., Mulpuri, R., Smith, W., Alpers, J., Costantini, C., Rohatgi, N., Yang, R., Haythem, A., Biren, S., Morris, M., Kass, F., Reese, D.E.: A noninvasive blood-based combinatorial proteomic biomarker assay to detect breast cancer in women under the age of 50 years. Clin. Breast Cancer **17**(7), 516–525 (2017). https://doi.org/10.1016/j.clbc.2017.05.004
24. Levenson, V.V.: Biomarkers for early detection of breast cancer: what, when, and where? Biochim. Biophys. Acta **1770**(6), 847–856 (2007). https://doi.org/10.1016/j.bbagen.2007.01.017
25. Dua, D., Taniskidou, E.K.: UCI Machine Learning Repository (2017). http://archive.ics.uci.edu/ml
26. Patrício, M., Pereira, J., Crisóstomo, J., Matafome, P., Gomes, M., Seiça, R., Caramelo, F.: Using Resistin, glucose, age and BMI to predict the presence of breast cancer. BMC Cancer **18**(1), 1–8 (2018). https://doi.org/10.1186/s12885-017-3877-1
27. Agatonovic-Kustrin, S., Beresford, R.: Basic concepts of artificial neural network (ANN) modeling and its application in pharmaceutical research. J. Pharm. Biomed. Anal. **22**(5), 717–727 (2000). https://doi.org/10.1016/S0731-7085(99)00272-1
28. Riesel, D.: Selecting an activation function (2007). https://doi.org/10.1016/S0140-6736(95)92880-4
29. Duch, W., Jankowski, N.: Survey of neural transfer functions. Neural Comput. Surv. **2**, 163–212 (1999). ftp://ftp.icsi.berkeley.edu/pub/ai/jagota/vol2_6.pdf
30. Flores, D.L., Gómez, C., Cervantes, D., Abaroa, A., Castro, C., Castañeda-Martínez, R.A.: Predicting the physiological response of Tivela stultorum hearts with digoxin from cardiac parameters using artificial neural networks. BioSystems **151**, 1–7 (2017). https://doi.org/10.1016/j.biosystems.2016.11.002
31. Jiménez, F.M.: Redes neuronales y preprocesado de variables para modelos y sensores en bioingeniería. PhD thesis, Universidad Politécnica de Valencia (2012). https://riunet.upv.es/bitstream/handle/10251/16702/tesisUPV3874.pdf
32. Hagan, M.T., Demuth, H.B., Beale, M.: Neural Network Design (2014)
33. Erb, R.J.: Introduction to backpropagation neural network computation. Pharm. Res. **10**(2), 165–170 (1993)
34. Chrislb. (https://commons.wikimedia.org/wiki/File:ArtificialNeuronModel.png), "ArtificialNeuronModel". https://creativecommons.org/licenses/by-sa/3.0/legalcode
35. Shanker, M., Hu, M.: Cutoff values for two-group classification using neural networks (1996). http://www.personal.kent.edu/~mshanker/personal/Zip_files/im-1996.PDF
36. Turki, T., Wei, Z.: Boosting support vector machines for cancer discrimination tasks. Comput. Biol. Med. **101**(July), 236–249 (2018). https://doi.org/10.1016/j.compbiomed.2018.08.006
37. Xiao, Y., Wu, J., Lin, Z., Zhao, X.: A deep learning-based multi-model ensemble method for cancer prediction. Comput. Methods Programs Biomed. **153**, 1–9 (2018). https://doi.org/10.1016/j.cmpb.2017.09.005

38. Richter, A.N., Khoshgoftaar, T.M.: A review of statistical and machine learning methods for modeling cancer risk using structured clinical data. Artif. Intell. Med., vol. 90, pp. 1–14 (2018). https://doi.org/10.1016/j.artmed.2018.06.002
39. El Houby, E.M.F.: A survey on applying machine learning techniques for management of diseases. J. Appl. Biomed. **16**(3), 165–174 (2018). https://doi.org/10.1016/j.jab.2018.01.002
40. R Core Team: R: A Language and Environment for Statistical Computing. R Foundation for Statistical Computing. Vienna, Austria, (2014). http://www.R-project.org/
41. Sardouk, F., Durub, A., Bayatc, O.: Classification of breast cancer using data mining. Am. Sci. Res. J. Eng. Tech. Sci. ASRJETS. **51**(1), 38–46 (2019). https://www.google.com.mx/url?sa=t&rct=j&q=&esrc=s&source=web&cd=4&cad=rja&uact=8&ved=2ahUKEwiA2azMhOXiAhWKw1QKHayeB3wQFjADegQIBxAC&url=http%3A%2F%2Fasrjetsjournal.org%2Findex.php%2FAmerican_Scientific_Journal%2Farticle%2Fdownload%2F4585%2F1618&usg=AOvVaw2Nz-ktI_dBfW7aARwA1910
42. Yixuan, L., Zixuan, C.: Performance evaluation of machine learning methods for breast cancer prediction. Appl. Comput. Math. **7**(4), 212–216 (2018). https://doi.org/10.11648/j.acm.20180704.15

Measuring Periodicity Perturbations in Pathological Voice: General-Purpose Software vs. Custom-Tailored Methods

Reinier Rodríguez-Guillén and Carlos A. Ferrer-Riesgo(✉)

Central University "Marta Abreu" of Las Villas,
C. Camajuaní km 5½, 52830 Santa Clara, Cuba
reinierrg@uclv.cu, cferrer@uclv.edu.cu

Abstract. The acoustic measurement of the severity of the symptoms present in pathological voice is an active research area, for being inexpensive and non invasive. Periodicity perturbations are among the most frequently used, requiring the previous extraction of the individual glottal pulse boundaries. In this paper we explore the performances of methods for detecting glottal pulse boundaries as implemented by freely available software (Praat, intended for phonetic studies) vs. a research-grade pulse cycle detector (reported as a super-resolution method). We compare the sequences of pulse markers as obtained by two of Praat's internal implementations and the super-resolution method against the hand-marked reference sequence in a dataset of pathological sustained vowels from a well-known database. A group of performance measures is extracted from this comparison, using a Dynamic-Time Warping alignment procedure. The measures obtained show the pros and cons of each alternative. Researchers and clinicians must be aware of the benefits of selecting either approach.

Keywords: Vocal Quality · Jitter · Shimmer · Praat · PDAs · Real signals

1 Introduction

Speech is the result of the coordination of many anatomical and cognitive systems, therefore a wide range of pathologies manifest in the way it is emitted. Speech is arguably the most natural and effective means of human communication, and its alteration causes severe handicaps in the social insertion of the affected person. Objective means of measurement of the severity of different symptoms of speech disorders have been devised, and the search for reliable markers is still an area of research. Instrumental methods have been based on different physical principles depending on the magnitude used [1], among them:

- Acoustic measures working over the sound wave
- Electric measures working over the transconductance across the glottis (electroglottogram) or muscles electromyographic signals
- Mechanical measures working over accelerometers signals
- Optical measures made over still or moving images obtained with cameras.

© Springer Nature Switzerland AG 2020
C. A. González Díaz et al. (Eds.): CLAIB 2019, IFMBE Proceedings 75, pp. 56–62, 2020.
https://doi.org/10.1007/978-3-030-30648-9_8

This paper deals with acoustic measures, which have been preferred for been non-invasive and widely available (the sensor required, a microphone, is ubiquitous in everyday-use devices like smartphones and personal computers). Considering the smallest language units where the pathology can be perceived in the speech, the alterations can be classified in three levels:

- Vocal Quality: When the alteration can be perceived from individual sounds (phones) onwards. Vocal Quality is a multidimensional construct typically equated to the definition of Timbre [2], and more specifically in the clinical setting to Hoarseness [3, 4]. There is a vast proliferation of instrumental acoustical measures of Vocal Quality, with more than 500 methods reported in [5], a couple decades ago.
- Articulation: When the alteration requires the occurrence of transitions between sounds to be perceived. Smallest language unit required is the syllable. A typical example of a measure of articulation adequacy is the Voice Onset Time (VOT) [6–8], differentiating among voiced and unvoiced consonants.
- Prosody: Includes alterations of rhythm, intonation, and tempo, and requires the speaker to utter larger language units, like phrases, sentences, and larger. A straightforward example of measure is the Speech Rate [9, 10], measured in language units per time.

Vocal Quality has been the subject of most research efforts, arguably due to the relatively easier to model patterns of normal emission. In voiced sounds like vowels and several consonants, for instance, the acoustic waveform can be conceived within some time limits (frames of around 20 ms duration) [11] to be the vocal tract response to a quasi-periodic repetition of glottal pulses. The measurements of different types of deviations from this assumed periodicity are grouped within the term Periodicity Perturbations, and include jitter (variability in glottal pulses' durations), shimmer (variability in glottal pulses amplitudes) and additive noise. An initial requirement for all these measurements is the location of glottal pulse boundaries, performed by a special type of method called Pitch Detection Algorithm (PDA), of which there is also a broad proliferation of alternatives [12, 13], since no PDA can be assumed to work reliably for all situations [12].

Praat [14] is a computer program developed for performing phonetic studies, but the diversity of algorithms implemented (including several higly configurable PDAs) together with its support for running external scripts and its ability for batch processing has attracted its use in the clinical setting, with some standard measures programmed on it [15–18]. However, general purpose software like Praat can lack the fine tuning that some particular PDAs can achieve, which is the issue we explore in this paper.

2 Materials and Methods

Praat provides several implementations of two types of PDAs: short-term and cycle-to-cycle. The functioning of Praat's cycle-to cycle PDAs depends on the previous result of a short-term PDA, providing the frame-based estimate of T0 (TE) over which the search for the individual pulse duration is performed in the cycle to cycle PDA. The

cycle-to-cycle PDAs implemented in Praat are Peak Picking (denoted P-P in the remainder of the document) and Cross Correlation (denoted C-C). Praat P-P PDA departs from the most relevant maximum (or minimum) at the center of the voiced segment, and searches to the left and to the right for similar points in the TE ± 20% vicinity. It is provided for compatibility with other commercial systems, but its use is not encouraged. Praat C-C, being a waveform-matching PDA, is more robust to noise than the previous [19] evaluating the pulse as a whole and not a single point in the search for the periodicity. Praat C-C searches for the lag τ which minimizes the cost function:

$$J(\tau) = \frac{\sum_{n=1}^{T_E} |x(t_i+n)x(t_i+\tau+n)|^2}{\sqrt{\sum_{n=1}^{T_E} |x(t_i+n)|^2}\sqrt{\sum_{n=1}^{T_E} |x(t_i+\tau+n)|^2}} \quad (1)$$

The search range for τ is restricted to ±20% of T_E as in the P-P PDA, and cannot be modified in the Praat environment. The T_E is obtained in Praat by means of autocorrelation analysis of a frame containing at least three pulses [14].

Both Praat cycle-to-cycle PDAs are compared in this paper vs. the Super-resolution (denoted S-R) PDA described in [20], which has shown to perform better than many other cycle-to-cycle PDAs in several studies [21–23]. The cost function for S-R is slightly different from Eq. (1):

$$J(\tau) = \frac{\sum_{n=1}^{\tau} \left|x(t_i+n) - a_{\tau,t_i}x(t_i+\tau+n)\right|^2}{\sum_{n=1}^{\tau} x(t_i+n)^2} \quad (2)$$

In the case of Eq. (2), both segments are contiguous and of varying length, something made possible by setting their lengths equal to τ, in opposition to the constant length of T_E in Eq. (1).

The performances of the three PDAs were evaluated using real signals. In this paper we have used the same subset of recordings from the sustained vowel 'a' exercise, selected in [23] from the MEEI/Kay Database [24], chosen in a way that the signals were both, representative for comparing PDAs performances, and as few as to be feasible to hand-mark. The hand marking process was performed on 29 signals in total, producing 4695 pitch markers (average F0 = 161 Hz).

As measures of performance we also used the ones resulting from the Dynamic-Time-Warping (DTW) procedure described in [23], namely β, a measure of inter contour normalized error, in %, the number of pulse insertions (PI) and deletions (PD) and the number of contour shifts to the left (SL) or to the right (SR) of the detected pulse boundaries $P_d(n)$ as compared to the reference, hand-marked contour $P_r(n)$. The algorithm to obtain all measures is schematically depicted in Fig. 1:

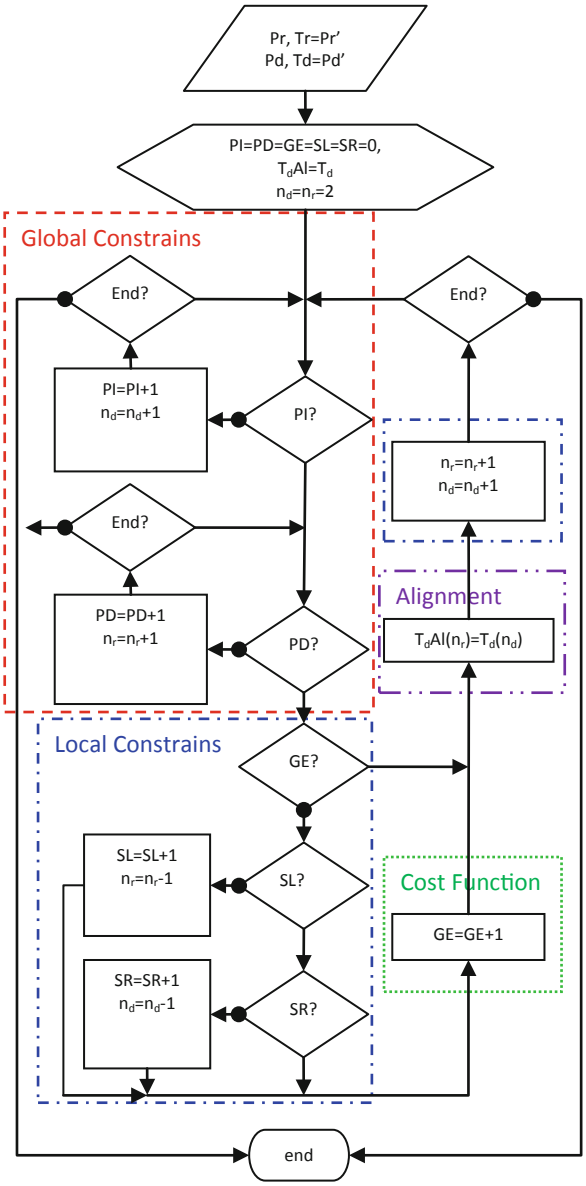

Fig. 1. Flowchart used for calculating the measures of performance reported in this paper. Basic inputs are the reference and detected pulse boundary positions $P_r(n)$ and $P_d(n)$. Bounding labeled squares indicate the relevant stages on a DTW procedure. Positive outcomes in the conditional blocks have been signaled by a black circle in the corresponding corner of the rhombus.

The values of PI, PD, SL & SR are completely determined once the algorithm ends, while the value of β is given by:

$$\beta = \frac{1}{N}\sum_{n=1}^{N}\frac{|T_dAl(n) - T_r(n)|}{T_r(n)} * 100 \quad (3)$$

being $T_dAl(n)$ the aligned contour/vector of position separations (differences) obtained in the "Alignment" square in the diagram.

3 Results and Discussion

The results for the 29 hand-marked signals have been aggregated in Table 1, with each measure as column. Statistical pair-wise differences (Wilcoxon Signed-Rank test) were found between S-R and any of the Praat variants for the β, PI and PD measures, and our discussion will focus on these results.

Table 1. Averaged results across the 29 pathological recordings for the PDAs considered. *: value with significant differences to the rest at the 0.01 level.

PDAs	β	PI	PD	SL	SR
C-C	8.84	0.03	18.69	0.62	2.00
P-P	11.74	0.00	15.31	1.03	1.79
S-R	**2.10***	**0.62***	**0.00***	.169	2.38

The first conspicuous outcome is that S-R boundary sequences are more similar to the hand-marked reference, with normalized errors (β) four times smaller than the closest Praat PDA, the C-C variant. If we consider β as a measure of the amount of perturbation introduced by the PDA, S-R is superior, possibly due to the different cost function used.

A second relevant result is the opposite asymmetries found between the PDAs in Praat (C-C y P-P) and the S-R approach regarding the PI and PD measures. In the Praat PDAs the asymmetry found is that PI << PD, while in the S-R it turns out that PI >> PD. These results could be explained by the fact that Praat's short-term PDA stage, prior to C-C or P-P, can mark some frames as non-periodic (unvoiced) causing all the pulses in that frame to be deleted (hence, reported as PD by the DTW procedure). On the other hand, S-R seems to be prone to introduce pulses. A possible cause is that in the real signals there can be actually missing pulses, but the S-R method always reports a pulse boundary (the most likely, even if the likelihood is low) on its search range, and hence it is reported as PI by the DTW.

Either way, the results of both Praat implementations fall below the performance of the S-R approach if we consider insertions and deletions as a whole.

A final remark should be made regarding the poor performance of the PP approach. Since the human hand-marking procedure follows basically the position of the main

peak in the pulse, as the peak picking PDAs do, it could be expected that the latter performances were favored. The results show the opposite, with the reason being that once the PP-PDA loses track of the position where the main peak in the pulse should have occurred, its performance is more severely affected than the ones of the waveform matching approaches, less dependent of a single point position.

4 Conclusions

The results of the PDAs considered facing pathological-grade had-marked real signals show that general purpose PDAs can perform worse than methods conceived to work completely with voiced signals. Discarding highly irregular segments/frames as unvoiced produces a tendency to underestimate jitter measures, as guessed elsewhere [25, 26].

It must be stressed that the procedures introduced in Praat to perform a frame-wise voiced/unvoiced decision are by no means wrong or unjustified, but devised to fit slightly different purposes than the measurement of Periodicity Perturbations in single sounds (e.g. sustained vowels). The decision is intended to deal with running speech recordings, where sounds are not necessarily voiced as a whole. Researchers and clinicians should be aware of the advantages and disadvantages of both assumptions when performing measurements of Periodicity Perturbations.

Acknowledgements. This work was partially supported by an Alexander von Humboldt Foundation Fellowship granted to one of the authors (Ref 3.2-1164728-CUB-GF-E).

References

1. Baken, R.J., Orlikoff, R.F.: Clinical Measurement of Speech and Voice, 2nd edn. Cengage Learning (2000)
2. Kreiman, J., Gerratt, B.R.: Measuring vocal quality. In: Kent, R.D., Ball, M.J. (eds.) Voice Quality Measurement, pp. 73–112. Singular, San Diego (2000)
3. Dejonckere, P.H., et al.: A basic protocol for functional assessment of voice pathology, especially for investigating the efficacy of (phonosurgical) treatments and evaluating new assessment techniques: Guideline elaborated by the Committee on Phoniatrics of the European Laryngolo. Eur. Arch. Oto-Rhino-Laryngology **258**(2), 77–82 (2001)
4. Dejonckere, P.H.: Assessment of voice and respiratory function. In: Remacle, M., Eckel, E. H. (eds.) Surgery of Larynx and Trachea, pp. 11–26. Springer, Heidelberg (2010)
5. Buder, E.H.: Acoustic analysis of voice quality: a tabulation of algorithms 1902–1990. In: Kent, R.D., Ball, M.J. (eds.) Voice Quality Measurement, pp. 119–244. Singular, San Diego (2000)
6. Ng, M.L., Wong, J.: Voice onset time characteristics of esophageal, tracheoesophageal, and laryngeal speech of cantonese. J. Speech Lang. Hear. Res. **52**, 780–789 (2009)
7. Karlsson, F., Olofsson, K., Blomstedt, P., Linder, J., Nordh, E., van Doorn, J.: Articulatory closure proficiency in patients with Parkinson's disease following deep brain stimulation of the subthalamic nucleus and caudal zona incerta. J. Speech. Lang. Hear. Res. **57**, 1178–1190 (2014)

8. Pouplier, M., Marin, S., Waltl, S.: Voice onset time in consonant cluster errors: can phonetic accommodation differentiate cognitive from motor errors? J. Speech Lang. Hear. Res. **57**, 1577–1588 (2014)
9. Borrie, S.A., Liss, J.M.: Rhythm as a coordinating device: entrainment with disordered speech. J. Speech Lang. Hear. Res. **57**, 815–824 (2014)
10. Skodda, S., Grönheit, W., Schlegel, U.: Intonation and speech rate in Parkinson's disease: general and dynamic aspects and responsiveness to levodopa admission, J. Voice 25(4) (2011)
11. Ní Chasaide, A., Yanushevskaya, I., Gobl, C.: Voice source dynamics in intonation. In: Proceedings of 17th International Congress of Phonetic Sciences (ICPhS 2011), pp. 1470–1473 (2011)
12. Hess, W.J.: Pitch Determination of Speech Signals. Springer, Berlin Heidelberg (1983)
13. Hess, W.J.: Pitch and voicing determination of speech with an extension toward music signals. In: Benesty, J., Sondhi, M.M., Huang, Y.A. (eds.) Springer Handbook of Speech Processing. Springer. Heidelberg, pp. 181–212 (2008)
14. Boersma, P.: PRAAT, a system for doing phonetics by computer. Glot Int. **5**(9/10), 5 (2002)
15. Barsties, B., Latoszek, V., Maryn, Y., Gerrits, E., De Bodt, M.S.: "The acoustic breathiness index (ABI): a multivariate acoustic model for breathiness, J. Voice (2017, in press)
16. Uloza, V., Latoszek, B.B.V., Ulozaite-Staniene, N., Petrauskas, T., Maryn, Y.: A comparison of Dysphonia severity index and acoustic voice quality index measures in differentiating normal and dysphonic voices. Eur. Arch. Oto-Rhino-Laryngology **275**(4), 949–958 (2018)
17. Latoszek, B.B.V., Ulozaitė-Stanienė, N., Petrauskas, T., Uloza, V., Maryn, Y.: Diagnostic accuracy of dysphonia classification of DSI and AVQI. Laryngoscope (2018)
18. Latoszek, B.B.V., De Bodt, M., Gerrits, E., Maryn, Y.: The exploration of an objective model for roughness with several acoustic markers. J. Voice **32**(2), 149–161 (2018)
19. Boersma, P.: Should jitter be measured by peak picking or by waveform matching? Folia Phoniatr. Logop. **61**(5), 305–308 (2009)
20. Medan, Y., Yair, E., Chazan, D.: Super resolution pitch determination of speech signals. IEEE Trans. Signal Process. **39**(1), 40–48 (1991)
21. Bagshaw, P.C., Miller, S.M., Jack, M.A.: Enhanced pitch tracking and the processing of F0 contours for computer aided intonation teaching. In: 3rd European Conference on Speech Communication and Technology EUROSPEECH 1993, pp. 1003–1006 (1993)
22. Parsa, V., Jamieson, D.G.: A comparison of high precision F0 extraction algorithms for sustained vowels. J. Speech. Lang. Hear. Res. **42**(1), 112–126 (1999)
23. Ferrer, C., Torres, D., Hernández-Díaz, M.E.: Using dynamic time warping of T0 contours in the evaluation of cycle-to-cycle pitch detection algorithms. Pattern Recognit. Lett. **31**(6), 517–522 (2010)
24. Disordered Voice Database v1.03. Kay Elemetrics Corp (1994)
25. Hosokawa, K., Ogawa, M., Hashimoto, M., Inohara, H.: Statistical analysis of the reliability of acoustic and electroglottographic perturbation parameters for the detection of vocal roughness. J. Voice **28**(2), 263.e9–263.e16 (2014)
26. Manfredi, C., Giordano, A., Schoentgen, J., Fraj, S., Bocchi, L., Dejonckere, P.H.: Validity of jitter measures in non-quasi-periodic voices. part II: the effect of noise. Logop. Phoniatr. Vocology **36**(2), 78–89 (2011)

Estimation of Heart Rate and Respiratory Rate via Blind Estimation from Smartphone-Based Contact Image Photoplethysmography

Rodrigo García-López(✉), Javier Benítez-Benítez, Daniel Ulises Campos-Delgado, and Bersaín A. Reyes

Faculty of Science, Autonomous University of San Luis Potosi, 78295 San Luis Potosi SLP, Mexico
rodrigogarcialopez@hotmail.com

Abstract. Heart rate (HR) and respiratory rate (RR) vital signs provide useful cardiorespiratory information, and their monitoring is routinely carried out in clinical settings via electrocardiography, photoplethysmography, and capnography. However, these and other specialized biomedical devices are not easily translated to everyday use outside clinical and research settings. Hence, there is still a need for HR and RR monitoring devices that could be used on a daily basis by the general population. In this study, we employed a contact approach to estimate both HR and RR directly from image plethysmography (iPPG) signals extracted from smartphone-acquired videos. Video recordings of the fingertips from eight ($N = 8$) volunteers were acquired with an Android smartphone while the subjects performed metronome breathing maneuvers. The iPPG waveform was extracted via the Extended Blind End-member and Abundance Extraction (EBEAE) algorithm. Simultaneous ECG recordings were used to compute reference HR and RR time series. We found that iPPG-based estimates are highly correlated by those from ECG-derived ones (HR: $\rho = 0.9953$, RR: $\rho = 0.9733$ with low normalized root-mean-square errors (HR: $NRMSE = 0.0855$, RR: $NRMSE = 0.3074$ for both HR and RR estimation. The obtained results corroborate the feasibility of using contact iPPG methods to accurately estimate not only HR, but also RR without specialized biomedical devices.

Keywords: Image photoplethysmography · Smartphone · Heart rate · Pulse rate · Respiratory rate

1 Introduction

Heart rate (HR), defined as the number of cardiac cycles per unit of time, is the most widely used vital sign to monitor cardiac status and is usually expressed in beats-per-minute (BPM). It is recognized that HR could serve as an index of propensity to cardiovascular diseases [1]. Furthermore, the motoring of breathing status has been recognized as relevant to identifying and predicting adverse cardiorespiratory events [2] where the respiratory rate (RR) is a basic monitoring parameter that refers to the number of breaths per unit of time, commonly expressed in breaths-per-minute (bpm).

© Springer Nature Switzerland AG 2020
C. A. González Díaz et al. (Eds.): CLAIB 2019, IFMBE Proceedings 75, pp. 63–70, 2020.
https://doi.org/10.1007/978-3-030-30648-9_9

Clinical and research methods for continuous monitoring of HR and RR include electrocardiography (ECG), photoplethysmography (PPG), transthoracic impedance, capnography, inductance plethysmography and acoustical monitoring. Each method has shown its utility and has its own advantages and disadvantages, e.g. such HR and RR monitors are not easily translated for daily use by the general population.

It is well known that smartphones are ubiquitous devices with their hardware and software capabilities being continuously updated. Given the number of cost-effective sensors already embedded in smartphone devices, they have been used in vital signal monitoring applications. To this end, smartphones have been employed for HR estimation using contact and non-contact optical image photoplethysmography (iPPG) methods [3]. In the contact approach, the smartphone's video camera is employed analogously to the photoreceptor in traditional PPG, while the light emitting diode (LED) is employed as the source of illumination [4]. Hence, HR, also known as pulse rate (PR) in PPG, could be estimated by capturing a video sequence at the fingertips of the subjects and extracting the blood pulsations synced with each heartbeat [5]. In addition, it is known that ECG and PPG signals contain components synced with respiratory rhythms that modulate both their amplitude and frequency. Hence, RR can also be estimated from iPPG smartphone-acquired signals [6], e.g. by exploiting the respiratory information present in the pulse wave velocity and dispersion [7], as well as from respiration-induced amplitude and frequency modulations (AM and FM).

There have been limited efforts to simultaneously estimate HR and RR using the same smartphone device, e.g. using the frontal camera for RR non-contact estimation from thoracic movements and the rear camera for HR contact estimation [8], or by using only non-contact estimation as in the Philips VitalSigns Camera (www.ip.philips.com). However, in these efforts just the average heart rate and average respiratory rate are provided. In this work, we propose a novel algorithm for simultaneous estimation of HR and RR time series, i.e. their evolution over time using a single smartphone camera via a contact iPPG approach. The obtained results were compared to ECG-derived HR and RR considered as reference.

2 Materials and Methods

2.1 Experimental Protocol

Eight ($N = 8$) healthy volunteer subjects with ages ranging from 18 to 24 years old were recruited for this study. Each volunteer provided their informed consent to participate in the study in agreement with the Declaration of Helsinki. The wireless acquisition system Shimmer3 Consensys ECG Development Kit (Shimmer, Dublin, Ireland) was used to acquire the ECG signals from volunteers at a sampling rate of 1024 Hz. Adhesive Ag/AgCl electrodes (3 M HealthCare, Maplewood, MN, United States) were placed on the subjects' thorax at locations that mimic the traditional Lead II. Prior to electrode placement, attachment skin sites were cleaned with 83% ethanol. Simultaneously with ECG signals, video recordings were obtained with a Samsung Galaxy S4 Android device (Samsung Electronics, Seoul, Korea).

Volunteers were asked to place their left index finger over the rear camera so that it also covered the flash LED and at a pressure level high enough to keep the finger in place, i.e. not move it, displace it or remove it from the camera and LED. The video sequence was recorded at 30 frames-per-second (fps) using a 1280 × 780-pixel resolution. Volunteers were asked to perform the following metronome respiratory maneuvers: (1) 3 bpm for one minute, (2) 6 bpm for one minute, and (3) 18 bpm for one minute. A mobile metronome application (Natural Metronome, Single Minded Productions LLC, Google Play Store) was employed to audiovisually guide the volunteers at each fixed respiratory rate, which in turn were selected to cover a normal range during resting conditions. Two minutes of rest were provided in between consecutive metronome breathings. The acquired signals and videos were stored for further processing in MATLAB (The MathWorks, Natick, MA, USA). The experimental setup is shown in Fig. 1.

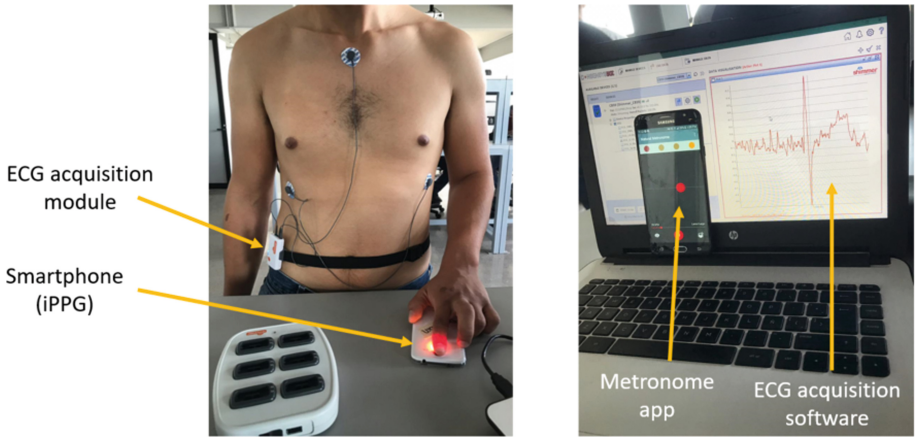

Fig. 1. Experimental setup for the simultaneous acquisition of ECG and iPPG signals during metronome breathing maneuvers.

2.2 Extraction of Image Photoplethysmograph Signal

Traditionally, average intensity RGB channels are used to compute the iPPG signal. There is still no consensus regarding which channel color performs better for all smartphone devices, but the green and red channels appear to be the most commonly used for this goal. In this work, we employed information from the green channel together with a more robust estimation approach than the average value, an approach based on the recently developed Extended Blind End-member and Abundance Extraction (EBEAE) algorithm [9]. In order to apply the EBEAE algorithm, the green channel was extracted from each frame of the video sequence containing a total of NF frames and down-sampled at half the pixel resolution to reduce the computational burden. Then, each green channel frame was reshaped as a 1 × (640 × 390) row vector, and finally an ensemble matrix of size NF × (640 × 390) was generated. Consequently, the temporal information is provided by the matrix rows, while its columns supply the spatial

information. Hence, the columns in the ensemble matrix are non-negative vectors describing the temporal response of each spatial pixel per frame. Finally, the ensemble matrix was used to feed the EBEAE algorithm described below [9].

2.3 Blind End-Member and Abundance Extraction Algorithm

In the EBEAE formulation [9], a set of non-negative vectors (columns in the ensemble matrix) is assumed as available measurements for the analysis. First of all, the measurements are scaled to sum-to-one to provide a common ground for the numerical analysis, and a linear mixing model is considered to reproduce each scaled measurement. This linear mixing model is characterized by a set of linearly independent end-member vectors, which are common to all the dataset. The contributions of the end-members are denoted as their abundances, which are limited to the interval [0,1]. A constrained quadratic optimization process estimates the end-members and their abundances per column in the ensemble matrix [9], where due to the nonlinear interaction between end-members and abundances, an alternated least squares methodology is pursued to provide an iterative optimization scheme. Thus, in this alternated structure, the abundances are estimated first per measurement in the dataset (*local perspective*), and the end-members are then obtained by using the whole dataset (*global perspective*) until convergence. In our study, a second-order linear mixing model was adopted to reproduce each column in the ensemble matrix and the first optimal end-member was regarded as the iPPG signal.

2.4 Heart Rate and Respiratory Rate Estimation

For comparison purposes, the iPPG signal was resampled at 1024 Hz, using cubic splines, to achieve the same sample frequency as the ECG signal. Then, due to different starting times and delays in the ECG and smartphone systems, simultaneous ECG and iPPG signals were manually aligned using corresponding peaks between both signals with the aid of a custom designed graphical user interface. The reference ECG signal was then bandpass filtered using a zero-phase 4th order Butterworth filter between 0.5 and 40 Hz, applied in forward and reverse fashion to minimize start and end transients. Furthermore, the iPPG signal was lowpass filtered at 5 Hz using a zero-phase 4th order Butterworth filter. An example of the resampled, aligned and filtered ECG and iPPG signals is shown in Fig. 2.

The HR time series was obtained by processing the ECG signal as follows. First, the R-peaks were automatically detected using an algorithm based on filter banks [10]. Then, the R-peaks' locations were used to compute an Rpeak-to-Rpeak interval time series, which was interpolated at 4 Hz using cubic splines. Furthermore, the PR time series from the processed iPPG signal was obtained by automatically detecting the local maxima of the signal using a custom designed algorithm [11], then generating a peak-to-peak interval time series, and finally interpolating at 4 Hz.

Regarding the estimation of the RR time series, the spectrogram (SP) of the HR and PR time series was employed. This time-frequency representation corresponds to the short-time Fourier transform given by

$$SP(t,w) = \left| \frac{1}{\sqrt{2\pi}} \int s(\tau) h(\tau - t) e^{-jwt} d\tau \right|^2 \quad (1)$$

where $s(t)$ represents the HR or PR signal of interest, $h(t)$ denotes the analysis window, and t and w correspond to the time and frequency variables, respectively. Hamming windows of 10 s were employed. Finally, RR time series were obtained for each SP via the first order moment (center of gravity) in frequency as follows

$$RR(t) = \frac{\int_0^{\frac{w_s}{2}} wSP(t,w)dw}{\int_0^{\frac{w_s}{2}} SP(t,w)dw} \quad (2)$$

where w_s corresponds to the sampling frequency ($2\pi \cdot 4$ rad/s), and $SP(t,w)$ to the spectrogram of the HR or RR time series. This time-frequency approach resulted in respiratory rate signals from ECG and iPPG, denoted as RR_{ECG} and RR_{iPPG}, respectively.

2.5 Performance Indices

To quantify the performance of the iPPG-based HR and RR estimates in comparison to the ECG-based ones, the cross-correlation coefficient (ρ) and the normalized root-mean-square error (NRMSE) were employed. In the case of the heart rate estimation (HR and PR, from ECG and iPPG respectively), these indexes correspond to

$$\rho_{HR} = \frac{\sum_{k=1}^{M} HR(k) \cdot PR(k)}{\sqrt{\sum_{k=1}^{M} (HR(k))^2 \cdot \sum_{k=1}^{M} (PR(k))^2}} \quad (3)$$

$$NRMSE_{HR} = \sqrt{\frac{\sum_{k=1}^{M} (PR(k) - HR(k))^2}{\sum_{k=1}^{M} (HR(k))^2}} \quad (4)$$

where M denotes the sample length of the HR and RR time series. Similar equations hold for the case of the RR estimation, but now between the RR_{ECG} and RR_{iPPG} time series.

3 Results and Discussion

Figure 3 shows an example of the HR estimated from ECG, and the PR estimated from iPPG, while Fig. 4 shows the corresponding RRs extracted by applying the time-frequency method to the HR and PR signals. Observe that heart rate modulation due to metronome respiration at 6 bpm is very evident in the HR and PR time series, and that RR estimates oscillate around the mean (6 bpm). The performance results for the heart rates and respiratory rates for all volunteers are summarized in Table 1, in terms of ρ and NRMSE mean $\pm$ SD values. For all metronome maneuvers, we found high average

correlation values equal to $\rho_{HR} = 0.9953$ and $\rho_{RR} = 0.9733$, and low average NRMSE equal to $NRMSE_{HR} = 0.0855$ BPM and $NRMSE_{RR} = 0.3074$ bpm.

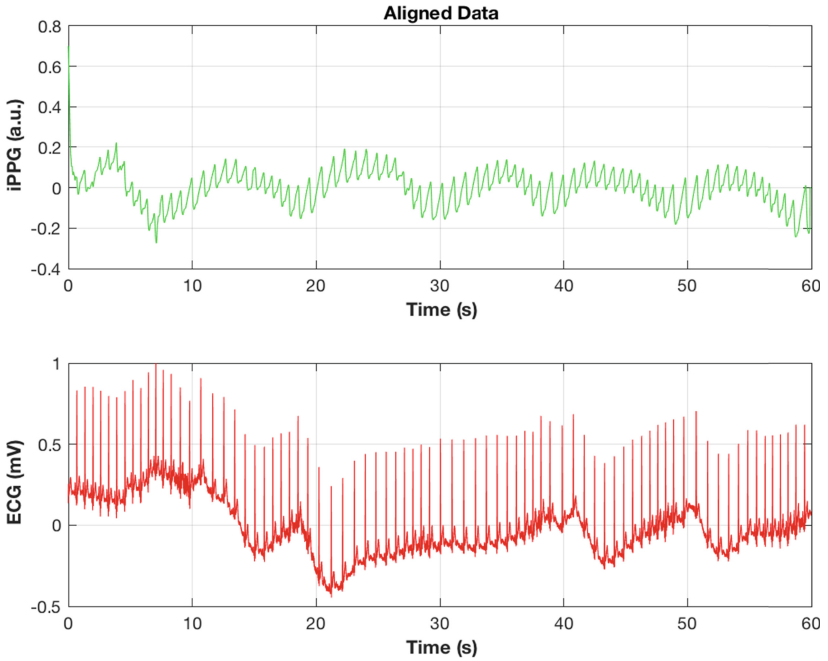

Fig. 2. Example of processed ECG and iPPG signals after resampling, alignment and filtering.

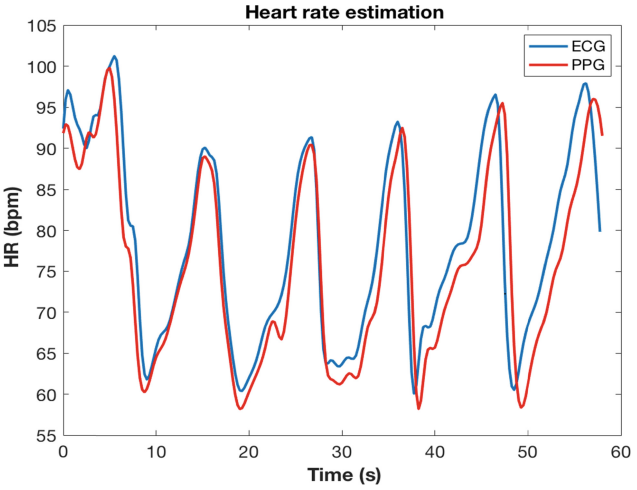

Fig. 3. Example of heart rate estimation from ECG signal (blue line) and from smartphone-acquired iPPG signal (red line).

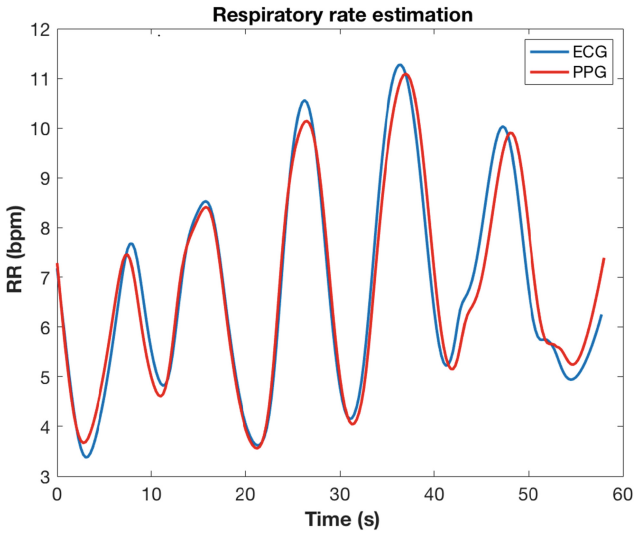

Fig. 4. Example of respiratory rate estimation from ECG signal (blue line) and from smartphone-acquired iPPG signal (red line). Volunteer was breathing at 6 bpm.

Table 1. Performance evaluation of heart rate and respiratory rated derived from iPPG signals compared to ECG-derived ones (N = 8)

Maneuver	ρ_{HR} (unitless)	$NRMSE_{HR}$ (BPM)	ρ_{RR} (unitless)	$NRMSE_{RR}$ (bpm)
3 bpm	0.9928 ± 0.0090	0.1060 ± 0.0794	0.9586 ± 0.0302	0.3520 ± 0.0878
6 bpm	0.9965 ± 0.0031	0.0750 ± 0.0378	0.9821 ± 0.0279	0.1796 ± 0.1326
18 bpm	0.9966 ± 0.0031	0.0755 ± 0.0423	0.9792 ± 0.0293	0.3907 ± 0.4209

4 Conclusions

In this work, we employed a contact approach for the simultaneous estimation of HR and RR using image photoplethysmograph signals from smartphone-acquired video sequences. We were able to accurately estimate HR and RR with high correlation coefficients and low NRMSE, in comparison to those derived via an ECG sensor. Besides the good results, our study had some limitations; for example, the reduced number of volunteers, the data acquisition while volunteers were resting, and the acquisition in indoor light conditions. We are currently working to improve the sample size and acquire data during other respiratory maneuvers and light conditions, e.g. during exercise and with high ambient light. As future work, our aim is to develop a smartphone application so that the estimation is provided on site. We consider that this and similar efforts could enable the general population to take more active control of their own healthcare with a potential improvement in costs, convenience, and quality.

Acknowledgments. The authors would like to thank CONACYT for the financial support through a Basic Science Grant (Ref. # 254637).

Conflicts of Interest. The authors declare no conflicts of interest.

References

1. Kannel, W.B., Kannel, C., Paffenbarger, R.S., Cupples, L.A.: Heart rate and cardiovascular mortality: the Framingham Study. Am. Heart J. **113**, 1489–1494 (1987). https://doi.org/10.1016/0002-8703(87)90666-1
2. Cretikos, M.A., Bellomo, R., Hillman, K., Chen, J., Finfer, S., Flabouris, A.: Respiratory rate: the neglected vital sign. Med. J. Aust. **188**, 657 (2008). https://doi.org/10.5694/j.1326-5377.2008.tb01825.x
3. Sun, Y., Thakor, N.: Photoplethysmography revisited: from contact to noncontact, from point to imaging. IEEE Trans. Biomed. Eng. **63**, 463–477 (2016). https://doi.org/10.1109/TBME.2015.2476337
4. Jonathan, E., Leahy, M.: Investigating a smartphone imaging unit for photoplethysmography. Physiol. Meas. **31**, N79 (2010). https://doi.org/10.1088/0967-3334/31/11/N01
5. Grimaldi, D., Kurylyak, Y., Lamonaca, F., Nastro, A.: Photoplethysmography detection by smartphone's videocamera. In: Intelligent Data Acquisition and Advanced Computing Systems (IDAACS), 2011 IEEE 6th International Conference, pp. 488–491. IEEE Press, New York (2011). https://doi.org/10.1109/idaacs.2011.6072801
6. Lázaro, J., Nam, Y., Gil, E., Laguna, P., Chon, K.H.: Respiratory rate derived from smartphone-camera-acquired pulse photoplethysmographic signals. Physiol. Meas. **36**, 2317 (2015). https://doi.org/10.1088/0967-3334/36/11/2317
7. Lázaro, J., Gil, E., Bailón, R., Mincholé, A., Laguna, P.: Deriving respiration from photoplethysmographic pulse width. Med. Biol. Eng. Comput. **51**, 233–242 (2012)
8. Nam, Y., Kong, Y., Reyes, B., Reljin, N., Chon, K.H.: Monitoring of heart and breathing rates using dual cameras on a smartphone. PLoS ONE **11**, e0151013 (2016). https://doi.org/10.1371/journal.pone.0151013
9. Campos-Delgado, D.U., Gutierrez-Navarro, O., Jo, J.A.: Linear unmixing of optic signals by extended blind end-member and abundance extraction. In: Latin America Optics and Photonics Conference 2018, p. Tu4A.12. OSA Publishing, Washington, D.C. (2018). https://doi.org/10.1364/laop.2018.tu4a.12
10. Vidaurre, C., Sander, T.H., Schlögl, A.: BioSig: the free and open source software library for biomedical signal processing. Comput. Intell. Neurosci. **2011**, 1–12 (2011). https://doi.org/10.1155/2011/935364
11. Lee, J., Reyes, B.A., McManus, D.D., Mathias, O., Chon, K.H.: Atrial fibrillation detection using an iPhone 4S. IEEE Trans. Biomed. Eng. **60**, 203–206 (2013). https://doi.org/10.1109/TBME.2012.2208112

Characterization of Forearm Electromyographic Signals for Automatic Classification of Wrist Movements

Milagros G. Salazar-Medrano(✉), Bersaín A. Reyes, Marco Mendoza, and Isela Bonilla

Faculty of Science, Autonomous University of San Luis Potosi, 78295 San Luis Potosi, SLP, Mexico
milagros.salazar@outlook.com

Abstract. In this work, three different classification methods (multilayer perceptron, support vector machine and decision tree) were used to automatically discern between six wrist movements (palmar flexion, palmar extension, radial deviation, ulnar deviation, supination and pronation of the hand) via time-domain and time-frequency features extracted from electromyographic signals (EMG) of the forearm muscles acquired in a multichannel fashion (eight channels). EMG signals of thirty ($N = 30$) healthy volunteers were acquired while they were performing consecutive repetitions of the six different wrist movements. Data processing included filtering, signal segmentation, feature extraction and classification using the above-mentioned methods. Finally, the results obtained with both time-domain and time-frequency features were compared. In the tests carried out with time-domain features up to 98% of correct classifications were obtained and up to 95% were obtained with the time-frequency features. These results look promising and we are currently working on their implementation in a robotic wrist rehabilitation system.

Keywords: Electromyography · Classification · Time-domain features · Time-frequency features

1 Introduction

In recent years, great importance has been given to research focused on helping people with disabilities through contributions for the control of prostheses and orthoses (exoskeletons), where one of the most important factors has been the ability to intuit the user's intention to perform a certain activity [1]. One of the tools that has been used the most to achieve this objective is the EMG signals coming from the muscles involved in the generation of a certain type of movement. Thus, EMG has become a very important tool in pattern recognition because it can be easily and non-invasively acquired, and it provides temporal and spectral information about neuromuscular activity present in the active

© Springer Nature Switzerland AG 2020
C. A. González Díaz et al. (Eds.): CLAIB 2019, IFMBE Proceedings 75, pp. 71–78, 2020.
https://doi.org/10.1007/978-3-030-30648-9_10

muscle, which corresponds to the spatio-temporal sum of the activity of smaller motor units. Currently, research in this area is aimed at finding algorithms for processing, characterization and classification of EMG signal patterns that allow the analysis and determination of the type of movement [2].

In 2011, Ahsan et al. extracted EMG signals using mean absolute value (MAV), zero crossing (ZC), slope sign change (SSC), root mean square (RMS), variance (VAR) and standard deviation (SD), and reported the detection of different hand motions (left, right, up and down) using an artificial neural network (ANN) with an average classification efficiency of 88.4% [3]. In 2015, Gokgoz and Subasi presented a framework for classification of EMG signals using multiscale principal component analysis (MSPCA) for denoising, discrete wavelet transform (DWT) for feature extraction and decision tree algorithms for classification and achieved the best performance using k-fold cross-validation with 96.67% total classification accuracy [4]. In 2018, Oluwarotimi et al. proposed a set of time-domain features to characterize EMG patterns by classifying arm movements in amputees, achieving an average classification accuracy of $92 \pm 3.11\%$ [5]. The present proposal is oriented to the recognition of 6 movements that seek significant improvements in the average success percentage. In this work, forearm EMG signals were analyzed in order to identify movement intention (flexion-extension, abduction-adduction, supination-pronation) by characterizing these with temporal and time-frequency techniques and comparing both results for their future implementation in assistive devices.

2 Methods and Materials

2.1 Acquisition of EMG Signals

Signals from thirty ($N = 30$) healthy volunteers between 20 and 25 years old were acquired. The Myo Armband (Thalmic Labs, Canada) was used for the acquisition of the EMG signals, which is a device that has eight electromyographic non-invasive medical grade sensors, a gyroscope, accelerometer and three-axis magnetometer, as well as an amplification and filtering system for the acquisition of EMG signals, with a sampling frequency of 200 Hz and information transfer using Bluetooth 4.0 technology [6]. Although the sampling frequency seems to be low for EMG applications, it was higher when provided by the Myo Armband system, which in turn has been used for classification purposes. Acquired signals were transmitted via Bluetooth from the Myo Armband to a personal computer using the Myo Data Capture software provided by the manufacturer (Thalmic Labs, Canada).

The maneuvers performed in the protocol were: (1) palmar flexion and extension in the wrist, (2) radial and ulnar deviation, and (3) supination and pronation of the hand. 10 consecutive repetitions were performed at a frequency of 55 repetitions per minute for each movement with a resting time of 10 seconds between each maneuver. In Fig. 1 the acquisition protocol is illustrated and, as an example, some acquired signals are shown.

2.2 Pre-processing of EMG Signals

Each of the eight EMG signals was rectified and normalized, then segmented and labeled for each repetition of the movements. The algorithm extracts the EMG envelope by means of a second order Butterworth low pass filter with a cutoff frequency of 2 Hz. Subsequently, the signal was thresholded by a lower and upper level, which were established according to the mean of baseline noise for the first seconds of acquisition while resting the forearm. In order to define the muscle activity segments, a threshold of 80 samples was established, representing 400 ms of muscle activity, which is sufficient for the identification of movement patterns [7]. As a result, a rectangular signal was generated indicating the existence of muscular activity within the threshold range. Based on the computed activity indices, each type of movement was labeled for each segment.

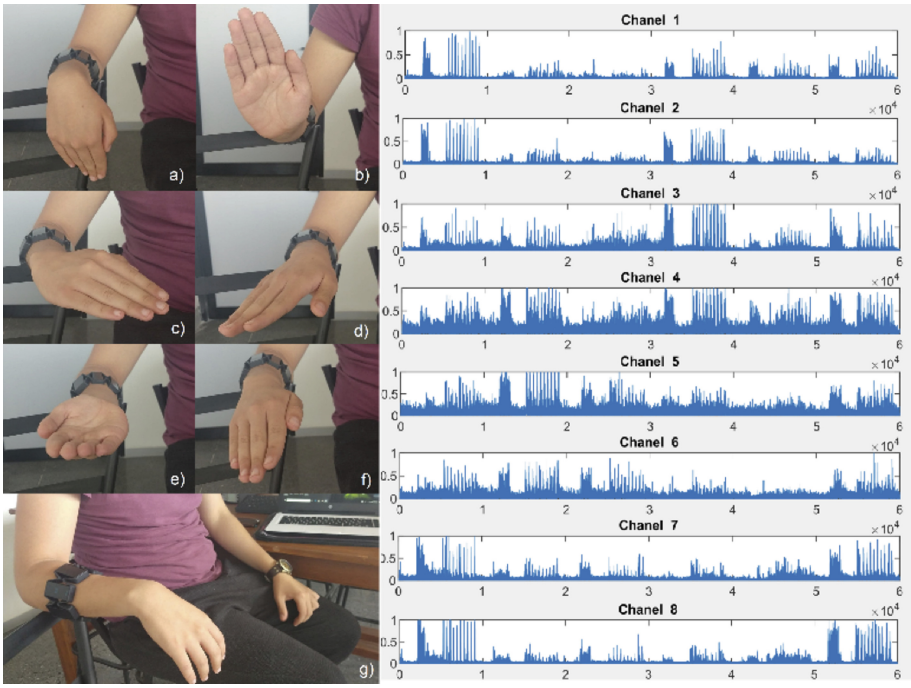

Fig. 1. Movements performed during the acquisition protocol (left): (a) Flexion, (b) Extension, (c) Radial deviation, (d) Ulnar deviation, (e) Supination, (f) Pronation, (g) Repose. Forearm EMG signals acquired through the eight channels of the Myo Armband (right), which appear rectified and normalized.

2.3 Temporal Characterization of EMG Signals

Each labeled EMG segment was characterized in time by the following parameters: (1) mean absolute value (MAV), (2) standard deviation (σ), (3) variance (σ^2), and

(4) root mean square (RMS), whose definitions can be found in the traditional literature [8].

2.4 Time-Frequency Characterization of EMG Signals

The time-frequency characterization was performed from the gray level co-occurrence matrix (GLCM) of the time-frequency representation given by the spectrogram (SP), which in turn is defined as the squared magnitude of the short-time Fourier transform (STFT), i.e.,

$$\mathrm{SP}\,(t, w) = \left| \frac{1}{\sqrt{2\pi}} \int s(\tau)\; h(\tau - t) e^{-jwt} d\tau \right|^2 \tag{1}$$

where $h(t)$ represents the analysis window used to focus on a temporal and spectral area of the signal $s(t)$, and t and w correspond to time and frequency variables, respectively. Thus, the SP of each labeled EMG segment was obtained (see Fig. 2) using Hamming windows of 100 ms, while the number of frequency bins was set to 1024.

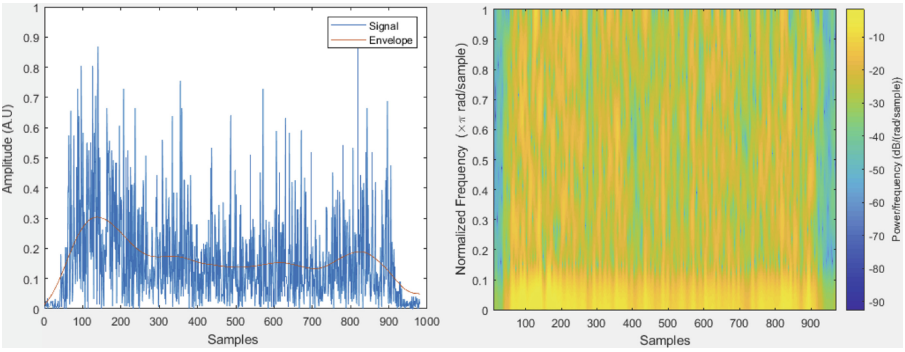

Fig. 2. Muscle activation segment (blue line) and envelope (red line) (left). Spectrogram of muscle activation segment (right).

The GLCM describes the frequency at which a gray level value appears in a specific spatial relationship with another gray value within the area of a given window [9]. For each SP obtained, the GLCM was calculated in four directions (0, 45, 90 and 135°). Once the GLCM (denoted by $C_{i,j}$) were obtained, the time-frequency characterization was carried out by calculating the following measurements in each direction:

– **Energy.** Measurement of local homogeneity described by:

$$C_1 = \sum_{i,j} {C_{i,j}}^2 \tag{2}$$

– **Entropy.** This measures the randomness of an image, reaching its maximum when all the elements of the co-occurrence matrix are equal. It is described by:

$$C_2 = \sum_{i,j} -C_{i,j} \log_2 [C_{i,j}] \tag{3}$$

– **Inertia (contrast).** This is a measurement of local variation in an image described by:

$$C_3 = \sum_{i,j} (i-j)^2 C_{i,j} \tag{4}$$

– **Correlation.** This measures the similarity of an image with itself but displaced and it is described as:

$$C_4 = \frac{C_2 - H_{xy}}{\max(H_x, H_y)} \tag{5}$$

where

$$H_x = -\sum_i S_x(i) \log_2 [S_x(i)], \qquad S_x(i) = \sum_j C_{i,j} \tag{6}$$

$$H_y = -\sum_j S_y(j) \log_2 [S_y(j)], \qquad S_y(j) = \sum_i C_{i,j} \tag{7}$$

$$H_{xy} = -\sum_{ij} C_{i,j} \log_2 \left[S_x(i) S_y(j) \right] \tag{8}$$

2.5 Classification of Movements from EMG Signals

The classification of wrist movements was carried out with the free software Weka (University of Waikato, Hamilton, New Zealand), where three types of classifiers were used: neural networks, support vector machines and decision trees, which are described below. As a performance measurement of the classifiers, accuracy was used in the classification of each pair of complementary movements (flexion-extension, abduction-adduction and supination-pronation). A k-fold cross validation scheme ($k = 10$) was employed to evaluate the performance of the classifiers.

Neural Network (Multilayer Perceptron). This has a non-linearity in the output and layers of hidden neurons using supervised training. It uses the back-propagation algorithm of error based on error-correction learning [10]. A network with two layers of hidden neurons with 11 and 6 neurons, respectively, was used.

Support Vector Machine. This is based on the projection of a n-dimensional data set to a higher dimensional space by applying a kernel function [11]. From the new created space, the data will be operated as a linear problem without

considering the dimensionality of the data. The Polynomial Kernel was used and is described by:

$$k(x, y) = (\alpha x^T y + c)^d \tag{9}$$

where α is a user-specified scalar parameter, x represents the vector of features, y is the support vector data, and $c \geq 0$ is a free parameter trading off the influence of higher-order versus lower-order terms in the polynomial [12]. In particular, a linear model ($d = 1$) was employed. Radial basis function kernel was also employed but better results were obtained with the polynomial kernel, which are reported in this paper.

Decision Tree. Non-parametric supervised inductive learning technique where logical construction diagrams are built from a database which serve to categorize a series of conditions that occur repetitively for the solution of a problem [13]. A J48 algorithm that built a tree with 8 leaves and 15 nodes was used.

3 Results and Discussion

Classification was performed on a channel basis. The average results obtained for the eight EMG channels are presented by the time-domain (Table 1) and time-frequency (Table 2) features for the 30 test volunteers below. For the support vector machine, the model parameters which provided better results were $\alpha = [-4.2021, 1.982, -1.5316, -1.4258]$ and $c = 1.3971$.

Table 1. Classification accuracy (%) obtained by time-domain features for all channels ($N = 30$ volunteers).

Classifier	Flexion-Extension	Abduction-Adduction	Supination-Pronation
Multilayer perceptron	84.482 ± 10.12	72.268 ± 7.41	71.703 ± 6.97
Support vector machine	84.084 ± 9.54	72.829 ± 7.43	71.062 ± 6.88
Decision tree	83.907 ± 10.24	73.109 ± 7.45	70.115 ± 6.55

Values presented as mean $\pm$ standard deviation.

It is observed that on average the lowest classification performance was obtained for the supination-pronation movements. Statistical comparison between accuracies from temporal and time-frequency features were performed via paired t-test with $p < 0.05$ considered as significant. In general, except for the supination-pronation movements, the classification accuracy obtained using temporal features for the analyzed signals were not statistically significantly superior to the results obtained using time-frequency features. In the particular case of abduction-adduction classification, the obtained p-value for the multilayer perceptron was $p = 0.04$.

Table 2. Classification accuracy (%) obtained by time-frequency features for all channels ($N = 30$ volunteers).

Classifier	Flexion-Extension	Abduction-Adduction	Supination-Pronation
Multilayer perceptron	79.166 ± 7.67	67.823 ± 6.18 #	68.320 ± 6.98 #
Support vector Machine	80.555 ± 8.81	69.085 ± 5.87	69.084 ± 5.98 #
Decision tree	79.629 ± 10.4	69.791 ± 6.062	67.557 ± 5.61 #

Values presented as mean ± standard deviation.
# denotes statistically significant differences in comparison with time domain features ($p < 0.05$).

4 Conclusions

The use of tools such as the Myo Armband in conjunction with the classification techniques studied in this work can be very useful for the control of assistive devices, since the bracelet provides relevant information related to forearm and wrist movements. This is due to the fact that the eight channels almost completely encompass the area and easily capture EMG signals from a large part of the muscles involved in the movements, as well as its structure and practicality being a wireless device that does not cause user discomfort.

In this work, three types of complementary movements were explored (flexion-extension, abduction-adduction, supination-pronation), and the classification was performed in pairs of complementary movements for each channel. As each channel acquires a different EMG signal for each movement, it is necessary to recognize the channel number that provides more useful information in order to make a more successful classification for a particular movement.

The use of temporal features provides favorable classification results and due to their easy implementation, they can be very useful in real-time classification algorithms. In the literature it has been mentioned that the use of time-frequency features has improved results in EMG-signal pattern recognition; however, in this project the same performance between both types of features was obtained in general, except for supination-pronation movements which in turn appear to be the most challenging case. As future work, it is intended to integrate a real-time EMG classification algorithm for the control of a robotic device for wrist rehabilitation.

Conflict of Interest. The authors declare that there is no conflict of interest.

References

1. Hussein, S.E., Granat, M.H.: Intention detection using a neuro-fuzzy emg classifier. IEEE Eng. Med. Biol. Mag. **21**(6), 123–129 (2002). https://doi.org/10.1109/MEMB.2002.1175148

2. Ferguson, S., Dunlop, G.R.: Grasp recognition from myoelectric signals. In: Proceedings of the Australasian Conference on Robotics and Automation, vol. 1, Auckland, New Zealand (2002)
3. Ahsan, M.R., Ibrahimy, M.I., Khalifa, O.O.: Neural network classifier for hand motion detection from EMG signal. In: 5th Kuala Lumpur International Conference on Biomedical Engineering 2011, Kuala Lumpur, Malaysia, pp. 536–541. Springer, Heidelberg (2011). https://doi.org/10.1007/978-3-642-21729-6_135
4. Gokgoz, E., Subasi, A.: Comparison of decision tree algorithms for EMG signal classification using DWT. Biomed. Signal Process. Control **18**, 138–144 (2015). https://doi.org/10.1016/j.bspc.2014.12.005
5. Samuel, O.W., Zhou, H., Li, X., Wang, H., Zhang, H., Sangaiah, A.K., Li, G.: Pattern recognition of electromyography signals based on novel time domain features for amputees' limb motion classification. Comput. Electr. Eng. **67**, 646–655 (2018). https://doi.org/10.1016/j.compeleceng.2017.04.003
6. Yang, C., Chen, J., Chen, F.: Neural learning enhanced teleoperation control of baxter robot using IMU based motion capture. In: 2016 22nd International Conference on Automation and Computing (ICAC), pp. 389–394. IEEE, Colchester (2016). https://doi.org/10.1109/IConAC.2016.7604951
7. Birkedal, L., Collet, T., Dagilis, S., Delavernhe, G., Emborg, J., Jørgensen, A.: Pattern recognition of upper-body electromyography for control of lower limb prostheses. Aalborg University, Institute of Electronic Systems (2002)
8. Torres-Hernández, A., Amaro-Amaro, B., Ramírez-Vera, V., Mendoza-Gutiérrez, M., Bonilla-Gutiérrez, I.: Cuantificación del avance en terapia de rehabilitación de miembros superiores mediante el uso de una interfaz háptica y realidad aumentada. In: Memorias del Congreso Nacional de Ingeniería Biomédica. vol. 2, pp. 297–300 (2015), https://doi.org/10.24254/CNIB.15.48
9. Presutti, M.: La matriz de co-ocurrencia en la clasificación multiespectral: tutorial para la enseñanza de medidas texturales en cursos de grado universitario. 4ª Jornada de Educação em Sensoriamento Remoto no Âmbito do Mercosul (2004)
10. Haykin, S.: Neural Networks: a Comprehensive Foundation. Prentice Hall PTR, Englewood Cliffs (1994)
11. Alpaydin, E.: Introduction to Machine Learning. MIT press, London (2009)
12. Achirul Nanda, M., Boro Seminar, K., Nandika, D., Maddu, A.: A comparison study of kernel functions in the support vector machine and its application for termite detection. Information **9**(1), 5 (2018). https://doi.org/10.3390/info9010005
13. Solarte-Martínez, G.R., Soto-Mejía, J.A.: Árboles de decisiones en el diagnóstico de enfermedades cardiovasculares. Scientia et technica **16**(49), 104–109 (2011)

Correlation of EEG Brain Waves in a Time Perception Task

Sergio Rivera-Tello[1], Rebeca Romo-Vázquez[2(✉)], and Julieta Ramos-Loyo[1]

[1] Instituto de Neurociencias, CUCBA, Universidad de Guadalajara, Guadalajara, Mexico
[2] Departamento de Ciencias Computacionales, CUCEI, Universidad de Guadalajara, Guadalajara, Mexico
rebeca.romo@academicos.udg.mx

Abstract. The perception of time is a fundamental part of our daily life. Several studies have reported that time estimation involves the communication and synchronization of neural assemblies that decode the duration of time. Therefore, the purpose of the present study is to evaluate the interaction between different brain areas during time estimation. Brain electrical activity was recorded during a time perception task and correlation matrices were calculated using different frequency bands. Graph networks show an important contribution of fronto-central regions and left hemisphere. The estimation of time could involve the recruitment of attentional resources and the inhibition of motor responses to make a temporal prediction, by this way possibly monitoring the "flow of time".

Keywords: Time perception · Brain activity · EEG · Connectivity · Correlation

1 Introduction

The human brain is a complex network of interconnected fibers that communicate between each other through electrical oscillations. This synchronic activity inside a neuronal network can be detected with electrophysiological techniques such as the electroencephalogram (EEG) [1]. The construction of informative networks that reflect brain connectivity requires the establishment of nodes and statistical dependencies, where each node represents a neural population [2]. Usually the functional connectivity uses correlation, phase synchronization, coherence, among other measures to trace the links that show the degree of connection between these neural populations.

Traditionally, the Pearson's correlation coefficient is used to calculate the similarity between two EEG signals, therefore, a possible functional connection between them. In order to observe the global functionality of the brain, it is necessary a connectivity matrix, obtained from the Pearson's correlations coefficients of several electrodes placed across the scalp. Once the connectivity matrix is calculated, it is required to set a threshold to determine an adjacency matrix [3]. This matrix represents the connections of a pair of electrodes, so the values that surpass a determined threshold are the ones

© Springer Nature Switzerland AG 2020
C. A. González Díaz et al. (Eds.): CLAIB 2019, IFMBE Proceedings 75, pp. 79–84, 2020.
https://doi.org/10.1007/978-3-030-30648-9_11

that will be represented in a graph network. However, functional connectivity of specific cognitive process could require the subtraction of a basal state, in favor of representing only the process of interest and in this way calculate the corresponding adjacency matrix.

To determine functional connectivity from electrophysiological data it is only required the EEG signals of interest. Nevertheless, one interesting approach is separating the EEG signal into different frequency waves. By filtering the entire EEG signal into different frequency bands, more information related to oscillatory activity can be observe and in this way reflecting the functional organization of the bran in specific cognitive processes, such as time perception.

The perception of time is a fundamental aspect of our daily life, it is involved in various cognitive processes and in the timing of motor actions. However, time itself is an intangible thing that the brain is unable to perceive, making it a subjective construct dependent of the level of attention [4, 5]. Humans anticipate and deploy their attention when an important event is expected, this feeling of expectancy of the immediate future and remembrance of near past is what gives the sense of flowing time [6]. Among species, being able to predict the future improves the chances of survival and evolution has selected the neural structures and mechanisms that allow it [7].

The estimation of time involves a complex network of cortical and subcortical structures, where it has been described a thalamocortical network as responsible for the timing of motor actions [8]. This network involves structures such as thalamus, basal ganglia, prefrontal cortex, posterior parietal cortex and cerebellum. Studies in monkeys reveals and important contribution of the putamen, which triggers beta activity towards the motor cortex [9]. Recently, the supplementary motor area (SMA) has been demonstrated to be at the core of timing actions in humans, where alpha and beta waves play and important role in the expectancy and inhibition of precise temporal movements [10]. However, it is still unclear the exact nature of the flow of information in different frequency bands across the cortex.

2 Materials and Methods

2.1 Participants

Ten healthy right-handed male individuals participated (n = 10), age between 22–30 years old as the inclusive requirements to participate in the study. None had any history of neurological or psychiatric disorders according to a clinical questionnaire and with no musical education (due to possible high temporal production experience). All subjects signed an informed consent form before participating in this research. The study was approved by the ethical committee of the Institute of Neuroscience, where all the experimental procedures were implemented.

2.2 Brain Electrical Activity Recording

Electrodes were placed in 32 locations according to the 10–10 International System, using an Electro-Cap: Fp1, Fp2, Afz, F7, F3, Fz, F4, F8, FT7, FC3, FCz, FC4, FT8,

T7, C3, Cz, C4, T8, TP7, CP3, CPz, CP4, TP8, P7, P3, Pz, P4, P8, POz, O1, Oz and O2, with linked earlobes as references. The amplifier used was a Neuronic Medicid®, impedances were kept below 10 kΩ at 500 Hz of sampling rate and line filters between 0.5–50 Hz. EEG activity was recorded in experimental (time production task, Fig. 1) and basal condition or resting state (participants were asked to keep eyes open and to make minimum movement for one minute before the start of the task).

Fig. 1. EEG equipment and participant performing the time production task during signal recording.

2.3 Time Production Task

The task used consisted in estimating a duration interval of 2.5 s, by clicking a button of a computer at the start and end of such time interval [10]. We used a time interval of 2.5 s due to the importance of measure a subjective cognitive process and because this interval makes it difficult for participants to count. In a monitor the participants could see a gray circle, this circle turned to green when they click the beginning of the time interval and it returned to gray every time they finished their estimation. The start of each trial was voluntary, every time the individual wanted to start and feel ready to estimate. They were asked to make the minimum movement or eye blinking as possible. The task consisted of 40 trials, which only 30 free artifact windows were analyzed. Before the experimental session the participant were trained (50 trials) to produce the 2.5 intervals by giving them visual feedback of their accuracy, five circles presented in the monitor indicated the precision after each trial, the middle circle represented a response between 2.4–2.6 s, while left and right circles represented 2.2–2.4 and 2.6–2.8 and extreme left and right circles represented less or more than 2.2 and 2.8 respectively.

2.4 EEG Analysis

Epochs consisted in 500 ms before the start of the trial to 3000 ms after and they were free of eye blinking and movement artefacts. In a first step the Pearson's correlation (Eq. 1) coefficients of a 32 × 32 matrix were calculated (Fig. 2) with the EEG data averaged by trial and then by subject with all the frequencies (0.5–50 Hz).

$$\rho(A,B)=\frac{1}{N-1}\sum_{i=1}^{N}\left(\frac{\overline{A_i-\mu_A}}{\sigma_A}\right)\left(\frac{B_\iota-\mu_B}{\sigma_B}\right) \quad (1)$$

where (*A, B*) are a pair of electrodes.

After, the epochs were filtered and separated by different frequency bands: delta (1.5–3.5 Hz), theta (4–7.5 Hz), alpha (8–12 Hz), beta (13–29 Hz) and gamma (30–40 Hz), using a Butterworth filter of fourth order. Correlation matrices were calculated of the resulting filtered epochs and then the average of correlation coefficients by trial and then by subject were calculated. After computing correlation matrices of different frequency bands, the same procedure was used for basal EEG data. Later, correlation matrices of time estimation condition of each frequency band were subtracted by the ones of basal condition ($\Delta_r = r_{te} - r_b$, time perception r_{te} and basal condition r_b). The distribution of this correlation difference is presented in Fig. 2. Adjacency matrices of correlation differences were calculated by thresholding the Δ_r values upper to zero, color scale was set from zero to two standard deviations, so the strong yellow colors represent the most significant connections. Graphs were obtained with the adjacency matrices using a MATLAB toolbox [11].

3 Results

Connectivity matrix of EEG data of all frequency bands reveals an important correlation between fronto-central regions and in the same way between occipital areas, whereas between temporal regions show low correlation and between fronto-occipital region none correlation at all (see Fig. 2). However, the difference of correlation coefficients of time estimation and basal conditions in separated frequency bands shows different patterns. The delta and alfa bands exhibit correlation between frontal and central regions. Theta band displays these same frontocentral correlation, but in a lesser

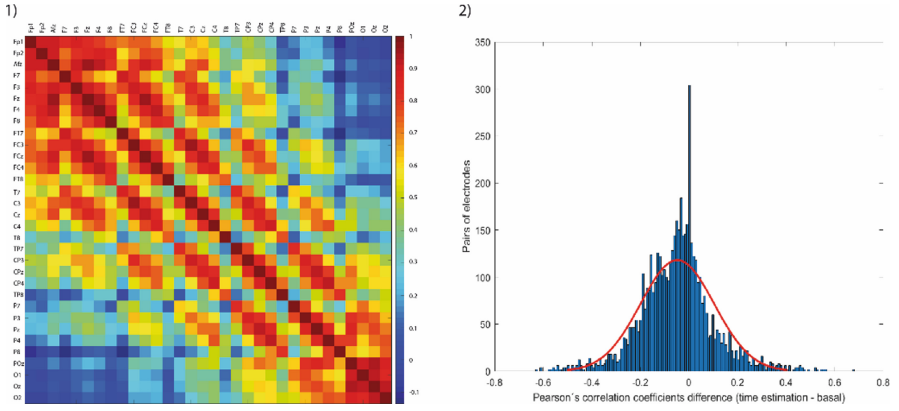

Fig. 2. Correlation matrix of 32 electrodes of EEG data with all frequency bands in the time perception condition. Warm colors represent a higher correlation coefficient. (2) Distribution of Pearson's correlation coefficient difference $\Delta_r = r_{te} - r_b$, time perception (r_{te}) and basal condition (r_b) of the five frequency bands.

extent. Furthermore, beta and gamma bands exhibit connections between fronto-central regions, particularly, beta band shows higher correlation within the left hemisphere. Graphs obtained from the adjacency matrices for each frequency band are represented with a scale from blue to yellow colors, representing the strength of the connection; yellow colors represent higher correlation than the blue colors (see Fig. 3). Graphs reveal and important correlation of fronto-central areas, especially it seems to be an important hub for delta, alpha and gamma bands.

Behavioral results show an overestimation of the fixed 2.5 s interval in the average of 40 trials per subject (*M = 3.14, SD = 0.47*). However, it is observed a low variability between trials, but high variability between individuals.

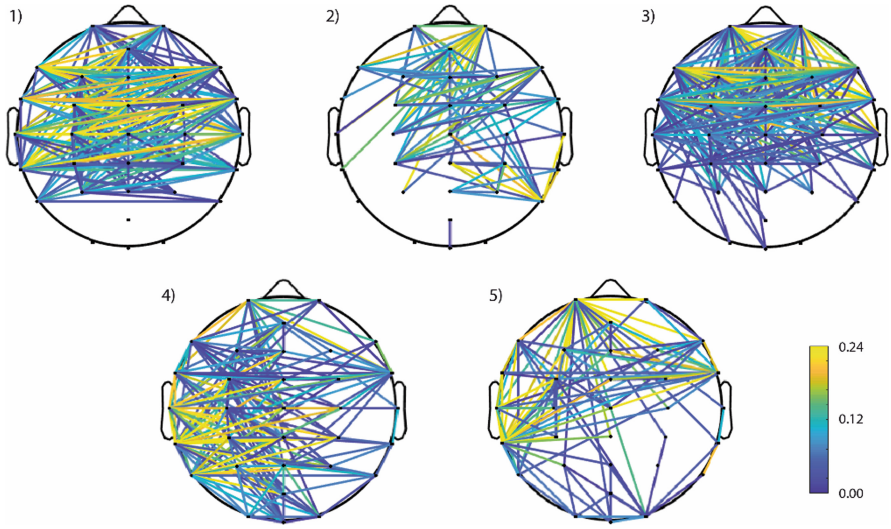

Fig. 3. Graphs representing adjacency matrix of correlation between pairs of electrodes. Each network represents delta (1), theta (2), alpha (3), beta (4) and gamma (5) frequency bands. Yellow colors represent higher Δ_r correlation coefficients that the blue colors.

4 Conclusion

The differentially coordination of the frequency bands reveals and important role of frontal areas in realization of the consciously estimation of time. Probably due to the high level of attention and alertness required in this task, executive functions could play and important role, in particular, the delta, alpha and gamma frequency bands and in a lesser extent theta band. Also, important to note is that these frontal regions show high correlation with central areas, where motor cortex plays and important role in the timing of motor actions by producing time intervals. Interestingly, it seems to be a left coordination in beta and gamma activity, probably related to motor beta by producing finger clicking as participants were right handed.

The correlation coefficient reflects statistical linear dependencies between two signals, by calculate them for several frequency bands hidden information related to specific cognitive processes comes out. However, it is needed to study how this information behaves with other measures, such as phase locking value [12] and coherence [1], due to previous reports finding similarities between them [13].

In conclusion, the estimation of time involves the recruitment of attentional resources to make a temporal prediction, where frontal areas coordinate executive functions to maintain some level of alertness and possibly monitoring the "flow of time" with some working memory mechanisms. Moreover, an important role of pre-motor area (left fronto-central) is observed, possibly because a constant participation of a mechanisms of motor inhibition, which is involve in the expectancy of near future events.

References

1. Bowyer, S.: Coherence a measure of the brain networks: past and present. Neuropsychiatric Electrophysiol. **2**, 1 (2016). https://doi.org/10.1186/s40810-015-0015-7
2. Sporns, O.: Networks of the Brain, 1st edn. MIT Press, Cambridge (2010)
3. Jaili, M., Knyazeva, M.: Constructing brain functional network from EEG: partial and un-partial correlations. Integr. Neurosci. **10**(02), 213–232 (2011). https://doi.org/10.1142/S0219635211002725
4. Eaglemann, D.: Human time perception and its illusions. Curr. Opin. Neurobiol. **18**(2), 131–136 (2008). https://doi.org/10.1016/j.conb.2008.06.002
5. Treisman, M.: Temporal discrimination and the indifference interval: Implications for a model of the "internal clock". Psychol. Monogr. Gen. Appl. **77**(13), 1–31 (1963). https://doi.org/10.1037/h0093864
6. Buonomano, D.: Your brain is a time machine. The neuroscience and physics of time. 1st edn. W. W. Norton & Company (2017)
7. Rovelli, C.: The Order of Time. 1st edn. Riverhead books (2018)
8. Buhusi, C., Meck, W.: What makes us tick? functional and neural mechanisms of interval timing. Nat. Rev. Neurosci. **6**(19), 755 (2005). https://doi.org/10.1038/nrn1764
9. Bartolo, R., Merchant, H.: Beta oscillations are linked to the initiation of sensory-cued movement sequences and the internal guidance of regular tapping in the monkey. J. Neurosci. **35**(11), 4635–4640 (2015). https://doi.org/10.1523/JNEUROSCI.4570-14.2015
10. Kononowicz, T., Van Rijn, H.: Single trial beta oscillations index time estimation. Neuro-Psychologia **75**, 381–389 (2015). https://doi.org/10.1016/j.neuropsychologia.2015.06.014
11. Connected topoplot Graph toolbox MathWorks Homepage. https://la.mathworks.com/matlabcentral/fileexchange/32563-connected-topoplot. Accessed 04 May 2019
12. Lachaux, J., Rodriguez, E., Martinerie, J., Varela, F.: Measuring phase synchrony in brain signals. Hum. Brain Mapp. **8**(4), 194–208 (1999). https://doi.org/10.1002/(SICI)1097-0193(1999)8:4%3c194:AID-HBM4%3e3.0.CO;2-C
13. Mazeiova, K., Palus, M.: Comparison of coherence and phase synchronization of the human sleep electroencephalogram. Clin. Neurophysiol. **123**(9), 1821–1830 (2012). https://doi.org/10.1016/j.clinph.2012.01.016

Estimation of Beta Burst Durations from Subthalamic Nucleus Local Field Potentials in Parkinson's Disease Through Hilbert and Continuous Wavelets Transforms

Arnaldo Fim Neto[1,4(✉)], Julia Baldi De Luccas[1,4], Bruno Leonardo Bianquenti[1,4], Tiago Paggi Almeida[5], Maria Sheila Rocha[2], Takashi Yoneyama[5], Fabio Luiz Franceschi Godinho[1,2,3], and Diogo Coutinho Soriano[1,4]

[1] Center of Engineering, Modeling and Applied Social Sciences (CECS), Federal University of ABC (UFABC), São Paulo, SP, Brazil
arnaldo.fim@ufabc.edu.br
[2] Neurology and Functional Neurosurgery, Santa Marcelina Hospital, São Paulo, SP, Brazil
[3] Functional Neurosurgery Division, University of São Paulo, São Paulo, SP, Brazil
[4] Brazilian Institute of Neuroscience and Neurotechnology (BRAINN), Campinas, SP, Brazil
[5] Signal Processing Laboratory, Aeronautics Institute of Technology, Sao Jose dos Campos, Brazil

Abstract. Parkinson's disease (PD) has a high impact on motor and cognitive impairment. Recent studies have suggested that abnormal beta band activity (13–35 Hz) in local field potentials (LFP) within the Subthalamic Nucleus (STN) are associated with PD's symptoms. Moreover, these oscillations are characterized by non-stationary behavior throughout the LFP defined as beta bursts. Despite of the currently widespread framework for evaluating beta bursts based on Continuous Wavelet Transform (CWT) coefficients, a carefully methodological investigation is required, especially when dealing with shorter intraoperative recordings in the context of deep brain stimulation (DBS). Aiming to investigate methodological dependence in beta burst detection, this work presents a comparison between wavelets analysis *vs*. Hilbert Transform (HT) magnitude for beta bursts duration evaluation considering different percentiles thresholds. Signals from 17 hemispheres of 12 tremor dominant PD patients undergoing stereotaxic surgery under rest and movement conditions were investigated. Bursts durations evaluated by both methods were capable of detecting significant differences between rest *vs*. movement conditions, depending on the adopted percentile threshold. These results point to a better comprehension of beta burst activity under daily motor tasks as also reveals a methodological dependence on burst characterization, being the HT method more prone to detect beta bursts with shorter durations in contrast to CWT.

Keywords: Parkinson's disease · Deep brain stimulation · Beta burst · Morlet wavelet · Hilbert transform

© Springer Nature Switzerland AG 2020
C. A. González Díaz et al. (Eds.): CLAIB 2019, IFMBE Proceedings 75, pp. 85–90, 2020.
https://doi.org/10.1007/978-3-030-30648-9_12

1 Introduction

Parkinson's disease (PD) entails in progressive motor and cognitive impairment, being the Deep Brain Stimulation (DBS) procedure accepted as the standard treatment for controlling the motor symptoms and improving life quality for pharmacological-resistant patients [1, 2]. Intraoperative procedure for electrodes implanting allows access of local field potentials (LFPs) in the motor portion of the Subthalamic nucleus (STN), which is valuable for defining electrophysiological markers modulated under different conditions (rest, movement, pharmacological treatment, etc.) in PD. Recently, it has been shown that intermittent elevated STN beta activity (13–35 Hz) – the beta bursts - is associated with motor impairment [3, 4], being the bursts durations and amplitudes crucial on this condition. In particular, different beta sub-bands - low beta (13–22 Hz) and high beta (22–35 Hz) seems to play a key role under rest [5] and movement [6] conditions and may define the cornerstone for the proposal of an adaptive DBS system. The beta burst activity in these sub-bands has been analyzed in terms of Morlet wavelet analysis, although a carefully methodological approach is still required for characterizing the effect of different strategies and thresholds for bursts evaluation, especially when different experimental procedures for accessing STN signals are considered. This work aims to present a comparison between low and high beta bursts durations in PD patients during rest and movement conditions by means of Continuous Wavelet Transform (CWT) and Hilbert Transform (HT) methods under different thresholds for burst definition. Whereas the CWT has been employed as standard approach to describe temporal evolution of the beta bursts [3–6], the HT classically outlines for LFP signal envelope evaluation, which has not been deeply investigated. In fact, as CWT and HT imply in convolving the signal with different functions, it is natural that methodological dependences could raise on beta burst evaluation, as shown here. These methodological differences may lead to parameters adjustment requirements (e.g. beta burst threshold definition) and to deal with different burst duration distributions, in which significant differences between movement and rest conditions can still be detected but in different burst duration bins.

2 Materials and Methods

2.1 Electrophysiological Study and Data Collection

All patients were clinically diagnosed with PD by a specialist at Movement Disorders Outpatient Clinic at Santa Marcelina Hospital (São Paulo, Brazil). All patients were classified either as Tremor Dominant (TD) or as tremor and postural instability/gait difficulty (PIGD) following the "Unified Parkinson's Disease Rating Scale" from the "Movement Disorders Society" (MDS-UPDRS). The study was approved by the local ethical committee (CAAE: 62418316.9.2004.0066). Only TD patients were included in this study. The cohort was composed of 8 males and 4 females with mean age of 55 years (range of 41 until 69) in which 5 of these PD patients the LFP were bilaterally recorded (i.e. both right and left brain hemispheres), implying in 17 electrophysiological signals, typically characterized by an increase in both signal baseline and spikes

firing rate. Intraoperative MRI and tomography scans were used to define the trajectory towards the STN sensorimotor region and guide the stereotaxic surgery in all patients.

Signals were recorded within the anatomical target through (1 kΩ) macroelectrodes (Medtronic – Minneapolis – USA) [2] during the rest and movement conditions. The LFP were recorded during 60 s at 24 kHz, band-pass filtered (0.5–5.0 kHz) and downsampled (decimation method) to 1 kHz, followed by a notch filter at 60 Hz and a band-pass filter (6th order Butterworth, 2–400 Hz). This range of frequencies to filter the signal was chosen primarily to preserve all the main LFP sub-bands from lower (e.g. *theta* and *alpha*) until gamma bands (35–200 Hz). Signal processing were performed in Matlab 2015b.

2.2 Beta Burst Duration Estimates

Both HT and CWT were evaluated for the LFP signals. For CWT, the LFP signal was further filtered at both low and high beta frequencies and, thereafter, convolved regarding the Morlet wavelet - a complex exponential function modulated by a Gaussian envelope - being the number of cycles (width) and the length of the used Morlet wavelet in standard deviations of the implicit Gaussian kernel (gwidth) set in 10 cycles and 5, respectively. These parameters are related to time and frequency resolutions. The wavelets coefficients obtained after convolution operation at each frequency-time point were averaged in frequency concerning low (13–22 Hz) and high beta bands (22–35 Hz) for each time instant. The CWT scenario used here is similar to the same introduced by in [3–6]. On the other hand, the same LFP signal filtered at low and high beta bands were convolved regarding the $1/\pi t$ function, in which t represents time, in order to provide the HT envelope. Both methods provide an estimate for beta power behavior over a spectral range of the LFP signal and its dynamical features. For each method, the bursts were defined based on a threshold defined based on different statistical ranging the percentiles (i.e., 55th to 90th, with a step of 5th), being the coefficients (either HT or CWT) higher than the percentile threshold defined as a burst. Bursts of at least 100 ms were considered (Fig. 1). For CWT analysis, the toolbox Fieldtrip were used for coefficients evaluation.

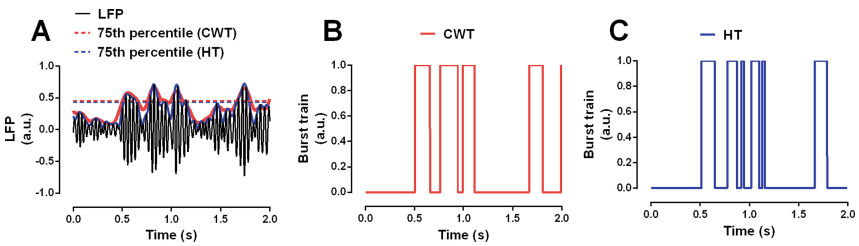

Fig. 1. Beta bursts evaluation. **(A)** High-beta bandpass filtered LFP signal and estimated HT envelope (blue continuous) and by the CWT (red continuous). Dashed lines: respective 75th percentiles. **(B)** The resulting beta train pulses for the activity that exceeds the threshold (*i.e.*, 75th percentile) for CWT and **(C)** for HT magnitude.

2.3 Statistical Analysis

Histograms of beta burst durations were evaluated for CWT and HT, comparing rest *vs*. movement conditions. The fractional durations amount was computed for: (i) each TD patient; (ii) each method (CWT and HT); (iii) each beta sub-band (low and high) and statistical percentile steps. This data are presented as mean ± standard deviation (SD). Statistical significance difference was confirmed for paired t-test when $p < 0.05$.

3 Results

Figure 2 depicts the distribution of beta burst durations for all patients across the 17 recordings for low beta sub-band, evaluated for the 65th and 90th percentiles, and by CWT and HT grouped in resting vs. movement conditions. Lower percentiles are sensitive to shorter bursts (200 ms, $p = 0.02$) when comparing rest and movement using the CWT approach, whereas HT has shown significant differences for longer bursts (300 ms, $p = 0.01$). The HT approach led to distributions presenting bursts with lower durations in contrast to CWT. Additionally, the 75th percentile - typically employed as a threshold in the aforementioned works - was not effective in detecting significant differences between movement *vs*. rest, neither in low nor in high beta sub-band.

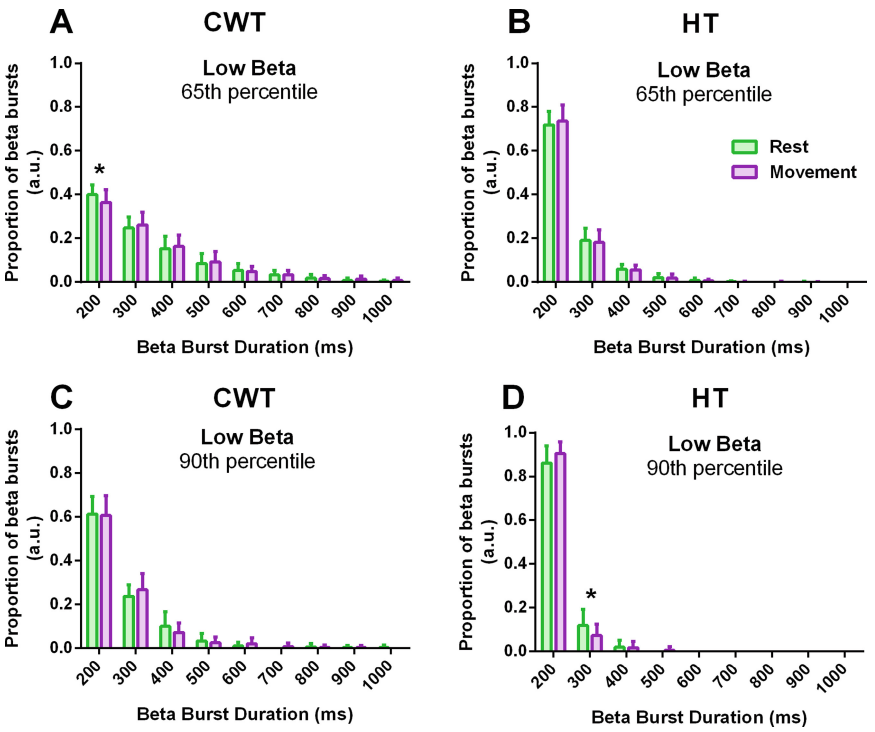

Fig. 2. Distributions of low beta burst durations (ms) across the 17 recordings during rest and movement for CWT **(A)** and HT **(B)**, and for the 65th (C) and 90th percentiles (**D**). *$p < 0.05$ (rest *vs*. movement).

4 Discussion and Conclusion

Exaggerated burst activity from STN LFP have been extensively presented as a hallmark in PD [3–6]. Furthermore, the recently the thorough subdivision of the beta into other sub-bands (low and high beta sub-bands) are of particular interest regarding DBS protocols [5]. The CWT has been employed to analyze the beta bursts and in the present cohort, this method was able to measure more evenly a wide range of bursts durations when compared to the HT. The latter method has been shown to be more sensitive to detect beta bursts of shorter durations. However, no differences were found in burst durations at low and high beta sub-bands at 75th percentile [6]. These differences from current literature may be related to: (1) particular spectral characteristics of the cohort considering exclusively TD patients [7], which may suggest the relevance of considering PD subtypes on the analysis; (2) The shorter duration of the LFP (60 s) when compared to other non-intraoperative experiments in which LFP is acquired ($\sim$360 s) [3, 4], which would allow a better distribution characterization with higher percentiles. As major conclusions, both CWT and Hilbert were capable of estimating beta burst durations for a range of percentiles at low and high beta sub-bands, which probably requires adjustments under shorter recordings. Hilbert approach also leads to shorter bursts when compared to CWT, being also possible to detect differences under rest and movement conditions depending on threshold.

5 Conflicts of Interest and Grants

All authors approved the manuscript submission with warranty of producing an original work. Moreover, this work neither received prior publication nor is under consideration for publication elsewhere. The authors have no conflict of interest. This work was financially supported by FAPESP, grants no 2018/14283-8 (BLB), no 2018/14285-0 (JBL) and 2017/00319-8 (TPA), CNPq, grants no 305616/2016-1 (DSC), BRAINN, grants no 2013/07559-3 (DSC) and Capes, grants no 2019/1814368 (AFN).

References

1. Mahlon, R., DeLong, M.D., Thomas Wichmann, M.D.: Circuits and circuits disorders of the basal ganglia. Arch. Neurol. **64**, 20–24 (2007)
2. Godinho, F., Thobois, S., Magnin, M., Guenot, M., Polo, G., Benatru, I., Xie, J., Salvetti, A., Garcia-Larrea, L., Broussolle, E., Mertens, P.: Subthalamic nucleus stimulation in Parkinson's disease. J. Neurol. **253**(10), 1347–1355 (2006)
3. Tinkhauser, G., Pogosyan, A., Little, S., Beudel, M., Herz, D.M., Tan, H., Brown, P.: The modulatory effect of adaptive deep brain stimulation on beta bursts in Parkinson's disease. Brain **140**(4), 1053–1067 (2017)
4. Tinkhauser, G., Pogosyan, A., Tan, H., Herz, D.M., Kühn, A.A., Brown, P.: Beta burst dynamics in Parkinson's disease OFF and ON dopaminergic medication. Brain **40**(11), 2968–2981 (2017)

5. Oswal, A., Beudel, M., Zrinzo, L., Limousin, P., Hariz, M., Foltynie, T., Litvak, V., Brown, P.: Deep brain stimulation modulates synchrony within spatially and spectrally distinct resting state networks in Parkinson's disease. Brain **139**(5), 1482–1496 (2016)
6. Lofredi, R., Tan, H., Neumann, W.J., Yeh, C.H., Schneider, G.H., Brown, P.: Beta bursts during continuous movements accompany the velocity decrement in Parkinson's disease patients. Neurobiol. Dis. **18**(127), 462–471 (2019)
7. Telkes, L., Viswanathan, A., Jimenez-Shahed, J., Abosch, A., Ozturk, M., Gupte, A., Jankovic, J., Ince, N.F.: Local field potentials of subthalamic nucleus contain electrophysiological footprints of motor subtypes of Parkinson's disease. Proc. Nat. Acad. Sci. **115**(36), E8567–E8576 (2018)

A Comparative Study of Time and Frequency Features for EEG Classification

Cesar Ortiz-Echeverri[1(✉)], Omar Paredes[2], J. Sebastian Salazar-Colores[1], Juvenal Rodríguez-Reséndiz[1], and Rebeca Romo-Vázquez[2]

[1] Universidad Autónoma de Querétaro, 76010 Santiago de Querétaro, Mexico
cesarortiz1983@gmail.com
[2] CUCEI, Departamento de Ciencias Computacionales, Universidad de Guadalajara, Av. Revolución 1500, Guadalajara, Jalisco, Mexico
rebecca.romo@academicos.udg.mx

Abstract. Despite the different nature of sounds and electrophysiological potentials, there are certain similarities between these two kinds of signals. Therefore, feature extraction methods used in both cases are based on similar signal processing concepts. In this work, we used a set of audio features based on time, and frequency domains, including Mel-Frequency Cepstral Coefficients ($MFCC$), which were applied to electroencephalographic signals (EEG) recorded for Motor Imagery (MI) tasks. A classification stage using Multilayer Perceptron (MLP) was implemented, to evaluate the accuracy to differentiate two task of Motor Imagery, for each proposed descriptor, as well as for groups of descriptors. Moreover, the influence of the length size windows was studied with this approach. The results suggest that $MFCC$ are more robust than other descriptors through different window lengths, achieving high classification accuracy both individually and in the group of MFFC filters.

Keywords: Feature extraction · Audio descriptors · Mel-Frequency Cepstral Coefficients · Multilayer Perceptron

1 Introduction

Brain-Computer Interfaces (BCI) allows the control of external devices using the brain activity. The common inputs for BCI applications are the cerebral signals recorded by the electroencephalogram (EEG) using electrodes on the scalp according to the 10–20 International system [1]. BCI is composed commonly of three stages: (i) preprocessing; where the signals are conditioned to minimize the effect of noise and artifacts; (ii) feature extraction, where meaningful information, known as features, is obtained while redundant information is discarded; and, (iii) feature classification, where linear or nonlinear classifiers are implemented in order to identify a proper control signal for external devices such as wheelchairs, robotics arms or legs prostheses, etc. In the present work, we focus on the feature extraction stage; the goal is to evaluate a set of features from the

© Springer Nature Switzerland AG 2020
C. A. González Díaz et al. (Eds.): CLAIB 2019, IFMBE Proceedings 75, pp. 91–97, 2020.
https://doi.org/10.1007/978-3-030-30648-9_13

recorded EEG signals, that represents important characteristics of the original data, pondering the differences and minimizing the redundancy at the same time by reducing the dimensionality of EEG channels.

We propose to work with three groups of features**:** time-domain, frequency-domain, and the Mel-Frequency Cepstral Coefficients ($MFCC$), that are filter banks that model the ability of the human ear to set the sounds [2,3]. However, for EEG feature extraction, has not been used extensively. Some reported works about the use of $MFCC$ in EEG signals are, for example, a Motor Imagery (MI) task classification using Power Spectral Density (PSD) and $MFCC$ for the feature extraction. The authors summarized that the Perceptron model trained with Mel-frequency band structure-based features has yielded a higher classification accuracy, above 90% [2]. Another example is an Artificial Immune System–Negative Selection Classification Algorithm (NSCA) for Four Class Electroencephalogram (EEG) Signals, where the feature extraction based on $MFCC$ is enhanced by combining with an immune classifier inspired algorithm. In this work is mentioned the influence of the number of $MFCC$ filters in the recognition accuracy of the classes [4]. There is another study where $MFCC$ filters were implemented and their impact evaluated, they focused on filter bank approaches, using a linear frequency scale for EEGs, since there is no physiological evidence that a log scale is meaningful [5]. Our methodology consists of analyzing the behavior of each descriptor individually, in groups, and as a whole, for different time window sizes using the same classifier in each case.

2 Background and Methods

To test the proposed method, EEG recordings provided by Laboratory of Brain-Computer Interfaces (Graz, Austria) were used. In this open access data-set, 14 participants had the task of performing kinaesthetic MI of the right hand (class1) and of the feet (class2). During the task, EEG was recorded with a biosignal amplifier and active Ag/AgCl electrodes with their placement designed for obtaining three Laplacian derivations. Center electrodes at positions C3, Cz, and C4 and four additional electrodes around [6].

Feature Extraction. A feature extraction step was implemented. The features proposed in this work are widely used in the field of audio processing [7,8], and correspond to the time and the frequency domains. The used library was developed by [9] and the main equations and definitions are listed in Table 1.

Classification. The Artificial Neural Network (ANN) was inspired by the biological neural networks. These structures are based on a collection of connected units or nodes called artificial neurons that are activated when recognized features. One of most popular ANN is known as feedforward neural network, that is a fully connected network in which all the input neurons are connected with all neurons in the first hidden layer as well as the outputs of these neurons are

Table 1. Audio descriptors

Feature	Description	Equation
1. Zero-crossing	Rate of sign-changes of the signal during the frame	$Z(i) = \frac{1}{2L}\sum_{i}^{L} \lvert sgn[x_i(n)] - sgn[x_i(n-1)]\rvert^2$ with $sgn(\cdot)$ the sign function
2. Energy	Defined as the area under the squared magnitude of the signal	$E(i) = \frac{1}{L}\sum_{i}^{L} \lvert x_i(n)\rvert^2$ with $x_i(n)$ the fragment of vector
3. Entropy of energy	Measure of abrupt changes in the wave energy	$H(i) = -\sum_{j=1}^{k} e_j log_2(e_j)$ where e_j is the division between $EsubFrame_j$ and $EshortFrame_i$
4. Spectral centroid	Center of 'gravity' of the spectrum	$C_i = \frac{\sum_1^{Wfl} kX_i(k)}{\sum_1^{Wfl} X_i(k)}$ with $X_i(k)$ the magnitude of the spectrum
5. Spectral spread	Second central moment of the spectrum	$S_i = \sqrt{\frac{\sum_1^{Wfl} (k-C_i)^2 X_i(k)}{\sum_1^{Wfl} X_i(k)}}$ with C_i the spectral centroid
6. Spectral entropy	Measure of abrupt changes in the spectrum energy	$H(i) = -\sum_{f=0}^{L-1} n_f log_2(n_f)$
7. Spectral flux	Spectral change between two successive frames	$Fl_{(i,i-1)} = -\sum_{f=1}^{Wf_L} (EN_i(k) - EN_{i-1}(k))^2$ with $EN_i(k)$ as the kth DFT coefficient
8. Spectral rolloff	Frequency below the spectrum is concentrated	$\sum_{k=1}^{m} X_i(k) = C\sum_{k=1}^{Wf_L} X_i(k)$ with mth DFT coefficient the spectral rolloff
9. $MFCC$	Cosine Transform distributed according to the Mel-scale	$c_m = \sum_{k=1}^{L} (log(O_k))cos\left[m\left(k-\frac{1}{2}\right)\frac{\pi}{L}\right]$ with O_k, the power at the output of the kth filter

also fully connected with the neurons of the next layer. A single unity is known as perceptron, and their equation is given by

$$y_N = f(WX + b) \tag{1}$$

where y_N is the output of the neuron, X is the vector of inputs, W is the weights parameters, b is the bias, and f is the activation function. Then, the output of each neuron is a linear combination of all their inputs, with an adjust of threshold given by the bias value, and finally the resultant output is evaluated by the activation function that commonly is a nonlinear operator such as the $tanh(y_N)$. The combination of perceptrons in different layers are known as Multilayer Perceptron (MLP), this neural network architecture has been widely used as a classifier in EEG signals [10,11].

Proposed Method. In the dataset, each frame of MI consist on 15 channels and four seconds with sampling rate of 512 Hz. The 21 features are calculated for each channel, using window sizes of 2.0 s, 1.5 s, 1.0 s, and 0.2 s. Therefore, the input of the classifier is $15x21 = 315$ feature vectors which contain spatial, temporal and frequential information. A MLP with seven neurons in the hidden layer was used. To train the network, gradient descent with momentum and

adaptive learning rate was employed. Inputs were divided in 60% for training, 20% for validation, and 20% for test once the net has been trained. In Fig. 1 is shown a general scheme of the proposed method.

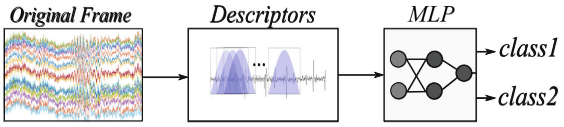

Fig. 1. Proposed methodology

Metrics. To evaluate the performance of proposed method, accuracy, sensitivity (true positive rate), specificity (true negative rate), and F1 score (measure of a test's accuracy) are calculated using the expresions 3, 4, and 5 respectively.

$$Accuracy = \frac{TP + TN}{TP + TN + FP + FN} \tag{2}$$

$$Sensitivity = \frac{TP}{TP + FN} \tag{3}$$

$$Specificity = \frac{TN}{TN + FP} \tag{4}$$

$$F1Score = \frac{2TP}{2TP + FP + FN} \tag{5}$$

With TP true positive, TN, true negative, FP false positive, and FN false negative cases.

3 Results

In Table 2 a first analysis was performed using only a subject (S01), to study the behaviour of individual descriptors, as well as for groups of descriptors. It can be noticed that the accuracy percentage is deficient for single descriptors except in the case of the $MFCC_5$ which achieved a 76.6% and 69.4% for 2.0 and 1.5 seconds respectively. For 1.0 second in window size, $MFCC_8$ achieved 73.5%. That can suggest the competence of the $MFCC$ descriptors for EEG signal feature extraction. The higher performance in the classification was achieved with the group corresponding to $MFCC$ features (group 3), for 2.0, 1.5, and 1.0 window size. Such results exhibit that these features properly discriminate between the studied classes. This leads to think that the filtering in the Mel scale are suitable to identify the frequency ranges that maximized the difference between both movements, which could be electrophysiological bands. The influence of window size in the feature extraction also studied and showed in Fig. 2. We can

notice that for the group 3 ($MFCC$ descriptors) the accuracy of the different window size is similar, that is, there are not influenced by the size in the classification results. On the other hand, for the group 1 (time-domain descriptors) and group 2 (frequency-domain descriptors) the results of classification change considerably with regards to the window size.

Table 2. Accuracy percentage (test) generated by individual descriptor, group of descriptors, and all descriptors at different time window (subject S01)

Descriptor	Window size			
	2.0 s	1.5 s	1.0 s	0.2 s
1. Zero-crossing	16.8	56.8	55.0	37.1
2. Energy	52.2	33.5	51.9	25.0
3. Entropy of energy	61.3	52.5	42.9	54.9
4. Spectral centroid	32.5	61.1	41.3	58.8
5. Spectral spread	43.6	49.0	54.0	55.9
6. Spectral entropy	44.2	64.3	55.0	51.3
7. Spectral flux	35.8	50.7	59.5	43.8
8. Spectral rolloff	29.6	31.5	49.0	47.9
9. $MFCC_1$	46.6	47.6	62.6	60.0
10. $MFCC_2$	49.5	44.0	61.5	67.0
11. $MFCC_3$	48.8	40.2	54.7	69.6
12. $MFCC_4$	44.9	55.4	51.1	69.1
13. $MFCC_5$	**76.6**	**69.4**	62.9	51.2
14. $MFCC_6$	48.6	46.1	54.5	50.9
15. $MFCC_7$	48.6	54.7	66.8	40.8
16. $MFCC_8$	44.1	53.9	**73.5**	37.0
17. $MFCC_9$	48.9	59.3	58.3	48.1
18. $MFCC_{10}$	58.3	63.1	48.0	48.1
19. $MFCC_{11}$	68.8	58.9	51.5	39.6
20. $MFCC_{12}$	45.3	51.8	47.7	39.6
21. $MFCC_{13}$	46.3	48.8	37.0	43.6
Group 1	33.6	52.3	44.9	52.8
Group 2	34.7	41.1	52.3	51.3
Group 3	**90.8**	**86.7**	**84.4**	49.7
All descriptors	**92.8**	88.4	71.6	44.6

According to results in Table 2, we select a window size of 2.0 seconds, to evaluate the 14 subjects of the dataset for the three groups of descriptors. In Table 3 are the classification accuracy, sensitivity, specificity, and F1 score, for each subject and each group of features, where group 3, the group of the MFCC features,

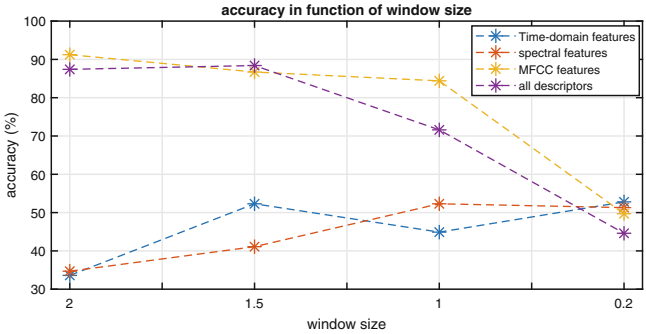

Fig. 2. Accuracy in function of window size

presents the highest values with 76.1%, 75.9%, 81.7%, and 78.1% respectively, ranked the MFCC features as features to consider in other brain activity classification. In this study, we used the $MFCC$ with the standard parameters adjusted to music and speech recognition, i.e, the number of coefficients, or logarithmic Mel-scale constants were not adjusted to electrophysiological cases. For future work, we propose an study of the hyper-parameters of the mentioned coefficients in order to take advantage of a greater number of $MFCC$ filters and improve the classification values, as well as the inclusion of a preprocessing step before the feature extraction which could improve the results obtained in this work.

Other MI classification works that used the same dataset reported mean validation accuracy of 63.4%, using online Fourier Transform (DFT) and Random Forest (RF); 76.1% using Common Spatial Patterns (CSP) and RF; and 73.2% using CSP and Linear Discriminant Analysis (LDA), [12]. Compare with these results, the accuracy of MFCC feature classification is better, and could be improved in further work with more robust machine learning algorithms.

Table 3. Accuracy, sensitivity and specificity for each group of descriptors

	Group 1		Group 2		Group 3		ALL	
	Mean	Std	Mean	Std	Mean	Std	Mean	Std
Accuracy	58.7	15.2	55.7	13.8	**76.1**	12.7	68.0	14.8
Sensitivity	60.6	18.0	59.3	17.5	**75.9**	13.4	67.7	15.1
Specificity	57.7	16.3	53.7	24.0	**81.7**	12.5	69.4	22.4
F1 score	55.9	19.0	57.5	21.3	**78.1**	9.7	70.9	13.2

4 Conclusion

In this work, we studied the feature extraction of EEG signals for the case of two class MI, using time, and time-frequency descriptors commonly used in audio and

speech recognition. According with our experimentation, the $MFCC$ descriptors showed the best performance in both cases, individually and as a group. However, there are some $MFCC$ that do not support the discrimination between classes, probably because their parameters are adjusted for speech and audio applications instead the frequency ranges corresponding to electrophysiological activities. In future works the adjust of $MFCC$ parameters according with electrophysiological nature of signals it must be done. Also the inclusion of a prepossessing step as BSS for artefacts and noise cancelling must be implemented.

Acknowledgements. The authors wish to thank the faculties of computer science and engineering at Universidad Autónoma de Querétaro and the Universidad de Guadalajara, as well as to CONACyT for the support scholarship.

References

1. Sanei, S., Chambers, J.A.: EEG Signal Processing, p. 10 (2007)
2. Paulraj, M., Teh, J.: Mel-frequency band structure based features for motor imagery task classification. J. Teknol. **76**(12) (2015)
3. Li, D., Sethi, I.K., Dimitrova, N., McGee, T.: Classification of general audio data for content-based retrieval. Pattern Recogn. Lett. **22**(5), 533–544 (2001)
4. Rashid, N., Iqbal, J., Mahmood, F., Abid, A., Khan, U.S., Tiwana, M.I.: Artificial immune system-negative selection classification algorithm (NSCA) for four class electroencephalogram (EEG) signals. Front. Hum. Neurosci. **12**, 439 (2018)
5. Harati, A., Golmohammadi, M., Lopez, S., Obeid, I., Picone, J.: Improved eeg event classification using differential energy. In: 2015 IEEE Signal Processing in Medicine and Biology Symposium (SPMB), pp. 1–4. IEEE (2015)
6. Steyrl, D., Scherer, R., Förstner, O., Müller-Putz, G.R.: Motor imagery brain-computer interfaces: random forests vs regularized LDA-non-linear beats linear. In: Proceedings of the 6th International Brain-Computer Interface Conference, pp. 241–244 (2014)
7. Muda, L., Begam, M., Elamvazuthi, I.: Voice recognition algorithms using mel frequency cepstral coefficient (MFCC) and dynamic time warping (DTW) techniques. arXiv preprint arXiv:1003.4083 (2010)
8. Hasan, M.R., Jamil, M., Rahman, M., et al.: Speaker identification using mel frequency cepstral coefficients. Variations **1**(4) (2004)
9. Giannakopoulos, T., Pikrakis, A.: Introduction to Audio Analysis: A MATLAB® Approach. Academic Press, Cambridge (2014)
10. Lotte, F., Congedo, M., Lécuyer, A., Lamarche, F., Arnaldi, B.: A review of classification algorithms for eeg-based brain-computer interfaces. J. Neural Eng. **4**(2), R1 (2007)
11. Orhan, U., Hekim, M., Ozer, M.: Eeg signals classification using the k-means clustering and a multilayer perceptron neural network model. Expert Syst. Appl. **38**(10), 13475–13481 (2011)
12. Steyrl, D., Scherer, R., Faller, J., Müller-Putz, G.R.: Random forests in non-invasive sensorimotor rhythm brain-computer interfaces: a practical and convenient non-linear classifier. Biomed. Eng./Biomed. Tech. **61**(1), 77–86 (2016)

Cortical Auditory Evoked Potentials Elicited by Spanish Words: An Equivalent Current Dipoles Clustering Study

Norma Castañeda-Villa(✉), Pilar Granados-Trejo, and Juan Manuel Cornejo-Cruz

Departamento de Ingeniería Eléctrica,
Universidad Autónoma Metropolitana-Iztapalapa, Mexico City, Mexico
ncv@xanum.uam.mx

Abstract. Cortical Auditory Evoked Potential (CAEP) has been used to understand the base of physiological processes of speech perception; in order to establish objectively speech-feature discrimination abilities in a subject. The aim of this work was to localize the brain areas of CAEPs activated when four disyllabic Spanish words were used on a passive listening paradigm in normal hearing adults. The clustering of Equivalent Current Dipoles, based on Independent Component Analysis, was used to localize brain areas activated with four words; which were selected from a list of words with a linguistic frequency approach. Our results show a clear division between words: (1) two with an anterior and posterior cingulate location both, and (2) two located at the Wernicke's area; those areas are involved on speech comprehension. This study could contribute in understanding of the neuronal substrates involved in the perception of words in Spanish and it could be used to measure objectively the performance of subject native speakers of Spanish, users of Hearing Aids and/or Cochlear Implants.

Keywords: Cortical Auditory Evoked Potentials · Independent Component Analysis · Equivalent Current Dipole · Spanish words

1 Introduction

Cortical Auditory Evoked Potentials (CAEPs) are a response of the Central Nervous System to long-term auditory stimuli, >5 ms duration [1]. These potentials are generated by the physical characteristics of the stimulus (amplitude, frequency, duration and rate repetition) [2]. CAEPs have been used to estimate auditory sensitivity at specific frequencies in people with hearing loss, users of Hearing Aids (HAs) and Cochlear Implants [3, 4]. The location of CAEPs generators elicited by phonemes, syllables and speech has been a widely tool used in the area of neurosciences to explain the neurological relationships involved in both speech perception and discrimination [1]. In this respect, it is important to highlight that diverse authors have utilized Independent Component Analysis (ICA) not only for separating the typical artifacts from EEG recording as blinking, muscle activity and cardiac pulse artifact, but also to determinate the cortical location of the Equivalent Current Dipoles (ECDs) of the

© Springer Nature Switzerland AG 2020
C. A. González Díaz et al. (Eds.): CLAIB 2019, IFMBE Proceedings 75, pp. 98–103, 2020.
https://doi.org/10.1007/978-3-030-30648-9_14

CAEPs. The above to evaluate the brain dynamics behind the relationship between auditory perception and language development [5]. In order to solve the *EEG inverse problem*, ICA decomposition proposes carry out inverse modeling of the individual Independent Components (ICs) estimated by this analysis. IC scalp maps are modeled as single or bilateral ECDs; location and orientation of those dipoles within a specific 3-D head model, establish the theoretical scalp projection of the dipole's electric field. This way to modeling ICs is useful to: (1) localize particular brain region which contribute to sensorial activity of interest and (2) to evaluate and visualize the spatial homogeneity of IC process across subjects [6]. Although there are several studies in this sense, most use syllables or short words of English, German, etc. [7, 8]; there are even studies using English-Spanish syllabic contrast in Mexican infants [9] and brain measures of phonetic discrimination in Spanish-English bilingual subjects [10]. From our point of view the work proposed in this paper would be the first one to carry out the ECD Clustering, based on ICA, of CAEPs elicited by speech stimuli in Spanish; this to determinate the brain areas of CAEPs activated by these stimuli.

2 Materials and Methods

The subject group consisted of 10 Spanish-speaking adults (5 males and 5 female) with a mean age of 23.67 ± 3.56 years; participants reported no sensorial or neurological disorders. All participants had average hearing thresholds <20 dBHL between 125 and 8000 Hz. This study was approved by the Ethical committee of the UAM and prior to the experiment subjects provided signed informed consent on a document approved by Audiology Laboratory of UAM-I. Disyllabic words used as stimuli were selected from a corpus for speech audiometry in Spanish [11]. The selected words were /bota/ - "boot", /papa/ - "potato", /lobo/ - "wolf" and /sabor/ - "flavor" with duration of 480, 354, 456 and 481 ms respectively. STIM software (Neuroscan, Inc.) was used to present stimuli binaurally to participants via an Interacoustic AC-40 audiometer and TDH-39 headphones; intensity approximately 75 dBSPL.

A passive listening paradigm was conducted in a sound-treated booth; participants were sat in a comfortable reclining armchair. Twenty electrode channels (FP1/2, F3/4, C3/4, P3/4, O1/2, F7/8, T3/4, T5/T6, Cz, Pz, Fz and AFZ as ground) were used to acquire the EEG data; additionally two electrodes M1 + M2 were used as reference. Data analysis was performed in EEGLAB [12]; ~400 trials were averaged separately for the four word stimuli. Trials from −100 to 600 ms were filtered with a second order FIR band-pass filter (1–30 Hz). A detailed analysis of the time characteristics - latency and amplitude - and the spatial distribution - Topographic maps - of the peaks of CAEPs elicited with these words was performed in a previous work [13]. Infomax ICA decomposition [14] was performing on each dataset; this ICA algorithm is widely used to decompose EEG recording; ICA gives the scalp projection of the sources. EEGLAB DIPFIT toolbox freely available at https://sccn.ucsd.edu/wiki/A08:_DIPFIT was used to fit single ECDs for the ICs using Boundary Element Method (BEM) which is based on the Montreal Neurological Institute template head model. ICs associated

with EEG artifacts were removed by visual inspection before clustering. Only ICs with residual variance <20% were preserved for subsequent clustering. ICs were grouped by k-mean algorithms (k = 7) to get cluster across subjects for each word.

3 Results

Waveforms, topographic maps and clusters of single dipolar sources fit of 6 IC clusters related to the CAEPs are shown in Fig. 1. Different Broadmann areas (BAs) were identified from Talairach atlas; those areas were searched using the cluster centroids coordinates where CAEPs were recognized (see Table 1). Two clusters were identified using the word /lobo/, located at right BA (24) and BA (23), IC3-/lobo/ and IC6-/lobo/respectively. IC3-/lobo/ included from 9 to 10 subjects while IC6-/lobo/ included 7. The topographic map distributions of IC3-/lobo/ and IC6-/lobo/ showed right-frontal and posteromedial distributions. Word /papa/activated the BA (41); IC6-/papa/ contained ICs from 8 of 10 subjects. The topographic map of this cluster showed a right-temporal distribution. Two cortical areas were active when word /sabor/ was used as stimulus, these located close to right-BA (32) and left-BA (23), IC3-/sabor/ and IC6-/sabor/ respectively. IC3-/sabor/ included from 8 to 10 subjects whilst IC6-/sabor/ included 9. The topographic map distributions of IC3-/sabor/ and IC6-/sabor/ showed right-frontal and posteromedial distributions. Finally, left BA (21) was activated using word /bota/; IC5-/bota/ contained ICs from 8 of 10 subjects. The topographic map of this cluster showed a left-temporal distribution.

Table 1. Brodmann areas, anatomical structure and location of ICs centroids for four different words

Cluster-/Word/	Hemisphere	Anatomical structure	BA	X medial-lateral	Y anterior-posterior	Z superior-inferior	R.V: %
IC3-/lobo/	Right	Anterior cingulate gyrus	24	2	30	1	7.59
IC6-/lobo/	Right	Ventral posterior cingulate	23	4	−48	17	6.42
IC6-/papa/	Right	Prim Auditory	41	43	−27	8	10.12
IC3-/sabor/	Right	Anterior cingulate gyrus	32	10	30	−1	4.92
IC6-/sabor/	Left	Ventral posterior cingulate	23	−8	−61	12	6.15
IC5-/bota/	Left	Temporal gyrus	21	−51	−37	9	9.86

BA: Brodmann area, R.V: Residual variance

Post-hoc Tukey-Kramer HSD tests showed significant mean differences between six clusters locations: C3-/lobo/ and C6-/papa/ (MD = 20.4990 and p = 0.0095), C3-/lobo/ and C6-/sabor/ (MD = 34.5159 and p << 0.05), C3-/lobo/ and C5-/bota/ (MD = 32.7554 and p << 0.05), C6-/lobo/ and C6-/sabor/ (MD = 25.2122 and p = 0.0006), C6-/papa/ and C3-/sabor/ (MD = 22.4698 and p = 0.0048), and C3-/sabor/and C5-/bota/ (MD = 34.7261 and p << 0.05). Finally, C3-/lobo/ and C3-/sabor/ (MD = 1.9707 and p = 0.9994), C6-/lobo/ and C6-/papa/ (MD = 2.7425 and p = 0.9971), C6-/lobo/ and C6-/sabor/ (MD = 11.2743 and p = 0.3553), C6-/lobo/ and C5-/bota/ (MD = 9.5139 and p = 0.6288), C6-/papa/ and C6-/sabor/ (MD = 14.0168 and p = 0.1706), C6-/papa/ and C5-/bota/ (MD = 12.2564 and p = 0.3816), and C6-/sabor/-and C5-/bota/ (MD = 1.7604 and p = 0.9997) location comparisons were not significant.

4 Discussion and Conclusions

In this study, ECD Clustering, based on ICA was used to identify cerebral cortex areas activated of CAEPs. Six different clusters of activation were found in our study, four related to the right hemisphere, BA (23), BA (24), BA (32) and BA (41) and two related to left hemisphere BA (21) and BA (23). The majority of the clusters where located at the right hemisphere which is consistent with reported by other authors in both adults [15]. In a previous study, we observed mainly a topographic maps distribution at fronto-central for the word /lobo/ and /sabor/. However, our most recent results, show not only a frontal cluster BA(24) and BA(32) – anterior cingulate gyrus- but also an additional cluster for these two words in BA(23) – posterior cingulate- which is in accordance with the findings of other authors [16]. In both words /lobo/ and /sabor/ in contrast to the words /papa/and /bota/, there is a clear difference between the two syllables that form them, which could explain the fact of the activation of the anterior cingulate reported by other authors with respect to syllable discrimination [17].

ECD Clustering allowed locating not only frontal cortical area, on the cingulate gyrus as expected, but also areas on PAC and the middle temporal gyrus; both are part of the Wernicke's area. Cingulate gyrus is a region involved on the speech comprehension while Wernicke's area responds to the acoustic complexity of the stimuli and is involved too on speech comprehension.

The foundations are laid to begin to understand the neuronal substrates involved in speech-feature perception of disyllabic words in Spanish. These words could be used in an objective test to measure speech perception in Spanish; it could be used to measure objectively the performance of subject user of Hearing Aids and /or Cochlear Implants. The passive paradigm used in this study could be extended to a paradigm such as oddball, using the minimal pairs of words mentioned above, to evaluate auditory memory in Spanish.

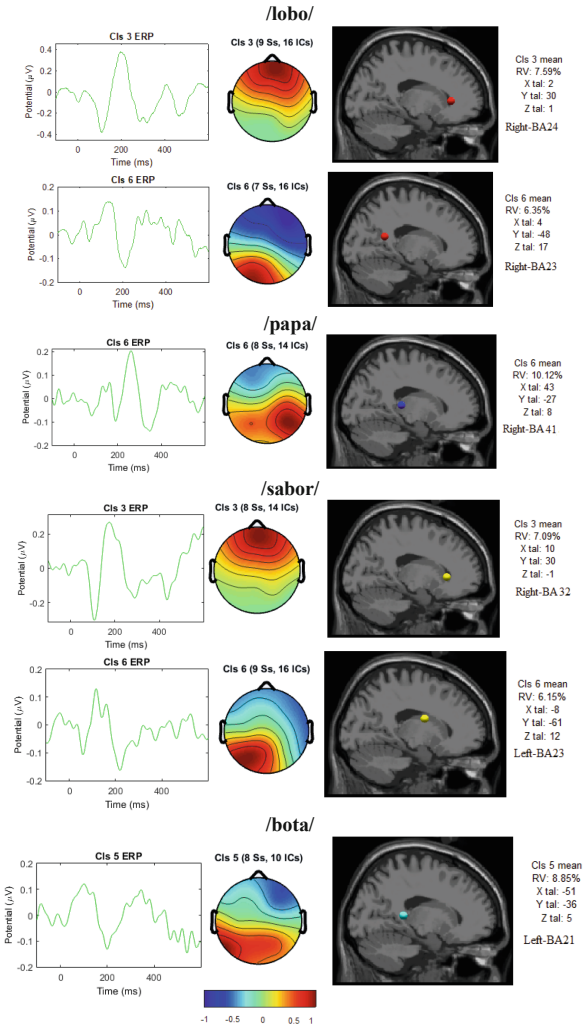

Fig. 1. Waveforms (left column), topographic maps (central column) and dipolar sources fit to ICs – MRI sagittal view - (right column) associated with the CAEP. X-Y-Z tal (Talairach centroid locations).

References

1. Picton, T.W., et al.: Guidelines for using human event-related potentials to study cognition: recording standards and publication criteria. Psychophysiology **37**(2), 127–152 (2000)
2. Purdy, S.C., Kelly, A.S.: Cortical auditory evoked potential testing in infants and young children. New Zeal. Audiol. Soc. Bull. **1**, 1–8 (2001)
3. Tremblay, K.L., Kalstein, L., Billings, C.J., Souza, P.E.: The neural representation of consonant-vowel transitions in adults who wear hearing AIDS. Trends Amplif. **10**(3), 155–162 (2006)

4. Sharma, A., et al.: P1 latency as a biomarker for central auditory development in children with hearing impairment. J. Acad. Audiol. **16**(8), 564–573 (2005)
5. Onton, J.A., Makeig, S.: Information-based modeling of event-related brain dynamics. Prog. Brain Res. **159**, 99–120 (2006)
6. Onton, J., Westerfield, M., Townsend, J., Makeig, S.: Imaging human EEG dynamics using independent component analysis. Neurosci. Biobehav. Rev. **30**(6), 808–822 (2006)
7. Christmann, C.A., Berti, S., Steinbrink, C., Lachmann, T.: Differences in sensory processing of German vowels and physically matched non-speech sounds as revealed by the mismatch negativity (MMN) of the human event-related brain potential (ERP). Brain Lang. **136**, 8–18 (2014)
8. Ortiz-Mantilla, S., Hämäläinen, J.A., Benasich, A.A.: Time course of ERP generators to syllables in infants: a source localization study using age-appropriate brain templates. Neuroimage **59**(4), 3275–3287 (2012)
9. Rivera-Gaxiola, M., Garcia-Sierra, A., Lara-Ayala, L., Cadena, C., Jackson-Maldonado, D., Kuhl, P.K.: Event-related potentials to an English/Spanish syllabic contrast in Mexican 10–13-month-old infants. ISRN Neurol. **2012**, 702986 (2012)
10. Garcia-Sierra, A., et al.: Bilingual language learning: an ERP study relating early brain responses to speech, language input, and later word production. J. Phon. **39**(4), 546–557 (2011)
11. Martínez A., Rufiner L., Cornejo J. M., Cadena M., and Herrera E.: Análisis Espectral de una Lista de Palabras. An. del VIII Congr. la Asociación Mex. Audiol. Foniatría y Comun. Humana 1–6 (1997)
12. Delorme, A., Makeig, S.: EEGLAB: an open source toolbox for analysis of single-trial EEG dynamics including independent component analysis. J. Neurosci. Methods **134**(1), 9–21 (2004)
13. Granados-Trejo, P., Castañeda-Villa, N., Cornejo-Cruz, J.M.: Características temporales y distribución topográfica de los potenciales evocados auditivos corticales evocados por palabras en español en una población adulta. Rev. Mex. Neurocienc. **17**(2), 42–49 (2015)
14. Bell, A.J., Sejnowski, T.J.: An information-maximisation approach to blind separation and blind deconvolution. Neural Comput. **7**(6), 1129–1159 (1995)
15. Crottaz-Herbette, S., Menon, V.: Where and when the anterior cingulate cortex modulates attentional response: combined fMRI and ERP evidence. J. Cogn. Neurosci. **18**(5), 766–780 (2006)
16. Ardila, A., Bernal, B., Rosselli, M.: The role of Wernicke's area in language comprehension. Psychol. Neurosci. **9**(3), 340–343 (2016)
17. Witteman, J., Goerlich-Dobre, K.S., Martens, S., Aleman, A., Van Heuven, V.J., Schiller, N. O.: The nature of hemispheric specialization for prosody perception. Cogn. Affect. Behav. Neurosci. **14**, 1104–1114 (2014)

Classification of Heart Health by LPC and MFCC Coefficients and Statistical Features

Manuel A. Soto-Murillo(✉), Karen E. Villagrana Bañuelos, Julieta G. Rodriguez-Ruiz, Jared D. Salinas-González, Carlos E. Galván-Tejada, Hamurabi Gamboa-Rosales, and Jorge I. Galván-Tejada

Universidad Autónoma de Zacatecas, 98000 Zacatceas, Zacatecas, Mexico
alejandro.somu@gmail.com, gatejo.somu@uaz.edu.mx

Abstract. This article presents a human heart health status classification based on a public database that contains hospital recordings of various heart sounds using a digital stethoscope. Three different sounds were analyzed in this study; normal heart sounds, heart murmur sounds and extra systolic sounds. Ten general and statistical features and 16 parameters of the classical techniques; Linear Predictive Coding (LPC) and Cepstral Frequency-Mel Coefficients (MFCC) were calculated to create a numerical database. Through the genetic algorithm Galgo, the most significant features of all cardiac audio samples were extracted. These features were analyzed with three different classification methods; Logistic Regression (LN), Neural Networks (NN) and Suport Vector Machine (SVM). The area under the curve (ROC) and the accuracy (ACC) were the metrics used to evaluate the classifiers. The Neural Network classifier with the data normalized gave the best results with a ROC = 0.7558. While the same classifier with the data not normalized gave the worst results with a ROC = 0.6571.

Keywords: LPC · MFCC · Logistic-regression · Support Vector Machine · Neural-Networks

1 Introduction

In 2016, The World Health Organization attributed ischemic heart disease as the leading cause of mortality worldwide [13], the National Institute of Statistics and Geography in 2017 found the same results [8].

Differentiating a healthy heart from an unhealthy heart, is a challenge in clinical practice even among highly experienced personnel. It has been found that the clinical ability of physicians to identify patients with potential risk of malignant ventricular arrhythmias in the course of an acute myocardial infarction is low [2].

© Springer Nature Switzerland AG 2020
C. A. González Díaz et al. (Eds.): CLAIB 2019, IFMBE Proceedings 75, pp. 104–112, 2020.
https://doi.org/10.1007/978-3-030-30648-9_15

The first sound of the heart (S1) has long duration, it is described as "tum" sound [6], and it is caused by the closing of the atrioventricular valves. It is usually heard as a unique noise. The second sound (S2) is due to the closing of the sigmoid valves (aortic and pulmonary) [9], and it is described as "ta" sound [6]. The S2 is altered in inspiration, what is known as splitting of the second noise, and in expiration is perceived as a unique noise [9].

Generally, the sounds described above are known as "normal" sounds, there may appear acoustic phenomena such as the third sound (S3) which occurs normally in children, adolescents and during pregnancy [6]. In people over 30 years old it is considered a pathological finding; it is a sound that coincides with rapid ventricular filling [9].

The fourth sound (S4) is usually an atrial noise, it is known as a pathological sound and it is found in myocardial ischemia, hypertrophy or rigidity due to the infiltration of foreign substances [9].

The murmurs are noises that have been compared by Laenec to the noise of a bellows when fanning fire [5]. They are of particular relevance because they can show a valvular cardiac injury in the majority of cases. The sounds are produced by a turbulent flow, and can appear in all the phases of the cardiac cycle [9].

The extrasistolic sounds are described as premature or "advanced" beats. They anticipate the appearance of the automatic rhythm commanded by the sinus node, blocking it and generating a "compensatory" pause. Extrasystoles are most common within arrhythmias, usually do not cause symptoms, and are harmless. Although certain diseases of the heart can cause extrasystoles, there may also be extrasystoles due to stress, too much exercise or excessive caffeine or nicotine [17].

Through cardiac auscultation, it is possible to identify various cardiac diseases. This can be done using a digital stethoscope, which generates a phonocardiogram (a waveform of cardiac sounds). Due to the auscultation is a simple, economical and primordial technique for the inspection of the heart, it is necessary to develop a technique that allows analyzing and characterizing heart sounds automatically. The researches that have been developed on analysis of cardiac sounds, focus on the segmentation of each heart sound by separately and then characterize each one of them [3,7,11,12,15]. Therefore, it is essential to characterize or model the sound of the healthy and unhealthy heart, and thus be able to automatically identify the health of the heart.

The research, discovery and invention of any method that provides alternatives to differentiating an unhealthy heart from a healthy one is likely to provide a significant decrease in heart disease related deaths. Rationale for this, is the likely increase of referrals to specialized healthcare facilities for treatment, as well as timely and effective rehabilitation.

The structure of this paper is divided on; materials and methods, results and conclusions sections.

2 Materials and Methods

2.1 Heart Sounds Database

A public database was used, which can be found in: http://www.peterjbentley.com/heartchallenge/#taskoverview [14]. Using the digital stethoscope DigiScope different data from a clinical trials in hospitals was collected. The database consists of 312 ".wav" independent audio files from different individuals. 200 individuals presented normal heart sounds, 66 presented heart murmur sounds and the remaining 46 presented extrasystolic sounds. The normal sounds were considered as the set of healthy hearts and the other two types of sounds formed the unhealthy heart set. For better learning classification the number of healthy and unhealthy cases needed to be balanced, therefore only 112 sounds of the 200 healthy sounds were taken into account, providing an equal number of cases of healthy and unhealthy heart sounds for analysis.

2.2 General and Statistical Features

Different general and statistical features were calculated for each of the 224 audio samples, such as:

- Duration: time in seconds that the audio files last.
- Mean: represents the average energy of the audio signals.
- Median: sample energy that represents the medium value of energy among all those present in the audio signal.
- Standard Deviation: indicates how scattered are the energy samples that make up the audio signal with respect to its mean.
- Variance: standard deviation squared.
- Kurtosis: determines the degree of concentration that the energy samples of the audio signal have around their mean.
- Skewness: symmetry of the distribution of the energy samples of the audio signal with respect to its arithmetic mean.
- Min: minimum energy value in the audio signal.
- Max: maximum energy value in the audio signal.
- Dynamic Range: range of energy between the minimum and the maximum energy values.

2.3 Coefficients LPC y MFCC

The sounds produced by the heart are stochastic, that is, their frequency content and energy level vary over long periods of time, preventing analysis. In order to analyze the cardiac audio signals, it is necessary that they be stationary. Thus, a segmentation and windowing prepossessing step was applied to the audio signals. They were segmented into "frames" of 25 ms to consider them as a quasi-stationary signals. Each frame was overlapped 50% with the adjacent frame to generate smooth transitions between frames. Later, the window was applied

(Hamming window), to eliminate the problems caused by rapid changes of the cardio audio signal at the ends of each frame. This prepossessing step is applied to each cardio sound before computing its LPC and MFCC coefficients.

Linear Predictive Coding (LPC) is based on the fact that each sound sample can be predicted or represented by a linear combination of several samples passed, that is, that each sound sample $s(n)$ at a time n, can be approximated as a linear combination of the samples of previous sound:

$$s(n) \approx a_1 s(n-1) + a_2 s(n-2) + \cdots + a_p s(n-p), \tag{1}$$

where p is the prediction order and $a_1, a_2, \cdots, a_p$ are the prediction coefficients that must be calculated. The basic scheme for calculating LPC is composed of three blocks according to [4]: pre-processing, autocorrelation and LPC analysis.

A matrix that contains each of the overlapped and windowed frames, is obtained from the pre-processing block. Each frame is autocorrelated to analyze the periodicity of the samples that comprise them. In the last block, each of the autocorrelated frames is converted into a set of LPC parameters by the Levinson-Durbin autoregressive algorithm. The LPC coefficients represent the information of the short-time spectral envelope of the sound signals according to [18]. 16 LPC coefficients were calculated per frame and a matrix of coefficients is obtained as shown in Fig. 1. This matrix represents the 16 coefficients per frames of all the frames of the cardio sound under analysis. This type of matrix is obtained for each of the 224 heart sounds.

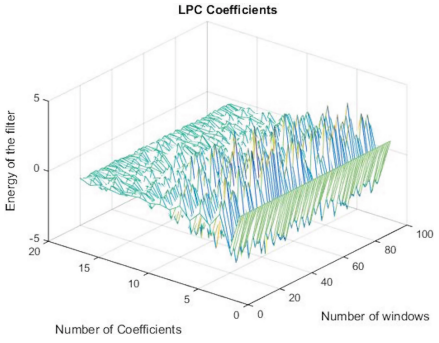

Fig. 1. LPC matrix of 16 coefficients.

Once the matrix of LPC coefficients of each cardiac sound was obtained, all the values of each column of each matrix were averaged to obtain a vector of 16 coefficients that will represent each one of the 224 cardiac sounds.

Cepstral Frequency-Mel Coefficients (MFCC) is a characteristic extraction technique that is based on the perception of the human auditory system, specifically the variation of the bandwidths of the critical frequencies of the human ear. The basic method for the extraction of the MFCC is composed of

four blocks according to [10]; FFT, filter bank, logarithm, and DTC. In the first block, the Fast Fourier Transform (FFT) is calculated to each one of the frames of the cardiac audio signal, previously pre-processed and the magnitude and the power spectral density (DEP) of each frame is obtained. This transformation is done to identify what frequencies each frame contains. The DSP frequencies should be grouped in regions and summed to know how much energy exists in those regions. This is done by Mel filter bank, composed of triangular filters that are distributed in Mel scale. The filter bank is calculated with the Eq. 2.

$$B(m,k) = \begin{cases} 0 & si \quad k > f(m-1), \\ \frac{k-f(m-1)}{f(m)-f(m-1)} & si \; f(m-1) \leq k \leq f(m), \\ \frac{f(m+1)-k}{f(m+1)-f(m)} & si \; f(m) \leq k \leq f(m+1), \\ 0 & si \quad k > f(m+1), \end{cases} \tag{2}$$

where $B(m,k)$ is the matrix of the filter bank, m the number of bank filters and k the number of analysis windows. A filter bank is obtained for each window of the voice signal. The first filter obtained is very narrow and indicates how much energy exists near 0 Hz. As the frequencies increase, the filters expand and the variations are smaller. To know the energy of the filter banks, we must multiply each bank of filters by the power spectral density windows and then add the coefficients:

$$E(m,k) = \sum_{m=1}^{M} B(m,k)P(k) \qquad k = 1, 2, \cdots, K, \tag{3}$$

where $P(k)$ is the power spectral density and k represents the number of windows that go from the first to the K-th window of the cardiac audio signal. Subsequently, the logarithm of the filter bank energies is calculated. This operation makes the obtained characteristics a closer match to what humans actually hear.

$$E_{log}(m,k) = log\left(\sum_{m=1}^{M} B(m,k)P(k)\right) \tag{4}$$

In the last block, the discrete cosine transform of the logarithm of the filter bank energies is calculated to obtain the MFCC [1]. The use of the discrete cosine transform (DCT) is used to reduce computational expenditure [16]. The DCT is defined by:

$$MFCC(n) = \sum_{m=1}^{M} E_{log}(m,k) cos\left[n\left(m-\frac{1}{2}\right)\frac{\pi}{M}\right], \tag{5}$$

where M represents the total number of MFCC coefficients that varies with respect to n, m represents the number of filters in the bank and k represents the number of the analysis window. As in LPC, 16 MFCC coefficients were calculated per frame and a matrix of coefficients is obtained as shown in Fig. 2.

As in LPC, a vector of 16 coefficients MFCC that will represent each one of the 224 cardiac sounds was calculated.

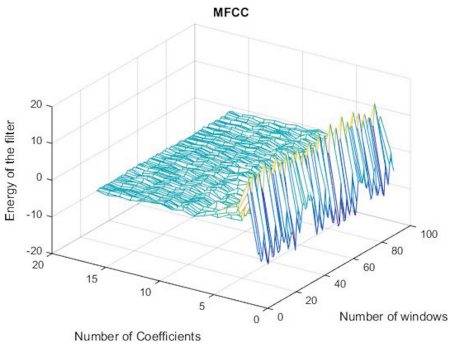

Fig. 2. MFCC matrix of 16 coefficients.

2.4 Database

Once the ten general and statistical features, the 16 LPC coefficients and the 16 MFCC coefficients for each of the cardiac audio signals were calculated, a database was created with 214 samples (112 healthy and 112 unhealthy) and the 42 calculated features.

The genetic algorithm Galgo was used to obtain which of the 42 features were the most significant of the data base, and the following features were obtained: Mean, Kurtosis, MFCC4, MFCC5, MFCC16 and LPC15. These six features were taken as the most significant according to its high fitness, logistic regression was used as the classification method in the internal procedure of Galgo.

2.5 Classification Methods

Three different classification methods were used: Logistic Regression (LR), Neural Networks (NN) and Suport Vector Machine (SVM), which were applied to the database formed by the 224 samples of cardiac sound and its six most significant characteristics (normalized and not normalized). To evaluate these classification methods, the area under the curve (ROC) and the accuracy (ACC) were used as evaluation metrics. The accuracy is computed by the Eq. 6. The ROC is a graph that represents the specificity (true negative rate) against sensitivity (true positive rate) and they are calculated as in Eqs. 7 and 8 respectively.

$$ACC = \frac{TruePositives + TrueNegatives}{TotalExamples} \tag{6}$$

$$Spec = \frac{TrueNegatives}{FalsePositive + TrueNegative} \tag{7}$$

$$Sens = \frac{TruePositives}{FalseNegative + TruePositives} \tag{8}$$

Table 1. ROC obtained from the classification methods

Classification method	ROC	ACC
LR - Normalized	0.7359	0.6670
LR - Not Norm.	0.7419	0.6492
NN - Normalized	0.7558	0.6712
NN - Not Norm.	0.6571	0.6155
SVM - Normalized	0.7426	0.6715
SVM - Not Norm.	0.7504	0.6624

3 Results

The results obtained by the ROC and ACC evaluation metrics, for the different classification methods are shown in Table 1.

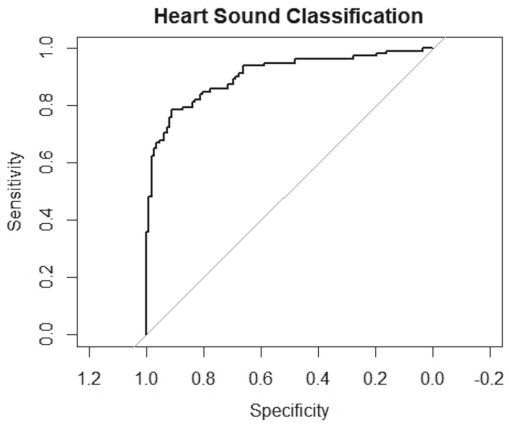

Fig. 3. ROC of the normalized data classified by the Neural Networks method

4 Discussion

Using LPC and MFCC coefficients and statistical features to classify a healthy or unhealthy heart according to the sounds it produces, was possible with the three different classification methods proposed. However, only 6 of the 42 computed features were significant according to the Galgo algorithm. To improve the obtained evaluation metrics values, would be necessary to calculate some other more significative acoustic features, and be able to model the functioning of the heart according to its sounds.

5 Conclusions

The classification method with the best area under the curve was Neural Networks when the data was normalized, as shown in Fig. 3. In turn, the same classification method presented the worst area under the curve, when the data was not normalized. Logistic Regression and Support Vector Machine showed good area under the curve results, but they were a little below the ones resolved by Neural Networks.

Conflict of Interest. The authors declare that they have no conflict of interest.

References

1. Bezoui, M., Elmoutaouakkil, A., Beni-hssane, A.: Feature extraction of some Quranic recitation using mel-frequency cepstral coeficients (MFCC). In: 2016 5th International Conference on Multimedia Computing and Systems (ICMCS), pp. 127–131. IEEE (2016)
2. Walter, C., Tortajada, G., Varela, G.: Predictores de arritmias ventriculares en el infarto agudo de miocardio. Rev. Uruguaya de Cardiol. **29**(1), 122–127 (2014)
3. Deperlioglu, O.: Segmentation of heart sounds by re-sampled signal energy method. BRAIN Broad Res. Artif. Intell. Neurosci. **9**(1), 17–28 (2018)
4. Feraru, S.M., Zbancioc, M.D.: Emotion recognition in Romanian language using lpc features. In: 2013 E-Health and Bioengineering Conference (EHB), pp. 1–4. IEEE (2013)
5. H. Jinich, A. Lifshitz, J.A.G., Ramiro, M.: Síntomas y signos cardinales de las enfermedades. 7 edn. El Manual Moderno S. A. de C.V. (2017)
6. Cruz Ortega, H.A., Calderón Monter, F.X.: "El corazón y sus ruidos cardíacos normales y agregados" una somera revisión del tema. Rev. Fac. Med. UNAM **59**(2), 49–55 (2016)
7. Ibarra, R.F., Alonso, M.A., Villarreal, S., Nieblas, C.I.: A parametric model for heart sounds. In: 2015 49th Asilomar Conference on Signals, Systems and Computers, pp. 765–769. IEEE (2015)
8. INEGI: Características de las Defunciones registradas en México durante 2017 (2018). http://www.beta.inegi.org.mx/contenidos/saladeprensa/boletines/2018/EstSociodemo/-DEFUNCIONES2017.pdf. Accessed 27 Apr 2019
9. L. Martin-Abreu, Martín-Armendariz, L.G.: Fundamentos del Diagnóstico. 11 edn. Méndez Editores (2008)
10. Mascorro, G.A.M., Torres, G.A.: Reconocimiento de voz basado en mfcc, sbc y espectrogramas. Ingenius **10**, 12–20 (2013)
11. Nieblas, C.I., Alonso, M.A., Conte, R., Villarreal, S.: High performance heart sound segmentation algorithm based on matching pursuit. In: 2013 IEEE Digital Signal Processing and Signal Processing Education Meeting (DSP/SPE), pp. 96–100. IEEE (2013)
12. Oliveira, J., Castro, A., Coimbra, M.: Exploring embedding matrices and the entropy gradient for the segmentation of heart sounds in real noisy environments. In: 2014 36th Annual International Conference of the IEEE Engineering in Medicine and Biology Society, pp. 3244–3247. IEEE (2014)

13. OMS: Muertes por causa, edad, sexo, por país y por región 2000-2016. https://www.who.int/es/news-room/fact-sheets/detail/the-top-10-causes-of-death (2016). Accessed 27 Apr 2019
14. Bentley, P., Nordehn, G., Coimbra, M., Getz, R.: Classifying Heart Sounds Challenge. http://www.peterjbentley.com/heartchallenge/#taskoverview (2011). Accessed 1 Feb 2019
15. Pedrosa, J., Castro, A., Vinhoza, T.T.: Automatic heart sound segmentation and murmur detection in pediatric phonocardiograms. In: 2014 36th Annual International Conference of the IEEE Engineering in Medicine and Biology Society, pp. 2294–2297. IEEE (2014)
16. REIG ALBIÑANA, D.: Implementación de algoritmos para la extracción de patrones característicos en Sistemas de Reconocimiento De Voz en Matlab. Ph.D. thesis (2015)
17. Villarroel, H.: Arritmias cardíacas: un manual para estudiantes de medicina y médicos de atenciíon primaria (2006)
18. Wang, L., Chen, Z., Yin, F.: A novel hierarchical decomposition vector quantization method for high-order LPC parameters. IEEE/ACM Trans. Audio Speech Lang. Process. **23**(1), 212–221 (2015)

Nonlinear, Time-Varying and Frequency-Selective Analysis During the Orthostatic Challenge in Patients with Vasovagal Syncope

Laura E. Méndez-Magdaleno[1(✉)], Guadalupe Dorantes-Méndez[1], Sonia Charleston-Villalobos[2], and Tomás Aljama-Corrales[2]

[1] Faculty of Sciences, Universidad Autónoma de San Luis Potosí, San Luis Potosi, Mexico
lauraeu23@gmail.com

[2] Electrical Engineering Department, Universidad Autónoma Metropolitana, Mexico City, Mexico

Abstract. In this study, dynamics of the response to an orthostatic challenge was investigated by the combination of an Empirical Mode Decomposition based method and the time varying nonlinear Point Prediction Error algorithm, used for the analysis of heart rate variability (HRV) calculated from time series of beat-to-beat intervals (BBI), and systolic blood pressure (SBP) in patients with vasovagal syncope (VVS) and healthy subjects to provide more information on the mechanisms leading to changes of the autonomic nervous system. This study included 7 young female patients with vasovagal syncope and 7 age-matched female controls. The subjects were enrolled in a head-up tilt (HUT) test, breathing normally, including 5 min of supine position, 15 s of head-up tilting and 18 min of 70° orthostatic phase. This time-variant, frequency-selective nonlinear analysis seemed to be suitable to distinguish between patients and healthy subjects even in the transition phase. The results allowed us to differentiate the response of patients with VVS and healthy subjects, mainly in the HF band of both the BBI and the SBP time series.

Keywords: Heart rate variability · Nonlinear analysis · Signal-adaptive decomposition · Time-variant analysis · Vasovagal syncope

1 Introduction

Vasovagal syncope (VVS) is a transient loss of consciousness characterized by triggers such as emotional stress (extreme emotions, fear, severe pain, etc.) or orthostatic stress and it is often preceded by symptoms such as excessive sweating, paleness and nausea. During this type of syncope, the cardiovascular reflexes

© Springer Nature Switzerland AG 2020
C. A. González Díaz et al. (Eds.): CLAIB 2019, IFMBE Proceedings 75, pp. 113–120, 2020.
https://doi.org/10.1007/978-3-030-30648-9_16

that control circulation are inadequate intermittently, resulting in a vasodilation and/or bradycardia and additionally a fall in blood pressure and cerebral perfusion [1,2].

VVS is the most frequent type in young people, and its presence is too variable. Typical vasovagal syncope usually begins during early ages, with a higher prevalence in patients between 10 and 30 years old [1].

In clinical practice, the evaluation of the autonomic function associated with vasovagal syncope is mainly carried out through the head-up tilt (HUT) test, which allows the reproduction of symptoms in a controlled environment. The main determinants to generate the syncope are the table inclination angle and duration of the test [3]. After a certain time in the orthostatic position and close to syncope, this test increases parasympathetic activity and reduces sympathetic activity, generating bradycardia, vasodilation and hypotension. It is a particularly useful technique for the diagnosis of atypical vasovagal syncope, since it distinguishes syncope from seizures, psychogenic pseudo-syncope, orthostatic hypotension and postural orthostatic tachycardia syndrome [2].

The analysis of the autonomic nervous system (ANS) response to the orthostatic challenge in healthy subjects and in subjects with VVS has been studied mainly from a linear and in an univariate perspective [4–6]. However, the analysis of the cardiovascular variability signals considering their nonlinear origin can generate information to better elucidate the physiological phenomena that occur in normal and pathological conditions.

In addition, standard approaches assume stationary observations and, therefore, fail to follow the time-varying changes in nonlinear information transfer, as presented in physiological systems. For this reason, time-varying techniques have been applied to physiological signals in order to better evaluate the response of such systems, such as the Point Prediction Error (PPE) [7] algorithm, as well as its combination with the complete empirical mode decomposition as a non-linear, time-variant and frequency-selective examination [8].

The aim of this work is to perform a time-varying analysis to better describe the changes that occur during the orthostatic challenge, that is, the early and late response of regulation of the systems involved, as well as including the analysis of the transition phase of the posture change. Former studies found in the literature evaluate each inclination stage individually, excluding the transition phase due to its short duration.

2 Methods

2.1 Subjects and Experimental Protocol

In this study, time series of successive beat-to-beat intervals (BBI) and systolic blood pressure (SBP) amplitude were selected of 7 female patients diagnosed with VVS with a mean age of 26 ± 8 years and 7 age-matched female controls [9]. Controls were healthy volunteers with no syncope or presyncope history and negative HUT test. None of the healthy subjects presented signs of autonomic

disorders or took any medication, including contraceptives in women. All subjects refrained from drinking coffee or alcoholic beverages for at least one week prior to the study.

The signals were acquired through the HUT test, carried out at the National Institute of Cardiology (NIC). First, the subjects were placed on the table in a supine position to guarantee a stable initial condition. The test started with a rest period of 5 min in the supine position, and then during 15 s, the subject underwent a 70° head-up tilt.

The duration of the following orthostatic phase varied between 30 and 40 min in case of the controls. Regarding patients, the HUT test was aborted by returning the tilt table back to supine position if the patient developed symptoms of presyncope during orthostatic phase. This reduced the maximal comparable duration of orthostatic phase between patients and controls down to 18 min. Studies were approved by the Ethics Committee of the NIC and performed under informed consent according to the Declaration of Helsinki.

2.2 Cardiovascular Variability Analysis

The Complete Ensemble Empirical Mode Descomposition with Adaptive Noise (CEEMDAN) has been used to calculate the frequency components of the signals, which have been subsequently analyzed using the time variant algorithm PPE. In this way, the heart rate characteristics, as well as the systolic blood pressure can be analyzed in a time-varying way and selectively in frequency.

Complete Ensemble Empirical Mode Decomposition. Empirical Mode Decomposition (EMD) is a method that has been applied to study the nonlinear and non-stationary properties of a time series. EMD method separates time-series into intrinsic oscillations called an Intrinsic Mode Functions (IMFs) using local temporal and structural characteristics of the data.

The computation of an IMF by the iterative EMD algorithm [10] can be summarized as follows.

1. Identification of all the extrema (maxima and minima) of the series X.
2. Generation of the upper and lower envelope via cubic spline interpolation among all the maxima and minima, respectively.
3. Point by point averaging of the two envelopes to compute a local mean series m.
4. Subtraction of m from the data to obtain a IMF candidate $h = X - m$.
5. Check the properties of h:
   - if h doesn't satisfy the IMF properties, replace X with h and repeat the procedure.
   - if h satisfy the IMF properties, evaluate the residue $r = X - h$.
6. Repeat the procedure from Steps 1 to 5 by sifting the residual signal. The sifting process ends when the residue r satisfies a predefined stopping criterion.

The criterion to stop the sifting process is defined in Eq. 1.

$$SD = \sum_{t=0}^{T} \frac{(|h_{k-1}(t) - h_k(t)|)^2}{h_{k-1}^2(t)} \tag{1}$$

where SD is the difference between the previous and the current IMF, h is the IMF and k represents the iteration number during the sifting process.

The Ensemble EMD relies on averaging the modes obtained by EMD applied to several realizations of Gaussian white noise added to the original signals and solves the EMD mode mixing problem [11]. However, the Complete Ensemble EMD provides a better spectral separation of the modes by adding white noise realizations of finite variance at each stage of the decomposition [12]. Due to its advantages, the CEEMDAN algorithm was used to separate the series of BBI and SBP into IMFs.

The sum of IMFs corresponding to the bands of high (HF), low (LF) and very low (VLF) frequencies was performed, and the time variable analysis was carried out through the Point Prediction Error algorithm.

Point Prediction Error. The IMFs preserve the non-linear properties of the signal, allowing the combination of CEEMDAN with a non-linear measure dependent on time as Point Prediction Error [7]. This algorithm is developed as follows: a one dimensional signal $x(t)$ is transformed into a multidimensional phase space by means of a time delay according to

$$T(t) = \{x(t), x(t-\tau), ..., x(t-(D_e-1)\cdot\tau\} \tag{2}$$

where $T(t)$ is the trajectory in the phase space, τ is the time delay, and D_e is the embedding dimension. A time delay of $\tau = 3$ and an embedding dimension of $D_e = 4$ were used for our analysis. The false nearest neighbor approach was used to set a sufficient embedding dimension while the time delay was estimated depending on the mutual information.

The analysis is based on the approach of Wolf et al. [13] for the estimation of the largest Lyapunov exponent, but measures the local exponential divergence of trajectories in the phase space. The nearest Euclidean neighbor must be searched for each point on a trajectory in the phase space and changes in the distance between these points are evaluated after evolving a specific time step by

$$PPE(t) = \frac{f_s}{k} \log_2 \frac{D(t+k)}{D(t)} \tag{3}$$

where t is the actual time point, $PPE(t)$ is the resulting sequence of locally estimated $PPEs$, f_s is the sampling frequency, k is the evolved time steps, $D(t)$ is the Euclidean distance to the next neighbor in the phase space at the time point t, and $D(t+k)$ is the evolved distance at time point $t+k$. Equation 3 reflects the degree of stability of any time point in relation to its initial condition.

A positive PPE is equivalent to a divergence of neighboring points in the phase space and indicates a low predictability, while a negative or vanishing PPE describes convergence in the phase space and indicates a high predictability [8].

The time series analysis was performed taking into account 3 min of the baseline, 15 s of the transition phase and 10 min of the orthostatic phase. The time series of BBI and SBP were separated into IMFs using the CEEMDAN algorithm with a noise standard deviation equal to 0.1. Subsequently, the IMFs sum corresponding to the HF, LF and VLF bands, as well as the original time series of BBI and SBP, were analyzed using the PPE algorithm with different values of the k parameter and those results that presented more statistical differences are shown.

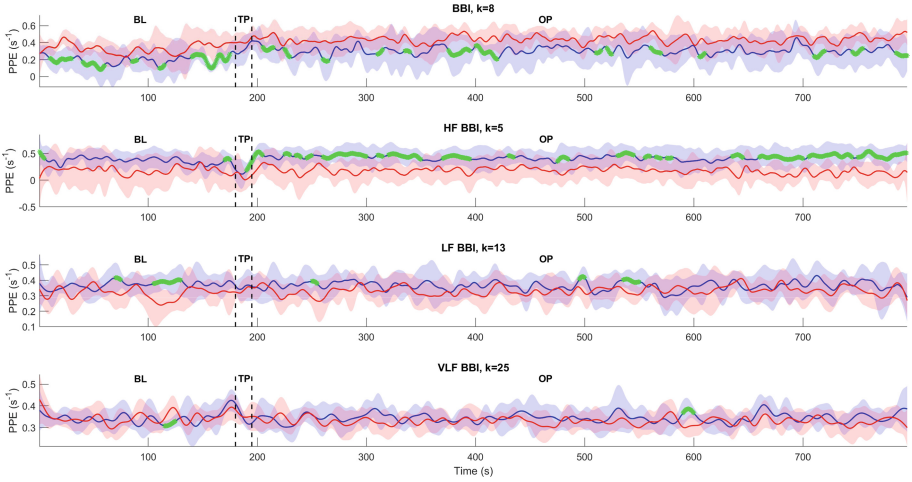

Fig. 1. Mean PPE of the original BBI time series, as well as its HF, LF and VLF bands. Red line shows the results of the patients with VVS and blue line shows the results of the control subjects. BL: baseline. TP: transition phase. OP: orthostatic phase. Green bold line indicate significant differences between healthy subjects and patients with VVS ($p < 0.05$).

2.3 Statistical Analysis

The normality criterion of the time series resulting from PPE was evaluated in windows of 5 s, through the lilliefors test. The differences between the two populations were evaluated using the Student's t-test for 2 independent samples, as well as the Wilcoxon test for the values that did not present a normal distribution. Statistically significant differences were considered with $p < 0.05$.

3 Results and Discussion

The results of the PPE of the BBI series and their respective HF, LF and VLF bands are shown in Fig. 1. The results of the BBI series showed significant differences between both groups mainly during the baseline and at some time instants

of the orthostatic phase. Despite not finding differences during the transition phase, an increase in the PPE of control subjects is observed throughout this phase, which indicates that the BBI becomes more variable. Additionally, the PPE values of the HF band significantly decreased in the VVS patients with respect to healthy subjects before and during transition phase and throughout most of the orthostatic phase, this indicates that the response in HF of VVS patients have less variability throughout the entire test. This result could suggest that there is a decrease in the vagal activity of VVS patients with respect to healthy subjects throughout the entire HUT test.

In the LF band few significant differences are found during baseline and orthostatic phase. However, the LF response of VVS patients is slightly diminished during the test with respect to healthy subjects, so it's suggested that the sympathetic response also decreases in VVS patients but this is not conclusive because there are very few statistical significances in orthostatic phase. In the case of VLF, there is uncertainty regarding the physiological mechanisms responsible for activity within this band. The heart's intrinsic nervous system appears to contribute to the VLF rhythm and the sympathetic nervous system influences the amplitude and frequency of its oscillations, but may also be generated by physical activity, thermoregulatory, renin-angiotensin, and endothelial influences on the heart [14]. In the results of the VLF band of the BBI, we can see that the response of both study groups is overlapped, and that only very few instants are significantly different between them.

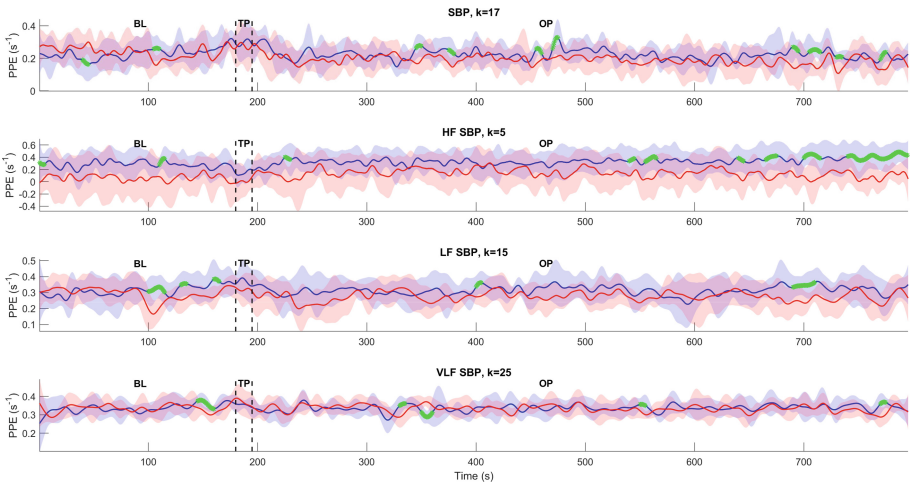

Fig. 2. Mean PPE of the SBP time series, as well as its HF, LF and VLF bands. Red line shows the results of the patients with VVS and blue line shows the results of the control subjects. BL: baseline. TP: transition phase. OP: orthostatic phase. Green bold line indicate significant differences between healthy subjects and patients with VVS ($p < 0.05$).

The PPE results of the SBP are shown in Fig. 2. In this case, neither the results of the SBP nor those of its HF, LF and VLF bands showed significant differences during the transition phase. SBP and its bands HF, LF and VLF of control subjects were significantly different from VVS patients in some time instants of the baseline and the orthostatic phase, particularly in the HF band, where a decrease in the PPE values of the VVS patients is more evident, as in the results of the HF band of the BBI time series, which suggest that the mechanical influence of respiration from VVS patients decreases during HUT test.

4 Conclusion

The performed analysis presents a combination of time-varying, frequency-selective methods, by which specific non-linear HRV properties of patients with VVS and healthy subjects can be revealed even from the transition phase. The main advantage of this methodology is that it allows us to analyze the predictability changes of the signals of interest throughout the entire test.

Significant differences were found between healthy subjects and VVS patients, mainly during baseline and orthostatic phase. In addition, the frequency separation allowed to find significant differences between both groups even during the transition phase. This may suggest that VVS patients have a different response to orthostatic stress from the first instants of the HUT test, and not only until a late phase of orthostatic phase where pre-syncope symptoms are already generated.

It is important to consider that the results are dependent on the correct selection of parameters, so it is suggested to propose new strategies for the appropriate selection of parameters used in the PPE algorithm, as well as to extend the study to a larger population in order to evaluate whether the time-varying and frequency-selective analysis is a method that would allow to detect changes in the response of VVS patients even from transition phase.

Conflict of Interest. The authors declare that they have no conflict of interest.

References

1. Moya, A., et al.: Guidelines for the diagnosis and management of syncope (version 2009). The task force for the diagnosis and management of syncope of the european society of cardiology (ESC). Eur. Heart J. **30**(21), 2631–2671 (2009). https://doi.org/10.1093/eurheartj/ehp298
2. Kenny, R., McNicholas, T.: The management of vasovagal syncope. QJM: Int. J. Med. **109**(12), 767–773 (2016). https://doi.org/10.1093/qjmed/hcw089
3. Parry, S., Kenny, R.: Tilt table testing in the diagnosis of unexplained syncope. QJM: Int. J. Med. **92**(11), 623–629 (1999). https://doi.org/10.1093/qjmed/92.11.623
4. Dickhaus, H., Maier, C., Khalil, M., Ulmer, H.: Short-term heart rate variability response to head-up tilt in young syncope patients and controls with respect to age. In: 2006 International Conference of the IEEE Engineering in Medicine and Biology Society, pp. 6430–6433 (2006). https://doi.org/10.1109/IEMBS.2006.260143

5. Maier, C., Magerl, M., Khalil, M., Ulmer, H., Dickhaus, H.: Age-dependent response of heart rate variability parameters to head-up tilt tests in young syncope patients and controls. In: 2006 Computers in Cardiology, pp. 861–864 (2006)
6. Kochiadakis, G.E., Lees, P.J., Kanoupakis, E.M., Igoumenidis, N.E., Manios, E.G., Vardas, P.E.: Spectral analysis of heart rate variability in the analysis of autonomic nervous system activity during tilt-table testing in patients with unexplained syncope. Comput. Cardiol. **1997**, 367–369 (1997). https://doi.org/10.1109/CIC.1997.647909
7. Schwab, K., Groh, T., Schwab, M., Witte, H.: Nonlinear analysis and modeling of cortical activation and deactivation patterns in the immature fetal electrocorticogram. Chaos: Interdisc. J. Nonlinear Sci. **19**(1), 015111 (2009). https://doi.org/10.1063/1.3100546
8. Schiecke, K., Wacker, M., Piper, D., Benninger, F., Feucht, M., Witte, H.: Time-variant, frequency-selective, linear and nonlinear analysis of heart rate variability in children with temporal lobe epilepsy. IEEE Trans. Biomed. Eng. **61**(6), 1798–1808 (2014). https://doi.org/10.1109/TBME.2014.2307481
9. Reulecke, S., Charleston-Villalobos, S., Voss, A., González-Camarena, R., González-Hermosillo, J., Gaitán-González, M., Hernández-Pacheco, G., Schroeder, R., Aljama-Corrales, T.: Orthostatic stress causes immediately increased blood pressure variability in women with vasovagal syncope. Comput. Methods Program. Biomed. **127**, 185–196 (2016). https://doi.org/10.1016/j.cmpb.2015.12.005
10. Huang, N.E., Shen, Z., Long, S.R., Wu, M.C., Shih, H.H., Zheng, Q., Yen, N.C., Tung, C.C., Liu, H.H.: The empirical mode decomposition and the Hilbert spectrum for nonlinear and non-stationary time series analysis. Proc. Roy. Soc. London A: Math. Phys. Eng. Sci. **454**(1971), 903–995 (1998). https://doi.org/10.1098/rspa.1998.0193
11. Wu, Z., Huang, N.E.: Ensemble empirical mode decomposition: a noise-assisted data analysis method. Adv. Adaptive Data Anal. **01**(01), 1–41 (2009). https://doi.org/10.1142/S1793536909000047
12. Torres, M.E., Colominas, M.A., Schlotthauer, G., Flandrin, P.: A complete ensemble empirical mode decomposition with adaptive noise. In: 2011 IEEE International Conference on Acoustics, Speech and Signal Processing (ICASSP), pp. 4144–4147 (2011). https://doi.org/10.1109/ICASSP.2011.5947265
13. Wolf, A., Swift, J.B., Swinney, H.L., Vastano, J.A.: Determining lyapunov exponents from a time series. Phys. D **16**(3), 285–317 (1985). https://doi.org/10.1016/0167-2789(85)90011-9
14. Shaffer, F., Ginsberg, J.: An overview of heart rate variability metrics andnorms. Front. Public Health **5**, 258 (2017). https://doi.org/10.3389/fpubh.2017.00258

Feature Selection and Machine Learning Applied for Alzheimer's Disease Classification

Ana Gabriela Sánchez-Reyna(✉), Carlos H. Espino-Salinas, Pablo C. Rodríguez-Aguayo, Jared D. Salinas-Gonzalez, Laura A. Zanella-Calzada, Elda Y. Martínez-Escobar, José M. Celaya-Padilla, Jorge I. Galván-Tejada, Carlos E. Galván-Tejada, and for the Alzheimer's Disease Neuroimaging Initiative

Unidad Académica de Ingeniería Eléctrica, Universidad Autónoma de Zacatecas, Jardín Juarez 147, Centro, 98000 Zacatecas, Zac, Mexico
ing.agsreyna19@gmail.com, gatejo@uaz.edu.mx
http://uaz.edu.mx

Abstract. Alzheimer disease (AD) is the most common type of dementia and one of the most serious mental health problems. Based on data analysis for classification of dementia, it is possible to distinguish the subjects into three groups: cognitively normal (CN), mild cognitive impairment (MCI) and AD. In this paper, the information of 628 patients from the Alzheimer's Disease Neuroimaging Initiative (ADNI) (Data used in preparation of this article were obtained from the Alzheimer's Disease Neuroimaging Initiative (ADNI) database (adni.loni.usc.edu). As such, the investigators within the ADNI contributed to the design and implementation of ADNI and/or provided data but did not participate in analysis or writing of this report. A complete listing of ADNI investigators can be found at: http://adni.loni.usc.edu/wp-content/uploads/how_to_apply/ADNI_Acknowledgement_List.pdf.) database was used which contains 2163 features in order to select the most significant features that allows to the classification of CN vs. MCI/AD, the genetic package GALGO was applied to the features in which four features were selected and four classification techniques were used: Logistic Regression (LR), Random Forest (RF), Artificial Neural Networks (ANN) and Support Vector Machines (SVM). A cross validation of 70% training 30% test. According to the results, the technique with the most significant area under the curve (AUC) for the classification the subjects was LR presenting a value of 0.842.

Keywords: Alzheimer disease · Feature selection · Classification · Logistic regression · Artificial Neural Network · Support Vector Machine · Random Forest

© Springer Nature Switzerland AG 2020
C. A. González Díaz et al. (Eds.): CLAIB 2019, IFMBE Proceedings 75, pp. 121–128, 2020.
https://doi.org/10.1007/978-3-030-30648-9_17

1 Introduction

According to the Alzheimer's Disease International (ADI), around 50 million people presented dementia worldwide in 2018. One of the types of dementia that increases its presence over time is Alzheimer's disease (AD), mainly affecting elder adults. Every year the ADI reports the global impact of dementia, estimating that by the year 2050 the incidence of people with some type of dementia will increase three times, reaching around 152 million people [1,2].

AD is the most common neurodegenerative disease and it is mainly associated with the aggregation of β-amyloid, hyperphosphorylated tau, synaptic dysfunction and neuronal loss. The development of biomarkers for early detection of AD can help to start treatment early and thus have better control of the disease [3,4]. For the detection of Alzheimer's disease it is necessary to go through a series of interviews, tests and laboratory analysis. Using algorithms for data analysis, it is workable to analyze the Alzheimer's Disease Neuroimaging Initiative (ADNI) database, with it is possible to detect changes related to Alzheimer's disease.

1.1 Related Work

Different approaches has been applied for the AD disease using machine learning models one of the most used are the Deep Learning architectures for the followings specific purposes:

- Classify AD patients from CN.
- Classify patients with MCI form the prodromal stage of AD.
- Predict the conversion of MCI to AD.

These models used MRI data where Deep Learning architectures were applied for the image processing, feature selection and the diagnostic classification of the disease. Because Deep Learning architectures works better with a high amount of data for obtaining the best accuracy performances without overfitting the classification [5]. On our approach, the ADNI dataset database was used as our data source for the feature selection genetic algorithm was proposed for identifying the best features that describes the AD disease, and for the classification more simply machine learning's models were used such as LR. This approach is less complex computational that deep learning architectures.

2 Materials and Methods

The methodology proposed in this work is contained by four main stages. Initially, the data are obtained from the ADNI database. Then, a data preprocessing is applied for a subsequent feature selection based on a genetic algorithm, using four different classification techniques, logistic regression (LR), artificial neural networks (ANN), support vector machine (SVM) and random forest (RF).

Fig. 1. Flowchart of the methodology proposed. The green squares refer to the data processing methodology while the gray squares detail the task involved in each step.

Finally, a validation is carried out using different metrics to determine the performance of each technique (Fig. 1).

Data used in the preparation of this article were obtained from the Alzheimer's Disease Neuroimaging Initiative (ADNI) database (adni.loni.usc.edu). The ADNI was launched in 2003 as a public-private partnership, led by Principal Investigator Michael W. Weiner, MD. The primary goal of ADNI has been to test whether serial magnetic resonance imaging (MRI), positron emission tomography (PET), other biological markers, and clinical and neuropsychological assessment can be combined to measure the progression of mild cognitive impairment (MCI) and early Alzheimer's disease (AD). For up-to-date information, see www.adni-info.org.

All processing and analysis performed in this research was carried out in R (version 3.5.3) [6], which is a *free software environment for statistical computing and graphics*. The libraries used are the following: *GALGO* (version 1.2-01) [7], *randomForest* (version 4.6-14) [8], *e1071* (version 1.7-0) for SVM [9] and *pROC* (version 1.11.0) [10].

Dataset Description

Data used in the preparation of this article were obtained from the Alzheimer's Disease Neuroimaging Initiative (ADNI) database (adni.loni.usc.edu). The ADNI was launched in 2003 as a public-private partnership, led by Principal Investigator Michael W. Weiner, MD. The primary goal of ADNI has been to test whether serial magnetic resonance imaging (MRI), positron emission tomography (PET), other biological markers, and clinical and neuropsychological assessment can be combined to measure the progression of mild cognitive impairment (MCI) and early Alzheimer's disease (AD).

From the above database, we used the *ADNI baseline data* [11], containing information which corresponds to certain brain areas, Mini-Mental State Examination (MMSE), ApoE4 [12], gender(264 Female/364 Male), age (75.16 +/− 6.68 years) and diagnosis (CN/MCI/AD) of the subjects (AD = 133, CN = 190, MCI = 305). For this work MCI and AD are joined in order to present a binary problem.

Data Preprocessing
For this stage, two main steps were applied: the conversion of the output data into a binary format and the manual reduction of non-useful features. When the patient diagnosis presents absence of MCI or AD disorder, a "0" is assigned, if the patient diagnosis presents MCI or AD, a "1" is assigned. Finally, a standard normalization is applied to the data in order to present a mean value of zero and a standard deviation value of one.

Feature Selection
The objective of the feature selection is to avoid overfitting during the classification analysis, as well as improving its performance, through the reduction of the features.

Due to the large number of characteristics (2163 features), looking for the model that allows to the classification of healthy and sick subjects, becomes a very complex problem, so it was decided to use an evolutionary approach that would allow to select only those features that, in conjunction, obtain the best classification of the subjects.

In this step, the genetic algorithm GALGO (GA) was used to select the top four features. GA presents a schematic representation of a multivariate variable selection of two classes, which involves the combination of genes or features, (chromosomes that represent the multivariable model) that allows to distinguish between classes based on a classification method, where a number of models that perform this processing are generated multiple times. Due to the stochasticity of the data, these models may differ from the genetic content, but with similar classification accuracy. Where the genes that appear multiple times differ in the models that suggest the important features for the classification of the problem in context. Finally, a forward selection and backward elimination steps are applied, obtaining the most representative model that generates the smallest error.

Classification Analysis
During the classification analysis, the ADNI database (Sect. 2) is divided into two subsets: training and testing. The training subset consists on 70% of the data and the subset of tests on 30%. The distribution of the data is generated pseudo-randomly.

For this step four techniques were applied: RL, ANN, SVM and RF.

3 Validation

Finally, the results were validated through the following metrics: accuracy, sensitivity, specificity, area under the curve and F1 score, establishing a relationship between the results obtained and thus determining which of the different classification algorithms is the most optimal to identify patients with Alzheimer's and what characteristics are more meaningful to obtain the most successful results.

4 Results and Discussion

After the feature selection, from the 2163 initial features the most important were selected, being: *MMSE*, *mean.curvature..median.1006*, *mean.curvature..mean.1006* and *FreeSurfer.thickness..kurtosis.1017*, represented in Fig. 2 where a graph of the frequency of appearance of each feature is shown, being the features in black those with the highest rank.

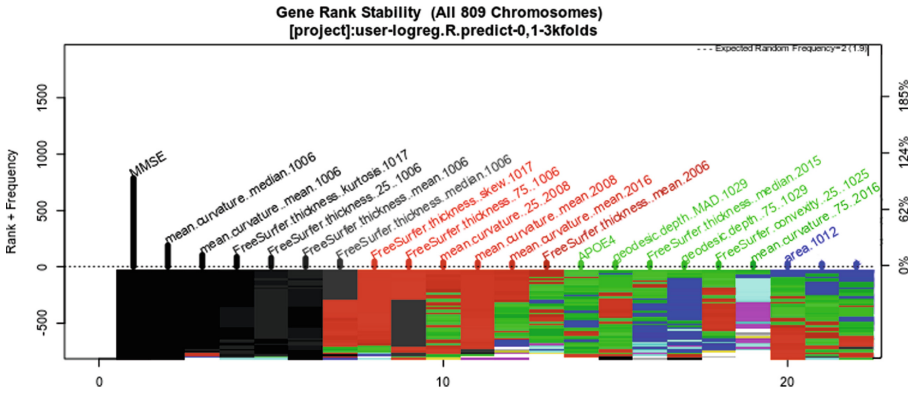

Fig. 2. Most relevant features obtain out of the Genetic Algorithm.

The results obtained are shown in Table 1. Based on these results, it can be observed that in each of the comparative validation metrics (Accuracy, Sensitivity, Specificity, AUC and F1 Score), the logistic regression within a set of applied techniques of supervised machine learning obtains the best performance for a classification of patients with AD / MCI since their index is higher each of these metrics.

Table 1. Metrics obtain out the selected features applied on each ML model of the test dataset.

Metrics	LR	ANN	SVM	RF
Accuracy	0.856	0.845	0.840	0.818
Sensitivity	0.912	0.904	0.910	0.870
Specificity	0.742	0.725	0.707	0.701
AUC	0.842	0.829	0.830	0.785
F1 score	0.894	0.887	0.881	0.870

As a validation metric for the model with the best accuracy was generated an AUC. Although the AUC of the ANN, LR and SVM models are similar, the value

with the highest AUC is 0.842, this value corresponds to the logistic regression model. The value of AUC has the capacity to differentiate patients from each other; this means that among the 188 test patients, 115 were diagnosed as NC and 46 as MCI/AD. To each of the models (ANN, LR, RF, SVM) the same type of AUC validation metric was applied, as shown in the Fig. 3.

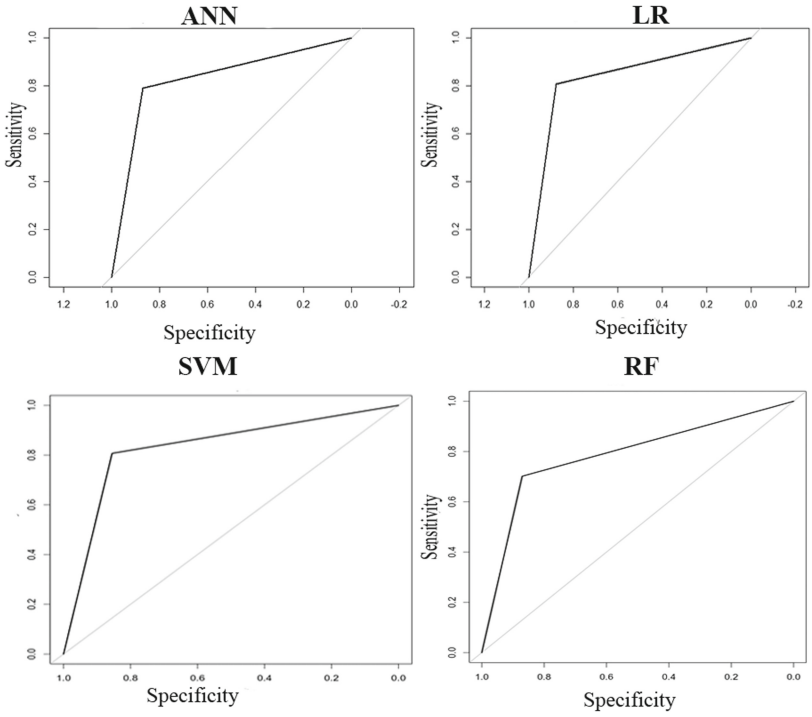

Fig. 3. Comparison of the ROC curves of the different models applied.

5 Conclusions and Future Work

Based on these results, the use of machine learning models with emphasis in LR can be used for the classification and identification of patients with presence of AD, for this reason specialized software and hardware can be developed for the analysis and control of this illness. The selected features by GA can be used as well for searching recognition patterns in order to have a better comprehension of the Alzheimer disease. As future work, it is proposed to increase the number of iterations through the GA so that in the data processing phase the models results will be more accurate compared to this iteration, also to apply a principal component analysis (PCA) in order to select the best relevant features based on a covariance analysis.

Acknowledgments. Data collection and sharing for this project was funded by the Alzheimer's Disease Neuroimaging Initiative (ADNI) (National Institutes of Health Grant U01 AG024904) and DOD ADNI (Department of Defense award number W81XWH-12-2-0012). ADNI is funded by the National Institute on Aging, the National Institute of Biomedical Imaging and Bioengineering, and through generous contributions from the following: AbbVie, Alzheimer's Association; Alzheimer's Drug Discovery Foundation; Araclon Biotech; BioClinica, Inc.; Biogen; Bristol-Myers Squibb Company; CereSpir, Inc.; Cogstate; Eisai Inc.; Elan Pharmaceuticals, Inc.; Eli Lilly and Company; EuroImmun; F. Hoffmann-La Roche Ltd and its affiliated company Genentech, Inc.; Fujirebio; GE Healthcare; IXICO Ltd.; Janssen Alzheimer Immunotherapy Research & Development, LLC.; Johnson & Johnson Pharmaceutical Research & Development LLC.; Lumosity; Lundbeck; Merck & Co., Inc.; Meso Scale Diagnostics, LLC.; NeuroRx Research; Neurotrack Technologies; Novartis Pharmaceuticals Corporation; Pfizer Inc.; Piramal Imaging; Servier; Takeda Pharmaceutical Company; and Transition Therapeutics. The Canadian Institutes of Health Research is providing funds to support ADNI clinical sites in Canada. Private sector contributions are facilitated by the Foundation for the National Institutes of Health (www.fnih.org). The grantee organization is the Northern California Institute for Research and Education, and the study is coordinated by the Alzheimer's Therapeutic Research Institute at the University of Southern California. ADNI data are disseminated by the Laboratory for Neuro Imaging at the University of Southern California.

References

1. Prince, M., et al.: World Alzheimer report 2015 the global impact of dementia an analysis of prevalence, incidence, cost and trends. Technical report, Alzeimer's Disease International, United Kindom (2015). www.alz.co.uk/worldreport2015corrections
2. Patterson, C.: World Alzheimer report 2018 - the state of the art of dementia research: new frontiers; World Alzheimer report 2018 - the state of the art of dementia research: New frontiers. Technical report, pp. 1–8. Alzheimer's Disease International (ADI), London (2018). https://www.alz.co.uk/research/WorldAlzheimerReport2018.pdf
3. Casanova, R., et al.: Alzheimer's disease risk assessment using large- scale machine learning methods. PLoS One **8**(11), e77949 (2013). https://doi.org/10.1371/journal.pone.0077949. Ed. by Stephen D Ginsberg
4. Hinrichs, C., et al.: Predictive markers for AD in a multi-modality frame- work: an analysis of MCI progression in the ADNI population. Neuroimage **55**, 574–589 (2011)
5. Jo, T., Nho, K., Saykin, A.J.: Deep learning in Alzheimer's disease: diagnostic classification and prognostic prediction using neuroimaging data. arXiv e-prints, May 2019. http://arxiv.org/abs/1905.00931
6. R Core Team: The R Project for Statistical Computing (2019). https://www.r-project.org/
7. Trevino, V., Falciani, F.: GALGO An R package for genetic algorithm searches (customized for variable selection in functional genomics). Technical report (2005). http://www.wag-inc.org
8. Liaw, A., Wiener, M.: Classification and Regression by randomForest. Technical repot, vol. 3, pp. 18–22 (2002). https://www.r-project.org/doc/Rnews/Rnews2002-3.pdf

9. Meyer, D.: Support vector machines * the interface to LIBSVM in pack- age e1071. Technical report, pp. 1–8. FH Technikum, Wien (2019). http://www.csie.ntu.edu.tw/~cjlin/papers/ijcnn.ps.gz
10. Robin, X., et al.: pROC: an open-source package for R and S+ to analyze and compare ROC curves. BMC Bioinform. **12**(1), 77 (2011). https://doi.org/10.1186/1471-2105-12-77. https://bmcbioinformatics.biomedcentral.com/articles/10.1186/1471-2105-12-77
11. ADNI - Alzheimer's Disease Neuroimaging Initiative (2003). http://adni.loni.usc.edu/
12. Honea, R.A., et al.: Impact of APOE on the healthy aging brain: a voxel- based MRI and DTI study. J. Alzheimers Dis. **18**, 553–564 (2009)

Fuzzy Logic as a Control Strategy to Command a Deep Brain Stimulator in Patients with Parkinson Disease

Gabriel Martín Bellino[1,2(✉)], Carlos Rodolfo Ramirez[1], Alejandro Miguel Massafra[1], and Luciano Schiaffino[1,2]

[1] Faculty of Engineering, National University of Entre Ríos, Ruta 11, Km 10, Oro Verde, Argentina
gabriel.bellino@gmail.com
[2] Faculty of Life and Health Sciences, Autonomous University of Entre Ríos, Alem 217, Paraná, Argentina

Abstract. Deep brain stimulation (DBS) of the subthalamic nuclei (STN) is the most used surgical treatment to improve motor skills in patients with Parkinson's disease (PD) who do not respond well to pharmacological treatment. Currently, DBS operates in open-loop mode stimulating with constant parameters. A way to improve the therapy is modeling a closed-loop DBS system that automatically adjusts the stimulation parameters based on the clinical and/or neural state of the patient. Fuzzy logic was used to design three models: two *Mamdani*-type models, varying the defuzzification method, and a *Sugeno*-type one. The inputs for all models were the beta oscillation power calculated from local field potential and the magnitude of the acceleration recorded from a smart watch. Total electrical energy delivered (TEED) and theoretical charge density in the STN (Q) was calculated in order to evaluate the performance of the algorithms. The model with the lowest TEED was the *Mamdani*-Bisector type with 136.80 ± 59.07 μW, followed by the *Mamdani*-Centroid type with 138.90 ± 57.22 μW, being 66% lower than open loop DBS. *Mamdani*-Centroid had the lowest maximum Q and a smooth output for the *trials* tested, with gradual changes in the control surface. Therefore, the *Mamdani*-Centroid model resulted to be the best control strategy to implement a closed-loop DBS system in our study.

Keywords: Fuzzy logic · Closed-loop deep brain stimulation · Parkinson's disease

1 Introduction

Parkinson's disease (PD) is a chronic neurodegenerative disorder manifested by 4 common motor symptoms: bradykinesia, rigidity, tremor at rest and postural instability. Deep Brain Stimulation (DBS) is an effective therapy to treat the symptoms of PD and consists in the release of a pulsed electrical current in a deep structure of the brain. The implantable pulse generator (IPG) delivers these pulses with controllable amplitude,

© Springer Nature Switzerland AG 2020
C. A. González Díaz et al. (Eds.): CLAIB 2019, IFMBE Proceedings 75, pp. 129–137, 2020.
https://doi.org/10.1007/978-3-030-30648-9_18

frequency and pulse width, through a stimulation electrode implanted in the subthalamic nucleus (STN) or in the globus pallidus in its internal segment (GPi) [1].

The current DBS devices work by stimulating the STN/GPi with constant parameters fixed in the postoperative stage by a trained neurophysiologist. Programming these devices in order to find the appropriate stimulation parameters may require up to 6 months. In addition, an inadequate programming may lead to tissue damage or induce psychological and cognitive side effects if the recommended charge density of 30 $\mu C/cm^2$ is exceeded [2]. The battery life of IPG depends on the programmed stimulation parameters and the tissue impedance checks [2].

Although DBS provides an acceptable solution for PD symptoms, it works by constantly stimulating without relying on the clinical and/or neural state of the patient in real time, a method called open-loop DBS. DBS therapy can be significantly improved by automatically adjusting the stimulation in response to biological signals such as neuronal states and signs of motor abnormalities called biomarkers. This way of operating is known as closed-loop DBS, or adaptive DBS.

In 2013, Little et al. presented the first report on the use of closed-loop DBS in eight patients with PD. The device was controlled by a brain-computer interface that analyzed the local field potentials (LFP) activity in the beta frequency band and activated the stimulation when exceeding a threshold. Closed-loop DBS showed improvements of 49.7% to 66.2%, and decreased the time of on-stimulation by 56%, compared to open loop DBS [3]. In 2017, Herron et al. conducted experiences in patients using inertial records obtained from a smart watch as a feedback variable for a closed-loop algorithm. In this work, a 53.2% and 84.5% reduction in the energy used by the IPG was achieved, with regard to the open-loop DBS [4].

Although the results of [3, 4] are encouraging, the biomarkers used characterize some of the cardinal symptoms of the disease, leaving the others out of study. In the present work, different control models were designed to operate in a closed-loop manner to command a DBS.

2 Materials and Methods

Based on the state of the art of closed-loop DBS and experimental tests performed by the authors of this study, it is proposed to use two biomarkers, combining an internal biomarker (IB) and an external one (EB). The adopted IB is the power of the beta frequency band (BP) obtained from an LFP register [3], which represents the oscillatory electrical activity of a neuronal population close to the electrode, and the selected EB is the magnitude of the acceleration (MA) obtained by inertial sensors [4], as can be seen in Fig. 1. The LFP have the advantage that no other surgical intervention is needed to implant recording electrodes, as they can be obtained by the same stimulation electrodes. On the other hand, inertial registers as EB are not invasive and can be acquired by portable devices, such as smart watches.

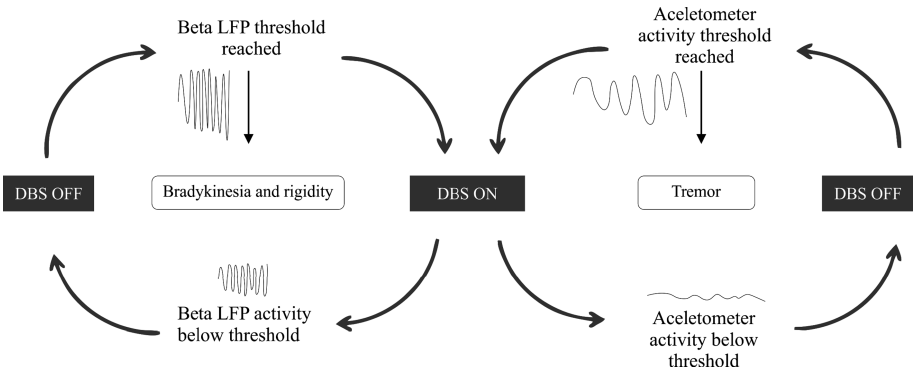

Fig. 1. Closed loop DBS system where stimulation is triggered whenever one or both biomarkers cross independent thresholds and is terminated whenever both biomarkers have fallen below their thresholds.

2.1 Acquisition and Processing of Biomarkers

The LFP were recorded by microelectrodes recordings implanted in both STNs of 5 hemi-parkinsonian rats, in which PD was induced only in one cerebral hemisphere, following the procedure described in [5]. The LFPs were pre-amplified by an Astro-Med Grass P55 with 100x gain and then amplified with the Cibertec Ampli4G21 with a 10x gain. Line filters of 50 Hz and a bandpass between 0.3 and 300 Hz were applied in the amplifier. A DT9812 launchpad with a sampling frequency of 15151.52 Hz was used to digitize the records. In an off-line analyses, Matlab® was used to obtain the BP following the methodology proposed by [6], applying a Butterworth band pass filter between 3 and 100 Hz and estimating the power spectral density using the Welch method with 1 s Hanning windows and 50% of overlap.

For the inertial signals, a Samgung Gear Fit 2 (SGF) was used, running a software designed to acquire acceleration signals on all three axes. For the acquisition of the inertial signals, the SGF was placed on the wrist of 3 healthy subjects that simulated tremor performing pronation-supination movements with different intensities, in 1-minute routines. Each subject evaluated performed the routines simulating three tremor intensities, classified in low, medium and high. The records are composed of periods of rest and periods of simulated tremor, interleaving 10 s between one another until completing the minute. Records were divided into 1 s windows and the magnitude of acceleration (MA) was calculated according to Eq. (1), where a_x, a_y and a_z is the acceleration on the x-axis, y-axis and the z-axis, respectively. Finally, MA was normalized by subject.

$$MA = \sqrt{a_x^2 + a_y^2 + a_z^2} \tag{1}$$

2.2 Design of the Control Model

After studying different control strategies through exploratory tests, fuzzy logic was adopted, which has been reported with good results for the detection of tremor episodes [7]. Two types of fuzzy inference were implemented: *Mamdani* and *Sugeno*.

A fuzzy controller is formed by different modules: fuzzification module of the input and output variables; the knowledge base; the inference engine, and the defuzzification module. The modules and their elements are shown in Fig. 2.

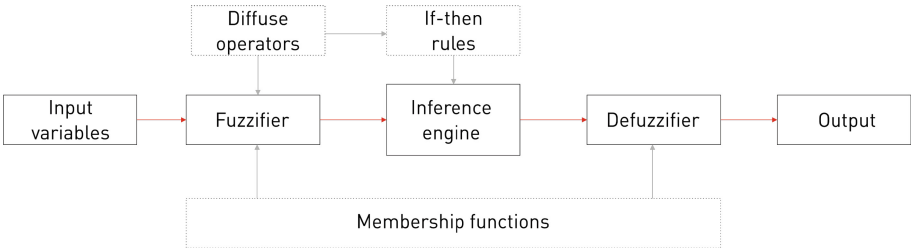

Fig. 2. Fuzzy controller blocks diagram.

The input variables to the system are BP, MA and their derivatives. As they are indicators of changes in inputs, they enrich the control system by providing information that allows the stimulation to be adjusted gradually.

The output variable of the system represents a percentage of the maximum stimulation amplitude of the DBS. It has been shown that the variation in the stimulation voltage is the most important factor for the relief of the disease symptoms [2].

Subsequently, the membership functions (MFs) that would transform inputs and outputs into fuzzy sets were designed. The MFs used are detailed in Table 1 and integrate the fuzzification module.

Table 1. Number and types of MFs used for each characterized variable.

Inputs and output	Number of MFs	Type of MF
Input 1: MA	3	Two-sided Gaussian
Input 2: BP	3	Two-sided Gaussian
Input 3: Derivative of MA	4	Two-sided Gaussian
Input 4: Derivative of BP	4	Two-sided Gaussian
Output: Amplitude percentage of the stimulator	5	Triangular

The knowledge base was formed with rules that govern the stimulator's control. In order to define them: the behavior of the input variables were studied in detail; professionals specialized in programming DBS devices were consulted; and the effectiveness reported in the state of the art on the variation stimulation parameters was consulted [2].

For the fuzzy inference system, 3 models were designed using the Matlab® *fuzzy logic designer* toolbox:

- *Mamdani*-Centroid model: *Mamdani* type inference system, with centroid defuzzification method.
- *Mamdani*-Bisector model: *Mamdani* type inference system, with bisector defuzzification method.
- *Sugeno* model: *Sugeno* type inference system, with weighted averages defuzzification method.

2.3 Analysis of Fuzzy Inference Models

10 *trials* of 1 min each were generated as inputs to the 3 proposed models. Each *trial* contained:

- MA and its derivative: fragments of MA of different intensities were generated, interleaved by periods of rest.
- BP and its derivative: fragments of parkinsonian BP and healthy BP were generated, from the same baseline record of different rodents.

The output of each model was analyzed for each *trial* by measuring the total electrical energy delivered (TEED) by the IPG. The TEED of a DBS system in an arbitrary period of time is determined by the stimulation parameters and the STN impedance according to the Eq. (2) [8].

$$TEED_{1s} = \frac{V^2 f\, pw}{imp} 1s \tag{2}$$

Where V is the amplitude of the stimulation pulse in Volts, f is the stimulation frequency in Hz, pw is the pulse width in μs and imp is the STN impedance, established in 500 Ω as an average value for PD patients [9]. The average voltage over time was taken to be evaluated, as proposed by [8].

Another performance indicator of the models is the theoretical charge density received in the STN (Q) calculated by Eq. (3) [9].

$$Q = \frac{V\, pw}{imp\, A} \tag{3}$$

Where A is the area of the geometrical surface of the electrode, set at 0.06 cm^2 for a typical electrode (Medtronic Model 3389®) [9]. The Q value must not exceed the maximum limit of 30 $\mu C/cm^2$ in any case.

The stimulation parameters were selected according to the average reported in the bibliography:

- Maximum amplitude: 4 V.
- Frequency: 130 Hz.
- Pulse width: 100 μs.

Given that the result of TEED with the same *trials* in each model are paired samples, and that they do not follow a normal distribution (Kolmogorov-Smirnov with p-value < 0.05), the Friedman statistical test was used and then Nemenyi as a post-hoc test. All statistical calculations were made using the Matlab® *Statistics Toolbox*.

3 Results and Discussion

Applying the methodology proposed in Sect. 2.2, a knowledge base with 88 rules was made by combining the different inputs and their ranges of variation. Figure 3 presents the control surfaces as a result of each model, built with 2 of the 4 input variables, where it can be seen that all the models show gradual changes in the output and tend to take higher stimulation values as MA and BP increase. The *Mamdani*-Bisector model presents an abrupt change as it varies MA, in the area between 0.4 and 0.6 indicating an undesired behavior.

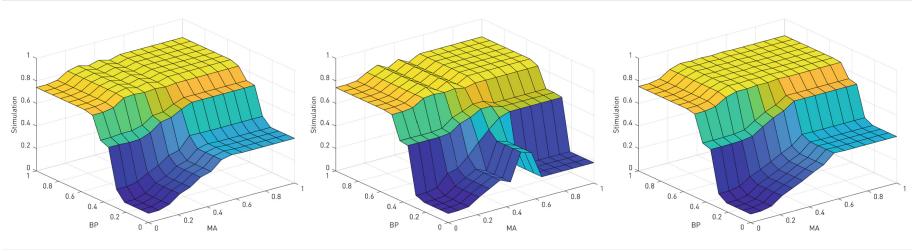

Fig. 3. From left to right, *Mamdani*-Centroid, *Mamdani*-Bisector and *Sugeno* control surfaces; for MA and BP as normalized inputs.

Figure 4 shows the response of all the models with *trial* 6, where it can be observed that the answers are coherent according to the behavior of the entries, anticipating the changes of MA and BP. Also, it is observed that in *Mamdani*-Bisector model the response of the system presents certain variability in the lapse of 48 to 58 s, that may lead to induce paresthesia in patients. It is important to mention that the *Mamdani*-Centroid model presents a smoother behavior.

Table 2 shows the average values of TEED, Q and maximum Q as a result of the output of each closed-loop models and open-loop DBS, using the 10 *trials* proposed in Sect. 2.3.

The three proposed models have similar values of TEED, where *Mamdani*-Bisector has the lower value. An average TEED decrease of 67% is observed in regards to the open-loop DBS. The results of the TEED obtained are similar to the ones obtained by Little et al. in 2016, which was 223 ± 31.00 μW in closed-loop DBS [10].

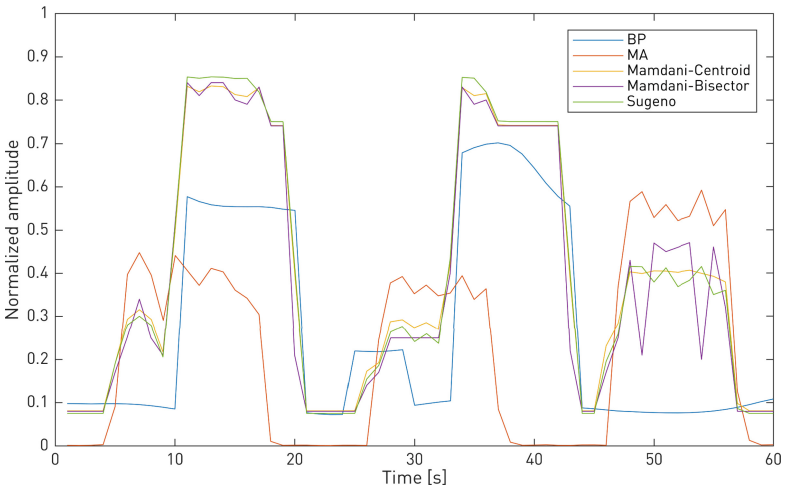

Fig. 4. MA and PB as inputs to the system; and the response of each model for *trial* 6.

Table 2. TEED, Q and maximum Q values calculated for each model and open-loop DBS.

Evaluated model	TEED [μW]	Average Q [μC/cm^2]	Maximum Q [μC/cm^2]
Mamdani-Centroid	138,90 ± 57,22	7,56 ± 1,57	11,11
Mamdani-Bisector	136,80 ± 59,07	7,49 ± 1,62	11,20
Sugeno	142,41 ± 59,99	7,65 ± 1,63	11,46
Open-loop DBS	416,00	15,00	15,00

In 2017, Rosa et al. obtained a TEED of 44.6 ± 47.90 μW. Although it is lower than the TEED obtained in the present work, it is possible that this difference is due to the stimulation parameters used [11]. An optimized DBS system model should generate maximum clinical benefit at the lowest TEED, resulting in an extended battery life and decreasing complications related to stimulation.

The Q and maximum Q values obtained for the proposed models did not exceed the density limit of 30 μC/cm^2 in any of the *trials*. The closed-loop DBS models presented an average Q 50% lower than open-loop DBS, in which the *Mamdani*-Centroid model resulted in the one with the lowest maximum Q. Q values have not been reported in other studies so it is not possible to make a comparison. We consider it is important to include this indicator to prevent any tissue damage, particularly in the first weeks after the implantation surgery, since the edema may generate variations in the STN impedance and consequently in the charge density [2].

The Friedman test for the TEED value showed a global significance with $p = 0.0055$. Then, the Nemenyi test is presented in Table 3 where a statistically significant difference is observed ($p < 0.01$) between the *Mamdani*-Bisector model and the *Sugeno* model. It is possible that this can be attributed to the variability in the control surface observed for the *Mamdani*-Bisector model.

Table 3. *p*-values of the paired comparisons between the fuzzy inference models proposed.

Model 1	Model 2	*p*
Mamdani-Centroid	*Mamdani*-Bisector	0,64383
Mamdani-Centroid	*Sugeno*	0,06526
Mamdani-Bisector	*Sugeno*	0,00497

The rejection of the null hypothesis for the statistical comparison of *Mamdani*-Centroid and *Sugeno* is weak ($p = 0.06526$) whereas the *Mamdani*-Centroid and *Mamdani*-Bisector models clearly showed no statistically significant differences for TEED ($p = 0.64383$), so they could be control strategy options for a closed loop DBS system.

4 Conclusion

The results obtained indicate that it is possible to use fuzzy logic as a control strategy to command a closed-loop DBS by using LFP registers and inertial signals. Unlike other studies, the proposed models present four input variables, combining IB and EB that describe the main motor symptoms of PD. Of the models designed, *Mamdani*-Centroid did not present statistically significant differences for TEED compared to *Mamdani*-Bisector. In addition, *Mamdani*-Centroid has the lowest maximum Q and a smooth output with gradual changes in the control surface. Therefore, we believe that under the experimental conditions of this study the *Mamdani*-Centroid model is the appropriate control strategy to implement a closed-loop DBS system.

Acknowledgements. English language editing services supplied by Prof. Diana Waigandt and Área de Asesoramiento Interdisciplinar (Facultad de Ingeniería - Universidad Nacional de Entre Ríos - Resolución CD N° 137/19).

Funding. This research was funded by the National University of Entre Rios (UNER - research project number 6169) and by the Autonomous University of Entre Rios (UADER – Res. CS 067/2018).

Conflicts of Interest. The authors declare no conflict of interest. The funders had no role in the design of the study; in the collection, analyses, or interpretation of data; in the writing of the manuscript, or in the decision to publish the results.

References

1. Bellino, G., Schiaffino, L., Battisti, M., Guerrero, J., Rosado-Muñoz, A.: Optimization of the KNN supervised classification algorithm as a support tool for the implantation of deep brain stimulators in patients with Parkinson's disease. Entropy **21**, 346 (2019). https://doi.org/10.3390/e21040346

2. Wagle Shukla, A., Zeilman, P., Fernandez, H., Bajwa, J.A., Mehanna, R.: DBS programming: an evolving approach for patients with Parkinson's disease. Parkinson's Dis. **2017**, 1–11 (2017). https://doi.org/10.1155/2017/8492619
3. Little, S., et al.: Adaptive deep brain stimulation in advanced Parkinson disease: adaptive DBS in PD. Ann. Neurol. **74**, 449–457 (2013). https://doi.org/10.1002/ana.23951
4. Herron, J.A., et al.: Chronic electrocorticography for sensing movement intention and closed-loop deep brain stimulation with wearable sensors in an essential tremor patient. J. Neurosurg. **127**, 580–587 (2017). https://doi.org/10.3171/2016.8.JNS16536
5. Kaminer, J., Thakur, P., Evinger, C.: Frequency matters: beta-band subthalamic nucleus deep-brain stimulation induces Parkinsonian-like blink abnormalities in normal rats. Eur. J. Neurosci. **40**, 3237–3242 (2014). https://doi.org/10.1111/ejn.12697
6. Henrich, M.C., Tepper, Á.: Diseño de un sistema de soporte para cirugías de implantación de electrodos en terapias DBS de pacientes con Enfermedad de Parkinson, p. 214 (2016)
7. Wang, C.-F., et al.: A proof-of-principle simulation for closed-loop control based on preexisting experimental thalamic DBS-enhanced instrumental learning. Brain Stimul. **10**, 672–683 (2017). https://doi.org/10.1016/j.brs.2017.02.004
8. Swann, N.C., et al.: Adaptive deep brain stimulation for Parkinson's disease using motor cortex sensing. J. Neural Eng. **15**, 046006 (2018). https://doi.org/10.1088/1741-2552/aabc9b
9. Itakura, T.: Deep Brain Stimulation for Neurological Disorders: Theoretical Background and Clinical Application. Springer, New York (2015)
10. Little, S., et al.: Bilateral adaptive deep brain stimulation is effective in Parkinson's disease. J. Neurol. Neurosurg. Psychiatry **87**, 717–721 (2016). https://doi.org/10.1136/jnnp-2015-310972
11. Rosa, M., et al.: Adaptive deep brain stimulation controls levodopa-induced side effects in Parkinsonian patients: DBS controls levodopa-induced side effects. Mov. Disord. **32**, 628–629 (2017). https://doi.org/10.1002/mds.26953

Cerebral Cortex Atlas of Emotional States Through EEG Processing

Alejandro Gómez[1(✉)], O. Lucia Quintero[1], Natalia Lopez-Celani[2], and Luisa Fernanda Villa[3]

[1] Mathematical Modelling, Universidad EAFIT, Medellín, Colombia
agomez13@eafit.edu.co
[2] Gabinete de Tecnologia Medica - CONICET, Universidad Nacional de San Juan, San Juan, Argentina
[3] Arkadius, Universidad de Medellín, Medellín, Colombia

Abstract. This paper addresses the cerebral cortex maps construction from EEG signals getting an information simplification method for an emotional state phenomenon description. Bi-dimensional density distribution of main signal features are identified and a comparison to a previous approach is presented. Feature extraction scheme is performed via windowed EEG signals Stationary Wavelet Transform with the Daubechies Family (1–10); nine temporal and spectral descriptors are computed from the decomposed signal. Recursive feature selection method based on training a Random forest classifier using a one-vs-all scheme with the full features space, then a ranking procedure via gini importance, eliminating the bottom features and restarting the entire process over the new subset. Stopping criteria is the maximum accuracy. The main contribution is the analysis of the resulting subset features as a proxy for cerebral cortex maps looking for the cognitive processes understanding from surface signals. Identifying the common location of different emotional states in the central and frontal lobes, allowing to be strong parietal and temporal lobes differentiators for different emotions.

Keywords: Emotion · EEG · Cerebral cortex · Atlas · Feature selection

1 Introduction

Define the emotions is a difficult matter [10], but for convenience, we consider the emotions as states, and these emotional states are the neurological answer to an external stimulus. The study of these responses to external stimuli is important because it allows establishing a psychological profile of the person which it is useful for the diagnosis of the psychopathology of the individual, allowing to create optimal treatment strategies [8,11]. In recent years, some research reported with the premise of decoding brain areas, in which start or separate certain mental states, actions or responses to an environment [6]. Detect emotions using EEG

© Springer Nature Switzerland AG 2020
C. A. González Díaz et al. (Eds.): CLAIB 2019, IFMBE Proceedings 75, pp. 138–144, 2020.
https://doi.org/10.1007/978-3-030-30648-9_19

signals is important, because these signals are related to brain activity, allowing a mapping from emotional states to the different areas of neuronal activity. The emotional map of the cerebral cortex allows psychologists to validate or determine emotional states by studying the behavior of the activation patterns of certain brain areas, the identification of mental disorders, a feedback loop before treatments, or integrating into an artificial intelligence system to decide about the emotional state of a user, without requiring the user to perform a phonetic activity or facial expression which can be useful with infants, users with paralysis, autism or phonetic problems [9]. A different approach that has reported in recent years for detection of emotional states is by analyzing the electroencephalographic signals [3,4]. This paper is organized as follows: Sect. 2 presents a brief explanation about the previous cerebral cortex atlas and addresses the main contributions on surface signals and introduces our proposed methodology from the feature extraction, feature selection and classification schemes. Section 3 discusses widely our findings and provide insights about the usefulness of our proposal.

2 Cerebral Cortex Atlas

Our proposal is go a step further in the emotion recognition, and analyze the resultant features as indicators of the importance of each electrode in the EEG emotion recognition task and the construction of emotional maps in the cerebral cortex obtaining an minimum relevant information methodology for an emotional state phenomenon description. Bi-dimensional density distribution of reduce set of features are identified and a comparison to a previous approaches is presented. Recursive feature selection method is based on the training of a Random forest classifier in an one-vs-all scheme with the full features space, then a ranking procedure via gini importance is performed eliminating the bottom features and restarting the entire process over the new subset. Stopping criteria is the maximum accuracy. The main contribution is the analysis of the resulting subset features as proxy to cerebral cortex maps looking for the cognitive processes understanding from surface signals.

Studies whose direct purpose is the construction of maps of the cerebral cortex, referring to an emotional state, have not been developed. Some approaches can be found in investigations that select a set of EEG channels as main sources of information to recognize emotions, in which the use of the electrodes corresponding to the frontal, central lobes and the left and right lobes can be identified [2,12].

To construct the cerebral cortex atlas of emotional states through EEG processing, we proposed a method of five stages: (1) Pre-processing of the EEG signals by segmentation with a window function [1], (2) A wavelet decomposition using the Stationary Wavelet Transform with the complete family Daubechies [4], (3) Feature space construction through feature extraction using a set of temporal and spectral estimators [1,3], (4) Feature space reduction with a recursive feature selection using random forest classifier [5,7] and (5) Cerebral cortex atlas

estimation through the analysis of the reduce feature space as the source of significant information. The Fig. 1 present these five stages scheme.

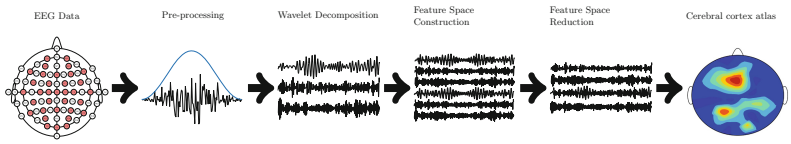

Fig. 1. Proposed method to cerebral cortex atlas construction based on EEG processing, consist in five stages

3 Bi-dimensional Density Distribution

The cerebral cortex atlas that we proposed correspond to the bi-dimensional density distribution of features in the cerebral cortex surface. First we calculate the quantity of features per EEG channel, with the following expression:

$$h_{ch} = \frac{|featuresubset \in ch|}{|featuresubset|} \tag{1}$$

Then we calculate a cubic spatial interpolation in order to obtain the bi-dimensional density distribution from each subset of features.

3.1 Final Features Analysis

The final subset of features was analyzed by the distribution of features in function of the wavelet used, and the extracted feature for each emotional state. In Fig. 2, we present the feature distribution in function of the Wavelet used and

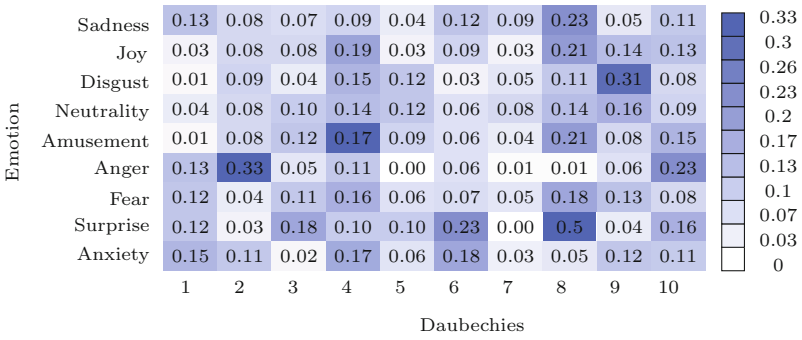

Fig. 2. Feature distribution in function of the Wavelet used and the emotional state

the emotional state. It is possible to identify that the feature distribution has a behavior quasi-uniform, but it is noticeable that the wavelets Db4, Db6, Db8, Db9, and Db10 have a marked protagonism in this feature distribution, contrary to what happens with the wavelets Db1 and Db7.

In Fig. 3, we present the feature distribution in function of the extracted features and each emotional state, we find a high concentration of features in a small subset of features: rms, standard deviation and mean frequency. These features are associated with the energy of the signal, and it can be found that being relevant in all the emotional states, this allows us to infer that one of the keys to recognizing emotions in EEG signals corresponds to the study of the energy of the signals. In contrast to the distribution of characteristics as a function of the wavelet, a subset of features that have an insignificant contribution to the description of the phenomenon of an emotional state is clear, this corresponds to the wavelength, the number of zero crossing and the maximum value of the spectral power.

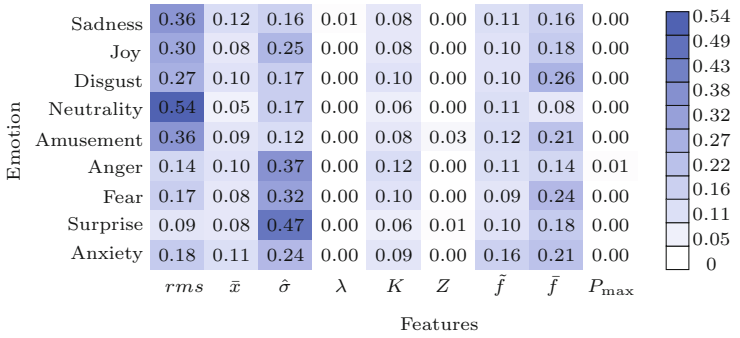

Fig. 3. Feature distribution in function of the extracted features and the emotional states

3.2 Bi-dimensional Density Distribution of Information on Cerebral Surface

Finally, it is presented in Fig. 4, the bi-dimensional density distribution in function of the EEG channels and each emotional state. These density distributions represent the minimal information that allows classifying each emotional state. Independently it is possible to identify that Sadness is condensed in the right temporal lobe, right frontal lobe, and the central-left parietal lobe. Happiness has intensity peaks in the central and temporal lobe and a concentrated region at the parietal lobe. Disgust seems to be exclusive of the right parietal lobe, with a small activity in the occipital lobe. The neutral state seems to be the one with the greater intensity in the parietal and occipital lobes, however, this emotional state is the one with the smallest maximum value of intensity, which can be contrasted with emotional states with a high arousal as disgust, anger, and surprise. Amusement is dense at the central and parietal lobe, with a peak in the occipital lobe.

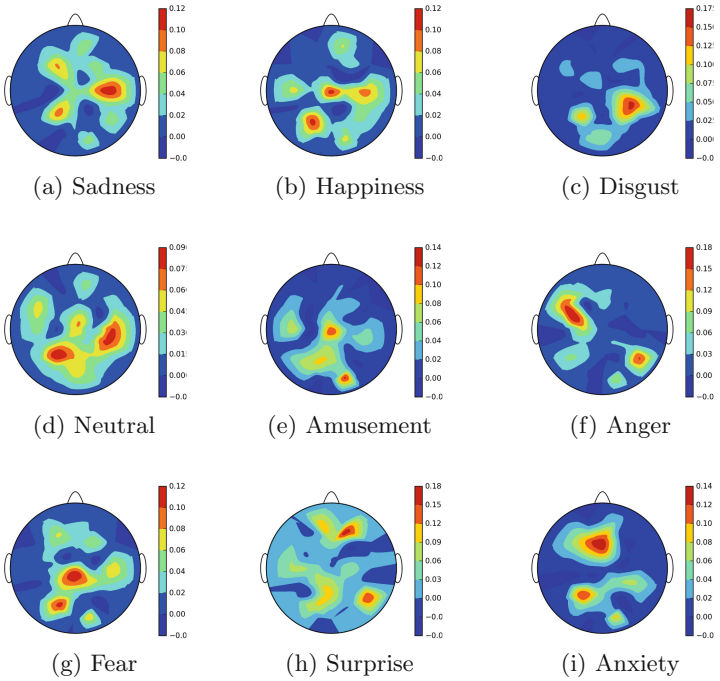

(a) Sadness (b) Happiness (c) Disgust

(d) Neutral (e) Amusement (f) Anger

(g) Fear (h) Surprise (i) Anxiety

Fig. 4. Bi-dimensional density distribution of information on cerebral surface for Sadness, Happiness, Disgust, Neutral, Amusement, Anger, Fear, Surprise and Anxiety are represented with red the regions with higher intensity and with blue the regions with intensity equal to zero.

Anger is divided into two main regions: between the left frontal, temporal and central lobes and the right central-parietal lobe. Fear is condensed at the central lobe with an important participation between the left parietal and occipital lobe. Surprise has a quasi-uniform distribution in the cerebral cortex, but it is possible to identify intensity peaks at the frontal lobe, and between the central and right parietal lobe. Anxiety has a lite intensity peak between the left parietal and occipital lobe, with the major concentration in the middle of the frontal lobe. In a comparative way it is notorious that each emotional cerebral cortex atlas has in common the activation of the central lobe, however, there is not the principal region in the emotional states of disgust and anger. It is also clear that the emotional states of happiness and amusement share the high intensity in the central, parietal and occipital lobe, being able to differentiate happiness for the high activity in the right frontal and temporal lobe. In addition, it is possible to identify a pattern corresponding to emotional states with a positive valence, these emotional states have an intensity peak at the left temporal lobe, that is absent in emotions with a negative valence. Also, it is possible to identify that the emotions with a small arousal such as Sadness, Neutral, and Happiness have theirs intensity peak between the central and temporal right lobe and another peak in the central lobe with a tendency towards the left parietal lobe.

4 Conclusion

We demonstrated from surface signals and a proper mathematical treatment, the relevance of the frontal, central and occipital lobes for the recognition of emotions, being consistent with what is reported in the literature, however it is possible to identify a high intensity in the different density functions in the temporal lobes, which have not been reported in studies of EEG signals, but indirectly influencers in the fMRI studies. It is important to highlight that the extracted features that have a more important role in the recognition of emotions are related to the energy of the EEG signals, being this an indicator on the possible description of the phenomenon of the identification of an emotional state, from the analysis of the EEG signals.

Acknowledgment. The authors would like to thank to the APOLO for the support to this project. This work has been partially funded by Colciencias Young researcher 2017 grant.

References

1. Chaparro, V., Gomez, A., Salgado, A., Quintero, O.L., Lopez, N., Villa, L.F.: Emotion recognition from EEG and facial expressions: a multimodal approach. In: IEEE Engineering in Medicine and Biology Society (EMBS) (2018)
2. Chen, M., Han, J., Guo, L., Wang, J., Patras, I.: Identifying valence and arousal levels via connectivity between EEG channels. In: 2015 International Conference on Affective Computing and Intelligent Interaction, ACII 2015, pp. 63–69 (2015)
3. Gómez, A., Quintero, L., López, N., Castro, J.: An approach to emotion recognition in single-channel EEG signals: a mother child interaction. J. Phys.: Conf. Ser. **705**(1), 012051 (2016)
4. Gómez, A., Quintero, L., López, N., Castro, J., Villa, L., Mejía, G.: An approach to emotion recognition in single-channel EEG signals using stationary wavelet transform. In: IFMBE Proceedings, Claib 2016, pp. 654–657 (2017)
5. Guyon, I., Weston, J., Barnhill, S., Vapnik, V.: Gene selection for cancer classification using support vector machines. Mach. Learn. **46**(1–3), 389–422 (2002)
6. Kragel, P.A., LaBar, K.S.: Decoding the nature of emotion in the brain. Trends Cogn. Sci. **20**, 1–12 (2016)
7. Menze, B.H., Kelm, B.M., Masuch, R., Himmelreich, U., Bachert, P., Petrich, W., Hamprecht, F.A.: A comparison of random forest and its Gini importance with standard chemometric methods for the feature selection and classification of spectral data. BMC Bioinform. **10**(1), 213 (2009)
8. Restrepo, D., Gomez, A.: Short research advanced project: development of strategies for automatic facial feature extraction and emotion recognition. In: 2017 IEEE 3rd Colombian Conference on Automatic Control (CCAC), pp. 1–6. IEEE, October 2017
9. Scherer, R., Moitzi, G., Daly, I., Muller-Putz, G.R.: On the use of games for noninvasive EEG-based functional brain mapping. IEEE Trans. Comput. Intell. AI Games **5**(2), 155–163 (2013)
10. Tracy, J.L., Randles, D.: Four models of basic emotions: a review of Ekman and Cordaro, Izard, Levenson, and Panksepp and Watt. Emot. Rev. **3**(4), 397–405 (2011)

11. Uribe, A., Gomez, A., Bastidas, M., Quintero, O.L., Campo, D.: A novel emotion recognition technique from voiced-speech. In: 2017 IEEE 3rd Colombian Conference on Automatic Control (CCAC), pp. 1–4. IEEE, October 2017
12. Zheng, W.: Multichannel EEG-based emotion recognition via group sparse canonical correlation analysis. IEEE Trans. Cogn. Dev. Syst. **9**(3), 281–290 (2017)

Estimation of the Very Low Frequency Components in Heart Rate Variability During Hemodiafiltration

Raul Martínez-Memije[1(✉)], Brayans Becerra-Luna[1], Raul Cartas-Rosado[1], Oscar Infante-Vázquez[1], Claudia Lerma[1], Hector Pérez-Grovas[2], and Jóse Manuel Rodríguez-Chagolla[2]

[1] Electromechanical Instrumentation Department, NIC 'Ignacio Chávez' Juan, Badiano 1, Sección XVI, Tlalpan, 14080 Mexico City, Mexico
raulmmemije@yahoo.com
[2] Hemodialysis Unit, Nephrology Department, NIC "Ignacio Chávez" Juan, Badiano 1, Sección XVI, Tlalpan, 14080 Mexico City, Mexico

Abstract. Heart rate variability (HRV) has been used to indirectly assess and study the autonomic nervous system (ANS). For the analysis of HRV, two different time windows are recommended.

For certain physiological conditions, neither of the standard time windows are appropriate for evaluating the very low frequency (VLF) band of HRV. In this work, we evaluate HRV using two different time windows, one of 5 min and the other of 50 min. Analyses were conducted in both the time and frequency domains, with an emphasis on VLF content. Ten patients with chronic kidney disease participated in this study. The electrocardiogram signal was measured during their hemodialysis therapy. Time domain parameters such as the mean heart rate, mean R-R intervals, standard deviation of normal-to-normal intervals (SDNN), and root mean square of standard deviations (RMSSD) are reported, along with frequency domain parameters such as mean power of the very low frequency (VLF), low frequency (LF) and high frequency (HF) bands, as well as the LF/HF ratio.

Significant differences were found in the SDNN for 5 min as compared to 50 min (41.13 ± 5.40 ms, 52.85 ± 2.63 ms, $p < 0.000$), and the VLF power spectra for 5 and 50 min were 1271.54 ± 406.52 ms^2 and 1561.99 ± 170.62 ms^2 ($p = 0.02$), respectively.

Keywords: Very low frequency · HRV · Autonomous nervous system

1 Introduction

Heart rate variability (HRV) has been used to study the modulatory effects of the autonomic nervous system (ANS) over the cardiac system. To perform a frequency domain analysis of HRV, the power spectral density (PSD) is required. Guidelines provided by the Task Force of the ESC and the NASPE [1] recommend two time windows to perform this analysis: one of 5 min length (short window) and the other of 24 h length (long window). When the short window is used, the guidelines establish

© Springer Nature Switzerland AG 2020
C. A. González Díaz et al. (Eds.): CLAIB 2019, IFMBE Proceedings 75, pp. 145–150, 2020.
https://doi.org/10.1007/978-3-030-30648-9_20

that it is possible to evaluate the low frequency (LF: 0.04–0.15 Hz) and high frequency (HF: 0.15–0.4 Hz) bands of HRV with high certainty, but not the very low frequency (VLF: 0.003–0.04 Hz) band. The LF and HF bands are associated with sympathetic and vagal activities, respectively [2, 3], while the VLF is thought to be related to the activity of the sympathetic nervous system, temperature regulation and renin-angiotensin-aldosterone (RAAS) system [4–6].

The estimation of VLF is particularly interesting in patients with kidney disease. Patients with chronic kidney disease (CKD) who undergo maintenance hemodialysis (HD) experience changes in their homeostasis that overexcite the RAAS, which in turn involves dysfunction of the ANS to some degree [7]. To evaluate HRV, and in particular, the changes occurring in the VLF band during hemodialysis, neither of the recommended epochs are appropriate. In previous work, it was shown that the minimum time window required to evaluate the VLF with certainty is 50 min [8]. The aim of this work is to show the differences in estimating the spectral and time domain parameters of the VLF, LF and HF bands using a 300 s (5 min) window and a 3000 s (50 min) window in patients during hemodialysis therapy

2 Methods

This is a cross-sectional and quasi-experimental study conducted at the National Institute of Cardiology "Ignacio Chávez" in accordance with the principles of the Declaration of Helsinki. The protocol was approved by the institutional ethics committee with register number 17-1014 A total of 10 patients (6 female and 4 male) receiving maintenance hemodiafiltration (HDF) thrice per week were included. Mean age and mean body mass index of our population were 38.9 ± 15.66 y.o. and 24.19 ± 3.40, respectively. All participants were duly informed about the protocol and were asked to sign an informed consent. The study was performed in the first morning shift in a controlled temperature room set at 20 °C. Each participant was in a sitting position and was instructed to not ingest caffeine or any anti-hypertensive medication, which may alter their nervous ratings.

Dietary recommendations were also given as an effort to control the intradialytic gain weight before the study. The same HD machine (model 4008, Freseniuss Medical Care) was used in all the sessions. Ultrafiltration rate was fixed to 800 ml/h for the 3-h therapy. Electrocardiographic recordings used to extract the HRV were acquired using a Holter recorder model DMS300-7 with a sampling rate of 128 samples/s.

2.1 Data Analysis

The ECG signal was resampled to 256 samples/second with a linear interpolation, the R-wave detection and R-R interval measurements were carried out according to a previous work, where the second derivative algorithm was used for the detection [9], In this study, the algorithm was rewritten in Matlab language. The resulting series were visually inspected to check for and manually correct misidentified or missing R-waves.

The series of R-R intervals were resampled to 4 samples/s using Kubios HRV Premium and the trend was removed by adjusting a third order polynomial. The resulting

tachograms were split into 18 non-consecutive and non-overlapped 5-min epochs, and also into 7 overlapped 50-min epochs for the analysis. According to the work of Becerra-Luna et al. [8], two overlapped 50-min epochs can be considered statistically independent if the overlapping between them is of 30 min or less. Independence was evaluated using the cross-correlation function. For the time domain analysis the following parameters were calculated: mean RR, RMSSD (Root Mean Square Standard Deviation) and SDNN (Standard Deviation of Normal to Normal interval). For the frequency domain analysis, the power in the VLF, LF and HF bands along with the LF/HF ratio are reported.

Spectral analyses were performed using the Welch method with 50% overlap. Analysis was performed using Kubios HRV Premium.

Polynomial regression curves were fitted for each bandwidth to evaluate the non-linear correlation and dependence between power and time. The coefficient of determination (R^2) and *p*-values were calculated using the unpaired t-test.

Table 1. Mean, standard deviation (SD), minimum and maximum values of age, initial weight, final weight, weight lost, height and Body Mass Index (BMI) for the 10 subjects participating in this study.

N = 10 (6 F, 4 M)	Age (y.o.)	Initial weight (kg)	Final weight (kg)	Weight lost Δ (kg)	Height (m)	Starting BMI
Mean	38.90	63.27	61.27	2.33	1.62	24.19
SD	15.66	10.63	10.63	0.82	0.08	3.40
Minimum	19.00	48.30	46.30	1.40	1.50	18.87
Maximum	68.00	79.70	77.70	3.70	1.76	30.37

3 Results

Table 1 contains the descriptive statistics of our population, where it can be seen that a wide range of ages and physical compositions were included in our study. Figure 1 shows the results obtained from the frequency domain analysis using both window times. Each plot includes the second-order curve fitted to the VLF, LF and HF bands as well as its corresponding equation. The curve fitted to the sympathovagal balance (LF/HF ratio) corresponds to a linear equation. Table 2 lists the results obtained from the statistical analysis for both time and frequency domains. In the time domain, we found statistical differences ($p << 0.05$) in the SDNN when its value for 5-min window (41.13 ± 5.40 ms) was compared against its value for 50-min window (52.85 ± 2.63 ms). In the frequency domain, only the VLF showed statistical significance ($p = 0.02$) when its mean power estimated at 5-min (1271.54 ± 406.52 ms^2) was compared against the estimation at 50-min (1561.99 ± 170.62 ms^2).

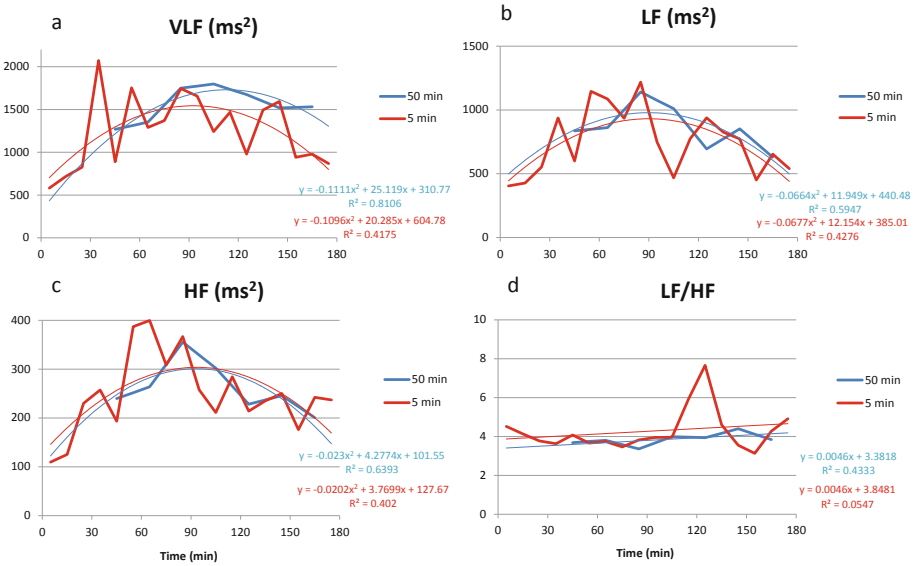

Fig. 1. Mean spectral power from the group of patients evaluated. Each plot corresponds to the VLF (a), LF (b), HF (c) bands plus the LF/HF ratio (d). Red traces correspond to 5 min window, and blue traces correspond to 50 min window.

Table 2. Mean values for the evaluated parameters from the HRV analysis. The results shown are for the 5 min and 50 min windows. The values are reported as mean ± SD

Parameter	50 min	5 min	Stat signif
Mean (ms)	816 ± 25	818.92 ± 19.15	p = 0.668
HR (bpm)	75.4 ± 2.52	75.03 ± 1.94	p = 0.511
SDNN (ms)	41.13 ± 5.40	52.85 ± 2.63	**p < 0.000**
RMSSD (ms)	21.19 ± 2.90	22.30 ± 1.73	P = 0.511
VLF (ms^2)	1271.54 ± 406.52	1561.99 ± 170.62	**p = 0.021**
LF (ms^2)	797.66 ± 266.15	855.46 ± 162.84	p = 0.227
HF (ms^2)	243.27 ± 74.14	262.03 ± 49.38	p = 0.633
LF/HF	4.34 ± 0.84	3.85 ± 0.29	p = 0.156

4 Discussion

The guidelines for the analysis of HRV recommend the use of only two possible time windows of either 5 min or 24 h [1]. In certain medical conditions such as in patients with CKD undergoing hemodialysis maintenance, a window longer than 5 min but shorter than 24 h is required for the analysis, because the activity in the VLF band is relevant and vital, and a short time window is not enough while a long time window is not feasible. Here, we propose the extension of the length of the analysis window up to 50 min.

This window size was chosen to increase the spectral analysis, especially in the VLF band. It was shown by Becerra-Luna et al. [8] that a short time window (5-min window) does not have enough resolution to estimate spectral components close to 0.003 Hz, which is the lower limit of the VLF band, but this size is enough to evaluate the upper limit of the VLF band (0.015 Hz). Previous work using short windows for the analysis of the LF and HF bands from HRV before and after hemodialysis therapy [6, 10], have shown that the activity of the LF band increases after the therapy has concluded. Our results using a 5-min window suggest that the activity in the VLF band increases during the first half of the therapy and decreases during the second half. It is worth noting that our results obtained during the 50-min epoch suggest that the power increases at the end of the therapy. The spectral power in the LF and HF bands did not show differences when they were estimated using either the 5-min or 50-min window, which yielded low statistical significance. This may be due to the fact that neither window is enough to cover the spectrum of these two bands. One limitation of our work is the small number of patients participating in our study. In future work we plan to use power estimators involving time-frequency analysis such as the wavelet transform or the Hilbert Huang transform, which is computationally faster to carry out spectral decomposition.

5 Conclusions

In some clinical conditions such as patients with CKD, it is necessary to monitor changes in the renin-angiotensin-aldosterone system, temperature regulation, and other mechanisms that are influenced by the behavior of the VLF band and hence the behavior of the HRV. Changes in this band lead us to consider the use of an adapted analysis window different from those recommended by the literature.

The differences found in our results in time and frequency with respect to previous published works, where short windows were used, suggest that a 5-min time window is not long enough for the analysis, and that estimation of the VLF content using this window results in a wrong estimation of the power contained in the LF and HF band.

Conflict of Interests. The authors declare no conflict of interest for the realization of this work.

References

1. Task Force of the ESC and the NASPE: Heart rate variability: standards of measurement, physiological interpretation and clinical use. Eur. Heart J. **17**, 354–381 (1996)
2. Brotman, D.J., Bash, L.D., Qayyum, R., Crews, D., Whitsel, E.A., Astor, B.C., Coresh, J.: Heart rate variability predicts ESRD and CKD related hospitalization. J. Am. Soc. Nephrol. **21**, 1560–1570 (2010)
3. Karas, M., Lacourcière, Y., LeBlanc, A.R., et al.: Effect of the renin–angiotensin system or calcium channel blockade on the circadian variation of heart rate variability, blood pressure and circulating catecholamines in hypertensive patients. J. Hypertens. **23**(6), 1251–1260 (2005)

4. Virtanen, R., Jula, A., Kuusela, T., Helenius, H., Voipio-Pulkki, L.M.: Reduced heart rate variability in hypertension: associations with lifestyle factors and plasma renin activity. J. Hum. Hypertens. **17**, 171–179 (2003)
5. Houle, M.S., Billman, G.E.: Low-frequency component of the heart rate variability spectrum: a poor marker of sympathetic activity. Am. J. Physiol. **276**(1), H215–H223 (1999)
6. Taylor, J.A., Carr, D.L., Myers, C.W., Eckberg, D.L.: Mechanisms underlying very-low-frequency RR-interval oscillations in humans. Circulation **98**(6), 547–555 (1998)
7. Hildreth, C.M.: Prognostic indicators of cardiovascular risk in renal disease. Front. physiol. **2**, 1–6 (2011)
8. Becerra-Luna, B., Martínez-Memije, R., Cartas-Rosado, R., Infante-Vázquez, O., Sánchez-García, J.C., Sánchez-Pérez, G.: Optimal window for the estimation of very low frequency content in heart rate variability analysis. In: Lhotska, L., Sukupova, L., Lacković, I., Ibbott, G. (eds.) World Congress on Medical Physics and Biomedical Engineering 2018. IFMBE Proceedings, vol. 68/2 (2019)
9. Infante, O., Valenzuela, F., Polo, S.: Algoritmo que utiliza la segunda derivada para identificar el complejo QRS en tiempo real. Rev Mex Ing Bioméd **13**, 23–32 (1992)
10. Barnas, M.G., Boer, W.H., Koomans, H.A.: Hemodynamic patterns and spectral analysis of heart rate variability during dialysis hypotension. J. Am. Soc. Nephrol. **10**(12), 2577–2584 (1999)

NeuroMoTIC: An Smart Tool to Support Pediatric Epilepsy Diagnosis

Rubiel Vargas-Canas[1(✉)], Maria Eugenia Mino-Arango[2], and Diego Mauricio Lopez-Gutierrez[3]

[1] Physics Deparment, Universidad del Cauca, Popayan, Colombia
rubiel@unicauca.edu.co
[2] Pediatrics Deparment, Universidad del Cauca, Popayan, Colombia
[3] Telematics Deparment, Universidad del Cauca, Popayan, Colombia

Abstract. According to the World Health Organization, 50 million people have epilepsy with 80% of them living in low- and middle-income countries. Three quarters of these do not receive the treatment they need due to delays in interpreting electroencephalograms (EEGs). This paper presents a Machine learning model to support the diagnosis of pediatric epilepsy in semi-automatic way. The model was built from more than 100 pediatric EEGs, with a diagnosis of epileptic seizure. The results achieved using the software were compared with annotations made by a pediatric neurologist, reaching up to 85% agreement. In addition, the neurologists stated that, during the evaluation of a 30-min EEG, the system allowed them to save up to half of the time that usually takes. The tool herein presented facilitates the study and evaluation of pediatric EEGs using a semi-automatic classification of EEG signals and it can be used in the diagnosis of pediatric epilepsy.

Keywords: Pediatric epilepsy · Automated seizure detection · Tele-EEG

1 Introduction

Epilepsy is a brain disorder predominantly characterized by recurrent and unpredictable interruptions of normal brain function, caused by imbalance of neuronal electrical activity in some areas of the brain [1]. Clinical manifestations consist of transient and sudden abnormal phenomena, which may include alterations of consciousness, and motor, sensory, autonomic or psychic events [2]. According to the World Health Organization (WHO), approximately, 50 million people have epilepsy, around the world, and about 80% of these people live in low- and middle-income countries [3]. Three quarters out of them do not receive the treatment they need due to delays in interpreting the exams [3]. In Colombia, prevalence of epilepsy is 11.3 per 1,000 inhabitants, with only 30% of the population controlled [4]. The highest prevalence of epilepsy is found in children, being diagnosed for the first time before 18 years old in 71% of the population, and before 6 years old in only 28% of the cases [4].

Electroencephalography (EEG) analysis is the most common technique for diagnosing epilepsy. It measures the electrical activity of the cerebral cortex, however, these signals have a highly random nature, hence visual inspection becomes a complex

© Springer Nature Switzerland AG 2020
C. A. González Díaz et al. (Eds.): CLAIB 2019, IFMBE Proceedings 75, pp. 151–155, 2020.
https://doi.org/10.1007/978-3-030-30648-9_21

and time consuming task; it takes between 30 min and 2 h, interpreting a single exam, which reduces the opportunity for diagnosis and increases the time to obtain results for patients. To overcome the abovementioned difficulties, approaches based on digital signal processing [5, 6] and Machine Learning [7, 8] have emerged in order to detect and classify automatically epileptiform signals. Even though, these approaches focus on the detection of epileptic points, epileptic events (convulsions) and focal epilepsies, they are focus in normal and abnormal classification and do not have multiclass classification systems, which could be essential for the neurology specialist in exam inspection.

This paper presents a tool to support the diagnosis of pediatric epilepsy through a machine learning model that allows semi-automatic classification of EEG and clinical information; this tool was built and tested in a clinical environment.

2 Method

The research was carryout in four phases: Data collection, Data preparation and Feature Engineering, Model Building, and Model testing. These phases are detailed below:

2.1 Data Collection

More than 100 pediatric EEGs, with a diagnosis of epileptic seizure, were collected in a clinical environment (AXON PED S.A.S) using a BWII EEG electroencephalographic machine with a sampling frequency of 200 Hz and 25 channels; each exam was about 35 min long, reviewed and annotated (labeled) by a pediatric neurologist, and registered according to the different events of interest, normal and epileptiform abnormalities (spikes and poly-spikes); abnormalities vary in number from subject to subject. This procedure was performed in accordance with bioethics standards, where an informed consent was obtained for each EEG recording; the consent, and the whole study, were approved by the Ethics Committee of the Universidad del Cauca.

2.2 Data Preparation and Feature Engineering

In order to adapt the data for the Machine Learning process, the initial data set was split in segments of one second in length, which in turn were clean, standardized using Hamming windows and subjected to a process of feature extraction. The feature extraction was performed in both: time domain, where the signal is analyzed only in terms of the change of its amplitude, and the time-frequency domain obtained from the Discrete Wavelet Transform (DWT). In each domain, additional features were computed, i.e., Energy, Log energy entropy, Shannon Entropy, Katz's Fractal Dimension, Higuchi's Fractal Dimension and Hurst Exponent, Mel frequency coefficients, among others. The feature vector was composed of 141 features in total.

Next, the dimension of the feature vector was reduced to 15 using a ranking approach through consensus between: Information Gain, ANOVA, Squared chi, ReliefF algorithm, and Fast Correlation Based Filter (FCBF).

2.3 Model Building

In this phase, different techniques and classification algorithms were implemented and their results compared in order to select the one with the greatest overall accuracy; subject to a constrain, the selected algorithm has to accomplish multiclass classification, i.e., normal, spikes and poly-spikes. In this work, eleven different algorithms were compared: Random Forest, Naive Bayes, Support Vector Machines (SVM), Stochastic Gradient Descendent (SGD), AdaBoost, Neural Network, Trees, CN2 rule inducer, Logistic Regression, k-nearest neighbors (kNN), and Constant. To build the model, the dataset was split into three sets: training (60%), evaluation (10%), and test (30%) sets.

2.4 Model Evaluation

To evaluate the model, three metrics were used, i.e., the average accuracy, area under the ROC curve and recall. Furthermore, the confusion matrix was obtained in order to compute precision, specificity and sensitivity from the test dataset.

3 Results

The dataset contains 350 segments of one second length, where 181 are normal, 65 are spikes and 104 are poly-spikes segments. After feature engineering, the best 15 features ranked were included in the feature vector, i.e., Entropy of Gamma and Alpha waves, activity of Delta wave, variance and standard deviation of Gamma wave, Hurst Exponent of the channel and Theta wave, mobility, zero cross rate, crest factor, Reyi entropy of Gamma and Beta waves, complexity of the channel and Delta wave, and average frequency. A comparison of the overall accuracy, in classification, using the full data set and the reduced feature vector is shown in Table 1.

Table 1. Evaluation of the performance of the classifiers with the full dataset and with a reduced features vector. Indicators are CA overall accuracy, AUC area under de ROC curve, and recall.

Method	Using 141 features			Using the best 15 ranked		
	CA	AUC	Recall	CA	AUC	Recall
Random forest	0.926	0.986	0.926	0.914	0.983	0.914
Naive bayes	0.903	0.979	0.903	0.877	0.975	0.877
SVM	0.891	0.977	0.891	0.886	0.975	0.886
SGD	0.891	0.909	0.891	0.866	0.881	0.866
AdaBoost	0.889	0.910	0.889	0.877	0.903	0.877
Neural network	0.866	0.948	0.866	0.886	0.969	0.886
Tree	0.863	0.896	0.863	0.869	0.896	0.869
CN2 rule inducer	0.811	0.924	0.811	0.849	0.939	0.849
Logistic regression	0.660	0.790	0.660	0.746	0.852	0.746
kNN	0.586	0.774	0.586	0.743	0.893	0.743
Constant	0.514	0.500	0.514	0.514	0.500	0.514

Using the data in Table 1, the Random Forest was selected to build the machine learning model, which in turn was tested with 30% of the data (test dataset) achieving a performance of: CA 89.1%, AUC 97.5%, Recall 89.1%, and Precision 89.1%.

The confusion matrix and the ROC curve were also computed, from there, the concordance between the software and the neurologist was calculated using the Kappa index, which resulted in K = 0.855. According to Landis y Koch [9], it corresponds to an almost perfect or perfect agreement.

4 Discussion and Conclusions

The tool herein presented facilitates the study and evaluation of pediatric EEGs through collection, management and semi-automatic classification of EEG signals and clinical information associated with epileptic events and it can be used in the diagnosis of pediatric epilepsy. The system was tested with more than 100 pediatric EEGs, with a diagnosis of epileptic seizure, and the characteristics of abnormal electrical activity were determined in semi-automatic way using an intelligent software designed for this specific task. The results achieved using the software were compared with the annotations made by an expert pediatric neurologist reaching up to 85.5% agreement between the expert and the software. In addition, the neurologists stated that, during the evaluation of a 30-minute EEG, the intelligent system allowed them to save up to one hour in the study of each EEG. These kinds of systems can support the neurologist, which is reflected in better opportunities for the patient. The main issue is related to artifacts which can reduce the performance of the classifier. As future work, it is recommended to include artifacts in both, training and testing phases.

Acknowledgements. This work is funded by a grant from the Colombian Agency for Science, Technology, and Innovation – Colciencias – under Calls 715-2015, project: "NeuroMoTIC: Sistema móvil para el Apoyo Diagnóstico de la Epilepsia", Contract number FP44842-154-2016, and Call 647-2015.

References

1. Fisher, R.S., Boas, W.V., Blume, W., Elger, C., Genton, P., Lee, P., Engel, J.: Epileptic seizures and epilepsy: definitions proposed by the International League Against Epilepsy (ILAE) and the International Bureau for Epilepsy (IBE). Epilepsia **46**, 470–472 (2005)
2. Lauzán, D.P., Pozo Alonso, A.J.: Epilepsias y discapacidades neurológicas en el niño, Editorial Ciencias Médicas La Habana Cuba (2007)
3. World Health Organization Executive Board: Global burden of epilepsy and the need for coordinated action at the country level to address its health, social and public knowledge implications. World Health Organ. **136** (2015)
4. Amaya, L., Villegas, A., Chavarro, D., Matallana, M., Puerto, S., Ruiz, F., Vasquez, M.: Estudio de disponibilidad y distribución de la oferta de médicos especialistas, en servicios de alta y mediana complejidad en Colombia. Pontificia Universidad Javeriana (2013)

5. Alickovic, E., Kevric, J., Subasi, A.: Performance evaluation of empirical mode decomposition, discrete wavelet transform, and wavelet packed decomposition for automated epileptic seizure detection and prediction. Biomed. Signal Process. Control **39**, 94–102 (2018)
6. Lahmiri, S.: An accurate system to distinguish between normal and abnormal electroencephalogram records with epileptic seizure free intervals. Biomed. Signal Process. Control **40**, 312–317 (2018)
7. Gao, Z.-K., Cai, Q., Yang, Y.-X., Dong, N., Zhang, S.-S.: Visibility graph from adaptive optimal kernel time-frequency representation for classification of epileptiform EEG. Int. J. Neural Syst. **27**(4) (2017). Article no. 1750005
8. Verhoeven, T., Coito, A., Plomp, G., Thomschewski, A., Pittau, F., Trinka, E., Wiest, R., Schaller, K., Michel, C., Seeck, M., Dambre, J., Vulliemoz, S., van Mierlo, P.: Automated diagnosis of temporal lobe epilepsy in the absence of interictal spikes. NeuroImage Clin. **17**, 10–15 (2018)
9. Landis, J.R., Koch, G.G.: The measurement of observer agreement for categorical data. Biometrics **33**(1), 159–174 (1977)

Comparative Analysis of Alpha Power Spectral Density in Real and Virtual Environments

Fabian O. Romero-Soto, David I. Ibarra-Zárate, and Luz Maria Alonso-Valerdi(✉)

Tecnológico de Monterrey, Escuela de Ingeniería y Ciencias, Ave. Eugenio Garza Sada 2501, 64849 Monterrey, NL, Mexico
lm.aloval@tec.mx

Abstract. The virtual reality (VR) technology has been able to emulate physical places with realistic details, useful for multiple areas such as rehabilitation, education, entertainment, etc. This is possible because virtual environments can emulate the sense of "presence" that the user undergoes in the real world. The present study aimed to compare the typical videogame "Power Solitaire" in both scenarios, real and virtual one, by monitoring *presence* by estimating the alpha power spectral density on 14 electroencephalographic channels. As well, it was used three questionnaires ("Immersive Tendencies", "Presence", and "Slater Usoh-Steed") to check the level of *Presence*. For this study, seven volunteers were recruited, and an Occulus Rift Headset and a headset "Emotiv epoc" were used. The study showed that "Power Solitaire" videogame rendered in VR mode induced the similar sense of presence experienced in the real world in accordance with (1) a good movement and auditory response of VR, (2) high quality of user-system interaction, and (3) similar level of alpha neural synchrony over the frontal lobe, which reflects sensory decoding, level of attention, and readiness to perform a task.

Keywords: Virtual Reality · Alpha band · Presence · EEG

1 Introduction

The virtual reality (VR) is an emerging technology that simulates the physical presence at different places, from real to imaginary ones [1]. VR is a computational tool that has been applied in a wide variety of research fields, since it can achieve the sense of presence under controlled conditions. In other words, VR allows individuals to interact similarly to the real world, without facing the risks that could be run at the time of real human interactions. For example, the "AR Constructor" is a supportive educational tool to train people about the construction techniques, and thus facilitating and optimizing students' projects [2]. Another example is the webpage titled as "EEG AR: Things we have lost", which was created to render the possible appearance of ancient animals, empires and objects that do not currently exist [3].

Videogames have been particularly beneficiated by VR. An interesting example is "Robot & Robotnik", software created in the University of Valencia that narrates the story inspired on "Rossum's Universal Robots" written by Karel Capek [4]. Another

© Springer Nature Switzerland AG 2020
C. A. González Díaz et al. (Eds.): CLAIB 2019, IFMBE Proceedings 75, pp. 156–163, 2020.
https://doi.org/10.1007/978-3-030-30648-9_22

good example is “Mind-Mirror”, which is a system that reflects the user motion in accordance with the cortical arousal [5].

Medical care has been extremely beneficiated by VR, as well. For example, the psychotherapy based on VR to treat phobias, post-traumatic stress disorders, and pain management has been well-accepted treatments with important social impacts [6, 7]. Another relevant application of VR has concerned the evaluation and rehabilitation of cognitive processes such as visual perception and executive functions [7]. Regarding motor rehabilitation, VR has provided the circumstances to control systematically tridimensional, complex and dynamic stimuli within an immersive environment, making possible the hierarchical presentation and recreation of those stimuli [8–10]. VR has provided the possibility to render ecological and friendly cognitive environments [8]. In the same line of thinking, VR has been used as training method for surgical processes and as an educational tool for medical students, e.g., the training environment to acquire transcranial magnetic stimulation skills [11].

In the aforementioned projects (and many others), it is supposed that VR induces a high level of presence and immersion. However, although the sensory pathways of a human being are relatively inefficient, it is difficult to deceive the central nervous system because of the great efficiency of the neuronal processing. In the first VR applications, the sensory channel to have the sense of presence was the vision. However, the technological advances have extended the sensory stimulation to other channels such as audition, haptics and proprioception. By means of this technology, the sensation of a handshake [12], corporal control [13], and spatial orientation [14] has been rendered and studied over the past few years.

Along the sensorial improvement in VR, the evaluation of the sense of presence has attracted the attention of researchers. According to [15], the term of “presence” refers to the sensation of being or belonging in an environment, where psychophysiological reactions are induced. By way of illustration, in [16], it was found that prefrontal and parietal lobes established a regular communication when experiencing sense of presence induced by VR. In [17], it was showed that the insula is activated to modulate attention and self-awareness during virtual experiences. In [18], motor activity was detected and quantified at cortical level in 2D and 3D environments. Researchers demonstrated that power spectral density (PSD) in theta frequency band at fronto-central cortex was more prominent in the tridimensional environment than in the bidimensional one.

As VR has become a potential tool to emulate authentic interactions with the real world, the measurement of the sense of presence has been necessary. In this paper, it is proposed to quantify the level of synchrony of EEG signals of individuals when interacting with real and virtual environments. Both environments are based on the popular card game known as “solitaire”. The quantification of the EEG synchrony is based on the estimation of alpha PSD since alpha band has been related to (1) sensory decoding: identification and interpretation of environmental stimuli; (2) level of attention: selection of information, activation and mental effort, expectative; and (3) readiness to perform a task [19–21]. On this basis, it is hypothesized that alpha PSD should be similar in both real and virtual “solitaire” games since the sense of presence, which is defined in terms of sensory decoding, level of attention, and readiness, should be very similar as well.

2 Methodology

2.1 Sample

Seven males aged around 21.227 ± 1.901 years were recruited for this study. Participants were explained about the experimental procedure, and all of them gave their consent to participate voluntarily. All the participants were right-handed and none of them reported either neuropathological condition, or consumption of alcohol, tobacco or any hallucinogenic substance. The study was previously approved by the Ethical Committee of the Medicine School at Tecnologico de Monterrey (reference number: CONBIOETICA-19-CEI-011-20161017).

2.2 Materials

EEG signals were recorded by an Emotiv Epoc System of 14 channels distributed in accordance with the 10/20 System (AF3, AF4, F3, F7, F8, FC5, FC6, T7, T8, P7, P8, O1, O2), and at sampling frequency of 128 Hz. EEG signals were referenced using both ear lobes.

VR was rendered by a visor Oculus Rift with OLED panels of resolution: 2160x1200 pixels. VR software to play the "Solitaire" game was purchased in the virtual store Steam. By using the videogame scenario, the real one was constructed. See Fig. 1.

Fig. 1. Virtual (top image) and real (bottom image) scenarios used for the video game "power solitaire".

2.3 Experimental Procedure

The present study was undertaken as follows. First, a preliminary questionnaire was distributed in social networks at Tecnologico de Monterrey. Around 20 persons between 20 and 25 years provided information concerning their age, sex, health habits

(e.g., consumption of alcohol, tobacco, and hallucinogenic substance, and physical activity), clinical history (e.g., neurological deficits), and availability to participate in the study. From the 20 persons, 7 of them who reported healthy habits and no neurological deficits, and who agreed to take part in the experiment, were recruited. Second, these volunteers responded the "Edinburgh Handedness Inventory" to identify their dominant hemisphere [22]. In addition, they responded the "Immersive Tendencies Questionnaire" (Likert scale from 0 to 6, where 0 is "never" and 6 is "often") to estimate their immersion tendency [23]. Both questionnaires took around 5 min. Third, participants spent around 5 min to get familiarized with the Oculus Rift visor. Forth, they moved on to play the VR game for around 11 min. The session was distributed in 3 runs of 3 min each, and 2 breaks of 1 min each. Fifth, they moved on to play the same game, but now in real conditions, and in line with the same rules. Finally, they responded the "Presence Questionnaire" (Likert scale from 0 to 7 where 0 is "never/none" and 7 is "completely") [23], and the "Slater-Usoh-Steed Questionnaire" (Likert scale from 0 to 6 where 0 is "never/none" and 6 is "completely") [24]. The latter questionnaire concerned the technical aspects of the VR such as the image quality, audio fidelity and user-system interaction.

2.4 EEG Signal Processing

EEG signals were analyzed using the Matlab toolbox for processing electrophysiological data, EEGLAB [25]. The signal analysis pipeline was run as follows. First, signals were band-pass filtered from 8 to 13 Hz using a Butterworth design of 6th order. Second, EEG signals were visually scanned and transitory artifacts (e.g., head movement or pop-up electrodes) were rejected manually. Third, independent component analysis was applied to detect and remove blinks, eyes movements, and cardiac activity (if present). Finally, PSD was estimated as the power of the Fourier Transform magnitude (See Eq. 1). PSD estimates were normalized by the maximum value per channel.

$$Sxx\left(e^{j2\pi k}\right) = \left|\sum_{n=0}^{N-1} x_n e^{-j2\pi kn/N}\right|^2 k = 0, \ldots, N-1 \quad (1)$$

2.5 Statistical Evaluation

In terms of the questionnaires, mode was estimated. Regarding PSD comparison, Kruskal-Wallis test was applied. The significance level was set at 5%. The data analysis was performed using Minitab 18 (Minitab Inc., Pennsylvania, USA).

3 Results

Table 1 provides the central tendencies (along with their description) of the VR monitoring based on four questionnaires. In addition, Fig. 2 depicts the central tendency of alpha PSD in virtual and real environments. Main results are reported below.

3.1 Pre-experimental Evaluation

The "Edinburgh handedness inventory" showed that all the participants do 70% of their activities using their right hand, while the rest of their activities are undertaken either using right or left hand. The "Immersive tendencies" revealed that participants reported to feel partially immersed in scenarios such as T.V. series or movies (mode = 2/6), whereas they feel almost totally immersed in video games (mode = 5/6).

Table 1. Central tendencies of VR monitoring based on four questionnaires

	Questionnaire		Mode	Description
Pre-virtual experience	Edinburgh handedness inventory			70% of right-handed dominance
	Immersive tendencies	TV, movies	2/6	Videogames are higher immersive
		Videogames	5/6	
Post-virtual experience	Presence	Movements and sounds	5/7	Movements and sounds provide higher presence
		Vision	4/7	
	Slater-usoh-steed		6/6	High quality of VR in use

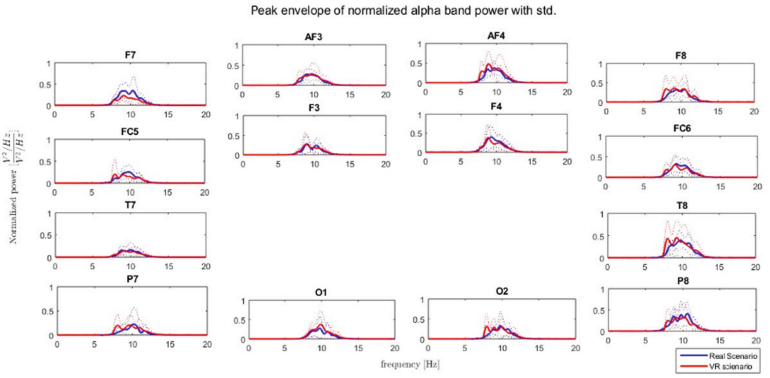

Fig. 2. Mean (solid lines) and standard deviation (dotted lines) of the normalized alpha PSD of the 7 participants for each EEG channel and in both real (blue) and virtual (red) environments.

3.2 EEG Evaluation Based on Alpha Band PSD

Figure 2 presents the mean (solid line) and the standard deviation (dotted line) of the normalized alpha PSD of the 7 participants for each EEG channel and in both real (blue) and virtual (red) environments. According to the Kruskal-Wallis test, mean PSDs in virtual and real environments were significantly different ($p > 0.0091$) across all the EEG channels, except for F3 ($p = 0.0614$). Alpha PSD on F3 channel is presented in Fig. 3.

3.3 Post-experimental Evaluation

In line with the survey "Presence", volunteers positively evaluated VR quality on movement, sound and reaction effects (mode = 5/7). On the other hand, VR quality on visual effects was less satisfactorily assessed (mode = 4/7). In accordance with the survey "Slater-usoh-steed", VR in use was 85.71% effective with a mode = 6/6.

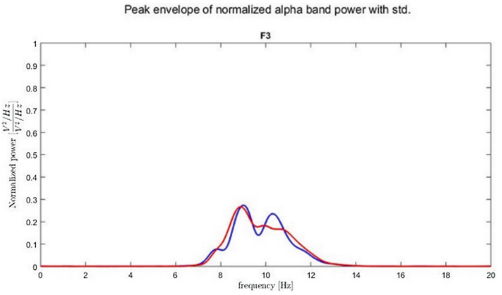

Fig. 3. Average normalized alpha PSD of the 7 participants on F3 channel and in both real (blue) and virtual (red) environments.

4 Discussion

VR is one of the most popular emerging technologies. VR is not only developed for immersive gaming, but they have also been applied as capacitation, rehabilitation and disorder treatment tool. All these advances have addressed to a key questioning: Is VR ready to replace real world? To move towards answering this question, the present work aims to compare the typical videogame "Power Solitaire" in both scenarios, real and virtual one, by monitoring presence. A notable feature of VR is embodiment and presence, which refer to the ability to feel inside a projected environment. In this work, presence was estimated by making use of three questionnaires, and estimating alpha band PSD of 14 EEG channels. Hereunder, main findings are discussed.

4.1 Pre-virtual Experience

According to the "Immersive tendencies" questionnaire, the willingness of virtual experiences of volunteers in terms of videogames was considerably high (mode = 5/6). This means that the user-system interaction in the present experimental protocol was somehow expected to be natural.

4.2 Virtual Experience

Average normalized alpha PSD over 14 EEG channels and across 7 individuals showed that the level of neural synchronization of alpha waves was significantly different in all of the recoding sites, except for F3. Having in mind that alpha waves synchronize in accordance with mental coordination, alertness and mind/body integration, their PSD

was considered a feasible parameter of presence. This finding indicates that presence (refers herein as to level of neural synchrony in alpha band) was only similar on F3 at the time of comparing virtual and real environments. In [16] and [17], it was demonstrated that most of cortical areas related to the sense of presence were found over right parietal and frontal lobes. In addition, dorsolateral left prefrontal cortex has been associated with action planning [26], a key feature to induce presence in VR. Finally, in [27], it was shown that both dorsolateral prefrontal cortexes were interconnected while experiencing presence in virtual environments. Specifically, left hemisphere was associated with self-reflective and independent thoughts. Based on those investigations, the alpha PSD similarity over F3 found on this study could be result of the sense of presence undergone by volunteers during "Power Solitaire" videogame. The particular tendency over the left hemisphere in this study may be also associated with the 70% of right-handed dominance in all the volunteers.

4.3 Post-virtual Experience

The "Presence" questionnaire showed that volunteers reported a good acceptance of motion and audition rendering of VR in use (mode = 5/7). Additionally, the "Slater-usoh-steed" questionnaire demonstrated that the interaction between volunteers and the VR was very satisfactory (mode = 6/6).

Taken together, these findings suggest that "Power Solitaire" videogame rendered in VR mode induced the similar sense of presence experienced in the real world in accordance with (1) a good movement and auditory response of VR, (2) high quality of user-system interaction, and (3) similar level of alpha neural synchrony over the frontal lobe, which reflects sensory decoding, level of attention, and readiness to perform a task.

5 Conclusion

VR experiences are moving towards being similar to those undergone in real world in terms of presence. In this study, user opinion was not only considered, but similar alpha neural synchrony over F3 was also found. Along the technological recent advances such as 3D spatial audition and haptic stimulation, VR could induce sense of presence as in real world at a cortical level.

References

1. Chon, J., Kaongoen, N., Jo, S.: EEG signal analysis for measuring the quality of virtual reality, Busan (2015)
2. Mesárošová, A., Hernández, M.F., Mes, P., Behún, M.: Mixing Augmented reality and EEG technology to create an unique learning tool for construction process (2017)
3. Freeman, J.C.: EEG AR: things we have lost (2018). https://johncraigfreeman.wordpress.com/eeg-ar-things-we-have-lost/
4. Mésárošová, A., Reality, A.A.: Art behind the mind exploring new art forms by implementation of the electroencephalography (2015)

5. Mercier-Ganady, J., Anatole, L.: The mind-mirror: see your brain in action in your head using EEG and augmented reality, vol. III, no. 8 (2014)
6. Riva, G.: Virtual reality in psychotherap: review, vol. VIII, no. 3, pp. 220-231 (2005)
7. Schultheis, M.T., Rizzo, A.A.: The application of virtual reality technology in rehabilitation. Rehabil. Psychol. **XLVI**(3), 296–311 (2001)
8. Rizzo, A., Buckwalter, J.G., van der Zaag, C., Neumann, U.: Virtual environment applications in clinical neuropsychology. In: Proceedings IEEE Virtual Reality, pp. 63–70 (2000)
9. Rizzo, A.A., Schultheis, M., Kerns, K.A., Mateer, C.: Analysis of assets for virtual reality applications in neuropsychology. Neuropsychol. Rehabil. **XIV**(1), 207–240 (2004)
10. Wiederhold, B.K., Rizzo, A.: Virtual reality and applied psychophysiology. Appl. Psychophysiol. Biofeedback **XXX**(3), 183–185 (2005)
11. Soeiro, J., Cláudio, A.P., Carmo, M.B., Ferreira, H.A.: Mobile solution for brain visualization using augmented and virtual reality (2016)
12. Perani, D., Fazio, F., Borghese, N.A., Tettamanti, M., Ferrari, S., Decety, J.: Different brain correlates for watching real and virtual hand actions. Neuroimage **14**, 749–758 (2001)
13. Nagamine, S., Hayashi, Y., Yano, S., Kondo, T.: An immersive virtual reality system for investigating human bodily self-consciousness, pp. 3–6 (2016)
14. Sharma, G., Daniel, R.V.: Brain connectivity in spatial orientation task, pp. 1–4 (2016)
15. Steuer, J.: Defining virtual reality: dimensions determining telepresence (1992)
16. Kober, S.E., Kurzmann, J., Neuper, C.: Cortical correlate of spatial presence in 2D and 3D interactive virtual reality: an EEG study. Int. J. Psychophysiol. **LXXXIII**(3), 365–374 (2012)
17. Clemente, M., Rodríguez, A., Rey, B., Alcañiz, M.: Assessment of the influence of navigation control and screen size on the sense of presence in virtual reality using EEG. Expert Syst. Appl. **XLI**(4), 1584–1592 (2014)
18. Slobounov, S.M., Ray, W., Johnson, B., Slobounov, E., Newell, K.M.: Modulation of cortical activity in 2D versus 3D virtual reality environments: an EEG study. Int. J. Psychophysiol. **XCV**(3), 254–260 (2015)
19. Benedek, M., Bergner, S., Konen, T., Fink, A., Neubauer, A.C.: EEG alpha synchronization is related to top-down processing in convergent and divergent thinking. Neuropsychologia **XLIX**(2), 3505–3511 (2011)
20. Kropotov, J.D.: Quantitative EEG, Event-Related Potentials and Neurotherapy. Academic Press-Elsevier, San Diego (2009)
21. Pineda, J.A.: The functional significance of mu rhythms: translating "seeing" and "hearing" into "doing". Brain Res. Rev. **L**, 57–68 (2005)
22. Oldfield, R.C.: The assessment and analysis of handedness: The Edinburgh inventory. Neuropsychologia **IX**(1), 97–113 (1971)
23. Witmer, B.G., Singer, M.J.: "Measuring presence in virtual environments: a presence questionnaire. Presence Teleoper. Virtual Environ. **VII**(3), 225–240 (1998)
24. Usoh, M., Catena, E., Arman, S., Slater, M.: Using presence questionnaires in reality. Presence Teleoper. Virtual Environ. **IX**(5), 497–503 (2000)
25. Delorme, A., Makeig, S.: EEGLAB: an open source toolbox for analysis of single-trial EEG dynamics including independent component analysis. Neurosci. Methods **134**, 9–21 (2004)
26. Davidson, R., Pizzagalli, D.: Parsing the subcomponents of emotion and disorders of emotion: perspectives from affective neuroscience. Handb. Affect. Sci. 8–24 (2003)
27. Baumgartner, T.: Feeling present in arousing virtual reality worlds: prefrontal brain regions differentially orchestrate presence experience in adults and children. Front. Hum. Neurosci. **2** (August), 1–12 (2008)

Analysis of Cardiorespiratory Variations During Sleep in Shift Workers by Univariate and Multivariate Detrended Fluctuation Analysis

Raquel Delgado-Aranda[1(✉)], Guadalupe Dorantes-Méndez[1], and Martín Oswaldo Méndez[1,2]

[1] Faculty of Sciences, Universidad Autónoma de San Luis Potosí, San Luis Potosí, Mexico
r.delgadoaranda@gmail.com
[2] Laboratorio Nacional CI3M, San Luis Potosí, Mexico

Abstract. This paper presents a study of the heart rate variability (HRV) and respiratory rate variability (RRV) during daytime and nighttime sleep, considering the sleep stages. Eleven healthy female shift workers of 20–54 years old, were recorded during the sleep period. Detrended fluctuation analysis (DFA) was used to assess the short and long-range correlations of time series. Furthermore, the bivariate signal (HRV - RRV) was evaluated by means of the multivariate DFA. The results showed significant differences between the sleep stages. Nevertheless, the mean values of the HRV and RRV exponents did not show meaningful variability between daytime and nighttime sleep. The results suggest that there are changes in the central nervous system, in the regulation of heart and respiratory rate during the sleep stages. Also, the correlations of nighttime sleep are preserved during daytime sleep, which could be due to the adaptability of sleep to changes due to shifting work, keeping correlation properties of HRV and RRV.

Keywords: Detrended Fluctuation Analysis · Heart rate variability · Respiratory rate variability · Sleep

1 Introduction

The sleep can be defined as the physiological state that implies the reduction of vigil consciousness and response to the environment. Normal human sleep comprises two states, rapid eye movement (REM) and non REM (NREM) sleep, that alternate cyclically across a sleep episode. This one has functions of restoration and recovery of biological systems. Therefore, the absence or disturbance of sleep has serious physiological consequences, such as fatigue, work under-performance, depressed mood, a higher risk of metabolic syndrome, hypertension, cardiovascular diseases, among others [1].

© Springer Nature Switzerland AG 2020
C. A. González Díaz et al. (Eds.): CLAIB 2019, IFMBE Proceedings 75, pp. 164–171, 2020.
https://doi.org/10.1007/978-3-030-30648-9_23

Shifting the work-sleep cycle on the circadian rhythm can have consequences for the sleep and wake states. Since, the shift workers require a greater effort and time to recover. Most shift workers sleep less than 6 hours [2] and the sleep disturbance rate is 20–90%, compared to 10% in the case of day workers [3]. Therefore, the study of sleep in shift workers is considered important for the prevention and diagnosis of diseases. The standard method for sleep evaluation is polysomnography (PSG). However, it is expensive and needs the placement of several sensors on the patient. Therefore, alternative devices have been developed to acquire physiological signals in a non-invasive and non-obstructive manner, providing a more comfortable environment. One of these devices is the Pressure Bed Sensor (PBS) developed in the technical research center of Finland (VTT). This one allowed to obtain physiological signals such as the respiratory effort, heart rate, and movement activity [4,5].

The influence of shift work on heart rate variability (HRV) has been analyzed previously. Freitas et al. [6] analyzed a three-shift rotating work group and they found that the circadian rhythm of HRV seems to be predominantly related to sleep and wakefulness, independent of night-day cycle. Ito et al. [7] also reported that the circadian rhythm of cardiac autonomic activity is modified by the level of physical activity regardless of the shifts. However, Furlan et al. [8] observed that the continuous changes in the cardiac sympathetic and vagal autonomic control may play a role in the excessive rate of cardiovascular diseases in shift workers.

The aim of the present study was to assess the HRV and respiratory rate variability (RRV) by means of Detrended Fluctuation Analysis (DFA), in order to evaluate changes in the sleep autocorrelations of time series during daytime sleep with respect to nighttime sleep in shift workers. Moreover, the Multivariate Detrended Fluctuation Analysis (MVDFA) was used to evaluate the autocorrelation of the cardiac and respiratory systems in a bivariate way.

2 Methods

2.1 Database

At the sleep laboratory of Finnish Institute of Occupational Health, sleep recordings of 11 healthy shift working females (age 20–54 years) were performed. From the subjects, a total of 22 recordings were obtained, 11 during daytime sleep after a night shift of work and 11 during nighttime sleep [9]. All participants underwent a complete PSG recording and simultaneously recorded the signals with the PBS. The signals obtained from the PBS were filtered and processed with algorithms to extract respiration, HRV and movement or activity [4]. A pre-processing to the inter-beat interval signal (IBI) was performed, which consisted of applying an adaptive filter [10] to eliminate abnormal heartbeats. In addition, the respiration signal was sampled based on the R wave.

2.2 Detrended Fluctuation Analysis

DFA is a method for scaling the long-term autocorrelation of non-stationary signals [11]. The algorithm consists of first constructing the signal profile $y(i)$, of the time series $x(k)$ of length N, with mean μ

$$y(i) = \sum_{k=1}^{i} [x(k) - \mu], \quad i = 1, ...N \tag{1}$$

As a next step, the profile is divided into $N_n = [N/n]$ series $y_v(i)$ of length n. Subsequently, for each $y_v(i)$, $v = 1, ..., N_n$, the linear trend $t_v(i)$ is calculated, by a least-square fit. Finally, the fluctuation function of the DFA is obtained as

$$F(n) = \sqrt{\frac{1}{N} \sum_{i=1}^{N} [y_v(i) - t_v(i)]^2} \tag{2}$$

The fluctuation function $F(n)$ is plotted for all windows size n, on logarithmic axes ($log[F(n)]$ vs $log(n)$) and the DFA exponent, α is calculated as the slope of a linear fit of the graphic of the fluctuation function. The parameter α represents the correlation properties of the signal [11]: $0 < \alpha < 0.5$ an anti-correlated signal, $\alpha = 0.5$ an uncorrelated signal (white noise), $\alpha > 0.5$ mean positive autocorrelation in the signal, $\alpha = 1$ it is $1/f$ noise and $\alpha = 1.5$ Brownian noise.

DFA was applied to segments with a duration of 10 min, corresponding to deep and light sleep, which belong to the NREM sleep and REM sleep. The heart rate (HR) has two scale regions due to on short time scales, the physiological fluctuation of the heartbeat intervals is dominated by an oscillation associated with respiration [12]. Therefore, it was obtained α_1 ($4 \leq n \leq 16$) and α_2 ($17 \leq n \leq N/4$) associated with short-range and long-range fractal dynamics respectively [13]. For the respiration signal, the DFA was applied to the same 10 min segments corresponding to the sleep stages (deep and light sleep, REM sleep), obtaining an α_{RES} with $4 \leq n \leq N/4$.

2.3 Multivariate Detrended Fluctuation Analysis

MVDFA is an extensive version of DFA, aiming to explore the autocorrelation behavior of multivariate time series. The algorithm of MVDFA [14] considers a multivariate time series $y_{k,i}$ ($i = 1, 2, ..., p$), where p denotes the number of signals. For a scale s, the profile ($Y_{k,i}$) of the ith signal is calculated in the same way that the DFA

$$Y_{k,i} = \sum_{n=1}^{k} \left[y_{n,i} - \overline{y}_{.,i} \right] \quad k = 1, \ldots, N \tag{3}$$

where N is the number of samples in each signal and $\overline{y}_{.,i}$ is the average of the ith signal. Divide the profile of the ith signal into $N_s = (N/s)$ non-overlapping

segments of equal length s and repeat the segment procedure from the opposite end. Thereby, $2N_s$ segments ($v = 1, 2, ..., 2N_s$) are obtained altogether for the ith signal, with l_v as the elements of segment, where $l_v = (v-1)$ for $v = 1, 2, ..., N_s$ and $l_v = N - (v - N_s)$ for $v = N_s + 1, ..., 2N_s$. Calculate the local trend of each segment ($\tilde{Y}_{.,i}$) by a least-square fit of the series for each signal. Then determine the local variance of the multivariate time series for segment v

$$F^2(v,s) = \frac{1}{s}\sum_{t=1}^{s} ||(Y_{l_v+t,1}, Y_{l_v+t,2}, ..., Y_{l_v+t,p}) - (\tilde{Y}_{.,1}, \tilde{Y}_{.,2}, ..., \tilde{Y}_{.,p})||^2 \quad (4)$$

where $||\cdot||$ denotes the Euclidean norm. Average over all the local variances $F^2(v,s)$ to obtain the overall fluctuation function

$$F_{MVDFA}(s) = \left\{ \frac{1}{2N_s} \sum_{v=1}^{2N_s} [F^2(v,s)] \right\}^{1/2} \quad (5)$$

Repeat for the varied scales s and then the scaling behavior, α_{MVDFA} is determined with linear regression of the graph $log[F_{MVDFA}(s)]$ vs $log(s)$. If only short-range correlations or no correlations exist in the sequence, then the scaling exponent $\alpha_{MVDFA} = 0.5$; if $0.5 < \alpha_{MVDFA} < 1.0$, the long-range auto-correlations is persistent, and if $0 < \alpha_{MVDFA} < 0.5$, long-range auto-correlations with anti-persistent behavior is present. In order to evaluate in a bivariate way the fluctuations of HRV and the RRV, the MVDFA was applied to IBI and respiration signals.

2.4 Statistical Analysis

The Lilliefors test was used to determine if the data were normally distributed. According to the results of the previous test, the Kruskal-Wallis or one-way ANOVA test were applied to observe differences between the three stages of sleep. Also, the Wilcoxon rank sum test or two-sample t-test were used to find differences between the day and nighttime sleep data. For the previous tests, significant differences were considered with a value of $p < 0.05$.

3 Results and Discussion

The sleep duration during daytime sleep was approximately half of the hours with respect to nighttime sleep, this is shown in the Table 1, which is consistent with the results of [15]. During the daytime sleep a decrease in the percentage of REM sleep hours was observed and an increase in deep sleep, which could be interpreted as a body effort to achieve physical restoration, in shorter total sleep time.

On the other hand, the DFA results from the nocturnal records presented in Fig. 1, suggests that HR depends on the sleep stage, which agrees with the results found in [16]. A long-range correlation was obtained throughout sleep,

Table 1. Mean and standard deviation of sleep hours and duration of each stage in percentage.

	Daytime Sleep	Nighttime Sleep
Sleep hours	4.38 ± 0.59	7.92 ± 0.70
Deep sleep	$22.86 \pm 10.99\%$	$12.89 \pm 6.56\%$
Light sleep	$49.80 \pm 10.53\%$	$56.93 \pm 7.31\%$
REM sleep	$15.47 \pm 14.88\%$	$22.12 \pm 5.18\%$

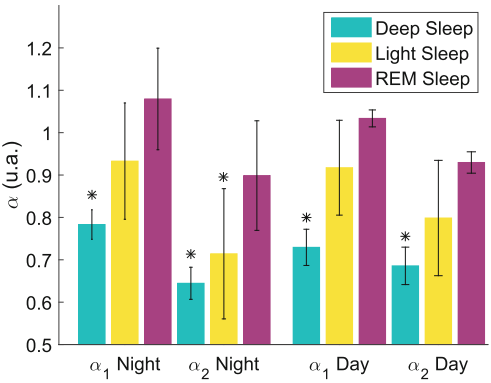

Fig. 1. Mean and standard deviation of the α exponent of the IBI signal of the nighttime and daytime sleep. The symbol $*$ indicates significant differences *vs* REM sleep ($p < 0.05$).

where REM sleep obtained a higher α exponent (α_1 and α_2) than deep sleep. This could be explained by the increase in the parasympathetic nervous system influence during NREM sleep. This behavior was observed during both daytime and nighttime sleep. In addition, α_2 value of REM sleep was significantly higher than deep sleep and light sleep during the nighttime sleep. The results of α_1 reflected a larger scale exponent for all stages of sleep with regard to α_2 because on short time scales HRV is affected by an oscillation associated with breathing [12]. There were no significant differences in α exponent of daytime sleep against those of nighttime sleep.

The results of the respiration signal are presented in Fig. 2, where a similar behavior to those of HRV was observed, as well as [17]. The NREM sleep was significantly smaller than REM sleep in the nighttime sleep, supporting the idea that there is different regulation of the RRV during NREM and REM sleep. Nevertheless, in the daytime sleep, only deep sleep was significantly less than REM sleep. There were no significant differences between the nighttime sleep and daytime sleep stages.

Regarding the results of the MVDFA, α_{MVDFA} was higher during REM sleep with respect to light and deep sleep of the nighttime sleep ($p < 0.05$), this can be

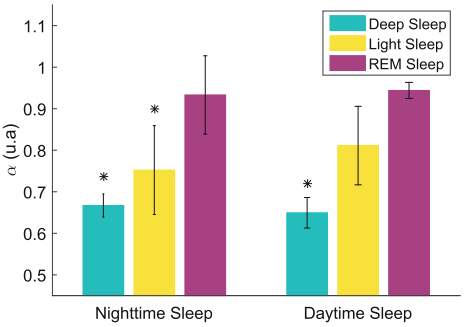

Fig. 2. Mean and standard deviation of the α exponent of the respiration signal of the nighttime and daytime sleep. The symbol $*$ indicates significant differences *vs* REM sleep ($p < 0.05$).

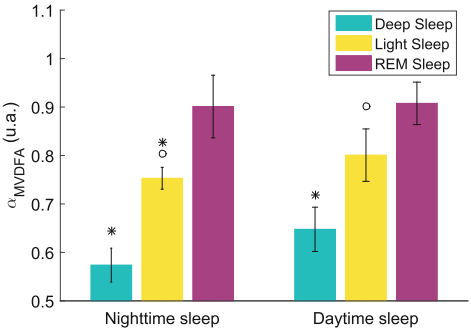

Fig. 3. Mean and standard deviation of the α_{MVDFA} exponent of the nighttime and daytime sleep. The symbols $*$ and $\circ$, indicates significant differences *vs* REM sleep and *vs* deep sleep respectively ($p < 0.05$).

seen in Fig. 3. In addition, deep sleep was significantly smaller than light sleep during nighttime and daytime sleep. On the other hand, during daytime sleep, the REM sleep was only significantly higher than deep sleep. The autocorrelation of the bivariate signal was lower during deep sleep, and higher during REM sleep. This result could be influenced by the respiratory sinus arrhythmia (RSA) phenomenon, where the IBI signal decreases when the amplitude of breathing increases and viceversa on exhalation. Then RSA is higher during deep sleep and lower during REM sleep [18].

4 Conclusions

The correlation properties of HRV and the RRV signals were assessed by means of DFA and MVDFA. The changes in IBI and respiration signals during the different sleep stages were very similar. In both IBI and respiration signals, when the brain is very active as in the REM sleep, the long-range correlation is

higher, in contrast to NREM sleep, this supports the idea of different autonomic regulation during REM and NREM sleep.

The MVDFA results of nighttime sleep, suggest that there is different regulation during each stage of sleep, since significant differences were found between sleep stages. However, during daytime light sleep was not different from REM sleep.

When comparing the results of the daytime sleep with the nighttime sleep, the analysis of sleep stage durations revealed that there are differences in the daytime sleep macrostructure, with a significant increase in deep sleep duration, and a decrease during REM sleep. However, when comparing the results of the DFA and MVDFA, there were no significant differences between daytime sleep and nighttime sleep. This suggests that despite the reduced daytime sleep the cardiorespiratory system is able to maintain the correlation properties, which suggests that the cardiorespiratory system is not altered by shift work. However, it could be interesting study this population in long term and to assess other indices to better characterize the cardiorespiratory function.

Conflict of Interest. The authors declare that there is no conflict of interest.

References

1. Jehan, S., Zizi, F., Pandi-Perumal, S.R., Myers, A.K., Auguste, E., Jean-Louis, G., McFarlane, S.I.: Shift work and sleep: medical implications and management. Sleep Med. Disord.: Int. J. **1**(2) (2017). https://doi.org/10.15406/smdij.2017.01.00008
2. Ahumada, H.T., Ortega, M.: Rotación de turnos, fatiga y trastornos del sueño en un grupo de trabajadores industriales. Rev. Cubana Salud Trabajo **6**(1), 27–31 (2005)
3. Montalvo, J.F., Piñol, E.: Horario laboral y salud: consecuencias psicológicas de los turnos de trabajo. Rev. psicopatol. psicol. clín. **5**(3), 207–222 (2000). https://doi.org/10.5944/rppc.vol.5.num.3.2000.3899
4. Mora, G.G., Kortelainen, J.M., Hernández, E.R.P., Tenhunen, M., Bianchi, A.M., Méndez, M.O.: Evaluation of pressure bed sensor for automatic sahs screening. IEEE Trans. Instrum. Meas. **64**(7), 1935–1943 (2014). https://doi.org/10.1109/TIM.2014.2366976
5. Guerrero, G., Kortelainen, J.M., Palacios, E., Bianchi, A.M., Tachino, G., Tenhunen, M., Mendez, M.O., Van Gils, M.: Detection of sleep-disordered breating with pressure bed sensor. In 2013 35th Annual International Conference of the IEEE Engineering in Medicine and Biology Society (EMBC), pp. 1342–1345. IEEE (2013). https://doi.org/10.1109/EMBC.2013.6609757
6. Freitas, J., Lago, P., Puig, J., Carvalho, M.J., Costa, O., de Freitas, A.F.: Circadian heart rate variability rhythm in shift workers. J. Electrocardiol. **30**(1), 39–44 (1997). https://doi.org/10.1016/S0022-0736(97)80033-7
7. Ito, H., Nozaki, M., Maruyama, T., Kaji, Y., Tsuda, Y.: Shift work modifies the circadian patterns of heart rate variability in nurses. Int. J. Cardiol. **79**(2–3), 231–236 (2001). https://doi.org/10.1016/S0167-5273(01)00439-9
8. Furlan, R., Barbic, F., Piazza, S., Tinelli, M., Seghizzi, P.: Modifications of cardiac autonomic profile associated with a shift schedule of work. Circulation **102**(16), 1912–1916 (2000). https://doi.org/10.1161/01.CIR.102.16.1912

9. Mendez, M.O., Palacios-Hernandez, E.R., Alba, A., Kortelainen, J.M., Tenhunen, M.L., Bianchi, A.M.: Detection of the sleep stages throughout non-obtrusive measures of inter-beat fluctuations and motion: night and day sleep of female shift workers. Fluctuat. Noise Lett. **16**(04), 1750033 (2017). https://doi.org/10.1142/S021947751750033X
10. Wessel, N., Voss, A., Malberg, H., Ziehmann, C., Voss, H.U., Schirdewan, A., Meyerfeldt, U., Kurths, J.: Nonlinear analysis of complex phenomena in cardiological data. Herzschrittmachertherapie Elektrophys. **11**(3), 159–173 (2000). https://doi.org/10.1007/s003990070035
11. Golinska, A.K.: Detrended fluctuation analysis (DFA) in biomedical signal processing: selected examples. Stud. Log. Gramm. Rhetor. **29**, 107–115 (2012)
12. Peng, C.K., Havlin, S., Stanley, H.E., Goldberger, A.L.: Quantification of scaling exponents and crossover phenomena in nonstationary heartbeat time series. Chaos Interdisc.: J. Nonlinear Sci. **5**(1), 82–87 (1995). https://doi.org/10.1063/1.166141
13. Castiglioni, P., Di Rienzo, M., Faini A.: Self-similarity and detrended fluctuation analysis of cardiovascular signals. In: Complexity and Nonlinearity in Cardiovascular Signals, pp. 197–232. Springer (2017). https://doi.org/10.1007/978-3-319-58709-7_7
14. Xiong, H., Shang, P.: Detrended fluctuation analysis of multivariate time series. Commun. Nonlinear Sci. Numer. Simul. **42**, 12–21 (2017). https://doi.org/10.1016/j.cnsns.2016.04.035
15. Åkerstedt, T.: Shift work and disturbed sleep/wakefulness. Occup. Med. **53**(2), 89–94 (2003). https://doi.org/10.1093/occmed/kqg046
16. Penzel, T., Kantelhardt, J.W., Grote, L., Peter, J.H., Bunde, A.: Comparison of detrended fluctuation analysis and spectral analysis for heart rate variability in sleep and sleep apnea. IEEE Trans. Biomed. Eng. **50**(10), 1143–1151 (2003). https://doi.org/10.1109/TBME.2003.817636
17. Kantelhardt, J.W., Penzel, T., Rostig, S., Becker, H.F., Havlin, S., Bunde, A.: Breathing during rem and non-rem sleep: correlated versus uncorrelated behaviour. Phys. A **319**, 447–457 (2003). https://doi.org/10.1016/S0378-4371(02)01502-9
18. Jurysta, F., Lanquart, J.P., Van De Borne, P., Migeotte, P.F., Dumont, M., Degaute, J.P., Linkowski, P.: The link between cardiac autonomic activity and sleep delta power is altered in men with sleep apnea-hypopnea syndrome. Am. J. Physiol. Regul. Integr. Comp. Physiol. **291**(4), R1165–R1171 (2006). https://doi.org/10.1152/ajpregu.00787.2005

Morphological and Temporal ECG Features for Myocardial Infarction Detection Using Support Vector Machines

Wilson J. Arenas[1(✉)], Silvia A. Sotelo[2], Martha L. Zequera[1], and Miguel Altuve[3]

[1] Electronics Department, School of Engineering, BASPI/FootLab, Bioengineering, Signal Analysis and Image Processing Research Group, Pontificia Universidad Javeriana, Bogotá, D.C., Colombia
warenas@javeriana.edu.co, mzequera@javeriana.edu.co

[2] Department of Basic Sciences, Pontifical Bolivarian University, Bucaramanga, Colombia
silvia.sotelo@upb.edu.co

[3] Faculty of Electrical and Electronic Engineering, Pontifical Bolivarian University, Bucaramanga, Colombia
miguel.altuve@upb.edu.co

Abstract. Myocardial infarction is a leading cause of death worldwide. A 12-lead electrocardiogram (ECG) recording is commonly performed to diagnose this pathology. In this paper, we explored temporal and morphological features extracted from multi-lead ECG signals to classify subjects from the PTB Diagnostic ECG database into healthy control and myocardial infarction using a support vector machine binary classifier. After delineating the 12-lead ECG signals with a wavelet transform-based method, a unique set of characteristic points was obtained for the ECG leads by suppressing outliers and by taking the average of the remaining points. Then, mathematical operations (average, standard deviation, skewness, etc.) performed to the P wave duration, QRS complex duration, ST-T complex, QT interval, T wave duration and RR interval were used as temporal features, and mathematical operations performed to ECG signals bounded by the P wave, QRS complex, ST-T complex and QT interval were used as morphological features. A 10-fold Monte Carlo cross-validation was employed to analyze the reproducibility of the classification results by randomly splitting the dataset into training (70%) and test (30%) sets with balanced classes. Mean classification accuracies above 93% were achieved when the SVM classifier uses only temporal ECG features, only morphological ECG features, and both temporal and morphological ECG features. The best classification performance was achieved when temporal and morphological ECG features are jointly considered by the binary SVM classifier (accuracy 96.67%, error rate 3.33%, sensitivity 97.33% and specificity 96.00%).

Keywords: Digital signal processing · Electrocardiography · Myocardial Infarction · Support vector machines

© Springer Nature Switzerland AG 2020
C. A. González Díaz et al. (Eds.): CLAIB 2019, IFMBE Proceedings 75, pp. 172–181, 2020.
https://doi.org/10.1007/978-3-030-30648-9_24

1 Introduction

Myocardial infarction (also known as heart attack) is one of the leading causes of death worldwide, negatively affecting health care systems and producing a significant economic burden for patients and for the nation, both in developed and developing countries, especially because of the aging of the population. The estimated costs of care of this disease vary between countries, for instance, it is around $12000 in USA [1], around € 3766 in Europe (€ 7450 in Italy vs € 396 in Hungary) [2] and around $20500 in Australia [3].

Myocardial infarction results from the blockage of blood supply to the heart muscle mostly due to a coronary artery occlusion, leading to the death of heart tissue. The diagnosis of myocardial infarction generally involves the analysis of the electrocardiogram (ECG) in the search for changes in the waveforms that make up the ECG, particularly the abnormal elevation of the ST segment above the baseline. The ECG still remains as the preferred observation tool of the cardiac electrical activity [4], by depicting the P wave (depolarization of the atria), QRS complex (depolarization of the ventricles) and T wave (ventricular repolarization).

Several methods have been proposed for the detection of myocardial infarction from single-lead and multiple-lead ECG recordings. These methods are mainly based on the application of digital signal processing techniques for noise reduction and signal enhancement, and the use of rule-based or machine learning techniques for diagnosis and classification [5–10]. The increase in computing power in the last decade and the availability of multi-channel ECG recordings in most hospitals have favored the access of different sources of information from several ECG channels with the aim of providing an accurate automatic diagnosis of myocardial infarction.

In this study, we are particularly interested in the detection of myocardial infarction by using morphological and temporal features extracted from multi-lead ECG recordings. In order to carry out this, first the different ECG channels were delineated using a wavelet transform method, outliers of the set of fiducial points marking the beginning, peak and end of the ECG waves in each ECG channel were removed by considering the interquartile range. Then, by considering the average of the fiducial points, a unique set of fiducial points was obtained from each wave in all ECG channels. Operations such as mean value, standard deviation, skewness and kurtosis of ECG time intervals (P wave duration, QRS complex duration, ST-T interval, QT interval, T wave duration and RR interval) and of portion of the ECG signal (P wave, QRS complex, ST-T complex and QT interval) were used inputs to an SVM classifier to classify ECG records from the Physikalisch-Technische Bundesanstalt (PTB) Diagnostic ECG database into two classes: Healthy Control (HC) and Myocardial Infarction (MI). Three binary classifiers were developed: one that considered temporal ECG features exclusively, another that considered morphological ECG features exclusively, and the final one included both temporal and morphological ECG features.

2 Materials and Methods

2.1 Multi-lead ECG Signal Database

Conventional 12-Lead ECG signals from the PTB Diagnostic ECG database [11,12] were used in this study: six limb leads (I, II, III, aVL, aVF, aVR) and six chest leads (V1, V2, V3, V4, V5 and V6). Those leads offer different angles of visualization of the propagation of cardiac action potentials through the heart's electrical conduction system by depicting a different morphology of the ECG signal in each channel. ECG signals were acquired at 1 kHz with 16 bits resolution over a range of ±16.384 mV. Two diagnostic classes (HC and MI) of the database were analyzed to perform a binary classification problem. To avoid the imbalanced class problem from the database, 50 subjects were randomly selected for each of the two diagnostic classes, and the diabetic subjects were excluded.

2.2 SVM-Based Myocardial Infarction Detector

The proposed classification approach is composed of three main stages: (*i*) ECG delineation, (*ii*) ECG feature extraction and (*iii*) ECG recording classification.

(*i*) **ECG delineation:** The baseline wandering of the ECG signals was reduced by subtracting the 10_{Th}-level approximation db4 wavelet transform decomposition from the original signal. A notch filter centered at 50 Hz and a seventh-order low-pass Butterworth filter with cutoff frequency of 100 Hz were used to remove the power-line interference and high-frequency noise components, respectively. Then, the Pan and Tompkins QRS complex detector [13] was implemented, on each ECG lead, to detect QRS complex fiducial points. These marks were posteriorly used by a wavelet-based ECG delineator [14] to find the reference points for the beginning, peak and end of the P wave, QRS complex, and T wave, on each ECG lead, it means, the instant location of P_{on} (beginning of P wave), P_{peak} (peak of P wave), P_{end} (end of P wave), QRS_{on} (beginning of QRS complex), Q_{peak} (peak of P wave), R_{peak} (peak of R wave), S_{peak} (peak of S wave),

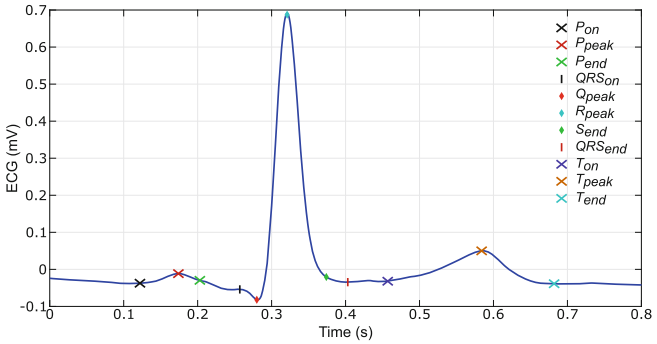

Fig. 1. Example of the automatic location of the reference points of each ECG wave.

QRS_{end} (peak of QRS complex), T_{on} (beginning of T wave), T_{peak} (peak of T wave), T_{end} (end of P wave). Figure 1 shows an example of the different reference points obtained for each ECG wave on an ECG lead.

Given the variability of the different reference points automatically found with the wavelet-based ECG delineator among the ECG leads, a unique reference point was estimated for each ECG indicator for all the 12 ECG leads by eliminating the marks that are considered outliers, it means, those marks that are outside $1.5 \times IQR$, where IQR is the interquartile range, and by taking the average value of the remaining points. Figure 2 shows an example of the estimation of the T_{end} location for all the ECG leads.

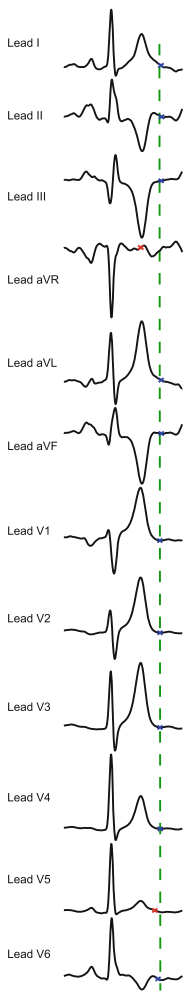

Fig. 2. Example of the variability of the T_{end} location among the different ECG leads. In red, two outliers are shown. The green line corresponds to the final T_{end} location after outliers removal and average operation.

(*ii*) **ECG feature extraction:** Two set of features were extracted from the multi-lead ECG recordings: temporal (time domain) features and morphological (related to the amplitude) features, as follows:

Temporal features: Once established the unique location of P_{on}, P_{peak}, P_{end}, QRS_{on}, Q_{peak}, R_{peak}, S_{peak}, QRS_{end}, T_{on}, T_{peak}, T_{end} among the 12 ECG leads, six time intervals were retained for feature extraction: P wave duration ($P_{end} - P_{on}$), QRS complex duration ($QRS_{end} - QRS_{on}$), ST-T complex ($T_{end} - QRS_{end}$), QT interval ($T_{end} - QRS_{on}$), T wave duration ($T_{end} - T_{on}$), and RR interval ($R_{peak}(i+1) - R_{peak}(i)$). To reduce the influence of the cardiac cycle length on the aforementioned time intervals (with the exception of the RR interval), these time intervals were normalized by dividing them by the RR interval. Then, the mean value, standard deviation, skewness and kurtosis of these time intervals were obtained for each subject. As a result, 24 features were reported (4 operations $\times$ 6 time intervals on the ECG).

Morphological features: For each ECG lead of each subject, a heartbeat template was created as the average value of the heartbeats on the ECG lead. Then, the amplitude, area under the curve (AUC), mean value, standard deviation, skewness and kurtosis of the ECG signals bounded by the P wave (from P_{on} to P_{end}), QRS complex (from QRS_{on} to QRS_{end}), ST-T complex (from QRS_{end} to T_{end}), QT interval (from QRS_{on} to T_{end}), and T wave (from T_{on} to T_{end}), on each ECG lead, were obtained. As a result, 288 features were reported (6 operations $\times$ 4 portions of the ECG signal $\times$ 12 ECG leads).

(*iii*) **ECG recording classification:** Three binary classifiers were developed in this study to classify the subjects into HC or MI. A first classifier that only considered temporal ECG features (24 features), a second one that only considered morphological ECG features (288 features) and a third one that considered both temporal and morphological ECG features ($288 + 24 = 312$ features).

Given the high dimensionality (up to 312 features) and nonlinearity of the feature space of the binary classification problem, a classifier based on SVM was implemented. In the scatter plot shown in Fig. 3 we can see that the data is not linearly separable by using, for instance, the AUC of the P wave and the AUC of the QT interval.

An SVM is a supervised machine learning technique that looks to maximize the distance or margin in the feature space between the separating hyperplane and the training data that are closest to this hyperplane. In addition, the feature space is mapped to a higher dimensional space to gain a linearity separation. A radial basis function (RBF) kernel was used in the SVM classifiers. The sequential minimal optimization algorithm was used to train the SVM [15]. For each classifier, the input data were standardized according to the z-score.

Signal processing and rhythm classification were carried out in MATLAB® R2018a (The MathWorks, MA, USA) using built-in functions from Signal Processing, and Statistics and Machine Learning toolboxes.

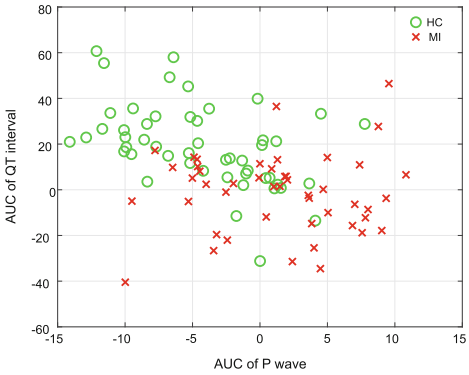

Fig. 3. Example of the nonlinearity separation of the classes by considering AUC of P wave and AUC of QT interval in the ECG lead II as feature space.

2.3 Performance Evaluation

Monte Carlo cross-validation of ten iterations was implemented to ensure the reproducibility of the classification results. In order to carry out this procedure, the subjects of the two classes (HC and MI) were randomly divided into two sets: training set, composed of 70% of the subjects of each class (35 HC and 35 MI), and test set, composed of 30% of the subjects for each class (15 HC and 15 MI). This procedure was repeated ten times.

Accuracy (ACC), error rate (Er), sensitivity (Se) and specificity (Sp) were the used metrics to evaluate the classification performance:

$$Acc = \frac{TP + TN}{TP + FN + FP + TN} \tag{1}$$

$$Er = \frac{FP + FN}{TP + FN + FP + TN} \tag{2}$$

$$Se = \frac{TP}{TP + FN} \tag{3}$$

$$Sp = \frac{TN}{FP + TN} \tag{4}$$

where TP, TN, FP and FN correspond to the number of true positives, true negatives, false positives and false negatives, respectively.

3 Results

Table 1 shows the mean classification performance of each classifier. We have obtained an average error rate below 10% and an average accuracy above 90% to classify the 30 subjects of the test set with the three SVM-based classifiers.

Although the mean accuracies were very similar when morphological and temporal ECG features were used separately by the classifiers, the classifier tends to be more specific (detect the control cases better) when only morphological ECG features were used, and it tends to be more sensitive (detect the myocardial infarction cases better) when only temporal ECG features were used. However, when both classifiers, temporal and morphological ECG features are integrated by the classifier, the classification performance improves: accuracy increases by 3% and error rate decreases by 3%.

Table 1. Classification performance of each SVM-based classifier, averaged over the iterations of the cross-validation process.

ECG feature	*TP*	*TN*	*FP*	*FN*	*Acc (%)*	*Er (%)*	*Se (%)*	*Sp (%)*
Morphological	13.8	14.1	0.9	1.2	93.00	7.00	92.00	94.00
Temporal	14.7	13.4	1.6	0.3	93.67	6.33	98.00	89.33
Morphological and temporal	14.6	14.4	0.6	0.4	96.67	3.33	97.33	96.00

4 Discussion

After the evaluation of the three classifiers based on SVM, it was found that the best classification performance (accuracy of 96.67% and error rate of 3.33%) was achieved when morphological and temporal features were jointly considered by the SVM classifier. Specifically, temporal ECG features facilitated the detection of the myocardial infarction cases (higher sensitivity) whereas morphological features eased the rejection of the myocardial infarction cases (higher specificity). According with the preliminary results obtained in this study, it seems that the information contained in the temporal and morphological ECG features explored in this study (up to 312 features) was successfully used by different SVM classifiers to classify the ECG of subjects into healthy control and myocardial infarction, with a classification performance (error rate below 10%, and accuracy, sensitivity and specificity above 90%) comparable with the literature [6,7,9]. For instance, Chang et al. obtained a classification performance of 85.71% in sensitivity and 79.82% in specificity using a Gaussian Mixture and a Gaussian kernel SVM approach to exploit statistical features obtained from the log-likelihood of each heartbeat's ECG given an HMM model [6], Arif et al. reported sensitivity of 99.97% and specificity of 99.9% using the K-Nearest Neighbors algorithm with T- and Q-wave amplitudes and ST-segment deviation as attributes [7], and Dohare et al. achieved sensitivity of 96.96% and specificity of 100% using a Gaussian kernel SVM approach that exploits morphological and temporal features extracted from a composite lead [9]. In this work, T wave duration, RR interval and morphological features of T wave were not included in the analysis.

The results obtained in this study can be attributed to the fact that myocardial infarction generates changes in the electrical activity of the heart beyond the modifications in the ST segment (usually used by physicians for diagnostic purposes). These modifications can be observed as changes in the duration of ECG waves and intervals and changes in ECG signals' amplitude per se. Most of the literature has focused on the detection of ST-segment elevation as the main feature for myocardial infarction classification, but, depending on the amount of ischemic and necrotic tissue, other ECG waveforms may also be altered. For instance, a myocardial infarction in the upper region of the right coronary artery affects only the sinus node, leading to the absence of P waves or alterations of the heart rhythm (high RR interval variability). A subendocardial myocardial infarction (the necrosis covers only the internal wall of the myocardium) produces a ST segment depression and an inversion or alteration in the morphology of T waves due to the decrease in ATP levels necessary for the repolarization of cardiomyocytes. Finally, a transmural myocardial infarction (the necrosis covers all or almost all the myocardium) produces a ST segment elevation, the QT interval is prolonged and its morphology is altered, because the time of ventricular conduction is increased, and exist a significant increase in the amplitude of the Q waves (negative). In general, the necrotic area caused by myocardial infarction does not have any electrical charge. This means that, if the necrotic area compromises ventricular depolarization, where the affected area is not disturbed by peripheral electrical changes, the QRS complex will be directly affected [16,17].

The use of multiple ECG leads enriches the information to be used by the classifier and minimizes the probability of errors thanks to the inclusion of redundant information. The elimination of outliers in the set of ECG characteristic points and the use of a unique reference mark per ECG indicator reduce the variability among the different ECG channels and facilitate the classification task.

Other features extracted from the multi-lead ECG recordings by signal transformations and mathematical operations as well as the reduction of the feature space by principal component analysis to perform the binary classification task can also be carried out to improve the classification performance. In addition, using the same set of features reported in this study, a multiclass classification system can be implemented on the same database to identify, for instance, subjects with myocardial infarction, cardiomyopathy/heart failure, bundle branch block, dysrhythmia, etc. Again, an SVM classifier might be well suited to this kind of classification problem. Our research team is currently working on these directions.

5 Conclusion

Three SVM classifiers that use: only temporal ECG features, only morphological ECG features and both temporal and morphological ECG features, extracted from 12-lead ECG recordings, were proposed in this paper to perform a binary classification task (healthy control vs myocardial infarction). By using a 10-fold

Monte Carlo cross-validation procedure (70% training, 30% test), an average error rate of 3.33% and an accuracy of 96.67% were achieved to classify 30 subjects from the PTB database. The main innovation of this study relays on the fact that using temporal and morphological features extracted from the ECG, instead of temporal features or morphological features associated with the ST segment, a classification performance comparable with the state of the art was obtained.

References

1. Nicholson, G., Gandra, S.R., Halbert, R.J., Richhariya, A., Nordyke, R.J.: Patient-level costs of major cardiovascular conditions: a review of the international literature. ClinicoEcon. Outcomes Res.: CEOR **8**, 495 (2016)
2. Tiemann, O.: Variations in hospitalisation costs for acute myocardial infarction-a comparison across Europe. Health Econ. **17**(S1), S33–S45 (2008)
3. Ioannides-Demos, L.L., Makarounas-Kirchmann, K., Ashton, E., Stoelwinder, J., McNeil, J.J.: Cost of myocardial infarction to the Australian community. Clin. Drug Invest. **30**(8), 533–543 (2010)
4. Hernández, A.I., Dumont, J., Altuve, M., Beuchée, A., Carrault, G.: Evolutionary optimization of ECG feature extraction methods: applications to the monitoring of adult myocardial ischemia and neonatal apnea bradycardia events. In: Gacek, A., Pedrycz, W. (eds.) ECG Signal Processing, Classification and Interpretation: A Comprehensive Framework of Computational Intelligence, pp. 237–273. Springer, London (2012)
5. Sun, L., Lu, Y., Yang, K., Li, S.: ECG analysis using multiple instance learning for myocardial infarction detection. IEEE Trans. Biomed. Eng. **59**(12), 3348–3356 (2012)
6. Chang, P.-C., Lin, J.-J., Hsieh, J.-C., Weng, J.: Myocardial infarction classification with multi-lead ECG using hidden Markov models and Gaussian mixture models. Appl. Soft Comput. **12**(10), 3165–3175 (2012)
7. Arif, M., Malagore, I.A., Afsar, F.A.: Detection and localization of myocardial infarction using k-nearest neighbor classifier. J. Med. Syst. **36**(1), 279–289 (2012)
8. Sharma, M., San Tan, R., Acharya, U.R.: A novel automated diagnostic system for classification of myocardial infarction ECG signals using an optimal biorthogonal filter bank. Comput. Biol. Med. **102**, 341–356 (2018)
9. Dohare, A.K., Kumar, V., Kumar, R.: Detection of myocardial infarction in 12 lead ECG using support vector machine. Appl. Soft Comput. **64**, 138–147 (2018)
10. Baloglu, U.B., Talo, M., Yildirim, O., San Tan, R., Acharya, U.R.: Classification of myocardial infarction with multi-lead ECG signals and deep CNN. Pattern Recogn. Lett. **122**, 23–30 (2019)
11. Bousseljot, R., Kreiseler, D., Schnabel, A.: Nutzung der EKG-signaldatenbank cardiodat der PTB über das internet. Biomedizinische Technik/Biomed. Eng. **40**(s1), 317–318 (1995)
12. Goldberger, A.L., Amaral, L.A., Glass, L., Hausdorff, J.M., Ivanov, P.C., Mark, R.G., Mietus, J.E., Moody, G.B., Peng, C.-K., Stanley, H.E.: PhysioBank, physiotoolkit, and physionet: components of a new research resource for complex physiologic signals. Circulation **101**(23), e215–e220 (2000)
13. Pan, J., Tompkins, W.J.: A real-time QRS detection algorithm. IEEE Trans. Biomed. Eng. **32**(3), 230–236 (1985)

14. Martínez, J.P., Almeida, R., Olmos, S., Rocha, A.P., Laguna, P.: A wavelet-based ECG delineator: evaluation on standard databases. IEEE Trans. Biomed. Eng. **51**(4), 570–581 (2004)
15. Fan, R.-E., Chen, P.-H., Lin, C.-J.: Working set selection using second order information for training support vector machines. J. Mach. Learn. Res. **6**, 1889–1918 (2005)
16. Klabunde, R.E.: Cardiac electrophysiology: normal and ischemic ionic currents and the ECG. Adv. Physiol. Educ. **41**, 29–37 (2017)
17. Cinca, J., Figueras, J., Tenorio, L., Valle, V., Trenchs, J., Segura, R., Rius, J.: Time course and rate dependence of Q-T interval changes during noncomplicated acute transmural myocardial infarction in human beings. Am. J. Cardiol. **48**, 1023–1028 (1981)

Window Functions Analysis in Filters for EEG Movement Intention Signals

C. Covantes-Osuna, O. Paredes, H. Vélez-Pérez, and R. Romo-Vázquez(✉)

Department Computer Sciences, CUCEI, Universidad de Guadalajara, Jalisco, Mexico
rebeca.romo@academicos.udg.mx

Abstract. The aim of this work is to compare the different windows performance in EEG signals related to movement intention, to find the adequate window in specific frequency bands filters. For this purpose, FIR filters using different window functions were implemented in two kinds of signals: a set of simulated signals and a dataset containing EEG movement intention records taken of PhysioNet. The movement intention could be understood as the product of the neuronal synchronization before the movement onset. The similarity of the results was measured using the Euclidean distance. The results obtained suggest the existence of a window function as the most suitable and robust for the EEG movement intention analysis.

Keywords: Digital filter · EEG · Movement intention · PhysioNet · Euclidian distance

1 Introduction

The window functions are commonly used in different digital signal processing (DSP) applications as signal preprocessing (denoising), analysis and estimation signal, digital filter design and speech processing. There are a large number of windows with completely different properties in time and frequency domains and that derive into a different enhancement of the studied signal. Some examples of these windows are Bartlett, Blackman, Hanning, Hamming, Kaiser, Rectangular, Triangular etc., [1–3], being the most popular and widely used in different DSP applications the Hanning, Hamming and Kaiser windows.

However, there is not a standard approach to select a window function. Every window offers advantages and disadvantage relative to the others; some are effective for specific types of signal and others improve the frequency resolution. Since the correct window choice depends on the signals nature and the applications, it is necessary to compare the performance of the different window functions to find the best one for the specific application. The objective of this work is to find the adequate window function that enhance the movement intention signals in electroencephalography (EEG).

© Springer Nature Switzerland AG 2020
C. A. González Díaz et al. (Eds.): CLAIB 2019, IFMBE Proceedings 75, pp. 182–190, 2020.
https://doi.org/10.1007/978-3-030-30648-9_25

The movement intention could be understood as the product of the neuronal synchronization before the movement onset. In movement intention, some features can be extracted as motor imagery (MI) and motor execution (ME) from upper and lower limbs [4–6]. Motor imagery (MI) is the ability to imagine performing a movement without executing it [7]. It has been shown that the imagination of a limb activation can modify brain electrical activity [8]. Depending on the MI task used, multiple neuro imaging studies have revealed the functional participation of motor, pre-motor, and supplementary motor cortices. In addition, other structures play an important functional role in motor imagery as it occurs with the cerebellum, the basal-ganglia, the superior and inferior parietal lobules, and the pre-cuneus [9].

The electroencephalogram (EEG) records the brain electric activity, usually described in five frequency oscillations known as brainwaves: delta (0.5–4 Hz), theta (4–8 Hz), alpha (8–13 Hz), beta (13–30 Hz), and Gamma (30–128 Hz) [10]. There is also the Mu (μ) rhythm that it is a sub-band of alpha (9–11 Hz) [10], this rhythm is directly related with the movement [11]. The EEG presents some characteristics such as the non-periodicity, non-standardized patterns, and small voltage amplitudes. These attributes lead to the EEG signal to be easily mixed up with noise, making it harder to recognize and extract meaningful information from the EEG signals, particularly electrophysiological information. Several factors can generate noise and distortions, *e.g.* room exposure, energetic radiation, electromagnetic couplings, heart rate, muscle movements, and eyes movements. Other parameters, such as a sudden change in phase and loss of signal amplitude, can also contribute to the signal contamination [12]. In this context, Finite Impulse Response (FIR filters) using different window functions have been widely used to reduce noise and distortions.

In this work, we compare the performance of six window functions (Barlett, Blackman, Kaiser, Hamming, Hann and Rectwin) in simulated signals to fix the function that retains the frequential band related to the movement intention activity (alpha). Then the choose window is applied in real EEG signals.

2 Method

The methodology implemented in this work has been divided into three steps: (i) Database (simulated and real signals), (ii) Window Analysis and, (iii) Similarity measure.

2.1 Real Signal Database

The dataset used was from PhysioNet [13]. PhysioNet contains a lot of different types of dataset. The database of interest was the EEG motor movement intention dataset (EEG Motor Movement/Imagery Dataset). This dataset was created and contributed to PhysioNet by the developers of the BCI2000 instrumentation system [14,15]. The database contains different 109 recording from

different subjects who perform motor/imaginary task for two minutes, using 64 channels as the international 10-10 system.

For this work, we considered four EEG records, with a low presence of artefacts. In these records, subjects performed motor/imaginary tasks over two minutes with a sampling frequency at 160 Hz. Each participant executed 3 tasks per recording with the annotation task (T0, T1 and T2). The task T0 corresponds to resting state, the T1 corresponds to open and close the left fist and T2 corresponds to open and close the right fist. We considered the electrode C3 for the task T2 and the electrode C4 for T1. Each EEG signal is 120 s long (seven T1 fragments and seven T2 fragments and each one is preceded by a T0 fragment). Figure 1 shows an example of the first 32 s in an EEG signal. The blue segment corresponds to the resting state (T0), the red color is related to the opening and closing of the left fist, while the orange fragment corresponds to the same movement but to the right fist.

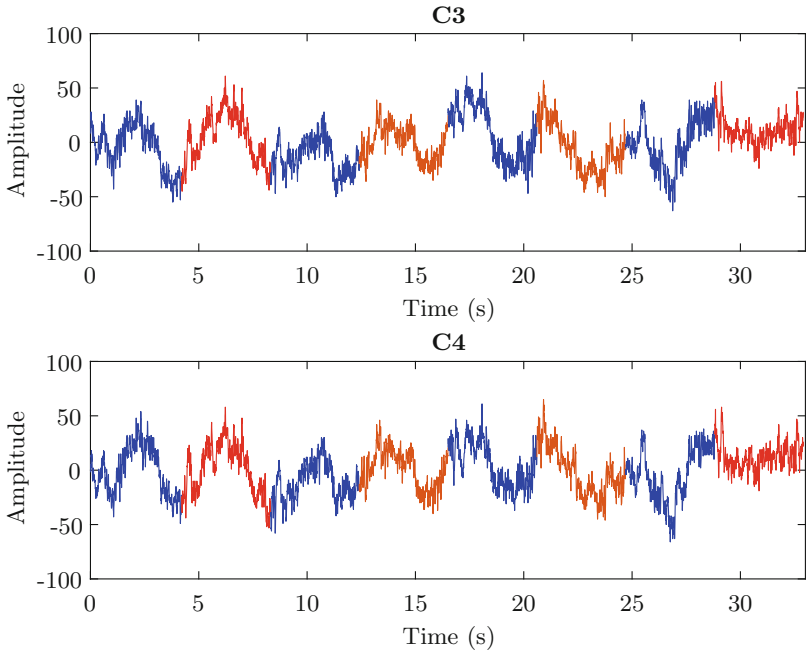

Fig. 1. Example of first 32 s of C3 and C4 EEG signals including the T0, T1, and T2 tasks.

The movement intention potential is found 2 s before T1 or T2 state starts that is, in the last 2 s of T0. The intention signal of the resting state in T0 (the signal before the last 2 s) is subtracted from the intention movement potential. This intention signal is present in the electrophysiological α band [11]. Each intention EEG signal recorded was normalized with respect to the mean and the

standard deviation before Fourier Transform estimation to know the frequencies in the signal. Figure 2 shows an EEG movement intention signal (A) with its spectra (B) and this EEG signal filter in alpha band (C) with its spectra (D).

2.2 Simulated Signal Database

In order to obtain the α band (where the intention movement signal is present) of the EEG electrophysiological band, it is necessary to implement a filter. It is imperative not to lose information. In this context, it is important to have the appropriate window for the filter restrict the attenuation of the frequency content in the α band and, consequently, improves the identification of the movement intention signal.

Thus, 20 random alpha frequency signals were computed to evaluate the windows Barlett, Blackman, Kaiser, Hamming, Hann and Rectwin with respect to the data sets *S00603.edf, S030R03.edf, S029R03.edf, S102R03.edf* from the PhysioNet database.

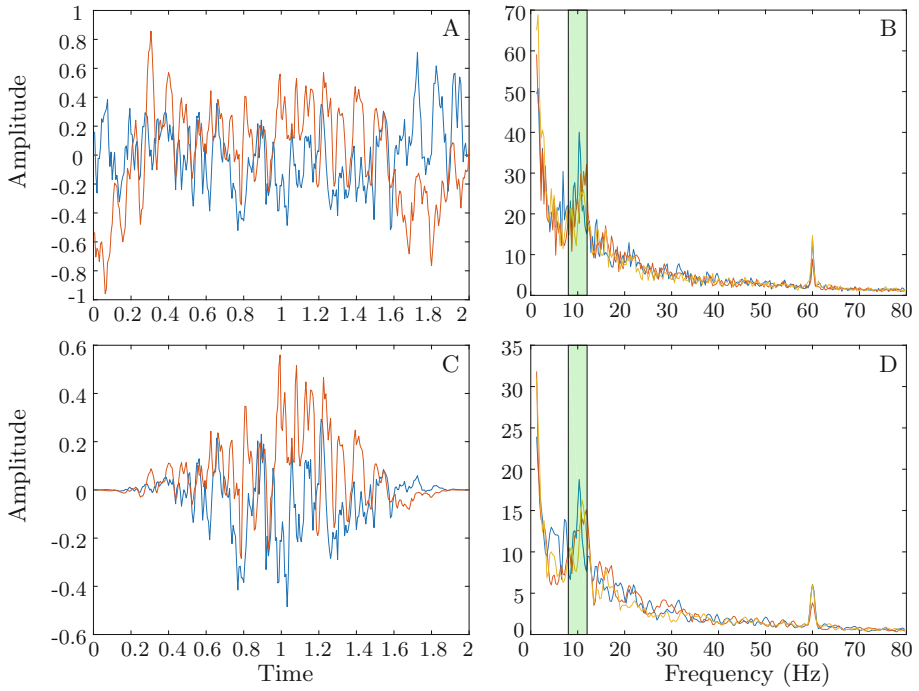

Fig. 2. (A) EEG movement intention signals (in blue the left movement and in orange is the right movement), (B) The corresponding spectra of each movement (the frequency band related to the movement intention is marked in green), (C) the signals convoluted with the Bartlett window to enhance the activity in the alpha band, (D) the spectra of both movement after the convolution with the Bartlett window.

2.3 Window Analysis

To evaluate the suitability of the window function, all signals (real and simulated) were convoluted with the six selected window functions (Barlett, Kaiser, Blackman, Hanning, Hamming and, Rectwin) and then transformed into the frequency domain using the Fourier Transform. All simulated signal was divided into the same segments as the real signals before the convolution process.

2.4 Euclidean Distance

Thereafter, to evaluate the performance of each window functions the Euclidean distance between the spectrum of non-convoluted simulated signal and the six convoluted simulated signals was estimated. In this work, the lower the Euclidean distance is, the lower the impact of the windows function to the signal; meaning that the information related to the frequency of interest (α band) is adequately retrieved. To probe the robustness of each window function, several evaluations of different non-convoluted and convoluted signals were performed. We look for the group of Euclidean with the lower scattering.

Firstly, the algorithm starts generating a random signal with components in alpha frequency band and noise was added. Then every simulated signal it is divided in differents parts and convoluted with the six window function to generate the set of convoluted simulated signal. The spectrum of each signal was computed (Eq. 1). Each simulated spectral signal were compared against the complete simulated signal reduced with the same length using the Euclidean distant (Eq. 2). The Euclidean distant represents how a signal stays in the same frequency. The algorithm was developed in Matlab® for its easy programming and operations between matrices, besides it provides the different windows already developed for its use. The procedure (pseudocode) to estimate the Euclidean distance is described in Algorithm 1.

$$X(K) = \frac{1}{N} \sum_{n=0}^{N-1} x_n e^{i2\pi k \frac{n}{N}} \tag{1}$$

$$D_{ij} = \sqrt{\sum_{k=1}^{n} (x_{ki} - x_{kj})^2} \tag{2}$$

Algorithm 1: Algorithm to calculate Euclidean distance

Input :
N; **Total simulated signal to be created**
name_file; **PhysioNet file**
type_event; **Type of the event tast (T1 or T2)**
Output:
total_result[N][total_windows]; **Result of N signal with respect on total_windows**

```
for i = 1 to N do
    X_i ← simulated_signal(alpha)
end
for i = 1 to total_simulated_signal do
    k ← number_segment(X_i);
    for j = 1 to k do
        part_signal_j ← simulated_signal(startS, endS);
        for z = 1 to z = window do
            result_window_zi ← part_singal_j * window_z;
        end
    end
    for j = 1 to j = window do
        len ← length(result_window_z);
        simulated_singal_i ← downsample(len);
        result1 ← fft(simulated_signal_i);
        vec_window ← mean(result_window_j);
        result2 ← fft(vec_window);
        total_result_ij ← Euclidian(result1, result2);
    end
end
```

3 Results and Discussion

The Euclidean distances between the non-convoluted and convoluted simulated signals are in the Fig. 3. Visual inspection allows verifying that the Bartlett is the window function that has the lowest scattering, even lower than the widely used Ham-ming window. The standard deviation is of 80.62, (see Table 1). Other interesting window is the Blackman that is the second lowest robust with a standard deviation of 81.01. The dispersion values represent the precision of the windows to estimate the spectrum of a signal, suggesting the Bartlett is the suitable window to study the spectral information of the movement intention in EEG records. The scattering of the windows may be the result of the amount of spectral leakage, a trend that is also showed in Fig. 3. In the case of the Rectangular is the window function that less handle the leakage in the spectrum.

Moreover, is also remarkable that the minimum value in the cloud of Euclidean distance, *i.e.* the accuracy, is not the Hamming window that is the most used in window analysis and filtering, but in the Bartlett and Blackman

Table 1. Mean and standard deviation of Euclidean distance between simulated signals and the simulated signals convoluted with the window functions.

	Hamming	Bartlett	Blackman	Hanning	Rectwin	Kaiser
Mean	1855	1850	1847	1854	1905	1902
STD	81.91	80.62	81.01	81.74	95.72	94.41

windows with mean distance of 1850 and 1847, respectively. This could suggest, besides the lower deviation of both them, that the latter are suitable windows to enhance the α band. It is necessary to emphasize that the worst window performance is the Rectangular with mean distance of 1905 and, standard deviation of 95.72. This is interesting because applying the rectangular window is equivalent to segment or slice the studied signal, a common praxis in signal processing, and our results show that is not the better one.

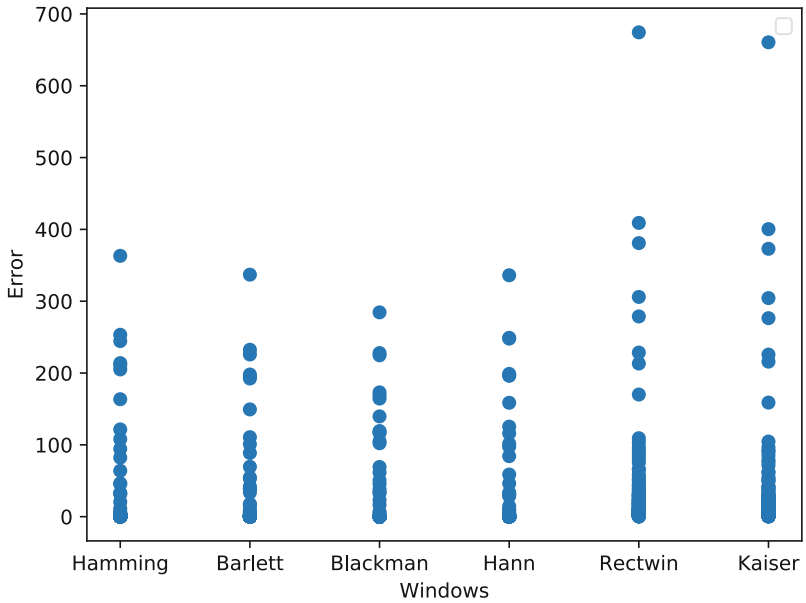

Fig. 3. Euclidean distance between simulated signals for six different windows.

In Fig. 3, the spectra of the two tasks of imaginary movement are displayed. It can be noticed that indeed the activity is distinguishable between the non convoluted signals and the filtered ones. In this work, only the implementation of fix window length was analyzed, in further work the effect of the window length should be studied.

4 Conclusion

The frequency analysis is a powerful tool to characterize brain activities through EEG data [16]. However, there are two principal constraints to use spectral analysis: the non-stationary nature of the EEG and the method itself (*i.e.* Discrete Fourier Transform - DFT, Fast Fourier Transform - FFT) [16]. To avoid these restrictions, the non-stationary EEG signals are convoluted with other functions called windows. The windows are functions that weight the analyzed EEG signals to minimize the spectral leakage and the variance in the obtained spectrum [17].

Despite that the window improves the spectrum, these functions do not cancel completely the spectral leakage. For this reason, there are several window functions that face to these constraints and which are characterized by many parameters (*i.e.* main lobe width; fall of sides lobe, equivalent noise bandwidth) [18]. Hence, choose a window function to calculate the spectrum of a signal, EEG signals in this work, is a crucial step in the signal processing.

For movement intention, the Bartlett window demonstrated to be the most suitable and robust window to study the spectral information of the movement intention. From the results, we could identify that there is a hint of the laterality of this study, but there is no certainty for the lack of information related to laterality of the subjects in the database. As future work, a new database could be recorded taking into account the laterality of the subjects to identify if the differences or similarities are significant in windows with movement intention and lateralization.

Acknowledgments. The authors wish to thank the National Council of Science and Technology (CONACYT) for the support received through the scholarship grant CVU-311539 and CVU-713526.

Conflicts of Interest. The author(s) declared no potential conflicts of interest with respect to the authorship and/or publication of this article.

References

1. Andreas, A.: Digital Signal Processing. McGraw-Hill, New York (2016)
2. Robert, M.: Introduction to Digital Signal Processing. Newnes, Oxford (2000)
3. Ramesh, R., Nathiya, R.: Realization of fir filter using modified distributed arithmetic architecture. Signal Image Process. **3**(1), 83 (2012)
4. Pfurtscheller, G., Da Silva, F.H.L.: Event-related EEG/MEG synchronization and desynchronization: basic principles. Clin. Neurophysiol. **110**(11), 1842–1857 (1999)
5. Müller, G.R., Neuper, C., Rupp, R., Keinrath, C., Gerner, H.J., Pfurtscheller, G.: Event-related beta EEG changes during wrist movements induced by functional electrical stimulation of forearm muscles in man. Neurosci. Lett. **340**(2), 143–147 (2003)
6. Huang, D., Lin, P., Fei, D.-Y., Chen, X., Bai, O.: Decoding human motor activity from EEG single trials for a discrete two-dimensional cursor control. J. Neural Eng. **6**(4), 046005 (2009)

7. Avanzino, L., Giannini, A., Tacchino, A., Pelosin, E., Ruggeri, P., Bove, M.: Motor imagery influences the execution of repetitive finger opposition movements. Neurosci. Lett. **466**(1), 11–15 (2009)
8. Gandevia, S.C., Rothwell, J.C.: Knowledge of motor commands and the recruitment of human motoneurons. Brain **110**(5), 1117–1130 (1987)
9. Alonso-Valerdi, L.M., González-Garrido, A.A.: Characterizing motor system to improve training protocols used in brain-machine interfaces based on motor imagery. In: Cognitive and Computational Neuroscience: Principles, Algorithms and Applications, p. 57 (2018)
10. Sanei, S., Chambers, J.A.: EEG Signal Processing. Wiley, Hoboken (2007)
11. Pfurtscheller, G., Aranibar, A.: Evaluation of event-related desynchronization (ERD) preceding and following voluntary self-paced movement. Electroencephalogr. Clin. Neurophysiol. **46**(2), 138–146 (1979)
12. Repovs, G.: Dealing with noise in EEG recording and data analysis. Informatica Medica Slovenica **15**, 18–25 (2010)
13. Goldberger, A.L., Amaral, L.A.N., Glass, L., Hausdorff, J.M., Ivanov, P.C., Mark, R.G., Mietus, J.E., Moody, G.B., Peng, C.-K., Stanley, H.E.: Physiobank, physiotoolkit, and physionet: components of a new research resource for complex physiologic signals. Circulation **101**(23), e215–e220 (2000)
14. PhysioNet: EEG motor movement/imagery dataset (2019). Accessed 09 Mar 2019
15. Schalk, G., McFarland, D.J., Hinterberger, T., Birbaumer, N., Wolpaw, J.R.: BCI 2000: a general-purpose brain-computer interface (BCI) system. IEEE Trans. Biomed. Eng. **51**(6), 1034–1043 (2004)
16. Dumermuth, G., Molinari, L.: Spectral analysis of the EEG. Neuropsychobiology **17**(1–2), 85–99 (1987)
17. Gautam, J.K., Kumar, A., Saxena, R.: Windows: a tool in signal processing. IETE Tech. Rev. **12**(3), 217–226 (1995)
18. Prabhu, K.M.M.: Discrete-time windows and their figures of merit. In: Window Functions and Their Applications in Signal Processing, pp. 145–188. CRC Press (2013)

Algorithm for Presumptive Diagnosis of Cardiac Murmurs over Auscultated Heart Signals

Andrea García-Cedeño[1(✉)], Eduardo Pinos[2], and Mónica Huerta[1]

[1] GITEL, Telecommunications and Telematics Research Group, Universidad Politécnica Salesiana, Cuenca, Ecuador
{agarciac,mhuerta}@ups.edu.ec

[2] GIIATA, Artificial Intelligence and Assistive Technologies Research Group, Universidad Politécnica Salesiana, Cuenca, Ecuador
epinos@ups.edu.ec

Abstract. The development of innovative cardiac assessment techniques has optimized heart conditions diagnosis, however it has led to a reduction of auscultation practice and hence its effectiveness. Furthermore, in public health systems it is not possible to meet the demand of patients who require the use of these new technologies, so auscultation is key in the process of evaluating cardiac subjects. Based on this situation, this document describes a proposal focused on the analysis and processing of the auscultated heart signal in order to generate a presumptive diagnosis of heart murmurs. The evaluation of the presence of a valvular lesion consisted in the identification of abnormalities in the relationship between the period of contraction and relaxation of the cardiac cycle. During the experimental phase of this work, acceptable results of sensitivity and specificity were obtained, reason why as future work it is planned its development as a tool of low cost to optimize the detection of valvular diseases.

Keywords: Auscultation · Heart murmurs · Audio acquisition · Audio processing

1 Introduction

In cardiovascular semiology, auscultation corresponds to the most significant and indispensable exploration, which depends directly on the knowledge and expertise of the physician in order to differentiate the acoustic cardiac phenomena perceptible by the human ear [9]. The main tool used in this process is the stethoscope; another equipment used for assessing the acoustic manifestation of the heart is the phonograph, which, by means of a piezoelectric microphone and an amplifier, records the acoustic vibrations, specifying the tone, intensity, location and duration of the captured noises [3,9]. In the case of Ecuador, the main methods used to diagnose heart disease are the electrocardiogram,

© Springer Nature Switzerland AG 2020
C. A. González Díaz et al. (Eds.): CLAIB 2019, IFMBE Proceedings 75, pp. 191–201, 2020.
https://doi.org/10.1007/978-3-030-30648-9_26

thoracic radiography and echocardiography. However, although cardiac auscultation is one of the most relevant maneuvers in cardiovascular exploration, its use has been reduced as the introduction of new technologies more reliable, but not economically accessible, are limiting for optimal implementation in Ecuador [2,4,11,12].

Within the area of pathology, the identification of murmurs is one of the main references for the diagnosis of valvular diseases also known as valvular lesions. These diseases at a severe level can affect the daily life of a cardiac patient, even under controlled treatment, confining the person to activities that require physical effort, as well as psychological [1]. At the same time they cause another type of disease called heart failure, which stands out in the high positions of the mortality tables in Ecuador [3,8–10].

As a contribution to the solution of the above problems, a proposal for the acquisition of heart acoustics and its analysis for the presumptive diagnosis of heart murmurs is described below, the result of which will be used for the prediction of valvular lesions.

From various existing proposals of phonocardiographs and heart audio information processing, we can establish that, as in this project, most opt for spectral analysis and wavelets theory for the separation of normal and pathological noises. However, at the time of determining the presence of a murmur is where different methodologies and hypotheses are established, either the application of the Hidden Markov Model [13] or even the use of machine learning techniques from extensive databases [7]. In this case, an algorithm is presented so that parameters such as low cost and low complexity can be met, differing from the approaches mentioned.

2 Methodology

For the current project, two general stages were established: acquisition of cardiac acoustics and their analysis for the identification of the presence of cardiac murmurs. The focus of this article corresponds to the description of the algorithm used for the latter, therefore each phase will be described in detail with respect to the study of an auscultated cardiac signal.

2.1 Acquisition and Conditioning of Cardiac Acoustic Signals

The data obtained during the audio acquisition corresponds to a type of sample that is not probabilistic due to the fact that it depends on the time dedicated to its capture. During 20 working days, a sample space of 11 patients was collected, auscultating the four cardiac focuses for a period of one minute each. The downside factor that reduced the sample size was the alterations in the data due to health conditions that generate an acoustic interposition and limitations from anatomapathological factors of each patient and their delicate state of health.

For the audio recording, a capacitive microphone with its respective amplification circuit based on an instrumentation amplifier was used due to the low

amplitude of the signals. Its common mode gain depends on the floating resistance RG used (4.7 KΩ) which resulted in a gain of 11.51. However, a potentiometer was used for calibration purposes. Said circuit was connected to the analogical port of an Arduino UNO and the transmission was done in serial mode with a value of 9600 bauds, while the sampling of the information by interruption was every 0.067 s, which is the period equivalent to the maximum sampling frequency reached of 150 Hz.

The acquired signal represents the acoustic phenomena recorded by the microphone with an offset of 1.02 V (Fig. 1). In order to solve this shift a clamper is implemented, which, in spite of being a continuous voltage, presents oscillations. This is the reason why a Least-Mean-Square adaptive filter is implemented as corrective level measure to eliminate said noise. Its coefficients were calculated based on a voltage divider that represents the offset correction made with the clamper, see Figs. 2.

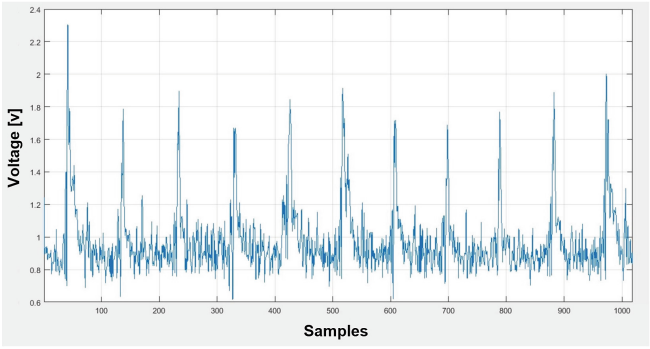

Fig. 1. Acquired audio sample from auscultation process before applying an adaptive filter.

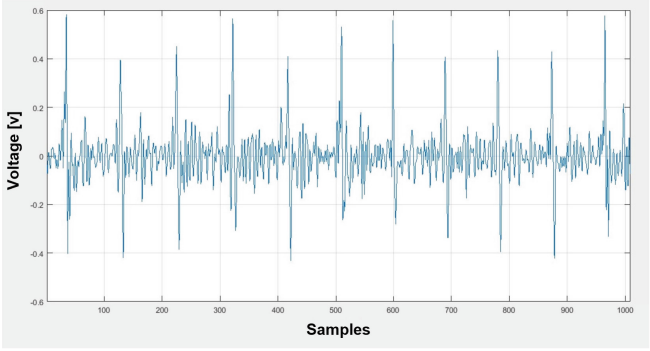

Fig. 2. Acquired audio sample from auscultation process after applying an adaptive filter.

2.2 Identification of the Presence of Heart Murmurs

The methodology for the presumptive diagnosis is based in normalizing and cleaning the acquired heart audio from noise produced by external phenomena. Subsequently, a Discrete Wavelet Transform is performed to obtain a simpler component of the signal and identify the location of the first and second heart noise, defining the sample space in which each phase of the heart cycle is contained. Once the sample position of systole and diastole has been established, the amplitude values of the signal corresponding to this position are extracted. Finally we perform a statistical analysis where, based on the determination of the significant differences between systole and diastole, the presence of a heart murmur can be considered.

As can be seen in Fig. 3, the procedures that constitute the general algorithm for the detection of heart murmurs are shown sequentially. Every phase consists in important procedures for the determination of the presence of murmurs, and each one is detailed below.

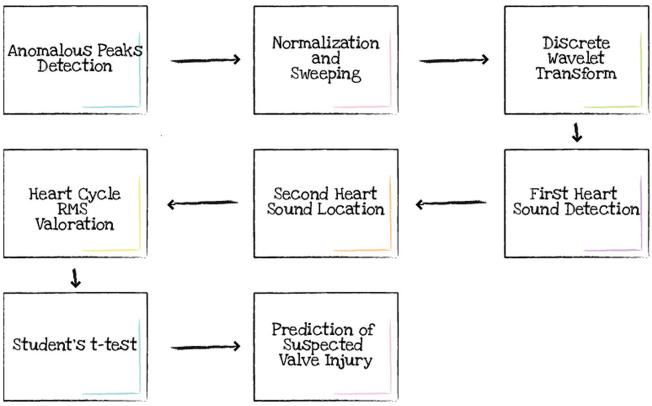

Fig. 3. Block diagram of the algorithm for heart murmur detection.

Anomalous Peaks Detection and Normalization. Abnormal peaks are considered to be those voltage levels whose amplitude is greater than the average and which do not occur periodically throughout the acquisition of the sample. These acoustic phenomena are usually caused by friction in the bell and chest-piece of the stethoscope at some point during auscultation. For a more detailed analysis of the presence of these values, the total sample is segmented into equal periods, thus the maximum peak value for each section is obtained, generating a vector of size equal to the number of segmentations performed. In this vector it is evaluated if there is one or more abnormal values in comparison with the own elements of the arrangement. Once these peaks are detected, they are replaced by the maximum value of the voltages within the normal range, Fig. 4a and b.

Normalization and sweeping is obtained by calculating the maximum between the normal values and then dividing it for all samples, thus, the voltage variation range is between −1 and 1 V, see Fig. 4c.

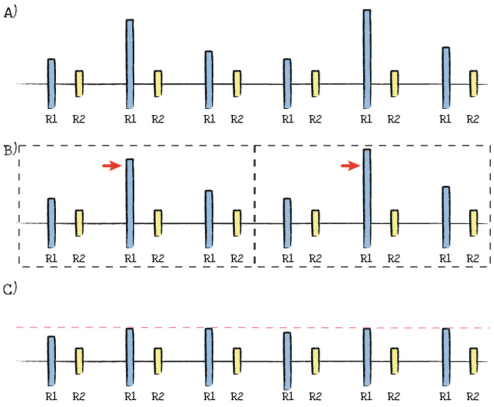

Fig. 4. Detection of anomalous peaks: (a) Sample with anomalous peaks, (b) Segmentation and identification of maximum peaks, (c) Substitution of anomalous peaks by normal maximum.

Discrete Wavelet Transform. Since the acquired data is a consequence of pressure variations in the heart chambers and corresponds to a biomechanical cardiac signal, it is considered a non-stationary stochastic signal, so the Discrete Wavelet Transform (DWT) is applied [6]. Figure 4 presents the data set of a sample of a healthy heart and its respective approximation 3 which becomes a signal easier to analyze, the filtered state of the signal can be verified through the spectrogram, see Fig. 5.

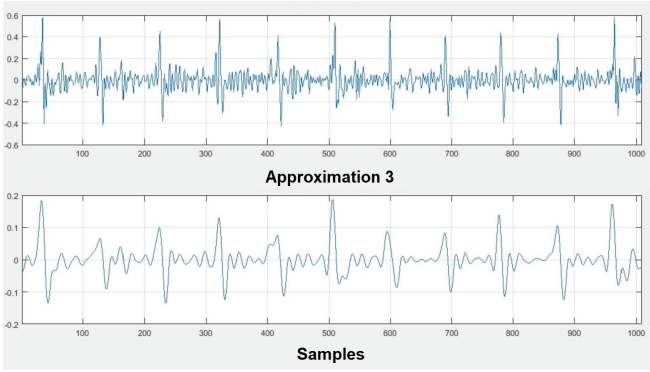

Fig. 5. Filtered audio sample and its approximation from the Wavelet transform.

First Heart Sound Detection. With the first Wavelet approximation, the detection of the first noise is obtained by searching for peaks greater than 50% of the amplitude of the maximum voltage of that group of data (Fig. 6). Once recognized, the distance between each of them is evaluated to identify which are consecutive, if there is no contiguity, the peaks found are established as R1, see Figs. 7 and 8.

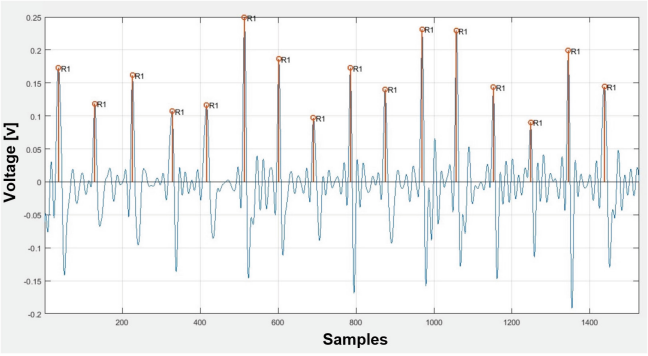

Fig. 6. First heart sound (R1) location within approximation wave. Sample without consecutive peaks.

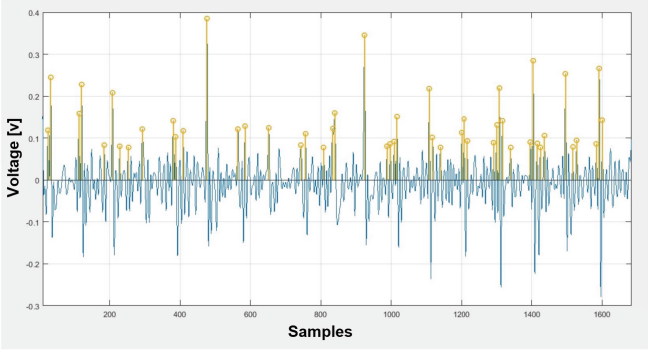

Fig. 7. Different sample with presence of consecutive peaks along first heart sound (R1) location area.

Second Heart Sound Location. Once the location of the first heart noise has been identified, the sampling space between each one is calculated and it is determined that R2 will be located in the sample corresponding to one third of the space between each R1, i.e. each cycle [5], as shown in Fig. 9. This calculation returns a vector with the voltage values of each R2 in the signal, and another vector with the sample number where each is located.

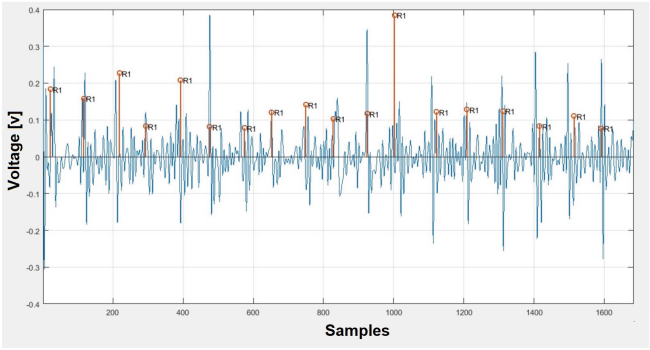

Fig. 8. First heart sound (R1) location within approximation wave. Sample with consecutive peaks.

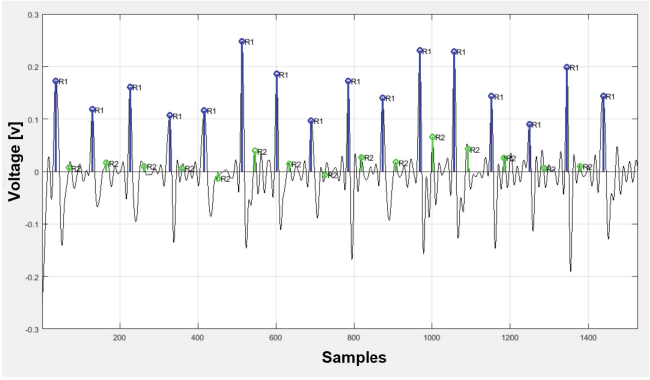

Fig. 9. Second heart sound (R2) location within approximation wave.

Heart Cycle RMS Valoration. Once acquired the vectors containing the numbers of the samples numbers of R1 and R2 location, Fig. 10; two cell type variables are generated, the first one with the arrangements of the location of each systole and the second one with the vectors of the location of each diastole. From the sampling spaces corresponding to systole and diastole, the values present in the space are extracted from the first detail resulting from the DWT, Fig. 11.

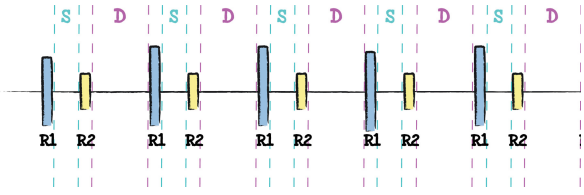

Fig. 10. Systole and diastole identification.

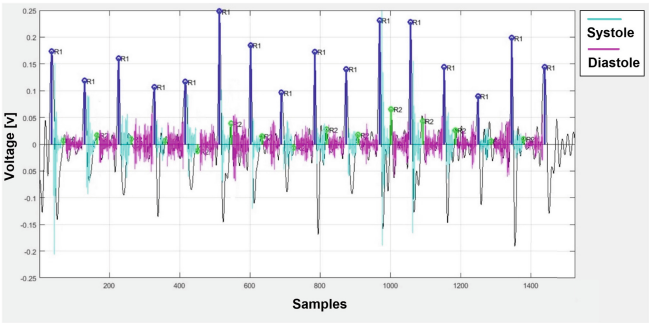

Fig. 11. Extraction of systole and diastole data from the first detail wave.

For each cycle the systole and the diastole are segmented in three parts (Fig. 12), then the Root Mean Square (rms) of each fragment of each cycle is calculated and averaged to have reference values of the whole sample; therefore, at the end a vector of three elements of rms values of the systole is obtained and in the same way of the diastole.

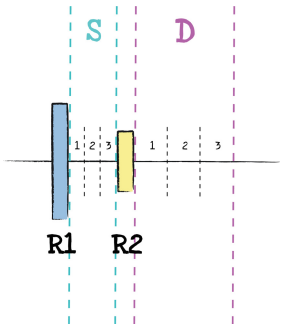

Fig. 12. Segmentation of systole and diastole into three sections.

Student's t-Test. In general, the different existing valvular lesions are characterized by the presence of systolic and diastolic murmurs that define them. In a healthy person, the spaces between tones are silent, while in a person with a clinical state of valvular disease, the supposedly empty spaces between R1 and R2 are altered by acoustic presences of different qualities. The specific application of the Student t-test in this project is for the determination of the relationship between two vectors: diastole and systole. To determine the relationship between them, the Matlab ttest2 command is used, where it is hypothesized that the two data samples come from populations with equal means. At the same time, a level of significance or acceptance of this statement is assigned; if the function returns "0" it means that it does not reject the hypothesis and therefore are related and

subject does not present murmurs, otherwise the command will return "1" indicating that there is an acoustic presence that represents a murmur. This method has been used to associate the non-relationship between the diastole and systole vectors as a murmur, since beforehand it has been ensured that all types of noise pollution not belonging to cardiac biomechanics are eliminated.

Prediction of Suspected Valve Injury. In this phase, the type of murmur and the valvular lesion it represents is identified through the evaluation of the systole and diastole rms vectors of each murmur positive sample. The vector of higher value denotes the cardiac cycle stage in which the sign is located in a more intense way. The magnitude of the values of each arrangement indicates the qualities of the signal to be compared with the characteristics of a valve disease.

3 Results

Analyzing the relationship between the diastole and systole vectors of each sample, the presence of murmurs is verified according to the acceptance or rejection of the hypothesis posed with the t-student test. The supposed presence of a murmur in one or several auscultation zones is a considerable factor in determining that the patient should actually be subjected to cardiac evaluation tests run by a specialist. However, it is not possible to specify the zone or category of a valve disease, nor can a definitive diagnosis be established.

Subsequently, it is established to identify not only the presence of the murmur, but also the auscultation focus where it is located. By means of a comparison between the results achieved by the system and diagnostic results verified by echocardiography, the analysis of false positives and false negatives is determined, see Table 1. As a result, the area of the murmur and, therefore, the anatomical region of the presumed valve lesion coincides in most cases with the actual state of the patient.

Table 1. Identification of heart murmurs results from the implementation of the proposed algorithm.

True negatives	False positives
31	3
False negatives	True positives
2	8

The system coincided with the anatomic location of most of the lesions being able to detect accurately healthy subjects as patients affected with different valvular injuries.

One patient from the sample who presented pulmonary stenosis, diagnosed by an specialist, was the first case of false negatives, due that the proposed algorithm predicted that there is no pulmonary lesion. Also, the presence of tricuspid and aortic lesions is identified, which also corresponds to false positives.

Another subject presented a medical diagnosis of aortic stenosis that coincides with the obtained result; however, the proposed method was also able to identify a pulmonary valvular disease that constitutes a false positive in the patient's examination. The sensitivity analysis indicates that the algorithm allows to correctly diagnose a patient as sick in 80%, while the specificity, presents a 91% probability of a correct diagnosis of healthy subjects.

4 Conclusions

This algorithm is a solution to the problem of the reduced practice of auscultation and, therefore, the auscultatory capacity of new doctors. Auscultation is an evaluation that must be carried out with great technicality and expertise, especially in public health systems where the correct diagnosis in general consultation is fundamental before assigning later examinations of greater complexity and less accessibility. In the case of rural areas, the implementation of this proposal will help to prioritize the assignment of specialists to people who present a presumptive diagnosis of murmurs.

The results of sensitivity and specificity were promising; this is a key factor in ensuring the health of patients. A low percentage of these values would give way to the progression of the disease and its fatal consequences or, if a healthy patient is detected with a heart condition, he would be unnecessarily medicated and would generate iatrogenic diseases.

As the title of this project indicates, the results consist of a presumptive diagnosis, which indicates that, despite its successful operation, the evaluation is not official and this method should not be used as a final examination, but is recommended to be used in conjunction with other complementary tests that the doctor may suggest.

Acknowledgment. The authors gratefully acknowledge the support of Eng. Leonardo Bueno MSc. for his collaboration during the signal acquisition process. Also, to Dr. Whiston Moreira, Dr. Ricardo Quizhpe and Dr. María Augusta Córdova for all the support provided by their expertise in the field of medicine. Finally, an expression of gratitude to all the patients who contributed to this study.

Conflict of Interest. The authors declare no conflicts of interest in preparing this article.

References

1. Aguilar Peris, J., Senent Pérez, F.: Cuestiones de física. Reverté, Barcelona (1980)
2. Argente, H.A., Álvarez, M.E. (eds.): Semiología médica. Médica Panamericana, Madrid (2005)
3. Baré, G.M., Califano, J.E.: Semiotecnia: maniobras de exploración. McGraw-Hill Interamericana, Mexico (1996)
4. Bickley, L.S., Szilagyi, P.G.: Bates guía de exploración física e historia clínica. Wolters Kluwer Health/Lippincott Williams & Wilkins, Philadelphia (2013)
5. Cano, A.: Fonocardiografía (fcg) - dalcame (2005). http://www.dalcame.com/fono.html#.XLSmmOhKhhE
6. Hillegass, E.: Essentials of Cardiopulmonary Physical Therapy. Elsevier Health Sciences (2016)
7. Kocuvan, P., Torkar, D.: Classification of the heart auscultation signals. In: HEALTHINF, pp. 534–539 (2015)
8. Llanio Navarro, R., Perdomo González, G.: Propedéutica clínica y semiología médica. Editorial Ciencias Médicas (2007)
9. Melloni, B.J., Dox, I., Eisner, G.M.: Diccionario médico ilustrado de Melloni. Reverté (1982)
10. Clínica Universidad de Navarra: Diccionario médico. Clínica Universidad de Navarra (2019). http://www.cun.es/es_EC/diccionario-medico
11. Ramírez, L.G.D., Vanegas, H.R.: Semiología médica integral. Universidad de Antioquia (2006)
12. Surós Batlló, A., Surós Batlló, J.: Semiología médica y técnica exploratoria. Elsevier Masson (2001)
13. Zhong, L., Wan, J., Huang, Z., Cao, G., Xiao, B.: Heart murmur recognition based on hidden markov model. J. Signal Inf. Process. **4**(02), 140 (2013)

Recurrence Analysis of EEG Power and HRV Time Series for Asynchronous BCI Control

Claudia Ivette Ledesma-Ramírez[1(✉)], Erik Bojorges-Valdez[2], Oscar Yanez-Suarez[3], and Omar Piña-Ramírez[2,3]

[1] PhD Programme in Engineering Sciences, Universidad Iberoamericana Ciudad de México (UIA), 01219 Mexico City, Mexico
claudia.ledram@gmail.com
[2] Engineering Studies for Innovation Department, Universidad Iberoamericana Ciudad de México (UIA), 01219 Mexico City, Mexico
[3] Electrical Engineering Department, Universidad Autónoma Metropolitana (UAM), 09340 Mexico City, Mexico

Abstract. Autonomic control evidenced in both heart rate variability (HRV) and electroencephalographic (EEG) oscillations, reflect the behaviour of the underlying physiological non-stationary dynamical systems. In order to assess the influence of autonomic changes in the performance of an asynchronous brain-computer interface, recurrence analysis of EEG spectral density time series and HRV feature sets were used in binary classifiers to detect rest state from mental calculation state. Results suggest that recurrence indices of HRV might contribute to improve activity episodes detection for BCI control as the highest performance was achieved with power spectral density features of EEG in combination with recurrence HRV features (AUROC $= 0.81 \pm 0.07$).

Keywords: Recurrence quantification analysis · BCI · EEG · HRV

1 Introduction

Non-invasive brain-computer interface systems (BCI) based on EEG (electroencephalography) allow the translation of brain signals into commands for communication or control of physical devices [5]. Ideally they must allow free alternation between idleness and intended control periods of the BCI. Towards this goal, changes in the dynamics of brain oscillations over EEG spectral bands might be elicited with specific mental tasks (motor imagery, auditory imagery or mental calculation) where no additional stimulation is required. However, to date, asynchronous BCI present important disadvantages: (1) training sessions could take from several days to weeks and (2) low classification accuracy (65–70%).

Recurrence quantification analysis (RQA) provides information of the dynamical behaviour of non-stationary systems. Recurrence Plots (RPs) graphically represent recurring states in phase space of dynamic systems and from

© Springer Nature Switzerland AG 2020
C. A. González Díaz et al. (Eds.): CLAIB 2019, IFMBE Proceedings 75, pp. 202–207, 2020.
https://doi.org/10.1007/978-3-030-30648-9_27

them, a variety of indices can be quantified. An RP corresponds to a binary matrix R where the entry $R_{i,j}$ is represented by a black pixel if two states at different times are similar in phase space within a specified neighbourhood. Otherwise, a white pixel is shown. In general, diagonal lines in RPs indicate a deterministic behaviour, vertical or horizontal lines represent changes on dynamics and patterns of parallel lines indicate periodicity [3].

In addition, heart rate variability (HRV) dynamics reflect Autonomic Nervous System (ANS) changes in some conditions as arousal and stress that have been suggested to negatively contribute to the overall performance of BCI systems. This work explores inclusion of RQA and HRV to achieve higher classification accuracy between periods of mental calculation versus idle state.

2 Materials and Methods

The dataset used in the present study is available through Physiobank [1,6]. It consists of simultaneous recordings of EEG signals and one ECG lead from 36 volunteers (mean age 18.25 ± 2.17 years old) during two sessions: rest state with closed eyes (180 s) and mental arithmetic task with eyes open (60 s). Data were recorded at 500 Hz using a Neurocom monopolar EEG 23-channel system (Ukraine, XAI-MEDICA). The EEG montage includes 19 channels (Fp1, Fp2, F3, F4, Fz, F7, F8, C3, C4, Cz, P3, P4, Pz, O1, O2, T3, T4, T5 and T6), with digital band-pass filter of 0.5–45 Hz. For the purpose of this study six subjects were excluded because of a corrupted ECG recording. Only the first 60 s of mental arithmetic task were used in order to process the same amount of data for each session.

The pre-processed EEG signals were detrended over the entire record and re-referenced to Common Average Reference (CAR). Welch's periodogram was used to calculate the relative power spectral density time series over the beta band (β_{PSD}, 12–30 Hz). HRV series were computed and linear features were calculated for both sessions (SDNN - standard deviation of RR intervals and LF/HF - low frequency/high frequency ratio). The differences between rest and arithmetic sessions were tested by a Wilcoxon rank sum test. Statistical significant values were set as $p < 0.05$.

Individual and joint RQA was performed for HRV and β_{PSD} series using the Cross-Recurrence Plot Toolbox for Matlab [2]. Dimension m, time delay τ and size of the neighbourhood ϵ were set to 3, 5, 0.4; respectively. These parameters are needed for RPs estimations. Thirteen features were extracted from RPs and the differences between rest and arithmetic sessions were statistically analysed by a Wilcoxon rank sum test (recurrence rate, determinism, averaged diagonal length, length of longest diagonal line, entropy of diagonal length, laminarity, trapping time, length of longest vertical line, recurrence time of first type, recurrence time of second type, recurrence period density entropy, clustering coefficient and transitivity). Figure 1 shows an example of rest and mental calculation HRV RPs for one subject.

Support vector machine (SVM) classifiers were built to test the discrimination capacity of selected features between mental calculation and rest sessions.

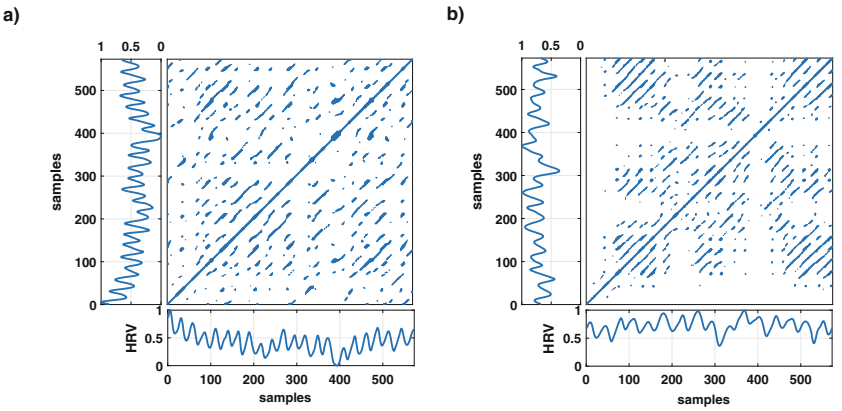

Fig. 1. HRV recurrence plots example for one subject. Dimension: 3, time delay: 5 and size of the neighbourhood: 0.4. Next to each RP, HRV series are shown. **(a)** HRV recurrence plot for rest condition. **(b)** HRV recurrence plot for mental calculation condition.

Feature selection was based on two criteria: (1) known brain areas were mental calculation is reflected and (2) significance level results from the statistical test. Five classifiers were built for different feature subsets as shown in Table 1. Linear kernel was used for all cases and no hyper parameter optimization was performed. Twenty fold cross validation was carried out to evaluate performance, using the area under receiver operating characteristic (AUROC) metric.

Table 1. Selected feature subsets for each classifier.

Classifier	Selected features
1	HRV: recurrence time of 2nd type
	HRV: recurrence period density entropy
	[a]EEG: mean value of β_{PSD}
2	LF/HF ratio
	SDNN
3	[a]EEG: mean value of β_{PSD}
4	HRV: recurrence time of 2nd type
	HRV: recurrence period density entropy
5	HRV, [a]β_{PSD}: joint recurrence time of 2nd type
	HRV, [a]β_{PSD}: joint recurrence period density entropy

[a]Selected EEG channels for all cases were: C3, C4, CZ and P3.

3 Results

From linear analysis of HRV, SDNN and LF/HF ratio resulted significantly different between rest and mental calculation conditions. SDNN with $p < 10^{-2}$ and LF/HF ratio with $p < 0.001$. SDNN has been suggested to reflect autonomic influence on HRV, whereas LF/HF may estimate the balance between sympathetic and parasympathetic nervous system activity.

Recurrence time of 2nd type and recurrence density entropy were the two RQA statistically different indices for HRV between rest and mental calculation conditions, with $p < 10^{-2}$ and $p < 0.05$, respectively. The first one is related to Lyapunov exponent, describing the scaling law behaviour of a multivariate system. Entropy provides information about complexity of the RP plot [3].

Figure 2a shows the scatter distribution of data from rest and mental calculation conditions with two features of classifier number one (β_{PSD} for channel C3 and HRV recurrence period density entropy). Figure 2b shows population performance of the selected classifiers. Classifier number one achieved the best performance (AUROC $= 0.81 \pm 0.07$) considering two recurrence features of HRV and four EEG features corresponding to the mean values of β_{PSD} from C3, C4, CZ and P3, as specified in Table 1. This classifier performance was significantly different from the remaining four with $p < 0.01$, after Bonferroni correction. The lowest and most dispersed performance was achieved by classifier number 5 (AUROC $= 0.63 \pm 0.14$) considering joint recurrence characteristics from HRV and β_{PSD}.

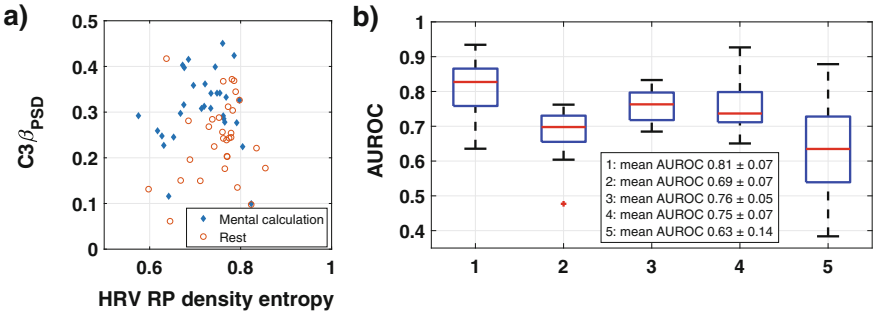

Fig. 2. **(a)** Distribution of mental calculation and rest features in recurrence period density entropy HRV and the mean β_{PSD} value from channel C3. **(b)** AUROC performance of classifiers. **1**: recurrence features of HRV in combination with mean values of beta power spectral density features. **2**: linear features of HRV. **3**: mean values of beta power spectral density features. **4**: HRV recurrence indices. **5**: HRV and β_{PSD} joint recurrence indices.

4 Discussion

Our results are consistent with previous studies where RQA reflects more sensibility than linear features to detect HRV changes between different conditions that alter the ANS (classifiers 2 and 4 performance in Fig. 2b) [4], suggesting that BCI classification methods could take advantage of this technique to enhance performance (classifier 1 in Fig. 2b). Although joint recurrence indices of β_{PSD}-HRV did not improve the description of HRV and EEG dynamics, joint recurrence between α_{PSD}-HRV and γ_{PSD}-HRV should still be explored as features from these frequency bands have shown important contributions to differentiate elicited mental tasks from rest for BCI control. Both, alpha and gamma bands were excluded for feature extraction since experimental conditions for database recording introduce distortions (eyes open/closed and limited bandwidth). It is important to emphasize that the present study exposes only population results, optimal feature selection for each subject must be addressed to a reliable BCI implementation.

For future work specific experiments might take place for the understanding of ANS contribution during BCI control, in order to improve classification accuracy of asynchronous BCI. Additionally, other non-linear methods might be explored such as symbolic dynamics.

5 Conclusion

Results suggest that RQA of HRV might contribute to improve detection of activity episodes for BCI control as it reflects changes in the ANS that affect BCI performance. Further studies should be done to determine the possible contribution of joint recurrence analysis of HRV and power spectral density over EEG bands.

Acknowledgement. This work is supported by Dirección de Investigación of Universidad Iberoamericana Ciudad de México (DINV), under research project on BCI.

Conflict of Interest. The authors declare that they have no conflict of interest.

References

1. Goldberger, A.L., Amaral, L.A.N., Glass, L., Hausdorff, J.M., Ivanov, P.C., Mark, R.G., Mietus, J.E., Peng, C.-K., Moody, G.B., Eugene Stanley, H.: Physiobank, physiotoolkit, and physionet: components of a new research resource for complex physiologic signals. Circulation **101**(23), e215–e220 (2000)
2. Marwan, N.: Cross Recurrence Plot Toolbox for Matlab. Potsdam Institute for Climate Impact Research (PIK), October 2016
3. Marwan, N., Carmenromano, M., Thiel, M., Kurths, J.: Recurrence plots for the analysis of complex systems. Phys. Rep. **438**(5–6), 237–329 (2007)

4. Schlenker, J., Socha, V., Riedlbauchová, L., Nedělka, T., Schlenker, A., Potočková, V., Malá, Š., Kutílek, P.: Recurrence plot of heart rate variability signal in patients with vasovagal syncopes. Biomed. Signal Process. Control **25**, 1–11 (2016)
5. Wolpaw, J.R., Birbaumer, N., McFarland, D.J., Pfurtscheller, G., Vaughan, T.M.: Brain-computer interfaces for communication and control. Clin. Neurophysiol.: Official J. Int. Fed. Clin. Neurophysiol. **113**, 767–791 (2002)
6. Zyma, I., Tukaev, S., Seleznov, I., Kiyono, K., Popov, A., Chernykh, M., Shpenkov, O.: Electroencephalograms during mental arithmetic task performance. Data **4**(1), 14 (2019)

Joint Exploitation of Hemodynamic and Electrocardiographic Signals by Hidden Markov Models for Heartbeat Detection

Nelson F. Monroy[1,2(✉)] and Miguel Altuve[2]

[1] Faculty of Systems Engineering and Informatics, Pontifical Bolivarian University, Bucaramanga, Colombia
nelson.monroy@upb.edu.co
[2] Faculty of Electrical and Electronic Engineering, Pontifical Bolivarian University, Bucaramanga, Colombia
miguel.altuve@upb.edu.co

Abstract. The detection of heartbeats is a fundamental task in the diagnosis of cardiovascular diseases. In a clinical setting, heartbeats are commonly detected from the electrocardiographic (ECG) signal, but it can also be estimated from hemodynamic signals, such as arterial blood pressure (ABP), pulmonary arterial pressure (PAP) and central venous pressure (CVP). In this paper, we conceived three HMM-based detectors that jointly exploit the information from ECG and ABP ($D_{ECG\&ABP}$), ECG and PAP ($D_{ECG\&PAP}$), and ECG and CVP ($D_{ECG\&CVP}$). The HMM-based detectors are based on the comparison of the difference of log-likelihoods of observation of two competing models that learned the dynamics of the presence and absence of a heartbeat, respectively. The detection performances of the bivariate centralized detectors were similar, but the detector that simultaneously considers ECG and ABP provide the best result (sensitivity = 98.91% and positive predictivity = 99.11%). These results agree when a univariate HMM-based detector only considers the ECG signal in the decision process. The centralized bivariate detection approach proposed in this paper make uses of redundant information in the decision process and is particularly useful when one of the signals is too noisy or missing.

Keywords: Hidden Markov model · Heartbeat · Detection algorithms · Electrocardiogram · Blood pressure

1 Introduction

The acquisition of several physiological signals for continuous monitoring purposes is a common task both in ambulatory and intensive care units. The objective of this multi-signal health monitoring system is not only to make available a greater quantity of information but also, since they are obtained from different sources, to increase the observability of the system and provide a better diagnosis

© Springer Nature Switzerland AG 2020
C. A. González Díaz et al. (Eds.): CLAIB 2019, IFMBE Proceedings 75, pp. 208–217, 2020.
https://doi.org/10.1007/978-3-030-30648-9_28

and treatment [1–3]. Electrocardiogram (ECG), respiratory rate, peripheral capillary oxygen saturation, and blood pressure are physiological signals typically observed in clinical environments.

In a clinical setting, heart rate is by far the most important monitored parameter because it can easily reveal whether a person is alive or not. Moreover, since heart rate is modulated by the autonomic nervous system through the sympathetic and parasympathetic branches, a deeper understanding of a disease can be obtained through the analysis of heart rate variability [4].

To estimate the heart rate, the heartbeat must be first detected. In an ECG trace, the heartbeat is generally detected by detecting the QRS complex, i.e. the signal with the largest amplitude. Once QRS complexes are detected, other ECG waveforms can be easily detected and employed for diagnostic purposes, such as the diagnosis of acute myocardial infarction by morphologic analysis of the ST segment [5]. Given that the different systems in the human body are interconnected, the heartbeat, and hence the heart rate, can be estimated from other physiological signals. Indeed, the robust detection of heartbeat in multimodal data is a current research topic particularly brought out by the PhysioNet/Computing in Cardiology Challenge 2014 [6]. In this sense, ECG, arterial blood pressure (ABP), photoplethysmogram, electroencephalogram, and electromyogram recordings can be jointly exploited to robustly detect heartbeats. However, given that heart rate and blood pressure are related through the baroreceptor reflex [7], it is more convenient to use blood pressure and ECG signals to detect heartbeats.

The detection of heartbeats by combining the information from ECG and ABP signals has been successfully carried out using hidden semi-Markov models [8], Bayesian networks and hidden Markov models [9], and fusion of individual detections [10]. However, the use of blood pressure obtained in different places, such as pulmonary arterial pressure (PAP) and central venous pressure (CVP), has not been so much exploited for heartbeat detection. One of the reason is the difficulty of obtaining PAP and CVP signals since they are collected invasively, in contrast to ABP which is measured noninvasively. Figure 1 shows the ECG, ABP, PAP and CVP signals, acquired simultaneously. It is clear the relationship between the ECG signal and the ABP, PAP and CVP signals in this figure.

In this paper we are thus interested in exploiting the information contained in ABP, PAP and CVP hemodynamic signals and ECG recordings to conceive a heartbeat detector. We used hidden Markov models (HMM) to jointly exploit, in an ECG signal and in one of the blood pressure signals, the dynamics that represent (*i*) the presence and (*ii*) the absence of heartbeats. The detection of the heartbeat is then based on the comparison of the log-likelihoods of observation of two competing HMM that characterize the presence and absence of the heartbeat [11].

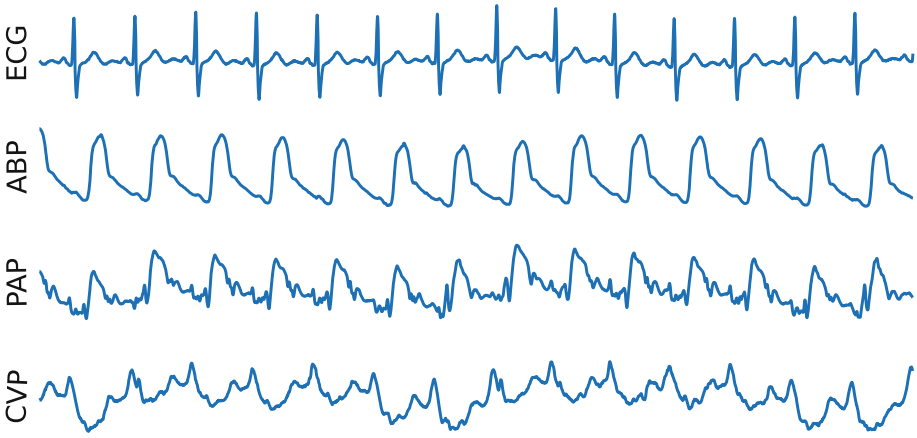

Fig. 1. Example of an electrocardiographic (ECG) and three hemodynamic signals (ABP, PAP and CVP). The signals were acquired simultaneously.

2 Methods

2.1 Physiological Signals

ABP, CVP, PAP and lead II ECG signals were taken from the MGH/MF Waveform Database [12,13]. The signals in this database, collected from 250 patients, have different durations (12–86 min), and different signal-to-noise ratios. In this work, we have considered the records with typical patterns of the signals ABP, CVP, PAP and ECG, in the first five minutes (learning period). This selection was made to prevent the HMM to learn patterns that do not belong to the signals but to noise. In this case, records named mgh004, mgh010, mgh012, mgh013, mgh020, mgh022, mgh035, mgh039, mgh040 and mgh134 were retained in this study. The duration of the selected record was 76.45 ± 13.53 min. The physiological signals in the database were sampled at 360 samples per second.

2.2 Heartbeat Detector Based on HMM

ABP, CVP, PAP and ECG signals were firstly filtered to reduce noise and enhance the dynamics of interest. On the one hand, ECG signals were filtered with a 400-order band-pass FIR filter with stop band cutoff frequencies of 4 and 30 Hz and pass band cutoff frequencies of 6 and 28 Hz. These frequencies bands agreed with the ones reported by other authors and are used to enhance the QRS complex dynamics [14]. On the other hand, a 4020-order high-pass FIR filter with stop band cutoff frequency of 0.3 Hz and pass band cutoff frequency of 0.5 Hz was applied to ABP signals to reduce baseline wandering and a 30-ms long moving average filter was applied to CVP and PAP signals to smooth them. FIR filters were designed using the Kaiser window method.

We used two HMM to characterize two dynamics: (*i*) the *presence* of a heartbeat and (*ii*) the *absence* of a heartbeat [11]. These dynamics are contained in observation sequences $O = \{o_1, o_2, \ldots, o_T\}$, where T is the duration of the sequence. In this study, we are interested in bivariate observation sequences, where one of the signals is ECG and the other one blood pressure (ABP, PAP or CVP). These bivariate signals are jointly exploited by HMM with the aim of characterizing the two dynamics. Therefore, one detector is composed of two competing HMM: one characterizing the presence of a heartbeat and another characterizing its absence. We conceived three detectors: (*i*) $D_{ECG\&ABP}$ that simultaneously exploits ECG and ABP signals, (*ii*) $D_{ECG\&PAP}$ that simultaneously exploits ECG and PAP signals, and (*iii*) $D_{ECG\&CVP}$ that simultaneously exploits ECG and CVP signals.

In the training phase, once the number of states M has been selected, the model is trained on a training dataset using the Baum-Welch algorithm [15]. For each detector, two training datasets were created, each one containing the dynamics of interest in observation sequences. The annotation files provided in the database with the location of QRS complexes were used to extract the observation sequences:

- O_{QRS}: Observation sequences containing the dynamics of the *presence* of a heartbeat were centered at the annotation marks in ECG and CVP signals but were placed 250 ms after the annotation marks in ABP and PAP signals. This delay was obtained by visual inspection of the dynamics of the ECG and pressures signals, and is a bit larger than the one used by Johnson et al. [16].
- O_{NQRS}: Observation sequences containing the dynamics of the *absence* of a heartbeat were randomly taken from the signals without overlapping with O_{QRS}.

In the test phase, once the models have been trained, observation sequences are passed through the models in order to obtain log-likelihoods of observations. These observations sequences were taken in a sliding window of length T and 30 ms of displacement. The detection of a heartbeat is signaled when the difference of log-likelihoods of two competing models is greater than the threshold $\alpha w(t)$, where $w(t)$ is the average value of the difference of log-likelihoods in the past 15 s and α is a multiplication factor (see [11] for more detail).

As recommended in [17,18], the heartbeat detectors were trained on the first five minutes of the records (learning period). Therefore, observation sequences of O_{QRS} and O_{NQRS} were randomly chosen from the learning period to train the models. The remainder of the records were used to test the detectors and compute the detection performances.

2.3 Heartbeat Detection Performance Metrics

The number of true positives (TP), false positives (FP), and false negatives (FN) were computed for each record in the database, where a detection is a TP if it lies within 150 ms from a reference annotation, otherwise, it is an FP. Sensitivity $\left(Se = \frac{TP}{TP+FN}\right)$, positive predictivity $\left(+P = \frac{TP}{TP+FP}\right)$,

detection error rate $\left(DER = \frac{FN+FP}{TP+FN}\right)$, and distance to perfect detection $\left(DPD = \sqrt{(1-Se)^2 + (1-+P)^2}\right)$ were also computed [11].

For each detector, the number of states of the HMM, M, was varied from 2 to 7 states. In addition, for each detector and for each M, the best α was chosen in the test phase as the one that produces the shortest DPD, as explained in [19]. The search space for α was [0.2, 1.5]. T was set to 120 ms as obtained in [11]. Observation sequences were multiplied by ten, both in training and in test; this multiplication increases the dynamic range of the observation sequences [11].

The experiments were repeated ten times with different random seeds. We have reported the best results obtained on each experiment.

3 Results

Table 1 shows the detection performances of the HMM-based detectors for the different number of states. The optimal values of α for each M were also shown. Figure 2 shows the DER metrics of the three detectors for different M. We can observe that the three HMM-based detectors have similar detection performances, being the joint exploitation of ECG and ABP signals by HMM the one that produces the best results, followed by the detector that jointly exploits

Table 1. Heartbeat detection performance for each value of M. α was optimized in the test phase, as explained in Sect. 2.3. In bold, the best detection performance per centralized detector, in terms of DER.

Detector	M	α	TP	FN	FP	Se (%)	$+P$ (%)	DER (%)	DPD
$D_{ECG\&ABP}$	2	0.47	54687	648	502	98.80	98.82	2.42	0.0192
	3	0.39	54770	565	375	98.91	99.11	**2.00**	0.0155
	4	0.36	54675	660	446	98.76	98.96	2.31	0.0180
	5	0.35	54322	1013	749	97.86	98.32	3.84	0.0288
	6	0.25	54717	618	1231	98.83	97.35	4.22	0.0320
	7	0.35	54764	467	1562	99.00	96.76	5.00	0.0357
$D_{ECG\&PAP}$	2	0.39	54469	866	475	98.24	98.81	**2.95**	0.0227
	3	0.32	54341	994	725	98.05	98.26	3.81	0.0299
	4	0.33	54532	803	925	98.10	97.87	4.27	0.0326
	5	0.29	54521	814	1034	98.29	97.48	4.31	0.0324
	6	0.21	54852	483	1302	98.93	97.14	4.33	0.0313
	7	0.23	54497	838	1117	98.29	97.31	4.64	0.0346
$D_{ECG\&CVP}$	2	0.26	54201	1134	1423	97.72	97.13	5.38	0.0426
	3	0.42	53340	1995	431	96.33	98.91	4.72	0.0398
	4	0.46	54063	1272	685	97.46	98.17	4.39	0.0334
	5	0.55	54662	673	721	98.51	98.25	**3.34**	0.0244
	6	0.66	54513	822	968	98.15	97.74	4.29	0.0313
	7	0.48	54100	1235	1231	97.57	97.25	5.55	0.0418

ECG and PAP signals by HMM. The best detection performance was achieved when ECG and ABP signals are taken together by the HMM with three states (375 false detections and 565 missed detections).

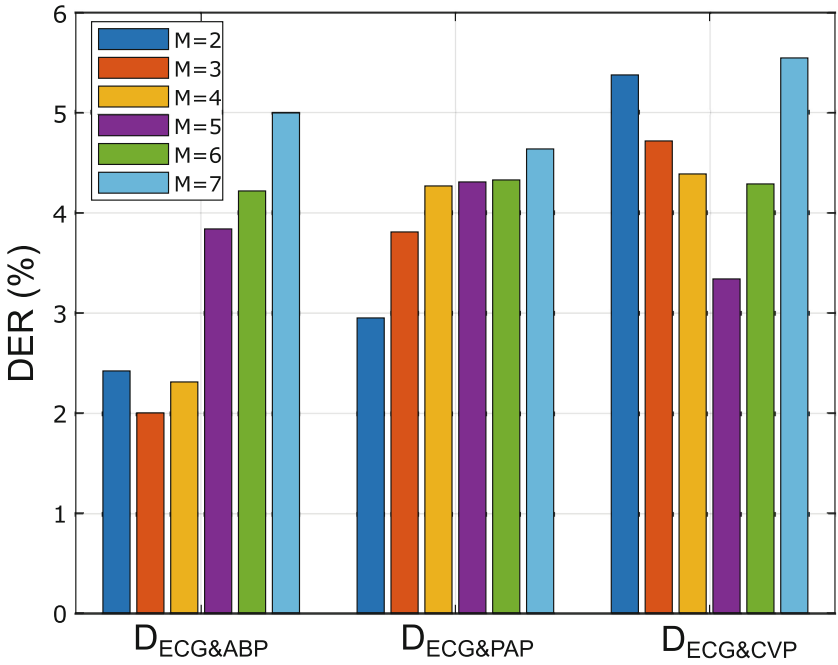

Fig. 2. Detection error rate (DER (%) for each HMM-based detector for different number of states M.

An example of the detection performance for each record of the dataset is shown in Table 2. We can see that the detection performance is similar among the subject ($DER < 4\%$) except for the record mgh040 that produces a $DER = 7.5\%$. Figure 3 shows an excerpt of the signals ECG, ABP, PAP and CVP of this particular record. We can observe that the annotations of the position of the QRS complexes after minute 68 were not available (the last 17 min of the record were not annotated), however, our detector incorrectly signal detections beyond minute 68, where the quality of the signals is bad. This resulted in a large number of FP on this interval (in green dotted lines in the figure).

Table 2. Heartbeat detection performance for $D_{ECG\&ABP}$ with $M = 3$ states and $\alpha = 0.39$, for each record of the dataset.

Record	TP	FN	FP	Se (%)	$+P$ (%)	DER (%)	DPD
mgh004	2886	53	40	98.19	98.63	3.16	0.0226
mgh010	8881	74	10	99.17	99.88	0.93	0.0083
mgh012	5682	126	26	97.83	99.54	2.61	0.0221
mgh013	6293	10	10	99.84	99.84	0.31	0.0022
mgh020	5980	123	30	97.98	99.50	2.50	0.0207
mgh022	6183	51	18	99.18	99.71	1.11	0.0086
mgh035	3842	16	8	99.58	99.79	0.62	0.0046
mgh039	5453	10	21	99.81	99.61	0.56	0.0042
mgh040	3618	75	202	97.96	94.71	7.5	0.0566
mgh134	5952	27	10	99.54	99.83	0.61	0.0048
Sum	**54770**	**565**	**375**				
Average				**98.91**	**99.11**	**2.00**	**0.0155**

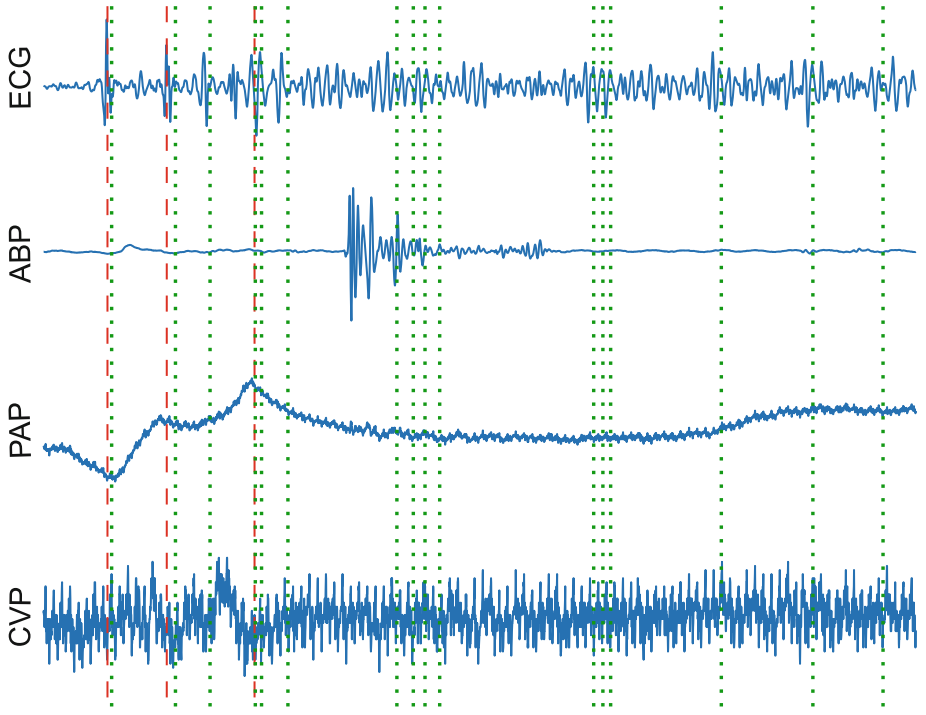

Fig. 3. An excerpt of the signals ECG, ABP, PAP and CVP of record mgh040. The annotations (red discontinuous line) provided in the database and the detections (green dotted lines) obtained with the detector $D_{ECG\&ABP}$ for $M = 3$ states are detailed.

4 Discussion

The slight variation in detection performances between the three HMM-based detectors could be due to similar dynamics of the presence and absence of a heartbeat embedded on the three pressures signals: ABP, PAP, and CVP. Therefore, we can say that the models characterize the dynamics in the bivariate signals in a similar way. However, as already shown in Fig. 1, there could be dynamics that are not represented in the three pressure signals, therefore, we think that the fusion of the three detectors could improve the overall detection performance as shown in [19]. Our research team is currently working in this direction. Another factor to consider is the location of the bivariate observation sequence extracted from the pressure signals: we have used a delay of 250 ms in the ABP and PAP with respect to the ECG signal. This delay is observed in these two pressure signals in Fig. 1 and was confirmed in our experiments. We decided not to delay the CVP signal with respect to the ECG since we observed that the dynamics were in phase (see Fig. 1). We are also currently working on optimizing the location of the observation sequences on the three hemodynamic signals to improve detection results.

Despite we have only used a portion of the available records on the MGH/MF Waveform database, we obtained similar detection performance results as obtained when only an HMM-based heartbeat detector that only processes ECG signals was considered [11]. We have observed that some signals on the database were to noise to process, and the long duration of the records (about an hour long) make it difficult to identify noisy segments.

Other researchers using different approaches have reported similar results on other databases. For instance, 94% sensitivity and 93% positive predictivity were achieved using HMM and Bayesian networks [9], 92.85% sensitivity and 94.29% positive predictivity were obtained using convolutional neural networks [20], and, by considering the quality of signals for choosing the signals to be used in a decentralized fusion scheme, 95.47% sensitivity and 96.06% positive predictivity were attained [21].

5 Conclusion

In this paper, we have shown that the joint exploitation by HMM of ECG and blood pressure signals, obtained at different locations, such as arterial blood pressure, pulmonary arterial pressure, and central venous pressure, resulted in detection results similar to the one obtained when only the ECG is taken into account. The advantage of the centralized bivariate detection approach is that the availability of redundant information can be used to provide detection when one of the signals is too noisy or missing.

Although the detection results were similar among the bivariate detectors that combine the ECG with the hemodynamic signals, the joint exploitation of the ECG and the ABP produces the best detection performance. In addition, even though PAP and CVP signals are invasively acquired, we believe that the fusion of detections of the three detectors could lead to better results.

References

1. Anliker, U., Ward, J.A., Lukowicz, P., Troster, G., Dolveck, F., Baer, M., Keita, F., Schenker, E.B., Catarsi, F., Coluccini, L., Belardinelli, A., Shklarski, D., Alon, M., Hirt, E., Schmid, R., Vuskovic, M.: AMON: a wearable multiparameter medical monitoring and alert system. IEEE Trans. Inf. Technol. Biomed. **8**(4), 415–427 (2004)
2. Saeed, M., Villarroel, M., Reisner, A.T., Clifford, G., Lehman, L.-W., Moody, G., Heldt, T., Kyaw, T.H., Moody, B., Mark, R.G.: Multiparameter intelligent monitoring in intensive care II: a public-access intensive care unit database. Crit. Care Med. **39**(5), 952–960 (2011)
3. Michard, F., Bellomo, R., Taenzer, A.: The rise of ward monitoring: opportunities and challenges for critical care specialists. Intensive Care Med. **45**(5), 671–673 (2019)
4. Saul, J.: Beat-to-beat variations of heart rate reflect modulation of cardiac autonomic outflow. Physiology **5**(1), 32–37 (1990)
5. Brady, W.J., Syverud, S.A., Beagle, C., Perron, A.D., Ullman, E.A., Holstege, C., Riviello, R.J., Ripley, A., Ghaemmaghami, C.A.: Electrocardiographic ST-segment elevation the diagnosis of acute myocardial infarction by morphologic analysis of the ST segment. Acad. Emerg. Med. **8**(10), 961–967 (2001)
6. Moody, G., Moody, B., Silva, I.: Robust detection of heart beats in multimodal data: the physionet/computing in cardiology challenge 2014. In: Computing in Cardiology 2014, pp. 549–552, September 2014
7. Ogoh, S., Fisher, J.P., Dawson, E.A., White, M.J., Secher, N.H., Raven, P.B.: Autonomic nervous system influence on arterial baroreflex control of heart rate during exercise in humans. J. Physiol. **566**(2), 599–611 (2005)
8. Pimentel, M.A., Santos, M.D., Springer, D.B., Clifford, G.D.: Heart beat detection in multimodal physiological data using a hidden semi-Markov model and signal quality indices. Physiol. Meas. **36**(8), 1717 (2015)
9. Zia, T., Arif, Z.: Probabilistic data fusion model for heart beat detection from multimodal physiological data. Turk. J. Electr. Eng. Comput. Sci. **25**(1), 449–460 (2017)
10. Johnson, A.E., Behar, J., Andreotti, F., Clifford, G.D., Oster, J.: R-peak estimation using multimodal lead switching. In: Computing in Cardiology 2014, pp. 281–284, September 2014
11. Monroy, N.F., Altuve, M.: Analysis of the observation sequence duration of hidden Markov models for QRS complex detection in single-lead ECG recordings. In: 2018 Computing in Cardiology (CinC), pp. 1–4, September 2018
12. Welch, J., Ford, P., Teplick, R., Rubsamen, R.: The Massachusetts general hospital-marquette foundation hemodynamic and electrocardiographic database-comprehensive collection of critical care waveforms. Clin. Monit. **7**(1), 96–97 (1991)
13. Goldberger, A.L., Amaral, L.A.N., Glass, L., Hausdorff, J.M., Ivanov, P.C., Mark, R.G., Mietus, J.E., Moody, G.B., Peng, C.-K., Stanley, H.E.: PhysioBank, physiotoolkit, and physionet: components of a new research resource for complex physiologic signals. Circulation **101**(23), e215–e220 (2000)
14. Elgendi, M., Jonkman, M., DeBoer, F.: Frequency bands effects on QRS detection. In: Proceedings of the Third International Conference on Bio-Inspired Systems and Signal Processing: BIOSIGNALS, (BIOSTEC 2010), INSTICC, pp. 428–431. SciTePress (2010)

15. Welch, L.R.: Hidden Markov models and the Baum-Welch algorithm. IEEE Inf. Theory Soc. Newslett. **53**(4), 10–13 (2003)
16. Johnson, A.E., Behar, J., Andreotti, F., Clifford, G.D., Oster, J.: Multimodal heart beat detection using signal quality indices. Physiol. Meas. **36**(8), 1665 (2015)
17. ANSI/AAMI EC38:1998: Ambulatory Electrocardiographs, American National Standard (1998)
18. ANSI/AAMI EC57:1998: Testing and Reporting Performance Results of Cardiac Rhythm and ST Segment Measurement Algorithms, American National Standard (1998)
19. Ledezma, C.A., Altuve, M.: Optimal data fusion for the improvement of QRS complex detection in multi-channel ECG recordings. Med. Biol. Eng. Comput. **57**, 1673–1681 (2019)
20. Chandra, B.S., Sastry, C.S., Jana, S.: Robust heartbeat detection from multimodal data via CNN-based generalizable information fusion. IEEE Trans. Biomed. Eng. **66**(3), 710–717 (2018)
21. Khavas, Z.R., Asl, B.M.: Robust heartbeat detection using multimodal recordings and ECG quality assessment with signal amplitudes dispersion. Comput. Methods Programs Biomed. **163**, 169–182 (2018)

Hand Movement Detection from Surface Electromyography Signals by Machine Learning Techniques

Jose Alejandro Amezquita-Garcia[1],
Miguel Enrique Bravo-Zanoguera[1(✉)],
Felix Fernando González-Navarro[2], and Roberto Lopez-Avitia[1]

[1] Facultad de Ingeniería, Universidad Autónoma de Baja California, Mexicali, Mexico
{jose.amezquita,mbravo}@uabc.edu.mx
[2] Instituto de Ingeniería, Universidad Autónoma de Baja California, Mexicali, Mexico

Abstract. Surface electromyography (sEMG) signals offer information on the natural control of muscle contraction but struggle to identify temporal pattern parameters for several degrees of motion of voluntary hand movements. The complex nature of these signals renders the movement prediction task difficult; therefore, feature extraction and selection algorithms are a natural choice to transform time domain data into a new space domain to enhance recognition. The purpose of this work was to conduct an analysis of a former forearm sEMG database to improve a model to classify 15 defined hand movements. A simpler classification model was created from algorithms, such as naive Bayes (NB), linear discriminant analysis (LDA), and quadratic discriminant analysis (QDA). Also, novel preprocessing of the EMG signal data was employed and modeled the movement in virtual simulation software. In the preprocessing, outliers were eliminated, and a scatter matrix algorithm was used to transform the data into a new space to increase the differentiation between distinct classes. The processing window was 62.5 ms to generate a classification and integrate one video frame movement. Experiments yielded promising results, achieving a 93.76% recognition rate in an independent test set. The biomechanical wrist model available in OpenSim was completed by adding the missing degrees of freedom of the fingers to simulate the movement generated from the proposed classification model. The sequence of movement was converted to a biomechanical model and constructed into a video object with the potential for real time use.

Keywords: Electromyography · Stochastic signal · sEMG array · Scatter matrix · Probabilistic model

1 Introduction

The interpretation of surface electromyography (sEMG) is an active area of research to examine the direction of muscle movement. The electronic control of devices aims to create control commands that are more comfortable and easier to use. Devices and their software applications have more functionalities, and more complex systems are needed

© Springer Nature Switzerland AG 2020
C. A. González Díaz et al. (Eds.): CLAIB 2019, IFMBE Proceedings 75, pp. 218–227, 2020.
https://doi.org/10.1007/978-3-030-30648-9_29

to control or access these functions. Currently, devices are being developed that are controlled with body movements, some using cameras and images [1, 2] and others using EMG signals directly [3–20]. These signals are used to estimate strength and changes in muscle activation caused by neuromuscular abnormalities and the control of medical devices [10]. With machine learning techniques, it is possible to develop models that interpret complex systems, such as the progression of the movement of the hand through forearm sEMG array data, to determine gradual finger motion responses given the input sequencing [5, 7, 10]. Although there are a considerable number of investigations into the processing of EMG data [3, 21–26], there is not a model in which the signal between movements is sufficiently differentiable to generate a simple classification model that can be used in real time processing. The objective of this work was to generate a recognition model using typically selected features and transforming these measurements into a new space, such as a scatter matrix, to increase the separation of measurements between classes. Experiments yielded promising results achieving a 93.76% recognition rate in an independent test set. This study is complemented by the use of OpenSim motion simulation software to simulate hand movement that has been predicted with the classification model. Achievements of this kind offer possible applications in multifunctional prosthesis, exoskeletons, rehabilitation therapies, and new technologies, such as hand gesture control.

2 Methodology

2.1 EMG Database of Predefined Fingers Movements

A previously created database repository found in a website [27] was analyzed. The database consisted of 15 hand movements monitored with a ring of eight surface electrodes on the forearm (Fig. 1). Eight normal subjects were evaluated; the characteristics of the subjects and the form and type of acquisition can be found in [28], along with the related ethical approval for that study. Fifteen types of flexion movements were evaluated, i.e., thumb (T), index (I), middle (M), ring (R), little (L), the combined T-I, T-M, T-R, T-L, I-M, M-R, R-L, I-M-R, M-R-L, and finally the hand close (HC) motion. Each movement was performed for 5 s, which produced 20,000 sample readings, and repeated twelve times by each subject.

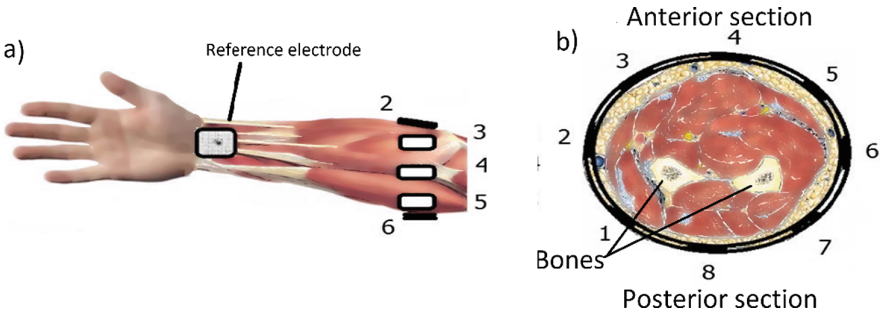

Fig. 1. Electrode position (a) Forearm (anterior section), (b) Forearm (cross-section).

2.2 Features Selected from Literature and Classification Issues

Time domain features have been widely used to extract useful information and improve the performance of classifiers. A major disadvantage of these features comes from the non-stationary property of the EMG signal, but typically, the data is assumed as a stationary signal [29]. It is desirable to have features that generate a differentiation between each of the evaluated classes and a decrease of the dispersion between the measurements of each class. Ten features in the time domain are proposed in this investigation as defined elsewhere [30]: mean absolute value, simple square integral, variance of EMG, temporal moments, waveform length, zero crossings, myopulse percentage rate, and slope sign change. Classification complications are commonly divided into two separate stages: the inference step, in which training data is used so that the model learns the probabilities of each of the classes, and the subsequent decision step, in which posterior probabilities are used for prediction based on variables independent of the class type.

Naive Bayes. This classifier is based on probabilistic theory in which the classification of n vectors is given, assuming that the data has a normal probability distribution. The prior probabilities are defined as $P(C_k)$, and the sum of the prior probabilities is $\sum_{k=1}^{N} P(C_k) = 1$. The prior probabilities indicate the likelihood that the vector belongs to a given class. Then, the probability of the class k given the vector x (posterior probability) is expressed as

$$p(c_k|x) = p(x|c_k)p(c_k)/p(x) \tag{1}$$

where $p(x) = \sum_k p(x|C_k)p(C_k)$. The vector belongs to the class C_k for which $C_k = argmaxp(C_k|x)$ [31]. As it is assumed that the data has a normal distribution, the density function can be written as

$$p(c_k|x) = \frac{1}{\sqrt{2\pi\sigma_k}} e \frac{-(x_k - \mu_k)^2}{2\sigma^2} \tag{2}$$

Thus, a function is defined for each class, and each class is selected with the highest quality argument. In this way, the class to which a new vector belongs is selected.

Discriminant Functions. As a probabilistic classifier, it assumes that different classes generate data based on different Gaussian distributions [32]. The model for discriminant analysis follows that each class *(Y)* generates data *(X)* using a multivariate normal distribution. In other words, the model assumes X has a Gaussian mixture distribution [32]. For linear discriminant analysis (LDA), the model has the same covariance matrix for each class; only the means vary. For quadratic discriminant analysis (QDA), both the mean and covariance of each class vary [32].

2.3 Preprocessing and Signal Processing Techniques

The raw EMG data of the 12 repetitions of each subject were evaluated for each movement. A non-overlapping rectangular window was used to process the raw EMG

signal data with a length of 250 samples per window (equivalent to 62.5 ms). The 10 selected features of each EMG channel were concatenated producing a vector of 80 data features in each window period per subject; one movement repetition equaled 80 windows. All the features for all the windows (a complete movement) were grouped and repeated 12 times producing a new feature database with 960 vectors. An algorithm for the elimination of outliers with chi-square distribution was used. Due to the dimensionality of the data, the features per window were evaluated with an algorithm for selecting the best features (method of sequential forward selections; SFS). Of the 80 given variables, those chosen increased the power of classification of the LDA classification algorithm, per the method presented in [33]. With the subset of the selected data, a transformation of our data was implemented to a new space with the display algorithm based on scatter matrices; a description of this method is detailed in [34] and a summary presented in Fig. 2.

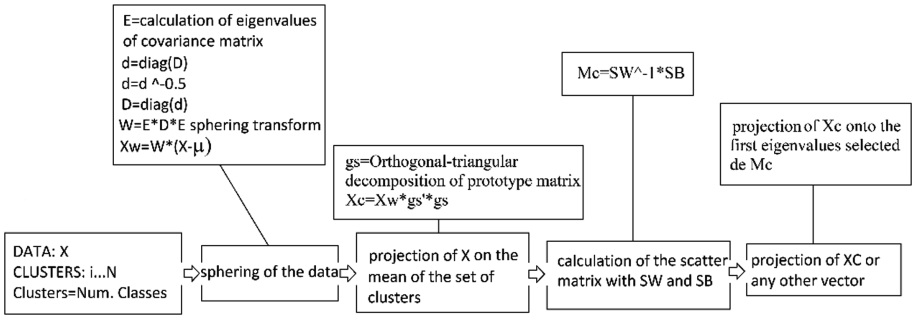

Fig. 2. Method of scatter matrices where X is the matrix of input data; g_s is the orthonormal set of basis vectors; E is the eigenvalue of the covariance matrix; and M^c is the scatter matrix, which is born from Sw and Sb, where Sw is the within-cluster matrix, and Sb is the between-scatter matrix.

2.4 OpenSim Model for Movement Simulation

OpenSim is a free biomechanical simulation program of the human body [35] that allows movement analysis and muscle evaluation with motion files. A limited wrist model is available in OpenSim SimTK [38] that has 10 degrees of freedom and a total of 23 actuator muscles with movement in the forearm, wrist, thumb (no flexion), and index fingers. This model of the wrist was modified, adding the missing degrees of freedom to the thumb, middle, ring, and little fingers to reproduce the complete movement of a real hand in simulation [37], accounting for 20 articulations. This more complete model was used for the simulation of the predicted movements of the hand motion classifier for a virtual visualization of each of the database movements. With each decision of the classifier, a certain degree of the articulation motion was advanced, creating a rotation vector. Video objects of the evaluated movements were created from the advancement of the rotation vectors.

3 Results

3.1 Preprocessing and Signal Processing Results

Method of Attribute Selection by SFS and Projection with a Scatter Matrix. After the removal of the outliers was applied, the SFS algorithm evaluated the performance of each attribute, and 52 of 80 attributes remained. With the subset of the selected data, the data was transformed into this new space (scatter matrix); these new features are grouped in regions defined between the classes (Fig. 3a).

Training, Validation, Testing and Opensim. The data, already selected and processed, was evaluated with three classification algorithms: NB, LDA, and QDA. Results were validated statistically through 10 × 10-fold cross-validation. The measurements were separated into 70% for training, 15% for validation, and 15% for testing. The first step was to assess the training measurements, which were randomized. Then, the training matrix was divided into 10 folds; the model was generated with nine folds and tested with the remaining fold. A recognition percentage in each tested classifier (NB, LDA, and QDA) was obtained 10 times, and an average was calculated. Then, the validation and training data were combined, and the same procedure was repeated. Average percentages of recognition were obtained. The model with the highest percentage was selected, and that model was tested with 15% of the testing data. This method of cross-validation was performed with a built-in function of MATLAB software (Fig. 4a). An error of 0.0624 was obtained for the most effective class differentiator, equivalent to 93.76% recognition in the test set for each subject individually (Table 1). Furthermore, a recognition percentage of 80.97% was obtained for the database created from the group of eight subjects (Table 2). Figure 4b presents the confusion matrix of the test set classification for the movements evaluated for a test subject. Every 62.5 ms (the duration time of the processing window), a new classifier output corresponded to an advance image frame of the movement. The advance vector corresponding to the degree of rotation for each of the joints of the biomechanical wrist model (Fig. 3b) created motion matrices. OpenSim used these motion matrices to visualize the virtual model. Movement files along with the videos can be found in [37].

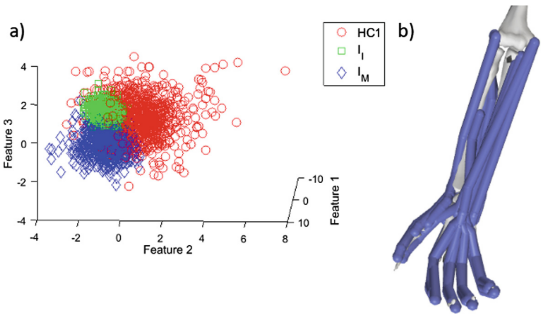

Fig. 3. (a) Visualization of three hand movements with scatter matrices, as a function of three new features, (b) Opensim wrist model.

a)

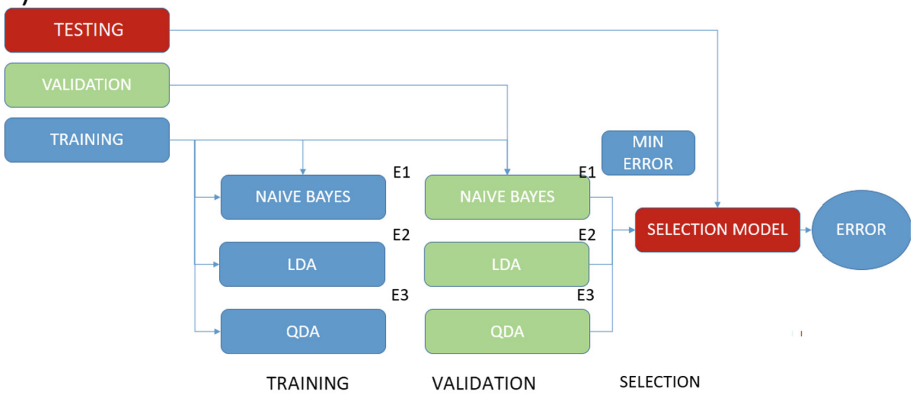

b)

	T	I	M	R	L	T-I	T-M	T-R	T-L	I-M	M-R	R-L	I-M-R	M-R-L	HC
T	102	0	0	0	0	0	0	4	0	0	0	1	0	0	0
I	0	122	0	0	0	1	0	0	0	0	3	0	0	0	1
M	0	0	139	0	0	1	0	0	0	0	0	0	0	0	2
R	0	0	0	146	0	0	0	0	0	0	0	0	0	0	1
L	0	0	0	0	111	1	0	0	2	1	0	0	1	0	0
T-I	0	3	1	0	0	140	0	0	0	0	0	0	0	0	0
T-M	0	0	0	4	0	0	137	0	0	0	0	0	0	0	0
T-R	0	0	0	0	0	0	0	112	0	0	0	0	0	0	0
T-L	0	0	0	1	1	0	2	0	121	1	0	1	0	6	0
I-M	0	1	0	0	5	0	0	0	0	127	0	0	0	0	3
M-R	0	5	0	0	0	0	0	0	0	0	123	0	1	0	2
R-L	0	0	0	0	0	0	0	0	0	0	0	134	0	0	0
I-M-R	0	0	5	0	1	1	0	0	0	0	7	0	110	0	0
M-R-L	0	0	0	0	0	0	0	0	5	0	0	0	0	117	0
HC	0	5	0	0	0	6	0	0	0	0	1	0	0	0	124

Fig. 4. (a) Sequence to select the most effective classification model through cross-validation, (b) Confusion matrix of the 15 movements evaluated for a test subject.

Table 1. Average recognition percentages of the models evaluated for the eight subjects separately through cross-validation. Training = TRN, validation = VAL, testing = TST, standard deviation = SD.

Algorithm	TRN		VAL		TST	
	Mean	SD	Mean	SD	Mean	SD
Naive bayes	86.13	7.84	85.92	8.10	–	
LDA	93.96	3.88	93.88	4.11	93.76	4.07
QDA	90.36	6.47	90.22	6.67	–	

Table 2. Average and standard deviation of recognition percentages of the models evaluated for the group of eight subjects through 10 × 10-fold cross-validation. Training = TRN, validation = VAL, testing = TST, standard deviation = SD.

Algorithm	TRN		VAL		TST	
	Mean	SD	Mean	SD	Mean	SD
LDA	81.12	0.88	81.36	0.78	80.97	1.11

4 Discussion and Conclusion

The machine learning techniques applied to real world EMG array data produced a recognition rate of 93.76% of the hand motions, satisfactory for a linear model classifier. Notably, the use of LDA as the classification algorithm in the attribute selection method may have contributed to the superior performance of LDA during training, validation, and testing against the other recognition models. However, other features not used, such as those in the frequency domain, may improve performance. In any case, it would be necessary to analyze the required processing time of any new features as response time is an issue. The time domain features measured for each electrode channel were 10 of the most commonly cited in the literature. From the initial 80-feature vector, 29 were removed for irrelevant or negative impact. Most of these removals corresponded to electrodes 7 and 8, which only retained two and three features, respectively, after the selection. This result may be due to the fact that the most defined movements were flexor movements, and those electrodes were in a region of extensor muscles. Therefore, only six electrodes contributed significantly and may be sufficient for the recognition process. The processing time for each window was 62.5 ms, equivalent to 250 measurements over time, while other studies, such as [36], have larger window sizes for an equal or lower percentage of recognition. The procedure presented here is a valid method to define specific movements from EMG measurements since it has short processing times and includes transformations to new spaces, resulting in a classification model already trained for a group of eight subjects. The percentage of recognition is comparable with models generated by other published studies, though only time domain features were used here. The large number of different movements evaluated here is another factor that affected the resolution of our classification algorithms. Since a future objective is to increase the number of defined movements, it is essential to find features that best differentiate between the classes or evaluate new transformation spaces that maximize the differentiation between the classes. The present work enhanced the biomechanical model of the wrist in OpenSim, which is necessary to simulate the movements detected with the proposed classification model. Thus, this study contributes to the application of the output of movement classification methods in a virtual system for the analysis of multifunctional prosthesis response.

Declaration of Conflicting Interest. The authors declare that there is no conflict of interest.

References

1. Liu, Y., Ning, Y., He, J., Li, S., Zhou, P., Zhang, Y.: Internal muscle activity imaging from multi-channel surface EMG recordings: a validation study. In: 2014 36th Annual International Conference of the IEEE Engineering in Medicine and Biology Society, EMBC 2014, pp. 3559–3561 (2014)
2. Sun, Y., Li, C., Li, G., Jiang, G., Jiang, D., Liu, H., Zheng, Z., Shu, W.: Gesture recognition based on kinect and sEMG signal fusion. Mob. Netw. Appl. **23**(4), 797–805 (2018)
3. Wahid, M.F., Tafreshi, R., Al-Sowaidi, M., Langari, R.: Subject-independent hand gesture recognition using normalization and machine learning algorithms. J. Comput. Sci. **27**, 69–76 (2018)
4. He, J., Sheng, X., Zhu, X., Jiang, C., Jiang, N.: Spatial information enhances myoelectric control performance with only two channels. IEEE Trans. Industr. Inf. **PP**(c), 1 (2018)
5. Saikia, A., Kakoty, N.M., Phuka, N., Balakrisxnan, M., Sahai, N., Paul, S., Bhatia, D.: Combination of EMG features and stability index for finger movements recognition. Proc. Comput. Sci. **133**, 92–98 (2018)
6. Resnik, L., Huang, H.H., Winslow, A., Crouch, D.L., Zhang, F., Wolk, N.: Evaluation of EMG pattern recognition for upper limb prosthesis control: a case study in comparison with direct myoelectric control. J. NeuroEng. Rehabil. **15**(1), 113 (2018)
7. Feng, N., Shi, Q., Wang, H., Gong, J., Liu, C., Lu, Z.: A soft robotic hand: design, analysis, sEMG control, and experiment. Int. J. Adv. Manuf. Technol. **97**(1–4), 319–333 (2018)
8. Menegaldo, L.L.: Real-time muscle state estimation from EMG signals during isometric contractions using Kalman filters. Biol. Cybern. **111**(5–6), 335–346 (2017)
9. Kim, M., Chung, W.K.: Spatial sEMG pattern-based finger motion estimation in a small area using a microneedle-based high-density interface. IEEE Robot. Autom. Lett. **3**(1), 234–241 (2017)
10. Sheibani, A., Pourmina, M.A.: Study and analysis of EMG signal and its application in controlling the movement of a prosthetic limb. Health Technol. **6**(4), 277–284 (2016)
11. Paleari, M., Di Girolamo, M., Celadon, N., Favetto, A., Ariano, P.: On optimal electrode conguration to estimate hand movements from forearm surface electromyography. In: Proceedings of the Annual International Conference of the IEEE Engineering in Medicine and Biology Society, EMBS 2015, pp. 6086–6089 (2015)
12. Castro, M.C., Arjunan, S.P., Kumar, D.K.: Selection of suitable hand gestures for reliable myoelectric human computer interface. BioMed. Eng. Online **14**(1), 111 (2015)
13. Kumar, D.K., Arjunan, S.P., Singh, V.P.: Towards identification of finger flexions using single channel surface electromyography – able bodied and amputee subjects. J. NeuroEng. Rehabil. **10**(1), 17 (2013)
14. Jeong, E.C., Kim, S.J., Song, Y.R., Lee, S.M.: Comparison of wrist motion classification methods using surface electromyogram. J. Cent. South Univ. **20**(4), 960–968 (2013)
15. Daley, H., Englehart, K., Hargrove, L., Kuruganti, U.: High density electromyography data of normally limbed and transradial amputee subjects for multifunction prosthetic control. J. Electromyogr. Kinesiol. **22**(3), 478–484 (2012)
16. Dennis, T., He, H., Todd, K.: Study of stability of time-domain features for electromyographic pattern recognition. J. NeuroEng. Rehabil. **7**, 21 (2010)
17. Arjunan, S.P., Kumar, D.K.: Decoding subtle forearm exions using fractal features of surface electromyogram from single and multiple sensors. J. NeuroEng. Rehabil. **7**(1), 110 (2010)

18. Walbran, S.H., Calius, E.P., Dunlop, G.R., Anderson, I.A.: A technique for optimizing electrode placement for electromyographic control of prostheses. In: Proceedings of the 31st Annual International Conference of the IEEE Engineering in Medicine and Biology Society: Engineering the Future of Biomedicine, EMBC 2009, pp. 1331–1334 (2009)
19. Ryait, H.S., Arora, A.S., Agarwal, R.: Study of issues in the development of surface EMG controlled human hand. J. Mater. Sci. Mater. Med. **20**(Suppl. 1), 107 (2009)
20. Smith, R.J., Tenore, F., Huberdeau, D., Cummings, R.E., Thakor, N.V.: Continuous decoding of nger position from surface EMG signals for the control of powered prostheses. In: 2008 30th Annual International Conference of the IEEE Engineering in Medicine and Biology Society, pp. 197–200 (2008)
21. Christov, I., Raikova, R., Angelova, S.: Separation of electrocardiographic from electromyographic signals using dynamic ltration. Med. Eng. Phys. **57**, 110 (2018)
22. Veer, K.: A flexible approach for segregating physiological signals. Meas. J. Int. Meas. Confed. **87**, 21–26 (2016)
23. Willigenburg, N.W., Daertshofer, A., Kingma, I., van Dieën, J.H.: Removing ECG contamination from EMG recordings: a comparison of ICA-based and other filtering procedures. J. Electromyogr. Kinesiol. **22**(3), 485–493 (2012)
24. Marque, C., Bisch, C., Dantas, R., Elayoubi, S., Brosse, V., Pérot, C.: Adaptive filtering for ECG rejection from surface EMG recordings. J. Electromyogr. Kinesiol. **15**(3), 310–315 (2005)
25. Kumar, D.K., Melaku, A.: Electrode distance and magnitude of SEMG. In: Proceedings of the Second Joint Engineering in Medicine and Biology, 24th Annual Conference and the Annual Fall Meeting of the Biomedical Engineering Society EMBS/BMES Conference, vol. 3, pp. 2477–2480 (2002)
26. Baratta, R.V., Solomonow, M., Zhou, B.H., Zhu, M.: Methods to reduce the variability of EMG power spectrum estimates. J. Electromyogr. Kinesiol. **8**(5), 279–285 (1998)
27. Repository of Dr. Rmi N. Khushaba online. http://www.rami-khushaba.com/electromyogram-emg-repository.html
28. Khushaba, R.N., Kodagoda, S.: Electromyogram (EMG) feature reduction using mutual components analysis for multifunction prosthetic fingers control, pp. 1534–1539. IEEE, December 2012 https://doi.org/10.1109/icarcv.2012.6485374
29. Lei, M., Wang, Z., Feng, Z.: Detecting nonlinearity of action surface EMG signal. Phys. Lett. Sect. A: Gener. Atom. Solid State Phys. **290**(5–6), 297–303 (2001). https://doi.org/10.1016/s0375-9601(01)00668-5
30. Phinyomark, A., Phukpattaranont, P., Limsakul, C.: Feature reduction and selection for EMG signal classification. Expert Syst. Appl. **6**(8), 7420–7431 (2012). https://doi.org/10.1016/j.eswa.2012.01.102
31. Havlik, J., Uhlir, J., Horcik, Z.: Comparison of k-means and bayes classifiers for human body motions classification. In: IFMBE Proceedings. FEE CTU (2009)
32. Fisher, R.A.: The use of multiple measurements in taxonomic problems. Ann. Eugen. **7**, 179–188 (1936)
33. Gutierrez-Osuna, R.: CSCE 666 Pattern Analysis—CSE@TAMU. http://courses.cs.tamu.edu/rgutier/csce666 f13/
34. Lisboa, P.J.G., Ellis, I.O.: Cluster-based visualisation with scatter matrices. Pattern Recogn. Lett. **29**, 1814–1823 (2008)
35. Seth, A., Habib, A.: SimTK Opensim, National Institutes of Health (NIH). https://simtk.org/projects/opensim
36. Oskoei, M.A., Hu, H.: Myoelectric control systems - to survey. Biomed. Signal Process. Control **2**(4), 275–294 (2007). https://doi.org/10.1016/j.bspc.2007.07.009

37. Amezquita-Garcia, J.A., Bravo-Zanoguera, M.E.: Bioingenieria, UABC. https://simtk.org/projects/moving-fingers
38. Gonzalez, R.V., Buchanan, T.S., Delp, S.L.: How muscle architecture and moment arms affect wrist flexion-extension moments. J. Biomech. **30**, 705–712 (1997)

Characterization of Intrinsic Mode Functions of the Electrical Cochlear Response

Norma Castañeda-Villa(✉), Pilar Granados-Trejo, and Juan Manuel Cornejo-Cruz

Departamento de Ingeniería Eléctrica,
Universidad Autónoma Metropolitana-Iztapalapa, Mexico City, Mexico
ncv@xanum.uam.mx

Abstract. The aim of this paper was to characterize the Intrinsic Mode Functions (IMFs) of the Electrical Cochlear Response (ECR) obtained by Ensemble Empirical Mode Decomposition. Sample Entropy was used to identify the IMFs related to background noise, Cochlear Implant artefact, and ECR. Finally, Noise Reduction Percentage was used to quantify the decrease of artefact in the ECR reconstruction.

Keywords: Electrical cortical response · Ensemble Empirical Mode Decomposition · Intrinsic Mode Functions · Sample entropy · Noise Reduction Percentage

1 Introduction

A Cochlear Implant (CI) is the only technological alternative to provide hearing to patient with profound bilateral neurosensorial deaf diagnosis. CI translate sound intensity and frequency into an electrical stimulation code which is sent to patient auditory nerve through an electrode array-up to twenty two electrodes- located along cochlea.

After surgical implantation patient success rehabilitation depends on factors such as age, general health condition and proper electrode array electric current dynamic range setting. For postlingual adult patient proper current adjustment is possible by getting feedback about sound quality provided by CI. However this is not the case for implanted children due to their short age and lack of alternative communication resources. Even though there are objective methods for predicting current level without conscious patient participation their predictive value is not good enough, so patient collaboration is still necessary. A major drawback of these methodologies is the obligated pediatric patient auditory behavioral observation period that reduce rehabilitation opportunities.

Alternative to actual objective methodologies Cornejo et al. propose the use of the so-called Electrical Cochlear Response (ECR) [1] which is the hearing tissue response to electrical stimulation every time CI processes an input sound. Its wave shape resembles sinusoidal positive phase which peak amplitude is related to sound intensity of incoming sound. ECR is an implanted patient electric intrinsic response and do not depend on the CI manufacturer.

© Springer Nature Switzerland AG 2020
C. A. González Díaz et al. (Eds.): CLAIB 2019, IFMBE Proceedings 75, pp. 228–233, 2020.
https://doi.org/10.1007/978-3-030-30648-9_30

ECR is obtained by averaging a number of 75 ms EEG epoch picked up time locked to variable intensity and frequency sound stimulus presentation, 20 ms "Pip", while patient is asleep inside a dark anechoic room and using CI in everyday operation mode. Hearing tissue response contained in EEG epochs recorded from scalp surface electrodes are noise contaminated due to various artifact sources: myogenic, spontaneous brain activity, EEG electrode-skin interface and operation device itself.

One of the most popular signals processing technique used to reduce artifact is Independent Components Analysis [2]; however, multichannel EEG recordings are necessary for its application, which it is not always available in clinical practice, including the ECRs which are recorded using only two EEG channels (see Materials and methods section for details).

Instead, Empirical Mode Decomposition (EMD) has demonstrate to be an efficient single-channel signal processing technique to decomposing nonstationary time series; originating from nonlinear systems in an adaptive approach without predefined basis function.

EMD generates a group of Intrinsic Mode Functions (IMFs) through an iterative process; decomposition is based on direct extraction of the energy associated with various intrinsic time scales [3]. Among the applications of EMD to processing single-channel biomedical signals are: (1) reduction of muscular artefact in EEG [4], (2) ECG enhancement and QRS detection [5], (3) reduction of heart sound interference from lung sound [6] and (4) detection of glottal closure on Electroglottograph (EGG) [7]; just to name a few examples.

EMD can be summarized in five steps:

1. Extrema identification (minimum and maximum) of signal *x(t)*.
2. Interpolating between minima and maxima to obtain the lower envelope, $e_{\min}(t)$, and upper envelope $e_{\max}(t)$
3. Compute mean between envelops, $m(t) = \frac{[e_{min}(t) + e_{max}(t)]}{2}$
4. Detail extraction of the so-called Intrinsic Mode Function (IMF), $d(t) = x(t) - m(t)$
5. Iterate on the residual $m(t)$

This process continues until each IMF extracted is defined as an oscillatory function with:

(1) Equal number of extrema and zero crossings (or at most differed by one) and
(2) The envelopes are symmetric with respect to zero; implying means value of each IMF equal to zero.

As any signal processing technique, EMD has advantages and disadvantages. Regarding advantages, EMD does not require any known basis function and is considered a fully data driven mechanism suited for nonlinear processes and nonstationary signals [3]. In contrast, one of the major disadvantages of the original EMD is the frequent appearance of mode mixing, which is defined as a single IMF either consisting of signals of widely different scales, or a signal of a similar scale residing in different

IMF components. When mode mixing occurs, an IMF can conclude to have physical meaning by itself, suggesting incorrectly that there may be different physical processes represented in a mode [8]. In order to solve the EMD mode mixing problem, alternative algorithms have been developed, for example: Ensemble Empirical Mode Decomposition (EEMD) [9]. In this work ECRs were decomposed using EEMD [8]. IMFs related to artifact and response were identified using Sample Entropy [10]. Finally, it was determined reduction of the artefacts in the reconstructed ECR through the Noise Reduction Percentage [11].

2 Materials and Methods

Eight ECRs from a group of six unilateral CI users were analyzed (two users of CI manufacture 1 and four users of CI manufacture 2; CI_{M1} and CI_{M2}, respectively). Figure 1 shows the methodology used in this research: (a) Pip sounds, (20 ms duration) @ 60 dBHL were presented via a loudspeaker located 1 m away from patient; pips frequency was varied according with the central frequency assign to individual electrode. Standard Auditory Brainstem Response (ABR) evoked potentials electrode montage was used: Cz(+), A1(−), A2(−) and Fpz as GND; EEG signal was recorded by using a Neuroscan, Synamps system, 20 kHz sampling rate and 0.1 to 300 Hz band pass filtering (b) ECR was obtained by averaging one hundred EEG epochs per central frequency. (c) Decomposition was carrying out for contralateral ECR, opposite side to CI location, for three different central frequencies/stimulation electrodes-F1, F2 and F4. (d) Characterization of IMFs was carried out by means of Sample entropy (*SampEn*) which measures statistics complexity and regularity of a time series [11].

SampEn was calculated in all IMFs obtained by EEMD algorithm; functions related to noise (I) and CI artefact (II) were eliminated and only functions related with the response (III) were used to the ECR reconstruction. e) Finally, one metrics was used to measure the performance of this procedure to reduce the artefacts of ECR: the Noise Reduction Percentage (NRP), as well known as the mean energy reduction criterion, NRP is defined by :

$$\mathrm{NRP}(\%) = \left\{ \frac{\mathrm{E}(\mathrm{RCE_o}(\mathrm{n})^2) - \mathrm{E}(\mathrm{RCE_R}(\mathrm{n})^2)}{\mathrm{E}(\mathrm{RCE_o}(\mathrm{n})^2)} \right\} * 100 \tag{1}$$

where $\mathrm{RCE_o}(\mathrm{n})$ is the original signal and $\mathrm{RCE_R}(\mathrm{n})$ is the reconstructed ECR without artefacts; n is the number of signal samples.

The experimental procedures involving human subjects described in this work were approved by the UAM-I Review Board. During ECR test pediatric patient was accompanied by parent who signs an informed consent before the study.

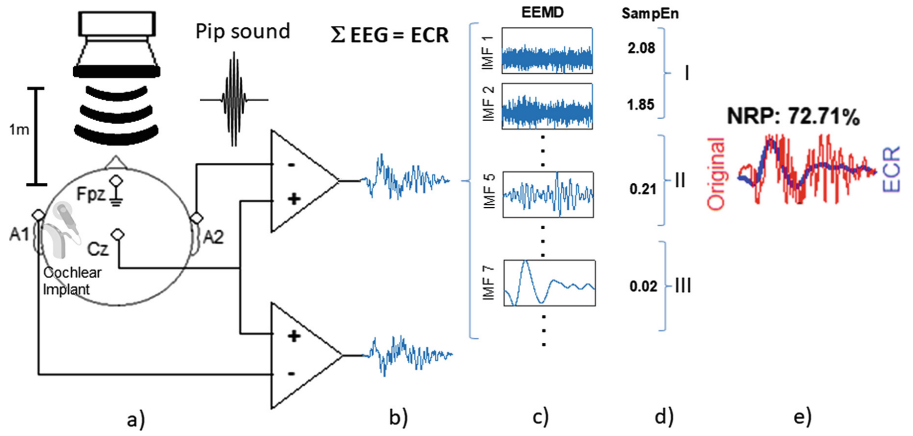

Fig. 1. Scheme of the proposed methodology: (a) by using pip stimuli EEG epochs time locked to stimulus are recorded by a bipolar electrode montage; (b) Ipsi and contralateral ECR is obtained by averaging 100 EEG epochs. (c) EEMD for decomposing ECR (d) *SampEn* index to characterize IMFs e) Finally NRP (%) to measure artefact reduction in response.

3 Results

Figure 2 shows an example of IMFs of ECR (**S5-CI$_{M2}$-F2**) - subject S5, manufacturer 2 and frequency F2-. Original ECR (up-left) was decomposed into 11 IMFs. By an expert visual inspection and *SampEn* values IMFs were categorized. In Fig. 2 IMFs **I** correspond to background noise (IMF1-2) which is present throughout the recording. IMFs **II** (CI artefacts) are generally associated with the stimulus presentation; notice

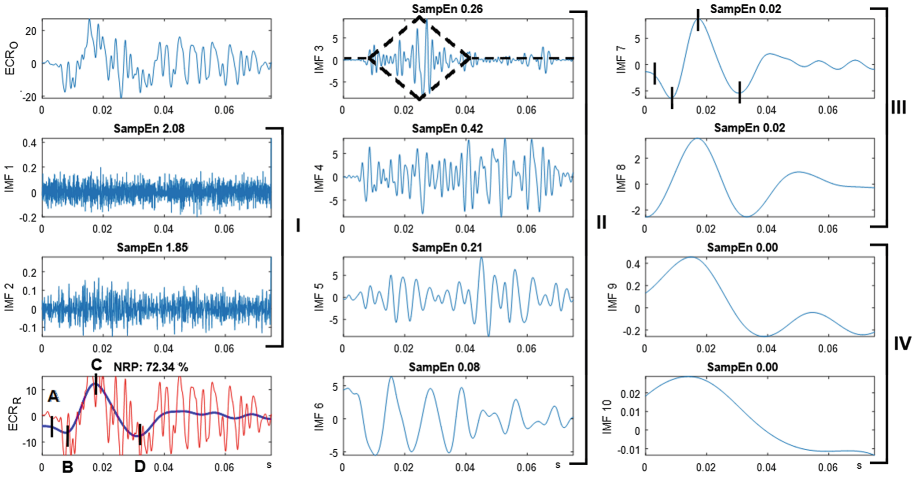

Fig. 2. Example of one ECR signals (S5-CI$_{M2}$-F2) decomposition. ECR$_O$: original signal, ECR$_R$: reconstructed signal. IMF: Intrinsic mode functions and *SampEn*: sample entropy.

IMF3 has waveform and time length of pip stimulus. IMFs **III** have the waveform expected for ECR, (IMF7-8) where it is possible to recognize the peaks sequence of the response. IMFs **IV** show *SampEn* close to zero, (IMF9-and 10). Finally, bottom-left graph corresponds to ECR reconstructed from non-artifact IMFs (blue line) overlapping on original signal (red line).

Table 1 shows quantitative analysis for eight ECR IMFs. Average *SampEn* of IMFs related to background noise is close to 2 (1.84 ± 0.15). On the other hand, IMFs related to stimulus have average values close to 0.2 (0.16 ± 0.10). Finally, IMFs with the ECR waveform have *SampEn* equal to 0.03 ± 0.00; average NRP% after eliminate artefactual IMFs was in average 68.36 ± 15.40.

Table 1. Decomposition quantitative analysis for eight different ECRs

EEMD	*SampEn*			*NRP*
Recording	I	II	III	*(%)*
S1-CI_{M1}-F1	1.72(3)	0.05(3)	0.03(2)	38.94
S1-CI_{M1}-F4	1.75(3)	0.09(3)	0.03(2)	59.60
S2-CI_{M2}-F1	1.72(2)	0.19(3)	0.03(2)	87.53
S3-CIB2-F1	1.70(3)	0.05(3)	0.03(2)	80.54
S4-CI_{M1}-F1	1.80(3)	0.14(3)	0.03(1)	60.44
S5-CI_{M2}-F1	1.95(2)	0.21(4)	0.03(1)	79.50
S5-CI_{M2}-F2	1.97(3)	0.25(4)	0.02(1)	72.34
S6-CI_{M2}-F1	2.12(1)	0.34(5)	0.03(2)	68.02
Average	1.84	0.16	0.03	68.36
±Std	0.15	0.10	0.00	15.40

SampEn: Sampling Entropy. EEMD: Ensemble EMD. S#: Subject number. CI_{M1}: Cochlear Implant manufacture 1 and CI_{M2}: Cochlear Implant manufacture 2. **I**: Background noise, **II**: Stimulus, and **III**: ECR. Values in parentheses indicate the number of IMFs in each block

4 Conclusion

In this research the ECR recordings were decomposed using EEMD. It was possible to characterized four groups of IMFs: (I) related to background noise (II) associated with stimulus presentation and (III) functions with the expected ECR waveform as observed for high frequency intracochlear electrodes, 1500 to 7500 Hz, located near top cochlea. Previous experimental work show that noise masks ECR mainly for intracochlear electrodes corresponding to cochlear implant low frequency band, 100 to 1500 Hz, located on cochlea base. Finally, (IV) functions associated with the tendency of the original signal. EEMD showed an adequate performance to decompose the ECRs. *SampEn* seems to be a useful parameter for IMFs identification; this has to be validating with recordings obtained at different stimulation frequency and intensities. Although it is necessary to increase analyzed dataset, it is possible the say that EEMD could help on detection of the ECR even in registers with a high level of noise.

Importance for denoising ECR is that a clinical expert make a judgment about proper CI programming and auditory rehabilitation strategy for pediatric implanted patient based on ECR minimum sound intensity level detection, wave shape and peak amplitude.

Conflict of Interest. The authors declare that there is no conflict of interest.

References

1. Cornejo-Cruz, J.M., Granados-Trejo P.: Method and apparatus for obtaining and registering an electrical cochlear response ("ECR") (2011)
2. Comon, P.: Independent component analysis, a new concept? Signal Process. **36**, 287–314 (1994)
3. Huang, N., et al.: The empirical mode decomposition and the Hilbert spectrum for nonlinear and non-stationary time series analysis. Proc. R. Soc. A Phys. Eng. Sci. **454**(1971), 904–993 (1998). https://doi.org/10.1098/rspa.1998.0193
4. Chen, X., Liu, A., Peng, H., Ward, R.K.: A preliminary study of muscular artifact cancellation in single-channel EEG. Sens. (Switzerland) **14**(10), 18370–18389 (2014). https://doi.org/10.3390/s141018370
5. Pal, S., Mitra, M.: Empirical mode decomposition based ECG enhancement and QRS detection. Comput. Biol. Med. **42**(1), 83–92 (2012). https://doi.org/10.1016/j.compbiomed.2011.10.012
6. Mondal, A., Bhattacharya, P.S., Saha, G., Mondal, A., Bhattacharya, P.S., Saha, G.: Reduction of heart sound interference from lung sound signals using empirical mode decomposition technique reduction of heart sound interference from lung sound signals using empirical mode decomposition technique. J. Med. Eng. Technol. **35**(6–7), 344–356 (2011). https://doi.org/10.3109/03091902.2011.595529
7. Colominas, M.A., Schlotthauer, G., Torres, M.E.: Improved complete ensemble EMD: A suitable tool for biomedical signal processing. Biomed. Signal Process. Control **14**(1), 19–29 (2014). https://doi.org/10.1016/j.bspc.2014.06.009
8. Wu, Z., Huang, N.E.: Ensemble empirical mode decomposition: a noise assisted data analysis method. Adv. Adapt. Data Anal. **1**(1), 1–41 (2009). https://doi.org/10.1142/S1793536909000047
9. Czarniak, L.J.: Effect of stimulus intensity on cortical potentials in cochlear implant recipients. Independent Studies andCapstones. Paper 630. Program in Audiology and Communication Sciences, Washington University School of Medicine (2011). http://digitalcommons.wustl.edu/pacs_capstones/630
10. Richman, J.S., Moorman, J.R.: Physiological time-series analysis using approximate entropy and sample entropy. Am. J. Physiol. Hear. Circ. Physiol. **278**, 2039–2049 (2000). https://doi.org/10.1152/ajpheart.2000.278.6.h2039
11. Hadjileontiadis, L.J., Panas, S.M.: Adaptive reduction of heart sounds from lung sounds using fourth-order statistics. IEEE Trans. Biomed. Eng. **44**(7), 642–648 (1997). https://doi.org/10.1109/10.594906

Remote Optical Estimation of Respiratory Rate Based on a Deep Learning Human Pose Detector

Isaac René Aguilar Figueroa(✉), Jesús Vladimir Martínez Nuño, and Eduardo Gerardo Mendizabal-Ruiz

Departamento de Ciencias Computacionales, Universidad de Guadalajara, Guadalajara, Jalisco, Mexico
{isaac.aguilar,vladimir.martinez}@alumnos.udg.mx, gerardo.mendizabal@academicos.udg.mx

Abstract. Respiratory rate (RR) is a handy parameter in the clinical field since it allows the timely detection of diverse pathologies. However, RR is currently acquired using expensive devices which are attached to the patients and therefore may be uncomfortable to use. In this paper, we present a method for the estimation of respiratory rate through a non-contact optical method based on a deep learning human pose detector. The proposed method is tested using a database of videos of subjects performing different respiratory maneuvers to obtain the respiratory signal, and the instantaneous respiratory rate automatically. The proposed method obtained a correlation of 0.8 on static breathing maneuvers with respect to the ground truth signal. For the instantaneous respiratory rate, it was observed through a time-frequency analysis, that the obtained signal shares the same frequency bandwidth as that contained in the ground truth, indicating that the information of both signals is on the same frequency band. Our results indicate the feasibility of employing the proposed method for estimation respiratory rate frequency.

Keywords: Deep learning · Breathing frequency · Computer vision

1 Introduction

The respiratory cycle is a vital process for the human being since it is in charge of the gaseous exchange of atmosphere and blood, the distribution of oxygen to the body tissues, and the ejection of carbon dioxide from it. The respiratory system is composed of a series of organs and muscles that work in synergy to complete the process. The lungs are responsible for carrying out said gaseous exchange, the respiratory tract is in charge of filtering the air that enters to the lung, and the intercostal muscles and the diaphragm which are the primary muscles of the process for controlling the total volume of the lung [1].

Respiratory rate (RR), which is one of the vital signs of humans, is measured by counting the number of breaths per minute (bpm). Under normal conditions

© Springer Nature Switzerland AG 2020
C. A. González Díaz et al. (Eds.): CLAIB 2019, IFMBE Proceedings 75, pp. 234–241, 2020.
https://doi.org/10.1007/978-3-030-30648-9_31

is set to 12 to 20 bpm in an adult person. A respiration rate under 12 or over 25 bpm while resting is considered abnormal [2].

Currently, there exist systems for the estimation of the RR such as the optic fiber breath rate sensor, the impedance pneumography, and the devices based in capnography. New techniques for automatically monitoring respiratory rate are in development, such as estimation of respiratory rate from the electrocardiogram, photoplethysmogram, and accelerometry signals [3].

Deep learning is one of the new topics in Machine Learning and Artificial Intelligence. Deep learning architectures have been applied in different areas of interest to solve complex problems with various degrees of difficulty. Deep learning has been used in biomedical research with exciting results including the decodification of neural activity and control activation of a person with quadriplegia [4], the recognition of physiological stress from breathing patterns [5], and the automatic detection of diabetic retinopathy and diabetic macular edema in retinal fundus photographs in [6].

In this paper, we propose a method for the remote optical estimation (ROE) of RR and the Instantaneous Respiratory Rate (IRR), through a non-contact optical method based on a deep learning human pose detector. Our method relies on the detection of the variations of light present in the thorax of the subjects recorded in a video while performing respiratory maneuvers. To keep track of those maneuvers, we use a deep learning algorithm as well as image and signal processing to acquire the breathing activity of each volunteer. Our results indicate the feasibility of using the proposed method for the estimation of respiratory rate.

2 Methods

The database consists of twelve videos from four volunteers (two men and two women) and is freely available for research [7]. The videos were taken with a camera of a smartphone with a resolution of 1920×1080 pixels and different sampling rates. The videos contained voluntaries performing different respiratory maneuvers, some of them controlled by a metronome, and others were spontaneous breathing. The database also included the reference respiratory signal (acquired from a thermal sensor placed around the mouth and nose of the volunteers at a sampling rate of 25 Hz).

The first two subjects performed the following maneuvers:

1. Spontaneous Breathing with Static Movement (SBSM) for two minutes.
2. Breathing with Static Movement (BSM) at 0.2 Hz for two minutes.
3. Breathing with Dynamic Movement (BDM) at 0.2 Hz for two minutes.

The remaining two subjects performed the following maneuvers:

1. Spontaneous Breathing with Dynamic Movement (SBDM) for two minutes.
2. BSM at 0.5 Hz for two minutes.
3. BDM at 0.5 Hz for two minutes.

The proposed method consists of five consecutive steps: (i) selection of the region of interest (ROI) on each frame of the video, (ii) aligning of the ROIs among all frames, (iii) the estimation of the respiratory rate signal, (iv) processing of the acquired signal, and (v) estimation of the RR and IRR.

2.1 Selection of the Region of Interest

OpenPose is a deep learning-based algorithm which allows real-time multi-person detection of the human body, hand, facial, and foot keypoints (in total 135 keypoints) on single images [8]. The implementation of this algorithm is freely available for research and non-commercial use [9].

The system takes each frame from the given a video as a RGB image input of a multi-stage Convolutional Neural Network (CNN) to jointly produce 2D locations of anatomical keypoints. The CNN produces a 2D set of confidence maps and 2D vector of part affinity fields (PAF), then a feedforward network is used to predict 2D confidence maps of anatomical keypoints as well as 2D vector fields of PAFs. From each of these vector fields, it is obtained a vector per limb, so each image location encodes a 2D vector. Finally, each confidence map and PAF are parsed using greedy inference to output the 2D keypoints (see Fig. 1b) for the subject in the video written in a JSON file [10].

To estimate the ROI on each frame of the video, we chose the chest keypoint from the JSON file, then a region of 260×150 pixels centered on the thoracic area of each subject was selected (Fig. 1).

Fig. 1. Example of OpenPose results on a single frame. (a) initial frame without processing. (b) OpenPose image output with 2D keypoints draw on the subject. (c) estimated ROI of 260×150 pixels for a single frame.

2.2 Aligning of the ROIs Among All Frames

Once the ROI has been selected on each frame, it is necessary to align the obtained images to eliminate the movements that had no relationship with

breathing. To perform this alignment, we used a motion model called "translation". An Affine transform is computed as a 2×3 sized warp matrix. Once this matrix is estimated for each frame, the images can be brought into alignment. The proposed alignment algorithm consist of the following steps:

1. Convert each frame to grayscale.
2. Use the motion model "translation".
3. Allocate space to store the motion model.
4. Define a termination criteria that tells the algorithm when to stop.
5. Estimate the warp matrix.
6. Apply the warp matrix to one of the images to align it with the other image.

In this case, our first image is our reference image, which is the selected ROI with the first frame of the video. All the following frames will seek to align with the reference image. It should be mentioned that the size of the ROI (260×150 pixels) is maintained after the image registration.

2.3 Estimation of the Respiratory Rate Signal

The proposed algorithm is designed to estimate the respiratory movement signal by analyzing the changes in the intensity of the reflected light caused by the breathing movements in the ROI captured in the videos. The algorithm to process the video after completing the alignment is to take the average intensity of the pixels in the red, green, and blue channels for each frame. As a result of the intensity analysis for each channel, the waveform of the respiration signal corresponding to each maneuver was obtained. Then, the average of the three channels intensities was calculated for each frame within the ROI, at each instant of time ($S(t)$), according to:

$$S(t) = \frac{1}{3D}\left(\sum_{(m,n)} i_R(m,n,t) + \sum_{(m,n)} i_G(m,n,t) + \sum_{(m,n)} i_B(m,n,t)\right) \quad (1)$$

where $i_x(m,n,t)$ is the intensity value of the pixel at the m-th row and n-th column of the red, green or blue channel within the ROI containing a total of D (260×150) pixels [11].

2.4 Processing of the Acquired Signal

The estimated signal is sampled to 25 Hz to match the sampling frequency of the reference signal. The spectrum of this signal was examined by calculating the Fast Fourier Transform (FFT). According to [12] the normal respiratory rate range goes from 0.1 Hz to 0.5 Hz corresponding to 5–60 bpm. Therefore, a second-order bandpass Butterworth filter was designed having the lower cutoff frequency at 0.1 Hz and the higher cutoff frequency at 0.5 Hz. Finally, the signal tendency was removed by subtracting the mean of it to itself.

To find the similarity between the obtained signal $S(t)$ and the available reference signal (i.e., ground truth) $Z(t)$ the correlation index was calculated according to:

$$\rho(S(t), Z(t)) = \frac{cov(S(t), Z(t))}{\sigma_S \sigma_Z} \tag{2}$$

where *cov* is the covariance, σ_S is the standard deviation of estimated signal, and σ_Z is the standard deviation of reference.

2.5 Instantaneous Respiratory Rate

For the estimation of the IRR, we computed the envelope of each estimated respiratory movement signal using the Hilbert transform. Initially removing the mean of the signal and add it back after the computation of the envelope. A further time-frequency analysis was done using spectrogram, dividing the signal input into 8 segments with 50% overlap and each segment was windowed with a Hamming window, to evaluate the bandwidth of the estimated IRR against the reference IRR.

The performance of the IRR estimation was measured on the test data using the normalized root-mean-squared error (NRMSE) between both signals (*IRREstimate* and *IRRreference*).

3 Results and Discussion

The changes in the intensity of the reflected light caused by the breathing movements in the ROI captured were calculated and analyzed, given that the estimated signal presented a non-linear tendency it was necessary to linearize such signal. In Fig. 2 it can be observed the comparison between a processed signal and a reference signal for a BSM at 0.2 Hz, starting with the calculated signal (dotted black), which presented noise from the video processing that was removed after the signal processing obtaining the processed signal (orange) which is highly correlated with the reference signal (blue).

As for the IRR, in Fig. 3, it can be observed the time-frequency analysis of an SBDM signal through a spectrogram, showing similar frequency behavior between the calculated and the reference IRR signal, which is corroborated by the NRMSE listed in Table 1.

By calculating the average of correlation of the two signals for each maneuver (see Table 1), it can be observed that in the cases in which the subjects were static, a more significant correlation is obtained speaking of the signal of the respiratory movement. This may be because although the image alignment was made, noise is still obtained due to lateral movements other than those of breathing when the subjects are in motion. Regarding the NRMSE obtained from the comparison of the IRRestimate and IRRreference signals, high values can be observed in DBM at 0.2 Hz and SBDM. This may be due to the same problem regarding the alignment of images or the respiratory rhythm of the subjects test.

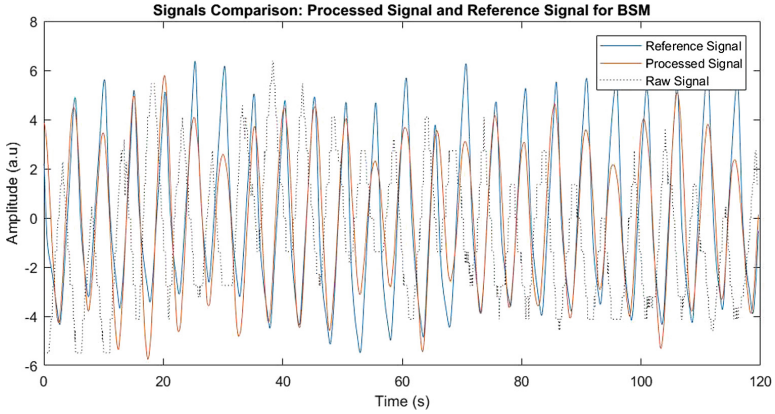

Fig. 2. Comparison between the estimated signal (raw Signal), the processed signal, and the reference Signal.

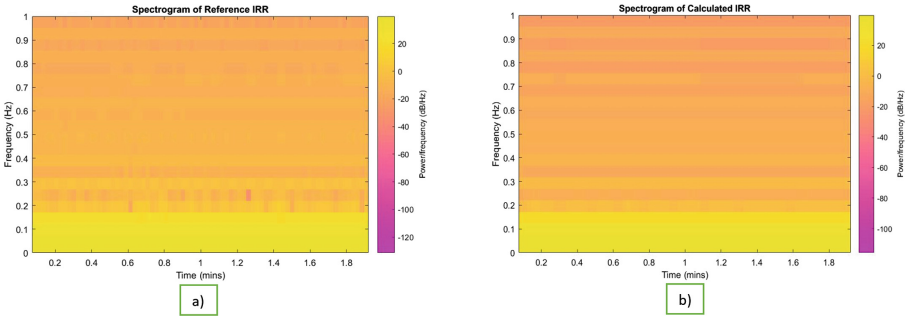

Fig. 3. Spectrogram comparison between IRR's. (a) spectrogram of reference IRR. (b) spectrogram of calculated IRR

Table 1. Performance results of estimated respiratory movement signal (average correlation) and instantaneous respiratory rate (average NRMSE).

Respiratory maneuvers	Average correlation	Average NRMSE
BSM at 0.2 Hz	0.85 ± 0.04	10.62 ± 3.58
SBSM	0.83 ± 0.05	7.15 ± 0.39
BSM at 0.5 Hz	0.73 ± 0.01	2.49 ± 0.07
BDM at 0.5 Hz	0.58 ± 0.11	4.41 ± 1.13
BDM at 0.2 Hz	0.57 ± 0.04	20.40 ± 4.18
SBDM	0.51 ± 0.02	21.57 ± 12.77

Regarding spontaneity, it can be because when the subject does not concentrate on breathing, they performed exaggerated lateral movements.

4 Conclusions

In this paper, we obtained the breathing activity of different subjects performing static and dynamic maneuvers through a non-contact optical method via an algorithm that automatically selects a ROI through a deep learning pose estimation method.

Based on the obtained results, most of the static movement maneuvers represent a highly-correlated result, but it is prominent the average correlation difference between static movement and dynamic movement maneuvers, this is due to the video processing, adding noise to the signal that is also contained in the breathing information frequency range. As for the IRR through the spectrogram analysis, it is notable that the calculated and reference signal share the same frequency bandwidth. For future work, it is proposed a separating multivariate signal processing technique hoping to separate the added video processing noise from the breathing activity signal without eliminating its information.

Acknowledgements. We want to acknowledge Rebeca Romo-Vazquez and Hugo Vélez Pérez for their assistance with the signal processing and comments that significantly improved the proposed work.

Conflict of Interest. The authors declare no conflict of interest.

References

1. Yoshikawa, M., Yamamoto, Y., Tomoda, K., Fujita, Y., Yamauchi, M., Osa, T., Uyama, H., Okamoto, N., Kurumatani, N., Kimura, H.: Prevalence of chronic obstructive pulmonary disease in independent community-dwelling older adults: The Fujiwara-kyo study. Geriatrics & Gerontology International, p. 17 (2017). https://doi.org/10.1111/ggi.13091.
2. Kozier, B., et al.: Fundamentos de enfermería. Conceptos, procesos y práctica, chapter 27, pp 539–561. McGraw-Hill
3. Al-Khalidi, F.Q., Saatchi, R., Burke, D., Elphick, H., Tan, S.: Respiration rate monitoring methods: a review. Pediatr. Pulmonol. **46**(6), 523–529 (2011). https://doi.org/10.1002/ppul.21416
4. Bouton, C.E., Shaikhouni, A., Annetta, N.V., et al.: Restoring cortical control of functional movement in a human with quadriplegia. Nature **533**, 247–250 (2016). https://doi.org/10.1038/nature17435
5. Cho, Y., Bianchi-Berthouze, N., Julier, S.J.: DeepBreath: Deep Learning of Breathing Patterns for Automatic Stress Recognition using Low-Cost Thermal Imaging in Unconstrained Settings (2017). https://doi.org/10.1109/ACII.2017.8273639.
6. Gulshan, V., Peng, L., Coram, M., et al.: Development and validation of a deep learning algorithm for detection of diabetic retinopathy in retinal fundus photographs. JAMA **316**, 2402–2410 (2016). https://doi.org/10.1001/jama.2016.17216
7. Vázquez-Segura, J.A,, Mejía-Rodríguez, A.R., Reyes, B.A.: Estimación Óptica Remota de la Actividad y Frecuencia Respiratoria durante Diversas Maniobras Respiratorias. In: Memorias del Congreso Nacional de Ingeniería Biomédica, vol. 5, no. 1, pp. 114–117, Mexico (2018). ISSN: 2395-8928

8. Cao, Z., Hidalgo, G., Simon, T., Wei, S.-E., Sheikh, Y.: OpenPose: realtime multi-person 2D pose estimation using Part Affinity Fields, arXiv preprint arXiv:1812.08008 (2018)
9. Hidalgo, G., et al.: OpenPose, GitHub repository (2019). https://github.com/CMU-Perceptual-Computing-Lab/openpose
10. Cao, Z., Simon, T., Wei, S.-E., Sheikh, Y.: Realtime multi-person 2D pose estimation using part affinity fields. In: IEEE Conference on Computer Vision and Pattern Recognition (CVPR), vol. 1, p. 7, arXiv:1611.08050 (2016)
11. Reyes, B., Reljin, N., Kong, Y., Nam, Y., Chon, K.: Tidal volume and instantaneous respiration rate estimation using a volumetric surrogate signal acquired via a smartphone camera. IEEE J. Biomed. Health Inform. **21**(3), 764–777 (2017). https://doi.org/10.1109/jbhi.2016.2532876
12. Jarchi, D., Salvi, D., Tarassenko, L., Clifton, D.A.: Validation of instantaneous respiratory rate using reflectance PPG from different body positions. Sensors **18**, 3705 (2018). https://doi.org/10.3390/s18113705

Respiratory Rate Estimation by a Non-invasive Optical Method Based on Video Image Processing

C. A. Hurtado-Otalora(✉), J. D. Pulgarin-Giraldo, and A. M. Gonzalez-Vargas

GBio Research Group, Universidad Autónoma de Occidente, 760030 Cali, Colombia
{cristian_aug.hurtado, jdpulgarin, amgonzalezv}@uao.edu.co

Abstract. Respiratory rate measurement and monitoring allow predicting adverse events on time. However, in clinical settings, it is performed with specialized devices that are always attached to the patient's body. The objective of this work was to estimate the instantaneous respiratory rate (IRR) and the respiratory movement (RM) using image processing techniques from a video. A smartphone recorded the videos, and the RM was estimated offline. An RM reference signal obtained in the same test with a thermal sensor around the nose and mouth was used to make comparisons with the computed signal. The remote optical estimation was evaluated on a pilot test with four volunteers in three different conditions of movement and breathing. We analyzed the correlation for the RM signals and the mean square error of the IRR between reference and estimated signals, obtaining a value of 0.737 and 0.091, respectively. These results are competitive with the ones founded in the bibliography. Moreover, the respiratory rate estimation has a precision of P = 0.98 and sensitivity S = 0.99, which makes our method superior. This outstanding performance is due to the proposed framework is robust in the presence of motion artifacts, even motion artifact that corrupts the reference signal from the thermal sensor.

Keywords: Digital image processing · Remote optical estimation · Respiratory rate

1 Introduction

When evaluating the condition of a person, four vital signs are analyzed: temperature, pulse, blood pressure, and respiratory rate. An anomaly that occurs in one of these indicates the need for urgent care [1]. In the case of the respiratory rate, its average value in a person at rest is 17 breaths per minute [2]. Different devices measure the respiratory rate: breathing monitors, spirometers, capnography. Also qualified personal by observation can measure it. Respiratory rate estimation by human observation depends on the expertise of the medical staff, resulting in value variations according to the professional who performs the test.

© Springer Nature Switzerland AG 2020
C. A. González Díaz et al. (Eds.): CLAIB 2019, IFMBE Proceedings 75, pp. 242–251, 2020.
https://doi.org/10.1007/978-3-030-30648-9_32

On the other hand, the mentioned devices must be attached to the patient. Nevertheless, when a patient moves abruptly, or the environment presents changes, artifacts will appear in the signal acquired [3]. What is more, in surgical or diagnostic imaging environments, these devices cannot be connected to the patient, so the remote estimation always remains in the visual monitoring by the healthcare personnel.

Currently, video acquisition and streaming are simple and easy to install in any environment, allowing to build a tool for remote estimation of variables in a simple way [4]. Even, smartphone video recording and streaming are used, so that the optical estimation of the respiratory frequency is a real possibility to measure the vital sign studied. Previous works using video processing showed the viability of this option, but they were limited by the distance of the camera, exposed skin, controlled light conditions, and a resting state of the patient [5]. So, a system that works with abrupt movements and active states of the patient, as well as changing conditions of the environment for remote monitoring of rate breathing is needed.

The mean goal of this work is to present a framework based on digital image processing and smartphone video recording for non-contact measure and remote monitoring of respiratory rate. This framework works although the patient presents lateral movements. Additionally, the method was tested by comparisons with reference signals obtained through a thermal sensor placed around the mouth and nose of the study subjects.

2 Experimental Setup

2.1 Database Description

We used an access-free database from [6]. It consists of 12 videos of 4 people: two men, and two women. Each subject has three videos with an approximate duration of 2 min each. The subjects are in different states, such as at rest or movement and breathing at a fixed rate or spontaneously. Table 1 shows the conditions of respiration and movement of the subjects in each video.

Table 1. Database movement and breathing conditions

Subject	Genre	Breathing	Movement state	Breaths per minute
Subject 1	Man	Fixed rate	Active	12
		Fixed rate	Resting	12
		Spontaneously	Resting	
Subject 2	Woman	Fixed rate	Active	12
		Fixed rate	Resting	12
		Spontaneously	Resting	
Subject 3	Woman	Fixed rate	Active	30
		Fixed rate	Resting	30
		Spontaneously	Active	
Subject 4	Man	Fixed rate	Active	30
		Fixed rate	Resting	30
		Spontaneously	Active	

2.2 Respiratory Movement Estimation from Video

Video frame extraction and image processing were done in MATLAB® (The MathWorks, Inc., Natick, Massachusetts, United States) [7]. To estimate the respiratory movement of the subjects, the steps described in Fig. 1 were done and explained below.

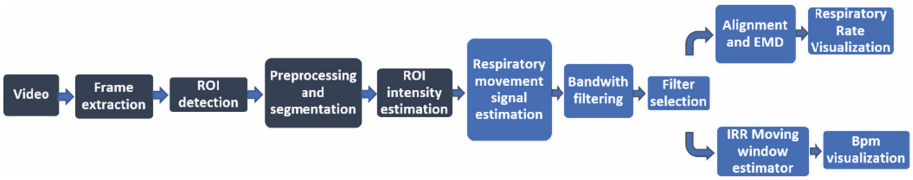

Fig. 1. Framework's blocks diagram. Dark blue ones to estimate respiratory movement. Light blue ones to estimate respiratory rate.

First, the method detects the Region of Interest (ROI). This ROI is established using a Viola-Jones algorithm [7] to detect the upper body (Fig. 2(b)). According to the proportionality of the upper body to the torso [8], we take as ROI the projection of this to the trunk, adjusting only its width to 0.75 centered. The height of the ROI remained the same.

a) b) c)

Fig. 2. (a) Original video frame, (b) upper body detection and, (c) ROI selected

Secondly, we did an image preprocessing on each frame that included: grayscale thresholding, binarization, and closing employing morphological operators.

Lastly, with ROI delimited, we computed the rate between ROI's mean intensity and ROI's total pixels for each n-th frame. Thus, for a video with N frames, we obtain a signal x(n) n = 1…, N.

2.3 Respiratory Rate Estimation

The signal x(n) obtained in the previous section was resampled at 25 Hz using linear resampling from [9]. Since each video had different framerate (15 or 25 frames per second), this stage was necessary to unify x(n) signal rate. Moreover, this 25 Hz framerate also was necessary to make comparisons with the reference signals from the thermal sensor in the Subsect. 2.4.

In order to capture the chest volume variation, the respiratory movement is obtained derivating *x(n)* as:

$$y(n) = x(n) - x(n-1), \text{ for } n = 1\ldots, N. \quad (1)$$

Subsequently, *y(n)* passes through a low-pass FIR filter with a cutoff frequency of 1 Hz to reduce the respiratory movement bandwidth [2]. In this part, we adjusted the length of our estimated signal. The reference signal length is shorter than it, so the estimated one is truncated to reference length.

Filter Selection. Due to the conditions of the capture of respiratory movement in each subject, we proposed a bank of filters. Here, we estimated the additive gaussian white noise presented in each signal *y(n)* as well its pseudo-period. With these values, we select the filter according to its noise level and natural frequency of interest. The values founded were: (1) adaptive threshold using the Stein's unbiased risk estimation, (2) global threshold using the Otsu method, and (3) pseudo-period estimation from autocorrelation [10]. Table 2 describes the range of values founded and the decision rules to assign the proper filter.

Table 2. Noise levels and pseudo-period values. If the three value conditions are met, the filter is assigned to process *y(n)*

Noise levels and pseudo-period values			Filter assigned
SURE adaptive threshold	Otsu global threshold	Autocorrelation period	FIR equiripple low-pass
SURE = 1	$\lambda < 0.3$	$N_{corr} < 20$	$fc(Hz) = 0.2$
SURE > 1	$\lambda > 0.25$	$N_{corr} > 100$	$fc(Hz) = 0.25$
SURE = 1	$\lambda < 0.2$	$70 < N_{corr} < 100$	$fc(Hz) = 0.3$
	$\lambda > 0.45$	$N_{corr} < 100$	$fc(Hz) = 0.5$
SURE > 1	$\lambda < 0.13$	$N_{corr} < 100$	$fc(Hz) = 0.6$

After filtering, the signal *y(n)* was normalized, storing the variable *rm(n)*. The respiratory rate estimation was inspired by the classic heart rate detectors which locate fiducial marks at the peak of each cycle [11]. Firstly, we proceed to detect the peaks on *rm(n),* taking into account a minimum distance between peaks of 0.8 s. The peaks

allow us to observe the algorithm accuracy in the respiratory rhythm detection against that given by the thermal sensor. Secondly, the inverse of the difference between consecutive peaks went to a moving window estimator. Finally, we obtained IRR per minute and compared it against the reference IRR.

Signal Alignment. In order to measure the performance of the optical estimator, the signals must be aligned with the references for making a fair comparison. This stage only must be considered when a request for comparing with another sensor (e.g., thermal sensor) is made. In our case, two measures: correlation index and normalized mean square error used reference signals. In case reference signals are not available, sensitivity and precision measures can be done with the estimated signals.

To do the signal alignment, we proceeded to perform temporal alignment and empirical mode decomposition (EMD) [12]. In the first place, the cross-correlation between the reference and the estimated signal *rm(n)* is calculated to determine the alignment point L between the first peak of each signal. Thus, we aligned the estimated RM as:

$$rm(n) = rm(n - L), \text{ for all } n = 1\ldots, N. \tag{2}$$

In the second place, based on the EMD decomposition of the reference signal, the modes that minimize the Euclidean distance between the reference signal and the estimated signal are added to the *rm(n)*. These modes capture the trend of the reference signal, so the estimation must incorporate this information to make a fair comparison.

2.4 Performance Analysis

As mentioned above, the two first measures compared our estimation with a reference signal from a different source. The first measure of performance calculated is the correlation between RM signals that was defined as:

$$\rho\left(RM_{ref}, RM_{est}\right) = \frac{1}{N-1}\sum_{i=1}^{N}\left(\frac{RM_{ref}(i) - \mu_{RM_{ref}}}{\sigma_{RM_{ref}}}\right)\left(\frac{RM_{est}(i) - \mu_{RM_{est}}}{\sigma_{RM_{est}}}\right). \tag{3}$$

The second measure was the normalized mean square error (NMSE) computed for IRR estimation [13]. These two measures require signal alignment.

Our framework was designed to detect each breath, so we also calculated sensitivity and precision with the estimated signal. The signal alignment was no needed in these other two measures. We labeled true positives (TP), false positives (FP), and false negatives (FN) in the estimated signals. The sensitivity and precision were defined as:

$$Sensibility = \frac{TP}{TP + FP}, \tag{4}$$

$$Precision = \frac{TP}{TP + FN}. \tag{5}$$

3 Results and Discussion

The results obtained in 11 of the 12 videos allow us to affirm that our framework estimates the respiratory rate adequately. In the subject 3 case, the reference information for both the RM and the IRR in spontaneous breathing conditions in the presence of lateral movements present several artifacts. These motion artifacts turn this record in an outlier, and we did not calculate NMSE for it. However, correlation, sensitivity, and precision were computed over the entire database (12 videos), as they are shown later in Table 3. To illustrate our framework scope Fig. 3(a) shows each breath location estimated as well as the reference. The remote estimation works as good as the thermal sensor located in the patient's nose and mouth. Figure 3(b) shows a slightly smooth IRR estimation compared to the reference, and the number of breaths per minute trend is well estimated.

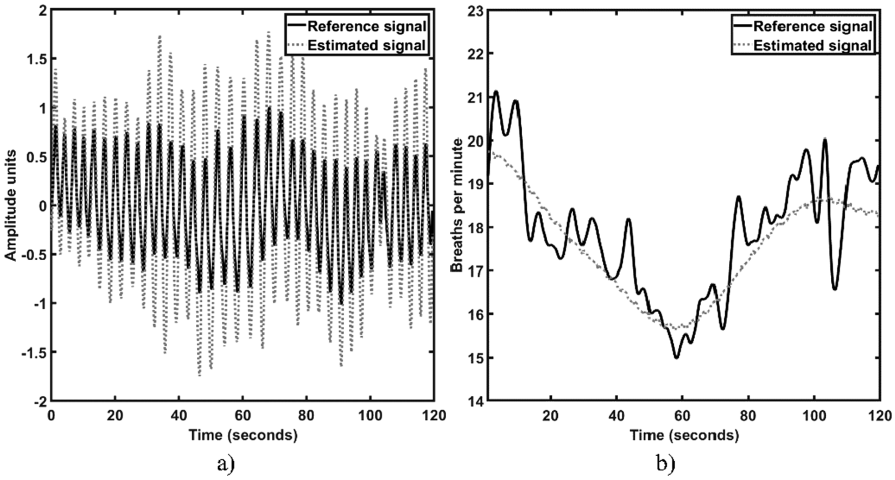

Fig. 3. Comparison between reference and estimated signals. Case: subject 1 in resting state and spontaneous breathing. (a) MR, (b) IRR

Figure 4 shows the reference signals of the video considered outlier. The reference RM signal in Fig. 4(a) has a non-linear baseline drift, possibly caused by movement artifacts due to an incorrect fixing of the thermal sensor. Even more, IRR reference in Fig. 4(b) dismissed several breaths and the breaths per minute plot does not match with reference RM. The time interval from 60 to 80 s shows this reference error. In this interval, RM does not have abrupt frequency changes, as is suggested by the IRR reference signal. Motion artifacts cannot be corrected by classic linear filters [10], so it is essential to define an adequate protocol for recording reference signals. On the other hand, our remote optical estimation is not affected by these artifacts and baseline drifts, resulting in a more linear trend estimation. Moreover, in the time interval from 60 to 80 s, our IRR estimation is visually more accurate according to RM reference information.

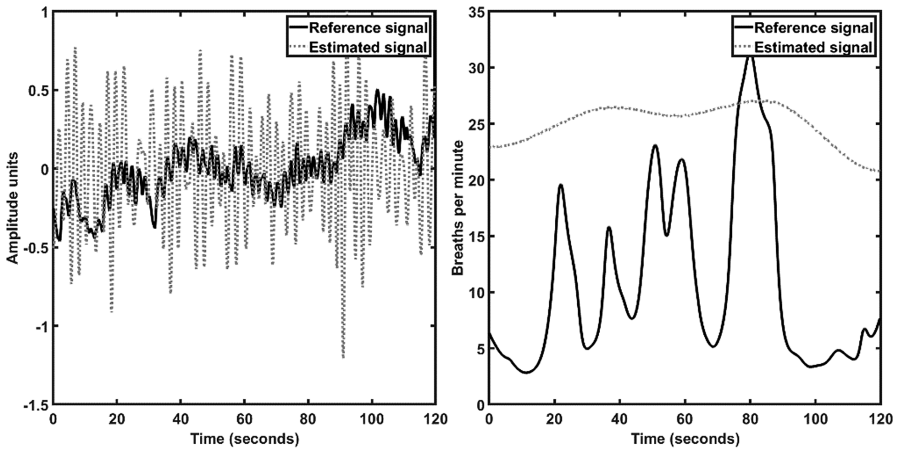

a) b)

Fig. 4. Comparison between reference and estimated signals. Case: subject 3 in movement and spontaneous breathing (a) RM, (b) IRR

Table 3 shows the results obtained from the analyzed videos regarding the correlation index and the normalized mean square error (NMSE). Our results are comparable with the obtained in [6, 14] respect to NMSE. Concerning to sensitivity and precision, our results are superior that [15] and equal to [16]. They reported 3.5 and 0.54 breaths/min error, respectively, while our test showed 0.5 breaths/min error.

Table 3. Number of breaths: reference ones (ground truth) and estimated ones, correlation index and NMSE

Subject	Breathing	Movement state	Breathings		Correlation index	NMSE
			R	E		
Subject 1	Fixed rate	Active	24	24	0.916	22%
	Fixed rate	Resting	23	23	0.919	8.5%
	Spontaneously	Resting	35	35	0.955	4.3%
Subject 2	Fixed rate	Active	23	24	0.822	14.7%
	Fixed rate	Resting	25	24	0.765	10.5%
	Spontaneously	Resting	31	30	0.755	9.7%
Subject 3	Fixed rate	Active	58	57	0.388	5.1%
	Fixed rate	Resting	58	54	0.749	10.1%
	Spontaneously	Active	56	50	0.529	—
Subject 4	Fixed rate	Active	59	59	0.590	3.5%
	Fixed rate	Resting	59	58	0.777	4.4%
	Spontaneously	Active	70	72	0.469	7.6%
Mean					0.737	9.1%

The correlation index measure revealed to us that we must improve the RM amplitude estimation. However, the individual breath localization works excellent, as shown in sensitivity and precision columns. Table 3 also specifies the volunteers of the database, the condition of respiration and movement condition, the total reference breaths (R) and estimated breaths (E). NMSE computation excludes the outlier signal of subject three mentioned at the beginning of Sect. 3.

Two more analyses were performed on the optically estimated signals to evaluate the reliability of the framework: sensitivity and accuracy for each of the 12 videos (Table 4). The mean sensitivity obtained was 0.99, and the precision was 0.98.

Table 4. Sensitivity (S) and precision (P) of optically estimated signals

Subject	State Movement and Breathing	TP	FP	FN	S	P
Subject 1	Fixed rate, Active	24	0	0	1	1
	Fixed rate, Resting	23	0	0	1	1
	Spontaneously, Resting	35	0	0	1	1
Subject 2	Fixed rate, Active	23	1	0	0.96	1
	Fixed rate, Resting	25	0	1	1	0.96
	Spontaneously, Resting	31	0	1	1	0.97
Subject 3	Fixed rate, Active	58	0	1	1	0.98
	Fixed rate, Resting	58	0	4	1	0.94
	Spontaneously, Active	56	0	6	1	0.90
Subject 4	Fixed rate, Active	59	0	0	1	1
	Fixed rate, Resting	59	0	1	1	0.98
	Spontaneously, Active	70	2	0	0.97	1
Mean					0.99	0.98

4 Conclusions

According to the results obtained in the four performance measurements made, our framework is competitive with the current approaches that also use remote optical methods [6, 14–16]. Specifically, our algorithm is competitive in NMSE results, and its excellent sensitivity and precision reached encourage us to improve correlation results.

Although this method visually does not fit RM and IRR reference signals, it should be noted that a rate estimator must detect each breath appropriately. As far as we are concerned, we insist on doing sensitivity and precision tests with each breath labeled in reference.

Overall, the developed framework can track the region of interest as the subject performs lateral movements. Even more, our method makes it possible to obtain the estimated signal at rest as well as moving with remarkable results. Last, our method does not require signal alignment because it is based on peak detection, and our respiratory rate estimation has no trends.

As future work, a pilot test must validate this framework, where an adequate protocol for recording reference signals (thermal sensor) must be defined. This protocol

will prevent motion artifacts that corrupt the reference signal. Moreover, a ground truth labeling of each respiration must be annotated by medical staff to make a fair comparison, especially in IRR. Concerning to the algorithms, improvements in filter design and selection must include advanced filter algorithms like Kalman, filters that can deal with non-linear trends in the signal.

Acknowledgments. This work is supported by the project 17INTER17385 "Desarrollo e implementación de herramientas de simulación para la enseñanza de la bioinstrumentación" funded by Universidad Autónoma de Occidente, by the program "Doctorados Nacionales 2014" financed by COLCIENCIAS, as well as partial Ph.D. financial support from Universidad Autónoma de Occidente.

Conflict of Interest. The authors declare that they have no conflict of interest.

References

1. Boron, W., Boulpaep, E.: Medical Physiology, 3rd edn. Elsevier Inc, Philadelphia (2017)
2. Patton, K., Thibodeau, G.: Anatomy and Physiology, 8th edn. Mosby Elsevier, St. Louis (2013)
3. Chan, A.: Biomedical Device Technology: Principles and Design, 2nd edn. Charles C Thomas Publisher, Springfield (2016)
4. Qi, J.A., Yang, P.A., Min, G.B., Amft, O.C., Dong, F.D., Xu, L.E.: Advanced internet of things for personalised healthcare systems: a survey. Pervasive Mobile Comput. **41**, 132–149 (2017). https://doi.org/10.1016/j.pmcj.2017.06.018
5. He, X., Goubran, R., Knoefel, F.: IR night vision video-based estimation of heart and respiration rates. IEEE Sensors Applications Symposium SAS, pp. 1–5, Glassboro, NJ (2017). https://doi.org/10.1109/sas.2017.7894087
6. Vázquez-Segura, J.A., Mejía-Rodríguez, A.R., Reyes, B.A.: Estimación Óptica Remota de la Actividad y Frecuencia Respiratoria durante Diversas Maniobras Respiratorias. In: Memorias del Congreso Nacional de Ingeniería Biomédica, vol. 5, no. 1, pp. 114–117, México (2018). https://doi.org/10.24254/cnib.18.12
7. MATLAB and Computer Vision Toolbox Release 2018b, The MathWorks, Inc., Natick, MA, United States
8. Osti, R.: Basic Human Anatomy: An Essential Visual Guide. Monacelli Studio, New York (2016)
9. MATLAB and Signal Processing Toolbox Release 2018b, The MathWorks, Inc., Natick, MA, United States
10. Pulgarin-Giraldo, J.D., Acosta, C., Castellanos, G.: Noise reduction by discrete mollification and wavelet thresholding. Scientia et Technica **13**(35), 55–60 (2007). https://doi.org/10.22517/23447214.5353
11. Orozco-Morales, R., Pérez-Sánchez, M.A., Lorenzo-Gironi, J.V., Grau-Ábalo, R., Ramos-Ramírez, R.: Evaluation of QRS morphological classifiers in the presence of noise. Comput. Biomed. Res. **30**(3), 200–210 (1997). https://doi.org/10.1006/cbmr.1997.1437
12. Reyes, B.A., Reljin, N., Kong, Y., Nam, Y., Chon, K.H.: Tidal volume and instantaneous respiration rate estimation using a volumetric surrogate signal acquired via a smartphone camera. IEEE J. Biomed. Health Inform. **21**(3), 764–777 (2017). https://doi.org/10.1109/JBHI.2016.2532876
13. Sayed, A.: Fundamentals of Adaptive Filtering. Wiley, New Jersey (2003)

14. Antognoli, L., Marchionni, P., Nobile, S., Carnielli, V., Scalise, L.: Assessment of cardio-respiratory rates by non-invasive measurement methods in hospitalized preterm neonates. In: IEEE International Symposium on Medical Measurements and Applications, pp. 1–5, Rome (2018). https://doi.org/10.1109/memea.2018.8438772
15. Liang, Q., Xu, L., Bao, N., Qi, L., Shi, J., Yang, Y., Yao, Y.: Research on non-contact monitoring system for human physiological signal and body movement. Biosensors **9**(2), 58–71 (2019). https://doi.org/10.3390/bios9020058
16. Liu, J., Liu, H., Jia, X., Guo, S.: Vision-based automatic detection method for non-contact respiratory rate. Chin. J. Sci. Instrum. **40**(2), 51–58 (2019). https://doi.org/10.19650/j.cnki.cjsi.J1804156

Computer Vision-Based Estimation of Respiration Signals

Maria Eugenia Paz Reyes[1], Jasiel Dorta_Palmero[1], Jessica Leon Diaz[1], Efren Aragon[1], and Alberto Taboada-Crispi[2(✉)]

[1] Computer Science, Universidad Central "Marta Abreu" de Las Villas, Santa Clara, Cuba
{mpaz, jdorta, jldiaz, earagon}@uclv.cu
[2] Informatics Research Center, Universidad Central "Marta Abreu" de Las Villas, Santa Clara, Cuba
ataboada@uclv.edu.cu

Abstract. Respiration movement and respiration rate have been used to monitor breathing status for diagnosis and fitness purposes. From a given video sequence of a person facing a camera, this system here automatically detects and tracks a region of interest (ROI) on the chest, using the Kanade-Lucas-Tomasi method, after applying the Viola-Jones algorithm and identifying the Harris-Stephens features for tracking the ROI across frames. The displacement in the vertical direction of the ROI (frame by frame) was used to estimate the respiration movement, after low-pass filtering at a proper cutoff frequency. Finally, the respiration rate is estimated from the respiration movement signal by a root MUSIC-based estimator. For the 12 video files provided, we obtained respiration movement signals with correlation indexes respect to the corresponding '*reference*s' of above 90%, in most cases, and respiration rate signals with normalized root mean-squared errors with respect to the *inst_freq* around 10%. A global ranking index of around 0.8 was consistently obtained. Computer vision algorithms are well-suited for estimating respiration movement and respiration rate signals from frontal video sequences.

Keywords: Respiration · Time-varying signals · Estimation/evaluation · Video processing · Computer vision algorithms

1 Introduction

Respiration time-varying signals can be useful to characterize the physiological condition of a subject in clinical and fitness applications. Respiration movement and respiration rate, illustrated in Fig. 1, are among the most important respiration signals. Respiration movement (V_T) is defined as a surrogate of respiratory effort and provides information about the relative respiration depth. The respiration rate (RR) expresses the number of breaths per unit of time, commonly given in breaths per minutes (bpm).

© Springer Nature Switzerland AG 2020
C. A. González Díaz et al. (Eds.): CLAIB 2019, IFMBE Proceedings 75, pp. 252–261, 2020.
https://doi.org/10.1007/978-3-030-30648-9_33

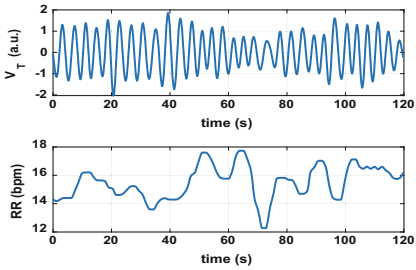

Fig. 1. Examples of respiration time-varying signals

Respiration movement can be measured directly from the tidal volume by spirometry [12], or estimated from other surrogated signals [2, 8, 15]. Respiration rate can be estimated as instantaneous frequency, from the signal V_T vs. t, by different methods [12].

In the presence of movements, we should track a region of interest (ROI) on the subject, from which to estimate the respiratory signals. Computer vision (CV) algorithms could accomplish this task. This paper deals with CV-based estimation of respiratory signals.

2 Materials and Methods

2.1 Database for Estimation and Evaluation

We use a database comprising 12 video files with associated references for respiration movement (V_T) and respiration rate (RR) signals: '*reference*' and '*inst_freq*', respectively [15]. Files were acquired from 4 different subjects, performing respiratory maneuvers: resting or moving, and breathing at a fixed respiratory frequency or at spontaneous rate.

2.2 Block Diagram of the Proposed System

To estimate the respiration movement and the respiration rate signals from a video sequence (Fig. 2), we first detect a region of interest (ROI) on the chest and features that can be tracked. From the ROI, we compute certain parameters of interest in every frame, obtaining a time series resembling the respiration movement signal. Finally, we estimate the instantaneous frequency.

For evaluation, we first align, prune/enlarge, and normalize the estimated V_T and RR signals to compare them with the '*reference*' and '*inst_freq*' signals, respectively. The correlation index (*CorrI*) is computed for V_T vs. *reference* and the normalized root mean squared error (*NRMSE*) for RR vs. *inst_freq*. A global index, *RI*, is estimated for the whole dataset.

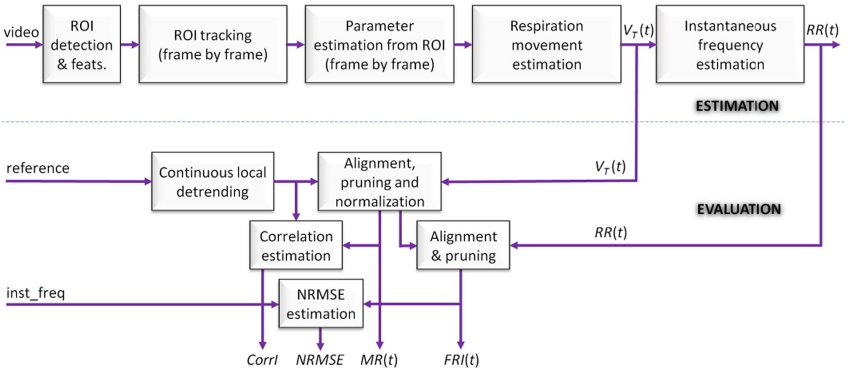

Fig. 2. Block diagram of proposed estimation and evaluation stages per file set

ROI Detection and Estimation of Features to Track

From a given video sequence, this system automatically detects a ROI using the Kanade-Lucas-Tomasi (KLT) method [13], as illustrated in Fig. 3. First, it detects the face, with the Viola-Jones algorithm [16]. By translating downwards the red bounding box (bbox) of the detected face with a face-to-chest distance proportion, fch, of 1.5, it obtains a ROI on the chest.

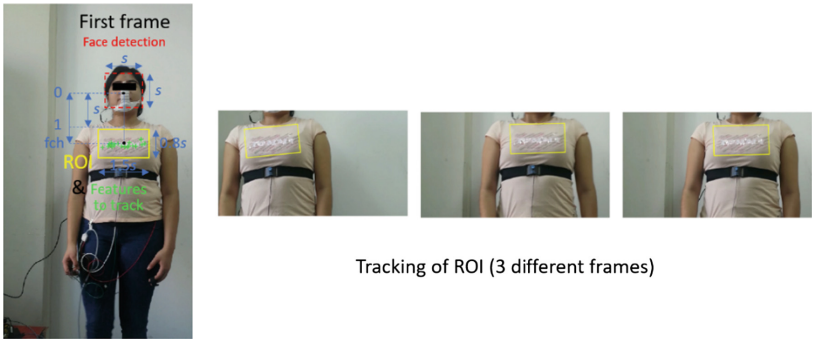

Fig. 3. Detection of ROI and tracking

Then, it identifies the features, which can be reliably tracked, for tracking the ROI across frames. We try several local feature detectors [14], such as Shi-Tomassi [10], FAST [9], Harris-Stephens [5], BRISK [6], SURF [3] and KAZE [1] algorithms.

ROI Tracking

This system creates a point tracker and enables the bidirectional error constraint to make it more robust in the presence of noise and clutter [13]. For each point in the previous frame, the point tracker attempts to find the corresponding point in the current frame. Then, it estimates the translation, rotation, and scale between the old points and

the new points of the bounding box around the ROI on the chest to obtain the displacement and the other parameters of interest for the whole video.

Parameter Estimation from ROI
Several signals were candidate parameters to be estimated, frame by frame, from the ROI, to get the information of the respiration movement (*reference*), and therefore, from which to estimate V_T:

- *Imean*: mean of the gray intensity levels [8, 15].
- *Ymean*: mean of the *Y* component of the Farneback optical flow [4]. Estimation of the optical flow was not successful here by using other methods: Lucas-Kanade, Lucas-Kanade derivative of Gaussian, and Horn-Schunck [7].
- *Omean*: the same as *Ymean*, but regarding the orientation information.
- *dy*: displacement in the vertical direction [2].
- *rY*: RLS adaptively filtered signal, using *dy* as main input and *dx* (displacement in the horizontal direction) as a reference input [11].

Respiration Movement Estimation
From the adequate raw signal, computed on the ROI of every frame, we estimated the respiration movement signal, by low-pass filtering it with an 8 order zero-phase Butterworth filter. The cutoff frequency is estimated as 25% above the frequency at a relevant peak of the PSD, between 0.1 Hz and 0.7 Hz. After this stage, the respiration movement (V_T) signal should be re-sampled, if needed, at 25 Hz.

Instantaneous Frequency Estimation
Finally, the *RR* signal was estimated from V_T by using the root MUSIC algorithm, with an analysis window of 128 samples, updated every 31 samples [12].

Continuous Local Detrending
There are low-frequency thermal drifts that should be removed from the *reference* signals before using them for assessment because those low-frequency components may considerably affect the correlation.

Alignment, Pruning/Enlargement and Normalization
In the evaluation process, we first align the estimated V_T signal with the *reference* to maximize the correlation. Then, we correct the lengths of V_T and *RR* to resemble the references. If the length of the aligned estimated signals exceeds the length of the references, they are pruned. Otherwise, we estimate the final samples of V_T by a 2^{nd}-order forward predictor and we extend the *RR* series with the same last value already estimated. Finally, we normalize V_T to better resemble the reference by computing

$$V_T = \frac{V_T \cdot \sigma_{reference}}{\sigma_{V_T}} \tag{1}$$

where $\sigma_{reference}$ is the standard deviation of the *reference* (after continuous local detrending), and σ_{VT} is the standard deviation of V_T.

Computing Quality Indexes

To evaluate the performance of the algorithms estimating the respiratory signals, we first compute the correlation index $\left(CorrI = \hat{\rho}_{xy}\right)$ between the *reference* (x) and the estimated V_T (y), assuming that x and y are stationary and jointly stationary, as well as previously aligned, then

$$CorrI = \hat{\rho}_{xy} = \frac{\hat{\gamma}_{xy}}{\sqrt{\hat{\gamma}_x \cdot \hat{\gamma}_y}} \cdot 100\%, \tag{2}$$

where $\hat{\gamma}_{xy}$ is the cross-covariance function between x and y, $\hat{\gamma}_x$ is the auto-covariance function of x.

We also compute, as a goodness of fit between the estimated *RR* signal and the *inst_freq* reference signal, the normalized root mean-squared error (*NRMSE*) as

$$NRMSE = \frac{\sqrt{MSE}}{\overline{inst_freq}} \cdot 100\%, \tag{3}$$

where $\overline{inst_freq}$ is the arithmetic mean of the *inst_freq* reference signal and the mean-squared error (*MSE*) is computed as

$$MSE = \frac{\|RR - inst_freq\|^2}{N}. \tag{4}$$

where, N is the number of samples, and $\|$ indicates the 2-norm of a vector. *NRMSE* is then a scalar value between 0 and 100%.

Actually, we estimate *CorrI* and *NRMSE* for every subject performing a respiratory maneuver (12 files) and then we compute an average global ranking index (*RI*), which could be between 0 (worst performance) and 1 (for perfect performance algorithms) as

$$RI = \frac{CorrI + 100 - NRMSE}{2 \cdot 100}. \tag{5}$$

3 Results and Discussion

In this section, we will critically discuss on the available database for estimation and evaluation of the respiratory signals, as well as all the results regarding the application of the CV algorithms.

3.1 On the Database

Table 1 reviews the main parameters of the data. Please, observe that the sampling frequencies (fs) of the video files are 25 Hz, 15 Hz, or 14.93 Hz, while the sampling frequency of the reference signals is always 25 Hz. Therefore, all the estimated signals

should be re-sampled. On the other hand, the duration T of the reference signals (approximately 120 s) is normally around 1 s shorter than the video sequences and they are not perfectly synchronized. Thus, we should post-process the estimated respiration movement and respiration rate signals.

Table 1. Database for estimation and evaluation of respiratory signals. fmov (frequency at which the subject is moving) is shown in smaller text when it is not intentionally introduced.

files (video & reference signals: *reference*, *inst_freq*)	fmov (Hz)	fo (Hz)	fmin (Hz)	fmax (Hz)	fs (Hz)	N	T (s)
s11_metro_02Hz_resting.mp4	0.580	0.200			25.00	3018	120.72
s11-metro-02Hz-resting-ref.mat		0.205	0.161	0.241	25.00	2992	119.64
s11_metro_02Hz_moving.mp4	0.510	0.200			25.00	3017	120.68
s11-metro-02Hz-moving-ref.mat		0.198	0.104	0.258	25.00	2995	119.76
s11_sponta_resting.mp4	0.290	0.280			25.00	3013	120.52
s11-sponta-resting-ref.mat		0.298	0.250	0.352	25.00	2987	119.44
s34_metro_02Hz_resting.mp4	0.200	0.200			14.93	1806	121.00
s34-metro-02Hz-resting-ref.mat		0.195	0.116	0.231	25.00	2994	119.72
s34_metro_02Hz_moving.mp4	0.380	0.200			14.93	1803	120.80
s34-metro-02Hz-moving-ref.mat		0.197	0.138	0.287	25.00	2994	119.72
s34_sponta_resting.mp4	0.250	0.260			14.93	1803	120.80
s34-sponta-resting-ref.mat		0.260	0.221	0.312	25.00	2996	119.80
s24_metro_05Hz_resting.mp4	0.210	0.490			14.93	1804	120.82
s24-metro-05Hz-resting-ref.mat		0.497	0.474	0.536	25.00	2994	119.72
s24_metro_05Hz_moving.mp4	0.510	0.490			14.93	1802	120.73
s24-metro-05Hz-moving-ref.mat		0.496	0.469	0.563	25.00	2994	119.72
s24_sponta_moving.mp4	0.410	0.500			14.93	1803	120.80
s24-sponta-moving-ref.mat		0.180	0.047	0.524	25.00	2994	119.72
s31_metro_05Hz_resting.avi	0.500	0.490			15.00	1812	120.80
s31-metro-05Hz-resting-ref.mat		0.493	0.473	0.574	25.00	2994	119.72
s31_metro_05Hz_moving.avi	0.490	0.490			15.00	1811	120.73
s31-metro-05Hz-moving-ref.mat		0.500	0.482	0.603	25.00	2994	119.72
s31_sponta_moving.avi	0.600	0.600			15.00	1812	120.80
s31-sponta-moving-ref.mat		0.619	0.521	0.829	25.00	2992	119.64

The mean of the respiration rate signal (fo), easily estimated from the provided *inst_freq* (e.g. 0.198 Hz for the *inst_freq* in s11-metro-02 Hz-moving-ref.mat), should be in the same order of the fo estimated as the frequency at which the maximum peak of the power spectral density (PSD) of the '*reference*' occurs. However, there is an unacceptable difference between those estimations for the s24-sponta-moving-ref.mat files. The minimum value associated to the *inst_freq* of this very example does not seem to reflect the real variations of '*reference*'.

In a closer look to the s24-sponta-moving-ref.mat signals (Fig. 4), we confirm the bad quality of these reference signals. One of the reasons of this bad quality signals is the extreme trending shown in the *reference*, which is not associated to physiological reasons but to a supposedly non-controlled thermal drift. Therefore, we suggest

ignoring the s24 spontaneous moving files for evaluation. Some other '*reference*' signals in the database would be benefited from a detrending process as well.

We decided to use a continuous local detrending algorithm which fits and subtracts a running line to the input data by local linear regression, as in "Chronux version 2.11" (http://chronux.org/, August 12, 2014), with a running window of 160 samples and a step-size of 4 samples.

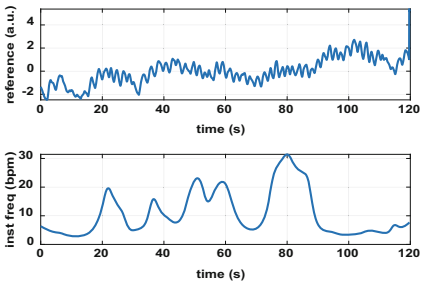

Fig. 4. References in s24-sponta-moving-ref.mat file

3.2 Local Features and Candidate Parameters

All the local feature detectors tried here (i.e. Shi-Tomassi, FAST, Harris-Stephens, Kanade, SURF and KAZE) successfully worked with most video sequences, but some failed for particular sequences. The most stable algorithms were the corner detectors (e.g. Harris-Stephens and Shi-Tomassi), maybe because of the clothing designs in the database, although they are not scale and rotation invariants.

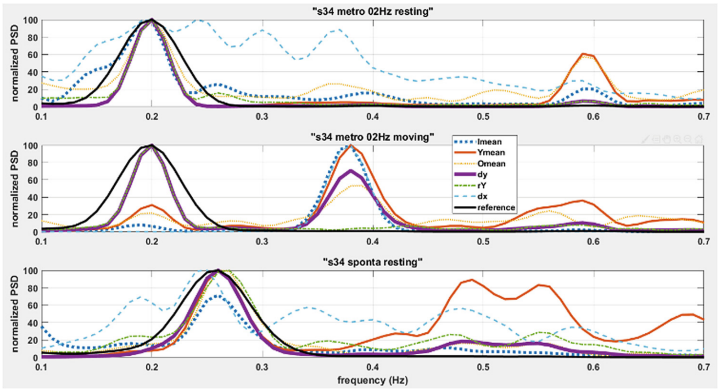

Fig. 5. Normalized power spectral density in the respiration frequency band (0.1 Hz–0.7 Hz) of parameters of interest

To certain extent, all the candidate parameters (*Imean*, *Ymean*, *Omean*, *dy*, and *rY*) carry the information of the respiratory respiration movement. Please, note in Fig. 5, that the power spectral densities (PSD) of those signals in the respiration frequency band (between 0.1 and 0.7 Hz) resemble the main component of the *reference*, although they comprise also some other components due to interferences such as the oscillatory movement of the subjects at *fmov* and more. However, we decided to work with the apparently more stable displacement in the vertical direction (*dy*).

3.3 Final Evaluation Results

Figure 6 and Table 2 review the results of the evaluation of the estimated respiratory signals. The global *RI* was around 0.80, even without discarding the outlier file s24-sponta-moving-ref.mat, already criticized in Sect. 3.1. If we discard it, *RI* increases to around 0.88, which can be considered as an acceptable global result.

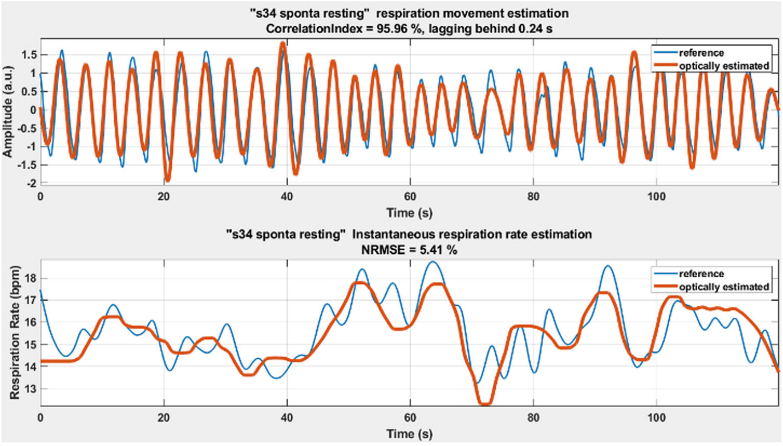

Fig. 6. Estimated respiratory signals compared to references

Note that the *CorrI* of the estimated respiration movement signals is higher than 90% for half (6/12) of the input files, and even higher than 95% for the best performing quartile (3/12). A similar result was achieved by estimating the instantaneous frequencies, *RR*, with 7/12 showing *NRMSE* lower than 10%, and a 3/12 with values lower than 5%. In addition, 7/12 files reached $RI > 0.9$.

Without applying the continuous local detrending to the *reference* signals, the *CorrI* decreases in the same proportion to the severity of the initial thermal drifts in them, slightly decreasing the *RI*, from around 0.8 to around 0.7.

These results are inferior than those in [8], but the database here seems more demanding, with lower fs and resolution, and several moving maneuvers. Results are comparable to [15], even when no moving maneuvers were included there.

Table 2. Results of evaluation of estimated respiratory signals

video files	*CorrI* (%)	*NRMSE* (%)	*RI*
s11_metro_02Hz_resting.mp4	92.73	11.30	0.91
s11_metro_02Hz_moving.mp4	85.64	17.30	0.84
s11_sponta_resting.mp4	95.29	5.10	0.95
s34_metro_02Hz_resting.mp4	95.51	9.77	0.93
s34_metro_02Hz_moving.mp4	94.87	10.10	0.92
s34_sponta_resting.mp4	95.71	5.55	0.95
s24_metro_05Hz_resting.mp4	91.59	2.40	0.95
s24_metro_05Hz_moving.mp4	64.72	6.83	0.79
s24_sponta_moving.mp4	23.78	146.00	-0.11
s31_metro_05Hz_resting.avi	84.74	2.66	0.91
s31_metro_05Hz_moving.avi	79.43	2.60	0.88
s31_sponta_moving.avi	49.55	14.90	0.67
Total Average	79.46	19.54	0.80
Average without outlier	**84.53**	**8.04**	**0.88**

Observe that the worst results were those for the sequences where the subjects are spontaneously breathing and moving at the same time (i.e. the outlier s24 sponta moving and s31 sponta moving), apparently in a coordinate way, because is almost impossible to isolate the respiration component from the other effects. However, resting subjects spontaneously breathing (s11 sponta resting and s34 sponta resting) consistently allow achieving excellent results of *CorrI* and *NRMSE* at the same time (around 95% and 5%, respectively). Therefore, the spontaneous sequences by themselves are not as demanding as supposed. Actually, it is the other way around, the algorithms perform the best with the more natural situations, i.e. spontaneous breathing at rest, which is highly convenient.

4 Conclusions and Recommendations

We can conclude that CV algorithms are well-suited for estimating the V_T and *RR* signals from video sequences. More specifically, the Viola-Jones algorithm can be used to detect the ROI on the chest, the local feature detectors (as the Harris-Stephens detector) can be used for detecting features to be tracked with a KLT algorithm.

Several parameters computed frame by frame on the ROI contain the main component of the respiration movement signal, from which it could be derived: based on the gray intensity levels, the Farneback optical flow, the displacement in the vertical direction and the RLS adaptively filtered signal using *dy* as main input and *dx* as a reference input, but we used here the displacement of the ROI in the vertical direction (*dy*). Future works could be focused on adaptive filtered versions of these signals.

The results are subject-dependent because of the differences in respiration patterns, clothing style, etc. However, by fine tuning the input parameter values, better results could be obtained.

Conflict of Interest. The authors declare that they have no conflict of interest.

References

1. Alcantarilla, P.F., Bartoli, A., Davison, A.J.: KAZE features. In: ECCV 2012, Part VI, LNCS 7577, p. 214 (2012). https://doi.org/10.1007/978-3-642-33783-3_16
2. Bartula, M., Tigges, T., Muehlsteff, J.: Camera-based system for contactless monitoring of respiration. In: Proceedings of 2013 35th Annual International Conference on IEEE Engineering Medicine and Biology Society, pp. 2672–2675 (2013). https://doi.org/10.1109/embc.2013.6610090
3. Bay, H., Ess, A., Tuytelaars, T., Van Gool, L.: SURF: speeded up robust features. Comput. Vis. Image Underst. (CVIU) **110**(3), 346–359 (2008). https://doi.org/10.1007/11744023_32
4. Farneback, G.: Two-frame motion estimation based on polynomial expansion. In: Proceedings of 13th Scandinavian Conference on Image Analysis, Sweden (2003). https://doi.org/10.1007/3-540-45103-x_50
5. Harris, C., Stephens, M.J.: A combined corner and edge detector. In: Proceedings of the 4th Alvey Vision Conference, pp. 147–152 (1988). https://doi.org/10.5244/c.2.23
6. Leutenegger, S., Chli, M., Siegwart, R.: BRISK: binary robust invariant scalable keypoints. In: Proceedings of IEEE International Conference on ICCV (2011). https://doi.org/10.1109/iccv.2011.6126542
7. Lucas, B.D., Kanade, T.: An iterative image registration technique with an application to stereo vision. In: International Joint Conference on Artificial Intelligence (1981)
8. Reyes, B.A., Reljin, N., Kong, Y., Nam, Y., Chon, K.H.: Tidal volume and instantaneous respiration rate estimation using a volumetric surrogate signal acquired via a smartphone camera. IEEE J. Biomed. Health Inform. **21**(3), 764–777 (2017). https://doi.org/10.1109/jbhi.2016.2532876
9. Rosten, E., Drummond, T.: Machine learning for high-speed corner detection. In: 9th European Conference on Computer Vision, vol. 1, pp. 430–443 (2006). https://doi.org/10.1007/11744023_34
10. Shi, J., Tomasi, C.: Good features to track. In: Proceedings of IEEE Conference on Computer Vision and Pattern Recognition, pp. 593–600 (1994). https://doi.org/10.1109/cvpr.1994.323794
11. Taboada-Crispi, A., Bazan-Prieto, C.A., Lorenzo-Ginori, J.V. et al.: Cancelador adaptativo de interferencias con mínima distorsión. Revista de Bioingeniería y Física Médica Cubana **4** (2), 27–32 (2003)
12. Taboada-Crispi, A., Rivera-Cruz, L., Barber-Perez, M.: Algorithms to estimate the instantaneous frequency of a respiratory time-varying sequence. In: International Conference on Information Processing "CIPI 2019", Cuba (2019)
13. Tomasi, C., Kanade, T.: Detection and Tracking of Point Features. Carnegie Mellon University Technical Report CMU-CS-91-132 (1991)
14. Tuytelaars, T., Mikolajczyk, K.: Local invariant feature detectors: a survey. Found. Trends Comput. Graph. Vis. **3**(3), 177–280 (2007). https://doi.org/10.1561/0600000017
15. Vázquez-Segura, J.A., Mejía-Rodríguez, A.R., Reyes, B.A.: Estimación Óptica Remota de la Actividad y Frecuencia Respiratoria durante Diversas Maniobras Respiratorias. In Memorias del Congreso Nacional de Ingeniería Biomédica **5**(1), 114–117, México (2018)
16. Viola, P.A., Jones, M.J.: Rapid object detection using a boosted cascade of simple features. In: IEEE CVPR (2001). https://doi.org/10.1109/cvpr.2001.990517

Processing of Biomedical Images

Computer-Aided Detection Systems for Digital Mammography

Marlen Perez-Diaz[1(✉)], Ruben Orozco-Morales[1], Eduardo Suarez-Aday[1], and Rosana Pirchio[2]

[1] Automatic and Computer Systems Department, Universidad Central "Marta Abreu de las Villas", Camajuani Road km 5 ½, 52830 Santa Clara, Cuba
mperez@uclv.edu.cu
[2] Medical Physics Department, Atomic Energy National Commission, Buenos Aires, Argentina

Abstract. Mammography is the typical diagnostic test for early detection of breast cancer. The presence of microcalcifications and masses in the images may be an indicator of the disease. The microcalcifications size is very small, so, in many cases, they are not visible from medical images by radiologists. On the other hand, masses can be also undetectable if image contrast is not good enough. The computer-aided detection (CAD) systems are useful tools in facilitating the physician´s diagnosis. The CAD system proposed in this work is aimed at improving image quality based on image processing. On these improved images, it segments the mammary gland and highlights the presence of microcalcifications and masses. The system improves image contrast by means of convolution filters, it also eliminates artifacts by means of morphological opening and closing and Laplacian filtering, and uses entropy-based methods for segmentation of the gland and morphological filtering and histogram readjustment to enhance microcalcifications in the image. Masses are detected using an iterative contrast increase method. The system was tested with an annotated database (DB) *MIAS*, in oblique lateral views of glandular, glandular-dense and predominantly adipose breasts, which included images of malignant and benign lesions and other breast images without them. The system was evaluated with respect to the DB annotation, for a sample of 115 images. The performance of the system revealed a sensitivity of 93.2%, a specificity of 85.3%, a precision of 90.4% and an accuracy of 92%.

Keywords: Computed Aided Diagnostic Systems (CAD) · Mammography · Microcalcifications and masses

1 Introduction

Mammography has proven to be the most effective method for early breast cancer detection. The presence of microcalcifications and masses are indicators of the disease.

Microcalcifications are difficult to detect due to their small size. Among the proposed solutions, in [1] the performance of five algorithms of enhancement of images has been analyzed. In particular, Local Range Modification and Redundant Discrete Wavelet have an effectiveness of 93.2% and 92.6%, respectively. Another relevant

© Springer Nature Switzerland AG 2020
C. A. González Díaz et al. (Eds.): CLAIB 2019, IFMBE Proceedings 75, pp. 265–271, 2020.
https://doi.org/10.1007/978-3-030-30648-9_34

solution was proposed in [2], using a knowledge-based system, which uses local features extracted with a filter bank. In [3] the use of the contour transform and simplified pulse coupling neural networks are introduced to achieve a sensitivity of 96.3% and a specificity of 94.7%. In the last decades, methods that include artificial intelligence have also been used [4].

The masses detection is another important aspect. However, its visualization can be very complex when the mass is very small or the breast tissue is very dense, since it does not produce a noticeable peak in the image histogram. Various methods have been proposed for segmentation of masses. Among them, a scheme in two parts that forms homogeneous blocks first and later uses a quantification of the intensities is introduced [5]; as well as a combination of the entropy of Havrda-Charvat with the method of Otsu's thresholding to obtain a sensitivity of 93% [6]. Recently, the principal component analysis has been used [7]. Also, a two-stage adaptive thresholding method has been proposed [3] with an average sensitivity of 93.5%.

Computer-Aided Diagnostic (CAD) systems have been developed to support and facilitate the radiologists' work. Most of these systems consist of four stages: pre-processing of images, segmentation of the previously described lesions and their extraction of characteristics and classification.

During the pre-processing stage, contrast enhancement techniques are useful since they guarantee a successful subsequent segmentation. In addition to classical methods, such as histogram equalization, transform-based methods, or those based on image decomposition, other strategies have been applied based on histogram optimization [8]. However, these methods are generally computationally expensive. Some examples are: [1, 9–11].

In this work, the efficacy for contrast enhancement in digital images of mammography for microcalcifications is evaluated based on morphological operations in gray scale, known as black top hat and white top hat [1]. These state-of-the-art methods have proven their effectiveness in other contexts. Furthermore, the performance of several methods of masses segmentation based on thresholding was examined by applying different entropy criteria, such as the two-dimensional Tsallis, and several implementations of Shannon entropy [12–15], but in the case of mammography is used for the first time.

2 Materials and Methods

The proposed System includes the pre-processing of the image, the segmentation of the gland, the extraction of lesions characteristics (masses and microcalcifications) and the evaluation of the system. During the pre-processing stage the contrast is enhanced by highlighting the regions of greatest interest. The convolution filters H1, H2, H3 and H4 of Matlab were used for this purpose. This achieves lighting effects, sharpening and edge enhancement.

The artifacts that are not of interest for the study are eliminated. A morphological opening procedure is applied, using a structure element (strel). To remove the labels, the image is converted to binary, using the Laplacian-based ridge [16]. For this purpose, several simple leveling methods (bi-class) based on the entropy of the image are

used for the first time in this case. The used entropy-based thresholding methods have been: maximum entropy (ME), based on the classical definition of *Shannon* entropy [6], the improved version of the *Kapur* method [5] and the two-dimensional implementation introduced from the *Tsallis* entropy [17]. To determine the optimal threshold, the opinion of an experienced radiologist was asked, just to guarantee that the visual appearance of images were not distant from the typical ones. With it, a fine adjustment was made, which consisted of modifying the threshold obtained with each method, multiplying them by a factor k. In addition, a readjustment of the image was made, extending the pixels to the whole gray scale in the histogram.

Then morphological filtering is used for the enhancement of microcalcifications images. To do this, a grayscale erosion is applied with a circular geometry strel with 3 pixels of radius and flat top to increase the size of these objects and make them brighter. The dilation operator increases the size of the bright regions and decreases the size of the objects and the dark regions in the image.

In order to enhance the contrast between the identified objects in the image, morphological transformations in white top-hat and black top-hat gray scale are used. For the mass image enhancement, it was also essential to determine the shape and size of the strel. To do this, an iterative procedure is implemented based on a gradual increase of the strel diameter in each iteration, determining in each case the value of the contrast increase ratio (CIR), until an optimum result is obtained with a value of 20 pixels. The process ends when the CIR of an iteration is less than the previous one. This procedure is also new in the mammography case.

$$CIR = \frac{\sum_{(x,y)\epsilon R}\left(C(x,y) - \hat{\mathrm{C}}(\mathrm{x},\mathrm{y})\right)^2}{\sum_{(c,y)\epsilon R} C^2(x,y)} \tag{1}$$

Where R is the region of interest, while C and $\hat{\mathrm{C}}$ are the local contrasts in the original and enhanced images respectively.

To evaluate the system, 115 images of the database (BD) MiniMammographic were used. In each image, a normal or abnormal region was selected to perform a forced observation task, by comparison with the DB annotation. To evaluate the performance of the designed system, the results that the radiologist detected against the BD annotation were compared. From these elements, the accuracy, precision, sensitivity and specificity of the system were calculated.

$$\text{Accuracy} : \frac{Vp + Vn}{Vp + Vn + Fp + Fn} \tag{2}$$

$$\text{Precision} : \frac{Vp}{Vp + Fp} \tag{3}$$

$$\text{Sensitivity} : \frac{Vp}{Vp + Fn} \tag{4}$$

$$\text{Specificity} : \frac{Vn}{Vn + Fp} \tag{5}$$

Where *Vp* are the true positive, *Vn* are the true negative, *Fn* are the false positive and *Fn* are the False negatives.

3 Results

The H4 filter displayed the best results of image contrast enhancement and edge enhancement and was the one selected to use with the images for the different levels of glandularity. The thresholding methods employed, based on entropy, showed different results. Some images were over-segmented but in others, a lot of extra tissue was included. The results of these methods were averaged obtaining the best results. Figure 1 shows an example of the system's performance up to this point. The values of the fine segmentation correction coefficient (k) were between 0.6–1.0.

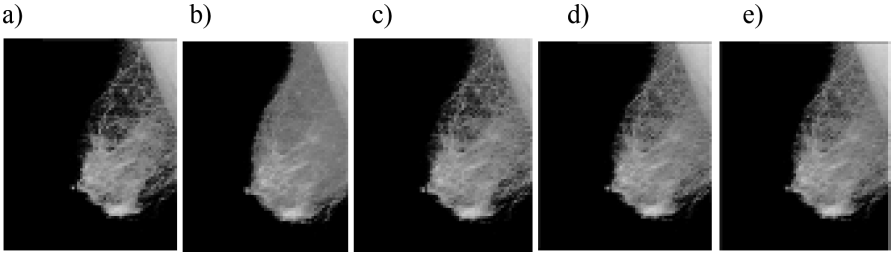

Fig. 1. Original image, enhanced and readjusted, with artifacts removed and subjected to different thresholding methods: (a) Method 1 Thr = 144 and k = 0.8, (b) Method 2 Thr = 127 and k = 1, (c) Method 3 Trh = 141 and k = 0.85, (d) Method 4, Thr = 138 and k = 0.8, (e) Average of the four methods.

Figure 2 shows the results provided by the proposed system up to the next step, for a dense glandular breast, where the microcalcifications are highlighted, using the morphological filtering (2c). The morphological dilation increased the size of the microcalcifications with the aim of focusing the visualization and localization of these anomalies by the radiologists; this is the most useful aspect of the system.

Figure 3 shows the original image of a breast that contains spiculated masses and the progress of the algorithm, showing the increase in contrast, until reaching the mass detection. For this image, the CIR reached its maximum value in 10 iterations.

The performance of the system is shown in comparison with the base annotation, from the 115 images evaluated by the radiologist using the proposed system (Table 1).

In [4] 100 cases of the same BD have been used, but under the paradigm of artificial intelligence. They have obtained 94 true positives, 4 false positives and 2 false negatives. Three different algorithms were used using machine learning [18] with 161 images from the MIAS database to classify breast lesions, using 5 different pixel size

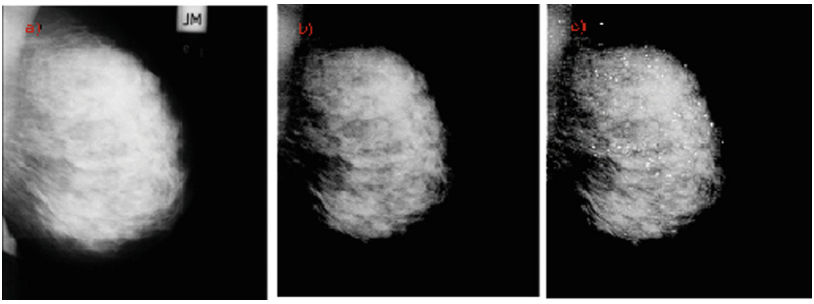

Fig. 2. (a) Original image. (b) Segmented image preprocessed, readjusted, cleaned of artifacts and with the microcalcifications detected in their real size. (c) Image with enhanced microcalcifications.

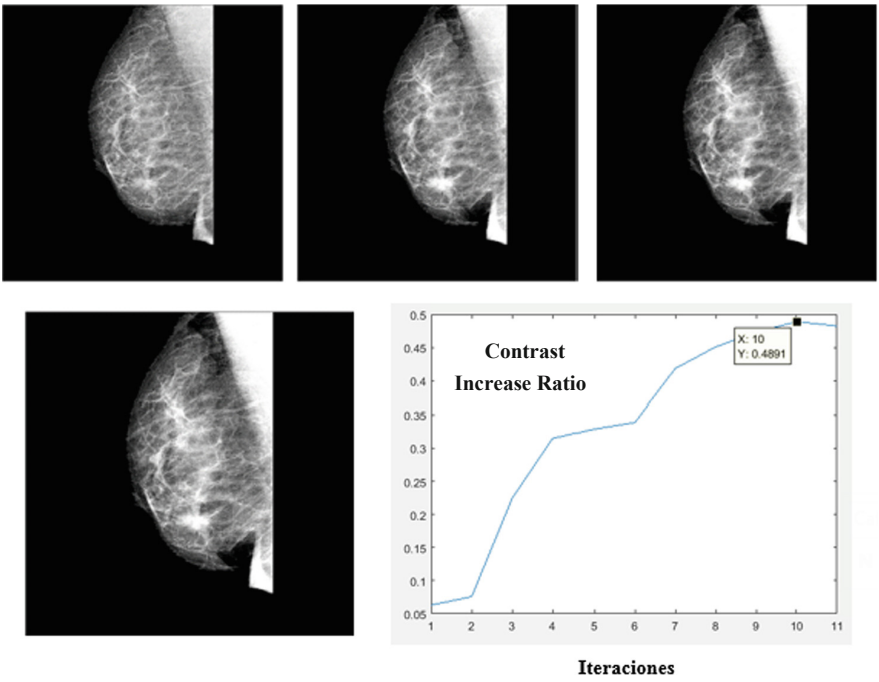

Fig. 3. Result of the detection algorithm and mass enhancement image.

Table 1. Evaluation of the performance of the proposed CAD system.

Accuracy (%)	Precision (%)	Sensitivity (%)	Specificity (%)
90.4	92	93.2	85.3

values and 5 methods of texture analysis, obtaining AUC values between 40 and 78%. The adaptive thresholding is used and 170 images from the BD MIAS [3] and they obtained a sensitivity of 93% and a rate of 0.62 false positives (microcalcifications) per image. In [17] they use segmentation of the gland in the 322 images of the MIAS BD by the Otsu method, thresholding with Wavelet focus and detection by one-dimensional Tsallis Entropy. They obtained AUC values between 87 and 92%. In [7] the 322 images of the MIAS BD were used again to detect masses, using a k-means conglomerate algorithm and analysis of principal components for classification. They obtained an accuracy of 92.7% in non-dense breasts and 79.17% in dense breasts; they also obtained 5 false positives and 2 false negatives for each type of breast. In this sense, it can be stated that the results of the proposed CAD system are in the environment of those reported by other authors using other methods of segmentation-detection and/ or classification, for the same database.

All the calculations were below 30 s, in a common laptop computer, with an Intel P6 Pro-crossover, with 6 GB of RAM. The proposed CAD system proved to be efficient and can be used under conditions of clinical routine to facilitate the diagnosis.

4 Conclusions

For the detection of breast lesions images in mammography a new CAD system was proposed. This system allowed the best edge enhancement with the convolution filter H4. With this, the spatial resolution was improved without introducing excessive noise. All the artifacts were satisfactorily eliminated from the combination of Laplacian segmentation, opening of binary areas and determination of binary related components. The mammary gland was successfully segmented from the average of three global thresholding methods, based on entropy and image readjustment. The microcalcifications were detected from the morphological filtering. The masses were satisfactorily detected after implementing an iterative method for the improvement of image contrast. The proposed CAD system presented good performance index.

Conflict of Interest. The authors declare no conflict of interests.

References

1. Papadopoulos, A., Fotiadis, D., Costaridou, L.: Improvement of microcalcification cluster detection in mammography utilizing image enhancement techniques. Comput. Biol. Med. **38**(10), 1045–1055 (2008)
2. Arnau, O., Torrent, A., Llado, X., Tortajada, M., Tortajada, L.S., et al.: Automatic microcalcification and cluster detection for digital and digitised mammograms. Knowl.-Based Syst. **28**(4), 68–75 (2012)
3. Anitha, J., Dinesh, P., Pandian, I.: A dual stage adaptive thresholding (DuSAT) for automatic mass detection in mammograms. Comput. Methods Programs Biomed. **138**(10), 93–104 (2017)

4. López, Y., Novoa, A., Guevara, M., Quintana, N., Silva, A.: Computer aided diagnosis system to detect breast cancer pathological lesions. In: Iberoamerican Congress on Pattern Recognition, pp. 453–460. Springer, Heidelberg (2008)
5. Maitra, I., Sanjay, N., Kumar, S.: Identification of abnormal masses in digital mammography images. Int. J. Comput. Graph. **2**(1), 17–24 (2011)
6. Burcin, K., Vasif, V., Turhan, K.: A novel automatic suspicious mass regions identification using Havrda & Charvat entropy and Otsu's N thresholding. Comput. Methods Programs Biomed. **114**(3), 349–360 (2014)
7. Oliveira-Silva, L., Kardec-Barros, A., Vinicius- Lopes, M.: Detecting masses in dense breast using independent component analysis. Artif. Intell. Med. **80**(7), 29–38 (2017)
8. Babu, P., Rajamani, V.: Evolutionary algorithm based optimized histogram modification for contrast enhancement of mammogram images. J. Med. Imaging Health Inform. **6**(2), 518–525 (2016)
9. Sundarama, M., Ramar, K., Arumugam, N., Prabin, G.: Histogram modified local contrast enhancement for mammogram images. Appl. Soft Comput. **11**(8), 5809–5816 (2011)
10. Mustra, M., Grgic, M.: Robust automatic breast and pectoral muscle segmentation from scanned mammograms. Sig. Process. **93**(10), 2817–2827 (2013)
11. Sheeba, J., Parasuraman, S., Kadirvelu, A.: Contrast enhancement and brightness preserving of digital mammograms using fuzzy clipped contrast-limited adaptive histogram equalization algorithm. Appl. Soft Comput. **42**(5), 167–177 (2016)
12. Chang, C., Du, Y., Wang, J., Guo, S., Thouin, P.: Survey and comparative analysis of entropy and relative entropy thresholding techniques. IEEE Proc. Vis. Image Signal Process. **153**(6), 837–850 (2006)
13. Yan, H., Liu, J., Yang, D., Wang, P.: An improved algorithm of the maximum entropy image segmentation. In: Fifth International Conference on Intelligent Systems Design and Engineering Applications, pp. 157–160. IEEE, Zhangjiajie (2014). https://doi.org/10.1109/isdea.2014.255
14. Kapur, J., Sahoo, P.: A new method for gray-level picture thresholding using the entropy of the histogram. Comput. Vis. Graph. Image Process. **29**(3), 273–285 (1985)
15. Prasanna, K., Gurdial, A.: Image thresholding using two-dimensional Tsallis–Havrda–Charvát entropy. Pattern Recogn. Lett. **27**(6), 520–528 (2006)
16. Abdulkader, H., Abiyev, R.: Shape and texture features for the identification of breast cancer. In: Proceedings of the World Congress on Engineering and Computer Science. Newswood, San Francisco (2016)
17. Mehdi, M., Gargour, B., Ayed, A., Masmoudi, D., Sellami, R.: An efficient microcalcifications detection based on dual spatial/spectral processing. Multimedia Tools Appl. **76**(11), 13047–13065 (2017)
18. Abdel-Nasser, M., Melendez, J., Moreno, A., Puig, D.: The impact of pixel resolution, integration scale, preprocessing, and feature normalization on texture analysis for mass classification in mammograms. Int. J. Opt. (2016). http://dx.doi.org/10.1155/2016/1370259. ID 1370259

Check for updates

Time Estimation of Topotecan Penetration in Retinoblastoma Cells Through Image Sequence Analysis

Debora Chan[1], Ursula Winter[2], Paula Schaiquevich[2], Rodrigo Ramele[3], and Juliana Gambini[1,3,4(✉)]

[1] Universidad Tecnológica Nacional, Regional Buenos Aires, Buenos Aires, Argentina
mchan@frba.utn.edu.ar
[2] CONICET - Hospital de Pediatría Prof. Dr. Juan P. Garrahan, Buenos Aires, Argentina
[3] Depto. de Ingeniería en Informática, Instituto Tecnológico de Buenos Aires, Buenos Aires, Argentina
mgambini@itba.edu.ar
[4] Depto. de Ingeniería en Computación, UNTreF, Buenos Aires, Pcia. de Buenos Aires, Argentina

Abstract. Retinoblastoma is the most common intraocular tumor in childhood. Topotecan has been widely used as an antineoplastic agent for retinoblastoma treatment. Topotecan penetration into living tumorspheres is quantified using confocal microscopy. This fluorescent drug dyes the living tissue and it can be recorded in a sequence of images over a period of time. The effective penetration of the drug depends on culture characteristics and requires a very specific timing. This penetration time is calculated empirically by an expert. The purpose of this work is to offer a statistical model to automatically estimate the penetration time of topotecan in the cell, based on the information obtained from a sequence of tumorsphere images.

Keywords: Sequence of confocal microscopy image · Statistical model · Tumorspheres · Retinoblastoma

1 Introduction

Retinoblastoma is the most frequent ocular tumor in childhood. It is characterized by the appearance of malignant cells in the retina. In Argentina, 45 new cases are detected per year, and 80% are referred for care to Prof. Dr. Juan Pedro Garrahan Hospital, Buenos Aires, where the current cure rate is over 98%. Worldwide, approximately 60% of cases of retinoblastoma occur unilaterally (only in one eye) while the remaining 40% compromises both eyes. In unilateral disease, the average age of onset in children is 2 years old, while in the bilateral case, it is 1 year old. For its treatment, Garrahan Hospital currently relies on a small number of drugs that are administered by different routes according to

© Springer Nature Switzerland AG 2020
C. A. González Díaz et al. (Eds.): CLAIB 2019, IFMBE Proceedings 75, pp. 272–280, 2020.
https://doi.org/10.1007/978-3-030-30648-9_35

the ophthalmologist's and oncologist's criteria, including: systemic (intravenous infusion), intravitreal and intra-arterial treatment. Each administration route has its advantages and disadvantages and the delivery of one treatment or the other depends on medical criterion. Local administration routes, such as intravitreal and intra-arterial routes have advantages over systemic chemoreduction, because they reduce the occurrence of serious adverse events such as severe myelosuppression [7,11]. One of the drugs used in retinoblastoma treatment is topotecan.

Several authors have studied retinal diseases using different types of medical images and statistical modeling. For example in [9] a study for tumor classification using a probabilistic framework is presented. In [12] a method for vessel segmentation using active contours is introduced. In [6] a work focused on retinoblastoma detection is presented and several processing techniques are reviewed, all of them based on different types of medical image processing. In [10], the authors contribute to understanding retinoblastoma by studying drug penetration and response to chemotherapy to optimize patient treatment. Inspired by that work, in this paper we focus on image sequences analysis and processing techniques combined with statistical analysis, in order to determine the penetration time of topotecan in tumor clusters (set of tumor cells).

The objectives of this work are:

1. To estimate the time that topotecan consumes in penetrating the whole tumorsphere by means of microscopy image sequence analysis. The tumorsphere is considered to have been totally penetrated when it has a homogeneous color in the central region. We work with live-cell imaging.
2. To compare the penetration rate of topotecan between types of tumorspheres from Patient 1 and Patient 2.
3. To Compare the penetration rate of topotecan between different sizes of tumorspheres, derived from the same patient.

This article unfolds as follows. In Sect. 2.1, the experiment and image processing techniques to segment the microscopy image sequence are described. In Sect. 2.2, a statistical analysis of topotecan fluorescence evolution based on a mixed model with fixed and random effects is performed. Section 3 shows the results and a discussion. Finally, in Sect. 4, final remarks and future works are presented.

2 Materials and Methods

The experiment consists of the following steps: two primary cell cultures are obtained from the intraocular tumor of two patients, which were enucleated due to the advanced nature of the disease. After signing the informed consent (Protocol # 904, Hospital de Pediatria J. P. Garrahan), once the enucleation is completed by the ophthalmologist, she/he takes tumor samples, which are placed in the middle of defined cultures for primary cell cultures. Once the cultures are

established and characterized according to the morphology and cellular markers of the retina, they are used to study the penetration speed of the drug, for more details, see [10].

The main advantage of having chosen topotecan is that its penetration can be quantified through its fluorescence emission by laser excitation. The microscope used is Olympus Fluoview FV1000 confocal laser scanning microscope (Olympus, Tokyio, Japan) with imaging software (Olympus Fluoview FV10-ASW v1.7c) and equipped with a UPlanSApo 20X/0.75 NA objective.

The cell cultures studied belong to two patients:

- Patient 1: the patient was enucleated in the first line of treatment without having previously received chemotherapy.
- Patient 2: the patient had received chemotherapy prior to the enucleation of the affected eye.

Obtaining tumor cell primary cultures is an important challenge due to stringent growth and maintenance conditions. These patient models are unique in Argentina and given the aforementioned conditions, there is a limited number of available models. These cell cultures, to which we refer to as tumorspheres, are classified, according to their size, into three categories: small, medium and large. Then, 1 μl of a 10 μg/ml solution of topotecan is injected to the cell culture and a sequence of microscopy images are taken. The penetration time of the drug in the tumorsphere is expected to be predicted according to the fluorescence evolution over time. Figure 1 shows an example of a sequence of microscopy images corresponding to a large size tumorsphere from Patient 1. It can be observed that gray levels of pixels become brighter as time passes by. As topotecan penetrates the cell, it takes on brighter gray levels.

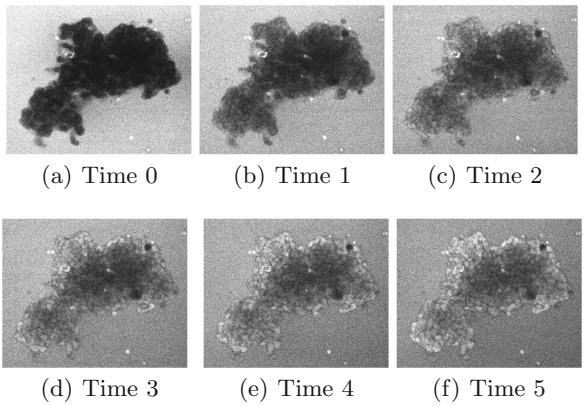

(a) Time 0 (b) Time 1 (c) Time 2

(d) Time 3 (e) Time 4 (f) Time 5

Fig. 1. Example of a sequence of microscopy images taken at 30 s intervals, corresponding to large size tumorsphere from Patient 1.

2.1 Image Sequence Analysis and Interpretation

In this section, the methods of image analysis used for automatic interpretation of a sequence of microscopy images are described.

The microscopy images are contaminated with noise which can be observed as a granulation. Figure 1 shows an example of a sequence of images where none image improvement technique was applied. Noise confuses automatic methods of image interpretation and it is necessary to eliminate it before starting the analysis. A method of noise removal with edge preservation called Anisotropic Diffusion method [5] is applied because it balances noise reduction, edge preservation and low computational cost [3]. Figure 2 shows the result of applying the method to the images of Fig. 1.

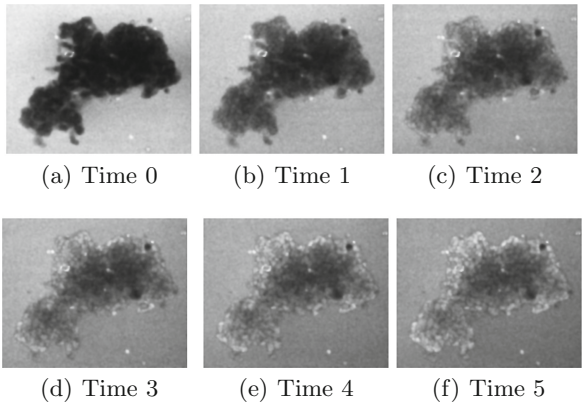

(a) Time 0 (b) Time 1 (c) Time 2

(d) Time 3 (e) Time 4 (f) Time 5

Fig. 2. Results of applying the Anisotropic Diffusion Method to the images of Fig. 1.

The main idea is to classify the pixels inside the tumorsphere in two classes, black and white. Black zones correspond to regions of the tumorsphere where topotecan did not penetrate. White zones correspond to regions of tumorspheres where topotecan penetrated. In order to classify the pixels inside the tumorsphere, the contour of the tumorsphere in the first image of the sequence is computed using an Active Contours algorithm, presented in [8]. This method was successfully modified for ultrasound image segmentation [2]. This procedure receives, as input data, an image I_1, the first image of the sequence and an initial region inside the object of interest. Then, it returns a list of pixels belonging to the contour of the object of interest, named C. It has several advantages over other methods of active contours because rather than solving differential equations, the contour is found through y the interchange between two lists of neighboring pixels, saving computational cost. This method is highly efficient since it determines the contour of the object with high precision and it can be used in applications with real time requirements or constrained computational resources. Figure 3(a) shows the initial region of the algorithm, chosen in a supervised way. Figure 3(b) shows the computed contour for a small tumorsphere of Patient 1. Given the contour of the cell, the set of pixels in the inner of the contour, TS are computed.

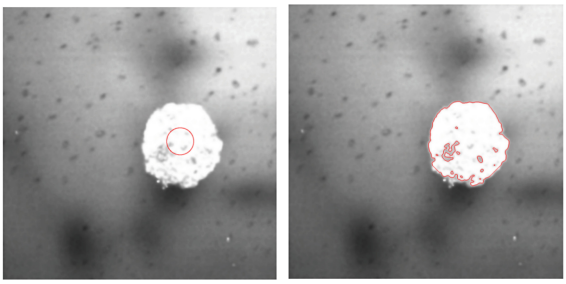

(a) Initial region. (b) Contour detection in red colour.

Fig. 3. Tumorsphere contour detection.

$$TS = \{(x, y) \in I/(x, y)\ is\ inside\ C\} \tag{1}$$

Then, we calculate the threshold to segment TS in two classes, by means of Otsu's thresholding method [4], obtaining two colors for region TS in the image called B_1. We use the same contour and the same threshold to analyze the entire sequence, obtaining $\{B_1, \ldots, B_n\}$, where n is the number of sequence images. Results are presented in Fig. 4(a)–(f). The background is excluded from the analysis.

We calculate the percentage of black pixels within the tumorsphere. The percentage decreases as time passes by, indicating that the topotecan penetrates in the cell. Table 1 shows the results for each image of the sequence of Fig. 4.

The percentage of black pixels for each image of the sequence is computed as:

$$p^j_{Black} = \frac{\#\{(x, y) \in TS/B_j(x, y) = 0\}}{M},\ j = 1, \ldots, n \tag{2}$$

where (x, y) is a pixel location and M is the total number of pixels of the object TS.

2.2 Statistical Analysis

In this section, a statistical model for time penetration prediction is performed using the results obtained in Sect. 2.1 for 11 tumorsphere samples from Patient 1 and 10 tumorsphere samples from Patient 2.

Generalized Mixed Models make it possible to predict the expected value of the response variable of the phenomena under study, considering the temporal variability and the correlation. With the mixed model both, fixed effects as tumorsphere sizes, and random effects, which are essential due to the biological variability between samples can be included in the same model [1]. In this case, the response variable is the penetration time, estimated from the black pixels rate.

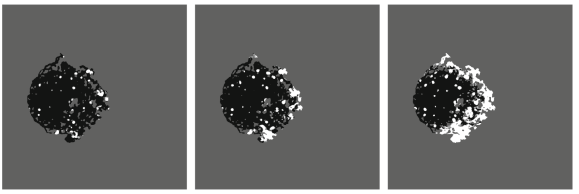

(a) Time 1 (b) Time 2 (c) Time 3

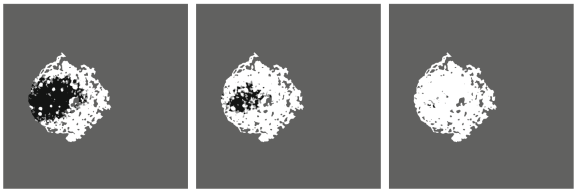

(d) Time 4 (e) Time 5 (f) Time 6

Fig. 4. Two-class tumorsphere classification.

Table 1. Percentage of black pixels within the tumorsphere for each image of the sequence of Fig. 4.

Image	Fig. 4(a)	Fig. 4(b)	Fig. 4(c)	Fig. 4(d)	Fig. 4(e)	Fig. 4(f)
p_{Black}	0.94%	0.87%	0.68%	0.39%	0.13%	0.005%

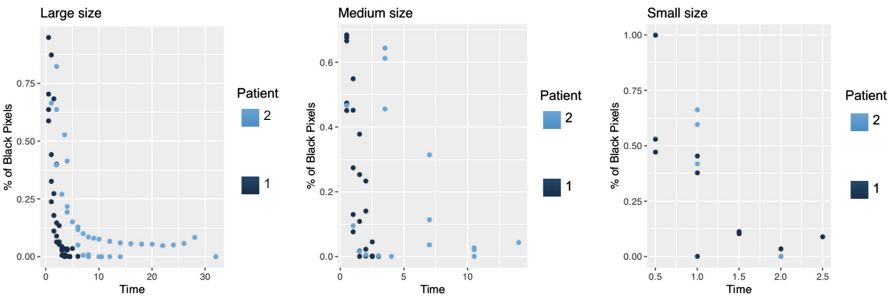

(a) Large size (b) Medium size (c) Small size

Fig. 5. Topotecan penetration evolution for different cell sizes.

Figure 5(a)–(c) show the evolution of the percentage of black pixels for both patients, for large, medium and small cells, respectively.

We propose the following statistical model

$$\widehat{Y}_{ij} = a_i + \beta_0 t_{j(i)}^{\beta_i} e^{(\alpha_L * L + \alpha_S * S) t_{j(i)}}$$

where

- i number of patient, $i \in \{1, 2\}$.
- β_0, a_i, β_i, $i = 1, 2$ are the unknown coefficients.
- Y_{ij} varies from 0 to 1 and is the black pixel rate inside the cell at the $t_{j(i)}$time, corresponding to the i-th patient, with $j \in \mathcal{N}$.
- $t_{j(i)}$ time in the j-th image of the sequence for patient i (1 or 2), whereas j is enclosed in parenthesis as a nested factor on i and references the time point in which the image was captured. This depends on each patient and each tumorsphere size.
- α_L and α_S coefficients correspond to Large and Small tumorspheres respectively.
- $L = 1$ if the size of the tumorsphere is large and $L = 0$ in other case. Likewise, $S = 1$ if the size of the tumorsphere is small and $S = 0$ in any other case. Hence, a middle-sized tumosphere is identified when $L = 0$ and $S = 0$.

3 Results and Discussion

In this section, the results of the statistical model and a discussion is presented. Microscopy images were taken at 30 s for some sequences and at 60 seconds for others. For some of them, the penetration time reached 210 s for Small tumorspheres while it took almost 1920 s for their Large counterparts. Therefore, time varies from 30 s to 1920 s. Coefficients α_L and α_S take values 0 or 1.

Black pixel rate plotting shows different curves for each one of the tumorsphere sizes and is different for the two patients. However, both plots have a decreasing tendency for increased time values. For this reason, a Γ family distribution was selected, due to their versatility and their ability to capture the variability per patient and per tumorsphere size.

Considering size, average penetration times are 164.4 s (Big), 144.6 s (Medium) and 1.83 m (Small) for the previously untreated patient, whereas 8.66 m (Big), 8.3 m (Medium) and 109.8 s (Small) for the patient who underwent a previous treatment.

Concerning the penetration time based on tumorsphere size and patient, ANOVA testing shows that differences are statistically significant.

The estimated coefficients are given by:

- Patient 1:
$$\widehat{Y}_{1j} = 0.3127 t_{j(1)}^{-0.251} e^{(0.0065*L - 0.0923*S)t_{j(1)}}$$
- Patient 2:
$$\widehat{Y}_{2j} = 0.5018 t_{j(2)}^{-0.205} e^{(0.0065*L - 0.0923*S)t_{j(2)}}$$

For both models, all coefficients are statistically significant. The residuals are approximately Gaussian distributed. The Levene test does not reject the homoscedasticity assumption of the model in any case. With this model comparisons can be between large - medium size and small - medium size. For each of the sizes of tumorspheres and for each patient considered, it is possible to compute the average time at which the percentage of blacks is less than 10%. Due to space constraints final results are not presented.

4 Conclusions

This work shows that a statistically significant model can be devised in order to predict the required penetration time of topotecan in a tumorsphere, depending on the type of patient. The model proposed here can offer complementary information to care givers about the penetration time, which can be accurately estimated. The conclusion of the study indicates that the larger the size of the tumorsphere, the longer the penetration time. In addition, the penetration time is longer in tumorspheres corresponding to Patient 2 than those corresponding to Patient 1. This result is not surprising as larger seeds consist of a greater number of cells arranged in multilayers around a central core. Therefore, spheres are not mere aggregates of cells but 3D structures that may hamper drug accessibility.

As future work, additional work should be conducted in order to verify alternative statistical models and to use neural networks to estimate penetration time.

Conflict of Interest. The authors declare that they have no conflict of interest.

References

1. Bates, D., Mächler, M, Bolker, B, Walker, S: Fitting linear mixed-effects models using lme4. arXiv preprint arXiv:1406.5823 (2014)
2. Bisso, I., Gambini, J.: Ultrasound image segmentation through a fast active contour based algorithm. In: VI Congreso Latinoamericano de IngenierÌa BiomÈdica (2014). https://doi.org/10.1007/978-3-319-13117-7_92
3. Haider, S.A., Cameron, A., Siva, P., Lui, D., Shafiee, M.J., Boroomand, A., Haider, N., Wong, A.: Fluorescence microscopy image noise reduction using a stochastically-connected random field model. Nature Scientific report, vol. 6, p. 20640 (2016). https://doi.org/10.1038/srep20640
4. Otsu, N.: A threshold selection method from gray-level histogram. IEEE Trans. Syst. Man Cybern. **9**, 62–66 (1979). https://doi.org/10.1109/TSMC.1979.4310076
5. Perona, P., Malik, J.: Scale-space and edge detection using anisotropic diffusion. IEEE Trans. Pattern Anal. Mach. Intell. **12**(7), 629–639 (1990). https://doi.org/10.1109/34.56205
6. Sadhana, S., Mallika, D.: A review of retina blood vessel detection using image segmentation techniques. Int. J. Innovative Res. Sci. Technol. **3**, 247–253 (2017)
7. Schaiquevich, P., Ceciliano, A., Millan, N., Taich, P., Villasante, F., Fandino, A.C., Dominguez, J., Chantada, G.L.: Intra-arterial chemotherapy is more effective than sequential periocular and intravenous chemotherapy as salvage treatment for relapsed retinoblastoma. Pediatr. Blood Cancer, 766–770 (2013). https://doi.org/10.1002/pbc.24356
8. Shi, Y.G., Karl, W.C.: A real-time algorithm for the approximation of level-set-based curve evolution. Image Process. **17**(5), 645–656 (2008). https://doi.org/10.1109/TIP.2008.920737
9. Tobin, K.W., Abdelrahman, M., Chaum, E., Govindasamy, V.P., Karnowski, T.P.: A probabilistic framework for content-based diagnosis of retinal disease. In: 29th Annual International Conference of the IEEE Engineering in Medicine and Biology Society, pp. 6743–6746 (2007). https://doi.org/10.1109/IEMBS.2007.4353909

10. Winter, U., Aschero, R., Fuentes, F., Buontempo, F., Zugbi, S., Sgroi, M., Sampor, C., Abramson, D., Carcaboso, A., Schaiquevich, P.: Tridimensional retinoblastoma cultures as vitreous seeds models for live-cell imaging of chemotherapy penetration. Int. J. Mol. Sci. **20**, 1077 (2019). https://doi.org/10.3390/ijms20051077
11. Winter, U., Nicolas, M., Sgroi, M., Sampor, C., Torbidoni, A., FandiÒo, A., Chantada, G., Munier, F., Schaiquevich, P.: Assessment of retinoblastoma rna reflux after intravitreal injection of melphalan. Br. J. Ophthalmol. **3**, 415–418 (2018). https://doi.org/10.1136/bjophthalmol-2017-310574
12. Zhao, Y., Rada, L., Chen, K., Harding, S.P., Zheng, Y.: Automated vessel segmentation using infinite perimeter active contour model with hybrid region information with application to retinal images. IEEE Trans. Med. Imaging **34**(9), 1797–1807 (2015). https://doi.org/10.1109/TMI.2015.2409024

A Comparative Study of Reinforcement Learning Algorithms Applied to Medical Image Registration

Ramiro F. Isa-Jara[1(✉)], Gustavo J. Meschino[2], and Virginia L. Ballarin[1]

[1] Image Processing Laboratory, ICYTE-CONICET, Universidad Nacional de Mar del Plata, Mar del Plata, Argentina
ramfer.isaj@gmail.com
[2] Bioengineering Laboratory, ICYTE-CONICET, Universidad Nacional de Mar del Plata, Mar del Plata, Argentina

Abstract. Nowadays, several medical procedures depend on the comparison and combination of images obtained in different modalities (magnetic resonance, computed tomography, PET, among others). Image registration is a geometric transformation process to align two or more images. It is necessary to have robust algorithms to find the best parameters of transformation in order to achieve accurate registrations. Reinforcement learning allows to train an agent through direct environment interaction, to achieve a goal. In this work, a comparison of the performance of Q-learning and Deep-Q with its variants is presented. Brain magnetic resonance images are used in 2D domain considering rigid deformations. The comparison is based on the reward values, computing the Pearson correlation factor in monomodal registration and Mutual information in multimodal registration, obtained during the learning process. It is also considered an error measure between the target parameters and the achieved ones. Finally, a backup memory criterion is proposed to train the Q-Network methods. Experimental results show a successfully behavior in all cases, but performance is improved when the proposed criterion is applied.

Keywords: Q-learning · Deep-Q Networks · Reinforcement learning · Image registration · Machine learning

1 Introduction

Reinforcement Learning (RL) is one of the three main paradigms of Machine Learning. RL is composed by: an agent, an environment and its model, a policy, a reward signal and a value function [1]. The main idea is that an agent can be trained through direct interaction with its environment, therefore it is a learning process to take actions to maximize a numerical reward signal [1, 2].

Registration is a geometrical aligning process between two or more images, taken in different times, views or modalities, for comparison and combination of information purposes [3]. In the medical field, this process has an important role, especially in

© Springer Nature Switzerland AG 2020
C. A. González Díaz et al. (Eds.): CLAIB 2019, IFMBE Proceedings 75, pp. 281–289, 2020.
https://doi.org/10.1007/978-3-030-30648-9_36

patient monitoring and treatment [4]. This requires robust algorithms that allow to obtain better results using reasonable time and computing resources.

The aim of this work is to apply RL algorithms, *Q-learning, Deep-Q-Network (DQN), Double DQN and Dueling DQN,* to image registration tasks in order to compare their performances. Moreover, a backup memory criterion, as a novel way to train a neural network, is introduced in order to improve the results of DQN algorithms. It is applied in Double DQN to analyze their performances.

This work is organized as follows: Sect. 2 summarizes the algorithms used; Sect. 3 describes their application in an image registration process; Sect. 4 shows the obtained results and Sect. 5 presents the conclusions and future work.

2 Reinforcement Learning Algorithms

2.1 General Description

Reinforcement learning is based on dynamic system theory for optimal control. Markov decision processes (MDPs) are used due its mathematical background. MPDs are the formalization of sequential decision making where actions can influence not just immediate rewards but also in future states and rewards [1].

A finite *Markov Decision process* is defined by a tuple $\langle S, A, T, R, E \rangle$, where S is the agent's state-space, A is the action-space, T is the dynamic transition in reference to $T(s, a, s')$ i.e. the probability to select an action a in current state s to obtain the next state s', R is the numeric reward value obtained when an agent change the state s to s' selecting an action, and E is the terminal states set to avoid future transitions where $E \subset S$ [5]. Thus, the probability of those values occurring at time t, given particular values of the state and actions, is defined as:

$$p(s', r|s, a) = \Pr\{S_t = s', R_t = r|S_{t-1} = s, A_{t-1} = a\}. \tag{1}$$

2.2 Q-Learning Algorithm

Q-learning is a RL technique derived from Temporal Difference (TD) methods. TD methods combine properties of Dynamic programming algorithms and Monte-Carlo methods. The goal is to learn a policy, which tells an agent what action to take in different states [6].

In order to adjust the polices, Watkins [7] introduced an *action-value function* $Q^{\pi}(s, a)$ which is the expected value in the initial state s, selecting an action a through the policy π. According to the Bellman equation, the Q function [8] for an optimal policy, is defined as:

$$Q^*(s, a) = \sum\nolimits_{s' \epsilon S} T(s, a, s')[R(s, a, s') + \gamma \max_{a'} Q^*(s', a')], \tag{2}$$

where, $0 \leq \gamma \leq 1$, is the discounting factor to evaluate how valuable is the immediate reward in terms of the expected final reward.

Function Q updating is simply performed with instantaneously available information, which is a function of the optimal actions (normally a greedy policy is used) [6]. The update of function Q at time t can be written as:

$$\begin{gathered}\delta_t = \left[r_{t+1} + \gamma \max_{a'} Q_t(s_{t+1}, a') - Q_t(s_t, a_t)\right] \\ Q_{t+1}(s_t, a_t) \leftarrow Q_t(s_t, a_t) + \alpha_t(s_t, a_t)\delta_t,\end{gathered} \tag{3}$$

where α is the learning rate, $\alpha \epsilon (0, 1]$.

2.3 Deep-Q Network Algorithm

The DQN algorithm, proposed by Mnih [9], uses a multilayer neural network that has an array of states S as input and an array of actions A as output. The *action-value function* will be $Q(s, .; \theta)$, where θ are the weights of the network called *Deep*. The function Q is calculated by updating θ based on experience [10, 11].

In this case, an agent learns the parameterized function $Q(s, a; \theta_t)$:

$$\theta_{t+1} = \theta_t + \alpha\left(Y_t^Q - Q(s_t, a_t; \theta_t)\right)\nabla_{\theta_t} Q(s_t, a_t; \theta_t), \tag{4}$$

where α is the learning rate and Y_t^Q are the target values computed by: $Y_t^Q = r_{t+1} + \gamma \max_a Q(s_{t+1}, a; \theta_t)$.

2.4 Double DQN Algorithm

If the same *action-value function* is used to evaluate and select an action a, it may lead to over-optimization. In the Double DQN algorithm, an agent learns two *action-value functions* through assignment of random experiences to obtain two sets of parameters or weights θ and θ' [10]. To update the function, one set of parameters is used to determine *the policy* and the other one is used to compute *the value.* The target values in Double DQN algorithms are computed as:

$$Y_t^{DoubleQ} = r_{t+1} + \gamma Q\left(\max_a Q(s_{t+1}, a; \theta_t); \theta_t^{'}\right). \tag{5}$$

2.5 Dueling DQN Algorithm

It is usually assumed that the choice of an action is always a priority, but there are some cases, especially in a free-model problem, where selecting an action or another does not affect the overall performance of the agent [12]. Therefore, *the action-value function* $Q(s, a; \theta_t)$ can be separated into its two main subfunctions:

$$Q(s, a; \theta, \alpha, \beta) = V(s; \theta, \beta) + A(s, a; \theta, \alpha), \tag{6}$$

where $V(s)$ is the *value function*, $A(s,a)$ is the *advantage function*, θ is the set of parameters of the neural network and α, β are the set of parameters corresponding to $V(s)$ and $A(s,a)$. The subfunctions are combined in the output layer in order to obtain the function Q [13].

3 Description of Problem and Applications of Algorithms

3.1 Medical Image Registration

Two images are considered during the registration process: the *target image* and the *moving image*. The moving image is deformed to align to the coordinate system of the target image [14].

A geometric transformation is estimated considering 3 parameters: *scale, orientation and translation.* Monomodal and multimodal registration are performed in the 2D domain with the translation parameter over the X and Y axes.

3.2 Image Description

The image dataset is composed of brain magnetic resonance images (MRI) in T1 and T2 modalities and SPECT images (Fig. 1). The images were provided by the Radiologic Institute of Mar del Plata, Argentina. In these images, only rigid deformations can occur during acquisition.

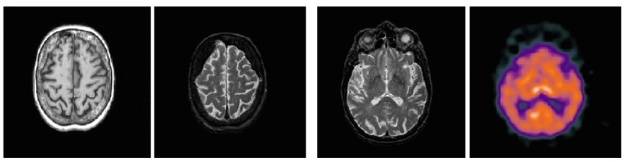

Fig. 1. Brain magnetic resonance images used in tests. **G1** - MRI of the same slide in T1 and T2 weighted modalities. **G2** - MRI of same slide in T2 weighted and SPECT modalities

T1 and T2 images are sized 256 × 256, 8 bits, grayscale. SPECT images have the same size, RGB color space, 8 bits per channel.

3.3 Software and Hardware Description

RL algorithms were implemented in *Python 3.6*, using *TensorFlow 1.10*. The tests were performed using a Core-i5 computer with 8 GB RAM and Debian operating system.

3.4 RL Algorithms in Image Registration

RL algorithms have been adapted for image registration taking the next considerations:

1. *Environment:* composed by the target image and the moving image. The moving images are created using the parameters of Table 1 as targets, in order to measure the error achieved by each algorithm.

Table 1. Parameters used to generate the testbench to test RL algorithms.

Registration modality	Test 1 $[s, \theta, t_x, t_y]$	Test 2 $[s, \theta, t_x, t_y]$
G1 T1 – T1	$[1.2, 29°, -10, 1]$	$[0.8, -29°, 10, -5]$
G1 T1 – T2	$[1.0, -15°, 0, -7]$	$[1.0, 15°, 8, 0]$
G2 T2 – T2	$[1.15, -10°, -5, -15]$	$[0.85, 10°, 7, 12]$
G2 T2-SPECT	$[1.1, -45°, -9, 6]$	$[0.9, 45°, -17, 12]$

2. *States:* described as the set $[s, \theta, t_x, t_y]$, where s is the scale value, θ is the orientation angle, and t_x and t_y are the values to move pixels over the X and Y axes. The initial state is set as $[1.0, 0°, 0, 0]$.
3. *Actions:* the total number of actions is $2^4 = 16$ because there are 4 transformation parameters and 2 possibilities for each one (increment or decrement). The parameter step is defined by $[\pm 0.05, \pm 0.25°, \pm 1, \pm 1]$.
4. *Reward:* Pearson correlation coefficient in monomodal registration and Mutual information in multimodal registration are considered. These similarity measures are maximized during the registration process. When an action produces a decrease in similarity, the agent receives a penalty of -0.1 and the algorithm restarts the learning process.

3.5 Backup Memory Criterion

In DQN algorithms, the agent experiences are stored in order to train the neural networks. A batch technique is used for this purpose [15]. In the backup memory proposed in this work, best experiences are saved, and they are only replaced by others with better reward values, which prevents these good solutions from being lost.

In a random position of the batch, current information is replaced by experiences of the backup memory. Therefore, the batch contains information from the database of experiences (good and bad ones) and from the backup memory (best experiences). In this work, backup memory is used with the Double DQN algorithm and the results show a good performance compared to the other algorithms.

4 Results

The initial parameters are the same for all algorithms. The number of epochs is 200 and the learning process runs 100 iterations, though it can end before if the agent receives a penalty. The tests are evaluated along 5 independent runs.

In Figs. 2 and 3, the mean values of the Pearson coefficient for monomodal registration are presented. In Fig. 3, the double-back_ algorithm, which uses the backup memory criterion, achieved a better correlation factor than the other algorithms.

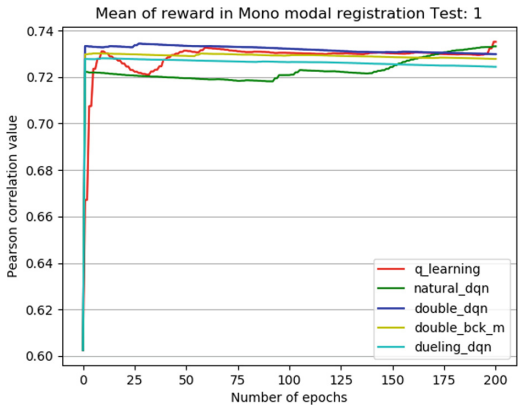

Fig. 2. Mean of monomodal registration results obtained according to parameters of Test 1.

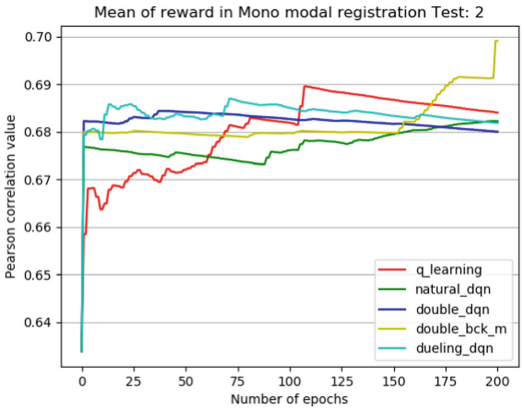

Fig. 3. Mean of monomodal registration results obtained according to parameters of Test 2.

In Figs. 4 and 5, the mean values of mutual information for multimodal registration are presented. The double-back_ algorithm shows a similar performance to other Deep Networks algorithms.

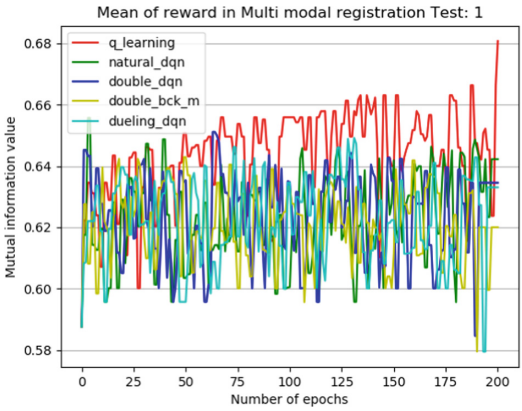

Fig. 4. Mean of multimodal registration results obtained according to the parameters of Test 1.

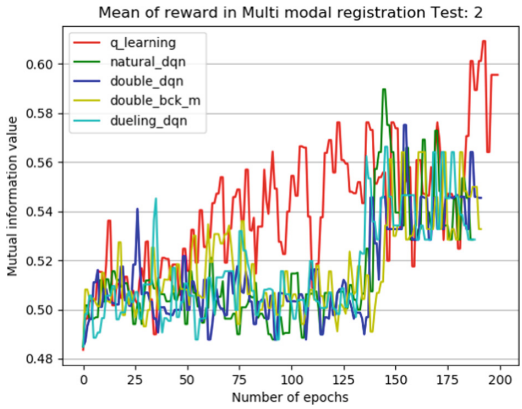

Fig. 5. Mean of multimodal registration results obtained according to the parameters of Test 2.

In Tables 2 and 3, the mean values of similarity measures and errors computed for monomodal and multimodal registration tests are presented. The tables show the performance of each algorithm through mean values of similarity measures and error between target and obtained parameters.

Table 2. Performance of RL algorithms achieved during Monomodal registration.

RL algorithms	Test 1		Test 2	
	Pearson value	% Error	Pearson value	% Error
Q-learning	0.54	0.27	0.63	0.36
Natural-DQN	0.51	0.48	0.49	0.25
Double-DQN	0.62	0.23	0.55	0.25
Double-back_	0.62	0.24	0.55	0.28
Dueling-DQN	0.61	0.37	0.52	0.72

Table 3. Performance of RL algorithms achieved during Multimodal registration.

RL algorithms	Test 1		Test 2	
	Mutual info	% Error	Mutual info	% Error
Q-learning	0.65	0.23	0.58	0.39
Natural-DQN	0.67	0.15	0.40	0.43
Double-DQN	0.67	0.16	0.42	0.76
Double-back_	0.66	0.16	0.58	0.37
Dueling-DQN	0.66	0.15	0.59	0.20

Finally, average of times spent during the tests are presented in Table 4.

Table 4. Average time spent by each algorithm during tests.

Algorithms	Test 1	Test 2
Q-learning	14.40 min	19.22 min.
Natural-DQN	20.60 min	22.46 min
Double-DQN	30.55 min	15.67 min
Double-back_	15.12 min	29.71 min
Dueling-DQN	61.27 min	55.46 min

5 Conclusions

In this work, the Reinforcement Learning paradigm is applied to medical image registration. A performance comparison study between four RL algorithms is presented. The registration process is an optimization problem where a similarity measure is maximized. RL allows that an agent could be trained in order to find the best parameters in medical images considering rigid deformations.

In all cases, the algorithms gave successfully results which allow a significant improvement in similarity between the target images and registered images. According to the results, Q-learning, Double-DQN and Double-DQN with backup memory show better performances than the others.

According to the results, the mean error obtained by Double-back is reduced around of 37% in Test1 and 35% in Test2 compared with the highest error achieved by each algorithm. Q-learning and Double-DQN reduce the mean error around of 24% in Test1 and 19% in Test2. Moreover, these algorithms also use a reasonable time for the training process which is important in reference to computational resources available.

Future work focuses on analyzing the optimum size of batch and backup memories to optimize the training of the deep neural networks which could improve their performance and to maximize the reward values. The RL paradigm could also be applied in nonlinear registration.

Conflict of Interest. The authors declare that they have no conflict of interest.

References

1. Sutton, R.S., Barto, A.G.: Reinforcement Learning: An Introduction, 2nd edn. (2017)
2. Kaelbling, L.P., Littman, M.L., Moore, A.W.: Reinforcement learning: a survey. J. Artif. Intell. Res. **4**, 237–285 (1996)
3. Zitová, B., Flusser, J.: Image registration methods: a survey. Image Vis. Comput. **21**, 977–1000 (2003)
4. Maintz, J.B.A., Viergever, M.A.: A survey of medical image registration. Med. Image Anal. **2**(1), 1–37 (1998)
5. Roderick, M., MacGlashan, J., Tellex, S.: Implementing the deep Q-network, November 2017
6. Sigaud, O., Buffet, O.: Markov decision processes in artificial intelligence (2010)
7. Watkins, C.J.C.H., Dayan, P.: Q-learning. Mach. Learn. **8**(3–4), 279–292 (1992)
8. Bellman, R.: A Markovian decision process (1957)
9. Mnih, V., et al.: Human-level control through deep reinforcement learning. Nature **518**(7540), 529–533 (2015)
10. van Hasselt, H., Guez, A., Silver, D.: Deep reinforcement learning with double Q-learning, September 2015
11. Lin, L.-J.: Self-improving reactive agents based on reinforcement learning, planning and teaching. Mach. Learn. **8**(3–4), 293–321 (1992)
12. Wang, Z., Schaul, T., Hessel, M., Com, M., Van Hasselt, H., Lanctot, M.: Dueling network architectures for deep reinforcement learning (2015)
13. Harmon, M.E., Baird, L.C., Klopr, A.H.: Advantage updating applied to a differential game. In: NIPS (1995)
14. Fitzpatrick, J.M., Hill, D.L.G., Maurer, C.R.: Image registration. In: Handbook of Medical Imaging. Medical Image Processing and Analysis, vol. 2, pp. 447–514 (2000)
15. Hoffer, E., Hubara, I., Soudry, D.: Train longer, generalize better: closing the generalization gap in large batch training of neural networks (2017)

Measurement of the Degradation Rate of Anodized AZ91 Magnesium Temporary Implants Using Digital Image Processing Techniques

Francisco Javier Buchelly[1(✉)], Martina Gomez[2], Silvia M. Cere[2], Josefina Ballarre[2], Virginia L. Ballarin[1], and Juan I. Pastore[1]

[1] Laboratorio de Procesamiento de Imágenes, ICYTE – UNMdP – CONICET, Mar del Plata, Argentina
fbuchelly@gmail.com, jpastore@fi.mdp.edu.ar
[2] División de Electroquímica Aplicada, INTEMA – UNMdP – CONICET, Mar del Plata, Argentina

Abstract. To be used as intracorporeal temporary orthopedic biomaterial, magnesium alloys have to be biocompatible but also to have an adequate and controlled corrosion rate. It means that its degradation accompanies the formation of bone tissue since it is expected that the material maintains its mechanical properties until it fulfills its function and then degrades in the body. The degradation of AZ91 magnesium alloy generates the release of hydrogen gas. It is important to quantify the hydrogen evolution since it is directly related to the Mg corrosion rate. Hydrogen evolution can be experimentally quantified with high associated errors. Digital image processing tools allow the evaluation frame by frame of the hydrogen release from the surface. In this work, we performed a set of digital image processing operations to determine the gas generation rate in the surface of metallic pieces of AZ91 magnesium alloy with and without a surface oxidation process, captured from an optical microscopy camera. The proposed approach detected gas bubbles in a region of interest and then it measured the present volume in each frame of the video sequence. Surface oxidized AZ91 samples showed a slow rate of hydrogen release at short immersion times, showing a retarding in corrosion or degradation of the sample at early times.

Keywords: Magnesium alloy degradation · Hydrogen release · Digital image processing

1 Introduction

Magnesium alloys provide potential advantages as a degradable biomaterial for osteosynthesis, because they provide good biocompatibility and high primary stability, avoiding so-called stress shielding [1]. The primary interest of these alloys is the ability of Mg alloys to biodegrade and the potential functional capacity of degradation

© Springer Nature Switzerland AG 2020
C. A. González Díaz et al. (Eds.): CLAIB 2019, IFMBE Proceedings 75, pp. 290–297, 2020.
https://doi.org/10.1007/978-3-030-30648-9_37

products to influence osteoconductivity and osteogenesis. To be used as a biomaterial, a control of the corrosion rate is required where its degradation accompanies the formation of bone tissue since it is expected that the material maintains its mechanical properties until it fulfills its function and then degrades in the body.

Magnesium and its alloys show a good corrosion resistance in absence of water. A MgO thin layer is growing on the surface of the material with just the air contact. But when H_2O is present, a reaction with the oxide is generating magnesium hydroxide and its ions in solution [2]. Metallic corrosion is an electrochemical process where electron transfer occurs from an interface to an electrolyte. It depends on the electrochemical potential of the reactions: in our case, Mg reaction in water is highly electronegative and it is produced spontaneously very fast.

$$\mathrm{Mg} + 2\,\mathrm{H_2O} \rightarrow \mathrm{Mg(OH)_2} + \mathrm{H_2}\;\mathrm{E}^{\circ} = -2.37\,\mathrm{V}\;(\mathrm{vs\;Standard\;Hydrogen\;Electrode})$$

The dissolution rate of Mg alloys can potentially be controlled by changes in metallurgy, microstructure and surface treatments. However, significant challenges still exist for biomaterials, including problems due to acute inflammation related to the release of hydrogen gas that accompanies the dissolution [3]. One of the strategies of surface modification to promote osseointegration and inhibit corrosion is through anodizing treatments. In this treatment, passive layers have been developed and perfected on valve metals for use in implantology, and it is expected that the generation of the layers in basic medium on magnesium will allow generating a partial barrier to magnesium degradation and hydrogen evolution, and also enhance its bioactive response [4, 5].

For temporary implants, life-time in service and early fixation times are needed to be estimated, so the measurement of corrosion or degradation rate of degradable metals is necessary to be obtained. For magnesium degradable alloys, the typical hydrogen evolution evaluations are related with experimental calculation of changes in the release gas pressure [6]. This measurement is influenced with several experimental errors related with the system being evaluated. Most of the time, the procedure requires manual precision and it is not accurate.

Digital image processing presents as a powerful tool to allow the evaluation frame by frame of the hydrogen release from the surface, as we showed in a previous work [7]. However, there are some limitations in bubble detection when they grow or move on a metallic surface: reflections on the surfaces, bright and shadows areas, transparence of the substances, etc. Related works [8, 9] used segmentation techniques to detect irregularities like water droplets, blister and scratch defects in a metallic surface assuming that it should be smooth.

In this work, we dealt with the mentioned limitations because surfaces were not always smooth, due to polishing or coating processes, as seen with the optical magnification. Thus, we performed a set of digital image processing operations to determine the gas generation rate in the surface of metallic pieces of AZ91 magnesium alloy with and without a surface oxidized treatment, captured from an optical microscopy camera. First, the proposed approach detected gas bubbles in a region of interest, and then it measured the present gas volume in each frame of the video sequence. Finally, some considerations about the bubbles growing and motion allowed for approximating

the instantaneous liberation rate in order to estimate the gas volume generated until a given time instant.

2 Materials and Methods

2.1 Sample Preparation

In this work AZ91 magnesium alloy was used as degradable material. Its composition is 9% weight aluminum, 1% zirconium and the balance is magnesium. Four samples were treated with anodizing process and four were maintained without treatment as control. Anodizing process was carried out starting with the AZ91 magnesium alloy, polished with 1000 grit paper. Each metal sample consisted of a rectangular piece (50 mm × 10 mm × 5 mm). Then the samples were immersed in a 5 mol/L KOH solution and a low constant voltage of 3 V was applied for 40 min. Samples were cleaned gently and dry prior to use.

2.2 Acquisition of the Video Sequences

A laboratory fixed clamp held each piece in vertical direction inside an empty glass container. The operator filled the recipient with Simulated Body Fluid (SBF) [10] and then the video capture started. A digital microscope camera [11], disposed with its optical axis horizontal, acquired the video sequences of the piece surface with a frame rate of 30 frames per second with enough optical zoom to see the gas bubbles growing in the surface, as we show in the results. We used fixed light sources around the camera to ensure a nearly uniform brightness distribution and to detect every bubbles contour. The video capture finished when no considerable changes were observed, depending on the sample ($\sim$1 min for anodized samples and $\sim$3 min for bare ones).

2.3 Detection of the Bubbles

We proposed the following image processing techniques for bubble detection, using the OpenCV library [12] in the NetBeans Integrated Development Environment:

Gray Level Conversion. We converted the original images to gray scale because there was no relevant color information to perform the bubble detection (see Fig. 1a).

Bubbles Enhancing. The lighting system produced a wide shadow inside each bubble. The substraction of the gray scale image from a smoothed image enhanced those circular shadows, as shown in Fig. 1b. We used a large square Gaussian kernel to obtain the smoothed image [12] (101 pixels width and 25 pixels of standard deviation).

Adaptive Thresholding. We applied a standard adaptive thresholding method [12] using a Gaussian square window (49 pixels width and 7.7 pixels of standard deviation) in order to obtain a binary image with the shadows segmentation (see Fig. 1c).

Morphological Filtering. Binary morphological filters were applied [13] after thresholding: first an opening removed noise and then a closing joins regions

Fig. 1. Bubble detection procedure: (a) Gray scale conversion, (b) Enhancing of the bubbles shadows, (c) Adaptive thresholding, (d) Morphological filtering and noise removing, (e) Approximation of the bubbles shape by means of circles.

corresponding to the same object (see Fig. 1d). The structuring element used in the morphological filters was cross-shaped (3 × 3 kernel).

Centroids and Radii Estimation. For each binary object i, we determined the spatial moments of the object contour [14] in order to get its centroid point. We obtained the radio r_i for each object by taking the mean of two distances: the average and the maximum distance between the centroid and each point in the object contour. In Fig. 1e, we show an example of the obtained circular approximation for the bubbles.

2.4 Data Analysis

We assumed a spherical shape for all bubbles, each one with a known radio as described in the previous section. The chemical reaction generated gas bubbles on the entire surface, then they grow and finally they detach to rise vertically. We analyzed a rectangular region of the image sequence, so some bubbles were generated there and other came from different regions. Next, we define some physical measurements in order to analyze the gas generation by the selected rectangular region:

Instantaneous Gas Volume (v_k). The analysis steps determined the gas volume present in the selected region of each video frame as the sum of the individual volumes:

$$v_k = \sum_{i=1}^{n_k} \frac{4}{3}\pi r_i^3 \tag{1}$$

In Eq. (1), the index k corresponds to the frame index in the video sequence, i.e., $k = 0, \ldots, N-1$, n_k is the bubbles count in the k-th frame, and N is the frame count of the video file.

Instantaneous Liberation Rate (*ILR*). This parameter represents the rate of gas production in a portion of the material surface in an infinitesimal time interval. Considering the sampling period Δt of the video with a constant frame rate, this measurement can be approximated as follows:

$$ILR_k = \begin{cases} -\left(\frac{v_k - v_{k-1}}{\Delta t}\right) & \text{if } v_k < v_{k-1} \\ 0 & \text{otherwise} \end{cases} \tag{2}$$

We can see that *ILR* is positive when the gas volume that leaves the rectangular region in an interval is higher than the gas volume retained by the surface. Also, ILR_k tends to smaller values when k is larger enough, as the gas generation decreases. The zero value in Eq. (2) is used to avoid negative generation rates that can appear due to the noisy nature of the v_k signal, thus Eq. (2) can be considered as a good approximation for the *ILR* calculation because the bubbles that come from different regions in the material will leave the region of interest in some few frames later.

Total Produced Volume (V_k). This is the instant cumulative volume of released until the instant k (or the time t, according to the frame rate), which results from the temporal integration of the *ILR* parameter. Then, a discrete approximation for this value in each time instant is proposed:

$$V_k = \sum_{n=o}^{k} ILR_n \tag{3}$$

3 Results

In this work, samples of the material with and without the anodizing treatment were analyzed with the proposed method and we compared differences in the volume of gas generated between the treated and untreated surfaces. The description of the final gas volume generated by the samples (V_k) is shown in Table 1. The recording time was set to 200 s and the analyzed area was ~ 1.0 mm^2 for all samples. Also, the magnification was different for treated and untreated samples because of the bubbles sizes: in treated samples, only a few small bubbles were slowly generated on the surface.

Table 1. Total gas volume generated by untreated and treated samples.

	Untreated				Treated			
Sample	1	2	3	4	1	2	3	4
Magnification (pix/mm)	190	190	190	190	309	309	309	309
Total volume (μL)	42.5	38.77	30.86	31.34	1.12	0.38	0.37	0.37

We can compare the gas generation in both situations starting from the volume variations, as seen in Fig. 2. As an example, we show the register of gas volume present in rectangular regions of the surface for an untreated and a treated sample (Fig. 2a). It can be seen that the gas volume had an exponential decay with time of immersion for the untreated pieces, as expected. On the other hand, anodized samples only presented small variations due to the generation of a few small bubbles at the beginning of the video recording. Then, the integration of the *ILR* parameter gave a near exponential curve that increases until they became constant at large time values (Fig. 2b).

Taking the ratio between the cumulative volumes (V_k) measured at the end of the recording for the example shown in Fig. 2, we can observe at the end of the recording interval that the total volume produced for the untreated sample is 37.9 times the

volume produced by the treated surface, but this ratio increases until the total degradation of the untreated material occurs several minutes later.

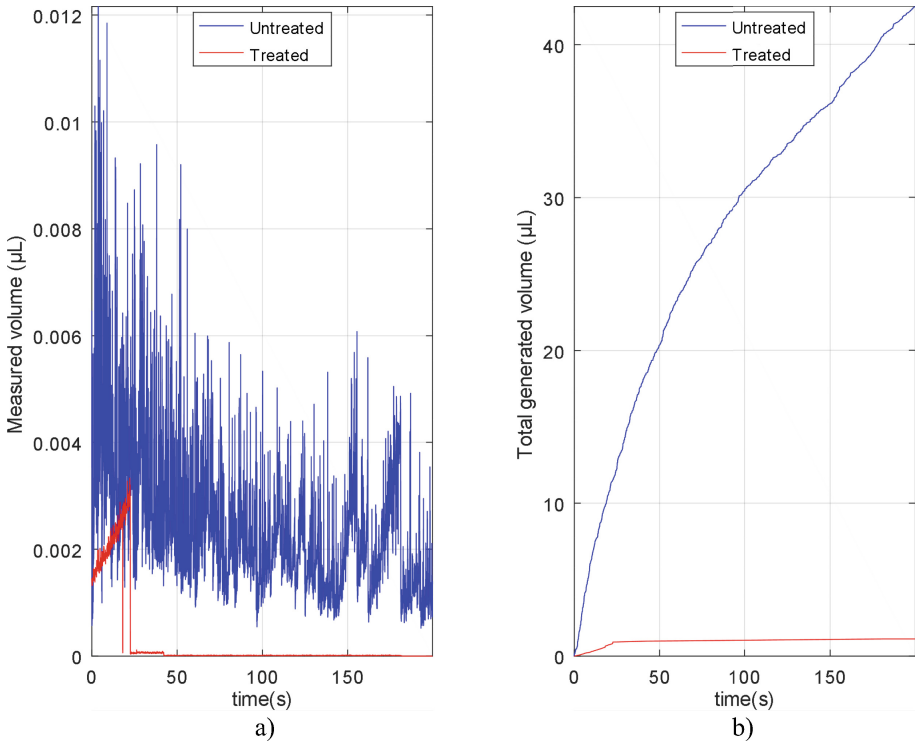

Fig. 2. Gas volume variations in a region of interest for the first untreated sample and the first treated sample from Table 1: (a) Present volume (v_k), and (b) Cumulative volume (V_k).

4 Conclusion and Discussion

Our previous work [7] showed that the anodizing process reduced the surface corrosion in the initial states of immersion in SBF and the formation of some compounds important to the biocompatibility of the implants. In this work, our proposed method quantified the corrosion and degradation rate of AZ91 magnesium alloy plates with and without anodizing surface treatment, by means of the automatic determination of the total volume of gas released by the material.

It is well known that gas production during AZ91 degradation has an exponential behavior with time, as we can observe in Fig. 2 for the untreated surface. The higher reaction rate took place during the first seconds of the surface reaction of the magnesium alloy with the SBF solution, i.e. the oxidation reaction of Mg, which turned into Mg^{2+} and water and generated gaseous H_2. For anodized samples, the hydrogen generation rate was low and only a small amount of bubbles was generated at the

beginning of the immersion until the generation of bubbles ended soon. Then, this situation was maintained in time due to the thin magnesium oxide/hydroxide layer that was created during anodizing process. As a result, the final gas volume produced by the anodized surfaces was significantly lower than the one obtained by untreated surfaces, as shown in Table 1.

We can compare the anodic oxide effect (anodizing treatment) of the proposed approach by quantifying the proportion of released gas in treated and untreated samples. In this way, the proposed method can be considered as a promising assay to estimate the degradation rate of the material by means of measuring the amount of hydrogen released by some areas of the surface. Although there is no literature regarding degradation of anodized AZ91 magnesium alloy, it is possible to state that our results are in the same order that the ones obtained by the funnel and burette method of collection [15]. In future works, the method will be applied in longer periods of time and hence the comparison with the traditional assays used to measure gas release of a corroding metal will be more feasible.

Finally, the estimation of the gas generation rate is a challenging task due to some factors: the bubbles detection must be done with appropriate lighting conditions to avoid false positive or false negative, the generation rate is an approximation obtained from the *ILR*, and the moving bubbles show high rising speed. To improve the method performance, standardized lighting conditions and acquisition protocols will be established. Also, other segmentation techniques could be tested to find the bubbles boundaries. Additionally, a robust tracker will be implemented in order to determine the exact amount of generated gas and to avoid errors due to the moving bubbles that come from other regions.

Conflict of interests. The authors declare that they have no conflict of interests.

References

1. Zhuang, J., Jing, Y., Wang, Y., Zhang, J., Xie, H., Yan, J.: Degraded and osteogenic properties of coated magnesium alloy AZ31; an experimental study. J. Orthop. Surg. Res. **11**, 1–6 (2016). https://doi.org/10.1186/s13018-016-0362-5
2. Esmaily, M., Svensson, J.E., Fajardo, S., Birbilis, N., Frankel, G.S., Virtanen, S., Arrabal, R., Thomas, S., Johansson, L.G.: Fundamentals and advances in magnesium alloy corrosion. Prog. Mater Sci. **89**, 92–193 (2017). https://doi.org/10.1016/j.pmatsci.2017.04.011
3. Heublein, B.: Biocorrosion of magnesium alloys: a new principle in cardiovascular implant technology? Heart **89**, 651–656 (2003). https://doi.org/10.1136/heart.89.6.651
4. Cere, S., Sanchez, A.G., Ballarre, J.: Anodisation and Sol–Gel coatings as surface modification to promote osseointegration in metallic prosthesis. In: Djokić, S. (ed.) Biomedical and Pharmaceutical Applications of Electrochemistry, pp. 197–265. Springer, Cham (2016). https://doi.org/10.1007/978-3-319-31849-3_3
5. Blawert, C., Dietzel, W., Ghali, E., Song, G.: Anodizing treatments for magnesium alloys and their effect on corrosion resistance in various environments. Adv. Eng. Mater. **8**, 511–533 (2006). https://doi.org/10.1002/adem.200500257

6. Song, G., Atrens, A.: Understanding magnesium corrosion. a framework for improved alloy performance. Adv. Eng. Mater. **5**, 837–858 (2003). https://doi.org/10.1002/adem.200310405
7. Gomez, M., Ballarre, J., Gomez Sanchez, A., Buchelly, F., Pastore, J.I., Ceré, S.: Estudio in vitro de implantes temporarios de aleación de magnesio (AZ91) modificados superficialmente mediante anodizado. In: 10° COLAOB Congresso Latino-Americano de Órgãos Artificiais e Biomateriais (2018)
8. Nand, G.K., Noopur, N.N.: Defect detection of steel surface using entropy segmentation. In: 11th IEEE India Conference: Emerging Trends and Innovation in Technology, INDICON 2014 (2014). https://doi.org/10.1109/indicon.2014.7030439
9. Tan, W.C., Goh, P.C., Causo, A., Chen, I.M., Tan, H.K.: Automated vision based detection of blistering on metal surface: for robot. In: IEEE International Conference on Automation Science and Engineering, pp. 74–79 (2017). https://doi.org/10.1109/coase.2017.8256078
10. Kokubo, T., Kushitani, H., Sakka, S., Kitsugi, T., Yamamuro, T.: Solutions able to reproduce in vivo surface-structure changes in bioactive glass-ceramic A-W3. J. Biomed. Mater. Res. **24**, 721–734 (1990). https://doi.org/10.1002/jbm.820240607
11. Andonstar: digital microscope A1. http://www.andonstar.com/e_products/digital-microscope-V1-1.html
12. OpenCV: OpenCV 3.0.0 Open Source Computer Vision. https://docs.opencv.org/3.0.0/
13. Shih, F.Y.: Image Processing and Mathematical Morphology. CRC Press, Boca Raton (2009)
14. Bigun, J.: Vision with Direction. Springer, Heidelberg (2006)
15. Atrens, A., Liu, M., Abidin, N.I.Z.: Corrosion mechanism applicable to biodegradable magnesium implants. Mater. Sci. Eng. B Solid-State Mater. Adv. Technol. **176**, 1609–1636 (2011). https://doi.org/10.1016/j.mseb.2010.12.017

Development of Eclipse Scripting API for Automatic Delineation of Femoral Head

Bruno Assumpção Gomes da Silva[1], Rodrigo Souza Dias[2], Antonio Cassio de Assis Pellizzon[3], Álvaro Luiz Fazenda[1], and Fabiano Carlos Paixão[1(✉)]

[1] Institute of Science and Technology, Federal University of Sao Paulo, Sao Jose dos Campos, SP, Brazil
fcpaixao@unifesp.br
[2] Sao Paulo Hospital, Federal University of Sao Paulo, Sao Paulo, SP, Brazil
[3] Department of Radiation Oncology, AC Camargo Cancer Center, Sao Paulo, SP, Brazil

Abstract. Contouring of organs at risk is an important but time consuming part of radiotherapy treatment planning. This procedure is usually performed by manual contouring and it may take several hours to delineate all structures of interest by radiation oncologists. This work presents an algorithm for automatic delineation of the femoral bone used as tool within Eclipse® software to save time of radiation oncologists. The Eclipse's script was successfully characterized in pelvic CT Scan DICOM files of prostate patients (n = 11) from two different hospitals, AC Camargo Cancer Center and Sao Paulo Hospital. The automatic delineation was compared with manual and approved delineation through blind test evaluated by a panel of seniors radiation oncologists (n = 9) from both hospitals and the overlapping evaluation was assessed using Dice similarity coefficient. Clinical experts considered that no corrections were needed in 77.8% and 67.8% of manual and automatic delineation respectively. A similarity of 0.94 ± 0.07 was achieved between manual and automatic delineation for the lesser trochanter, 0.91 ± 0.07 for femoral neck, and 0.86 ± 0.08 for femoral head. The results showed that the automated delineation was reproducible in all patient and its performance was similar to manual delineation. In conclusion, the script is capable to relieve the physician of time-consuming tasks and shows the great potential to be employed for automatic segmentation of organs at risks in pelvic or others anatomical body regions.

Keywords: Automatic delineation · Radiotherapy · Femoral head

1 Introduction

Delineation of target volumes and multiple organs at risk are hugely important in external beam radiation therapy due the current advances achieved in the treatment delivery to the oncology patients [1, 2]. Organ delineation is currently the most time-consuming part in radiotherapy planning [3]. This procedure is usually performed by manual contouring and it may take several hours to delineate all structures of interest by radiation oncologists [3, 4].

© Springer Nature Switzerland AG 2020
C. A. González Díaz et al. (Eds.): CLAIB 2019, IFMBE Proceedings 75, pp. 298–303, 2020.
https://doi.org/10.1007/978-3-030-30648-9_38

Although manual contouring is considered the gold standards in radiotherapy planning, regions of interest (ROIs) delineation still result in intra- and inter-observer variations [3]. Several automatic delineation methods have been proposed to address the aforementioned challenges such as deformable models, deformable registration, multi-atlas-based labeling, and deep learning [5, 6]. However, expert clinical eyes remain the gold standards due the poor performance of the all methods developed [5].

Prostate cancer is the second leading cause of cancer death, behind only lung cancer, in American men [5]. Manual delineation typically taking 27–33 min for an experienced radiation oncologist to delineate prostate (target) and four major organs at risk, including bladder, rectum and two femoral heads [5]. Radiation therapy based on inaccurate segmentation of these organs would result in severe side effects, such as persistent bleeding from the bladder and rectum and femoral head necrosis according to Gao *et al.* [5]. Accordingly, it is clinically desirable to develop a robust, accurate and automatic algorithm for the segmentation of major male pelvic organs from CT images.

The aim of this work were to develop an algorithm for automatic segmentation of femoral bone for prostate cancer radiotherapy planning. The developed script was applied to delineate the femoral bone, the results were compared with manual and approved delineation through blind test evaluated by radiation oncologists, and overlapping evaluation was assessed using Dice Similarity Coefficient (DSC) [7].

2 Introduction

2.1 Automatic Delineation Script

An Application Program Interface (API) composed by a set of routines, protocols, and tools was developed in C# programming language for an auto-segmentation software as a totally visual platform without the need to compile numerous individual algorithms. All set of pelvic CT images were assessed by the researchers using this software where all pre- and post-processing parameters to achieve the end segmentation were recorded by the researchers. The automated algorithm for automatic delineation was the composition of steps from the best results generated by the appropriated parameters chosen during the research segmentation procedure.

The script for automated delineation of femoral bone was developed as a tool inside of Eclipse® software (Varian Medical Systems, US) to save time of radiation oncologists and consisted of four steps: (i) Pelvic bones detection using K-means filtering ($K = 3$) and images binarization with constant threshold ($t = 200$) to remove soft pelvic tissues. Small holes and disconnected pixels were processed by appropriated binary morphology. Erosion kernel to remove small noisy pixels and Dilation connecting for disjointed regions; (ii) Delineation of lesser trochanter was detected following circularity pattern on the CT slices since femoral distal region provides similar geometry and low variance in the mass center; (iii) Delineation of femoral neck was achieved by a binary mask defined between lesser trochanter and femoral head, and erode morphology operation was used to remove small pixels disconnected; and (iv) Delineation of femoral head was obtained by fitting a dynamic circular pattern masks until the end of femoral bone.

2.2 Data Analysis

The script was applied to delineate the femoral bone of pelvic CT scan in eleven prostate patients from Sao Paulo Hospital (5 patients) and AC Camargo Cancer Center (6 patients). All experimental procedures were approved by the local Ethics Committee. The automatic delineations were compared with manual and approved delineation through blind test evaluated by a panel of seniors radiation oncologists from both hospitals (n = 9). Ten complete femoral delineation (5 manual and 5 automatic) were displayed for doctors and then asked to evaluate if the delineations need some changes (No, Minimal, Medium, or Large delineation fixes). Where minimal, medium, and large delineation corrections means the size of the area that needs to be changed to become a correct delineation. The overlapping between automatic and manual delineation was assessed using DSC as a quantitative analysis result.

3 Results

Figure 1 shows the sample of manual delineation made by radiation oncologists and the automatic delineation achieved by the script. The algorithm spend only 1.3 ± 0.1 s to perform femoral bone contouring for each patient.

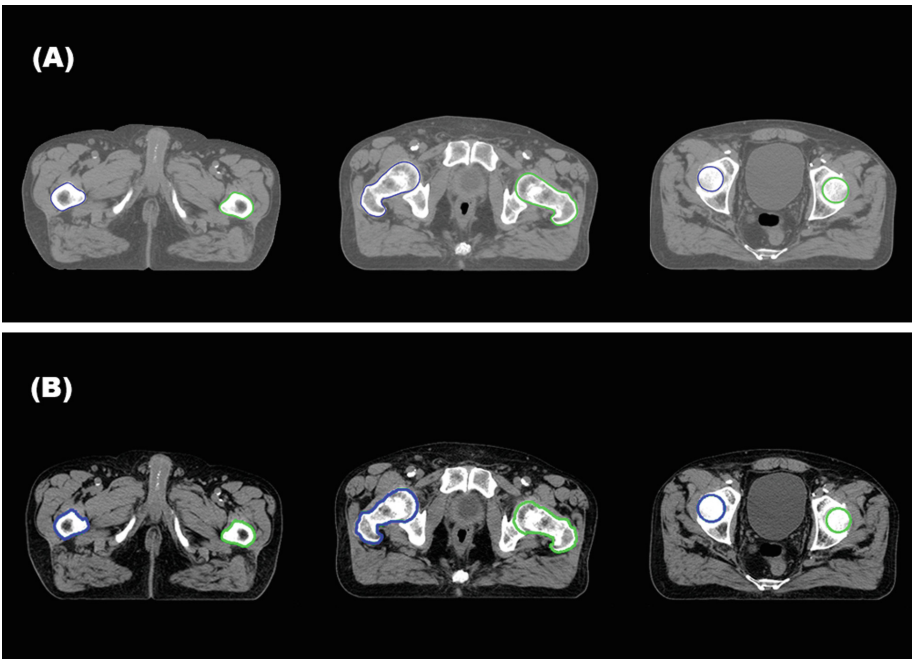

Fig. 1. Delineation of femoral bone (from the left to the right side: lesser trochanter, femoral neck, and femoral head) drawn by **(A)** radiation oncologists and **(B)** automatic delineation algorithm.

Figure 2 shows the evaluation of seniors radiation oncologists in the blind test comparison between the manual and automatic femur delineations, 77.8% of manual delineation and 67.6% of automatic delineation did not require any contouring correction, approximately 18% of manual and automatic delineation required minimal correction, 0.3% of manual delineation and 13.4% of automatic delineation required medium correction, and less than 1.0% of manual and automatic delineation required large correction.

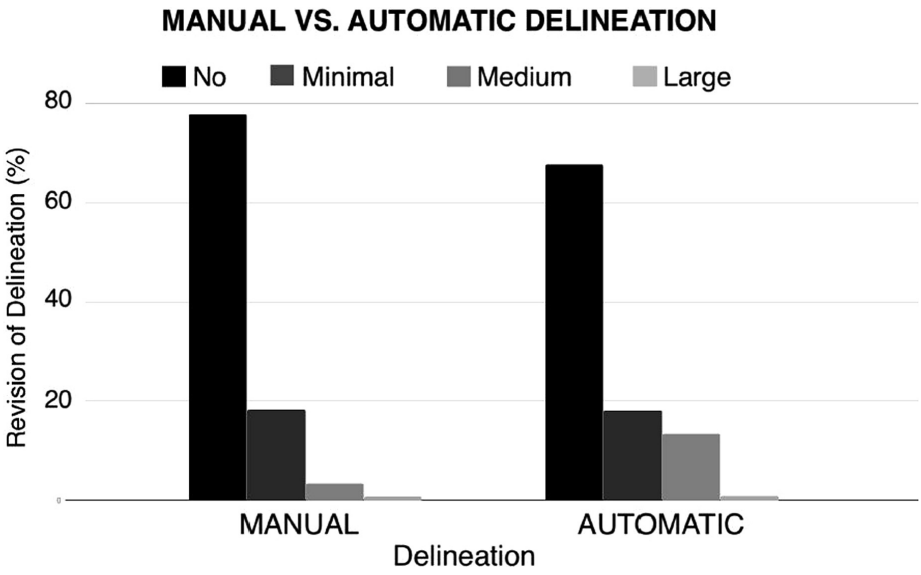

Fig. 2. Comparison between manual approved delineation (left) and automatic femoral bone delineation (right) evaluated through blind test by a panel of seniors radiation oncologists.

The Dice Similarity Coefficient, measuring overlapping area between manual approved delineation and automatic delineation for all patients, is shown in Table 1. This analysis shows the correlation between the blue and green circles obtained by doctors and automatic delineation algorithm.

Table 1. Dice Similarity Coefficient between manual approved delineation and automatic delineation obtained by the script.

Femoral Region	DSC
Femoral Head	0.86 ± 0.08
Femoral Neck	0.91 ± 0.06
Lesser Trochanter	0.94 ± 0.06

4 Discussion

The Eclipse's script developed presents the ability to delineate the femoral bone for 3D Radiotherapy Treatment Planning. The specialist blind test shows that automatic delineation has similar performance compared to manual delineation made by radiation oncologists.

According Pekar *et al.* [3], manual segmentation is considered the "gold standard", but cannot be considered the perfect ground truth, due to inter-observer variability. This may be seen when 18% of manual delineation needs a minimal correction according to the senior panel of radiation oncologists. On the other hand, less than 1% of manual and automatic delineation required large correction.

A satisfactory agreement of similarity coefficient between automatic and manual delineation performances was found as Table 1 shows. DSC greater than 0.7 is allegedly considered satisfactory index for good segmentation [8] and our values were always greater than 0.86.

The results obtained allow the organs at risk delineation, with appropriated image contrast, to be carried out automatically and then radiation oncologists make the contouring review and some minor corrections only, saving experts time and allowing a greater number of radiotherapy planning to be made in a shorter time with the same present human quality assurance.

5 Conclusion

The automatic delineation was reproducible in all patient and its performance was similar to manual delineation made and evaluated by a panel of senior radiation oncologist from two different hospitals. The Eclipse Scripting API developed for automatic femoral delineation shows great potential to be employed for automatic segmentation of others anatomical body regions and the results that have been achieved should be seen in a very positive light for further reduce the time of radiotherapy treatment planning, allowing the cost reduction for hospitals and increasing the number of patient to be treated in the same current spent time.

Acknowledgments. This work is part of an offset agreement between Varian Medical Systems and Brazilian Ministry of Health for the expansion of radiotherapy in Brazil. The authors would like to thank the Sao Paulo Research Foundation (FAPESP), AC Camargo Cancer Center, and Technology Park of Sao Jose dos Campos for financial support.

Conflict of Interest. The authors do not have any conflicts of interest to declare.

References

1. Whitfield, G.A., Price, P., Price, G.J., Moore, C.J.: Automated delineation of radiotherapy volumes: are we going in the right direction? Br. J. Radiol. **86**(20110718), 1–9 (2013). https://doi.org/10.1259/bjr.20110718

2. Pasquier, D., Lacornerie, T., Vermandel, M., Rousseau, J., Lartigau, E., Betrouni, N.: Automatic segmentation of pelvic structures from magnetic resonance images for prostate cancer radiotherapy. Int. J. Radiat. Oncol. Biol. Phys. **68**(2), 592–600 (2007). https://doi.org/10.1016/j.ijrobp.2007.02.005
3. Pekar, V., McNutt, T.R., Kaus, M.R.: Automated model-based organ delineation for radiotherapy planning in prostatic region. Int. J. Radiat. Oncol. Biol. Phys. **60**(3), 973–980 (2004). https://doi.org/10.1016/j.ijrobp.2004.06.004
4. Teguh, D.N., Levendag, P.C., Voet, P.W., Al-Mamgani, A., Han, X., Wolf, T.K., Hibbard, L. S., Nowak, P., Akhiat, H., Dirkx, M.L., Heijmen, B.J., Hoogeman, M.S.: Clinical validation of atlas-based auto-segmentation of multiple target volumes and normal tissue (swallowing/mastication) structures in the head and neck. Int. J. Radiat. Oncol. Biol. Phys. **81**(4), 950–957 (2011). https://doi.org/10.1016/j.ijrobp.2010.07.009
5. Gao, Y., Shao, Y., Lian, J., Wang, A.Z., Chen, R.C., Shen, D.: Accurate segmentation of CT male pelvic organs via regression-based deformable models and multi-task random forests. IEEE Trans. Med. Imaging **35**(6), 1532–1543 (2016). https://doi.org/10.1109/TMI.2016.2519264
6. Lustberg, T., van Soest, J., Gooding, M., Peressutti, D., Aljabar, P., van der Stoep, J., van Elmpt, W., Dekker, A.: Clinical evaluation of atlas and deep learning based automatic contouring for lung cancer. Radiother. Oncol. **126**(2), 312–317 (2018). https://doi.org/10.1016/j.radonc.2017.11.012
7. Dice, L.R.: Measures of the amount of ecologic association between species. Ecology **26**(3), 297–302 (1945). https://doi.org/10.2307/1932409
8. Zou, K.H., Warfield, S.K., Bharatha, A., Tempany, C.M.C., Kaus, M.R., Haker, S.J., Wells, W.M., Jolesz, F.A., Kikinis, R.: Statistical validation of image segmentation quality based on a spatial overlap index. Acad. Radiol. **11**(2), 178–189 (2004). https://doi.org/10.1016/S1076-6332(03)00671-8

Comparative Evaluation of Anisotropic Filters Used to Reduce Speckle in Ultrasound Images

Lucas Gonçalves Santos, Carlos Marcelo Gurjão de Godoy, Leopoldo de Jesus Prates, and Regina Célia Coelho(✉)

Science and Technology Institute, UNIFESP, São José dos Campos, SP, Brazil
reginaccoelho@gmail.com

Abstract. Image denoising in medical image processing is essential to improve the visual quality of the image and, consequently, the diagnosis. Speckle, a multiplicative noise that degrades the image, is common in ultrasound imaging as it tends to degrade the resolution and contrast in the image. Several filters have been developed to reduce this kind of noise. This paper presents a comparative evaluation of some anisotropic filters used to reduce the speckle noise in ultrasound images. The evaluated filters were Coherence-Enhancing Diffusion (CED), Speckle Reducing Anisotropic Diffusion (SRAD), Detail-Preserving Anisotropic Diffusion (DPAD), and Anisotropic Diffusion Filter with Memory Based on Speckle (ADMSS). The filters processed four phantom ultrasound images with speckle noise. The comparison performances of filters occurred by using Mean Square Error, Signal to Noise Ratio, Peak Signal Noise Ratio, and Structure Similarity Index. The results showed that ADMSS better reduces speckle noises in ultrasound images, compared to the other filters evaluated.

Keywords: Speckle noise · Despeckling · Ultrasound images

1 Introduction

Ultrasonography is one of the most powerful techniques for imaging of the human body, as it is a non-invasive and low-cost technique for medical diagnosis that does not use ionizing radiations. However, one disadvantage of this technique compared, for example, to magnetic resonance image (MRI) technique, is the poor quality of the image due to speckle noise. This noise, inherent in ultrasound images, is formed due to interferences produced by the deflection of the mechanical waves, also called backscattering. As it interferes with the perception and extraction of details from the image, the suppression of such noise using digital filtering improves the quality of the image obtained by ultrasound and, consequently, helps in the medical diagnosis.

There are several methods to reduce speckle noise in ultrasound images. In general, anisotropic diffusion filters present the best results in speckle suppression [1–4]. Given the relevance of choosing the suitable filter to improve the quality of ultrasonography images, the present work aims to assess the performance of some anisotropic filters used commonly in speckle noise correction in ultrasound images.

© Springer Nature Switzerland AG 2020
C. A. González Díaz et al. (Eds.): CLAIB 2019, IFMBE Proceedings 75, pp. 304–308, 2020.
https://doi.org/10.1007/978-3-030-30648-9_39

2 Speckle Noise Filters

Distinct from many filters that can damage the edges during the filtering process, Anisotropic Diffusion filtering detects the borders using gradient and attenuates the smoothing in that region. Coherence-Enhancing Diffusion (CED) filtering [1] combines ideas of non-linear diffusion filtering with orientation analysis by using tensor, where the non-linear diffusion process smoothens (anisotropic smoothing) the noise image by acting along the preferred structure direction (Fig. 1).

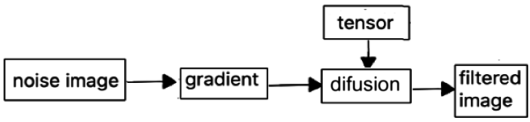

Fig. 1. Block diagram of CED filtering

Speckle Reducing Anisotropic Diffusion (SRAD) filter [2] uses adaptive filtering by exploiting the instantaneous coefficient of variation, which serves as speckle detector, instead of a tensor as in CED filtering (see Fig. 1). The function presents high values at edges and low values at homogeneous regions, ensuring the mean behavior in the homogeneous regions, and preserving and enhancing the edges.

Aja-Fernández and Alberola-López [3] proposed the Detail-Preserving Anisotropic Diffusion (DPAD) filter that has the same approach of SRAD, but it combines the Kuan filter with the instantaneous coefficient of variation. It also decouples the problem of noise estimation and image filtering by using different window sizes for each task.

Llordén-Ramos [4] proposed Anisotropic Diffusion Filter With Memory Based on Speckle Statistic (ADMSS) to solve over-filtering of images that can be caused by the loss of information of filtering. This filter uses a probabilistic model system to estimate the noise using memory, preserving the image area considered essential to the diagnosis, and filtering the other regions classified as irrelevant. If the region is essential (according to its statistic), the filter activates the stationary mode, preserving the area (see Fig. 2).

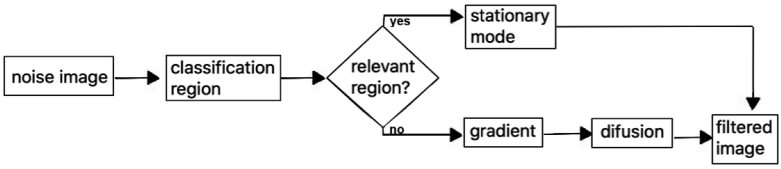

Fig. 2. Block diagram of ADMSS filtering.

3 Methodology

The Field II software [5] created a phantom ultrasound image (with speckle noise) from an MRI scan (Fig. 3(a)). It is possible to see that the phantom image is very noisy, which hinders visualizing some tissues.

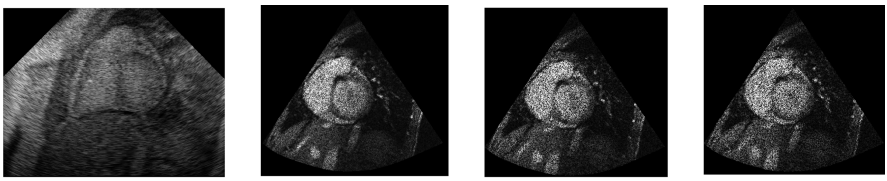

(a) (b) (c) (d)

Fig. 3. Images used in the tests. (a) phantom generated by Field II software; (b)-(d) images with *speckle* using $\sigma = 0.2$, $\sigma = 0.4$, and $\sigma = 0.6$, respectively.

The *imnoise* function of MatLab created another three noise ultrasound phantom images from MRI. It included different speckle noises in the MRI, whose variances were $\sigma = 0.2$, $\sigma = 0.4$, and $\sigma = 0.6$. Thus, the evaluation of filters consisted of experiments: (i) using an ultrasound simulated image (phantom), generated by Field II software (Fig. 3(a)), and (ii) using three phantoms with noises included by *imnoise* function (Fig. 3(b)–(d)). The first experiment evaluated filters that preserve more structures, whereas the second experiment assessed filters, which reduce noise more efficiently. The parameters used in the filters were the same as proposed by the authors.

The validation metrics were: Mean Squared Error (MSE), Signal to Noise Ratio (SNR), Peak Signal to Noise Ratio (PSNR), and Structural Similarity (SSIM). In the case of MSE, the lower the value, the better will be the result, whereas in the other metrics, the higher the value, the higher will be the filtering quality.

4 Results and Discussion

Table 1 presents the results of filters applied to images of Fig. 3. SRAD presented the worst outcome. The problem with this filter is that, with a few iterations, it does not exhibit good result (as shown in this work) and, with more iterations, it can even blur further the image. DPAD filter, in general, deteriorated some details of tissue (see SSIM values for this filter), but, as for Fig. 3(c), in some cases, it can present the best results for the MSE, SNR, and PSNR metrics. Thus, this filter can be better than the others for the removal of speckles in images presenting medium levels of noise. CED filter exhibited the second best result, being worse only concerning the ADMSS performance (not considering the validation metrics of Fig. 3(c) and MSE metric of Fig. 3(d)). This indicates that CED preserves the image structure during filtering, but sometimes it highlights the contour of the speckle noise.

Table 1. Results obtained with the filtering. The four values in each metric in each filter are referring to Figs. 3(a), (b), (c) and (d) respectively.

Method	MSE	SNR	PSNR	SSIM
ADMSS	0.0086; 0.0004; 0.0025; 0.0024	13.48; 21.75; 13.85; 13.84	23.64; 36.94; 29.10; 20.17	68.01; 94.48; 87.81; 87.06
CED	0.0098; 0.0015; 0.0028; 0.0039	13.01; 16.09; 13.42; 12.03	23.11; 31.15; 28.49; 27.09	55.53; 86.91; 83.67; 82.12
DPAD	0.0208; 0.0046; 0.002; 0.0036	10.90; 9.79; 14.96; 12.48	19.83; 26.38; 30.016; 27.41	64.07; 91.47; 84.88; 81.42
SRAD	0.0108; 0.0032; 0.0052; 0.0065	12.72; 13.12; 11.04; 10.16	22.66; 28.01; 25.82; 24.88	54.74; 84.14; 81.47; 80.31

As a whole, the ADMSS filter outperformed the others and proved to be robust in filtering very noisy images, presenting the lowest MSE and the best value of structural conservation (SSIM). Thus, ADMSS smoothes non-fundamental regions of the image structure, as it preserves interdependent regions. Figure 4 shows the resulting filtered images using this filter.

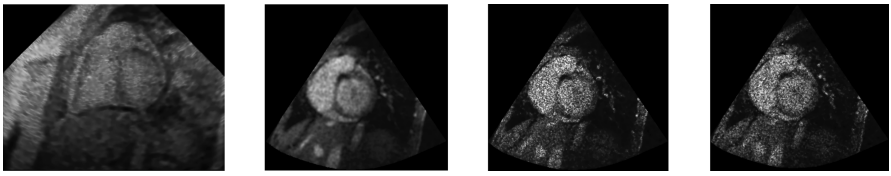

Fig. 4. Results of ADMSS filtering of the images in Fig. 3.

5 Conclusion

In general, the ADMSS despeckles images better than the other filters evaluated, as it is a robust filter, which preserves essential structures of the images (the higher SSIM) and provides higher similarity between the resulting and original images (the lowest MSE). Furthermore, this filter improves the quality of the images and, therefore, the diagnostic process performed by physicians.

The works of Finn [6] and Yang et al. [7] presented similar studies comparing filters for speckle noise reduction in an ultrasound image, but both did not test the ADMSS filter, which presented the best result in this paper. Also, they used fewer metrics than those used in the present work to evaluate the filters.

It is intended, in future experiments, to apply this filter before segmenting ultrasound images and compare the segmentation results with and without this filtering.

Acknowledgment. This work was supported by FAPESP (Proc. 2017/22949-3).

Conflict of Interest. The authors do not have any conflicts of interest to declare.

References

1. Weickert, J., Scharr, H.: A scheme for coherence-enhancing diffusion filtering with optimized rotation invariance. J. Vis. Commun. Image Represent. **13**(1), 103–118 (2002)
2. Yu, Y., Acton, S.T.: Speckle reducing anisotropic diffusion. IEEE Trans. Image Process. **11** (11), 1260–1270 (2002)
3. Aja-Fernandez, S., Alberola-Lopez, C.: On the estimation of the coefficient of variation for anisotropic diffusion speckle filtering. IEEE Trans. Image Process. **15**(9), 2694–2701 (2006)
4. Ramos-Llorden, G., Vegas-Sanchez-Ferrero, G., Martin-Fernandez, M., Alberola-Lopez, C., Aja-Fernandez, S.: Anisotropic diffusion filter with memory based on speckle statistics for ultrasound images. IEEE Trans. Image Process. **24**(1), 345–358 (2015)
5. Jensen, J.A.: Field: a program for simulating ultrasound systems. In: 10th Nordicbaltic Conference on Biomedical Imaging, vol. 4, Supplement 1, PART 1, pp. 351–353 (1996)
6. Finn, S., Glavin, M., Jones, E.: Echocardiograpic speckle Reduction Comparison. IEEE Trans. Ultrason. Ferroelectr. Freq. Control **58**(1), 82–101 (2011)
7. Yang, J., Fan, J., Ai, D., Wang. X., Zheng, Y., Tang., S., Wang, Y.: Local statics and non-local mean filter for speckle noise reduction in medical ultrasound image. Neurocomputing **195**, 88–95 (2016)

A System for High-Speed Synchronized Acquisition of Video Recording of Rodents During Locomotion

Cesar Ascencio-Piña[1], Marco Pérez-Cisneros[1], Sergio Dueñaz-Jimenez[2], and Gerardo Mendizabal-Ruiz[1(✉)]

[1] División de Electrónica y Computación, Universidad de Guadalajara, Guadalajara, Mexico
gerardo.mendizabal@academicos.udg.mx
[2] Departamento de Neurociencias, Universidad de Guadalajara, Guadalajara, Mexico

Abstract. The analysis of locomotion in laboratory rodents allow the study and understand the effects of diseases or conditions that affect the nervous system in the patterns of the rodents using qualitative and quantitative metrics. Many methods for the quantitative analysis of rodents' locomotion have been previously employed. These methods rely on the use of high-speed video sequence recording that is analyzed through the analysis of the translations of the joints of the extremities of interest along time. However, there does not exist a standard system that allows the acquisition of videos for such type of analysis. In this work, we describe a system and its components for the synchronized acquisition of multiple high-speed video recordings of rodents during locomotion, including the required post-processing image algorithms.

Keywords: Locomotion analysis · Laboratory rodents · Video acquisition

1 Introduction

Laboratory rodents such as rats and mice are commonly used as a biological model for the evaluation of the effects of diseases or the effectiveness of new drugs and treatments. The locomotion analysis in laboratory rodents allows the study and understand the effects of diseases or conditions that affect the nervous system in the patterns of the rodents using qualitative and quantitative metrics. Examples of applications of the locomotion analysis in rodents include understanding the motor defects in diseases such as osteoarthrosis [1], Parkinson's disease, Huntington's disease, and amyotrophic lateral sclerosis [2, 3], as well as the damage and recovery after peripheral and central nervous system injury [4]. Existing methodologies for the analyses of locomotion of laboratory rodents are based on the use of a treadmill for imposing the speed of gait (e.g., [5]), or based on letting the rodent freely to move at any speed on the ground or an activity wheel [4].

Various methodologies for the quantitative analysis of rodents' locomotion have been previously employed [6, 7]. These approaches rely on the use of high-speed video

© Springer Nature Switzerland AG 2020
C. A. González Díaz et al. (Eds.): CLAIB 2019, IFMBE Proceedings 75, pp. 309–314, 2020.
https://doi.org/10.1007/978-3-030-30648-9_40

sequence recording (i.e., in general above 90 frames per second) that are analyzed through the analysis of the translations of the joints of the extremities of interest along time. Currently there exist three commercially available systems for gait analysis using video recordings: TreadScan™ (CleverSys Inc., Reston, VA), CatWalk™ (Noldus Inc., Wageningen, The Netherlands), and DigiGait™ (Mouse Specifics Inc., Framingham, MA) that have been used for extracting parameters related to rodents locomotion [8–14]. However, those systems rely on the use of a single camera that records the rodents from the bottom of a Plexiglas tunnel to allow the detection of the rodent's paw positions, sizes, and intensities as a function of time [15], and do not perform any analysis related to the patterns of movement of the articulations of the extremities.

Therefore, currently, there does not exist a standard system that allows the acquisition of several video sequences at high speed from different angles that may allow the analysis of the patterns of movement of the articulations of the extremities.

In this work, we present a system that allows the synchronized recording of four cameras pointing to the rodents from different angles at high speed. Moreover, we present the image-processing algorithms required to calibrate the videos and be able to transform from pixel space to real-world space to enable the quantitative analysis of the locomotion patterns of the rodent's extremities. Finally, we present a method that performs automatic segmentation of the rodents on each video towards the automatic analysis of the locomotion patterns.

2 Materials and Methods

The proposed system consists of a crystal tunnel of size 0.1 × 0.1 × 1 m. that is set over a custom-made stand, which permits a clear view of the tunnel from any direction. A support made of PVC pipes is used to hold two fluorescent lights at a distance of 0.4 m. from the top of the tunnel. Additionally, the PVC structure is used to place three 3D printed camera holders that will hold cameras at different locations to cover the button, and left and right lateral views. A total of twelve markers are placed at every face of the tunnel at a distance of .4 and 0.8 m to define the corners of a rectangle, which will be the analysis area (Fig. 1).

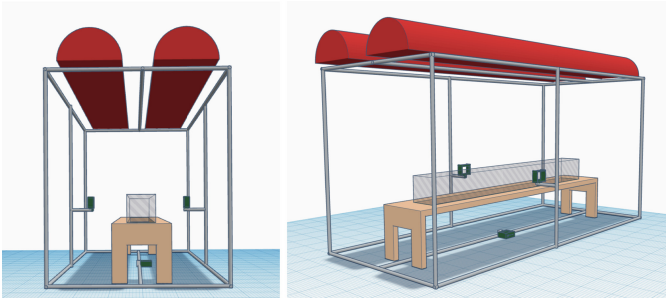

Fig. 1. Depiction of the acquisition system hardware configuration.

We employ three Xiaomi Yi 4K action cameras since they can record at 240 fps with a resolution of 1280 × 720 and they be controlled by using custom software based on the YI Open API SDK, which provides reference designs for software developers and hardware makers. The three cameras are configured with the firmware v1.0.179 that allows the synchronized trigger of the recording starts by a command that is sent by TCP protocol. We created a network consisting of the router, the three cameras, and a PC, which contained a script in Python 3.0 that allows sending the specific command that triggers the record-command of all the cameras simultaneously by pressing the spacebar.

The protocol for recording using the system consist of placing the rodents on one side of the tunnel and then start recording while the rodent is walking freely to the other side of the tunnel. Then, each video is post-processed to compensate for the misalignment of the cameras. For this, we created an algorithm that automatically computes the image position of every marker placed on each face of the tunnel. This algorithm consists of applying a Hough transform [16] to one selected frame of the image to obtain the pixels that are candidates to be the center of the circles corresponding to the markers. Then, the bounding box of each circle candidate is computed and the H, S, V normalized histograms of the patch are computed and compared with a histogram that represents the known distribution of the color intensities of the markers. Finally, for each evaluated patch, we keep the pixel that collected the larger numbers of votes in the Hough transform and that has the minimum difference with respect to the known color distribution of the marker.

Since we know the corresponding positions of these markers in the real world, it is possible to compute a homography matrix which is used to rectify the misalignment of the cameras with respect to the tunnel face and to convert from pixel coordinates to real-world coordinates. The homography is estimated by numerically solving a linear system of equations using the SVD algorithm [17].

Finally, we employ a background subtraction algorithm to perform automatic segmentation of the rodent while walking on the tunnel [18]. For this, we select the first frame of the video sequence as our baseline frame. Then, for every subsequent frame, we computed the Euclidean distance between the **R, G, B** values from the baseline image and the current frame. Finally, only those values with a distance larger than a given threshold **T** are considered to belong to the rodent. Then, an opening operation is applied to the image to eliminate noise and to fill the possible holes in the resulting image [19].

3 Results and Discussion

We build a tunnel according to the proposed configurations and performed experiments recording three female mice. Figure 2(a) depicts an example of each view as the cameras obtain it. Note that the cameras may not be wholly aligned with the faces of the tunnel. Figure 2(b) depicts an example of the frames after the homography correction. Note that the perspective has been corrected as expected. Figure 3 depicts an example of the segmentation result. Note that the mouse is isolated from the rest of the environment. Figure 4 depicts the results of translation patterns for three mice as

extracted automatically by the proposed method. Note the differences in the translation rate between the mice walks.

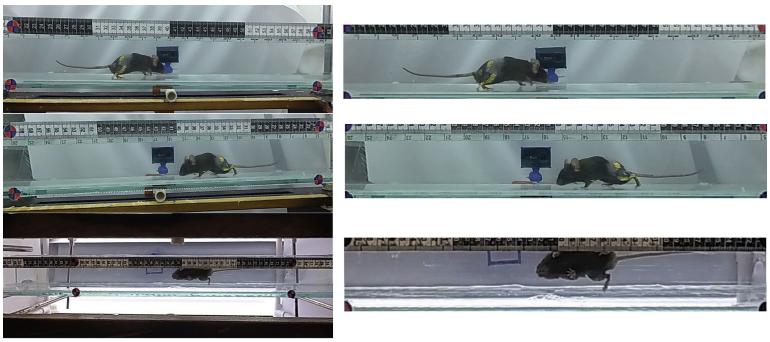

Fig. 2. Examples of a frame of a mouse walking on the proposed system before and after the correction (a and b, respectively).

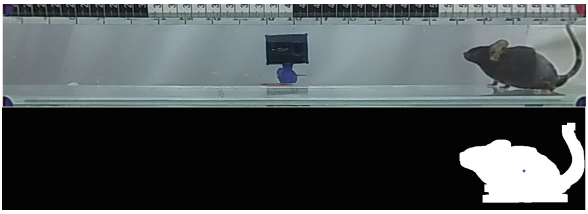

Fig. 3. Example of the segmentation result using the proposed background subtraction algorithm. The blue dot on the binary image of the mouse indicates the center of mass of the rodent.

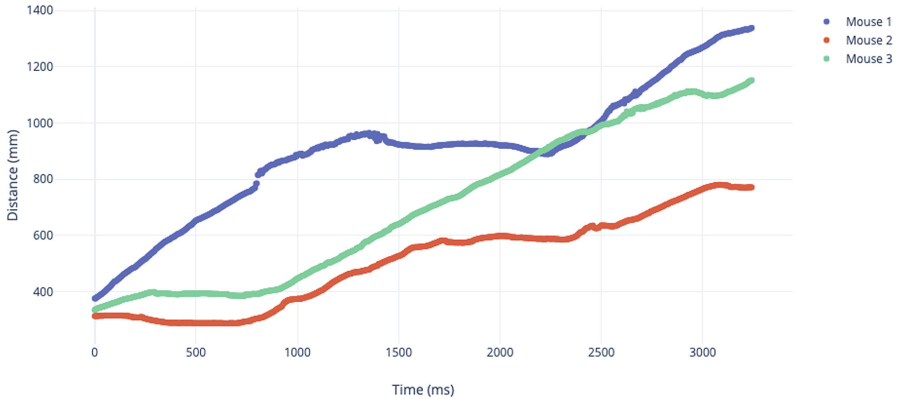

Fig. 4. Results of translation patterns for three mice as extracted automatically by the proposed method.

4 Conclusion

We have presented a system and its components for the synchronized acquisition of multiple high-speed video recordings of rodents during locomotion, as well as the required post-processing image algorithms to enable the quantitative analysis of the data. Our results indicate the feasibility of assembling the system using commercially available hardware allowing research groups to employ this type of analysis for their experiments. Future work includes the extraction of features that allow the analysis of the locomotion patterns of the extremities of the rodents.

Conflicts of Interest. Authors declares that there is no conflict of interest regarding the publication of this article.

References

1. Clarke, K., Heitmeyer, S., Smith, A., Taiwo, Y.: Gait analysis in a rat model of osteoarthrosis. Physiol. Behav. **62**(5), 951–954 (1997). https://doi.org/10.1016/S0031-9384(97)00022-X
2. Amende, I., Kale, A., McCue, S., Glazier, S., Morgan, J.P., Hampton, T.G.: Gait dynamics in mouse models of parkinson's disease and huntington's disease. J. Neuroeng. Rehabil. **2**(1), 20 (2005). https://doi.org/10.1186/1743-0003-2-20
3. Hampton, T.G., Amende, I.: Treadmill gait analysis characterizes gait alterations in parkinson's disease and amyotrophic lateral sclerosis mouse models. J. Motor. Behav. **42**(1), 1–4 (2009). https://doi.org/10.1080/00222890903272025
4. Osuna-Carrasco, L., López-Ruiz, J., Mendizabal-Ruiz, E., De la Torre-Valdovinos, B., Bañuelos-Pineda, J., Jiménez-Estrada, I., Dueñas-Jiménez, S.: Quantitative analysis of hindlimbs locomotion kinematics in spinalized rats treated with tamoxifen plus treadmill exercise. Neuroscience **333**, 151–161 (2016). https://doi.org/10.1016/j.neuroscience.2016.07.023
5. Beare, J.E., Morehouse, J.R., DeVries, W.H., Enzmann, G.U., Burke, D.A., Magnuson, D.S., Whittemore, S.R.: Gait analysis in normal and spinal contused mice using the treadscan system. J. Neurotrauma **26**(11), 2045–2056 (2009). https://doi.org/10.1089/neu.2009.0914
6. Kunkel-Bagden, E., Dai, H.-N., Bregman, B.S.: Methods to assess the development and recovery of locomotor function after spinal cord injury in rats. Exp. Neurol. **119**(2), 153–164 (1993). https://doi.org/10.1006/exnr.1993.1017
7. Santos, P., Williams, S., Thomas, S.: Neuromuscular evaluation using rat gait analysis. J. Neurosci. Methods **61**(1), 79–84 (1995). https://doi.org/10.1016/0165-0270(95)00026-Q
8. Timotius, I.K., Canneva, F., Minakaki, G., Pasluosta, C., Moceri, S., Casadei, N., Eskofier, B.: Dynamic footprints of α-synucleinopathic mice recorded by CatWalk gait analysis. Data Brief **17**, 189–193 (2018). https://doi.org/10.1016/j.dib.2017.12.067
9. Mock, J.T., Knight, S.G., Vann, P.H., Wong, J.M., Davis, D.L., Forster, M.J., Sumien, N.: Gait analyses in mice: effects of age and glutathione deficiency. Aging Dis. **9**(4), 634 (2018). https://doi.org/10.14336/AD.2017.0925
10. Möller, K.Ä., Svärd, H., Suominen, A., Immonen, J., Holappa, J., Stenfors, C.: Gait analysis and weight bearing in pre-clinical joint pain research. J. Neurosci. Methods **300**, 92–102 (2018). https://doi.org/10.1016/j.jneumeth.2017.04.011

11. Gonsalvez, D.G., Yoo, S., Craig, G.A., Wood, R.J., Fletcher, J.L., Murray, S.S., Xiao, J.: Myelin protein zero 180–199 peptide induced experimental autoimmune neuritis in C57BL/6 mice. In: Myelin. Humana Press, New York (2018). https://doi.org/10.1007/978-1-4939-7862-5_19
12. Haggerty, A.E., Bening, M.R., Pherribo, G., Dauer, E.A., Oudega, M.: Laminin polymer treatment accelerates repair of the crushed peripheral nerve in adult rats. Acta Biomater. **86**, 185–193 (2019). https://doi.org/10.1016/j.actbio.2019.01.024
13. Myers, S.A., Gobejishvili, L., Ohri, S.S., Wilson, C.G., Andres, K.R., Riegler, A.S., Whittemore, S.R.: Following spinal cord injury, PDE4B drives an acute, local inflammatory response and a chronic, systemic response exacerbated by gut dysbiosis and endotoxemia. Neurobiol. Disease **124**, 353–363 (2019). https://doi.org/10.1016/j.nbd.2018.12.008
14. Diogo, C.C., da Costa, L.M., Pereira, J.E., Filipe, V., Couto, P.A., Geuna, S., Armada-da-Silva, P.A., Maurício, A.C., Varejão, A. S. (2019). Kinematic and kinetic gait analysis to evaluate functional recovery in thoracic spinal cord injured rats. Neurosci. Biobehav. Rev. https://doi.org/10.1016/j.neubiorev.2018.12.027
15. Xu, Y., Tian, N.X., Bai, Q.Y., Chen, Q., Sun, X.H., Wang, Y.: Gait assessment of pain and analgesics: comparison of the DigiGait™ and CatWalk™ gait imaging systems. Neurosci. Bull., 1–18 (2019). https://doi.org/10.1007/s12264-018-00331-y
16. Duda, R.O., Hart, P.E.: Use of the hough transformation to detect lines and curves in pictures. Comm. ACM **15**, 11–15 (1972). https://doi.org/10.1145/361237.361242
17. Yang, Z.-G., Ren, L.: SVD-based camera self-calibration and 3-D reconstruction from single-view. In: Proceedings of 2004 International Conference on Machine Learning and Cybernetics, vol. 7. IEEE (2004). https://doi.org/10.1109/icmlc.2004.1384556
18. McIvor, A.M.: Background subtraction techniques. In: Proceedings of Image and Vision Computing, pp. 3099–3104 (2000)
19. Haralick, R.M., Sternberg, S.R., Zhuang, X.: Image analysis using mathematical morphology. IEEE Trans. Pattern Anal. Mach. Intell. **4**, 532–550 (1987). https://doi.org/10.1109/TPAMI.1987.4767941

An Entropy-Based Graph Construction Method for Representing and Clustering Biological Data

Leandro Ariza-Jiménez[1(✉)], Nicolás Pinel[2], Luisa F. Villa[3], and Olga Lucía Quintero[1]

[1] Mathematical Modeling Research Group, Universidad EAFIT, Medellín, Colombia
{larizaj,oquinte1}@eafit.edu.co
[2] Biodiversity, Evolution, and Conservation Research Group, Universidad EAFIT, Medellín, Colombia
npinelp@eafit.edu.co
[3] System Engineering Research Group, ARKADIUS, Universidad de Medellín, Medellín, Colombia
lvilla@udem.edu.co

Abstract. Unsupervised learning methods are commonly used to perform the non-trivial task of uncovering structure in biological data. However, conventional approaches rely on methods that make assumptions about data distribution and reduce the dimensionality of the input data. Here we propose the incorporation of entropy related measures into the process of constructing graph-based representations for biological datasets in order to uncover their inner structure. Experimental results demonstrated the potential of the proposed entropy-based graph data representation to cope with biological applications related to unsupervised learning problems, such as metagenomic binning and neuronal spike sorting, in which it is necessary to organize data into unknown and meaningful groups.

Keywords: Entropy · Graph · Clustering · Biological data · Spike sorting · Metagenomic binning.

1 Introduction

Finding simple representations that allow the underlying structure of biological data to be uncovered and portrayed is a non-trivial task [1]. Unsupervised methods are used to learn the inner structure from this kind of data, which can consist of unlabeled observations. However, conventional approaches proposed to accomplish this task rely on methods that make assumptions about data distribution (e.g., center-based clustering) and require the reduction of the original dimensionality of the input data (e.g., via principal component analysis). Understanding and mining biological datasets is currently a relevant activity because it offers the opportunity to obtain meaningful information, for instance,

© Springer Nature Switzerland AG 2020
C. A. González Díaz et al. (Eds.): CLAIB 2019, IFMBE Proceedings 75, pp. 315–321, 2020.
https://doi.org/10.1007/978-3-030-30648-9_41

in the context of biomedical research, for prevention, prognosis, and treatment of human diseases [2]. Graphs are an option for mathematically representing and analyzing the complex interactions between real-world entities [3], allowing the extraction of useful information from data. Graph-based methods for detecting structure in data have previously been reported, mainly based on similarity measures between data objects [1,4,5]. From an information theory perspective, there is a relationship between compactly describing a set of data and learning from the data themselves [6]. Accordingly, this work proposes the incorporation of entropy related measures into the process of constructing graph-based representations for biological datasets in order to uncover their inner structure. Experimental results demonstrated the potential of the proposed entropy-based graph data representation to cope with biological applications, such as metagenomic binning and neuronal spike sorting, in which it is necessary to organize data into unknown and meaningful groups.

2 Proposed Method

Given a dataset of N d-dimensional data objects $\mathbf{X} = \{\mathbf{x}_1, \mathbf{x}_2, \ldots, \mathbf{x}_N\}$, our goal is to use similarity-based entropy measures to construct a graph that allows us to represent and discover the inner structure of the input data; the latter is described as a K-partition of $\mathbf{X}$. The overall process of the proposed method, which consists of four stages, is detailed below.

First Stage - Each dimension of $\mathbf{X}$ is normalized in interval [0,1]. Then, similarity between every pair of objects $\mathbf{x}_i$ and $\mathbf{x}_j$ is calculated using a modified Gaussian-based function $S_{ij} = \exp\left(-\alpha\sqrt{D_{ij}}\right)$, where D_{ij} is the normalized Euclidean distance between $\mathbf{x}_i$ and $\mathbf{x}_j$. In particular, α is a data-driven scale parameter computed automatically as $\alpha = -\ln 0.5/\sqrt{D}$, where D is the average distance among data objects in $\mathbf{X}$. As a result, data points separated by a distance equal to D are assigned a similarity of 0.5.

Second Stage - The total entropy value at each object $\mathbf{x}_i$ with respect to all other objects in $\mathbf{X}$ is calculated as $\mathbb{H}_i = \sum_{j=1}^{N} H(S_{ij})$. In particular, $H(S_{ij}) = -S_{ij}\log S_{ij} - (1 - S_{ij})\log(1 - S_{ij})$ is a similarity-based entropy measure at $\mathbf{x}_i$ with respect to $\mathbf{x}_j$ [7]. To represent the structure in data compactly, a copy $\mathbf{X}^*$ of the original data set $\mathbf{X}$ is sampled by an iterative procedure based on the total entropy values. A sampled data object, henceforth referred as a "prototype", is obtained in each iteration. The first prototype $\mathbf{x}_{p_1}$ is the data object in $\mathbf{X}^*$ with the lowest total entropy value. This object is subsequently removed from $\mathbf{X}^*$ as well as all of its nearby neighbors $\mathbf{x}_i$ such that $S_{ip_1} > \beta$. Next, the object with the lowest total entropy value among the remaining objects in $\mathbf{X}^*$ is selected as the second cluster center $\mathbf{x}_{p_2}$, and then this object together with all of its close neighbors are removed from $\mathbf{X}^*$. This iterative procedure is performed until no data object remains in $\mathbf{X}^*$. Note that the parameter β in the second stage conditioned the number of prototypes found through the iterative procedure. Preliminary tests showed that setting $\beta = \bar{S}_{ij} + \gamma\sigma$, where $\bar{S}_{ij}$ and σ

are respectively the sample mean and standard deviation of all of the pairwise similarities S_{ij}, and γ is an integer constant, allowing selection of a large and representative number of data samples from $\mathbf{X}$.

Third Stage - Let $\mathbf{x}_{p_1}, \mathbf{x}_{p_2}, \ldots, \mathbf{x}_{p_K}$ be K prototypes sampled from $\mathbf{X}$, where $K \ll N$. Suppose that each prototype $\mathbf{x}_{p_l}$ is the center of a fuzzy cluster C_l, which is part of a fuzzy partition of $\mathbf{X}$ into K clusters, and let u_{lj} be the grade of membership of object $\mathbf{x}_j \in \mathbf{X}$ in cluster C_l. Prototypes are then used to build a fuzzy connectivity graph G [8], which is an undirected weighted graph able to represent the structure of the input data. To this end, each prototype is considered as the vertex of an empty graph G on K nodes, that is, $G = (V, E)$, where $V = \{\mathbf{x}_{p_1}, \mathbf{x}_{p_2}, \ldots, \mathbf{x}_{p_K}\}$ and $E = \emptyset$. To populate G with weighted edges, for each object $\mathbf{x}_j$, the two larger membership values u_{pj} and u_{qj} are identified, and the edge $\{\mathbf{x}_{p_i}, \mathbf{x}_{p_j}\}$ is created thereafter. If edge $\{\mathbf{x}_{p_i}, \mathbf{x}_{p_j}\}$ already existed, its current weight is increased by one; otherwise, a unitary weight is initially assigned on the edge.

Fourth Stage - Graph clustering is performed on the resulting fuzzy connectivity graph G to organize the original data set $\mathbf{X}$ into groups. Clusters on G are found by the so-called Louvain method [9]. Once prototype nodes in G are clustered, the cluster membership of each prototype is transferred to the remaining data objects that are not part of the graph. Let $\mathbf{x}_j \in \mathbf{X}$ be a non-prototype data object. If $i = \arg\max_{l=1,\ldots,K} u_{lj}$, then $\mathbf{x}_j$ is assigned to the same cluster to which prototype node $\mathbf{x}_{p_i}$ was assigned on graph G.

3 Experiments and Results

To demonstrate the usefulness and effectiveness of the proposed method, experiments were conducted on datasets from two different types of biological applications (Fig. 1), both related to problems in which data are organized into unknown and meaningful groups.

First, our approach was used to organize a mixture of genomic fragments, composing a given artificial metagenomic dataset, into groups or "bins" reflecting organismal origin, a process known as "binning" in metagenomics [10]. The binning ability of the proposed method was tested on 37 simulated datasets presented in [11] for benchmarking metagenomic binning methods. The metagenomic datasets vary in composition and structure. Each of them comprises contigs from either five or ten distinct genome sequences, which in turn have pairwise genetic relatedness, measured by average amino acid identity, in one of two possible ranges: $[25, 40)\%$ or $[40, 55)\%$. Moreover, datasets contained between 6443 and 33,199 contigs, with lengths equal to 1000 base pairs.

For a metagenomic dataset, let $\mathbf{X}$ be the set of N contigs of d-dimensional features, and let $\mathbf{x}_i$ denote the i-th contig. Binning on each dataset $\mathbf{X}$ was performed by our method, either directly or indirectly, based on the pentamer (5-mer) frequency profile of each genomic fragment (obtained as in [12]). In the direct approach, the i-th contig was described by a 512-length frequency

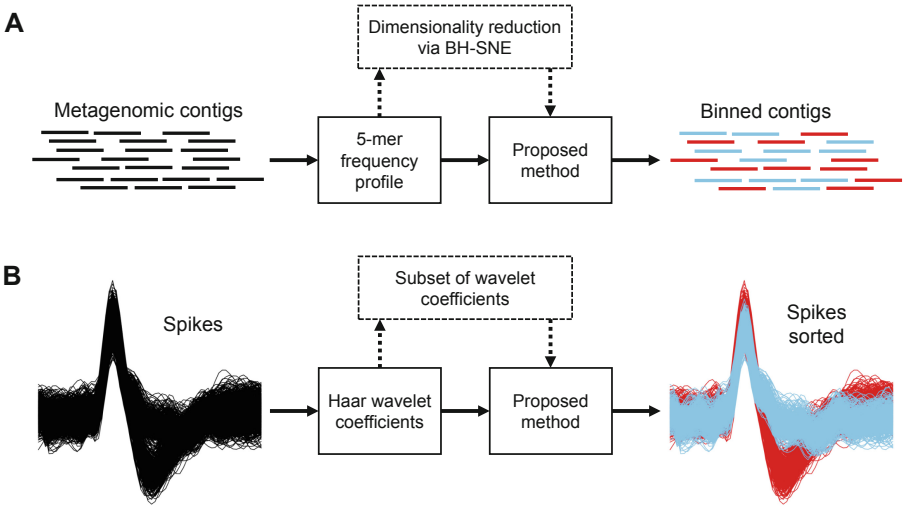

Fig. 1. Workflow of the experiments conducted on two biological applications of the proposed method. A: Metagenomic binning. B: Spike sorting. Dotted blocks and arrows represent experimental variations.

profile vector, namely $\mathbf{x}_i \in \mathbb{R}^{512}$. In contrast, in the indirect approach, prior binning, the above high-dimensional profiles were reduced via the Barnes-Hut t-Stochastic Neighbor Embedding (BH-SNE) algorithm [13] to either two or three dimensions [12], that is $\mathbf{x}_i \in \mathbb{R}^2$ or $\mathbf{x}_i \in \mathbb{R}^3$.

Figure 2A shows the binning performance of the proposed method on the ground-truth datasets, benchmarked against a reference method, in terms of the F-measure. In the indirect (low-dimensional) approach, the reference method, presented in [12], performed unsupervised binning on BH-SNE-based low-dimensional representations of metagenomic data using a combination of Subtractive and Fuzzy c-Means clustering algorithms with the Silhouette index. In the direct (high-dimensional) approach, the reference method was MetaCluster 3.0 [10], an unsupervised state-of-the-art binning method. The binning results indicated that the proposed method exhibited statistically significantly higher performance than the reference methods in both direct ($p \sim 10^{-7}$; t-test) and indirect ($p \sim 10^{-3}$; t-test) approaches. However, our results attested that as data dimensionality increased, the binning performance of our method significantly decreased ($p \sim 10^{-6}$; t-test). In particular, our method's parameter γ was set equal to two for all of the experiments and applications henceforward, except in the aforementioned indirect binning approach in which $\gamma = 1$.

As a second application, the proposed method was used for neuronal spike sorting. That is, given a set of recorded neuronal action potentials, or spikes, our purpose was to sort them according to which hypothetical neuron created them, based on features extracted from each spike waveform [14]. Experiments were conducted on simulated data, previously introduced in [15], namely, on 80

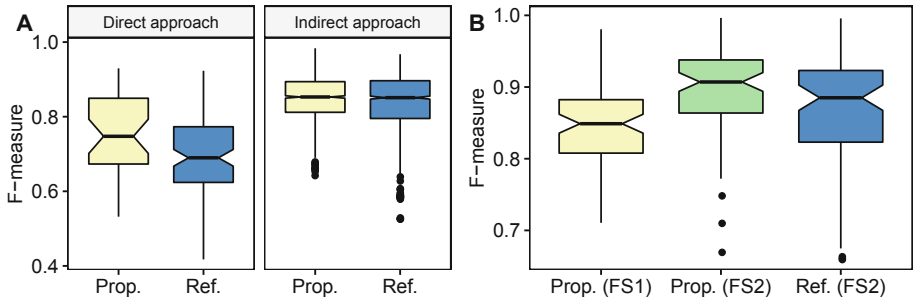

Fig. 2. Performance comparison of the proposed method and reference methods on different biological applications. A: Metagenomic binning. B: Spike sorting.

single-channel extracellular recordings of a varying number of neurons, ranging from 5 to 20. The reference method for this application was a state-of-the-art spike sorting software known as *Wave_clus* [14]. This software was used to detect and isolate spikes automatically from each simulated recording. The number of spikes obtained per simulated recording ranged between 1063 and 12,618.

Given a simulated recording, suppose that $\mathbf{X}$ is the set of N spikes of d-dimensional features, and let $\mathbf{x}_i$ denote the i-th spike. Spikes were sorted by our method based on two sets of wavelet-based features extracted from each spike waveform. The first set (FS1) consisted of all of the 64 coefficients extracted from the four-level wavelet decomposition of each spike waveform using the Haar wavelet, while the second one (FS2) was a variable subset of wavelet coefficients (between 10 and 29 out of 64) that were selected based on an automatic criterion implemented by *Wave_clus*. Therefore, for FS1, $\mathbf{x}_i \in \mathbb{R}^{64}$, and for FS2, $\mathbf{x}_i \in \mathbb{R}^d$, where $10 \leq d \leq 29$.

The performance, in terms of F-measure, of both spike sorting methods on simulated recordings is shown in Fig. 2B. Our method and *Wave_clus* presented slightly different results ($p = 0.094$; t-test) when the former used all 64 wavelet coefficients as inputs. However, when both methods sorted spikes in the same reduced feature space, our method's performance increased significantly ($p = 0.014$; t-test). Accordingly, for the proposed method, the achieved performance based on selected coefficients was significantly higher than the performance exhibited with 64 wavelet coefficients ($p \sim 10^{-6}$; t-test).

4 Discussion

An entropy-based graph construction method for representing and finding structure in biological data was proposed. Given a dataset, our method applies an iterative entropy-based data sampling approach to obtain a subset of representative data objects based on which a fuzzy connectivity graph is built, rather than using all of the data objects to obtain a graph-based representation (e.g., see [1,4,5]). Then, graph clustering is performed to detect structure in the data.

Experiments on biological datasets showed the usefulness and effectiveness of the proposed method on applications related to unsupervised learning problems, such as metagenomic binning and neuronal spike sorting, in which data is expected to be organized data into unknown and meaningful groups. Moreover, our proposed method does not require any prior knowledge of the input data, and it can outperform state-of-the-art methods in each of the aforementioned biological applications.

In particular, the proposed method furthers and integrates the ideas presented in previous reports [7,8]. Laskaris and Zafeiriou [8] suggested the concept of a fuzzy connectivity graph, derived from fuzzy over-clustering, and showed that it captures an abundance of topological information regarding the structure of an unlabeled dataset. However, they did not provide an automatic method for determining the proper number of prototypes or a method for identifying them. Yao et al. [7] introduced a method to calculate the entropy at each data object using similarity measures and a binary entropy function together. This method was initially intended to identify potential cluster centers on datasets. However, two main modifications were introduced here: a variation of the Gaussian kernel used as a similarity measure, and data-driven strategies that enable the method to automatically over-cluster the input datasets.

Since our method used a similarity-based entropy measure between data objects to characterize datasets, the interaction between similarity measures that are less prone to the curse of dimensionality than standard distance measures and this entropy measure should be addressed in future work, especially with regard to high-dimensional metagenomic datasets. Although the so-called Louvain algorithm performed well on clustering the fuzzy connectivity graphs, it only considered information regarding edge weights and not the entropy values that were available for prototypes as node attributes. Therefore, the combination of these "metadata" and the information from the fuzzy connectivity graph topology to guide and condition the graph clustering process is also a worthwhile subject of future research [16]. In addition, owing to the remarkable results on simulated datasets, we plan to extend our analyzes to real-world datasets, for example, metagenomic datasets obtained from the microbiome of an infant human gut [17].

Acknowledgments. This research was supported by Centro de Excelencia y Apropiación en Big Data y Data Analytics -Alianza CAOBA- and Universidad EAFIT.

Conflict of Interest. The authors declare that they have no conflicts of interest.

References

1. Vogt, J.E.: Unsupervised structure detection in biomedical data. IEEE/ACM Trans. Comput. Biol. Bioinforma. **12**(4), 753–760 (2015). https://doi.org/10.1109/TCBB.2015.2394408
2. Xu, R., Wunsch, D.C.: Clustering algorithms in biomedical research: a review. IEEE Rev. Biomed. Eng. **3**, 120–154 (2010). https://doi.org/10.1109/RBME.2010.2083647

3. Fortunato, S., Hric, D.: Community detection in networks: a user guide. Phys. Rep. **659**, 1–44 (2016). https://doi.org/10.1016/j.physrep.2016.09.002
4. de Arruda, G.F., Costa, L.D.F., Rodrigues, F.A.: A complex networks approach for data clustering. Phys. A Stat. Mech. Appl. **391**(23), 6174–6183 (2012). https://doi.org/10.1016/j.physa.2012.07.007
5. Zhang, H., Chen, X.: Network-based clustering and embedding for high-dimensional data visualization. In: 2013 International Conference on Computer-Aided Design and Computer Graphics, pp. 290–297. IEEE (2013). https://doi.org/10.1109/CADGraphics.2013.45
6. Grünwald, P.D.: The Minimum Description Length Principle. The MIT Press, Cambridge (2007)
7. Yao, J., Dash, M., Tan, S.T., Liu, H.: Entropy-based fuzzy clustering and fuzzy modeling. Fuzzy Sets Syst. **113**(3), 381–388 (2000). https://doi.org/10.1016/S0165-0114(98)00038-4
8. Laskaris, N.A., Zafeiriou, S.P.: Beyond FCM: graph-theoretic post-processing algorithms for learning and representing the data structure. Pattern Recognit. **41**(8), 2630–2644 (2008). https://doi.org/10.1016/j.patcog.2008.02.005
9. Blondel, V.D., Guillaume, J.L., Lambiotte, R., Lefebvre, E.: Fast unfolding of communities in large networks. J. Stat. Mech. Theory Exp. **2008**(10), P10008 (2008). https://doi.org/10.1088/1742-5468/2008/10/P10008
10. Leung, H.C., Yiu, S.M., Yang, B., Peng, Y., Wang, Y., Liu, Z., Chen, J., Qin, J., Li, R., Chin, F.Y.: A robust and accurate binning algorithm for metagenomic sequences with arbitrary species abundance ratio. Bioinformatics **27**(11), 1489–1495 (2011). https://doi.org/10.1093/bioinformatics/btr186
11. Ceballos, J., Ariza-Jiménez, L., Pinel, N.: Standardized approaches for assessing metagenomic contig binning performance from Barnes-Hut *t*-Stochastic neighbor embeddings. In: VIII Latin American Conference on Biomedical Engineering and XLII National Conference on Biomedical Engineering, pp. 761–768. Springer Nature Switzerland AG (2020). https://doi.org/10.1007/978-3-030-30648-9_101
12. Ariza-Jiménez, L., Quintero, O., Pinel, N.: Unsupervised fuzzy binning of metagenomic sequence fragments on three-dimensional Barnes-Hut t-Stochastic neighbor embeddings. In: 40th Annual International Conference of the IEEE Engineering in Medicine and Biology Society (EMBC), pp. 1315–1318. IEEE (2018). https://doi.org/10.1109/EMBC.2018.8512529
13. van der Maaten, L.: Accelerating t-SNE using tree-based algorithms. J. Mach. Learn. Res. **15**, 3221–3245 (2014). http://jmlr.org/papers/v15/vandermaaten14a.html
14. Chaure, F.J., Rey, H.G., Quian Quiroga, R.: A novel and fully automatic spike-sorting implementation with variable number of features. J. Neurophysiol. **120**(4), 1859–1871 (2018). https://doi.org/10.1152/jn.00339.2018
15. Pedreira, C., Martinez, J., Ison, M.J., Quian Quiroga, R.: How many neurons can we see with current spike sorting algorithms? J. Neurosci. Methods **211**(1), 58–65 (2012). https://doi.org/10.1016/j.jneumeth.2012.07.010
16. Newman, M.E., Clauset, A.: Structure and inference in annotated networks. Nat. Commun. **7**(May), 1–11 (2016). https://doi.org/10.1038/ncomms11863
17. Sharon, I., Morowitz, M.J., Thomas, B.C., Costello, E.K., Relman, D.A., Banfield, J.F.: Time series community genomics analysis reveals rapid shifts in bacterial species, strains, and phage during infant gut colonization. Genome Res. **23**(1), 111–120 (2013). https://doi.org/10.1101/gr.142315.112

Automatic Lid Segmentation in Meibography Images

Luis DelaO-Arévalo[1(✉)], Erik Bojorges-Valdez[1], Everardo Hernández-Quintela[2], Nallely Ramos-Betancourt[2], and Jesus H. Davila-Alquisiras[2]

[1] Universidad Iberoamericana Ciudad de México, 01219 Mexico City, Mexico
ldelaoa@gmail.com

[2] Asociación para Erradicar la Ceguera I.A.P., 04030 Mexico City, Mexico

Abstract. This work presents an evaluation of two machine learning schemes for lid segmentation on meibography images. Both schemes use same input features based on pixel gray levels, laplacian and entropy filters, and also distances to anatomical landmarks like pupil and eye lashes. The methods evaluated were support vector machines (SVM) with 4th degree polynomial kernel, a Neural Network (NN) with 60 neurons distributed on three layers and the intersection of both. Performance was evaluated with AUC on a bootstrapped cross validation (CV) tests of 20 folds. Dataset is conformed by 465 images for each fold entire dataset was split on 70% training and remainder for testing. Results of CV: SVM 0.851 ± 0.103, NN 0.713 ± 0.144 and SVM & NN 0.835 ± 0.118, suggest that SVM is a suitable model to be used for this task.

Keywords: Meibography · Machine learning · Image processing

1 Introduction

The meibomian glands are sebaceous glands located along lid margin posterior to lashes, they produce a lipidic secretion that retards tear evaporation [1]. Meibomian gland dysfunction (MGD) is one of the most common abnormalities in ophthalmic practice [2], resulting in an altered or reduced gland distribution thru the lid.

Meibography is a standard method for in-vivo evaluation of meibomian glands [3], this imaging study pictures everted lid under infrared (IR) light. Arita et al. [4] score changes in meibomian glands using a four-grade scale describing area of meibomian gland loss, but a standard scale is not fully accepted.

Although there has been some initial publications about user-free meibography [5,6], where an algorithm is able to evaluate and group meibomian glands in a non supervised system, manual lid segmentation is still required. This work is focused in automatic lid segmentation using machine learning (ML) approaches, as a first step for a fully user-free diagnosis tool of MGD.

© Springer Nature Switzerland AG 2020
C. A. González Díaz et al. (Eds.): CLAIB 2019, IFMBE Proceedings 75, pp. 322–326, 2020.
https://doi.org/10.1007/978-3-030-30648-9_42

2 Methodology

2.1 Data

For this work 465 meibography images were acquired at a third level ophthalmology hospital "Dr. Luis Sánchez Bulnes", at Mexico City, as part of routinely practices. Images were acquired by a trained physician with a Keratograph 5M (Oculus, Germany), with resolution of 1024 × 1064 pixels in 256 gray levels. Dataset is divided in 235 lower lid images and 230 upper lid images, clinical records remain anonymous.

2.2 Machine Learning Approaches

Lids in meibography images were segmented by two ML algorithms. Support vector machines (SVM) and neural networks (NN). An extra approach was proposed by combining both outputs with a logic AND operation.

Segmentation was conceived as two classes (lid vs no-lid) classification task pixel-by-pixel. Labeling was manually done by drawing lid area, creating a binary mask for each image.

This information was used to train an optimized Support Vector Machine Model (SVM) with a fourth degree polynomial kernel and a Forward Neural Network (NN) with 60 neurons distributed in 3 layers with Levenberg-Marquardt error function and Relu as activation function. All algorithms and evaluations were done in MATLAB ®19a (Mathworks, USA) under academic license.

2.3 Input Features for Machine Learning Models

To enhance lid segmentation is useful to locate anatomical and prior information elements such as:

Pupil coordinates. These provides information whether pupil is present in the image or not. If it is: PupilRow and PupilCol matches pupil's center coordinates. If it is not: both are set to zero.

Eyelashes coordinates. Eyelashes were considered as dark elements with high frequency components in the image. Eyelashes can be considered as a cluster that forms a polygon. Coordinates of corresponding polygon's centroid are used as features.

Probabilistic Maps (PM). By averaging manually selected lid areas of several images, upper and lower probabilistic maps can be created. With the highest value of each map times the corresponding pixel value in the original image, results in one value for upper (PM up) and one for lower (PM low), the difference between them matches the image lid type (up/low).

Table 1 shows a full list of input features base on values intensities and distances to previous described elements.

Table 1. Input features for ML models.

Values and intensities	Distances
Gray level value	Row and Col number
Gray values × PM median	Pupil Row and Col - Row and Col number
Gray value after border enhancement	Center of mass for PM up Euclidean distance
Gray value after entropy filter	Center of mass for PM low Euclidean distance
Gradient value in 9×9 window	Eyelash Row and Col - Row and Col number

2.4 Lid Area Definition

Each ML model output is a binary mask with same dimensions as input images. To optimize comparisons among models, the biggest area in the mask is selected and its perimeter smoothed by Savitzky-Golay filter [7].

2.5 Testing and Validation

Dataset contains images with artifacts like: existing and non existing pupil in the image, difference in eyelash structure (only upper, only lower, both present in the image), among others artifacts as fingers and cotton swabs. Training evaluation was assessed with bootstrapped cross-validation of 20 vias, using 70% of data as training set.

Performance validation computes area under curve of the receiver operating characteristic curve (AUROC) and evaluation time for each method in 139 images (30% of data) randomly selected. These images were compared versus manually segmented images by a trained single user. Tanimoto coefficient was also calculated to measure intersection between manual and each segmentation model [8].

3 Results

Figure 1 shows AUCROC results corresponding to all evaluations: NN 0.713 ± 0.144, SVM 0.851 ± 0.103 and NN & SVM 0.835 ± 0.118; with evaluation time NN $12\,\text{s} \pm 0.8\,\text{s}$ and SVM $40\,\text{s} \pm 1.1\,\text{s}$. On Fig. 2, upper and lower lid segmentation examples are shown using manual and automatic SVM, NN and NN & SVM segmentation. Tanimoto Index between manual and ML models reported following values: NN $= 0.3170 \pm 0.2122$, SVM $= 0.7131 \pm 0.1231$ and SVM $\cap$ NN $= 0.7135 \pm 0.1235$.

4 Discussion and Conclusion

According to AUCROC values shown in Fig. 1, SVM is the method with the highest performance. On several images NN presents chaotic behavior, suggesting that lack of pupil cause this classifications errors.

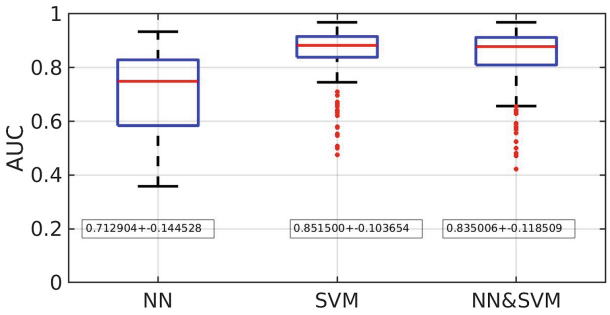

Fig. 1. AUC results

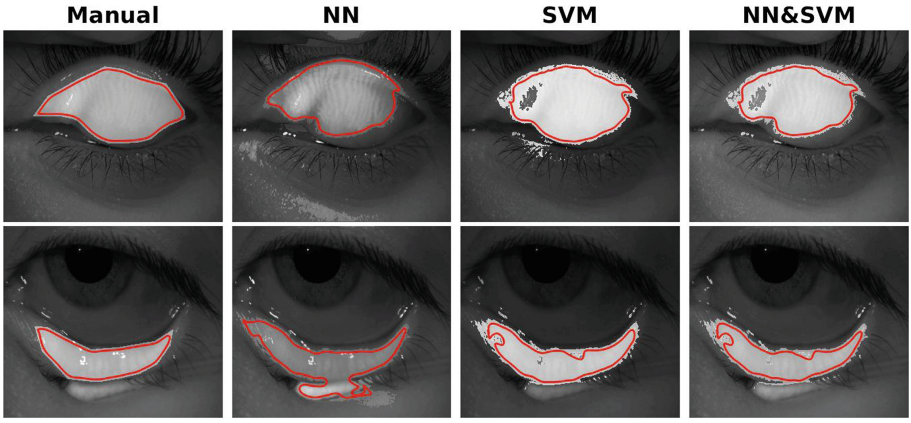

Fig. 2. First row shows and upper lid example and lower lid on the second. Each column shows manual, NN, SVM and NN & SVM output. Line describes the perimeter after Savitzky-Golay filtering

Future work includes a clinical validation, by certified physicians who will perform a manual lid segmentation. Accuracy, repeatability and inter observatory variability will be measured.

Although these algorithms will be on constant training and improvements (specially NN), clinical trials are already encouraged to be practiced. Following stages will focus on applying ML in meibomian gland segmentation and classification.

Acknowledgments. This work is financed by Instituto de Investigación Aplicada a la Tecnología (InIAT) of Universidad Iberoamericana Ciudad de México under the project CIDIBIO.

Conflict of Interest Declaration. Participant authors certify that they have NO affiliations with or involvement in any organization or entity with any financial interest or non-financial interest in the subject matter or materials discussed in this manuscript.

References

1. Wise, R.J.: Meibography: a review of techniques and technologies (2012). https://doi.org/10.1016/j.sjopt.2012.08.007
2. Foulks, G.N.: Meibomian gland dysfunction: a clinical scheme for description, diagnosis, classification, and grading. (2003). https://doi.org/10.1016/S1542-0124(12)70139-8
3. Driver, P.J.: Meibomian gland dysfunction (1996). https://doi.org/10.1016/S0039-6257(96)80064-6
4. Pult, H.: A review of meibography (2012). https://doi.org/10.1097/OPX.0b013e3182512ac1
5. Ebenezer, D.: Grading and baseline characteristics of meibomian glands in meibography images and their clinical associations in the dream study (2019). https://doi.org/10.1016/j.jtos.2019.04.003
6. Koh, Y.W.: Detection of meibomian glands and classification of meibography images (2012). https://doi.org/10.1117/1.JBO.17.8.086008
7. Orfanidis, S.J.: Introduction to Signal Processing (1996)
8. Rogers, D.J., et al.: A computer program for classifying plants (1960)

Brain Tortuosity as Biomarker to Classify Mild Cognitive Impairment and Control Subjects

Eduardo Barbará Morales[1(✉)], Karla C. Rojas Saavedra[2], Luis Jiménez Ángeles[3], and Verónica Medina Bañuelos[1]

[1] Universidad Autónoma Metropolitana, Unidad Iztapalapa, Mexico City, Mexico
eduardobm@xanum.uam.com
[2] Universidad del Valle de México, Campus Sur., Mexico City, Mexico
[3] Universidad Nacional Autónoma de México, Mexico City, Mexico

Abstract. Mild cognitive impairment (MCI) is an abnormal deterioration of cognitive functions, whose prevalence is considerable in adults older than 65 years old. Several of these cases will convert to Alzheimer's disease and therefore, MCI's simple, proper and opportune diagnosis continues to be a research field with great impact in public health. In this paper we propose tortuosity, which is defined as a shape measure that has been applied to quantify morphological changes in several anatomical structures, as a potential biomarker sensitive enough to depict early brain changes that appear in MCI subjects in comparison with healthy controls (HC). Also, a random forest (RF) classification strategy was implemented to discriminate between MCI and HC populations. A training population selected from the ADNI database and a test group of 21 mexican subjects were analyzed. Statistical analysis showed significant differences ($p < 0.05$) in tortuosity indices determined for MCI vs HC populations in most of the measured cortical structures. Classification rates increased by 6.7% during training and 4.77% during the test stage, when incorporating tortuosity to other image-based features set. This suggests that tortuosity is a promising morphological parameter to be considered for early stages of Alzheimer disease (AD) and that, combined with an RF classifier, it can adequately separate HC and MCI subjects.

Keywords: Tortuosity biomarker · Random forest · Mild Cognitive Impairment

1 Introduction

Alzheimer's disease (AD) is a neurodegenerative disorder that leads to irreversible gradual loss of cognitive and intellectual capabilities, thus limiting a subject's performance in daily activities. It has been reported that this illness gradually provokes changes in brain morphology, leading to loss of cognitive activities such as memory, orientation, language, among others. The National Institute on Aging and Alzheimer's Association recognize three principal phases of the progression of AD: Preclinical healthy stage, Mild Cognitive Impairment (MCI) and Dementia due to AD [1]. Mild cognitive impairment is a transitory stage between normal cognitive function and

© Springer Nature Switzerland AG 2020
C. A. González Díaz et al. (Eds.): CLAIB 2019, IFMBE Proceedings 75, pp. 327–333, 2020.
https://doi.org/10.1007/978-3-030-30648-9_43

dementia. It is characterized by memory disturbances followed by ample deterioration in multiple domains. Its prevalence is around 15% in adults older than 65 years, some of which remain stable on this condition (MCInc), while up to 50% can convert to AD (MCIc) [2, 3]. It is important to consider that biochemical changes trigger AD progression, followed by structural deterioration visible through neuroimaging techniques. Cognitive impairment appears later and can be assessed using neuropsychological tests, which are nowadays the most common diagnosis criteria.

Recent interest has arisen on the medical and neuroimaging communities to incorporate techniques taken from artificial intelligence and machine learning fields for AD diagnosis. Also, new image-extracted biomarkers have appeared for early detection of brain changes. Many studies focus on combining biomarkers (BMs) of different kinds and applying pattern recognition techniques to identify early symptoms of the disease, especially during the MCI stage [4].

On the other hand, tortuosity has been proposed as a useful measure to depict morphological changes in several medical applications. Tortuosity is an intrinsic property of curved surfaces that quantitatively reflects deformations of an object. It has been used to determine twists and turns, for instance in retinal and cerebral blood vessels [5] and in corneal nerve fibers [6].

Some pieces of research were recently reported on the classification of patients with AD in its different phases and describe the use of biomarkers and patterns' analysis to solve the problem of early detection of symptoms in subjects with MCI [7–10]. In this research the three-dimensional tortuosity measured in several cortical regions is proposed as a novel biomarker, sensitive to early changes of brain morphology. It is intended to be used as a complementary parameter that quantifies structural changes in different moments of the pathological process.

2 Materials and Methods

2.1 Participants

Data were obtained from the Alzheimer's Disease Neuroimaging Initiative (ADNI) database (adni.loni.usc.edu), according to inclusion/exclusion criteria of the ADNI protocol (http://www.adni-info.org/Scientists/ADNIStudyProcedures.aspx). In addition, two populations were constituted considering the completeness of the following information: MR volumes acquired in similar conditions (T1-weighted, at 1.5T, voxel resolution of $1.2 \times 0.93 \times 0.93$ mm^3), cognitive scores evaluated by clinical dementia rating (CDR) test, groups paired by age and all biomarkers recorded in nearby dates. The two selected populations were 30 Healthy Controls (HC) and 30 subjects with stable MCI, whose demographic and neuropsychological scores are shown in Table 1 (1st and 2nd columns). These groups were used as training data in the classification process.

A test population was recorded at the Research Center of Medical Instrumentation and Imaging in Mexico. It consisted of 13 HC and 8 MCI (mild and moderate) subjects, previously diagnosed by a geriatrician following several neurocognitive scores (Table 1, 3rd and 4th columns). MR volumes were acquired in similar conditions

Table 1. Demographic data and cognitive tests for training and test populations

ADNI training populations			Test populations	
	HC (N = 30)	MCI (N = 30)	HC (N = 13)	MCI (N = 8)
Age (yrs) ($\mu \pm \sigma$)	76.1 ± 3.9	74.0 ± 7.1	73.15 ± 6.0	81.25 ± 7.0
Gender (F/M)	16/14	13/17	13	8
CDR (sum of boxes) (rank/$\mu \pm \sigma$)	0	1.5–2.5 (1.87 ± 0.41)	0	1–2 (1.6 ± 0.51)

(T1-weighted, at 3T, voxel resolution of 0.42 × 0.42 × 5 mm^3). This group was used as a test population, to prove the generalization capability of the proposed classification strategy.

2.2 MR Images Processing

As a first step, global gray and white matters (GM, WM) were segmented from brain MR volumes; the former was also subdivided into several substructures, to separate parietal and temporal lobes (PL, TL), for right and left hemispheres (RH, LH) of all subjects. It has been demonstrated in several researches that these two lobes are the first to be affected during the degenerative process of AD [8, 11]. For this purpose, the "Statistical Parametric Mapping" (SPM) [12] tool was used, with the following sequence: volume orientation, image realignment/registration and segmentation.

2.3 Volume (V), Normalized Volume (NV) and Discrete Compactness (DC)

As a first step, an interpolation of MR volumes was applied, to have an isometric resolution of 1 mm^3. After segmentation, the volume is easily estimated by counting the number of voxels (n) that belong to regions of interest. Normalization was carried out by dividing the total number of voxels of a given structure by the intracranial volume, which is computed by adding those voxels corresponding to GM, WM and CSF.

Discrete compactness has been reported as a useful biomarker for the classification of HC, MCI and AD [8]. It is computationally simple to calculate, it varies in a range of zero (null compactness) and one (totally compact voxels) and it is invariant to rotation, scaling or translation, qualities that are useful to eliminate bias in the measurement. DC is computed by:

$$DC = \frac{n - \frac{A}{6}}{n - \left(\sqrt[3]{n}\right)^2} \tag{1}$$

where n is the number of voxels and A is the enclosing area.

2.4 Tortuosity (TR)

Normalized tortuosity has been reported by Bullit et al. [5] and is estimated by the Sum of Angles Metric (SOAM) method, with the following steps:

(i) A mesh is obtained from a 3D skeletonization process, constituting a set of N ordered points P_k, with coordinates (x_k, y_k, z_k); (ii) Vectors X, Y and Z are defined, containing respectively the set of x_k, y_k and z_k coordinates of the array of points; (iii) The following two-column, k-row arrays are conformed: T1 = [Y X], T2 = [Z Y] and T3 = [Z X]; (iv) Each array is normalized; (v) The following elements are computed:

$$\text{Plane angle}: \; IP_k = cos^{-1}\left((T1/|T1|) \cdot \left(\frac{T2}{|T2|}\right)\right) \tag{2}$$

$$\text{Total angle}: \; CP_k = \sqrt{(IP_k \times IP_k)} \tag{3}$$

$$\text{SOAM}: \; TR = \left(\sum_{k=1}^{N-3} CP_k\right) / \left(\sum_{k=1}^{N-1} |P_k - P_{k-1}|\right) \tag{4}$$

2.5 Statistical Analysis

We applied a Kruskal-Wallis test ($p <= 0.05$) between the two classes, since the calculated metrics do not follow a normal distribution. The objective of this statistical analysis was to find differences between the calculated biomarkers of the two populations.

2.6 Classification Strategy

To classify the studied populations into two groups, random forests (RF) were used. They are defined as a collection of classifiers structured as a tree [10], that are robust to overfitting and are considered more stable to outliers and high dimensional parameter spaces than other machine learning algorithms [13]. The RF algorithm was trained with the ADNI's 60 subjects of the two classes and tested with the recorded 21 cases, as described in Sect. 2.1.

Accuracy was first calculated during the training procedure (reported as central and dispersion measures obtained from a 10-fold cross validation) and was afterward determined for the test dataset.

The feature set included only image-extracted parameters because subjects were assigned, by expert neurologists, to HC or MCI populations according to the CDR score, that was considered the gold standard.

3 Results and Discussion

Absolute volume, normalized volume, discrete compactness and tortuosity were computed for all the segmented brain structures. Means and standard deviations are shown graphically in Fig. 1. Significant differences ($p < 0.05$) between HC and MCI

are marked with *. It can be observed that tortuosity determined for all brain structures (excepting global white matter) is a good discriminator between the two populations. Also, the Volume parameter differs significantly in five out of six of the segmented structures, while NV is different in four structures and DC only in the left temporal lobe. In order to test the discrimination capability of tortuosity, performance of RF classifier was obtained for several feature combinations (Table 2). The first three rows include only image-extracted parameters: previously reported measures (V, NV and DC, 18 features) in the first row; only TR (6 features) in the second; and all included (24 features) in the third. As expected, the combination of more morphological parameters allows an increase of 6.66% in the training set classification. For the test set, the best accuracy (71.43%) was obtained through the combination of all image-extracted parameters.

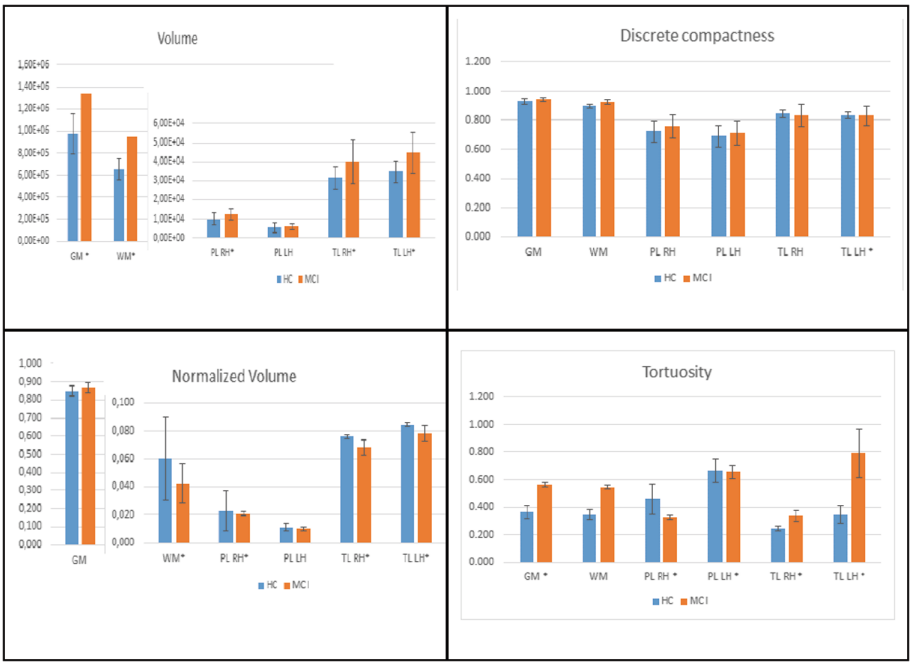

Fig. 1. Statistical analysis for image-extracted parameters. * ($p < 0.05$)

Considering that cognitive deterioration is the clinical gold standard for diagnosis, we have measured the classification capability of this parameter alone. In the fourth row of Table 2, it can be seen that CDR provides a classification rate of 73.33% in the training set, but only of 61.9% in the test set. Several pieces of research have demonstrated that the combination of different modalities increases classification capability [3, 7], and this is shown in the last row of Table 2, where all image and cognitive biomarkers are incorporated to attain a perfect assignation of the training set and up to

Table 2. Results of the classification process using RF for different BM combinations.

Performance					
V NV DC	TR	CDR	Number of features	Accuracy training set (N = 60) ($\mu \pm \sigma$)	Accuracy test set (N = 21)
✓			18	71.67 ± 0.33%	66.66%
	✓		6	75.00 ± 0.22%	52.38%
✓	✓		24	78.33 ± 0.33%	71.43%
		✓	1	73.33 ± 0.25%	61.90%
✓	✓	✓	25	100 ± 0.0%	80.95%

80.95% for the test set. Our results can also be contrasted with performances reported by Salvatore et al. [4] that show classification rates of 59% (HC vs MCI). Nanni et al. [14] report classification rates between 85.5% when comparing pairs of groups (MCI vs HC), but employing a large number of image features (2000) selected with several methods. In contrast, Dimitriadis et al. [9] report a 61.9% accuracy in the classification of four groups: HC, MCIc, MCInc and AD, but it must be noted that discriminating between MCIc and MCInc classes can cause the apparently low performance of their method.

4 Conclusions

The main contribution of this research is the introduction of tortuosity measure, as a promising morphological parameter to be considered in early stages of AD. Results show that tortuosity is sensitive to morphology changes appearing in several brain structures. because it shows significant differences for most of the analysed structures, allowing the discrimination between HC vs MCI. The classification strategy incorporates multimodal information and allows attaining an accuracy of 80.95% during the test stage with previously unseen data. These findings suggest that tortuosity can be considered as an image-extracted BM, helpful in the detection of early stages of AD.

Acknowledgments. Eduardo Barbará-Morales received financial support from CONACyT, scholarship number 593171. Data collection and sharing for this project was funded by the Alzheimer's Disease Neuroimaging Initiative (ADNI) (National Institutes of Health Grant U01 AG024904) and DOD ADNI (Department of Defense award number W81XWH-12-2-0012), adni.loni.usc.edu.

Conflicts of Interest. The authors have no conflicts of interest to disclose.

References

1. McKhann, G.M., Knopman, D.S., et al.: The diagnosis of dementia due to Alzheimer's disease: recommendations from the National Institute on Aging-Alzheimer's Association workgroups on diagnostic guidelines for Alzheimer's disease. Alzheimers Dement. **7**, 263–269 (2011). https://doi.org/10.1016/j.jalz.2011.03.005

2. Donnelly-Kehoe, P.A., Pascariello, G.O., Gomez, J.C.: Looking for Alzheimer's Disease morphometric signatures using machine learning techniques. J. Neurosci. Methods **302**, 24–34 (2018). https://doi.org/10.1016/j.jneumeth.2017.11.013
3. Yao, D., Calhoun, V.D., Fu, Z., Du, Y., Sui, J.: An ensemble learning system for a 4-way classification of Alzheimer's disease and mild cognitive impairment. J. Neurosci. Methods **302**, 75–81 (2018). https://doi.org/10.1016/j.jneumeth.2018.03.008
4. Salvatore, C., Castiglioni, I.: A wrapped multi-label classifier for the automatic diagnosis and prognosis of Alzheimer's disease. J. Neurosci. Methods **302**, 58–65 (2018). https://doi.org/10.1016/j.jneumeth.2017.12.016
5. Bullitt, E., Gerig, G., Pizer, S.M., Lin, W., Aylward, S.R.: Measuring tortuosity of the intracerebral vasculature from MRA images. IEEE Trans. Med. Imaging **22**, 1163–1171 (2003). https://doi.org/10.1109/tmi.2003.816964
6. Annunziata, R., Kheirkhah, A., Aggarwal, S., Hamrah, P., Trucco, E.: A fully automated tortuosity quantification system with application to corneal nerve fibres in confocal microscopy images. Med. Image Anal. **32**, 216–232 (2016). https://doi.org/10.1016/j.media.2016.04.006
7. Janousova, E., Vounou, M., Wolz, R., Gray, K.R., Rueckert, D., Montana, G.: Alzheimer's disease neuroimaging initiative, biomarker discovery for sparse classification of brain images in alzheimer's disease. Ann. BMVA **2012**, 1–11 (2012)
8. Perez-Gonzalez, J.L., Yanez-Suarez, O., Bribiesca, E., Cosío, F.A., Jiménez, J.R., Medina-Bañuelos, V.: Description and classification of normal and pathological aging processes based on brain magnetic resonance imaging morphology measures. J. Med. Imaging **1**, 034002 (2014). https://doi.org/10.1117/1.jmi.1.3.034002
9. Dimitriadis, S.I., Liparas, D., Tsolaki, M.N.: Random forest feature selection, fusion and ensemble strategy: combining multiple morphological MRI measures to discriminate among healhy elderly, MCI, cMCI and alzheimer's disease patients: from the alzheimer's disease neuroimaging initiative (ADNI) database. J. Neurosci. Methods **302**, 14–23 (2018). https://doi.org/10.1016/j.jneumeth.2017.12.010
10. Ramirez, J., Gorriz, J.M., Ortiz, A., Martinez-Murcia, F.J., Segovia, F., Salas-Gonzalez, D., Castillo-Barnes, D., Illan, I.A., Puntonet, C.G.: Ensemble of random forests One vs. rest classifiers for MCI and AD prediction using ANOVA cortical and subcortical feature selection and partial least squares. J. Neurosci. Methods **302**, 47–57 (2018). https://doi.org/10.1016/j.jneumeth.2017.12.005
11. Karas, G.B., Scheltens, P., Rombouts, S.A.R.B., Visser, P.J., Schijndel, R.A., Fox, N.C., Barkhof, F.: Global and local gray matter loss in mild cognitive impairment and Alzheimers disease. NeuroImage **23**, 708–716 (2004). https://doi.org/10.1016/j.neuroimage.2004.07.006
12. Alemán-Gómez, Y., Melie-García, L., Valdés-Hernandez, P.: IBASPM: toolbox for automatic parcellation of brain structures. Presented at the 12th Annual Meeting of the Organization for Human Brain Mapping (2006)
13. Sarica, A., Cerasa, A., Quattrone, A., Calhoun, V.: Editorial on special issue: machine learning on MCI. J. Neurosci. Methods **302**, 1–12 (2018). https://doi.org/10.1016/j.jneumeth.2018.03.011
14. Nanni, L., Salvatore, C., Cerasa, A., Castiglioni, I.: Combining multiple approaches for the early diagnosis of Alzheimers disease. Pattern Recogn. Lett. **84**, 259–266 (2016). https://doi.org/10.1016/j.patrec.2016.10.010

Classification of Handwritten Drawings of People with Parkinson's Disease by Using Histograms of Oriented Gradients and the Random Forest Classifier

João Paulo Folador[1(✉)], Adrian Rosebrock[2], Adriano Alves Pereira[1], Marcus Fraga Vieira[3], and Adriano de Oliveira Andrade[1]

[1] Centre for Innovation and Technology Assessment in Health, Postgraduate Program in Electrical and Biomedical Engineering, Faculty of Electrical Engineering, Federal University of Uberlândia, Uberlândia, Brazil
jpfolador@gmail.com, a.alves.pereira@uol.com.br, adriano@ufu.br

[2] PyImageSearch, University of Maryland Baltimore County (UMBC), Baltimore, USA
adrian@pyimagesearch.com

[3] Bioengineering and Biomechanics Laboratory, Federal University of Goiás, Goiânia, Brazil
marcus@ufg.br

Abstract. Parkinson's disease (PD) is a neurological disorder that is progressive and causes losses of dopaminergic neurons from the substantia nigra, a region in the human brain. The decrease of dopamine in this area elucidates the presence of motor symptoms, such as tremors, bradykinesia, rigidity, gait impairment, and non-motor symptoms, e.g., depression, loss of cognitive functions, sleep problems, and nerve pain. Among the motor symptoms, tremors can have the most impact on the social activities of people with PD. Furthermore, there is difficulty in diagnosing the underlying disorder that causes tremors. Thus, the study and development of methods to assess tremors and their severity is of paramount relevance for clinical practice. A typical clinical tool to evaluate tremor severity is the analysis of hand drawing shapes (e.g., spirals, circles, meanders, waves). The evaluation of these drawings is dependent on the experience of professionals, yielding a high variability of results. Aiming to contribute to the objective evaluation of hand drawing shapes of people with PD, this research proposes the application of the Random Forest Classifier to classify Histograms of Oriented Gradients (HOG) estimated from sinusoidal patterns collected from healthy individuals (n = 12) and from people with PD (n = 15). The highest accuracy, sensitivity and specificity classification success rates were of 83%, 85% and 81%, respectively. These results can be relevant for the early detection of pathological tremors, the follow-up of medical treatments and the diagnosis of parkinsonian conditions.

Keywords: Parkinson's disease · Tremor · Handwritten drawing classification · Random Forest Classifier · Histograms of oriented gradients

© Springer Nature Switzerland AG 2020
C. A. González Díaz et al. (Eds.): CLAIB 2019, IFMBE Proceedings 75, pp. 334–343, 2020.
https://doi.org/10.1007/978-3-030-30648-9_44

1 Introduction

Parkinson's disease (PD) is a neurological disorder that is progressive and causes losses of dopaminergic neurons from the substantia nigra, a region in the human brain. The decrease of dopamine in this area implies the worsening of motor symptoms such as tremors, bradykinesia, rigidity, gait impairment, and non-motor symptoms such as depression, loss of cognitive functions, sleep problems and nerve pain [1].

PD affects 1% of the world's population aged 60 years and over, and despite scientific advancement, the disease remains incurable. The diagnosis of PD is complex, with a seasoned specialist being necessary to make it [1, 2].

Tremors are a common symptom in PD and it can be classified into many types: resting tremor, postural tremor, kinetic, essential, cerebellar, and others. Each type manifests in different situations and frequency ranges [3].

Despite the existence of various clinical scales to assess motor symptoms in PD (e.g., Unified Parkinson's disease Rating Scale - UPDRS [2], Tremor Rating Scale – wTRS, and the Essential Tremor Rating Assessment Scale - TETRAS [3]), the understanding and quantification of tremors is important for the correct diagnosis of PD and for monitoring its progress [3, 4]. An alternative way to assess tremors is by using a scale of severity based on handwritten drawings. However, the scoring of these drawings is complex and dependent on the experience of the examiner.

Several methods have been proposed to automate the assessment of tremors in PD. For instance, Bravo et al. [5] analyzed postural tremor, action tremor and rest tremor from the hand index finger using a triaxial accelerometer to acquire the data. The data was analyzed via spectral power density (PSD). The study showed that the tremors decreased considerably with the use of medication, but they did not disappear completely.

Zhang et al. [6] employed principal component analysis (PCA) to discriminate the main features from Magnetic Resonance Imaging (MRI) data and Support Vector Machine (SVM) to classify the essential and PD tremors. The best classification success rate reported in the study was 93.75%.

Prince and de Vos [7] collected data from healthy individuals and people with PD, performing the task of hitting the index and middle fingers on a smartphone. Subsequently, they compared the data classification success rate between traditional algorithms and Deep Learning (DL), which outperformed traditional techniques.

According to Pereira et al. [8], another technique based on DL is Convolutional Neural Network (CNN), and it was used for the automatic discrimination between people with PD from healthy individuals. The data were acquired by using a pen with several attached sensors. The participants of the study drew spirals and meanders on a sheet of paper. The data from the sensors were converted into images for data classification and the CNN reached good accuracy.

Unlike the work done by Pereira et al. [8] that used the time series from different pens' sensors and built an image of these signals, this work proposes to classify images of handwritten drawings collected from healthy individuals and people with PD. The identification and discrimination of motor symptoms in PD is a fundamental step in the diagnosis and follow-up of the disorder

The remainder of this paper is organized as follows. Section 2 describes the experimental environment, the information about the participants of the study, and the feature extraction and classification methods. Section 3 shows the obtained results, and in Sect. 4 the discussion and conclusions are presented.

2 Materials and Methods

2.1 Computational Environment

The experiments were carried out in a machine with Intel Core i7 2.40 GHz, dual DDR3 with 8 GB RAM, 256 SSD of hard driver, and a 2 GB video card NVIDIA GeForce GT 650. The machine was configured with Microsoft Windows 7 Pro 64 bits, Python 3.6.5, the Scientific Python Development Environment (Spyder 3.3.2), and Keras that is a high-level API for building and training machine learning models.

2.2 Data Collection

Data was collected from 12 (twelve) healthy individuals and 15 (fifteen) individuals with Parkinson's disease. Table 1 shows information from the two groups. The Federal University of Uberlândia's Research Ethics Committee approved the research under the number 07075413.6.0000.5152.

Table 1. Characterization of the studied groups.

Group	Total	Sex (F/M)	Age (years)
Health	12	8/4	60.08 ± 6.13
PD	15	7/8	65.33 ± 9.17

The method based on severity scales was used to collect the data. In this method, the participants have to draw geometric shapes like spirals, sine waves, circles, or another different shape (e.g., Fig. 1).

2.3 Experimental Task

The participants involved in this research had to draw a specific image pattern similar to a sine wave. First, the person made the drawing following a printed pattern. A standard black pencil was used. After the participant learned how to draw the pattern, a new drawing was made, as illustrated in Fig. 1.

Each participant drew between three and four samples of sine waves. These drawings were digitalized, cleaned (the arrows were removed) and rescaled to a width of 512 pixels and automatic height (Gimp image manipulation software was used to preprocess the images).

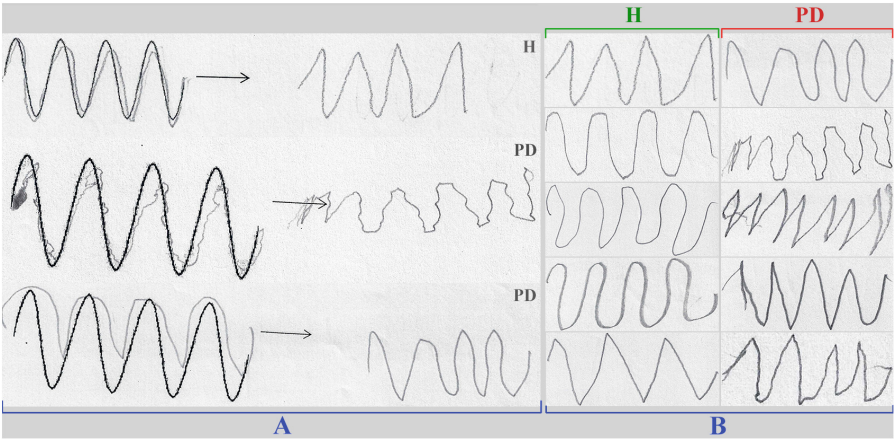

Fig. 1. (A) Samples of handwritten drawings collected from people with Parkinson's disease (PD) and healthy individuals (H); (B) Pre-processed images for each group (H and PD).

Figure 1(A) shows a sample of raw drawings made by a healthy person (H) and two distinct people with PD marked with (PD). Figure 1(B) shows drawing samples from each group.

In the study, 51 images were collected from each group, i.e., healthy individuals and people with PD. A total of 102 images were available.

2.4 Machine Learning

Machine learning is a subarea of artificial intelligence based on the idea that systems can learn from data, classify and identify patterns, and make decisions automatically. In this paper, we used some of these techniques to solve the problem of recognizing and classifying handwritten drawings between two different classes: drawings of healthy and Parkinson's disease subjects.

2.4.1 HOG Descriptor

The first step for image classification was to apply a method named histograms of oriented gradients (HOG). The HOG descriptor is commonly used to object detection. HOG allows the image to be described by the distribution of intensity gradients or edge directions. Figure 2 illustrates the wave detected with the intensity gradients and orientation [9, 10].

In Fig. 2 it is possible to notice that HOG divides the image into small areas named cells, which are of a predefined size, Fig. 2(B) in blue; the method estimates the histogram of the gradient orientations of each cell as shown in Fig. 2(C). Following this, normalization of the histograms in each cell is performed by comparing each block to the block of neighboring cells. Finally, a one-dimensional feature vector from the information in each cell is obtained [9–12]. The method scans and processes the entire image using the block to create the HOG that is presented in Fig. 2(D) as an output.

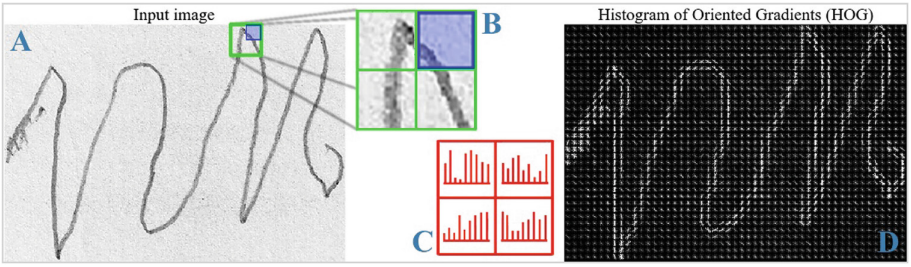

Fig. 2. Raw input image (A), the block of 2 × 2 cells (B), gradient histogram of each cell (C), and HOG feature extracted from the image input (D).

In this work, the input image was resized to 200 by 200 pixels (width and height). HOG was defined with 10 (ten) pixels per cell, blocks with 4 (four) cells (2 × 2 matrix), and the number of orientations was 9 (nine), meaning that nine bins were defined in the histogram with orientation between 0º and 180º degrees for each cell.

2.4.2 Random Forest Classifier

After HOG estimation, the data is ready to be classified by a Random Forest Classifier (RFC). RFC is a type of supervised machine learning algorithm based on ensemble learning, a method that makes it possible to join different types of algorithms or the same algorithm to set a more powerful prediction model. The random forest algorithm combines multiple decision-tree algorithms [13].

A decision tree (DT) is a tree in which a node represents a feature, each branch represents a decision and each leaf yields a result that can be a categorical or a continuous value [14, 15]. In addition, DT is a non-parametric supervised learning method commonly used for classification and regression [15, 16].

A Random Forest is a meta-estimator that fits multiple decision tree classifiers into manifold subsamples of the dataset and uses the mean to improve predictive accuracy and control overfitting. In general, an RFC takes N objects from the database, builds a decision tree with this data, and every tree in the forest predicts the category of the objects belonging to it. Finally, the new object is assigned to the category that wins the majority vote [13, 17, 18].

In this study, the Random Forest Classifier was structured with 100 and 200 decision trees and analyzed the model differences. The dataset was split into 70% of data for training and 30% for testing the model. Furthermore, the model was executed 10 times, 50 times and 100 times. Following that, an average of metrics was estimated and it was analyzed whether the model is able to classify the handwritten drawings of people with PD and healthy individuals.

2.4.3 Accuracy, Sensitivity and Specificity

These metrics are commonly used to describe if a test is good enough and reliable. The accuracy, sensitivity and specificity are the most used statistics to describe a diagnostic test [19]. Accuracy demonstrates the proportion of correct prediction of a given condition. Sensitivity evaluates how good the test is at detecting a positive disease. On the

other hand, the specificity shows us if a healthy subject has been correctly classified as without disease [16, 19].

The accuracy value is obtained by the number of correct assessments divided by the number of all assessments. Sensibility is calculated by the number of true positive assessments divided by the number of all positive assessments. Finally, the specificity is acquired through the number of true negative assessments divided by the number of all negative assessments [19].

3 Results

Table 2 describes the RFC results for each test. One test was arranged with 100 trees and it was executed in batches of 10, 50 and 100 times. For each one of these "total of runs", the average of the classification obtained was made and the lowest and highest classification rates were estimated. For these tests the highest accuracy was 0.83 (83% of success) and the average was 70%. Sensitivity reached the best value of 83% and an average of 69%. The highest specificity was 85% and its mean was 70%.

Table 2. Classification results for distinct configurations of the Random Forest Classifier.

Set of trees	Total of runs	Accuracy			Sensitivity			Specificity		
		Min	Max	Average	Min	Max	Average	Min	Max	Average
100	10	0.63	0.76	0.70	0. 64	**0.83**	0.71	0.61	0.79	0.70
	50	0.60	0.80	0.69	0.60	0.83	0.69	0.59	0.82	0.70
	100	0.57	**0.83**	0.70	0.57	0.82	0.69	0.56	**0.85**	0.70
200	10	0.67	0.77	0.72	0.67	0.75	0.70	0.67	0.79	0.74
	50	0.60	0.80	0.70	0.59	0.80	0.70	0.61	0.80	0.71
	100	0.60	0.80	0.70	0.61	0.80	0.70	0.58	0.80	0.72

The second configuration of the RFC was 200 trees. Table 2 shows the results. The highest value of accuracy was 80% and the average 71%. The highest sensitivity was 80% and the average was 70%. The highest specificity was 80% and the average was 72%.

The results are shown in Fig. 3 in confusion matrix (CM) format. It shows us the relation of true and false positives about the presence of tremor (T) in PD sufferers and the true and false negatives in healthy (H) subjects. The diagonal cells correspond to observations that are correctly classified, and the off-diagonal cells correspond to incorrectly classified observations. At the bottom right of the CM is the cell with the overall accuracy.

Figure 4 shows boxplots for each metric. Figure 4(A) shows a comparison between the accuracies obtained for three different batches for the RFC with 100 trees. A similar procedure was executed for sensitivity and specificity. Figure 4(B) presents results for the RFC with 200 trees.

Fig. 3. Confusion matrix test average. A1, A2, and A3 are from the RFC tests with 100 trees with 10, 50, and 100 runs, respectively. In the same way, RFC tests with 200 trees are represented by B1, B2, and B3, respectively in 10, 50, and 100 runs.

The data distribution in Fig. 4(A) is around 65-75% for all metrics. In Fig. 4(B) the accuracy and sensitivity behave the same way in (A), and specificity spread above 75%.

4 Discussion and Conclusion

In this work, the drawings collected from healthy individuals and people with PD were classified by RFC. The proposed method employed pencil drawings digitized from ordinary sheet of paper, making it very simple to be applied in the context of scarce financial resources. A major advantage of RFC is the low computational cost when compared to Deep learning.

Despite the small number of images in the available data set (51 per class), the obtained results were satisfactory and accurate by discriminating drawings of healthy people from those with PD (Fig. 3).

In the study, the HOG parameters were tested in default values (10 × 10 pixels per cell, 2 × 2 cells per block and 9 bins in the histogram with 0–180° orientation) focus on good performance showed by Dalal and Triggs [10] and the HOG result was passed to the classifier. In a future study, these parameters could be changed aiming to get the best ones to improve the model results.

The results shown in Table 2 and Fig. 4 suggest that there is a similarity regarding the number of trees used (100 and 200). The variability of all the metrics showed in

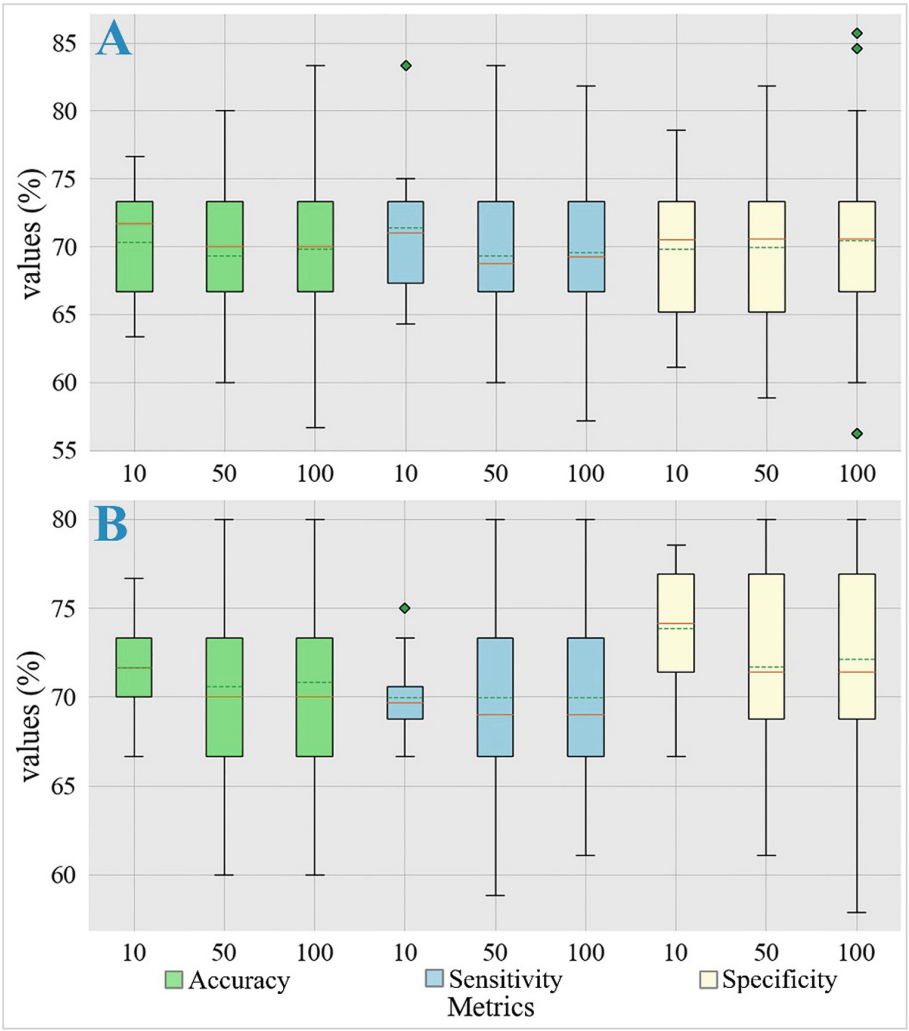

Fig. 4. Accuracy, sensitivity and specificity for each performance metric. (A) RFC with 100 trees and (B) RFC setup with 200 trees. The green dotted line is the average and the orange is the median.

Fig. 4 indicates that the diagnostic test is working correctly in discriminating between who has tremors and who does not.

This is the first reported study considering the application of HOG estimates in combination with the RFC applied to the automatic classification of data obtained from people with PD. This study is in the direction of related work [16] which analyzed data of people with dementia.

In the future, it will be necessary to obtain more image drawings and different shapes to increase the database [8]. In addition, it is relevant to test more parameters

and tune the proposed method as well as to implement other types of classifiers and compare them with RFC as proposed here.

Acknowledgment. The present work was carried out with the support of the National Council for Scientific and Technological Development (CNPq), Coordination for the Improvement of Higher Education Personnel (CAPES – Program CAPES/DFATD-88887.159028/2017-00) and the Foundation for Research Support of the State of Minas Gerais (FAPEMIG-APQ-00942-17). A. O. Andrade, A. A. Pereira and M. F. Vieira are a fellow of CNPq, Brazil (304818/2018-6, 310911/2017-6, and 306205/2017-3).

Conflicts of Interest. The authors declare no conflict of interest.

References

1. de Lau, L.M., Breteler, M.M.: Epidemiology of Parkinson's disease. Lancet Neurol. **5**, 525–535 (2006). https://doi.org/10.1016/S1474-4422(06)70471-9
2. Cancela, J., Mascato, S.V., Gatsios, D., et al.: Monitoring of motor and non-motor symptoms of Parkinson's disease through a mHealth platform. In: Proceedings of the Annual International Conference of the IEEE Engineering in Medicine and Biology Society, EMBS, pp. 663–666. IEEE (2016)
3. Andrade, A.O., Pereira, A.A., de Almeida, M.F.S., et al.: Human tremor: origins, detection and quantification. In: Andrade, A.O. (ed.) Practical Applications in Biomedical Engineering. InTech, Croatia (2013)
4. Chan, P.Y., Ripin, Z.M., Halim, S.A., et al.: An in–laboratory validity and reliability tested system for quantifying hand-arm tremor in motions. IEEE Trans. Neural Syst. Rehabil. Eng. **26**, 460–467 (2018). https://doi.org/10.1109/TNSRE.2017.2782361
5. Bravo, M., Bermeo, A., Huerta, M., et al.: A system for finger tremor quantification in patients with Parkinson's disease. In: Proceedings of the Annual International Conference of the IEEE Engineering in Medicine and Biology Society, EMBS, pp. 3549–3552. IEEE (2017)
6. Zhang, L., Liu, C., Zhang, X., Tang, Y.Y.: Classification of Parkinson's disease and essential tremor based on structural MRI. In: Proceedings - 2016 7th International Conference on Cloud Computing and Big Data, CCBD 2016, pp. 353–356. IEEE (2017)
7. Prince, J., de Vos, M.: A deep learning framework for the remote detection of Parkinson'S disease using smart-phone sensor data. In: Proceedings of the Annual International Conference on IEEE Engineering in Medicine and Biology Society, pp. 3144–3147 (2018). https://doi.org/10.1109/embc.2018.8512972
8. Pereira, C.R., Weber, S.A.T., Hook, C., et al.: Deep learning-aided Parkinson's disease diagnosis from handwritten dynamics. In: Proceedings - 2016 29th SIBGRAPI Conference on Graphics, Patterns and Images, SIBGRAPI 2016, pp. 340–346. IEEE (2017)
9. Chowdhury, S.A., Kowsar, M.M.S., Deb, K.: Human detection utilizing adaptive background mixture models and improved histogram of oriented gradients. ICT Express **4**, 216–220 (2018). https://doi.org/10.1016/j.icte.2017.11.016
10. Dalal, N., Triggs, B.: Histograms of oriented gradients for human detection. In: 2005 IEEE Computer Society Conference on Computer Vision and Pattern Recognition (CVPR 2005), pp. 886–893. IEEE (2018)

11. Li, T., Li, W., Yang, Y., Zhang, W.: Classification of brain disease in magnetic resonance images using two-stage local feature fusion. PLoS One **12**, 1–19 (2017). https://doi.org/10.1371/journal.pone.0171749
12. Ren, H., Li, Z.-N.: object detection using edge histogram of oriented gradient
13. Breiman, L.: Random forests. Mach. Learn. **45**, 1–33 (2001)
14. Quinlan, J.R.: Induction of decision trees. Mach. Learn. **1**, 81–106 (1986). https://doi.org/10.1007/BF00116251
15. Safavian, S.R., Landgrebe, D.: A survey of decision tree classifier methodology. IEEE Trans. Syst. Man Cybern. **21**, 660–674 (1991). https://doi.org/10.1109/21.97458
16. Maroco, J., Silva, D., Rodrigues, A., et al.: Data mining methods in the prediction of Dementia: a real-data comparison of the accuracy, sensitivity and specificity of linear discriminant analysis, logistic regression, neural networks, support vector machines, classification trees and random forests. BMC Res. Notes **4**, 299 (2011). https://doi.org/10.1186/1756-0500-4-299
17. Bernard, S., Heutte, L., Adam, S.: Influence of hyperparameters on random forest accuracy. In: Lecture Notes in Computer Science (Including Subseries Lecture Notes in Artificial Intelligence and Lecture Notes in Bioinformatics), pp. 171–180. Springer (2009)
18. Ramani, R.G., Sivagami, G.: Parkinson disease classification using data mining algorithms (2011)
19. Zhu, W., Zeng, N., Wang, N., et al.: Sensitivity, specificity, accuracy, associated confidence interval and ROC analysis with practical SAS implementations. NESUG Proc. Heal Care Life Sci. Balt. Maryl. **19**, 67 (2010)

Improving Myoelectric Pattern Recognition Robustness to Electrode Shift Using Image Processing Techniques and HD-EMG

Roberto Díaz-Amador[1(✉)], Miguel Arturo Mendoza-Reyes[2], and Carlos A. Ferrer-Riesgo[1]

[1] Centro de Investigaciones de la Informática, Universidad Central de Las Villas, Carretera a Camajuaní km 5 ½, Santa Clara, Cuba
{rdamador, cferrer}@uclv.edu.cu

[2] Departamento de Telecomunicaciones y Electrónica, Universidad Central de Las Villas, Carretera a Camajuaní km 5 ½, Santa Clara, Cuba
mmendoza@uclv.edu.cu

Abstract. Pattern recognition of myoelectric signals for prosthesis control has been extensively studied in research settings; however, its systems perform poorly in the presence of electrode shift, defined as the movement of surface electrodes with respect to the underlying muscles. In this paper, we present the results of using image processing techniques for gesture recognition in the presence of electrode shifts based on High-Density Electromyography (HD-EMG). Here the instantaneous sample of each EMG channel is represented as a pixel of an image that changes with different movements. In this image, various patterns are recognized as associated with specific gestures. We found that feature extraction based on image processing techniques can improve the accuracy of gesture classification from HD-EMG signals in the presence of the electrode shift.

Keywords: Electrode shift · Electromyography (EMG) · Pattern recognition

1 Introduction

Pattern recognition approach allows the use of a high-density electrode array forming a matrix of high-density electromyography signals (HD-EMG) that has been extensively studied in research settings. However, the clinical reliability of pattern-recognition-based myoelectric control systems is still challenged by some issues including effects of socket loading and limb orientation [1], variations in muscle contraction effort [2], and electrode shift during donning/doffing and daily use [3, 4]. In the current paper, we present the results of using image processing techniques for HD-EMG based gesture recognition in the presence of electrode shift. We represent the instantaneous sample of each EMG channel as a pixel of an image that changes with different movements. Then the set of pixels obtained in this way forms a pattern associated with the corresponding movement. Notice that the spatial resolution (number of pixels per unit area) is defined by the array electrodes, i.e., the number of electrodes and their inter-electrode distances.

© Springer Nature Switzerland AG 2020
C. A. González Díaz et al. (Eds.): CLAIB 2019, IFMBE Proceedings 75, pp. 344–350, 2020.
https://doi.org/10.1007/978-3-030-30648-9_45

This method seeks for an instantaneous spatial-temporal representation of the motor unit action potential (MUAP). The use of HD-EMG to analyze how muscle activation patterns are composed and distributed and the single MUAP behavior is not new in pattern recognition research [5, 6]. Recently, the use of electrode arrays was extended to classify gestures and decode the intention of motion [7–9].

The current works presents the use of features extracted from an image formed by HD-EMG from electrode patches for gesture classification. The results are compared with those obtained with the use of time-domain features computed channel by channel.

2 Materials and Methods

2.1 HD-EMG Signal Dataset

HD-EMG data were obtained from the sub-database DB-a in CapgMyo database [10]. These data were collected [10] using a non-invasive wearable device consisting of 8 acquisition modules, each of them containing a matrix-type (8×2) differential electrode array. Each electrode has a diameter of 3 mm and was arranged with an inter-electrode distance of 7.5 mm horizontally and 10.05 mm vertically. The silver wet electrodes were disposable and covered with conductive gel, with a contact impedance of less than 3 kΩ. The 8 acquisition modules were fixed around the right forearm with adhesive bands. The first acquisition module was placed on the extensor digitorum communis muscle at the height of the radio-humeral joint; others were equally spaced clockwise (viewing from the subject's perspective), forming an 8×16 electrode array. When collecting HD-EMG, no individual muscle is directly measured, but the combined superposition of all. In this way, each adjacent electrode contains redundant information.

The EMG signals were sampled at 1 kHz, digitized with a 16-bit analog to digital converter and band-pass filtered at 20–380 Hz. The EMG data from the 8 acquisition modules were packed in an ARM controller and transferred to a PC via WIFI [11]. The database contains 8 isometric and isotonic hand gestures obtained from 18 subjects. Subjects were asked to hold each gesture for 3 to 10 s. The considered gestures are shown in Fig. 1 and correspond to classes 13–20 in the NinaPro database [12]. Each gesture was recorded 10 times.

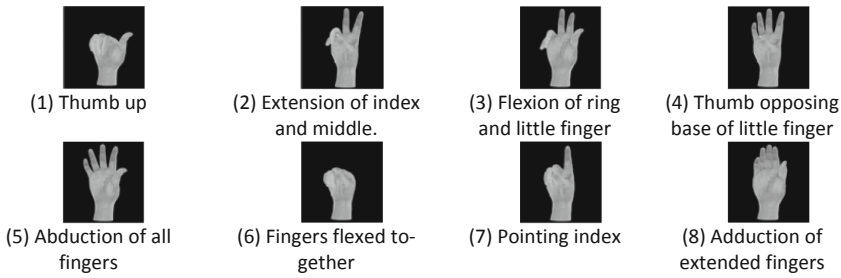

Fig. 1. Gestures considered in this study. Numbers in parenthesis represent the corresponding labels in the dataset.

Power-line interference was removed from the EMG signals by using a second-order Butterworth band-stop filter (45–55 Hz). To the purpose of the current research, only the static part of the movement (the middle one-second window for each trial) was used to train and to evaluate the recognition algorithms.

2.2 Features

The TD features used was proposed in [13] and it is described from Eq. (1) to Eq. (4).

Mean Absolute Value (MAV)

$$MAV = \frac{1}{N}\sum_{n=1}^{N} |x_n| \tag{1}$$

Zero-crossing (ZC)

$$ZC = \sum Ct;$$
$$Ct = \begin{cases} 1; & x_n > 0 \, and \, x_{n+1} < 0 \, and \, |x_n - x_{n+1}| > th \\ 1; & x_n < 0 \, and \, x_{n+1} > 0 \, and \, |x_n - x_{n+1}| > th \\ 0; & otherwise \end{cases} \tag{2}$$

Waveform Length (WL)

$$WL = \sum_{n=1}^{N} |\Delta x_n|; \Delta x_n = x_n - x_{n-1} \tag{3}$$

Slope Sign Changes (SSC)

$$SSC = \sum_{n=1}^{N} sgn[-(x_{n+1} - x_n) \cdot (x_{n+2} - x_{n+1})]; sgn = \begin{cases} 1, x > th \\ 0, x < th \end{cases} \tag{4}$$

In Eqs. (1) to (4), x_n represents the amplitude of the sample n of EMG, N is the length in samples of the analysis window, and th is a threshold taken as the 5% of the MAV on the analysis window.

The images-based the feature set consider in the current work was proposed in [14] and consists of:

– Pixel-based features: energy by block, maximum intensity value by block, the position of maximum intensity by block,

Equations (5) to (7) show the corresponding expressions:

Energy (En)

$$\mathrm{En} = \frac{1}{\mathrm{N_1 N_2}} \sum_{\mathrm{n_1}=1}^{\mathrm{N_1}} \sum_{\mathrm{n_2}=1}^{\mathrm{N_2}} \mathrm{x}^2_{\mathrm{n_1,n_2}} \tag{5}$$

Maximum Intensity Value (MIV)

$$\mathrm{MIV} = \max\left(x_{n_1,n_2}\right) \tag{6}$$

Position of Maximum Intensity (PMI)

$$\mathrm{PMI} = \operatorname{argmax}\left(x_{n_1,n_2}\right); \tag{7}$$

– Texture-based features: contrast, correlation, and homogeneity calculated from the co-occurrence matrix by block.

Equations (8) to (10), show expressions to calculate them:
Contrast

$$\mathrm{Ct} = \sum_{n_1,n_2=0}^{N-1} P_{n_1 n_2}(n_1 - n_2)^2 \tag{8}$$

Correlation

$$\mathrm{Cr} = \sum_{n_1,n_2=0}^{N-1} P_{n_1 n_2}\left[\frac{(n_1 - \mu_{n_1})(n_2 - \mu_{n_2})}{\sqrt{\left(\sigma_{n_1}^2\right)\left(\sigma_{n_2}^2\right)}}\right] \tag{9}$$

Homogeneity

$$\mathrm{Ho} = \sum_{n_1,n_2=0}^{N-1} \frac{P_{n_1 n_2}}{1 + (n_1 - n_2)^2} \tag{10}$$

In (8) to (10), P is the probability matrix from the co-occurrence matrix.

– Shape-based features: number of pixels actives by block, area, and the centroid of the major region active by block, after the image is binarized using the Otsu [15] method.

We computed the image-based features dividing the image into two blocks, i.e., two 8×8 arrays.

2.3 Experiments

The experiments conducted in the current research consist of computed the time-domain features of all the individual EMG channels and compared the results of the classification whit the results obtained when used the image-based features. The effects of the electrode shift were simulated by mean of a circular shift of the instantaneous matrix. The circular shift was repeated using an increment of $\Delta = \frac{L}{16}$, where L is the

perimeter of the forearm. Each circular shift corresponds with $\frac{\pi}{8}$ radians. The results were compared using the accuracy and F-score computed class bay class. Differences in performance using both features sets were doing by the Wilcoxon test, and a posthoc comparisons with a Bonferroni correction factor were analyzed for each statistically significant factor of interest.

3 Results and Discussion

Results of Accuracy and F-Score are showing in Table 1 using the image-based feature extraction. Results show that the class Thumb opposing base of the little finger (4th) presents the poorest performance.

Table 1. Results by class.

	Class							
	1	2	3	4	5	6	7	8
Acc	93.8	89.5	90.9	82.8	92.7	97.5	92.6	89.9
F-Sc	94.6	90.9	93.0	84.6	91.4	97.1	93.7	86.5

Acc: Accuracy, F-Sc: F-Score

A more important aspect is the variation of the performance while electrodes are shifting around the forearm. Figure 2 shows the results comparing the image-based feature extraction presented here whit respect to the time-domain feature extraction.

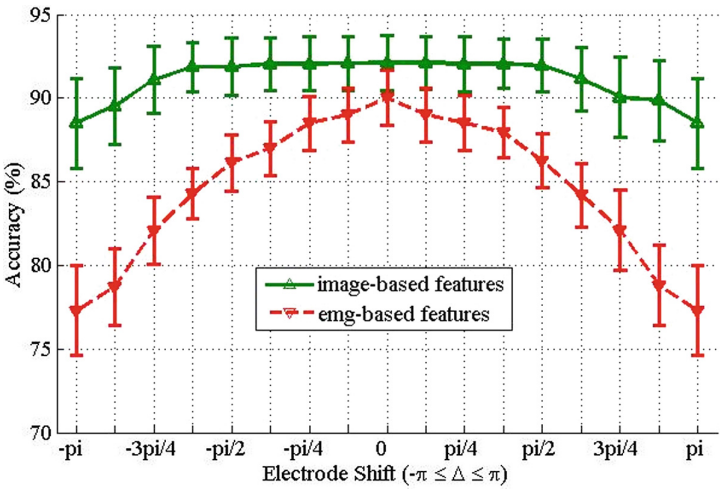

Fig. 2. Classification results using the proposed image-based feature extraction approach and the conventional time-domain feature set.

Results show how when the rotation is the half of the perimeter of the forearm the proposed feature extraction method presents a major behavior the conventional time-domain feature set. Around the 3Δ shift the degradation of the performance using a conventional time-domain feature set becomes evident.

The Wilcoxon test whit Bonferroni correction shows that in the critical shift the differences between both feature sets are significative.

4 Conclusions

We found that feature extraction based on image processing techniques can improve the accuracy of gesture classification from HD-EMG signals in the presence of the electrode shift. These results should be applicable for designing robust, clinically viable EMG pattern recognition systems, however, future experiment whit a larger data set will be conducted.

References

1. Scheme, E., Fougner, A., Stavdahl, O., Chan, A., Englehart, K.: Examining the adverse effects of limb position on pattern recognition based myoelectric control. In: Proceedings of 32nd Annual International Conference on IEEE Engineering Medicine Biology Society, Buenos Aires, Argentina, pp. 6337–6340 (2010)
2. Tkach, D., Huang, H., Kuiken, T.: Study of stability of time-domain features for electromyographic pattern recognition. J. Neuroeng. Rehabil. **7**(1), 21 (2010)
3. Hargrove, L., Englehart, K., Hudgins, B.: The effect of electrode dis-placements on pattern recognition based myoelectric control. In: Proceedings of 28th Annual International Conference on IEEE Engineering Medicine Biology Society, New York, pp. 2203–2206 (2006)
4. Young, A., Hargrove, L., Kuiken, T.: The effects of electrode size and orientation on the sensitivity of myoelectric pattern recognition systems to electrode shift. IEEE Trans. Biomed. Eng. **58**, 2537–2544 (2011)
5. Merletti, R., Holobar, A., Farina, D.: Analysis of motor units with high-density surface electromyography. J. Electromyogr. Kinesiol. **6**, 879–890 (2008)
6. Rojas-Martínez, M., Mañanas, M., Alonso, J., Merletti, R.: Identification of isometric contractions based on High Density EMG maps. J. Electromyogr. Kinesiol. **1**, 33–42 (2013)
7. Rojas-Martínez, M., Mañanas, M., Alonso, J.: High-density surface EMG maps from upper arm and forearm muscles. J. Neuroeng. Rehabil. **1**, 85 (2012)
8. Amma, C., Krings, T., Boer, J., Schultz, T.: Advancing muscle-computer interfaces with high-density electromyography. In: Proceedings of the 33rd Annual ACM Conference on Human Factors in Computing Systems, pp. 929–938 (2015)
9. Geng, W., Du, Y., Wenguang, J., Wentao, W., Jiajun. L.: Gesture recognition by instantaneous surface EMG images. Sci. Rep. **6**, 36571 (2016)
10. Du, Y., Wenguang, J., Wentao, W., Geng, W.: Surface EMG-based inter-session gesture recognition enhanced by deep domain adaptation. Sensors. **17**(3), 458 (2017)
11. Du, Y., Wenguang J., Wentao, W, Geng, W.: CapgMyo: A High Density Surface Electromyography Database for Gesture Recognition. http://zju-capg.org/myo/data/index.html

12. Atzori, M., Gijsberts, A., Castellini, C., Caputo, B., Hager, A.-G.M., Giatsidis, G., Bassetto, F., Müller, H.: Electromyography data for non-invasive naturally-controlled robotic hand prostheses. Sci. Data. **1**, 140053 (2014)
13. Hudgins, B., Parker, P., Scott, R.N.: A new strategy for multifunction myoelectric control. IEEE Trans. Biomed. Eng. **40**, 82–94 (1993)
14. Díaz-Amador, R., Ferrer-Riesgo, C.A., Lorenzo-Ginori, J.V.: Using image processing techniques and HD-EMG for upper limb prosthesis gesture recognition. In: Iberoamerican Congress on Pattern Recognition. Springer, Cham, pp. 913–921 (2018)
15. Otsu, N.: A threshold selection method from gray-level histograms. IEEE Trans. Sys. Man. Cyber. **1**, 62–66 (1979)

Classification of Plasmodium-Infected Erythrocytes Through Digital Image Processing

Juan Valentín Lorenzo-Ginori[1(✉)], Lyanett Chinea-Valdés[1], Yanela Izquierdo-Torres[1], Rubén Orozco-Morales[1], Niurka Mollineda-Diogo[2], Sergio Sifontes-Rodríguez[2], and Alfredo Meneses-Marcel[2]

[1] Universidad Central Marta Abreu de Las Villas, 54830 Santa Clara, Villa Clara, Cuba
juanl@uclv.edu.cu
[2] Centro de Bioactivos Químicos, 54830 Santa Clara, Villa Clara, Cuba

Abstract. The development of antimalarial drugs requires performing laboratory experiments that include the analysis of blood smears infected with *Plasmodium*. Analyzing visually the resulting microscopy images is usually a slow and tedious task prone to errors due to fatigue and subjectivity of the analysts. These facts have motivated the creation of digital image processing systems to automate this analysis. In this work a computer vision solution to process microscopy images of blood smears containing erythrocytes infected with *Plasmodium* is shown. This system performs tasks like illumination and color correction, image segmentation including splitting of clumped objects and extraction of color features. A set of different classifiers was tested and evaluated to find the best one in terms of indexes of effectiveness. A new feature named pixels fraction was introduced and used together with a number of other color-related features, from which a subset to classify cells into normal or infected was selected. The classifiers evaluated were: support vector machines (SVM), K-nearest neighbors (KNN), J48, Random Forest (RF), Naïve Bayes and linear discriminant analysis (LDA). All of them were evaluated in terms of correct classification rate, sensitivity, specificity, F-measure and area under Receiver Operating Characteristic (ROC) curve (AUC). The effectiveness of the pixels fraction as a new feature was demonstrated by the experimental results. In regard to classifiers, J48 and Random Forest showed the best results.

Keywords: Malaria · Image processing · Computer vision · Feature extraction · Classifiers

1 Introduction

Malaria is an infectious disease showing high degrees of morbidity and mortality, for which the World Health Organization estimated 219 million of infected people and 475000 deaths in 2017 [1]. This serious health problem demands new diagnose tools and anti-malarial drugs. Microscope analysis of large amounts of blood smears in order

© Springer Nature Switzerland AG 2020
C. A. González Díaz et al. (Eds.): CLAIB 2019, IFMBE Proceedings 75, pp. 351–360, 2020.
https://doi.org/10.1007/978-3-030-30648-9_46

to detect the presence of the *Plasmodium* parasite, both to diagnose the disease in humans as well as determining the infection rate in laboratory mice, is an issue of crucial importance during the process of developing anti-malarial drugs. The analysis of blood smears by human experts tends to be slow and tedious, and its results are prone to errors due to tiredness and subjectivity and to the frequently found low rate of positive cases (infected erythrocytes). This situation has motivated a research effort to develop solutions based on digital image processing (DIP) and computer vision (CV) for this process and this has been the objective of the present work.

There are a number of published works dealing with this problem. Diverse image processing methods have been developed to obtain appropriate image features which allow an effective classification of erythrocytes into normal and infected, examples of which can be found in [2–7]. These methods typically include tasks such as image conditioning (non-uniform illumination correction, filtering and color normalization), image segmentation, feature extraction and classification of erythrocytes. It is stressed that testing and selecting effective features and classifier algorithms constitute a key step in the design of the whole system [3]. The use of various classifiers for this purpose, like linear discriminant analysis (LDA), K-nearest neighbors (KNN), support vector machines (SVM), among others, have been reported in the literature [8–13].

The contribution of this research consists in defining new color features having high discriminating capabilities, as well as testing their use together with various classifier algorithms to find the best combination. A complete algorithm was developed, oriented mainly towards the applications in the development of anti-malarial drugs, where the analysis of blood smears from laboratory mice demands a low rate of false positives as a requirement.

2 Materials and Methods

2.1 Sample Images

In this research digital images obtained from Giemsa-stained blood smears from mice experimentally infected with *Plasmodium berghei* were used, as well as a Zuzi 122/148 tri-ocular microscope, equipped with a Microscopy 319 CU digital camera with 3.2 MP resolution and 8-bit RGB output without compression, producing a matrix having 2048 $\times$ 1536 pixels, with pixel size 3.2 $\times$ 3.2 μm, signal to noise ratio 43 dB and optical magnification 50$\times$. The digital images were saved in.tiff (tagged image file) format. An annotated database was created with the aid of two expert analysts from Centro de Bioactivos Químicos (CBQ). This database was intended to perform all the DIP-CV procedures to obtain the features, training the classifiers and performing tests to evaluate the classification effectiveness. A set of 211 images was obtained, from which 600 images of individual erythrocytes were formed, comprising 400 un-infected and 200 *Plasmodium*-infected cells, as shown in Fig. 1. Notice the reddish-purple spots inside individual erythrocytes that harbor the parasites.

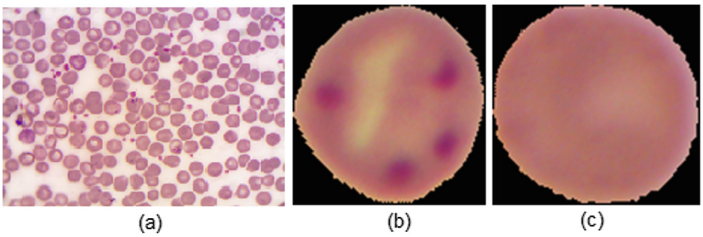

Fig. 1. Microscopy images employed. (a) Image of a blood smear showing multiple erythrocytes, (b) segmented, infected erythrocyte and (c) segmented, normal erythrocyte.

The size of the sample set was calculated from [14] as a minimum required to obtain a reasonable error when evaluating the correct classification rate CCR, which is expected to be above 0.95 for the classifiers tested. These numbers took into account also some class-imbalance. The images size for individual cells depends on their physical (variable) dimensions and can also be affected by the presence of the parasite.

2.2 Image Conditioning

The images used in this research were acquired with a Zuzi 319 CU camera coupled to a microscope. The photos were taken in the RGB color space at 8 bpp/channel. The intensity of the color components was normalized to the interval [0, 1] and converted afterwards to the HSI color space. Other pre-processing steps applied were [3 × 3] median filtering to the intensity component and a morphological *top hat* with an appropriate structuring element to compensate illumination imbalance. Conversion of the images to the L*a*b* space was made also after segmentation to allow obtaining more features. Information on color spaces is given in [15].

2.3 Segmentation

Segmentation of erythrocytes was performed in two steps. Firstly, a coarse segmentation using the Otsu's algorithm as in [2] was applied adaptively to the intensity component of the image, which was divided into 16 patches that were segmented independently. This coarse segmentation binarized the image into foreground objects (cells, including clumps) and background. Then the cell clumps were detected and segmented employing a version of the algorithm described in [16], using weighted outer distance and marker-controlled watershed transforms, with the regional maxima of the distance transform acting as internal markers. Other components of the blood smears like leukocytes and platelets were suppressed using the procedure described in [3]. Area opening allowed eliminating other artifacts as well, using a threshold derived from the median size of the erythrocytes.

2.4 Color Normalization

In microscopy images, color can be altered due to changes in the illumination source and to the procedure of preparing the samples. This led to the necessity of color normalization by means of DIP techniques. Here the method described in [5] was used for this purpose and the results are illustrated in Fig. 2.

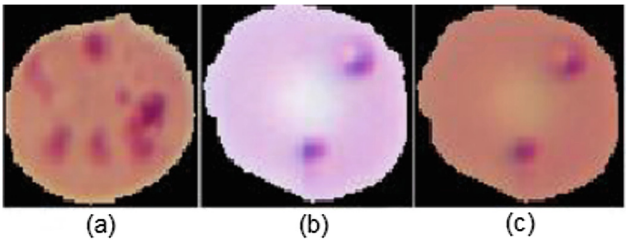

Fig. 2. Color normalization: (a) reference, (b) target and (c) color-corrected images.

2.5 Feature Extraction and Pixels Fraction

In this work, one main goal is achieving a fairly good classification result using only features derived from the color properties of the images. A total of 13 features were obtained for each of the RGB, HSI and L*a*b* color spaces. These were, for each color component: mean, variance and skewness as described in [17], as well as kurtosis and a new feature which is the main contribution of this work, called pixels fraction. For the three color spaces this led to 39 features in total.

The pixels fraction is defined here based on the relative coincidence of the pixel values in the three planes corresponding to the color channels respectively, for the color spaces employed. The reasoning behind this idea is that pixels having the color properties associated to the presence of the parasite in an erythrocyte, would be practically absent in the images of healthy erythrocytes. Only a minimum proportion of them could exist eventually due to the presence of artifacts in the images, like for example tiny spots created during the preparation of samples for the microscope. The pixels fraction was thought in this case to allow discriminating the presence of a real parasite from the occurrence of a colored artifact, thus improving the classification indexes of effectiveness when using features derived from the color properties of the images. Following this idea, a small set of regions of interest (ROI) were located inside the reddish-purple colored region characteristic of the parasites in a color-normalized erythrocyte, and taken as a reference, as shown in Fig. 3a. For these regions, the mean and standard deviation of the intensity in each color channel for the color spaces used was calculated. To illustrate this for the RGB color space, consider a cell being analyzed. Then the number of pixels is determined for it, whose three color components imC in which C can take the values R (red), G (green) or B (blue), fall simultaneously within the following intervals:

$$\mu_c = \begin{cases} imC > \mu_c - \sigma_c * 2 \\ imC < \mu_c + \sigma_c * 2 \\ 0, \ otherwise \end{cases} \quad (1)$$

In Eq. 1, μ_c is the mean value and σ_c the standard deviation of the component value inside the ROI and the indexes C indicate the color component to which they correspond. The factor 2 multiplying σ widens the acceptance intervals for a given component and was determined heuristically. The pixels fraction p_f is finally determined for the image of an erythrocyte in a specific color space by dividing the number of pixels n_f satisfying Eq. 1 by the total number N of pixels in the image.

$$p_f = \frac{n_f}{N} \quad (2)$$

The value of p_f was determined analogously in the HSI and L*a*b* color spaces. Figure 3b illustrates the general process followed to calculate the pixels fraction.

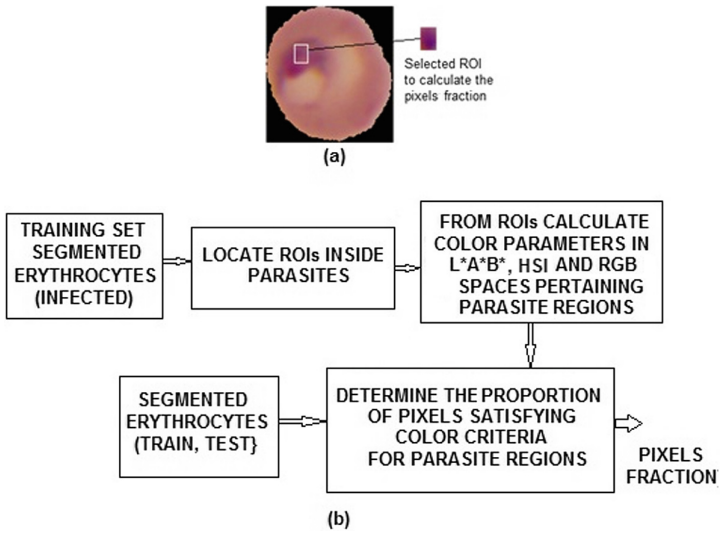

Fig. 3. Illustrating the procedure used to calculate the pixels fraction, (a) ROI selection within an infected erythrocyte, (b) block diagram illustrating steps to calculate the pixels fraction.

2.6 Feature Selection and Classification

Facilities provided by Weka 3.9 [18] were used here. Firstly, filtering (*CfsSubsetEval* with a greedy stepwise search method) was used to make a selection from the erythrocyte features previously described. This resulted in seven features. Three ranking alternatives were tested for classification: (*InfoGainAttributeEva*) using the first 20 ranked features and also the first 7 (to match the number selected through filtering), as well as all the features. Then the effectiveness of these alternatives were compared.

Classification was made using the following algorithms: SVM, KNN, J48, Random Forest (RF), Naïve Bayes (NB) and Linear Discriminant Analysis (LDA). In the case of SVM and KNN, various alternatives in their parameters (polynomial and PUK kernels in SVM, K = 1, 3, 5, 7 for KNN) were tested the best ones were used in the comparison to the rest of the classifiers. All the features were normalized previously.

The various classifiers were compared by ten-fold cross-validation and 1/3-2/3 percentage split. The indexes of effectiveness used were the correct classification rate (CCR), sensitivity (Se), specificity (Sp), F-measure and area under the receiver operating characteristic (ROC) curve, AUC. A more realistic experiment considered also the possibility of defining visually dubious cases as a third class, a situation often encountered in practice due to spurious colored pixels. In this case confusion matrices were used to express the results.

The general process of training the various classifiers evaluated and performing the classification process is illustrated in Fig. 4.

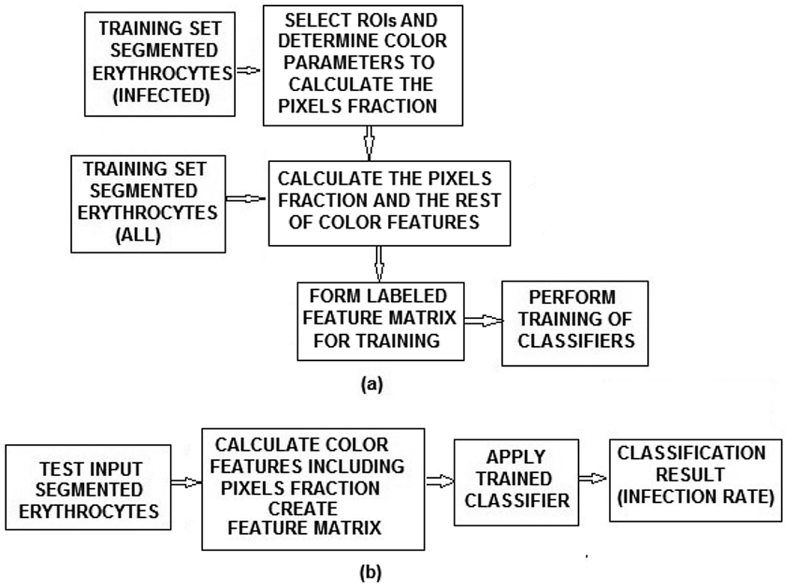

Fig. 4. Diagram of the general classification process. (a) Training the classifiers with the defined features, (b) classifying test erythrocytes.

3 Results and Discussion

The experimental work described in Sect. 2 was performed for the dataset composed of 600 erythrocytes previously mentioned. Special care was taken when building the (600 $\times$ 39) feature matrix corresponding to this dataset.

3.1 Feature Selection

Results from feature selection using the two methods (filter and ranking) are shown in Table 1. Notice that despite in general the seven first features ranked by the InfoGainAttributeEva method differ from those selected by CfsSubsetEval, the pixels fractions in all the color spaces were the first ones in the list, confirming their usefulness.

Table 1. Results of the feature selection process

CfsSubsetEval method		InfoGainAttributeEva, first 20 ranked features			
1	Pixels fraction HSI	1	Pixels fraction HSI	11	Variance, H
2	Pixels fraction L*a*b*	2	Pixels fraction RGB	12	Variance, R
3	Pixels fraction RGB	3	Pixels fraction L*a*b*	13	Skewness, R
4	Variance, G	4	Skewness, G	14	Skewness, L
5	Skewness, R	5	Skewness, a*	15	Skewness, H
6	Skewness, B	6	Skewness, S	16	Kurtosis, H
7	Mean, R	7	Variance, S	17	Kurtosis, R
8		8	Variance, a*	18	Kurtosis, L
9		9	Variance, G	19	Skewness, B
10		10	Variance, L	20	Skewness, b

3.2 Classification

Classification results when using 7 features obtained through ranking and filtering, are shown in Tables 2 and 3, respectively. In this case the performance measures used in a 10-fold cross-validation experiment were CCR, Se, Sp, F- measure and AUC. Classification results using the whole set of features or the first 20 in the ranking list were inferior to those shown in the tables and are not shown due to space limitations. This suggests that there is some degree of noisy behavior in the discarded features whose deletion improved the classification results. Some variants of SVM and KNN were disregarded previously in favor of those included in the tables, which exhibited better behavior. The best performance was obtained by the J48 and Random Forest classifiers, which yielded results close to 100%.

Table 2. Results of classification with features selected through InfoGainAttributeEva ranker, using the 7 best ranked features and ten-fold cross-validation

Classifier	CCR %	Sp	Se	F-measure	AUC
SVM	95.13	0.85	0.99	0.97	0.93
RF	99.95	1.00	1.00	1.00	1.00
J48	100.00	1.00	1.00	1.00	1.00
LDA	94.27	0.84	0.99	0.96	0.96
KNN, K = 1	96.20	0.91	0.97	0.97	0.95
KNN, K = 3	96.18	0.90	0.98	0.97	0.96
NB	98.50	0.95	0.98	0.99	0.99

The pixels fraction should be theoretically zero for a normal erythrocyte. However, the classification of a cell is not a trivial task: some spurious colored pixels could appear in practice and provoke an erroneous classification. Here a larger set of color-based features was employed to improve the classification results in this situation and a third "dubious" class was introduced. Table 4 shows the confusion matrix obtained in this case. This is especially important when determining the infection rate in laboratory mice through microscopy analysis, where dubious cells are usually disregarded by human analysts. In this case only four features (pixels fraction among them) were chosen by the filter selector. When using the J48 and RF classifiers, almost all dubious cases were correctly classified, all normal cells were still classified as normal and a small proportion of infected erythrocytes were classified as dubious. The success of these classifiers is consistent with the experience about their good behavior in numerous applications [19].

Table 3. Results of classification, features selected by CfsSubsetEval (Greedy Stepwise), 10-fold cross-validation

Classifier	CCR	Sp	Se	F-measure	AUC
SMO, con Puk	94.78	0.84	1.00	0.96	0.92
Random forest	99.93	1.00	1.00	1.00	1.00
J48	100.00	1.00	1.00	1.00	1.00
LDA	91.45	0.74	1.00	0.94	0.97
KNN, con K = 1	93.80	0.87	0.97	0.95	0.92
KNN, con K = 3	94.82	0.86	0.99	0.96	0.95
Naive bayes	98.67	0.96	1.00	0.99	0.99

Table 4. Confusion matrices from the classification results, considering a third class (dubious cases), J48 and RF classifiers

J48, %CCR = 98.667					Random Forest, %CCR = 98,5			
Classified as →		a	b	c		a	b	c
Normal	a	**400**	**0**	**0**	a	**400**	**0**	**0**
Infected	b	**0**	**159**	**7**	b	**0**	**159**	**7**
Dubious	c	**0**	**1**	**33**	c	**0**	**2**	**32**

4 Conclusion

Automated classification of erythrocytes to detect the presence of *Plasmodium* parasites in blood smears is currently an open area of research and this work presents two contributions to it. The first one has been an improvement of the use of color information in the classification process through a new feature, called the *pixels fraction*, whose effectiveness was proved by two facts. Firstly, the values obtained for it in the three color spaces involved (RGB, HSI and L*a*b*) were selected among the most

important features by both the filter and the ranker feature selectors used. Secondly, the classification results using the pixels fraction were remarkable, showing that it is worth to enhance the use of color information when defining the features for classification and this is just what was achieved through this new feature. Several classifier algorithms were tested, among which J48 and RF exhibited the best results in terms of the several evaluated measures of performance. The second contribution was linking a set of image processing steps with the classifiers, to complete a computationally efficient system to classify erythrocytes in malaria studies.

Acknowledgments. The authors express their gratitude to Dr. José Antonio Escario García Trevijano from the Faculty of Pharmacy, Universidad Complutense de Madrid, who kindly donated the Giemsa-stained blood smears from mice experimentally infected with *Plasmodium berghei* used in the reported experimental work.

Conflicts of Interest. The authors declare that they have no conflict of interest.

References

1. WHO World Malaria Report (2018)
2. Arco, J.E., Górriz, J.M., Ramírez, J., et al.: Digital image analysis for automatic enumeration of malaria parasites using morphological operations. Expert Syst. Appl. **42**, 3041–3047 (2015). https://doi.org/10.1016/j.eswa.2014.11.037
3. Abdul-Nasir, A.S., Mashor, M.Y., Mohamed, Z.: Colour image segmentation approach for detection of malaria parasites using various colour models and k-means clustering. WSEAS Trans. Biol. Biomed. **10**(1), 41–55 (2013)
4. Preedanan, W., Phothisonothai, M., Senavongse, W., Tantisatirapong, S.: Automated detection of plasmodium falciparum from giemsa-stained thin blood films. In: 2016 8th International Conferrence on Knowledge Smart Technology, KST, pp. 215–218 (2016). https://doi.org/10.1109/KST.2016.7440501
5. Tek, F.B., Dempster, A.G., Kale, I.: Parasite detection and identification for automated thin blood film malaria diagnosis. Comput. Vis. Image Underst. **114**, 21–32 (2010). https://doi.org/10.1016/j.cviu.2009.08.003
6. Das, D.K., Maiti, A.K., Chakraborty, C.: Automated system for characterization and classification of malaria-infected stages using light microscopic images of thin blood smears. J. Microsc. **257**, 238–252 (2015). https://doi.org/10.1111/jmi.12206
7. Xiong, W., Ong, S.H., Lim, J.H.: Malaria infection detection in color blood cell images using local regional features. In: Proceedings of the Second APSIPA Annual Summit and Conference, 14–17 December 2010, Biopolis, Singapore, pp. 753–756 (2010)
8. Di Ruberto, C., Dempster, A., Khan, S., Jarra, B.: Analysis of infected blood cell images using morphological operators. Image Vis. Comput. **20**, 133–146 (2002). https://doi.org/10.1016/S0262-8856(01)00092-0
9. Ajala, F.: Comparative analysis of different types of malaria diseases using first order features. Int. J. Appl. **8**, 20–26 (2015). https://doi.org/10.5120/ijais15-451297

10. Pinkaew, A., Limpiti, T., Trirat, A.: Automated classification of malaria parasite species on thick blood film using support vector machine. In: 2015 8th Biomedical Engineering International Conference BMEiCON, pp. 1–5 (2015). https://doi.org/10.1109/BMEiCON.2015.7399524
11. Loddo, A., Di Ruberto, C., Kocher, M.: Recent advances of malaria parasites detection systems based on mathematical morphology. Sensors **18**, 513 (2018). https://doi.org/10.3390/s18020513
12. Muralidharan, V., Dong, Y., Pan, W.D.: A comparison of feature selection methods for machine learning based automatic malarial cell recognition in whole slide images. In: 2016 IEEE-EMBS International Conference on Biomedical and Health Informatics (BHI), pp. 216–219. IEEE (2016)
13. Chavan, S., Nagmode, M.: Malaria disease identification and analysis using image processing. Int. J. Latest Trends Eng. Technol. (IJLTET). **3**(3), 263–269 (2016)
14. Walpole, R.E., Myers, R.H., Myers, S.L., Keying, E.Y.: Probability and Statistics for Engineers and Scientists. Pearson New International Edition, New York (2013). Pearson Higher Ed
15. Gonzalez, R.C.: Digital Image Processing. Prentice Hall, Upper Saddle River (2017)
16. Jierong, C., Rajapakse, J.C.: Segmentation of clustered nuclei with shape markers and marking function. IEEE Trans. Biomed. Eng. **56**, 741–748 (2009). https://doi.org/10.1109/TBME.2008.2008635
17. Saikrishna, T.V., Yesubabu, A., Anandarao, A., Rani, T.S.: A novel image retrieval method using segmentation and color moments. Adv. Comput. **3**, 75 (2012). https://doi.org/10.5121/acij.2012.3106.75
18. Bouckaert, R., Frank, E., Hall, M., et al.: WEKA Manual for Version 3-6-10. CreateSpace Independent Publishing Platform (2015)
19. Biau, G., Scornet, E.: A random forest guided tour. TEST **25**(2), 197–227 (2016). https://doi.org/10.1007/s11749-016-0481-7

Noise Reduction in Phase-Contrast Mammography Images with Synchrotron Radiation

Yusely Ruiz-Gonzalez[1(✉)], Javier D. Brizuela-Cardoso[2], and Marlen Pérez-Díaz[3]

[1] Informatics Research Center,
Universidad Central "Marta Abreu" de Las Villas, Santa Clara, Cuba
yuselyr@uclv.edu.cu
[2] Center for Genetic Engineering and Biotechnology (CIGB),
Sancti Spiritus, Cuba
javier.brizuela@cigb.edu.cu
[3] Automatic Department, Faculty of Electric Engineer,
Universidad Central "Marta Abreu" de Las Villas, Santa Clara, Cuba
mperez@uclv.edu.cu

Abstract. Phase-contrast mammography using synchrotron beams (PCI_SR) has shown quantitatively better results in terms of image contrast and detection of small details with respect to conventional digital techniques. However, this new technique has shown higher levels of random noise than common digital techniques. The objective of this work was to reduce noise in PCI_SR images to levels, similar to those of hospital equipment without significantly affecting the spatial resolution, contrast and visibility of fine details. Five filters: Wiener, Gauss, bilateral and coif and biord wavelets families, were used independently to reduce image noise. Image quality before and after filtering was estimated using objective indexes. The results showed increases in Signal-to-Noise Ratio (SNR) without impairing other quality indexes; which demonstrates the superiority in image quality of this innovative technique for the detection of small lesions such as microcalcifications and low contrast masses.

Keywords: Phase contrast mammography · Digital filter · Image quality

1 Introduction

Breast cancer is the most common invasive cancer in females worldwide. Mammography is a specialized medical imaging technique that uses low-dose X-ray system to see inside the breasts. Usually, radiologic studies are based only on absorption effects, so image contrast is entirely due to differences in the absorption properties of details inside an object. The breast tissues are soft tissues in which the absorption effects are not very different; so small X-ray absorption differences result in poor image contrast and the complete discrimination of diseased and healthy tissues could be difficult [1].

The use of synchrotron radiation (SR) is an innovative X-ray imaging practice that improves the identification of breast lesions due to the beam characteristic [2, 3].

© Springer Nature Switzerland AG 2020
C. A. González Díaz et al. (Eds.): CLAIB 2019, IFMBE Proceedings 75, pp. 361–366, 2020.
https://doi.org/10.1007/978-3-030-30648-9_47

Synchrotron sources generate X-ray beams that have sufficient spatial coherence to allow using free space propagation phase-contrast imaging (PCI) [4]. Also the phase-contrast images are not only sensitive to the X-ray tissues absorption, but also to the phase shift that X-ray experiences when passing through the matter. Thus, they allow accessing an additional pool of contrast, potentially much stronger than that based only on X-ray absorption [2].

Previous studies have reported the advantage of the mammography images obtained in the PCI modality using synchrotron radiation (PCI-SR) as compared with images obtained in digital mammography (DM) [3, 5]. However, noise levels at PCI-SR are still a problem [6–8]. Usually, digital mammography equipment in hospitals comprises post-processing software to improve the image quality and noise removal. To our knowledge, the beam line designed by the SYRMEP research group in Trieste, Italy, has not used any post-processing technique [4, 6, 9]. This work shows how to reduce the noise level of PCI-SR images to values similar to those obtained from hospital digital mammography using filtering techniques that could be easily implemented, without diminishing contrast, edge visibility or spatial resolution.

2 Materials and Methods

Images were obtained from the RMI 165 Anthropomorphic Breast phantom. This phantom provides the same attenuation characteristics as a human breast with 50% of glandularity and 50% of fat [10]. Data acquisition from hospital equipment and PCI-SR modality had been described in [8]. PCI-SR images were acquired in two exposure modalities (High dose, low dose) and 12 images on each modality. High dose modality (SR-HD) was around 1 mGy, and low dose modality (SR-LD) was around 0.6 mGy. Hospital digital mammography images were acquired in the automatic modes of the hospital equipment. In the Senographe DS (General Electric Healthcare, UK Version ADS 54.11), 3 images were acquired in contrast, standard and dose modes. In the Giotto Image 3DL (IMS, Bologna, Italy), 1 image was acquired in automatic mode.

2.1 Image Quality Analysis

Regions of interest (ROI) were selected to analyze filter influence in simulated breast tissues and edges (see Fig. 1, blue and red ROI, respectively). The number of pixels of the ROI was different in each mammography equipment due to differences in the pixel detector sizes, while covering approximately the same area. The studied parameters were Contrast, SNR area, Visibility and SNR edge. Contrast (C) and the SNR area were estimated for breast tissue ROI and Visibility (V) and SRN edge were estimated for edge ROI, as defined in [6]. Background ROI (see Fig. 1, magenta ROI) was also defined for simulated breast tissues and edges and they were used in the image quality indexes estimation previously described.

The MTF (Modulation Transfer Function) is a commonly used metric for characterizing spatial resolutions of imaging systems. The MTF of the original PCI_SR images and filtered images were estimated according to the algorithms described in [11], using slanted-edge ROI (see Fig. 1, green ROI) in order to check the filter spatial resolution effect.

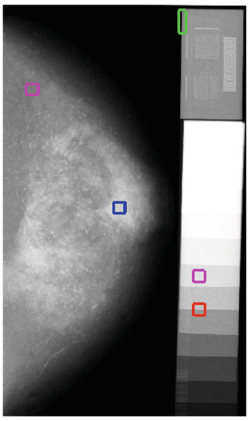

Fig. 1. Region of interest selected, blue = tissues, red = edges, green = MTF, magenta = background.

2.2 Filter Design

Two classical filters for image de-noising were used: Gaussian and Wiener filter [12]. A Gaussian filter is a general-purpose filter currently standardized for image processing. The MATLAB ® function "imgaussfilt" was used during the process and the standard deviation of the filter was 0.5. Wiener filter used a pixel-wise adaptive method based on statistics estimated from a local neighborhood of each pixel. It was implemented using the MATLAB ® function "wiener2", and window size 3.

Non-classical filters, like bilateral and wavelets families were also used. Bilateral filter smooth images while preserving edges [13] and wavelet filters are commonly used for noise reduction. The wavelet families selected were "coif1" and "bior1.3" [12].

Statistical significance of differences in contrast (C) and edge visibility (V) among filters was tested using a non-parametric Kruskal-Wallis test. The MATLAB function kruskalwallis was used to perform the test and the significance level was set to $p = 0.05$.

3 Results

Table 1 shows the values of image quality indexes for the hospital equipment images, original PCI_SR images and filtered images, where GE values are for images from DM Senographe DS, Giot for images from DM Giotto Image, SR-LD and SR-HD for images from low and high dose PCI-SR modality. Wie, Gau, Bi, Coif and Biord are for filtered PCI-SR images using Wiener, Gaussian, bilateral and wavelets filter (coif1 biord1.3 families) respectively in LD and HD modality.

Table 1. Estimated quality indexes, mean ± SD.

Index	GE	Giot[a]	SR-LD	SR-HD	Wie-LD	Wie-HD	Gau-LD
C	22.09 ± 2.07	10.39	24.21 ± 0.91	24.12 ± 0.89	24.36 ± 1.01	24.28 ± 0.60	24.36 ± 1.01
SNR_{area}	9.65 ± 0.15	4.52	7.73 ± 0.65	8.78 ± 0.39	12.39 ± 0.42	12.85 ± 0.20	12.94 ± 0.39
V	3.55 ± 0.24	3.02	4.53 ± 0.26	4.47 ± 0.33	4.38 ± 0.26	4.43 ± 0.20	4.35 ± 0.25
SNR_{edge}	10.17 ± 0.59	4.51	4.54 ± 0.83	5.71 ± 0.91	10.79 ± 1.81	13.20 ± 0.72	12.09 ± 1.43
Index	Gau-HD	Bi-LD	Bi-HD	Coif-LD	Coif-HD	Biord-LD	Biord-HD
C	24.28 ± 0.60	24.36 ± 1.01	24.28 ± 0.60	24.36 ± 1.01	24.27 ± 0.60	24.36 ± 1.01	24.28 ± 0.60
SNR_{area}	13.26 ± 0.20	12.87 ± 0.39	13.21 ± 0.19	13.12 ± 0.37	13.36 ± 0.21	12.56 ± 0.40	12.78 ± 0.22
V	4.40 ± 0.19	4.35 ± 0.25	4.41 ± 0.19	4.48 ± 0.32	4.50 ± 0.22	4.32 ± 0.28	4.39 ± 0.18
SNR_{edge}	14.41 ± 0.74	11.90 ± 1.43	14.18 ± 0.74	13.39 ± 1.63	16.09 ± 0.91	12.06 ± 1.44	14.59 ± 0.73

[a]Mean value, there was only one image

The results showed that SNRs of filtered images were higher than those at the original PCI-SR images and those obtained by the hospital equipment. The contrast index showed small increases for filtered images compared to original PCI-SR images. The visibility of filtered images had small decreases with respect to the PCI-SR image, but they are still higher than those from the hospital equipment.

The Kruskal-Wallis test comparing the contrast and visibility indexes from the five filters showed $p = 0.999$ and $p = 0.5185$ respectively. Former results revealed that there are no significant differences among the studied filters.

Figure 2 shows the MTF for original PCI_SR image and filtered images. The MTF was not affected by the filter process, so was not the spatial resolution of the images either. The main differences were in the second lobe of the curve, but the values were below 0.1, which is considered the detection limit of the MTF.

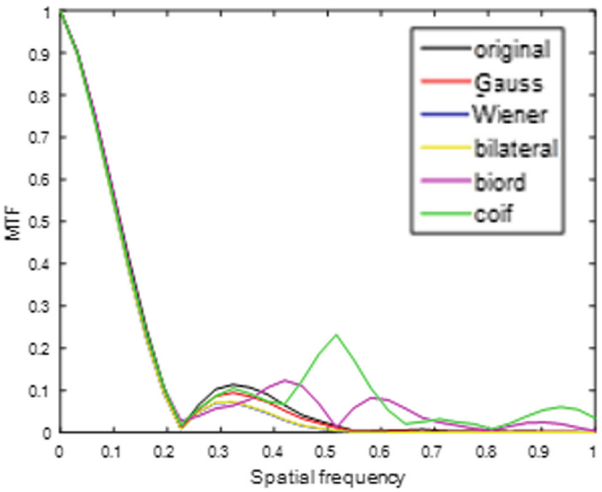

Fig. 2. MTF of the original and filtered images.

4 Conclusions

The Signal to Noise Ratio was increased to values higher than those from the hospital equipment, with small increases in the contrast index and small decreases of the visibility index. However, the visibility index of the filtered images was still higher than that from the hospital equipment.

In general, the results from the image quality indexes were similar for all the filters used in this experiment. Moreover, further research on filter design is advisable in order to obtain the best options when using filters since no significant differences among them were noticed at this stage of the research.

Previous works described the superiority of PCI-SR images, even though this new technique showed higher levels of noise than those obtained from the hospital digital mammography equipment [5, 6, 8]. Using filtering techniques, the SNR of the PCI-SR images can be improved to values higher than those from the hospital equipment, preserving the superiority on the contrast and visibility indexes. The results came to confirm the superiority in image quality of PCI_SR new technique.

Conflict of Interest. The authors declare that they have no conflict of interest.

References

1. Dance, D.R.: Diagnostic Radiology with X-rays. Adam Hilger, London (1988)
2. Lewis, R.A.: Medical phase contrast x-ray imaging: current status and future prospects. Phys. Med. Biol. **49**(16), 3573–3583 (2004)
3. Arfelli, F., et al.: Mammography with synchrotron radiation: phase-detection techniques. Radiology **215**(1), 286–293 (2000)
4. Dreossi, D., et al.: The mammography project at the SYRMEP beamline. Eur. J. Radiol. **68** (3), 58–62 (2008)
5. Castelli, E., et al.: Mammography with synchrotron radiation: first clinical experience with phase-detection technique. Radiology **259**(3), 684–694 (2011)
6. Ruiz-Gonzalez, Y., et al.: Objective measurements of image quality in synchrotron radiation phase-contrast imaging versus digital mammography. Int. J. Comput. Assist. Radiol. Surg. **11**(2), 181–188 (2016)
7. Ruiz-Gonzalez, Y., et al.: Initial steps of objective measurements of image quality in phase-contrast vs. digital mammography. In: Braidot, A., Hadad, A. (Eds.) VI Latin American Congress on Biomedical Engineering CLAIB 2014, Paraná, Argentina, 30–31 October 2014, vol. 49, pp. 341–344. Springer, Cham (2015)
8. Ruiz-Gonzalez, Y., et al.: Measurements of image quality in synchrotron radiation phase-contrast imaging versus digital mammography using anthropomorphic breast phantom. presented at the I international scientific convention, "UCLV 2017," Varadero, Cuba (2017)
9. Castelli, E., et al.: Clinical mammography at the SYRMEP beam line. Front. Detect. Front. Phys. Proc. 10th Pisa Meet. Adv. Detect. **572**(1), 237–240 (2007)
10. Gammex Rmi RMI 165 Anthropomorphic Breast Mammographic Phantom - Manufacturer specifications. http://www.medwow.com/med/phantom-mammographic/gammex-rmi/rmi-165-anthropomorphic-breast/21126.model-spec

11. Alaruri, S.D.: Calculating the modulation transfer function of an optical imaging system incorporating a digital camera from slanted-edge images captured under variable illumination levels: Fourier transforms application using MATLAB. Optik **127**(15), 5820–5824 (2016)
12. Gonzalez, R., Woods, R.: Digital Image Processing Using Matlab, 2nd edn. GP, New Delhi (2009)
13. Tomasi, C., Manduchi, R.: Bilateral filtering for gray and color images. In: Sixth International Conference on Computer Vision (IEEE Cat. No. 98CH36271), pp. 839–846 (1998)

Interface for Contour Extraction and Determination of Morphologic Parameters in Digital Images of Footprints Based on Hernandez-Corvo Protocol

H. A. Miranda C.[1], Luz Alejandra Flores Cu[1], Santiago Camacho López[2], Horacio Rostro González[3], and Miroslava Cano Lara[1(✉)]

[1] Depto. Mecatrónica, TecNM-Instituto Tecnológico Superior de Irapuato, Irapuato, GTO, Mexico
miroslava.cano@itesi.edu.mx
[2] Depto. Óptica, Centro de Investigación Científica y de Educación Superior de Ensenada, Ensenada, BC, Mexico
[3] Depto. Electrónica, Universidad de Guanajuato, Salamanca, GTO, Mexico

Abstract. This work presents the development of an interface to obtain the morphological parameters for the classification of the type of footprint of a person using the Hernandez-Corvo protocol. A digital photograph of the footprint is acquired with Matlab an algorithm which is applied to detect the contour of the footprint. Hernandez-Corvo protocol is applied through the interface to determine the morphological parameters, the distances of internal prominences of the forefoot and hindfoot are measured. The distance of the longest phalange and the extension of the metatarsal is obtained and the type of footprint is classified as flat, high and normal in different degrees. The ease of measurement of morphological parameters for the analysis of the pathology of the patient's foot is beyond a general study. The interface was tested, applying the protocol to the footprint of a child of 7 years-old which resulted in a percentage of 32.65 corresponds to a flat foot. The work time in the interface was approximately 4 min including to display the parameters of interest.

Keywords: Podoscanner · Footprint · Hernandez-Corvo protocol · Image processing

1 Introduction

The study of a person's footprint covers various parameters, both of them medical and engineering. Types of foot degrees can be diagnosed with engineering technology and numerical analysis [1], most of them are currently used podoscopes and a mirror that allows the observation. Another type of analysis is to cover the sole of the user's foot with ink to capture the footprint on a paper to observe the contour [2].

The detection of the flat foot can be made less subjective by employing engineering in the medical condition [3, 4] where the entire bottom of the foot gets in touch with the

© Springer Nature Switzerland AG 2020
C. A. González Díaz et al. (Eds.): CLAIB 2019, IFMBE Proceedings 75, pp. 367–376, 2020.
https://doi.org/10.1007/978-3-030-30648-9_48

ground due to the type of footprint of the person. There would be an absence or prominence of the plantar arch This condition means that according to the level of severity, there are discomforts at the time of walking during long periods of time [5]. Baropodometry benefited from the technological advance, using data acquisition algorithm, algorithms implemented as 2D or dynamic bio-feedback, which they must be handled by a specialist [6]. The use of automation systems makes the studies have an increase in price costing around $1000.00 pesos in Mexico plus the cost of the examination that can reach $800.00 pesos, it makes the treatment less accessible [7].

This analysis can be treated to obtain other values that enrich the static study such as the Clark angle, the Staheli index, the Valgo index, the Chippaux index and the angular deviation of the foot among others which can help the common user or in a sports area in the detection of problems that affect the performance of athletes [8].

The protocol used is precise for the determination of the type of footprint, this has been widely disseminated in the Latin American population, especially in the sports sector which is implemented manually, making the application impractical and limited to small groups [9]. Currently in the small clinics to determine the type of footprint tread consists of a visual or manual exploration, which weakens the valuation and accurate diagnosis of the type of tread patient. This work presents a graphical interface in the Matlab programming environment, shows the necessary steps for preliminary diagnosis of the patient footprint [10].

This work presents the technique where the image of the sole of the foot is obtained in a nadir plane trying to eliminate all the sections of the foot where pressure is not exerted on the tread, to perform the process in the same isolating the contour of the footprint with which you can apply different algorithms [11] to obtain more information about it, in this case the protocol of Hernandez-Corvo [12], in which by means of measurements of distances between characteristic points of the foot makes it possible to classify the state of the footprint in different categories considering deformations of flat foot and foot dig [13], the traces of the protocol are made on the contour of the footprint because the initial photograph may look unclear in specific points of interest, those where the applied pressure is lower as well as the brightness resulting from the luminance phenomenon; the thickness of the contour can affect the measurement because if the foot is not placed correctly on the edge, the measurements can be altered [9].

2 Methodology

The experimental methodology begins in a digital photograph that is acquired using a podoscanner. The podoscanner technique provides a better quality digital image for this study, in comparison than other techniques [14]. The metallic structure of podoscanner has a glass 6 mm thick with white LED lighting at the edges for transmitting light in the glass. A black cover fabric was used in patient's extremities to facilitate the acquisition of the digital image. The photograph was acquired with a Sony DSC-T300 10.1Mpx camera (See Fig. 1). The system used is round at a price of approximately $1500 pesos. The experimental tests were carried out on an 8 year-old boy with footwear number 20. The acquisition of the footprint of the plantar pressure is obtained in full, with the support of lighting and dark cover avoiding external affectations.

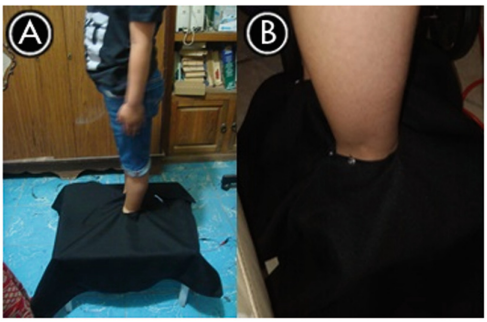

Fig. 1. Podoscanner system. (a) Application in the system. (b) Laying the cape around the child's ankle

The interface begins with the acquisition of the photography in the podoscanner system. The footprints are showed clearly, so then it extracts the contour and acquire the parameters of the Hernadez-Corvo protocol with the Matlab interface (see Fig. 2). It is observed that the image presents green tonality in the regions of the footprints and black for the exterior, thus achieving ease when it comes to digital image processing.

Fig. 2. Image obtained from the footprints of the test subject under controlled light conditions.

The graphical interface in which the processing of the photograph generated by the footprint of patient made. A first step the algorithm of the pseudo-color to extract the contour and to avoid that parts of the foot that contain noise in the image intervene in the measurement (see Fig. 3). The pseudocolor algorithm was used because it generates images with little noise and the thickness of the contour does not generate ambiguity in the measurements [9]. The pseudocolor algorithm converts the image into gray scale to

compare the 256 tonalities and color different pixel ranges to clearly observe the different shades of gray as seen in Fig. 3a. The area of interest is extracted, which is the range from 0 to 18 (in gray scale). The image obtained is a defined perimeter with a thin but continuous line [15], where the sole of the foot exerts pressure and the effective outline of the footprint is obtained. Finally, an applied anti-Gaussian filter noise is obtained (see Fig. 3b) with a continuous contour and defined lines that will help to take precise points for the measurements established in the protocol.

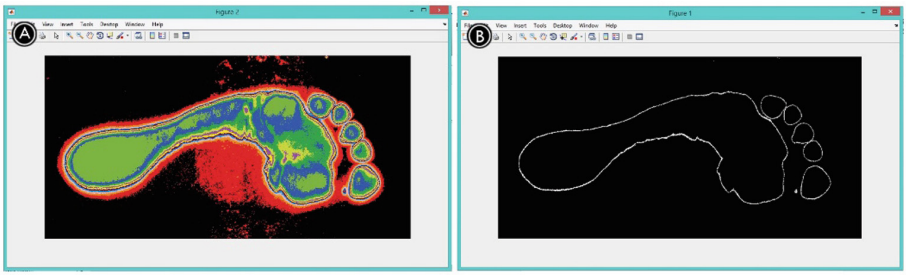

Fig. 3. Interface in Matlab (a) Graph of illuminance changes using pseudo-color technique. (b) Contour found using pseudo color technique.

Applying this method, the processing time lasts 63 s due the allowed time frame when processing an image of approximately 2500 × 1250 Pixels considering a frame to keep only the area of interest. The numerical techniques to acquire the patient's footprint and in turn the contour, facilitates and gives accuracy to a preliminary diagnosis of the type of footprint of the patient. The interface generates the results in a time of a few seconds to start the application of the Hernandez-Corvo protocol which is not easily achieved with manual or traditional techniques [11]. The measurements of the parameters of the HernadezCorvo protocol are made in the image of the generated contour of the footprint. Programming techniques are used to use the distance tool, an interactive line that can be manipulated in the interface helps to assign the parameters of interest of the fingerprint.

To obtain the classification of the footprint it is necessary to follow a sequence of steps described below [16] (See Tables 1 and 2).

This distance $\overline{d}$ is homologous to the variable "Y", that Hernandez-Corvo protocol shows us, to obtain the value "X", we use the formula (9),

$$X = \frac{|p(y2 - y1) + q(x1 - x2) + x1(y1 - y2) + y1(x2 - x1)|}{\sqrt{(y2 - y1)^2 + (x1 - x2)^2}} \tag{9}$$

The formula of the Hernandez-Corvo protocol for the classification of the foot by categories can be seen in Eq. (10),

Table 1. Steps in Hernandez-Corvo protocol.

Step	Image	Description
1		The upper points of the inner part of the hindfoot and forefoot are obtained Applying the formula (1) we draw the line that passes through these points
2		Detect the upper and lower point of the foot. These lines are drawn with formulas (2) and (3) Two perpendicular lines are drawn through the midfoot and forefoot with the formulas (5) and (6), spaced with the fundamental measure (mf) of the Eq. (4)
3		We find the most prominent external point and draw the line that passes through the point with the Eq. (7)
4		Mark the distance of the midfoot with the help of the reference line by applying Eq. (8)

$$\%X = \frac{X - Y}{X} * 100 \tag{10}$$

The protocol classifies the type of footprint in 6 [9], according to the percentage that is obtained, these can be:

Table 2. Equations for distances

Step	Equations
1	$y = \frac{y2 - y1}{x2 - x1}(x - x1) + y1$ (1)
	$y = \left(-\frac{x2 - x1}{y2 - y1}\right) * (x - a1) + b1$ (2) $y = \left(-\frac{x2 - x1}{y2 - y1}\right) * (x - a2) + b2$ (3) $mf = \sqrt{F - \left[\frac{\lvert(y1 - b1)(D) + (a1 - x1)(C)\rvert}{\sqrt{((C)^2 + (-D)^2)}}\right]^2}$ (4) Where: $C = y2 - y, D = x2 - x1, F = (x2 - a1)^2 + (y2 - b1)^2$ $y = \left(-\frac{x2 - x1}{y2 - y1}\right) * (x - a1 + mf) + b1$ (5) $y = \left(-\frac{x2 - x1}{y2 - y1}\right) * (x - a1 + 2 * mf) + b1$ (6)
3	$y = \left(\frac{y2 - y1}{x2 - x1}\right) * (x - p) + q$ (7)
4	$\bar{d} = \frac{\left\lvert\left(\frac{y2 - y1}{x2 - x1}\right)m2 - n2 + \left(-m1\left(\frac{y2 - y1}{x2 - x1}\right) + b1\right)\right\rvert}{\sqrt{\left(\frac{y2 - y1}{x2 - x1}\right)^2 + 1}}$ (8)

Table 3. Foot classification

%X	Type of foot
0–34	Flat
35–39	Flat-Normal
40–54	Normal
55–59	Normal-Dig
75–84	Strong dig
85–100	extreme dig

To improve and facilitate the experience in the Hernandez-Corvo algorithm developed in the MatLab environment, a graphic interface was designed that

exemplifies the steps to follow that has interactive elements which the user avoids performing manual calculations by making dynamics the generation of results.

3 Results

3.1 Hernandez-Corvo Diagnostic Interface

The interface designed in this work generates a dynamic management of the parameters of interest in the patient's footprint (see Fig. 4). The box with (number 1) shows the photo of the patient's foot and the protocol will be applied.

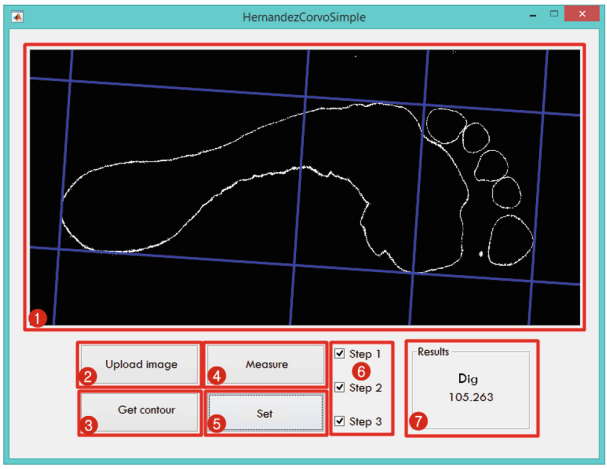

Fig. 4. Final interface for the Hernandez-Corvo protocol application.

The program management buttons (number 2) contain "Upload image" where we can select the photo, "Get contour" (number 2) applies the selective pseudocolor algorithm on the image, "Measure" (number 4) generates the imdistline objects to mark the points of interest, "Set" (number 5) draw the protocol strokes. The checkbox (number 6) indicates the sequence of steps in which the procedure is. In the marked section as (number 7) the results of the image that was worked as well as the classification in which the case is found are shown.

3.2 Obtaining Contour

In Fig. 5 you can see the comparison between both images (original and contour). The persistent noise in the outline of the trace is eliminated, the rest that was not eliminated does not affect the measurements in the image, since they are inside the contour.

The algorithm developed to obtain the contour can be used in general medicine, in the area of orthopedics or traumatology can be used for accurate visual diagnoses, replacing the most common in public services such as prediagnosis along with the use

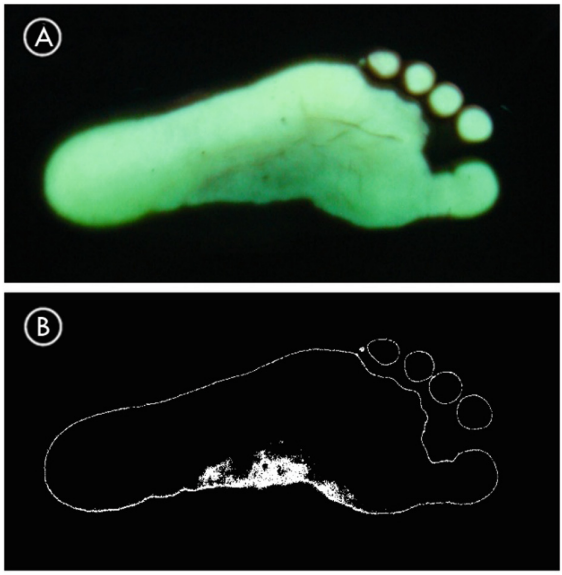

Fig. 5. Images acquired from the user's footprint. (a) Photograph with a green tone due to the scattering of light on the glass where the user is standing, coupled with the controlled environment of the system. (b) Contour extracted from the footprint.

of podoscopes [10]. In other areas of medicine it can be used to analyze other regions of interest involving detections contours.

3.3 Tests

The tests were carried out on an 8 year-old infant, who has a size 20. The initial photograph of the trace that is observed in Fig. 6a. The steps of the protocol were applied, resulting in Fig. 6b, where the guide lines of the protocol are shown and the results of Table 4.

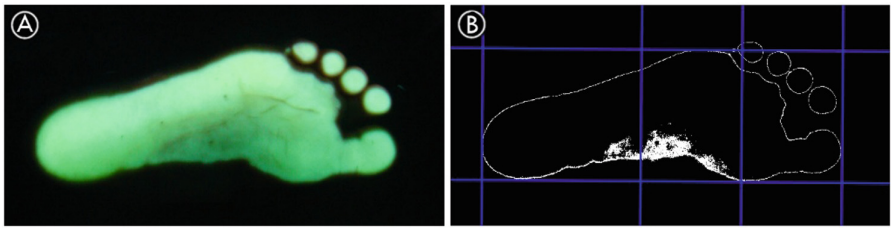

Fig. 6. (a) Photograph of the footprint of the child test. (b) Image of the child's footprint after applying the Hernandez-Corvo protocol.

Table 4. Fundamental measure of Hernandez-Corvo.

Parameter	Distance obtained (pixels)
Fundamental measure	542.0573
X	706.7349
Y	475.9821

Table 4 shows the parameters required in the application of the Hernandez-Corvo formula as well as the fundamental measure. With which, gives us a value of 32.6505, entering the classification of flat foot according to Table 3. In addition, obtaining the Chippaux index and the clarke angle with the same Hernandez-Corvo protocol technique described in the paper, the results of 0.63 and 24.55 respectively were obtained, so that the foot with each study is classified as flat, corroborating the result by Hernandez-Corvo. In [17] an automatic application system of the Hernandez-Corvo protocol is presented with a processing time of 409 s for an image of 1280 × 960 pixels. The interface shown in this paper used 60 s of processing, being within the acceptable time frame [17] when analyzing both feet simultaneously.

4 Conclusion

The programming interface shows a facility to obtain the morphological parameters that can be acquired through a digital image of the footprint of a person. This static study can be performed faster to a large population, with the obtaining of more accurate computational results for a evaluation of the patient. The interface is of great support in the medical area when carrying out a study of plantar pressure, since it can be managed without great difficulties. The images processing and the real-time program of the Hernandez-Corvo protocol allowed us to obtain the foot classification and the parameters of interest in an approximate time of 4 min, considering the time capture of the image. The manual corroboration of the protocol resulted from 30.55 placing the foot of the infant in the same classification of flat feet that shows the interface, obtaining a margin of error of 6.41% for manual tracing.

The computational interface, using the technique of trace measurements in the sole of the foot, can be adapted to generate these indexes and other necessary parameters in the baropodometry such as the Clark angle, the Chippaux-Smirak index, the arc index, as a complement of static orthopedic studies, etc.

Currently in public health services in Mexico, the diagnosis of these conditions are still made by hand, so with the current interface we present a simple way of giving less subjective diagnoses using computer technology.

5 Recognition

This research has been supported by the CONACYT project FC2016-1961 Neurociencia computacional: de la teoría al desarrollo de sistemas neuromórficos. Acknowledges to Lic. Karla Lizbeth Mejía Barrera for reviewing the manuscript.

References

1. Kahleel, A.L., Sadiq, G.Sh.: Manufacturing and analysis custom foot orthotic for flexible flatfoot. Int. J. Mech. Eng. Technol. **9**(13), 1253–1263 (2018)
2. Nurzynska, D., Di Meglio, F., Castaldo, C., Latino, F., Romano, V., Miraglia, R., Guerra, G., Brunese, L., Montagnani, S.: Flatfoot in children: anatomy of decision making. Ital. J. Anat. Embriol. **117**(2), 98–106 (2012)
3. Martínez Lozano, A.G.: Pie plano en la infancia y adolescencia. Conceptos actuales. Rev Mex Ortop Pediátr. **11**(1), 5–13 (2009)
4. Netter, F.: Atlas de anatomía humana. 6th edn. Elsevier, España (1989)
5. Halabchi, F., Mazaheri, R., Mirshahi, M., Abbasian, L.: Pediatric flexible flatfoot; clinical aspects and algorithmic approach. Iran J. Pediatr. **23**(3), 247–260 (2013)
6. Hasegawa, N., Takeda, K., Sakuma, M., Mani, H., Maejima, H., Asaka, T.: Learning effects of dynamic postural control by auditory biofeedback versus visual biofeedback training. Gait Posture **58**, 188–193 (2017)
7. La Cruz, A., Zeas, A.L., Quishpi, E.A., Campoverde, J.L., Guamán, H.K., Morocho, V.: Clinical validation of footprint analysis using the low cost Photo-podoscope. Jheca Nawe. Maskana, pp. 95–102 (2014)
8. Ozer, C.M., Barut, C.: Evaluation of the sole morphology of professional football players. Int. SportMed J. **13**(1), 8–17 (2012)
9. Sánchez, C.: Análisis de dos métodos de evaluación de la huella plantar: índice de Hernandez Corvo vs. Arch Index de Cavanagh y Rodgers. Fisioterapia **39**(5), 209–215 (2017)
10. Boffino, L., Meléndez, I., Rodriguez, A.: Pie plano pediátrico. Obtenido de Pie Plano pediátrico. Universidad del Salvador facultad de medicina catedra de ortopedia y traumatologia (2012)
11. Lara, D.S., Lara, S.A., Zagalaz-Sánchez, M.L., Martínez-López, E.: Análisis de los diferentes métodos de evaluación de la huella plantar. Retos. Nuevas tendencias en Educación Física, Deporte y Recreación **19**, 49–53 (2011)
12. Hernandez Corvo, R.: Morfología funcional deportiva. Sistema locomotor, 1st edn. Paidotribo, España (1987)
13. Luengas, L., Díaz, M., González, J.: Determinación de tipo de pie mediante el procesamiento de imágenes. Ingenium **17**(34), 147–161 (2016)
14. Ferrín, C., Magdalena, X., Loaiza, H.: Determinación semiautomática de parámetros morfológicos de la huella plantar mediante el procesamiento digital de imágenes. Revista S&T **11**(27), 9–26 (2013)
15. Khosravi, M., Rostami, H.: A new pseudo-color technique based on intensity information protection for passive sensor imagery. Int. J. Electron. Commun. Comput. Eng. **6**, 324–329 (2015)
16. Lehmann, C.H.: Geometría Analítica, 1st edn. LIMUSA, México (2007)
17. Ferrin, C., Magdalena, X., Loaiza, H., Lopez, S., Henao, S.: Sistema de extracción automática de parámetros morfológicos de la huella plantar mediante técnicas de visión por computador en un sistema embebido. Revista Colombiana de Tecnologías de Avanzada **1** (23), 80–86 (2014)

Cervix Type Classification Using Convolutional Neural Networks

Daniel A. Cruz(✉), Carmen Villar-Patiño, Elizabeth Guevara, and Marisol Martinez-Alanis

Facultad de Ingeniería, Universidad Anáhuac México,
52786 Huixquilucan, State of Mexico, Mexico
dcruz@arttech.com.mx, {maria.villar,
elizabeth.guevara, marisol.martinez2}@anahuac.mx

Abstract. Cervical cancer is still a significant cause of death, especially in developing countries. The detection and correct treatment of the disease is vital in its early stages. One of the key factors in selecting appropriate treatment is the identification of the cervix type. The objective of this work is to propose a Convolutional Neural Network (CNN) architecture to perform a classification of the cervix from a set of images published by Intel and MobileODT. The proposed architecture is combined with a preprocessing algorithm based on an assembly of color models to select the region of interest in the image. The obtained model provides better results than other models in which transfer learning is used or there is no preprocessing stage.

Keywords: Convolutional Neural Network · Cervical cancer · Color models · Adamax

1 Introduction

Although cervical cancer is one of the most treatable cancers if detected early, it still appears in fourth place for both incidence and mortality [1]. The mortality rate increases in developing countries, where access to opportune diagnosis and effective treatment is uncommon.

Important challenges in the treatment of cervical cancer are obtaining adequate tissue samples and determining the appropriate method of treatment. These tasks are affected by the physiological characteristics of the cervix. The cervix contains two kinds of cells: rectangular columnar cells and squamous cells. Columnar cells are constantly changing into squamous cells in an area of the cervix called the "transformation zone" (TZ). This zone is the most common place for abnormal cells to develop on the cervix. It is the origin of more than 90% of precancerous lesions, also called "squamous cervical intraepithelial" (CIN) lesions and cancers, hence its importance [2, 3].

The difference between various cervix types is quite small, depending specifically on the TZ. There are three types, according to the visibility of all or part of the upper limit of the squamocolumnar junction [4]. Figure 1(a) describes the main differences between the types of cervix, due to the TZ, and Fig. 1(b) displays sample images of the types of cervix, showing the difficulty of the classification problem.

© Springer Nature Switzerland AG 2020
C. A. González Díaz et al. (Eds.): CLAIB 2019, IFMBE Proceedings 75, pp. 377–384, 2020.
https://doi.org/10.1007/978-3-030-30648-9_49

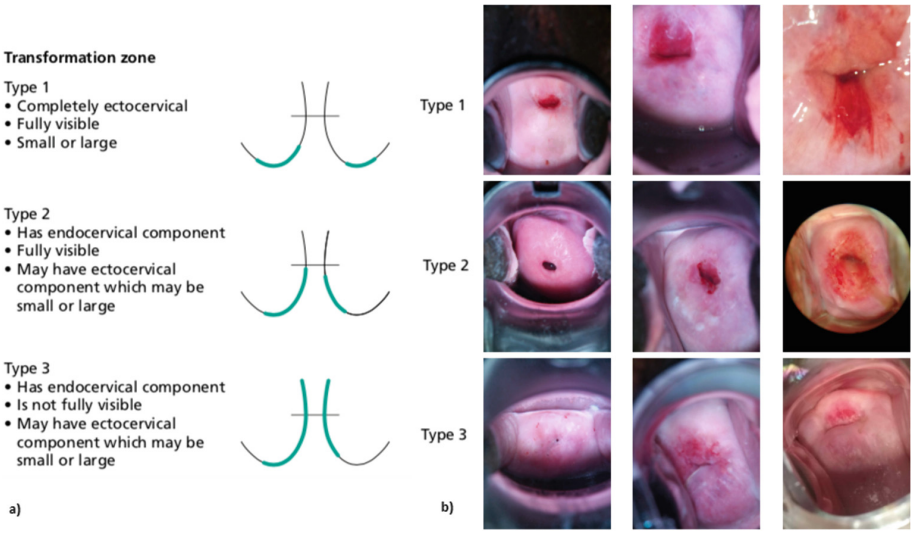

Fig. 1. **(a)** Transformation zone types [4], **(b)** sample images of the three cervix types [5].

In order to identify the type of cervix, it is necessary to obtain the corresponding images. The most common method of obtaining images is a colposcopy. Digital colposcopy is a low-cost alternative to traditional colposcopies [6], owing to portable mobile devices, which provide access to vulnerable populations [7]. However, the main drawback of this method is its low sensitivity for detection when carried out by untrained personnel [8].

If the wrong treatment is applied or the sample is not taken from the TZ, one may mistakenly believe that the patient is healthy or has been cured. This will have significant implications for their health. It is, therefore, crucial to automate the classification, based on colposcopy images, to assist health providers in improving diagnosis and treatment of the disease.

For this reason, researchers and developers are interested in using Machine Learning and Computer Vision to automate the analysis of digital colposcopies [9–12]. Intel and MobileODT have published a database of images that are labeled by cervix type [5]. Based on this dataset, the aim of this work is to propose an architecture that allows for the classification of cervical images in the precancerous stage, using Artificial Neural Networks (ANNs) and, more specifically, Convolutional Neural Networks (CNNs). The short-term objective is to use these results to develop a system that works with real images, obtained in hospitals in rural areas of Mexico.

2 Materials and Methods

The purpose of this work is to develop a procedure for classifying cervical images according to the TZ, using ANNs. The first stage of the classification process was the exploratory data analysis of the image database obtained from the website for the "Intel

& MobileODT Cervical Cancer Screening" competition [5]. The training set has 8 215 images, but a number of the images are duplicated (6.71%). Some of the images are in green color (9.08%); others do not show the cervix correctly (22.7%). These images were removed from the original dataset, leaving only 5 862 images for experiments. It is important to mention that image distribution with respect to the type of cervix is not uniform; type 2 cervix images represent 50% of the total images of the population, while type 1 and 3 constitute 20% and 30%, respectively.

The extraction of the region of interest (ROI), i.e., the cervix, is a vital step in the preprocessing phase. Correct ROI selection prevents the ANN from learning noise patterns, improving the performance of the classifier. The ROI selection is based on color, since the images have similar colors in the warm range: red, orange, yellow and pink.

The proposed algorithm locates the ROI by making an assembly with three color models: HSV, YCbCr and CIELAB [13]. For each model, a range of values per channel is established. These limits are shown in Table 1. The chosen models have a common characteristic: two channels for color definition and one channel (V, Y and L respectively) for controlling the impact of brightness, which usually represents a challenge in the identification and segmentation of color.

Table 1. Color model's values.

Color model	Minimum value	Maximum value
HSV	(H = 140, S = 28, V = 148)	(H = 180, S = 88, V = 255)
YCbCr	(Y = 0, Cr = 170, Cb = 0)	(Y = 255, Cr = 205, Cb = 171)
CIELAB	(L = 0, A = 149, B = 0)	(L = 219, A = 255, B = 171)

The assembly executes a logical OR with the results of each model in such a way that each model contributes with a layer to the final image. Refer to Fig. 2 for an example of the application of each color model and the obtained assembly.

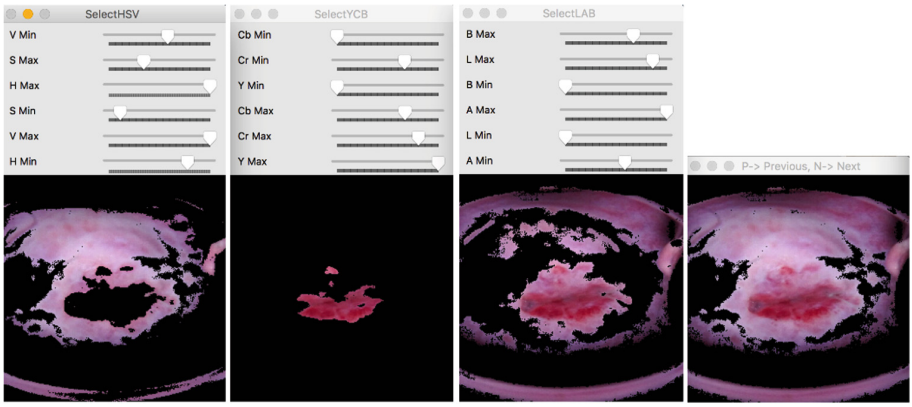

Fig. 2. Results of each color model and the obtained assembly.

The application of CNNs is popular in image classification. One difference between a CNN and an ANN is the way in which they work with images. While an ANN requires features that characterize the object to be detected, a CNN automatically learns and generalizes characteristics of the images.

Transfer learning is a useful technique for speeding up training and, in some cases, for improving the performance of a deep learning model for a problem where a large amount of data is not available (as in this case). The results obtained when applying this technique with the Xception model were not satisfactory. For this reason, a CNN architecture called "CXNN" was developed. The model VGG16 [14] inspired this architecture, which has sequential layers.

The main reason for relying on this model was its simplicity, as can be seen in Fig. 3. It works with images of 224 × 224 pixels in RGB format; therefore, it has a depth of three layers of data arrangement – one for each color. It has seven ConvLayers (hid-den layers), and the output layer has three fully connected layers. The last layer is formed by only three nodes, corresponding to each type of cervix. The filter size of all the ConvLayers is 3 × 3, and the filters implement a 1 × 1 stride and 1 × 1 padding. The last of these layers is the exception regarding the size of the filter, which is 2 × 2.

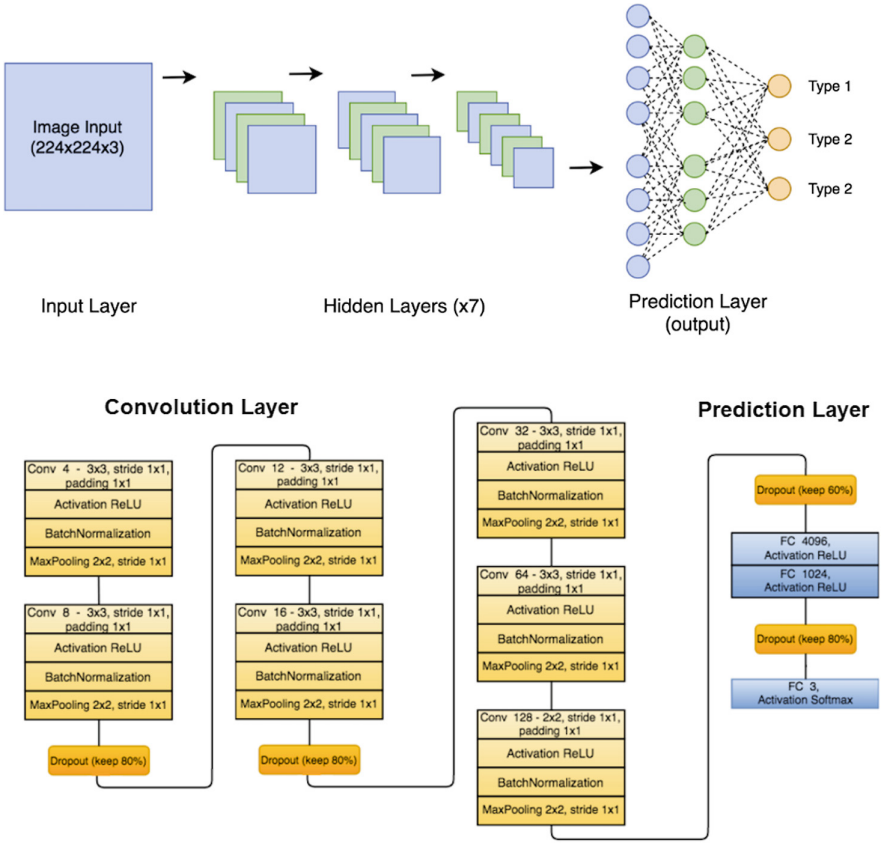

Fig. 3. CXNN Architecture and layers specifications.

A ReLU activation was also used with the batch normalization regularization technique. Max pooling was applied to reduce the size of the data. Dropout was used to avoid overfitting; the 80% of the neuronal activations was retained after layers 2 and 4, and, subsequent to Layer 7 (the last ConvLayer), a more aggressive dropout was applied, with a retention of only 60% of the activations. This process helped to improve the generalization capacity of the model. Finally, the Softmax activation function was applied, as it is commonly used in classification problems with more than two classes.

The model was built using open-source tools: TensorFlow and Keras. To increase the number of images of the dataset, a data augmentation technique was used, specifically the Keras function called "ImageDataGenerator". Variants of the images were created in the training dataset, applying a rotation range of 0.1, a horizontal flip and a zoom range of 0.2, increasing the training dataset to 9 200 images.

To deal with the problem of having an imbalanced dataset, the function called "compute_class_weight" of the "scikit-learn" framework was applied. This function implements an algorithm to manage rare events [15].

3 Results and Discussion

The hyperparameters used to train the CXNN with the Adamax optimization are the default values in Keras, with the exception of the learning-rate. These values are shown in Table 2.

Table 2. Hyperparameters for CXNN.

Type of hyperparameter	Hyperparameter	Value
Optimization	Learning rate	2×10^{-3}
	Decay	0
	Beta 1	0.9
	Beta 2	0.999
	Epsilon	10^{-3}
Training	Mini-batch size	32
	Epochs	100
	Steps per epoch	300
	Loss function	Categorical cross entropy

The results obtained using Adamax for the "accuracy" and "loss" metrics are presented in Fig. 4. For accuracy in training, an almost linear positive trend can be seen, which indicates that the increase in accuracy was progressive. This is not the case for the validation because it reaches a maximum in the trend between epoch 35 and 45, approximately, and begins to decay later, suggesting the beginning of overfitting. The training was stopped by the early stopping condition.

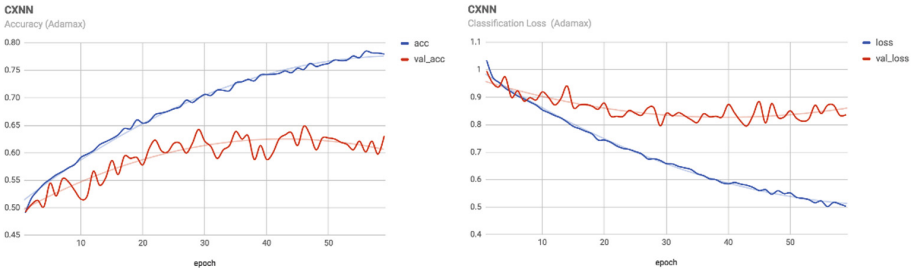

Fig. 4. CXNN accuracy and loss metric.

To validate the importance of the ROI selection, the CXNN was tested with images, without processing and with the selected ROI. The results obtained with other models are also presented. Figure 5 presents a comparison, which indicates that the best model was the CXNN-Adamax with ROI selection, with a loss metric during validation of 0.7956 and an accuracy of 0.6425.

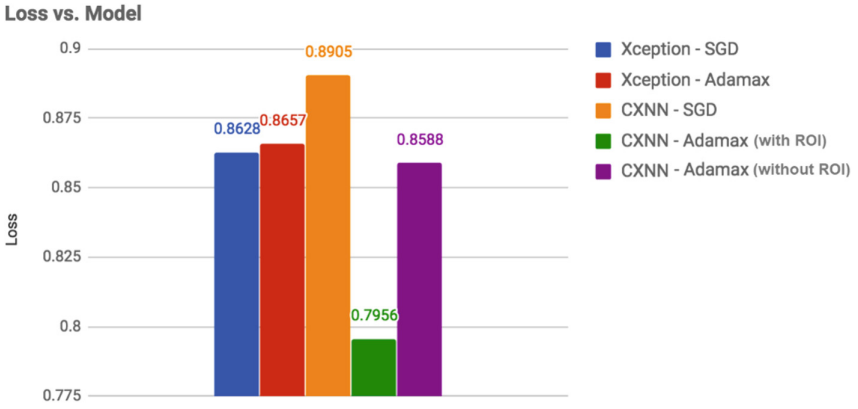

Fig. 5. Comparison of results with different models.

Due to the nature of the presented problem, there is a high level of interest in the development of novel methodologies that will help with the identification of the cervix type. As a result of the aforementioned competition, several methodologies have been proposed to help with the classification of the cervix.

Fernandes et al. [8] focused on the analysis of the different automated methods that exist today. They identified a series of challenges present in automating the classification of cervix images. One of these challenges focuses on the segmentation of the images in order to obtain a ROI. The aim of the majority of methodologies is to extract the ROI based on the morphology of the cervix. However, the presence of smooth transitions in parts of the cervix makes it difficult to achieve the correct segmentation. This work proposes a solution to this challenge by focusing on color extraction, exclusively, to obtain the ROI.

Yang et al. [16] proposed the use of a complex model combining four different CNNs in order to classify the cervix in preprocessed images with ROI extraction. In order to extract the ROI, they used a different combination of CNN models, which have to be retrained several times. As a result, they managed to obtain a loss of 0.808 with their proposed framework – higher than the loss presented in this paper (0.7956). Furthermore, by comparing the results of this work with the final ranking of the competition [5], the presented architecture would have ranked in second place among 261 places, based on the obtained loss. It should be noted that the official ranking was obtained with a private dataset (different to the public dataset that was released for the competition), and the details of the process for evaluation of the model performance were not known. Even so, these results indicate that the proposed architecture is effective for cervix classification and may become a useful tool in the correct diagnosis of cervical cancer.

After the competition ended, other frameworks and architectures have been proposed, using the same data. Zang and Zhao [17] proposed a Neural Network model based on CapsNet, which achieved a loss of 0.1593. Although this new model obtained better results than all previous works, it is important to note that they worked with images annotated by professionals in order to create the model that would extract the ROI.

Due to this previous identification of the ROI, an improvement on the classification results is expected. Also, the authors reported a problem with overfitting, which might explain the low loss obtained in their results. It would be interesting to combine their proposed model with the ROI extraction proposed by this work, which could help obtain better results in an automated way.

4 Conclusions

The proposed CXNN architecture provides a tool for classification of cervical images. The algorithm based on color models is a simple and effective means of finding the cervix in the images. This preprocessing stage decreased the noise and increased the accuracy of the classifier. The inclusion of this stage can be considered for other works where there is no ROI selection or where the selection is done manually.

The results also indicate better performance by a model that is designed to solve a specific problem, compared to one that is already trained for other types of problems.

Future work on this project will be to obtain images from digital colposcopy studies carried out in Mexico and to test the proposed solution, in order to improve the diagnosis and treatment of women in any area of the country, which could potentially save their lives.

Conflict of Interests. The authors of this work do not have any conflicts of interest to declare.

References

1. International Agency for Research on Cancer, Latest global cancer data: Cancer burden rises to 18.1 million new cases and 9.6 million cancer deaths in 2018. https://www.iarc.fr/wp-content/uploads/2018/09/pr263_E.pdf. Accessed 12 May 2019
2. Sellors, J.W., Sankaranarayanan, R.: Colposcopy and Treatment of Cervical Intraepithelial Neoplasia: A Begineer's Manual. International Agency for Research on Cancer, Lyon, France (2003)
3. Curiel-Valdés, J.J.: Vaginal cytology: the importance of the transformation zone and how to obtain an adequate sample. Gaceta Médica de México **138**(3), 259–265 (2002)
4. Jordan, J., Singer, A., Jones, H., Shafi, M.: The Cervix, 2nd edn. Wiley-Blackwell, London (2006). https://doi.org/10.1002/9781444312744
5. Kaggle, Intel & MobileODT Cervical Cancer Screening (2017). https://www.kaggle.com/c/intel-mobileodt-cervical-cancer-screening/. Accessed 12 May 2019
6. Spitzer, M.: The era of digital colposcopy will be here soon. J. Lower Genital Tract Dis. **19**(4), 273–274 (2015). https://doi.org/10.1097/LGT.0000000000000140
7. Lam, C.T., Krieger, M.S., Gallagher, J.E., Asma, B., Muasher, L.C., Scmitt, J.W., Ramanujan, N.: Design of a novel low cost point of care tampon (POCkeT) colposcope for use in resource limited settings. PLoS ONE **10**(9), e0135869 (2015). https://doi.org/10.1371/journal.pone.0135869
8. Fernandes, K., Cardoso, J.S., Fernandes, J.: Automated methods for the decision support of cervical cancer screening using digital colposcopies. IEEE Access **6**, 33910–33927 (2018). https://doi.org/10.1109/ACCESS.2018.2839338
9. Sato, M., Horie, K., Hara, A., Miyaoto, Y., Kurihara, K., Tomio, K., Yokota, H.: Application of deep learning to the classification of images from colposcopy. Oncol. Lett. **15**(3), 3518–3523 (2018). https://doi.org/10.3892/ol.2018.7762
10. Rani, R.A., Manie, R.K., Monisha, B., Ranichandra, V.: Convolution neural networks aiding colposcopy image classification. Int. J. Trend Res. Dev. **5**(2), 270–274 (2018)
11. Fernandes, K., Chicco, D., Cardoso, J.S., Fernandes, J.: Supervised deep learning embeddings for the prediction of cervical cancer diagnosis. Peer J. Comput. Sci. **4**, e154 (2018). https://doi.org/10.7717/peerj-cs.154
12. Payette, J., Rachleff, J., Van de Graaf, C: Intel and MobileODT Cervical Cancer Screening Kaggle Competition: cervix type classification using Deep Learning and image classification. Stanford University (2017)
13. Reinhard, E., Khan, E.A., Akyuz, A.O., Johnson, G.: Color imaging: fundamentals and applications. AK Peters/CRC Press, New York (2008). https://doi.org/10.1201/b10637
14. Simonyan, K., Zisserman, A.: Very Deep Convolutional Networks for large-scale image recognition. arXiv preprint 1409.1556 (2014). http://arxiv.org/abs/1409.1556. Accessed 12 May 2019
15. King, G., Zeng, L.: Logistic regression in rare events data. Polit. Anal. **9**(2), 137–163 (2001). https://doi.org/10.1093/oxfordjournals.pan.a004868
16. Yang, X., Zeng, Z., Teo, S.G., Wang, L., Chandrasekhar, V., Hoi, S.: Deep learning for practical image recognition: case study on kaggle competitions. In: Guo, Y., Farooq, F. (eds.) 24th ACM SIGKDD International Conference on Knowledge Discovery & Data Mining, pp. 923–931. ACM, London (2018). https://doi.org/10.1145/3219819.3219907
17. Zhang, X., Zhao, S.G.: Cervical image classification based on image segmentation preprocessing and a CapsNet network model. Int. J. Imaging Syst. Technol. **29**(1), 19–28 (2019). https://doi.org/10.1002/ima.22291

Comparative Analysis of Different Techniques to Determine Motility Parameters in Video Sequences of Ram and Buck Sperm

Francisco Javier Buchelly[1(✉)], Ramiro Fernando Isa Jara[1], Lucía Zalazar[2], Andreina Cesari[2], Juan I. Pastore[1], and Virginia L. Ballarin[1]

[1] Laboratorio de Procesamiento de Imágenes ICYTE CONICET-UNMdP, Mar del Plata, Argentina
fbuchelly@gmail.com, jpastore@fi.mdp.edu.ar
[2] Instituto de Investigaciones Biológicas IIB CONICET-UNMDP, Mar del Plata, Argentina

Abstract. In this paper we analyzed different techniques, included in the *Sperm Motility Tracker* (SMT) software, used to determine the standard motility parameters in video sequences of sperm. The commercial *Sperm Class Analyzer* (SCA) software was used as reference to evaluate the two proposed methods. Two tests were performed: first, samples of ram and buck sperm with a constant frame rate were analyzed and the linear correlation coefficient was found between the variables measured with each method and with the commercial SCA. In the second test, samples of ram sperm were acquired with three different frame rates and the parameters that depend on the smoothing procedure were compared. As a result of both tests, the measurements obtained with the SMT were very similar to the ones obtained with the SCA for the most of variables. As a particular case, one of the proposed methods showed a slightly better performance to measure the amplitude of lateral head oscillation (ALH), but the measures of the beat-cross frequency (BCF) present significant differences regarding the commercial SCA values.

Keywords: Spermatozoa trajectories · Measurement of motility parameters · Path smoothing

1 Introduction

Computer-Assisted Semen Analysis (CASA) systems have been used in several works with an increasing trend worldwide in the last 10 years, showing the importance of objective methodologies to evaluate semen quality and predict fertility [1, 2]. It is well-known that CASA systems are commonly used for determination of sperm quality from various species [3], cryopreservation effectiveness [4], toxicity bioassays, prediction of fertility potential or research related to sperm biology [5].

CASA systems provide sequential digital images of spermatozoa tracks allowing individual motion analysis, to obtain a rapid, precise and accurate assessment of several and meaningful kinetic measurements [2]. The most common motility parameters

© Springer Nature Switzerland AG 2020
C. A. González Díaz et al. (Eds.): CLAIB 2019, IFMBE Proceedings 75, pp. 385–392, 2020.
https://doi.org/10.1007/978-3-030-30648-9_50

based on the head displacement are: curvilinear velocity (VCL), average path velocity (VAP), straight-line velocity (VSL), linearity (LIN), straightness (STR), wobble (WOB), amplitude of the lateral head oscillation (ALH) and beat-cross frequency (BCF). Those motility parameters are considered as objective and reproducible, while using identical instrument settings. However, there are many factors affecting CASA performance [6], so the methodologies and system specifications (equipment, chamber, plate temperature and acquisitions details) have to be fully and clearly described. Moreover, the accuracy of CASA results is intrinsically dependent on the range of sperm concentrations analyzed [5].

Starting from a good detection and tracking scheme, several works show different methodologies for motility determination. The measurement of some parameters (VCL, VSL, LIN) do not depend on the trajectory smoothing and the methods are well defined [1] as they are described in the next sections. Currently, the methods to measure the other parameters are not standardized [1] and each approach adopts a different low-pass filtering technique, e.g. in [7], a moving average filter with a fixed size is used to determine the smoothed path; in [8], the original paths are downsampled and the smoothed path is found from the selected points by using the Bezier plane method; in [9], the smoothed path is found using a moving average filter but its size depends on the frame rate; and other systems like the commercial *Sperm Class Analyzer* (SCA) [10] let the user choose the desired settings for the path smoothing.

Some previous works of the authors determined the capabilities of the *Sperm Motility Tracker* (SMT) software. First, a suite of algorithms [11] was developed to detect and track ram sperm, showing a better performance compared with commercial SCA software. Then, some improvements in the algorithms and the development of a graphic interface [12] gave the users a friendly management to evaluate new ram and buck sperm samples, showing a good performance again. Finally, the SMT software was tested with fish sperm [4] to show the plasticity of the inner algorithms while being used with different species. Thus, the use of the software can be successfully extrapolated.

This paper describes the proposed calculation methods used in the SMT software to determine the common motility parameters. The methods were evaluated using the commercial SCA software as reference. The tests were performed with ram and buck sperm. Those samples are used as models, then the SMT software can be used in other species with similar sperm morphology such as bull, horse or even human, as shown in literature [13].

2 Materials and Methods

2.1 Sample Preparation and Video Acquisition

In this work, ram and buck semen samples were prepared as described in [12]. Chambers with a depth of 10 μm (Makler) or 20 μm (CellVu) were used. Videos were acquired with a phase contrast microscope. The acquired videos can be stored in AVI, MOV, MPG or MP4 formats to be loaded in the *Sperm Motility Tracker 2.0* software.

2.2 Software Settings

After loading a video, appropriate settings may be selected in the user interface to perform an adequate video processing: dark/bright contrast, detection parameters, time interval, region of interest, and length reference. Then, the video processing and motility analysis operations are performed when a button is pressed.

2.3 Video Processing

Image processing algorithms were developed in C++ using the OpenCV library [14] and the user interface was created using the Qt platform in the NetBeans IDE. The detection and tracking methods were described in a previous work [12]. The following operations are performed for each frame in the video: a top-hat transformation highlights the cells, a uniform threshold separates the cells from the background, and a morphological filter removes noise. Then, the cells centroids are determined to be tracked. In the tracking procedure, spermatozoa are modeled as points and a Kalman predictor is associated to each, in order to perform the temporal correspondence.

2.4 Motility Analysis

The eight standard motility parameters were determined automatically from the spermatozoa trajectories. Let $\overrightarrow{p_n} = (x_n, y_n)$ be the position of a head centroid at a discrete instant n, N the amount of points of the track, F the frame rate and L the length conversion factor from pixels to microns; then, the same methods shown in [8, 12, 15] are used to measure VCL, VSL and LIN as follows:

$$VCL = \frac{L \times F}{(N-1)} \sum_{n=1}^{N-1} \left\| \overrightarrow{p_n} - \overrightarrow{p_{n-1}} \right\| \tag{1}$$

$$VSL = \frac{L \times F}{(N-1)} \left\| \overrightarrow{p_{N-1}} - \overrightarrow{p_0} \right\| \tag{2}$$

$$LIN = \frac{VSL}{VCL} \tag{3}$$

The SMT software uses two methods to determine the remaining parameters: a fixed length filter to smooth the tracks with a spatial approach to analyze the oscillations, or a variable length filter with a frequential approach. The first method uses a moving average filter with a fixed length of five elements in order to obtain a new set of points, as shown in [7]:

$$\overrightarrow{s_n} = \frac{1}{5} \sum_{i=n-2}^{n+2} \overrightarrow{p_n}, n = 0, \ldots, N-1 \tag{4}$$

Then, the VAP, STR and WOB parameters are determined as follows:

$$VAP = \frac{L \times F}{(N-1)} \sum_{n=1}^{N-1} \left\| \overrightarrow{s_n} - \overrightarrow{s_{n-1}} \right\| \tag{5}$$

$$STR = \frac{VSL}{VAP} \tag{6}$$

$$WOB = \frac{VAP}{VCL} \tag{7}$$

According to the weak smoothing method mentioned in (4), the SMT software obtains the n_i curve portions between inflection (turning) points of each track in order to determine the ALH and BCF parameters. Thus, the ALH is approximated as the average of the oscillation amplitudes a_i between inflection points and the BCF is approximated as the mean turning frequency given by the amount of inflection points:

$$ALH = \frac{L}{n_i} \sum_{i=0}^{n_i - 1} a_i \tag{8}$$

$$BCF = \left(\frac{n_i - 1}{N-1} \right) F \tag{9}$$

On the other hand, the second method also uses a moving average filter for the smoothing procedure, but its size depends on the frame rate ($r = FPS/5$), similar to the one proposed in [9]:

$$\overrightarrow{s_n} = \frac{1}{2\mathrm{r}+1} \sum_{i=n-\mathrm{r}}^{n+\mathrm{r}} \overrightarrow{p_n}, n = 0, \ldots, N-1 \tag{10}$$

Then, the VAP, STR and WOB parameters are determined according to the Eqs. (5) to (7). However, the smoothing degree in (10) should not be ignored and different procedures are used to calculate AHL and BCF: the mean separation between the original and the smoothed path $d(n)$ is determined to find the AHL and a proximity function $g(\mathrm{n})$ is analyzed in the frequency domain to obtain the BCF:

$$d(\mathrm{n}) = \left\| \overrightarrow{p_n} - \overrightarrow{s_n} \right\| \cos \alpha_n \tag{11}$$

$$g(\mathrm{n}) = \max\left(\{d(n)\}_{0 \le n < N} \right) - d(n) \tag{12}$$

$$ALH = \frac{L}{N} \sum_{n=0}^{N-1} d(n) \tag{13}$$

$$BCF = \frac{F}{N} \underbrace{argmax}_{k} (|\mathcal{F}\{g(n)\}|) \tag{14}$$

In (11), α corresponds to the slope angle formed by the vector $(\overrightarrow{p_k} - \overrightarrow{s_k})$ and the unit vector perpendicular to the smoothed curve. In (14), $\mathcal{F}\{g(n)\}$ is the Fourier Transform of the proximity function, where k $(0 \leq k < N)$ is the frequency index [16].

3 Results and Discussion

In this work, two tests were done to evaluate the mentioned methods and the SCA software was used as reference, with similar settings than the ones used in [12].

In the first test, 10 samples of ram and buck sperm acquired at a constant frame rate of 25 FPS were analyzed with both, the SMT and the SCA. First, the motility parameters of each cell were determined with both methods; then the correspondence between tracks found with the SCA and the SMT were established; and finally, the linear correlation coefficient between the parameters obtained with each method and the SCA were determined. The means of the correlation coefficients of each variable are shown in Fig. 1. The motility parameters were labeled with numbers as follows: 1 for VCL, 2 for VSL, 3 for LIN, 4 for VAP, 5 for STR, 6 for WOB, 7 for ALH and 8 for BCF. The first 3 average correlation coefficients in Fig. 1 show a good correspondence

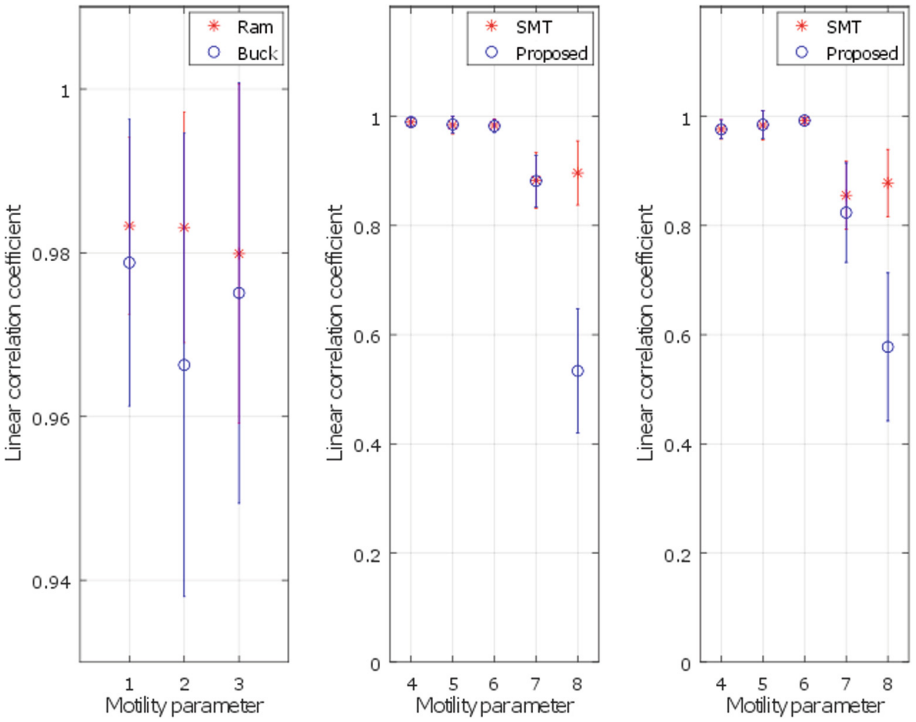

Fig. 1. Average correlation coefficients for the motility parameters determined between the described methods and the ones found with the SCA: parameters that do not depend on the smoothing procedure (left), parameters for ram samples (center) and parameters for buck samples (right). The errors shown in the plots correspond to the standard deviation of each variable.

of the variables measured with both software's. On the other hand, the other parameters do not show a significant difference between smoothing procedures, except for the BCF.

In the second test, 15 ram sperm samples were evaluated with the SMT, using both proposed methods, and the SCA. We analyzed some parameters with different frame rates, as shown in Fig. 2. In this test, only motile (non-static) spermatozoa were considered to evaluate the smoothing effect in the paths. For the VAP parameter, no significant variations were observed between the SMT and the SCA measures. For the ALH, the frequential approach shows closer results to the SCA mean values, and the results of the spatial approach are slightly lower. In the last case, the BCF values measured with the spatial approach and the SCA were similar, but the frequential approach shows lower average results, although their standard deviations are significantly lower. Also, the SCA approach for measuring VAP, ALH and BCF show a decreasing tendency with the frame rate, while the SMT approaches seem to present more stability.

The results obtained with both tests show that the measurement of the motility parameters of both methods used in the SMT software are reliable in general. For the BCF determination, the results obtained with the frequential method are different from the two others due to the Fourier approach. Equation (14) only determines the frequency where the spectrum of the oscillations has maximum intensity, but spermatozoa

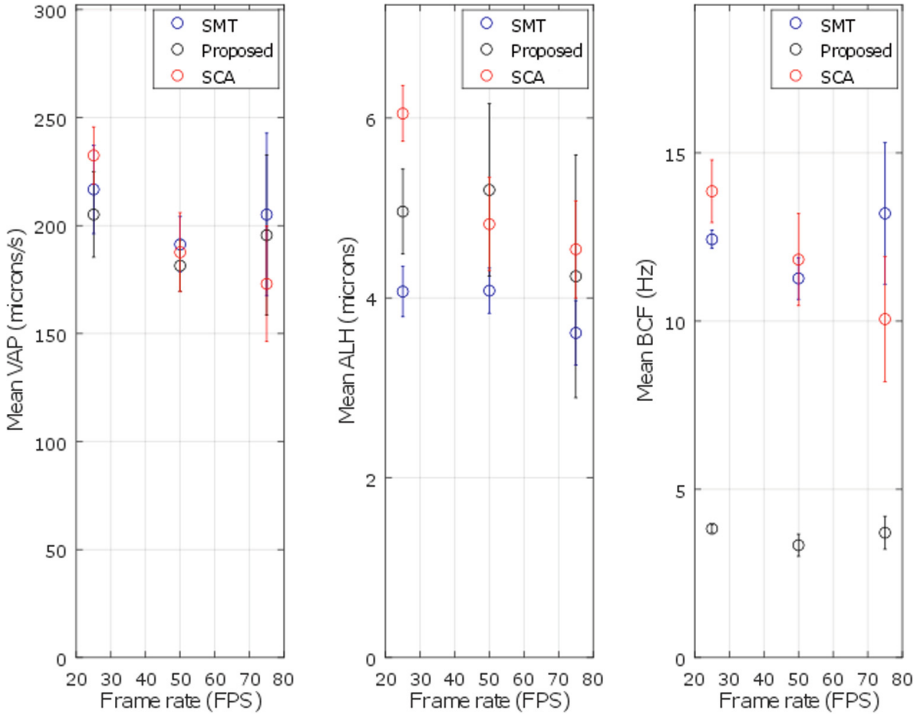

Fig. 2. Effect of the frame rate on the measurements that depend on the smoothing process. The three methods were tested with 5 videos of each frame rate (25, 50 and 75 FPS).

trajectories are usually complex and may contain several harmonics. On the other hand, the typical methods consider only a frequency that is closer to high values and it is susceptible to noise. In future works, the noise influence on the BCF parameter and the oscillatory harmonics of the spermatozoa tracks will be studied more deeply.

4 Conclusion

In this paper, two tests were performed in order to evaluate the two methods used for determining motility parameters in the Sperm Motility Tracker software with the commercial SCA software used as reference.

In the first test, high correlation coefficients were found for all measurements obtained with the spatial approach and the SCA at a constant frame rate. On the other hand, the frequential method also shows a good performance for most of the parameters, but the correlation coefficient has a lower value for the BCF calculation.

In the second test, some parameters that depend on the smoothing procedure were evaluated: the VAP measured with the three methods did not show significant variations according to changes in the frame rate; the ALH determined with the frequential approach presented slightly closer values to the SCA measures than the spatial approach; finally, the BCF measures are similar for the spatial approach and the SCA, but the obtained with the spatial method are significantly lower because of the nature of the proposed approach. However, this parameter could be analyzed with different samples to study its stability according to changes in the frame rate.

Future research work may analyze the meaning of the differences in the BCF values obtained with the frequential method and the harmonics found in the oscillatory spectrum of the spermatozoa tracks.

Conflict of Interests. The authors declare that they have no conflict of interests.

References

1. World-Health-Organization: WHO laboratory manual for the Examination and processing of human semen (2010)
2. Amann, R.P., Waberski, D.: Computer-assisted sperm analysis (CASA): capabilities and potential developments. Theriogenology **81**, 5–17.e3 (2014). https://doi.org/10.1016/j.theriogenology.2013.09.004
3. Giaretta, E., Munerato, M., Yeste, M., Galeati, G., Spinaci, M., Tamanini, C., Mari, G., Bucci, D.: Implementing an open-access CASA software for the assessment of stallion sperm motility: relationship with other sperm quality parameters. Anim. Reprod. Sci. **176**, 11–19 (2017). https://doi.org/10.1016/j.anireprosci.2016.11.003
4. Zalazar, L., Buchelly, F., Greco, M., López, A., Radonic, M., Pastore, J.I., Aristizabal, E., Cesari, A., Ballarin, V.: Preliminary semen sample management from Paralichthys Orbignyanus for sperm motility objective analysis by using a novel open-source suite of algorithms. In: Medicina Supplementary I (2017)

5. Muiño, R.: Evaluación de la Motilidad y Vialidad del Semen Bovino Mediante el Uso de Sistemas CASA y Citometría de Flujo: Identificación de Subpoblaciones Espermáticas (2008)
6. Broekhuijse, M.L.W.J., Šoštarić, E., Feitsma, H., Gadella, B.M.: Additional value of computer assisted semen analysis (CASA) compared to conventional motility assessments in pig artificial insemination. Theriogenology **76**, 1473–1486.e1 (2011). https://doi.org/10.1016/j.theriogenology.2011.05.040
7. Hidayatullah, P., Awaludin, I., Kusumo, R.D., Nuriyadi, M.: Automatic sperm motility measurement. In: 2015 International Conference on Information Technology Systems and Innovation (ICITSI), pp. 1–5. IEEE (2015). https://doi.org/10.1109/icitsi.2015.7437674
8. Rojas, H.A., Rojas, J.A., Zuleta, G.A., Madrigal, C.A.: Extraction of new features for classification of porcine sperm motility. In: STSIVA 2012 - 17th Symposium of Image, Signal Processing, and Artificial Vision, pp. 323–327 (2012). https://doi.org/10.1109/stsiva.2012.6340603
9. Wilson-Leedy, J.G., Ingermann, R.L.: Development of a novel CASA system based on open source software for characterization of zebrafish sperm motility parameters. Theriogenology **67**, 661–672 (2007). https://doi.org/10.1016/j.theriogenology.2006.10.003
10. MICROPTIC: SCA® Motility and concentration module. https://www.micropticsl.com/products/sperm-class-analyzer-casa-system/main-modules/sca-motility-concentration/
11. Buchelly, F., Zalazar, L., Pastore, J.I., Soler, A.J., Cesari, A., Ballarin, V.: Evaluation of motility quality in ram sperm by using a novel open - source suite of algorithms. In: Congreso Argentino de Bioingeniería - SABI 2017, Córdoba, Argentina (2017)
12. Buchelly Imbachí, F., Zalazar, L., Pastore, J.I., Greco, M.B., Iniesta-Cuerda, M., Garde, J.J., Soler, A.J., Ballarin, V., Cesari, A.: Objective evaluation of ram and buck sperm motility by using a novel sperm tracker software. Reproduction **156**, 11–21 (2018). https://doi.org/10.1530/REP-17-0755
13. Garner, D.L.: Flow cytometric sexing of mammalian sperm. Theriogenology **65**, 943–957 (2006). https://doi.org/10.1016/j.theriogenology.2005.09.009
14. OpenCV: OpenCV 3.0.0 Open Source Computer Vision. https://docs.opencv.org/3.0.0/
15. Gárate, D., Medina, R., Incahuanaco, F., Beltrán, C.: A heuristic model for determining the sperm motility grade by video. In: Proceedings - 2015 41st Latin American Computing Conference, CLEI 2015 (2015). https://doi.org/10.1109/clei.2015.7360039
16. Proakis, J.G., Manolakis, D.G.: Digital Signal Processing: Principles, Algorithms, and Applications. Prentice Hall, Englewood Cliffs (1996)

3D Kidney Reconstruction from 2D Ultrasound Images

Mariana Teresa Alvarez-Gutiérrez(✉), Aldo Rodrigo Mejía-Rodríguez, Ines Alejandro Cruz-Guerrero, and Edgar Román Arce-Santana

Faculty of Sciences, Universidad Autónoma de San Luis Potosí, 78295 San Luis Potosí, SLP, Mexico
marianaag22@hotmail.com

Abstract. The use and analysis of ultrasound images (US) is one of the safest and most accessible ways to monitor and diagnose illness; however, expert knowledge is required for the interpretation of these images. The aim of this project is to propose a practical and low cost alternative for the visualization of anatomical structures in 3D from 2D B mode US images acquired as a video. In particular, this project focused on the 3D reconstruction of the kidney, which is an organ of great importance in keeping the blood clean and maintaining the body's chemical balance. Our strategy consisted of acquiring the images with portable US equipment and applying digital image processing techniques such as filtering and segmentation in order, to then perform the 3D reconstruction of the anatomical structure of interest.

Keywords: Ultrasound images · 3D reconstruction · Kidney

1 Introduction

The kidney is an organ of great importance due to its principal function keeping the blood clean and chemically balanced. Normally, the two kidneys of the human body cyclically process around 190 L of blood to eliminate approximately 2 L of waste products and excess water through urination [1, 2]. Urine continuously goes down from the kidney through the ureters to the urinary bladder, where it is stored until it is expelled through the urethra [3]. Anatomically, each kidney is around 10 to 12 cm in height, 5 to 8 cm wide and 3 to 5 cm of thick, weighing approximately 170 g in a healthy adult. The external configuration of the kidney has the form of a bean seed whose hilum is medially oriented [4].

Kidney evaluations are usually carried out by means of medical imaging such as Radiography (Rx), Computed Tomography (CT), Magnetic Resonance Imaging (MRI) and Ultrasound (US) [5]. Particularly, US is the most simple, non-invasive and safe technique since it generates an image from the echoes produced by the different tissues when ultrasonic waves are applied; therefore, the use of US imaging is the first approach for the diagnosis and medical follow up of kidney diseases such as kidney cancer, kidney stones, and polycystic kidney diseases [2, 6].

© Springer Nature Switzerland AG 2020
C. A. González Díaz et al. (Eds.): CLAIB 2019, IFMBE Proceedings 75, pp. 393–400, 2020.
https://doi.org/10.1007/978-3-030-30648-9_51

US allows the visualization of the kidney's morphology and the evaluation of its health, possible the identification of solid masses such as tumors or cysts possible due to the differences in the composition of healthy and unhealthy tissues. However, US images analysis is usually carried out in 2D even though the anatomic structures of interest are three-dimensional, limiting the useful information that can be obtained by the specialist clinic [7]. This happens mainly because the edges of anatomic structures in US images are difficult to identify due to the presence of speckle noise in the image inherent to its acquisition.

For this reason, the aim of this work is to propose a semi-automatic methodology to generate a three-dimensional reconstruction of the kidney by applying digital image processing techniques (filtering, segmentation and 3D reconstruction) to a group of 2D images acquired with a portable US in B mode.

2 Materials and Methods

2.1 Experimental Protocol

Acquisitions of renal images of right and left kidneys from 10 volunteers (5 woman and 5 men) with an average age of 30.7 ± 14.9 years old were carried out. Before the acquisition, the protocol was explained to the volunteers and informed consent was obtained. All images were acquired using a portable US CHISON ECO 1 with a @ 3.5 MHz concave transduce.

During the acquisition of the images, volunteers had to lay down on a stretcher in prone decubitus position with their back uncovered. A mark was then placed at the height of the iliac fossa and between the 12th rib and the spine to be used as a reference for the location of the kidney [4]. The transducer was positioned above this mark in order to explore the surface of the kidney from a coronal perspective, where it is possible to observe different structures such as the renal cortex, which corresponds to the peripheral part of the kidney where the glomerular filtration is carried out, and the medulla located in the center where the pyramids and the renal columns are located (see Fig. 1a) [6].

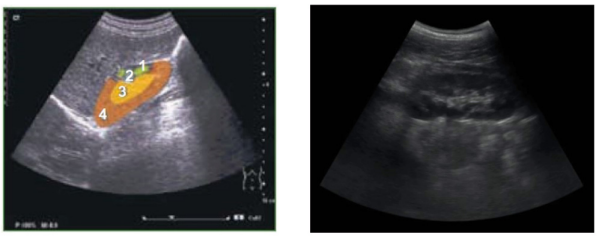

(a) **(b)**

Fig. 1. Anatomy of the kidney (a) 1. - Renal Pyramids 2. - Renal Column 3. - Medulla 4. - Renal Cortex [6]. (b) Longitudinal section of the kidney at the level of the iliac fossa.

Once the visualization of the structures previously mentioned was perceived, an angular scan was performed to locate the dimensions of the kidney and place the transducer on one of its edges. The volunteers were then asked to hold their breath in order to avoid the interference of breathing movements in the video acquired in one angular movement (scan). This procedure was performed for the both kidneys. The acquired videos were stored in .AVI format at 14 frames per second with a total duration of 10 s per video.

2.2 Generation of Volumetric US Images

For the generation of volumetric images, the acquired videos were transformed from .AVI format to .JPG images resulting in approximately 140 photograms per video for each kidney. Subsequently, the obtained photograms were compiled into a NifTI (Neuroimaging Informatics Technology Initiative .nii) file using the software MIPAV [8], which allowed us to generate a 3D US kidney image viewed from a coronal plane [9].

2.3 US Image Processing

For all 3D images a preprocessing stage was applied which consisted of the application of a non-local means filter (NLM) due to its efficiency in eliminating speckle noise, as well as calculating the weighted average of a similarity measure in the whole image [10, 11]. Due to the anatomic differences between the volunteers, the images presented inhomogeneities in terms of intensity and gray levels; therefore, the brightness and contrast parameters were adjusted manually by the MIPAV software in order to obtain a saturation of the image that allowed us to visualize the kidney structure of each volunteer. Once the .nii image had been modified, it was possible to identify the section of the 3D image with useful renal information, making it possible to reduce the total number of photograms per kidney to 50.

For the delimitation of the renal cortex, a modification of the semi-automatic algorithm based on the dynamic programing established in [12] was implemented, where it is necessary to determine manually the approximated contour of the organ of interest in the central frame of a 3D image, (represented by a binary image). This is carried out due to the fact that in the US image the contour of the renal cortex is not completely defined, and we need to help the algorithm with an initial delimitation. From this initial contour defined as μ, its respective center of mass was calculated in order to generate a new image y in polar coordinates with dimensions *[K, J]*. In this new image, the evolution of the contour depends in the minimization of the following operation:

$$F(\beta) = \sum_{j=1}^{J} f(\beta_j, j) + \lambda\left(\sum_{j=1}^{J-1} \beta_j - \beta_{j+1}\right)^2 + \sum_{j=1}^{J} G(\beta_j + p_j, j) \qquad (1)$$

where β is the set of selected boundaries (row) for all the columns of y, β_j are the rows where it is feasible to find the boundary for the *j-th* column, p_j is a vector with the position of the boundary μ in *j-th* column, and λ is a regularization constant. The first term in (1) makes a comparison of intensities between the initial contour and the US image to be analyzed, defined by

$$f(\beta_j, j) = \sum_{k=-r}^{r} \left(\mathrm{y}(k + \beta_j + p_j, \mathrm{j}) - \mu(k + p_j, j)\right)^2 \quad (2)$$

where r is a scalar that establishes a range $\{-r, \ldots, 0, \ldots, r\}$ where is feasible to find the contour. The second term in (1) corresponds to the comparison between the possible locations of β_j of the j-th column with respect to the next one. Finally, the third term represents a function that is inversely proportional to the gradient of the image, which is used as an attractor of the contour towards the regions with high gradient value. Once the initial contour is given, it evolves to localize the renal cortex at the actual frame, then it is propagated to the adjacent images as an initial contour and the segmentation process starts again, until the contours of the renal cortex in the whole volumetric US image are obtained.

Subsequently, the obtained contour of the renal cortex was used to trim the image and reduce the area where the segmentation of the medulla was made by means of the K-means approach [13]. In this case, the K-means algorithm works with 2 clusters (medulla and background) and the Euclidian distance was used as a similarity metric for the pixel clustering.

2.4 3D Reconstruction of the Anatomical Structures of Interest

The reconstruction of the 3D kidney model was carried out by defining an isosurface in MATLAB from a binary mask generated by the contour obtained by the segmentation. In this way, a representation of equidistant points is obtained in three-dimensional space; these points define the faces and vertexes of the isosurface connected by isovalues in order to create a graphic representation of the object of interest [14]. In this case, each renal structure was reconstructed individually; the renal cortex being the external structure of the kidney, it was visualized in transparent mode in order to be able to observe the internal structure of the kidney, which is the medulla.

3 Discussion and Results

Figure 2a shows a representation of the kidney as described in the literature [15], and Fig. 2b shows an example of the US image obtained, where it is possible to observe similarities in both kidneys structures, giving the idea that the proposed acquisition protocol is appropriate. In addition, Fig. 2c shows the result of the NLM filter where it

(a) (b) (c)

Fig. 2. (a) Kidney representation [15]. (b) Kidney ultrasound image. (c) Filtered image by means of NLM filter.

is possible to observe that the filter eliminates the speckle noise, facilitating the extraction of characteristics for the segmentation stage, highlighting the presence of the renal cortex and the medulla.

Figure 3 shows an example of the results of the segmentation of the renal cortex by the semi-automatic algorithm, based on dynamic programming, where it is possible to observe the manual delimitation of the renal cortex of a central frame for the initialization of the algorithm, the evolution, and the propagation of the contour in adjacent frames. Here we can observe that the proposed approach can properly delimit the border of the kidney in all the 2D images even if this border is not completely visible.

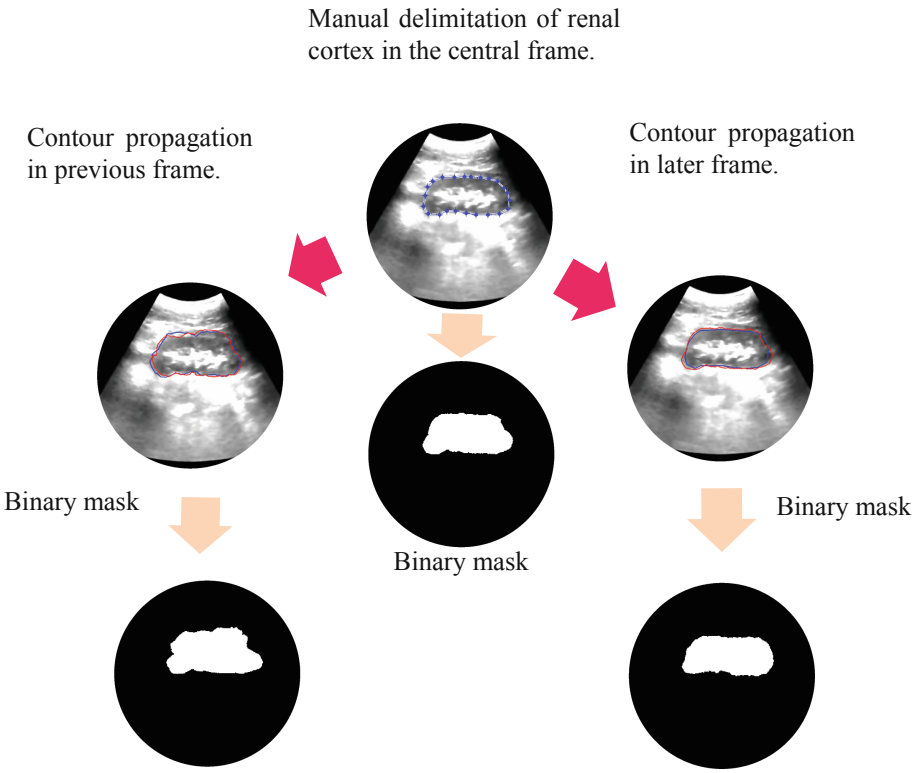

Fig. 3. Sequence to obtain the binary mask with the segmentation of the semiautomatic algorithm. Magenta arrows represent the propagation of the contour of a frame and pale pink arrows represent the binary mask of a frame.

Figure 4 shows an example of the 3D reconstruction of the kidney's renal cortex and medulla structures. In this case, a similarity can be observed between the morphology of the 3D reconstruction and the bean seed that it is commonly mentioned in the literature.

(a) (b)

Fig. 4. 3D reconstruction of a volunteer's kidneys. (a) Right kidney. (b) Left Kidney.

In order to validate the proposed strategy, a clinic expert performed a manual delimitation of the renal cortex in one of the volunteers' volumetric images, and a comparison between the obtained result and the manual segmentation was made by means of the estimation of similarity metrics such as the DICE similarity coefficient and the Average Symmetric Distance (ASD) [16]. For the DICE index a value of 0.90 was obtained in the right kidney and 0.86 for the left kidney, which indicates that the superposition between surfaces is a good match. For the case of the ASD, the index has values of 6.11 pixels in the right kidney and 8.50 in the left kidney; and if this value is transformed into centimeters, it gives us a result of 0.18 and 0.25 cm of mean error

Table 1. Perimeter, Area and Volume of the kidneys from the different volunteer's

Volunteers		Right Kidney		Perimeter	Area	Volume	Left Kidney		Perimeter	Area	Volume
		X (High)	Y (Width)	cm	cm^2	cm^3	X (High)	Y (Width)	cm	cm^2	cm^3
Volunteer 1	Pixels/Voxels	348	170			1789010	275	175			1934451
	Physical Dimensions	12.29	6.01	36.92	73.84	279	9.72	6.18	30.03	60.06	241
Volunteer 2	Pixels/Voxels	213	146			1089166	281	147			1506538
	Physical Dimensions	7.52	5.16	19.41	38.81	136	9.93	5.19	25.78	51.55	188
Volunteer 3	Pixels/Voxels	264	128			1601427	251	127			1413100
	Physical Dimensions	9.33	4.52	21.09	42.18	200	8.87	4.49	19.89	39.79	176
Volunteer 4	Pixels/Voxels	240	133			1449281	269	144			1573465
	Physical Dimensions	8.48	4.7	19.92	39.84	181	9.5	5.09	24.17	48.35	196
Volunteer 5	Pixels/Voxels	279	94			1074837	217	94			950163
	Physical Dimensions	9.86	3.32	16.37	32.73	134	7.67	3.32	12.73	25.46	119
Volunteer 6	Pixels/Voxels	250	124			1421323	264	122			1435068
	Physical Dimensions	8.83	4.38	19.35	38.69	177	9.33	4.31	20.1	40.2	179
Volunteer 7	Pixels/Voxels	250	161			1370417	283	156			1565738
	Physical Dimensions	8.83	5.69	25.12	50.24	214	10	5.51	27.55	55.1	244
Volunteer 8	Pixels/Voxels	280	132			1279805	286	115			1416890
	Physical Dimensions	9.89	4.66	23.06	46.13	200	10.1	4.06	20.52	41.05	177
Volunteer 9	Pixels/Voxels	256	120			1409404	264	105			1322205
	Physical Dimensions	9.04	4.24	19.17	38.34	176	9.33	3.71	17.3	34.6	165
Volunteer 10	Pixels/Voxels	253	104			1022020	240	105			1173915
	Physical Dimensions	8.94	3.67	16.42	32.84	128	8.48	3.71	15.73	31.45	147

respectively. It can be interpreted that a good correspondence between contours exists and that the proposed approach properly delimits the renal cortex from US images.

Finally, a relation between the obtained pixels along and across the kidney was made to obtain their respective physical dimension such as perimeter, area and volume in centimeters. The obtained values of each volunteer can be observed in Table 1. This information could be useful for a clinical expert in the diagnosis and monitoring of renal diseases.

4 Conclusion

In the present work an alternative for generating a three-dimensional reconstruction of the kidney using 2D ecographic images acquired with a portable US was implemented.

The results obtained suggest that the proposed acquisition protocol and the image processing strategy, a filtering process (NLM) followed by a segmentation approach (assisted dynamic programming and K-means) and a 3D reconstruction process, can be used to provide useful information in the diagnosis and medical monitoring of renal diseases, offering a morphological 3D visualization of the kidney, and the possibility to estimate the dimensions of the anatomical structure of interest.

As future work, we need to explore other image processing techniques in order to optimize the proposed methodology by studying other image filtering, segmentation and registration approaches that could allow us to have a better volumetric representation of the kidney. In addition, we need to extend our US images database and validate all of our results with the help of a clinical expert, analyze images from patients with specific renal diseases, and compare our results with state of the art algorithms.

Conflict of Interest. The authors declare not conflict of interest for the realization of this work.

References

1. Restrepo, C.A., et al.: Anatomy and renal physiology. Basic Nephrology, 2nd edn., vol. 2, Editorial La Patria S.A. Colombia (2012)
2. National Institute of Diabetes and Digestive and Kidney Diseases. https://www.niddk.nih.gov/health-information/informacion-de-la-salud/enfermedades-rinones/rinones-como-funcionan. Accessed 19 Apr 2019
3. KidsHealth. https://kidshealth.org/es/parents/kidneys-urinary-esp.html?view=ptr&WT.ac=p-ptr. Accessed 09 Jun 2019
4. Pró, E.A.: Clinical Anatomy. Editorial Panamericana, Buenos Aires (2014)
5. Merck, S.: Diagnostic procedures (MSD). Merck Sharp & Dohme de España, S.A. Madrid, España (2005)
6. Devesa, R.M., et al.: ABC of Abdominal Ultrasound Theory and practice, 2 edn., Editorial Medica Panamericana (2011)
7. Rivera Gorrin, M., Rodriguez-Navarro, Q.C.: The ultrasound performed by the nephrologist: our experience. Nephrology [Internet], vol. 2, no. 1 (2009)
8. MIPAV. https://mipav.cit.nih.gov/. Accessed 19 Apr 2019

9. NIFTI. https://nifti.nimh.nih.gov/. Accessed 19 Apr 2019
10. Liu, H., et al.: Denoising 3D MR images by the enhanced non-local means filter for Rician noise. Magn. Reson. Imaging **28**(10), 1485–1496 (2010). https://doi.org/10.1016/j.mri.2010.06.023
11. Sawatzky, A.: (Nonlocal) total variation in medical imaging (2011)
12. Xiberta, P., et al.: A semi-automatic and an automatic segmentation algorithm to remove the internal organs from live pig CT images. Comput. Electron. Agric. **140**, 290–302 (2017). https://doi.org/10.1016/j.compag.2017.06.003
13. Dhanachandra, N., Manglem, K., Chanu, Y.J.: Image segmentation using K-means clustering algorithm and subtractive clustering algorithm. Procedia Comput. Sci. **54**, 764–771 (2015). https://doi.org/10.1016/j.procs.2015.06.090
14. MathWorks. https://www.mathworks.com/help/matlab/ref/isosurface.html. Accessed 19 Apr 2019
15. American Cancer Society. https://www.cancer.org/es/cancer/cancer-de-rinon/acerca/que-es-el-cancer-de-rinon.html. Accessed 06 May 2019
16. Aldo, M.: Deformable image registration for radiotherapy monomodal applications. Dissertation, Italy (2013). http://hdl.handle.net/10589/82803

Mask R-CNN to Classify Chemical Compounds in Nanostructured Materials

Carlos Cabrera[1(✉)], David Cervantes[1], Franklin Muñoz[1], Gustavo Hirata[2], Patricia Juárez[3], and Dora-Luz Flores[1]

[1] Facultad de Ingeniería Arquitectura y Diseño, Universidad Autónoma de Baja California, 22860 Ensenada, Mexico
carlos.cabrera31@uabc.edu.mx
[2] Centro de Nanociencias y Nanotecnología, Universidad Nacional Autónoma de México, 22860 Ensenada, Mexico
[3] División de Biología Experimental y Aplicada, Centro de Investigación Científica y de Eduación Superior de Ensenada, 22860 Ensenada, Mexico

Abstract. Nowadays artificial intelligence has become the iron horse in high-performance computing, solving problems that were impossible 10 years ago. This work uses a deep learning technique named Mask Region-Convolutional Neural Network (Mask R-CNN) using images of nanostructured materials obtained from a transmission electron microscope (TEM) at a nanoscale spatial resolution. In those images, we observed different regions with specific structure correspond to yttrium silicate and silicon oxide materials system. The architecture Mask R-CNN was trained with TEM images, and performs the classification, location, and segmentation of chemical compounds with a data set of 26 images, reaching scores above 90% of accuracy.

Keywords: Deep learning · CNN · Mask R-CNN · Nanostructured material

1 Introduction

In the last two decades, humanity has witnessed a significant development in the areas of nanotechnology [1] and artificial intelligence [2], stimulated by scientific and technological advances in microscopy and high-performance computing, respectively.

In this work, artificial intelligence algorithms were developed to perform identification and classification of chemical compounds characterized in an image acquired with transmission electron microscopy of nanometric size material structure. Nanoscience and nanotechnology involve studying and working with matter on a nanometric scale (1×10^{-9} m) [1]. Nanoscience is the study and manipulation of matter at atomic and molecular scales, where the properties differ significantly from those at a macroscale. Nanotechnology is the design, synthesis, characterization, production, and application of structures, devices, and systems at the nanometric scale [3].

On the other hand, artificial intelligence (AI) was hard to define over the years. During the last 70 years, AI had significant changes and opportunities, but nowadays we understand the AI as the science that mimics the human brain using computers [4] with artificial neural networks. Convolutional neural networks (CNN) used in deep learning (DL) are a branch of AI [2].

© Springer Nature Switzerland AG 2020
C. A. González Díaz et al. (Eds.): CLAIB 2019, IFMBE Proceedings 75, pp. 401–411, 2020.
https://doi.org/10.1007/978-3-030-30648-9_52

2 Background

2.1 Deep Learning

Deep learning allows the algorithm to learn multiple levels of abstraction through multiple layers (see Fig. 1). These algorithms improved the state of the art in speech recognition, visual object recognition, medical imaging, object detection, and other applications like drug discovery and genomics [2].

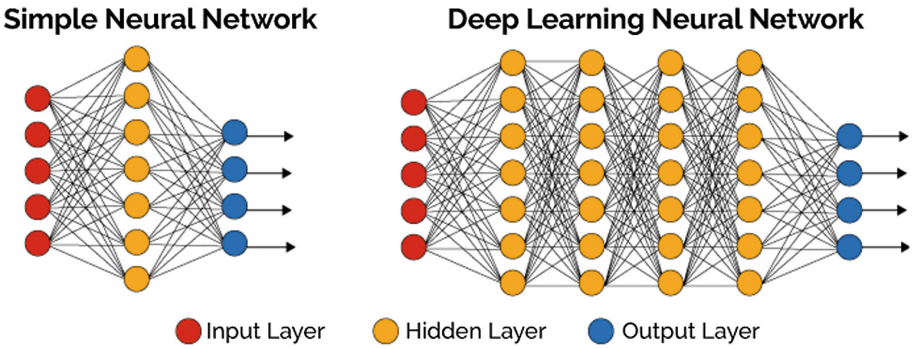

Fig. 1. Neural networks containing input, hidden and output layers, and nodes in each layer. With more nodes, the network becomes complex, and with more layers, the network becomes deep.

Deep learning is a subset of machine learning, and it has an outstanding performance in Artificial Intelligence, also is a supervised learning approach, in which the network architecture is trained using labeled data (Fig. 2a), meaning that the data is already tagged with the correct answer [2], to predict classes in data which labels do not exist [5]. Deep neural networks (DNN) started with object detection, searching for how to classify objects in an image [6]. Following the way of improving DNN, semantic segmentation appears as the new challenge associating each pixel of an image with a class label (car, truck, house, person, etc.). In the last couple of years, instance segmentation did the most complex job of classifying each object in a scene. This method requires the correct detection at a pixel level of each object in an image, combining elements of traditional computer vision as object detection and location inside a bounding box. Also, DNN uses semantic segmentation to classify each pixel into a set of categories. The goal of instance segmentation is to differentiate between similar objects [7].

Convolutional Neural Networks

This type of artificial neural network is widely used in image recognition. It's a powerful method in deep learning, with an outstanding performance. CNN's are neural networks that limit its neurons only to connect with a subset of the image at each layer, instead of using a fully connected layer.

All the neurons use the same weights and connect to a small square matrix of pixels according to the weights. These weights are convolved over the entire image on each layer and are updated every epoch working as a filter (learnable) over the image, generating the feature maps.

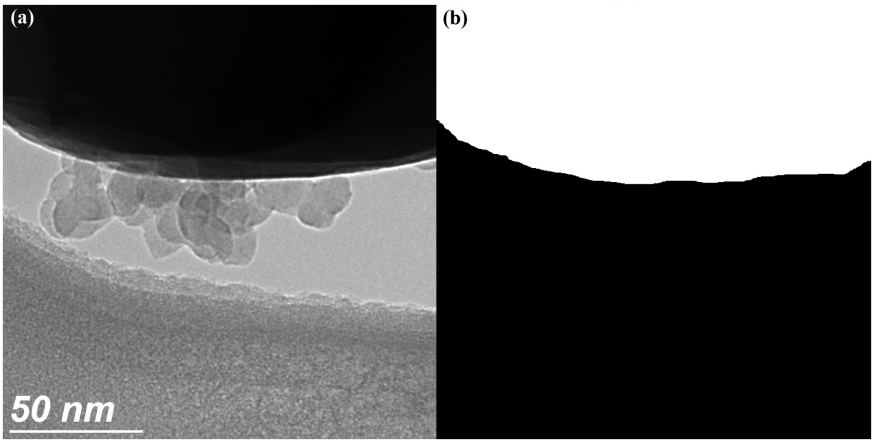

Fig. 2. Supervised learning trained the network with the original image (a) and data labeled and segmented with the name of the class that belongs to yttrium silicate, showing the ground truth (white region) in (b).

2.2 Mask R-CNN

CNN's were designed to process multi-dimensional arrays of data; images are ideal to be used in CNN's because an image is 2D data matrix and has three channels of color (R, G, B). In mathematics, the main entities of linear algebra are scalar, vector, matrix, and tensor. A scalar is just a number (real or integer), a vector is an array of scalars, a matrix is an array of vectors, and a tensor is an array of matrices. In that sense, a multidimensional array of data can be a large set of images, video streaming, or image sequences in time.

The AlexNet architecture was introduced to ImageNet Challenge, and won the challenge with a deep network of eight layers and is considered one of the most influential papers in computer vision [7]. This network was based on Yann LeCun model [8], which used the original CNN architecture of "neocognitron" [6]. Improved CNN's outperform humans.

The architecture R-CNN [9, 10] was introduced to perform object detection inspired by Hinton's research. R-CNN takes the image and finds the object locations, each within a bounding box. It uses the method of Selective Search over region proposals to find the bounding box. This architecture uses the region proposal and warps that region to a standard size and then pass to AlexNet. The last layer of R-CNN adds a Support Vector Machine that classifies the object. The last step applies a linear regression model over region proposals to generate tighter bounding boxes coordinates.

The architecture Fast R-CNN [10, 11] improved the speed up of R-CNN adding some modifications to that architecture, introducing the Region of Interest Pooling (RoIPool), which reduce the computation of network.

The new architecture Faster R-CNN [12] improved the region proposal speed up by changing the selective search method using the convolution layer in two ways, as the region proposal, and as a classifier. They found the bottleneck in Selective Search method overall process.

The architecture Mask R-CNN [7], was introduced to perform instance segmentation. This architecture is the last of the family of R-CNN and is an extension of Faster R-CNN (Fig. 3). Mask R-CNN add a branch to predict the mask of an object. That means, predict the location of exact pixels over each Region of Interest (RoI), with the bounding box, the mask using the ground truth to generate the image segmentation prediction.

Figure 3 shows the network architecture of Mask R-CNN with a fully connected network at the pixel level, for instance segmentation.

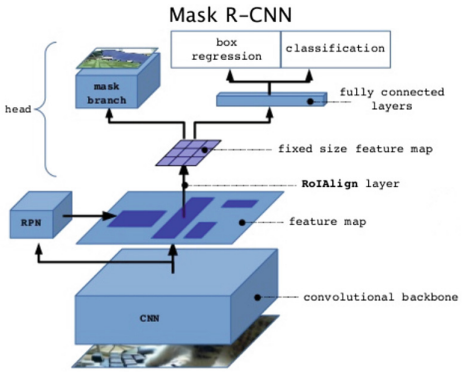

Fig. 3. Architecture of Mask R-CNN.

Instance Segmentation

We understand instance segmentation as the problem to solve more efficiently the object detection and the semantic segmentation at the same time. The goal is to locate a single object from a class (ground truth, see Fig. 2) or a set of classes and to infer the correct class. Furthermore, this method provides a mask prediction (see Fig. 5) giving the values that belong to the class and which not [13].

Mean Average Precision (MAP Metric)

The MAP is an extensive method used (by Mask RCNN) to measure the recall of object location and segmentation, computing the average precision value over the 0's and 1's on the image. The precision value tells us how accurate is the prediction; recall is the

metric of how good are all the true positives. The mathematical definition follows the next equations [13]:

$$Accuracy = \frac{\text{True Positive}}{\text{True Positive} + \text{False Negative}}$$

$$Precision = \frac{\text{True Positive}}{\text{True Positive} + \text{False Positive}}$$

$$Recall = \frac{\text{True Positive}}{\text{True Positive} + \text{False Negative}}$$

2.3 Process of Nanostructured-Imaging

Materials science is focused in to understand and apply properties of the matter. The scientists of the matter study the structure of materials, its properties, synthesis methods, characterization, and perform in applications in real life. Researching advances to creating artificial light are nowadays in progress. Solid-state-lighting offers safety and energy efficiency with light-emitting diodes, LEDs [14].

Applications in antireflective coatings use silica deposited as a thin layer. This kind of silica (SiO_2) coating is used to produce core/shell structures that improve the luminescent properties of phosphor material [15].

The images used are the results of material composed of Y_2SiO_5 (YSO) doped with Ce and Tb ions to produce two-color emission. These materials were synthesized by combustion and by sol-gel methods and coated with colloidal silica [15].

Synthesis by PACS (*Pressure-Assisted Combustion Synthesis*). This method performs a violent exothermic reaction according to stoichiometric amounts of reagents in a chemical equation. Precursors were mixed in 30 ml of distilled water and stirred for 20 min, and hydrazine was added inside a glove box pre-purged with N_2 to prevent the violent reaction. Then, the reagent mixture was introduced into a reactor heated to 403 K during 20 min to evaporate the water. The outlet valve was closed, and argon was introduced into the reactor to reach 3.44 MPa. Following the process, the reactor temperature was increased to 623 K, and then the heating was interrupted by a cooling system. The exit valve was opened to release the pressure. When the temperature downed to 333 K, the product was extracted as a foamy powder, which was annealed in the air in an alumina crucible in two samples one at 1373 K and other at 1623 K for 2 h obtaining the crystal phases X1-YSO and X2-YSO, respectively [5].

Synthesis by Sol-Gel. This method mixes the reagents with tartaric acid as a chelating agent, and the amounts of reagents are mixed in a nitric acid solution according to a stoichiometric reaction. The reagents were dissolved in 30 ml of the nitric acid solution, then mixed with the tartaric acid solution under stirring by 24 h at room temperature. Then, the mixture was heated to 353 K by 2 h and then increased to 393 K until the solvent was evaporated and the product was placed into an alumina crucible and annealed at 1373 and 1623 K separated in two samples by 2 h [15].

Colloidal Silica Coating. Powders of YSO:Ce, Tb are dispersed in water, and different concentrations of silica molar are incorporated into the dispersion. The solutions are stirred for 12 h to incorporate the silica nanoparticles over the YSO:Ce, Tb particles surface. The solution was centrifuged at 6000 rpm to recover the solid, which then was washed three times with ethanol, dried at 483 K, and then annealed at 1623 K for 6 h [15].

3 Methods

3.1 Transmission Electron Microscopy Imaging

The images acquired from TEM were visually checked and separated, then we have selected a dataset of 26 images for training and evaluation; and another dataset of 11 images for inference at the highest resolution of 1024 × 1024 pixels.

3.2 Ground Truth Imaging

The open software GIMP 2.10.8 (GNU Image Manipulation Program) was used to generate the ground truth (Fig. 2b) according to the number of images used for training and evaluation. This software is free and contains all the tools needed to easily manipulate images. All images were created, manipulated, and displayed as JPEG format.

Two classes were created with the ground truth (silica and yttrium silicate). The metadata files describe the class that belongs to each mask in JSON format.

Images processed during training were down-sampled to 512 × 512 pixels. At a low resolution, there is a difficulty in processing the interface limits between chemical compounds of yttrium silicate and silica. As a result, the optimal resolution found was at 512 × 512 pixels. At lower image resolutions, the architecture is confused with the interfaces between chemical compounds.

3.3 Software Programming Framework and GPU Computing

We used Mask R-CNN architecture implemented in Python. The Python version used was 3.6.5, with all the utilities from Anaconda® default installation and OpenCV to read and write images files.

The network was trained in a laptop ASUS ROG with Intel Core i7, 32 GB RAM, and NVIDIA GPU GTX 1080 8 Mb RAM, under Windows 10 operating system.

3.4 Training and Inference

The training was performed running 20, 50, and 100 epochs using Mask R-CNN architecture (see Fig. 3 and Table 1). The dataset consists of 26 images, as well, creating 26 ground truth images (Fig. 2b) to the classes of yttrium silicate and silicon oxide. Furthermore, were created 26 files with metadata annotations containing the corresponding class in JSON format. From those 26 images, 18 were used for training and 8 for evaluation. Another set of 11 images was used for inference.

4 Results

After training the supervised network, the resulting weights were used to run the inference network with a different set of images. Each epoch computes an average of 47 s.

Table 1. Showing errors of RPN and Mask R-CNN after 20, 50, and 100 epochs.

Training loss functions	20 epochs	50 epochs	100 epochs
rpn_class_loss	0.000336	0.000186	0.000142
rpn_bbox_loss	0.009100	0.000114	0.000034
mrcnn_class_loss	0.002700	0.008100	0.006200
mrcnn_bbox_loss	0.011400	0.000559	0.000056
mrcnn_mask_loss	0.037700	0.022500	0.019000
loss	0.061300	0.031500	0.025000

Table 1 shows the performance of the same architecture running at different epochs (20, 50, 100). The left column shows the legends for error calculated during the training, where:

rpn_class_loss: means how well the region proposal network (RPN) separates the background from objects.

rpn_bbox_loss: means how well the RPN localize objects.

mrcnn_class_loss: means how well the Mask R-CNN recognize each class of object.

mrcnn_bbox_loss: means how well the Mask R-CNN localize objects.

mrcnn_mask_loss: means how well the Mask R-CNN segment objects.

The Fig. 4 shows the total loss function and how the network converged to an optimal performance in the inference for bounding box, classification and segmentation. On the other hand, Fig. 5 depicts the distribution, showing how the error fluctuates around the zero value.

Results in Table 1 shows the error in "mrcnn_mask_loss" is decreasing as the number of epochs increase in the mask prediction. Figure 6 shows the prediction of two different classes: (a) silicon oxide with a probability of 99% of certainty and (b) yttrium silicate with a probability of 97% of certainty. Both masks are located with accuracy.

In general, the loss function is the sum of all error values, meaning that perform the computing of more epochs in our case, the error is decreasing.

On the other hand, we found that "mrcnn_class_loss" (see Table 1) its error is increasing in object classification as the epochs increase, this could be possible to the reduced dataset of images and classes we defined.

As future work, there is a need in increasing the size of the data bank of TEM images for training and extending the detection of classes over these nanostructured systems.

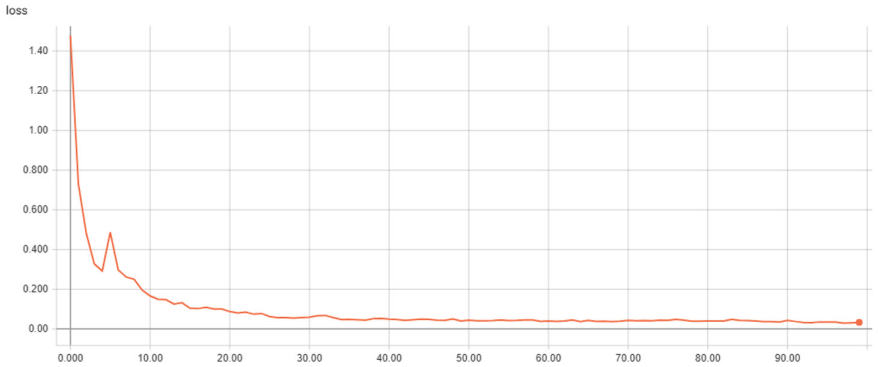

Fig. 4. Time series of the total error (loss function) approximated by the Mask R-CNN architecture. Loss function is the sum of the errors of class, bounding box and segmentation.

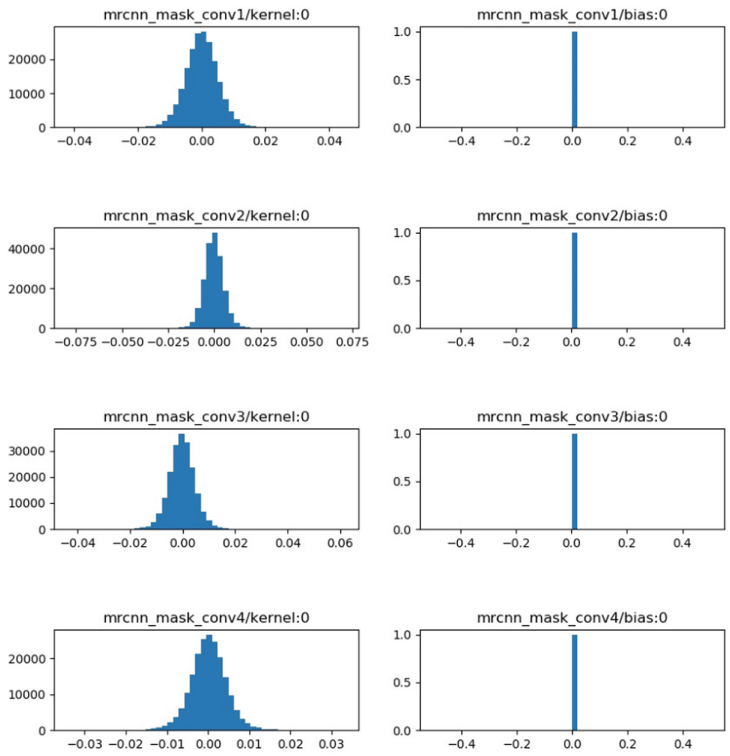

Fig. 5. Histograms show how the error values are performed close to zero, with a normal distribution, in four convolution layers in segmentation task. Right panels, show the error bias.

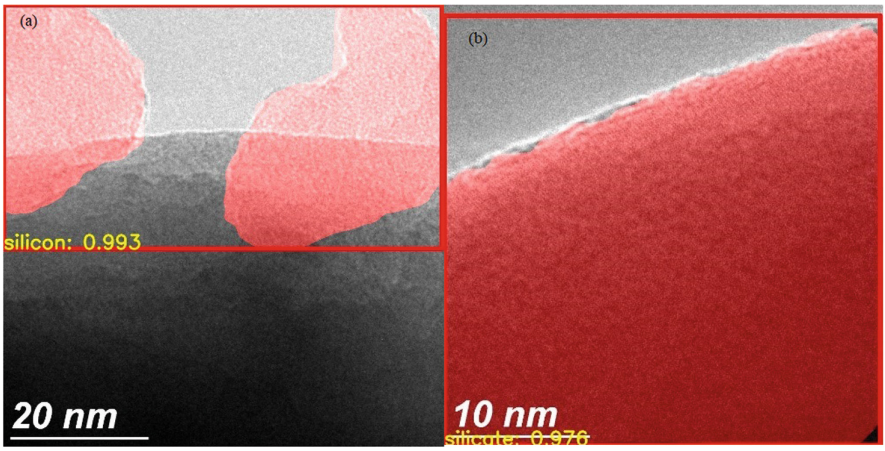

Fig. 6. Nanostructured systems classified and segmented. (a) Silicon oxide with 99% of accuracy, and (b) yttrium silicate with 97% of accuracy. These images were not used in training nor evaluation with Mask R-CNN architecture.

5 Discussion

Artificial intelligence has a big challenge to change and revolutionize the way we see the world and how the world works [5]. From multiple systems of data acquisition as sensors, cameras, microscopy, satellites, scanners, cars, cell phones, medical devices related to multiple systems of structured and unstructured data, data processing, data management, data curation, data labeling that feed hundreds of algorithms in supervised and unsupervised learning, transfer learning, reinforcement learning. All those new approaches to data analytics talk efficiently with the newest high-performance computing that brings the human being to a new level in their life.

In science, AI can play an important role in a wide variety of scientific areas. Nanotechnology use widely AI analyzing images from microscopies in several forms, since post-processing data imaging from TEM, SEM, AFM microscopy, to the analysis on data acquired on the fly with artificial intelligence methods [16] with the capability using adaptive methods to obtain pattern recognition and classification in materials without human hand and be able to analyze and locate different regions of a nanostructured system composed of different materials when the sample is been analized with the microscopy technique.

On the side of post-processing, this work follows the automatic classification and segmentation in the area of nanostructured materials. As well this type of microscopy imaging, finding new challenges, and new classes to predict. After the experiments, we found that it is necessary to improve some of the results, like to make some adjustments to the ground truth to improve the certainty during network training, evaluation, and inference. And, we need some data augmentation and work with new ground truth to improve the classification and mask prediction in the no labeled dataset for testing.

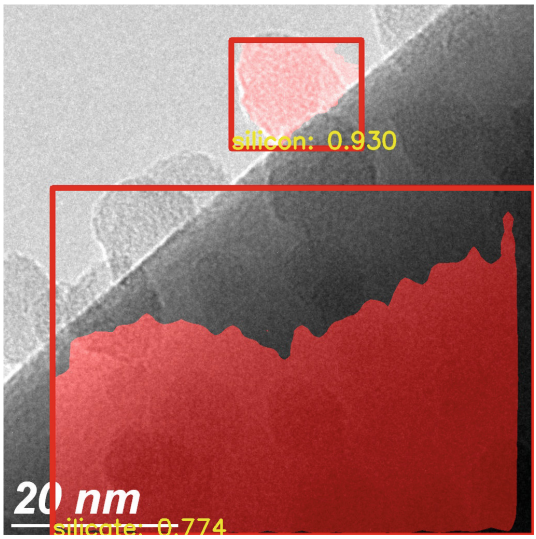

Fig. 7. Nanostructured systems classified and segmented, detecting two classes, two bounding boxes, and two segmentations. Small bounding box belongs to silica, and the big bounding box belongs to yttrium silicate. These images were not used in training nor evaluation with Mask R-CNN architecture

Figure 7 shows how the architecture trained infers two different classes. Silica was detected correctly, but silicate class has a low probability, as we mentioned before, our conclusion at this point is that we need to use more images and ground truth mask to augment the accuracy and recall between all classes and make new training.

This kind of nanostructured materials creates a thin film that must be classified. The coating shows how the silica nanoparticles were melted to the surface of the yttrium silicate. This method of artificial intelligence will help the scientist of materials to analyze the microscopy images in automatic form.

Acknowledgments. We thank Jose Hernan Sandoval Heredia for the exhaust work of creating the ground truth images.

Conflict of Interest. The authors declare that there are no conflicts of interest.

References

1. Nanoscience and nanotechnologies: opportunities and uncertainties. Roy. Soc. Roy. Acad. Eng. (2004). ISBN 0 85403 604 0
2. LeCun, Y., Bengio, Y., Hinton, G.: Deep learning. Nature **521**, 436–444 (2015)
3. Filipponi, L., Sutherland, D.: Interdisciplinary Nanoscience Center (iNANO). Aarhus University, Denmark (2010)
4. Hopgood, A.: Artificial intelligence: Hype or Reality? IEEE Computer Society (2003)

5. Gadepally, V., Goodwin, J., Kepner, J., Reuther, A., Reynolds, H., Samsi, S., Su, J., Martinez, D.: AI Enabling Technologies: A Survey. MIT, Boca Raton (2019)
6. Fukushima, K.: Neocognitron: a self-organizing neural network model for a mechanism of pattern recognition unaffected by shift in position. Biol. Cybern. **36**, 193–202 (1980)
7. He, K., Gkioxari, G., Dollar, P., Girshick, R.: Mask R-CNN, arXiv:1703.06870v3 (2018)
8. LeCun, Y., Boser, B., Denker, J.S., Henderson, D., Howard, R.E., Hubbard, W., Jackel, L. D.: Backpropagation applied to handwritten zip code recognition. Neural Comput. **1**, 541–551 (1989)
9. Girshick, R., Donahue, J., Darrel, T., Malik, J.: Rich feature hierarchies for accurate object detection and semantic segmentation, arXiv:1311.2524v5 (2014)
10. Parthasarathy, D.: A brief history of CNN's in image segmentation: From R-CNN to Mask R-CNN. https://blog.athelas.com/a-brief-history-of-cnns-in-image-segmentation-from-r-cnn-to-mask-r-cnn-34ea83205de4. Accessed 22 Apr 2017
11. Girshick, R.: Fast R-CNN, arXiv:1504.08083v2 (2015)
12. Ren, S., He, K., Girshick, R., Sun, J.: Faster R-CNN: Towards Real-Time object Detection with Region Proposal Networks, arXiv:1506.01497v3 (2016)
13. Pinto, J.: Masknet: An Instance Segmentation Algorithm, Dept of Signals and Systems, Chalmers University of Technology, Sweden (2017)
14. Flores, D.L., Gutierrez, E., Cervantes, D., Chacon, M., Hirata, G.: White-light emission from $Y_2SiO_5:Ce^{3+}$, Tb^{3+} and $Sr_2Si_5N_8:Eu^{2+}$ phosphor blends: a predictive model. Micro & Nano Lett. **12**(7), 500–504 (2017)
15. Cervantes-Vasquez, D., Contreras, O.E., Hirata, G.A.: Quantum efficiency of silica-coated rare earth doped yttrium silicate. J. Lumin. **143**, 226–232 (2013)
16. Huang, B., Li, Z., Li, J.: Artificial Intelligence Atomic Force Microscope Enabled by Machine Learning, arXiv:1807.09985 (2018)

Follow-up of Cutaneous Leishmaniasis by Three-Dimensional Reconstruction Based on Photogrammetry: Proof of Concept

Caren Garzón-Márquez[1], Manuela Gómez-Ramírez[1], Javier D. Murillo[2], Sara Robledo[2], A. Hernandez[1], Benjamín Castañeda[3], and Sandra Pérez-Buitrago[3](✉)

[1] Instituto Tecnológico Metropolitano, Medellín, Colombia
[2] Programa de Estudios y Control de Enfermedades Tropicales - PECET, Universidad de Antioquia, Medellín, Colombia
[3] Departamento de Ingeniería, Pontificia Universidad Católica del Perú, Lima, Peru
sm.perez@pucp.edu.pe

Abstract. Cutaneous leishmaniasis is a parasitic disease transmitted by a vector prevalent in tropical rural areas affecting people with low economic resources. Treatments for this disease have significant adverse effects and a different therapeutic response in patients; therefore, accurate follow-up is necessary. Although there has been an increased interest in generating other options for treatment efficiency, the follow-up does not have standardized quantitative methods that allow an accurate estimation of the area and volume of the ulcer in the different phases of the disease. In this work, the proof of concept of a methodology based on photogrammetry was carried out to perform the quantitative follow-up of the treatment of cutaneous leishmaniasis ulcers in hamsters. For this, several stages were implemented, from the acquisition of videos by an in-house artificial vision system, to the measurement of ulcers using a commercial image processing software.

Keywords: Cutaneous leishmaniasis · Ulcer · Three-dimensional reconstruction · Photogrammetry

1 Introduction

Cutaneous leishmaniasis (LC) is the most common form of leishmaniasis which produces skin lesions on exposed areas of the body, especially ulcers, which leave scars for life and are a cause of severe disability. Approximately 95% of cases of cutaneous leishmaniasis occur in the Americas, the Mediterranean basin, the Middle East and Central Asia. More than two-thirds of the new cases appear in six countries: Afghanistan, Algeria, Brazil, Colombia, the Islamic Republic of Iran and the Syrian Arab Republic. It is estimated that between 0.6 million and 1 million new cases occur in the world every year [1].

© Springer Nature Switzerland AG 2020
C. A. González Díaz et al. (Eds.): CLAIB 2019, IFMBE Proceedings 75, pp. 412–420, 2020.
https://doi.org/10.1007/978-3-030-30648-9_53

Currently, one of the first options for treatment of cutaneous leishmaniasis is the use of pentavalent antimonials, generally administered intramuscularly and intravenously. For these first-line drugs, a high frequency of adverse effects; such as, nephrotoxicity, hepatotoxicity, headache, lethargy, cardiotoxicity, among others, have been reported [2].

In the follow-up of the treatment, the behavior of metrics; such as, area, perimeter, depth and volume can indicate the evolution of the ulcers and the effectiveness of the treatment [1].

In the clinical practice, measurements of the ulcer size and the photographic record are made manually, which depend on the experience of the person performing them and the traceability of the data is not ensured. Therefore, proposing strategies is necessary for the quantitative control of the disease. The 3D information of wounds is useful to measure the volume of the ulcer cavity; this measurement is a significant criterion in the evaluation of the lesion since the reduction in volume is an indicator of healing [2, 3]. This technique could replace the conventional measurement method that is qualitative and subjective. The effectiveness of the treatment can be improved and the healing period can be shortened if changes in the parameters of the wound are observed with regularity and precision [4]. The characteristics of depth, shape, and color can be extracted from the three-dimensional model and the methods used are critical to achieve accurate results [5].

Therefore, in this work, the proof of concept of a methodology based on photogrammetry for 3D reconstruction of cutaneous ulcers in hamsters is proposed to perform quantitative monitoring of the treatment.

2 Methodology

2.1 Animal Model

Hamsters were bred and inoculated in the Tropical Disease Study and Control Program - PECET. The endorsement of the Ethics Committee for Experimentation with Animals of the University of Antioquia was obtained as stated in the record No. 110 of May 17, 2017.

Two groups of subjects infected with leishmaniasis were included in the project: Group 1, eighteen hamsters treated with the experimental drug. Group 2, twenty hamsters under Glucantime treatment. From these animals, four hamsters were chosen for the proof of concept; from Group 1 a hamster with experimental treatment and another one without treatment, from Group 2 a hamster infected with leishmaniasis Brazilienzis and another hamster infected with leishmaniasis Panamensis. To identify the hamsters, they were stained in an area of the skin with a swab soaked in picric acid with marks: Right Anterior Member (MAD), Left Anterior Member (MAI), Right Posterior Member (MPD) and Left Back Member (MPI) – all initials correspond to the names in Spanish. At the end of the experiment, the hamsters were sacrificed by inhalation of CO_2 under anesthesia.

2.2 Acquisition of Ulcer Videos Using a Rotating Platform

The video recorder used for hamsters was the SONY NEX-5T camera of 16 megapixels with a recording format compatible with JPEG HD.

A mobile rotating platform attached to a static surface was developed. There, the hamster was positioned by turning it manually 360° to obtain a record of the ulcer at a focal length of 50 mm. The camera was placed on a flat surface supported by a tripod, tilted at an angle of 80° in order to obtain a working distance projected towards the ulcer. Additionally, the camera's depth of field was determined, showing a window with appropriate focus points to visualize the area of interest with high resolution.

A 1 cm pattern was added to the field of view as a base scale to determine the size of the ulcer after the 3D-reconstruction.

2.3 Three-Dimensional Reconstruction of Ulcers

For the reconstruction and processing of the 3D volumes of ulcers, the commercial software Agisoft PhotoScan was used. This is an advanced image-based 3D modeling solution, designed to create quality 3D content from static images [6].

After the acquisition of the video, 50 frames were extracted for 3D reconstruction. This number was selected as a compromise between higher resolution and computation cost. The 50 frames were loaded in Agisoft PhotoScan and the three-dimensional reconstruction was carried out using the different work tools presented by the software: (1) camera calibration, (2) loading point cloud in high mode, (3) add reference markers, (4) optimizing the line of the camera alignment, (5) build dense cloud, (6) build mesh, (7) build texture, (8) build tile model, (9) 3D model save in an XYZ format, (10) build orthomosaic and, finally (10) build the Digital Elevation Model (DEM).

2.4 Measurements of Ulcers

The metrics were obtained from the 3D model using Agisoft PhothoScan. This software allowed to analyze the values of the area and the volume of a selected area with a polygon, as well as the measurement of the sizes of the ulcers by measuring distances in the model [4].

3 Results and Discussion

3.1 System for Acquisition of Videos of Ulcers

The platform allowed reducing the time for acquisition of videos for each hamster. They were positioned to obtain a stable display and accuracy in the camera without leaving any part of the hamster suspended while the manual rotation was performed, as shown in Fig. 1. In addition, the camera allowed a focus of the ulcer with a resolution of 16 megapixels thus allowing a better reconstruction.

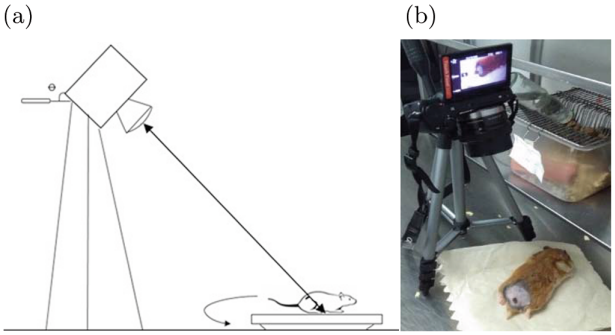

Fig. 1. Acquisition system (a) Scheme, (b) Picture.

3.2 Three-Dimensional Reconstruction of Ulcers

The 50 frames provided an appropriate quality in the 3D reconstructions with Agisoft PhotoScan, which allowed obtaining three-dimensional reconstructions with low noise and similar to 2D images, as shown in Fig. 2.

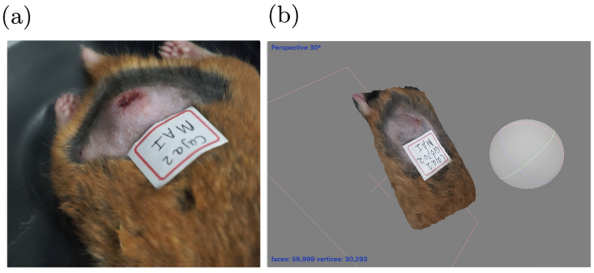

Fig. 2. (a) Photo of the hamster ulcer of box 762, left anterior limb (MAI). (b) 3D reconstruction using Agisoft commercial software from the same hamster.

3.3 Measurement of Area and Volume

Hamsters 756 MAD with experimental treatment and 757 MAD without treatment correspond to group 1 (strain L. Braziliensis). Hamster 762 MAI (strain L. Braziliensis) and hamster 766 MAD (strain L. Panamensis) treated with commercial treatment (Glucantime) belong to group 2. They began treatment in week 3 after inoculation and ended on week 7.

The most common method to measure the surface of wounds is to make an approximation using a ruler to measure centimeters in order to measure length and width calculating then its approximate surface. Although it is one of the most used methods, and even recommended due to its simplicity and clinical effectiveness, it has limitations. For example, it does not take into account the variation of the behavior of the surface since this measurement can vary if the surface is irregular. Thus, when using this rule, measurement conditions cannot be standardized for all wounds due to the variety of their characteristics [4].

Therefore, it is significant to use a method that accurately quantifies the measurements obtained from the ulcer. For this purpose, in this study the area and total volume metrics were made during the treatment follow-up in 15 weeks for the four selected hamsters (see Figs. 3 and 4).

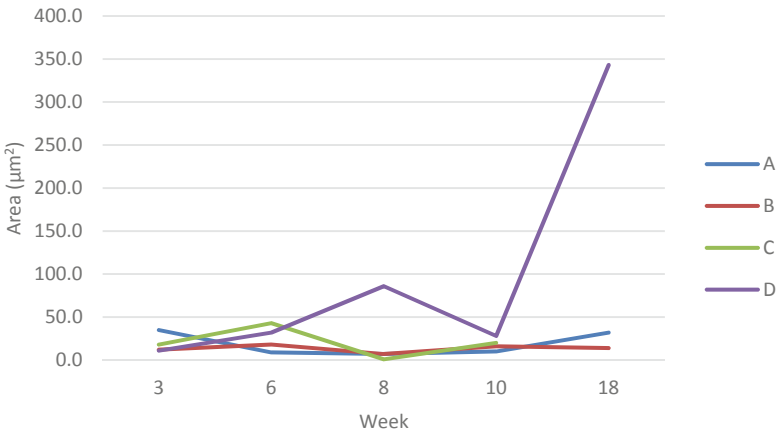

Fig. 3. Evolution of the area in the four hamsters during 15 weeks. (A) 756 MAD, (B) 757 MAD, (C) 762 MAI, (D) 766 MAD.

Figure 4 shows that once the two treatments fulfill their therapeutic action the volume decreases due to the granulation process of the ulcers since this is a mechanism that depends on hemostasis and an initial inflammatory state, caused by the injury [5, 6]. This stage is known as the acute phase [7]. Subsequently, it enters a proliferative phase of epidermal, endothelial and fibroblast cells, generating an initial granulation tissue [7, 8]. Then a late inflammatory phase appears, characterized by neovascularization and dependent on regulatory factors. Finally, a scar is formed where granulation tissue remodeling occurs with the generation of new collagen fibers and the differentiation of fibroblasts in myofibroblasts that increases the tensile strength and allows the approximation of the edges of the lesion [8–10]. An important structural element of the extracellular matrix are the proteoglycans (PGs) which, in addition to fulfilling a structural function by absorbing water and filling the spaces between collagen and elastin fibers, have regulatory functions by influencing proliferation, migration and cell adhesion [11].

When filling the spaces between collagen and elastin fibers, the volume (understood as the depth of the ulcer) decreases over time, and the area (understood as the surface of the skin) increases in the healing process [12]. In this sense, the volume could be an indicator of clinical utility for physicians and for the development of new treatments for leishmanisis. Figure 3 shows that ulcers caused by the two strains of leishmaniasis have different behaviors in terms of area; identifying that the wound of the strain L. Braziliensis has a smaller area than the L. Panamensis strain. For this reason, it is

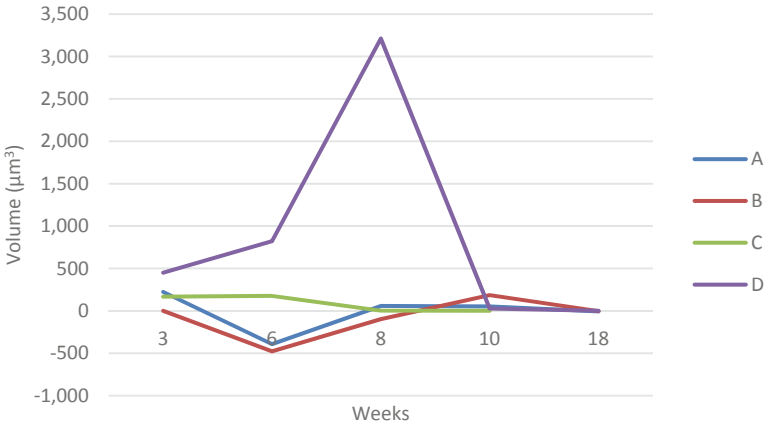

Fig. 4. Evolution of the volume for the ulcers of the four hamsters during 15 weeks. (A) 756 MAD, (B) 757 MAD, (C) MAI, (D) 766 MAD.

observed that hamster 757 MAD and 762 MAI, whose lesions healed, have an area that decreased in comparison with hamster 756 MAD that did not heal and its area is greater than them having Fig. 5 as reference that allows to have a detailed visual analysis of the evolution of the lesion.

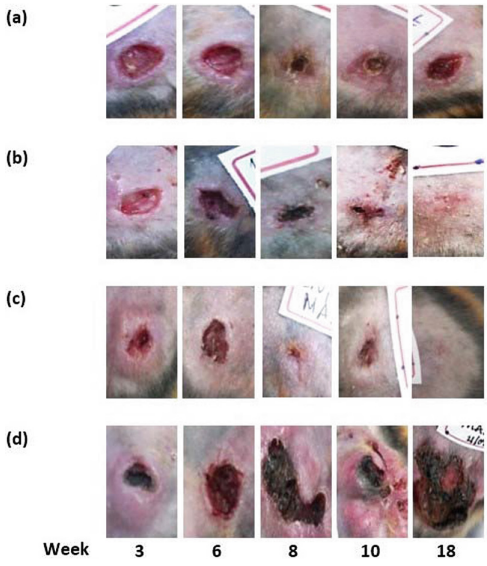

Fig. 5. Evolution of the lesion in each hamster (a) 756 MAD with experimental treatment, (b) 757 MAD without treatment, (c) 762 MAI with commercial treatment (Glucantime), (d) 766 MAD with commercial treatment (Glucantime).

3.4 Evolution of Lesions Size

In Fig. 6 the size results for the four ulcers are observed using the manual method with calipers and the measurement system based on the three-dimensional reconstruction by photogrammetry.

Up to know, the measurements taken manually have been obtained by direct vision, for which there is no standardized method and it is susceptible to include subjectivity and errors that depend on the criteria and experience of each physician [1]. For this reason, this proof of concept allowed us to evaluate the ulcers follow-up in a quantitative and precise way, without need of using complex instrumentation, minimizing subjectivities and having the evidence of the three-dimensional models as support, achieving results that can be useful in the assessment, treatment follow-up and cost-effectiveness [4].

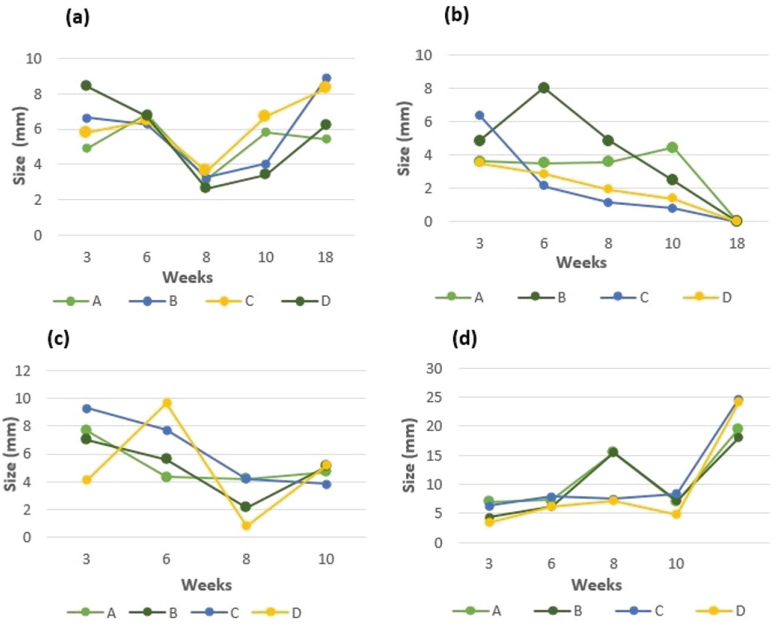

Fig. 6. Comparison between the sizes: A, C measured manually with vernier calipers and B, C calculated from the three-dimensional reconstruction. For hamsters (a) 756 MAD, (b) 757 MAD, (c) 762 MAI, (d) 766 MAD.

4 Conclusions

The purpose of this work was to perform a proof of concept of the treatment follow-up of cutaneous leishmaniasis by means of a quantitative tool. Two groups of hamsters were studied, inoculated with L. Braziliensis and L. Panamensis. It was identified that for each of the strains, the reaction to the treatment is different as well as the evolution of the injury in the course of time.

A rotating platform was developed to have a work area where the ulcer can be observed in different rotation angles, without blurring the image and studying the lesion superficially.

With the implementation of the 3D reconstruction methodology by photogrammetry, the ulcer could be analyzed superficially, the cloud of points could be exported and the lesion evaluated with greater specificity analyzing their metrics (volume, depth, area and perimeter). Finally, the evolution of the lesion was quantified over time.

All the development carried out in this work can be replicated for the follow-up of ulcers in other hamsters with cutaneous leismaniasis.

In the future, the results should be analyzed with a wider population to confirm the results obtained.

Acknowledgments. The authors are grateful for the support provided by Dr. Jorge Arévalo from the Universidad Peruana Cayetano Heredia, the English edition to Ada Tresierra García from Pontificia Universidad Católica del Perú and the financial support provided by the Administrative Department of Science and Technology of Colombia - COLCIENCIAS, Metropolitan Technological Institute, University of Antioquia, Universidad Pontificia Bolivariana and Kinetics Systems SAS (Medellín-Colombia), under project number 57186.

References

1. Zvietcovich Zegarra, J.F.: Estimación de volumen de lesiones producidas por leishmaniasis cutánea utilizando un escáner láser de triangulación 3D. Pontificia Universidad Católica Del Perú (2011)
2. Zvietcovich, F., Castaneda, B., Valencia, B., Llanos-Cuentas, A.: A 3D assessment tool for accurate volume measurement for monitoring the evolution of cutaneous leishmaniasis wounds. In: Proceedings of Annual International Conference on IEEE Engineering Medicine Biology Society, pp. 2025–2028 (2012). https://doi.org/10.1109/EMBC.2012.6346355
3. Casas, L., Castaneda, B., Treuillet, S.: Imaging technologies applied to chronic wounds: a survey. In: Proceedings of the 4th International Symposium on Applied Sciences in Biomedical and Communication Technologies, pp. 167:1–167:5. ACM, New York (2011)
4. Restrepo-Medrano, J.C., Verd, J.: Medida de la cicatrización en úlceras por presión, Con qué contamos. Gerokomos **22**, 35–42 (2011). https://doi.org/10.4321/S1134-928X2011000100006
5. Conway, K.P., Price, P., Harding, K.G., Jiang, W.G.: The role of vascular endothelial growth inhibitor in wound healing. Int. Wound J **4** (2007). https://doi.org/10.1111/j.1742-481X.2006.00295.x
6. Reinke, J.M., Sorg, H.: Wound repair and regeneration. Eur. Surg. Res. **49**, 35–43 (2012). https://doi.org/10.1159/000339613
7. Wilgus, T.A.: Immune cells in the healing skin wound: influential players at each stage of repair. Pharmacol. Res. **58**, 112–116 (2008). https://doi.org/10.1016/j.phrs.2008.07.009
8. Diegelmann, R.F., Evans, M.C.: Wound healing: an overview of acute, fibrotic and delayed healing. Front. Biosci. **9**, 283–289 (2004)
9. Singer, A.J., Clark, R.A.F.: Epstein1999_Woundhealing. N Engl. J. Med. **341**, 738–746 (1999)

10. Kumar, S., Wong, P.F., Leaper, D.J.: What is new in wound healing? Turkish J. Med. Sci. **34**, 147–160 (2004)
11. Prathiba, V., Gupta, P.D.: Cutaneous wound healing: significance of proteoglycans in scar formation. Curr. Sci. **78**, 697–701 (2000). https://doi.org/10.1111/j.1752-1688.2001.tb03624.x
12. Fundación Universitaria del Área Andina CV (2015) Cicatrización: Proceso de reparación tisular. Aproximaciones terapéuticas. Rev. Investig. Andin. **12**, 85–98

Image-Based Analysis of Human Tissue Regeneration During Therapy Based on Photobiostimulation and Natural Latex Biomembranes

Mayla dos Santos Silva(✉), Lorena de Sousa Moreira, Franciéle de Matos da Silva, Wellington Rodrigues, Breno Amadeus Sales Marinho de Sousa, Luiz José Lucas Barbosa, Cristiano Jacques Miosso, and Suélia de Siqueira Rodrigues Fleury Rosa

University of Brasilia, UnB-Gama Campus, Brasilia, DF 72444-240, Brazil
mayla.s@hotmail.com

Abstract. Diabetes often results in severe ulceration of lower limbs' tissues, a condition described as *diabetic foot*. Recent research has shown that therapy combining photobiostimulation and the use of natural latex biomembranes can significantly improve tissue regeneration and promote healing in otherwise difficult to treat diabetic foot wounds. We propose a method using image processing techniques to supervise wound healing during therapy using photobiostimulation and latex biomembranes. The proposed method analyzes visual aspects related to ulcer's inflammation and tissues regeneration. The algorithms, implemented in Python, are based on digital filters and post-processing techniques that extract the regions of interest (ROIs) and estimate the total ulcer area and tissues characteristics over the treatment sessions. The experimental results suggest that the method can be used to automatically monitor tissue regeneration during the treatment, which can in the future assist the treatment by providing automatic feedback.

Keywords: Wound healing · Diabetic foot · Image processing · Photobiostimulation · Latex membranes

1 Introduction

Severe ulcerations, most commonly affecting the lower limbs, often result from Diabetes Mellitus (DM) and constitute one of the serious chronic conditions that impact DM patients' quality of life. These ulcerations characterize the so-called *diabetic foot* and have great socioeconomic impacts [1,2]. On the individual level, it is responsible for several complications, including limitations in moving and performing work, and amputations.

Recent research has shown that, by combining photobiostimulation with the use of membranes made of natural latex, it is possible to significantly increase

© Springer Nature Switzerland AG 2020
C. A. González Díaz et al. (Eds.): CLAIB 2019, IFMBE Proceedings 75, pp. 421–425, 2020.
https://doi.org/10.1007/978-3-030-30648-9_54

the rate of success in healing the wounds associated to the diabetic foot [5,6]. A project developed at the University of Brasília, called RAPHA®, explores these methods and resulted in a novel piece of equipment that has been investigated for the treatment of wounds, with impacting results [4–6]. The project compares several photobiostimulation protocols and details the procedures for producing and using the latex membranes.

The RAPHA® uses a light emitting diode (LED) and latex biomembranes in specific protocols, combining two techniques that had previously been used in isolation, with validated tissue regeneration and neoformation properties [3–7].

However, the performance evaluation of photobiostimulation and of the use of latex membranes, as a means to enhance diabetic foot wounds' treatment, is usually based on the clinical observation by trained health professionals. An automatic method for evaluating this performance could benefit both the patient, who would receive feedback on his condition and the research on the area, as it could provide objective metrics when comparing different protocols. We propose using digital images taken from diabetic foot, at different treatment stages, in order to evaluate the progress provided by photobiostimulation and the latex membranes. With the impact of digital image processing on science, researchers have sought methods to process and analyze biomedical images [8], both for treatment planning and evaluation. In particular, wound image processing seeks to assist health professionals with appropriate diagnoses and treatments, highlighting the importance of sound and well-established assessments [9].

In this context, we evaluate the use of images taken from the diabetic foot wounds in order to determine the possible correlation between extracted image characteristics and the current treatment stage. The idea is that, since the wound area changes as the treatment advances, our method can allow for the health professional to promote a more acute intervention, if needed, or to change the used protocols, depending on the parameters we extract from the images.

Therefore, our method focuses on estimating the reduction of wound size according to the applied protocol, the improvement rate, the skin appearance, and other aspects, which we supervise using ImageJ®, with scripts in Python.

2 Methods

The study is based on a double-blind randomized controlled trial approved by the local Ethics Committee (protocol 052/2012-2016 – CEP/SES/DF). The intervention uses latex biomembranes and red LED light ($\lambda = 636 \pm 20$ nm) applied over diabetic foot ulcers. We performed the clinical research at the Regional Hospital of Ceilândia (HRC-DF) clinic, in Brasília, Brazil.

For evaluating the DM wounds, the research team registered the treatment using digital images taken on a weekly basis, using a Sony DSCH70 digital camera with a resolution of 16.1 megapixels.

The participant selected for the image analysis belongs to the experimental group and was treated on a daily basis using RAPHA® equipment.

We used ImageJ® version 1.51r, from the National Institute of Health, Bethesda, MD, USA, in order to process and analyze several morphological parameters in the sequence of images obtained from the participant.

In the first processing stage, we performed image filtering under Python 3.6, in order to emphasize and then automatically extract the wound's edges. The filters were based on color differentiation, by computing the Hue-Saturation-Luminance (HSL) representation of each image. We then applied a thresholding over the hue values, in order to separate the regions corresponding to inflamed areas; the threshold was empirically set beforehand, by varying the values from the minimum to the maximum hue, and registering the resulting images. Next, we used the ImageJ analyze/measure command, in order to estimate the perimeter of each wound. The entire areas surrounding the lesions were excluded.

3 Results

During the clinical trial, all participants experienced the plastic with the RAPHA® protocol. The patient selected for the study was No. 12, who obtained accelerated and effective healing when compared to patients submitted to other conventional methods of treatment.

Figure 1 shows the images we obtained by applying the filters described in Sect. 2 to the pictures taken from patient 12 at the beginning of the treatment, after 21 days, and at the end of the treatment. Note that the wound area is emphasized with respect to the surrounding tissue, in the patient's lower limb. In the filtered images, tones of red were proposed to represent different levels of wound inflammation. We can clearly observe a decrease of points with higher levels of inflammation, 21 days after the beginning the proposed protocol.

Figure 2 shows the original pictures taken from the patient. By comparing Figs. 1 and 2, we observe that the proposed filters corrected highlighted the wound areas, and allowed us to differentiate the existing levels of inflammation.

Based on the extracted surfaces shown in Fig. 1, the analyze/measure command in ImageJ allowed us to compute the corresponding wound areas, as shown in Table 1. Note the wound area reduction during the applied treatment.

Table 1. Measured lower limb wound areas for patient 12, during the phototherapy protocol associated with latex biomembranes. The areas were estimated using ImageJ® applied to the wound areas extracted by our proposed method.

Treatment day	Area (cm^2)
01	19.0
21	16.6
46	11.6

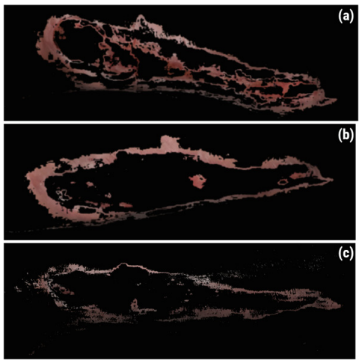

Fig. 1. Wound edges from the participant's lower limb, as extracted using the proposed image filters and using different tones of red to represent different levels of inflammation: (a) result when applying the filters to the image obtained in the first contact with the patient, as he started the phototherapy treatment associated with latex membrane; (b) result after 21 days, with a clear reduction of the affected area and a decrease in the total area with high level of inflammation; (c) the final result, with controlled inflammation and important healing effect.

Fig. 2. The original images taken from patient 12, at (a) the beginning of the treatment, (b) after 21 days, and (c) at the end of the treatment.

4 Conclusion

The healing of diabetic foot ulcers is the subject of great research aiming at efficient cure methods and good quality of the resulting tissue. In this context, the use of image processing techniques may provide objective metrics to evaluate the healing process and compare the efficiency of different treatment protocols.

In order to improve and guarantee the quality of image processing, simple and easy-to-apply methods are recommended so that healthcare professionals can perform them without requiring much time and effort. Patients may also directly benefit from automatic feedback regarding the ulcer evolution.

The developed and evaluated process facilitates the identification of the ulcer, showing the evolution of wound healing using the Rapha® protocol.

Conflict of Interest. The authors declare that they have no conflict of interest.

References

1. Narres, M., Kvitkina, T., Claessen, H., Droste, S., Schuster, B., Morbach, S., Rümenapf, G., Van Acker, K., Icks, A.: Incidence of lower extremity amputations in the diabetic compared with the non-diabetic population: a systematic review. PLoS ONE **12**(8), e0182081 (2017). https://doi.org/10.1371/journal.pone.0182081
2. Santos, K.P.B., Luz, S.C.T., Mochizuki, L., d'Orsi, E.: Burden of disease from lower limb amputations attributable to diabetes mellitus in Santa Catarina State, Brazil, 2008–2013. Cad. Saúde Pública **34**(1), e00013116 (2018). https://doi.org/10.1590/0102-311x00013116
3. Parker, C.N., Van Netten, J.J., Parker, T.J., Jia, L., Corcoran, H., Garrett, M., Kwok, C.F., Nather, A., Que, M.T., Srisawasdi, G., Wraight, P., Lazzarini, P.A.: Differences between national and international guidelines for the management of diabetic foot disease. Diabetes Metab Res Rev. **35**(2), e3101 (2019). https://doi.org/10.1002/dmrr.3101
4. Nunes, G.A.M.A., Reis, M.C., Rosa, M.F.F., Peixoto, L.R.T., Rocha, A.F., Rosa, S.S.R.F.: A system for treatment of diabetic foot ulcers using led irradiation and natural latex. Res. Biomed. Eng. **32**(1), 3–13 (2016). https://doi.org/10.1590/2446-4740.0744
5. Rosa, S.S.R.F., Rosa, M.F.F., Fonseca, M.A.M., Luz, G.V.S., Avila, C.F.D., Domínguez, A.G.D., Dantas, A.G.D., Richter, V.B.: Evidence in practice of tissue healing with latex Biomembrane: integrative review. J. Diabetes Res. **1–17** (2019). https://doi.org/10.1155/2019/7457295
6. Rosa, S.S.R.F., Rosa, M.F.F., Marques, M.P., Guimarães, G.A., Motta, B.C., Macedo, Y.C.L., Inazawa, P., Dominguez, A., Macedo, F.S., Lopes, C.A.P., da Rocha, A.F.: Regeneration of diabetic foot ulcers based on therapy with red LED light and a natural latex biomembrane. Ann. Biomed. Eng. **47**(4), 1153–1164 (2019). https://doi.org/10.1007/s10439-019-02220-5
7. Silva, F.M., Moreira, L.S., Silva, M.S., Rodrigues, W., Rosa, S.S.R.F.: Uso de Fototerapia para cicatrização de feridas de pés diabéticos. Hegemonia-Revista Eletrônica do Programa de Mestrado em Direitos Humanos, Cidadania e Violência/Ciência Política do Centro Universitário Unieuro Especial (27), 7–27 (2019)
8. Schindelin, J., Ruedene, C.T., Hiner, M.C., Eliceiri, K.W.: The ImageJ ecosystem: an open platform for biomedical image analysis. Mol. Reprod. Dev. **82**, 518–529 (2015). https://doi.org/10.1002/mrd.22489
9. Kumar, K.S., Reddy, B.E.: Wound image analysis classifier for efficient tracking of wound healing status. Signal Image Process. Int. J. **5**(2), 15–27 (2014)

Semantic Segmentation of Lung Tissues in HRCT Images by Means of a U-Net Convolutional Network

Sarahí Hernández-Juárez[1(✉)], Aldo R. Mejía-Rodríguez[1], Edgar R. Arce-Santana[1], S. Charleston-Villalobos[2], A. T. Aljama-Corrales[2], R. González-Camarena[3], and M. Mejía-Ávila[4]

[1] Faculty of Sciences, Autonomous University of San Luis Potosi, San Luis Potosí, S. L. P., Mexico
sarahihj@hotmail.com
[2] Electrical Engineering Department, Metropolitan Autonomous University, Iztapalapa, Mexico City, Mexico
[3] Health Sciences Department, Metropolitan Autonomous University, Iztapalapa, Mexico City, Mexico
[4] National Institute of Respiratory Diseases, Mexico City, Mexico

Abstract. In this work, a strategy for the segmentation of Interstitial Lung Diseases (ILD) from a High-Resolution Computed Tomography (HRCT) volumetric image by means of a U-Net convolutional network is presented. In particular, the delimitation of Idiopathic Pulmonary Fibrosis (IPF), Pulmonary Emphysema (PE) and Healthy Lung Tissue (HLT) were carried out. The key idea of the proposed strategy is that the U-Net training was performed using three slices from the HRCT. The results of the segmentation of all tissues at once in the whole volumetric image were: 93.6% of accuracy; 80% for the intersection over union (IoU) metric; and above 0.9 for HLT, around 0.8 for IPF and PE in terms of the DICE similarity coefficient. These results suggest that the proposed approach could be used to properly segment different lung tissues at the same time, using only partial data from the HRCT image instead of a large dataset for the training of the U-Net.

Keywords: Convolutional network · Interstitial lung diseases · Semantic segmentation · U-Net

1 Introduction

Semantic segmentation is a deep learning algorithm that associates a label or category to each pixel in an image. The segmentation task is different from classification because it requires predicting a class for each pixel, instead of only one class for the whole image [1]. In other words, the classification must consider what is in the input (context). However, semantic segmentation needs to recover not only what is in the input, but also its spatial location, which means a

© Springer Nature Switzerland AG 2020
C. A. González Díaz et al. (Eds.): CLAIB 2019, IFMBE Proceedings 75, pp. 426–434, 2020.
https://doi.org/10.1007/978-3-030-30648-9_55

classification at pixel level. Semantic segmentation is used in many applications, especially in medical image processing where it is very useful to combine location and context information to recognize the pixels that make up different regions.

Recently, a new architecture based on a modified Full Convolutional Network (FCN), known as U-Net, has been designed to classify and segment images with precision using a reduced dataset for the training of the network. U-Net has a large number of function channels which allow the propagation of context information to higher resolution layers, making it particularly suitable for different segmentation problems. To our knowledge, the U-Net architecture has only been used with microscopy images for biomedical applications [2].

From a clinical point of view, the characterization of different tissues (healthy or pathological) present in medical imaging is desirable for a better understanding of a disease. In particular, the understanding of Interstitial Lung Diseases (ILD) is still an open problem due to the difficulty to properly differentiate tissues from different ILD, considering that their information in terms of intensity and texture have similarities [3].

Previous works have shown that the use of an automatic classification approach might facilitate the differentiation of ILD, considering that the clinical expert may not perceive a disease at an early stage using only medical imaging information [4]. However, despite the automatic classification, a segmentation approach is still needed for the characterization of images. In addition, it is known that in these types of techniques, it is necessary to have an extensive amount of data for training; in real clinical scenarios having a reliable large database to train a classification algorithm might be complicated.

Therefore, in this work we present a strategy for the segmentation of Healthy Lung Tissue (HLT) and two ILDs at the same time on a High-Resolution Computed Tomography (HRCT) image using a U-Net architecture, which might represent a useful tool to provide visual and accurate information for the follow up of ILD. In particular, we focus on obtaining good results using a few slices of HRCT to train the U-Net, which can be useful in cases with limited information.

2 Methods

2.1 Dataset

To perform the segmentation of ILD through the use of a U-Net network, a set of HRCT 2D thorax images belonging to a patient diagnosed with idiopathic pulmonary fibrosis (IPF) and pulmonary emphysema (PE) was used. This data set was provided by the head of the interstitial diseases ward of the National Institute of Respiratory Diseases (INER, for its acronym in Spanish) in Mexico City. In each image, the structures of the lungs is observed with the characteristics of healthy tissue (also considering the bronchial branches) and the tissue from both diseases. The data volume consists of an HRCT scan with a size of $512 \times 512 \times 55$ voxels, and a voxel size of $0.6328 \times 0.6328 \times 9.00$ per slice.

To characterize the tissues of IPF and PE, a sub-volume of 11 central slices of the data set were selected, since these slices had important characteristic tissues

of both ILDs; few of them were used to train the network. The images of the sub-volume were pre-processed before being used in the network. The pre-processing consisted of the manual delimitation of the pulmonary region in order to only use the information of the pulmonary tissues during the training.

2.2 Network Architecture

The architecture of the U-Net comes from the FCN and is modified in such a way that it produces a better segmentation of medical images [2]. Compared to the FCNs, the U-Net is symmetric and in the connections between the sub-sampling path and the sampling one, it applies a concatenation operator. These connections have the function of providing local information to the global information while the sampling is being carried out.

The architecture of the network consists of three parts: a contraction path (sub-sampling), a bottleneck, and an expansion path (up-sampling). The contraction path consists of 4 blocks, where each block is formed by the repeated application of two 3×3 convolutions filters, followed by a rectified linear unit (ReLU), and finally, a 2×2 size pooling layer.

During each step along the contraction path, the map of characteristics (channels) is duplicated in each group. At the beginning of the first block, there are 64 characteristic, 128 in the second, and so on. The purpose of this path is to capture the context of the input image in order to perform the segmentation of regions of interest.

The bottleneck is between the contraction and expansion paths. This part is constructed by two convolutional layers, each with its respective ReLU, and by a neuron deactivation stage in a random way (Dropout) in order to avoid overfitting in the training process.

On the other hand, the expansion path (also composed of 4 blocks) consists of up-sampling the map of features obtained along the previous layers; furthermore, it allows a precise location when it is combined with the information from the contraction path. This path consists of a convolutional transposed layer (up convolution) with a 2×2 kernel, which reduces the number of feature channels by half; a concatenation with the map of characteristics corresponding to the contraction path, and two convolutional 3×3 size layers followed by a ReLU.

Finally, a 1×1 convolutional layer is used in order to assign each characteristic channel to the desired number of classes, and the softmax activation function to normalize the output of the layer to sum one. Segmentation is carried out in a pixel classification layer, which provides a categorical label for each pixel on the image. Considering the above, the U-Net is made up of a total of 58 layers.

2.3 Training

In 1986, the introduction of the back-propagation algorithm finally solved the training problem of the multilayer neural network. This algorithm provided a systematic method to determine the error of the hidden nodes since it propagates the output error backward from the output layer [5].

For this, forward propagation must be performed where the weighted sum S is calculated in each of the j-th intermediate neurons. The weighted sum S passes to the non-linear activating element, which applies a sigmoid function $f(S)$. This output becomes the input for each i-th neuron of the output layer, which in turn calculates a weighted sum of its inputs.

The next step is to calculate the error of the output layer δ_j (backward propagation), which is computed as:

$$\delta_j = (t_j - y_j)\, f'(S_j), \tag{1}$$

where t_j is the desired output and y_j the actual output of the j-th neuron, $f'(S_j)$ is the derivative of the sigmoidal function at point S_j; this is the weighted sum of the inputs to the j-th neuron.

Then, the error value δ_j is computed for each intermediate neuron. For this, the weighted sum of the output errors is calculated using the interconnection weights (w) between the intermediate j-th neuron and each k-th output one

$$\delta_j = \left(\sum_k \delta_k w_{kj} \right) f'(S_j). \tag{2}$$

Next, the increase in the weights w_{ji} is computed as follows

$$\Delta w_{ji} = \delta_j a_i \eta, \tag{3}$$

where δ_j is the error value of the subsequent neuron, a_i the actual output value of the previous neuron, and η the learning rate, which determines how much the weights change over time.

Sometimes, the convergence of the network is accelerated by introducing the term momentum (α) in the adjustment equations. This term is a kind of memory that allows weight changes to be smooth because they include information about the previous process. Therefore, learning stability improves resulting in an increase in the learning rate. Considering the above, Eq. (3) can be expressed as

$$\Delta w_{ji}(n) = \delta_j a_i \eta + \alpha \Delta w_{ji}(n-1). \tag{4}$$

The α-value varies in the interval $[0, 1]$; in this work to train the network a value of 0.9 was chosen, while the initial learning rate was set at 0.05.

There are different schemes to improve the learning of the network [6]. One of them is the stochastic gradient descent (SGD), which computes the error for each available data in the training and adjusts the weights.

Another scheme is the batch method, where a single average error is calculated for the training data, and it is used to adjust the weights. This method uses all the training data and is updated only once.

The last scheme is a mixture between the previous ones and is called the 'mini-batch method'. This method selects a part of the training data set and uses it to train in batch mode, that is, it calculates the weight updates of the selected data and trains the network with the average of the updates.

In this work, the mini-batch method was used in the training of the network, where the number of training processes (or iterations) for each epoch varies depending on the number of points given in each batch. One epoch is the number of training cycles completed for all training data.

Deep networks, with many convolutional layers and different routes through the network, need a good initialization of the weights. Otherwise, some parts of the network may give excessive activation, while other parts may never contribute [2].

2.4 Experiment

The input images and their corresponding labels are needed to carry out the training of the network. Considering that the patient had two interstitial diseases, four classes were then defined: background, IPF, PE, and HLT.

Experiments were performed using 10%, 20% and 30% (1, 2 and 3 slices respectively) of the sub-volume selected as training data to the network, where manual segmentations were available, previously reviewed and validated by a clinical expert (MD head of the interstitial diseases ward of the INER). The experiment with 30% showed the most favorable results qualitatively; hence, we decided to use this proportion of slices to carry out the quantitative analysis of the segmentation. The training data correspond to top, middle and bottom slices of the HRCT sub-volume in order to have representative information from different heights of the lung.

To generate the mini-batches for the network training, a data store was created with the input slices and their labels. This is because during training pairs of patches are extracted from the training images and labels. In each iteration, for each training image, a set of 50 batches were generated, which correspond to different regions. For each one of them, 5 random transformations: rotation, scaling and reflection, were also generated (mini-batches). This gives a total of 750 patches used for training from the 3 slices of HRCT data. The number of epochs was set to 10, so the network was trained with 1500 iterations.

Once the network was trained, the slices of the sub-volume were segmented which, as already mentioned, include the HLT, IPF and PE tissue patterns (test data).

In addition, to validate the performance of the U-Net, metrics used for the evaluation of semantic segmentations were calculated between the obtained segmentations and their respective manual labels. The metrics were: accuracy, intersection over union (IoU), also known as the Jaccard similarity coefficient, and the DICE similarity coefficient [7,8].

It is important to mention that the training of the network and the segmentation of the chosen slices was carried out in the MATLAB® software.

3 Results/Discussion

Figure 1 shows the architecture of the U-Net network, the contraction path (green blocks), the bottleneck (yellow blocks) and the expansion path (blue blocks).

In addition, it is possible to observe the slices of the HRCT volume used as input images with their respective manual labels, as well as the results of the segmentations obtained from some slices of the sub-volume through the network compared to the original images.

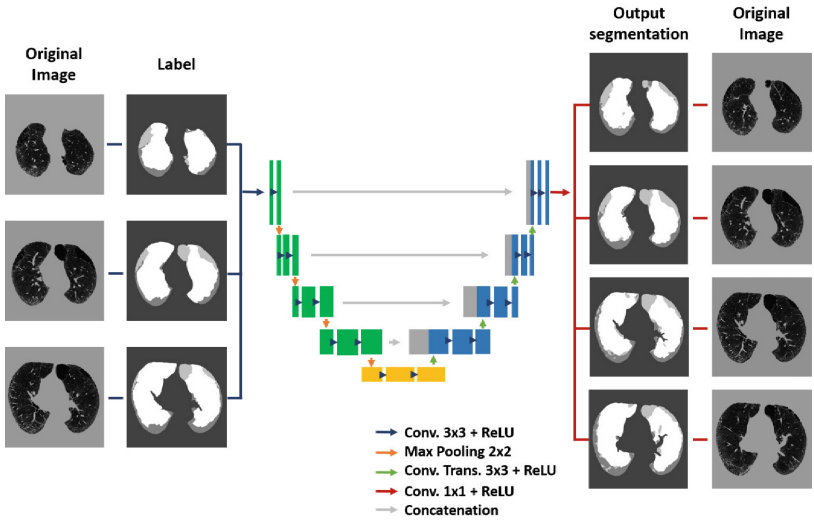

Fig. 1. Outline of the U-Net architecture where the input images to the network are shown in conjunction with the labels, as well as output segmentations compared to the original image slices.

Table 1 contains the results of the calculated accuracy metric for all images and classes. Accuracy is the percentage of correctly identified pixels in the image. As can be seen, all classes obtained an accuracy above 88%, which means a good classification of the pixels corresponding to each class. It could be said that in general the network has an average performance of 93.6% classification of true pixels.

Table 2 shows the results of the IoU metric. IoU is a class evaluation that estimates the proportion of pixels correctly classified according to the total number of real pixels and the predicted pixels of the image. The IPF and PE classes showed values below 80%, which may be due to the fact that the network classified pixels in those classes when they do not belong to them. In the case of PE, this occurs in the last slices where the regions of the bronchial branches and HLT are confused with the disease, which is verified by IoU values of less than 50%. For the classification of HLT, good results were obtained, since there are IoU values very close to 1 (mean IoU of 89%). The overall performance with respect to this index was 80%.

Finally, Table 3 contains the DICE coefficient estimated between the results obtained from the segmentation and the manual labels of the HRCT volume.

Table 1. Accuracy calculation results for all slices and classes.

Slice	IPF	PE	HLT
1	0.9044	0.9529	0.8979
2	0.9216	0.9722	0.9162
3	0.9270	0.9605	0.8988
4	0.9183	0.9540	0.8727
5	0.9147	0.9753	0.9172
6	0.9194	0.9786	0.9108
7	0.8306	0.9725	0.9032
8	0.8369	0.9858	0.8808
9	0.8703	0.9635	0.8930
10	0.8736	0.9259	0.9001
11	0.7771	0.9528	0.9322
	0.8812 ± 0.0487	0.9631 ± 0.0166	0.9021 ± 0.0169

Table 2. IoU metric obtained from the comparisons between the resulting segmentation and labels.

Slice	IPF	PE	HLT
1	0.5566	0.7761	0.8911
2	0.6908	0.7226	0.9090
3	0.6634	0.6508	0.8940
4	0.6134	0.6256	0.8690
5	0.7047	0.7807	0.9101
6	0.6862	0.7714	0.9057
7	0.6504	0.6912	0.8910
8	0.6646	0.6133	0.8696
9	0.6830	0.5108	0.8813
10	0.6963	0.5080	0.8871
11	0.6988	0.4221	0.9099
	0.6644 ± 0.0445	0.6430 ± 0.1215	0.8925 ± 0.0151

The DICE index is a measurement of global overlap between the regions to be compared, which may have values between 0 (no overlap) and 1 (perfect overlap). In this case, for HLT we could say that the network does a good job in classifying it with a DICE average value of 0.94. For IPF and PE, the DICE values are slightly below 0.8, meaning a good overlap for these ILD; however, as with the IoU metric, the DICE index is low in PE in the last slices.

Table 3. Results of the calculation of the DICE similarity coefficient.

Slice	IPF	PE	HLT
1	0.7151	0.8739	0.9424
2	0.8171	0.8390	0.9523
3	0.7977	0.7884	0.9441
4	0.7604	0.7697	0.9299
5	0.8268	0.8769	0.9529
6	0.8139	0.8710	0.9505
7	0.7882	0.8174	0.9424
8	0.7985	0.7603	0.9303
9	0.8117	0.6762	0.9369
10	0.8210	0.6738	0.9402
11	0.8227	0.5937	0.9528
	0.7975 ± 0.0334	0.7764 ± 0.0941	0.94320 ± 0.0085

Although low indexes were obtained in some of the slices, the results obtained suggest that the U-net network performed well in segmenting different lung tissues at the same time (Accuracy: 93.6% vs 85.5% obtained in [4]).

4 Conclusion

In this work, a strategy for the segmentation of HLT and two ILDs, IPF and PE in a volumetric HRCT image using a U-Net approach was presented. The performance of the segmentation was evaluated by means of accuracy, IoU and DICE indices, and the results obtained suggest that the proposed approach could be useful for the characterization of several lung tissues.

We performed the training of the U-Net with few slices of the volumetric image in order to facilitate the segmentation of pulmonary diseases through the network, making the proposed approach particularly useful in cases where a reduced amount of data is available.

In this case, we obtained favorable results by using only 3 HRCT slices during the training stage, which are comparable with the results of strategies found in the literature in terms of accuracy and IoU where extensive databases are used [2,4].

As future work, we will consider the evaluation of new images from diagnosed patients with ILD available at the INER in order to obtain more evidence regarding the performance of our approach. In addition, different setups for the training stage of the U-Net will be studied in order to improve the accuracy of the segmentation.

Conflict of Interest. The authors declare that they have no conflict of interest.

References

1. Long, J., Shelhamer, E., Darrell, T.: Fully convolutional networks for semantic segmentation. In: Proceedings of the IEEE Conference on Computer Vision and Pattern Recognition, pp. 3431–3440 (2015). https://doi.org/10.1109/CVPR.2015.7298965
2. Ronneberger, O., Fischer, P., Brox, T.: U-net: convolutional networks for biomedical image segmentation. In: International Conference on Medical Image Computing and Computer-Assisted Intervention, pp. 234–241. Springer, Heidelberg (2015). https://doi.org/10.1007/978-3-319-24574-4_28
3. Kim, N., Seo, J.B., Lee, Y., et al.: Development of an automatic classification system for differentiation of obstructive lung disease using HRCT. J. Digital Imaging **22**(2), 136–148 (2009). https://doi.org/10.1007/s10278-008-9147-7
4. Anthimopoulos, M., Christodoulidis, S., Ebner, L., et al.: Lung pattern classification for interstitial lung diseases using a deep convolutional neural network. IEEE Trans. Med. Imaging **35**(5), 1207–1216 (2016). https://doi.org/10.1109/TMI.2016.2535865
5. Rumelhart, D.E., Hinton, G.E., Williams, R.J.: Learning internal representations by error propagation. In: Parallel Distributed Processing: Explorations in the Microstructure of Cognition, vol. 1, pp. 318–362. MIT Press, Cambridge (1986)
6. Kim, P.: MATLAB Deep Learning: With Machine Learning, Neural Networks and Artificial Intelligence. Apress (2017). https://doi.org/10.1007/978-1-4842-2845-6
7. Csurka, G., Larlus, D., Perronnin, F., et al.: What is a good evaluation measure for semantic segmentation? In: Proceedings of the British Machine Vision Conference, vol. 27, pp. 32.1–32.11. BMVA Press (2013). https://doi.org/10.5244/C.27.32
8. Faggiano, E., Fiorino, C., Scalco, E., et al.: An automatic contour propagation method to follow parotid gland deformation during head-and-neck cancer tomotherapy. Phys. Med. Biol. **56**(3), 775 (2011). https://doi.org/10.1088/0031-9155/56/3/015

Fast Optic Disc Localization Using Viola-Jones Algorithm

Yainet García García[1(✉)], Reinier Rodríguez Guillén[2], Y. García[3], and Alberto Taboada-Crispi[1]

[1] Universidad Central "Marta Abreu" de Las Villas, Santa Clara, Cuba
yagarcia@uclv.cu
[2] "Jesús Menéndez" Factory, Sagua la Grande, Cuba
[3] Provincial Meteorology Center, Camagüey, Cuba

Abstract. This paper proposes the implementation of the Viola-Jones algorithm for the Optic Disc (OD) localization in eye fundus images. A robust classifier for the detection of the region of interest (ROI), which contains the OD through the Viola-Jones algorithm was trained, and the center of the ROI for the OD localization was found. A 8776-image dataset for training (7300) and testing (1476) the detector was conformed with images from public databases: DRIVE, DRIONS, ROC, HRF, MESSIDOR, DIARETB0 and DIARETB1. A success rate of 99.6% was obtained for the OD localization in an average time of 474 ms. The Viola-Jones algorithm results a fast, accurate and low-computational cost algorithm for the OD localization and it is applicable in the detection and localization of other structures as the macula and fovea. The results are comparable with those of the state-of-the-art algorithms and, in addition, they could be improved in future works and may be applied in eye computer-aided diagnosis or periodic evaluations of the eyes in real-time mobile applications.

Keywords: Eye fundus images · OD localization · Viola-Jones algorithm

1 Introduction

Digital retinal images or eye fundus images are possible due to the presence in the human eye of transparent structures, which allow viewing directly the interior and back portion of the eye through the pupil. In the eye fundus, anatomical structures of the eyeball such as blood vessels, the macula, the fovea and the optic disc (OD) [1] can be observed. The study of these structures is essential for the diagnosis of several pathologies. The OD is one of the main structures for medical analysis, and its localization plays a decisive role in the automatic analysis of eye fundus images. The OD is a brighter area than the rest of the retina, varying in color from yellowish red to pinkish in normal eye fundus images. The OD has a slightly oval or round shape, roughly one-sixth of the width of the image in diameter [2], which represents approximately 90 to 100 pixels in an image of 565 × 584 dimensions.

© Springer Nature Switzerland AG 2020
C. A. González Díaz et al. (Eds.): CLAIB 2019, IFMBE Proceedings 75, pp. 435–441, 2020.
https://doi.org/10.1007/978-3-030-30648-9_56

The proposed algorithms for the OD localization, initially, focused its efforts in accomplishing operations of image processing that allow using the anatomic characteristics of the OD. These algorithms select a particular color space like LUV [3] or HIS [4]. The RGB color space is the most commonly used, generally with the green channel, although [5, 6] proposed to use the red channel, while [2] uses a combination of both channels for enhancing the illumination characteristics of the OD. [4, 7] used Hough Circular Transform for the segmentation of the OD by geometric shape. These steps are usually followed by morphological operations and edge detection for segmentation using a threshold. The success rate of these methods depend on the image quality and the presence of anomalous characteristics. Other works used the relationships between the OD and other structures like a macula or blood vessel. [8] determines the OD position by finding a convergence point between two parabolas drawn by the geometry of blood vessels, while [9] used this option like a validation method to ensure correct OD detection.

Actually, it is a trend to use computer vision methods in order to solve the problem of OD localization and segmentation. These methods imply learning the OD characteristics, generally supervised like a template-matching or deep learning techniques, offer high success rate. [10, 11] are examples of articles in this field, archiving a success rate of 99.1% and 97.0%, respectively, for the OD localization. Therefore, to find a robust algorithm, which satisfies the requirements of speed, accuracy and low-computational cost for this task, remains a challenge and a need. That is the motivation for the following study.

A supervised learning algorithm with high prestige in computer vision is the Viola-Jones algorithm [12, 13]. This algorithm was proposed in 2001 for the object detection, principally, for the faces detection in images and videos. In recent works, its performance is compared with another algorithm, [14] compared the Haar features with the Convolutional Neural Networks (CNN) for the surgical material detection. [15] combines both algorithms in the signal traffic detection and [16] explains that this combination may reduce the big memory space and the expensive implementation that CNN requires. This algorithm can be applied to detect objects characterized by typical patterns [17] and enables its use in mobile devices, for high speed and real-time, justifying its implementation in several programming languages. Hence, this algorithm was thought due to the peculiarities of the OD, which could be useful to train the algorithm for its localization. The main contribution of this paper is the implementation of the Viola-Jones algorithm for automatic OD localization in eye fundus images, allowing the creation of a robust detector, which can be a help for the automatic diagnosis of eye diseases by computers or the future implementation of real-time mobile applications.

2 Materials and Methods

For the development of this study, a dataset with 8776 eye fundus images, taken from different public database, was gathered. 1476 test images and 7300 training images were used, with 7300 positive images and 200 000 negative images obtained through rotations with different angles:

DRIVE (40, [565 × 584]) [18], DIARETB0 (130, [1500 × 1152]) [19], DIARETB1 (89, [1500 × 1152) [20], MESSIDOR (1200, [1440 × 960, 2240 × 1488, 2304 × 1536]) [21], DRIONS-DB (110, [600 × 400]) [22], HRF (81, [3504 × 2336, 3888 × 2592, 5184 × 3456]) [23], ROC (100, [768 × 576, 1058 × 1061, 1380 × 1381, 1386 × 1383, 1386 × 1391, 1394 × 1301]) [24] and images acquired by us. The study was run on a Soneview Laptop, with Intel Dual Core, 4 GB of RAM, 2.10 GHz and 64-bit Windows 10 operating system. MatLab®, version 8.5.0.197613 (R2015a) with the Computer Vision System Toolbox that was used here.

The methodology applied for this study is shown in Fig. 1. The algorithm firstly extracts information of interest from the image by combining the Haar features with the Integral Image, which brings speed. Then, a supervised learning algorithm based on AdaBoost was used, which allows to take a series of weak classifiers and combine them to build a strong classifier. For detection of the objects, increasingly complex classifiers are combined in a cascade, providing statistical guarantees to quickly discard regions with low probability of containing the object of interest [12]; if the requested object is not found in any step of the cascade, the detector rejects the region.

For the training of the classifier are needed positive and negative images. The positive images comprise the region of interest (ROI), which contains the OD; for which the ROI is marked using the MatLab® Image Labeler App in rectangular form, because this way more information is obtained in that region [10]. The `trainCascadeObjectDetector` function automatically generates negative samples from a negative images set constituted by the rest of the image without the ROI. The function returns an XML file that constitutes the detector, and it is used in the `vision.CascadeObjectDetector` function. The `step` function allows applying the detector to the input image.

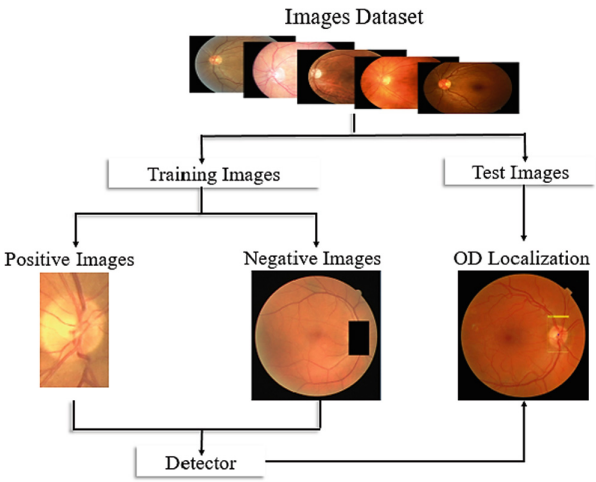

Fig. 1. Block diagram of proposed method.

2.1 Post-processing

In order to correct multiple detections of the ROI, or to detect it in the cases where it was not found, a simple post-processing was performed. The incorrect regions, of sizes below the minimum or above the maximum ones, estimated from the average size of the OD in eye fundus image, were discarded. For the poor cases, where multiple detections were kept, a validation method was made to select the correct bbox of the OD, determining the orientation of the blood vessels via a simple segmentation using morphologic operations. Considering the limitations of the Viola-Jones algorithm regarding position and illumination [16], rotations at different angles were made in the images where the ROI were not detected. Experimentally, it was determined that the angles of 45 and 180 degrees offer better results.

3 Results

The object detector cascade was trained in 10 stages with a 0.01 `FalseAlarmRate`, and other default parameters. The input image can be a grayscale or RGB, which evidences the robustness of our algorithm. As a result of the detection, the ROI is obtained enclosed by a yellow bounding box (bbox). The bbox is a vector of four elements with the pixel coordinates [x y width height], marking in green the central pixel of the bbox, which in turn constitutes the OD localization. One of the advantages of the proposed algorithm is the fast and easy localization of the OD, because the bbox obtained in the detection is similar to the bbox utilized for the training of the detector that offers the possibility of finding correctly the OD localization as the central point of it. Figure 2a–g shows the OD localization in different public databases: DIARETB0, DIARETB1, DRIVE, DRIONS-DB, ROC, HRF and MESSIDOR, respectively. Figure 2h–k shows the cases where the localization was incorrect, while Fig. 2l and m did not detect the ROI.

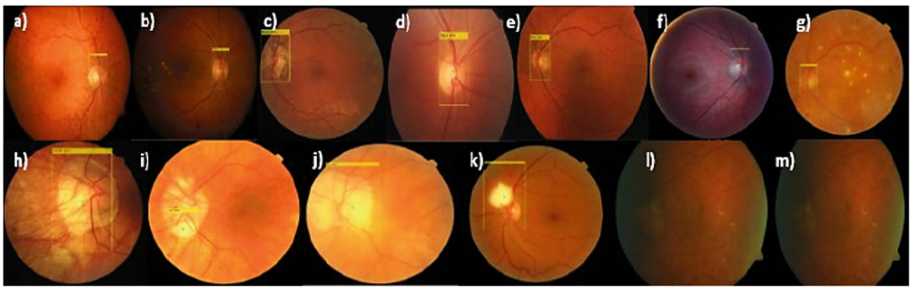

Fig. 2. OD localization in different public databases.

Table 1 shows that the success rate of the proposed algorithm for OD localization of the test images is 99.6%, i.e. in only six images of the ample dataset, with several characteristics and the presence of considerable number of anomalies, the OD localization was incorrect. Our algorithm archives an average time inferior to one second,

only in HRF database the time is superior to one second because this database contains the highest resolution images. The incorrect localizations may be improved by using simple methods of image processing and, in the case of multiple and incorrect detections of the ROI, the results can be improved by using a bigger number of stages of training, increasing the number of training images or experimentally adjusting other parameters. The correct ROI was detected in 99.8% of the cases, which evidences the importance of a correct selection of the bbox during the post-processing. In fact, the results of this study can be improved applying a simple post-processing focused in the convergence of blood vessels to determine the OD center, which would gain at precision, with a minimum spend of time. Only in two images, where the OD presents evident problems of illumination, ROI were not correctly detected, while in another image where the OD is anomalous, only a small fragment of the ROI is detected. Considering these 3 cases as incorrect detection, the proposed algorithm presents a high success rate for the ROI detection, which means that the global performance of our algorithm may be superior to that of other state-of-the-art OD localization and segmentation algorithms, shown in Table 2.

Table 1. OD localization using the Viola-Jones algorithm.

Dataset	Our	Drive (40)	DIARETB0 (130)	DIARETB1 (89)	MESSIDOR (1200)	DRIONS (110)	HRF (81)	ROC (100)	Total
Training images	7026	20	62	44	98	–	–	50	7300
Test images	–	20	68	45	1102	110	81	50	1476
Localized ODs	–	19	66	45	1099	110	81	50	1470
Sucess rate (%)	–	95.0	97.1	100.0	99.7	100.0	100.0	100.0	**99.6**
Av. Time (ms)	–	70	301	345	429	62	1739	377	**474**

Table 2 shows the performance of the proposed method compared to recent papers, including the CNN-based OD localization algorithm, demonstrating that accuracy, precision and speed of the proposed method are comparable to other state-of-the-art

Table 2. Success rates (in %) for OD localization using different methods on several databases.

Dataset	Methods					
	Meng [10]	Wen Lin [25]	Gui [26]	Jacob [4]	Kamble [27]	**Proposed method**
DRIVE	100.0	97.5	100.0	95.0	100.0	**95.0**
DIARETB0	98.5	–	–	96.9	97.7	**97.1**
DIARETB1	100.0	96.9	–	96.6	97.8	**100.0**
MESSIDOR	–	99.3	99.2	–	99.8	**99.7**
DRIONS-DB	–	–	–	100.0	–	**100.0**
HRF	–	–	–	93.3	100.0	**100.0**
ROC	–	–	–	–	–	**100.0**
STARE	98.8	–	86.4	–	95.1	–
ONHSD	–	–	–	–	99.0	–
HEIMED	–	–	–	–	98.8	–
Av. Success rate	99.1	99.1	98.5	97.3	99.2	**99.6**
Time (ms)	15000	1080	980	536	–	**474**

algorithms. These characteristics, along with the low computational cost of the proposed algorithm, could allow its implementation in computer-aided diagnosis or periodic evaluations of ocular diseases in real-time mobile applications.

4 Conclusions

The Viola-Jones algorithm enables the fast, accurate and low-computational cost detection of structures of the eye fundus like an OD. The success rate of the ROI detection is very high (99.6% as an average), which means that the global performance of our algorithm may be superior to some other state-of-art OD localization and segmentation algorithms. It is essential to select the correct bbox. The OD localization, is acceptably fast for searching the center of the bbox, although using known methods of image processing, these results can be optimized. The performance of the proposed method (regarding accuracy, precision and speed) is comparable or even better than those that have being reported in recent papers, including the CNN-based OD localization algorithm. These characteristics along with the low computational cost could allow implementing eye computer-aided diagnosis in real-time mobile applications. The obtained results may be improved in future research, where more efficient parameters for the algorithm could be intended to select.

Conflict of Interest. "The authors declare that they have no conflict of interest".

References

1. García, Y., Rodríguez, R.: Mapeo de imágenes digitales de fondo de ojo atendiendo a rasgos de textura. Revista Cubana de Ciencias Informáticas **11**(1), 106–121 (2017)
2. Elbalaoui, A., Kokare, Y.: Segmentation of optic disc from fundus images. In: 2018 International Conference on Computing Sciences and Engineering (ICCSE) (2018). https://doi.org/10.1109/iccse1.2018.8374223
3. Wisaeng, K., Hiransakolwong, N.: Automatic detection of optic disc in digital retinal images. Int. J. Comput. Appl. **90**(5) (2014)
4. Devasia, T., Jacob, P.: Automatic optic disc localization in color retinal fundus images. Adv. Comput. Sci. Technol. **11**(1), 1–13 (2018)
5. Rajput, G.G., Reshmi, B.M.: Automatic detection of optic disc based on mathematical morphology in retinal fundus images. Int. J. Comput. Appl. (2015)
6. Devasia, T., Jacob, P.: Automatic optic disc localization and segmentation using swarm intelligence. World Comput. Sci. Inf. Technol. J. **5**(6), 92–97 (2015)
7. Bhat, S.H., Kumar, P.: Segmentation of optic disc by localized active contour model in retinal fundus image. In: Smart Innovations in Communication and Computational Sciences, pp. 35–44. Springer (2019). https://doi.org/10.1007/978-981-13-2414-7_4
8. Wu, X., Dai, B.: Optic disc localization using directional models. IEEE Trans. Image Process. **25**(9), 4433–4442 (2016). https://doi.org/10.1109/TIP.2016.2590838
9. Zou, B., Chen, Ch.: Classified optic disc localization algorithm based on verification model. Comput. Graph. **70**, 281–287 (2018). https://doi.org/10.1016/j.cag.2017.07.031

10. Meng, X., Xi, X.: Fast and effective optic disk localization based on convolutional neural network. Neurocomputing **312**, 285–295 (2018). https://doi.org/10.1016/j.neucom.2018.05.114
11. Al-Bander, B., Al-Nuaimy, W.: Multiscale sequential convolutional neural networks for simultaneous detection of fovea and optic disc. Biomed. Signal Process. Control **40**, 91–101 (2018). https://doi.org/10.1016/j.bspc.2017.09.008
12. Viola, P., Jones, M.: Robust real-time object detection. Int. J. Comput. Vision **4**(4), 34–47 (2001)
13. Viola, P., Jones, M.: Rapid object detection using a boosted cascade of simple features. In: CVPR, vol. 1, no. 1, pp. 511–518 (2001)
14. Murillo, P.C., Jiménez, R.: Comparison between CNN and haar classifiers for surgical instrumentation classification. Contemp. Eng. Sci. **10**(28), 1351–1363 (2017). https://doi.org/10.12988/ces.2017.711157
15. Jose, A., Thodupunoori, H.: A novel traffic sign recognition system combining Viola–Jones framework and deep learning. In: Soft Computing and Signal Processing, Advances in Intelligent Systems and Computing, vol. 900, pp. 507–517 (2019). https://doi.org/10.1007/978-981-13-3600-3_48
16. Enriquez, K.: Faster face detection using Convolutional Neural Networks & the Viola-Jones algorithm (2018)
17. Kaur, J., Sharma, A.: Performance analysis of face detection by using Viola-Jones algorithm. Int. J. Comput. Intell. Res. **13**(5), 707–717 (2017)
18. Staal, J., Abràmoff, M.D.: Ridge-based vessel segmentation in color images of the retina. IEEE Trans. Med. Imaging **23**(4), 501–509 (2004). https://doi.org/10.1109/TMI.2004.825627
19. Kauppi, T., Kalesnykiene, V.: DIARETDB0: evaluation database and methodology for diabetic retinopathy algorithms. Lappeenranta University Technology (2006)
20. Kauppi, T., Kalesnykiene, V.: Diaretdb1 diabetic retinopathy database and evaluation 84 protocol. Technical report (2007)
21. Decenciere, E.: Feedback on a publicly distributed image database: the Messidor database. Image Anal. Stereology, 231–234 (2014). https://doi.org/10.5566/ias.1155
22. Carmona, E.J., Rincón, M.: Identification of the optic nerve head with genetic algorithms. Artif. Intell. Med. **43**(3), 243–259 (2008). https://doi.org/10.1016/j.artmed.2008.04.005
23. Budai, A., Bock, R.: Robust vessel segmentation in fundus images. Int. J. Biomed. Imaging (2013). https://doi.org/10.1155/2013/154860
24. Niemeijer, M., Ginneken, B.V.: Retinopathy online challenge: automatic detection of microaneurysms in digital color fundus photographs. IEEE Trans. Med. Imaging **29**(1), 185–195 (2010). https://doi.org/10.1109/TMI.2009.2033909
25. Lin, J.W., Weng, Q.: Fast fundus optic disc localization based on main blood vessel extraction. In: Proceedings of the 2018 10th International Conference on Machine Learning and Computing (2018). https://doi.org/10.1145/3195106.3195162
26. Gui, B., Shuai, R.J.: Optic disc localization algorithm based on improved corner detection. Procedia Comput. Sci. **131**, 311–319 (2018). https://doi.org/10.1016/j.procs.2018.04.169
27. Kamble, R., Kokare, M.: Localization of optic disc and fovea in retinal images using intensity based line scanning analysis. Comput. Biol. Med. (2017). https://doi.org/10.1016/j.compbiomed.2017.04.016

Biosensors

Recording and Analysis of the Vestibulo-Ocular Reflex with Pendular Movement in the Vertical Plane

Geovanny Palomino Roldán(✉) and Ernesto Suaste Gómez

IE-Bioelectronics, CINVESTAV, Mexico City, Mexico
{gpalominor, esuaste}@cinvestav.mx

Abstract. The study of the vestibulo-ocular reflex (VOR) has been mainly focused on horizontal responses because it is the plane in which the human being is more accustomed to movements. With the use of sensors (accelerometer and gyroscope) as well as a video camera, the response of the VOR in the vertical plane was recorded. Using image processing techniques, the displacement of the eyeball was obtained and with the sensor (accelerometer and gyroscope) it was possible to record the movement of the head. Tests were performed with pendular movement in the vertical plane to obtain the gain of the vestibulo-ocular reflex. Although it is possible to record the horizontal responses, the tests were planned to register a greater alteration in the vertical plane. It was observed that it is possible to record in the vertical plane the responses of the VOR, which can be very useful in different areas such as sports medicine, aviation medicine for the detection of problems associated with posture and balance.

Keywords: Vestibulo-ocular reflex · Accelerometers · Gyroscopes

1 Introduction

The human being is more accustomed to experiencing movements in the horizontal plane, however, for some activities such as in the case of a pilot or a gymnast the responses of the VOR in the vertical plane must be studied and analyzed to avoid problems as the spatial disorientation or the loss of balance. The VOR is integrated with other systems to maintain orientation and balance in space. The vestibular apparatus of the inner ear, the proprioceptive signals and the organ of vision complement each other to allow us to orient ourselves in space [1, 2]. The vestibulo-ocular reflex is responsible for fixing the gaze during the rotation of the head, stabilizing the image in the retina and generating a rotation of the eye with an amplitude equal and opposite to the direction of movement of the head [3, 4].

For the detection of the movements of the eyeball video oculography is very useful which is a non-invasive technique that with the use of algorithms and image processing allows to obtain the changes in the position of the pupil [5–8].

In this work is aimed to determine and analyze if it is possible to register the vertical VOR response using sensors (accelerometer and gyroscope) for recording the

© Springer Nature Switzerland AG 2020
C. A. González Díaz et al. (Eds.): CLAIB 2019, IFMBE Proceedings 75, pp. 445–448, 2020.
https://doi.org/10.1007/978-3-030-30648-9_57

movement of the head, as well as a video camera (VC) for recording eye movements. To determine the presence or absence of the vertical VOR, the gain of this is obtained, which is defined as the change in the angle of the eye divided by the change in the angle of the head [9]. The ideal gain of the VOR is 1, if the gain has a close value it means the presence of the VOR.

2 Methodology

An accelerometer - gyroscope was used to register the movements of the head and the swing and a VC was used to record the movements of the eyeball as described below.

2.1 Detection of Head Movements

To record the movement of the head and the swing, the MPU6050 sensor was used, which included a three-axis accelerometer and a gyroscope (six degrees of freedom in total). This sensor has three 16-bit analog-to-digital converters (ADC's) to digitize the gyroscope outputs and three 16-bit ADC's to digitize the accelerometer outputs. An Arduino Uno card was used to acquire the data through Labview where the signal was filtered with the help of a Kalman type filter. The data obtained by the sensor indicated the displacement in degrees and Matlab was used to graphically represent them [9].

2.2 Detection of Eye Movements

For the recording of eye movements, a VC and video-oculography were used, for which a program was implemented in Labview that tracked the movements of the eyeball. The first stage of the developed program was the acquisition of the image, then a template was created where the region of interest (centroid of the iris) was selected. Afterwards, the image was processed to obtain it in gray scale and then, with the help of the template, the movement of the eyeballs was tracked to finally store the position. Thanks to the fact that the distance from the video camera to the eyeball was known, it was possible to process the data in Matlab to obtain the displacement in degrees and thus be able to analyze them with the data obtained from the sensors.

The VC was configured to take 60 frames per second, it was placed on a support that was always attached to a helmet so that it was focused on the movements of the eyeball and did not affect the movement of the head to record them.

2.3 Tests

The tests were performed on a swing where the movements of the swing, head and eyes were recorded while the subject was swinging in the vertical plane. The subject was asked to keep the gaze fixed at a point that was placed at 1.26 m, this in order to record the VOR while swinging. The final assembly of the tests performed is illustrated in Fig. 1.

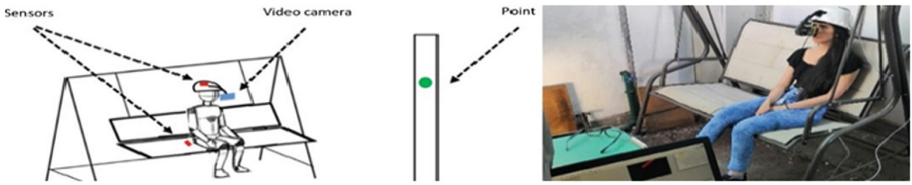

Fig. 1. Final assembly for the tests.

3 Results

The responses of the movements corresponding to the eyeball, head and swing were graphed. In Fig. 2 the movements corresponding to the vertical plane are shown.

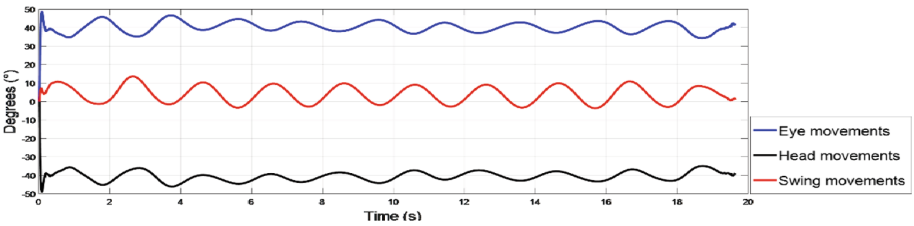

Fig. 2. Vertical movements.

In the case of the vertical movements of the swing a constant behavior is shown because the subject was balancing in the vertical plane. The movements of the head and the eye show greater amplitude by the movement of the swing.

Although the test is mostly focused on vertical movement, the horizontal movement responses were also plotted as are shown in Fig. 3.

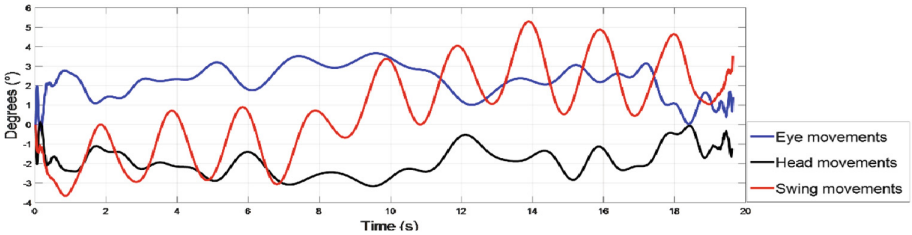

Fig. 3. Horizontal movements

The movement that was recorded in the horizontal plane corresponding to the swing could be due to the vibrations of the swing and not precisely to the VOR.

4 Discussions and Conclusions

In Fig. 2 the presence of the VOR can be observed. To verify that the amplitude was the same as in the VOR, a value of 0.99784202 was obtained as the gain of the VOR that is close to 1, which indicates the presence of the VOR in the vertical plane. The movements in the horizontal plane were also analyzed, a value of 1.21415308 was obtained in the gain, so the gain is not close to 1 which indicates the absence of the VOR.

According to the results shown, it was determined that it is feasible to register the vertical VOR with the methodology used. With these records it is possible to complement and help document studies of movement and human reflexes such as VOR and its relation to body movements, which is important for the early detection of the presence of a vestibular pathology such as Meniere's disease or problems associated with disorientation in space, involuntary movements, posture, walking and loss of balance and even studies in people suffering from nystagmus in which the affectation could be determined according to the VOR gain and the condition that causes the problem.

Conflict of Interest. The authors declare that we have no conflict of interest.

References

1. Federal Aviation Administration: Aeromedical Factors. In: Pilot's Handbook of Aeronautical Knowledge, FAA-H-8083-25B. Chapter 17 (2016)
2. Pauwels, L.W., Akesson, E.J., Stewart, P.A.: Cranial Nerves, Anatomy and Clinical Comments. B.C. Decker Inc. (1988)
3. Zangemeister, W.H.: Fixation suppression of the vestibular ocular reflex and head movement correlated EEG potentials. In: Eye Movements from Physiology to Cognition, pp. 247–256 (1987). https://doi.org/10.1016/b978-0-444-70113-8.50037-0
4. Rodenburg, M.: Coordination of head and eye position during fixation. In: Eye Movements from Physiology to Cognition, pp. 211–218 (1987)
5. Villalobos-Castaldi, F.M., Suaste-Gómez, E.: A new spontaneous pupillary oscillation-based verification system. Expert Syst. Appl. (2013)
6. Suaste, E., Sánchez, A.: Biomedical instrumentation to analyze pupillary responses in white-chromatic stimulation and its influence on diagnosis and surgical evaluation. In: Hudak, R. (ed.) Biomedical Engineering - Technical Applications in Medicine (2012)
7. Stark, L., Zangemeister, W.H.: Simulation of head movement trajectories: model and fit to main sequence. Biol. Cybern. **41**, 19–32 (1981)
8. Suaste-Gómez, E., et al.: Instrumental methodology for the measurement of the pupil cycle time using a chromatic slit lamp. In: IFMBE, vol. 49, pp. 20–22. Springer (2015)
9. Suaste, E., Palomino, G.: 15th International Conference on Electrical Engineering, Computing Science and Automatic Control (CCE), Mexico City, Mexico (2018)

Fabrication of PPy/PVC Electrodes for ECG Monitoring

Ernesto Suaste-Gómez(✉), Ilian Pérez-Solís, and Grissel Rodríguez-Roldán

Department of Electrical Engineering, Section of Bioelectronics, CINVESTAV, Mexico City, Mexico
esvaste@cinvestav.mx

Abstract. The detection of biosignals includes the use of biomedical electrodes. As the obtention of biosignals is vital for medical diagnosis, electrodes with good performance must be used. In this paper, electrodes made of Polypyrrole (PPy) and Polyvinyl chloride (PVC) were fabricated in order to record ECG signals. Besides, a methodology of their fabrication is presented as well as a comparison between the ECG signal measured with commercial Ag/AgCl electrodes and PPy/PVC electrodes. The results showed a good performance of the PPy/PVC electrodes compared to the commercial ones, making this type of polymeric electrodes a very reliable tool to acquire any type of biosignal.

Keywords: Conductive electrodes · ECG · PPy · PVC

1 Introduction

The growing development of new technologies has encouraged the study of smart polymers because of their mechanical properties as well as their fascinating behavior (stimulus-response). The features of smart polymers has promoted the development of new techniques and applications in different fields such as biotechnology and biomedicine, creating new fields of research and new areas of opportunity and giving scientists and engineers the search for new solutions as well as the improvement of those already known. Nowadays, conductive polymers are one of the most studied and investigated polymers due to their low oxidation potential, their high conductivity [1, 2], as well as their long-term environmental stability [3–7]. Different electronic devices have been developed with this type of polymers, for example, PPy has been used to measure physiological parameters, which are flexible and of great durability [8]. Also, it has been reported conductive bioelectrodes to obtain ECG records [9].

At present, there is a complexity in the design of bioelectrodes due to the specific requirements these must have to obtain records depending on their application. Thus, the challenge is to fabricate electrodes with longer durability, flexibility and easy to manufacture. The goal is to obtain long-term records, and reduce the noise in the biosignal making it more reliable, thus, providing better quality and efficiency in medical care [3, 10].

© Springer Nature Switzerland AG 2020
C. A. González Díaz et al. (Eds.): CLAIB 2019, IFMBE Proceedings 75, pp. 449–452, 2020.
https://doi.org/10.1007/978-3-030-30648-9_58

1.1 Fabrication

In order to fabricate the electrodes, two milliliters of Chloroform were added to 0.1 g of Polypyrrole (PPy) in powder from Sigma Aldrich. The solution was sonicated for two hours and it was left until Chloroform was evaporated. Subsequently, the obtained powder passed through milling and sieving with a mesh size of 149 μm. Then, two milliliters of Dodecylbenzenesulfonic acid (DBSA) were added little by little to this powder until obtaining an emulsion. Later, this emulsion was sonicated for 3 h in order to be homogenized and it was left to rest for 24 h. In the process of shaping the electrodes a PVC sheet with a thickness of approximately 4 μm was placed on a glass surface, then, a layer of the PPy solution with a thickness of approximately 260 μm was placed over the PVC sheet. A small copper wire was placed as a contact inside this mixture, and finally, it was left to dry. Once dried, circles of 1 cm in diameter were cut.

1.2 ECG Measurement

ECG records were obtained using a KT88-2400 Digital 24-Channel EEG, which is a very useful tool for clinical diagnosis. It contains 19 channels of EEG and 5 multi-parameter channels (ECG, EMG, respiration and EOG). This device collects the signal via integrated amplification, A/D transformation, PC auto-analysis and FFT. In order to collect the signal, the PPy/PVC electrodes were placed using the configuration shown in Fig. 1.

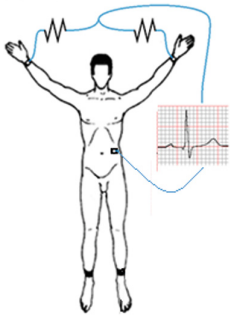

Fig. 1. Placement of electrodes for ECG

2 Results and Discussion

Figure 2 shows an example of an electrode fabricated with PPy and PVC. As it can be seen, it is smaller than the commercial ones and can be adaptable to any surface of the skin.

Figures 3 shows the recorded ECG signal using commercial Ag/AgCl electrodes and Fig. 4 the obtained signal using the PPy/PVC electrodes. As it can be seen, the amplitude in both images is the same and all ECG waveforms are clearly appreciated.

Fig. 2. PPy/PVC electrode, a small copper wire was placed as a contact inside the electrode with 1 cm of diameter.

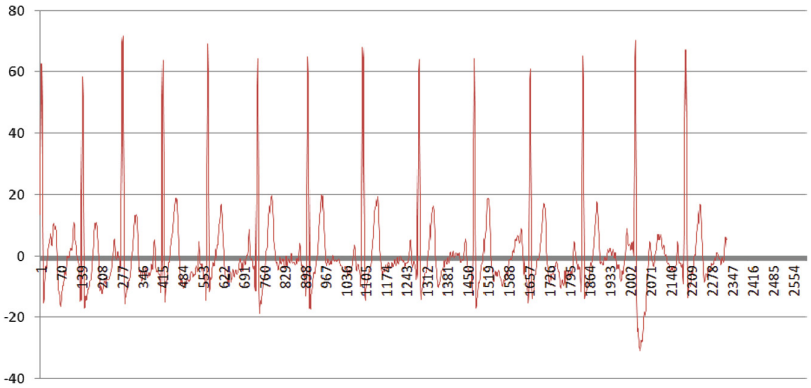

Fig. 3. ECG signal acquired with commercial Ag/AgCl electrodes

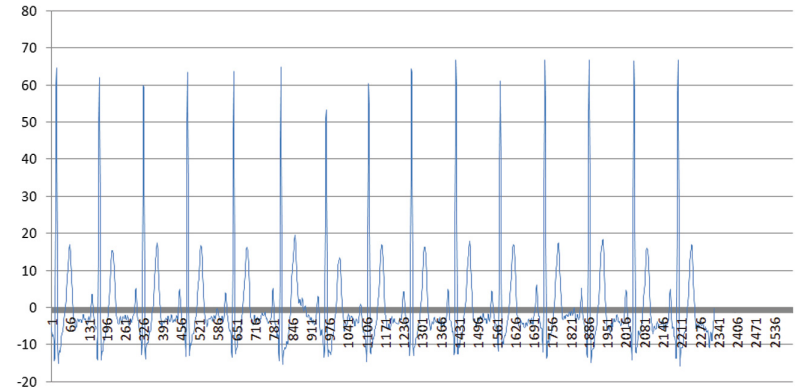

Fig. 4. ECG signal acquired with PPy/PVC electrodes

3 Conclusions

The monitoring of physiological signals at the present time is growing due to the new innovations in the field of materials and electronics. In this work, PPy/PVC electrodes were fabricated satisfactorily. The ECG signals acquired with conventional electrodes (Ag/AgCl) and PPy/PVC electrodes didn't show significant differences. However, the PPy/PVC electrodes present some other advantages among the commercial ones such as flexibility, reusability and durability. They are also biocompatible and present low oxidation potential and high conductivity [1, 2]. These electrodes showed to be very reliable in the measurements of ECG and can be used to measure another kind of biosignal. Something that is glimpsed, is in regard to its manufacture in industrial quantities PPy/PVC electrode would be more feasible to automate resulting in a more economical electrode.

References

1. Chronakis, I.S., Grapenson, S., Jakob, A.: Conductive polypyrrole via electrospinning: electrical and morphological properties. Polymer **47**, 1597–1603 (2006)
2. Baumhardt-Neto, R., De Paoli, M.A.: Mechanical degradation of polypropylene: effect of UV irradiation. Polym. Degrad. Stab. **40**, 59–64 (1993)
3. Kang, T.S., Lee, S.W., Joo, J., Lee, J.Y.: Electrically conducting polypyrrole fibers spun by electrospinning. Synth. Met. **153**, 61–64 (2005)
4. Balint, R., Cassidy, N.J., Cartmell, S.H.: Conductive polymers: towards a smart biomaterial for tissue engineering. Acta Biomater. **10**(6), 2341–2353 (2014)
5. Ateh, D.D., Vadgama, P., Navsaria, H.A.: Culture of human keratinocytes on polypyrrole-based conducting polymers. Tissue Eng. **12**, 645–655 (2006)
6. Misoska, V., Price, W.E., Ralph, S.F., Wallace, G.G., Ogata, N.: Synthesis, characterisation and ion transport studies on polypyrrole/deoxyribonucleic acid conducting polymer membranes. Synth. Met. **123**, 279–286 (2001)
7. West, K., Zachau-Christiansen, B., Jacobsen, T., Skaarup, S.: Electrochemical characterization of conducting polymers: polypyrrol. Mater. Sci. Eng. **B13**, 229 (1992)
8. Terán-Jiménez, O., Rodríguez-Roldán, G., Hernández-Rivera, D., Suaste-Gómez, E.: Sensors based on conducting polymers for measurement of physiological parameters. IEEE Sens. J. **17**, 2492–2497 (2017)
9. Pani, D., et al.: Fully textile, PEDOT: PSS based electrodes for wearable ECG monitoring systems. IEEE Trans. Biomed. Eng. **63**, 540–549 (2016)
10. Petrova, G.I.: Influence of electrode impedance changes on the common-mode rejection ratio in bioimpedance measurements. Physiol. Meas. **20**, N11–N19 (1999)

Implementation of the NEURONIC INFANTIX Newborn Hearing Screening System

José Carlos Santos-Ceballos(✉), Jorge German Pérez-Blanco, Yosvani Pantoja-Gómez, Francisco Martín-González, Alejandro Torres-Fortuny, Eduardo Eimil-Suarez, and Ernesto Velarde-Reyes

Cuban Center for Neuroscience (CNEURO), Havana, Cuba
jsantosceballos@gmail.com

Abstract. Hearing loss is an important health problem. It affects about six per 1,000 live births worldwide. Hence, the implementation of a newborn hearing screening program represents a goal of a good health system. For the effective implementation of an efficient hearing-screening program, appropriate technologies are needed to make objective physiological measurements. Within these types of technologies, the most commonly used are Otoacoustic Emissions (OAE), Automated Auditory Brainstem Response (AABR) and the quite new Auditory Steady State Response (ASSR). This paper presents the NEURONIC INFANTIX Newborn Hearing Screening System for implementing these techniques. The main characteristics of the hardware architecture, its Control Module, Auditory Evoked Potential Record Module and Otoacoustic Emissions Module are depicted. Finally, a prototype and a validation experiment of the AABR technique are shown.

Keywords: Newborn screening · Microcontrollers · Hearing loss

1 Introduction

Data from the World Health Organization (WHO) reflect that the incidence of congenital hearing loss, in any of its grades and throughout the world, is no less than six per 1,000 live births [1]. The condition of hearing loss from birth can imply a delay in the acquisition of oral language which can affect the normal development of the child. The late diagnosis of hearing loss constitutes a serious problem, considering that there is an optimal and non-recoverable period to begin the treatment or rehabilitation of a hearing-impaired child. Between 5 and 6 months of age they would be established naturally, if there was adequate stimulation of the areas of the cerebral cortex dedicated to the language [2].

Therefore, it is very important to begin the rehabilitation of the hearing-impaired child before reaching 6 months and then, it is necessary to carry out a previous and effective diagnosis, which is only possible through the proper implementation of newborn auditory screening programs. An increasing number of countries develop

© Springer Nature Switzerland AG 2020
C. A. González Díaz et al. (Eds.): CLAIB 2019, IFMBE Proceedings 75, pp. 453–459, 2020.
https://doi.org/10.1007/978-3-030-30648-9_59

programs and laws that regulate newborn auditory screening. These programs focus on testing all children at risk of hearing loss or all children universally. It should be considered that 50% of hearing-impaired newborns do not present any known risk condition and would never be detected in a selective screening [3].

For the effective implementation of any newborn auditory screening program, suitable technologies are required. Within these types of technologies, the most frequently used are Otoacoustic Emissions (OAE), Automated Auditory Brainstem Response (AABR) and the relatively recent Auditory Steady State Response (ASSR). Because of its relative low cost and speed, the OAE technique is the most used in the first screening level [4]. AABR and ASSR allow a more complete study of the auditory pathway, but require the use of contact electrodes in addition to the patient's previous preparation. That is the reason why these techniques are usually applied at a second level of screening to infants who did not pass the OAE test or to those who present a risk factor [5].

The objective of this paper is to present the implementation of a System capable of developing all the auditory screening techniques which is called NEURONIC INFANTIX Newborn Hearing Screening System.

2 System Implementation

The NEURONIC INFANTIX System was conceived as a modular system, with physical modules for the different test types, as shown in Fig. 1. This way, the System could be distributed according to the required function, facilitating the emergence of forthcoming functions.

The designed system consists of a Control Module, an Auditory Evoked Potential (AEP) Recorder Module and an Otoacoustic Emissions (OAE) Recorder Module. Figure 1 also shows a Wireless Portable Printer as optional equipment. The functions of each module are described below.

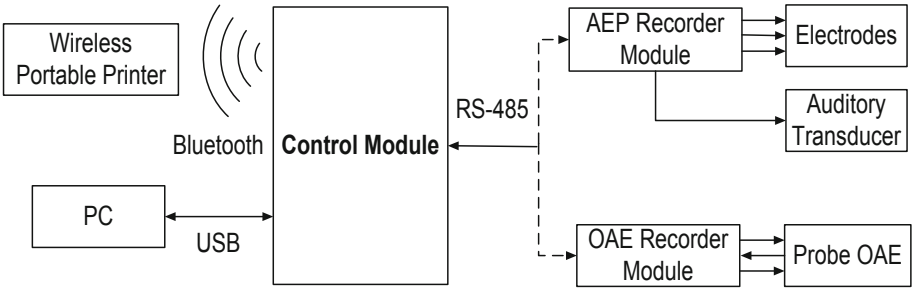

Fig. 1. NEURONIC INFANTIX Newborn Hearing Screening System

2.1 Control Module

The key function of the control module is to regulate the rest of the modules of the system. It must be able to record user data on a touch screen, graph biosignals, and apply methods of digital signal processing. In addition, it can send and receive commands to the rest of the modules, as well as managing the power of the system. This element is composed of the blocks shown in Fig. 2.

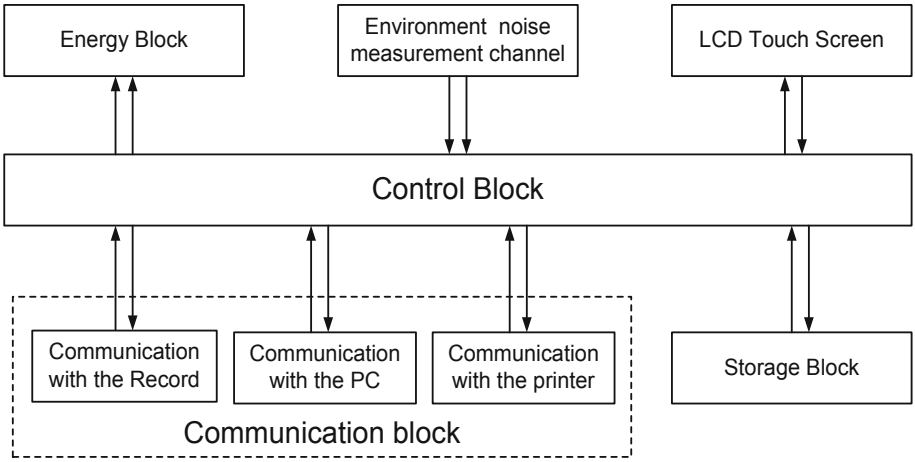

Fig. 2. Block diagram of the Control Module

Within the Control Module, a control block is located; whose main function is the handling of the other components of the module. For this, it uses the different interfaces provided by the STM32F429 microcontroller, which has a 32-bit RISC processor with ARM Cortex-M4 architecture. It can function at a frequency up to 180 MHz. It also has a floating-point unit (FPU) and a set of instructions for digital signal processing (DSP). This feature facilitates both the processing of recorded bioelectric signals and the implementation of screening techniques.

In order to save the patient data, tests, the general configuration of the system, and to increase the non-volatile storage capacity, a microSD memory card is used. This memory card is controlled by a secure digital input/output (SDIO) interface.

Communication with the Record Module is accomplished through one of the UART interfaces present in the microcontroller, using the RS-485 standard. In order to attain this, an integrated transducer circuit converts the TTL voltage logic levels, coming from the microcontroller, to the levels of this standard. The microcontroller enables this circuit when it is necessary to establish this communication.

Communication with the PC is carry out via USB. The microcontroller communicates through the USB Full Speed interface (12 Mbits/s). In the Control Module, this communication was implemented, using two kinds of USB device: mass storage (USB MSC) that allows access to microSD data from the PC, and communication device (USB CDC) that is used for the transmission of information between the Control Module and an application on the PC. On the other hand, the USB port recharges the internal batteries of the system, using an integrated battery charger circuit.

The Bluetooth module SPBT2632C2A of STMicroelectronics, which receives the commands to be sent from the microcontroller via a UART interface, establishes the communication with the wireless portable printer. The power supply of the module is provided by the power supply block.

The function of the energy block is to supply energy to the components of the Control Module. It is composed of different integrated circuits that ensure different voltage levels for the correct operation of the device. The microcontroller will enable these integrated circuits only when the system needs it, seeking greater energy savings. For instance, the circuit that powers the Bluetooth module will be enabled only when communication with the wireless printer is established. As a result, greater control over the energy consumption of the device is achieved. The system is powered by three AA (1.2 V) rechargeable nickel-metal hydride (Ni-MH) batteries.

The environment noise measurement channel is composed of operational amplifiers, which has the purpose of conditioning the signal recorded by the ABM-703-RC microphone of PROSIGNAL. This signal is then digitized by one of the 12-bit analog-digital (A/D) converters of the microcontroller. To obtain the result of the measurement in dBA, a digital frequency weighting was performed using a filter A.

The screen is made up of an LCD and a touch panel. The former is managed by the microcontroller through an LTDC interface, while a touchscreen controller, which in turn communicates with the microcontroller through an I2C interface, manages the second. For the implementation of the graphical user interface (GUI) the emWin graphic library was used, which was designed so that it could be used independently of the processor and the LCD screen.

2.2 Auditory Evoked Potential (AEP) Recorder Module

The function of this module is to record the electrical biosignals of the patient's brain in a synchronized manner with an auditory stimulus that the module generates. The module has to digitize these biosignals and send them to the Control Module. In Fig. 3, the blocks that integrate this module are shown.

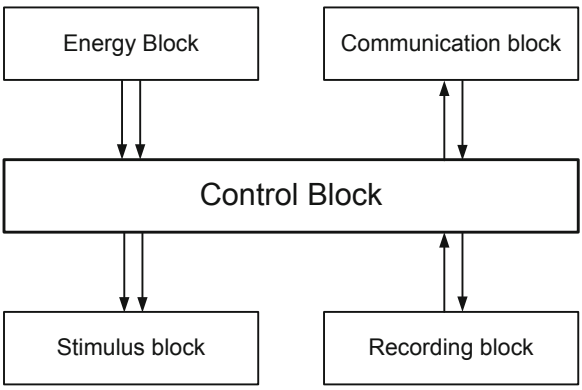

Fig. 3. Block diagram of the AEP Record Module

The main component of the control block is the STMicroelectronics STM32F405 microcontroller, which like that of the Control Module has a Cortex-M4 processor. The difference lies on peripherals available. This block has the function of managing the rest of the module blocks.

The recording block should be able to record the electrical EEG brain activity by three electrodes placed on the neonate's head. For this, the block has an amplification stage and an A/D converter. The amplification stage is differential and has a theoretical gain of 4096. The bandwidth of this amplifier is between 1 Hz and 4 kHz.

For the analog-digital conversion the AD7767 A/D converter was employed, which has a resolution of 24 bits. This converter samples the signal coming from the amplification stage at a sampling frequency of 500 kHz, then decimating it by 32, to finally deliver the signal to the microcontroller with a sampling frequency of 15,625 kHz. A unique feature of this converter is that its signal input is differential, increasing the Common-Mode Rejection Ratio (CMRR) of the signal acquisition system.

The aim of the stimulus block is to generate the auditory stimuli that induced the evoked potentials. The block is composed of a digital-analog converter (D/A) and two audio amplifiers (one for each stimulation channel). The stimuli are stored in the flash memory of the microcontroller and sent to the D/A converter via an SPI interface, at a sampling frequency of 48 kHz. The D/A converter has two channels and a resolution of 16 bits. The signals generated by the D/A converter's channels are amplified by their respective audio amplifiers, which are connected to a jack connector.

The communication block is responsible for establishing the serial communication (RS485) with the Control Module. This block is composed by a UART interface of the microcontroller and a transducer to convert the TTL logic levels to the RS-485 standard, similar to that of the Control Module. Through the cable that supports this interface, power is also received (5.2 V) from the Control Module.

The energy block consists of integrated circuits that convert the supply voltage (5.2 V) to the different voltage levels used in the rest of the components of the AEP Recorder Module.

2.3 Otoacoustic Emissions (OAE) Recorder Module

This module is responsible for generating the necessary stimuli to evoke the otacoustic emissions and the registration of these biosignals synchronized to the stimulus itself. The records obtained are digitized, and sent to the Control Module for processing. The module has a probe where a microphone for recording and two small speakers for stimulation are located.

The internal architecture of the OAE Recorder Module is similar to the AEP Recorder Module, so its block diagram matches the one shown in Fig. 3.

The control block includes as core element the STM32F405 microcontroller from the manufacturer STMicroelectronics, the same one used in the AEP Recorder Module. This block has the function of controlling and coordinating the operation of the rest of the parts that make up the module.

The register block consists of a high sensitivity microphone, an amplification stage and an A/D converter. The sound pressure level of the otoacoustic emissions is in the

range of −20 to 20 dB SPL approximately, which requires a high sensitivity microphone for its registration.

The amplification stage conditions the signal coming from the microphone that has a wide dynamic range, since it should record both the otoacoustic emissions, which cause a response in the microphone of the order of microvolts, as well as the stimulus itself, whose response is in the order of millivolts. The theoretical gain of this stage is 90 and its bandwidth is between 100 Hz and 11 kHz. The converter used is the Texas Instruments ADS8681, whose 16-bit resolution is suitable for the application. A sampling frequency of 24 kHz was used for the acquisition of the samples that are sent to the microcontroller of the Control Block through the SPI interface that includes the converter.

The stimulation block is composed of a D/A converter, two audio amplifiers and two speakers. The microcontroller integrates a D/A converter, whose resolution is 12 bits, which are enough to achieve the audio quality required in the application. Two converter channels were used and a frequency of 48 kHz was used to update the samples in the D/A.

The communication and energy blocks are very similar and hold the same functionality as their counterparts belonging to the AEP Recorder Module.

3 System Validation

For the validation of the NEURONIC INFANTIX Newborn Hearing Screening System, an experiment was performed, using a prototype similar to the one shown in Fig. 4. To validate, an auditory screening test was performed on AABR in 14 babies (7 females and 7 males, between 0 and 19 weeks of birth). As a whole, 28 ears were studied.

Fig. 4. View of the NEURONIC INFANTIX Newborn Hearing Screening System prototype

The validation experiments were carried out in the neurophysiology room of the "Ramón González Coro" Obstetric-Gynecological Hospital in Havana. Informed consent from the mothers or guardians of the neonates was received. The AABR tests were performed using a click-type stimulus, at a frequency of 71 repetitions per second and an intensity of 30 dB nHL. Prior to the test, babies were tested for AABR looking for hearing thresholds using an Audix 5 device from Neuronic S.A.

The results were reported as PASS, in case the baby passed the test satisfactorily; as REFER if auditory brainstem auditory evoked potential was not recorded; and as REPEAT in the event that the residual noise at the end of the test was greater than 40 nV. Out of the 28 ears studied, three reported thresholds greater than 50 dB nHL with the Audix 5 equipment and were reported as REFER upon performing the test. The remaining 25 ears gave thresholds equal to 30 dB nHL with Audix 5 and then resulted in PASS. With the sample studied, the NEURONIC INFANTIX Newborn Hearing Screening System achieved a Specificity and a Sensitivity of 100%.

4 Conclusions

The NEURONIC INFANTIX Newborn Hearing Screening System was presented in this paper. This system is able to carry out the techniques of AABR, ASSR and the different variants of OAE. A description of the different hardware modules was made and finally a validation experiment was explained. Based on the validation experiment, it is concluded that the System fulfills the purpose of auditory screening with a Specificity and Sensitivity of 100% for the experimental sample with which the validation was performed. Further work is proposed to conduct experiments with a larger sample, as well as with the diverse techniques that this system is capable of implementing.

Conflict of Interest. The authors declare that they have no conflict of interest.

References

1. Olusanya, B., Wirz, S., Luxon, L.: Community-based infant hearing screening for early detection of permanent hearing loss in Lagos, Nigeria: a cross-sectional study. Bulletin of the World Health Organization [Internet], 17 August 2008 (2016). http://www.who.int/bulletin/volumes/86/12/07-050005/en/
2. Moore, J.K.: Maturation of human auditory cortex: implications for speech perception. Ann. Otol. Rhinol. Laryngol. **111**(Part 2 of 2), 7 (2002)
3. US Preventive Services Task Force. Universal screening for hearing loss in newborns: US Preventive Services Task Force recommendation statement. Pediatrics (122) (2008)
4. Gorga, M.P., Preissler, K., Simmons, J., Walker, L., Hoover, B.: Some issues relevant to establishing a universal newborn hearing screening program. J. Am. Acad. Audiol. **12**, 101–112 (2001)
5. American Academy of Pediatrics JCoIH: Year 2007 position statement: Principles and guidelines for early hearing detection and intervention programs. Pediatrics **120**(4), 898–921 (2007)

Prototype Sensor with Optical Principle for Measuring Strength of the Fingers

Jessica Ferreira[1(✉)], Catherine Moreno[1], A. Ramírez[1], and Ricardo Espinosa[2]

[1] Universidad Manuela Beltrán, Bogotá, Colombia
[2] Seedbed of Research in Rehabilitation and Modelling Applied in Physiological Systems, ECCI University, Biomedical Engineering Program, Bogotá, Colombia
respinosam@ecci.edu.co

Abstract. The loss of strength in the hand caused by different pathologies, accidents or injuries, affects the development and performance of the daily activities of the subject and if they are not treated properly they can generate a permanent atrophy in the functionality of the hand. Currently, there are different therapy options and high-cost technological alternatives that focus on the rehabilitation of strength and the coordination of hand movements. Therefore, we propose the development of a prototype technology that measures the strength of the fingers through a modern system, which uses an optical principle sensor, as a low cost alternative, that can be implemented in physical rehabilitation therapies. This to get the strength and coordination of fingers of the hand. The main elements of the prototype are: plastic pieces that go in the fingertips and distal phalanges, palmar coating, a distance sensor (composed of a photoresistor, a led encapsulated in a tube), springs that provide three levels of resistance, a microcontroller and a graphic interface that allows the user and the specialist to know the progress of the patient during therapy.

Keywords: Strength · Technology · Therapy · Fingers · Optical principle · Sensor

1 Introduction

The hand is a complex system, which intervenes in vital functions for the development of the human being, such as: the development of tools (aimed at carrying out work), the search for food and survival, the communication (because hands are used for writing, expression through gestures and allow the creation of language to blind and deaf), the interaction with the environment, and helps the expression of feelings of people [1–3]. The hand can perform all these functions thanks to its structure consisting of 27 bones, more than 20 articulations, more than 30 muscles and specialized nerves that arise from the brachial plexus, which is responsible for examining the sensations and controlling movement with surprising ease and apparent minimum effort [4].

The hand participates in several activities, this is why it is also exposed to several risks such as physical injuries, work accidents, fractures, pathologies such as the carpal tunnel, median nerve injury, Quervain tendinitis, and rheumatoid arthritis. This hinder

© Springer Nature Switzerland AG 2020
C. A. González Díaz et al. (Eds.): CLAIB 2019, IFMBE Proceedings 75, pp. 460–468, 2020.
https://doi.org/10.1007/978-3-030-30648-9_60

activities of daily, such as turning a door knob, using a screwdriver, drinking a cup of coffee, carrying, moving or using objects with their hands, feeding, grooming and even being unable to work [5–7]. When a person has a hand disability attends the specialist in physical therapy, who uses different methods to assess the functional status of the hand, several variables are considered, such as clamp functions, functional capacity, mobility, strength and the flexion of the fingers [8].

Strength is one of the most common variables in the evaluation of the functional state of the hand. This is observed in the study conducted by Chen et al. [9] in 2010, which consisted in the design of a glove capable of sensing the movement made by the hand of a subject, quickly and accurately, thus determining the muscular strength developed during the session. The device allowed the specialists to perform an evaluation, diagnosis and more effective treatments. On the other hand, Agraz et al. [10] in 2013, they developed a system to sense and visualize by through a graphical interface, the isometric force of each finger and the grip movement made by the upper extremity, which allowed a better analysis by the specialist. Likewise, Lambercy et al. [11] in 2007, they designed a robotic interface to train and control the strength of the wrist and hand. The training consisted of simulating grasping/releasing, in combination with the pronation/supination movements of the forearm, to reduce muscle weakness, improve tactile sensitivity and coordination in the movement of the hand. The subject carried out the movements in a virtual reality environment.

The technological alternatives involve sensors that directly measure strength, such as strain gages, flexiforce and force sensors based on Tekscan resistance technology. However, these sensors have some drawbacks related to the conditioning of the sensor on the hand, because the hand is a complex mobile anatomical structure, this causes a deformation of the sensor, adhered on the curves of the hand, alter the measure of the force, a more accurate measurement requires a completely smooth surface [12]. We propose a sensing alternative for the strength of fingers, embedded in a glove that allows to measure and quantify in real time the strength of each finger of the hand during the grip movement. The glove uses springs that have a mechanic resistance to the bending movement of each finger, the deformation of the spring generates a change in distance between a photoresistive sensor and a light source. We propose a sensing alternative for the strength of fingers, embedded in a glove that allows to measure and quantify in real time the strength of each finger of the hand during the grip movement. The glove uses springs that have a mechanic resistance to the bending movement of each finger, the deformation of the spring generates a change in distance between a photoresistive sensor and a light source. The sensor information is conditioned and transmitted to a user interface. The interface allows the user to observe the maximum strength values, the average strength and the successful repetitions made.

2 Methodology

2.1 Structure of the Supports for Thimbles and Phalanges

The plastic pieces that cover the distal (“Thimble”) and proximal (“Phalange”) of each finger were designed using Autodesk Inventor® software and 3D printing was made on

Filaflex material, the objective of these pieces is to support the measuring system. The two pieces can be adapted to the shape of the finger because they have two side tabs that are attached to an elastic band that allows adjustment according to the size of the finger, in turn prevents the movement of the piece during movement. In addition, they have in the upper part a guide tunnel where the springs pass, in the case of the thimble piece (see Fig. 1A) this tunnel has a larger diameter, because in this part the spring is fixed with a pin. The phalange piece (see Fig. 1B) the diameter is smaller since in this way it is ensured that the spring does not move sideways.

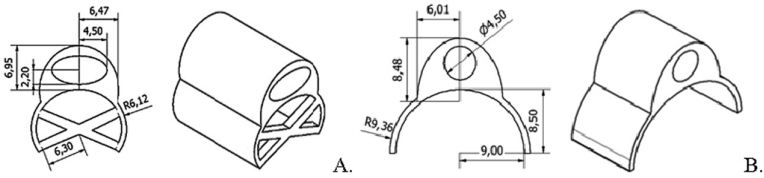

Fig. 1. A. Thimble design. Piece located in the distal phalanx of the finger, has at the upper end a barrier in the form of X to allow it to retain its position when performing the movements. B. Phalanx design. Piece located in the proximal phalanx, has a lower depth so as not to interfere with the movements made by the fingers.

2.2 Covering Back and Palm of the Hand

The covering of the back and the palm of hand is fundamental in the design of the prototype since it provides the support system for the measurement mechanisms. The material of the coating is neoprene, with a thickness of 2.5 mm to ensure firmness and avoid excessive movement, when the movement is made using the glove. The neoprene fabric provides flexibility and comfort to the user. The Fig. 2 shows the design of the coating on the back and palm of hand, as well as the adjustment elements.

Fig. 2. Adjustment system for the coating of the palm and back of the hand. Made of neoprene, it has Velcro bands that allow it to adapt to the shape of the hand.

2.3 Measurement Mechanism

The measurement system consists of fifteen springs separated into 3 groups, each group consists of 5 springs, one for each finger, the springs of each group have different

characteristics, which allows having different levels of resistance. Optical sensors along with LEDs inside black plastic tubes. Inside the tube, of 30 mm long and 10 mm in diameter, at the bottom is located the fixed led, a photoresistor supported by a wire that runs through the interior of the spring, which in turn is attached to the thimble piece, when the finger makes some movement this pull the wire and the photoresistor moves away or approaches the led, varying the value of the electrical resistance. In synthesis, the mechanism works by detecting the variation of light intensity, which is proportional to the displacement of the sensor inside the tube. This displacement depends on the force with which each finger, when flexing, deforms the spring (see Fig. 3).

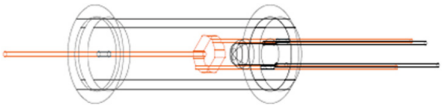

Fig. 3. Distance sensor. Composed of a tube that inside has a photoresistor (element color orange) and a fixed LED (element color black).

The Fig. 4 shows the final integration of the components of the prototype that fits the hand. In general, the following parts are named: the thimbles, phalanges, the covering and the tube (measurement mechanism).

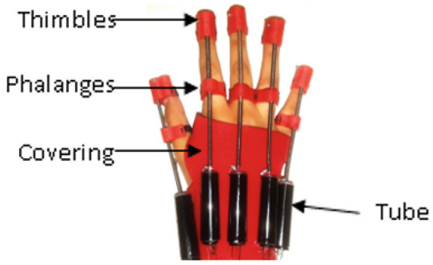

Fig. 4. Final prototype. The integration of the systems described in the glove.

2.4 Conditioning, Transmission and User Interface

The variation of the light intensity captured by the photoresistive sensor was characterized (details in the Results section) and related to the force that the patient performs when flexing each finger. This information is transmitted through a microcontroller (Arduino UNO) to a user interface, made in LabView®. The interface has sections that allow the user: registration of basic information (Name, date of birth, identification,) data of the therapy (session number, type of movement, repetitions to be performed, strength to be overcome). A second window shows the value of force in real time, the repetitions made, the maximum value of force reached and the way to perform the chosen movement.

3 Results

The results of this work are aimed at obtaining force data by implementing a system that varies the distance of an optical sensor with respect to the light source. The relation of displacement (generated by a spring) with force is given by Hooke's law, which represents elastic phenomena, the force exerted on the springs, is proportional to the length of its stretch [13, 14].

3.1 Distance Sensor Characterization

The characterization was done using a tape measure, a multimeter and a video camera. The tape measure was used to measure the distances (in millimeters) between the photoresistor and the light source. With the multimeter, it was measured the voltage variation that the conditioning of the photoresistor presented at each moment of separation with the source. The video camera was used to record the data of voltages obtained, in this way corroborate the measurements observed vs. digital data record. The measurements for each distance value were measured four times, the average was calculated to obtain a reference value. Values of 0 to 0.03 meters were taken for each tube (details in literal C of the Methodology section) corresponding to each finger. Figure 5 shows the curves obtained from the displacement vs. voltage, in the spring and optical sensor assembly.

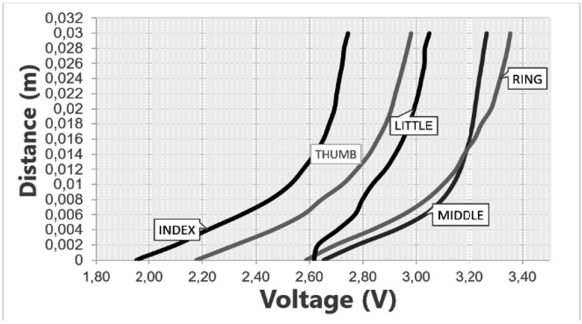

Fig. 5. Characteristic curves. In the figure we can observe the exponential behavior of the photoresistors.

3.2 Springs Characterization

The design uses springs made of stainless steel that are attached from one end to the thimble of the glove and passes through the guide of the phalanx piece. Each spring has a different length depending on the finger on which it will be located. To perform the characterization of the springs, masses and a tape measure were used. Following this, the springs were placed vertically in a universal support, different masses were hung in the springs and the elongation of these was measured. Once all the measurements had been taken, the different delta values (final position - initial position) of the variations in

the length of each spring were calculated, the data obtained for each one of the springs were averaged, thus obtaining the displacement. To calculate the force, we obtained the value of the masses measured on a digital bascule, Ohaus brand, which gave data in grams, which were converted into kilograms and these were multiplied by 9.8 m/s^2, complying with the weight formula, which indicates the weight is equal to the product of the mass by gravity (where the weight is the force with which the gravity of the earth attracts a body). From Figs. 6, 7, 8 and 9 the relation between the force exerted by the weights on the springs and their respective displacements are shown. The curves obtained are different for each finger, because the lengths of the springs are different for each finger.

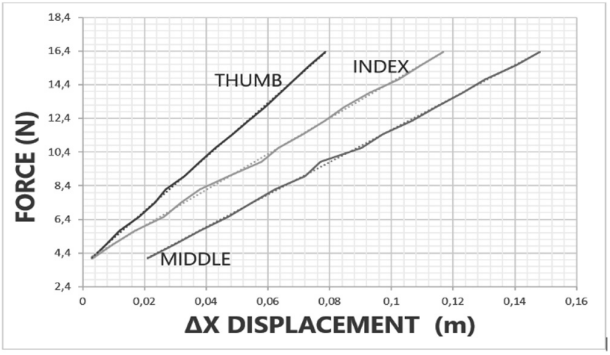

Fig. 6. Characterization of springs, low effort level: thumb (k = 160,47), index (k = 107,06) y middle (k = 96,262)

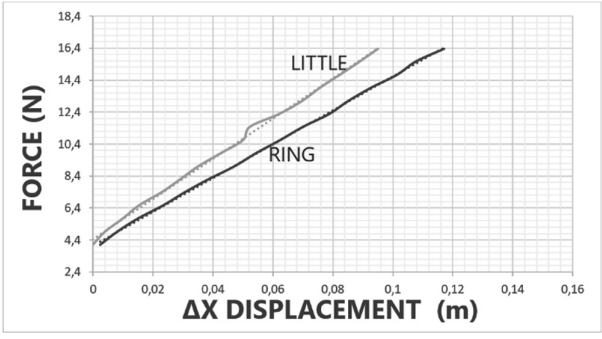

Fig. 7. Characterization of springs, low effort level: ring (k = 105.85) and little finger (k = 125.52)

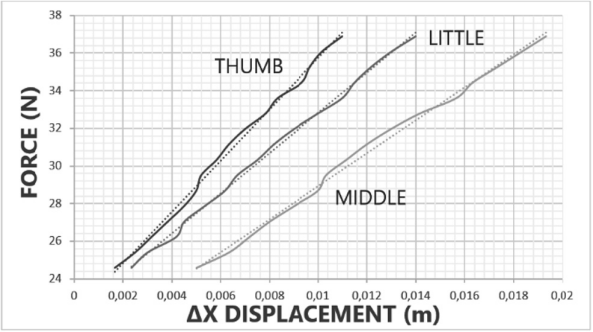

Fig. 8. Characterization of springs, high effort level: thumb (k = 1162.76), middle (k = 1104.59) and little finger (k = 1127.26)

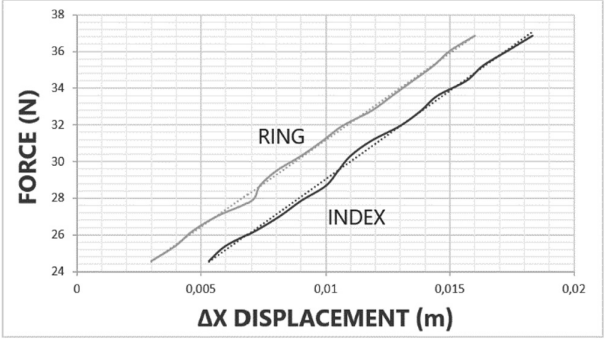

Fig. 9. Characterization of springs, high effort level: index (k = 1113.47) and ring finger (k = 1115.25)

4 Discussion

The design was based on the structure of a glove, which takes into account: The width of the back of the hand, which is adjusted thanks to two straps that it has in the palm. The length of the fingers, which is adjusted by the piece called thimble. The design of the structure was made in Inventor® software because it is oriented to the mechanical design of 3D objects that includes parametric modeling and assembly of parts. The construction of the glove used different materials, for the dorsal and palmar coating, neoprene was used in conjunction with velcro and the pieces called thimbles and phalanges were printed in 3D filaflex material. One of the objectives of carrying out the generation of the pieces through of this printing mechanism, was to provide the best ergonomics when using the glove and at the same time to generate adjustable parts so that the anthropometric differences present between one person and another, so not affect the comfort when using the prototype.

The built prototype employs springs in its design, as previously conducted studies that highlight applications whit springs in the implementation of technologies that bring benefits such as muscle tone recovery, provide strength and stability, constant retention force and as actuators that lead to more compact designs [15, 16]. The characterization of the distance sensor results in a non-linear sensor behavior, thus demonstrating the exponential behavior of the photoresistors. In the development of the project, polynomial equations of degree 4 were obtained by means of an analysis carried out in the Excel program using the function of linear estimation with the curve option, these equations represent the ideal behavior of the curves. This analysis was made in order to accomplish an adjustment of greater precision, which was achieved since a coefficient of determination of value 1 was obtained and this represents a perfect correlation. The equations were entered in the Labview® program for the digital processing of the signal.

For the feeding of the optical sensor, a voltage regulator of 3.3 volts was implemented, that guarantees the voltage and current necessary for the correct functioning of the system. This element was used to ensure that the LED and the photoresistor always reached a standard voltage value, minimizing the error caused by voltage discharge and current flow, due to the number of components connected in parallel. Considering in this way, that in future applications different means of energy supply are used, as could be the case of batteries.

5 Conclusion

An initial prototype is presented, with the projection that the proposed system can become a support instrument for specialists, used in finger strength recovery therapies, with the benefits of the existing technologies that employ springs. This support tool focuses on the quantification of the strength of the fingers of the hand by means of a measurement system, whose operating principle is Hooke's law. The system has a proposed distance sensor, consisting of: a led and a photoresistor encapsulated in a plastic tube and three resistance levels determined by the constants of the springs. The force of fingers is measured and visualized, through a user interface, variables such as maximum force, average strength, number of repetitions and successful attempts according to a programmed limit, in order to identify the progress of the user.

The design of a force measurement system, low cost, accessible and simultaneous to other technologies, which will adapt to the mobility of the hand and measure the force in the fingers necessary to providing to counteract the opposition movement generated by the spring. It was the main achievement of this work, generating in this way a future application in the field of measurement and rehabilitation, focused on training and recovery of strength in the hand, which considers normal parameters within age ranges and physical frame.

Declaration of Conflict of Interest. The authors declare that they don't have conflicts of interest.

References

1. Engels, F.: El papel del trabajo en la transformación del mono en hombre (2011)
2. Monreal, R.: The hand, its origin, evolution and role in society. Revista Cubana de Ortopedia y Traumatología **21**(2) (2007)
3. Orts, A.P.: La mano, admirable don del hombre. Universidad de Alicante (1992)
4. Arias, L.: Biomecánica y patrones funcionales de la mano. Morfolia **4**(1), 14–24 (2012)
5. Caballero, C.V., Chalem, P., Londoño, J.D., (eds.) Guías para el tratamiento de la artritis reumatoidea. Asociacion Colombiana de Reumatologia (2002)
6. Brotzman, S.B., Manske, R.C.: Rehabilitación ortopédica clínica + ExpertConsult: Un enfoque basado en la evidencia. Elsevier Health Sciences (2012)
7. Murad, R.A., Discapacidad, N.: Colombia Encuesta nacional de demografía y salud, pp. 135–149 (2015)
8. Halic, T., Sinan, K., Demirel, D., Willey, M., Eichelberger, K.: MoMiReS: mobile mixed reality system for physical & occupational therapies for hand and wrist ailments. In: 2014 IEEE Innovations in Technology Conference, pp. 1–6. IEEE, Warwick (2014)
9. Chen, H., Wang, Q., Cao, L.: Design of the workstation for hand rehabilitation based on data glove. In: 2010 IEEE International Conference on Bioinformatics and Biomedicine Workshops (BIBMW), pp. 769–771. IEEE, Hong Kong (2010)
10. Agraz, J., Robert, P.: LabVIEW based control software for finger force sensor instrumentation design. In: 2013 IEEE AUTOTESTCON, pp. 1–6. IEEE, Schaumburg (2013)
11. Lambercy, O., Dovat, L., Johnson, V., Salman, B., Wong, S., Gassert, R., Milner, T., Leong, C., Burnet, E.: Development of a robot-assisted rehabilitation therapy to train hand function for activities of daily living. In: 2007 IEEE 10th International Conference on Rehabilitation Robotics, Noordwijk, pp. 678–682 (2007)
12. Alonso, C.: Análisis comparativo entre instrumentación clásica de galgas extensiométricas y sensores ópticos para la monitorización en una célula de carga. Undergraduate tesis, Telecommunication Eng. Program. Universidad de Cantabria, Cantabria (2015)
13. Serway, R., Jewett, J.: Física para ciencias e Ingeniería, 9th edn. Cengage Learning, pp. 171–173 (2015)
14. Matar, M., Parodi, M., Repetto, C., Roatta, A.: Linear modelization of a real spring-mass system. Revista Brasileira de Ensino de Física **40**(2) (2018)
15. Perry, J., Trimble, S., Castilho, L., Schoroeder, J., Belloso, A., Rodriguez, C., Keller, T.: Design of a spring-assisted exoskeleton module for wrist and hand rehabilitation. In: 2016 38th Annual International Conference of the IEEE Engineering in Medicine and Biology Society (EMBC), pp. 594–597. IEEE, Orlando (2016)
16. López, R., Torres, J., Salazar, S., Lozano, R.: Desarrollo de un exoesqueleto para rehabilitación de tobillo y rodilla. Revista mexicana de Ingeniería Biomédica **35**(1), 13–28 (2014)

A Rapid and Low-Cost Lung Function Testing Method Based on an Optical Flow Sensor

Markus Höglinger[1], Bianca Wiesmayr[2], Werner Baumgartner[1], and Anna T. Stadler[1(✉)]

[1] Institute of Biomedical Mechatronics, Johannes Kepler University Linz, Altenberger Straße 69, 4040 Linz, Austria
anna.stadler@jku.at

[2] LIT Cyber-Physical Systems Lab, Johannes Kepler University Linz, Altenberger Straße 69, 4040 Linz, Austria
http://www.jku.at/mmt

Abstract. Chronic obstructive pulmonary disease was the fifth highest cause of death in 2002 and it is projected to be the fourth highest cause of mortality by 2030 [1]. It is a heterogeneous disease, but the basic abnormality in all patients is airflow limitation, a value that could be easily assessed by pulmonary function tests. These tests are not readily available in low and middle income countries. Reasons include high equipment costs and the need for trained personnel. In this work, we present a lung function test that measures three highly relevant values: the forced vital capacity; the forced expiratory volume in one second and their ratio; the Tiffeneau-Pinelli index. The sensor is based on an optical detection principle. Light is coupled into a silicone fiber, that consists of a core and a cladding with low refractive index contrast to ensure high bending sensitivity. All parts of the sensor are low-cost, the silicone fiber can be both disposed and autoclaved.

Keywords: Rapid lung function testing · Optical measurement principle · FEV1/FVC ratio

1 Introduction

Chronic lung diseases are some of the most threatening medical conditions in the world. One preventable chronic respiratory illness is chronic obstructive pulmonary disease (COPD) [2]. Primary causes are tobacco smoke (second hand), and air pollution (both indoor and outdoor) [3]. The Global Initiative for Obstructive Lung Diseases (GOLD) has defined COPD based on spirometric criteria using the forced expiratory volume in one second (FEV1) and its ratio to the forced vital capacity (FVC), the so-called Tiffeneau-Pinelli index (T-index) [4]. The main criterion for COPD is a T-index smaller than 70%.

Spirometry is a noninvasive, well-established diagnostic tool to measure and record lung function. By assessing breathing patterns, lung diseases like COPD

© Springer Nature Switzerland AG 2020
C. A. González Díaz et al. (Eds.): CLAIB 2019, IFMBE Proceedings 75, pp. 469–477, 2020.
https://doi.org/10.1007/978-3-030-30648-9_61

can be detected. There is no cure for COPD, but an early detection can help to improve quality of life and reduce the risk of early death. However, spirometers are not readily available among general practitioners, particularly in low and middle income countries.

High effort is made to improve this situation and develop low-cost, point-of-care testing (PoCT) devices. Smartphone-based systems are popular. Bhattacharjee et al. [5] propose a humidity sensor to monitor breathing frequency and peak-flow rate. The SpiroSmart [6] assesses lung function parameters via the smartphone's microphone - a promising method as no additional sensor would be necessary; however, systematic errors occur with this method and therefore to date no accurate measurement is feasible. Michailidis et al. [7] directly attached a turbine-flow spirometer to a smartphone. Recently, a low-cost spirometer [8] based on an optical mouse was presented; it was not clear though how the sensor could be sterilized to avoid cross-contamination. Cantilever systems to measure lung function were studied previously [9,10], both struggled with accuracy issues. A promising technology that was not yet tested in humans though is based on quartz crystal microbalance arrays [11].

In this study, we sought to design a simple, low-cost, and rapid pulmonary function test (PFT) based on an optical measurement principle. Light is coupled into an elastomer waveguide. When airflow deflects the waveguide, light is lost, and hence less photons are detected by a highly sensitive photodiode. The resulting output voltage depends quadratically on the flow velocity. The specific objectives of this study were: (1) to manufacture a highly sensitive sensor that can be sterilized; (2) to assess the T-index; (3) to design a high-quality and low-cost prototype; and (4) to evaluate the functionality of the flow sensory system.

2 Materials and Method

An optical measurement principle (schematic description in Fig. 1) for the flow sensor was chosen: Red light (peak wavelength at 625 nm) is coupled into a polydimethylsiloxane (PDMS) fiber consisting of a core and a cladding. For the core Sylgard 184 (Dowsil, USA) was used; the cladding was fabricated with RTV 165 (Momentive, USA). The two materials have almost identical properties and show similar mechanical behavior. At a wavelength of 625 nm, the refractive indices amounted to 1.4299 (Sylgard 184) and 1.4286 (RTV 615) [12]. (This small refractive index contrast guarantees high bending sensitivity.) Additionally, a sealing layer (Sylgard 170, Dowsil, USA) was applied to shield the waveguide from ambient light. The light is guided through the fiber and detected by a high-sensitivity, low-capacitance photodiode (BPX61, Osram, Germany). When air flow bends the fiber, optical losses are produced that can be related to the flow velocities.

The measurement setup consists of a light-emitting diode (LED), an optical fiber and a photodiode with amplifier. The basic prototype design was already described in detail in our previous work [13,14]. To meet the requirements for

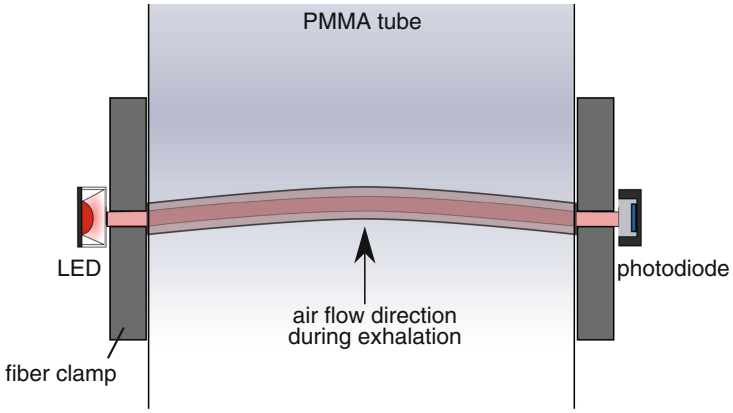

Fig. 1. Schematic description of the optical flow sensor, after [14]. Light is coupled into the PDMS fiber by means of an LED. The air flow bends the fiber, and therefore light is lost. Less photons reach the photodiode. The light loss and hence the flow velocity can be determined.

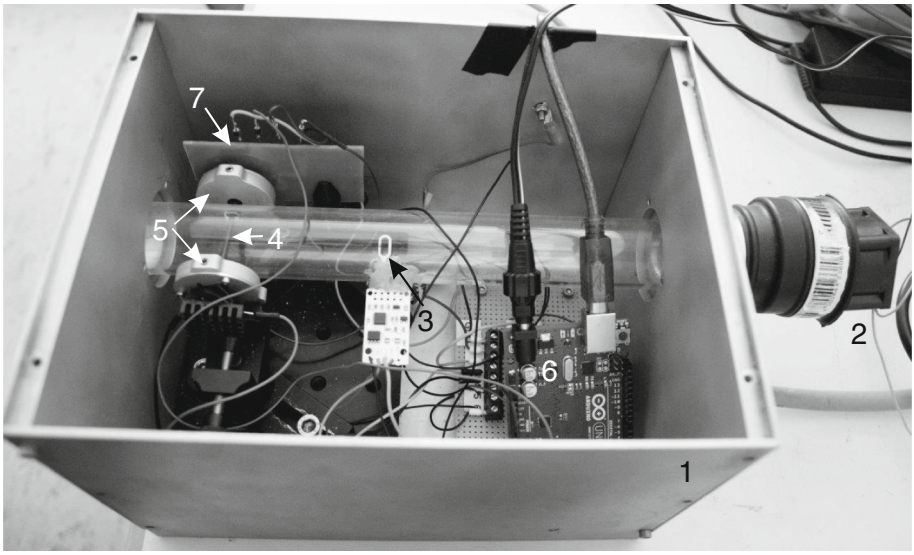

Fig. 2. Measurement setup in the shielding cage (1). A fan (2) simulates the air flow; the flow velocity is measured by the wind sensor (3) and the optical fiber (4). Fiber clamps (5) fix the fiber. An Arduino^{TM}UNO (6) records the data from the photodiode amplifier (7) and converts it to a digital signal.

PFT, the setup was adapted accordingly. The fiber has a circular cross-section, a core diameter of 1.5 mm and a cladding diameter of 2 mm to reach higher bending sensitivity; it is 30 mm long to fit into standard spirometric tubes. The fabrication process of the fiber was outlined in [13]. Various LEDs were tested, and the Osram LED (LR T68F, Osram Opto Semiconductors GmbH, Germany) was found to display the highest bending sensitivity in combination with a 20 mA current source.

The PFT prototype (Fig. 2) comprises a Poly(methyl methacrylate) (PMMA) pipe holding the optical fiber and a wind sensor (Rev-P, Modern Device, USA) for calibration and as a reference. Fiber clamps guarantee reproducible fixation of the elastic fiber without twisting or squeezing it. The electronic evaluation unit comprises an Arduino^{TM}UNO to record both the data from the wind sensor and the photodiode amplifier, and converts the data to a digital signal (analogue/digital conversion). The Arduino^{TM}UNO is connected to a computer via USB. A GUI was programmed in MATLAB (R2015b, Mathworks, USA) to start/stop recording and to save, plot, and evaluate the measurement results. To evaluate the performance of the prototype, a fan (San 24 Ace 36, Sanyo Denki, Germany) was connected at the end of the PMMA tube. The wind speed was increased from 0 m/s to 10 m/s and subsequently decreased by means of a power supply. Three cycles consisting of 36 individual measurements each were performed. Data were recorded for 10 s, and the mean value was calculated.

After the positive evaluation of the prototype, a PFT cycle, consisting of three measurements each, was recorded with six testers. For each cycle, a pulmonary function filter mouthpiece (MicroGard^{TM}II, CareFusion, Germany) was used to guarantee highest viral and bacterial efficiency, while still offering a low breathing resistance [15]. To calculate the values of the forced vital capacity (FVC) and the forced expiratory volume in one second (FEV1), the volume flow (in m^3/s)

$$Q = v \cdot A, \tag{1}$$

was integrated over time. Here, v denotes the airflow velocity in m/s and A the cross-section in m^2 of the airflow tube. FVC and FEV1 values were calculated from the digitized data as follows:

$$FVC = \sum_{i=1}^{N} v(i) \cdot A \cdot \Delta t, \tag{2}$$

and

$$FEV1 = \sum_{i=1}^{k} v(i) \cdot A \cdot \Delta t, \tag{3}$$

where N denotes the total number of data points, k the number of data points in one second, and $\Delta t = t(i) - t(i-1)$ is the time between two data points. From these two spirometric values, the T-index T was calculated

$$T = \frac{FEV1}{FVC}. \tag{4}$$

3 Results and Discussion

3.1 Prototype Evaluation

Before we conducted the PFT, the prototype was tested by means of a fan. Although the support voltage at the fan was set to the same values for each measurement cycle, the velocities at the wind sensor varied slightly. Therefore the standard deviation could not be calculated. To test if the fiber can be fixed reproducibly, we conducted three measurement cycles. After each cycle, the fiber was manually removed and fixed subsequently. The results are illustrated in Fig. 3. The three measurement cycles show similar behavior but differ slightly at higher flow velocities. The reason can be found in the fixation method. A torque wrench to tighten the screws at the clamps with a defined tightening torque would be necessary. The findings however reveal that within one measurement cycle the fiber can be reproducibly deflected.

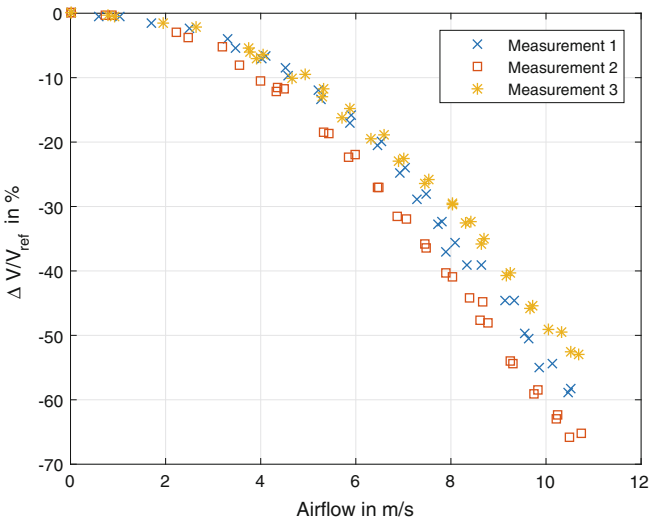

Fig. 3. Three measurements to determine the reproducibility of the fiber. The fiber was newly fixed with the fiber clamps after each measurement. All three measurements showed similar behavior, slight differences can be observed at higher flow velocities. The mean relative voltage change at 10 m/s was approximately –55%.

The experiments illustrate that the light loss depends quadratically on the flow velocity. The fiber is highly sensitive to bending, i.e. changes in flow velocities. A mean relative voltage change of up to 60% at 10 m/s was achieved.

3.2 Pulmonary Function Tests

When the first experiments with test subjects were conducted, unwanted effects occurred at the output of the sensor. We observed both a delayed response and a small unexpected decline at the sensor output.

After eliminating all possible causes that could introduce the unwanted effects, we determined rising temperature and humidity as the interfering factors.

The optical fiber is made of PDMS. This material is widely regarded as hydrophobic [16]. Studies showed however that PDMS materials are known to allow permeation of gas and water vapor [17]. Also, the material has a thermal expansion coefficient.

To reduce humidity, we put silica gel into the mouthpiece; temperature was stabilized by cooling the mouthpiece prior to the lung function tests.

Table 1. Pulmonary function values of 6 testers and the T-index reference values [18].

	Test subjects	FVC [L]	FEV1 [L]	T (T_{ref}) [%]
1	Male, 27, non-smoker	5.34	4.38	82.03 (82.35)
2	Female, 27, non-smoker	5.81	4.42	76.84 (83.97)
3	Female, 34, non-smoker	5.54	4.91	89.11 (82.64)
4	Male, 31, non-smoker	5.64	4.42	79.05 (81.63)
5	Female, 48, smoker	2.74	2.34	84.61 (79.98)
6	Male, 31, heavy smoker	6.25	4.15	66.52 (81.63)

In Table 1, the measurement results of six test subjects are shown. While there was a noticeable inter-person variability concerning the FVC and FEV1 values, the T-index (see Eq. 4) was in the expected range. The reason for the differences in the values compared to the reference values may be found in the inconsistent behavior of the test subjects.

The reference values T_{ref} presented in Table 1 were calculated from the equations suggested in [18] and depend on age, gender, weight, height, and ethnicity. Smoking behavior is not considered in the presented equations. Therefore the last candidate's T-index is dramatically lower than the expected value. One can also notice that the FVC and FEV1 values in tester 5 are remarkably lower than in the other testers. One reason is certainly the difference in age. Nevertheless, both FVC and FEV1 values are lower than expected ($FVC_{ref} = 3.13$ and $FEV1_{ref} = 2.68$). In this case our rapid test would recommend a more detailed analysis of the lung function to determine the reasons for the low values.

In Fig. 4 a representative measurement of a forced expiration is illustrated. The setup fulfills the recommendations for spirometry regarding the volume (0.5 L – 8L) and flow range (0 L/s – 14 L/s) [19], and could be a promising sensor for future applications.

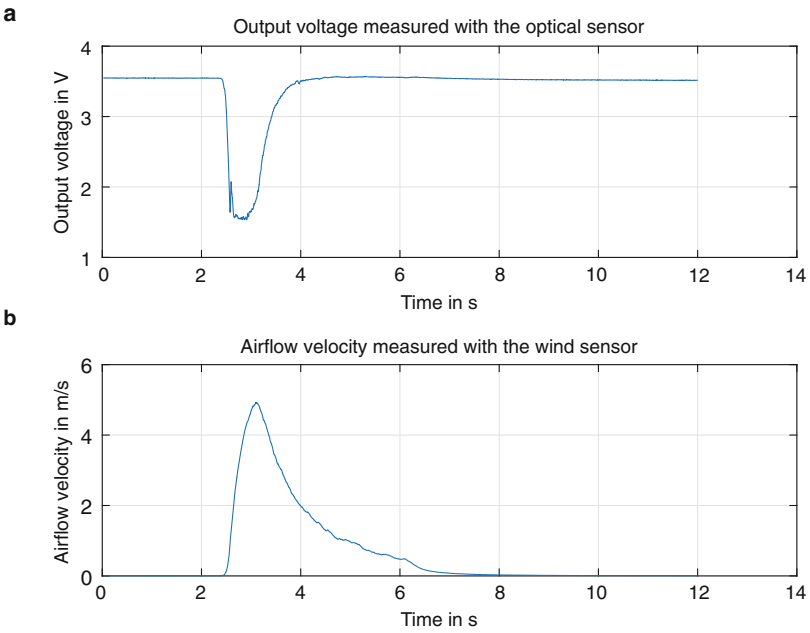

Fig. 4. One representative measurement of a forced expiration. **a** Output voltage of the optical flow sensor, and **b** airflow velocity of the wind sensor.

4 Conclusion

The purpose of this study was to investigate an optical flow sensor to demonstrate its applicability in lung function testing. We focused on (i) simple handling, and (ii) the design of a low-cost device. The sensor only displays three values, the FVC, the FEV1, and their ratio, the T-index. With these values, a detection of airflow limitations and hence detection of chronic lung diseases is feasible. The PDMS fiber can be both disposed and autoclaved, and the whole sensor setup is designed with low-cost parts.

The current issues with temperature and humidity influence must be solved to develop a professional device for PFT.

To avoid permeation of water vapor, the fiber sealant could be dispersed with collagen powder. Collagen is an important protein and is often used in medical products due to its water-holding capacity, biocompatibility, and flexibility [17]. The interfering effects due to temperature seem to be more difficult to control. The linear coefficient of thermal expansion for Sylgard 184 is $310{\cdot}10^{-6}1\,^{\circ}\mathrm{C}$. The maximum temperature difference observed was 10 °C. If, for example, the temperature rises from 20 to 30 °C during a PFT measurement, the fiber with a length of 30 mm would expand 0.1 mm.

Possible solutions could be to heat the system up to a constant temperature equal to the breathing temperature or cool the breathing temperature down to

ambient temperature. In future work we will also focus on compensating the effect in the output signal, which needs a profound understanding and precise calculation of the temperature influence.

At present, measurements were controlled and evaluated via a laptop for reasons of convenience. The programming of an application for smartphones or tablets is feasible and will be included in our future work.

Acknowledgment. The authors thank the colleagues from the Center for Surface and Nanoanalytics (ZONA) at JKU for their professional assistance in drafting and fabricating the measurement setup; in particular Philip Lindner for designing the fibre clamps (Institute of Semiconductor and Solid State Physics and ZONA, both JKU), Robert Leimlehner (ZONA and Institute of Experimental Physics, both JKU) for his great help in planning the measurement setup, and Bianca Ratzenböck (ZONA) for fabricating essential parts of the setup.

Conflict of Interest. The authors declare that they have no conflict of interest.

References

1. Mathers, C.D., Loncar, D.: PLoS Med. **3**(11), e442 (2006). https://doi.org/10.1371/journal.pmed.0030442
2. Bousquet, J. (eds.): WHO. Global Surveillance, Prevention and Control of Chronic Respiratory Diseases: A Comprehensive Approach. WHO, Geneva (2007)
3. Ford, E.: J. Allergy Clin. Immunol. **115**(5), 897 (2005). https://doi.org/10.1016/j.jaci.2004.11.050
4. NHLBI: WHO, Global strategy for the diagnosis, management, and prevention of chronic obstructive pulmonary disease. Technical report, NHLBI (2011)
5. Bhattacharjee, M., Nemade, H.B., Bandyopadhyay, D.: Biosens. Bioelectron. **94**, 544 (2017). https://doi.org/10.1016/j.bios.2017.03.049
6. Larson, E.C., Goel, M., Boriello, G., Heltshe, S., Rosenfeld, M., Patel, S.N.: Proceedings of the 2012 ACM Conference on Ubiquitous Computing - UbiComp 2012, p. 280. ACM Press, Pittsburgh (2012). https://doi.org/10.1145/2370216.2370261
7. Michailidis, C., Smanis, I., Stamatis, K., Bergeles, C., Kouris, A.: Proceedings of the 4th International Conference on Wireless Mobile Communication and Healthcare - Transforming Healthcare through Innovations in Mobile and Wireless Technologies (ICST, Athens, Greece) (2014). https://doi.org/10.4108/icst.mobihealth.2014.257512
8. Bagchi, S., Sengupta, S., Mandal, S.: IEEE Sens. J. **17**(7), 2065 (2017). https://doi.org/10.1109/JSEN.2017.2664889
9. Ambastha, S., Umesh, S., Maheshwari, K.U., Asokan, S.: J. Lightwave Technol. **34**(24), 5682 (2016). https://doi.org/10.1109/JLT.2016.2627017
10. Ghafar-Zadeh, E., Gholamzadeh, B., Ayala-Charca, G., Raveri, P.B., Matynia, M., Sawan, M., Awwad, F., Magierowski, S.: Microsyst. Technol. **23**(10), 4591 (2017). https://doi.org/10.1007/s00542-016-3200-0
11. Selyanchyn, R., Wakamatsu, S., Hayashi, K., Lee, S.W.: Sensors **15**(8), 18834 (2015). https://doi.org/10.3390/s150818834
12. Schneider, F., Draheim, J., Kamberger, R., Wallrabe, U.: Sens. Actuators, A **151**(2), 95 (2009). https://doi.org/10.1016/j.sna.2009.01.026

13. Stadler, A.T., Wiesmayr, B., Krieger, M., Baumgartner, W.: Sensors and measuring systems. In: 19th ITG/GMA-Symposium, pp. 1–4 (2018)
14. Wiesmayr, B., Höglinger, M., Krieger, M., Lindner, P., Baumgartner, W., Stadler, A.T.: Sensors **19**(4), 925 (2019). https://doi.org/10.3390/s19040925
15. CareFusion, Microgard II Datasheet. Datasheet, CareFusion Germany 234 GmbH (2012)
16. Harley, S.J., Glascoe, E.A., Maxwell, R.S.: J. Phys. Chem. B **116**(48), 14183 (2012). https://doi.org/10.1021/jp305997f
17. Zhang, Y., Ishida, M., Kazoe, Y., Sato, Y., Miki, N.: IEEJ Trans. Electr. Electron. Eng. **4**(3), 442 (2009). https://doi.org/10.1002/tee.20429
18. Quanjer, P.H.: European coal and steel community. In: European Respiratory Society Standardized Lung Function Testing: Report; Official Statement of the European Respiratory Society, vol. 16, Munksgaard, Copenhagen (1993)
19. Miller, M.R.: Eur. Respir. J. **26**(2), 319 (2005). https://doi.org/10.1183/09031936.05.00034805

A New Approach to Cardiovascular Screening in Newborn

Rene Gonzalez-Fernandez(✉), Luis Reyes-Morales, Alejandro Torres-Fortuny, and Hany Pazos-Espinosa

Cuban Neuroscience Center, 190 Street, 11600 Havana, Cuba
rigf58@yahoo.com

Abstract. The aim of this paper is to present the main features of a new approach to cardiovascular screening in newborns. The proposed system is made up of the Recorder and the Analyzer. The former is a medical device able to acquire two channels of pulse oximetry data and lead II from the standard ECG simultaneously. Data transmission to the Analyzer is supported by the Bluetooth standard. The Analyzer is an Android application run in a mobile device to analyze several ECG and plethysmography parameters that allows newborn's classification as cardiovascular "healthy" and "no healthy". QRS complexes are detected as the first step to study the cardiac rhythm looking for arrhythmia events. QT interval duration is measured to check if the studied newborn is prone to sudden death. Pulse oximetry values are measure in finger and leg to detect dangerous differences. PWTT index computation offers an indirect estimation of cardiac output; this index is inversely proportional to the cardiac output. A prototype was developed and tested at laboratory level. Results indicate that the developed device is safe according to the IEC 60601-1 standard, and sensitivity in QRS complex detection was 99.36%, enough for the intended use of the proposed system.

Keywords: Cardiovascular screening · ECG in newborns · Newborn oximetry

1 Introduction

It is globally recognized that newborn screening provides an opportunity to reduce morbidity and mortality in the first years of life [1, 2]. This is the reason why many governments provide significant resources to apply these procedures as part of their public health policies. Several cardiovascular diseases can be identified with simple tests before newborns are discharged from hospital; hence, their life quality can be guaranteed without large investments.

Congenital heart defects occur in approximately eight of every 1,000 live births according to information published by the U.S. Department of Health and Human Services [3]. Also, other disturbances such as dangerous ventricular arrhythmias and propensity to sudden death could be identified in the first hours of life. In the absence of early detection of these cardiac conditions, infants are at risk for serious complications or death within the first weeks of life.

© Springer Nature Switzerland AG 2020
C. A. González Díaz et al. (Eds.): CLAIB 2019, IFMBE Proceedings 75, pp. 478–485, 2020.
https://doi.org/10.1007/978-3-030-30648-9_62

Typically, cardiovascular screening of newborns is based on pulse oximetry or standard twelve-lead electrocardiogram (ECG). These techniques are inexpensive, noninvasive and well known by physicians [4, 5]. Pulse oximetry is preferred by many specialists because low oxygen saturation values indicate hypoxemia, an early clinical sign of critical congenital heart defects, as well as other disorders that require immediate follow-up. Moreover, other disturbances can be detected studying plethysmography signal (PPG). Nonetheless, other specialists favor ECG because a deeper arrhythmia analysis can be done, the signal morphology provides important information about the cardiovascular system and the QT interval can be studied as a very important sudden death predictor. The main ECG disadvantage is the number of electrodes as the newborn skin is fragile and ten electrodes seem to be a high damage risk.

Pulse oximetry and standard ECG are useful for cardiovascular screening, so the combination of both techniques would be a powerful tool. If the ECG is reduced to one channel, the number of required electrodes decreases from ten to three, even two, thus minimizing its main disadvantage. The ability to study the ECG morphology from different electrical point of view is lost, but it is possible to examine the cardiac rhythm and the QT interval, recognized as an important sudden death predictor.

The aim of this paper is to discuss the main characteristics of a new approach to the cardiovascular screening based on the analysis of two simultaneous pulse oximetry measurements and a one-channel ECG.

2 Materials and Methods

The proposed system is composed of the Recorder and the Analyzer. The Recorder is a medical device that allows the acquisition of II from the standard ECG and two channels of pulse oximetry information simultaneously. The Analyzer is a mobile device application that processes and stores the whole data. Both components communicate through a Bluetooth interface, as shown in Fig. 1.

Fig. 1. Representation of the proposed approach.

The proposed procedure is as follow: The physician checks the Recorder's setup to verify all data is correct. A nurse prepares the newborn and places the electrodes,

previously connected to the Recorder, on the newborn's skin. Once the nurse turns on the Recorder, it automatically connects, by Bluetooth, to the Analyzer. The physician selects the general data of the studied newborn and starts the signal acquisition by sending a command to the Recorder. Samples of the PPG signals and the ECG are sent together with oxygen saturation and pulse rate to the Analyzer to be displayed in real time. In addition, ECG is filtered using a band pass FIR approach with cut-off frequencies of 0.6 Hz and 37 Hz. When an electrode disconnects, the Recorder sends a command to the Analyzer to restart the data acquisition. All data is processed and stored in a database.

The Recorder's electronic design has the following blocks: the processing unit, the power supply, the oximetry modules and the ECG amplifier, as presented in Fig. 2.

The STM32F407 microcontroller was selected as the processing unit of the Recorder due to its high level of integration and performance, embedded memories and rich peripheral set. This microcontroller guarantees the necessary level of computing power and peripherals for all the tasks to be performed.

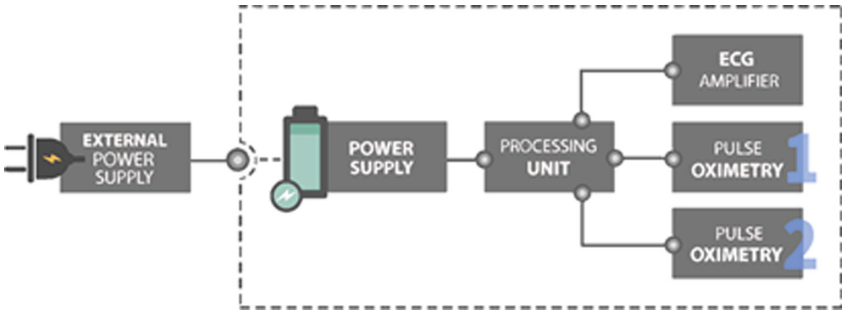

Fig. 2. The recorder divided in functional blocks.

The main features of the processing unit are the following:

- A SD memory controller that stores all the data corresponding to each studied patient. It provides a backup to restore Analyzer's database.
- A programmable timer to synchronized events and activities such as data acquisition and serial communication.
- Internal memory that allows storing Recorder's setup data.
- A fully integrated Bluetooth serial port module.
- An UART (Universal Asynchronous Receiver & Transmitter) controller for serial communication that enables to read data from oximetry modules.
- A driver for input/out lines used in the implementation of communication protocols.
- A twelve-bit analogue to digital converter for ECG acquisition.

The power supply block is composed of two elements. The first component is an external medical grade power supply that is able to guarantee the requested electrical isolation and the Recorder's power consumption. This external power supply works with input voltages from 90 V to 240 V and its output voltage is 12 V DC. The second

element is an electronic circuit implemented into the Recorder to get 5 V and 3.3 V from the 12 V previously mentioned. These voltages are required for other Recorder's blocks.

The Recorder includes two oximetry modules to measure oxygen saturation in the right hand and on one of the feet of the studied newborn simultaneously. Many pulse oximetry modules are available in the market, so it is better to select one instead of start a new design to measure this variable. The E305654 module from Mindray, an acknowledged Chinese medical devices manufacturer, was selected because of its high performance in previous monitoring devices developed by the authors.

The communication between the processing unit and the pulse oximetry modules is implemented as a serial channel for each one; data transmission rate is 115200 bauds following a protocol set by the module's manufacturer. Pulse rate value, oxygen saturation value and samples of the digitized plethysmography signals are transmitted.

Lead II from de standard ECG is sampled at 250 Hz while pulse oximetry information, signal samples and parameter values, are read from the modules. A digital moving average filter is applied to each ECG sample to minimize the noise negative effects. Data acquisition time is set between one and five minutes in the Recorder's setup.

The Recorder's goal is the acquisition of high quality signals to guarantee a reliable data input to the processing algorithm. On the other hand, the Analyzer is focused on the processing of the incoming cardiovascular data to extract the following information:

- Cardiac rhythm: Events such as bradycardia, tachycardia, asystole and ventricular arrhythmias can be detected when ECG samples are analyzed.
- QT interval duration: This parameter is recognized as a sudden death predictor [6].
- Pulse oximetry values: A difference of 3% of oxygen saturation between the right hand and any foot is an indicator of cardiovascular disturbance.
- PPG wave shape: A small amplitude might be associated with a low perfusion index, a negative condition for the metabolism. In addition, the PWTT (Pulse Wave Transit Time) index is computed to identify important changes in cardiac output.

All the signal processing, excluding digital filtering, is done off-line, at the end of the signal acquisition process. Cardiovascular signals, pulse rate and oxygen saturation values are displayed on the Analyzer's screen during the data acquisition process.

The ECG processing starts with QRS complex detection. The Teager operator is computed for each ECG sample and these values are integrated into a moving window to emphasize the high energy zones associated with the QRS complexes. Two thresholds are applied; the first one set a frontier between signal segments candidates to be a QRS complex and the rest of the signal. The second threshold is combined with the signal slope to identify the onset and offset for each QRS complex. The expression 1 shows how to compute the Teager operator in time domain.

$$T(i) = \mathrm{x(i)}^2 - \mathrm{x(i-1)} * \mathrm{x(i+1)} \tag{1}$$

Where:
T(i): Teager operator for each sample.
x(i): ECG sample.

When QRS complexes are detected, RR interval duration is computed for each complex and a mean value is calculated to get the heart rate value. RR interval duration is the primary information to define if a QRS complex is premature.

The QRS complexes are classified as normal (N), ventricular premature (VP) and other complexes (OC). It is essential because QT interval duration and PWTT index are measured in N complexes only while VP complexes are related to dangerous arrhythmias. A QRS complex will be considered as N when its duration is between the 80% and 120% of the mean duration and the complex is not premature. A VP complex will be premature, wide and different in amplitude from the mean of the studied signal. QRS complexes that are not classified as N or VP will be considered as OC.

The arrhythmia analysis is based on the duration of RR intervals and the QRS classification results. The fulfillment of the following criteria is sought:

- Bradycardia: When heart rate value is below a preset limit.
- Tachycardia: When heart rate is higher than a preset limit.
- Asystole: Absence of QRS complexes in a preset period.
- Frequent VP: When the VP rate is higher than a preset limit.

The cardiac rhythm is normal when none of the above conditions is met. Other disturbances such as edema and intraventricular conduction disorders are studied. Edema is associated with low voltage QRS complexes while a continuous wide QRS complex pattern with a stable rhythm is related to the cited conduction disorders.

QT interval duration for each normal QRS complex is measured. This process is based in an algorithm described by the authors in previous papers [7, 8]. The essence of the algorithm is to find the moment after the T wave peak when the difference between the baseline and the ECG stops decreasing. If the signal voltage is very low, this parameter is not measured to avoid measurement errors.

PWTT index is computed combining features of the ECG and PPG waves; it is measured only for normal QRS complexes. The R wave peak is used as start point to find the maximum positive slope in the plethysmography wave before the next QRS complex, the distance between these points is the PWTT index. In addition, pairs of pulse oximetry values and their differences are studied to detect cardiovascular disturbances according to findings reported previously [4, 5].

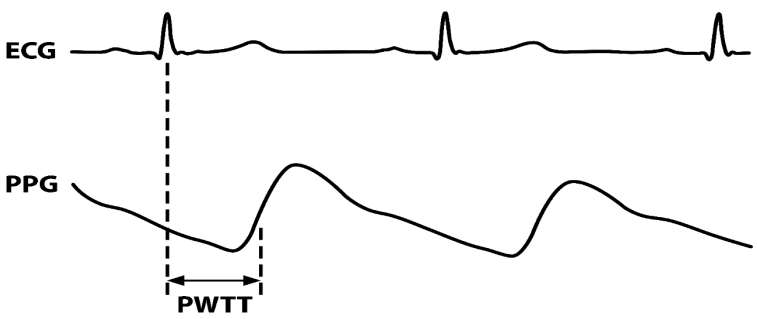

Fig. 3. PWTT index as the time from the R wave peak to the most positive slope of the PPG cycle.

When all the measures and analysis described above indicate normal results, the analyzed newborn is classified as "cardiovascular healthy". If any of the analyzed measures is out of their respective normal ranges, the corresponded test should be repeated or a more detailed tests and analysis should be indicated (Fig. 3).

3 Materials and Methods

A prototype of the proposed solution has been developed and tested at laboratory level because national regulatory body approval is mandatory for the application of medical technology to humans. Currently, the authors are working in compliance with the requirements demanded by the regulatory body.

The Recorder has been tested as a whole according to the IEC 60601-1 general safety standard. However, pulse oximetry modules are supported by international certifications, such as CE mark, guarantying compliance with current standards. The most significant technical results are shown in Table 1.

Table 1. Main technical results according to IEC 60601-1 standard.

Test	Result
Dynamic input range	±5 mV
Input impedance	Greater than 2,5 MΩ
Maximum DC input level	320 mV
Internal noise	21 μV
Patient auxiliary current	Less than 0,01 mA
Common mode rejection rate	Greater than 90 dB

All technical results meet the applied standard but it was impossible to show them all due to the limits of the paper. Combining certified pulse oximetry modules, a certified medical power supply and a well-designed ECG amplifier, the authors have developed a safe medical device.

The detection of QRS complexes was tested using the MIT-BIH Arrhythmia Database which is considered as a gold standard for this purpose. Table 2 shows the results for each ECG. These signals include a representative variety of waveforms and artifact that any detector could encounter in routine clinical use.

The sensitivity of the proposed QRS complex detection algorithm was 99.36%. This measure was over 99% in 38 ECGs and never was less than 98.30%. The algorithm performance was highly stable; it is very important for the intended use of the proposed solution. Newborns are non-cooperative patients and signal acquisition process could be hard, although MIT-BIH database includes signals acquired in worse conditions.

Table 2. Results detecting QRS complexes from MIT-BIH Arrhythmia Database.

Record	QRS	TP	Sensitivity	Record	QRS	TP	Sensitivity
100	2273	2273	100.00%	201	1963	1960	99.85%
101	1863	1861	99.89%	202	2136	2127	99.58%
102	2187	2160	98.77%	203	2980	2963	99.43%
103	2084	2084	100.00%	205	2656	2624	98.80%
104	2229	2220	99.60%	207	1860	1833	98.55%
105	2572	2549	99.11%	208	2955	2933	99.26%
106	2027	2007	99.01%	209	3005	2996	99.70%
107	2137	2120	99.20%	210	2650	2631	99.28%
108	1762	1741	98.81%	212	2748	2746	99.93%
109	2532	2507	99.01%	213	3251	3220	99.05%
111	2124	2111	99.39%	214	2262	2241	99.07%
112	2539	2538	99.96%	215	3363	3360	99.91%
113	1795	1794	99.94%	217	2208	2177	98.60%
114	1877	1860	99.09%	219	2154	2136	99.16%
115	1953	1951	99.90%	220	2048	2046	99.90%
116	2412	2398	99.42%	221	2427	2407	99,18%
117	1535	1520	99.02%	222	2483	2466	99.32%
118	2278	2253	98.90%	223	2605	2581	99.08%
119	1987	1981	99.70%	228	2053	2018	98.30%
121	1863	1861	99.89%	230	2256	2253	99.87%
122	2476	2475	99.96%	231	1571	1568	99.81%
123	1518	1516	99.87%	232	1780	1772	99.55%
124	1619	1592	98.33%	233	3079	3036	98.60%
200	2601	2576	99.04%	234	2753	2750	99.89%

QRS complex classification process was not evaluated with the same criteria used in MIT-BIH database because the authors are focused on normal and ventricular beats only. The evaluation of the QRS complex classification was implemented using the conclusions of a specialist as golden rule. A software tool was developed by the authors for the ECG reviewing process and the specialist classified the QRS complexes in the same groups as the proposed solution: normal (N), ventricular contractions (VC) and other contractions (OC). It is impossible to include the complete results, but the authors summarized the evaluation in the following sentences:

- Regarding the classification of N type QRS complexes, there was a full coincidence between the algorithm's conclusions and criteria emitted by the specialist. However, there were 32 QRS complexes classified as OC by the algorithm that the specialist considered as N. This error is not determinant in the effectiveness because QRS complexes type OC do not influence the final evaluation of the analyzed newborns.
- Regarding the classification of VC type QRS complexes, there was a full coincidence in all those who were premature. The proposed algorithm was not able to classify the non-premature ventricular QRS complexes, but this kind of complexes are exceptions. Nevertheless, authors will work to solve this weakness in the future.

The results obtained confirm that the QRS complex classification process is appropriate for the intended use.

A complementary test was developed with the Preterm Infant Cardio-respiratory Signals (PICS) database available in Physionet website [9]. Only QRS complex detection have been tested and sensitivity was 99.21%; very close to the result with MITBIH Arrhythmia Database shown previously. The next step will be test the QRS complex classification process with the same data.

The algorithm to compute PWTT index was tested with simulated signals. A ProSim 8 Vital Signs Simulator was used to generate ECG and PPG signals simultaneously with heart rate between 100 and 180 beats per minute. The identification of R wave peak was always correct as well as the moment of maximum slope in the PPG, so the PWTT index measurement was successful.

The proposed solution seems a useful approach to the cardiovascular newborn screening because advantages of ECG and oximetry ate mixed in a single method while patient discomfort is minimized. PWTT index can provide valuable information on the cardiovascular system of the studied newborn. More tests are necessary, but the results obtained to date are very promising.

References

1. Bruno, J., Havranek, T.: Screening for critical congenital heart disease in newborns. Adv. Pediatr. **62**, 211–226 (2015)
2. Zeltser, I., Cannon, B., Silvana, L., Fenrich, A., George, J., Schleifer, J., Garcia, M., Barnes, A., Rivenes, S., Patt, H., Rodgers, G., Scott, W.: Lessons learned from preparticipation cardiovascular screening in a state funded program. Am. J. Cardiol. **110**, 902–908 (2012)
3. Hoffman, J.L., Kaplan, S.: The incidence of congenital heart disease. J. Am. Coll. Cardiol. **39**(12), 1890–1900 (2002)
4. Vetter, V.L.: Should electrocardiographic (ECG) screening of all infants, children and teenagers be performed? Circulation **130**, 688–697 (2014)
5. Schwartz, P.J., Kotta, M.: Sudden infant death syndrome and genetics. J. Am. Coll. Cardiol. **71**(11) (2018)
6. Lupoglazoff, J.M., Denjoy, I., Villain, E., Fressart, V., et al.: Long QT syndrome in neonates. J. Am. Coll. Cardiol. **43**(5) 2004
7. Gonzalez-Fernandez, R.: Computerized analysis of the electrocardiogram. Caderno de Engenharia Biomédica **13**, 139–148 (1997)
8. Gonzalez-Fernandez, R., Rodriguez-Gomez, A., Almeida-Verdaguer, R.: QT dispersion monitoring as a coronary disturbance prediction tool. Comput. Cardiol. **32**, 507–510 (2005)
9. Gee, A.H., Barbieri, R., Paydarfar, D., Indic, P.: Predicting bradycardia in preterm infants using point process analysis of heart rate. IEEE Trans. Biomed. Eng. **64**(9), 2300–2308 (2017)

Graphene Nanosensor for NO Metabolites Detection

Andrés Fuentes-Aranda[1(✉)], Carlos Maya-Escamilla[1], Columba Rentería-Montoya[1], Mercedes Teresita Oropeza-Guzmán[1], Oscar Vázquez-Mena[3], and Viviana Sarmiento[2,3]

[1] Centro de Graduados e Investigación en Química, Tecnológico Nacional de México/Instituto Tecnológico de Tijuana, 22414 Tijuana, B.C., Mexico
carlosmayalike@gmail.com
[2] Universidad Autónoma de Baja California, 22427 Tijuana, B.C., Mexico
[3] Department of NanoEngineering, University of California San Diego, La Jolla, San Diego, CA 92093, USA

Abstract. In the present study, we present the design, manufacture and analytical performance of a graphene sensor (SLG/SiO_2/Si) for the *in situ* detection of HNO_3 as a substitute measure of NO in aqueous conditions. Our electrochemical and FET studies demonstrate that the CVD graphene, which is applied as a sensing platform, can respond rapidly to NO metabolites in physiological environments with a micromolar sensitivity. These results are promising in the development of a sensor that allows real-time monitoring of the physiological levels of NO in cultured cells and plasma.

Keywords: Chip · Graphene · Real-time · NO · Metabolites electrochemical detection

1 Introduction

Nitric oxide (NO) is an intracellular messenger molecule involved in functions of the immune system, cardiovascular system, and communication in nervous system [1–7]. The major pathway for NO metabolism is the stepwise oxidation to nitrite and nitrate [8]. In plasma or other physiological fluids or buffers NO is oxidized almost completely to nitrite, where it remains stable for several hours [9, 10]. Thus, nitrite is a central homeostatic molecule in NO biology and serves as an important signaling molecule in its own right [11, 12]. Nitrite and nitrate in blood has been widely used as an index of endothelial NO synthase activity [13, 14] as routine indirect measures of NO levels. Monitoring the evolution of NO concentration over time and with spatial resolution on the micrometer scale is crucial to elucidating the metabolic pathways and biological processes in which NO participates. There are several methods for determining NO and its products/metabolites in biological fluids, many of which have been described in review articles [15–18]. However, a comprehensive methodological description for the detection of NO and it products/metabolites in blood as well as multiple tissues and other compartments is still missing.

© Springer Nature Switzerland AG 2020
C. A. González Díaz et al. (Eds.): CLAIB 2019, IFMBE Proceedings 75, pp. 486–493, 2020.
https://doi.org/10.1007/978-3-030-30648-9_63

Electrochemical sensing is best suited for real-time NO detection in biological samples because it requires only small volumes of analyte and is capable of providing spatially resolved NO concentration data at low analyte concentration [19]. Recently, graphene materials based working electrodes have emerged as a promising alternative because of their electrochemical stability, high specifics surface area and demonstrated catalytic properties toward a wide variety of analytes [20]. Chemical vapor deposition (CVD) graphene has higher electrical conductivity and fewer defects than graphene prepared using wet-chemical methods [21]. Due to its excellent sorption properties and carrier mobility CVD graphene has been widely investigated for use in the development of chemical sensors for the detection of various chemical species, including levodopa [22], glucose [23], L-ascorbic acid (AA), dopamine (DA), uric acid (UA), tryptophan (Trp), and nitrite (NO_2^-) [24]. In the present study, we the report the design, fabrication and analytical performances of a CVD graphene sensor (SLG/SiO_2/Si) for the detection of HNO_3 as a surrogate measurement of NO in aqueous conditions. The design should allow real-time monitoring of the levels and ratios of important but unstable NO and could serve as an important diagnostic tool in biomedical research as well as in primary care situations.

2 Methodology

2.1 Preparation of SL Graphene on Silicon Chip

CVD graphene grown on copper foils was used in these experiments. SLG was obtained from ACS Material. The material was transferred onto silicon chips (525 mm thick) with a 280 nm thick thermal oxide (Fig. 1A). Graphene layers were transferred using the PMMA polymer assisted wet transfer technique by spin coating PMMA dissolved in chlorobenzene on the copper foils. Copper was etched away by floating the PMMA/graphene/copper on the surface of an 0.1 M $(NH_4)_2S_2O_8$ solution for 3 h. After etching the copper, the PMMA/graphene film was moved to 3 subsequent fresh deionized water baths for 10 min each to clean the surface of graphene. Then, the PMMA/graphene film was picked up by the bare Si/SiO_2 substrate and air dried over 12 h. The PMMA was removed by acetone and isopropanol, 10 min each.

2.2 Raman Analysis

Raman spectra of the samples before and after NO detection were carried out using a Renishaw Invia Raman microscope spectrometer. SLG/SiO_2/Si was directly placed on a microscope glass slide, which was then mounted under the objective lens of a Raman microscope. Samples were excited with a 532 nm green laser at 5 mW laser power for data collection.

2.3 X-Ray Photoelectron Spectroscopy (XPS)

XPS measurements of samples were obtained using a AXIS Supra by Kratos Analytical UK with an Aluminum monochromatic x-ray source (1486.6 eV) at 15 kV.

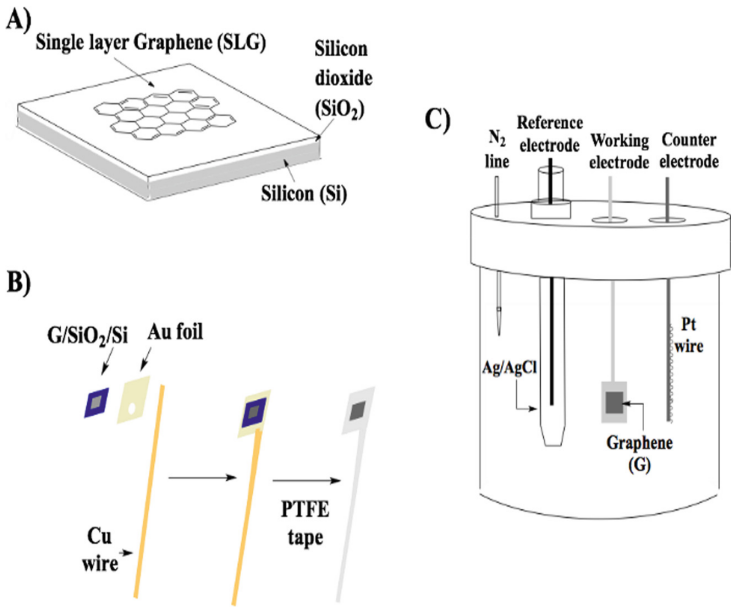

Fig. 1. Electrochemical instrumentation. (A) Single layer graphene silicon chip (SLG/SiO_2/Si). (B) Working electrode scheme. Working electrode was assembled using a Golden foil (Au), a copper (Cu) wire, the SLG/SiO_2/Si, and Polytetrafluoroethylene (PTFE) tape. C) Diagram of the three-electrode electrochemical cell (80 mL) used in the NO analysis, consisting of a working electrode, a Pt foil counter electrode and an Ag/AgCl electrode as reference electrode.

Survey and region scans were performed at 15 mA with a spot size of 300 × 700 μm. Chamber was maintained at a base pressure below 6×10^{-8}.

2.4 Electrochemical Analysis

Electrochemical experiments were done using a potentiostat/galvanostat Epsilon-BAS coupled to a computer system for recording data. Voltammetric plots were recorded using a three-electrode system in an 80 ml electrochemical cell. The working electrode was SLG/SiO_2/Si contacted to a golden foil that was assembled into a copper wire as shown in Fig. 1B. Then the electrode was coated using polytetrafluoroethylene (PTFE) film tape exposing the graphene area (1×2 mm^2); Ag/AgCl (saturated KCl) was used as a reference electrode and platinum wire as counter electrode (Fig. 1C). Working electrodes were washed with isopropyl alcohol under sonication for 30 s, then air dried and rinsed with 1X PBS. Different HNO_3 concentrations were additionated to assess the sensitivity of the chip by cyclic voltammetry (CV) in 1X PBS solution at room temperature. The potential of the working electrode was swept between +0.35 V and −0.6 V at 100 mV/s. After de experiment, the graphene samples were rinsed with water, followed by a 5 s sonication in acetone. After sonication the electrodes were again rinsed in water.

2.5 Conductance Sensing

SLG were electrically contacted by pre-deposited gold electrodes on the SiO_2/Si chip for electrical measurements using a probe station with a Keithley Sourcemeter applying a 500 mV DC bias voltage. Current vs gate voltage characteristics were obtained using the bulk silicon as gate and the 280 nm thick SiO_2 as gate dielectric.

3 Results

Figure 2A, exhibits the typical characteristics of CVD monolayer graphene, the minimal D peak at $\sim$1350 cm^{-1}, a G peak at $\sim$1560 cm^{-1} and 2D peak at $\sim$2660 cm^{-1}. Moreover Fig. 2B shows the C1 s spectra, of the bare SLG/SiO_2/Si with a peak at 284.4 eV corresponding to C-C bonds in graphene.

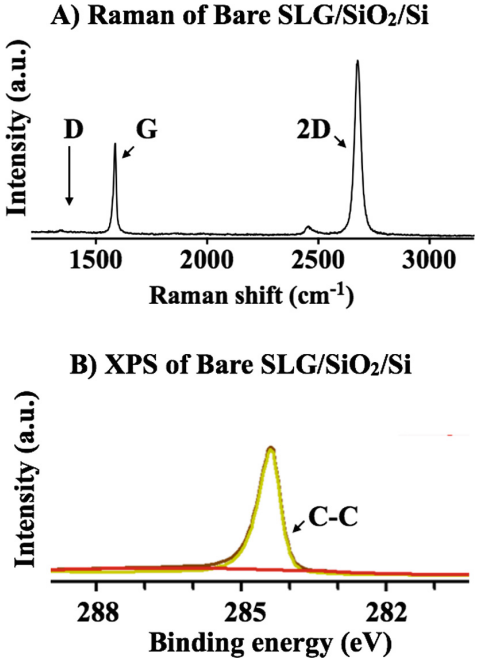

Fig. 2. Characterization of SLG/SiO_2/Si chip. (A) Raman spectrum of SLG/SiO_2/Si chip. and (B) XPS C1 s of SLG/SiO_2/Si chip.

The voltammetry analysis displayed in Fig. 3 shows the cathodic and anodic waves, that increase as the NO concentration increased.

The conductance of SLG/SiO_2/Si to detect the effect of HNO_3 interaction on SLG is displayed in Fig. 4. The samples kept their linear ohmic behavior, with changes in conductance as the HNO_3 concentration increased.

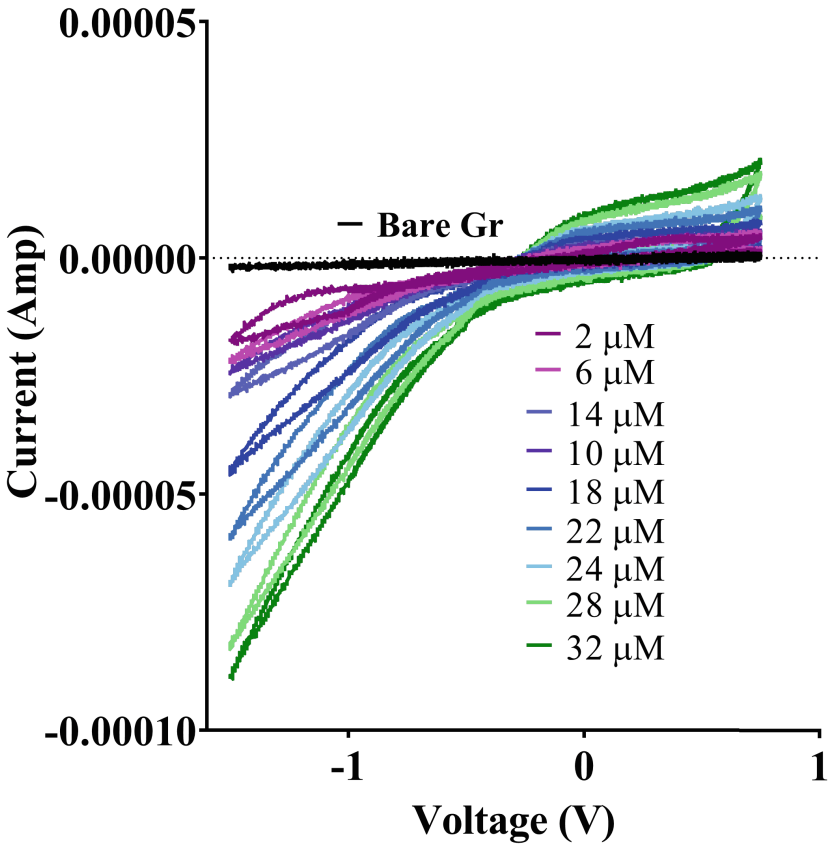

Fig. 3. Cyclic voltammograms of HNO_3 detection by SLG/SiO_2/Si chips in a PBS solution (pH 7.4) at a scan rate of 100 mV s^{-1}.

4 Discussion/Conclusions

The quality and uniformity of the SLG/SiO_2/Si was characterized by Raman spectroscopy and XPS. The Raman spectrum, in Fig. 2A, exhibits two principle peaks, the G and 2D peaks. The G peak is a result of in-plane vibrations of sp^2 bonded carbon atoms whereas the 2D peak is the result of a phonon lattice vibrational process (is used to determine graphene layer thickness). A third peak, the D peak may also be apparent in graphene when defects within the carbon lattice are present. Thus, the lower intensity of G peak (at $\sim$1560 cm^{-1}), as compared to the symmetric 2D peak at $\sim$2660 cm^{-1}, and the minimal D peak prove high-quality of the single layer graphene samples [26]. These results were confirmed by XPS. The C1s spectrum of the bare SLG/SiO_2/Si, in Fig. 2B, displays an asymmetric peak at 284.5 eV corresponding to sp^2 hybridization of C-C bonds. [25]

Cyclic voltammograms of HNO_3 detection by SLG/SiO_2/Si chips in a PBS solution (pH 7.4) at a scan rate of 100 mV s^{-1} are displayed in Fig. 3. Cathodic and anodic

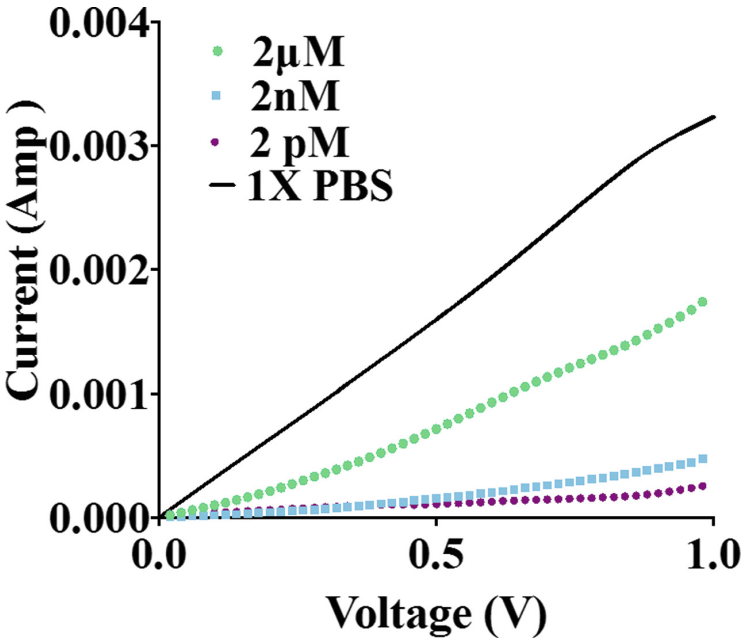

Fig. 4. Electrical test of HNO_3 detection by SLG/SiO_2/Si chips. Current vs Voltage curve of the SLG/SiO_2/Si in presence of HNO_3.

waves are observed in the samples that increase as the NO concentration increased. In general, the peak current of a voltammogram must increase with the scan rate.

For 0.1 μM and 1 μM HNO_3 cathodic and anodic waves were not observed probably because the HNO_3 not being reduced to NO^{+2} in an appropriate amount during the scanning in the reduction of Eq. (1).

$$HNO_2 + 3H^+ + e^- \rightarrow NO + H_2O \tag{1}$$

Consequently, the reduction current of nitrous acid increases explosively in the negative scanning direction. These reactions take place when the concentration of nitric acid is higher than 10 μM. The residual nitrous acid after the oxidation of the nitrous acid results higher reduction peaks in the negative scanning direction, as displayed in Fig. 3, through the autocatalytic reaction of nitrous acid according to Eqs. (2) to (4).

$$HNO_2 + H^+ + e^- \rightarrow NO + H_2O \tag{2}$$

$$NO + NO_3^- + 2H^+ + e^- \rightarrow 2HNO_2 \tag{3}$$

$$HNO_3 + 2NO + H_2O \rightarrow 3HNO_2 \tag{4}$$

Moreover, the effect of HNO_3 exposition on the current density–voltage was tested. Figure 4 illustrates the ohmic I/V curves, displaying clear reductions in conductance of

SLG after exposing to NO, that might be attributed to an influence of the electron withdrawing NO metabolites adsorbed on the SLG chip surface.

We demonstrated a graphene-based NO metabolites sensor on a silicon substrate. The electrochemical characterization of SLG/SiO_2/Si chip displayed an apparent reduction current of nitric acid to nitrous acid. The nitrous acid was rapidly and easily reduced to nitric oxide by an autocatalytic reaction that resulted in increased reduction peaks. Further, in the electrical test, the conductance of the SLG/SiO_2/Si decreased in presence of HNO_3, as a result of de HNO_3 metabolites adsorbed on the SLG surface. Further measurements are required to test the specificity using biology samples (red cells) and comparing CV and conductivity sensing measurements will allow to determine the advantages of using high mobility CVD graphene. However, we believe that our initial capabilities of 2.0 μg/ml are promising for NO detection and hold a great promise for develop an *in situ* biochemical sensor compatible with an electronic interface readout.

Acknowledgment. V.S. acknowledge support from CONACyT in the form of fellowship grant. M.T.O.G. gratefully acknowledge financial support from CONACyT-FORDECyT Project No. 282227-2017.

F.A.A; C.M.E; C.R.M: we thank V.S. and M.T.O.G, for allowing us to participate in this research work and for the opportunities for growth in this field.

Conflict of Interest. We have received proper clearance from all the authors and institution. No conflicts of interest to disclose.

References

1. Brunton, L.L., Lazo, J.S.: Goodman y Gilman's The Pharmacological Basis of Therapeutics, vol. 11, pp. 395–397. McGraw-Hill Companies, Inc.
2. Centelles, J.J., Redondo, C.E., Imperial, S.: Óxido nítrico, vol. 23, pp. 11–160. Elsevier, Offarm (2004)
3. Nathan, C.F., Hibbs Jr., J.B.: Role of nitric oxide synthesis in macrophage antimicrobial activity. Curr. Opin. Immunol. **3**, 65–70 (1991). https://doi.org/10.1016/0952-7915(91)90079-g
4. Lincoln, J., Hoyle, C.H., Burnstock, G.: Nitric Oxide in Health and Disease, p. 226. Cambridge University Press, Cambridge (1997)
5. Stuart Ira Fox: Fisiología Humana, p. 451. McGraw-Hill Companies, Inc. (2013)
6. Praveen Buddiga, M.D.: Cardiovascular System Anatomy. Medscape. https://emedicine.medscape.com/article/1948510-overview
7. Stuart Ira Fox.: Fisiología Humana, pp. 418–419. McGraw-Hill Companies, Inc. (2013)
8. Yoshida, K.: Biotransformation of nitric oxide, nitrite and nitrate. Int. Arch. Occup. Environ. Health **52**, 103–115 (1983). https://doi.org/10.1007/BF00405415
9. Grube, R., et al.: The biology of nitric oxide. In: Moncada, S., et al. (eds.) Enzymology, Biochemistry, and Immunology, pp. 201–204. Portland Press, London (1994)
10. Kelm, M., et al.: The Biology of nitric oxide. In: Moncada, S., et al. (eds.) Physiological and Clinical Aspects, pp. 319–322. Portland Press, London (1992)

11. Bryan, N.S.: Nitrite in nitric oxide biology: cause or consequence? A systems-based review. Free Radic. Biol. Med. **41**(5), 691–701 (2006). https://doi.org/10.1016/j.freeradbiomed.2006.05.019
12. Bryan, N.S.: Nitrite is a signaling molecule and regulator of gene expression in mammalian tissues. Nat. Chem. Biol. **1**(5), 290–297 (2005). https://doi.org/10.1038/nchembio734
13. Kleinbongard, P.: Plasma nitrite reflects constitutive nitric oxide synthase activity in mammals. Free Radic. Biol. Med. **35**(7), 790–796 (2003). https://doi.org/10.1016/S0891-5849(03)00406-4
14. Lauer, T., et al.: Plasma nitrite rather than nitrate reflects regional endothelial nitric oxide synthase activity but lacks intrinsic vasodilator action. In: Proceedings of the National Academy of Sciences, USA, pp. 12814–12819 (2001). https://doi.org/10.1073/pnas.221381098
15. Pelletier, M.M.: The measurement of blood and plasma nitrite by chemiluminescence: pitfalls and solutions. Free Radic. Biol. Med. **41**, 541–548 (2006). https://doi.org/10.1016/j.freeradbiomed.2006.05.001
16. Rassaf, T., Feelisch, M., Kelm, M.: Circulating NO pool: assessment of nitrite and nitroso species in blood and tissues. Free Radic. Biol. Med. **36**, 413–422 (2004). https://doi.org/10.1016/j.freeradbiomed.2003.11.011
17. Tsikas, D.: Methods of quantitative analysis of the nitric oxide metabolites nitrite and nitrate in human biological fluids. Free Radic. Res. **39**, 797–815 (2004). https://doi.org/10.1080/10715760500053651
18. Yang, B.K.: Methodologies for the sensitive and specific measurement of S-nitrosothiols, iron-nitrosyls, and nitrite in biological samples. Free Radic. Res. **37**, 1–10 (2003). https://doi.org/10.1080/1071576021000033112
19. Bedioui, F., Quinton, D., Griveau, S., Nyokong, T.: Designing molecular materials and strategies for the electrochemical detection of nitric oxide, superoxide and peroxy-nitrite in biological systems. Phys. Chem. Chem. Phys. **34**, 9976–9988 (2010). https://doi.org/10.1039/c0cp00271b
20. Shao, Y.Y.: Graphene based electrochemical sensors and biosensors: a review. Electroanalysis **22**, 1027–1036 (2010). https://doi.org/10.1002/elan.200900571
21. Nguyen, D.D., et al.: Macroscopic, freestanding, and tubular graphene architectures fabricated via thermal annealing. ACS Nano., 3206–3214 (2015). https://doi.org/10.1021/acsnano.5b00292
22. Kim, H., Park, J.-H., Suh, M., Real Ahn, J., Ju, S.: Horizontally aligned ZnO nanowire transistors using patterned graphene thin films. Appl. Phys. Lett. **100** (2012). https://doi.org/10.1063/1.3684614
23. Jang, J.: Low-temperature-grown continuous graphene films from benzene by chemical vapor deposition at ambient pressure. Sci. Rep. **5**, 17955 (2015). https://doi.org/10.1038/srep17955
24. Wang, X., Gao, D., Li, M., Li, H., Li, C., Wu, X., Yang, B.: CVD graphene as an electrochemical sensing platform for simultaneous detection of biomolecules. Sci. Rep. **7**(1), 7044 (2017). https://doi.org/10.1038/s41598-017-07646-2
25. Ermolieff, A., Chabli, A., Pierre, F., Rolland, G., Rouchon, D., Vannuffel, C., Vergnaud, C., Baylet, J., Séméria, M.N.: XPS, Raman spectroscopy, X-ray diffraction, specular X-ray reflectivity, transmission electron microscopy and elastic recoil detection analysis of emissive carbon film characterization. Surf. Interface Anal. **31**, 185–190 (2001). https://doi.org/10.1002/sia.955
26. Liao, C.-D., Lu, Y.-Y., Tamalampudi, S.R., Cheng, H.-C., Chen, Y.-T.: Chemical vapor deposition synthesis and raman spectroscopic characterization of large-area graphene sheets. J. Phys. Chem. A **117**, 9454–9461 (2013). https://doi.org/10.1021/jp311757r

Bioinstrumentation and Micro-Nanotechnologies

Heart Rate Monitor for Athletes in Activity

Gisella Borja[1(✉)], Evert De Los Ríos[2], José Ledesma[2], and Glayder Viloria[2]

[1] Centro de Bioingeniería, Universidad Autónoma del Caribe, Barranquilla, Colombia
Gissella.borja25@uac.edu.co
[2] Grupo de Investigación en Electrónica y Telecomunicaciones, Universidad Autónoma del Caribe, Barranquilla, Colombia

Abstract. The current work presented in this paper is focused on the development of a heart rate (HR) monitoring system which allows the coach and/or a physical trainer to monitor in real time the HR of all his athletes while they are in an exercise activity, through an application developed on Android. The system has the possibility of sending the data of one or more athletes to a single module via Zigbee, and then retransmit them using the 3G network to a remote display and processing unit that does not require high-cost equipment. The system consists of a unit of acquisition and transmission of HR, a Gateway, and a monitoring and analysis unit. For the acquisition of the HR, which in a high performance athlete is estimated between 40–195 BPM (beats-per-minute), a chest strap is used including a HR sensor, which is connects to a microcontroller that detects the heartbeat as a High/Low pulse. The microcontroller is responsible for calculating the HR and the packing of the data for transmission to the Zigbee module. The Gateway is the sink node of the network where all the data coming from the different acquisition and transmission units of the HR is received. The Gateway manages the 3G module and the Zigbee module, and a microcontroller establishes the connection with the communications manager program hosted on the remote server and keeps it operative automatically. The mobile device consults the database and, through an interface, graphs of HR behavior are generated during the training.

Keywords: Heart Rate · Athletes · Wireless monitoring

1 Introduction

The Heart Rate (HR) can be applied with the aim to monitor exercise intensity, estimate energy expenditure, and detect and prevent over training [1]. The HR is an excellent way of control the workload, so for an individual application of the exercise is registered during the development of the itself [2]. Although there are a large number of devices for the detection of HR and monitoring systems, these require expensive mechanisms and units. Currently the physical trainers do not have technological tools to evaluate the physical performance of their athletes in an objective way, while they are training or in a competition. Furthermore, they are not designed to send information over long distances, and do not allow data from several users can be monitored

© Springer Nature Switzerland AG 2020
C. A. González Díaz et al. (Eds.): CLAIB 2019, IFMBE Proceedings 75, pp. 497–500, 2020.
https://doi.org/10.1007/978-3-030-30648-9_64

simultaneously by a single person (Trainer) [3, 4, 5]. Therefore, the current work is focused on the development of an HR monitoring system that sends the data to a single module via Zigbee, and then retransmits them using the 3G network to a remote display and a processing unit. The monitoring system simultaneously allows the coach and/or physical trainer to monitor in real time the HR of all his athletes while they are in activity, through an application developed on Android. The monitoring can be done remotely, that is, without the athletes in the same place. In addition, it can be useful for one or more athletes who are in the same place of training or playing in different places at distance.

2 Materials and Methods

The heart rate monitor for athletes in activity is composed by one or more HR acquisition and transmission units, a Gateway, and a monitoring and analysis unit (See Fig. 1).

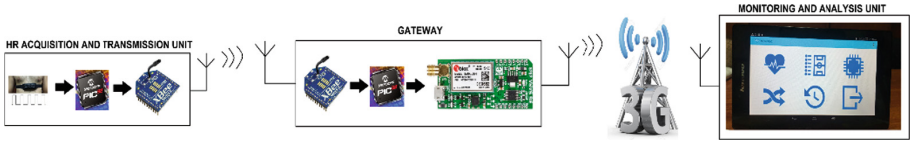

Fig. 1. Process of acquiring information from the HR of one or more athletes to the storage of information on a server.

2.1 HR Acquisition and Transmission Unit

The acquisition and transmission unit consists of a band that includes a HR sensor, a microcontroller and a Zigbee module. The HR sensor sends the signal as a High/Low pulse train that reaches the PIC32MX2 microcontroller, and is programmed to calculate the HR by analyzing the pulse train. In addition, it's responsible for the packing of the data for the transmission to the Zigbee module.

2.2 Gateway

The Gateway is composed of a Zigbee module, a microcontroller and a 3G module. It´s the sink node of the network where all the data are received from the different acquisition and transmission units of the HR. The Gateway manages the 3G module (Ublox SARA - U201) and the Zigbee module. The PIC32Mx7 microcontroller establishes the connection with the communications manager program hosted on the remote server and keeps it operating automatically. Once the link is established, the microcontroller appropriately formats the data coming from the Zigbee network to the communications manager program.

2.3 Monitoring and Analysis Unit

The monitoring and analysis unit is composed of a modem, a server, a communications manager program, a database and a mobile device. The communications manager program allows the connections of the remote nodes to later exchange frames with them, check the integrity of the data to detecting the validity of them and discard those that arrive with errors, analyze and section for later write them in the fields of the database once you have established the connection with it. In addition, the communications manager program takes a metric of the number of packets that have arrived, the number of defective packets, and the number of reconnections that a node has made, and is responsible for eliminating inactive connections. The mobile device consults the database and through an interface displays the HR data of each player or athlete. The Android application is designed in order to visualize the data of maximum HR and minimum HR of each player simultaneously, and generate the graphics of behavior of the HR during the training of the athlete selected. In addition, the Android application is configured to generate alarms when a player is below or above his minimum and maximum HR, which are calculated before each workout. The application allows to consult the history of the data of each player and generate statistics.

3 Results

We can obtain a record of the HR, performing tests on two soccer players while they were in a training practice (See Fig. 2). In the figure you can see the measurement of HR of all athletes simultaneously measured in BPM, and the limits of maximum heart rate (HRmax) and minimum heart rate (HRmin). In addition, you can see the graphics of one of athletes selected, where the blue line represents the measurement of HR and the red line the HRmax and the yellow line the HRmin. It should be noted to generate the alarm, HRmax and HRmin are established for each athlete. The HRmin is calculated in the idle state, and the HRmax is calculated with the Ball State formula [2] after the trainer enter the data (sex and age) of each athlete.

Fig. 2. Monitoring display.

$$For\ men:\ 209 - (0.7 * age) \tag{1}$$

$$For\ women:\ 214 - (0.8 * age) \tag{2}$$

We proved that the system is capable of: (a) Capturing the contractions of the heart through the HR sensor; (b) Send the signal in the form of an High/Low pulse train to the microcontroller and calculate the HR; (c) Pack the data and transmit them using the Zigbee network from the sensor nodes to the Gateway node (d) Establish the connection with the communications manager hosted on the remote server; (e) Format the data coming from the HR sensor network to the communications management program; (f) Establish connection with the database and write the data; (g) Consult the database; and h) Display the HR data in a graphical interface.

4 Conclusion

This article demonstrated the feasibility of implementing HR wireless monitoring systems, which allow the coach to evaluate the performance of athletes in real time and simultaneously, while they are in a training or a competition activity also. In the same way, this type of systems can be implemented in various field sports disciplines.

5 Discussion

The use of HR monitoring systems of active athletes, by trainers and/or physical trainers, will allow them to act objectively when making important decisions in a competition, such as replacing a player due to exhaustion. Likewise, the physical trainer will be able to evaluate the individual performance of each athlete in order to improve their training routines, taking them to reach their maximum capacity.

Conflict of Interest Declaration. The authors declare that they have no competing interests.

References

1. Achten, J., Jeukendrup, A.E.: Heart rate monitoring: applications and limitations. Sports Med. **33**(7), 517–538 (2003)
2. Marins, J.C., Delgado, M.: Empleo de ecuaciones para predecir la frecuencia cardíaca máxima en carrera para jóvenes deportistas. Archivos de Medicina del Deporte **XXIV**(118), 112–120 (2007)
3. Pérez, N.: La Frecuencia Cardiaca. http://www.frecuencia-cardiaca.com/pulsometros.php. Accessed 11 Aug 2017
4. Garmin. http://gbr.garmin.com/winter-training/_downloads/advice/Full-Potential-Training-Using-Heart-Rate-SPAIN.pdf. Accessed 11 Aug 2017
5. 郭鹏程, 冯勇: Sistema De Monitoreo En Tiempo Real Especifico Para Entrenamiento De Fútbol, CN204319729 (2015)

Instrumented Footwear for Diabetic Foot Monitoring: Foot Sole Temperature Measurement

Sofía D. Rodríguez-Sáenz[1(✉)], Sarahí S. Franco-Pérez[1], Aurora Espinoza-Valdez[2], Ricardo A. Salido-Ruiz[2], and Fátima B. Curiel-López[2]

[1] Departamento de Electrónica del Centro Universitario de Ciencias Exactas e Ingenierías de la Universidad de Guadalajara, Guadalajara, Jalisco 44430, Mexico

[2] Departamento de Ciencias Computacionales del Centro Universitario de Ciencias Exactas e Ingenierías de la Universidad de Guadalajara, Guadalajara, Jalisco 44430, Mexico

aurora.espinoza@academicos.udg.mx

Abstract. Diabetes is a huge and growing problem, the costs to society are high and increasing, as well as affecting in a considerable way, the quality of life of diabetic patients. One of the main complications of diabetes is the high probability of developing some kind of neuropathic ulceration, particularly of the feet. Among the most common methods for early detection of ulceration, is without a doubt, the continuous temperature monitoring on the bottom foot area. The goal of this research is the early detection of ulcers development in subjects with diabetes. A device with four temperature sensors was designed to continuously monitor the foot temperature and reduce the likelihood of amputations. Tests were performed using the device in 35 subjects with diabetes, we observed temperature variations on the different plantar regions studied here. We concluded that continuous, independent and simultaneous monitoring is critical, as it can provide preventative information for possible ulceration development.

Keywords: Diabetic foot · Temperature sensor · Ulceration · Prevention

1 Introduction

According to the International Diabetes Federation (IDF), the incidence of diabetes in Mexico in 2017 was 14.8% in adults between 20 and 79 years, that is approximately 12 million people. Mexico is in the 5th place of the world ranking, just behind China, India, U.S.A., and Brazil. It is estimated that around 425 million people have diabetes and an increase of 48% is expected for 2045 (approx. 629 million people), thus, this condition is a serious global public health problem [1].

The IDF defines diabetes mellitus as a chronic condition that occurs due to the high glucose levels in the blood, since the body is unable to produce enough insulin or cannot use it effectively to regulate the glucose concentrations. Diabetes is classified as

© Springer Nature Switzerland AG 2020
C. A. González Díaz et al. (Eds.): CLAIB 2019, IFMBE Proceedings 75, pp. 501–507, 2020.
https://doi.org/10.1007/978-3-030-30648-9_65

type 1, 2 or gestational. Among the symptoms of this condition are: fatigue/lack of energy, blurred vision, heavy urination, excessive thirst, etc. [1].

One of the greatest concerns is the high frequency of metabolic and neurological complications [2]. Among these are: retinopathy, nephropathy, cardiovascular morbidity and mortality, hypertension, infections, neuropathies or diabetic foot [3].

Diabetic foot, as defined by the World Health Organization (WHO), is the infection and/or destruction of deep tissue in the lower limb, related to peripheral neuropathies [4]. The infection in the diabetic foot is the main cause of hospitalization in diabetic people [5]. Twenty percent out of the people with complications due to diabetic foot will require limb amputation, from which 70–80% are preceded by chronic ulcers [6]. Ulcers cause sensibility and mobility loss, which implies complications in the daily tasks' performance. On the other hand, if ulcerations are not treated promptly, it will be required the amputation of some part of the lower limb; significantly decreasing the quality of life of the patient. It is estimated that every 30 s a lower extremity or part of it, is lost by amputation somewhere in the world [1]. Based on the above, diabetic foot constitutes one of the most common reasons for mortality in diabetic patients [7]. Therefore, is very important to have effective and reliable methods for the prevention of diabetic foot ulceration.

It has been shown that when foot temperature is higher than normal (around 30 °C) [8, 9], it could be associated with the ulceration development in the diabetic foot due to lack of oxygen. This fact has motivated other authors investigating the correlation between plantar foot temperature and diabetic neuropathy through the use of infrared thermic image techniques [8]. Plantar foot temperature monitoring in diabetic patients is so important that a revision of wearable technology for this purpose has been presented in [10]. Moreover, there are some patents describing systems for the monitoring of plantar foot temperature in diabetic patients such as the one presented by [11, 12]. Concerning the development of computational tools for early diagnosis of diabetic foot, the authors in [13] present a computational system support based on different data acquisition that is uploaded to an on line database for further analysis.

Some of the above-mentioned works have inspired us to develop an instrumented footwear for diabetic foot monitoring. In order to verify if this phenomenon occurs in people diagnosed with diabetes, we have recorded the foot sole temperature. In this paper we present the first results of temperature monitoring in certain areas of the foot sole, obtained by a prototype of instrumented footwear designed for this purpose. Results for mobile device applications are subject of other research.

2 Methodology

An insole with four LM35 temperature sensors was built (this sensor responds to variations of 10 mV per Celsius degree), placed in specific places [14] on the inner surface of the sandal. The points in which the sensors were placed, can be seen in Fig. 1, it was decided to position them there since those are the points of the greatest impact or greater support of a foot and therefore with greater probability of developing ulcers [14]. The footwear consists of a pigskin insole, which aims to provide comfort and safety to the patient.

Fig. 1. Sensors placement. Each sandal contains sensors on the four points shown.

Both the main strap and heel leash were made with Velcro so it can adjust and prevent discomfort. The sensors outputs are connected to the analog inputs of Arduino Nano®, which is a free hardware and software platform, based on an ATMEL® AVR® ATmega328P 8-bit micro-controller. Arduino Nano® was chosen since its small dimensions allow us to optimize the instrumented area. Once the signals of the temperature sensors have been acquired, they are sent via serial port to the computer using a wireless communication module (Bluetooth). For this purpose, we selected the Bluetooth module HC-05. The data is acquired, stored and processed by MatLab®, (i.e. the statistical parameters of the data are stored, averaged and obtained). In Fig. 2 we can see the connection diagram between the sections that make up the device.

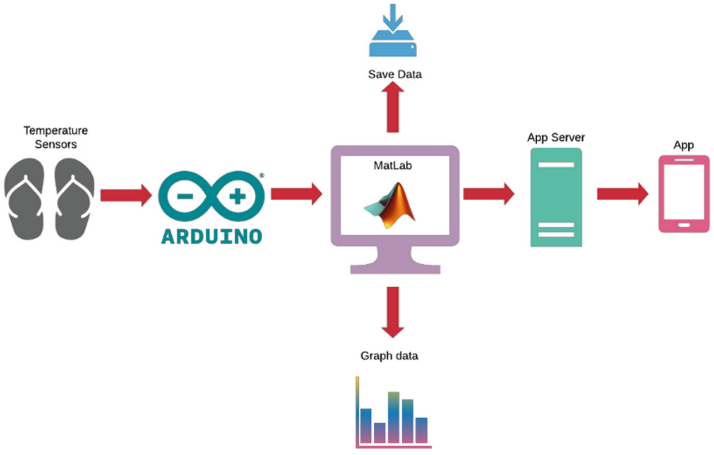

Fig. 2. Prototype scheme.

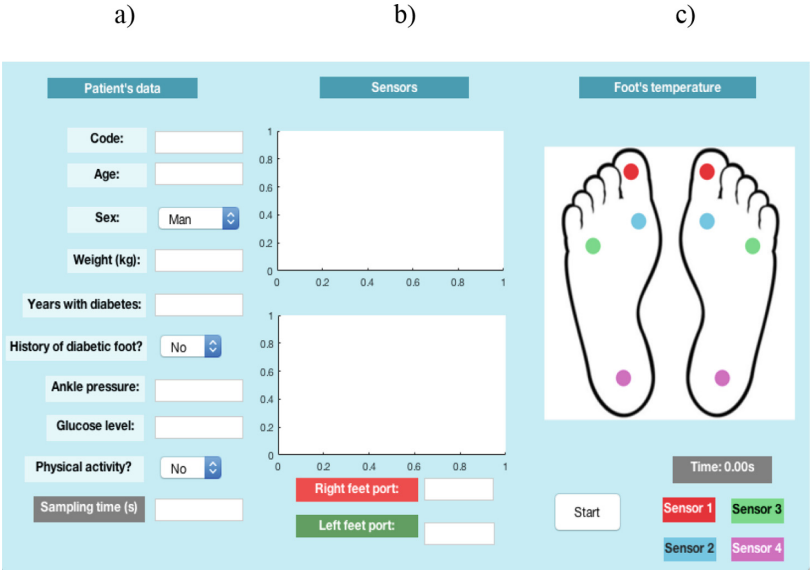

Fig. 3. MatLab's Interface. Patient's data (a), sensor registration (b) and foot's temperature in the measured area (c).

In the "Patient's data" section, (Fig. 3a) full data must be provided, the program will not allow to entry data in this form if it is not completely filled out. In the next section, "Sensors" (Fig. 3b) we find two graphs, where the temperature sensors signals will be plotted. The upper graph shows the temperature from the right foot and the lower one from the left foot. We record both feet to rule out any possibility of ulceration, because the temperature recorded on one foot is not related to changes in temperature on the other. The section "Foot's temperature" (Fig. 3c) shows the sensors' location. In the "Time" label shown in Fig. 3c, the time elapsed during the data capture will be indicated. The "Start" button will begin the data capture.

3 Results

Temperatures were measured on both feet, during 60 s, in 35 individuals (27 women and 8 men) between 36 and 83 years. The male subjects reported an average of 11.4 years suffering from diabetes, while the women reported 7.4 years. Figure 4a shows the graph corresponding to the average temperature in both genders in the right foot while in Fig. 4b it is shown for the left foot.

The average temperature on each foot are shown in Table 1. We can see that almost all the temperature sensors have similar lectures in the studied regions of the foot except in sensor 2, placed at the first metatarsal in right foot. In order to perform an equitable study by gender, 8 women out of the original 27 subjects, were randomly

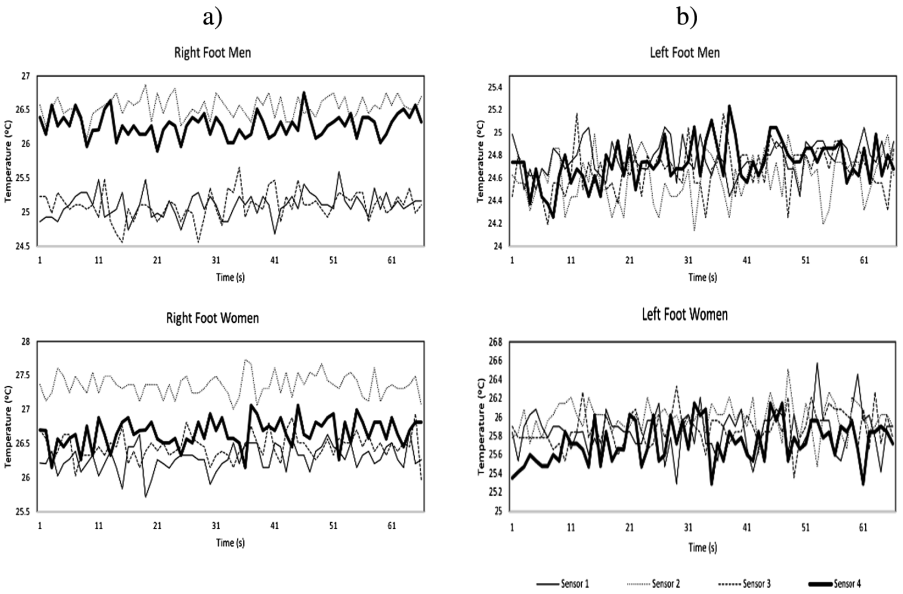

Fig. 4. Average temperature in men and women in right foot (a) and left foot (b).

selected from the database to compare the values between men and women. Table 2 shows the average temperatures in both sexes, with respect to each foot and each sensor. From this, it is possible to observe that right foot temperature in both genders is lower than the left foot temperature; however, this temperature difference between feet is less in women than in men, who present the lowest temperature. The average temperature between feet and for each sensor show that women have a slightly higher temperature than men. Sensor 2 in right foot (first metatarsal) displays the highest temperature values: 27.36 °C in women and 26.54 °C for men.

Table 1. Average temperature on both feet by sensor.

	Right foot	Left foot
Sensor 1	25.99 ± 0.101	25.69 ± 0.364
Sensor 2	27.07 ± 0.092	25.72 ± 0.095
Sensor 3	26.14 ± 0.098	25.60 ± 0.102
Sensor 4	26.44 ± 0.086	25.43 ± 0.100

Note: Sensor 1 (Hallux), Sensor 2 (1st Metatarsal), Sensor 3 (4th y 5th Metatarsal) y Sensor 4 (Calcaneus).

Table 2. Average temperature by gender.

		Right foot	Left foot	Average
Women	*S1*	26.29 ± 0.19	25.98 ± 1.02	26.13 ± 0.51
	S2	27.36 ± 0.16	25.99 ± 0.17	26.68 ± 0.11
	S3	26.41 ± 0.39	25.88 ± 0.19	26.15 ± 0.23
	S4	26.66 ± 0.21	25.73 ± 0.22	26.20 ± 0.16
Men	*S1*	25.10 ± 0.18	24.78 ± 0.15	24.94 ± 0.12
	S2	26.54 ± 0.16	24.60 ± 0.21	25.57 ± 0.13
	S3	25.10 ± 0.21	24.68 ± 0.20	24.89 ± 0.15
	S4	26.28 ± 0.17	24.74 ± 0.19	25.51 ± 0.14

4 Discussion

Based on the results, we can see in the graphs that women exhibit a higher temperature in relation to men, about 1.07 °C. From what can be seen in the Fig. 4 and Tables 1 and 2, the great difference is due to the variation that exists in the right foot specially in sensor 2 (first metatarsal), unlike the left foot (both groups have, on average, the same temperature range). Concerning the somewhat higher temperature on the right foot's first metatarsal for both genders, it is possible that this foot region, where foot pressure is concentrated, has greater contact to the sensors, unlike other regions and thus the temperature is better estimated or that this specific sensor is, to some degree, biased due to the quality errors. Nevertheless, this can be corrected by using high quality components. On the other hand, if these lectures are correct and no bias errors are present, they show us that is possible to differentiate the temperature in the studied regions of the foot. Thus, we can say that monitoring both feet independently it is of great importance. The temperature of both groups is not within the range reported for the development of ulcers according to the reference [15].

5 Conclusion

One of the most frequent problems for society is undoubtedly, the occurrence of diabetes, whose complications include ulcerations in the feet.

The developed device provides an effective and alternative way to combat this problematic. With the constant use of this footwear, it is possible to observe temperature changes in both feet simultaneously and independently, in order to prevent or reduce the likelihood of developing ulcers in diabetic people and thereby increase the quality of life of those who suffer from this condition.

References

1. International Diabetes Federation: IDF Diabetes Atlas, 8th edn. Brussels, Belgium: International Diabetes Federation (2017). http://www.diabetesatlas.org

2. Camacho, J.: Prevalencia de neuropatía periférica en pacientes con diabetes mellitus tipo 2, atendidos en la Clínica Hospital del ISSSTE en Mazatlán. Sinaloa. Revista de Especialidades Médico-Quirúrgicas **16**(2), 71–74 (2011)
3. Tripathi, B.K., Srivastava, A.K.: Diabetes mellitus: complications and therapeutics. Med. Sci. Monit. 12(7), RA130–RA147 (2006). Epub 2006 Jun 28
4. Rincón, Y., Gil, V., Pacheco, J., Benítez, I., Sánchez, M.: Evaluación y tratamiento del pie diabético. Revista Venezolana de Endocrinología y Metabolismo **10**(3), 176–187 (2012)
5. Martínez De Jesús, F., et al.: Diagnóstico, clasificación y tratamiento de las infecciones en el pie diabético. Cirujano General. **34**(3), 199–205 (2012)
6. Mendoza, M., Ramírez, M.: Abordaje multidisciplinario del pie diabético. Revista de Endocrinología y Nutrición **13**(4), 165–179 (2005)
7. Macioch, T., Sobol, E., Krakowiecki, A., Mrozikiewicz-Rakowska, B., Kasprowicz, M., Hermanowski, T.: Health related quality of life in patients with diabetic foot ulceration—translation and Polish adaptation of Diabetic Foot Ulcer Scale short form. Health Qual. Life Outcomes **15**(15) (2017). https://doi.org/10.1186/s12955-017-0587-y
8. Bagavathiappan, S., Philip, J., Jayakumar, T., Raj, B., Rao, P., Varalakshmi, M., Mohan, V.: Correlation between plantar foot temperature and diabetic neuropathy: a case study by using an infrared thermal imaging technique. J. Diabetes Sci. Technol. **4**(6), 1386–1392 (2010)
9. Houghton, V.J., Bower, V.M., Chant, D.C.: Is an increase in skin temperature predictive of neuropathic foot ulceration in people with diabetes? A systematic review and meta-analysis. J. Foot Ankle Res. **6**(1), 31 (2013)
10. Martín-Vaquero, J., et al.: Review on wearables to monitor foot temperature in diabetic patients. Sensors **19**(4), 776 (2019)
11. Lavery, L.A., et al.: Foot temperature and health monitoring system. U.S. Patent No. 6,767,330, 27 July 2004
12. Leyerer, R., Schaff, P., Wetter, O.: Device for prevention of ulcers in the feet of diabetes patients. U.S. Patent No. 5,642,096, 24 June 1997
13. Torres, I.A., et al.: Computational support system for early diagnosis of diabetic foot. In: 2018 Global Medical Engineering Physics Exchanges/Pan American Health Care Exchanges (GMEPE/PAHCE). IEEE (2018)
14. Franco, S., Salido, R.A., Espinoza, A.: Análisis de las zonas con mayor probabilidad de desarrollo de úlceras en el pie diabético. In: Avances de la ciencia en México. Centro de investigaciones en óptica
15. Nardin, R.A., Fogerson, P.M., Rutkove, S.B.: Foot temperature in healthy individuals: effects of ambient temperature and age. J. Am. Podiatr. Med. Assoc. **100**(4), 258–264 (2010)

Analysis of the Thermal Distribution Generated by a Thermal Patch to Evaluate Its Feasibility to Treat Patient's Pain Relief

Luis A. Castellanos-Rivera[1], Edgar A. Mandujano-García[1], Antonio Ruiz-Morán[1], Melany Barrón-Salazar[1], Benjamín A. Morales-Ruiz[1], and Citlalli J. Trujillo-Romero[1,2(✉)]

[1] Machina Innovation Lab S.A.P.I. de C.V., Liverpool 174, 06600 Juarez, Mexico City, Mexico
ctrujillo@machina.in
[2] Arenal de Guadalupe, Mexico-Xochimilco 289, 14389 Mexico City, Mexico

Abstract. Pain is considered a world problem; several options to release pain have been used. Although thermal patches are commonly used to release pain, there are not enough information to validate if they produce a real therapeutic effect. The present study was done in order to evaluate the effectiveness of a patch designed to keep a constant and uniform temperature through the treatment. 3D human models were generated to evaluate the thermal distribution generated by the patch located over different regions. The effect over fat, muscle and bones was analyzed. Temperature patch from 40 °C to 48 °C and treatment times from 900 s to 1800 s were included in this study. Results show that the thickness of fatty tissue is strongly related with the penetration depth of heat and the effectiveness of the pain therapy. Patch temperatures over 44 °C are the best option to treat regions even with a thick layer of fatty tissue.

Keywords: Pain relief · Thermal therapy · Pain treatments · FEM models

1 Introduction

The World Health Organization report that the chronic and acute pain are considered a worldwide health issue. Between 20%–25% of the world population suffer some kind of chronic pain [1]. In Mexico, more than 28 million of people are suffering chronic pain [2]. Moreover, acute pain is the main reason of medical consultation. Pain (muscle, ligament or tendon) is considered one of the biggest reasons of inability to work [3–6]. Pain produces a negative impact in health as well as in physical and emotional well-being of people; moreover, it causes an economic impact in the country.

Drugs and thermotherapy are the most common treatments for pain. However, drugs provoke several health issues; they can generate a physical dependence and produces the withdrawal syndrome. Moreover, this can cause several symptoms like gastrointestinal damage, anxiety, irritability, and even tachycardia [7]. Thermotherapy

© Springer Nature Switzerland AG 2020
C. A. González Díaz et al. (Eds.): CLAIB 2019, IFMBE Proceedings 75, pp. 508–518, 2020.
https://doi.org/10.1007/978-3-030-30648-9_66

is a therapeutic application of any substance that helps to increase tissue temperature, blood flow, metabolism and connective tissue extensibility [8–11]. The blood circulation stimulates the tissue recovery by supplying the site of the injury with oxygen, nutrients, proteins, etc., while metabolites and carbon dioxide are removed from the system. A $\Delta T = 1$ °C in tissue is associated with an increase of 10–15% of local metabolism [8, 10]. This change aids to the recovery process by increasing the catabolic and anabolic reactions necessary to metabolically degraded and removed products from tissue damage; moreover, it promotes the natural healing process. Thermotherapy also modifies the skin temperature activating the thermoreceptors that initiate nerve signals that block nociception (pain signal process) inside the spine. Furthermore, the proprioceptors are also activated; these ones inhibit the transmission of signals from nociceptors to the brain. The activation of these receptors reduces muscle tone, decreases muscle pain and increases tissue blood flow [12].

In thermotherapy, the greatest temperature increase occurs in skin and subcutaneous tissue (5 mm deep). Therapeutic temperatures at depths around 1.2 cm occur slowly and require more exposition time (15–30 min) [10, 13, 14]. The tissue heating is strongly related with its thermal properties, as well as with the blood perfusion in each tissue [15]. It is important to remark that due to its properties, the fat layer is considered as an insulator. Therefore, tissues under a large amount of fat are minimally affected by surface heating agents. Hot compresses around 42 °C–48 °C are the most used in thermotherapy to treat pain [9, 10]. Even high-performance athletes use this therapy due to its high degree of effectiveness. However, the traditional procedure to applicated it, even in hospitals, is complicated and less effective. Its inefficiency is because in some cases, it is necessary to use a thermal bath at very high temperatures in order to heat them up to 45 °C. In addition, it is impossible to keep a constant and uniform temperature throughout the therapy, i.e. due to the heat loss produced by the interaction with the environment, the compress temperature starts to decrease after some minutes of starting the treatment. If a conventional patch is used, to keep a constant and uniform temperature through the whole treatment is a problem. To solve it, new designs of thermal patches have been proposed; like the splint reported in [16]. It is important to address that, although there are several models to evaluate the efficiency of devices for thermal therapy to treat cancer [17–19], nowadays none of the devices to treat pain relief has a modeling study to evaluate the heat distribution over the tissues.

This work describes the 3D models of a patch designed to keep a constant and uniform heat distribution through the whole pain treatment. Moreover; a multi-patch option to cover a biggest region was analyzed. A uniform heating of the patch would help to ensure that the applied temperatures to the target area are the same, and that the degree of effectiveness of the therapy is only due to the anatomical characteristics of the people under treatment (tissues thickness). The thermal effect generated by the patch over the different tissue layers was analyzed.

2 Materials and Methods

2.1 Thermal Patch

The patch dimensions allow it to be used to treat the most affected regions (shoulder and neck). The patch has a width of 96 mm and a length of 202 mm. It has a special design that allows to use one of them or a multi-patch system, to treat different sized regions. Some possible configurations are depicted in Fig. 1. The patch has internally a thermo-electric mesh to keep it at a constant temperature around 40 °C–48 °C through the whole pain treatment (15–30 min). The designed patch is depicted in Fig. 1(e) and (f).

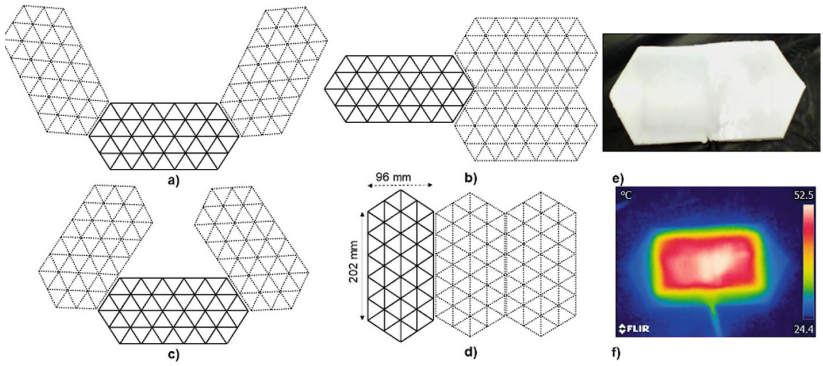

Fig. 1. Possible configurations used to treat pain of different sized body regions with the patch, (a) Shoulder-neck-shoulder region, (b) Knee (front and back), (c) Knee (front) without affecting the patella. (d) Lower back, (e) Proposed patch, (f) Thermal distribution generated by the patch.

2.2 Human Body Models

The 3D models were generated by using medical images that were selected from an available set of files. License-free software was used to develop such models. To be able to use these models in the finite element software (COMSOL-Multiphysics), a special process was implemented. First, the tissue segmentation was done in *3D-slicer* by using a set of computed tomography (CT). All tissues were segmented by using different layers; each layer correspond to a specific tissue. To avoid problems in the mesh generation, the final segmentation must not have air gaps or overlaps between tissues. Each tissue was saved as a solid in a STL format. These files were processed in MeshMixer; where a mesh size reduction was implemented. It was important to reduce the mesh without affecting the anatomical shape of the 3D model. This process gave us an easier model to manipulate in the finite element software. The last step was implemented in FreeCAD; this was used to convert from surfaces (.STL) to solids (.STEP). The files were imported to the finite element software. Figure 2 shows the 3D human models.

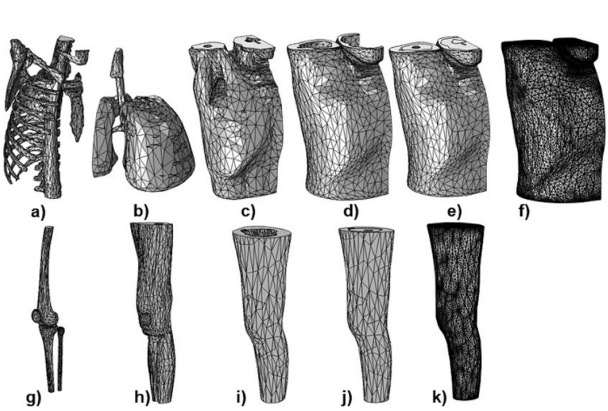

Fig. 2. 3D models generated to simulate the thermal pain treatment in torso and leg. (a) Vertebral column, scapula, clavicle and ribs, (b) Lungs and larynx, (c) Muscle, (d) Fat, (e) 3D model, (f) Mesh for the FEM model, (g) Femur, patella, tibia and fibula, (h) Muscle, (i) Fat, (j) 3D model, (k) Mesh for the FEM model.

2.3 Thermal Models

To emulate the behavior of the designed patch, 3D thermal models were implemented. Figure 2 depicts the 3D models as well as the tissue layers considered in this study. A patch to emulate a treatment over the knee, leg, shoulder and low back pain was modeled. According to the literature, to treat pain with thermotherapies; it is necessary to use temperatures around 38–48 °C [10]; moreover, a deep of minimum 5 mm must be achieved. However, due to the variety of people that use this treatment, it is not possible to ensure such a thing; especially, because of the difference in the thickness of tissue layers between people. Therefore, this study was done in order to know the effect of our patch over a specific region. The modeling was done with the finite element method software, COMSOL-Multiphysics (COMSOL Multiphysics Inc., USA).

The Pennes Bioheat equation was used to model the thermotherapy in a human body [20]. This equation describes the thermal distribution in tissues due to an external source (thermal patch). The equation is described as:

$$\rho c \frac{dT}{dt} = \nabla * (k \nabla T) + [-\rho_b w c_b (\mathrm{T} - T_b)] + Q_m + Q_{ext} \tag{1}$$

where c (J/kg/K) represents heat capacity, ρ (Kg/m^3) density, k (W/m/K) thermal conductivity, C_b (J/kg/K) heat capacity of blood, W (kg/m^3/s) blood perfusion, T_b (K) blood temperature, Q_m (W/m^3) rate of heat generated by metabolism and Q_{ext} the heat generated by the patch. The patch was fixed at different temperatures around 42 °C–48 °C; the temperature was kept constant through the whole treatment time. The analyzed treatment times were 15 min (900 s), 20 min (1200 s), 25 min (1500 s) and 30 min (1800). This study was done to analyses the thermal effect over the tissues. In order to emulate a treatment, thermal tissue properties, blood perfusion and metabolism were considered, see Table 1.

Table 1. Properties used in the model [21].

Tissue	Thermal conductivity [W/(m*K)]	Caloric capacity [J/(kg*K)]	Perfusion [ml/min/kg])	Metabolism [W/m^3]	Density (kg/m^3)
Fat	0.21	2348	33	3.9	911
Muscle	0.49	3421	37	716	1090
Bone	0.32	1313	30	368.3	1908

To evaluate the thermal effect produced by the patch, the reached temperatures at the tissue layers were obtained. The volume of tissue with a ΔT = 1 °C was analyzed. This helps us to evaluate if it is possible to produce a therapeutic effect.

3 Results

3.1 Thermal Effect

Figure 3 shows the volume of tissue that reaches a ΔT = 1 °C when the patch was located over the knee. The fatty tissue was the most affected. Treatment time and patch temperature played an important role to achieve enough heat penetration depth. The fat volume with a ΔT = 1 °C varied between 176.72 cm^3–296.42 cm^3, for a 40 °C patch and 900 s of treatment and 48 °C patch and 1800 s of treatment, respectively. To get a therapeutic effect, the muscle tissue must be affected also by the temperature. However, depending on the fat tissue layer thickness, treatment time and temperature patch, the muscle can be barely affected. Patch temperatures over 42 °C must be used to heat

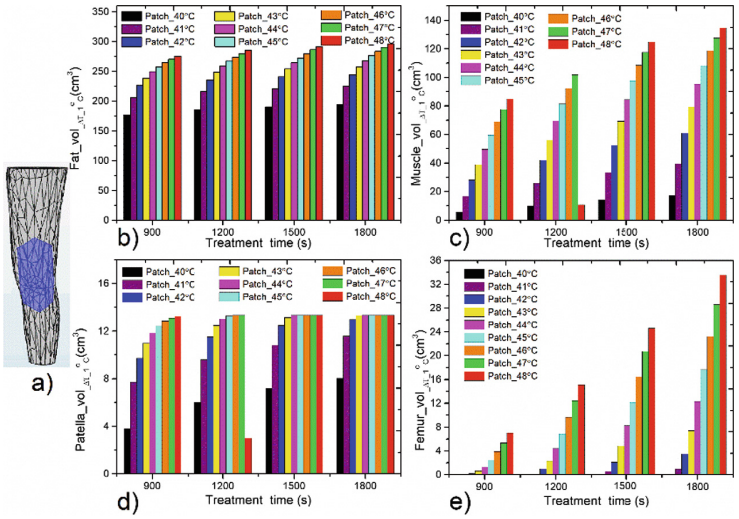

Fig. 3. Time dependent volume of tissue with a ΔT = 1 °C, reached with different patch temperatures. (a) Patch over the knee, (b) Volume of fat with a ΔT = 1 °C, (c) Volume of muscle with a ΔT = 1 °C, (d) Volume of bone with a ΔT = 1 °C (patella), (e) Volume of bone with a ΔT = 1 °C (femur).

muscle. Treatment times over 900 s gives better results; however, to avoid tissue thermoregulation, no more than 1800 s must be used. The volume of bone (patella and femur) affected by the temperature increase was lower; however, to avoid this, another patch configuration can be proposed.

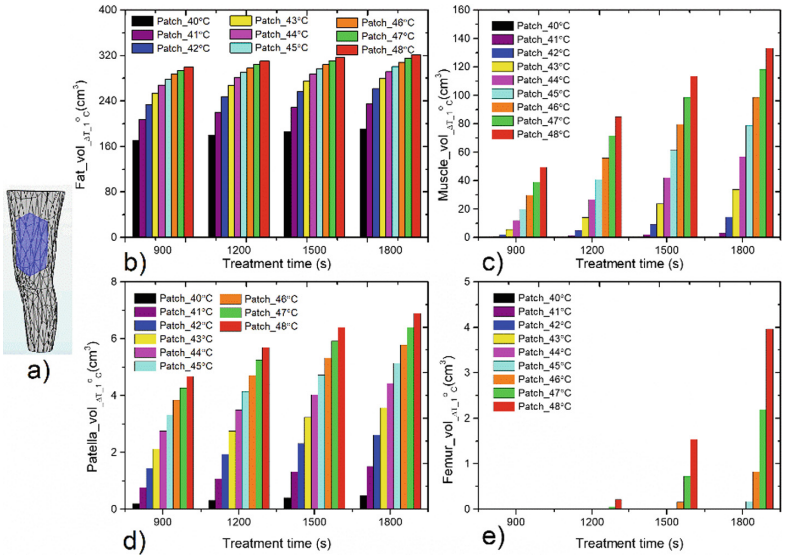

Fig. 4. Time dependent volume of tissue with a $\Delta T = 1$ °C, reached with different patch temperatures. (a) Patch over the leg, (b) Volume of fat with a $\Delta T = 1$ °C, (c) Volume of muscle with a $\Delta T = 1$ °C, (d) Volume of bone with a $\Delta T = 1$ °C (patella), (e) Volume of bone with a $\Delta T = 1$ °C (femur).

Figure 4 shows the results for a patch located over the leg, a region with more quantity of fatty tissue. To treat this region and to produce a thermal effect in muscle, a patch with temperatures higher than 43 °C must be used, as can be observed in Fig. 4(c). Bones are less affected by the temperature, reaching the maximum volumes of 6.89 and 3.95 cm^3 with a $\Delta T = 1$ °C (48 °C patch and 1800 s) in patella and femur, respectively.

Figure 5 depicts the behavior of the patch used to treat the shoulder region. To generate an effect in muscle, it must be used a patch with temperatures higher than 43 °C (See Fig. 5c)); moreover, treatment times higher than 1200 s must be considered. In this case, the volume of muscle affected by the temperature seems to be lower; however, it is important to remark that in this region the muscle tissue is skinny.

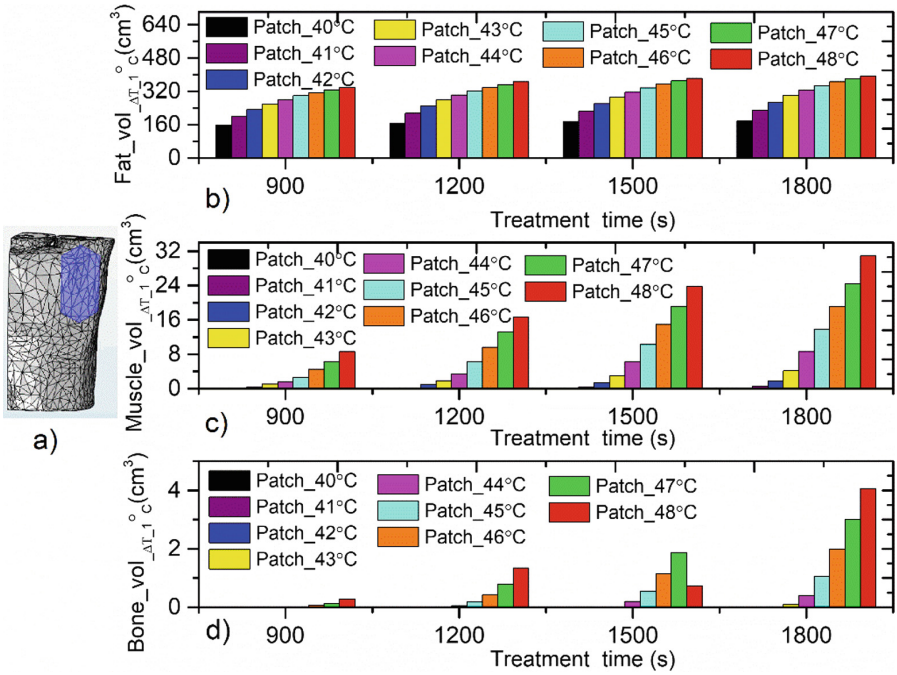

Fig. 5. Time dependent volume of tissue with a $\Delta T = 1$ °C, reached with different patch temperatures. (a) Patch over the shoulder, (b) Volume of fat with a $\Delta T = 1$ °C, (c) Volume of muscle with a $\Delta T = 1$ °C, (d) Volume of bone with a $\Delta T = 1$ °C.

Figure 6 shows a configuration used to treat pain in the lower back, three patches were used. Once more, the fatty tissue was the most affected and its thickness can really affect the amount of muscle affected by the patch temperature. Figure 6(c) shows that with a 43 °C patch and 900 s, a muscle volume of 11.87 cm^3 will reach a $\Delta T = 1$ °C. However, with a 44 °C patch and 1500 s and 1800 s, muscle volumes with $\Delta T = 1$ °C of 20.08 cm^3 and 34.67 cm^3 were achieved, respectively. Bone was barely affected, volumes lower that 3 cm^3 were achieved.

Figures 7(a)–(h) represent the regions of tissue affected with a $\Delta T = 1$ °C when a 44 °C patch was used for 900 s and 1800 s, for each case-scenario analyzed. In all cases, longer treatment times generate higher volumes of tissue with a $\Delta T = 1$ °C. However, 900 s could be enough to generate a therapeutic effect in the 4 case scenarios analyzed.

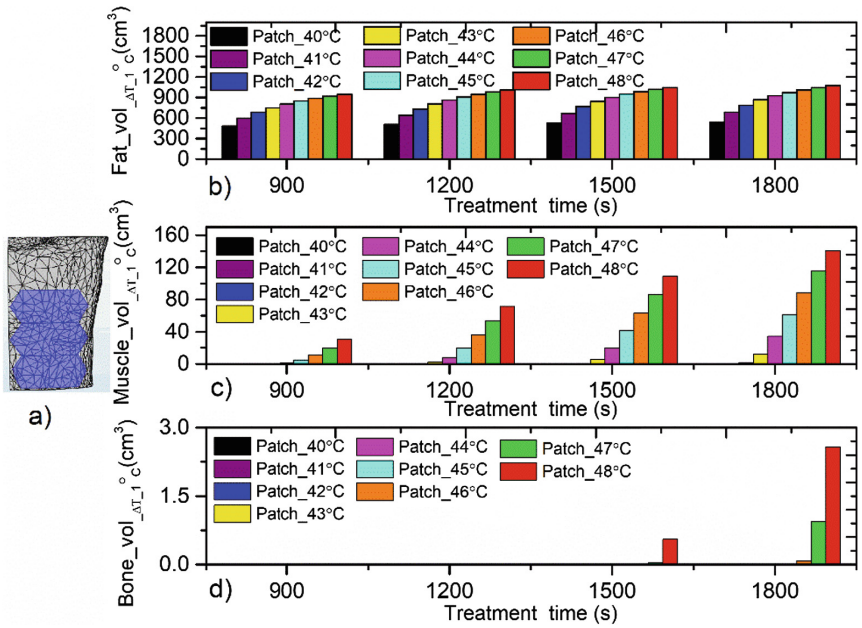

Fig. 6. Time dependent volume of tissue with a $\Delta T = 1$ °C, reached with different patch temperatures. (a) Patch over the lower back, (b) Volume of fat with a $\Delta T = 1$ °C, (c) Volume of muscle with a $\Delta T = 1$ °C, (d) Volume of bone with a $\Delta T = 1$ °C.

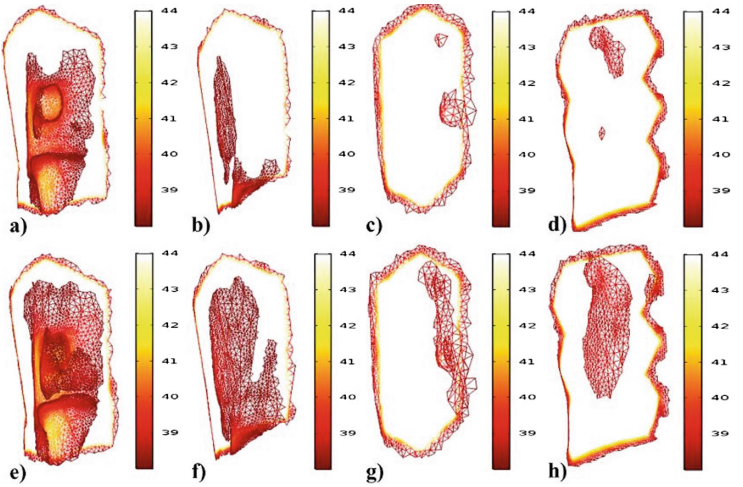

Fig. 7. Regions affected with a $\Delta T = 1$ °C in each case scenario. The white region represents the most superficial one (near to the patch), while the red ones represent the deeper tissues (muscle and bones). A 44 °C patch and treatment times of 900 s and 1800 s are shown. (a) Patch over the knee (900 s), (b) Patch over the leg (900 s), (c) Patch over the shoulder (900 s), (d) Patch over the low back (900 s), (e) Patch over the knee (1800 s), (f) Patch over the leg (1800 s), (g) Patch over the shoulder (1800 s), (h) Patch over the low back (1800 s).

4 Discussion

A 3D model to evaluate the thermal effect produced by a patch that is able to keep its temperature uniform and constant through the whole treatment was proposed. As it was described before, there are not enough information to say under which conditions the use of this kind of devices will have positive therapeutic effects. It is important to evaluate the effect of the proposed patch over each tissue layer, to evaluate the deep penetration. The results showed that fatty tissue is a problem, because it works as an insulator avoiding that the muscle can be affected by the temperature. Although it is necessary to perform some experimental test to validate these models, it is important to remark that they can be considered a good approximation because blood perfusion and metabolism were included. It is important to remark that to our understanding, until now, there are none information about 3D models implemented to describe the thermal effect that a patch (for pain relief) can produce over different tissue layers. Although the technic is quite used in several institutions, the analysis of its efficiency has been proved just by clinical trials. However, it is hard to find a standardized protocol to apply it. This work describes a first model to evaluate in a quantitative mode the efficiency of the patch.

5 Conclusions

This study was made to analyze the thermal effect of a patch designed to keep its temperature constant and uniform through the whole treatment. The analysis includes different patch temperatures and treatment times. Literature describes that in order to increase the local metabolism (metabolism of the damaged region) and to produce a therapeutic effect a temperature increase of 1 °C must be achieved. However, to reach this increment in muscle tissue can be difficult, especially because the fat thickness works as an insulator. Our results show that in order to produce a real therapeutic effect, it is not possible to treat all the body regions with the same patch temperature and treatment times. However, a patch temperature higher than 44 °C can be considered enough to generated therapeutic effects in most of the cases. If the treated region is covered by a huge fat layer, then the treatment time could be longer than 900 s. If the fat tissue layer is small, more muscle tissue will be heated up, then a real therapeutic effect will be generated in the local region.

Acknowledgment. Authors thank to the Mexican National Council for Science and Technology (CONACYT) and to the Technology Innovation Fund (FIT) for the financial support of the project B-S-95714.

Declaration of Interest Statement. The authors report no declarations of interest.

References

1. Goldberg, D.S., McGee, S.J., Ollila, E., Gureje, O., Von, K.M., Simon, G., et al.: Pain as a global public health priority. BMC Public Health [Internet] **11**(1), 770 (2011). http://bmcpublichealth.biomedcentral.com/articles/10.1186/1471-2458-11-770
2. Covarrubias-Gómez, A., Guevara-López, U., Gutiérrez-Salmerón, C., Betancourt-Sandoval, J.A., Córdova-Domínguez, J.A.: Epidemiología del dolor crónico en México. Rev. Mex. Anestesiol. **33**(4), 207–213 (2010)
3. AAPM Facts and Figures on Pain [Internet]. The American Academy of pain medicine. http://www.painmed.org/patientcenter/facts_on_pain.aspx
4. Wynne-Jones, G., Cowen, J., Jordan, J.L., Uthman, O., Main, C.J., Glozier, N., et al.: Absence from work and return to work in people with back pain: a systematic review and meta-analysis. Occup. Environ. Med. **71**(6), 448–458 (2014)
5. Osterweis, M., Kleinman, A., Mechanic, D.: Pain and Disability: Clinical, Behavioral, and Public Policy Perspectives (1987)
6. The Cost of Pain to Business and Society Due to Ineffective Pain Care [Internet]. The American Academy of pain medicine (2018). http://www.painmed.org/patientcenter/cost-of-pain-to-businesses/
7. López-Forniés, A., Iturralde-Garcia de Diego, F., Clerencia-Sierra, M., Ortiz-de Landázuri, J.G.: Concepto de dolor. In: Tratado de Geriatría para residentes (2011)
8. Nadler, S.F., Weingand, K., Kruse, R.J.: The physiologic basis and clinical applications of cryotherapy and thermotherapy for the pain practitioner. Pain Phys. **7**(3), 395–399 (2004)
9. Tepperman, P.S., Devlin, M.: The therapeutic use of local heat and cold. Can. Fam. Phys. [Internet]. **32**(5), 1110–1114 (1986). http://www.pubmedcentral.nih.gov/articlerender.fcgi?artid=2327914&tool=pmcentrez&rendertype=abstract
10. Hayes, K.W.: Heat and cold in the management of rheumatoid arthritis. Arthritis Care Res (Hoboken) [Internet]. **6**(3), 156–166 (1993). http://doi.wiley.com/10.1002/art.1790060308
11. Yurdanur, D.: Non-pharmacological therapies in pain management. In: Pain Management-Current Issues and Options (2012)
12. Defrin, R., Ohry, A., Blumen, N., Urca, G.: Sensory determinants of thermal pain. Brain **125** (3), 501–510 (2002)
13. Garra, G., Singer, A.J., Leno, R., Taira, B.R., Gupta, N., Mathaikutty, B., et al.: Heat or cold packs for neck and back strain: a randomized controlled trial of efficacy. Acad. Emerg. Med. **17**(5), 484–489 (2010)
14. Mordeniz, C.: Pain perception within consciousness. Neuro Quantol. **14**(2), 439–446 (2016)
15. Habash, R.W.Y., Bansal, R., Krewski, D., Alhafid, H.T.: Thermal therapy, part 2: hyperthermia techniques. Crit. Rev. Biomed. Eng. **34**(6), 491–542 (2006)
16. Naranjo-Rosas, A., Sandoval-Gonzalez, O., González-Sánchez, E., Trujillo-Romero, C., Martinez-Mendez, R., Flores-Cuautle, A.: Férula auxiliar en el tratamiento del dolor articular por medio de termoterapia resultados preliminares. Rev. Fisioter. **1**(1), 23–30 (2017)
17. Denzi, A., Strigari, L., Di Filippo, F., Botti, C., Di Filippo, S., Perracchio, L., et al.: Modeling the positioning of single needle electrodes for the treatment of breast cancer in a clinical case. Biomed. Eng. Online **14**(Suppl 3), 1–14 (2015)
18. Liu, Z., Ahmed, M., Sabir, A., Humphries, S., Goldberg, S.N.: Computer modeling of the effect of perfusion on heating patterns in radiofrequency tumor ablation. Int. J. Hyperth. **23**, 49–58 (2007)

19. Karampatzakis, A., Kühn, S., Tsanidis, G., Neufeld, E., Samaras, T., Kuster, N.: Heating characteristics of antenna arrays used in microwave ablation: a theoretical parametric study. Comput. Biol. Med. [Internet]. **43**(10), 1321–1327 (2013). https://doi.org/10.1016/j.compbiomed.2013.07.013
20. Pennes, H.H.: Analysis of tissue and arterial blood temperatures in the resting human forearm. J. Appl. Physiol. **85**, 5–34 (1948)
21. Hasgall, P., Neufeld, E., Gosselin, M., Klingenbock, A., Kuster, N.: IT'IS database for thermal and electromagnetic parameters of biological tissues [Internet] (2012). http://www.itis.ethz.ch/itis-for-health/tissue-properties/overview/

Prototype of a Multivariable Measurement System

Israel Sánchez-Domínguez(✉), Paul Erick Méndez Monroy, and Ernesto Pérez-Rueda

UNAM IIMAS – Unidad Mérida, Mérida, Yucatán, Mexico
israel.sanchez@iimas.unam.mx

Abstract. In this work we present the guidelines for the construction of a prototype for general purpose measurements. The goal for this prototype of a virtual instrument is to achieve measurements at macro- or micro-scales, depending on the variables. The measurements will be made through sensors from a personal computer without having to resort to commercial instruments. The system consists of a development platform (Arduino), an adapter to adjust the sensors and a graphical interface. The acquisition card has the specifications required for the correct functioning of the sensors, whereas the adapter consists of different plug-and-play inputs. In our development phase, the regulation of voltage and frequency was tested, as was the communication required for correct readings from the sensors. We obtained a system and an interface capable of recognizing the connected sensors and that showed the measurements in the interface developed in LabVIEW; our system also allowed saving the information (input and output).

Keywords: Measurement · Sensors · Virtual instrument · Arduino · LabVIEW

1 Introduction

Advances of technology for multivariable measurement systems now allow increasingly easy access to development of such systems; however, such advances do not always lead to the best option for a specific problem. The present work begins with the development of systems using a simple technology, the development platform of Arduino [3], and observations on its compatibility for scaling this system with various sensors all integrated under the same development platform. Since this work is in the prototype stage, it serves to verify the functionality of Arduino and, depending on the results, to show the possibilities for migrating to other platforms, such as Raspberry Pi. The need to perform measurements immediately, accurately, safely and with the appropriate instruments has generated increasingly sophisticated instruments now on the market [2]. However, these instruments do not always solve the problem of signal acquisition, because in most cases more than one instrument is required to complete the tasks that must be performed. In addition, it is necessary to move from the macro- to the micro-scale, which entails investments in instruments with different measurement scale ranges and different input variables; these changes lead to the need for more than one instrument. It is worth mentioning that the availability of more-sensitive and

© Springer Nature Switzerland AG 2020
C. A. González Díaz et al. (Eds.): CLAIB 2019, IFMBE Proceedings 75, pp. 519–523, 2020.
https://doi.org/10.1007/978-3-030-30648-9_67

manipulable sensors in recent years has increased significantly their accessories, as has the emergence of different platforms that are easy to program. Altogether, these improvements allow robust development of instruments with *ad hoc* measurements superior functionalities and escalation compared to the counterpart commercial instruments [4–6]. In the present work, we propose the development of a general purpose measurement system that allows the improvement of functionality, interconnectivity and scalability. This system allows measurements of diverse parameters, with different scale ranges and units, embedded in a single system that relies on both software and hardware tools. In addition, the system provides to the user the possibility of diverse measuring instruments in a single system, relevant to the intended medical application, because it guarantees portability, escalation and is user-friendly. The advantage that such a system offers is that can be adapted according to the requirements of the measurement and/or the task. In Fig. 1, we show the implemented system that performs different measurements, based on a plug-and-play concept. Thus, by using recent technology, accessible via a wide field of configurations, we found that Arduino in any of its versions, as well as the range of sensors associated with it, is a viable option in the design of the proposed measurement system [7, 8].

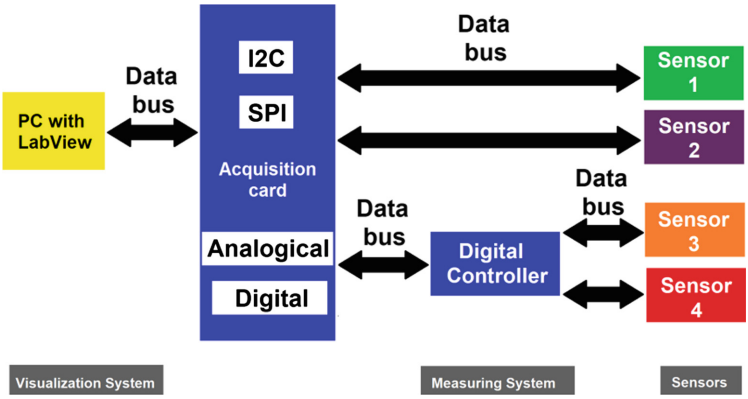

Fig. 1. General scheme of the measurement system.

2 Methodology

From Fig. 1, the characteristics that are measured with different sensors are considered. These characteristics can be modified, from the input voltage to the communication protocol, due to the disposition presented by the Arduino UNO platform, because it has analog and digital inputs/outputs and manages different communication protocols, such as Serial, SPI or I2C. Those features allow use of switches, with a frequency up to 20 kHz for data acquisition. The control and power modules of the system are shown in Fig. 2. The measurement system has standard connectors for the sensors and related hardware; however, the characteristics for each sensor change, since it can be analog or digital, working at 5 v (TTL) or 3.3 v (CMOS) or even communicating through I2C,

SPI or serial protocols. This is the reason that the CI 74HC4066 was used, which is a bilateral analog quadruple-switch module. In this context, the input is configured for an analog or digital sensor. To carry out the functionality tests, four sensors were used, at different times, in terms of both electrical and communication protocols. The sensors we considered were for temperature, ultrasound, humidity and current. Because the design of the system was focused on making a stage B prototype, the assembly of all the associated electronics was developed. The Arduino and connection of the sensors were assembled in a breadboard, and later a simple PCB was constructed, for the best performance of the circuit. Finally, the prototype B was assembled in a "black box".

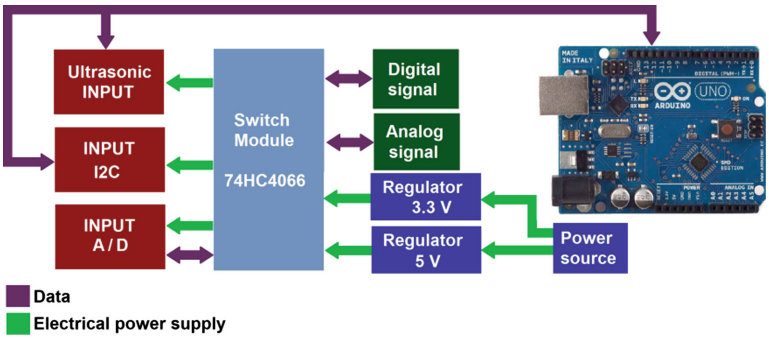

Fig. 2. Control and supply modules of the system

3 Results

The functionality of the system was achieved by testing the operation with four different sensors, for temperature, current, humidity and distance, verifying that the interface displayed the information measured by the sensors. This system was designed to perform bio-medical measurements, from sensors; however, it can be used for other types of measurements. Figure 3 shows the input interface to the system, where the connected sensors are identified and the user can select specific information or employ all at the same time.

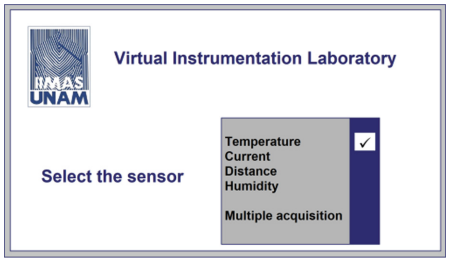

Fig. 3. Interface of the measurement system

Figure 4 shows the interfaces for the sensor. This was intended to be simple, and provide clear and concise information appropriate for the type of task. That is, it could be alphanumeric, graphic or combined. It is worth mentioning that the user may select each interface separately or in combination.

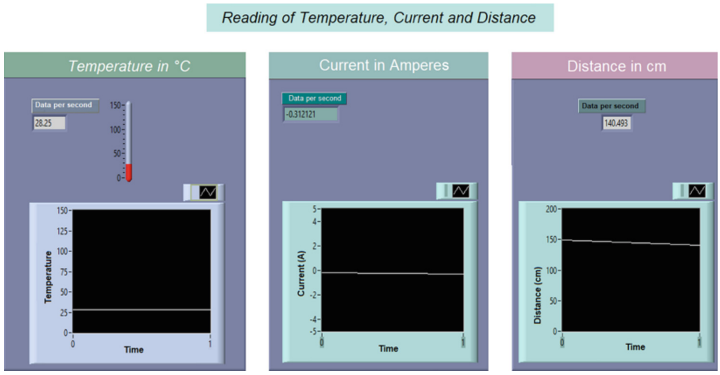

Fig. 4. Interface for the sensors

In order to verify that the system was able to work with every sensor or with all of them simultaneously, that the information could be displayed in the interface developed in LabVIEW [1], and finally, that measurements could be saved, all sensors were connected as needed. In Fig. 5b, we show the connections and the way in which the data can be saved.

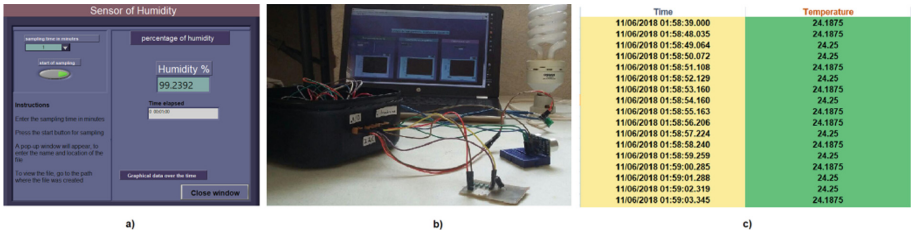

Fig. 5. System functionality, (a) measurement of one sensor, (b) test connecting of diverse sensors, (c) data storage test (option to save the measurements)

4 Conclusions

It was possible to design, build and validate the prototype for a virtual measurement system, for each of its parts (hardware and software) involved in the coupling between the transducers, Arduino, and LabVIEW, to show the measures acquired by the sensors, individually or in combination, without generating failure in the system. Therefore, for the intended medical applications, the system can be used as an ad-hoc

instrument for simultaneous measurements. Another tool that helps to guarantee the good portability, improvement and escalation options is the LabVIEW software, which allows incorporation of intuitive interfaces, that are user-friendly and with the facility of being able to show several screens at the same time with different modes of deployment and with the capacity to store the information, making it the appropriate complement for the realization of such a system and ad-hoc tool for the user. Finally, there are still several improvements we are working on, such as the miniaturization, feeding part, and connection of the Arduino, the possibility of scaling the platform to a Raspberry and the possibility of expanding the number of sensors. All these improvements will be beneficial in the medical area, such as in signal acquisition and processing. In this context, tools for the data analysis, must be developed and incorporated into the system.

Acknowledgements. We thank to Joaquin Morales, Sandra Sauza and Fatima Cocom for their technical support. Project was funded by DGAPA-Universidad Nacional Autónoma de México (IN-201117) and CYTED (P918PTE0261) to EP-R; and (IA-104218) to PEM-M.

References

1. LabVIEW User Manual: National Instruments (2003)
2. Ni USB-6008/6009 Bus Powered Multifunction DAQ USB Device National Instruments (2015)
3. Arduino Uno R3: Arduino (2018)
4. Mosterman, P.J., Campbell, J.O., Brodersen, A.J., Bourne, J.R.: Design and implementation of an electronics laboratory simulator. IEEE Trans. Educ. **39**, 309–313 (1996)
5. Shen, H., Xu, Z., Dalager, B., Kristiansen, V., Strum, O.: Conducting laboratory experiments over the internet. IEEE Trans. Educ. **42**(3), 180–185 (1999)
6. Chen, S.H., Chen, R., Ramakrishnan, V., Hu, S.Y., Zhuang, Y., Ko, C.C., Chen, B.M.: Development of remote laboratory experimentation through internet. In: IEEE Hong Kong Symposium on Robotics and Control, vol. 2, pp. 756–760 (1999)
7. Callejas Tavera, A.: Sistema de Adquisición y registro de datos autónomo con aplicación de hidrófono. Facultad de Matemáticas, Universidad Autónoma de Yucatán (2018). Tesis de Licenciatura
8. Nah, F.Y.C.: Desarrollo de un laboratorio de instrumentación virtual abierto para sistemas de medición con distintos sensores. Facultad de Matemáticas. Universidad Autónoma de Yucatán (2018). Tesis de Licenciatura

Development and Pilot Testing of a New Electromyography Device

Douglas Crochi(✉), Tiago R. S. Silva, André Silva, Marcello F. Santos, Natasha H. Ota, Paulo Daudt, Silvia C. Martini, Silvia R. M. S. Boschi, Terigi A. Scardovelli, and Alessandro P. Silva

Technology Research Center, University of Mogi das Cruzes, Mogi das Cruzes, São Paulo, Brazil
douglascrochi@gmail.com

Abstract. In recent years, no other aspect of muscle loading has been more investigated in the literature than eccentric movement. However, issues involving muscle responses from eccentric training are not fully understood. Thus, the objective of this study is to develop and test a new electromyography device (EMG Lavita) capable of assisting researchers and clinicians in understanding the muscular responses from eccentric contraction. An electronic circuit composed by an INA118P, a 30 to 150 Hz bandpass filter and a rectifier was developed. The analog signal is converted into a digital signal using a 10-bit A/D converter that is part of the Atmega328p microcontroller which sends the data through a serial communication to a supervisory system which them processes and shows the data in graphic way. A pilot test was performed and simultaneously recorded the EMG signals from the brachial biceps muscle using two different electromyography devices, a Commercial EMG and EMG Lavita. For this test one researcher performed 5 data collections consisting of 10 repetitions of the elbow flexion movement with one-minute interval between them. After the data collection, a statistical test was performed to verify the Pearson correlation coefficient to compare the RMS values of the devices. The EMG Lavita behaved similarly to commercial EMG, presenting (r = 0.86) which shows a good to excellent correlation. The EMG Lavita device showed strong correlation with the commercially used device.

Keywords: Electromyography · EMG · Device

1 Introduction

In high-performance sports, physiotherapists are subject to numerous pressures and charges so that the athlete returns to their sports practice as soon as possible [1]. In this way, several training techniques have been used to optimize the rehabilitation process [2]. In recent years, no other aspect of muscle loading has been more investigated in the literature than eccentric movement [3]. It is known that this stimulus causes a decline in the ability to produce strength, release of creatine kinase, edema, and late-onset muscle pain, suggesting muscle injury [4, 5]. However, it was observed that a three weeks

© Springer Nature Switzerland AG 2020
C. A. González Díaz et al. (Eds.): CLAIB 2019, IFMBE Proceedings 75, pp. 524–529, 2020.
https://doi.org/10.1007/978-3-030-30648-9_68

protocol performing eccentric exercise was effective in promoting hypertrophy, without any muscular damage being observed, allowing the athlete a safe and early return to his training routine [6].

Questions involving muscle responses to eccentric training are not fully understood. Thus, the development of a device that allows to analyze the behavior of muscular activity during eccentric contractions, would aid researchers and clinicians in understanding the physiological mechanisms that involve this type of contraction. So, the objective of this study was to develop and test a new electromyography device capable to record the intensity and duration of eccentric contractions.

2 Materials and Methods

To collect the signal of muscular activity an acquisition system was developed, represented by Fig. 1.

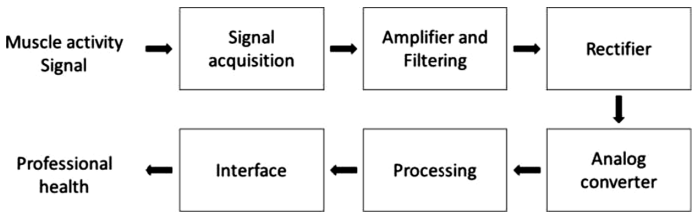

Fig. 1. Function diagram of the EMG Lavita device.

The electronic circuit was powered by batteries, which made the circuit portable and avoided noise from the electrical network. The myoelectric signals were captured by self-adhesive contact electrodes. Then, an INA118P instrumentation amplifier was used to collect and amplify the electrode signal. The signal is then filtered by a first order Butterworth 30 to 150 Hz bandpass filter, and then amplified, generating a final gain of 400 times the original signal. After the filtering process, the signal is rectified so that the negative signals become positive, ensuring that the Arduino Nano A/D converter can capture all the signal variations, convert the signals and send them via serial communication. Upon receiving the collected signals, the supervisory system developed by the MatLab® Software designer App uses an Average Moving Filter to filter the signal. With the filtered signal, the system finds the upper and lower positions peaks of each repetition and calculates the time in seconds between each peak. With this data it is possible to calculate the number of repetitions performed during the exercise.

2.1 Experimental Protocol

A pilot test was performed, and the EMG signals were recorded simultaneously using two different electromyography devices, EMG Commercial (EMG System of Brazil, SAS2000V12-WF) and EMG Lavita (developed in this study). Both devices were adjusted to a sampling rate of 2000 Hz. The electrode positioning procedure on the

biceps brachii muscle and the skin preparation followed the SENIAM recommendations [7]. The data were collected 5 times, with an interval of 1 min between them. For each data collected, the subject performed 10 repetitions of the elbow flexion movement with a 2 kg halter. To analyze the data was performed a Pearson correlation test between the root mean square (RMS) variables of the Commercial EMG and EMG Lavita [8].

3 Results

The Fig. 2 illustrates the final model of the device.

Fig. 2. Final model

3.1 Pilot Test

Table 1 shows the RMS values of the 5 data collections performed by the researcher.

Table 1. RMS values

Data collect	EMG system	EMG Lavita
1	396,0972	377,6468
2	332,8503	344,285
3	326,9942	296,4334
4	402,5563	385,355
5	378,1988	341,0584

Using the data from Table 1, a Pearson correlation coefficient analysis was performed, presenting ($r = 0.86$) between the RMS values of commercial EMG and EMG Lavita, which shows a good to excellent correlation [8].

3.2 Supervisory System

The supervisory system presents to the user the gross signal, segmented signal, intensity and duration of the eccentric contractions (Fig. 3).

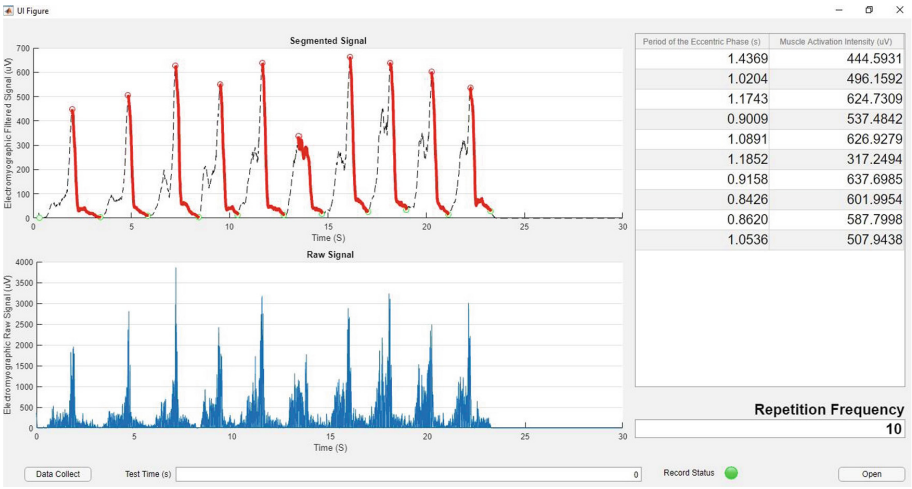

Fig. 3. EMG supervisory screen

Table 2 shows the intensity values of the eccentric contractions collected during the test.

Table 2. Intensity of contraction (uV)

Data collect	Contraction										Average	Standard deviation
	1	2	3	4	5	6	7	8	9	10		
1	268,95	287,14	369,53	349,18	381,29	322,18	419,48	392,03	365,10	498,70	365,35	62,63
2	380,22	282,31	413,47	458,73	399,48	416,39	355,38	422,34	624,59	475,41	422,83	84,58
3	359,53	239,84	208,82	268,51	402,19	291,41	381,31	457,56	423,69	420,32	345,31	82,25
4	269,14	383,46	463,74	467,75	368,47	443,55	413,34	305,22	496,01	433,81	404,44	69,47
5	444,59	496,15	624,73	537,48	626,92	317,24	637,69	601,99	587,79	507,94	538,25	95,94

Table 3 shows the elapsed time of the eccentric contractions during the test.

Table 3. Duration of each eccentric contraction (s)

Data collect	Contraction										Average	Standard deviation
	1	2	3	4	5	6	7	8	9	10		
1	0,86	0,66	0,88	0,81	0,76	0,77	0,78	0,66	0,74	1,16	0,80	0,13
2	1,10	0,88	0,90	0,88	0,86	1,18	0,76	1,11	0,84	1,25	0,97	0,15
3	0,68	1,03	1,54	1,03	0,69	1,33	0,99	0,76	0,73	0,72	0,95	0,28
4	0,73	0,93	0,62	0,96	1,00	0,97	0,81	1,28	1,07	1,02	0,93	0,17
5	1,43	1,02	1,17	0,90	1,08	1,18	0,91	0,84	0,86	1,05	1,04	0,17

Based on the values presented by the system, clinicians and researchers will be able to perform a detailed analysis on muscular responses to different eccentric contraction protocols.

4 Discussion/Conclusion

In recent years, the use of eccentric exercises in sports rehabilitation has been intensely studied [9]. For Goldspink [10] the eccentric contraction is considered one of the most damaging stimuli to the muscles, due to the increase in tension in the z-line of sarcomeres. However, Batista et al. [11] demonstrate that eccentric training improves athletes' performance and flexibility, as well as promoting a significant gain in strength when compared to concentric exercises [12]. However, the mechanisms by which this process occurs are still not completely clear. In order to better understand muscle responses to eccentric contraction, this study developed a device that differs from commercially available electromyography equipment by individually demonstrating the intensity and duration of each muscle contraction, as well as the number of repetitions performed, which facilitates the interpretation of data by the evaluator. With this, clinicians and researchers have a better direction in their decision making, since this device can be used as a method to evaluate or compare the effectiveness of intervention protocols. Therefore, it is possible to concluded that this study developed and tested a new electromyography device capable of assisting researchers and clinicians in understanding muscular responses from eccentric exercise. Although the pilot test has shown that it tends to behave as a commercial EMG device, further testing is required to confirm its results.

Acknowledgment. The São Paulo Research Foundation – FAPESP, grant #2017/16292-1.

Declaration of Conflict of Interest. The authors declare no conflict of interest.

References

1. Caparrós, T., Pujol, M., Salas, C.: General guidelines in the rehabilitation process for return to training after a sports injury. Apunts. Medicina de l'Esport. **52**(196), 167–172 (2017)
2. Sewry, N., Verhagen, E., Lambert, M., et al.: Exercise-based interventions for injury prevention in tackle collision ball sports: a systematic review. Sports Med. **47**(9), 1847–1857 (2017)
3. Neto, A., Preis, C.: A valorização do treinamento muscular excêntrico na fisioterapia desportiva. Fisioterapia em Movimento **18**(1), 19–26 (2005)
4. Warren, G., Lowe, D., Armstrong, R.: Measurement tools used in the study of eccentric contraction-induced injury. Sports Med. **27**, 43–59 (1999)
5. Clarkson, P., Hubal, M.: Exercise-induced muscle damage in humans. Am. J. Phys. Med. Rehabil. **81**(11), 52–69 (2002)
6. Flann, K., LaStayo, P., McClain, D., et al.: Muscle damage and muscle remodeling: no pain, no gain? J. Exp. Biol. **214**, 674–679 (2011)
7. SENIAM. http://seniam.org/bicepsbrachii.html. Accessed 22 Apr 2019

8. Jang, M., Ahn, S., Lee, J., et al.: Validity and reliability of the newly developed surface electromyography device for measuring muscle activity during voluntary isometric contraction. Comput. Math. Methods Med. (2018)
9. Pull, M., Ranson, C.: Eccentric muscle actions: implications for injury prevention and rehabilitation. Phys. Ther. Sport **8**(2), 88–97 (2007)
10. Goldspink, G.: Changes in muscle mass and phenotype and the expression of autocrine and systemic growth factors by muscle in response to stretch and overload. J. Anat. **194**(Pt 3), 323–334 (1999)
11. Batista, L., Camargo, P., Oishi, J., et al.: Efeitos do Alongamento ativo excêntrico dos músculos flexores do joelho na amplitude de movimento e torque. Revista Brasileira de Fisioterapia **12**(3), 176–182 (2008)
12. Ferreira, A., Marujo, A., Folgado, H., et al.: Programas de exercício na prevenção de lesões em jogadores de futebol: uma revisão sistemática. Revista Brasileira de Medicina Esportiva **21**(3), 236–241 (2015)

Initial Approaches for Manipulation of Human Lens for Irradiation in a Solar Simulator: A Study for Cataract

Fernanda Oliveira Duarte[1(✉)], Andre Fragalli[1], Mauro Masili[1], Sidney Julio de Faria e Sousa[2], and Liliane Ventura[1]

[1] Departamento de Engenharia Elétrica, Universidade de São Paulo (EESC), Av. Trabalhador Saocarlense 400, São Carlos, SP 13566 590, Brazil
ferduarte@usp.br

[2] Banco de Olhos – Hospital das Clínicas/Faculdade de Medicina de Ribeirão Preto, Universidade de São Paulo (FMR-USP), Av. Bandeirantes 3900, Ribeirão Preto, SP 14040 900, Brazil

Abstract. There are evidences that ultraviolet radiation has an intimate relationship with cataract in the human lens. However, there is no complete proof that ultraviolet radiation is the cause of cataracts or either acceleration of this pathology. This disease is characterized by increased absorption and scattering of light through at the lens which leads to decreased light transmission to the retina, resulting in poor vision, and eventually leading to blindness. The objective of this study is to analyze the spectroscopy of a human lens and different culture media to determine which solution is most suitable for the development of a future experimental protocol for solar irradiation of the lens. A holder to accommodate the lens was developed, since there is no consensus on the best way to manipulate the lens to avoid its opacification. We performed the spectroscopy of a human lens and three different culture media (saline solution, TC199 with phenol-red and TC199 without phenol). The preliminary result of the lens spectroscopy is in agreement with one described in the literature, demonstrating that the lens holder did not interfere in the measurement. In conclusion, the lens holder can be used to avoid lens manipulation and probable opacification. Among the analyzed media, the saline solution proved to be the most adequate because it does not absorb light in the ultraviolet range and therefore can be used in a solar simulator, as a strategy to prevent dryness of the lens. These findings are important for future experiments involving the human lens and solar irradiation to determine if the effects of chronic exposure of the eyes to ultraviolet solar radiation has any relation with cataract development.

Keywords: Human lens · Ultraviolet radiation · Spectroscopy · Cataract · Transmittance

© Springer Nature Switzerland AG 2020
C. A. González Díaz et al. (Eds.): CLAIB 2019, IFMBE Proceedings 75, pp. 530–537, 2020.
https://doi.org/10.1007/978-3-030-30648-9_69

1 Introduction

Since the 19th century, the possibility of developing cataracts due to long exposure to ultraviolet radiation (UVR) from the sun has been discussed. In this context, current scientific studies have shown that UVR is potentially dangerous to the structure of the eyes, particularly the cornea, lens, and retina [1–3]. The spectral energy increases inversely with to the wavelength, and the potential damage to the eye increases exponentially [4]. Solar UVR, subdivided in UVA and UVB, are the shortest wavelengths that reach the human eyes and, are absorbed, especially by the cornea and the lens.

The cornea absorbs most of the UV radiation, completely blocking solar UVR with wavelengths shorter than 290 nm; around 45% on 320 nm, 34% on 360 nm and continues to decrease with longer wavelengths reaching the lens with range from 300 nm onwards [5, 6]. However, even though UV levels are low, the cumulative exposure for many decades may negatively affect the lens [7]. Indeed, solar UV radiation penetrating the eye is one of the major factors causing oxidative stress in the lens [8, 9]. Photochemical reactions occurring within the lens can induce post-translational modifications of lens crystallins proteins, resulting in their coloration, aggregation, and insolubilization. These processes may eventually lead to the development of cataracts. Therefore, the highly ordered and densely compacted arrangement of the crystallins present in the lens help to keep its transparent state, being the cataract an irreversible opacification of these proteins [9–11].

Protection against UVR is performed by molecular UV filters present in the lens. The UV absorption in UVA and visible regions by human lens proteins increases substantially with age. The near infrared radiation transmitted by the cornea is also absorbed, and is age-dependent [8]. Therefore, older human lens absorb most of the wavelengths of UVA and blue light. In this case, the absorption of the lens extends at wavelengths in the visible region up to 550 nm [8]. Thus, although UVB may have a greater potential to cause damage, the amount of UVA that reaches the human lens is about two orders of magnitude higher [7]. In addition, according to Zelentsova et al. (2017) [9], it can be assumed that increased age-related absorption of the crystalline protein weakens the UV protection of the lens, especially against UVA radiation. These findings raise concerns about eye health from exposure to UVR and its possible damage to the lens.

Besides the possible damage that chronic exposure to UVR can cause to human lenses, there is another concern when we think of eye health. Beyond the endogenous protection, the use of sunglasses can be an ally in the protection of the lens against the UVR, regardless of age. However, there is a concern with sunglasses, since in studies developed in our laboratory, we have demonstrated non-compliance of some sunglasses with the ISO 12312-1 standard [12–20], even before the solar simulator exposure test [21]. These data are important because they add to the researches that estimate the amount of exposure to UVR for a particular occupation or lifestyle under the sun [9, 21–25]. On the other hand, cataract can be induced in experimental animals by many agents, but with few exceptions, it is not clear whether the lens opacification routes in the laboratory have parallels with the human population [26].

In this sense, a literature review makes it clear that some studies show correlations of cataract incidence with exposure to UV sunlight, while others do not, making the results inconclusive. In addition, most studies are conducted in animals, which means that the lens are not sufficiently similar to the human lens [1, 6, 11, 26, 27]. Moreover, methods of extraction and manipulation of the lens can affect its proteins, changing the composition and architecture, resulting in opacification of the tissue, which also limits the studies. Because UV doses received by the eyes accumulate throughout direct and diffuse exposure [28], it is essential and urgent investigate the real effect of UVR on the eyes.

Therefore, studies that mimic the natural environment should be performed to verify the effect of UVR on the human lens. However, for future studies to be carried out, it is necessary to minimize the negative effects of lens manipulation and to standardize the use of culture media in order to increase the lifetime of these delicate structures. For all that, the objective of this study is analyze spectroscopically a human lens and different culture media to determine which solution is most suitable for the development of a future experimental protocol for irradiation of the lens, within a solar simulator.

2 Materials and Methods

2.1 Ethics Committee

This research was approved in the Human Research Ethics Committees of the Centro Universitário Central Paulista – UNICEP (CAAE: 99432718.4.0000.5380) and in the Hospital das Clínicas da Faculdade de Medicina de Ribeirão Preto (CAAE: 99432718.4.3001.5440).

2.2 Biological Material and Crystalline Lens Collection

The human lens used in this project was donated by the Eye Bank of the HCRP-FMRP-USP. After dissection of the cornea for donation, the lens was removed from the eyeball and allocated in specific support, adapted from Duarte et al. [29], to avoid excessive manipulation during the development of the experimental protocol. The crystalline contained in the support was maintained in TC199 preservative solution at 36 °C to simulate body temperature.

2.3 Spectral Transmittance

The spectroscopy was made using an UV-Vis-NIR spectrophotometer (CARY 5000, VARIAN) in the range of 200 to 800 nm with 1 nm resolution, in air, and at 23 °C. The lens analysis was made without the conservative solution and with the lens sample inside the designed holder.

3 Results

3.1 Spectral Transmittance of Culture Media and Saline Solution

The transmittance spectra of the saline solution and TC199 with and without phenol-red are shown in Fig. 1. At this point, our region of interest is the UVA range because nearly all UVB frequencies are absorbed by previous ocular structures. In this sense, we observed that both the saline solution and the medium culture TC199 without phenol-red presented low absorption in the UVA region. The saline solution presented non-negligible UVB transmittance, and the TC199 with phenol-red showed very low transmittance in both UVA and UVB ranges.

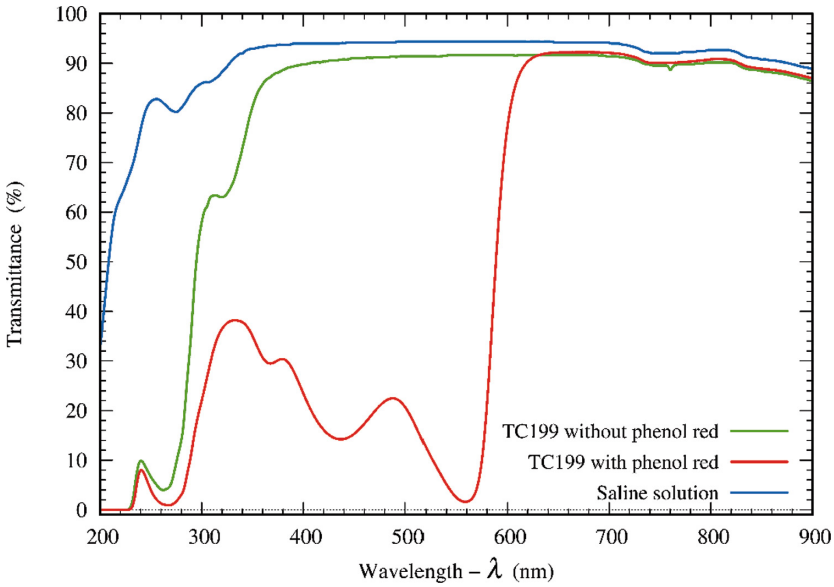

Fig. 1. Transmittance spectra of the three considered media, i.e., saline solution and TC199 with and without phenol red.

3.2 Spectral Transmittance of the Human Lens

The spectroscopy was made with the lens inside the designed holder and the transmittance spectrum is shown in Fig. 2. We observe very low transmittance in the UVA and UVB ranges. The lens absorbed UVR up to approximately 390 nm. The visible light is almost not absorbed by the lens, with peak values in the red region.

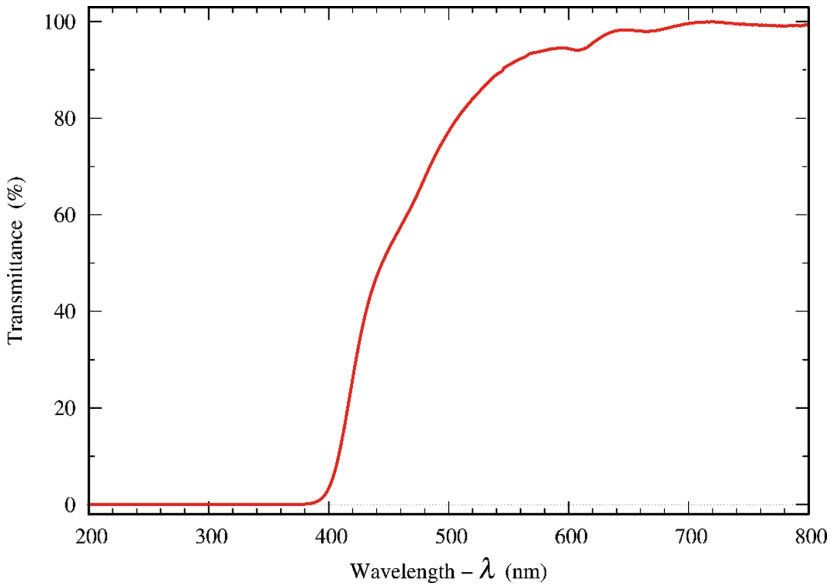

Fig. 2. Transmittance spectrum of the human lens sample.

4 Discussion

The main result obtained in this study was to determine the best solution for the future lens irradiation inside a solar simulator to avoid its dryness. In addition, it can be seen from the transmittance analysis that the human lens absorbs much of the radiation in the UV band, which adds concern about the correlation between UV absorption by the lens and cataract. Besides this, the profile of the curve obtained is in agreement with the findings of Artigas et al. [30], who carried out measurements of the transmittance on human lenses using an integrating sphere. It is worth mentioning that our findings allow us to state that the specific support previously developed [29] does not interfere with the transmittance measurements of the human lens and that the probability of problems due to manipulations are lowered.

It is evident the need and the importance of future studies about the human lens, since the chronic exposure of UVA radiation seems to be related to the development of cataract in humans. In fact, studies have shown this possible relationship but, due to a large number of controversial results, in both human and animal lens studies, there is no conclusive evidence. Furthermore, another result obtained in this study is that a saline solution can be used to avoid dryness of the lens during the irradiation period in a solar simulator once it does not considerably absorb radiation in the UV region.

Thus, we will be effectively able to observe if there will occur a degeneration of the lens, and if this is the case, be able to quantify it as a function of the exposure to the UVR. The development of this preliminary study of the human lens has scientific importance, because new experimental protocols can be developed aiming at understanding the relationship between UVR and ocular health. The results may contribute to

a safe standard for use of sunglasses in our tropical country [14, 15, 17]. Although the efforts of our team have been progressively achieved, the Brazilian standard NBR15111: 2013 [21] was revoked in 2015, for the convenience of the industries. Thus, this work comprises one of the many systems that our laboratory is developing [12, 13, 16, 18, 19], focusing on the effects caused by UVR on the human lens and in the eye health.

5 Conclusion

From the results obtained in this study, future experiments involving human lens will be developed, allowing a quantification of the effects of chronic exposure to ultraviolet solar radiation upon the eyes. Future results could to contribute to the suitability of standards and ISOs associated with the use of sunglasses, ensuring that they have an adequate UV protection, which is an important strategy to prevent the development of related eye diseases.

Acknowledgments. The authors are grateful for the financial support of the Coordenação de Aperfeiçoamento de Pessoal de Nível Superior (CAPES) - Financing Code 001 (Fernanda Oliveira Duarte and Mauro Masili).

Conflict of Interest. The authors declare that there is no conflict of interest.

References

1. Löfgren, S.: Solar ultraviolet radiation cataract. Exp. Eye Res. **156**, 112–116 (2017)
2. Mercede, M., Milani, B.Y., Asadolah, M., Lisa, W., Ali, R.D.: The role of ultraviolet radiation in the ocular system of mammals. Photonics **1**(4), 347–368 (2014). https://doi.org/10.3390/photon-ics1040347
3. Sliney, D.H.: Photoprotection of the eye - UV radiation and sunglasses. J. Photochem. Photobiol., B **64**(2–3), 166–175 (2001)
4. van Norren, D., Gorgels, T.G.: The action spectrum of photochemical damage to the retina: a review of monochromatic threshold data. Photochem. Photobiol. **87**(4), 747–753 (2011). https://doi.org/10.1111/j.1751-1097.2011.00921.x
5. Pajer, V., Tiboldi, A., Bae, N., Li, K., Kang, S.U., Hopp, B., Kolozsvári, L., Lubec, G., Nógrádi, A.: The molecular background of the differential UV absorbance of the human lens in the 240–400 nm range. Photochem. Photobiol. **89**(4), 856–863 (2013). https://doi.org/10.1111/php.12063
6. Krutmann, J., Béhar-Cohen, F., Baillet, G., de Ayguavives, T., Ortega, G.P., Peña-García, P., Remé, C., Wolffsohn, J.: Towards standardization of UV eye protection: what can be learned from photodermatology? Photodermatol. Photoimmunol. Photomed. **30**(2–3), 128–136 (2014). https://doi.org/10.1111/phpp.12089
7. Andley, U.P., Malone, J.P., Townsend, R.R.: Inhibition of lens photodamage by UV-absorbing contact lenses. Invest. Ophthalmol. Vis. Sci. **52**(11), 8330–8341 (2011). https://doi.org/10.1167/iovs.11-7633
8. Söderberg, P.G., Talebizadeh, N., Yu, Z., Galichanin, K.: Does infrared or ultraviolet light damage the lens? Eye (Lond) **30**(2), 241–246 (2016). https://doi.org/10.1038/eye.2015.266

9. Ekaterina, A.Z., Lyudmila, V., Yanshole, A.Z.F., Yuri, P.T.: Optical properties of the human lens constituents. J. Photochem. Photobiol., B **173**, 318–324 (2017). https://doi.org/10.1016/j.jphotobiol.2017.06.00
10. Tamara, S.O., Yanshole, L.V., Yanshole, V.V., Fursova, A.Z., Stepakov, D.A., Novoselov, V.P., Tsentalovich, Y.P.: Spatial distribution of metabolites in the human lens. Exp. Eye. Res. **143,** 68–74 (2016). https://doi.org/10.1016/j.exer.2015.10.015
11. Hightower, K.R.: A review of the evidence that ultraviolet irradiation is a risk factor in cataractogenesis. Doc. Ophthalmol. **88**(3–4), 205–220 (1994–1995)
12. Mauro, M., Liliane, V.: Building a resistance to ignition testing device for sunglasses and analysing data: a continuing study for sunglasses standards. Biomed. Eng. Online **16**, 1–10 (2017)
13. Artur, L.D., Leoardo, G.L., Liliane, V.: Transmittance variations analysis in sunglasses lenses post sun exposure. J. Phys. Conf. Ser. (Print) **733**, 012028 (2016)
14. Mauro, M., Liliane, V.: Equivalence between solar irradiance and solar simulators in aging tests of sunglasses. Biomed. Eng. Online (Online) **15**, 86–98 (2016)
15. Mauro, M., Homero, S., Liliane, V.: Contribution to the radiation protection for sunglasses standards. Radiat. Prot. Dosimetry. **164**, 435–443 (2015)
16. Márcio, M.M., Victor, L.A.C., Liliane, V.: Self-service kiosk for testing sunglasses. Biomed. Eng. Online (Online) **13**, 45 (2014)
17. Liliane, V., Nobre, A., Toschi, J.A.: ABNT NBR 15111:2013 - Óculos para proteção solar, filtros para proteção solar para uso geral e filtros para observação direta do sol. ABNT **1**, 1–47 (2013)
18. Márcio, M.M., Liliane, V.: Cálculo da transmitância visível e semafórica com função de ponderação alternativa. Revista Brasileira de Física Médica (Online) **7**, 99–104 (2013)
19. Victor, L.A.C., Liliane, V., Sidney, J.F.S.: Ultraviolet analysis of donated corneas: a portable prototype. Appl. Opt. **49**, 4890–4897 (2010)
20. International Organization for Standardization 2013 Eye and face protection—sunglasses and related eyewear Part 1: sunglasses for general use Geneva: ISO 12312–1:2013
21. Mauro, M., Fernanda, O.D., White, C.C., Liliane, V.: Degradation of sunglasses filters after long-term irradiation within solar simulator. Eng. Fail. Anal. **1**, 1 (2019)
22. Taylor, H.R., West, S.K., Rosenthal, F.S., Muñoz, B., Newland, H.S., Abbey, H., Emmett, E.A.: Effect of ultraviolet radiation on cataract formation. N. Eng. J. Med. **319**(22), 1429–1433 (1988)
23. West, S.: Ocular ultraviolet B exposure and lens opacities: a review. J. Epidemiol. **9**(6 Suppl), S97–101 (1999)
24. McCarty, C.A., Nanjan, M.B., Taylor, H.R.: Attributable risk estimates for cataract to prioritize medical and public health action. Invest. Ophthalmol. Vis. Sci. **41**(12), 3720–3725 (2000)
25. Sasaki, H., Kawakami, Y., Ono, M., Jonasson, F., Shui, Y.B., Cheng, H.M., Robman, L., McCarty, C., Chew, S.J., Sasaki, K.: Localization of cortical cataract in subjects of diverse races and latitude. Invest. Ophthalmol. Vis. Sci. **44**(10), 4210–4214 (2003)
26. Truscott, R.J., Friedrich, M.G.: The etiology of human age-related cataract. Proteins don't last forever. Biochim. Biophys. Acta. **1860**(1PtB), 192–198 (2016). https://doi.org/10.1016/j.bbagen.2015.08.016
27. Hoeijmakers, J.H.: Genome maintenance mechanisms for preventing cancer. Nature **411** (6835), 366–374 (2001)
28. Rifai, K., Hornauer, M., Buechinger, R., Schoen, R., Barraza-Bernal, M., Habtegiorgis, S., Glasenapp, C., Wahl, S., Mappes, T.: Efficiency of ocular UV protection by clear lenses. Biomed. Opt. Express. **9**(4), 1948–1963 (2018). https://doi.org/10.1364/boe.9.001948

29. Duarte, F.O., Mello, M.M., Masili, M., Ventura, L.: Set up for irradiation and performing spectroscopy for human lenses. In: Lhotska, L., Sukupova, L., Lacković, I., Ibbott, G. (eds.) World Congress on Medical Physics and Biomedical Engineering 2018, IFMBE Proceedings, vol. 68/3. Springer, Singapore (2019). https://doi.org/10.1007/978-981-10-9023-3_53
30. Artigas, J.M., Felipe, A., Navea, A., Fandiño, A., Artigas, C.: Spectral transmission of the human crystalline lens in adult and elderly persons: color and total transmission of visible light. Invest. Ophthalmol. Vis. Sci. **53**(7), 4076–4084. https://doi.org/10.1167/iovs.12-9471 (2012)

Wearable Spine Postural Monitoring Embedded System for Occupational Health in Sitting Position

Edisson Pugo-Méndez, Juan Cabrera-Zeas, Luis Serpa-Andrade(✉), Eduardo Pinos-Vélez, and Freddy Bueno-Palomeque

GIIB, Research Group on Biomedical Engineering, Universidad Politécnica Salesiana, Cuenca, Ecuador
{epugo, jcabrera}@est.ups.ecu.ec, {lserpa, epinos, fbueno}@ups.ecu.ec

Abstract. This document presents the design and construction of an embedded system to alert the position of the back in order to improve the occupational health of users who remain long in sedentary positions. The proposed system is an alternative to monitor and alert the spine posture of people whose daily activities demand to remain long period of time in a sitting posture, in order to avoid problems in the medium or long term. The wearable system consists of a flexible resistive sensory surface that molds to the shape of the spine in order to measure its position. The sensors are located in a vest that is easy to use to improve the comfort of the user. The system uses a Bluetooth BLE communication to send the data sensed to a mobile device, which monitor and save the position of the user and be able to alert if it is in an incorrect position that can affect their health. In addition, the data is saved in an online database, creating a history of postural compartment of each user. The app also suggests exercise routines such as active pauses to improve worker performance that reduces work fatigue, improves joint mobility, prevents and reduces stress, and reduces the risk of occupational diseases.

Keywords: Bad posture · Wearable system · Spine · Occupational health

1 Introduction

The goal of postural hygiene is to try to avoid bad posture, which can influence the appearance of musculoskeletal injuries. Additionally, a bad posture can directly influence in the development of the diary activities. The variables associated to a bad posture can be related to the ergonomics of the workplace and the people postural habits; however, one of the main reasons is the leak of active pauses during a working day. People, who perform the work tasks in a sitting position in any work areas, hold a sedentary posture relatively long time in that position. In this scenario, our system is aimed as a technological tool to register the posture during the working day in order to alert people about a bad stance; furthermore, with a day register of the posture, it is possible to design a personalized active pause program for each worker in function of the register of the posture.

© Springer Nature Switzerland AG 2020
C. A. González Díaz et al. (Eds.): CLAIB 2019, IFMBE Proceedings 75, pp. 538–542, 2020.
https://doi.org/10.1007/978-3-030-30648-9_70

Back pain caused by poor posture is a problem that can affect 80% of people in a general population or working population at some point in their lives, that is, out of every 10 people 9 will have back problems in sometime. Although the problems in some cases are solved and do not occur again, in a low proportion they can become chronic. In the workplace, back pain is a pathology causing absenteeism at work, in some cases only with absence and in others reaching disability [1].

When people stay or perform their daily tasks sitting for a long time tend to generate bad postures at the level of the back, these bad postures in some cases become bad habits, generate discomfort and lead to develop diseases of the spine, in addition to Inadequate movements and forces are performed, these factors can help the appearance of muscle-skeletal fatigue [2–4].

The most frequent diseases that related to occupational health generated by adopting ergonomic positions for relatively long periods, by erroneous efforts to lift weight, perform repetitive activities [2]. According to García Cardona [5], "about 80% of people have experienced muscle pain at some point in their lives, becoming common pathologies in the population of productive age" [2].

Currently, the rates of postural changes in children and young people up to 15 years have increased because the health system does not have a program to detect and prevent this situation, which must be of vital importance since in this age the body adopts habits in the development of its position [6].

Bad posture affects the health and condition of the body in different ways, therefore, it is important to maintain a postural balance, a correct posture is where there is alignment of the whole body and presents biomechanical efficiency [1, 7, 8]

The American Academy of Orthopedics considers posture as a balance between muscles and bones [1]. An alteration in the posture, is due to unfavorable habits or postural vices, the human being adapts a posture according to the activity that is being carried out, the time that develops it, the developed force and the movements [1, 7, 9].

In the workplace, there are associated risks in the physical, psychosocial and medical aspects, which generates work absenteeism. That is why among the work postures that generate more problems are the handling of loads and work in a sedentary position. The importance of the position is in the magnitude of pressure on the intervertebral discs, which vary according to the posture of the spine. Good posture will prevent the appearance of back pain and may reduce the incidence of musculoskeletal disorders [1, 8, 10].

Back pain caused by a neurological function, which activates the nerves that transmit pain, and this triggers a muscle contracture and inflammation [1, 7, 11].

2 System Architecture and Functionality

The proposal submitted must meet with different requirements such as: be adaptable to each user, the interface has to be easy to use, and it should be comfortable. The system consists of three stages. The first stage is responsible for sensing the movements of the back at the spine level (sensory surface). The second stage corresponds to the connection between the sensor area and the microprocessor, which, through a Bluetooth module send the data to an Android Application (app). The app runs on a Smartphone

or Tablet showing the user data as graphical interface, indicating the position sensors, as well as archiving census data. The proposed system is summarized in the diagram in Fig. 1, in which we see the blocks: sensory area (block 1), data process (block 2) and the application and data storage (block 3).

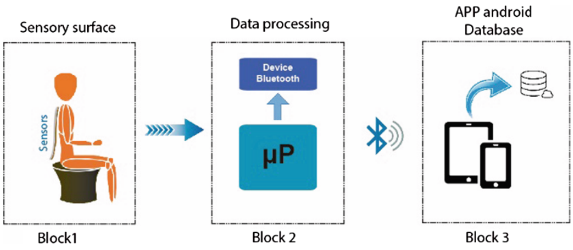

Fig. 1. System architecture to measure the position of the back.

3 Experiments and Preliminary Results

The development of tests was focused to evaluate aspects related to the prototype design and the communication during many hours. The first test on the user 1 used the system with a configuration without alerts over a period of 8 h, registering a vector of 2880 points. The online saved data is presented creating a history of the position of the back of each user, the same procedure was done in each position of the back, obtaining the following results shown in Fig. 2.

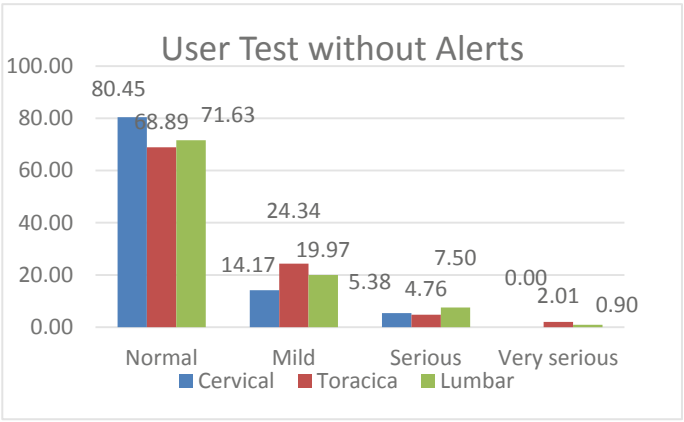

Fig. 2. Test developed using the system without alarms configured. The values are showed in percentages.

As noted in Fig. 2 we can see that the user has an important percentage with a mild and serious bad position in the daily work and it is probably that it can evoke a back

pain at the end of the day. After this test, we developed another but using the systems with alerts configured, during the same number of hours (Fig. 3).

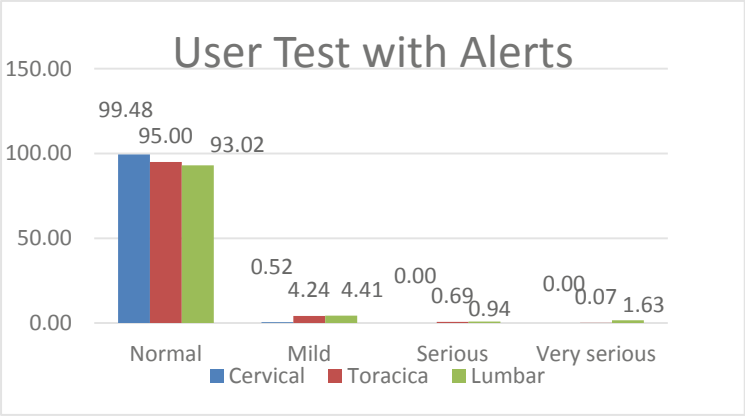

Fig. 3. Test developed using the system with alarms configured. The values are showed in percentages.

As shown in Fig. 3 the data obtained from the test performed give us reference that the system helps to improve posture users because the user is alerted to take better posture and thus to generate a habit with a correct posture.

4 Conclusions

Validation tests were conducted in the company Proquímica, allow us to conclude that the system is well accepted by users, taking comfort in their daily activities, tests were performed with and without alerts. When testing without alerts, the system is only sensing the postural position of the user and it is possible to see that there are many bad habits during the workday. When configuring the alerts in the system, we can say that the system lead users to choose a correct position during the day. Thus, with the use of the system for a long period, it is possible that it helps people to generate the habit of improving their position in their activities, improving the quality of life, reducing the risk of having problems caused by poor posture.

Our system is proposed as a tool for monitoring, recording and giving feedback about the position of the users, focused on improving posture system, preventing bad formations or illness on the back for incorrect positions on the field labor. We worked with people who develop administrative processes in sedentary position for prolonged times, but could perform tests with people who spend most of their time they spend sitting, for example, drivers, students, disabled, etc. focused on improving the posture and prevent any injury to short, medium or long term.

Conflict of Interest. "The authors declare that they have no conflict of interest".

References

1. Herrero, T.M.V.: Lumbago prevention, damage assessment and rehabilitation work 1.a ed, Lettera, Spain (2011)
2. Alvarez, G.M.A., Carrillo, S.A.V., Rendon, C.M.T.: Major musculoskeletal pathologies related to ergonomic risk arising from administrative work activities. CES Rev. Public Health **2**(2), 196–203 (2011)
3. Luttmann, A., Jager, M., Griefahn, B.: Preventing musculoskeletal disorders in the workplace. Be. Prot. TRAb Health **5**, 1–30 2004
4. Parra, M.: Occupational health (2003)
5. Professional writing team: Parties back. Educ. Mag. (2017). https://www.partesdel.com/partes_de_la_espalda.html. Accessed 06 Dec 2017
6. Nacional, U.: San MDE and Medical EAPDET, Postural alterations of the lumbar spine back and dynamic balance in children of third and fourth grade of primary school of St. Augustine in the district of Comas, 2012 (2014)
7. GSZV Adviser: Postural alterations of the lumbar spine back and dynamic balance in children of third and fourth grade of primary school of St. Augustine in the district of commas. National University Saint Mark, Lima Peru, p. 129 (2014)
8. Gómez-Conesa, A.: Labor Postural Risk factors for health. Physiotherapy **24**, 23–32 (2002)
9. Kendall, F.P., McCreary, E.K., Provance, P.G., Rodgers, G.M., Romani, W.A.: Kendalls Musculos Functional Tests Posture and Pain, Quinta. Marban, Madrid (2007)
10. De Alba, C.R., Mark, M.P., Street, C.M.: The cervical pain in primary care consultation. Form FMC Medica Contin. Aten. Primary **19**(9), 521–528 (2012)
11. Miñarro, P.A.L.: Body posture and spinal loads (2009)

Non-invasive Ultrasonic Stimulator Applied in the Treatment of Urinary Incontinence in Women

Aurelio H. Heredia J.[1(✉)], Karim Tapia Q.[1], María del R. L. Cabrera L.[2], Germán Barrientos C.[3], Roberto C. Ambrosio L.[4], and Mario Moreno M.[5]

[1] Ingeniería Biónica, UPAEP, 21 sur 1103 Col. Santiago, Puebla, Puebla, Mexico
aureliohoracio.heredia@upaep.mx, ktapiaq@hotmail.com
[2] Licenciatura en Estomatología CESES, Puebla, Puebla, Mexico
leticiacabreralara00@gmail.com
[3] Facultad de Medicina, UPAEP, Puebla, Puebla, Mexico
german.barrientos@upaep.edu.mx
[4] Electrónica BUAP, Puebla, Puebla, Mexico
[5] Electrónica INAOE, San Andrés, Cholula, Puebla, Mexico

Abstract. This work proposes a non-invasive ultrasonic device for stimulation of the pelvic floor in women suffering from urinary incontinence (UI), which is an extremely common pathology in older women.

The device is composed of an oscillator with a frequency range of 1 to 5 MHz, the time of application of the ultrasonic waves is determined by a frequency of 10 to 50 Hz. The pelvic floor is stimulated by the waves generated by the oscillator, together the frequencies have an energy of 15 mJ. The main contribution of this work is the development of a low cost, non-invasive device for the treatment of urinary incontinence.

Keywords: Urinary incontinence (UI) · Device · Ultrasound · Pelvic floor · Non-invasive

1 Introduction

The intraurethral or extraurethral UI is the involuntary loss of urine [1]. There are two types of UI: stress and urgency. The stress UI is due to the increase of the urethrovesical angle caused by the relaxation of the pelvic musculature. Loss of detrusor muscle function causes urgency UI [2].

There are different methods of stimulation of the pelvic floor. Vaginal, anal needles or surface electrodes are invasive methods based on manual therapy or electrical stimulation.

Currently there are very few and limited non-invasive ultrasonic device for the treatment of (UI). These methods return the functionality to the detrusor muscle with the subsequent recovery of the urethrovesical angle [3].

© Springer Nature Switzerland AG 2020
C. A. González Díaz et al. (Eds.): CLAIB 2019, IFMBE Proceedings 75, pp. 543–547, 2020.
https://doi.org/10.1007/978-3-030-30648-9_71

The parameters that use existing stimulators and those indicated on this treatment depend on the type of incontinence: low frequencies (10–20 Hz) for urge incontinence and high ones (50 Hz) for stress incontinence [4, 5].

We propose the stimulation of the muscles of the internal inferior pelvic surface through ultrasonic devices with controlled parameters of frequency, intensity, and duration of the pulses, being a non-invasive alternative, unlike the current methods. The instrument must comply with the following characteristics to ensure that the pelvic floor muscles and ligaments recover functionality, the mentioned parameters were established based on the existing devices:

- The Frequency range between 1 and 5 MHz that reaches the pelvic region
- Outgoing stimulation energy of the transducer in the pelvic floor greater than 15 mJ. Considering the absorptions of the different anatomical components present in the area.
- The frequency of pulse duration for different types of UI is from 10 to 50 Hz.

2 Methods

Ultrasonic waves need a medium for their propagation, based on the transport of energy, which is absorbed by the muscle tissue becoming heat, the absorption is directly proportional to the frequency applied, ultrasonic waves transfer their energy and momentum as they propagate through the tissues, increasing the local pressure in the medium.

The oscillations of particles increase local pressure. These oscillations of particles cause harmonic pressure variations and pressure waves that propagate as neighboring particles.

The pressure waves move in parallel (longitudinal wave) or perpendicular (transverse wave) to the direction of the propagation of the wave. Sound passes through the different types of tissues with variable speed. Considering this fact, the average speed of sound through the tissues is 1,540 m/s, like the speed of propagation in water.

The ultrasound beam loses intensity as it moves through the tissues. The loss per unit length is called attenuation. Attenuation is a result of the inhomogeneity of the medium and the absorption, refraction, and reflection of the different tissues; the attenuation is directly proportional to the frequency.

The “one rule” is used to measure the attenuation. It establishes that there is attenuation of 1 dB for every MHz, for each centimeter that the wave travels. Absorption is the conversion of US mechanical energy into heat. Absorption coefficient (α) expresses the amount that occurs in different tissues. Tissues with abundant structural proteins and collagen absorb US energy. This energy increases proportionally with frequency. Depth is inversely proportional to frequency. Lower frequencies produce lower resolution and greater depth in the body.

3 Results

For uterus, and bladder (deep organs) the frequencies are restricted in a range between 1 and 5 MHz. For superficial structures and in children applications the frequencies range are between 4 and 10 MHz. In this last case, they have a better axial and lateral resolution.

This work proposes the design of a prototype of a device with the characteristics of frequency and intensity for the stimulation of the pelvic musculature with ultrasound, for the non-invasive treatment of UI, applying a frequency between 1 and 5 MHz, considering the presence of adjacent structures such as skin, bone, ligaments. See Table 1.

The stimulation parameters to be considered were calculated from the power and energy equations, taking into account the minimum and maximum values of the electrical stimulation parameters, according to Eqs. 1 and 2.

$$P = V \cdot I \tag{1}$$

$$E = P \cdot t \tag{2}$$

Where:

P = electric power, V = voltage, I = electric current, E = energy, T = time.

Considering the parameters that are used by electrical stimulation:

I = 1 a 100 mA, V = 600 Vpp, t = 200 a 500 µs, obtaining 15 mJ energy.

The parameters were obtained from Eq. 2, considering the absorption of the tissues adjacent to the pelvic musculature (Table 1) to achieve a non-invasive stimulation.

$$I = I_o e^{-x\propto} \tag{3}$$

Where:

I = final intensity, Io = initial intensity, x = tissue length, ∝ = Tissue absorption coefficient

Table 1. Absorption of different biological tissues at 3 MHz

Tissue	Absorption coefficient (dB/cm)
Blood	*0.084*
Nervous tissue	*0.6*
Blood vessel	*1.2*
Fat tissue	*0.42*

A direct approach is required to avoid the absorption by structures adjacent to the pelvic musculature. The proposed devise contains is shown in Fig. 1.

The frequency generator is a 36 Vac relaxation oscillator, as shown in Fig. 2.

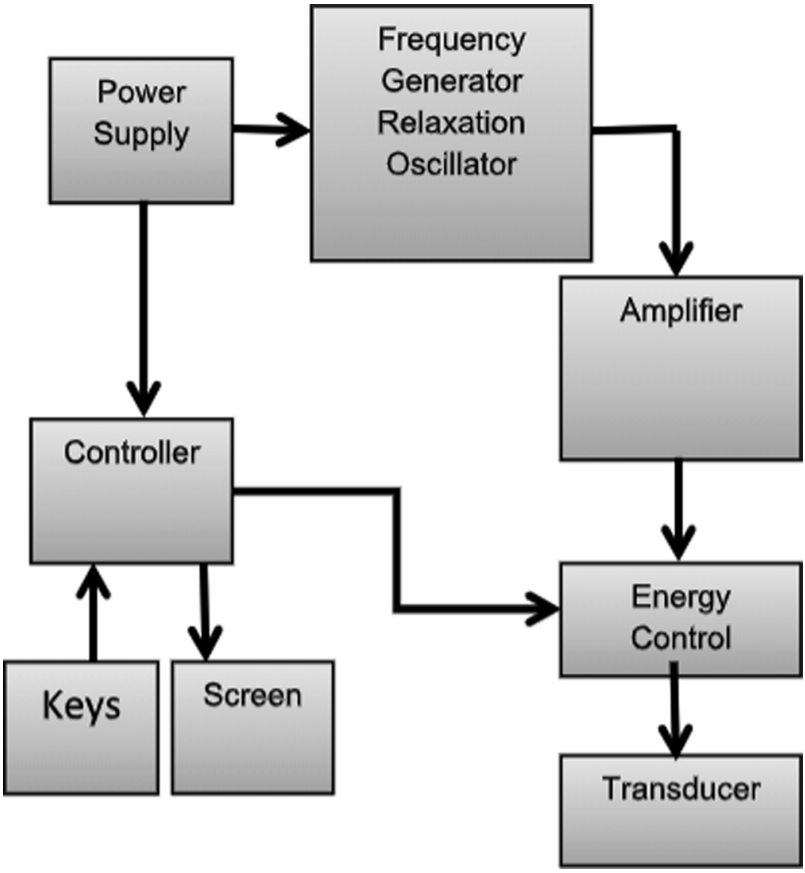

Fig. 1. Block diagram of the proposed device.

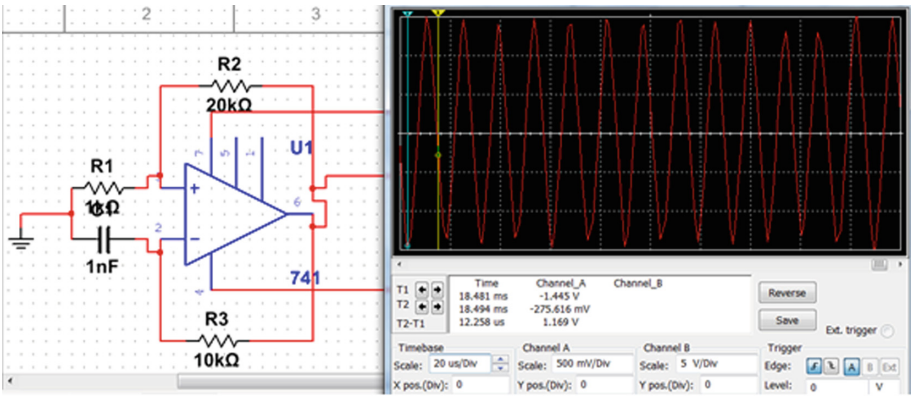

Fig. 2. Relaxation oscillator

Its frequency is determined by Eq. 4, with a real stimulation frequency between 10 to 50 Hz direct to the pelvic floor. It depends on the type of UI and provides stimulation energy of up to 15 mJ.

$$f = \frac{0.455}{RC} Hz \tag{4}$$

4 Discussion

Acoustic energy interacts with body tissues. This energy slightly modifies molecules and passes from one molecule to another.

The acoustic energy moves through the tissue by longitudinal waves. The molecules of the transmission medium oscillate in the same direction of the wave. Piezoelectric crystals generate ultrasonic waves. The relaxation oscillator excites the piezoelectric crystals.

5 Conclusions

Based on the analysis of energy of 15 mJ and frequency of 1 to 5 MHz, the initial parameters are established to obtain stimulation in the pelvic floor using non-invasive techniques. After we develop the prototype, we will be able to obtain final results and to carry out tests.

References

1. Milsom, I., Gyhagen, M.: The prevalence of urinary incontinence. Climacteric **22**(3), 217–222 (2019)
2. Haag-Molkenteller, C.C., Jenkins, B.: U.S. Patent Application No. 15/354, 263 (2017)
3. Dumoulin, C., Hunter, K.F., Moore, K., Bradley, C.S., Burgio, K.L., Hagen, S., Chambers, T.: Conservative management for female urinary incontinence and pelvic organ prolapse review 2013: summary of the 5th international consultation on incontinence. Neurourol. Urodyn. **35**(1), 15–20 (2016)
4. Susset, J., Galea, G., Manbeck, K., Susset, A.: A predictive score index for the outcome of associated biofeedback and vaginal electrical stimulation in the treatment of female incontinence. J. Urol. **153**(5), 1461–1466 (1995)
5. Yamanisha, T., Yasuda, K.: Electrical stimulation for stress incontinence. J. Urol. 1 62(3-lS,) 970 (1999)

SpO_2 Alarm: A Tool for Health Care

Nancy Lisset Domínguez-Hernández(✉),
Lady María Murrieta-Brígido, and Pablo Samuel Luna-Lozano

Facultad de Instrumentación Electrónica, Universidad Veracruzana,
Xalapa, Veracruz, Mexico
tevi.14549@gmail.com, LadyMurrieta@outlook.com,
paluna@uv.mx

Abstract. The continuous measurement of the level of oxygen concentration in blood (SpO2) and the heart rate (HR) may help verify the state of health of the cardiovascular system. SpO2 Alarm is a wearable technological tool that consist of a SpO2 and HR measurement device and a mobile-device application that collects, via Bluetooth, the information obtained from the MAX30102 module once processed through the ATMega328P microcontroller (included in the Arduino Nano board), and allows real-time visualization of both parameters. The SpO2 Alarm was intended to be used by patients with a risk of suffering low levels of SpO2, which then sends an alert with the exact location of the user to a designated contact in case of detecting a low concentration of oxygen in blood. The goal of the SpO2 Alarm is to facilitate the detection and timely medical attention of cardiovascular diseases and emergencies.

Keywords: SpO_2 · Cardiovascular health · Oximetry · Heart rate

1 Introduction

The advance of technology in recent years has allowed the development of devices to monitor biological variables in a continuous and non-invasive manner. These devices, together with the communication facilities provided by a smartphone, allows the creation of technological tools available to anyone.

A wearable device, as its name indicates, is designed to be worn, and usually allows access to information in real time, so it makes monitoring of various variables through the incorporation of sensors more efficient.

On the other hand, continuous signals monitoring is based on obtaining and processing uninterrupted data from a sensor.

In this work we present a wearable tool, SpO2 Alarm, for the continuous monitoring of the heart rate (HR) and the oxygen level in blood.

The heart rate refers to the number of contractions or heartbeats per unit of time. The parameters of an adequate rhythm depend on the age of the patient and the physical activity that he or she carries out.

On the other hand, the percentage of concentration of oxygen in the blood (SpO2) is an indicator of the amount of oxygen transported by hemoglobin, that is, with a saturation of 96% each globule will have 96% oxygen. Adequate levels of SpO2 must

© Springer Nature Switzerland AG 2020
C. A. González Díaz et al. (Eds.): CLAIB 2019, IFMBE Proceedings 75, pp. 548–559, 2020.
https://doi.org/10.1007/978-3-030-30648-9_72

be between 95% and 100% for a person to be healthy. When there is a concentration below 90%, there are various symptoms such as dizziness, respiratory difficulties, abdominal distension, weakness, confusion, sleep disturbances, numbness and tingling in the arms or around the mouth, muscle wasting, hands or feet, chest pain and palpitations, among others, hence the importance of having constant monitoring of these variables in an efficient and real-time manner [1]. Table 1 shows the necessary medical action according to the level of oxygen saturation in the blood [2].

Table 1. Medical action according to the percentage of oxygen [2].

% saturation	Medical action
Greater than 95%	Without immediate action
Between 95 and 90%	Immediate treatment and monitoring of response, according to this, assess referral to the hospital. Patients with chronic respiratory disease tolerate saturations well around these values
Less than 90%	Seriously ill. Severe Hypoxia Oxygen therapy, treatment and transfer to the hospital
Less than 80%	Evaluate intubating and mechanical ventilation
Less than 92% in children	Refer to the hospital even if they show improvement with initial maneuvers, since their response to treatment is more uncertain

The principle of operation of the oxygen-saturation-measuring devices, also called oximeters, is based on the transmission of an optical signal, in the range of red and infrared (IR), and its absorption by oxygenated hemoglobin (HbO2) and reduced hemoglobin (Hb). HbO2 mainly absorbs infrared light and Hb absorbs red light.

A conventional transmittance oximeter leaves the tissue in the middle of the light emitters and reflectors (Fig. 1A), on the other hand, a reflectance oximeter has the emitter and the light receiver on the same face of the tissue [3] (Fig. 1B).

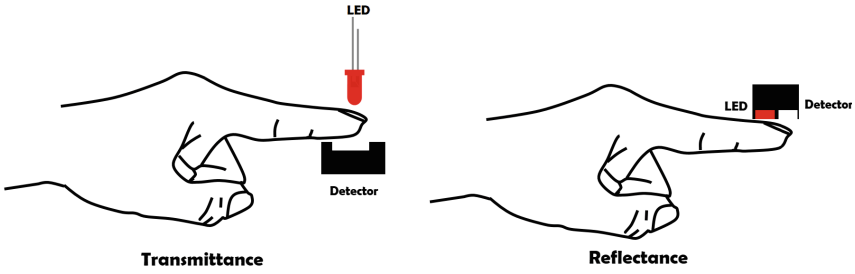

Fig. 1. Oximetry techniques for pulse: (a) conventional oximeter by transmittance and (b) oximeter by reflectance.

2 Materials and Methods

2.1 MAX30102 Module

The MAX30102 (Maxim Integrated) module integrates a heart rate meter and pulse oximetry by reflectance. It contains LEDs, photodetectors, optical elements and low noise electronics to detect the presence of oxygen in the blood. Its design is adjusted to the application proposed to be a wearable device, in addition to having a low cost in the market.

The MAX30102 [4] has red and infrared LED controllers and can be configured to supply electrical power up to 50 mA with pulse width between 69 µs and 411 µs. It also has an ambient light canceller (ALC), an 18-bit continuous-time sigma-delta analog-to-digital converter (ADC) of up to 3200 samples per second and a discrete-time filter. Figure 2 shows the functional diagram of the MAX30102.

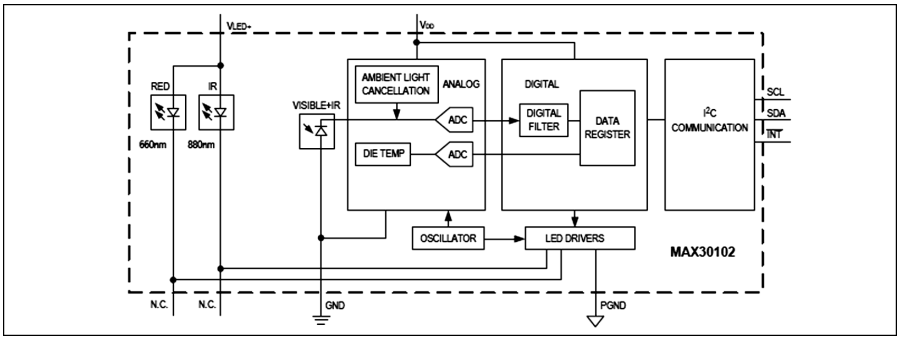

Fig. 2. Functional diagram of the MAX30102.

2.2 Bluetooth Module HC-05

The oximeter communicates with the smart phone by Bluetooth with the HC-05 module. It is a module that has the serial port protocol (SPP), with version 2.1 + EDR of the Bluetooth Core specification. Due to its physical characteristics, shown in Fig. 3, the HC-05 module perfectly matches the "SpO2 Alarm" design.

Fig. 3. Bluetooth module HC-05.

2.3 Arduino Nano Board with ATMega328P Microcontroller

The control of the oximeter and communication with the mobile was made with an Arduino Nano board with an ATMega328P microcontroller. This card has a compact design that includes 14 digital input/output pins (six can be used as PWM), six analog inputs, a 16 MHz crystal oscillator, Mini-USB connection, terminals for ICSP connection and a reset button [5].

The algorithm used for reading the sensor and sending and receiving data is shown in Fig. 4. In the first place, all variables used throughout the code are declared, the sensor is initialized, to determine if it is in operation, and the serial port is also initialized, to allows the use of the Bluetooth module.

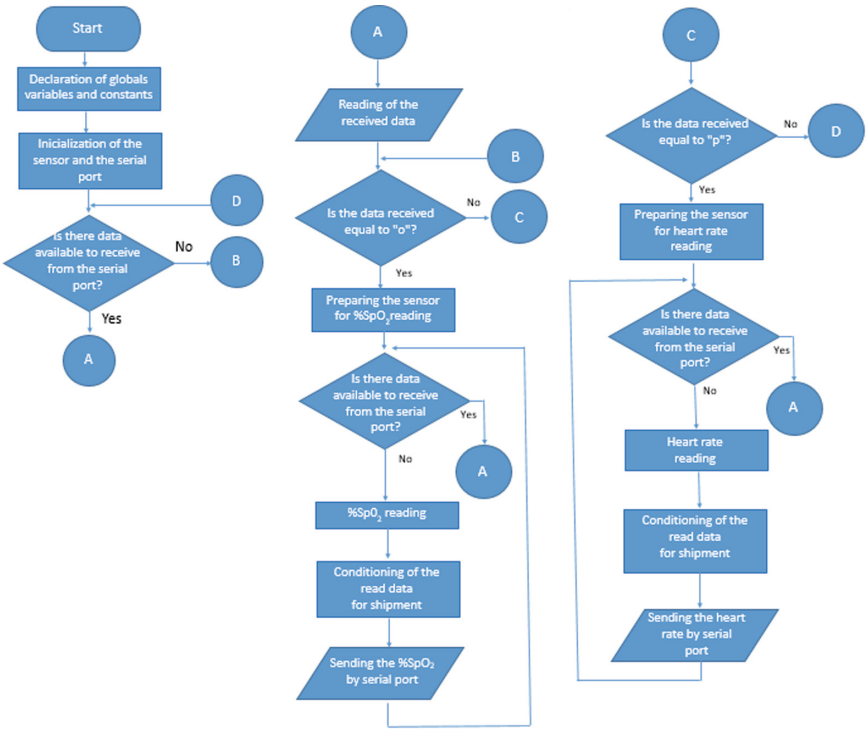

Fig. 4. Flow diagram of the microcontroller.

Afterwards, the microcontroller starts to read the data provided by the sensor. Since two variables will be read, it is necessary to define an identification character that will be sent by the application depending on what the user wants to read. Initially, this data has a value without relevance in the code so that the microcontroller keeps waiting for the arrival of the identification character.

If the microcontroller receives the identification character corresponding to the SpO2 or HR reading, the sensor is configurated with the respective parameters, the reading is performed, the data is conditioned and sent by serial. This is done until the microcontroller receives another identification character from the application, which means that the user has requested the other variable and the procedure is repeated.

2.4 SpO_2 Alarm App

The SpO_2 Alarm application was programed in the App Inventor 2 platform.

The interface of the mobile application is dynamic and intuitive, focused on being used by different age groups; It has 5 screens: welcome screen, menu, pulse or heart rate display, oxygen levels and a personal information form.

The design of the screens was made through the elements offered by App Inventor 2 such as buttons, tables, lists, text boxes, memory storage, among others. App Inventor 2 uses a type of visual programming that is based on a design screen and a block editor, each element that is placed on the design screen has predetermined blocks that can be manipulated in the editor, each block constitutes one function or characteristic of the element and these can be related through control blocks, logical, mathematical, variables, text, among other things.

The platform allows access to the sensors and functions of the smart phone such as the location sensor, the clock, the sending of text messages and the bluetooth communication, all of which were used to develop "SpO2 Alarm".

The home screen was designed with an image element placed in the center and two invisible elements that are the clock and a canvas, programmed so that when the clock counts 5 s, or when the user touches the canvas, the app changes to the menu screen, which consists of three buttons related to the remaining three screens.

The form or personal information screen consists of text boxes in which the user should enter his or her name and the name and phone number of two contacts to whom the alert will be sent in case of detecting abnormal levels of oxygen concentration. This is done by the invisible element "TinyDB", which allows to store data obtained from the application in the phone's memory. The data is labeled to access it at any time. The name and contact information can be modified or replaced when the user decides.

The pulse screen displays the pulse waveform. It contains the TinyDB element to access the user's registered name to make it a user-friendly application. It also contains a selection list that is linked (through the invisible element "Blue-toothClient") with the list of devices previously linked to the mobile phone, which allows to choose the Bluetooth module connected to the microcontroller.

When selecting the Bluetooth device to which the application will connect, the application sends an identification character to the microcontroller to send the corresponding information to the SpO2 or HR. To synchronize the reception, the clock element is used. When the application receives a number larger than or equal to 2 B, data reading starts. To draw the pulse waveform, the received data is plotted in the canvas and joined with lines, since each received value corresponds to a pixel number on the canvas.

Finally, the oxygen levels screen reads the SpO2 value and sends the alert when necessary. It has a drop-down list to select the linked Bluetooth device. When the connection is made, the application sends the identification character to ask the microcontroller to send the SpO2 information. The data is received as a single 1 B number and the value is displayed in a text box. The synchronization is performed with a clock. When several SpO2 values lower than 90% are received, the application accesses the phone memory through the TinyDB to extract the registered contact numbers and send a text message, through the "Texting" element, which contains an alert message and the location of the user that is obtained through the location sensor.

This screen also has the option of disabling the alerts in case of not wanting continuous monitoring.

2.5 Housing Design

The housing of the device was printed on a 3D printer (Fig. 5) to contain the MAX30102 and HC-05 modules and the Arduino Nano board. The design was made in SolidWorks (SolidWorks Corp.) looking for a comfortable and functional housing for the user.

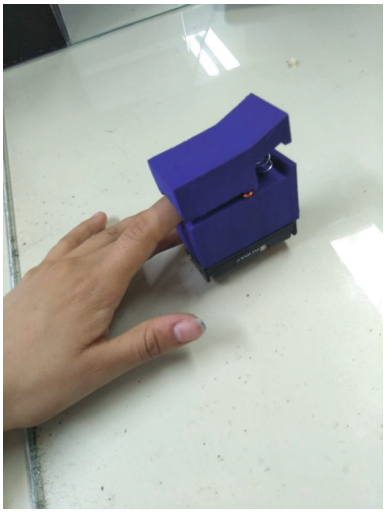

Fig. 5. Oximeter housing printed in 3D.

In addition, the housing includes a 9 V battery for the power supply of the Arduino Nano board.

3 Results and Discussion

The SpO_2 Alarm application consist of five screens, which are shown in Fig. 6.

a) b) c)

d) e)

Fig. 6. "SpO2 Alarm" screens: (a) Home screen, (b) Menu, (c) Oxygen levels, (d) Pulse and (e) Personal information form.

In Fig. 6A the logo of the application is shown, which is displayed for five seconds or until the user touches the screen. This will direct the user to the menu screen, shown in Fig. 6B. This screen provides access to the three remaining screens through the three buttons: “My pulse”, “My oxygen levels” and “Add information”.

On the Oxygen Levels screen (Fig. 6C) the percentage of oxygen concentration in blood and a drop-down list to select the Bluetooth device you want to connect to and a check box to enable or disable the alerts is shown.

The pulse waveform is displayed in the Pulse screen (Fig. 6D). It was designed with a wide margin since its position on the canvas changes with the user’s breathing.

Finally, in the Information screen (Fig. 6E) the user may register his or her name and two emergency contacts. This information is stored in the memory of the phone. If low level of oxygen is detected during a time and the alert is enabled, the “SpO2 Alarm” sends an emergency message to the defined contacts. The message contains the exact location where the device is located. Figure 7 shows an example of the emergency message.

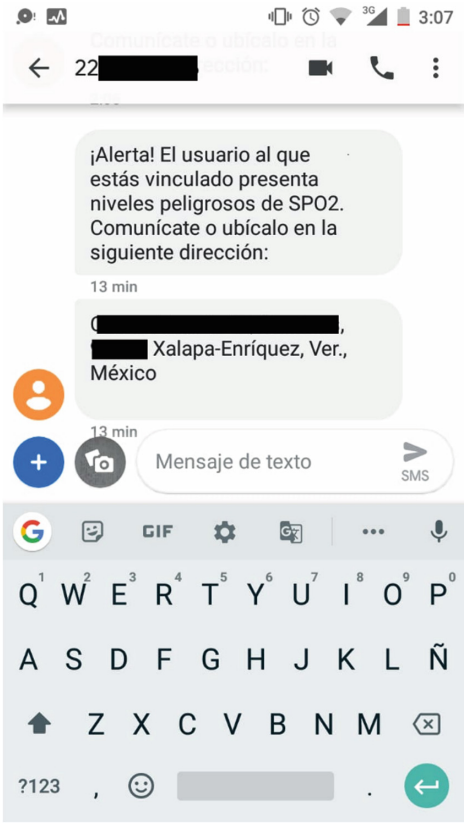

Fig. 7. Example of alert message received.

We tested SpO2 Alarm on healthy volunteers at rest. All volunteers found the housing comfortable and the app intuitive. For almost all users, the measurement of heart rate and SpO2 was performed satisfactorily. Some users placed their finger incorrectly the first time and it was necessary to repeat the measurement.

To evaluate the alert function of the SpO2 Alarm, a situation of low oxygen level was simulated. The simulation consisted of moving the finger away from the sensor in such a way that it did not reach a correct measurement and the values displayed were low. Our current work is focused on testing our development in real life situations with patients at risk of low SpO2 level.

a) b)

Fig. 8. User using SpO_2 Alarm in: (a) Movement (b) Rest.

For its characteristics the SpO2 Alarm is an example of a wearable device, among these is the design of a housing that the user can wear, this in conjunction with the application developed for smart devices allows the user to view the data of his or her heart rate and percentage of blood oxygen in real time even when he or she is in motion with a minimum percentage of noise in the collection of data.

In Fig. 8, the device is observed already assembled and being used by a person in two conditions: movement and rest. Focusing on Fig. 8b shows how wireless transmission of oxygen levels in the blood is being done and its display in the SpO_2 Alarm application. Also one can see that the device can be used on any of the two index fingers (left or right hand) considering that the user can be left or right handed, so the user can place the device in the hand that he or she uses less.

In Fig. 9 monitoring of the heart rate of a person in movement (walking) in the mobile application is observed. Compared with Fig. 6d, where the heart rate measurement of a person at rest is observed, in Fig. 9 more noise is seen due to the movement made by the user, however this does not produce a considerable effect on the measurement since the signal is only deformed when very abrupt movements are made but it is re-established in a short time.

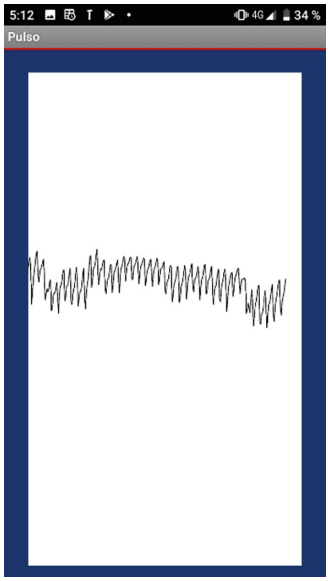

Fig. 9. Heart rate monitoring of a moving user using an SpO_2 Alarm.

On the other hand, Fig. 10 shows the monitoring of blood oxygen saturation of a person walking. This measurement was not affected by the movement due to the fact that a possible sensor error was already considered, since in the algorithm of the Arduino board a validation constant is used that indicates whether the sensor

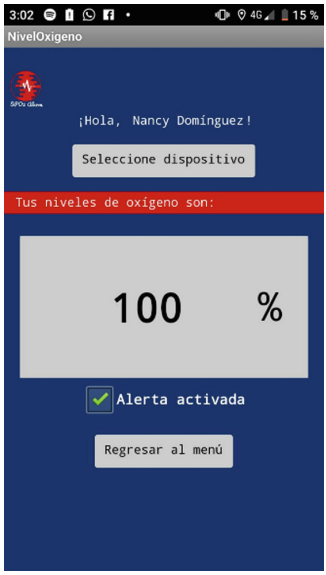

Fig. 10. Oxygen saturation in blood monitoring of a moving user using an SpO_2 Alarm.

measurement is correct or not. Considering this constant, in the algorithm of the application a sample time is established before sending the alert message.

Tests were done in which the user underwent heavier physical activity. Figure 11 shows how the device is being used while the user is running at a speed of 10 km/h and how it monitors his or her heart rate through the application.

Fig. 11. A user running at 10 km/h while his heart rate is monitored using an SpO_2 Alarm.

In Fig. 12 a record of uninterrupted data of a user with an oxygen percentage between 97 and 100% is appreciated, adequate levels for a person in good health. Showing the continuous monitoring that a SpO_2 Alarm carries out. This continuous monitoring allows that although the user leaves the application, it continues to collect data uninterrupted, as long as the bluetooth communication is maintained.

Archivo Edición Formato Ver Ayuda

100 100 100 100 99 99 99 99 99 99 99 100 100 100 99 99 100 99 99 99 99 99 99 99 100 100 100
100 100 100 99 99 99 99 99 99 100 100 100 100 100 98 98 99 98 99 99 99 99 99 100 100 100 100
100 100 99 99 99 99 99 99 100 100 100 100 100 98 98 99 98 99 100 100 100 99 99 100 99 99 99 99 99
97 97 98 98 98 98 98 98 98 98 99 99 99 99 99 99 99 100 100 100 100 100 98 98 99 98 99 100 100 100 99
98 98 98 98 98 98 99 100 100 100 100 100 100 99 99 99 99 99 98 99 100 100 100 99 100 100 99 99 99 99
99 99 100 100 100 100 100 98 98 99 98 99 100 100 100 99 99 100 99 99 99 99 99 97 97 98 98 98 98 98
98 98 98 98 98 99 98 99 99 99 97 97 97 99 99 99 99 99 99 99 99 99 99 99 100 100 100 100 100 98 98 99
98 99 100 100 100 99 00 100 100 100 100 98 98 99 98 99 100 98 98 99 98 99 100 100 100 99 99 100 99
99 99 99 99 99 99 99 99 99 99 100 100 100 100 100 98 98 99 98 99 100 100 100 99 98 98 98 98 98 98
99 100 100 100 100 100 100 99 99 99 99 99 98 99 100 100 100 99 100 100 99 99 99 99 99 99 100 100 100
100 100 98 98 99 98 99 100 100 100 99 99 100 99 99 99 99 99 97 97 98 98 98 98 98 98 98 98 99 98
99 99 99 97 97 97 99 99 99 99 99 99 99 99 99 99 99 100 100 100 100 100 98 98 99 98 99 100 100 100 99 100
100 100 100 100 98 98 99 98 99 100 98 98 99 98 99 100 100 100 99 99 100 99 99 99 99 99 98 99 98 99 100
100 100 99 99 100 99 99 99 99 |

Fig. 12. Record of continuous data monitoring.

4 Conclusion

The contribution that SpO_2 Alarm offers is the creation and implementation of an original algorithm that covers the information processing of biological signals (heart rate and percentage of oxygen in the blood) through the MAX30102 module and the sending of these through bluetooth communication, in this way we have an algorithm capable of receiving information, processing it and at the same time sending it to a mobile application for viewing. In addition, the algorithm of the mobile application provides the user with the opportunity to choose from his or her cell phone which variable he or she wants to read without having to load a new programming code to the Arduino board.

Another important contribution is the original design of a 3D printed housing where the different devices that make a SpO_2 Alarm can be placed in a way that it is comfortable for the user and, above all, wearable.

Finally, the contribution that is considered the most important of the project is the continuous monitoring of the percentage of oxygen in the blood, because thanks to this an algorithm can be developed to generate alerts messages to predefined contacts that are sent when the device detects that the oxygen saturation is below normal levels, which could put the user's health at risk.

With this work we are taking advantage of the small, low cost and highly powerful technology available today. SpO_2 Alarm links smart oximeters, wireless communication and a mobile application to continuously monitoring biological variables.

The development of this technological tool will allow the population to maintain a continuous control of their health state and to be sure that in case they cannot request help for themselves the application will do it for them.

We are currently working to design a more ergonomic housing, to improve the heart rate display interface and to test the tool with real patients and potential users.

Declaration of Interest Conflicts. There are no interest conflicts.

References

1. Mimoonline: Qué es la saturación de oxígeno y cuáles son los niveles normales (2019). http://grupolasmimosas.com/mimoonline/saturacion-de-oxigeno/. Accessed 10 May 2019
2. Noguerol-Casado, M.J., Seco-González, A.: "Pulsioximetría", Coruña (España). https://www.fisterra.com/material/tecnicas/pulsioximetria/pulsioximetria.pdf. Accessed 09 May 2019
3. López-Herranz, G.: Oximetría de pulso: A la vanguardia en la monitorización no invasiva de la oxigenación. Revista Médica del Hospital General de México **66**, 160–169 (2003)
4. Maxim Integrated Products: MAX30102 High-Sensitivity Pulse Oximeter and Heart-Rate Sensor for Wearable Health (2018). https://datasheets.maximintegrated.com/en/ds/MAX30102.pdf. Accessed 14 May 2019
5. Arduino.cl: Arduino Nano. http://arduino.cl/arduino-nano/. Accessed 14 May 2019

Development of a Device Based on Oscillometry and Photoplethysmography for Measuring Blood Pressure

Haydeé Alicia Yáñez-Ocampo[1], Brayans Becerra-Luna[2(✉)], Raúl Cartas-Rosado[2], Raúl Martínez-Memije[2], and Oscar Infante-Vázquez[2]

[1] Universidad La Salle, ULSA, Mexico City, Mexico
[2] Departamento de Instrumentación Electromecánica, Instituto Nacional de Cardiología, Mexico City, Mexico
bbecerral0500@alumno.ipn.mx

Abstract. Blood pressure is a very important physiological parameter given it provides information about the state of the cardiovascular system. The present work describes the development of an electromechanical device to measure the systolic and diastolic blood pressure in the digital artery. The measurements are based on the onset of the photoplethysmographic pulse signal when the artery is decompressed during the deflation of a neonatal cuff placed on the middle finger. The device consists of an optical sensor, a pressure transducer, an electronic system based on an Arduino development board and a graphical computer interface written in Matlab. To validate our device we used a Portapres® system. Simultaneous pressure measurements made with our device and the Portapres® were continuously recorded from 9 subjects in sitting and standing positions. The systolic (SBPDA) and diastolic (DBPDA) blood pressures measured from the digital artery were analytically compared. Results obtained for the SBPDA yielded R^2 values of 0.59 and 0.76, as well as 0.59 and 0.85 for the DBPDA for the sitting and standing positions evaluated. A comparison of SBPDA values using the Bland-Altman plot yielded mean values of $\mu = 3.88 \pm 11.97$ mmHg and $\mu = -0.6 \pm 9.59$ mmHg for the sitting and standing position, respectively.

Keywords: Systolic pressure · Diastolic pressure · Photoplethysmography · Digital artery

1 Introduction

Mexico has the largest worldwide prevalence of arterial hypertension (AHT), according to ENSANUT 2012 [1]. It is estimated that 450,000 new cases of AHT are diagnosed annually [2], and this number could double because the AHT is considered a silent disease [2]. Given these circumstances, it is very important to have reliable and easy-to-use devices for measuring blood pressure that could help to prevent diseases associated with high blood pressure. At clinical facilities, blood pressure is commonly measured by detecting the Korotkoff sounds by using the ear, which makes the technique

© Springer Nature Switzerland AG 2020
C. A. González Díaz et al. (Eds.): CLAIB 2019, IFMBE Proceedings 75, pp. 560–566, 2020.
https://doi.org/10.1007/978-3-030-30648-9_73

dependable on the auditory capacity of the person performing the auscultation. Some clinical devices use the oscillometric method, which is good for measuring the mean pressure but also limited for performing other measurements such as the systolic and diastolic blood pressures given that they are estimated by algorithms provided by each manufacturer [3, 4]. Published algorithms related to the calculation of blood pressure parameters show disagreements between them, and pressure monitors manufacturers consider their algorithms are of proprietary, keeping them in secret and making impossible the verification of their validity for a wide range of health statuses [5]. Other methods based on the photoplethysmographic (PPG) pulse and oscillometric method are good for measuring the systolic pressure [5–7]. According to the aforementioned pros and cons we consider that it is possible to combine the PPG and oscillometric signals for determining the systolic and diastolic blood pressure. In this work we propose the design of a semi-automatic device for measuring the digital systolic blood pressure (DSBP) and digital diastolic blood pressure (DDBP) from the digital artery using a PPG sensor, a pressure sensor, and a neonatal insufflation cuff placed on the finger to temporarily occlude the digital artery for measuring purposes. The system follows the auscultation and oscillometric standard methods.

2 Methodology

2.1 Device Description

The device integrates a PPG module (PPGM) and a pressure measurement module (PMM). The PPGM consists of an infrared (IR) LED (960 nm) and a red LED (660 nm) to detect the photoplethysmographic pulse wave by reflectance, in order to attenuate the influence of breathing it is proposed a bandpass filter (0.6 – 45 Hz), and according to the disposition of the PPG sensor it is proposed an amplification stage (G = 22) in order to have a greater range of operation in the ADC, given the characteristics of the PPG signal [3]. The PMM consists of a neonatal cuff, a NXP MPX5050dp pressure transducer, a bandpass filter (0.4 – 15 Hz), an amplification stage (G = 5), and a pneumatic system for automatically inflating/deflating the cuff. To obtain the oscillometric pulse wave, the bandpass of the filter used in the PMM is narrower than the one used in the PPGM (Fig. 1). The signals were acquired using an Arduino UNO development board sampling at a rate of 100 samples per second and sent to a computer through a USB 2.0 interface. Using MATLAB environment, a computer application based on MATLAB R2013b (MathWorks Ltd.) was developed for controlling and processing purposes.

2.2 Subjects

A total of nine subjects (N = 9) were recruited for testing the device, from which five were women and four were men with mean age 38.11 ± 13.94 y.o. and mean body mass index of 27.77 ± 5.54. No exclusion criteria regarding health status or age was applied in order to have a wider range of measurements.

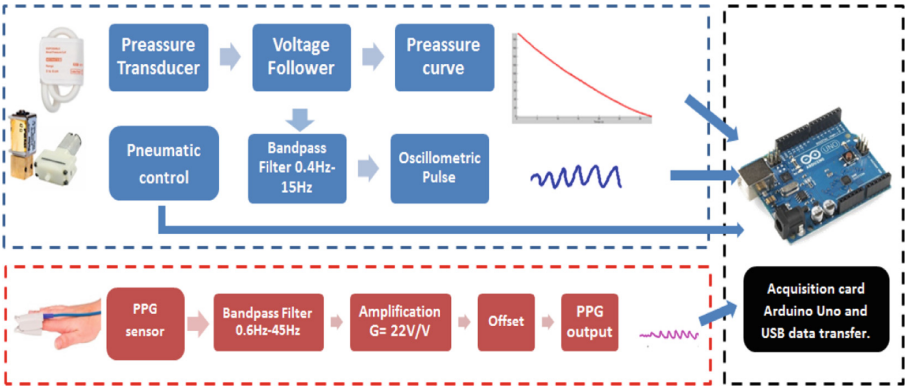

Fig. 1. Block diagram of the developed device. The PPGM is enclosed in a dashed red line, the PMM is enclosed in a blue dashed line, and the development board is enclosed using a black dashed line.

2.3 Recordings

A Portapres (Finapres Medical Systems®) device, which is a clinically tested ambulatory blood pressure monitoring, was used as reference. The protocol was explained to the subjects before performing the tests. Their age, weight, height, and sex were registered in the Portapres® database as well as in an Excel file. The subjects were firstly asked to be in sitting position and rest during 2 min to allow for the stabilization of the hemodynamics variables before the measurements were made. The left arm was used for performing the measurements and was placed at heart level using a sling. Recordings were made according to the official Mexican standard for the measurement of blood pressure NOM-030-SSA [8]. The Portapres ® finger cuffs were connected in the index and ring fingers, the neonatal cuff was placed in the proximal phalanx of the middle finger, and the PPG sensor in the medium phalanx of the same finger. Pressures were recorded firstly in sitting position and then in standing position for a total of 7 min, from which 4 min were used for recording (2 min in standing position and 2 for sitting position) and 3 min between recordings were employed for resting. The recordings were saved in a text format using a TOSHIBA laptop computer with Intel CORE i7 processor, 8 GB RAM, and Windows 10 operating system.

2.4 Data Analysis

Measurements made with our device were compared against measurements obtained with the Portapres® [9], which is a validated equipment and a gold standard for measuring systolic and diastolic blood pressure [10, 11]. Data recorded was processed using MATLAB R2013b. To register the blood pressure with our device, first the neonatal cuff is compressed until reaching a suprasystolic pressure (in this work 180 mmHg), afterwards the control system performs the task of slow deflation of the neonatal cuff, allowing to observe the appearance of the first pulse, followed by a pulse of greater amplitude, which is taken as the highest point for systolic pressure

measurements. The DSBP of our device was calculated as the average of three pressure measurements made with the neonatal cuff: one corresponding to the highest trace of the PPG, plus the one before and the one after. To determine the central pulse for the calculation of the DDBP it is verified that the oscillometric signal has been attenuated 40% of its maximum amplitude, after that moment the following 5 PPG were considered to evaluate the magnitudes of amplitude which were subsequently averaged, taken as the central pulse the one that has an amplitude less than or equal to the value obtained from the average of these. Once the central pulse was determine, DDBP's value was calculated by the feet of three stable pulses were taken for its calculation instead of the peaks. The DSBP and the DDBP from the Portapres® were calculated as the average of 7 continuous measurements, where the central pulse of the measurements was synchronized with the central pulse taken by our device for its calculations. A correlation was made between the measurements of both devices by means of a regression assuming a lineal model. A Bland-Altman plot was generated to check for the agreement between the measurements obtained with the Portapres® and our device. The plot was generated by placing the mean of the measurements on the abscissa and the differences between them on the ordinate [12].

3 Results

A device with two electronic sub-systems operating at 12 volts was designed. One subsystem records the PPG signal using 2 LEDs (IR and red), a phototransistor, an amplifier with gain G = 22, and a bandpass filter with cut-off frequencies of 0.6 Hz and 45 Hz. The second sub-system records the pressure using a neonatal cuff, a NXP MPX5050dp pressure transducer whose range response goes from 0 up to 375 mmHg [13], an automatic pneumatic system, a bandpass filter with cut-off frequencies of 0.4 Hz and 15 Hz, and an amplifier with gain G = 5. Table 1 shows the averages for the DSBP and DDBP obtained with both systems. The comparison using the Bland-Altman plot yielded mean values for the DSBP of $\mu = 3.88 \pm 11.97$ mmHg and $\mu = -0.6 \pm 9.59$ mmHg in sitting and standing position, respectively (See Fig. 2). Results obtained yielded R^2 values of 0.59 and 0.76 for the DSBP, as well as 0.59 and 0.85 for the DDBP for the sitting and standing positions, respectively.

Table 1. Mean values and standard deviations (SD) for the systolic (DSBP) and diastolic (DDBP) blood pressure measurements made in the digital artery with our device (DD) and the Portapres.

Position	Parameter	DSBP DD (mmHg)	DDBP DD (mmHg)	DSBP Portapres® (mmHg)	DDBP Portapres® (mmHg)
Sitting	Mean	108.57	68.45	104.69	61.40
	SD	17.62	13.30	17.75	14.46
Standing	Mean	111.54	62.28	104.52	65.90
	SD	17.51	15.54	19.48	13.16

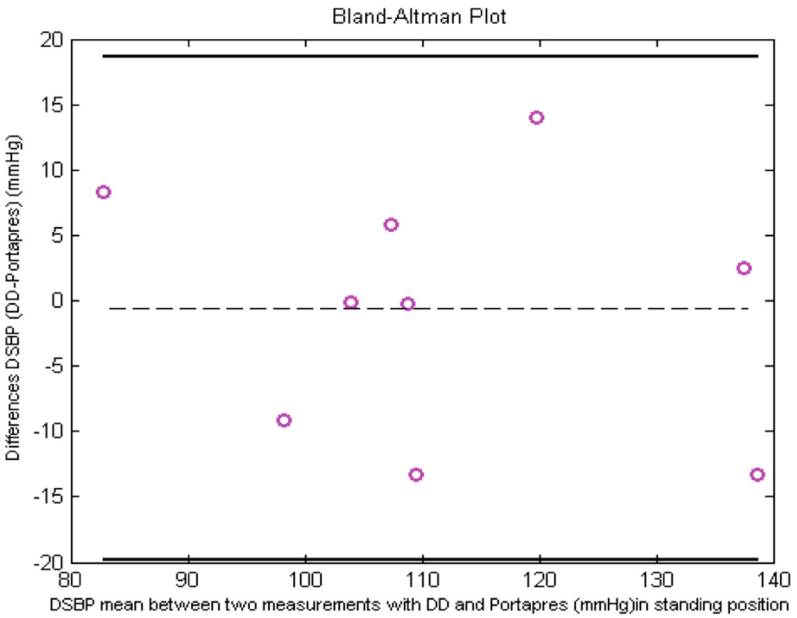

Fig. 2. Bland-Altman plot for the systolic blood pressure measured in the digital artery (DSBP) by our device (DD) and the measurements obtained with the Portapres®

4 Discussion

An Arduino UNO development board was used for building an affordable device for measuring blood pressure in the digital artery. Using Arduino has several advantages such as it incorporates an ATmega328P principal microcontroller and ATmega16u2 which can deliver via USB the digital values acquired through its analog to digital converter; its modularity design, and the fact that the modules can be modified through programming under a Creative Commons license, which enables the possibility to freely distribute the code of the pressure meter [14]. On the other hand, the use of Matlab for processing the signals has the disadvantage of a high licensing price and limitations related to the priority assigned by the computer. Since computers are multitasking systems and Matlab is an interpreter language, its priority is not high for the operative system. An important advantage of its use is that it can simultaneously perform different tasks such as storage, retrieval, and mathematical processing. It is worth mentioning that in this work we visually selected the PPG pulses used in the calculation of the DSBP and DDBP, but it has been planned, in a future work, to fully automatize the measurements and redesign the system by using low power surface mount components in order to reduce the device's dimension as well as its energy consumption.

5 Conclusions

The results show that our device has a good performance in terms of measurements, given that the pressure values obtained are clinically acceptable since they are being compared to a gold standard in this case Portapres®, which has been validated in research and clinic. According to the linear regression employed for the a comparison between both systems when measuring the DSPB a high positive correlation was obtained ($R^2 = 0.59$, $R = 0.76$) in sitting and standing position ($R^2 = 0.75$, $R = 0.86$), which suggests a high association between them in both positions, likewise, high associations were found in DDBP in sitting position ($R^2 = 0.59$, $R = 0.76$) and standing position ($R^2 = 0.85$, $R = 0.92$), however to verify the agreement of the DSBP values measured Bland-Altman plot was used, which showed in this case that the average differences of the DSBP in sitting position was $\mu = 3.88 \pm 11.97$ mmHg and de $\mu = -0.6 \pm 9.59$ mmHg in standing position. According to the interpretation of these results, the smallest average difference close to zero ($\mu = -0.6$) is in standing position, as shown in the Bland-Altman plot. The system shows limitations related to the noise shown by the PPG sensor. Additionally, our system has the advantage of a low electronic complexity design and uses an open source system such as Arduino.

Conflict of Interest. The authors declare that there is no conflict of interest.

References

1. Instituto Nacional del Seguro Social. http://www.imss.gob.mx/prensa/archivo/201707/203. Accessed 18 Oct 2018
2. Campos, I., Hernández-Barrera, L.: Hipertensión arterial en adultos mexicanos: prevalencia, diagnóstico y tipo de tratamiento. Ensanut MC 2016, Salud Pública Mex, vol, 60, pp. 233–234 (2018)
3. Webster, J.: Medical Instrumentation: Application and Design. Wiley, New York (1998)
4. Heyward, V.: Evaluación de la aptitud física y prescripción del ejercicio. 5th edn. Editorial Médica Panamericana. España, Madrid (2008)
5. Bello, J.: Método fotopletismográfico para la medición incruenta de la presión arterial sistólica a nivel de la arteria digital. In: Memorias del Congreso Nación de Ingeniería Biomédica on Trabajos Libres, SOMIB, México, pp. 72–75 (2014)
6. Jilek, J., Fukushima, T.: Oscillometric blood pressure measurement: the methodology, some observations, and suggestion. Biomed. Instrum. Technol. **3**(39), 237–241 (2005)
7. Chandrasekhar, A.: An iPhone application for blood pressure monitorng via the oscillometric finger pressing method. Sci. Rep. **8**, 1–6 (2018)
8. Norma Oficial Mexicana NOM-030-SSA-1999
9. Finapres Medical Systems, Finometer TM User's Guide (2005)
10. Castiglioni, P.: Broad-band spectral analysis of 24 h continuous finger blood pressure: comparition with intra-arterial recording. Clin. Sci. **97**, 129–139 (1999)
11. Bogert, L.W.J.: Non-invasive pulsatile arterial pressure and stroke volume: changes from the human finger. Exp. Physiol. **90**, 437–446 (2005)
12. Bland, J.M.: Statistical methods for assessing agreement between two methods of clinical measurement. Int. J. Nurs. Stud. **47**(8), 931–936 (2010)

13. NXP, FreeScale Semiconductors Inc. https://www.nxp.com/docs/en/data-sheet/MPX5050.pdf. Accessed 10 Apr 2019
14. Romano, P. https://www.semiconductorstore.com/blog/2014/Arduino-Development-Kits-Advantages-and-Features/811/. Accessed 12 Apr 2019

Treatment of Abdominal Hypertension: Development of an Original Non-invasive Device ABDOPRE

Alicia Schandy[1(✉)], Francisco Pracca[2], and Franco Simini[1]

[1] Núcleo de Ingeniería Biomédica de las Facultades de Medicina e Ingeniería, Universidad de la República, Montevideo, Uruguay
aliciaschandywood@gmail.com, simini@fing.edu.uy

[2] Departamento de Medicina Intensiva del Hospital de Clínicas, Universidad de la República, Montevideo, Uruguay

Abstract. ABDOPRE is a device that reduces the abdominal pressure of intensive care patients with intraabdominal hypertension. The controlled reduction following a time protocol is consequence of the application of an external negative pressure inside a vacuum bell affixed to the patient's abdomen. Originally developed in 2007, **ABDOPRE** was tested in four intensive care patients with intrabdominal pressures (12 to 15 mmHg). In three of these patients a reduction of 5 mmHg, 3 mmHg and 2 mmHg was accomplished. Afterwards, a new, cheaper, smaller and lighter version of **ABDOPRE** was developed using an ARDUINO UNO board for the control system and an ARUINO UNO SHIELD for the electrical interface. This version has an optimized Software and includes two bell sizes of 14 and 24 L respectively.

Keywords: Abdominal hypertension · Intra-abdominal pressure · Clinical instrument

1 Introduction

Intraabdominal hypertension (IAH) and abdominal compartment syndrome (ACS) are associated with pathologies that frequently affect intensive care patients. It is paramount to monitor and control these conditions as they have numerous pathophysiological implications. IAH is defined as a sustained or repeated pathological increase in intraabdominal pressure (IAP) above 12 mmHg. ACS is defined by a sustained increase in IAP above 20 mmHg that is associated with organ dysfunction or failure [1, 2]. In both cases, IAP elevation may have consequences in the nervous, cardiovascular, respiratory, hepatic, gastrointestinal, renal or endocrine system as well as potentially damaging the abdominal wall [3, 4]. Both IAH and ASC may cause a multi-organic failure and therefore increase the patient's mortality risk. Nowadays, the usual practice for reducing IAP when other non-surgical methods fail, is decompressive laparotomy [2]. Nevertheless, this is an invasive procedure and therefore there is large consensus [3] in searching for alternative less traumatic methods for reducing IAP that avert the potential complications inherent to any surgery. **ABDOPRE** was developed in 2007 [5] in response to this need, enabling a

© Springer Nature Switzerland AG 2020
C. A. González Díaz et al. (Eds.): CLAIB 2019, IFMBE Proceedings 75, pp. 567–574, 2020.
https://doi.org/10.1007/978-3-030-30648-9_74

controlled and non-invasive reduction of IAP through the application of a negative external pressure (NEXAP) above the patient's abdomen. Research has been done on the use of NEXAP to treat HIA [6, 7]. However, a specific device that allows a controlled reduction of IAP is yet to be developed. This paper analyses the different stages in the development of such a device, **ABDOPRE,** since its conception to the latest version on trial, describing its subsequent updates.

2 Operating Principle

ABDOPRE is based on the idea that IAP can be reduced through the controlled application of an external negative pressure. In previews works [8] we modelled the abdomen as a cuboid body filled with gases and liquids whose only compressible wall is its anterior wall. Assuming the abdomen is a compressible body which obeys the isothermal compression equation, we showed that changes in the pressure inside the bell are inversely proportional to abdominal volumen changes. Then, assuming abdominal gases obey the Ideal Gas Law, we proved that a reduction in the pressure inside the bell leads to a reduction in IAP which is the main idea behind **ABDOPRE** [8].

The system has four main functional blocks: a vacuum chamber or bell affixed to the patient's abdomen, a vacuum pump, a signal acquisition and control module and a graphical user interface. **ABDOPRE** has two pressure transducers, one that senses IAP through an intravesical catheter and another one that measures the pressure in the bell.

The clinical staff chooses the treatment protocol that consists in applying repeated positive and negative pressure slopes with pauses without applied pressure and periods of maximum applied pressure [9]. The simplest protocol is specifying the initial patient's IAP, the target IAP, the tolerance margin for the IAP and the duration of the treatment. Let IAP_o be the patient´s initial IAP, IAP_f the target IAP and $t_{treatment}$ the duration of the treatment, the control system creates the following linear reduction pattern for the IAP:

$$\mathrm{r(t)} = \frac{-\left(IAP_o - IAP_f\right)}{t_{treatment}} \times t + IAP_o \tag{1}$$

2.1 Protocol for Reducing and Maintaining IAP

Let ΔIAP_{max} be the maximum tolerance for the IAP, the control system turns the vacuum pump On and Off according to the following criteria:

$$If\ IAP(t) > r(t) + \Delta IAP_{max} \rightarrow PumpON$$

$$If\ IAP(t) \leq r(t) - \Delta IAP_{max} \rightarrow PumpOFF$$

The pump creates partial vacuum inside the chamber that in turn causes abdominal distension and therefore a reduction in the IAP. Once the target IAP is achieved, the

linear reduction pattern is replaced by a plateau and the control system keeps commanding the pump in order to maintain the IAP within the target range [9].

3 ABDOPRE 2007

The first prototype, **ABDOPRE** 2007 [5], included a PIC 16F687 microcontroller [10] as the control system which received the analog pressure values form the two transducers 143PC03D [11] and communicated bidirectionally with the PC through the UART port. The PIC controlled the functioning of the vacuum pump CZ-79600-02 [12] and sounded an alarm in case the chamber was misplaced which was deduced from a time analysis of the variables. The power supply for the transducers used to measure IAP and pressure in the chamber was delivered from an external medical-grade power source whereas all the other parts of the system were powered by a mains connected power source. The 2007 prototype included only one chamber size. The chamber was made with acrylic and its edges were covered with polyphon surrounded by vulcanized silicon in order to ensure a soft and hypoallergenic contact with the patient's skin. The Software displayed the IAP, the pressure in the chamber and the target IAP according to the chosen protocol. It was developed in Scilab with a total of 1075 lines of code. The **ABDOPRE** cabinet had a volume of 2520 cm^3, weighted 1.6 kg, and was linked to the chamber and the medical-grade power source. **ABDOPRE** 2007 costed 714USD without considering the development cost of 1400 person-hours.

4 Clinical Trials of ABDOPRE 2007

ABDOPRE was tested in four intensive care patients with IAP between 12 and 15 mmHg. An example of the application of **ABDOPRE** to a patient is presented in Fig. 1.

Three of the patients treated with **ABDOPRE** showed a reduction of 5 mmHg, 3 mmHg and 2 mmHg in IAP, while a fourth patient showed a 38% increment in IAP with respect to the initial IAP. What happened was that, as the patient was obese, the chamber was intromitted in the abdominal wall reducing the abdominal volume and consequently causing the IAP to increase. The three patients in which **ABDOPRE** was successfully applied showed an average 25% reduction in the IAP with respect to its original value for a period of one hour. In all cases the treatment lasted 10 min and a pressure of -35 mmHg was needed in the chamber in order to achieve the target PIA. The remaining case encouraged the redesign of the chamber in order to adapt it to different abdominal sizes and therefore avoid the 'Ventosa effect' with paradoxical increase [13].

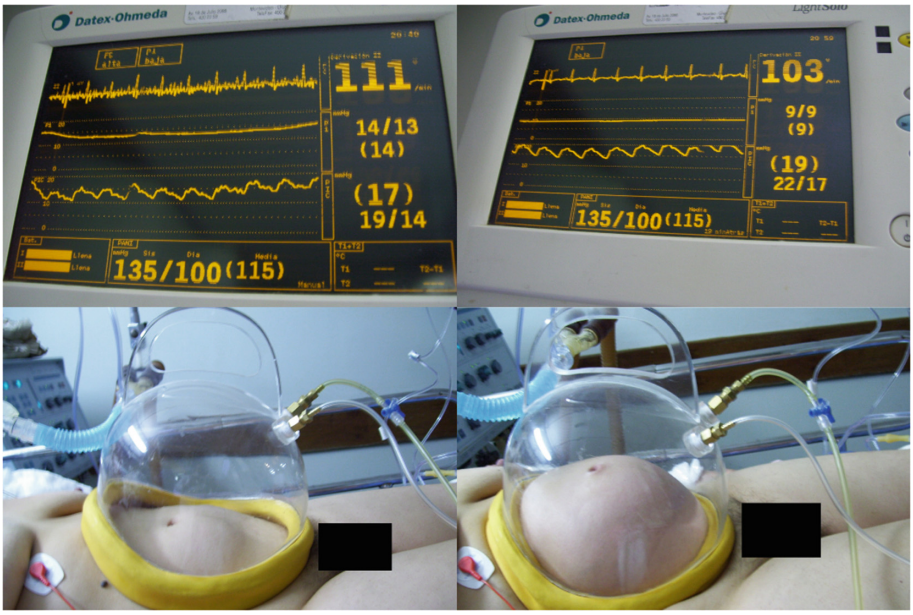

Fig. 1. **ABDOPRE** applied to a patient. The patient's abdomen distends when an external negative pressure is applied. In the picture in the left the patients has an IAP of 14 mmHg while in the picture in the right the patient has an IAP of 9 mmHg [13].

5 Redesign of the Bell

To ensure the proper function of **ABDOPRE** it is of extreme relevance to guarantee that the chamber is secured upon firm footholds: the iliac crests, the sternum, the pelvic bone and the costal arcs. Only one chamber size may be too small for some patients and the chamber may get intromitted in the abdominal wall when the negative pressure is applied, as was the case in the 2011 clinical trial [13]. In order to lift this restriction and enable **ABDOPRE** to be applied to as many patients as possible, the bell was redesigned in collaboration with Industrial Design students and staff of the Escuela Universitaria Centro de Diseño (EUCD) of the Faculty of Architecture. A sample of 19 intensive care patients were measured to determine how many chamber sizes were needed. This data was mapped in a histogram that revealed that two sizes were enough to fit all the measured patients. Then, 19 more patients were measured to make sure their abdomen fitted one of the two sizes. Based on this information, two new transparent methacrylate chambers were designed weighting 250 or 370 g and of capacities of 14 or 20L respectively [14].

6 ABDOPRE 2016

The circuitry and code of **ABDOPRE** were redesigned in 2016 in order to reduce the size, weight and cost of the device and to improve its performance. The original transducers were replaced with Argon DTXPlus TNF-R transducers [15] which are frequently used in intensive care. Additionally, the control system was implemented in an ARDUINO UNO board and the electrical interface in a SHIELD ARDUINO UNO [16] due to its low cost, versatility and ease of duplication. The ARDUINO UNO board communicates with the PC, samples the IAP and the pressure in the bell and commands the pump. Likewise, the SHIELD ARDUINO UNO supplies power to the pump and transducers and amplifies the transducer signals. Finally, for practical reasons and to ensure the patient's electrical safety, the power source was replaced by a battery. All the components fitted in a 3D-printed PVC box of 378 cm^3 and 200 grs. **ABDOPRE** 2016 cost less than USD 450. A comparison between the original and the latest cabinet, made in 2017, is presented in Fig. 2.

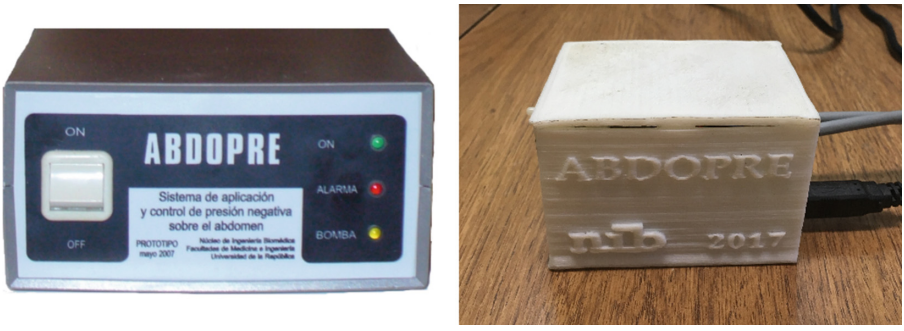

Fig. 2. **ABDOPRE** cabinet in 2007 [9] and 2017. Volume was reduced from 2520 cm^3 to 378 cm^3.

7 Trial Phantoms

Several phantoms were designed to test **ABDOPRE**. In the early stages of the development of **ABDOPRE**, water and beer bottles where used to calibrate the pressure measurements taken with the transducers. The bottles were insufflated with different amounts of air using a bicycle pump in order to simulate the positive pressure inputted to the transducers. Then, the pressure in the bottles was simultaneously measured with an analog water column pressure gauge, a digital EXTECH HD750 [17] pressure gauge and the evaluated transducer. The results obtained validate the reliability of the pressure measurements taken with the transducers.

Furthermore, a phantom was specially designed to assess the global performance of **ABDOPRE**. This phantom is a semi-sphere made of acrylic that has rigid walls and an upper part made from a rubber membrane that simulates the abdominal wall. The phantom has a tight fit with the vacuum chamber. In order to emulate the different

conditions of distensibility and content of the abdominal wall, the phantom has a plug that can be extracted to fill it with different amounts of water and a valve to insufflate it with different amounts of air. Moreover, it has an opening through which a catheter can be introduced to measure the internal pressure. This phantom enables the analysis and adjustment of **ABDOPRE** without having to involve a patient [9]. Figure 3 shows **ABDOPRE** applied to this trial phantom.

Fig. 3. **ABDOPRE** 2007 bell applied to the phantom and rear part of the cabinet [9].

8 Results and Discussion

We developed a first version of **ABDOPRE** in 2007 which proved to be effective in reducing the IAP of three intensive care patients. Subsequently, based on a statistical analysis we designed two bell sizes aimed to fit most patients. We also developed several trial phantoms in order to asses and adjust **ABDOPRE** without having to involve a patient. In 2016 we developed a second version of **ABDOPRE** which is more than six times smaller, eight times lighter and costs half the price of the original version.

A recent study [18] with 491 intensive care unit (ICU) patients from 15 different clinical settings showed that IAH occurred in almost half of all subjects. In addition, the presence and severity of IAH during the first 2 weeks of the ICU stay significantly increased 28- and 90-day mortality. Ten years have passed since the conception of

ABDOPRE and IAH and ACS remain to be concerning and prevalent medical conditions usually treated invasively. **ABDOPRE** offers a non-invasive and practical alternative for progressively reducing IAP. The first clinical results of **ABDOPRE** original version suggest its ability to reduce IAP. Further research will include clinical trials of the latest version to confirm our findings and assess its clinical effectiveness in preventing and treating IAH.

9 Conclusions

This paper aimed to gather every contribution made throughout the years in pursuit of the original development and the improvement of **ABDOPRE.** Despite a decade has passed, **ABDOPRE** is still a disruptive project since no descriptions of similar devices were found neither in the literature nor on the market. Moreover, it represents a clear example of what may arise from the synergy between medicine and engineering since the clinical need and idea were introduced by an intensive care medical team in cooperation with biomedical engineering staff. Development was done as master′s theses by Electrical Engineering students assisted by Industrial Design students. This close interdisciplinary collaboration resulted in an efficient, safe, ergonomic and therefore useful system. With the evidence of successful clinical trials of the latest version, **ABDOPRE** has the potential of becoming the usual therapy for controlled IAP reduction during the treatment of IAH.

Acknowledgments. The authors acknowledge the work done for the initial development by Marcelo David, Cedric Zoppolo and Guillermo Sánchez, as well as continuing support by Professor Alberto Biestro, Head of the Department of Intensive Medicine. Subsequent work was done by María José González Franco and Martín Arregui. Special thanks are also expressed to Luciana Urruty, Sylvia Díaz and Florencia Peirano for research and craftsmanship of **ABDOPRE** bells. This paper was checked for correct language format by Valerie Best, educated at the British Schools, Montevideo, Uruguay. The authors are deeply grateful for her advice.

Conflict of Interest. The authors declare that they have no conflict of interest with respect to the biomedical instrumentation research described in this paper.

References

1. Malbrain, M., Cheatham, M., Kirkpatrick, A., et al.: Results from the international conference of experts on intra-abdominal hypertension and abdominal compartment syndrome. Intensive Care Med. **32**, 1722–1732 (2006)
2. Kirkpatrick, A., Roberts, D., Malbrain, M., et al.: Intra-abdominal hypertension and the abdominal compartment syndrome: updated consensus definitions and clinical practice guidelines from the World Society of the Abdominal Compartment Syndrome World Society of the Abdominal. Intensive Care Med. **39**, 1190–1206 (2013)
3. Malbrain, M.: Is it wise not to think about intraabdominal hypertension in the ICU? Current Opinion in Critical Care **10**, 132–145 (2004)

4. Groen, R., Malbrain, M., Peul, W., et al.: The significance of intra-abdominal pressure in neurosurgery and neurological diseases: a narrative review and a conceptual proposal. Acta Neurochir. **161**, 1–10 (2019)
5. Pracca, F., Zoppolo, C., David, M., et al.: Negative pressure device for intra-abdominal pressure reduction. J. Phys. Conf. Ser. **90** (2007)
6. Fossali, T., Bottino, N., Guglielmi, M., et al.: Effects of continuous negative extra-abdominal pressure on cardiorespiratory function during abdominal hypertension: an experimental study. Intensive Care Med. **31**, 105–111 (2004)
7. Valenza, F., Bottino, N., Canavesi, K., et al.: Intra-abdominal pressure may be decreased non-invasively by continuous negative extra-abdominal pressure (NEXAP). Intensive Care Med. **29**, 2063–2067 (2003)
8. David, M., Pracca, F., Simini, F.: Non-invasive negative pressure system to treat abdominal hypertension. In: IFMBE Proceedings, vol. 37, pp. 211–214 (2011)
9. David, M., Sánchez, G., Zoppolo, C.: ABDOPRE Sistema de aplicación y control de presión negativa sobre el abdomen para la reducción de la presión intrabdominal. Thesis, Universidad de la república, Montevideo, Uruguay (2007)
10. Micro Chip: 20-Pin Flash-Based, 8-bit CMOS Microcontrollers, PIC16F687 datasheet (2004)
11. Honeywell: Board Mount Pressure Sensors 7 V-16 V 5.0psi Differ Transducer, 143PC03D datasheet (2006)
12. Cole Parmer: Miniature OEM Vacuum/Pressure Pumps, cz-79600-02 datasheet (2004)
13. Pracca, F., Biestro, A., Gorrassi, J., et al.: ABDOPRE: dispositivo de aplicação externa para redução da pressão intra-abdominal: Experiencia clínica preliminar. Revista Brasileira de Terapia Intensiva **23**, 238–241 (2011)
14. Urruty, L., Simini, F., Pereyra, M., et al.: Non-invasive treatment of abdominal hypertension: a new vacuum chamber. In: 36th Annual International Conference of the IEEE Engineering in Medicine and Biology Society, Chicago, IL USA (2014)
15. Medco Health Care: Argon DTX PlusTM Disposable Pressure Transducer Sets, Argon DTXPlus TNF-R datasheet (2013)
16. ARDUINO Homepage. https://www.arduino.cc/. Accessed 11 Jun 2019
17. Extech: Differential Pressure Manometers, Extech HD750 datasheet (2008)
18. Blaser, A.R., Regli, A., De Keulenaer, B., et al.: Incidence, risk factors, and outcomes of intra-abdominal hypertension in critically III patients-a prospective multicenter study (IROI study). Crit. Care Med. **47**, 535–542 (2019)

Portable Wireless Monitoring Center Designed in LabVIEW and myRIO 1900

Héctor García-Estrada[1(✉)], Karen Jazmín Mendoza-Bautista[1], María Guadalupe Ramírez-Sotelo[2], and Agustín Ignacio Cabrera-Llanos[1]

[1] Departamento de Bioprocesos, Unidad Profesional Interdisciplinaria de Biotecnología, Instituto Politécnico Nacional, Mexico City, Mexico
hectorgaes@gmail.com, aicllbuda@yahoo.com
[2] Departamento de Bioingeniería, Unidad Profesional Interdisciplinaria de Biotecnología, Instituto Politécnico Nacional, Mexico City, Mexico

Abstract. This work shows the design and development of a portable wireless monitoring center that connects to three vital sign monitors, with each providing electrocardiogram (EKG), partial oxygen saturation (SaO2), and breath signals and heart rate, breath rate, and temperature values. Each signal and value is stored in a variable library in each monitor. The monitors are connected to a Wi-Fi network with the WPA2 security protocol generated by the center. The center accesses the variable libraries of each monitor using the target IP direction. Then, the center groups the data into clusters and connects with a PC to deploy the variables in a virtual instrument with a general screen for deploying the EKG and the values of all of the monitors and specific screens for each monitor. For portability, the center's power source is 8 AA batteries.

Keywords: Monitoring center · Vital sign monitor · Wireless

1 Introduction

During the 2011 Haiti earthquake, nearly 300,000 people required medical care (3% of the country population). Among the deaths, 20% occurred during the first two weeks after the earthquake due to medical complications. Also, medical teams mostly performed emergency procedures, while leaving post-operatory care out of the equation. In fact, only 400 beds were available for post-operatory care for the entire population during the disaster [1]. Since post-operatory care was a problem because the lack of personnel for this task, a monitoring center could have been an alternative to optimize the reach of the nurses and physicians. This fact shows the need for a monitoring system capable of operating in disaster zones, meaning without a continuous electric supply, compact, using the fewest consumables possible, and with expandable connection characteristics. An example is changeable connection cables for each monitor with a Wi-Fi network.

© Springer Nature Switzerland AG 2020
C. A. González Díaz et al. (Eds.): CLAIB 2019, IFMBE Proceedings 75, pp. 575–581, 2020.
https://doi.org/10.1007/978-3-030-30648-9_75

1.1 Vital Sign Monitor

A vital sign monitor is a medical device that continually acquires, processes, and displays multiple physiological parameters of a patient [2]. Different kinds of vital sign monitors exist, according to the physiological parameters a monitor shows and the area where it is used. The classification is as follows:

- Fixed vital-sign monitors:
  - Advanced
  - Intermediate
  - Simple
  - Anesthesiologists

A portable monitor has a battery power supply and measures EKG, plethysmography, breath curve, heart rate, breath rate, and SaO_2 [3]. Vital sign monitors are important for patient care since their application allows a patient's development to be watched continuously over time and find applications in emergency rooms, intensive care units, surgery rooms, and post-operatory care rooms [4].

1.2 Monitoring Center

A monitoring center is a medical device that continuously obtains and displays the parameters of one or more vital sign monitors, allowing one to observe the status of multiple patients from one site. Depending on the transmission form, monitoring centers can be direct (physical transmission) or telemetric (wireless transmission) [5]. Monitoring centers should be able to display the parameters of all of the monitors connected to them or the parameters of a specific monitor [6]. Monitoring centers optimize vigilance over multiple patients since one nurse or physician can observe multiple patients from a single location. This quality is extremely useful, mainly in intensive care units, in which this quality is vital [4].

1.3 LabVIEW

LabVIEW is a development environment with a graphic coding language produced by National Instruments (NI). It was designed to develop virtual instruments with options for real-time applications using NI's acquisition boards and others [7]. The graphic coding language makes it easier to design interfaces according to the developer's needs. LabVIEW comes with multiple acquisition, signal-processing and control toolkits, allowing the development of various implementations [8].

1.4 NI myRIO 1900

The NI myRIO 1900 acquisition board belongs to the Reconfigurable Input/Output family of control and acquisition hardware of NI. It was designed as a mobile device for control, robotics, and mechatronics applications in academic environments [9]. The NI myRIO 1900 has multiple input/output digital channels, 2 differential analog inputs, 8 single-ended analog inputs, a Wi-Fi module (with the ability to connect or

generate a network), and a dual-core ARM Cortex-A9 microprocessor, making it ideal for embedded and remote system applications [10].

2 Methodology

The center was developed in three stages: Wi-Fi network generation, library design and variable transmission, and power supply. The monitors used for this project were developed previously and are described in [11]. These monitors provide the signals and values of a portable vital sign monitor as defined by [3]. In addition, these monitors can also measure temperature and can use a battery power supply.

The power supply for the boards during the trials was 8 rechargeable AA batteries connected in series, with a total voltage of 12 V and a 2300 mAh charge [12].

2.1 Wi-Fi Network Generation

For the Wi-Fi network, each monitor has to transmit the data to the center; then, the center has to group the data and broadcast them to the PC with the visualization screen. For this purpose, a star network topology was chosen, with a NI myRIO 1900 (now and on the center) used as the access point. Since the connection and transmission depend on the center acting as an access point, the failure of one of the monitors does not imply the failure of the entire network (Fig. 1).

Fig. 1. Information flow diagram

The Wi-Fi network and its connections were generated in three stages. For the first stage, a NI myRIO 1900 was configured using the NI-MAX software, allowing the board's settings to be modifiable [10]. To create the network, the Wireless setting has to

be changed from "Disabled" to "Create Wireless Network"; to connect, the setting has to be changed to "Connect to a Wireless Network." Once the configuration is changed, the network settings can be modified. For the center, the network received the name UCI (from the Spanish for "intensive care unit"), a WPA2 security protocol for connection, and a dynamic assignment of IP addresses with the IPv4 protocol. Since it is the access point of the network, it receives the first IP address.

The second stage was to connect each monitors' NI myRIO 1900 to the center. The difference was that the "Connect to Wireless Network" option was chosen. In order to avoid future identification problems, the monitors' IP addresses were configured as static, giving terminations 2, 3, and 4 to each monitor.

Finally, for the third stage, the PC was connected to the network with a dynamic IP address. This address type was chosen because the project is saved in a PC.

2.2 Library Design and Signal Transmission

After the monitors and the PC were connected to the center, a LabVIEW project was created in the PC, with the "Connected over Wi-Fi" option used to assign the boards to the project. Since the project wizard only allows one target to be chosen, the center was taken as the main board of the project. The monitors were added to the project manually, using their IP addresses for identification. This allowed all of the NI myRIOs to be controlled from a single project.

When all of the boards were on the project, the variable libraries were generated for each monitor. Each variable library had the EKG, breath, plethysmography, SaO_2, heart rate, breath rate, and temperature variables and was named according to the monitor to which it belonged. Additionally, a fourth variable library was created in the center with a general stop button. For the signals and the numeric values, the variables were created as numeric variables with 64 bits of precision. Although the center accessed the libraries using each target's IP address, the names of the variables were not repeated in the project.

The center retrieves the data from the library and regroups it into clusters for display on the PC with the virtual instrument, generating two clusters per monitor: one for the general screen and the other for each specific screen. The variables of the general screen cluster were EKG, heart rate, breath rate, SaO_2, and temperature. For the specific screens, they were EKG, breath, plethysmography, heart rate, breath rate, SaO_2, and temperature. Then, the PC displays the EKG, breath, and plethysmography in graphs and the heart rate, breath rate, SaO_2, and temperature in numerical indicators. The structure of the project is shown in Fig. 2.

The monitors acquire and process the signals in situ and then publish them in the variable libraries. The center accesses the libraries and displays the signals and the numeric values on different screens, with a general screen for all of the monitors and specific screens for each monitor.

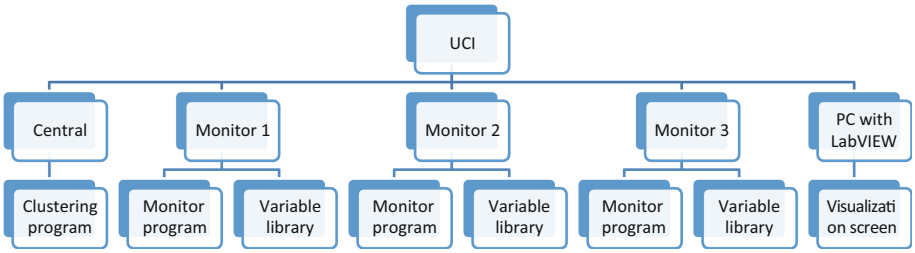

Fig. 2. Center's project structure

3 Results

Before the center was tested, a single monitor was used with the power supply described in the methodology section to observe its behavior. The monitor worked continuously in a six-hour period and performed adequately, with the batteries being changed.

The center was tested with three probe subjects connected to the monitors in a three- hour period. During this time, there was no need to change the batteries. The main screen of the front panel of the virtual instrument shows the EKG, heart rate, breath rate, SaO_2, and temperature from the three monitors (Fig. 3).

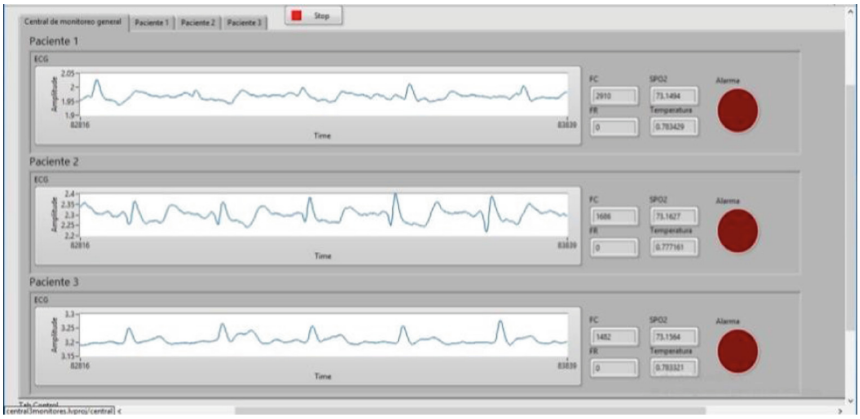

Fig. 3. Central main screen

The center also allows the option to watch all of the parameters (EKG, SaO_2, breath curve, heart rate, breath rate, temperature, and plethysmography) of only one monitor (Fig. 4).

When the measurements were being taken, a delay between acquisition and display was noted. This delay was measured (Table 1).

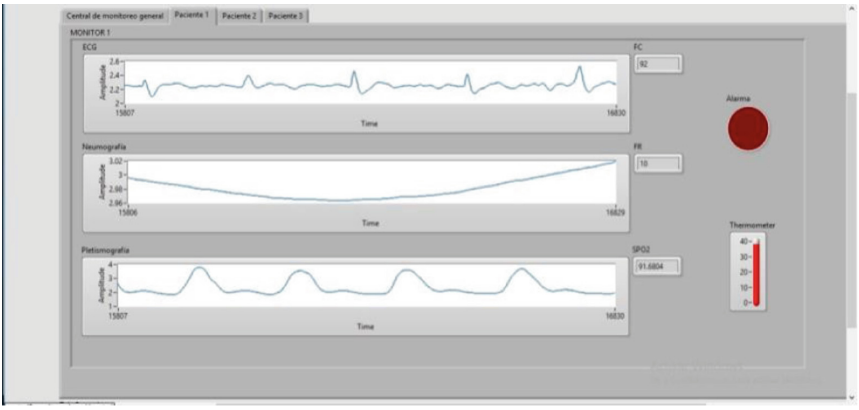

Fig. 4. Specific monitor screen

Table 1. Delay time

Measurement	Time (seconds)
1	1.85
2	1.65
3	1.87
4	1.60
5	1.85
6	1.92
Mean	1.785

4 Conclusions

A wireless monitoring center for three monitors was developed with PC visualization and a mean transmission delay of 1.785 s. The Wi-Fi network allows for communication among the center, the monitors, and the PC. The in situ processing of the monitors allows them to work with or independently from the center. The variables being grouped into libraries and different targets being configured in one project help with controlling and programming the entire system. The batteries used had adequate performance during the test of the center, which proves that a battery power supply is viable and could be used in the absence of an electric line supply. However, other kinds of batteries should be tested to maximize the operational time of the prototype.

References

1. Organización Panamericana de la Salud, La respuesta de salud al terremoto de Haití Enero de 2010: Enseñanzas que deben aprenderse para el próximo desastre repentino de gran magnitud, Organización Panamericana de la Salud, Washington D.C. (2012)

2. CENETEC: CENETEC, Enero (2005). http://www.cenetec.salud.gob.mx/descargas/biomedica/guias_tecnologicas/13gt_monitores.pdf
3. CENETEC: CENETEC, 19 Mayo 2010. http://www.cenetec.salud.gob.mx/descargas/CETpdf/monitores/Monitotraslado.pdf
4. Kipnis, E., Ramsingh, D., Bhargava, M., Dincer, E., Broccard, A., Vallet, B., Bendjelid, K., Thibault, R.: Monitoring in the intensive care. Crit. Care Res. Pract. (2012)
5. CENETEC: CENETEC, Junio 2006. http://www.cenetec.salud.gob.mx/descargas/biomedica/guias_tecnologicas/ 24gt_centrales_monitoreo.pdf
6. CENETEC: CENETEC, 2010 Mayo 2010. http://www.cenetec.salud.gob.mx/descargas/CETpdf/centrales_monitoreo/telemetria.pdf
7. National Instruments: National Instruments (2019). http://www.ni.com/es-mx/shop/labview.html
8. Vizcaíno, J.R.L., Sebastiá, J.P.: LabVIEW: Entorno gráfico de programación. Marcombo, Madrid (2011)
9. National Instruments: National Instruments (2019). http://www.ni.com/es-mx/support/model.myrio-1900.html.
10. National Instruments: National Instruments, Junio 2018. http://www.ni.com/pdf/manuals/376047d.pdf
11. García, H., Pastrana, A., Linares, O., García, J., Ramírez, M., Cabrera, A.: Monitor de signos vitales con comunicación inalambrica Wi-Fi para unidad de cuidados intensivos desarrollado en LabVIEW y la tarjeta myRIO-1900. Res. Comput. Sci. **147**(12), 203–212 (2018)
12. Energizer: Energizer Recharge® Rechargeable Batteries (2019). https://www.energizer.com/batteries/energizer-rechargeable-batteries. Último acceso: 4 25 2019

Design of a Suitable NIR System for Monitoring Hemodynamic Changes in the Brain Prefrontal Cortex

Miguel Angel Santiago Gorostieta-Esperon(✉) and Luis Jiménez-Ángeles

Biomedical Systems Engineering Department, Engineering Faculty, National Autonomous University of Mexico (UNAM), Mexico City, Mexico
goros95@comunidad.unam.mx, luis.jimenez@ieee.org

Abstract. Near infrared systems (NIRS) are able to detect hemodynamic changes in the brain cortex and offer several advantages to be considered as a suitable technology to address problems in medicine. The objective of this work was to design a NIRS prototype for monitoring the dorsolateral prefrontal cortex activity related with tobacco addiction. An analysis of the needs of potential users helped us to establish the design of a device with a safe optoelectronic circuit mounted on an adaptable and portable chase (size of 7 cm × 7 cm × 4 cm and weight of 100 g). Our device is capable to acquire two signals (750 nm and 850 nm) continuously while a subject makes arithmetic tasks. Both signals follow a reliable behavior and are in agreement with the reports from the literature. A clinical protocol comparing non-smokers vs smoker subjects is in progress to validate the results of our device.

Keywords: NIRS · Hemodynamic response · Prefrontal cortex · Tobacco

1 Introduction

Near-infrared systems (NIRS) works based on the principle that light passing through a tissue is variably attenuated depending on the levels of oxy-hemoglobin (HbO_2) and deoxy-hemoglobin (Hb). NIRS are very sensitive to these changes and are considered as non-invasive devices that can be used to measure brain activity with a high spatial resolution. Additionally, NIRS are more portable than other medical image modalities, can be used for long periods and are not restricted to motionless acquisitions [1, 2]. Brain activity in the dorsolateral prefrontal cortex (DLPFC) has been commonly implicated in the modulation of subjective and behavioral response of subjects exposed to drug-associated cues [3]. The objective of this work was to design a suitable NIRS to monitor hemodynamic changes in the DLPFC, based on specifics requirements, so that in the future the proposed device can be used as an objective and quantifiable tool for the treatment of tobacco cessation.

© Springer Nature Switzerland AG 2020
C. A. González Díaz et al. (Eds.): CLAIB 2019, IFMBE Proceedings 75, pp. 582–587, 2020.
https://doi.org/10.1007/978-3-030-30648-9_76

2 Materials and Methods

2.1 Requirements and Specifications

Requirements of the NIRS were obtained from interviews with 3 potential clinical users, a market analysis and a comparisons of similar devices. Six main requirements were selected for the design of the proposed NIRS considering that can be used by any adult subject (adaptable) in a non-restricted environment (portable) to obtain high accuracy measurements (reliable) of hemodynamic changes in the frontal cortex, while subject perform a task (continuous), safely and with minimal user interaction (easy). Requirements were tailored to prioritized technical specifications (see Table 1) following the methodology described in [4].

Table 1. Design requirements for the proposed NIRS.

Requirement	Technical specification	Units	Max value
Adaptable	Diameter of the head	cm	20
Safety	Number and kind of components	#	4
Safety	Contact surface of the device with the head	cm^2	628
Easy operation	Number of controls	#	4
Reliability	Correlation	%	5
Continuous monitoring	Operation time	hours	1
Portable	Device weight	g	150
Portable	Device size	cm^3	2094

2.2 Optoelectronic Circuit

The proposed NIRS was based on a previous report [5] since it is adaptable to future applications, enables spatial distribution of the hardware and allows direct output for signal processing. A block diagram of the proposed NIRS is shown in Fig. 1. The light stimulation-detection block contains four NIR light sources. Each light source is a bi-color LED mounted on a lead frame with a clear epoxy lens emitting at wavelengths of 750 and 850 nm in a common-anode connection (L750/850-04A, Marubeni). A dual N-channel MOSFET (IRF7303, International Rectifier) in a source-follower/grounded-gate configuration was used to regulate the light output intensity of each NIR-LED. The NIR light detector was a monolithic photodiode with on-chip transimpedance amplifier (OPT101, Texas Instruments), having an output voltage linearly dependent with respect to the light intensity. The NIR light detector was assembled in a basic configuration using an internal 1 Mega Ohm feedback resistance as described in [6]. The NIR light detector was located at the center and the four NIR-LEDs were placed at opposite corners at equal distances of 30 mm.

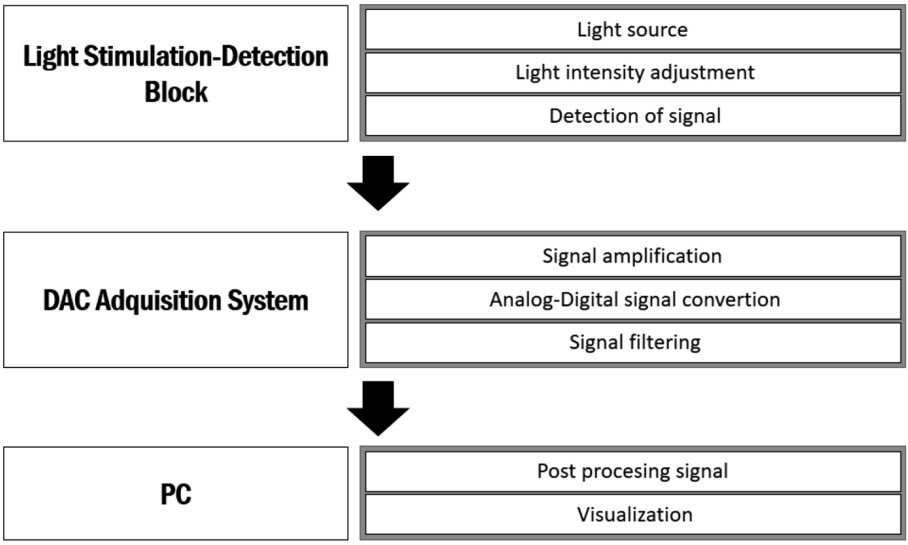

Fig. 1. Block diagram of the proposed NIR system.

2.3 Mechanical Design

The proposed NIRS was designed to register the metabolic activity at DLPFC and should meet the portable and non-invasive requirements. To adjust the optoelectronic circuit perpendicularly to the surface head of an adult subject, a chase module design was based on a spherical approximation of the head considering 20 cm of diameter. The design of the chase module (see Fig. 2) was carried out using Siemens NX 9.0 CAD software (Siemens PLM software).

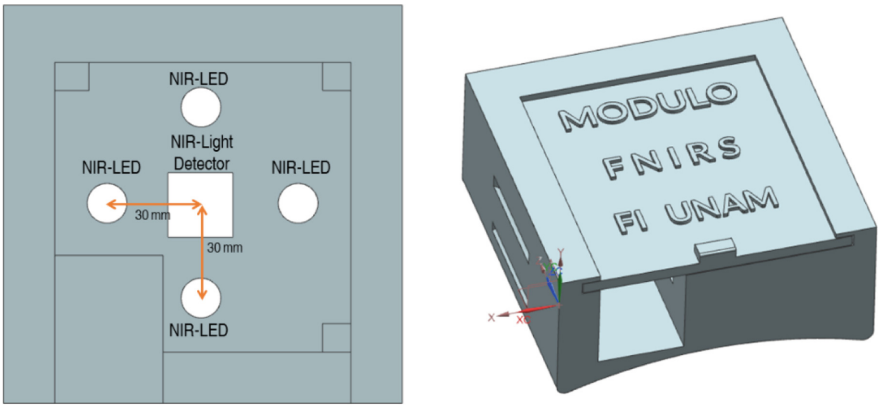

Fig. 2. Arrangement of LEDs (left) and conceptual design of the chase (right).

2.4 Mental Task Stimulation

To validate the operation of the NIRS prototype, twenty control subjects (10 men and 10 women, with 23 ± 3 years old) with no report of mental and cognitive impairment were voluntary invited to perform mental arithmetic tasks while the NIRS signal was acquired. A mental task block consists of an initial rest period followed by a stimulus period. The stimulus period consisted of six images (five seconds per image) containing mathematical equations to be solved. During the resting period only arithmetic and equation symbols were presented but not solved. Resting period had the same time duration as the stimulus. Five mental task blocks were presented to the subject, followed by a final rest period. The mental task stimulation had a total time of 330 s. The NIR-light detector was placed on the DLPFC (point F7 according to 10–20 electrode placement system for electroencephalography).

2.5 NIRS Signal Acquisition and Processing

The signal output of the NIR-light detector was amplified with a constant gain of 1000 and digitalized by a 12-bit DAQ card (LabQuest Mini, Vernier) using a sampling rate of 1000 Hz. The digital signal was processed with a low-pass Butterworth filter using a 3 dB cut-off frequency of 2 Hz and 30 dB at 5 Hz.

3 Results and Discussion

Figure 3 shows the printed circuit board (PCB) with surface-mount, through-hole technology and the final chase fabricated with black acrylonitrile butadiene styrene (ABS) by fused deposition modelling. The PCB and chase were 4.9 cm × 4.9 cm and 7 cm × 7cm × 4 cm, respectively. The device weights 100 g and satisfies the requirement of portability. Safety requirement was satisfied due to the fact that there is not electrical connection between the device and subject, only optical coupling was

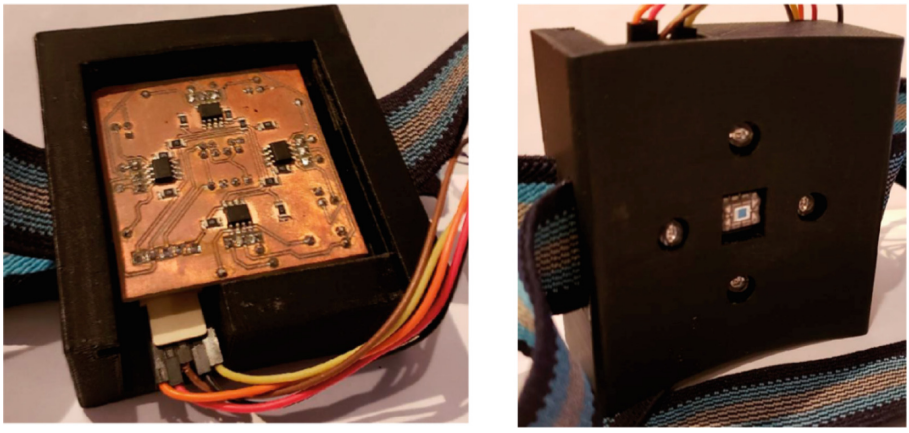

Fig. 3. PCB and chase result of the proposed NIRS

established and a well regulated current supplied by MOSFETS protects from burns by heat dissipation. The spherical approximation of the head, considering 20 cm of diameter, allow us to adapt the device to any adult subject.

Signal filtering was performed using Logger Pro® software (Vernier Software & Technology) whereas post processing and visualization was performed using Matlab® software (R2015a, The MathWorks Inc). Signal changes at 750 nm (Hb) and 850 nm (HbO_2) in two consecutive blocks are shown in Fig. 4. A difference in the signal amplitude was evident when resting and stimulus periods were compared. We observed signal changes during the stimulus periods that correlates with the evoked pattern of the hemodynamic response as previously reported [7]. Also, the signal frequency increase during stimulus periods as a function of heart rate as has been reported [8]. All these findings confirm the reliability of our measurements.

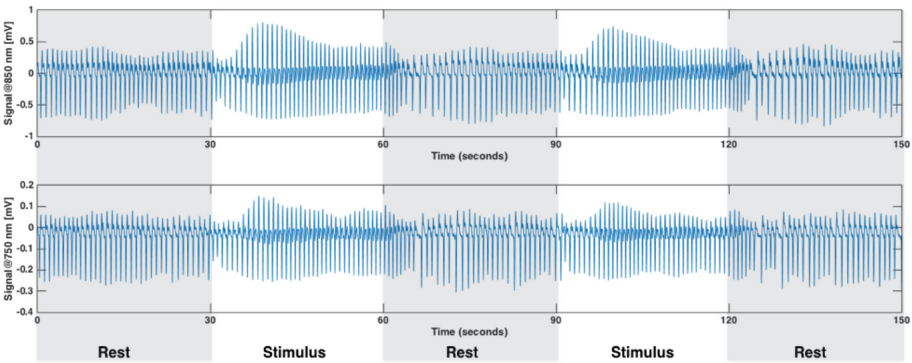

Fig. 4. Signal changes at 850 nm and 750 nm reflects changes in oxi-hemoglobin and deoxi-hemoglobin during the resting period and mental task.

4 Conclusions

The main contribution of this work was to design a suitable prototype to perform continuous monitoring of the brain activity. The design was based on specific requirements of potential users that need a tool to evaluate the brain activity in the DLPFC related to tobacco addiction. The design of the light stimulation-detection block complies the requirements of safety while the chase size and weight offer an adaptable and portable prototype. Signals of HbO_2 and Hb were acquired continuously while the subject makes specific task and follows a reliable behavior. No specific training is required to use of the prototype however, the need of algorithms and software to analyze the signals in a friendly user platform should be addressed. A clinical protocol (non-smokers vs smoker subjects) is in progress and a positive correlation of NIRS vs functional magnetic resonance imaging needs to be completed to validate the results of the proposed device.

Acknowledgments. To DGAPA-UNAM project PAPIIT 2017-IA106917 "Sistema de registro no invasivo de la actividad cerebral relacionada al consumo de tabaco" and to Dr. Alejandro Santos for his help preparing this manuscript.

References

1. Ferrari, M., Quaresima, V.: A brief review on the history of human functional near-infrared spectroscopy (fNIRS) development and fields of applications. Neuroimage **63**(2), 921–935 (2012). https://doi.org/10.1016/j.neuroimage.2012.03.049
2. Scholkmann, F., Kleiser, S., Metz, A.J., Zimmermann, R., Mata Pavia, J., Wolf, U., Wolf, M.: A review on continuous wave functional near-infrared spectroscopy and imaging instrumentation and methodology. Neuroimage **85**, 6–27 (2014). https://doi.org/10.1016/j.neuroimage.2013.05.004
3. Janes, A.C., Pizzagalli, D.A., Richardt, S., deB Frederick, B., Chuzi, S., Pachas, G., Culhane, M.A., Holmes, A.J., Fava, M., Evins, A.E., Kaufman, M.J.: Brain reactivity to smoking cues prior to smoking cessation predicts ability to maintain tobacco abstinence. Biol. Psychiatry **67**(8), 722–729 (2010). https://doi.org/10.1016/j.biopsych.2009.12.034
4. Ulrich, K., Epinger, S., Madrigal, R.: Diseño y desarrollo de productos, 5a edn. Mcgraw-Hill, México (2013)
5. von Lühmann, A., Herff, C., Heger, D., Schultz, T.: Towards a wireless open source instrument functional near-infrared spectroscopy in mobile neuroergonomics and bci applications. Front. Hum. Neurosci. **9** (2015). https://doi.org/10.3389/fnhum.2015.00617
6. OPT101 – Texas Instruments. www.ti.com/lit/ds/symlink/opt101.pdf
7. Pfurtscheller, G., Bauernfeind, G., Wriessnegger, S.C., Neuper, C.: Focal frontal (de) oxyhemoglobin responses during simple arithmetic. Int. J. Psychophysiol. **76**(3), 186–192 (2010). https://doi.org/10.1016/j.ijpsycho.2010.03.013
8. Themelis, G., D'Arceuil, H., Diamond, S., Thaker, S., Huppert, T., Boas, D., Franceschini, M.: Near-infrared spectroscopy measurement of the pulsatile component of cerebral blood flow and volume frontal arterial oscillations. J. Biomed. Opt. **12**(1), 014033 (2007). https://doi.org/10.1117/1.2710250

A Prototype for Automatically Blood Pressure Measurement with Wireless Communication to a Graphical User Interface in MATLAB

Alicia Sofía Virueña-Vázquez[1(✉)], Haydeé Alicia Yáñez-Ocampo[1], Sebastián Aguiñaga-González[1], Juan Pablo Matadamaz-Castro[1], María del Carmen Arquer-Ruiz[2], María Guadalupe Flores-Sánchez[1], and José Israel Hernández-Oropeza[1]

[1] Faculty of Engineering, Universidad La Salle, Mexico City, Mexico
aliciasvv@gmail.com, jose.hernandez@lasalle.mx
[2] UMAE Pediatric Hospital, Centro Médico Nacional Siglo XXI, IMSS, Mexico City, Mexico

Abstract. High blood pressure and its pathologies are among the main diseases suffered by Mexicans. Many people may consider themselves prone by inheritance or lifestyle, so monitoring this biometry could help for early diagnosis. As part of the treatment, hypertensive people must keep a record that the doctor can consult periodically about the behavior of the patient blood pressure. In this work, a prototype that automatically takes blood pressure and communicates the data to a PC through a graphical user interface (GUI) in MATLAB is proposed. The values of systolic and diastolic pressures set from the prototype were compared against measurements using a digital wrist baumanometer, obtaining a percentage error less than 4%. Therefore, it can be concluded that the prototype gives not only precise, but also exact values of blood pressure.

Keywords: Hypertension · Prototype · Blood pressure monitor · Graphical user interface

1 Introduction

According to the World Health Organization (WHO), blood pressure is the force exerted by the blood against the walls of the arteries when being pumped by the heart [1]. Blood pressure is expressed by two numbers, the first number is the systolic pressure, which is the pressure when the heart beats; the second number, the diastolic pressure, is the pressure when the heart rests between beats [2]. The normal systolic blood pressure is 120 to 129 mmHg, while the diastolic pressure is 80 to 84 mmHg [3, 4].

When the systolic and diastolic pressures are equal to or greater than 140 mm Hg and 90 mm Hg, respectively, it is considered as arterial hypertension, which is defined as the constant elevation of the pressure in the blood vessels; the higher it is, the more work is done by the heart to efficiently pump blood in the body [4, 5].

© Springer Nature Switzerland AG 2020
C. A. González Díaz et al. (Eds.): CLAIB 2019, IFMBE Proceedings 75, pp. 588–592, 2020.
https://doi.org/10.1007/978-3-030-30648-9_77

Currently, hypertension is one of the causes of mortality in Mexico and the world, due to its lack of symptoms, it is the main risk factor that causes other diseases, especially cardiovascular, and is detected until the person has health complications [6, 7]. The National Survey of Health and Nutrition 2016 (ENSANUTMC 2016) reported that in Mexico the prevalence of hypertension is 25.5%, and approximately 40.0% of these people were unaware that they had this disease [8, 9].

Due to hypertension is the result of a multifactorial process, if a person who is prone to develop hypertension modifies its habits in a positive way, these actions could significantly to prevent the disease from appearing [10, 11]. It should be extremely helpful that the population at any age take its blood pressure regularly with the aim of diagnose the disease at an early stage and avoid future complications [12, 13].

This project seeks to respond to the fore problem through a prototype that automatically measures blood pressure without the need of assistance of any kind. In addition, the values of the biometry are calculated by MATLAB and not by a reading subject. The importance of the project also lies in the automatic storage of the values of systolic and diastolic pressures which ensure the integrity of the registration in case that consultation was necessary.

2 Materials and Methods

2.1 Signal Conditioning

We used the MPX2200 pressure sensor which measures in a range from 0 to 29 psi, with a maximum output voltage of 40 mV. A differential amplification was performed with a G = 1000, from which the pressure signal of the arm cuff was obtained. After the amplification, the signal was taken to a pass band filtering stage with a lower cutoff frequency from 0.4 to 14.4 Hz, delimited by beats per minute in hypertensive patients with tachycardia (150 bpm) and hypotension (50 bpm), the signal obtained by the filter is the oscillation signal of the arm cuff. An amplification was performed with a G = 5 in order to be better appreciated by the Arduino.

2.2 Automatic Pneumatic Control

The system has an automatic pneumatic control for inflating and deflating the cuff, for this an activation circuit was performed with a Darlington pair using a TIP31C and a BC547 transistors to have a current gain.

2.3 Arduino Programming

The inflation control of the cuff was carried out up to 170 mmHg and its subsequent deflation with the electrovalve, as well as the recording of the pressure signal and the oscillometric signal with a sampling frequency of 100 samples per second.

2.4 Zigbee Wireless Connection

For the acquisition of data, two Zigbee modules were used (transmitter and receiver), which work with radio frequency, the transmitter was connected to the Arduino through the pins of the Serial and the other module it connects directly to the USB port of the computer [14].

2.5 Graphical User Interface (GUI) and Pressure Measurement in MATLAB

A graphical user interface (GUI) was made in MATLAB. The GUI allows the measurement and acquisition of the signals into the computer. Obtaining the systolic and diastolic pressure requires aligning both signals and showing the points where the blood flow changes behavior. For this, it is necessary to detect the moment, in the deflation of the arm cuff, where the pulses are again noticeable and the point where the pulse has greater magnitude during the deflation of the bracelet (systolic and diastolic pressure respectively). Both moments in the pressure signal mark the values corresponding to the biometry.

3 Results

We performed 25 series of characterization measurements within the range of 0 to 200 mmHg, with gain of 1000. We calculated the margin of error of the voltage (converted to mmHg) against an analog manometer used as reference, obtaining an error of 2.8%. Then, with the values from the characterization, we proceeded to set the linear regression equation. Once the characterization was made and after having obtained the equation of the line, we started reading in mmHg in the Arduino IDE. The filter is of second order, for its characterization a shift of frequencies from 0.1 to 16 Hz was performed, obtaining a lower cutoff frequency of 0.37 Hz and higher than 14.82 Hz, taking as error 1.4%.

The pressure signal of the bracelet was sent to the Arduino and also the one previously described to be the result of the filter, once this part of both signals was obtained both signals align in time and the detection of the first pulse and the largest pulse was obtained programmatically in MATLAB.

Subsequently, both signals were plotted and aligned since both have the same length. The area of interest is comprised by the part of the deflation of the bracelet, so attention was focused on this area since where the systolic and diastolic pressures are obtained (see Fig. 1). When both signals were obtained, the first pulse and the largest pulse were detected by programming in MATLAB. The Zigbee communication was used because the serial communication protocol is the same as that handled by Arduino to MATLAB.

It was decided to use a MATLAB GUI for the compatibility of the software with both Arduino and Zigbee and to facilitate the understanding of the system to the user. The program developed in MATLAB to extract the data wirelessly was based on reading the impressions made by the Arduino main program.

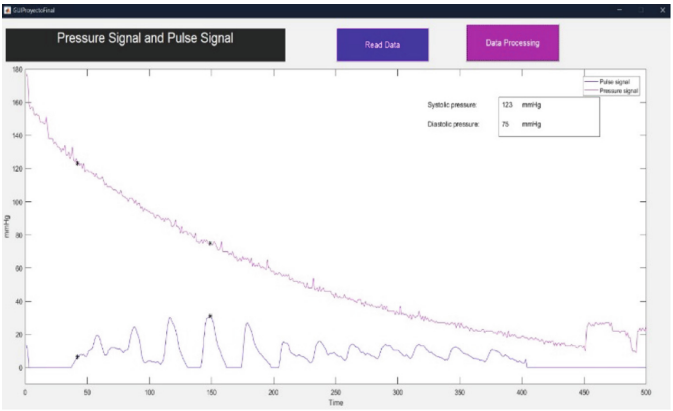

Fig. 1. Systolic and diastolic pressures shown by the GUI made in MATLAB.

The project as a physical system, consists of several parts to carry out its operation, this requires two actuators for inflation and deflation, the MPX2200 sensor, the circuit with amplification and filter and finally the Arduino UNO.

4 Conclusions

The MPX2200 sensor was used for the characteristics and the range of operation it offers, only a differential amplification being necessary due to the sensitivity of the Arduino UNO. After the first tests with a time interval of inflation it was found that from person to person the pressure reached was changed; to have an established threshold that would be met in any person, inflation time was established as determined by the recorded pressure; that is, the sleeve is inflated until 170 mmHg is reached. The values of systolic and diastolic pressures set from the prototype were compared against measurements using a digital wrist baumanometer, obtaining a percentage error less than 4%. Since both tests could not be performed simultaneously, it is considered acceptable. In addition, it can be concluded that the prototype gives not only precise, but also exact values of blood pressure.

References

1. World Health Organization Homepage. https://www.who.int/topics/hypertension/es/. Accessed 07 Jan 2019
2. American Heart Association Homepage. https://www.heart.org/-/media/data-import/downloadables/whatishighbloodpressure_span-ucm_316246.pdf. Accessed 07 Jan 2019
3. Segura-Vega, L.: Nuevas cifras de la presión arterial en las poblaciones peruanas de altura y la nueva guía americana de hipertensión arterial. Rev Peru Ginecol Obstet **64**(2), 185–190 (2018)

4. Ritchey, M., Keming, Y., Gillespie, C., Zhang, G., Ostchega, Y.: Development and validation of a hypertension prevalence estimator tool for use in clinical settings. J. Clin. Hypertens. **18**(8), 750–761 (2017)
5. Instituto Mexicano del Seguro Social Homepage. http://www.imss.gob.mx/prensa/archivo/201707/203. Accessed 07 Jan 2019
6. Secretaría de Salud Homepage. https://www.gob.mx/salud/prensa/hipertension-arterial-causa-de-muerte-en-mexico-y-el-mundo. Accessed 07 Jan 2019
7. Rosas-Peralta, M., Arizmendi-Uribe, E., Borrayo-Sánchez, G.: What do adults die in Mexico? Impact on the economic and social development of the nation. The global burden of cardiovascular disease. Rev. Med. Inst. Mex. Seguro Soc. **55**(1), 98–103 (2017)
8. Secretaría de Salud Homepage. https://www.gob.mx/cms/uploads/attachment/file/209093/ENSANUT.pdf. Accessed 14 May 2019
9. Encuesta Nacional de Salud y Nutrición de Medio Camino 2016 Homepage. https://www.gob.mx/cms/uploads/attachment/file/209093/ENSANUT.pdf. Accessed 07 Jan 2019
10. Huerta-Robles, B.: Factores de riesgo para la hipertensión arterial. Arch. Cardiol. Mex. **71**(1), S208–210 (2001)
11. James, P.A., Oparil, S., Carter, B.L., et al.: 2014 evidence-based guideline for the management of high blood pressure in adults: report from the panel members appointed to the eighth joint national committee (JNC 8). JAMA **311**(5), 507–520 (2013)
12. Guijón-Conde, T.: Use of ambulatory blood pressure monitoring. Hipertensión y Riesgo Vascular **34**(2), 15–18 (2018)
13. González-Rivas, J.: Optimizando la medición de la presión arterial en la consulta. Revista Venezolana de Endocrinología y Metabolismo **14**(3), 179–186 (2016)
14. Peng, C., Qian, K.: Development and application of a ZigBee-based building energy monitoring and control system. Sci. World J. **2014**, 1–13 (2014)

Development of Auricular Transcutaneous Vagal Stimulation Device Integrated with Signal Monitoring

Eugênia Gonzales Lopes[1(✉)], Eleonora Tobaldini[2], Nicola Montano[2], Karina Rabello Casali[1], and Henrique Alves de Amorim[1]

[1] Universidade Federal de São Paulo, São José dos Campos, Brazil
eugenia.lopes@geb.inatel.br
[2] Università degli Studi di Milano, Milan, Italy

Abstract. The paper consists of the development of a transcutaneous vagal stimulation device triggered by respiration and responsible for monitoring two physiological signals, the Electrocardiogram (ECG) and the Respiratory Cycle (RC). The device is used for some pathologies, such as Alzheimer, obesity and hypertension. The advantages reached by the device include a non-invasive method for vagal modulation and presents the option to synchronize the stimulation with the exhalation phase of RC. It is described the stages of development, which are Recording and Control Interface using an application for mobile devices, Stimulation System for the electrical pulses generation and Synchronization System to trigger the stimulation with the RC wave. In addition, it is shown the device as wearable equipment, by the use of a costumed t-shirt. The results of this development include a validation of the algorithm for peak detection, the pattern of the pulses generated on System Stimulation confirmed and the device is considered as a promising alternative therapy for certain diseases.

Keywords: Transcutaneous Vagal Nerve Stimulation · Wearable device · Auricular branch · Heart Rate Variability

1 Introduction

The Vagal Stimulation has been used as alternative and promising therapy in the treatment of several pathologies such as epilepsy, cardiovascular diseases, Alzheimer's disease, treatment-resistant anxiety, obesity, migraine and chronic pain. As an example, we have before this picture that "Epilepsy is one of the most common serious disorders of the brain, affecting about 50 million people worldwide" [1]. As for Alzheimer's disease: "Alzheimer's disease (AD) is characterized by progressive cognitive decline leading to dementia. It has been estimated that over 35.6 million people have dementia worldwide." [2]. Furthermore, it has been demonstrated through clinical cases that the decrease in cardiac vagal activity and the increase in heart rate are prognostic of the high mortality rate caused by heart problems [3].

© Springer Nature Switzerland AG 2020
C. A. González Díaz et al. (Eds.): CLAIB 2019, IFMBE Proceedings 75, pp. 593–600, 2020.
https://doi.org/10.1007/978-3-030-30648-9_78

Traditional techniques for performing vagal activation involve the implantation of a subcutaneous device in the left breastplate that is connected to the left vagal nerve. This device provides pulses for a given time at a frequency established in the literature [4, 5]. The Vagal stimulation therapy was approved as an additional treatment in refractory epilepsy in 1994 in Europe and in 1997 in the USA and Canada, resulting in the implantation of more than 100,000 devices in approximately 80,000 patients worldwide [6]. In 2005, the US Food and Drug Administration (FDA) approved invasive vagal stimulation as an additional treatment for recurrent and chronic depression after the study by Rush AJ et al. (2005) to demonstrate positive results in 205 subjects with a diagnosis of depression resistant pressure conventional treatment [7].

Despite the significant increase in the number of prescriptions for this type of therapy, the most widely used vagal stimulation systems still have limitations, especially because they are invasive in nature, such as the above procedure [6]. Other limitations are related to side effects, such as cough, hoarseness, voice changes and shortness of breath. In order to solve these problems, some devices seek similar results using a noninvasive model, Transcutaneous Vagal Nerve Stimulation (TVNs). TVNs devices induce depolarization in the atrial vagal branch, which anatomically provides better access for direct non-invasive stimulation of the vagus nerve through the X branch [6, 8, 9].

Additionally, recent studies from a group demonstrated optimization of vagal nerve activation and analgesic results through breath modulation. These studies were performed in patients with migraine, chronic or hypertensive pain and achieved significant results. The realization of the modulation is achieved through a group of individual devices: a pacing device, a device controller computer for sending the acquired breath signal through a pneumatic belt to the computer, and the Powerlab DAQ (AD Instruments) system for acquiring the signals of electrocardiogram (ECG) and respiration [10–13].

The aim of this study is to present the development of a unique wearable device capable of transcutaneous vagal stimulation in a noninvasive way and acquire process and store physiological signals in real time. The ECG signal is used posteriorly to obtain the Heart Rate Variability (HRV) and the breathing signal is used to initiate the stimulation. As a result, it is expected that the device will be compared to gold-standard equipment, but with the advantages of breathing modulation and integration into the same portable device.

2 Materials and Methods

2.1 Overview

The development of the transcutaneous vagal feedback stimulator was organized in three stages, being these separated by the electrical circuits of – Registry Interface and Control, Stimulation and Synchronization System; each module will be described in sub-items of the present chapter. Beyond the Transcutaneous Vagal Stimulation Device, the Project focuses a Portable and Wearable System. To satisfy these criteria, an elastic fabric shirt (polyester microfiber) was implemented with the following ornaments: sewn channels to organize the cables (Fig. 1.1) and a latex belt to obtain the breathing movement (Fig. 1.2 and 1.3.a).

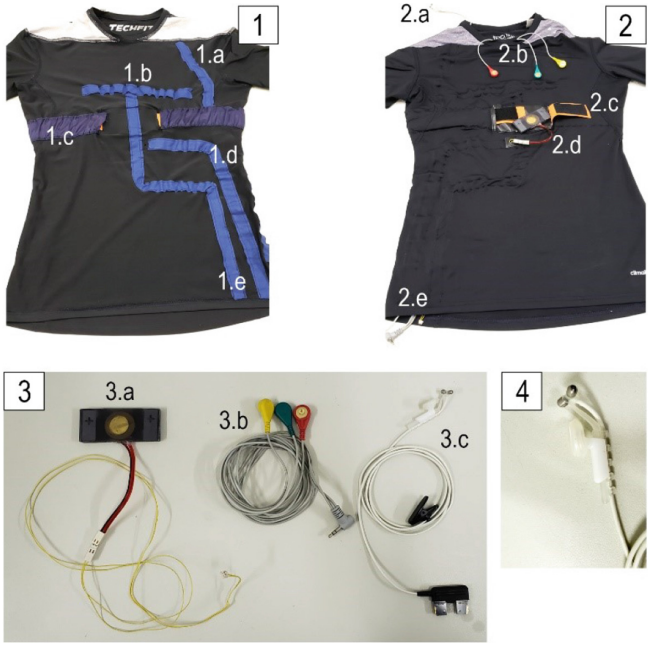

Fig. 1. Shirt with wearable technology and accessories. 1.1 - Shirt inverted. 1.2 Latex shirt, straps and belt; 1.3.a Breathing Transducer; 1.3.b ECG Cable and Breathing; 1.3.c and 1.4 Bipolar tympanic electrode.

The wearable model guarantees the autonomy of the patient during their daily use. Under experimental conditions, the model provides implementation of pilot testing and analysis response in remote monitoring (outside the laboratory environment). The use of the jacket is not mandatory for the experiment in a controlled environment. The accessories used for data collection and stimulation are shown in Fig. 1, which include the Breathing Transducer based on a piezoelectric sensor (see Fig. 1.3.a), made to respond as a comparative parameter for bioimpedance measurement; the transcutaneous vagal stimulation electrodes (see Fig. 1.3.c and 1.4 - the same electrodes used in Nemos® [14]); and the patient cable for electrocardiogram and bioimpedance measurements. The transducer, electrodes, and main acquisition specifications are detailed in this section.

2.2 Interface of Registry and Control

The integration interface between the user (patient, doctor and/or researcher) and the stimulation system is designed for viewing on mobile devices (smartphones and tablets). This design facilitates the distribution of updates, eases access and reduces equipment costs, and enables the remote monitoring of the routine of use by health professionals.

The communication protocol between the mobile device and the pacing system is performed through Bluetooth technology and the application was returned in MIT App Inventor, an open source application (see Fig. 2). There are two options that can be selected for the type of stimulation, the classic protocols described in the literature [6] or the vagal stimulation synchronized with the respiratory cycle. For the first option, you can select the parameters of: 1 or 25 Hz frequencies, stimulation current intensity (from 0.1 mA to 5.0 mA), duration of the stimulation train and the inter-train interval (ITI). Both options allow you to choose the length of the section.

Fig. 2. Application interface developed in MIT App Inventor

Physiological Signal Recording. The device performs the collection of two physiological signals: Respiratory cycle (CR) and Electrocardiogram (ECG). The electronic circuit for reading ECG and CR (through thoracic bioimpedance) has a main component called ADS1292R, the 24-Bit Analog Front-End for Biopotential Measurements of Texas Instruments®. Due to movement artifacts, a second wave of CR is obtained from a different system, which uses a belt having a transducer based on the piezoelectric sensor. The belt is attached to a custom shirt. Unlike the CR signal, the ECG does not act directly on the pacing system, but is an important parameter, since the signal is used for spectral analysis applied to heart rate variability (data to prove vagal modulation). In addition to this circuit, the analog filters and the 32-bit ARM Cortex-m3 microcontroller can be cited.

2.3 Stimulation System

This stage consists in the implementation of an electronic circuit responsible for the generation of electric pulses for activation of the auricular branch of the vagus nerve (ABVN). Recent research indicates that a current amount of 0.7 mA to 1.4 mA is enough to achieve the therapeutic effects cited in the Introduction [15]. The pain threshold varies among users and the amount of current should be adjusted according to medical advice. The modulation of the parameters is managed by a second Arm Cortex-m3 32bits microcontroller, without the need to use voltage transformers.

The microcontroller is used to receive information sent by the signal conditioning microcontroller and to define settings, such as operating mode (stimulation from literature or synchronized with CR). See Fig. 3 for complete circuit. Segment 1 converts a continuous current signal into a periodic square wave. Segment 2 is a quadruple voltage multiplier, with the objective of increasing the potential difference that will be switched to the stimulus train. Segment 3, on the other hand, is responsible for increasing or decreasing the signal strength and is connected to the PWM output of the microcontroller. Segment 4 is used to amplify the signal and, finally, segment 5 monitors the current applied to the patient.

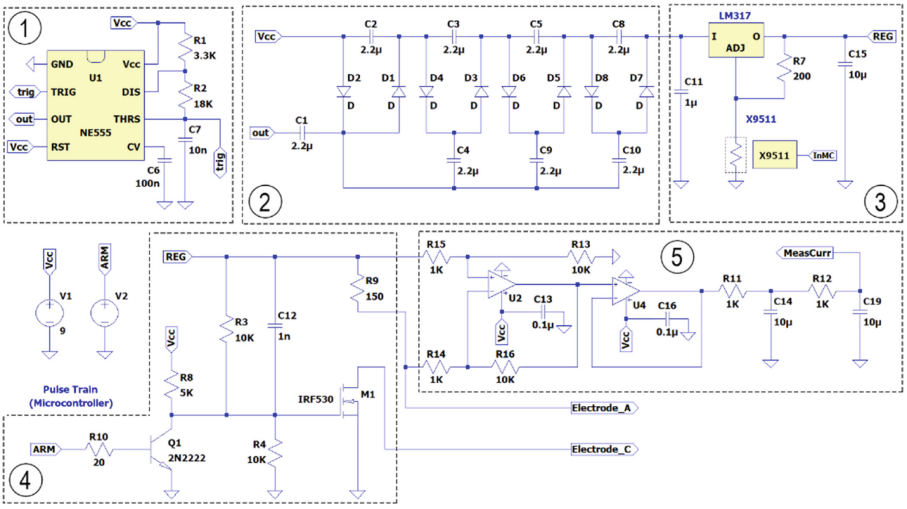

Fig. 3. Stimulation system electrical circuit

2.4 Synchronization System

The stimulation model synchronized with the RC will be the most explored protocol in this project. To detect the maximum peak of the exhalation phase of breathing, a real-time method was used. The first stage consists of removing the low-frequency fluctuation by deriving the recorded signal and this process eliminates the offset, but increases the action of the high-frequency noises. To attenuate this influence, a processing window of 20 points was defined and then a first order linear regression was calculated, and with the parameters of the extracted line, the variation rate of the angular coefficients obtained with each interaction was calculated, window of 20 points. The result was an amplitude gain in the expression of the maximum points of CR. Finally, we considered as target points, the peaks located in a portion 80% higher than the average amplitude of the 05 targets previously collected.

3 Preliminary Results

The device is under the final phase of development. In a first stage, the systems described were tested and validated individually and on the next stage, the integrated test were realized. Both stages produced satisfactory results. The RC signal was recorded by different sensors and compared, resulting in correlations with metabolic activity and correlation between sensors. There were identified artefacts on both technical models during a mechanical movement and new methodologies elaboration are in progress. The algorithm for peak detection satisfies the criteria of processing time and toughness during the analysis in rest period (see Fig. 4). The pattern of the pulses generated on System Stimulation were confirmed and the device is a promising alternative in hypertension and other pathologies.

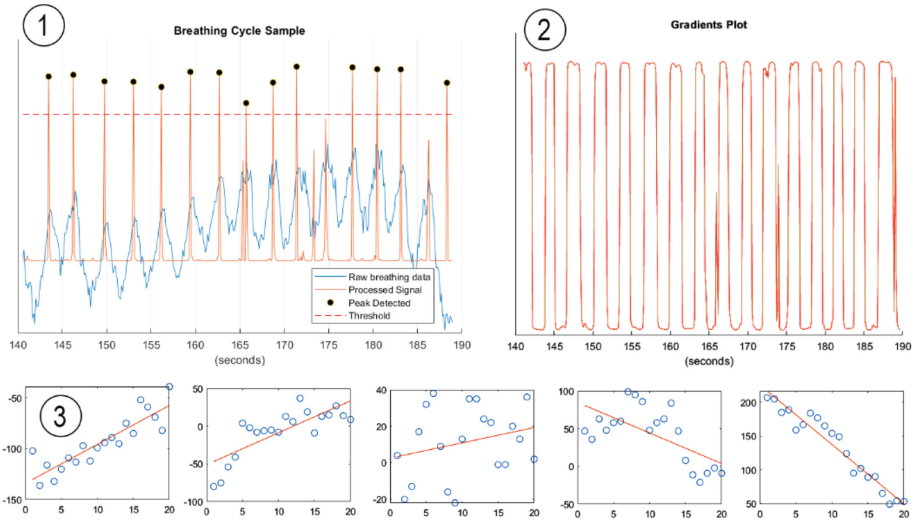

Fig. 4. Method for detecting the maximum peak of the exhalation phase of RC. 4.1 Raw signal, processed signal, peak detected and threshold; 4.2 Graph of linear regression gradients; 4.3 Clusters of the window to obtain the linear regression.

Vagal modulation was validated in a pilot study by spectral analysis of Heart Rate Variability (HRV), following the protocol described by Montano et al. [16]. The pilot study compared the proposed equipment to vagal stimulation equipment (without feedback) of the company Vitos tVNS Technologies GmbH. The signals were recorded on different days. The increase of high-frequency percentage (0.15 Hz to 0.4 Hz) of HRV, Vagal modulation response, was verified in both types of equipment, as shown in Table 1. The analyses were performed in the PowerLab software. The research next stage will extend the protocol to a greater number of volunteers to provide available data to statistical analyses.

Table 1. Parameters of the HRV analysis

Protocol	Segment	Length (sec.)	RR LF (%)	RR HF (%)
Vitos (Commercial)	Basal	95.32	25.97	**67.19**
Vitos (Commercial)	Stimulus	96.24	17.26	**78.26**
Developing prototype	Basal	130.70	29.91	**64.56**
Developing prototype	Stimulus	155.95	13.31	**81.51**

4 Conclusion and Discussion

The Current Equipment for Vagal Activation is mostly invasive. The closer equipment models, which are also non-invasive and portable, do not evaluate the physiological signals in real time and are not synchronized with the breath for optimization of the vagal activation, being less effectiveness. Furthermore, the presently existing equipment does not have worldwide manufactured and are not marketed directly in non-European countries, hindering the access of patients to the use of this technology. Another major advantage is that the equipment is easy to handle, wearable and can be controlled via mobile phone, which makes the utilization widely simple in the present day.

Conflicts of Interest Statement. The authors whose names are listed certify that they have no affiliations with or involvement in any organization or entity with any financial interest or non-financial interest in the subject matter or materials discussed in this manuscript.

References

1. Jennum, P., et al.: Welfare consequences for people with epilepsy and their partners: a matched nationwide study in Denmark. Seizure **49**, 17–24 (2017)
2. Lawrence, E., Vegvari, C., Ower, A., Hadjichrysanthou, C., De Wolf, F., Anderson, R.M.: A systematic review of longitudinal studies which measure Alzheimer's disease biomarkers. J. Alzheimer's Dis. **59**(4), 1359–1379 (2017)
3. Verrier, R.L., Tan, A.: Heart Rate, Autonomic Markers, and Cardiac Mortality (2009)
4. Meisenhelter, S., Jobst, B.C.: Neurostimulation for memory enhancement in epilepsy. Curr. Neurol. Neurosci. Rep. **18**(6), 1–9 (2018)
5. Engineer, C.T., et al.: Pairing speech sounds with vagus nerve stimulation drives stimulus-specific cortical plasticity. Brain Stimulation **8**(3), 637–644 (2015)
6. Cyberonics Inc.: Annual Report. VNS therapy system physician's manual. Houston, TX. http://dynamics.cyberonics.com/manuals. Accessed 25 July 2018
7. Rush, A.J., et al.: Vagus nerve stimulation for treatment-resistant depression: a randomized controlled acute phase trial. Biol. Psychiatry **58**(5), 347–354 (2005)
8. Clancy, J.A., et al.: Non-invasive vagus nerve stimulation in healthy humans reduces sympathetic nerve activity. Brain Stimulation **7**(6), 871–877 (2014)
9. Kraus, T., Kiess, O., Hösl, K., Terekhin, P., Kornhuber, J., Forster, C.: CNS BOLD fMRI effects of sham-controlled transcutaneous electrical nerve stimulation in the left outer auditory canal - a pilot study. Brain Stimulation **6**(5), 798–804 (2013)

10. Frangos, E., Ellrich, J., Komisruk, B.R.: Non-invasive access to the vagus nerve central projections via electrical stimulation of the external ear: fMRI evidence in humans. Brain Stimulation **8**(3), 624–636 (2015)
11. Busch, V., Zeman, F., Heckel, A., Menne, F., Ellrich, J., Eich-Hammer, P.: The effect of transcutaneous vagus nerve stimulation on pain perception - an experimental study. Brain Stimulation **6**, 202–209 (2013)
12. Sclocco, R., Garcia, R.G., Gabriel, A., Kettner, N.W., Napadow, V., Barbieri, R.: Respiratory-gated auricular vagal afferent nerve stimulation (RAVANS) effects on autonomic outflow in hypertension. In: 39th Annual International Conference of the IEEE Engineering in Medicine and Biology Society (EMBC) (2017)
13. Fisher, H., Stowell, J., Garcia, R., Sclocco, R., Goldstein, J., Napadow, V., Barbieri, R.: Acute effects of respiratory-gated auricular vagal afferent nerve stimulation (RAVANS) in the modulation of blood pressure in hypertensive patients. In: Computing in Cardiology, vol. 45 (2018)
14. NEMOS® t-VNS for treatment of drug-resistant epilepsy. http://cerbomed.com. Accessed 25 July 2018
15. Gancheva, S., et al.: Constant hepatic ATP concentrations during prolonged fasting and absence of effects of Cerbomed Nemos® on parasympathetic tone and hepatic energy metabolism. Mol. Metab. **7**, 71–79 (2018)
16. Montano, N., et al.: Heart rate variability explored in the frequency domain: a tool to investigate the link between heart and behavior? Neurosci. Biobehav. Rev. **33**, 71–80 (2008)

Development of a Bimodal Electronic Resuscitator Prototype for Adult Patients

Andrea Paola Pineda-Espinosa[1(✉)], Ana Paulina Barba-Muñoz[1], Rodrigo Antonio Sánchez-Mateos[1], María del Carmen Arquer-Ruiz[2], and José Israel Hernández-Oropeza[1]

[1] Faculty of Engineering, Universidad La Salle, Mexico City, Mexico
andype28@hotmail.com, jose.hernandez@lasalle.mx
[2] UMAE Pediatric Hospital, Centro Médico Nacional Siglo XXI, IMSS, Mexico City, Mexico

Abstract. Resuscitators are devices that favor resuscitation in two types of arrests: respiratory and cardiopulmonary. The correct application of resuscitation can save lives and prevent neurological sequelae; however, few people are trained to give this kind of medical attention. In this work, we present the development of a bimodal electronic resuscitator prototype for adult patients focused on automating the process of respiratory and cardiopulmonary ventilation. For the prototype development, the verification of the compatibility of the working range for adult patients and the pump control completion, that determines the insufflation required by the patient, were regarded. The insufflation has a feedback system to measure the pressure that is provided to the patient and correctly regulate it. The action of the pump generates two treatment options depending on the type of procedure that is required. The prototype considered safety parameters to avoid health consequences and assure the security of the patient. The electronic resuscitator prototype is automatic and portable.

Keywords: Electronic resuscitator · Prototype · Respiratory arrest · Pulmonary arrest

1 Introduction

A resuscitator is a device that favors resuscitation and life support. It essentially consists of a mask, a self-inflating bag or balloon, a reservoir bag or an oxygen connection and a PEEP valve to maintain positive pressure during expiration [1].

There are two operating modes in these devices: in the presence of pulse or in its absence. This implies giving treatment at two different situations, a patient in respiratory arrest and a patient in cardiopulmonary arrest. A respiratory arrest implies an interruption in the pulmonary gas exchange. When it occurs for more than 5 min it could cause irreversible damage to vital organs such as the brain [2]. For this type of arrest, it is necessary to perform 1 compression every 5 or 6 s. Cardiorespiratory arrest refers to an abrupt, unexpected and reversible interruption of the mechanical activity of the heart and respiration [3]. To reverse the process, it is necessary to perform cardiopulmonary resuscitation (CPR) maneuvers. For adults, 2 insufflations for every 15 compressions, with a total of 100 to 120 compressions per minute [4].

© Springer Nature Switzerland AG 2020
C. A. González Díaz et al. (Eds.): CLAIB 2019, IFMBE Proceedings 75, pp. 601–605, 2020.
https://doi.org/10.1007/978-3-030-30648-9_79

Both respiratory and cardiopulmonary arrests are two medical emergencies that have high impact within the mortality statistics of Mexico. On one hand, 70% of heart at-tacks occur at home or in public spaces, of which only 5% are treated with CPR [5]. On the other hand, respiratory diseases are in tenth place in causes of death, this includes respiratory arrest [6]. Based on the above, the National Center for Health Technology Excellence (CENETEC) states that the possibility of surviving in case of an emergency of these types increases by 30% if adequate resuscitation is received [7]. Community training in basic CPR and public access to an automated external defibrillator (AED) can save lives and prevent disabling neurological sequelae [8].

Therefore, this project seeks to facilitate the task of resuscitation by automating the ventilations that are provided to the patient during the application of this technique, considering safety parameters, such as the critical pulmonary pressure. These parameters are important because could prevent neurological sequels and bronchoaspiration.

2 Materials and Methods

This project was developed in the Electromedicine Laboratory of the Faculty of Engineering of Universidad La Salle. For the design of the electronic resuscitator prototype, specific parameters for adults were considered and an artificial lung was used to perform the tests. Five stages were contemplated in the methodological strategy: signal reading, conditioning, analog-digital conversion, processing and control and visualization of the signal in real time and correlation of the signals.

Concerning the reading of the signal, a piezoresistive silicon pressure sensor was used. The sensor was characterized, and its linear behavior was verified. The linearity of the sensor was confirmed considering the working range. The signal obtained was then conditioned using an operational amplifier in a differential configuration. Subsequently the analog-digital conversion was carried out with the help of an Arduino UNO. Finally, signal processing was performed to control the air pump that provides mechanical ventilation to the patient with signal feedback emitted by the inflation of the lung.

3 Results

A feedback was performed in a physical manner by adapting the output of the pump in which the mask would be placed to a system of hoses. When the tests were carried out, the hose system allowed to verify the measurement of the insufflation of the test lung with a Homecare Duplex 2600 manometer in addition to connecting to the pressure sensor. Ten measurements of three different control values were taken for the prototype (20, 30 and 40 mmHg) through the adjustment of the sensor with a Homecare Duplex 2600 baumanometer. These parameters contemplate a safety ventilation for an adult patient. First, the given voltage was noted without any alteration, being 2.522 V the reference for the positive output feeding the circuit to 5 V. For the first metric 20 mmHg was measured which corresponds to a value of 27.2 cmH_2O for an average adult whose normal pressure is between 25 and 30 cmH_2O [9]. Then it was measured

with 30 mmHg, equivalent to 40.8 cmH_2O, that is, a high level, and then at 40 mmHg, which corresponds to the limit level to avoid endangering the patient from a bronchoaspiration [3], with a value of 54.4 cmH_2O. The results are shown in Table 1, considering the average voltage of each parameter.

Table 1. Experimental average voltage

Pressure (mmHg)	Average voltage (V)
20	2.4999
30	2.5029
40	2.5061

From the linear regression analysis of the experimental data, Eq. (1) resulted:

$$y = 0.0003x + 2.4937 \tag{1}$$

where x represents the pressure in mmHg and y is the average voltage in V.

The value of $R^2 = 0.9997$ obtained from the analysis confirmed the linearity of the sensor in the range of pressures in which it was required to function. Regarding the conditioning stage of the signal, the amplification was carried out with an operational amplifier in differential configuration. The analogue-digital conversion for the signal processing and for the control of the pump was made through the Arduino UNO connection. A voltage of 5 V and the resolution of the Arduino UNO, of 1023 bits, were considered. For the coupling of the pump, a Darlington pair was used. Also, a connection of hoses that feed back to the sensor, as well as used for the artificial lung in the prototype proves. Arduino programming was required to control the pump according to the type of arrest. The pump is turned on and off according to the times established in each type of arrest as can be seen in Fig. 1.

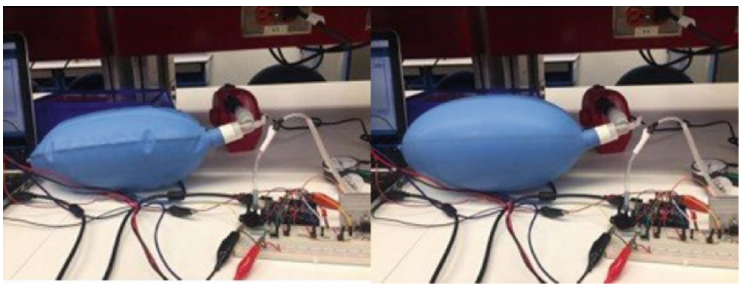

Fig. 1. Emptying the artificial lung at a pressure greater than 20 mmHg (left) and filling the artificial lung at a pressure equal or less than 20 mmHg (right).

A code was developed in Arduino, which includes the Arduino UNO connection, the analog-digital conversion; along with the evaluation of patient safety parameters and pump control for both types of arrest.

In the case of respiratory arrest, a cycle was developed in which the signal coming from the sensor was constantly measured during the 4 s in which the exhalation is performed, so that, if the pressure value is lower than the readjustment of the voltage value corresponding to approximately 20 mmHg, it contemplates 2 s of insufflation. For the other operating mode, it started by giving two insufflations of approximately 1.5 s each (considering the readjustment of pressure), and a cycle was performed that considers the constant pressure measurements during the 15 s in which the compressions are performed. With respect to the pump, the power supply is the crucial factor to avoid exceeding the appropriate insufflation pressure level and consequently avoid lung injury, for this reason the alarm and patient safety control system is an essential part of both sections of the code, that is, in both types of arrests.

On the other hand, the power circuit contemplates the power values for the entire main circuit; however, in a second version of the prototype it would be necessary to consider a charger circuit to recharge the 12 V batteries that the prototype uses.

The generated pulses depend of the arrest type. For respiratory resuscitation, the pulses had a ratio of 1:2; that means expiration lasts twice as long as inspiration. On the other hand, two pulses were required to perform cardiopulmonary resuscitation. All of these, considering that the techniques are equivalent to the timing that is carried out during a manual resuscitation.

For the portable implementation of the bimodal electronic resuscitator prototype, the power was supplied by two 12 V batteries in serial connection. The voltages required were 5, 7 and −7 V, being regulated from the battery supply. The electronic components and the pump were placed inside a wooden box to which two metal handles were added for easier transportation. The complete device can be seen in Fig. 2.

Fig. 2. Internal (left) and external (right) views of the prototype.

In Fig. 2 (left) it is noticed that there is a surplus in the dimensions; however, this is necessary due to the placement of the pump inside the box. Although the prototype design of the bimodal electronic resuscitator shown is functional and lightweight, as seen in Fig. 2 (right), in the second version the reduction in size and improvement of the position of use with the implementation of a mask and longer hose, is being considered for patient comfort.

4 Conclusions

The determining factors in the development of the project were the characterization and control of the air pump to establish the adequate ventilatory response according to the required operation mode. The control values considered for the development of the bimodal electronic resuscitator prototype are very important because they serve as safety parameters. The developed electronic resuscitator prototype avoided the over-expansion of the artificial lung through a control of the supplied pressure, implying that the prototype could help by automating the ventilations that is provided to the patient during the application of this technique. Both types of ventilation, respiratory and cardiopulmonary, considered parameters of conventional manual techniques, established in the code in order to apply a correct resuscitation for each type of arrest. However, despite the fact that the portable implementation of the prototype was achieved and that both the interaction with the user through LEDs and push buttons and the bimodal control were carried out in a satisfactory manner, it was identified that the mechanical design of the prototype could improve, since it was not so comfortable for users. Finally, the control could be improved from the observed parameters, in such a way that when the sensor captured a signal different from that of the pump, the flow and the pressure supplied reduce or increase. For this to happen it would be necessary to implement a coupling circuit that allows the handling of the pump by PWM; in this way an intelligent system could be made that would detect the adequate flow for each patient.

References

1. Iberomed Homepage. https://www.iberomed.es/blog/2018/02/28/que-son-y-para-que-sirven-los-resucitadores-manuales/. Accessed 07 Jan 2019
2. Manual MSD Homepage. https://www.msdmanuals.com/es-mx/professional/cuidados-cr%C3%ADticos/paro-respiratorio/revisi%C3%B3n-sobre-el-paro-respiratorio. Accessed 20 Aug 2018
3. Nodal-Leyva, P.E., López-Hector, J.G., De la Llera-Domínguez, G.: Paro cardiorespiratorio (PCR). Etiología. Diagnóstico. Tratamiento. Rev Cubana Cir 45(3–4) (2006)
4. Meaney, P., et al.: Calidad de la reanimación cardiopulmonar: mejora de los resultados de la reanimación cardíaca intra y extrahospitalaria. https://cpr.heart.org/idc/groups/heart-public/@wcm/@ecc/documents/downloadable/ucm_464150.pdf. Accessed 19 Aug 2018
5. El Universal Homepage. http://www.eluniversal.com.mx/articulo/nacion/sociedad/2017/04/21/ataques-cardiacos-primera-causa-de-muerte-en-mexico. Accessed 19 Aug 2018
6. INEGI Homepage. http://www3.inegi.org.mx/rnm/index.php/catalog/407. Accessed 19 Aug 2018
7. CENETEC Homepage. http://www.cenetec-difusion.com/CMGPC/IMSS-633-13/ER.pdf. Accessed 19 Aug 2018
8. Publimetro México Homepage. https://www.publimetro.com.mx/mx/noticias/2017/04/28/cruz-roja-quiere-establecer-record-guinness-reanimacion-cardiopulmonar-rcp.html. Accessed 19 Aug 2018
9. Tobin, M.J.: Principles and practice of mechanical ventilation, 3rd edn. McGraw-Hill, China (1994)

System to Continuous Differential Acquisition of Arterial Blood Pressure During Tilt Test

Carmenchu Regueiro-Busoch[1(✉)], Carmen Busoch-Morlán[1], René Joaquín Díaz-Martínez[2], and Angel Regueiro-Gómez[1]

[1] Universidad Tecnológica de La Habana (CUJAE), La Habana, Cuba
carmenchu@automatica.cujae.edu.cu
[2] Tecnologico de Monterrey, Monterrey, Mexico

Abstract. This work discusses the design of a new method for the continuous differential record of the variable Arterial Blood Pressure (PSA) for noninvasive method (oscillometric) to be employed during the study of the vasovagal syncope in subjects with problems of peripheral circulation during the tilt test. We analyze the different sections of the proposed system, it includes the selection and characterization of the pressure transducer for the differential measurement of the variable; as well as the blocks of the analog channel (multiplexer, amplifier, and filters) and the ARDUINO ONE platform to achieve the control of the acquisition of the data; the control of the filling and emptying of cuffs and besides the communication with a station of processing and control through an interface developed in C #. The obtained results evidence adequate linearity and frequency response, allowing to the study of the variable PSA during the development of Tilt test.

Keywords: Tilt test · Continuous differential record · Arterial blood pressure

1 Introduction

The Tilt test (Fig. 1) is a clinical tool to cardiovascular diagnoses, specialty during the determination of vagal syncope (neurocardiogenic syncope) [1–3]. In this test most of the patients without cardiogenic and with syncope of unknown cause, reproduce the vasovagal symptoms (bradycardia and hypotension) before the "orthostatic stress". The neurocardiogenic syncope happens when the part of the nervous system that controls the blood flow changes the heart rhythm and it reduces the arterial pressure for a short time; then, less blood flows to the brain and the result is a faint of people. The clinical exam has been used for more than 20 years and studies are reported with diverse protocols to explain the variability of the results [4].

The test consists typically of two stages: a spontaneous one and a pharmacological one, both varying the grades of inclination. The subject is placed in the bed (0°) and some basal vital signs are previous measured, and then the clinical specialist proceeds to the controlled inclination. In the spontaneous phase, the arterial pressure is measured every five minutes when the subject has more symptoms frequently. If the patient develops syncope, pre-syncope or hypotension and/or bradycardia symptomatic, the test is considered positive and it concludes in that instant. If the symptoms don't appear

© Springer Nature Switzerland AG 2020
C. A. González Díaz et al. (Eds.): CLAIB 2019, IFMBE Proceedings 75, pp. 606–610, 2020.
https://doi.org/10.1007/978-3-030-30648-9_80

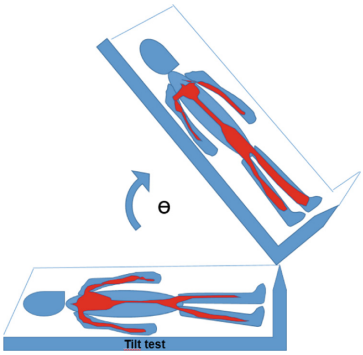

Fig. 1. Representation of a clinical tilt test (blood pressure changes with different positions).

after thirty minutes of inclination, the patient is returned to the decubitus position and clinical specialist proceeds to the pharmacologic stage where apply certain drugs to the patient.

During the cardiovascular study of patients in tilt test is necessary to characterize the recording of physiologic variables, among those variables is the arterial blood pressure (ABP) [5, 6]. Nowadays it is possible the intermittent measurement of the ABP for noninvasive methods by means of the use of a pressure transducer and cuff (manual or automatic) [7–9]; but in the cardiovascular studies it is necessary to know and study in continuous way the behavior of this important variable during the interval of time that the tests are applied in the bed on the peoples under study in the different work positions.

2 Materials and Method

The Fig. 2 shows the fundamental blocks of system proposed for the differential continuous measurement of the ABP variable in tilt tests, starting from the employment of two cuffs placed in the extremities (arm and leg) of people during the tests.

Two P2000-501G transducers were selected as sensor of pressure (0-32 kPa), and they are together to its respective cuffs and coupled to an analogical multiplexer (CI4052), which permits to take alternating samples of each one according to the sampling frequency (fm = 500 Hz). An instrumentation amplifier (AD620) and pass-band filters (0,5 Hz < Bw < 40 Hz) allow to signal conditioning, giving the appropriate levels to the A/D converter of the platform selected with 10 b of resolution ($error_t$ < 2 mmHg). The acquired samples are sent (USB way) to the PC station for their representation.

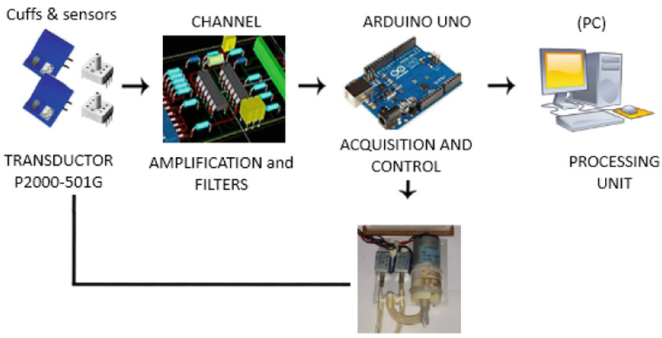

Fig. 2. Functional blocks of proposed system to continuous differential acquisition of ABP during tilt test.

3 Results and Discussion

Figure 3 shows the good linearity and the bandwidth obtained during the verification of acquisition channel using resistors and capacitors with 5 and 20% of tolerances.

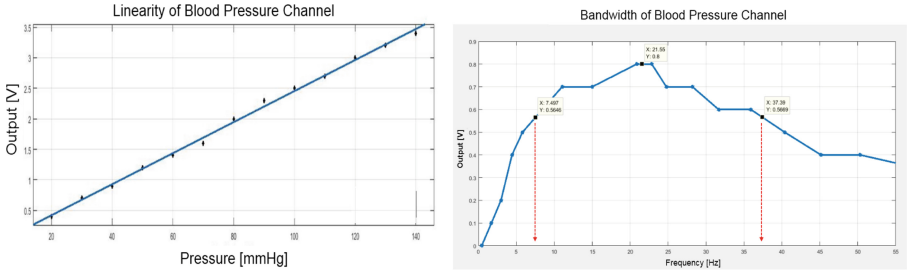

Fig. 3. Linearity and bandwidth of blood pressure channel.

Figure 4 shows the interface development in C# to obtain the graphic representation of acquired data during the tilt test.

In the higher section exits the possibility to introducing some data for the appropriate recording of the received information, among them the used communication port, the name and last names of the patient, the place where it is preferred to store the data and also, it is automatically included Date and Time of the acquisition. In the higher right section exists two boxes: Start and Stop, which are used to give the beginning orders or detention of data records related with ABP in both corporal sections. In the center of the developed interface, two windows are shown with the pressure registers obtained during the tilt test.

The information stored in the computer can be analyzed with other mathematical tools of more power, like it can be MATLab to facilitate the spectral-time analysis of different physiological variables obtained during the cardiovascular studies on tilt test.

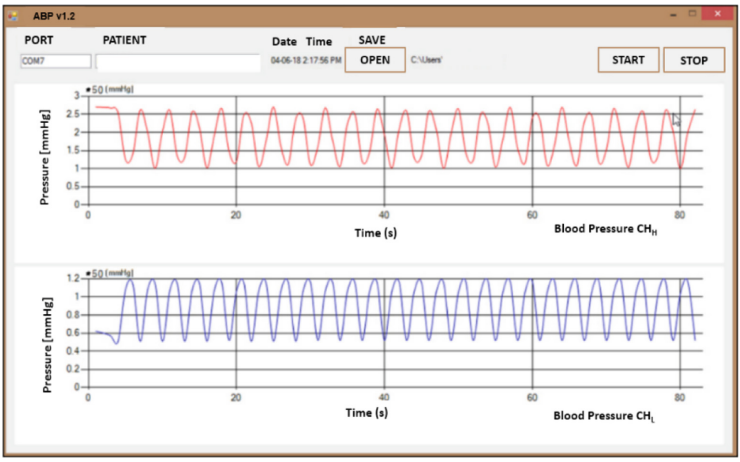

Fig. 4. Interface developed to show the ABP signals related with patients during tilt test.

4 Conclusion

In the development of the system for differential continuous acquisition of ABP different sections have been verified with good results: good linearity and answer of frequency of the channel, easy handling of the control of fill-casting of the cuffs starting from the employment of digital terminals of the platform of development employee; as well as a simple interface has been developed that allows the development of future spectral-time analysis with the acquired information of the ABP variable.

References

1. Teodorovich, N., Swissa, M.: Tilt table test today - state of the art. World J. Cardiol. **8**(3), 272–282 (2016)
2. Eza-Nunez, P., et al.: Comparison of three diagnostic tests in detecting vestibular deficit in patients with peripheral vestibulopathy. J. Laryngol. Otol. **130**(2), 145–150 (2016)
3. Naik, C.: Investigating a patient of vertigo: where do we stand today? Indian J. Otol. **23**(2), 63–66 (2017)
4. Nova, P.: Cerebral blood flow, heart rate, and blood pressure patterns during the tilt test in common orthostatic syndromes. Neurosci. J. 1–20 (2016)
5. Shirley, L., et al.: A review on non-invasive hypertension monitoring system by using photoplethysmography method. Mov. Health Exerc. **6**(1), 47–57 (2017)
6. Cohen, Z., Haxha, S.: Optical based sensor prototype for continuous monitoring of the blood pressure. IEEE Sens. J. 1–12 (2017)

7. Zheng, D., et al.: Effect of respiration on Korotkoff sounds and oscillometric cuff pressure pulses during blood pressure measurement. Med. Biol. Eng. Comput. **52**, 467–473 (2014)
8. Zhang, G., et al.: Hybrid optical unobtrusive blood pressure measurements. Sensors **17**, 1–12 (2017)
9. Kiselev, A., et al.: Comprehensive assessment of cardiovascular autonomic control using photoplethysmograms recorded from the earlobe and fingers. Phys. Meas. **37**, 580–595 (2016)

Assessment of AMR-ACB System Using Maghemite Nanoparticles in Theranostic Concentration

Leopoldo de Jesus Prates[1], Fabiano Carlos Paixão[1], Marli Leite de Moraes[1], Regina Célia Coelho[1], Robson Rosa da Silva[2], and Carlos Marcelo Gurjão de Godoy[1(✉)]

[1] Institute of Science and Technology, UNIFESP, São José dos Campos, SP, Brazil
gurjaogodoy@gmail.com
[2] Institute of Chemistry, UNESP, Araraquara, SP, Brazil

Abstract. Alternating current biosusceptometry assembled with anisotropic magnetoresistive sensor (AMR-ACB) is a radiation-free technique that can enable the real-time monitoring of magnetic nanoparticles in biomedical applications. The aim of this study is to assess the capability of a multi-channel AMR-ACB system in detecting maghemite nanoparticles (MN) in concentrations used in therapeutic and diagnostic (theranostic) applications, such as oncology, multimodal anticancer therapy, or magnetic resonance imaging. The axial sensibility of the AMR-ACB system was successfully characterized in a bench-top study using MN in different concentrations and distances. The MN sample was aligned with the detection axis of the AMR-ACB system, and then it was moved at fixed distances from 0 to 16 mm. The test was repeated with different MN concentrations. The results show that the AMR-ACB system is capable of detecting samples of MN with a concentration of 0.3 mg/mL, and the output signal is directly proportional to the MN concentration. The output signal exhibits exponential decaying with distance, where the signal amplitude at 8.5 mm is approximately 10% of the signal at 0 mm. This work shows that the AMR-ACB system has adequate sensibility to be employed in in vivo studies to detect MN in theranostic concentrations as well as demonstrates the potential of this magnetic method as a possible tool for future diagnosis.

Keywords: Maghemite nanoparticle · AC Biosusceptometry · Magnetoresistive sensor

1 Introduction

Magnetic resonance imaging (MRI) and magnetic particle imaging (MPI) are expensive technologies that require superparamagnetic iron oxide nanoparticles as contrast agents [1]. A suitable low-cost imaging technique, known as AC biosusceptometry (ACB), is a radiation-free method that enables real-time monitoring of magnetic nanoparticles in the bloodstream [2]. The device presented by Paixão et al. [3] serves as an innovative magnetic device that combines an anisotropic magnetoresistive (AMR) sensor and

© Springer Nature Switzerland AG 2020
C. A. González Díaz et al. (Eds.): CLAIB 2019, IFMBE Proceedings 75, pp. 611–615, 2020.
https://doi.org/10.1007/978-3-030-30648-9_81

ACB to evaluate gastrointestinal motility in dogs. This device, known as the AMR–ACB System, replaced ACB detection coils by an array of AMR sensors, thereby increasing spatiotemporal resolution and improving the evaluation of the digestive tract [3] using ferrite powder as magnetic contrast agents. Although the AMR–ACB System has been successfully characterized to assess physiological parameters, its sensibility has not been evaluated yet to detect magnetic nanoparticles. As maghemite nanoparticles (MN) can exhibit low toxicity [4] and, at appropriate concentrations, can be used for simultaneous therapy and diagnosis (theranostics) applications [4, 5], the present work aims to evaluate the aforementioned system's capability to detect MN at theranostic concentrations. Further, it seeks to quantify the lower concentration, and the greater distance of the MN sample can be detected by the AMR–ACB System. Moreover, the preliminary study will support the kind of applications that can be developed using this technology, such as cardiology, nephrology, oncology, or some form of brain study.

2 Methods

2.1 AMR-ACB System

The said system is composed of two excitation coils arranged coaxially, and an array of 36 AMR sensors is arranged in a first-order gradiometric configuration with just one reference sensor (Fig. 1). The excitation coils were made with 140 winds, and the detection system was composed with a one-axis AMR sensor (HMC1001, Honeywell Inc, US). A complete description of this device has been provided by Paixão et al. in an earlier work [6], and the entire electronic innovation developed is under the "patent pending" status (BR PI-1000419-0).

Fig. 1. (A) Photo of the AMR–ACB System; (B) Schematic diagram where 1 represents an array of 36 AMR sensors, 2 denotes the reference sensor, while 3 and 4 are the excitation coils.

2.2 Nanoparticles

The ionic ferrofluid produced in our laboratory comprises MN with a diameter of 11.2 nm (estimated as crystal domain averaged by X-ray diffraction) and an initial concentration of 6 mg/mL (1.65×10^{15} particles/mL, determined by the phenolphthalein method). Based on earlier works that demonstrate maghemite concentrations suitable for theranostic applications [4, 5], the samples tested were 1 mL-aliquot at the

concentrations of 1.2, 0.75, 0.6, and 0.3 mg/mL. Furthermore, the MN were placed in Eppendorf vials to perform system characterization.

2.3 Bench Top Experiments

Characterization of the AMR–ACB System was performed in order to ascertain the dependence profile of the magnetic field at different distances and MN concentrations. For axial sensitivity tests, the MN sample (1.2 mg/mL) was aligned with the detection axis of an AMR sensor, and subsequently, it was moved at fixed distances from 0 to 16 mm (step of 0.5 or 1 mm), which is a feasible distance for mouse and/or rat organs. For the characterization of sensitivity pertaining to MN concentration, an MN sample (as detailed above) was placed in front of the magnetometer, and the signals were recorded. Moreover, a fixed plastic pachymeter was used to position each MN sample in front of the AMR sensor meticulously. The collected data measurements were processed using Matlab routines (MathWorks Inc., USA). It is important to mention that only one AMR sensor was used in this work

3 Results

The magnetic signal decays exponentially with the increasing distance between the MN sample and the magnetometer. Figure 2A depicts the normalized signal indicating this behavior. The signal detected for the MN sample fixed at 8.5 mm from the magnetometer is approximately 10 times lesser than the sample placed in front of the sensor. The magnetic signal measured increases directly with the expansion of the MN sample concentration (Fig. 2B). Further, the increase in the magnetic signal demonstrates a linear behavior at the concentration assessed. Figure 2C shows a sample of the magnetic signal recorded by the AMR sensor for the 0.3 and 1.2 mg/mL MN samples placed directly in front of it. The graphic representation shows the signal and electronic noise amplitude.

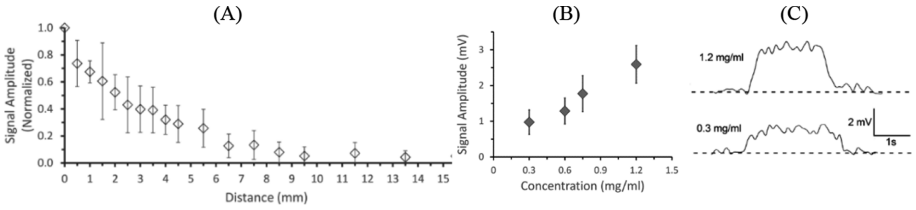

Fig. 2. Variation of the magnetic field detected by the ACB–AMR System as a function of the (A) axial distance between the MN sample (1.2 mg/mL) and the magnetometer; (B) the MN sample concentration placed in front of the AMR sensor (average ± SD, n = 10); (C) Sample of the output signal recorded for the 0.3 and 1.2 mg/mL MN samples placed in front of the magnetometer. The signal amplitude (Vrms) of the two samples are 1.35 and 2.82 mV, respectively.

4 Discussion

This work presents a characterization of the AMR–ACB System in order to detect the MN. The recorded signal's exponential decay is in accordance with that of the previous work [3]. The results showed that at a higher concentration, the MN sample allowed the improvement of the signal-to-noise ratio. Further, they show that the ACB–AMR System was capable of detecting MN samples with a concentration of 0.3 mg/mL placed in front of the sensor, and the output signal is directly proportional to the MN concentration. The said signal demonstrates exponential decaying with the distance, wherein the signal amplitude at 8.5 mm is approximately 10 times lesser than the sample in front of the sensor. Although the AMR–ACB System's sensitivity seems to be lesser than the traditional ACB built with coil detection [2], the former presents the advantage of having more detector sensors in the same area than only one coil, as discussed by Paixão et al. [3], and it has the capability to capture real-time magnetic images [6]. The MN used in this work show size (diameter of 11.2 nm) and concentration (0.3–1.2 mg/mL) compatible with those of theranostic applications in MRI [5], oncology, and multimodal anticancer therapy [4].

5 Conclusion

The results show that the AMR-ACB system can be used to detect and assess magnetic maghemite nanoparticles at concentration levels suitable for theranostic applications, allowing this technology to be applied in animal studies beyond the proven performance in the gastroenterology field.

Funding. The Brazilian agencies FINEP and FAPESP have supported this work.

Conflict of Interest. The authors do not have any conflicts of interest to declare.

References

1. Wu, L.C., Zhang, Y., Steinberg, G., Qu, H., Huang, S., Cheng, M., Bliss, T., Du, F., Rao, J., Song, G., Pisani, L., Doyle, T., Conolly, S., Krishnan, K., Grant, G., Wintermark, M.: A review of magnetic particle imaging and perspectives on neuroimaging. Am. J. Neuroradiol. **40**(2), 206–212 (2019)
2. Próspero, A.G., Quini, C.C., Bakuzis, A.F., Fidelis-de-Oliveira, P., Moretto, G.M., Mello, F.P.F., Calabresi, M.F.F., Matos, R.V.R., Zandona, E.A., Zufelato, N., Oliveira, R.B., Miranda, J.R.A.: Real-time in vivo monitoring of magnetic nanoparticles in the bloodstream by AC biosusceptometry. J. Nanobiotechnol. **15**(1), 22 (2017)
3. Paixão, F.C., Corá, L.A., Américo, M.F., Oliveira, R.B., Baffa, O., Miranda, J.R.A.: Development of an AMR-ACB array for gastrointestinal motility studies. IEEE Trans. Biomed. Eng. **59**(10), 2737–2743 (2012)
4. Kuchma, E.A., Zolotukhin, P.V., Belanova, A.A., Soldatov, M.A., Lastovina, T.A., Kubrin, S.P., Nikolsky, A.V., Mirmikova, L.I., Soldatov, A.V.: Low toxic maghemite nanoparticles for theranostic applications. Int. J. Nanomed. **12**, 6365–6371 (2017)

5. Kluchova, K., Zboril, R., Tucek, J., Pecova, M., Zajoncova, L., Safarik, I., Mashlan, M., Markova, I., Jancik, D., Sebela, M., Bartonkova, H., Bellesi, V., Novak, P., Petridis, D.: Superparamagnetic maghemite nanoparticles from solid-state synthesis – their functionalization towards peroral MRI contrast agent and magnetic carrier for trypsin immobilization. Biomaterials **30**(15), 2855–2863 (2009)
6. Paixão, F.C., Fonseca, P.R., Grossklauss, D.B.B.S., Baffa, O., Miranda, J.R.A.: Development of an automated alternating current biosusceptometer to acquire magnetic images. In: 1st Annual IEEE Healthcare Innovation Conference of the IEEE EMBS, Houston, TX, USA, pp. 139–142 (2012)

Fabrication and Study of Organic Nanomaterials as Photosensitizers for Photodynamic Therapy

Nelly Monjaraz-Carrillo[1(✉)], Alejandro Valdez-Calderón[2], Yunuén D. Solorio-Cendejas[2], Gabriel Ramos-Ortiz[2], and Mario Rodríguez[2(✉)]

[1] División de Ciencias Ingenierías, Universidad de Guanajuato, 37000 León, Guanajuato, Mexico
ng.monjarazcarillo@ugto.mx
[2] Centro de Investigaciones en Óptica A.C., A.P. 1-948, 37000 León, Guanajuato, Mexico
mrodri@cio.mx

Abstract. During the last decade, organic nanomaterials have emerged as an exciting research area due to their chemical, magnetic, and optical properties. In biomedicine, the possibility of the nanomaterials to produce reactive oxygen species (ROS) and their luminescence properties are used for the diagnostic and treatment of some specific diseases. Photodynamic therapy (PDT) is an unintrusive procedure that involves the photoactivation, with a specific wavelength, of a photosensitizer (PS) to produce ROS, especially singlet oxygen, which is the responsible for provoking damage to precise cells; however, its performance would increase if we developed the photosensitizers as nanoparticles. In this work, we reported the study and fabrication of silica core-shell nanoparticles (SNP). These nanomaterials were manufactured by a microemulsion method using an inert or photoluminescent polymer as a core. The surface of the nanoparticle was functionalized with Thionine colorant, which was previously tested as a photogenerator of ROS. The optical and morphological properties of nanoparticles were evaluated by UV-Vis spectroscopy, photoluminescence, and scanning electron microscopy (SEM). Finally, the generation of singlet oxygen was evaluated using an indirect test, by using as an excitation source, a green laser (532 nm). The results indicate that the photoluminescent SNPs generate singlet oxygen so they could be considered as a PS.

Keywords: Nanoparticles · Photodynamic Therapy · Photosensitizer · Singlet oxygen

1 Introduction

Since the first clinical application of photodynamic therapy (PDT) for cancer treatment in the 1960s [1, 2], this methodology showed several advantages. Photodynamic therapy (PDT) is a non-intrusive procedure that involves the photoactivation, with a specific wavelength, of a photosensitizer (PS) to produce ROS, especially singlet

© Springer Nature Switzerland AG 2020
C. A. González Díaz et al. (Eds.): CLAIB 2019, IFMBE Proceedings 75, pp. 616–623, 2020.
https://doi.org/10.1007/978-3-030-30648-9_82

oxygen, which is then responsible for provoking damage to a specific tissue. PDT is used predominantly in oncological pathologies, such as high-grade dysplasia, carcinoma in situ (buccal, cervix, skin, among others) and some other malignancies [3].

1.1 Photodynamic Therapy as a Novel Treatment

PDT consists of a non-surgical and non-invasive means, which provides an efficient way to selectively eradicate the tissues avoiding damage and side effects in healthy tissues. It includes three components: a chemical photosensitizer (PS), a light source of a specific wavelength, and molecular oxygen. None of these components is individually toxic, but together, they initiate a photochemical reaction that culminates in the generation of a highly reactive species called singlet oxygen ($^1O_2$) [4]. The antitumor effects of these reactive species are based on three possible mechanisms: cytotoxic effects that produce an apoptotic response directly in the cancer cell, damage to the vasculature of the tumor and the induction of an immune process that causes an inflammatory response [5, 6].

PDT consists of supplying PS, either topically or systemically, and when it is concentrated in the tissue, it is irradiated with an appropriate wavelength to excite (PS*), after that energy transference from PS* to intracellular oxygen molecules in ground state ($^3O_2$), and through an intersystem crossing, singlet oxygen is produced. Then, the photosensitizer returns to its basal state. The effectiveness of PDT can be affected by the concentration of oxygen in the tissue, the dose of light, and the distribution of the PS [7].

1.2 Major Disadvantage of the Photosensitizers

The limited clinical application of PDT is due to the PS characteristics; these latter ones are currently based on a porphyrin ring and its derivatives [3, 8]. Numerous researches have shown that factors such as the hydrophobicity or poorly solubility in water, short half-life in the tissue, and slow elimination of the body, making it very difficult to find or develop any drug that can qualify as an ideal PS [9].

In order to increase its efficiency, a photosensitizing agent should be a compound with excellent photochemical stability, with a high absorption band between 500 and 800 nm to allow a deeper penetration of the light in the tissues without causing damage, and it must also have a high quantum efficiency of $^1O_2$ production (Φ_Δ) [10].

The path that most researches have taken for the development of PS revolves around the development of the porphyrinoid structure, but several non-porphyrin chromogens exhibit photosensitize activity. Phenothiazines (Fig. 1) such as methylene blue (MB) and thionine (THI) have been part of several studies of their optical properties and their ability to be a sensitizer [11–14].

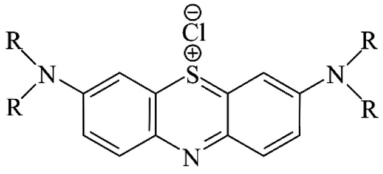

Fig. 1. Chemical structure of thionine with R = H, and methylene blue with R = CH_3.

Literature shows that methylene blue and thionine have a quantum efficiency of singlet oxygen generation (Φ_Δ) similar to hematoporphyrin derivatives. Φ_Δ of thionine in ethanol, and methylene blue, hematoporphyrin IX, and protoporphyrin IX in buffer are: $\Phi_{THI} = 0.62 \pm 0.03$, $\Phi_{MB} = 0.49 \pm 0.03$, $\Phi_{HP} = 0.74 \pm 0.04$, $\Phi_{PPIX} = 0.54 \pm 0.04$, respectively [15, 16]. However, further investigation of Φ_{THI} in other media is needed; as in buffer or a conjugated of the photosensitizer with nanomaterials, for example.

1.3 Using Nanotechnology to Improve the Application

Although PDT is already in use, PS that has been approved for clinical use do not meet all the requirements. If we go a little further, we can take advantage of nanotechnology to eradicate many of these disadvantages.

The benefits provided by the use of nanoparticles are that they can be engineered to transport multiple theragnostic agents, increasing the bioavailability of the PS. Also, their surface can be functionalized to change the physical and biological properties, optimizing its stability in water, and controlling the specificity of administration, among other properties [17].

There is a wide variety of reports about nanoparticles used to solubilize, encapsulate, and deliver PS to both tumors and microbial cells [18, 19]. However, it is of our particular interest the passive transport mediated by silica core-shell nanoparticles (SNP), as seen in several studies [20–23], the SiO_2 polymer shell can provide:

- Drug encapsulation to reduce toxicity, increase biocompatibility and solubility, and prevent agglomeration.
- Possibility of biofunctionalization, from antibodies to PS.
- Slowing down the elimination of the body before they arrive at the target cells.
- Enhanced biodistribution.
- Administration of light to the core due to their optical transparency.

Therefore, the carried mediated supply increases the accumulation of PS at the destination site, minimizing the amount of precision needed in the supply of light, and thus improving its clinical administration.

2 Materials and Methods

2.1 Nanoparticle Fabrication and Bioconjugation

The fabrication of the silica nanoparticles (SNP) was based on the microemulsion method, described by Aparicio-Ixta *et al.* [24], which consists in forming a soft core of either an inert or fluorescent polymer, the one used in this experiment is POH, a synthetized polymer with absorption in 455 nm. Followed by the formation of the silica shell by the aggregation of VTES and APTES reactive species. The addition of APTES allows the modification of the surface of the nanoparticle with propyl amino fragments for its next bioconjugation process.

Using succinic anhydride as a linker, amino groups on the periphery were modified to carboxyl units, in order to form a covalent bond between the linker and the photosensitizer (Thionine).

The optical and morphological characterization of the bioconjugated nanoparticles was carried out to confirm the amide bond of the photosensitizer and nanoparticle surface.

2.2 Determination of Singlet Oxygen Generation

The $^1O_2$ production was evaluated using an indirect method, briefly consist of the quantification of the degradation of a specific chemical trap 1, 3-diphenylisobenzofuran (DPBF). Suspensions of SNP are first saturated with oxygen; after that, the suspension was irradiated with a diode-laser (532 nm) for three minutes intervals. The absorbance was measured after each irradiation, recording the maximum absorption of DPBF at 411 nm.

The determination of Φ_Δ for nanoparticles (Φ_{SNP}) was calculated by Eq. 1, described by Rossi *et al.* [25] where the relationship between the time for the decay of the chemical trapper is compared with thionine in solution (t_{THI}) and the SNP bioconjugated (t_{SNP}), and multiplied by the quantum efficiency of thionine in solution (Φ_{THI})

$$\phi_{SNP} = \phi_{THI} \frac{t_{THI}}{t_{SNP}} \tag{1}$$

It provides a measure of its singlet oxygen delivery efficiency (ϕ_{SNP}).

3 Results and Discussion

3.1 Silica Nanoparticles Morphology

Figure 2 shows the micrographs obtained by SEM microscopy corroborating the fabrication of silica nanoparticles with a polymeric nucleus made of POH; the nanoparticles were obtained with a uniform spherical shape and an average size of 70 nm; this parameter is not modified after the bioconjugation process. Tang *et al.* reported the fabrication of SNP using a variation of the same technique for layer assembly of silica shell on a PS template, with sizes of 190 nm [26].

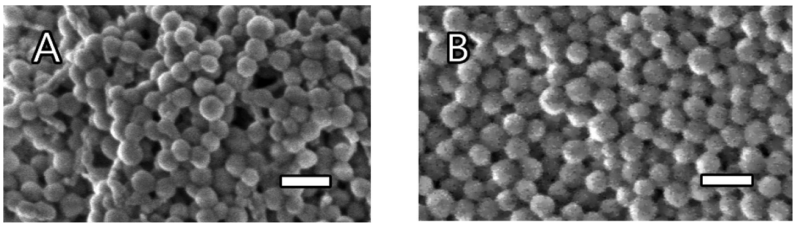

Fig. 2. (A) SEM micrograph of silica nanoparticles doped with POH (B) Micrograph of bioconjugated nanoparticles with the photosensitizer. Scale bar (A, B) = 100 nm.

For fabrication of SNPs, there are several reports about their chemical and thermal stabilities and also the size control by keeping constant the proportions of the materials [27, 28].

3.2 Optical Properties of Nanoparticles

The photoluminescence and absorption spectra of thionine (PS), fluorescent polymer (POH) in solution and the manufactured nanoparticles were obtained. The analysis of the optical properties of the fluorophore shows that its emission band (588 nm) overlaps with the absorption band of the photosensitizer (604 nm) (see Fig. 3A), which could be used to activate the generation of singlet oxygen via fluorescence resonance energy transfer (FRET) process.

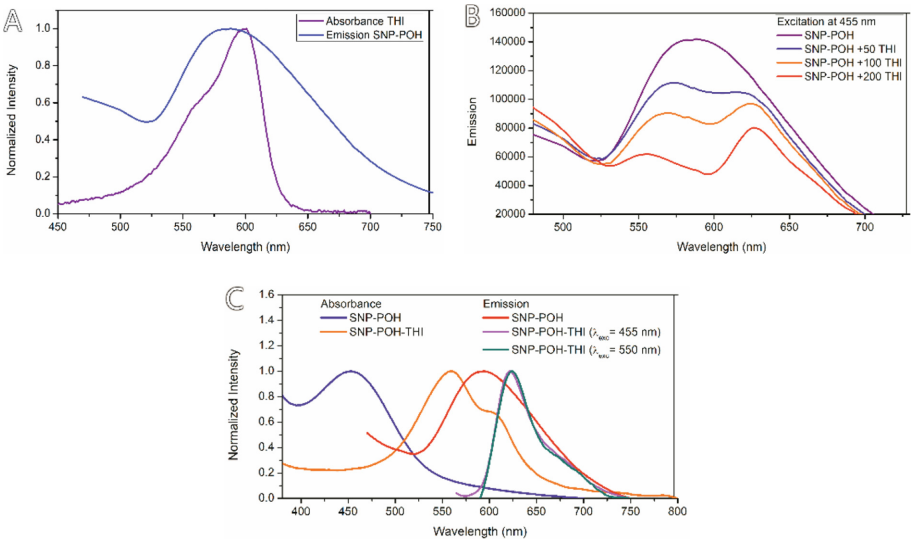

Fig. 3. (A) Spectral overlap of THI and POH fluorophore. (B) Emission spectrum of SNP-POH and the gradual addition of THI in solution. (C) Spectrum of absorption and emission of bioconjugated SNP, in which both the photosensitizer and the fluorophore were excited.

In order to analyze the possible energy transference from the fluorophore to the photosensitizer, it was compared to the emission spectra of the nanoparticle's suspension (SNP-POH) and the absorption band of Thionine (PS). Also, emission spectra of SNP-POH show a gradual change after THI in solution was added, the SNP-POH band at 588 nm decreases as the band at 624 nm appears it which is assigned to the Thionine emission (see Fig. 3B).

Kim *et al.* previously reported organically modified silica nanoparticles, encapsulating a PS (HPPH) and a two-photon FRET donor (BDSA), that effectively produced singlet oxygen exciting the BDSA, followed by energy transfer to HPPH [29]. Cheng *et al.* also demonstrated this, in which research, they encapsulated a TPA dye (FITC)

and the PS (PdTPP), using hexagonal mesoporous silica nanoparticles and resulted in high $^1O_2$ production and efficient TPE PDT for both in vitro and in vivo studies [30].

Afterward, the suspension of bioconjugated nanoparticles (SNP-POH-THI) emission spectrum was measured by exciting the absorption length of the fluorophore POH (455 nm) and another exciting the PS (550 nm), in both spectra, the emission bands have the same form and position (see Fig. 3C). The difference between the spectrum of SNP-POH and SNP-POH-THI bears out the annulment of the POH emission band, so thionine's band is established, regardless of whether the POH is activated directly or not. The nullification of the peak band led us to understand that the FRET transfer is carried out successfully.

3.3 Photogeneration of Singlet Oxygen

Singlet oxygen generation of thionine was first demonstrated in solution when is excited at 532 nm (see Fig. 4A). Thus, it was set the generation of $^1O_2$ using SNP-THI (see Fig. 4B) to observe if the SNP were capable of keeping the singlet-oxygen photogeneration.

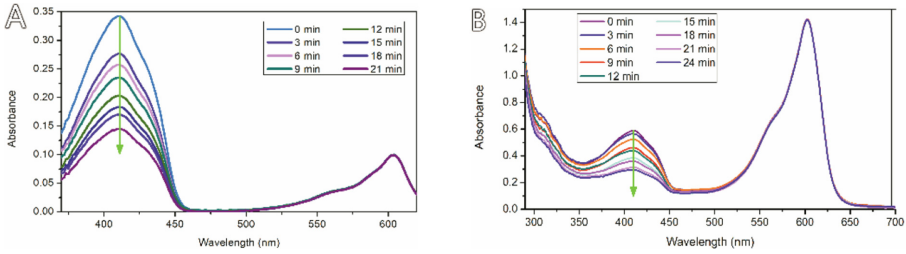

Fig. 4. Absorbance spectrum of photogeneration of singlet oxygen using: (A) THI in solution as the photosensitizer and (B) SNP-THI aqueous suspension.

Although the quantum efficiency of singlet oxygen was reduced from thionine in solution to SNP-THI, these nanomaterials proved to maintain photogeneration. Subsequently, it was established that SNP-POH-THI could also generate $^1O_2$ in aqueous suspension.

4 Conclusion

Through SEM microscopy, it was corroborated the fabrication of nanomaterials with spherical morphology, with diameters close to 70 nm. By absorption and emission spectroscopy the presence of the fluorophore and the photosensitizer in the nanoparticles was corroborated, the possible energy transfer process was also demonstrated.

The singlet oxygen generation was established by an indirect method which confirms the possibility of the use of these nanomaterials as photosensitizers.

References

1. Lipson, R.L.: The photodynamic properties of a particular hematoporphyrin de-rivative. Arch. Dermatol. **82**(4), 508 (1960). https://doi.org/10.1001/archderm.1960.01580040026
2. Gray, M.J., Lipson, R., Maeck, J.V.S., Parker, L., Romeyn, D.: Use of hematoporphyrin derivative in detection and management of cervical cancer. Am. J. Obstet. Gynecol. **99**(6), 766–771 (1967). https://doi.org/10.1016/0002-9378(67)90392-4
3. Van Straten, D., Mashayekhi, V., de Bruijn, H., Oliveira, S., Robinson, D.: Oncologic photodynamic therapy: basic principles, current clinical status and future directions. Cancers **9**(12), 19 (2017). https://doi.org/10.3390/cancers9020019
4. Foote, C.S.: Type I and type II mechanisms of photodynamic action. In: Light-Activated Pesticides, pp. 22–38 (1987). https://doi.org/10.1021/bk-1987-0339.ch002
5. Henderson, B.W., Dougherty, T.J.: How does photodynamic therapy work? Photochem. Photobiol. **55**(1), 145–157 (1992). https://doi.org/10.1111/j.1751-1097.1992.tb04222.x
6. Castano, A.P., Mroz, P., Hamblin, M.R.: Photodynamic therapy and anti-tumour immunity. Nat. Rev. Cancer **6**(7), 535–545 (2006). https://doi.org/10.1038/nrc1894
7. Sirotkina, M.A., Matveev, L.A., Shirmanova, M.V., Zaitsev, V.Y., Buyanova, N.L., Elagin, V.V., Gelikonov, S.S., Kuznetsov, E.B., Kiseleva, A.A., Moiseev, S.V., Gamayunov, E.V., Zagaynova, F.I., Gladkova, N.D.: Photodynamic therapy monitoring with optical coherence angiography. Sci. Rep. **7**(1) (2017). https://doi.org/10.1038/srep41506
8. Pushpan, S., Venkatraman, S., Anand, V., Sankar, J., Parmeswaran, D., Ganesan, S., Chandrashekar, T.: Porphyrins in photodynamic therapy - a search for ideal photosensitizers. Current Med. Chem.-Anti-Cancer Agents **2**(2), 187–207 (2002). https://doi.org/10.2174/1568011023354137
9. Castano, A.P., Demidova, T.N., Hamblin, M.R.: Mechanisms in photodynamic therapy: Part three—Photosensitizer pharmacokinetics, biodistribution, tumor localization and modes of tumor destruction. Photodiagn. Photodyn. Ther. **2**(2), 91–106 (2005). https://doi.org/10.1016/s1572-1000(05)00060-8
10. Agostinis, P., Berg, K., Cengel, K.A., Foster, T.H., Girotti, A.W., Gollnick, S.O., Hahn, S.M., Hamblin, M.R., Juzeniene, A., Kessel, D., Korbelik, M., Moan, J., Mroz, P., Nowis, D., Piette, J., Wilson, B.C., Golab, J.: Photodynamic therapy of cancer: an update. CA Cancer J. Clin. **61**(4), 250–281 (2011). https://doi.org/10.3322/caac.20114
11. Leonardo, M., Juliana, P., Paula, A., Severino, D., Regina, M., de Oliveir, H.P.M.: Phenotiazinium dyes as photosensitizers (PS) in photodynamic therapy (PDT): spectroscopic properties and photochemical mechanisms. Adv. Aspects Spectro. (2012). https://doi.org/10.5772/48087
12. Chen, Y., Zheng, W., Li, Y., Zhong, J., Ji, J., Shen, P.: Apoptosis induced by methylene-blue-mediated photodynamic therapy in melanomas and the involvement of mitochondrial dysfunction revealed by proteomics. Cancer Sci. (2008). https://doi.org/10.1111/j.1349-7006.2008.00910.x
13. Lu, Y., Jiao, R., Chen, X., Zhong, J., Ji, J., Shen, P.: Methylene blue-mediated photodynamic therapy induces mitochondria-dependent apoptosis in HeLa Cell. J. Cell. Biochem. **105**(6), 1451–1460 (2008). https://doi.org/10.1002/jcb.21965
14. Ormond, A., Freeman, H.: Dye sensitizers for photodynamic therapy. Materials **6**(3), 817–840 (2013). https://doi.org/10.3390/ma6030817
15. Bryce-Smith, D.: Photochemistry, vol. 2. Royal Society of Chemistry, Cambridge (2007)
16. Fernandez, J.M., Bilgin, M.D., Grossweiner, L.I.: Singlet oxygen generation by photodynamic agents. J. Photochem. Photobiol., B **37**(1–2), 131–140 (1997). https://doi.org/10.1016/s1011-1344(96)07349-6

17. Lucky, S.S., Soo, K.C., Zhang, Y.: Nanoparticles in photodynamic therapy. Chem. Rev. **115** (4), 1990–2042 (2015). https://doi.org/10.1021/cr5004198
18. Master, A., Livingston, M., Sen Gupta, A.: Photodynamic nanomedicine in the treatment of solid tumors: perspectives and challenges. J. Controlled Release **168**(1), 88–102 (2013). https://doi.org/10.1016/j.jconrel.2013.02.020
19. Abrahamse, H., Hamblin, M.R.: New photosensitizers for photodynamic therapy. Biochem. J. **473**(4), 347–364 (2016). https://doi.org/10.1042/bj20150942
20. Chang, Y.-C., Shieh, D.-B., Chang, C.-H., Chen, D.-H.: Conjugation of monodisperse chitosan-bound magnetic nanocarrier with epirubicin for targeted cancer therapy. J. Biomed. Nanotechnol. **1**(2), 196–201 (2005). https://doi.org/10.1166/jbn.2005.021
21. Salahuddin, N., Galal, A.: Improving chemotherapy drug delivery by nanoprecision tools. Nanostruct. Cancer Ther., 87–128 (2017). https://doi.org/10.1016/b978-0-323-46144-3.00004-0
22. Amirthalingam, T., Kalirajan, J.: Use of silica-gold core shell structured nanoparticles for targeted drug delivery system. J. Nanomed. Nanotechnol. **02**(06) (2011). https://doi.org/10.4172/2157-7439.1000119
23. Zhang, J.L., Srivastava, R.S., Misra, R.D.K.: Core−shell magnetite nanoparticles surface encapsulated with smart stimuli-responsive polymer: synthesis, characterization, and LCST of viable drug-targeting delivery system. Langmuir **23**(11), 6342–6351 (2007). https://doi.org/10.1021/la0636199
24. Aparicio-Ixta, L., Ramos-Ortiz, G., Pichardo-Molina, J.L., Maldonado, J.L., Rodríguez, M., Tellez-Lopez, V.M., Barbosa-García, O.: Two-photon excited fluorescence of silica nanoparticles loaded with a fluorene-based monomer and its cross-conjugated polymer: their application to cell imaging. Nanoscale **4**(24), 7751 (2012). https://doi.org/10.1039/c2nr31925j
25. Rossi, L.M., Silva, P.R., Vono, L.L.R., Fernandes, A.U., Tada, D.B., Baptista, M.S.: Protoporphyrin IX nanoparticle carrier: preparation, optical properties, and singlet oxygen generation. Langmuir **24**(21), 12534–12538 (2008). https://doi.org/10.1021/la800840k
26. Tang, W., Xu, H., Kopelman, R., Philbert, M.: Photodynamic characterization and in vitro application of methylene blue-containing nanoparticle platforms. Photochem. Photobiol. **81**(2), 242 (2005). https://doi.org/10.1562/2004-05-24-ra-176.1
27. Echeverri, M., Giraldo, L.F., López, B.L.: SÍNTESIS Y FUNCIONALIZACIÓN DE NANOPARTÍCULAS DE SÍLICA CON MORFOLOGÍA ESFÉRICA. Scientia Et Technica, vol. XIII, número 036, pp. 169–173 (2007)
28. Li, Y., Shi, J.: Hollow-structured mesoporous materials: chemical synthesis, functionalization and applications. Adv. Mater. **26**(20), 3176–3205 (2014). https://doi.org/10.1002/adma.201305319
29. Kim, S., Ohulchanskyy, T.Y., Pudavar, H.E., Pandey, R.K., Prasad, P.N.: Organically modified silica nanoparticles co-encapsulating photosensitizing drug and aggregation-enhanced two-photon absorbing fluorescent dye aggregates for two-photon photodynamic therapy. J. Am. Chem. Soc. **129**(9), 2669–2675 (2007). https://doi.org/10.1021/ja0680257
30. Cheng, S.-H., Hsieh, C.-C., Chen, N.-T., Chu, C.-H., Huang, C.-M., Chou, P.-T., Lo, L.-W.: Well-defined mesoporous nanostructure modulates three-dimensional interface energy transfer for two-photon activated photodynamic therapy. Nano Today **6**(6), 552–563 (2011). https://doi.org/10.1016/j.nantod.2011.10.003

Biomaterials, Molecular, Cellular and Tissue Engineering

Evaluation of Titanium-Niobium Alloy as a Possible Material to Manufacture Endodontic Files

Javier Nino-Barrera(✉), Oscar Rodriguez-Montano, and Carlos Cortes-Rodriguez

Department of Mechanical Engineering and Mechatronics, Engineering Faculty, Universidad Nacional de Colombia, Bogotá, Colombia
javinino40@gmail.com

Abstract. In order to avoid fractures of endodontic instruments within the root canal, rotary endodontic files have been manufactured in nickel titanium alloy, either conventional or with different thermal treatments. However, fatigue fractures continue to occur, preventing root canal cleaning and shaping. In our research we explored the possibility that titanium niobium alloy may be useful in the manufacture of endodontic rotary files due to its resistance to fatigue fracture. Simulations of the fatigue failure were made by means of finite elements in wires with the properties of the proposed alloys and they were validated experimentally finding similar results. Likewise, simulations of fatigue failure were made of models of the F2 file of Protaper series® with the same mechanical properties tested on the wires but only the rotary file composed of nickel titanium alloy was experimentally validated.

It was found that the niobium titanium alloy virtual file was more resistant to fatigue failure than the nickel titanium alloy file, therefore with the limitations of the present study, it can be concluded that titanium-niobium could be an alternative material for the manufacture of endodontic files.

Keywords: Nickel-Titanium · Rotary file · Titanium-Niobium

1 Introduction

As a consequence of caries, trauma or iatrogenic restorative procedures, the dental pulp can be irreversibly injured and end up leading to the death of the dental pulp. The procedure indicated in this case is root canal treatment which consists in cleaning and shaping of complete root canal [1]. In this way the necrotic tissue and debris is eliminated, allowing the alveolar bone and the periodontal ligament health or prevent the appearance of periapical disease [2].

In this treatment, small-caliber instruments called endodontic files are used conventionally. The endodontic files have been manufactured historically by carbon steel (1950–1960) [3, 4], stainless steel (1960-nowadays) [5] and nickel titanium (ni-ti) alloy (1988-nowadays) [6]. Carbon steel was characterized by its rigidity and lack of flexibility [4], which resulted in the presence of procedural accidents (deviations of the root canal and/or perforations) [7, 8], additionally it was common to observe fractured

© Springer Nature Switzerland AG 2020
C. A. González Díaz et al. (Eds.): CLAIB 2019, IFMBE Proceedings 75, pp. 627–636, 2020.
https://doi.org/10.1007/978-3-030-30648-9_83

instruments of carbon steel inside the root canal [8]. The endodontic files made with stainless steel alloy presented better characteristics than carbon steel, such as increase in flexibility and less tendency to fracture [4, 9]. In 1988 Walia *et al.* introduced the nickel titanium (ni-ti) alloy in endodontics [6]. This alloy was previously used in orthodontic treatments and had even better flexibility characteristics than stainless steel files decreasing its probability of fracture and allowing the appearance of rotary files [6].

However, the problem of fractured endodontic files is still present [10–12] and the research was focused in improving the fracture resistance of nickel titanium files enhancing their mechanical properties. This was made with help of thermic treatments on the material [13, 14]. In this way appeared the M-wire® and the CM wire® as better alloys than original nickel titanium alloy [15, 16].

The main problem of a fractured instrument inside the root canal is that it acts as a blockage that prevents its cleaning and shaping, then with an untreated infection and a disease in progress, the situation would put the affected tooth in front of two possible treatments: Endodontic surgery or dental extraction, both invasive procedures with consequent discomfort for the patient [10].

Since the nickel titanium alloy was introduced, no new alloys have been proposed as alternatives in the manufacture of endodontic instruments. This thinking is different from that in other areas of dentistry, such as orthodontics, where new alloys such as titanium niobium (ti-nb) have been used [17].

Among the most relevant features of titanium niobium alloy, there are modulus of elasticity of approximately 40 GPa, a high tensile strength, super elasticity and good ductility, it has been reported that its effect of super elasticity is similar to the one presented by the nickel titanium alloy [18].

In the same way as alternative materials such as nickel titanium, used in orthodontics, were proposed in the 1980s for endodontic use, the present research aim is to determine if the titanium niobium alloy used in orthodontics could become useful as a material for the manufacture of endodontic files.

2 Materials and Methods

2.1 Selection of Material

Orthodontic wires with rectangular shape in their transversal design were used in two different types of alloys: Alloy nickel titanium of 0.40 mm (0.016 in.) × 0.55 mm (0.022 in.). and titanium niobium alloy of 0.45 mm (0.018 in.) × 0.55 mm (0.022 in.).

2.2 Cyclic Fatigue Test of Orthodontic Wires

The assembly of a numerical control device was performed to decrease and calibrate the speed of the continuous rotation of each sample, which was at 375 revolutions per minute (RPM). This assembly was made directly on a bore that had a speed control system. An optocoupler with an Arduino® circuit was used to measure the revolutions.

This device was programmed with an RPM frequency meter on the card (Arduino Mega®) by displaying directly on the Arduino® software, which recorded the RPM reading of the serial monitor. To perform the cyclic fatigue test, the wire was confined to a simulated stainless steel canal (length: 30 mm, Diameter: 1.5 mm, curvature: 86° [19]. Each wire had a length of 50 mm and 10 repetitions were made per group: Group 1: ni - ti alloy; Group 2: ti - nb alloy.

To observe if there is a statistically significant difference between groups, a U Mann Whitney test was used to determine which group was different.

2.3 Cyclic Fatigue Test of Rotary File F2 Protaper® Series

With the same root canal simulated in stainless steel at 86° of curvature, 12 rotary files F2 Protaper series® at 300 RPM were used with the help of an Xsmart Plus® motor (Dentsply Maillefer®).

2.4 Mathematical Model Construction of Orthodontic Wires and Border Conditions

Mathematical models were built with the real dimensions of each wire with Inventor® (Autodesk®), then the models were imported inside Ansys® software. The mechanical properties of the two alloys evaluated were taken from the literature [17, 18, 20, 21] and introduced in each of the corresponding wire mathematical models.

The models of the wires were meshed with 4476 and 4768 elements and 26534 and 28247 nodes respectively, subsequently a displacement was applied on a corner at one end of the wire model until a curvature of 86° was achieved, at the other end of the wire, a fixed restriction was placed (Fig. 1).

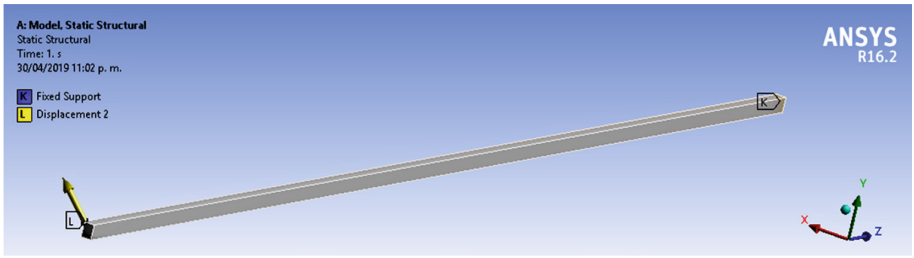

Fig. 1. Boundary conditions for the simulation of wires.

Once the static simulation was resolved, the Ansys® fatigue module was used and the time in seconds between each of the wire alloys and the experimental result was compared.

2.5 Mathematical Model Construction of Rotary Files Protaper Series F2® and Border Conditions

A reverse engineering process was performed with help of the metrology laboratory at the School of Engineering of Universidad Nacional de Colombia. Measurements of nickel titanium rotary file F2 Protaper series® were taken with a Carl Zeiss Jenna® profile projector, with a resolution of 0.01 mm, it was made for geometric characterization and contour plotting of the files (Fig. 2). In the same way as it was performed with the wire models, the rotary file F2 Protaper series® models were built in Inventor® next imported into Ansys® with the same mechanical properties of the alloys used in the wires. The models of the rotary file F2 Protaper series® were meshed with 6482 elements and 12766 nodes. The boundary conditions were similar to those used in the wires, that is, a displacement was placed at the tip of the file, obtaining a curvature of 86° and placing a fixed restriction on the other end (Fig. 3). Finally, once the static analysis was carried out, the Ansys® fatigue module was used and the time in seconds as well as the number of cycles due to fatigue failure were recorded and compared.

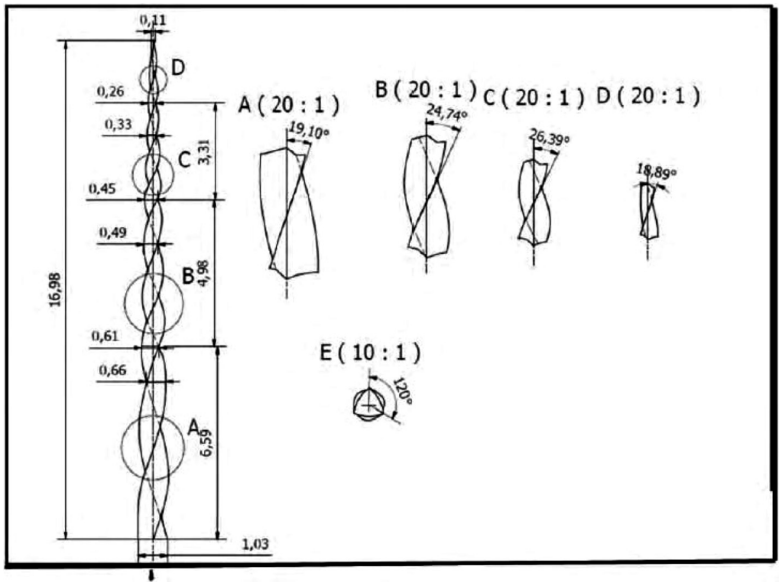

Fig. 2. Plane of the rotary file Protapér series F2.

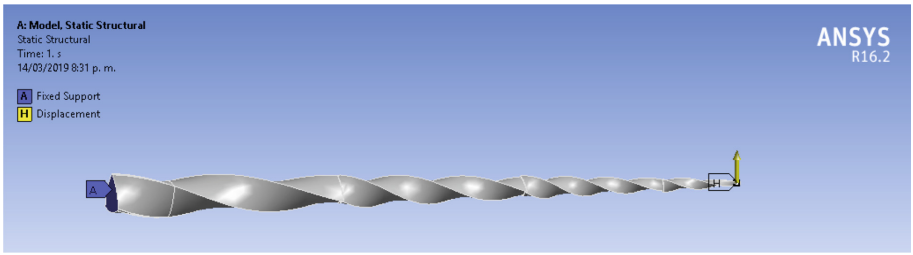

Fig. 3. Boundary conditions for the simulation of rotary file F2 Protaper series®.

3 Results

The results of the experimental test of the wires are presented in Table 1, it is observed that the ti-nb alloy wire is significantly more resistant to fatigue than the nickel titanium alloy ($p = 0.0002$). The results of the experimental test with the rotary files F2 Protaper series® shows a mean of 84 s of fracture failure resistance and 420 cycles to fracture (Table 2).

Table 1. Number of seconds and cycles of each repetition with a speed of 375 RPM. Ti-nb alloy is significantly more resistant to fracture than ni-ti alloy ($p = 0.0002$).

Repetitions	Group 1: ni-ti		Group 2: ti-nb	
	Seconds	*Cycles to fracture	Seconds	*Cycles to fracture
1	9.75	61	14.99	94
2	9.67	60	1503	94
3	10.8	68	14.25	89
4	9.81	61	15.11	94
5	9.78	61	15.05	94
6	8.9	56	15.23	95
7	9.92	62	15.13	95
8	9.95	62	14.86	93
9	9.5	59	14.93	93
10	9.88	62	14.95	93
Mean		61.2		93.4
Standard deviation	3.01		1.71	

$$*Cycles = \frac{375\,RPM \times Time(seconds)}{60}$$

The results of the simulation by means of the finite element analysis for the wires of the two alloys and the experimental results are observed in Table 3, it is also possible to observe the approximation that exists between these results. The results of the simulation for theoretical ti-nb rotary file F2 Protaper® series are presented in Table 3.

Table 2. Cycles and time to fracture (sec) of F2 nickel titanium rotary files in simulated canal with 86° curvature.

Time to fracture (Sec)	*Cycles to fracture
86	430
49	245
131	655
78	390
104	520
59	295
70	350
98	490
68	340
93	465
90	450
82	410
Mean: 84 s	Mean: 420 Cycles*

$*Cycles = \frac{300\,RPM \times Time(seconds)}{60}$

Table 3. Comparative table of FEM results between the evaluated alloys for mathematical model, F2 Protaper series® and experimental results.

	Nickel	Titanium	Titanium	Niobium
	Wire (exp. Res)	Rotary File F2 (exp. Res)	Wire (exp. Res)	Rotary File F2
Stress (Mpa)	2273	1234	2206	1169
Strain (mm/mm)	0,07	0,06	0,04	0,05
Fatigue (Cycles)	52,02(61,2)	415,8(420)	83,17(93,4)	455
Fatigue (Seconds)	11,56(9,79)	92,39(84)	18,12(14,95)	116

4 Discussion

The purpose of the present research was to evaluate niobium titanium alloy as a possible material for the manufacture of endodontic rotary files. Since it is not possible nowadays to find endodontics files with the alloy of ti-nb, thus experimental tests were initially performed comparing this alloy with wires of orthodontic nickel titanium alloy because this material is commonly used in the manufacture of endodontic files. We found better results with the wire ti-nb than with the wire of ni-ti. With base in this results in a second stage we proceeded to manufacture virtual models of the rotary files and setting the mechanical properties of the tested alloys. In this way in order to accomplish our aim, we designed and implemented an experimental and theoretical study employing both orthodontic wires and rotary files mathematical models.

Nowadays the research has been oriented to improve the mechanical properties of ni-ti alloy by means of various thermal treatments [22]. Improvements include decreasing its modulus of elasticity, which makes the alloy more ductile and with control of the shape memory effect. The files manufactured with these alloys have been reported to have greater resistance to cyclic fatigue than those manufactured using conventional ni-ti alloy [23].

Ti-nb is an alternative alloy that have properties similar to the ni-ti alloy after the latter has been subjected to thermal treatments, such properties as a minor modulus of elasticity and good ductility, have been characterized for give a good resistance to cyclic fatigue [17, 18]. When performing the cyclic fatigue test for both alloys, we compared the number of cycles to fatigue fracture and we found that the ti-nb alloy was significantly more resistant to cyclic fatigue than ni-ti alloy.

Among the limitations included in this research were that the dimensions in which ti-nb alloy was obtained were not the same as those of the ni-ti alloy, this fact is not new in researches with ti-nb alloys [24], in our case it wasn't possible to get the ti-nb wire with adequate dimensions, however, the dimensions of both of the wires are very close with very little difference between them and moreover, it has been reported that resistance to cyclic fatigue of rotary files is inversely proportional with its transverse area [25, 26] then, taken into account that the resistance to cyclic fatigue decreases significantly when the angle of curvature increases [26], as it is the case of the present study (86°) it can be said that, although it would have been ideal to compare wires with the same dimensions, in our study the wire of more caliber was precisely the ti-nb alloy which despite the factors mentioned above, showed the greatest resistance to cyclic fatigue. The good toughness of ti-nb alloy is possible because of its good ductility [23], and both properties decreases the stress levels [27], which would explain in part the increase in the resistance to cyclic fatigue in a severe curvature as it was in this case.

Due to the good results of the alloy of ti-nb wire in the experimental test, we decided to test this alloy with a mathematical model of a rotary file, for this case we use the model of a file F2 Protaper series® and we compared its resistance to cyclic fatigue with the same model with the ni-ti alloy tested before. It's also worth noting the close approximation of the result of the experimental assay of the file ni-ti alloy F2 Protaper series ® with the simulation in the fatigue module of Ansys® (84 vs 92.39 s). Montalvao *et al.* also used the Ansys® fatigue module but with the GT® and Profile® rotary files, finding agreement between the fatigue simulation and the experimental result, that similarity between the experimentation and the simulation with fatigue module of Ansys® agrees with our findings [15].

Both the reverse engineering process and the use of finite element analysis have previously been used in research similar to ours and its utility to propose new designs and alloys is clearly demonstrated [20, 28].

Lee *et al.* correlated von Mises stresses results with cyclic fatigue experimental, this correlation is given between the high stresses of von Mises and the low resistance to fatigue and vice versa, this relationship coincides with that reported in our study where we found in all cases, either with the models of the wires. and the models of the rotary files and their respective experimental results, a high number of stresses of von Mises associated with a lower resistance to fatigue and viceversa [28]. This last result means that a lower number of cycles to the fracture is related with less time of resistance to the

fracture in seconds. In this way were validated experimentally the results of the simulations of the wires and additionally we could infer that the fatigue resistance of a virtual rotary file of ti-nb alloy was higher than fatigue resistance of a virtual rotary file of alloy of ni-ti alloy.

Due to its good properties, ti-nb alloy has been used in other biomedical areas such as orthodontics and medical implants [17, 29]. Niimomi found that the fatigue resistance of the ti-nb alloy is high and allows it to be used for biomedical applications [30], which agrees with our results, consequently due to its resistance to cyclic fatigue, the ti-nb alloy could be proposed as a material for the manufacture of rotary endodontic files.

Finally, it is clear that the geometric design is very important in a rotary file and that together with the alloy, it gives to the file not only resistance to fatigue but resistance to the torsional fracture [31], therefore as a future work it is proposed to test the ti-nb alloy with other designs of endodontics files to analyze their mechanical behavior, and someday be able to make a real rotary file of ti-nb alloy.

5 Conclusion

The alloy of ti-nb can be proposed for the manufacture of endodontic files. The fatigue module of Ansys® simulated adequately the fracture to fatigue process.

Conflict of Interest. The authors declare that they have no conflict of interest.

References

1. Schilder, H.: Cleaning and shaping the root canal. Dent. Clin. North Am. **18**(2), 269–296 (1974)
2. Seltzer, S., Soltanoff, W., Sinai, I., Goldenberg, A., Bender, I.B.: Biologic aspects of endodontics part III. periapical tissue reactions to root canal instrumentation. 1968. J. Endod. 30(7), 491–499 (2004). Discussion 489–490
3. Gallegos, A.G., Bertolotti, R.L.: Effect of sodium hypochlorite on the strength of carbon steel endodontic instruments. J. Endod. **7**(9), 423–425 (1981)
4. Craig, R.G., Mc Ilwain, E.D., Peyton, F.A.: Comparison of theoretical and experimental bending and torsional moments of endodontic files and reamers. J. Dent. Res. **46**(5), 1058–1063 (1967)
5. Darabara, M., Bourithis, L., Zinelis, S., Papadimitriou, G.D.: Assessment of elemental composition, microstructure, and hardness of stainless steel endodontic files and reamers. J. Endod. **30**(7), 523–526 (2004)
6. Walia, H.M., Brantley, W.A., Gerstein, H.: An initial investigation of the bending and torsional properties of Nitinol root canal files. J. Endod. **14**(7), 346–351 (1988)
7. Riggans Jr., J.W.: The case history of a root perforation and a method for its prevention. Dent. Digest **77**(5), 275–279 (1971)
8. Chernick, L.B., Jacobs, J.J., Lautenschlager, E.P., Heuer, M.A.: Torsional failure of endodontic files. J. Endod. **2**(4), 94–97 (1976)
9. Camps, J.J., Pertot, W.J.: Relationship between file size and stiffness of stainless steel instruments. Endod. Dent. Traumatol. **10**(6), 260–263 (1994)

10. Bahcall, J.K., Carp, S., Miner, M., Skidmore, L.: The causes, prevention, and clinical management of broken endodontic rotary files. Dent. Today **24**(11), 74, 76, 78–80, quiz 80 (2005)
11. Fu, M., Zhang, Z., Hou, B.: Removal of broken files from root canals by using ultrasonic techniques combined with dental microscope: a retrospective analysis of treatment outcome. J. Endod. **37**(5), 619–622 (2011)
12. Sattapan, B., Nervo, G.J., Palamara, J.E., Messer, H.H.: Defects in rotary nickel-titanium files after clinical use. J. Endod. **26**(3), 161–165 (2000)
13. Kaval, M.E., Capar, I.D., Ertas, H.: Evaluation of the cyclic fatigue and torsional resistance of novel nickel-titanium rotary files with various alloy properties. J. Endod. **42**(12), 1840–1843 (2016)
14. Kaval, M.E., Capar, I.D., Ertas, H., Sen, B.H.: Comparative evaluation of cyclic fatigue resistance of four different nickel-titanium rotary files with different cross-sectional designs and alloy properties. Clin. Oral Invest. **21**(5), 1527–1530 (2017)
15. Montalvao, D., Shengwen, Q., Freitas, M.: A study on the influence of Ni-Ti M-Wire in the flexural fatigue life of endodontic rotary files by using Finite Element Analysis. Mater. Sci. Eng. C Mater. Biol. Appl. **40**, 172–179 (2014)
16. Rodrigues, C.T., Duarte, M.A., de Almeida, M.M., de Andrade, F.B., Bernardineli, N.: Efficacy of CM-Wire, M-Wire, and nickel-titanium instruments for removing filling material from curved root canals: a micro-computed tomography study. J. Endod. **42**(11), 1651–1655 (2016)
17. Miyazaki, S., Kim, H.Y.: 2 - basic characteristics of titanium–nickel (Ti–Ni)-based and titanium–niobium (Ti–Nb)-based alloys. In: Miyazaki, S., Kim, H.Y. (eds.) Shape Memory and Superelastic Alloys, pp. 15–42. Woodhead Publishing (2011)
18. Saito, T., Furuta, T., Hwang, J.H., Kuramoto, S., Nishino, K., Suzuki, N., et al.: Multifunctional alloys obtained via a dislocation-free plastic deformation mechanism. Science **300**(5618), 464–467 (2003)
19. Rodrigues, R.C., Lopes, H.P., Elias, C.N., Amaral, G., Vieira, V.T., De Martin, A.S.: Influence of different manufacturing methods on the cyclic fatigue of rotary nickel-titanium endodontic instruments. J. Endod. **37**(11), 1553–1557 (2011)
20. Nino-Barrera, J.L., Aguilera-Canon, M.C., Cortes-Rodriguez, C.J.: Theoretical evaluation of Nickel-Titanium Mtwo series rotary files. Acta Odontol. Latinoam.: AOL **26**(2), 90–96 (2013)
21. Cheung, G.S., Zhang, E.W., Zheng, Y.F.: A numerical method for predicting the bending fatigue life of NiTi and stainless steel root canal instruments. Int. Endod. J. **44**(4), 357–361 (2011)
22. Braga, L.C., Faria Silva, A.C., Buono, V.T., de Azevedo Bahia, M.G.: Impact of heat treatments on the fatigue resistance of different rotary nickel-titanium instruments. J. Endod. **40**(9), 1494–1497 (2014)
23. Acosta, E.C., Resende, P.D., Peixoto, I.F., Pereira, E.S., Buono, V.T., Bahia, M.G.: Influence of cyclic flexural deformation on the torsional resistance of controlled memory and conventional nickel-titanium instruments. J. Endod. **43**(4), 613–618 (2017)
24. Murakami, T., Iijima, M., Muguruma, T., Yano, F., Kawashima, I., Mizoguchi, I.: High-cycle fatigue behavior of beta-titanium orthodontic wires. Dent. Mater. J. **34**(2), 189–195 (2015)
25. Sekar, V., Kumar, R., Nandini, S., Ballal, S., Velmurugan, N.: Assessment of the role of cross section on fatigue resistance of rotary files when used in reciprocation. Eur. J. Dent. **10**(4), 541–545 (2016)
26. Pruett, J.P., Clement, D.J., Carnes Jr., D.L.: Cyclic fatigue testing of nickel-titanium endodontic instruments. J. Endod. **23**(2), 77–85 (1997)

27. Figueiredo, A.M., Modenesi, P., Buono, V.: Low-cycle fatigue life of superelastic NiTi wires. Int. J. Fatigue **31**(4), 751–758 (2009)
28. Lee, M.H., Versluis, A., Kim, B.M., Lee, C.J., Hur, B., Kim, H.C.: Correlation between experimental cyclic fatigue resistance and numerical stress analysis for nickel-titanium rotary files. J. Endod. **37**(8), 1152–1157 (2011)
29. Chapala, P., Acharyya, S.G., Shariff, S.M., Naik, G.: Novel Ti-Nb alloys with improved wear resistance for biomedical implant application. Conference proceedings. In: Annual International Conference of the IEEE Engineering in Medicine and Biology Society IEEE Engineering in Medicine and Biology Society Annual Conference 2016, pp. 4208–4211 (2016)
30. Niinomi, M.: Fatigue performance and cyto-toxicity of low rigidity titanium alloy, Ti-29Nb-13Ta-4.6Zr. Biomaterials **24**(16), 2673–2683 (2003)
31. Baek, S.H., Lee, C.J., Versluis, A., Kim, B.M., Lee, W., Kim, H.C.: Comparison of torsional stiffness of nickel-titanium rotary files with different geometric characteristics. J. Endod. **37** (9), 1283–1286 (2011)

Formation of Tumor Spheroids by Spontaneous Cellular Aggregation in Incubation: Effect of Agarose as a Compaction Agent

Christian Chapa-González(✉), Marcos Bryan Valenzuela-Reyes, Lizbeth Lucero Alemán-Miranda, Laura Elizabeth Valencia-Gómez, Adeodato Israel Botello-Arredondo, and Esmeralda Saraí Zúñiga-Aguilar

Instituto de Ingeniería y Tecnología de la Universidad Autónoma de Ciudad Juárez, 32310 Ciudad Juárez, CH, Mexico
christian.chapa@uacj.mx

Abstract. Tumor spheroids is a 3D culture of cancer cells. This type of cell culture is a great tool for the evaluation of novel nanomedicine systems and in other areas of biomedical engineering. The main advantage over monolayer cell cultures is the biomimetic microenvironment which is appropriate for recapitulating tumor complexity. However, current tumor spheroids obtention methods require sophisticated and expensive equipment and are time-consuming. It is possible to obtain these tumor spheroids by centrifugation of the suspended cancer cells in round-bottom tubes and using compaction agents, for example agarose, which is a polysaccharide well known for its function of forming gels. Herein, we developed a method for obtaining cancer spheroids varying the centrifugation time and the concentration of agarose. The variation in spheroid size was analyzed. No significant changes were observed in the morphology or in the initial size and growth of the spheroids; except in those obtained with the shortest centrifugation time. The cell viability of spheroids that showed growth as a function of incubation time was evaluated. Viability greater than 80% was presented, however, the cell viability does not grow when the size of the spheroidal tumor increases. This simple and effective method for obtaining in vitro tumors represents a tool to further studies in Nanomedicine systems or the development of new anticancer drugs.

Keywords: Cancer · Tumor spheroid · Cell viability

1 Introduction

Cell culture methods have spread prolifically within a century [1]. Cell culture has represented a powerful tool to progress on investigation cellular responses to drugs [2] and novel anticancer nanomedicine systems [3, 4]. In 2D culture systems, cells are grown as monolayers on a flat solid surface, missing cell interactions that are present in native organs or tumors. In contrast, 3D culture systems encourage cell aggregation and

© Springer Nature Switzerland AG 2020
C. A. González Díaz et al. (Eds.): CLAIB 2019, IFMBE Proceedings 75, pp. 637–642, 2020.
https://doi.org/10.1007/978-3-030-30648-9_84

compaction which mimics tumors *in vivo*. As fields such as nanomedicine advance there is an increasing need to develop cell culture models to study the uptake of nanomaterials systems by tumor cells. Recently, it was shown that cancer spheroids are appropriate for studying the effect of nanoparticle physicochemical properties on the penetration and the uptake into tumors *in vitro* [5]. Cell spheroids offers the advantage of better imitating the complexities of tumors as compared to conventional monolayer culture systems [6]. However, multicellular spheroid fabrication methods employ sophisticated techniques such acoustofluidics [7], laser direct-write (LDW) bioprinting [8], microfluidic system [9, 10], and self-filling microwell arrays (SFMAs) [11] which are costly, and of intensive-labor, as well as time-consuming.

Mechanical agitation of suspended cells is a simple and effective technique to obtain cell spheroids. In this method the individualized cells are seeded in a culture medium, followed by centrifugation. The cells spontaneously aggregate themselves to form spheroids while remaining attached. Gentle agitation during incubation at 37 °C promotes the cells to remain anchored in the aggregate. However, to achieve the best cellular viability, growth, and homogeneity of spheroids formed it is still necessary to evaluate experimental variables such as time of centrifugation and the addition of molecules that allow the aggregation when obtaining tumor spheroids.

In the present study, we have developed a convenient methodology to assess the formation and growth of tumor spheroids. We have examined and compared the effects of the time of agitation and the addition of agarose on the viability as well as the compaction of cancer cells. From these several results, we aim to recognize the conditions that ease the formation of the tumor spheroids.

2 Materials and Methods

2.1 Spheroid Culture

Cervical cancer cells were grown in DMEM supplemented with 10% fetal bovine serum, and 100 U/ml penicillin at 37 °C in a humidified 5% CO_2 atmosphere. The medium was replaced every 3–4 days. The cells were detached using trypsin and counted in the Countess, Automated Cell Counter (Invitrogen) using trypan blue staining. Then, 1.5×10^4 viable cells were placed in six Eppendorf tubes containing cell culture medium with 20 μL of RPMI 1640 and 50 μl of agarose (1.5% w/v). Agarose was previously sterilized in a water bath. Other six tubes were prepared, but without containing agarose. Then three tubes containing agarose and three without agarose were centrifugated at 1500 rpm for 6 min while the other six tubes were centrifuged for 15 min. Then, the precipitate was incubated at 37 °C in a humidified 5% CO_2 atmosphere for 4 days. The medium (500 μL) was replaced with the fresh one every 24 h.

2.2 Morphology and Growth of the Cancer Spheroids

The spheroids obtained after the centrifugation of the cancer cells were kept in moderate agitation for 1 h and then transferred to a sterile culture plate. The size and shape of cancer spheroids were recorded by using an inverted light microscope. Spheroids

were imaged daily for 4 days by using an Axiocam ERc 55 of the Zeiss Vert A1-Ax10 microscope. The pictures were analyzed, and the diameter of spheroids was determined by measuring their cross-sectional area.

2.3 Cell Viability Assay

Spheroids were transferred from the tubes into wells of an uncoated 24-well plate. The medium surrounding the spheroids was removed out, and the spheroids were washed twice with PBS 1x, pH 7.4. The spheroid was dissociated with trypsin to obtain a suspension of cells. At the same time, 1.5×10^4, 3.0×10^4, 4.5×10^4, 6.0×10^4, and 7.5×10^4 cells were also moved to a 96-well plate to perform a calibration curve on them. MTT reagent was added to each well and the plate was incubated at 37 C, 5% CO_2 for 1 h. The absorbance of the plate was read at 540 nm by using a NanoDrop™ 2000 Spectrophotometer (Thermo Fisher Scientific).

3 Results and Discussion

Images of the aggregates were taken and then the average diameter was calculated (n = 12). In Fig. 1 it is observed representative tumor spheroids formed after two days of incubation. Some of the aggregates did not have a defined spheroidal shape, regardless of whether the culture medium contained agarose or not. This means that the addition of this polysaccharide does not modify the obtained morphology. However, the measurements were made in those aggregates with spheroidal morphology. It was also not observed that the centrifugation time favored the formation of multicellular aggregates with spheroidal morphology. Regardless of the centrifugation time, spheroidal and other irregular morphologies were observed in the cultures. The formation of aggregated tumor spheroids consists of four stages of formation which are compaction, segmentation, division and proliferation. The compaction stage occurs at the beginning on day 1, during this stage the initial compaction of the cancer cells occurs. In addition, on day 1, a high compaction of the cancer cells occurs that allows the formation of the spheroid structure.

We further characterized the growth of aggregates as a function of incubation time with the initial seeding density of 15 000 cells. It was expected that the size of spheroids was proportional to the initial cell numbers. However, a significant difference in the initial size and in the size growth of the tumor spheroids were noted in those obtained in culture medium lacking agarose with a centrifugation time of 6 min. In Fig. 2 it can be noted that the tumor spheroids tend to decrease in size depending on the incubation time, except for the case mentioned above. The spheroid diameter was approximately approaching 150 μm on day 1 with a low variation. While the initial average size of the spheroids in the highlighted method was 687 μm. Moreover, it was seen a growth of almost 3 times the average of the initial size while the average of the tumor spheroids diameter of the remaining methods decreased. It is possible that the agarose prevents the passage of nutrients and the aggregation of more cells, and this affects the observed size. Apparently, increasing the centrifugation time does not increase the initial average size of the aggregates, on the contrary it is reduced almost 4 times.

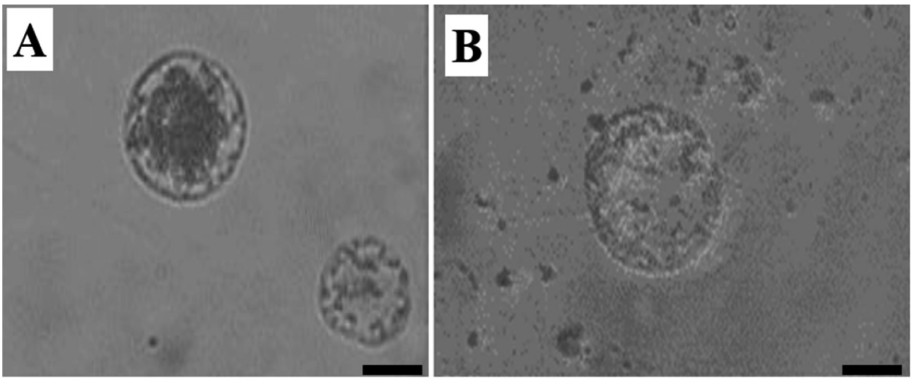

Fig. 1. Representative images were taken in the microscope (20X) where the tumor spheroids are observed (A) Tumor spheroid formed with cell media containing agarose, centrifuged 15 min at 1500 rpm. (B) Tumor spheroid formed with cell media without agarose, centrifuged 15 min at 1500 rpm. Culture days = 2. Scale bar = 100 μm

If it is considered that the physiological state of cells in a spheroid depends on its spheroid size, we must verify that the growth of the tumor spheroid is due to the aggregation of viable cells. The MTT assay was performed in order to obtain the cell viability of the multicellular spheroids (Fig. 3). Results showed that cells aggregates have a cell viability greater than 80%. A decrease in viability occurs in day 2 which can be attributed to the compaction stage. The stage of the segmentation takes place from the second day of incubation where the formation of the three specific zones of the cancer spheroids takes place: the zone of proliferation, the zone of senescence, and the necrotic zone. Cancer cells divide and proliferate with a low cell density which allows the formation of these zones which affects the cell viability as it can be seen.

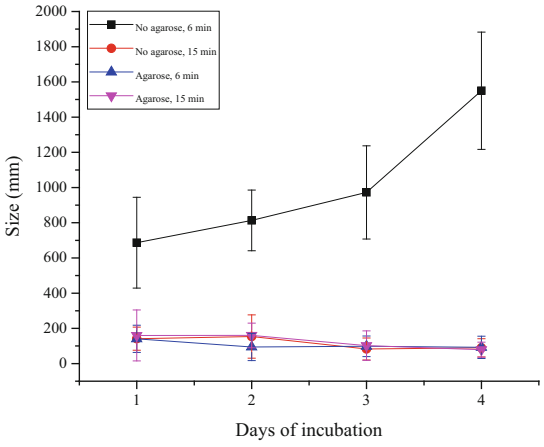

Fig. 2. Graph of variation of the average diameter of the tumor spheroids (n = 12) as a function of the incubation time.

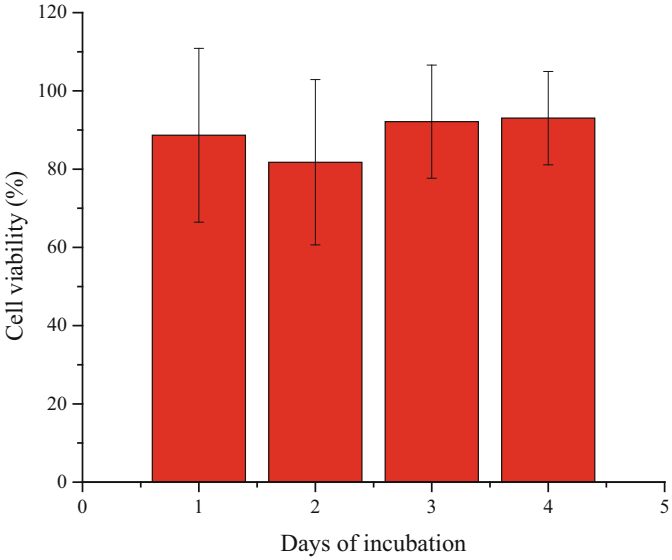

Fig. 3. Cell viability of the cells in tumor spheroids that have a growth in the average diameter, that is, those obtained in a culture medium without agarose and with a centrifugation time of 6 min. Viability is the average of 5 measurements of absorbance in the MTT assay with 100% viability control

Although there is an increase in the size, and therefore in the number of cells, the cell viability does not vary. The aggregates grow in diameter, but the proliferation zone no longer increases in size, because the oxygen and nutrients do not reach deeper areas of the aggregates. The necrotic zone causes that the cellular viability to decrease. It could even get to diminish more due to conditions like lack of oxygen in the center areas of the spheroid and depletion of the nutrients.

4 Conclusion

In conclusion, cancer cells were found to spontaneously form the spheroids in round-bottomed tubes when centrifugation time was varied from 6 min to 15 min. Agarose was used to evaluate the influence of these polymer on the compaction and growth of multicellular spheroids, and no significant differences were found in growth nor morphology of tumor spheroids. A bigger average size of the tumor spheroid was obtained in a medium lacking agarose that was centrifuged for 6 min. The growth of the spheroids is due to the aggregation of viable cells. However, the cell viability does not increase due to the formation of the necrotic zone. Therefore, the obtention of cancer spheroid described in this work would offer useful tool for nanomedicine applications.

References

1. Yao, T., Asayama, Y.: Animal-cell culture media: history, characteristics, and current issues. Reprod. Med. Biol. **16**(2), 99–117 (2017)
2. Kalashnikova, I., Albekairi, N., Ali, S., Al Enazy, S., Rytting, E.: Cell culture models for drug transport studies. In: Drug Delivery, pp. 131–151. Wiley, Hoboken (2016)
3. Lugert, S., et al.: Cellular effects of paclitaxel-loaded iron oxide nanoparticles on breast cancer using different 2D and 3D cell culture models. Int. J. Nanomed. **14**, 161–180 (2018)
4. Solomon, M.A., Lemera, J., D'Souza, G.G.M.: Development of an *in vitro* tumor spheroid culture model amenable to high-throughput testing of potential anticancer nanotherapeutics. J. Liposome Res. **26**(3), 246–260 (2016)
5. Tchoryk, A., et al.: Penetration and uptake of nanoparticles in 3D tumor spheroids. Bioconjug. Chem. **30**(5), 1371–1384 (2019)
6. Nunes, A.S., Barros, A.S., Costa, E.C., Moreira, A.F., Correia, I.J.: 3D tumor spheroids as in vitro models to mimic in vivo human solid tumors resistance to therapeutic drugs. Biotechnol. Bioeng. **116**(1), 206–226 (2019)
7. Chen, B., et al.: High-throughput acoustofluidic fabrication of tumor spheroids. Lab Chip **19**(10), 1755–1763 (2019)
8. Kingsley, D.M., et al.: Laser-based 3D bioprinting for spatial and size control of tumor spheroids and embryoid bodies. Acta Biomater, February 2019
9. Kwak, B., Lee, Y., Lee, J., Lee, S., Lim, J.: Mass fabrication of uniform sized 3D tumor spheroid using high-throughput microfluidic system. J. Control. Release **275**, 201–207 (2018)
10. Belgorosky, D., et al.: Analysis of tumoral spheres growing in a multichamber microfluidic device. J. Cell. Physiol. **233**(9), 6327–6336 (2018)
11. Seyfoori, A., et al.: Self-filling microwell arrays (SFMAs) for tumor spheroid formation. Lab Chip **18**(22), 3516–3528 (2018)

Synthesis and Characterization of Hydrogels Cross-Linked with Gamma Radiation for Use as Wound Dressings

Paola Bustamante(✉), Carolina Anessi, Natalia Santoro, Nazarena Ciavaro, and Celina Horak

Radiation Processes Department, Biological Applications Division, National Commission of Atomic Energy, Camino Real Presbítero González y Aragón 15, B1802AYA Ezeiza, Buenos Aires, Argentina
paolaabustamante@cae.cnea.gov.ar

Abstract. In this work, the synthesis of cross-linked PVA/PVP 10% w/v hydrogels was carried out by using ionizing energy at a dose of 30 kGy from a Co60 source in order to be used as dressings for skin wounds. These hydrogels were characterized by various tests such as swelling, dehydration, surface pH, Fourier Transform Spectroscopy (FTIR), Scanning Electron Microscopy (SEM) and Cytotoxicity. The results of these tests allowed us to evaluate the physical, chemical and biological properties of these and ensure that these hydrogels are a good tool for the treatment of skin burns.

Keywords: Hydrogels · Gamma radiation · Biocompatibility · Wound dressings · Crosslinking

1 Introduction

Burns are skin wounds that manifest themselves according to its degree from erythemas to ulcers and tissue necrosis [1]. It has been shown that in general the pH of the wounds tends to be basic (ph from 6.9 to 8). This is due to the activity of proteases that are produced by the same wound and as a final product of some bacteria. A treatment that involves reducing the pH of this type of injury could generate a benefit because it would reduce the toxicity generated by bacteria and their products, increasing fibroblastic activity and controlling enzymatic activity [2].

Considering in the referenced bibliography [2–4] that one of the methods that benefit the healing of wounds is the reduction of its pH and that also this affirmation was validated by health professionals specialized in burns treatment, with wide experience in the management of these, we decided to develop hydrogels with acid pH which not only allow the control of the moisture in the wound, necessary to prevent cell desiccation, promote autocatalytic debridement and generate thermal isolation [4] but also reducing the pH would promote angiogenesis and stimulate the synthesis of collagen, this improves the quality of healing [2].

Hydrogels are described as cross-linked polymer networks that constitute three-dimensional structures with the capacity to modify their volume in the presence of

© Springer Nature Switzerland AG 2020
C. A. González Díaz et al. (Eds.): CLAIB 2019, IFMBE Proceedings 75, pp. 643–651, 2020.
https://doi.org/10.1007/978-3-030-30648-9_85

water [5]. These materials possess excellent biocompatibility properties, for this they are of great interest in biomedical applications such as scaffolds for cell growth, wound dressings and drug delivery [6].

There are different methods to synthesize hydrogels. Some involve the use of chemical initiators that generate covalent crosslinking between the polymer chains, these give rise to chemical gels [5, 7], others use thermal cycling to initiate the formation of hydrogen bridges, Van der Waals forces or hydrophobic effect that allow the generation of physical hydrogels [5, 8]. Finally, another method of synthesis of hydrogels corresponds to the use of ionizing radiation as an initiator, which allows the formation of covalent bonds to give rise to thermostable hydrogels [6, 9, 10]. The synthesis of hydrogels by ionizing radiation involves a process in which the energy of this radiation is transferred to the material by ionization, generating the release of free radicals that induce active sites in the polymer chains, leading to the formation of macroradicals. Those recombine themselves to macromolecules that constitute the network of cross-linked polymers [11, 12]. It is important to consider that during the irradiation of the polymer solution to produce the hydrogel, two simultaneous processes need to occur: one that leads to the increase of the molecular weight through the crosslinking of the chains and the other that leads to a decrease of the molecular weight through the degradation of the polymer [6]. One of them always prevails.

In our country, there are no companies or institutions that develop hydrogels. Therefore, the objective is to obtain affordable products available to the most vulnerable population. As a result of this, the use of ionizing radiation for the preparation of hydrogels was considered as a simultaneous method of crosslinking and sterilization, fast, safe and friendly to the environment.

In this work, we develop hydrogels of poly (vinyl pyrrolidone) (PVP) and poly (vinyl alcohol) (PVA) cross-linked by gamma radiation at a dose of 30 kGy and a dose rate of 7.5 kGy h^{-1}. The resulting hydrogels were tested by the swelling test in order to know the percentage of swelling and the mechanism of water diffusion in the gel. There are three types of diffusion mechanisms that are representative in hydrogels; they are based on the relative rate of water diffusion in the polymer matrix, the relaxation rate of the polymer chains, the swelling of the gel and the drug delivery in the swollen polymer [13]. These mechanisms are as follows (1) Fickian diffusion in which the diffusion rate of the solvent is much less than the relaxation of the gel matrix, (2) Case II diffusion in which the transport mechanism is controlled only by diffusion which it is faster in comparison with the processes of relaxation of the polymeric network and (3) Non-Fickian diffusion also called Anomalous diffusion which arises from the simultaneous and comparable contribution of the phenomenon of diffusion of the molecules of the bioactive agent and the relaxation of the polymeric chains [14]. The analysis of these mechanisms is realized considering the diffusional exponent n that is obtained by the equation following [15, 16]:

$$Ms = kt^n \tag{1}$$

Where k is a constant that depends on the diffusion coefficient and the material thickness, t is the time and Ms equals $H\ (i)$ shown in the Eq. 2 which is calculated

according to the swelling equation as a function of time, where *i* is the amount of data acquired.

$$H(i) = ((w(i) - w(0))/w(0)) * 100 = kt^n \quad (2)$$

Here, *w (i)* is the weight increased at one time *i* and *w0* is the weight of the xerogel.

The natural logarithm is applied to Eq. 2 and a straight line is obtained whose slope is the diffusional exponent. For the case of thin films, when the value of *n* is 1 the diffusion mechanism is Case II, if the value of n is between 0 and 1, the transport mechanism of the water follows an Anomalous behavior, and if the *n* is 0.5, the diffusion follows the laws of Fick so it is the diffusion is Fickian [13, 16].

In addition, to characterize the hydrogels, the pH of the surfaces was measured, FTIR spectra were obtained, the hydrogels images were analyzed by SEM to determine porosity and pore density and dehydration tests were realized at room temperature and in hospitals conditions of a general care room for adult patients with skin burns, this involves imitating the temperature (32 °C +/− 1.5 °C) and humidity (50% +/− 8%) of this rooms.

2 Materials and Methods

We used PVP k90 of Solkem of 99.98% and PVA with a hydrolysis degree of 99% of Sigma Aldrich. A 10% w/v PVA:PVP (1:1) solution was prepared. The polymers were dissolved in deionized water at 90 °C with stirring for 2 h. The mixture was placed in the corresponding casts inside multilaminated bags. Subsequently, the solution was subjected to gamma irradiation from a Co60 source at a dose of 30 kGy, with a dose rate of 7.5 kGy h^{-1}.

The resulting hydrogels were evaluated by a swelling test according to ASTM 570. In this test, the hydrogels were taken to xerogel in an oven at 50 °C for 24 h. Then, the samples were placed in a container with sterile distilled water and weight measurements were performed for 72 h. With the data obtained, the percentage of swelling and the diffusional exponent was calculated, this data allowed the analysis of the type of water diffusion mechanism in the gel.

The dehydration test was performed at room temperature and under hospital conditions. In the first case, the hydrogel samples were placed in a petri dish maintained at a temperature of 23 °C +/− 1 °C, in the second case, the samples were placed at 36 °C +/− 1 °C and humidity of 50% +/− 1% and the entire surface of the hydrogel was covered with adherent film to imitate the treatment given to this type of wounds. The weights of the samples were recorded for 72 h and the percentage of dehydration was calculated from the data obtained. The pH was measured with a surface pH meter at different points of the elaborated hydrogels. The FTIR test was performed on a sample of xerogel and on the polymers of PVP and PVA separately so that they serve as a comparative base. The fracture surface of the hydrogel was visualized in the SEM at low vacuum.

The cytotoxicity of the material was evaluated with a VERO cell line through the MTT test with three extraction vehicles: physiological solution (PS), phosphate buffer

(PBS) and culture medium with serum (MEM) under the guidelines of ISO 10993-5 which establishes that viability greater than 70% indicates that the sample analyzed is non-cytotoxic.

3 Results

The results showed that the hydrogels (see Fig. 1) were easily manipulated and easily removable. The results of the characterization tests are shown below.

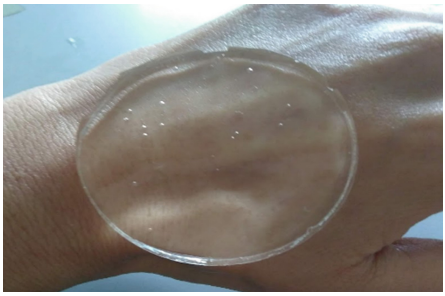

Fig. 1. PVA/PVP hydrogel crosslinked by gamma radiation.

3.1 Swelling Test

The (Fig. 2) shows the increase in the swelling percentage as a function of the time of hydrogels. It can be seen that at 48 hs the swelling reached saturation with a percentage of 636.58% +/− 5.09% with respect to the original weight. The calculated *n* exponent was 0.5, indicating that the diffusion mechanism of the water molecules in the hydrogel responds to a Fickian behavior, which implies that the diffusion speed of the water molecules in the hydrogel is less than the relaxation rate of the polymer matrix.

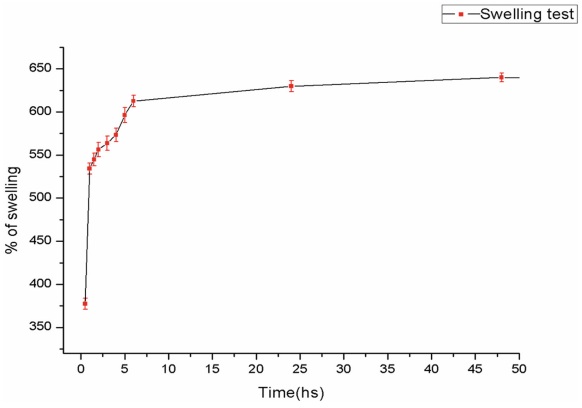

Fig. 2. Swelling in hydrogels samples

3.2 Dehydration Test at Room Temperature

In the (Fig. 3), the graph of the dehydration percentage as a function of time is observed. The dehydration percentage reached 88.18% +/− 0.35% at 48 h and stabilized at that value. In the graph it can be seen that within the first 6 h the dehydration percentage reached 29.83% +/− 3.83%.

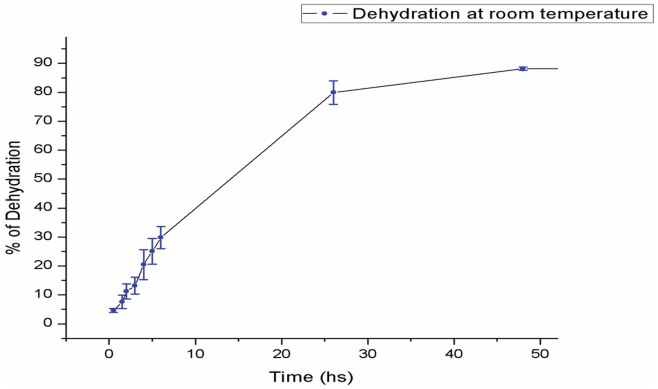

Fig. 3. Dehydration of hydrogel samples in a test at room temperature.

3.3 Dehydration Test in Hospital Conditions

In the (Fig. 4) the variation of the dehydration percentage over time is exhibited. In this graph the dehydration rate is slower. Within the first 6 h the dehydration percentage is 12.7% +/− 0.70%. Just after 24 h dehydration percentage reached 28.4% +/− 3.13%, getting the maximum dehydration of 56.85% +/− 5.17 at 72 h.

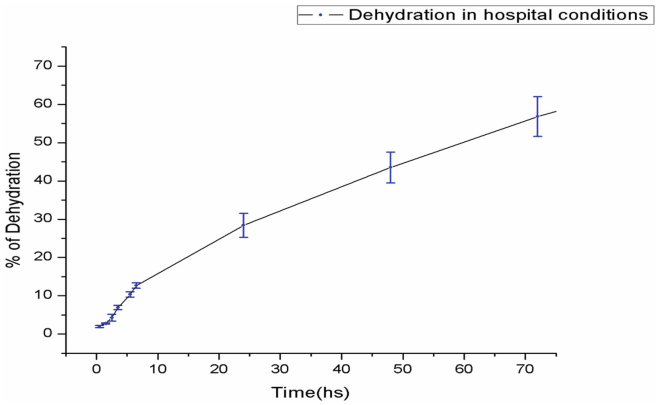

Fig. 4. Dehydration of hydrogel samples in hospital conditions.

Comparing the results of the dehydration it can be observed that the conditioning of the samples simulating a hospital environment had a great influence on the results, reducing in more than 30% the dehydration of the hydrogels.

3.4 pH Test

An average pH value of 5.63 +/− 0.025 was obtained.

3.5 Fourier Transform Infrared Spectroscopy (FTIR)

In the (Fig. 5) the hydrogel spectrum is shown. It can be seen that the absorbance bands characteristic of each polymer are present [17, 18]. The peak at 3370 cm^{-1} appears in both polymers and corresponds to the OH^{-} group. The band at 2925 cm^{-1} also appears in both polymers and corresponds to the C-H. The peak at 1659 cm^{-1} appears in the PVP and is associated with C = 0. The bands in 1462 cm^{-1} and 1441 cm^{-1} appear in the PVP and are associated to the deformation of the CH. The band at 1291 cm^{-1} appears in the PVP and is due to the C-N bond. The peak at 1089 cm^{-1} corresponds to the vibrational stretching of the C-O and is associated with the PVA.

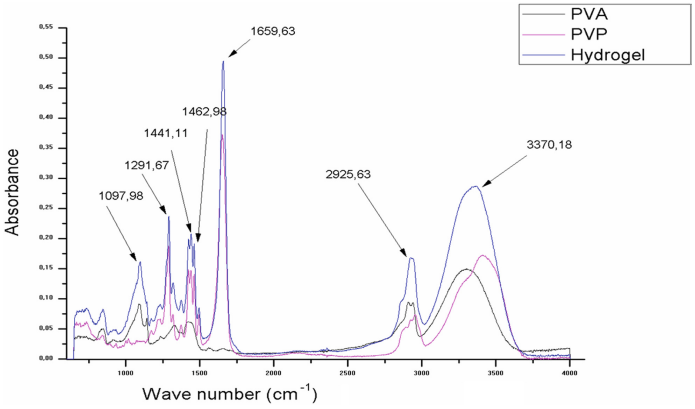

Fig. 5. Spectra of hydrogel (blue color), PVP (magenta color) and PVA (black color)

3.6 Scanning Electron Microscopy (SEM)

In the (Fig. 6) an SEM image of the hydrogel fracture surface is shown. By analyzing it with the ImageJ® software it was obtained that the porosity range covers from 0.625 μm to 2.075 μm. The pore size that appears most frequently is 1.17 μm and the average pore size calculated was 1.16 μm +/− 0.38 μm.

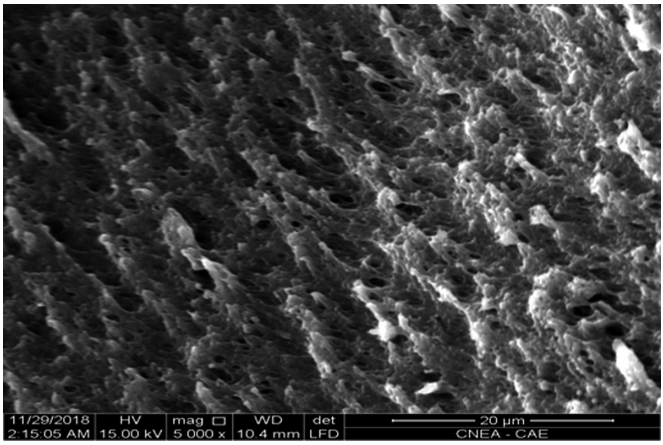

Fig. 6. Image of the fracture surface of a hydrogel with magnification of 5000X

3.7 Cytotoxicity Test

The cytotoxicity test showed the following cell viability percentages: PBS 103.72% +/− 0.03%; MEM 101.55% +/− 0.02% and PS 102.84% +/− 0.05% which indicates that the hydrogels are non-cytotoxic.

4 Discussion

The hydrogels that resulted from the radiation crosslinking process compared to those generated by other methods such as the chemical or physical method, have greater advantages from the point of view of the ease and speed in the generation of the product that occurs simultaneously with the sterilization. The procedures for obtaining physical hydrogels by thermal cycling are extensive since at least more than two cycles are needed to generate a hydrogel and this implies a time greater than 48 h [19]. Another advantage of the hydrogels generated by radiation in the absence of toxic elements, this is one of the main disadvantages of chemical processes [12]. Also other advantage is that these hydrogels have thermostability compared to physical hydrogels which dissolve at certain temperatures, therefore they would not support a process of heat sterilization.

The hydrogels characterization is crucial to demonstrate that they are apt to be used as a medical product. The swelling test is of great importance to know how much liquid the gel can absorb and how are the transport mechanisms with which they are moving in the hydrogel mesh. The dehydration tests in two conditions could demonstrate that under laboratory conditions (room temperature) similar to those in hospital conditions, the hydrogels have the capacity to have a minimum dehydration during the first 8 h of treatment, which is the duration of a conventional bandage.

The analysis of the FTIR spectra allows us to appreciate that only the absorbance bands of the polymers that make up the hydrogel appear, with this we demonstrate that

there is no other chemical element that can result from the synthesis process and that can generate toxicity. Both polymers present supplier certification as biocompatible materials; however in the final product the cytotoxicity test verified that the hydrogel is non-cytotoxic therefore is suitable for use as a medical product.

Finally, surface pH measurements indicate that hydrogels generated with PVA/PVP polymers present acidic surfaces that could reduce the basic environment present in wounds as a result of bacterial and enzymatic activity.

5 Conclusions

The hydrogels generated in this project present a simple, economical synthesis procedure alternative, which is independent of the use of chemical substances for the generation of hydrogels, friendly to the environment, biocompatible and with acid surface pH characteristics that could induce an accelerated recovery of patients with dermal wounds.

Interest Conflict Declaration. Our research group considers that this work does not present conflicts of interest.

References

1. Singer, A., Clark, R.: Cutaneous wound healing. N. Engl. J. Med. **341**(10), 738–746 (1999)
2. Gethin, G.: The significance of surface pH in chronic wounds. Wounds UK **3**(3), 52 (2007)
3. Andrades, P., Sepúlveda, S., González, J.: Curación avanzada de heridas. Rev Chil Cir **56**(4), 396–403 (2004)
4. Greener, B., Hughes, A., Bannister, N., Douglass, J.: Proteases and pH in chronic wounds. J. Wound Care **14**(2), 59–61 (2005)
5. Hoffman, A.: Hydrogels for biomedical applications. Adv. Drug Deliv. Rev. **64**, 18–23 (2012)
6. Rosiak, J., et al.: Radiation formation of hydrogels for biomedical application. Radiation synthesis and modification of polymers for biomedical applications, 5 (2002)
7. Crescenzi, V., et al.: Novel hydrogels via click chemistry: synthesis and potential biomedical applications. Biomacromol **8**(6), 1844–1850 (2007)
8. Echeverri, C.E., et al.: Síntesis y caracterización de hidrogeles de alcohol poli vinílico por la técnica de congelamiento/descongelamiento para aplicaciones médicas. Revista EIA (12) (2009)
9. Tawfik, E.K.: Radiation effect on characterization and physical properties of polymer nano composites (2013)
10. Clough, R.L.: High-energy radiation and polymers: a review of commercial processes and emerging applications. Nucl. Instrum. Methods Phys. Res., Sect. B **185**(1–4), 8–33 (2001)
11. Sakurada, I., Ikada, Y.: Effects of cobalt-60 gamma radiation on poly (vinyl alcohol) (III): effects of gamma radiation on water-swollen films and aqueous solutions (special issue on physical, chemical and biological effects of gamma radiation, II) (1961)
12. Rosiak, J., Ulański, P.: Synthesis of hydrogels by irradiation of polymers in aqueous solution. Radiat. Phys. Chem. **55**(2), 139–151 (1999)

13. Singh, B., et al.: Radiation crosslinked psyllium and polyacrylic acid based hydrogels for use in colon specific drug delivery. Carbohyd. Polym. **73**(3), 446–455 (2008)
14. Benítez, J.L., et al.: Cinética de absorción y transporte del agua en hidrogeles sintetizados a partir de acrilamida y anhídrido maleico. Revista Latinoamericana de Metalurgia y Materiales **35**(2), 242–253 (2015)
15. Ritger, P., Peppas, N.: A simple equation for description of solute release I. Fickian and non-fickian release from non-swellable devices in the form of slabs, spheres, cylinders or discs. J. Controlled Release **5**(1), 23–36 (1987)
16. Ritger, P., Peppas, N.: A simple equation for description of solute release II. Fickian and anomalous release from swellable devices. J. Controlled Release **5**(1), 37–42 (1987)
17. Sadahira C.: Caracterização dos hidrogéis do álcool polivinílico (PVA) processados por método químico e radiação gama. Anais do 9o Congresso Brasileiro de Polímeros, vol. 17 no. 4. Paraiba (2007)
18. Mishra, R., Datt, M., Banthia, A.: Synthesis and characterization of pectin/PVP hydrogel membranes for drug delivery system. AAPS PharmSciTech **9**(2), 395–403 (2008)
19. Stauffer, S., Peppast, N.A.: Poly (vinyl alcohol) hydrogels prepared by freezing-thawing cyclic processing. Polymer **33**(18), 3932–3936 (1992)

Morphology and Viability of Nerve Cells Cultured on Plasma Polymerized Polypyrrole-Coated Scaffolds

Diana Osorio-Londoño[1], J. Rafael Godínez-Fernández[2], Ma. Cristina Acosta-García[3], Juan Morales-Corona[4], and Roberto Olayo-González[4(✉)]

[1] Posgrado en Ciencias (Ingeniería Biomédica), Universidad Autónoma Metropolitana, Iztapalapa, Mexico City, Mexico
dmol@xanum.uam.mx
[2] Departamento de Ingeniería Eléctrica, Universidad Autónoma Metropolitana, Iztapalapa, Mexico City, Mexico
gfjr@xanum.uam.mx
[3] Departamento de Biología de la Reproducción, Universidad Autónoma Metropolitana, Iztapalapa, Mexico City, Mexico
acostagmc@xanum.uam.mx
[4] Departamento de Física, Universidad Autónoma Metropolitana, Iztapalapa, Mexico City, Mexico
{jmor,oagr}@xanum.uam.mx

Abstract. In this work, neural cell interactions with previously fabricated and characterized polylactic acid (PLA) fibrillar scaffolds, randomly- and aligned-oriented, coated with plasma-synthesized polypyrrole (PPPy) and polypyrrole doped with iodine (PPPy/I) were studied by three-dimensional culture of cells from a neural cell line on the scaffolds, analysis of their morphologic response by scanning electron microscopy and their viability by measuring the metabolic activity of the cells directly seeded on the scaffolds. Cells attached to the composite scaffolds and projected filopodia towards neighboring cells and fibers. Randomly-oriented scaffolds allowed for greater cell population on the scaffolds than did the aligned scaffolds. Greater average cell viability, adequate membrane ultrastructure and even neurite-like processes were observed on PPPy- and PPPy/I-coated scaffolds. These results suggest that PPPy/I and aligned PPPy-coated scaffolds provide a permissive substrate for the growth and survival of neural cells, with potential for supporting the processes of neural tissue repair and regeneration.

Keywords: Composite scaffolds · Tissue engineering · 3D cell culture

1 Introduction

Tissue engineering, as a promising strategy to assess nerve tissue injuries, relies on the design and physicochemical properties of biomaterials promoting cell–biomaterial interactions [1]. In vitro three-dimensional (3D) cell culture is an approach for studying

© Springer Nature Switzerland AG 2020
C. A. González Díaz et al. (Eds.): CLAIB 2019, IFMBE Proceedings 75, pp. 652–655, 2020.
https://doi.org/10.1007/978-3-030-30648-9_86

cell–cell and cell–environment interactions in controlled and more easily-monitored conditions than animal models, presenting a more realistic strategy for evaluating cellular processes than 2D cultures [2].

Cell line-based models afford advantages over primary cell-based models, such as the use of clearly-defined types of cells comprising known characteristics, without the complexity, maintenance cost and ethical implications of primary cultures. The neuroblastoma-glioma hybrid cell line NG108-15 expresses properties of the neuron used to study processes, such as adhesion, migration, cytoplasmic neurite-like processes, cytocompatibility and the effect of topography on cells [3, 4]. To evaluate neural cell response to fibrillar composite scaffolds, 3D in vitro models were designed and evaluated by scanning electron microscopy (SEM) and the MTT metabolic assay for cell viability.

2 Materials and Methods

The NG108-15 cell line (ATCC, HB-12317™) was cultured in standard conditions [4]. The cells were then detached mechanically by pipetting and seeded onto UV-sterilized randomly- and aligned-oriented PLA scaffolds, coated with PPPy and PPPy/I, as fabricated and characterized in our previous work [5]. For the SEM studies, 2 × 104 cells were seeded on each scaffold and maintained for 15 days. Samples were then fixed in 3.5% glutaraldehyde in 0.1 M PB at 4 °C, washed with 7.4 pH PB at 4 °C, post-fixed in OsO4, dehydrated by immersion in ascending concentrations of ethanol in water (30–100%) and critical-point dried. Samples were mounted on SEM holders using conductive carbon tape and graphite paint, and coated with gold.

For the viability test, 1.65 × 104 cells were seeded on each scaffold and maintained for 5 days. Samples and controls (scaffolds without cells) were then transferred to a 96-well microplate, washed in PBS, and 0.5 mg/ml MTT (Sigma, M 5655) solution in PBS was added. After 2 h, DMSO (Sigma) was added and left for 2 h in the dark. Absorbance from samples and controls was recorded in an Epoch Microplate Spectrophotometer at 580 nm. Measurement of metabolic activity was obtained by subtracting the absorbance of the controls from the corresponding absorbance of scaffolds with cells. Since viable cells reduce MTT by metabolic activity, the absorption from dissolved MTT reduction product, which is proportional to the number of viable cells [7], was used to estimate cell viability.

3 Results and Discussion

In general, the cells attached and grew on the scaffolds; however, as shown in Fig. 1, there were morphologic differences between them. Randomly-oriented scaffolds allowed more cell bodies to populate the scaffolds' inner fibers, due to the pores formed during the electrospinning process, as opposed to the more packed structure of the oriented scaffolds in which the pores extend longitudinally.

The NG108-15 cell line extended filopodia all over the plasma membrane in general, which searches for integrin adhesion sites to move the rest of the cells [4], in

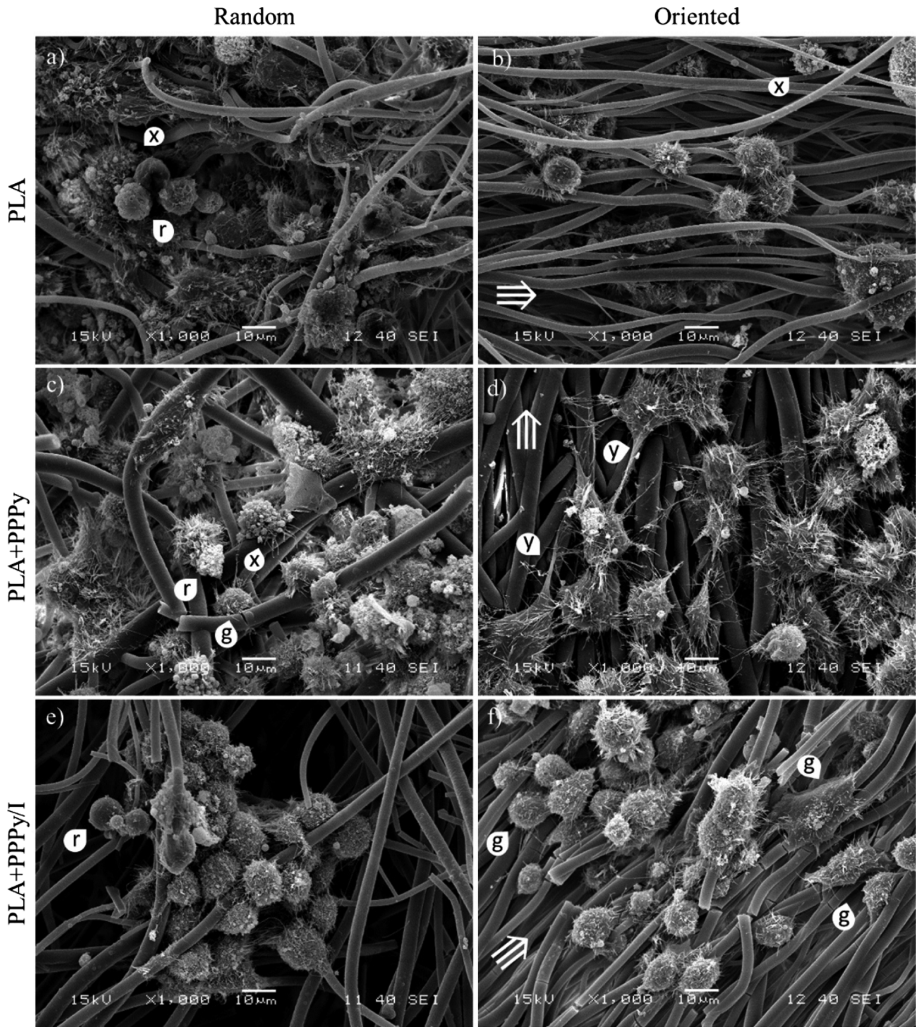

Fig. 1. SEM images of NG108-15 cell line on the scaffolds. Amplification × 1000, bar = 10 µm. "X" indicates blebbed membranes; "r," cells with altered membrane without filopodia; "g," adequate plasma membrane; "y," neurite-like processes; and triple arrows, direction of the fibers.

this case using the fibers to attach and migrate, and in many cases, forming dense cytoplasmic processes toward the fibers. Aligned PPPy-coated scaffolds induced elongation of neurite-like processes, following the path of the oriented fibers, as shown in Fig. 1d.

In PLA and random PPPy-coated scaffolds, some cells have blebbed membrane (Fig. 1a–c), suggesting cell death processes [6]. Other cells show an altered plasma membrane without filopodia (Fig. 1, indicated by "r"), thus losing the ability to attach to the substrate. Although these events are normal in biologic systems, cell blebbing also

occurs when cells are exposed to noxious stimuli [6]. By contrast, in PPPy/I and aligned PPPy-coated scaffolds, the cells display adequate membrane structure in general.

Table 1 shows preliminary results of the MTT assay as mean ± SD (n = 3). These results suggest that PPPy and PPPy/I-coated scaffolds serve as more permissive substrate for cell survival than uncoated scaffolds, in accordance with SEM images showing better cell membrane structure when seeded on PPPy (aligned) and PPPy/I-coated scaffolds, thus suggesting cell preference towards PPPy/I surfaces and an aligned topography.

Table 1. Average viable cell absorbance on the scaffolds

	PLA	PLA + PPPy	PLA + PPPy/I
Random	0.274 ± 0.332	0.355 ± 0.0756	0.714 ± 0.789
Aligned	0.317 ± 0.193	0.964 ± 0.243	1.14 ± 0.637

4 Conclusion

Aligned fibrillar PPPy-coated scaffolds induced morphologic changes in the cells, which developed neurite-like processes, while aligned PPPy/I-coated scaffolds provided the more permissive substrate for a greater average number of viable cells. These results suggest that aligned fibrillar PPPy and PPPy/I-coated scaffolds have the physicochemical properties for neural cell adhesion, survival and neurite outgrowth, and thus, the potential for supporting neural tissue repair and regeneration.

Acknowledgments. We thank Dr. Carlos E. Orozco Barrios for his support. This work was financially supported by the National Council for Science and Technology (CONACyT).

Conflict of Interest Statement. The authors declare that they have no conflict of interest.

References

1. Chen, L., Yan, C., Zheng, Z.: Functional polymer surfaces for controlling cell behaviors. Mater. Today **21**(1), 38–59 (2018). https://doi.org/10.1016/j.mattod.2017.07.002
2. Zhuang, P., Sun, A.X., An, J., et al.: 3D neural tissue models: From spheroids to bioprinting. Biomaterials **154**, 113–133 (2018). https://doi.org/10.1016/j.biomaterials.2017.10.002
3. Hamprecht, B.: Structural, electrophysiological, biochemical, and pharmacological properties of neuroblastoma-glioma cell hybrids in cell culture. Int. Rev. Cytol. **49**, 99–170 (1977). https://doi.org/10.1016/S0074-7696(08)61948-8
4. NG108-15 [108CC15] ATCC® HB-12317™. https://www.atcc.org. Accessed 18 May 2019
5. Osorio, D.M., Godínez, J.R., Morales, J., Olayo, R.: Desarrollo y Caracterización de Andamios para Aplicaciones en Sistema Nervioso. In: Memorias del Congreso Nacional de Ingeniería Biomédica, pp. 298–301 (2018). https://doi.org/10.24254/cnib.18.58
6. Zhang, Y., Chen, X., Gueydan, C., Han, J.: Plasma membrane changes during programmed cell deaths. Cell Res. **28**, 9–21 (2018). https://doi.org/10.1038/cr.2017.133
7. Stoddart, M.J.: Mammalian Cell Viability. Humana Press, Totowa (2011). https://doi.org/10.1007/978-1-61779-108-6_8

Analysis and Quantification of Bone Tissue Around Anodized Zirconium Implants

Guillermo Abras[1(✉)], Maria Rosa Katunar[2], Josefina Ballarre[2], Virginia L. Ballarin[1], and Juan Ignacio Pastore[1]

[1] Laboratorio de Procesamiento de Imágenes ICYTE – CONICET, Mar del Plata, Argentina
{gabras, jpastore}@fi.mdp.edu.ar
[2] División de Electroquímica Aplicada – INTEMA – CONICET-UNMDP, Mar del Plata, Argentina

Abstract. Characterization of newly formed bone tissue around surface modified Zr implants is one way to determine and quantify the bioactive response of these generated surfaces. The objective of the present work is to evaluate if the surface modification treatment, by the anodizing technique, has an effect on histomorphometric bone tissue parameters such as mass of bone or bone density, in an in vivo model. For this purpose, a clustering algorithm was designed for the segmentation of trabecular bone tissue in histological images. The experimental results show that anodizing treatment at 30 V produce a significant increase in bone volume. This is evident because the number and thickness of trabeculae increase and the separation between them decreases.

Keywords: Bone tissue · Image segmentation · Implants

1 Introduction

The use of cementless implants is increasing worldwide. Modifications at the surface level have been the subject of research in recent years in order to promote the process of osseointegration and long-term fixation [1]. Chemically modified surfaces increase the adhesion and proliferation of ontogenic lineage cells, favoring the expression of genes and proteins associated with bone tissue. Zirconium (Zr) is a promising material with regard to permanent implants, with good wear resistance, osseointegration capacity, low corrosion rate and therefore low ion release [2].

The objective of the present work is to evaluate if the surface modification treatment by the anodizing technique has an effect on histomorphometric bone tissue parameters such as bone mass or bone density, in an *in vivo* model.

The classic evaluation of morphological parameters is usually done with a commercial or free software [3], but the choice of the evaluation zone and the principal parameters have to be settled by the operator. In this work, the evaluation of the surface treated implants regarding bone volume and osseointegration was carried out by applying Digital Image Processing techniques in order to measure the trabecular bone tissue around the implant.

© Springer Nature Switzerland AG 2020
C. A. González Díaz et al. (Eds.): CLAIB 2019, IFMBE Proceedings 75, pp. 656–662, 2020.
https://doi.org/10.1007/978-3-030-30648-9_87

In particular, the ability to detect structures with certain characteristics within an image, such as, for example, bone tissue [4, 5], constitutes a fundamental aspect for the automation of different types of applications. This type of procedure, known as image segmentation, allows the decomposition of an image into significant regions, according to each particular application [6].

A paradigm widely used for segmentation consists of the grouping or classification of pixels using various techniques of pattern recognition. The pixels are characterized by numerical vectors that identify them with some criteria, their components being called characteristics or descriptors, which are extracted from the images to be segmented [7, 8]. The selection of a good set of descriptors is the key in any classification process to achieve a later adequate segmentation [9].

The clustering algorithm proposed for the segmentation of the trabecular tissue generated around modified Zr implants, is based on a variant of the k-means called weighted K-means algorithm [10].

Once the segmentation is done, the information can be used by the specialists to compare volumes, morphologies and characteristics of these tissues with normal ones.

2 Materials and Methods

2.1 Sample Preparation

The characteristics of the surrounding bone tissue were studied with Zr implants without treatment (Zr0) and with anodized treatment at 30 V (Zr30).

Pure zirconium metal samples (99.9% w/w Cordes SA, Argentina) were used in nail like shape (0.9 mm diameter). Samples were used bare or treated with an anodising treatment with constant voltage (30 V) for 60 min in phosphoric acid.

All the experiments were approved by the Bioethics Committee HIEMI-HIGA, (Mar del Plata, October 2011). Twelve-week male WKAH/Hok rats (n = 6) weighting 300 g–330 g were used in this study. The animals were divided in two groups for each type of surface treatment: control and anodised. All animals were housed in a temperature controlled room with 12 h. alternating light-dark cycle and were given water and food *ad libitum* throughout the study.

Rats were anaesthetized with fentanyl citrate and droperidol (Janssen-Cilag Lab, Johnson and Johnson, Madrid, Spain) according to their weight and the surgery region was cleaned with antiseptic soap. The animals were placed in a supine position and the implantation site was exposed through the superior part of the tibia's internal face. A region of around 0.5 cm diameter was scraped in the tibia and femur plateau and a hole was drilled using a hand drill with a 0.15 cm diameter bur at low speed. The implantation site was irrigated with physiological saline solution during the drilling procedure for cleaning and cooling purposes. The control and anodised implants were placed by press fit into the tibia extending into the medullar canal for 30 days. Conventional X-ray radiographs were taken after surgery for control purposes (Fig. 1). Animals were sacrificed and the tibias were fixed, decalcified and included in paraffin and the sections colored with hematoxylin-eosin.

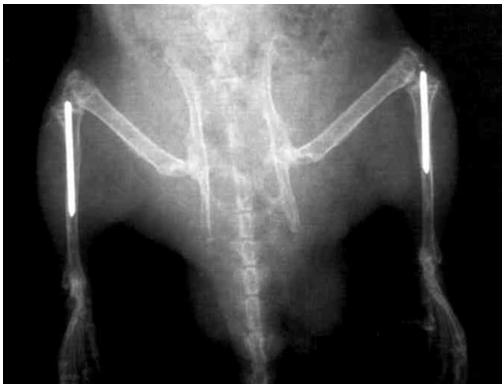

Fig. 1. Conventional X-ray radiographs were taken after surgery.

2.2 Images to Process

Proximal tibia cross-sections transversal to the central long axis of the tibia were prepared and cut as described above. Three sections from the proximal region were selected and stained with hematoxylin-eosin to allow for observations and identifications/discriminations of tissues (bone and bone marrow for example), in particular at the metal-implant interface in a light microscope (Nikon Eclipse Ti, Tokyo, Japan).

2.3 Digital Image Processing: Classification Method

To estimate the area of the bone tissue generated around the anodized zirconium implant, we propose a segmentation method based on an unsupervised classification algorithm in a region of the image bounded by a ring around the implant. Given the staining that was performed on the histological samples, the images obtained are color images, so the method is based on the use of this descriptor for segmentation. In the next section we describe the classification method used.

2.4 Weighted K-Means

Clustering is one of the unsupervised pattern recognition techniques that have been widely used to identify regions in an image. They are deterministic methods for grouping data according to different types of characteristics, when the level of prior information that is available is very low. One of the most widespread methods of clustering is the k-means algorithm [9].

In summary, given a set Ω with an ideal partition $W = \{W_1, W_2, \ldots, W_p\}$ where each subset W_i is called a class and being F a n-dimensional vector of characteristics, a new partition $H = \{H_1, H_2, \ldots, H_p\}$ in R^n is defined as $D(F) = H_i$ where D is a measure of similarity. The measure of similarity is usually determined by the proximity of the points in R^n according to a defined distance function, although it can be based on

other properties [9]. One of the most used distance functions is the Euclidean. The smaller the distance, the greater the similarity.

In particular, the k-means algorithm is based on the minimization of a criterion function which, in this case, consists of the sum the Euclidean distances between all the points of one cluster to its center, squared. Each sample is assigned to the cluster which distance to centroid is minimum. The center of each cluster is recalculated, minimizing the criterion function. The algorithm ends when the cluster centroid not change. Initial centers of each cluster are randomly chosen. The behavior of the k-means algorithm is little influenced by the choice of the initial centers so no prototypes are needed, because they arise from the data [10].

In this work, we use a special variant of the k-means algorithm, called weighted k-means, in which the number of times that appears in a given pattern is taken into account for the calculation of the cluster centers. A weighted average is used in the calculation of the centers [10].

2.5 Segmentation Method for Estimating the Trabecular Tissue Area Around the Implant

In this section, the algorithm proposed to segment the bone tissue generated around the naked implant is semiautomatically described. The bone color images present different objects whose tonalities vary from red to bordeaux, with different textures (granulated, curvilinear, etc.) of great complexity, combined with white, black and non-textured parts.

Since in the images the information that allows to differentiate the objects to be segmented is not conveniently distributed in the RGB space, through color space transformations, the RGB image is modeled in the YIQ and YUV spaces. These spaces were chosen since the luminosity or brightness are clearly differentiated [11, 12].

The variability of the values of the components of the matrices and the purpose of homogenizing the weight of each of them in the grouping algorithm, all are normalized by means of a map to the interval [0,1]. The matrices now represent images in gray levels. In addition, in order to soften the textures, each of them is applied to a low-pass average spatial filter [6].

Each position pixel (s,t) in the original color image, will be represented by a vector of characteristics $F = \{f_1(s,t), f_2(s,t), \ldots, f_n(s,t)\}$, where $f_i(s,t)$ is each of the gray levels of the component images of the same position as the pixel. Therefore, each feature vector F represents a point (or pattern) in the space R^n, and will be characteristic of the weighted K-means algorithm to perform the segmentation.

The steps of the proposed algorithm are the following:

- *Step 1:* conversion of the bone color image from the RGB space to the YIQ and YUV spaces and normalization and filtering of the obtained matrices to convert them to gray level images.
- *Step 2*: application of the classification algorithm to the images obtained in step 1, with the characteristic vector defined by $F = \{f_1(s,t), f_2(s,t), \ldots, f_n(s,t)\}$ where each component represents the filtered image by $n = 6$.

- *Step 3:* assignment of the patterns to one of the three clusters or groups H_1, H_2 and H_3, which represent the different kinds of objects: bone tissue, implant and the rest of the tissues that make up the image (Fig. 2(b)).
- *Step 4*: generation of a ring that is used as a mask. The internal diameter of the implant is the morphological gradient of the implant and the outer diameter is determined in such a way that the area of the implant increases by 10% (Fig. 2(f)).
- *Step 5:* The image segmented in step 3 is multiplied by the mask generated in step 4, in order to delimit the region of interest around the implant, on which the measurement and calculation of the covered area are made (Fig. 2(g)).
- *Step 6:* calculation of the percentage of the area covered by the ring. This is done by the sum of pixels belonging to the bone tissue class.

The proposed method is a semi-automatic method, thus, the user selects the initial cluster centroids from the screen in the original image.

To illustrate the steps of the proposed algorithm, Fig. 2 shows the results obtained in the different stages of segmentation in a histological image of bone tissue. Figure 2 (a) shows the original image stained with hematoxylin-eosin. Figure 2(b) shows the result of the segmentation obtained with the weighted K-means algorithm and Fig. 2(c) the class corresponding to trabecular bone tissue. Figure 2(d) and (e) show the class of the trabecular tissue and the rest of the classes applied to the original image respectively. Figure 2(f)–(i) show the ring on which the analysis of bone integration is performed.

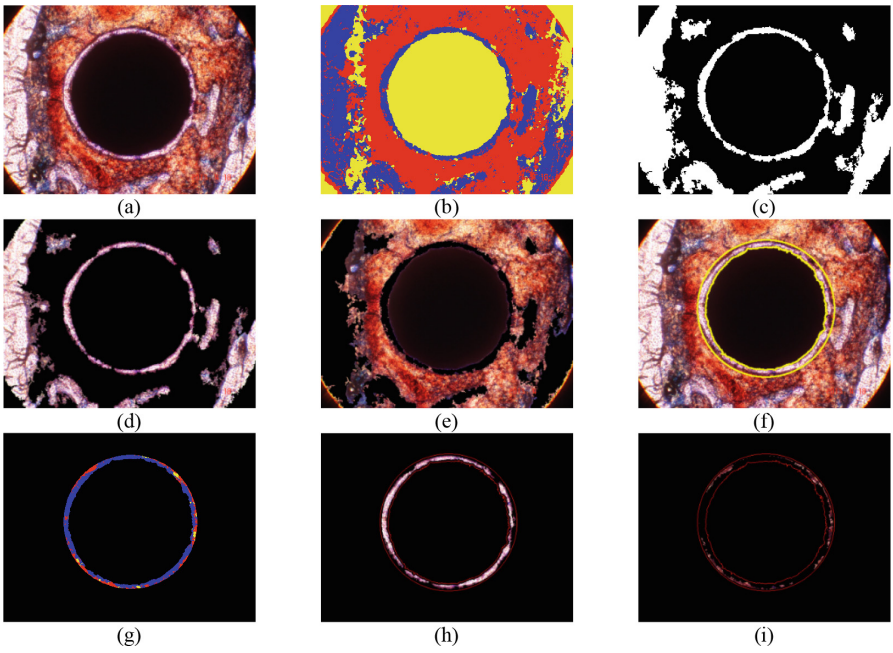

Fig. 2. Results obtained in the different stages of the proposed method.

For this image the resulting area within the ring corresponding to the trabecular bone tissue generated around the implant is 76.46%.

In the following section, the results obtained on two samples are presented.

3 Results

Table 1 shows the results obtained on a total of 64 images, of which 32 correspond to the bare material and 32 to the material with anodized treatment. Results revealed that anodizing treatment at 30 V could produce a significant increase in bone volume reflected in an increase in the number of trabeculae, their thickness and in a smaller separation between them. With this, it could be inferred that the anodizing treatment at 30 V would enhance the development of a trabecular bone with a more stable morphology for future mechanical and functional performance.

Table 1. Results obtained on a total of 64 images

Samples	Mean area	Standard deviation
Implants with treatment (Zr30)	91,6%	6,4%
Implants without treatment (Zr0)	71,2%	7,8%

4 Conclusion and Discussion

The segmentation of histological images of bone tissue is a complex process due to their fuzzy boundaries, different textures and tonalities making the objects extraction a difficult task. With the proposed method, an efficient semi-automatic image segmentation can be achieved, helping the work of the specialist and reducing the subjectivity of the analysis. With the proposed method it is possible to quantify the area of the bone tissue around the implants. Although the method is not totally automatic, since the user must select the initial centroids from the screen, similar papers reported in the state of the art use commercial software, where the user intervention is necessary also for segmentation and objects measurement [13]. Therefore, results are not reproducible, with great intra- and inter-user variability.

Results revealed that anodizing treatment at 30 V could produce a significant increase in bone volume reflected in an increase in the number of trabeculae, their thickness and in a smaller separation between them. As future work, we propose to develop an interface in order to supply the specialist with a friendly graphic environment.

References

1. Bauer, S., Schmuki, P., von der Mark, K., Park, J.: Engineering biocompatible implant surfaces: part I: materials and surfaces. Prog. Mater. Sci. **58**(3), 261–326 (2013)

2. Katunar, M.R., Gomez Sanchez, A., Santos Coquillat, A., Civantos, A., Martinez Campos, E., Ballarre, J., Vico, T., Baca, M., Ramos, V., Cere, S.: In vitro and in vivo characterization of anodised zirconium as a potential material for biomedical applications. Mater. Sci. Eng. C **75**(2017), 957–968 (2016)
3. Rasband, W.S.: Image J.U.S. National Institutes of Health; Bethesda, Maryland, USA (2009). http://rsb.info.nih.gov/ij/
4. Abras, G.N., Ballarin, V.L., González, M.L.: Segmentación de Imágenes de Biopsias de Médula Ósea utilizando técnicas de Reconocimiento de Patrones y transformaciones de Espacios Color. VI Congreso Latinoamericano de Ingeniería Biomédica (CLAIB 2014), 29, 30 y 31 de octubre de 2014. Paraná, Argentina
5. Abras, G.N., Katunar, M.R., Ballarre, J., Pastore, J.I., Ballarin, V.: Reconocimiento de patrones en imágenes color: análisis micro-estructural de tejido óseo alrededor de implantes de circonio. XXI Congreso Argentino de Bioingeniería (SABI 2017), 25, 26 y 27 de octubre de. Córdoba, Argentina (2017)
6. González, R., Woods, R.: Digital Image Processing. Addison Wesley, Boston (2002)
7. Wu, G., Shen, D., Sabuncu, M.R.: Machine Learning and Medical Imaging, p. 481. Academic Press, Cambridge (2016). ISBN: 978-0-12-804076-8
8. Torrents-Barrena, J., Piella, G., Masoller, N., Gratacós, E., Eixarch, E., Ceresa, M., Ballester, M.Á.G.: Segmentation and classification in MRI and US fetal imaging: recent trends and future prospects. Med. Image Anal. **51**, 61–88 (2019)
9. Duda, R., Hart, P., Stork, D.: Pattern Classification and Scene Analysis. Wiley, New York (2000)
10. Abras, G., Ballarin, V.: A weighted k-means algorithm applied to brain tissue classification. J. Comput. Sci. Technol. **5**, 121–126 (2005)
11. Trémeau, A., Tominaga, S., Plataniotis, K.N.: Color in image and video processing: most recent trends and future research directions. J. Image Video Process. **2008**, 1–26 (2008)
12. Wyman, C., Sloan, P., Shirley, P.: Simple analytic approximations to the CIE XYZ color matching. J. Comput. Graph. Tech. **2**(2), 1 (2013)
13. Gao, Y., Luo, E., Hu, J., Xue, J., Zhu, S., Li, J.: Effect of combined local treatment with zoledronic acid and basic fibroblast growth factor on implant fixation in ovariectomized rats. Bone **44**(2), 225–232 (2009). ISSN 8756-3282

In Situ Mechanical Characterization of Skin: Participation in the Program Nodos Binacionales de Salud

Michelín Alvarez-Camacho[1,2(✉)], Ana Laura Pérez-Medina[1], Paris Joaquín Velasco-Acosta[2], Andreas Schoetz[3], and Citlalli Jessica Trujillo-Romero[2,3]

[1] Ingeniería en Sistemas Biomédicos, Facultad de Ingeniería UNAM, Mexico City, Mexico
mich_address@hotmail.com
[2] Instituto Nacional de Rehabilitación Luis Guillermo Ibarra Ibarra, Mexico City, Mexico
[3] Mentor Tecnológico de Monterrey/CONACyT/National Science Foundation, Mexico City, Mexico

Abstract. A research project focused on skin elasticity evaluation, was started at the request of burn physicians at the Instituto Nacional de Rehabilitación, to collect information on tissue quality and the efficiency of interventions. As data collection progressed, it was sought to transfer the results to the market, allowing diffusion and use. Thus, it was decided to participate in the Nodos Binacionales de Salud program. Although research at the Mexican National Institutes of Health focuses on solving patient health requirements, the question was how these projects can lead to a sustainable success on the market. During the program we follow the Lean Startup methodology that consists in finding potential market by getting out of the building to do interviews; the main tool used was the Business Model Canvas and mentor support on how to validate business hypotheses. Throughout the program we realized that the initial product did not meet the needs of the physicians and it was decided to make a pivot. A new business model focused on injectable cosmetic treatments was developed, due to its economic viability. In this market, the validation of most of the business model and field of development were achieved, through the discovery of a new product soon to be available in the market. Although the decision of not to advance the cosmetic technology was taken, the primary research project, focused on burn patients do continue in progress, with a new understanding of the relevant information for the customers ecosystem.

Keywords: Business model · Nodos Binacionales de Innvación · Technology validation · Skin elasticity

1 Introduction

Healthy skin experience strain and displacement to allow movement of the body. Once the skin has suffered an injury, such as a burn, the ability to deform is compromised, which causes contractures. At the Instituto Nacional de Rehabilitación Luis Guillermo

© Springer Nature Switzerland AG 2020
C. A. González Díaz et al. (Eds.): CLAIB 2019, IFMBE Proceedings 75, pp. 663–669, 2020.
https://doi.org/10.1007/978-3-030-30648-9_88

Ibarra Ibarra, our group is developing a research project focused on the measurement of mechanical deformation and the displacement of the skin. In this paper we present the experience of participation in the Nodos Binacionales de Salud program, to highlight the importance of technological validation from an early stage of research projects.

1.1 Project Potential

The research project started from the approchement between the Centro Nacional de Investigación y Atención a Quemados and the Laboratorio de Ingeniería de Rehabilitación, to solve the specific need to obtain evidence on tissue quality and efficiency of different interventions. The project is at an TRL2 development stage. The volume and type of data obtained in this research exceeds the capacities of scientific publications to show relevant results, so we looked from this initial stage of the project, a transfer strategy that allows diffusion and use of the results. Thus, it was decided to participate in the Nodos Binacionales de Innovación en Salud program.

1.2 Business Model Canvas

The Business Model Canvas (BMC) [1] is composed of nine basic sections whose purpose is to logically describe how a company should operate and how it pretends to generate money. These blocks cover the four main areas for a business: customers, offer, infrastructure and financial viability.

The blocks are:

1. Value Propositions. Reasons why customers prefer your product. They are aggregations, or a set of benefits aimed at a specific customer segment. They solve a specific customer problem or satisfy one of their needs.
2. Customer Segments. They are the multiple groups of people that a company tries to reach and serve. Without them, the company cannot survive. To satisfy them, they must be better separated into different segments with common needs, common behaviors or other attributes. For this it is necessary to obtain the customer archetype.
3. Channels. Ways in which the company communicates and reaches its customers to deliver a Value Proposition. They are the points of contact with customers and there are three types: sales, to acquire the product or service; distribution, to make delivery; and support, to maintain contact with the customer after the purchase.
4. Customer Relationships. Connections that the company creates with a specific Customer Segment and are motivated by getting, keeping and growing customers and, therefore, sales.
5. Revenue Streams. Money generated by each Customer Segment. It should be asked, "what value is the customer paying for?". The price of the product should not be based on production costs, but on the perception that customers have about the Value Proposition.
6. Key Partnerships. Companies that provide essential elements for the enterprise to be successful. They are created to optimize business models, reduce risk, acquire resources or complement your product. It must be a bidirectional relationship, that is, both must obtain a benefit.

7. Key Resources. Most critical assets to start the business, and to allow the startup to offer a Value Proposition, reach markets, create and maintain relationships with customers, and earn revenue. They can be physical, financial, intellectual or human.
8. Key Activities. Critical actions to execute the business model. It is a to do list to obtain money and have a successful company.
9. Costs Structure. Costs focused on the project and not on the product. They can be calculated after defining Key Resources, Key Activities and Key Partnerships.

1.3 Iterative Validation Process

In addition to the BMC, other tools were also available, such as the Lean Startup methodology [2], which consists in decreasing the development time of a product by performing experiments based on hypotheses and validating them through an iterative process that aims to obtain a feedback from potential clients. It involves open-ended questions in face-to-face interviews of at least 10 clients per hypothesis or until a tendency is discovered. The information obtained with this process serves to generate conclusions that enrich and corroborate the information of each of the blocks of the business model. In addition, we counted on the direct advice of the professors of the course, of a mentor with business experience, and a software platform for registration and documentation of the progress.

2 Methodology

The objective of the application of the I-Corps methodology [3] through the Nodos Binacionales course is that each research project can determine how ready they are to reach commercialization. As well as allowing the teams to develop a clear decision to go or no-go, based on viability for commercialization. In addition, a transition plan is developed to advance the technology, in case the team decides to do so. The methodology implies that the researchers change their way of working, leave their laboratories to meet the market and thus, validate their hypotheses to continue with their research.

2.1 Development Stages

During the kick-off week, the methodology was presented; a BMC with initial hypotheses to be tested were generated, and the market discovery was put into practice following the Lean Startup methodology. Subsequently, in each week, the main topics of different sections of the Canvas were studied in detail, and the hypotheses proposed for each of the sections were refined.

2.2 Construction of the Business Model

The initial business model proposed did not met burns specialists needs, as it was discovered that the elasticity measurement will be used only for research. Moreover, the technology product proposed for their use (a virtual patient) was not fully useful.

Therefore the application spectrum of the technology was open to both healthy skin and burn treatments. In addition, an alternative business model had to be developed from the results of the interviews. In this model, a new value proposition was established for clients in the area of cosmetic medicine, with a new target market. Needs, limitations, preference in channels to receive the product, use, payment and support requirements were detected.

3 Results

In addition to conducting interviews, an investigation was carried out on the size of the national and international market of cosmetics industry. We reviewed the literature related to treatments, both surgical and non-surgical; duration of the effect of different treatments, frequency of application, costs and future trends. At this stage, the participation of a mentor with experience in the pharmaceutical and cosmetic industry, who gave us access to relevant industry information, was crucial.

3.1 Initial Canvas

The first Canvas was integrated by 51 hypotheses. In Fig. 1, the general diagram of the first BMC is shown. The technological product to validate consisted of a virtual patient (Fig. 1a) to visualize the mechanical-functional behavior of the skin; with the intention of being used as a guide (Fig. 1b) by surgeons, rehabilitators and researchers, to improve the success of the treatment of burned patients (Fig. 1e–h).

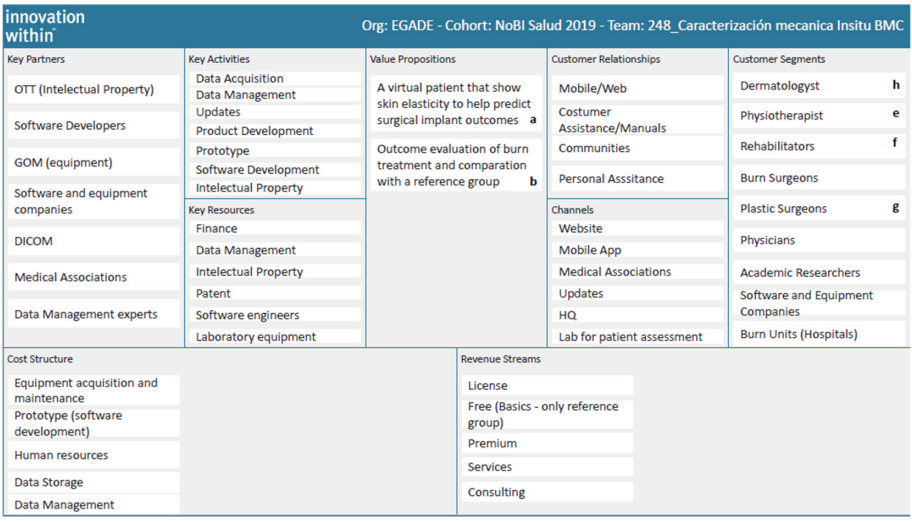

Fig. 1. Initial canvas. (a) and (b) Initial product and value proposition. (e)–(h) Initial customer segments.

3.2 Shifts and Pivots

During the course, 107 interviews were conducted with surgeons and rehabilitation specialists in burns, developers of cosmetic products and dermal covers, patients, plastic surgeons, dermatologists, internists, dentists, maxillofacial surgeons and distributors of medical devices related to care of the skin as laser, among others. The clients were located in hospitals with burn care units, dermatological clinics, private practices and through the attending of a scientific meeting in burn care in the city of Aguascalientes. Of the 107 interviews conducted, 88.7% were in-person, 7.6% were by telephone, and 3.7% were video calls.

The BMC with the pivots and shifts is shown in Fig. 2, validate hypothesis are in green, invalidates hypothesis in red and pending to be validated in white. During the course 24 new hypotheses were added to the model (47%), of which five were not validated (9.8%). 35 hypotheses (68.6%) were invalidated, mainly those generated in the first BMC. Four hypotheses (7.8%) were modified to integrate two ideas that had originally been presented separately. Of the original hypotheses, six were pending to be validated (11%). At the end of the course, the total of validated hypotheses was 17, which corresponds to 33%.

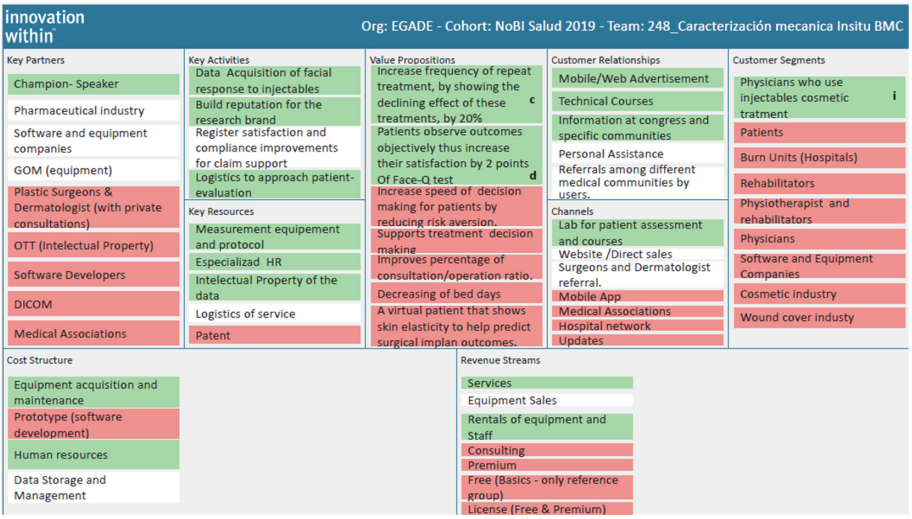

Fig. 2. Final Business Model Canvas. Validated hypotheses are marked in green, invalidated hypothesis in red and pending of validation in white.

3.3 Final Canvas

It was decided to focus the product on nonsurgical cosmetic treatments, specifically in injectables, because they have two great advantages: they are very popular and the patient frequently returns to evaluation and re-application of the treatment (Fig. 2c and d), since they are temporary interventions. The interviewed physicians agreed in the

interest of buying or renting a small equipment that could be installed in their offices, which allowed them to measure their patients to show the changes before-after the treatment, and maintain a photographic record for follow-up, as some treatments have a very noticeable result, while others do not (Fig. 2i).

3.4 Validation

This last step was not expected. However, the last week of the program, we found through a cosmetic equipment distributor that the brand they represented will launch a product to the market with features very close to those we developed during the market discovery process.

Value propositions: A mechanical and photographic evaluation of the skin to help the diagnosis and follow-up of patients undergoing cosmetic treatments.

Clients: Plastic surgeons, dermatologists and cosmetic professionals.

The commercial product also has characteristics that were yet not fully resolved in our product, such as physical presentation: small and portable equipment, integration of cameras, light sources and support for the patient's face; and support functions: safety storage and processing of a large volume of images.

This finding allowed us to validate the work done in the course. However, due to the complexity of competing with a product fully developed, with a distribution network, pre- and post-sales support, the decision not to continue with the development of the project to a further stage was made. Therefore, the conclusion of the course was a "no-go" of the business.

4 Discussion

A business model of a technological product, relevant to the market, was developed. The business model was constructed by making a set of interviews with decision makers from different areas related with skin, for either diseases treatment, scars and healthy skin. The initial results showed that both, the concept of the initial product and the value proposition, did not cover the whole expectations of the clients for whom the technological product was developed. This was unexpected because the customers were involved in the design process of the initial concept [4]. Besides this, we found out that the initial technology application, to analyses burn scars, was not enough to initiate an independent business. The main reason of this was that physicians were focused on the use of the product only as a research tool. Moreover, due to the cost of burns treatment, it is unlikely that patients consider paying extra for a non-vital evaluation.

In order to initiate a real business, it was necessary to pivot and find a new area with enough financial resources, where our technology could be applied. This new market must appropriate our technology in order to be a viable field of development. These characteristics are important, as it has been observed that factors such as availability, feasibility and cost are important to match the technology with the market [5].

Fortunately, we manage to observe and document requirements of the cosmetic industry and to validate our findings.

During the process of business model construction, as researchers in the biomedical engineering area, we found that it is important to increase our knowledge about the market readiness, in order to develop a product with the potential to be a successfully commercial [6]. It is important to remark that this is the first time that the Instituto Nacional de Rehabilitación participates in a program like this and further experience is needed to advance the project.

Finally, we consider that a long-term mentoring program would be helpful to enrich the work of biomedical engineering teams involved in R&D, to consider the validation processes of medical devices products. For the development of a business model, we found out that to have a multi-disciplinary team with expert people in business was important to make an effective research-market integration and enriched the research. For this project, the primary research activity, focused on burn patients, is still under development. Although we found out that it is not a scalable business, the original product is better focused on the validated requirements of the consumers.

References

1. Osterwalder, A., Pigneur, Y.: Business Model Generation. Wiley, New Jersey (2010)
2. Nobel, C.: Teaching a 'Lean Startup' Strategy. Harvard Business School|Working knowledge, pp. 1–2 (2011)
3. ¿Qué es I-Corps? http://www.nobiu.unam.mx/?page_id=691. Accessed 13 May 2019
4. Schwab, T., Fassl, B., Langell, J.: The importance of design validation in global health surgical innovation. Surg. Innov. **25**(6), 563–569 (2018)
5. MacLachlan, M., McVeigh, J., Cooke, M., Ferri, D., Holloway, C., Austin, V., Javadi, D.: Intersections between systems thinking and shaping for assistive technology: the SMART (Systems-Market for Assistive and Related Technologies) thinking matrix. Int. J. Environ. Res. Public Health **15**, 2627 (2018)
6. Malkin, R.: Barriers for medical devices for the developing world. Expert Rev. Med. Devices **4**(6), 759–763 (2017)

Residual SDS Reducing Methods in the Process of Decellularization of Muscle Tissue

Christian Chapa-González[1(✉)], Miguel Ángel Alfaro-Zapata[1], Joseph Kinsella[2], Adeodato Israel Botello-Arredondo[1], and Esmeralda Saraí Zúñiga-Aguilar[1]

[1] Instituto de Ingeniería y Tecnología de la Universidad Autónoma de Ciudad Juárez, CH 32310 Ciudad Juárez, Mexico
christian.chapa@uacj.mx
[2] Department of Bioengineering, Mc Gill, Quebec H3A 0C3, Canada

Abstract. Developing bioinks that are biocompatible and well-suited with the printing process is crucial for the progress of 3D bioprinting tissue engineering field. Decellularized extracellular matrix (dECM) bioink is considered a promising material for bioprinting applications due to its inherent composition. However, the laboratory protocols for obtaining this bioink involve the use of sodium dodecylsulphate (SDS) detergent which is widely known as an agent that causes lysis of the cell membrane. This study reports the fabrication of decellularized matrix gels and the comparison between the morphology and rheological behavior of the extracellular matrix gels treated with different SDS elimination methods. These dECM gels were treated with PBS, acetone or trichloroacetic acid (TCA). Scanning electron microscopy revealed that the PBS washes and the acetone treatment maintained the porous gel structure. The flow curve of the three gels was also studied and determined that the bioinks has a pseudoplastic behavior and that the viscosity of the TCA treated gel is relatively lower (0.08 Pa·s) than the acetone and PBS treated dECM, 0.2 Pa·s 0.3 Pa·s respectively. Even though the dECM gels treated with acetone and TCA encourages the cell survival, the storage modulus of acetone-treated bioink is above the loss modulus indicating that the microstructure is able to resist the shear stress and hold its conformation.

Keywords: Tissue engineering · Bioprinting · dECM bioink · Sodium dodecyl sulfate (SDS)

1 Introduction

One of the most emerging techniques in tissue engineering is bioprinting. The bioprinting process consists of the precise deposition of biomaterial and cells layer-by-layer in pre-defined computer-aided designs. The bioprinting methods are classified into three main groups, according to the operating mechanisms: extrusion-, droplet-, and laser-based process. The comparison of bioprinting techniques in terms of the operating principles, the components, as well as the advantages and disadvantages of each one is described elsewhere [1]. Although, recent advances in the printing of skin

© Springer Nature Switzerland AG 2020
C. A. González Díaz et al. (Eds.): CLAIB 2019, IFMBE Proceedings 75, pp. 670–678, 2020.
https://doi.org/10.1007/978-3-030-30648-9_89

[2, 3], cardiac cells [4, 5], neural tissue [6], cartilage and bone [7, 8], and stem cell derived tissues [9] have been reported, and in all cases, the suitable bioink features are crucial. Therefore, improving bioinks remains one of the main challenges in tissue engineering for research groups.

One of the most important goals in bioprinting is achieving bioinks whose rheological properties are compatible with the printing method, in addition to maintaining the conditions for cellular function and tissue formation. Encapsulated cells in individual extracellular matrix (ECM) components such as collagen, fibrin, gelatin, hyaluronic acid, etc. are largely adopted for bioink research [10–12]. However, the decellularized extracellular matrix (dECM) based-bioinks promote the cell viability, proliferation, differentiation, migration and morphological changes by growth factors [13].

The dECM bioink is obtained by the elimination of cellular residues through the use of chemical, physical and enzymatic methods. Sodium dodecyl sulfate (SDS) is a detergent commonly used in the protocols for obtaining dECM [14, 15]. The SDS solubilizes the cell and nuclear membrane, plus it efficiently removes the cell content of dense tissues. The impact of SDS on the tissue decellularization process is explained elsewhere [16]. Likewise, the effect of SDS on cell behavior has recently been reported [17]. Because the effect of SDS on cellular and ECM integrity is well known, it is necessary to implement new methods to minimize the remnant of this detergent in the dECM.

Once the dECM is obtained, it is solubilized to the desired concentration, which results in a gel-like substance which must meet several important properties for suitable for bioprinting. The rheological nature of the resulted bioink has a considerable impact on the printability and cellular viability. In consequence, the viscosity of the bioink should be adjustable according to the requirements of the selected printing method.

In the present work, we describe practical methods for reducing the SDS concentration in dECM-based bioink. Reduction of SDS concentration in dECM based-bioinks was enhanced with three different types of treatments. These treatments are the use of acetone (Ac), trichloroacetic acid (TCA), and phosphate buffer solution (PBS). Final SDS concentration, rheological properties and cell viability of fabricated dECM bioinks were also determined and compared.

2 Materials and Methods

2.1 dECM Bioink Preparation

A PBS 10x saline solution was prepared, dissolving 80 g of sodium chloride (NaCl, J. T. Baker), 2 g of potassium chloride (KCl, J.T. Baker), 14.4 g of sodium phosphate dibasic (Na_2HPO_4, J.T. Baker), and 2.4 g potassium phosphate monobasic (KH_2PO_4, Sigma-Aldrich) in distilled water to a final volume of 1 L. To obtain a PBS 1x solution, 100 ml of stock mix was diluted in 900 ml of distilled water. The mixture used to eliminate the cellular content was prepared with 10 g of SDS (Research Products International, IL, USA) dissolved in PBS 1x to a final volume of 1 L.

A porcine muscular tissue sample, obtained from a local meat supplier, was weighted and cut into pieces (up to 8 mm^3). The adipose tissue was removed to avoid

its interference with the detergents. The decellularization of skeletal muscle and vascular tissues was conducted according to the protocol described by Pati *et al.*, 2014 [15] with modification. Briefly, the tissue was stirred in 1% SDS solution (400 ml) for 48 h followed by a treatment with 1% Triton X-100 solution for 30 min. The SDS solution was replaced by the new one at 24 h. Then, the tissue slurry was treated with Tris–HCL solution (pH 7.4) for 4 h followed by 3 washes with PBS solution for 24 h.

2.2 Treatments for the Removal of SDS and Residual Quantification

The samples were weighed and divided in three equal parts named dECM-Ac, dECM-PBS, and dECM-TCA, according to the applied treatment. dECM-Ac sample was shaken vigorously in acetone for 10 min in an ice bath. The sample was centrifuged at 6000 rpm for 5 min. The supernatant was discarded, and the precipitated was transferred to a 35 mm petri dish and dried for 12 h followed by PBS for 24 h. dECM-TCA sample was mixed with 33 ml of trichloroacetic acid (Sigma-Aldrich) (60% in PBS) at room temperature and it was incubated through the night. The sample was centrifugated at 6000 rpm for 5 min. Subsequently, 200 ml of acetone were added for 20 min. Finally, it was washed in PBS for 24 h. The dECM-PBS sample was treated with three consecutive washes of 200 ml of PBS 1x for 24 h each.

The three samples were shaken for 2 h in 250 ml with vigorous agitation of the following: peracetic acid solution (1%), ethanol (4%), and deionized water. After this moment, the samples were manipulated under sterile conditions inside a biosafety cabinet class 2. All samples were rinsed with a sterile PBS solution for 24 h.

The samples were lyophilized for 12 h. Afterward, the samples were weighed and 100 ml of HCl 0.01M were added for each gram in the sample, as well as pepsin. The mixture was maintained with agitation for 48 h and afterwards treated with a NaOH 0.1M solution to obtaining a final pH 7.4. The samples were filtered with a nylon mesh of 100 μm (Corning). Subsequently, 6 μL of solubilized gel were mixed with 594 μl of a methylene blue solution (Fisher Scientific), along with 1200 μl of chloroform (J. T. Baker). The absorbance of the samples was measured at 650 nm (Thermo Scientific NanoDrop 2000) and quantified by referring to a standard curve made in advance with SDS.

2.3 Morphology Characterization

The morphology of dECM samples was characterized using a Scanning Electron Microscope SEM (JEOL6010 PLUS/LA) operating at 5.0 kV. The dECM sample was instantly frozen in liquid nitrogen for 2 min and lyophilized for 24 h before being cut into small pieces with a sharp blade. The samples were deposited onto an aluminum holder before SEM observation.

2.4 Rheological Characterization

A rotational rheometer (AR-2000, TA Instruments) with cone geometry (60 mm diameter, 500 μm gap) and a solvent trap was used to evaluate rheological properties such as viscosity (η) and storage modulus (G′) of the dECM-based bioinks. A shear rate

sweep was done in a range of 0.01 s^{-1} to 100 s^{-1} and the apparent viscosity was registered. In addition, it was conducted a temperature sweeps from 8 °C to 36 °C, by simulating a transition from the refrigerator to the incubator. The storage module of the material was measured in function of time. Every measurement was taken in triplicate under the same temperature conditions.

2.5 Cell Culture on Gels

Cell cultures were performed by using breast cancer cell line MDA-MB-231, which expresses the green fluorescent protein (GFP) in its nucleus. The treated gels were mixed with the cell line at a concentration of 2×10^6 cells/ml. A 96-well plate was seeded with 75 μL of the mixture and allowed to incubate at 37 °C for one hour and a 2 ml of culture media was added. The plate was kept in an incubator at 37 °C and 5% CO_2. Changes of culture medium were made every 3 days for a week and then every 2 days since the cell population had increased.

An inverted microscope, U-HGLGPS lighting system, a cubic filter set for GFP and the Metamorf Advance software (IX-83, Olympus, Japan) were used to monitor cell culture growing. The lamp was set to a light intensity of 6% and the images were captured with an exposure time of 100 ms, with a separation between images on the z-axis of 5 μm. The range where the cells were located was searched manually and between 40 and 150 photographs were taken from each well, during days 4, 8 and 17 after starting the cell culture. The files were saved in .TIFF format and the contrast and lighting were adjusted using the ImageJ tool. To show representative results of the cell population throughout the gel, a sum of the images was performed. For this, the Z-Projection tool was used with a maximum intensity projection, which shows the maximum value of the pixels parallel to the z-axis.

3 Results and Discussion

During the decellularization process changes in color and consistency of the muscular tissue were observed. The dECM product is shown in Fig. 1, and the changes are due to the detergent's action which removes blood, lipids and cell content. Once the decellularization process and the methodology implementation to eliminate the SDS were finished, the PBS washed sample was filtered, and the acetone and TCA treated samples were dried. The PBS-treated product did not show any changes after the washes. On the other hand, the acetone precipitated pregel was reduced in size, and it adopted a yellowish color and, once rehydrated, it recovered its initial appearance.

The SDS concentration in the solubilized dECM-treated bioink was measured by adding chloroform and methylene blue to the sample, and the absorbance of the organic phase was measured and compared with the absorbances of the known concentrations. As seen in Table 1, the PBS-treated gel showed a higher SDS concentration, whereas the acetone-treated gel showed the lowest concentration.

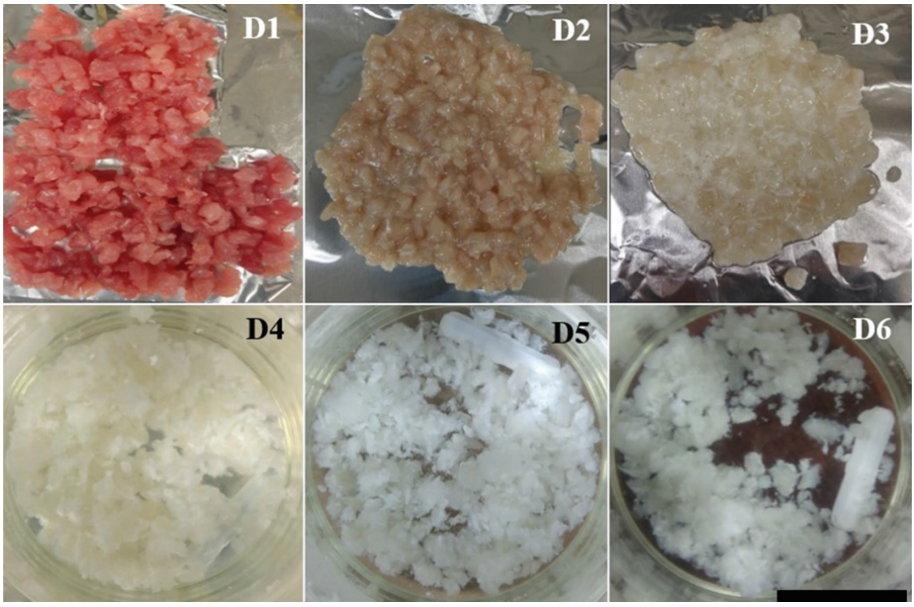

Fig. 1. Images of a native and decellularized muscular tissue sample. The changes were monitored for 6 days. The 1% SDS solution was replaced by the fresh one at 24 h. Scale bar = 45 mm

Table 1. Residual concentration of SDS in dECM inks after treatments

Treatment	Absorbance	Concentration, % (m/V) 10^{-3}
Acetone	0.206[a]	3
Trichloroacetic acid	0.240[b]	5
Phosphate buffer solution	0.325	9

[a]Acetone-treated gel presented an absorbance lower than the LOD
[b]TCA-treated gels showed values below the LOQ, previously calculated.

SEM images are shown in Fig. 2 and demonstrate porous morphology in the PBS-dECM and Ac-dECM while TCA-dECM shows a morphology with no pores. Intermolecular coalescence of unfolding protein is derived from the exposure of the non-polar surface produced by TCA [18] which causes the proteins to form macromolecular aggregates, and avoids the formation of pores.

The results of the flow curves of three different dECM bioinks (Fig. 3) suggest that the dECM gels are suitable for bioprinting techniques compatible with low-viscosity bioinks, as jetting-based printing (3.5–12 mPa·s), and droplet-based printing (<15 mPa·s). However, the dECM bioink treated with TCA was ineffective to form stable porous morphology due to its relatively low viscosity, whereas the PBS-dECM and Ac-dECM with relatively higher viscosity formed a stable porous morphology.

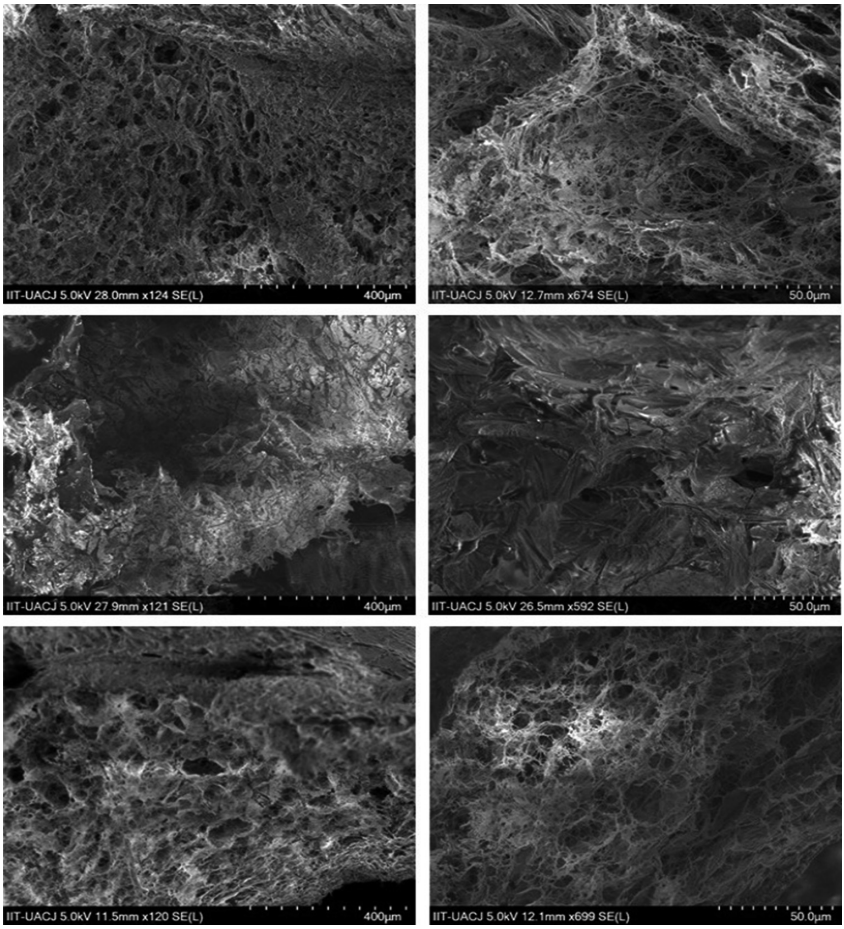

Fig. 2. Representative SEM micrographs of PBS-dECM (top), TCA-dECM (middle), and Ac-dECM (bottom)

The inherent mechanical properties of the biomaterials have a crucial role in the printability of the material, resolution of the impression and cell viability. The information obtained from the flow curve, and the temperature step indicate a modification in the structure of the proteins. This increases the viscosity of the solution at low shear rates and accelerates the gelation process. As shown in Fig. 4, the loss modulus of the bioinks dipped below the storage modulus, due to the thermal gelation properties of dECM. However, the storage modulus is always above the loss modulus in Ac-dECM. This result indicates that although the bioink may flow above 36 °C, the porous microstructure is able to resist the shear stress and hold its conformation.

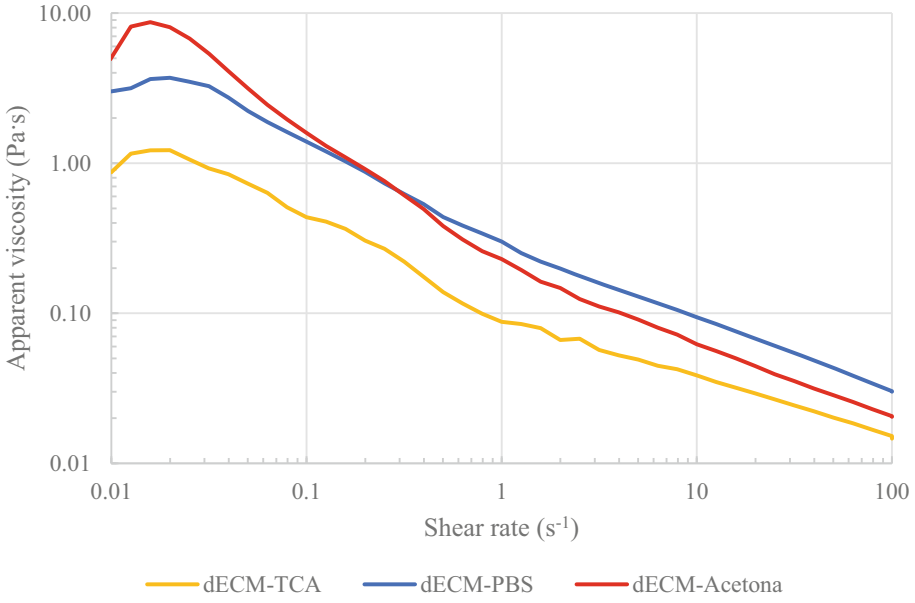

Fig. 3. Flow curves of three different dECM bioinks

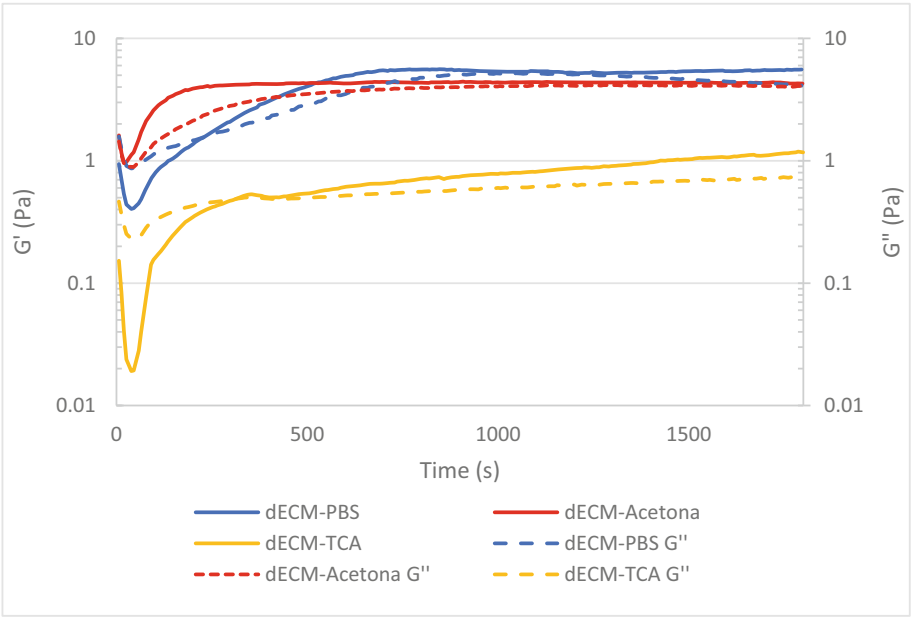

Fig. 4. Storage and loss modulus after a temperature step

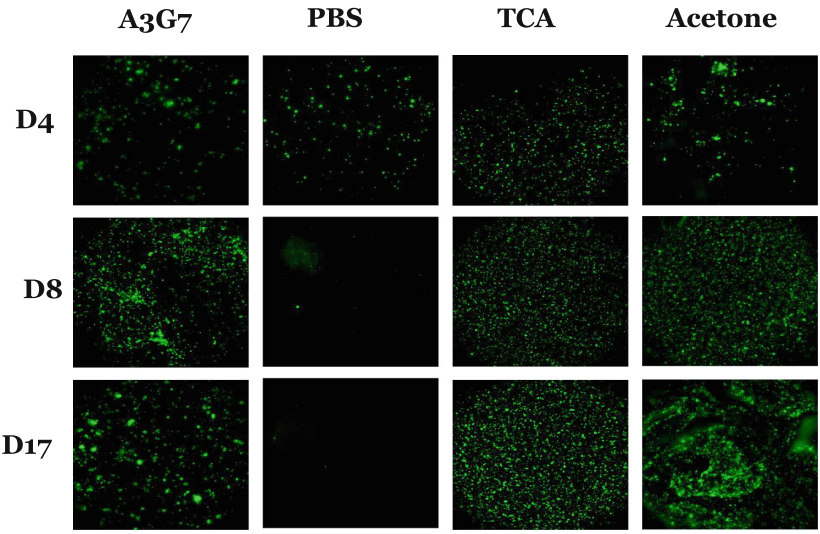

Fig. 5. Cell cultures in extracellular matrix gels from day 4 to day 17. Column from right to left: Ac-dECM, TCA-dECM, PBS-dECM and A3G7. The images were captured at 10× magnification

As shown in Fig. 5, a gel of 3% alginate and 7% gelatin (A3G7) was used as control on cell cultures. The development of tumor spheroids was observed, as previously reported [19]. The cell population increased during the 17 days of cell culture in the control gel, and in the gels treated with acetone and TCA. On the other hand, the culture performed in gels washed with PBS had negative effects on the cell population, since it practically eliminated the number of green spots on day 17. What indicates the presence of a cytotoxic element in the gel that was not removed by the PBS washes and that correlates with the highest concentration of SDS measured in the colorimetric test. When comparing the dECM gels treated with acetone and TCA with the control, a greater number of green points was observed on day 17, suggesting that the dECM gels treated with acetone and TCA encourages the development of the cell population. It was also found that the cells proliferated throughout the dECM gel while the cells in the control gel were kept in groups, forming tumor spheroids.

4 Conclusion

This study has suggested a viable strategy to remove SDS from dECM from muscular tissue. The final SDS concentration was below detectability levels, as confirmed after cell culture. Although modified, the rheological are suitable for bioprinting with different printing systems. This finding confirms the usefulness of acetone as a treatment to reduce the SDS concentration in the dECM. Moreover, the method proposed has a clear advantage over the treatment of removing SDS by several washes with PBS as reported in previous literature.

References

1. Noh, S., Myung, N., Park, M., Kim, S., Zhang, S.-U., Kang, H.-W.: 3D bioprinting for tissue engineering. In: Clinical Regenerative Medicine in Urology, pp. 105–123. Springer, Singapore (2018)
2. Yan, W.-C., et al.: 3D bioprinting of skin tissue: from pre-processing to final product evaluation. Adv. Drug Deliv. Rev. **132**, 270–295 (2018)
3. Augustine, R.: Skin bioprinting: a novel approach for creating artificial skin from synthetic and natural building blocks. Prog. Biomater. **7**(2), 77–92 (2018)
4. Cheung, D.Y.C., Duan, B., Butcher, J.T.: Bioprinting of cardiac tissues. In: Essentials 3D Biofabrication Translation, pp. 351–370 (2015)
5. Kuss, M., Duan, B.: 3D bioprinting for cardiovascular tissue engineering. In: Rapid Prototyping in Cardiac Disease, pp. 167–182. Springer, Cham (2017)
6. Gu, Q., Tomaskovic-Crook, E., Wallace, G.G., Crook, J.M.: Engineering Human Neural Tissue by 3D Bioprinting, pp. 129–138. Humana Press, New York (2018)
7. Chen, C., et al.: Research trends in biomimetic medical materials for tissue engineering: 3D bioprinting, surface modification, nano/micro-technology and clinical aspects in tissue engineering of cartilage and bone. Biomater. Res. **20**(1), 10 (2016)
8. Park, S.-H., Jung, C.S., Min, B.-H.: Advances in three-dimensional bioprinting for hard tissue engineering. Tissue Eng. Regen. Med. **13**(6), 622–635 (2016)
9. Tasnim, N., et al.: 3D bioprinting stem cell derived tissues. Cell. Mol. Bioeng. **11**(4), 219–240 (2018)
10. Parak, A., Pradeep, P., du Toit, L.C., Kumar, P., Choonara, Y.E., Pillay, V.: Functionalizing bioinks for 3D bioprinting applications. Drug Discov. Today **24**(1), 198–205 (2019)
11. Hospodiuk, M., Dey, M., Sosnoski, D., Ozbolat, I.T.: The bioink: a comprehensive review on bioprintable materials. Biotechnol. Adv. **35**, 217–239 (2017)
12. Jang, J., Park, J.Y., Gao, G., Cho, D.-W.: Biomaterials-based 3D cell printing for next-generation therapeutics and diagnostics. Biomaterials **156**, 88–106 (2018)
13. Nam, S.Y., Park, S.-H.: ECM Based Bioink for Tissue Mimetic 3D Bioprinting, pp. 335–353. Springer, Singapore (2018)
14. Deepak, C., Han Win, T., Tianyi, W., May Win, N.: Organ-derived decellularized extracellular matrix: a game changer for bioink manufacturing? Trends Biotechnol. **36**(8), 787–805 (2018)
15. Pati, F., et al.: Printing three-dimensional tissue analogues with decellularized extracellular matrix bioink. Nat. Commun. **5**(1), 3935 (2014)
16. Crapo, P.M., Gilbert, T.W., Badylak, S.F.: An overview of tissue and whole organ decellularization processes. Biomaterials **32**, 3233–3243 (2011)
17. White, L.J., et al.: The impact of detergents on the tissue decellularization process: a ToF-SIMS study HHS. Acta Biomater. **50**, 207–219 (2017)
18. Rajalingam, D., Loftis, C., Xu, J.J., Kumar, T.K.S.: Trichloroacetic acid-induced protein precipitation involves the reversible association of a stable partially structured intermediate. Protein Sci. **18**(5), 980 (2009)
19. Jiang, T., et al.: Directing the self-assembly of tumour spheroids by bioprinting cellular heterogeneous models within alginate/gelatin hydrogels. Sci. Rep. **7**(1), 4575 (2017)

Modeling and Simulation

Animation of Atrial and Ventricular External Walls of a Virtual 3D Heart Based on Echocardiogram Images

Gabriela Colares Ali Ganem, Regina Célia Coelho, and Carlos Marcelo Gurjão de Godoy(✉)

Institute of Science and Technology, UNIFESP, São José dos Campos, SP, Brazil
gurjaogodoy@gmail.com

Abstract. The advance of the three-dimensional (3D) computational simulation resulted in high-fidelity virtual heart models, which are useful for implementation in medical educational tools. These computational tools help the study of cardiac anatomy and function and are of interest to many medical professionals. As the appearance of the heart surface is relevant for the comprehension of cardiac movements, the aim of the present work was the development of an animation of the external atrial and ventricular walls, during the heartbeat in a virtual 3D heart, according to physiological data. The animation used data extracted from echocardiogram images of healthy human hearts and ECG timing. The results show that displacements of the epicardial walls measured manually and wall displacements generated by the animation were comparable. Thus, the implemented animation of the atrial and ventricular external walls of the 3D virtual heart complied with those of echocardiogram images, being useful for future implementation in cardiac teaching and (or) learning tools.

Keywords: Atrial wall · Ventricular wall · 3D virtual heart

1 Introduction

The significant growth of the three-dimensional (3D) computational simulation resulted in high-fidelity virtual heart models [1]. Heart models that provide realistic visualization of the heart are concerned with physiological heart movements observed in medical exam images, such as echocardiograms [2].

The main appeal of developing such computational tools is to help medical and educational professionals in the study of cardiac anatomy and function [2–4]. As the appearance of the heart surface is naturally crucially important to comprehending cardiac physiological movements, the aim of the present work was the development of an animation of the atrial and ventricular external walls of a 3D virtual heart simulator based on measurements taken from echocardiogram images. Similar to a previous work developed by the authors [2], the distinguishing feature of the present work is essentially the use of ECG timing and image analyses for heart simulation.

© Springer Nature Switzerland AG 2020
C. A. González Díaz et al. (Eds.): CLAIB 2019, IFMBE Proceedings 75, pp. 681–684, 2020.
https://doi.org/10.1007/978-3-030-30648-9_90

2 Methods

The general approach consisted of animating a 3D human heart model (https://www.turbosquid.com/3d-models/free-ma-mode-heart/548944) in a virtual environment. Based on the study of Coelho and colleagues [2], the animation used physiological displacements extracted from echocardiogram images. The time references (0.1 and 0.3 s for the atrium and ventricle movements, respectively) correspond to ECG wave durations concomitant with the contraction and relaxation of atrial and ventricular chambers in a cardiac cycle.

2.1 Data Extraction

The parasternal long, apical four-chamber, and short-parasternal echocardiographic planes are concordant with the Cartesian plane, at x, y, and z respectively. The data consisted of displacement measures of the atrial and ventricular walls extracted from 15 echocardiographic videos obtained from the Internet (YouTube), five of which referred to each of the plans mentioned above. The measurements of the walls occurred in a sequence of video frames of the cardiac cycle. The wall measurements excluded the region of the valves and the border that delimits the cone representing the image of the echocardiogram. Once the reliable region for the measurements was delineated, the next step was manually obtaining the measurements (from the top of the inner wall of the endocardium to the epicardium) with the help of an echocardiogram specialist.

2.2 Implementation

The animation's implementation consisted of applying the morphing technique to the virtual 3D heart. For a given chamber, the morphing technique interpolated two images of the 3D heart, one being the deformation in the virtual model equivalent to the systole (contraction) visualized and measured on the echocardiogram, the other being the model without deformations, equivalent to diastole (relaxation). Thus, the interpolation deformation (morphing) in the virtual 3D model represented the appearance of the heart at different moments of the complete heartbeat cycle (systole and diastole). The software used for the morphing (Maya AutoDesk) generated the transition of movements automatically according to the minimum (relaxation) and maximum (contraction) displacement values inserted (values measured from echocardiogram videos). It also generated the displacement curve of each cardiac chamber (left or right ventricle or atrium) automatically in the animation. The curve served to compare the animation movement automatically generated by the morphing technique to the movement extracted from the echocardiogram videos. The Unity 3D software synchronized the temporal data with the period of atrial and ventricular contraction. In the simulation, 13 frames refer to the atrial cycle, which is equivalent to 0.1 s, whereas 23 frames refer to the ventricular cycle, which is equivalent to 0.3 s (time references are the ECG wave durations related to contraction and relaxation of atrial and ventricular chambers). The animation of a 1s-cardiac cycle generated 30 frames as, physiologically, atrial relaxation occurs during ventricular contraction.

3 Results

Figure 1(a) and (b) show the results of the atrial and ventricular wall movements and (c) and (d) show the displacement measured manually and displacement curve obtained from the animation. It is possible to verify that the displacement obtained manually and from the animation are comparable.

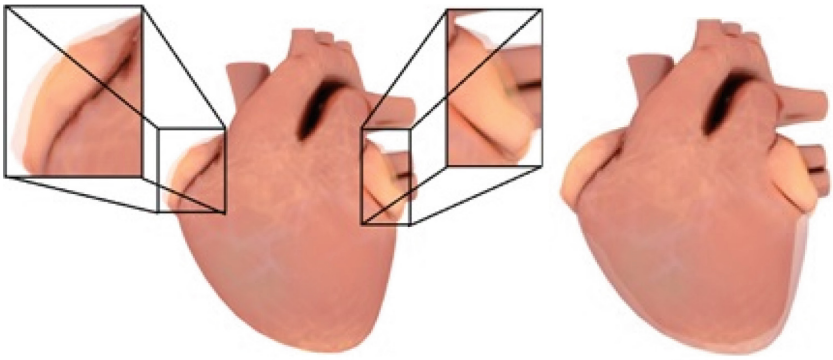

(a) (b)

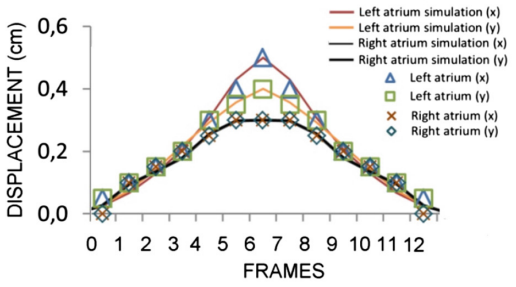

(c)

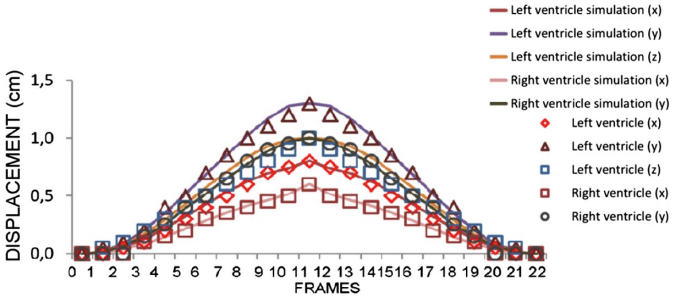

(d)

Fig. 1. Displacement of heart chambers: (a) and (b) illustrate atria and ventricles displacements; (c) displacement graph of Cartesian axes x and y of the external left atrial wall measured manually and the curve obtained from animation; (d) displacement graph of Cartesian axes x, y and z of the external ventricular walls measured manually and curve obtained from animation. The graphs refer to atrial and ventricular displacement periods in a cardiac cycle.

4 Discussion

In this work, the physiological movements of the human heart were appropriately implemented in a virtual 3D heart. The animation followed the movement of the walls according to actual echocardiogram image data and ECG timing.

Even though revisions of the similar works stress out the complexity of modeling both cardiac mechanical and electrical activities [3, 4], the result of the present work will help to improve the 3D heart animation concerning, at least, its external physiological appearance during the cardiac cycle.

Finally, the results showed that it was possible to extract manual measurements of ventricular and atrial wall movements. However, there are controversial opinions among cardiologists about the appropriate way to measure heart walls and their movement, making it difficult to compare clinical measurements in different approaches [5]. Thus, in addition to the aforementioned inherent difficulty, further clinical validation tests of the developed animation are necessary.

5 Conclusion

The results indicate that the implemented 3D animation of the external cardiac walls fairly represents the atrial and ventricular movements observed in actual echocardiograms and could be useful for future implementation in cardiac teaching/learning tools.

Acknowledgment. This work was supported by FAPESP (Proc. 2017/22949-3).

Conflict of Interest. The authors do not have any conflicts of interest to declare.

References

1. Prakosa, A., Arevalo, H.J., Deng, D., Boyle, P.M., Nikolov, P.P., Ashikaga, H., Blauer, J.J.E., Ghafoori, E., Park, C.J., Blake, R.C., Han, F.T., Macleod, R.S., Halperin, H.R., Callans, D.J., Ranjan, R., Chrispin, J., Nazarian, S., Trayanova, N.A.: Personalized virtual-heart technology for guiding the ablation of infarct-related ventricular tachycardia. Nat. Biomed. Eng. **2**, 732–740 (2018)
2. Coelho, R.C., Lourenço, N.C.G., Godoy, C.M.G.: A mobile device tool to assist the ECG interpretation based on a realistic 3D virtual heart simulation. Simul. T. Soc. Sim. **94**, 465–476 (2018)
3. Lopez-Perez, A., Sebastian, R., Ferrero, J.M.: Three-dimensional cardiac computational modelling: methods, features and applications. Biomed. Eng. **14**, 35 (2015)
4. Lopez-Perez, A., Sebastian, R., Izquierdo, M., Ruiz, R., Bishop, M., Ferrero, J.M.: Personalized cardiac computational models: from clinical data to simulation of infarct-related ventricular tachycardia. Front. Physiol. **10**, 580 (2019)
5. Chetrit, M., Roujol, S., Picard, M.H., Timmins, L., Manning, W.J., Rudski, L.G., Levine, R.A., Afilalo, J.: Optimal technique for measurement of linear left ventricular dimensions. J. Am. Soc. Echocardiogr. **32**, 476–483 (2019)

Mathematical Model of the Oculomotor System

Jesica Talero(✉), Karen Leiva, and Ricardo Espinosa(✉)

Seedbed of Research in Rehabilitation and Modelling Applied in Physiological Systems, ECCI University, Biomedical Engineering Program, Bogotá, Colombia
{jesical.talerom,respinosam}@ecci.edu.co

Abstract. Mathematical modeling of eye movement contributes to the learning of the oculomotor system and the development of technologies for device control. We propose in the present article a representative model of the different movements and rotation of the eye (adduction, abduction, elevation and descent) taking into account the anatomical properties of the extraocular muscles, strength-elongation relationship, and the action of the agonist muscles and antagonists. An easy to understand model is presented that allows the analysis of applied forces in muscle contraction, the conversion of length of elongation (or shortening) of the muscle, which generates rotation of the eye, and the vector interpretation of the direction in the space of towards where the eye directs the sight. In addition, an interface was made that allows the user to vary the Force applied to the extraocular muscles and obtain the spatial movement of the eye, with the anatomical and physiological considerations of the oculomotor system. The proposed model allows a simplified understanding, compared to other models, of the physiology of the oculomotor system, and its implementation in computational simulation systems results in faster executions with lower computational cost. The implementation of the proposed model will serve in the future in the control of devices or development of technologies that depend on eye movements or that imitate these movements.

Keywords: Mathematical model · Extraocular muscles · Linear model muscle · Field of view

1 Introduction

The mathematical models of prediction of eye movements are studied and used in the understanding of the oculomotor system, as well as in the control of devices applied in rehabilitation or in the development of bio-inspired technologies.

In the medical field, the models of the oculomotor system have been used by Hoerantner and Kaltofen in 2007, for the correction of pathologies such as, strabismus and high axial myopia through simulations of oculomotor mechanics, these simulators allow to improve diagnostic skills and facilitate treatment planning, by analyzing the action of oblique and extraocular rectus muscles in disorders caused by an elongated eyeball, which generates orientation difficulties with respect to the visual axis [1].

Technologies created dependent on eye movements are also developed, such as the specialized glasses for research in neurology and eye movements, presented

© Springer Nature Switzerland AG 2020
C. A. González Díaz et al. (Eds.): CLAIB 2019, IFMBE Proceedings 75, pp. 685–693, 2020.
https://doi.org/10.1007/978-3-030-30648-9_91

byExtraocular muscles of human Charfreitag in 2008, where an experimental model of eye movement was applied to measure the dynamic position of the head using algorithms, that detect the pupil of eye as a center for recognition of eyeball movements [2].

Bioinspired technologies associated with eye movements are presented even more frequently, in cameras fitted in specific places with the monitoring function, or in cameras placed on robots that simulate the function of vision.

The mathematical model of eye movement considers: the biomechanical action of the main extraocular muscles (superior rectus, inferior rectus, medial rectus and lateral rectus); the analysis of applied forces in muscle contraction, represented in a classic way using the Hill model reported in 1938 [3], which incorporates passive mechanical elements such as springs, dampers and active elements; a spherical mass, which represents the eye, and a system of vectors or angles dependent on the variation of the length of the eye muscles.

The mathematical models of the oculomotor plant have been studied and represented by Holland and Komogorstev in 2013, where they describe the characteristics of the eye and the extraocular muscles responsible for the vertical and horizontal movement of the eye. They also made a comparison between the saccades movements of the normal eye and a simulation of two-dimensional eye movements linearly oriented using the model proposed by the authors [4].

Another model, very popular, for the movement of the eye is that of Bahill in 1980, where it introduces the muscular model of Hill (skeletal muscle represented as a mechanical system) and reveals the values of the passive elements that make up the mechanical system [5]. Both models are similar, and make use of the state matrix to incorporate the necessary variables that result in the vertical and horizontal movements of the eye. The mathematical analysis of these models can be complex and limit their application in the real field.

In the present study, we propose a mathematical model of eye movement using an alternative linear model of the muscle, considering the anatomical properties of the extraocular muscles, simplifying the necessary equations that relate the variables involved in the physiological process of muscular activation, and that finish in the movements of the eye in the different directions of space. In addition, we performed a computational simulator with user interface (using the proposed model) to demonstrate the changes in eye movement caused by the variation of the force applied in the contraction of extraocular muscles. In future works, we want to make validations that allow us to refine the model to obtain results equivalent to the eye movements of a normal subject.

2 Materials and Methods

In this section, we describe the anatomical considerations of the oculomotor system, composed of extraocular muscles and the eyeball. As well as the necessary components for the creation of the mathematical model of eye movement and the development of a simulator that would allow to demonstrate the behavior of the model.

2.1 Design Model of the Human Eye in 3D

The solid structure of the eyeball and the extraocular muscles was modeled in 3D, to be incorporated into a computational simulator (see Fig. 1). The information of the dimensions used in the 3D model of the eye are also a source of information for the mathematical model proposed in this work. The following physiological dimensions of the eye were considered: eyeball (Radius: 1.2 cm), cornea (Radius: vertically 0.5 cm and horizontally 0.6 cm), pupil (Radius: 0.15 cm–0.225 cm), medial rectus muscle (Length: 4.1 cm), lateral rectus muscle (Length: 4.1 cm), superior rectus muscle (Length: 4.2 cm) and inferior rectus muscle (Length: 4.0 cm).

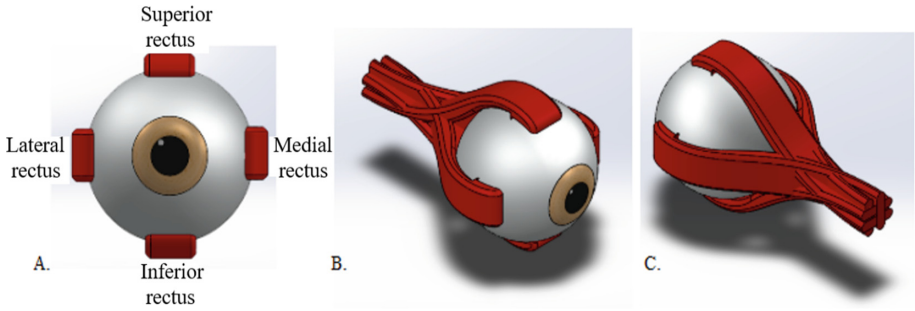

Fig. 1. Extraocular muscles of human eye, A. Front view, B. Upper lateral and C. posterior

2.2 Mathematical Modeling of Extraocular Muscles

The physiological model of the muscle reported by [6], a variation of the mechanical system of the classic Hill model, was used to determine the force vs. elongation. The Fig. 2 shows the muscle model used, this incorporates the same elements interpretively similar to Hill's muscle model, but in a different configuration. The muscle model used represents the behavior of a voluntary contraction muscle and relates to F real force that occurs in the muscle, taking into account its mechanical properties, the value of the maximum contractile force corresponds to 100 gt; Fo is the force developed by the active contractile element of the muscle, can be considered as a percentage of the maximum force, according to [7], in this study Fo equals 0.26% of F.

The elastic element in series (Ce) represents the elasticity of the cross-linkage of actin-myosin of muscle fluted fibers, with a value of 2.5 gt/° [5], while the parallel elastic element (Cp) describes elastic properties of connective tissue (of the extraocular muscles), with a value of 0.9 gt/°, and R the viscous damping present in the tissue, equal to 0.06 gt-sec/° [5]. In this work the responses of four extraocular muscles were considered: medial rectus, lateral rectus, superior rectus and inferior rectus.

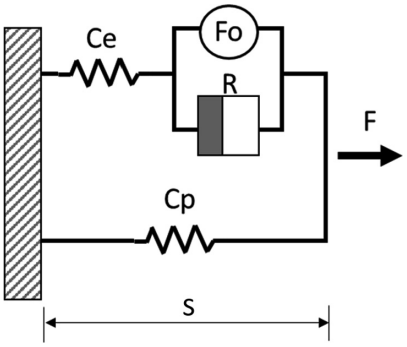

Fig. 2. Linear model of muscular mechanics

The differential equation resulting from the mechanical system of Fig. 2 is described in Eq. (1) and represents the behavior of the muscle action on contracting. When a force F is applied at the entrance of the mechanical system, a variation of the length of the muscle S, is generated.

$$\frac{dF}{dt} + \frac{1}{RC_e}F = \left(\frac{1}{C_e} + \frac{1}{C_p}\right)\frac{dS}{dt} + \frac{1}{RC_eC_p}S + \frac{F_0}{RC_e} \tag{1}$$

We apply the Laplace Transform to the differential equation and we find the variable S(s), which corresponds specifically to the shortening length of the contracting agonist muscle and which corresponds to the same stretch length in the antagonist muscle is:

$$S(s) = \frac{\frac{F(s)}{RCe} + sF(s) - \frac{Fo(s)}{RCe}}{\frac{1}{RCeCp} + \left(\frac{1}{Ce} + \frac{1}{Cp}\right)s} \tag{2}$$

The dynamic balance of the extraocular muscles allows the eye to maintain a forward facing position. The Fig. 3A show an illustrated example of the action of the superior and inferior rectus muscles.

The Fig. 3B shows the contraction of the agonist muscle (for this example the inferior rectus muscle), the muscle contracts a distance S, while the antagonist relaxes (superior rectus). The action of the mass of the eyeball is considered null, because the mechanical system does not drag the mass, only rotates it certain angles, in average of low value. In addition, the mass is held by four muscles, which implies a weight distribution.

If we consider the eyeball, seen from the sagittal plane, as a circumference, we can say that, the turn of the eye is caused by the drag of the muscle when contracting a distance S, without distorting the eyeball.

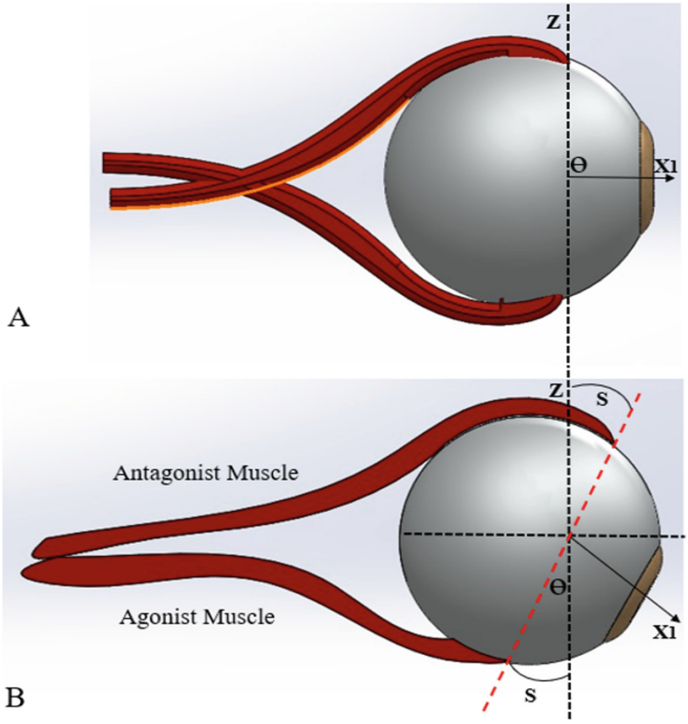

Fig. 3. A. Scheme of the eye on the main axis (X1), B. Scheme of the eye representative of ocular movement

Therefore, there is a relationship between S (seen as the arc of the circumference) and the angle that indicates the movement of the eye with respect to the equilibrium axis (see Fig. 3B). The Fig. 4A shows the relationship of the following variables: Arc length S, is calculated by the Laplace inverse transform of Eq. (2), R is the radius of the eyeball equal to 1.2 cm and the angle θ can be calculated by the following equation:

$$\theta = \frac{S * 180^{\circ}}{\pi * R} \tag{3}$$

The above is described equally for the action of the lateral muscles (medial and lateral rectus). The Fig. 4A shows the sagittal and transverse planes of the eyeball and the orientation of the view represented by the vector X1.

The superior and inferior rectus muscles allow the pupil to move up and down, on coordinates Y and Z axes, while the lateral muscles allow the pupil to move to the right and left, on coordinates X and Y axes. In both cases, one of these axes is shared, which is common for eye movements.

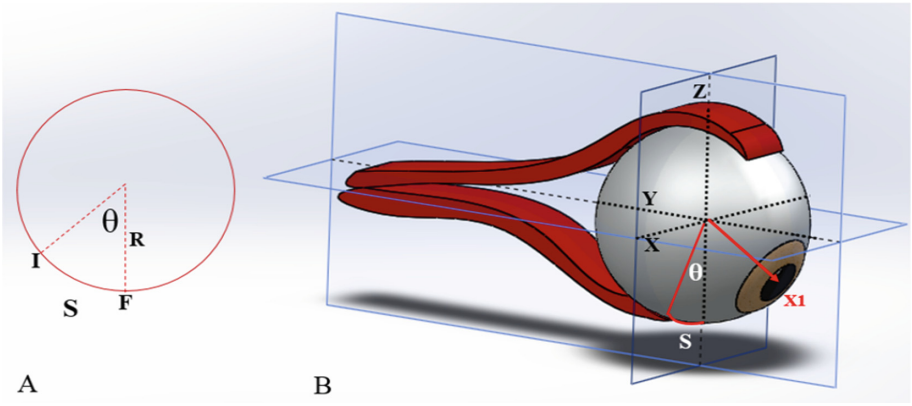

Fig. 4. A. Arc of circumference, B. Three-dimensional plane in eye movement

The angle θ obtained by the action of the superior and inferior rectus muscles is called elevation angle. The angle α obtained by the action of the lateral and medial rectus muscles is called the horizontal sweep angle. The conversion of these spherical coordinates to cartesian can be given by the following equations:

$$X = r * cos(\theta) * cos(\alpha) \tag{4}$$

$$Y = r * cos(\theta) * sin(\alpha) \tag{5}$$

$$Z = r * cos(\theta) \tag{6}$$

2.3 Graphical Interface Development

A graphic interface was developed in MATLAB® to analyze the application of force to the system of Fig. 2, obtaining the distance S of shortening and stretching of the

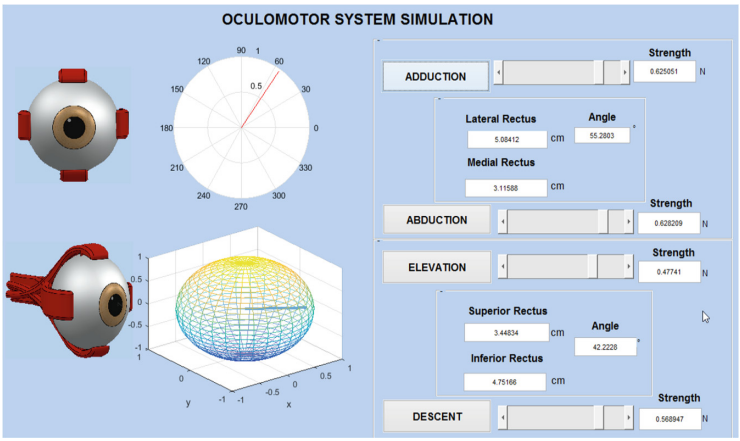

Fig. 5. Interface and simulation of extraocular muscles from primary position.

extraocular muscle, associated in turn, to the circumference arc to find the angle of movement of the pupil of eye, in movements of adduction, abduction, elevation and descent (Fig. 5).

3 Results

The modeling of the oculomotor system allowed to identify the maximum strength ranges required to perform a movement (see Fig. 6), as well as the angles corresponding to these movements.

For the movements of vertical rotation, in the case of the movement of elevation, the maximum angle in vertical direction upwards is 42º (with a range of 33° to 56°) [8]. For this situation the application required a force of 0.47 N corresponding to the maximum angle of 42°, for which, the superior rectus contracted reaching a length of 3.44 cm and the inferior rectus was stretched reaching a length of 4.75 cm. The ranges of force applied to the elevation movement were from 0.37 N to 0.63 N.

For the descent movement, the maximum angle of the downward eye rotation is 50º (with a range of 33º to 62º) [8]. For this movement, the applied force ranges were (0.37 N–0.70 N), and a force of 0.56 N corresponding to the maximum angle of 50° was required, for which, the superior rectus was stretched until reaching a length of 5.09 cm, while the inferior rectus contracted reaching a length of 3.10 cm.

In horizontal rotation movements, the maximum angle in the lateral direction is approximately 55° (with a range of 45° to 65°) [8], for which, the application of a force ranges (of 0.51 N–0.73 N) was required, which allowed to simulate adduction and abduction movements. For the movement of adduction, in which the eye turns towards the nose, it was required to apply a force of 0.61 N to reach an angle of 50°, for which, the medial rectus contracted until reaching a length of 3.11 cm, and the lateral rectus was stretched to a length of 5.08 cm. To perform an abduction movement, a force of 0.62 N was applied and the medial rectus muscle stretched reaching a length of 5.08 cm while the lateral rectus contracted reaching a length of 3.10 cm.

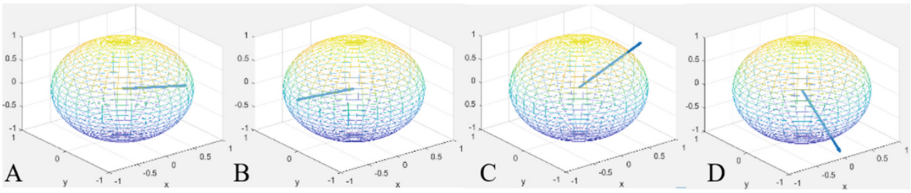

Fig. 6. Eye movement representation graphics; A. Adduction, B. Abduction, C. Elevation and D. Descent.

In the developed model the activity of the superior-inferior and lateral-medial rectus muscles was considered, to identify the muscle that acted as an agonist, which contracted, which allowed to associate it physiologically as a collaborator in the execution

of the movement, that pulling the eyeball in the required direction, while the other muscle acted as antagonist, stretching and resisting traction.

The computational simulator allowed the analysis of the maximum strength ranges used to perform a normal eye movement, this brought us closer to a theoretically compare the effects of the modifications in certain parameters, as: force and radius of the eyeball, given that in cases of extraocular muscle weakness, as in strabismus, poor control occurs when performing an eye movement and the eyes do not align in the same direction.

The analysis of coordinated movements in both eyes allowed to identify that, while in the right eye there is a movement of abduction by the action of the agonist muscle (lateral rectus), in the same situation and simultaneously, in the left eye, the lateral rectus acts as an antagonist and generates an adduction movement.

4 Discussion and Conclusion

During an eye movement the trajectory can be identified by the displacement of the pupil due to the action of four extraocular muscles (superior rectus, inferior rectus, lateral rectus and medial rectus) allowing movements of adduction, abduction, elevation and descent, in the which generate angle changes with respect to the main axis, which by compensation correspond to the angle formed between the shortening distance of the agonist muscle (in contraction) with respect to the main axis X1.

The model proposed in this paper is a simple model that is easy to understand and implement because it incorporates variables from other traditional models, such as the muscle dynamics proposed by Hill, as well as the nonlinear force-elongation relationship, the Bahill model classic and the variables, such as: viscous damping and elastic elements in series and parallel. Which allowed the analysis of the action of the lateral and medial rectus muscles in horizontal rotation and the action of superior and inferior rectus muscles in vertical rotations. Also, the proposed model allowed to identify the relationship between the application of force in a mechanical system to simulate the behavior of each extraocular muscle, obtaining the final length of the agonist muscle after the contraction and the final stretch length of the antagonist muscle.

The extraocular muscle activity generates a movement in the eyeball, modeled in this work as a sphere. The effect of only one pair of muscles (superior-inferior or lateral-medial) was considered to calculate the angle formed between the main axis X1 and the equilibrium position by the relation of the circumference arc and the radius of the eyeball. The collection of the obtained angles and cartesian coordinates of the main axes of rotation (X, Y, Z), generated by the activity of superior-inferior and lateral-medial rectus muscles, allow to represent in a coherent way the real physiological behavior of the eye movement caused by the oculomotor system.

The mathematical models of the oculomotor system are useful in the accurate prediction of eye movement by providing information on the ranges of maximum force applicable to the eyeball to perform a movement, useful in the medical field for the detection or future treatments of pathologies such as strabismus, in the which deviates from the normal visual line of the eyes.

The development of the eye movement simulator proposed in this work, integrates the mathematical modeling of the eye and the 3D model of eye structures, which facilitates the understanding and analysis of the oculomotor system. The possible applications of the proposed model focus on the use of maximum force ranges to simulate an eye movement and three-dimensional representation, in future projects for the simulation and detection of saccades movements and fixation movements, as well as computer simulations of the effects of pathologies of the oculomotor system, applied to control and optimization in the development of technologies that depend on eye movements or that imitate these movements.

The proposed model allows a simplified understanding of the oculomotor system, compared to other more complex models, and is useful in the learning and interpretation of extraocular muscle activity through the integration of mathematical model and graphic representation of structures of eye in 3D, in a user friendly simulator, designed for the future development of eye tracking technology. The designed simulator shows that it can be improved and used as application in the control of devices since its implementation in computational simulation systems would allow faster executions with less impact and computational cost.

Declaration of Conflict of Interest. The authors declare that they don't have conflicts of interest.

References

1. Hoerantner, R.: Model-based improvements in the treatment of patients with strabismus and axial high myopia. IOVS **48**(3), 1133–1138 (2007)
2. Charfreitag, J., Hozman, J., Cerny, R.: Specialized glasses - projection displays for neurology investigation. In: 4th European Conference of the International Federation for Medical and Biological Engineering Conference 2008, IFMBE, vol. 22. Springer, Belgium (2009)
3. Hill, A.V.: The heat of shortening and the dynamic constants of muscle. Philos. Trans. Roy. Soc. Lond. B **126**, 136–195 (1938)
4. Holland, D., Komogortsev, O.V.: Complex eye movement pattern biometrics: analyzing fixations and saccades. In: Conference 2013, IEEE/IARP International Conference on Biometrics (ICB) (2013). https://doi.org/10.1109/icb.2013.6612953
5. Bahill, A.T.: Development, validation, and sensitivity analyses of human eye movement models. Crit. Rev. Bioeng. **4**(4), 311–355 (1980)
6. Khoo, M.C.K.: Physiological Control Systems: Analysis, Simulation and Estimation. Control Systems, 1st edn. Wiley, Hoboken (2000)
7. Aguado, X., Grande, I., Lopez, J.: Consideraciones sobre conceptos y clasificaciones de la fuerza muscular desde el punto de vista mecánico. Universidad de Castilla la mancha, Consejo superior de deportes. Serie ICd, n 2 (2011)
8. Álvarez, A.: Visión y trabajo. Instituto nacional de seguridad e higiene en el trabajo (Guía de notas técnicas de prevención) NIPO: 792-08-008-8 (2008)

Route to Chaos in a Nonlinear Model of HIV Dynamics with Antiretroviral Treatment

Lorena de Sousa Moreira(✉), Rodrigo Andres Miranda Cerda, and Ronni Geraldo Gomes de Amorim

University of Brasília, UnB-Gama Campus, Brasília, DF 72444-240, Brazil
moreira.lorena@ymail.com

Abstract. Here we present a numerical study of a nonlinear model of HIV dynamics. The model describes the dynamics of T4 lymphocytes cells, HIV virus and opportunistic infection, and includes the effect of HIV treatment. We show that, as the efficacy of the antiretroviral treatment is reduced, the model display a transition from orderly to chaotic dynamics via a period-doubling cascade. The chaotic regime is interrupted by regions of periodic dynamics known as periodic windows.

Keywords: Nonlinear dynamics · Chaos · HIV

1 Introduction

The human immunodeficiency virus (HIV) is a non-taxonomic and historical term referring to any of two species, HIV-1 and HIV-2 [1]. The HIV has as main target as $CD4^+$ T lymphocytes. These cells mature in the thymus and are responsible for coordinating the immune response against microorganisms, for example, viruses. Reduction of $CD4^+$ T cells results in widespread damage to the functioning of the immune system as a whole. The weakened organism becomes more susceptible to the appearance of opportunistic infections, for example, herpes, pneumonia, and toxoplasmosis.

The global statistics released by the Joint United Nations Program on HIV/AIDS [2] estimated that in 2017 around 36.9 million people are living with HIV worldwide. Based on these statistics, there is a need to further study the progression of the disease, as well as the more effective treatment and opportunistic diseases that may arise.

Theoretical studies can contribute to our understanding of the dynamics of the HIV virus. A number of studies have focused on nonlinear models that describe the interaction between the HIV and populations of immune system cells, in particular, $CD4^+$ T lymphocytes. For example, Anderson and May [3] proposed a simplified model which accounts for the complex dynamical behavior between the HIV and the immune system. This model was studied by Lund

© Springer Nature Switzerland AG 2020
C. A. González Díaz et al. (Eds.): CLAIB 2019, IFMBE Proceedings 75, pp. 694–698, 2020.
https://doi.org/10.1007/978-3-030-30648-9_92

et al. [4] who demonstrated that the virus dynamics can become chaotic via a periodic-doubling cascade. Perelson et al. [5] analyzed a model of three populations of T cells, namely, uninfected T cells, latently infected T cells and actively infected T cells, and their interaction with the free virus. They demonstrated that HIV cytopathicity is a major factor that leads to the quantitative features of HIV infection. Wang [6] studied HIV mathematical model with uninfected T cells, infected T cells and free virus. Their study associated the interaction between HIV virus and $CD4^+$ T cells with treatments, namely, inhibitors reverse transcriptase and protease inhibitors. Li and Wang [7] studied a mathematical model that describes the viral dynamics of HIV with anti–retroviral treatments.

These works have demonstrated that numerical studies of nonlinear models can provide reliable predictions about the interaction between the HIV and the immune system, and the development of HIV and opportunistic diseases, and can help determine the most appropriate treatment, as well as contribute to the elaboration of public policies. This work may contribute to the most appropriate intervention to be stipulated by public policies aimed at the treatment and viral suppression of HIV-infected persons by predicting the number of infected cells, viral load and antiretroviral efficacy [8,9].

In this paper, we analyze a simplified model of HIV dynamics in the presence of an opportunist infection. The effect of two antiretroviral treatments is also included. By applying nonlinear systems tools we demonstrate that a transition from orderly to chaotic dynamics occurs when the effectiveness of the antiretroviral treatment is reduced. This paper is organized as follows The nonlinear model is described in Sect. 2. Section 3 presents numerical results. The conclusion is given in Sect. 4.

2 Methods

We study a simplified model based on Lund et al. [4] which describes the nonlinear dynamics of the population of non-infected and non-activated T_4 lymphocytes P, non-infected and activated T_4 lymphocytes X, infected T_4 lymphocytes Y, free HIV virus V and an opportunistic infection I. Following Wang [6] we included antiretroviral treatment by inserting two parameters, namely, σ_1 and σ_2, which represent the reverse transcriptase inhibitors and the protease inhibitor, respectively. The physical interpretation of σ_1 and σ_2 is given below. The model is described by the following set of ordinary differential equations

$$\dot{P} = \Lambda - \mu P - \gamma PV, \tag{1}$$

$$\dot{X} = \gamma PV + rX - \beta XV - dX^2 + kIX, \tag{2}$$

$$\dot{Y} = \sigma_1 \beta XV - \alpha Y, \tag{3}$$

$$\dot{V} = \sigma_2 \lambda \alpha Y - bV - \delta(X + Y)V - \sigma XV, \tag{4}$$

$$\dot{I} = cI - hIX, \tag{5}$$

where Λ represents the rate of production of P cells, μ represents the cell death rate, γ is the rate of cell removal from the pool through cell division of the number

of P cells, r is the rate of cell division of X cells, β represents the rate of decrease population of activated lymphocytes when the activated cells become infected by HIV, d is the rate of decrease of activated cells by saturation phenomenon, k is the rate of cell division, α stands for the rate of decrease in the population of Y cells, $\lambda\alpha$ is the rate of new HIV buds from the surface of infected T4 cells, b represents the HIV population death rate, δ is the rate of decrease of V through absorption by activated and infected cells, σ is the rate of elimination through the immune response, c represents the rate of increase of I trough proliferation, h represents the rate of decrease of I through the effect of the immune response, σ_1 involves inhibitors reverse transcriptase and σ_2 involves protease inhibitors.

Equations (1)–(5) are obtained by describing the interaction between T cells and HIV virus using a nonlinear predator-prey model. These models can successfully reproduce several characteristics observed in infected patients such as long transient periods of dormancy, depletion of healthy T cells and exponential grow rates of HIV virus and opportunistic infections [3–5]. Following Lund et al. [4] we set the model parameters as $\Lambda = 1.0$, $\mu = 0.1$, $\gamma = 0.01$, $r = 1.0$, $\beta = 1.0$, $d = 0.001$, $k = 0.01$, $\alpha = 2.0$, $\lambda\alpha = 10.0$, $b = 1.0$, $\delta = 0.01$, $\sigma = 0.1$, $c = 1.0$, $h = 0.01$.

The effectiveness of reverse transcriptase inhibitor treatment is given by $1-\sigma_1$ and the effectiveness of protease inhibitor treatment is given by $1 - \sigma_2$ [6]. A value of $\sigma_1 = 0$ represents 100% effectiveness of reverse transcriptase inhibitor treatment, whereas $\sigma_1 = 1$ represents 0% effectiveness. Similarly, a value of $\sigma_2 = 0$ represents 100% effectiveness of protease inhibitor treatment, whereas $\sigma_2 = 1$ represents 0% effectiveness. Note that the σ_1 parameter can be also interpreted as the probability that an activated T cell become infected. Lund et al. [4] showed that Eqs. (1)–(5) exhibit a period-doubling route to chaos when σ_1 increases. In this paper we focus on the effect of the antiretroviral treatment, therefore we set $\sigma_1 = 1$ and let σ_2 be the control parameter.

The numerical integration of Eqs. (1)–(5) is performed using the `lsoda` package which is a variable-step integrator [10]. The initial conditions are $P = X = Y = V = I = 0.1$, unless otherwise stated.

3 Results

We investigate the effect of the efficacy of the protease inhibitor treatment σ_2 on the HIV dynamics. Figure 1 displays the bifurcation diagram of the virus population V for $\sigma_1 = 1$ and $\sigma_2 \in [0, 1]$. The bifurcation diagram was constructed by defining the Poincaré surface of section $I(t) - 40V(t) = 0$ and $\dot{I} > 0$ in variable space, and selecting the points of the orbit of Eqs. (1)–(5) that intersect with the Poincaré section. The asymptotic solutions were obtained by discarding the initial transient points until $t = 1000$. Figure 1 depicts a similar route to chaos described by Lund et al. [4] in terms of the β parameter. At $\sigma_2 \sim 0.05$ the orbit converges to a limit-cycle represented by a period-1 attractor. At $\sigma_2 \sim 0.2$, the period of the limit cycle is doubled. By increasing the value of σ_2 (i.e., decreasing the efficacy of the protease inhibitor treatment), the virus dynamics undergoes a

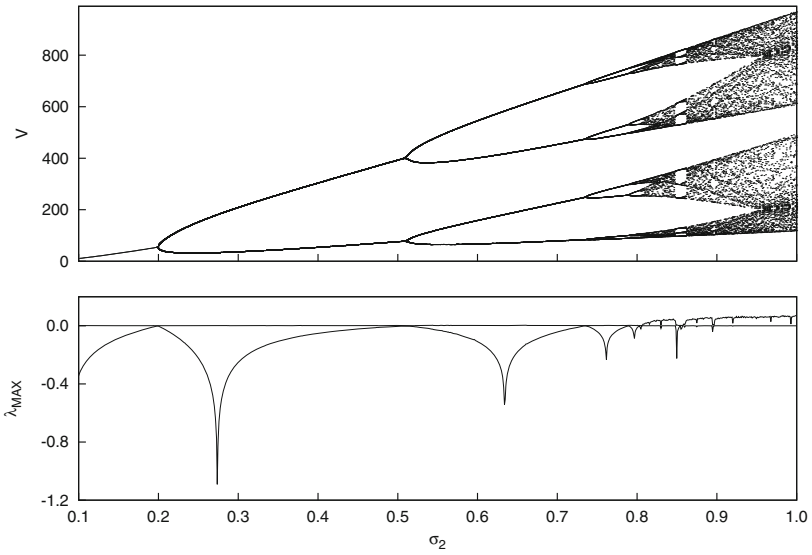

Fig. 1. Upper panel: Bifurcation diagram of V as a function of σ_2. Lower panel: The maximum Lyapunov exponent λ_{MAX} as a function of σ_2.

period-doubling cascade. At $\sigma_2 \sim 0.8$, the virus dynamics become chaotic. The chaotic regime ($\sigma_1 > 0.8$) is occasionally interrupted by periodic windows. This figure demonstrates that the virus dynamics can become unpredictable if the effectiveness of the treatment is reduced.

In order to validate the different regimes displayed by the bifurcation diagram we computed the maximum non-zero Lyapunov exponent [11] as a function of the bifurcation parameter σ_2. The result is presented in the lower panel of Fig. 1. It is clear that the periodic dynamics are characterized by $\lambda_{\mathrm{MAX}} < 0$, whereas chaotic behavior corresponds to $\lambda_{\mathrm{MAX}} > 0$ as expected.

4 Conclusion

A nonlinear model of HIV dynamics which includes antiretroviral treatment and an opportunistic infection has been studied numerically. By decreasing the efficiency of the treatment we observe a transition from regular to chaotic dynamics via a periodic-doubling cascade, leading to a chaotic regime. The chaotic regime is occasionally interrupted by periodic windows. The computation of the maximum non-zero Lyapunov exponent demonstrates the transition from regular (periodic) to irregular (chaotic) dynamics. Our results can contribute to understand the HIV dynamics and contribute to defining protocols for public policies focused on HIV treatment.

Conflict of Interest. The authors declare that they have no conflict of interest.

References

1. BVS: Health sciences descriptors: DeCS (2017). http://decs.bvsalud.org/I/homepagei.htm
2. UNAIDS: Global HIV&AIDS statistics–2018 fact sheet (2018). http://www.unaids.org/en/resources/fact-sheet
3. Anderson, R.M., May, R.M.: Complex dynamical behavior in the interaction between HIV and the immune system. In: Cell to Cell Signalling, from Experiments to Theoretical Models. Academic Press, New York (1989)
4. Lund, O., Mosekilde, E., Hansen, J.: Periodic doubling route to chaos in a model of HIV infection of the immune system. Simul. Pract. Theor. **1**, 49–55 (1993)
5. Perelson, A.S., Kirschner, D.E., de Boer, R.: Dynamics of HIV infection of CD4+ T cells. Mathe. Biosci. **114**, 81–125 (1993)
6. Wang, L.: Global dynamical analysis of HIV models with treatments. Int. J. Bifurcat. Chaos **22**(9), 11 (2012). 1250227
7. Li, M.Y., Wang, L.: Backward bifurcation in a mathematical model for HIV infection in vivo with anti-retroviral treatment. Nonlinear Anal. Real World Appl. **17**, 147–160 (2014)
8. Bain, L.E., Nkoke, C., Noubiap, J.J.N.: As metas 90-90-90 do UNAIDS para acabar com a epidemia de AIDS até 2020 não são realistas: comente: "A meta do UNAIDS 90-90-90 pode ser alcançada? Uma análise sistemática das cascatas nacionais de tratamento do HIV". BMJ Glob Health **2**(2) (2017)
9. UNAIDS. 90–90–90 An ambitious treatment target to help end the AIDS epidemic (2014). https://www.unaids.org/sites/default/files/media_asset/90-90-90_en.pdf
10. Petzold, L.R.: Automatic selection of methods for solving stiff and non-stiff systems of ordinary differential equations. SIAM J. Sci. Stat. Comput. **4**, 136 (1983)
11. Wolf, A., Swift, J.B., Swinney, H.L., Vastano, J.A.: Determining Lyapunov exponents from a time series. Phys. D **16**, 285–317 (1985)

Automatic Control Applied to Servosystems. Influence of the State Transition Matrix in Functional Variables of DC Motors Used in Myoelectric Prostheses

Carlos Alvarez Picaza(✉), C. R. Ferrari, J. I. Veglia, and M. A. Ulibarrie

Universidad Nacional del Nordeste, 3400 Corrientes, Argentina
cpicaza@gmail.com

Abstract. Participation of Engineering in sciences that affect people's lives has generated relatively new disciplines. Rehabilitation is the biomedical area that produces most impact. Technological developments help people with some functional losses and encourage them to participate in their societies. We present an alternative mathematical analysis applied to servomotors that drive biomechanical prostheses by using the State Transition Matrix according to modern control criteria. It allows work in state-space where it´s possible to find new information to enrich conclusions of research. Some properties quantification are required to perform necessary movements in agreement to manipulation of control signal variables that must be implemented. Work points placed on the left side of the complex plane, relevant theoretical gains, as well as time response graphs, will be new parametric indicators. Obtained results show the importance of the state transition matrix used as a control tool in functional analysis of drive systems applied to prostheses, as much as it is needed to each particular case, meaning to each individual patient.

Keywords: Transition · State-space · Gains

1 Introduction

Contribution of Biomedical Engineering in the rehabilitation area consists in useful device designs to automate the different therapies and give patients the necessary autonomy for a better social development [1]. Assistive devices and technologies such as wheelchairs, prosthetics, mobility aids, hearing aids, visual aids, specialized computer programs and increased hardware mobility, hearing, vision and communication skills, are the most used. However, in many low and middle income countries, only 5% to 15% of people who require support devices and technologies have access to them [2]. Access to rehabilitation can reduce the consequences of illness or injury, improve health and life quality, even decrease the use of health services. As engineers, we apply mathematical laws and physics to solve problems, such as those mentioned above. Through the Modern Control Theory any problematic situation can be treated by means of state equations. Some mathematical rules, just like superposition principle, present in

© Springer Nature Switzerland AG 2020
C. A. González Díaz et al. (Eds.): CLAIB 2019, IFMBE Proceedings 75, pp. 699–708, 2020.
https://doi.org/10.1007/978-3-030-30648-9_93

recursive algorithms are excluded in this new approach. The consequent developments will be reflected in new findings, giving value to new concepts such as Controllability and Stability [3].

Once the prosthesis for people with disabilities are finished, it is essential to evaluate previous cases related with an efficient model of energy management and exhibit an optimal servomotor regulator designed to generate movements of a robotic arm joint for the rehabilitation of a patient, in order to arrive at a useful application model.

The design of artificial limbs requires full knowledge not only of the mechanics of the mechanisms, but also a clear understanding of electromechanical devices, among which driving motors play a key role in the area of prostheses. The maximal speed, force and stability of the anatomical limb are still unparalleled by the artificial prosthesis. These limitations are due to physical restraints of current technology to achieve the properties which the natural limb exhibits. Matching muscle speed and force with technological actuator is not an easy task, mainly when choosing a driving motor with the appropriate speed-torque relationship [4]. Instability of driving motors adds to the complexity of proper prosthesis design.

It is known that many theories in the physical sciences are based or expressed in terms of optimality. In the field of motor control, optimality also plays a key role. The optimization processes give rise to a specific motor system under investigation (adaptation, development, evolution, recovery). These processes cause the system to perform better and better. In the area of theoretical investigations, it is natural to search for the limits of optimal performance of motor control [5].

In 2012 Musa and Muawia used the state transition matrix to investigate the performance of DC motors [6]. Also, another study about LQR problem (energy optimization) is analytically determined by this method, getting an explicit solution [7].

Specific kinematics of a mechanical arm studies the analytical description of the robot space displacement as a time function, particularly, and relations between articulation variables position and robot arm orientation.

Direct kinematic tries to determine the position coordinates from the articulation variables knowledge, i.e. from the angles between them. The cartesian coordinates depend on the joint coordinates.

Inverse kinematic seeks to determine the angles that each joint must establish to bring the arm to a desired position (or coordinates). It is possible to try to choose some method that allows us to control the manipulator. This control tends to locate the final effector in a certain position, and with a given orientation, to perform some task.

Reaching any X point of the manipulator accessible space means to locate the kinematic pairs, which in this type of robot are all of the rotating type, in a given angular position. If we wish to move to another X1 point of space, what must be done is to calculate which angle will be necessary to rotate all the joints.

Since the solution to the problem is not unique, some kind of strategy should be used to perform the movements, both in its sequence and in its value. It is unlikely that these movements can be done all together, but rather one at a time. Movements acceleration and speed must also be controlled, in order not to exceed certain maximum values.

DC motors are used in systems that require a lot of precision and they are low power ones.

The aim of this work is to prove the influence of the State Transition Matrix in order to find desired theoretical work points of the servomotor, trying to drive the movements of the manipulator arm as efficiently as possible.

2 Methodology

The elbow is an upper limb joint, which carries out the mechanical union between the first segment, the arm and the second segment, the forearm and allows the upper extremity to be oriented in the three planes of space thanks to the shoulder. The elbow represents a single joint; there is only one articulation cavity. On the other hand, physiology allows us to distinguish two different functions:

- Pronation-Supination, which sets in motion the superior radio-ulnar joint, the trichoid.
- Flexion-Extension, which requires the assistance of two articulations: the humerus-ulnar articulation and the humerus-radial articulation.

Being a trochlear, it has a single degree of freedom of movement on a transverse axis, and performs the flexion-extension motion in a sagittal plane. From now on, we will work with the motor model, responsible for artificially performing the muscles actions.

2.1 Servomotor Model

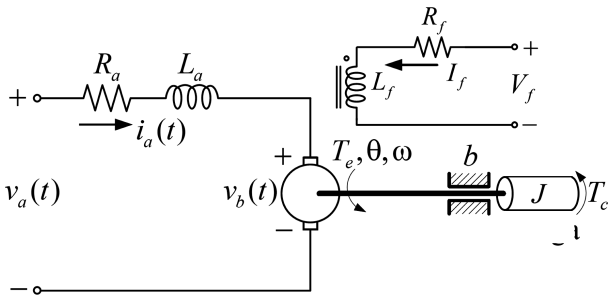

Fig. 1. Electrical diagram of the servomotor.

It is considered the DC motor from Fig. 1 that drives a load through a rigid shaft. If the field current is kept constant in a value I_f, or the field flux comes from a permanent magnet, this machine can be controlled only by the voltage $v_a(t)$ applied to the armature [8].

As it has been described in previous works [9, 10], this machine can only be controlled by the supply voltage $v_a(t)$, when the field current I_f is kept constant or the flow comes from a permanent magnet. The relationship between the torque electric

torsion $T_e(t)$ and the armature current $i_a(t)$ is the torque constant K_t, as it is indicated in Eq. (1).

$$T_e(t) = K_t i_a(t) \tag{1}$$

When the motor propels the load, a counter electro-motive power is developed in the armature circuit, which opposes to the applied voltage $v_a(t)$. The angular velocity ω of the shaft is directly proportional to the voltage $v_b(t)$.

$$v_b(t) = K_b \frac{d\theta(t)}{dt} \tag{2}$$

where K_b is the motor speed constant. The moment of total inertia of the load is J and θ the angular displacement, b is the coefficient of viscous friction and T_c is the torque produced by the load.

In the armature circuit, it is verified that

$$v_a(t) = u(t) = R_a i_a(t) + L_a \frac{di_a(t)}{dt} + K_b \frac{d\theta(t)}{dt} \tag{3}$$

where R_a and L_a represent the impedance of the armature windings.

We choose to work in the state-space, whose equations contain internal dynamic information of the system, they allow to include the initial conditions easily and they are of simple resolution.

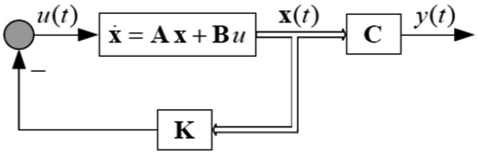

Fig. 2. Servosystem model in space-state.

We choose as state variables of the system to

$$\begin{aligned} x_1 &= \dot{\theta}(t) = \omega(t) \\ x_2 &= i_a(t) \end{aligned} \tag{4}$$

The matrix representation remains as:

$$\begin{aligned} \begin{bmatrix} \dot{\omega}(t) \\ \dot{i}_a(t) \end{bmatrix} &= \begin{bmatrix} \frac{-b}{J} & \frac{K_t}{J} \\ \frac{-K_b}{L_a} & \frac{-R_a}{L_a} \end{bmatrix} \begin{bmatrix} \omega(t) \\ i_a(t) \end{bmatrix} + \begin{bmatrix} 0 \\ \frac{1}{L_a} \end{bmatrix} u(t) \\ y &= \begin{bmatrix} 1 & 0 \end{bmatrix} \begin{bmatrix} \omega(t) \\ i_a(t) \end{bmatrix} \end{aligned} \tag{5}$$

A control system like

$$\begin{aligned} \dot{\mathbf{x}} &= \mathbf{A}\mathbf{x} + \mathbf{B}\,u \\ y &= \mathbf{C}\mathbf{x} + Du \end{aligned} \tag{6}$$

The control signal is selected as

$$u = -\mathbf{K}\mathbf{x} = [\,K_1 \quad K_2 \quad \ldots \quad K_n\,][\mathrm{x}_1, \mathrm{x}_2, \ldots, \mathrm{x}_n]^{\mathrm{T}} \tag{7}$$

A system like this is known as a *regulator system*.
When it is replaced

$$\dot{\mathbf{x}} = (\mathbf{A} - \mathbf{B}\mathbf{K})\mathbf{x} \tag{8}$$

The eigenvalues of $\mathbf{A} - \mathbf{B}\mathbf{K}$ are called regulator poles.

Working points of the servomotor system are found by using the pole location method, which consists of two stages:

(a) desired location of the roots belonging to the characteristic equation of the closed-loop system, and
(b) gain calculation to locate those roots in definite places.

The characteristic equation of the closed loop system of Fig. 2 is given by:

$$det[s\,\mathbf{I} - \mathbf{A} + \mathbf{B}\mathbf{K}] = 0 \tag{9}$$

If this determinant is developed, it becomes a polynomial of n power in Laplace's space that contains the gains of the matrix **K**.

2.2 State Transition Matrix

The matrix $e^{\mathbf{A}t}$ is called State Transition Matrix and is denoted by

$$\mathbf{\Phi}(t) = e^{\mathbf{A}t} = (\mathbf{I} + \mathbf{A}t + \frac{1}{2!}\mathbf{A}^2t^2 + \frac{1}{3!}\mathbf{A}^3t^3 + \ldots) \tag{10}$$

It commands over the states trajectories in a finite interval time t. It's the natural response of the system.

The dynamics of the output signal depends on the eigenvalues of the matrix $(\mathbf{A} - \mathbf{B}\mathbf{K})$. If all eigenvalues (closed loop poles) of this matrix have a negative real part or are on the left half plane of the Laplace's space, then for any initial state $\mathbf{x}(0)$ other than zero, the system output will tend to a desired value when $t \to \infty$.

Therefore, if the pair $[\mathbf{A}\mathbf{B}]$ is controllable, it's possible to find a gains matrix **K** in such a way to locate the eigenvalues of $(\mathbf{A} - \mathbf{B}\mathbf{K})$ in desired positions. There is a restriction on $u(t)$, which can limit the speed with which the output tends to the desired value.

The function that determines the system natural response is given by

$$\mathbf{x}=\mathbf{\Phi}(t)\mathbf{x}(0) \tag{11}$$

In the state-space this function represents the trajectory, transition from one state to another.

3 Results

Data for the servomotor simulation model, developed in a previous section, were obtained from an actual engine (RE model Maxon® 40–40 mm) [11] previously used to drive biomechanical prostheses [12]. The following values were taken from the manufacturer catalog:

R_a = Armature Resistance = 1,16 Ω.
L_a = Armature Inductance = 0,329 mH.
K_t = Torque Constant = 60,3 mNm/A.
K_b = Constant Rate = 158 rpm/V.
B = Friction coefficient of the bearings = 3,04 rpm/mNm.
J = Inertia moment of the motor and load = 138 gcm^2

The system natural poles are

$$\mathrm{P} = [-1,7739 + 14,3797\mathrm{i};\ \ -1,7739 - 14,3797\mathrm{i}]$$

We carried the normal work points to other positions, moving along and across of Laplace's complex plane.

Real part (abscissa axis):

$$\mathrm{P1} = [-1 + 14,3797\mathrm{i}\,;\ \ -1 - 14,3797\mathrm{i}]$$
$$\mathrm{P2} = [-3 + 14,3797\mathrm{i}\,;\ \ -3 - 14,3797\mathrm{i}]$$

The needed gains to reach those points gave

$$\mathbf{K}1 = [-1,5911 \quad -0,5092]$$
$$\mathbf{K}2 = [4,3660 \quad 0,8068]$$

These gains are the necessary ones to move the original poles P to the desired positions P1 and P2.

Figure 3 shows that when taking the work points furthest away from the ordinate axis (P2, **K**2), the temporary response of the system becomes more stable (red color). The location of the poles (P1, **K**1) results in an oscillatory response (middle graph) [13].

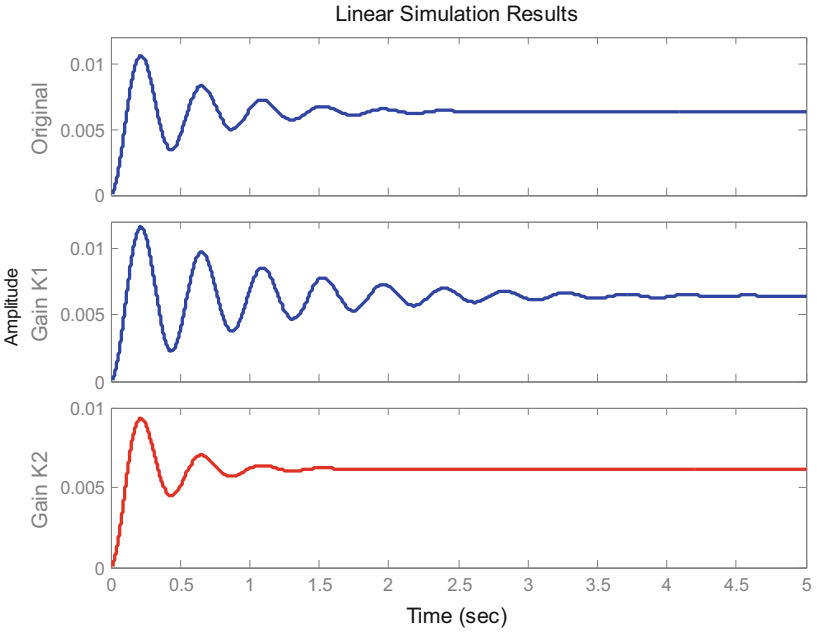

Fig. 3. Response time graph (real)

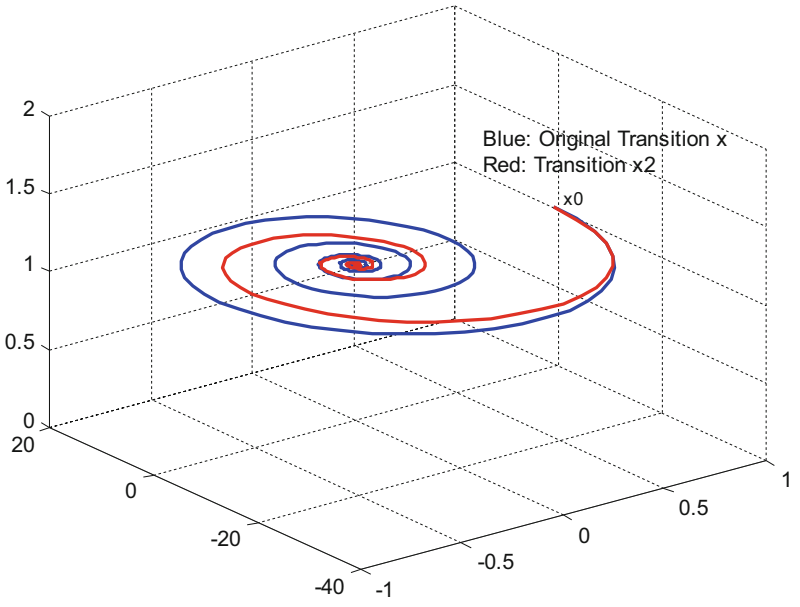

Fig. 4. State transition graph (real).

$$\mathbf{x}2 = [a/b * \exp(-3 * \mathrm{t}) * c\hat{}(1/2) * \sin(1/d * f\hat{}(1/2) * \mathrm{t}) + \exp(-3 * \mathrm{t}) * \cos(1/g * h\hat{}(1/2) * \mathrm{t});$$
$$-j/m * \exp(-3 * \mathrm{t}) * n\hat{}(1/2) * \sin(1/q * r\hat{}(1/2) * \mathrm{t}) + \exp(-3 * \mathrm{t}) * \cos(1/v * w\hat{}(1/2) * \mathrm{t})]$$

This is the function that defines the trajectory **x**2.

Figure 4 shows the transition in the state-space corresponding to the original system in blue and to **x**2 (P2, **K**2) of red color, that being a more stable system, its trajectory to reach the state of balance is more enclosed.

Imaginary part (ordinate axis):

$$\mathrm{P1i} = [-1,7739 + 10\mathrm{i}\,;\ -1,7739 - 10\mathrm{i}]$$
$$\mathrm{P2i} = [-1,7739 + 20i\,;\ -1,7739 - 20\mathrm{i}]$$

The gain values,

$$\mathbf{K}1\mathrm{i} = [-80,3957\ \ 0]$$
$$\mathbf{K}2\mathrm{i} = [145,4849\ \ 0]$$

These gains are necessary to move the original poles along the ordinate axis, reaching the positions of P1i and P2i.

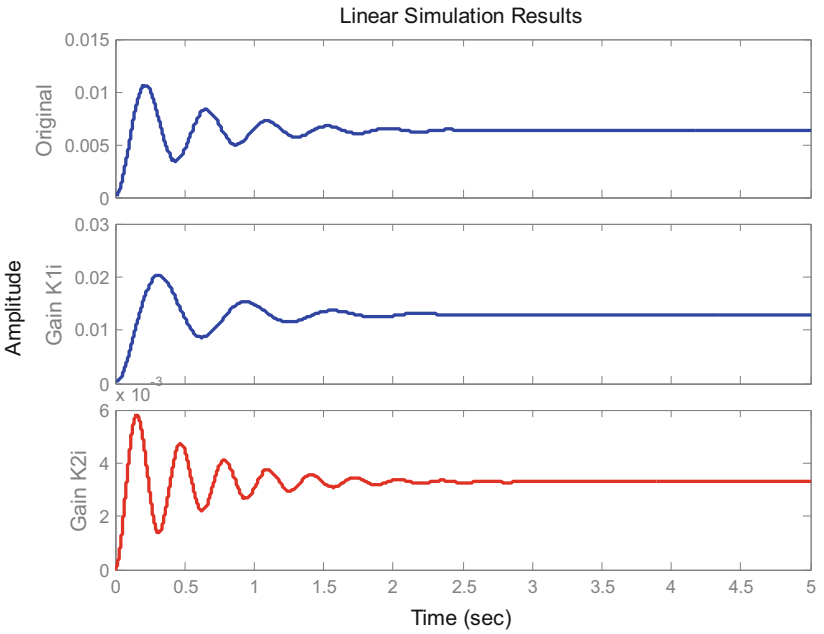

Fig. 5. Response time graph (imaginary).

The response of the system in red color of Fig. 5 belongs to the pole-gain pair (P2i, **K**2i). Now, unlike the previous case, the poles (red color) were located away from the abscissa axis, becoming a quite oscillatory response.

As in the real case, the value of the function **x**2i (P2i, **K**2i), is quite complex and indicates the red path in Fig. 6. In this case, longer compared to the original system trajectory **x** in blue.

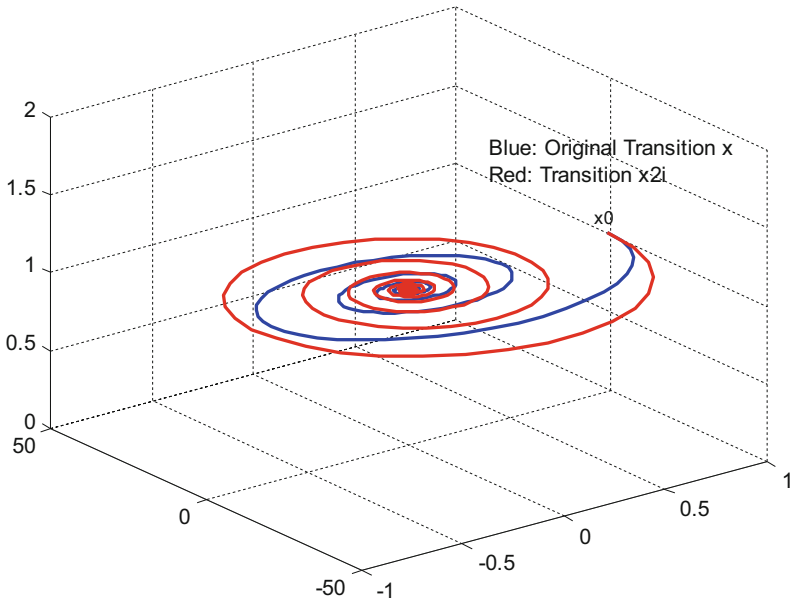

Fig. 6. State transition graph (imaginary).

4 Conclusions

The treatment of events in the state-space gives us the advantage of being able to observe dynamic behaviors that would not be visible in the time space or frequency space. According to the results we can conclude that the work points that are closest to the abscissas axis and farther away from the ordinates axis respond to a much more stable and less oscillatory behavior.

It's important to note that the matrices $\mathbf{\Phi}(t)$ y **K** are not unique to a given system, but depend on the desired positions of the poles in closed loop (which determine the speed and damping of the response). It should be considered that these work points selection, or of the desired characteristic equation, is a compromise between response speed and sensitivity to disturbances. That is, if the response speed increases, the adverse effects of disturbances and noise in measurement are generally increased.

Therefore, when determining gain matrix **K** for a given system, it is convenient to examine by computer simulations the characteristics of the system response for several different matrices and choose the one that offers better overall behavior.

Acknowledgment. This work responds to the 18F011 Research Project funded by the General Secretariat of Science and Technology of the Universidad Nacional del Nordeste.

A special acknowledgment to Eng. Ana María Marder for her contribution in the drafting of this paper.

Conflicts of Interest. We have not had any conflicts of interest in the preparation of this document: Automatic Control applied to Servosystems. Influence of the State Transition Matrix in Functional Variables of DC Motors used in Myoelectric Prostheses.

References

1. El libro blanco de la robótica en España Investigación, tecnologías y formación. Ministerio de Ciencia e Innovación. Gobierno de España. CEA comité español de automática. 1ª Edición (2011)
2. Discapacidad Y Salud Nota Descriptiva N°352 Septiembre De 2013. http://www.Who.Int/Mediacentre/Factsheets/Fs352/Es/
3. Cortes, Reyes F.: Robótica, control de robots manipuladores. Alfaomega Grupo Editor, Mexico (2011)
4. Weir, R.F.ff.: Design of artificial arms and hands for prosthetic applications. In: Myer, K. (ed.) Standard Handbook of Biomedical Engineering and Design. Mcgraw-Hill Publisher, New York (2003)
5. Todorov, E., Li, W.: Optimal control methods suitable for biomechanical systems. In: EMBS- IEEE Proceedings of the 25th Annual International Conference, vol 2, pp. 1758–1761 (2003)
6. Musa, A.A.A., Muawia, M.A.: Analysis of the DC motor speed control using state variable transition matrix. Int. J. Sci. Res. (IJSR) **3** (2012)
7. Ghaffari, V.: A state transition based approach to explicit solution of the LQR problem. In: 5th International Conference on Control, Instrumentation, and Automation (ICCIA), IEEE Conferences, pp. 234–237 (2017)
8. Ogata, K.: Ingeniería de Control Moderna, 4th edn. Pearson, London (2003)
9. Alvarez Picaza, C., Pisarello, M.I., Monzón, J.E.: Model of optimal energy regulation for the articulation of a robotic manipulator. In: VI Latin American Congress on Biomedical Engineering, CLAIB, pp. 908–911. Springer, Heidelberg (2014)
10. Alvarez Picaza, C., Pisarello, M.I., Monzón, J.E.: Análisis teórico de la regulación de energía de servomotores utilizados en manipuladores biomecánicos. In: Annals of the XX Congreso Argentino de Bioingeniería, IX Jornada de Ingeniería Clínica (2015)
11. RE 40 ∅40 mm, Graphite Brushes, 150 Watt. Catálogo. http://www.maxonmotor.com/medias/sys_master/root/8816798990366/15-142-EN.pdf. Accessed May 2018
12. Alvarez Picaza, C., Pisarello, M.I., Monzón, J.E.: Analysis of the stability control of motors used in biomechanical prostheses. In: VII Congreso Latinoamericano Ingeniería Biomédica, CLAIB 2016 (2016)
13. Phillips, C.L., Harbor, R.D.: Feedback Control Systems, 4th edn. Prentice Hall, Upper Saddle River (2000)

SCHSim: A Simulator of Elastic Arterial Vessels Using Windkessel Models

Andrew Guimarães Silva[1(✉)], Daniel G. Goroso[1], and Robson Rodrigues Silva[1,2]

[1] Technological Research Center,
University of Mogi das Cruzes, Mogi das Cruzes, Brazil
andrewguimaraessilva@gmail.com
[2] Center for Biomedical Engineering,
State University of Campinas, Campinas, Brazil

Abstract. The use of simulators that represent characteristics of the physiological system has great utility for students and researchers in the medical field since they allow a better understanding of the dynamics in this complex system. These simulators are also an important tool for performing "in-silico" experiments, which aim to visualize the body's response to new drugs and treatments. In this context, we present SCHSim, a computational tool with didactic purposes, that mimics the basic behavior of elastic arterial vessels by means of equivalent electrical circuits based on Windkessel models. SCHSim allows the user to interact with the model by changing some parameters of the system: heart rate, peripheral resistance, arterial compliance and blood inertia. As a result, it is possible to visualize graphs referring to the behavior of blood pressure and blood flow, thus demonstrating the dynamics in this type of system. SCHSim has, in addition to the simulation elements, didactic tools, with information about Human Circulatory System (HCS) theory and instructions for using the software. Through these tools, it is expected that the simulator can be used by students in the basic physiology of (HSC) teaching.

Keywords: Arterial physiology · Elastic arterial vessels · Human Circulatory System · Windkessel models · Equivalent electric models

1 Introduction

Cardiovascular diseases are one of the leading causes of death in the world, according to the World Health Organization (WHO) it is estimated that 17.7 million people died of cardiovascular disease in 2015, this represents 31% of all deaths at the global level [1]. In Brazil alone, according to the Brazilian Society of Cardiology (SBC), it is estimated that 349,000 people died from heart disease in the year 2016 [2]. This death toll is a cause for concern and has increased over the last few years.

Understanding the functioning of the heart and the whole system in which it is inserted is vitally important so that studies around the development of treatments for cardiopathies can progress. To support these studies, one of the most promising tools is the use of mathematical models to simulate from the stochastic behavior of the ionic

© Springer Nature Switzerland AG 2020
C. A. González Díaz et al. (Eds.): CLAIB 2019, IFMBE Proceedings 75, pp. 709–717, 2020.
https://doi.org/10.1007/978-3-030-30648-9_94

channels to the functioning of the structures of the Human Circulatory System (HCS) [3]. From these models, several simulators with an educational focus have already been developed, such as: MarkoLAB [3, 4], which simulates the stochastic behavior of the main ion channels present in the ventricular myocyte; the MioLAB [5, 6] which describes the properties of ionic currents and contractile forces for the rat ventricular myocytes and the CircAdapt [7] developed from a mathematical model that describes the general circulation of the human heart.

In this context, based on mathematical models that mimic HCS, the objective of this work is to present the SCHSim simulator, which was implemented in the platform MATLAB®, allowing the user to perform tests of comparison between the three mathematical models that simulate the variations in the behavior of the blood pressure from changes in the basic physiological parameters, such as heart rate, arterial compliance, peripheral resistance and blood inertia. The simulator also has didactic tools that allow the study of the basic concepts of HCS.

1.1 Initial Concepts

Among the models that describe the HCS stand out the Windkessel models. This model was described by Otto Frank in 1899 and describes the HCS as a closed hydraulic circuit (Fig. 1) [8]. This circuit is formed by a pulsatile pump connected to a reservoir full of water, except for a small portion containing air. As the water is pumped through the circuit, the air is compressed in the reservoir. When there is no water ejection by the pump, the air pushes the water out of the reservoir, completing a closed circuit. The behavior of this hydraulic circuit can be compared to the HCS. The compressibility of the air in the chamber simulates the elasticity of the large arteries that dilate as the blood is pumped through the ventricles. The resistance encountered by the water passing through the circuit back to the pump emulates the resistance found by blood to flow from the great arteries to the smaller arteries, arterioles, and capillaries. This is due to the decrease in vessel diameter [9].

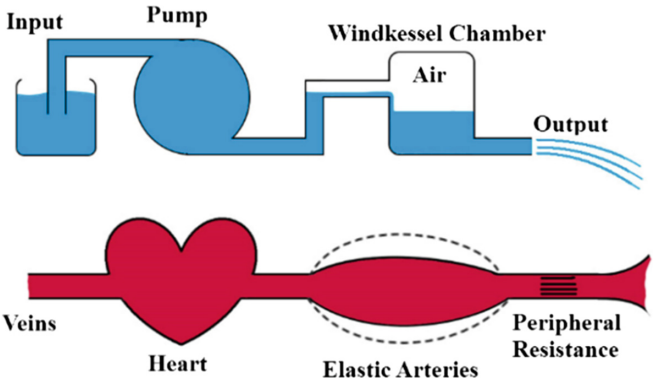

Fig. 1. Relation between hydraulic circuit and HCS

An equivalent electric circuit can also represent the behavior of the hydraulic circuit, where each property of the mechanical system is characterized by an electric component. Figure 2 shows the correlation between the hemodynamics in a blood vessel and the aspects of an electric circuit. The blood flow in the vessel is represented by the electric current; blood pressure is equivalent to an electric voltage; the vessel compliance can be compared to the capacitance of the circuit and the inertia of the blood as it traverses the vessel is equivalent to the inductance of the electric model [8].

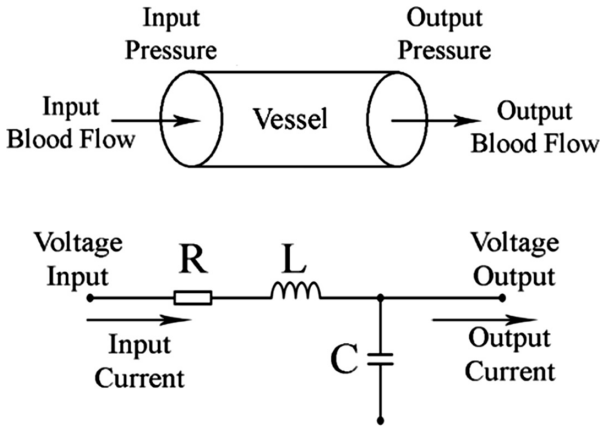

Fig. 2. Correlation between a blood vessel and an equivalent electric circuit

2 Materials and Methods

2.1 Implemented Models

The implementation of the SCHSim simulator was based on the Windkessel models [8]. These models are characterized by working with lumped parameters, simplifying the system, because they do not consider the spatial variations of the dependent variables, different from the distributed parameter models in which the dimensions of the system are considered, this approach allows to reduce the degree of complexity of the system making it possible to solve them by means of ordinary differential equations (ODE) [10]. In this way, the models implemented were the Windkessel models of two, three and four elements. Figure 3 shows the circuit of the three models implemented.

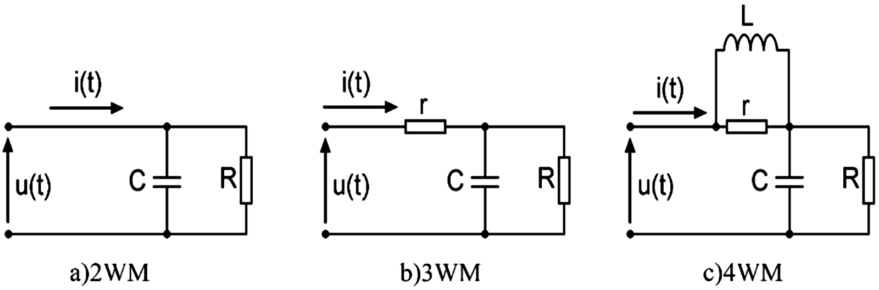

Fig. 3. The three Windkessel models

Two-Element Windkessel Model (2WM)
The first model is that of two elements (Fig. 3a), this is formed by a capacitor and a resistor connected in parallel. In this model the resistor (R) represents the peripheral resistance and the capacitor (C) represents the arterial compliance.

The electric modeling of this circuit is represented by Eq. (1), where i(t) represents the blood flow as a function of time, u(t) represents blood pressure, (R) corresponds to peripheral resistance, and (C) represents arterial compliance.

$$i(t) = \frac{u(t)}{R} + C\frac{du(t)}{dt} \tag{1}$$

Three-Element Windkessel Model (3WM)
In the three-element model (Fig. 3b), another resistive element (r) is added in series with the set formed by the capacitor (C) and the resistor (R) connected in parallel. This resistor (r) represents the resistance of blood to flow through the arterial valve. The electric modeling of this circuit is represented by Eqs. (2) and (3).

$$i(t) = \frac{u_c(t)}{R} + C\frac{du_c(t)}{dt} \tag{2}$$

$$u(t) = i(t).r + u_c(t) \tag{3}$$

Four-Element Windkessel Model (4WM)
The third model implemented is the four-element model (Fig. 3c). This model is an adaptation of the 3WM and adds to the circuit an inductor (L) in parallel with the resistive element (r). This inductor (L) represents the blood inertia existing in the artery. The 4WM is described by Eqs. (4), (5) and (6).

$$\frac{du_C(t)}{dt} = \frac{-1}{R.C} \cdot u_C(t) + \frac{1}{C} \cdot i(t) \tag{4}$$

$$i(t) = i_L(t) + \frac{L}{r} . \frac{di_L(t)}{dt} \tag{5}$$

$$u(t) = u_C(t) + r.(i(t) - i_L(t)) \tag{6}$$

2.2 Development of the Simulator SCHSim

The implementation of the Windkessel models [8] was performed on the MATLAB® (2017b). To solve the differential equations presented in the previous section, we used the ODE Solver tool, which allows solving differential equations by the numerical method. As the aim of the simulator is to become a didactic tool that can be used by students, it was used in the creation of graphical interfaces the Graphical User Interfaces Development Environment (GUIDE) tool also available on the MATLAB® platform. The development of the simulator was performed considering the importance

of the instructional elements. To make the user experience educational, we added help menus that describe the physiological functioning of HCS with mathematical models analogous to HCS and a section that describes how to perform the simulations in the software.

2.3 Simulation Protocol

To solve the differential equations, it is necessary to establish a function i(t), which represents the blood flow in the artery. In the implementation of this model, we adopted the parameters described in [8], in which the signal generated by the function generator is divided into two parts. The first part of the signal represents the period of systole, where blood ejection occurs in the artery, represented by the variable Ts. In the second part, the diastole movement occurs where the signal is equal to zero because it represents the moment when the heart valve closes and, blood flow is interrupted. The systole period and the diastole period form a cardiac cycle, represented by the variable T. The amplitude of the signal is denoted I0 and represents the peak blood flow in the artery. The signal i(t) is described by the following equation:

$$i(t) = \begin{cases} I_0.sin^2\left(\frac{\pi.t}{T_s}\right) set \in (0, T_s) \\ 0 \, set \in (T_s, T) \end{cases} \quad (7)$$

The simulation protocols used in this project refer to the systemic circulation. This protocol includes the values of peripheral resistance (R), arterial compliance (C), resistance of the aortic valve (r) and blood inertia (L). For the maximum blood flow value I0 = 500 mL was used, the systolic period Ts = 0.3 s, the period of the cardiac cycle received T = 0.8 s and the simulation time equal to 4 s. All values are based on characteristics of a healthy adult human and can be seen in Table 1.

Table 1. Parameter values of a healthy adult human for Windkessel models [8]

Parameters	2WM	3WM	4WM
R (mmHg.s/mL)	1,000	1,000	1,000
C (mL/mmHg)	1,000	1,000	1,000
r (mmHg.s/mL)	x	0,050	0,050
L (mmHg.s^2/mL)	x	x	0,005

3 Results

3.1 The Simulator SCHSim

Figure 4 shows the initial screen of the SCHSim simulator. This screen has three buttons that allow the user to access the main functions of the simulator and select the default language (English or Portuguese).

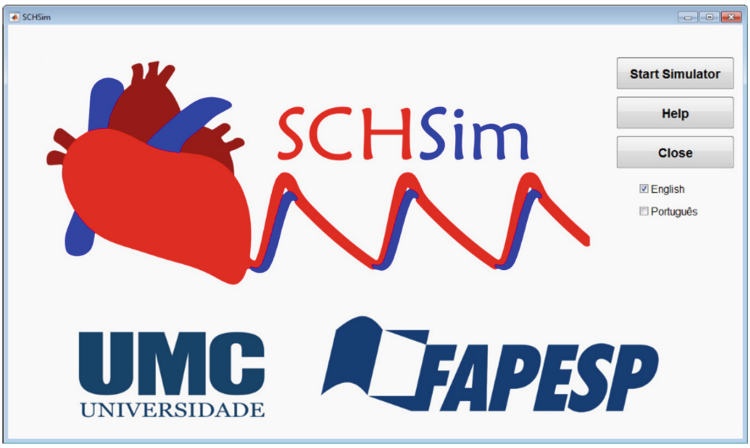

Fig. 4. The initial screen of the SCHSim simulator

Pressing the (Help) button displays the screen shown in Fig. 5. This screen contains a menu to the right that allows you to navigate among the information that the user wants to access.

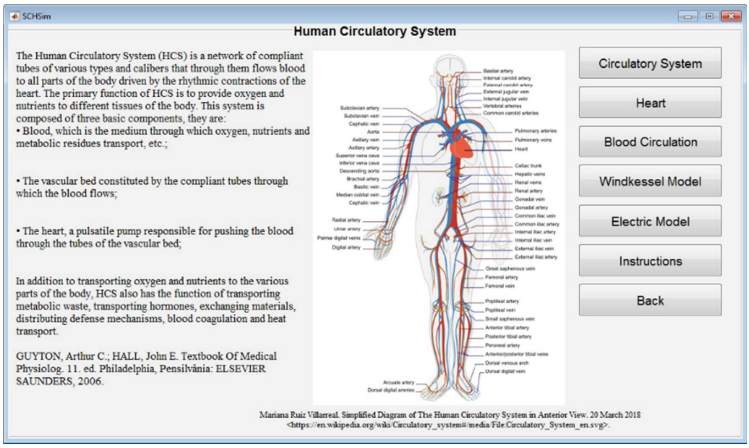

Fig. 5. Help screen of the simulator: allows the user to have access to didactic information

Figure 6 shows the simulation screen. This interface is divided into six fields: (A) Toolbar; (B) Model selection tabs; (C) Graphs; (D) Data input; (E) Results; (F) Execution buttons.

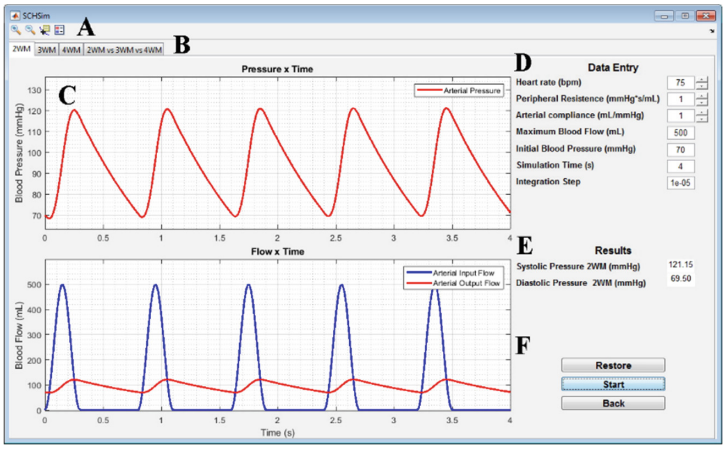

Fig. 6. Screen to change parameters and display results in SCHSim

Figure 7 shows the comparison screen of the models. The values obtained for 2WM, 3WM, and 4WM were respectively: 121.19/69.46 mmHg, 133.46/70.73 mmHg and 116.87/70.66 mmHg.

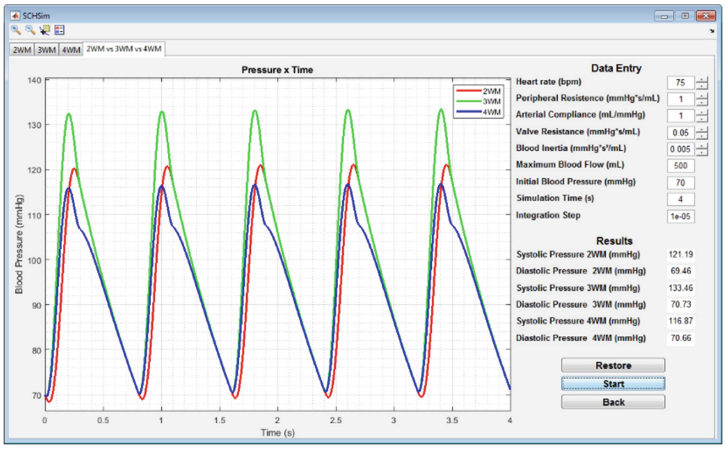

Fig. 7. Comparison of blood pressure obtained by 2WM, 3WM and 4WM models

To access the SCHSim, one can download the source code or the executable file available at the link: https://goo.gl/forms/ZTAMRKTKQRTo7QAz1. The executable file does not require the installation of MATLAB and runs on the Windows® operating system.

4 Discussion

As can be seen in Fig. 7, the 2WM and 4WM models have a systolic pressure close to 120 mmHg, a coherent value when compared to healthy adult blood pressure values, according to [11], 120 mmHg for systolic pressure and 80 mmHg for diastolic pressure, differing only as regards the value of diastolic pressure which for the two and four-element models was close to 70 mmHg, a little distant from the ideal 80 mmHg. When observing the results obtained by the 3WM model, it was observed that the systolic pressure obtained was 133.46 mmHg, a value outside the expected 120 mmHg, however its diastolic pressure was 70.73 mmHg, showing close to the other models. Analyzing the graphs generated by the models it is verified that the 2WM and 3WM models were not able to reproduce the dicrotic notch presented by the 4WM model. This occurrence is because the 4WM model has more elements capable of representing the effect, thus allowing a closer description of the phenomena in question.

It is also observed that the signals present unrealistic curves due to the simplifications of the models, which work with lumped parameters not considering all the spatial variables existing in the real HCS [10]. The main limitations of the models are their incapability to represent effects of local vascular changes, wave transition phenomena and blood flow distribution [12]. Thus, the results obtained by these simulations are simplified, but serve as the basis for the understanding and development of more complex models.

About the didactic elements of SCHSim, it is important to highlight the insertion of instructive elements of the theory addressed in the simulator, a fact not observed in the CircAdapt simulator [7], although it was implemented in a more complete model, it does not have didactic tools included. The didactic aspect is important, since due to the complexity of the subject addressed, instructional tools can provide a better user experience.

5 Conclusion

Based on the results obtained, it is expected that SCHSim can contribute to the teaching of the basic principles of the complex theory of the cardiovascular system, making it easier to visualize the dynamics in the system.

The present work served as a basis for the development of the second version of SCHSim. This new version is based on a more robust model capable of representing the entire HSC, including certain types of diseases of the heart valves. Activities with fixation questions and new data visualization tools will be implemented to help teaching the basic concepts of cardiovascular system. Its development is being done in the programming language R and will be available with didactic tools via web platform.

Acknowledgments. The authors are grateful for the financial support of the University of Mogi das Cruz-es (OMEC/UMC) and the Foundation for Research Support of the State of São Paulo (FAPESP) Grants # 2013/20220–5 and # 2016/18422–7.

Conflict of Interests. The authors state that there are no undisclosed financial or personal relationships that might results in conflict of interest with respect to this study.

References

1. Doenças Cardiovasculares: Organização Mundial da Saúde (OMS). https://www.paho.org/bra/index.php?option=com_content&view=article&id=5253:doencas-cardiovasculares&Itemid=1096. Accessed 12 May 2019
2. Cardiômetro: Mortes por Doenças Cardiovasculares no Brasil. Sociedade Brasileira de Cardiologia (SBC). http://www.cardiometro.com.br/. Accessed 15 May 2017
3. Silva, R.R., Goroso, D.G., Bers, D.M., Puglisi, J.L.: MarkoLAB: a simulator to study ionic channel's stochastic behavior. Comput. Biol. Med. **87**, 258–270 (2017)
4. Pessoa, C.A., Junior, R.A.R., Souza Filho, O.B., Goroso, D.G., Puglisi, J.L., Silva, R.R.: MARKOLAB WEB: Uma plataforma online para estudo do comportamento estocástico dos canais iônicos. 2017. In: V Congresso Brasileiro de Eletromiografia e Cinesiologia e X Simpósio de Engenharia Biomédica. Universidade Federal de Uberlândia (2017)
5. Silva, R.R., Goroso, D.G., Bissaco, M.A.: MioLab: simulator for cardiac myocyte contractile force of rat based on the dynamics of calcium. Med. Eng. Phys. **35**, 338–349 (2013)
6. Silva, R.R., Bissaco, M.A., Goroso, D.G.: MioLAB, a rat cardiac contractile force simulator: applications to teaching cardiac cell physiology and biophysics. Comput. Methods Programs Biomed. **122**(3), 480–490 (2015)
7. Lumens, J.: Creating your own virtual patient with CircAdapt simulator. Eur. Heart J. **35**, 335–337 (2014)
8. Hlaváč, M.; Holčík, J.: Windkessel model analysis in MATLAB. Student Electrical Engineering, Information and Communication Technologies, Brno (2004)
9. Kerner, D.R.: Solving Windkessel Models with MLAB, pp. 1–2 (2014)
10. Shi, Y., Lawford, P., Hose, R.: Review of zero-D and 1-D models of blood flow in the cardiovascular system. BioMed. Eng. OnLine **10**, 33 (2011)
11. Guyton, A.C., Hall, J.E.: Textbook of Medical Physiology, 11th edn. Elsevier Saunders, Philadelphia (2006)
12. Westerhof, N., Lankhaar, J., Westerhof, B.E.: The arterial windkessel. Med. Biol. Eng. Comput. **47**, 131–141 (2009)

Effects of Astaxanthin on Pulse Rate Variability of Mice Under Chronic Stress

Daniel Escutia-Reyes[1(✉)], Rigoberto Oros-Pantoja[1], José Javier Reyes-Lagos[1], Adriana Cristina Pliego-Carrillo[1], Claudia Ivette Ledesma-Ramírez[1], Daniela Rodríguez-Muñoz[2], and Eugenio Torres-García[1]

[1] Faculty of Medicine, Autonomous University of the State of Mexico (UAEMex), 50180 Toluca, Mexico
seyerder@hotmail.com
[2] Faculty of Medicine, CUS XXI, 51350 Zinacantepec, Mexico

Abstract. This exploratory study aims to evaluate the autonomic cardiovascular effects of the astaxanthin on pulse rate variability (PRV) of chronically stressed mice.

We used male CD1 mice that were divided into four groups: l-control (Ct, n = 3), ll-chronic restraint stress (St, n = 4), III-supplemented with astaxanthin (Astx, n = 4) and IV-supplemented and stressed (Astx + St, n = 5). Astaxanthin (4 mg/kg for 21 consecutive days) in the corresponding groups was orally administered. In the last day, the pulse rate signals were recorded by photoplethysmography. One minute of pulse-to-pulse time series (P-P) were constructed for all the groups. The P-P time series were processed to estimate relevant linear and nonlinear PRV parameters. It was found that in stressed mice, astaxanthin produced: (1) decreased heart rate; (2) increased complexity in the P-P time series and (3) increased fractal behavior in the pulse rate fluctuations. These results suggest that astaxanthin may attenuate the autonomic cardiac imbalance produced by chronic stress.

Keywords: Astaxanthin · Pulse rate variability · Autonomic nervous system · Chronic stress

1 Introduction

The ketocarotenoid astaxanthin has several applications in industries such as aquaculture, food, cosmetics, nutraceuticals, and pharmaceuticals. It is a micronutrient which is attributed numerous beneficial properties in health issues. The astaxanthin is considered the most potent antioxidant that exists in the natural environment. Furthermore, it is known that astaxanthin exerts, directly or indirectly, cardioprotective effects due to its anti-inflammatory, antihypertensive, antiobesogenic and lipid-lowering agent properties [1, 7]. Interestingly, some studies have demonstrated that long-term astaxanthin administration to isoproterenol-induced rats produces significant cardioprotection by minimizing the alterations in the activities of the antioxidant enzymes. These effects could be due to membrane protective action of astaxanthin by scavenging the free radicals and its antioxidant action [2].

© Springer Nature Switzerland AG 2020
C. A. González Díaz et al. (Eds.): CLAIB 2019, IFMBE Proceedings 75, pp. 718–723, 2020.
https://doi.org/10.1007/978-3-030-30648-9_95

Although psychological stress is considered a typical response to ensure survival and restore homeostasis, in a chronic way can lead to allostasis [3], which is related to metabolic imbalances (e.g., oxidative stress, dyslipidemia, hyperglycemia, changes in energy redistribution mediated by gluconeogenesis and glycogenolysis), and hemodynamic changes, which together can enhance cardiovascular risk [4].

It is well known that chronic stress causes autonomic imbalance, characterized by increased sympathetic activity and changes in parasympathetic activity [5]. Additionally, a noninvasive tool to assess the cardiac autonomic nervous system (ANS) is the analysis of pulse rate variability (PRV). Noteworthy, some authors have considered the PRV as a surrogate of heart rate variability (HRV) analysis [6]. Indeed, results speak in favor of enough accuracy of PRV to estimate HRV when subjects are at rest [7].

With this background, the present study aimed to evaluate the autonomic cardiovascular effects of the astaxanthin on pulse rate variability of chronically stressed mice. We hypothesize that cardioprotective effects of astaxanthin attenuate the cardiac autonomic imbalance produced by chronic stress in mice.

2 Materials and Methods

We used Male CD1 mice of 9–10 weeks old (30–5 g). Rodents were kept with water and food *ad libitum* under bioterium standard conditions (light/dark cycles 12/12 h, 20–24 °C, humidity 40–65%), and randomly allocated into four groups: l–control (Ct, n = 3), ll-chronic restraint stress (St, n = 4), III-supplemented with astaxanthin (Astx, n = 4) and IV-supplemented and stressed (Astx + St, n = 5).

The St and Astx + St groups were stressed 3 h daily for 21 consecutive days, by confining them into rodent restrainers (2.36 in. long × 1.4 in. of diameter). Cyanotech Astaxanthin (2.5% microbeads presentation) was dissolved in water and tween-20% (5%), and it was orally administered (4 mg/kg) for 21 consecutive days in the corresponding groups. To avoid circadian cycle changes, the procedures were performed in a set schedule (8:00 a. m. ±1 h), and to prevent adaptation to stress model; randomly stimuli were applied for 30 s every 20 min (restrainer's inclination, rotation, and vibration). In the last day, continuous pulse rate signals were recorded at rest mice by a photoplethysmography system (BP-2000 Blood Pressure Analysis System, Visitech Systems, Inc., USA).

One minute of pulse-to-pulse time series (P-P) was calculated and filtered for all the groups using Matlab® software (the MathWorks, Inc. Natick, Massachusetts, USA). The P-P time series were processed to estimate relevant parameters such as the standard deviation of the PP intervals (SDPP), the heart rate (HR), the root mean square of the successive differences (RMSSD), the sample entropy (SampEn) and the short-term fractal scaling exponent (α_1) for the four groups using Kubios software [8].

Ordinary one-way ANOVA was used to assess the effect of astaxanthin in the chronic stressed mice on linear PRV and SD measures. Normality was verified with the Shapiro-Wilk test. Data were further analyzed by Uncorrected Fisher's LSD test for multiple comparisons. $\alpha = 0.05$ was considered as the significance level. GraphPad software (Prism 7.0) was used to assess the statistical analyses. In all tests, the null hypothesis was rejected when $P < 0.05$.

3 Results

The results are presented as mean ± standard deviation (SD, Fig. 1). A significant decrement of SDPP was found in the St group in comparison with the Ct group (8.75 ± 2.66 vs 4.86 ± 0.78 ms, $F_{St\ versus\ Ct} = 2.451$, $P < 0.05$; Fig. 1a). Also, statistical differences were found between them for RMSSD (5.43 ± 2.68 vs 2.54 ± 0.67 ms, $F_{St\ versus\ Ct} = 2.262$, $P < 0.05$; Fig. 1c).

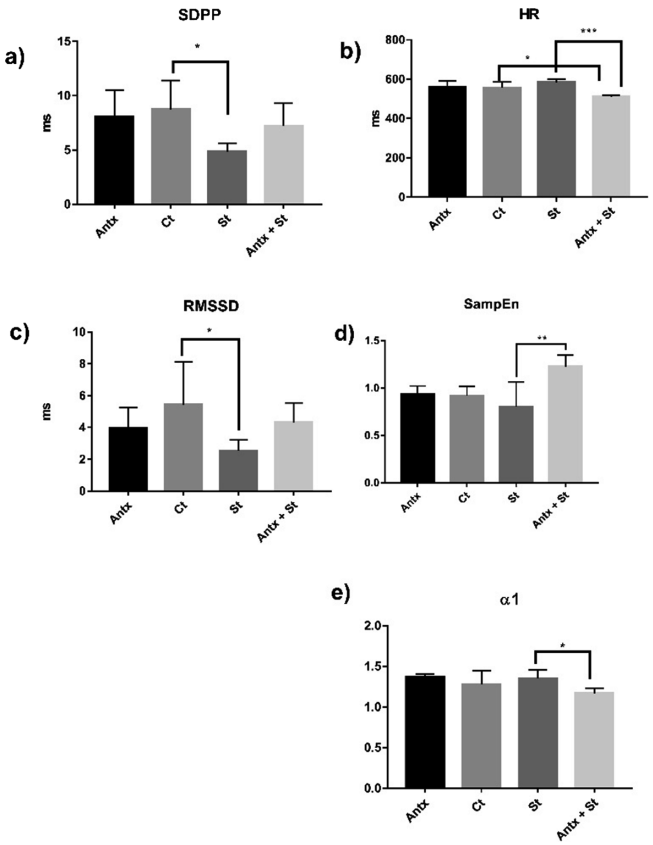

Fig. 1. Bar graphs of linear and nonlinear pulse rate variability (PRV) parameters of four groups of mice: control (Ct, n = 3), chronic restraint stress (St, n = 4), supplemented with astaxanthin (Astx, n = 4) and supplemented and stressed (Astx + St, n = 5): (a) the standard deviation of the PP intervals (SDPP); (b) the heart rate (HR); (c) the root mean square of the successive differences (RMSSD); (d) the sample entropy (SampEn) and (e) the short-term fractal scaling exponent (α1). *P < 0.05, **P<0.01 and ***P<0.001

Furthermore, a significant decrement of HR is noted in the Astx + St group compared with St group (584.3 ± 14.9 vs 510.6 ± 8.49 bpm, $F_{St\ versus\ Astx+St} = 9.899$, $P < 0.001$; Fig. 1b). The same parameter showed a considerable difference between Ct and Astx St (557.2 ± 28.42 vs 510.6 ± 8.49, $F_{Ct\ versus\ Astx+\ St} = 9.899$, $P < 0.05$; Fig. 1b).

Finally, the group St showed significant differences versus the Astx + St group for SampEn and for α_1 (0.80 ± 0.26 vs 1.23 ± 0.12, $F_{Ct\ versus\ Astx+\ St} = 5.826$, $P < 0.01$; Fig. 1d) and (1.35 ± 0.11 vs 1.17 ± 0.06, Fig. 1e), respectively.

4 Discussion

At present, there are many advances in astaxanthin research related to cardiovascular health and diseases, due to its direct antioxidant, indirect antioxidant, anti-inflammatory, and anti-hypertensive properties [9]. On the other hand, it is well known that chronic stress is associated with a reduction of the autonomic modulation or sympathovagal balance modification and it is thereby considered by some authors to provoke cardiac autonomic dysregulation [10]. To our best knowledge, this is the first study documenting the effects of astaxanthin on the ANS. The key contribution of this work is to show that astaxanthin exert cardioprotective effects under chronic stress conditions as a result of enhanced autonomic cardiac modulation.

Recent studies have shown that astaxanthin supplementation improves parameters associated with brain health (neuro-inflammation and cognition), that data suggested that natural astaxanthin supplementation reduces negative mood state parameters (depression and fatigue) and improves global mood state and supports mental wellness [11]. Thus, we can speculate that astaxanthin is effective to attenuate stress. Additionally, other results suggest that astaxanthin can modulate the oxidative condition and may improve vascular elastin and arterial wall thickness in hypertension [12].

Our findings are in line with studies that indicate that supplementation with astaxanthin may modify autonomic function [13] and also protects the myocardium when is administered both orally or intravenously before the induction of the ischemic event [14]. On the one hand, relevant linear parameters such as SDPP and RMSSD shoed decreased values in chronically stressed mice group compared with a control group. These findings show that there is effectively a decrease in parasympathetic activity. Moreover, we observed a decreased values of HR in the astaxanthin supplemented mice, compared with both the Ct group and the St group, being this difference more noticeable in the group St. This findings may suggest that astaxanthin supplementation has a major effect under a stress condition. Finally, we found an increment of SampEn in the Astx + St group, it could be associated with more complexity in the time series. These indirect determinations are associated with compensatory response or adverse cardiovascular effects [15].

In future studies, we will verify the effects of astaxanthin on HRV and increase the number of subjects.

5 Conclusion

Chronic stress caused a decrease in PRV, accompanied by a decrease in parasympathetic cardiac activity.In addition, we found that in stressed mice, astaxanthin caused: (1) decreased heart rate; (2) increased complexity in the P-P time series and (3) increased fractal behavior in the pulse rate fluctuations. Concretely these results suggest that astaxanthin may exert potential cardioprotective effects under chronic stress conditions. Our results indicate that astaxanthin may attenuate the autonomic cardiac imbalance produced by chronic stress in mice increasing the parasimpathetic tone.

Conflicts of Interest. All coauthors have no financial conflicts or other conflicts of interest in this area.

References

1. Régnier, P., Bastias, J., Rodriguez-Ruiz, V., Caballero-Casero, N., et al.: Astaxanthin from haematococcus pluvialis prevents oxidative stress on human endothelial cells without toxicity. Mar. Drugs **13**(5), 2857–2874 (2015)
2. Abdalla-Hussein, M.: Cardioprotective effects of astaxanthin against isoproterenol-induced cardiotoxicity in rats. J. Nutr. Food Sci. **5**, 1–6 (2015)
3. Pilnik, S.D.: El concepto de alostasis: un paso más allá del estrés y la homeostasis. Rev. del Hosp. Ital. **30**, 7–12 (2010)
4. Sikora, M., Konopelski, P., Pham, K., Wyczalkowska-Tomasik, A., Ufnal, M.: Repeated restraint stress produces acute and chronic changes in hemodynamic parameters in rats. Stress **19**(6), 621–629 (2016)
5. Thayer, J.F., Yamamoto, S.S., Brosschot, J.F.: The relationship of autonomic imbalance, heart rate variability and cardiovascular disease risk factors. Int. J. Cardiol. **141**, 122–131 (2010)
6. Pellegrino, P.R., Schiller, A.M., Zucker, I.H.: Validation of pulse rate variability as a surrogate for heart rate variability in chronically instrumented rabbits. Am. J. Physiol. Heart Circ. Physiol. **307**, 97–109 (2014)
7. Schäfer, A., Vagedes, J.: How accurate is pulse rate variability as an estimate of heart rate variability? Int. J. Cardiol. **166**(1), 15–29 (2013)
8. Tarvainen, M.P., Niskanen, J.-P., Lipponen, J.A., Ranta-Aho, P.O., Karjalainen, P.A.: Kubios HRV - heart rate variability analysis software. Comput. Methods Programs Biomed. **113**(1), 210–220 (2014)
9. Visioli, F., Artaria, C.: Astaxanthin in cardiovascular health and disease: mechanisms of action, therapeutic merits, and knowledge gaps. Food Funct. **8**(1), 39–63 (2017)
10. Kim, H.G., Cheon, E.J., Bai, D.S., et al.: Stress and heart rate variability: a meta-analysis and review of the literature. Psychiatry Investig. **15**, 235–245 (2018)
11. Talbott, S., Hantla, D., Capelli, B., et al.: Astaxanthin supplementation reduces depression and fatigue in healthy subject. EC Nutr. **14**(3), 239–246 (2019)
12. Hussein, G., Goto, H., Oda, S., Sankawa, U., Matsumoto, K., Watanabe, H.: Antihypertensive potential and mechanism of action of astaxanthin: III. Antioxidant and histopathological effects in spontaneously hypertensive rats. Biol. Pharm. Bull. **29**(4), 684–688 (2006)
13. Fassett, R.G., Coombes, J.S.: Astaxanthin: a potential therapeutic agent in cardiovascular disease. Mar. Drugs **9**, 447–465 (2011)

14. Haensel, A., Mills, P., Nelesen, R., Ziegler, M., Dimsdale, J.: The relationship between heart rate variability and inflammatory markers in cardiovascular diseases. Psychoneuroendocrinology **33**, 13051312 (2008)
15. Imai, A., Oda, Y., Ito, N., Seki, S., Nakagawa, K., Miyazawa, T., et al.: Effects of dietary supplementation of astaxanthin and sesamin on daily fatigue: a randomized, double-blind, placebo-controlled, two-way crossover study. Nutrients **10**(3), 281 (2018)

Criticism of Baroreflex Estimation Methods in Time Domain

Juan Carlos Perfetto[1(✉)] and Aurora Graciela Ruiz[2]

[1] Biomedical Engineering Institute, Buenos Aires University, Paseo Colon 840, Buenos Aires, Argentina
jperfet@fi.uba.ar
[2] Fernández Hospital, Cerviño 3356, C1425 AGP Buenos Aires, Argentina

Abstract. This article analyzes the simplifications made by methods for assessing baroreflex sensitivity in the time domain, and also discuss the reason to apply them since by using other techniques, better results are achieved.

The sequence method should be not applied without checking arterial blood pressure excursion. Using a linear model, as the majority of time-domain methods do, the error increases significantly when the pressure range increases. Additionally, with this novel approach, real curve points can be computed by grouping data, and consequently two important parameters like the setpoint and the gain peak can be obtained.

Keywords: Baroreflex sensitivity · Inter-beat interval · Systolic arterial pressure · Time domain

1 Introduction

The baroreflex is the main adaptation mechanism of the cardiovascular system. The vagal component of the baroreflex can be studied by evaluating inter-beat interval variations in response to arterial pressure variations. This sigmoid curve is often referred to as the baroreflex function curve [1, 2].

The slope of the curve at each point represents baroreflex sensitivity, or gain. At very low pressures (below 50 mmHg) [3], the gain tends to be zero, but it becomes saturated at pressures around 160–200 mmHg [4].

The sensitivity is maximal in the middle part of the curve. It corresponds to a certain arterial pressure, which can itself be assumed to correspond with the set value to be stabilized. Among other approaches, all of which involve searching baroreflex sequences, baroreflex sensitivity can be estimated using time domain methods [5–8] (Fig. 1).

To search baroreflex sequences, computerized scanning is applied to find linear correlations between RR Intervals (RR) and Blood Pressure (BP) changes. Then, the slope of the linear correlation between the RR and BP of each sequence is added as a point of the baroreflex curve. Underlying assumptions are:

(1) The linear part of the baroreflex curve is wide in men; moderate increases of the delta p-value (of 20 mmHg) are limited to this part of the curve.

© Springer Nature Switzerland AG 2020
C. A. González Díaz et al. (Eds.): CLAIB 2019, IFMBE Proceedings 75, pp. 724–728, 2020.
https://doi.org/10.1007/978-3-030-30648-9_96

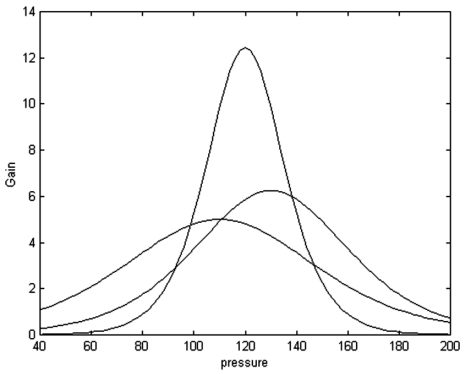

Fig. 1. Simulated gain curves with different pressure mid-values and different range of pressure variation to mimic subject variability.

(2) BP varies shortly from the mid-value, and, therefore, the gain does not change significantly.

As this method is applied to people of different age, sex, and pathologies, the question is: "Can this simplification be sustained?"

2 Materials and Methods

2.1 Experimental Data

All records used in this study were from the EuroBavar Dataset, acquired from 21 patients (four men and 17 women) in supine and standing positions. The patients were noninvasively monitored, and continuous arterial blood pressure (CBPC) and electrocardiogram (ECG) signals were acquired. The sample rate was 500 samples per second; both signals were available in text format; and each study was approximately ten minutes in length.

2.2 Data Preprocessing

Two series are needed: beat to beat intervals and beat to-beat systolic BP, which were obtained from the EuroBavar Dataset's ECG and CBPC measurements, respectively. This involved finding the R wave in ECG signals to compute intervals between the R waves and determine the maximum blood pressure for every cardiac cycle in CBPC measurements. The Pan-Tompkins [9] algorithm was used to detect the R waves in ECGs, and the intervals between the R waves were used to make the RR event series. Another method [10] was utilized to detect systolic arterial blood pressure from CBPC. From these points, the SBP series was constructed.

2.3 Baroreflex Sequences Detection

For this research, the authors adopted the sequential method criteria [11]. Using the time series created, three or more consecutive cycles of blood pressure increments, coupled with RR interval concordant changes, were identified. To assure linear relationship between point serial pairs, only correlation coefficient values greater than 0.85 between both point series were included. The quotient between segments was the gain, and the minimum increment considered was 1 mmHg for arterial pressure. For each ramp, not only the gain was registered, but also the corresponding arterial pressure. A lag of one beat between ramps was allowed.

2.4 Data Binning

As the number of sequences that could be detected was limited, and because the sequences varied greatly, the solution was to average all gain points obtained from the selected ramps. An alternative procedure was to cluster points based on similar arterial pressure and average only those points belonging to the same class. The pressure range from 60 mmHg to 170 mmHg was then segmented into non-overlapping windows, 10 mmHg wide. To choose the range of pressures, possible values from a physiological point of view were considered. 12 gain values were computed within each window. The maximum gain and the systolic arterial blood pressure of the corresponding class were extracted. This pressure value corresponded to the systolic arterial pressure setpoint. Depending on the subject, only a few of the classes had elements, so the others were allowed to be empty. For comparison, all the slopes were also averaged.

2.5 Systolic Arterial Pressure Setpoint Using Histogram

The goal of the baroreflex is to stabilize blood pressure at a given value; therefore, if the baroreflex works as it should, blood pressure levels should be close to this given value more often than they are to any other value. Therefore, using systolic arterial blood pressure series, histograms were obtained in this research, and the pressure corresponding to the maximum of each histogram was taken as a second estimate of the systolic arterial blood pressure setpoint and used to validate the other estimate. If the estimates did not match, it was concluded that the baroreflex was damaged. This could be used to diagnose damage to the baroreflex.

3 Results

All the processes explained in the previous section were accomplished using 21 records from the EuroBavar Dataset, corresponding to the supine position. In one case, no baroreflex sequence was detected, and this case was removed. Another case likely corresponded to a patient with impaired baroreflex because the gain was extremely low, and only one bin had sequences. In all other cases, three or more bins were involved in the calculations.

Gain, estimated by the sequence method and averaging all the slopes, was 14 ± 14.3 ms/mmHg. In the second approach, each class was formed by grouping arterial pressure points into 12 bins, corresponding to different pressure ranges. The maximum gain from these 12 measurements was 16.9 ± 14.3 ms/mmHg. One case involved gains that could be considered outliers; with this record excluded, the gains were 11 ± 5.09 ms/mmHg and 14.1 ± 7.54 ms/mmHg, respectively. The correlation coefficient between estimates of the systolic arterial pressure setpoint was 0.91. Arterial Blood Pressure Setpoint 1 corresponded to the blood pressure of the bin with the greatest gain; values were 118 ± 21.9. Arterial Blood Pressure Setpoint 2 corresponded to the peak of the histograms for systolic arterial blood pressure; values were 119 ± 17.7 mmHg.

4 Discussion

The EuroBavar Dataset was non-homogenous. One subject was a diabetic with autonomic neuropathy, and another had received a heart transplant. Of the remaining 19 subjects, 12 were normotensive; three were hypertensive; and four were healthy. Real data analysis showed that the range of pressure changes was not as small as supposed when applied to a diverse group of subjects, leading the researchers to consider the nonlinear nature of the baroreflex curve. Then, slopes corresponding to different operating points of the curve, and, consequently, different pressure values, were averaged. In this way, the sensitivity was sub-estimated, as can be seen in the Results section. On the other hand, with very little extra processing, this provided an opportunity to add information about the corresponding blood pressure setpoint and to calculate peak gain, in addition to the traditional gain estimated across the "linear" region of the relation.

5 Conclusion

In most cases, the sequence method sub-estimates the maximum gain. The sequence method should be not applied without checking the BP excursion. Using a linear model, the error increases significantly when the pressure range increases.

Rearranging the data collected via standard procedures of assessing baroreflex gain in the time domain can enhance analysis of the results incorporating new features—such as the set pressure to be stabilized, as well as the peak gain, which is greater than the average gain. Those features are not obvious in traditional analysis. However, with the novel method proposed in this research, both setpoint and peak gain are exposed, which could be very useful in further studies of cardiovascular diseases.

References

1. deBoer, R.W., Karemaker, J.M., Strackee, J.: Hemodynamic fluctuations and baroreflex sensitivity in humans: a beat-to-beat model. Am. J. Physiol. **253**(3 Pt 2), H680–H689 (1987)

2. Koch, E.: Die reflektorische Selbststeuerung des Kreislaufes, vol. 1. Theodor Steinkopff, Dresden (1931)
3. Berne, R.M., Levy, M.N.: Cardiovascular Physiology, vol. vi, 6th edn, p. 298. St. Louis, Mosby-Year Book (1992)
4. Donald, D.E., Shepherd, J.T.: Autonomic regulation of the peripheral circulation. Annu. Rev. Physiol. **42**(1), 429–439 (1980)
5. Bertinieri, G., et al.: Evaluation of baroreceptor reflex by blood pressure monitoring in unanesthetized cats. Am. J. Physiol. **254**(2 Pt 2), H377–H383 (1988)
6. Bertinieri, G., et al.: A new approach to analysis of the arterial baroreflex. J. Hypertens. **3** (Suppl 3), S79–S81 (1985)
7. Gouveia, S., et al.: Time domain baroreflex sensitivity assessment by joint analysis of spontaneous SBP and RR series. Biomed. Signal Process. Control **4**(3), 254–261 (2009)
8. Westerhof, B.E., et al.: Time-domain cross-correlation baroreflex sensitivity: performance on the EUROBAVAR data set. J. Hypertens. **22**(7), 1371–1380 (2004)
9. Pan, J., Tompkins, W.J.: A real-time QRS detection algorithm. IEEE Trans. Biomed. Eng. **3**, 230–236 (1985)
10. Perfetto, J.C., et al.: Robust algorithm to extract systoles and diastoles from continuous blood pressure signal. In: Proceedings of the 25th Annual International Conference of the IEEE Engineering in Medicine and Biology Society, 2003. IEEE (2003)
11. Parati, G., Di Rienzo, M., Mancia, G.: How to measure baroreflex sensitivity: from the cardiovascular laboratory to daily life. J. Hypertens. **18**(1), 7–19 (2000)

Bioinformatics and Computational Biology

A Preliminary Comparison of P-Tool Consistency

Javier Murillo[1(✉)], Flavio Spetale[1], Elizabeth Tapia[1], Flavia Krsticevic[6], Olivier Cailloux[2], Serge Guillaume[3], Gustavo Vazquez[4], Tamara Fernandez[4], Sebastien Destercke[5], Sergio Ponce[6], and Pilar Bulacio[1]

[1] CIFASIS-CONICET, Univ. Nacional de Rosario, Rosario, Argentina
murillo@cifasis-conicet.gov.ar
[2] Université Paris-Dauphine, CNRS, Paris, France
[3] ITAP, Irstea, Montpellier SupAgro, Univ. Montpellier, Montpellier, France
[4] Universidad Católica del Uruguay, Montevideo, Uruguay
[5] Université de Technologie de Compiègne, Compiegne, France
[6] Universidad Tecnológica Nacional, Regional San Nicolás, Buenos Aires, Argentina

Abstract. Many Bioinformatics tools, known as p-tools, have been developed to predict the effect of single nucleotide polymorphisms (SNPs) on gene functionality, in an effort to reduce the need for *in-vivo* assays. However, the large number of p-tools available and the heterogeneity of their output make their selection and comparison difficult. To study the consistency of predictions across p-tools, here we present two indices and test them on five p-tools whose predictions are based on different types of background information. For this test, SNPs from well-known organism *Drosophila melanogaster* are considered.

Keywords: SNP · Gene functionality · Missense nonsense mutation

1 Introduction

A main factor underlying the conformation of proteins is their amino acid sequence. An individual nucleotide change, also called a Single Nucleotide Polymorphism (SNP), is a *missense mutation* when it causes a different protein, or a *nonsense mutation* when it causes a short and non-functional protein. The degree to which a SNP affects protein function is a key point, but its prediction remains an open problem.

Next-Generation Sequencing (NGS) technologies have made it possible to detect thousands of SNPs [1], but wet-lab studies needed to associate these SNPs with phenotypic traits are costly. To narrow down the list of candidate SNPs, several Bioinformatics tools, hereafter referred to as p-tools, have been developed to predict the impact of SNPs *in-silico*. P-tools can be based on information from amino acid sequences, protein structure, context, functional parameters and evolutionary information [2]. For instance, for sequence conservation

© Springer Nature Switzerland AG 2020
C. A. González Díaz et al. (Eds.): CLAIB 2019, IFMBE Proceedings 75, pp. 731–735, 2020.
https://doi.org/10.1007/978-3-030-30648-9_97

analysis, conserved amino acids—known to be relevant for protein function—are identified by alignment, and SNPs on these positions are identified as likely deleterious. Structure information is also used to infer sites with likely impact on protein function: SNPs in ligand-binding domains or active sites typically modify protein function. Based on this information, p-tools can be designed using either expert knowledge or machine learning techniques. P-tools not only vary in nature, but their outputs also vary in syntax and semantics, which makes comparison between them tricky. To tackle this problem, most strategies normalize predictions, forcing them into two classes, to evaluate classical performance metrics like accuracy, sensibility, sensitivity and ROC curves [4].

In this work, consistency across p-tools is evaluated by means of two proposed indices. For two given p-tools, the indices quantify the systematic disagreement between each pair of SNPs, i.e., count pairs of predictions ordered differently in each p-tool scale, without performing any scale normalization. An experimental study was carried out using five widely-used p-tools [3]. These were selected based on the diversity of knowledge or learning method they are based on, as well as the possibility to be run online with standard parameters. The consistency across p-tools was tested with SNPs from model organism *D. melanogaster*, a common starting point for data analysis.

2 Materials and Methods

The method to evaluate consistency across p-tools has two stages. The first one ponders, for each p-tool i, the order of two SNP effect predictions, (m_1, m_2): m_1 can be more damaging than m_2, the opposite can be true, or two mutations can be equally damaging. This preference relation is noted as follows:

- $m_1 \prec_i m_2$ if p-tool i considers m_1 to be less damaging than m_2;
- $m_1 \sim_i m_2 \iff \neg(m_1 \prec_i m_2) \wedge \neg(m_2 \prec_i m_1)$, if p-tool i cannot assert m_1 to be less or more damaging than m_2.

To value the three possible orders for a pair m_1, m_2, let $r_i(m_1, m_2)$ be defined as follows:

$$r_i(m_1, m_2) = \begin{cases} 1 \text{ if } m_1 \prec_i m_2 \\ -1 \text{ if } m_2 \prec_i m_1 \\ 0 \text{ if } m_2 \sim_i m_1 \end{cases} \tag{1}$$

The second stage values the degree of (dis)agreement of relative orders—given by all pairs of mutations—between two p-tools, i and j, through two indices (Eqs. 2 and 3): K_{all} is the ratio of mutations pairs ordered differently by both p-tools to all mutation pairs, considering all disagreements; K_{strong} is analogous but considers only opposite orderings.

$$K_{\text{all}} = \frac{|\{(m_1, m_2) \mid r_i(m_1, m_2) \neq r_j(m_1, m_2)\}|}{\binom{|M|}{2}} \tag{2}$$

$$K_{\text{strong}} = \frac{|\{(m_1, m_2) \mid r_i(m_1, m_2) \neq 0 \wedge \ r_i(m_1, m_2) = -r_j(m_1, m_2)\}|}{\binom{|M|}{2}} \tag{3}$$

For the case of discrete outputs, predictions are ordered according to labels, e.g. {*benign, possibly deleterious, probably deleterious*} and a preference relation: *benign* $\prec$ *possibly deleterious* $\prec$ *probably deleterious*. When dealing with numerical outputs t_i, an inequality threshold δ_i is introduced, such that the preference relation for p-tool i is defined as follows: $m_1 \prec_i m_2 \iff t_i(m_2) - t_i(m_1) > \delta_i,\ \delta_i \geq 0$. Hence, $m_1 \sim_i m_2 \iff |t_i(m_2) - t_i(m_1)| \leq \delta_i$.

P-Tools: Selected p-tools have the following main features.

- PolyPhen2[1] uses protein sequences on a trained Naïve Bayes model to predict SNP sites which code for a protein's structure or function.
- Provean[2] is based on a model that evaluates evolutionary information from protein sequence.
- Align-GVGD[3] uses biophysical characteristics of amino acid and protein multiple sequence alignments on an evolutionary conservation model.
- Strum[4] values changes in folding stability induced by SNPs based on a gradient boosting of Gibbs free-energy with different sequence and structure properties.
- Cupsat[5] evaluates changes in protein stability induced by SNPs based on structure information of wild-type and mutant proteins.

Data: SNPs were analyzed on gene *vermilion*, locus *Dmel_CG2155*, on *D.mel.*

3 Results and Discussion

P-tools are compared pairwise with the K_{all} and K_{strong} indices and different equality thresholds. All possible SNPs in each sequence position of the *vermilion* gene are considered. See Fig. 1. Small index values represent similar pairwise outputs. For all pairwise comparisons, as the threshold increases, the K_{all} value first increases and then decreases when outputs became similar ($r_i(m_1, m_2) = 0$). **Polyphen2-Provean** follows that behavior after a threshold of 40% (data not shown). On the other hand, K_{strong} has a monotonically decreasing behavior. Two cases are possible when comparing pairwise p-tool outputs t_i, t_j with pairwise SNPs m_1 and m_2: (1) $t_i(m_1) < t_i(m_2)$ and $t_j(m_1) < t_j(m_2)$ or (2) $t_i(m_2) < t_i(m_1)$ and $t_j(m_1) < t_j(m_2)$ ($t_i(m_1) \simeq t_i(m_2)$ or $t_j(m_1) \simeq t_j(m_2)$ are a middle step between these cases and are also analyzed). In case (1), there is an agreement according to K_{all}. When the threshold increases up to level $\delta_i = |t_i(m_1) - t_i(m_2)|$, $t_i(m_1) \simeq t_i(m_2)$ and $t_j(m_1) < t_j(m_2)$, making K_{all} count this as a disagreement. When the threshold reaches $\delta_j = |t_j(m_1) - t_j(m_2)|$, $t_j(m_1) \simeq t_j(m_2)$ and both tools agree again. In this case, the error will increase after δ_i and decrease after δ_j. Clearly, when δ is 100%, all pairs will be considered

[1] http://genetics.bwh.harvard.edu/pph2/.
[2] http://sift.jcvi.org/.
[3] http://agvgd.hci.utah.edu/agvgd_input.php.
[4] https://zhanglab.ccmb.med.umich.edu/strum/.
[5] http://cupsat.tu-bs.de.

equal. In case (2), there is a disagreement according to K_{all}. After δ_i is reached, $t_i(m_1) \simeq t_i(m_2)$ and $t_j(m_1) < t_j(m_2)$, meaning they still disagree. Only after δ_j is reached, the two p-tools agree. In this case, the error decreases monotonically. An analogous analysis can be done with K_{strong}. In case (1), since both p-tools never give opposite results, K_{strong} evaluates outputs as an agreement, regardless of the threshold. In case (2), after δ_i is reached, the outputs are no longer opposite and are therefore equal according to K_{strong}. In both cases, the error can only decrease for increasing thresholds. While K_{all} has a monotonically decreasing behaviour with δ only in case (2), K_{strong} has such a behaviour for both cases, making it less sensitive to the equality threshold.

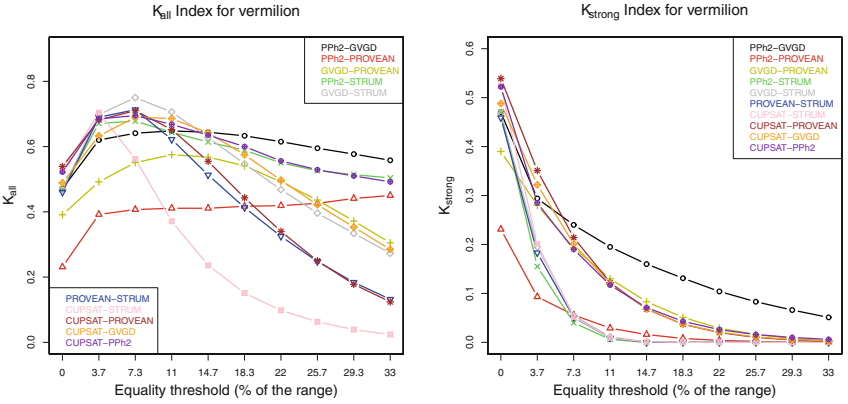

Fig. 1. Pairwise p-tool comparison. K_{all} (left) and K_{strong} (right), δ from 0% to 33%. Outputs scales: AlignGVGD $[5, 215]$; Provean $[-15, 3]$; PolyPhen-2 $[0, 1]$; Strum $[-10, 11]$, and Cupsat $[-23, 20]$, *D.mel.* gene *vermilion*

Note that even for $\delta \sim 10\%$, pairwise p-tool comparison with K_{strong} varies from 0.05% to 20% in the worst case. The two tools which agree the most across all δ are **Strum** and **Cupsat**, which makes sense since both work with similar knowledge, namely gene energy functions. On the other hand, the two tools which disagree the most are **PolyPhen2** and **Align-GVGD**, which also makes sense since one is based on structure and the other on evolutionary information.

4 Conclusions

Two indices were proposed to compare p-tools considering their most informative output. The indices do not require any normalization process. The comparison on *D.mel.* gene *vermilion* shows that predictions vary widely depending on the p-tool. Still, different outputs are not necessarily a problem, since they enable outputs to be integrated to achieve a more accurate prediction of SNP effects.

References

1. Wadapurkar, R., Vyas, R.: Computational analysis of next generation sequencing data and its applications in clinical oncology. Inform. Med. Unlocked **11**, 75–82 (2018)
2. Choi, Y., Sims, G.E., Murphy, S., Miller, J.R., Chan, A.P.: Predicting the functional effect of amino acid substitutions and indels. PLOS ONE **7**(10), e46688 (2012)
3. Thusberg, J., Olatubosun, A., Vihinen, M.: Performance of mutation pathogenicity prediction methods on missense variants. Hum. Mutat. **32**(4), 358–368 (2011)
4. Hicks, S., et al.: Prediction of missense mutation functionality depends on both the algorithm and sequence alignment employed. Hum. Mutat. **32**(6), 661–668 (2011)

DNA-MC: Tool for Mapping and Clustering DNA Sequences

Valeria Ramírez(✉), Israel Román-Godínez, and Sulema Torres-Ramos

Departamento de Ciencias Computacionales, CUCEI - Universidad de Guadalajara, Guadalajara, Jalisco, Mexico
vrmz@hotmail.com, sulema.torres@academicos.udg.mx

Abstract. As a result of the increasing interest on genomic signal processing, there is the necessity of develop computational software that combines different tools for signal processing and automatic analysis. This paper presents a computational tool for mapping and clustering DNA sequences. Several DNA numerical representations, a feature extraction method, the K-means algorithm and different clustering evaluation metrics were implemented. This software allows to researchers to perform genomic signal analysis through a graphical user interface, without need programming skills. The tool is prepared to increase their capabilities by implementing different algorithms or modules. Also, a comparative analysis of eleven DNA numerical representation is presented. The results show that Electron-ion and Voss present the best performances when clustering genomic signals using K-means. The clusters quality was measure using the ARI metric.

Keywords: DNA numerical representations · Genomic signal processing · Clustering

1 Introduction

To assess the genetic relationship between organisms or species is a very important task in bioinformatics. Traditionally, this task has been addressed using sequence alignment algorithms, which identifies similarities between DNA or protein sequences [1].

Recent studies [2–5] have been shown that, among other applications, it is possible to measure the similarity between DNA sequences using the theory and methods of digital signal processing (DSP). This approach is known as Genomic Signal Processing (GSP), defined as an engineering discipline which analyzes, processes and uses genomic signals to discover biological knowledge [6], in order to diagnose genetic diseases [7, 8], identify DNA regions [9], make gene predictions [10], among others. By genomic signal it is understood the numerical representation of genomic data (e.g. DNA sequences). Due to the DNA sequences are digitally represented by letter strings in which each letter could be A, T, C and G which stands for adenine, thymine, cytosine, and guanine, respectively, it is necessary to map these letter string into one or more numerical sequences. These mapping methods are known as DNA numerical representations (DNRs).

© Springer Nature Switzerland AG 2020
C. A. González Díaz et al. (Eds.): CLAIB 2019, IFMBE Proceedings 75, pp. 736–742, 2020.
https://doi.org/10.1007/978-3-030-30648-9_98

The importance of GSP reside in the application of numerous powerful, flexible and efficient DSP-based tools that can be used for the analysis of genomic data [11]. Also, recent studies combines GSP with machine learning tools in order to automatically look for underlying patterns hidden in the biological data [3, 7, 8, 12]. One of these tools is clustering, used for grouping genomic signals by applying the K-means algorithm [3].

However, the tool presented in [3] is not licensed as open source, it only allows one mapping type for DNA sequences and, do not evaluate the clusters cohesiveness. This papers presents DNA-MC, an open source system that allows the automatic processing of genomic signals, using diverse DNRs along with K-means clustering algorithm. Also, this paper presents a quantitative analysis of the implemented DNRs based on the quality of the clusters using the ARI metric.

2 Materials and Methods

DNA-MC tool was designed under the object-oriented paradigm (OOP) and using a modular architecture in order to make it scalable. The programming language used was Python. The six modules that constitute the DNA-MC software are presented as follow.

2.1 Input Module

This module receives one or more FASTA files [13] that can contain a single sequence or several sequences per file. To read the files the module uses Bio.SeqIO, a Biopython library [14] which facilitates the data extraction, specifically the header, which contains a description of the sequence, and the DNA sequence itself.

2.2 Mapping Module

The DNA sequences received as input for this module will be transformed into a numerical representation. Eleven DNRs (Voss, Tetrahedron, Integer, Real, Complex, Quaternion, Electron-ion, Atomic Number, Paired Numeric, DNA Walk and Z-Curve) [15] were implemented.

To carry out the mapping, the sequences are divided in batches in order to execute this task using two threads, making it parallel. The mapping method takes each character and transforms it into a number, obtaining a numerical representation for each DNA sequence.

The resulting genomic signal could be a one or multi-dimensional vector, it depends on the chosen numerical representation. For example, Fig. 1 depicts the mapping of a fragment of DNA sequence using the one-dimensional numerical representation Atomic Number; while in Fig. 2 the Voss mapping is used for the same sequence fragment. The latter generates a genomic signal formed by a multidimensional vector.

```
Sequence = [A, T, G, T, T, C, G, C, C, G, A, C, C, G, T, T, G, A, C, T]

Signal = [70, 66, 78, 66, 66, 58, 78, 58, 58, 78, 70, 58, 58, 78, 66, 66, 78, 70, 58, 66]
```

Fig. 1. Example of the numerical representation *Atomic Number*.

```
Sequence = [A, T, G, T, T, C, G, C, C, G, A, C, C, G, T, T, G, A, C, T]

Signal = [ Gn[0, 0, 1, 0, 0, 0, 1, 0, 0, 1, 0, 0, 0, 1, 0, 0, 1, 0, 0, 0]
           An[1, 0, 0, 0, 0, 0, 0, 0, 0, 0, 1, 0, 0, 0, 0, 0, 0, 1, 0, 0]
           Cn[0, 0, 0, 0, 0, 0, 1, 0, 1, 1, 0, 0, 1, 1, 0, 0, 0, 0, 0, 1, 0]
           Tn[0, 1, 0, 1, 1, 0, 0, 0, 0, 0, 0, 0, 0, 0, 1, 1, 0, 0, 0, 1] ]
```

Fig. 2. Example of the numerical representation *Voss*.

2.3 Characterization Module

In the field of machine learning, the characterization consists in obtaining a set of features or characteristics that represents an element. This module obtains the genomic signal characteristics through the fast Fourier transform [16].

The libraries of Spectrum [17], NFFT [17], and Numpy [18] from Python were used to execute all the necessary methods to carry out the Fourier analysis in each dimension of the genomic signal. The resulting feature vectors are concatenated into a one-dimensional vector. The final output are the feature vectors that represent the signals in terms of their frequency spectra.

2.4 Machine Learning Module

The clustering is done using the genomic signals characterized and the K-means algorithm. To do this, the Scikit-learn library [19] was used. This module requires that the user enters parameters such as: the number of clusters to be found, the number of replicas and iterations. K-means returns the groups found in the signals according to the similarity between them.

2.5 Evaluation Module

This module evaluates the results obtained in the Machine Learning Step, that is, it verifies the quality of the generated clusters. To do so, two metrics were implemented: Silhouette evaluates the cohesiveness of the clusters, and Adjusted Rand Index compares each cluster against a gold standard, which is not generated by K-means.

Silhouette receives the genomic signals and their automatic assigned cluster, returning a score for each signal, which indicates how similar a genomic signal is to its own cluster (cohesion) compared to other clusters (separation). The range score is between −1 to 1. Where score near to 1 means high cohesiveness of the genomic signal in its assigned cluster and high separation of the neighbor clusters. A score near to −1 suggests that at the average distance, the element should be grouped in a different cluster [20].

The ARI metric receives the automatic assigned clusters and requires that the user enters the predefined group for each genomic signal. To do so, the module allows to load a txt file containing the header and the gold standard group of each genomic signal.

Adjusted Rand Index returns one score for all the clusters, it indicates the similarity of the two assignments. The range score is [0, 1], where values closer to zero indicate a bad clustering, similar clustering have a positive value where 1 is the perfect match score [21].

2.6 Graphical User Interface Module

The design of the graphic interface was made thinking that the system would be practical and easy to use. The GUI was implemented using the wxPython library [22]. One of the capabilities of DNA-MC is to allow the selection of any number of FASTA files through a file dialog. Furthermore, it provides options to choose the numerical representation and the results evaluation metric.

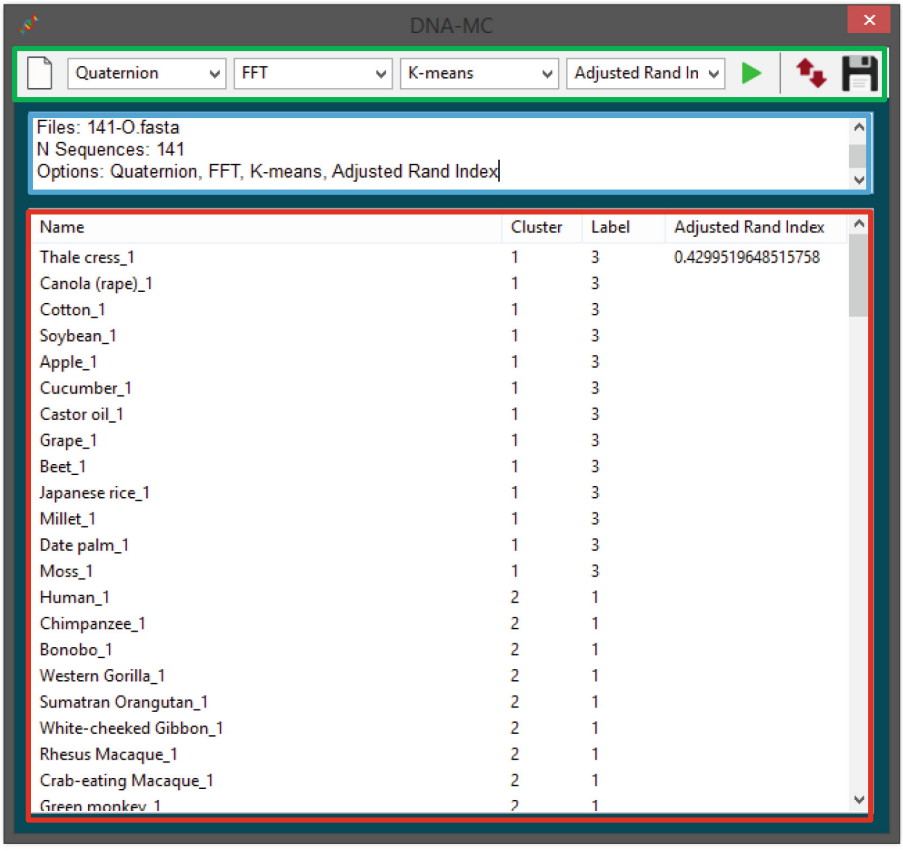

Fig. 3. Output of the ARI metric for the Quaternion numerical representation.

Figure 3 depicts the system view. The upper side (framed on green), corresponds to the configuration options (file selection, DNR, characterization method, machine learning algorithm and evaluation metric) necessary to perform the analysis. The blue frame presents general information about the selected configuration, and the red one shows the obtained results. Observe that the "Name" column lists the sequences headers (obtained from the Fasta file), the "Cluster" column indicates the cluster assigned to each sequence by K-means, and the last column shows the results of the selected evaluation metric. The "Label" column only is shown when the ARI metric is selected, and it presents the predefined group assigned for each sequence (see Sect. 2.5).

3 Results and Discussion

DNA-MC was tested using the dataset presented in [3], which consists of 141 DNA sequences from several organisms. The sequences were mapped using the eleven DNRs described in Sect. 2.2, and the resulting clusters were evaluated using the ARI metric described in Sect. 2.5. This metric was selected because of it allows to determine which numerical representation, in conjunction with k-means, find groups that are closer to the biological taxon.

Table 1 presents three experiments assigning three different values of K (6, 17, and 35) corresponding to the organism's hierarchical category of kingdom, phylum, and class, respectively. The bolded numbers corresponds to the three greater scores for each experiment. The best DNR where K equal to 6 corresponds to Electro-ion (0.51), Atomic number (0.50), and Voss (0.46) and the worst case to DNA Walk (0.03) and Z-curve (0.06). Electro-ion and Atomic number are mapping methods based on physicochemical properties of the DNA sequences while Voss is a multidimensional arbitrary mapping method. Setting K equal to 17, corresponding to the phylum category in the data set, the best three DNA numerical representations correspond to Electro-ion (0.46), Voss (0.46), and Integer (0.39). Again, Electro-ion is one of the best along with Voss. Finally, when K is equal to 35, the best scores are presented by Integer (0.51), Electro-ion (0.47) and Voss (0.44).

Comparing the obtained results with those presented in [4], it could be observed that the DNRs that better behave are Electro-ion and Voss. On the other hand, it is consistent with [4] that the worst DNRs are the DNA Walk and Z-curve which are categorized as cumulative DNRs.

Finally, one of the conclusions presented in [4] is that the multidimensional DNRs are more appropriate for the similarity computation between genomic signals. Even though the latter is consistent with our results (in which Voss appears in the best three results for all experiments), other DNRs that consider physicochemical properties, as Electro-ion, are also a good option for similarity computation.

Table 1. ARI scores for each DNA numerical representation for three different values of K.

DNA numerical representation	K = 6	K = 17	K = 35
Voss	**0.45**	**0.46**	**0.44**
Tetrahedron	0.44	0.28	0.31
Integer	0.45	**0.39**	**0.51**
Real	0.24	0.36	0.36
Complex	0.26	0.34	0.30
Quaternion	0.21	0.38	0.37
Electron-ion	**0.51**	**0.46**	**0.47**
Atomic Number	**0.50**	0.26	0.40
Paired Numeric	0.26	0.24	0.36
DNA Walk	0.03	0.05	0.07
Z-curve	0.06	0.11	0.07

4 Conclusions

Using DNA-MC tool it is possible to process, group and evaluate DNA sequences, through the processing of genomic signals using clustering. The software implements eleven DNRs, one characterization method, one machine learning algorithm, and two evaluation metrics. The main advantage of the presented tool is that not only performs clustering, but also presents an evaluation of the clusters' quality.

As can be seen in the results, the evaluation of the ARI metrics allows bioinformatics researchers to analyze the behavior of the different DNRs and identify which of them is the best or most appropriate to work with the GSP methods, in this case, our results suggest that Electron-ion and Voss are the DNRs with better performance.

Some applications of the presented tool are automatic generation of DNA sequences groups to find relationships between organisms, which is particularly useful for phylogenetic analysis.

As future work, it is proposed to implement different methods in the characterization module, machine learning algorithms, and DNRs.

Conflict of Interest. The authors declare that they have no conflict of interest.

References

1. Chang, X., Escobar, F.A., Valderrama, C., Robert, V.: Exploring sequence alignment algorithms on FPGA-based heterogeneous architectures. In: IWBBIO, pp. 330–341 (2014)
2. Hou, W., Pan, Q., Peng, Q., He, M.: A new method to analyze protein sequence similarity using dynamic time warping. Genomics **109**(2), 123–130 (2017)
3. Mendizabal-Ruiz, G., Román-Godínez, I., Torres-Ramos, S., Salido-Ruiz, R.A., Vélez-Pérez, H., Morales, J.A.: Genomic signal processing for DNA sequence clustering. PeerJ **6**, e4264 (2018)

4. Mendizabal-Ruiz, G., Román-Godínez, I., Torres-Ramos, S., Salido-Ruiz, R.A., Morales, J. A.: On DNA numerical representations for genomic similarity computation. PLoS ONE **12**(3), e0173288 (2017)
5. Borrayo, E., Mendizabal-Ruiz, E.G., Vélez-Pérez, H., Romo-Vázquez, R., Mendizabal, A.P., Morales, J.A.: Genomic signal processing methods for computation of alignment-free distances from DNA sequences. PLoS ONE **9**(11), e110954 (2014)
6. Dougherty, E.R., Shmulevich, I., Chen, J., Wang, Z.J.: Genomic Signal Processing and Statistics, vol. 2. Hindawi Publishing Corporation, New York (2005)
7. Liu, D.W., Jia, R.P., Wang, C.F., Arunkumar, N., Narasimhan, K., Udayakumar, M., Elamaran, V.: Automated detection of cancerous genomic sequences using genomic signal processing and machine learning. Future Gener. Comput. Syst. **98**, 233–237 (2019)
8. Shen, T., Nagai, Y., Udayakumar, M., Narasimhan, K., Shriram, R.K., Mohanraj, N., Elamaran, V.: Automated genomic signal processing for diseased gene identification. J. Med. Imaging Health Inform. **9**(6), 1254–1261 (2019)
9. Weighill, D., Macaya-Sanz, D., DiFazio, S.P., Joubert, W., Shah, M., Schmutz, J., Jacobson, D.: Wavelet-based genomic signal processing for centromere identification and hypothesis generation. Front. Genet. **10**, 487 (2019)
10. Mabrouk, M.S., Naeem, S.M., Eldosoky, M.A.: Different genomic signal processing methods for eukaryotic gene prediction: a systematic REVIEW. Biomed. Eng.: Appl. Basis Commun. **29**(01), 1730001 (2017)
11. Anastassiou, D.: Genomic signal processing. IEEE Signal Process. Mag. **18**(4), 8–20 (2001)
12. Yu, N., Li, Z., Yu, Z.: Survey on encoding schemes for genomic data representation and feature learning—from signal processing to machine learning. Big Data Min. Analytics **1**(3), 191–210 (2018)
13. NCBI. https://www.ncbi.nlm.nih.gov/. Accessed 14 May 2019
14. BioPython. https://biopython.org/. Accessed 14 May 2019
15. Kwan, H.K., Arniker, S.B.: Numerical representation of DNA sequences. In: IEEE International Conference on Electro/Information Technology EIT2009, pp. 307–310. IEEE (2009)
16. DSP Guide. http://www.dspguide.com/. Accessed 14 May 2019
17. The Python Package Index (PyPI). https://pypi.org/. Accessed 14 May 2019
18. NumPy Package. http://www.numpy.org/. Accessed 14 May 2019
19. Scikit-learn. https://scikit-learn.org/stable/. Accessed 14 May 2019
20. Rousseeuw, P.J.: Silhouettes: a graphical aid to the interpretation and validation of cluster analysis. J. Comput. Appl. Math. **20**, 53–65 (1987)
21. Santos, J.M., Embrechts, M.: On the use of the adjusted rand index as a metric for evaluating supervised classification. In: International Conference on Artificial Neural Networks ICANN 2009, pp. 175–184. Springer, Heidelberg (2009)
22. The wxPython. https://wxpython.org/. Accessed 14 May 2019

Using Convolutional Neural Networks with Direct Acyclic Graph Architecture in Segmentation of Breast Lesions in US Images

Marly Guimaraes Fernandes Costa[1(✉)], João Paulo Campos Mendes[1], Wagner C. A Pereira[2], and Cicero F. F. Costa Filho[1]

[1] Centro de P&D de Tecnologia Eletrônica e da Informação-CETELI, Universidade Federal do Amazonas, Manaus, AM, Brazil
ccosta@ufam.edu.br
[2] Programa de Engenharia Biomédica/COPPE/Universidade Federal do Rio de Janeiro, Rio de Janeiro, RJ, Brazil

Abstract. Outlining lesion contours in Breast Ultrasound (BUS) images is an important step in breast cancer diagnosis. Malignant lesions infiltrate the surrounding tissue, generating irregular contours, with spiculations and angulated margins, while benign lesions produce contours with a sharp outline and elliptical shape. In breast imaging, the majority of the existing publications focus on using Convolutional Neural Networks (CNNs) for segmentation and classification of lesions in mammographic images. In this study we propose CNNs with direct acyclic graph (DAG) architecture for breast lesion segmentation in US images. We also compare the performance of these two proposed architectures with a series architecture. The best results were obtained with the DAG architecture. The following mean values were obtained for the metrics used to evaluate the segmented contours: Global accuracy = 9593%; IOU = 87.92%; BF score = 68.77%; and Dice coefficient = 89.11%.

Keywords: Breast lesion · Ultrasound images · Convolutional neural networks

1 Introduction

Breast cancer alone accounts for 30% all new cancer diagnoses in women (Siegel et al. 2017). According to World Cancer Report 2014, breast cancer had the highest incident rate (43.4 per 100) among women (Stewart and Wild 2014). Studies have shown that detection of early-stage breast cancers, followed by appropriate treatment, was responsible for 38% mortality drop rate from 1989 to 2014 (Siegel et al. 2017). Digital mammography (DM) and Ultra-sound (US) are two commonly used techniques for breast lesion detection. Although DM is considered the most effective technique (Akin et al. 2012), US imaging has the advantage of being safer, more versatile and sensitive to lesions located in dense areas (Stavros et al. 1995). US imaging, compared to DM, is heavily dependent on the radiologist's experience.

© Springer Nature Switzerland AG 2020
C. A. González Díaz et al. (Eds.): CLAIB 2019, IFMBE Proceedings 75, pp. 743–751, 2020.
https://doi.org/10.1007/978-3-030-30648-9_99

Outlining lesion contours in US breast images is an important step in breast cancer diagnosis. Malignant lesions infiltrate the surrounding tissue, generating irregular contours, with spiculations and angulated margins, while benign lesions produce contours with a sharp outline and elliptical shape (Stavros et al. 1995). On the other hand, low-contrast images associated with speckle noise generate spurious borders that impede obtaining lesion outlines and hinder accurate diagnosis.

Inspired by the success of machine learning and image processing in computer vision applications, many attempts have been made to build automatic Computer-Aided Diagnosis (CAD) systems for breast lesion segmentation (Jiang et al. 2012; Torbati et al. 2013; Zhao et al. 2014; Liu et al. 2015; Daoud et al. 2016).

Considering the huge popularity of Deep Learning and, in particular, convolutional neural networks (CNNs) in segmenting and classifying objects, naturally the following question arises: using a relatively small image dataset, such as those available in a medical dataset, can a CNN outperform traditional machine learning techniques in segmentation of lesions in breast ultrasound (BUS) imaging?

Considering breast lesion detection techniques presented in the literature, the majority of the existing publications focus on using CNNs in x-ray mammography images: Dhungel et al. (2015) used deep learning for segmentation of masses; Mordang et al. (2016) proposed the use of CNNs in microcalcification detection, and Ahn et al. (2017) proposed the use of CNNs in breast density estimation. More recently, the study of Yap et al. (2018) focuses on using CNNs for automatic segmentation of breast lesions in BUS imaging. The authors compared the performance of three CNN architectures: Le-Net (Thulasiraman and Swamy 2011), U-Net and Fully Convolutional Network (FCN) Alex-Net (Krizhevsky et al. 2012); with three machine learning techniques: Rule-Based Region Ranking, Multifractal Filtering, and Radial Gradient Index (RGI) filtering.

In this study our main concern is to assess the ability of CNNs in detecting contour irregularities in breast lesion US images. With this aim, we propose a CNN with direct acyclic graph (DAG) (Thulasiraman and Swamy 2011) architecture and compare its performance with a CNN with series architecture.

2 Methodology

2.1 Dataset

The BUS images were acquired by National Cancer Institute (INCa) of Rio de Janeiro, during routine breast diagnostic procedures. The dataset was compiled by researchers in the US Lab from the Biomedical Engineering Program of Federal University of Rio de Janeiro, Brazil. The dataset consists of 387 images. Based on the results of histopathologic exams, there are 208 benign lesions and 179 malignant lesions. The images were acquired by a Sonoline Sienna® ultrasound machine. They are grayscale images (8-bit depth resolution). All images were resized to 160 × 160 pixels.

2.2 Convolutional Neural Network Architectures

The first CNN proposed in this study for lesion segmentation in BUS image, CNN1, has a series architecture. In this architecture, the input of each layer is the output of the previous layer. Figure 1 shows the proposed CNN1 architecture. It was obtained empirically through several experiments. The network contains eleven convolutional layers. The receptive fields of the first ten equal to 3×3 pixels and of the last one is 1×1 pixel; both padding and stride hyper-parameters are equal to one. All convolutional layers, except the last one, have 64 feature maps. The last convolutional layer produces two feature maps, since pixels will be classified in two classes: (0) background, (1) lesion. All weights of the convolution layers were initialized according to a Gaussian distribution with mean 0 and standard deviation of 0.01. The biases were initialized as constants, with zero as default value.

Each convolutional layer is followed by a Rectifier Linear Unit (ReLU) layer, which applies an activation function to neurons defined as $f(x) = \max(0, x)$ where x is a single neuron input. MaxPooling layers progressively reduces the input spatial size in order to reduce the number of parameters and computation in the network. All these have 2×2-sized filters applied with a stride of 2 and padding of 0, down sampling every depth slice in the input by 2 along both width and height, discarding 75% of the activations. The MAX operations take the max value from a 2×2 pixel region. The depth dimension remains unchanged. The Dropout layer reduces overfitting by preventing complex co-adaptations in training data. A Dropout ratio parameter sets the probability that any given unit is dropped. In this work, the dropout ratio parameter was set to 0.5. In order to speed up training of convolutional neural networks and reduce the sensitivity to network initialization, a Batch Normalization layer is used between convolutional layers and nonlinearities, such as ReLU layers. It normalizes each input channel across a mini-batch. The Deconvolution layers performs an up-sampling in order to obtain a predictive map of pixel classification with same size as the input; in other words, it predicts the class to which each pixel belongs. All the Deconvolution layers use filters with receptive fields of 4×4 pixels. It works inversely to the convolutional layer. It reuses the convolution layer parameters, but in the opposite direction, that is; the padding is removed from the output rather than added to the input, and the stride results in an up-sampling rather than a sub-sampling.

The Softmax layer calculates both the softmax and the multinomial logistic loss operations, which saves time and improves numerical stability. It takes two inputs, the first one being the prediction of the prior layer (Conv2) and the second one being the label layer. It computes the loss function value, which is used by a backpropagation algorithm to calculate the gradients with respect to all weights in the network.

The second CNN proposed in this study for breast lesion segmentation in US image, CNN2, have a DAG architecture. A DAG architecture has layers arranged as a directed acyclic graph. A DAG architecture is a more complex architecture than a series architecture, in which layers have inputs from multiple layers and outputs to multiple layers. When applied to image processing, these architectures aggregate information of pixel localization contained in initial layers into final layers. In semantic tasks, it is expected that this procedure enhances fine image details. The study of Chen et al. (2016) used a DAG network to segment neuronal structures in Electron Microscope

Images. Figure 2 shows the proposed CNN with a DAG architecture. The main network path is like CNN1.

In CNN2, information from the three sub-sampling modules, after the second convolution layer of each one, is aggregated before the last convolution layer of the network. To implement aggregation, it is necessary that the data representation in both inputs be the same size. Once the data dimension after the two convolution operations of the first sub-sampling module is 160 × 160, and after the last convolution layer of the network is also 160 × 160, no dimension change is necessary. Once the data dimensions after the two convolution operations of the second and third sub-sampling module are 80 × 80 and 40 × 40, respectively, an us-sampling operation, in the first case, and two up-sampling operations, in the second case, are used to convert the dimensions to 160 × 160. The number of layers of CNN1 and CNN2 are 52 and 68, respectively.

We evaluated the performance of the proposed architectures applying some hyper parameter adjustments. The dataset was split in 50% for training and 50% for testing. For CNN training, the stochastic gradient descent with momentum (SGDM) algorithm was used. The initial learning rate was set in 0.001 and the momentum in 0.9. Due to limitations in GPU memory, batch size was set to 5. Stop condition was set in 150 epochs. This maximum was selected observing the convergence of the CNN training.

A quantitative analysis of the performance of the three architectures is performed using the following metrics: accuracy, global accuracy, Jaccard coefficient (intersection over union – IOU), BF score (Boundary F1 -measure) and Dice similarity coefficient (DC).

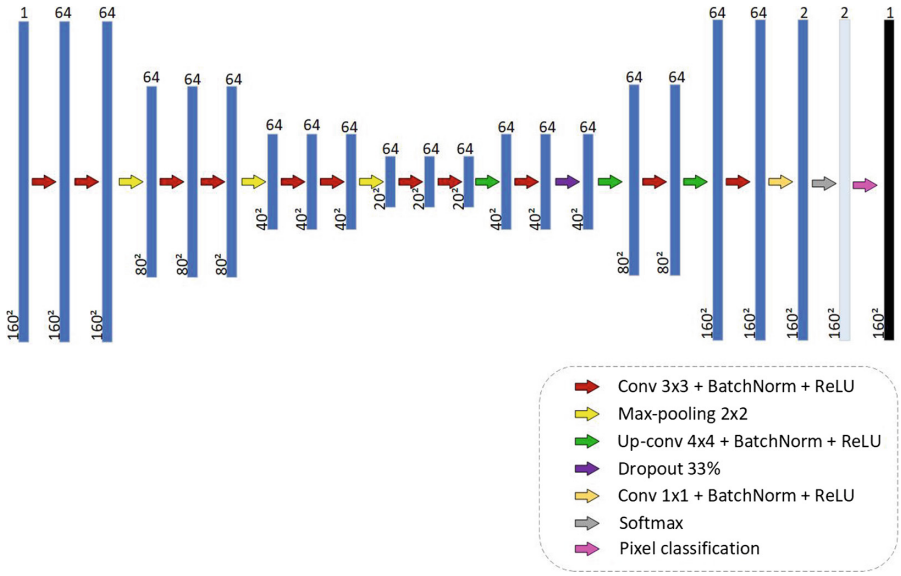

Fig. 1. CNN1: series architecture proposed for breast lesion segmentation in US images.

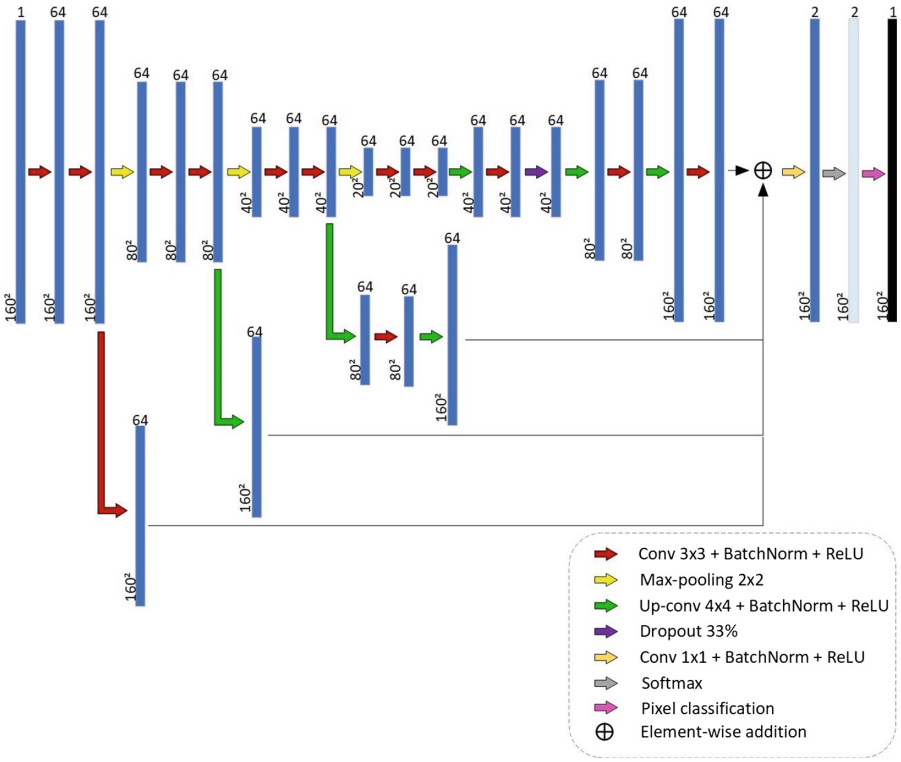

Fig. 2. CNN2: DAG architecture proposed for breast lesion segmentation in US images

2.3 Work Environment

Experiments were performed in MatLab® 2017b (9.3.0.713579). The computer used was equipped with a DELL® motherboard with 128 GB RAM, Intel® Core™ i5-7200U CPU @ 2.50 GHz. The graphics processing unit used was a Nvidia® GeForce 940MX, with 4 GB RAM and 384 CUDA cores. The computer operating system was Microsoft Windows 10®.

3 Results and Discussion

Figure 3 shows examples of segmentations performed by the three architectures in three breast lesions in US images. As observed, the contours obtained by CNN1 are smoother than the contours obtained by the DAG architectures. The contours obtained with the DAG architecture have more details and irregularities, like the gold-standard contours. The reason is that this architecture aggregates, in the last layers, information from initial layers, thus preserving pixel localization in the original image.

Figure 4(a) and (b) shows a quantitative analysis of a benign and a malignant lesion, respectively. The pink color pixels correspond to false positive pixels (pixels outside the ground-truth contour that are considered as inside, in the obtained contour), while green color shows false negative pixels. The contour with lower number of false positives and false negatives pixels is the one obtained with CNN2. Below each image is shown the metrics of each contour. As shown, the best metrics values are also obtained with CNN2.

A summary of the metric values (mean values) obtained for the test set is shown in Table 1.

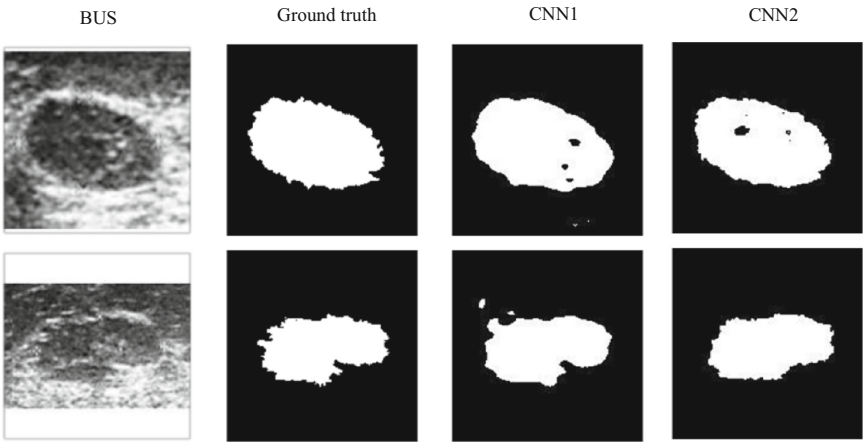

Fig. 3. Examples of contours obtained by the two CNN architectures.

In this study we evaluate the performance of CNN architectures in the task of breast lesion segmentation in US images. Our main concern was to assess the ability of CNNs in detecting contour irregularities in breast lesion US images. A qualitative analysis showed that DAG networks better represent the irregularities present in the gold-standard contours traced by a specialist. The best results were obtained with the more complex DAG architecture. With this architecture, the following mean values were obtained in the test set: Accuracy: 93.36%, Global accuracy: 95.93%; IOU: 87.92%; BF-Score: 68.77%; Dice coefficient: 89.11%.

Comparing our results with the results of Yap et al. (2018), using CNNs for automatic segmentation of lesions on BUS imaging, we have that the best results reported by the authors in the datasets used (A and B), was the sensitivity of 0.99 and 0.93, respectively, resulting in a mean sensitivity of 0.96. The best sensitivity obtained in our study was 0.96, with CNN1. However, we emphasize that a strict comparison could not be made between results obtained in both studies, because the datasets are different.

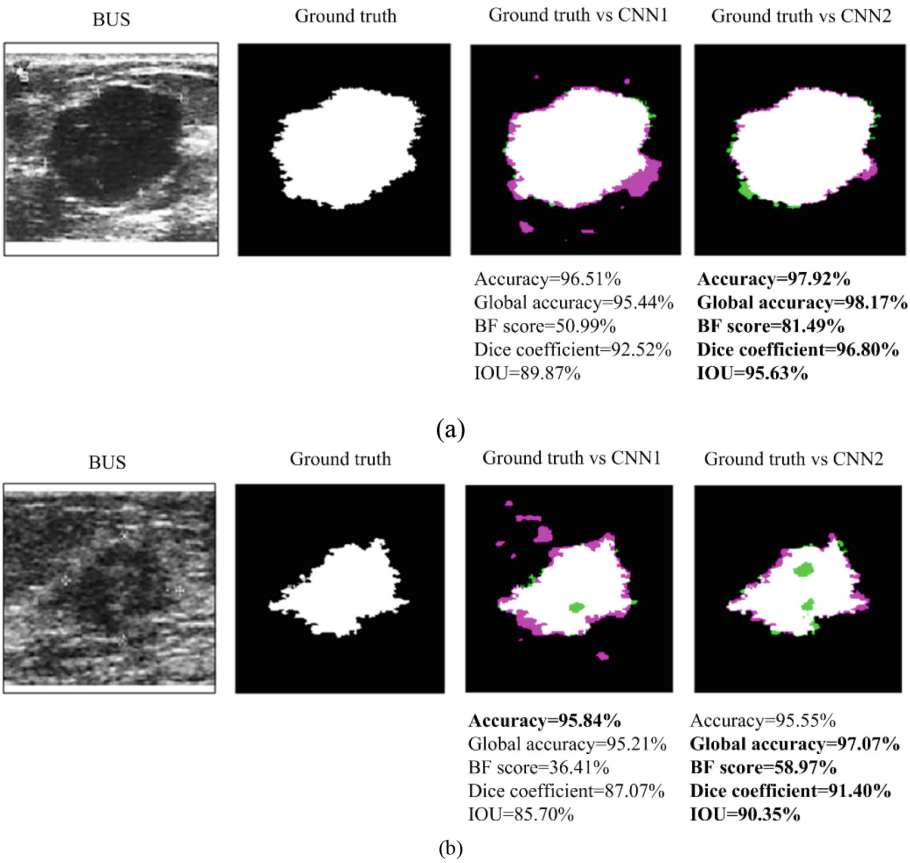

Fig. 4. Quantitative analysis of two segmentations obtained with the three CNN architectures. (a) benign lesion; (b) malignant lesion. Pink color represents false positive pixels, while green color represents false negative pixels. Metric values for each contour are shown below each image.

Table 1. Mean values of the metrics for the test set.

Architecture	Metrics					
	Accuracy	Global accuracy	IOU	Sensitivity	BF score	Dice coefficient
CNN1	94.24	95.46	86.92	**96.05**	63.04	88.17
CNN2	93.36	**95.93**	**87.82**	94.6	**68.77**	**89.11**

The lack of a public standard dataset in breast US research prevents the comparison of different algorithms. The quality of breast US images is highly dependent on the acquisition process and there is a wide variability between different US systems. The appearance, size and location of lesions also affect the results.

For future work, we plan to evaluate DAG architectures in a large database, which would enable a better network generalization. We also intend to extend the work to breast ultrasound lesion classification, evaluating the performance of the complete CAD system.

Acknowledgment. This work was supported in part by the Samsung Electronica da Amazonia Ltda through the terms of the Brazilian Federal Law under Grant 8.387/91, in part by the Coordenação de Aperfeiçoamento de Pessoal de Nível Superior-Brasil (CAPES)–Funding Code 001, in part by the Fundação de Amparo a Pesquisa do Estado do Amazonas (FAPEAM), under Grant 062.00710/2016–PAPAC, and in part by The National Institute for Science and Technology-Medicine Assisted by the Scientific Computing (INCT-MAAC) under Grant CNPq 465586/2014-7. Jim Hesson proofread the manuscript (https://www.academicenglishsolutions.com).

Conflicting of Interests. The authors declare that they have no conflicting of interests.

References

Ahn, C.K., Heo, C., Jin, H., Kim, J.H.: A novel deep learning-based approach to high accuracy breast density estimation in digital mammography. In: Medical Imaging 2017: Computer-Aided Diagnosis, SPIE, p. 101342O (2017)

Akin, O., Brennan, S., Dershaw, D.D., et al.: Advances in oncologic imaging. CA Cancer J. Clin. **62**, 364–393 (2012). https://doi.org/10.3322/caac.21156

Chen, H., Qi, X., Cheng, J.-Z., Heng, P.-A.: Deep contextual networks for neuronal structure segmentation. In: Proceedings of the Thirtieth AAAI Conference on Artificial Intelligence, pp. 1167–1173 (2016)

Daoud, M.I., Atallah, A.A., Awwad, F., Al-Naja, M.: Accurate and fully automatic segmentation of breast ultrasound images by combining image boundary and region information. In: 2016 IEEE 13th International Symposium on Biomedical Imaging (ISBI), pp. 718–721. IEEE (2016)

Dhungel, N., Carneiro, G., Bradley, A.P.: Deep learning and structured prediction for the segmentation of mass in mammograms. In: Lecture Notes in Computer Science (Including Subseries Lecture Notes in Artificial Intelligence and Lecture Notes in Bioinformatics), pp. 605–612. Springer Verlag (2015)

Jiang, P., Peng, J., Zhang, G., et al.: Learning-based automatic breast tumor detection and segmentation in ultrasound images. In: Proceedings - International Symposium on Biomedical Imaging, pp. 1587–1590 (2012)

Krizhevsky, A., Sutskever, I., Hinton, G.E.: ImageNet classification with deep convolutional neural networks. In: Proceedings of the 25th International Conference on Neural Information Processing Systems - Volume 1, pp. 1097–1105. Curran Associates Inc., USA (2012)

Liu, L., Qin, W., Yang, R., et al.: Segmentation of breast ultrasound image using graph cuts and level set. In: 2015 IET International Conference on Biomedical Image and Signal Processing (ICBISP 2015), Institution of Engineering and Technology (IET), pp. 1–4 (2015)

Mordang, J.-J., Janssen, T., Bria, A., et al.: Automatic microcalcification detection in multi-vendor mammography using convolutional neural networks. In: Tingberg, A., Lång, K., Timberg, P. (eds.) Breast Imaging, pp. 35–42. Springer International Publishing, Cham (2016)

Siegel, R.L., Miller, K.D., Jemal, A.: Cancer statistics, 2019. CA Cancer J. Clin. **69**, 7–34 (2017). https://doi.org/10.3322/caac.21551

Stavros, A.T., Thickman, D., Rapp, C.L., et al.: Solid breast nodules: use of sonography to distinguish between benign and malignant lesions. Radiology **196**, 123–134 (1995). https://doi.org/10.1148/radiology.196.1.7784555

Stewart, B.W., Wild, C.P.: World cancer report 2014, 1st edn. International Agency for Research on Cancer, Lyon – France (2014)

Thulasiraman, K., Swamy, M.N.S.: Directed graphs. In: Graphs: Theory and Algorithms, pp. 97–125. Wiley (2011)

Torbati, N., Ayatollahi, A., Kermani, A.: Ultrasound image segmentation by using a FIR neural network. In: 2013 21st Iranian Conference on Electrical Engineering (ICEE), Mashhad, Iran, pp. 1–5. IEEE (2013)

Yap, M.H., Pons, G., Martí, J., et al.: Automated breast ultrasound lesions detection using convolutional neural networks. IEEE J. Biomed. Health Inform. **22**, 1218–1226 (2018). https://doi.org/10.1109/JBHI.2017.2731873

Zhao, F., Li, X., Biswas, S., et al.: Topological texture-based method for mass detection in breast ultrasound image. In: International Symposium on Biomedical Imaging, pp. 685–689. Institute of Electrical and Electronics Engineers (IEEE) (2014)

Spatial Visual Perceptions by Means of Simulated Prosthetic Vision

Diego Lujan Villarreal[1(✉)] and Wolfgang H. Krautschneider[2]

[1] Escuela de Ingenieria y Ciencias, Tecnologico de Monterrey, Monterrey, Mexico
diego.lujan@tec.mx
[2] Hamburg University of Technology, TUHH, Hamburg, Germany

Abstract. Visual prostheses electrically stimulate nearby neurons to generate artificial vision in patients blinded by retinal degenerative diseases. Despite some notable progress in the generation of small dot-like percepts induced by electrical stimulation, the physical aspects of phosphenes demand a better understanding. This present work is part of the feasibility assessment of the activation area introduced elsewhere used for estimating the size and shape of the phosphenes elicited by electrical stimulation. Electrical stimulation of retinal ganglion cells was simulated in a realistic 3D reconstruction of the retina. To ensure cell activation, the dynamics of the ionic channels in cell were considered. Visual perceptions elicited by stimulating electrodes reported by Klauke et al. 2011 in clinical trials were directly compared with our simulation framework. The wide range of visual responses formerly described by subjects is highly correlated with our simulation-based findings. Prior to device implantation, simulation-based findings of the activation area can be advantageous to comprehend the physical aspects of phosphenes and to develop an electrode array for generating spatially-localized perception of light.

Keywords: Physical aspects of phosphenes · Simulating visual prosthetics · Visual percepts

1 Introduction

Artificial vision is built upon phosphenes [1]. A phosphene is defined as any visual sensation described as a spot of light in the visual field caused by methods other than stimulation of the visual system by light. Humayun et al. [2], Keserü et al. [3], Zrenner et al. [4], and Klauke et al. [5] reported the generation of recognizable symbols and simple shapes from multiple stimulated phosphenes. Phosphenes have been reported as doughnut shapes [2], "round" spots of light [2, 5], elongated shapes [3, 5], lines [5], oval shapes [5], and more complicated patterns [5]. Concerns in advanced retinal implants include the eliciting of atypical patterns of retinal activity [6]. Percepts induced by electrical stimulation are variable [2, 3, 5, 7] and support only limited visual function [5, 6]. Current clinical trials demonstrate that patients do not obtain a complete visual scene composed of simultaneously presented phosphenes. Recent clinical trials associated with Argus II developed by Second Sight Medical Products in the United States exhibited a best measured visual acuity of 20/1260 in 7 out of 30 test volunteers

© Springer Nature Switzerland AG 2020
C. A. González Díaz et al. (Eds.): CLAIB 2019, IFMBE Proceedings 75, pp. 752–760, 2020.
https://doi.org/10.1007/978-3-030-30648-9_100

[6]. Similar conclusions have lately been reached by Alpha IMS developed by Retina Implant AG in Germany that reported a best visual acuity of 20/546 in 2 out of 9 test volunteers [8]. Visual prostheses would ideally reproduce accurately natural spatiotemporal patterns of activity in the retinal ganglion cells (RGCs). This requires the capacity of each electrode to reach single-cell selectively. In other words, RGCs are tightly-packed in the ganglionic layer, mainly at the fovea. Unique characteristics of the visual space are sent to the brain by temporal patterns of activity in RGC types that are spatially mixed. Hence, RGCs that are close to each other frequently transmit very different signals [9]. Current strategies for single-cell selectivity have proven to be inadequate [6, 8]. To evoke a narrow spot of light that resembles a natural signal to the brain and can serve as a building block for the pattern of phosphenes, each electrode should activate a nearby cell [9]. Electrode array topology influences the shape and breadth of the phosphenes while the retina is electrically stimulated [9]. That is, by applying a given value of peak stimulus amplitude, the current spread varies according to the topology of the electrode array and the position of the active and ground electrodes. This could lead in changes in the area of stimulation, thereby causing the generation of phosphenes with shapes other than a small spot of light. As artificial vision is currently in an early-stage of maturity, the physical basis of phosphenes in prosthetic vision demands a better understanding. Together with a grasp of attaining single-cell selectivity would be then a requirement to align retinal stimulation with a high-stage of maturity. Hence, prior to device implantation at the retina, life-like situations of phosphenes must be understood. This work is part of the feasibility assessment of the activation area introduced in [9] used to estimate the size and shape of the phosphenes induced by stimulation. In this study, the experimental findings by Klauke et al. [5] of specific spatial patterns of percepts on the array are used to prove the activation area.

2 Materials and Methods

The algorithm of the activation area is as shown in Fig. 1 [9]. The processing steps are explained as follow. In essence, the activation area is defined as a space on the retina where the stimulus initiated at the active electrode in effect triggers a response of some cells. The activation area can estimate the amount of cells activated and identify the size and shape of the phosphenes. The criterion of the activation area states that a cell located inside the activation area is activated by the respective electrode. Otherwise, the cell is not activated by this electrode.

2.1 Electric Field Response

A 3D computational model for electrical stimulation was implemented in Comsol Multiphysics (Comsol, AB., Sweden, Version 4.4). The model consists of a realistic 3D spherical reconstruction of the retina, representing a segment of the human eye, Fig. 2(a). The description values [11, 12] and geometric parameters are listed in Tables 1 and 2. Biphasic pulses of uniform current are injected from the active to ground electrodes to drive single or nearby RGC stimulation. The voltage across the electrodes and current delivered by the active electrode were extracted from post processing steps.

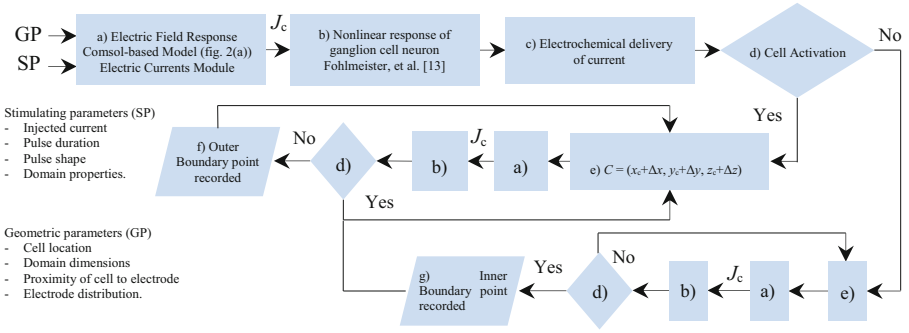

Fig. 1. Algorithm of the activation area. Steps showing letters are related to the corresponding actions in the algorithm. (See [9] for more information).

2.2 Nonlinear Response of Cell Neurons and Electrochemical Safety

RGC responses to electrical stimulation were inspected in Comsol by incorporating the parameters and equations that describe the dynamics of the ionic channels in the circuit modeling of the RGC [13]. Peak boundary current density in the cell membrane was assumed as the input parameter. Recent works used this modelling assumption for axonal activation [14] and for RGC stimulation [9]. All information of the circuit model was kept as in the original model [13]. Safety is related to avoid electrolysis of water, the formation of corrosion and excessive tissue heating. A Matlab script organized the extracted data of the voltage across the electrodes and current delivered to the electrode and performed several tasks to obtain the heat dissipated by the device and charge density on the electrode. Local charge density was obtained by integrating the current delivered by the active electrode over time and dividing it by the electrode area. Neural heating from the retinal implant is calculated as seen in [15].

2.3 Cell Activation, Shifting and Boundary Point Recording

Comsol Multiphysics investigated the stimulation of an RGC by shifting it around the horizontal direction (*x* or *y axis*). For the proper operation of the algorithm, the initial values of cell location (x_c, y_c, z_c) should be such that the cell is placed inside the RGC layer, exactly below the center of the active electrode. Electrochemical safety is checked first before the user can step forward (step (c)). If activation is reached, the RGC is shifted in the ganglion layer as (Δx, Δy, Δz), (Fig. 2b and step (e)), and the algorithm is iterated until the outer boundary of activation is found. Next, this boundary point is recorded, step (f). If activation is not reached, two possibilities can occur. A percept where the surface forms an opened geometry is created, e.g. ring-shaped percept or there is no electrical stimulation. For the former case, the cell is shifted inside the ganglionic layer and the algorithm is iterated until the inner boundary of activation is found. Then, the boundary point can be recorded, step (g). For the latter case, an increase on the injected current must be implemented. The algorithm is executed until the activation area is an enclosed geometry. In summary, the activation area

is defined as a triggering boundary where the spreading current is sufficient to stimulate a single or nearby cell. That is, a cell located inside the activation area is activated by the respective electrode. Otherwise, the cell is not activated. The activation area can be related to the visual sensations represented as a phosphene [9]. For more data of the activation area, supporting evidence and limitations, see [9].

2.4 Stimulating Parameters

Stimulating parameters per subject in [5] were implemented in the model. Peak current amplitude, pulse width and pulse train frequency were kept constant except where expressly varied at 13 μA, 94 μs and 100 Hz, all respectively. Single charge-balanced biphasic current pulse was delivered to the electrodes. 25-stimulating electrodes were arranged in a hexagonal array with an electrode diameter of 100 μm and 500 μm center-to-center distance. The array is reconstructed in a 2 by 4 mm^2 substrate and placed for epiretinal stimulation. Nearby electrodes were activated separately per simulation approximating a pulse train frequency of 100 Hz. That is, a period of 10 ms is enough for the membrane voltage to return to its resting potential. The appearance of the total elicited phosphene is the result of the summation of the phosphenes elicited per pair of electrodes. Experimental evidence suggests that two temporal components of brightness fading are present: a rapid fading within <0.5 s (5–60 Hz stimulating rate) [16] and 0.18 s (16 Hz rate) [17], as well as a slower reduction in brightness within several seconds (5–60 Hz rate) [16] and 14 s (16 Hz rate) [17]. Freeman [18] suggested that the reduction of firing rate over time may contribute to the fading of brightness. This suggests that the stimulation rate of 100 Hz in [9] produced percepts that persisted during the complete period of stimulation of 1.5 s.

3 Results

Table 3 lists the results that were organized as follows. First and second columns show the spatial stimulation patterns and the comparison with the activation area, respectively. Rows in such table are designated to each subject. In the first column neighboring electrodes in red for subjects 3 and 2 (only 3e) correspond to the spatial patterns of stimulation. For subject 3 at 3(c), upper electrode in a set of adjacent pair of stimulating electrodes corresponds to the active. Subjects 1, 2 and 6, electrodes in red and gray correspond to active and ground, respectively. Visual percepts reported by the subjects are indicated below each spatial stimulation pattern. In the second column, all results except 3(f) are related to the corresponding spatial patterns. Figures 3(a), (b), (e) show a single elicited percept of one electrode pair and the summation of visual data. For 3(a), (b), (e), (f) and (g), purple, blue, green and orange elicited percepts are related to 10, 100, 150 and 200 μm of proximity. For 3(d), blue and green percepts are related to lower and higher percepts. For 3(c), blue and orange percepts are related to a displacement angle of the array width of 2° and 4°, all resp. Figure 3(f) shows the possibility to restore a visual percept by changing the proximity, conductivity around the RGC and peak current amplitude. All results satisfy electrochemical safety.

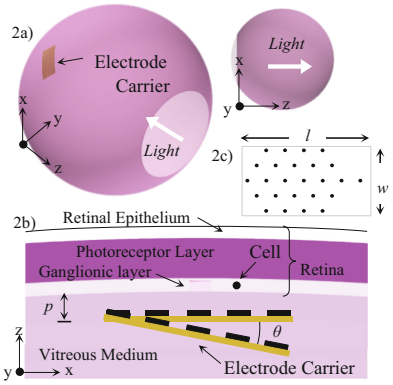

Fig. 2. (2a) Simulation model built in Comsol Multiphysics. Figure (2b) shows a zoom-in view of the layers included in the model. p corresponds to the proximity of cells to the electrodes. θ is the angle of displacement along the width of the array. The electrodes are in contact with the retinal surface layer. (2c) Twenty-five stimulating electrodes are arranged in a hexagonal array (Data from [5]). Complete information of the model is listed in Tables 1 and 2.

Table 1. Description of the values in simulations

Layer	Conductivity [S/m]	Permittivity [-]	Thickness [µm]
Polyimide carrier	1e-17	1	65
Vitreous humor	1.5	98	22e3[a]
Epithelium layer	2e-3	1	65
Photoreceptor layer	28.5e-3	1	200
Intracellular space	100e-3	3.98e-11	30
PEDOT-NaPSS coating	400	1	0.2
Contact conductivity	321	–	–
Cell membrane	1e-8	8.8e-11	0.001[b]
Ganglionic layer	100e-3	1	65

[a]Value of vitreous humor is its diameter, [b]Value is the thickness of cell membrane.

Table 2. Geometric values of the retina

Layer	Inner surface diameter $Ø_i$ [mm]	Outer surface diameter $Ø_o$ [mm]
Epithelium	22.265	22.33
Photoreceptor	22.065	22.265
Ganglionic	22	22.065
Vitreous humor	–	22

4 Discussion

4.1 Proximity of RGCs to the Electrodes

The closeness of RGCs to the electrodes influences the shape and scope of the percepts [9]. Body cells can be triggered with low stimulus amplitudes within close proximity. This produces small regions of stimulation at the retina. Increasing the proximity results in a broader area of activation because stimulus amplitude must increase to activate some body cells, thereby expanding the size of the phosphenes [9]. In this study, however, the proximity of RGCs to the electrodes increased while the peak current amplitude remained fixed. This progressively leads the current to become insufficient to trigger a response of RGCs. Hence, the elicited visual percept becomes smaller as the proximity increases, figs. 3(b), (e) and (f). The fact that larger visual percepts occur for close proximity is not surprising since a larger activation area of retinal neurons are activated, fig. 3(a).

4.2 Angle of Displacement of the Electrode Array

Epiretinal implants are located near to the retinal surface to ensure lower thresholds of activation and a more precise stimulating area [9, 11, 12]. However, natural movements of the eye may relocate the electrode array in the vitreous cavity [19] and displace the array with an angle that changes the orientation of stimulation. Frequently, the eyes make rapid‖ shifts in position about 2–3 times per second [18]. This would affect the stimulation of RGCs, particularly single cells. In this study, the electrode array was displaced with an angle of 2° and 4° with proximity of the electrodes of 200 μm. This small displacement was sufficient to modify the activation area generated by the electrode stimulus, producing complex percepts as an arc-, triangle- and an egg-shape fig. 3(c). The plausible reason is that the current spread cannot generate a symmetric stimulating area on the retina because regions in the electrode array are closer to the target neurons. This will lead to changes in the area of stimulation, thereby causing the generation of percepts with shapes other than round dot-like phosphene. These results suggest that a highly sensitive response to stimulation is present to produce visual phosphenes similar to a spot of light.

4.3 Orientation of Stimulus Pattern

The appearance of the elicited phosphene is related to the spreading direction of current density that follows the position of the active to ground electrodes [9]. This will lead variations in the area of stimulation around the stimulating and return electrodes, figs. 3 (d), (e), (g). The fact that visual percepts occur in the surrounding or close to the active and ground electrodes are not surprising because of the stimulus exits and entries in such electrodes. This could be, however, invalid for distant proximities between RGCs and electrodes and large angles of displacement.

4.4 Electrode Topology and Degenerate Retina

Electrode array topology and electrode features influence the shape and breadth of phosphenes. Simulation-based findings in [9] revealed that single and multiple topologies of stimulating electrodes form different shapes of percepts, e.g. hash mark- and circular-shapes. A plausible reason for such forms is the far location of the ground to the active electrode, causing deep down current flow into the tissues that activate cells in its path to ground. Experimental findings using different electrode topology revealed dissimilar shapes of phosphenes other than a small spot of light [2, 3, 5]. Cell density in the degenerate retina influences the shape and formation of percepts. Keserü [3] found variabilities of thresholds in experimental stimulation and was attributed to the varying degree of retinal degeneration. This can influence the shape of the visual perception since gaps of dark vicinities would be displayed at locations of cell depletion [9].

4.5 Peak Stimulus Amplitude

The breadth of the elicited percept and the amount of peak current amplitude are well-associated. That is, far-localized RGCs can be activated by increasing the injected current. Experimental findings by Rizzo [20] in human volunteers found a direct relationship between the stimulus charge and the size of the percept. Figure 3(h) demonstrates that the elicited percept can be restored by doubling the peak stimulus despite having different proximities.

Table 3. Relationship between stimulation patterns and simulations. Spatial patterns in the first column are not drawn to scale. Simulated visual percepts highlighted in dark brown (in background), yellow and orange in figure 3(h) are generated with current amplitudes and proximities of 13 µA and 25 µm, 26 µA and 50 µm, and 13 µA and 50 µm. Conductivities of ganglionic layer and intracellular space were decreased with a factor of 10 due to different data found in [10–12]. Sizes of visual percepts are related to the surface of the retina.

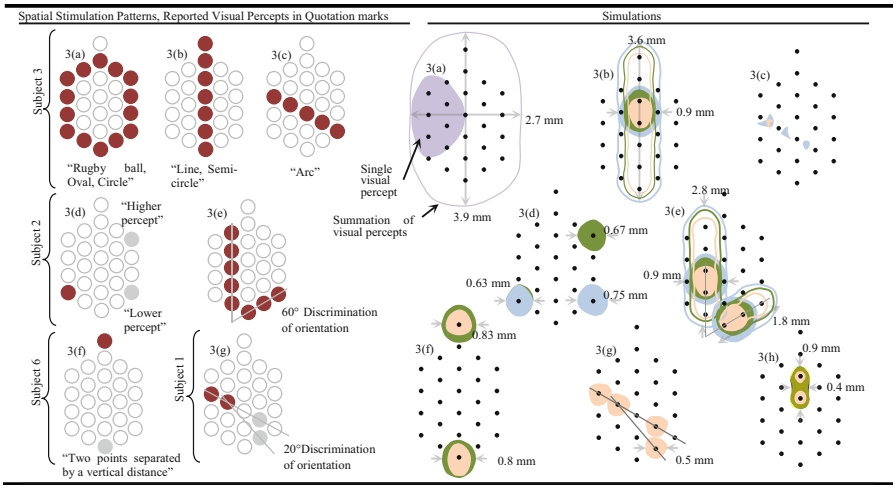

4.6 Phosphene-Based Prosthetic Vision

Visual prosthesis elicit phosphenes by exciting the visual cortex, optic nerve or the retina along the visual pathway. Recent psychophysical research have demonstrated that visual prostheses are able to provide visual perception to people and visual function can be partly recovered with phosphene-based prosthetic vision. Perez-Yus [21] developed computer vision algorithms to evoke phosphene-based stimuli with semantic meaning for real data indoor environments. Sanchez-Garcia [22] explored image recognition using convolutional neural network to understand different indoor environments under prosthetic vision considerations. Denis [23] developed real-time text localization algorithm to improve text accessibility. Guo [24] used contrast enhancing under simulated prosthetic vision, edge detection and zooming technique to improve significantly the accuracy of object recognition. Recently, Abraham [25] used active photonic sensing of image scanning and control text size to increase word recognition rate.

5 Conclusion

The activation area can be categorized as a valuable tool to understand the response of RGCs for a set of stimulating parameters, to estimate the size and shape of visual percepts using an arbitrary electrode array and to develop an arrangement of electrodes for eliciting spatially-localized perception of light. It provides an understanding into the underlying neural mechanisms to move towards to a precise analytical modelling of elicited percepts. Prior to device implantation, simulation-based findings of the activation area can be advantageous to comprehend the physical aspects of phosphenes and to develop an electrode array for generating perception of light with high resolution.

Conflict of Interest. "The authors declare that they have no conflict of interest".

References

1. Chen, S.C., Suaning, G.J., Morley, J.W., Lovell, N.H.: Simulating prosthetic vision: I. Visual models of phosphenes. Vision Res. **49**, 1493–1506 (2009)
2. Humayun, M.S.: Visual perception in a blind subject with a chronic microelectronic retinal prosthesis. Vision Res. **43**, 2573–2581 (2003)
3. Keseru, M., Feucht, M., Bornfeld, N., Laube, T., Walter, P., Rossler, G., Velikay-Parel, M., Hornig, R., Richard, G.: Acute electrical stimulation of the human retina with an epiretinal electrode array. Acta Ophthalmol. **90**, e1–e8 (2012)
4. Zrenner, E., Besch, D., Bartz-Schmidt, K.U., Gekeler, F., Gabel, V.P., Kuttenkeuler, C., et al.: Subretinal chronic multi-electrode arrays implanted in blind patients. Invest. Ophthalmol. Vis. Sci. **47**, 1538 (2006)
5. Klauke, S., et al.: Stimulation with a wireless intraocular epiretinal implant elicits visual percepts in blind humans. Invest. Ophthalmol. Vis. Sci. **52**, 449–455 (2011)
6. Humayun, M., et al.: Interim results from the international trial of second sight's visual prosthesis. Acta Ophthalmol. **119**(4), 779–788 (2012)

7. Perez Fornos, A., Sommerhalder, J., Da Cruz, L., et al.: Temporal properties of visual perception on electrical stimulation of the retina. Invest. Ophthalmol. Vis. Sci. **53**(6), 2720–2731 (2012)
8. Stingl, K., Besch, D., Braun, A., Hipp, S., Schatz, A., Peters, T., et al.: Artificial vision with wirelessly powered subretinal electronic implant alpha-IMS. Proc. R. Soc. B: Biol. Sci. **280** (175), 20130077 (2013)
9. Villarreal, D.L., Schroeder, D., Krautschneider, W.H.: A treatise of the physical aspects of phosphenes and single-cell selectivity in retinal stimulation. Int. J. Comput. Neural Eng. **4** (2), 55–70 (2017)
10. Dokos, S., et al.: A bidomain model of epiretinal stimulation. IEEE Trans. Neural Syst. Rehabil. Eng. **13**(2), 137–146 (2005)
11. Abramian, M., Lovell, N.H., Morley, J.W., Suaning, G.J., Dokos, S.: Computational model of electrical stimulation of a retinal ganglion cell with hexagonally arranged electrodes. In: Proceedings 34th Annual International Conference of the IEEE EMBS (2012)
12. Kasi, H., et al.: Simulation of epiretinal prostheses - evaluation of geometrical factors affecting stimulation thresholds. J. Neuro Eng. Rehabil. **8**, 44 (2011)
13. Fohlmeister, J., et al.: Modeling the repetitive firing of retinal ganglion cells. Brain Res. **510**, 343–345 (1989)
14. Joucla, S., et al.: Current approaches to model extracellular electrical neural micro stimulation. Front. Comput. Neurosci. **8**, 13 (2014)
15. Luján, Villarreal D., et al.: Feasibility study of a 1000+ electrode array in epiretinal prosthesis. Int. J. Pharma Med. Biol. Sci. **5**(3), 163–170 (2016)
16. Perez Fornos, A., Sommerhalder, J., Pelizzone, M.: Dynamics of visual perception upon electrical stimulation of the retina (abstract). Invest. Ophthalmol. Vis. Sci. **51**, 3057 (2010)
17. Freeman, D.K., Fried, S.I.: Multiple components of ganglion cell desensitization in response to prosthetic stimulation. J. Neural Eng. **8**, 016008 (2011)
18. Freeman, D.K., Rizzo 3rd, J.F., Fried, S.I.: Encoding visual information in retinal ganglion cells with prosthetic stimulation. J. Neural Eng. **8**, 035005 (2011)
19. De Balthasar, C., Patel, S., Roy, A., Freda, R., Greenwald, S., Horsager, A., Mahadevappa, M., Yanai, D., McMahon, M.J., Humayun, M.S., Greenberg, R.J., Weiland, J.D., Fine, I.: Factors affecting perceptual thresholds in epiretinal prostheses. Invest. Ophthalmol. Vis. Sci. **49**, 2303–2314 (2008)
20. Rizzo, J.F., et al.: Perceptual efficacy of electrical stimulation of human retina with a microelectrode array during short-term surgical trials. Invest. Ophthalmol. Vis. Sci. **44**, 5362–5369 (2003)
21. Perez-Yus, A., Bermudez-Cameo, J., Lopez-Nicolas, G., Guerrero, J.: Depth and motion cues with phosphene patterns for prosthetic vision (2017). https://doi.org/10.1109/ICCVW.2017.179
22. Sanchez-Garcia, M., Martinez-Cantin, R., Guerrero, J.: Structural and object detection for phosphene images (2018)
23. Denis, G., Jouffrais, C., Mailhes, C., Mace, J.-M.: Simulated prosthetic vision: improving text accessibility with retinal prostheses. In: 2014 36th Annual International Conference of the IEEE Engineering in Medicine and Biology Society, EMBC 2014, pp. 1719–1722 (2014). https://doi.org/10.1109/embc.2014.6943939
24. Guo, F., Yang, Y., Gao, Y.: Optimization of visual information presentation for visual prosthesis. Int. J. Biomed. Imaging **2018**, 1–12 (2018). https://doi.org/10.1155/2018/3198342
25. Abraham, C., Farah, N., Gerbi-Zarfati, L., Harpaz, Y., Zalvesky, Z., Mandel, Y.: Active photonic sensing for super-resolved reading performance in simulated prosthetic vision. Biomed. Opt. Express **10**(3), 1081–1096 (2019)

Standardized Approaches for Assessing Metagenomic Contig Binning Performance from Barnes-Hut *t*-Stochastic Neighbor Embeddings

Julian Ceballos[1], Leandro Ariza-Jiménez[2(✉)], and Nicolás Pinel[1]

[1] Biodiversity, Evolution, and Conservation Research Group, Universidad EAFIT, Medellín, Colombia
{jceballosc,npinelp}@eafit.edu.co
[2] Mathematical Modeling Research Group, Universidad EAFIT, Medellín, Colombia
larizaj@eafit.edu.co

Abstract. The performance of unsupervised methods for metagenomic binning is often assessed using simulated microbial communities. The lack of well-characterized evaluation protocols and approaches to community construction cognizant of biological realities impedes the rigorous assessment and standardization of the binning process. This work attempted to standardize performance evaluation using benchmark communities constructed according to the genome similarity metric Average Amino Acid identity. This approach allowed us to extend and deepen our previous research on the unsupervised binning of metagenomic sequence fragments based on low-dimensional embeddings of pentamer frequency profiles. Experimental results evidenced our method's potential for the binning of metagenomic contigs to become an alternative to state-of-the-art methods such as MetaCluster 3.0.

Keywords: Metagenomics · Binning · Embeddings · Fuzzy clustering · Internal cluster validity index · Benchmark

1 Introduction

Metagenome reconstruction from sequences obtained with high throughput technologies requires assembly and binning. The lack of prior knowledge about the number of microbial groups and their relative abundance makes the binning procedure challenging. Unsupervised binning strategies, which are required when studying communities that are poorly represented in existing genome databases, rely on the extraction and group construction based on taxon-specific features, using machine learning methods such as clustering and dimensionality reduction [1]. The performance of binning methods is assessed using artificially labeled datasets. The lack of well-characterized evaluation protocols and approaches

© Springer Nature Switzerland AG 2020
C. A. González Díaz et al. (Eds.): CLAIB 2019, IFMBE Proceedings 75, pp. 761–768, 2020.
https://doi.org/10.1007/978-3-030-30648-9_101

to community construction cognizant of biological realities impedes the rigorous assessment and standardization of the binning process. MetaSim [2] is a metagenomic sequence simulator that permits the *ad hoc* construction of read datasets for method development, as used in [3,4]. While it enables the selection of genomes according to the NCBI taxonomy, the latter is a poor descriptor of biological boundaries when applied to prokaryotic microorganisms, and by extension a poor predictor of a binning algorithm's separation abilities. This, and the paucity of rigorous evaluations of binning algorithm in terms of their consistency, resolution, and accuracy, motivated us to attempt to standardize performance evaluation using communities constructed according to the genome similarity metric *Average Amino Acid identity (AAI)* [5] and a systematic group delimiting performance assessment with multiple internal clustering validity indices.

This work makes two main contributions. First, it presents a strategy to generate synthetic datasets that can be used as a benchmark against which the effectiveness of methods for binning metagenomic contigs can be assessed. Second, it uses this benchmark to extend our previous research on the unsupervised binning of metagenomic sequence fragments on low-dimensional Barnes-Hut t-Stochastic Neighbor Embeddings (BH-SNE) [6]. Specifically, this paper: (1) explores the effect of first reducing the data dimensionality through Principal Component Analysis (PCA) and then using the reduced data as an input to the BH-SNE algorithm; (2) presents additional experimental results on several simulated datasets with different lengths of sequence and various numbers of genomes, and reflecting diverse ranges of phylogenetic relatedness; and (3) performs a more statistically rigorous evaluation of the experimental results.

2 Materials and Methods

Simulated Datasets - Forty six complete/near-complete genome sequences for human intestinal microorganisms were retrieved from the Human Microbiome Project (HMP) [7] data portal (http://hmpdacc.org/HMRGD/). Pairwise AAIs were calculated from the translated coding regions for all possible genome pairs, using the online calculator at http://enve-omics.ce.gatech.edu/aai/. Simulated communities (SC) were constructed using a graph theory-based approach, where each genome sequence was considered as a vertex of a complete weighted graph in which all genome sequence pairs were connected via edges whose weights were given by the AAI among connecting members. Four sub-graphs were derived from the complete graph such that edges in each graph had AAI weights in the ranges of $[25, 40)\%$, $[40, 55)\%$, $[55, 70)\%$, or $[70, 85)\%$. Here, k-vertex cliques, that is, a subset of k vertices such that every two distinct vertices in the subset were adjacent, were identified in each sub-graph and considered as candidate SC of k sequence genomes having pairwise AAI values in the same range. For a given k and AAI range, a random set of ten candidate SC, representing pseudo-biological replicates, were selected by imposing the condition that no pair of SC within the set shared more than two or six community members for the five-genome and ten-genome datasets, respectively. This last condition was introduced to increase

the independence of the candidate SC. Contigs of 600, 1000 or 10,000 base pairs (bp), of random starting points, were generated from each genome to achieve a 1× or 0.5× genome sequence coverage for the 1000/10,000 bp and the 600 bp sets, respectively. The number of contigs in each SC varied according to the constituent genomes' sizes. Pentamer (5-mer) frequency profiles per SC were obtained as reported previously [6].

BH-SNE-Based Dimension Reduction - BH-SNE was used to generate low-dimensional embeddings of the 5-mer frequency profiles. As in previous studies [6,8], default values for the input parameters of BH-SNE were used. The perplexity and the speed-accuracy trade-off parameter θ were set to 30 and 0.5, respectively. Two- and three-dimensional BH-SNE embeddings, with or without prior dimensionality reduction by PCA, were generated. Henceforth, the term "treatment" will refer to how the embeddings were obtained. The notations 2D, 3D, 2DPCA and 3DPCA will be used to refer to each of these treatments, depending on whether PCA was used as a preprocessing step. For 2DPCA and 3DPCA, the scores of the first 50 principal components were used to initialize the BH-SNE algorithm. As in [6], a set of 11 replicate embeddings were generated for each embedding treatment applied to a particular SC to take into account the non-deterministic nature of the BH-SNE.

Unsupervised Binning and Performance Evaluation - A method that we previously reported [6] was used to bin the low-dimensional embeddings of simulated metagenomic datasets. This unsupervised method uses the Fuzzy c-Means algorithm to cluster the embedded data based on different cluster center estimations provided by the Subtractive algorithm, and then internal cluster validity indices are used to determine the best clustering for the embedded data. Indices considered here were Silhouette (S), Calinski-Harabasz (CH), David-Bouldin (DB), and Dunn (D). Configuration parameters of the method were set similarly to those in a previous study [6]. The F-measure was used, as described elsewhere [3,4], to assess the performance of our binning method on the benchmark datasets. Here, the F-measure was computed on the resulting (hard) binning obtained by this method for each SC embedding treatment replicate, according to a cluster validity index.

An overall block diagram that outlines the flow of this work is shown in Fig. 1.

3 Results and Discussion

The benchmark datasets synthesized in this work totaled 41 SC. For both $[25, 40)\%$ and $[40, 55)\%$ AAI ranges, ten five-genome SC were obtained as expected. In the case of the ten-genome SC, ten and seven were constructed for each of the above ranges, respectively. For $[55, 70)\%$ and $[70, 85)\%$ AAI ranges, it was only possible to synthesize three and one three-genome SC, respectively. Fewer SC (made up of fewer distinct genomes) than expected were obtained due to the nature of the input genomic data, which limited the underlying process of identifying k-vertex cliques.

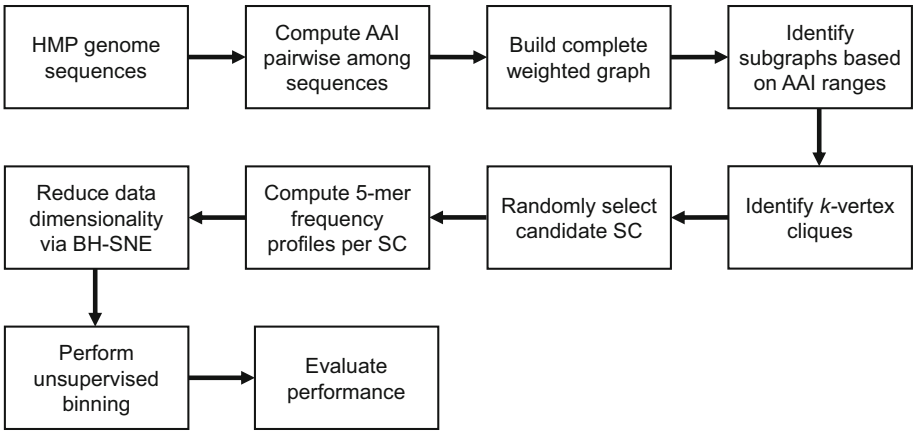

Fig. 1. Overall block diagram that outlines the flow of this work.

Based on the available SC and under the experimental conditions previously described, a total of 5412 embeddings were generated and then processed in this work by our unsupervised binning method. Figure 2 shows a two-dimensional embedding of a five-genome SC. In the left panel, colors represent the organismal origin of the genomic fragments. The remaining panels present the group assignments suggested by our method as a function of the various cluster validity indices implemented. Sequences assigned to the wrong genome by said indices are colored in black.

Table 1 describes the binning performance of our method for all of the experiments conducted on the benchmark datasets. Median F-measure values (F) are reported to summarize the overall performance on binning contigs among the embedding treatment replicates of each SC. The coefficient of variation (CV) is used to specify the variability of the accuracy measures. For each combination of AAI range, number of genomes (NG), and embedding treatment, the best binning performance achieved by the method, based on different cluster validity indices, is highlighted in bold. Conversely, the worst performance values are enclosed in parentheses. The Wilcoxon signed rank test was used to determine significant differences in the results. With few exceptions (6 out of 72 cases), mostly due to over-clustering, the highest binning accuracy was obtained when our method was matched with the S index. Moreover, whenever CH, D, and DB indices allowed better binning results to be obtained, S index always coincided in leading to the same condition. In particular, CH produced the worst accuracy values in more than half of the experiments conducted on 10,000 bp SC. In [9,10], DB and D indices were reported, respectively, as leading to better effectiveness in binning. However, DB usually yielded the worst binning performance on three-genome SC in the two highest AAI ranges for any contig length; meanwhile D, was the index that more often led to worse results and less often led to better results, and the one with the highest reported CV values (per instance).

Table 1. Binning performance on the benchmark datasets

AAI-NG	Treatment	CH		D		DB		S		MC3	
		F	CV	F	CV	F	CV	F	CV	F	CV
600 bp											
2540-5	2D	**0.84**	**0.12**	(0.71)	(0.31)	**0.82**	**0.15**	**0.82**	**0.15**	0.81	0.13
	2DPCA	0.86	0.12	(0.76)	(0.31)	**0.88**	**0.08**	**0.88**	**0.14**		
	3D	**0.85**	**0.15**	(0.74)	(0.29)	**0.84**	**0.15**	**0.85**	**0.15**		
	3DPCA	**0.89**	**0.08**	(0.79)	(0.24)	**0.9**	**0.09**	**0.9**	**0.11**		
2540-10	2D	**0.8**	**0.16**	(0.64)	(0.24)	**0.77**	**0.14**	**0.75**	**0.24**	0.62	0.17
	2DPCA	0.82	0.05	(0.73)	(0.22)	**0.85**	**0.06**	**0.85**	**0.06**		
	3D	0.76	0.26	(0.69)	(0.22)	**0.78**	**0.16**	**0.78**	**0.23**		
	3DPCA	**0.87**	**0.04**	(0.78)	(0.16)	**0.86**	**0.05**	**0.86**	**0.05**		
4055-5	2D	**0.78**	**0.12**	(0.69)	(0.26)	**0.77**	**0.3**	**0.77**	**0.14**	0.69	0.18
	2DPCA	**0.83**	**0.09**	(0.72)	(0.4)	**0.81**	**0.14**	**0.8**	**0.1**		
	3D	**0.78**	**0.13**	(0.73)	(0.27)	**0.78**	**0.25**	**0.78**	**0.12**		
	3DPCA	**0.84**	**0.11**	(0.79)	(0.24)	**0.8**	**0.09**	**0.82**	**0.11**		
4055-10	2D	**0.69**	**0.08**	(0.53)	(0.24)	0.65	0.09	0.56	0.17	0.5	0.16
	2DPCA	**0.72**	**0.06**	(0.63)	(0.26)	**0.72**	**0.06**	**0.72**	**0.12**		
	3D	(0.52)	(0.22)	(0.61)	(0.21)	**0.68**	**0.09**	0.63	0.17		
	3DPCA	0.73	0.12	(0.62)	(0.25)	**0.74**	**0.05**	**0.75**	**0.06**		
5570-3	2D	0.59	0.09	0.36	0.51	(0.1)	(0.36)	**0.61**	**0.06**	0.7	0.03
	2DPCA	0.61	0.08	(0.33)	(0.56)	(0.16)	(0.76)	**0.62**	**0.06**		
	3D	**0.67**	**0.06**	0.5	0.55	(0.04)	(1.83)	**0.67**	**0.06**		
	3DPCA	**0.63**	**0.04**	**0.63**	**0.26**	(0.61)	(0.74)	**0.63**	**0.04**		
7085-3	2D	**0.54**	**0**	(0.25)	(0.69)	(0.16)	(0.38)	**0.54**	**0**	0.67	–
	2DPCA	**0.33**	**0.29**	(0.15)	(0.64)	(0.12)	(0.36)	**0.43**	**0.16**		
	3D	**0.53**	**0**	0.2	0.75	(0.07)	(1.2)	**0.53**	**0**		
	3DPCA	**0.44**	**0.12**	(0.29)	(0.61)	(0.22)	(0.93)	**0.44**	**0.12**		
1000 bp											
2540-5	2D	**0.85**	**0.07**	(0.77)	(0.35)	**0.86**	**0.07**	**0.86**	**0.08**	0.77	0.13
	2DPCA	0.83	0.09	(0.76)	(0.33)	**0.87**	**0.07**	**0.87**	**0.08**		
	3D	**0.86**	**0.09**	(0.79)	(0.21)	**0.86**	**0.1**	**0.88**	**0.09**		
	3DPCA	0.87	0.06	(0.84)	(0.19)	**0.92**	**0.08**	**0.92**	**0.07**		
2540-10	2D	**0.85**	**0.04**	(0.75)	(0.26)	**0.86**	**0.06**	**0.87**	**0.06**	0.75	0.11
	2DPCA	0.86	0.07	(0.77)	(0.27)	**0.88**	**0.06**	**0.89**	**0.04**		
	3D	**0.89**	**0.05**	(0.8)	(0.25)	**0.89**	**0.05**	**0.89**	**0.04**		
	3DPCA	**0.91**	**0.03**	(0.87)	(0.19)	**0.91**	**0.04**	**0.91**	**0.04**		
4055-5	2D	**0.79**	**0.08**	(0.72)	(0.3)	**0.79**	**0.19**	**0.8**	**0.09**	0.78	0.15
	2DPCA	0.78	0.08	(0.72)	(0.39)	**0.8**	**0.07**	**0.81**	**0.07**		
	3D	0.8	0.12	(0.75)	(0.19)	**0.82**	**0.08**	**0.81**	**0.1**		
	3DPCA	0.83	0.05	(0.79)	(0.27)	**0.87**	**0.06**	**0.87**	**0.05**		
4055-10	2D	**0.76**	**0.06**	(0.65)	(0.31)	0.75	0.06	0.75	0.1	0.64	0.13
	2DPCA	0.76	0.06	(0.62)	(0.28)	0.77	0.04	**0.78**	**0.05**		
	3D	**0.78**	**0.15**	(0.67)	(0.23)	**0.78**	**0.06**	**0.79**	**0.07**		
	3DPCA	0.78	0.04	(0.75)	(0.18)	**0.81**	**0.04**	**0.81**	**0.03**		
5570-3	2D	**0.63**	**0.18**	0.47	0.39	(0.12)	(0.51)	**0.63**	**0.16**	0.69	0.02
	2DPCA	0.64	0.16	0.46	0.45	(0.19)	(0.81)	**0.68**	**0.09**		
	3D	**0.74**	**0.1**	0.56	0.49	(0.04)	(0.48)	**0.74**	**0.12**		
	3DPCA	**0.77**	**0.06**	(0.66)	(0.27)	0.69	0.32	**0.78**	**0.06**		
7085-3	2D	**0.35**	**0.13**	0.25	0.52	(0.07)	(0.36)	**0.37**	**0.15**	0.65	–
	2DPCA	**0.38**	**0.31**	(0.18)	(0.68)	(0.13)	(0.34)	**0.45**	**0.19**		
	3D	**0.53**	**0.1**	(0.43)	(0.65)	(0.21)	(0.75)	**0.53**	**0.16**		
	3DPCA	**0.53**	**0.09**	(0.45)	(0.45)	0.53	0.74	**0.53**	**0.09**		

(*continued*)

Table 1. (*continued*)

AAI-NG	Treatment	CH		D		DB		S		MC3	
		F	CV	F	CV	F	CV	F	CV	F	CV
10000 bp											
2540-5	2D	(0.86)	(0.18)	0.95	0.19	**0.96**	**0.05**	**0.96**	**0.04**	0.69	0.16
	2DPCA	(0.8)	(0.32)	0.96	0.2	**0.97**	**0.04**	**0.97**	**0.04**		
	3D	(0.92)	(0.07)	0.97	0.15	**0.99**	**0.03**	**0.99**	**0.03**		
	3DPCA	(0.96)	(0.08)	**0.99**	**0.11**	**0.99**	**0.03**	**0.99**	**0.02**		
2540-10	2D	(0.84)	(0.15)	0.91	0.14	**0.96**	**0.02**	**0.96**	**0.02**	0.65	0.07
	2DPCA	(0.54)	(0.26)	0.92	0.16	**0.96**	**0.02**	**0.96**	**0.02**		
	3D	(0.95)	(0.05)	0.95	0.09	**0.97**	**0.01**	**0.97**	**0.01**		
	3DPCA	(0.91)	(0.07)	0.96	0.11	**0.97**	**0.01**	**0.97**	**0.01**		
4055-5	2D	(0.86)	(0.19)	0.87	0.23	**0.96**	**0.05**	**0.96**	**0.06**	0.72	0.13
	2DPCA	(0.82)	(0.18)	0.88	0.2	**0.95**	**0.06**	**0.95**	**0.06**		
	3D	(0.92)	(0.08)	(0.95)	(0.13)	**0.97**	**0.02**	**0.97**	**0.02**		
	3DPCA	(0.9)	(0.1)	(0.95)	(0.22)	**0.97**	**0.02**	**0.97**	**0.02**		
4055-10	2D	(0.77)	(0.11)	0.81	0.13	**0.88**	**0.06**	**0.88**	**0.05**	0.59	0.11
	2DPCA	(0.72)	(0.13)	0.87	0.14	**0.89**	**0.06**	**0.89**	**0.06**		
	3D	(0.84)	(0.05)	0.89	0.11	**0.92**	**0.02**	**0.92**	**0.03**		
	3DPCA	(0.83)	(0.06)	0.9	0.11	**0.91**	**0.03**	**0.91**	**0.04**		
5570-3	2D	**0.91**	**0.03**	(0.7)	(0.44)	**0.91**	**0.03**	**0.91**	**0.03**	0.71	0.03
	2DPCA	**0.91**	**0.02**	(0.78)	(0.54)	**0.91**	**0.02**	**0.91**	**0.02**		
	3D	**0.91**	**0.01**	(0.42)	(0.89)	(0.06)	(1.17)	0.9	0.6		
	3DPCA	**0.91**	**0.02**	(0.08)	(1.16)	0.9	0.43	(0.08)	(1.18)		
7085-3	2D	**0.61**	**0.06**	0.43	0.47	(0.09)	(0.06)	**0.61**	**0.04**	0.74	–
	2DPCA	**0.6**	**0.4**	**0.48**	**0.58**	(0.11)	(0.06)	**0.6**	**0.51**		
	3D	**0.62**	**0.03**	(0.05)	(1.4)	(0.05)	(0.09)	(0.05)	(0.09)		
	3DPCA	**0.64**	**0.03**	0.52	0.76	(0.06)	(0.08)	(0.06)	(0.08)		

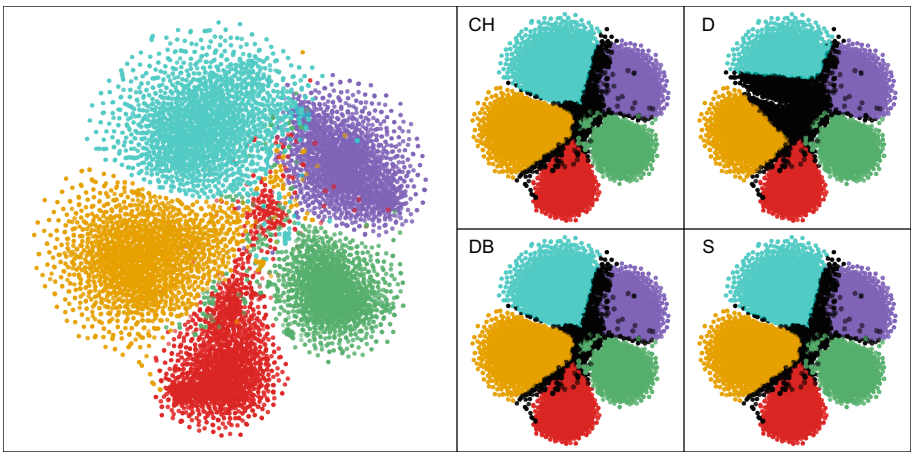

Fig. 2. A two-dimensional BH-SNE-based embedding of a five-genome SC (left panel). Colors represent the organismal origin of the embedded data. Sequences erroneously grouped, as a function of distinct cluster validity indices, are colored in black.

Table 1 also evidences that, as the contig length increased, the method's performance increased, which is reflected through larger median F-measure values and smaller CV values. For S and DB indices, for example, the number of instances with $F \geq 0.9$ increased from 1 in 600 bp to 16 in 10,000 bp, while the number of cases with $CV \leq 0.1$ increased from 9 in 600 bp to 21 in 10,000 bp. This could be associated with the reduction in the number of contigs to bin as the contig length increases in simulated datasets. Additional comparisons among binning results indicated that binning accuracy on BH-SNE-based mappings of SC could be improved when data have been previously preprocessed using PCA. This circumstance was observed when our method was matched with DB and S indices to bin both 600 and 1000 bp SC on the first two AAI ranges ($[25, 40)\%$ and $[40, 55)\%$). Finally, comparison against MetaCluster 3.0 (MC3) [11] demonstrated that, for all of the embedding replicate treatments, our binning method associated with the S index almost always outperforms this state-of-art unsupervised binning method, except for some SC on the last two AAI ranges (see Table 1).

4 Conclusions

This paper presents a benchmark strategy to improve the assessment of binning methods, using simulated metagenomic datasets that vary in composition and structure. This benchmark was used for testing a previously developed method for the unsupervised fuzzy binning of metagenomic sequence fragments from BH-SNE mappings. Ground truth-based benchmarks suggested that, in some instances, the quality of binning performed on low-dimensional BH-SNE-based embeddings of metagenomic data can be improved when data have been previously preprocessed using PCA. Experimental results also indicated that the Dunn index and the Silhouette index are the least and most reliable indices, respectively, for guiding an unsupervised binning method on simulated microbial communities. Finally, the consistency with which our binning approach performed across varying community structures demonstrates the method's potential to become an alternative to current methods for the clustering of metagenomic data, such as MetaCluster 3.0. One identified weakness with the work presented herein is the low number of synthetic communities with member reciprocal AAI values above 55%. Our rationale in selecting the data sources was to include in each SC genomic populations that were likely to co-occur. Consequently, we limited the genome sequences to organisms from the human intestinal microbiome sequenced by the HMP [7], among which we were unable to find sufficient genomes at high AAI. During the final stages of the present work, new human intestinal microbiome databases were published [12], expanding greatly the availability of genomic sequences of relevance to our design. As future work, we plan to incorporate more complex simulated datasets into the proposed benchmark and to extend our analyses to real-world metagenome datasets.

Acknowledgements. This research work was supported by Centro de Excelencia y Apropiación en Big Data y Data Analytics -Alianza CAOBA- and Universidad EAFIT.

Conflict of Interest. The authors declare that they have no conflicts of interest.

References

1. Sedlar, K., Kupkova, K., Provaznik, I.: Bioinformatics strategies for taxonomy independent binning and visualization of sequences in shotgun metagenomics. Comput. Struct. Biotechnol. J. **15**, 48–55 (2017). https://doi.org/10.1016/j.csbj.2016.11.005
2. Richter, D.C., Ott, F., Auch, A.F., Schmid, R., Huson, D.H.: MetaSim–a sequencing simulator for genomics and metagenomics. PLOS ONE **3**(10), 1–12 (2008). https://doi.org/10.1371/journal.pone.0003373
3. Girotto, S., Comin, M., Pizzi, C.: Metagenomic reads binning with spaced seeds. Theor. Comput. Sci. **698**, 88–99 (2017). https://doi.org/10.1016/j.tcs.2017.05.023
4. Vinh, L.V., Lang, T.V., Binh, L.T., Hoai, T.V.: A two-phase binning algorithm using l-mer frequency on groups of non-overlapping reads. Algorithms Mol. Biol. **10**(1), 1–12 (2015). https://doi.org/10.1186/s13015-014-0030-4
5. Konstantinidis, K.T., Tiedje, J.M.: Towards a genome-based taxonomy for prokaryotes. J. Bacteriol. **187**(18), 6258–6264 (2005). https://doi.org/10.1128/JB.187.18.6258
6. Ariza-Jiménez, L., Quintero, O., Pinel, N.: Unsupervised fuzzy binning of metagenomic sequence fragments on three-dimensional Barnes-Hut t-Stochastic neighbor embeddings. In: 2018 40th Annual International Conference of the IEEE Engineering in Medicine and Biology Society, pp. 1315–1318 (2018). https://doi.org/10.1109/EMBC.2018.8512529
7. The Human Microbiome Project Consortium: Structure, function and diversity of the healthy human microbiome. Nature **486**(7402), 207–214 (2012). https://doi.org/10.1038/nature11234
8. Laczny, C.C., Pinel, N., Vlassis, N., Wilmes, P.: Alignment-free visualization of metagenomic data by nonlinear dimension reduction. Sci. Rep. **4**, 4516 (2014). https://doi.org/10.1038/srep04516
9. Lux, M., Sczyrba, A., Hammer, B.: Automatic discovery of metagenomic structure. In: 2015 International Joint Conference on Neural Networks (IJCNN), pp. 1–8 (2015). https://doi.org/10.1109/IJCNN.2015.7280500
10. Gisbrecht, A., Hammer, B., Mokbel, B., Sczyrba, A.: Nonlinear dimensionality reduction for cluster identification in metagenomic samples. In: 2013 17th International Conference on Information Visualisation, pp. 174–179 (2013). https://doi.org/10.1109/IV.2013.22
11. Leung, H.C.M., Yiu, S.M., Yang, B., Peng, Y., Wang, Y., Liu, Z., Chen, J., Qin, J., Li, R., Chin, F.Y.L.: A robust and accurate binning algorithm for metagenomic sequences with arbitrary species abundance ratio. Bioinformatics **27**(11), 1489–1495 (2011). https://doi.org/10.1093/bioinformatics/btr186
12. Forster, S.C., Kumar, N., Anonye, B.O., Almeida, A., Viciani, E., Stares, M.D., Dunn, M., Mkandawire, T.T., Zhu, A., Shao, Y., Pike, L.J., Louie, T., Browne, H.P., Mitchell, A.L., Neville, B.A., Finn, R.D., Lawley, T.D.: A human gut bacterial genome and culture collection for improved metagenomic analyses. Nat. Biotechnol. **37**(2), 186–192 (2019). https://doi.org/10.1038/s41587-018-0009-7

Understanding Ventricular Tachyarrhythmias Related to Acute Myocardial Ischemia: A Computational Modeling Approach

Andrés Mena[1], José Felix Rodríguez-Matas[2], Ana González-Ascaso[2], and José M. Ferrero[3(✉)]

[1] Universidad de Zaragoza, Zaragoza, Spain
[2] Politécnico di Milano, Milan, Italy
[3] Universitat Politècnica de València, Valencia, Spain
cferrero@ci2b.upv.es

Abstract. This paper describes a computational approach designed to study ventricular tachyarrhythmias arising from acute myocardial ischemia. Since these cardiac disorders can frequently lead to sudden cardiac death, understanding their mechanisms is key to improving their diagnosis and therapy. The use of computational simulations based on multiscale mathematical modeling has proved to be a powerful tool in unraveling the causes of this phenomenon. In the first part of this work, we reformulated a model of the ischemic human ventricular cell to simulate the features of the action potentials during acute ischemia. We then incorporated the model into an electrophysiologically-detailed three-dimensional virtual human heart, which was able to reproduce the typical ventricular tachyarrhythmias in the first 15 min of ischemia with rhythms resembling ventricular fibrillation. The results suggest that the extracellular potassium concentration and the presence of a wash-out subendocardial zone are key factors in the vulnerability of the ischemic myocardium to arrhythmias.

Keywords: Computational modeling · Myocardial ischemia · Ventricular tachyarrhythmias · Action potential · Hyperkalemia

1 Introduction

Acute myocardial ischemia is one of the leading causes of mortality all over the world [1]. Indeed, sudden cardiac death is a frequent consequence of acute myocardial ischemia in the first 10 to 15 min after the onset of coronary artery occlusion. The reason is the appearance of potentially mortal ventricular tachyarrhythmias such as ventricular fibrillation (VF) [2]. The ischemia-related development of hypoxia (i.e. lack of oxygen), hyperkalemia (i.e. accumulation of potassium in the extracellular medium) and acidosis (i.e. reduced pH) alters the characteristics

© Springer Nature Switzerland AG 2020
C. A. González Díaz et al. (Eds.): CLAIB 2019, IFMBE Proceedings 75, pp. 769–776, 2020.
https://doi.org/10.1007/978-3-030-30648-9_102

of the cellular action potentials (AP) and the myocardial substrate, increasing the likelihood of the appearance of reentrant arrhythmias such as VF [3].

Since the acute phase of myocardial ischemia is a highly unstable situation (both from the metabolic and electrophysiological point of view), it is very difficult (or even impossible) to completely understand the mechanisms that lead to the appearance of reentry by purely experimental means. For instance, the direct influence of hypoxia, hyperkalemia and acidosis on the likelihood of suffering an arrhythmia cannot be determined experimentally. However, computational simulations have proven to be a powerful aid in understanding the intricate mechanisms of ischemia-induced arrhythmias [4]. Since the first mathematical models of the acutely ischemic cardiac cell were developed [5–7], they have been used to throw light in the electrophysiologic basis and consequences of the pathology [4].

The aim of this work was therefore to (a) reformulate a cellular model of acute ischemia and adapt it to human cardiac cells, and (b) study the mechanisms of VF in a three-dimensional model of human cardiac ventricles, including the relevant myocardial anatomical and structural features (i.e. fiber orientation and central and border ischemic zones).

2 Materials and Methods

2.1 Background of the Computational Modeling Approach

Considerable efforts have been made in the last twenty-five years to adapt AP models to simulate acute ischemia (see [4] for review). Previous approaches have focused on reformulating and/or adapting existing AP models of different animal species (e.g. guinea pig, rabbit and dog) to account for ischemic features, mainly the effects of hypoxia on the ATP-sensitive K^+ current ($I_{K(ATP)}$) [5–7], the causes of hyperkalemia [8], and the effects of acidosis [7,9,10]. These models have then been used to study the effects of ischemia in realistic virtual 3D models of the heart [9–11]. However, although these models were based on human non-ischemic current data, the formulation of important ischemic-related currents, such as the $I_{K(ATP)}$, were based on data from other animal species, and the effects of ATP, ADP and other ischemia-related metabolites on the ATP-dependent pumps were not included.

2.2 Single Ischemic Cell Model

In order to develop a more comprehensive ischemic model of the human ventricular cell, a modified version [12] of the O'Hara model of the ventricular human AP [13] was used as the basal model in the present study. Since the original model was not intended to simulate acute ischemia, we incorporated new currents and reformulated others to account for the changes exerted by hypoxia, hyperkalemia and acidosis.

Hypoxia reduces intracellular ATP ($[ATP]_i$) and rises intracellular ADP ($[ADP]_i$). To introduce these changes into the model, we first did so in a model

of the ATP-sensitive K^+ current ($I_{K(ATP)}$) based on the formulation proposed by Ferrero et al. [5]. In order to adapt this model to human ventricular cells, we changed the maximum conductance and the sensitivity to $[ATP]_i$ and $[ADP]_i$, using experimental data from Babenko et al. [14]. Following the model proposed by Cortassa et al. [15], we also introduced different multiplication factors that depended on $[ATP]_i$ and $[ADP]_i$ in the formulations of the ATP-dependent pumps (i.e. the Na^+/K^+, sarcolemmal Ca^+ and SERCA pumps). The values of the parameters related to the ATP and ADP effects are shown in Table 1. In order to account for acidosis, we introduced multiplying factors that depend on intracellular and extracellular pH and LPC into the fast and late Na^+ currents, the L-type Ca^+ current and the Na^+/K^+ pump. Finally, to account for hyperkalemia, we raised the extracellular potassium concentration ($[K^+]_o$) to typical acutely ischemic levels.

Table 1. Ischemia-related parameters in the model compared to the previous model [10]. Data for $I_{K(ATP)}$ corresponds to $[ADP]_i = 0$. Last column shows source of the model parameters.

Ionic current	Parameter	Ref. [10]	Our model	Data from
$I_{K(ATP)}$	$K_{m,ATP}$	0.035 mM	0.017 mM	[14]
	H	1.5	0.9	[14]
I_{NaK}	K_{ATP}	Absent	0.163 mM	[15]
	K_{ADP}	Absent	0.002 mM	[15]
SERCA	K_{ATP}	Absent	5.100 mM	[15]
	K_{ADP}	Absent	0.140 mM	[15]
I_{pCa}	K_{ATP}	Absent	0.230 mM	[15]
	K_{ADP}	Absent	1.000 mM	[15]

The stimulation protocol consisted of delivering a train of pulses 1 millisecond in duration with an amplitude 50% above diastolic threshold. The cell was paced at a basic cycle length (BCL) of 800 ms, which corresponds to a cardiac frequency of 75 beats per minute, for 10 min in order to achieve a steady-state. The APs shown in Fig. 2 and the values of action potential duration at 90% repolarization (APD_{90}) are those of the last AP of the series. The model was solved using Matlab(R) software.

2.3 Three-Dimensional Heart Model

The anatomically-based model of the human heart was similar to a model previously developed by our group [10]. Based on DT-MRI images, it accurately represents the geometry of both ventricles of a healthy human subject, including realistic fiber orientation. It also includes transmural electrophysiologic heterogeneity, which was introduced into the model by defining three distinct zones

(endocardium, midmyocardium and epicardium), as described in [10], in each of which the appropriate version of the O'Hara model was used.

To simulate acute regional ischemia, a central ischemic zone (CZ) was defined to mimic the proximal occlusion of the left anterior descending coronary artery (LAD). Surrounding the CZ, ischemic border zones (BZ) of different widths were defined as described in [7,10]. The BZ for $[ATP]_i$ and $[ADP]_i$ had a width of 1 mm [16], while the width of the BZ for pH, LPC and $[K^+]_o$ was 1 cm [16]. Gradients of the relevant ischemic-related parameters were introduced into each BZ as proposed in [16] (see Fig. 1(A)). A wash-out zone was included in some simulations, consisting of a normal (i.e. non-ischemic) zone in the subendocardium 100 μm in width [17].

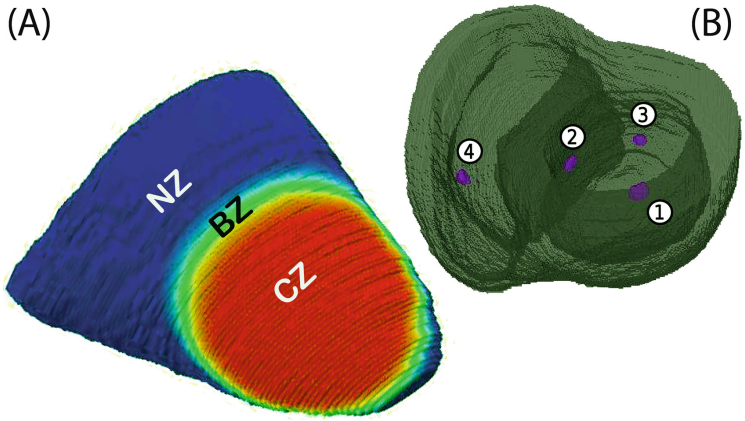

Fig. 1. (A) Three-dimensional human bi-ventricular model seen from the right epicardium. CZ: central ischemic zone; BZ: ischemic border zone; NZ: normal zone. Color indicates gradients of the ischemic-related parameters in each zone. (B) Sites of pacing for normal sinus activation.

The heart was paced for 1 min in four selected locations in the subendocardium (see Fig. 1(B)) to mimic sinus activation, and an extra-stimulus was delivered at different locations within the BZ to simulate the initiation of an ectopic beat [2]. The extra-stimulus was delivered at different coupling intervals (CI) (i.e. time after the onset of the last sinus beat), and the vulnerable window (VW) for reentry was defined as the range of CIs within which an extra-stimulus elicits reentrant activity (as in [7]). The model was solved by using the Finite Element Method as described in [10].

3 Results and Discussion

3.1 Effects of Ischemia at the Cellular Level

Figure 2 shows APs corresponding to control (i.e. normoxic) conditions (blue thin curve) and acutely ischemic conditions (red thick curve). In the control

simulation, the values chosen for the ischemia-related parameters were $[ATP]_i = 7$ mmol/L, $[ADP]_i = 15\,\mu$mol/L, $pH_i = 7.2$, $pH_o = 7.4$, $[LPC]_i = 2\,\mu$mol/L, and $[K^+]_o = 5.4$ mmol/L. In the ischemic case, values corresponded to 15 min of ischemia ($[ATP]_i = 2.3$ mmol/L, $[ADP]_i = 140\,\mu$mol/L, $pH_i = 6.2$, $pH_o = 6.4$, $[LPC]_i = 5\,\mu$mol/L, and $[K^+]_o = 10$ mmol/L). The values of APD_{90} were 270 ms and 135 ms, respectively.

The AP waveforms shown in the figure closely resemble the waveforms of experimentally measured APs in control and ischemic conditions [18]. The upstroke of the ischemic AP is divided into two phases, with the first one carried by sodium current through the ischemic-depressed fast Na^+ current, whilst the second one is sustained by calcium current flowing through the L-type Ca^{2+} current. The values of APD_{90} are in accordance with those measured in human normoxic and ischemic APs [19].

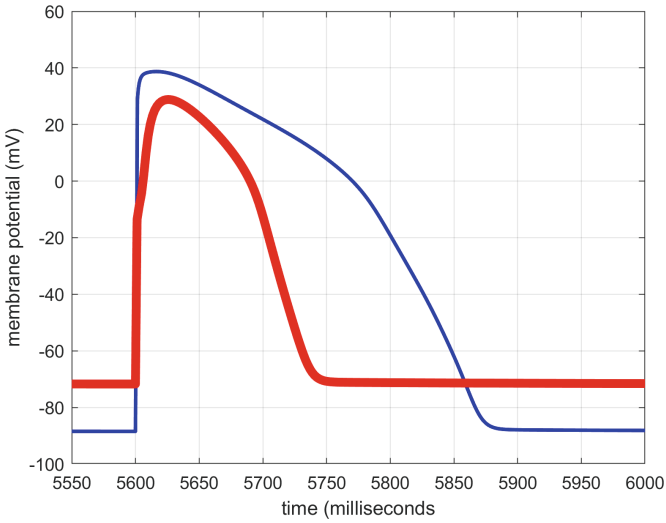

Fig. 2. Action potentials under control conditions (blue thin curve) and 15-min of myocardial ischemia (red thick curve). See text for details.

3.2 Reentrant Arrhythmias in a 3D Model of the Human Ventricles

We then incorporated the cellular ischemic model into the 3D heart model described in the Methods section and carried out simulations as described therein. Reentrant activity was elicited when we introduced an extra-stimulus within a certain range of CIs. Figure 3 shows an example of such reentry. At 2688 millisecond, an activation wavefront initiated by the extra-stimulus travels counterclockwise around and partially invades the CZ. This wavefront completes a 270° rotation at 2760 ms and 2832 ms and gives rise to a rotor-like reentry (2904 ms), which is typical in acute myocardial ischemic arrhythmias [18].

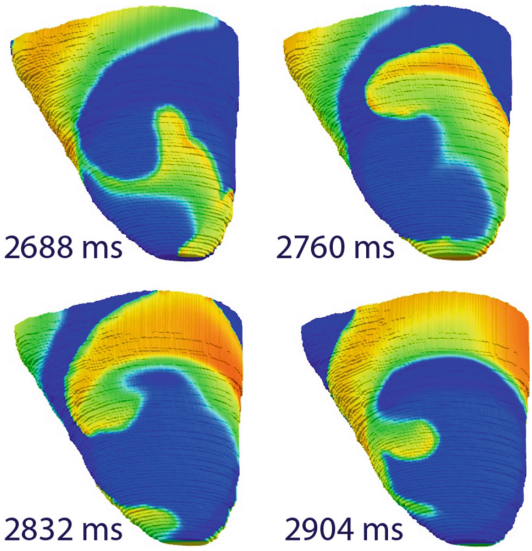

Fig. 3. Example of simulated reentrant activity in the acutely ischemic heart. See text for details

Table 2. Beginning (CI_{ini}) and ending (CI_{fin}) of the vulnerable window, and value (VW) of the vulnerable window, for different simulation conditions.

Wash-out zone	$[K^+]_o$ (mM)	CI_{ini} (ms)	CI_{fin} (ms)	VW (ms)
Yes	7.5	250	270	20
	8.5	265	280	15
	9.5	–	–	0
No	7.5–9.5	–	–	0

Once it was clear that the model was able to reproduce typical ischemia-related reentrant activity, we used it to quantify the VW duration under different conditions. The results are shown in Table 2. When the wash-out zone was included in the model, the duration of the VW for sustained reentry was approximately 20 ms for a value of $[K^+]_o = 7$ mmol/L. When more severe hyperkalemia was simulated ($[K^+]_o = 8$ mmol/L), the size of the VW decreased to 15 ms, indicating that the myocardium was less vulnerable to arrhythmias in this case. No reentrant activity was found for $[K^+]_o = 9$ mmol/L.

Finally, the effect of the presence of the subendocardial wash-out zone was assessed. When this was removed from the model it was impossible to obtain reentrant activity in the simulations for $[K^+]_o = 7$ mmol/L, $[K^+]_o = 8$ mmol/L or $[K^+]_o = 9$ mmol/L, indicating that the wash-out zone has a protective effect

during acute myocardial ischemia. These results agree with those in [10], while the differences are due to the fact that the present model was based on human $I_{K(ATP)}$ current data and the effects of ATP and ADP on the ATP-dependent pumps were included.

4 Conclusions

The results obtained indicate that an anatomically-based 3D model of the acutely-ischemic human ventricles is able to reproduce the reentrant activity typically found in experimental and clinical observations that can lead to sudden cardiac death. The model shows that the degree of hyperkalemia is a key factor in determining the vulnerability of the myocardium to arrhythmias, with moderate hyperkalemia ($[K^+]_o = 7$ mmol/L) being the worst scenario, while the presence of the subendocardial wash-out normoxic zone protects the myocardium against arrhythmias.

Acknowledgments. This work was partially supported by the "Programa Salvador de Madariaga 2018" of the Ministerio de Ciencia, Innovación y Universidades of Spain (Grant Reference PRX18/00489).

References

1. Mozaffarian, D., Benjamin, E.J., Go, A.S., Arnett, D.K., Blaha, M.J., Cushman, M., Das, S.R., de Ferranti, S., Després, J.P., Fullerton, H.J., Executive Summary: Heart Disease and Stroke Statistics Subcommittee: Executive summary: heart disease and stroke statistics–2016 update. Circulation **133**(4), 447–454. https://doi.org/10.1161/CIR.0000000000000366
2. Zipes, D.P., Wellens, H.J.: Sudden cardiac death. Circulation **98**(21), 2334–2351 (1998)
3. Carmeliet, E.: Cardiac ionic currents and acute ischemia: from channels to arrhythmias. Physiol. Rev. **79**(3), 917–1017 (1999). https://doi.org/10.1152/physrev.1999.79.3.917
4. Ferrero, J.M., Trenor, B., Romero, L.: Multiscale computational analysis of the bioelectric consequences of myocardial ischaemia and infarction. Europace **16**(3), 405–415 (2014). https://doi.org/10.1093/europace/eut405
5. Ferrero, J.M., Sáiz, J., Ferrero, J.M., Thakor, N.V.: Simulation of action potentials from metabolically impaired cardiac myocytes. Role of ATP-sensitive K+ current. Circ. Res. **79**, 208–221 (1996). https://doi.org/10.1161/01.RES.79.2.208
6. Shaw, R.M., Rudy, Y.: Electrophysiologic effects of acute myocardial ischemia: a theoretical study of altered cell excitability and action potential duration. Cardiovasc. Res. **35**(2), 256–272 (1997). https://doi.org/10.1016/s0008-6363(97)00093-x
7. Ferrero, J.M., Trénor, B., Rodríguez, B., Sáiz, J.: Electrical activity and reentry during regional myocardial ischemia: insights from simulations. Int. J. Bifurcat. Chaos **13**(12), 3703–3715 (2003). https://doi.org/10.1142/S0218127403008806
8. Rodríguez, B., Ferrero, J.M., Trénor, B.: Mechanistic investigation of extracellular K+ accumulation during acute myocardial ischemia: a simulation study. Am. J. Physiol. Heart Circulatory Physiol. **283**(2), H490–H500 (2002). https://doi.org/10.1152/ajpheart.00625.2001

9. Dutta, S., Mincholé, A., Zacur, E., Quinn, T.A., Taggart, P., Rodriguez, B.: Early afterdepolarizations promote transmural reentry in ischemic human ventricles with reduced repolarization reserve. Prog. Biophys. Mol. Biol. **120**(1–3), 236–248 (2016). https://doi.org/10.1016/j.pbiomolbio.2016.01.008
10. Mena Tobar, A., Ferrero, J.M., Migliavacca, F., Rodríguez Matas, J.F.: Vulnerability in regionally ischemic human heart. Effect of the extracellular potassium concentration. J. Comput. Sci. (2017). https://doi.org/10.1016/j.jocs.2017.11.009
11. Mena, A., Ferrero, J.M., Rodriguez Matas, J.F.: GPU accelerated solver for nonlinear reaction-diffusion systems. Appl. Electrophysiol. Probl. Comput. Phys. Commun. **196**, 280–289 (2015). https://doi.org/10.1016/j.cpc.2015.06.018
12. Mora, M.T., Ferrero, J.M., Romero, L., Trenor, B.: Sensitivity analysis revealing the effect of modulating ionic mechanisms on calcium dynamics in simulated human heart failure. PLOS ONE **12**(11), e0187739 (2017). https://doi.org/10.1371/journal.pone.0187739
13. O'Hara, T., Virág, L., Varró, A., Rudy, Y.: Simulation of the Undiseased human cardiac ventricular action potential: model formulation and experimental validation. PLoS Comput. Biol. **7**(5), e1002061 (2011). https://doi.org/10.1371/journal.pcbi.1002061
14. Babenko, A.P., Gonzalez, G., Aguilar-Bryan, L., Bryan, J.: Reconstituted human cardiac KATP channels: functional identity with the native channels from the sarcolemma of human ventricular cells. Circ. Res. **83**(11), 1132–1143 (1998)
15. Cortassa, S., Aon, M.A., O'Rourke, B., Jacques, R., Tseng, H.-J., Marbán, E., Winslow, R.L.: A computational model integrating electrophysiology, contraction, and mitochondrial bioenergetics in the ventricular Myocyte. Biophys. J. **91**(4), 1564–1589 (2006). https://doi.org/10.1529/biophysj.105.076174
16. Coronel, R., Fiolet, J.W., Wilms-Schopman, F.J., Schaapherder, A.F., Johnson, T.A., Gettes, L.S., Janse, M.J.: Distribution of extracellular potassium and its relation to electrophysiologic changes during acute myocardial ischemia in the isolated perfused porcine heart. Circulation **77**(5), 1125–1138 (1988)
17. Wilensky, R.L., Tranum-Jensen, J., Coronel, R., Wilde, A.A., Fiolet, J.W., Janse, M.J.: The subendocardial border zone during acute ischemia of the rabbit heart: an electrophysiologic, metabolic, and morphologic correlative study. Circulation **74**(5), 1137–1146 (1986)
18. Kléber, A.G., Janse, M.J., van Capelle, F.J., Durrer, D.: Mechanism and time course of S-T and T-Q segment changes during acute regional myocardial ischemia in the pig heart determined by extracellular and intracellular recordings. Circ. Res. **42**(5), 603–613 (1978)
19. Sutton, P.M.I., Taggart, P., Opthof, T., Coronel, R., Trimlett, R., Pugsley, W., Kallis, P.: Repolarisation and refractoriness during early ischaemia in humans. Heart **84**(4), 365–369 (2000). https://doi.org/10.1136/heart.84.4.365

Evaluation of Linked Determinants Between Diabetes and Caries

Nubia M. Chavez-Lamas, Laura A. Zanella-Calzada, Carlos Eric Galván-Tejada(✉), Hamurabi Gamboa-Rosales, Jorge I. Galván-Tejada, José M. Celaya-Padilla, and Huizilopoztli Luna-García

Academic Unit of Electric Engineering, Universidad Autónoma de Zacatecas, Jardín Juarez 147, Centro, 98000 Zacatecas, ZAC, Mexico
ericgalvan@uaz.edu.mx

Abstract. Dental caries and diabetes mellitus, represent two chronic diseases of public health that present statistics of high prevalence worldwide. One of the main problems that affect these conditions is demography, since the least developed countries are those that have less access to public health services and are limited by the economic costs that represent the treatments. In this work is presented the univariate analysis, of a set of demographic determinants obtained from the National Health and Nutrition Examination Surveys (NHANES), in order to identify those that present the most significant information related to estimation of these diseases. According to the results, the age of the subjects is the main determinant describing the simultaneous presence of these diseases, obtaining an area under the curve (AUC) value ≥ 0.846, concluding that age can be used as tool for their preventive diagnosis.

Keywords: Dental caries · Diabetes · Demographic determinants · NHANES · Univariate analysis · General linear model

1 Introduction

Recent years have seen a rapid increase in global technological and economic potential and, as a result, the capacity to overcome problems related to poverty and poor health has increased. However, in many developing countries, the health situation has deteriorated, largely due to the reappearance of infectious diseases and the increased burden of non-communicable diseases such as caries and diabetes [3].

Oral health rarely endangers the existence of people, however, it directly affects their quality of life and their self-esteem, which establishes their importance as a fundamental part of the integral life of the population. Dental caries is a transmissible, infectious and multifactorial chronic disease, with a prevalence of 94% of people worldwide, regardless of age or socioeconomic level, represents a public health problem throughout the world [3,17].

© Springer Nature Switzerland AG 2020
C. A. González Díaz et al. (Eds.): CLAIB 2019, IFMBE Proceedings 75, pp. 777–783, 2020.
https://doi.org/10.1007/978-3-030-30648-9_103

Currently, diabetes is considered a genetic-based chronic metabolic syndrome, caused by a partial or total deficiency of insulin that leads to a decrease in tolerance to carbohydrates, hyperglycemia, glucosuria, polydipsia, polyphagia, polyuria and alteration of the intermediate metabolism of lipids and proteins, among others. Because its severity may change over time, hyperglycemia is considered a marker of the severity of the underlying metabolic state rather than the nature of the process itself. Worldwide, more than 140 million people suffer from diabetes, which makes it one of the most frequent causes of undeclared diseases [15].

In Mexico, 12.03 million people present the condition of diabetes mellitus, being the 6^{th} country in high prevalence in the world ranking [5] and the 1^{st} in global obesity [4]. Diabetes mellitus is considered a social disease, not only because of its high frequency, but also because of the economic cost it represents for governments and families of those who suffer from it. This disease is influenced by different determinants, for example, some of the cultural and economic factors that predispose the patient's behavior towards the disease and change their own family, work and community context [14].

The state of oral health in diabetic patients has been the subject of numerous studies over the last few years. The risk of finding dental caries more frequently in patients with diabetes is being more controversial, since, according to Lalla et al., dental caries represent an oral affection related to diabetes in 91.4% of cases [8]. Then, some studies found more caries in diabetics and explained that they had a worse metabolic control but the higher risk of dental caries is related to certain factors such as following bad oral hygiene or a lack of glycemic control, this last factor may be produced for an incorrect diet or for a bad control of insulin doses with respect to physical exercise or meal times [11].

In addition, it is well known that several socioeconomic and demographic determinants are linked between these two multifactorial diseases [2,18], and some of them are shared between diabetes and caries, simultaneously [19], according to different sources of information, such as the National Survey of Health and Nutrition Examination (NHANES). The NHANES is a national program of the United States (USA) that designs surveys based on surveys to evaluate the nutritional and health status of adults and children of different ethnic groups, supporting the development of research related to clinical, para-clinical and demographic features [6].

Therefore, due to the difficulty of controlling the incidence of dental caries and diabetes mellitus since they depend on a multiple amount of variables, recent studies have implemented algorithms and performed analyzes based on computer-aided diagnosis (CADx) to develop prediction and classification models for the preventive diagnosis and the reduction of its high prevalence, looking for the main factors that affect these conditions [16].

1.1 Related Work

Among the approaches that have been undertaken to identify different determinants that affect the risk of developing caries and diabetes, is the work of

Lam et al. [9] where it was found that a set of determinants associated with the accumulation of plaque based on visits to the dentist, the frequency of brushing, the low importance perceived by parents on milk teeth and weaning on solids they are determinants associated with the accumulation of plaque. Fernandes et al. [7] proposed a cross-sectional study of children and their mothers based on demographic/socioeconomic status, where a Poisson regression was used to find that dental caries is mostly present in mothers of one-year-old children, which demonstrates a relationship between the analyzed features and caries with children. In addition, some risk factors that are generally associated with caries are genetic and dietary, since according to the work of Lips et al. [10], an association between genetic polymorphisms and the risk of dental caries for most salivary proteins is demonstrated. On the other hand, diabetic and hypertensive patients have risk factors in the diet that could lead to oral health problems, according to the work of Ahmed et al. [1], a statistical analysis was carried out with clinical data based on the characteristics related to the diet of the participants, clearly identifying that patients with dental problems of gold are hemodynamically stressed.

Therefore, for this research, a set of five demographic determinants that, according to the literature, are the most significant to estimate the simultaneous presence of dental caries and diabetes, are analyzed individually through their univariate modeling to identify the main factors that they are affected according to a validation process, in order to support preventive diagnosis and reduce the prevalence of these conditions.

2 Materials and Methods

The methodology of this work consists of three main stages: data preprocessing, classification analysis and validation. All the analysis is performed using R [13].

2.1 Data Description

For the development of this work, the information obtained from NHANES surveys (2013–2014 collection) is used. These surveys contain several interviews and physical examinations collected each year, including data related to the demographics of the subjects, from which the five determinants analyzed in this approach were obtained, which are described below.

- **DMQMILIZ:** Have you ever served on active duty in the U.S.?
- **DMDEDUC3:** Highest grade or level of school completed.
- **DMDHSEDU:** Household reference person's spouse's education level.
- **RIDEXAGM:** Age in months at the time of examination.
- **RIDAGEYR:** Age in years of the participant at the time of screening.

On the other hand, the output feature used presents two possible values related to the conditions of dental caries and diabetes, where "1" represents the presence of both and "0" represents the absence.

The dataset contains the observations of 3,552 subjects (1,813 men and 1,740 women/3,041 controls and 511 cases), located in an age range from zero to 80 years old.

2.2 Data Preprocessing

The preprocessing of data consists in the imputation of the missing data, according to the random forest technique, where the missing data are replaced by the value of the median of the column that is subsequently updated through the iterations of the trees. In addition, a standard standardization is applied to relocate the data and have an average of zero and one standard deviation of one, which can be calculated by the Eq. 1, where x_i represents the data, mu represents the average value and $sigma$ represents the standard deviation.

$$X = \frac{x_i - \mu}{\sigma} \tag{1}$$

2.3 Classification Analysis

For the classification analysis, the technique of the general lineal model (glm) based on the logit function is implemented for each characteristic, in order to develop a set of univariate generalized models that allow classifying the subjects according to the two possible outcomes.

The logit function is the natural register, Ln, of the probabilities that the output characteristic is equal to the possible categories, as shown in the Eq. 2, where P is the probability that the output equals 1, X_k are the input characteristics and $beta_k$ are coefficients.

$$Ln(\frac{P}{1-P}) = \beta_0 + \beta_1 X_1 + \beta_2 X_2 \ + ... + \ \beta_k X_k \tag{2}$$

2.4 Validation

The validation consists on measuring the area under the curve (AUC) of the receiver operating characteristic (ROC) curve of each model, in order to evaluate the sensitivity/specificity rate.

Sensitivity is referred to the proportion of data belonging to a condition and being classified as positive. It is calculated with Eq. 3, where TP represent true positives and FP represent false positives.

$$sensitivity = \frac{TP}{TP + FP} \tag{3}$$

Specificity is referred to the proportion of data that doesn't belong to a condition and it's classified as negative. It is calculated with Eq. 4, where TN represent true negatives and FN represent false negatives.

$$NPV = \frac{TN}{TN + FN} \tag{4}$$

3 Results and Discussion

The results indicate a greater vulnerability to dental caries in patients with diabetes. In the Fig. 1 the ROC curves obtained for each univariate model are presented, where it is possible to observe that all the characteristics present statistically significant AUC values; however, the curves (C) and (E), which are related to the age of the subjects, present the best performance.

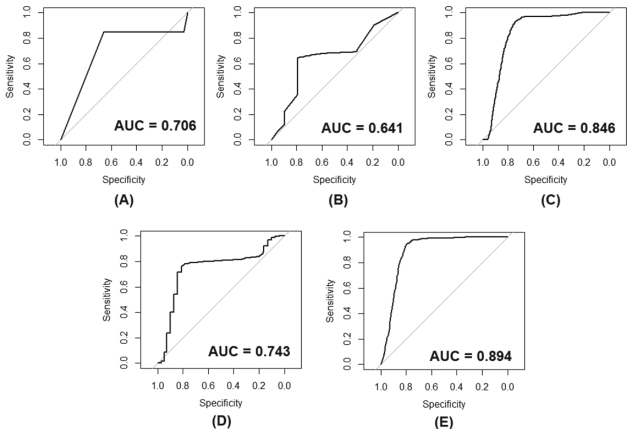

Fig. 1. ROC curves obtained for each model, (A) "DMQMILIZ", (B) "DMDHSEDU", (C) "RIDEXAGM", (D) "DMDEDUC3", (E) "RIDAGEYR".

Dental caries is an infectious disorder that involves multiple factors that coincide at a given point and at a given time, where the basic factors are the presence of the causative microorganism, the host (tooth), substrate (diet) and immune capacity of the patient. Moore et al. [12] reported a higher prevalence of caries in diabetics, relating this observation with the age of the patients since they usually present a greater gingival recession. In addition, it is known that diabetic patients tend to develop caries since saliva has been identified as a factor related to the appearance of dental caries.

Therefore, the features "RIDEXAGM" and "RIDAGEYR", which are specifically defined as the age in years and the age in months of the participants, respectively, show that they are the two determinants that present the best model in relation to the presence of caries and diabetes, allowing to identify that of the group of previously selected factors, age is the most important.

4 Conclusions

On the basis of the results obtained, it is concluded that the univariate analysis of a series of specific factors that support the description of the presence of dental

caries and diabetes allows to identify the age of the subjects as the main determinant that affects these conditions, which It can be used with a determinant diagnosis of preventive diagnosis.

Therefore, the methodology proposed in this work can represent a preliminary tool of low cost that helps in the diagnosis of dental caries and diabetes as a whole, making possible the prediction of them according to the developed models, having as main objective the regions of low socioeconomic and educational level, seeking to reduce its high incidence and avoid high cost treatments that represent these conditions.

References

1. Ahmed, A., Ikram, K., Masood, H., Urooj, M.: Identification of relationship between oral disorders & hemodynamic parameters. Pak. Oral Dent. J. **37**(2) (2017)
2. Alcalá-Rmz, V., Zanella-Calzada, L.A., Galván-Tejada, C.E., García-Hernández, A., Cruz, M., Valladares-Salgado, A., Galván-Tejada, J.I., Gamboa-Rosales, H.: Identification of diabetic patients through clinical and para-clinical features in Mexico: an approach using deep neural networks. Int. J. Environm. Res. Public Health **16**(3) (2019). https://doi.org/10.3390/ijerph16030381. http://www.mdpi.com/1660-4601/16/3/381
3. Allard Soto, R.: El acceso a los medicamentos: conflictos entre derechos de propiedad intelectual y protección de la salud pública. Acta Bioethica **21**(1), 83–91 (2015)
4. Barriguete-Meléndez, J., Hercberg, S., Galán, P., Parodi, A., Baulieux, J.: Nutrinet-salud méxico. Prospective study online: 2018–2028. Relationship between nutrition and health and determinants of dietary habits and nutritional status. Cirugia y cirujanos **86**(1), 8–19 (2018)
5. Dávila-Torres, J., González-Izquierdo, J.D.J., Barrera-Cruz, A.: Obesity in Mexico. Revista Médica del Instituto Mexicano del Seguro Social **53**(2), 240–249 (2015)
6. Centers for Disease Control for Health Statistics (NCHS), P.C.N.C.: National health and nutrition examination survey data. https://wwwn.cdc.gov/nchs/nhanes/ContinuousNhanes/Default.aspx?BeginYear=2013
7. Fernandes, I., Sá-Pinto, A., Marques, L.S., Ramos-Jorge, J., Ramos-Jorge, M.: Maternal identification of dental caries lesions in their children aged 1–3 years. Eur. Arch. Paediatr. Dent., 1–6 (2017)
8. Lalla, E., Cheng, B., Lal, S., Kaplan, S., Softness, B., Greenberg, E., Goland, R.S., Lamster, I.B.: Diabetes mellitus promotes periodontal destruction in children. J. Clin. Periodontol. **34**(4), 294–298 (2007)
9. Lam, C.U., Khin, L., Kalhan, A., Yee, R., Lee, Y., Chong, M.F., Kwek, K., Saw, S., Godfrey, K., Chong, Y., et al.: Identification of caries risk determinants in toddlers: results of the gusto birth cohort study. Caries Res. **51**(4), 271–282 (2017)
10. LIps, A., Antunes, L.S., Antunes, L.A., Pintor, A.V.B., Santos, D.A.B.D., Bachinski, R., Küchler, E.C., Alves, G.G.: Salivary protein polymorphisms and risk of dental caries: a systematic review. Braz. Oral Res. **31** (2017)
11. Miralles, L., Silvestre, F.J., Hernández-Mijares, A., Bautista, D., Llambes, F., Grau, D.: Caries dental en diabéticos tipo 1: Influencia de factores sistémicos de la enfermedad en la instauración de la caries dental. Medicina Oral, Patología Oral y Cirugía Bucal (Internet) **11**(3), 256–260 (2006)

12. Moore, P.A., Weyant, R.J., Etzel, K.R., Guggenheimer, J., Mongelluzzo, M.B., Myers, D.E., Rossie, K., Hubar, H., Block, H.M., Orchard, T.: Type 1 diabetes mellitus and oral health: assessment of coronal and root caries. Commun. Dent. Oral Epidemiol. **29**(3), 183–194 (2001)
13. R Core Team: A Language and Environment for Statistical Computing. R Foundation for Statistical Computing, Vienna, Austria (2018). https://www.R-project.org/
14. Ramón, C.L., Ávalos García, M.I.: Diabetes mellitus hacia una perspectiva social. Revista Cubana de Salud Pública **39**(2), 331–345 (2013)
15. Sanz-Sánchez, I., Bascones-Martínez, A.: Diabetes mellitus: Su implicación en la patología oral y periodontal. Avances en odontoestomatología **25**(5), 249–263 (2009)
16. Singh, P., Pal, A.B., Anburajan, M., Kumar, J.: Computer-aided diagnosis of type 2 diabetes mellitus using thermogram of open mouth. In: Progress in Advanced Computing and Intelligent Engineering, pp. 167–177. Springer (2018)
17. Zanella-Calzada, L.A., Galván-Tejada, C.E., Chávez-Lamas, N.M., Galván-Tejada, J.I., Celaya-Padilla, J.M.: Multivariate features selection from demographic and dietary descriptors as caries risk determinants in oral health diagnosis: data from nhanes 2013–2014. In: 2018 International Conference on Electronics, Communications and Computers (CONIELECOMP), pp. 217–224. IEEE (2018)
18. Zanella-Calzada, L.A., Galván-Tejada, C.E., Chávez-Lamas, N.M., Rivas-Gutierrez, J., Magallanes-Quintanar, R., Celaya-Padilla, J.M., Galván-Tejada, J.I., Gamboa-Rosales, H.: Deep artificial neural networks for the diagnostic of caries using socioeconomic and nutritional features as determinants: data from nhanes 2013–2014. Bioengineering **5**(2) (2018). https://doi.org/10.3390/bioengineering5020047. http://www.mdpi.com/2306-5354/5/2/47
19. Zanella-Calzada, L.A., Galván-Tejada, C.E., Chávez-Lamas Nubia M., R., Celaya-Padilla, J.M., Galván-Tejada, J.I.: A preliminary approach to find linked determinants between diabetes and caries using genetic algorithms. Res. Comput. Sci. (2018, in press)

Evaluation of Kernels Applied in Support Vector Machines in the Data Analysis of Organochlorines Exposure in Study of Biomarkers

Jorge Alejandro Lopera-Rodríguez[1(✉)], Martha Zuluaga[2], and Jorge A. Jaramillo-Garzón[3]

[1] Instituto Tecnológico Metropolitano, Medellín, Colombia
alejandrolopera@itm.edu.co
[2] Universidad Nacional de Colombia, Manizales, Colombia
[3] Universidad de Caldas, Manizales, Colombia

Abstract. One of the biggest concerns in metabolomic data analysis is adopting good predictive models in cases of asymmetric databases and few samples. As a result, more studies should evaluate statistical methods that can produce adequate analyses despite those limitations. Support vector machines (SVMs) can be an alternative. This study assesses the behavior of SVMs and the application of different kernels in order to propose a strategy for biomarker recognition in cases of organochlorine exposure.

The database used in this study comes from an original experiment previously published, in which a HepG2 cell line was exposed to four different organochlorine pesticides, a mixture, and a control. The database consists of 153 identified and 246 unidentified metabolites. First, a partial least squares discriminant analysis (PLS-DA) was applied to the database to obtain the top ten candidate biomarker metabolites. Subsequently, an SVMs algorithm was implemented using four different kernels: linear, sigmoid, polynomial, and radial basis function (RBF). Afterward, a methodology based on recursive feature elimination (SVM-RFE) was adopted in order to obtain the top ten metabolites. Finally, PLS-DA and SVMs were compared.

It was demonstrated that SVMs have a good predictive power when they are trained with few samples. The sigmoid and linear kernels with hard and soft margin showed the best performance. Moreover, the SVM-RFE strategy can rapidly identify candidate biomarker metabolites using a limited number of training samples.

Keywords: Support vector machines · Organochlorine exposure · Metabolomics · Biomarkers

1 Introduction

Metabolomics is an important growing area of biological studies because it can explain the metabolic behavior of any organism during a specific event. Many statistical analysis strategies have been reported to handle the large amounts of data produced in

© Springer Nature Switzerland AG 2020
C. A. González Díaz et al. (Eds.): CLAIB 2019, IFMBE Proceedings 75, pp. 784–791, 2020.
https://doi.org/10.1007/978-3-030-30648-9_104

metabolomics studies. Strategies based on machine learning have been adopted in multivariate analysis of metabolite datasets in order to reduce the dimension of the variables and facilitate the interpretation [1]. Currently, the most widely used unsupervised methods are principal components analysis (PCA), hierarchical clustering, and heat maps. In turn, PLS-DA and orthogonal partial least square discriminant analysis are the most commonly reported supervised methods [2–4].

However, those methodologies are suitable when the data come from controlled experiments such as cell cultures [5]. When the data are obtained from a non-controlled population or complex matrices like blood or tissue, their probability of exhibiting a non-linear distribution is greater. As a consequence, the accuracy of said methodologies may decrease [5]. Additionally, when training dataset has few samples available, overfitting may occur in the construction of the predictive models [6].

Despite the fact that many multivariate algorithms can perform metabolomics data analysis, some concerns remain about the data overfitting, collinearity, and linear assumption of many of those multivariate methods [2]. Nevertheless, methods that use SVMs could overcome such difficulties because they can interpret multivariate data better and deal with non-linear relationships between the metabolomic data and the variable of interest [7, 8]. In addition, they can optimize their analysis through the implementation of kernel functions [9]. The latter can amplify the analysis capacity of SVMs processing non-linear data. Another advantage is that they can construct predictive models using few samples [6]. For that reason, they are proposed as a solution to analyze highly complex data. Therefore, this study focuses on the evaluation of SVMs with different kernels for metabolomic data analysis in order to compare their performance with that of classical methods. For that purpose, the authors used a metabolomic database obtained from an *in vitro* assay using a HepG2 cell line [10].

This work is divided into four sections: (1) evaluation of the performance of PLS-DA; (2) evaluation of SVMs with four different kernels; (3) comparison between PLS-DA and SVM methodologies; and (4) discussion and conclusions.

2 Materials and Methods

2.1 Database

The metabolomic database was obtained from an original study into HepG2 cell line cultures exposed to four different organochlorine pesticides: aldrin, DDT, endosulfan, and lindane [10]. In that case, to evaluate the effects, 36 samples of HepG2 cells were exposed to said organochlorines and a mixture of them, and the control group was exposed to dimethyl sulfoxide (DMSO). Six samples were subjected to each combination. Endogenous metabolites were extracted and analyzed by GC/MS-TOF. The corresponding chromatograms were automatically deconvolved using the software CromaTOF. Subsequently, the retention width of the peaks was filtered and calculated using the BinBase algorithm described by Fiehn et al. [11]. The results of that analysis were compared with the Fiehn mass spectral library. The spectral data that did not match the Fiehn library were considered new metabolites or unknown compounds. In total, 1081 signals were extracted from the GC/MS TOF analysis. Those with a ratio of

missing values above 30% in the observations were selected; thus, 399 spectra related to metabolites and their corresponding abundances in each sample were obtained. From that dataset, 153 metabolites were identified, while 246 remained unidentified. The complete protocol can be consulted in the study by Zuluaga et al. [10].

In this study, the database was divided into three different analysis groups: (1) all metabolites, (2) unidentified metabolites, and (3) identified metabolites. Each one of those groups was subdivided into five subgroups in which each organochlorine was paired with the control group. Therefore, fifteen subgroups were created in total.

The raw data was first normalized in order to facilitate the statistical analysis, correct the systematic variation between the samples, and enable the comparison between them. That process included logarithmic transformation and Pareto scaling. The application Metaboanalyst 4.0 was employed for such normalization [12].

2.2 PLS-DA

A supervised PLS-DA model was applied to each subgroup of data using Metaboanalyst 4.0. K-fold cross validation was implemented to evaluate the predictive power of the model. The parameters measured in the PLS-DA were accuracy, Q2, and R2.

2.3 SVMs

The fifteen normalized subgroups were used for this analysis. An SVM algorithm was implemented using R [13], the RStudio environment [14], and the package e1071 [15]. Subsequently, the SVMs were applied with linear, polynomial, sigmoid, and RBF kernels. Four vector margin penalties were also implemented: 1e100, 1e10, 1, and 1e-10.

To identify the training and predictive power of each kernel, the SVMs were trained starting with two samples and progressively adding two more until the training set had 10 samples. The number of remaining samples in each trial served to test the predictive power of the SVM model. K-fold cross validation was utilized, and the accuracy was reported.

2.4 Biomarkers

After the SVM with the best kernel was identified, an SVM-RFE-based strategy was implemented. Such methodology uses the training of an SVM with a linear kernel that iteratively removes the features with the smallest decision hyperplane value given in the SVM. In that way, the metabolites are ordered from highest to lowest with respect to their own decision value in the hyperplane [16]. Kernels with 100% accuracy were used to implement this methodology.

Finally, the accuracies achieved with the PLS-DA and the SVM were compared. Furthermore, the metabolite rankings obtained with the two methodologies were also contrasted.

3 Results

3.1 Normalization and PLS-DA

All the fifteen subgroups achieved an acceptable normal distribution. The models constructed by the PLS-DA methodology presented an accuracy of 100%. The details of the tests are listed in Table 1.

Table 1. Performance of the PLS-DA methodology.

Parameter	Aldrin	DDT	Endosulfan	Lindane	Mixture
All metabolites					
Accuracy	1.0030	1.0	1.0	1.0	1.0
R2	0.9594	0.98433	0.97572	0.97602	0.99391
Q2	0.88724	0.95379	0.95053	0.85183	0.97613
Unidentified metabolites					
Accuracy	1.0	1.0	1.0	1.0	1.0
R2	0.93362	0.97902	0.96422	0.96552	0.98856
Q2	0.84121	0.95639	0.93881	0.82281	0.9565
Identified metabolites					
Accuracy	1.0	1.0	1.0	1.0	1.0
R2	0.98544	0.98503	0.98681	0.97504	0.99624
Q2	0.94223	0.92412	0.96653	0.80682	0.97542

3.2 SVMs

The details of the implementation of the four kernels can be consulted in Table 2.

The SVM with the linear kernel reached a 100% predictive power when the training included 6 samples and margin penalties of 1, 1e10, and 1e100. Such 100% was maintained when the training was conducted with more samples, except with a margin penalty of 1e-10.

According to the k-fold parameter, the SVM with the polynomial kernel does not reach a 100% predictive power, only 90% in the training with 8 samples; and it achieves a better performance with margin penalties of 1e10 and 1e100. In turn, the SVM with the RBF kernel reached a 100% predictive power when the training was carried out with 6 samples and margin penalties of 1e10 and 1e100. However, that performance was not maintained in the training sessions with 8 and 10 samples, when the maximum predictive power was 98.64%.

Like the SVM with the linear kernel, those implemented with the sigmoid kernel reached a 100% predictive power when the training was performed with at least 6 samples and margin penalties of 1, 1e10, and 1e100. Such behavior was maintained when the training included more samples. It should be noted that, with said kernel, even in the training using 4 samples and margin penalties of 1e10 and 1e100, a 90% predictive power was reached.

Table 2. Performance of the four kernels (in percentages).

Kernels			Linear	Polynomial	RBF	Sigmoid
Global mean of k-fold by kernel			**54.74**	**28.19**	**41.85**	**55.61**
Samples used in SVM training and accuracy for each margin penalty	2	Margin	**0**	**0**	**0**	**0**
		1e-10	0	0	0	0
		1	0	0	0	0
		1e10	0	0	0	0
		1e100	0	0	0	0
	4	Margin	**60**	**25**	**27.5**	**64.17**
		1e-10	0	0	0	0
		1	80	10	20	76.67
		1e10	80	45	45	90
		1e100	80	45	45	90
	6	Margin	**70.59**	**18.75**	**53.75**	**70.59**
		1e-10	0	0	0	0
		1	100	9.09	68.18	100
		1e10	100	83.33	100	100
		1e100	100	83.33	100	100
	8	Margin	**72.22**	**35.14**	**63.33**	**72.22**
		1e-10	0	0	0	0
		1	100	33.33	95	100
		1e10	100	90	95	100
		1e100	100	90	95	100
	10	Margin	**75**	**60.33**	**74**	**75**
		1e-10	0	0	0	0
		1	100	61.33	98.67	100
		1e10	100	90	98.67	100
		1e100	100	90	98.67	100

3.3 Comparison Between Methodologies

In order to identify variations in the metabolite rankings generated with the two methodologies, PLS-DA and SVM-RFE, the percentage of matches of the first ten metabolites in the same position was quantified (Table 3). Moreover, the percentage of matches of the first ten metabolites included in both rankings regardless of their position was calculated (Table 4). The ranking of aldrin presented the highest percentage of matches in the same position.

Table 3. Percentage of metabolite matches in the same position in both rankings.

Datasets	Aldrin	DDT	Endosulfan	Lindane	Mixture
All metabolites	20%	10%	30%	10%	10%
Unidentified metabolites	30%	10%	10%	10%	10%
Identified metabolites	40%	10%	0%	10%	20%

Table 4. Percentage of metabolites included in both rankings.

Datasets	Aldrin	DDT	Endosulfan	Lindane	Mixture
All metabolites	90%	90%	80%	50%	60%
Unidentified metabolites	70%	90%	90%	50%	60%
Identified metabolites	70%	60%	60%	60%	80%

4 Discussion

4.1 SVMs and Kernels

The present work confirmed the capacity of SVMs to deal with complex samples. In addition, it was possible to work with a large number of variables and few samples. The linear and sigmoid kernels applied to the SVMs achieved the best performance, followed by the RBF and, finally, the polynomial. It should be noted that, when the margin penalty of the SVM was set to 1e-10, the predictive power was completely lost. This finding did not depend on the kernel that was used.

On the other hand, to achieve a 100% predictive power, the linear and sigmoid kernels needed 6 samples and a margin penalty equal or greater than 1. Regarding the RBF kernel, the results show a poor performance, possibly because its dispersion parameter needed further adjustment; however, it is strongly recommended in situations where the data is not linearly distributed. Using such kernel has been one of the most popular methodologies in various studies. One of them was conducted by Zheng et al. [17]. In another work, said kernel was found to be superior compared to its polynomial counterpart [18]. It has been reported that the polynomial kernel does not generally present a satisfactory solution, which has led to the implementation of special normalization techniques to improve its performance [19]. In addition, the data normalization process in the present study could have influenced the performance of the polynomial kernel.

4.2 Comparison Between PLS-DA and SVM

The models obtained by PLS-DA achieved a 100% predictive power. However, all the samples were required for the construction of such models. Therefore, the SVMs have a

clear advantage because they achieve their training using few samples. This was previously described by Mahadevan et al. [6].

Moreover, the rankings generated by the two methodologies present a similarity between 50% and 90% (see Tables 3 and 4). Both rankings had at least one metabolite in the same position, except for the metabolites identified with endosulfan. In previous studies, when the samples were few, the order of priority of the metabolites in the rankings of PLS-DA and SVM was different. Mahadevan et al. found that the PLS-DA model omitted a key feature, creatinine, which was important to differentiate between men and women. Nevertheless, the ranking produced by the SVM included it [6].

4.3 Limitations

Although the SVM methodology exhibited a good behavior, no additional samples were available to expand the evaluation of the predictive power and the generation of rankings. In future studies, such strategy should be validated using databases with a greater number of samples.

4.4 Conclusions

It was demonstrated that SVMs have a good predictive power when they are trained with few samples. The sigmoid and linear kernels with hard and soft margin achieved the best performance. The SVM-RFE strategy demonstrated its capacity to rapidly identify candidate biomarker metabolites using few training samples.

Acknowledgments. The authors appreciate the help received from the ITM Language Center in the proofreading of this paper.

Declaration of Interests. The authors of the present study declare that there are not conflicts of interest that affect the results of this work.

References

1. Xia, J., Wishart, D.S.: Web-based inference of biological patterns, functions and pathways from metabolomic data using MetaboAnalyst. Nat. Protoc. **6**, 743 (2011)
2. Worley, B., Powers, R.: Multivariate analysis in metabolomics. Current. Metabolomics **1**, 92–107 (2013)
3. Yamamoto, H., Yamaji, H., Abe, Y., Harada, K., Waluyo, D., Fukusaki, E., et al.: Dimensionality reduction for metabolome data using PCA, PLS, OPLS, and RFDA with differential penalties to latent variables. Chemometr. Intell. Lab. Syst. **98**, 136–142 (2009)
4. Zuluaga, M., Robledo, S., Osorio-Zuluaga, G.A., Yathe, L., Gonzalez, D., Taborda, G.: Metabolomics and pesticides: systematic literature review using graph theory for analysis of references. Nova **14**, 121–138 (2016)
5. Heinemann, J., Mazurie, A., Tokmina-Lukaszewska, M., Beilman, G.J., Bothner, B.: Application of support vector machines to metabolomics experiments with limited replicates. Metabolomics **10**, 1121–1128 (2014)

6. Mahadevan, S., Shah, S.L., Marrie, T.J., Slupsky, C.M.: Analysis of metabolomic data using support vector machines. Anal. Chem. **80**, 7562–7570 (2008)
7. Boser, B.E., Guyon, I.M., Vapnik, V.N.: A training algorithm for optimal margin classifiers, pp. 144–152. ACM (1992)
8. Maldonado, S., Weber, R.: A wrapper method for feature selection using support vector machines. Inf. Sci. **179**, 2208–2217 (2009)
9. Shawe-Taylor, J., Cristianini, N.: Kernel Methods for Pattern Analysis. Cambridge University Press, Cambridge (2004)
10. Zuluaga, M., Melchor, J.J., Tabares-Villa, F.A., Taborda, G., Sepúlveda-Arias, J.C.: Metabolite profiling to monitor organochlorine pesticide exposure in HepG2 cell culture. Chromatographia **79**, 1061–1068 (2016)
11. Fiehn, O., Wohlgemuth, G., Scholz, M., Kind, T., Lee, D.Y., Lu, Y., et al.: Quality control for plant metabolomics: reporting MSI-compliant studies. Plant J. **53**, 691–704 (2008)
12. Chong, J., Soufan, O., Li, C., Caraus, I., Li, S., Bourque, G., et al.: MetaboAnalyst 4.0: towards more transparent and integrative metabolomics analysis. Nucleic Acids Res. **46**, W486–W494 (2018)
13. R Core Team: R: a language and environment for statistical computing (2013)
14. RStudio Team: RStudio: integrated development for R, vol. 700. RStudio. Inc., Boston, MA (2015)
15. Meyer, D., Dimitriadou, E., Hornik, K., Weingessel, A., Leisch, F., Chang, C.-C., et al.: Package 'e1071'. R J. (2019)
16. Guyon, I., Weston, J., Barnhill, S., Vapnik, V.: Gene selection for cancer classification using support vector machines. Mach. Learn. **46**, 389–422 (2002)
17. Zheng, H., Zheng, P., Zhao, L., Jia, J., Tang, S., Xu, P., et al.: Predictive diagnosis of major depression using NMR-based metabolomics and least-squares support vector machine. Clin. Chim. Acta **464**, 223–227 (2017)
18. Feizizadeh, B., Roodposhti, M.S., Blaschke, T., Aryal, J.: Comparing GIS-based support vector machine kernel functions for landslide susceptibility mapping. Arab. J. Geosci. **10**, 122 (2017)
19. Wan, V., Campbell, W.M.: Support vector machines for speaker verification and identification, vol. 2, pp. 775–784. IEEE (2000)

Diagnosis of Type 2 Diabetes and Pre-diabetes Using Machine Learning

Erika Severeyn[1(✉)], Sara Wong[2], Jesús Velásquez[1], Gilberto Perpiñán[3], Héctor Herrera[4], Miguel Altuve[5], and José Díaz[6]

[1] Departamento de Termodinámica y Transferencia de Calor, Universidad Simón Bolívar, Caracas, Venezuela
severeynerika@usb.ve
[2] Departamento de Electrónica y Circuitos, Universidad Simón Bolívar, Caracas, Venezuela
[3] Faculty of Electronic and Biomedical Engineering, Antonio Nariño University, Cartagena, Colombia
[4] Departamento de Tecnología de Procesos Biológicos y Bioquímicos, Universidad Simón Bolívar, Caracas, Venezuela
[5] Faculty of Electrical and Electronic Engineering, Pontifical Bolivarian University, Bucaramanga, Colombia
[6] Departamento de Ingeniería Eléctrica y Computación, Universidad Autónoma de Ciudad Juarez, Ciudad Juarez, Mexico

Abstract. The type-2 diabetes (T2D) is a multifactorial chronic disease that reduces the quality of lifestyle and produces the death of a large percentage of the population worldwide. Before the development of T2D a series of symptoms are presented even years before T2D diagnosis. This condition that appears before the development of T2D is called prediabetes. Prediabetes and T2D are diagnosed from the oral glucose tolerance test (OGTT). The OGTT consists in the measurement of glucose and insulin in five-time intervals, the first after 8 h of fasting (0 min) and the other four measurements after taking 75 g of oral glucose in 30-minutes intervals (30, 60, 90 and 120 min). Some parameters have been used to improve the efficiency in the diagnosis of prediabetes and T2D, for example: the area under the glucose (AUC_G) and insulin (AUC_I) curve during OGTT has been used as a parameter for the diagnosis of prediabetes, T2D and obesity. The aim of this study is to assess the *k*-means clustering algorithm in the classification of subjects with prediabetes and T2D using the AUC_G and AUC_I. A database of 188 subjects (male = 88 subjects, age = 42.11 ± 14.91 years old) with values of plasma glucose and insulin during OGTT was used. The *k*-means clustering performed for AUC_G presents acceptable results since the silhouette coefficient is above 0.6 in all cases. The findings in this study indicate that the *k*-means applied in the AUC_G classify subjects with T2D, prediabetes and control. Furthermore, it could even predict those subjects with high probabilities of developing T2D.

Keywords: *k*-means · Oral glucose tolerance test · Area under the insulin curve · Area under the glucose curve · Statistical analysis

© Springer Nature Switzerland AG 2020
C. A. González Díaz et al. (Eds.): CLAIB 2019, IFMBE Proceedings 75, pp. 792–802, 2020.
https://doi.org/10.1007/978-3-030-30648-9_105

1 Introduction

Type-2 diabetes (T2D) is a multifactorial chronic disease that reduces the quality of lifestyle and produces the death of a large percentage of the population worldwide [1]. The T2D imposes an enormous economic burden to the global health systems [2]. The total annual expenses of this disease range between US$ 141.6 million and 174 billion, and it is estimated that the health expenditure of T2D patients is at least twice the expenditure of healthy people [3–5].

The T2D has become entrenched in developing countries, and in very recent years, more than 80% of the deaths caused by this disease have occurred in low and middle-income countries. Moreover, their morbidity burden is estimated that it will increase worldwide and particularly in developing countries [6–8]. Currently, the global prevalence of T2D in people older than 18 years has increased from 4.7% (108 million people) in 1980 to 8.5% (400 million people) in 2017 and this increase has been faster in middle and low-income countries [8]. Even more, the global prevalence of T2D is projected to increase to more than 600 million affected persons by the year 2035, and the 70% of that global estimation will be placed in developing countries [8].

T2D is a progressive disease that even years before its diagnosis a series of symptoms are present. This condition that appears before the development of T2D is called prediabetes [9]. Prediabetes and T2D are diagnosed from the oral glucose tolerance test (OGTT). The OGTT consists in the measurement of glucose and insulin concentrations in five-time intervals (5-samples OGTT), the first measurement is taken after 8 h of fasting (0 min) and the other four measurements after taking 75 g of liquid glucose in 30-minute intervals (30, 60, 90 and 120 min) [10]. T2D is diagnosed according to the World Health Organization if fasting glucose is above 125 mg/dL and/or postprandial glucose (120 min of OGTT) is above 200 mg/dL [9]. Prediabetes is diagnosed according to the ADA if fasting glucose ranges between 100-125 mg/dL, which is known as impaired fasting glucose (IFG) and/or postprandial glucose range between 140–200 mg/dL, which is known as impaired glucose tolerance (IGT) [9].

Prediabetes can be controlled, even reversed through very simple treatments or changes in lifestyle; otherwise, when T2D is diagnosed it is not possible to reverse it. Furthermore, it can only be controlled with more expensive treatments that diminished the patient life quality [11]. Therefore, the diagnosis of the prediabetic diseases is crucial to prevent the development of diabetes and thus reduce public health spending [12]. On the other hand, it is known that early diagnosis of T2D can prevent the progression of the disease to other related conditions such as diabetic neuropathy, atherosclerosis, and diabetic foot [13].

There are studies that have used different methodologies to classify prediabetes, T2D and its related diseases (metabolic syndrome and insulin resistance). Some studies have used *k*-means to differentiate diabetic subjects from normal subjects, achieving accuracy classification above 80% [14, 15]. Other studies have designed indices that include anthropometric variables [16], biochemical variables [17] and heart rate variability parameters [18] to classify subjects with insulin resistance, prediabetes and metabolic syndrome, obtaining receiving operating characteristics curves with areas above 0.70 [19]. On the other hand, the area under the glucose (AUC_G) and insulin

(AUC_I) curves during OGTT have also been used to improve the efficiency in the diagnosis of prediabetes, T2D and obesity [20, 21].

The aim of this study is to assess the *k*-means clustering algorithm using AUC_G and AUC_I in the classification of subjects with prediabetes and T2D. A database of 188 subjects with values of glucose and insulin during OGTT was used. In the next section the methodological procedure will be explained. In section three and four, results and discussion will be shown. And finally, in section five, the conclusions and future works proposals will be presented.

2 Methodology

2.1 Database

At the Clinical Research Laboratory of the Venezuela Central University, 188 adults were enrolled (male = 88 subjects, age = 42.11 $\pm$ 14.91 years old), between the years 2010 and 2013. Each participant underwent the 5-samples OGTT. In the OGTT of five samples, insulin and glucose levels were measured in the five different blood samples: a sample in fasting of 8 h (G_0, I_0) and four others after oral intake of 75 g of glucose at 30 min (G_{30}, I_{30},), 60 min (G_{60}, I_{60}), 90 min (G_{90}, I_{90}),and 120 min (G_{120}, I_{120}).

Every participant was classified as T2D according to WHO criteria ($G_0 > 125$ and/or $G_{120} \geq 200$) [22], as prediabetic according to ADA criteria ($140 \leq G_{120} < 200$ and/or $100 \leq G_0 \leq 125$) [9] and as a control group if it does not meet the criteria for T2D or prediabetes. The characteristics of the database are shown in Table 1. The clinical protocol adhered to the principles of the Declaration of Helsinki and it was approved by the Bioethical Committee of the Medical Science Faculty of Venezuela Central University; all the subjects signed a written informed consent.

2.2 *k*-Means Clustering Method

In this investigation the *k*-means clustering algorithm is used to classify the one-dimensional observations [23]. *k*-means technique goal is the partition of the dataset into different clusters, so that observations in each cluster share some similar characteristics. The distance between observations and centroids were calculated by squared Euclidean distance and it was repeated 10 times to avoid local minima. The silhouette coefficient (SC) was used to evaluate the assignment of the dataset into the cluster [24].

Two experiments were carried out using the AUC_I, and two more experiments using the AUC_G. The AUC_G was calculated from the curve constructed with the glucose values of 30, 60 and 90 min of the OGTT. The glucose values of 0 min and 120 min from the OGTT are dismissed because they are dependent variables in the diagnosis of T2D and prediabetes. The AUC_I was calculated from the curve constructed with the insulin values of 0, 30, 60, 90 and 120 min of the OGTT.

Table 1. Glucose and insulin values of the OGTT, AUC_I and AUC_G for prediabetic, diabetic and control groups.

Variables	Control[e] Male = 33, n = 87	Prediabetic Male = 51, n = 85 IGT = 35, IFG = 72 IGT and IFG = 22	T2D Male = 4, n = 16	p-value[a]
Age [years]	35.78 ± 13.02[f] 18.00–75.00[g] 33.05–38.52[h]	46.32 ± 14.69 20.00–78.00 43.20–49.44	54.19 ± 10.24 42.00–72.00 49.17-59.20	<0.01[b,c,d]
G_0 [mg/dl]	90.74 ± 6.23 75.00–99.00 89.43–92.04	104.18 ± 7.45 77.00–119.00 102.59–105.76	134.25 ± 22.17 99.00–187.00 123.39–145.11	<0.01[b,c,d]
G_{30} [mg/dl]	134.10 ± 24.97 85.00–202.00 128.86–139.35	163.54 ± 27.22 100.00–230.00 157.75–169.33	214.81 ± 48.63 135.00–312.00 190.98–238.64	<0.01[b,c,d]
G_{60} [mg/dl]	125.54 ± 31.54 73.00–227.00 118.91–132.17	167.19 ± 39.45 80.00–256.00 158.80–175.58	243.44 ± 53.62 136.00–349.00 217.16–269.71	<0.01[b,c,d]
G_{90} [mg/dl]	111.67 ± 27.45 58.00–198.00 105.90–117.44	149.75 ± 37.47 71.00–245.00 141.79–157.72	243.03 ± 53.63 114.00–326.00 216.75–269.31	<0.01[b,c,d]
G_{120} [mg/dl]	100.03 ± 20.21 51.00–139.00 95.79–104.28	133.52 ± 29.46 72.00–194.00 127.25–139.78	231.69 ± 54.47 105.00–346.00 205.00–258.38	<0.01[b,c,d]
I_0 [μUI/ml]	6.76 ± 8.18 2.00–55.00 5.04–8.48	12.50 ± 20.36 2.00–154.00 8.17–16.82	15.70 ± 15.50 2.00–57.90 8.10–23.29	<0.01[b,c,d]
I_{30} [μUI/ml]	65.38 ± 55.50 12.00–293.00 53.72–77.04	80.15 ± 56.93 16.80–300.00 68.04–92.25	63.38 ± 58.96 15.00–233.00 34.48–92.27	<0.01[b,d]
I_{60} [μUI/ml]	72.22 ± 67.32 5.00–300.00 58.07–86.37	99.60 ± 69.67 10.00–300.00 84.79–114.41	87.14 ± 73.39 26.00–300.00 51.18–123.11	<0.01[b,c,d]
I_{90} [μUI/ml]	64.43 ± 64.74 8.79–300.00 50.83–78.03	96.32 ± 66.42 7.00–300.00 82.20–110.44	94.57 ± 74.13 26.00–300.00 58.25–130.89	<0.01[b,c,d]
I_{120} [μUI/ml]	53.74 ± 54.59 3.76–300.00 42.27–65.22	86.88 ± 62.35 7.00–300,00 73.63–100.14	100.87 ± 88.02 20.00–300.00 57.74–144.00	<0.01[b,c,d]
AUC_I [(μUI/ml) min]	6968.43 ± 6056.84 1248.60–31780.50 5695.68–8241.17	9772.55 ± 6137.39 2055.00–31087.50 8467.79–11077.31	9101.12 ± 7424.06 2385.00–30358.50 5463.33–12738.91	<0.01[b,d]
AUC_G[i] [(mg/ml) min]	7452.76 ± 1591.46 4425.00–12435.00 7118.34–7787.18	9715.06 ± 1967.07 5175.00–13905.00 9296.88–10133.24	14170.78 ± 2956.88 7815.00–19650.00 12721.91–15619.65	<0.01[b,c,d]

[a]Statistically significant difference if p-value < 0.01.
[b]Statistically significant differences between control and prediabetic group.
[c]Statistically significant differences between control and diabetic group.
[d]Statistically significant differences between prediabetic and diabetic group.
[e]Control subjects are those who do not belong to any of the groups with pathology.
[f]Average and standard deviation.
[g]Maximum and minimum value.
[h]95% confidence interval.
[i]The AUC_G was calculated from the glucose values of 30, 60 and 90 min from OGTT since the values of glucose of 0 and 120 min from OGTT are dependent variables of prediabetes and T2D diagnosis.

The two experiments using AUC_I and AUC_G were made as follow:

i. First experiment: The number of clusters used was set to k = 2, in order to see if the algorithm is able to group the observations into subjects with and without T2D.
ii. Second Experiment: The number of clusters used was set to k = 3 to group observations according to T2D, prediabetes and control group.

To evaluate the performance of *k*-means algorithm clustering to group T2D, prediabetic and control subjects, the accuracy (ACC), precision (P) and recall (R) were computed in each experiment [25].

2.3 Statistical Analysis

Two nonparametric statistical tests were used in this study:

i. The Kruskal-Wallis nonparametric statistical test was used to find significant differences between groups of three or more variables.
ii. The Mann-Whitney U test was used as post-hoc to determine the differences between groups of two.

A p value less than or equal to 5% was considered to be statistically significant [26]. The data in the text and in the tables are presented as values of mean and standard deviation, minimum and maximum values and 95% confidence interval.

Table 2. Best clustering results for k = 2, k = 3, accuracy, precision, recall and SC using AUC_I.

AUC_I		SC	T2D (n = 16)	Prediabetic (n = 85)	Control (n = 87)
k = 2 ACC = 0.79[g] P = 0.49 R = 0.50	Cluster 1 (n = 162)	0.71 ± 0.19	14[a] 87.5%[b]	70[c] 82.4%[d]	78[e] 89.7%[f]
	Cluster 2 (n = 26)		2 12.5%	15 17.6%	9 10.3%
k = 3 ACC = 0.55 P = 0.44 R = 0.42	Cluster 1 (n = 135)	0.64 ± 0.18	11 68.8%	53 62.4%	71 81.6%
	Cluster 2 (n = 12)		2 12.5%	6 7.1%	4 4.6%
	Cluster 3 (n = 41)		3 18.8%	26 30.6%	12 13.8%

[a]Number of subjects belongs to the T2D group and classify to a respective cluster.
[b]Percentage of subjects belongs to the T2D group and classify to a respective cluster.
[c]Number of subjects belongs to the prediabetic group and classify to a respective cluster.
[d]Percentage of subjects belongs to the prediabetic group and classify to a respective cluster.
[e]Number of subjects belongs to the control group and classify to a respective cluster.
[f]Percentage of subjects belongs to the control group and classify to a respective cluster.
[g]To construct the confusion matrix for the calculation of accuracy, precision and recall, the assignment of each cluster was made as follow: In the case of k = 2, the cluster 1 and cluster 2 were assigned as a predicted control-prediabetic and cluster 2 predicted T2D group, respectively. In the case of k = 3, the cluster 2, cluster 3 and cluster 1 were assigned as s predicted T2D, prediabetics and control groups, respectively.

Table 3. Best clustering results for k = 2, k = 3, accuracy, precision, recall and SC using AUC_G.

AUC_G		SC	T2D (n = 16)	Prediabetic (n = 85)	Control (n = 87)
k = 2 ACC = 0.76[g] P = 0.62 R = 0.83	Cluster 1 (n = 60)	0.60 ± 0.18	15[a] 93.8%[b]	39[c] 45.9%[d]	6[e] 6.9%[f]
	Cluster 2 (n = 128)		1 6.3%	46 54.1%	81 93.1%
k = 3 ACC = 0.70 P = 0.65 R = 0.75	Cluster 1 (n = 78)	0.62 ± 0.19	1 6.3%	55 64.7%	22 25.3%
	Cluster 2 (n = 80)		1 6.3%	16 18.8%	63 72.4%
	Cluster 3 (n = 30)		14 87.5%	14 16.5%	2 2.3%

[a]Number of subjects belongs to the T2D group and classify to a respective cluster.
[b]Percentage of subjects belongs to the T2D group and classify to a respective cluster.
[c]Number of subjects belongs to the prediabetic group and classify to a respective cluster.
[d]Percentage of subjects belongs to the prediabetic group and classify to a respective cluster.
[e]Number of subjects belongs to the control group and classify to a respective cluster.
[f]Percentage of subjects belongs to the control group and classify to a respectively cluster.
[g]To construct the confusion matrix for the calculation of accuracy, precision and recall, the assignment of each cluster were made as follow: In the case of k = 2, the cluster 2 and cluster 1 were assigned as a predicted control-prediabetic group and predicted T2D group, respectively. In the case of k = 3, the cluster 3, cluster 1 and cluster 2 were assigned as a predicted T2D, prediabetics and control groups, respectively.

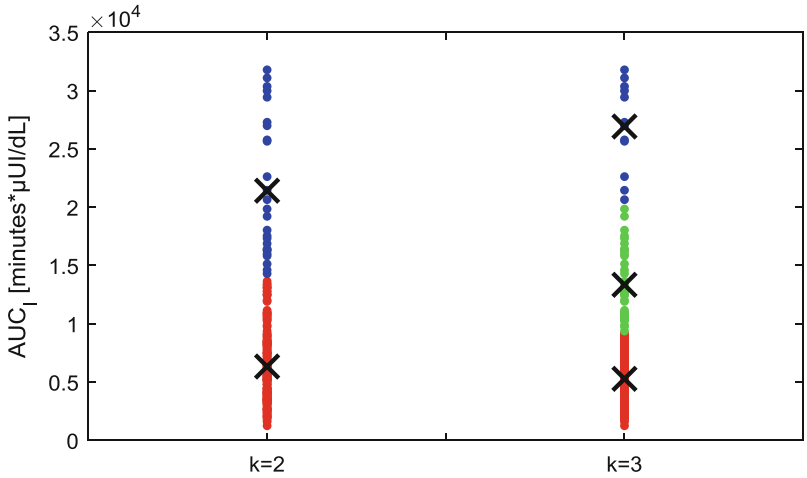

Fig. 1. Assignment of individuals (circles) to clusters for k = 2 and k = 3, using AUC_I. For k = 2, red circles belong to cluster 1 and blue circles to cluster 2, while for k = 3, red circles belong to cluster 1, blue circles to cluster 2 and green circles to cluster 3. Cluster centroids are represented by the character X.

3 Results

Table 1 reports the glucose and insulin values of the OGTT, the values of AUC_I and the modified version of AUC_G for the subjects with prediabetes, T2D and the control group. The database consists of 188 subjects, 46.6% belongs to the control group, 45.2% belongs to the prediabetic group and 8.5% endure T2D. Additionally, 25.9% of the subjects from the prediabetic group suffer from IGT and IFG in concomitance.

Tables 2 and 3 show the best clustering results of AUC_I and AUC_G, additionally, they report the silhouette coefficient, accuracy, precision and recall for k = 2 and k = 3. In the case of k = 2, to estimate the accuracy, precision and recall, the control and the prediabetics subjects were unified as one only group.

Figures 1 and 2 show the assignment of individuals to clusters for k = 2 and k = 3, using AUC_I and AUC_G, respectively, and the character X represents the centroids in each cluster.

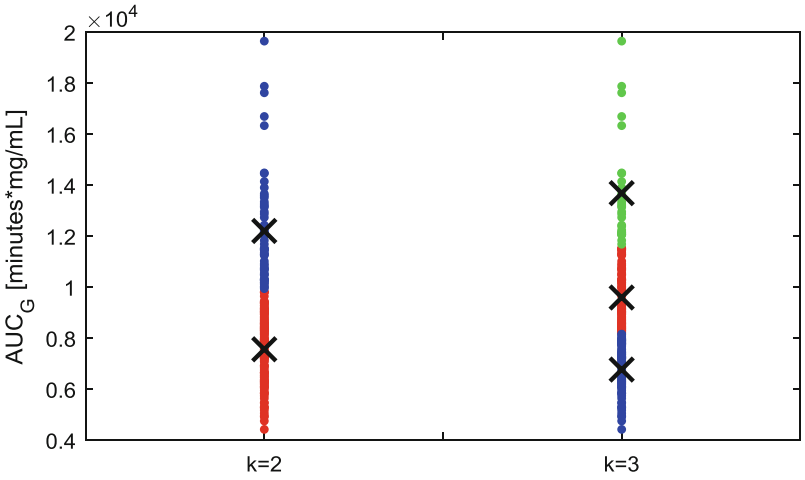

Fig. 2. Assignment of individuals (circles) to clusters for k = 2 and k = 3 using AUC_G. For k = 2, red circles belong to cluster 1 and blue circles to cluster 2, while for k = 3, red circles belong to cluster 1, blue circles to cluster 2 and green circles to cluster 3. Cluster centroids are represented by the character X.

4 Discussion

Table 1 shows significant statistical differences in the ages between all groups. The subjects with T2D show higher values of age than the prediabetic subjects, and these have a higher age than the control subjects. This could indicate that the prevalence of T2D as well as the risk of developing diabetes increase with age [27].

On the other hand, the AUC_I of the control and T2D subjects have not statistically significant differences, nevertheless, in the AUC_G, the T2D subjects have a higher AUC_G than the control subjects. All this indicates that control and T2D subjects have a similar insulin production; however, that is not reflected in the metabolism of glucose. This is consistent with researches that indicate the production of insulin does not ensure the correct metabolization of glucose [28]. In the same sense, it could be observed that prediabetic subjects have higher values of AUC_I compared to control subjects. It was also observed that the AUC_G is significantly higher in the prediabetic subjects compared to the control subjects. All this indicates that alterations in glucose absorption can be seen even in a prediabetic phase [29].

The *k*-means clustering performed for AUC_I and AUC_G presents acceptable results since the SC is above 0.6 in all cases. In Table 2, it can be seen that the *k*-means from the AUC_I values are not able to differentiate between prediabetic, T2D and the control subjects. In the case of k = 2, most of the T2D (87.5%), prediabetic (82.4%) and the control (89.7%) subjects are located in cluster 1. In the case of k = 3, most of the T2D (68.8%), prediabetic (62.4%) and the control (81.6%) subjects are located in cluster 2. On the other hand, it can be stated that although the AUC_I can identify the subjects without T2D, which explains the high accuracy in the case of k = 2 (ACC = 0.79), it cannot detect the subjects with T2D, which it is reflected in the low recall and precision values (P = 0.49, R = 0.50).All these indicate that the *k*-means method is not capable to differentiate between prediabetic, T2D and control with the AUC_I in this sample.

In Fig. 1, it can be observed that the subjects with higher AUC_I are in the cluster 1, and the subjects with lower AUC_I in the cluster 2, it is known that the higher AUC_I is related with the insulin resistance [30]. Insulin resistance is a condition that can appear in normal subjects, prediabetics subjects, or T2D subjects indistinctly. These facts suggest that the incapability of AUC_I *k*-means clustering to differentiate subjects with T2D and prediabetes could be due to the presence of insulin resistance in the three groups that bias the results [30].

Table 3 shows that AUC_G *k*-means clustering was able to classify the T2D, prediabetic and control subjects with accuracy and recall above 0.70 and precision above 0.60. Additionally, in the case of k = 2, in cluster 1 was located the 93.8% of the T2D subjects and 45.9% of prediabetic subjects; in cluster 2 was located the 93.1% and 54.1% of control and prediabetics subjects respectively. The prediabetic subjects located in cluster 1, 56% endure IFG and IGT in concomitance, also indicating that the *k*-means method was able to differentiate those subjects with high probabilities of developing T2D [30]. In the case of k = 3, it could be observed that 87.5% of the T2D subjects were located in cluster 3, 72.4% of the control subjects were located in cluster 2 and 64.7% of the prediabetic subjects were located in cluster 1. The 16.5% of prediabetics subjects located in cluster 3 suffer from IFG and IGT in concomitance; also they have the highest values of AUC_I and AUC_G. All these are in consistency with the findings with the k = 2 *k*-means clustering, where it was observed that the *k*-means method classifies as diabetic those subjects with high probabilities of developing T2D [31].

5 Conclusions

The findings in this study indicate that the *k*-means applied in the AUC_G classify subjects with T2D, prediabetes and the control group. Furthermore, it could even predict those subjects with high probabilities of developing T2D.

On the other hand, it was observed that the classifier does not work in the case of the AUC_I. This could be due to the fact that the T2D and the control subjects could produce comparable amounts of insulin, thus, the difference is not perceptible in the insulin values but in the values of glucose, because although they produce insulin, the correct metabolism of glucose does not occur. Another explanation is the presence of other associated diseases such as insulin resistance in all groups that could be biasing the results.

In this work, an unsupervised machine learning technique was used to identify subjects with T2D and prediabetes, other machine learning techniques such as neural networks and support vector machine will be explored in the future to assess the T2D diagnosis. Additionally, since the increment of the age has a direct proportional relationship with the prevalence of T2D, it would be interesting to investigate machine learning techniques using the age as a variable for the study.

Acknowledgments. This work was funded by the Research Vice-rectorate of the University Antonio Nariño, and the Research and Development Deanery of the Simón Bolívar University (DID) and Pontifical Bolivarian University.

References

1. Rowley, W.R., Bezold, C., Arikan, Y., Byrne, E., Krohe, S.: Diabetes 2030: insights from yesterday, today, and future trends. Popul. Health Manage. **20**(1), 6–12 (2017)
2. Nathanson, D., Sabale, U., Eriksson, J.W., Nyström, T., Norhammar, A., Olsson, U., Bodegård, J.: Healthcare cost development in a type 2 diabetes patient population on glucose-lowering drug treatment: a nationwide observational study 2006–2014. PharmacoEconomics-open **2**(4), 393–402 (2018)
3. Islam, S.M.S., Lechner, A., Ferrari, U., Laxy, M., Seissler, J., Brown, J., Holle, R.: Healthcare use and expenditure for diabetes in Bangladesh. BMJ Glob. Health **2**(1), e000033 (2017)
4. Eshwari, K., Kamath, V.G., Rao, C.R., Kamath, A.: Annual cost incurred for the management of type 2 diabetes mellitus—a community-based study from coastal Karnataka. Int. J. Diabet. Dev. Countries **39**(3), 590–595 (2019)
5. Karter, A.J., Parker, M.M., Solomon, M.D., Lyles, C.R., Adams, A.S., Moffet, H.H., Reed, M.E.: Effect of out-of-pocket cost on medication initiation, adherence, and persistence among patients with type 2 diabetes: the diabetes study of Northern California (DISTANCE). Health Serv. Res. **53**(2), 1227–1247 (2018)
6. Misra, A., Gopalan, H., Jayawardena, R., Hills, A.P., Soares, M., Reza-Albarrán, A.A., Ramaiya, K.L.: Diabetes in developing countries. J. Diabetes **11**(7), 522–539 (2019)
7. Narayan, K.V., Fleck, F.: The mysteries of type 2 diabetes in developing countries. Bull. World Health Organ. **94**, 241–242 (2016)

8. Dagogo-Jack, S.: Primary prevention of type 2 diabetes: an imperative for developing countries. In: Diabetes Mellitus in Developing Countries and Underserved Communities, pp. 7–31. Springer, Cham (2017)
9. American Diabetes Association2: Classification and diagnosis of diabetes: standards of medical care in diabetes—2018. Diabetes Care, **41**(Suppl. 1), S13-S27 (2018)
10. Kim, J.Y., Michaliszyn, S.F., Nasr, A., Lee, S., Tfayli, H., Hannon, T., Arslanian, S.: The shape of the glucose response curve during an oral glucose tolerance test heralds biomarkers of type 2 diabetes risk in obese youth. Diabetes Care **39**(8), 1431–1439 (2016)
11. Hays, L.M., Hoen, H.M., Slaven, J.E., Finch, E.A., Marrero, D.G., Saha, C., Ackermann, R.T.: Effects of a community-based lifestyle intervention on change in physical activity among economically disadvantaged adults with prediabetes. Am. J. Health Educ. **47**(5), 266–278 (2016)
12. Khan, T., Tsipas, S., Wozniak, G.: Medical care expenditures for individuals with prediabetes: the potential cost savings in reducing the risk of developing diabetes. Popul. Health Manage. **20**(5), 389–396 (2017)
13. Zheng, Y., Ley, S.H., Hu, F.B.: Global aetiology and epidemiology of type 2 diabetes mellitus and its complications. Nat. Rev. Endocrinol. **14**(2), 88 (2018)
14. Qu, H.Q., Li, Q., Rentfro, A.R., Fisher-Hoch, S.P., McCormick, J.B.: The definition of insulin resistance using HOMA-IR for Americans of Mexican descent using machine learning. PLoS One **6**(6), e21041 (2011)
15. Patil, B.M., Joshi, R.C., Toshniwal, D.: Hybrid prediction model for type-2 diabetic patients. Expert Syst. Appl. **37**(12), 8102–8108 (2010)
16. Velásquez, J., Severeyn, E., Herrera, H., Encalada, L., Wong, S.: Anthropometric index for insulin sensitivity assessment in older adults from Ecuadorian highlands. In: 12th International Symposium on Medical Information Processing and Analysis, vol. 10160, p. 101600S. International Society for Optics and Photonics, January 2017
17. Velásquez, J., Herrera, H., Encalada, L., Wong, S., Severeyn, E.: Análisis dimensional de variables antropométricas y bioquímicas para diagnosticar el síndrome metabólico. Maskana **8**, 57–67 (2017)
18. Velásquez, J., Severeyn, E., Herrera, H., Astudillo-Salinas, F., Wong, S.: Dimensional analysis of heart rate variability parameters for metabolic dysfunctions diagnosis. In: 2017 IEEE Second Ecuador Technical Chapters Meeting (ETCM), pp. 1–6, October 2017
19. Severeyn, E., Velásquez, J., Herrera, H., Wong, S.: Random sub-sampling cross validation for empirical correlation between heart rate variability, biochemical and anthropometrics parameters. In: Conference on Information Technologies and Communication of Ecuador, pp. 347–357. Springer, Cham (2018)
20. Potteiger, J.A., Jacobsen, D.J., Donnelly, J.E.: A comparison of methods for analyzing glucose and insulin areas under the curve following nine months of exercise in overweight adults. Int. J. Obesity **26**(1), 87 (2002)
21. Abdul-Ghani, M.A., Lyssenko, V., Tuomi, T., DeFronzo, R.A., Groop, L.: The shape of plasma glucose concentration curve during OGTT predicts future risk of type 2 diabetes. Diabetes/Metab. Res. Rev. **26**(4), 280–286 (2010)
22. World Health Organization: Definition and diagnosis of diabetes mellitus and intermediate hyperglycaemia: report of a WHO/IDF consultation (2006)
23. Hartigan, J.A., Wong, M.A.: Algorithm as 136: a kmeans clustering algorithm. J. Roy. Stat. Soc. Ser. C (Appl. Stat.) **28**(1), 100–108 (1979)
24. Rousseeuw, P.J.: Silhouettes: a graphical aid to the interpretation and validation of cluster analysis. J. Comput. Appl. Math. **20**, 53–65 (1987)
25. Powers, D.: Evaluation: from precision, recall and F1-measure to ROC, informedness, markedness and correlation (2011)

26. Marusteri, M., Bacarea, V.: Comparing groups for statistical differences: how to choose the right statistical test? Biochem. Medica: Biochem. Medica **20**(1), 15–32 (2010)
27. Menke, A., Casagrande, S., Geiss, L., Cowie, C.C.: Prevalence of and trends in diabetes among adults in the United States, 1988–2012. JAMA **314**(10), 1021–1029 (2015)
28. Tangvarasittichai, S.: Oxidative stress, insulin resistance, dyslipidemia and type 2 diabetes mellitus. World J. Diabetes **6**(3), 456 (2015)
29. Burgeiro, A., Cerqueira, M., Varela-Rodríguez, B., Nunes, S., Neto, P., Pereira, F., Carvalho, E.: Glucose and lipid dysmetabolism in a rat model of prediabetes induced by a high-sucrose diet. Nutrients **9**(6), 638 (2017)
30. Vintimilla, C., Wong, S., Astudillo-Salinas, F., Encalada, L., Severeyn, E.: An aide diagnosis system based on *k*-means for insulin resistance assessment in eldery people from the Ecuadorian highlands. In: 2017 IEEE Second Ecuador Technical Chapters Meeting (ETCM), pp. 1–6, October 2017
31. Anjana, R.M., Rani, C.S.S., Deepa, M., Pradeepa, R., Sudha, V., Nair, H.D., Mohan, V.: Incidence of diabetes and prediabetes and predictors of progression among Asian Indians: 10-year follow-up of the Chennai urban rural epidemiology study (CURES). Diabetes Care **38**(8), 1441–1448 (2015)

Biomechanics

Development of a Protocol for the Evaluation of the Mechanical Behavior of a Transtibial Prosthesis by Infrared Thermography

Natali Olaya Mira[1,2(✉)] and Carolina Viloria Barragán[1]

[1] Grupo de Investigación e Innovación Biomédica, Instituto Tecnológico Metropolitano (ITM), Medellín, Colombia
{nataliolaya, carolinaviloria}@itm.edu.co
[2] Laboratorio de Biomecánica y Rehabilitación, Instituto Tecnológico Metropolitano (ITM), Medellín, Colombia

Abstract. Temperature is one of the most common indicators of the structural health of devices and components. In recent times, infrared thermography has become a mature and widely accepted monitoring technique to measure temperatures in real time in a non-contact manner. In the clinical context, it is also used to study some diseases or the mechanical behavior of endoprostheses. However, the assessment of exoprostheses has been limited to gait analysis or the study of their interaction with residual limbs. The aim of this work is to assess thermography as a tool for evaluating mechanical stresses in a transtibial prosthesis through the development of a protocol that allows the identification of critical points. A transtibial prosthesis was recorded undergoing mechanical stress during the stance phase using a device that simulates the human gait and a thermal camera. A protocol was developed to detect critical thermal points that could reveal areas with the greatest concentration of such stress in a gait test. It can be concluded that thermography can be used as tool for assessing lower limb prostheses in dynamic tests because it is a non-invasive method and its results can be obtained in real time.

Keywords: Thermography · Prosthesis · Mechanical stress · Gait simulation

1 Introduction

The study of lower limb prostheses has been limited to the evaluation of prosthetic walking performance and biomechanical assessments of gait kinematics, plantar foot pressure, and contact interface between the residual limb and the prosthetic socket. Nevertheless, the behavior of prostheses must be evaluated in terms of prosthetic component design and prosthetic alignment to make them cost-effective for clinical applications [1–3].

Some approaches using modern computational techniques have gained popularity, especially in cases where detailed and complex information about the behavior of the prostheses should be obtained but also validated by experimental models [2]. Mechanical stress is difficult to assess in complex experimental situations, but thermography can be a

© Springer Nature Switzerland AG 2020
C. A. González Díaz et al. (Eds.): CLAIB 2019, IFMBE Proceedings 75, pp. 805–811, 2020.
https://doi.org/10.1007/978-3-030-30648-9_106

useful tool to validate theoretical results, providing information about the mechanical behavior [4].

Thermography has been applied in the mechanical field as a non-destructive, real-time, and non-contact testing technology. Some methods have been developed over the years in order to correlate growing temperatures to physical processes of damage and failure in materials [5, 6]. The use of Infra-Red Thermography (IRT) to study thermal effects in mechanics requires knowledge of the material (e.g., the emissivity of its surface and melting point, among others) as well as controlling external and environmental parameters (e.g., temperature, pressure, and humidity) [7, 8].

Therefore, a novel IRT protocol is needed to assess the mechanical behavior of lower limb prostheses in a gait simulation device to complement regular assessment methods regarding walking performance devices.

2 Materials and Methods

The objective of the approach proposed in this work is to characterize the critical points in a prosthesis simulating the stance phase of gait by observing important changes in its temperature and revealing mechanical stress with an IR camera.

The walking cycle was simulated by a prototype device applying 980 N to the prosthesis supported on a tilting platform with a cadence of 90 steps/min. The movement was synchronized by the configuration of two different pneumatic actuators. The first one applied the simulated weight to the prosthesis, while the second one moved the platform according to the ground reaction force vector during the stance phase [9], its speed affects the calculation of the cadence.

A FLIR A655SC thermal camera (FLIR systems Inc., Portland, U.S.) was used to record temperature changes in the long wavelengths of the infrared band from 7.5 to 14 μm with a spatial resolution of 640 × 480 pixels, an accuracy of ±2 °C, a NETD under 30 mK, and a FOL25 lens. Said camera uses the software FLIR R&D 3.3.

The protocol was implemented in a laboratory with controlled atmospheric temperature (22 °C) and relative humidity (42%). These measurements were made with instruments external to the camera as a way to test the reliability of the temperature measurements.

3 Results

The protocol developed in this work represents a non-destructive and non-contact measurement technique that offers high resolution in real time for IR images. Such images allow the identification of relevant zones where important thermal changes occur due to the mechanical stress the prosthesis undergoes.

3.1 Initial Setup

The most important factor in this test is extensive knowledge of the material properties of the prosthesis under evaluation because that information is needed to configure the protocol. Such properties include emissivity, reflected temperature, and object distance; in this test, those parameters were 0.97, 22.9 °C, and 0.84 m, respectively.

The camera must be turned on and left unoperated for some time so that it stabilizes and the registered temperature equals room temperature. Subsequently, it is important to define geometric parameters depending on the region of interest and the object distance reported above, making sure that the selected area is not affected by external elements.

3.2 Spatial Setup

The prosthesis was aligned to reproduce ankle kinematics during gait. The foot was slightly shifted forward and, therefore, the camera was placed in a specific configuration not to interfere with the temperature measurement. Six camera positions were defined to record short videos in the frontal and rear planes of the device, thus establishing three strategic positions which, together, offer a complete view of the prosthesis. The side views were not recorded due to the interference of the platform axis with the acquisition of the image (See Fig. 1).

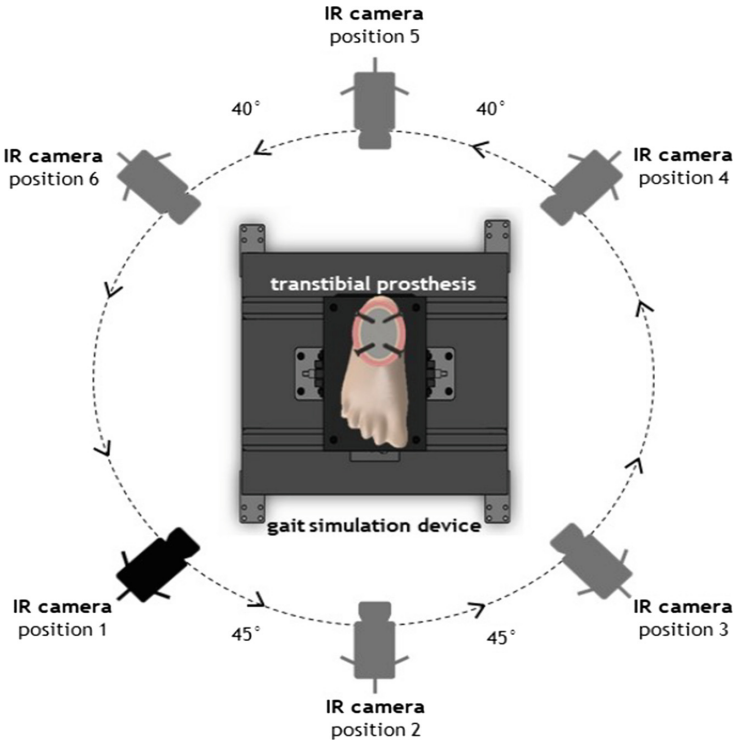

Fig. 1. Camera positions around the prosthesis.

3.3 Temporal Setup

The duration of the short videos depended on the gait parameters established above. Cadence indicated the number of steps by means of a time unit. Hence, the aim was to record at least three gait cycles to analyze the frames in the middle of the recording. Likewise, the limit record rate had to be defined by the frequency of frames and recording some footage during the initial contact and terminal stance of gait. A series of 15 s videos was recorded in each position, with a 5 min interval every hour. Such time intervals were defined in order to acquire the videos and analyze temperature changes as the number of cycles increased.

3.4 Image Acquisition

A series of frames was selected from the recorded videos for analysis. After only one hour of motion simulation, images were acquired in each position, as shown in Figs. 2 and 3, where different isothermal areas can be observed. The areas where the prosthesis underwent the greatest stresses, by repetition and load, display temperatures between 27 and 30 °C, while in the gait device or the regions of less stress they fluctuate between 21 and 25 °C. Furthermore, all the critical points in the prosthesis during the dynamic test simulating human gait can be identified by TIR analysis.

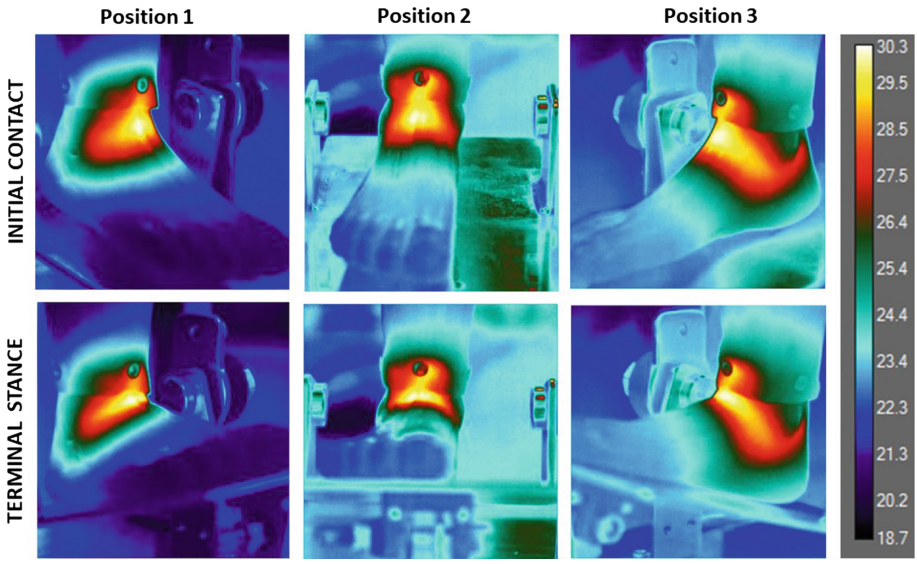

Fig. 2. Thermal images - frontal plane

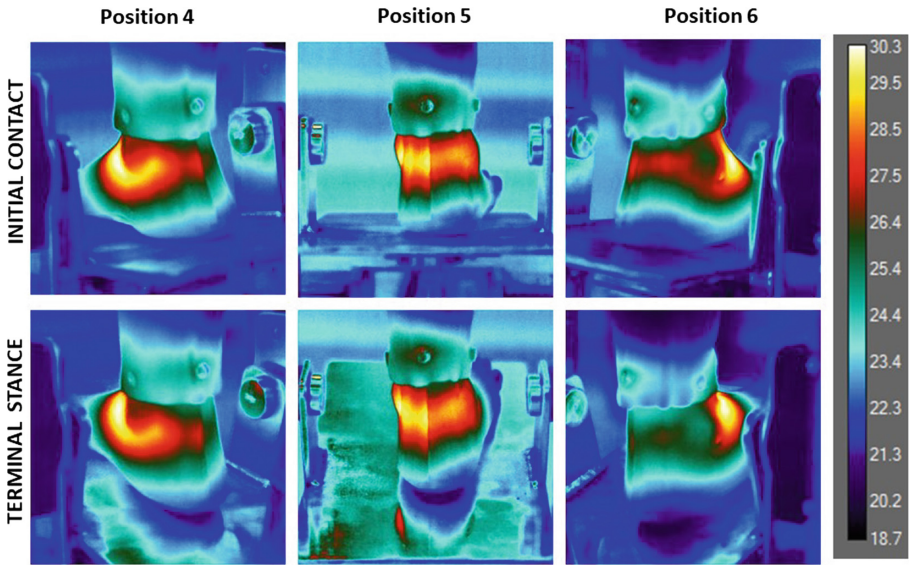

Fig. 3. Thermal images - rear plane

4 Discussion

Several authors have published studies on thermography applications for monitoring structures in mechanical, electrical, and electronic fields, as well as for the diagnosis and characterization of diseases in the medical area or the behavior of endoprostheses under stress [10–13]. In such studies, adequate measures were taken to acquire reliable infrared thermal images under different conditions for accurate IRT measurement [14]. Those measures were intended to address procedural, technical, and environmental factors such as the view angle of the camera, characteristics of the object under investigation, and external conditions. Almost all those parameters were taken into account in the present protocol.

The results of this protocol show temperature changes over a one-hour test. A longer test would enable researchers not only to identify points but also track changes in said points, thus data vs. number of gait cycles could be graphed and even extrapolated to predict fatigue [5, 7, 12, 13].

Moreover, regarding the materials of the prosthesis studied in this work, the vulcanized rubber foot attached to the high density polyethylene cylinder exhibited changes of around 4 °C after only one hour of testing. Accordingly, polymers are very sensitive to the strain rate; hence, the higher the strain rate, the greater the stress and the more likely the temperature changes [7].

5 Conclusions

Thermography is an optimal method to identify isothermal areas in real time. In this work, such fast and non-invasive technique was employed to monitor the mechanical behavior of a prosthesis using a gait simulation device. The area of maximum stress concentration and increases in temperature are immediately visible during the dynamic test.

Therefore, an image acquisition protocol should be established to provide guidance on the variables that influence the test results. This protocol provides a global view of the prosthesis during the application of loads in a gait cycle and, therefore, it allows the identification of the area of greatest stress and the assessment of different prosthesis designs.

This protocol complements regular lower limb prosthesis evaluation methods, because basic gait parameters evaluated in other methodologies are the inputs in this original method making possible to give additional specific information about mechanical performance of prosthesis, which is not traditionally analyzed in prosthetic devices assessment.

Acknowledgments. This work was carried out as part of project P17204 funded by Instituto Tecnológico Metropolitano through its 2016 internal call for proposals. We also thank our colleague Ph.D. Gloria María Díaz Londoño, who provided insights and expertise that greatly assisted our work.

Conflict of Interest. None declared.

References

1. Luengas Contreras, L.A., Camargo Casallas, E., Guardiola, D.: Modelagem e simulação da marcha protética usando modelo em 3D de uma prótese transtibial. Rev. Ciencias la Salud **16** (1), 82–100 (2018). https://doi.org/10.12804/revistas.urosario.edu.co/revsalud/a.6492
2. Omasta, M., Paloušek, D., Návrat, T., Rosický, J.: Finite element analysis for the evaluation of the structural behaviour, of a prosthesis for transtibial amputees. Med. Eng. Phys. **34**(1), 38–45 (2012). https://doi.org/10.1016/j.medengphy.2011.06.014
3. Junqueira, D.M., Gomes, G.F., Silveira, M.E., Ancelotti, A.C.: Design optimization and development of tubular isogrid composites tubes for lower limb prosthesis. Appl. Compos. Mater. **26**(1), 273–297 (2019). https://doi.org/10.1007/s10443-018-9692-2
4. Chrysochoos, A.: Infrared thermography applied to the analysis of material behavior: a brief overview. Quant. Infrared Thermogr. J. **9**(2), 193–208 (2012). https://doi.org/10.1080/17686733.2012.746069
5. Wang, X.G., Crupi, V., Guo, X.L., Zhao, Y.G.: Quantitative thermographic methodology for fatigue assessment and stress measurement. Int. J. Fatigue **32**(12), 1970–1976 (2010). https://doi.org/10.1016/j.ijfatigue.2010.07.004
6. Chandraprakash, C., Krishnamurthy, C.V., Balasubramaniam, K.: Thermomechanical phenomenon: a non-destructive evaluation perspective. Trans. Indian Inst. Met. (2019). https://doi.org/10.1007/s12666-019-01656-6

7. Pieczyska, E.A., Maj, M., Kowalczyk-Gajewska, K., Staszczak, M., Urbanski, L., Tobushi, H., et al.: Mechanical and infrared thermography analysis of shape memory polyurethane. J. Mater. Eng. Perform. **23**(7), 2553–2560 (2014). https://doi.org/10.1007/s11665-014-0963-2
8. Duchene, P., Chaki, S., Ayadi, A., Krawczak, P.: A review of non-destructive techniques used for mechanical damage assessment in polymer composites. J. Mater. Sci. **53**, 7915–7938 (2018). https://doi.org/10.1007/s10853-018-2045-6
9. Marasović, T., Cecić, M., Zanchi, V.: Analysis and interpretation of ground reaction forces in normal gait. WSEAS Trans. Syst. **8**(9), 1105–1114 (2009). ISSN 1109-2777
10. Shah, S., Zdero, R., Schemitsch, E.H., Rahim, E., Bougherara, H., Dubov, A.: A preliminary biomechanical assessment of a polymer composite hip implant using an infrared thermography technique validated by strain gage measurements. J. Biomech. Eng. **133**(7), 074503 (2011). https://doi.org/10.1115/1.4004414
11. Bougherara, H., Saleem, M., Shah, S., Toubal, L., Sarwar, A., Schemitsch, E.H., et al.: Stress analysis of a carbon fiber-reinforced epoxy plate with a hole undergoing tension: a comparison of finite element analysis, strain gages, and infrared thermography. J. Compos. Mater. **52**(19), 2679–2689 (2018). https://doi.org/10.1177/0021998317752501
12. Jourdan, F., Muracciole, J.-M., Chrysochoos, A., Huon, V., Wattrisse, B., Peyroux, R.: Use of full-field digital image correlation and infrared thermography measurements for the thermomechanical analysis of material behaviour. Strain **46**(1), 117–130 (2009). https://doi.org/10.1111/j.1475-1305.2009.00635.x
13. Skozrit, I., Frančeski, J., Tonković, Z., Surjak, M., Krstulović-Opara, L., Vesenjak, M., et al.: Validation of numerical model by means of digital image correlation and thermography. Proc. Eng. **101**(C), 450–458 (2015). https://doi.org/10.1016/j.proeng.2015.02.054
14. Bagavathiappan, S., Lahiri, B.B., Saravanan, T., Philip, J., Jayakumar, T.: Infrared thermography for condition monitoring - a review. Infrared Phys. Technol. **60**, 35–55 (2013). https://doi.org/10.1016/j.infrared.2013.03.006

Assessment of Changes in the Pressure Distribution While Sitting in an Instrumented Cushion During an Undergraduate Class

Freddy L. Bueno-Palomeque(✉), Carlos A. Tamay-Crespo, and Richard M. Ramos-Tituana

Grupo de Investigación en Ingeniería Biomédica GIIB-UPS, Universidad Politécnica Salesiana, Cuenca 010102, Ecuador
fbueno@ups.edu.ec
http://www.ups.edu.ec

Abstract. Acquiring a sedentary posture to develop diary activities is considered like an usual activity in the professional or the educational field. However, a lot of people do not know that this posture causes a high pressure between the seat and the person, which is associated with problems and pain in the low back. This work presents the analysis of the pressure variation between the chair and the user during an hour of undergraduate class; with the goal to provide quantitative information to strengthen the importance of active pauses during a class. To measure, monitor, and save the pressure levels generated, we developed an electronic system using five force sensors. The tests were carried out in the Universidad Politécnica Salesiana (Cuenca-Ecuador) with 10 undergraduate volunteers during 50 ± 6 min. The registered pressure levels were visualized through a graphic user interface in Matlab. The higher pressures were registered on the ischial tuberosities with an average pressure of 16.31 kPa without a backrest and 8.89 kPa with a backrest. In addition, it was developed a finite elements simulation to estimate the contact pressure levels generated between the ischial tuberosity and the muscle tissue, with a maximum pressure calculated of 1.27 MPa, distributed over a 4.49 cm^2 area. The objective of this study is to measure the pressures generated between the chair and the buttocks and to quantitatively characterize the sedentary posture of undergraduate students.

Keywords: Pressure distribution · Sedentary posture · Force sensors · Ischial tuberosity

1 Introduction

In a sedentary posture the body weight is supported by the ischial tuberosities and as a consequence of a long time in the same position, an incorrect posture could induce pain at the low level of the back, even increase the risk of pressure

© Springer Nature Switzerland AG 2020
C. A. González Díaz et al. (Eds.): CLAIB 2019, IFMBE Proceedings 75, pp. 812–821, 2020.
https://doi.org/10.1007/978-3-030-30648-9_107

ulcers development. Commonly, most of the body weight is supported by soft tissue without other points of support to reduce the impact. Here, the pelvis transfers the load to the chair surface. During the professional or scholar diary activities, habitually, it is necessary to hold a sedentary posture; however, many people do not know that this posture, beyond the human biomechanical factors and the physical structure of the seat, is one of the main causes of pain at the low level of the back. Combining an incorrect stance with the development of different diary activities could increase the likelihood of suffering lumbago, herniated disc, arthritis, inflamed tendons, etc. [1]. These medical disorders are related to the lack of movement of the people during the diary activities. To reduce this problem, some authors recommend active pauses of several minutes per every work hour [2,3].

Extensive researches about the pressure distribution on a sedentary posture have shown different methods based on sensors or simulations. Huang et al. [4] used an instrumented seat with 1600 sensors over a 50.8×50.8 cm area on a rigid seat. Ten asymptomatic people were asked to acquire a comfortable stance, registering an average pressure (AP) of 7.64 kPa and maximum pressure of 53.75 kPa. Moes et al. [5], analyzed the pressure distribution and location of the point with maximum pressure on people sat on a rigid, flat and horizontal surface. Using a Kistles platform, the pelvis rotation angle was registered on 20 participants (21.60 ± 2.50 years-old and a body mass of 67.50 ± 9.20 kg). The maximum pressure registered was 170 kPa and the AP on the left ischial tuberosity was 56 kPa and 85 kPa on the right. This study used multiple regression to determine the relation between the pressure generated in a sedentary posture and the body anthropometric characteristics, as well as the influence of the pelvis rotation.

Lewis et al. [6], used a pressure mat to measure the pressure when the people play sports using a wheelchair as a movement device. The results obtained by wheel chair racing athletes, comparing the pressure on a static stance before to start the competition, showed pressures between 7.27 and 16.05 kPa with maximum levels that exceeded the sensor capability of 34.70 kPa. Cazho-Tobar et al. [7], using capacitive sensors, registered an AP of 55.91 kPa on the ischial tuberosity area on people who use a wheelchair as a movement support, distributed on a 12 cm^2 area, which could make them more prone to pressure ulcers development and tissue damaged.

Other researches showed results in the same range. Swain [8] evidenced that pressures oscillate between 8 kPa and 19.50 kPa. Rivas [9] determined that depending on the region of register, it can be between 20 kPa and 70 kPa. In this perspective, the sedentary posture will generally lead to the application of an overload on the contact tissue area and over time it could injure muscles and nerves in the area.

The reduced contact area and the high load supported, leads to a blood circulation reduced through tissues, causing a discomfort sensation and fatigue to the people. These inconveniences make it impossible to hold a static sedentary posture, provoking changes or posture movements to relieve and reduce the pressure. Tamay-Crespo et al. [10] analyzed the sedentary posture of ten students

throughout a period between 8 and 15 min. The results showed that students change their posture approximately 4 min after the test began and additionally determined which are the points where a high pressure is present.

In the scholar environment, Çakmak et al. [11], carried out a descriptive analysis based on polls on 1552 university students. The results evidenced that 40.90% of the participants felt pain at lumbar level. This study allowed to show a relation between the pain at the lumbar area and the people age. Smith et al. [12] researched the prevalence and the different musculoskeletal disorders in students of fourth year of medicine in China. It was collected data through poll to 207 students. The results showed that 31.90% of the students have some kind of medical disorder, 40.10% of theirs had pain at the low back, followed by neck pain (33.80%) and shoulders (21.70%). In Ecuador there are not similar studies focused in identify the relation between musculoskeletal disorders and the sedentary level in undergraduate students. Additionally, it is important to mention the anthropometric differences among Latin Americans and different populations of the world, as a factor that could alter the pressure distribution during a class.

Based on the studies exposed, it is evident the importance of researching and developing new alternatives that allow us to characterize quantitatively the sedentary posture, the pressure generated and its impact on the task development in different activities and fields like the scholar. This study proposes an electronic tool based on force sensors to quantify the pressure levels on sedentary posture and to analyze its variation throughout an academic class.

2 Materials and Methods

This research registered and analyzed the pressure distribution on sedentary posture of 10 volunteer asymptomatic students (age: 23 ± 4 years-old, weight: no more than 85 kg and average height: 173 ± 8 cm) along 50 ± 6 min, inside the Universidad Politécnica Salesiana campus (Cuenca-Ecuador). The volunteers did not evidence pain at low back level during the tests, which were executed at an university classroom in different academic sessions.

The pressure distribution registered between the chair and the volunteer were measured using an electronic system developed by the Grupo de Investigación en Ingeniería Biomédica GIIB-UPS [10]. The system consists of 5 round force sensors located under the ischial tuberosities regions (sensor 1 and 2), under the thighs (sensor 3 and 4) and on the anterior region of the chair, between the legs to detect an incorrect sedentary posture. This non-invasive device facilitates a free position change of the volunteers during the tests.

During the tests the volunteers were asked to hold a stance with the back straight, shoulders back and an angle between the thighs and the backbone of 90° for two minutes. The remaining time of the test, the participants were asked to hold a free posture to attend the academic session. The chairs used did not have adjustable arms and it was not possible to adjust the chair backrest. The test was divided in 4 stages, each one lasting around 11.3 min, according to the results presented by Tokuhama et al. [13], who demonstrated that students can hold an active and stable attention for an period of 10 to 20 min.

In order to estimate the internal stress distribution on soft tissue when people are on sedentary posture, it was used a finite elements model of the pelvis and the muscle tissue. It was developed a three-dimensional (3D) model of the pelvis based on computed tomography scan (CT) of an asymptomatic woman (age: 21 years-old, weight: 56 kg, and height: 172 cm) [14]. This model was meshed using 34068 Tet4 elements and 6665 nodes. The 3D muscle model was meshed using 8000 Hex8 elements and 9261 nodes. The meshed models were exported to Febio v2.0 [15] software for biomechanical analysis using finite elements. The pelvis was characterized as a rigid body with density 1.8e-9 tonne/mm [16]. The muscular tissue was represented using a "Mooney-Rivlin Hyper-elastic" model with 0.38 MPa as the first coefficient (C1), 0.31 MPa for the second coefficient (C2) [17] with density de 1e-9 tonne/mm [18]. A force (F) of 230 N was applied on the pelvis model taking in account the body weight and its impact in a sedentary posture.

3 Results and Discussion

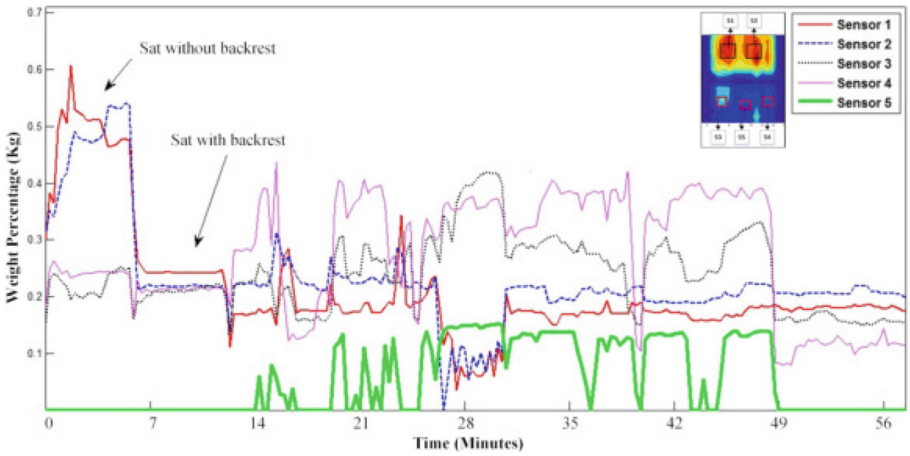

Fig. 1. Normalized pressure distribution on five force sensors during 1 h of class.

Tests developed in this study allowed to register the pressure levels generated in undergraduate students on a sedentary posture in class. The data were normalized considering the maximum weight of the volunteers (39.20 kg) as 1. Figure 1 shows the variation of normalized pressure registered on the ischial tuberosities (sensor 1 and 2) during the tests. Comparing the first period when volunteers did not used a backrest with the second one, sensors 3 and 4 registered a minimum variation with a standard deviation (SD) = ±0.0161 and ±0.0154 kPa respectively and the sensor 5 registered a continuous variation. Figure 2 shows

the AP on each sensor using the backrest and not. Data shows a better pressure distribution when people use the backrest or a lumbar support on a sedentary posture. To determine the pressure distribution symmetry on the sensor 1 and 2, the results obtained on each sensor were statistically compared using *t distribution*, in order to quantify its relation. Results showed that seven out of ten volunteers have a non-significant difference ($p > 0.05$) between sensor 1 and 2; hence, we analyze just the data registered on sensor 2 considering its similarity with the sensor 1. The analysis was made on the data of the seven volunteers with no-statistically significance and the complete register was divided in four stages.

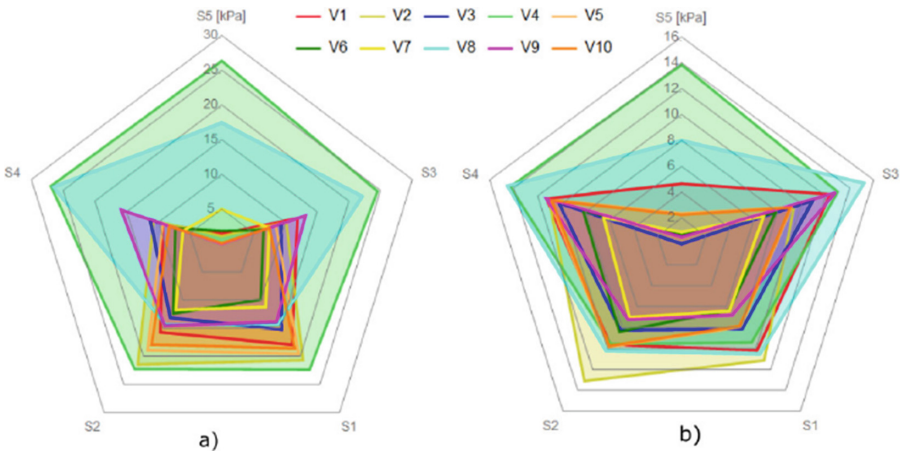

Fig. 2. Averaged pressure on 10 volunteers (V1, V2, .. V10): (a) sat without backrest and (b) sat with backrest.

On the other hand, considering the biomechanical model, Fig. 3a shows the contact area between the 3D model of the pelvis and the muscle. Applying a force (230 N) on the pelvis model, we observed how it is transmitted to the muscular tissue, provoking the generation and distribution of pressure (Fig. 3c). Figure 3b shows the contact pressure generated between the ischial tuberosity and the muscular tissue, with a maximum pressure of 1.27 MPa on a 44.49 cm^2 area. This results support the importance of this kind of studies about the pressure generated on internal tissues on people who stay long time periods on a sedentary posture due the superficial measurements do not reveal the real internal pressure which could provoke damages in the tissues.

The results show that using a backrest or a lumbar support on a sedentary posture, it is possible to redistribute and reduce the pressure generated between the seat and the person mainly on the ischial tuberosities area. This study registered an AP of 16.31 kPa without backrest and 8.89 kPa using it. S1 and S2 registered different pressure values, associated with the lateral tilt of the

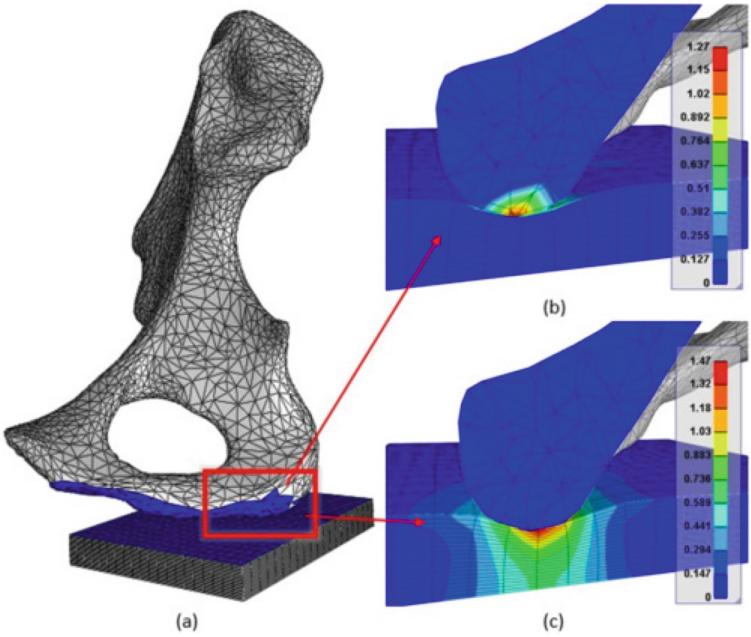

Fig. 3. Finite elements simulation of the contact between the pelvis and the muscle tissue. (a) Pelvis constructed using CT images, (b) contact region when applying a load and (c) maximum pressure generated on the muscle tissue.

volunteers' mass center, distributing asymmetrically the pressure on the ischial tuberosities. Huang et al. [4] found an AP of 7.64 kPa and a maximum pressure of 53.75 kPa. Moreover, Swain [8] evidenced pressure levels between 8.00 kPa and 19.50 kPa on the ischial tuberosities. Moes et al. [5] registered high pressure levels compared with our results; due the straight posture of the volunteers; however, when used a backrest the AP decreased round 8.00 kPa considered a safe pressure level which cannot damage the tissue [6]. This evidence sustain the importance of use a backrest on a sedentary posture to reduce the pressure applied on the different tissues. Contrary to this results, all subjects in our study were asked to get a comfortable stance with no restriction on the movements.

Figure 4a shows the normalized AP and the SD on the ischial tuberosities area (S2) on seven volunteers during the four stages of the test. As shown in Stage 1 the SD values are around 0.02, which is a non-considerable change on the posture in this stage. On stage 2 the normalized AP on volunteers 3 and 5 increase and decrease respectively and for the rest of the volunteers, the AP did not change significantly. Three out of seven volunteers showed an SD over 0.02. Stage 3 and 2 are similar, with the difference that volunteers 1 and 3 showed an increment in the AP. Stage 4 showed an increment on the AP on volunteers 3 and 5 associated with an abrupt change on the sedentary posture; the rest of volunteers' registers were similar to the stage 3.

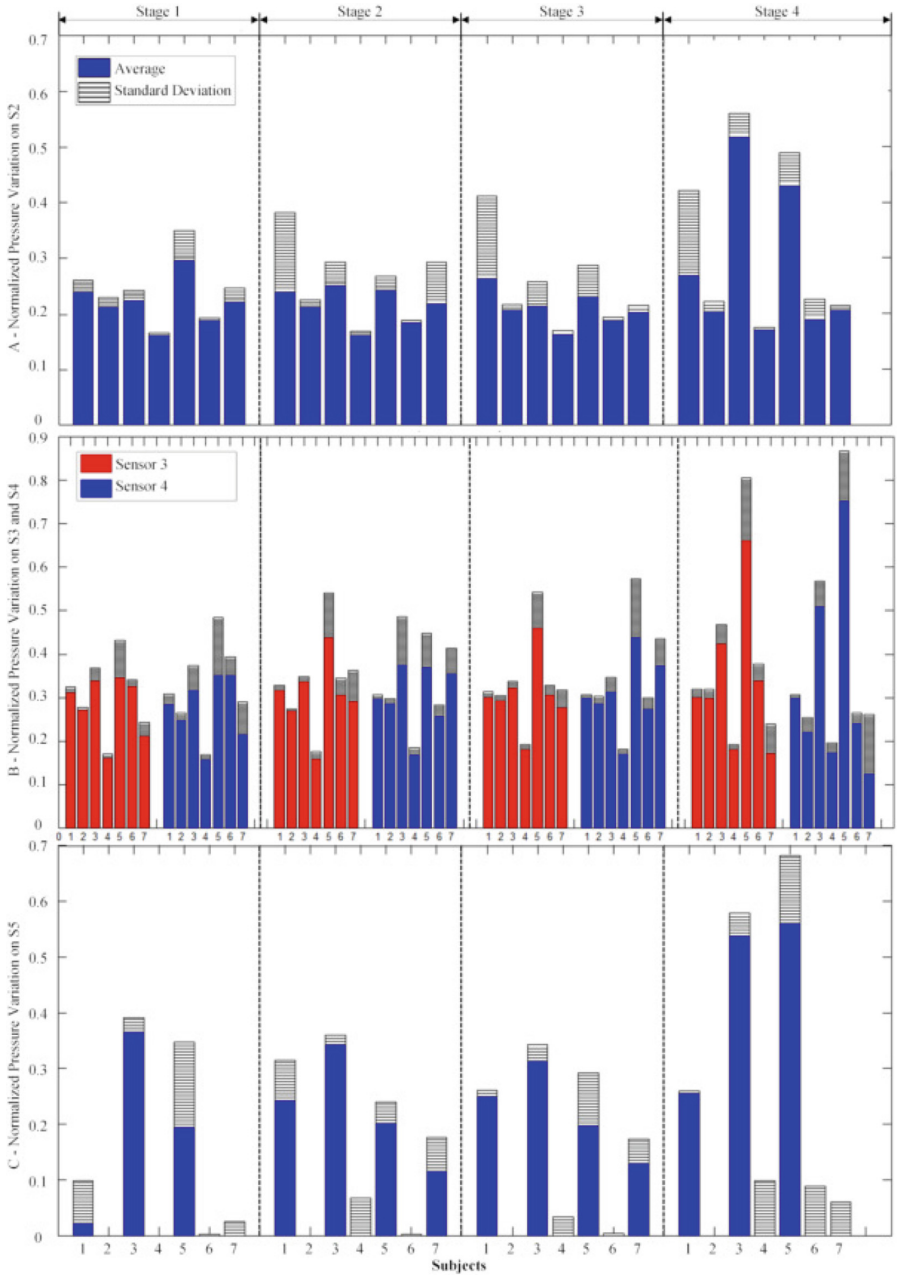

Fig. 4. Normalized AP and SD of the five sensors data registered on seven volunteers during the four stages of an hour of class.

The AP and the SD registered under the thighs (S3 and S4) on seven volunteers is shown in Fig. 4b. The stage 1 shows a similar AP on S3 and S4 but S4 shows a bigger data dispersion. On the stage 2 it is possible to see a postural change, translated in a unequal pressure distribution; additionally, the stage 3 shows that the pressure distribution does not present important changes more than a SD reduction on six out of seven volunteers. Finally, the stage 4 shows again a pressure imbalance between S3 and S4; moreover, the SD values increased due to a postural change and thigh movements. As shown in Fig. 4c, the S5 allows to see when a volunteer is a wrong posture, sat near the anterior border of the chair.

The superficial pressure levels registered using the system allows to recognize and evaluate the risks present when people hold on a sedentary posture; however, according to the simulation results about the internal tissue behavior, there is a high pressure applied on the internal tissues under the ischial tuberosities. As show on Fig. 3, the pressure calculated on the internal tissue (1.27 MPa) is higher than the pressure registered on the chair (8.89 kPa) and its located just under the ischial tuberosities in accordance with the scientific literature [27]; however, the simulation results revealed a pressure seven times higher than other studies. Oomens et al. [19] applied 200 N to the pelvis model and found a pressure of 170 kPa between the internal tissue and the ischial tuberosities decreasing until disappearing 46 mm from the maximum pressure point. Li et al. [20] found a maximum pressure of 150 kPa between the same structures when a load of 150 N was applied. The pressure level decreased in function of the cushion used. This high difference is due the 3D models and the finite elements simulation are sensible to the mechanical properties assigned; furthermore, the 3D pelvis model was developed from CT images, thus the contact region depends on the subject's anthropometric characteristics. Another important factor is the fact that the simulation just considers the contact between the bone and muscular tissues; however, the muscular tissue, in a real scenario, is vascularized and could have nerve fibers around the region. The high pressure level calculated in the simulation is related with the discomfort generated when people hold a sedentary posture along a long period.

4 Conclusion

In this study the pressure generated between a volunteer and a chair was registered, using a force sensors system; additionally, a finite elements simulation was developed to estimate the pressure generated at tissue level. All subjects in this tests presented a high pressure on the ischial tuberosities. The high pressure levels are associated with the continuous posture changes probably associated with the class attention. As the time passed, all subjects changed their posture more frequently and the first 11.30 min (stage 1) was the period where the volunteer showed a low posture change and probably a minor distraction.

The results show that the pressure generated on the chair surface are correctly distributed as long as the person get a correct sedentary posture supporting their

back. This will allow to the person improve the body weight distribution with no overloading the ischial tuberosities. Data registered suggest take in account the periods when people stay in the same posture. In this context, to do an active pause during the academic sessions or work activities is an important habit to prevent from back pain and discomfort on the underlying tissue.

Future work in this research line will have as a main objective to accurately estimate the time to do an active pause during an academic session in order to improve the comfort through a class, reducing the distraction caused by discomfort. A limitation in this study was the number of volunteers, so it is necessary to increase the number of tests and use different chair geometries to improve the results and propose more adequate solutions.

Conflict of Interest. The authors do not have any conflicts of interest.

References

1. Lueder, R.: Ergonomics of seated movement a review of the scientific literature. Ergonomics Review of Humanics Ergosystems, Inc. (2004)
2. Castillo, J.A., Ramírez, B.A.: El análisis multifactorial del trabajo estático y repetitivo. estudio del trabajo en actividades de servicio. Revista Ciencias de la Salud **7**(1) (2009)
3. Thosar, S.S., Bielko, S.L., Mather, K.J., Johnston, J.D., Wallace, J.P.: Effect of prolonged sitting and breaks in sitting time on endothelial function. Med. Sci. Sports Exerc. **47**(4), 843–849 (2015). https://doi.org/10.1249/mss.0000000000000479
4. Huang, S., Zhang, Z., Xu, Z., He, Y.: Modeling of human model for static pressure distribution prediction. Int. J. Ind. Ergon. **50**, 186–195 (2015). https://doi.org/10.1016/j.ergon.2015.09.017
5. Moes, N.C.: Variation in sitting pressure distribution and location of the points of maximum pressure with rotation of the pelvis, gender and body characteristics. Ergonomics **50**(4), 536–561 (2007). https://doi.org/10.1080/00140130601138585
6. Lewis, A.R., Haydon, D.S., Phillips, E.J., Grimshaw, P.N., Robertson, W.S., Portus, M.: Monitoring seating interface pressure in wheelchair sports. Sports Eng., 1–9 (2018). https://doi.org/10.1007/s12283-018-0272-3
7. Cazho-Tobar, J., Barbecho-Sarango, J., Bueno-Palomeque, F.: Pressure ulcer prevention system based in capacitive sensors. In: International Conference on Applied Human Factors and Ergonomics, pp. 518–525. Springer (2017). https://doi.org/10.1007/978-3-319-60597-5_49
8. Swain, I.: The measurement of interface pressure. In: Pressure Ulcer Research: Current and Future Perspectives, pp. 51–71. Springer, Berlin (2005). https://doi.org/10.1007/3-540-28804-X_5
9. Rivas, R.R.: Ergonomía en el diseño y la producción industrial. Nobuko (2007)
10. Tamay-Crespo, C.A., Ramos-Tituana, R.M., Bueno-Palomeque, F.L., Serpa-Andrade, L.J.: Análisis de la postura al sentarse utilizando sensores de fuerza. In: el Portatítulo, G. (ed.) Avances y aplicaciones de sistemas inteligentes y nuevas tecnologías, Chap. 12, pp. 179–187. Mérida, Venezuela, primera edn. (2016)
11. Çakmak, A., Yücel, B., Özyalçn, S.N., Bayraktar, B., Ural, H.I., Duruöz, M.T., Genç, A.: The frequency and associated factors of low back pain among a younger population in turkey. Spine **29**(14), 1567–1572 (2004). https://doi.org/10.1097/01.BRS.0000131432.72531.96

12. Smith, D.R., Wei, N., Ishitake, T., Wang, R.S.: Musculoskeletal disorders among chinese medical students. Kurume Med. J. **52**(4), 139–146 (2005). https://doi.org/10.2739/kurumemedj.52.139
13. Tokuhama-Espinosa, T.: Mind, Brain, and Education Science: A Comprehensive Guide to the New Brain-based Teaching. WW Norton & Company (2010)
14. Harris, M.D., Anderson, A.E., Henak, C.R., Ellis, B.J., Peters, C.L., Weiss, J.A.: Finite element prediction of cartilage contact stresses in normal human hips. J. Orthop. Res. **30**(7), 1133–1139 (2012). https://doi.org/10.1002/jor.22040
15. Maas, S.A., Ellis, B.J., Ateshian, G.A., Weiss, J.A.: Febio: finite elements for biomechanics. J. Biomech. Eng. **134**(1), 011005 (2012). https://doi.org/10.1115/1.4005694
16. Alfonzo-González, M.A., et al.: Simulación y análisis computacional del conducto medular del fémur en presencia de una prótesis de cadera. Revista de la Facultad de Ingeniería **28**(4) (2016)
17. Abraham, A.C., Moyer, J.T., Villegas, D.F., Odegard, G.M., Donahue, T.L.H.: Hyperelastic properties of human meniscal attachments. J. Biomech. **44**(3), 413–418 (2011). https://doi.org/10.1016/j.jbiomech.2010.10.001
18. Meier, P., Blickhan, R.: Fem-simulation of skeletal muscle: the influence of inertia during activation and deactivation. In: Skeletal Muscle Mechanics: From Mechanisms to Function, vol. 12, pp. 207–233 (2000)
19. Oomens, C.W.J., Bressers, O., Bosboom, E., Bouten, C., Bader, D.: Can loaded interface characteristics influence strain distributions in muscle adjacent to bony prominences? Comput. Methods Biomech. Biomed. Eng. **6**(3), 171–180 (2003). https://doi.org/10.1080/1025584031000121034
20. Li, S., Zhang, Z., Wang, J.: A new custom-contoured cushion system based on finite element modeling prediction. J. Mech. Med. Biol. **13**(04), 1350051 (2013). https://doi.org/10.1142/S0219519413500516

Assessment of the Ground Reaction Forces on Metatarsal Foot Bones Due to Changes on Pinball Region Contact

Roberto González-Navarrete(✉), Natali Mancera-Campos, Agustin Vidal-Lesso, and Elías Ledesma-Orozco

Universidad de Guanajuato, Salamanca, Guanajuato, Mexico
{roberto.gonzalez,n.manceracampos}@ugto.mx,
{agustin.vidal,elias}@ugtomx.onmicrosft.com

Abstract. With the aim to determine the importance of considering the contact between bodies, in this work, has been developed a numerical three dimensional model of the foot, which includes 28 bones, 504 thin ligaments, 48 plantar ligaments and the posterior tibial tendon; to find the values of the pinball region contact between each pair of bones, which at the same time, helps to achieve a correct distribution of body weight and, thus, highlight the importance of taking into account the configuration of the contact parameters between two bodies, to perform a correct characterization of the biomechanical effect of the foot. First, the validation of the model was carried out, determining the reaction forces of the metatarsals with the ground, and comparing them with the experimental reaction forces, subsequently, this validation was used to compare the variation of the reaction force once the contacts were modified. It was observed that by varying the value of the pinball region the reaction forces with the ground (GRF) can achieve significant changes (up to 159% in the fifth metatarsal into this work) and generates a wrong or a better prediction.

Keywords: Pinball region radius · Finite element · Validation · Ground reaction forces (GRF) · Contact

1 Introduction

Currently, several works have been carried out [1–9] in which the researchers have developed numerical models of the human foot that allow analyzing and understanding the biomechanical behavior of this member. In these works, different forms of validation and applications are shown for each one of the developed models.

Budhabhatti et al. [10] for his research on the hallux limitus, considered bones rigid and the soft tissues as a hyperelastic material, his validation was made in the Push-off phase. Chen et al. [11] for a parametric study of template design, considered for his foot model properties of bone and soft tissue as elastic, his validation was in the phase Quasi-static mid stance until push off. Cheung et al. [12] reported a parametric study of the plantar fascia rigidity, they considered the soft tissue as a hyperelastic material, his validation was performed in the Quiet-stance phase. Moreo et al. [13], in his parametric

© Springer Nature Switzerland AG 2020
C. A. González Díaz et al. (Eds.): CLAIB 2019, IFMBE Proceedings 75, pp. 822–830, 2020.
https://doi.org/10.1007/978-3-030-30648-9_108

study of configurations and bones geometries, performed the separation between the cortical and trabecular bones, his qualitative validation was against a computational model of the literature.

These models have been developed with a lot of variations between them, such as the simplifications made according to the analysis of interest. There are many variables that must be taken into consideration for a correct analysis and a correct finite element simulation like mechanical properties, load and boundary conditions. However, the influence of the modification of the contact parameters on the results obtained and the predictions made with each model is not addressed due to the complexity involved in the numerical analysis.

When the contact between two bodies or two surfaces in a numerical model is created it is possible to specify the distance that the contact surface will have.

There are several types of contact that can be specified between two bodies or two surfaces, including No separation, Bonded, Frictional, or Frictionless. The way to specify the distance between the bodies in contact can be through the options in the program, Program Controlled, Automatic Detection Value or the Region of pinball [14].

The pinball region is a contact element parameter that differentiates between the state of a far open field and the state of a close open field. It can be thought of as a spherical boundary that surrounds each point of contact detection, see Fig. 1. If a node on the target surface is located within the sphere, ANSYS Workbench® considers it in close contact and will supervise more closely its relationship with the contact detection point if the contact is established. The nodes on the target surface that are outside of this sphere will not be monitored so closely, for that specific point of contact detection.

Therefore, this work aims to acknowledge the importance of considering the configuration of the parameters of the contacts between two bones, in a numerical model of the foot, for the general characterization of its biomechanical effect. Mainly, the influence of the contact radius that produces considerable variations in the results. The proposal of the work is to find the radio contact values between each pair of bones that achieve a correct validation of the foot model used.

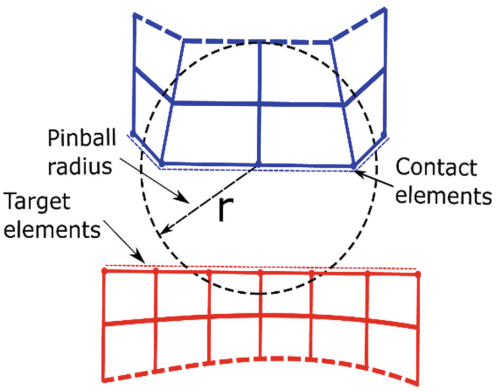

Fig. 1. Pinball region.

2 Materials and Methods

2.1 Foot Model Validation

A fundamental part for a correct analysis of results, is the validation of the model that is being used. In this work, it was developed a three dimensional finite element model with high order tetrahedral elements of the foot, composed of 28 bones (26 bones of the foot, tibia and fibula), and with the main ligaments and soft tissues involved in the gait cycle (504 fine ligaments, 48 between plantar ligaments and 10 that form the plantar fascia), which were added manually, based on the literature [15–19] and on the opinion of experts in the foot area.

The validation of this model was carried out in the "midstance" phase of the gait cycle and divided into three parts, the first was the validation of the load percentages in the front and back of the foot (forefoot and hindfoot), the second was the fall of the medial longitudinal arch [20, 21] and the third on which this work is focused, was the validation of load percentages on the head of the metatarsals of the foot with the ground also called the ground reaction forces (GRF).

For the above, it was necessary to establish the experimental load distributions that are generated in the areas of interest (metatarsals), these distributions were obtained from the literature [1, 22].

2.2 Load Distributions and Simulation with Automatic Contacts

According to Isvilanonda [1], the experimental load distributions on the metatarsals of the foot during the "mid stance" support of the gait cycle are the ones shown in the graph of Fig. 2. Where it can be seen that reach a value of up to 30% of the total, for the case of the third metatarsal.

The load percentages obtained experimentally were used as a reference for the validation of the model presented here.

Thus, once the load percentages in each metatarsal obtained experimentally were known, it proceeded to calculate those obtained through simulation with the developed numerical foot model. Once this was done, the comparisons of the percentages of load obtained with the numerical model and the obtained experimentally were made, and it could be noted that the results differed significantly. Figure 2 shows the comparison between the experimental and simulation results (Finite element model). It is worth mentioning that for this simulation it was used the automatic contacts generated by the finite element software.

Figure 3 shows the finite element model error percentage for each of the metatarsals, calculated comparing the GRF obtained through simulation with the experimental data, all of this according to Eq. (1)

$$error\ \% = \frac{GRF_{exp} - GRF_{sim}}{GRF_{exp}} * 100 \tag{1}$$

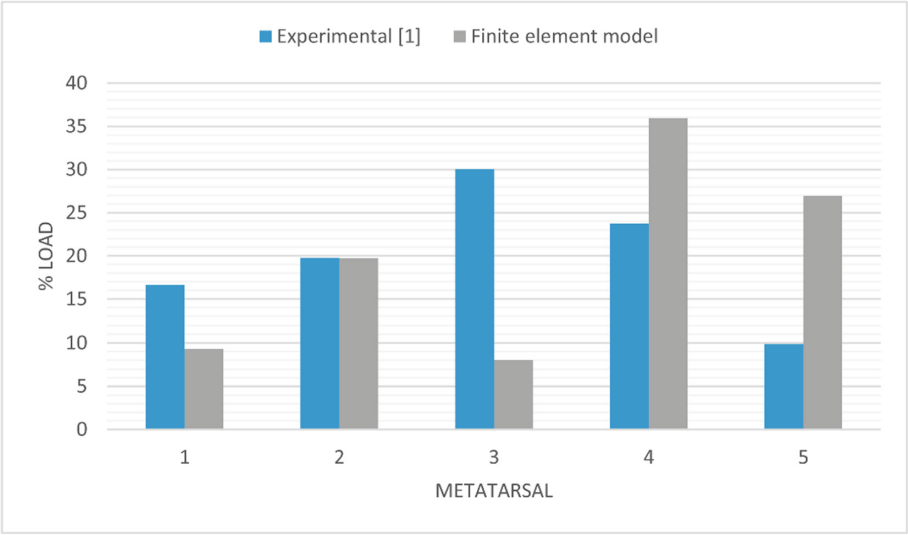

Fig. 2. First load comparison in the metatarsal bones.

This error percentage was obtained for each one of the metatarsals, finding a higher percentage error at the 5th metatarsal.

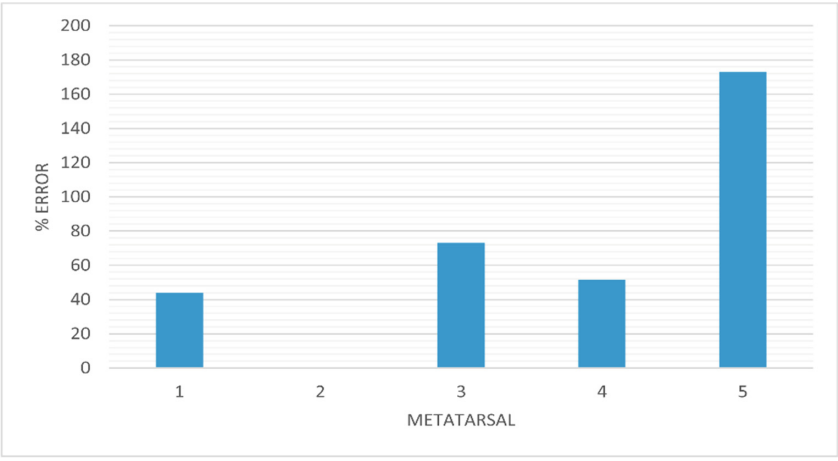

Fig. 3. Error percentage for each metatarsal without modifying the radius of the pinball region.

Based on the load percentages obtained experimentally, work was begun on the modification of the contact radius between the bones of the numerical model to reduce the error percentages generated between both models.

2.3 Determination of the Contact Radius and Comparison Between Models, Experimental and Numerical

Once established that the behavior of the contacts between bodies is the cause of the difference between the results obtained with both models, it was proceeded to specify a contact value between each pair of bones. Since, by not doing so, the ANSYS Workbench® software automatically applies an arbitrary value, in order to complete the simulation, without considering the effect of that value on the analysis to be performed.

Figure 4 shows an example of the contact radius established between the navicular and lateral cuneiform bones.

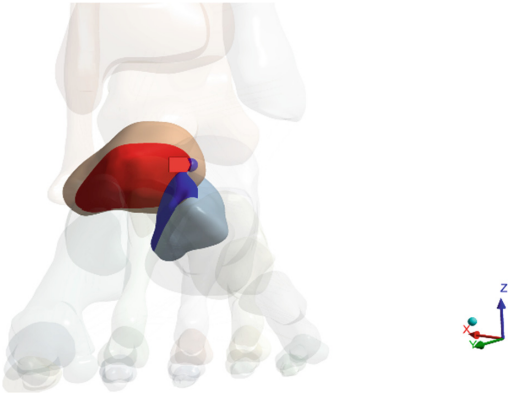

Fig. 4. Pinball region between navicular and lateral cuneiform bones.

The assignment of a suitable value for the pinball region between each pair of bones was made based on the movement of these during the "midstance" support phase of the gait cycle, in order to achieve an adequate reaction in the base of the metatarsals. To do this, each of the contacts value was varied, until determining those that were most significant or that had the greatest influence on the reaction of the metatarsals.

In Fig. 5, the contact regions determined as the most significant of the model are shown.

The pinball region radius variation was carried out until finding those parameters for which the percentage of error between the results obtained with the numerical model and the experimental model was reduced until considered insignificant.

The value of the pinball region radius of the most significant pairs of bones showed in Fig. 5 was varied until the results of the reactions were as close as possible to the experimental values, without forgetting considering that in each value influences the movement of the foot model. A very large pinball value led to greater rigidity and at the same time, to a less natural movement of the simulation. It continued to vary this

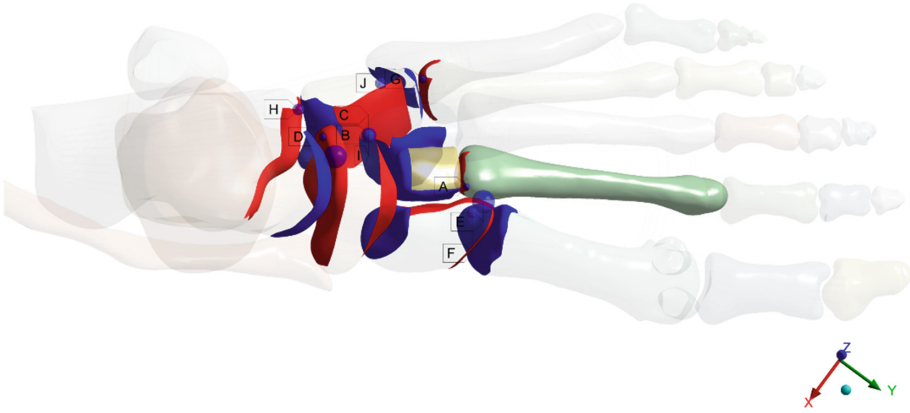

Fig. 5. Most significant pinball regions of the model.

pinball value until the reaction and movement of the foot model were as expected. It is important to mention that the contact algorithm to solve the contact problem for all cases was the Lagrange Augmented Method.

3 Results Analysis

3.1 Foot Model Validation

As mentioned above, in Fig. 5 the pairs of bones that have a greater effect on the reactions of the metatarsals are shown and to reduce the error percentage showed in graph of Fig. 3, it was started with a minimum value for the pinball that was varied until finding the pinballs radius that gave the best results in the reactions. In Fig. 6 are shown the comparisons between the experimental results, those of the simulation with the generation of automatic contacts and those obtained from the simulation by varying the contact radius.

Figure 6 also shows, how by varying the contact radius between each pair of bones, it is possible to bring closer the results of the ground reaction force of the metatarsals obtained from the simulation to those obtained experimentally by Isvilanonda [1].

Figure 7 shows the reduction in the percentage of error between numerical models, once the contact radius is modified. It is evident that, by varying the contact radius, always taking care that this radius resembles the natural movements of the bones at the analyzed stage of the cycle; it is possible to reduce the error rate by up to 159% in the most significant case.

It was possible to determinate this error percentage comparing the GRF present in each one of the metatarsals of the two numerical models analyzed respect to the GRF determined with the experimental data. Thus, the higher error reduction with respect to the experimental model, once the contacts were modified, it was observed for the 5th metatarsal with 159%.

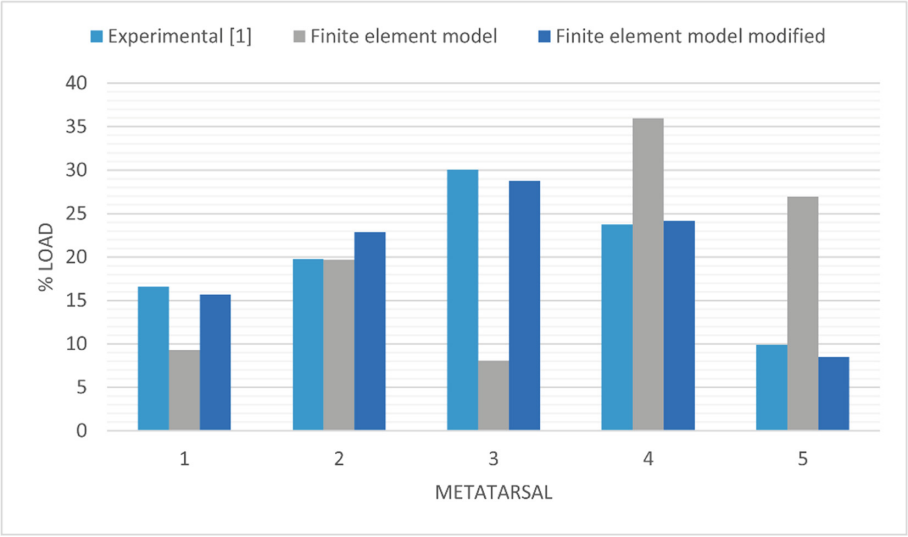

Fig. 6. Load comparisons in the metatarsals between experimental and numerical models when the radius of pinball region is changing.

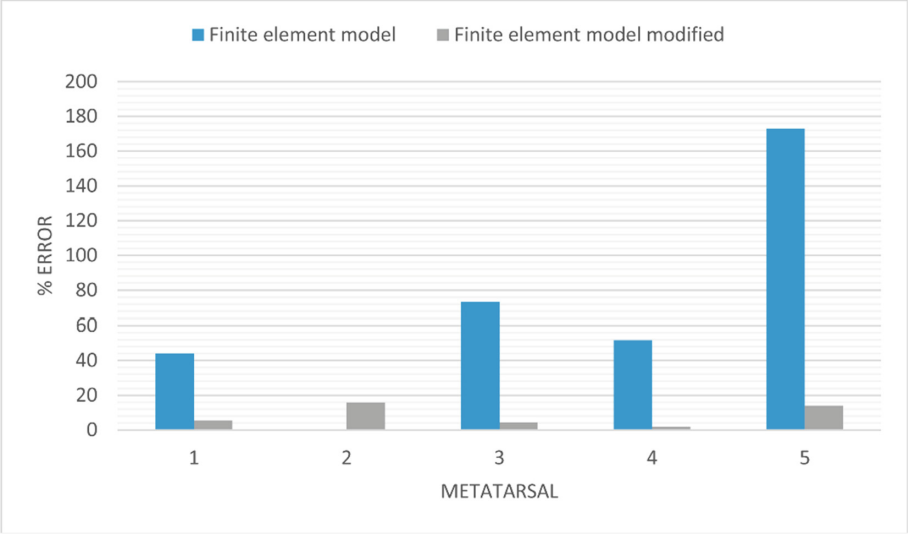

Fig. 7. Error percentage comparison between finite element models, with and without the pinball region modified on each metatarsal.

4 Discussion and Conclusions

The pinball region can be considered as a space between a pair of bodies that allows detecting how close or far one body is from the other by varying its radius.

During the realization of this work, it was observed that the contact sphere of the pinball region has a great impact on the distribution in the reaction's percentages and in the general behavior of the simulation.

From the first simulation, it was observed (Fig. 3) that the percentages of error between the experimental data and the simulation data with the unmodified pin-ball region are high, the largest being the error in the reaction of the 5th metatarsal. By modifying the pinball radius between the pairs of bones with the greatest effect on the results, the error percentages were significantly reduced, where the most significant reduction was in the 5th metatarsal with a reduction of 159%, achieving thus, closer to the experimental values.

Thus, this work shows the importance of the contacts and their parameters, since even a change of tens of millimeters can significantly change the final results due to the sensitivity of the pinball. Finally, the results found in this work suggest that all contact parameters must be reviewed and validated before continuing with a finite element simulation.

Conflict of Interest. The authors declare that they have no conflict of interest.

References

1. ReserchWorks Archive. http://hdl.handle.net/1773/33203. Acceddesd 13 June 2019
2. Morales, E., Bayod, J., de las Casas, E.B.: Computational foot modeling: scope and applications. Arch. Comput. Methods Eng. **23**(3), 389–416 (2016). https://doi.org/10.1007/s11831-015-9146-z
3. Wang, Y., Wong, D.W.C., Zhang, M.: Computational models of the foot and ankle for pathomechanics and clinical applications: a review. Ann. Biomed. Eng. **44**(1), 213–221 (2015). https://doi.org/10.1007/s10439-015-1359-7
4. Spratley, E., Matheis, E., Hayes, C., Adelaar, R., Wayne, J.: Validation of a population of patient specific adult acquired flatfoot deformity models. Orthop. Res. **31**(12), 1861–1868 (2013). https://doi.org/10.1002/jor.22471
5. Netter, F.: Atlas de Anatomía Humana, 5th edn. Elsevier Inc., Barcelona (2014)
6. Qiu, T., Teo, E., Yan, Y., Lei, W.: Finite element modeling of a 3D coupled foot boot model. Med. Eng. Phys. **33**(10), 1228–1233 (2011). https://doi.org/10.1016/j.medengphy.2011.05.012
7. Cheung, J., Zhang, M.: Finite element modeling of the human foot and footwear. In: 2006 ABAQUS Users' Conference, Boston, pp. 145–159 (2006)
8. Gefen, A., Megido, M., Itzchak, Y., Arcan, M.: Biomechanical analysis of the three dimensional foot structure during gait: a basic tool for clinical applications. J. Biomech. Eng. **122**(6), 630–639 (2000). https://doi.org/10.1115/1.1318904
9. Cavanagh, P., Rodgers, M., Iiboshi, A.: Pressure distribution under symptom-free feet during barefoot standing. Foot Ankle **7**(5), 262–276 (1987). https://doi.org/10.1177/107110078700700502

10. Budhabhatti, S., Erdemir, A., Petre, M., Sferra, J., Donley, B., Cavanagh, P.: Finite element modeling of the first ray of the foot: a tool for the design of interventions. J. Biomech. Eng. **129**(5), 750–756 (2007). https://doi.org/10.1115/1.2768108
11. Chen, W., Tang, F., Ju, C.: Stress distribution of the foot during mid-stance to push-off in barefoot gait: a 3D finite element analysis. Clin. Biomech. **16**(7), 614–620 (2001). https://doi.org/10.1016/S0268-0033(01)00047-X
12. Cheung, J., Phil, M., Zhang, M.: A 3-dimensional finite element model of the human foot and ankle for insole design. Arch. Phys. Med. Rehabil. **86**(2), 353–358 (2005). https://doi.org/10.1016/j.apmr.2004.03.031
13. Moreo, P., García-Aznar, J.M., Doblaré, M.: Bone ingrowth on the surface of endosseous implants. Part 1: mathematical model. J. Theor. Biol. **260**(1), 1–12 (2009). https://doi.org/10.1016/j.jtbi.2008.07.040
14. Academia. www.academia.edu/7033061/ANSYS_13.0_Introduction_to_contact. Accessed 19 June 2019
15. Drake, R., Volg, W., Mitchell, A.: GRAY Anatomía para Estudiantes, 1st edn. Elsevier Inc., Madrid (2005)
16. Siegler, S., Block, J., Schneck, C.: The mechanical characteristics of the collateral ligaments of the human ankle joint. Foot Ankle Int. **8**(5), 234–242 (1988). https://doi.org/10.1177/107110078800800502
17. Wright, D., Rennels, D.: A study of the elastic properties of plantar fascia. J. Bone Joint Surg. **46**(3), 482–492 (1964). https://doi.org/10.2106/00004623-196446030-00002
18. Zaragoza, K., Fernández, S.: Ligamentos y tendones del tobillo: anatomía y afecciones más frecuentes analizadas mediante resonancia magnética. Anal. Radiol. Méx. **12**(2), 81–94 (2013)
19. Cheung, J., Zhang, M., Leung, A., Fan, Y.: Three dimensional finite element analysis of the foot during standing–a material sensitivity study. J. Biomech. **38**(5), 1045–1054 (2005). https://doi.org/10.1016/j.jbiomech.2004.05.035
20. Franch, M., Infante, M., Albiol, J.: Cronología de osificación del pie. Radiogoniometría. El Peu **24**(3), 148–158 (2004)
21. Bandholm, T., Boysen, L., Haugaard, S., Zebis, M.K., Bencke, J.: Foot medial longitudinal-arch deformation during quiet standing and gait in subjects with medial tibial stress syndrome. J. Foot Ankle Surg. **47**(2), 89–95 (2008). https://doi.org/10.1053/j.jfas.2007.10.015
22. Lamm, B., Stasko, P., Gesheff, M., Bhave, A.: Normal foot and ankle radiographic angles, measurements, and reference points. J. Foot Ankle Surg. **55**(5), 991–998 (2016). https://doi.org/10.1053/j.jfas.2016.05.005

Biomechanical Evaluation of Hemiarthroplasty in First Metatarsal Bone

Mario Alberto Madrid[1,3(✉)], Ricardo Becerro de Bengoa Vallejo[2], and Javier Bayod López[1]

[1] Escuela de Ingeniería y Arquitectura, Universidad de Zaragoza, Zaragoza, Spain
jbayod@unizar.es
[2] Escuela de Enfermería, Fisioterapia y Podología, Universidad Complutense de Madrid, Madrid, Spain
ribebeva@enf.ucm.es
[3] Facultad de Ingeniería, Universidad Autónoma de Chihuahua, Chihuahua, Mexico
mmadrid@uach.mx

Abstract. Hallux valgus and hallux rigidus are the most common pathologies of the first metatarsophalangeal joint. Despite advances in the treatment of hallux valgus and hallux rigidus, no one technique can address the various stages of these pathologies. To alleviate these pathologies there are destructive techniques such as cheilectomies, arthrodesis and arthroplasties, and there are non-destructive techniques such as certain osteotomies. Hemiarthroplasty in the first metatarsal bone allows to recover the mobility of the first ray as well as to eliminate the pain caused by hallux valgus and hallux rigidus. However, there are no studies that allow us to know the biomechanical effect that the implant researched in this article produces on the human foot. Finite element analysis is a good technique that allows to understand these biomechanical effects. The objective of this work is to make a biomechanical evaluation of the HemiCAP®Toe DF by Arthrosurface and in that way to know the effects that this type of devices produces in the foot. To do this a finite element model of the foot after having performed a hemiarthroplasty in the first metatarsal bone was developed. It was detected a loss of capacity to support load in the first ray after introducing the implant, as well as an increase of principal stresses in the second and third ray. Effects of the hemiarthroplasty might cause postoperative medical complications. It was found loss of passive windlass mechanism in the model, leading to a loss of effectiveness in walking.

Keywords: Hallux rigidus · First metatarsophalangeal join · Hemiarthroplasty · Finite element analysis

1 Introduction

Hallux valgus is the most common chronic deformity of the first ray of the foot. The first metatarsal is deviates in varus while the first proximal phalanx (hallux)

© Springer Nature Switzerland AG 2020
C. A. González Díaz et al. (Eds.): CLAIB 2019, IFMBE Proceedings 75, pp. 831–840, 2020.
https://doi.org/10.1007/978-3-030-30648-9_109

is deviated in valgus, having thus an increase in four angles of the first ray of the foot. The first one is formed by the longitudinal axis of the metatarsal bone with the longitudinal axis of the first proximal phalanx, this angle is known as the hallux valgus angle and is considered normal if it is less than 15°. The second one is the intermetatarsal angle, which measures the opening between the first and second metatarsal bone, and it is considered normal if it does not exceed 9°. The third one is the distal articular set angle, which is formed with the joint surface and the axis of the first metatarsal and is usually it is not greater than 10°, and the fourth one is formed by the longitudinal axes of the phalanges of the great toe, also known as interphalangeal angle, which is considered normal when it is less than 10°. The different stages of this pathology are classified according to the measurements of the previously mentioned angles [1,2].

The second most common pathology of the first metatarsophalangeal joint is hallux rigidus [3]. This pathology is characterized by a decrease in dorsiflexion in the first metatarsophalangeal join, caused both by the dorsal osteophytes and by the retraction of plantar soft tissues [4]. Núñez-Samper [5] says that hallux rigidus is a process that evolves fundamentally in three phases, each of which presents a different symptomatology and radiological semiology, which will condition, consequently, the treatment. Some other authors prefer to consider the classification of Coughlin et al. [6,7]. These authors base their classification on subjective finding and objective clinical data and radiographs.

There are many treatments for hallux valgus and hallux rigidus, but to date none can be applied to the different stages of these pathologies. Many kinds of osteotomies are considered nondestructive surgical techniques and there are many destructive surgical techniques like arthrodesis, arthroplasty, and cheilectomy. Arthroplasty is a surgical procedure that consists in realigning, remodeling or replacing the skeletal muscle surface of an articular joint. The hemiarthroplasty in the first metatarsal remains in debate among surgeons because it allows the patient to recover the mobility of the first metatarsophalangeal join and eliminates pain, but it is a destructive technique. To date there is no biomechanical evaluation with the type of hemi implant studied in this paper and surgeons insert these types of implants according to their own experience.

On the other hand Finite element analysis is a good methodology to solve this type of biomechanical evaluations in the foot [8,9]. The objective of this article is to perform a biomechanical evaluation by a finite element model of the foot after having developed a hemiarthroplasty in the first metatarsal bone using the hemi-implant HemiCAP®Toe DF by Arthrosurface, and in that way, to understand how the implant works, and to know the effects that this kind of implants make in patients.

2 Methods

2.1 Hemiarthroplasty in First Metatarsal Model

The model presented in this paper was developed by the Applied Mechanics and Bioengineering group (AMB) from the University of Zaragoza (Spain).

To develop the model 93 separate computed tomography (CT) were generated every 2 mm in DICOM format. To generate the volumes from the tomographies, we used a volume extrapolation program called g1.exe developed by the Advanced Computing Group (GIGA) of the University of Zaragoza. The scanned foot belongs to a person of 36 years old free of any pathology. The 93 CT was processed in MIMICS software to make volumes of cortical and trabecular bones as well as cartilage in STL format. The implant was placed using Softimage software and the resection in the first metatarsal bone was developed with MIMICS software. The mesh for the model was generated with ICEM software of ANSYS. The maximum element size in the implant was 0.5 mm avoiding in that way loss of geometry due to mesh and to solve the problem of mesh convergence.

The model contains 28 cortical and trabecular bones and contain too cartilages that make a connection between bones, these bones are: talus, cuboid, scaphoid, 3 cuneiforms, 5 metatarsals, 2 major phalanges, 12 minor phalanges and 2 sesamoids embedded in the first metatarsal. After having obtained the tetrahedral elements, MATLAB programming was used to add soft tissues such as; thin ligaments, plantar ligaments, muscles and tendons. In this model, thin ligaments between the first metatarsal and the first proximal phalanx as well as the muscles and tendons of; flexor hallucis brevis, capsularis, pedio, hallux adductor and hallux abductor were disinserted as a recommendation of the podiatrist PhD. Ricardo Becerro de Bengoa Vallejo [10], remaining in the model only the muscles and tendons of; extensor hallucis longus, extensor hallucis longus expansion, flexor hallucis brevis, flexor digitorum longus and flexor digitorum brevis. In Fig. 1 can be seen components for this model. This model contains 611,349 nodes and 3,386,602 elements.

The model presented in this article is in toe-off stage because of this stage generates the maximum efforts to the first ray of the foot [11]. This model contains ligaments that were modeled as truss elements because they only experiment a displacement in their extreme nodes when the model is loading, another kind of elements in this model, such some muscles and tendons, were modeled as beam elements due to they receive directly a pretension force due to the toe-off stage. Figure 2 shows the implant and the mesh obtained from it.

2.2 Mechanical Properties and Boundary Conditions

In the model presented in this paper we assume that we are working only with small deformations and small displacements because of all elements are considered as homogeneous, isotropic and linearly deformable elastic. For this model cortical bones have a Young's modulus of 17 GPa and trabecular bones have a elasticity modulus of 700 MPa, both materials have a Poisson ratio of 0.3 [9]. For cartilage we consider an elastic limit of 10 MPa and a Poisson's coefficient of 0.4 [12]. Muscles and tendons are capable to resist bending and they have a circular cross section with 2 mm radius and a young's modulus of 450 MPa with a Poisson ratio of 0.3 [13]. In this model the ligaments only can support axial forces. For thin ligaments we use a cross section of 0.045 mm^2 in each element and an elasticity modulus of 260 MPa. For plantar ligaments (plantar ligaments

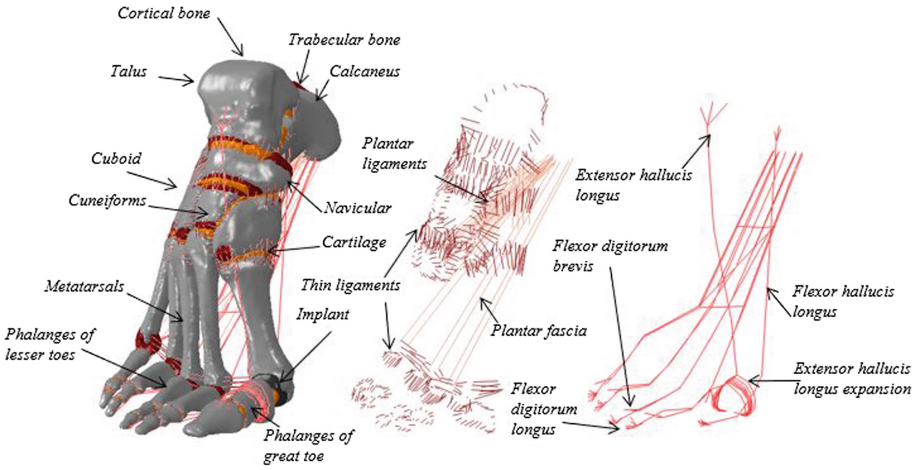

Fig. 1. Elements of the model.

Fig. 2. Implant, and mesh generated from implant.

and plantar fascia, see Fig. 1) we use a cross section in every element of 7.35 mm^2 and a Young's modulus of 350 MPa. For both groups of ligaments we use a Poisson ratio of 0.3 [14]. The HemiCAP®Toe DF Contoured Articular Prosthetic is an implant composed by two parts. The articular resurfacing component is made of cobalt-chronium alloy (Co-Cr-Mo) and the taper post is titanium alloy (Ti-6Al-4V). For the articular resurfacing component we use a elasticity modulus of 210 Gpa and Poisson's coefficient of 0.29 and for the taper post we use a Young's modulus of 113.8 GPa and a Poisson ratio of 0.29 [15,16]. The summary of the mechanical properties for this paper can be seen in Table 1.

On the other hand it is well known the human gait is a dynamic problem but traditionally human gait cycle has been divided in 6 stages [12]. In the present work the toe-off stage was reproduced. The analysis was made in the software

Abaqus 6.13–5 and it contains 2 steps. In the first step a fixed support was used on; the insertion surface of the Achilles tendon, the first and second phalanx, for the lesser toes translation and rotation on vertical axis were restricted in distal phalanges and pre-tension forces of 2% was applied on the muscles [17]. In the second step acts too the self-weight of the person represented by a force of 1805 N vectorially discomposed in the global axes of the model as can be seen in Fig. 3. This force due to self-weight of the person is applied in a group of 361 nodes located in the area where fibula and tibia contact talus [8]. In the second step pretension forces in muscles were maintained.

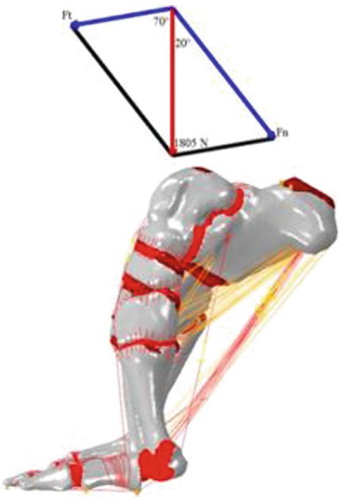

Fig. 3. Load condition for the model.

Table 1. Mechanical properties of bones, soft tissues and prosthesis

Materials	Elasticity modulus (MPa)	Poisson's ratio
Cortical bone	17000	0.3
Trabecular bone	700	0.3
Cartilage	10	0.4
Muscles	450	0.3
Thin ligaments	260	0.3
Plantar ligaments	350	0.3
Prosthesis (Co-Cr)	210000	0.29
Prosthesis (Ti-6Al-4V)	113800	0.29

3 Results

In Fig. 4 can be seen the maximum absolute principal stress values. The maximum absolute principal stresses appear in calcaneus in the zone of the insertion surface of the Achilles tendon (fixed support in the model). It can be noted that the second and third rays are responsible for transmitting the load in the toe-off stage when a hemiarthroplasty in first metatarsal bone has been developed. Respect to the proximal phalanges of the second and third ray of the foot, the dorsal zone is working in tension (positive stresses) and the plantar zone is working in compression (negative stresses). Respect to the first ray of the foot, only in the support points appear a little concentration of stress. The displacements in the first ray of the foot are almost null while the displacements in lesser toes are responsible for carrying out the impulse produced in the cycle of the human march in toe-off stage. In Fig. 4 can be noted that the second ray of the foot is the most loaded and the first ray is the least loaded. The maximum principal stress value in the toes appears in the second proximal phalanx in the zone of support points. Figure 5 shows the values of von Mises stress in the hemi implant studied in this research. The summary of the stresses in the model can be seen in Table 2.

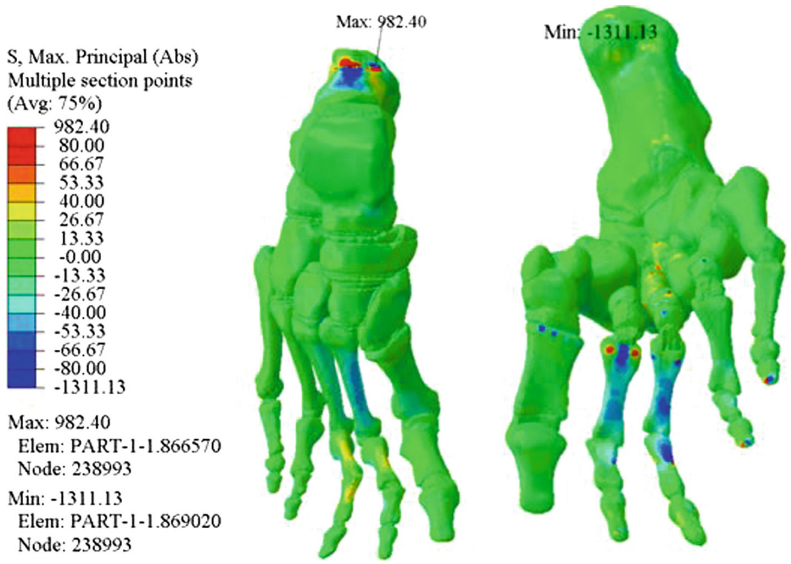

Fig. 4. Principal stresses in hemiarthroplasty model.

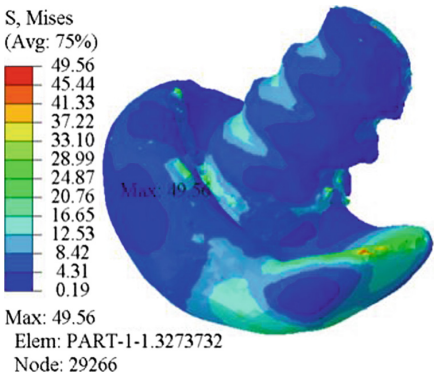

Fig. 5. Von Mises stresses in implant.

Table 2. Values of stresses in the model.

Zone	Kind of stress	Value (MPa)
Calcaneus (Fixed support in the model)	Absolute principal stress	1311.13
Second ray of the foot	Absolute principal stress	462.06
Implant	Von Mises stress	49.56

4 Discussions and Conclusions

Ulusal et al. used the HemiCAP®resurfacing implant by Arthrosurface in their study and report 14 patients with no bilateral case of hallux rigidus, of the 14 patients, 5 were male and 9 were female, with a mean age of 58.7 ± 7.4 with a range from 52 to 75 years. The mean preoperative VAS score for pain was 8.4 ± 0.9 with a range from 7 to 10 cm and had decreased to 1.21 ± 1.2 with a range from 0 to 5 cm at the final follow-up visit. The mean preoperative AOFAS score was 33.9 ± 9.8 with a range from 22 to 59 points and had increased to 81.6 ± 10.1 with a range from 54 to 96 points at the final follow-up visit. The mean preoperative of the range of motion in the first metatarsophalangeal join was 22.8° with a range from 15° to 45° and had increased to 69.6° with a range form 50° to 90° at the final follow-up. One patient's implant was removed, and arthrodesis of the first metatarsophalangeal join was performed because of ongoing pain and immobility [18].

The HemiCAP®Toe DF Contoured Articular Prosthetic is used in the treatment of patients with degenerative and post-traumatic arthritis in the first metatarsal joint in the presence of good bone stock along with critical conditions of hallux valgus or hallux rigidus. This implant has the advantage of to obtain pain relief and improve function of the first metatarsophalageal join, but

contraindications include inadequate skin, musculontendinus or neurovascular system status and chronic instability or deficient soft tissues and other support structures [19]. Despite the advantages of the use of implants, such as recovery of joint mobility and pain relief, no studies has been developed to evaluated the biomechanical properties of this kind of implants through the use of finite elements [20].

In this article a model of finite elements standing in the toe-off stage have been presented. This model analyses a foot of a 36-years-old person with 60 kg of weight after having developed hemiarthroplasty in first metatarsal bone. It was found that when the hemiarthroplasty is developed, the first ray of the foot loses the capacity to support the person's weight, causing an increase of stresses in rays 2 and 3 of the foot. It was also observed that the first distal phalanx loses the passive windlass mechanism after the surgical procedure was performed (see Fig. 6). Due to we recommend to surgeons to evaluate the active windlass mechanism in patients during postoperative follow-up.

In Fig. 6 can be contemplated that the metatarsal bone tends to down and the proximal phalanx seems to have no move due to the support points in the model. The passive Windlass mechanism gives impulse to the human gait by an upward movement in first distal phalanx, but the results in the model have showed that this impulse is lost as a consequence of hemiarthroplasty in first metatarsal bone. Take in mind that a part of the process of hermiarthoplasty in the model consist in disconnect muscles and tendons of; flexor hallucis brevis, capsularis, pedio, hallux adductor, hallux abductor and thin ligaments between the first metatarsal and the first proximal phalanx.

Garcia-Aznar et al. have shown that when the first ray of the foot loses the capacity to support the person, the others rays are overloaded, thus increasing the risk of metatarsalgia [21,22]. This study demonstrates that hemiarthroplasty in first metatarsal bone generates an overload on the second ray of the foot. The overload of the proximal phalanges of lesser toes can cause hammertoe, claw

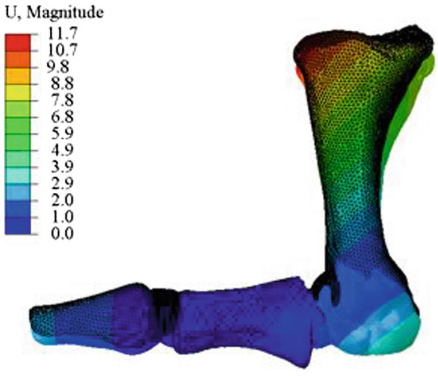

Fig. 6. Lost of passive windlass mechanism due to hemiarthroplasty. Units in millimeters.

toe or tendonitis in the lesser toes [22]. Unfortunately, there are no computational models in the literature that report a biomechanical evaluation after having developed an hemiarthroplasty in the first metatarsal bone using the implant studied in this paper, so the model of hemiarthroplasty cannot be confirmed with other models. However, the contraindications of this implant include chronic instability or deficient soft tissues and other support structures [19].

The model presented in this paper has some limitations. It is well-known that the soft tissues are hyper-elastic materials, but due to we are working with small displacements the soft tissues were modeled like elastic materials. This project focuses on the hard tissues and hemi implant, and due to we avoid the computational cost of modeling soft tissues, such as beam and truss elements, which consist of an elastic material. For soft and hard tissues, it is important to know the main maximum principal stresses, while for the implant, because it is a ductile metal, it is important to know the maximum Von Mises stresses.

The results obtained in the analysis have a qualitative value, instead of quantitative because all people have a different foot size and weight but all have the same skeletal muscle system. Therefore, the distribution of stress and strain is similar for different people, which indicates that the results can be extrapolated. Due it we only report the value of the von Mises stress in the implant researched in this article. The tensile strength yield for CrCo alloy is 410 MPa [23] and the tensile strength yield for Ti-6Al-4V alloy is 880 MPa [16]. The maximum value of von Mises stress in the implant was 49.56 MPa (see Fig. 5). This indicates that failure for this implants may be due to fatigue problems.

Acknowledgment. The authors gratefully acknowledge the support of the Ministry of Economy and competitiveness of the Government of Spain through the project DPI2016-77016-R.

Conflict of Interest Statement. The authors declare no conflict of interest.

References

1. Koller, U., Willegger, M., Windhager, R., Wanivenhaus, A., Trnka, H.-J., Schuh, R.: Plantar pressure characteristics in hallux valgus feet. J. Orthop. Res. Official Publ. Orthop. Res. Soc. **32**(12), 1688–1693 (2014). http://www.ncbi.nlm.nih.gov/pubmed/25130961
2. Bauer, T., Biau, D., Lortat-Jacob, A., Hardy, P.: Percutaneous hallux valgus correction using the Reverdin-Isham osteotomy. Orthop. Traumatol. Surg. Res. **96**(4), 407–416 (2010). https://doi.org/10.1016/j.otsr.2010.01.007
3. Asunción, J., Poggio, D., Pellegrini, M.J., Melo, R., Ríos, J.: Evaluation of first metatarsal head declination through a modified distal osteotomy in hallux rigidus surgery. A cadaveric model. Foot Ankle Surg. **21**, 187–192 (2014)
4. Asunción Márquez, J., Martín Oliva, X.: Hallux rígidus: Etiología, diagnóstico, clasificación y tratamiento. Revista Espanola de Cirugia Ortopedica y Traumatologia **54**(5), 321–328 (2010)
5. Núñez-Samper, M., Llanos Alcázar, L.F.: Biomecánica, medicina y cirugía del pie, primera ed. Masson, Barcelona (2000)

6. Polzer, H., Polzer, S., Brumann, M., Mutschler, W., Regauer, M.: Hallux rigidus: joint preserving alternatives to arthrodesis - a review of the literature. World J. Orthop. **5**(1), 6–13 (2014). http://www.pubmedcentral.nih.gov/articlerender.fcgi?artid=3952696&tool=pmcentrez&rendertype=abstract
7. Coughlin, M.J., Shurnas, P.S.: Hallux Rigidus. J. Bone Joint Surg. **85**–**A**(11), 2072–2088 (2003)
8. Bayod, J., Losa-Iglesias, M., de Bengoa-Vallejo, R.B., Prados-Frutos, J.C., Jules, K.T., Doblare, M.: Advantages and drawbacks of proximal interphalangeal joint fusion versus flexor tendon transfer in the correction of hammer and claw toe deformity. A finite-element study. J. Biomech. Eng. **132**(5), 51 002–51 007 (2010)
9. Martínez Bocanegra, M.A., Bayod Lopez, J., Vidal-Lesso, A., de Bengoa Vallejo, R.B., Lesso-Arroyo, R.: Structural interaction between bone and implants due to arthroplasty of the first metatarsophalangeal joint. Foot Ankle Surg. https://doi.org/10.1016/j.fas.2017.10.002
10. de Bengoa Vallejo, R.B., Losa Iglesias, M.E., Jules, K.T.: Tendon insertion at the base of the proximal phalanx of the Hallux: surgical implications. J. Foot Ankle Surg. **51**(6), 729–733 (2012)
11. Morales-Orcajo, E., Bayod, J., de Bengoa-Vallejo, R.B., Losa-Iglesias, M., Doblare, M.: Influence of first proximal phalanx geometry on hallux valgus deformity: a finite element analysis. Med. Biol. Eng. Compu. **53**(7), 645–653 (2015)
12. Enrique Morales Orcajo: Influencia de la geometría de la falange proximal en la formación de juanetes. Ph.D. dissertation (2012)
13. Ramos, A.R.: Construcción e Instalaciones Industriales. Ph.D. dissertation (2006)
14. Bocanegra, M.A.M., Lopez, J.B.: IMECE2015-53525, pp. 1–7 (2015)
15. Çelik, I.: Influence of CrN coating on electrochemical behavior of plasma Nitrided Pure Titanium in Bio-simulated environment, pp. 150–155 (2016)
16. Tanner, K.E.: Titanium in medicine, vol. 216, no. 3 (2002). http://pih.sagepub.com/lookup/doi/10.1243/0954411021536432
17. García-González, A., Bayod, J., Prados-Frutos, J.C., Losa-Iglesias, M., Jules, K.T., de Bengoa-Vallejo, R.B., Doblaré, M.: Finite-element simulation of flexor digitorum longus or flexor digitorum brevis tendon transfer for the treatment of claw toe deformity. J. Biomech. **42**(11), 1697–1704 (2009)
18. Ulusal, A.E., Akseki, D.: Short-term clinical outcomes after first metatarsal head resurfacing hemiarthroplasty for late stage hallux rigidus go. J. Foot Ankle Surg. **54**, 173–178 (2015)
19. Systems, I.: Technique Guide
20. DeHeer, P.A.: The case against first metatarsal phalangeal joint implant arthroplasty. Clin. Podiatr. Med. Surg. **23**(4), 709–723 (2006)
21. García-Aznar, J.M.: Load transfer mechanism for different metatarsal geometries: a finite element study. J. Biomech. Eng. **131**(2), 021011 (2008). http://biomechanical.asmedigitalcollection.asme.org/article.aspx?doi=10.1115/1.3005174
22. Bayod, J., de Bengoa Vallejo, R.B., Losa Iglesias, M.E., Doblaré, M.: Stress at the second metatarsal bone after correction of hammertoe and claw toe deformity: a finite element analysis using an anatomical model. J. Am. Podiatr. Med. Assoc. **103**(4), 260–273 (2013). http://www.ncbi.nlm.nih.gov/pubmed/23878378
23. Dolgov, A., Dikova, N.T., Dzhendov, D., Pavlova, D., Simov, M.: Mechanical properties of dental CO-CR alloys fabricated via. In: Scientific Proceedings Ii International Scientific-Technical Conference "Innovations in Engineering" 2016, vol. 33, pp. 29–33 (2016)

Comparative Study of Biomechanical Model of the L4-L5 Lumbar Section with Mechanical Fixation

Eduardo Osquel Pérez-Rivero[1], Raide Alfonso González-Carbonell[1(✉)], Armando Ortiz-Prado[2], and Victor Hugo Jacobo-Armendáriz[2]

[1] Mechanical Engineering, Universidad de Camagüey, Camagüey, Cuba
eduardoosquel@hotmail.com, raidel977@gmail.com
[2] UDIATEM, Universidad Nacional Autónoma de México, Coyoacán, DF, Mexico
armandoo@unam.mx, vicjacobo@yahoo.com.mx

Abstract. The risk of fixation loosening by the pedicle failure during or after the screw insertion surgery is high, causing fracture of the bone tissue due to the high stress concentration. The purpose of this paper is study the influence of osteoporosis on the bone-screw interface, based on a 3D biomechanical model of the lumbar section. The Finite Element (FE) method was used. Mechanical properties in health vertebra (HV) and osteoporotic vertebra (OV) were defined. A compression load of 500 N and a moment of 7.5 Nm were assumed in four load scenarios: compression, flexion, flexion-extension and axial rotation. The bone-screw interaction zone and the posterior of vertebra and pedicles were susceptible to bone tissue failure, because the higher equivalent stress were close to bone failure stress. The HV stresses were higher than OV stresses. The higher stress was 8.83 MPa. Opposite to stresses results, the strains were higher in OV than in HV, being the OV strain more than 2 times higher than HV strain.

Keywords: L4-L5 lumbar section · Biomechanics · Mechanical fixation

1 Introduction

Trans-pedicular vertebral fixation is a common technique used in the treatment of vertebral disorders [1]. Its purpose is to obtain a solid arthrodesis to relieve the patient's pain [2]. In this technique, the pedicle screws are inserted in the vertebral body and are joined to bars to create a solid union and release an injured section (vertebra or intervertebral disc).

This procedure has gained acceptance for the treatment of degenerative diseases of the lumbar spine and it has shown advantages in the decompression of nerves and the restoration of the intervertebral disc, the stabilization and the reinforcement of the damaged region of the spine [3–5]. However, in osteoporotic patients the risk of pedicle failure during or after the screw insertion surgery is high [4], causing fracture of the bone tissue due to the stress concentration.

© Springer Nature Switzerland AG 2020
C. A. González Díaz et al. (Eds.): CLAIB 2019, IFMBE Proceedings 75, pp. 841–849, 2020.
https://doi.org/10.1007/978-3-030-30648-9_110

The study of the behavior of the bone-screw interface allows the anticipation of possible failures. The objective of this work is to study the influence of mechanical properties of vertebrae in the bone-screw interface, based on a 3D biomechanical model of the L4-L5 lumbar section.

2 Materials and Methods

The Finite Element Method (FEM) was used to analyze the biomechanical model. The geometry, material and loads and boundary conditions were taken into account for model definition, which allowed the succeeding analysis (post - processing) [6].

2.1 3D Geometry of the Model

The L4-L5 lumbar section was selected as the region under analysis. For geometrical reconstruction, images in DICOM format from the Computed Tomography Scanner GE LightSpeed VCT (120 kV/89.40 mAs, pixel 0.773 mm, 512 × 512, slice 5 mm) installed on the National Institute of Rehabilitation of México were used.

In order to obtain the geometric model, it was used the 3D-Slicer software (http://www.slicer.org) while the medical images manipulation and the 3D geometry reconstruction were made. The meshed surfaces with triangular elements were generated and exported in STL file extension [7].

The Blender software (http://www.blender.com) was used in the transformation of the meshed surfaces of the vertebrae into an editable polygon model. The smooth surfaces were also conducted. The intervertebral disc was obtained from both delimited surfaces and the contour of L4 and L5 vertebral plates. In order to avoid parts interferences, a Boolean operation was executed.

A generic hardware (bar and screw model) was selected. Assembly was conducted in Solidworks Premium 2018 (Dassault Systemes SOLIDWORKS Corp., MA, USA).

2.2 Loads and Boundary Conditions

Four load scenarios were defined: compression, flexion, flexion-extension, and axial rotation (see Fig. 1), according to criteria of Rohlmann et al. [8]. A compression load of 500 N and a moment of 7.5 Nm were assumed. The compression was applied at the upper plate of the L4 vertebra and the rotation at a reference point of the same vertebra. All degrees of freedom in the screws head were restricted.

2.3 Mechanical Properties

A linear elastic model was used. The mechanical properties (modulus of elasticity and Poisson's coefficient) in healthy vertebrae (HV) bone were 12 GPa and 0.3 respectively [9–11], while in osteoporotic vertebrae (OV) bone they were 4.014 GPa and 0.3 [12]. The mechanical properties of a titanium base material (7074) were used.

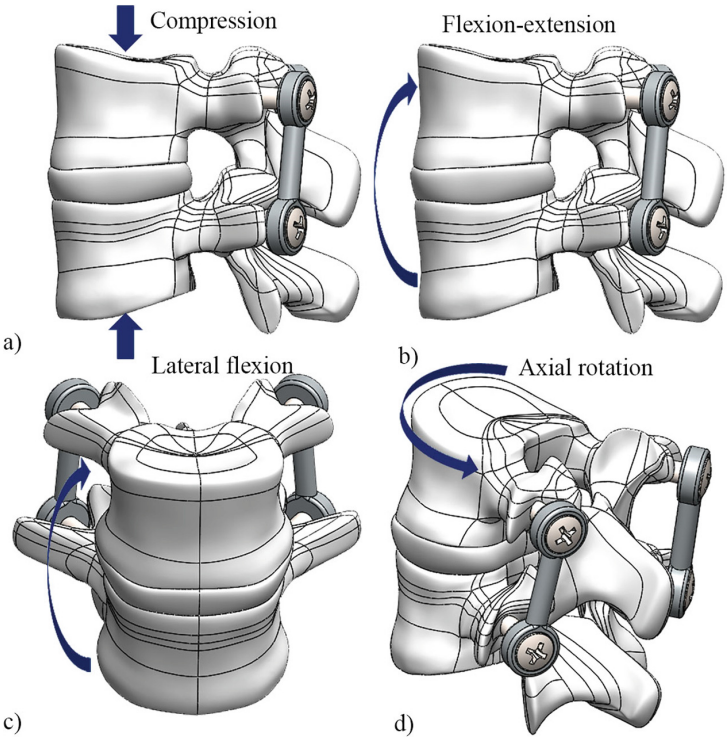

Fig. 1. Loads scenarios defined to the model. (a) Compression load, (b) Flexion-extension, (c) Lateral flexion, and (d) Axial rotation.

2.4 Mesh

The assembly was meshed by using an automatic mode. The high order tetrahedral elements of 1.5 mm were used. The 16-point Jacobian formulation was also used. A total of 426613 nodes and 299453 elements was obtained, with an aspect ratio less than 5 in all the elements.

3 Results and Discussion

In the geometry of the intervertebral disc, the stress was maximum in the compression scenario, 3.45 MPa in the osteoporotic vertebrae (OV) and 3.29 MPa in the healthy vertebrae (HV). Stress was distributed towards the edge, leaving the nucleus pulpous free (Fig. 2). This result could be influenced by the boundary conditions imposed on the model, which simulate a total rigidity of the hardware. The stress in the lateral flexion was 3.18 MPa (OV) and 2.91 MPa (HV). In the rotation and the flexion-extension, the stress did not reach 50% of the previous results.

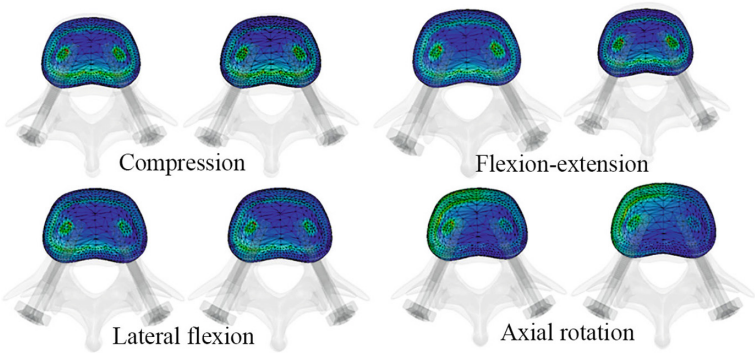

Fig. 2. Equivalent von Mises stress in the intervertebral disc in the four loads scenarios.

In the geometry of vertebrae under compressive loads, the higher stress 8.02 MPa (HV) and 5.81 MPa (OV) was located in the posterior region and in the pedicles of the vertebrae. This result coincides with Xu et al. [9]. Stress was located below the bone-screw interface of L4 vertebra, while it was in the upper plate of L5 vertebra. The zone that contained the highest stress was the one located between the mechanic fixation (from upper screws to the lower screws) (Fig. 3a).

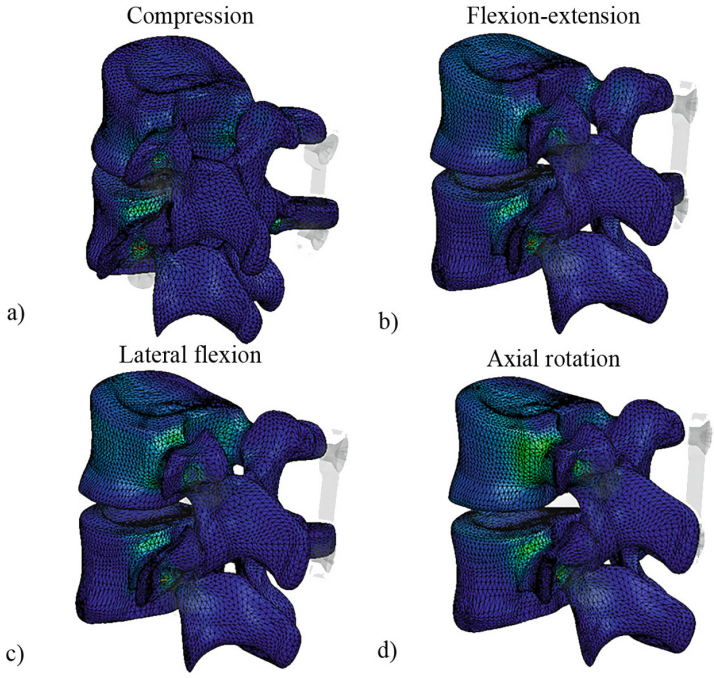

Fig. 3. Distribution of von Mises equivalent stress in the four scenarios and in health bone. Posterior vertebra and pedicle was the higher stress zone: (a) compression load, (b) flexion-extension, (c) lateral flexion, and (d) axial rotation.

In the flexion-extension movement, L5 vertebra experimented higher equivalent stress than L4 vertebra. It was 3.63 MPa in HV and 3.34 MPa in OV (Fig. 4). It reached the maximum value of stress in the zone of the bone-screw interface (Fig. 3b), which agrees with Cheng et al. [13].

In lateral flexion movement, the stress exceeded the compression scenario, 8.83 MPa (HV) and 6.05 MPa (OV) (Fig. 4). The zone near to bone-screw interface and near the direction of movement experienced higher stress than the rest of the posterior part of the vertebra. The pedicular channels were the most affected (Fig. 3c). In this scenario, the vertebrae movement occurred in one direction and it is dangerous because a complex system of loads appeared. In the rotation scenario, the stress was higher in the left of the sagittal plane (orientation of the loads) (Fig. 3d). It was 1.97 MPa in HV and 1.39 MPa in OV (Fig. 4).

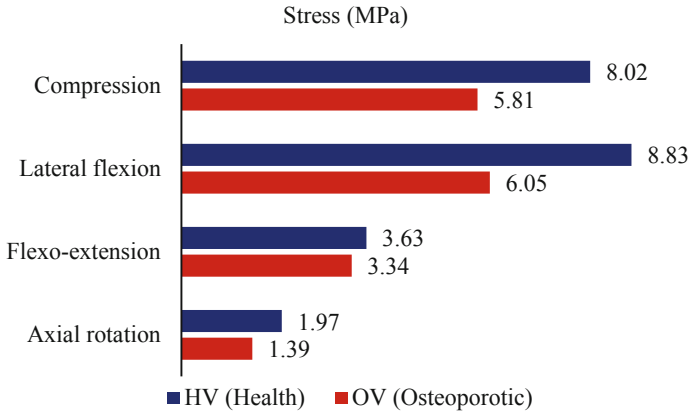

Fig. 4. Results of equivalent von Mises stress in the four scenarios. Compression and lateral flexion of health bone showed higher state of stress.

Notice that HV stress was higher than OV stress (Fig. 4). This was due to the lower modulus of elasticity of the OV bone. Those stresses were in the range reported in the literature (2 to 10 MPa) [14, 15].

When the patient experiences a flexion or axial rotation movement of the spine, the screws may come out of the bone. In addition, the patient's weight produces a perpendicular load to the screws axis and it may fail at shear stress. Furthermore, if the patient carries out heavy activities, the forces acting on the mechanical fixation may increase its magnitude, producing equivalent stress higher than the failure limit of the bone. In consequence, the contact area in the bone-screw interface is susceptible to bone failure.

According to the results of the stress analyses, the patients should be oriented not to carry out heavy activities, as should be considered a risk factor for the treatment stability, directly affecting the functionality of the arthrodesis system. In this respect, it is compulsory to avoid the occurrence of stresses close to the failure limit because high stress may produce the loosening of the screw-bone interface, extraction, and insufficiency of

the instruments after the lumbar arthrodesis (the catastrophic screw or hardware failure), three of the common problems of the implant's failure [16].

A bone modifies its structure to supports load conditions (Wolff's Law). The stress, strain and deformation energy density influence the bone adaptation. Then, strain is an important factor to consider because this mechanical signal constitute the trigger of bone remodeling [17, 18].

Opposite to stresses results, the strains were higher in OV than in HV, being the OV strain more than 2 times higher than HV strain (Fig. 5). In the compression load scenario, the strain was 0.000508 in HV when the stress was 8.02 MPa. While it was 0.00134 in OV (2.63 times of HV strain), when the stress was 5.81 MPa, just the 72% of HV. In flexion-extension scenario, the strain was 0.000249 (HV) and 0.0007 (OV). OV strain was 2.81 times higher than HV (Fig. 5). The influence of strain was highly perceptible on the left pedicular channels and at the center on the upper plate of L4 vertebra.

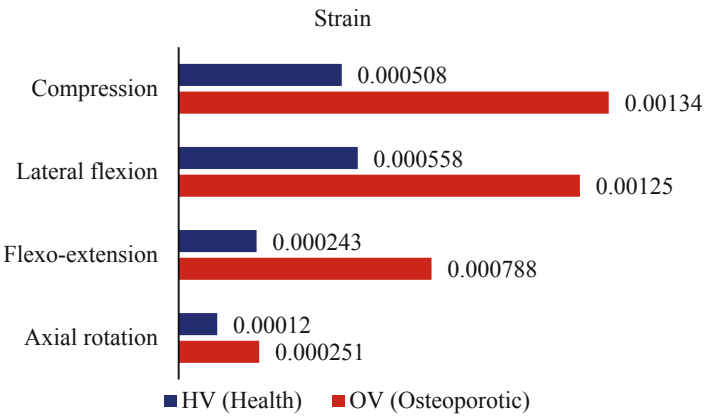

Fig. 5. Results of maximum strain in the four load scenarios. Compression and lateral flexion showed higher strain in osteoporotic bone.

In lateral flexion, the strain was 0.00055 in HV and 0.00125 in OV (2.72 times of HV strain), following similar stress-strain dependence such as in the two previous cases. In the rotation movement, strain was 0.00012 in HV and 0.00025 in OV (2 times of HV strain).

In regards to the displacements, they were 0.0116 mm (HV) and 0.0219 mm (OV) in compressive load. The zone of the highest displacements was the posterior region of the vertebra, while the smallest displacement was identified in the apophysis. The displacements in flexion-extension were 0.0144 mm (OV) and 0.00711 mm (HV). Once again, the influence of the displacements had more risks in the diseased vertebra; the value was 10 times higher in OV. In lateral flexion, displacement have the same direction of the applied load, while the values were even higher than the case of compression 0.0141 mm (HV) and 0.031 mm (OV) (Fig. 6).

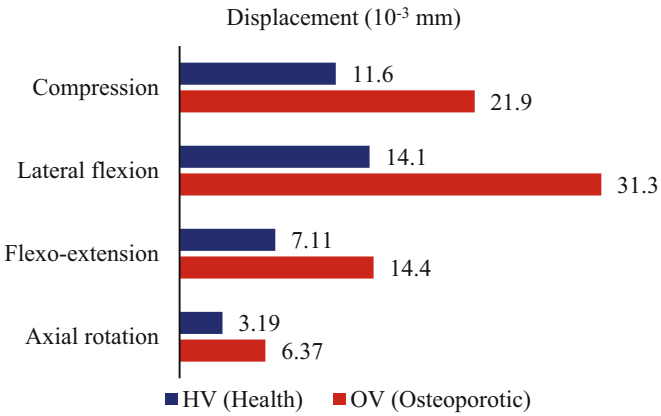

Fig. 6. Results of maximum displacements in the four load scenarios. Compression and lateral flexion showed higher displacement in the osteoporotic bone.

Several biomechanical models have been used in the simulation of spine regions. Von Farell et al. [19] studied a lumbar section with different levels of intervertebral disc degeneration. They assigned mechanical properties to the cancellous bone through a density-stiffness relationship and they defined homogeneous mechanical properties to the cortical bone. They did not use mechanical fixators. Rohlmann et al. [8] investigated the influence of an implant on the intervertebral rotation, the facet joint forces, and intra-disc pressure. They did not take into account the vertebrae displacement and defined a rigid model of the vertebrae, supposing that most of the spinal movement occurred in the intervertebral discs. Elmasry et al. [10] performed the study of the thoracolumbar region with different fixation systems. They defined constant mechanical properties in both cortical and trabecular bone.

In this work, we used a model of a posterior mechanical fixation which differs from the ones used by Elmasry et al. [10] and it is similar to the spine fixation hardware used by Rohlmann et al. [8]. The mechanical properties were not dependent to bone density as stated in the study by Von Farell et al. [19], but constant as stated by Elmasry et al. [10]. However, a comparison of healthy and osteoporotic behavior of the vertebrae was carried out by defining not only two mechanical properties for each one the healthy and the osteoporotic bone, but also four load scenarios: compression, flexion, flexion-extension and axial rotation. In further analysis, adjacent segments of the spine, mechanical properties and bone density relationship and the effect of fatigue through cyclic loads should be included.

4 Conclusions

In this paper, the L4-L5 lumbar section under four scenarios of loads and two mechanical properties (Health Vertebra HV and Osteoporitic Vertebra OV) of the bone was simulated. The model was sufficiently refined to accurately represent the geometry. The bone-screw interaction zone and the posterior of vertebra and pedicles were

susceptible to bone tissue failure, because the higher equivalent stress was close to bone failure stress. The HV stress was higher than OV stress. The higher stress was 8.83 MPa. Opposite to stress results, the strain was higher in OV than in HV, being the OV strain more than 2 times higher than HV strain.

Acknowledgment. The authors would like to thank Dr. Armando Alpizar Aguirre (Instituto Nacional de Rehabilitación de México) for providing image data. The authors acknowledge the assistance of UDIATEM. This research was supported by the Universidad Nacional Autónoma de México through the projects PAPIIT (IN115015, IN115415) and the Universidad de Camagüey through the project INI

Conflict of Interest. The authors declare no competing interests.

References

1. Morales Ávalos, R., Elizondo Omaña, R.E., Vílchez Cavazos, F., et al.: Fijación vertebral por vía transpedicular. Importancia de los estudios anatómicos y de imagen. Acta Ortop. Mex. **26**(6), 402–411 (2012)
2. Lv, C., Li, X., Zhang, H., et al.: Comparative effectiveness of two different interbody fusion methods for transforaminal lumbar interbody fusion: cage versus morselized impacted bone grafts. BMC Musculoskelet Disord **16**(207), 1–6 (2015). https://doi.org/10.1186/s12891-015-0675-2
3. Xue, H.M., Tu, Y.H., Cai, M.W.: Comparison of unilateral versus bilateral instrumented transforaminal lumbar interbody fusion in degenerative lumbar diseases. Spine **12**(2012), 209–215 (2012). https://doi.org/10.1016/j.spinee.2012.01.010
4. Rao, P.J., Mobbs, R.J.: The, "TFP" fusion technique for posterior 360° lumbar fusion: a combination of open decompression, transforaminal lumbar interbody fusion, and facet fusion with percutaneous pedicle screw fixation. Orthop. Surg. **6**(1), 54–59 (2014). https://doi.org/10.1111/os.12086
5. Liu, J., Tang, J., Liu, H.: Comparison of one versus two cages in lumbar interbody fusion for degenerative lumbar spinal disease: a meta-analysis. Orthop. Surg. **6**(3), 236–243 (2014). https://doi.org/10.1111/os.12119
6. Cisneros Hidalgo, Y.A., González Carbonell, R.A., Ortiz Prado, A., et al.: Posibilidad de aplicación de la simulación computacional de tejido óseo en niños con torsión tibial. Rev. Cubana Ortop. Traumatol. **30**(2), 193–200 (2016)
7. González Carbonell, R.A., Ortiz Prado, A., Jacobo Armendáriz, V.H., et al.: Consideraciones en la definición del modelo específico al paciente de la tibia. Rev. Cubana Inv. Bioméd. **34**(2), 157–167 (2015)
8. Rohlmann, A., Nabil Boustani, H., Bergmann, G., et al.: Effect of a pedicle-screw-based motion preservation system on lumbar spine biomechanics: a probabilistic finite element study with subsequent sensitivity analysis. J. Biomech. **43**(15), 2963–2969 (2010). https://doi.org/10.1016/j.jbiomech.2010.07.018
9. Xu, G., Fu, X., Du, C., et al.: Biomechanical effects of vertebroplasty on thoracolumbar burst fracture with transpedicular fixation: a finite element model analysis. Orthop. Traumatol.: Surg. Res. **100**(4), 379–383 (2014). https://doi.org/10.1016/j.otsr.2014.03.016
10. Elmasry, S., Asfour, S., Travascio, F.: Implications of spine fixation on the adjacent lumbar levels for surgical treatment of thoracolumbar burst fractures: a finite element analysis. J. Spine Care **1**(1), 1–5 (2016). https://doi.org/10.15761/JSC.1000105

11. Ibarz, E., Herrera, A., Más, Y., et al.: Development and kinematic verification of a finite element model for the lumbar spine: application to disc degeneration. Biomed. Res. Int. **2013**, 1–18 (2013). https://doi.org/10.1155/2013/705185
12. Wagnac, E., Arnoux, P.J., Garo, A., et al.: Finite element analysis of the influence of loading rate on a model of the full lumbar spine under dynamic loading conditions. Med. Biol. Eng. Comput. (2012). https://doi.org/10.1007/s11517-012-0908-6
13. Cheng, I., Arnold, P.M., Harris, J., et al.: Multilevel kinematic assessment of immediate and simulated long-term stabilization of novel inline cervical interbody devices with intervertebral screw, anchor, or blade fixation. Spine J. **17**(10), S101 (2017). https://doi.org/10.1016/j.spinee.2017.07.083
14. Wang, J., Zhou, B., Liu, X.S., et al.: Trabecular plates and rods determine elastic modulus and yield strength of human trabecular bone. Bone **72**(Suppl. C), 71–80 (2015). https://doi.org/10.1016/j.bone.2014.11.006
15. Chen, Y., Ma, H.T., Liang, L., et al.: A simulation study on marrow fat effect on biomechanics of vertebra bone. In: 37th Annual International Conference of the IEEE Engineering in Medicine and Biology Society (EMBC), pp. 3921–3924. IEEE EMBS, Milán (2015). https://doi.org/10.1109/EMBC.2015.7319251
16. Alkaly, R.N., Bader, D.L.: The effect of transpedicular screw design on its performance in vertebral bone under tensile loads: a parametric study. Clin. Spine Surg. **29**(10), 433–440 (2016). https://doi.org/10.1097/BSD.0b013e3182a03c70
17. González-Carbonell, R.A., Ortiz-Prado, A., Jacobo-Armendáriz, V.H., et al.: A CT-based and mechanobiologic model for the simulation of rotation of tibia deformities during patient's immobilization treatment. In: Torres, I., Bustamante, J., Sierra, D.A. (eds.) VII Latin American Congress on Biomedical Engineering, CLAIB 2016, vol. 60, pp. 449–452. Springer, Singapore (2017). https://doi.org/10.1007/978-981-10-4086-3_113
18. González-Carbonell, R.A., Ortiz-Prado, A., Jacobo-Armendáriz, V.H., et al.: 3D patient-specific model of the tibia from CT for orthopedic use. J. Orthop. **12**(1), 11–16 (2015). https://doi.org/10.1016/j.jor.2015.01.009
19. Von Forell, G.A., Stephens, T.K., Samartzis, D., et al.: Low back pain: a biomechanical rationale based on "patterns" of disc degeneration. Spine (Phila Pa 1976) **40**(15), 1165–1172 (2015). https://doi.org/10.1097/BRS.0000000000000982

Biomechanical Analysis of Weeding Labor in Mexican Farmers Through the Simultaneous Use of Photogrammetry and Accelerometry

Lázaro Morales-Acosta[1(✉)], Armando Ortiz-Prado[1], Victor Hugo Jacobo-Armendáriz[1], and Raide Alfonso González-Carbonell[2]

[1] Universidad Nacional Autónoma de México/UDIATEM, Coyoacán, DF, Mexico
lazaroo.fi@gmail.com, armandoo@unam.mx, vicjacobo@yahoo.com.mx

[2] Universidad de Camagüey/Mechanical Engineering, Camagüey, Cuba
raidel977@gmail.com

Abstract. The purpose of the paper is to study the biomechanics of sickle weeding, thus this study becomes an analytical tool for understanding the causes of injuries. Ten people with experience in sickle weeding were studied. Photogrammetry was used to define the start and end of the movement cycle under study, and accelerometry was also used to obtain the dynamic behavior of the 3D movement for sickle weeding. Accelerations recorded in the neck, cervical, trunk, and lumbar regions are characterized by movements that begin with slight oscillations. The curve moved up to reach two peaks of acceleration approximately at the 25% and the 80% of the cycle. The average acceleration for these points was fenced to 1.3 g. The highest acceleration was at the lumbar vertebra. Farmers took a bending position with the back arched up most of the time during weeding. That position provoked compression at the front of the intervertebral discs and that configuration combined with the time that they remained in this position could be an important factor in the development of low back pain.

Keywords: Low back pain · Weeding · Biomechanics

1 Introduction

Manual labor in agriculture is a work activity where injuries occur very frequently [1, 2]. Farming is an occupation that requires physical activities such as bending, kneeling, lifting, and carrying loads, among others [3]. The repetition of these actions expose workers to the development of musculoskeletal disorders [2, 4].

Sickle weeding is a common manual agricultural activity in developing countries that demands unfavorable positions for workers. According to [4], developing efficient strategies of injury prevention requires the identification of both the agricultural

© Springer Nature Switzerland AG 2020
C. A. González Díaz et al. (Eds.): CLAIB 2019, IFMBE Proceedings 75, pp. 850–857, 2020.
https://doi.org/10.1007/978-3-030-30648-9_111

activities associated with pain and the characterization of the biomechanical basis in these activities.

The development of photogrammetry and accelerometry allowed the authors to study human biomechanics. Low back pain was one of the most common musculoskeletal disorders [5]. There are reports on biomechanical research of the flexion of the spine in individuals sitting on stable [6] and unstable chairs [7]. In both studies, the range of mobility of the spine of subjects with and without injury has been compared. The range of mobility of healthy and injured individuals behaved differently. Although studies related to the occurrence of injuries in agriculture-related activities have been developed, a few biomechanical studies have been related to injuries with one type of activity [4]. The objective of this paper is to study the biomechanics of sickle weeding so that it can serve as an analytical tool for understanding the causes of the occurrence of injuries.

2 Materials and Methods

The combination of photogrammetry and accelerometry was used as a tool to monitor the sickle weeding cycle. Photogrammetry was used to identify kinematic variables of the trunk and leg and the markers path over time, the triaxial accelerometers were used to capture the orthogonal components of acceleration, following the methodology explained in [8].

2.1 Participants

Ten people with experience in sickle weeding were studied. The participant population in the study had an age range between 29 and 65 years (Table 1). The experiments were conducted in a sowing field on normal workday conditions.

The Ethics Committee of the Universidad Nacional Autónoma de Mexico passed the study protocol and obtained the informed consent from the subjects prior to testing according to the ethical standards of the responsible committee on human experimentation.

Table 1. Baseline characteristics of subjects.

Subject (n = 10)	
M/F, n	9/1, 10
Age in years: mean (SD)	47 (13)
BMI in: kg/m^2 mean (SD)	26.2 (3.7)

M: male; F: female; BMI: body mass index.

2.2 Instruments and Software

A high-speed camera (StreamView-LR portable Gigabit Ethernet) was used for photogrammetry. Four accelerometers of Zstar3 System (Freescale™ Semiconductor MMA7455L, dynamic range 2, ±4 a ±8 g, frequency response ±5%, noise level

0.0025 g 2 Hz–25.000 Hz, sensibility 64 LSB/g at 2 g. 64 LSB/g at 8 g in 10-bit mode, temperature range from −40 °C to 85 °C, current 400 μA and voltage from 2.4 V to 3.6 V) were used for accelerometry data acquisition. Dartfish ProSuite v8.0 (Friburgo, Suiza) was used for the processing of photogrammetry data, Mathematica (Wolfram Research, Boston, MA, USA) was used for the data processing and plotting.

2.3 Marker and Accelerometer Positions

Passive and reflective markers of 30 mm of diameter were placed on the right side of the workers as shows (Fig. 1). The accelerometers were enclosed on a 30 mm-diameter cylindrical white box that also served as reflective markers. Four axial accelerometers located on the neck, C7, T5, and L2 vertebrae. They were used to capture the numerical data.

Fig. 1. Position of the markers and accelerometers used to capture the numerical data.

2.4 Data Analysis

The farmworkers were doing sickle weeding. That activity consisted of abduction-adduction movements of the arm, forearm, and leg and forward bending of the trunk. Participants were recorded five times as they passed in front of the background plane (from left to right) as well as three of their sickle wedding cycle each time. Measurements were performed on Los Reyes de Juárez, Puebla.

Photogrammetry data were recorded at 640 × 480 images and 200-fps with <1% dropped frames. Data were standardized as a percentage of the cycle of sickle weeding (normalized time) in the x-axis. A e = 14 m-length and d = 2.2 m-height black cloth was placed as the background plane. Two spheres were used as a reference located at a distance

c = 2.95 m from the background plane. The high-speed camera StreamView-LR was positioned horizontally, at a height a = 1.1 m from the floor and at a distance b = 14 m from the center of the background plane.

The data from the accelerometers were captured by radio frequency at a data rate of 60 Hz and were standardized as a percentage of the cycle (normalized time) in the x-axis too (Eq. 1). Photogrammetry and accelerometry data were acquired at real time. The internal clocks of measurement equipment were synchronized.

$$\%c = \frac{(t - t_{start})}{(t_{end} - t_{start})} \times 100 \tag{1}$$

where:

t: is the time to transform into $\%c$,
t_{start}: is the time at the cycle start, and
t_{end}: is the time at the cycle end.

2.5 Statistical Analysis

Data was saved in CSV format and used as input in a series of scripts written using R (R Foundation for Statistical Computing, Vienna, Austria) for the statistical analysis. The significant level was set at 0.05. Data were tested for normality by using the Shapiro–Wilk test. The difference between knee and neck angles and between lumbar, neck, and knee acceleration were tested by using t-test for normally distributed data and Wilcoxon signed rank test for not normally distributed ones. Each participant was evaluated by the same examiner. The intra-class correlation coefficient (ICC) was used. ICC indicated variations in the population sample within and among participants [6, 9].

3 Results and Discussion

Both techniques, the sequential photogrammetry and the accelerometry, were combined. The authors considered that the combination of sequential photogrammetry and accelerometry techniques constituted a contribution to study the degree of mobility of the spine, particularly when performing an agricultural activity. In this research, photogrammetry was used to define the start and the end of the movement cycle under study; while accelerometry was used to obtain the dynamic behavior of the 3D movement of sickle weeding.

According to the results of photogrammetry, the start of the weeding cycle was established for the movement analysis. The cycle began with the farmer in a hunched over position, with his right legs on the furrow and left leg slightly ahead of the other. The arm performed flexion and extension movements and the hand did lateral rotations, combined with drag movements from front to back (these rotational and drag movements of the hand are known as weeding). After two or three continuous weeding movements of the arm, the right leg that was in the posterior position stepped forward. The cycle was completed after both legs took a step forward (Fig. 2).

Fig. 2. Characterization of the wedding cycle through photogrammetry. A bending position of the farmers' trunk for most of the time was observed, analogous to a cantilever beam in engineering.

According to [10], low back disorder risk is multi-factorial and it is influenced by the interactions between genetic, psychosocial, and workplace factors. The agricultural industry is distinguished by the exposure of workers to high-risk workplace factors. Fathallah et al. [11] stated that the agricultural stooped works represent a situation where farmers commonly perform works in open fields with little space restrictions, do not involve the use of equipment or substantial lifting. Their study showed that not only the trunk flexion was an important workplace factor associated with LBP [11], but also the time spent in a flexed posture of the trunk.

In this study, a bending position of the farmers' trunk for most of the time was observed, even when the workers moved forward while weeding. This position was analogous to what is known in engineering as a cantilever beam. This type of configuration caused the highest moment at the lower back region; thus, the tissues were more stressed. Also, this position provoked compression of the intervertebral discs. Longtime forward bending produced an increase of compression loads of spinal segments, together with the cyclic loads, could reduce the answer of spinal tissues to failure limit and fatigue life. As Adam [12] stated, the bending position of the farmers for most of the time was a position where the loads were requirements for the occurrence of injuries.

Table 2. Inter-class correlation coefficient (ICC), mean and standard deviation (SD) of angular displacements and accelerations.

Acceleration data	ICC	Mean	SD
Angular displacement data			
Neck	0.893	65.246	14.761
Knee	0.815	134.65	19.537
Acceleration data			
Neck	0.74	1.019	0.103
Cervical	0.65	1.033	0.083
Trunk	0.5	1.022	0.068
Lumbar	0.54	1.069	0.087

Significance level was set at $P < 0.05$

The neck and knee angular displacements showed a high reliability (ICC = 0.815 – 0.893, $p < 0.01$) (Table 2). The mean angles values are shown in Fig. 3. The knee angle curve of the right leg (Fig. 3a) started with a maximum value; later, it started to decrease up to 60% of the cycle. The minimum angle was at the 90% of the cycle when the leg swings during the step forward and later reached the maximum angle again. The neck curve (Fig. 3b) moved like a sinusoidal curve, both the maximum and the minimum of the curve were approximately at the 25% and the 80% of the cycle. These points corresponded to the time that workers took a step forward. The range of motion of the knee was higher than that of the neck ($p < 0.05$).

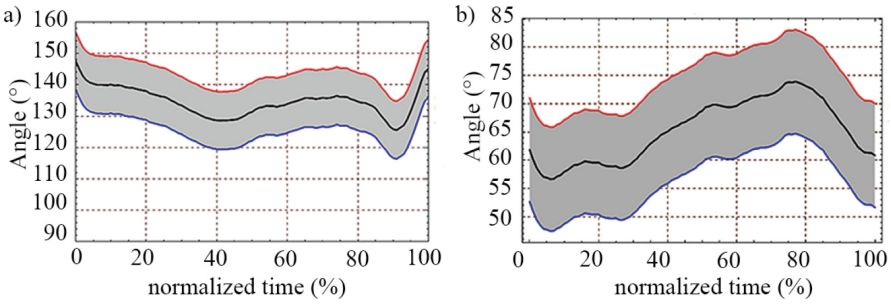

Fig. 3. Angular displacements: (a) the neck, (b) the knee.

The accelerometers results were expressed as the resultant vector of x, y, and z components. This way, the errors that could be influenced by the location of the accelerometers from one participant to another were suppressed. The acceleration data acquired from all accelerometers showed good reliability (ICC = 0.5 – 0.74, $p < 0.01$) (Table 2). The mean acceleration values for the four accelerometers are shown in Fig. 4.

The accelerations recorded in the neck, cervical, trunk, and lumbar regions were characterized by movements that began with slight oscillations. The four points where the markers were placed, move up and down at about the same time. The curve moved up to reach two peaks of acceleration approximately at the 25% and the 80% of the cycle. The average value of acceleration for these points was fenced to 1.3 g. Both points corresponded to the time that workers took a step forward and to the minimum and maximum of the neck angle. The decline between the two peaks occurred when the trunk was moving down and the arm made the movements for weeding. This occurred at the beginning and end of the cycle.

The highest acceleration was reported in the lumbar region because it was the section of the spine that was closest to the legs, so the acceleration was greater affected by the flexion and extension of the legs. Generally, accelerations were relatively low because workers accommodated their movements so that they were able to get through the workday with less discomfort. The acceleration changes produced dynamic forces that must be absorbed by the musculoskeletal system and they increased the effect of the forces in the area of the lower back.

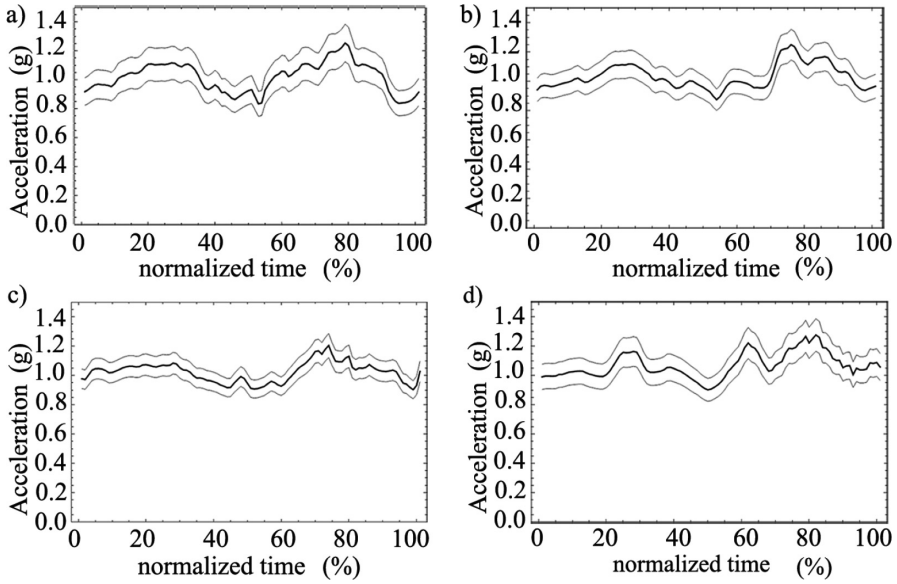

Fig. 4. Graphs of the acceleration behavior for each accelerometer positioned on: (a) the neck, (b) the C7 vertebra, (c) the T5 vertebra and (d) the L2 vertebra.

Finally, LBP is common in agricultural workers which perform manual works in an awkward posture, such as the sickle wedding, in both developing and developed countries, which stay for long periods of time with their trunks in a bending position [13]. Although the individuals selected for the study did not report suffering from episodes of LBP, they stated that at the end of the workday, they were suffering from fatigue and back problems. Intuitively participants performing the activity of weeding used the other arm as support to lessen the effect of the cantilever beam and to reduce efforts in the lumbar segment. This supporting point also helped the back to make less abrupt movements and reduced the stress in the lower back.

4 Conclusion

The use of the accelerometers placed on anatomical landmarks of the spine, allowed the authors to record the behavior of the acceleration magnitude at each position and to generate information to identify future changes in the behavior of workers. The accelerations were relatively low because workers had accommodated their movements so that they could get through the work day with less discomfort. The points where the markers were placed, moved up and down at about the same time. The farmers take a bending position with the back arched up most of the time, even when they step forward as the weeding activity progresses. This position combined with the time that they remained in this position can be an important factor in the development of lower back pain.

Acknowledgments. The authors acknowledge the farmers who participated in this project and the collaboration of professor Albertina Ortega Palma from the Escuela Nacional de Antropología e Historia. This research was supported by the Universidad Nacional Autónoma de México through the projects PAPIIT AI105115 and PAPIIT IN113710.

Conflict of Interest. Authors declare no competing interests.

References

1. McMillan, M., Trask, C., Dosman, J., et al.: Prevalence of musculoskeletal disorders among saskatchewan farmers. J. Agromed. **20**(3), 292–301 (2015). https://doi.org/10.1080/1059924X.2015.1042611
2. Mora, D.C., Miles, C.M., Chen, H., et al.: Prevalence of musculoskeletal disorders among immigrant Latino farmworkers and non-farmworkers in North Carolina. Arch. Environ. Occup. Health (2014). https://doi.org/10.1080/19338244.2014.988676
3. Weigel, M.M., Armijos, R.X., Beltran, O.: Musculoskeletal injury, functional disability, and health-related quality of life in aging Mexican immigrant farmworkers. J. Immigr. Minor. Health **16**(5), 904–913 (2014). https://doi.org/10.1007/s10903-013-9788-6
4. Fethke, N.B., Merlino, L.A., Gerr, F., et al.: Musculoskeletal pain among Midwest farmers and associations with agricultural activities. Am. J. Ind. Med. **58**(3), 319–330 (2015). https://doi.org/10.1002/ajim.22398
5. Traeger, A.C., Moseley, G.L., Hübscher, M., et al.: Pain education to prevent chronic low back pain: a study protocol for a randomised controlled trial. BMJ Open **4**(6), 1–7 (2014). https://doi.org/10.1136/bmjopen-2014-005505
6. Hidalgo, B., Gilliaux, M., Poncin, W., et al.: Reliability and validity of a kinematic spine model during active trunk movement in healthy subjects and patients with chronic non-specific low back pain. J. Rehabil. Med. **44**(9), 756–763 (2012). https://doi.org/10.2340/16501977-1015
7. Freddolini, M., Strike, S., Lee, R.Y.W.: Stiffness properties of the trunk in people with low back pain. Hum. Mov. Sci. **36**, 70–79 (2014). https://doi.org/10.1016/j.humov.2014.04.010
8. Morales-Acosta, L., Ortiz-Prado, A., Jacobo-Armendáriz, V.H., et al.: Analysis and characterization of the normal gait phases of walking Warmblood horses as a tool for the diagnosis of lameness. Pesq. Vet. Bras. **38**(3), 536–543 (2018). https://doi.org/10.1590/1678-5150-PVB-4496
9. Wolak, M.E., Fairbairn, D.J., Paulsen, Y.R.: Guidelines for estimating repeatability. Methods Ecol. Evol. **3**(1), 129–137 (2012). https://doi.org/10.1111/j.2041-210X.2011.00125.x
10. Wai, E.K., Roffey, D.M., Bishop, P., et al.: Causal assessment of occupational lifting and low back pain: results of a systematic review. Spine J. **10**, 554–566 (2010). https://doi.org/10.1016/j.spinee.2010.03.033
11. Fathallah, F.A., Miller, B.J., Miles, J.A.: Low back disorders in agriculture and the role of stooped work: scope, potential interventions, and research needs. J. Agric. Saf. Health **14**(2), 221–245 (2008). https://doi.org/10.13031/2013.24352
12. Adams, M.A.: Biomechanics of back pain. Acupunct. Med. **22**(4), 178–188 (2004). https://doi.org/10.1136/aim.22.4.178
13. Ojha, P., Kwatra, S.: An ergonomic study on the assessment of work related musculoskeletal disorder risks among agriculture workers of Uttarakhand. India Int. J. Sci. Eng. Res. **5**(1), 188–191 (2014)

Virtual Training System for Mechanical Transhumeral Prostheses

Andrea Montero(✉), Andrea Gutiérrez, and Carlos Galván Duque

Universidad Iberoamericana, 01219 Mexico City, Mexico
andreamonteroc2@hotmail.com, carlos.galvan@ibero.mx

Abstract. In Mexico, transhumeral amputation occurs due to traumatic etiology and represents 4% of all the amputations. These amputations occur during an active period of life, which limits work options and increase user demotivation. It is known that pre-prosthetic and post-prosthetic rehabilitation provides the necessary tools to improve range of motion, increase muscle strength and restore the sense of control to perform activities of daily living. For this reason, virtual therapy environments have been developed for myoelectric prostheses, leaving aside body-powered prostheses. This paper presents the design and development of virtual training system for body-powered transhumeral prostheses in pre-prosthetic therapy. The created device has allowed to efficiently simulate the control of the body-powered transhumeral prosthesis for the user and provides a tool with specific routines of occupational therapy to the therapist. Thus, this provide the opportunity to increase the acceptance of a prosthesis at a higher level.

Keywords: Amputation · Transhumeral · Prosthetic therapy · Virtual simulation

1 Background

In Mexico, there were 935,000 amputees in 2014. Transhumeral amputations (above elbow) represent 4% of them, and their etiology is mainly traumatic. It is said, that the loss of an upper limb (or part of it), results in a 50% of disability. This is more relevant if we consider that this kind of amputations, usually occur while people is economically active [1].

Upper limb amputees can perform much of their activities with the use of prostheses. Nevertheless, this kind of prostheses have a high rate of rejection and consequent abandonment. Transhumeral prostheses have a 57% rate of rejection. This is associated to several factors, such as the skill developed by the patient with the healthy hand, lack of training, the insufficient ability to use the prosthesis, a poorly fabricated prosthesis, among others [2].

In order to obtain successful outcomes in rehabilitation for the upper limb amputee, multiple factors must be addressed, including patient-directed prosthetic training and a multidisciplinary approach rehabilitation [3]. This group of specialists provide tools

© Springer Nature Switzerland AG 2020
C. A. González Díaz et al. (Eds.): CLAIB 2019, IFMBE Proceedings 75, pp. 858–865, 2020.
https://doi.org/10.1007/978-3-030-30648-9_112

such as occupational and physical therapies, helping to improve range of motion and muscle strength, and to restore the sense of control to perform activities of daily living.

Different studies have shown that the use of virtual reality for stroke rehabilitation, carried out with traditional occupational therapy, provides efficient results, and patients show satisfaction, motivation and improvement in functional activity [4–6].

In the prosthetic field, these kinds of therapies have been only used for training with myoelectric prostheses, which had positive results, for example, in the treatment of the phantom limb, increasing the user's motivation and decreasing the rejection rate [7, 8]. However, there is not a virtual reality application for therapy with body-powered prostheses, which are the most used kind of prostheses due to costs.

Therefore, a virtual training system for body-powered transhumeral prostheses (BPTHP) was created for pre-prosthetic therapy and evaluated with the User Satisfaction Evaluation Questionnaire.

2 Methodology

The virtual training system consists of a hardware that simulates the control mechanism of a BPTHP, by means of a harness and a force sensor. Additionally, it has a software, that displays the measured values, allows to program training routines, provides biofeedback and generates a database of patients.

2.1 Hardware

2.1.1 Bracelet and Harness

The bracelet simulates the socket of a BPTHP, which can be adapted to different stump circumferences, without affecting the distribution of the sensors. It has two main segments:

(1) *Terminal device*. Is in the most distal part, it controls the hook and the mechanic elbow. A load cell gauge (YZC-131 20 kg) was used to determinate the tension force exerted on the control cable that generates the opening of the hook or the flexion of the elbow.
(2) *Simulation of locking and unlocking of the elbow*. A pull chain switch, located on the anterior side in the middle third of the bracelet, was employed to simulate the locked or unlocked status of the elbow. The status was selected by pulling the chain through scapular retraction or shoulder extension.

A Northwestern transhumeral harness, was used to control the prototype and as suspension system. This type of harness is less restrictive to the movement and easy to adapt to the patient's dimensions.

2.1.2 Data Acquisition

The acquisition of the force data and the calculation of the positions of both, the terminal device and the elbow, were made with an Arduino Uno microprocessor (Fig. 1). The conditioning of the signal obtained from the force sensor, was done by a module (HX711), which has a default data frequency of 10 Hz. This module was

connected to analog inputs of the microprocessor, which calculates the opening angle of the hook, as well as the angle of elbow flexion and extension.

The elbow status, defines if the force applied to the control cable generates an opening of the hook or a flexion of the elbow. A digital "zero" from the pull chain switch indicates an "unlocked" status, while a digital "one", refers to a "locked" status. When the elbow is unlocked, the force is used for the flexion of the elbow; when the elbow is locked, the force is used for the opening of the hook. This digital input enters to the digital port of the microprocessor.

The opening angle of the hook was estimated using, as reference, the forces reported by Smit et al. for Hosmer Model 5XA Hook. [9] The flexion of the elbow was obtained using the arm length and the hook weight reported by manufacturers. The user, through the graphic interface, provides these two parameters.

The communication between the microprocessor and a computer (Dell Intel ® Pentium ®, CPU N3710 @ 1.6 Hz, operating system Windows 10) was made by the USB port.

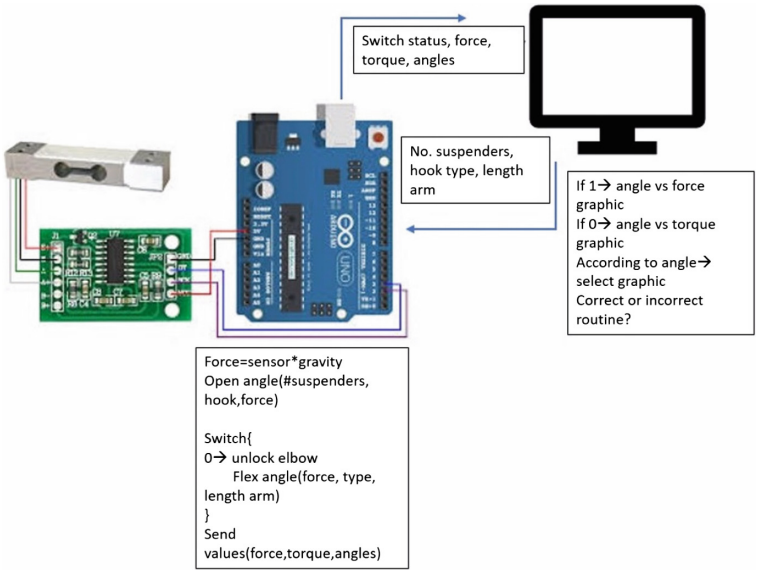

Fig. 1. General scheme of data acquisition by the force sensor.

2.2 Software

A relational and entity-relationship model was used to establish the structure of the database in MySQL. The entities that were managed were:

(1) *Therapist:* which includes the data of the therapist, user and password.
(2) *Patient*: personal data of the patient, height, arm length, observations.
(3) *Hook:* displays a list of predefined commercial hooks and features.

(4) *Routine:* gives the option to choose the number of tension bands, the waiting time to validate each movement and the total routine time.
(5) *Actions:* shows the list of actions that the patient can perform, for example, open hook, close hook, elbow flexion, elbow extension.

The software includes a method for evaluation of the patient's performance in which the therapist assigns a qualification.

The Eclipse software was used to design the graphic interface for both, the therapist and the patient. This interface consists of 3 main screens:

(1) "*Log in screen"* The therapist logs in to his account or registers a new user.
(2) *"Main screen"*. Collects the necessary patient information, the characteristics of the hook, and the routine to be performed, selected by the therapist.
(3) *"Patient Screen"*. The patient is able to observe the movement that is being executed of the prosthesis by means of images.

The therapist has the option to stop, pause or skip instructions and generate a report with the patient information.

2.3 User Satisfaction Evaluation Questionnaire

The "User Satisfaction Evaluation Questionnaire" (USEQ) was used to evaluate the virtual reality system, specifically for rehabilitation. It consists in 6 questions rated on a Likert scale of 5 points. This questionnaire was used because users have reported that it is easy to understand, and since it is a short questionnaire they did not get distracted while they answered it. In addition, the USEQ was developed specifically for evaluation of virtual rehabilitation systems [10, 11].

The tests were done with ten healthy volunteers. The tests consisted in making use of the harness and the software (in both roles, therapist and patient). All parts of the process were tested, from the placement of the harness, to connect it to the computer and the use of the graphic interface. The volunteers were instructed in the use of the software and they were left to interact with it before the test. The questionnaire (see Table 1) was answered at the end of the test anonymously via Survey Monkey ®.

Table 1. The *"User Satisfaction Evaluation Questionnaire"* (USEQ) [11]

Question	Response
	Not at all – very much
1. Did you enjoy your experience with the virtual training system?	1 2 3 4 5
2. Were you successful using the virtual training system?	1 2 3 4 5
3. Were you able to control the virtual training system?	1 2 3 4 5
4. Is the information provided by the virtual training system clear?	1 2 3 4 5
5. Did you feel discomfort during your experience with the virtual training system?	1 2 3 4 5
6. Do you think that the virtual training system will be helpful for rehabilitation?	1 2 3 4 5

3 Results

The harness is shown in Fig. 2 (for the right side), the four quick release buckles allow to adjust the harness to the size of the patient and to couple to right or left bracelet. This harness provides suspension to the bracelet and simulation of the control system of a BPTHP. It has two bracelets; one for each side (right or left), this prevents the components from moving and alter their functionality.

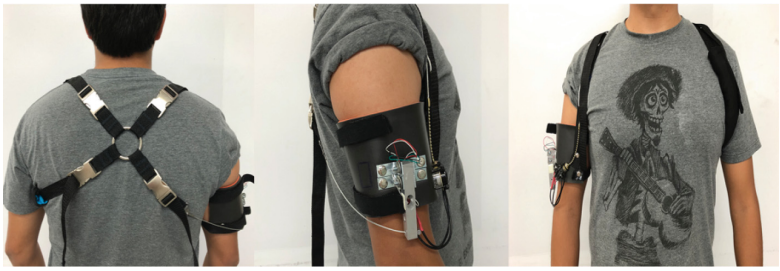

Fig. 2. The Northwestern transhumeral harness as BPTHP control and suspension system. The bracelet has 3 main elements, pull chain switch, force sensor and module.

Figures 3 and 4 illustrate the screens of the graphic interface: log in screen, main screen and patient screen.

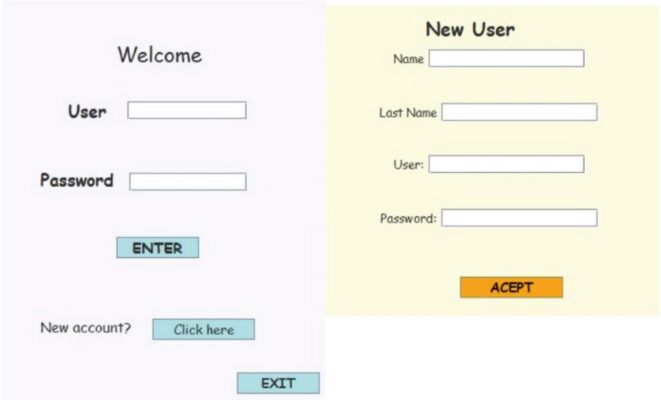

Fig. 3. "*Log in screen*". The therapist creates a new account (right) or login (left) in order to access to his patient's clinical records, or manage a new one.

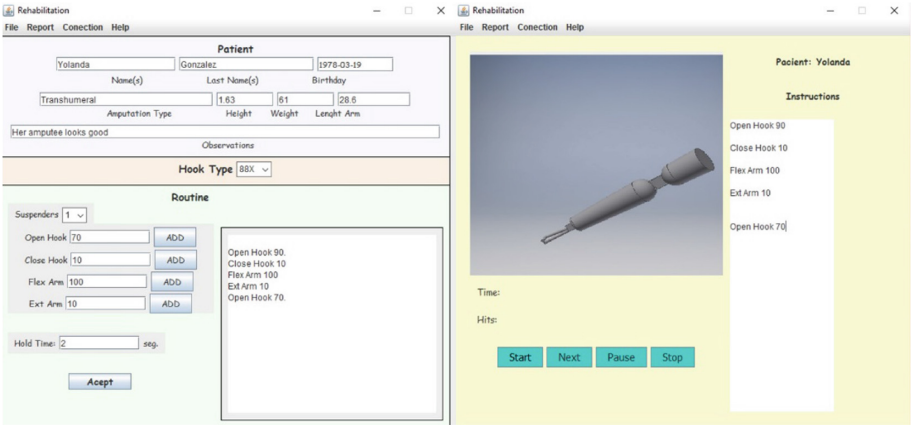

Fig. 4. Left "*Main screen*". Therapist enters all the relevant data of the patient, selects the type of hook to use in the tests, creates a unique routine for each patient. Right, "*Patient screen*". Allows to the patient and therapist to observe the movements in real time, a qualification is assigned to each task by therapist.

Results of USEQ by ten healthy volunteers are shown on Table 2. Although the number of users is not enough to statistically conclude the satisfaction of the system, these initial tests are promising. The prototype, without counting question 5, has a global average of 4.12 of 5.00.

The users demonstrated to enjoy the use of the prototype (Q1, mean ± SD = 4.20 ± 0.42); and considered the information provided by the prototype is clear (Q4, mean ± SD = 4.50 ± 0.53). Question five, refers to the disconformity of the prototype in general, which the subjects answered with a low rating (Q5, mean ± SD = 2.1 ± 0.74), it means that they did not feel important discomfort. One user commented that the harness was mismatched after a while using it. Two subjects expressed that the cables are annoying, and one said that he would like that the communication would be via Bluetooth.

Table 2. Mean and SD.

Question	Result (N = 10)	
	Mean	SD
1. Did you enjoy your experience with the virtual training system?	4.20	0.42
2. Were you successful using the virtual training system?	3.90	1.10
3. Were you able to control the virtual training system?	3.90	0.74
4. Is the information provided by the virtual training system clear?	4.50	0.53
5. Did you feel discomfort during your experience with the virtual training system?	2.10	0.74
6. Do you think that the virtual training system will be helpful for rehabilitation?	4.10	1.29

4 Discussion

The bracelets adapt to different stump sizes. This allows their adjustment to people with different stump lengths and volumes, as well as amputated side, simulating the socket of the prosthesis for a wide variety of patients.

The Northwestern type harness has the ability to modify to different sizes of people and meets the typical characteristics of the fastening and control systems of the BPTHP. In addition, the location of the force sensor and the switch, allows to simulate, in a realistic way, the control of the prosthesis through scapular retraction and shoulder extension. The hardware was adequate to capture the movements of the patient in order to control the BPTHP.

USB communication transmits the data (in both directions) and permits the system to processes the information obtained from the hardware in an efficient way for the user's interaction. The virtual system can be adjusted for different arm lengths, types of hooks and number of elastic bands, providing a wide variety of prosthetic configurations and modes of use. The graphical interface lets the therapists to create different routines of exercises for the patient, to evaluate the performance and to generate reports of the therapy sessions, which can be used for the follow up of each patient. The interface is designed for friendly use and intuitive learning, and the volunteers were able to use it after a short instruction.

USEQ shows that the virtual system was entertaining for the volunteers (4.2 ± 0.42), this suggest that it can improve the motivation and therapy adherence of the patients. The volunteers also reported that the system can be successfully used and controlled, therefore, its implementation in a rehabilitation center could be possible in future stages of the project. The provided information for the use of the system was clear (4.5 ± 0.53), this indicates that the design of the graphic interface fulfills the user's needs. Although most of the users reported not to feel discomfort with the virtual system, the adjustment of the harness was lost during the test for one user. This happened because the tape used for the axilla loop of the harness was softer than the rest of the bands; this caused less traction in the buckles so the tape slipped. The other complain about the system was reference to the cables. The actual version of the system uses cables for communication with the computer, however, it is planned to change to a Bluetooth communication in the next versions to improve the comfort.

5 Conclusions

The high rejection rate of the upper limb prosthesis makes necessary to look for playful and functional alternatives, for the training of the use of body-powered prostheses, and to increase the motivation of the user.

The developed device allows a simple way to simulate the control of a BPTHP, and offers a tool to perform specific therapy routines before the prosthesis is fabricated. Preliminary tests suggest that the use of this device could improve motivation of the patients for therapy. Future work includes the realization of tests with BPTHP users, as well as the generation of a virtual environment to achieve a greater immersion of the patient in the therapy simulation system.

References

1. Vázquez, E.: Los amputados y su rehabilitación, un reto para el estado, 1a ed. Academia Nacional de Medicina de México, México (2016)
2. Resnik, L., Ekerholm, S., Borgia, M., Clark, M.A.: A national study of Veterans with major upper limb amputation: Survey methods, participants, and summary findings. PLoS One **14**(3), 1–24 (2019)
3. American Academy of Orthopaedic Surgeons: Atlas of Amputations and Limb Deficiences. Surgical, Prosthetic, and Rehabilitation Principles, 3a ed. American Academy of Orthopaedic Surgeons, Illinois, Estados Unidos (2004)
4. Sou, A.H., Hassani, M.A., Amini, M., Sheikhi, M.: The effects of virtual reality on upper limb function in chronic stroke patients: a clinical trial. Iran. Rehabil. J. **17**(1), 81–89 (2019)
5. Mejía, J.A.: Upper limb rehabilitation therapies based in videogames technology review. In: Global Medical Engineering Physics Exchanges/Pan American Health Care Exchanges (GMEPE/PAHCE), Buenos Aires, Argentina, pp. 1–5 (2019)
6. Saposnik, G., Levin, M.: Virtual reality in stroke rehabilitation. Stroke **42**(5), 1380–1386 (2011)
7. Singhal, A.S.M., Smita, E., Sreenivas, S., Appaji, A.M.: Virtual reality in rehabilitating amputees suffering from phantom limb pain. In: 11th International Conference on Communication Systems and Networks (COMSNETS), Bengaluru, India, pp. 801–806 (2019)
8. Sturma, A., Hruby, L.A., Prahm, C., Mayer, J.A., Aszmann, O.C.: Rehabilitation of upper extremity nerve injuries using surface EMG biofeedback: protocols for clinical application. Front. Neurosci. **12**, 906 (2018)
9. Smit, G., Bongers, R.M., Van der Sluis, C.K., Plettenburg, D.H.: Efficiency of voluntary opening hand and hook prosthetic devices: 24 years of development? J. Rehabil. Res. Dev. **49**(4), 523–534 (2012)
10. Gil-Gómez, J.-A., Manzano-Hernández, P., Albiol-Pérez, S., Aula-Valero, C., Gil-Gómez, H., Lozano-Quilis, J.-A.: USEQ: a short questionnaire for satisfaction evaluation of virtual rehabilitation systems. Sensors **17**(7), 1589 (2017)
11. Gil-Gómez, J.-A., Gil-Gómez, H., Lozano-Quilis, J.-A., Manzano-Hernández, P., Albiol-Pérez, S., Aula-Valero, C.: SEQ: suitability evaluation questionnaire for virtual rehabilitation systems. Application in a virtual rehabilitation system for balance rehabilitation. In: Proceedings of the 7th International Conference on Pervasive Computing Technologies for Healthcare (PervasiveHealth 2013), pp. 335–338 (2013)

Energy Harvesting from Fingers Motions Using a Wearable System: An Experimental Analysis

Omar Méndez-Lira(✉), Ernesto Sifuentes, and Rafael González-Landaeta

Universidad Autónoma de Ciudad Juárez, 32310 Ciudad Juarez, Chihuahua, Mexico
all83006@alumnos.uacj.mx

Abstract. An experimental analysis is presented in order to assess the best conditions for energy harvesting from the movement of the fingers using a glove-shape wearable system. Polyvinylidene Fluoride (PVDF) piezofilms were used as piezoelectric generators; they were mounted on the glove so they coincide with different interphalangeal joints on both sides of each finger of the right hand. Two scenarios have been carried out for five minutes each and the root-mean-square (rms) voltage of each piezofilm was measured. Scenario 1 consisted in the use of a computer mouse for browsing different web-sites on the internet; scenario 2 consisted in the use of a keyboard to write a text of 190 words. Scenario 2 produced the greater voltage because the number of keys depressed was higher in comparison with the number of clicks on the computer mouse. In the Scenario 1, the greater voltage was obtained from the piezofilm located on the thumb which is a finger not involved with the click action when using a computer mouse so, in this case, it is possible to harvester energy from three fingers instead of two, as have been reported in previous studies. From the results obtained in both scenarios, the best location to place the piezofilms to increase energy harvesting is the posterior side of each finger, specifically on the proximal interphalangeal and metacarpophalangeal joints. Placing the piezofilms on the fingertips did not produce an increase in the generated voltage.

Keywords: Energy harvesting · Biomechanical energy · Fingers motions · Wearable system

1 Introduction

Continuous progress in reducing the size and power consumption of electronic systems has allowed a fast-growing development of wearable technology. One of the aims of wearable systems is to offer basic healthcare monitoring to the people in nonhospitalary environments. However, if long-term monitoring is desired, the limited power source (typically a battery) becomes a handicap. Thus, there is a tradeoff between the operating time and the mass of the system because of the size of long-term batteries [1]. Additionally, some batteries cause other problems due to their short-life cycle, high maintenance costs, and their environmental impact because of toxic materials that they

© Springer Nature Switzerland AG 2020
C. A. González Díaz et al. (Eds.): CLAIB 2019, IFMBE Proceedings 75, pp. 866–873, 2020.
https://doi.org/10.1007/978-3-030-30648-9_113

contain. To tackle these, in the last decades, energy harvesting systems have been proposed in order to develop more autonomous systems [2].

Energy harvesting consists in transform the environment energy into electrical energy to be stored later. The main sources for energy harvesting are light, temperature differences, electromagnetic radiation, and movement; each one with its respective advantages and disadvantages [3]. Starner [4], published one of the first works that discuss the possibility of harvest energy from human activities such as: movement of the upper and lower limbs, breathing, blood pressure, body heat and the movement of the fingers. Numerous wearable biomechanical energy harvesters have been reported. To name a few, there has been mounted piezoelectric generators in shoes [5–8], backpacks [9, 10], watchstraps [8] and clothes [11, 12], all of them oriented to harvester energy from the movement of different parts of the human body. Recently, there have been efforts to collect energy from the movement of the fingers when a subject manipulates a keyboard or a computer mouse, which are daily common activities of many people. For this, glove-shape wearable systems have been developed, where piezoelectric generators are placed on the fingers [13–15], being the common options the use of Lead Zirconate Ti-tanate (PZT) and Polyvinylidene Fluoride (PVDF). The PZT is a ceramic characterized for having good piezoelectric coefficients, but it is brittle, which is an unwanted feature for a wearable system. The polymer-based PVDF exhibits excellent mechanical flexibility, which makes it a good option to be integrated into wearable systems, but it has lower piezoelectric coefficients [16].

Many efforts have been made to improve the performance of harvesting systems, focusing on the materials, circuits, and conversion methods [2]. However, few studies have focused on determining the optimal placement of the piezoelectric generators on a glove-shape wearable system. In this work, the amount of voltage generated is evaluated when the piezofilms are placed on the distal, proximal and metacarpal interphalangeal joints of the right hand including both anterior and posterior side of the fingers. The intention is to determine the best location of the piezofilms on the fingers to increase the generation of voltage. The results obtained in this work are the starting point to assess the best conditions to increase the energy harvesting from fingers motions that allow us to supply a batteryless wearable system that detects the cardiac activity in the wrist or, in the worst case, to extend the period of battery replacement used as a power source of the system.

2 Energy Harvesting

At first instance, some energy can be produced when depressing the keys of a keyboard or the buttons of a computer mouse. According to [4], a typical keyboard requires between 40 and 50 g of mass to depress a key, which represents forces between 0.392 and .490 N. According to [17], the minimum force necessary to activate a button of a standard size computer mouse is about 0.65 N. So, it is possible to estimate the power, P, that can be generated when using a keyboard or a computer mouse, that is:

$$P = F \cdot d \cdot \left(\frac{\#\ keystrokes\ or\ \#\ clicks}{s} \right) \text{mW}, \tag{1}$$

where F is the force necessary to depress a key of a keyboard or a button of a computer mouse the distance d necessary to register a keystroke or a click. The greater the number of keystrokes or clicks the greater the power generated.

3 Materials and Methods

The piezoelectric generators used in this work are the LDT1-028K from Measurement Specialties. This is a multi-purpose PVDF piezoelectric film commonly used for detecting physical phenomena such as vibration and impact. This piezofilm produce a voltage (Voltage Mode) or a charge (Charge Mode) in the direction i according to the intensity and the direction j of the deformation of the active area. The main characteristics of the piezofilms used are presented in Table 1.

Table 1. Electrical characteristics and dimensions of the LDT1-028K [18].

Property	Value	Units
Output resistance, R_o	10 (max)	MΩ
Capacitance, C_o	1.38	nF
Piezoelectric voltage constant, g_{ij}	$g_{31} = 216 \times 10^{-3}$ $g_{33} = -330 \times 10^{-3}$	Vm/N
Piezoelectric charge constant, d_{ij}	$d_{31} = 23$ $d_{33} = -33$	pC/N
Large	41.40	mm
Width	16.26	mm
Thickness	28	μm

We used the piezofilms in Voltage Mode in order to estimate the voltage generated in each test. For this, the output of each piezofilm was connected independently to the analog inputs of a 16 bits Data Acquisition System USB-6341 from National Instruments. The system was connected to a laptop and was configured to acquire data during 5 min at 1 kSa/s. The procedure was repeated 5 times for each test and the data were stored in a laptop for further analysis.

In order to assess the voltage generated by the piezofilms located on the fingers, two different test scenarios were carried out: Scenario 1: the subject browsed different web-sites on the internet using a computer mouse M310 from Logitech for 5 min. There were no restrictions about the number of clicks executed by the subject. Scenario 2: the subject used a laptop keyboard Inspiron 7559 from Dell to write a text of 190

words for 5 min (3.97 keystrokes/s). According to [4], the subject who made both tests is considered a moderately skilled QWERTY typist.

The piezofilms were mounted on a right-hand glove; once the glove was put on the right hand of the subject, the positions of the piezofilms coincide with different interphalangeal joints of the hand. The interphalangeal joints used in each test were (Figs. 1 and 2):

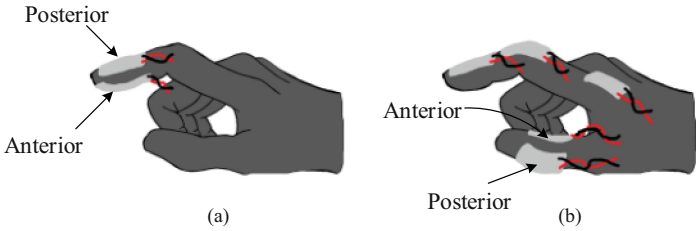

Fig. 1. Configuration of the piezoelectric generators on the glove used for the computer mouse test: (a) $ADIP_i$ and $PDIP_i$; (b) $PPIP_i$, $PMCP_i$ $PDIP_i$, $APPIP_t$ and $PPIP_t$.

Scenario 1: Using a computer mouse

(a) Anterior distal interphalangeal joint ($ADIP_i$) and posterior distal interphalangeal joint of the index finger ($PDIP_i$) (Fig. 1a).
(b) Posterior proximal interphalangeal joint of the index finger ($PPIP_i$) (Fig. 1b).
(c) Posterior metacarpophalangeal joint of the index finger ($PMCP_i$) (Fig. 1b).
(d) Anterior proximal interphalangeal ($APIP_t$) and posterior proximal interphalangeal of the thumb ($PPIP_t$) (Fig. 1b).

Scenario 2: Using a computer keyboard:

(a) Anterior distal interphalangeal joint of the index, medium, ring and little fingers ($ADIP_f$) and anterior proximal interphalangeal joint of the thumb ($APIP_t$) (Fig. 2a).
(b) Posterior distal interphalangeal joint of the index, medium, ring and little fingers ($PDIP_f$) and posterior proximal interphalangeal joint ($PPIP_t$) (Fig. 2b).
(c) Posterior proximal interphalangeal joint of each one of the five fingers (PPIP) (Fig. 2c).
(d) Posterior metacarpophalangeal joint of the index, medium, ring and little fingers ($PMCP_f$) and posterior proximal interphalangeal joint ($PPIP_t$) (Fig. 2d).

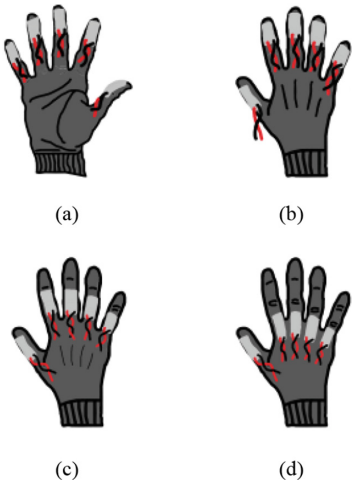

Fig. 2. Configuration of the piezoelectric generators for the computer keyboard test: (a) $ADIP_f$ and $APIP_t$; (b) $PDIP_f$ and $PPIP_t$; (c) PPIP; (d) $PMCP_f$ and $PPIP_t$.

4 Results

The use of the computer keyboard produced more rms voltage than that produced with the use of the computer mouse. According to (1), this is an expected result because, during the tests, the number of keystrokes was greater than the numbers of clicks. In the Scenario 1, the piezofilm located on the posterior side of the index finger produced a root-mean-square (rms) voltage of 0.834 V, while the voltage obtained from the piezofilm located on the anterior side (fingertips) was 0.847 V. One would expect to obtain a much higher voltage from the piezofilm located on fingertips, where the impact between the finger and the surface of the mouse button is sensed. However, the results reveals that there is no significant difference between the voltages obtained when the piezofilms were placed on the anterior and on the posterior side of the index finger.

Figure 3 shows the average and the standard deviation of the rms voltage obtained from each piezofilm in the scenario 1, where some interesting conclusions can be drawn. Paradoxically, the greater rms voltage (1.218 V) was obtained from the piezoelectric generator located on the posterior side of the thumb, which is a finger that is not involved with click action of the computer mouse, so (1) does not apply here. This result can be attributed to the muscular activity involved in the process of moving the mouse, where slight movements of the wrist and of the ring and thumb fingers are required, being the thumb one of the most used finger. With this finger, a significant difference was obtained between the rms voltage obtained from the piezofilm located on the posterior side of the thumb and that located on the anterior side. In regards to the index finger, the higher voltage (0.944 V) was generated when the piezofilm was located on the posterior distal interphalangeal joint.

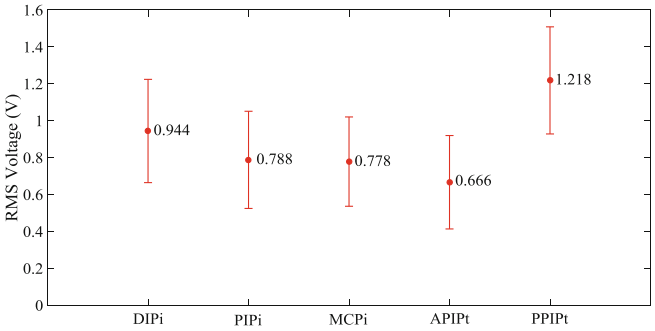

Fig. 3. RMS voltage generated by each piezofilm located at different interphalangeal joints on the posterior side of the index finger and on the anteroposterior sides of the thumb at the proximal interphalangeal joint. Test: Scenario 1.

Figures 4 and 5 show the results obtained in the Scenario 2, where in Fig. 4 are presented the average and the standard deviation of the rms voltage generated from each piezofilm located on the anterior side of each finger, while Fig. 5 shows the results obtained when the piezofilms were located on the posterior side of each finger. Firstly, comparing the results of both figures, there is a significant difference between the rms voltages generated. We obtained 2.329 V from the piezofilms located on the anterior side and 1.180 V from the piezofilms of the posterior side of the proximal interphalangeal joint of the thumb. That is, changing the side of the location of the piezofilm in the same finger and interphalangeal joint, we gained 1.149 V. Secondly, the higher rms voltages were obtained from the piezofilms located on the posterior side of the metacarpophalangeal and the proximal interphalangeal joints of the other four fingers. In our case, the highest voltage was produced with the piezofilm located on the proximal interphalangeal joint of the little finger (3.044 V). The average rms voltage obtained in this test is greater than that presented in [15], where PZT generators (with

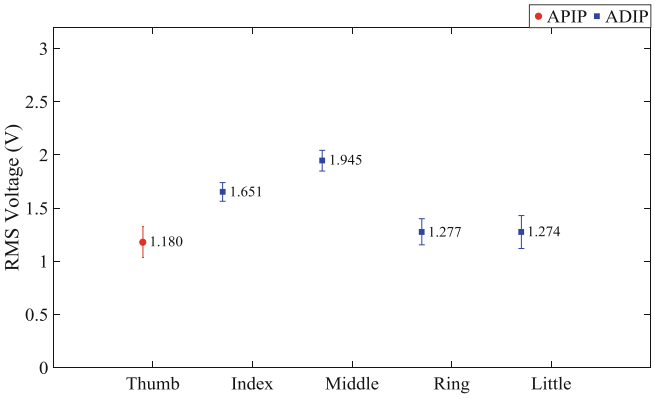

Fig. 4. RMS voltage generated by each piezofilm located at different interphalangeal joints on the anterior side of each of the five fingers. Test: Scenario 2.

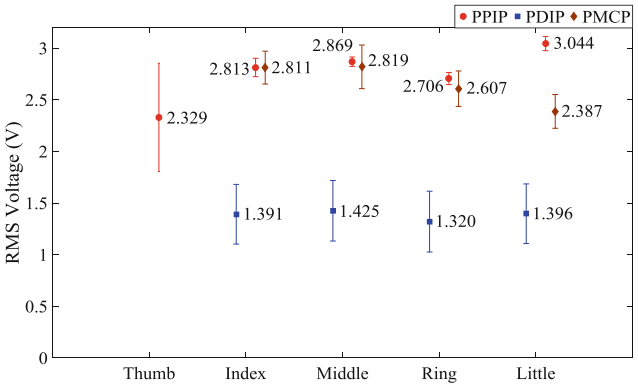

Fig. 5. RMS voltage generated by each piezofilm located at different interphalangeal joints on the posterior side of each of the five fingers. Test: Scenario 2.

higher piezoelectric coefficients) were placed on the fingertips of a QWERTY typist who wrote a text of 602 words. The fact of placing the piezofilms on the fingertips, makes it difficult for them to make correct contact with the keys of the keyboard due to the design of the glove [15]; therefore, placing the piezofilms on the posterior side of the fingers gives more freedom to the subject to use the keyboard without any restrictions.

5 Conclusions

In this work, we assessed the best conditions to increase the voltage generated from the movement of the fingers using piezoelectric generators when a subject use a computer mouse and a keyboard. In both scenarios, the greater rms voltages were obtained when the piezofilms were located on the posterior sides of the fingers, specifically on the proximal interphalangeal and the metacarpophalangeal joints. When the subject used the computer mouse, the greater voltage was obtained from the piezofilm located on the thumb, which is a finger not involved with the click action, but it does contribute to the movement of the mouse where a not negligible force must be applied by the ring and the thumb fingers. This reveals that, in this scenario, a quantifiable energy can be harvested not only from the fingers involved with the click action as has been reported in [15], but also from the fingers involved with the movement of the mouse. Placing the piezofilms on the posterior side of the fingers, not only achieves more rms voltage, but also does not restrict the use of the keyboard or the computer mouse to depress a key or a click.

Acknowledgment. This work has been partially funded by PRODEP and UACJ, Mexico.

Conflict of Interest. The authors declare that they have no conflict of interest.

References

1. Magno, M., Boyle, D.: Wearable energy harvesting: from body to battery. In: 12th International Conference on Design and Technology of Integrated Systems in Nanoscale Era (DTIS), pp. 1–6 (2017)
2. Yang, Z., Zhou, S., Zu, J., Inman, D.: High-performance piezoelectric energy harvesters and their applications. Joule **2**(4), 642–697 (2018)
3. Mitcheson, P.D., Yeatman, E.M., Rao, G.K., Holmes, A.S., Green, T.C.: Energy harvesting from human and machine motion for wireless electronic devices. Proc. IEEE **96**(9), 1457–1486 (2008)
4. Starner, T.: Human-powered wearable computing. IBM Syst. J. **35**(3.4), 618–629 (1996)
5. Shenck, N.S., Paradiso, J.A.: Energy scavenging with shoe-mounted piezoelectrics. IEEE Micro **21**(3), 30–42 (2001)
6. Paradiso, J.A., Starner, T.: Energy scavenging for mobile and wireless electronics. IEEE Pervasive Comput. **4**(1), 18–27 (2005)
7. Zhao, J., You, Z.: A shoe-embedded piezoelectric energy harvester for wearable sensors. Sensors **14**(7), 12497–12510 (2014)
8. Jung, W.-S., Lee, M.-J., Kang, M.-G., Moon, H.G., Yoon, S.-J., Baek, S.-H., et al.: Powerful curved piezoelectric generator for wearable applications. Nano Energy **13**(4), 174–181 (2015)
9. Granstrom, J., Feenstra, J., Sodano, H.A., Farinholt, K.: Energy harvesting from a backpack instrumented with piezoelectric shoulder straps. Smart Mater. Struct. **16**(5), 1810 (2007)
10. Lund, A., Rundqvist, K., Nilsson, E., Yu, L., Hagström, B., Müller, C.: Energy harvesting textiles for a rainy day: woven piezoelectrics based on melt-spun PVDF microfibres with a conducting core. npj Flex. Electron. **2**(1), 9 (2018)
11. Proto, A., Fida, B., Bernabucci, I., Bibbo, D., Conforto, S., Schmid, M., et al.: Wearable PVDF transducer for biomechanical energy harvesting and gait cycle detection. In: IEEE EMBS Conference on Biomedical Engineering and Sciences (IECBES), pp. 62–66 (2016)
12. Proto, A., Vlach, K., Conforto, S., Kasik, V., Bibbo, D., Vala, D., et al.: Using PVDF films as flexible piezoelectric generators for biomechanical energy harvesting. Lékař Tech.-Clin. Technol. **47**(1), 5–10 (2017)
13. Cha, Y., Hong, J., Lee, J., Park, J.-M., Kim, K.: Flexible piezoelectric energy harvesting from mouse click motions. Sensors **16**(7), 1045 (2016)
14. De Pasquale, G., Kim, S.-G., De Pasquale, D.: GoldFinger: wireless human–machine interface with dedicated software and biomechanical energy harvesting system. IEEE/ASME Trans. Mechatron. **21**(1), 565–575 (2016)
15. Psoma, S., Tzanetis, P., Tourlidakis, A.: A practical application of energy harvesting based on piezoelectric technology for charging portable electronic devices. Mater. Today: Proc. **4**(7), 6771–6785 (2017)
16. Choi, Y.-M., Lee, M., Jeon, Y.: Wearable biomechanical energy harvesting technologies. Energies **10**(10), 1483 (2017)
17. Komandur, S., Johnson, P.W., Storch, R.: Relation between mouse button click duration and muscle contraction time. In: 30th Annual International Conference of the IEEE Engineering in Medicine and Biology Society, pp. 2299–2301 (2008)
18. Measurement Specialties Inc. Technical manual, p. 28 (2008)

Assessment of Plantar Pressure in a Foot Finite Element Model Considering a Sliding Contact Between Soft Tissues

Marco A. Martínez Bocanegra[1,2(✉)], Javier Bayod[2], Agustín Vidal-Lesso[1], Ricardo Becerro de Bengoa Vallejo[3], and Andrés Mena Tobar[2]

[1] División de Ingenierías Campus Irapuato-Salamanca, Universidad de Guanajuato, Salamanca, Guanajuato, Mexico
marco.890310@hotmail.com, agustin.vidal@ugto.mx
[2] Escuela de Ingeniería y Arquitectura, Universidad de Zaragoza, Zaragoza, Spain
jbayod@unizar.es, andresmt77@gmail.com
[3] Facultad de Enfermería, Fisioterapia y Podología, Universidad Complutense de Madrid, Madrid, Spain
ribebeva@enf.ucm.es

Abstract. Currently, most finite element models of the foot in literature have simplifications, mainly in terms of real and complete modeling of soft tissues and their proper transmission of the force, causing limitations in the response of the model. A deficient transmission of the force among muscles, tendons and plantar fascia occurs due to unions with other tissues or excessive displacement. These kinds of problems can be fixed, doing the separation among tissues and applying appropriated contacts or displacement constraint conditions.

Therefore, the objective of this study is to evaluate changes in plantar pressure in a three-dimensional model of finite elements of a foot in the second rocker of gait when considering the relative displacement and load transmission between muscles, tendons and plantar fascia.

Through scanning and 3D processing, the geometries of the tissues were obtained. First-order tetrahedral elements were used for meshing and were considered models of linear elastic and hyperelastic material. The fixed connections among tissues were separated, and in some of these areas, contacts were simulated, allowing a relative sliding of the tissues and proper transmission of force.

Results obtained into this work showed a maximum contact pressure localized under the calcaneus of 0.1925 MPa for the sliding contact model (SCM) and 0.1710 MPa for the non-sliding contact model (N-SCM). These numerical values mean a variation of the plantar pressure between both models of up to 12.57%.

Analysis suggests that including sliding contacts on the foot model had a significant improvement in the qualitative plantar pressure response.

Keywords: Finite Element Method (FEM) · Computed Tomography (CT) · Magnetic Resonance Imaging (MRI) · Contact pressure

© Springer Nature Switzerland AG 2020
C. A. González Díaz et al. (Eds.): CLAIB 2019, IFMBE Proceedings 75, pp. 874–883, 2020.
https://doi.org/10.1007/978-3-030-30648-9_114

1 Introduction

Currently, in the literature, there are a wide variety of models of finite elements of the foot, some more complex and complete than others. The peculiarity of most of the models reviewed is that the ligaments, tendons, muscles, or plantar fascia are modeled with unidimensional elements (trusses). Recently, some foot models are already beginning to reincorporate some soft tissues with realistic geometry [1, 2], but there is not a simulation of contacts among these tissues. In some other cases is not considered the skin and much less there is a distinction between the cortical and trabecular bone [3–13]. These simplifications in the models can be for different reasons, such as the objective in which the research is centered, the lack of specialized equipment for the generation and solution of the model or ease in convergence. However, the use of simplified models can cause that the quantitative and qualitative response is limited.

Nowadays, in the literature, the most complete foot model is the model developed by Enrique Morales et al. [14]. This foot incorporates most of the muscles and tendons with more realistic geometry. Besides, it includes plantar fascia, skin, and makes the distinction between the cortical and trabecular tissue of the bones.

However, the main problem with this type of models so complete is to make the muscles and tendons properly transmit their load to the surrounding tissues. This because of unions that are presented on the tissues of the foot model owing to the kind of mesh used (shared). The shared mesh creates fixed connections through the nodes shared among elements of the mesh of the tissues in contact. These unions generate a constraint of movement that limits the transmission of the load to other elements.

One of the ways to correct the problem of the wrong transmission of the load among muscles and tendons is to make the separation among the meshes and use appropriated contacts. However, is essential to know that there is a large number of interacting tissues, whose behavior, in some cases, is influenced by other tissues. So, using too many contacts can cause long times in the solution and even severe difficulties to achieve model convergence. For these reasons, simulating the right response of each of them is a great challenge.

Therefore, the objective of this research seeks to evaluate the behavior of the plantar pressure in a three-dimensional finite element model of a foot, correcting the main limitations of the models found in the literature, mainly, the improper functioning of muscles, tendons, and plantar fascia.

2 Materials and Methods

2.1 Obtaining Tissues Geometries

The working group of Applied Mechanics and Bioengineering (AMB) of the engineering and architecture school of the University of Zaragoza provided the foot model. The geometries of tissues were created by Morales *et al.* [14]. as part of a research project. The right foot of an individual of 40 years of age, 1.70 m in height and 70 kg of weight in the gait of the second rocker (standing position) was scanned to obtain the images of the tissues. In the process, CT and MRI scanning techniques were used to get

hard and soft tissue images, respectively. Subsequently, in MIMICS (Materialize, Leuven, Belgium), a 3D medical image processing program, the images were treated to generate the geometries of the tissues.

The model is made up of twenty-eight bones (with cortical and trabecular part): fourteen phalanges (medial, proximal and distal), five metatarsal bones, two sesamoids, three cuneiforms (medial, intermediate and lateral), cuboids, navicular, calcaneus, talus and part of the tibia and fibula. Tendons as extensor digitorum longus (EDL), extensor hallucis longus (EHL), extensor digitorum brevis (EDB), fibularis brevis (FB), fibularis longus (FL), tibialis anterior (TA), tibialis posterior (TP), flexor digitorum longus (FDL), flexor hallux longus (FHL), and flexor digitorum brevis (FDB). Several muscles as: flexor hallux brevis (FHL), abductor hallucis (ABDH), adductor hallucis (ADDH), quadratus plantae (QP), abductor digiti minimi (ABDDM), lumbricals interossei (LI), plantar interossei (PI) and dorsal interossei (DI). The foot model also includes the plantar fascia (central, PFC and lateral, PFL), skin and cartilages.

2.2 Meshing

The mesh was generated using an ANSYS module, identified as ICEM CFD (ANSYS Inc., Canonsburg, PA, USA). Tetrahedral elements of the first order were used for the mesh the tissues of the foot model, with a size that varies from 1 to 4 mm.

The meshing method employed gave two severe problems in the areas of contact among tissues, the first one, irregularities in the mesh. These irregularities consisted of an incorrect assignment of the elements in the meshes and the generation of inadequate elements in the borders of the tissues, causing the loss of their geometry.

A fix of the mesh in I-DEAS (SDRC, Milford, CT, USA) for each tissue was doing. The fix of the mesh consisted of the elimination of inadequate elements, the generation of new elements, and the relocation of wrongly assigned elements. These, to avoid problems of concentration and incorrect distribution of stress on the tissues.

The second one was that when using shared mesh, the meshing software in the contact area adapts the size of elements of the mesh of one of the geometries (larger mesh) to the size of the mesh of the other (smaller mesh)—making that in the interface among geometries there was a sharing of nodes, generating fixed connections. These unions among tissues cause a constraint of movement, provoking a progressive loss of load towards the insertion areas, furthermore, to transmitting additional effects to other tissues that should not exist.

A program that works with the information of the tissues (groups of nodes, groups of elements and coordinates of the nodes) was created to repair the problem of the shared nodes. This program duplicates the group of shared nodes between two tissues, assigning them the same position as the primary nodes, but with another identification label (ID). Subsequently, the new group of nodes is assigned to one of the meshes of the tissues while the group of initial nodes remains in the other tissue. In this way it was possible to remove the movement constraint, allowing independent movement between tissues. In Fig. 1 the foot model can be seen.

It is important to mention that priority was given to the repair of the fixed connections among muscles and tendons (of greater relevance for the analysis) with those tissues with greater rigidity (bone tissue and muscles) that making it difficult the partial

or complete transmission of the load. Only the shared mesh was left at the insertion points and with some soft tissues (muscles, skin, and tendons), to prevent the tissues suffered a large displacement, adopting another position in the model. Accordingly, the union with soft tissues leads to a loss of load. However, it is considered that those soft tissues having a hyperelastic behavior, the loss of load is not so significant in comparison with a union with cortical tissue. It was decided not to apply movement constraints through groups of nodes to avoid stress concentration on the tissues.

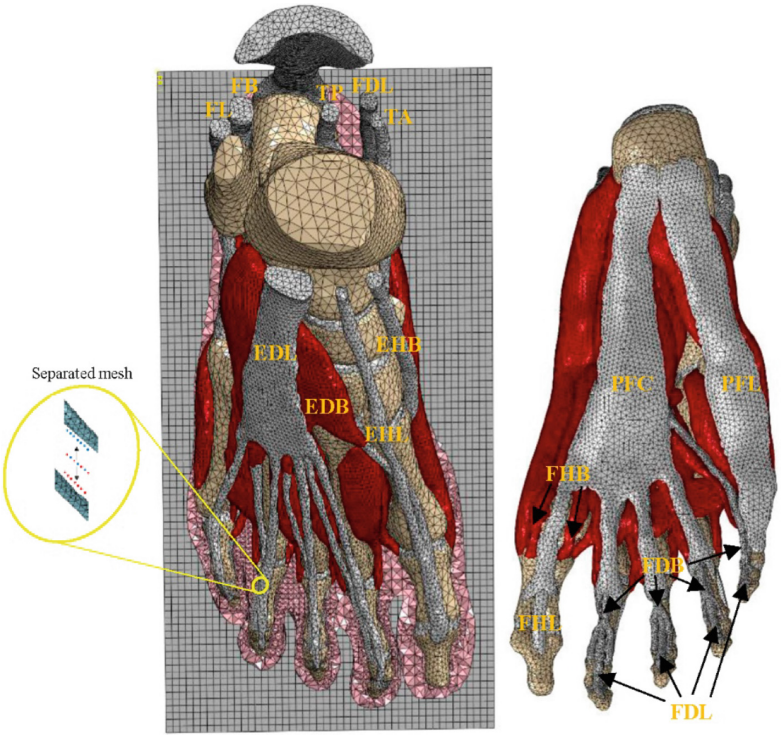

Fig. 1. Finite element model.

2.3 Mechanical Properties of the Foot Model Tissues

From the literature were taken all the mechanical properties of the tissues used in the simulation. Cortical bone (CB), trabecular bone (TB), hard cartilage (HC), soft cartilage (SC) and contact surfaces were modeled with an isotropic, homogeneous and linearly elastic mechanical behavior [14]. While the rest of the tissues were modeled with an isotropic, homogeneous and hyperelastic behavior defined by a fourth-order Ogden model for the lateral plantar fascia (LPF), a fifth-order reduced polynomial model for the central plantar fascia (CPF) [15], a model second-order polynomial for the skin (S) [14] and a first-order Ogden hyperelastic model for muscles (M) [16] and tendons (T) [17]. In Table 1 the values used into this work are showed.

Table 1. Mechanical material parameters. Units for elastic and sharing parameters (E, μ_n, C_n) are in MPa, while for the compressibility (D_n) are in mm^2N^{-1}.

Tissues	E					ν				
CB	17000					0.3				
TB	700					0.3				
HC	10					0.4				
SC	1					0.4				
	μ			α		D				
M	0.057			28.82		1.20710^{-4}				
T	33.1622			24.899		1.210^{-4}				
	C_{10}	C_{01}	C_{20}	C_{11}	C_{02}	D_1	D_2			
S	0.086	-0.058	0.039	-0.023	0.009	3.652	0			
	μ_1	α_1	μ_2	α_2	μ_3	α_3	μ_4	α_4		
LPF	1.210^6	-3.7	-5.710^5	0.2	-1.410^6	-11.4	7.710^5	-15.4		
	C_{10}	C_{20}	C_{30}	C_{40}	C_{50}	D_1	D_2	D_3	D_4	D_5
CPF	9.9	908.2	8943.1	-9.510^4	2.210^5	0	0	0	0	0

2.4 Boundary Conditions and Loads

Displacement constraints in the tibia and fibula area were applied through a group of nodes, simulating an embedment. A platform (rigid body) was added under the sole to simulate the interaction of the foot with the ground. Which during the simulation is moved perpendicularly by the action of a load that is generated at the moment the foot supports with the ground. Finally, were applied eight forces in eight of the main tendons that stabilize the foot during the gait. The load magnitudes were taken from research made by Morales et al. [14]. In Table 2 the magnitudes of these loads can be seen.

Table 2. Loads applied on the tendons of the foot model.

Element	Load (N)	Number of nodes
Ground	350	1
Aquilles tendon	150	156
Tibialis posterior	30	18
Fibularis brevis	12	28
Fibularis longus	24	25
Extensor hallucis longus	15	12
Flexor hallucis longus	15	20
Extensor digitorum longus	7.5	66
Flexor digitorum longus	7.5	51

2.5 Contact Definition

Trough shell surfaces created between tissues, frictionless contacts were applied on the large muscles, tendons (long and short extensor, long and short flexor) and fascia plantar to generate relative sliding and normal load transmission. While the rest of muscles and tendons, only the separation work was done to ensure a free displacement. Finally, a friction contact with a coefficient of 0.6 [2, 4, 7] was applied between the sole and the platform to simulate the interaction with the ground.

3 Results

ABAQUS (ABAQUS Inc., Pawtucket, RI, USA) in the high-performance computing cluster (HERMES) of Zaragoza University was used to solve the finite element model.

The validation of the results was carried out using a baropodometric study of the patient from which the model was obtained in which were taken the values of the plantar pressure of his right foot in the standing position [14]. A comparison of plantar pressure was also made with experimental data of several patients found in the literature [6–8, 14, 18].

The maximum contact pressure obtained for the SCM, N-SCM and baropodometric study (BS) on the sole of the foot under calcaneus and metatarsals, as well as the percentages of error between the finite element models and the experimental test can be seen in Table 3.

Table 3. Plantar pressure. Sole under calcaneus (SUC) and sole under metatarsals (SUM).

Area	SCM (MPa)	N-SCM (MPa)	BS (MPa)	% SCM/N-SCM	% SCM/BS
SUC	0.1925	0.1710	0.17	12.57	13.24
SUM	0.1283	0.1425	0.16	9.96	19.81

Finally, the distribution of contact pressure on the sole between the N-SCM and SCM can be seen in Fig. 2.

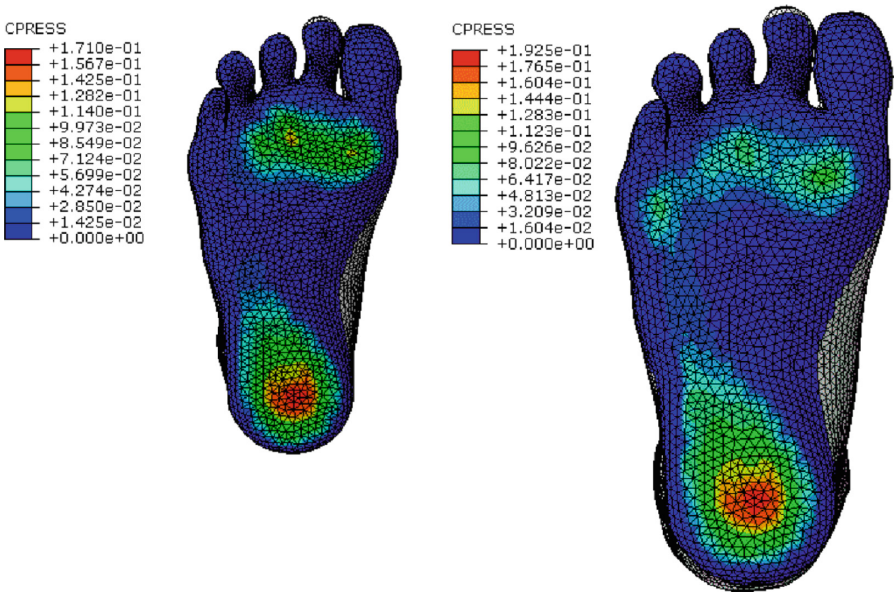

Fig. 2. Contact pressure: (a) Non-sliding contact model, and (b) Sliding contact model.

4 Conclusions

With the work done in the soft tissues of the model, a more realistic contact pressure distribution was obtained in the SCM (Fig. 2b) compared to the N-SCM (Fig. 2a), whose distribution in the latter seems to come from a pathological foot.

The concentration of the maximum contact pressure of the SCM was recorded under the calcaneus as suggested by the baropodometric study. Besides existing a better distribution of pressure under the head of the metatarsals in compared with N-SCM.

Regarding the magnitudes of the contact pressure obtained in the SCM, they are a little high in the area of the calcaneus and low in the metatarsals, in comparison with the pressures recorded in the experimental test (BS) [14]. This variation is attributed to a change in the effect of the load on the model by eliminating the fixed connections of some of the main stabilizing tendons with soft and hard tissues (bones, muscles, and tendons) of the midfoot and hindfoot, leaving only the insertions with the forefoot. This change in the way of acting of the load caused a rotation of the model in the sagittal plane. Allowing a rise of the forefoot and a drop of the hindfoot that caused the concentration of the pressure on the sole of the foot below the calcaneus to increase and reduce the pressure below the metatarsals.

Acknowledgment. The authors gratefully acknowledge the support of the Ministry of Economy and competitiveness of the Government of Spain through the project DPI2016-77016-R and the University of Guanajuato for all facilities to this work.

Conflict of Interest.

29th april, 2019

Congreso Latinoamericano de Ingeniería Biomédica

CLAIB 19

We certify that there is not a conflict of interest with any financial organization regarding the material discussed in the manuscript entitled: "Assessment of plantar pressure in a foot finite element model considering the contact sliding between soft tissues."

Sincerely,

MSc. Marco Antonio Martínez Bocanegra

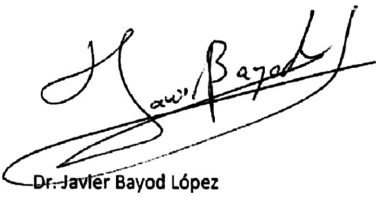

Dr. Javier Bayod López

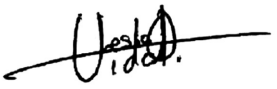

Dr. Agustín Vidal Lesso

Ph. D. Ricardo Becerro de Bengoa Vallejo

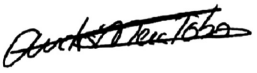

Dr. Andrés Mena tobar

References

1. Chen, W.M., Park, J., Park, S.B., Shim, V.P., Lee, T.: Role of gastrocnemius-soleus muscle in forefoot force transmission at heel rise-a 3D finite element analysis. J. Biomech. **45**, 1783–1789 (2012)
2. Cifuentes, C., Larrainzar, R., Bayod, J.: Biomechanical stress analysis of the main soft tissues associated with the development of adult acquired flatfoot deformity. Clin. Biomech. **61**, 163–171 (2019)
3. Wong, D.W., Wang, Y., Leung, A.K., Yang, M., Zhang, M.: Finite element simulation on posterior tibial tendinopathy: load transfer alteration and implications to the onset of pes planus. Clin. Biomech. **51**, 10–16 (2018)
4. Isvilanonda, V., Dengler, E., Iaquinto, J.M., Sangeorzan, B.J., Ledoux, W.R.: Finite element analysis of the foot: model validation y comparison between two common treatments of the clawed hallux deformity. Clin. Biomech. **27**, 837–844 (2012)
5. Garcia, A., Bayod, J., Prados, J., Losa, M., Jules, K., Becerro de Bengoa, R., Doblaré, M.: Finite-element simulation of flexor digitorum longus or flexor digitorum brevis tendon transfer for the treatment of claw toe deformity. J. Biomech. **42**, 1697–1704 (2009)
6. Chen, T.L., Wong, D.W., Wang, Y., Lin, J., Zhang, M.: Foot arch deformation and plantar fascia loading during running with rearfoot strike: a dynamic finite element analysis. J. Biomech. **83**, 260–272 (2019)
7. Zhang, M., Yu, J., Cong, Y., Wang, Y., Cheung, J.T.-M.: Foot model for investigating foot biomechanics and footwear design. In: Computational Biomechanics of the Musculoskeletal System. 1st edn. CRC Press, Boca Raton (2014)
8. Li, S., Zhang, Y., Gu, Y., Ren, J.: Stress distribution of metatarsal during forefoot strike: a finite element study. Comput. Biol. Med. **91**, 38–46 (2017)
9. Cheung, J.T.-M., Zhang, M., Leung, A.K.-L., Fan, Y.-B.: Three-dimensional finite element analysis of the foot during standing – a material sensitivity study. J. Biomech. **38**, 1045–1054 (2005)
10. Mao, R., Guo, J., Luo, C., Fan, Y., Wen, J., Wang, L.: Biomechanical study on surgical fixation methods for minimally invasive treatment of hallux valgus. Med. Eng. Phys. **46**, 21–26 (2017)
11. Zhang, Y., Aurejsewicz, J., Szymanowska, O., Shen, S., Zhao, X., Baker, J.S., Gu, Y.: Effects of severe hallux valgun on metatarsal stress and metatarsophalangeal loading during balanced standing: a finite element analysis. Comput. Biol. Med. **97**, 1–7 (2018)
12. Wang, Y., Li, Z., Wong, D.W.-C., Cheng, C.-K., Zhang, M.: Finite element analysis of biomechanical effects of total ankle arthroplasty on the foot. J. Orthop. Transl. **12**, 55–65 (2018)
13. Martinez, M., Bayod, J., Vidal, A., Becerro de Bengoa, R., Lesso, R.: Structural interaction between bone and implants due to arthroplasty of the first metatarsophalangeal joint. Foot Ankle Surg. **25**, 150–157 (2019)
14. Morales, E., Souza, T., Bayod, J., Barbosa, E.: Non-linear finite element model to assess the effect of tendon forces on the foot-ankle complex. Med. Eng. Phys. **49**, 71–78 (2017)
15. Guo, J., Liu, X., Ding, X., Wang, L., Fan, Y.: Biomechanical and mechanical behavior of the planatr fascia in macro and microstructures. J. Biomech. **76**, 160–166 (2018)
16. Petre, M., Erdemir, A., Panoskaltsis, V.P., Spirka, T.A., Cavanagh, P.R.: Obtimization of nonlinear hyperelastic coefficients for foot tissues using a magnetic resonance imaging deformation experiment. J. Biomech. Eng. **135**(6), 061001–061012 (2013)

17. Morales, E., Becerro de Bengoa, R., Losa, M., Bayod, J., Barbosa, E.: Foot internal stress distribution during impact in barefoot running as function of the strike pattern. Comput. Methods Biomech. Biomed. Eng. **21**(7), 1–8 (2018)
18. Chen, W.M., Lee, T., Lee, P.V.-S., Lee, J.W., Lee, S.-J.: Effects of internal stress concentrations in plantar soft-tissue – a preliminary three-dimensional finite element analysis. Med. Eng. Phys. **32**, 324–331 (2010)

Boccia Assistant Biomechanics: A Case Study

Juan Pablo Angel-Lopez[1(✉)], Julialba Castellanos-Ruiz[1(✉)], Leidy Tatiana Rojas-Lopez[1(✉)], Daniela Ramirez-Restrepo[1(✉)], Andrea Gomez-Alzate[1(✉)], Yenny Marcela Orozco-Ocampo[1(✉)], Carlos Andres Aguirre-Ospina[2(✉)], and Maria Camila Hoyos-Restrepo[1(✉)]

[1] Universidad Autonoma de Manizales, Manizales, Colombia
{jangel,jcastellanos,daniela.ramirezr,agomez, yorozco,maria.hoyosr}@autonoma.edu.co, tatianarojas2705@gmail.com, agomezalzate@gmail.com, mcamilahoyosr@gmail.com
[2] Liga Caldense de Parálisis Cerebral, Manizales, Colombia
krlos.aguirre@hotmail.com

Abstract. This paper presents and assesses a case study regarding to Boccia, which in present has been constituted in a Paralympic sport that integrates athletes with different degrees of disability and that has aroused a remarkable interest during the last decade. However, according to the topic review from a biomechanical perspective, it has been detected that information about the movements of assistants or coaches is scarce, which is identified as an important information gap, specifically for the BC3 category of said sport. This is why the goal is to develop a biomechanical analysis of the movements of a Boccia coach/assistant during the ramp configuration tasks. The development of the present study consists of four periods: characterization of the coach, positioning of markers under a protocol of upper limbs, 3D motion capture and biomechanical analysis. The results suggest that due to the nature of the movements developed by the coach, he is at high risk of worsening different injuries already existing in his body, and the ergonomic difficulties of the equipment used for the practice of this sport also plays a role in these issues.

Keywords: Motion capture · Ergonomics · Boccia ramp

1 Introduction

Boccia is a precision ball sport, that combines strategy and skill. The plays are made by athletes with cerebral palsy and other severe disabilities affecting motor skills. Accompaniment by the coaches or assistants is as important as the players' technique, given that assistants are the ones who guide the sporting gesture of the participant in trainings and follow player's instructions so their launches are as accurate as possible. In this sense, when inquiring about the background

© Springer Nature Switzerland AG 2020
C. A. González Díaz et al. (Eds.): CLAIB 2019, IFMBE Proceedings 75, pp. 884–893, 2020.
https://doi.org/10.1007/978-3-030-30648-9_115

associated with the biomechanics of the game and the sporting gesture made by the coach or assistant, no references were found. This may be due to the diversity of health conditions and degrees of disability presented by the players of the different categories and not considering the coach or assistant as the object of analysis.

As part of the studies that refer to the topic of Boccia from the biomechanical perspective, in [1] they tried to demonstrate that the lower launch is more effective compared to the upper launch. They also aimed to define a correct posture and technique for the player, in order to suggest modifications for this activity. Based on the findings, the target was to improve the results of the studied subject in terms of strength and direction and also improving the accuracy of the launches. The subject of this study was male, with spastic cerebral palsy and spastic tetraparesis of 80%. Six launching techniques were evaluated and photogrammetry was used for motion kinematics, through a videographic analysis. Additionally, a measurement system (control object) was registered in order to obtain 3D coordinates that allowed biomechanical calculations.

More recently, the development of a simulator with virtual reality of the Boccia Paralympic game, called "Boccia Game Simulator" was also found. The use of several simulated accessories was included within the game experience. The simulator allows the player to observe a Boccia court, the ball launch platform and also allows the participation of two players; this simulation is obliged at all times by the rules of the game for BC3 players. People in that range need external assistance to place the boccia ball on a launching ramp and to orient this device in the desired direction. Twenty-four men and thirteen women participated in this study, all of them without limitations at motor or cognitive level and most of them were right handed. A positive evaluation was registered, which allowed to establish that the simulator is fulfilling the main target of realism and usability [2].

On the other hand, in the final report made by [3], sought to verify the effectiveness in quantitative and qualitative terms of a method of Boccia training, applied to people with cerebral palsy, using a seven-week training program, whose objective was to determine the degree of improvement in accuracy, strength control and direction, in three Boccia players, BC3 category. During the training sessions they worked from the tactical and technical points of view, involving the decision making at each moment of the game, the study of the strengths and weaknesses of the opponent, the way of communication with the assistant, in addition to the correct orientation and position of the player, including the optimization of the throwing technique.

In another study they systematized the experience of Boccia's training in a group of children with cerebral palsy, with the purpose of relating changes in gross motor function, functional independence and quality of life of this population. The authors aimed to propose and justify transformations at the level of educational policy and public health to favor the inclusion of this population in the social environment. To do this, a pre-test and post-test intrasubject study was carried out on ten children and young people from the Colombian team of Boccia. The findings showed significant changes in gross motor function and

functional independence of the study group. Therefore, it can be affirmed that the practice of Boccia promotes belonging to a group, the acceptance of disability and stimulates the promotion of motor skills favoring sports practice even in people with severe disability conditions [4].

Broadly speaking, there are not many references found specifically on Boccia biomechanics; in addition to this, the references found are specifically focused on athletes, leaving aside the coach or assistant. Consequently, the aim of this work is to develop a biomechanical analysis of the movement of a Boccia's coach/assistant during the ramp configuration test and apply the protocol with a subject to write a case study, given that its analysis and understanding will help to perform further studies with the purpose of identifying deficiencies, secondary functional limitations to the practice of sports gesture generated by forced positions, deficient use of body mechanics, unnecessary energy expenses and repetitive movements executed during training sessions and competitive encounters.

2 Equipments and Methods

2.1 Subject

This case study was focused on a 29 year old male Boccia coach/assistant, 1.67 m tall and body mass of 70 kg. Right handed, with experience of 6 years as a Boccia trainer. This subject, among other tasks, claims to do "anything required as a trainer, delegate, sports assistant, daily life auxiliary, 'psychologist', 'physiotherapist', etc.". He also informed about suffering from wrists tendinitis, low back pain and sciatic pain.

2.2 MoCap Registries

The motion capture sessions were recorded with an Optitrack^{TM} system composed of a rectangular arrange of 12 *Flex 3* cameras at a rate of 100 *FPS*, inside a closed space. The subject proceeded to assemble a Boccia ramp in four different configurations, each depending on the length of the ramp (which affects the speed and reach distance of the thrown ball). Every ramp setup was recorded from the first contact with the ramp to the moment the ball was placed on the ramp for it to be shooted by the player. The five configurations used for this test were classified according to the boccia ball's placing, being named the following ways: high, mid high, mid low, low and very low.

2.3 Markers

Following the guidance of [5,6], a maker setup (Fig. 1(a)) was designed in order to calculate all relevant variables for describing the range of movement of the upper body joints. The computed data from this protocol showed the following angles from each side of the body and the trunk:

- Shoulder stumps: anteposition, retroposition.
- Shoulders: flexion, extension, abduction, adduction.
- Forearms: pronation, supination.
- Elbows: flexion.
- Wrists: flexion, extension, ulnar deviation, radial deviation.
- Back: lateral tilt, anteroposterior tilt.

There were also a set of markers placed on the ramp (Fig. 1(b)) in order to track the traveled distance of the accessories and times of assembly for further studies. The ramp used during the MoCap sessions has a main base for tilting and orientating, two elongation accessories and the boccia ball's holder.

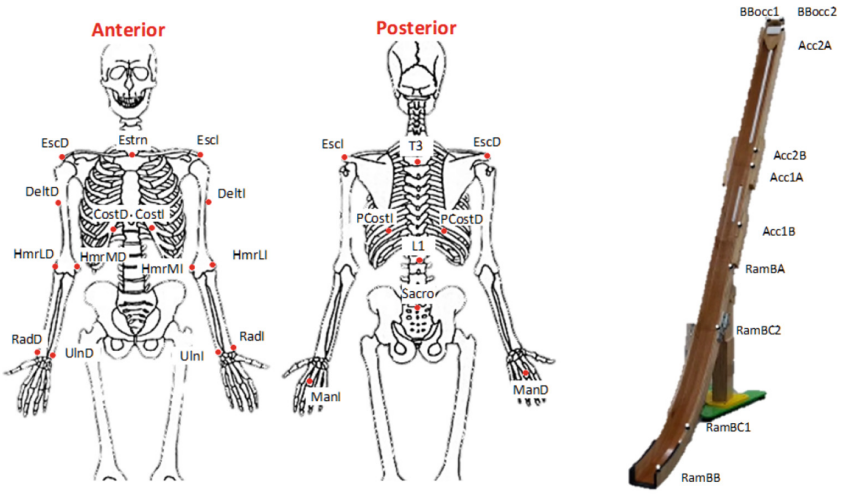

Fig. 1. Markers placing. (a) On the subject. (b) On the Boccia ramp.

3 Results

The data showed all movements (listed in Sect. 2.3) were performed among normal ranges for all the joints, according to [7]. Despite of that, the movements of flexion and extension of the wrists (Fig. 2) and pronosupination (Fig. 3) generated particular interest in this research, because of a high frequency behaviour observed during all the tests.

3.1 Step 1. Break the Plane

Besides the numerical analysis, there is also observed information about the ergonomics and gestures performed by the assistant. In this matter, there are

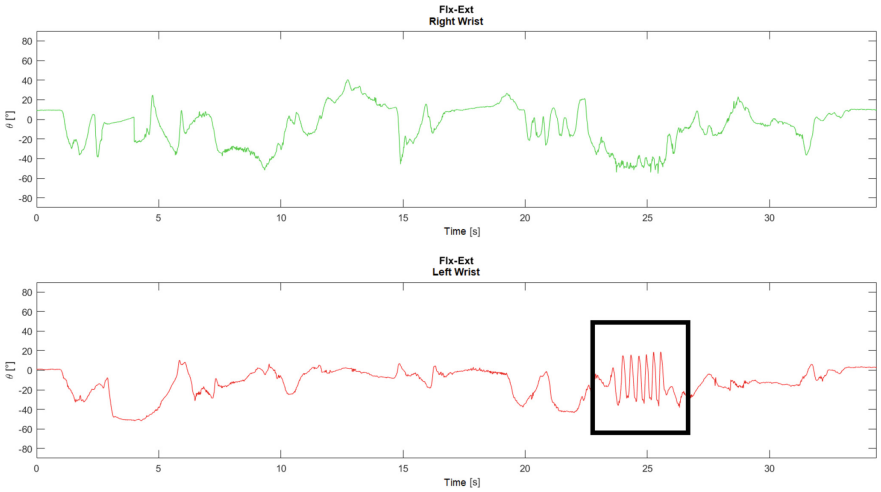

Fig. 2. Example of flexion and extension of the wrist. A high frequency behaviour is closed inside a box.

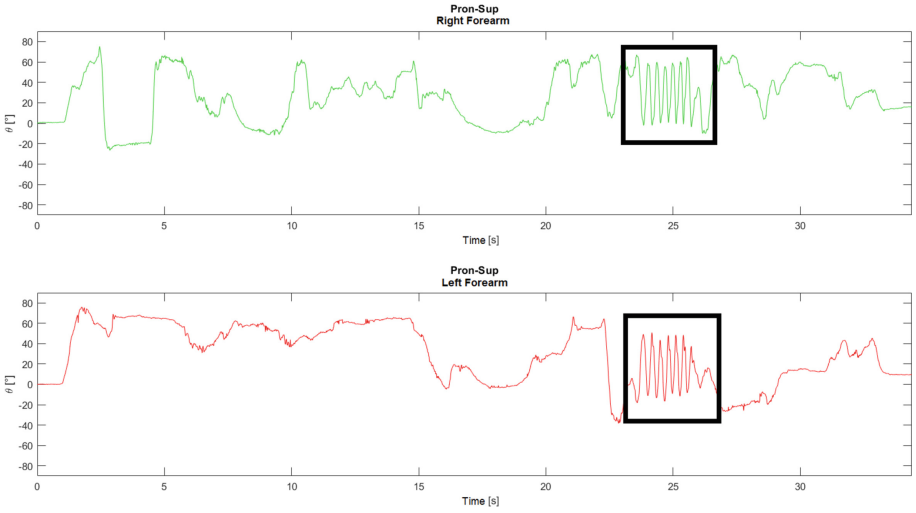

Fig. 3. Example of pronosupination. A high frequency behaviour is closed inside a box.

some identified steps for this kind of analysis. In the first step the coach assumes a frontal-lateral inclination posture and extends the opposite arm to the ramp (Fig. 4(a)) which allows him to hold it while raising the frontal part of the ramp from the floor. This elevation involves the use of both arms, in this case, the right arm is doing elbow flexion and the left arm is doing elbow extension, this is required to move the auxiliary material. The assistant must move the ramp at least 20 cm to each side, as demanded by the BISFed[1], to break the launch plane (Fig. 4(b)). This step is completed by positioning the ramp as indicated by the player and adopting the initial sedentary position (Fig. 4(c)). This movement must be made at the beginning of the game, each time the player leaves the playing area and when a penalty is given.

Fig. 4. Step 1. Break the plane.

3.2 Step 2. Boccia's Support Assembly

In a seated position and with a lateral inclination, the assistant clutches the extension of the ramp that will be used during the play. With the opposite hand the assistant holds the support element for the boccia ball, which must be attached to the extension (Fig. 5(a)). The assistant must make use of his lower extremities to support the extension as he assembles the element, with one of his hands he holds the extension and with the other one he puts in place the boccia ball's support, this involves a rotatory movement of his upper limb joints (Fig. 5(b)). Finally, it is essential that the assistant exert pressure on the boccia ball's support to fully install it on the ramp extension (Fig. 5(c)).

3.3 Step 3. Ramp Extension Assembly

Coupling the extension with the ramp denotes lifting the shoulder and flexing the elbows (Fig. 6(a)), which allows the assistant to adjust the extension on the guide

[1] Boccia International Sports Federation.

Fig. 5. Step 2. Boccia's support assembly.

rails that the ramp has. For this activity the total use of upper body members is required. The total extension of the upper limbs also entails a tilt of the torso as the extension rail and the ramp rail align (Fig. 6(b)), throughout the process shoulder lifting as well as frontal tilt of the torso is required (Fig. 6(b)). The extension in its maximum length implies greater effort for the assistant because the arm-shoulder coordination is also affected by the weight of the ramp, the part of the ramp that the assistant clutches is the lower part, which requires greater effort for its alignment and adjustment (Fig. 6(d)).

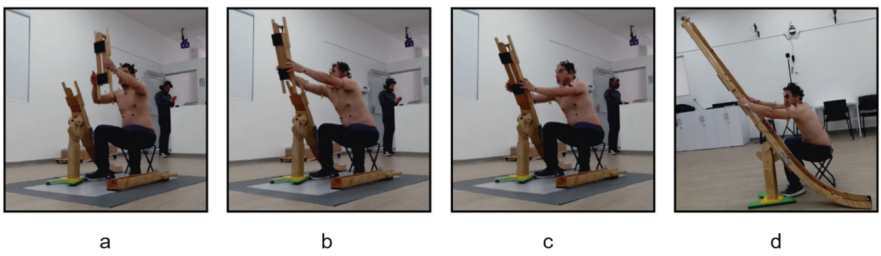

Fig. 6. Step 3. Ramp Extension Assembly.

3.4 Step 4. Rounding of the Boccia Ball

While in a sedentary position with total frontal-lateral inclination, the coach extends his arm to grab hold of the ball with its respective container (Fig. 7(a)). The rounding of the bochas requires rotating wrist-forearm movement and bending of the elbows with a separation from the medial line of the body (Fig. 7(b)), this rotating movement is performed 10 to 15 times per Boccia ball.

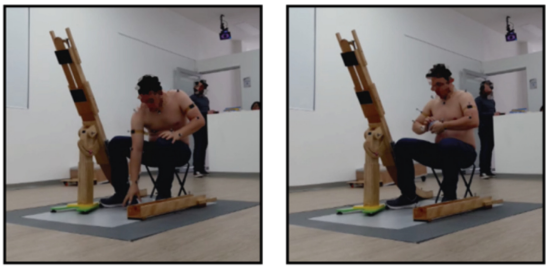

Fig. 7. Step 4. Rounding of the Boccia Ball.

3.5 Step 5. Position Bocha in Ramp

The assistant is in a position where his body is in total frontal-lateral inclination, with his arm extended so he can place the container of the boccia ball (bocha or boccia) on the floor (Fig. 8(a)). A visual inspection of the surface of the ball is made in order to determine the precision angle of the ball before it is placed in the support, which is located in the ramp extension. The assistant is flexing his elbows, they are separated from the medial line of the body as he is in a seated position (Fig. 8(b)). The kinetic chain of arm and trunk flexion to the side allows the assistant to reach the support located on the ramp, he must bend the elbow of his opposite arm and rest it on his leg to gain stability (Fig. 8(c)). When using the maximum extension on the ramp, the assistant must leave the sitting position and stand up so he can carry out the kinetic chain of forearm, arm and shoulder extension; at the same time, he performs shoulder elevation, trunk extension and planti-flexion to achieve the necessary reach while resting on the metatarsus of the foot, opposite to the direction of the extension, this is done to achieve balance (Fig. 8(d)).

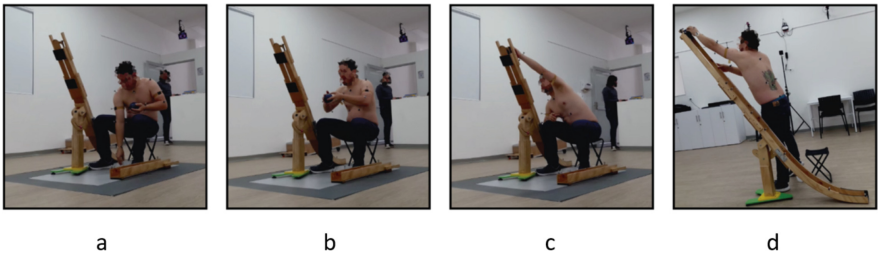

Fig. 8. Step 5. Position Bocha in Ramp.

4 Conclusion

BC3 Boccia player's assitant has a major role during training and competition; he is the one who has to rearrange the ramp and position it, according to the required play indicated by the athlete; this demands that during the game the coach must adopt different postures that go from inclinations to partial and total extensions of his or her body. This pattern of movements, observed over the tests performed during this research, indicate that there is a risk of injury, mostly to the lower back; this also explains the lower back pain the coach claimed to feel.

The Step 4 (Sect. 3.4) is the one related to that high frequency present in Figs. 2 and 3. This repetitive movement, despite showing joint angles within normal ranges, also represents a risk of injury to the coach and even explains the coach's wrists tendinitis. Further studies must explore this pattern and possibly suggest designs for some kind of mechanism or device that helps in this task (essential for the game), preventing injuries.

Thanks to the data given by the marker placed near the sacrum, it was possible to track hip's height (and by default the chair's height also). This information showed that the coach's seated position does not correspond to ergonomic parameters and this may explain the sciatic pain that the subject claimed to feel. The chair used by the coach during competitions should be reconsidered due to its influence in a possible injury.

Conflict of Interest. The authors whose names are listed immediately below the title of this document certify that they have NO affiliations with or involvement in any organization or entity with any financial interest (such as honoraria; educational grants; participation in speakers' bureaus; membership, employment, consultancies, stock ownership, or other equity interest; and expert testimony or patent-licensing arrangements), or non-financial interest (such as personal or professional relationships, affiliations, knowledge or beliefs) in the subject matter or materials discussed in this manuscript.

References

1. Calverol, T.: Estudio Biomecánico de los Lanzamientos de Boccia, June 1999
2. Machado-Ribeiro, J.: Boccia Game Simulator - Applications for Training Cerebral Palsy Patients. MA thesis. Universidade do Porto, January 2017. https://repositorio-aberto.up.pt/handle/10216/102572
3. Moreno-González, M.: Boccia: Design and implementation of an assessment and training program. Universidade de León, July 2015
4. Ramón-Cuellar, M., Ortega-Arellano, C.: Entrenamiento deportivo en relación con la función motora gruesa y la independencia funcional en niños y jóvenes con parálisis cerebral pertenecientes a la selección Valle de Boccias. MA thesis. Universidad de Manizales, April 2010. http://ridum.umanizales.edu.co:8080/xmlui/handle/6789/611.10

5. Wu, G., Cavanagh, P.R.: ISB recommendations for standardization in the reporting of kinematic data. J. Biomech. **28**(10), 1257–1261 (1995). https://doi.org/10.1016/0021-9290(95)00017-C. http://www.sciencedirect.com/science/article/pii/002192909500017C. ISSN: 0021-9290
6. Wu, G., et al.: ISB recommendation on definitions of joint coordinate systems of various joints for the reporting of human joint motion-Part II: shoulder, elbow, wrist and hand. J. Biomech. **38**(5), 981–992 (2005). https://doi.org/10.1016/j.jbiomech.2004.05.042. http://www.sciencedirect.com/science/article/pii/S002192900400301X. ISSN: 0021-9290
7. Kapandji, A.I., Lacomba, M.T.: Fisiología Articular Obra Completa. Fisiología Articular. Editorial Medica Panamericana Sa (2011). ISBN: 817903770

Validation of the Foot Base for Measuring the Control of Ankle Movements

Juan M. Gomez-Gonzalez[1(✉)], Molina Cecilia[2], and Braidot Ariel[2]

[1] Faculty of Engineering, National Autonomous University of México, México City, Mexico
juan@dctrl.fi-b.unam.mx
[2] Biomechanics Laboratory, Faculty of Engineering, National University of Entre Ríos, Oro Verde, Argentina

Abstract. From the design of a Foot Base [1] (FB), in which a Smartphone (SP) connected to a computer application [2] is used, the movements of inversion, eversion, plantar flexion and dorsiflexion of the ankle are measured. Two types of (SP) are validated, one of medium range and another of low range, to know the precision that they have when measuring the angle of the ankle in the stages of the application. The measurement is made with a high precision system, composed of eight cameras (OPTITRAC® flex-13 from Natural Point Inc.) and simultaneously recording the angle measured by the SP accelerometers, yielding the precisions reported in this document. This validation will allow proposing a measurement scheme in the control of the ankle without load.

Keywords: Ankle · Smartphone · Rehabilitation

1 Introduction

The ankle is a joint adapted to support large loads, however, the fine motor control allows the individual to adapt the gait to different ground conditions. When the ankle suffers an injury or its mobility is affected, one of the strategies used by health personnel to rehabilitate the ankle is the repetition of movements. Rehabilitation is achieved from several factors, such as the therapeutic frequency and motivation of the patient, however many of the diagnostic methods use scales based on experience, so they are subjective.

Electronic systems that measure the control of the ankle, allow health personnel to observe the evolution of the ankle and the therapy itself. These systems can be used in patients with sprained ankles, patients with ankle pain, patients with reduced mobility of the ankle due to cerebrovascular accidents or cerebral palsy.

Additionally, the use of smartphones (SP) has been popularized, systems that have a great power of computation and have been instrumented with sensors that allow to measure movements [3]. Although they are not ergonomic devices, they can be mounted on devices or equipment designed to measure different signals or movements of biomechanical origin [4].

In recent years, the use of smartphones in health-related matters has been favored, particularly taking advantage of their easiness of interconnectivity [5] (internet, voice

© Springer Nature Switzerland AG 2020
C. A. González Díaz et al. (Eds.): CLAIB 2019, IFMBE Proceedings 75, pp. 894–906, 2020.
https://doi.org/10.1007/978-3-030-30648-9_116

calls, text messages) [6]. These devices include sensors, such as GPS, accelerometers and gyroscopes, which can monitor from the position of the user, or specific movements, such as follow-up of cardiac patients, gait studies or physical rehabilitation [7].

The vast majority of SPs are ergonomically inadequate to use as wearable devices, due to their size. However, its capacity for calculation, registration, accuracy of sensors and connectivity, together with its massive use, makes them a tool in which important opportunities are visualized in areas of remote monitoring and use as the measurement tool.

The developed Foot Base [1] is a semi-spherical platform in which the foot is placed and the SP is used as a joystick. This tool allows to measure the angle of the ankle joint with the SP accelerometer, shown in Fig. 1 the system indicated in the neutral position of the ankle.

Fig. 1. The SP mounted on the BP measures the inclination of the ankle, from the built-in accelerometer.

For the evaluation of a subject the leg is kept fixed and the movement of the Foot Base is recorded from the values of the triaxial accelerometer of the SP, which are transmitted to a computer. A specific computer software evaluates the angle of the ankle and transforms this data into movement of a virtual sphere in a hexagonal circuit (Fig. 2), with the help of visual feedback from the computer screen the subject must move his ankle to move the sphere in this hexagonal circuit trying not to get out of this line. For an adequate evaluation of the movement of the ankle, it is necessary to know the precision and accuracy of the SP accelerometer used [8]. The objective of the work is to analyze and recommend the use of a particular SP or to make the appropriate adjustments in the software so that the measurement of the ankle angle reaches the accuracy and precision required to assess the mobility of the ankle.

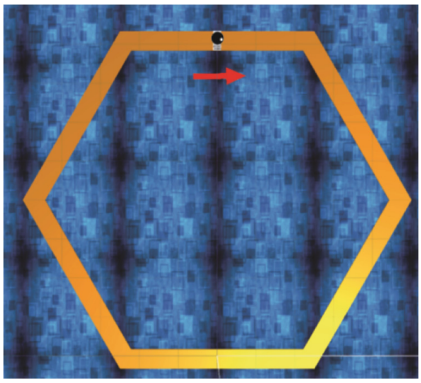

Fig. 2. Virtual circuit that is covered with the movements of the ankle.

For registration and rehabilitation of the ankle (without force) robotic platforms have been developed, such as "anklebot, Rutgers Ankle Platform, IntelliStretch" [9], while our platform, the FB, measures the fine control of the ankle; and Isokinetic Ankle Platform (IAP) [10], which was designed to know inter-limb learning.

Our proposal intends for health personnel to have access to an easily accessible measurement tool, where the measuring instrument can be an SP.

This work is part of a larger project that includes the use of the Foot Base (FB) for the rehabilitation of patients with pathologies that affect the movement of the ankle. In this stage, the validation of a low range SP and a mid-range SP is presented, in order to evaluate the performance of both SPs in the use of this tool.

2 Methods

To know the accuracy of the accelerometers incorporated in the SP, the inclination of each SP was measured by rotating it on the X axis and the Y axis separately (Fig. 3). In order to have control over the measurements, each of the SPs were placed in the BP in which each axis to be measured was aligned perpendicular to a graphic scale (Fig. 3).

The inclination of the SP is registered with an interface programmed in C# on a PC and in the SP simultaneously. In the computer, the triaxial reading of the accelerometer is received at a sampling rate of 50 mps.

The measurement of the SP inclination was made observing the calculated angle with the registered data of the accelerometer turning it with a slow and continuous movement. It started from 0° until reaching −45° and returning to 0°, without stopping the movement. After doing three times the same route, the measurement is modified by 5°, this is from 0° to −40° and so on, so that measurements are taken covering from −45° to 45°. In Fig. 4 the result of the record taken with the mid-range SP is shown.

As a reference (gold standard) an 8-camera system Optitrack®, Flex 13 and a Motive® image acquisition and processing system used in a biomechanics laboratory were used. The system allows 3D tracking at a frequency of 120 mps of movements, using retro-reflective passive markers. This system has an error in the measurement of

spatial coordinates less than 0.2 mm. With this system the movement of the SP was recorded, referenced to the same coordinate system of the printed scale (Fig. 3).

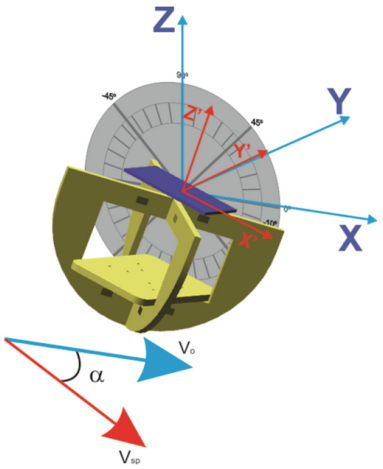

Fig. 3. The SP is mounted on the FB, aligning the axis to be measured perpendicular to the printed scale.

With this procedure the angle of inclination was obtained from the record of the SP accelerometers and another record measured with the gold standard system in order to make the comparison.

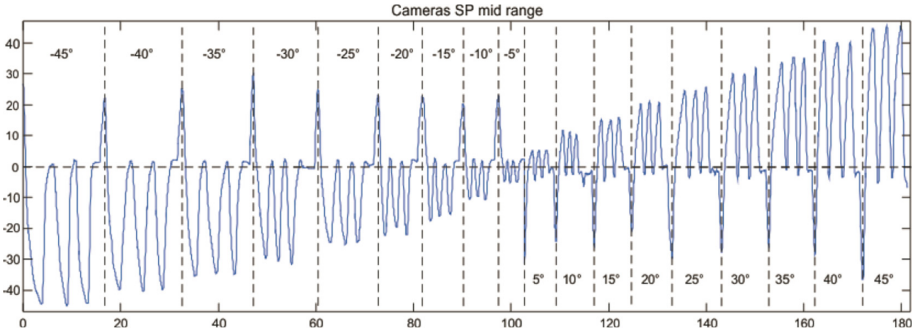

Fig. 4. Records of angle vs. time of the SP of medium range, continuous movement, slow, varying in 5° the maximum angle to measure every three repetitions.

The calculation of the angle of the SP was made from the reading of the triaxial accelerometer, applying trigonometric expressions (Eq. 1), which records the value of the force of gravity mainly, considering that the acceleration of the sensor is disregarded taking into account that it moves at very low speed. The initial position of the

SP is horizontal, so that the acceleration recorded by the accelerometer on the Z axis is a normalized reading of 1 (corresponding to 9.81 m/s2), while on the X and Y axes the reading is zero. According to the inclination that the SP takes, each axis registers the respective component of the acceleration of gravity. When the SP is turned around the Y axis at a very low speed, the reading obtained from the accelerometer is equal to zero for this axis (Y) and for the X and Z axes a reading proportional to the recorded slope. Equivalently, the measurement is obtained by rotating the SP on the X axis by registering the corresponding components on the Y and Z axes.

$$|M| = \sqrt{X^2 + Y^2 + Z^2}$$
$$\delta = \left(\frac{X}{M}\right) \tag{1}$$

Where:

$\|M\|$	Accelerometer reading module.
X, YyZ	Value of each axis of the accelerometer reading.
δ	Angle calculated from each accelerometer reading

The data registered with the Optitrack system, are three-dimensional positions of markers used in biomechanics, to calculate the inclination of the SP two coordinate systems were defined: one fixed (X,Y,Z) and the other (X',Y',Z') that rotates with the SP position (Fig. 3). For each coordinate system, two vectors v_o corresponding to the fixed system and v_{sp} to the SP system are calculated, with the spatial positions of both the rotation matrix between the systems is obtained and the angle α between them is calculated as a gold value standard to compare with the values registered with the SP.

To validate the measurements obtained from the SP, the root mean square error (RMS) was calculated taking the movement records for each of the axes, according to Eq. 2,

$$RMS = \sqrt{\frac{\sum_i^n (\delta_{oi} - \delta_{si})^2}{n}} \tag{2}$$

Where:

δ_o	Angle calculated with the measurement by the Optitrack® system.
δ_s	Angle calculated with the measurement by SP.
n	Number of samples

The RMS allowed to evaluate the accuracy of the SP measurement. To know the accuracy, we analyzed the data dispersion obtained for the ranges of angles shown in Table 1.

Table 1. Ranges used to evaluate the accuracy of the measurement of the SP angle.

−45.01 < angle < −44.99	4.99 < angle < 5.01
−40.01 < angle < −39.99	9.99 < angle < 10.01
−35.01 < angle < −34.99	14.99 < angle < 15.01
−30.01 < angle < − 29.99	19.99 < angle < 20.01
−25.01 < angle < −24.99	24.99 < angle < 25.01
−20.01 < angle < −19.99	29.99 < angle < 30.01
−15.01 < angle < −14.99	34.99 < angle < 35.01
−10.01 < angle < −9.99	39.99 < angle < 40.01
−5.01 < angle < −4.99	44.99 < angle < 45.01
−0.01 < angle < 0.01	

3 Results

3.1 Low Range Smartphone

The record of the X-axis inclination (Fig. 5), which shows the rotation of the XZ plane, in the range calculated with the accelerometer from −45° to 45°, the RMS calculated for each range of angles is shown in Table 2, where it is observed that the RMS is between 2.0° < ECM < 12.4°, on average we have $\overline{RMS} = 6.8°$. Figure 5 shows the complete record and the segment of the measurement corresponding to −45°.

When observing the records it can be seen that the SP did not really measure the angles of greater amplitude, having a higher error.

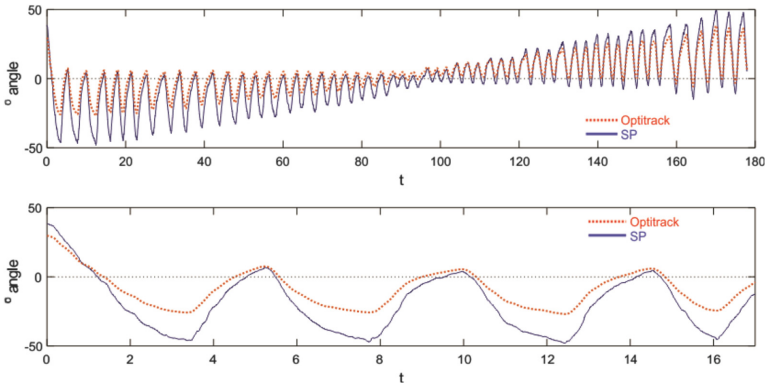

Fig. 5. Record of the low range SmartPhone, the SP rotation of the X axis is shown

Table 2. Root mean square error of the tests performed in the rotation of the X axis of the low range SP.

Angle	RMS	Angle	RMS
$-45 < \alpha < 0$	12.42	$0 < \alpha < 45$	6.57
$-40 < \alpha < 0$	12.72	$0 < \alpha < 40$	6.19
$-35 < \alpha < 0$	10.87	$0 < \alpha < 35$	4.81
$-30 < \alpha < 0$	10.02	$0 < \alpha < 30$	4.17
$-25 < \alpha < 0$	9.66	$0 < \alpha < 25$	3.40
$-20 < \alpha < 0$	8.94	$0 < \alpha < 20$	2.70
$-15 < \alpha < 0$	7.62	$0 < \alpha < 15$	2.86
$-10 < \alpha < 0$	6.60	$0 < \alpha < 10$	2.81
$-5 < \alpha < 0$	5.57	$0 < \alpha < 5$	4.15

The measurements for the rotation of the Y axis of the low range SP are shown in Fig. 6, in Table 3 it is observed that the RMS is found $2.2° < RMS < 9.6°$, with an average of $\overline{RMS} = 5.1°$. As for the X axis, it is observed that for angles of greater amplitude the error also increase

3.2 Medium Range Smartphone

The measurements for the rotation of the X axis of the medium range SP are shown in Fig. 7, the RMS is found ECM between $0.32° < \text{ECM} < 0.84°$, with an average of $\overline{RMS} = 0.44°$ (Table 4), and for the plane YZ (Fig. 8), $0.37° < \text{ECM} < 0.55°$, with an average of $\overline{RMS} = 0.45°$ (Table 5).

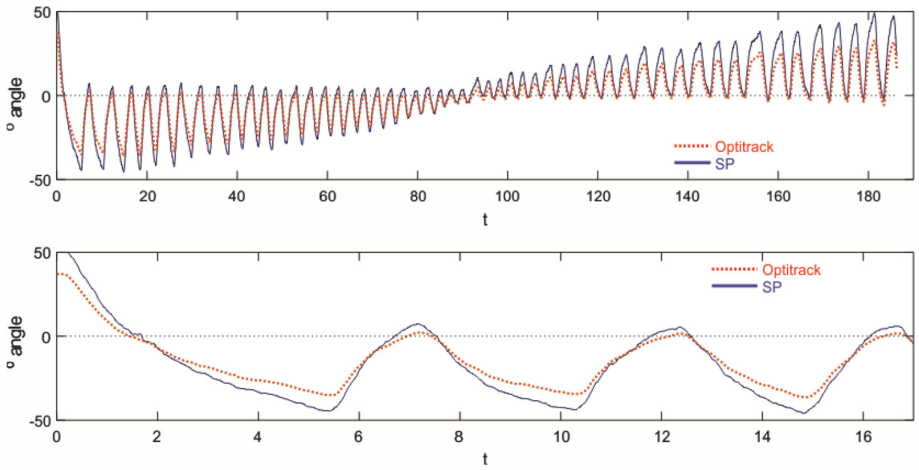

Fig. 6. Register of the low range Smartphone, the rotation of the Y axis of the phone is shown.

Table 3. RMS of the tests performed in the rotation of the Y axis of the low range SP.

Angle	RMS	Angle	RMS
$-45 < \alpha < 0$	12.42	$0 < \alpha < 45$	6.57
$-40 < \alpha < 0$	12.72	$0 < \alpha < 40$	6.19
$-35 < \alpha < 0$	10.87	$0 < \alpha < 35$	4.81
$-30 < \alpha < 0$	10.02	$0 < \alpha < 30$	4.17
$-25 < \alpha < 0$	9.66	$0 < \alpha < 25$	3.40
$-20 < \alpha < 0$	8.94	$0 < \alpha < 20$	2.70
$-15 < \alpha < 0$	7.62	$0 < \alpha < 15$	2.86
$-10 < \alpha < 0$	6.60	$0 < \alpha < 10$	2.81
$-5 < \alpha < 0$	5.57	$0 < \alpha < 5$	4.15

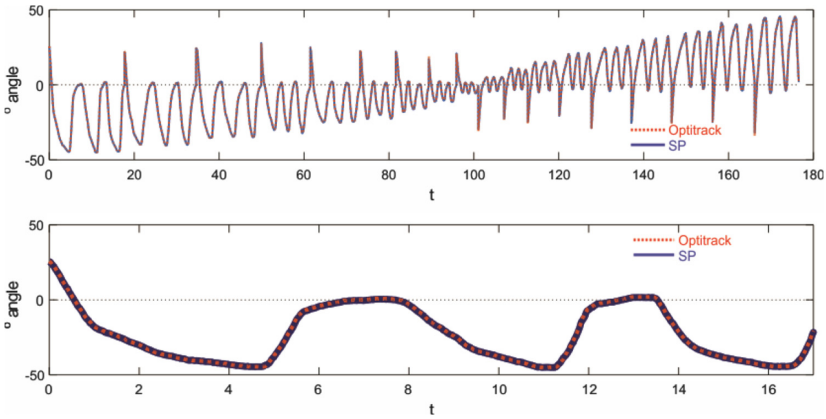

Fig. 7. Record of the medium range SmartPhone, the SP rotation of the X axis is shown.

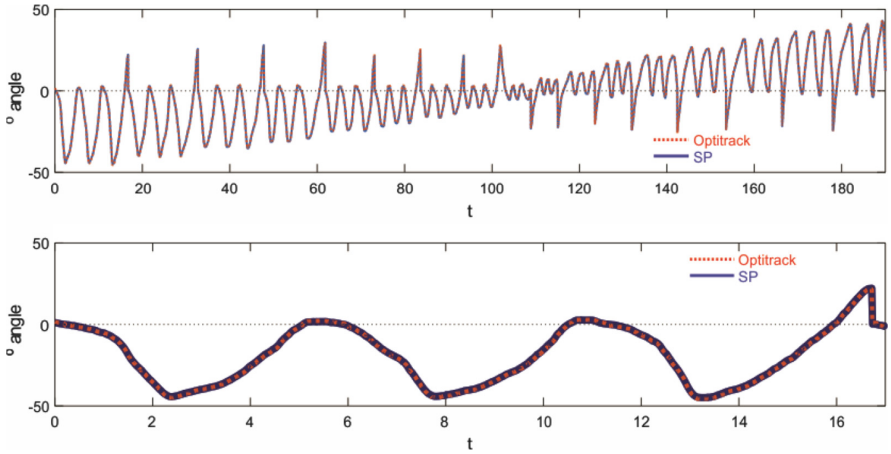

Fig. 8. Register of the medium range Smartphone, the rotation of the Y axis of the phone is shown.

Table 4. Root mean square error of the tests performed in the rotation of the X axis of the medium range SP.

Angle	RMS	Angle	RMS
$-45 < \alpha < 0$	0.34	$0 < \alpha < 45$	0.52
$-40 < \alpha < 0$	0.39	$0 < \alpha < 40$	0.46
$-35 < \alpha < 0$	0.37	$0 < \alpha < 35$	0.49
$-30 < \alpha < 0$	0.68	$0 < \alpha < 30$	0.41
$-25 < \alpha < 0$	0.84	$0 < \alpha < 25$	0.37
$-20 < \alpha < 0$	0.45	$0 < \alpha < 20$	0.32
$-15 < \alpha < 0$	0.32	$0 < \alpha < 15$	0.37
$-10 < \alpha < 0$	0.35	$0 < \alpha < 10$	0.35
$-5 < \alpha < 0$	0.43	$0 < \alpha < 5$	0.44

Table 5. Root mean square error of the tests performed in the rotation of the Y axis of the medium range SP.

Angle	RMS	Angle	RMS
$-45 < \alpha < 0$	0.37	$0 < \alpha < 45$	0.48
$-40 < \alpha < 0$	0.43	$0 < \alpha < 40$	0.51
$-35 < \alpha < 0$	0.52	$0 < \alpha < 35$	0.55
$-30 < \alpha < 0$	0.46	$0 < \alpha < 30$	0.49
$-25 < \alpha < 0$	0.39	$0 < \alpha < 25$	0.46
$-20 < \alpha < 0$	0.39	$0 < \alpha < 20$	0.40
$-15 < \alpha < 0$	0.39	$0 < \alpha < 15$	0.47
$-10 < \alpha < 0$	0.43	$0 < \alpha < 10$	0.46
$-5 < \alpha < 0$	0.37	$0 < \alpha < 5$	0.51

It is observed that the medium range SP has a greater accuracy in the measurement than low range SP throughout the measurement range.

3.3 Dispersion

The accuracy of each of the SPs was evaluated in the ranges of angles presented in Table 1, a dispersion between the data acceptable for both telephones was obtained (Table 6, Fig. 9). It is observed that although for the low range SP, its measurements are not exact; they are repeatable with little dispersion.

Table 6. Root mean square error of the tests performed in the rotation of the Y axis of the medium range SP.

Lowrange SP						Medium range SP					
Angle	X	Y	Angle	X	Y	Angle	X	Y	Angle	X	Y
−45			5	0.40	1.15	−45	0.05	0.02	5	0.33	0.39
−40			10	0.50	1.83	−40	0.09	0.16	10	0.24	0.33
−35			15	0.61	1.38	−35	0.35	0.11	15	0.38	0.15
−30			20	0.86	1.30	−30	0.43	0.27	20	0.40	0.22
−25	0.26	0.90	25	1.15	0.81	−25	0.21	0.30	25	0.19	0.25
−20	0.81	1.66	30	0.38	0.21	−20	0.29	0.35	30	0.21	0.15
−15	1.16	1.78	35			−15	0.67	0.30	35	0.28	0.32
−10	0.67	1.10	40			−10	0.47	0.37	40	0.14	0.09
−5	0.4	1.24	45			−5	0.32	0.28			
0	0.43	1.22				0	0.20	0.27			

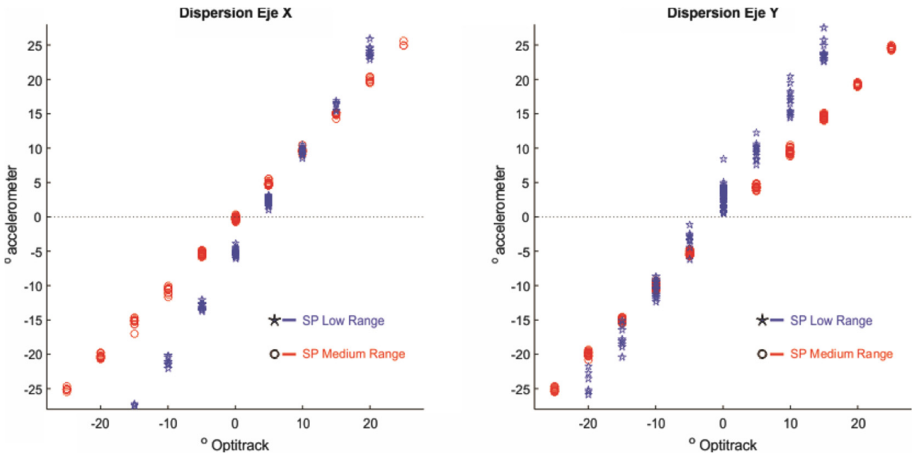

Fig. 9. Dispersion of the data in the measurements made on the two axes of the accelerometers (X and Y) of both SP, in the graph we can see that both SP are accurate.

3.4 Correlation Coefficient

To know the linear association between the measured angle and the real angle, the correlation coefficient was calculated. For the low range SP it was divided into three intervals $\alpha < -30^{o}$, $-30^{o} < \leq \alpha \leq < 30^{o}$ y $\alpha > 30^{o}$, obtaining (Table 7):

Table 7. Correlation coefficient of the tests performed in the rotation of the X and Y axis of the low range SP.

Angle	X-axis correlation coefficient	Y-axis correlation coefficient
$\alpha < -30^{o}$	0.9902	0.970
$-30 < \leq \alpha < 30^{o}$	0.997	0.991
$\alpha > 30^{o}$	0.997	0.988

For the mid-range SP, the correlation coefficient of the whole record was calculated, obtaining for the X and Y axis 0.999. The result shows a strong linear relationship for both SP.

4 Discussion

It can be seen that there is a significant difference between the measurements made with the low range SP and the medium range SP. The results show that a medium range SP can be used to measure the movements of a joint, such as the ankle, with a maximum error of 0.55°, which results in adequate precision for the movements that you want to measure.

It is important to consider the maximum average range of the rotation of an ankle that can be reached in a healthy subject Table 8 [11].

Table 8. Maximum angles that a healthy ankle can reach on average.

Movement	Angle
Dorsiflexion	29.8
Plantar flexion	45.8
Inversion	22
Eversion	17

In the measurement of the angle of rotation of the ankle, with the SP accelerometer mounted on the FB, the inversion-eversion movement has to be recorded with the angle measured of the X axis of SP, while dorsiflexion and plantar flexion with the inclination of the accelerometer on its Y axis. The error that would represent using the low range SP can be up to 30% on the X axis and up to 17% on the Y axis, while on the SP medium range for the X axis is 2.6% and for the Y axis 1.5%.

It is important to have a reliable measuring instrument to register the movement of ankles with some motor deficiency, caused by a sprained ankle or by poor control of the nervous system. The present work shows that it is possible to use mid-range SP in this type of applications.

The objective of the work was to validate the registration system used for the developed Foot Base [1] used in the rehabilitation control of patients with deficiencies in the movement of the ankle. It is important to note that the medium range SP complies with the accuracy and precision required both for the visual feedback of the ankle movement (Fig. 2) and for evaluating the angle of the joint. The low range SP would also allow the use as a visual rehabilitation tool of the ankle movement considering accuracy despite not being accurate measurement.

The correlation coefficient of the IAP base [10] (designed with potentiometers) is 0.955, while the coefficient of the low range SP is 0.99, and the mid-range coefficient is 0.999 (used in the FB), both Platforms work like a joystick.

5 Conclusion

With low error and correlation coefficients very near to the unit, we can affirm that the accelerometer of an SP can be used, to measure the movement of the ankle with acceptable precision.

The massive use of smartphones allows health personnel and users to have a platform that helps them evaluate ankle control with relatively accessible items at moderate costs.

The FB is not reported in this work, however, we have begun to record the movements of the ankle (plantar flexion, dorsiflexion, eversion and inversion) in healthy volunteers and with sprains. With the aim of proposing indexes of evaluation of the ankle control, which will help health professionals observe the progress in the improvement of the ankle in rehabilitation processes.

Another application is the use of the tools developed in the learning process for cases of stroke, in stages where rehabilitation has already established the recovery of the movement of the ankle.

References

1. Meana A., Negrete-Rojas D., Nava-Gomez R.A., Ruiz Diaz J.A., Vega-Gonzalez A., Gomez-Gonzalez J.M.: Assessment of ankle movements through a game-based sphere: proof of concept. In: VII Latin American Congress on Biomedical Engineering CLAIB 2016. IFMBE Proceedings, vol. 60, p. 166. Springer, Singapore (2017). https://doi.org/10.1007/978-981-10-4086-3
2. Choi, Y.H., Ku, J., Lim, H., Kim, Y.H., Nam-Jong, P.: Mobile game-based virtual reality rehabilitation program for upper limb dysfunction after ischemic stroke. Restor. Neurol. Neurosci. **34**(3), 455–463 (2016). https://doi.org/10.3233/RNN-150626
3. Reyes, A., Qin, P., Brown, C.: A standardized review of smartphone applications to promote balance for older adults. Disability and Rehabilitation **40**(6), 690–696 (2018). https://doi.org/10.1080/09638288.2016.1250124. Taylor & Francis
4. Nussbaum, R., Kelly, C., Quinby, E., Mac, A., Parmanto, B., Dicianno, B.E.: A systematic review of mobile health applications in rehabilitation. Arch. Phys. Med. Rehabil. **100**, 115–127 (2019). https://doi.org/10.1016/j.apmr.2018.07.439
5. Zmily, A., AbuSaymeh, D.: Alzheimer's Disease rehabilitation using smartphones to improve patients' quality of life. In: 7th International Conference on Pervasive Computing Technologies for Healthcare and Workshops, pp. 393–396, Venice (2013). https://doi.org/10.4108/pervasivehealth.2013.252248
6. Bisio, I., Delfino, A., Lavagetto, F., Sciarrone, A.: Enabling smartphone-centric platforms for in-home rehabilitation: a comparison among movement recognition approaches. In: IEEE International Conference Communications (ICC), pp. 1–6 (2016). https://doi.org/10.1109/icc.2016.7511596
7. Longoni, L., Brunati, R., Sale, P., Casale, R., Ronconi, G., Ferriero, G.: Smartphone applications validated for joint angle measurement: a systematic review. Int. J. Rehabil. Res. **42**, 11–19 (2019). https://doi.org/10.1097/MRR.0000000000000332
8. Bittel, A.J., Elazzazi, A., Bittel, D.C.: Accuracy and precision of an accelerometer-based smartphone app designed to monitor and record angular movement over time. Telemed. e-Health **22**(4), 302–309 (2016). https://doi.org/10.1089/tmj.2015.0063

9. Xiangfeng, Z., Guoli, Z., Mingming, Z., Sheng, Q.: reviewing clinical effectiveness of active training strategies of platform-based ankle rehabilitation robots. J. Healthc.Eng. **2018**, 1–12 (2018). https://doi.org/10.1155/2018/2858294. Article ID 2858294
10. Morris, T., Newby, N.A., Wininger, M.: Novel interfaces for training neuromotor control of the upper and lower limb. Exp. Brain Res. **192**, 33–42 (2009). https://doi.org/10.1007/s00221-008-1547-x
11. Tsoi, Y.H., Xie, S.Q.: Design and control of a parallel robot for ankle rehabiltation. In: 15th International Conference on Mechatronics and Machine Vision in Practice, pp. 515–520, Auckland (2008). https://doi.org/10.1109/mmvip.2008.4749585

Protocol for the Functional Evaluation of Patients with Knee Injury Treated in a Local Rehabilitation Centre

Camila Ileana Duré[1(✉)], Julio Savio[2], Bruno Marengo[2], Germán Perotti[2], Paola Catalfamo Formento[1,3], and Claudia Edith Bonell[1]

[1] Facultad de Ingeniería, Laboratorio de Investigación en Movimiento Humano, Universidad Nacional de Entre Ríos, Concepción del Uruguay, Argentina
camiiladure6@gmail.com,
cbonell@ingenieria.uner.edu.ar
[2] Centro Médico de Rehabilitación, Nogoyá, Entre Ríos, Argentina
[3] Centro de Investigaciones y Transferencia de Entre Ríos (CITER), Consejo Nacional de Investigaciones Científicas y Técnicas (CONICET) y Universidad Nacional de Entre Ríos (UNER), Oro Verde, Entre Ríos, Argentina

Abstract. The pathologies and injuries of the knee are a common problem in the clinical field. There are numerous tests that allow to evaluate in a standardized way the results of the rehabilitation, nevertheless in the medical center where the present work was developed, the evaluation was carried out by treating clinicians without following protocolized and documented criteria. For this reason, a protocol was developed that consisted of a first part that uses the IKDC test and a conventional videographic method to obtain spatio-temporal parameters. The protocol was applied for six patients attending the rehabilitation centre, the indices proposed by the IKDC test and the spatio-temporal parameters were calculated: step time, stance time, cadence and symmetry. It was concluded that the IKDC test provided useful information that allowed recording the evolution in the rehabilitation, to document it, and to complement the patient's clinical history. Spatio-temporal parameters, on the other hand, did not provide more information for the patients studied. However, the information provided by these parameters contributed tools to quantify the qualitative observations made in patients by treating physicians. Finally, a survey was carried out to the personnel of the institution to evaluate the proposed protocol, which resulted in the decision to implement it routinely for the assessment of the patients of the institution.

Keywords: Analysis of Human Movement · IKDC · Videography

1 Introduction

The total or partial limited mobility of the lower limbs, and in particular those due to an injury in the knee joint, is a pathological condition that often requires rehabilitation treatments. The objectives of the treatments are to restore the mobility of the joint and to diminish or eliminate the associated pain [1, 2].

© Springer Nature Switzerland AG 2020
C. A. González Díaz et al. (Eds.): CLAIB 2019, IFMBE Proceedings 75, pp. 907–912, 2020.
https://doi.org/10.1007/978-3-030-30648-9_117

Different tools of Analysis of Human Movement have been proposed for the evaluation of the rehabilitation treatments. Particularly for the evaluation of knee rehabilitation, tests such as IKDC (International Knee Documentation Committee Knee Form), WOMAC (Western Ontario and McMaster Universities Osteoarthritis Index), KOOS (Knee injury and Osteoarthritis Outcome Score) and others have been proposed [3]. These tests evaluate the degree of pain, the ability to perform activities and in some respect the quality of life through the impact of the disability in the physical, psychological and social involvement. The tests include questionnaires for the patient himself or for the clinician. In this respect, the final mark of the evaluated items strongly depends on the experience of the observer and the proper perception of the patient [4].

Also, instrumented gait analysis that provides kinematic and kinetic information has been proposed as alternatives for the evaluation of rehabilitation [2, 5]. Unfortunately, often the optical systems needed for instrumented gait analysis are expensive and require especial characteristics for their installation (for example, equipments are not portable and the gait lab should be large enough to allow an accurate measurement). Alternative methods, which are portable, with a relatively low cost and easy to use are more practical for local clinical environments [4]. For example, basic temporal parameters have been proposed and validated using conventional videography [6].

The use of temporal parameters in combination with tests specifically designed for the appraisal of the knee, appear as an appealing option for the assessment of rehabilitation treatments of patients with knee injury in local clinical environments. However, they have yet not been evaluated in situ.

Currently, at the CMR, standardized methods are not applied to record and document the rehabilitation of patients, as well as validated tests are not implemented. For this reason, a protocol was developed. It consisted of the IKDC test and a conventional videographic method to obtain spatio-temporal parameters. The results obtained were compared against the evaluation of the clinicians and the feasibility of using the protocol was evaluated using a questionnaire for the clinicians.

2 Methods

Six patients (a women, five men, mean age: 35 $\pm$ 17,07 years old) who were in rehabilitation treatment at the local Rehabilitation Centre participated of the study. All of them had an unilateral injury of the knee and they were at different stages of the rehabilitation treatment.

The selected protocol included two measurement techniques. The first one consisted of implementing Part 3 and Part 6 of the IKDC test [7]. Part 3 consists of a questionnaire for the patient, who needs to rate the perceived pain and the difficulty in performing different activities (such as kneeling or walking up the stairs). Once the patient complete the questionnaire, a final scoring was calculated as proposed in the form itself [7]. Results vary from 0% to 100%, interpreted as a measure of function

such that higher scores represent higher levels of function and lower levels of symptoms. A score of 100 is interpreted to mean no limitation with activities of daily living or sports activities and the absence of symptoms.

Part 6 consists of measuring certain characteristics of the joint and its mobility, normally performed by the physiotherapist. Section 2 of Part 6 measures the passive motion deficit in flexion and extension angles of the knee (measured by a goniometer). Results vary in a scale from A to D, where A is normal and D is severely abnormal.

The second measurement technique was the estimation of temporal parameters using conventional videography. For this, a video of the patient while they are walking is recorded. And using methods previously validated [6], the time of the first contact of the foot with the floor (inicial contact, IC) and the time of the brake of contact (foot off, FO) are visually estimated. Then, the following temporal parameters were calculated:

- Step time (StT): time between the IC of one foot until the IC of the contralateral foot.
- Cadence (Cad): steps performed in a given time, usually expressed as steps per minute.
- Stance time (ST): time elapsed between the IC of one foot and the FO of the same foot.
- Symmetry index (SI): calculated using the maximum and minimum of Stance Time, which could be right (STR) or left (STL) as:

$$S.I(\%) = (min(STR, SPL)/max(STR, SPL)) * 100 \quad (1)$$

For this, a camera (Nikkon 3300) was positioned at 1 m high and 3 m away from the walking path for capturing the videos.

Each patient walked twelve times in both directions at their self selected speed. The estimation of IC and FO was performed on the leg nearest to the camera, using the software KINOVEA.

Participants were measured twice, with a difference of two months between the first and second measurement. The results from the IKDC test and temporal parameters were cualitatively compared in this pilot study against the evaluations performed from the treating physiotherapist.

Finally, a questionnaire was given to the clinicians to evaluate the feasibility of using the protocol in their center.

3 Results

The results of the application of the protocol are presented in the Table 1 and Table 2. For each take, the value obtained from Sect. 3 of the IKDC test (subjective analysis) and Part 6 of the same test (physiotherapist analysis) are reported, in addition to the values of the calculated spatio-temporal parameters.

Table 1. Results obtained in the first application of the protocol. (STL: stance time of the injured leg). (STN/L: stance time of the healthy leg).

Parameters	Patient 1	Patient 2	Patient 3	Patient 4	Patient 5	Patient 6
Score IKDC	39,08%	87,36%	57,47%	32,18%	75,86%	71,26%
Degree IKDC	–	–	–	–	–	–
STL [ms]	637,3	647,7	658,8	585	578,2	576,6
STN/L [ms]	666,3	648,8	667,7	587,5	587,3	588,8
Symmetry index	95,63%	99,82%	98,66%	99,57%	98,45%	97,92%
StT [ms]	604,5	566,6	607,7	527,5	547,2	557,7
Cadence [step/min]	99,25	105,8	98,72	113,7	109,6	107,5

Table 2. Results obtained in the second application of the protocol. (STL: Stance time of the injured leg). (STN/L: Stance time of the healthy leg).

Parameters	Patient 1	Patient 2	Patient 3	Patient 4	Patient 5	Patient 6
Score IKDC	31%	91,95%	70%	51,72%	62%	100%
Grade IKDC	B	B	B	A	B	A
STL [ms]	599,0	712,0	656,6	572,2	661,6	712,5
STN/L [ms]	599,0	700,0	658,3	582,2	676,6	703,7
Symmetry index	100%	98,31%	99,74%	98,28%	97,78%	98,77%
StT [ms]	527,0	621,0	598,3	521,1	591,6	658,7
Cadence [step/min]	113,8	96,62	100,3	115,1	101,4	91,08

Patient 1 presented a lesion characterized by the presence of intermittent pain, a fact that was referred by the physiotherapist during the interview, so he opted for 10 points in frequency of pain (constant) with an intensity of 8 points. In the physiotherapist report he obtained grade B, and the patient was not yet discharged in his rehabilitation. The videography shows a possible improvement of the patient between both sessions: the support times of both extremities are the same, and presents high symmetry and greater cadence.

Patients 2 and 3 present improvements according to medical analysis. An increase of the IKDC score is observed, but in the physiotherapist examination they obtained grade B, both continue the rehabilitation process. Patient 2 increased the stance time of the injured leg although the step time is longer which leads to a lower cadence value. In patient 3, the spatio-temporal parameters are similar in both cases.

Patients 4 and 6 had already been discharged between the two applications of the protocol. For subject 4 although the percentage of IKDC does not come close to 100%, it increased between both instances. No changes are observed regarding spatio-temporal parameters. In subject 6 the IKDC test indicates a greater degree of rehabilitation, grade A and 100% IKDC. However, the spatio-temporal parameters show an increase in support times between both takes and a decrease in cadence.

Patient 5 left the rehabilitation after the first evaluation and returned to it in the second take due to pain and discomfort. This corresponds to the value obtained in the IKDC index, being the similar symmetry in both sessions compared to stance times of the injured leg and healthy leg which were larger.

4 Discussion

As a first activity, a literature review of validated and standard tools available for the evaluation of knee function was performed. The IKDC test was the first choice out of the review [1]. Also, a test not involving the subjective view of the patient was thought as a complement for the analysis [2], in this case a validated protocol for the estimation of temporal parameters using conventional videography was selected [8].

It is not possible to compare the IKDC test between subjects. The subjective view of the patient was evident in the results of the test, given that patients who practice a sport regularly achieved better results that those who did not have an sport activity. This is because, the test includes questions regarding activities with increasing difficulty, and the most difficult were sport activities. Patients, who did not practice a sport regularly, did not complete those questions, so they were not feasible to achieve the maximum level of the test (100%). During the measurements, the clinicians suggested that it is important to consider the emotional state of the subject in order to interpret the IKDC results. In terms of Part 6 of the test, the results agreed with the physiotherapist analysis of the case. Patients that were finishing the treatment obtained a grade A, while patients who had to continue their rehabilitation obtained a grade B.

Temporal parameters could have had an improvement in terms of an increase in stance time of the injured leg, in cadence and in the symmetry of stance time. However, all the values where within the normal values reported in the literature for both days [8]. Four of the patients who presented improvement in the rehabilitation process, showed an increase in stance time of the injured leg but symmetry was normal at the time of the first measurement. The measurement of cadence was influenced by the previous activity performed by the subject.

Two clinicians (one physiotherapist and one orthopaedic surgeon) evaluated the application of the protocol. They considered that it was an useful tool for the evaluation of the rehabilitation process, that could be reported in the clinical history of the patient, and they could make use of the measurements for extending or terminating the treatment and/or modify the treatment according to the results.

5 Conclusion

In this study, a protocol for the evaluation of the rehabilitation process in patients with knee injury was designed and applied in a local rehabilitation centre. The centre did not have a standard criteria for the assessment or the documentation process for the rehabilitation treatments. The protocol was applied to patients with knee pathologies of the institution and health personnel very useful for documentation of rehabilitation.

The application of the protocol in the rehabilitation center will continue and other protocols will be added to complement the evaluation.

Conflict of Interest. The authors declare no conflicto of interest.

References

1. Leguizamon, J.H., Braidot, A., Formento, P.C.: Assessing the progress of rehabilitation in patients with ACL reconstruction using the international knee documentation committee subjective knee form. J. Phys. Conf. Ser. **332**(1), 1–21 (2011)
2. Biggs, P.R., Whatling, G.M., Wilson, C., Holt, C.A.: Correlations between patient-perceived outcome and objectively-measured biomechanical change following total knee replacement. Gait Posture **70**, 65–70 (2019)
3. Castellet Feliu, E., Vidal, N., Conesa, X.: Rating scales in orthopaedic surgery and traumatology. Trauma Fund Mapfre **21**(supl 1), 34–43 (2010)
4. Rodriguez-Merchan, E.C.: Knee instruments and rating scales designed to measure outcomes. J. Orthop. Traumatol. **13**(1), 1–6 (2012)
5. Angthong, C., Veljkovic, A.: Relationships among subjective patient-reported outcome, quality of life, and objective gait characteristics using wearable foot inertial-sensor assessment in foot–ankle patients. Eur. J. Orthop. Surg. Traumatol. **0123456789**, 1–5 (2018)
6. De Grucci, C., Ewins, D., Shaheen, A., Catalfamo Formento, P.: Evaluation of a visual method to calculate temporal parameters. In: IEEE Argencon, no. Ic (2016)
7. International Knee Documentation Committee: IKDC Knee Forms, pp. 1–21 (2000)
8. Vasco, P., Herriko, E., España, U.: Análisis de la marcha : sus fases y variables espacio-temporales Gait analysis: phases and spatio-temporal variables Doctor en Fisiología del Ejercicio, Universidad del País Vasco . Resumen Introducción (2011)

Biomark: A Toolbox for Visualization and Kinematic Gait Analysis

Francisco J. Alvarado-Rodríguez[1], Cesar Covantes-Osuna[1], Erick Guzmán-Quezada[1,2], Rebeca Romo-Vázquez[1], Sandra Guevara-Vega[3], Paola Ruiz-Padilla[3], and Hugo Vélez-Pérez[1(✉)]

[1] Department of Computer Sciences, CUCEI, Universidad de Guadalajara, Guadalajara, Jalisco, Mexico
hugo.velez@academicos.udg.mx
[2] Department of Electronics, Universidad Autónoma de Guadalajara, Guadalajara, Jalisco, Mexico
[3] Gait Analysis Laboratory, Centro de Rehabilitación Infantil Teletón, Guadalajara, Jalisco, Mexico

Abstract. Visualization and kinematic analysis of gait with computer programs and quantitative metrics are nowadays essential tools for the characterization of normal and pathological patterns, as well as for the diagnosis and rehabilitation in gait alterations. However, most of the software that is used for the acquisition systems in the gait labs, estimates a predetermined and restricted number of parameters, conditioning and limiting the work of the medical specialists, either in follow-up studies of individual cases or in the gait description between populations. The objective in this work, is to implement a computational tool that accesses the records of the databases generated by gait analysis equipment, for the visualization and obtaining of quantitative metrics from these kinematic studies, facilitating in this way, the identification of normal and pathological gait patterns, as well as facilitate the statistical estimation inter- and intra-patient in the development of comparative studies.

Keywords: Kinematic Gait Analysis · Gait Analysis Lab · Toolbox · Matlab · CRIT

1 Introduction

Gait Analysis (GA) is a technique used to describe the kinematics in the stages of human progression. Despite the fact that the movement science field has been present for several years [1], with the development of computer systems, gait has been studied more accurately providing important advances in understanding the movement for applications in various areas, including biometric identification [2], medical diagnostic and therapeutic tools.

The term *human gait cycle* refers to the completion by a unique set of movements that in sequence make up the motion of walking; which are divided into

© Springer Nature Switzerland AG 2020
C. A. González Díaz et al. (Eds.): CLAIB 2019, IFMBE Proceedings 75, pp. 913–920, 2020.
https://doi.org/10.1007/978-3-030-30648-9_118

two main periods: Stance and swing [3], both are subdivided into eight phases that meet the three tasks that must perform each limb [4,5], which can be seen in Fig. 1. A complete gait cycle begins with the contact of the heel until a new contact of this. The gait cycle is evaluated with respect to each lower limb, obtaining quantifiable data corresponding to each of the joints in the lower extremity [6].

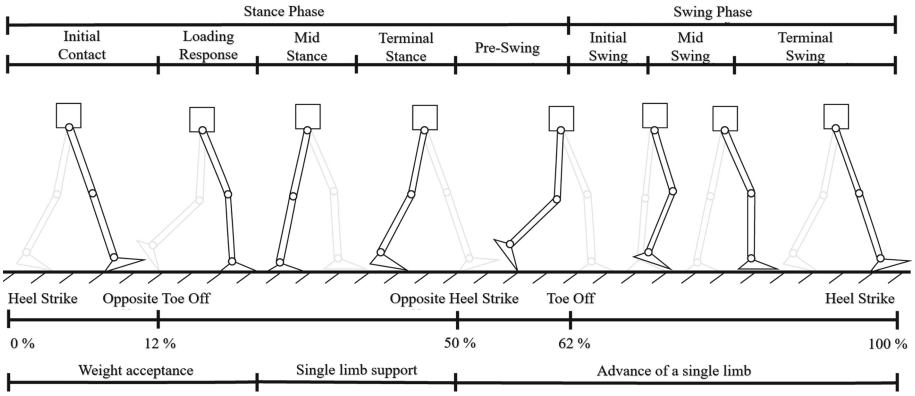

Fig. 1. Representation of the phases, stages and tasks of a normal gait cycle (image edited from [5]).

The most used tools to obtain kinematic values of the gait are the motion capture systems (MoCap). These systems were implemented around the 80's, and currently maintain the same basic operating principles, although they have improved their speed, accuracy and reliability [7].

During a study, some reflective markers, corresponding to anatomical bone points, are placed on the patient indicating the movement of the joints that are under them [4]. These markers are stroboscopically illuminated and detected by infrared cameras. The marker detection by two or more cameras, as well as the knowledge of the position and orientation, makes possible to detect the markers position in three dimensions. Currently, the Gait Analysis Laboratories (GAL) use as minimum of six cameras and operate at a minimum frequency of 100 Hz, making it possible to detect several tens of markers between 9 and 25 mm [8]. In addition, the movement study is completed by actively recording the electrical activity of the muscles, using dynamic telemetric electromyography (EMG), through electrodes placed on the skin in the muscles involved in the movement [9]. All this information is visualized in a report where the clinical expert, by empirical knowledge, diagnoses the patient.

Despite the importance of laboratories for GA, several limitations have been observed. For example: restrict the marker acquisition to only a few steps per trial [10], select a single cycle empirically and ignoring the rest of the information, in the reports generated by these analysis systems. Likewise, the restricted practicality in the manipulation of information hinders the follow-up in individual cases (intra-patients), or the treatment progress analysis in groups of patients

with the same pathology (inter-patients). Given these limitations, several systems for the analysis of markers have been proposed and developed in México [10–12]. However, these systems are rudimentary compared to the acquisition systems that are already in the international market [13].

In this context, this work presents Biomark, a toolbox developed in MatLab®, for the reading and processing of records acquired by the existing systems for GA, and in this way, extracts patterns and useful characteristics for the records of the gait, both by subject and by group. In this way, it offers the possibility of generate tracking reports by case, as well as the possibility perform statistical studies among various groups in patients of interest more easily.

2 Methodology

2.1 Database

In this work, 11 records from patients with alterations walking pattern, selected and provided by the GAL of the *Centro de Rehabilitación Infantil Teletón de Occidente* (CRIT), were used [14]. Each record contains only the values of the spatial coordinates of the markers and the angular movements and was previously analyzed and evaluated by the specialists of the GAL. The kinematic parameters presented in this work were estimated from these data. The research protocol implemented was reviewed and approved by the Ethics Committee of the CRIT.

2.2 Biomark Description

Biomark focuses on the estimation and visualization of the most important indices used to study the gait cycle, indicated by the specialists of the CRIT which are: The stance time, swing time and the double support (time reported in percentage); the stance time, swing time and the stride time (reported in seconds); the cadence (steps for minute reported in frequency); the step length, stride length and the step width (reported in meters), and the velocity, swing velocity and the mean velocity (reported in m/s). These indexes are estimated from records that were previously analyzed by the specialist doctor, in which the beginning of the cycle, the beginning of the swing stage, and the end of the gait cycle of both limbs, were indicated. The records were converted from the original format of the analysis system to a MatLab® compatible format.

2.3 Estimated Rates

Stance time (S_t) is calculated through the subtraction of the beginning time from gait cycle (St_b), to the swing start time (Sw_b) as follows (Eq. 1):

$$S_t = Sw_b - St_b \tag{1}$$

where b represents the initial time, t the stance, and w the swing.

In the same way, the swing time (S_w) is estimated by subtracting the swing start time (Sw_b) at the end of the gait cycle (St_e) as (Eq. 2):

$$S_w = St_e - Sw_b \tag{2}$$

where e is the end of the gait cycle.

The duration of each step (S) is obtained by subtracting in the end of the gait cycle (St_e) the initial time of the gait cycle (St_b) in each limb (Eq. 3):

$$S = St_e - St_b \tag{3}$$

The percentages (DS) in each value are obtained by dividing the time of each stage (Sw_{bc} and St_{ei}) over the total time (S). To obtain the percentage value of the double support the difference between the start time in the contralateral step and the beginning of the swing in the ipsilateral step is made (Sw_{bc}-St_{ei}) (Eq. 4):

$$DS = \frac{Sw_{bc} - St_{ei}}{S} \tag{4}$$

where c is the contralateral limb, and i is the ipsilateral limb.

On the other hand, the cadence (Cad) is estimated by calculating the inverse of the time obtained from averaging duration of the right and left step in a minute (Eq. 5):

$$Cad = \frac{240}{S_l + S_r} \tag{5}$$

where r is the right cycle and l is the left cycle.

The distance indexes are obtained from the foot marker location at the instants of the time defined by the beginning of the gait cycle (St_b), the beginning of the swing (Sw_b) and the end of the gait cycle (St_e). The first index is the step length and represents the displacement distance in each step. The index step length ($Step$) is calculated by the difference between the distances of the feet after each step in a contralateral way, that is: for the right step the distance progression is estimated with respect to the left foot, and for the left step the distance is estimated from the right foot (Eq. 6).

$$Step = Sl_{ei} - Sl_{ec} \tag{6}$$

Strike length index ($Strike$) is obtained by estimating the covered progression distance from the beginning (Sl_b) until the completion of a step (Sl_e) (Eq. 7).

$$Strike = Sl_e - Sl_b \tag{7}$$

Gait speed (V) represents the relationship between the strike length and the time required for this (Eq. 8).

$$V = \frac{Strike}{S} \tag{8}$$

The swing speed (V_s) is equal to the ratio of the progression shift ($Strike$) over swing time (S_w) (Eq. 9).

$$V_s = \frac{Strike}{S_w} \tag{9}$$

Finally, the average speed (V_m) is obtained by estimating the average of the progression displacement in a complete march cycle, divided by the average progression time in each limb (Eq. 10).

$$V_m = \frac{Strike_r + Strike_l}{S_r + S_l} \tag{10}$$

The data obtained by Biomark and the equipment of the GAL were compared using the t-student and the Pearson's correlation tests.

3 Results

In order to present a simple and intuitive design, Biomark interface has been structured into three large sections as shown in Fig. 2. The first section (top left) allows the search of previously saved records. From these data, the indices values described in the Sect. 2.3 are estimated and displayed by limb (right and left). In addition, these indices were arranged in two groups of parameters: temporal and distance. For a better reference, the standard values of these indices were also included.

At the bottom of the interface is the second section dedicated to the visualization of the main cinematic plots: Pelvic obliquity, tilt and rotation; Hip rotation, abduction-adduction and flexion-extension; Knee flexion-extension and valgus-varus; Ankle dorso-plantar flexion and foot progression. These plots are extracted from the records and plotted by clicking the button "Visualize Kinematics".

In the third section (top right), 3D kinematic markers visualization was implemented in a skeletal representation. To display these animated graphics, it is necessary to click the "Visualize Marks" button. These views show three projection angles by default: lateral, frontal and superior. However, the graphics can be edited and rotated freely by users according to their needs. Finally, with the aim of moving the skeletons frame by frame or selecting a particular frame, a scroll bar was also included.

As mentioned above, the first step was to convert the data from the records of the equipment format to a format compatible with MatLab®. The next step was to verify that the data had been completely and correctly converted. Due to its programming, the Biomark toolbox managed to extract most of the parameters of interest requested by the medical specialists, which are used for the generation of clinical reports and listed in Table 1. To verify that the format conversion was correct and that the indices correspond to the values estimated by the lab equipment, Table 1 presents a comparative example between the indices calculated by Biomark and those estimated by the software of the GAL equipment.

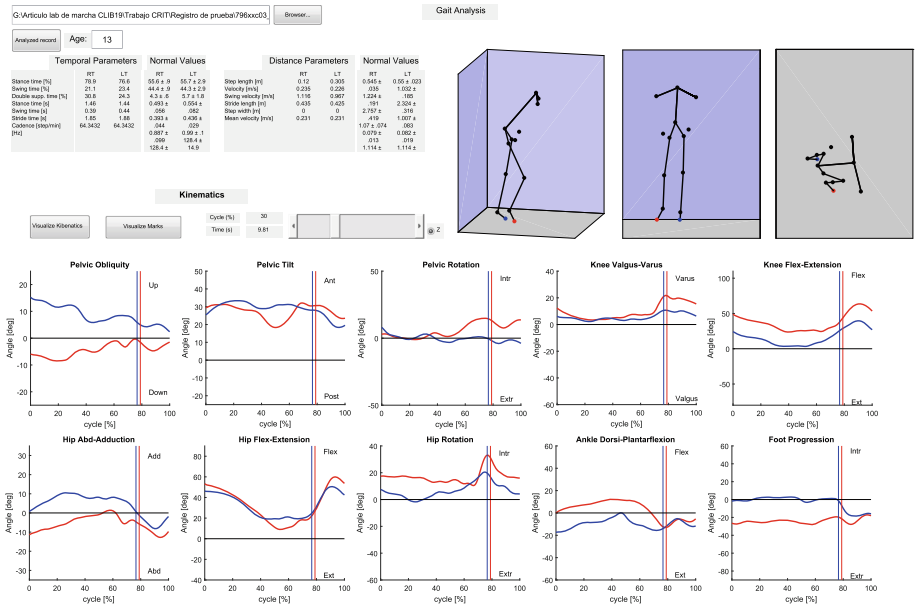

Fig. 2. Visualization of the data obtained from the records previously analyzed by specialists in Biomark.

As can be seen, the values estimated by Biomark are similar to those obtained by the equipment and are within the allowed error margins in the deviations of the "Normal Values" in Fig. 2.

The analysis of the parameters calculated by Biomark against the parameters generated with the gait laboratory equipment, shows the following results. In the temporal parameters a Pearson's correlation of 1 was obtained, which was the expected result however, in the t-student a $p = 0.99$ value was observed, this was mainly caused by the cadence estimates, since it presented an average estimation error of 0.001 ± 0.007 Hz. Regarding the distance parameters, a correlation of 0.99 and a p-value were obtained in the t-student test of $p = 0.97$, mainly due to the estimation of the step length that presented an average error of estimation of 0.02 ± 0.01 m.

4 Conclusion

The kinematics quantitative analyses applied in gait using computational tools are essentials to identify normal and pathological patterns to improve the diagnosis in diseases and plan better rehabilitation strategies. However, the studies and diagnoses of the specialists depend on a limited number of parameters estimated by the equipment software. This paper presents the computational tool called Biomark developed in MatLab®, software widely used for the acquisition,

Table 1. Comparison of the indices estimated by Biomark VS the GAL equipment.

Parametric	Unit	Biomark		GAL equipment	
		RT	LT	RT	LT
Stance time	Percentage %	78.9	76.6	78.9	76.6
Swing time	Percentage %	21.1	23.4	21.1	23.4
Double support time	Percentage %	30.8	24.3	30.8	24.3
Stance time	Seconds s	1.46	1.44	1.46	1.44
Swing time	Seconds s	0.39	0.44	0.39	0.44
Stride time	Seconds s	1.85	1.88	1.85	1.88
Cadence	Step/min Hz	64.343		64.343	
Step length	Meters m	0.12	0.305	0.131	0.307
Velocity	Meters/second	0.235	0.226	0.236	0.226
Swing velocity	Meters/second	1.116	0.967	1.118	0.964
Stride length	Meters m	0.435	0.425	0.436	0.424
Mean velocity	Meters/second	0.231		0.231	

processing and visualization of data. In our case, these data were generated from software that does not allow in direct way, the extraction of characteristics of interest in the GAL.

As we saw in Sect. 3, Biomark focuses on the extraction of the necessary parameters to estimate the indices required by medical experts for the diagnosis and development of therapies and research on gait patterns in healthy or pathological subjects, and to evaluate the rehabilitation processes in a quantitative way. The proposed tool was able to extract a significant amount of information from the few running cycles that are generated in each test in the gait lab, which is presented as other important limitation by the optokinetic registers.

Biomark presented a simpler and efficient option for data analysis. It also offers specialists, the advantage of not staying in the gait lab to perform their clinical diagnoses and interpretations, it would be enough to install Biomark on a personal computer or laptop. Biomark has been conceived to become an application as complete as possible for the reading, visualization, graphing and estimation of parameters in biomechanical and kinematic gait studies. The Biomark tool presented in this work corresponds to a beta version and does not include the statistics section, since more records are needed to become a robust tool. However, a section for statistical comparisons is planned for the next version and the analyzes that it includes will depend on the needs of the specialists. We hope that this toolbox plays an important role in advancing research in the sciences of human movement analysis.

Acknowledgments. We thank the Gait Analysis Laboratory of the *Centro de Rehabilitación Infantil Teletón de Occidente* for providing the records used to implement and test Biomark. Also we thank the National Council of Science and Technology (CONACyT) for the support received through the scholarship CVU-311539 and CVU-746539.

Conflict of Interest. The authors declare no potential conflicts of interest with respect to the authorship and/or publication of this article.

References

1. Baker, R.: The history of gait analysis before the advent of modern computers. Gait and Posture **26**(3), 331–342 (2007)
2. Nixon, M.S., Tan, T., Chellappa, R.: Human Identification Based on Gait, vol. 4. Springer, Heidelberg (2010)
3. Hesse, S., Uhlenbrock, D., et al.: A mechanized gait trainer for restoration of gait. J. Rehabil. Res. Dev. **37**(6), 701–708 (2000)
4. Perry, J., Davids, J.R., et al.: Gait analysis: normal and pathological function. J. Pediatr. Orthop. **12**(6), 815 (1992)
5. Dollar, A.M., Herr, H.: Lower extremity exoskeletons and active orthoses: challenges and state-of-the-art. IEEE Trans. Robot. **24**(1), 144–158 (2008)
6. Gage, J.R., Deluca, P.A., Renshaw, T.S.: Gait analysis: principles and applications. JBJS **77**(10), 1607–1623 (1995)
7. Mündermann, L., Corazza, S., Andriacchi, T.P.: The evolution of methods for the capture of human movement leading to markerless motion capture for biomechanical applications. J. Neuroeng. Rehabil. **3**(1), 6 (2006)
8. Baker, R.: Gait analysis methods in rehabilitation. J. Neuroeng. Rehabil. **3**(1), 4 (2006)
9. Mordaunt, P., Zalzala, A.M.S.: Towards an evolutionary neural network for gait analysis. In: Proceedings of the 2002 Congress on Evolutionary Computation, CEC 2002 (Cat. No. 02TH8600), vol. 2, pp. 1922–1927. IEEE (2002)
10. Herrera-Hernández, A.R., Sánchez-Uresti, A.: Sistemas de captura y análisis de datos de la marcha. In: Memorias del Congreso Nacional de Ingeniería Biomédica, vol. 5, pp. 362–365 (2018)
11. Arellano-González, J.C., Medellín-Castillo, H.I., Cárdenas-Galindo, J.A.: Analysis of the kinematic variation of human gait under different walking conditions using computer vision. Rev. Mexicana de Ingeniería Bioméd. **38**(2), 437–457 (2017)
12. Gutiérrez-Martínez, J., González-Leyva, A., Ortiz-Espinosa, A., Núñez-Gaona, M.A., Barraza-López, E.F., Piña-Ramírez, O.: Design and development of a system for analysis of movement of the hand and wrist. Rev. Mexicana de Ingeniería Bioméd. **32**(1), 7–11 (2011)
13. Cutti, A.G., Ferrari, A., Garofalo, P., Raggi, M., Cappello, A., Ferrari, A.: Outwalk: a protocol for clinical gait analysis based on inertial and magnetic sensors. Med. Biol. Eng. Comput. **48**(1), 17 (2010)
14. CRIT-Occidente: Teletón méxico (2019). https://www.teleton.org/home/informacion-crit/CRIT-Occidente. Accessed 28 Feb 2019

Results of the Use of Personalized Insoles for the Treatment of Cavus Foot and Comorbidities

Paola Hernández-Gandarillas(✉), Sergio Luis Orozco-Villaseñor, José de Jesús Mayagoitia-Vázquez, Israel Miguel-Andrés, José Pablo Herrera-Rangel, and Karla Daniela de la Cruz-Alvarado

Laboratory of Biomechanics, Centro de Innovación Aplicada en Tecnologías Competitivas CIATEC, A.C. León, GTO, Mexico
{phernandez, sorozco, jmayagoitia}@ciatec.mx

Abstract. It has been found several cases of anterior cavus foot. Because of that, it is needed the manufacturing of the costume-made orthoses for the plantar foot region and with this the musculoskeletal deformation of the foot can be corrected, reducing the symptom and/or helping the structure.

In order to make sure that the insoles were working properly, a survey was performed in a sample of 60 people, from the participants just six of them did not continue wearing the insoles due to different personal reasons. The study did not consider those participants who did not wear the insoles. All persons who participated in the survey and those who wore the insoles for more than one month evidenced positive results in the foot structure.

Keywords: Baropodometry · Cavus foot · Plantar orthosis

1 Background

Foot functions during the static posture or dynamic movement are associated with differences in foot structure. The pathologies of the foot are of biomechanical origin and associated with the foot type, being this a clinical concept to simplify the anatomical complexities of the human foot [1]. Among the features that indicate a normal foot is the angle of Moreau - Costa - Bartani of 120–130°, the angle of Kite in radiographic projections of profile of 15° and 20° in dorsoplantar. The longitudinal angles of the foot decrease progressively from 18 to 25° in the first radius to 5° for the fifth radius.

When the patient has the cavus foot pathology, these parameters are modified, an excess of height in the internal and external longitudinal arch characterizes it. It can be associated with varus deviation of the calcaneus and retraction of the fingers (claw toes). Its development is associated with muscle weakness, neuromuscular imbalance, shortening of the Achilles tendon, among other causes.

© Springer Nature Switzerland AG 2020
C. A. González Díaz et al. (Eds.): CLAIB 2019, IFMBE Proceedings 75, pp. 921–932, 2020.
https://doi.org/10.1007/978-3-030-30648-9_119

The clinical manifestations are conditioned by the excessive pressure of the metatarsal heads and the fingers that produce calluses in those areas. Chronic pain in the forefoot or heel in the form of metatarsalgia or plantar fasciitis is common [2]. According to the position in the sagittal plane can be anterior, posterior or mixed.

The cavus foot is often attributed to neuromuscular disorders affecting the brain, spinal cord or peripheral nerves; among the pathologies developed are hereditary sensory and motor neuropathies such as Charcot – Marie – Tooth disease (CMT), cerebral palsy, spina bifida, poliomyelitis, muscular dystrophy or apoplexy. The patients with cavus feet often have tight calves and a short and tight gastrocnemius leading to increase of the plantar pressures in the forefoot and the plantar fascia acts as a deforming hindfoot inverting forces [3].

A comorbidity is the presence of different additional diseases that have existed or may occur during the clinical course of a patient with a major disease (main attention disease), either acute or chronic [4, 5]. Among the signs or symptoms present in a cavus foot are hammered or claw toes, callus in the forefoot, hindfoot or lateral part, instability due to the inclination of the heel inward, which causes ankle sprains. However, there are patients who experience a foot drop due to weakness of the foot and ankle muscles resulting in foot drag during the gait cycle [6].

There are non-surgical treatments for the cavus foot pathology: shoe modifications, orthopedic devices and orthotic devices. An example of these are the insoles or plantar orthoses that aim to correct and/or compensate the functional and morphological alterations of the feet [7]; they decrease the vertical pressure and redistribute the support of the foot affected by anatomical deformities.

A foot with mechanical alterations is painful at the moment that it rests against the ground and supports the weight of the body in an inadequate way or during march. That is why the distribution of the plantar loads is especially important when there is a cavus foot, since the only support that the foot performs is in the heel and the metatarsal area [8]. For this reason, the insoles promote an integrity of the joints of the lower limbs. The functional insoles can be classified into:

- Realignment or deformity control insoles: rigid or semi-rigid and elastic density is used to avoid muscle atrophy.
- Insoles of discharge or distribution of pressure: of soft or semi – soft density, redistribute the pressure and re-establish the horizontal support on the ground.
- Mixed templates: combine rigid and soft densities [9].

The goal of the insoles is achieved when abnormal compensatory movement are avoided, a good forefoot posture is controlled, the rearfoot is maintained in neutral keeping the correct anatomical angle between the forefoot and hindfoot, between the leg and the horizontal plane of the ground with the purpose of achieving normal movements in the gait cycle without pain in each of the phases of gait.

2 Method

For the manufacturing of the insoles, it is needed to perform a biomechanical test, Baropodometry, it is a technique that consists in measuring and analyzing the reaction forces exerted on the foot when it is subjected to loads, using pressure sensors that analyze the distribution of loads and pressure of the feet [10]. The Bioethics Committee of CIATEC, AC with registration in the National Bioethics Commission **No.: CONBIOETICA11CEI00620131108** approved this study. It consists of performing four tests.

2.1 Static Phase

The image of the footprint is recorded for 10 s, location of the barycenter, maximum pressure points of each limb and distribution of loads between forefoot and hindfoot is recorded (see Fig. 1).

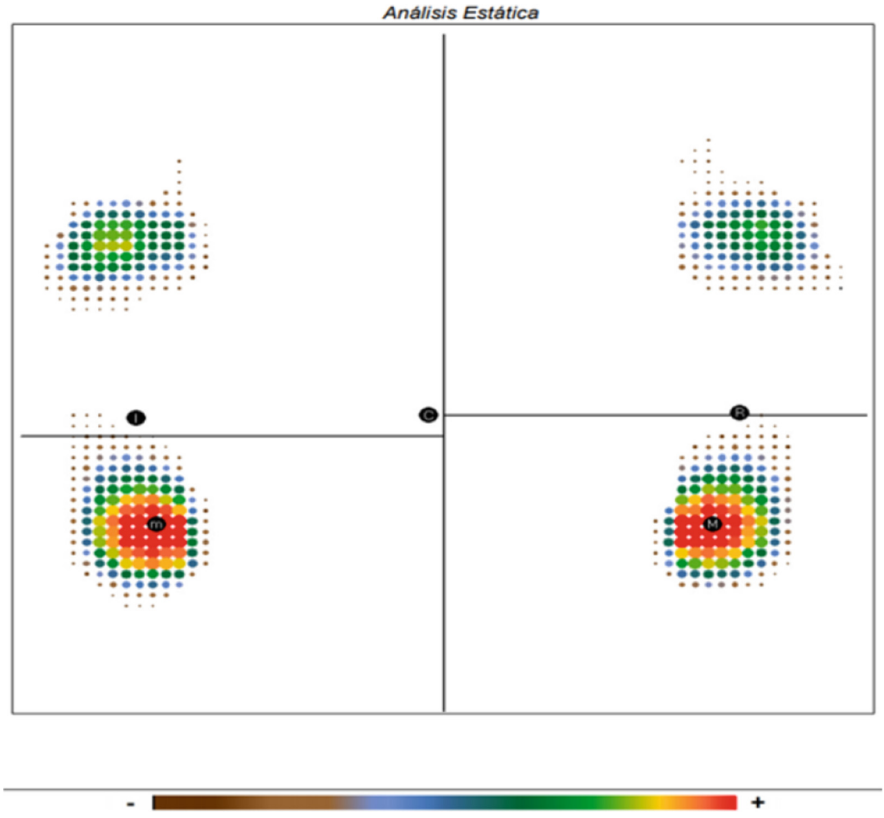

Fig. 1. Static phase performed on a patient with cavus foot.

2.2 Dynamic Phase

It allows the visualization of a consecutive record as a function of time, of data relative to the foot during the cycle of the gait as it is the surface that is covered between each step, the maximum pressure exerted in each individual phase during the development of the step, the speed of movement of the foot in each phase and peak pressure exerted by the weight during the stance phase (see Fig. 2).

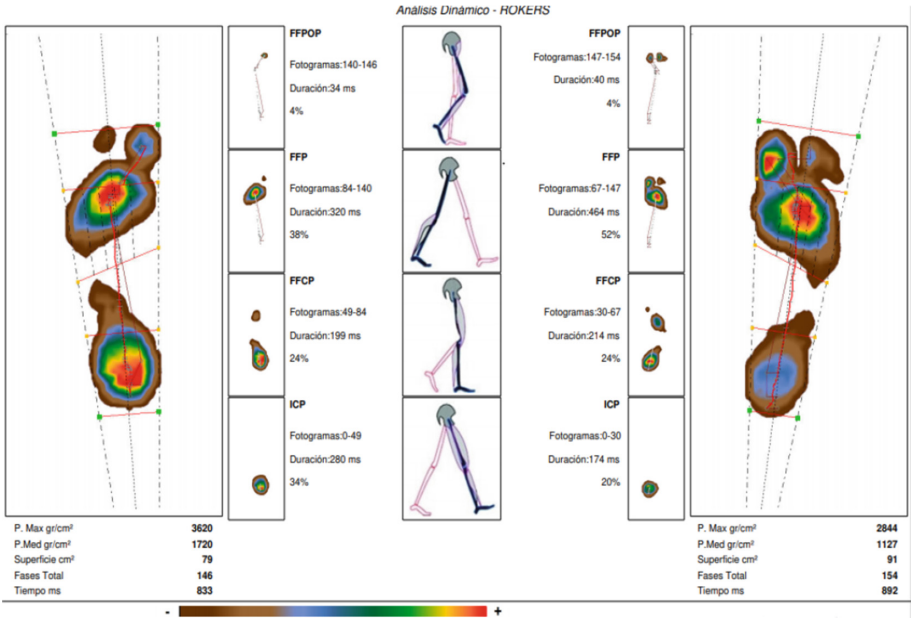

Fig. 2. Plantar pressure distribution analysis during the stance phase on a patient with cavus foot.

2.3 Posturographic Phase

The posturography or stabilometry is the study of the balance that allows analyzing and defining postural control, the average position of the body and its relationship with the stability in the bipedal position, as well as the tiny movements [11]. The platform physically measures the position of the pressure load center, measure the stability of the subject in environment and makes a recording with opened and closed eyes since they are the most used condition to compare the response of the evaluated subjects. The participants usually changes tactics when they close their eyes, being less precising the control of movements [12] (see Fig. 3).

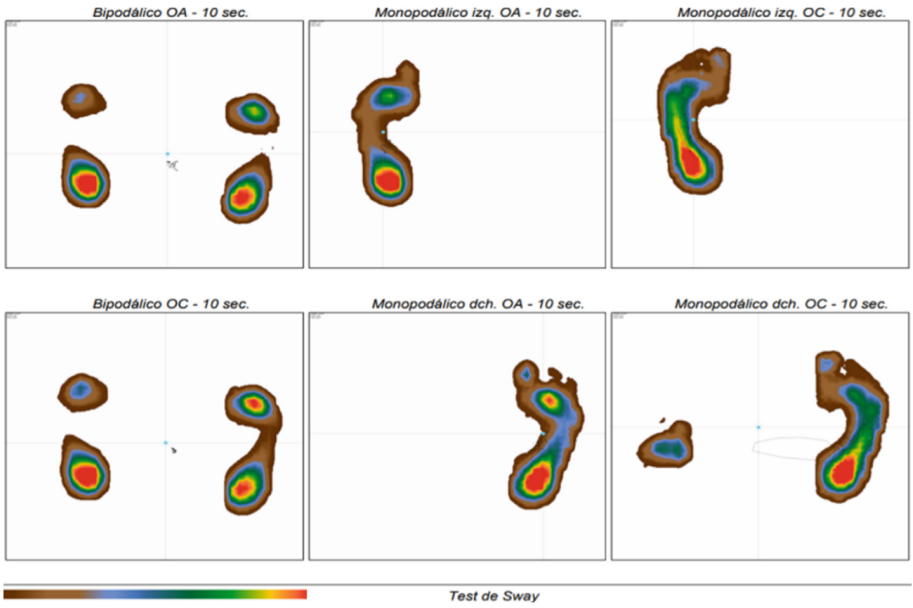

Fig. 3. Posturographic analysis performed on a patient with cavus foot.

2.4 Digital Podoscopic Image

It is a digital podoscope that allows the evaluation of the footprint in standing position, possible pathologies, highlighted areas of higher pressure, angles and lengths of the sole of the feet [13] (see Fig. 4).

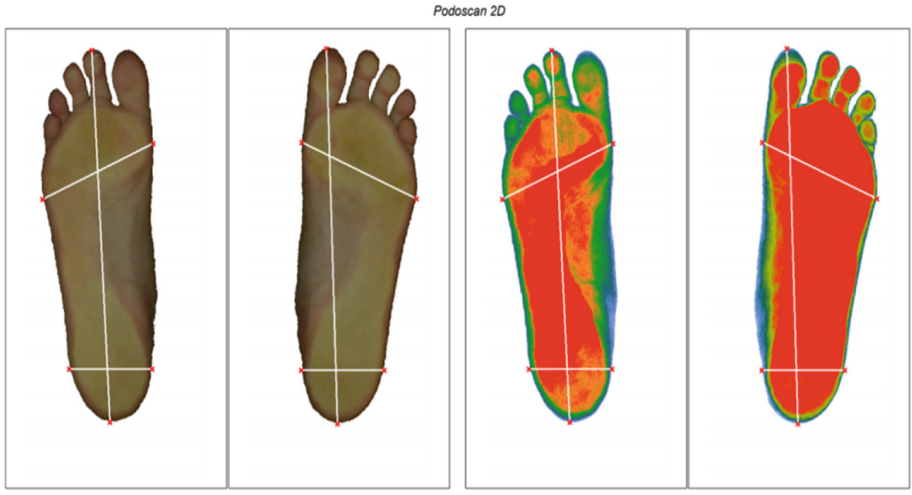

Fig. 4. Digital image taken by the Podoscan 2D.

Having the results of the study and the basis in the diagnosis and interpretation of the orthopedic specialist in foot and ankle, then, the design of the insoles is performed. These are completely costume-made in the patient and for this; the dynamic study footprint is considered since a person is normally in motion and does not stand completely for a long time.

When the design is finished, we proceed to the manufacturing of the insoles in a material with different densities called Ethylene-Vinyl-Acetate (EVA), then, the Computer Numerical Control (CNC) equipment starts the process. At the end of the process, it continues to give the finishing to the insoles on the basis of the desired footwear, they are lined up considering the type of footwear and if the person practices sport or has diabetes, the insoles requires a leather interface, finally, the insoles receives the final polish.

After being used for a period of time, we get in touch with the patient for feedback; and based on this we notice if the person has been doing well with the insoles or if there is a modification in case of suffering from a blister, discomfort or pain. Then, a survey was carried out within a sample of 60 people to see the effects of the insoles on the feet, the sample was selected by convenience.

3 Results

The survey consists of 10 simple and quick subjective questions that allow us to know the level of satisfaction of the use of the insoles and the result in daily use. Of the 60 people who were taken as a sample, only 6 patients did not use them and 54 patients used them with the results presented below through their corresponding graphs.

Among the evaluated variables, we found that age and gender were necessary as basic information, besides, it can be useful to observe the percentage of the population that suffer from previous cavus foot pathology. As shown in Figs. 5 and 6.

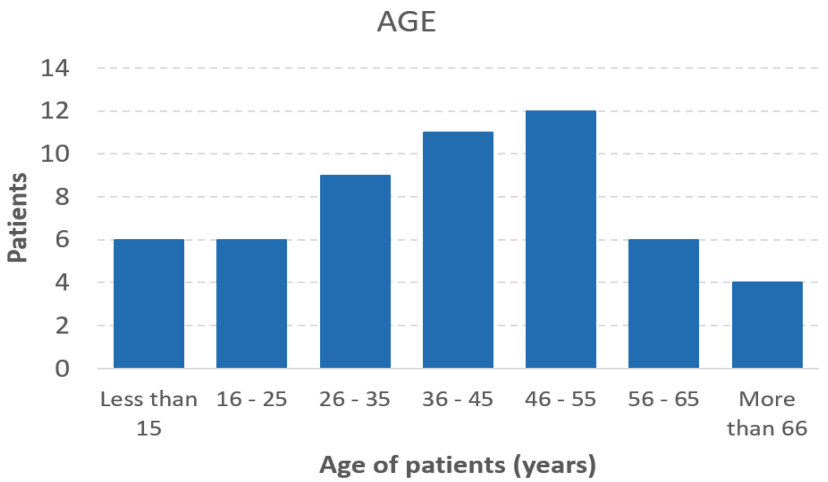

Fig. 5. Ages of the patients surveyed in 10-years ranges.

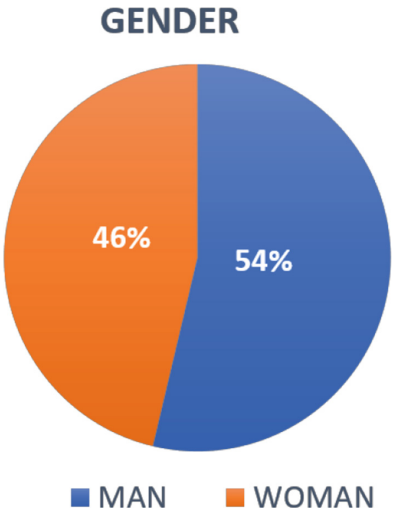

Fig. 6. Gender of the people surveyed.

Having already the age and gender, it is necessary to know what were the problems or ailments suffered by the patients before and after the use of the insoles, so that a graph was made with the most frequent discomforts or if there were no signs of pain, (see Fig. 7). It shows the results before the use of the insoles, pain in the knees or heels was the most frequent alteration, so that, after using the insoles, the discomfort is drastically reduced, since most of the patients no longer feel any ailment.

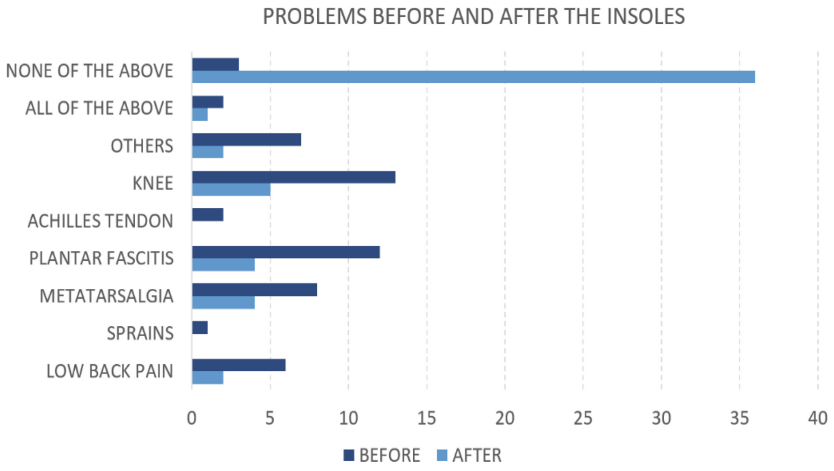

Fig. 7. Results of the insoles before and after being used, showing the location of the pain.

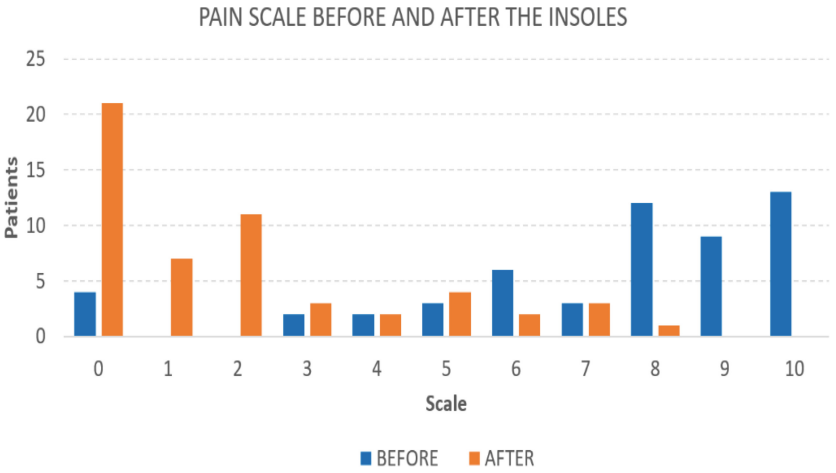

Fig. 8. Results of the pain before and after using the insoles.

Having found the regions where the discomfort is located, it is also important to know how much pain people presented, so they were asked from 0 to 10 how much pain they presented (being 0 no pain and 10 too much pain). Based on the results, a bar chart was made showing how much pain the patients presented before and after the use of insoles (see Fig. 8). The Table 1 shows the responses in more detail.

Throughout the survey, we noticed that most people have more than 6 months using the insoles, as shown in Fig. 9; this was a good sign due to the fact that the patients should be adapted to the insoles after one month without suffering any discomfort or blister. In general, it is necessary that after 8 months the persons can renew the orthosis. The results showed in Fig. 10 indicates that the 22% of the sample had renewed the insoles two times, 17% three or more times and 62% of the population used the insoles for the first time.

Finally, they were asked how the plantar orthosis behaved and if they thought that the insoles had improved their quality of life for very little or that it had changed their system of life completely, so that, the answers of the patients are shown in a graph, Fig. 11. Something that is also very important for us is to know if they would recommend our products, so in Fig. 12, the opinions of the 54 people surveyed during this project were included.

Table 1. Results of the question about the pain scale before and after the insoles.

Scale	Before	After
10	10	7
	10	7
	10	7
	10	4
	10	3
	10	3
	10	2
	10	2
	10	0
	10	0
	10	0
	10	0
	10	0
9	9	8
	9	6
	9	6
	9	5
	9	5
	9	1
	9	0
	9	0
	9	0
8	8	5
	8	4
	8	3
	8	2
	8	2
	8	2
	8	1
	8	1
	8	0
	8	0
	8	0
	8	0
7	7	2
	7	1
	7	0
6	6	2
	6	2
	6	1
	6	1
	6	0
	6	0
5	5	5
	5	1
	5	0
4	4	2
	4	2
3	3	2
	3	0
0	0	0
	0	0
	0	0
	0	0

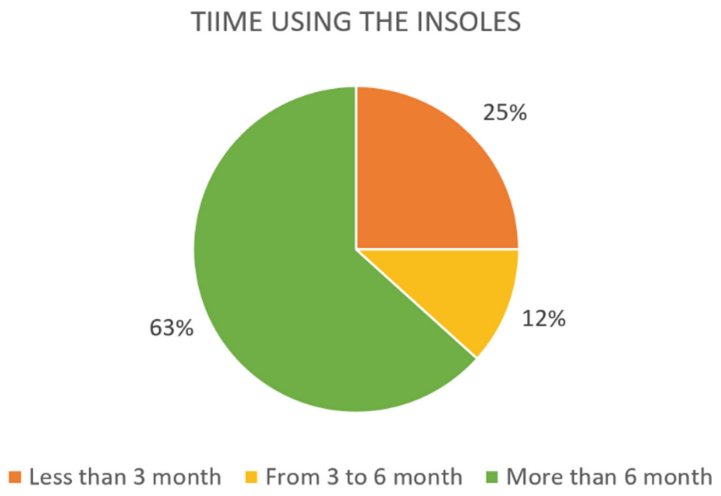

Fig. 9. Time of use of the insoles by the people surveyed.

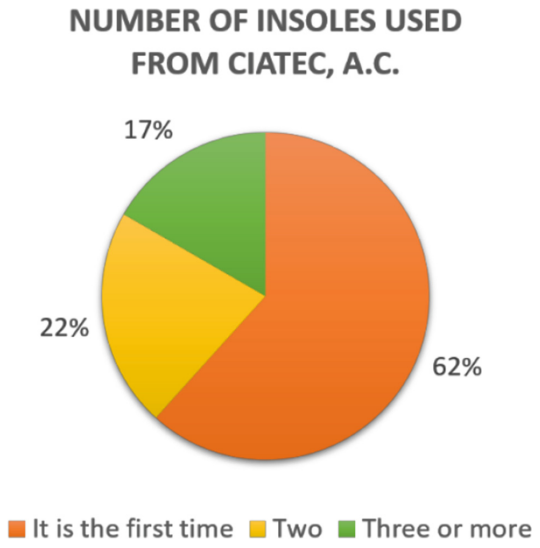

Fig. 10. Number of insoles used by the patients.

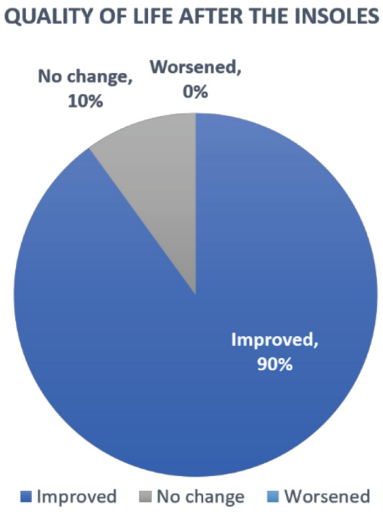

Fig. 11. Quality of life of the people who used the insoles of CIATEC, AC.

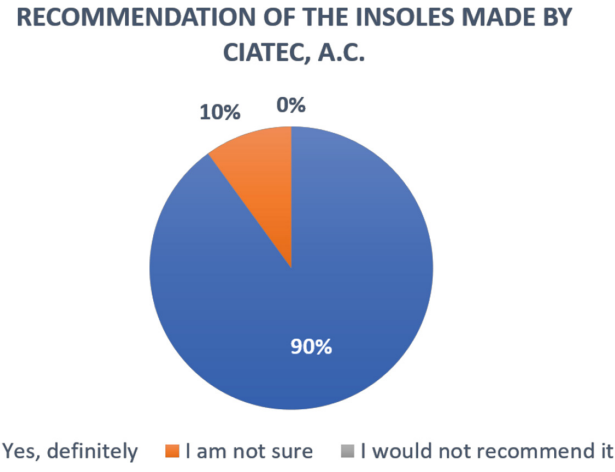

Fig. 12. The graph shows if users would recommend the insoles from CIATEC, AC.

4 Discussion and Conclusion

Cavus foot is a problem that affects part of the population and prevents them from continuing their daily activities because of the pain (in many cases unbearable). The insoles designed for the deformity of the anterior cavus foot (the most common pathology) have several specific functions among which are supporting the internal longitudinal arch, enthesitis control, plantar fasciitis, insertional and not insertional tendinopathies, correct and stabilize the hindfoot in neutral, support the Achilles tendon

for the association in most cases to functional shortening of the tendon itself, distribute the axial loads exerted by the body axes through the rigid materials of the own insoles and protect the joint areas of the foot in its different areas.

With the use of the insoles, it can be noticed from the survey that the inconveniences decrease drastically or in most cases disappear. That is why we can conclude that the goal of using the insoles to overcome the cavus foot pathology has been fulfilled, they are really a treatment proven to alleviate the pain, besides, and they are completely personalized and are used to correct the problem.

Conflict of Interest. The authors declare that they have no conflict of interest.

References

1. Hillstrom, H., Song, J., Kraszewski, A., Hafer, J., Mootanah, R., Dufour, A., Chow, B., Deland, J.: Foot type biomechanics part 1: structure and function of the asymptomatic foot. Gait Posture **37**(3), 445–451 (2013)
2. Estévez, A., García, Y., Licea, M., Fundora, A., Álvarez, H.: Identification of foot deformities in diabetes mellitus patients, a strategy to prevent amputation. Rev. Cubana Endocrinol. **24**(3), 1 (2013)
3. Maynou, C., Szymanski, C., Thiounn, A.: The adult cavus foot. EFORT Open Rev. (2), 1–9 (2017)
4. Fried, L., Ferrucci, L., Darer, J., Williamson, J., Anderson, G.: Untangling the concepts of disability, frailty, and comorbidity: implications for improved targeting and care. J. Gerontol. Med. Sci. **59**(3), 255–263 (2004)
5. Blanco, M., Shunchao, K., Xueqing, L.: Comorbidity and its value for the general doctor in Internal Medicine. Rev. Haban. Cienc. Med. **16**(1), 1 (2017)
6. Cornell, K., Godhania, V., Romero, C., Pytowski, D.: Pie cavo (pie de arco alto), pp. 1–2. American College of Foot and Ankle Surgeons, Austin (2007)
7. Giner, G.: https://www.esalud.com/plantillas-ortopedicas/. Accessed 15 June 2019
8. García, I., Zambudio, R.: Órtesis, calzado y prótesis. Tratado de pie diabético. Jarpyo Editores, Madrid (2002)
9. Cohí, O., Salinas, F.: Ortesis Plantares. Rev. Esp Reumatol **30**(9), 508–513 (2003)
10. Echeverry, L., Velásquez, S., Castaño, P., Valderrama, S., Ruiz, M.: Anthropometry and baropodometry as foot characterization techniques and tools that provide criteria for ergonomics and comfort in footwear design and manufacture: a systematic review. Prospectiva **16**(1), 7–17 (2018)
11. Petrocci, K., Cárdenas, R.: La medición del control postural con estabilometría – Una revisión documental. Rev. Col. Med. Fis. Reh. **10**(1), 16–24 (2011)
12. González, R., Keglevic, V.: Análisis del Centro de Presión en Posturografía en Pacientes con Síndrome de Dolor Lumbar Crónico. Tesis, pp. 1–66. Facultad de Medicina Universidad de Chile, Santiago de Chile (2004)
13. Sensor Medica. https://www.sensormedica.com/SM_catalogue_2017.pdf. Accessed 15 Apr 2019

Implementation of Novel Technologies and CAD Software to the Improve and Reduce of Costs in Orthotics Adaptation

Isaac F. Nava-Vázquez(✉), Eduardo de Avila-Armenta, Lorena Espinoza-Bermúdez, Estefani Esquivel-Cordero, Viviana Chora-López, Jorge I. Galván-Tejada, Carlos E. Galván-Tejada, and Hamurabi Gamboa-Rosales

Unidad Académica de Ingeniería, Universidad Autónoma de Zacatecas, 98000 Zacatecas, Zacatecas, Mexico
gatejo@uaz.edu.mx

Abstract. In this paper is presented the manufacturing process of an Ankle-Foot Orthosis (AFO) model for the treatment of foot drop. To recreate the model were used three-dimensional (3D) printing, three-dimensional (3D) scanning techniques and a computer-aided design (CAD) software. The final result was a prototype Ankle-Foot Orthosis for foot drop patient.

Keywords: Ankle-Foot Orthosis (AFO) · 3D printing · CAD software

1 Introduction

Foot drop, is a symptom that muscular activities around the ankle become weak due to the paralysis of the neural system. These patients show abnormal gait patterns, in which the dorsiflexion and eversion of the ankle do not occur voluntarily. These inefficient gait patterns result in slow walking speed and increased energy consumption [1,2]. Therefore, increases the risk of tripping and affects safety when walking, leading to a bad quality of life [3]. An option for treating and improving the gait pattern in patients with foot drop is the implementation of a support device as an Ankle-Foot Orthosis (AFO) [1,4]. An orthosis is defined as any external applied device on the human body, which is used to modify the functions of the neuromusculoskeletal systems, in order to maintain, improve or recover the function [5].

An AFO was recreated based on a commercial orthotic model and the use of novel technologies, such as 3D scanning, 3D printing and CAD software [6].

2 Materials and Methodology

Based on the particular measurements in a piece of athletic footwear (the main type of footwear used by the patient) lengths were determined by taking as a

© Springer Nature Switzerland AG 2020
C. A. González Díaz et al. (Eds.): CLAIB 2019, IFMBE Proceedings 75, pp. 933–938, 2020.
https://doi.org/10.1007/978-3-030-30648-9_120

main reference the measures of the junction piece, placing half of that piece in the middle of the length of the footwear, where the curvature in the sole of the reference footwear is found (curvature that implies an unstable base) according to Lison "it has been recently pointed out that specific variations of unstable sole constructions differently challenged the postural control system. Consequently, an extrapolation of established changes in the spine kinematics and trunk muscle activity while wearing a particular unstable shoe model to other types of related footwear design would be constrained from this viewpoint" the lengths are determined based on the curvature of the reference foot to perform the extrusion of the rectangle with the corresponding cuts which based on the original part follow the principle.

The measurements defined for the junction piece were based on a square centimeter of thickness estimated and two centimeter of depth at both ends, so the base piece was obtained where it was split to make the measurements relevant for the missing parts.

The function "Sketch Picture", from SolidWorks, and an image of the base model (FS3000) profile were used in order to develop a sketch of its contour to extrude the 12 cm required in this particular case for the upper rear part.

After obtaining the main piece, the U-shaped back piece is developed using the same image command for sketches for both extrusion and reference: With a picture of a tennis shoe seen from above, adjusting to the scale that matches the shoe size used by the patient, so the relevant cuts were made on the extrusion to obtain the U-shape respecting to the curvature of an "average" tennis shoe.

The U-shaped frontal piece was developed by means of the extrusion of a rectangle with its respective cuts and the use of "flexion" command, applying angles of 45° for the elevation according to the final height of the junction piece which is the one that allows joining the pieces back with the front. The Shoelace Holder piece (Which its function is to fasten the front part of the orthosis to the footwear) was developed based on the U-shaped front piece. The Showlace holder should be embraced by cinches to the holes for the shoe laces.

The main piece was separated into 3 fragments using the "Cut" function from SolidWorks. Proceeded to make a cut halfway through the lower curve piece, observed from a front view, thus optimizing the printing process ensuring faster time for printing of each piece, as well as a lower range of error and waste of materials in that case.

Finally, the assembly was made in SolidWorks to validate that the measurements matches, obtaining an error of 0.5 cm extra wide in the U-shaped frontal piece. However, this error range was not considered due to the properties of polylactic acid (PLA) that allow us to use hot water to mold it once the piece is printed, thus obtaining a more ergonomic model, then passing to the ergonomic fitting test.

A test on the patient's foot to check precision in accordance to the measurements that have been taken on count before is subsequently performed. The size of the developed prototype respect to the patient's is checked as well as the

errors on the measurements of the frontal U piece length and the curvature, and the length error on the upper back piece.

Then, in the molding phase, where the pieces were submerged in water at boiling point for the material to change its composition and so the molding process becomes easier [7,8]. These tests were done with caution, avoiding burning or causing any damage to the patient, so the calf holder piece (the piece that clings to the gastrocnemius muscle area) had to be molded separately from the leg of the patient until this piece is perfectly adjusted to the area (Fig. 1).

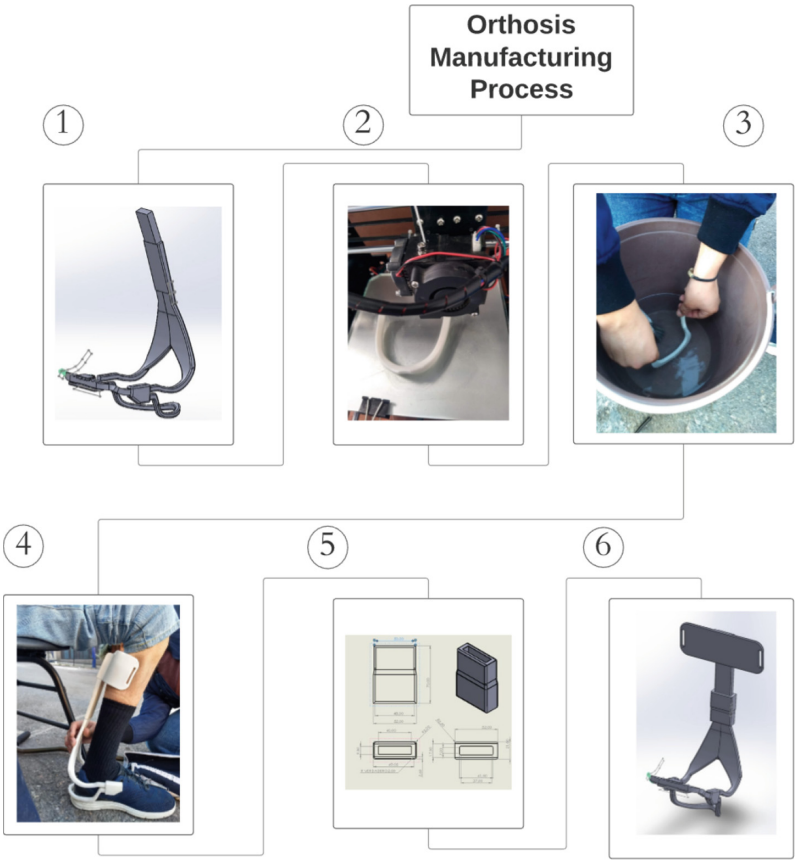

Fig. 1. Orthotic Manufacturing Process: (1) First design, (2) Printing process, (3) Molding phase, (4) Ergonomic fitting test, (5) Coupler piece design, (6) Final Model.

3 Results and Discussion

After a thoroughly research, it was found that the acrylonitrile butadiene styrene (ABS), a thermoplastic that is more complex than common plastics, such as the

polioleofinas (polyethylene, polypropylene), which has properties such as rigidity, resistance to chemical attack, stability to high temperature as well as hardness, toughness, mechanical resistance, was the best option for the development of this work [7,9]. The left and right curved pieces were printed both with this material. For the pieces that require a greater rigidity, due to they have a higher load, it was decided to use an alloy with polylactic acid (PLA) and carbon fiber, those pieces are: U shaped piece, back U shaped piece, upper back piece and joints as well as the calf brace piece. Therefore, the main fabrication is thermoplastic, which is formed by polymers. The main features of the latter are focused on comfort and usability as they are external and easy to adapt to footwear.

On the other hand, the verification of measures was conducted in real patient and observed that the main piece (including the calf brace piece) was 2 cm above with regard to the measures envisaged, which held a straight cut on the center-line of the upper part of the piece, seen from a side view, and taking into account a slight change in thickness covered in the 2 supposed cm cut in the work-piece. The parts were thus obtained lower curve piece and the top piece due the mentioned cut.

A coupler piece was designed taking into account 2 cm cut above. This piece was designed proportionally respect to the average thickness of 1 cm referred to since the beginning of the project, to obtain a mechanically functional coupler. Finally it was obtained a final model composed of ten pieces, as shown in Fig. 2.

Fig. 2. Final printed model.

After proceeding with the three-dimensional impressions, it was possible to realize that some pieces had a weak structure, being necessary to change the conditions of these impressions, such as the increase of some conditions like a

hundred percent in the infill and 0.06 mm height between the layers obtaining a major quality and considerable structure.

Finally, taking into account that the developed project was based on the model Turbomed FS3000, following the requirements to treat the foot drop, it is important to mention that one of the main advantages of this work in comparison with the Turbomed FS3000 is the price, since this prototype follows a low-cost approach.

4 Conclusion

In conclusion, thanks to the novel technologies mentioned before, it is possible to have an approach to the industry but on a smaller scale with this work, and it depends on the vision and the ability in this kind of processes that each person can obtain. This type of technologies allows to have a considerably cost reduction of many process that can helps people to deal with motor conditions or muscular weakness, as it is "drop foot" in this case.

Also, we can conclude that the experimentation and the research regarding of materials plays an important role, allowing to have the piece made of the suitable material. It is also necessary to consider a possible future development techniques and more appropriate materials to develop a better prototype.

When looking for a product with greater strength and a better structure, the coupler parts are needed, since they provide greater rigidity and mechanical stability. Then, this type of pieces needs to be printed with an adequate material and with higher qualities (100% fill and 0.06 mm of high layer) that the printer we are using can provide us.

References

1. Kim, J., Hwang, S., et al.: Development of an active ankle foot orthosis to prevent foot drop and toe drag in hemiplegic patients: a preliminary study. Appl. Bionics Biomech. **8**, 377–384 (2011)
2. Donatelli, R., Hurlbert, C., Conaway, D., et al.: Biomechanical foot o orthotics: a retrospective study. J. Orthop. Sports Phys. Ther. **10**, 205–212 (1988)
3. Chin, R., Hsiao-Wecksler, E., et al.: A pneumatic power harvesting ankle-foot orthosis to prevent foot-drop. J. NeuroEng. Rehabil. **6**, 6–19 (2009)
4. Kluding, P., Dunning, K., et al.: Foot drop stimulation versus ankle foot orthosis after stroke. Stroke **44**, 1660–1669 (2013)
5. Villa-Parra A., et al.: Sistema de control para Asistir el Movimiento de Dorsiflexión de Pie Caído en la Fase de Oscilación de la Marcha en Pacientes Hemipljico (2011). http://repositorio.educacionsuperior.gob.ec/bitstream/28000/978/1/T-SENESCYT-0382.pdf
6. Borghese, N., Ferringo, G., et al.: Autoscan: a flexible and portable 3D scanner. IEEE Comput. Graphics Appl. **18**, 38–41 (1998)
7. Tian, X., Liu, T., et al.: Interface and performance of 3D printed continuous carbon fiber reinforced PLA composites. Compos. Part A Appl. Sci. Manufact. **88**, 198–205 (2016)

8. Mi, H., Salick, M., et al.: Characterization of thermoplastic polyurethane/polylactic acid (TPU/PLA) tissue engineering scaffolds fabricated by microcellular injection molding. Mater. Sci. Eng. C **33**, 4767–4776 (2013)
9. Galina, M., et al.: CARACTERIZACIÓN DE LAS PROPIEDADES MECÁNICAS DE LOS CUERPOS DE PRUEBA ABS CONFECCIONADOS CON DIFERENTES PARÁMETROS DE EXTRUSIÓN VÍA IMPRESIÓN 3D. Revista Iberoamericana de Polímeros **17**, 303–308 (2016)

Biomechanical Model to Evaluate Movement Characteristics in Infants

Virginia Bueyes-Roiz[1(✉)], Ivett Quiñones-Uriostegui[1], Karen L. Cortés-García[2], and Yannick Quijano[1]

[1] National Institute of Rehabilitation LGII, Calzada México-Xochimilco 289, 14389 Mexico City, Mexico
vbueyes@hotmail.com
[2] Universidad Iberoamericana, Prol. Paseo de la Reforma 880, 01219 Mexico City, Mexico

Abstract. Brain development occurs before and after birth, it is important to determine if an infant would present a developmental disorder such as cerebral palsy. If the case, it is important to start rehabilitation and get to the fullest functional capacity they could at young age. There are different methods to determine a possible developmental disorder such as brain imaging and clinical assessments. One of the methods that has resulted in positive outcomes is based on the spontaneous movements presented by the infants known as General Movements, one of the problems with this method is that is based on the clinician expertise. 3D motion analysis is a technology that allow us to evaluate any movement on all their axis and obtain kinematic characteristics such as velocity, acceleration and smoothness. In this work we proposed a biomechanical model of the full body of the new born to determine if we could study the movement pattern characteristic presented on young infants, we only presented the circular movement pattern on both feet created by a full-term 2-month-old during 5 min obtaining similarities on smoothness, and differences on velocity and acceleration. The results obtained on this study encourage us to create a pilot study in order to assess the general movements presented on infants and to determine the specific characteristics of these movements, with the future aim to evaluate pre-term infants and know if there is a possible developmental disorder.

Keywords: 3D movement analysis · Biomechanics · Young infant assessment

1 Introduction

Substantial part of brain development occurs before and after birth throughout childhood, in which age-specific characteristics can help as important predictors for developmental disorders at early age [1]. When predicting developmental disorders there are different techniques which include clinical methods, neurological assessments and the use of technical equipment for brain imaging between others; additionally there also exists a clinical method which consist on the study of movements that are age

© Springer Nature Switzerland AG 2020
C. A. González Díaz et al. (Eds.): CLAIB 2019, IFMBE Proceedings 75, pp. 939–944, 2020.
https://doi.org/10.1007/978-3-030-30648-9_121

specific, in case of showing or lacking movements a predictor of a disorder specially cerebral palsy can be made with a sensitivity and specificity of 95%, this method was proposed by Prechtl, the problem with this method relays on the experience that the medical examiner possess. That is why, in recent years there has been an increase on the research or early motor skill of infants using different technology [1–3].

It is important to make an early diagnosis of possible developmental risk which will help provide an early intervention service to the infant, which will take him to the best quality of life based on the limitations they pose [4].

As stated, the movement infants present are age-specific, fetus and young infants present movements that consist of a series of gross movements with variable speed and amplitude involving all the parts of the body and lacks a distinctive sequence these movements are known as General Movements (GM), movements increase by number and variety approximately every three months since infants increases muscular tone and their capacity to overcome gravity force. Between birth at full term (36–38 weeks) and the first three months the GM are known as writhing movements that have been described as slower with low participation of the pelvis and trunk, from the third month to the fifth month after birth the GM as known as fidgety movements which consists of continuous flow of small movements occurring irregularly all over the body in which limbs participate to a similar extent sometimes the small movements can be superimposed with large and fast movements, the characteristics in both cases are that the movements tend to be circular [1].

One of the technologies that has been proposed to study the GM consist on 3D movement analysis with the use of infrared cameras that allows the spatial detection and movement quantification with the following benefits: movement is stored in 3D, the movement is independent to medical examiner impressions, it allows to extract quantitative variables regarding movement such as velocity, acceleration and trajectories that will help describe the movement besides we can calculate smoothness, straightness index, mid-line crossing and head turns [5].

The objective of this paper consists on the development of a biomechanical model with the use of an infrared camera system that will allow to describe circular movement patterns that are present on healthy infants and, in a future, to be able to evaluate infants with possible predictor of a disorder.

2 Methodology

2.1 Subject

We measure one full-term baby girl of 2 months old, with no apparent concern of developmental disorder. Previous to the study the parents where provided with an informed consent approved by the ethics committee.

2.2 Experimental Setup

We followed the methodology proposed by Prechtl and others to assess General Movements which consist on the baby with only the diaper placed on a supine position on a flat surface in this case a wood table, the infant was not irritated, with the diaper recently change so we could measure her at her calm and normal movements without having external factors that could affect her movement, around the infant we place 12 Optitrack® (Natural Point, Oregon, United States) Flex 13 Cameras, so we could be able to record from all angles the baby and the reconstruction could be easy, we record the baby movement for 5 min on the Motive:Body (Natural Point, Oregon, United States) software.

2.3 Instrumentation

We created a biomechanical model that consisted on eleven 9-mm markers for the full body, the markers were placed on the head above both eyes, both shoulders on the acromion, trunk placed at the sternum, both hands on the third metacarpal articulation, pelvis on both anterior superior iliac spine and on both feet on center of the dorsal part.

2.4 Data Processing

Markers were named on the Motive:Body software and the coordinates on the 3 axis were obtained this data was exported and the following processing was carried out on MATLAB® (MathWorks, Massachusetts, United States).

We created an algorithm that is able to find every circular movement presented by the infant based on the location of the marker on feet and hands respectively. After obtaining the circular movement patterns presented on each limb, we calculated velocity, acceleration and smoothness calculated as the length of the spectral arc of the Fourier magnitude spectrum of the velocity of each limb, the patterns were normalized to the length of the trajectory to be able to do comparisons and in the future be able to apply statistical analysis.

3 Results

We obtained the circular pattern trajectories of all the limbs, in this case the trajectories presented on the right foot during the circular movement pattern in 3D perspective are shown on Fig. 1. We normalized the trajectories based on the largest, as shown on Fig. 2 the beginning of the circular patter movement is smaller and gets to a peak of length that decrement as the pattern tends to stop. Finally, on Table 1 the results of mean velocity, mean acceleration and mean smoothness for both feet are presented.

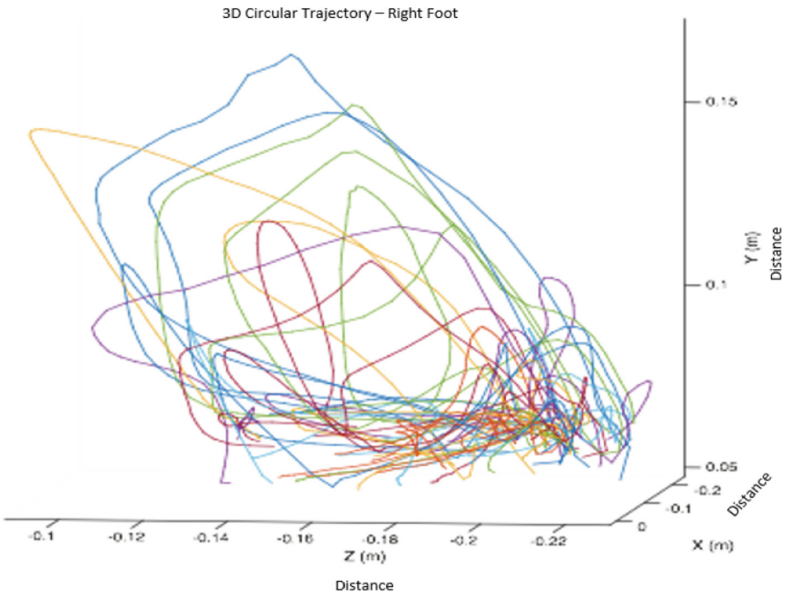

Fig. 1. Circular pattern trajectories presented on the right foot

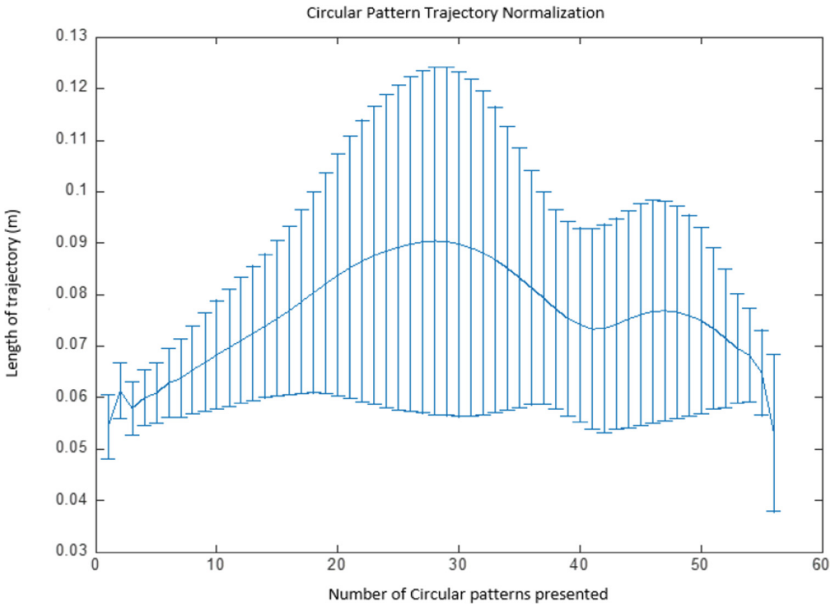

Fig. 2. Normalization of the circular movement trajectories based on length through the pattern presented on the right foot

Table 1. Kinematic characteristics of the circular patterns presented on both feet

Kinematic variables	Right foot	Left foot
Velocity (m/s)	0.074	0.055
Acceleration (m/s^2)	0.025	0.038
Smoothness	−2.33	−2.22

4 Discussion and Conclusion

With the methodology proposed we were able to segment the trial and find the circular movements regardless of the duration and length presented on all the limbs based on the position of the markers as it is shown on Fig. 1 during the 5 min that the test last, from all of these circular movement patterns we calculated their smoothness, velocity and acceleration with their mean values presented on Table 1, to be able to find and report this kinematic characteristics of the circular patterns was important since the GM are based on the description, as stated on the introduction the writhing movements are slower than the fidgety that is the reason why the acceleration and velocity is important, the flow of the movement is important to differentiate between writhing and fidgety that is why we calculated smoothness, finally fidgety movements tend to be small which is why trajectory is important.

Even though the patterns seem to be identical on both feet, and both feet are moving at the same time, the results obtained from the kinematic values shows that the acceleration and velocity are different, while the right foot goes faster (velocity of 0.074 m/s vs velocity of 0.055 m/s), there are more changes in velocity on the left foot (acceleration of 0.038 vs 0.025 m/s^2), it seems that the patient has more control on the right foot based on these results, based on this results we were expecting the smoothness to also being different on both feet, being smoother the circular patterns presented on the right foot, however the smoothness presented on both feet is similar with a better smoothness value presented on the left foot, this made us think that the discrepancies shown between acceleration and velocity could be an indication of the laterality that the baby is going to show in the future, this needs to be verified with a longitudinal clinical trial.

The circular pattern was not presented through the length of all the test, there exists a time when the infant starts moving with this pattern then stops, and then do it again. As shown on Fig. 2 it is an example when the circular pattern was shown on the test. We noticed that when the pattern begins the circles are with a small length that starts to increment as time passes, it arrives to a peak length and then this length will start to decrement until the pattern stops to show.

The results obtained from the measurement of this infant give us great hopes for our future work with the evaluation of GM, since the model proposed let us obtained the kinematic characteristics, view differences between both feet, we still need to analyze the characteristics that are found on the upper limb, and on all limbs to find different patterns and describe their characteristics. After that measure healthy infants with low probability of developmental disorder to know the normal values and be able to compare it to infants with probability of developmental disorder.

References

1. Hadders-Algra, M.: General movements: a window for early identification of children at high risk for developmental disorders. J. Pediatr. **145**, S12–S18 (2014)
2. Einspieler, C., Prechtl, H.F.: Prechtl's assessment of general movements: a diagnostic tool for the functional assessment of the young nervous system. Ment. Retard. Dev. Disabil. Res. Rev. **11**(1), 61–67 (2005)
3. van der Soares, D., Kamp, J., et al.: The effect of a short bout of practice on reaching behavior in late preterm infants at the onset of reaching: a randomized controlled trial. Res. Dev. Disabil. **34**(12), 4546–4558 (2013)
4. Murphy, N., Such-Neibar, T.: Cerebral palsy diagnosis and management: the state of the art. Curr. Probl. Pediatr. Adolesc. Health Care **33**(5), 146–169 (2013)
5. Heinze, F., Hesels, K., Breitbach-Faller, N., et al.: Movement analysis by accelerometry of newborns and infants for the early detection of movement disorders dur to infantile cerebral palsy. Med. Biol. Eng. Comput. **48**(11), 765–772 (2010)

Surface Representation of the Urinary Bladder and Bio-mechanical Analysis by Linear Dynamic Model

Keith Guzman-Diaz[1], Aurora Alvarado-Gonzalez[1], Daniela Herrera[1], Ana Hernandez-Reynoso[2], Sergio Rodríguez-Reynoso[1], and Alejandro Garcia-Gonzalez[1(✉)]

[1] Tecnologico de Monterrey, Escuela de Medicina y Ciencias de la Salud, Ave. Morones Prieto 3000, 64710 Monterrey, N.L., Mexico
alexgargo@tec.mx
[2] Department of Bioengineering, University of Texas at Dallas, Richardson, TX, USA

Abstract. The biomechanical characterization of Urinary Bladder is essential to create new therapeutic tools as artificial tissue replacement or electrical stimulators. In this paper, we applied a linear model, the so-called viscoelastic Voigt's model to calculate the viscosity and elasticity in three regions of a bladder under the experimental condition of tensile stresses. Additionally, we acquired the tridimensional surface of urinary bladders by a cloud of points that were processed in digital format. Viscosity and elasticity are represented on the surface reconstruction. Three bovine bladders were processed with an average sample viscosity of 89.33×10^{-6} Ns/mm^2 and average elasticity of 1.3×10^{-3} N/mm, the isotropic condition was evaluated. The digital representation includes a cloud of points of 9×10^6 elements on average. These results are the base of a future computational simulation platform.

Keywords: Urinary bladder · Biomechanical modeling · Surface acquisition

1 Introduction

Urinary bladder (UB) is a hollow organ which stores urine (up to 400 mL), UB can keep pressure nearly constant due to the stress relaxation property of its wall [1]. The stress urinary incontinence (SUI) is a problem that affects the adult population. The involuntary loss of urine during coughing or physical activity is caused by weak pelvic floor or urethral sphincter. Developing new therapies requires the knowledge of mechanical properties of UB, for instance, the use of implantable electronic stimulators and the use of engineered tissue for substitution [2]. For this reason, it is necessary to develop methods for the calculation of biomechanical parameters of the tissue, that allows us to understand its behavior under mechanical stress condition. We propose a method to derive the biomechanical parameters of elasticity and viscosity for UB tissue under tensile conditions, considering a linear dynamic Voigt's model [3], this information is associated to the digital representation of the UB surface. The process

© Springer Nature Switzerland AG 2020
C. A. González Díaz et al. (Eds.): CLAIB 2019, IFMBE Proceedings 75, pp. 945–949, 2020.
https://doi.org/10.1007/978-3-030-30648-9_122

includes the sample preparation, the standardization of the capture routine, and the mechanical test conditions.

2 Methodology

2.1 Cloud of Points Acquisition of UB Surface

The experiments were run, using three male bovine bladders from an abattoir within less than two hours of slaughtering the animal. Bladders were frozen for transportation at –2 °C. The defrosting occurred at room temperature for two hours. For each of the three experiments the bladder cleans and fills up with water up to maximum volume, then empties to distend. Connective tissue and adipose tissue were removed from the outer surface of UB. Bladder was continuously hydrated with saline solution at 0.9%. The organ is allocated over a solid three-dimensional base structure that emulates the anatomy of UB, such structure was designed and printed with Polylactic Acid (PLA). Marker points were added to the outer surface of the UB, two points on each region, separated 1 cm, to identify the part used for the tensile test. The point cloud of the bladder's surface was obtained using a 3D scanner EinScan-SE from SHINING 3D and the software EinScan-S series v2_7.0.6 installed in a Laptop with a RAM of 16 GB, i7 processor, graphic memory 4 GB NVIDIA with a spatial resolution of 0.2 mm. The cloud of points filled with a triangular mesh geometry. The mesh was configured with high resolution (0.17 mm) and sharpen texture, filled and saved as a 3D object.

2.2 Mechanical Characterization of the Tissue

We dissect the UB sample considering the methodology described in [1]. UB is divided in three parts: superior, middle and inferior, see Fig. 1a. We designed a template (Fig. 1b) to achieve size standardization of every sample cut from the UB with measures (test area of 150 mm^2 and a grip zone of 352.5 mm^2). The UB muscular tissue was dissected by placing the printed template (3D printed) over the tissue and cutting around it. Thickness of each sample is registered. The stress-strain testing involved a 200 N loads using a stress machine Univert by Cellscale ™, data acquisition occurred at a period of 1 ms. Stress-strain curves were obtained using Microsoft Excel and Mathworks Matlab a2017.

Mechanical Model and Parameter Identification. Voigt's model was used for the characterization of the UB mechanical parameters [3], with a viscosity parameter (η), parallel to an elastic component (E). The strain (ε) is considered the same for both elements and the total stress (σ) is the summation of independent stresses for each component Eq. (1). The transfer function of the differential equation is considered for the parametric identification Eq. (2), the data of stress and strain from the tensile test was used in the Identification System toolbox of Matlab for this purpose.

a) b) c)

Fig. 1. (a) Dissection of the bovine bladder with a mark for each region. (b) template and obtained samples per region, (c) tensile test experimental setup.

$$\sigma = \sigma_{E+}\sigma_{\eta} = E\varepsilon + \eta\frac{d\varepsilon}{dt} \tag{1}$$

$$H(s) = \frac{\varepsilon(s)}{\sigma(s)} = \frac{1}{\eta s + E} \tag{2}$$

3 Results and Analysis

The surface reconstruction process is shown in Fig. 2. Figure 2a shows the UB before of the cleaning and distension process. The samples had an average maximum volume of 300 ml. Figure 2b shows the cleaned sample during the scanning, UB is allocated over a printed base of 200 ml capacity. Meshing the sample resulted in the reconstructed surface shown in Fig. 2c. We compare the measures from the digital representation with the real sample to assess if the reconstruction was accurate. Size of this UB resulted in 74.5 × 126.32 × 78.65 mm.

a) b) c)

Fig. 2. (a) Sample organ cleaned and partially dissected. (b) UB allocated over a designed support. (c) Sample UB after meshing the cloud of points (6,355,097 points and 12,711,042 triangles). Marker points can be seen in the reconstruction.

After the scanning process, the samples for tensile testing were dissected as is shown in Fig. 1(a), one sample for each section of the bladder: upper, middle and the lower region are obtained, Fig. 1a. In Fig. 1b the printed template to cut the samples is showed, as well as the samples for each region. Figure 1c shows the tensile test experimental setup. To calculate the stress, the thickness is measured in order to calculate the cross-sectional area. This area has a value of 45.835 mm^2 on average. In Fig. 3 an example of the obtained stress-strain graphics is presented, as can be seen the tissue sample endured a maximum force of approximately 0.077 N/mm^2 with a displacement of 43 mm. After this point, the sample breaks, which is observed in Fig. 3 when the stress falls.

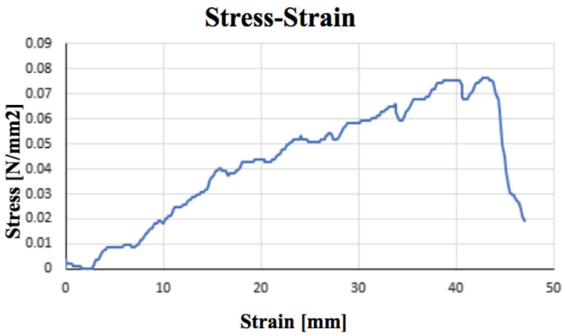

Fig. 3. Example of stress-strain graph for the tensile stress test for one of the tissue samples. After deformation of 43 mm, the stress falls, after the break point.

Stress and Strain time series were used by the system identification toolbox, we obtained elasticity (E) and the damping constant (η). We obtained that the lower region has the most elastic tissue (1.76×10^{-3} N/mm) of the three regions and the upper the most viscous one with 2×10^{-4} Ns/mm^2, similar results have been found by other authors [4, 5], but with different magnitudes due to the use of porcine bladder instead of bovine. The average values of the samples resulted in 1.3×10^{-3} N/mm for the elastic constant and 89.33×10^{-6} Ns/mm^2 for the viscos constant.

4 Conclusions

A cloud point of the surface bovine UB was obtained using tridimensional scanning, it was possible to reconstruct the UB surface. The viscosity and elasticity parameters were characterized for tissue samples of bladder, using a linear dynamic mechanical model; the lower region had the most elastic tissue, and the upper region the most viscous, under isotropic conditions. A current research is carried out considering the anisotropy of the tissue and, frequency response.

References

1. Jokandan, M.S.: Bladder wall biomechanics: a comprehensive study on fresh porcine urinary bladder. J. Mech. Behav. Biomed. Mater. **79**, 92–103 (2018)
2. Ouyang, Z., Sperry, Z.J., Barrera, N.D., Bruns, T.M.: Real-time bladder pressure estimation for closed-loop control in a detrusor overactivity model. IEEE Trans. Neural Syst. Rehabil. Eng. **27**(6), 1209–1216 (2019)
3. Park, J., Lakes, R.S.: Biomaterials: An Introduction, 3rd edn. Springer, New York (2007)
4. Morales-Orcajo, E., Siebert, T., Böl, M.: Location-dependent correlation between tissue structure and the mechanical behaviour of the urinary bladder. Acta Biomater. **75**, 263–278 (2018)
5. Barnes, S.C., Shepherd, D.E.T., Espino, D.M., Bryan, R.T.: Frequency dependent viscoelastic properties of porcine bladder. J. Mech. Behav. Biomed. Mater. **42**, 168–176 (2015)

Classification of Lower Limb Amputees Gait Using Machine Learning Algorithms

Eduardo de Mendonça Mesquita[1], Adriano Pericles Rodrigues[1], Adriano de Oliveira Andrade[2], and Marcus Fraga Vieira[1(✉)]

[1] Federal University of Goiás, Goiânia, Goiás 74690-900, Brazil
marcus@ufg.br
[2] Federal University of Uberlândia, Uberlândia, Minas Gerais 38408-100, Brazil

Abstract. Human gait data, as well as other biological signals, follow distinguishable and measurable patterns that are important for the evaluation and analysis of movement. In this paper, we used spatiotemporal gait data for classification of lower limb amputee groups (transtibial and transfemoral) and individuals without amputation (control). The classification was made using algorithms based on machine learning, KNN (K-nearest neighbors) and RF (random forest). Three treadmill walking conditions were analyzed: horizontal (0º), uphill (+8%) and downhill (–8%). These conditions were important to establish in which scenarios the data are more discriminating. The classification of the data with all conditions together provided an accuracy of 75.8% and 77.7% for KNN and RF, respectively. The best classification result was obtained using the RF algorithm with the data in the downhill condition, indicating that this condition imposes greater motor demands to the participants, showing greater differences between the extracted variables.

Keywords: Classification · Spatiotemporal gait variables · Amputees · K-nearest neighbors · Random forest

1 Introduction

Biomechanics is a science that study and analyze the patterns of human posture and locomotion through variables such as: spatiotemporal (support phase, swing phase, step length, etc.), kinematics (linear and angular displacements, etc.) and kinetics (reaction forces, torque in the joints, etc.). The evaluation of these variables may, therefore, contribute to the identification and understanding of adaptations and limitations of patterns of posture and locomotion [1].

Given the importance of using these variables to compare and identify differences in the physical aspects of different groups, several studies have processed data to discriminate them, such as: individuals with Parkinson's disease versus healthy individuals, older versus young adults, obese versus athletes, etc.

Using nonlinear characteristics [2], kinetic data [3] and spatiotemporal data [4] it is possible to extract characteristics that allow this discrimination.

Statistical tools are quite useful in the analysis of data discrimination, some of the most used methods are the classification algorithms coming from machine learning

© Springer Nature Switzerland AG 2020
C. A. González Díaz et al. (Eds.): CLAIB 2019, IFMBE Proceedings 75, pp. 950–954, 2020.
https://doi.org/10.1007/978-3-030-30648-9_123

techniques. The algorithm KNN (K nearest neighbor) and LDA (linear discriminant analysis) was used to classify the movements of the hand fingers using EMG (electromyography) signals [5]. SVM (support vector machine) was applied for an automatic classification of the gait in young and older adults, which was obtained using minimum foot clearance (MFC) data [6]. In [7] artificial neural networks were applied for gait classification of post-stroke patients, and in [8] neural networks were used for recognition of emotions in gait patterns.

Thus, the purpose of this study is to discriminate three groups, walking in different conditions, using spatiotemporal gait features: a transtibial amputees group, a transfemoral amputees group, and a control group of individuals without amputation. The analysis was done using supervised classification algorithms.

2 Methods

In this study, three groups of individuals were classified based on their physical condition (transfemoral and transtibial amputees, and healthy subjects) using gait spatiotemporal data. These groups are: 14 individuals with transfemoral amputation, 11 individuals with transtibial amputation and 15 control individuals.

Data collection was conducted with participants walking on a treadmill at a preference walking speed (PWS). Three conditions were assessed: level treadmill, uphill +8% and downhill –8%. All protocols were approved by the local ethics committee for human research, and the participants signed an informed consent form.

Kinematic data were obtained using a 3D capture system (Vicon Oxford Metrics, Oxford UK) with 10 infrared cameras. Spatiotemporal variables were extracted from the kinematic data: step width (mm), support phase duration (s), swing phase duration (s), double support phase duration (s), step frequency and normalized step length (by individual leg length).

The classification was done using KNN and random forest (RF) algorithms because they are methods widely used in task classification. KNN is a simple supervised learning algorithm for working with a large number of classes. The classification is based on how similar a data is from a neighboring set. The number K indicates how many individuals belong to the desired neighborhood and the metric used is the Euclidean distance between the individuals [9].

RF is a supervised learning algorithm in which a forest is created randomly. This forest is created by a combination (ensemble) of random trees. This algorithm consists in the use of randomly selected characteristics or by combinations in each node for the creation of decision trees [10].

3 Results and Discussion

3.1 Classification

Each algorithm accuracy, considering all walking conditions, is presented in Table 1.

Table 1. Accuracy of each algorithm in classification of spatiotemporal data considering all walking conditions.

Algorithms	Accuracy (%)
KNN	75.8
RF	77.7

Using data from all walking conditions to discriminate the groups, the RF algorithm has the best accuracy and the highest classification power. The data were then analyzed in the different walking conditions and the results can be seen in Subsect. 3.2.

3.2 Classification Using the Different Walking Conditions

The accuracy of each algorithm in data classification in the three walking conditions (horizontal, uphill and downhill) is presented in Table 2.

Table 2. Accuracy of each algorithm in classification of spatiotemporal data in each walking condition.

Algorithms	Horizontal	Uphill	Downhill
KNN	73.3%	72.8%	83.8%
RF	75.9%	74.0%	86.3%

The algorithms presented the best results in the downhill condition, which was better than those using all walking condition data simultaneously. Uphill walking condition produced the worst results. RF algorithm presented better results compared to KNN algorithm in all walking conditions.

The results suggest that the downhill condition imposes a greater challenge in the gait of individuals with amputation, producing more distinguishable data from those extracted from control individuals. This is supported by the fact that all participants have reported that the downhill walking condition was more challenging from a biomechanical point of view. It is more difficult to negotiate in favor of gravity, controlling the greater impact magnitude at each foot strike and the friction demands, than in the uphill or level walking condition.

The results also suggest that the adaptation of individuals with amputation may be better evaluated in conditions of downhill walking, since in this situation the classifiers presented a better performance.

4 Conclusion

In this study, groups with lower limb amputation (transtibial and transfemoral) and without amputation (control) were classified using gait spatiotemporal variables collected in three treadmill walking conditions (horizontal, uphill +8% and downhill –8%).

RF algorithm produced better results compared to KNN algorithm for all walking conditions. The performance of both algorithms was greater in the downhill walking condition, in which the accuracy reached 86.3% and 83.8% for the RF and the KNN, respectively. Horizontal and uphill walking conditions produced similar accuracy, below 80%. This analysis indicates that the downhill condition imposes greater demands to the gait, producing more discriminating data than the other walking conditions. This suggests that amputees are less able to negotiate with such demands in downhill walking condition than control individuals. RF algorithm produced better results in discriminating amputees from control individuals, using gait spatiotemporal variables extracted from kinematic data collected during downhill walking condition.

This study demonstrates the potential use of classification algorithms in an automatic diagnosis system for discrimination of amputees based on gait spatiotemporal parameters. This may be useful for assessment of the adaptation to the prosthesis and gait recovery in subjects with lower limb amputation. However, although the classifiers analyzed here are promising to the construction of an automatic diagnosis system, its performance should be improved, either using a larger sample or selecting other gait features.

Acknowledgments. The authors are grateful to CNPq-Brazil and Fapeg for financial support, and CAPES-Brazil for EMM and APR scholarship. AOA and MFV are a fellow of CNPq-Brazil (304818/2018-6, 306205/2017-3).

Conflict of Interest. There are no conflicts of interest to declare.

References

1. Winter, D.: Human balance and posture control during standing and walking. Gait Posture **3**, 193–214 (1995). https://doi.org/10.1016/0966-6362(96)82849-9
2. Fatmehsari, Y.R., Bahrami, F.: Assessment of parkinson's disease: classification and complexity analysis. In: Proceedings of 2010 17th Iranian Conference of Biomedical Engineering (ICBME) (2010). https://doi.org/10.1109/icbme.2010.5704930
3. Zeng, W., Yuan, C., Wang, Q., Liu, F., Wang, Y.: Classification of gait patterns between patients with Parkinson's disease and healthy controls using phase space reconstruction (PSR), empirical mode decomposition (EMD) and neural networks. Neural Netw. (2019). https://doi.org/10.1016/j.neunet.2018.12.012
4. Halgamuge, S., Ackland, D.C., Begg, R.K., Wahid, F., Hass, C.J.: Classification of parkinson's disease gait using spatial-temporal gait features. IEEE J. Biomed. Health Inform. (2015). https://doi.org/10.1109/jbhi.2015.2450232
5. Fandakli, S.A., Aydemir, Ö.: A fast and highly accurate EMG signal classification approach for multifunctional prosthetic fingers control. In: 2017 40th International Conference on Telecommunication Signal Process. TSP 2017, pp. 395–398, January 2017. https://doi.org/10.1109/tsp.2017.8076013
6. Begg, R.K., Palaniswami, M., Owen, B.: Support vector machines for automated gait classification. IEEE Trans. Biomed. Eng. (2005). https://doi.org/10.1109/TBME.2005.845241

7. Kaczmarczyk, K., Wit, A., Krawczyk, M., Zaborski, J.: Gait classification in post-stroke patients using artificial neural networks. Gait Posture. **30**, 207–210 (2009). https://doi.org/10.1016/j.gaitpost.2009.04.010
8. Janssen, D., Schöllhorn, W.I., Lubienetzki, J., Fölling, K., Kokenge, H., Davids, K.: Recognition of emotions in gait patterns by means of artificial neural nets. J. Nonverbal Behav. **32**, 79–92 (2008). https://doi.org/10.1007/s10919-007-0045-3
9. Clarke, M.R.B., Duda, R.O., Hart, P.E.: Pattern classification and scene analysis. J. R. Stat. Soc. Ser. A. **137**, 442 (2006). https://doi.org/10.2307/2344977
10. Cutler, A., Cutler, D.R., Stevens, J.R.: Random forests. Ensemble Mach. Learn. Methods Appl. 157–175 (2012). https://doi.org/10.1007/9781441993267_5

Musculoskeletal Modeling as a Tool for Biomechanical Analysis of Normal and Pathological Gait

Manuel Cardona[1,2(✉)] and Cecilia García Cena[1]

[1] Centro de Automática y Robótica, Universidad Politécnica de Madrid, Madrid, Spain
cecilia.garcia@upm.es
[2] Universidad Don Bosco (UDB), Soyapango, El Salvador
manuel.cardona@udb.edu.sv

Abstract. In this paper, a 3D lower limb musculoskeletal model and simulation of multiple sclerosis disease is presented. The Model was developed using the Musculoskeletal Modeling Software (MSMS), MSMS has the advantage that the model can be exported directly to Simulink allowing us to generate Functional Electrical Stimulation (FES) and evaluate different injuries. From the simulations, is possible to obtain the joint range of motion, joint torque, muscle-tendon length, force and moment arm, this is important not only to perform biomechanical analysis but also to design exoskeleton robots for rehabilitation and to generate reference trajectories for control purposes. In order to validate the results, a study case of a normal and pathological gait is presented, then, the results are compared with the literature and with real data obtained from a low cost, and a professional gait capture system.

Keywords: Biomechanics · Lower Limb · Multiple sclerosis · Musculoskeletal Modeling · Muscle-tendon · Pathological gait

1 Introduction

Musculoskeletal Models have been used successfully in many applications such as injuries analysis, surgeries evaluation, and Biomechanical analysis to determine Forces and Torques. Piazza and Delp [1] have used a model to predict the motions of knee implants during a step-up activity, Cazzola et al. [2], created a model to evaluate Cervical Spine Injuries, Paul et al. [3] have used a model to study the effects of spinal cord injury on locomotor abilities, Arnold et al. [4], used a musculoskeletal model to estimate muscle-tendon length of the hamstrings and Iliopsoas in patients with cerebral palsy in order to predict the biomechanical effect of a surgical intervention, Reinbolt et al. [5], and Rasmussen et al. [6], have used a model to evaluate sport performance.

The main importance of the musculoskeletal model is that allows us to predict muscle-tendon activity without having to use patients which would imply using

© Springer Nature Switzerland AG 2020
C. A. González Díaz et al. (Eds.): CLAIB 2019, IFMBE Proceedings 75, pp. 955–963, 2020.
https://doi.org/10.1007/978-3-030-30648-9_124

invasive Electromyography Sensors (EMG), because non-invasive EMG has a low sensitivity to discriminate between voluntary motor activity and deep muscle activity involved during limb movement. However, invasive EMG is not feasible due ethic conflict with the international guidelines of biomedical investigation with human beings [7]. On the other hand, the model allows to include electronics sensors such as: Inertial Measurement Units (IMU), force sensors or encoders, or using signals from motion analysis systems such as: Cartesian Optoelectronic Dynamic Anthropometer (CODA).

Most of the models have been implemented using OpenSim, SIMM or AnyBody software. All of these are exclusively for biomechanical simulation, however these models cannot be exported directly to a mechanical design tool, therefore for our research propose, we implemented a new one under MSMS-MATLAB environment, enabling a wide range of features such as sensor integration, control strategies testing, FES simulations and the integration of the all well know MATLAB's toolboxes.

The aim of this paper is to present a human lower limb modeling and simulation of multiple sclerosis disease. Furthermore, the model allows us not only to perform a biomechanical analysis for both normal and pathological gait but also kinematics and dynamics analysis for dimensioning and selection of actuators in order to develop rehabilitation mechanisms. Thus, the model will allow us to study differences in muscle synergies of a pathology and compare them with a normal gait which is crucial for the optimized mechanical design of powered lower limb robotic exoskeletons.

2 Materials and Methods

The model presented in this paper was created based on the anatomical dataset reported by Arnold et al. [8] and Ward et al. [9], and have been implemented using Musculoskeletal Modeling Software (MSMS). MSMS has the advantage that the model can be exported directly to Simulink allowing us to generate Functional Electrical Stimulation (FES) signals for muscle-driven and send these signals to MSMS via UDP. A musculoskeletal model is composed of bones, muscle-tendon segments, ligaments and wrapping objects. The correct activation of each muscle group allows the motion of each joint. Some previous work using MSMS have been reported for the upper limb [10], however, for the lower limb, there are a few incomplete and very basic related works [11], without any kind of validation.

On the other hand, the model allows to include electronics sensors such as Inertial Measurement Units (IMU), force sensors or encoders, using signals from motion analysis systems such as Cartesian Optoelectronic Dynamic Anthropometer (CODA) or other third-party software.

2.1 Musculoskeletal Model

The model is composed of 44 muscle-tendon actuators per leg, each actuator was modeled as a 3-element Hill-Type muscle-tendon unit [12] as depicted in

Fig. 1. For muscle-tendon with complex geometry (Adductor magnus, gastrocnemius, gluteus maximus, gluteus medius, gluteus minimus) the whole muscle was divided into multiple segments and the constraint of the muscle-tendon path was modeled by moving points and wrapping objects.

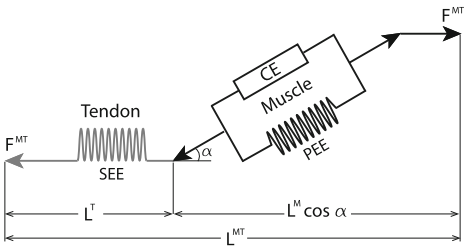

Fig. 1. Hill-Type Muscle-tendon model. CE: Contractile Element, PEE: Parallel Elastic Element, SEE: Serial Elastic Element, α: pennation angle.

The Hill-type muscle model defines the muscle force generation, MSMS Software implements this model and requires the following morphometrics parameters: optimal Fascicle Length, Optimal Tendon Length, Maximum muscle-tendon length, muscle mass, and the origin and insertion point for each muscle-tendon unit. The cadavers from which muscle-tendon architecture parameters were measured [9] had an average weight of 82.7 $\pm$ 15.2 kg and height of 168.4 $\pm$ 9.3 cm, the complete model is depicted in Fig. 2.

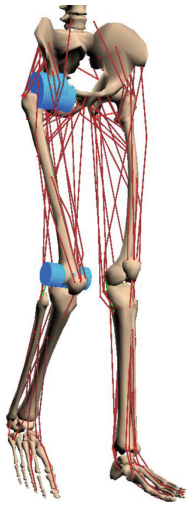

Fig. 2. Musculoskeletal Model of the Lower Limb in MSMS software. The blue components are the wrapping objects.

The model has 6 joints (hip, knee, ankle, subtalar, metatarsophalangeal, patellofemoral) allowing 10 degrees of freedom (DoF) per leg. The hip joint was modeled as a spherical joint allowing 3 DoF. The knee, ankle, metatarsophalangeal and subtalar were modeled as a revolute Joints, allowing one degreed of freedom per Joint. The Range of Motion (ROM) were taken from Kapandji [13], Delp et al. [14], and Arnold et al. [8] and are presented in Table 1.

Table 1. Joints and Range of Motion (ROM). MTP: Metatarsophalangeal

Joint	Action	ROM
Hip	Extension/Flexion	$-30°/120°$
	Abduction/Adduction	$-50°/30°$
	External/Internal Rotation	$-40°/40°$
Knee	Flexion/Extension	$-120°/0°$
Ankle	Plantar/Dorsal Flexion	$-40°/30°$
Subtalar	Eversion/Inversion	$-30°/30°$
MTP	Extension/Flexion	$-20°/20°$

3 Results

One of the unique features of MSMS is the ability to export the model directly to Simulink. This represents a huge advantage because it allows: set activation signals (muscle-driven simulation), measure angles, speeds, accelerations, torques and forces in the joints, integrate sensors, as well as apply control strategies and integrate all the well-know MATLAB's toolboxes.

Once the model was exported to Simulink, the muscle-tendon was excited by applying activation signals to them. The signals correspond to a 0 to 1 pulse train with a pulse-width of 50%. An active delay between each signal is set in order to shift agonist-antagonist muscles interactions. The amplitude of the signals corresponds with the percentage of muscle activation (0% to 100%). That is, 100% for a healthy subject.

Figure 3 shows the Simulink and MSMS Integration. The MSMS integration allow us to see the motion evolution in the avatar while the simulation is being performed. The communication between Simulink and MSMS is established via UDP.

A study case was performed by simulating the range of motion for a gait cycle of healthy persons and persons with multiple sclerosis, the activation profile for the affected muscles was taken from the literature. Furthermore, the results of the simulation were compared with those obtained by the Cartesian Optoelectronic Dynamic Anthropometer (CODA) at Physiotherapy School ONCE, Madrid, and those obtained from our own motion capture system (Fig. 4), that consist of three

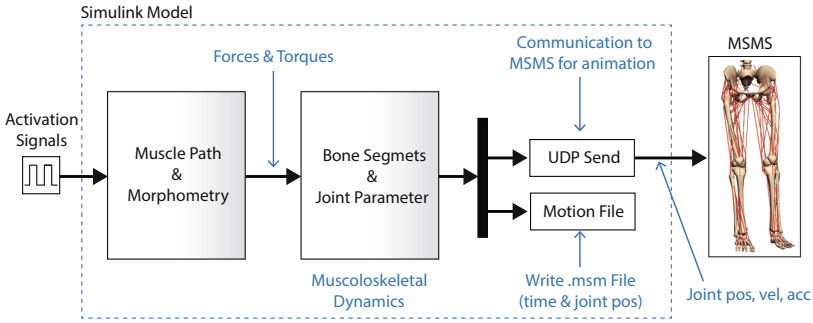

Fig. 3. Simulink Model and MSMS communication

wireless 9-axis inertial measurement unit (IMUs) modules, each module consists of a high-precision 3-axis gyroscope, 3-axis accelerometer, 3-axis geomagnetic sensor, and a 32 bits high-performance MCU, allowing us to solve the current real-time motion posture quickly with a high accuracy (0.05°).

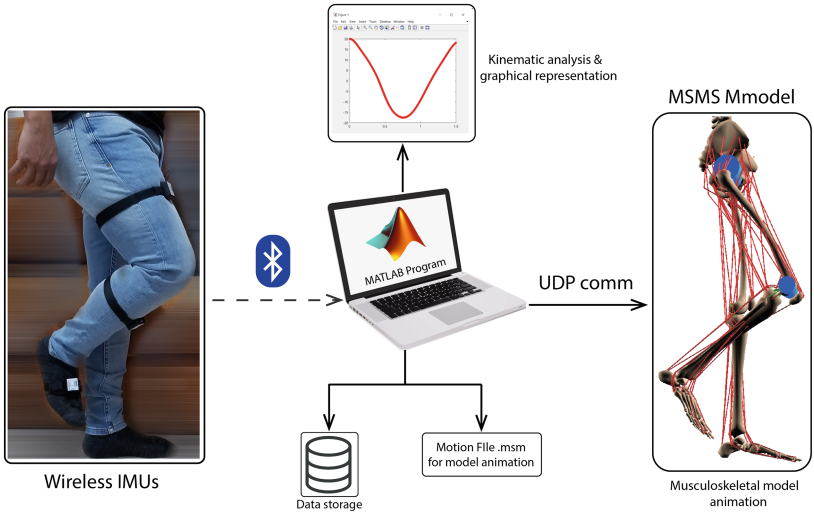

Fig. 4. Our own wireless gait capture system. The IMU sends the data via Bluetooth to MATLAB, the data is stored in a .xslx file and a MSMS motion file (.msm) is also created, then, the data is plotted instantaneously and send to MSMS via UDP.

Figure 5 shows the hip flexion/extension angle and Fig. 6 the knee flexion/exten-sion angle, during a gait cycle for a healthy subject (HS) and a person with multiple sclerosis (PwMS).

As we can see in Figs. 5 and 6, the model predicts successfully for both normal and pathological subjects, indeed our results follow very close the IMU Data

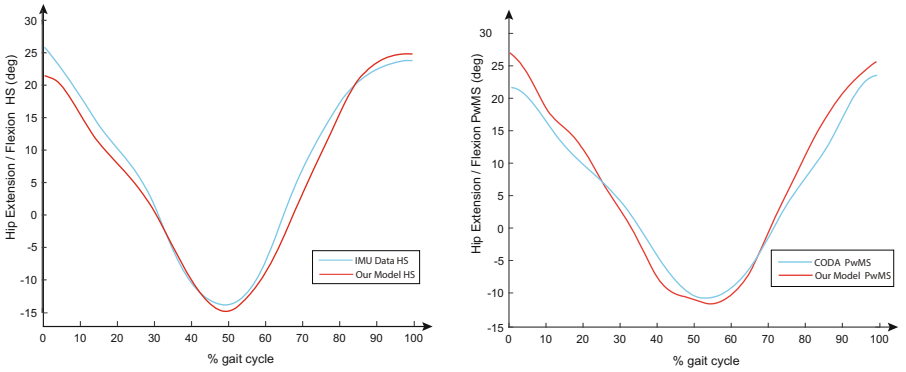

Fig. 5. Hip flexion/extension for a healthy subject (HS) and a person with multiple sclerosis (PwMS) for a gait cycle

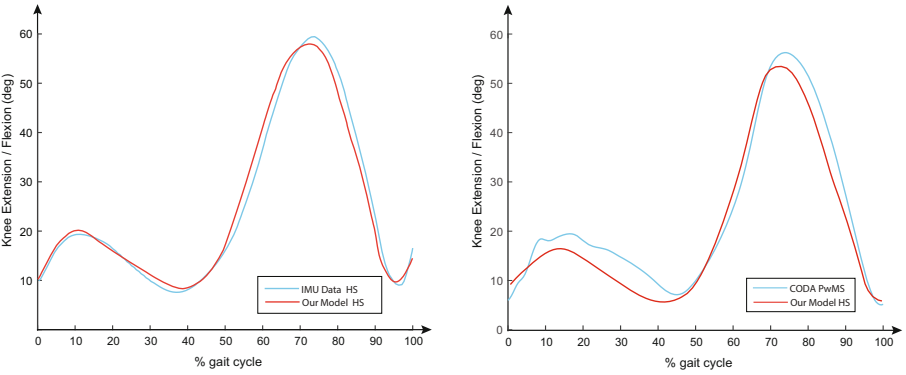

Fig. 6. Knee flexion/extension for a healthy subject (HS) and a person with multiple sclerosis (PwMS) for a gait cycle

and CODA values. On the other hand, the Root Mean Square Error (RMSE) and the Normalized Mean Square Error (NMSE) were evaluated. For hip flexion/extension the NMSE was 2.74% and the RMSE was 2.22° for HS, whereas for PwMS the NMSE was 3.65% and the RMSE was 2.54° respectively. In the case of the knee flexion/extension the NMSE was 0.752% and the RMSE was 2.79° for HS, whereas for PwMS the NMSE was 1.73% and the RMSE 3.68° respectively. Thus, the values obtained show the goodness-of-fit of the model. In addition, the gait sequence for a PwMS is shown in Fig. 7.

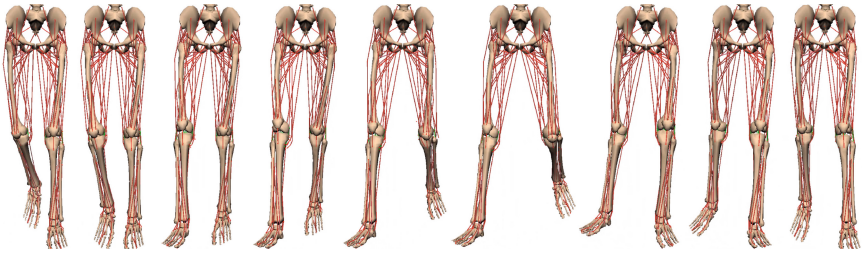

Fig. 7. Gait cycle simulation in MSMS for a PwMS. Data send from Simulink via UDP.

3.1 Application to Robotic Exoskeleton Controller Design

A musculoskeletal model is an important tool not only for exoskeleton design but also for evaluation of control strategies. In the design stage is a useful tool to analyze the maximum joint torques required to produce a desired motion and evaluate actuators sizing. On the other hand, the model allows us to include the dynamics of a subject injured in the control loop with the aim to design the best suitable control architecture. In this sense, our research team uses robot theory merged with biomechanical theory in order to personalize the mechanism design, Fig. 8 shows the methodology used by our research group.

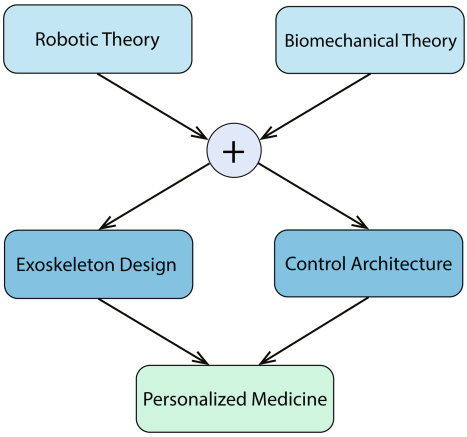

Fig. 8. Methodology used for robotic exoskeleton design.

Furthermore, following this methodology, the exoskeleton dynamics (from exoskeleton design) and the musculoskeletal model is included in the control loop in order to test different control strategies. For instance, Fig. 9 shows a general control schema architecture with the musculoskeletal model in the loop.

In the control scheme, the injured subject model is combined with the exoskeleton dynamics to adapt the joint torques to subject pathology, a feedforward controller which can be derived from the musculoskeletal model is used to compensate predictable perturbations in an anticipatory way.

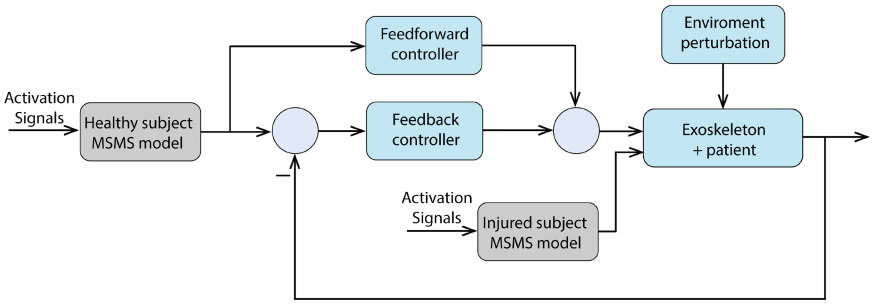

Fig. 9. A general controller architecture with MSMS model in the loop.

4 Conclusions

We have presented a musculoskeletal model of the lower limb using MSMS software, the model presented is an important tool since allow to perform biomechanical analysis and determine muscle-tendon synergies without using patients. One of the most significant advantage of our study is the Simulink model obtained since allow to predict muscle-tendon activity for both healthy and pathological patient by activating the synergists muscle group and setting the muscle activation level. Also, using the equivalent model in Simulink we are able to estimate joint position, velocity and acceleration; joint forces and torques; and muscle-tendon lengths and forces.

As we can see in Figs. 5 and 6, the model predicts successfully for both normal and pathological subjects. For instance, in the case of the hip flexion/extension the Normalized Mean Square Error (NMSE) was 2.74% for HS and 3.65% for PwMS, whereas for knee flexion/extension the NMSE was 0.752% for HS and 1.73% for PwMS. Thus, the values obtained shown the goodness-of-fit of the model presented.

Finally, the model is an important tool not only to perform a complete biomechanical analysis or to evaluate kinematics and dynamics in order to design exoskeleton rehabilitation robots but also to design the best suitable control strategy.

Acknowledgments. The authors would like to thanks to Physiotherapy School ONCE, Madrid and the Faculty of Medicine, Universidad Autónoma de Madrid. Manuel Cardona would like to thank to Fundación Carolina and Universidad Don Bosco for their support during this research.

References

1. Piazza, S., Delp, S.: Three-dimensional dynamic simulation of total knee replacement motion during a step-up task (2001). https://doi.org/10.1109/MIS.2014.27
2. Cazzola, D., Holsgrove, T.P., Preatoni, E., Gill, H.S., Trewartha, G.: Cervical spine injuries: a whole-body musculoskeletal model for the analysis of spinal loading (2017)

3. Paul, C., Bellotti, M., Jezernik, S., Curt, A.: Development of a human neuro-musculo-skeletal model for investigation of spinal cord injury (2005)
4. Arnold, A.S., Asakawa, D.J., Delp, S.L.: Do the hamstrings and adductors contribute to excessive internal rotation of the hip in persons with cerebral palsy? (2000)
5. Reinbolt, J.A., Seth, A., Delp, S.L.: Proceedings of the 11th conference of the International Sports Engineering Association, ISEA 2016, Elsevier, pp. 281–287 (2016)
6. Rasmussen, J., Holmberg, L.J., Sørensen, K., Kwan, M., Andersen, M., de Zee, M.: Performance optimization by musculoskeletal simulation (2012)
7. CIOMS, International ethical guidelines for biomedical research involving human subjects. Report, Council for International Organizations of Medical Sciences (2002)
8. Arnold, E.M., Ward, S.R., Lieber, R.L., Delp, S.L.: A model of the lower limb for analysis of human movement (2010)
9. Ward, S.R., et al.: Are current measurements of lower extremity muscle architecture accurate? (2009)
10. Destarac, M.A., Cena, C.E.G., Pazmiño, R.J.S., Urbina, M.J.R., López, J.L., Gómez, R.E.: Modeling and simulation of upper brachial plexus injury (2016)
11. Chauhan, R., Vyas, J.: Lower limb musculoskeletal modeling by using musculoskeletal modeling software (2013)
12. Millard, M., Uchida, T., Seth, A., Delp, S.: Flexing computational muscle: Modeling and simulation of musculotendon dynamics (2013)
13. Kapandji, A.: Fisiología Articular, vol. 2, 6th edn. Editorial Panamericana, France (2010)
14. Delp, S.L., Loan, J.P., Hoy, M.G., Zajac, F.E., Topp, E.L., Rosen, J.M.: An interactive graphics-based model of the lower extremity to study orthopaedic surgical procedures (1990)

Quantification of Coordination Variability During Gait in Fallers and Non-fallers Older Adults at Different Speeds

Guilherme Augusto Gomes De Villa[1], Adriano de Oliveira Andrade[2], and Marcus Fraga Vieira[1(✉)]

[1] Federal University of Goiás, Goiânia, GO 74690900, Brazil
marcus@ufg.br
[2] Federal University of Uberlândia, Uberlândia, MG 38408100, Brazil

Abstract. The aim of the present study was to analyze segments coordination and coordination variability during gait of fallers and non-fallers older adults at different speeds (preferred walking speed (PWS), 120% of PWS and 80% of PWS) through vector coding technique (VC). Thirty-one young adults, 22 non-fallers and 17 fallers older adults participated in the study. All participants practice exercise regularly at least three times a week. They performed a protocol of three 1-min walking on a treadmill at each speed for data collection, in a randomized order. For thigh-leg segments pair, angles were computed during four gait phases (first double support, single support, second double support and swing phase). Data was exported and analyzed with a custom MatLab code (R2018a, MathWorks, Natick, MA). There were significant differences in thigh-leg segments pair coordination pattern, with the greatest differences observed at 80% and 120% PWS for all groups, with emphasis on the older adults groups.

Keywords: Coordination · Variability · Vector coding

1 Introduction

Coordination can be defined as a process in which motion components are sequentially organized over time, and their relative magnitude determined in the sense of producing a functional movement pattern or a synergy [1]. Coordination variability quantify the variety of movement patterns that an individual uses during a task and can provide a measure of the flexibility/adaptability of individual's motor system [2]. In order to quantify coordination variability, there are some nonlinear techniques that can be useful. This includes vector coding technique, adopted here for its versatility, requiring less rigor in data processing and, more important, shorter data collection time when compared to other traditional techniques, an essential characteristic for the target groups analyzed here. On the other hand, fall can be defined as an unintentional displacement of the body to a level lower than the initial position, with inability to correct in a timely manner, determined by multifactorial conditions that compromise stability [3], including a coordination impairment.

© Springer Nature Switzerland AG 2020
C. A. González Díaz et al. (Eds.): CLAIB 2019, IFMBE Proceedings 75, pp. 964–969, 2020.
https://doi.org/10.1007/978-3-030-30648-9_125

While several gait parameters (speed reduction, stride length and increased double support time, among others) are strategies to reduce the risk of falls, the variability of the gait is the indicator that better represents the postural instability [4, 9]. It is not known exactly how many gait cycles are required to reliably estimate coordination variability during gait. The recent literature estimates that at least five [6], ten [7] to fifteen [8] gait cycles are required. However, there is a consensus that less than five gait cycles are a very small number and the reported values cannot be representative of the true coordination variability of an individual or group. Thus, for more reliable results, in this study the entire time series was used, a total of 25 gait cycles for each individual.

Therefore, the aim of the present study is to quantify the coordination variability of pairs of anatomical segments in fallers and non-fallers older adults during gait at different speeds, testing their potential use as a predictor of fall risk in the older population. For this, it was analysed the coordination variability of the thigh-leg segment in sagittal plane at different speeds (preferred walking speed (PWS), 120% of PWS and 80% of PWS), using vector coding technique (VC).

2 Materials and Methods

2.1 Participants

A control group of thirty-one young adults (17 males, 14 females – control group), and two experimental groups of 22 non-fallers (9 males, 13 females) and 17 (10 males, 7 females) fallers older adults were enrolled in this study. The older adults were characterized as fallers if they had three or more falls in the last 24 months (in this study, all fallers older adults had fallen more than 3 times in the last 24 months). All participants practice exercise regularly at least three times a week. The timed up and go (TUG) and International Physical Activity Questionnaire (IPAQ) tests were applied to evaluate the level of activity of all groups. All protocols were approved by the local ethics committee for human research, and the participants signed an informed consent form.

2.2 Equipment

Sixteen reflective markers were fixed at specific places according to Vicon's lower body plug-in-gait model (Vicon, Oxford Metrics, Oxford, UK), for movement registration. A 3D motion capture system comprising 10 infrared cameras operating at 100 Hz was used. The data were low pass filtered at 8 Hz.

2.3 Protocol

The preferred walking speed (PWS) on a treadmill was determined according to a previously reported protocol [9]. A 4-min walking on the treadmill for familiarisation was allowed. After a 2-min rest period, the participants executed three 1-min walking at PWS, 80% PWS and 120% PWS, in a randomized order. The thigh-leg segment pair was analysed for 25 strides, normalized with 100 points, for each 1-min walking, in four phases of the gait cycle: first double support, single support, second double

support and swing phase. Segment angles were calculated in relation to the laboratory global coordinate system. Coupling angles represent the segments coordination pattern, while the standard deviation of the coupling angle at each instant of the gait cycle represents the segments coordination variability [10].

2.4 Calculation of Coupling Angle

The coupling angles were calculated as the angle of a vector connecting consecutive data points, according to the following Eqs. (1) and (2):

$$\gamma_i = \tan^{-1}\left(\frac{\theta_{D(i+1)} - \theta_{D(i)}}{\theta_{P(i+1)} - \theta_{P(i)}}\right).\frac{180}{\pi} \quad \text{for} \quad \theta_{P(i+1)} - \theta_{P(i)} > 0 \tag{1}$$

$$\gamma_i = \tan^{-1}\left(\frac{\theta_{D(i+1)} - \theta_{D(i)}}{\theta_{P(i+1)} - \theta_{P(i)}}\right).\frac{180}{\pi} + 180 \text{ for} \quad \theta_{P(i+1)} - \theta_{P(i)} < 0 \tag{2}$$

where $0 \leq \gamma \leq 360°$, in which i represent the consecutive samples in a normalized gait cycle, and γ_i was calculated on the basis of the distal segmental angles (θ_D, $\theta_{D(i+1)}$) and proximal segment angles ($\theta_{P(i)}$, $\theta_{P(i+1)}$).

The coupling angle γ_i is corrected to show the value between 0° and 360° according to the Eq. (3):

$$\gamma_i = \begin{cases} \gamma_i + 360 & \gamma_i < 0 \\ \gamma_i & \gamma_i \geq 0 \end{cases} \tag{3}$$

The mean of the coupling angle γ_i should be computed using circular statistics.

For an individual (n) and then for a group, γ_i is calculated from the horizontal ($\bar{x}_i$) and vertical ($\bar{y}_i$) Cartesians components along multiple cycles of gait j, for each instant i of the gait cycle according to the Eqs. (4) and (5):

$$\bar{x}_i = \frac{1}{n}\sum_{j=1}^{n}\left(\cos\gamma_{ji}\right) \tag{4}$$

$$\bar{y}_i = \frac{1}{n}\sum_{j=1}^{n}\left(\sin\gamma_{ji}\right) \tag{5}$$

The mean of the coupling angle $\bar{\gamma}_i$ is corrected to show the value between 0° e 360°, following the Eq. (6):

$$\bar{\gamma}_i = \begin{cases} \tan^{-1}\left(\frac{\bar{y}_i}{\bar{x}_i}\right).\frac{180}{\pi} & \bar{x}_i > 0, \bar{y}_i > 0 \\ \tan^{-1}\left(\frac{\bar{y}_i}{\bar{x}_i}\right).\frac{180}{\pi} + 180 & \bar{x}_i < 0 \\ \tan^{-1}\left(\frac{\bar{y}_i}{\bar{x}_i}\right).\frac{180}{\pi} + 360 & \bar{x}_i > 0, \bar{y}_i < 0 \end{cases} \tag{6}$$

The length of the mean coupling vector is then defined according the Eq. (7):

$$\bar{r}_i = \sqrt{\bar{x}_i^2 + \bar{y}_i^2} \tag{7}$$

Finally, the variability of the coupling angle CAV_i, is calculated according to the Eq. (8):

$$CAV_i = \sqrt{2.(1 - \bar{r}_i)}.\frac{180}{\pi} \tag{8}$$

The coupling angles were computed in four phases of the gait cycle: first double support, single support, second double support, and swing phases.

2.5 Statistical Analysis

As all the results presented a normal distribution (Shapiro-Wilk test, ($p > 0.05$)), repeated measure analysis of variance (ANOVA) with mixed design was used to compare the three groups, the main effect of speed, and the interaction effect between groups and speed, followed by post-hoc test with Bonferroni correction. The TUG and IPAQ tests were compared using one-way analysis of variance (one-way ANOVA). Statistical analysis was performed using SPSS software, version 23 (SPSS Inc., Chicago, IL, USA), with a significant level set at $p < 0.05$.

3 Results and Discussion

The young adults, non-fallers and fallers older adults groups did not present significant differences regarding height, body mass, IMC and IPAQ. However, young adults presented significant higher PWS than older adults ($p = 0.014$), as shown in the Table 1.

With respect to the coordination variability, statistical differences were found for all groups at speeds of 80% of PWS and 120% of PWS. For the sagittal thigh segment and sagittal leg segment, the statistical differences between young adults and non-fallers older adults occurred in the first double support and swing phase at 120% of PWS, with the variability being higher in the young group.

Table 1. Characteristics of the groups: Young adults, Non-Fallers and Fallers older adults.

	Groups		
	Young (n = 31)	Non-Fallers (n = 22)	Fallers (n = 17)
PWS (km/h)*	4,78 ± 0,67	3,98 ± 0,55	3,79 ± 0,96
IPAQ	1,78 ± 0,64	1,67 ± 0,12	1,62 ± 0,35
TUG(s)	5,98 ± 0,94	9,56 ± 1,68	11,02 ± 2,85

Values expressed as mean ± standard deviation. PWS (Preferred Walking Speed); IPAQ (International Physical Activity Questionnaire); TUG (timed up and go). *Significant difference (one-way ANOVA, p = 0.014)

Comparing young adults with fallers older adults, there were significant differences in the first double support phase at 80% of PWS, the variability being greater in the young adults group.

Table 2 shows the results of mains effects of group and speed, and interaction effect on the coordination variability for each gait phase.

Table 2. Effects of group and speed on coordination variability for each gait phase.

Effect	Phases of Gait	F	p	η^2
Group	First Double Support	4,956	**0,010**	0,150
	Single Support	3,925	**0,025**	0,123
	Second Double Support	7,399	**0,001**	0,209
	Swing	21,091	**<0,001**	0,430
Speed	First Double Support	NS	NS	NS
	Single Support	7,859	**0,002**	0,123
	Second Double Support	NS	NS	NS
	Swing	10,431	**<0,001**	0,157
Group vs. Speed	First Double Support	2,731	**0,033**	0,089
	Single Support	NS	NS	NS
	Second Double Support	6,513	**<0,001**	0,189
	Swing	5,054	**0,001**	0,153

Mixed repeated measures ANOVA. F is used to test the overall fit of a regression model to a data set; p is the significance of the test; η^2 is a measure of the effect size; NS = Not Significant.

Finally, when comparing non-fallers with fallers older adults, differences in the first double support phase occurred at 80% and 120% PWS, in the second double support phase at 80% and 120% of PWS, and in the swing phase at 120% of PWS; in this case, the variability was always higher for non-fallers compared to fallers older adults. The analyzed segments had rotation in the same direction, being, therefore, in-phase.

4 Conclusions

There were significant differences in all analyzed segments, however the greatest differences were observed at 80% of PWS and 120% of PWS, with variability being higher for the non-fallers older adults in comparison with the fallers older adults. Thus, there are differences between fallers and non-fallers older adults with respect to segmental coordination variability that can be used as a potential predictor of fall risk. Reduced coordination variability in fallers older adults can be an indicative of reduced adaptability and increased risk of fall. Future studies may examine what leads to this difference in coordination variability, and assess physical exercises focusing on increasing coordination variability to decrease the risk of falls.

Acknowledgments. The authors are grateful to CNPq-Brasil and Fapeg for financial support, and CAPES-Brasil for GAGV scholarship. AOA and MFV are a fellow of CNPq-Brasil (304818/2018-6, 306205/2017-3).

Conflict of Interest Declaration. There are no conflicts of interest to declare.

References

1. Scholz, J.P.: Dynamic pattern theory—some implications for therapeutics. Phys. Ther. **70**, 827–843 (1990). https://doi.org/10.1093/ptj/70.12.827
2. Hafer, J.F., Boyer, K.A.: Variability of segment coordination using a vector coding technique: reliability analysis for treadmill walking and running. Gait Posture **51**, 222–227 (2017). https://doi.org/10.1016/j.gaitpost.2016.11.004
3. Masud, T., Morris, R.O.: Epidemiology of falls. Age Ageing **30**, 3–7 (2001). https://doi.org/10.1093/ageing/30.suppl_4.3
4. Priest, A.W., Salamon, K.B., Hollman, J.H.: Age-related differences in dual task walking: a cross sectional study. J. Neuroeng. Rehabil. **5**, 29 (2008). https://doi.org/10.1186/1743-0003-5-29
5. Torres, J.L.: Influência da dupla tarefa nos parâmetros espaço-temporais da marcha de idosos: uma revisão da literatura [Monografia de especialização]. Univ. Fed. Minas Gerais, Esc. Educ. Física, Fisioter. e Ter. Ocup. (2010)
6. Hafer, J.F., Freedman Silvernail, J., Hillstrom, H.J., Boyer, K.A.: Changes in coordination and its variability with an increase in running cadence. J. Sports Sci. **34**, 1388–1395 (2016). https://doi.org/10.1080/02640414.2015.1112021
7. Miller, R.H., Chang, R., Baird, J.L., Van Emmerik, R.E.A., Hamill, J.: Variability in kinematic coupling assessed by vector coding and continuous relative phase. J. Biomech. **43**, 2554–2560 (2010). https://doi.org/10.1016/j.jbiomech.2010.05.014
8. Heiderscheit, B.C., Hamill, J., van Emmerik, R.E.A.: Variability of stride characteristics and joint coordination among individuals with unilateral patellofemoral pain. J. Appl. Biomech. **18**, 110–121 (2002). https://doi.org/10.1123/jab.18.2.110
9. Dingwell, J.B., Marin, L.C.: Kinematic variability and local dynamic stability of upper body motions when walking at different speeds. J. Biomech. **39**, 444–452 (2006). https://doi.org/10.1016/j.jbiomech.2004.12.014
10. Robertson, E.G., Caldwell, G.E., Hamill, J., Kamin, G., Whittlesey, S.N.: Research Methods in Biomechanics. Human Kinetics, Champaign (2004)

Center of Pressure Periodic Displacement with Alternate Current Unilateral Vestibular Stimulation

Pliego Adriana[1,2(✉)], Vega Rosario[2], and Soto Enrique[2]

[1] Autonomous University of the State of Mexico, Toluca, Mexico
acpliegoc@uaemex.mx
[2] Meritorious Autonomous University of Puebla, Puebla, Mexico

Abstract. Various studies describe the postural response and ocular movements produced by transmastoid galvanic vestibular stimulation (GVS). To take advantage of this response in a noninvasive vestibular prosthesis, a unilateral configuration would be a practical design for users. However, the locomotor response to unilateral GVS on physiological functions related to the vestibular system has not been thoroughly described. To determine the postural effects of unilateral GVS, sine, square and triangle waveforms of 0.3, 0.6 and 0.9 Hz were used to transcranially stimulate the vestibular system of 12 healthy subjects (0.4–2.3 mA). Center of pressure (COP) oscillations were recorded with a stabilometric platform. The largest mean COP trajectory length in the mediolateral axis was produced while stimulating with a sine waveform of 0.3 Hz, followed by stimulation with a square waveform of 0.3 Hz. Oscillation of COP followed stimulation frequency in the mediolateral axis when a sine waveform of 0.6 Hz was used. Root means square (RMS) value and the area of an ellipse calculated from COP displacement recordings, decreased with increasing frequency when stimulating with square and sine waveforms. No changes in these variables were observed when using triangle (symmetric) waveforms. Amplitude of spectral analysis increased notoriously for sine wave stimulation of 0.3 Hz. In future studies, a larger range of frequencies with square and sine waveforms, may be used to study postural response in relation to stimulation frequency. Results suggest that it is possible to include low frequency square and sine waveforms with unilateral GVS in a noninvasive vestibular prosthesis.

Keywords: Vestibular prosthesis · Unilateral galvanic vestibular stimulation · Center of pressure

1 Introduction

Galvanic vestibular stimulation (GVS) is a safe and noninvasive method to produce vestibular reflexes by applying electrical current of >1 mA over the mastoid process [1]. Stimulation with a periodic signal using transmastoid (bilateral bipolar) GVS has been previously used to study the integrity of the vestibulospinal pathway [2], the vestibulo-ocular reflex [3] and the autonomic function related to vestibular activation [4]. However, the physiological response on these three neural systems using the

© Springer Nature Switzerland AG 2020
C. A. González Díaz et al. (Eds.): CLAIB 2019, IFMBE Proceedings 75, pp. 970–974, 2020.
https://doi.org/10.1007/978-3-030-30648-9_126

unilateral bipolar GVS configuration has not been studied. Additionally, various stimulation signals using transmastoid GVS have proven to improve postural stability in a pathological population. Sinusoidal waveform of 0.5 Hz and 0.5–3 mA alternate current (AC) reduced postural imbalance provoked by an external multisensory perturbation in elders [5]. Long-term noisy GVS (0.02–10 Hz, 0–1000 μA) improved balance in patients with bilateral vestibulopathy [6]. This study aims to determine if unilateral bipolar GVS modulates postural displacement in a way to be included in a noninvasive vestibular prosthesis, such as that proposed by our research group [6].

2 Methods

Twelve healthy subjects, 4 women and 8 men, age between 18–25 years, participated in this study. All participants signed an informed consent. Experimental trials were done in accordance with ethical principles laid down in the Helsinki Declaration. Stimulation electrodes (Ag-AgCl, 6 cm diameter) were placed over the right mastoid process and the mid-distance between the nasion and the mastoid process. Stimulation current intensity was set to the maximum tolerated by subjects (0.4–2.3 mA-rms). Stimulation (stim) parameters included sine, square and triangle waveforms of 0.3, 0.6 and 0.9 Hz. Subjects performed 10 trials of 25 s duration each: one control (no-stim) and one trial with each waveform and frequency selected (10 s pre-stim, 10 s stim, 5 s post-stim). COP displacement was recorded with a Wii Balance Board and a custom-made software [7, 8], in the mediolateral and anteroposterior axis. Calculations were made to estimate the RMS value of displacement. An ellipse was drawn including 95% of the points recorded in the cartesian plane of the stabilometric platform. Mean RMS value and mean area of the ellipse were compared among recordings with a Kruskal-Wallis one-way analysis of variance on ranks.

3 Results

Unilateral vestibular stimulation with a periodic stimulation signal produces larger COP oscillations than those recorded without stimulation. The frequency of this oscillation is notoriously different from that of natural COP movement during quiet stance (Fig. 1). Mean RMS displacement value and mean ellipse area obtained from recordings were compared statistically (n = 12). It was found that these stabilometric parameters decreased with increasing stimulation frequency, when using sine and square stimulation signal. The mean RMS and mean ellipse area increased compared to control (Table 1).

Table 1. Mean RMS and ellipse area in control and under GVS with various waveforms.

	Control	Sine 0.3 Hz	Sine 0.6 Hz	Sine 0.9 Hz	Square 0.3 Hz	Square 0.6 Hz	Square 0.9 Hz	Trian 0.3 Hz	Trian 0.6 Hz	Trian 0.9 Hz
RMS	0.84 ± 0.4	1.2 ± 0.9	1.1 ± 0.4	0.9 ± 0.2	1.3 ± 0.9	1.2 ± 0.7	1.1 ± 0.5	1.0 ± 0.2	0.9 ± 0.3	1.1 ± 0.9
Area	9.3 ± 6	15 ± 28	10.3 ± 8.7	7.3 ± 3.9	18.2 ± 3	14.5 ± 15	12 ± 9.2	8.8 ± 3.9	8.4 ± 5.5	9.5 ± 8.9

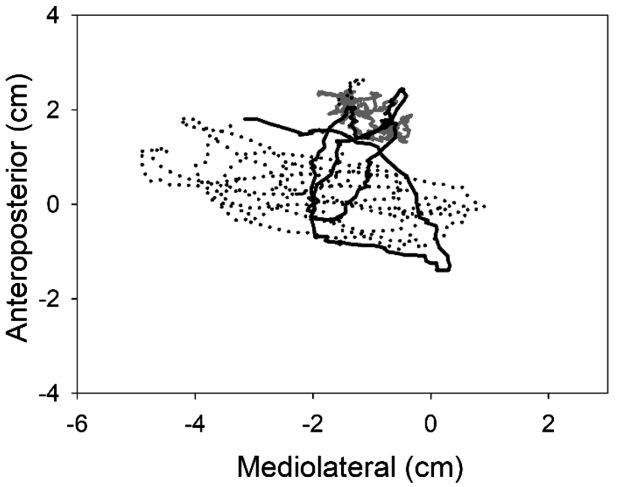

Fig. 1. Stabilometric recording with square 0.3 Hz frequency stimulation signal: Solid gray - no stim period (10 s), dotted - stim period (10 s), solid black – post-stim (5 s).

No significant changes were detected when using triangle stimulation signal compared to control (RMS value P = 0.89, ellipse area P = 0.943). The longest mean trajectory was provoked with sine stimulation of 0.3 Hz, followed by the trajectory length using square stimulation of 0.3 Hz (Fig. 2).

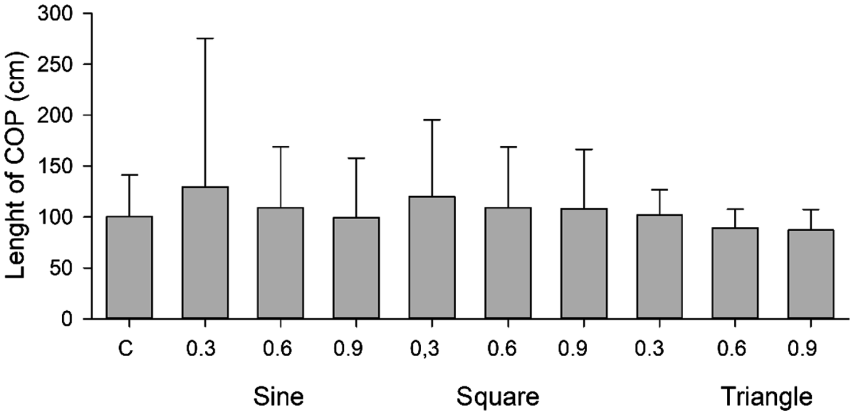

Fig. 2. Mean length of COP trajectory in control and under GVS with various waveforms.

Amplitude of spectral analysis increased for sine wave stimulation of 0.3 Hz in the mediolateral axis, and when using square 0.3 Hz stimulation, also in the mediolateral axis. The only peak frequency of COP displacement that was coherent with stimulation frequency occurred with sine 0.6 Hz stimulation signal in the mediolateral axis (Fig. 3).

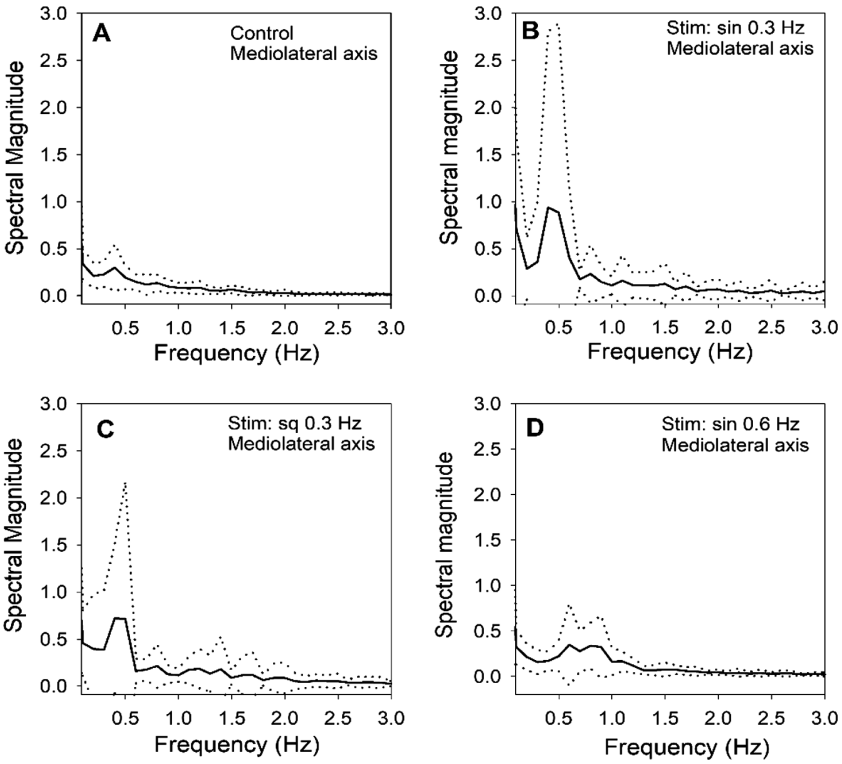

Fig. 3. Spectral analysis (mean) shows a magnitude increase around stimulation frequency for both sine and square stimulation waveform. A, spectral analysis of COP movement on the mediolateral axis, no stimulation was applied, peak frequency = 0.4 Hz. In this and following graphs solid line shows the mean power spectra and dotted lines standard deviation intervals. B, spectral analysis of COP movement on the mediolateral axis with sine stimulation signal of 0.3 Hz, peak frequency = 0.4 Hz. C, spectral analysis of COP movement on the mediolateral axis with square stimulation signal of 0.3 Hz, peak frequency 0.5 Hz. D, spectral analysis of COP movement on the mediolateral axis with sine stimulation signal of 0.6 Hz, peak frequency 0.6 Hz.

4 Discussion

This study was aimed to determine if unilateral GVS is capable to modulate posture. Also, if there is an optimal waveform that produces COP displacement following the frequency of the stimulation signal. Our results support observations reported in previous studies with transmastoid GVS and invasive methods where low frequency stimulation produces the largest response in ocular and postural movements. Vestibular implants (invasive vestibular prosthesis) use balanced bipolar square pulse train as stimulation signal directly applied to the ampulla of the semicircular canals, however, it is not clear if this waveform is the best suited to produce the desired response with the less collateral effects. Sine wave stimulation should not be dismissed for it produced a

similar displacement than that with square stimulation. Additionally, subjects' COP oscillation followed the stimulation frequency only for the sine stimulation waveform. Further studies should define if COP displacement is particularly sensible to a stimulation frequency in the range between 0.3 and 0.9 Hz using unilateral GVS.

5 Conclusion

Unilateral GVS produces postural displacement in tune with a periodic stimulation signal. Square and sine low frequency stimulation waveforms are more efficient causing displacement of the COP in humans. The amplitude of oscillations decreased with increasing frequency as observed with mean RMS displacement and the mean ellipse area calculated from mediolateral and anteroposterior stabilometric recordings. Results show that, in the design of a noninvasive unilateral vestibular prosthesis, it would be reasonable to include sine and square low frequency waveforms to modulate users' posture. In the future, the response evoked with unilateral GVS in a prosthetic device may contribute to improve balance loss in patients and in extreme conditions, such as microgravity [9].

References

1. Fitzpatrick, R.C., Day, B.L.: Probing the vestibular system with galvanic stimulation. J. Appl. Physiol. **96**(6), 2301–2316 (2004)
2. Matos Cunha, L.C., Campelo Tavares, M., Tierra Criollo, C.J., et al.: Contribution of galvanic vestibular stimulation for the diagnosis of htlv-1-associated myelopathy/tropical spastic paraparesis. J. Clin. Neurol. **4**, 252–528 (2013)
3. Gensberger, K.D., Kauffman, A.K., Dietrich, H., Branoner, F., et al.: Galvanic vestibular stimulation: cellular substrates and response patterns of neurons in the vestibulo-ocular network. J. Neurosci. **36**(35), 9097–9110 (2016)
4. Cohen, B., Martinelli, G.P., Xiang, Y., Raphan, R., Yakushin, S.B.: Vestibular activation habituates the vasovagal response in the rat. Front. Neurol. **8**, 83 (2017)
5. Eikema, D.J., Hatzitaki, V., Tzovaras, D., Papaxanthis, C.: Application of intermittent galvanic vestibular stimulation reveals age-related constraints in the multisensory reweighting of posture. Neurosci. Lett. **561**, 112–117 (2014)
6. Goel, R., Kofman, I., Jeevarajan, J., De Dios, Y., Cohen, H.S., Bloomberg, J.J., Mulavara, A. P.: Using low levels of stochastic vestibular stimulation to improve balance function. PLoS ONE **10**(8), e0136335 (2015)
7. Soto, E., Vega, R., Alexandrova, T., Alexandrov, V., Reyes, M., Pliego, A., Guerrero, W.: Vestibular Prosthesis. US8855774B2 (2014)
8. Soto, E., Vega, R., Salinas, E., Robles, P.: Posturographic system using a balance board Patent Office of the United States. US 2014/0081177 (2014)
9. Aleksandrov, V.V., Alexandrova, T.B., Bugrov, D.I., Lebedev, A.V., Lemak, S.S., Tikhonova, K.V., Reyes, R.M., Soto, E., Vega, R.: Mathematical modeling of output signal for the correction of the vestibular system inertial biosensors. In: IEEE Proceedings ISISS, pp. 109–112 (2014)

Leonardo Da Vinci, the Great Innovator in Cardiovascular Biomechanics

Ricardo Armentano[1,2,3(✉)]

[1] EMBS IEEE Technical Committee on Cardiopulmonary Systems, Buenos Aires, Argentina
armen@ieee.org
[2] I2C Grupo de Investigación en Ingeniería Cardiovascular, Montevideo, Uruguay
[3] GIBIO Grupo de Investigación y Desarrollo en Bioingeniería, Buenos Aires, Argentina

Abstract. Five hundred years after his death, the figure of Leonardo da Vinci continues transmitting his tireless desire to know and learn. *Leonardo* is the symbol of a century in which progress impacted, shattering the thickness of dogmas. In the *Quattrocento*, the doors were definitely opened, ideas spread and still feed us, clear our path and enlighten us. Florence, in Leonardo's time, was the Silicon Valley of the Renaissance. Leonardo studied the dynamics of water flow in rivers, using colors to show the flow patterns, thus defining the continuous stress on the side walls of the river. He determined, with different colors, the flow characteristics in the center and near the edges of the rivers and extrapolated those findings to the blood that flows in the arteries. Leonardo studied the coronary artery and veins, heart and bronchia in detail and made several assumptions about the cause of atherosclerosis, based on his previous hydrodynamic studies of water flow. Leonardo theorized that diseases were derived from some imperfection in the structure of the human body and addressed the issue of atherosclerosis and its correlation with aging. He accurately described a case of portal hypertension with liver cirrhosis as well as pulmonary circulation and chronic obstructive pulmonary disease. Leonardo was the great innovator in Biomechanics of the cardiovascular system: heart, lungs and circulation.

Keywords: Innovation · Biomechanics · Cardiovascular

1 Introduction

1.1 Brief History

Leonardo who was born on April 15, 1452 in his father's family property in An-chiano, in the small town of Vinci, embodied in the Renaissance atmosphere. He died in France in 1519 and was buried in the Château d'Amboise in the Loire Valley. The last three years of his life were spent in the service of the king of France, Francis I. Through his research and with the scarce resources available at that time, Leonardo anticipated and foresaw topical phenomena such as ecology, nuclear destruction, and the use of

© Springer Nature Switzerland AG 2020
C. A. González Díaz et al. (Eds.): CLAIB 2019, IFMBE Proceedings 75, pp. 975–981, 2020.
https://doi.org/10.1007/978-3-030-30648-9_127

sciences for war purposes [1]. His focus, imagination and power of observation have left their mark on modern engineering. His most precious legacy is not the 21 paintings or the almost 100,000 drawings and sketches he left, but his creation of a new way of thinking. On the other hand, his ability to interconnect diverse fields of knowledge, increasing their cognitive potential tenfold when interwoven, is a good example of "interdisciplinarity" (to use a modern expression) that constitutes a fundamental basis for the bioengineers of the present [1].

Leonardo embodied the Renaissance ideal of the multi-talented sage—painter, sculptor, narrator, musician, scientist, mathematician, architect, engineer—with an insatiable curiosity and thirst for knowledge. Through his research and with the scarce resources available at that time, Leonardo anticipated and foresaw topical phenomena such as ecology, nuclear destruction, the use of sciences for war purposes [1]. His focus, imagination and power of observation have left their mark on modern engineering [2].

1.2 Leonardo and His Prophecies

In his modest house of Florence, Leonardo lived in the shadow of the palaces' splendor. In the heart of the night, he imagined the distant world to come, posing hypotheses that would take science many centuries to verify, intuitions that surprise us due to their conceptual power and prophetical precision [3]. Water is "the blood of the Earth", he wrote, "the main and essential element of the cycle where all forms of life articulate". It is Leonardo who stated that "the man is made of earth, water, air and fire, like the earthly body" [4]. That the whole cellular metabolism is based on aqueous exchanges was a completely unthinkable idea at that time. He was the pioneer of ecologists! He sensed that the water cycle, both in our whole planet and in the essence of any living organism, must be based on an inalterable balance; otherwise, we run the risk of a disaster. He foresaw a world where this essential cycle of vital water would be altered. From his 16th-century Florence, Leonardo foresaw the polluted big cities of our time. He sensed the poisoning of the air, the nauseating and dangerous substances that kill the oceans. And the war… a terrible war, of flame and steel, a war he speaks of in terms of "rupture of the matter in the most intimate elements…" Was he foreseeing the division of the atom? [5].

1.3 Leonardo the Innovator

Leonardo's greatest innovation was taking well-established concepts and bringing them under direct verification of phenomena, always using his great capacity of observation, equipped with his extraordinary ability to transform what he saw in a graphic schematization of processes [5]. Leonardo laid the foundations of new experimental sciences; he stepped away from mere empirism to precepts of applied science which was apt for the general application in the industrial world. In this regard, he was the first modern engineer. Leonardo was less influential because his writings did not have enough diffusion and some were lost. What if Galileo and Kepler had met him? The more his legacy is studied, the more that prodigious dimension of the great Florentine is understood [2].

In those days, being an innovator was not as simple as it is today. At the beginning of the 1500's, Inquisition became more and more strict to counteract the new thoughts and ideas coming from Germany, where intolerance was growing against the power of Rome: an intolerance that a few years later brought about Martin Luther's thesis against indulgences presented in Wittenberg, which officially sparked the Protestant Reform. Probably, Leonardo was not allowed to publish all his work even though he could have had time and support to do it. In his notes, next to the drawings of the heart and blood circulation, he wrote: "…I could say more if I were allowed to…" William Hunter (1718–1783) could observe and study Leonardo's drawings and notes on anatomy [6]. He defined Leonardo as the best anatomist of his time and, probably, of all times. He tried, unsuccessfully, to publish Leonardo's work. The interest in Leonardo in modern times has fascinated and it is still fascinating. It is an indefinable attraction. Most people place this attraction in the many intuitions, discoveries and ideas he had, looking to future horizons. In some way, Leonardo da Vinci is out of this world, his strange genius directs him to all the fields of knowledge and works that today we would call "engineering". Very early, he reveals himself as a universal spirit, his view of the world is that of a visionary in the real world [3].

2 Results

Leonardo was authorized to dissect corpses in the Santa Maria Nuova Hospital in Florence [6]. His diaries' notes include detailed studies of the human skull, human fetus, a woman's internal organs, muscles, tendons, skeleton, cardiovascular system, etcetera. During the Middle Age, human dissections were rare because of many reasons, among them was religion and the fear of disease transmission. To all those facts, we must add the "Ecclesia Abhorret a Sanguine" bull (1163) and the Papal bull entitled "De Sepolturis" (1299), which practically forbade touching corpses after death [8].

2.1 Leonardo and the Arteries

He studied the flow dynamics of water in rivers [6], using colors to show the flow patterns, defining the continuous stress on the lateral walls of the river, "… the water continuously bounces against the riverbank… And as time passes by, the course of "the river gets more tortuous…" He determined, with different colors, the flow characteristics in the center and near the edges of the rivers and extrapolated those findings to the blood that flows in the arteries [8].

2.2 Leonardo and the Heart

Leonardo stated that the heart is a muscle that spontaneously contracts and that the aorta supplies blood, calories and energy across the body through the arterial blood that comes up to the skin through the capillaries. Leonardo studied the anatomy of the coronary artery and the veins in detail, concluding that the heart is self-feeding. He noticed that both atria contract when the ventricles dilate, which explains the transport of blood from the atria to the ventricles. The left atria and ventricle are larger than their

right counterparts. In parallel, he made several wax moulds of bulls' hearts and, based on those, he built glass models to study the hydraulic characteristics of the blood flowing through the heart and its valves, an in vitro circulation model to imitate human circulation. Seeds were used to visualize the turbulences and blood flow [8].

2.3 Leonardo and the Bronchial Tubes

He examined the bronchial tubes in detail including their smallest branches, noticing that each of them is accompanied by a small branch of the pulmonary artery. Therefore, he posed the hypothesis that the bronchial arteries receive *freshness* from the bronchial tubes, filled with air, and that the venous blood receives *freshness* from the lungs, before returning to the heart [8].

2.4 Leonardo and the Valves

Having a special interest in hydraulic engineering, Leonardo studied the anatomy of the cardiac valves which "… are covered by the endocardium in the top part and the muscles in the lower part…". He concluded that the 4 valves must open and close completely; otherwise, the heart will not work properly, with blood regurgitation in the atria from the ventricles.

At that time, diseases were considered a punishment from God by the public at large, and a humor imbalance by the experts, who closely followed Galen's theories. The most common remedy for most diseases, regardless of their nature, was continuous venous bleeding. Leonardo theorized that diseases were the result of some kind of imperfection in the human body structure [8].

2.5 Leonardo and Atherosclerosis

Leonardo made several assumptions about the cause of atherosclerosis, based on his previous hydrodynamic studies on water flow in rivers, speaking of "… the continuous stress on the arterial walls" and "… the lack of nutrition of the media of the artery, far from the blood that nurtures it." In 1505, Leonardo met a man at Santa Maria Nuova, in Florence, who was more than 100 years old. Leonardo wrote: "… this man was wise, happy despite his old age." "I performed an autopsy to understand the causes of this pacific death and discovered that it was caused by the weak blood flow and a failure in the artery that feeds the heart and the other limbs". He clarified the concept of atherosclerosis and its correlation with old age "when vessels get old, they lose the straightness in their branches and become more tortuous or winding and stiff…" and "… one [can] ask why the vessels in old people become quite long and those which were previously straight become tortuous, and their skin becomes thicker in order to occlude and prevent blood flow…". Leonardo also performed an autopsy of a 2-year-old boy and found that "… all the arteries are soft and straight… different from those of an old man…" [9].

2.6 Leonardo, Cirrhosis and Portal Hypertension

He accurately described a case of portal hypertension with liver cirrhosis, possibly in the same autopsy in which he accurately described arteriosclerosis, "… the artery and the vein which extend from the spleen to the liver become so big that they block the blood coming from the mesenteric vein; the latter vein dilates so much and becomes so tortous as a snake that the liver dries and becomes like frozen bran, both in color and consistency…" [9].

2.7 Leonardo, Pulmonary Circulation and Chronic Obstructive Pulmonary Disease

When Leonardo was painting a fresco at the Santa Maria Novella church, a middle-aged man was preparing colors for his frescos. The man, breathing the vapors of the colors, developed a severe chronic obstructive pulmonary disease, with severe restrictive lung disease and the associated dyspnea at rest. Leonardo asked the man to be the model for Saint Jerome in the desert. The painting shows Saint Jerome, who lived the life of a hermit in the desert, in great suffering. The muscles of the neck, chest and face are shown in the spasmodic contraction. When the man died, Leonardo performed the autopsy in order to understand the reasons behind such suffering. He found lung emphysema and noted down the possibility of correcting those alterations. Based on his engineering knowledge, he stated the hypothesis that the lungs were dilated because the air could not be properly expelled [9].

2.8 Leonardo and the Mechanics of Venous Circulation in the Lower Limb

Leonardo was interested in the venous circulation of the lower limbs. Varicose veins have been described since the old days, but Leonardo had the intuition of understanding the importance of muscle contraction in facilitating the return of venous blood. He described the presence of collaterals in the superficial and deep venous system in the lower limb. In Italian anatomy, the perforator group of veins around and right below the knee are connected by the so-called Leonardo's vein [9].

3 Conclusions

Leonardo moved slowly among the accepted theories that he learned in books, but they were adapted to his new ideas and based on his own experiments. He wrote: "the heart is a muscle which contracts spontaneously". He understood that the aorta supplies blood, calories and energy across the body through arterial blood which comes up to the skin through the capillaries. He examined the bronchial tubes in detail up to their smaller branches, noticing that each of them is accompanied by a small branch of the pulmonary artery [8]. Interestingly, following his collaboration with scientists from Pavia, a series of new theories on blood circulation were proposed in the university by

Realdo Colombo and Andrea Cisalpino. Those theories were then reinforced by Fabrizio Acquapendente in the nearby University of Padua and were almost kept in secret.

Willian Harvey, a young student at Cambridge, studied in Padua as an assistant of Fabrizio Acquapendente. He graduated in 1602, before returning to London. In 1628, William Harvey published Exercitatio anatomica de motus cordis et sanguinis, which constitutes the foundation of modern cardiovascular physiology. The concept of oxigenation was defined by Marcello Malpighi, professor of theoretical medicine at the University of Bologna, when he published, in 1661, De Pulmonibus, anatomical observations where he described the concepts of venous blood oxigenation in the lungs before returning to the heart, thus completing William Harvey's previous theory [8].

Leonardo was a man in continuous psychological agitation who tried to understand the world that surrounded him and, above all, to get an understanding of himself. His desire to understand human nature is confirmed by the efforts he made to correlate psychological conditions with alterations in the human body and vice versa. He analyzed the condition of the heart in many dissections, trying to correlate the person's psychology with the general condition of the body. Leonardo understood the influence of the overt and the hidden psychological factors in heart diseases. Sigmund Freud, the father of psychoanalysis, was the first person to understand this aspect of Leonardo and tried to define Leonardo's personality. Freud found himself lost in a sea of sensations in his efforts. Leonardo seems so simple, but impossible to define. Scientists, whether consciously or not, find his message that science and art can work together attractive [1]. He possesses the unstoppable strength of the freedom that a man should always seek to conquer, persistently maintaining the creative fervor and the fierce need to know, not to leave the world as it is, but to change it [7]. It was not easy for Leonardo to express his daring ideas freely in the tumultuous environment of the Italian Renaissance and therefore his life continues to be a big puzzle which has not yet been completed, with many things still to be discovered [4]. A high level of erudition would be required. There are thousands of brochures written from right to left, blueprints, sketches, diagrams, which sleep in several large libraries around the world. Nobody has dared to gather them and make a vast summary of this huge amount of pending material and one cannot stop wondering how a man, who is one of the world's greatest painters, was able to accumulate such amount in a single lifetime. It is possible that Leonardo, due to the oneiric dimension of his research, still surpasses us.

References

1. Isaacson, W.: Leonardo Da Vinci. Simon & Schuster, New York (2017)
2. Birkett, D.: Leonardo: artist & engineer. Eng. Technol. **11**(1), 68–71 (2016)
3. Bortolon, L.: The Life and Times of Leonardo. Paul Hamlin, London (1967)
4. Burckhardt, J.: The Civilization of Renaissance in Italy. Trans S.G.C, Middlemore, New Zealand (1878)
5. Burke, P.: The Italian Renaissance: Culture and Society in Italy. Princeton University Press, Princeton (1999)
6. Kirby, R., et al.: Engineering in History. Dover Publications Inc., New York (1990)

7. West, J.B.: Leonardo da Vinci: engineer, bioengineer, anatomist, and artist. Am. J. Physiol. Lung Cell. Mol. Physiol. **312**, L392–L397 (2017)
8. Sterpetti, A.: Cardiovascular research by Leonardo da Vinci (1452–1519). Circ. Res. **124**, 189–191 (2019)
9. Sterpetti, A.: Cardiovascular physio-pathology by Leonardo Da Vinci (1452–1519). Circ. Res. **124**(4), 472–474 (2019)

Biorobotics

Design and Development of 3D Printed Electromyographic Upper Limb Prosthesis

Osmar Vazquez[1], Mariel Alfaro-Ponce[2(✉)], Isaac Chairez[1], and Barbara Arteaga-Ballesteros[2]

[1] Instituto Politecnico Nacional, Unidad Profesional Interdisciplinaria de Biotecnologia, Mexico City, Mexico
[2] School of Engineering and Science, Tecnologico de Monterrey, Calle del Puente 222, Col. Ejidos de Huipulco Tlalpan, 14380 Mexico City, Mexico
marielalfa@gmail.com

Abstract. Three-dimensional printed prostheses have gain popularity due to their cost, customization capabilities and rapid prototyping, which allows researchers to implement over them various control and classification techniques that make them more functional for the users. This paper presents the design, construction and instrumentation of an electromyographic (EMG) active upper limb prosthesis, with a set of distributed PD controllers that ensures tracking of trajectories corresponding to different arm movements. The proposed rehabilitation device employs an artificial neural network to exert the classification of EMG signals which drive the activity of the prosthesis. The classifier defines the reference trajectories which must be tracked by the PD controllers. Finally, the complete integration of the system is presented, as well as the results obtained by each of its parts.

Keywords: Active upper limb prosthesis · Neural networks · Electrophisiological signal classifier · Three-dimensional printing

1 Introduction

In the field of prosthetic devices, three-dimensional printing (3DP) provides a low cost, affordable and reliable methodology to develop rehabilitation devices for those needing patients [10]. Among other advantages, the characteristics of materials employed in 3DP (polylactic acid or PLA and acrylonitrile butadiene styrene or ABS) result in strong rigid parts with longer durability [12].

As a result, 3DP prosthesis designs are available for general population at lower cost compared to conventional manufacturing options. Despite the evident benefits of providing 3DP prosthesis to patients, most of the existing designs are aimed to construct passive prosthesis with null or limited mobility. Generally, for the design of an active 3DP prosthesis, there are some developing requirements that should be taken into account. These requirements consider factors related to

© Springer Nature Switzerland AG 2020
C. A. González Díaz et al. (Eds.): CLAIB 2019, IFMBE Proceedings 75, pp. 985–992, 2020.
https://doi.org/10.1007/978-3-030-30648-9_128

the extremity to be replaced, such as kinematics, range of movement, amputation site, and some others. Once the medical issues appeared, electromechanical and constructions characteristics must be considered such as type of actuation and control strategies, number of joints, weight, materials and 3D printer limitations.

The upper limb (UL) is a structure of the human body that extend from the deltoid to the hand anatomical section. The hand is an important sensory tool, its opossable thumb allows the development of fine movements. In social interaction this part of the body plays an important role [1]. There are different levels of amputation of the UL, that can be classified as transcarpal, wrist disarticulation, transradial, elbow disarticulation, transhumeral, shoulder disarticulation and forequarter [4].

According to [11] there are three levels of 3D printed prostheses for the UL: hand, forearm and upper arm. In the specific case of active UL prostheses there are different types of control that can be electroencephalography (EEG); electromyography (EMG); voice controlled; flexing the thumb, wrist or elbow.

The active prosthesis presented in [6] was designed for transradial limb amputation patients, with the capability of movement in the 5 fingers and independent movement of the thumb. The prosthetic device presented in [13], is a low cost mechanical shoulder prosthetic, that assist the patient in the performance of bi-manual activities.

This work presents the design, construction and instrumentation of a 3DP UL transhumeral prosthesis implementing artificial neural networks (ANN) for EMG signals classification as part of the control for the different movements of the device. The paper is organized as follows; Sect. 2, describes the mechanical designs and parts of the ULP, Sect. 3 is the actuators and control algorithm selected for the ULP, Sect. 4 the proposed Neural Network and its performance, Sect. 5 are the results from all previous sections and Sect. 6 closes the study with some conclusions.

2 Mechanical Design

The mechanical proposal of the ULP was developed with computer-aided design (CAD) software. This part of the process included the degrees of freedom (DoF) selection (Fig. 1a), the prosthesis structure, the analysis of the materials (including the evaluation of mechanical stress, unitary displacements, torsional resistance), the class of actuators and sensors used in the prosthetic system and others.

The different sections of the ULP were modeled in SolidWorks. The entire ULP model was exported to Matlab to evaluate the controller efficiency. The ULP was divided into five main sections: phalanges, palm and wrist, thumb, forearm, elbow and distal humerus (Fig. 1b). The components of each section are described ahead:

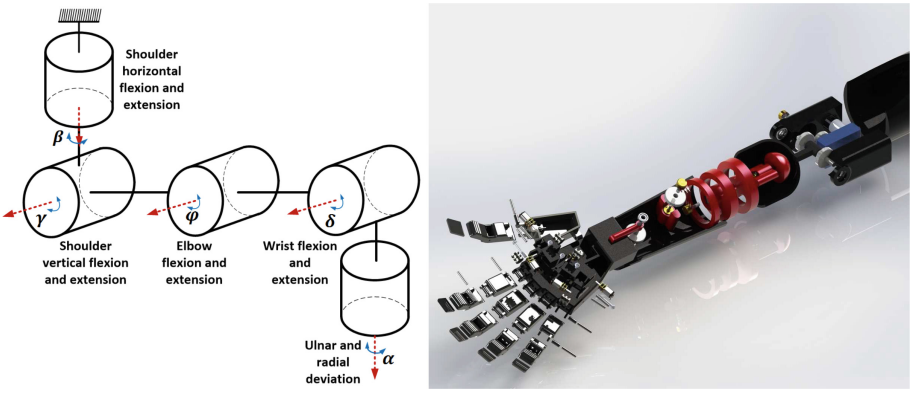

(a) (b)

Fig. 1. (a) Degrees of freedom in the ULP design, (b) Render of active ULP with full actuators

2.1 Phalanges Design

For the proximal and middle phalanges, a single piece with an inclination of 30° was designed. For the distal phalanx, an extra piece was created. For the assembly of the fingers, two steel cables functioned as hand ligaments. These cables exerted the agonist-antagonist structure.

2.2 Palm and Wrist Design

The palm and wrist are divided into: a main base carrying the joints corresponding to the distal part of the phalanges. This section also contains the proximal part of the wrist which is connected with the forearm. A second piece gives the direction to the threads that serve as tensor to generate the finger flexion and extension. A third piece allows fixing all the actuators, pulleys and feedback instrumentation (potentiometers) belonging to the control system. A lid covers the entire electromechanical system from the external elements (dust, wind, humidity, etc.).

2.3 Thumb Design

The factors to be considered for the design of the thumb were the angle of natural separation established between phalanges (20°). A mechanical rotational joint on the palm established the movement of 50° corresponding to flexion and metacarpophalangeal total extension. This articulation defines the clamp function with all the other phalanges.

2.4 Forearm Design

The part of the forearm is made up of two parts: the first is equivalent to the case of the distal and medial part of the forearm, and the section corresponding to the proximal part of the forearm. This section serves to exert the forearm pronation and supination movements (turn from 0 to 180°).

2.5 Elbow and Distal Humerus

This design considered that the elbow articulation can perform a movement from 0 to 150° over its own axis.

3 Instrumentation and Control

For proposed ULP, a Proportional Derivative (PD) controller was employed. A controller, in a system like the ULP, determines the action of the actuators based on the obtained error signal. In the case of a PD-type action controller, both the tracking error and its derivative forms part of the feedback design. This design considered the implementation of a robust and exact differentiator to recover the tracking error derivative. The actuators implemented for the ULP are described in Table 1. This table also summarizes the actuator used at each articulation.

Table 1. Actuator tech specifications for the different PODs.

Component	Quantity	Localization
Metal Gearmotor	3	Shoulder and Elbow
Micro Metal Gearmotor	1	Wrist
Micro Metal Gearmotor	1	Ulnar and Radial deviation
CTX2480 Gear Motor	1	Elbow
Pololu Metal Gearmotors	6	Finger
Pololu Metal Gearmotors	2	Wrist and forearm

Also for the implementation of the PD control, 2 PIC18F4550 that work in parallel were employed. The microcontrollers are responsible for receiving the NN output, measuring the position of the potentiometer, performing the control of the PD and moving the actuators according to the PD response.

4 Neural Network for EMG Classification

An ANN is a computational model inspired in the biological neuron an the way neurons are connected each others [8,9]. The main characteristics of ANNs

are their ability to reproduce complex nonlinear input-output relationships, and self-adaptation to the input data [3].

For the classification of the EMG signals, a multilayer neural network with a supervised backpropagation training was employed. For the purposes of this study, the used ANN can be found in the MATLAB Neural Networks Toolbox [2]. The inputs u injected into the ANN are the EMG signals, and in order to classify the signal once a pattern is fed to the ANN at the output layer the preponderated sum of the input of the j^{th} node is:

$$N_j = \sum \omega_{i,j} x_j + \omega_j \tag{1}$$

Here ω_j is the bias node weighted value with value of 1 and ω represented the weight matrix between two neurons, the value of ω was updated until the training process is over. This value is employed as activation potential for the artificial neuron mathematical function. The evaluation of these functions determined the neurons output. This value was also the one fed to the next layer of neurons as in the case of biological models. The typical activation function represented as sigmoid equation [5] (2) was considered in this study:

$$O_j = x_k = \frac{1}{1 + e^{-N_j}} \tag{2}$$

The following equations were employed for the calculation of the error and the weights updating at the output layer of the proposed ANN. First the difference between the output node O_k and the expected output t_k is calculated by

$$\Delta_k = t_k - O_k \tag{3}$$

And the error for the output layer is given by

$$\delta_k = (t_k - O_k) O_k (1 - O_k) \tag{4}$$

where $O_k(1-O_k)$ is the derivative of (2). The weights $\omega_{j,k}$ dynamics were driven by the error at node k multiplied by the activation node j

$$\Delta W_{j,k} = 1_r \delta_k X_k \tag{5}$$

Here $\Delta W_{j,k}$ is the learning rate. At the hidden layer, the local training error was given by

$$\delta_k = (t_k - O_k) O_k \sum (\omega_{j,k} - \delta_k) \tag{6}$$

In this case, the updating laws for the weights were

$$\Delta W_{j,k}^n = 1_r \delta_k X_k + \Delta W_{j,k}^{(n-1)} \mu \tag{7}$$

If the ANN was correctly trained, the global training error E should tend to zero with

$$E = \frac{1}{2} \sum \left(\sum (t_k - O_k)^2 \right) \tag{8}$$

The training process is repeated for each of the classes formin up the EMG signals database. At the end a parallel ANN is constructed in order to make the EMG classification process, forming a class of multi-binary classifier ensemble.

The training of the ANN used an annotated database of EMG signals. The database was taken from [7] in it you can find a complete description of the database. The database contains EMG signals taken from eight men and two women, with ages between 20 and 35 years. The data was recorded with a DE2x 2 EMG channels from Delsys, even though the database is made up of ten different classes. For this work, only four of the classes where employed. The selected classes describe the hand movements of Hand Close(HC), Thumb-Index (TI), Thumb (T), Thumb-Little (TL).

5 Results

5.1 Construction and Instrumentation

Figure 3b shows the physical model of the full ULP, including the electronic instrumentation. The full ULP have a total weight of 9.5 kg and a total size from the distal humerus to the phalanges of 71.7 cm.

The total weight of the device consider the full instrumentation of the system. To achieve the movement of the fingers cane thread was used, that worked as the ligaments in the human body, the hand open and close movement was controlled by the small motors located at the base of the palm.

5.2 Neural Network

The implemented NN had an accuracy of 95% for the classification of the 4 different movements of the hand. Figure 2A depicts an EMG signals made of 4 random EMG (HC, TI, T and TL) segments. Figure 2B, C and D the performance of the NN for the different signals.

Once the NN classified a signal, its output activates the desired trajectories used to exert the PD control.

5.3 PD Control

The ULP has variable resistors at all of its joints. The divided voltage obtained from the resistors provide the trajectory signals that are used for PD control. Figure 3a shows the signal that is obtained from the resistors and how the control works tracking the selected reference signal provided by the ANN classifier.

For testing the full system several trials were performed, where a random EMG signal was taken from the database, the signal as mentioned before correspond to one of the four possible movements. The signal is the entrance of the NN; the NN classifies it into one of the 4 possible trajectories that the complete system can perform.

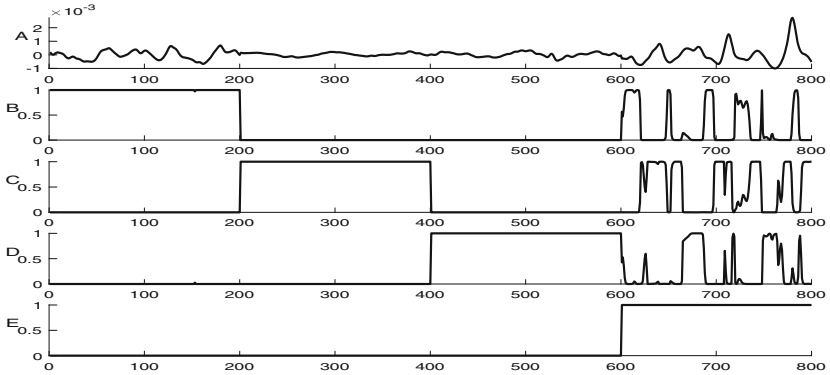

Fig. 2. Performance of the proposed ANN, in all of the signals the x axes show samples and the y axes the amplitude. (A) is a EMG test signal. (B) NN for HC, (C) NN for TI, (D) ANN for T, (E) NN for TL

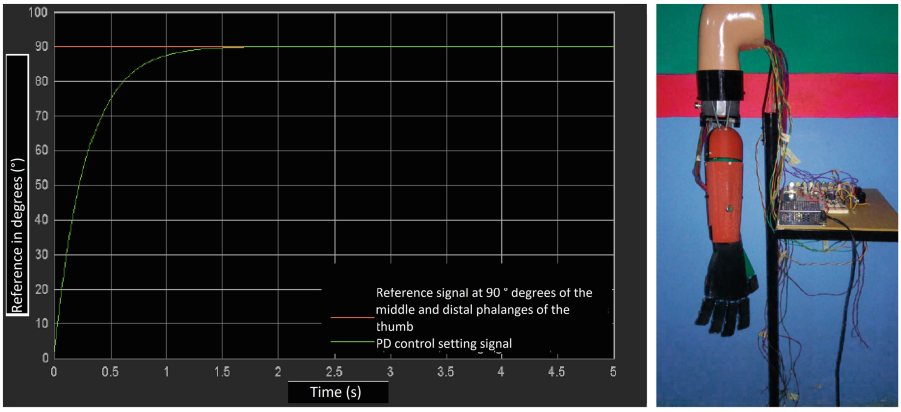

(a) (b)

Fig. 3. (a) Performance of the proposed control algorithm with the simulated trajectories, (b) 3D printed full instrumented ULP

Once the NN select the adequate trajectory, the PD control that is performed by the microcontrollers starts to work, the PD control employs the potentiometers placed in each joint of the ULP as references. Finally, the conjugation of each of the sections that make up this active ULP allows its correct functioning.

6 Conclusion

The 3D printing manufacturing process represents a way to develop accessible prosthesis for the general population. Even though there are other prosthetic devices that are developed with 3D printers, not many of them are active or integrated an EMG classifier for the selection of the movements of the device. This work demonstrated the general methodology for developing an ULP prototype, that works with a suitable NN classifier of 4 different EMG signals. The distributed PD control structure ensures the correct tracking of the reference trajectories selected by the ANN classifier. The integration of the different sections guaranteed the proper functioning of the proposed device.

References

1. Alpenfels, E.J.: The anthropology and social significance of the human hand. Artif. Limbs **2**(2), 4–21 (1955)
2. Câmara, D.: Bio-Inspired Networking. Elsevier (2015)
3. Canakci, A., Varol, T., Ozsahin, S.: Artificial neural network to predict the effect of heat treatment, reinforcement size, and volume fraction on alcumg alloy matrix composite properties fabricated by stir casting method. Int. J. Adv. Manuf. Technol. **78**(1–4), 305–317 (2015)
4. Cordella, F., Ciancio, A.L., Sacchetti, R., Davalli, A., Cutti, A.G., Guglielmelli, E., Zollo, L.: Literature review on needs of upper limb prosthesis users. Front. Neurosci. **10**, 209 (2016)
5. Cybenko, G.: Approximation by superpositions of a sigmoid function. Math. Control Signals Syst. **2**, 303–314 (1989)
6. Gretsch, K.F., Lather, H.D., Peddada, K.V., Deeken, C.R., Wall, L.B., Goldfarb, C.A.: Development of novel 3D-printed robotic prosthetic for transradial amputees. Prosthet. Orthot. Int. **40**(3), 400–403 (2016)
7. Khushaba, R., Kodagoda, S., Takruri, M., Dissanayake, G.: Toward improved control of prosthetic fingers using surface electromyogram (EMG) signals. Expert Syst. Appl. **39**, 10731–10738 (2012)
8. Liu, Y., Chuan Zhu, J., Cao, Y.: Modeling effects of alloying elements and heat treatment parameters on mechanical properties of hot die steel with backpropagation artificial neural network. J. Iron Steel Res. Int. **24**(12), 1254–1260 (2017)
9. Maren, A., Harston, C., Pap, R.: Handbook of Neural Computing Applications. Academic Press, Cambridge (2014)
10. Prince, D.: 3D printing: an industrial revolution. J. Electron. Resour. Med. Libr. **11**(1), 39–45 (2014)
11. ten Kate, J., Smit, G., Breedveld, P.: 3D-printed upper limb prostheses: a review. Disabil. Rehabil. Assistive Technol. **12**(3), 300–314 (2017). PMID: 28152642
12. Tymraka, B., Kreigerb, M., Pearce, J.: Mechanical properties of components fabricated with open-source 3-D printers under realistic environmental conditions. Mater. Design **58**, 242–246 (2014)
13. Zuniga, J.M., Carson, A.M., Peck, J.M., Kalina, T., Srivastava, R.M., Peck, K.: The development of a low-cost three-dimensional printed shoulder, arm, and hand prostheses for children. Prosthet. Orthot. Int. **41**(2), 205–209 (2017). PMID: 27117013

Prototype of a Surgical Robot with Contact Force Feedback

Misael Sánchez-Magos[1(✉)], Caridad Mireles-Pérez[2], Kenny Pérez[2], Francisco Medina[2], Mariana Ballesteros[2], David Cruz-Ortiz[2], Ivan Salgado[1], and Isaac Chairez[2]

[1] CIDETEC, Instituto Politécnico Nacional, Mexico City, Mexico
msanchezm1204@alumno.ipn.mx
[2] UPIBI, Instituto Politécnico Nacional, Mexico City, Mexico

Abstract. Surgical and medical robotics had become an interesting field of research joining disciplines such as biomedical engineering, mechatronics and automatic control. One of the main design issues of surgical robots is the interaction (contact force) between the end effector and the biological tissue. This manuscript presents the design, instrumentation and control of a surgical robot prototype (SRP) with two robotic arms of three degrees of freedom (DoF) attached to a cartesian robot, getting a total of five DoF per arm. The end effector consists of a robotic scalpel instrumented with force sensors to interact with the biological tissue resulting in more precise cuttings and avoiding, at the same time, damage of surrounding areas. An output-feedback proportional derivative hybrid controller is applied to track the trajectories aimed to realized precise cut. Simulations and experimental results show the performance of the SRP.

Keywords: Surgical robotics · Tissue-robot interaction · Hybrid control

1 Introduction

Medical robotics represent one of the fastest growing sectors in the medical devices industry due to they different applications. For example, surgery, therapy and home assistance [1]. Nowadays, the current surgical robotic devices exert tele-operation tasks allowing the surgeon to control all the movements realized by the robot, even though when the surgeon is not in the operation room [2]. These robots track the reference movements of the surgeon's hands. This process involves the implementation of a detailed and high-resolution interface, which guides the robot activity. Most medical robots are multi-body manipulators with a refined robotic scalpel (RS) as an end effector [3]. Since the beginning of this century, some RSs have contributed to develop efficient minimally invasive procedures in different medical disciplines. The most important advantages of the use of a surgical robot are: (1) reduced patient trauma and brief periods of

© Springer Nature Switzerland AG 2020
C. A. González Díaz et al. (Eds.): CLAIB 2019, IFMBE Proceedings 75, pp. 993–1001, 2020.
https://doi.org/10.1007/978-3-030-30648-9_129

hospitalization after surgery, (2) specific mechanical and instrumentation designs for maximizing the surgery performance, (3) superior spatial accuracy and lower vibration amplitudes of the instruments in contact with the patient, (4) artificial increment of the available degrees of freedom (DoF) compensating for spatial restriction of laparoscopic surgery and (5) the option to integrate either, force or torque measurement devices to *record* environment contact forces along the manipulation of the tissue [4,5].

Precise movements and robustness against external disturbances or uncertainties are desirable characteristics in new designs of RS. This characteristics yield in more complex robotic configurations, sophisticated instrumentation and the ability of exerting accurate movements when the end-effector interacts with the tissue [6,7]. Indeed, the ultimate goal of RS is to integrate reliable mechanical designs, electronic instrumentation, advanced digital signal processing and automatic controllers to extend the surgeons capabilities and, if necessary, to correct errors or to track some spatial points of interest and motions, as well as offering a realistic feedback to the user. The design of automatic controllers is still deserving interest from the practitioners and researchers because of the trade-off between performing a precise tracking of the reference movements induced by the surgeon and executing efficient force control when the scalpel interacts with the tissue. This aspect is of paramount importance due to the patient's safety, which is a primordial issue in the RSs performance [8,9].

The aforementioned issues constitute the main motivation to build a device that ensure the patient greater security when a RS interacts with it trough the surgeon. This manuscript proposes a surgical robotic prototype (SRP) with 11 DoF aimed to execute precise movements by means of an hybrid control algorithm that (a) drives the robotic arms to a desired position near to the patient with a proportional derivative (PD) scheme and a robust exact differentiator and (b) when the pressure sensor detects the tissue of interest, the control switches into a force feedback control to make the incision.

2 Desing of the SRP

The design of the robotic system was carried out in three sections: (A) the support platform, (B) the manipulator arm and (C) the final effector (see Fig. 1).

The support platform has two independently cartesian robots that holds each robotic arm. The platform was constructed using commercial aluminum channels, this structure has a base on which the biological tissue will be placed where the incision will be made.

Each robotic manipulator has three DoF and considers a modular structure. The design was made in a CAD software and they were manufactured in 3D-PLA-printing technique.

Figure 2 depicts the design of the end-effectors that contemplates the accomplishment of different tasks. The first one is a gripper designed to hold the sampled to be cut. The dimensions and design can be appreciated in the same figure. The second end-effector is designed to cut the biological tissue. The RS

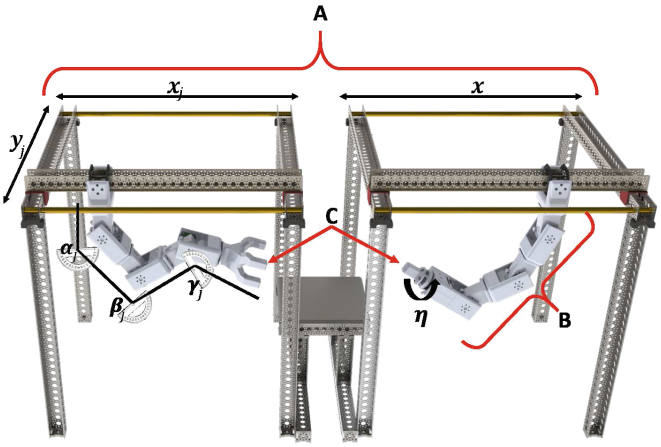

Fig. 1. Complete design of the surgical robot prototype, (A) support plataform, (B) the manipulator arm, (C) the final effector.

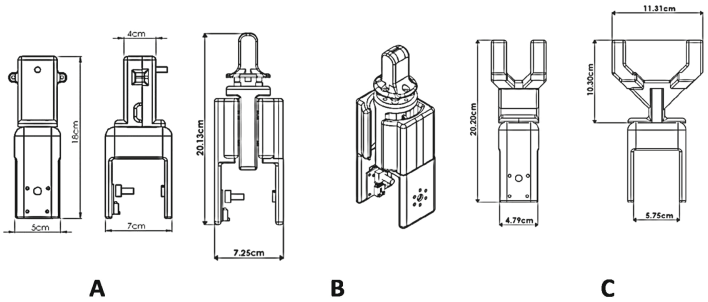

Fig. 2. Design of motor covers (A) and end-effectors (B, C)

design allows inversion to the patient tissue at any direction by using a mechanism with a 300° rotational configuration. This characteristic allows the SRP to make incisions in any direction. The RS has a mesh of force sensors to identify the contact with the biological tissue.

Table 1 shows the angular ranges of each Dof in the robotic arm as well as the distances covered by the cartesian robot.

3 Instrumentation

Figure 3 presents a block diagram describing the complete instrumentation details used in the SRP. The instrumentation is divided in two stages: the digital and the power ones, see in Fig. 3.

Table 1. Movement ranges.

Link	Angular range (deg)	Linear range (cm)
x	0	0–46
y	0	0–50
α	0–200	0
β	0–210	0
γ	0–220	0
η	0–300	0

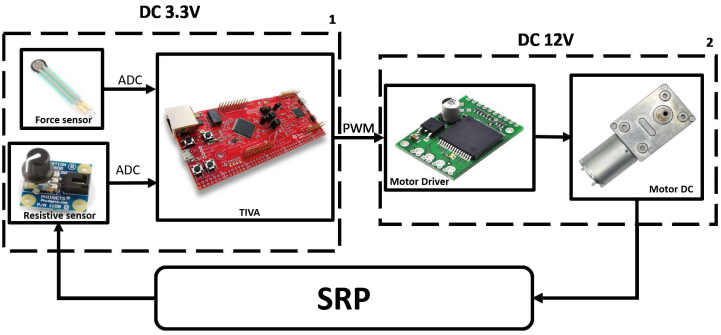

Fig. 3. General scheme of the electronic instrumentation

1. Two direct current (DC) motors actuate the cartesian robot. Optical distance sensors are used to obtain the actual position of the cartesian robot where the robotic manipulators are hold. A motor drive capable of managing a total current 12 amperes control the DC motors.
2. The robotic arms are actuated by DC motors with a transmission box at 90° and their position is gotten from rotational resistive sensors. Motors drivers managed the DC motors from a digital Pulse With Modulation (PWM) control.
3. The RS has a total of four pressure resistive sensors to formulate a mesh that describes the interaction of the RS with the patient. A DC motor actuates the movement of the RS in a range of 300°.

The digital instrumentation consists of two digital microcontrollers *TIVA C Series 1294* responsible for acquiring the physical measurements as well as to perform the robust control algorithms (described below) to manage the complete movements of the SRP.

4 Control

The control scheme satisfies a hybrid scheme: a position control and an admittance control. The switching function is obtained from the measurements in

the force sensors mesh allowing the surgeon to perform a precise cut without damage surrounding tissue. Figure 4 describes the complete control algorithm for the position stage. To solve the problem of tracking trajectories and force, proportional derivative (PD) controller with the derivative term obtained by a super-twisting algorithm (STA) is proposed as follows

$$u_i(t) = -k_{P_i} e_i(t) - k_{D_i} \delta_i(t), \qquad i = 1:11 \tag{1}$$

Where k_{P_i} and k_{D_i} are the proportional and derivative gains for each individual control acting each DoF. e_i is the tracking error for each joint and it is defined as $e_i = q_i - q_i^*$, where $q_i = [\alpha_j, \beta_j, \gamma_j, \eta, x_j, y_j]^\top$ is the real position, $j = [1, 2]$ and q_i^* is the reference position. The term δ_i is the estimated of the derivative of the tracking error in each joint obtained with the STA defined as

$$\begin{aligned} \delta_i(t) &= \beta_{2,i}(t) - \lambda_{1,i} |\beta_{1,i}(t) - e_i(t)|^{\frac{1}{2}} sign(\beta_{1,i}(t) - e_i(t)) \\ \dot{\beta}_{2,i}(t) &= -\lambda_{2,i} sign(\beta_{1,i}(t) - e_i(t)) \\ \dot{\beta}_{1,i}(t) &= \delta_i(t) \end{aligned} \tag{2}$$

Here $\delta_i(t)$ constitutes the output id the robust exact differentiator (RED). $\dot{\beta}_1(t)$ is the estimation of the error tracking $\lambda_{1,i} \in R^+$ and $\lambda_{2,i} \in R^+$ are the gains to ensure the convergence of the set of 11 differentiators.

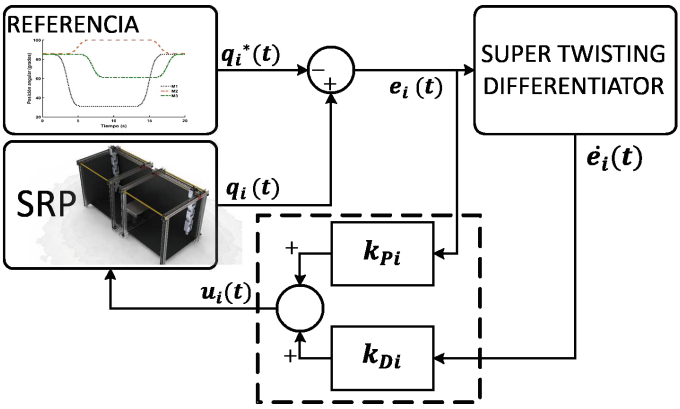

Fig. 4. Controller structure

Once the desired positions are reached, the second stage of the hybrid control starts, that is, the moment when the RS makes contact with the tissue, the force sensors activates the admittance control. That means, instead of follow a position reference, a force reference is switching and tracking to avoid the damage of surrounded tissue.

5 Results

Figure 5 depicts the final version of the SRP printed with the 3D technique and placed on the platform with the cartesian robot.

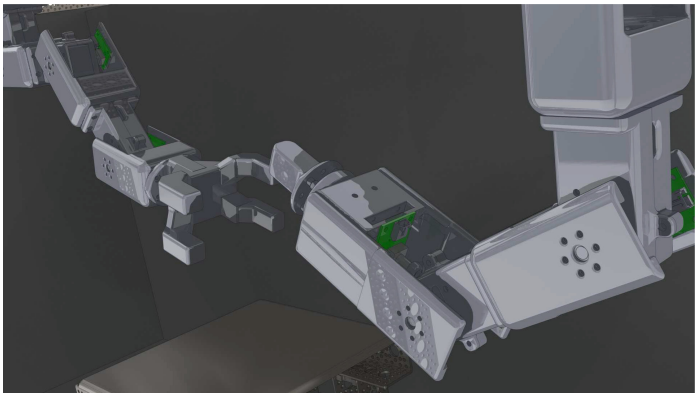

Fig. 5. Final construction of the SRP

There is a sub-platform in the workspace of the SPR when the sample is placed to execute the incision. Each real robotic arm is shown in Fig. 6. Subfigure 6a depicts the gripper to hold the sample. Subfigure 6b shows the RS mounted into the mesh of force sensors. Figure 7 shows the numerical simulation and experimental results. Simulation results Subfig. 7a were obtained from the SimMechanics® toolbox in Matlab® simulating 30 s with a fixed step of 0.1 ms. After 23 s arrives to the desired position to execute the incision on the biological tissue. Subfigure 7b shows the experimental results driving the SRP

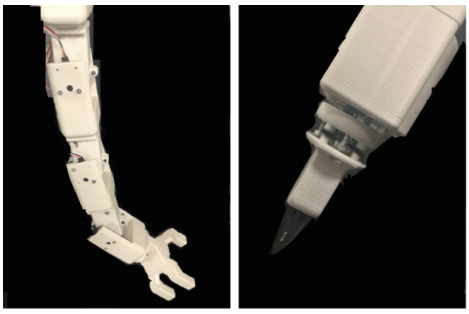

(a) Robotic manipulator (b) Robotic scalpel

Fig. 6. Real robotic system design

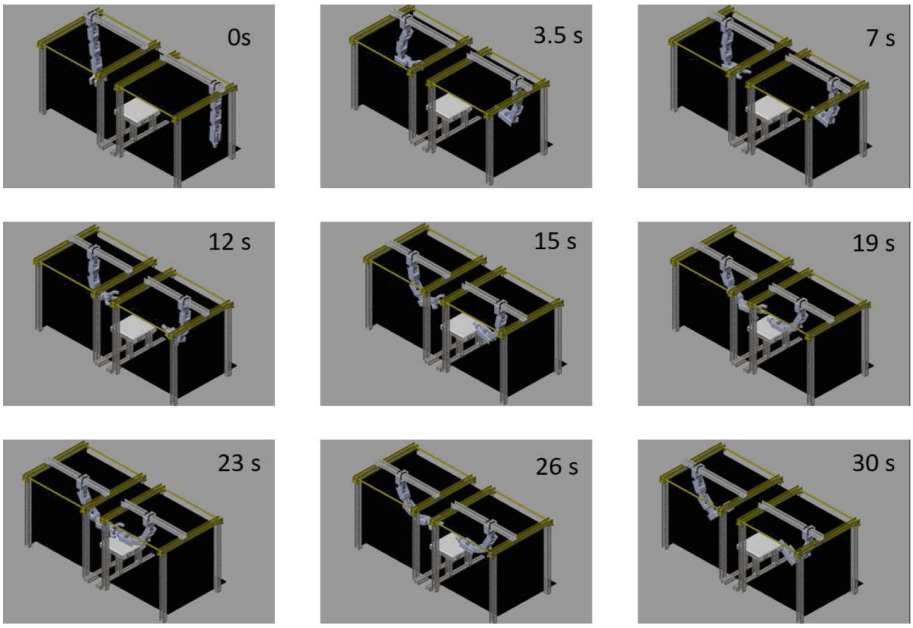

(a) Simulation secuence of robotic system

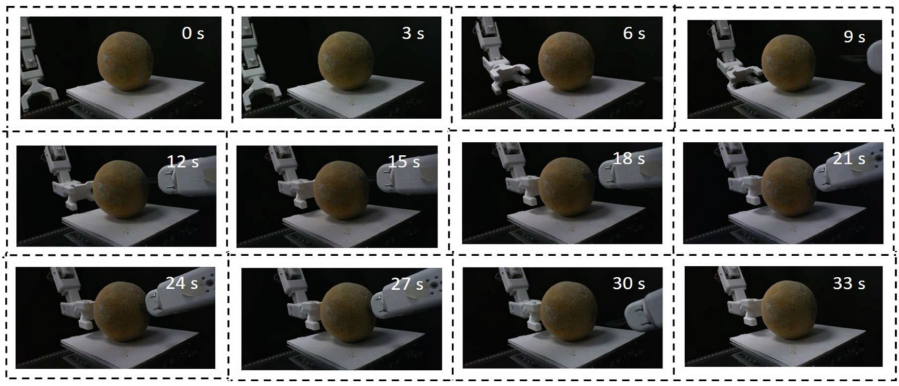

(b) Real tracking trayectory of robotic system

Fig. 7. Simulation and experimental results.

with the same trajectories as in simulation but making a closer view to the end effectors. In the first 15 s the robotic arm is positioned near the biological tissue selected as a *melon*. The measurements obtained in the pressure sensors triggers the admittance control to perform a precise cut on the fruit. Once the incision is finished (in the second 30), the robotic arms return to their initial position.

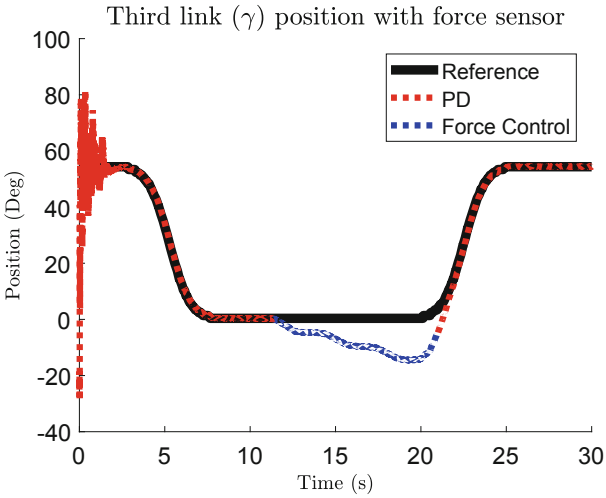

Fig. 8. Numeric simulation of the tracking trajectory with the force sensor

Finally, Fig. 8 describes the trajectories obtained in the position of the end effector. After twelve seconds, the RS makes contact with the biological tissue and changes into the admittance controller depicted by a blue continuous line. When the mesh of resistive force sensors detects a decrease in the measurement, near to zero, the control algorithm switch into the position control algorithm.

6 Conclusions

The developed SPR seems to be a preliminary solution to finally characterize the interaction between the RS an the patient. This first version accomplished the task of making precise incisions by means of an hybrid control scheme. The results showed how the switching threshold obtained with a mesh of resistive force sensors triggered an adequate sequence of control tasks alternating between a position control algorithm and an admittance control one.

The configuration design allowed to increase the work space using a pair of Cartesian robots and three DoF robotic arms. The track/error control problem was solved with a PD controller using the derivative provided by a set robust exact differentiators.

Conflict of Interest. The authors declare that they have no conflict of interest.

References

1. Guang-Zhong, Y., James, C., Kevin, C., et al.: Medical robotics-regulatory, ethical, and legal considerations for increasing levels of autonomy. Sci. Robot. **2**, 8638 (2017)
2. Kiaii, B., Douglas, B.W., Rayman, R., et al.: Robot-assisted computer enhanced closed-chest coronary surgery: preliminary experience using a Harmonic Scalpel® and ZEUS^{TM}. Heart Surg. Forum **3**, 194–197 (2000)
3. Tobias, O., Holger, W., Volkmar, F.: Design requirements for a new robot for minimally invasive surgery. Ind. Robot Int. J. **31**, 493–498 (2004)
4. Nabil, Z., Guillaume, M., Tobias, O., Nicolas, B.: Mechatronic design of a new robot for force control in minimally invasive surgery. IEEE/ASME Trans. Mechatron. **12**, 143–153 (2007)
5. Peter, K.: Safety design for medical robots. In: 2009 Annual International Conference of the IEEE Engineering in Medicine and Biology Society, IEEE, pp. 7208–7211 (2009)
6. Shi, P., Bin, C., Ye, Z., et al.: A soft tissue scalpel cutting robotic system with sucker fixation. In: 2018 IEEE 14th International Conference on Control and Automation (ICCA), IEEE, pp. 1162–1167 (2018)
7. Gregg-Smith, A., Mayol-Cuevas, W.W.: The design and evaluation of a cooperative handheld robot. In: 2015 IEEE International Conference on Robotics and Automation (ICRA), IEEE, pp. 1968–1975 (2015)
8. Opie, J., Jaiprakash, A., Ploderer, B., Crawford, R., Brereton, M., Roberts, J.: Understanding the challenges and needs of knee arthroscopy surgeons to inform the design of surgical robots. In: Proceedings of the 30th Australian Conference on Computer-Human Interaction, ACM, pp. 458–462 (2018)
9. Eduardo, D.C., Roemi, F., Manuel, A., Felipe, G.: A research review on clinical needs, technical requirements, and normativity in the design of surgical robots. Int. J. Med. Robot. Comput. Assist. Surg. **13**, e1801 (2017)

Proportional and Simultaneous Control Strategy for 3 DoF of Hand

J. Cuadros-Acosta, J. Perez-Guerra, V. Herrera-Ruiz, M. Garcia-Florez, and J. Murillo-Escobar(✉)

Instituto Tecnológico Metropolitano, GI2B, Medellín, Colombia
juanmurillo@itm.edu.co

Abstract. Amputation is a physical deficiency affecting indiscriminately the world population, representing a high cost for social security systems in health, in order to improve the life quality of amputees, is necessary obtain prosthesis that simulate the movement of the hand as naturally as possible. This paper, shows a methodology for the continuous and simultaneous control of 3 degrees of freedom (DoF) of the hand, for further applications on prostheses control. The position of the flexion/extension of the wrist (DoF1), Metacarpophalangeal (MCP) joint for tri-digital grasp (DoF2) and penta-digital grasp (DoF3) were estimated, based on surface Electromyography (sEMG) and Support Vector Regression (SVR), using time domain features widely applied in the processing of sEMG signals, like the Hudgin's feature set. Intersubject and Intrasubject model were assessed, finding that Intrasubjects models had the best performance with R^2 of 0.73, 0.49 and 0.51 for DoF1, DoF2 and DoF3, respectively. Our approach was able to estimate the target motion profile within **22.5**° with a low memory usage and minimum computational complexity.

Keywords: sEMG · Proportional control · Simultaneous control · SVR · Prosthesis control

1 Introduction

The United Nations in the Convention on the Rights of Persons with Disabilities of 2006 defines disability as "An evolving concept and that disability results from the interaction between people with disabilities and attitude and environmental barriers that hinders their participation full and effective in society on an equal basis with others" [1]. In 2008, there were around 10 million people threatened by an amputation [2]. In the United States, according to 2005 statistics, there were 1.6 million people with amputations, and it is estimated that by 2050 this number will double [3]. Amputations represent a high cost for social security systems in health, while a study of the International Labor Organization estimates that every year there is an economic loss of 4% of the global gross domestic product due to amputations [4].

© Springer Nature Switzerland AG 2020
C. A. González Díaz et al. (Eds.): CLAIB 2019, IFMBE Proceedings 75, pp. 1002–1011, 2020.
https://doi.org/10.1007/978-3-030-30648-9_130

There are three main approaches to enhance a prosthesis control. The on/off control, which is based on thresholds and allows to perform actions through a single surface Electromyography (sEMG) channel [5]. Secondly, the Pattern recognition method, consist in extracting features to classify between defined motion patterns [6]. These strategies are useful, although, they do not allow an adequate, dexterous and intuitive control by the user [7], thus, strength or final position of the prosthesis can not be accurate controlled, due to its restricted to pre-programmed motions. This is far from the capacity of the natural human hand skills [8]. In fact, a literature review shows that for a greater number of simultaneous patterns to recognize, the performance of the classifier decreases e.g., using the Ninapro database it is observed that with 52 movements the classification error increases to $20.3 \pm 6.9\%$ in contrast to using only three movements $7.5 \pm 7.2\%$ [9,10]. Currently, the trending strategy is the proportional control, in which the user can control at least one mechanical output of the prosthesis (e.g. force, velocity, position, or any function thereof) [11]. For this reason, the proportional control is a relevant strategy, owing to its capacity for achieving a dexterous hand control. However, the proportional control applied to upper limp control is in development stage and according to [5,12,13], there are no commercial prostheses based on this technology.

The aim of the present study is to assess a methodology for continuous and simultaneous control of 3 Degrees of Freedom (DoF) of the hand (flexion/extension of the wrist and metacarpophalangeal joint) based on sEMG and Support Vector Regression (SVR) with synthetic position signals, this mean use predefined movements with the goal to not employ any instrumentation to measure angles.

2 Materials and Methods

The proposed methodology is based in three stages: Data Acquisition, Characterization and Angle Estimation, Fig. 1, illustrated the flow chart.

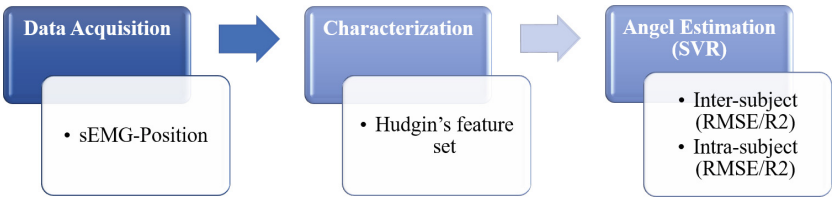

Fig. 1. Proposed methodology.

2.1 Data Acquisition

Eight able-bodied (7 male, 1 female; age range: 20–27 years) subjects participated, all right-handed with no history of neuromuscular disorders. Subjects

were required to perform dynamic motions associated with the extension/flexion of the wrist (DoF1), as well as two hand movements: tri-digital and penta-digital grasps. It is worth to mention, that thumb was not analyzed, because its movements have a high complexity, therefore, it was neutrally set in opposition to the remaining fingers. The DoF2 is the flexion of the MCP joint for index and middle finger, used to perform a tri- digital grasp, while, the DoF3 is flexion of the MCP joint of the ring and little finger, the simultaneous activation of DoF2 and DoF3 is a penta-digital grasp. Combinations of the wrist and hand motions were performed as well. An instructor guided the subjects to execute the five movements shown in Table 1. The shoulder was around neutral position and the elbow was flexed approximately $90^{c}irc$. Each motion was repeated 5 times.

Table 1. Motion profiles studied.

Motion ID	Description
M1	Wrist Flexion/Extension
M2	Tri-digital grasp
M3	Penta-digital grasp
M4	M1 + M2
M5	M1 + M3

During the execution of movements, sEMG signal was recorded using a wireless electromyography acquisition device (FreeEMG Wireless 4G, BTS Bioengineering Corp. Quincy, MA 02169 USA), six channels of sEMG were collected, positioning to acquire the upper limb sEMG signals for transradial prostheses [14]. The electrodes where placed proximal to the elbow joint at 1/3 of the forearm, specifically on the muscles flexor carpi ulnaris, palmaris longus, flexor carpi radialis, extensor digitorum longus, extensor carpi radialis longus and braquiorradialis. Muscles were identified according to the European Standards recommendation for sEMG placement [15]. The wireless bipolar sEMG electrodes, where placed on each muscle. The sampling rate of sEMG was set to 1 kHz with a 16 bit ADC resolution. Each channel was filtered using a 8^{th} Order Butterworth filter between 20 Hz and 400 Hz. The data transmission was based on the standard IEEE 802.15.4 for Wireless network. Regarding to the position, angle was not measure using any instrumentation equipment, instead, we create synthetic signals which correspond to the performed movements. These signals were generated based on literature reports on hand biomechanics [16], where maximum angles of each joint are establish. The execution time changes regarding to the movement (neutral position, reaching the maximum joint value and the combination of gestures) Fig. 2.

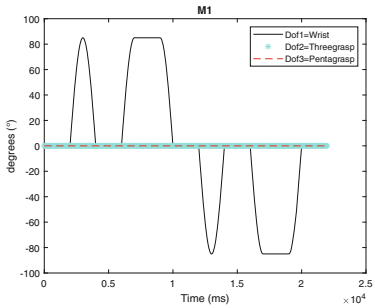

(a) M1

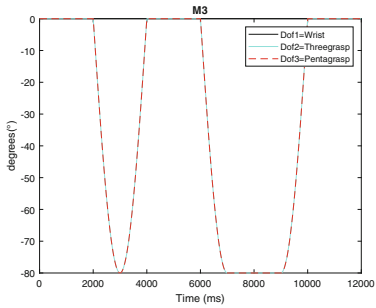

(b) M3

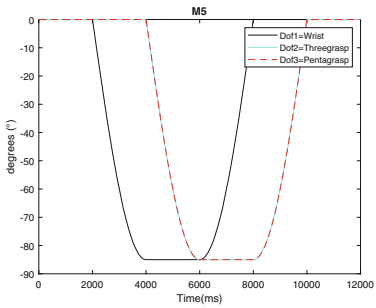

(c) M5

Fig. 2. Description of movements: M1 contemplates the movements of flexion and extension of the DoF1, in both gestures two cycles are made, and each cycle with a different time of execution. In M2 and M3 the same bending movement is done in M1, only with DoF2 and DoF3 respectively. M4 and M5 are gestures where the movement of the DoF1 and joint MCP is combined, M4 combines DoF1 flexion and DoF2 flexion, M5 combines DoF1 flexion and DoF3 clamp flexion.

2.2 sEMG Characterization

The literature reports several sEMG features, however, the most used and recommended is the time domain feature set proposed by Hudgins, due to its low computational cost, since no transformations to other domains are required [17]. Hudgins set includes Mean Absolute Value (MAV), Mean Absolute Value Slope, Zero Crossing (ZC), Slope Sign Changes (SSC) and Waveform Length. Another relevant features with extended usage in proportional and simultaneous control are Root Mean Square (RMS), Willison Amplitude (WA), Variance (VAR), Integrated EMG (IEMG) and Standard Deviation (SD) [18]. In this regard, we employed the features described in Table 2.

2.3 Angle Estimation

The angle estimation was conducted for every DoF using the SVR algorithm, in this context, for a given training data set $U = \{(x_1, y_1), (x_2, y_2), \cdots (x_n, y_n)\}$

Table 2. Computed sEMG features.

Feature	Formula
RMS	$\sqrt{\frac{1}{n}\sum_{i=1}^{n} x_i^2}$
VAR	$\frac{1}{n-1}\sum_{i=1}^{n} x_i^2$
WA	$\sum_{i=1}^{n-1} f\left(\lvert x_i - x_{i+1}\rvert\right)$
MAV	$\frac{1}{n}\sum_{i=1}^{n} \lvert x_i\rvert$
ZC	$\sum_{n=1}^{N} Z(x[n], x[n+1])$
SSC	$\sum_{i=2}^{N-1} f(x_i * x_{i+1})$
IEMG	$\sum_{i=1}^{N} \lvert x_i\rvert$
STD	$\sqrt{\frac{1}{n-1}\sum_{i=1}^{n} (x_i - \bar{x})^2}$

where y_i is the target value of an input vector x_i, the objective of SVR is to find a function that satisfies the expression $f(x_i) \approx y_i$ for all the training data. SVR uses an ϵ-insensitive loss function that constrains $f(x)$ to errors below ϵ [19]. Such a function can be obtain solving the following dual optimization problem:

$$\begin{gathered} \max -\frac{1}{2}\sum_{i,j=1}^{n}\left(\alpha_i - \alpha_i^*\right)\left(\alpha_j - \alpha_j^*\right)\Phi(x_i, x_j) \\ -\epsilon\sum_{i=1}^{n}\left(\alpha_i + \alpha_i^*\right) + \sum_{i=1}^{n} y_i\left(\alpha_i - \alpha_i^*\right) \\ \text{Subject to: } \begin{cases} \sum_{i=1}^{n}\left(\alpha_i - \alpha_i^*\right) = 0 \\ \alpha_i, \alpha_i^* \in [0, C] \end{cases} \end{gathered} \tag{1}$$

where α_i and α_i^* are Lagrange multipliers, $C > 0$ is the cost constant that control the trade-off between the model's complexity and the maximum level of deviation above ϵ. The Kernel function $\Phi(x_i, x_j)$ returns the dot product between the pairwise in a high-order dimensional space without explicitly mapping the data. We employ the Radial Basis Kernel, which function is $\Phi(x_i, x_j) = e^{\gamma\lvert x_i - x_j\rvert^2}$, where γ is a free parameter that controls the amplitude of the function.

Initially, we trained a SVR for each DoF and motion, then, we trained a SVR for each DoF combining all motions. Finally, we carried a comparison between Intrasubject and Intersubject models. Intrasubject make reference to train a model for each participant, while Intersubject reference to train a single model for all participants. Performance was assessed in therms of the correlation coefficient (R^2) and Root Mean Square Error (RMSE), computed as:

$$\text{RMSE} = \sqrt{\frac{1}{n}\sum_{i=1}^{n}\left(\hat{y}_i - y_i\right)} \qquad \text{R2} = 1 - \frac{\sum_{i=1}^{n}(y_i - \hat{y}_i)^2}{\sum_{i=1}^{n}(y_i - \bar{y})^2} \tag{2}$$

where y_i is the actual angle, $\hat{y}_i$ is the estimated angle and $\bar{y}$ the corresponding to mean of actual angle, calculated in (i = 1 ,2, 3, ..., n).

3 Results and Discussion

In order to characterize the sEMG features, we computed 8 features (RMS, VAR, WA, MAV, ZC, SSC, IEMG and STD) for the 6 acquired channels, obtained a total set of 48 features.

In order to estimate the angle for the 3 Assessed DoFs, we employed a SVR algorithm, trained models for Intrasubject and Intersubject comparison, as well for every motion and its combination.

Table 3 contains the performance for the Intersubject models for all the motions, finding that for DoF1, the best performance is reached using the Combined model, while for DoF2 and DoF3 is reached in the model for M5 motion.

Table 3. Intersubject performance.

Movement	DoF1		DoF2		DoF3	
	R2	RMSE	R2	RMSE	R2	RMSE
M1	0.54	34.51	–	–	–	–
M2	–	–	0.25	31.41	–	–
M3	–	–	0.33	29.63	0.33	29.63
M4	0.66	21.83	0.36	31.16	–	–
M5	0.67	20.67	0.55	26.01	0.55	26.01
Combined	0.73	21.63	0.49	33.81	0.51	16.29

Table 4, shows the performance for DoFs angle estimation using Intrasubjects models. Unlike DoF1 for Intersubject models, the best performance was reached for M4 motion. For DoF2 and DoF3, the best performance was obtained for M5 motion.

Table 4. Intrasubject performance.

Movement	DoF1		DoF2		DoF3	
	R2	RMSE	R2	RMSE	R2	RMSE
M1	0.76	33.44	–	–	–	–
M2	–	–	0.53	30.74	–	–
M3	–	–	0.57	29.88	0.57	29.88
M4	0.85	19.34	0.66	29.28	–	–
M5	0.84	19.57	0.75	25.46	0.75	25.46
Combined	0.78	19.95	0.56	31.56	0.58	16.08

Comparing the performance of Intrasubject and Intersubject models, it can be seen that Intersubject model overperforms, for all evaluated motions. This suggest that this control should be trained for each user.

Despite the best performance was reached for M4 and M5 (Intrasubject Model), combined motion represent the most realistic scenario for proportional and simultaneous control of a prosthetic hand, given that during the usage of a prosthesis is not necessary to define a control mode. For this reason, we graphically assessed the quality of the estimated angles using combined motions, Fig. 3 shows the actual and estimated angle for the 3 DoFs during M5. It can be appreciated that estimation for DoF1 is accurate, while for DoF2 and DoF3, is necessary improve the quality of the estimations, this is reflected in the R^2, that is above of 0.6 for DoF2 and DoF3, while for DoF1 almost reach 0.8.

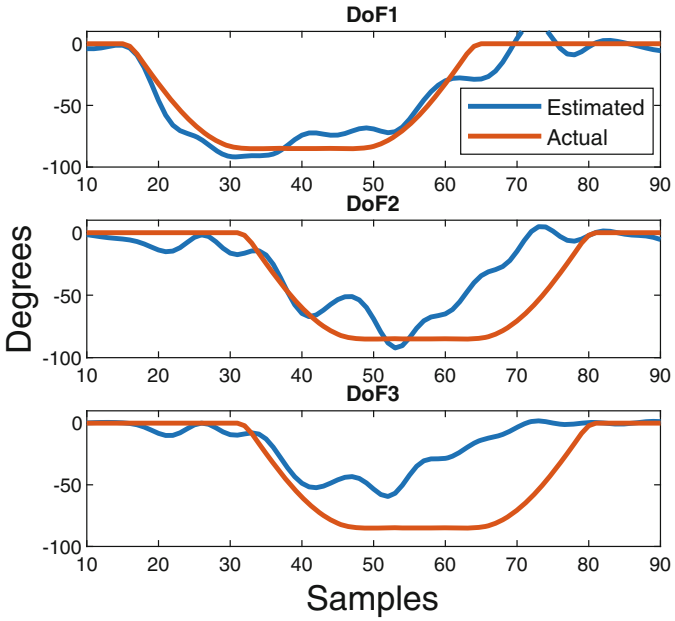

Fig. 3. Estimated angle using Intrasubject models and combined motions for M5.

Despite of the difficult to establish a direct comparison with other works, due to physical magnitude (e.g. angle, force or speed) and the same motion, Table 5 shows the performance reported in others studies in the same topic for the assessed DoFs. Our results are comparable for the 3 DoFs, overperforming several approaches like Artificial Neural Networks (ANN), Kernel Ridge Regression (KRR) and Support Vector Regression (SVR). In DoF1, we obtain R2 values over 0.84 for M4 and M5, which is above of the values reported in literature [18,20], while for Combined motions the R2 (0.78) is only 0.01 below of another SVR study [8]. In other hand, the mean R2 for DoF2 and DoF3 (0.62) is below of the performance reported in literature [21,22].

Despite of using synthetic signals to generate position labels, the results are comparable with those reported in the state of the art, so our research provides

a valuable contribution to the literature, demonstrating that the proposed strategy, can be used to train prosthetic controls without using any equipment to measure angles.

Table 5. Reported performance for studied joints.

Joint	R2	RMSE	Method	Studies
DoF1	0.66	18.25	ANN	[18,20]
	0.83	14.90	KRR	[18]
	0.79	–	SVR	[8]
DoF2-DoF3	0.71	–	ANN	[22]
	0.79	–	KRR	[21]

4 Conclusion

This application of proportional and simultaneous control based on sEMG and SVR was able to estimate the target motion profile within 22.5°. The synthetic labeling approach, showed that is possible to obtain performance comparable with current literature, without the need of specialized equipment to measure hand kinematics. Furthermore, the proposed methodology has a low memory usage and minimum computational complexity, which is quite convenient. DoF2 presented the lower performance, which could be attributed to lower activation of the muscle fibers responsible for movement, obtaining lower action potentials compared to DoF1. Besides, our study provides a benchmark for the angle estimation of the 3 DoFs. Further evaluation of our results with amputee subjects and real-time control are required to establish the clinical applications. However, to improve the performance, it is necessary to use goniometers or inertial sensors for measuring the angle in order to decrease the uncertainty of the results.

Conflict of Interest. Authors state there is not any conflict of interest. As well, not animals or humans were not hurt in the development of this work.

References

1. United Nations: Convention on the Rights of Persons with Disabilities. Eur. J, Health Law (2007)
2. Leblanc, M.: "Give Hope - Give a Hand" - The LN-4 Prosthetic Hand (2015)
3. Ziegler-Graham, K., Mackenzie, E.J., Ephraim, P.L., Travison, T.G., Brookmeyer, R.: Estimating the prevalence of limb loss in the United States: 2005 to 2050. Arch. Phys. Med. Rehabil. **89**(3), 422–429 (2008)

4. Isabel, A.B., Margarita, A., Pérez-garcía, C.: Costos directos e indirectos por amputaciones en mano derivadas de accidentes de trabajo **48**(4), 367–375 (2010)
5. Roche, A.D., Rehbaum, H., Farina, D., Aszmann, O.C.: Prosthetic myoelectric control strategies: a clinical perspective. Curr. Surg. Rep. **2**(3), 44 (2014). https://doi.org/10.1007/s40137-013-0044-8
6. Scheme, E., Englehart, K.: Electromyogram pattern recognition for control of powered upper-limb prostheses: state of the art and challenges for clinical use. J. Rehabil. Res. Dev. **48**(6), 643 (2011). http://www.rehab.research.va.gov/jour/11/486/pdf/scheme486.pdf
7. Jiang, N., Lorrain, T., Farina, D.: A state-based, proportional myoelectric control method: online validation and comparison with the clinical state-of-the-art. J. Neuroeng. Rehabil. **11**, 110 (2014)
8. Li, S., Chen, X., Sheng, X., Zhu, X.: Preliminary study on proportional and simultaneous estimation of hand posture using surface EMG based on synergy concept. In: EMBS, pp. 6199–6202 (2013)
9. Atzori, M., Gijsberts, A., Heynen, S., Hager, A.g.M., Deriaz, O., Smagt, P.V.D., Castellini, C., Caputo, B., Henning, M.: Building the N INAPRO Database: A Resource for the Biorobotics Community (Section II) (2012)
10. Atzori, M., Gijsberts, A., Castellini, C., Caputo, B., Hager, A.G.M., Elsig, S., Giatsidis, G., Bassetto, F., Müller, H.: Electromyography data for non-invasive naturally-controlled robotic hand prostheses. Sci. Data **1**, 1–13 (2014)
11. Fougner, A.L., Stavdahl, Ø., Kyberd, P.J.: System training and assessment in simultaneous proportional myoelectric prosthesis control. J. NeuroEng. Rehabil. **11**(1), 1–13 (2014)
12. Yang, D., Gu, Y., Thakor, N.V., Liu, H.: Improving the functionality, robustness, and adaptability of myoelectric control for dexterous motion restoration. Exp. Brain Res. (2018)
13. Iqbal, N.V., Subramaniam, K.: A review on upper-limb myoelectric prosthetic control. IETE J. Res. **2063**, 1–13 (2017)
14. Atoufi, B.: Toward proportional control of myoelectric prostheses with muscle synergies. J. Med. Biol. Eng. **34**(5), 475 (2014)
15. Stegeman, D., Hermens, H.: Standards for surface electromyography: the european project surface emg for non-invasive assessment of muscles (SENIAM). Roessingh Research and Development, Enschede, pp. 108–112 (2007)
16. Teresa, M., Carrere, A., Álvarez, A., Peñaranda, Y.F.: Biomecánica clínica Biomecánica de la Extremidad Superior Exploración de la Mano **3**(4), 1–21 (2011)
17. Hudgins, B., Parker, P., Scott, R.N.: A new strategy for multifunction myoelectric control. IEEE Trans. Biomed. Eng. **40**(1), 82–94 (1993)
18. Bakshi, K., Manjunatha, M., Kumar, C.S.: Estimation of continuous and constraint-free 3 DoF wrist movements from surface electromyogram signal using kernel recursive least square tracker. Biomed. Signal Process. Control **46**, 104–115 (2018). https://doi.org/10.1016/j.bspc.2018.06.012
19. Murillo-Escobar, J., Sepulveda-Suescun, J., Correa, M., Orrego-Metaute, D.: Forecasting concentrations of air pollutants using support vector regression improved with particle swarm optimization: case study in aburrá valley, colombia. Urban Clim. **29**, 100473 (2019)
20. Sebelius, F., Eriksson, L., Balkenius, C., Laurell, T.: Myoelectric control of a computer animated hand: a new concept based on the combined use of a tree-structured artificial neural network and a data glove. J. Med. Eng. Technol. **30**(1), 2–10 (2006)

21. Krasoulis, A., Vijayakumar, S., Nazarpour, K.: Evaluation of regression methods for the continuous decoding of finger movement from surface EMG and accelerometry. In: EMBS 2015-July (May 2016), pp. 631–634 (2015)
22. Ngeo, J.G., Tamei, T., Shibata, T.: Continuous and simultaneous estimation of finger kinematics using inputs from an EMG-to-muscle activation model. J. NeuroEng. Rehabil. **11**(1), 122 (2014)

Biopsy Robot Design for Breast Cancer Identification

Joav Madrid(✉), Tatiana Álvarez, and Ángel Luis Rodriguez

Centro de Física Aplicada y Tecnología Avanzada,
Universidad Nacional Autónoma de México, 76230 Mexico City, QRO, Mexico
j.madrid.ayala@outlook.com,
talvarez.alvarado@outlook.com,
alrodriguez@fata.unam.mx

Abstract. Nowadays breast cancer is one of the main problems that affect women worldwide. In Mexico, this disease is considered the second cause of death of productive age women, and the first cause of death worldwide. This death rate, as well as the incidence, have been ascending in the last years; however, the correct interpretation of test analysis could play a key part in the process. Biopsy procedures are successful only for 78% of cases, which leaves 22% of patients in danger of receiving wrong diagnoses which include false negatives, leading towards late treatment and therefore fewer survival possibilities. This project aims to increase the successful biopsy results by implementing the usage of biomedical robotics. The development consists of a Delta type robot, equipped with infrared sensors for cancerous breast pathology localization, trucut type biopsy needle, thermal image projection, artificial intelligence for optimum trajectory and positioning over the patient. This equipment offers a live detection with infrared technology and a precise incision controlled by the health professional. Therefore, this system offers a more accurate precision reaching the tumour, achieving a better extirpation of suspicious tissue for histopathological analysis, reducing the number of false negatives and, therefore, acting directly over the death rate.

Keywords: Breast cancer · Robotics · Biopsy · Thermography

1 Introduction

Breast cancer is a disease that affects mainly women worldwide; it has been increasing in both incidence and mortality mostly in Middle- and Low-income countries. Each year there are 1,38 million of new cases and 458 000 deaths by breast cancer worldwide [1]. A correct diagnosis is crucial for a patient's treatment. However, when it comes to biopsy, human error, as well as tumor size, lead to a 22% of erroneous identification including false negatives [2]. In these cases, the patient is unable to be treated opportunely and therefore increasing the risk of unsuccessful treatment. For this problematic biomedical engineering can develop a solution. In this work, we will show a Delta type robot for a more accurate biopsy procedure, that includes thermal detection technology as well as a precision control for more accurate sampling.

© Springer Nature Switzerland AG 2020
C. A. González Díaz et al. (Eds.): CLAIB 2019, IFMBE Proceedings 75, pp. 1012–1022, 2020.
https://doi.org/10.1007/978-3-030-30648-9_131

2 Background

2.1 Breast Cancer

In the last years, breast cancer has increased within the population, expanding the age range in which it is detected. This type of cancer is known to appear at two main locations. The most common type is ductal carcinoma which develops in the milk ducts that connect the lobules with the excretory milk valve in the nipple. The other location for breast cancer is in the lobules, called lobular carcinoma. This type of cancer can be classified by its biological activity in in-situ or infiltrating.

2.2 Panorama

The increase of breast cancer patients urges for an early and accurate diagnosis, therefore a screening with image-based technology such as mammography or ultrasound is recommended. If there is a finding during screening it may be required to extract a sample to give the accurate diagnosis. The finding will be categorized by the BI-RADS (Breast Image Report and Data System) provided by the ACR (American College of Radiology). It's been reported that near 78% of the biopsies performed were successful. However, the rest were procedures on which the tumor was not penetrated, causing the consequent tumor volumetric increase due to the lack of timely treatment [2].

2.3 Biopsy

A biopsy is a procedure in which a sample tissue is extracted for a histopathological analysis. It is an invasive procedure as it penetrates the patient's skin and obtain one or several samples [3]. Biopsies can be made manually or robotically assisted. The National Comprehensive Cancer Network (NCCN) recommends the practice of a core needle biopsy rather than a surgical incision when a histopathological analysis is needed [4]. There are three different types of biopsies. The core needle biopsy, or trucut, is based on a two steps needle in which the inner needle that has a cavity in its structure, enters first into the tumor and then the secondary needle covers the first one, making a precise internal cut [2]. Another type of biopsy, not recommended by the NCCN given the aggressiveness of its procedure, is the aspiration biopsy that uses a vacuum-like needle that extracts tissue from inside the tumor [5]. The third type is the most common technic, but limited to size and location of the target, is the surgical biopsy where a surgeon removes a tissue sample [3].

2.4 Medical Robotics

Due to the inaccuracy of biopsy procedures the development of a robotic assistant was made. There are other medical robotic developments that have proven to be helpful in medical procedures, however none of them are designed for a biopsy procedure. The FDA approved in 2000 the use of Da Vinci's robot as a method for performing microsurgeries, since then, robotic assistance in minimum invasive surgeries and low-risk procedures has been increasing. There are around 4000 Da Vinci´s stations around

the world, with near 750,000 operations performed per year. Besides, the ZEUZ robot was also approved as a computer motion surgeon assistant. All the approved robots follow the master-slave teleoperation, limited to a same room environment, including the surgeon console and the robot, even though a transatlantic surgery experiment has been successfully achieved [6].

Currently, robotic assisted surgery stands as top of the line in terms of precision, recovery time and minimum invasiveness. Even though the Da Vinci system is the most famous, there are other robotic systems in development, such as SurgyScope for neurosurgery at Humboldt University, Berlin; or the Stereotactic system for breast biopsies which is an ad-on for Mammography systems, currently found in hospitals.

Specialized robots for breast biopsies are currently under develop in order to satisfies the deficiencies the stereotactic method has, such as limited axis approach or changing position once the original is lost due a patient involuntary movement. The robot here presented will cover this gap at the medical and robotics overlap. One of the main advantages of this is the thermal imaging which can identify the lesion position helping the operator to identify accurately the area of incision and therefore perform a better sampling. This will improve the biopsies with better accuracy than the current methods, the directed purpose of this robot will make a specialized contribution to medical robotics.

2.5 Thermal Imaging

Thermal image used as a screening technique has proven its efficiency in recent investigations at Centro de Física Aplicada y Tecnología Avanzada (CFATA), which is a facility for scientific and high-tech research at Universidad Nacional Autónoma de Mexico (UNAM), with more than 15,000 analyzed patients [7].

Cancerous cell's growth is rapid and uncontrolled, deriving in an accelerated metabolism causing a substantial thermal increase. This technic consists of identifying zones with high-temperature contrast that are characteristic of patients with cancerous cells growth. By using this technic, it is possible to have a real-time approach to the feasible cancerous region and being able to perform a biopsy [8].

3 Materials and Methods

3.1 Design Specifications

The design of the system is composed of four main blocks, the stretcher for patient positioning; the robot; the control and instrumentation for infrared analysis. The specifications of the robot and infrared systems are (Tables 1 and 2):

Table 1. Robot specifications

Specification	Measure
Precision	0.001 m
Accuracy	5%
Repeatability	0.01/100
Force control	Punctual over z
Applied force	10 kgf
Maximum allowed oscillation	0.2 Hz
Workspace volume	2L
Materials for sterilization	Titanium/INOX steel

Table 2. Infrared sensor

Specification	Measure
Wavelength	540 nm
Opening cone	3.8 mm
Sensibility	1.2×1.2 mm^2
Bandwidth	1 Hz
Source	5 V
Data acquisition card (10 MHz)	NI USB 6009

3.2 Conceptual Design

Given the specifications and the system's complexity it is required the elements to be designed in a modular way. Generating a design proposal for each of the main features of the system. The positioning of the patient shown in Fig. 1, the spatial location of the needle as the effector of the robot, the manual control, and the infrared identification system are addressed individually.

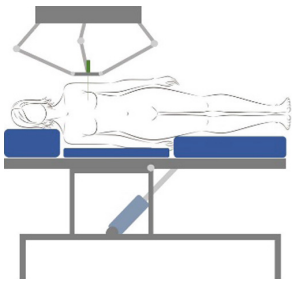

Fig. 1. Whole biopsy system diagram, displaying the stretcher, patient positioning, robot position and insertion

Also, a specialized stretcher was developed to cover the necessary specs for the proposed procedure. A linear medical-grade actuator allows patients to stand upright in front of the stretcher, after 1:30 min, reaching a horizontal position of lateral decubitus, providing greater safety and comfort. It also has collapsible lateral pallets, allowing thus, perform the procedure perpendicular to the thorax, avoiding the risk of tearing the pleura.

Needle Location

The use of a parallel robot was proposed to deal with the needle positioning problem, this robot has a linear displacement of 25 cm, achieving greater stability, repeatability and strength, than a linear proposal. These characteristics were probed by the dynamic analysis of the system in situations that resemble the aspects of a real biopsy procedure.

At the time of performing this procedure, the needle faces changes in density and hardness, which represents changes in the needle's effort against displacement. The Delta type parallel robot demonstrates to have a higher resistance to the change of hardness, compared to serial robots, since it has the force of 3 actuators applied at the same time. The position of the patient and the needle is shown in Fig. 2:

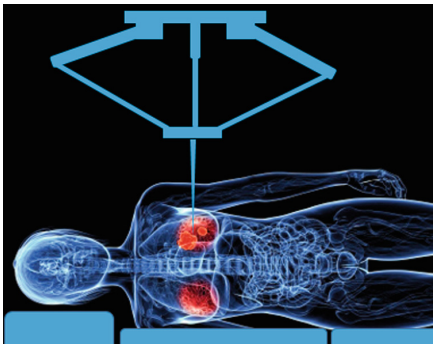

Fig. 2. Needle insertion and patient positioning during biopsy procedure

Thermography

To show the global position of the extraction area, an ultrasound device is used to provide information about the location of the lesion; however, it doesn't define the surface area, generating a possible error at insertion. The strategy used is thermal imaging, the system can perform a thermic sweep of the thoracic area, locating the area with a possible lesion as shown in Fig. 3. This radically improves the surface positioning of the cutting needle.

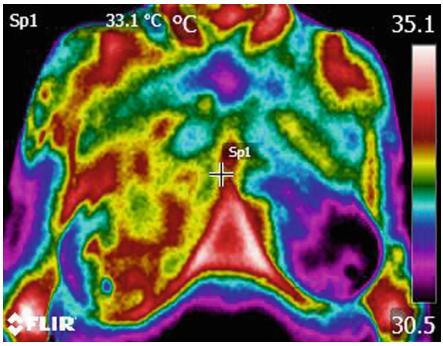

Fig. 3. Thermal image of a patient with cancer where a tumor can be observed at the left breast

4 Development

4.1 Design Evaluation

Robot System

Robot's main feature is performing the biopsy with control, after a sweep of the sensor on the patient, it can obtain a thermal-image of the torso and thus locate the pathology correctly [9, 10]. The necessary mathematical analysis was carried out to arrive at the values of precision, accuracy and repeatability determined in the specifications. The dynamic equation of the movement of a parallel robot is:

$$\tau = M_1(q)\dot{\rho} + C_1(q,\dot{q})\rho + Y_1(q,\dot{q},\dot{q}_d,\ddot{q}_d)\theta_1 \tag{1}$$

Where M is the inertia matrix, C is the vector of the Coriolis, centrifugal and gravity torques, Y is the inverse dynamics model, and q is the leg dynamics.

In Fig. 4 we can observe the free body diagram of the robot:

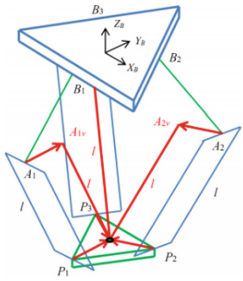

Fig. 4. Free body model of a delta type robot

The design of the control diagram with backstepping is shown in Fig. 5:

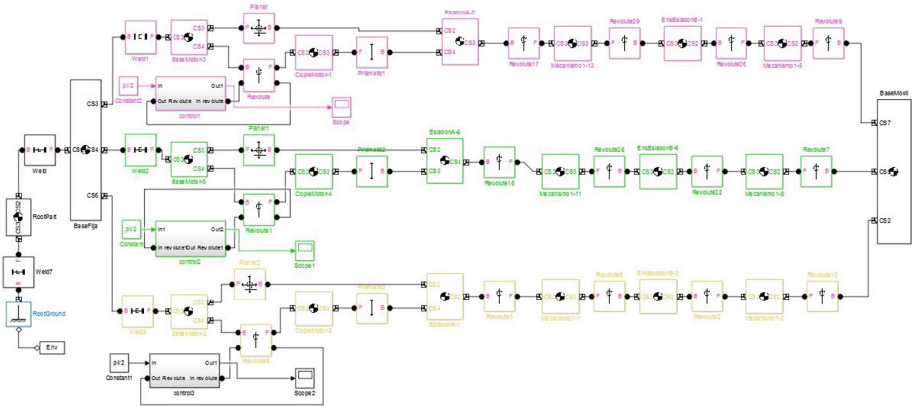

Fig. 5. Block diagram of proposed control with backstepping (SimMechanics)

4.2 Control Model

Considering the primary function of this robot, performing a biopsy would only be possible with software capable of analyzing the images obtained after a sensor covers the torso area of the patient and localizing the target area correctly.

Lyapunov theorem indicates:

$$\begin{cases} V \text{ is positive definite} \\ V \text{ is negative semi} - \text{definite} \end{cases} \rightarrow V \in L_\infty$$

Assuming $V(0)\varepsilon L_\infty$, we can deduce:

$$V(t) - V(0) = \int_0^1 \left(\frac{1}{2} e^t e + \frac{1}{2} \rho^T M_1(q) \rho + \frac{1}{2} \tilde{\theta}_1^T \beta_1 \tilde{\theta}_1 + \frac{1}{2} \tilde{\theta}_7^T \beta_2 \tilde{\theta}_7 \right) d\omega \in L_\infty \quad (2)$$

$$\rightarrow \begin{cases} e \in L_2 \\ \rho \in L_2 \\ \tilde{\theta}_1 \in L_2 \\ \tilde{\theta}_7 \in L_2 \end{cases} \text{and} \begin{cases} e \in L_\infty \\ \rho \in L_\infty \\ \tilde{\theta}_1 \in L_\infty \\ \tilde{\theta}_7 \in L_\infty \end{cases}$$

By writing Barbalat's Corollary as it follows:

$$\dot{V} = -e^T k_1 e - \rho^T (d - Dsgn(\rho)) - \rho^T k_2 \rho \leq -e^T k_1 e = -g^2 \quad (3)$$

Where $= \sqrt{k_1}e$, taking the derivative of g and elaborating for $\dot{e}$:

$$\dot{g} = \sqrt{k_1}\dot{e} = \sqrt{k_1}\left(Y_7\tilde{\theta}_7 + \widehat{J_T}\rho - k_1 e\right) \tag{4}$$

According to the fourth equation:

$$\dot{g} = \sqrt{k_1}(Y_7\tilde{\theta}_7 + \widehat{J_T}\rho - k_1 e) \in L_\infty \rightarrow g \text{ is uniformly continuous}$$

$$e \in L_2 \rightarrow g = \sqrt{k_1}e \in L_2 \tag{5}$$

Consequently, ll Barbalat's corollary conditions are satisfied. With this last, applied to Lyapunov, we go to the conclusion that $g = \sqrt{k_1 e} \rightarrow 0, omot \rightarrow \infty$

Introducing these results to the equation $\tau = Y_1\widehat{\theta}_1 - \hat{J}_T^T e - k_2\rho$;

$$\tau \in I_\infty \tag{6}$$

Consequently, all control τ entry elements can be constructed, all the values designed and measurable are delimited and the control τ entry is implementable. Therefore, control is implementable. This control was programmed on Matlab using the adaptive Back-stepping laws where the algorithm allows us adjusting the controller parameters (Fig. 5), which means it's possible to maintain asymptotic stability in the presence of force variability associated to the tumour penetration.

4.3 Kinetic Analysis

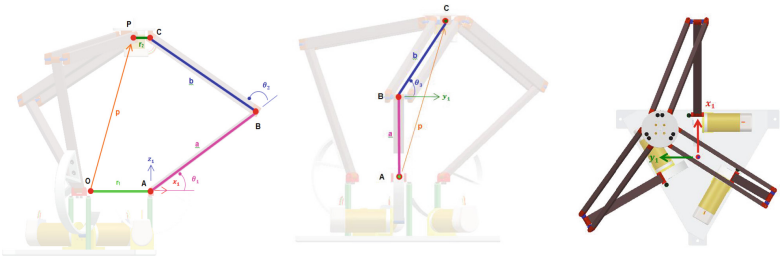

Fig. 6. Lateral and upper robot diagram displaying segments and angles

In Fig. 6 as reference, the robot can be described by segments as follows:

$$\overline{OA} + \overline{AB} + \overline{BC} = \overline{OP} + \overline{PC} \tag{7}$$

Which can be rearranged in:

$$\overline{AB} + \overline{BC} = \overline{OP} + \overline{PC} - \overline{OA} \tag{8}$$

Each term can be written as a matrix as follows:

$$\overline{OA} = \begin{bmatrix} r_1 \\ 0 \\ 0 \end{bmatrix}, \overline{AB} = \begin{bmatrix} aCos\theta_1 \\ 0 \\ aSen\theta_1 \end{bmatrix}, \overline{BC} = \begin{bmatrix} bCos(\theta_1 + \theta_2)Sen\theta_3 \\ bCos\theta_3 \\ bSen(\theta_1 + \theta_2)Sen\theta_3 \end{bmatrix},$$

$$\overline{PC} = \begin{bmatrix} r_2 \\ 0 \\ 0 \end{bmatrix}, \overline{OP} = \begin{bmatrix} Cos\varphi_i & Sen\varphi_i & 0 \\ -Sen\varphi_i & Cos\varphi_i & 0 \\ 0 & 0 & 1 \end{bmatrix} \begin{bmatrix} P_x \\ P_y \\ P_z \end{bmatrix} = \begin{bmatrix} P_xCos\varphi_i + P_ySen\varphi_i \\ -P_xSen\varphi_i + P_yCos\varphi_i \\ P_z \end{bmatrix}$$

By this last, its seen that φ_i shows the orientation of the robots legs from the X axis to the r_1, with values of 0° for leg $i = 1$, 120° for leg $i = 2$, and 240° for leg $i = 3$.

5 Results

The results can be summarized in the development of a Delta type Robot system with the equipment required to fulfill its functions in the identification of areas with considerable thermal differences, optimal positioning in the insertion area and cutting biopsy procedure. As well as, the development of a specialized stretcher system and the implementation of the controller for the execution of trajectories. The results of the driver simulation indicate that there is millimeter precision and trajectory tracking higher than that required in a biopsy procedure. In the following section the robot's design will be detailed as well as the performance simulation results, meaning the robot workspace, velocity and precision.

5.1 Robot Design and Construction

The robot was designed as a parallel delta type, resulting in a more precise procedure, and therefore performing the biopsy better than a manual operation. This robot has 3 degrees of freedom (DOF), Fig. 7 shows the SimMechanics model while Fig. 8 shows the actual robot prototype.

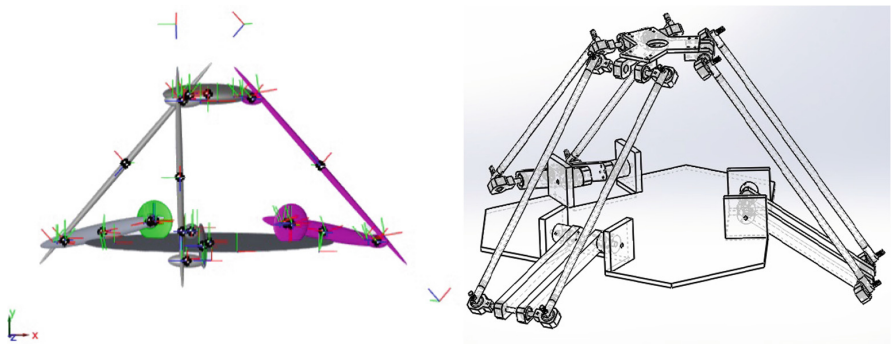

Fig. 7. Robot modelling at SimMechanics and Solid Works showing the 3 DOF coordination

Fig. 8. Delta type robot prototype with control and power unity developed

With this 3 DOF prototype the workspace of the actuator was tested giving the results shown in Fig. 9 in subsection (a) with a cylindrical space of 0.2 m^3, compared to other robot's workspace; subsection (b) belongs to the SYLVIO development and (c) to the ARABIA II. The workspace of our development is shown to be enough for the biopsy procedure to be done despite just having 3 DOF.

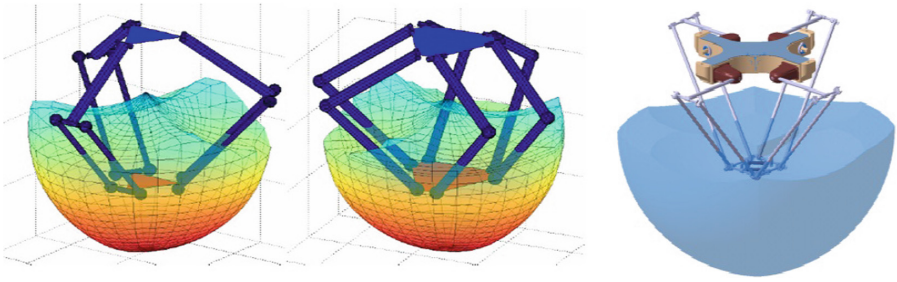

Fig. 9. Robot's workspace: (a) 3 DOF (OURS), (b) 6 DOF (SYLVIO), (c) 4 DOF (ARABA II) showing a similar workspace nevertheless the DOF

Subsequently the performance of the robot was simulated, the results are shown in the following graphs. These show the behavior of the auto adjustment feature of the robot, Fig. 10 subsection (a) shows the positions of the robot within 10 s, and subsection (b) shows the velocity.

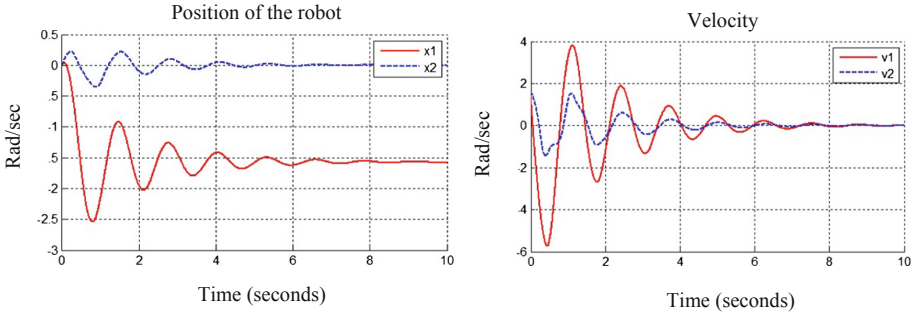

Fig. 10. Behavior of the robot for entries with 0 torque and initial conditions $x_1(0)$, $x_2(0)$, $v_1(1.5)$ $v_2(1.5)$

Please notice that within the 10 s of simulation the velocities decrease to 0 and the desired position is achieved.

6 Conclusion

The evaluation of the robotic biopsy system allows us to open a space within the interventionist robotics on one of the pressing needs among health issues in Mexico. Technological development improves processes by partially eliminating human error and therefore the inherent reduction of false negatives, which in some cases results in a costly procedure due to late diagnosis and, in other cases, in the irreparable loss of human life. Further challenges are the development of a prototype with surgical standard materials as well as the improvement of the surgeon console. This first approach to interventionist robotics allows us to glimpse a growing opportunity niche where Mexican technological developments become internationally competitive.

Disclaimer. None of the authors claimed a conflict of interest for the development of this research.

References

1. Youlden, D.R., Cramb, S.M., Dunn, N.A.M., Muller, J.M., Pyke, C.M., Baade, P.D.: The descriptive epidemiology of female breast cancer: an international comparison of screening, incidence, survival and mortality. Cancer Epidemiol. **36**(3), 237–48 (2012). http://dx.doi.org/10.1016/j.canep.2012.02.007
2. Dahabreh, I.J., Wieland, L.S., Adam, G.P., Halladay, C., Lau, J.T.T.: Core Needle and Open Surgical Biopsy for Diagnosis of Breast Lesions : An Update to the 2009 Report. Comp Eff Rev No 139. AHRQ Publication No. 14-EHC040-EF (2014)
3. IARC: IARC Handbooks of Cancer Prevention - Breast Cancer Screening, vol. 15, IARC Handbooks of Cancer Prevention, p. 482 (2016)
4. Hukkinen, K., Kivisaari, L., Heikkilä, P.S., Von Smitten, K.: Unsuccessful preoperative biopsies, fine needle aspiration cytology or core needle biopsy, lead to increased costs in the diagnostic workup in breast cancer (2009)
5. Lucero, J.R., Espinosa, C., Franco, M., Arnedo, M.G., Neuman, J., Vaselli, I.: Estudio de la subestimación histológica e incidencia de falsos negativos en biopsias de mama por vacío con guía estereotáxica. Rev. Argentina Radiol. **75**(2), 123–130 (2011)
6. Speich, J.E., Rosen, J.: Medical robotics. In: Wnek, G., Bowlin, G. (eds.) Encyclopedia of Biomaterials and Biomedical Engineering, pp. 983–993. Marcel Dekker, New York (2004)
7. Bastida, M.B., Cabello, M.E.: Sistema de apoyo para la toma de decisiones en termografía de glándulas mamarias **38**(1), 166–187 (2017)
8. Bland, K.I., Copeland, E.M.: The Breast, Comprehensive Management of Benign and Malignant Diseases, 4th edn., vol. 91, pp. 399–404. Elsevier Inc. (2017)
9. Zou, J., Schueller, J.K.: Adaptive backstepping control for parallel robot with uncertainties in dynamics and kinematics. Robotica. **32**(6), 2 (2014)
10. Pisla, D., Gherman, B., Vaida, C., Suciu, M., Plitea, N.: An active hybrid parallel robot for minimally invasive surgery. Robot. Comput. Integr. Manuf. **29**(4), 203–221 (2013)

Development of a Lower-Limb Exoskeleton for Assistance of Movements in the Sagittal Plane

Itzel García, Lourdes Luna(✉), Marco Mendoza, Aldo Mejía-Rodríguez, Isela Bonilla, and Guadalupe Dorantes-Méndez

Faculty of Science, Autonomous University of San Luis Potosi, 78295 San Luis Potosi, SLP, Mexico
itzel.gcz_28@hotmail.com, lourdeslunardz_2895@outlook.com

Abstract. Currently, exoskeletons can be categorized according to the part of the human body they are focused on, their purpose and the type of mechanisms used for their operation. This paper presents the development of an exoskeleton to assist lower-limb motion during human gait and uses the electromyographic (EMG) signals as data acquisition and control system. In addition, the system has an anthropomorphic and adjustable design to serve a larger number of patients and thus make it affordable for a larger sector of the population. In order to verify the suitable operation of the exoskeletal system, experimental tests were carried out with a volunteer and some of the obtained results are presented.

Keywords: Lower-limb exoskeleton · Electromyography · Human gait

1 Introduction

The human gait is the product of a succession of periodic and synchronized movements that keep the individual in a dynamic equilibrium and allow movement from one place to another, with low effort and minimal energy consumption. The human gait is an activity of excessive difficulty, since it demands complex and coordinated interactions of the joints of the human body, particularly of the lower limb joints [1]. The gait cycle or stride consists of two phases: stance and swing of a limb, and it can be described by some characteristic angular displacements and muscular actions, which allow to identify any change or alteration in the pattern of this cyclic movement [2]. Human gait can be restricted or modified by diseases, old age, injuries, accidents or tasks that require a higher load capacity; in order to solve these problems, a large number of auxiliary devices have been developed.

In recent years, the development of robotic platforms for assistance has been the subject of innumerable research works worldwide. Among the main advances are the exoskeletal systems, which consist of an external mechanical structure

© Springer Nature Switzerland AG 2020
C. A. González Díaz et al. (Eds.): CLAIB 2019, IFMBE Proceedings 75, pp. 1023–1030, 2020.
https://doi.org/10.1007/978-3-030-30648-9_132

coupled to a person and designed to support, assist movements and/or increase the capabilities of the human body. The contact between the user and the exoskeleton allows a transfer of mechanical power and exchange of information, so they are designed to be as ergonomic as possible. According to the state of the art on the development of exoskeletons [3,4], these systems are classified as performance or military, rehabilitation and mobile-medical exoskeletons.

One of the most important works in military exoskeletons is known as BLEEX (Berkeley Lower Extremity Exoskeleton), which aims to provide soldiers, rescuers and emergency personnel the ability to carry heavy loads in the back with a minimum effort while moving on any kind of terrain [5]. On the other hand, a system designed for people with motor disabilities due to muscle weakness is the HAL exoskeleton, which is not only used in rehabilitation but also for strength amplification. In [6], the general features of HAL are described, we can highlight that it is an exoskeleton with adjustable structure and that like BLEEX has an anthropomorphic design with kinematics similar to the human leg. Therefore, in this context, this paper presents the design, construction and start-up of a lower-limb exoskeleton, with three degrees of freedom: one passive in the hip and two active for knee and ankle, in order to assist the movements of flexion-extension of knee and ankle during human gait. The main objective of the proposed exoskeleton is to have an experimental platform that allows to innovate in the design of impedance control schemes based on the angular and EMG patterns characteristic of human gait.

2 Methods and Materials

2.1 Acquisition Protocol

A male adult carried out the acquisition, who gave his written, informed consent to participate. This subject after performing some high intensity physical activity suffers from an inflammation in the ligaments of the left ankle joint. Angular movements and surface feet contact during the gait were acquired through the Biometrics system (Biometrics Ltd., Newport, UK), which consists of an acquisition module (DataLOG MWX8 Bluetooth®), two SG150 goniometers, a SG110/A goniometer, and a contact pressure sensor with four digital inputs (FS4 Contact Switch). The acquisition was performed using the manufacturer's software (DataLOG Software v8.51). All the maneuvers of the protocol were performed on an electric treadmill (Athletic Works, AR, USA).

The goniometers were placed on the external lateral side of the left lower limb, the SG150 goniometers were placed on the hip and knee joints, while the SG110/A goniometer on the ankle joint. The contact sensor terminals were placed in the metatarsal area and the heel of each sole of the foot. The acquisition was divided into two stages: first, when the subject was without any injury, and then when the subject had performed physical activity the previous day. In both cases, the subject was instructed to walk on the treadmill at 2.5 and 0.8 km/h speeds, respectively, in the most comfortable and appropriate way for him. The signals were acquired at a sampling frequency of 1 kHz and stored for further

processing in Matlab (The MathWorks, MA, USA). The acquisitions made with the Biometrics system were used to establish the angular pattern characteristic of the subject's gait.

2.2 Identification of Angular Pattern

For identification of the gait phases, the movements of flexion/extension for each joint were analyzed. The signals were automatically segmented by means of the pressure sensor information and the average behavior for each joint was calculated, as suggested in the literature [7].

In order to simplify the real time implementation of the control algorithm for the exoskeleton, the angular pattern of hip joint is used as a reference to determine the subject gait stage's. Then, a polynomial representation of the angular patterns was made by using cubic polynomials of the form $at^3 + bt^2 + ct + d = e$, where t corresponds to the current time instant, e represents the current angular position of the hip and the constants a, b, c and d correspond to data interpolation obtained in the characterization. Finally, from the polynomial resulting from the hip joint, the root t_1 of the polynomial $at_1^3 + bt_1^2 + ct_1 = e - d$ was used to identify at what gait stage the subject is.

2.3 Kinematics Model of Lower Limbs

By considering the flexion and extension movements in the sagittal plane, for the hip, knee and ankle joints, the forward kinematics model of the lower limbs is divided into two stages. The first stage corresponds to the stance phase, in which it is considered that the displacement of the ankle joint is almost null, setting the reference system 0 in the ankle (see Fig. 1a). Therefore, the forward kinematics for stance phase consists of computing the position and orientation of the trunk's center of gravity with respect to the reference frame located in the ankle. Therefore, the homogenous transformation matrix of stance phase is

$$T_3^0 = \begin{bmatrix} \cos(q_1 - q_2 + q_3) & \sin(q_1 - q_2 + q_3) & 0 & c_x \\ -\sin(q_1 - q_2 + q_3) & \cos(q_1 - q_2 + q_3) & 0 & c_y \\ 0 & 0 & 1 & 0 \\ 0 & 0 & 0 & 1 \end{bmatrix} \tag{1}$$

where

$$c_x = L_s \sin(q_1) + L_t \sin(q_1 - q_2) + L_c \sin(q_1 - q_2 + q_3) \tag{2}$$

$$c_y = L_s \cos(q_1) + L_t \cos(q_1 - q_2) + L_c \cos(q_1 - q_2 + q_3) \tag{3}$$

with q_1, q_2 and q_3 representing the angular motion of ankle, knee and hip, respectively. While, L_s is the length of shin, L_t is the length of thigh, and L_c is the distance from hip to trunk's center of gravity.

On the other hand, the second stage corresponds to the swing phase, where it is considered that the displacement of the hip joint is almost null, setting the

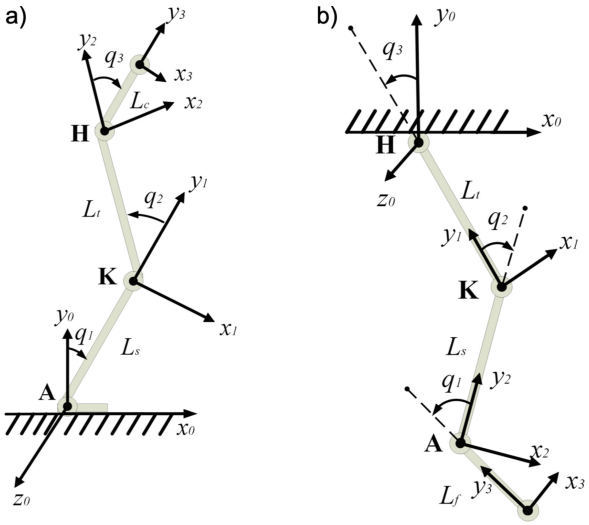

Fig. 1. Assignment of reference systems for kinematic analysis of the lower limbs during human gait: (a) Stance phase, (b) Swing phase.

reference system 0 in the hip (see Fig. 1b). Therefore, the forward kinematics for swing phase consists of computing the position and orientation of the foot with respect to the reference frame located in the hip. Therefore, the homogenous transformation matrix of swing phase is

$$T_3^0 = \begin{bmatrix} \cos(q_1 - q_2 + q_3) & -\sin(q_1 - q_2 + q_3) & 0 & f_x \\ \sin(q_1 - q_2 + q_3) & \cos(q_1 - q_2 + q_3) & 0 & f_y \\ 0 & 0 & 1 & 0 \\ 0 & 0 & 0 & 1 \end{bmatrix} \tag{4}$$

where

$$f_x = L_s \sin(q_3) + L_t \sin(q_3 - q_2) + L_f \sin(q_1 - q_2 + q_3) \tag{5}$$

$$f_y = -L_s \cos(q_3) - L_t \cos(q_3 - q_2) - L_f \cos(q_1 - q_2 + q_3) \tag{6}$$

with L_f being the length of foot.

2.4 Design and Manufacture of the Exoskeleton

The biomechanical features considered to design the mechanical structure, as well as the selection of actuators, were: (1) Degrees of freedom of each lower-limb joint in sagittal plane, (2) Range of motion of the lower-limb joints during human gait, (3) Characteristic joint torques of the hip, knee and ankle [2]. Likewise, it was essential to know the average weight and anthropometric measurements of lower limbs for mexican male population, which is reported in [8,9].

Based on the above, the mechanical structure of the exoskeleton for assistance of left lower limb is composed of three mechanisms arranged in a serial chain, where each joint corresponds to the motion in sagittal plane of hip, knee and ankle, respectively, i.e. the robot has three degrees of freedom; the first is passive and the remaining two are active. The axis or rotation center of each joint in the robot coincides with those of the lower limb. The ranges of motion of robot joints are: hip (±90°), knee (±90°), ankle (±45°), which allows no restrictions caused by the mechanisms on the motion.

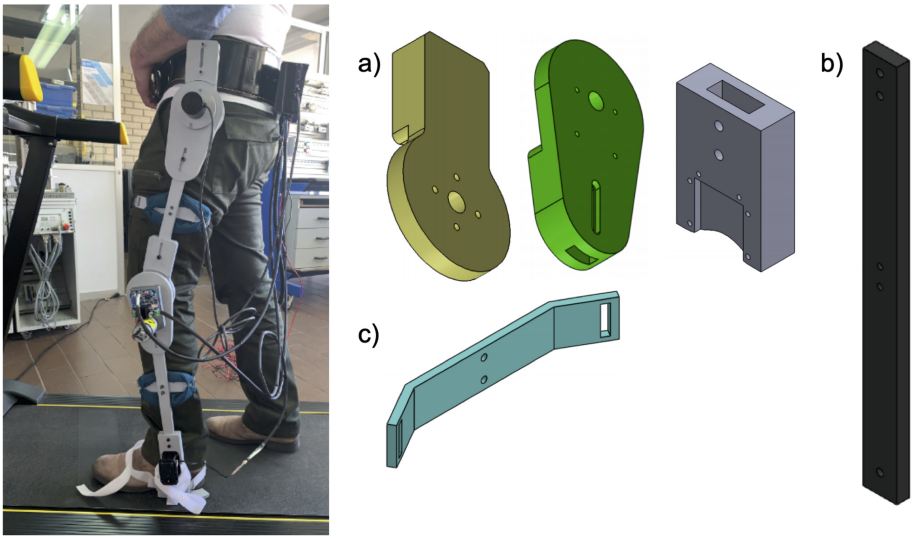

Fig. 2. Lower-limb exoskeleton for assistance of motion in the sagittal plane. Parts designed in SolidWorks: (a) Supports for the joints, (b) Links, (c) Leg adjustment structure.

Figure 2 shows the proposed exoskeleton prototype, its mechanical structure consists of 4 main parts: (1) *Hip support*, which is composed of a belt that allows the exoskeleton to be held in the user's lumbar area and whose passive joint moves freely (using a bearing) and includes a position sensor (incremental rotary encoder with a resolution of 1024 pulses per revolution) YUMO E6B2-CWZ3E, to measure the flexion/extension motion of the leg during the gait cycle. (2) *Knee support*, which is an active rotational joint of one degree of freedom driven by the servomotor WINGXINE ASMC-03B (with maximum torque of 90 kg · cm at 12 V) and it allows the flexion/extension motion of the knee. (3) *Ankle support*, it is an active rotational joint of one degree of freedom driven by the servomotor ROBOTIS Dynamixel MX-64AT (with maximum torque of 64 kg·cm at 12 V) and allows to perform the flexion/extension motion of the ankle. (4) *Linking bars or links*, the supports are linked by adjustable bars getting the robot adaptable to different lengths of lower limbs (within the average mexican male population),

the bars are attached to the lower limbs by means of an adjustment structure with textile pad and velcro tapes, so that it is comfortable and does not harm the user. In the particular case of the ankle, there is a footboard where the user places his foot for a better adjustment. The main parts of the exoskeleton (Fig. 2) were designed using the SolidWorks® software, and the material that was selected for its manufacture (using lathe/milling machines) was Nylamid.

In order to use electromyographic (EMG) signals to control the active joints of the exoskeleton, an impedance control scheme derived from [10] was used, given by

$$\mathbf{q}_r = \mathbf{q}_d - \mathbf{q}_f \tag{7}$$

where $\mathbf{q}_r$ are reference trajectories for knee and ankle joints, respectively, $\mathbf{q}_d$ is the vector of desired joint trajectories (angular patterns) and the torque filter

$$\mathbf{q}_f = (K_d + B_d s + M_d s^2)^{-1} \tau_e \tag{8}$$

with s being the Laplace complex variable, K_d, B_d and M_d being the matrices of stiffness, damping and inertia, respectively. The normalized exerted torque τ_e is related to the EMG signal, therefore, the muscle activity during the gait will be defined between 0 and 1, where 0 represents that the subject did not make any effort and 1 that the maximum effort necessary to generate the movement was made. Thus,

$$\tau_e = T(\mathbf{EMG}_p - \mathbf{EMG}) \tag{9}$$

where $\mathbf{EMG}_p$ is the vector containing the envelopes of the EMG gait pattern signals (for semitendinosus and gastrocnemius muscles defined in [11]), **EMG** is the vector containing the envelopes of the current EMG signals and T is a diagonal matrix whose elements are the characteristic torques of each joint, which is used to normalize the exerted force according to the units used by the force filter implemented.

Arduino MEGA 2560 platform was used to control the system. The serial communication protocol required to control the Dynamixel MX-64AT servomotor was implemented using the Dynamixel Serial library. The prototype has an emergency stop button for user safety and the connection plates between the encoder, servomotors, power supply system, stop button and the Arduino were designed. The power supply system consists of two stages: a 12 V power supply for servomotors and a 9 V rechargeable battery for the rest of the components.

3 Results and Discussion

In order to verify the correct operation of the exoskeleton, experimental tests were carried out following the specifications of the acquisition protocol. It should be noted that the speed was gradually increased until reaching 2.5 km/h, allowing the subject to adapt to the system. The volunteer's left leg dimensions are: 52 cm from hip to knee, 41 cm from knee to ankle, 8 cm from ankle to foot sole, 26 cm of foot length, 10 cm of foot width, 53 cm of thigh diameter and 36 cm of calf diameter. Therefore, the exoskeleton was adjusted to these dimensions.

For tests in passive mode, the control of the exoskeleton senses the angular position using the encoder placed in hip joint, in order to obtain the gait phase in real time and to determine the trajectories to be followed by the servomotors located in knee and ankle joints. The data recorded during the tests in an average stride can be seen in Fig. 3, where the angular pattern trajectories for the three joints are the pink lines and the trajectories calculated via polynomials from data obtained by the encoder are the blue lines.

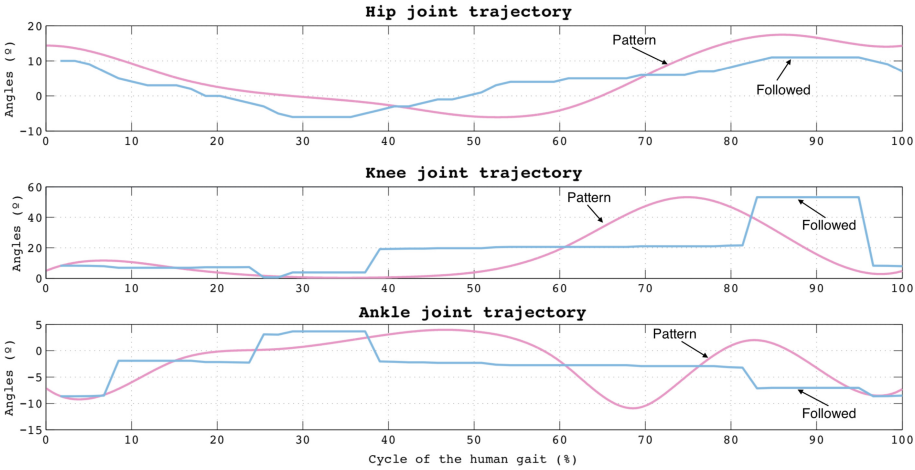

Fig. 3. Angular trajectories in the sagittal plane of the hip, knee and ankle joints, respectively.

In Fig. 3, it can be observed that the trajectory registered with the encoder presents some differences in amplitude and phase with respect to the hip pattern trajectory. It can be seen at the beginning, when the heel contacts the treadmill surface, the hip registers a flexion of approximately 10° while the pattern trajectory registers a flexion of approximately 15°. Additionally, at 50% of the gait cycle (final stance phase) the hip joint extends up to −5° in the pattern trajectory, while with the encoder has such extension but in 30% of the cycle. Finally, in the pattern trajectory between 60% and 85% of the cycle, hip is flexed up to 18° while in the trajectory acquired with the sensor such flexion occurs at 40% of the cycle and reaches a maximum of approximately 10°. Such differences in the trajectory recorded by the encoder cause modifications in the trajectories that the servomotors of the knee and ankle should follow, because the trajectory of the hip determines the phase of the limb's movement.

4 Conclusions

Based on the results obtained in experimental tests, it can be concluded that the stages of design, manufacture and operation of the lower-limb exoskeleton of three degrees of freedom were satisfactory. However, it is necessary to perform

experimental tests with a greater number of volunteers. The main features to highlight about the developed system are the detection system of the gait phases with a minimum number of sensors and the EMG-based impedance control that allows to assist the user according to his/her mobility characteristics.

Finally, in order to improve the characteristics of the system, it is planned to integrate another sensor for the detection of gait phases and to convert the hip into an active joint to drive of the exoskeleton.

Conflict of Interest. The authors declare that there is no conflict of interest.

References

1. Osorio, J.H., Valencia, M.H.: Bases para el entendimiento del proceso de la marcha humana. Archivos de Medicina **13**(1), 88–96 (2013)
2. Nordin, M., Frankel, V.H.: Basic Biomechanics of the Musculoskeletal System. Lippincott Williams & Wilkins, Philadelphia, USA (2012)
3. Chávez-Cardona, M.A., Rodríguez-Spitia, F., Baradica-López, A.: Exoskeletons to enhance human capabilities and support rehabilitation: a state of the art. Revista Ingeniería Biomédica **4**(7), 63–73 (2010)
4. Low, K.: Robot-assisted gait rehabilitation: from exoskeletons to gait systems. In: 2011 Defense Science Research Conference and Expo (DSR), IEEE, New York, USA, pp. 1–10 (2011). https://doi.org/10.1109/DSR.2011.6026886
5. Zoss, A., Kazerooni, H., Chu, A.: On the mechanical design of the berkeley lower extremity exoskeleton (BLEEX). In: 2005 IEEE/RSJ International Conference on Intelligent Robots and Systems, IEEE, Canada, pp. 3465–3472 (2005). https://doi.org/10.1109/IROS.2005.1545453
6. Jansen, O., Schildhauer, T.A., Meindl, R.C., Tegenthoff, M., Schwenkreis, P., Sczesny-Kaiser, M., Grasmücke, D., Fisahn, C., Aach, M.: Functional outcome of neurologic-controlled hal-exoskeletal neurorehabilitation in chronic spinal cord injury: a pilot with one year treatment and variable treatment frequency. Glob. Spine J. **7**(8), 735–743 (2017). https://doi.org/10.1177/2192568217713754
7. Hoyos-Daza, H.: Muscle Activity Patterns in Lower Limbs During the Human Gait under Body Load Relief Conditions. Bachelor's thesis, Facultad de Ingeniería, Pontificia Universidad Javeriana, Colombia (2014)
8. Ávila, R., Prado, L., González, E.: Dimensiones antropométricas de la población latinoamericana. México, Universidad de Guadalajara, Centro Universitario de Arte, Arquitectura y Diseño, División de Tecnología y Procesos, Departamento de Producción y Desarrollo, Centro de Investigaciones en Ergonomía (2007)
9. Lefton, J., Malone, A.: Anthropometric Assessment. ADA Pocket Guide to Nutrition Assessment, pp. 160–161, 2nd edn. American Dietetic Association, Chicago (2009)
10. Mendoza, M., Bonilla, I., Reyes, F., González-Galván, E.: A lyapunov-based design tool of impedance controllers for robot manipulators. Kybernetika **48**(6), 1136–1155 (2012)
11. García, I., Luna, L., Reyes, B., Dorantes-Méndez, G., Mejía-Rodríguez, A., Mendoza-Gutiérrez, M.: Aplicación de técnicas en el dominio del tiempo y la frecuencia para el análisis de la marcha humana usando señales de electromiografía. Memorias del Congreso Nacional de Ingeniería Biomédica. **4**, 114–117 (2017). https://doi.org/10.24254/CNIB.17.126

Design for Additive Manufacturing of a Robotic Hand with Two Thumbs

Horacio León(✉)

Universidad Politécnica del Valle de México,
Av. Mexiquense & Universidad Politécnica, Col. Villa Esmeralda,
Tultitlán, 54910 Fuentes del Valle, Mexico State, Mexico
hleon@cinvestav.mx

Abstract. This paper shows the mechanical design by additive manufacturing (DFAM) of a robotic hand with 5 fingers, where the little finger is replaced with a thumb. The aim of this work is trying to look for a mechanical perspective, in order to develop a functional prototype that allows us to visualize and identify all the advantages that we could get with an object's grip through a hand with two thumb fingers. Also, we pretend since the prototype manufacturing by Fused Deposition Modeling (FDM) show the design technique application based in divergent and convergent remix on digital models of robotic hands like Inmoov and Parloma. Several prototypes were made to obtain as a result robotic hand called Kool, which has advantages of mechanical design, from weight, shape, and cost compared to previous prototypes.

Keywords: Remix · Design · Robotic hand · Print 3D · Thumbs · Kool hand

1 Introduction

It's known in the scientific community related to the study of the human body, that the most important advances on the grip of objects, are in the possibility of oppose the thumb towards the other fingers of the human hand. This is given covering two aspects: (1) Precision grip, and (2) Power grip. The thumb is so important that has an impact on 60% of the functionality of the hand [1], and, it has the most interdependence with the other fingers, since it's used in 90% of the grip positions [2].

The passion and research by the human hand, has left aside, and/or in a limited way, the biomimetic study, that takes advantage of diverse conditions of nature, and it's impacts on other possible meta-capabilities in the design of grip objects. As an example, is found in the study of mammals like, panda bear, mole, and koala bear, this last with two thumbs (Prepollex), which emphasizes strength capabilities that must have to sustain its own weight [3], and it is comparable in the human's hands because they show a thumb duplication and this one of the most common congenital anomaly, and it happens in 1.4 of each 1000 births [4], furthermore, exist other extraordinary human structural configurations such as those generated by polydactyly, which have not been taken into account for the study of mobility and grip in the hand.

The impact of replacing the little finger with a thumb, could improve the conditions of gripping, in the design of prostheses, and even influence the mood of a person

© Springer Nature Switzerland AG 2020
C. A. González Díaz et al. (Eds.): CLAIB 2019, IFMBE Proceedings 75, pp. 1031–1034, 2020.
https://doi.org/10.1007/978-3-030-30648-9_133

suffering from a hand amputation. The above implies making changes in the structure design of robotic palm. A quick and low cost way to make modifications and prototypes, is using the Design for Additive Manufacturing, (DFAM), which refers to technology, or additive process of successive deposition of layers of material, one on top of the other, producing a final three-dimensional product, where a wide variety of materials can be used, from polymers, ceramics, glass, concrete, and metals, [5]. The targets of DFAM methodology are (1) Resource Reduction, like print time, weight and cost; (2) Quality Enhancement, like, strength, aesthetic and functionality.

In the creative domain, the re-use of knowledge is a common practice known as "remixing". A remix is defined as a three-dimensional design that includes references to other designs on which it is based. There are 8 remix patterns grouped into divergent and convergent classes, which are used to explore the feasibility of making modifications to the remixes, [6]. Inmoov is a prototype of a robotic hand, that exist in the web, like open source, with 36 components, and 17 degree of freedom (DOF's), meets the parameters of aesthetic similarity with the human hand. Parloma Hand, is a remix (R1) better than Inmoov, with 22 DOF's. The carpal bones in the human hand, capitate, lunate, trapezium, and scaphoid bones, are considered key to establishing an analysis of symmetry in the hand palm. This allows to consider the possibility of removing the little finger, and replace with another thumb, but requires size modifications over the bones and the palm edge.

2 Methodology

An own methodology is used, following the next steps: (1) Inspiration; (2) Ideation, and (3) Implementation. Step 2 includes (a) DFAM with Prusa i3 and Anycubic 4 Max printers 3D; (b) Remix patterns [4], and Redesign; see Fig. 1.

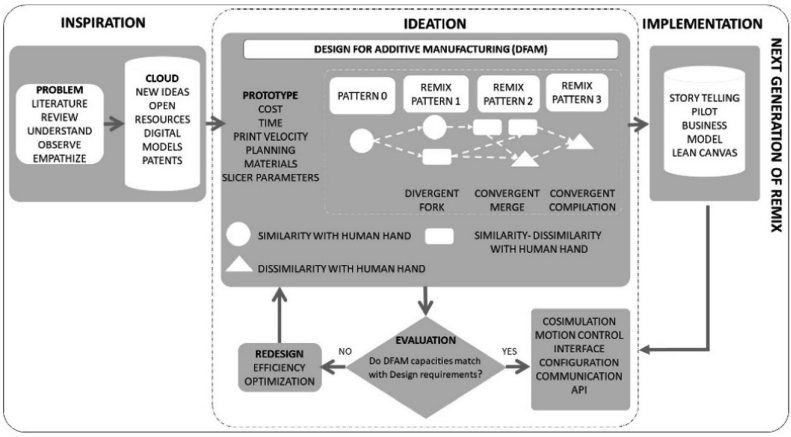

Fig. 1. Methodology of DFAM using remixes.

2.1 Problem and Conceptual Design

For a long time, prostheses and robotic hand research have been focused on some skill improvements for instance the devices guided through the mechatronics, as well as the relationship between aesthetic appearance and the human appearance. We consider there is a lack of information, as well as, we think it hasn't been considered biomimetic, anatomical special and functional conditions as the incorporation of additional fingers or the replacement of one of them. Likewise, the design of the human palm, the study is limited since the structural configuration. The problem that involves to replace the little finger instead of the thumb finger implicates: (1) Consider the osseous structure in the metacarpal of the robotic hands; (2) the fastest way to accelerate the prototype development is on the basis of the last models such as Inmoov and Parloma, for it, we require some piece of information such as available data, open and completed digitals in good conditions in order to reconfigure and redesigns; (3) At the moment we didn't find any studies that they have a relationship with the present studies.

The goal of conceptual design is to identify mechanical behavior, performance, anthropometry, anthropomorphism, existence of digital data for 3D printing. Access to files CAD must be in good condition, and complete.

3 Results

Some factors that influencing the remix process include: (a) number of components; (b) DOF's; (c) time; (d) cost; (e) appearance; and (f) security, Fig. 2. Functionality is improved with a simple mechanism for thumb, indeed, the number of components it's reduced in the last remix, Kool Hand, with respect to the parent prototype, and remix Parloma (R1). Regarding mobility, Kool, increase the DOF's, respect to Inmoov prototype, but they are reduced with respect Parloma, which has more DOF's, and its more complex. The additive manufacturing time, it's reduced from 19 h to 15 h on Kool Hand, due to les number of components, and a gain in knowledge and experience over parameter handling in Cura software, which impacts on manufacturability of prototype. Table 1 gives a summary of parameters that influence the design.

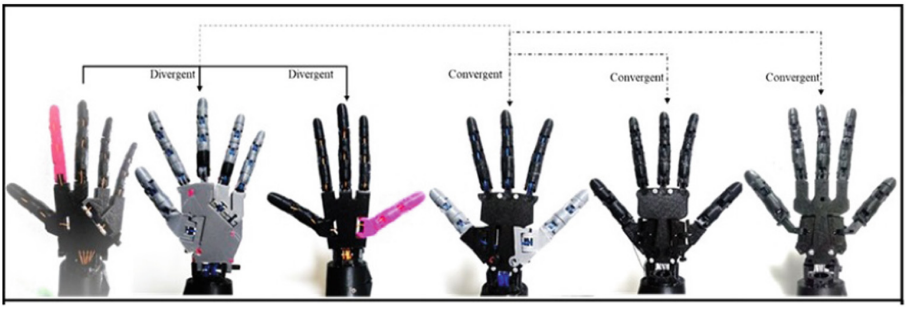

Fig. 2. Remix (Inmmov, Parloma, Remix 1, Remix 2, Remix 3, Kool Hand)

Table 1. Parameters that influence the remix.

Parameters	Inmoov	Parloma	R2	R3	R4	Kool
Number of components	36	34	44	40	33	33
Degree of freedom	17	22	15	17	19	19
Time [hr]	19	17	21	18	19	**15**
Weight [gr]	290	316	249	237	240	**227**
Printing rate [gr/min]	0.25	0.31	0.20	0.22	0.21	0.25
Cost [MX$]	1996	1808	2227	1914	2041	**1611**

4 Conclusions

The findings that have been identified in this research conclude that there are new functionalities generated by the rapid development of prototypes, by including a second thumb, modifying the size and form of the palm, reducing numbers of components, improving mobility, reducing time, weight, cost, and increasing the level of experience over DFAM. Finally, the added value is generated in the design of the prototype Kool, since there is no similar one in open digital and online communities. In forward research, we will analyze the grasp attributes, like, dexterity, precision, sensitivity, stability, and security, in a hand with two thumbs fingers.

References

1. Swanson, A., Hagert, C., Swanson, G.: Evaluation of impairment of hand function. J. Hand Surg. **8**, 709–722 (1983). https://doi.org/10.1016/S0363-5023(83)80253-6. Accessed 6 May 2019
2. Cotugno, G., Althoefer, K., Nanayakkara, T.: The role of the thumb: Study of finger motion in grasping and reachability space in human and robotic hands. IEEE Trans. Syst. Man Cybern. Syst. **47**, 1061–1070 (2016). https://doi.org/10.1109/TSMC.2016.2531679
3. Kücken, M., Newell, A.: Fingerprint formation. J. Theor. Biol. **235**, 71–83 (2005)
4. Manske, M., Kennedy, C., Huang, J.: Classifications in Brief: The Wassel Classification for Radial Polydactyly. Clin. Orthop. Relat. Res. **475** (2016)
5. Attaran, M.: The rise of 3-D printing: the advantages of additive manufacturing over traditional manufacturing. Kelley School of Business, Indiana University. Published by Elsevier Inc. (2017)
6. Flath, C.M., Friesike, S., Wirth, M., Thiesse, F.: Copy, transform, combine: exploring the remix as a form of innovation. J. Innov. Technol. **32**, 306–325 (2017). https://doi.org/10.1057/s41265-017-0043-9. Accessed 6 May 2019
7. Langevin, G.: Inmoov Hand Robot. https://www.thingiverse.com/Gael_Langevin/collections/inmoov-parts-and-derivatives. Accessed 5 June 2019
8. Parloma Hand v1 beta 2. https://www.thingiverse.com/thing:701446. Accessed 5 June 2019

Neural Engineering

Automatic Recognition and Feature Extraction of Motor-Evoked Potentials Elicited by Transcranial Magnetic Stimulation

Jose E. Tecuapetla-Trejo[1], Jessica Cantillo-Negrete[2], Raquel Valdés-Cristerna[3], Paul Carrillo-Mora[4], Oscar Arias-Carrion[5], Emmanuel Ortega-Robles[5], and Ruben I. Carino-Escobar[2,3(✉)]

[1] School of Engineering, Universidad La Salle, 09340 Mexico City, Mexico
enriquettip@gmail.com
[2] Division of Research in Medical Engineering, Instituto Nacional de Rehabilitación, 14389 Mexico City, Mexico
{jcantillo,ricarino}@inr.gob.mx
[3] Electrical Engineering Department, Universidad Autónoma Metropolitana Iztapalapa, 09340 Mexico City, Mexico
raquel.valdesc@gmail.com
[4] Neuroscience Division, Instituto Nacional de Rehabilitación, 14389 Mexico City, Mexico
neuropolaco@yahoo.com.mx
[5] Movement and Sleep Disorders Unit, Hospital General Dr. Manuel Gea González, 14080 Mexico City, Mexico
arias@ciencias.unam.mx, emmanuel_mpg40@yahoo.com.mx

Abstract. Transcranial magnetic stimulation can be used as a tool for assessment of corticospinal tract integrity by extracting features from elicited motor evoked potentials (MEPs). However, the selection of MEPs from recordings that present them, and the computation of amplitude and latency are usually performed manually. A methodology based on computing summed power calculated by means of the Discrete Fourier Transform in 10-ms windows was used for automatization of this process and compared to manual measurements. Results showed that MEP selection coincided in 69% of cases, and amplitude and latency had average differences of 7% between methods. Therefore, automatization of MEP computations is feasible using frequency-based features.

Keywords: Electromyogram · Corticospinal tract · Primary motor cortex · TMS

1 Introduction

Transcranial magnetic stimulation (TMS) is a technique which stimulates the brain cortex by inducing an electrical current in a short time lapse (approximately 1 ms) using a specialized coil. TMS is used for studying cortical interactions in the body [1]. To apply a TMS pulse, the coil is placed tangential to the subject's scalp and,

© Springer Nature Switzerland AG 2020
C. A. González Díaz et al. (Eds.): CLAIB 2019, IFMBE Proceedings 75, pp. 1037–1042, 2020.
https://doi.org/10.1007/978-3-030-30648-9_134

depending on the muscle target, is oriented in a specific angle. Motor-evoked potentials (MEP's) are a biphasic activity with a specific latency and amplitude detected by electromyography, which can be elicited in the target muscle as a consequence of a TMS pulse over the primary motor-cortex [2]. MEP features, such as amplitude and latency (stimulus-response time) are used for corticospinal tract assessment in diseases where brain damage is presented, such as stroke (neurological lesion caused by an obstruction or hemorrhage within the brain's blood vessels) [3].

For MEP recordings, the smallest muscles of the hand, such as the first dorsal interosseous (FDI) or abductor pollicis brevis muscles can be recorded without eliciting polyphasic waveforms [4]. These polyphasic waveforms increase the difficulty of extracting MEP features, and are usually in recordings from larger muscles, such as the ones located in the forearms. In addition, FDI is localized and identifiable by palpitation and, in clinical practice, this muscle is one of the most frequently examined by its easer TMS hotspot localization in the primary motor cortex.

There is no established method for MEPs automatic processing, making analysis a mostly manual procedure. For example, Groppa [4] described how TMS is used for diagnostic purposes by the interpretation of its derived features using visual strategies. Feature extraction of MEPS by a visual procedure is a long and subjective process, requiring manual inspection. This manual process makes it difficult to correctly extract MEP features and the interpretation of these measures. Examples of MEP recordings whose features need to be extracted are shown in Fig. 1.

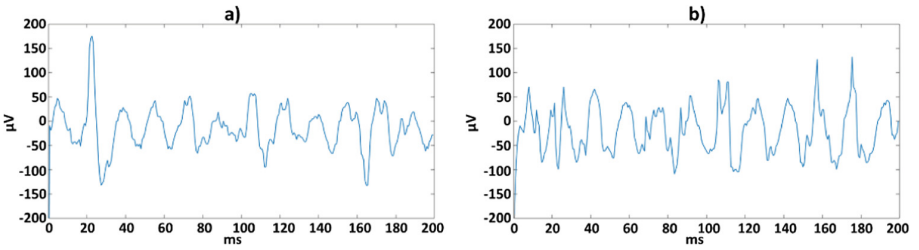

Fig. 1. MEP's signals examples. (a) Recording where the MEP can be easily identified. (b) Recording where the MEP is not easily identified.

MEP digital processing also varies according to different studies. Genschow et al. [5] used a high-pass filter to record MEP signals for offline analysis and digitized them at 2 kHz. The records of Biabani [6] and Pellegrini [7] were sampled at 1000 Hz and applied a band-pass filtering from 10–500 Hz. Only Rábago *et al.* [8] have reported an automated processing for MEP using time features, however, their algorithm did not select trials automatically based on the detection of MEPs within recordings.

In this work, different TMS sessions were recorded in stroke patients (central nervous system lesion due to a circulatory affection) as part of an ongoing study involving a new therapy intervention [9]. EMG recordings produced during TMS were used for validation of an automatic methodology for MEP recognition and feature extraction.

2 Materials and Methods

Bipolar EMG was recorded on the first dorsal interosseous (FDI) muscle for both hands of 5 stroke patients, using two passive surface electrodes on each muscle and a reference electrode located above the olecranon bone, for the corresponding extremity. Afterwards, an 8-bit analog-digital converter was used for acquisition of the trials with a sample frequency of 1500 Hz and 200 ms duration. A bandpass filter of 20 to 10 kHz was applied to the EMG signals. Figure 2 shows the coil orientation technique during a TMS session for FDI stimulation with the positioning of EMG electrodes. All patients signed an informed consent approved by the ethical commission of the National Institute of Rehabilitation in Mexico City, as part of a larger study. In total, 150 trials, 30 for each patient, were recorded using a MAGSTIM Rapid^2 stimulator with a figure-of-eight coil. Unaffected hemispheres were used for testing the proposed method since not all patients presented MEPs over their affected hemispheres due to stroke. The proposed method for MEP analysis comprised these stages:

(1) A zero-phase digital filter, of 8th order, type IIR Butterworth was used for Notch filtering of the signal, since it allowed to increase filter rejection using an IIR design without affecting the original signal phase.
(2) The filtered signal was then segmented in 69 overlapping windows of 10 ms to find which window had the highest summed power within a 0–234 Hz range, since most of the frequency power of MEPs was within this frequency range. Windows were overlapped by 9 ms. Power spectrum was computed by means of the Discrete Fourier Transform (DFT), within 5–50 ms of the trial to avoid initial artifacts and posterior TMS responses [4].
(3) The window with the highest summed power spectrum was identified as the segment of the trial containing the MEP. Latency (first time point of the window with highest power) and amplitude (computed from maximum and minimum peaks of the recording within the window's time segments) of the MEP were calculated.
(4) The algorithm discarded 10 trials out of 30 [6] by a criterion comprised by the division of the summed power spectrum of the window with the highest power, between the median of the summed power spectrum of all the trial's windows.

The automatic MEP selection and feature extraction algorithm was compared to manual measurements, performed by a single person from visual inspections of the MEPs traces for each trial. Amplitude, latency, and trials which should be discarded were manually obtained. The percentage of trials selected or discarded by both the manual and automatic methods was calculated, and a Wilcoxon rank-sum test was used for assessing if amplitudes and latency medians were significantly different ($\alpha = 0.05$) between methods, for each patient. Relative errors of amplitude and latency were also determined by considering the manual method outputs as the standard measurement.

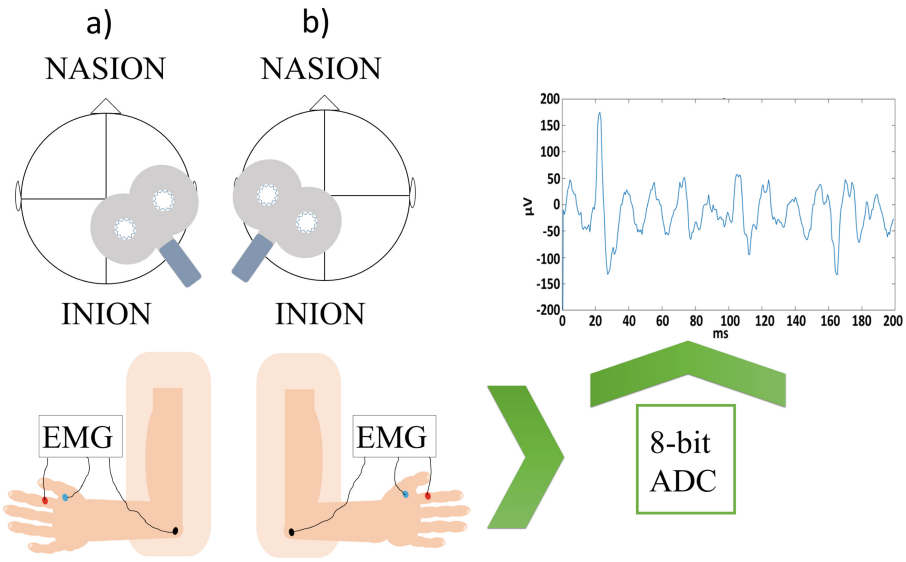

Fig. 2. Coil orientation during a TMS session for each hand with electrode location for the record of FDI activity by EMG. (a) Left hand MEP acquisition with a figure-of-eight coil on the right side of the brain cortex. (b) Right hand MEP acquisition with a figure-of-eight coil on the left side of the brain cortex.

3 Results

Figure 3 shows two MEP trials. In the first trial (a), the automatic method correctly recognized the MEP location within the trace. In the second one (b), the method recognized the waveform within the trial which resembled most a MEP. The summed power from 0–234 Hz of the maximum window of the trial with a MEP (a) was 32 times higher than the median summed power for all windows (c), while for the trial without a MEP (b) the window with maximum power was only 1.5 times higher than the median (d).

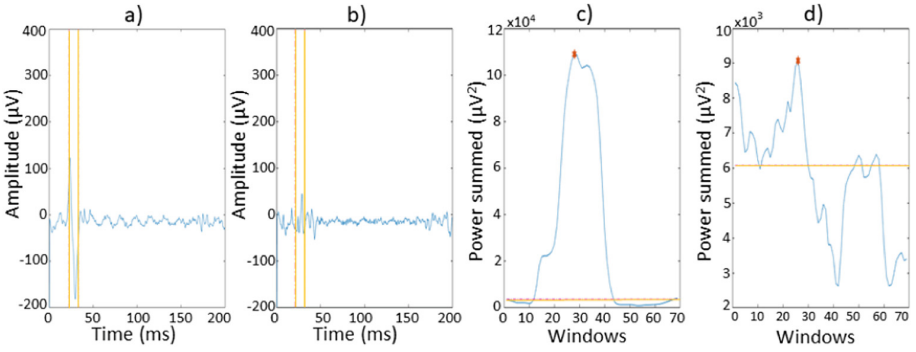

Fig. 3. (a) Trial with a MEP elicited by TMS, (b) Trial without a MEP that should be discarded, (c) and (d) Windows of summed power plotted continuously for both trials.

The percentage of trials that were recognized by both methods as trials with MEPs or without them, and mean amplitude and latency for each patient are shown in Table 1. On average, both methods coincided in 69% of their trial's selection. For each patient, computed MEP amplitudes were not significantly different (P1: $p = 0.07$, P2: $p = 0.22$, P3: $p = 0.68$, P4: $p = 0.69$, P5: $p = 0.74$) between both methods. Latency was not significantly different for 3 patients (P1: $p = 0.8$, P3: $p = 0.61$, P5: $p = 0.14$) between both methods, while significant differences (P2: $p = 0.03$, P4: $p = 0.04$) were observed for the other patients. Mean relative errors between the proposed method and the manual method were below 10% for both amplitude and latency computation.

Table 1. Comparison between automatic and manual MEP trial selection and amplitude and latency measurements. Significantly different measurements are shown (*).

ID	Trial coincidence (%)	MEP amplitude (μV)			MEP latency (ms)		
		Automatic	Manual	Relative error (%)	Automatic	Manual	Relative error (%)
P1	66.7	173.4	180.2	3.73	24.3	23.2	4.82
P2	66.7	382.3	327.8	16.62	18.8*	17.5*	7.65
P3	73.3	129.7	133.0	2.47	17.2	17.5	1.88
P4	70.0	193.7	203.2	4.66	24.8*	22.2*	11.74
P5	70.0	150.2	166.5	9.83	20.9	23.1	9.55
Mean (STD)	69.3(±2.8)	206(±101)	202(±74)	7.4(±5)	21.2(±3)	20.7(±3)	7.1(±4)

4 Conclusion

The automatic and manual methods coincided in the selection of most trials, showing that selecting trials with frequency-based criteria makes feasible the automatic task of discarding irrelevant trials in TMS studies. However, for approximately 30% of the trial sample, both methods did not coincide in their selection, which could be caused by the subjective nature of manual selection used for validation. The average MEP amplitudes computed with both methods were within the range reported using a 105% motor threshold reported by Pellegrini [7] (250 ± 300 μV). Latencies with both methods were close to the range of 27.6 ± 2.7 ms reported by Van Doren [2] in healthy subjects. Possible reasons for this difference could be stroke patients' cortical excitability differences compared to healthy subjects, and variability in manual measurements. MEP peak to peak amplitude measurements were not significantly different between methods, while computed latency was significantly different for 2 patients; again, a possible reason could be the subjective nature of manual measurements. Amplitude and latency relative errors were of approximately 7.5% using the automatic method, implying that the automatic method could replace manual inspection if a difference of less than 10% and higher than 5% is regarded as acceptable. Limitations of this study were a small sample and that only one person performed manual MEP assessments. If manual observations of more users were analyzed, the effect of the manual method's

subjectivity could be better assessed. However, obtained results suggest the feasibility of MEP automatic selection and feature extraction using information in the frequency domain.

Conflicts of Interest Statement. Authors declare that they have no conflicts of interest regarding the publication of this study.

References

1. Rotenberg, A., Horvath, J., Pascual-Leone, A.: Transcranial Magnetic Stimulation, 1st edn. Humana Press, New York (2014). https://doi.org/10.1007/978-1-4939-0879-0
2. Van Doren, J., Langguth, B., Schecklmann, M.: TMS-related potentials and artifacts in combined TMS-EEG measurements: comparison of three different TMS devices. Neurophysiol. Clin. **45**, 159–166 (2015). https://doi.org/10.1016/j.neucli.2015.02.002
3. Bath, P.M., Lees, K.R.: Acute stroke. West. J. Med. **173**, 209–212 (2000). https://doi.org/10.1136/ewjm.173.3.209
4. Groppa, S., Oliviero, A., Eisen, A., et al.: A practical guide to diagnostic transcranial magnetic stimulation: report of an IFCN committee. Clin. Neurophysiol. **123**, 858–882 (2012). https://doi.org/10.1016/j.clinph.2012.01.010
5. Genschow, O., Bardi, L., Brass, M.: Anticipating actions and corticospinal excitability: a preregistered motor TMS experiment. Cortex **106**, 81–92 (2018). https://doi.org/10.1016/j.cortex.2018.04.014
6. Biabani, M., Ferrell, M., Zoghi, M., et al.: The minimal number of TMS trials required for the reliable assessment of corticospinal excitability, short interval intracortical inhibition, and intracortical facilitation. Neurosi Lett. **674**, 94–100 (2018). https://doi.org/10.1016/j.neulet.2018.03.026
7. Pellegrini, M., Zoghi, M., Jaberzadeh, S.: The effect of transcranial magnetic stimulation test intensity on the amplitude, variability and reliability of motor evokes potentials. Brain Res. **1700**, 190–198 (2018). https://doi.org/10.1016/j.brainres.2018.09.002
8. Rábago, C., Lancaster, J., Narayana, S., et al.: Automated-parameterization of the motor evoked potential and cortical silent period induced by transcranial magnetic stimulation. Clin. Neurophysiol. **120**, 1577–1587 (2009). https://doi.org/10.1016/j.clinph.2009.04.020
9. Carino-Escobar, R., Carrillo-Mora, P., Valdés-Cristerna, R., et al.: Longitudinal analysis of stroke patient's brain rhythms during an intervention with a brain-computer interface. Neural. Plast. **2019**, 1–11 (2019). https://doi.org/10.1155/2019/7084618

Preliminary Design of a Regions-Based BCI Speller for Locked-in Patients

Lucas Baldezzari[1,2(✉)] and Gerardo Gabriel Gentiletti[2]

[1] Dpto. Río Negro, Entre Ríos, Universidad Tecnológica, Barrio Anglo, Ruta Panorámica Augusto Hoffman y Zabala, Padrón 3716, 65000 Fray Bentos, Uruguay
lucas.baldezzari@utec.edu.uy

[2] Facultad de Ingeniería, Universidad Nacional de Entre Ríos, Ruta Prov. No 11 – Km 10, Oro Verde, 3100 Parana, Prov. de Entre Ríos, Argentina
ggentiletti@ingenieria.uner.edu.ar

Abstract. An important application for Brain-Computer Interfaces (BCI) is using them for spelling task in subjects with severe motor disabilities. Most BCI spellers are based on the matrix proposed by Farwell and Donchin [1] or variations of these. Several defects of those, were resolved by other authors. In this project, an improvement of the regions-based matrix of Fazel-Rezai [2] is proposed to better realize the user experience and the speller performance. This is a preliminary design of a region-based speller using BCI to record electroencephalographic (EEG) signals, taking in mind Locked-in patients. We developed a computer based system which generate a two levels stimulation matrix. The first level has ten (10) regions with alphabet characters, numbers, some short words and a region with the capacity of propose words or phrases, in base of previous letter or words spelled by the user. The second level has only six symbols or words/phrases belonging to the region selected by the patient in the first stimulation level. The Application Module of the system, designed to detect P300 signal, was developed using the BCI2000 software [3] and the framework BCPy2000 [4]. The results of preliminary in vivo trials showed that the enhanced matrix can elicit P300 and the recognition module exhibited an average accuracy in characters' identification, ranging 75–89% and reaching 100% in one of the trials.

Keywords: Computer interfaces · P300 · Region-based stimulation · Speller

1 Introduction

Different diseases such as Amyotrophic Lateral Sclerosis, Multiple Sclerosis, cerebral palsy, muscular dystrophies, traumatic accidents, and others, can alter the neuronal channels that control the muscles, generating different levels of motor disabilities. In some cases, the person completely loses its ability to perform movements on its own, remaining in a state known as Locked-in State (LIS).

In the world, more than a billion people live with some kind of motor disability, 200 million of these have severe motor difficulties and it is estimated that this number will continue to grow [5].

© Springer Nature Switzerland AG 2020
C. A. González Díaz et al. (Eds.): CLAIB 2019, IFMBE Proceedings 75, pp. 1043–1050, 2020.
https://doi.org/10.1007/978-3-030-30648-9_135

One procedure to restore these lost functions is providing a new form of communication and control without using conventional nerve pathways or muscles. Patients affected by these types of diseases generally retain their cognitive capacity intact, which includes the ability to plan and transmit orders.

Brain Computer Interfaces (BCI) are devices that translate brain activity into messages and control signals [6]. At present, the electroencephalogram (EEG) is widely used for recording brain activity since it is a non-invasive, simple and inexpensive technique.

The BCI Spellers make it possible to patients with motor disabilities or even with LIS communicate with other people. The best known and used speller is the Farwell and Donchin speller [1]. It is a 6 × 6 matrix with letters and numbers arranged in rows and columns. The rows and columns were illuminated in a random and infrequent way, and the patients focused on the letter he/she wanted to spell evoking a P300. Over the years, the Farwell and Donchin matrix has been subject of numerous studies, all in the search of improving the Information Transfer Rate (ITR) [7–13]. Different studies show some perceptual errors associated with the Farwell and Donchin matrix such as problems of adjacency between symbols, repetition blindness, illusory conjunction, among others, which are potential sources of error in the detection of P300 [2, 14–16].

In 2010 Fazel-Rezai proposed a novel speller, also based on P300, called Region Based Paradigm (RBP). His method displayed 7 regions on a screen, where each of these contained 7 symbols (letters, numbers and special characters), making a total of 49 symbols (13 symbols more than in the Farwell and Donchin conventional matrix). With this new paradigm the perception problems generated in the Farwell and Donchin matrix are reduced as well as some advantages are obtained, namely, it is possible to increase the distance between regions in the first level screen and between symbols in the second level screen, decreasing the problems of adjacency; also, the same region does not light up two consecutive times as it can happen in the Farwell and Donchin matrix, decreasing the blindness for repetition. Also, the expectation (by the observer) of a single region appearing is decreased. As a consequence, the P300 amplitude is greater [7].

In this work we added several advantages to the Fazel-Rezai matrix method. We augmented the regions up to 10, in order to increase the P300 amplitude. Other improvement we made was the introduction of autocompleting the words departing of single selected characters by the observer.

2 Materials and Methods

2.1 Stimulation Matrix

For the matrix development and implementation, the BCI2000 software [15 bci2000 homepage] and a framework called BCPy2000 were used [16 bcpy2000 homepage].

The BCI2000 software has four fundamental modules: acquisition module, signal processing module (PM), application module (AM) and operator module.

In the present work, the AM was developed from zero, which would be used as a stimulation matrix. The AM code can be seen in [17].

The developed matrix contains 2 levels of stimulation. The first level consists of 10 regions. Of this total of regions, 9 of them are constituted by a group of 9 characters ranging from the letter A to Z, numbers from 0 to 9, special features such as "RR"-"CH"-"LL"-"."(dot)-","(comma) and certain words of the type "what", "how", "why", and similar. The tenth region contains possible words that the subject would like spell. These words are obtained from a Python package called *autocomplete* (v 0.0.104) [18 package autocomplete] which uses n-grams and distribution of probabilities to determine the possible words considering the already spelled letters, as well as the last one the bracket previously spelled. Each of these regions it was illuminated individually, infrequent and randomly. When a region was selected, the system showed a second level of stimulation which contain the symbols of the previous regions that had been selected. The Fig. 1 show the screens for the first and second levels of stimulation.

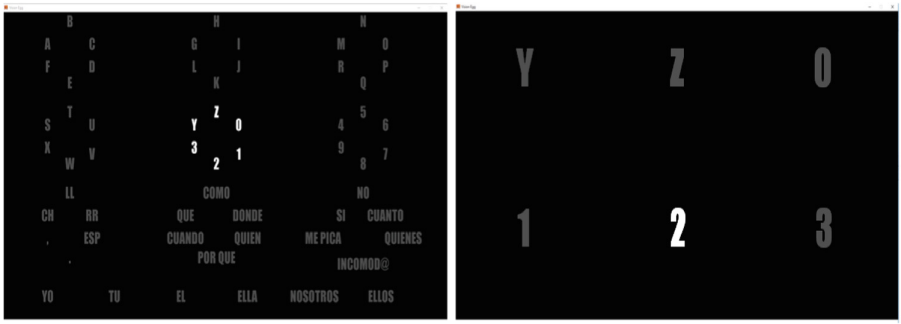

Fig. 1. A shows the screen with the 10 regions corresponding to the first level of stimulation (the 5th region is shown enlighted, 10th region is the lower row, with frequently used words). B shows the screen for the second level of stimulation, with the symbols of the 5th region (the character 2 appears enlighted).

AM receives control signals from PM. During one epoch, AM is illuminating regions in an individually, infrequent and randomly way. When a P300 is detected by PM, due to the subject was focusing his gaze in one of the region, this region was storage. After repetition of 6 epochs (see below) the focus region is validated and level 2 stimulation proceed following a similar pattern. Validation of focus region after level 2 produce identification of the character.

2.2 Volunteers

Two healthy subjects between 20 and 30 years old participated in the online tests. None of them had vision problems when they were tested. On the other hand, none of them had experience in BCI tests.

2.3 Data Acquisition

The EEG recording was performed using the gMOBIlab + device [19 gtec homepage] with 8 channels with a sampling frequency of 256 [Hz] per channel. The electrodes were positioned according to the 10–20 system. The positions used were, FZ (channel 1), CZ (channel 2), PZ (channel 3), OZ (channel 4), O1 (channel 5), O2 (channel6), C3 (channel 7) and C4 (channel 8). The reference and ground channels were placed on the left and right mastoid bones, respectively.

2.4 Experimental Procedures

Offline Session
Corrections and tuning between the algorithm written in Python and BCI2000, including the autocomplete module, were performed in the offline tests, using the tools of the BCI2000. Once the performance of the system was assessed, online records were carried out on the volunteers.

Online Session
The online experimentation phase was divided into 4 sessions

1. *Testing session of the simulation matrix*

First experimentation session consisted of using the BCI2000 and the developed matrix in order to see if P300 were generated, for this, the BCI2000 was configured to work in the CopyMode mode. In this modality, the software tells the subject in which region (for the first level) or in which symbol (for the second level) the subject must focus. The subjects were asked to freely choose three words, which would be used under this modality. Table 1 shows the election of each of the volunteers.

Table 1. Words used by the volunteer subjects in the test session

Subject	Word 1	Word 2	Word 3
Subject 1	RAMIRO	HERNAN	RAMIRO
Subject 2	GIULIANA	TIARA	FABI

2. *Linear classifier training session*

In the second session the linear classifier provided by BCI2000 called P3Classifier was trained. The P3Classifier is a tool that allows to train and test a linear classifier for the detection of evoked potentials.

The linear classifier training was made using the P3Speller application of BCI2000. Each subject used the same words of Table 1 under the CopyMode modality.

3. *Testing session using the developed matrix and the trained linear classifier*

Each subject was asked to pay attention to the three up regions of the stimulation matrix and then to items 1, 2 or 3 corresponding to each region, that is, during the first trial the subject had to focus and mentally count the times when region 1 was illuminated, when the region was selected by the system, the subject had to focus on item number 1 of the second level of stimulation and mentally count the times it was illuminated. Then proceed to the second trial where the same should be done, but focusing on region 2, then symbol 2 and so on until completing the test for region 3.

BCI200 was configured so that the processing module made a classification after six (6) epochs, the duration between stimuli was 125 ms and the duration of one stimulus was 62.5 ms.

4. *Free session*

Last session was made over voluntary subject 2 only, where he was asked to try to spell some words of its choice. In case the computed region (in the first level) by the PM after the end of an epoch was incorrect, the user should focus on some of the items (in the second region) of the region incorrectly determined and report if the item computed by the PM corresponded or not with that observed by the volunteer.

3 Results

Figure 2 shows P300 evoked for both volunteers using the stimulation matrix developed. These curves represent the coefficient of determination, which is a statistical measure computed on a pair of distribution samples, giving a measure of how strong the means of two distributions differ in relation to their variances. (Eq. 1).

$$r^2 = \frac{cov(x,y)^2}{var(x)var(y)} \tag{1}$$

Tables 2 and 3 show the success percentages for sessions 3 and 4, respectively.

Table 2. Percentages of hits for the session number 3 for voluntaries 1 and 2.

Subject	Trial 1	Trial 2	Trial 3
Subject 1	66,7%	50,0%	66,7%
Subject 2	83,3%	83,3%	100%

Table 3. Success rate for free mode in the test session for subject 2.

Spelled words	Word 1 GIULI	Word 2 FABI	Word 3 BRANCA
Hit percentage	70%	75%	83%

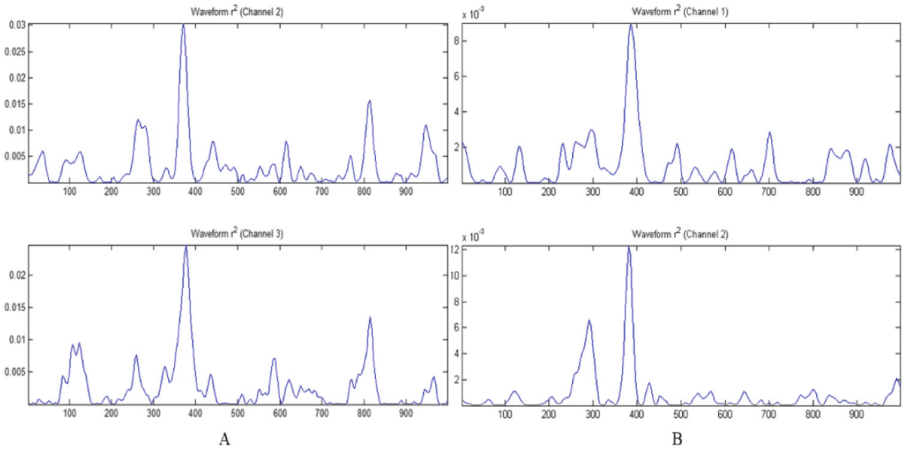

Fig. 2. Figures A and B show the presence of P300 in channels 2 and 3 for subject 1 and channels 1 and 2 for subject 2. The *x-axis* is time in milliseconds and *y-axis* is the r^2 value.

4 Discussions

Figure 2 shows that the developed matrix generates P300 potentials after averaging over six epochs, which makes it suitable to be used as a stimulation method. The training time for each volunteer was less than 10 min. Tables 2 and 3 present the results about the voluntary subjects. The free session was performed for only one user. It is important to note that the percentages of correct answers are based on computing the characters correctly determined by the system versus the total of characters in the word that the volunteer wanted to spell.

In the present work, the design, development and testing of a region-based stimulation matrix was proposed to be used as a speller in a BCI as an alternative to the Farwell and Donchin matrix. It was proposed to add a region where words proposed by the system were presented as the user spelled, in this way, the user could select a complete word instead of having to spell it, similar to [11] and thus increase the ITR.

However, during the development of the online tests, some problems were found between the BCPy2000 module and BCI2000, such as, for example, loss of state variables that the application module (in BCPy200) must send and they are used by the processing module (in BCI2000), which translates into a bad classification. This is associated with a high computational demand on the part of the module programmed in Python.

5 Future Works

In order to validate and compare the present design with those from other authors [8–11], more tests should be performed on a large number of voluntary subjects, without motor disabilities as well as Locked-in patients.

It is necessary perform more online testing in order to corroborate the good performance of the autocomplete module and see if it is useful to improve the ITR. Operation tests were performed in offline mode only.

To avoid loss of state variables between the application and processing modules, a solution would be to develop the MP over the binary files of the BCI2000, in C++ language, to then compile the complete program, thus increasing the system's performance.

An alternative to BCI spelling using P300 evoked potentials is to use Steady State Visual Evoked Potentials, as implemented in [10]. In the future, the matrix proposed here could be developed so that each region of the first level and its associated symbols in the second level flash following a sinusoidal function with a certain frequency and phase.

It is important to note that the based regions paradigm can be used not only to spell, but also for the control of a wheelchair, control of household appliances, electronics, and others, simply by changing the regions with letters of the alphabet, by symbols or drawings representative of this actions.

Acknowledgments. To Dr. Leonardo Nicola Siri, for his contributions and his patience.

References

1. Farwell, L.A., Donchin, E.: Talking off the top of your head: toward a mental prosthesis utilizing event-related brain potentials. Electroencephalogry Clin. Neurophysiol. **70**(6), 510–523 (1988)
2. Fazel-Rezai, R., Ahmad, W.: P300-Based Brain-Computer Interface Paradigm Design. Submitted: 31 May 2010. Published: 4 February 2011. https://doi.org/10.5772/14858
3. BCI200 Homepage. http://www.schalklab.org/research/bci2000
4. BCPy2000 Homepage. http://bci2000.org/downloads/BCPy2000/BCPy2000.html
5. World Health Organization: World report on disability (2011)
6. Wolpaw, J.R., Birbaumer, N., McFarland, D.J., Pfurtscheller, G., Vaughan, T.M.: Brain–computer interfaces for communication and control. Clin. Neurophysiol. **113**, 767–791 (2002)
7. Allison, B.Z., Pineda, J.A.: ERPs evoked by different matrix sizes: implications for a brain computer interface (BCI) system. IEEE Trans. Neural Syst. Rehabil. Eng. **11**, 2 (2003)
8. Takano, K., Komatsu, T., Hata, N., Nakajima, Y., Kansaku, K.: Visual stimuli for the P300 brain computer interface: a comparison of white/gray and green/blue flicker matrices. Volúmen **120**, 1562–1566 (2009)
9. Chen, X., Wang, Y., Nakanishi, M., Gao, X., Jung, T.-P., Gao, S.: High-speed spelling with a noninvasive brain–computer interface. PNAS **112**(44), E6058–E6067 (2015)
10. Chen, X., Chen, Z., Gao, S., Gao, X.: A high-ITR SSVEP-based BCI speller. Brain Comput. Interfaces **1**, 181–191 (2015)
11. Akram, F., Han, H.-S., Kim, T.-S.: A P300-based brain computer interface system for words typing. Comput. Biol. Med. **45**, 118–125 (2014)
12. Brunner, P., Ritaccio, A.L., Emrich, J.F., Bischof, H., Schalk, G.: Rapid communication with a "P300" matrix speller using electrocorticographic signals (ECoG). Front Neurosci. **5**, 5 (2011)

13. Cecotti, H.: Spelling with non-invasive brain-computer interfaces-current and future trends. J. Physiol. Paris **105**(1–3), 106–114 (2011)
14. Fazel-Rezai, R.: Human error in P300 speller paradigm for brain-computer interface. In: 29th Annual International Conference of the IEEE Engineering in Medicine and Biology Society, pp. 2516–2519, 22–26 (2007)
15. Salvaris, M., Sepulveda, F.: Perceptual errors in the Farwell and Donchin matrix speller. In: 4th International IEEE/EMBS Conference on Neural Engineering (2009)
16. Townsend, G., LaPallo, B.K., Boulay, C.B., Krusienski, D.J., Frye, G.E., Hauser, C.K., Schwartz, N.E., Vaughan, T.M., Wolpaw, J.R., Sellers, E.W.: A novel P300-based brain-computer interface stimulus presentation paradigm: moving beyond rows and columns. Clin. Neurophysiol. **121**(7), 1109–1120 (2010)
17. Application module code source. https://github.com/lucasbaldezzari/BCI-usingBCpy2000
18. Package Autocomplete Homepage. https://pypi.org/project/autocomplete/0.0.104/, último acceso, 16/04/2019
19. Gtec Homepage. http://www.gtec.at/Products/Hardware-and-Accessories/g.MOBIlab-Specs-Features
20. Gao, S., Wang, Y., Gao, X., Hong, B.: Visual and auditory brain-computer interfaces. IEEE Trans. Biomed. Eng. **61**(5), 1436–1447 (2014)

Real-Time Home-Devices Control Based on Pupil Position

Cristian E. Ordoñez(✉), Eduardo L. Blotta, and Juan Pastore

Departamento de Electrónica, Laboratorio de Procesamiento Digital de Imágenes, Facultad de Ingeniería, ICYTE-CONICET, UNMDP, Mar del Plata, Argentina
ordonez@fi.mdp.edu.ar

Abstract. This paper proposes a Real-Time Home Devices Control System based on the processing of the user's pupil position. A low-cost method is proposed to assist people with reduced mobility, unable to handle any type of device manually. The system was tested using a television and the software "Plaphoons" as test devices. It is capable of identifying up to six different action commands. The method allows to identify if the user is looking towards the screen and uses this information to determine if you want to perform some command. Each time a command is identified, a signal is sent to an electronic interface that allows to operate a universal remote control adapted for that purpose.

The system was successfully tested in real cases by patients of the Cilsa ONG institution. The tests performed showed that the system is capable of being used successfully by users of different ages and with different degrees of motor disability.

Keywords: Real time · Digital image processing · Remote control · Pupil position · Home devices

1 Introduction

In 2018, the National Institute of Statistics and Censuses of the Argentine Republic (INDEC) revealed that 10.2% of the Argentine population has some type of disability. In absolute terms, this represents an estimation of more than 3,5 million people. Segmenting the information by type of disability, it was found that 42.7% have motor difficulties that cause them great difficulty or impossibility to grab and lift small objects with their hands or arms, or great difficulty or impossibility to walk or climb stairs [1]. These figures encourage the development of inclusive technology with the purpose of improving the quality of life of these people.

Nowadays, we are surrounded of technology that can be controlled wirelessly. This technology is usually manually operated through a control, for example a remote control of television, audio equipment, air conditioner, or a cell phone application. This means that a large number of people with different degrees of motor disability are unable to use this type of technology which is increasingly used.

© Springer Nature Switzerland AG 2020
C. A. González Díaz et al. (Eds.): CLAIB 2019, IFMBE Proceedings 75, pp. 1051–1059, 2020.
https://doi.org/10.1007/978-3-030-30648-9_136

Existing methods that allow people to control home devices without using their hands can be divided into four categories according to the technology on which they are based: bio-potential, voice, body movement, and image analysis.

Anu et al. [2] propose a system based on biopotential signals. They present a non invasive electroencephalograph control in order to control smart home applications using a sensing headset, a data processing unit and a home appliance controller.

Some researchers use voice control to develop this type of technology. Rathnayake et al. [3] uses a Kinect sensor, the Microsoft Speech Recognition Engine and an electronic interface based on Arduino board to control home appliances.

Wang et al. [4] proposes a smart home control system using the head and the mouth movement. The system combines the Adaboost algorithm and ASM algorithm for face detection and feature-point calibration to detect the user's head movements and mouth status information.

Finally, some authors like Bonino et al. [5] employs an image analysis approach. They propose an eye-based interface using the requirements of smart environments, already outlined in a public Recommendation issued by the COGAIN European Network of Excellence [6]. The software prototype is based on the ETU universal driver [7], thus is potentially capable to operate on a variety of eye trackers.

Some issues that can be found in the works that are shown in the literature, are that often can be uncomfortable to use, expensive, and not always work properly.

In this work, a low-cost Real-Time Home Devices Control System based on the spatial position of the user's pupil is presented. The system focuses on people with difficulties or impossibility to handle any type of remote control manually.

The proposed method analyzes the spatial position of the user's pupil in order to identify up to six possible action commands. To achieve this goal, a portable computer, an electronic interface and a modified universal remote control are used. To evaluate the system performance a TV and the software Plaphoons [15] were used as test devices.

This paper is organized as follows: Sect. 2 presents the description of the hardware used. In Sect. 3 the implemented method is developed and finally, in Sect. 4, the results obtained are shown.

2 Materials and Methods

2.1 Hardware Description

The proposed system employs a standard specifications PC laptop to run the algorithm that analyze the user's pupil position, an electronic interface based on an Arduino Nano V3.0 board and a modified universal remote (RVTC RM-014S +) control that allows to handle practically any model and brand of LED/LCD TV, see Fig. 1.

Fig. 1. Proposed system.

3 Implementation

The proposed method is composed of three stages as shown in Fig. 2: Identification and Transmission of commands, Signal Conditioning and Execution.

The identification and transmission stage is an algorithm that runs on the PC and is responsible for analyzing the spatial position of the user's pupil in order to generate the command signal. This signal is sent to the signal conditioning stage which is an electronic interface that translates the software´s orders to the remote control. Finally, the execution stage represents the activation of the remote control.

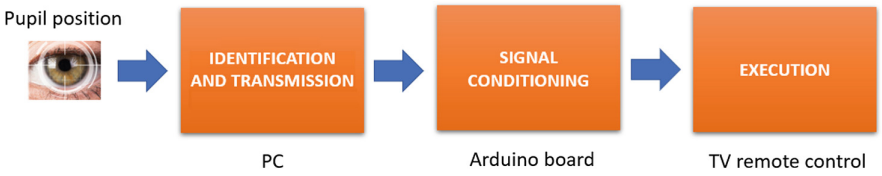

Fig. 2. Stages of the proposed method.

3.1 Identification and Transmission

This stage receives the information referred to the spatial position of the user's pupil. This position is obtained by processing the video frames acquired by a camera that is mounted on the eye tracking glasses, see Fig. 1. This processing is performed by a pupil tracking algorithm developed by Ordoñez et al. [8–11], which is based on the Hough Transform and the dark pupil effect.

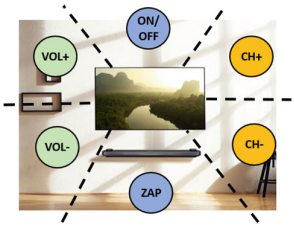

Fig. 3. Gaze direction to perform each command.

The Command Identification and Transmission stage allows to identify up to six possible commands based on the position of the user's pupil: turn up the volume, lower the volume, upload a channel, download a channel, zap and deactivate/activate the tracking. In order to execute these commands, the user must hold the gaze off the screen for two seconds, pointing to any of the six regions shown in Fig. 3.

An initial calibration is necessary so that the software can correctly identify each of the commands. This process seeks to identify the pupil positions that are generated when the user looks towards the center and towards the four corners of the screen. This calibration process allows the system to determine if the user is looking at the screen or outside the screen. The calibration process is performed as soon as the software is started and is performed as follows:

1. Initially the software shows the video signal captured by the camera and asks the user to look at the center of the screen for a few seconds, see Fig. 4. The red box represents the processing region.
2. Then, as Fig. 5 shows, the user must look for a few seconds towards the upper left corner of the screen. The video signal captured by the camera is displayed at the top, the red cross represents the detected pupil position, the green box represents the processing window and a yellow text shows the number of frames processed per second.
3. The process detailed in 2 is repeated for the rest of the three corners.
4. Finally, using a criterion of spatial distribution of the detected positions, it is established whether the calibration was correct. If so, a message is displayed indicating that the calibration was successful, if not, steps 1 to 4 must be repeated.

Fig. 4. Initial software interface.

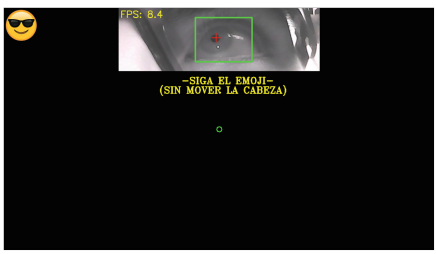

Fig. 5. Software interface during the calibration process.

Once the calibration process is completed, a set of points is obtained and used to generate, using affine transformations, a map of regions like the one shown in Fig. 6, which has the following features:

1. In the center of the map appears a rectangle with rounded edges. This curve represents the region of pupil position associated with the area of the screen. That is, when the user looks at the screen, the detected pupil position will reside in this region. The set of points x_i, y_i that are inside the rectangle represent the pupil positions that were obtained in the calibration process.
2. Outside the previous region, there are six additional regions that represent the pupil positions associated with each of the six commands. That is, when the user looks away from the screen, trying to perform some command, the detected pupil position will reside in one of these six regions.
3. In order to implement this map, an array of 3600 elements is generated. This array stores in polar form the phase and amplitude that the pupil position must have to fall inside of the command regions.

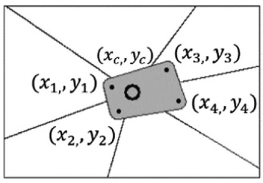

Fig. 6. Map of regions generated through the calibration process.

Following the calibration process, an interface like the one shown in Fig. 7 appears.

The video signal captured by the camera is displayed at the top and below the map of regions mentioned. The detected pupil position is represented by a red dot.

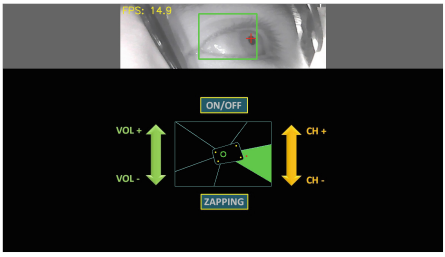

Fig. 7. Software interface after the calibration process.

In order to determine if any of the six possible commands is being performed, the following procedure is done:

1. The phase and amplitude of the vector representation of the obtained pupil position is calculated (taking as origin the central position obtained in the initial calibration process).
2. The array generated through the map of regions is consulted as a lookup table.
3. If the detected pupil position is inside of any of the six possible regions and the command is held for more than two seconds, it is considered as valid.
4. Then, the detected command is sent as a string to the electronic interface through a USB port.

3.2 Signal Conditioning

This stage is based on an Arduino Nano board that is described in the section "Materials and Methods" and is responsible for establishing the communication between the software and the remote control.

The signal conditioning stage processes the messages sent by the USB port of the personal computer in order to identify if any command is performed. The signal conditioning is achieved using an integrated circuit that operates as a quadruple bilateral digital key (CD4066). Through this set of digital keys, it is possible to generate a signal that simulates the operation of the remote-control buttons.

3.3 Execution

The execution stage uses a universal remote control that is able to operate practically any brand and model of LCD/LED TV.

In order to be able to control the volume and channel buttons of the remote control a small molex connector is added. As shown in Fig. 1, this connector has 6 pins which communicate with the tracks of the buttons to operate.

4 Results

As mentioned, the performance of the system was evaluated using a television as a test device.

CILSA ONG, as part of the bases of the APPcesible 2018 contest, gave us the possibility of carrying out some tests at its headquarters in Mar del Plata with people with different degrees of motor disability. Table 1 shows the results obtained by six users with different degrees of motor disability, which takes values from one to three, where 1 means mild, 2 moderate and 3 severe. Also, shows the training time required by each patient to learn how to use the system successfully, and the number of commands correctly identified for a total set of twenty commands. Figure 8 shows one of users that tested the system at Cilsa [13, 14].

Table 1. Test results.

User	Degree of motor disability	Training time	Identified commands
1	1	10 m	95%
2	1	5 m	90%
3	2	20 m	85%
4	2	20 m	60%
5	3	2 sessions of 30 m each	65%
6	3	3 sessions of 30 m each	60%

Fig. 8. User testing the system.

The initial results show that people with a higher degree of disability require more training time in order to use the system correctly, as expected. This does not prevent them from being able to use the system properly, after a suitable training time.

It is difficult to compare the results obtained with the works that can be found in the literature, that is, to find a common parameter under controlled variables in order to quantify the response of each method. Each one has its advantages and disadvantages, the advantages of this method lie in its low cost, it is simple to use, able to control different devices, and according to the tests performed works satisfactorily.

As shown in [12] the system can also be used to handle software designed for people with different types of disability, such as "Plaphoons" [15]. The video shows how the software is able to position and click on six different positions on the screen, allowing people with any speech disorder to use these plaphoons to select different messages which can be configured according to the needs of the user.

As mentioned, the proposed system was presented in the APPcesible 2018 contest, developed by Cilsa ONG along with Microsoft company. After being evaluated by different juries, composed of referents from sectors linked to technology, disability, business and institutions, the project was selected as one of the winners in the "Disruptive Technology" category.

5 Conclusions

A real time control system of home devices based on pupil detection, capable of interpreting up to six possible action commands was implemented. Depending on the user's ability to perform the necessary pupil movements, it is possible to increase the number of commands that can be performed.

The system also allows controlling the mouse of a computer which can be used to control basic programs developed for people with diverse types of disabilities.

To evaluate the performance of the system a TV was used as a test device, however, these results can be extrapolated to any other electronic home device. Depending on the device to be controlled, a signal adaptation stage connected to the interface output may be necessary.

The tests performed showed that the system is capable of being used successfully by users of different ages and with different degrees of motor disability. They also showed that each user needs a different training time to be able to use the system properly.

It is important to mention that some types of motor disability generate that the person does not have enough control of the eye movement to use this type of technology. In addition, it is likely that the user may experience some level of exhaustion, especially in the adaptation stage, if he tries to perform too many commands in a short period of time.

As future work, it is proposed to perform a greater number of tests with users of different ages and different degrees of motor disability in order to learn from their experiences and make the system more robust and easier to use. In addition, it is proposed to optimize the Interpretation and Command Transmission stage in order to have more processing time to reduce the number of false positives.

Acknowledgment. The authors wish to thank all the people of Cilsa for the goodwill shown at all times, the project support provided and mainly for allowing us to test our project on potential users of the system. In addition, we want to thank Bibiana Barreneche for opening the doors of her house and contribute to the project performing several tests of the system.

Conflict of Interest. The authors declare that they have no conflict of interest.

References

1. Estudio Nacional sobre el Perfil de las Personas con Discapacidad Instituto Nacional de Estadística y Censos (INDEC). Dirección Nacional de Estadísticas Sociales y de Población (DNESyP). ISBN: 978-950-896-519-6
2. Anu, K.E., Joseph, J., Narayanan, S., George, S., Joy, M.M.: Non invasive electroencephalograph control for smart home automation. In: National Conference on Recent Advances in Electrical & Electronics Engineering (NCREEE 2016), ISSN (Online), pp. 2278–8875, vol. 5, Special Issue 3, March 2016

3. Rathnayake, K.A.S.V., Diddeniya, S.I.A.P., Wanniarachchi, W.K.I.L., Nanayakkara, W.H. K.P., Gunasinghe, H.N.: Voice operated home automation system based on Kinect sensor. In: 2016 IEEE International Conference on Information and Automation for Sustainability (ICIAfS), Galle, pp. 1–5 (2016). https://doi.org/10.1109/iciafs.2016.7946530
4. Wang, X., Liang, L., Deng, T., Wang, Z.: Smart home control system for the disabled using the head and the mouth movement. In: Proceedings of the 29th Chinese Control Conference, Beijing, pp. 3527–3530 (2010)
5. Bonino, D., Castellina, E., Corno, F., De Russis, L.: DOGeye: controlling your home with eye interaction. Interact. Comput. **23**(5), 484–498 (2011)
6. COGAIN homepage. https://www.cogain.org/
7. Špakov, O.: University of Tampere in Finland. https://www.tobiipro.com/siteassets/tobii-pro/about/app-market/app-market/tobii-test-of-eye-tracking-universal-driver/
8. Gonzalez, R.C., Woods, R.E.: Digital Image Processing, 2nd edn. Prentice Hall (2002)
9. Bruno, J.S.: Reconocimiento de burbujas en formularios inteligentes aplicando la Transformada de Hough. FRBA-UTN, Buenos Aires, Argentina, 2005
10. Ballard, D.H.: Generalizing the Hough transform to detect arbitrary shapes. Pattern Recogn. **13**(2), 111–122 (1981)
11. Ordoñez, C., Pastore, J., Blotta, E.: Real-time gaze-tracking embedded-system. Congreso Argentino de Sistemas Embebidos (CASE2017). Ciudad de Buenos Aires, 9 al 11 de agosto de 2017
12. Open Eye Tracker sample video. https://www.facebook.com/2005046846227837/videos/332311554198501/
13. Cilsa homepage. https://www.cilsa.org/
14. APPcesible contest, Desarrollar inclusion homepage. https://desarrollarinclusion.cilsa.org/
15. Proyecte fresa homepage. http://projectefressa.blogspot.com/

Parkinson's Disease Classification Using Artificial Neural Networks

Carlos Castro[1(✉)], Eunice Vargas-Viveros[1], Alejandro Sánchez[2], Everardo Gutiérrez-López[2], and Dora-Luz Flores[1]

[1] Facultad de ingeniería, Arquitectura y Diseño, Universidad Autónoma de Baja California, 22860 Ensenada, Baja California, Mexico
I.carlos.castro@uabc.edu.mx

[2] Facultad de Ciencias, Universidad Autónoma de Baja California, 22860 Ensenada, Baja California, Mexico

Abstract. An artificial neural network multi-layer perceptron classifier was developed to make a diagnosis of Parkinson's disease (PD) using a dataset obtained from the UCI Machine Learning Repository. The dataset consists of voice recordings from patients with PD and a control group. Multiple networks were trained to vary the number of neurons in the hidden layer between 10 and 6000 in steps of 10. The network with 280 neurons in the hidden layer had the best performance showing an accuracy of 95.23%, a precision of 96.40%, a recall of 97.10%, a specificity of 90.19%, and a F1-score of 96.75%. Artificial neural networks can be used to differentiate if a patient has PD using speech-related features. Furthermore, machine learning methods could predict other neurological diseases if the biomedical information is available.

Keywords: Artificial neural networks · Medical diagnosis · Parkinson's disease

1 Introduction

Parkinson's disease (PD) is a neurological disorder where different motor and non-motor features negatively impact the normal functions of the patients who suffer the disease [1]. PD is caused by the loss of neuronal cells in the brain area known as the substantia nigra [1,2]. There is a neurotransmitter called dopamine that is involved in the control of movements and coordination. As neurons die, the amount of dopamine in the brain decreases and the person's capability to coordinate and make movements becomes affected [3]. Therefore, PD patients commonly have difficulty in walking, speaking and writing or completing simple tasks [3,4].

PD affects a significant percentage of the population and its diagnosis is difficult at an early stage due to the slow progression of the disease [5]. As PD can pass unnoticed until it is too late, early diagnosis becomes especially important, in order to find appropriate treatments [3,6]. Even thought neuroimaging

© Springer Nature Switzerland AG 2020
C. A. González Díaz et al. (Eds.): CLAIB 2019, IFMBE Proceedings 75, pp. 1060–1065, 2020.
https://doi.org/10.1007/978-3-030-30648-9_137

techniques can be useful in the diagnosis of PD, there is a need to improve the resolution and sensitivity using neuroimaging approaches [1]. Another approach consists of speech analysis as an indicator of PD, in order to make an early diagnosis [7], due to 90% of patients with PD developing some kind of speech problems [8].

Machine learning algorithms are powerful computational techniques that can be designed to treat medical information and are being successful with high dimensional data and large datasets, excelling when statistical models cannot produce good results [9]. Artificial neural networks (ANNs) are a machine learning method capable of predicting an output, making calculations and learning from a set of input data [10]. In addition, classification is the process where two or more output variables are separated. Classification is commonly used to perform a diagnosis, separating the data of healthy patients from the data of patients that have the disease [6].

In this study, a classification model was developed using ANNs, in order to predict if a patient has PD or not using speech recordings as the model input features.

2 Methods

2.1 Dataset

The dataset was obtained from the UCI Machine Learning Repository [11]. The data contains information from 188 patients with PD (107 men and 81 women) with ages ranging from 33 to 87, and 64 healthy individuals (23 men and 41 women) with ages varying between 41 and 82. The data consists of recordings that were processed using time-frequency features, Mel frequency cepstral coefficients, wavelet transform based features, vocal fold features and tunable Q-factor wavelet transform features [8]. The final dataset used was 756 values x 754 input features.

2.2 Experimental Setup

ANNs were developed using Python 3.7, with the scikit-learn machine learning library. The neural network classifier created uses a multi-layer perceptron trained with backpropagation. The net was trained using the "relu" activation function, the "lbfgs" solver, 1000 maximum number of iterations and "constant" learning rate; other values for those parameters were tested but they did not show better results against the results obtained by the values mentioned above (data not shown). The number of neurons in the hidden layer was varied between 10 and 6000 in steps of 10 to determine the number of neurons in the hidden layer with the best performance because the number of neurons can greatly change the performance of the network [12,13]. Each specific configuration was performed ten times, resulting in 6,000 nets trained. The input data was randomly partitioned into a training and test set of 75% and 25% of the data respectively.

2.3 Metrics

The confusion matrix is a graphical and common graphical representation of a classifier's accuracy. A confusion matrix consists of: positive samples correctly predicted (TP), negative samples correctly predicted (TN), positive samples wrongly predicted (FN) and negative samples wrongly predicted as positive (FP) [14]. Alongside the confusion matrix, there are four metrics that help to determine classification performance. Accuracy (1), precision (2), recall (3), specificity (4) and F1-score (5) are metrics commonly used in classification tasks [14].

$$Accuracy = \frac{TP + TN}{TP + FP + TN + FN} \tag{1}$$

$$Precision = \frac{TP}{TP + FP} \tag{2}$$

$$Recall = \frac{TP}{TP + FN} \tag{3}$$

$$Specificity = \frac{TN}{FP + TN} \tag{4}$$

$$F1\text{-}score = \frac{2 * Precision * Recall}{Precision + Recall} \tag{5}$$

3 Results

Figure 1 shows the average accuracy obtained for each configuration of neurons in the hidden layer, where the red dot is the best average accuracy obtained (2940 neurons). As shown in Fig. 1, when the number of neurons is low, the accuracy

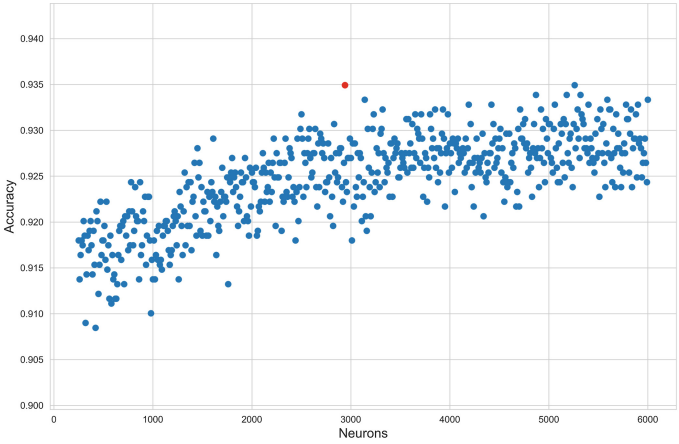

Fig. 1. Variation of the accuracy of the classifier as the number of neurons in the hidden layer increases.

obtained by the classifiers increases with the number of neurons. After the initial rise in accuracy, the performance shows similar levels and stops increasing even when the number of neurons in the hidden layer increases. As the accuracy maintains similar levels in almost all the range of neuron values, is possible that the accuracy will not increase when adding more neurons to the hidden layer.

The best overall network was selected based on the performance metrics mentioned in the previous section, prioritizing the accuracy level and the confusion matrix. Table 1 shows the metrics obtained by the networks with the highest and lowest performance, resulting in 280 neurons in the hidden layer for the network with the higher accuracy and 10 neurons in the hidden layer for the network with the lowest accuracy. These results match the values shown in Fig. 1 where the network with the smallest amount of neurons in the hidden layer performed more poorly than the networks with more number of neurons. All metrics showed values greater than 0.90, meaning that the classifier can correctly predict if a person has PD or not.

Table 1. Metric values for the best and worst networks obtained

	Accuracy	Precision	Recall	Specificity	F1-score
280 neurons	0.9523	0.9640	0.9710	0.9019	0.9675
10 neurons	0.8730	0.9191	0.9057	0.7843	0.9144

In addition, Fig. 2 shows the confusion matrix obtained by the neural classifier with the best performance metrics. The network with 280 neurons in the hidden layer had the best confusion matrix alongside the accuracy for the classification of PD. As can be seen, the majority of instances were correctly classified, thus, making a correct diagnosis of PD.

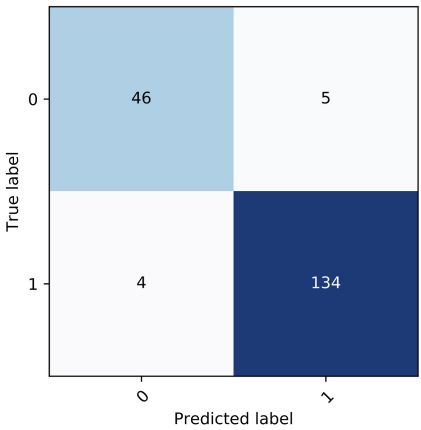

Fig. 2. Confusion matrix for the network with the best performance.

4 Discussion

As can be seen in Table 1, there is a considerable gap between the values of the metrics obtained for the classifier with 280 and 10 neurons, especially for the accuracy. This means that a higher number of neurons can be beneficial for the network performance. However, a considerable range of values for the neurons in the hidden layer was tested and the results were similar for almost all of those values. Nonetheless, as mentioned in [13], an excessive number of neurons can be problematic and this is another reason why the network with 280 neurons was chosen as the best, so a high number of neurons will not improve the performance of the models. The next step is to add more hidden layers to the network to test if the accuracy and other metrics improve.

The results obtained by the net classifier are highly promising, proving that speech analysis is a proper approach to discriminate between patients with or without PD, obtaining an accuracy of 95.23%, which is considerably higher than the results reported by Sakar et al. [8] using the same dataset, where a best accuracy of 86% was obtained with a support vector machine using a radial basis function.

The high metric values confirm that ANNs are a suitable technique to carry out classification tasks with biomedical data. In order to successfully accomplish that, the data needs to be pre-processed exactly as described in Sakar et al. [8].

Machine learning methods have the capability to help professional physicians to make a more accurate diagnosis of PD, but also in other diseases where accurate diagnosis is difficult. As future work, the accuracy of the network can be improved performing a feature selection algorithm to determine which features are the most important. Furthermore, networks with multiple hidden layers can be created.

In addition, neural networks and other machine learning methods require a high amount of data to create highly accurate models that can help to make an early diagnosis. Nonetheless, public, free and globally available medical data are often non-existent, therefore, in order to improve patient's quality of life, there is a need for hospitals and research groups to gather and share their data.

Conflicts of Interest. The authors declare that there are no conflicts of interest with respect to the publication of this research.

References

1. Blochberger, A., Jones, S.: Parkinson's disease clinical features and diagnosis. Clin. Pharmacist **3**, 361–366 (2011). https://doi.org/10.1136/jnnp.2007.131045
2. Tolosa, E., Wenning, G., Poewe, W.: The diagnosis of Parkinson's disease. Lancet Neurol. **5**, 75–86 (2006). https://doi.org/10.1016/S1474-4422(05)70285-4
3. Gokul, S., Sivachitra, M., Vijayachitra, S.: Parkinson's disease prediction using machine learning approaches. In: 5th International Conference on Advanced Computing, pp. 246–252 (2014). https://doi.org/10.1109/ICoAC.2013.6921958

4. Mathur, R., Pathak, V., Bandil, D.: Emerging trends in expert applications and security. Emerg. Trends Expert Appl. Secur. **841**, 357–363 (2019). https://doi.org/10.1007/978-981-13-2285-3
5. Alqahtani, E.J., Alshamrani, F.H., Syed, H.F., Olatunji, S.O.: Classification of Parkinson's disease using NNge classification algorithm. In: 21st Saudi Computer Society National Computer Conference, pp. 1–7 (2018). https://doi.org/10.1109/NCG.2018.8592989
6. Kubota, K., Chen, J., Little, M.: Machine learning for large-scale wearable sensor data in Parkinson's disease: concepts, promises, pitfalls, and futures. Mov. Disord. **31**, 1314–1326 (2016). https://doi.org/10.1002/mds.26693
7. Klempir, O., Krupicka, R.: Machine learning using speech utterances for Parkinson disease detection. Lekar a Technika **48**, 66–71 (2018)
8. Sakar, C., Serbes, G., Gunduz, A., Tunk, H.C., Nizam, H., Sakar, B.E., Tutuncu, M., Aydin, T., Isenkul, M.E., Apaydin, H.: A comparative analysis of speech signal processing algorithms for Parkinson's disease classification and the use of the tunable Q-factor wavelet transform. Appl. Soft Comput. J. **74**, 255–263 (2019). https://doi.org/10.1016/j.asoc.2018.10.022
9. Fatima, M., Pasha, M.: Survey of machine learning algorithms for disease diagnostic. J. Intell. Learn. Syst. Appl. **9**, 1–16 (2017). https://doi.org/10.4236/jilsa.2017.91001
10. Flores, D.-L., Gómez, C., Cervantes, D., Abaroa, A., Castro, C., Castañeda-Martínez, R.A.: Predicting the physiological response of Tivela stultorum hearts with digoxin from cardiac parameters using artificial neural networks. BioSyst. **151**, 1–7 (2017). https://doi.org/10.1016/j.biosystems.2016.11.002
11. Parkinson's Disease Classification Data Set. http://archive.ics.uci.edu/ml/datasets/Parkinson%27s+Disease+Classification
12. Mateo, F., Gadea, R., Medina, A., Mateo, R., Jiménez, M.: Predictive assessment of ochratoxin A accumulation in grape juice based-medium by Aspergillus carbonarius using neural networks. J. Appl. Microbiol. **107**, 915–927 (2009). https://doi.org/10.1111/j.1365-2672.2009.04264.x
13. Sheela, K.G., Deepa, S.N.: Review on methods to fix number of hidden neurons in neural networks (2016). https://doi.org/10.1155/2013/425740
14. Boukenze, B., Mousannif, H., Haqiq, A.: Performance of data mining techniques to predict in healthcare case study: chronic kidney failure disease. Int. J. Database Manage. Syst. **8**, 1–9 (2016). https://doi.org/10.5121/ijdms.2016.8301

Design and Implementation of a Multifunctional Myoelectric Control for Upper Limb Prostheses

Gonzalo Oviedo[1], Mariano Sosa[1], Juan Manuel Fontana[1,3(✉)], Eric Laciar[2,3], and Leonardo Molisani[1]

[1] Grupo de Acústica y Vibraciones, Facultad de Ingeniería, Universidad Nacional de Rio Cuarto, 5800 Rio Cuarto, Córdoba, Argentina
juanmfontana@ing.unrc.edu.ar
[2] Gabinete de Tecnología Médica, Facultad de Ingeniería, Universidad Nacional de San Juan, San Juan, San Juan, Argentina
[3] Consejo Nacional de Investigaciones Científicas y Técnicas (CONICET), Godoy Cruz 2290, C1425FQB Cuidad Autónoma de Buenos Aires, Argentina

Abstract. The myoelectric control of upper limb prostheses from surface EMG signals is characterized by the ease of data collection and by being non-invasive. Multiple functions of a prosthesis can be activated from the signals generated by a voluntary muscle contraction. In this work, we present a system that activates four functions of a hand prosthesis with two EMG channels by means of a command strategy based on the maximum voluntary contraction (MVC). Experiments were performed on five healthy subjects and one amputee to evaluate the feasibility of this strategy. The results showed a fluid and intuitive strategy, justified by an accurate performance of the subjects controlling the prosthetic functions.

Keywords: Myoelectric control · EMG · Upper limb prosthesis

1 Introduction

The use of electromyography signals (EMG), originated from a muscle contraction, allows people to control directly and voluntarily the functions of a certain device [1–3]. This type of signals have been widely studied by the scientific community for its implementation in myoelectric control of upper limb prosthesis [4]. In proportional myoelectric control, the amputee can select and modulate a function of the prosthesis by performing gestures involving the contraction of muscles groups located in the remaining limb. [5, 6]. Generally, surface myoelectric sensors are placed in antagonistic muscle groups to control two different functions of the prosthesis [7]. The disadvantage of this control is that the number of functions to be controlled is reduced, since each group of muscles could control only a single function. Furthermore, the number of antagonist muscles that can be used is limited in amputees due to the available space and the presence of the crosstalk phenomenon [8]. In this paper, we present the development of a myoelectric interface to voluntarily control multiple

© Springer Nature Switzerland AG 2020
C. A. González Díaz et al. (Eds.): CLAIB 2019, IFMBE Proceedings 75, pp. 1066–1072, 2020.
https://doi.org/10.1007/978-3-030-30648-9_138

functions of an upper limb prosthesis. Specifically, we present a strategy to command four functions of a robotic hand through two EMG channels located in antagonist muscles of the forearm.

2 Materials and Methods

2.1 Capture and Processing of EMG Signals

In this work, EMG signals were non-invasively captured using surface electrodes and MyoWare sensors (www.advancertechnologies.com). The electrodes were located on the surface of the forearm, separated 3 cm each. For the implementation of the control strategy, the envelope EMG signal delivered by the sensor was used.

Six non-amputees (28 ± 7 years old) and one person with short transradial amputation (26 years old) participated in an experiment designed to evaluate the proposed control strategy and obtain information about the user's experience. To carry out the experiments, a sensor (EMG1) was placed on the posterior part of the forearm of the non-amputees, in the region of the extensor muscles of the wrist. Another sensor (EMG2) was located in the anterior part of the forearm, in the area of the flexor muscles of the wrist. For the case of the amputee, the location of the sensors was based on the level of amputation and the muscular contractions that he was able to perform. Therefore, the EMG1 sensor was placed in the upper part of the remaining limb and the EMG2 sensor in the anterior part. Figure 1 shows the location of the sensors. The obtained EMG signals were sent to an Arduino board, with an ATmega 2560 microcontroller, to carry out the scanning and post-processing of the signals.

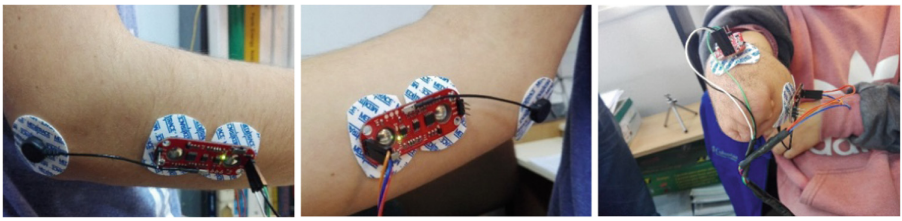

Fig. 1. Location of the electrodes in the extensor muscles (left) and wrist flexors (center). Location of electrodes in amputee user (right).

2.2 Control Strategy for the Functions of the Prosthesis

From the EMG signals a control strategy was developed to command the different functions of a prosthesis. The strategy used was based on detecting the user's intention from the maximum voluntary contraction (MVC). The system monitored the level of muscle contraction through the sensors, thus when it exceeded a preset threshold (dynamic and configurable according to the value of the MVC) a function of the prosthesis was executed.

Two antagonist muscles were monitored in order to reduce the crosstalk phenomenon and to be able to control two functions. To increase the number of functions to be controlled using the same number of sensors, a strategy was implemented in order to change the "state" of the system (from "State 1" to "State 2" and vice versa). Particularly, in the State 1, the opening and closing of a robotic hand was controlled. In State 2, the movement of the thumb was controlled. In this way, four functions of the prosthesis hand were controlled using only two EMG channels. The change of state was generated by a fast contraction of one of the two antagonistic muscles ("switch" signal). This type of contraction is characterized by its steep slope at the beginning of the transient state, which can be detected by calculating the temporal derivative of the signal.

2.3 Strategy Implementation

With the chosen sensor arrangement, the flexion of the wrist was selected to activate both hand closing in State 1 and the movement of the thumb inward in State 2. On the other hand, the extension of the wrist was selected to activate both the hand opening in State 1 and the movement of the thumb outward in State 2. Finally, a fast flexion of the wrist produced the "switch" signal to change the system's state. For the amputee, the movements used to control the functions of the prosthesis were pronation and supination of the remaining limb, while a fast pronation changed the state of the system.

A configuration routine was implemented in order to determine the parameters that each user needed to activate a function. These parameters were: (a) the mean absolute value of the EMG signal corresponding to the MVC of the flexion and extension of the wrist (pronation and supination of the remaining limb in the case of the amputee); (b) the peak value of the derivative of the EMG signal corresponding to fast flexion of the wrist (fast pronation in case of the amputee). From these values, the decision thresholds were calculated, which ranged between 60% and 70% of the MVC depending on the subjects. The threshold for the change of state was established as the average of three peak values of the derivative. Once the configuration was done, the acquired EMG signals were normalized with respect to the MVC of each channel. The use of thresholds for the activation of the functions determines a control of the ON/OFF type [9].

2.4 Prosthesis Used

The prosthesis used to evaluate the proposed system was developed by the Group of Acoustics and Vibrations (GAV) from the Faculty of Engineering of the National University of Rio Cuarto, Argentina (Fig. 2) [10]. This prosthesis consists on a robotic hand printed with 3D technology, which design resembles shape and size of an adult hand [11]. One of the main advantages of this device is the implementation of a mechanism for thumb opposition, which allows the hand to perform three different grasp configurations. Cylindrical, pinch, and lateral grasping options were implemented to facilitate the realization of the activities of daily living.

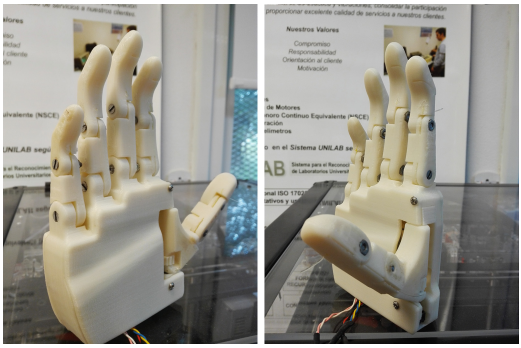

Fig. 2. Illustration of the robotic hand used in the experiments. The prototype was developed by the Group of Acoustics and Vibrations (GAV) of the National University of Rio Cuarto, Argentina [10].

3 Experiments

Experiments were conducted to evaluate the control strategy proposed. Each experiment was divided into three parts. In the first part, the system configuration routine mentioned in Sect. 2.3 was carried out in order to determine the control parameters for each participant. In the second part, each person was asked to activate ten times the function controlled by each movement. In other words, the person repeated flexion or pronation until he/she activated ten times the function related to that movement. Subsequently, the sequence for the extension of the wrist or supination of the remaining limb was repeated. Finally, fast flexion or fast pronation was repeated until ten changes in the state of the system were achieved. Five series of this part of the experiment were carried out. In each series, the number of attempts needed to reach ten successful activations of the functions was recorded. Visual displays were used to indicate to the person if he succeeded activating a function. Finally, a third part was implemented, where a robotic hand command routine was carried out. It consisted of closing the hand, opening it and then making a change of state of the system to later move the thumb laterally from one end to the other. The time required to execute the routine was recorded for each subject.

4 Results

The results obtained were separated into two parts. The first part reflects the number of attempts needed to activate the function associated to each movement in each of the five series. Figure 3 (left) shows the average number of attempts of the five non-amputee subjects and Fig. 3 (right) shows the attempts needed for the amputee. In the second part, a table shows a ranking of the times taken for each subject to perform the routine with the robotic hand (Table 1).

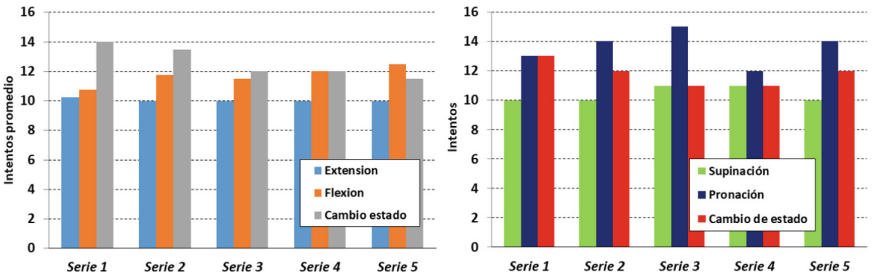

Fig. 3. Average number of attempts of the 5 non-amputated subjects to activate the output functions (left). Number of attempts of the amputee subject (right).

Table 1. Table of execution positions of the robotic hand command routine.

ID subject	Runtime of the routine
1	16.81 [s]
6	17.72 [s]
4	22.22 [s]
5	22.87 [s]
3	24.23 [s]
2	46.25 [s]

5 Discussions

The results of Fig. 3 show that, on average, non-amputees managed to satisfactorily achieve the objective associated with the extension movement without exceeding ten attempts. This result was repeated throughout the five series, which indicates that the control strategy worked correctly for this movement and that the subjects had no greater difficulties to activate the corresponding function. Similar performance was observed for the case of the flexion movement, where the average number of attempts was 11 for the first series and continued with a slight increase until reaching a maximum of 12.5 attempts in the last series. This increase in the number of attempts with respect to that obtained for the extension movement may be due to the fact that the signal from the sensor EMG2 was weaker than the signal from the sensor EMG1, which caused a difficulty for the person to control the level of contraction needed to activate the function. Finally, for the fast flexion of the wrist, the average number of attempts started at 14 but decreased until reaching 11.5 in the fifth series. For this case, it is observed that the subjects learned to control the change of state of the system throughout the series due to the training given by the repetition of the movement.

For the case of the amputee, the results indicate that he did not present major difficulties to fulfill the objective associated with the supination movement of the remaining limb. However, the pronation movement was more complex to perform since it took between 12 and 15 attempts to achieve 10 successes. For fast pronation,

which changed the state of the system, he required between 11 and 13 attempts, achieving an improvement from the first series to the fourth.

The robotic hand routine was aimed at performing a test of specific use of a prosthesis, which entails an association of voluntary muscular contraction with the movement performed by it. In Table 1, ID 6 corresponds to the amputee who was the second fastest person to complete the routine. In the case of the last subject (ID 2), the measured time included an error in the execution of the routine, so he was asked to repeat it without restarting the timer.

The amputee achieved an acceptable adaptation to the system, considering that he rarely uses the muscles involved in the experiment. The strategy of changing the state of the system through a fast contraction was fluid and improved as the series of the experiment went on.

The configuration of the parameters to activate the output functions is of great importance. In different series performed by the same subject, the number of attempts varied when the configuration parameters of the system varied since they define the activation thresholds.

6 Conclusions

In this paper, the development and implementation of a myoelectric control strategy for voluntary control of upper limb prostheses was presented. Such strategy was able to command four functions of a prosthesis (hand open/close, opposition of the thumb inwards/outwards) using only two EMG channels located on forearm muscles. Experiments were carried out on healthy subjects and amputees to evaluate the feasibility of the strategy and obtain information about the degree of acceptability of the subjects when controlling a robotic hand. Considering that users had only a short training period (i.e. less than 50 min during the sensor configuration stage); the obtained results provide initial information that validate the presented work and results useful to guide future improvements of the strategy.

Acknowledgments. This work was partially supported by a PPI 2016-2018 research grant from the Science and Technology Secretary, National University of Rio Cuarto and for a PID research grant from the Ministry of Science and Technology of Córdoba, Argentina.

Conflict of Interest. The authors declare that there is no conflict of interest.

References

1. Saikia, A., Mazumdar, S., Sahai, N., Paul, S., Bhatia, D., Verma, S., Rohilla, P.K.: Recent advancements in prosthetic hand technology. J. Med. Eng. Technol. **40**, 255–264 (2016). https://doi.org/10.3109/03091902.2016.1167971
2. Krausz, N.E., Rorrer, R.A.L., Weir, R.F.f: Design and fabrication of a six degree-of-freedom open source hand. IEEE Trans. Neural Syst. Rehabil. Eng. **24**, 562–572 (2016). https://doi.org/10.1109/TNSRE.2015.2440177

3. Tavakoli, M., Benussi, C., Lourenco, J.L.: Single channel surface EMG control of advanced prosthetic hands: a simple, low cost and efficient approach. Expert Syst. Appl. **79**, 322–332 (2017). https://doi.org/10.1016/j.eswa.2017.03.012
4. Romo, H.A., Realpe, J.C., Jojoa, P.E.: Análisis de Señales EMG Superficiales y su Aplicación en Control de Prótesis de Mano. Rev. Av. En Sist. E Informática **4**, 127–136 (2007)
5. Jiang, N., Lorrain, T., Farina, D.: A state-based, proportional myoelectric control method: online validation and comparison with the clinical state-of-the-art. J. NeuroEng. Rehabil. **11**, 110 (2014). https://doi.org/10.1186/1743-0003-11-110
6. Fougner, A., Stavdahl, O., Kyberd, P., Losier, Y., Parker, P.: Control of upper limb prostheses: terminology and proportional myoelectric control - a review. IEEE Trans. Neural Syst. Rehabil. Eng. (2012). https://doi.org/10.1109/TNSRE.2012.2196711
7. Subasi, A., Alaskandarani, A., Abubakir, A.A., Qaisar, S.M.: sEMG signal classification using DWT and bagging for basic hand movements. In: 2018 21st Saudi Computer Society National Computer Conference (NCC), IEEE, Riyadh, pp. 1–6 (2018). https://doi.org/10.1109/NCG.2018.8593010
8. Talib, I., Sundaraj, K., Lam, C.K., Hussain, J., Ali, Md.A.: A review on crosstalk in myographic signals. Eur. J. Appl. Physiol. **119**, 9–28 (2019). https://doi.org/10.1007/s00421-018-3994-9
9. Geethanjali, P.: Myoelectric control of prosthetic hands: state-of-the-art review. Med. Devices Auckl. NZ **9**, 247–255 (2016). https://doi.org/10.2147/MDER.S91102
10. Lasheras, G., Castro, N., O'Brien, R., Molisani, L., Laciar, E., Fontana, J.M.: Diseño de una mano artificial antropomórfica para aplicaciones protésicas. In: 2016 IEEE Biennial Congress of Argentina (ARGENCON), pp. 1–5 (2016). https://doi.org/10.1109/ARGENCON.2016.7585335
11. Mutlu, R., Alici, G., in het Panhuis, M., Spinks, G.M.: 3D printed flexure hinges for soft monolithic prosthetic fingers. Soft Robot. **3**, 120–133 (2016). https://doi.org/10.1089/soro.2016.0026

Post-stroke Injured Cerebral Cortex: Frequency Analysis of the Desynchronization of Its Sensorimotor Rhythms During Motor Intent

Carolina B. Tabernig[1(✉)], L. Carolina Carrere[1], Gerardo G. Gentiletti[1], and Erika G. Spaich[2]

[1] Laboratory of Rehabilitation Engineering and Neuromuscular Research (LIRINS), Faculty of Engineering, National University of Entre Ríos, Oro Verde, Argentina
ctabernig@ingenieria.uner.edu.ar
[2] Integrative Neuroscience Group, Department of Health Science and Technology, Aalborg University, Aalborg, Denmark

Abstract. During a motor intent, desynchronization of sensorimotor rhythms of the cerebral cortex takes place. This physiological phenomenon, called event related desynchronization (ERD), is used for the development of Brain Computer Interfaces (BCI) for motor recovery. Stroke survivors suffering complete or partial loss of mobility usually require therapy for motor rehabilitation. The damage of the sensorimotor cortex that follows a stroke can compromise the brain rhythms that encode motor states. Therefore, this study assessed the ERD behavior during movement and motor intent in post-stroke patients.

Eight electroencephalogram channels were recorded in seven chronic ischemic stroke patients during rest and movement or motor intent of their hands. The spectra of the coefficient of determination r^2 were estimated between 8 and 30 Hz.

The median of r^2 reached 0.05 during motor intent of the corresponding affected hand; so it is a real value to be taken into account in BCI developments for people who have suffered a stroke. However, there was no evidence of a common pattern for the ERD. It was also observed that stroke survivors have discrimination capacity in the injured hemisphere during the motor intent of their affected limb.

Keywords: Event related desynchronization · Stroke · Motor intent · Brain Computer Interfaces

1 Introduction

During movement or motor intent (MI), the desynchronization of the sensorimotor rhythms (SMR) of the electroencephalogram (EEG) is produced. This phenomenon, called Event Related Desynchronization (ERD), is evidenced as a decrease in the amplitude of the EEG signal related to the resting state [1]. The cortical region where

© Springer Nature Switzerland AG 2020
C. A. González Díaz et al. (Eds.): CLAIB 2019, IFMBE Proceedings 75, pp. 1073–1078, 2020.
https://doi.org/10.1007/978-3-030-30648-9_139

the ERD happens is surrounded by areas that show an increase in the SMR amplitude, a phenomenon known as Event Related Synchronization (ERS) [2].

The fact that the ERD happens during an MI is very interesting in the context of the systems based on Brain Computer Interfaces (BCI) because it provides a means to detect the user's intention, that can be used to control an actuator [3]. These BCI systems can then be used by patients with motor disabilities, e.g. patients with sequels of stroke, who cannot perform voluntary movements. For many of these patients, a motor command becomes a MI with little or no movement result due to the injury of the sensorimotor cortices. Since these patients are one of the possible users of the BCI systems, it is necessary to characterize the behaviour of the ERD during MI in post-stroke people to use this information in the design of BCI.

Although there are reports describing the temporal and topographic behaviours of the ERD of ipsilesional motor cortex after stroke [4–6], there is no literature describing its frequency behaviour. This paper presents a descriptive study of this ERD behaviour of post-stroke volunteers during upper limb MI.

2 Materials and Methods

Seven volunteers with chronic ischemic stroke and left hemiparesia participated in the study (mean age: 61.2 ± 19 years). All of them gave their informed consent.

2.1 Protocol

Volunteers sat comfortably in front of a screen and were asked to relax, observe the screen, and avoid blinking. They were instructed, both verbally and through a visual demonstration, how to move their hands while the presentation of a visual cue on the screen.

EEG was recorded using the protocol proposed by Schalk and Mellinger [7], (see the temporal sequence of the protocol in Fig. 1). During the cue, the volunteer had to perform the MI (wrist and finger extension) or rest.

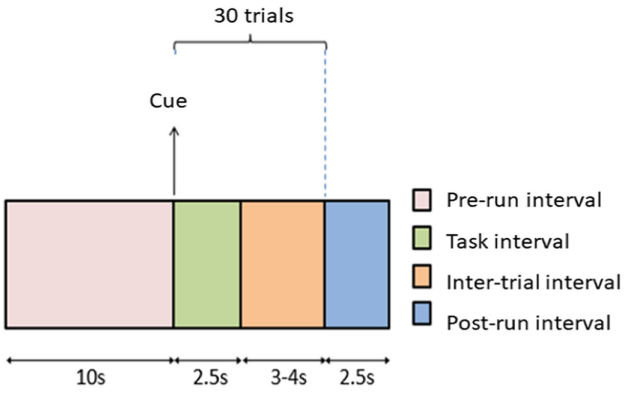

Fig. 1. Protocol for EEG recording: temporal sequence of a run.

Each trial contained data from 3 runs of 20 min of duration with rest periods of 1 to 2 min. Each run included 30 trials, 10 of each of three different tasks of 2.5 s of duration: rest and MI of the right and left hands following the visual cue. The three tasks were randomly repeated 10 times during each run, separated by inter-trial interval varying randomly between 3 and 4 s, with uniform probability for all intermediate values. During the inter-trial interval, a white screen was presented and the subjects were instructed to relax. Then, 120 EEG records for each volunteer were obtained.

2.2 EEG Recording System

Eight EEG channels were recorded using a monopolar configuration with the g. MOBIlab+® amplifier (Guger Technologies, Austria), with a sampling frequency of 256 Hz, 16 bits of resolution, filters between 0.5 and 100 Hz, and a sensitivity of 500 μV. In the platform BCI2000, a 50 Hz notch filter to suppress line interference and a band pass filter between 0.5 and 40 Hz were configured [7].

Passive Ag/AgCl electrodes located according to the extended version of the 10–20 system were employed using the g.GAMMA cap (Guger Technologies, Austria). Taking into account the cortical areas of interest for the study, positions C3, C4, T7, T8, Pz, F3, F4 and Cz were selected. The ground and reference electrodes were placed on the right and left mastoids, respectively.

2.3 Signal Processing

The EEG signals were processed using "BCI2000 Offline Analysis", available on the BCI2000 platform [7]. Common average reference spatial filtering and frequency analysis of the EEG signal contrasting MI and rest, were performed. The spectra of the coefficients of determination r^2 for rest versus each MI task were obtained [8]. If the value of the r^2 coefficient approaches 1, it indicates very good discrimination between the MI and rest, while values close to 0 indicate poor discrimination [7].

The spectra of the r^2 coefficients of all volunteers were then processed in order to obtain the box plots and the median of r^2 for each frequency of the SMR (μ: 10–12 Hz; β: 18–30 Hz). These spectra were obtained for channels C3, C4 and Cz; as they correspond to the sensorimotor cortex of upper and lower limbs respectively.

3 Results

Figure 2 shows the box plots of the r^2 spectra for the SMR during the MI of the affected hand, for the electrodes placed on the sensorimotor cortex (C3, Cz and C4). The frequency of maximal ERD, i.e. frequency at which the greatest positive difference is found between C4 and Cz and between C4 and C3, was 8 Hz (β rhythm) with a median at r^2 close to 0.04. The outlier values reveal the dispersion in the population of r^2; some volunteers were able to desynchronize with very large r^2 values, as observed for example at 22 Hz at the C4 electrode (r^2 close to 0.25). The maximum value of the median of the r^2 coefficients was reached in the contralateral side to the affected hand

(C4) and was close to 0.05. The r^2 values in the ipsilateral, non-lesioned, hemisphere (C3) were smaller than 0.02.

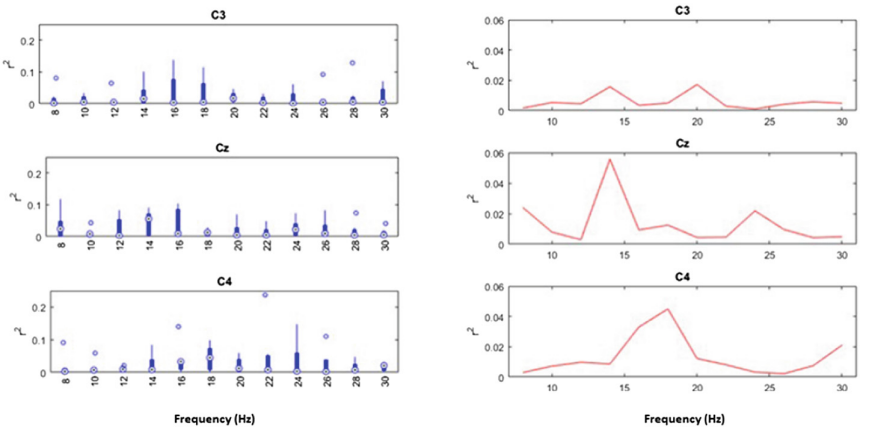

(a) Box plots (b) Medians

Fig. 2. r^2 spectra for the SMR during the MI of the left affected hand for the electrodes C3, Cz and C4. In (a): in a circle with a central point, the median; in full bar, the first and third quartile; in an empty circle, the outlier values; and in a thin line, the maximum and minimum values; in (b): the medians of the r^2 coefficients.

Figure 3 shows the box plots of the r^2 spectra for the SMR during the movement of the non-affected right hand, for the electrodes placed on the sensorimotor cortex (C3, Cz and C4). When performing a MI of the right hand, the ERD was manifested in C3, with maximum r^2 values larger than those of the affected left hand. The frequency of maximal ERD, i.e. the frequency at which the greatest positive difference is found between C3 and Cz and between C3 and C4, was 20 Hz (β rhythm) with a median close to 0.03 (Fig. 3(b)). r^2 medians in the contralateral hemisphere to the right hand (C3) were higher than those at the ipsilateral hemisphere (C4).

4 Discussion and Conclusions

The frequency behaviour of the ERD during MI in post-stroke patients was reported in this study. The values of the r^2 coefficients were maximal in the area corresponding to the hand involved in the MI task. For the same frequency of maximal ERD, the r^2 values were minimal, even close to zero, in the surrounding electrodes. This indicates that people who suffered a stroke also present the phenomenon of ERD with surrounding ERS, as reported by Pfurtscheller and Lopes da Silva [8] and Neuper, Wörtz and Pfurtscheller [3].

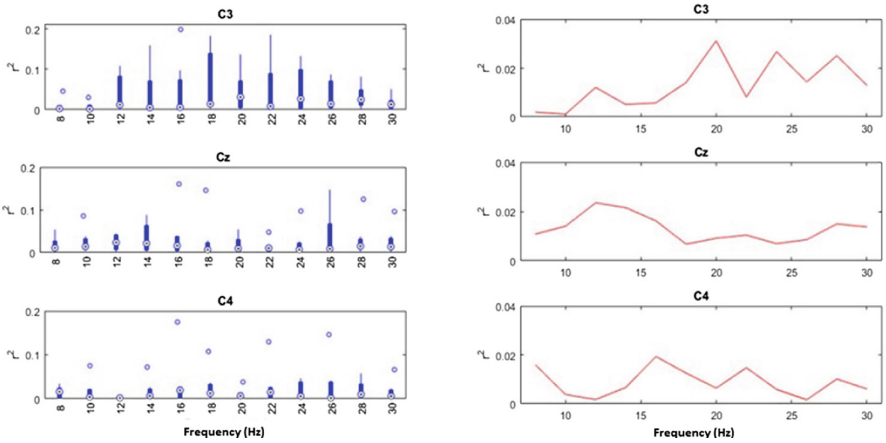

(a) Box plots (b) Medians

Fig. 3. r^2 spectra for the SMR during the MI of the right non-affected hand for the electrodes C3, Cz and C4. In (a): in a circle with a central point, the median; in full bar, the first and third quartile; in an empty circle, the outlier values; and in a thin line, the maximum and minimum values; in (b): the medians of the r^2 coefficients.

The r^2 coefficients found during MI of the affected hand (maximal median equal to 0.05 in C4, Fig. 2b) had similar values to those of the non-affected hand (maximal median equal to 0.04 in C3, Fig. 3b) and within the range of values reported by Antelis et al. [9]. In this paper, the authors showed values of r^2 smaller than 0.05 in the affected hemisphere and close to 0.1 in the non-injured hemisphere, during MI of the affected limb.

These similar median values of r^2 obtained in the contralateral hemispheres to MI (C4 in Fig. 2 and C3 in Fig. 3) evidenced that the volunteers showed a similar ability to discriminate independently of whether MI was performed by the affected or healthy limb.

The outlier values reveal great dispersion in the population of coefficients r^2. This behaviour supports the fact that there is not a common pattern for the ERD of stroke survivors, as reported by Scherer et al. [5]. Mc Crimmon et al. also reported dispersion of median ERD of 9 stroke survivors and a significant increase of this median ERD after a BCI-FES therapy aimed to improve dorsiflexion [10].

Our results showed that it is possible to identify ERD, both spatially and in the frequency domain, in brain-injured individuals. According to Kaiser et al. [4], this might be possible because the brain injury could have happened in deep cerebral structures and thus, the sensorimotor cortex related to the movement was not directly affected.

Although the sample size was small in this study, the results obtained are promising and suggest the feasibility of extracting EEG features from stroke survivors that can be used in BCI systems for rehabilitation purposes.

Acknowledgment. The authors would like to thank the "Fundación Rosarina de Neurorehabilitación", who facilitated access to the patients; and the "Área de Asesoramiento Interdisciplinar", Faculty of Engineering - National University of Entre Ríos, which supplied the English language editing services.

Conflict of Interest. The authors declare that they have no conflict of interest.

References

1. Pfurtscheller, G., Lopes da Silva, F.H.: EEG event-related desynchronization (ERD) and event-related synchronization (ERS). In: Schomer, D.L.; da Silva, F.H.L. (eds.) Niedermeyer's Electroencephalography: Basic Principles, Clinical Applications, and Related Fields,. Lippincott Williams & Wilkins., Filadelfia, Pensilvania, Estados Unidos, pp. 937–948 (2011)
2. Neuper, C., Wörtz, M., Pfurtscheller, G.: ERD/ERS patterns reflecting sensorimotor activation and deactivation. In: Progress in Brain Research-Event-Related Dynamics of Brain Oscillations, pp. 211–222 (2006)
3. Wolpaw, J.R., Wolpaw, E.W.: Brain-Computer Interfaces: Principles and Practice. Oxford University Press, Oxford (2012)
4. Kaiser, V., Daly, I., Pichiorri, F., Mattia, D., Müller-Putz, G.R., Neuper, C.: Relationship between electrical brain responses to motor imagery and motor impairment in stroke. Stroke **43**, 2735–2740 (2012). https://doi.org/10.1161/STROKEAHA.112.665489
5. Scherer, R., Mohapp, A., Grieshofer, P., Pfurtscheller, G., Neuper, C.: Sensorimotor EEG patterns during motor imagery in hemiparetic stroke patients. Int. J. Bioelectromagnetism **9**, 155–162 (2007)
6. Carrere, L.C., Tabernig, C.B.: Detection of foot motor imagery using the coefficient of determination for neurorehabilitation based on BCI technology. In: IFMBE Proceedings - CLAIB 2014, vol. 49, pp. 944–947 (2015). https://doi.org/10.1007/978-3-319-13117-7_239
7. Schalk, G., Mellinger, J.: A Practical Guide to Brain-Computer Interfacing with BCI2000. Springer, New York (2010)
8. Pfurtscheller, G., Lopes da Silva, F.H.: Event-related EEG/MEG synchronization and desynchronization: basic principles. Clin. Neurophysiol. **110**, 1842–1857 (1999). https://doi.org/10.1016/S1388-2457(99)00141-8
9. Antelis, J.M., Montesano, L., Ramos-murguialday, A., Birbaumer, N., Minguez, J.: Decoding upper limb movement attempt from EEG measurements of the contralesional motor cortex in chronic stroke patients. IEEE Trans. Biomed. Eng. **64**(1), 99–111 (2017)
10. McCrimmon, C.M., King, C.E., Wang, P.T., Cramer, S.C., Nenadic, Z., Do, A.H.: Brain-controlled functional electrical stimulation therapy for gait rehabilitation after stroke: a safety study. J. Neuroeng. Rehabil. **12** (2015). https://doi.org/10.1186/s12984-015-0050-4

Evaluating Strategies for Improving the Detection of Auditory Steady-State Responses in the AUDIX System

Isabel Arnaiz(✉), Eduardo Martínez-Montes, and Alejandro Torres-Fortuny

Cuban Center for Neurosciences, 198 St 19818, Havana, Cuba
{isabel.arnaiz,eduardo,fortuny}@cneuro.edu.cu

Abstract. A preliminary comparison was carried out among three novel strategies for automatic detection of ASSR versus the current alternatives implemented in AUDIX system. Two of the proposed strategies were faster in detecting the response and they did it robustly in the majority of the data set, even in subjects where current alternatives failed. This work provides evidence that improvements can still be done in the detection of ASSR by using appropriate statistical assumptions and averaging procedures.

Keywords: Auditory steady-state · Response detection · Hotelling's T2

1 Introduction

Detection of auditory steady-state responses (ASSR) remain as a non-expendable tool for hearing assessment, especially in patients with poor or no collaboration at all during an auditory evaluating session. It is also useful for objectively evaluating suprathreshold hearing and monitoring the state of arousal during anesthesia. Auditory steady-state responses are oscillatory evoked potentials whose discrete frequency components remain constant in amplitude and phase during the presentation of the stimuli. See [1] for a detailed explanation of its physiological origin, recording, analysis, and clinical applications. The detection of ASSR implies a precise synchronization among auditory stimulation and the electroencephalogram (EEG), as well as the combination of averaging procedures with powerful statistical methods for assessing the presence of the physiological response. Averaging in time domain many consecutive sweeps[1] obtained from the segmentation of continuous recordings, have been the classical procedure for extracting the evoked responses from the noisy EEG signal. Nonetheless, other averaging procedures have been specifically proposed for the extraction of the ASSR: weighted averaging and sorted averaging [2, 3], with promising results on the improvement of the signal-to-noise ratio and thus, on the faster detection of the response.

[1] Sweeps are N-samples-long segments of recordings which are also divided in N_1 epochs with N_2 samples each. Thus $N = N_1 * N_2$.

© Springer Nature Switzerland AG 2020
C. A. González Díaz et al. (Eds.): CLAIB 2019, IFMBE Proceedings 75, pp. 1079–1084, 2020.
https://doi.org/10.1007/978-3-030-30648-9_140

The presence of ASSR is commonly analyzed in the frequency domain by means of a Fast Fourier Transform (FFT) procedure. The FFT algorithm converts the set of values that change in amplitude over time to a set of complex values that vary with frequency. The magnitude of the complex value corresponding to the exact frequency of stimulation is taken as the amplitude of the ASSR (response-peak or signal), while all other frequencies are assumed to reflect 'noise' (which includes electrical activity from other brain sources, muscles of the face, scalp and neck, and measurement errors). The estimation of whether the signal is significantly different form noise depends on a statistic test, selected according to which information of signal and noise (amplitude, phase, or both) will be considered for the statistical analysis. The most frequently used statistic in ASSR detection is the Hotelling's T2, since it is a multivariate test on two-dimensional vectors formed by the real and imaginary parts of FFT values, effectively considering information from both the amplitude and phase. Mathematically, the Hotelling's T2 statistic is described as:

$$T2 = \mathrm{N}\left(\overline{X_{peak}} - \overline{X_{noise}}\right)' S^{-1} \left(\overline{X_{peak}} - \overline{X_{noise}}\right) \quad (1)$$

Where the combined covariance matrices of the signal and noise is $S = S_{peak} + S_{noise}$ and $N = \frac{N_1 N_2}{N_1 + N_2}$ with degrees of freedom of 2 (length of the vectors) and $N_1 + N_2 - p - 1$.

Given a set of two-dimensional vectors of response and noise with N1 and N2 samples respectively, one can calculate the T2 statistic to determine whether the measured means of response and noise significantly differ. In practice, this statistic has been simplified in terms of comparing only one sample of the response-peak versus a limited number of noise samples around the response-peak (known as 'T2H'). Even more, in 1991, Victor and Mast proposed a simpler variant, called the 'circular T2 test' (T2C) assuming equivalent variance in the real and imaginary dimensions of response and a zero mean for the noise. An important similarity between these simplified versions was that both assumed zero covariance (i.e. statistical independence) between the real and the imaginary parts for the response, and additionally for the noise in the case of T2H. Although there are arguments in favor of this selection [4], this was mainly aimed at decreasing computational load, but it might be also a constraint for a more precise and faster detection of the response.

The AUDIX system (NEURONIC S.A Havana), allows hearing assessment with ASSR by using the classical averaging procedure and the T2H or T2C statistics (as selected by the user). Although a good performance of the system has been widely validated, current research is devoted to improving the system by finding ways for a faster detection of the response.

This article presents a preliminary comparison among the current methods implemented in the AUDIX system and novel strategies based on combining different averaging procedures with the more general T2 statistic. This was calculated with the assumption that the response has a preferential phase in all epochs, therefore the covariance between the Real and Imaginary parts could not be discarded as in current implementations.

2 Methods and Materials

The dataset consisted in eight recordings from normal-hearing (24.1 ± 3.7 years) subjects acquired by an AUDIX system at 920 Hz sampling rate. All recordings correspond to a simultaneous and multiple-frequency stimulation protocol[2]. Sweeps were 8192-samples long with 16 epochs of 512 samples. Each sweep was filtered by a Butterworth Bandpass with 85 and 120 Hz as cutoff frequencies and no gain in the passband.

The three novel strategies differ in the type of averaging procedure for extracting the ASSR: classical (C-T2), weighted (W-T2) and sorted (S-T2) averaging. Weighted and sorted averaging were implemented as described in [2] and [3], respectively. Averaging is done sequentially in the detection procedure: the statistic is computed in the first sweep, then in the average of sweep 1 and 2, then in the average of sweeps 1, 2 and 3, and so on. This leads to increasing signal-to-noise ratio in every new "mean sweep" making the detection of the response easier. Prior to averaging, in the "weighted" version every epoch is divided by its variance while in the "sorted" version the sweeps are rearranged according to the descendent order of their root-mean-square (rms) amplitudes. The 16 epochs of each mean sweep are transformed to the frequency domain by means of the Fast Fourier Transform. In each epoch, we obtain a complex value for the response at the frequency of interest, and all other 256-8 complex values represent the noise samples (i.e. discarding also the other 7 response frequencies due to the multiple-frequency stimulation). To sum up, 16 complex samples for response and 3968 complex samples for the noise are statistical analyzed using the T2 statistic, with 2 and 3981 degrees of freedom and without the assumption of zero covariance between Real and Imaginary parts in both the response and noise samples.

In practice, the response is considered as "detected" if the T2 value is significant in three consecutive mean sweeps with a significance level of 0.05. Since responses should be detected in all recordings of our database (normal-hearing subjects), a comparison between pairs of strategies can be done in terms of two error quantities: Error I corresponds to the number of subjects for which one strategy is able to detect the response and the second strategy is not, while Error II is defined in the other way around.

The performances of the proposed strategies were compared to those of the current strategies implemented in the AUDIX system (T2C AUDIX and T2H AUDIX) based on the number of mean sweeps needed for detecting the response and the behavior of Error I and Error II along the 40 first averages. All the preprocessing of the recordings and subsequent analyses were carried out in MATLAB 8.5 (R2015a) 64-bits.

[2] Amplitude-modulated tones. Right Ear: carrier tone of 500 Hz (modulated at 93.44 Hz), 1000 Hz (100.63 Hz), 2000 (107.81 Hz), 4000 Hz (115 Hz). Left Ear: 500 Hz (89.84 Hz), 1000 Hz (97.03 Hz), 2000 (104.22 Hz), 4000 Hz (111.41 Hz). See [5] for a more detailed explanation of the stimulation protocol and the recording conditions.

3 Results

Table 1 shows the number of mean sweeps needed by each strategy to detect the response at four stimulation frequencies. All proposed strategies achieved better results than the current strategies in the AUDIX system; needing much less mean sweeps for detecting the response. In addition, all of them could detect the responses at specific frequencies in a difficult subject.

Table 1. Average number (maximum in parenthesis) of mean sweeps needed to detect the responses in different stimulation frequencies among the 8 subjects.

	89.84 Hz	100.63 Hz	104.22 Hz	115 Hz
C-T2	5 (13)	4.5 (12)	3.9 (7)	5.6 (10)
W-T2	3.1 (4)	3.8 (5)	3.5 (6)	7.4 (26)
S-T2	3.1 (4)	5 (10)	4.5 (13)	4.5 (6)
T2H AUDIX	11.0 (22)	12.3 (24)*	16.4 (49)*	11.0 (32)
T2C AUDIX	10.9 (22)	12.1 (25)*	12.6 (28)	13.4 (42)

(*) one subject was not taken into account as detection took more than 50 sweeps.

Error I and Error II were computed only for the response at 89.84 Hz. Pairwise comparisons between the novel strategies showed that they have similar detection capabilities, although S-T2 had a slightly better performance than W-T2, which in turn offered slightly better results than C-T2. Note that sorted averaging needs to be performed off-line, requiring long recordings and massive storage for prior rearranging of sweeps, while weighted and classical averaging can be done on-line. Future implementations of partial reordering during online recording would allow us to benefit from the S-T2 capabilities for detecting the response. Finally, the performance of S-T2 and C-T2 were compared to those of T2H AUDIX and T2C AUDIX, as shown in Fig. 1.

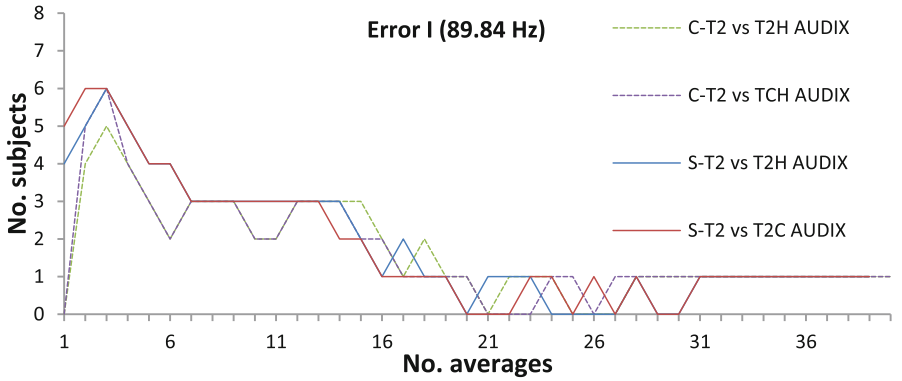

Fig. 1. Error I for pairwise comparisons between novel strategies and the current strategies in the AUDIX system along the 40 first averages.

Both novel strategies were able to detect responses -in the first 5 averages- that were not detected by AUDIX methods in more than half the subjects. None of the currently available methodologies in the AUDIX system were capable of detecting any response missed by some of the proposed strategies, being Error II equals zero in all comparisons.

4 Discussion

Previous studies have focused on the comparison among the most frequently used strategies for ASRR detection[6, 7]. Particularly, in [6], no significant differences were found between performances of T2H and T2C, and neither between these statistics and other less frequently used as CSM and F. In addition, [7] reflected a similarly well performance of T2C and T2H and it also reaffirmed the potentialities of ASSR for screening purposes due to the strength of such statistical indicators in the automatic detection. It is worth to note that both studies were carried out on a real data sample. However, such previous works considered only the classical averaging method for the extraction of the evoked potential. The proper combination of averaging procedure and statistic turns out to be relevant for a faster detection of ASSR, because the statistic can detect a significant response-peak easier if there is a high signal-to-noise ratio. This is why several averaging procedures were included in the present study in the first place.

A strength of the novel strategies is their higher degrees of freedom respect to the current alternatives, in which one sample of the response-peak was statistically compared with the samples of noise in a vicinity (T2H) or several samples of response-peaks were compared with a zero-mean noise (T2C). Although we have only studied here the detection of responses (sensitivity), we hypothesize that the higher statistical power of the novel strategies implies a higher precision and it might lead to a better specificity. Future studies with more general databases including hearing-impaired subjects, should be carried out to study this topic in detail.

In addition, we explored the covariance values between Real and Imaginary parts for the entire sample at some random number of averages, finding that they were of the same order of magnitude as the variances in the response samples, while only one order lower than variances in the noise samples. Variance of Real and Imaginary parts for response and noise samples also differed. Such behavior does not support the assumption of [4] that calls for equivalent variance in the Real and Imaginary parts of the response-peak, based on the stationary behavior of the noise and the additive property of the evoked potential and the noise. Therefore, taking into account all the variance and covariance values in the general T2 statistic, might be the key for the higher detection capabilities of the proposed strategies, suggesting that the use of the original definition of T2H leads to a proper selection of statistical thresholds for response detection.

As conclusions, we have found that the novel strategies based on sorted, weighted and classical averaging procedures and the original definition of Hotelling's T2 statistic, allow a high sensitivity and faster detection of the ASSR than the current strategies implemented in the AUDIX system.

Conflict of Interest. The authors declare that there is no conflict of interest.

References

1. Picton, T.W., et al.: Human auditory steady-state responses: Respuestas auditivas de estado estable en humanos. Int. J. Audiol. **42**(4), 177–219 (2003)
2. John, M.S., Dimitrijevic, A., Picton, T.W.: Weighted averaging of steady-state responses. Clin. Neurophysiol. **112**(3), 555–562 (2001)
3. Rahne, T., Verhey, J.L., Mühler, R.: Sorted averaging improves quality of auditory steady-state responses. J. Neurosci. Methods **216**(1), 28–32 (2013)
4. Victor, J., Mast, J.: A new statistic for steady-state evoked potentials. Electroencephalogr. Clin. Neurophysiol. **78**, 378–388 (1991)
5. Fortuny, A.T., et al.: Stopping criteria for averaging the multiple auditory steady-state response. Acta Otorrinolaringol. (English Edn.) **62**(3), 173–180 (2011)
6. Valdes, J.L., et al.: Comparison of statistical indicators for the automatic detection of 80 Hz auditory steady state responses. Ear Hear. **18**(5), 420–429 (1997)
7. Mijares, E., et al.: Comparing statistics for objective detection of transient and steady-state evoked responses in newborns. Int. J. Audiol. **52**(1), 44–49 (2013)

Reusable, Cased and Mechanically Held Graphite-Based Dry ECG Electrodes

Rodrigo Soto Domínguez(✉), Uriel Anguiano Piña, and Bersaín A. Reyes

Faculty of Science, Autonomous University of San Luis Potosi, 78295 San Luis Potosi, SLP, Mexico
Rodrigo.SotoD@hotmail.com

Abstract. In this work, we proposed the coupling of graphite pencil lead (GPL) electrodes with a custom designed 3D printed case and adjusting Velcro straps for the task of ECG acquisition. The proposed electrode and its attachment procedure were intended to provide reusable, easy-to-apply and long-lasting results in comparison to traditional adhesive electrodes, while simultaneously protecting the graphite-based electrode against mechanical stress. To this end, ECG data from twenty ($N = 20$) healthy volunteers were simultaneously acquired using commercial adhesive Ag/AgCl electrodes and the proposed cased and mechanically held graphite-based electrodes. The performance of the proposed electrodes was studied during still conditions via signal quality from ECG template signals as well as from heart rate (HR) time series. We found high correlation coefficients for the signal quality ($\rho = 0.9942$) and HR estimation ($\rho = 0.9495$). The obtained results look promising and shown the feasibility of developing reusable, simple, low cost, and waste-free ECG electrodes alternatives to traditional disposable, adhesive ones.

Keywords: Graphite · Dry electrode · ECG monitoring · Reusable electrode

1 Introduction

The electrocardiogram (ECG) is the noninvasive record of the electrical activity of the heart muscle, during its active (systole) and passive (diastole) phases. It can be easily recorded from at least two electrodes placed on either side of the heart, e.g. on the chest or on the left and right arms. Nowadays, it is well recognized that the ECG provides meaningful information regarding the performance and functionality of the heart [1], and that it supports the diagnosis and management of patients with abnormal cardiac rhythms [2]. Among the information derived from the ECG signal, the heart rate (HR) is the most widely used measurement [3]. However, other relevant physiological information can be deduced from morphological changes in the ECG waveforms, as it has extensively been documented in the literature.

ECG and HR monitoring are common in both clinical and research applications. While commercially available adhesive Ag/AgCl electrodes can be easily used in short term recordings, these electrodes falter in long term recordings as they require a proper

© Springer Nature Switzerland AG 2020
C. A. González Díaz et al. (Eds.): CLAIB 2019, IFMBE Proceedings 75, pp. 1085–1092, 2020.
https://doi.org/10.1007/978-3-030-30648-9_141

wet electrolyte to function properly, i.e. the adhesive ECG electrodes have an electrolyte sponge or a layer of hydrogel which dries relatively quickly, leading to signal quality degradation with sweat, bacterial proliferation and skin irritation [4, 5].

The need for a dry, reusable, simple to fabricate, and cost-effective electrode has been subject of several works. For example, polymer-carbon-based dry electrodes have even been proposed for underwater ECG monitoring applications [6]. Among the proposed efforts, graphite pencil lead (GPL) has been preferred due to its performance, low cost and easy accessibility on an everyday basis for the general population. Previous studies have evaluated dry GPL electrodes for underwater ECG measurement obtaining promising results [7]. However, the previously proposed GPL electrodes suffer from the lack of a proper attachment method and possess a relatively high fragility. Current attachment methods, such as adhesive tape, tend to fail, increasing motion artifacts and degrading signal quality. Unfortunately, there is a lack of methodological studies regarding comparison between attachment methods for dry ECG electrodes. Furthermore, traditional dry GPL-based electrodes tend to break while in use.

In this work, we have developed an attachment method using a computer-aided design (CAD) casing and adjustable Velcro straps. The proposed casing protection of the electrodes provides them with an increased stability and durability against mechanical stress when used consecutively on several volunteers. Performance of the proposed electrodes were tested considering commercially available adhesive Ag/AgCl electrodes as reference, in terms of quality of ECG morphology as well as of HR time series.

2 Materials and Methods

2.1 GPL Electrodes Fabrication

The fabrication procedure was based on previous work from Thap et al. as reported in 2016 [7], which can be summarized as follows. First, the pencil leads are cut into pieces, each piece must have a length greater than the desired electrode diameter. Then, the pieces are flattened to form a rounded rectangle shape. The resultant rectangles are arranged in a parallel manner and attached to each other by an ethyl cyanoacrylate bond. A metal cap is placed and attached on top. Finally, the edge is trimmed to obtain a circular shape with the desired diameter. For this work, the fabricated electrodes had a 10 mm diameter and 1 mm thickness. Three electrodes were fabricated to allow ECG acquisition in common leads systems used in academic and research environments.

2.2 Case Design and Implementation

The protection case was designed using SolidWorks CAD software (SolidWorks Corp., Waltham, MA, USA). Several parameters were considered during the designing process, including mechanical protection, size, shape and coupling with the adjustable straps. At the end, the design offered protection around the electrode borders and included structures meant for the strap adjustment and attachment, as shown in Fig. 1.

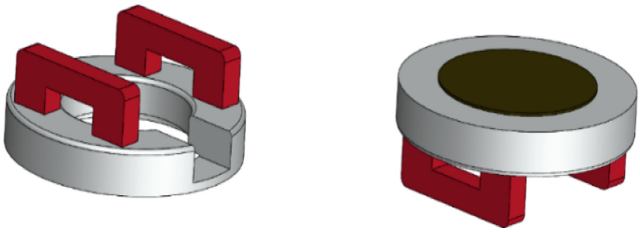

Fig. 1. (Left) Protection case model as seen from above. The arches (in red) allow coupling with the adjustable straps. (Right) Case model as seen from below. The electrode border is completely protected by the case, preventing damage and rupture from mechanical stress.

Finally, the case was fabricated using the Fused Filament Deposition (FFD) printing technique which is a rapid and low-cost 3D printing technique consisting in depositing successive fine layers of melted printing material to conform a three-dimensional object. The printing material was Acrylonitrile Butadiene Styren (ABS). The cost per case was around 2 USD. Velcro straps were cut in order to allow coupling, and their final dimensions were 90 cm long and 1 cm wide. Total cost of the proposed electrodes, including cases and straps, was around 10 USD. Figure 2 shows one of the final cased dry electrodes that were fabricated.

Fig. 2. Different views of the fabricated cased GPL electrodes. The dimensions of the active area were 10 mm diameter and 1 mm thickness.

2.3 Experimental Protocol

Data Acquisition. Twenty ($N = 20$) healthy volunteer subjects with ages ranging from 18 to 24 years old (21.1 $\pm$ 1.44; mean $\pm$ SD) were included. Prior to data acquisition, volunteers provided their informed consent to participate in the study in agreement with the Declaration of Helsinki. The wireless acquisition system Shimmer3 Consensys ECG Development Kit and the software ConsensysPRO (Shimmer, Dublin, Ireland) were used to acquire the ECG signals from volunteers for both commercial adhesive Ag/AgCl electrodes (3M HealthCare, Maplewood, MN, United States) and the proposed cased GPL electrodes. A sampling rate of 512 Hz was employed with a resolution of 24 bits-per-sample.

ECG signals were simultaneously acquired using two Shimmer Bluetooth modules for a minute while the subject remained seated in calm and breathing normally. Prior to electrode placement, attachment skin sites were cleaned with 83% ethanol. Electrodes were placed in three pairs with enough pressure to keep them in the thoracic area, at locations that mimics the traditional Lead II. Each pair consisted of a GPL and a commercial Ag/AgCl electrode, placed as close as possible to each other. As shown in Fig. 3, GPL electrodes were attached by wrapping them around the thoracic area with the Velcro straps while Ag/AgCl electrodes were attached using their embedded adhesive tape. Acquired data was transferred to a personal computer for further processing in MATLAB (The MathWorks, Natick, MA, USA).

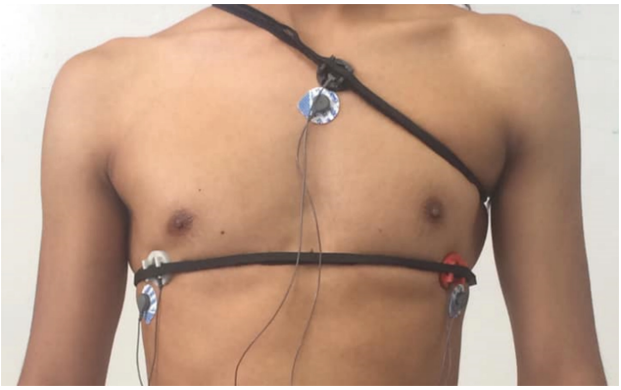

Fig. 3. Placing of electrodes during ECG signal acquisition.

Signal Processing. A zero-phase 4th order bandpass Butterworth filter, with a passband between 0.5–40 Hz, was applied in forward and reverse scheme to minimize start and end transients. Then, both simultaneous ECG signals from the two acquisition devices, i.e. with Ag/AgCl and GPL electrodes, were automatically aligned employing a cross-correlation function approach [6]. After filtering and alignment, R-wave peaks were automatically detected in each ECG signal using a robust algorithm [8].

2.4 Performance Evaluation

Regarding the ECG signal quality, ECG templates $\overline{ECG}$ were generated for Ag/AgCl ($\overline{ECG}_{Ag/AgCl}$) and GPL electrodes ($\overline{ECG}_{GPL}$), by creating an ECG ensemble matrix aligned with respect to the R-peak detected locations for each recording. Then, cross-correlation coefficient ρ between both ECG templates was calculated as follows

$$\rho_{\overline{ECG}} = \frac{\sum_{k=1}^{M} \overline{ECG}_{Ag/AgCl} \cdot \overline{ECG}_{GPL}}{\sqrt{\sum_{k=1}^{M} \left(\overline{ECG}_{Ag/AgCl}\right)^2 \cdot \sum_{k=1}^{M} \left(\overline{ECG}_{Ag/AgCl}\right)^2}} \quad (1)$$

where M refers to the sample length of the templates. In addition, the peak-to-peak amplitude VPP of the ECG templates was obtained for both electrodes ($VPP_{Ag/AgCl}$ and VPP_{GPL}) to quantify possible amplitude reductions due to the electrodes.

Finally, to analyze the performance of GPL electrodes for heart rate analysis, HR time series were obtained by using the detected R-peaks location to create a RR intervals time series, interpolating it via cubic splines at 4 Hz, obtaining its reciprocal, and finally converting it from Hz to beats-per-minute units. A new cross-correlation coefficient was calculated between HR time series from Ag/AgCl ($HR_{Ag/AgCl}$) and GPL electrodes (HR_{GPL}) using the same equation form given in Eq. (1).

3 Results and Discussion

An example of the acquired ECG signals using the proposed GPL electrodes and attachment procedure is shown in Fig. 4 (top), together with its corresponding ECG from commercial adhesive Ag/AgCl electrodes. The corresponding ECG template obtained for the GPL electrode is also in Fig. 4 (bottom). In addition, Fig. 5 shows an example of the HR time series obtained from both types of electrodes. As can be seen, from Figs. 4 and 5, the results from GPL electrodes closely resemble the ones from commercially available Ag/AgCl electrodes, and hence, heart rate variability (HRV) parameters from GPL electrodes are not expected to be statistically significant different from the corresponding ones from Ag/AgCl electrodes. Similar results were obtained for all volunteers in the study. The performance results for ECG signal quality, HR time series, and amplitude reduction are presented in Table 1 (mean ± SD). Regarding the amplitude reductions results, we found that data do not follow a normal distribution and, accordingly, their median ± Inter-Quartile Range (IQR) values are also presented. No statistically significant differences ($p = 0.07$) were found in terms of ECG amplitude reductions, using a Wilcoxon rank sum test and considering $\alpha = 0.05$. The corresponding boxplot for peak-to-peak amplitude of ECG templates is shown in Fig. 6.

Table 1. Performance evaluation of GPL electrodes compared to Ag/AgCl electrodes ($N = 20$)

Performance index	Mean ± SD	Median ± IQR
$\rho_{\overline{ECG}}$	0.994 ± 0.005	
ρ_{HR}	0.949 ± 0.102	
$VPP_{Ag/AgCl}$	0.607 ± 0.104	0.594 ± 0.151
VPP_{GPL}	0.551 ± 0.078	0.540 ± 0.078

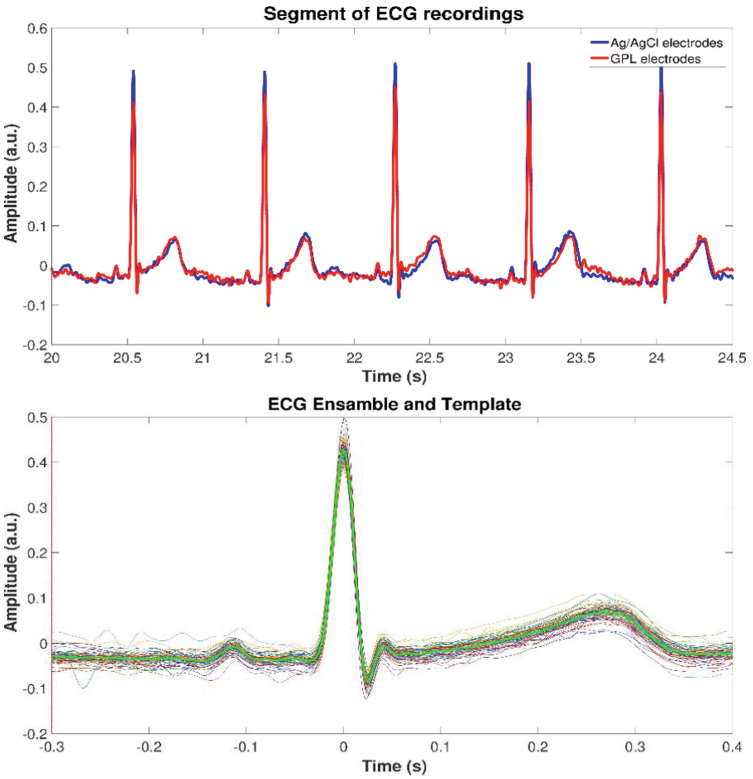

Fig. 4. Acquired ECG signals from a volunteer using the proposed dry GPL electrodes. (Top) ECG obtained with commercial Ag/AgCl electrodes (blue line) and GPL electrodes (red line). (Bottom) ECG ensemble and template obtained with GPL electrodes.

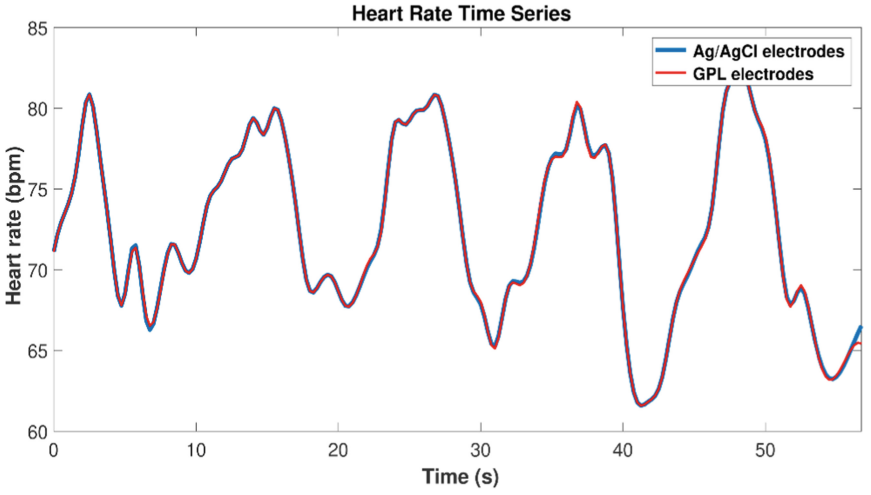

Fig. 5. Heart rate time series obtained from a volunteer using the proposed dry electrodes. HR obtained with commercial Ag/AgCl electrodes (blue line) and GPL electrodes (red line).

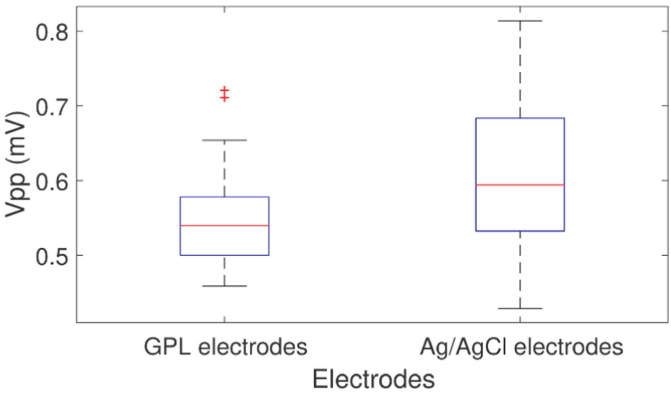

Fig. 6. Distribution of peak-to-peak amplitude of ECG templates obtained with proposed cased GPL electrodes and commercial adhesive Ag/AgCl electrodes ($N = 20$).

4 Conclusions

In this work, we designed and tested cased graphite-based ECG electrodes and compared its performance considering adhesive Ag/AgCl electrodes as reference. High cross-correlation coefficients during the ECG signal acquisition were obtained, just as reported in previous work [6]. Furthermore, we did not find statistically significant amplitude reductions when acquiring ECG data using the proposed GPL electrodes and the results also show that acquisition is more consistent with GPL electrodes, when compared to Ag/AgCl ones, as indicated by their median and IQR values.

In contrast to previous studies, GPL electrodes were designed for easy use considering the protection of fragile graphite material. Regarding the reusability and costs, only three GPL electrodes were used to acquire ECG signals from twenty volunteers, in contrast to sixty disposable electrodes Ag/AgCl. Although total cost was higher for the GPL electrodes ($5USD for sixty Ag/AgCl electrodes, $10 USD for three GPL electrodes), GPL electrodes were still in good condition and could be used in more ECG acquisition, making them more cost effective in the long term. It is also worth mentioning that the protective case of the electrodes appears to be properly working as the fabricated units remain in proper condition and their functionality is reflected by the good performance indexes obtained from first to last volunteer of the study. We are currently investigating if mechanical attachment still provides good results compared to adhesive-based attachment during long-lasting exercise conditions, where the latter is expected to fail due to sweat. Future work also includes evaluation performance for tasks different than HR monitoring and in underwater conditions. We consider that this and similar efforts in developing reusable, dry electrodes could result beneficial in academic environments where students can easily design their own electrodes and keep using them through their college life.

Conflict of Interest. The authors declare no conflict of interest.

References

1. Carroll, D.: Electrocardiogram (EKG). Encyclopedia of Behavioral Medicine. Springer, Heidelberg (2013)
2. Hampton, J.: The ECG Made Easy. Elsevier Health Sciences, Amsterdam (2013)
3. Mundt, C.W., et al.: A multiparameter wearable physiologic monitoring system for space and terrestrial applications. IEEE Trans. Inf Technol. Biomed. **9**(3), 382–391 (2005). https://doi.org/10.1109/TITB.2005.854509
4. Joutsen, A.S., Kaappa, E.S., Karinsalo, T.J., Vanhala, J.: Dry electrode sizes in recording ECG and heart rate in wearable applications. In: EMBEC & NBC 2017, IFMBE Proceedings, pp. 735–738. Springer, Singapore (2017). https://doi.org/10.1007/978-981-10-5122-7_184
5. Jung, H.C., et al.: CNT/PDMS composite flexible dry electrodes for long-term ECG monitoring. IEEE Trans. Biomed. Eng. **59**, 1472–1479 (2012). https://doi.org/10.1109/TBME.2012.2190288
6. Reyes, B.A., et al.: Novel electrodes for underwater ECG monitoring. IEEE Trans. Biomed. Eng. **61**, 1863–1876 (2014). https://doi.org/10.1109/TBME.2014.2309293
7. Thap, T., Yoon, K.-H., Lee, J.: Graphite based electrode for ECG monitoring: evaluation under freshwater and saltwater conditions. Sensors **16**, 542 (2016). https://doi.org/10.3390/s16040542
8. Vidaurre, C., Sander, T.H., Schlögl, A.: BioSig: the free and open source software library for biomedical signal processing. Comput. Intell. Neurosci. **2011**, 1–12 (2011). https://doi.org/10.1155/2011/935364

Bio-Signal Acquisition Analysis for Stress Level Determination

Sergio Alfonso Sánchez-Manzo[1(✉)], Ricardo Antonio Salido-Ruiz[2], O. Rocío Manzo-Palomera[3], Ángel Alfredo Sánchez-Michel[3], and Guillermo Alonso Cervantes-Cardona[4]

[1] Departamento de Electrónica del Centro Universitario de Ciencias Exactas e Ingenierías de la Universidad de Guadalajara, 44430 Guadalajara, Jalisco, Mexico
sergio.smanzo@alumnos.udg.mx
[2] Departamento de Ciencias Computacionales del Centro Universitario de Ciencias Exactas e Ingenierías de la Universidad de Guadalajara, 44430 Guadalajara, Jalisco, Mexico
ricardo.salido@academicos.udg.mx
[3] Departamento de Odontología para la Preservación de la Salud del Centro Universitario de Ciencias de la Salud, Universidad de Guadalajara, 44430 Guadalajara, Jalisco, Mexico
[4] Departamento de Disciplinas Filosóficas, Metodológicas e Instrumentales del Centro Universitario de Ciencias de la Salud, Universidad de Guadalajara, 44430 Guadalajara, Jalisco, Mexico

Abstract. Stress and illness have a complex relationship, that's why stress is considered a precursor of illness, so it is important to study about it to reduce deceases and even prevent early death. In this work we employ two methods to measure stress: a subjective one known in the literature as Depress, Anxiety and Stress Scale (DASS) and an objective one proposed here based on the acquisition and analysis of certain bio-signals. The former is based on tests about how people feel, and the latter is based on bio-signal acquisition of temperature and galvanic skin response. In this paper, we use the Depress, Anxiety and Stress Scale method on its reduced version of 21 items as a reference to compare objective methods based on measurements of temperature and galvanic skin response of undergraduate students of High and Low Stress levels during three different conditions (i.e., closed eyes, open eyes and relaxation). We found that inter-individual variability of temperature and galvanic skin response does not allows us to show significant differences for subjects having low or high stress levels. In the other hand, for an intra-subject analysis differences among temperature or galvanic skin response shows significant differences between subjects having low or high stress levels.

Keywords: Stress measure · Bio-signal · DASS

© Springer Nature Switzerland AG 2020
C. A. González Díaz et al. (Eds.): CLAIB 2019, IFMBE Proceedings 75, pp. 1093–1100, 2020.
https://doi.org/10.1007/978-3-030-30648-9_142

1 Introduction

Stress is cataloged as a precursor of disease, in fact, it exist a complex relationship between illness and stress depending on the person affected [1]. Stress can even cause death, people having high stress levels and depression are 48 percent more likely to die or have a heart attack, compared with people having low stress levels and depression [2]. In this context we believe that it is important to study more about stress and how to measure it. There are two methods to measure stress: subjective and objective. In subjective methods, there are several ways to measure; most of them consist in tests with different questions about how the person is feeling during the test. The best way to apply these tests is with the presence of a medical specialist, for example a psychologist. In objective methods, there are some techniques to measure, however they are less in number than in subjective methods. One method used to measure stress is a cortisol test, this hormone is associated to stress because cortisol tend to increase when a person is taken to a stressful situation. And the ways to get cortisol are by blood test, and saliva test [3]. Other ways to measure stress are based on bio-signal analysis, for example heart rate measure devices. Among these devices, there are modern wearables for example, smart watches or devices placed on areas where is possible to measure the pulse [4]. Other bio-signal is obtained from Galvanic Skin Response (GSR) sensors, this response is associated with stress because sweat in our body is present when performing stressful activities [5]. Another measurement associated is temperature, in specific peripheral temperature, which shows a good biofeedback to analyze stress [6]. There are several works in this field of bio-signal processing for example in [7], the authors use skin conductance, photoplethysmography and skin temperature to classify stress levels. Another work presented in [8] where the authors want to measure stress is done by comparing other bio-signals such as EEG and ECG to a saliva cortisol test. In this work, we compare two objective methods to determine the level of stress. We used as reference the subjective method Depression Anxiety Stress Scale (DASS) [9] in order to associate the subject stress perception to a numerical value. The original scale consist on 42 items corresponding to anxiety and stress in a single factor, and depression in second factor. A short version of this scale is known as DASS-21, and it was used in this study. The two objective methods compared here are GSR, Temperature [10]. A related study is [11], were they measure a stress level normalizing some stress parameters: Breathing, EMG, GSR, position, cortisol and prolactin.

2 Materials and Methods

We applied DASS-21 to 200 undergraduate students ranging in age from 20 to 25 years old. Also, to get general status and personal information a questionnaire. General data and DASS-21 items where obtained based on the research presented in [12]. Among these candidate subjects, only the ones showing higher and lower stress levels were selected in this study to be part of the posterior bio-signal acquisition protocol. Thus, 46 subjects were selected, 23 with higher and 23 with lower stress levels.

The bio-signal acquisition protocol consisted in recording: GSR and Temperature signals in three distinct conditions: open eyes (OE), closed eyes (CE) and relaxation (R) for subjects with higher stress (HS) and lower stress (LS) levels. The OE condition was a basal state register, CE condition consisted on a cognitive challenge to apply some stressful conditions, and the R condition consisted on regulated deep breaths. The GSR sensor was placed on middle and index fingers on left hand to measure the resistance of the skin. Temperature sensor was placed on the index finger on right hand to measure peripheral temperature. Signals from each student were recorded during 2 min with a sample frequency of 2 samples per second, then were saved for further analysis. We employ the Analysis of Variance (one-way-ANOVA test) to measure if there is a significant difference between the means of the bio-signal average values from both groups: HS and LS.

3 Results

The one-way ANOVA resulting from the comparison of mean values of measured bio-signals (GSR and Temperature) between the above mentioned groups HS and LS is present in Fig. 1. We observe non-significant differences ($p > 0.05$) between means for any of the bio-signals tested here among both groups. Moreover, in HS the GSR signal for OE, CE and R conditions we observe a significant number of outliers which clearly indicate the great variability between subjects belonging to the same group and condition. We also observe that mean GSR responses for group HS and OE, CE and R conditions are slightly lower than for those presented in group LS for the same conditions. In the other hand for temperature sensor the variability for subjects in the same group and condition is not so big (Fig. 1(b)); however, even if we can see that the means among groups (for the three conditions) are slightly higher in the HS group than for the LS group this difference is still non-significant ($p > 0.05$).

The bio-signals behavior between subjects in HS and LS were analyzed. We observed the great variability of GSR and Temperature values respectively among subjects. We choose the OE condition to perform this analysis because this is the basal state of each subject. In Fig. 2(a) we show that HS subjects present GSR values above 20 KΩ and under 35 KΩ and even among these subjects some of them presents significant differences ($p < 0.05$). In Fig. 2(b) we show that LS subjects present GSR values above 20 KΩ and under 60 KΩ and also, among these subjects some of them presented significant differences ($p < 0.05$). In this context it is confirmed that there exists an overlap in GSR values between HS and LS groups from 20 KΩ to 35 KΩ; however we also observed that most of the subjects in LS presented higher GSR values ranging from 35 KΩ to 60 KΩ approx.

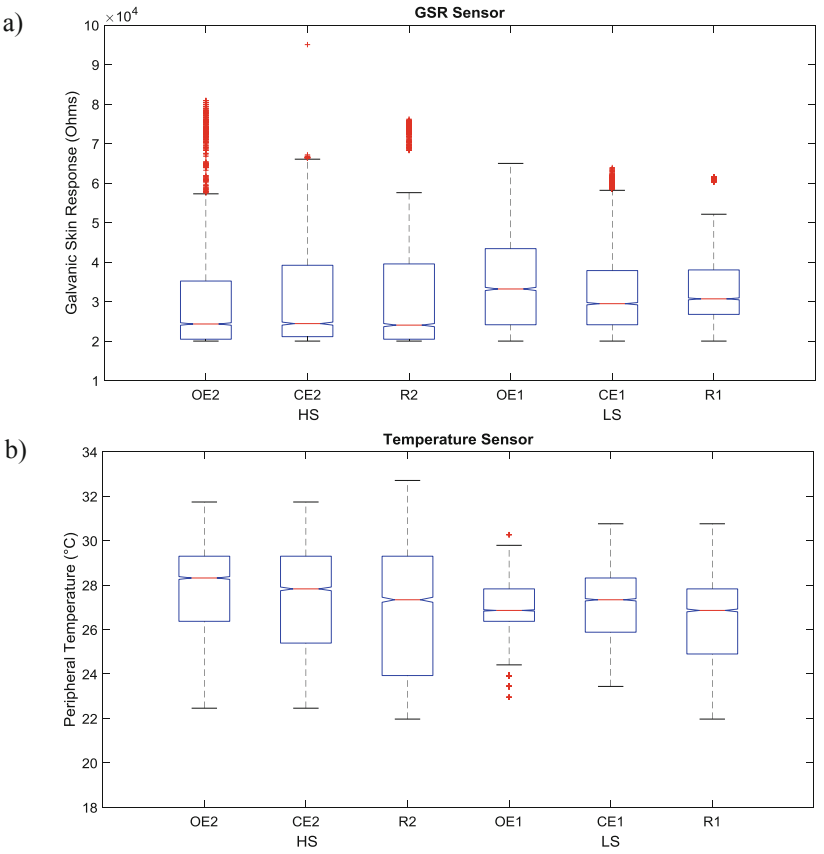

Fig. 1. Box plot of differences in mean values for (a) GSR and (b) Temperature bio-signals among HS group on three conditions: OE, CE, R and LS group on three conditions: OE, CE and R.

In Fig. 3(a) for Temperature analysis values in HS group showed that most of the subjects were above 28 °C and under 32 °C and as same as GSR values these subjects also presented significant differences ($p < 0.05$) between their temperature mean values. In Fig. 3(b) in LS group the subjects presented temperature values above 25 °C and under 30 °C, even some of them presented significant differences ($p < 0.05$) between their temperature mean values. In this temperature context it is confirmed that there exists an overlap in temperature values between HS and LS groups from 25 °C to 30 °C; more overlapping than the obtained for GSR values.

Intra-subject analysis, here two subjects one from each group were selected according the following criteria: the values for GSR and temperature of the chosen subjects must be close to the average values obtained among all other subjects in their respective groups. In this case, the subject representing the HS group was subject 9 and

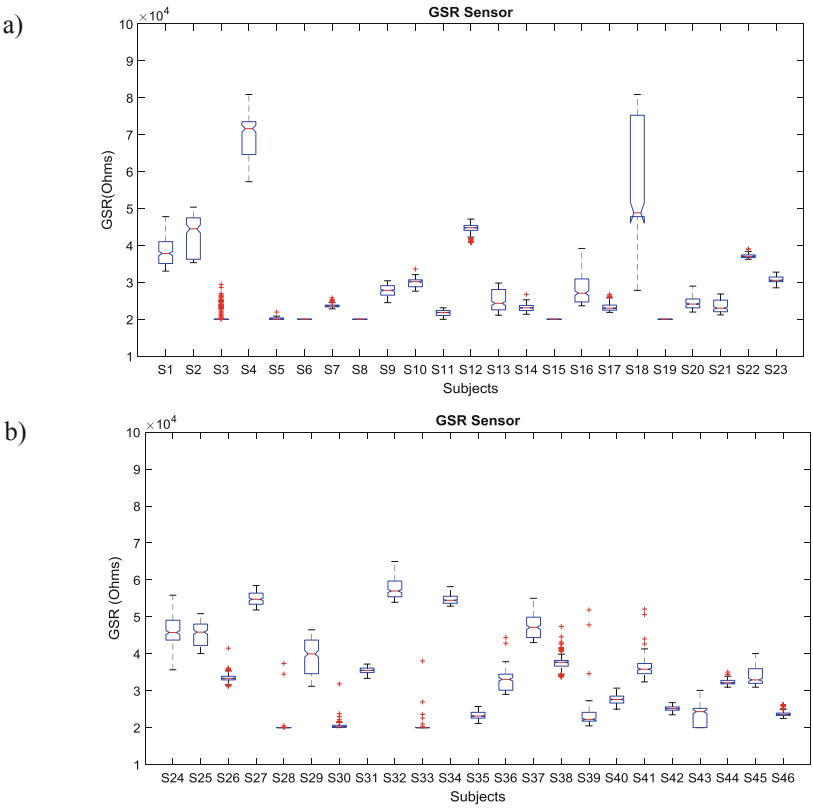

Fig. 2. Box plot of differences in mean values for every single student in this test for GSR values in (a) HS group and (b) LS group on the OE condition.

representing the LS group was subject 29. During the three conditions HS subject 9 showed no significant differences ($p > 0.05$) among their GSR response (Fig. 4(a)) while these differences were more evident for their peripheral temperature values (Fig. 4(b)) for the same conditions. In other hand, analysis intra-subject for LS subject 29 found significant differences ($p < 0.05$) between CE and R conditions while it showed no significant differences ($p > 0.05$) between OE and R conditions. Peripheral temperature showed no significant differences ($p > 0.05$) for LS subject 29, however is clear that for R condition temperature was lower.

Comparison from subjects 9 and 29 for GSR and Peripheral Temperature during three conditions is presented in Fig. 4(a) and (b) respectively. Significant differences ($p < 0.05$) between HS subject 9 and LS subject 29 for OE, and R conditions in the GSR measurements while there is not for CE condition, in this condition we can infer that skin for both higher and lower stress subjects presented similar behavior due to the cognitive challenge.

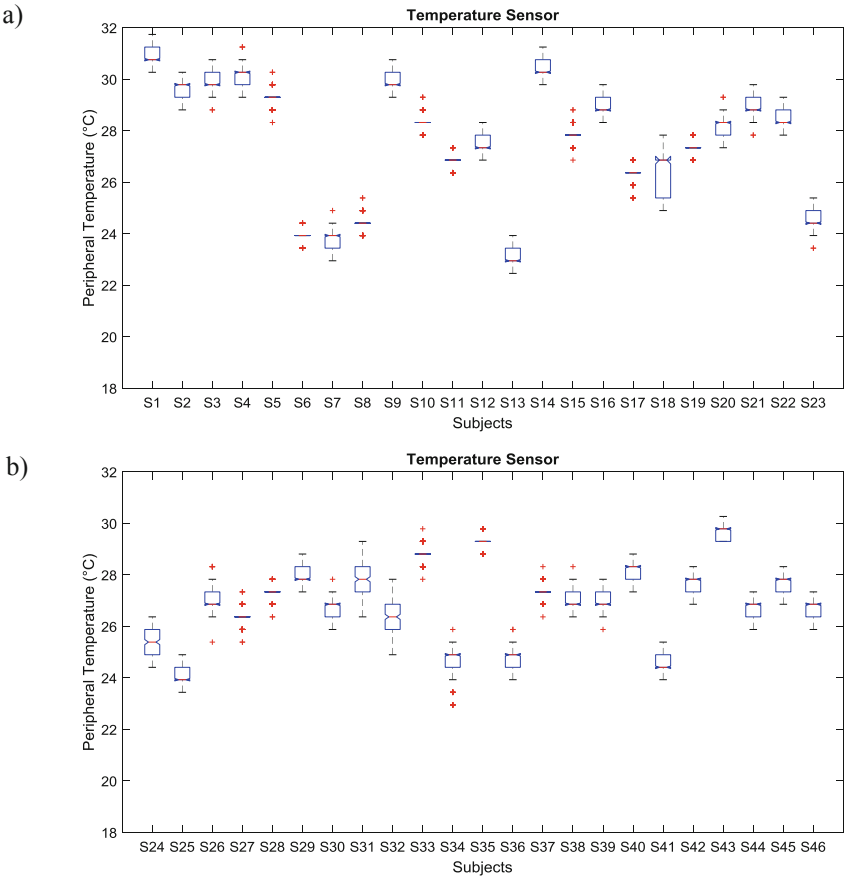

Fig. 3. Box plot of differences in mean values for every single student in this test for temperature values in (a) HS group and (b) LS group on the OE condition.

In bio-signals analysis we found interesting data, comparing one to one High and Low Stress subjects we observed bigger differences (Figs. 2 and 3). In general, people with higher stress present lower levels of skin resistance, and higher temperature levels, this can be associated with a natural skin response of sweating when the temperature of our body increases.

Also we can infer that some of the HS subjects had difficulties to control themselves as we observed for subject 9 in the R condition. In Fig. 4, we can see that HS subject 9 and LS subject 29 stress subjects behave almost the same (i.e., GSR values decrease, and temperature rises), but at the time of the R condition, LS subject 29 showed more control and regulate their bio-signals and returned to their basal state values (OE condition) or even lower.

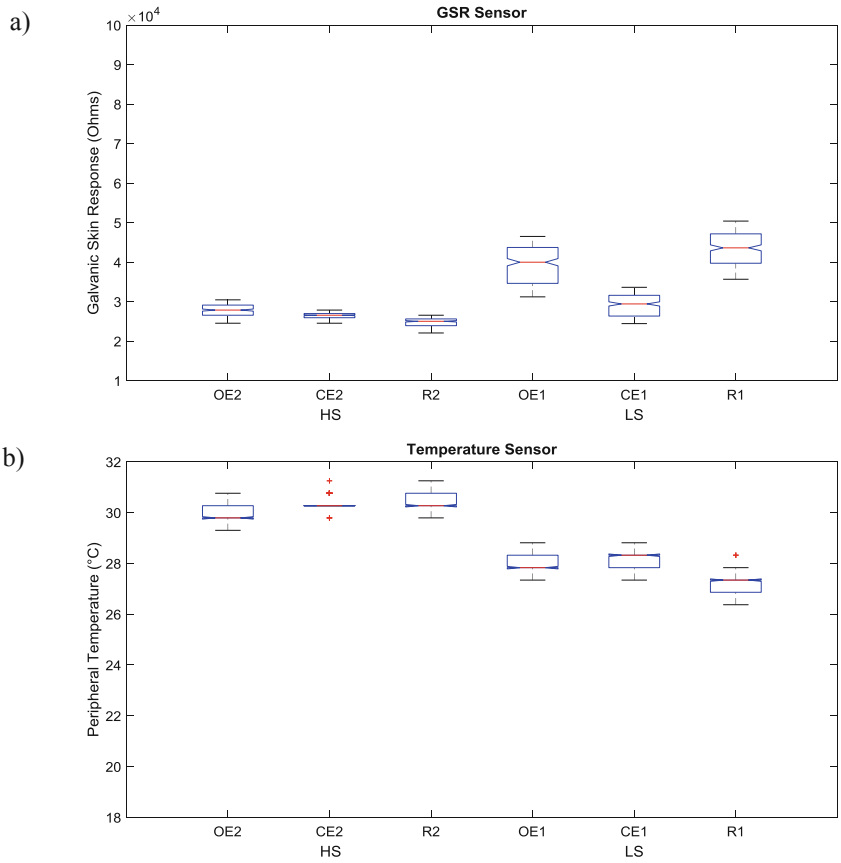

Fig. 4. Box plot of differences in mean values for HS subject 9 and LS subject 29 in every single condition for (a) GSR and (b) Temperature respectively.

4 Discussion and Future Work

Results showed that there are small differences between higher and lower stress levels in the subject population tested here according to DASS-21, for example, their mean values are close as observed in Fig. 1, and this is due to the high variability among these measured parameters. Probably subgroups of these two populations show significant differences in stress levels comparison. An intra-subject analysis showed that most of the subjects are on their respective stress level group, of course with their respective exceptions. For example most of the HS level subjects belong to that group, but there are 6 out 23 subjects in the HS level group that probably belong to the LS level group if we look at their measured bio-signals. A probably explanation could be that at the time they made DASS-21 they were stressed and when they made the device test they were a little bit calmer.

Finally, with this work we infer some new hypothesis to continue studying stress and discover how it can vary through each person. Hybrid researches between quantitative and qualitative assessments help us to confirm and reaffirm subjective stress measurement methods with objective methods because we can complement subjective results.

References

1. Razali, M.: Life event, stress and illness. Malays J. Med. Sci. **15**, 9 (2008)
2. Alcántara, C.: Perfect storm, concurrent stress and depressive symptoms increase risk of myocardial infarction or death. Circulation: cardiovascular quality and outcomes, https://www.ahajournals.org/doi/full/10.1161/CIRCOUTCOMES.114.001180. Accessed 29 Apr 2019
3. Konkel, L.: Every day health. https://www.everydayhealth.com/cortisol/guide/. Accessed 23 Apr 2019
4. Stress tracking tech: heart rate monitoring and guided breathing devices, Wearable. https://www.wareable.com/wearable-tech/stress-beating-tech-to-keep-you-sane. Accessed 23 Apr 2019
5. Villarejo, M., Garcia, B.: A Stress sensor based on galvanic skin response (GSR) controlled by ZigBee. Sensor (Basel) **12**, 6075–6101 (2012)
6. Dominguez, B.: Monitoreo no invasivo de la temperatura periférica en la evaluación y tratamiento psicológico, Research Gate. https://www.researchgate.net/publication/275951248_Monitoreo_no_invasivo_de_la_temperatura_periferica_en_la_evaluacion_y_tratamiento_psicologico. Accessed 23 Apr 2019
7. Cho, D., Ham, J., Oh, J., Park, J., Kim, S., Lee, N-K., Lee, B.: Detection of stress levels from biosignals measured in virtual reality environments using a kernel-based extreme learning machine. Sensors, MDPI, NCBI (2017). https://www.ncbi.nlm.nih.gov/pmc/articles/PMC5677291/. Accessed 13 June 2019
8. Seo, S.: Detection of chronic stress using bio-signals. Ind. J. Sci. Technol. **9**(46) (2016). http://www.indjst.org/index.php/indjst/article/download/107866/76210. Accessed 13 June 2019
9. Psychology Foundation of Australia. http://www2.psy.unsw.edu.au/dass/over.htm. Accessed 24 Apr 2019
10. Sánchez S.: Diseño e implementación de un sistema para medir estrés. Universidad de Guadalajara (2018)
11. Acevedo, M.E., Acevedo, M.A., de Luca, A.: Sistema de medición de estrés. Rev. Mexicana de Ingeniería Bioméd. **XXII**(1), 6 (2001)
12. Manzo R.: Estrés Ansiedad y Depresión en estudiantes en el Centro universitario de Ciencias de la Salud (CUCS). In: Armendariz, J. (ed.) XVIII CIAM, vol. 8, pp. 232. Revista en ciencias de la salud (2016)

Therapainting: Interactive Art-Therapy Tool Based on Head Movements and Eye Blinks

Fernando González-Martínez(✉), Luz María Alonso-Valerdi, and David I. Ibarra-Zárate

Tecnológico de Monterrey, Escuela de Ingeniería y Ciencias, Ave. Eugenio Garza Sada 2501, 64849 Monterrey, NL, Mexico
A01192751@itesm.mx, lm.aloval@tec.mx

Abstract. *Therapainting* is a system based on head movements and eye blinks that allows the artistic expression for therapeutic purposes. Head movements and eyes blinks are respectively detected by accelerometers and electroencephalographic electrodes mounted on the headband MUSE developed by InteraXon from Toronto, Canada. On the basis of different exercises for people with spinal cord injuries, *Therapainting* makes use of head movements to move a paint brush across a screen, and eye blinks to select randomly different colors. *Therapainting* has been tested in non-controlled environments and by users of all ages at the Modern Art Museum, and at a high school of Autonomous University of Nuevo Leon in Monterrey, Mexico. User evaluation were carried out through the User Experience Questionnaire, which showed that *Therapaining* was considered as an interesting, exciting, innovative and leading edge system.

Keywords: EEG-based technology · Head movements · Eye blinks · Accelerometers · Art-therapy

1 Introduction

American Art Therapy Association (AATA) establishes that art-therapy is a psychotherapeutic technique that assists in developing social skills, solving conflicts, controlling behavior, reducing stress, and enhancing self-esteem by artistic expression [1]. On this basis, *Therapainting* was conceptualized as an art-therapy tool that allows to generate brush strokes on a blank screen in wide variety of colors by monitoring head movements and eye blinks. Figure 1 presents an example of artistic expression (on left side), and users interacting through *Therapainting* (on right side).

Therapainting was originally designed to improve the quality of life of quadriplegics. Quadriplegia is a condition caused by a spinal cord injury, where different body parts are affected depending on the injury level. Injuries located from cervical vertebras from C1 to C3 provoke limited head movements, while injuries below C4 affect different body parts depending on the injury level. However, the person still has full head and neck movement in this latter condition [2]. In terms of assistive technology for people with quadriplegia, there are no interactive systems that can strengthen head and neck muscles, and grant the possibility for artistic expression, what

© Springer Nature Switzerland AG 2020
C. A. González Díaz et al. (Eds.): CLAIB 2019, IFMBE Proceedings 75, pp. 1101–1106, 2020.
https://doi.org/10.1007/978-3-030-30648-9_143

Fig. 1. *Therapainting*: interactive art therapy tool based on head movements and eye blinks.

can help to reduce stress and enhance self-esteem according to AATA [3, 4]. In line with different exercises for people with spinal cord injuries proposed in [5], *Therapainting* was designed to make use of head movements and eye blinks to respectively move a paint brush across a computer screen, and randomly select different colors. Although the present project was conceived to implement a dynamic and interactive physical and psychological therapeutic alternative for people with quadriplegia, *Therapainting* is now an art-therapy tool for people of all ages with different types of mental and physical conditions. Hereunder, the system implementation and evaluation is described.

2 Methods

Therapainting is a prototype built on the MUSE headband [6] and Processing programming language [7]. The prototype was tested in non-controlled environments by users of all the ages. In this section, design, implementation and test conditions are described.

2.1 Design

Therapainting aims to allow artistic expression by head movements and eye blinking. Head movements are detected by accelerometers of the MUSE headband and are employed to move a paint brush across a computer screen. On the other hand, eye blinks detected by prefrontal electroencephalographic (EEG) electrodes of the MUSE headband are used to randomly change the stroke color. The movements that are decoded to move the paint brush around were selected from [5], where are specified different exercises for people with spinal cord injuries, including flexion, extension and lateral flexion of the neck. See Fig. 2a. However, the prototype is not limited to quadriplegics as is discussed in last section.

2.2 Data Acquisition

The MUSE headband distributed by InteraXon (from Toronto, Canada) is used as recording system. This headband has five EEG electrodes and three accelerometers that provide special location in three axes: X, Y, and Z. Two of the five EEG electrodes are placed on the prefrontal lobe (AF7 and AF8), and two other electrodes are placed on

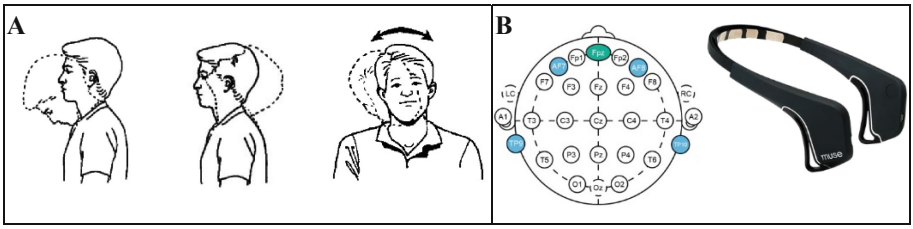

Fig. 2. Design and implementation of *Therapainting*. On the left (A), flexion and extension neck movements employed to interact through *Therapainting* are depicted. On the right (B), recording system is specified. On one side, EEG layout of MUSE is shown: blue electrodes refer to prefronto-temporal recording sites, and green one refers to the ground. On the other side, MUSE headband is illustrated.

the temporal lobe (TP9 and TP10). The remaining one is used as ground (Fpz). See Fig. 2b. The communication between the headband and the computer is established via Bluetooth at a sampling rate of 220 Hz, and Processing programming language retrieves MUSE information by User Datagram Program (UDP) protocol.

2.3 System Implementation

To establish UDP communication, Processing makes use of the library oscP5. The processing program is executed in four steps. Firstly, variables are declared and a white canvas is created. Secondly, events coming from the accelerometers are detected and stored in variables "accelX" and "accelY". These events are applied to smoothly move the paint brush across the canvas and limit its position inside the canvas. For this purpose, Processing drawing functions are used. Thirdly, EEG activity is taken to set a RGB color, and eye blink detection is employed to apply such color. Lastly, the canvas is reset every time the key "R" is pressed. The Processing program can be found in [8].

2.4 Prototype Test

Two field tests were undertaken in non-controlled environments and with users of all ages. The first field test was done in the exposition titled as "Neural Interfaces" organized by the Neuroengineering and Neuroacoustics Research Group at Modern Art Museum from September 24th to 28th, 2018 in Monterrey, Mexico [9]. During the exposition, the prototype was tested by more than 50 museum visitors of all ages, and who provided feedback through a survey designed by the research group [10]. See Fig. 3. The second field test was done at a high school of the Autonomous University of Nuevo Leon in Monterrey (Mexico) in October 17th, 2018 during a Neuroscience conference. The prototype was tested by 12 teenagers who were around 15 years old. All of them responded a short version of the User Experience Questionnaire (UEQ) [11].

Fig. 3. Setup, explanation and use of *Therapainting*.

3 Results

3.1 Field Test 1: Modern Art Museum

In line with the survey results, *Therapainting* was the most accepted prototype by visitors. Figure 4 shows how *Therapainting* was the favorite one over all of the other prototypes by almost a third of the visitors (29%), and around 90% of the visitors showed interest in the exposition about "Neural Interfaces".

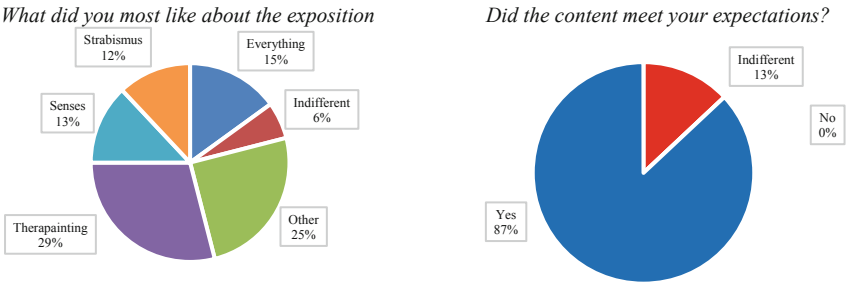

Fig. 4. Self-design survey responses from around 50 visitors at Modern Art Museum (on the left) and UEQ responses from 12 teenager users at a high school of the Autonomous University of Nuevo Leon in Monterrey, Mexico (on the right).

3.2 Field Test 2: High School

Short version of the UEQ was applied to 12 high school students. The questionnaire has 6 items, and each item has two opposite choices on a scale from 1 to 7. The higher the number chosen is, the more preferred the option on the right is. Figure 5 presents the mean UEQ results. It can be seen from the figure that the system is very exciting, inventive and revolutionary.

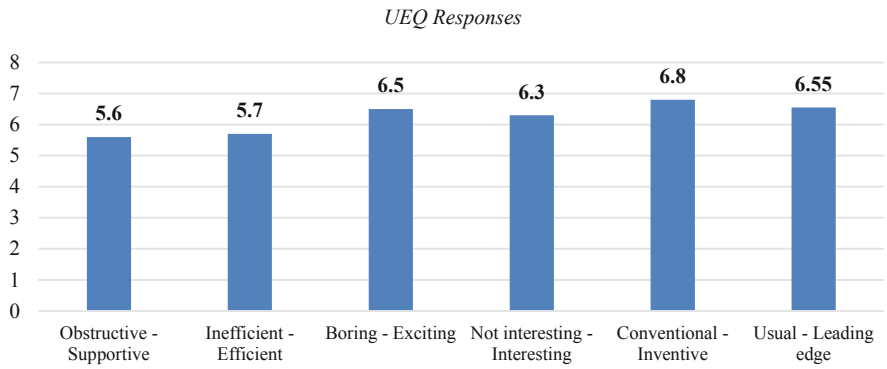

Fig. 5. Average results from the short version of the UEQ applied to 12 high school students.

4 Discussion and Conclusion

Therapainting is an interactive art-therapy tool that allows artistic expression through head movements and eye blinks. Field tests reveal that *Therapainting* catches attention of all type of possible end-users and is considered as an interesting, exciting, innovative and leading edge system. Although the system was originally conceived as a dynamic and interactive physical and psychological therapeutic alternative for people with quadriplegia, it is highly suitable for multiple purposes such as neck pain relief of office workers and entertainment tool.

References

1. AATA: American Art Therapy Association, Website design by Vandenberg DC (2017). https://arttherapy.org/about/
2. Avery Biomedical Devices: Understanding Quadraplegia and Spinal Cord Injury. Ascent Digital Media, New York (2012–2019)
3. Floris, L., Dif, C., Le Mouel, M.A.: The tetraplegic patient and the environment. In: Surgical Rehabilitation of the Upper Limb in Tetraplegia, WB Sauders, Medical, pp. 45–55 (2002)
4. Spinalpedia: Assistive Technology - At Home & Driving. Determined2Heal Foundation, New York (2019)
5. S. C. I. R. Program: Range of motion: a guide for you after spinal cord injury. Hamilton Health Sciences, (2011). http://www.cdss.ca.gov/agedblinddisabled/res/VPTC2/8%20Paramedical%20Services/Range_of_Motion.pdf
6. Przegalinska, A., Ciechanowski, L., Magnuski, M., Gloor, P.: Muse headband: measuring tool or a collaborative gadget? In: Collaborative Innovation Networks, pp. 93–101. Springer, Cham (2018)
7. Reas, C., Fry, C.: Processing: programming for the media arts. AI Soc. **20**(4), 526–538 (2006)
8. González-Martínez, F.: Therapainting, Monterrey (2019). https://gist.github.com/fernando-gzz-mtz/021ac5852d05d974145140f1944d458a

9. Neuroengineering and Neuroacoustics, Interfaces Neuronales en MARCO, Monterrey (2018). https://www.facebook.com/events/2458352520849259/
10. Neuroengineering and Neuroacoustics, Expectativas Finales, Monterrey (2018). https://docs.google.com/forms/d/e/1FAIpQLSfEY8Pg9MVig8SNSVf1OT4o6sXitQ1eqCtLm-oW0ooZdIHOoQ/viewform
11. Schrepp, M., Hinderks, A., Thomaschewski, J.: Design and evaluation of a short version of the user experience questionnaire (UEQ-S). Int. J. Interact. Multimed. Artif. Intell. **4**(6), 103–108 (2017)

Analysis of Alternating Hand Movement in Parkinson's Disease Patients

Williams Saraguro[1], Boris Barzallo[1], Andrea García-Cedeño[1], Juan Carlos Guillermo[1], Catalina Punín[1], Ángel Soto[1], David Rivas[2], Roger Clotet[3,4], and Mónica Huerta[1(✉)]

[1] GITEL, Telecommunications and Telematics Research Group, Universidad Politécnica Salesiana, Cuenca, Ecuador
wsaraguro@est.ups.edu.ec,
{bbarzallo,agarciac,jguillermo,bpunin,asoto,mhuerta}@ups.edu.ec
[2] Universidad de las Fuerzas Armadas ESPE, Sangolquí, Ecuador
drrivas@espe.edu.ec
[3] Networks and Applied Telematics Group, Universidad Simón Bolívar, Caracas, Venezuela
clotet@usb.ve,roger.clotet@campusviu.es
[4] Valencian International University, Valencia, Spain

Abstract. In Parkinson's disease the symptoms of motor disability predominate, generating consequences in their quality of life, psychological, social and economic stability. The Unified Parkinson's Disease Rating Scale is considered as a clinical evaluation method, that is a compendium of subjective interpretations. Alternatively a system called LEEPark is proposed, capable of quantifying the speed of the test of Alternating Hand Movement. The system uses Kinect V2 for data acquisition and features extraction, the results are stored in a database that is subjected to statistical analysis, grouped by degree of disease and by upper extremities. The analysis methods used were: ANOVA, linear regression and quantification of improvement, applied to data collected during 6 sessions from 6 patients: 4 with Parkinson's disease and 2 control subjects. The results showed contrasts in hand speed, being able to find significant differences between grade 1 and 2 of the disease. It was also possible to establish the decrease in speed as the degree of disease progresses and the percentage of improvement when comparing the effects of medication on the speed of the hands.

Keywords: Parkinson's Disease · Alternating hand movements · Kinect sensor · Medical application

1 Introduction

In the course of time, great technological advances have been evidenced in various areas of science. However, there are exceptions to this fact as is the case of neurodegenerative diseases. Currently, innovation in neurology has not been able

© Springer Nature Switzerland AG 2020
C. A. González Díaz et al. (Eds.): CLAIB 2019, IFMBE Proceedings 75, pp. 1107–1116, 2020.
https://doi.org/10.1007/978-3-030-30648-9_144

to determine the origin, prevention and cure of several of its pathologies. Due to the growing affected population, most of which is elderly, medical research has focused on slowing the progression of these diseases and improving the living conditions of people who suffer from them [6,9]. This group of disorders represent progressive and chronic affections that compromise the central nervous system and therefore cognitive domains and motor performance. Among this classification is Parkinson's Disease (PD), the second neurogenerative condition that most affects the adult population after Alzheimer's [1,4,7,9]. Worldwide, more than 10 million people suffer from it. In Ecuador, the prevalence of PD ranges from 300 to 600 patients per 100,000 inhabitants; and, as in various studies, it is shown that the presence of the disease is more prevalent in people over 61 years of age, more commonly in men than in women [7,13].

PD arises at a gradual level with symptoms of motor disability which may vary by patient, however it generates significant limitations in his quality of life [15,16]. The majority of those who suffer it have a life expectancy of 15 years from its detection until death, as a result of causes derived from motor conditions: falls, fractures, infections, etc. [1,11].Its diagnosis is based merely on clinical fundamentals, even for an experienced neurologist, the detection of PD in its initial stages is a challenge since its presence in a patient cannot be assumed only by the manifestation of tremors [8,11]. Based on these complications, the medical community has established different methods to standardize the assessment including the commonly used Unified Parkinson's Disease Rating Scale (UPDRS) [12].

The UPDRS corresponds to a clinical method classified into three specific sections: mentation, behavior and mood; daily activities and motor examination. This evaluation, carried out throughout the subject's illness, gives indications of the history of the disease and the influence of the treatments used. However, this test is based on subjective interpretations and is therefore considered inaccurate [10,12]. In the motor section of the UPDRS there is an item called "Rapid alternating movements", an activity carried out with the purpose of evaluating the postural tremor of the hands and their performance before and after medication [12]. Is this exercise the motivation for the present proposal, which is focused on quantifying the speed of Alternating Hand Movements through the LeePark system, capable of recognising motions of hands in PD patients [14]. The aim is to expose a support tool for physicians with the goal of optimizing the UPDRS motor evaluation process and, consequently, eliminating the disadvantages of a subjective and imprecise assessment. The present implementation of said LeePark system, corresponds to a continuation of the work referenced in [14]. Nonetheless, this article makes reference to the recognition of the alternating movement of hands. The obtained data will be used for a population analysis regarding the degree of the disease, speed differentiation and evidence of PD progression in each limb, through an Analysis Of Variance (ANOVA) and Linear Regression [17].

2 Related Works

Different UPDRS assessment and analysis technologies or systems for PD patients have been developed to exclude the conventional clinical assessments used by physicians [2]. With these existing technologies, it is possible to achieve high assessment accuracy, monitor all stages of PD, and provide a much more accurate diagnosis. The systems closely related to our study are detailed below.

Dror et al. propose a non-invasive system with an Human Machine Interface (HCI) for the evaluation of motor activities according to the UPDRS scale such as hand movements (open-closed, pronation-supination and finger tapping), using a 3D depth sensor, similar to a Kinect v2. The data acquisition is obtained in 4 matrices of 986 by 274 pixels with a speed of 24 frames per second through a 3D camera based on Time of Flight (TOF) technology. The automatic classification between healthy and sick patients is carried out using machine learning techniques with the acquired data. For the final diagnosis, the manual action of the most unfavourable case is chosen, so if at least one of these actions presents PD, the patient will be classified as a person with Parkinson's disease [3].

AVIPARK: Web system for the evaluation and analysis of hand movements (finger tapping, hand opening - closing and pronation - supination), using artificial vision techniques with Kinect version 1 of people with EP based on the UPDRS scale. The interface allows to visualize statistical graphs with time values, repetitions and average speed of each movement of the left and right hands and fingers of each of the patients registered in the system, in order to evaluate in a quantitative way the evolution of the rehabilitation process, as well as to evaluate the effect of the different pharmacological treatments of the patient over time [8].

Ferraris et al. propose a low-cost HCI system for the automated evaluation of hand movements of a PD patient according to the UPDRS scale at home. This system is based on an RGB-Depth optical device and replicable software. The interface allows gestural interactions with visual feedback and allows the characterization of hand movements by the kinematic parameters of its trajectories. The correlation between selected parameters and UPDRS clinical patient performance scores is used to evaluate instances of new tasks using an automatic learning approach based on supervised classifiers [5].

LeePark: Web system capable of analysing hand movements in patients with PD with medication (Onstate) and without medication (Off state), using the Kinect v2 device based on the UPDRS scale to valuate finger tapping movements. The system measures the variations in the position of a patient, these displacements are interpreted as an increase in the intensity of the tremors. The application allows to visualize the acquired data or interpretations in a graphical interface. The difference of our proposal with the Leepark system is that it is mainly focused on quantifying the speed of alternating hand movement and in turn analyzing and inferring on the data collected with the ANOVA method, linear regression and quantification of improvement in patients with medicated and non-medicated PD [14].

3 Materials and Methods

The inclusion of technology to society suffering from PD seeks to incorporate tools, programs and applications that allow and facilitate the specialist to give a more accurate diagnosis, an appropriate therapy and, especially, to administer the required dose of medication. The study of alternating hand movements performed in this article is a continuation of LeePark project and is carried out in four phases: Acquisition, Processing, Visualization and Statistical Analysis, see Fig. 1.

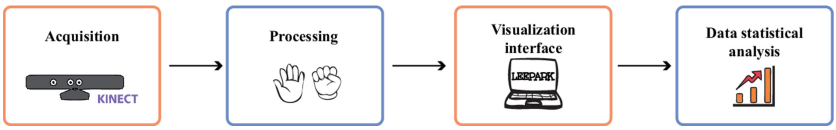

Fig. 1. Block diagram for detection of alternating hand movements using Kinect v2.

3.1 Acquisition

For the patients evaluation process, the system was applied in six subjects from 60 to 89 years of age from the Universidad del Adulto Mayor (UAM); four of them suffer from Parkinson's disease and two individuals are healthy. All participants signed a letter of informed consent to proceed with the examination, which was carried out when patients were on medication (ON status) or without medication (OFF status).

The exercise to be tested corresponded to the alternating movement of the hands where the subject opened and closed the hand repeatedly as fast as possible. The purpose was to count the number of repetitions performed by the patient in the time assigned by the specialist.

It is important to consider some parameters of the evaluation environment before testing such as height, distance between the patient and the device, posture and lighting as shown in Fig. 2.

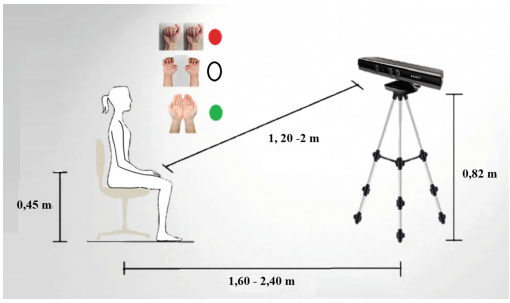

Fig. 2. Distances on scenario during testing.

In Table 1, the characteristics of the patients are presented in terms of age, sex and disease degree.

Table 1. Patient data.

Patient	Age	PD	Gender	Disease degree
P1	82	Yes	Male	3
P2	72	Yes	Female	3
P3	83	Yes	Female	2
P4	87	Yes	Male	1
P5	89	No	Female	–
P6	62	No	Female	–

3.2 Processing

During the opening and closing hand movements, the system used the KinectPv2 Processing library, which detects the change of state of the hands (opening and closing) to a person within the measuring range.

The state of the hands is represented by a circle, where if the hands are closed, the circumference is red, while when the hands are open, the circumference turns green. However, when the hands are not in the correct position, the circumference turns white indicating that the hands are out of place.

The results are stored in a database using MySQL server, the PHP is used for connection and interaction with the database using web server XAMPP (version 3.2.2).

3.3 Visualization Interface

Over the visualization interface, as shown in Fig. 3, the user can access to the historical data of the evaluations recorded by session, which can be consulted by patient and by date. The information of each subject is visualized through dynamic graphs composed by the speeds of exercise execution in ON and in OFF state.

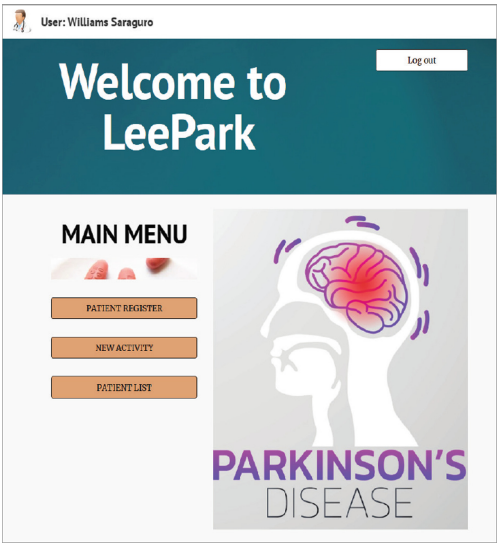

Fig. 3. LEEPARK system registration interface [14].

3.4 Data Statistical Analysis

In order to carry out a proper interpretation of the obtained results, different statistical and mathematical techniques were used. The first analyses correspond to population comparisons through ANOVA and Linear Regression; with the first one, a relationship hypothesis is tested to determine significant differences between groups that have been classified by disease degree; in the second case, thanks to the linear adjustment, the progression of PD in each extremity is evidenced. Finally, in order to demonstrate the evolution of each patient, a percentage representation is established.

4 Results

The database collected from the LeePark system is subjected to statistical analysis with the objective of quantifying the state of each patient and of the total sample, grouping them by degree of disease (Grade 0 to Grade 3) and by their upper limbs (right and left). The methods used were: ANOVA with a 95% confidence interval, linear regression and quantification of improvement; the first method is used to determine differences in velocities between the degrees of disease and between the upper limbs, the second method establishes the progress of the disease and the third method stipulates the level of improvement in each patient.

For the first calculation the patients in Off state were grouped and labeled according to their PD degree, where healthy patients were classified as Degree 0. Four groups of patients were established (Degree 0 to Degree 3), to which

ANOVA was calculated, under the null hypothesis that there is no difference in velocities during the alternating movement of the hands test between PD degrees. Its result of F (73.55) > critical value (3.10) rejects the null hypothesis, accepting the alternative hypothesis that at least one of the groups differs in speed with respect to the rest, the results of the calculation are shown in Table 2.

Table 2. ANOVA of speeds between the degrees of disease.

Origin of variations	Squares sum	Freedom degrees	Squares average	F	Probability	Critical value for F
Between groups	1379.77	3	459.92	73.55	5.59E–11	3.10
Within groups	125.06	20	6.25			
Total	1504.83	23				

The ANOVA calculation was repeated for the following groupings: Degree 0 – Degree 1, Degree 1 – Degree 2 and Degree 2 – Degree 3, in order to determine how much difference exists between consecutive groups. The result of the calculation determined that there are no significant speed differences between the groups: Degree 0 – Degree 1 and Degree 2 – Degree 3. While the grouping Degree 1 – Degree 2 evidenced a high differentiation due to the fact that F (59.68) > Critical value (4.96).

A new ANOVA calculation was applied between the right and left hand speeds, considering only patients diagnosed with PD. The result from Table 3 indicated that there is no difference in the velocities of the two limbs, as F (0.14) < Critical value (5.99).

Table 3. ANOVA of speeds between the upper limbs.

Origin of variations	Squares sum	Freedom degrees	Squares average	F	Probability	Critical value for F
Between groups	8	1	8	0.14	0.72	5.99
Within groups	332.33	6	55.39			
Total	340.33	7				

Although no difference in velocity between the extremities was demonstrated, Fig. 4 illustrates the average velocities during each patient's 6 sessions, grouped by degree of disease and demarcating data from the right and left extremities. Figure 5 also show the application of lineal regression to the data, which show a decay of speed in each limb as the degree of disease progresses.

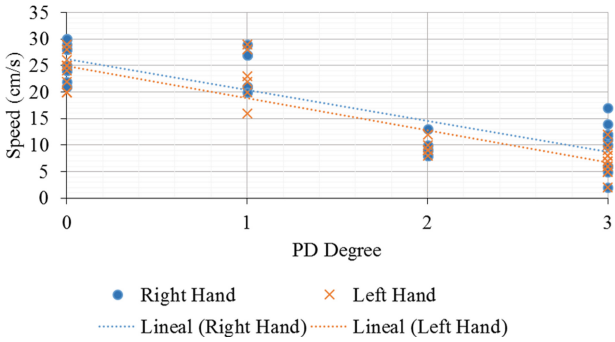

Fig. 4. Lineal regression of the upper limbs.

Figure 5 shows the percentage improvement of each limb in PD patients, comparing the average velocities during the 6 sessions between Off and On states. Patients 1, 2 and 3 show significant improvements over 20%, while patient 4 (Degree1) has the lowest improvement in the group, 8.28% in the right hand and 15.84% in the left hand. The data shows that the percentage does not depend on the degree of disease, nor is it exclusive of gender or age; a more exhaustive and complete analysis would make it possible to know the incidence of the drugs in the progress of improvement.

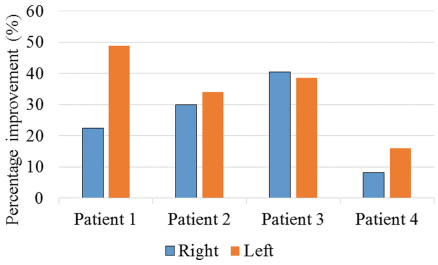

Fig. 5. Percentage improvement of each limb in PD patients.

5 Conclusions

The LEEPark system made it possible to quantify the speed of the alternating movement of the hands. The collected data was subjected to a population analysis on the degree of disease, speed differentiation and evidence of PD progression in each limb; through: ANOVA, Linear Regression and calculation of the difference of speeds, without medication and with medication of the patients, thus achieving that the physician evaluates in a quantitative way the progress of the disease. The system is a medical tool that optimizes the motor evaluation within the UPDRS.

The applied statistical analysis allowed to quantify with more precision the differences between the groupings of the sample, excluding the subjective opinion and standardizing the results. Given that in Ecuador there are 229 cases of PD registered according to the National Institute of Statistics and Censuses, a sample of 68 patients is calculated for measurement with the system and subsequent analysis, under a 95% confidence level and a 10% margin of error.

The results of the ANOVA calculations determined that the alternating hand movement test does not allow differentiation of motor speeds between the upper extremities (right or left), but can be used to differentiate the first signs and stages of PD, being able to find significant differences between Degree 1 and 2 disease.

Linear regression to the velocity distribution of all patients showed that there is a relationship between the degree of disease and the speed of alternating hand movement. The speed decreases as the degree of PD advances, although its values tend to increase in each patient during each session.

It was also possible to compare the velocities between the Off and On states of patients with PD, the results are part of the indicators of the effectiveness of medication in their body, as well as a quantitative result from medical history.

The system is intended to implement a module for statistical analysis with the results, as well as to realte the processing and calculation of the Finger Tapping test, previously performed in the LeePark system. It is hoped to achieve concise and accurate results that will allow further automation of the UPDRS quantitative motor analysis.

Ethical Statement. All subjects gave their informed consent for inclusion before they participated in the study. The study was conducted in accordance with the Declaration of Helsinki, and the protocol was approved by the Ethics Committee of Comité de Ética de Investigación en Seres Humanos USFQ (2019-011E).

References

1. Batista, P., Pereira, A.: Impact and Prevention of Neurodegenerative Diseases in Society: Alzheimer and Parkinson. Neurodegenerative Diseases (2016)
2. Bermeo, A., Bravo, M., Huerta, M., Soto, A.: A system to monitor tremors in patients with parkinson's disease. In: 2016 38th Annual International Conference of the IEEE Engineering in Medicine and Biology Society (EMBC), pp. 5007–5010. IEEE (2016)
3. Dror, B., Yanai, E., Frid, A., Peleg, N., Goldenthal, N., Schlesinger, I., Hel-Or, H., Raz, S.: Automatic assessment of parkinson's disease from natural hands movements using 3D depth sensor. In: 2014 IEEE 28th Convention of Electrical Electronics Engineers in Israel (IEEEI), pp. 1–5, December 2014
4. Organización Médica Colegial de España: Las enfermedades neurodegenerativas afectan a más de un millón de personas en España (2014). http://www.medicosypacientes.com/articulo

5. Ferraris, C., Nerino, R., Chimienti, A., Pettiti, G., Cau, N., Cimolin, V., Azzaro, C., Albani, G., Priano, L., Mauro, A.: A self-managed system for automated assessment of UPDRS upper limb tasks in parkinson's disease. Sensors **18**(10), 3523 (2018). https://doi.org/10.3390/s18103523
6. Garcés, M.: Estudio sobre las enfermedades neurodegenerativas en españa y su impacto económico y social. Universidad Complutense y Estudio Neuroalianza, Madrid (2016)
7. Herdoíza, J.P.M., Perero, P.S.M., Toala, L.E.A., Mercado, E.R.I., Moreira-Vera, D.V.: Prevalencia de la enfermedad de parkinson: Estudio puerta-puerta en la provincia de manabí-ecuador. prevalence of parkinson's disease: Door-to-door study in manabi-ecuador. Rev. Ecuatoriana de Neurol. **26**(1) (2017)
8. Jefferson Rubio, B.V.: Valoración y análisis de los movimientos de las manos de un paciente de Parkinson según la escala UPDRS usando técnicas de visión artificial con Kinect. Tesis de Grado - FIEC (2015). http://www.dspace.espol.edu.ec/xmlui/handle/123456789/30706
9. Jennekens, F.G.: A short history of the notion of neurodegenerative disease. J. Hist. Neurosci. **23**(1), 85–94 (2014)
10. MacKinnon, A.: Statistical comparison of results from the timed up and go test, Unified Parkinson's Disease Rating Scale, Falls Efficacy Scale, and force plate balance measures concerning risk of falls among patients with Parkinson's Disease. Ph.D. thesis, University of Prince Edward Island (2018)
11. World Health Organization: Neurological disorders: public health challenges. World Health Organization (2006)
12. Rosenbaum, R.B.: Understanding Parkinson's disease: a personal and professional view. Greenwood Publishing Group (2006)
13. Salvador, A., Alfonso, E.: Validación clínica del Montreal Cognitive Assessment (MOCA) en pacientes con Parkinson en la ciudad de Quito. B.S. thesis, Quito: Universidad de las Américas 2018 (2018)
14. Saraguro, W., Barzallo, B., Guillermo, J., García-Cedeño, A., Soto, A., Rivas, D., Clotet, R., Huerta, M.: Analysis of hand movements in patients with parkinson's disease using kinect. In: IEEE International Conference on E-health Networking, Application & Services (2019)
15. Serrano-Dueñas, M., Martínez-Martín, P., Vaca-Baquero, V.: Validation and cross-cultural adjustment of PDQL-questionnaire, spanish version (ecuador) (PDQL-EV). Parkinsonism Relat. Disord. **10**(7), 433–437 (2004)
16. Today, P.N.: Parkinson's disease statistics (2019). https://parkinsonsnewstoday.com/parkinsons-disease-statistics/
17. Urdan, T.C.: Statistics in Plain English. Routledge (2011)

BCI for Meal Assistance Device

Brayan Camilo Castro Sánchez[1,2],
Laura Camila Loaiza Carvajal[1,2(✉)],
Fitzgerald Leonard Gerardo Toro Quitian[1,2],
and Juan Manuel López López[1]

[1] Escuela Colombiana de Ingeniería Julio Garavito, Bogotá 111166, Colombia
{brayan.castro, laura.loaiza,
fitzgeral.toro}@mail.escuelaing.edu.co,
juan.lopezl@escuelaing.edu.co
[2] Universidad Del Rosario, Bogotá 111221, Colombia

Abstract. Nowadays, in Latin America, a huge amount of people are in a motor disability condition. This phenomenon generates difficulties to execute daily tasks, such as the feeding process. To mitigate the daily difficulties, assistance devices are needed. This paper describes the evaluation of a brain-computer interface (BCI) for meal assistance, based on the sensorimotor rhythm (SMR), characteristic of the movement intention. The electroencephalographic (EEG) signals were acquired and processed to extract features in the frequency and time domain. These features train a classification model that separates the movement intention from any other cerebral activity. The study was made with ten healthy people who were subjected to a test that corresponds to feed themselves ten times. The results obtained show that average time to activate the meal assistance device is less than 10 s, furthermore, the accuracy of the tests performed was 81.6%, i.e. there is a good differentiation between a movement intention from another activity. Finally, it was concluded that the purposed meal assistance device achieves the goal of allowing an autonomous feeding and leaves as a precedent an alternative to implementing assistance devices through a BCI.

Keywords: BCI · EEG · Meal assistance · Movement intention

1 Introduction

The human body makes a movement by the falling order of the motor cortex to the muscles through the spinal cord and the motor neurons. Statistics reveal that more than one thousand millions of people around the world suffer a disability condition due to some damages in the spinal cord, nerves or muscles [1], it is equivalent to 15% of the world population. From this amount, in Latin America and the Caribbean, there are near to 85 millions of people in a motor disability condition. The number is increasing in many countries of this region; mainly as a result of the aging, chronic diseases and traumatisms caused by violence [2]. Part of this population has reduced mobility in their upper limbs, affecting their ability to perform basic movements, such as the hand-mouth pattern which allows the autonomous feeding process [3]. In fact, eating is one

© Springer Nature Switzerland AG 2020
C. A. González Díaz et al. (Eds.): CLAIB 2019, IFMBE Proceedings 75, pp. 1117–1121, 2020.
https://doi.org/10.1007/978-3-030-30648-9_145

of the most important daily activities. Therefore, solving the problem of carrying food to the mouth without the help of another subject could increase independence and improve the quality of life of the affected population.

On the other hand, brain-computer interfaces (BCIs) have been used widely in areas from rehabilitation engineering to entertainment. The main goal of a BCI is to translate brain activity into orders for a external device. Based on the scenario from above, in this study an electroencephalographic (EEG) BCI for meal assistance has been proposed.

2 Materials and Methods

The goal of this study was to implement a BCI based on sensorimotor rhythm (SMR) for controlling a mechanic meal assistance device that allows a user the action of lifting up or lifting down a spoon to receive food. SMR has been used extensively in the development of movement intention BCIs [4]. This activity occurs in the primary motor cortex, located between the parietal lobe and the frontal lobe. It has more power in the 8 Hz–12 Hz band. This device is formed by an EEG acquisition system, a processing unit, a microcontroller unit (MCU) and a mechanical device (Fig. 1).

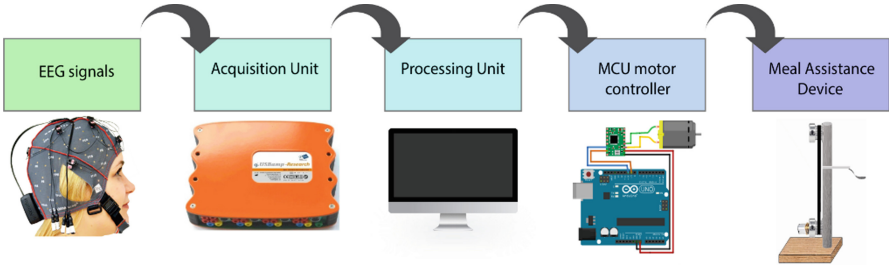

Fig. 1. General design diagram.

2.1 EEG Acquisition

The g.USBamp Research device was used for the acquisition of the EEG signals. Four electrodes were placed in the area closest to the sensorimotor cortex, following the 10–20 standard, in the C3, Cz, C4 and Pz locations, with reference in A2 and ground in Fpz. Signals were acquired using a sampling frequency of 512 Hz and 24 bits of resolution.

2.2 Mechanical Device for Meal Assistance

The device consists of a two pulley's system fixed to the ends of a vertical axle. The simultaneously rotatory movement of the pulleys is due to a distribution belt that allows the displacement of support in the vertical axle. The support is attached to a spoon.

The movement is generated by a DC gear motor that activates the system when the control signal is sent from the MCU, then, the spoon lifts up or down, depending on if the subject's desire is to receive or take up food, respectively.

2.3 Signal Processing

Features Definition. EEG data were windowed (5 s square windows, with 50% overlapping) and analyzed in the time domain and the frequency domain. The features extracted in the time domain were Hjorth's parameters (activity, mobility, complexity) [5]. According to studies, they have been used to detect the movement intention, because offer a way to quantify the statistical characteristics of an EEG signal [6, 7]. In addition, the features extracted in the frequency domain were the relative powers for the δ (0.4–4 Hz), θ (4–8 Hz), μ (8 – 12 Hz) and β (12–31 Hz) bands, computed from the power spectral density (PSD), obtained by Welch method.

Classification Algorithm. The classification algorithm implemented was based on supervised learning, using a linear support vector machine, for finding the best hyperplane that separates all data points of a class differentiating it from another class [8]. The parameters in the SVM of box constraints and kernel scale were 1 and 3.37 respectively.

Real Time Processing. The real time processing has a window of 2 s (1024 samples), i.e. every 2 s a vector with features is obtained. This vector is analyzed by the model and it generates a value. This value indicates the class to which an action belongs depending on whether it is a movement intention (class 1) or static intention (class 2). The prediction value (or class), is sent by means of a serial communication to the MCU, whose function is to activate the device depending on the order given by the participant.

2.4 Experiment

A total of 10 healthy participants were recruited, with average age of 22.5 years old. 8 men and 2 women. After their arrival, participants read and accepted the informed consent. Then, the electrodes were placed and the impedance of each channel was verified.

Training Stage. This stage consists on a set of tasks executed by the participant while the EEG signals are acquired. Three requested tasks are to think about lifting up, lifting down and leave static the spoon. To improve the performance, a visual feedback was implemented by activating the mechanical device for the movement commands, while for the third task (static), the participants were instructed to focus their attention in a non-related activity (like talking about their day). It is important to clarify that these three tests are made in fifteen s trials and nine times each one.

System Test. To start the implementation of BCI in real time, participants were asked to activate the device within a time less than 30 s, time recording starts when task is requested to the participant until the device is activated. In addition, the participants

were asked to kept the spoon static for at least 30 s, time recording stops if the device is activated before the stablished time. Each of these tests were made 10 times by participant.

3 Results

Table 1 shows the activation times of each task from participants, for the tasks as lifting up and lifting down the spoon, the average time is less than 10 s for activation, however, the average time of non-activation of the device is close to the time set by the investigators (30 s). Moreover, the Receiver Operating Characteristic (ROC) area can be interpreted as the probability that a classifier will sort or score an instance correctly [9], as can be seen in Table 1. These values are between 0.87 and 0.99.

Table 1. Accuracy times table.

	Accuracy time (s)			ROC area	Accuracy
	Lifting up	Lifting down	Non-activation		
U01	7,5	9,3	16,4	0,93	0,9
U02	15,8	7,6	24	0,87	0,79
U03	8,6	9,8	25,8	0,92	0,86
U04	6	6,8	26,5	0,96	0,92
U05	7,5	6,6	16,2	0,95	0,9
U06	11,8	16,5	24,9	0,92	0,87
U07	11,5	13,2	28,9	0,91	0,85
U08	8	7,7	26	0,98	0,98
U09	8,3	6,1	22,1	0,99	0,95
U10	10,4	8,1	21,9	0,93	0,88
Average	9,54	9,17	23,27	0,936	0,89

Designed system had and accuracy of 81.6%, whit a sensitivity of 98% and a specificity of 49%.

4 Conclusion/Discussion

A BCI controlled device was developed to enable people to feed themselves. The reported results are similar to those reported by Looned et al. [10], because in there the time to perform a specific arm-hand movement is measured. Moreover, they propose an assistive drinking BCI- controlled wearable robot, but it is important to say that in that BCI the EEG signals are processed by the emotiv EPOC Headset.

Steady-state visual evoked potentials represent a common way to develop BCIs, but depending on the application it could not be the best way to develop a BCI. The problematic mentioned in this paper is based on the autonomous feeding process, so it

would be better if a subject had freedom to look at where he wanted than watching strobe lights in a screen and exiting the retina by a visual stimulus to activate a meal assistance device as similar to Chiu et al. [11].

This study represents a good precedent for the implementation of a BCI based on SMR because from that rhythm could be applied to the activation of assistance robots or rehabilitation robots, such as exoskeletons or prosthesis.

Conflict of Interest. The authors declare no conflict of interest.

References

1. Hochberg, L., Serruya, M., Friehs, M.: Neuronal ensemble control of prosthetic devices by a human with tetraplegia, pp. 164–171 (2006)
2. OMS Homepage. https://www.who.int/features/factfiles/disability/es/. Accessed 15 May 2019
3. Jimenez, C.: Involves in the Elderly and Other Dysfunctions of Neurological Origin. Masson, Barcelona (1999)
4. Pfurtscheller, G., Brunner, C., Schlogl, A., Lopes da Silva, F.: Mu rhythm (de) synchronization and EEG single-trial classification of different motor imagery tasks, pp. 1–7. Elsevier (2006)
5. Hjorth, B.: EEG analysis-based contributions on time domain properties, pp. 306–310. Elsevier, 30 January 1970
6. Hurtado, J., Rojas, S., Ricardo, Y., Alvarez, A., Castellanos, G.: Motor imagery classification using feature relevance analysis: an emotiv-based BCI system, pp. 1–5, January 2015
7. Vidaurre, C., Krämerc, N., Blankertz B., Schlögl A.: Time domain parameters as a feature for EEG-based brain computer interfaces, pp. 1313–1319. Elsevier (2009)
8. Fan, R., Chen, P., Lin, P.: Working set selection using second order information for training support vector machines. J. Mach. Learn. Res. **6**, 1889–1918 (2005)
9. Wen, Z., Nancy, Z., Ning, W.: Sensitivity, specificity, accuracy, associated confidence interval and ROC analysis with practical SAS implementations. In: Health Care and Life Sciences, pp. 1–9. NESUG (2010)
10. Looned, R., Webb, J., Zheng X., Menon, C.: Assisting drinking with an affordable BCI-controlled wearable robot and electrical stimulation: a preliminary investigation. J. Neuroeng. Rehabil. 1–13 (2014). 12th edn.
11. Chiu, C.-Y., Singh, A.K., Wang, Y.-K., King, J.-T., Lin, C.-T.: A Wireless Steady State Visually Evoked Potential-based BCI Eating Assistive System, pp. 3003–3007. IEEE, May 2017

Rehabilitation

A Setup for Lower-Limb Post-stroke Rehabilitation Based on Motor Imagery and Motorized Pedal

Teodiano Bastos-Filho(✉), M. A. Romero, V. Cardoso, A. Pomer, B. Longo, and D. Delisle

Universidade Federal do Espírito Santo, 29075-910 Vitoria, Brazil
teodiano@ele.ufes.br

Abstract. This work presents a low-cost solution for a neuro-rehabilitation system of stroke patients through a motorized pedal, as pedaling has the potential to provide a high number of flexion and extension repetitions of the lower limb. Stand-alone hardware and software were developed to control the motorized pedal, and the motor imagery recognition is done through a BCI, which analyzes EEG patterns on the motor region, related to feet movements and rest state. From this BCI, an avatar is triggered into an immersive virtual reality environment together the motorized pedal. sEMG signals collected on Rectus femoris (RF), Biceps femoris (BF), Tibalis Anterior (TA) and Gastrocnemius muscles (GM) allow identifying the muscle onset and offset when a force is exerted on the pedals, and force sensors are used to generate biofeedback for the subject. As a first result of this setup, the maximum accuracy reached with our BCI was 94.41%.

Keywords: Stroke · Motorized pedal · Brain-computer interface

1 Introduction

Stroke is a neurological syndrome with high prevalence in adults and elderly and one of the main causes of mortality in the world [1]. Neurological injury after stroke frequently leads to hemiparesis or partial paralysis and, despite labor-intensive conventional rehabilitation therapies, more than half of stroke survivors report disability in activity of daily living (ADL) [2].

A recent study in the literature [3] has shown that eight paraplegics with chronic spinal cord injury undergoing 12-month neurorehabilitation training based on BCI and using virtual reality system and ultra-high cost exoskeleton, experienced neurological improvements in somatic sensation (pain location, touch fine/gross and proprioceptive sensitivity) in addition to motor improvements. That system may also be used for rehabilitation of hemiparesis after stroke, however, its high cost is quite prohibitive. In this work, a motorized pedal commanded by a BCI from motor imagery is proposed to be used as low-cost robotic assistance for rehabilitation therapies in stroke patients.

Pedaling is a repetitive, functional activity that has potential benefit when it is used as an adjunct to therapy after stroke. Currently, there are many motorized exercise

© Springer Nature Switzerland AG 2020
C. A. González Díaz et al. (Eds.): CLAIB 2019, IFMBE Proceedings 75, pp. 1125–1129, 2020.
https://doi.org/10.1007/978-3-030-30648-9_146

bikes that are commercially available and that can provide a preprogrammed speed for the rider [4, 5]. Other related works include the use of Inertial Measurement Unit (IMU) to control and monitor the activation and deactivation of a system of Functional Electrical Stimulation (FES) to stimulate individual's lower limbs, considering the measurement of strength and angular speed during pedaling [6]. When using motor imagery (MI), the BCI can use the cognitive task of imagining the performance of a given movement or specific task without physically executing it. In fact, studies using these techniques have allowed observation of cortical activation in motor areas during MI, and neuroimaging studies have shown that there is cortical reorganization after MI in stroke patients [6].

2 Methodology

Figure 1 shows the general diagram of our low-cost setup, which includes a motorized pedal (Exerpeutic 7101 Activcycle Motorized Pedal Exerciser), a signal acquisition equipment (BrainNet BNT 36), a virtual reality oculus (HTC VIVE), PC and Raspberry, and a customized inertial sensor (IMU – Inertial Measurement Unit). The classifiers used to identify motor imagery run on MATLAB, and a Graphical User Interface (GUI), written in Python, is displayed to the patients. A control system was designed to command the motorized pedal from the classifier outputs. Hardware used in this work includes Raspberry PI 3B with Wi-Fi- and Bluetooth connection; Quad-core 64-bit ARM Cortex A53 CPU clocked at 1.2 GHz; 400 MHz VideoCore IV multimedia GPU; and 1 GB LPDDR2-900 SDRAM Memory. The virtual reality is implemented through an oculus HTC VIVE, which interacts with the user and with the control software to monitor the process and feedback the rehabilitation advances to the patient, and an IMU, which is the sensor used to monitor the neurorehabilitation process.

A serious game (SG) using the HTC VIVE was designed to the rehabilitation process, which uses a recumbent tricycle, so the player does not need to worry about its balance. This game consists of a road where the patient needs to pedal to move forward with his/her tricycle (Fig. 2). The player (patient) starts in the initial checkpoint, and flags are placed beside the road to mark the sequential checkpoints. Every time the player passes thought a checkpoint, time is registered and shown on the GUI. The session ends when the player crosses the final checkpoint. The distance is set by the health professional, which can be adjusted, making the SG adjustable for the patient's needs. A score tab is shown in the beginning and end of every session to inform the patients about their achievements, promoting motivation.

A protocol for the neuro-rehabilitation system was also designed, which has as an objective to evaluate four parameters: (1) relationship between the programmed velocity to be executed by the motorized pedal and the actual velocity executed; (2) relationship between the velocity executed by the motorized pedal and the user's weight and height; (3) pedal's stop position during the full cycle of 360 degrees; (4) onset and offset detection, through sEMG on Rectus femoris (RF), Biceps femoris (BF), Tibialis Anterior (TA) and Gastrocnemius (GM) muscles, during the full cycle of pedaling. Those parameters are used to evaluate the pedal's control and synchronize the pedal velocity with the virtual environment.

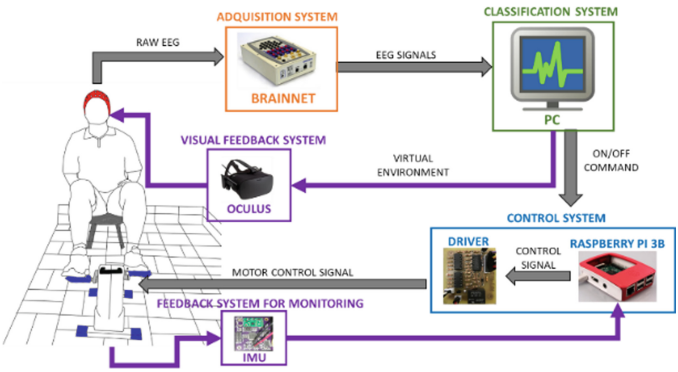

Fig. 1. Proposed neuro-rehabilitation system.

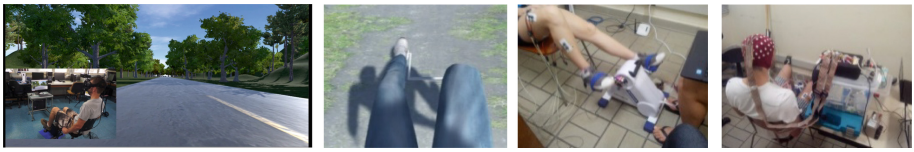

Fig. 2. Experiments using the virtual road designed to the neuro-rehabilitation process.

The inclusion criteria (only healthy subjects) were: without neurologic diseases or lower-limb impairments, with cognitive, language, hearing, and visual skills to understand and follow instructions. Eight subjects (65 males, mean 27, SD 2.37 years; 3 females, mean 28, SD 4.24 years) participated in the experiments. Regarding stroke patients, some of the main features of their hemiparesis are limitations in knee flexion and dorsiflexion, usually due to their flexor patterns, such as TA and BF weakened and spastic quadriceps and GM [7]. This way, onset and offset of these muscles were detected during the pedaling whereas the force of the movement was imposed. Four channels of sEMG were considered in the following muscles: RF (responsible for knee extension), BF (responsible for knee flexion), TA (responsible for dorsiflexion), GM (responsible for plantar flexion), with a reference electrode on the ankle. For the experiments, the subject sat comfortably in a chair and started the feet movements after a beep. For each participant the seat was suitably positioned, so that the knee flexion angle was between 70 and 80° (referring to knee extension at 0° of the cycle) when the ankle is in the neutral position (i.e., foot and tibia in an angle of 90°). The BCI used to recognize the motor imagery uses the Riemannian Kernel (RK) for feature extraction and the following classifiers: Linear Discriminant Analysis (LDA), Regularized Discriminant Analysis (RDA) and Support Vector-Machine (SVM), which recognize two classes: rest state and feet movement. EEG signals are recorded from the following scalp locations: Fz, FC3, FC1, FCz, FC2, FC4, C5, C3, C1, Cz, C2, C4, C6, CP3, CP1, CPz, CP2, CP4, P1, Pz, P2, POz. A total of 72 trials were analyzed, and the time window was from 0.5 to 2.5 s after the cue.

3 Results and Discussion

Table 1 shows the BCI performance for eight subjects to recognize the rest state and imagination of feet movements. The BCI shows a good performance (mean ACC > 83% for all classifiers) and maximum ACC = 94.14% with SVM. SVM got the best ACC for five subjects (A01, A03, A05, A06, and A07). LDA presented ACC values close to SVM, but LDA has lower computational cost.

Table 1. Results of the BCI to recognize rest state and feet movements.

Subjects	Linear Discriminant Analysis (LDA)				Regularized Discriminant Analysis (RDA)				Support Vector Machine (SVM)			
	ACC	Kappa	TPR	FPR	ACC	Kappa	TPR	FPR	ACC	Kappa	TPR	FPR
A01	89.51	78.99	80.28	1.39	90.21	80.41	85.92	5.56	90.21	80.24	81.69	1.39
A02	74.83	49.53	57.75	8.33	65.73	31.67	87.32	55.56	74.83	49.51	54.93	5.56
A03	79.02	58.07	84.51	26.39	79.72	59.47	85.92	26.39	80.42	60.84	81.69	20.83
A04	93.75	87.50	90.28	2.78	92.32	84.72	93.06	8.33	84.03	68.06	80.56	12.50
A05	74.83	49.61	69.01	19.44	74.83	49.80	95.77	45.83	80.42	60.78	69.01	8.33
A06	90.91	81.84	1.00	18.06	90.91	81.84	1.00	18.06	94.41	88.82	1.00	11.11
A07	83.92	67.78	73.24	5.56	86.71	73.42	84.51	11.11	85.31	70.61	80.28	9.72
A08	83.22	66.37	69.01	2.78	84.62	69.21	78.87	9.72	83.22	66.41	77.46	11.11
Mean	**83.75**	**67.46**	**65.64**	**10.59**	**83.13**	**66.32**	**76.55**	**22.57**	**84.11**	**68.16**	**65.83**	**10.07**

All values are presented in percent. ACC (Accuracy); TPR (True Positive Rate); FPR (False Positive Rate).

4 Conclusions

This work introduced a setup for stroke-patients neuro-rehabilitation. A stand-alone hardware and software were developed to control a motorized pedal. The motor imagery uses EEG patterns from the motor region related to feet movements and rest state. The BCI showed a good performance for healthy subjects (mean ACC > 83% for all classifiers), with the BCI based on SVM reaching the best result (ACC = 94.41%). sEMG signals are collected on RF, BF, TA and GM to identify the muscle onset and offset when a force is exerted on the motorized pedal, and force sensors are used on the pedals to generate bio-feedback. The next step of this work is to conduct long term experiments with stroke patients, evaluating the hypothesis of movement recovery.

References

1. World Health Organization (WHO): Stroke, cerebrovascular accident. http://www.who.int/topics/cerebrovascular_accident/en. Accessed 10 Dec 2018
2. Steinisch, M., Tana, M., Comani, S.: A post-stroke rehabilitation system integrating. IEEE Trans. Neural Syst. Rehabil. **21**(5), 849–859 (2013)
3. Donati, A., Shokur, S., Morya, E., et al.: Long-term training with a brain-machine interface-based gait protocol induces partial neurological recovery in paraplegic patients. Nature **6**, 30383 (2016)

4. Mohammadi, H., Ridgel, A., Discenzo, F., et al.: Design and development of a smart exercise bike for motor rehabilitation in individuals with Parkinson disease. Trans. Mech. **21**(3), 1650–1658 (2014)
5. Rodríguez, M., Iáñez, E., Ortíz, M., et al.: Personalized offline and pseudo-online BCI models to detect pedaling intent. Front. Neuroinform. **11**, 1–12 (2017)
6. Guerra, Z., Lucchetti, A., Lucchetti, G.: Motor imagery training after stroke. J. Neurol. Phys. Ther. **41**(4), 205–214 (2017)
7. Lucareli, P., Greve, J.: Alteration of the load-response mechanism of the knee joint during hemiparetic gait following stroke analyzed by 3-dimensional kinematic. Clinics **61**(4), 295–300 (2006)

A Robotic Lower-Limb Exoskeleton for Rehabilitation

Arlindo Elias-Neto[1], Ana Cecilia Villa-Parra[2], Thomaz Botelho[3], A. Frizera-Neto[1], and Teodiano Bastos-Filho[1(✉)]

[1] Assistive Technology Group (NTA), Universidade Federal do Espírito Santo, Vitoria 29075-910, Brazil
teodiano.bastos@ufes.br
[2] Biomedical Engineering Research Group (GIIB), Universidad Politécnica Salesiana, Cuenca 010107, Ecuador
[3] Instituto Federal do Espirito Santo (IFES), Electrotechnical Commission, São Mateus 29932-540, Brazil

Abstract. The use of robotic lower-limb exoskeletons for rehabilitation of individuals with motor impairments is currently a tendency in several research groups, as they can be used to improve therapies in many applications in the field of physiotherapy. The main reasons are that they are safe, allow accurately controlling the range of movement of the individual's lower-limbs, and can vary their speed and torque to make the movements, according to physiotherapist instructions. This work introduces the exoskeleton ALLOR (Advanced Lower Limb Orthoses for Rehabilitation), which was developed at UFES/Brazil, and presents an experimental protocol to be applied to rehabilitation of individuals with motor impairments. The proposed protocol is progressive and explores the different control strategies implemented in ALLOR: passive, mobilization, assisted, active and resisted, which are suitable for individual's rehabilitation in three scenarios addressed in this work: stroke, total knee arthroplasty, and anterior cruciate ligament reconstruction. Clinical and functional parameters are also proposed to assess improvements in motion characteristics and its impact over general quality of life, locomotion and pain in the individuals.

Keywords: Lower-limb rehabilitation · Robotic exoskeleton · Protocol

1 Introduction

The possibility of performing an interface between the human nervous system with mechatronic systems, and use them to restore human motor capacities, has been a fascinating field for scientists [1]. However, only in the last decades, due to the technological advances in sensors, actuators and processing signal techniques, it was when promising results began to appear in this field.

Early versions of robots for rehabilitation were obtained through the adaptation of industrial robots brought to the clinical setting [2, 3]. This brought questions regarding acceptability, usability and, mainly, safety. In this context, Pons [4] proposed the

© Springer Nature Switzerland AG 2020
C. A. González Díaz et al. (Eds.): CLAIB 2019, IFMBE Proceedings 75, pp. 1130–1136, 2020.
https://doi.org/10.1007/978-3-030-30648-9_147

concept of Wearable Robots (WR) as user-oriented devices, and thus, more adapted to the interaction with users [4]. These robots are dressed by the user to supplement the lost function of a member, intrinsically exhibiting a physical interaction [5] and cognitive [6] intense with the user.

Research on the use of exoskeletons for rehabilitation of individuals with functional impairments have focused on the application for recovery from gait, with a view to provide user's independence [4]. Different models of exoskeletons have been presented in the literature, among which are the Hybrid Assistive System (HAL) [7], the Smart Step [8] and the one developed by Human Neuromechanics Laboratory [9], among many other prototypes. The design of the models varies from exoskeletons for the entire lower limb up to smaller for the control of specific joints, such as the knee or the ankle.

The strategies of assistance to locomotion also vary greatly among these investigations [10]. Most of the exoskeletons described in the literature act as alternative devices for individuals with severe disabilities, particularly in cases of severe neurological disorders, such as spinal cord injury or stroke. However, these studies present failures related to low sampling, methodological failures and heterogeneous training [11, 12]. In addition, surveys on monoarticular exoskeleton-assisted rehabilitation (knee and ankle, particularly) have not yet been developed for patients orthopedic, both in conservative and postoperative treatment. This way, verifying the effect of these devices to improve rehabilitation is a fertile field for the research when using robotics.

This work presents a research protocol for rehabilitation assisted by a monoarticular knee-exoskeleton. Initially, a description of the exoskeleton model is provided, and then a methodology to be implemented in the trials is described, as well as the main clinical and biomechanical parameters to be measured.

2 Methodology

The exoskeleton used in this work is termed ALLOR (Advanced Lower Limb Orthoses for Rehabilitation), which has three joints (3 degrees of freedom) in its physical structure: one active in the knee, one passive in the hip (which is responsible for connecting the thigh with the structure of support in the user's hip), and a passive ankle, responsible for the support of the user's foot (Fig. 1).

For its conception, an active joint EXO-H1R (Technaid, Spain) is used in this research, such as done by other research groups [13, 14]. This joint has force sensors capable of measuring the torque in knee extension and flexion movements, formed by 4 strain gages (model 632-180 of RS Pro), fixed at the proximal side respect to the knee joint of the leg segment, in the sagittal plane. The articulation also has a potentiometer of precision (model 10 K from Vishay), capable of determining the degree of flexion between the two extremities of the user's leg, ranging from 0 to 90°. The engine used to carry out exoskeleton movements is a flat Brushless 408057 motor (model EC 60 from Maxon), which has a harmonic drive CSD-20-160-2A-GR (from Harmonic Drive LCC) as reduction box, providing a very good trade-off between dimension, torque and reduction. A control system (AZBH12A8 from Advanced Motion Controls) is used for

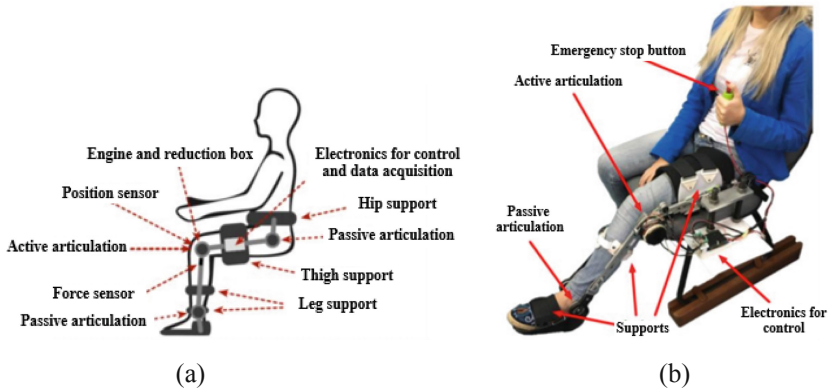

Fig. 1. (a) Details of the exoskeleton ALLOR; (b) User executing rehabilitation tasks with the exoskeleton ALLOR.

motor control, which operates in voltage mode, providing control signal up to ±10V. In addition, there is an internal control mode of speed (PID).

The exoskeleton has mechanical limitation at 0 and 90°, restricting the movements of leg's extension and flexion (as a safety way), in addition to an emergency stop button that interrupts the motor current immediately. The use of a harmonic drive in ALLOR (as a reduction box) provides safety to users, due to, in case of lack of electric current to the motor, it is possible to easily handle the exoskeleton to the right position. Figure 1 shows details of ALLOR.

3 Control of Knee's Flexion and Extension

To control the flexion/extension (F/E) of the knee, the control algorithm shown in Fig. 2 was implemented. The inputs q_{min} and q_{max} represent the limits of the F/E movement. Additionally, the inputs downtime and uptime define the periods of time (t) in seconds, in which the leg stays during the extension and flexion movements, respectively.

Additionally, in the F/E movement, a strategy to increase/decrease the speed and/or torque was designed, which implements, by software, the following hyperbolic function:

$$A = 1 \pm \tanh(k\tau) \tag{1}$$

where k is a constant that represents the wished speed to the individual, and τ is the interaction torque between the individual and the exoskeleton. The hyperbolic tangent function allows increasing the gain to stop and begin the movement when the user wishes. The value of k is determined for each user, based on his/her physical condition, and under the supervision of the physiotherapist, as different torques are necessary for each situation.

As part of the velocity control, a transfer function of first order that relates the input force with other variables as torque, inertia, and the damping was introduced to implement an active-resisted control approach, which is expressed as:

$$\dot{q}_a(s) = \tau(Ms + D) \tag{2}$$

where $\dot{q}_a$ is the output velocity, τ is the interaction torque, M is the inertia and D is the damping. The control strategy was implemented in a PC-104 embedded computer in real time Matlab/Simulink.

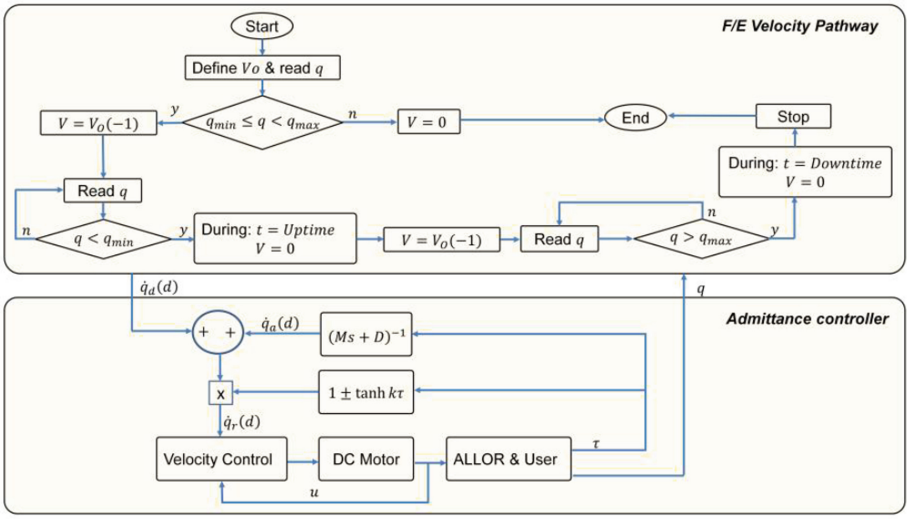

Fig. 2. Control strategy used in the exoskeleton ALLOR.

4 Characteristics of Participants

This study addresses the impact of rehabilitation assisted by ALLOR in three scenarios of clinical conditions of rehabilitation: stroke, total knee arthroplasty, and anterior cruciate ligament reconstruction. The study evaluates participants presenting the following general inclusion criteria: dysfunction of the lower left limb; ages between 18 and 80 years; stable general clinical condition; good understanding and able to follow directions from physiotherapists; good tolerance to standing (even with the use of support).

Stroke individuals are included when in subacute phase (4 to 31 days post-injury). Among the participants, the following subjects are excluded: score above 2 on the Ashworth Scale; autonomic dysreflexia; pressure ulcers; thrombosis; peripheral neuropathy; permanent stiffness of the knee; other surgical antecedents in lower-limb in the last 6 months; osteoporotic fractures at the last two years; severe osteoporosis; non-controlled

epilepsy; very limited visual ability; and who do not sign the informed consent for experiments.

The subjects will be recruited from our partners in this research: Center for Physical Rehabilitation of Espirito Santo (CREFES); UFES's Clinical Hospital and Municipal Center of Victory Specialties. The sample calculation for each of the groups was performed using the software G* Power version 3.1 [15].

As the objective of the protocol is to compare parameters before and after the procedures, the experiments were performed using the Student's t-test (for dependent samples), with alpha = 0.05, beta = 0.80 and moderate effect size (0.6). The results of the analysis suggest 24 participants in each clinical group.

All participants will be submitted to a clinical and functional assessment, according to the following parameters: Barthel scale (for evaluation of activities of daily living); visual analogue scale (for quantification of perceived pain in the lower limb); knee injury and Osteoarthritis Outcome Score – KOOS (for evaluation of the domains pain, symptoms, daily function, function in the sport and quality of life relative to the knee).

The parameters that will be obtained directly through of the exoskeleton sensors are: maximum extension torque, maximum bending torque, and maximum flexion-extension angles for the knee. For individuals with stroke and with reconstruction of the anterior cruciate ligament, the maximum amplitude may exceed the limits of the device (90°), thus, manual goniometry will also be used by all participants.

The tests that will be used in the protocol to assess the participant's mobility are the following: 6-min walk test (measures the distance traveled in this period); 10-m test (measures the time to travel 10 m); Timed Up and Go – TUG (test the time the subject gets up from a chair, walk 3 m, turn around and sit again).

At the end of the experimental protocol, participants will be asked to answer the QUEST form [16], which measures the satisfaction index of use of that assistive technology. All scales and tests used in this research are validated in Brazil and traditionally used in similar researches, and even in our previous work [17].

5 Protocol

Participants will be previously selected and examined in the rehabilitation institutions to ensure that are within the inclusion criteria of the study. The proposed rehabilitation protocol aims to gradually improve the joint amplitude, force (during extension and flexion) and speed of movement of the knee. To this end, subjects will undergo training of 30 min, varying between the following movements:

- Passive: the exoskeleton performs the movement within the predefined range
- Active-assisted: the patient initiates movement, and the exoskeleton helps it in the later stages of joint amplitude
- Active: strategy where the movement is performed completely by the patient
- Active-resisted: strategy where the movement is performed by the individual against a resistance produced by the exoskeleton

The training sessions will be held in a same time, 3 times a week for 8 weeks, guided by a physical therapist. Each training session will be divided into 5 min of

heating (passive movement through the maximum user's angle range), 10 min of active or active-assisted movement, 10 min of active-resisted motion, and finally 5 min of passive movement as a stretching routine.

The asset-resisted strategy will be based on percentages of the initial maximum force and will be every week to evaluate possible progression. The breadth of maximum motion will also be evaluated to adjust the progression for each individual.

Although the structure of the sessions is similar in all 3 clinical groups, there are particularities and objectives in each scenario. Individuals in the group in the subacute stage of the lesion will need to resume the active motor control of the knee. In this case, the objective is to gain active movement and joint amplitude.

Individuals with complete knee arthroplasty will need to quickly to re-gain joint amplitude and muscle strength to avoid post-surgery complications and loss of their quality of life. In that group, strength training is highlighted. Lastly, individuals with reconstruction of the anterior cruciate ligament will need to recover their range of motion and strength but cannot exert excessive force of extension in the first 3 months after the surgery, in order to minimize the risk of injury again the ligament.

For all these scenarios, different control strategies will be used in the exoskeleton. At the end of the 8-week period, individuals will be again submitted to clinical and functional assessment to determine if there was improvement of their physical parameters. All the parameters of the study will produce quantitative variables related of the knee joint (amplitude, torque, velocity), whose comparison between the parameters before and after the application of the protocol will be performed through Student's T-test to matched samples, with an adjusted level of significance to 0.05.

It is worth to comment that all participants of this study must agree and sign the informed consent form prior to the start of the rehabilitation protocol. This research was approved by the Ethics Committee in research of UNESA/Brazil, with CAAE number: 51685515.3.0000.5284.

6 Conclusions

This work introduced the exoskeleton ALLOR and presented a research protocol to be applied for motor rehabilitation of the knee joint with ALLOR, aiming at providing a progressive rehabilitation to individuals with motor impairment. This rehabilitation protocol can be adapted to individuals in three clinical scenarios (with stroke, total knee arthroplasty, and anterior cruciate ligament reconstruction). Clinical and functional parameters of the proposed protocol were selected, which will be used to evaluate not only the improvement of the individuals' movements using a robotic device for rehabilitation, but also the impact in their general quality of life and the improvements in their locomotion, muscles recovery and knee pain reduction.

Acknowledgments. Authors would like to thank FAPES/Brazil (218/2017) for supporting this research.

References

1. Chapin, J.K., Moxon, K.A.: Neural Prostheses for Restoration of Sensory and Motor Function. CRC Press, London (2000)
2. Dallaway, J.L., Jackson, R.D., Timmers, P.H.: Rehabilitation robotics in Europe. IEEE Trans. Rehabil. Eng. **3**, 35–45 (1995)
3. Carroza, M.C., Laschi, C., Micera, S., et al.: Research on rehabilitations engineering at ARTS lab. In: International Conference on Rehabilitation Robotics, pp. 590–600 (2007)
4. Pons, J.L.: Wearable Robots. Biomechatronic Exoskeletons. Wiley, Hoboken (2008)
5. Rocon, E., Ruiz, A.F., Raya, R., et al.: Human-robot physical interaction. In: Pons, J.L. (ed.) Wearable Robots: Biomechatronic Exoskeletons, pp. 127–164. Wiley, Hoboken (2008)
6. Bueno, L., Brunetti, F., Frizera-Neto, A. et al.: Cognitive human-robot interaction in wearable robots. In: International Conference on Robotics and Automation (ICRA), Januray 2008
7. Herr, H.: Exoskeletons and orthoses: classification, design challenges and future directions. J. Neuroeng. Rehabil. **6**, 21 (2009)
8. Ferris, D., Czerniecki, J., Hannaford, B.: An ankle-foot orthosis powered by artificial pneumatic muscles. J. Appl. Biomech. **21**, 189–197 (2005)
9. Smart Step Homepage. www.medgadget.com/archives/2005/06/the_smartstep_g.html. Accessed 10 Dec 2018
10. Cheung, E.Y.Y., Ng, T.K.W., Yu, K.K.K., et al.: Robot-assisted training for people with spinal cord injury: a meta-analysis. Arch. Phys. Med. Rehabil. **98**(1), 2320–2331 (2017)
11. Villa-Parra, A.C., Delisle-Rodríguez, D., López-Delis, A.: Towards a robotic knee exoskeleton control based on human motion intention through EEG and sEMG signals. Proc. Manuf. **3**, 1379–1386 (2015)
12. Young, A.J., Ferris, D.P.: State of the art and future directions for lower limb robotic exoskeletons. IEEE Trans. Neural Syst. Rehabil. Eng. **25**(2), 171–182 (2017)
13. Bayon, C., et al.: CPWalker: robotic platform for gait rehabilitation in patients with cerebral palsy. In: International Conference on Robotics and Automation (ICRA), pp. 3736–3741 (2016)
14. Figueiredo, J., Moreno, J.C., Santos, C.P.: Assistive locomotion strategies for active lower limb devices. In: Portuguese Meeting on Bioengineering, pp. 611–695 (2017)
15. Faul, F., Erdfelder, E., Lang, A.G., et al.: G*Power 3: a flexible statistical power analysis program for the social, behavioral and medical sciences. Behav. Res. Methods **39**(2), 175–191 (2007)
16. Carvalho, K.E.C., Gois-Júnior, B., Sá, K.N.: Tradução e validação do Quebec User evaluation of satisfaction with assistive technology (QUEST 2.0) para o idioma português do Brasil. Rev. Bras. Reumatol. **54**(4), 260–267 (2014)
17. Parra, A.C.V., Lima, J., Delisle, D., Bastos, T.F.: Stance control with the active knee orthosis ALLOR for post-stroke patients during walking. In: 4th International Symposium on Wearable Robotics (WeRob2018)/International Conference on Neurorehabilitation (ICNR 2018), Pisa. Proceedings of the 4th International Symposium on Wearable Robotics, pp. 196–200 (2018)

Development of a Sip-and-Puff Interface for Communication and Control of Devices

José Cláudio da Silva Junior(✉) and Walter Germanovix

Londrina State University, Londrina, PR 10011, Brazil
joseclaudio.silvajr@gmail.com, w.germanovix@uel.br

Abstract. People with severe motor dysfunctions need regular support to perform daily activities. Commercially are few affordable solutions that allow the control of everyday devices such as lamps, fans, and computers by tetraplegic. Thus, based on the concepts of assistive technology, this paper presents the development of a sip-and-puff interface that enables communication and control of devices. A hysteresis comparator circuit converts pressure signals into digital commands of sip-and-puff. The ARM Cortex - M4 STM32F429 microcontroller interprets the desirable actions and controls the graphical user interface on a VGA display. The system allows the activation of electrical equipment by relays and the operation of a computer through a virtual mouse and keyboard. Moreover, the invention handles a prototype of an adjustable bed, in which puff actions move DC motors that shift the structure. The results obtained with the prototype are satisfactory evaluating the ease of operation and its cost. These results encourage further studies with quadriplegic patients.

Keywords: Assistive technology · Tetraplegia · Pressure sensors

1 Introduction

People with severe motor dysfunctions need regular support to perform daily activities. Immobility and the consequent lack of autonomy can lead to poor self-esteem and health problems, such as pressure ulcers. In this context, researchers have been developing solutions focused on assistive technology to ensure the functional independence of the disabled [1,2]. With remaining capabilities, the user can control equipment by movements of head [3], eyes [4], and tongue [5], as well as by voice commands [6] and sip-and-puff [7–10].

The best solution depends on the severity of spinal cord injury (SCI), lesion site and the number of impaired nerve fibers. People with injuries on thoracic level preserve upper limbs function, on the other hand, tetraplegic have lesions on cervical nerves [11]. High cervical injuries that demand mechanical ventilation prevents the use of sip-and-puff interfaces. However, this approach is more

© Springer Nature Switzerland AG 2020
C. A. González Díaz et al. (Eds.): CLAIB 2019, IFMBE Proceedings 75, pp. 1137–1146, 2020.
https://doi.org/10.1007/978-3-030-30648-9_148

affordable, practical and user-friendly for the tetraplegic that exhibits adequate respiratory function, but has communication difficulties.

Usually, sip-and-puff devices perform only actions of on-off, communication [9,12] or control of specific equipment, such as wheelchairs [7] and adjustable beds [10]. Thus, there is a lack of solutions that thoroughly meet the user's need. Hence, this work presents a functional sip-and-puff interface that enables communication and control of devices such as computers, lamps, fans and adjustable bed by tetraplegic users.

The prototype of an adjustable bed is also a proposal for health maintenance, since disabled people may develop pressure ulcers due to lack of movement. Intense and constant pressures interrupt the bloodstream and breed lesions that can range from redness to deep ulcers [13,14]. So, the primary preventive practices are the repositioning every two hours [15] and stimulation of the most affected areas [16]. Therefore, the prototype presents both methods, since it permits the user's repositioning, as well as stimulates their skin by the activation of an electric massager.

2 Materials and Methods

2.1 System Description

The proposed system can be grouped into specific blocks, as shown in Fig. 1. The first is responsible for acquiring and conditionate sip-and-puff signals to the microcontroller. A second involves the logical device developed to execute tasks and the graphical user interface, VGA - $640 \times 480 - 60$ Hz. The user's command block, lastly, is divided into actions of relays (illumination, electric massager, fan and help alarm), communication and operation of the adjustable bed (upper and lower limbs). For detection of sip-and-puff signals, this project uses the MPX5100 - Case 867C piezoresistive transducer, which generates an analog voltage that is proportional to the applied pressure from 0 to 100 kPa.

The 32F429IDISCOVERY development kit with a STM32F429ZIT6 microcontroller (*ARM*® *Cortex*® *M4* - 168 MHz) manages the received signals and performs the respective tasks. This device exhibits capability for native USB 2.0, which allows the emulation of computer peripherals like mouse and keyboard through the human interface device (HID) class. By mirror apps, this system offers an extension to other devices apart from PC, such as smartphones.

2.2 Conditioning of Pressure Signals

User's respiratory function defines system responsiveness, so an exclusive calibration is required. Although not differential, the sensor detects negative pressures (suction) by an attenuation of standby voltage. In the experiments, was recorded: 0.17 V (standby), 0.09 V (suction) and 0.20 V (puff). For amplification, it was used a non-inverting amplifier with gain 11. Further, there is a Schmitt trigger stage responsible for the digitalization of pressure signals with two outputs to the microcontroller (sip, puff), as shown in Fig. 2(a).

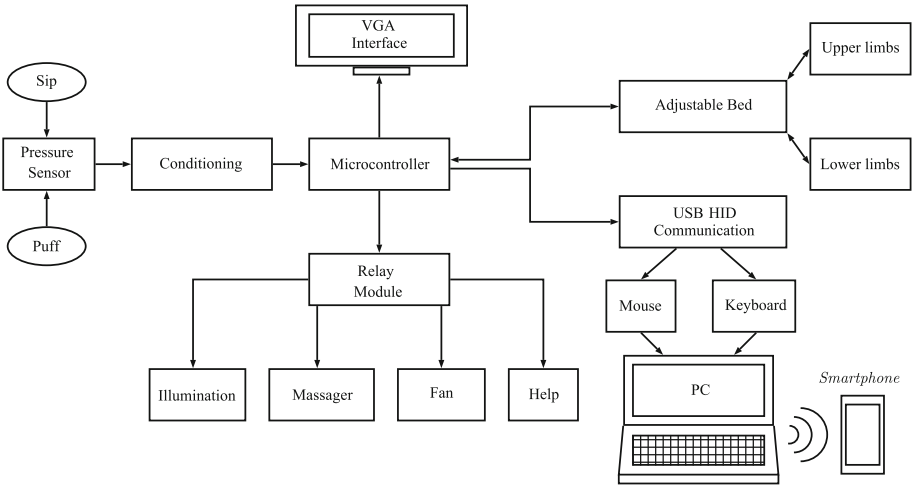

Fig. 1. System diagram.

Schmitt trigger reduces interference of external noises, such as those arising from breathing process. A non-inverting Schmitt trigger detects puffs with a switching threshold between 2 V and 2.15 V, while an inverting configuration indicates sips with a threshold between 1.3 V and 1.45 V.

Figure 2(b) exposes the printed circuit board (PCB) for conditioning of pressure signals. Trimpots define the reference voltages of the circuit, which adjust the hysteresis depending on the intensities of user's sips and puffs.

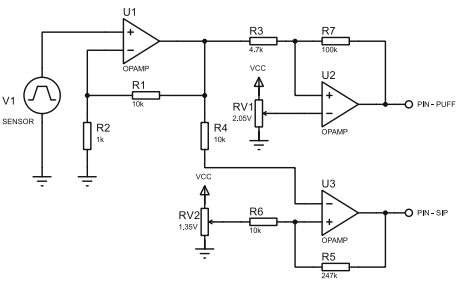

(a) Schematic.

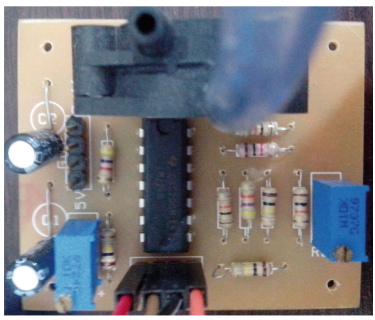

(b) PCB for conditioning signals.

Fig. 2. Conditioning circuit

2.3 Logical Block

A counter is activated if the microcontroller receives an external interrupt by pressure signals, which generates a timer interrupt of 1.5 s. The timer overflow

leads the system to check the number and sequence of sip and puffs, so it resets the counter and disables the time trigger. Combinations accepted are one or two puffs, one or two sips, sip and puff, puff and sip. Table 1 describes their respective functions.

Table 1. Actions of sip and puff.

Action	Description
One puff	The indicator moves to the next item of the menu or sub-menu
Two puffs	It modifies the states of control variables, such as ON/OFF in relay devices, besides sends data via USB and changes the bed inclination
One sip	The indicator moves to the previous item of the menu or sub-menu
Two sips	It returns to main menu
Puff and sip	The indicator moves one line up in sub-menus of the mouse, keyboard, and adjustable bed
Sip and puff	The indicator moves one line down in sub-menus of the mouse, keyboard, and adjustable bed

The graphical user interface presents the commands on a VGA display - 640×480 pixels, 60 Hz. This standard is typical in monitors and features an inexpensive implementation. As the VGA receives analog signals (0.7 V_{MAX} - 75 Ω), there was a need to perform the digital-to-analog conversion of the RGB outputs (3 V logic). We adopted an 8-bit color format - RGB332, that is, 3 bits reds, 3 green and 2 blue. So, each digital color set is converted to analog by a resistive network.

2.4 Relay Module

The interface enables activation of electrical equipment by puff signals. The module with four independent relays supports devices up to 250 V–10 A. With two puffs, the microcontroller toggles the output pins to ensure two distinct states in the loads (ON/OFF).

2.5 USB Communication

The STM32F429ZIT6 features native USB communication. Manufacturer provides the essential libraries for peripheral's configuration. The mouse and keyboard integrate the HID class (input devices). This standard does not require external drivers and works on several operating systems. Code structures known as descriptors characterize the USB communication.

Devices such as mouse and keyboard have predefined descriptors in HID class [17,18]. With two puffs, the interface sends vectors declared in the report descriptor with required address and data to the output buffer. Data can be from mouse (scrolling, directional, right and left button) or keyboard (Any key or key combination).

2.6 Prototype of the Adjustable Bed

The mechanical prototype of the adjustable bed frame, Fig. 3, has worm drives that allow the structure to move only by the motors drive. Two 12 V DC motors are used via an H-bridge. Gears transmit the movement to stems that bend the structure, which is articulated and segmented into blocks to the lumbar/cervical (upper) and legs (lower).

Potentiometers are used to measure angular change by variation of resistance and following voltage verified in the resistive divider. Thus, through the analog to digital converters, it is possible to check the current position of the axes.

For the headboard, we defined angles of 0°, 30°, 45° and 60°. The lower limbs section presents only two states (horizontal or inclined). At the power-up, system checks and records bed positions. By default, these values refer to a headboard's slope of 0° and horizontal position for lower limbs. When the user performs a change of bed's angle, the system compares the voltage of the desired position with the current voltage and moves the structure to it.

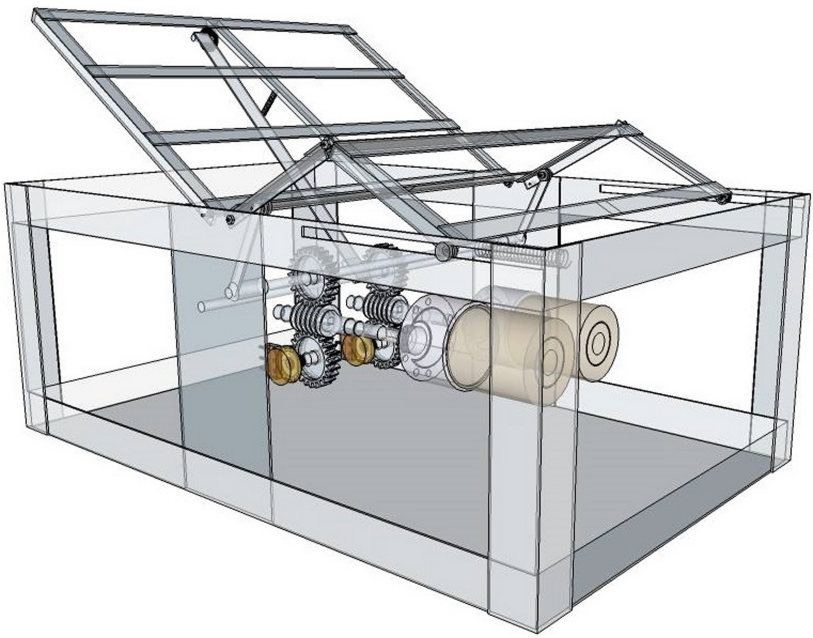

Fig. 3. 3D model of the adjustable bed.

3 Results and Discussion

The drawback of slow pressure response to a stimulus was not critical in the developed interface, which compensates this characteristic by the simple execution of operations. The system executes commands with 1.5 s, so it takes about 3 s to activate the ambient light at the startup. However, the user might notice some sensation of dryness in the throat after prolonged and uninterrupted use of the interface. Therefore, the user must keep his breathing constant and take breaks if he feels any fatigue.

The user accesses home screen of the graphical interface at the system startup, which displays the main menu at the left and sub-menu of options at the right. Figure 4 shows a sub-menu of the adjustable bed control, note that the user must perform two consecutive puffs to enter in sub-menu and a puff-sip action to execute the described situation. A green button indicates that the user is in the respective item of the main menu and the blue button exhibits the current indicator's position.

Fig. 4. Menu of the adjustable bed.

Figure 5 exposes the mouse feature, which enables the use of right and left buttons, screen scrolling, and cursor movement. Two puffs start or stop the cursor shift, and the arrows define a direction.

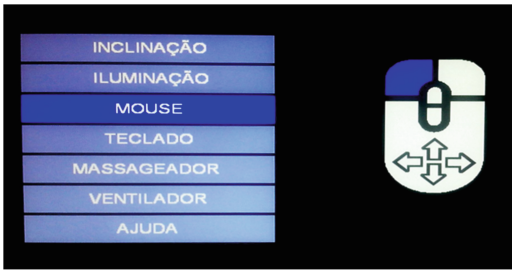

Fig. 5. Main menu - Mouse position.

Figure 6(a) presents the keyboard interface, which allows writing of texts directly on the PC. A blue target on the monitor exhibits the written characters.

Computer access provides a variety of opportunities for the user. Mouse and keyboard allow the execution of programs, write of texts, search, access to e-mails and social networks. Further, the user can handle a smartphone through any mirror app, as shown in Fig. 6(b).

(a) Virtual keyboard. (b) Text.

Fig. 6. Social network communication through the PC.

The remaining functionalities are related to the operation of relays. Two puffs change the device's state (ON/OFF). Figure 7 indicate the lamp and fan states, respectively. Finally, Fig. 8 displays all possible bed slope configurations, achievable through the proposed interface.

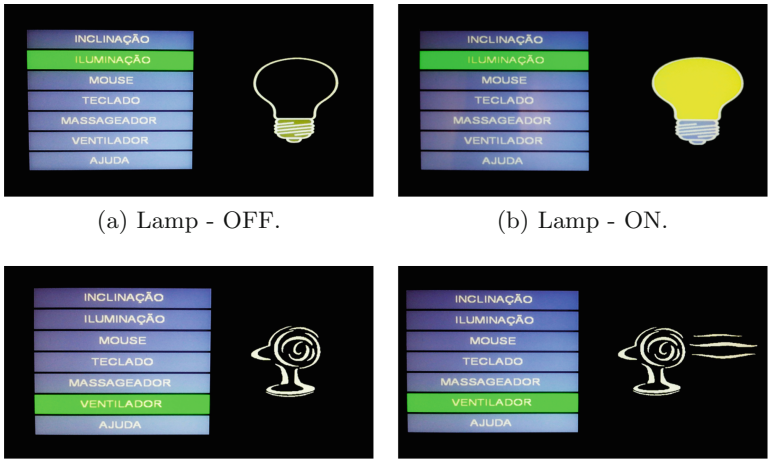

(a) Lamp - OFF. (b) Lamp - ON.

(c) Fan - OFF. (d) Fan - ON.

Fig. 7. ON/OFF menu.

(a) Flat frame.

(b) Inclined lower limbs.

(c) Upper: 30^o - Lower: Horizontal.

(d) Upper: 30^o - Lower: Inclined.

(e) Upper: 45^o - Lower: Horizontal.

(f) Upper: 45^o - Lower: Inclined.

(g) Upper: 60^o - Lower: Horizontal.

(h) Upper: 60^o - Lower: Inclined.

Fig. 8. Inclinations of the adjustable bed.

4 Conclusion

This work presents the development of a pressure-controlled interface (sip and puff) for control of devices and communication with the external environment as a relevant assistive technology for individuals with severe motor dysfunctions. Commands based on sip, puff and the combination of both sought to be logical and intuitive, aiming an affordable use. Although a healthy user tested the system, it was designed to satisfy people with disabilities. Thus, detection of commands has a good sensitivity of response that can also be adjusted in the Schmitt trigger circuit. Noises or involuntary signals, such as breathing, was barely perceptible.

If the user is conscious and lucid and has at least a condition to perform blows and suctions, this may have some commands available that will give more freedom to small actions, such as requesting help, turning on and off some equipment, changing the position of the bed, both in relation to the lower and upper limbs. Besides, the patient can access internet and email services. Another proposal of the system is in case the patient needs to leave some judicial message since the system can store reports issued by the user.

The VGA graphical interface reduces the system cost since it does not need any integrated indicative device. It also facilitates the understanding and execution of offered functions. Virtual mouse and keyboard ensure a complete experience on the PC, such as write, searches, and access to social networks. The activation of electrical equipment by relays also reflects a gain of independence.

In total, the electronic interface developed cost US$ 90, however, this value does not consider expenses with manpowers, infrastructure, marketing and taxes, which makes it impossible to compare with a final commercial device. A commercial sip-and-puff ON/OFF devices are sold for up to US$ 450 and up to US$ 1500 with mouse emulation.

As this project is in its first phase of development, there was not enough time to recruit volunteers who could perform a real test, even though it should be submitted to the ethics committee. However, testing with sane people proved the initial proposal of project functionality.

Authors requested the system's intellectual property through the Agency of Technological Innovation - Londrina State University (AINTEC/UEL).

References

1. Federici, S., Scherer, M.J.: Assistive Technology Assessment Handbook. Rehabilitation Science in Practice Series, 2nd edn. CRC Press, Boca Raton (2018)
2. Bastos-Filho, T., Ferreira, A., Cavalieri, D., Silva, R., Muller, S., Perez, E.: Multimodal interface for communication operated by eye blinks, eye movements, head movements, blowing/sucking and brain waves. Universidade Federal do Espirito Santo (UFES) (2012)
3. Nasor, M., Rahman, K.K.M., Zubair, M.M., Ansari, H., Mohamed, F.: Eye-controlled mouse cursor for physically disabled individual. In: 2018 Advances in Science and Engineering Technology International Conferences (ASET), pp. 1–4, February 2018

4. Molina-Cantero, A.J., Vazquez, C.L., Monge, M.M., Tabares, R.Q., Garcia, J.A.C., Gonzalez, I.M.G.: Communication technologies based on voluntary blinks: assessment and design. IEEE Access **7**(99), 70770–70798 (2019)
5. Struijk, L.N.S.A., Lontis, R.: Comparison of tongue interface with keyboard for control of an assistive robotic arm. In: 2017 International Conference on Rehabilitation Robotics (ICORR), pp. 925–928, July 2017
6. Umchid, S., Limhaprasert, P., Chumsoongnern, S., Petthong, T., Leeudomwong, T.: Voice controlled automatic wheelchair. In: 2018 11th Biomedical Engineering International Conference (BMEiCON), pp. 1–5, November 2018
7. Mougharbel, I., El-Hajj, R., Ghamlouch, H., Monacelli, E.: Comparative study on different adaptation approaches concerning a sip and puff controller for a powered wheelchair. In: Science and Information Conference (2013)
8. Rojhani, S., Stiens, S.A., Recio, A.C.: Independent sailing with high tetraplegia using sip and puff controls: integration into a community sailing center. J. Spinal Cord Med. **40**, 471–480 (2016). https://doi.org/10.1080/10790268.2016.1198548
9. Aigner, B., David, V., Deinhofer, M., Veigl, C.: FLipMouse: a flexible alternative input solution for people with severe motor restrictions, pp. 25–32 (2016)
10. de Freitas Marinho, D.: Proposta de uma cama funcional controlada por sensor de pressão. Departamento de Engenharia Elétrica da Universidade Estadual de Londrina (2014)
11. Brodwin, M.G., Siu, F.W., Howard, J., Brodwin, E.R., et al.: Medical, Psychosocial and Vocational Aspects of Disability, 4th edn. Elliott & Fitzpatrick, Inc., Athens (2014)
12. Mulfari, D., Celesti, A., Fazio, M., Villari, M., Puliafito, A.: Using embedded systems to spread assistive technology on multiple devices in smart environments. In: IEEE International Conference on Bioinformatics and Biomedicine (2014)
13. Stansby, G., Avital, L., Jones, K., Marsden, G.: Prevention and management of pressure ulcers in primary and secondary care: summary of nice guidance. BMJ **348**, g2592 (2014). https://www.bmj.com/content/348/bmj.g2592
14. Black, J.: Pressure ulcer prevention and management: a dire need for good science. Ann. Intern. Med. **162**(5), 387–388 (2015). https://doi.org/10.7326/M15-0190
15. Bock, E., Araki, S., Souza, R., Ronei, D., Hernandes, M., Frantz, J., Martins, D., Campos, A.: Integrated supervisory system to control a reconfigurable platform of assistive technology, pp. 444–447 (2017)
16. Bandala, A.A., Apelo, L.K.G., Dimalanta, T.C., Macatangay, J.A.V.V., Miciano, J.E.S., Sayo, M.L.C.: Development and design of automated hospital bed with incremental panels for bedsore prevention. In: TENCON 2014 - 2014 IEEE Region 10 Conference. IEEE, October 2014. https://doi.org/10.1109%2Ftencon.2014.7022411
17. Bergman, M., Peurach, T., Schmidt, T., McGowan, S., Crowe, J., Dezmelyk, R., Zimmermann, R., Flandern, M.V., Nathan, B., Davis, M., Rayhawk, J.: Device Class Definition for Human Interface Devices (HID). Lakeview Research LCC (2001)
18. Axelson, J.: USB Complete - The Developer's Guide, 5th edn. Lakeview Research LCC, Madison (2015)

Development of a Feeding Device for Patients with Motor Impairment in Upper Limbs

Natacha H. Ota, Tiago R. S. Silva, Douglas Crochi(✉), Cecilia P. Muffo, Silvia C. Martini, Alessandro P. Silva, Terigi A. Scardovelli, and Silvia R. M. S. Boschi

Technology Research Center, University of Mogi das Cruzes, Mogi das Cruzes, SP, Brazil
douglascrochi@gmail.com, boschi@umc.br

Abstract. Patients with neurological injury rarely recover the functionality of upper limbs to the point of using it in an effective way in their daily life activities, such as personal hygiene and feed, becoming dependent of a third-party assistance. Thus, the objective of this study is to develop an assistive device to support the feeding of patients with motor impairment in upper limbs. Initially it was made the virtual prototyping of the device, split in a support base compounded by a bar which could be adjusted by the M6 screw coupled to a handle, three movable rods, and a cutlery base which the spoon is fixed allowing the feed of the individual. The device has four axis, the first one allows the device to rotate 360°, the second one adds freedom movement in the vertical axis, the third one allows movement in the horizontal axis so that the spoon could be directed to the patient's mouth, and the last one keeps the spoon stable on the horizontal axis so that the food doesn't fall. With this study, it was possible to develop a device capable of enabling patients with upper limbs motor impairment to feed themselves independently.

Keywords: Assistive device · Feed · Upper limb

1 Introduction

The paralysis of the upper limb has been reported as the main consequence of the neurologic diseases, happening in more than 80% of the cases [1], and only 6% of them present a functional arm [2].

In particular, patients with neurological lesions have difficulty to recover the upper limb functionality to the point of using it effectively in their daily activities, such as hygiene and feeding [3], making them dependent on the help of third parties.

To help them to become more independent in these practices, a lot of robotic devices were developed [4–6]. In a study made with 233 physiotherapist and Occupational Therapist indicated that a robotic device for the upper limb should make a lot of movements of the arm more easily. It should also be useful at home, in seated position, and adapt to the user needs [7].

Therefore, the goal of this study is to develop an assisted device to help the feeding of the patients with motor impairment upper limbs.

© Springer Nature Switzerland AG 2020
C. A. González Díaz et al. (Eds.): CLAIB 2019, IFMBE Proceedings 75, pp. 1147–1152, 2020.
https://doi.org/10.1007/978-3-030-30648-9_149

2 Materials and Methods

All the device structure was made in polylactic acid (PLA) plastic of 1,75 mm of diameter, black color, by 3D printer of Fusion and Deposition Modeling (FDM). For the assembly it was used bolts and butterfly nuts M5 and M6.

2.1 Virtual Prototyping

The virtual prototype of the device was made using the modeling software 3d Autodesk® Inventor 2019 (Fig. 1).

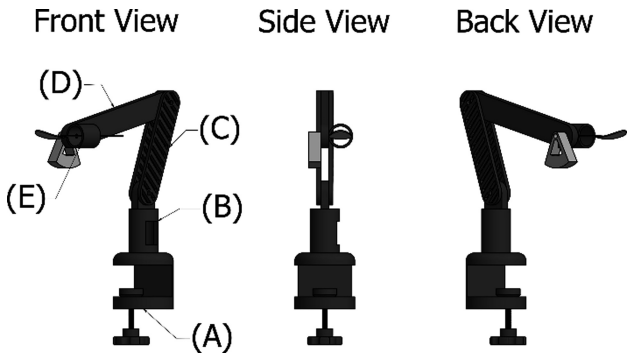

Fig. 1. Tridimensional Modeling of the device: A - Support base; B - Lower rod; C - Middle rod; D - Upper rod; E - Cutlery stand

2.2 Support Base

It was developed in a support base composed by a thread-adjustable rod M6 coupled to a handle, which allows the fixation of the device in different types of surfaces (Fig. 1A).

2.3 Movable Rods

The device presents three movable rods. The lower rod has an end fixed to the support base, and the other articulated with the middle rod (Fig. 1B). The middle rod has one of the ends articulated with the lower rod and the other one with the upper rod (Fig. 1C). In the upper rod there is a cutlery holder, where it was fixed a spoon which allows the feeding of the individual (Fig. 1D). The lower rod makes a 360° movement, the middle rod makes the vertical movement, and the upper rod makes the horizontal movement of the spoon in the direction of the patient's mouth. To help in this movement, an elastic was inserted into the rods, which keeps a constant strength to support the user in the elevation of the cutlery.

2.4 Cutlery Support

A spoon was fixed to a support attached to the upper rod. To keep the spoon balance during the rod rise movement, it was manufactured a metal pendulum and added in the opposite side of the spoon to stabilize it (Fig. 1E).

3 Results

3.1 Axis and Device Workspace

The device presents an area range of 40 cm height, and 30 cm in the laterals, which allows a satisfactory reach for the feed. To achieve this work area, the device has 4 axis. The axis 1 allows the 360° rotation of the device, which allows it to be installed anywhere on the table, the axis 2 adds freedom movement in the vertical plane, the axis 3 allied to the axis 2 makes the movement in horizontal plane so that the spoon can go to the individual's mouth, and the axis 4 keeps the spoon stable in the horizontal plane so the food doesn't fall from the cutlery (Fig. 2).

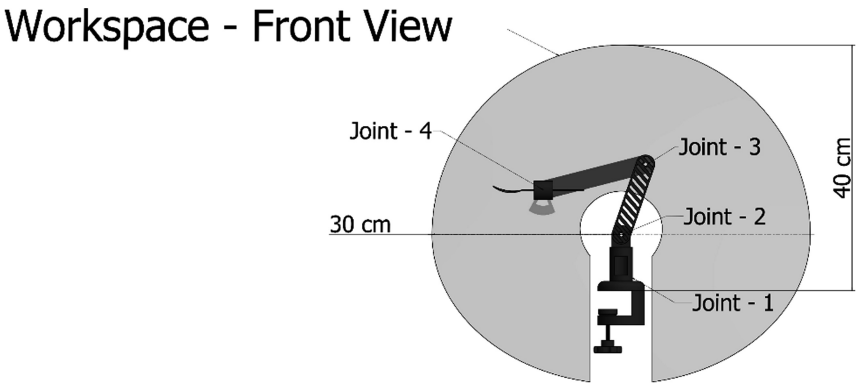

Fig. 2. Device's working area and its respective axes

3.2 Device Finished

The Fig. 3 shows the image of the final version of the device, it is made of plastic by the 3D printer. The image shows how to utilize it.

The device should be secured to the surface of a table, and positioned next to the hemiparetic member of the patient. The user will sit in front of the equipment and use his three stems and four axes to carry the cutlery to the plate, fill it with food, and then take it to his mouth.

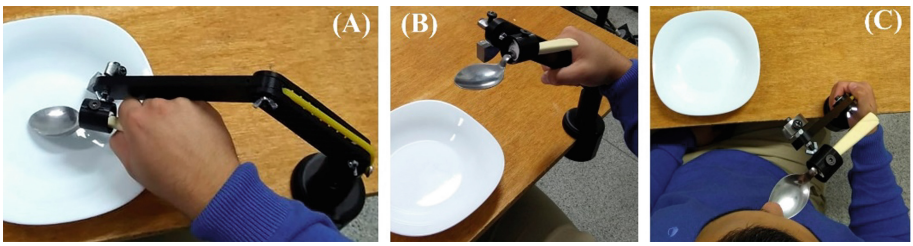

Fig. 3. Final version of the device: (A) Image simulating the position of the cutlery close to the plate. (B) Image simulating the movement of the cutlery. (C) Image simulating the final position of the cutlery in direction of the individual's mouth.

4 Discussion/Conclusion

Individuals with upper limb paresis experience a reduction in their life quality and are prone to give up rehabilitation programs. Thus, given that motivation is a determining factor in treatment outcomes [8], the use of self-directed devices that enable the patient to perform his tasks without the direct supervision of a therapist or caregiver could give the patient the sensation of feeling active again, favoring their adherence to therapy.

Taking it into consideration, several robots devices have been developed to allow individuals an interactive rehabilitation and promoting their participation (into society) [9–11]. However, although the use of these devices has shown significant improvement in the functions results, also in the motor abilities of the patients and in their motor skills, the devices assist indirectly in the individuals activities in their daily life, With this in mind, several robotic devices have been developed to allow the individual an interactive rehabilitation, promoting their participation [9–11]. However, although the use of these devices has shown significant improvement in the functional results and in the motor skills of the patients, they indirectly support the activities of daily living, since once more control of the upper limb is gained, this may help the patient in their food and hygiene. However, these devices were not developed for a specific function, different to this study, which designed a device that directly assists the user's feeding.

For Huang and Krakauer et al. [12] the recovery of function is achieved by the practice of repetitive movements specific to a given task. Thus, the development of a device that assists the patient to carry the cutlery towards the mouth, besides allowing the individual to feed independently without the help of third parties, can also contribute to the functional recovery of this movement, making with which in the near future, the use of external tools for their food is no longer necessary.

Thus, to assist the patient in their feeding, an elastic was inserted into the rods of the device. This elastic maintains a constant force in the rods, which makes the movement of elevation of the cutlery to the mouth easier. Therefore, the force applied by the individual on the rods to perform this movement is smaller, optimizing the energy expenditure of the activity.

In the Song and Kim study [13], an assistive robot was developed to feed people with physical disabilities. However, this device consists of two robotic arms, where one is responsible for picking up the food and putting it in a spoon, and the other for

bringing that spoon up to the user's mouth. There is also the possibility of using only the robotic arm that takes the spoon to the individual's mouth, but in this case it is necessary for a caregiver to fill the spoon. Thus, unlike the Song and Kim robot [13], the device developed in the present study is composed of a single mechanical arm, which allows the individual to fill the spoon, and take it independently to the mouth, leaving the person free of third-party assistance.

Furthermore, the robotic arm used by Song and Kim [13] to take the spoon to the patient's mouth has 3 degrees of freedom, while the device developed in this study has 4, which facilitates a variety of arm movements, and adapts to the needs of the user.

Another important point is that the device was projected for the patient to utilize it in a domestic environment, also in a sitting position, fulfilling in this way all the specifications described by Lu et al. [7], which state that robotics tools used in rehabilitation of upper limb should facilitate a variety of arms movements, be useful at home, utilizable in a sitting position, and adaptable to the user's needs.

Through this study it was possible to develop a device capable of helping patients with upper limbs motor impairment to feed themselves independently.

Declaration of Conflict of Interest. The authors declare no conflict of interest.

References

1. Sommerfeld, D., Eek, E., Svensson, A., et al.: Spasticity after stroke: its occurrence and association with motor impairments and activity limitations. Stroke **35**(1), 134–139 (2004)
2. Broeks, J., Lankhorst, G., Rumping, K., et al.: The long-term outcome of arm function after stroke: results of a follow-up study. Disabil. Rehabil. **21**(8), 357–364 (1999)
3. Shelton, F., Volpe, B., Reding, M., et al.: Motor impairment as a predictor of functional recovery and guide to rehabilitation treatment after stroke. Neurorehabil. Neural Repair **15**(3), 229–237 (2001)
4. Lum, P., Burgar, C., Shor, P., et al.: Robot-assisted movement training compared with conventional therapy techniques for the rehabilitation of upper-limb motor function after stroke. Arch. Phys. Med. Rehabil. **83**(7), 952–959 (2002)
5. Lum, P., Burgar, C., Van der Loos, M., et al.: MIME robotic device for upper-limb neurorehabilitation in subacute stroke subjects: A follow-up study. J. Rehabil. Res. Dev. **43**(5), 631–642 (2006)
6. Masiero, S., Celia, A., Rosati, G., et al.: Robotic-assisted rehabilitation of the upper limb after acute stroke. Arch. Phys. Med. Rehabil. **88**(2), 142–149 (2007)
7. Lu, E., Wang, R., Hebert, D., et al.: The development of an upper limb stroke rehabilitation robot: identification of clinical practices and design requirements through a survey of therapists. Disabil. Rehabil. Assist. Technol. **6**(5), 420–431 (2011)
8. Colombo, R., Pisano, F., Mazzone, A., et al.: Design strategies to improve patient motivation during robot-aided rehabilitation. J. Neuroeng. Rehabil. **4**, 3 (2007)
9. Susanto, E., Tong, R., Ockenfeld, C., et al.: Efficacy of robot-assisted fingers training in chronic stroke survivors: a pilot randomized-controlled trial. J. NeuroEng. Rehabil. **12**(1), 42 (2015)

10. McCabe, J., Monkiewicz, M., Holcomb, J., et al.: Comparison of robotics, functional electrical stimulation, and motor learning methods for treatment of persistent upper extremity dysfunction after stroke: a randomized controlled trial. Arch. Phys. Med. Rehabil. **96**(6), 981–990 (2015)
11. Brokaw, E., Nichols, D., Holley, R., et al.: Robotic therapy provides a stimulus for upper limb motor recovery after stroke that is complementary to and distinct from conventional therapy. Neurorehabil. Neural Repair **28**(4), 367–376 (2014)
12. Huang, V., Krakauer, J. Robotic neurorehabilitation: a computational motor learning perspective. J. Neuroeng. Rehabil. **6**(5) (2009)
13. Song, W., Kim, J.: Novel Assistive Robot for Self-Feeding. Robotic Systems – Applications, Control and Programming (2012)

Comparison of Assessment Methods Using Virtual Games for Balance Rehabilitation

Fabiana R. S. de M. Cavalcanti(✉), Silvia R. M. da S. Boschi, Cecilia Muffo, Alessandro P. da Silva, Terigi A. Scardovelli, and Silvia C. Martini

Technology Research Center, University of Mogi das Cruzes, Mogi das Cruzes, SP, Brazil
fabianarodrigues.smcavalcanti@gmail.com, cicamuffo@gmail.com

Abstract. Body balance is an important basic sensory-motor skill. As technology advances, several forms of rehabilitation have been emerging. Thus, virtual reality games have increasingly been used in balance rehabilitation. This paper aims to present a literature review on the interventions performed with the use of balance games and their benefits for motor development. This theoretical study consists of a literature review. Original studies in English were included, as published in full in scientific journals, available in the following electronic databases: Bireme Virtual Health Library (VHL), PubMed, Medline and Cochrane. A total of 22 studies were found, out of which 8 articles were excluded, since they were duplicated, and another 2 ones, since they were directed to adults. Therefore, 12 articles were read in full. When reviewing the studies, it was possible to observe that rehabilitation with games in balance can be used for chronic non-evolving spastic encephalopathy, Down Syndrome or Developmental Deficit, as long as the child or adolescent has cognition and the possibility of staying in an orthostatic position, and Nintendo Wii™ and Microsoft Kinect™ can be used with the same objective. A higher number of studies using Nintendo Wii™ were observed in the literature. The review of the studies proved to be effective in the rehabilitation of balance with several pathologies. There has been much study on the use of games, not only to work balance, but also towards motor coordination and social development.

Keywords: Evaluation methods · Games · Postural balance · Children

1 Introduction

Body balance is an important basic sensory-motor skill. Without the ability to maintain balance, a person cannot walk, stand and sit down without the aid of devices for more than a few seconds. Thus, balance plays an important role in the daily life of each individual [1].

Its lack diminishes the postural adjustment during the performance of daily tasks. Some factors influence balance, such as the sensory information obtained from somatosensory systems, visual vestibular systems and motor responses, range of motion and joint strength [2].

© Springer Nature Switzerland AG 2020
C. A. González Díaz et al. (Eds.): CLAIB 2019, IFMBE Proceedings 75, pp. 1153–1161, 2020.
https://doi.org/10.1007/978-3-030-30648-9_150

Motor evaluation performed by a physiotherapy professional establishes a resource that allows obtaining information about children or a specific population, so that it is possible to make valid decisions about their motor development, establish diagnostic evaluation as the primary point for an intervention in order to improve motor skills and allow higher levels of functioning in daily activities [3].

During the rehabilitation process, repetitive practice can lead to the automation of this specific skill, such as, the ability to improve speed, precision, stability and fluency, and when the new movements are learned, we should be able to connect them to adequate contextualization, such as objects, tasks or environments; thus, rehabilitation with games provides us with information to extract and spread their attention throughout the spatial picture, without any apparent decreased performance [4].

As technology advances, several forms of rehabilitation have been emerging, such as interactive games being used for the treatment of several diseases that cause motor disorders, also used as a possibility of treatment of stroke, Parkinson's Disease, as well as in diseases affecting children [5].

Marston et al. [6] address the potential of Microsoft Kinect and Nintendo Wii in the care of children and the positive impact on their physical and mental health, showing that in recent years, video game consoles, such as Nintendo Wii™ and Microsoft Kinect™, have been added to the care of children as part of a rehabilitation resource, being used in several types of rehabilitation, such as maintenance of physical conditioning, promotion of mental well-being, encouragement to social interaction and physical and mental rehabilitation.

Thus, virtual reality games have been increasingly used in the rehabilitation of balance, since they have functional results in several patients. Training with games proves to be effective, moving from traditional rehabilitation to interactive rehabilitation as a motor impairment response [7].

While conventional active video games offer children an attractive experience, they are not designed for therapy. Therefore, research during rehabilitation has become increasingly common. Due to the higher number of people with disabilities in the world, increased virtual reality is spreading in the rehabilitation field. There is a wide variety of studies to test the efficiency of virtual rehabilitation systems aimed at helping people with disabilities, employing different interactive tasks [8].

What has been observed in some areas of Biomedical Engineering is the development of specific and peripheral games to help the rehabilitation of patients; therefore, studies are needed to confirm the effectiveness of rehabilitation using virtual reality through interactive games [9].

2 Material and Method

This theoretical study consists of a systematic review, which includes articles reporting balance games for children and adolescents, the game name, the devices used, intervention time, number of patients, evaluation methods and evaluation of articles using the PEDro scale.

This review included original studies in English, published in full in scientific journals and available in electronic databases: the Bireme Virtual Health Library (VHL), PubMed, Medlin and Cochrane. A research period was not determined because this is a recent methodology used for rehabilitation. The terms used were methods and evaluation, games, balance and posture in children, while the Boolean operator used was (AND).

The data extracted from each study used the PICOS technique (participants, interventions, comparators, outcomes, and study design) to formulate the hypothesis of the review, which would be "Are balance games effective when used for balance training in children and adolescents? If so, what is the necessary intervention time and what are the best games to be used?"

In order to verify the quality of the articles cited in this review, the PEDro (Physiotherapy Evidence Database) scale [10] was used to assess the methodological quality of studies related to physiotherapy interventions. In all, there are 11 questions, but the first question is not scored, with a maximum score of 10, according to Table 1.

Table 1. Peter scale criteria

1.	eligibility criteria were specified	no ❑ yes ❑ where:
2.	subjects were randomly allocated to groups (in a crossover study, subjects were randomly allocated an order in which treatments were received)	no ❑ yes ❑ where:
3.	allocation was concealed	no ❑ yes ❑ where:
4.	the groups were similar at baseline regarding the most important prognostic indicators	no ❑ yes ❑ where:
5.	there was blinding of all subjects	no ❑ yes ❑ where:
6.	there was blinding of all therapists who administered the therapy	no ❑ yes ❑ where:
7.	there was blinding of all assessors who measured at least one key outcome	no ❑ yes ❑ where:
8.	measures of at least one key outcome were obtained from more than 85% of the subjects initially allocated to groups	no ❑ yes ❑ where:
9.	all subjects for whom outcome measures were available received the treatment or control condition as allocated or, where this was not the case, data for at least one key outcome was analysed by "intention to treat"	no ❑ yes ❑ where:
10.	the results of between-group statistical comparisons are reported for at least one key outcome	no ❑ yes ❑ where:
11.	the study provides both point measures and measures of variability for at least one key outcome	no ❑ yes ❑ where:

3 Results

A total of 22 studies were found, 8 of which were excluded, since they were duplicates, and 2 another ones, since they were directed to adults. Thus, 12 articles were read in full.

Table 2 illustrates the authors of the articles, the sample number, the target audience, the sample diagnosis, the game used to stimulate balance, the intervention time and the evaluation method used by them.

Table 2. Articles included in this review.

Publication	Target audience (n. of sample)	Diagnostic	Game	Intervention Time	Evaluation method
Abdel et al. (2010)	30 Children and adolescents aged 10 to 17 years	Down syndrome	Wii Fit	6 weeks, 2x by 35′ with rest interval	Test motor the Bruininks-Oseretsky. Performed before and after each
Andrysek et al. (2012)	10 Children and adolescents (8 to 18 years)	Transfemoral unilateral amputation (Osteosarcom a)	Jogo Wii Fit	4 weeks, for 20′ (home)	Questionnaire on the use of the game, at the beginning of the study (session 1), immediately after the intervention
Ramstrand et al. (2012)	18 children and adolescents (aged 8 to 17 years)	Cerebral Palsy	Wii Fit and Wii balance	5 weeks (5x weekly. 30′)	Gross Motor Function Classification (GMFCS score)
Salem et al. (2012)	40 children (39 to 58 months of age)	Delay in development	Nintendo WiiSports™	10 weeks (2x week)	Gross Motor Function Measurement (GMFM)
Hammond et al. (2013)	52 children (aged 7 to 10 years)	Development Coordination Disorder (DCD)	Wii Fit	Phase 1: 4weeks, 1 h, 3x without Phase 2: after 2 months, 4 weeks, 1 h 3x	Development Coordination Disorder Questionnaire
Sheehan et al. (2013)	64 Children in the 4th primary year	No motor change	Wii Fit Plus	6 weeks, 34 min, 4 and 5x a week	Equilibrium Platform: BT4 balance trainer (Test in the first and last week)

(*continued*)

Table 2. (*continued*)

Publication	Target audience (n. of sample)	Diagnostic	Game	Intervention Time	Evaluation method
Larsen et al. (2014)	54 children and adolescents (10 to 14 years)	No motor change	Nintendo Wii Board (NWB)	1 day	Test CHAMPS-Study DK
Tatla et al. (2014)	3 children and adolescents (5 to 18 years)	Acquired brain injury	Wii balance board	1 week (5x weekly. 1 h)	Test Timed up and timed go
Tarakci et al. (2016)	38 Children and adolescents (aged 5 to 18 years)	Cerebral Palsy	Jogo Wii Fit + Balance Board	12 week (2x weekly 50′)	Functional Forward Reach (FFRT); Timed Get Up and Go; Sit-To- Stand Test (performed at the beginning and end of each session)
Meyns et al. (2017)	11 children and adolescents (age 5 to 18 years)	Cerebral Palsy	WiiBalance Board	6 week	Trunk Control M easurement Scale (TCMS); Visual Analog Scale (EVA) Performed
Bonnechere et al. (2017)	10 Children and adolescents (between 5 and 15 years)	Cerebral Palsy	Wii Balance Board e Kinect sensor Xbox 360	4 game sessions, 1 x weekly 30′ by 4 weekly	Qualitative Motorized Trunk Control Scale (TCMS), test before and after each session
Chiu et al. (2018)	20 Children and adolescents (6 to 12 years)	Cerebral Palsy	Wii Fit	8 weeks (at home for 20 min, 3x weekly)	Gross Motor Function Classification System (GMFCS), One-Legged Stance Test, 10 m Walk

Table 3: Illustrates the evaluation of articles using the PEDro scale.

Table 3. Score of articles evaluated by the PEDRo scale

Publication	Question 1 (YES/NO)	Question 2 (YES/NO)	Question 3 (YES/NO)	Question 4 (YES/NO)	Question 5 (YES/NO)	Question 6 (YES/NO)	Question 7 (YES/NO)	Question 8 (YES/NO)	Question 9 (YES/NO)	Question 10 (YES/NO)	Question 11 (YES/NO)	Score
Abdel et al. (2010)	Yes	Yes	No	Yes	No	No	No	Yes	Yes	Yes	Yes	(0/6)
Andrysek et al. (2012)	Yes	No	No	Yes	No	No	No	Yes	Yes	Yes	Yes	(0/5)
Ramstrand et al (2012)	Yes	No	No	Yes	No	No	No	Yes	Yes	Yes	Yes	(0/5)
Salem et al. (2012)	Yes	Yes	Yes	Yes	Yes	No	No	Yes	Yes	Yes	Yes	(0/8)
Hammond et al. (2013)	Yes	No	No	Yes	No	No	No	Yes	Yes	Yes	Yes	(0/5)
Sheehan et al. (2013)	Yes	Yes	No	Yes	No	No	No	Yes	Yes	Yes	Yes	(0/6)
Larsen et al. (2014)	Yes	No	No	Yes	No	No	No	Yes	Yes	Yes	Yes	(0/5)
Tatla et al. (2014)	Yes	No	No	Yes	No	No	Yes	Yes	Yes	Yes	Yes	(0/6)
Tarakci et al. (2016)	Yes	Yes	No	Yes	No	No	No	Yes	Yes	Yes	Yes	(0/6)
Meyns et al. (2017)	Yes	Yes	No	Yes	No	No	No	Yes	Yes	Yes	Yes	(0/6)
Bonneckère et al. (2017)	Yes	Yes	No	Yes	No	No	No	Yes	Yes	Yes	Yes	(0/6)
Chiu et al. (2018)	Yes	No	No	Yes	No	No	No	Yes	Yes	Yes	Yes	(0/5)

4 Discussion

Traditional rehabilitation often uses repetitive exercises for a certain time, being effective in its results. The motor gains obtained contribute to motor learning, creating new sensory skills, visual feedback and the body adjustments provided by balance games, since patients demonstrate better interaction in each session [20].

In general, most evaluations involved a small number of subjects with specific characteristics, requiring a larger number of samples and a more heterogeneous group to compare the same game with different pathologies [9].

When reviewing the studies, it was possible to observe that rehabilitation with games in balance can be used for chronic non-evolving spastic encephalopathy, Down Syndrome or Developmental Deficit, as long as the child or adolescent has cognition and the possibility of staying in the orthostatic position, and Nintendo Wii™ and Microsoft Kinect™ can be used with the same objective. A higher number of studies using Nintendo Wii™ were observed in the literature.

Regarding the evaluation methods, there is a vast possibility of functional testing and the platform for analyzing the functionality of balance games. Therefore, when compared to functional tests and the platform, all patients were analyzed, using the Timed Get Up and Go tests, the Qualitative Trunk Control Motorized Scale (TCMS), the Gross Motor Function Measurement (GMFM), CHAMPS-Study DK Test and the Development Coordination Disorder Questionnaire before and after its session to prove the method effectiveness.

Given this, the development of games aimed at rehabilitation in the balance of children and adolescents is being viewed with great optimism, since there is a visual technological incentive, and the ease of being administered at home, as suggested in the studies of ANDRYSEK et al. [13] and CHIU et al. [2], where all of such authors show that the rate of adherence to the proposed treatment is successfully followed by improvement presented in all patients.

5 Conclusion

In this case, the analysis of the studies proved to be effective in balance rehabilitation with several pathologies; however, most studies evaluate a small number of patients with basically the same characteristics. Although it is a relatively new rehabilitation procedure, much has been studied about the use of games not only to work balance, but also towards motor coordination and social development. Therefore, after the review, it is believed that the development of more specific games brings benefits to patients when submitted to treatment as much as conventional rehabilitation; however, the adherence of balance rehabilitation with games is higher due to the interactivity it provides patients with.

Acknowledgements. The authors are grateful to the University of Mogi das Cruzes (UMC), Foundation for Teaching and Research Support (FAEP/UMC), grant #2017/14016-7, São Paulo Research Foundation (FAPESP) and Coordination for the Improvement of Higher Education Personnel (CAPES) for the financial support.

Declaration of Conflict of Interest. The authors declare that there are no conflicts of interest.

References

1. Kliem, A., Wiemeyer, J.: Comparison of a traditional and a video game based balance training program. Int. J. Comput. Sci. Sport. **9**, 80–91 (2010)
2. Chiu, C., Ada, L., Lee, S.: Balance and mobility training at home using Wii Fit in children with cerebral palsy: a feasibility study. BMJ Open. **8** (2018)
3. Rosa, G.K.B., Marques, I., Paspt, J.M., Gobbi, L.T.B.: Desenvolvimento motor de criança com paralisia cerebral: avaliação e intervenção. Rev. Bras. Ed. Esp. **14**(2), 163–176 (2008)
4. Bonney, E., Jelsma, D., Ferguson, G., Engelsman, S.B.: Variable training does not lead to better motor learning compared to repetitive training in children with and without DCD when exposed to active video games. Res. Dev. Disabil. **62**, 124–136 (2017)
5. Bonnechère, B., Jansen, B., Omelina, L., Degelaen, M., Wermenbol, V., Rooze, M., Jan, S. V.S.: Can serious games be incorporated with conventional treatment of children with cerebral palsy? A review. Res. Dev. Disabil. **35**(8), 1809–1926 (2014)
6. Marston, R.H., Greenlay, S., Hoof, V.J.: Understanding the Nintendo Wii and Microsoft Kinect consoles in long-term care facilities. Technol. Disabil. **25**, 77–85 (2013)
7. Meyns, P., Harlaar, J., Pol, V.L., Barkhof, F., Buizer, A.: Can virtual reality games improve scores on clinical balance scales in children with cerebral palsy: preliminary results of a randomized controlled clinical trial. Gait Posture **57**(1), 234–235 (2017)
8. Gomez, R., Murillo, R., Sibaja, A., Hernandez, G., Lasserre, A., Fernandez, M.: An interactive system for fine motor rehabilitation. Rehabil. Nurs., 1–10 (2016)
9. Ni, L., Biddiss, E.: Design and evaluation of virtual reality-based therapy games with dual focus on therapeutic relevance and user experience for children with cerebral palsy. Games Health J. **3**(3), 162–171 (2014)
10. Tannus, L., Ribas, D.: Evaluation of gross motor function before and after virtual reality application. Fisioter. Mov. **29**(1), 131–136 (2016)
11. Shiwa, S., Costa, L., Moser, A., Aguiar, I., Oliveira, L.: PEDro: the physiotherapy evidence database. Fisioter Mov. **24**(3), 523–533 (2011)
12. Abdel, S., Abdel, R.: Efficacy of virtual reality-based therapy on balance in children with down syndrome. World Appl. Sci. J. **10**(3), 254–261 (2010)
13. Andrysek, J., Klejman, S., Steinnagel, B., Torres, R., Zabjek, K., Salbach, N., Moody, K.: Preliminary evaluation of a commercially available videogame system as an adjunct therapeutic intervention for improving balance among children and adolescents with lower limb amputations. Arch. Phys. Med. Rehabil. **93** (2012)
14. Salem, Y., Gropack, S., Coffin, D., Godwin, E.: Effectiveness of a low-cost virtual reality system for children with developmental delay: a preliminary randomised single-blind controlled trial. Physiotherapy J. **98**(3), 189–195 (2012)
15. Hammond, J., Jones, V., Hill, E., Green, D., Male, I.: An investigation of the impact of regular use of the Wii Fit to improve motor and psychosocial outcomes in children with movement difficulties: a pilot study **40**(2), 165–175 (2013)
16. Sheehan, P., Dwayne., L.: The effects of a daily, 6-week exergaming curriculum on balance in fourth grade children. J. Sport Health Sci. **2**, 131–137 (2013)
17. Larsen, L., Jorgensen, M., Junge, T., Juul-Kristensen, B., Wedderkopp, N.: Field assessment of balance in 10 to 14 year old children, reproducibility and validity of the Nintendo Wii board **14**(144) (2014)

18. Tarakci, D., Huseyinsinoglu, B., Tarakci, E., Ozdincler, A.: Effects of Nintendo Wii-Fit video games on balance in children with mild cerebral palsy. Pediatr. Int. **58**, 1042–1050 (2016)
19. Tatla, S., Radomski, A., Cheung, J., Maron, M., Jarus, T.: Wii-habilitation as balance therapy for children with acquired brain injury. Dev. Neurorehabilitation **17**(1), 1–15 (2014)
20. Bonneche're, B., Omelina, L., Janse, B., Jan, S.: Balance improvement after physical therapy training using specially developed serious games for cerebral palsy children: preliminary results. Disabil. Rehabil. **39** (2017)
21. Koenig, K., Rudney, S.: Performance challenges for children and adolescents with difficulty processing and integrating sensory information: a systematic review. Am. J. Occup. Ther. **64**(3), 430–442 (2010)

A Wireless BCI-FES Based on Motor Intent for Lower Limb Rehabilitation

L. Carolina Carrere(✉), Leandro Escher, and Carolina Tabernig

Laboratory of Rehabilitation Engineering and Neuromuscular Research (LIRINS), Faculty of Engineering, National University of Entre Ríos, Oro Verde, Entre Ríos, Argentina
ccarrere@ingenieria.uner.edu.ar

Abstract. Recent investigations have proposed brain computer interfaces combined with functional electrical stimulation as a novel approach for upper limb motor recovery. These systems could detect motor intention movement as a power decrease of the sensorimotor rhythms in the electroencephalography signal, even in people with damaged brain cortex. However, these systems use a large number of electrodes and wired communication to be employed for gait rehabilitation. In this paper, the design and development of a wireless brain computer interface combined with functional electrical stimulation aimed at lower limb motor recovery is presented. The design requirements also account the dynamic of a rehabilitation therapy by allowing the therapist to adapt the system during the session. A preliminary evaluation of the system in a subject with right lower limb motor impairment due to multiple sclerosis was conducted and as a performance metric, the true positive rate was computed. The developed system evidenced a robust wireless communication and was able to detect lower limb motor intention. The mean of the performance metric was 75%. The results encouraged the possibility of testing the developed system in a gait rehabilitation clinical study.

Keywords: Brain computer interface · Gait rehabilitation · Motor intention

1 Introduction

Different neurological condition such as stroke, multiple sclerosis, spinal cord injury, traumatic brain damage can cause motor impairment of limbs. The advance of technology has enabled to propose Brain Computer Interfaces (BCI) as a tool for rehabilitation therapy [1]. These systems could use motor intention (MI) detected through event related desynchronization (ERD) of sensorimotor rhythms (SMR) in the electroencephalography signal, as a control signal [1]. The ERD could be observed as a decrease in the power of the SMR (*mu:* 8 to 12 Hz, and *beta*: 18 to 30 Hz) over the motor cortex [1]. Recent researches have shown that it is possible to detect lower limb ERD from the electroencephalography signal [2, 3], even in the damaged brain cortex [4].

Several studies have reported using a BCI and upper limb MI ERD from the brain damaged by a stroke to control a functional electrical stimulation (FES) device as an

© Springer Nature Switzerland AG 2020
C. A. González Díaz et al. (Eds.): CLAIB 2019, IFMBE Proceedings 75, pp. 1162–1170, 2020.
https://doi.org/10.1007/978-3-030-30648-9_151

upper limb rehabilitation system [1, 5–7], since this type of intervention could restore the motor function and promote neural plasticity. However, there is limited evidence of using BCI combined with FES based on lower limb motor intention for gait rehabilitation purposes. A study has proposed a BCI combined with FES for foot drop due to stroke and demonstrated the feasibility of using this system in a single stroke subject [4]. Although the proposed system employed a large number of EEG electrodes, the patient was seated in front of a computer and the setup involved wired communication. Another study presented a BCI combined with FES therapy for gait rehabilitation in stroke patients, but the EEG was recorded by means of 32 electrodes [8]. There are amplifiers that could record EEG with a minimum number of electrodes located by the researcher, and transmit wireless the data to the computer using radio frequency signals [9, 10]. Nevertheless, the problem related to the communication between the BCI and the FES device remains by wires.

Additionally, the design of a BCI for neurorehabilitation should focus on the patient's relearning to control ERD of the ipsilesional motor cortex. It should also account the dynamic of a rehabilitation therapy in which the therapist gives cues to the patient considering the patient's ability, concentration and motivation. Therefore, the BCI design should consider that the therapist/operator can update the classifier and be adapted to the user [6, 11]. With this regard, the classification block of the BCI can be adapted by updating for instance a classification threshold calculated from the selected features of MI ERD [5–7].

In order to implement a rehabilitation intervention for lower limb motor recovery, this paper describes the design, development and preliminary evaluation of a wireless BCI combined with FES (BCI-FES) intended for lower limb rehabilitation.

2 Design Requirements

The design of the wireless BCI-FES considered implementing a system, which records the EEG signal using a minimum number of electrodes while the patient performs a foot dorsiflexion motor intention in response to a verbal cue (MI task). This motor intention consists of the residual movement execution using the impaired limb. The data are transmitted wireless to the computer and processed to identify lower limb MI ERD. Then the selected features of MI ERD are classified and a command signal is generated, which is sent wireless to an interface that triggers a FES device and stimulates the common peroneal nerve to contract the anterior tibialis and produce dorsiflexion, allowing the patient to make a step forward. To avoid wrong feedback in idling intervals, the system remains off during these periods. In order to adequate to possible changes in SMR modulation, the BCI-FES can be updated during the session after each MI task.

3 Design Development

The structure of the BCI-FES is shown in Fig. 1 and consisted of 5 modules: Sensing and Conditioning, Control Signal Generator, Control Signal Adapter, Wireless Interface and FES device.

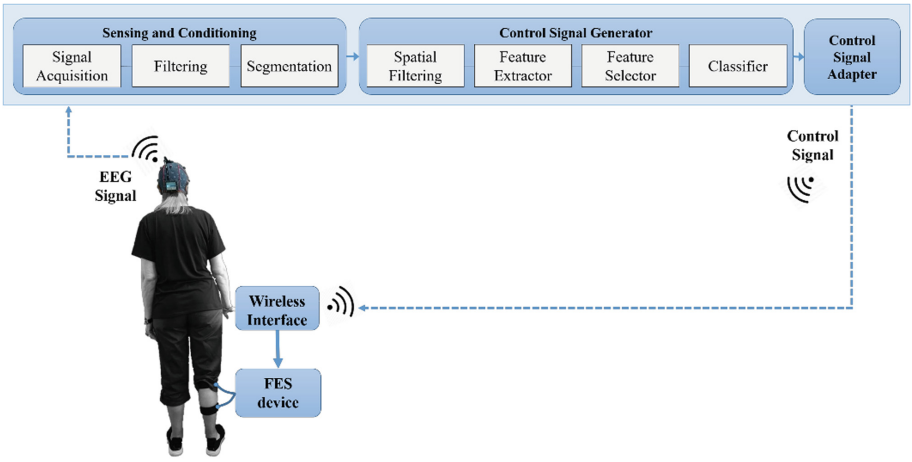

Fig. 1. Structure of BCI-FES, with its modules: sensing and conditioning; control signal generator, control signal adapter, wireless interface and FES device (dash arrow: wireless communication, solid arrow: wired communication)

3.1 Sensing and Conditioning

The first module comprised the following blocks: Signal Acquisition, Filtering and Segmentation. The Sensing and Conditioning module consisted of the wireless amplifier and A/D converter g®.Nautilus [9] and the BCI2000 platform [12]. The EEG was recorded by means of 8 active electrodes g®.Ladybird [9]. The data were digitized with a resolution of 24 bits and sampling frequency of 250 Hz. The amplifier transmitted the data using a radio frequency module in the 2.4 GHz band. The EEG was filtered with a digital band-pass filter between 0.1 Hz and 40 Hz and frequency power line filter at 50 Hz. The data from each channel were segmented and sent in blocks of 8 samples (31.25 ms of duration) to the next module.

3.2 Control Signal Generator

In the Control Signal Generator module, the following blocks were implemented: Spatial Filtering, Feature Extractor and Selector, and Classifier. In the Spatial Filtering block, a Laplacian spatial filter was implemented to improve the signal to noise ratio and to enhance the signal from the foot cortical position, Cz. Then, in the Feature Extractor block, the amplitude spectrum was computed in 500 ms signal epochs via an AR model of order 16 estimated by Burg Method [1]. It was estimated in the range of

0–30 Hz, discreetly in bins of 3 Hz. In the Feature Selector block, the amplitude spectrum at the f_{ERD} was selected resulting in 64 values of EEG amplitude per MI task. These processing steps were performed through the BCI2000 platform [12]. In the Classifier block, an application developed in MATLAB® 7.10 (R2010a) computed the mean of the EEG amplitude in f_{ERD} corresponding to the MI task and compared it with a threshold (ERD_threshold) to generate the control signal. The initial ERD_threshold was calculated as the mean EEG amplitude in f_{ERD} corresponding to the first trial of the MI task. If the mean was greater than the ERD_threshold in the next MI task; then the user was in the state of "rest" and the FES device was not activated. In the opposite case, it interpreted that the user had achieved the ERD related to the foot MI and activated the FES.

3.3 Control Signal Adapter

This module was developed in C++ using MATLAB® 7.10 (R2010a). It established Bluetooth® communication between the computer and the Wireless Interface. It generated the control signal, which collected the information about the onset and duration of electrical stimulation. The onset was given by the output of the Control Signal Generator and the duration was set by the therapist.

3.4 Wireless Interface

This communication interface received information from the computer through a Bluetooth® connection and sent it to the FES device using an RJ-45 connection. It consisted of an Arduino Nano Rev3® board, an opto-isolator (4N28, Motorola Inc.), a lithiumpolymer battery of 2400 mA and its charger. All the components were integrated into a custom PCB board and housed using a 3D printing enclosure. The Arduino comprised an ATmega328P microcontroller and a HC-06 Bluetooth® module configured as slave and connected by I^2C protocol. The output signal of this interface was a 5 V pulse which activated the FES device.

3.5 FES Device

The FES device (Flexicar S.A.) is a two channels controlled stimulator designed to stimulate the neuromuscular system in order to generate a muscular contraction. It has skin surface electrodes and generates biphasic rectangular pulses of 0.2 ms duration, a frequency of 25 pps and a maximal current intensity of 60 mA. These parameters can be set prior to use by the therapist.

4 Preliminary Evaluation

The evaluation of the developed BCI-FES was in one subject with relapsing-remitting multiple sclerosis who presented right lower limb impairment. The experimental protocol was approved by the Ethical Comitee of the Fundación Rosarina de Neurorehabiltación, Rosario, Santa Fe, Argentina; and written informed consent was obtained

from the patient. The designed BCI-FES detected the MI dorsiflexion ERD of the affected limb, being inactive during idling intervals. This resulted in an only class system so the true positive rate (TPR) was computed as performance metric. The evaluation entailed 17 sessions using the BCI-FES, each session was divided in two stages: Calibration and Feedback.

In both stages, the EEG signal was recorded with 8 channels, which were placed on the scalp according to the international 10-20 system: C3, C4, T7, T8, Pz, F3, F4 and Cz. Ground and reference electrodes were positioned in the right and left mastoids, respectively.

The Calibration stage was to identify MI dorsiflexion ERD from the offline analysis of the EEG and the f_{ERD} to be used in the BCI-FES. The subject was comfortable seated and was asked to remain still, avoid blinking and swallowing during the recording. Before starting, the subject was instructed in the MI task, and was asked to perform the MI dorsiflexion guided by a verbal cue given by the therapist. The EEG was recorded based on the experimental protocol suggested by Schalk [12], and lasted 20 min approximately, divided in 3 runs with rest intervals between 1 or 2 min long. Each run included 2 different tasks, the foot dorsiflexion of right and left foot. Every task was repeated 10 times randomly during each run, separated by a random inter-trial interval of 3 to 4 s of duration. During the inter-trial intervals subjects were asked to relax.

EEG recording signals between 8 Hz and 30 Hz were processed using BCI2000 Offline Analysis tool available in BCI2000 Platform [12], configured to make a frequency analysis of EEG using a common average spatial filter and compare the MI task of the affected limb and rest. ERD was studied using the spatial distribution of the coefficient of determination r^2 for a specific frequency represented in topographic maps and encoded in colors. This estimator of the ERD can be computed from the EEG signal spectra associated with rest and limb MI. Values of r^2 close to 1 indicate a very good discrimination of both conditions, while values of r^2 close to 0 are associated to conditions that can be scarcely distinguished [2]. The cortical localization of the ERD related to foot's MI can be identified using the EEG at Cz position [1]. The frequency with highest r^2 at Cz was selected, through visual inspection of the maps, as the f_{ERD} to be used in the BCI-FES.

In the Feedback stage, the BCI-FES was also guided by a verbal cue. The MI task had 3 s of duration. To detect the ERD, the BCI-FES compared the mean EEG amplitude in f_{ERD} during the MI task, which should be lower than the mean EEG amplitude for f_{ERD} in the resting state, with the ERD_threshold configured by the therapist. In order to adequate to possible changes in SMR modulation, the ERD_threshold was updated during the session after each MI task, and it was computed as the mean EEG amplitude in f_{ERD} of the last MI task. If ERD was detected, the FES was activated.

5 Results

The integrated wireless BCI-FES under the first session of use is presented in Fig. 2. It is observed that the Wireless Interface and the FES device are on the table next to the therapist. These two modules could be worn by the patient during gait. The rest of the BCI-FES modules are merged in the computer.

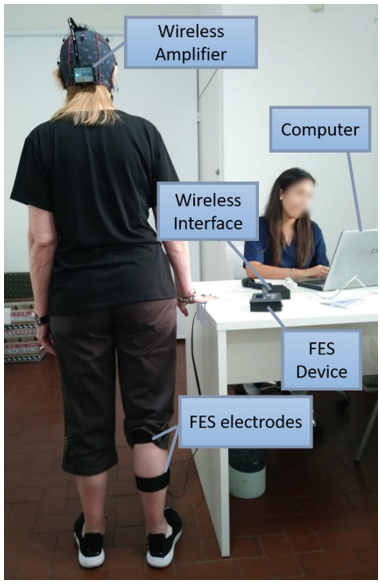

Fig. 2. The wireless BCI-FES in the first session of use of the subject.

In Fig. 3, it is shown the topographic map from the first session Calibration stage, as an example of foot ERD cortical localization. The subject evidenced ERD of the affected limb (right foot) in Cz at f_{ERD} = 8 Hz with r^2 = 0,12.

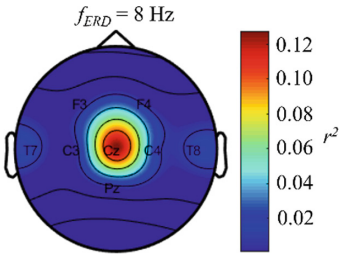

Fig. 3. Topography map corresponding to the identified f_{ERD} corresponding to the affected lower limb at the first session Calibration stage.

The preliminary evaluation of the BCI-FES showed that the patient was able to trigger the FES by performing dorsiflexion MI during a session therapy. The results of the performance metric over the sessions, from the only class available, are presented in Fig. 4. The mean of the TPR was 75 ± 13% and the mean of MI tasks performed in a session was 29 ± 8%. It is observed in Fig. 3 that the TPR fluctuated between sessions and presented a growing trend between the first and the last session.

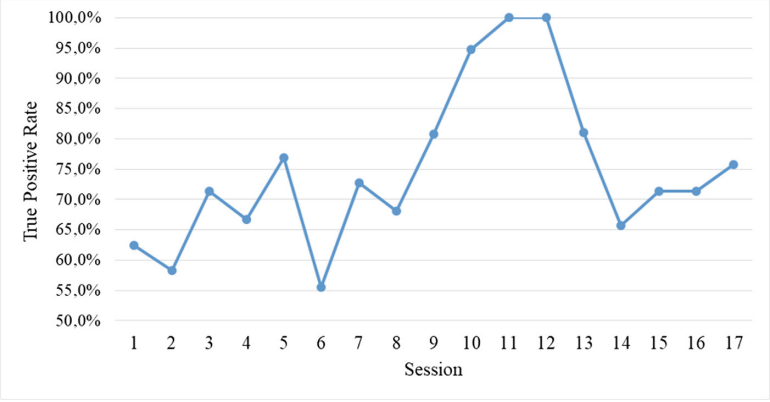

Fig. 4. True positive rate over sessions of using the BCI-FES

6 Conclusions

This paper presented a wireless BCI-FES aimed at lower limb rehabilitation that accomplished the proposed design requirements. The developed system was able to detect lower limb MI ERD in a patient with a neurological condition, and trigger a FES device to give feedback to the user.

BCI combined with FES have been recently developed with neurorehabilitation purposes and promising results, but they were mostly intended for upper limb motor recovery [6, 7]. Additionally, a study presented a portable low-cost BCI with 4 recording electrodes, which can be paired with portable effectors like a FES device, but its performance has been reported only for upper limb [13]. Hence, this paper introduced a novel approach for lower limb motor recovery. Moreover, the robust wireless communication allowed the patient to move freely and encouraged the idea of testing the developed system during gait.

The TPR results obtained from the preliminary evaluation of the wireless BCI-FES in a subject with multiple sclerosis are similar to the results informed by other authors for clinical studies using a BCI combined with FES for upper limb motor recovery in stroke patients. Tabernig et al. [7] informed a mean TPR of 85.4%, the patient who participated in the preliminary evaluation achieved TPR higher than that value in three sessions. Biasiucci et al. [6] presented results of TPR between 73.8% and 93.54%, the patient involved in the preliminary evaluation evidenced TPR in that range in seven of the sessions. Furthermore, the performance metric showed an improvement between

the first and the last session. These results suggest that the proposed system and the methodology for updating the classification threshold, using the last trial of the MI task, could adapt the wireless BCI-FES to patient's dynamic during the session.

In future work, it is possible to evaluate the performance of the BCI-FES in patients with gait impairment to investigate the effects of its use as a tool to promote motor recovery.

Acknowledgment. The authors would like to thank the Fundación Rosarina de Neurorehabilitación, who facilitated access to the patient.

References

1. Pfurtscheller, G., Mcfarland, D.: BCIs that use sensorimotor rhythms. In: Wolpaw, J.R., Wolpaw, E. (eds.) Brain-Computer Interfaces: Principles and Practice, pp. 227–240. Oxford University Press (2012)
2. Carrere, L.C., Tabernig, C.B.: Detection of foot motor imagery using the coefficient of determination for neurorehabilitation based on BCI technology. IFMBE Proc. **49**, 944–947 (2015). https://doi.org/10.1007/978-3-319-13117-7_239
3. Sannelli, C., Vidaurre, C., Müller, K.R., Blankertz, B.: A large scale screening study with a SMR-based BCI: categorization of BCI users and differences in their SMR activity (2019)
4. Do, A.H., Wang, P.T., King, C.E., Schombs, A., Cramer, S.C., Nenadic, Z.: Brain-computer interface controlled functional electrical stimulation device for foot drop due to stroke, pp. 6414–6417 (2012)
5. Ramos-Murguialday, A., Broetz, D., Rea, M., Yilmaz, Ö., Brasil, F.L., Liberati, G., Marco, R., Garcia-cossio, E., Vyziotis, A., Cho, W., Cohen, L.G., Birbaumer, N.: Brain-Machine-interface in chronic stroke rehabilitation: a controlled study. Ann. Neurol. **74**, 100–108 (2014). https://doi.org/10.1002/ana.23879.Brain-Machine-Interface
6. Biasiucci, A., Leeb, R., Iturrate, I., Perdikis, S., Al-Khodairy, A., Corbet, T., Schnider, A., Schmidlin, T., Zhang, H., Bassolino, M., Viceic, D., Vuadens, P., Guggisberg, A.G., Millán, J.D.R.: Brain-actuated functional electrical stimulation elicits lasting arm motor recovery after stroke. Nat. Commun. **9**, 1–13 (2018). https://doi.org/10.1038/s41467-018-04673-z
7. Tabernig, C.B., Lopez, C.A., Carrere, L.C., Spaich, E.G., Ballario, C.H.: Neurorehabilitation therapy of patients with severe stroke based on functional electrical stimulation commanded by a brain computer interface. J. Rehabil. Assist. Technol. Eng. **5**, 205566831878928 (2018). https://doi.org/10.1177/2055668318789280
8. McCrimmon, C.M., King, C.E., Wang, P.T., Cramer, S.C., Nenadic, Z., Do, A.H.: Brain-controlled functional electrical stimulation therapy for gait rehabilitation after stroke: a safety study. J. Neuroeng. Rehabil. **12** (2015). https://doi.org/10.1186/s12984-015-0050-4
9. g.Nautilus wireless biosignal acquisition Homepage. http://www.gtec.at/Products/Hardware-and-Accessories/g.Nautilus-Specs-Features
10. Emotiv EpocFlex flexible wireless EEG system Homepage. https://www.emotiv.com/epoc-flex/
11. Vuckovic, A., Wallace, L., Allan, D.: Hybrid brain-computer interface and functional electrical stimulation for sensorimotor training in participants with tetraplegia: a proof-of-concept study. J. Neurol. Phys. Ther. **39**, 3–14 (2015)

12. Schalk, G., McFarland, D.J., Hinterberger, T., Birbaumer, N., Wolpaw, J.R.: BCI2000: a general-purpose brain-computer interface (BCI) system. IEEE Trans. Biomed. Eng. **51**, 1034–1043 (2004). https://doi.org/10.1109/TBME.2004.827072
13. McCrimmon, C.M., Fu, J.L., Wang, M., Lopes, L.S., Wang, P.T., Karimi-Bidhendi, A., Liu, C.Y., Heydari, P., Nenadic, Z., Do, A.H.: Performance assessment of a custom, portable, and low-cost brain-computer interface platform. IEEE Trans. Biomed. Eng. **64**, 2313–2320 (2017). https://doi.org/10.1109/TBME.2017.2667579

Development of a Serious Game Controlled by Myoelectric Signals

Mariano Sosa[1], Gonzalo Oviedo[1], Juan Manuel Fontana[1,3(✉)], Ronald O'Brien[1], Eric Laciar[2,3], and Leonardo Molisani[1]

[1] Grupo de Acústica y Vibraciones, Facultad de Ingeniería, Universidad Nacional de Rio Cuarto, 5800 Rio Cuarto, Córdoba, Argentina
juanmfontana@ing.unrc.edu.ar
[2] Gabinete de Tecnología Médica, Facultad de Ingeniería, Universidad Nacional de San Juan, San Juan, Argentina
[3] Consejo Nacional de Investigaciones Científicas y Técnicas (CONICET), Godoy Cruz 2290, C1425FQB Cuidad Autónoma de Buenos Aires, Argentina

Abstract. This work presents the initial steps for the development of a serious game aimed at training users of upper limb prosthesis. In this initial phase, a virtual environment consisting of a soccer stadium was developed using Unity game engine. The game emulated the situation of a penalty kick where the users were able to control the direction to which the ball was kicked by contracting the muscles of the forearm. Experiments were performed on able-body subjects to assess their performance executing three series of ten penalties each. A score scale was implemented and the time needed to kick the penalties was measured. The results showed an intuitive and easy to play game, which was determined by the highly satisfactory performance of the subjects controlling the different functions of the game.

Keywords: Myoelectric control · Rehabilitation · Upper limb prosthesis

1 Introduction

Serious games are designed for a different purpose than pure entertainment. They are played according to specific rules and use the entertainment as a way to promote some type of training (i.e. education, health, public policies, etc.) [1]. In the particular case of health [2], these games provide the users useful skills for improving a person's motor ability: (1) they can provide a fun task with incremental levels of difficulty to motivate and prolong the patient's training; (2) they can be customized allowing remote guidance by a therapist or doctor; (3) they can incorporate augmented feedback to optimize learning [3–5].

In particular, serious games with a myoelectric interface (also called myogames) allow controlling different functions of a game using muscular contractions. This type of games represents a suitable alternative both to rehabilitate the upper limb in patients with motor impairment and to train a person's skills for prosthetic use. For that reason, one of the main applications of the myogames is related to the rehabilitation of patients with brain injuries, multiple sclerosis or that have suffered a stroke [6, 7].

© Springer Nature Switzerland AG 2020
C. A. González Díaz et al. (Eds.): CLAIB 2019, IFMBE Proceedings 75, pp. 1171–1177, 2020.
https://doi.org/10.1007/978-3-030-30648-9_152

Myogames are also used for helping amputees to train myoelectric control of an upper limb prosthesis [8, 9]. As an example of this type of myogames, researchers have worked on games that involve playing notes on a guitar, shooting balloons or spacecrafts [10, 11]. Besides making important technological contributions, these studies demonstrated that the incorporation of videogames in the training process has the potential to be more attractive and fun than traditional training paradigms. They can also provide a quantitative feedback of the performance to the user. Likewise, the exercise of practicing myoelectric control in this way could improve the control of complex movements that require more skills.

This paper presents the initial phase on the development of a serious game with a myoelectric interface designed to teach users to control the functions of an upper-limb prosthesis and to strengthen their muscles in order to improve such control. In this initial phase, a virtual environment was developed using Unity, a cross-platform game engine. It consisted of a penalty kick scenario where the users controlled the direction of the soccer ball by contracting the muscles of the forearm. Experiments on non-amputees were performed for tuning and evaluating the overall performance of the game. In addition, both a custom score scale and the time needed to accomplish the task were used as the initial metrics to evaluate the performance of subjects during game playing.

2 Materials and Methods

In this work, a tool was developed to teach and train the skills required to control different functions of a video game using voluntary contractions of the forearm muscles. This game is intended to create an innovative and attractive training process for people to learn to effectively control the functions of an upper-limb prosthesis (i.e. opening and closing the hand). It consisted of a virtual environment and a human-machine interface for myoelectric control, which are described in detail in the following sections.

2.1 Virtual Environment

The virtual environment was implemented in a personal computer using the Unity 3D game engine (https://unity3d.com/), which is an open access tool that allows the development of serious games, also called learning games. With this software, different types of stages can be emulated in which the person can learn and exercise myoelectric control. Specifically, a virtual environment was created in order to simulate a penalty kick in a soccer match (Fig. 1). In such environment, a person was able to control the following functions:

- *Horizontal function (HF)*: the horizontal position of a circular black cursor located in the soccer goal.
- *Vertical function (VF)*: the vertical position of the cursor mentioned above.
- *Kicking function (KF)*: the kick of the ball towards a certain point indicated by the final position of the cursor.

Both HF and VF functions were controlled by the contraction of the flexor and extensor muscles of the wrist located in the forearm. The KF function was controlled by a contraction of high amplitude and short duration of the same flexor muscles. The extensors and the flexors are antagonistic muscles, so the contraction of one of them commanded the movement in one direction whereas the contraction of the other muscle commanded the movement in the opposite direction. Thus, this control strategy decreases the probability of a combined contraction that would cause an undesired movement.

The game consisted of a series of ten penalties kicks where the objective was to get the highest score. At the beginning of each penalty, a circular white and red target was placed in a random position within the soccer goal (Fig. 1). First, the player controlled the HF with the flexion and extension of the wrist and then the VF using the same movements. Each player had to place the black cursor (located initially at the center of the soccer goal) in the center of the target in order to achieve the highest score. The change between the HF and the VF was made by a contraction of short duration and high amplitude, similar to the one used to kick the ball. The myoelectric control strategy implemented for this game was able to control up to 5 functions (move cursor up, down, left, and right and kick the ball) using only two EMG channels as inputs. This is a potential advantage that would allow controlling multiple functions of a prosthesis with a low cognitive burden.

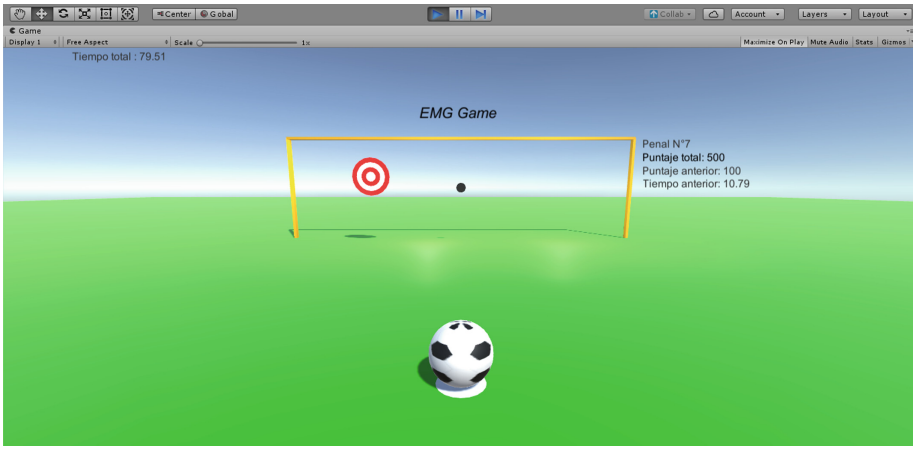

Fig. 1. Virtual environment that simulates a penalty kick scenario. The user can control (a) the position of the black indicator located in the goal; and (b) the moment to kick the penalty.

2.2 Human-Machine Interface

A simple human-machine interface was developed to serve as the input for the virtual environment. As mentioned in the previous section, the contraction of the flexor and extensor muscles of the wrist was used to control the HF and VF functions of the game. These contractions generated an electrical signal, known as electromyography signal

(EMG), captured on the surface of the skin. Therefore, the objective of this interface was to register and process the EMG signals and then transmit them to the PC, where they were used by the virtual environment.

Two MyoWare sensors (www.advancertechnologies.com) along with surface electrodes were used for the acquisition of EMG signals. Each MyoWare sensor contains an instrumentation amplifier connected in a differential configuration that outputs the envelope signal of the raw EMG. This signal was digitized and processed by an AT Mega 2560 microcontroller located on an Arduino board.

Before starting the game, a subject went through a configuration routine to determine the contraction levels needed to activate HF, VF and KF functions. Thresholds were established for HF and VF, which were obtained from the value of the maximum voluntary contraction (MVC) corresponding to the flexion and extension of the wrist. In all cases, such thresholds were established between 60% and 70% of the MVC. The threshold for KF was obtained as the average of the peak value of the derivative of the EMG signal corresponding to three repetitions of a wrist flexion (short duration and high amplitude contraction).

During game playing, the EMG signals were sampled at 10 Hz and processed by the microcontroller to determine the type of movement performed by the subject (wrist flexion or extension) based on the thresholds previously determined. The final decision was transmitted to a PC through a serial communication and served as input to the serious game to control the functions on the screen.

2.3 Experiments

Experiments were carried out for tuning and evaluating the overall performance of the game. There was also a preliminary evaluation of the performance of the players in terms of the score obtained after playing the game and the time necessary to execute a penalty. A total of 5 healthy non-amputees (25 ± 7 years old) participated in the experiments where they performed three series of 10 penalties each. For each penalty, the time taken by the player to kick the ball was recorded. Also, the score obtained after each penalty was also registered, which depended on the proximity of the indicator to the center of the target.

3 Results

The results obtained in the experiments are shown in Table 1. For each series of penalties, the average time required for kicking the penalties was calculated. Such time was measured from the time a subject started to move the cursor towards the center of the target to the time in which the ball was kicked. The table also shows the score obtained by each subject on a maximum of 1000 points for the series of 10 penalties. For each penalty, a score of 100 points was given when the cursor was located at the center of the target and a score of 0 points when the cursor was not located within the target.

Table 1. Results obtained for experiments on five non-amputee subjects. Each subject played three series of 10 penalty kicks each.

Subject	Age	Trial 1		Trial 2		Trial 3	
		$t_{average}$ [s]	Score	$t_{average}$ [s]	Score	$t_{average}$ [s]	Score
1	37	7.758	825	9.088	900	7.924	850
2	25	7.94	1000	6.587	975	7.15	975
3	21	8.879	1000	9.38	1000	7.552	1000
4	20	11.436	850	10.03	875	13.711	950
5	22	13.61	825	14.155	950	12.584	675
Mean	***25.0***	***9.92***	***900***	***9.85***	***940***	***9.78***	***890***
St. Dev.	***7.0***	***2.53***	***91.86***	***2.74***	***51.84***	***3.11***	***132.99***

4 Discussions and Conclusions

In this work, the initial development of a serious video game with a myoelectric interface was presented. The overall objective is to develop an intuitive and easy to use tool that can help users in their training and using of hand prostheses. At this initial stage, a game was developed, consisting of a virtual environment and a human-machine interface for the myoelectric control of the game. The purpose of the virtual environment was to teach users to modulate the muscle contraction levels in order to control an object in the screen. This was facilitated by the visual feedback displayed on the screen, which allowed the users to receive quantitative information about their performance.

Experiments were conducted to determine the reliability and robustness of the game as well as to have an indication of the players' performance. One of the metrics selected to evaluate subjects was a custom score scale that measured how close the cursor was from the center of the target. This score was intended to provide a measure of the subjects' ability to voluntarily control a function. The other metric was the time required to place the black cursor on the target before kicking the penalty (Fig. 1). Such metric was implemented to indicate if the subject improved their control skill over the trials. The results of the experiments (Table 1) showed high scores in all trials (more than 890 points on average over a total of 1000 points) and a slight improvement in the average time as the series progressed. These results may point out that subjects learned the methodology of the game and also learned to control the levels of muscle contractions required to activate the game functions. The most representative cases were subject 2 and 3, which obtained high scores in all trials and significantly improved the average time between the first and the last trial.

In concordance with the experiments, the functions responsible of controlling the horizontal and vertical movement of the cursor responded correctly according to the intentions of the users. This may be an indication of an intuitive and easy to play game. However, two undesired situations were observed during game playing. First, towards the end of the trials, the game did not respond properly to the player intention. This may be due to muscle fatigue, which caused that the amplitude of the EMG signal did not exceed the previously configured threshold and caused a delay in the positioning of

the indicator. Second, due to the sequential programming of the game, subjects were not able to change the position of the cursor once it was set in a specific point. That is, subjects were able to move the cursor first horizontally and then vertically and finally kicking the ball without the possibility of return to the previous step. These undesired situations during the game will be considered to continue developing the game.

The movements trained for playing the developed serious game would subsequently be translated to control a certain function of prosthesis (i.e. hand opening/closing). The contraction of high amplitude and short duration trained to kick the ball and change between functions would be implemented as an EMG switch that could allow the user to change from one function to another of the prosthesis.

Acknowledgments. This work was partially supported by a PPI 2016-2018 research grant from the Science and Technology Secretary, National University of Rio Cuarto and for a PID research grant from the Ministry of Science and Technology of Córdoba, Argentina.

Conflict of Interest. The authors declare that there is no conflict of interest.

References

1. Zyda, M.: From visual simulation to virtual reality to games. Computer **38**, 25–32 (2005). https://doi.org/10.1109/MC.2005.297
2. Graafland, M., Schraagen, J.M., Schijven, M.P.: Systematic review of serious games for medical education and surgical skills training. BJS **99**, 1322–1330 (2012). https://doi.org/10.1002/bjs.8819
3. Rahmani, E., Boren, S.A.: Videogames and health improvement: a literature review of randomized controlled trials. Games Health J. **1**, 331–341 (2012). https://doi.org/10.1089/g4h.2012.0031
4. Holden, M.K.: Virtual environments for motor rehabilitation: review. Cyberpsychol. Behav. **8**, 187–211 (2005). https://doi.org/10.1089/cpb.2005.8.187
5. Garcia-Agundez, A., Folkerts, A.-K., Konrad, R., Caserman, P., Tregel, T., Goosses, M., Göbel, S., Kalbe, E.: Recent advances in rehabilitation for Parkinson's disease with exergames: a systematic review. J. NeuroEng. Rehabil. **16**, 17 (2019). https://doi.org/10.1186/s12984-019-0492-1
6. Ghassemi, M., Triandafilou, K., Barry, A., Stoykov, M.E., Roth, E., Mussa-Ivaldi, F.A., Kamper, D.G., Ranganathan, R.: Development of an EMG-controlled serious game for rehabilitation. IEEE Trans. Neural Syst. Rehabil. Eng. **27**, 283–292 (2019). https://doi.org/10.1109/TNSRE.2019.2894102
7. Sadeghi Esfahlani, S., Muresan, B., Sanaei, A., Wilson, G.: Validity of the Kinect and Myo armband in a serious game for assessing upper limb movement. Entertain. Comput. **27**, 150–156 (2018). https://doi.org/10.1016/j.entcom.2018.05.003
8. Smith, P.A., Dombrowski, M., Buyssens, R., Barclay, P.: Usability testing games for prosthetic training. In: 2018 IEEE 6th International Conference on Serious Games and Applications for Health (SeGAH), pp. 1–7 (2018). https://doi.org/10.1109/SeGAH.2018.8401376
9. van Dijk, L., van der Sluis, C.K., van Dijk, H.W., Bongers, R.M.: Task-oriented gaming for transfer to prosthesis use. IEEE Trans. Neural Syst. Rehabil. Eng. **24**, 1384–1394 (2016). https://doi.org/10.1109/TNSRE.2015.2502424

10. Armiger, R.S., Vogelstein, R.J.: Air-guitar hero: a real-time video game interface for training and evaluation of dexterous upper-extremity neuroprosthetic control algorithms. In: 2008 IEEE Biomedical Circuits and Systems Conference, pp. 121–124 (2008). https://doi.org/10.1109/BIOCAS.2008.4696889
11. Anderson, F., Bischof, W.F.: Augmented reality improves myoelectric prosthesis training. Int. J. Disabil. Hum. Dev. **13**, 349–354 (2014). https://doi.org/10.1515/ijdhd-2014-0327

Design of a Portable Electric-Stimulation System to Reduce the Essential Tremor on the Hand

Reynol García-Guadarrama[1(✉)] and Rigoberto Martínez-Méndez[2]

[1] Faculty of Medicine,
Autonomous University of the State of Mexico (UAEM), 50180 Toluca, Mexico
arnol_l00_8@hotmail.com
[2] Faculty of Engineering,
Autonomous University of the State of Mexico (UAEM), 50180 Toluca, Mexico
rigo@ieee.org

Abstract. The essential tremor syndrome is a nerve disorder affecting around 77 million people worldwide. The causes are still not completely clear and there is no cure. Essential tremor is characterized by an uncontrollable "shaking" that affects greatly the quality of life of patients. The main treatments nowadays are drugs or surgery which have collateral effects, are expensive and does not fit to all the patients. Electrostimulation has emerged as an alternative treatment, however, the main drawback of this technique is the fatigue caused on the stimulated muscles as well as the difficult to make natural movements due to the stimulation. In this work is proposed a portable transcutaneous electrostimulation device based on a new type of stimulation that reduces the muscle fatigue by stimulating afferents pathways instead the muscle. The proposed device generates a bipolar current signal, 100 Hz pulse width of 30 μs and current from 0 to 20 mA. In this work is presented the methodology of design, preliminary results of the proposed circuit and the mechanical design of the portable device. The main contribution of this work is the design of a portable stimulator aiming to expand the research related to this technique.

Keywords: Portable device · Essential tremor · Afferent pathways stimulation

1 Introduction

Essential tremor (ET) is a movement disorder that causes an oscillation in one or more parts of the body, due to a contraction that occurs between the agonist and antagonist muscles [1]. The origin of this disorder is still not completely understood, however it has a strong link with genetics load [2]. ET usually affects several body segments such as upper extremities, head, jaw, larynx, trunk, face and lower extremities [3]. The tremor usually starts with the beginning of voluntary movements and rarely appears during the rest.

It is estimated that the ET affects 1% of the world population, is the most common tremor and it is 20 times more frequent that Parkinson tremor [4]. Although ET is not a

© Springer Nature Switzerland AG 2020
C. A. González Díaz et al. (Eds.): CLAIB 2019, IFMBE Proceedings 75, pp. 1178–1183, 2020.
https://doi.org/10.1007/978-3-030-30648-9_153

life treat disease, this disorder heavily reduce the quality of life in patients, causing depression, loss of autonomy and impairs, sometimes completely, the execution of natural motor tasks [3].

The etiology of the disease is not completely defined. Several factors such as environment, exposure to toxic agents, coexistence with pets and even the use of medications, such as intravenous aminophylline and immobilization of the wrist, have been postulated as possible detonating causes or the origin of essential tremor, but to date, there is not a clear cause-effect relationship [5]. Thus, to date there is no cure for essential tremor and, patients only have two main type of treatments: medication or surgery.

Aiming to find an alternative treatment for ET, several proposals have emerged based on biomedical technology, electronics and control. Approaches such as suppression of tremor by mechanical loading [6] reduce the tremor but must be designed specifically for each patient, and this technique cause muscle fatigue. Other technique is the electro stimulation, which stimulates the agonist and antagonist muscles controlling the stiffness of the limb and thus, reducing the tremor [7]. However, this approach also causes muscle fatigue and unnatural movements. Recently, it was proposed the stimulation of afferent pathways as an alternative [8]. This technique avoids the muscle fatigue, the stiffness of the limb, thus allowing more natural movements and is less invasive for patients.

The methodology employed by this new type of stimulation uses a 100 Hz squared wave, a width pulse between 400 and 300 μs with currents low enough to avoid muscle stimulation, depending on the subjects (below 20 mA). The signals onset was driven by electromyography signals detecting the tremor from the muscles. The researchers concluded from their work that it was achieved around 75% of tremor suppression but also, that further research is required to completely validate their technique [8]. One of the drawbacks of this Dideriksen *et al.* work [8] is the necessity of several commercial devices to apply the stimuli, thus limiting the application of this technique only to laboratory environments.

In this work is proposed the design of a portable electronic device to provide such stimulation technique aiming to contribute in two ways: to improve the application of the technique, allowing to apply it in environments outside laboratory and to reproduce the technique in more patients diagnosed with ET.

2 Methods

The proposed system is based on the block diagram from Fig. 1. It is based on two main stages, an electromyography signal detector to synchronize the stimulation signals and an electrical pulse generator.

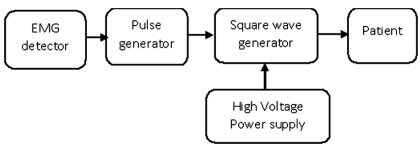

Fig. 1. Block diagram of the process for electrical stimulation

The pulse generator relies on a high voltage (more than 80 V) to generate current pulses higher enough to stimulate the afferent pathways.

The EMG signal acquisition circuit is based on that proposed by Wang *et al.* [10] (see Fig. 2).

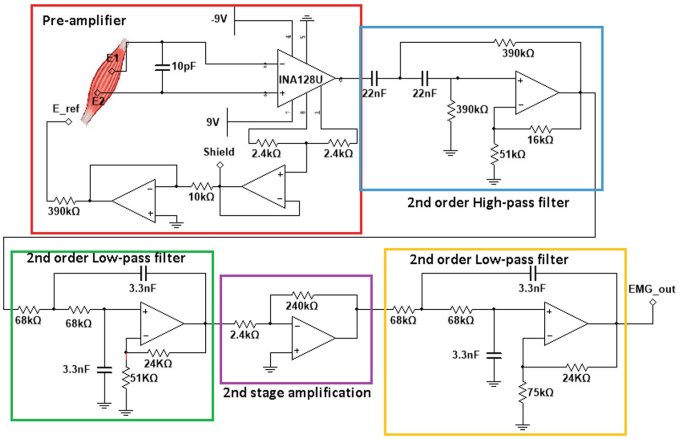

Fig. 2. Circuit diagram for the acquisition of the EMG signal, modified from [10].

The signal obtained from the EMG circuit should be rectified (this stage is not shown in this paper) and feed to a comparator to detect the muscle activation by threshold comparison. The output of the comparator activate the current pulse generator. Both, the comparator and the pulse generator are implemented using an Arduino Uno board. The Arduino also generates complementary pulses to drive a circuit similar to a modified H-bridge to generate a square wave to stimulate to the patient. This circuit is shown in Fig. 3 and is based on the work proposed by Leyva *et al.* [11]. This circuit is capable to control the current applied to the patient by modifying the amplitude of the control pulses (P1 and P2).

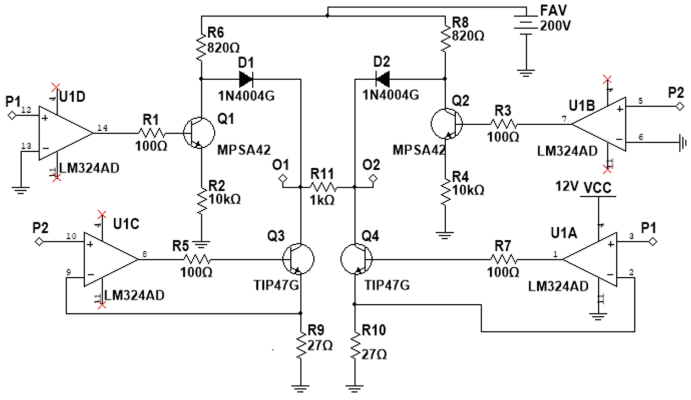

Fig. 3. Electronic diagram of the circuit to generate the stimuli signal.

The control of the duration of pulses P1 and P2 allow to generate different patterns and frequencies of a square wave to stimulate the patient. The control of the amplitude of P1 and P2 allow to control the current applied to the patient. According to the work of Dideriksen *et al.* [8], in order to apply an afferent pathways stimulation, it is required a bipolar signal of 100 Hz, pulse width variable between 0 and 30 μs with variable current from 0 mA to 20 mA. The current level for each patient is determined manually, first is applied a stimulation increasing the current level until the patient start to feel the stimuli sensation, then, the current level is decreased until the patient does not feel the stimulation anymore. Thus, the stimulation will be only for the afferent pathways without causing fatigue in the patient.

The high voltage source is implemented using a boost topology as shown in Fig. 4.

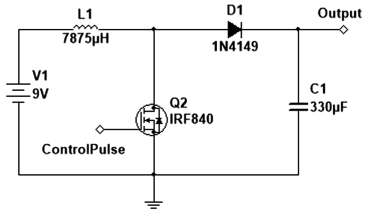

Fig. 4. Boost circuit for the high voltage power supply.

The control pulse will be generated using the Arduino board aforementioned, thus the output voltage can be controlled if required.

3 Results

The proposed circuitry was implemented and tested. Figure 5 shows and example of the generated waveforms. In this figure can be see a biphasic square signal, 100 Hz in frequency, pulse width of approximately 62 μs and 61 V peak to peak. For this test the square wave was applied to a 1 kΩ resistance, thus, the current applied was around 30 mA peak. Thus, it can be inferred that the designed circuit is capable to apply stimulation signals as suggested by [8].

The whole system is proposed to be encapsulated in a plastic case that should be attached to the arm. The device will have the necessary buttons and knobs to control the frequency, current and voltage amplitude necessary for each patient. The stimulation electrodes and EMG electrodes should be attached to the patient on the wrist flexor and extensor muscles. Figure 6 shows the preliminary design of the proposed device. This design was developed in SolidWorks (Dassault Systèmes, ver. 2018). The blue arrow points to the case of the device, red arrows point to the position of the electrodes. It is proposed that the electrodes are made of fabric substrate in order to reduce the possible discomfort to the patient. This part of the project is still under development.

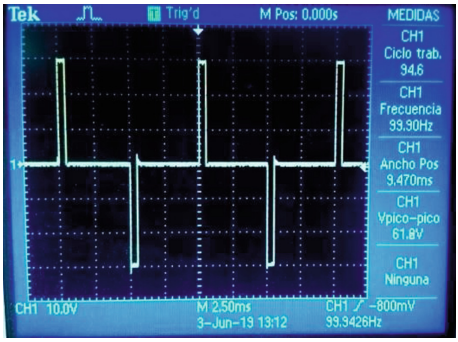

Fig. 5. Rectangular wave signal with an amplitude of 100 V peak to peak developed at Multisim

Fig. 6. Diagram of the case to fit the patient's arm.

4 Discussion and Conclusions

This work presents the design and preliminary results of an electronic circuit to stimulate patients suffering from essential tremor. The presented approach makes it possible to implement a new stimulation technique in a less intrusive way, compared to the original methodology, which requires several separated devices (EMG acquisition systems, electrical stimulators, etc.) [8]. The main advantage of this new stimulation technique [8] is the reduction of fatigue on the muscles of the patients, as occurs using conventional electrical stimulations such as those reported in several works [7, 9, 12].

The proposed device was designed in accordance with anthropometric measures recommended for a Latin American population from 20 to 29 years [13], so that the device is aimed to be ergonomic and to fit to Latin American patients. The final design of the proposed device must comply with the electrical safety standards, such as IEC60601-2-10, however, due to the currently stage of the project, this is not addressed in this paper.

The main limitation of the stimulation technique until now, according to the original proponents [8], is that it reduced the tremor only for the 75% of the subjects treated. However, as the authors stated, it is necessary to carry out further research on this technique in a larger population (they only applied the technique in 9 patients).

Thus, the development of the device proposed in this paper will be useful to extend this research in more patients in a more comfortable way and in environments outside laboratories, it could be applied in small clinics, or even in the patient's home.

Our results, although still limited to the electrical stimulator, allow us to infer that it is possible to develop a low-cost, portable transcutaneous electrical stimulation system for patients with ET. As it is known, electrical stimulation is a temporary treatment to reduce tremor, so a portable and low-cost design of this stimulation technique will contribute to a better quality of life in the ET patient.

References

1. National Tremor Foundation: What is Essential Tremor (ET)? (2018). https://tremor.org.uk/what-is-essential-tremor.html. Accessed 13 May 2019
2. Clark, L.N., Louis, E.D.: Essential tremor. Handb. Clin. Neurol. **147**, 229–239 (2018)
3. Venegas, P.F., Gómez, R.R., Sinning, O.M.: Temblor esencial: Una revisión crítica. Rev. Chil. Neuro-Psiquiatr. **48**(1), 58–65 (2010)
4. Louis, E.D., Ferreira, J.J.: How common is the most common adult movement disorder? Update on the worldwide prevalence of essential tremor. Mov. Disord. **25**(5), 534–541 (2010)
5. De La cruz-Estrada, E., Otero-Siliceo, E.: Temblor esencial. Arch. Neurosci. **11**(3), 194–204 (2006)
6. Rocon, E., Manto, M., Pons, J., Camut, S., Belda, J.M.: Mechanical suppression of essential tremor. Cerebellum **6**(1), 73–78 (2007)
7. Popović Maneski, L., et al.: Electrical stimulation for the suppression of pathological tremor. Med. Biol. Eng. Comput. **49**(10), 1187–1193 (2011)
8. Dideriksen, J.L., et al.: Electrical stimulation of afferent pathways for the suppression of pathological tremor. Front. Neurosci. **11**, 178 (2017)
9. Heo, J.-H., et al.: Sensory electrical stimulation for suppression of postural tremor in patients with essential tremor. Biomed. Mater. Eng. **26**(s1), S803–S809 (2015)
10. Wang, J., Tang, L., Bronlund, J.E.: Surface EMG signal amplification and filtering. Int. J. Comput. Appl. **82**(1), 15–22 (2013)
11. Leyva-Gutierrez, A.-E.: Diseño e implementación de la etapa de potencia para un sistema de estimulación eléctrica funcional/medular para rehabilitacion de miembro superior. Universidad Autónoma del Estado de México, Toluca, Estado de México (2018)
12. Grimaldi, G., Camut, S., Manto, M.: Functional electrical stimulation effect on upper limb tremor. Int. J. Bioelectromagn. **13**, 123–124 (2011)
13. Chaurand, R.Á., León, L.R.P., Muñoz, E.L.G.: Dimensiones antropométricas de población latinoamericana : México, Cuba, Colombia, Chile, 2da edición. Universidad de Guadalajara, Centro Universitario de Arte, Arquitectura y Diseño, Guadalajara, Jalisco, México (2007)

Mechanomyography Spasticity Assessment of Flexor and Extensor Wrist Muscles for the Classification of Boccia Athletes in Para Sports: A Pilot Study

Elgison da Luz dos Santos[1(✉)], Maria de Fátima Fernandes Vara[1], Maira Ranciaro[1], Gustavo Tanaka Zelaga[2], Amanda Mayara Pereira Gomes[2], Isabel Cristina Bini[2], Guilherme Nunes Nogueira Neto[1], Eddy Krueger[3], and Percy Nohama[1,4]

[1] Pontifícia Universidade Católica do Paraná, Curitiba, Paraná, Brazil
elgisantos20@gmail.com, percy.nohama@gmail.com
[2] Centro Universitário UniDomBosco, Curitiba, Paraná, Brazil
[3] Universidade Estadual de Londrina, Londrina, Paraná, Brazil
[4] Universidade Tecnológica Federal do Paraná, Curitiba, Paraná, Brazil

Abstract. The Paralympic boccia is a sport played by athletes with spasticity and severe impairment in the four limbs. Three (BC1, BC2, and BC3) of the four classes in boccia allow People with Cerebral Palsy (CP) to participate. The ranking is performed manually through the American Spasticity Scale. Like all qualitative scales, however, this evokes controversy among the evaluation board members who apply it, altering the classification of the athletes. A helpful option would be the use of mechanomyography (MMG), a method of acquiring muscle vibrations quantitatively based on accelerometers. Thus, the objective of this article was to conduct a pilot study analyzing the differences in the MMG signals of flexors and extensors muscles between two groups: 6 boccia athletes with spasticity and 6 non-impaired. Volunteers remained seated on the wheelchair, with their elbow bent close to 90°. They were verbally stimulated to perform the manual grip by pressing the evaluator's hand while the MMG signals were recorded and stored. The mean MMG_{RMS} descriptor was calculated for each signal. The experimental tests indicated differences between the two groups. For the spasticity group: 0.4058 and 0.4258 mV for the left flexor and extensor wrist muscles, respectively; 0.4215 and 0.4529 mV for the right flexor and extensor wrist muscles, respectively. For the non-impaired group, the MMG_{RMS} was 0.3694 and 0.3945 mV for the left flexor and extensor wrist muscles, respectively; 0.35033 and 0.3728 mV for the right flexor and extensor wrist muscles, respectively. Thus, these results indicate greater spasticity for the spastic group and so, volunteers classification in lower levels.

Keywords: Mechanomyography · Spasticity · Wrist · Boccia

© Springer Nature Switzerland AG 2020
C. A. González Díaz et al. (Eds.): CLAIB 2019, IFMBE Proceedings 75, pp. 1184–1190, 2020.
https://doi.org/10.1007/978-3-030-30648-9_154

1 Introduction

Paralympic boccia is a sport played by athletes with severe impairment in all four limbs and spasticity. Three of the four classes in boccia allow People with Cerebral Palsy to participate. Athletes of classes BC1 and BC2 hold the ball to the throw. In class BC3, assistive devices, such as a ramp, are allowed – in this case, the athlete may have strength, but not enough coordination to throw a ball manually [1]. These classifications are based on functional evaluations carried out by skilled physiotherapists using the ASAS scale (Australian Spasticity Assessment Scale), but still in a qualitative manner, which sometimes leads to disagreement among physiotherapists as to which class an athlete can belong to. This may have an impact on winning a Paralympic medal. Faced with the subjectivity of the evaluation process, quantitative data are performed and recommended. Quantitative measures of spasticity can be taken by biomechanical and neurophysiological approaches [2–4]. The biomechanical approaches use high-cost devices (such as isokinetics), a restriction that frequently makes their use infeasible in places of classification before the competition. The neurophysiological approaches take into account the neural aspects, so that further clarification of the correlation between this approach and clinical findings is still required. Thus, there are few quantitative studies on the analysis of spasticity of boccia athletes, which could abate or moderate the divergence during classification.

One option for quantitative analysis, which is currently being studied, is mechanomyography (MMG). MMG is a non-invasive technique that, by means of accelerometric sensors, registers muscle vibrations, and has been used in several studies to provide information on muscle strength production, mechanical properties of the muscular system, motor control, muscular atrophy, spasticity, muscular fatigue and other applications [5]. Authors such as Beck et al. [6] and Alves et al. [7] have already demonstrated the effectiveness of MMG for the analysis of muscle contraction.

Therefore, the goal of this study was to investigate the feasibility of using MMG as a quantitative method to evaluate the spasticity in wrist flexors and extensors muscle of boccia athletes during manual gripping.

2 Methods

This study is part of a larger project approved by the Human Research Ethics Committee of Pontifícia Universidade Católica do Paraná (CEP-PUCPR) under register 2.745.072/2018. For all procedures, instruction and familiarization were offered when necessary. Data collection was carried at Association of Physically Disabled People of Paraná (ADFP).

Twelve volunteers were selected, divided into two groups: (i) Cerebral Palsy Group (CP), (n = 6, 3 male, 3 female), including Paralympic athletes BC2 and BC3, of both genders, with spasticity; (ii) non-impaired group (NI), (n = 6, 4 male, 2 female), including healthy individuals, ages between 18 and 70 years, of both genders.

2.1 Mechanomyography Acquisition System

For data collection, an MMG equipment, developed by Nogueira-Neto [8] was used, composed by a Freescale MMA7260Q triaxial accelerometers (13 × 18 mm, 0.94 g) with the sensitivity of 800 mV/G (in 1.5 G mode and G = 9.8 $m.s^{-2}$). The custom hardware provided 2x amplification and a 3rd order 5–50 Hz Butterworth filter. A LabVIEW® virtual instrument acquired the MMG signals through a National Instruments™ NI USB-6221 acquisition board at a sampling frequency of 1 kHz.

2.2 Data Collection

Two MMG sensors were positioned on the volunteer. Sensor 1 was fixed on the skin surface, on the motor point of the wrist flexors and sensor 2, on the motor point of the wrist extensors (Fig. 1-A).

The volunteer remained seated in the wheelchair, with their elbow bent close to 90°, forearm in neutral position and stabilized by the wheelchair's backrest (Fig. 1-B). The volunteer was instructed to maintain the muscles as maximally relaxed as possible for 3 s and, after this period, he/she was verbally stimulated to perform the manual grip by pressing the evaluator's hand. Simultaneously, the MMG signals were recorded and stored. The test was performed in two replicates and considered the mean of both MMG_{RMS} signals.

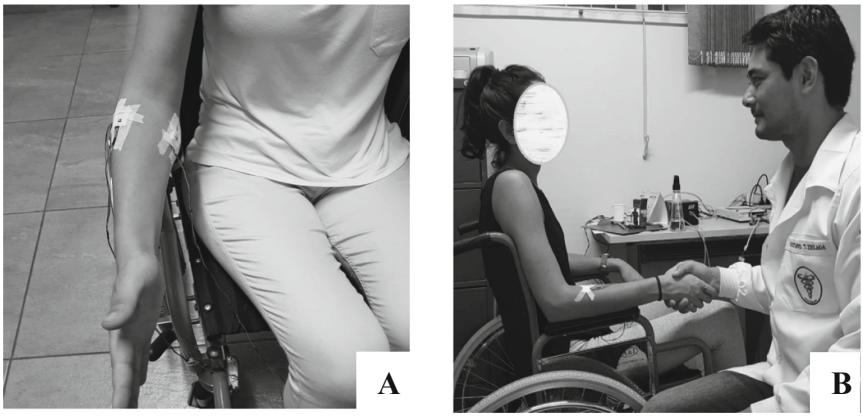

Fig. 1. Volunteer's position during the data collection (A) and sensor position (B).

2.3 Data Processing

Signals were selected and processed using MATLAB® software (MathWorks®, Inc. v. R2017b). The analysis window was in the range 1–4 s, with 4000 samples. The triaxial MMG sensor registered vibrations in three orthogonal directions: perpendicular (Z), transverse (X) and longitudinal (Z) to muscle fibers. The MMG_{RMS} was determined for each axis. Then, the MMG_{RMS} 3D module was determined for both CP and NI groups.

3 Results

Figures 1 and 2 show the acquisition of the MMG signals, without processing, for the three axes of muscle vibration of a volunteer. Figure 2 shows the MMG signal for the flexor and extensor muscles of a NI group's volunteer. Figure 3 shows the MMG signal of the flexor muscle and extensor muscle of a CP group's volunteer. These figures were generated to illustrate the differences of the signals between the investigated volunteers and also between the muscular groups.

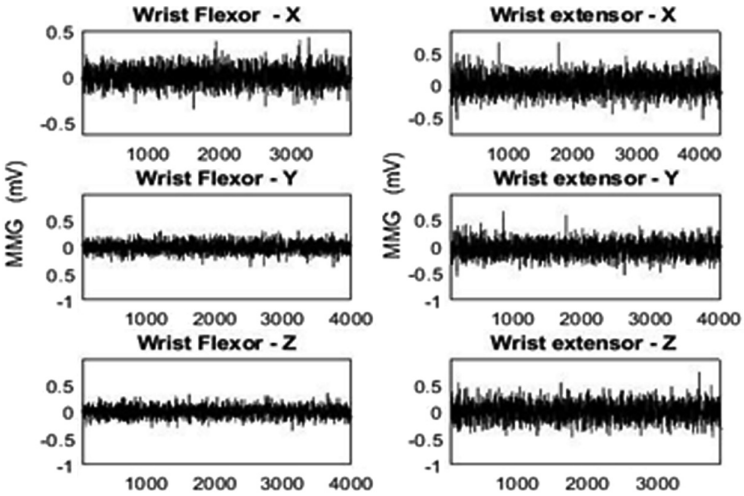

Fig. 2. MMG signal of muscle vibration of a non-impaired (NI) volunteer.

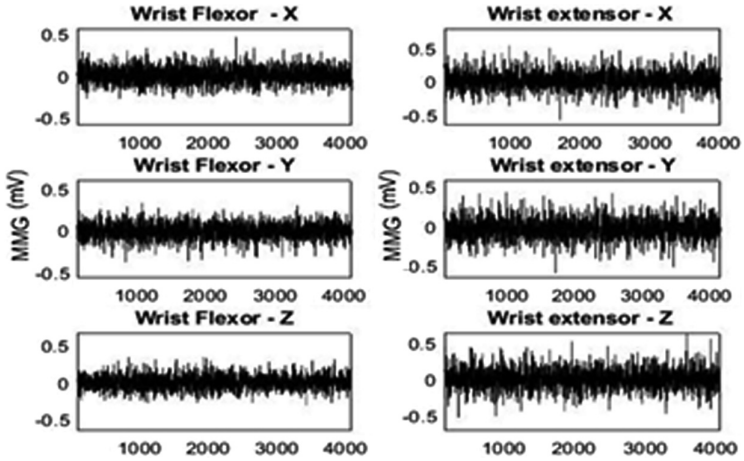

Fig. 3. MMG signal of muscle vibration of a CP volunteer.

Table 1 shows the magnitude of the MMG_{RMS} for each volunteer, followed by the MMG_{RMS} 3D module for each volunteer of both CP and NI groups.

Table 1. MMG_{RMS} 3D module for NI and CP groups.

Group	Volunteer	Flexor left (mV)	Extensor left (mV)	Flexor right (mV)	Extensor right (mV)
CP group	CP_1	0.5119	0.5204	0.5342	0.5420
	CP_2	0.5178	0.5508	0.5618	0.5473
	CP_3	0.4776	0.4827	0.3912	0.4093
	CP_4	0.2624	0.2854	0.4281	0.4432
	CP_5	0.3646	0.3851	0.2813	0.3486
	CP_6	0.3001	0.3301	0.4043	0.4269
Mean CP group		**0.4058**	**0.4258**	**0.4335**	**0.4529**
NI group	NI_1	0.1585	0.2312	0.1603	0.2165
	NI_2	0.3259	0.3496	0.3621	0.3883
	NI_3	0.4864	0.4999	0.3874	0.4016
	NI_4	0.4148	0.4190	0.3580	0.3611
	NI_5	0.40422	0.4113	0.4944	0.4934
	NI_6	0.4269	0.4558	0.3305	0.3761
Mean NI group		**0.3694**	**0.3945**	**0.3503**	**0.3728**

4 Discussion

The goal of the research described in this article was to investigate possible differences in the MMG signal of wrist flexors and extensors muscles between boccia athletes who present spasticity and non-committed athletes, in order to assist, in the future, in the classification of the athlete for the Paralympic Games, since the traditional manual testing cause divergences due to its subjectivity. It is possible to observe in Table 1 that the resultant mean MMG_{RMS} equivalent voltage for CP group was 0.4058 mV to the left wrist flexor muscles and 0.4258 mV to left wrist extensor muscles, 0.4215 mV to the right wrist flexor muscles and 0.4529 mV to right wrist extensor muscles. Still in Table 1, the mean MMG_{RMS} modulus of NI group was 0.3694 mV to left wrist flexor muscles, 0.3945 mV to left wrist extensor muscles, 0.3503 mV to right wrist flexor muscles, and 0.3728 mV to right wrist extensor muscles.

Mean MMG_{RMS} 3D module of the CP group was greater than the NI group. These results show that MMG can identify the difference between the vibration of muscles of healthy people and people with spasticity. This can also be observed in Fig. 1 so that the amplitude of the signals without processing of the NI group is larger than the CP group. This difference may be related to the changes in muscle mechanical properties and which may influence muscle vibration. Thus, the results corroborate previous studies that investigated the correlation between the assessment of spasticity by the manual test and the mechanomyography signals [9–11].

The data were not analyzed statistically because the small sample, but with the sensitivity of the sensor, variations are observed in relation to the mean of the signals, showing the differences between the muscular contractions of volunteers with and without spasticity.

Table 1 also shows that there are differences between the volunteers of the CP group, in which volunteer CP_1 presents a MMG_{RMS} value greater than the others, for both arms, indicating greater spasticity. On the other hand, volunteers CP_3 and CP_5 have greater spasticity in the left wrist than in the right one. The opposite occurred with volunteers CP_4 and CP_6 since both had greater spasticity in the right wrist. In the para sport classification, these volunteers are classified as B2 or B3, volunteer CP_1 to CP_3 are classified as B3, whereas volunteers CP_4 to CP_6 are classified as B2. For this classification other functional movements are also taken into account. Therefore, a larger study, with more muscles analyzed, is necessary to correlate MMG with this classification.

According with Krueger et al. [9], the amplitude of MMG signals increased significantly in subjects with some degree of spasticity (MAS "2", for instance) compared to subjects without spasticity (MAS "0"). Santos et al. [10] investigated the correlation between MAS groups and MMG signals in both time and frequency domains and showed correlation between MAS levels and MMG amplitude in the time domain. Wang et al. [11] used MMG and EMG to evaluate the spasticity of the elbow of post-stroke patients in association with a vector support machine (SVM) and showed correlation between MAS and level of spasticity. However, authors mentioned above didn't investigate wrist flexor and extensor muscles regarding the spasticity, neither in relation to boccia athletes.

Based on this pilot study, it is possible to observe that MMG is sensitive to identify differences between muscle contractions of NI and CP subjects, and some differences between the CP classes for spasticity in each limb. Finally, the use of MMG as an extra resource for clinical evaluation of spasticity is intended to help prevent divergences between evaluators, and contribute to higher safety from rehabilitation to the classification of functionality in sports.

5 Conclusion

There are few studies that related the mechanomyographic signals between Cerebral Palsy and those with no impairment, and no study attempting to use this technology with athletes. Considering the results of this study, it is possible to observe that the MMG signal presented differences between the two groups, during the movement of adhesion, being greater in the CP group, besides differences among CP volunteers. More studies will be necessary to determine the spasticity difference between CP persons and CPs and non-impaired groups, and to use MMG as a means for defining category levels in the Paralympic Games.

Acknowledgment. The authors would like to thank the National Council for Scientific and Technological Development (CNPq) and Araucária Foundation (FA) for the scholarships and

financial resources. This study was financed in part by the Coordenação de Aperfeiçoamento de Pessoal de Nível Superior - Brasil (CAPES) - Finance Code 001.

References

1. BISFED – Boccia International Sports Federation. Classification Rules. http://www.bisfed.com/wp-content/uploads/2014/02/Boccia-Classification-Rules-3rd-Edition-2017.pdf. Accessed 11 May 2019
2. Gordon, L.M., Keller, J.L., Stashinko, E.E., Hoon, A.H., Bastian, A.J.: Can spasticity and dystonia be independently measured in cerebral palsy? Pediatr. Neurol. **35**(6), 375–381 (2006)
3. Pandyan, A.D., Price, C.I., Rodgers, H., Barnes, M.P., Johnson, G.R.: Biomechanical examination of a commonly used measure of spasticity. Clin. Biomech. **16**(10), 859–865 (2001)
4. Lee, H.M., Chen, J.J.J., Ju, M.S., Lin, C.C.K., Poon, P.P.W.: Validation of portable muscle tone measurement device for quantifying velocity-dependent properties in elbow spasticity. J. Electromyogr. Kinesiol. **14**(5), 577–589 (2004)
5. Krueger, E., Scheeren, E.M., Nogueira-Neto, G.N., Button, V.L.S.N., Nohama, P.: Advances and perspectives of mechanomyography. Braz. J. Biomed. Eng. **30**(4), 384–401 (2014)
6. Beck, T.W., Housh, T.J., Cramer, J.T., Weir, J.P., Johnson, G.O., Coburn, J.W., Malek, M. H., Mielke, M.: Mechanomyographic amplitude and frequency responses during dynamic muscle actions: a comprehensive review. BioMed. Eng. OnLine **4**(67), 1–23 (2005)
7. Alves, N., Sejdić, E., Sahota, B., Chau, T.: The effect of accelerometer location on the classification of single-site forearm mechanomyograms. BioMed. Eng. OnLine **9**(23), 1–14 (2010)
8. Nogueira-Neto, G.N.: Viabilidade do emprego de mecanomiografia no controle motor artificial em lesados medulares empregando estimulação elétrica neuromuscular. Tese de Doutorado - Programa de Pós-Graduação em Engenharia Elétrica - Universidade Estadual de Campinas, Campinas/SP, Brazil (2013)
9. Krueger, E., Scheeren, E.M., Nogueira-Neto, G.N., Button, V.S.N., Nohama, P.: A new approach to assess the spasticity in hamstrings muscles using mechanomyography antagonist muscular group. In: 34th Annual International Conference of the Institute of Electrical and Electronics Engineers Inc. (IEEE): Engineering in Medicine and Biology Society (EMBC), pp. 2060–2063. IEEE, San Diego (2012)
10. Santos, E.L., Santos, M.C., Krueger, E., Nogueira-Neto, G.N., Nohama, P.: Mechanomyography signals in spastic muscle and the correlation with the modified Ashworth scale. In: 38th Annual International Conference of the Institute of Electrical and Electronics Engineers Inc. (IEEE): Engineering in Medicine and Biology Society (EMBC), pp. 3789–3792. IEEE, Orlando (2016)
11. Wang, H., Wang, L., Xiang, Y., Zhao, N., Li, X., Chen, S., Lin, C., Li, G.: Assessment of elbow spasticity with surface electromyography and mechanomyography based on support vector machine. In: 39th Annual International Conference of the Institute of Electrical and Electronics Engineers Inc. (IEEE): Engineering in Medicine and Biology Society (EMBC), pp. 3860–3863. IEEE, Seogwipo (2017)

Postural Tremor Reduction System Design for Parkinson's Disease Patients

María José Enciso Lopez[1]
and Ángel Luis Rodríguez Morales[2(✉)]

[1] Licenciatura en Tecnología, Universidad Nacional Autónoma de México, Querétaro, Mexico
mjell996@gmail.com
[2] Centro de Física Aplicada y Tecnología Avanzada, Universidad Nacional Autónoma de México, Querétaro, Mexico
alrodriguez@fata.unam.mx

Abstract. Parkinson's Disease is a neurodegenerative disease that affects fine movement control. It is generated by cellular death in the *subtantia nigra* which causes a decrement on the levels of dopamine in the body.

Most treatments are based on the dosage of dopamine precursors or substitutes. These treatments alleviate the symptoms, such as the postural tremor, which is the most common in Parkinson's disease. The downside to these treatments is, after approximately five years of usage, it turns ineffective, having to increment the dosage. It also has second-hand effects, such as vomit, loss of memory and dementia.

Other treatments include movement therapy for bradykinesia and the use of orthosis for tremor suppression.

The current orthosis has a constant opposition to the movement. This opposition generates fatigue and after time, muscular injury.

To avoid muscular fatigue and reduce the tremor, an orthotic system with an adaptable friction coefficient was designed to diminish the tremor amplitude in upper limbs produced by Parkinson's disease in the first and second stages. We developed a mathematical model to describe the arm's biomechanical dynamics, simulated in MATLAB, and validated with a prototype and an oscillatory entrance. We applied a PI controller and tested different reduction systems in order to find a reduction method adequate and comfortable for a Parkinson's Disease patient.

Keywords: Tremor · Amplitude · Frequency · Reduction · Patients

1 Introduction

Parkinson's disease (referred from now on just as Parkinson) is a neurodegenerative process, caused by cellular death in the *Subtantia nigra*, provoking a decrease in dopamine production. This chemical imbalance generates a lack of control in the fine movements giving place to Parkinson's symptoms [1–3].

The most characteristic symptoms are hypertonia, bradykinesia, and postural tremor [2, 4, 5]. The first one, hypertonia, refers to the excess of muscle tone. Bradykinesia is

© Springer Nature Switzerland AG 2020
C. A. González Díaz et al. (Eds.): CLAIB 2019, IFMBE Proceedings 75, pp. 1191–1199, 2020.
https://doi.org/10.1007/978-3-030-30648-9_155

the reduction of a patient's movement velocity. Postural tremor, present in 70% of Parkinson cases [3, 6], is an involuntary, uncontrolled oscillating movement. Parkinson's tremor at rest has a frequency between 3 and 7 Hz, while postural tremor has a frequency between 5 and 12 Hz, with an amplitude up to 30° at the elbow [7, 8], while in healthy people with a stable movement the frequency is between 4–12 Hz and an amplitude less than 1° [7–11]. These characteristics make impossible doing daily activities for Parkinson patients, making them dependent on other people, diminishing life's quality for the patients and the people surrounding them. This illness affects 0.3% of the whole world population and over 1% of the population over 55 years old. The main risk factor is age, being more common to present Parkinson symptoms when a person is 60 years old or more, but there are cases where they appear since a young age (less than 45 years old). When this happens, it is known as Juvenile Parkinson [12]. It usually represents less than the 5% of Parkinson's cases, but in Mexico, this number goes over 15% of the cases [3, 6, 12]. For 2030, the number of Parkinson patients will increase three times, only considering aging as a factor. All this makes it the second most common neurodegenerative disease [3, 6, 13].

Parkinson is an illness that affects the familiar economy of the patients and their families, due to the pharmacy costs, rehabilitation, check-ups, and the productivity impairment, which represents 49.4% of the total costs, according to the WHO [6, 14].

Nowadays, there's no standard treatment, but the most common is the symptomatic control with a dosage of Levodopa and Carbidopa. These treatments are not completely effective, and over time, it stops functioning. They have severe secondary effects, such as dyskinesia or dementia [1, 9, 14]. Alternative methods for tremor control are rehabilitation therapy and the use of orthosis. Each of Parkinson symptoms requires a different approach, rehabilitation focuses on recovering limb's control for bradykinesia and hypertonia. While orthosis usage is mainly focused on controlling gait for lower limbs and tremor suppression for upper limbs [2].

An orthosis is a mechanical system that applies forces to the body with a therapeutic benefit. These systems may resist or assist motion, transfer force or protect a body part in a functional way to improve the occupational performance of the user [15, 16]. Orthotic systems are designed according to the needs and characteristics of the patients, such as their age, routine, effort tolerance, and anthropologic characteristics; simplicity, functionality, wearability, and aesthetics, should also be taken into account [16]. One of the main characteristics to consider when designing an orthosis are comfort, alignment, and the forces applied. Most orthoses have one main force and two counterforces but they may have more depending on the system [15].

For tremor reduction, the orthotic systems used are focused on movement resistance, even when it may cause muscular fatigue. Thus, it is not recommended their usage unless it is absolutely necessary [17].

Although there's no certainty about Parkinson's progression mechanisms, we can analyze Parkinson tremors as a two degree of freedom biomechanical system with mass concentrated at centroid and inertia with an oscillatory perturbation. Simplifying the tendon, muscular and bone complex of the arm and forearm into two rigid segments and two joints (elbow and shoulder) [18].

According to Belda-Lois, we can consider each joint independently from each other, with voluntary movements generated by a central system which is altered at

some unspecified point with an oscillatory perturbation. This movement is activated with an internal moment and may be altered externally by a dynamic controller on the joint [7].

1.1 Problem

As mentioned before, an orthosis is used to restrain Parkinson's tremors, but after continuous usage, they can generate muscular fatigue and joint wear.

The constant friction also represents a problem as the illness progresses. Also, due to the variability of the different movements of the joints, the orthosis has to be continuously adapted and changed.

Hence the need to make an adaptable, comfortable and simple orthotic system to reduce Parkinson tremors, but that doesn't impede voluntary movements to the user.

1.2 Objectives

Develop a dynamic control system for the reduction of postural tremor amplitude for Parkinson in stages 1 and 2, without altering the limb's natural movement.

1.3 Hypothesis

The dynamic orthosis progressively attenuates tremor amplitude, keeping the natural movement, avoiding muscular fatigue and joint atrophy.

2 Materials and Methods

We designed, simulated and made an ergonomic and functional prototype for a tremor reduction system made up of the movement of Parkinson postural tremor in the first and second stages for upper limbs. To do this, first, we had to analyze the behavior of the system, based on the biomechanical model of the arm, similar to a lever with a fixed point and deduced the most general mathematical model. Also, we analyzed the movement through image processing of a video in MATLAB, which was captured from a patient in the first stage of Parkinson. We obtained the parameters and adapted the previous equation system, so it approximated the Parkinson's movement.

Introducing the equations obtained in MATLAB and Mathematica, and modifying the parameters, we observed the system's dynamics, getting a vector field, determining the importance of each factor studied. We enforced an oscillatory input and generated a control equation for the model to simulate the whole system, and compared the responses with the control and without it.

We designed an orthosis that adapted to the conditions established by the control system previously obtained, by proposing an adjustable system. To achieve this, we tested different energy dissipation methods, including fluid-based dampers, electromechanical actuators, and pneumatic actuators.

Based on the standard anthropological measurements reported by Avila-Chaurand, Prado-Leon, and Gonzalez-Muñoz in [19] for Latin-American people, we designed a

basic supporting structure to reduce the tremor on the wrist. This structure was adapted to the dissipation method selected to be tested. The structure was worn by a subject who qualified the efficiency perceived, comfort and wearability. At the same time, we compared the resulting movement with the movement previously measured, searching for an adequate ratio between the subjects feedback and the reduction.

3 Results

To understand Parkinson postural tremor, we expressed the state equation as the following:

$$F = \left(\frac{P}{\omega}\right)\theta\sin\left(\frac{n\pi}{2}\right) = ml^2 * \left(g + \ddot{\theta}\right) + d\dot{\theta} \tag{1}$$

Then, using Mathematica, we analyzed the systems stability and the most important factors that affected the conditions of the tremors through a series of simulations.

We observed the relation between muscle's power (P), the angular velocity magnitude (ω) and direction (positive or negative) of the movement, this was reduced in the coefficient k ($k \equiv P\omega$) and the rate of the limb's mass and length, expressed as coefficient c ($c \equiv ml^2$).

$$F = k\,\theta\sin\left(\frac{n\pi}{2}\right) = c * \left(g + \ddot{\theta}\right) + d\dot{\theta} \tag{2}$$

Figure 1, consists of three phase diagrams. In 1a, obtained with a negative k, we can observe that the limb's movement is marginally stable. While in 1b, obtained with a positive k, it is unstable. For 1c, we modified the friction coefficient and observed that, while adding a damping coefficient proportional to k and c, the system turned stable.

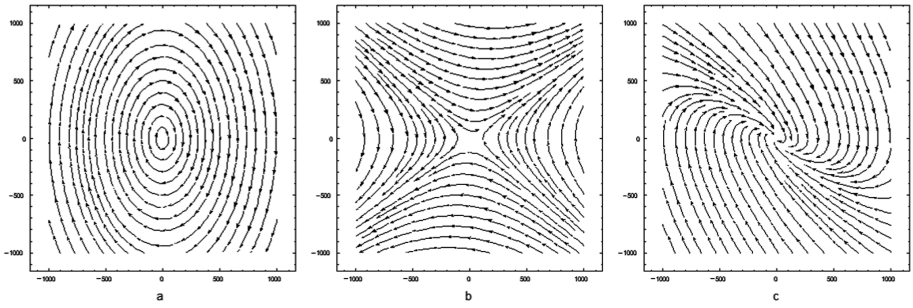

Fig. 1. In **a**, we observe that the vector field orbits the origin, meaning the movement is marginally stable. While in **b** the vector field diverges, which means the movement is unstable. For **c** we observed that the system converges, so it is steady.

Using the previous model, we designed a control system adapted to the needs previously described. The flowchart seen in Fig. 2 describes the process followed by the system. First, each patients' movements are characterized to determine specific tremor parameters and measures, then we classify them using tremor's amplitudes and frequencies described in The Handbook of Human Vibration of Griffin [11] and in the Kinematic Analysis of Upper Limb Trajectories in Parkinson Disease of Flash [8] as a basis to differentiate Parkinson originated movements from voluntary movements. Having obtained this parameter range for pathological tremors for each patient, movements characteristics are monitored and the information is fed to a Proportional-Integral control (PI) to calculate the correction needed to the movement and sending a signal to the actuator.

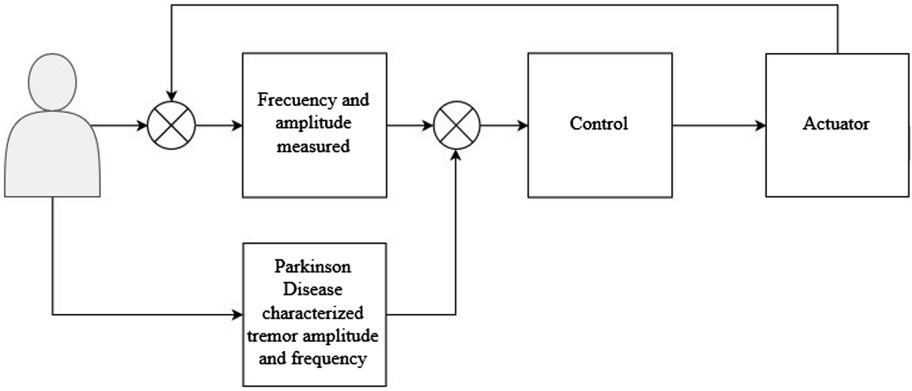

Fig. 2. Box diagram of the reduction system. Patients movements are characterized, monitored and analyzed by a PI control to apply the adequate correction using an actuator.

In Fig. 3 we can distinguish the amplitude reduction when applying the variable damping system, designed for our model.

Having the foundation for our design, we outlined a mechanism for the main force with a variable vibration damper and a support structure.

We tried three different types of reduction systems, based on electro-mechanic, pneumatic and magnetorheological fluid damping systems. We qualitatively analyzed these methods looking for durability and patient's comfort. The first one was based on an electro-mechanic actuator, using the counter electromechanical force. It was attached to an external joint (Fig. 4a). The second consists of a magnetorheological fluid rotational damper, controlled by the exposition to a magnetic field of variable intensity. This was used as a joint for the structural pieces (Fig. 4b). The third is a pneumatic actuator with an electronic valve which regulates the entrance and exit of air to the cylinders compartments (Fig. 4c) with a flexible elastomer piece, instead of a rigid joint, attached to the basic structure (Fig. 4d).

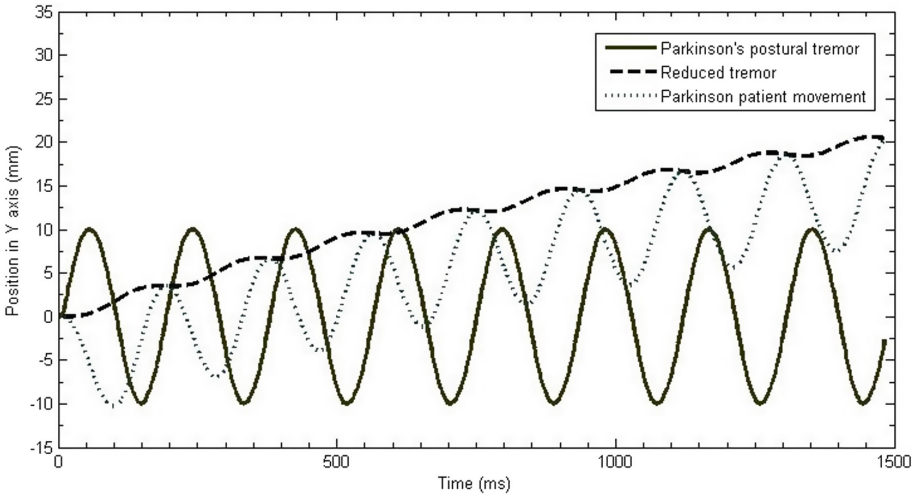

Fig. 3. Comparative simulation of the movement of a Parkinson Disease patient under different conditions: Postural tremor (continuous line) and tremor while moving limb upwards, with applied control (dashed line) and without it (dotted line).

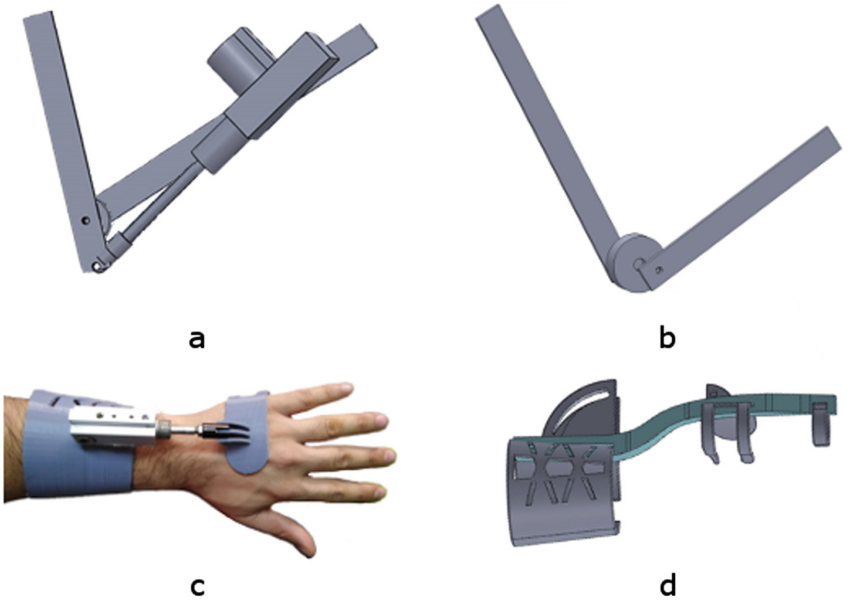

Fig. 4. Reduction systems evaluated. First, we can observe the 3D model with the main force based on an electro-mechanical actuator on a mountable structure as shown in **a**. Next to it, labeled with letter **b** is the 3D design of mountable rotational magnetorheological damper as the main force, which is located in the joint. On the second row, the first image denoted with letter **c** is the subject's hand wearing an adapted version of the structure to support a pneumatic cylinder. Finally, on **d**, we observe the elastomer pieces assembled with the modified structure.

The system selected was the last one, due to the durability of the system and the relation between the actuator's size and the force it can apply to reduce the tremor. It is activated when an inertial module detects a Parkinson postural tremor.

Parkinson's patient movement is detected by an accelerometer, measuring the inertia moments and classifying between a normal movement and a Parkinson postural tremor. As an anchor for the mechanism, we designed a solid structure (Fig. 5a), composed of 3 main parts: a ring (Fig. 5b), a handpiece (Fig. 5c) and a bracelet (Fig. 5d). These were designed to keep an adequate lateral articular alignment and to reduce Parkinson postural tremor on the wrist.

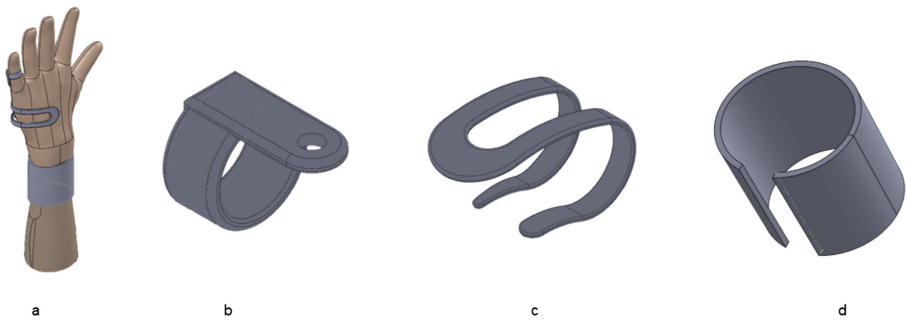

Fig. 5. Computer 3D designs of the solid structure of the orthosis. Shown the individual pieces: ring, handpiece, and bracelet marked as **b**, **c** and **d** respectively and the assembly labeled as **a**.

These pieces were 3D printed in PLA. To test how comfortable it was to wear the structure, various subjects wore them and gave us their opinion. We adapted the pieces, so they were convenient and comfortable to wear. They were worn by a subject who gave feedback on the wearability of each of the pieces and the whole structure.

After being accepted by the subject, we tested three different reduction mechanisms on the same subject who gave feedback on the reduction perceived, effort to do natural movements, comfort, and simplicity.

4 Conclusion and Discussion

Through the mathematical analysis, we compared the different variables that defined the stability of the movement, permitting us to understand that the system's stability changed according to k, which is the relation between P and ω; we can interpret this as the muscular power used and the kind of movement exerted. If the limb flexes k is negative, and if extended, k is positive, which fits with the observations made on patients movement. When the arm contracted, the postural tremor intensity reduced, but when the limb extended, the vigor if the tremor increased. This was consistent with empirical observations of a Parkinson patient.

The result obtained in the simulations for the control proposed was comparable with the ones obtained by Gebai et al. [20] who designed a system for two joints instead of one and to the results of [21].

As for the main force sources, compared to the fluid-based dampers, the electromechanical system and the pneumatic system had more durability. Comparing these last two, we chose the pneumatic system because it is smaller and less bulky, making it more comfortable when being worn.

References

1. Parkinson's Foundation Treatment. In: Parkinson's Foundation webpage. https://www.movementdisorders.org/MDS/About/Movement-Disorder-Overviews/Parkinsons-Disease–Parkinsonism.htm
2. México: Secretaría de Salud: Diagnóstico y tratamiento de la Enfermedad de Parkinson inicial y avanzada en el tercer nivel de atención (2010)
3. Martínez-Fernández, R., Gasca-Salas, C.C., Sánchez-Ferro, Á., Ángel Obeso, J.: Actualización en la enfermedad de parkinson. Rev. Méd. Clín. Las Condes **27**, 363–379 (2016). https://doi.org/10.1016/j.rmclc.2016.06.010
4. Prats, B.: Enfermedad de Parkinson. Guia Paciente Inicial. CETRAM (1927)
5. World Health Organization: Neurological disorders : public health challenges. World Health Organization (2006)
6. WHO: Neurological disorders: a public health approach. World Health Organ. pp. 41–176 (2006). https://doi.org/10.1001/archneurol.2007.19
7. Belda-lois, J.M., Belda, J.M., Atienza Vicente, C., et al.: Principios biomecánicos para la supresión del temblor por medios ortésicos. Universidad Politécnica de Valecia (2009)
8. Flash, T., Inzelberg, R., Schechtman, E., Korczyn, A.D.: Kinematic analysis of upper limb trajectories in Parkinson's disease. Exp. Neurol. **118**, 215–226 (1992). https://doi.org/10.1016/0014-4886(92)90038-R
9. Hosseini, R., Firoozbakhsh, K., Naseri, H.: Optimal design of a vibration absorber for tremor control of arm in Parkinson's disease. J. Comput. Appl. Res. Mech. Eng. **3**, 85–94 (2014)
10. Zill, D.G.: A First Course on Complex Analysis with Applications (2006)
11. Griffin, M.J., Erdreich, J.: Handbook of human vibration. J. Acoust. Soc. Am. **90**, 2213 (2005). https://doi.org/10.1121/1.401606
12. UNAM: En México es alta la incidencia de menores dE 40 años afectados por parkinson. Boletín UNAM-DGCS-218 (2015)
13. El costo de tener Parkinson. In: Ideas Pharma (2017). https://ideaspharma.com/2017/04/11/el-costo-de-tener-parkinson/
14. Solano, L.P.: Parkinson, enfermedad costosa, mal detectada y aún incurable. La Jorn (2013)
15. Edelstein, J.E., Bruckner, J.: Orthotics: a comprehensive clinical approach. Slack, Thorofare (2002)
16. Tapia, Z.L., Meneses, D.M.I., Bañados. C.M.E., et al.: Manual De Órtesis. 45 (2011)
17. Bernhofer, L., Assoc, D.-I., Gahleitner, R., Doughty, T.: Parkinson's assistive technology (2016)
18. Hashemi, S.M., Golnaraghi, M.F., Patla, A.E.: Tuned vibration absorber for suppression of rest tremor in Parkinson's disease. Med. Biol. Eng. Comput. **42**, 61–70 (2004). https://doi.org/10.1007/BF02351012

19. Avila-Chaurand, R., Prado-Leon, L.R., Gonzalez-Muñoz, E.L.: Dimensiones antropométricas de población latinoamericana. Universidad de Guadalajara, Centro Universitario de Arte, Arquitectura y Diseño, División de Tecnología y Procesos, Departamento de Producción y Desarrollo, Centro de Investigaciones en Ergonomía (2007)
20. Gebai, S., Hammoud, M., Hallal, A., Khachfe, H.: Tremor reduction at the palm of a Parkinson's patient using dynamic vibration absorber. Bioengineering **3**, 21 (2016). https://doi.org/10.3390/bioengineering3030018
21. Taheri, B., Case, D., Richer, E.: Active tremor estimation and suppression in human elbow joint, pp. 115–120 (2012). https://doi.org/10.1115/dscc2011-6185

Contribution of Virtual Environments to the Perception of Balance Rehabilitation Tasks: A Psychophysiological Study

Oscar I. Caldas[1], Juan D. Abril[1], Oswaldo Rivera[1], Carlos Rodriguez-Guerrero[2], and Oscar F. Avilés[1(✉)]

[1] Universidad Militar Nueva Granada, Bogotá 110111, Colombia
{oscar.caldas, u3900253, u3900248, oscar.aviles}@unimilitar.edu.co

[2] Vrije Universiteit Brussel, Boulevard de la Plaine 2, 1050 Ixelles, Belgium
carlos.rodriguez.guerrero@vub.be

Abstract. About half of the people with disabilities in Colombia manifest having impairments in the lower extremities, which requires them to perform any kind of physical rehabilitation, mainly balance recovery sessions. Often, these processes become tedious and monotonous for patients. Therefore, to address this issue, it is necessary to determine how emotional and psychophysiological responses are related to rehabilitation activities. We present a study performed by 13 healthy participants that includes the use of emotional self-reports and simultaneous psychophysiological measuring (15 features extracted) for two balance tasks, one based on regular rehab procedures and the other into a 3D virtual reality game. Results from this study shows that arousal (44%) and valence (24%) as well as heart rate (85%), skin conductance responses (40%) and respiratory rate (80%) outcomes tend to increase in the second task compared to first one. Though preliminary, these results indicate that rehabilitation process carried out through combination of VR environments, serious games and innovative technologies could improve balance recovery sessions, turning them into an enjoyable activity for participants.

Keywords: Virtual rehabilitation · Psychophysiology · Balance

1 Introduction

According to the report published by the office of Social Promotion of the Ministry of Health and Social Protection in 2018 [1], the number of people with disabilities in Colombia was 1'379.001, which corresponds to 2.6% of the total population. About half of them manifest having difficulty performing daily activities such as walking, running and jumping, which suggests involvement in the lower extremities. Musculoskeletal complaints, for instance, represent more than 315 million outpatient visits per year and more than 20% of all outpatient visits in the United States. The Center for Disease Control and Prevention estimate that 22.7% (52.5 million) of the US population has diagnosed arthritis and 22 million have significant functional limitations [2].

© Springer Nature Switzerland AG 2020
C. A. González Díaz et al. (Eds.): CLAIB 2019, IFMBE Proceedings 75, pp. 1200–1207, 2020.
https://doi.org/10.1007/978-3-030-30648-9_156

This motor disorders as well as others not only need to be diagnosed effectively, but also need to be treated mostly through rehabilitation processes, which seeks that to stop the progress of those disorders and provide the patients with strategies to recover partially or completely from the symptoms. In rehabilitation processes, it is common to find repetitive tasks, which in most cases tend to be perceived by patients as monotonous and boring; thus tasks tend to be omitted, performed in a wrong way or abandoned [3–6], causing rehab processes to be inefficient and their progress to depend on other factors instead of those proposed by the healthcare provider [7].

The implementation of innovative technologies integrated with virtual reality (VR) and serious games to promote motivation and engagement, such as in [3–6], generates benefits for both patients and therapists, helping to increase psychomotor learning through more repetitions and promoting neuroplasticity [8]. Besides, studies have shown that this integration also helps to measure the patient progress through the acquired data (biomechanical and task performance) by providing a more accurate information to the therapist, just to mention one extra benefit [9].

The present study proposes a setup to provide a 3D virtual rehabilitation for balance recovery, as a mandatory step in lower-limb motor rehabilitation. In this setup it is hypothesized that the multisensory stimuli and feedback, as well as the possibility of enhanced environmental interaction, will end up on most desired emotional states.

The study was performed by 13 healthy participants and included the use of emotional self-reports and simultaneous psychophysiological measuring (15 features extracted) for two balance tasks. The first one was a voice-guided balance session, and the second one was a VR serious game that ask the subject to perform the same set of movements with the same duration. The following sections describe the selected materials and methods as well as the results and discussion, ending with conclusions.

2 Materials and Methods

2.1 Subjects

Thirteen (13) healthy subjects were recruited to perform the tasks, 7 males and 6 females with age range 27–36. None of the participants reported previous undesired neurological conditions, such as epilepsy, vertigo or tendency to convulsions, nor cognitive disorders that implicate difficulties to understands or perform de tasks.

Three days before the session, all subjects performed a previous test to identify motion sickness. The exercise was a 3D-VR journey on a boat through a slow river, while seated safely. All participants were tested with the Virtual Simulation Sickness Questionnaires (VSSQ) designed by [10] before and after the virtual experience, as well as 24 h later. All of them obtained the required minimum score to continue.

2.2 Study Protocol

All sessions were conducted in the Davinci research group laboratory of Universidad Militar Nueva Granada at Bogotá, Colombia. At the start of the session, the study purpose and procedure were explained to participants via an informed consent. After

participants answered an initial questionnaire with demographic information, physiological sensors were placed on the subject as described below in the hardware subsection. A preliminary 1-min physiological measure was carried out to determine a baseline, intended to be used for each participant's outcomes normalization.

The study was divided in two tasks. The first one, was a voice guided balance task in which the participant performed 28 movements for 150 s over a balance board, such as in regular rehabilitation setups. The second task was guided by a VR serious game with a simple storytelling that ask the subject to perform the same movements while playing it, during the same period.

After each task, participants were asked to fill out the Self-Assessment Manikin Test (SAM) [11], reporting their experienced dimensional emotions (arousal, valence and dominance). Physiological measures were recorded during both tasks.

2.3 Hardware

A Wobble Balance Board was used as the haptic interface, with 35 mm of diameter and holding up to 135 kg. It was fixed in such a way that it only allowed pitch and roll when standing and no translations. In the middle of the board a 3-axis gyroscope was located to measure rotations (range of motion: −11° to 11°). The subject is properly attached to a structure to avoid falls and provide sense of security (see Fig. 1).

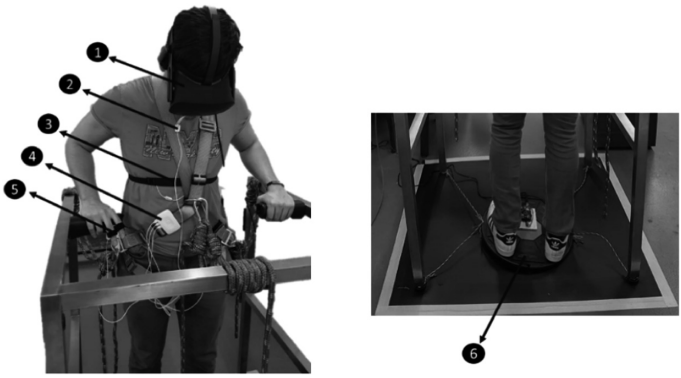

Fig. 1. A subject performing the task. The left picture shows the HMD (1), ECG sensor connected to the chest electrodes (2), respiration strap (3), sensing device (4) and SC electrodes on the fingers (5). The right picture shows the wobble board with the gyroscope (6).

Audiovisual stimuli and feedback were given by means of an Oculus Rift Head Mounted Display (HMD), which provided a full 3D immersion experience with acceptable features of tracking, latency, refreshment rate, resolution and field of view.

Physiological signals were acquired via a BiosignalsPlux Explorer research kit, at sampling rate = 1 kHz and resolution = 16 bits. This wearable sensing platform was used to measure electrocardiogram (ECG), Skin Conductance (SC) and Respiration. ECG was sampled by 3 surface electrodes placed on the upper-right part of the chest,

the downer-left part of the chest and the left part of the thorax, over the floating ribs (ground). SC was measured by a Galvanic Skin Response (GSR) sensor and 2 surface electrodes placed on the index and middle fingers of the non-dominant hand. Respiration was measured with a piezoelectric sensor in an elastic strap around the chest.

2.4 Virtual Task

As can be seen in Fig. 1, the subject inclines the balance board according to the received instructions during the second experimental stage. As the HMD allows first person interaction and enhanced presence, the subject is highly engaged as the player, which is a sky diver who is asked to pass through well marked rings during its fall to ground (see Fig. 2). The jump from the helicopter and the parachute deployment are automatically displayed, so the player is only required to move to all four directions (back, forward, right and left) in order to catch the eight (8) rings and finally fall over a target in a deserted island. Each correct pass through a ring gives ten (10) points and falling over the target gives 20 extra point, being 100 the maximum score.

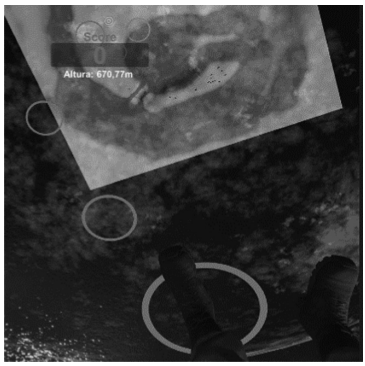

Fig. 2. First-person view in the virtual environment while subject is performing the task

2.5 Self-report Questionnaires

As mentioned before, all participants were asked to pass a previous stage for determining chances to develop simulation sickness by using the self-report VSSQ.

At the beginning of the test, participants were provided with an 8-questions multiple-option questionnaire intended to obtain demographic information for statistical purposes, including gender, age, previous experience with videogames and virtual reality, and records of neuromotor disorders.

Besides, after each of the experimental setups, subjects were asked to answer a graphical 9-point scale test for emotional states, called Self-Assessment Manikin (SAM). This subjective instrument allowed subjects to rate their experience in terms of the dimensional emotions: arousal (mental alertness), valence (pleasure) and dominance (control), with the advantage of being easy to apply due to its non-verbal graphic

depiction. It is important to remark that according to [12], SAM test has shown comparable results compared with other more complex self-report scales.

2.6 Feature Extraction

Fifteen features were extracted from the measured signals at each task: one (1) from task performance and fourteen (14) from physiological data. Considering the differences between subjects, features were normalized as the relative value to the corresponding baseline.

- **Task performance.** Performance was measured as success in the virtual reality task by means of percentage of collected rings (plus the target bonus).
- **Psychophysiology.** The psychophysiological features were extracted from three signals recorded during the study: ECG, SC and respiration. The time between two normal heartbeats (NN intervals) were used for calculating heart rate (HR) from ECG, as well as its maximum and minimum (*meanHR, maxHR* and *minHR*); HR variability was also calculated: *standard deviation of NN intervals (SDNN)* and the *root of the mean squared differences of successive NN intervals (RMSSSD)*. Skin conductance was measured as two components: skin conductance level (SCL) and skin conductance responses (SCR). *mean SCL* and *final SCL* were calculated for the first component, while *number of SCR*, *mean SCR amplitude*, *mean SCR risetime*, *standard deviation of SCR amplitude* and *standard deviation of SCR risetime* were obtained for the second one. The last two features were extracted from the respiration sensor: *mean respiratory rate (meanRR)* and *standard deviation of respiratory rate (SDRR),* as the corresponding variability indicator.

3 Results and Discussion

In order to realize how each data set behaves, boxplots analyses were carried out. This analysis helps to find how data are spread out, besides of common statistical measurements. Figure 3 shows the subjects' reports on the dimensional emotions, showing that arousal and valence increased for all the subjects when comparing exercise one (Ex. 1) (no VR) and exercise two (Ex. 2) (with VR). Arousal showed the greatest increment, mostly because the first exercise was considered as much lesser exciting. Although valence didn't have such a strong increment, it showed high values on both exercise, which shows general approval with the moving tasks. Dominance decreased on the VR task, which might be due the feeling of being restricted to move only to the rings position.

The next graphs show the behavior of the dimensional emotions and the most representative psychophysiological signals, i.e. values in exercise 1 vs exercise 2. All features extracted from the subjects are relative to their specific baseline.

The features related with HR and RR variability didn't show significant changes between exercises, so it is hard to perform conclusive analyses from them. However, HR variability (SSDNN and RMSSD) decreased lightly from baseline, which could be explained with the end of expectation, associated with anxiety and arousal.

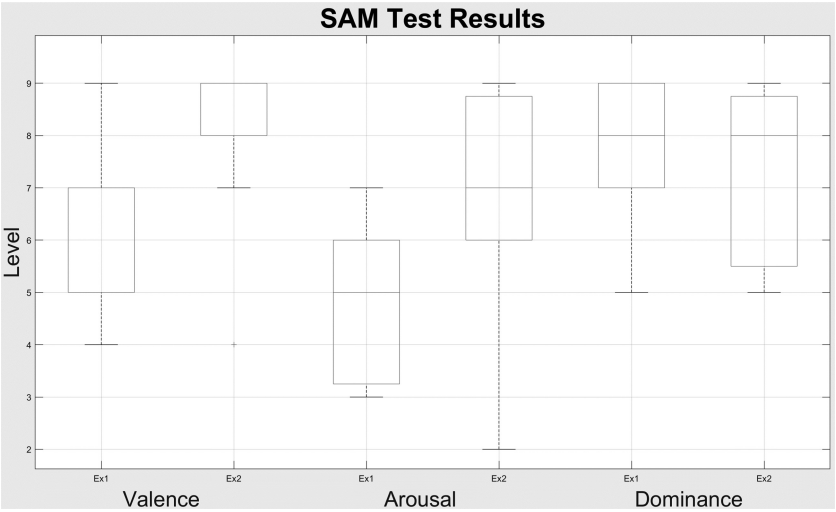

Fig. 3. Dimensional emotions between the two balance tasks

Several other features changed significantly. On one side, heart rate and skin conductance features increased as follows: meanHR by 85.36%, minHR by 2.6%, maxHR by 127.66% as well as meanSCL by more than 5 times, finalSCL by more than 6 times and NumberSCR to the double. The mean SCL and RR increase the most, which represents a probable relation with arousal. Heart rate and the number of skin conductance responses described a less pronounced increment but over high values, just as the behavior of valence (Figs. 4 and 5).

Fig. 4. Changes in heart rate between the two-balance task

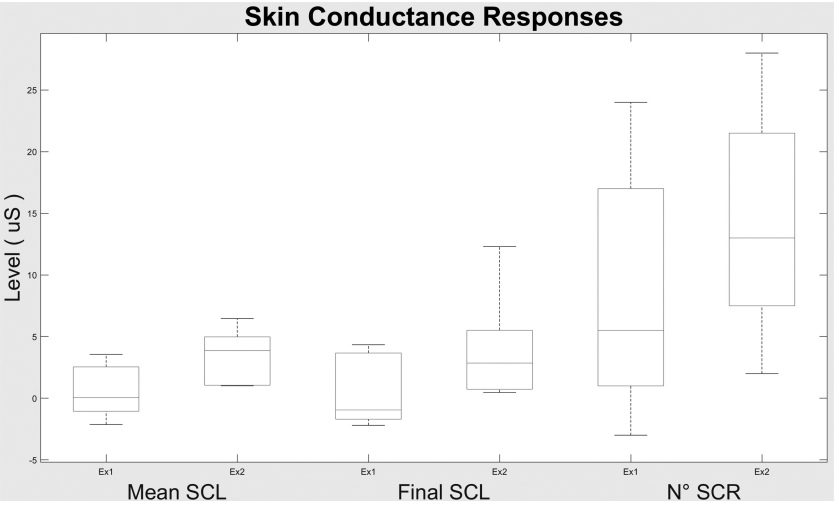

Fig. 5. Changes in skin conductance between the two balance tasks

Results shows that rehabilitation processes carried out through combination of VR environments, serious games and innovative technologies enhance affective response reflect on SAM test: arousal (44%) and valence (24%). Nonetheless, even when mean dominance stayed similar in both tasks (decreased by only 3.6%), some participants reported troubles performing the second activity. It is believed that lack of experience in VR and discomfort caused by wired Head-mounted Display are the main reasons for dominance results.

In another hand, it can be concluded that the system developed, turns common balance rehabilitation process in an enjoyable activity for participants, supported on self-reports and psychophysiological responses. Further work leads to carry out bigger studies that include variable levels and voice commands to guide participants inside the serious game, looking for enhance or decrease psychophysiological and emotional responses.

Acknowledgment. This research received financial support from Universidad Militar Nueva Granada, as part of the research project IMP-ING-2657.

References

1. Ministerio de Salud y Protección Social Oficina de Promoción Social: Sala situacional de las Personas con Discapacidad (PCD) 2018
2. World Health Organization and the World Bank: World Report on Disability 2011 (2011)
3. Rastegarpanah, A., Saadat, M., Borboni, A., Stolkin, R.: Application of a parallel robot in lower limb rehabilitation: a brief capability study. In: International Conference on Robotics and Automation for Humanitarian Applications, RAHA 2016 - Conference Proceedings (2017)

4. Kharboutly, H., Ma, J., Benali, A., Thoumie, P., Pasqui, V., Bouzit, M.: Design of multiple axis robotic platform for postural stability analysis. IEEE Trans. Neural Syst. Rehabil. Eng. **23**, 93–103 (2015)
5. Patanè, F., Cappa, P.: A 3-DOF parallel robot with spherical motion for the rehabilitation and evaluation of balance performance. IEEE Trans. Neural Syst. Rehabil. Eng. **19**, 157–166 (2011)
6. Schouten, A.C., Boonstra, T.A., Nieuwenhuis, F., Campfens, S.F., Van Der Kooij, H.: A bilateral ankle manipulator to investigate human balance control. IEEE Trans. Neural Syst. Rehabil. Eng. **19**, 660–669 (2011)
7. Roth, E., Mitra, R.: Chapter 10: stroke rehabilitation. In: Principles of Rehabilitation Medicine. McGraw-Hill Education, New York
8. Gobron, S.C., et al.: Serious games for rehabilitation using head-mounted display and haptic devices. Springer, Cham, pp. 199–219 (2015)
9. Van Diest, M., Lamoth, C.J., Stegenga, J., Verkerke, G.J., Postema, K.: Exergaming for balance training of elderly: state of the art and future developments. J. Neuro Eng. Rehabil. **10**, 101 (2013)
10. Kim, H.K., Park, J., Choi, Y., Choe, M.: Virtual reality sickness questionnaire (VRSQ): motion sickness measurement index in a virtual reality environment. Appl. Ergon. **69** (October 2017), 66–73 (2018)
11. Bradley, M.M., Lang, P.J.: Measuring emotion: The self-assessment manikin and the semantic differential. J. Behav. Ther. Exp. Psychiatry **25**(1), 49–59 (1994)
12. Goljar, N., et al.: Psychophysiological responses to robot training in different recovery phases after stroke. In: IEEE International Confernce on Rehabilitation Robotics (2011)

Medical Physics and Nuclear Medicine

Retinal Illuminance and the Relationship with Color

Nataly A. Garcia-Morales and Ernesto Suaste-Gómez(✉)

CINVESTAV, Mexico City, Mexico
esuaste@cinvestav.mx

Abstract. The pupillary reflex reacts to the light dilating or contracting the pupil depending on different factors like the image, or the light. These changes on the size of the pupil let us to identify the amount of light that impacts into the eye. To correlate the light and the pupillary contraction it is necessary define the Retinal Illuminance, which the product of luminance, pupillary area and a constant that belongs to the dispersion of the light on the ocular media. This research is focused on the Retinal Illuminance in presence of color (RGB). For the study it was developed a stimulator capable of control the luminance in order to make it constant for each color. The study was made in a dark environment on healthy persons between 25 and 50 years old following the guidelines of Helsinki Declarations. It have been measured the maximum contraction of the pupil for each subject and each color. The results exhibited that Retinal Illuminance is color dependent and not only luminance dependent. The study was made on healthy subjects, this study can help us to establish which are the normal values of Retinal Illuminance to detect diseases that affect the color vision.

Keywords: Retinal Illuminance · Isoluminent stimulus · Chromatic response

1 Introduction

Retinal Illuminance is the energy that the photoreceptors detect. The Illuminance that retina receives is expressed in the Eq. 1

$$E = dF/dS \tag{1}$$

Which is the total luminous flux (dF) that is received by the pupil (dS) in any direction. It can be assumed that light is uniform, the retinal image is perfect, and the light missing by the ocular media is considerate as a constant. Following a model for the Retinal Illuminance (see Fig. 1) it can been made some consideration using luminous flux and the dispersion and refraction, the image on the retina, and the theoretical eye we can express Retinal Illuminance as [1] a Luminance (L), Pupilar area (SP) and a factor ($\tau\lambda$):

$$E = 0.0036\ L\ Sp\ \tau\lambda \tag{2}$$

© Springer Nature Switzerland AG 2020
C. A. González Díaz et al. (Eds.): CLAIB 2019, IFMBE Proceedings 75, pp. 1211–1215, 2020.
https://doi.org/10.1007/978-3-030-30648-9_157

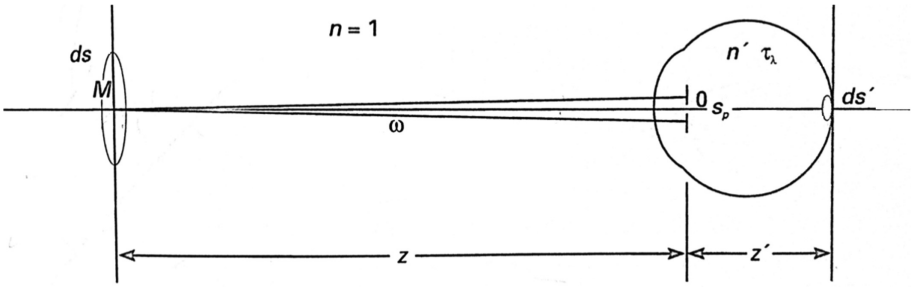

Fig. 1. Geometrical representation for the calculation of retinal Illuminance.

The dispersion of the ocular media and the refraction are constant for the same individual, it can be presented as a constant K.

$$E = K\,L\,Sp \tag{3}$$

Expressing the retinal Illuminance as a product of a constant (K), luminance (L) in cd/m^2 and pupillary area (Sp) in mm^2, and is independent of the distance of source (z).

The product of the area and the luminance can justify the definition of a new magnitude: Troland (Td), which is defined by the product of a Luminance of 1 cd/m^2 and the pupillary area of 1 mm$^{2.}$

On these equation and definition of Retinal Illuminance, the luminance and pupillary area are the only causes that affect the amount of light that the retina receives, but there are factors like color that are involved on this phenomenon [2]. It have been studied the Luminance, the changes of it and its relationship with the pupil, this changes can lead a reflex that modifies the pupillary area [3].

With this background we wanted to know if the color has an impact on the Retinal Illuminance. In order to explore that, it has been proposed a study in which was developed a stimuli isoluminent using 4 different colors [4, 5]. The subjects were on a dark room and stimulated with the isoluminent light and with a video-oculography method in order to record the response of the pupillary reflex [6, 7]. The study was made following the guidelines of the Helsinki Declaration.

2 Material and Method

The study recorded the pupillary reflex using four different colors obtained of the surface of 4 filters (Dark Blue 470 nm BG14, Red 610 nm RG510, Green 500 nm VG6) with constant luminance. The record of the pupillary reflex was made using video-oculography technique [8, 9]. The pupillary area was measured during the stimulus and 10 s after to ensure the dilatation of the pupil [10].

The system displays a stimulus of 10 ms. The luminance of the emitted light was 131.8 cd/m^2 with a standard deviation of 0.8 cd/m^2 measured with the photometer Gauge Coherent model IL1400, the system has three principals sections (see Fig. 2):

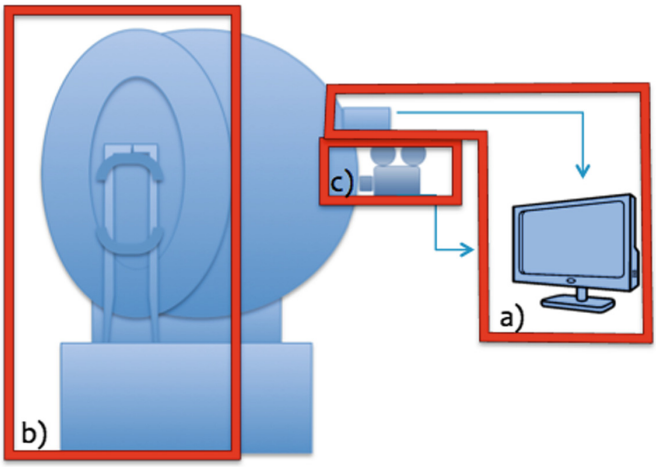

Fig. 2. Schematic representation of the system and its components. (a) Specialist section. It is form by a screen and the control of the stimulus (b) Patient section. (c) Video-oculography section

1. Specialist section: Allows the specialist to follow and to control the study.
2. Patient section: contains the stimulator and a modified Goldman perimeter [11].
3. Video- Oculography section: for recording the pupillary reflex.

The subject made the subjective test with the Ishihara cards to determinate if they have normal vision. The subject was dark adapted by 10 m. Then a pattern was placed under the eye for subsequent reconstruction. The subject placed their head on the opthalmological support. The patient was stimulated for 10 ms while the pupillary response was recorded. After that, the pupil has recorded for 10 s to wait dilatation and then next color stimulus was activated giving a total of 4 stimuli for each subject.

The study was made on 10 persons between 25 and 50 years old.

3 Results

The response was normalized in order to make a comparison of the morphology of the curve. It has been observer that color blue presented a bigger contraction than the other colors, therefore a minor Retinal Illuminance (Table 1). Another interesting finding is that in 8 of 10 subjects the red was the color with minor contraction. The white and green color had similar contraction. The morphology was similar on all the subjects. It can be observed the typical response of color for one subject on Fig. 3.

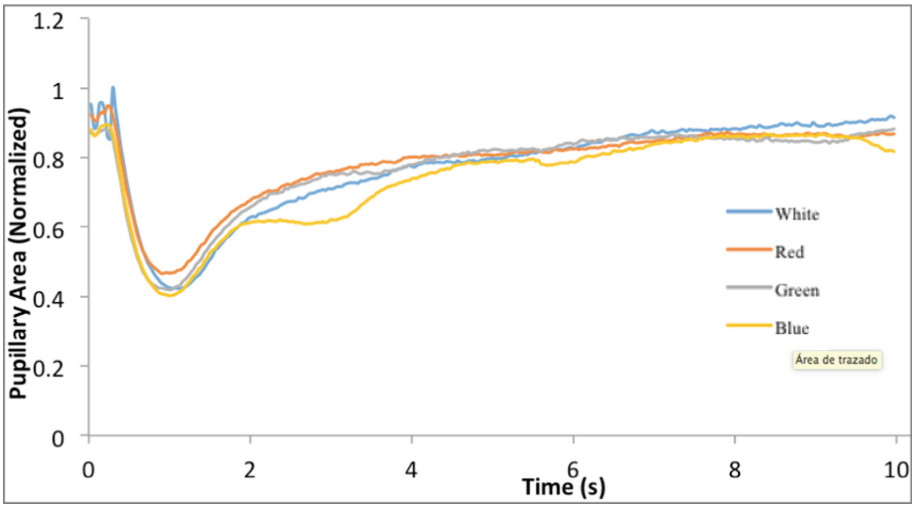

Fig. 3. Typical curve of the pupillary reflex, it can be observed that blue presented a greater contraction above the four colors.

Table 1. Average of Retinal Illuminance Troland (Td) for each color

Color	White	Red	Green	Blue
Luminance (cd/m^2)	131.8	131.8	131.8	131.8
Pupillary Area (mm^2)	21.85	24.97	21.40	20.38
Retinal Illuminance (Td)	2879.83	3291.046	2820.52	2686.084

Note: The Retinal Illuminance was calculated as the product of Luminance, which was constant for the four colors, the Pupillary Area, for this, area was the average of the 10 subjects and the constants of the ocular media. The standard deviation for the luminance was 0.8 and the standard deviation for the area was 7.24 for white 6.69 for red 7.26 for green and 7.71 for blue. The resolution of the camera gave us the opportunity to obtain the area of two decimals of millimeter.

4 Conclusions and Discussion

The retinal Illuminance is luminous energy that a retina receives. This quantity is dependent on the luminance of the stimulus and the pupillary area caused by the pupillary reflex, but the color of the stimulus is a factor that nowadays is not described in this phenomenon. After observing and analyzing the pupillary response it was objectively quantified that color shows different effects in pupillary area, which affects directly the Retinal Illuminance. The blue color presents a minor retinal Illuminance. In this context if the chromatic luminance is constant in the same subject the Retinal Illuminance will depends only of the pupillary response. Thus in study it was found in and objective way that the pupillary area changes depending only on color that the

stimuli emits. The results lead to think that the wavelength of the visible spectrum is an important factor that changes Retinal Illuminance. The following study will include a larger population and will take in count more factors like age, refractive problems, etc. This will have the purpose of establish normal Retinal Illuminance for each color in healthy subjects. It is necessary make this study with patients any color disabilities [12]. This study will lead us to a better understanding of the eye, the physical phenomenon of the chromatic vision and in a future can help to detect diseases in color vision [13].

References

1. Perea, P.C., Felipe, A., Ramo, J.P., Artigas, J.M.: Optica Fisiologica, 1st edn. Mc Graw-Hill, Madrid (1995)
2. Waldman, G.: Introduction to Light: The Physics of Light, Vision, and Color. Prentice Hall, New York (2002)
3. Hart, W., Schiefer, U.: Clinical Neuro-Ophthalmology: A Practical Guide. Springer, Berlin (2007)
4. Stiles, W.S., Wyszecki, G.: Color Science: Colors and Methods, Quantitative Data and Formulae. Wiley Interscience Publication, Hoboken (1967)
5. Malacara, D.: Color Vision and Colorimetry Theory and Applications. Spie, Bellingham (2002)
6. Mora-Martinez, R., Suaste-Góme, E.: Pupillary reflex associated with isoluminant chromatic stimuli. In: Arno, F. Rein, E. (eds.) Recent Progress in Eye Research, Chapter 5, Nova, pp. 231–264 (2017)
7. Villalobos-Castaldi, F.M., Suaste Gómez, E.: A new spontaneous pupillary oscillation-based verification system. Expert Syst. Appl. **40**, 5352–5362 (2013)
8. Sánchez, A.S., Suaste, E., Villarreal, E.: Isoluminant chromatic high speed video-oculography to study the dynamic of the pupillary response. In: IFMBE, vol. 49, pp. 465–467. Springer (2015). https://doi.org/10.1007/978-3-319-13117-7_119
9. Suaste-Gómez, E., Mora-Martínez, R., Villarreal-Calva, E., Sánchez Sánchez, A.S.: Instrumental Methodology for the measurmente of the pupil cycle time using a chromatic slit lamp. In: IFMBE, vol. 49, pp. 20–22. Springer (2015). https://doi.org/10.1007/978-3-319-13117-7_6
10. Cooper, C., Ashe, J., Weinberger, N.: Effects of stimulus omission during habituation of the pupillary dilation reflex. Physiol. Psychol. **6**(1), 1–6 (1978)
11. Suaste, E., Solís, L., Rivera, P.: Fiber optic for perimetry-based on video-oculography. In: Harrington, J.A., Harris, D.M., Katzir, A., Milanovich, F.P. (eds.) Biomedical Fiber Optic Instrumentation, vol. 2131, pp. 180–189. SPIE, Bellingham (1994)
12. Loza-Pacheco, D., Suaste-Gómez, E., de la Cruz-Burelo, E.: Blindness and low vision, an overview of opportunities for health services and preventive medicine. Int. J. Adv. Med. Sci. **3**(1), 33–36 (2015)
13. Gouras, P.: The Perception of color, Vision and Visual Dysfunction, vol. 6. CRC Press, London (1991)

Application of Structured Light Illumination and Compressed Sensing to High Speed Laminar Optical Fluorescence Tomography

Ichiro Sakuma[1(✉)], Toshiki Kobayashi[1], Hiroshi Seno[1], Yuki Akagi[1], Keiichi Nakagawa[1], Masatoshi Yamazaki[1], and Naoki Tomii[2]

[1] School of Engineering, The University of Tokyo, Bunkyo-ku, Tokyo 113-8656, Japan
sakuma@bmpe.t.u-tokyo.ac.jp
[2] Faculty of Medicine, The University of Tokyo, Bunkyo-ku, Tokyo 113-8656, Japan

Abstract. We constructed experiment system to verify the principle of CLOT using optical phantoms containing fluorophore. We used a digital mirror device (DMD) with high speed pattern switching capability (with interval of 1 ms). Fluorescent dye contained in a capillary with internal diameter of 1.4 mm was immersed in light scattering and absorbing medium contained intralipid. Location of the fluorophore was estimated by the proposed method. The reconstruction accuracy at the deep position (depth: 1.9 mm) was less than 0.4 mm. while the error was as large as 1 mm for the shallow position (depth: 0.6 mm) It is considered that accurate measurement of the optical constant is required for better reconstruction accuracy.

Keywords: Optical mapping · Laminar Optical Tomography · Compressed sensing · Spiral wave · Arrhythmia

1 Introduction

The study of the spatial organization and dynamics of reentrant activity in three-dimensional (3D) cardiac muscle is important to the understanding arrhythmia such as ventricular tachycardia and fibrillation. Spiral reentry in three dimensional space is called a scroll wave, and the scroll wave turns around a filament having a string shape connecting the centers of vortices of a two-dimensional [1, 2]. Optical mapping using voltage sensitive dye together with high-speed video camera enables measurement with high spatial resolution and has been used in electrophysiological studies [3]. Optical mapping method can only acquire signals from surface layer ($\sim$250 μm) of a cardiac tissue. Several attempts to visualize scroll waves in actual myocardial tissues have been reported [4, 5]. Laminar optical tomography (LOT) can be applied to the optical mapping of electrophysiological action potential propagation by utilizing voltage-sensitive dyes [6, 7]. The objective of this research is to develop 3-dimensional diffusion tomography combining high-speed structured illumination with new optical

© Springer Nature Switzerland AG 2020
C. A. González Díaz et al. (Eds.): CLAIB 2019, IFMBE Proceedings 75, pp. 1216–1219, 2020.
https://doi.org/10.1007/978-3-030-30648-9_158

system for diffusion tomography and compressed sensing technology (Compressed Laminar Optical Tomography: CLOT) [8]. We constructed an experimental system to verify the principle of CLOT using optical phantoms containing fluorophore.

2 Methods

2.1 Compressed Laminar Optical Tomography (CLOT)

Details of the method is available in the references [6, 8]. The excitation light laser enters at the position r_s. The incident light diffuses inside the tissue and excites the dye located at position r where fluorescence is generated which also scatters inside the tissue and exits from the position r_s on the tissue surface. The fluorescence in the stationary state measured can be described as:

$$F_{x,m}(r_d - r_s, \mathrm{t}) = \int p_{x,m}(r,t) H_x(r - r_s) E_m(r_d - \mathrm{r}) d^3 r \tag{1}$$

$H_x(r - r_s)$ represents the excitation light intensity at location r originated from the incident excitation light with unit intensity at location r_s. $E_m(r_d - \mathrm{r})$ represents the intensity of fluorescence light scattered in the tissue detected at location r_d originated from fluorescence with unit intensity at location r. $p_{x,m}(r,t)$ is a function of membrane action potential $V(r,t)$ at location r. Thus the $p_{x,m}(r,t)$ can be expressed as:

$$p_{x,m}(r,t) = wV(r,t) \tag{2}$$

where w is a scaling factor. The volume of tissue is discretized, change in fluorescence intensity can be linear equation that is solved by compressed sensing method.

2.2 Experimental System of CLOT

The experimental optical measurement system as shown in Fig. 1 consisted of an excitation laser (SSL-532-1000-10TM-D-LED, Shanghai Sanctity Laser Technology, max output power: 1 W), a laser expander (BEHP-10-532, Optosigma), a dichroic mirror (DM) (Di 02- EM CCD camera (ADT-100, Flovel), a Digital Mirror device (DMD) (DLP 6500, Texas Instruments), and lens system. The random pattern of 6 mm square generated by DMD was then enlarged to 10 mm square by an objective lens and was reflected by the dichroic mirror and irradiated onto the measurement object every 1 ms. Fluorescence light passed through a dichroic mirror and a long pass filter and was recorded by the EMCCD camera.

2.3 Phantom Preparation

Optical phantom mimicking biological tissue with fluorophore was prepared. Fluorescent dye contained in a capillary with internal diameter of 1.4 mm was immersed in light scattering and absorbing medium contained intralipid. The specification of the phantom and its optical constant are shown in Table 1. The capillary was placed at depth of 0.6 mm and 1.9 mm from the surface.

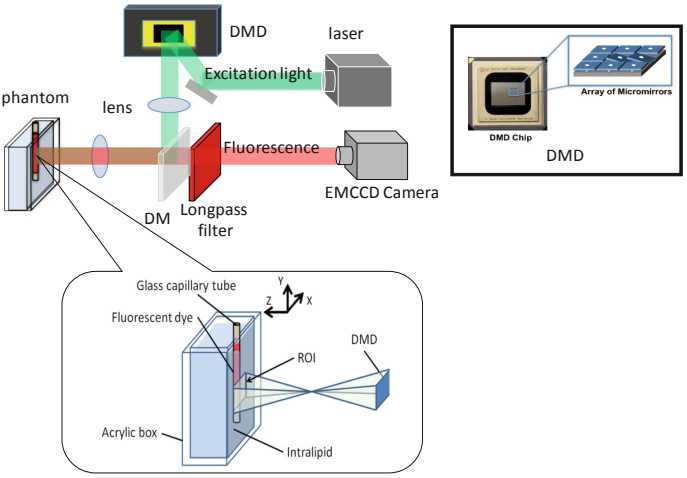

Fig. 1. Experimental optical system for clot

Table 1. Specification of the phantom and its optical constant of experimental phantom

Fluorescence dye	DY-521 XL (Excitation : 523nm, fluorescence : 668nm)
capillary	Outer 1.5mm, inner 1.3mm, thick 0.2mm, length 75mm
Intralipid	Intralipid 10% (0.5%)

Wavelength	Absorption coefficient [mm^{-1}]	Scattering coefficient [mm^{-1}]	Anisotropic parameter
532nm	0.2670	0.4600	0.9
610nm	0.1098	0.4240	0.9

2.4 Random Excitation Light Pattern Illumination and Signal Pre-processing

The position of illumination points and fluorescence detection points are registered with affine transformation. Then the 10 mm × 10 mm region of interest (ROI) was illuminated by random illumination patterns with 32 × 32 dots patterns. The measured image was down-sampled to square with 32 × 32 areas by taking the median value at pixel enclosed by each region in the extracted measurement image. The image data corresponding to the ROI was them down sampled into 32 × 32 data array. Two different illumination patterns were used.

3 Results

The estimated positions of the center of fluorophore both in experiments and computer simulation studies with assumed optical properties and errors compared with the true values (depth: 0.6 mm and 1.9 mm) are shown in Fig. 2.

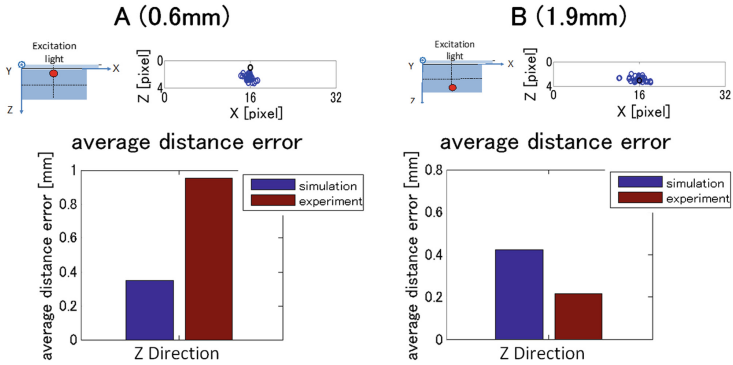

Fig. 2. Reconstruction of clot for experimental data

4 Discussion and Conclusion

We have constructed an optical system for CLOT with random excitation illumination patterns generated by a digital mirror device (DMD) with high speed pattern switching capability (every 1 ms). The CLOT was applied to identify the location of capillary obtaining fluorophore immersed in optical scattering medium with intralipid. The reconstruction accuracy at the deep position (depth: 1.9 mm) was less than 0.4 mm. On the other hand, that at the shallow position was as large as 1 mm. Variation in fluorescence luminance value might be influenced by optical absorption properties. Thus it is necessary to accurately measure the optical constant of the object to improve reconstruction accuracy.

References

1. Pertsov, A., Vinson, M.: Phil. Trans. R. Soc. Lond. A **347**, 687–701 (1994)
2. Qu, Z., Kil, J., Xie, F., Garfinkel, A., Weiss, J.N.: Biophys. J. **78**, 2761–2775 (2000)
3. Efimov, R., Nikolski, V.P., Salama, G.: Circ. Res. **95**, 21 (2004)
4. Bernus, O., Mukund, K.S., Pertsov, A.M.: J. Biomed. Opt. **12**, 014035 (2007)
5. Walton, R.D., Mitrea, B.G., Pertsov, A.M., Bernus, O.: Annual International Conference of the IEEE, pp. 4523–4526 (2009)
6. Hillman, E., Bernus, O., Pease, E., Bouchard, M.B., Pertsov, A.: Opt. Express **15**, 17827–17841 (2007)
7. Hillman, E.M., Burgess, S.A.: Laser Photonics Rev. **3**, 159–179 (2009)
8. Harada, T., Tomii, N., Manago, S., Kobayashi, E., Sakuma, I.: Biomed. Opt. Express **8**, 2339–2358 (2017)

A Method to Automate the Metabolite Postprocessing and Quantification on Magnetic Resonance Spectroscopy Signals

Francisco López-Caracheo[1(✉)], Carlos Andres Perez-Ramírez[1], Arturo Hernández-Medina[1,2], Roberto E. Mercadillo-Caballero[2], and Erick H. Pasaye-Alcaraz[3]

[1] Universidad Autónoma de Querétaro, Querétaro, Qro., Mexico
francisco.lopez.caracheo@gmail.com
[2] Universidad Autónoma Metropolitana – Iztapalapa, Mexico City, Mexico
[3] Unidad de Resonancia Magnética – UNAM, Juriquilla, Qro., Mexico

Abstract. In this paper, an automatic method to process and quantify the metabolites of a magnetic resonance spectroscopy signal is presented. Signals obtained from a region of the left thalamus were analyzed. The obtained results were compared with the ones obtained using a Phillips' commercial magnetic resonance software. Three features of the signal corresponding to five different metabolites (NAA, Cr, Cho, Glx, Cr2) were obtained: width, height and area of the curve corresponding to each peak. The obtained results showed a maximum relative error of over 20%, indicating the potential that the proposal has. Further refinements are required to reduce the error.

Keywords: H-NMR · MRS · Spectroscopy · Metabolites · FID · Spectro · ECC · Automatic signal postprocessing · Automatic spectroscopy quantification

1 Introduction

Magnetic resonance spectroscopy (MRS) is a technique that allows the evaluation of the tissue's properties, in health and risky situations, in vivo or in vitro. MRS is used to analyze tumors [1–3], psychiatric diseases such as schizophrenia, depressive disorders [4] and even multiple sclerosis [5], as well as benign pathologies, such as tuberculomas, metabolic and demyelinating brain diseases [1] due to the results obtained are similar to the ones obtained in biopsies [6]. To perform this task, MRS measures metabolites such as: n-acetyl aspartate (NAA), choline (Cho), creatine (Cr), Glutamate and Glutamine (Glx), among others [4], where their presence can allow the generation of biomarkers that could be used to predict the disease behavior [6] such as pediatric tumors [7–9]. To detect the metabolites, a signal known as free induction decay (FID) is analyzed using the Fourier Transform [10], where the positions in the x- and y-axes of the observed peaks in the spectrum indicates the type of metabolite and their concentration, respectively. Considering all the above mentioned advantages, it is necessary to develop an algorithm that can process a raw MRS signal in an automatic way. This paper presents a proposal that processes raw MRS signals and its non-water suppressed version to perform the Eddy current correction.

© Springer Nature Switzerland AG 2020
C. A. González Díaz et al. (Eds.): CLAIB 2019, IFMBE Proceedings 75, pp. 1220–1225, 2020.
https://doi.org/10.1007/978-3-030-30648-9_159

2 Materials and Methods

2.1 Data Acquisition Protocols

The data used in this work was provided by Universidad Nacional Autónoma de México. The obtention of this data followed the bioethical protocol from the bioethics committee. The MRS signals were acquired through a 3T Philips MRI scanner in a region of the left thalamus with a single-voxel technique. For each signal, a repetition time (TR) of 2000 ms, an echo time (TE) of 30 ms, 96 averages, 2048 points of resolution and a voxel size of $20 \times 20 \times 20$ mm^3 with a PRESS sequence and CHESS water suppression were used. All data processing was performed in MATLAB 2018a.

2.2 Signal Post-processing

The processing of the MRS signal improves both, the visualization of the signal data, as well as the estimation values closer to the real ones. To this purpose, it is important to execute each step in proper order because an incorrect order could affect the result. The postprocessing stage of the present work included eddy current correction, apodization and zero filling, frequency alignment, residual water suppression, phase correction and baseline correction.

Eddy Current Correction (ECC)
Eddy currents are generated by the magnetic field gradients sudden change in time, affecting the study quality since the resulting signal is distorted [11], as the resonant frequency shifts its value. This correction was performed by subtracting the signal phase with the signal generated without water correction phase at each point. The Klose's method describes mathematically this behavior [12]:

$$Sc = abs(Ss)\left(\frac{e^{-i\theta s}}{e^{-i\theta w}}\right) \tag{1}$$

where Sc is the signal after ECC, Ss is the signal before ECC, $e^{-i\theta s}$ is the Ss signal phase, and $e^{-i\theta s}$ is the phase of the signal without water suppression.

Apodization and Zero Filling
Usually, the acquisition of the relevant data is finished before the study concludes, making necessary to filter the signal in order to avoid a ripple phenomenon in the resulting spectrum. An appropriate procedure, known as apodization, consists in applying a filter that has a value of 1 in the first sample and then starts decaying to zero. In this work, an exponential filter was employed since it fulfills with the abovementioned features, which is described by:

$$\text{Signal Out} = \text{Signal} * \exp(-\text{pi} * \text{FWHM} * \text{t}) \tag{2}$$

where FWHM value, the full width at half maximum of the exponential filter (Hz), was set to 1.05543a in order to describe a Hamming window [13] since an optimal filter in terms of ripple reduction and line broadening can be approximated that window [14].

On the other hand, by adding zeros after the FID last data point, an increase in the digital resolution was achieved. Apodization should be performed prior to zero filling avoid increasing the ripple phenomena.

Frequency Alignment
This step aligns the x-axis (parts per million) of the obtained signal spectrum. To perform this operation, as the value in the x-axis of the two highest peaks (metabolites) is defined, a new vector, created with the afore mentioned values was created. In particular, both water and NAA were used as a reference, with the values of 4.7 and 2.02, respectively.

Residual Water Suppression (RWS)
The presence RWS in the spectrum often increase the complexity of the signal analysis and generates accuracy errors in the quantification. Even when water suppression (WS) can be done during data acquisition, including WS in the postprocessing stage is recommended. In this work, the Hankel-Lanczos Singular Value Decomposition with Partial Reorthogonalization (HLSVD-PRO) technique was employed. A subspace-based method for modeling a sum of exponentially damped sinusoids (Lorentzians), which can be used as a frequency-selective filter [15], was used for perform WS. The filter order was set to 25.

Phase Correction
When FT is applied to the MRS signal, the resulting signal has a real part, known as absorption mode line, and an imaginary part, known as Lorentzian scattering mode [16]. Usually, at the beginning, Sx(t) (the real part of the FID), should be a maximum and Sy(t) (the imaginary part of the FID), zero. When this scenario is not possible, a two-step phase correction is required. Chen et al. [17] proposed a method for the two-step compensation based on entropy minimization, which was employed in this work, since good results were obtained even in the presence of considerable noise.

Baseline Correction
The estimation and correction of the baseline must be done because it can produce many systematic errors in quantification due to its superposition with the peaks of interest. In this work, the Golotvin's method was used to correct the baseline, where the order of the smoothing filter, the number of spectral points in the artificial rectangle, the noise factor and its definition were 20, 31, 4 and 100, respectively. It should be noticed that this values were selected using the guidelines provided in [18].

2.3 Quantification

Once the H-RMS signal is processed, the metabolite quantification can be safely done. Peaks corresponding of each metabolite need to be identified in order to calculate its respective area. Table 1 shows the ppm range used in this work to find the peak of each metabolite. To estimate the area of the metabolites peaks both a peak integration or a peak adjustment can be performed [19]. In this work, peak integration technique was used to reduce the number of variables controlled by the user, while at the same time maintaining algorithm automation.

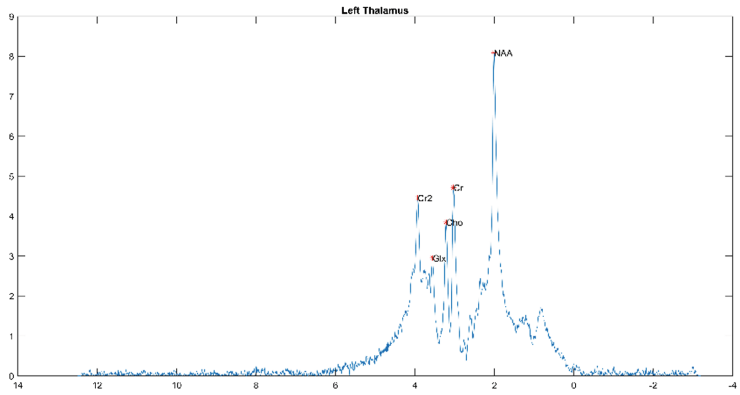

Fig. 1. Signal spectrum of a left region of a patient's thalamus after postprocessing and quantification stages. In the quantification stage, the first step is to identified the peaks (red indicator) and the curve corresponding of each metabolite to measure. Then, the area corresponding to the curve is calculated by the peak integration method.

3 Results

The proposed algorithm quantification results were compared with the results of a quantification analysis performed in a Philips magnetic resonance software. Thalamus signals were analyzed. Three characteristics of the signal corresponding of five different metabolites (NAA, Cr, Cho, Glx, Cr2) were obtained: width, height and area of the curve corresponding to each peak. From the table, it can be seen that the proposal method obtained similar results to the commercial software. Figure 1 shows the signal spectrum analyzed after the post-processing and quantification stages. Notice that the peaks corresponding to each quantified metabolite are marked with a red indicator. Full results of the comparations between the proposed method and the Philip software can be observed in Table 1.

Table 1. Comparation of the obtained results between Philip's software and proposed algorithm.

Thalamus metabolite	Chemical shift (ppm/x-axis) Tolerance = ±0.1	Philip software (area)	Proposed algorithm (area)	Absolute difference between methods (area)
NAA	2.02	0.648	0.6518	0.0038
Cr	3.02	0.359	0.24434	0.11466
Cho	3.20	0.337	0.32432	0.01268
Glx	3.70	0.211	0.26171	0.05071
Cr2	3.90	0.417	0.46679	0.04979

4 Discussion

This paper proposes an automatic process of MRS signal postprocessing and quantification. The obtained results can be considered as satisfactory, as a maximum absolute error of 0.11 is obtained. It is evident that further adjustments can be done in order to reduce the error, where a peak adjustment method should be developed. Future work will include a greater number of signals from diverse regions of the brain, suppress in a better way, the tails of some non interest metabolites to reduce error, and a greater number of quantified metabolites in each signal.

Conflict of Interest. The researcher claims no conflicts of interest.

References

1. Verma, A., Kumar, I., Verma, N., Aggarwal, P., Ojha, R.: Magnetic resonance spectroscopy - revisiting the biochemical and molecular milieu of brain tumors. BBA Clin. **5**, 170–178 (2016)
2. Preul, M., et al.: Accurate, noninvasive diagnosis of human brain tumors by using proton magnetic resonance spectroscopy. Nat. Med. **2**, 323–325 (1996)
3. Majós, C.: Espectroscopia por resonancia magnética de protón en el diagnóstico de tumores cerebrales. Radiologia **47**, 1–2 (2005)
4. Bustillo, J.R.: Use of proton magnetic resonance spectroscopy in the treatment of psychiatric disorders: a critical update. Dialogues Clin. Neurosci. **15**, 329–337 (2013)
5. Davie, C.A., et al.: Serial proton magnetic resonance spectroscopy in acute multiple sclerosis lesions. Brain **117**, 49–58 (1994)
6. Setzer, M., et al.: Diagnostic impact of proton MR-spectroscopy versus image-guided stereotactic biopsy. Acta Neurochir. (Wien) **149**(4), 379–385 (2007)
7. Orphanidou-Vlachou, E., et al.: Metabolite levels in paediatric brain tumours correlate with histological features. Pathobiology **85**(3), 157–168 (2018)
8. Wilson, M., et al.: Magnetic resonance spectroscopy metabolite profiles predict survival in paediatric brain tumours. Eur. J. Cancer **49**(2), 457–464 (2013)
9. Babourina-Brooks, B., et al.: Glycine: a non-invasive imaging biomarker to aid magnetic resonance spectroscopy in the prediction of survival in paediatric brain tumours. Oncotarget **9**(27), 18858–18868 (2018)
10. Garcia Osorio, I.M.: Advanced Signal Processing for Magnetic Resonance Spectroscopy, November 2011
11. Lin, C., Wendt, R.E., Evans, H.J., Hedrick, T.D., Leblanc, A.D., Rowe, R.M.L.: Eddy current correction in volume- localized MR spectroscopy. J. Magn. Reson. Imaging **4**, 823–827 (1994)
12. Klose, U.: In vivo proton spectroscopy in presence of eddy currents. Magn. Reson. Med. **30**, 26–30 (1990)
13. Weisstein, E.: WolframMathWorld (2019). http://mathworld.wolfram.com/FullWidthatHalfMaximum.html
14. Jiru, F.: Introduction to post-processing techniques. Eur. J. Radiol. **67**(2), 202–217 (2008)
15. Poullet, J.B., Sima, D.M., Van Huffel, S., Van Hecke, P.: Frequency-selective quantitation of short-echo time 1H magnetic resonance spectra. J. Magn. Reson. **186**(2), 293–304 (2007)
16. Keeler, J.: Fourier transformation and data processing (2004)

17. Chen, L., Weng, Z., Goh, L.Y., Garland, M.: An efficient algorithm for automatic phase correction of NMR spectra based on entropy minimization. J. Magn. Reson. **158**(1–2), 164–168 (2002)
18. Golotvin, S., Williams, A.: Improved baseline recognition and modeling of FT NMR spectra. J. Magn. Reson. **146**(1), 122–125 (2000)
19. Ernst, T., Chang, L.: Data Processing and Interpretation

Effects of Poor Junctions on the Effectiveness of Electromagnetic Shields of MRI Rooms

Rafael Navet de Souza[1,2] and Sérgio Santos Muhlen[1(✉)]

[1] Department and Center of Biomedical Engineering, University of Campinas, Campinas, Brazil
navet_r@yahoo.com.br, smuhlen@unicamp.br
[2] Siemens Healthineers Brazil, Rio de Janeiro, Brazil

Abstract. Nuclear magnetic resonance is a technique that produces high resolution volumetric images of the body without using ionizing radiation. The quality of images is significantly affected by electromagnetic fields in the environment, especially radio frequency signals and magnetic fields of 50/60 Hz, which results in the need for shielding of the room where the magnetic resonance imaging (MRI) equipment is installed. This study was undertaken to quantify the effects of poor shielding connections on image quality of MRI equipment. We compared the influence of poor connections on shielding effectiveness (SE) for magnetic fields of alternating currents in MRI cabinets with either ferromagnetic shielding (Fe-Si alloy non-oriented grain – NGO) or conductive shielding (Al). A computer simulation was compared to experimental measurements that used a metallic box with a volume of 1 m^3 and gaps of 0.5 mm in the sheet's connections. The SE of the Al shield was influenced more by the presence of gaps than the Fe-Si NGO shield.

Keywords: Magnetic shielding · Hospital environment · MRI

1 Introduction

Magnetic resonance imaging (MRI) equipment uses magnetic fields and radiofrequency (RF) waves. The technique is based on the phenomenon of nuclear magnetic resonance (NMR), discovered in 1938 and used since then for the analysis of chemical components. NMR is a physical phenomenon in which the nucleus of an atom or a given substance absorbs and emits energy in the form of radio waves in the presence of an external magnetic field. It is possible to determine the properties of the analyte by correlating the energy absorbed in each frequency of the electromagnetic spectrum (in the MHz range), such as a spectrometer [1].

When MRI equipment is installed in a hospital environment, magnetic shielding is often required to prevent uncontrolled exposure of the surroundings to any leakage of the magnetic field of the equipment and also to reduce the influence of local magnetic fields on the homogeneity of the magnetic field of the equipment [2]. This shielding is usually constructed of either ferromagnetic sheets or high-conductivity metals, such as Al or Cu. The preferred ferromagnetic material is an alloy of Fe-Si non-oriented grains (NGO), but the non-linearity of its magnetic properties must be considered in the design [3].

© Springer Nature Switzerland AG 2020
C. A. González Díaz et al. (Eds.): CLAIB 2019, IFMBE Proceedings 75, pp. 1226–1232, 2020.
https://doi.org/10.1007/978-3-030-30648-9_160

For MRI equipment, any reduction in the shielding effectiveness (SE) can result in artifacts in the image, produced by RF or by parasitic currents induced in the shielding or in any conductive part of the MRI apparatus. If these electromagnetic interferences are not mitigated, as required in the setup design, the resulting field within the shield will influence the RF signals or the gradient field.

When the RF signals coincide with the signals picked up by the reception coils, lines are generated as "zipper" artifacts in the images. Foucault (eddy) currents generate field gradients that coincide with the image gradient pulses. As the actual gradients experienced by the rotations in the image objects are not exactly the same as those programmed to produce and reconstruct the image, this error in the gradients, (which are not taken into account by the image reconstruction software), produces geometry distortions in the final images [4], as shown in Figs. 1a and b.

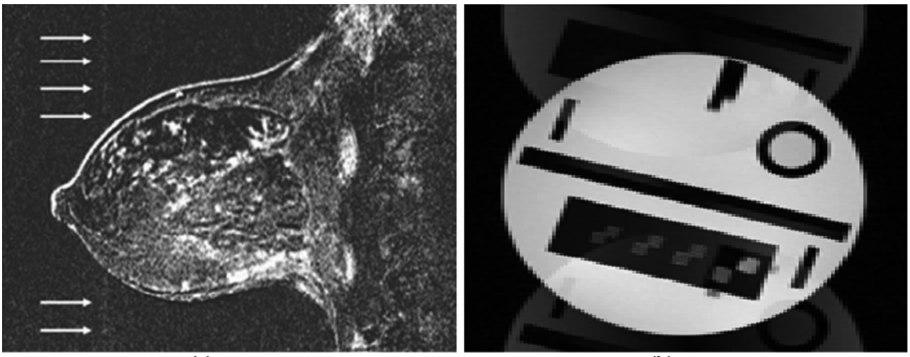

Fig. 1. (a) Vertical line artifact that runs in the direction of phase encoding [5]; (b) The image acquired with flat echo images from a single shot shows a N/2 phantom, a typical result of phase error.

Figures 2a and b show examples of gaps and poor junctions that are usually found in the shielding for MRI systems.

Fig. 2. Poor joints and connections between the plates create unwanted gaps (white arrows). (a) Fe-Si shield NGO; (b) Al shielding.

A shield can be specified in terms of the reduction of magnetic field strength, in decibels (dB). The use of decibels allows for the attenuation of the shield resulting from various effects to be calculated by summing the individually calculated effects for one or more mechanisms of attenuation in the same material. The shielding effectiveness is defined for magnetic flux density as follows [6]:

$$SE = 20 \log \frac{B_0}{B_i} \tag{1}$$

where SE [dB] = shielding effectiveness; B_0 = incident field; B_i = intensity of transmitted field emerging from the other side of the shield.

The aim of this study was to evaluate the influence of small gaps and imperfections on the shielding effectiveness of the AC magnetic field that can directly or indirectly affect the quality of the images produced by the MRI equipment. This study was motivated by the high demand for installation of MRI equipment in Brazil and the diversity of techniques used to construct and install the shielding among the many manufacturers of shielding. Often, they do not make the correct connections and unions as requested by the manufacturers of MRI systems.

2 Materials and Methods

The experiments and computational simulation were undertaken using both ferromagnetic and conductive materials for the shielding of the AC magnetic fields. In our experiments we used "1200 Al alloy" as the conductive material and "Fe-Si NGO E185" as the ferromagnetic material. These alloys are commonly used in the shielding of MRI examination rooms due to their availability in Brazil. The "1200Al alloy" features high thermal conductivity, very good weldability, very good resistance to atmospheric corrosion, an ease of bending and a high anodizing capacity [7]. Fe-Si Non-oriented grain E185 has excellent magnetic permeability, low losses and good magnetic properties in all directions [8].

2.1 Experiments

The objective of the experiments was to compare the influence of imperfections on Al and Fe-Si NGO shields in a controlled environment. The experiments consisted of performing measurements of the intensity of a 60 Hz magnetic field by varying the distance between the measurement point and the source of the magnetic field, also the thickness and metallic material of the shield.

The experimental shield structure was a metallic cubic frame (1 m-side) to which the plates of the shielding materials (Al or Fe-Si NGO) were fastened, in order to make it easier to change the number of plates (total thickness) and the type of material. The joints on the edges of the shield were kept open to create a small gap. Figure 3 shows the prototype with the gaps in the plate edges.

Fig. 3. Cubic structure covered with metallic plates with small gaps (white arrows) in the edge joints used in the experiments.

The measuring points P3-P5 (Fig. 4) represent the distances of 3 to 5 m from the source of the magnetic field in 1 m increments, while the thickness of the shield ranged between 0.5 and 2.0 mm. Measurements of shielding effectiveness were performed using a triaxial magnetic field sensor (magnetometer) mounted on a tripod inside the cubic shield and connected to a computer via a coaxial cable. The density of magnetic flux $\vec{B}$ obtained by the magnetometer was expressed in nanotesla [nT]. Figure 4 shows the electrical circuit used on the computational and experimental setup.

The 60 Hz magnetic field was generated by a coil of a single rectangular turn (19 m $\times$ 12 m loop), implemented with a flexible cable (ϕ 4 mm^2) suspended 60 cm from the ground. This cable supplied a resistive load (2 heaters) to generate a current of 18.4 A_{rms}.

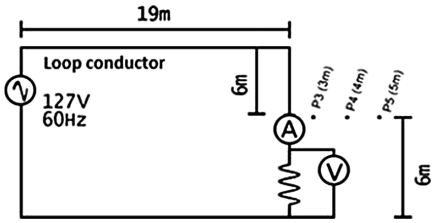

Fig. 4. Circuit used for computational simulation and experiments design. A rectangular coil (conductor loop) was used to generate the magnetic field, and the points P3-P5 are the measuring points representing the position of the center of the shield.

2.2 Computational Simulation

A computational simulation was performed for the installation of a cable that conducts a known current, and a cubic metal box with a thickness of 0.5 mm on the edges of all the plates, as was done in the experiments.

In addition to the simulations considering the imperfections in the shield (gaps), simulations were also performed considering a perfect shield, without gaps in the joints. Due the low density of magnetic flux [nT], we did not consider the non-linearities of Fe-Si NGO, assuming that the relative permeability was constant. The parameters used on the simulations are shown in Table 1 and the material properties are shown in Table 2.

Table 1. Parameters used in simulation.

Description	Value
Frequency f	60 Hz
Temperature T	20 ºC
Current I	18.4 A_{rms}
Thickness t	0.5 to 3 mm
Distance d	1 to 5 m

Table 2. Material properties.

Material	Electrical conductivity [10^6 S/m]	Relative permeability [H/m] @1.5 T
Al	34.5	1
Fe-Si NGO	2.6	1530

3 Results

The results shown in Fig. 5 represent the SE [dB] obtained from both the computational simulation and the experiments with gap, and SE [dB] of a perfect shield for (a) an Al shield; and (b) a shield composed of Fe-Si NGO.

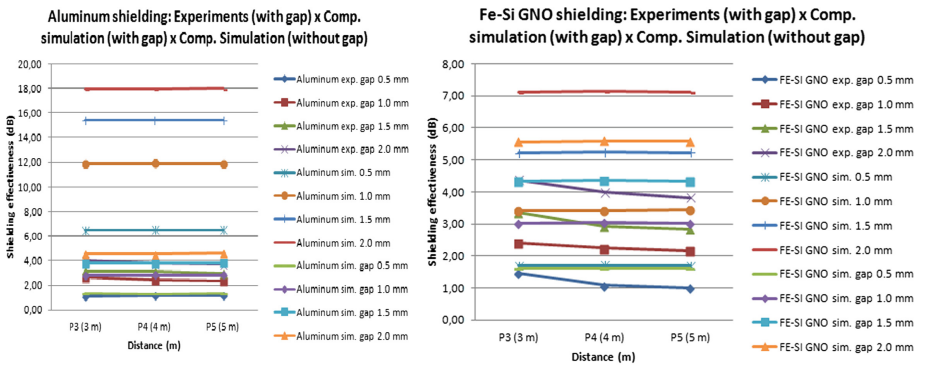

Fig. 5. Results obtained by computational simulation (sim.) and experiments (exp.) For the shielding effectiveness with different thicknesses and distances from the magnetic field source. (a) Al shield; (b) Fe-Si NGO shield.

4 Discussion

Poor joints connections in the Al shield caused a reduction in the shielding effectiveness from 5 to 15 dB, depending on the thickness of the shield, while the influence of those imperfections in the Fe-Si NGO shield caused a decrease in the shielding effectiveness of 1 to 5 dB, also depending on the thickness of the shield.

The results of the simulation of the Fe-Si NGO did not demonstrate any decrease of SE when the distance between the source and the shielding increased. This was because the non-linearities of Fe-Si NGO were not taken into account; it was assumed that the relative permeability was constant. This explains the differences between the results of the computational simulations and those of the experiments.

Al shields are known to be more effective than Fe-Si NGO for AC magnetic field shielding. However, gaps in the installation of Al shielding considerably reduced the SE, rendering it less effective than shielding with ferromagnetic materials. Nevertheless, conductive materials are lighter and usually easier to bend. weld or rivet than Fe-Si NGO, and maintain, as they do not rust.

These are the practical aspects that need to be considered in the construction and installation of magnetic shields for MRI rooms, and their long-term maintenance.

5 Conclusion

Imperfections in the construction of shielding for AC magnetic fields can affect the image quality of MRIs due to the production of artifacts, since these devices have maximum AC tolerance of the order of hundreds of nT. Our experiments and computational simulations demonstrated that small gaps due to imperfections in the construction of the metal shields can have a significant negative influence on shielding effectiveness.

References

1. Souza, R.N., Muhlen, S.S.: Advantages in the application of conductive shielding for AC magnetic field in MRI exam rooms. In: World Congress on Medical Physics and Biomedical Engineering. IFMBE Proceedings, vol. 68/3, pp. 577–580, May 2018
2. Noguchi, S., Ishiyama, A.: Optimal design method for MRI superconducting magnets with ferromagnetic shield. IEEE Trans. Magn. **29**(2), 1240–1244 (1993)
3. Yoshizawa, K., Noguchi, S., Igarashi, H.: Influence of magnetic property of ferromagnetic shield on high field magnet analysis. IEEE Trans. Appl. Superconducivity **21**(3), 2088–2091 (2011)
4. Erasmus, L.J., Hurter, D., Naudé, M., Kritzinger, H.G., Acho, S.: A short overview of MRI artefacts. SA J. Radiol. 13–17 (2004)
5. Hendrick, R.E.: Breast MRI: Fundamental and Technical Aspects. Springer, New York (2008)
6. Ott, H.W.: Electromagnetic Compatibility Engineering, 1st edn. Wiley (2009). ISBN 9780470189306

7. SMITH METAL. Technical Datasheet 1200 Aluminium. https://www.smithmetal.com/pdf/aluminium/1xxx/1200.pdf
8. Aperam South America. Aços Elétricos de Grão Orientado e de Grão Não-Orientado. https://brasil.aperam.com/wp-content/uploads/2015/08/A%C3%A7os-El%C3%A9tricos-GO-e-GNO.pdf

Thermography as a Diagnostic Tool for Early Detection of Diabetic Foot Ulceration Risk: A Review

Cesar A. Salazar(✉) and Martha L. Zequera Díaz

Electronics Department, School of Engineering, BASPI/FootLab,
Bioengineering, Signal Analysis and Image Processing Research Group,
Lab focused on Diabetes research,
Pontificia Universidad Javeriana, Bogotá D. C., Colombia
cesar_salazarc@javeriana.edu.co, mzequera@javeriana.edu.co

Abstract. Type 2 Diabetes Mellitus (DM2) is a disease that affects the following physiological systems: the central nervous system (CNS), the peripheral nervous system (PNS), the vascular system (VS), and the peripheral vascular system (PVS). When the PNS and PVS are affected, those complications are well known as diabetic neuropathy (DN) and diabetic vasculopathy (DV) respectively. These complications may cause lesions on the feet such as ulcers and are associated with other risk factors such as plantar pick pressure, friction from not wearing ergonomics footwear, the presence of biomechanics foot alterations, or significant temperature changes on the foot producing tissue infection that may cause lower limb amputation. The most important physiopathologies reported on the feet caused by the DN and DV are hypoesthesia and hyperthermia. These complications cause the loss of sensitivity and increase in temperature at the plantar surface respectively, and with continuously applied pressure, may initiate an ischemic or inflammatory problem. This multicausal condition of DM2 is known as Diabetic Foot Syndrome (DF), one of the main complications of the disease. Several studies have reported the correlation between ulcers and high temperatures under the plantar surface of the foot. Those temperature changes may be detected by using different methods. According to literary reviews, thermography is one of the methods most implemented by different researchers in laboratory environments. This method seems accurate in detecting temperature changes in the plantar foot anatomical regions by using image processing techniques, computer vision, and intelligent systems for improving ulcer detection in early stages of DF. The aim of this study is to define the benefits of using thermography as a future diagnostic tool for DF in a clinical environment based on the systematic literary review done in the last 15 years by BASPI-FootLab research group. Preliminary results of our review are reported in this paper.

Keywords: Type 2 Diabetes Mellitus · Diabetic foot · Image processing techniques · Protocol · Region of interest · Thermography

© Springer Nature Switzerland AG 2020
C. A. González Díaz et al. (Eds.): CLAIB 2019, IFMBE Proceedings 75, pp. 1233–1252, 2020.
https://doi.org/10.1007/978-3-030-30648-9_161

1 Introduction

Type 2 Diabetes Mellitus (DM2) is a pandemic disease, which is found to affect the metabolism of carbohydrates, the central nervous system (CNS), the peripheral nervous system (PNS), the vascular system (SV), and the peripheral vascular system (PSV). When the upper and lower extremities are affected it is known as diabetic neuropathy (DN) and diabetic vasculopathy (DV). These complications of DM2 are the precursors of the main cause of physical disabilities in diabetic patients due to biomechanical alterations in the biological systems involved on in motion, balance control, perception, and regulation of temperature related to metabolic disorders [1–3]. Among the changes at the neurological and vascular level associated with this disease, the loss of sensitivity and the increase in temperature was also found on the plantar surface respectively. Combined with other alterations such as the sustained presence of peak pressure on the plantar region, continuous friction due to the use of unsuitable footwear, the presence of osteomuscular deformities in the feet, among others, lead to the cause of imperceptible lesions that evolve rapidly. If these manifestations are detected at an earlier stage, more serious damage could be prevented such as ulcers, and therefore, amputations could be decreased. Those conditions combined with metabolic disorders due to the presence of DM2, also referred to as Diabetic Foot Syndrome (DFS), is the main cause of amputation in patients with DM2 in the world [4,5].

The complications of DM2 can be microvascular or macrovascular. The microvascular complications are lesions in the small blood vessels of the body. In these we find retinopathy, nephropathy, neuropathy, vasculopathy, DF, among others. In contrast, macrovascular complications are lesions in the larger blood vessels such as cardiovascular diseases [6].

In this way, the pathophysiology of DFS that affects the sensory systems of the body, known as DN, produce a direct relationship between DM2 and neuropathy, which is evident as the conduction of action potentials through the sural nerves and medial plantar decrease, which leads to hypoesthesia (decreased sensitivity); one of the main causes for the appearance of an ulcer [7–9]. At the same time, the pathophysiology of DFS induced by sustained hyperglycemia generates DV, which shows a degeneration of the vascular structure in the feet, arising from a thickening of the vascular structure blocking blood flow, causing hyperthermia (temperature increase) and anatomical and functional alterations in the sensory, motor, and autonomous systems [10–12]. With this, the DN and DV creates a relationship between the generation of tissue lesions and the increase in temperature at a continuously applied pressure, which initially produces damage to the deep tissue, and continues with cutaneous and subdermal damage, ultimately leading to the generation of ulcers based on pressure [13].

Statistics show that DM2 is among the 10 leading causes of death worldwide, equivalent to more than 80% of all deaths from noncommunicable diseases. Its prevalence between ages 20 and 79 corresponds to 425 million people and this in turn represents 8.8% of the world. Additionally, the number of deaths is 4 million people. One of the complications of DM2 is DFS which, associated with the DN and the DV, causes hypoesthesia and hyperthermia respectively on the plantar surface in anatomical regions of interest such as the toes, the metatarsal heads, the medial plantar region, the lateral plantar region, the tibial plantar region, among others, where significant alterations of body temperature generated from high levels of pressure applied continuously have been reported. This causes ischemia resulting in ulcers, and when infected ends in amputation. Furthermore, it is reported that its prevalence is between 16% and 66%, and the risk of amputations is 10 to 20 times more frequent compared to people who do not suffer from DN [14,15].

In conclusion, when the surface of the foot is losing sensitivity due to the DN, there is no perception of the pain caused by mechanical pressures applied continuously inside the shoes, while at the same time the DV causes an increase of temperature that may produce different lesions on the foot (ulcers), managing to generate loss of members.

2 Methodology and Methods

Previous studies have reported that thermography is an important technique in the detection of temperature changes [16,17]. In the DFS, significant temperature changes are detected on different anatomical regions of interest previously mentioned by means of image processing techniques, computer vision, and intelligent systems [18]. The normal values for temperature distribution in a healthy foot are defined as the "butterfly pattern" [19], but it has been shown that even without having a specific temperature value as a reference, the correlation between both feet is used where if the temperature difference is greater than 2.2 °C, there is a high risk of ulceration [20].

Below is a diagram that, after a systematic search of approximately 30 articles indexed in the last 15 years (2006–2019), will describe the progress, relevance, relationship, and implementation of thermography in detecting temperature changes for the prevention of possible areas of ulceration on the plantar surface of the diabetic foot (Fig. 1). Similarly, a detailed description is included of each protocol implemented for the acquisition of thermal images and videos, the use of various thermal imaging cameras, and the different regions of interest studied for each investigation implemented with thermography.

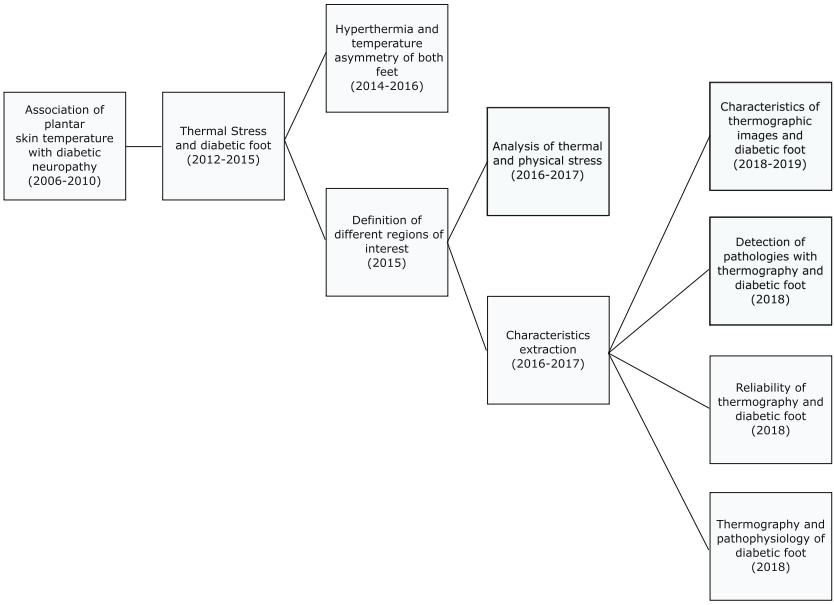

Fig. 1. Research timeline.

3 Thermography and the Diabetic Foot

It has been found according to literary review, that thermography is a technique which contributes to the detection of temperature changes in the biomedical areas such as breast cancer, varicocele, inflammatory diseases, skin abnormalities, among others. In the specific case of DFS, thermography detects temperature changes which may correspond to ischemic or inflammatory problems due to DV on possible anatomical regions of interest. These are obtained from image processing techniques, computer vision, and intelligent classification systems [21]. In addition, through the implementation of a good acquisition protocol which should be taken as reference from the "International Academy of Clinical Thermology (IACT)" [22], a non-profit organization committed to research, education, and the establishment of both standards and delineation in clinical thermography, where they demonstrate that thermography is completely non-invasive and does not require the use of radiation.

3.1 Association of Plantar Skin Temperature with Diabetic Neuropathy

The first studies between 2006 and 2010 (Table 1) showed that there is a relationship between temperature and DN through the design and implementation of a protocol, which should focus on the measurement of temperature in a certain number of regions of interest with the objective of being able to characterize the foot.

Table 1. Association of plantar skin temperature with diabetic neuropathy.

Reference (Year)	Study group	Protocol	Regions	Camera
Sun *et al.* (2006) [23]	25 control subjects and 29 (of 69) diabetic patients	Measurements in the mornings to eliminate the diurnal influence of the patients, remain in a sitting position for 15 to 20 min in a room temperature of 21 ± 1 °C	6 regions of interest (hallux, lesser toes, forefoot, arch, lateral sole and heel)	Spectrum 9000 MB (640 × 480 pixels)
Armstrong *et al.* (2007) [24]	225 high-risk diabetic patients with neuropathy and deformity in the structure of the foot, or with a history of ulceration or partial amputation	No protocol	6 regions of interest	Infrared skin thermometer TempTouch
Bagavathiappan *et al.* (2010) [25]	112 subjects with DM2	Remove both shoes and socks, remain in a supine position on a sofa for 5 min in a room with controlled temperature of 25 °C (air conditioning)	6 regions of interest (hallux, lesser toes, arch, lateral sole, forefoot, and heel)	No camera

Sun *et al.* [23] were the first research group that reported finding a relationship between the temperature of the plantar skin and the DN in a clinical study. The Sympathetic Skin Response (SSR) was found in both feet. They concluded that there was a significant abnormality in sweating with respect to thermoregulation over early sympathetic damage in the DFS. On the other hand, Armstrong *et al.* [24] evaluated the efficiency of measuring temperature to decrease the incidence of ulcers. Patients who presented a temperature difference between both feet higher than 2.2 °C, had to decrease their activity until the temperature normalized. For this measurement the opposite extremity was used as a control since both feet were exposed to the same stress during walking. In other words, they evaluated the efficiency of reducing the incidence of ulcers mainly in patients who had subsequently developed some type of ulcer. Similarly, Bagavathiappan *et al.* [25] reviewed the correlation between foot plantar temperature and DN. They found that patients with DN had higher temperatures on their feet compared to patients without neuropathy and also a correlation between the big toe of the right and left foot.

3.2 Thermal Stress and Diabetic Foot

During the period from 2012 to 2015 (Table 2), studies on thermal stress were started using image processing and thermographic video with the purpose of evaluating the recovery time generated by thermoregulation in response to VS in certain regions of interest.

Table 2. Thermal stress and diabetic foot.

Reference (Year)	Study group	Protocol	Regions	Camera
Barriga *et al.* (2012) [26]	8 people (3 controls, 3 diabetics without neuropathy and 2 diabetics with neuropathy)	Clean feet after removing shoes and socks, apply reflective markers and measure initial temperatures in the regions of interest with a thermometer, record a video for 2 min to get the base thermal signal (reference), submerge feet for 5 min in cold water (13 °C–14 °C), measure again with a thermometer and record a video for 15 min	6 regions of interest (great toe, third toe, third metatarsal, medial arch, lateral arch and heel)	FLIR SC305 (320 × 240 pixels)
Balbinot *et al.* (2013) [27]	20 patients (10 diabetics and 10 controls)	Recommendations given by The American Academy of Thermology, remain in a face-down position for 15 min in a controlled environment between 23 °C and 24 °C, apply a cold stress in order to increase the sensitivity in the diagnosis of neuropathy, by submerging feet in cold water (15 °C) for 60 s, obtain a base (reference) before thermal stress and then 10 min after applying thermal stress	5 regions of interest (big toe, first metatarsal, third metatarsal, fifth metatarsal and heel)	IRISYS® IRI 4010 (160 × 120 pixels)
Agurto *et al.* (2015) [28]	12 patients (7 controls and 5 diabetics)	Apply a cold stimulus on feet to lower the temperature to 13 °C in order to trigger the thermoregulation, make a video for 15 min to capture the recovery time	Spatial regions that were relevant for the classification of DM2	FLIR SC305 (320 × 240 pixels)

With reference to the above table, Barriga *et al.* [26] presented a computer-based system for the analysis of thermal images with the aim of detecting preclinical states of peripheral neuropathy. They monitored thermal videos of

microcirculatory recovery in the sole of the foot. They concluded that the magnitude of recovery was significantly different in the 2 study groups. Similarly, Balbinot *et al.* [27] used infrared thermography as a complementary diagnosis in distal diabetic neuropathy. They applied a cold stress in order to increase the sensitivity in the diagnosis of neuropathy, with the purpose of evaluating the induced thermoregulation response based on thermal stress (cold). In the same way, Agurto *et al.* [28] characterized the DN by using an infrared imaging device and Independent Component Analysis (ICA). They separated the temporal and spatial components to be able to represent the thermoregulation in response to the cold stimulus between control and diabetic patients, identifying the spatial regions that were relevant for the classification of DM2.

3.3 Definition of Different Regions of Interest on the Diabetic Foot

Already aware of the temperature relationship in the DFS and the first indications that there is a correlation between the temperature of both feet, in 2015 (Table 3), D. Hernández *et al.* began to perform a variety of studies of foot characterizations using different methods based on thermographic image processing.

Table 3. Definition of different regions of interest on the diabetic foot Part 1.

Reference (Year)	Study group	Protocol	Regions	Camera
Hernandez-Contreras *et al.* (2015) [29]	44 participants (24 non-diabetics and 20 diabetics)	Recommendations given by the International Academy of Clinical Thermology: remove shoes and socks, clean feet with a humid towel, remain in a supine position for 15 min in a temperature-controlled room of 21 ± 1 °C	Regions with higher temperature)	Spectrum 9000 MB (640 × 480 pixels)
Hernandez-Contreras *et al.* (2015) [30]	60 participants (30 non-diabetics and 30 diabetics)	Recommendations given by the International Academy of Clinical Thermology: removing shoes and stockings, clean feet with a damp towel, remaining in a supine cube position for 15 min in a temperature-controlled room of 21 ± 1 °C, use an obstructive device of infrared light to separate the temperature of the feet from the rest of the body	No regions	FLIR E60 (320 × 240 pixels)

In the first study [29], they presented a preliminary classification method to detect temperature patterns based on thermal image processing. They identified areas of higher temperature related to the high risk of patients by acquiring the thermal images of the areas of interest in isolation, followed by an analysis of these areas for their classification. In the second study [30], they characterized and identified temperature patterns in thermographic images of the sole of the foot, identifying the areas of higher temperature. They were able to establish characteristic vectors based on the patterns of the spectrum and the relative position of their 3D morphology, creating a system to quantify and discriminate characteristics using a neural network with which they obtained a classification rate of 94.33% in the extractions.

That same year (Table 4), studies continued in relation to the different regions, and in turn, with its correlation (asymmetry) between the temperature of both feet, reached the definition of different regions based on various studies of temperature, all this, using thermographic image processing techniques.

Table 4. Definition of different regions of interest on the diabetic foot Part 2.

Reference (Year)	Study group	Protocol	Regions	Camera
Neves *et al.* (2015) [31]	44 volunteers (22 women and 22 men) with DM2	Temperature and humidity controlled at 20 ± 1 °C and 55% respectively by using a thermohydrometer	3 regions of interest (the first finger, the fifth finger and the heel)	FLIR SC2000 (320 × 240 pixels)
Nandagopan and Bhargavi Haripriya (2016) [32]	20 people (10 diabetics and 10 controls)	Keep feet on a bench, cover the wall with a black cloth to eliminate the reflection radiation and cover feet with a black cardboard box to eliminate the body temperature	No regions	FLIR SC305 (320 × 240 pixels)

In this way, Neves *et al.* [31] conducted a cross-sectional study. The region with more asymmetric temperatures in comparison between both feet (regions greater than 2.2 °C) was selected for the DFS risk analysis, showing that there was a correlation between the temperatures of both feet. The next year, Nandagopan and Bhargavi Haripriya [32] implemented two techniques for segmentation of thermal images of the foot. They compared the soles of the feet with the help of asymmetrical temperatures, in order to try to identify ulcers in patients at an early stage.

3.4 Hyperthermia and Temperature Asymmetry of both Feet

During 2014, 2015 and 2016 (Table 5) different results were published corresponding to studies in thermography applied to the early detection of ulcers, in which the concept of hyperthermia was defined in the DFS to relate to the temperature correlation (asymmetry) of both feet through the development of different protocols for the acquisition of thermographic images.

Table 5. Hyperthermia and temperature asymmetry of both feet.

Reference (Year)	Study group	Protocol	Regions	Camera
Vilcahuaman *et al.* (2014) [33]	85 diabetic people	Stay for 15 min in the controlled temperature environment of 23 ± 3 °C to reach the thermodynamic equilibrium, cover feet by a black cover (polyurethane foam) to eliminate the temperature of the body	No regions	FLIR i5 (100 × 100 pixels)
Vilcahuaman *et al.* (2014) [34]	82 diabetic patients in a pre-ulcerative	Stay for 15 min in the controlled temperature environment of 23 ± 3 °C by eliminating external infrared sources to reach the thermodynamic equilibrium and cover feet with a black cover (polyurethane foam) to eliminate the body temperature	No regions	FLIR i5 (100 × 100 pixels)
Liu *et al.* (2016) [35]	60 diabetic patients	Stay for 15 min in the controlled temperature environment of 23 ± 3 °C to reach the thermodynamic equilibrium and cover feet with a black cover (polyurethane foam) to eliminate body temperature	No regions	FLIR i5 (100 × 100 pixels)

Two out of three studies were demonstrated by Vilcahuaman *et al.*, in the first one (2014) [33], proposed a simple way to detect hyperthermia. They developed a dedicated analysis of the thermographic images, which consisted of a contour detector on both feet using Chan-Vese active contours associated with the Rigid Interactive Closest Point registration technique. In this way, they were able to detect the hyperthermia in the DFS in the regions of interest which corresponded to the areas that had a temperature greater than 2.2 °C when compared on both feet. In the second one (2015) [34], analyzed the variation of temperatures. They developed an image processing software, performing 3 types of analysis. First, the average temperature of the plantar surface of the feet based on the segmentation of Chan-Vese active contours. Second, the absolute average difference between the 2 ft using a registration method based on Rigid Interactive Closest Point. And third, in the regions of interest which determined the hyperthermia, they highlighted the areas where the absolute difference in comparison of both feet was greater than 2.2 °C. One year later, Liu *et al.* [35] developed a system which processed essential medical images by segmentation, localization and regionalization based on an adaptive algorithm of active contours, acquiring the absolute average temperature in seven different regions (four plantar angiosomes), where hyperthermia was studied comparing both feet in the regions mentioned above.

3.5 Characteristics Extraction on the Diabetic Foot

In parallel and as a complement to the studies realized with the definition of different regions of the foot and implementation of protocols in 2016 and 2017 (Table 6) the characteristics extraction based on different regions was continued by D. Hernández *et al.* in three studies. They evaluated the correlation (asymmetry) between the temperatures of both feet.

Table 6. Characteristics extraction on the diabetic foot.

Reference (Year)	Study group	Protocol	Regions	Camera
Hernandez-Contreras *et al.* (2016) [36]	No study group	Remove shoes and socks, and remain seated in a supine position during 15 to 20 min in order to reach the thermal equilibrium	No regions	No camera
Hernandez-Contreras *et al.* (2017) [37]	140 patients (40 controls and 100 diabetics)	Recommendations given by the International Academy of Clinical Thermology: remove shoes and socks, clean feet with a damp towel to remove any particles or product, remain in a supine position for 15 min to reach the thermodynamic equilibrium in a temperature-controlled room of 21 $\pm$ 1 °C, use an obstructive infrared light device to separate the temperature of the feet of the rest of the body	4 angiosomes (medial plantar artery, lateral plantar artery, medial calcaneal and lateral calcaneal artery)	FLIR E60 (320 $\times$ 240 pixels)
Hernandez-Contreras *et al.* (2017) [38]	135 volunteers (35 controls and 100 diabetics)	Remove shoes and socks, clean feet with a damp towel and remain in a supine cube position for 15 min, place feet in an upright position in order not to affect the temperature by the blood pressure	Temperature distribution that may cause some complication	FLIR E60 (320 $\times$ 240 pixels)

In the first one (2016) [36], the relationship between temperature variation and DFS problems was demonstrated using infrared thermography. They presented a literature review corresponding to different protocols, regions of interest, methods of analysis with their respective advantages and disadvantages, analysis of asymmetrical temperatures between both feet of each method, and the potential of infrared thermography for DFS. In the second study (2017) [37], spatial temperature patterns dividing the foot into four angiosomes was identified. They proposed a quantitative method of measurement on temperature changes in the plantar region with participants diagnosed with DM2. This demonstrated a great diversity in the spatial distribution of DFS identifying common characteristics.

Therefore, they defined the concept of the "butterfly pattern" to describe the temperature distribution of the control group and to arrive at a comparison with the diabetic group. They concluded that the asymmetry of the temperatures of both feet had its limitations at the moment in which the patient had similar complications in both feet. In the third study (2017) [38], they identified changes in the distribution of plantar temperatures related to DFS complications. Based on the divergences of Kullback-Leibler and Jesen-Shannon they identified changes in the distribution of the plantar temperature in 82% of the 200 samples in which they presented a distribution that may cause some complications.

3.6 Analysis of Thermal and Physical Stress on the Diabetic Foot

That same year (2017), an analysis of thermal and physical stress was again carried out using thermography. This time, it was a comparison of different techniques where the objective was to study the reaction of the body's thermoregulation system in an environment where thermal stress (apply cold or hot water), and/or physical stress (running or walking) was applied.

Based on the above, Adam *et al.* [39] performed an exploration of physiopathology, conventional evaluation methods, infrared thermography and infrared thermography based on the CAD analysis (Computer-Aided Diagnosis) of the DFS was performed, deepening the infrared thermography analysis. In this they presented a literature review corresponding to the analysis of the temperature of the lower limbs, the analysis of the asymmetrical temperatures, the analysis of the temperature distribution, and the analysis of both thermal and physical stress. Included in the description of the analysis of asymmetrical temperatures is a proposal for the detection of inflammation and prediction of ulcers by using infrared thermography through an asymmetry analysis, an analysis based on a scalable scanning technique of asymmetry, with the purpose of comparing both feet of different sizes and shapes. In addition, a method with which they evaluated the temperature of the skin by means of taking the average of the temperatures between the right and left foot was included, showing the possibility of being a good marker to determine the necessity of treatment. For the analysis of the temperature distribution, they commented on an observational study where the temperature distribution of a healthy foot is described as symmetrical known as the "butterfly pattern," and they commented on a proposal for a method of characterization of thermal plantar patterns based on the concept of plantar angiosomes. Finally, the analysis of thermal and physical stress, where they describe that the pattern of abnormal temperature changes is classified into 3 types: increasing, decreasing, and flat. The cold induced in infrared thermography helps in the evaluation of the peripheral atherosclerosis condition and identification of patients with microvascular abnormalities. Likewise, they confirm that the low recovery rate in diabetic patients is for peripheral arterial sclerosis, abnormal blood coagulation (fibrinolysis), sympathetic nerve dysfunction, and the correlation between plantar stress and the increase in temperature in the sole of the foot after exercising through the use of infrared thermography.

3.7 Characteristics of Thermographic Images and Diabetic Foot

At present, in 2018 and 2019 (Table 7), different lines of research are defining the use of infrared thermography. The first study focuses on the continuation of the extraction of characteristics and segmentation of thermographic images of the foot.

Table 7. Characteristics of thermographic images and diabetic foot.

Reference (Year)	Study group	Protocol	Regions	Camera
Adam *et al.* (2018) [40]	33 healthy people and 33 individuals with DM2	Removed shoes and socks, clean feet, remain in a supine position for 15 min in a controlled temperature and humidity room of 21 ± 1 °C and 55 ± 5% respectively	No regions	VarioCAM® HD (640 × 480 pixels)
Astasio-Picado *et al.* (2018) [41]	277 diabetic patients	No protocol	4 regions of interest (head of the first metatarsal bone, head of the fifth metatarsal bone, heel and first finger pulp)	FLIR E60bx (320 × 240 pixels)
Bandalakunta Gururajarao *et al.* (2019) [42]	82 patients (62 diabetics and 20 controls)	Remove shoes and socks, remain seated or in a supine position for 15 to 20 min in order to reach thermal equilibrium	6 regions of interest (region of the big toe, region given by the other fingers, region of the plantar arch, region of the lateral medial plant, internal region of the heel and external region of the heel)	No camera
van Doremalen *et al.* (2019) [43]	32 participants with DM2	Sit in a supine position for 5 min at room temperature to reach the temperature equilibrium of the foot	9 regions of interest (big toe, first, third and fifth metatarsal head, metatarsal cuneiform joint, cuboid, third and fifth toe and lateral cuneiform metatarsal joint)	FLIR ONE (160 × 120 pixels), FLIR SC305 (320 × 240 pixels)

As stated by Adam *et al.* [40], who carried out a study of the thermograms of the sole of the foot, they managed to acquire images which were treated with the techniques of Discrete Wavelet Transform and Higher-Order Spectra, extracting different characteristics of texture and entropy, obtaining a precision of 89.39%,

a sensitivity of 81.81%, and a specificity of 96.67% with only 5 characteristics. Likewise, Astasio-Picado *et al.* [41] studied the use of infrared thermography finding that there was a correlation (asymmetry) when comparing the temperature of both feet in diabetic patients. As a result, they made an analysis of the temperature variability in the feet, achieving segmentation of the sole of the foot, and concluding the importance of the use of infrared thermography in the assessment of the risk of DFS.

Similarly, Bandalakunta Gururajarao *et al.* [42] used medical infrared thermography and Deep Learning algorithms for evaluation of DFS, where they extracted abnormal regions by qualifying the level of complexity and making decisions to suggest some additional action based on the processing output. They studied the patterns of the distribution of the surface of the sole of the foot in the control group (butterfly pattern) and the diabetic groups (with and without complications) and the correlation between regions of interest where the temperature was higher than 2.2 °C when being compared in both feet to finally establish temperature differences capable of making an early diagnosis. In the same way, van Doremalen *et al.* [43] used two smartphone cameras for DFS evaluation capturing the infrared images with both cameras. They found contralateral temperature differences in the whole sole of the foot by the implementation of the correlation coefficients between classes (asymmetry of temperatures higher than 1.35 °C between the lateral parts of both feet and temperatures higher than 2.2 °C between the parts against the sides of both feet) and the Bland-Altman graphs. They concluded that the infrared smartphone camera shows an excellent validation of the DFS evaluation.

3.8 Detection of Pathologies with Thermography and Diabetic Foot

The following group of studies (Table 8) is based on the detection and comparison of the DFS against different pathologies; either DM2 or any other disease that affects peripherals, mainly in the lower extremities.

Adam *et al.* [44] proposed an automatic system for the detection of DFS in diabetics with and without neuropathy. They segmented the thermograms of the sole of the foot by decomposing them into coefficients using the Double Density-Dual Tree-Complex Wavelet Transform (DD-DT-CWT). The developed a system with 93.16% of accuracy, 90.91% of sensitivity and 98.04% of specificity using only 4 characteristics of Local Sensitivity Discriminant Analysis (LSDA). Similarly, Gatt *et al.* [45] investigated the heat emitted by the feet. They used thermographic images and automatically segmented regions extracted by the temperature data finding significant differences between both groups, mainly in diabetics, based on the correlation (asymmetry) of the temperature difference of both feet (values higher than 2.2 °C).

Table 8. Detection of pathologies with thermography and diabetic foot.

Reference (Year)	Study group	Protocol	Regions	Camera
Adam *et al.* (2018) [44]	51 healthy individuals and 66 diabetics (33 with and 33 without neuropathy)	Remove shoes and socks, clean feet, and remain in a supine position for 15 min in a controlled temperature and humidity room of 21 ± 1 °C and 55 ± 5% respectively	No regions	VarioCAM® HD (640 × 480 pixels)
Gatt *et al.* (2018) [45]	84 patients with DM2 and Peripheral Arterial Diseases (PAD)	Recommendations given by American Academy of Thermology: remain in a supine position for 15 min in a room with controlled temperature of 22.63 ± 2.28 °C and a relative humidity of 33.50 ± 8.10%, avoiding external air sources and sunlight on the camera lens	6 regions of interest (5 toes and mean forefoot)	FLIR SC7200 (320 × 250 pixels)

3.9 Reliability of Thermography and Diabetic Foot

Another current line (Table 9) focuses on the reliability during the acquisition of thermographic images, which shows that thermography has been and continues to be a very important tool for studies related to DFS.

Table 9. Reliability of thermography and diabetic foot.

Reference (Year)	Study group	Protocol	Regions	Camera
Silva *et al.* (2018) [46]	51 diabetic patients	Remain in the supine cube position for 15 min, during this time do not touch feet, electronic equipment that could modify the measurement was removed, controlled room of 23 °C, place a black box on feet in order to eliminate the heat generated by the body	9 regions of interest (first, third and fifth toe, first, third and fifth metatarsal head, cuboid, internal region of the heel and external region of the heel and heel)	FLIR E60 (320 × 240 pixels)

(*continued*)

Table 9. (*continued*)

Reference (Year)	Study group	Protocol	Regions	Camera
Seixas *et al.* (2018) [47]	13 diabetic patients with DM2	Take the photos in the morning away from air and infrared sources, take 10 min of acclimatization for the room with a controlled temperature of 23.3 ± 0.6 °C and a relative humidity of 54.4 ± 5.5%	6 regions of interest (the sole foot and 5 angiosomes: anterior tibial artery, posterior tibial artery, peroneal artery, medial calcaneal artery and lateral plantar artery)	FLIR E60 (320 × 240 pixels)

Silva *et al.* [46] rated the intra-reliability and inter-reliability of the images evaluated by infrared thermography of the plantar surface. They found a 95% correlation in all the points analyzed. In addition, Seixas *et al.* [47] evaluated the intra-reliability and inter-reliability of foot skin temperature analysis based on the angiosome concept. They associated skin temperature in 6 different sizes of RoI (Regions of Interest). They performed the respective evaluation of the study using the Intraclass Correlation Coefficient (ICC) and the measurements agreed upon by Bland and Altam and the Standard Error Measurement (SEM).

3.10 Thermography and Pathophysiology of Diabetic Foot

Finally, the last line of study (Table 10) focuses on the comparison and relationship of thermography with the pathophysiology of DFS, by relating changes in sensitivity and temperature-related lesions.

Table 10. Thermography and pathophysiology of diabetic foot.

Reference (Year)	Study group	Protocol	Regions	Camera
Renero-C (2018) [48]	186 patients with DM2	Recommendations given by the Academy of Clinical Thermology Standards and Protocols	No regions	FLIR E6 (320 × 240 pixels)

Renero-C [48], identified different regions of the plantar skin with deficiencies in the blood supply and the behavior of the thermoregulation process. By means of analysis of local regions with low and high temperatures they identified that these corresponded to ischemia or inflammatory problems, and in turn, the distribution of temperature in normal regions of the foot did not vary more than 2.2 °C when both feet were compared (asymmetry). Finally, they found specifically in two patients during a follow-up session a considerable increase in temperature, loss of sensitivity, and development of ulcers in the regions identified above.

4 Discussion

As described above, the implementation of the different protocols since 2006 (Tables 1, 2, 3, 4, 5, 6, 7, 8, 9 and 10), shows us a clear idea of the importance in having a rigorous protocol in thermography. The evolution of these protocols tells us that taking a good thermographic image is required in a controlled environment (temperature) as described by [23,25,29–31,33–35,37,40,44–47], and at the same time, a relaxing position for the patients like the supine position described by [25,29,30,36–38,40,42–46] is required in order to reach thermal equilibrium.

Thermal and physical stress described by [23,26–28,39] are useful to analyze the recovery time and the dynamic temperature of the foot. As it is known that the alterations generated by diabetes increases this recovery time compared with a healthy foot, it's important to improve the actual protocols as well as the protocols that analyze the static temperature in a thermal image.

In addition, these studies used a variety of thermal cameras with different thermal image sizes but didn't appear to need to calibrate each camera sensor according to its specifications (emissivity and reflected temperature) to get a good temperature measurement.

Despite being performed with few patients, several studies show us a good complementation when using the distribution of temperatures in the healthy foot described by [20,37,39,42] known as the "butterfly pattern," with the help of the correlation that exists when comparing the different temperatures in both feet as described by [19,25,39,41,42,45,48], in order to detect and classify DFS in different regions of interest. This include 3 regions according to [31], 4 regions according to [37,41], 6 regions according to [23–27,42,45,47] and 9 regions according to [43,46]. The distribution of temperatures and the correlation when comparing both feet are the most transcendental characteristics for the detection of possible areas of risk of ulceration based on heat maps. In addition, thermography is a non-invasive technique, simple to implement, and easy for patients to accept. For those reasons it is a technique that requires and deserves further exploration.

5 Conclusions

Based on the literature research reported in this paper seems that thermography could be a relevant diagnostic tool for early detection of diabetic foot ulceration risk. The first reason could be due to the relationship between thermography and DFS documented in previous studies, and in addition it was found associations between Hypoesthesia and hyperthermia with the pathophysiology of DFS, which is affecting the nervous and vascular systems, producing a loss of sensitivity and increase temperature, and leading to the appearance of ulcers. The second reason is because thermography is a non-invasive method that may easily detect temperature changes on the sole of the foot at low cost. In the other hand, it was mentioned initially of this paper highlighting of the importance to implement of a good protocol for the acquisition of the plantar surface thermographic images and video, taking into account all the parameters described

in this review such as a: controlled environment and a relaxed position for the patient, defined the anatomic foot areas of interest were the main Author Proof Thermography: also a review was made of 17 studies in images processing and computer vision; the better the capture is made, the less processing must be done on the image. It was concluded that is possible to implement those studies at our research FootLab in Colombia in order to use thermography as a diagnostic tool for the early detection of diabetic foot ulceration risk in our region.

Acknowledgment. The authors acknowledge Pontificia Universidad Javeriana, BASPI-FootLab, Research and Innovation Staff Exchange (RISE), H2020-MSCA-RISE and the project *STANDUP* #777661 *"Smartphone Thermal Analysis for Diabetic foot Ulcer Prevention and treatment STANDUP"*.

References

1. American Diabetes Association (ADA): Standards of medical care in diabetes - 2016. Diabetes Care. J. Clin. Appl. Res. Educ. (2016)
2. Shubrook, J., Butts, A., Chamberlain, J.J., Johnson, E.L., Leal, S., Rhinehart, A.S., Skolnik, N., Bradley, S., Jaffa, F.M., Herman, W.H., Kalyani, R.R., Cherrington, A.L., Coustan, D.R., De Boer, I., James, R., Feldman, H., Florez, H.J., Koliwad, S., Maryniuk, M., Neumiller, J.J., Wolfsdorf, J., Berg, E.G., McAuliffe-Fogarty, A.H., Ratner, R.: Standards of medical care in diabetes-2017 abridged for primary care providers. Clin. Diabetes **35**, 5–26 (2017)
3. American Diabetes Association (ADA): Standard medical care in diabetes 2018. J. Clin. Appl. Res. Educ. (2018)
4. Alavi, A., Sibbald, R.G., Mayer, D., Goodman, L., Botros, M., Armstrong, D.G., Woo, K., Boeni, T., Ayello, E.A., Kirsner, R.S.: Diabetic foot ulcers: part I. Pathophysiology and prevention (2014)
5. Alavi, A., Sibbald, R.G., Mayer, D., Goodman, L., Botros, M., Armstrong, D.G., Woo, K., Boeni, T., Ayello, E.A., Kirsner, R.S.: Diabetic foot ulcers: part II. Management (2014)
6. WHO—World Health Organization. http://www.who.int/
7. Im, S., Kim, S.R., Park, J.H., Kim, Y.S., Park, G.Y.: Assessment of the medial dorsal cutaneous, dorsal sural, and medial plantar nerves in impaired glucose tolerance and diabetic patients with normal sural and superficial peroneal nerve responses. Diabetes Care **35**, 834–839 (2012)
8. Zeng, J., Xu, Y., Shi, Y., Jiang, C.: Inflammation role in sensory neuropathy in Chinese patients with diabetes/prediabetes. Clin. Neurol. Neurosurg. **166**, 136–140 (2018). https://www.sciencedirect.com/science/article/pii/S0303846718300374?via%3Dihub
9. Park, J.H., Won, J.C.: Patterns of nerve conduction abnormalities in patients with type 2 diabetes mellitus according to the clinical phenotype determined by the current perception threshold. Diabetes Metab. J. **42**, 519–528 (2018). https://doi.org/10.4093/dmj.2018.0068
10. Ahmad, J.: The diabetic foot. Diabetes Metab. Syndr. Clin. Res. Rev. **10**(1), 48–60 (2016). http://linkinghub.elsevier.com/retrieve/pii/S0011384016300739, http://linkinghub.elsevier.com/retrieve/pii/S1871402115000302
11. Lepäntalo, M.J., Kallio, M., Albäck, A.: Diabetic foot. In: Vascular Surgery: Cases, Questions and Commentaries (2018)

12. Boulton, A.J.: The diabetic foot (2019)
13. Kokate, J.Y., Leland, K.J., Held, A.M., Hansen, G.L., Kveen, G.L., Johnson, B.A., Wilke, M.S., Sparrow, E.M., Iaizzo, P.A.: Temperature-modulated pressure ulcers: a porcine model. Arch. Phys. Med. Rehabil. **76**, 666–673 (1995)
14. International Diabetes Federation: IDF Diabetes Atlas, 8th edn. Belgium, Brussels (2017). http://www.diabetesatlas.org/
15. Cho, N.H., Shaw, J.E., Karuranga, S., Huang, Y., da Rocha Fernandes, J.D., Ohlrogge, A.W., Malanda, B.: IDF diabetes atlas: global estimates of diabetes prevalence for 2017 and projections for 2045. Diabetes Res. Clin. Pract. **138**, 271–281 (2018)
16. Childs, C.: Body temperature and clinical thermometry. In: Handbook of Clinical Neurology (2018)
17. Law, J., Morris, D.E., Budge, H., Symonds, M.E.: Infrared thermography. In: Handbook of Experimental Pharmacology (2019)
18. Roback, K.: An overview of temperature monitoring devices for early detection of diabetic foot disorders (2010)
19. Chan, A.W., MacFarlane, I.A., Bowsher, D.R.: Contact thermography of painful diabetic neuropathic foot. Diabetes Care **14**, 918–922 (1991)
20. Liu, C., van der Heijden, F., Klein, M.E., van Baal, J.G., Bus, S.A., van Netten, J.J.: Infrared dermal thermography on diabetic feet soles to predict ulcerations: a case study. In: Advanced Biomedical and Clinical Diagnostic Systems XI (2013)
21. Nola, I.A., Kolanc, D.: Thermography in biomedicine. In: Proceedings Elmar - International Symposium Electronics in Marine, vol. 2015, pp. 17–20, November 2015
22. IACT—International Academy of Thermology. https://www.iact-org.org/
23. Sun, P.C., Lin, H.D., Jao, S.H.E., Ku, Y.C., Chan, R.C., Cheng, C.K.: Relationship of skin temperature to sympathetic dysfunction in diabetic at-risk feet. Diabetes Res. Clin. Pract. **73**, 41–46 (2006)
24. Armstrong, D.G., Holtz-Neiderer, K., Wendel, C., Mohler, M.J., Kimbriel, H.R., Lavery, L.A.: Skin temperature monitoring reduces the risk for diabetic foot ulceration in high-risk patients 120. Am. J. Med. **120**, 1042–1046 (2007)
25. Bagavathiappan, S., Philip, J., Jayakumar, T., Raj, B., Rao, P.N.S., Varalakshmi, M., Mohan, V.: Correlation between plantar foot temperature and diabetic neuropathy: a case study by using an infrared thermal imaging technique. J. Diab. Sci. Technol. **4**, 1386–1392 (2010)
26. Barriga, E.S. Chekh, V., Carranza, C., Burge, M.R., Edwards, A., McGrew, E., Zamora, G., Soliz, P.: Computational basis for risk stratification of peripheral neuropathy from thermal imaging. In: Proceedings of the Annual International Conference of the IEEE Engineering in Medicine and Biology Society, EMBS (2012)
27. Balbinot, L.F., Robinson, C.C., Achaval, M., Zaro, M.A., Brioschi, M.L.: Repeatability of infrared plantar thermography in diabetes patients: a pilot study. J. Diab. Sci. Technol. **7**, 1130–1137 (2013)
28. Agurto, C., Barriga, S., Burge, M., Soliz, P.: Characterization of diabetic peripheral neuropathy in infrared video sequences using independent component analysis. In: IEEE International Workshop on Machine Learning for Signal Processing, MLSP (2015)
29. Hernandez-Contreras, D., Peregrina-Barreto, H., Rangel-Magdaleno, J., Ramirez-Cortes, J., Renero-Carrillo, F., Avina-Cervantes, G.: Evaluation of thermal patterns and distribution applied to the study of diabetic foot. In: Conference Record - IEEE Instrumentation and Measurement Technology Conference, vol. 2015, pp. 482–487, July 2015

30. Hernandez-Contreras, D., Peregrina-Barreto, H., Rangel-Magdaleno, J., Ramirez-Cortes, J., Renero-Carrillo, F.: Automatic classification of thermal patterns in diabetic foot based on morphological pattern spectrum. Infrared Phys. Technol. **73**, 149–157 (2015)
31. Neves, E.B., Almeida, A.J., Rosa, C., Vilaca-Alves, J., Reis, V.M., Mendes, R.: Anthropometric profile and diabetic foot risk: a cross-sectional study using thermography. In: 2015 37th Annual International Conference of the IEEE Engineering in Medicine and Biology Society (EMBC), pp. 1–3 (2015). http://ieeexplore.ieee.org/document/7445519/
32. Nandagopan, G.L., Bhargavi Haripriya, A.: Implementation and comparison of two image segmentation techniques on thermal foot images and detection of ulceration using asymmetry. In: International Conference on Communication and Signal Processing, ICCSP (2016)
33. Vilcahuaman, L., Harba, R., Canals, R., Zequera, M., Wilches, C., Arista, M.T., Torres, L., Arbañil, H.: Detection of diabetic foot hyperthermia by infrared imaging. In: 2014 36th Annual International Conference of the IEEE Engineering in Medicine and Biology Society, EMBC (2014)
34. Vilcahuaman, L., Harba, R., Canals, R., Zequera, M., Wilches, C., Arista, M.T., Torres, L., Arbañil, H.: Automatic analysis of plantar foot thermal images in at-risk type ii diabetes by using an infrared camera. In: IFMBE Proceedings (2015)
35. Liu, Y., Polo, A., Zequera, M., Harba, R., Canals, R., Vilcahuamán, L., Bello, Y.: Detection of diabetic foot hyperthermia by using a regionalization method, based on the plantar angiosomes, on infrared images. In: Proceedings of the Annual International Conference of the IEEE Engineering in Medicine and Biology Society, EMBS (2016)
36. Hernandez-Contreras, D., Peregrina-Barreto, H., Rangel-Magdaleno, J., Gonzalez-Bernal, J.: Narrative review: diabetic foot and infrared thermography. Infrared Phys. Technol. **78**, 105–117 (2016)
37. Hernandez-Contreras, D., Peregrina-Barreto, H., Rangel-Magdaleno, J., Gonzalez-Bernal, J.A., Altamirano-Robles, L.: A quantitative index for classification of plantar thermal changes in the diabetic foot. Infrared Phys. Technol. **81**, 242–249 (2017)
38. Hernandez-Contreras, D., Peregrina-Barreto, H., Rangel-Magdaleno, J., Orihuela-Espina, F., Ramirez-Cortes, J.: Measuring changes in the plantar temperature distribution in diabetic patients. In: I2MTC 2017 - 2017 IEEE International Instrumentation and Measurement Technology Conference, Proceedings (2017)
39. Adam, M., Ng, E.Y., Tan, J.H., Heng, M.L., Tong, J.W., Acharya, U.R.: Computer aided diagnosis of diabetic foot using infrared thermography: a review. Comput. Biol. Med. **91**, 326–336 (2017). http://linkinghub.elsevier.com/retrieve/pii/S0010482517303566
40. Adam, M., Ng, E.Y., Oh, S.L., Heng, M.L., Hagiwara, Y., Tan, J.H., Tong, J.W., Acharya, U.R.: Automated characterization of diabetic foot using nonlinear features extracted from thermograms. Infrared Phys. Technol. **89**, 325–337 (2018)
41. Astasio-Picado, A., Escamilla Martínez, E., Martínez Nova, A., Sánchez Rodríguez, R., Gómez-Martín, B.: Thermal map of the diabetic foot using infrared thermography. Infrared Phys. Technol. **93**, 59–62 (2018)
42. Bandalakunta Gururajarao, S., Venkatappa, U., Shivaram, J.M., Sikkandar, M.Y., Al Amoudi, A.: Infrared thermography and soft computing for diabetic foot assessment. In: Machine Learning in Bio-Signal Analysis and Diagnostic Imaging (2019)
43. van Doremalen, R.F., van Netten, J.J., van Baal, J.G., Vollenbroek-Hutten, M.M., van der Heijden, F.: Validation of low-cost smartphone-based thermal camera for diabetic foot assessment. Diabetes Res. Clin. Pract. **149**, 132–139 (2019)

44. Adam, M., Ng, E.Y., Oh, S.L., Heng, M.L., Hagiwara, Y., Tan, J.H., Tong, J.W., Acharya, U.R.: Automated detection of diabetic foot with and without neuropathy using double density-dual tree-complex wavelet transform on foot thermograms. Infrared Phys. Technol. **92**, 270–279 (2018)
45. Gatt, A., Cassar, K., Falzon, O., Ellul, C., Camilleri, K.P., Gauci, J., Mizzi, S., Mizzi, A., Sturgeon, C., Chockalingam, N., Formosa, C.: The identification of higher forefoot temperatures associated with peripheral arterial disease in type 2 diabetes mellitus as detected by thermography. Prim. Care Diabetes **12**, 312–318 (2018)
46. Silva, N.C., Castro, H.A., Carvalho, L.C., Chaves, É.C., Ruela, L.O., Iunes, D.H.: Reliability of infrared thermography images in the analysis of the plantar surface temperature in diabetes mellitus. J. Chiropractic Med. **17**, 30–35 (2018)
47. Seixas, A., Azevedo, J., Pimenta, I., Ammer, K., Carvalho, R., Vilas-Boas, J.P., Mendes, J., Vardasca, R.: Skin temperature of the foot: reliability of infrared image analysis based in the angiosome concept. Infrared Phys. Technol. **92**, 402–408 (2018)
48. Renero-C, F.J.: The abrupt temperature changes in the plantar skin thermogram of the diabetic patient: looking in to prevent the insidious ulcers (2018)

Frequency Parametric Study for a HIFU Transducer Intended for Bone Tumor Treatment

Juan Carlos García-López[1], Raquel Martínez-Valdez[1(✉)], Citlalli J. Trujillo-Romero[2], Arturo Vera[3], and Lorenzo Leija[3]

[1] Department of Biomedical Engineering, Universidad Politecnica de Chiapas, Suchiapa, Chiapas, Mexico
{jgarcial53l, rmartinez}@ib.upchiapas.edu.mx
[2] Division of Medical Engineering Research, National Institute of Rehabilitation, Mexico City, Mexico
cjtrujillo@inr.gob.mx
[3] Electrical Engineering Department, Bioelectronics Section, CINVESTAV-IPN, Mexico City, Mexico
{arvera, lleija}@cinvestav.mx

Abstract. Over the last year, bone tumor accounted leastwise than 1% of all new cancers diagnosis. The diagnosis is not usually opportune due to the few symptoms that patients present, and the options for treatment are generally invasive, like surgery or chemotherapy and radiotherapy, involved risk to the patient. In recent years, new therapies for treatment of bone tumors have being studied, such as high intensity focused ultrasound. This technology allows energy concentration at a specific point, named focus, which yields on a temperature increase in a short time. In this work, a parametric study of the acoustic propagation modeling in water of a spherical bowl transducer was evaluated in a frequency range from 1 to 10 MHz. The radiator geometry was established according to a commercial transducer with 4 MHz operating frequency. From the preliminary results, frequencies from 2 to 6 MHz were selected to analyze the acoustic propagation when cortical bone tissue with different thicknesses was added to the model. This study presented a shortening of focus for both different frequencies and bone thickness compared to the acoustic propagation of the transducer in water. The best results were frequencies from 3 to 5 MHz with bone thickness of 0.5 mm. Furthermore, the results gave an overview in the analysis of possible frequencies and bone thicknesses that could be used with more specific conditions to those described in this work.

Keywords: Acoustic propagation modelling · Cortical bone · Focused ultrasound · HIFU · Parametric study

© Springer Nature Switzerland AG 2020
C. A. González Díaz et al. (Eds.): CLAIB 2019, IFMBE Proceedings 75, pp. 1253–1260, 2020.
https://doi.org/10.1007/978-3-030-30648-9_162

1 Introduction

In bone, even when constant changes are not observed in cells, sometimes they can uncontrollably grow forming tumors [1]. Bone tumors may be benign or malignant and these differ on their interaction with other tissues. Benign tumors are called osteomas and their particular characteristics are low metastasis capacity with inactive biological behavior. Malignant tumors, also called sarcomas, have origin inside the bone structure and spread to the consecutive tissues. Some tumors grow up without causing any pain, so their early detection is complicated. On the other hand, there are tumors which develop aggressively due to their high metastasis and pain is the most common symptom detected in the affected bone followed by the presence of a lump on the tumor location [1].

Generally, bone tumors are classified according to their biological behavior from of a structure that encloses the lesion called capsule to the compartmental boundaries formed by cortical bone, periosteum and articular cartilage [2]. Hence, it can be classified as intracapsular, extracapsular and extracompartmental; the last one causing the bone cortex destruction [2]. The most common malignant bone tumors are osteosarcoma, chondrosarcomas, Edwing's tumor and fibrosarcomas [2]. For 2019, it was estimated that more people would be detected with some kind of bone tumors, usually between 19 to 51 years old [1, 2].

Bone tumors detection is made from a histological diagnosis by means of X-rays, bone scan, computerized axial tomography (CAT), positron emission tomography (PET), biopsy and blood test. The treatments given are invasive, specifically surgical; such as bone resection, curettage, and amputation [2]. The use of preoperative chemotherapy (CTP) is proposed in order to protect the affected member, in addition, to prevent the progression of tumor cells [2]. Radiotherapy is another alternative for the treatment of bone tumors that is not common; it occurs when the patient refuses to amputation and the tumor location is non-surgical, for example, in flat bones.

In recent decades, new methods are being studied for their possible application in treatments of bone tumors, for example microwave ablation and ultrasonic ablation [1, 3, 4]. These techniques are based on the use of hyperthermia (temperature increase between 40 °C and 45 °C) and thermal ablation (temperature above 56 °C) [3, 5, 6]. The purpose of applying heat to the affected area is to cause irreversible damage to the cells within the tissue. The previous techniques have been considered as minimally invasive techniques because their application does not involve an open surgery. The microwave hyperthermia therapy comprises the use of interstitial antennas in the target region, thus, achieving a temperature increment [3].

Ultrasound ablation for treatment in tumors can be used in frequencies from 2 MHz to 20 MHz [4, 7]. The technology used is High Intensity Focused Ultrasound (HIFU) [5, 6], which concentrates the acoustic energy in a specific point named focus. The structure of the cortical bone allows a temperature increase to produce thermal damage [4]. According to [8], the use of ultrasound in patients with bone tumors decreases the pain sensation caused by cancer [4].

In this paper, a parametric study of acoustic propagation by means of the finite element method (FEM) for a concave HIFU transducer with different frequencies was

made in order to reach a focal distance close to 100 mm [9]. The best results were used to evaluate the acoustic propagation with the presence of cortical bone considering two arbitrary distances with respect to the average thickness of the cortical bone [10].

2 Materials and Methods

From a 4 MHz HIFU commercial transducer (model 4-30-100/4, Onda Corporation®, Ø30 mm) with a focal length of 100 mm, a 2D-axisymmetric model was performed to obtain the acoustic propagation in water [9]. The radiator dimensions configured at the model were 14.991 mm of radius and 1.13 mm of depth (See Fig. 1a). The resonance frequency was varied from 1 to 10 MHz with 1 MHz increments. The model was solved by using the acoustics module of COMSOL Multiphysics®. The time-harmonic wave equation for pressure acoustic propagation was

$$\nabla^2 p + \left(\omega^2/c_s^2\right)p = 0 \tag{1}$$

where p is the acoustic pressure (Pa), ω is the angular frequency (rad/s), and c_s is the sound velocity (m/s).

The best results with similar focal distances to that of the commercial transducer were used for modeling the acoustic propagation with the presence of cortical bone. Figure 1b shows the geometry used for the acoustic propagation modeling in bone; it was divided in subdomains that simulated the acoustic properties of the involved materials [9] (See Table 1). The subdomain for the cortical bone was placed at the focal length where the maximum acoustic pressure was reached for each selected frequency. Cortical bone subdomain geometry was a rectangular shape with 20 cm length; while the thicknesses of the bone were configured as 0.5 and 3.1 mm, according to [10].

The boundaries used in the model for the acoustic propagation in both water and with cortical bone (See Fig. 1a and b) were configured as: boundary 1, radiator; 2, sound hard wall; boundaries 3 and 4, acoustic impedance and boundary 5 was established as symmetry axis. The acoustic impedance boundary was used considering that the geometry was immersed in water for both cases in order to decrease wave reflection [4, 9].

The acoustic impedance is defined by

$$Z = p * c_s \tag{2}$$

where p is the acoustic pressure (Pa) and c_s is the sound velocity (m/s).

The FEM model was solved by using a mesh size of 8 triangular elements per wavelength defined as

$$\mathrm{E_{size}} = \lambda/8 \tag{3}$$

where E_{size} is the mesh size and λ is the wavelength in the medium.

As the parametric study was performed in the frequency range from 1 to 10 MHz, the number of elements constituting the mesh varied from 232,514 to 36,731,673 elements, respectively. The meshes of the parametric study in which cortical bone was included in the model geometry consisted of 1,469,759 and 13,265,542 triangular elements, respectively. The models were solved on a PC with Intel® Core™ i5-6500 CPU @ 3.20 GHz processor and 32 GB on RAM [11].

Results of the parametric study of the transducer frequency in a range of 1 to 10 MHz were evaluated where the maximum pressure was reached. Furthermore, dimensions of the focus were estimated in both length and diameter by the full length at half maximum (FLHM) and the full width at half maximum (FWHM) [4, 11]. The previous values should be close to the commercial transducer parameters at its nominal frequency (4 MHz and 10 cm focal length), without snappish changes in the focus shape and radiation patterns.

Table 1. Acoustic properties used in the model.

Material	Density [kg/m^3]	Sound velocity [m/s]	Acoustic impedance [MRayls]
Water	1000 kg/m^3	1500 m/s^2	1.5
Cortical bone	1908 kg/m^3	3514.9 m/s^2	6.75

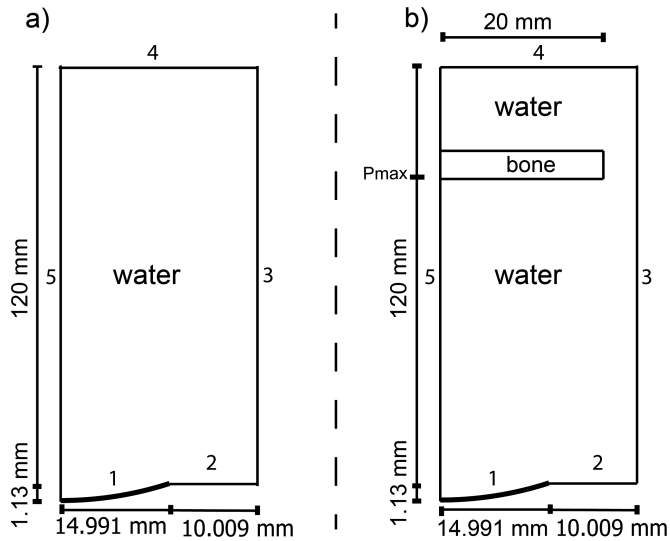

Fig. 1. (a) 2D axisymmetric geometry for acoustic propagation modeling in water. Boundary 1, radiator; boundary 2, sound hard wall; boundaries 3 and 4, acoustic impedance and 5, as symmetry axis. (b) 2D axisymmetric geometry for acoustic propagation modeling with cortical bone. The boundaries were considered in the same order as the model in water. In this model was included cortical bone structure placed at the maximum pressure obtained by each case selected

3 Results

Figures 2 and 3 show the acoustic field and the distribution of the acoustic pressure in z-axis for the simulation in a lossless medium: water. It can be observed that in the case of 4 MHz, the focal distance agrees with that of the commercial transducer. The best results for the frequency variation for the proposed geometry were observed from 2 MHz to 6 MHz (See Fig. 2).

Results were evaluated from the distance at which the maximum pressure was reached (See Table 2). In order to compare the focus dimensions, the FLHM the FWHM were calculated (See Table 2).

Table 2. Focal distance and focus dimensions

Frequency [MHz]	FLHM [mm]	FWHM [mm]	Focal distance [mm]
1	53.49	3.558	76.52
2	46.38	2.196	88.03
3	35.10	1.588	93.88
4	26.72	1.269	98.14
5	19.00	0.985	98.04
6	18.48	0.608	98.10
7	6.69	0.448	98.33
8	5.28	0.301	98.33
9	5.23	0.176	98.42
10	1.77	0.311	98.42

From these data, frequencies from 2 to 6 MHz were chosen to be evaluated in the model that includes the bone geometry due to their focal distance and the focus dimensions [11]. The results showed high pressure variation in the region close to the bone-water interface. A change in the ultrasonic propagation can be observed due to the impedance difference between water and bone [4]. Moreover, it can be observed that the ultrasonic waves, even if attenuated, penetrate the cortical bone. Based on this analysis, it was determined that the frequencies with the best results were 3 MHz, 4 MHz and 5 MHz. Figure 3 depicts the normalized acoustic propagation along the z-axis for the frequency range from 3 to 5 MHz with cortical bone subdomains added with the two different thicknesses for each case: 0.5 mm and 3.1 mm.

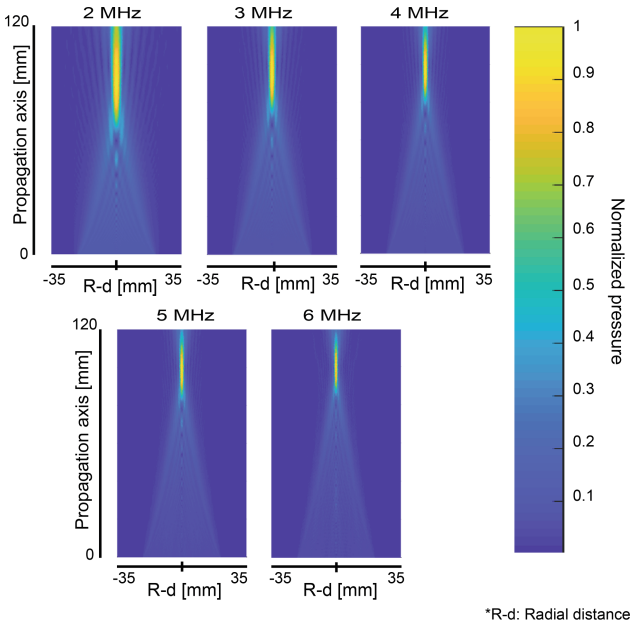

Fig. 2. Acoustic field for the best cases of the frequency variation study for acoustic propagation in water. Frequencies from 2 to 6 MHz showed similar characteristics (focal length, FLHM and FWHM) to the commercial transducer.

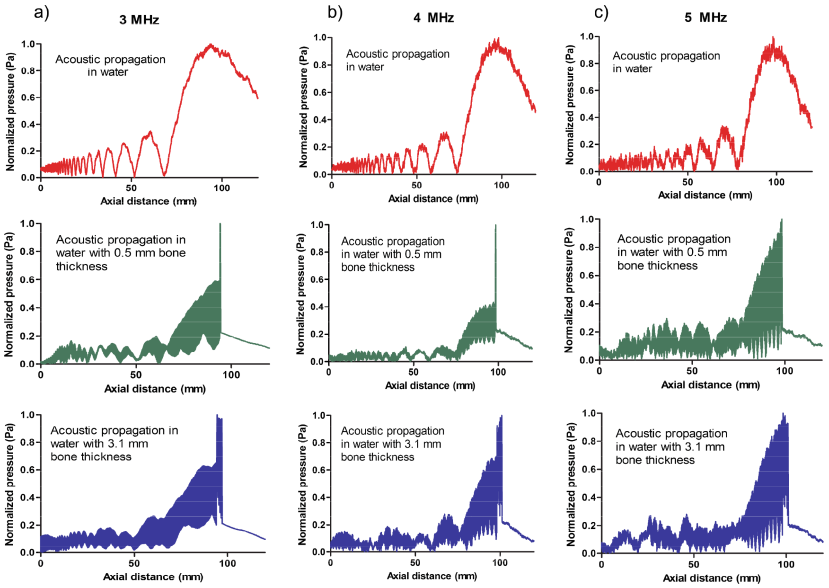

Fig. 3. Distribution of normalized acoustic pressure for the acoustic propagation model with cortical bone of 0.5 and 3 mm thicknesses. (a) 3 MHz, (b) 4 MHz, (c) 5 MHz. In the 3.1 mm thickness cases, a change in the morphology of the ultrasound beam close the interface with the cortical bone can be observed; hence, causing reflections towards the radiator boundary.

4 Discussion and Conclusion

This work presented results of the variation in frequency for the same geometry of a HIFU transducer. The frequency parametric study of the acoustic propagation modeling for the same proposed geometry showed that the best frequencies were from 2 to 6 MHz. This frequency range presented similar results to the commercial transducer (model 4-30-100/4, Onda Corporation®, Ø30 mm) (See Table 2) [11].

Frequencies of 1 and from 7 to 10 MHz showed an irregular acoustic propagation, generally in the near field. Moreover, by modifying the size of the proposed geometry a focal distance as the required could be reached; also, the dimensions of the focus can be changed. However, other factors and parameters involved in the structure of the transducer should be considered; hence, an analysis considering these conditions will be proposed in the future. The results of acoustic propagation of the transducer for the selected frequencies and the inclusion of cortical bone showed that frequencies from 3 to 5 MHz were the most suitable. The results indicated that, for this geometry, the frequencies of 3 MHz, 4 MHz and 5 MHz can be analyzed for the study for its feasibility of use in bone tumors treatments.

In addition, the acoustic propagation modeling results with the cortical bone inclusion contributes in the analysis of the behavior on that tissue. Moreover, it is important to highlight that this study was made in a stationary time; thus, transient analysis of the best cases could be considered as future work. Therefore, temperature increases as a function of time can be analyzed in order to observe thermal ablation phenomenon in the tissue. On the other hand, for future studies, the evaluation of cortical bone thicknesses that are among the values proposed in this work is considered. Also, irregularities of the tissue, as well as the inclusion of cancellous bone with specific properties, will be considered.

Acknowledgment. Authors thank the CINVESTAV-IPN and Universidad Politecnica de Chiapas for the facilities for the development of the work presented. R. Martinez-Valdez and J.C. Garcia-Lopez thank the PRODEP project number 511-6/17-10587.

Declaration of Interest Statement. The authors report no declarations of interest.

References

1. American Cancer Society: What are the Key Statistics About Bone Cancer? (2019)
2. Alvarez, A., Morote, C.C., Garc, Y., Mar, D., Paneque, E., Cl, H.P., Domenech, M.A., Especialista, M.G.I.I.I.I.: Tumores óseos primarios. Rev. Electrónica Arch. Médico Camagüey. **7**, 215–229 (2007)
3. Trujillo-Romero, C.J., Rico-Martínez, G., Gutiérrez-Martinez, J.: Thermal ablation : an alternative to bone cancer. Investig. en Discapac. **7**, 36–47 (2018)
4. Martinez-Valdez, R., Trujillo-Romero, C.J., Castellanos, L., Gutierrez-Martinez, J., Vera-Hernandez, A., Ramos, A., Leija, L.: Feasibility of the microwave and ultrasound ablation as alternatives to treat bone tumors. In: 2017 Global Medical Engineering Physics Exchanges/Pan American Health Care Exchanges (GMEPE/PAHCE), pp. 1–6. IEEE (2017)

5. Habash, R.W.Y., Bansal, R., Krewski, D., Alhafid, H.T.: Thermal therapy, part III: ablation techniques. Crit. Rev. Biomed. Eng. **35**, 37–121 (2007). https://doi.org/10.1615/CritRevBiomedEng.v35.i1-2.20
6. Quadri, S.A., Waqas, M., Khan, I., Khan, M.A., Suriya, S.S., Farooqui, M., Fiani, B.: High-intensity focused ultrasound: past, present, and future in neurosurgery. Neurosurg. Focus **44**, E16 (2018). https://doi.org/10.3171/2017.11.FOCUS17610
7. Rauch, M., Marinova, M., Schild, H.H., Strunk, H.: High intensity focused ultrasound for the treatment of advanced liver cancer. Dig. Liver Dis. **47**, 989–990 (2015). https://doi.org/10.1016/j.dld.2015.06.016
8. Al-Bataineh, O., Jenne, J., Huber, P.: Clinical and future applications of high intensity focused ultrasound in cancer. Cancer Treat. Rev. **38**, 346–353 (2012). https://doi.org/10.1016/j.ctrv.2011.08.004
9. Martínez-Valdez, R., Ramos Fernández, A., Vera Hernandez, A., Leija Salas, L.: Design of a low power hybrid HIFU applicator for haemostasis based on acoustic propagation modelling. Int. J. Hyperth. **32** (2016). https://doi.org/10.3109/02656736.2015.1112437
10. Mano, I., Horii, K., Hagino, H., Miki, T., Matsukawa, M., Otani, T.: Estimation of in vivo cortical bone thickness using ultrasonic waves. J. Med. Ultrason. **42**, 315–322 (2015). https://doi.org/10.1007/s10396-015-0617-5
11. Garcia-Lopez, J.C., Martinez-Valdez, R., Trujillo-Romero, C.J., Vera, A., Leija, L., Castellanos, L., Ramos, A.: Parametric study of a conical applicator for 4 MHz HIFU transducer for its possible application in bone tumour ablation therapy. In: 2019 Global Medical Engineering Physics Exchanges/Pan American Health Care Exchanges (GMEPE/PAHCE), pp. 1–5. IEEE (2019)

Photothermal Signature Characterization of Breast Microcalcifications Ex-Vivo by Photoacoustic Method

Lizbeth Anahí Serrano-Aguilar[1,2], Rosa María Quispe-Siccha[2(✉)], Argelia Pérez-Pacheco[2], Roberto Mosiñoz-Montes[3], Gregorio Quintero-Beuló[3], Azcary Vázquez-Tinajero[3], Fernando Lara-González[3], Mercedes Hernández-González[4], Joselín Hernández-Ruíz[5], and Juan C. López-Alvarenga[6]

[1] UPIBI, Instituto Politécnico Nacional, Av. Acueducto, Barrio La Laguna Ticomán, 07340 Mexico City, Mexico
Lserranoa0900@gmail.com
[2] Unidad de Investigación y Desarrollo Tecnológico, Hospital General de México "Dr. Eduardo Liceaga" (HGMDEL), Dr. Balmis 148, Col Doctores, 06726 Mexico City, Mexico
rosa.quispe@gmail.com
[3] Servicio de Oncología, HGMDEL, Dr. Balmis 148, Col Doctores, 06726 Mexico City, Mexico
[4] Servicio de Patología, HGMDEL, Dr. Balmis 148, Col Doctores, 06726 Mexico City, Mexico
[5] Farmacología Clínica, HGMDEL, Dr. Balmis 148, Col Doctores, 06726 Mexico City, Mexico
[6] South Texas Diabetes and Obesity Institute/School of Medicine, The University of Texas Rio Grande Valley, ERAHC 2.212, Edinburg, TX, USA

Abstract. Photothermal signatures of microcalcifications (MC) represented an important marker, that possibly later using the pulsed photoacoustic technique, this anomaly could be detected in early stages. Currently, MC are diagnosed by radiological images, however, their resolution is an impediment to detect smaller MC (<1 μm). For these reasons, this work presents pulsed photoacoustic technique as a possible method for microcalcifications early detection of and is also a non-invasive method. This method consists of irradiating the sample with near infrared light, and part of this light is absorbed by the microcalcifications, where these are heated causing a thermoelastic effect which generates mechanical waves that propagate at the sound speed and are detected by ultrasound sensors. The mechanical waves transmit information of the MC optical properties and when analyzing the amplitude, the delay time of the PA signal, and the vibrational modes of the frequency spectrum (FFT), it was possible to obtain the photothermal signature characteristic of microcalcifications and its depth in the breast tissue.

Keywords: Pulsed photoacoustic · Photothermal signature · Mammary microcalcifications

© Springer Nature Switzerland AG 2020
C. A. González Díaz et al. (Eds.): CLAIB 2019, IFMBE Proceedings 75, pp. 1261–1272, 2020.
https://doi.org/10.1007/978-3-030-30648-9_163

1 Introduction

The photoacoustic effect (PA) was discovered by Alexander Graham Bell in 1880, after noticing that thin selenium discs emit a sound when exposed to a beam of cut sunlight. The principle of this is that incident light is converted into kinetic energy, produces local heating and generates pressure waves. Although PA method is not a recent discovery, clinical applications are relatively new [1–3]. Currently, pulsed photoacoustic technique in near-infrared (NIR) is mainly used in biological material due to its ability to penetrate dense samples [4–8]. As for example, microcalcifications (MC) are commonly found in breast tissue; approximately 40% in patients diagnosed with breast cancer, 80% with ductal carcinoma in situ and 60% to 80% in the cases of cancer studied after the histological review. Although most of these are benign and does not need treatment, there are others malignant and their presence makes breast cancer common marker [8, 9]. MC physicochemical composition is calcium deposits of approximately 0.1–1.0 mm in diameter (average of 0.3 mm), which makes diagnosis difficult with conventional methods, such as mammography and ultrasound images [10, 11]. The main components of benign MC are apatite and calcium carbonate, and malignant ones contain additional calcium oxalate and calcium phosphate (high concentrations). The majority of MC is not detected by conventional methods (ultrasound and mammography) due to their size (<1 μm), composition and distribution of MC. For the reasons mentioned above, there are studies to detect microcalcifications by the photoacoustic pulsed method thanks to their high detection sensitivity, for this, they used phantoms as breast simulators [12–14]. One of the main contributions of this work is the detection of photothermal signatures of microcalcifications in *ex-vivo* mammary tissue of patients of the Hospital General de México "Dr. Eduardo Liceaga" (HGMDEL); using the photoacoustic technique pulsed in the near infrared due to its high sensitivity, it is non-invasive and inexpensive.

2 Methodology

In this work, the pulsed photoacoustic technique in the near infrared was used to obtain the photothermal signature or photoacoustic signals (PA) of microcalcifications contained in ex-vivo mammary samples of oncological patients, which were programmed for breast surgery by the Oncology Service of HGMDEL with previously signed informed consent of patient.

PA signatures of the microcalcifications were measured at the Unidad de Investigación y Desarrollo Tecnológico (UIDT) of the HGMDEL. This work is part of a bigger project (N ° DI/12/111/4/017) which is approved by the Ethics and Research Committees of the same institution.

Mammary samples with MC before the photoacoustic measurements were washed with a custodiol solution (HTK), in order to avoid the noise in the PA signal caused by the superficial blood of sample. Since HTK is used for organs preservation, a more reliable PA signature of MC is obtained.

Photoacoustic experimental setup that was used to obtain the PA signals of MC is shown in Fig. 1.

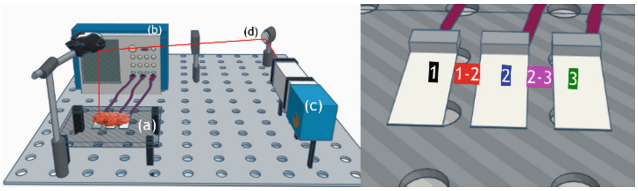

Fig. 1. Left **Side:** PA experimental setup to obtain the PA signature of MC. (a) Sample in direct contact with the three sensors of polyvinylidene fluoride (PVDF), (b) a digital phosphor oscilloscope (Tektronix: DPO5204B, 2 GHz) for the registration of PA signatures, (c) a Nd: YAG laser, λ = 1064 nm, F = 10 Hz, τ = 6 ns, E = 30 mJ and (d) optical arrangements. **Right Side:** Arrangement of the three PVDF sensors and five exposure positions of the laser light on the sample: P1, P1-2, P2, P2-3 and P3.

For PA measurements, it was essential to have the samples well coupled with piezoelectric PVDF sensors to avoid the noise of different frequencies that might be traveling in the air. Sample was placed on the three sensors (S1, S2 and S3) trying to occupy the largest possible area, then this sample was beamed with laser light in 5 positions, as observed on the right side of Fig. 1. Each position exposed by laser light was repeated 3 times, both from the front and back of tissue; so that a total of 30 PA signals were obtained per sensor and the sum of the three sensors would give us a total of 90 signals.

It should be noted that we obtained radiological images of mammary samples with MC from each patient provided by the experts. Images gave us a reference of size, shape and distribution of MC, which when comparing the irradiated position of sample with the PA signal, indicated whether there were microcalcifications or not, as we showed in the results.

PA signatures of MC were obtained from the analysis of PA signals in the space of time and the frequency (Fast Fourier Transform, FFT); with the purpose of obtaining a characteristic pattern of MC as well as their depth within the mammary sample.

3 Results

Photothermal signatures of seven samples were obtained according to the amplitude versus time and their frequency spectrum (FFT). In this work, we show the photothermal signature of four most representative samples according to its distribution and size. In Fig. 2 we present a breast tissue sample with microcalcifications of a 65-year-old patient (sample 1). The surface area containing MC is approximately 153.98 mm^2 and the MC sizes range between 0.32 mm–1.09 mm.

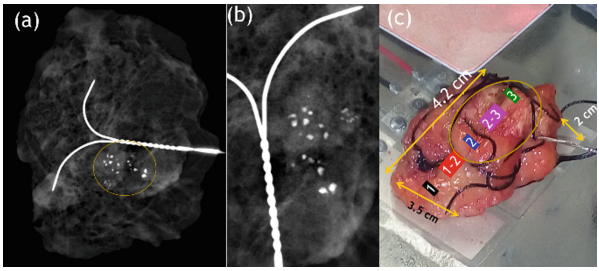

Fig. 2. Sample 1: (a) Mammography image, (b) Microcalcifications distribution (zoom of (a)), and (c) Positions of laser light exposure on the sample.

In Fig. 3 the PA signals of MC are clearly identifiable in the positions: P2, P2-3 and P3. The delay time that leads to the PA signal of the MC to the sensor according to their position were of 11.4 µs, 11.6 µs and 6.26 µs respectively. The MC depth calculated by the equation of the propagation velocity, v = d/t, where v = 1500 m/s (sound speed in water), correspond to: 1.71 cm, 1.74 cm and 0.9 cm respectively. With respect to Fig. 4, representative peaks (vibrational modes) between 1.07 MHz and 4.1 MHz are shown.

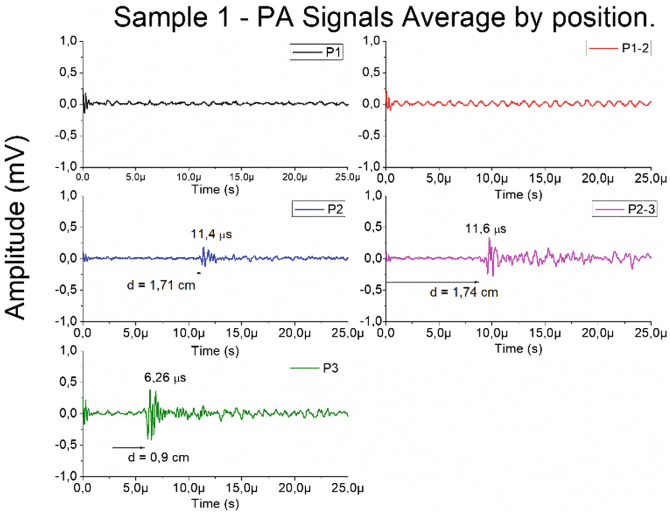

Fig. 3. Sample 1: each position is the average of 18 PA signals.

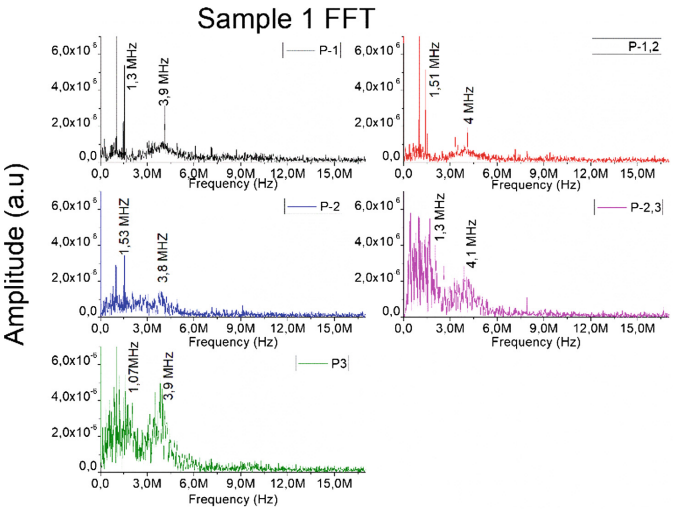

Fig. 4. Sample 1: frequency spectrum (FFT) per position of PA signals shown in Fig. 3.

In Fig. 5 we present a breast tissue sample with microcalcifications of a 51-year-old patient (sample 2). The surface area containing MC is approximately 168.02 mm^2 and the MC sizes range between 0.55 mm to 2.26 mm.

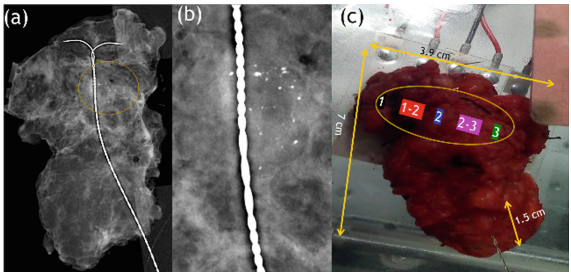

Fig. 5. Sample 2: (a) Mammography image, (b) microcalcifications distribution (zoom of (a)), and (c) Positions of laser light exposure on the sample.

Figure 6 observable PA signals are over P2 at 6.52 µs, corresponding to 0.97 cm and PA signal of P3 at 6 µs, corresponding to 0.9 cm.

In Fig. 7, representative vibrational modes in the frequency spectrum are between 1.1 MHz and 4.1 MHz are observable in all positions.

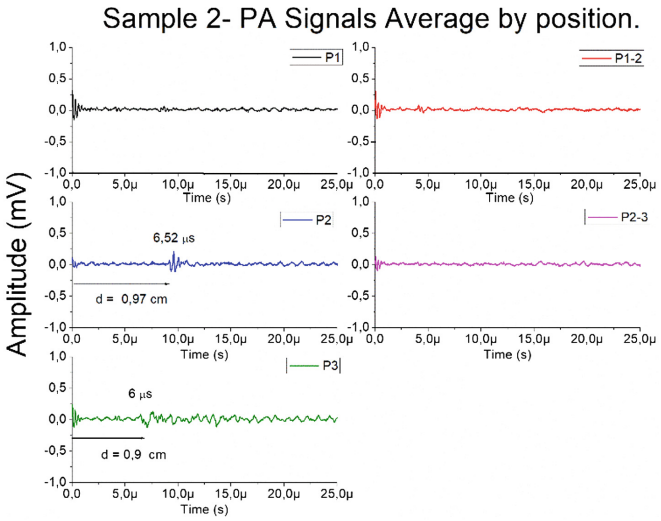

Fig. 6. Sample 2: each position is the average of 18 PA signals

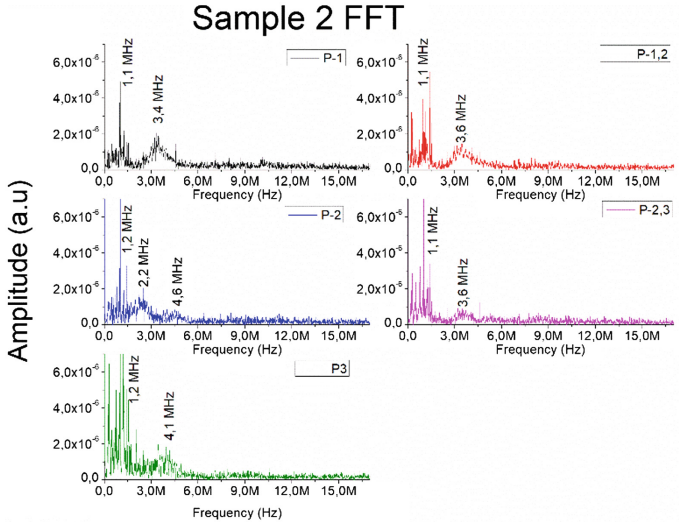

Fig. 7. Sample 2: frequency spectrum (FFT) per position of PA signals shown in Fig. 6.

In Fig. 8 we present a breast tissue sample with microcalcifications of a 51-year-old patient (sample 3). The surface area containing MC is approximately 168.02 mm^2 and the MC sizes range between 0.55 mm–2.26 mm, radiology image is opaque due to composition and density of tissue.

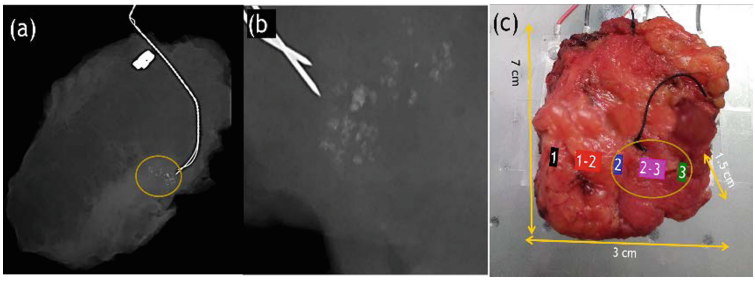

Fig. 8. Sample 3: (a) Mammography image, (b) microcalcifications distribution (zoom of (a)), and (c) Positions of laser light exposure on the sample.

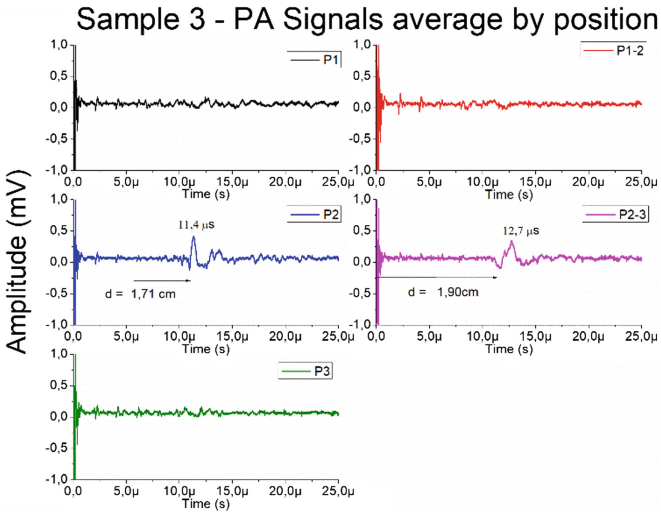

Fig. 9. Sample 3: each position is the average of 18 PA signals

In Fig. 10 the vibrational modes are observed in all the positions, however in the PA signals it can only be observed in the positions P1, P1-2 and P3. The representative vibrational modes are between 3.06 and 16.17 MHz for this reason it is important to obtain its frequency spectrum in case it cannot be distinguished in the PA

In Fig. 11 we present a breast tissue sample with microcalcifications of a 49-year-old patient (sample 4). The surface area containing MC is approximately 306.51 mm^2 and the MC sizes range between <1 µm to 0.46 mm (Fig. 13).

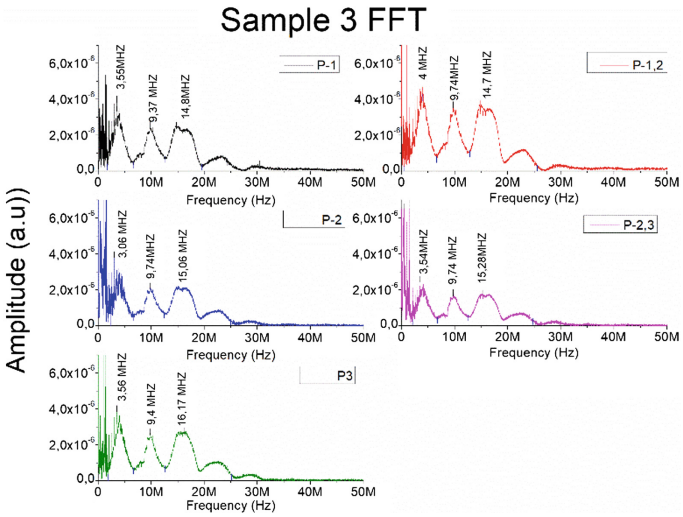

Fig. 10. Sample 3: frequency spectrum (FFT) per position of PA signals shown in Fig. 9.

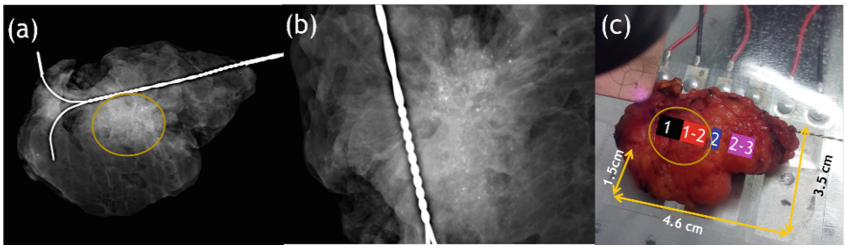

Fig. 11. Sample 4: each position is an 18 PA signals by position average

In Fig. 12, the representative PA signal is observed in the P1 position, and the MC peak is in 8.6 μs corresponding to a depth of 1.29 cm. With respect to the frequency spectrum, its vibrational modes are observed in all positions, similar to what happened with the sample 3. The vibrational modes are in a range of 4.06 MHz to 15.06 MHz.

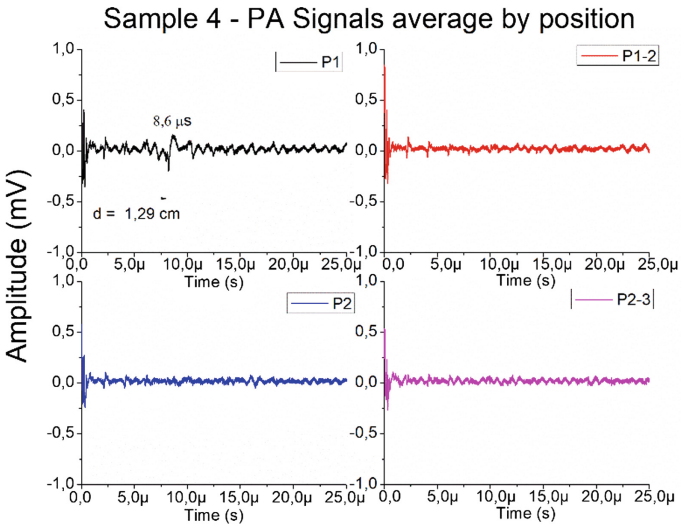

Fig. 12. Sample 4: each position is an 18 PA signals by position average

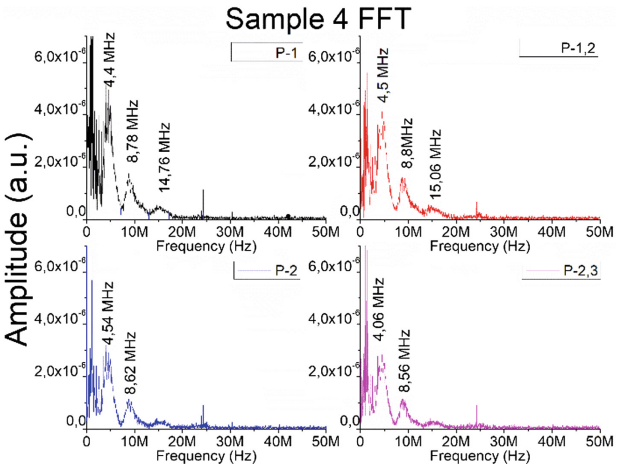

Fig. 13. Sample 4: frequency spectrum (FFT) per position of PA signals shown in Fig. 8.

4 Discussion

Of the seven samples measured by photoacoustic, we chose to present four that are the most representative. PA signal shape of sample 1 represents the structural form of MC, and the amplitude is related to MC components absorption; in this case there is higher absorption in positions: P2, P2-3 and P3 because laser light coincided with the MC particles, and in P3 position coincided with one of the larger particles, that is why it has a greater amplitude, as observe in Fig. 3. With respect to its frequency spectrum (FFT),

vibrational modes that indicate MC presence is at 1.07 MHz and 3.9 MHz as shown in Fig. 4, most representatives being positions: P2, P2-3 and P3 for PA signals. However, in positions: P1 and P1-2 vibrational modes can be also observed, but with lower resolution. This shows that although the peak of MC particles in the PA signal is not seen in those positions due to their low resolution, FFT will be able to identify them as long as there is MC presence, in this case FFT would be equal to sensor signal, and we verified it was different to sensor's.

PA signal shape of sample 2 is similar to sample 1, although these have different sizes are distributed separately. PA signal amplitude is smaller because the MC are smaller, however, in this sample, MC peak is observed for all positions, very small in P1, P1-2 and P2-3, and the most representative in P2 and P3. According to its FFT, MC vibrate in 1.2 and 4.1 MHz for all the positions, being the most representative the position P3, for the peak width it could be interpreted that biggest MC correspond to the bigger PA signal.

Sample 3 presents another type of microcalcifications (called *popcorn* by its shape), as seen in Fig. 8. and this is reflected in the photothermal signature, i.e. the peak of PA signal is wider. It was possible to identify these MC in all positions, being the most representative in positions P2 and P2-3, however in its FFT we can see their vibrational modes in all positions. Width of the vibrational mode is due to MC thickness; in this sample MC size is larger compared with samples 1 and 2.

Referring us to sample 4, MC size have a very wide range and are smaller compared to the other samples, some of it are smaller than 1 μm; this type of MC is known as diffuse. Most representative photothermal signature is presented in P1 position, and although in the other positions these do not distinguish very well, in its frequency spectrum the presence of MC can be observed. The shape of vibrational modes in this case, represent how MC particles are grouped, since these are very close to each other, as shown in Fig. 11.

Delay time variation indicates the depth in which MC are located within mammary sample, obtaining it from the equation of the propagation velocity: $v = d/t$, where $v = 1500$ m/s, is the sound speed through the water. We decided to use this data since the sample contains a considerable amount of water, and average of sound speed of glandular tissue and fat approximates that to the water.

PA technique, as we can see, is promising to characterize photothermal signatures of some mammary lesion, in this case microcalcifications. Apart from obtaining PA signature, one can also obtain the approximate depth of MC within breast tissue.

In order to have a reliable characteristic pattern, we would need a broader database, as well as a good filtering of the PA signal (glandular tissue, fat and water) in order to identify MC with major accuracy.

5 Conclusion

It was possible to obtain the photothermal signature representative of macrocalcifications in breast tissue using the pulsed photoacoustic method. Photothermal signatures represented by the PA signal and its frequency spectrum (FFT), gave us information of shape, size, distribution and MC depth of each mammary sample; by means of the

bandwidth, shape and delay time of representative PA signals peaks o, as well as representative vibration modes of their frequency spectrum (FFT).

We continue working on the obtention of PA signals to improve our database in order to prove and characterize method, and so soon, this photoacoustic method can arrive to make a complementary method of detecting microcalcifications in early stages.

Conflict of Interest. All authors declare that there is no conflict of interest.

References

1. Gould, T., Wang, Q., Pfefer, T.J.: Optical-thermal light-tissue interactions during photoacoustic breast imaging. Biomed. Opt. Express **5**(3), 832 (2014). https://doi.org/10.1364/boe.5.000832
2. Garcia-Uribe, A., Erpelding, T.N., Krumholz, A., Ke, H., Maslov, K., Appleton, C., Wang, L.V.: Dual-modality photoacoustic and ultrasound imaging system for noninvasive sentinel lymph node detection in patients with breast cancer. Sci. Rep. **5**(15748), 1–8 (2015). https://doi.org/10.1038/srep15748
3. Lin, X., Liu, C., Sheng, Z., Gong, X., Song, L., Zhang, R., Sun, M.: Highly sensitive fluorescence and photoacoustic detection of metastatic breast cancer in mice using dual-modal nanoprobes. ACS Appl. Mater. Interfaces. **10**(31), 26064–26074 (2018). https://doi.org/10.1021/acsami.8b09142
4. Menke, J.: Photoacoustic breast tomography prototypes with reported human applications. Eur. Radiol. **25**(8), 2205–2213 (2015). https://doi.org/10.1007/s00330-015-3647-x
5. Heijblom, M., Steenbergen, W., Manohar, S.: Clinical photoacoustic breast imaging: the twente experience. IEEE Pulse **6**(3), 42–46 (2015). https://doi.org/10.1109/mpul.2015.2409102
6. Yang, S., Gao, X., Yan, J., Song, H., Ju, Y., Zhang, G., Shu, R.: Do we have to suffer pain in breast exams? Compare the pain between digital screening mammography, automated breast ultrasound and hand-held ultrasound. Ultrasound Med. Biol. **43**, S21 (2017). https://doi.org/10.1016/j.ultrasmedbio.2017.08.1008
7. Jiang, Y., Pu, K.: Molecular fluorescence and photoacoustic imaging in the second near-infrared optical window using organic contrast agents. Adv. Biosyst. **2**(5), 1700262 (2018). https://doi.org/10.1002/adbi.201700262
8. Lee, C., Lee, D., Zhou, Q., Kim, J., Kim, C.: Real-time near-infrared virtual intraoperative surgical photoacoustic microscopy. Photoacoustics **3**(3), 100–106 (2015). https://doi.org/10.1016/j.pacs.2015.08.002
9. Scimeca, M., Bonanno, E.: Imaging Diagnostic and Pathology in the Management of oncological-patients (2018)
10. Chiara, A.: Breast Microcalcifications: A Focus (2015). https://doi.org/10.4172/2157-7013.s8-e101
11. Sainz de Cea, M.V., Nishikawa, R.M., Yang, Y.: Locally adaptive decision in detection of clustered microcalcifications in mammograms. Phys. Med. Biol. **63**(4), 045014 (2018). https://doi.org/10.1088/1361-6560/aaaa4c
12. Rubio, Y., Montiel, O., Sepúlveda, R.: Quantum inspired algorithm for microcalcification detection in mammograms. Inf. Sci. **480**, 305–323 (2019). https://doi.org/10.1016/j.ins.2018.12.040

13. Klosner, M., Sampathkumar, A., Chan, G., Wu, C., Gross, D., Heller, D.F.: Advanced laser systems for photoacoustic imaging. In: Photons Plus Ultrasound: Imaging and Sensing 2015 (2015). https://doi.org/10.1117/12.2077780
14. Kang, J., Kim, E., Kim, G.R., Yoon, C., Song, T., Chang, J.H.: Photoacoustic imaging of breast microcalcifications: A validation study with 3-dimensional ex vivo data and spectrophotometric measurement. J. Biophotonics **8**(1–2), 71–80 (2013). https://doi.org/10.1002/jbio.201300100

Innovation of Technologies for Health

HOMA-IR Assessment for Impaired Glucose Tolerance, Impaired Fasting Glucose and Insulin Resistance Diagnosis

Erika Severeyn[1(✉)], Jesús Velásquez[1], Gilberto Perpiñán[2], Héctor Herrera[3], Sara Wong[4], José Díaz[5], and Miguel Altuve[6]

[1] Departamento de Termodinámica y Transferencia de Calor, Universidad Simón Bolívar, Caracas, Venezuela
severeynerika@usb.ve
[2] Faculty of Electronic and Biomedical Engineering, Antonio Nariño University, Cartagena, Colombia
[3] Departamento de Tecnología de Procesos Biológicos y Bioquímicos, Universidad Simón Bolívar, Caracas, Venezuela
[4] Departamento de Electrónica y Circuitos, Universidad Simón Bolívar, Caracas, Venezuela
[5] Departamento de Ingeniería Eléctrica y Computación, Universidad Autónoma de Ciudad Juarez, Ciudad Juarez, Mexico
[6] Faculty of Electrical and Electronic Engineering, Pontifical Bolivarian University, Bucaramanga, Colombia

Abstract. Impaired glucose tolerance (IGT), impaired fasting glucose (IFG) and insulin resistance (IR) are prediabetic conditions diagnosed by glucose and insulin values measured by oral glucose tolerance test (OGTT). In the OGTT, insulin and glucose levels are measured in five different blood samples: a sample in fasting (minute 0) and four others after oral intake of 75 gr of glucose, at intervals of 30 min (minute 30, 60, 90, and 120). The values of glucose at 0 and 120 min from OGTT are used for the diagnosis of IFG and IGT, respectively. The HOMA-IR is the most used method of determining IR in large population-based studies; it is mathematically derived from fasting glucose and insulin measurements from OGTT. One of the limitations of HOMA-IR is the difficulty of predicting IR in populations with IGT. The aim of this study is to evaluate the capability of a HOMA-IR and modified version of HOMA-IR (HOMA-IR calculated from glucose and insulin of 30, 60, 90 and 120 min of OGTT) to diagnose IGT, IR, and IFG. Receiver operating characteristic (ROC) curves and area under the ROC curve (AUC) were performed to assess the predictive capacity of HOMA-IR and modified versions. The present study demonstrated that modified versions of HOMA-IR calculated using glucose and insulin from 60 and 90 min of OGTT are alternative indexes (AUC $\geq$ 0.70) for IGT, IFG and IR detection.

Keywords: HOMA-IR · ROC curves · Impaired fasting glucose · Impaired glucose tolerance · Insulin resistance

© Springer Nature Switzerland AG 2020
C. A. González Díaz et al. (Eds.): CLAIB 2019, IFMBE Proceedings 75, pp. 1275–1283, 2020.
https://doi.org/10.1007/978-3-030-30648-9_164

1 Introduction

Impaired glucose tolerance (IGT) is an intermediate metabolic state between normal and diabetic glucose homeostasis [1]. This condition is the precursor of diabetes, but the progression to overt the disease is not straight-forward [2]. The IGT is diagnosed with postprandial glucose of 140–199 mg/dL [3]. Studies corroborate that patients who have been diagnosed with IGT have a high risk of developing diabetes in the next decade after the diagnosis, which is why early diagnosis of this condition is very important [4].

The IGT is a metabolic disorder that is highly related to other metabolic pathologies, such as impaired fasting glucose (IFG) and insulin resistance (IR). The IFG is defined as fasting glucose levels of 100–125 mg/dL [5]. Studies reveal that these diseases are in many cases in concomitance worsening the patient's prognosis making them more prone to the development of diabetes. The Hoorn Study [6] revealed that 33% of patients with IFG, but not impaired glucose tolerance (IGT), and 64.5% of patients with IFG and IGT developed diabetes over a follow-up of 5.8–6.5 years.

The IR diagnosis is made through the homeostatic model assessment (HOMA-IR). HOMA-IR is the most used method of determining IR in large population-based studies; and it is mathematically derived from fasting glucose and insulin measurements. The IR is diagnosed when the HOMA-IR $\geq$ 2.5. HOMA-IR has been used to assess longitudinal changes in insulin resistance in persons with type 2 diabetes of various ethnic groups in order to examine the natural history of diabetes and to assess the effects of treatment [7]. It can also be utilized in non-diabetic populations as it allows comparisons of insulin sensitivity among persons with IGT and in longitudinal assessment of people who later develop IGT [8].

Studies have suggested that HOMA-IR may not be a good predictor of insulin resistance in all individuals. Indeed, several investigators report that HOMA-IR and insulin action do not correlate highly or significantly, particularly in individuals with IGT and IFG [9, 10]. There are many methods that have been designed to diagnose IR. Some methods, such as Avignon and Matsuda [11], use glucose and insulin values during the oral glucose tolerance test (OGTT). These methods have been shown to be better predictors of IR than HOMA-IR in populations with IGT and normal values of fasting glucose and insulin [11]. Since HOMA-IR use the glucose and insulin fasting values to calculate insulin sensitivity, we found interesting to explore a modified version of HOMA-IR (constructed from the use of glucose and insulin during OGTT) in order to assess the capability in the diagnosis of IGT, IFG, and IR.

The receiver operating characteristic (ROC) curve had been used in bioengineering to assess the diagnostic capability of a binary classifier. The ROC curve analysis is a statistical method to determine the diagnostic accuracy of a classifier. In general, the roc curve is used for: (i) determining the cut-off point of a continuous scale in which the highest sensitivity and specificity is reached [12], and (ii) evaluating the discriminative capacity of a diagnostic test, that is, its ability to differentiate healthy versus sick subjects. ROC curves have been used to evaluate the HOMA-IR in the diagnosis of diabetes and obesity [12]. Also, with the ROC curves, it had been determined the optimal cut-off points of HOMA-IR in the insulin resistance determination on different types of populations according to ethnic origin [13] and age [14].

Table 1. Glucose and insulin values of the OGTT and the values of HOMA-IR_0 for the subjects with IGT, IFG, IR and control group.

Variables	Control[e] Male = 9, n = 53	IGT Male = 15, n = 29	IFG Male = 30, n = 55	IR Male = 19, n = 39
Age[a, c, d] [years]	37.15 ± 14.62[f] 14.00–75.00[g] 33.22–41.09[h]	48.10 ± 13.42 20.00–72.00 43.22–52.99	49.69 ± 14.24 15.00–78.00 45.93–53.45	41.03 ± 12.78 15.00–66.00 37.02–45.04
G_0[a, b] [mg/dL]	90.66 ± 5.74 80.00–99.00 89.11–92.21	100.17 ± 9.32 77.00–115.00 96.78–103.57	106.31 ± 5.13 100.00–118.00 104.95–107.66	100.26 ± 10.16 77.00–117.00 97.07–103.44
G_{30}[a] [mg/dL]	134.11 ± 21.75 87.00–186.00 128.26–139.97	170.17 ± 29.28 100.00–230.00 159.52–180.83-	165.69 ± 27.56 113.00–230.00 158.41–172.97	160,77 ± 32,51 89.00–230.00 150.57–170.97
G_{60}[a] [mg/dL]	125.21 ± 26.85 73.00–184.00 117.98–132.44	183.03 ± 33.79 80.00–231.00 170.74–195.33	164.42 ± 39.51 95.00–256.00 153.98–174.86	158.64 ± 41.87 77.00–227.00 145.50–171.78
G_{90}[a, b, c, d] [mg/dL]	110,83 ± 23,91 53,00–181,00 104,39–117,27	175.07 ± 34.14 85.00–245.00 162.64–187.49	144.53 ± 38.85 71.00–245.00 134.26–154.80	140.23 ± 41.21 67.00–245.00 127.30–153.16
G_{120}[a, b, c, d] [mg/dL]	104.08 ± 17.74 64.00–139.00 99.30–108.85	161.66 ± 15.13 140.00–192.00 156.15–167.16	125.42 ± 26.71 72.00–181.00 118.36–132.48	119.64 ± 29.02 67.00–181.00 110.53–128.75
I_0[a, c, d] [μUI/mL]	3.86 ± 2.10 2.00–10.30 3.30–4.43	8.91 ± 5.66 2.00–22.00 6.84–10.97	9.62 ± 6.42 2.00–28.00 7.93–11.32	17.97 ± 8.17 9.55–55.00 15.41–20.54
I_{30}[a, b, c, d] [μUI/mL]	54.50 ± 37.00 12.70–189.00 44.54–64.46	76.09 ± 66.41 21.40–276.00 51.92–100.26	87.70 ± 57.77 16.80–276.00 72.43–102.96	120.53 ± 68.41 25.60–293.00 99.06–142.00
I_{60}[a, b, c, d] [μUI/mL]	62.75 ± 40.91 10.80–193.00 51.74–73.77	97.81 ± 80.38 26.30–300.00 68.55–127.07	110.64 ± 69.70 10.00–300.00 92.21–129.06	151.81 ± 85.53 5.00–300.00 124.96-178.65
I_{90}[a] [μUI/mL]	51.67 ± 28.24 8.26–137.00 44.07–59.28	110.57 ± 79.52 12.70–300.00 81.63–139.51	104.43 ± 68.16 12.70–300.00 86.42–122.45	136.81 ± 82.69 34.00–300.00 110.86–162.77
I_{120}[a] [μUI/mL]	46.21 ± 21.78 5.63–101.00 40.35–52.08	110.55 ± 72.31 27.50–300.00 84.23–136.87	86.80 ± 62.06 19.70–300.00 70.40–103.20	104.98 ± 73.72 21.90–300.00 81.84–128.11
HOMA-IR_0[a, c, d]	0.87 ± 0.48 0.40–2.44 0.74–1.00	2.27 ± 1.52 0.42–5.60 1.72–2.82	2.55 ± 1.73 0.50–7.60 2.09–3.00	4.39 ± 1.73 2.52–10.59 3.85–4.93

[a]Statistically significant differences between the control group and each pathology group (IGT, IFG, and IR).
[b]Statistically significant differences between IFG and IGT group.
[c]Statistically significant differences between IGT and IR group.
[d]Statistically significant differences between IFG and IR group.
[e]Control subjects are those who do not belong to any of the groups with pathology.
[f]Average and standard deviation.
[g]Maximum and minimum value.
[h]95% confidence interval.

The aim of this study is to evaluate the capability of a HOMA-IR and the modified version of HOMA-IR to diagnose IGT, IR, and IFG. A database of 137 subjects with values of glucose and insulin during OGTT was used. To assess the predictive capacity of HOMA-IR, ROC curves were performed. In the next section the methodological procedure will be explained. In section three and four, results and discussion will be presented. And finally, in section five, the conclusions and future work proposals will be presented.

2 Methodology

2.1 Database

Between 2010 and 2013, 137 adults (male = 48 subjects) between 14 and 78 years old without diabetes were enrolled at the Clinical Research Laboratory of the Venezuela Central University. Each participant underwent the 5-sample-OGTT. In the 5-sample OGTT, insulin and glucose levels are measured in five different blood samples: a sample in fasting of 8 h (G_0, I_0) and four others after oral intake of 75 gr. of glucose at 30 min (G_{30}, I_{30}), 60 min (G_{60}, I_{60}), 90 min (G_{90}, I_{90}),and 120 min (G_{120}, I_{120}) [15–17].

Every database's subject was diagnosed of IGT according to the WHO criteria ($140 \leq G_{120} \leq 199$ mg/dL) [5], IFG to ADA criteria ($100 \leq G_0 \leq 125$ mg/dL) [3], and IR with a HOMA-IR ≥ 2.5 [18]. The characteristics of the database are shown in Table 1. The clinical protocol adhered to the principles of the Declaration of Helsinki and was approved by the Bioethical Committee of the Medical Science Faculty of Venezuela Central University; all the subjects gave a written informed consent.

2.2 HOMA-IR Assessment

In this investigation, five indexes (HOMA-IR and four indexes constructed from calculating the HOMA-IR with the glucose and insulin values at the 30, 60, 90, and 120 min points of the OGTT) were used to assess the IGT, IFG and IR diagnosis. For IGT diagnosis the HOMA-IR_0, HOMA-IR_{30}, HOMA-IR_{60}, and HOMA-IR_{90} ROC curves were constructed. The HOMA-IR_{120} ROC curve was not created for IGT because the IGT diagnosis has a dependent functionality with postprandial glucose. In IFG and IR the HOMA-IR_{30}, HOMA-IR_{60}, HOMA-IR_{90}, and HOMA-IR_{120} ROC curves were constructed. In this case, the HOMA-IR_0 ROC curves were not built because the IFG and IR diagnosis have dependent functionality with fasting glucose. The expressions of the five indexes are presented in the Eqs. (1), (2), (3), (4), and (5).

$$HOMA{-}IR_0 = \frac{I_0 G_0}{405} \tag{1}$$

$$HOMA{-}IR_{30} = \frac{I_{30} G_{30}}{405} \tag{2}$$

$$HOMA{-}IR_{60} = \frac{I_{60} G_{60}}{405} \tag{3}$$

$$HOMA{-}IR_{90} = \frac{I_{90}G_{90}}{405} \tag{4}$$

$$HOMA{-}IR_{120} = \frac{I_{120}G_{120}}{405} \tag{5}$$

Where I_0, I_{30}, I_{60}, I_{90} and I_{120} are the values of insulin at 0, 30 60, 90 and 120 min of the 5-samples-OGTT, and G_0, G_{30}, G_{60}, G_{90} and G_{120} are the values of glucose at 0, 30, 60, 90 and 120 min of the 5-samples-OGTT.

2.3 Performance Measurements

To assess the HOMA-IR (HOMA-IR$_0$), and the modified versions (HOMA-IR$_{30}$, HOMA-IR$_{60}$, HOMA-IR$_{90}$, and HOMA-IR$_{120}$), ability for IGT, IR, and IFG detection, the ROC curves and the area under the ROC curve (AUC) were estimated. To construct and analyze the ROC curves, the sensitivity (SEN), specificity (ESP), positive predictive value (PPV), and negative predictive value (NPV) were calculated for each subject. An AUC $\geq$ 0.70 was considered as an acceptable predictive value [19]. The optimal cut-off point was defined as the shortest distance between the ROC curve and the point [0,1] of the ROC curve plot.

2.4 Statistical Analysis

Non-paired samples were handled with a different distribution than normal. To determine the differences between groups of two, the non-parametric Mann-Whitney U test was used, and between groups of three or more, the non-parametric statistical test of Kruskal Wallis were used; a p-value less than 0.01 was considered statistically significant [20]. The data in the text and in the tables are presented as values of mean and standard deviation, minimum and maximum values and 95% confidence interval.

3 Results

Table 1 reports the glucose and insulin values of the OGTT and the values of HOMA-IR$_0$ for the subjects with IGT, IFG, IR, and control group. The database consists of 137 subjects, 21.1% of subjects have two or more of the pathologies in concomitance (6.6% subjects of the total database with IFG, IGT and IR, 9.5% with IFG and IR, 5.1% with IGT and IFG, and none with IGT and IR).

Figure 1(a), (b), and (c) show the ROC curves of HOMA-IR$_0$, HOMA-IR$_{30}$, HOMA-IR$_{60}$ and HOMA-IR$_{90}$ for IGT diagnosis, and ROC curves of HOMA-IR$_{30}$, HOMA-IR$_{60}$ HOMA-IR$_{90,}$ and HOMA-IR$_{120}$ for IR and IFG diagnosis. Table 2 shows the AUC as well as the sensitivity, specificity, positive predictive value, and negative predictive value for the optimal detection cut-off point for each HOMA-IR version.

Table 2. HOMA-IR ROC curves for the predictability of IGT, IR and IFG.

HOMA-IR		SEN	SPE	PPV	NPV	Optimal cut-off point	AUC
IGT	0 min	0.68	0.59	0.30	0.88	1.50	0.58
	30 min	0.61	0.45	0.22	0.82	17.85	0.50
	60 min	0.68	0.54	0.27	0.87	22.56	0.59
	90 min	0.75	0.66	0.36	0.91	24.88	0.72
IR	30 min	0.75	0.76	0.56	0.88	26.85	0.80
	60 min	0.75	0.78	0.58	0.88	34.06	0.80
	90 min	0.70	0.72	0.51	0.86	25.98	0.77
	120 min	0.75	0.63	0.45	0.86	17.09	0.69
IFG	30 min	0.61	0.74	0.62	0.73	25.98	0.69
	60 min	0.68	0.70	0.60	0.76	25.16	0.70
	90 min	0.73	0.57	0.54	0.76	19.25	0.67
	120 min	0.59	0.72	0.59	0.72	20.19	0.66

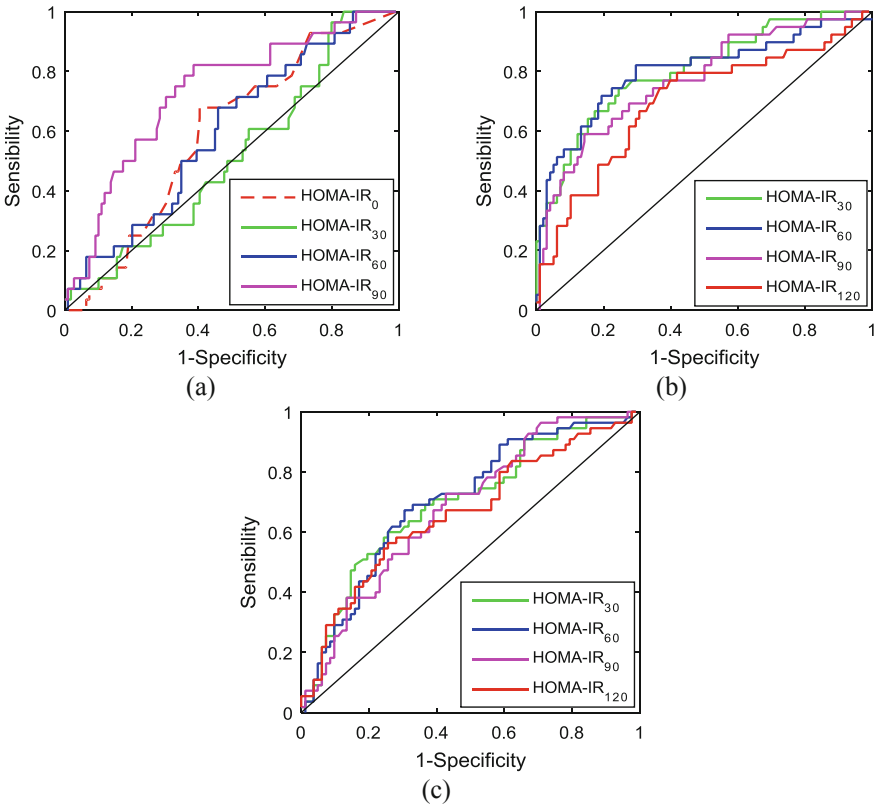

Fig. 1. HOMA-IR$_{0,30,60,\text{ and }90}$ ROC curves for the predictability of (a) IGT, HOMA-IR$_{30,60,90,\text{ and }120}$ ROC curves for the predictability of (b) IR and (c) IFG.

4 Discussion

Subjects with IGT have a HOMA-IR_0 of 2.27 ± 1.52 (Table 1), and in this group, there were no subjects with IR. On the other hand, the subjects who showed IFG and IR reported a HOMA-IR_0 of 3.98 ± 1.13, which is higher ($p < 0.001$) than the one reported in the group with IFG (2.55 ± 1.52, see Table 1). Furthermore, from the total database, there were subjects who had the three pathologies in concomitance. This group obtained a HOMA-IR_0 of 4.47 ± 1.56. All these facts could suggest that IGT could be the starting point for IR followed by metabolic disorders associated with altered fasting glucose and insulin values. Studies corroborate that to have two or more prediabetic conditions (IFG, IGT, and IR) is a sign that the metabolic dysfunction is getting worse [5, 6].

Age plays an important role in the development of pre-diabetic condition. Control subjects (Table 1) have a lower average age ($p < 0.001$) than subjects who have already developed any of the three pathologies. No significant differences were found between the IGT and IFG. All these facts imply that prediabetic conditions tend to increase their prevalence with increasing age [21].

Studies have suggested that using OGTT glucose and insulin values could improve the predictability of methods that measure insulin sensitivity [11]. In this case, the ROC curves with the best predictability for the pathologies studied (AUC $\geq$ 0.70) were the HOMA-IR_{90} for the case of IGT and the HOMA-IR_{60} for the case of IR and IFG. This implies that the HOMA-IR improves its predictability to prediabetic disorders if it is calculated from glucose and insulin values of OGTT that are not the fasting ones. Additionally, the glucose values at 60 min of the OGTT have been explored in the predictability of diabetes obtaining an AUC $\geq$ 0.80 [22]. In this work, the glucose and insulin values were able to determine subjects with IR and IFG with an AUC of 0.8, and 0.7, respectively. All these findings imply that glucose and insulin values at 60 min of OGTT could predict diabetes and prediabetes [23].

On the other hand, it can be observed that the curves with the best AUC (HOMA-IR_{90} for IGT diagnosis, HOMA-IR_{60} for IR, and IFG diagnosis) have a higher negative predictive value (NPV = 0.91 for IGT diagnosis, NPV = 0.88 for IR diagnosis and NPV = 0.76 for IFG diagnosis) than their corresponding positive predictive value (PPV = 0.36 for IGT diagnosis, PPV = 0.45 for IR diagnosis, and PPV = 0.59 for IFG diagnosis). These results suggest that all methods detect normal subjects more efficiently than subjects who are suffering from the pathologies (Table 2).

While analyzing the optimal cut-off points obtained from the best detectors for IR (HOMA-IR_{60}), and IFG (HOMA-IR_{60}), it may be seen that the cut-off point for IFG ($HOMAIR_{60} > 25.16$) is lower than the cut-off point for IR ($HOMAIR_{60} > 34.06$). These facts indicate that when a subject is diagnosed with IR, is automatically diagnosed with IFG. These results corroborate some studies that suggest there is a high prevalence of IFG in subjects with IR [24].

5 Conclusion

The OGTT is an important tool that allows the study of glucose metabolism, and the design of new indexes that allow extracting information from the OGTT is one of the most explored objectives by physicians nowadays. The present study demonstrated that modified versions of HOMA-IR which are calculated using glucose and insulin from 60 and 90 min of 5-samples-OGTT could be used as a diagnostic method for IFG, IGT, and IR.

In future works, the modified versions of the HOMA-IR could be compared with other methods that use glucose and insulin during the OGTT, such as Avignon method, whose correlation with the hyperinsulinemic-euglycemic clamp is 0.89 [11].

References

1. Richter, B., Hemmingsen, B., Metzendorf, M.I., Takwoingi, Y.: Intermediate hyperglycaemia as a predictor for the development of type 2 diabetes: Prognostic factor exemplar review. Cochrane Database Syst. Rev. (5) (2017)
2. Bansal, N.: Prediabetes diagnosis and treatment: a review. World J. Diab. **6**(2), 296 (2015)
3. American Diabetes Association. Diagnosis and classification of diabetes mellitus. Diabetes Care, 37, S81-S90 H (2014)
4. Nichols, G.A., Hillier, T.A., Brown, J.B.: Progression from newly acquired impaired fasting glucose to type 2 diabetes. Diab. Care **30**(2), 228–233 (2007)
5. World Health Organization. Definition and diagnosis of diabetes mellitus and intermediate hyperglycaemia: report of a WHO/IDF consultation (2006)
6. de Vegt, F., Dekker, J.M., Jager, A., Hienkens, E., Kostense, P.J., Stehouwer, C.D., Heine, R.J.: Relation of impaired fasting and postload glucose with incident type 2 diabetes in a Dutch population: the Hoorn study. JAMA **285**(16), 2109–2113 (2001)
7. Wallace, T.M., Levy, J.C., Matthews, D.R.: Use and abuse of HOMA modeling. Diab. Care **27**(6), 1487–1495 (2004)
8. Wongwananuruk, T., Rattanachaiyanont, M., Leerasiri, P., Indhavivadhana, S., Techatraisak, K., Angsuwathana, S., Dangrat, C.: The usefulness of homeostatic measurement assessment-insulin resistance (HOMA-IR) for detection of glucose intolerance in Thai women of reproductive age with polycystic ovary syndrome. Int. J. Endocrinol. (2012)
9. Festa, A., D'Agostino, R., Hanley, A.J., Karter, A.J., Saad, M.F., Haffner, S.M.: Differences in insulin resistance in nondiabetic subjects with isolated impaired glucose tolerance or isolated impaired fasting glucose. Diabetes **53**(6), 1549–1555 (2004)
10. Saad, M.F., Anderson, R.L., Laws, A., Watanabe, R.M., Kades, W.W., Chen, Y.D.I., Bergman, R.N.: A comparison between the minimal model and the glucose clamp in the assessment of insulin sensitivity across the spectrum of glucose tolerance. Diabetes **43**(9), 1114–1121 (1994)
11. Gutch, M., Kumar, S., Razi, S.M., Gupta, K.K., Gupta, A.: Assessment of insulin sensitivity/resistance. Indian J. Endocrinol. Metab. **19**(1), 160 (2015)
12. Salazar, M.R., Carbajal, H.A., Espeche, W.G., Dulbecco, C.A., Aizpurúa, M., Marillet, A.G., Reaven, G.M.: Relationships among insulin resistance, obesity, diagnosis of the metabolic syndrome and cardio-metabolic risk. Diab. Vascular Dis. Res. **8**(2), 109–116 (2011)

13. Yamada, C., Moriyama, K., Takahashi, E.: Optimal cut-off point for homeostasis model assessment of insulin resistance to discriminate metabolic syndrome in non-diabetic Japanese subjects. J. Diab. Inv. **3**(4), 384–387 (2012)
14. Madeira, I.R., Carvalho, C.N.M., Gazolla, F.M., Matos, H.J.D., Borges, M.A., Bordallo, M.A.N.: Cut-off point for Homeostatic Model Assessment for Insulin Resistance (HOMA-IR) index established from Receiver Operating Characteristic (ROC) curve in the detection of metabolic syndrome in overweight pre-pubertal children. Arquivos Brasileiros de Endocrinologia & Metabologia **52**(9), 1466–1473 (2008)
15. Velásquez, J., Wong, S., Encalada, L., Herrera, H., Severeyn, E.: Lipid-anthropometric index optimization for insulin sensitivity estimation. In: 11th International Symposium on Medical Information Processing and Analysis, vol. 9681, p. 96810R. International Society for Optics and Photonics, December 2015
16. Velásquez, J., Severeyn, E., Herrera, H., Encalada, L., Wong, S.: Anthropometric index for insulin sensitivity assessment in older adults from Ecuadorian highlands. In: 12th International Symposium on Medical Information Processing and Analysis. International Society for Optics and Photonics, 10160, 101600S, January 2017
17. Farina, P.V.R., Severeyn, E., Wong, S., Turiel, J.P.: Study of cardiac repolarization during oral glucose tolerance test in metabolic syndrome patients. In: 2012 Computing in Cardiology, pp. 429–432. IEEE, September 2012
18. Matthews, D.R., Hosker, J.P., Rudenski, A.S., Naylor, B.A., Treacher, D.F., Turner, R.C.: Homeostasis model assessment: insulin resistance and β-cell function from fasting plasma glucose and insulin concentrations in man. Diabetologia **28**(7), 412–419 (1985)
19. Reitsma, J.B., Glas, A.S., Rutjes, A.W., Scholten, R.J., Bossuyt, P.M., Zwinderman, A.H.: Bivariate analysis of sensitivity and specificity produces informative summary measures in diagnostic reviews. J. Clin. Epidemiol. **58**(10), 982–990 (2005)
20. Marusteri, M., Bacarea, V.: Comparing groups for statistical differences: how to choose the right statistical test? Biochemia medica: Biochemia medica **20**(1), 15–32 (2010)
21. Mayega, R.W., Guwatudde, D., Makumbi, F., Nakwagala, F.N., Peterson, S., Tomson, G., Ostenson, C.G.: Diabetes and pre-diabetes among persons aged 35 to 60 years in eastern Uganda: prevalence and associated factors. PLoS ONE **8**(8), e72554 (2013)
22. Kuang, L., Huang, Z., Hong, Z., Chen, A., Li, Y.: Predictability of 1-h postload plasma glucose concentration: a 10-year retrospective cohort study. J. Diab. Invest. **6**(6), 647–654 (2015)
23. Alyass, A., Almgren, P., Akerlund, M., Dushoff, J., Isomaa, B., Nilsson, P., Meyre, D.: Modelling of OGTT curve identifies 1 h plasma glucose level as a strong predictor of incident type 2 diabetes: results from two prospective cohorts. Diabetologia **58**(1), 87–97 (2015)
24. Kaya, A., Turan, E., Uyar, M., Bayram, F., Turan, Y.: The prevalence of insulin resistance in the Turkish population: a study conducted with 3331 participants. EJMO **1**(4), 202–206 (2017)

System for Monitoring Environmental Variables in a Pharmacy Area Using an Alternative IoT Architecture (a Pilot Study)

Jefferson Sarmiento-Rojas[1(✉)], John-Sebastian Sanchez-González[1,2], Pedro-Antonio Aya-Parra[1], and Daniel-Alejandro Quiroga-Torres[1]

[1] School of Medicine and Health Sciences, GiBiome Research Group, Universidad del Rosario, Bogotá, Colombia
jefferson.sarmiento@urosario.edu.co
[2] Biomedical Engineering Department, Escuela Colombiana de Ingeniería Julio Garavito, Bogotá, Colombia

Abstract. Hospitals and health centers that own a pharmacy area require continuous and safe monitoring of environmental variables. The rigorous control of temperature and relative humidity allows the physical and chemical properties of the medicines to be conserved, according to the suggestion of suppliers and current laws that regulate the conservation of medicines. The Internet of things (IoT) allows for monitoring and controlling specific areas by obtaining and publishing relevant data directly in the cloud, enabling intelligent systems to make early decisions when an abnormality is present in the area. However, for the IoT to fulfill its purpose, there must exist a permanent connection of things to the Internet, which is a challenge when there is low or no connection. Therefore, the purpose of this work is to implement a monitoring system for environmental variables under the condition of low or no Internet connectivity, using alternative technologies such as (GSM) for transferring data to the cloud. As a result of this work, the design and implementation of a continuous monitoring system for environmental variables in the hospital pharmacy area is presented. This system guarantees the integrity and security of the acquired data due to the standardized communication protocols that were implemented and the alternative IoT architecture under which the system was designed.

Keywords: Internet of Things · IoT architecture · GSM · Clinical engineering · Hospital

1 Introduction

Although the concept of the Internet of Things (IoT) has existed for about only a decade [1, p. 3], it has become a fundamental element in what is now called the fourth industrial revolution because of its important advances in applications related to smart devices with Internet connection. It is estimated that by the year 2035, approximately one trillion "things" will be connected to Internet, thus generating an extensive volume of data to be processed and enough information to contribute to the automation of

© Springer Nature Switzerland AG 2020
C. A. González Díaz et al. (Eds.): CLAIB 2019, IFMBE Proceedings 75, pp. 1284–1291, 2020.
https://doi.org/10.1007/978-3-030-30648-9_165

processes and decision making in real time [2]. The IoT paradigm intends that all everyday objects that provide us with relevant information from a specific environment are connected to Internet. Therefore, the IoT has an exponential growth not only in the consumer sector but also in the industrial sector in fields such as transportation, manufacturing, agriculture, telecommunications, energy and health [3].

Most IoT applications that focus on health are related to the remote monitoring of patients; these include applications that measure vital signs via remotely generating alerts for detecting an abnormality in the human body, applications that address the elderly and active aging [4], and IoT applications that focus on hospital management regarding medical equipment or hospital areas.

Hospital environments and health centers require constant monitoring in the pharmacy area that is responsible for the acquisition, preservation, delivery and, in some cases, manufacturing of medication. Environmental and specifically temperature and humidity controls must be carried out, as these variables are important in guaranteeing the safety, purity and efficacy of the medicines [5]. Previous works attempted to address temperature and humidity controls by implementing a system based on an IoT architecture using an Internet connection; however, due to the lacking availability of an Internet connection, this was not possible at the hospital.

The purpose of this work is to design and implement a temperature and humidity acquisition system for managing information in the hospital pharmacy area, which allows for transmitting these variables in an environment with low or no Internet connectivity.

2 Materials and Methods

In this paper, an architecture composed of two stations was proposed: one for the collection and sending of data located in the hospital pharmacy area and another for the reception, storage and visualization of information located in the laboratories of the Universidad del Rosario, which have networks for IoT applications. Both stations are separated by a geographical distance of 4.2 km.

2.1 Data Capture and Sending Station

This station was responsible for the continuous monitoring of temperature and humidity variables. The variables were acquired every minute; after an hour, the data was averaged, and the result was sent to the reception station. This station consists of an MKR 1400 board developed by Arduino company and whose primary feature is to use GSM technology and connectivity with the powerful Microchip ATSAMD21 and U-blox SARA-U201 GSM module [6], an activated SIM card featuring a country communications operator and the temperature and humidity sensor DHT 22 developed by Adafruit company and characterized by its high accuracy: ± 0.5 °C for temperature and $\pm 2\%$ for relative humidity [7]. The connection schematic is illustrated (see Fig. 1).

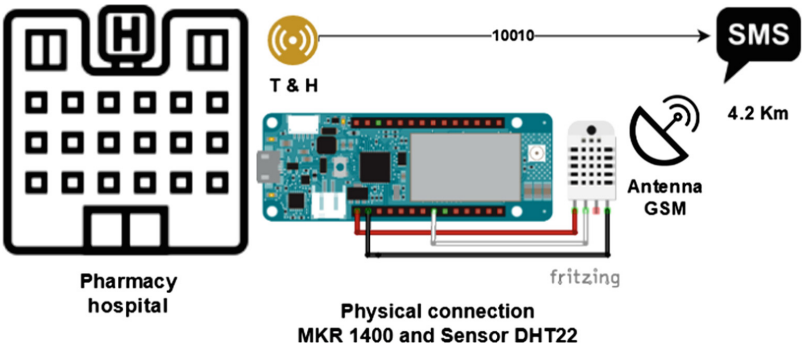

Fig. 1. Architecture of the sending station.

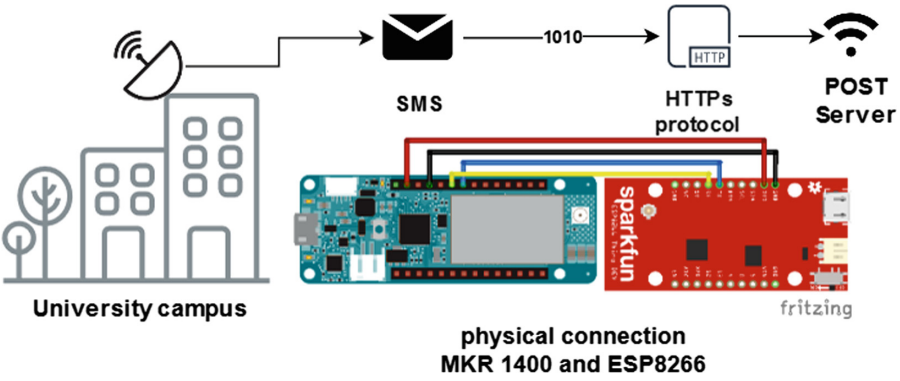

Fig. 2. Architecture of the station for receiving.

2.2 Station for Receiving

The station was responsible for receiving the data sent by the information capture station, using a GSM communication network (*Global System for Mobile*), receiving temperature and humidity data via text messaging or SMS (*short message service*) (see Fig. 2). This station uses an MKR 1400 board, which guarantees that the information comes from a reliable source. Once the information is received, it is sent through a serial communication to the development board ESP8266, developed by Sparkfun company, whose primary characteristic is its easy and safe connection to the Internet [8]. Finally, this board sends the data received using an Internet connection, an HTTP communication protocol, and an SSL security certificate to a web application hosted on a server in the cloud (see Fig. 3).

2.3 Storing and Displaying Information

Likewise, a web application was designed to store and query the data in a MySQL relational database for IoT [9, p. 195]; in addition, the application uses the Google Chart API to display the temperature and humidity status [10] of the last 12 h on a chart and two-gauge charts. Finally, the application offers a service of early alerts via email when abnormalities are present in the measurements. A preview of the developed interface can be observed in Fig. 3, and a demo of the application can be viewed at https://urbiomedeng.com/FarmaciaMederi/.

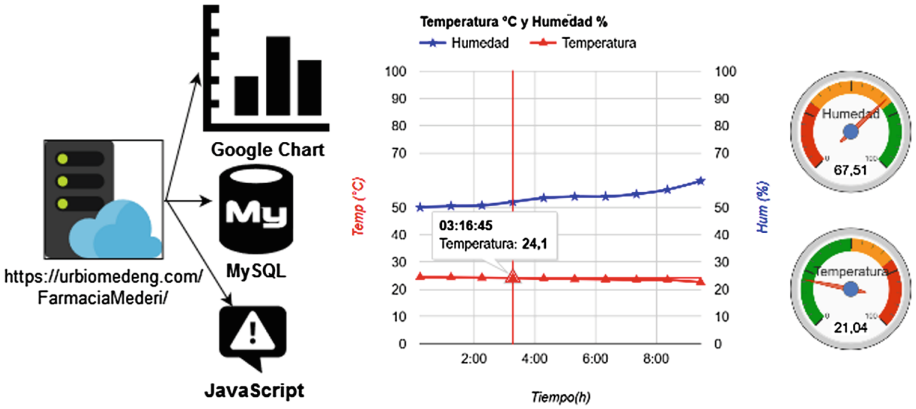

Fig. 3. Architecture for web application.

A statistical analysis was performed on the data collected by the system and the data collected manually. In the first instance, a descriptive analysis of the variables temperature and humidity was developed. Afterward, an inferential analysis of the data was conducted, the Shapiro Wilk normality test was applied, and a comparison of means was made between the data collected manually and the data measured by the system, for which a *t*-test was used. Finally, the error between the data collected manually and the data measured by the system was calculated. Statistical analysis was performed using the software SPSS V 25.

3 Results

To verify the reliability of our system, an analysis of the data collected for four days was performed. The manual records contain the measurements provided by the institution's thermohydrometer, which were compared with the measurements captured by the proposed system. In Tables 1 and 2, one can observe the descriptive statistics of the data manually acquired by the healthcare personnel in addition to what was registered by the proposed system.

Table 1. Descriptive statistics of manual temperature and humidity records

n	Mean ± SD[a]	Median	Shapiro-Wilk (***p*-value**)
12	23.66 ± 1.61 °C	23.50 °C	0.60
12	54.75 ± 4.04%	55%	0.86

[a]SD: Standard Deviation

Table 2. Descriptive statistics of temperature and humidity measured by the system

n	Mean ± SD	Median	Shapiro-Wilk (***p*-value**)
12	23.94 ± 1,70 °C	24.37 °C	0.183
12	55.18 ± 5.14%	54.34%	0.709

The value of statistical significance in the above tables is greater than 5%; for this reason, the null hypothesis is not rejected. This indicates that the temperature and humidity values for the mentioned cases follow a normal distribution. Therefore, a *t*-student test (see Table 3) of related measures was used to determine the degree of significance.

Table 3. Manual records against those measured by the system

Variable	Statistical T	gl	*p*-value
Temperature	−1.252	11	0.236
Humidity	−0.445	11	0.665

Based on the above table, it can be concluded that no statistically significant differences are found between the temperature and humidity measurements taken manually against the temperature and humidity measurements recorded by the system. This allows us to confirm the measurements delivered by the IoT system with a range of error lower than the 10% in each of the variables measured hourly (see Table 4).

An alternative IoT architecture applicable to any type of environment or industry in which the Internet connectivity is low or zero was designed and implemented (see Figs. 1 and 3). This system is presented with an open-source technologies solution that assures the traceability of temperature and humidity variables in a defined time interval, in addition to making a secure and reliable record in a database hosted in the cloud, which guarantees correct information management. The distribution of temperature and humidity data per day is presented in Fig. 4.

It can be observed in Fig. 4 above that the system detects that normal temperature values are between 23 °C and 25 °C; besides, it detects other temperature values within the limits established by the guidelines for the storage of medicines [11].

Likewise, in the humidity chart (see Fig. 5), some outliers were presented in the measurements, which indicates that on May 10, 13 and 14, some values were presented outside the average of the other values. However, these are contemplated in the regulations as tolerable values.

Table 4. Error manual records against those measured by the system

Month	Day	Hour	T Manual	T System	H Manual	H System	Error T	Error H
May	10	8	21	19.93	62	66.69	5%	8%
		12	24	24.71	56	56.73	3%	1%
		21	25	24.71	55	53.38	1%	3%
	11	8	22	21.96	58	58.15	0%	0%
		12	23	23.28	58	60.59	1%	4%
		21	26	25.42	54	54.39	2%	1%
	12	8	22	23.48	53	52.05	7%	2%
		12	25	25.01	49	49	0%	0%
		22	24	25.42	45	47.58	6%	6%
	13	8	23	23.38	57	56.53	2%	1%
		12	23	24.04	55	54.3	5%	1%
		21	26	26.03	53	52.8	0%	0%
	14	8	21	19.83	65	67.3	4%	6%
		12	23	23.48	56	56.73	1%	2%
		21	24	25.4	54	54.39	1%	6%

*T: Temperature, H: Humidity

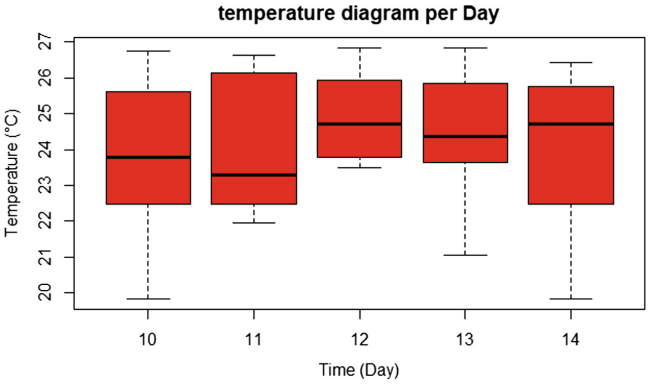

Fig. 4. Distribution of temperature per day.

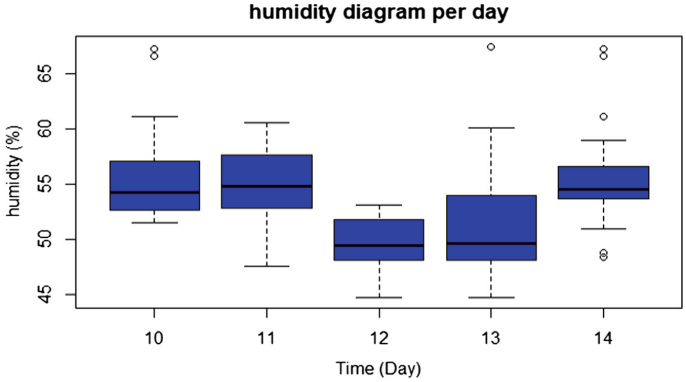

Fig. 5. Distribution of humidity per day.

To better detail the distribution of the temperature and humidity data per hour delivered by the system, an analysis was performed by means of a box diagram that is presented in the following graph.

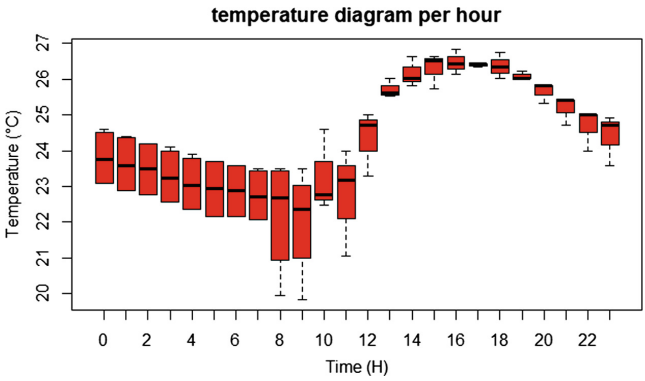

Fig. 6. Distribution of temperature per hour.

The box diagrams displayed in Fig. 6 reveal that, during the afternoon hours, the system detected a considerable increase in the environment's temperature, with ranges between 25 °C and 27 °C; in the night and morning hours, however, are ranges between 21 °C and 24 °C.

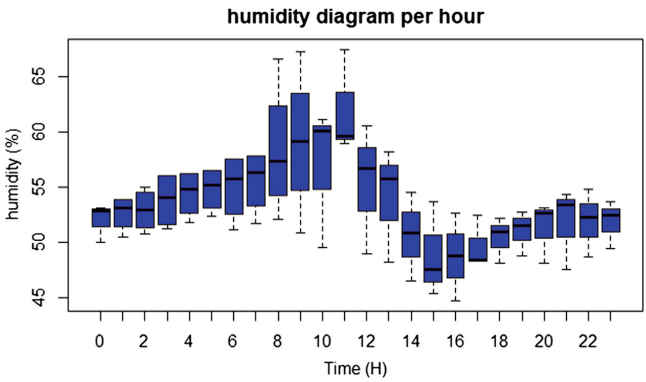

Fig. 7. Distribution of humidity per hour.

Similarly, the environment's relative humidity (see Fig. 7) ranged from 50% to 65% humidity and from 45% to 50% humidity during the afternoon.

4 Conclusions

It was possible to develop and implement a prototype system that guarantees the traceability of temperature and humidity in the pharmacy area, as it is continuously operated in the hospital, allowing for safely storing information in the cloud. Likewise, the system generates alerts to the responsible personnel in the event of an unusual change in these two variables. Moreover, Fig. 1 displays the proposed architecture expandable to all industrial sectors in which there is little or no Internet connectivity. The system is currently in operation in the hospital and continues capturing information to generate a statistical report of the accuracy and sensitivity of the system.

One of the limitations presented in this study is the amount of data with which the statistical tests were conducted. In future work, we intend to perform this same analysis using a minimum of six months of acquired data that will guarantee the accuracy, precision and sensitivity of the system and conduct a safety study.

Conflict of Interest. The authors report no conflicts of interest.

References

1. Hassan, Q.F.: Internet of Things A to Z: Technologies and Applications. Wiley (2018)
2. Sparks, P.: The route to a trillion devices. White Pap. ARM (2017)
3. Almada-Lobo, F.: The industry 4.0 revolution and the future of manufacturing execution systems (MES). J. Innov. Manag. **3**(4), 16–21 (2016)
4. Islam, S.M.R., Kwak, D., Kabir, M.H., Hossain, M., Kwak, K.: The internet of things for health care: a comprehensive survey. IEEE Access **3**, 678–708 (2015)
5. Ziance, R., Chandler, C., Bishara, R.H.: Integration of temperature-controlled requirements into pharmacy practice. J. Am. Pharm. Assoc. **49**(3), e61–e69 (2009)
6. Arduino MKR GSM 1400. https://store.arduino.cc/usa/mkr-gsm-1400. Accessed 19 Apr-2019]
7. Rachana, M., Abhilash, B., Meghana, P., Mishra, V., Rudraswamy, S.B.: Design and deployment of sensor system—envirobat 2.1, an urban air quality monitoring system. In: 2017 International Conference on Electrical, Electronics, Communication, Computer, and Optimization Techniques (ICEECCOT), pp. 412–415 (2017)
8. Schwartz, M.: Internet of Things with ESP8266. Packt Publishing Ltd. (2016)
9. Bell, C.: MySQL for the Internet of Things. Apress (2016)
10. Blackstock, M., Lea, R.: IoT mashups with the WoTKit. In: 2012 3rd IEEE International Conference on the Internet of Things, pp. 159–166 (2012)
11. Directrices para el almacenamiento de los medicamentos esenciales y otros insumos de salud. http://apps.who.int/medicinedocs/es/m/abstract/Js16726s/. Accessed 10 Jun 2019

Development a Virtual Game to Stimulate Grip and Pinch Movements

Domingo L. Cancela[1,2], Douglas Crochi[1(✉)], Fabiana R. S. M. Cavalcante[1], Alessandro P. Silva[1], Silvia C. Martini[1], Terigi A. Scardovelli[1], and Silvia R. M. S. Boschi[1]

[1] Technology Research Center, University of Mogi das Cruzes, Mogi das Cruzes, S.P., Brazil
douglascrochi@gmail.com, boschi@umc.br
[2] Centro Paula Souza, ETEC, Poá, São Paulo, Brazil

Abstract. By using new technologies in electronic games, virtual environments come up with the proposal of simulating daily routines. This research has intended to design a virtual game focused on performing palmar grip, cylindrical grip and tip-to-tip pinch movements. A virtual game was designed in three different stages, the first of which stage aiming to stimulate the palmar grip movement, the second one stage to stimulate the tip-to-tip pinch movement, while the third stage focused on furthering the cylindrical grip movement. The game features a timer, which determines three minutes for each stage, while the player's performance is recorded in order to measure his or her progress in performing each movement. In order to activate the virtual game, it is required using a device to capture hand movements, named Leap Motion controller. By doing that, it is possible to interact with and move characters in the game. During software engineering tests, no operational problems were found in the system. The virtual game is able to stimulate in a playful manner the grip and pinch movements and can be a tool used for training such movements.

Keywords: Virtual game · Grasping · Movement

1 Introduction

The hand is a very important organ, with great mobility, where the movements performed by the wrist and fingers allow for a variety of functions, especially grip and pinching movements, used to handle tools and performing daily activities [1, 2]. Control over these movements is fundamental to perform daily tasks, by promoting individuals' independence [3]. However, due to its complexity, the hand is one of the most difficult members to be rehabilitated [4] and when there is impairment, this causes loss of function, decreases performance in daily activities and changes in quality of life [5–7].

Among the many resources currently available towards recovery and treatment of patients, virtual rehabilitation offers unique opportunities for motor experience, in a playful, pleasurable way in order to enable the use of this virtual game, as well its

© Springer Nature Switzerland AG 2020
C. A. González Díaz et al. (Eds.): CLAIB 2019, IFMBE Proceedings 75, pp. 1292–1297, 2020.
https://doi.org/10.1007/978-3-030-30648-9_166

functional performance as a whole [3]. Boschi et al. [8] refer to the importance of grip movements for daily chores, having designed in their study a device to assist the hand rehabilitation process. According to studies [9], the use of Virtual Environments towards the rehabilitation of hand movements has been growing due to their playful aspect that eventually show a fabulous potential, since they entertain patients while in therapy. Therefore, Friedman et al. [10] developed a sensorized glove that controls a virtual game by the grip and pinch movements. Thus, recent studies have resorted to virtual reality as a means of motivating such patients, making therapy sessions more pleasurable [11–14]. Accordingly, this paper purports to develop a virtual game to stimulate palmar grip, cylindrical grip and tip-to-tip pinch movements.

2 Materials and Methods

In order to design the game, the cascade life cycle model was used, which includes the requirement analysis, analysis and design, implementation, tests and maintenance stages [15].

2.1 Graphic Design

The game is called "Crazy Scavenger Hunt". The entire scenario of the game was developed using a 2D graphic interface, through the resources of the C# programming language, which enabled communication between hardware and software. In addition, the SDK game development library made available by the interaction device manufacturer (Leap Motion) [16] and Corel Draw X6 graphic design software were used to create and vector the images.

2.2 Interface and Interaction

In order to access to the game stages, the user must first enter his or her name and date of birth on the login screen. The player's interaction with the virtual game occurs through the Leap Motion device, by means of which the individual uses hand movements to control the game. The user can stop, pause, change the stage or just leave the game anytime. At the end, the user will be able to view his performance scoring.

2.3 Game Stages

The first stage is comprised by a "worm" character that appears on apples scattered on a tree. With the grasp movement, the player must hit the worm as many times as possible in 3 min, and changes his or her position every 7 s. In the second stage, through the pinch movement, the individual will have 3 min to hold a dart, aim at the target, and release a missile to reach it. Every 7 s the target changes position. In the last stage, performing the grasp movement, the player will have 3 min to direct the rudder of a ship to rescue the largest number of divers at the sea.

2.4 Software Testing

Software tests were conducted by one of the researchers. Through the Visual Studio software, applying the white box test was possible to check and search for potential internal flaws in the game source code. Then, the black box test was also conducted on the game, which was manually applied in order to check for potential operational errors, as well as the information flow to use the game as a whole. Tests were split into four stages. The first one consisted of checking communication during the player's in the game database, in search of registration errors or any kind of inconsistency. The second step included clicking on all buttons displayed in the game to identify link errors. The third step, the loading time of screens and click responses were recorded. Finally, the entire game was tested, as if a volunteer were starting an exercise session.

3 Results

3.1 Game Design

Figure 1 shows a volunteer's home and registration screens. Initially, the volunteer is supposed to register by providing basic information, such as Name, Age, Gender and registration date in order to be able to log in as a player. It can be seen that the game main screen contains the 3 game stages, the enable/disable sound button, as well as the registration, change user, credits and exit buttons.

Fig. 1. Main screen and user's registration screen.

In Fig. 2A depicts the graphical interface of Phase 1, where by means of the palmar grip movement, the player must hit the highest number of "worms" that appear in the "apples". The volunteer has up to 7 s to hit the target, a time that requires and encourages greater attention from the player. That that time is over, the "worm" disappears and then reappears in another position.

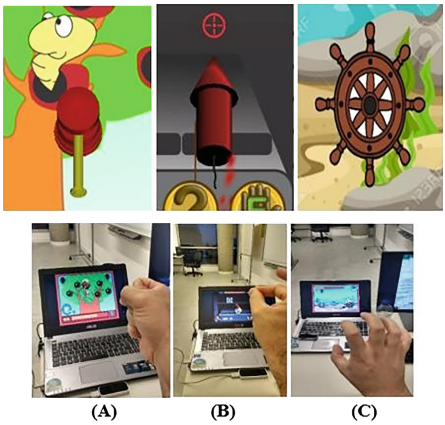

Fig. 2. (A) The Phase 1 and palmar grip movement screen; (B) The Phase 2 and tip-to-tip pinch movement screen; (C) The Phase 3 and cylindrical grip movement screen.

Figure 2B displays the graphical interface of Phase 2 and the "tip-to-tip pinch" movement performed by the player. In this stage, named "Hit the Target", by using the pinch movement, the player must hold the "missile", aim and release it to reach the target. As in stage 1, he or she will have 7 s to perform this action, since after that time the target disappears and then reappears in another position. The graphical interface of Phase 3 and the cylindrical grip movement that must be performed by the player are in Fig. 2C. In the last stage of the game, the "cylindrical grip" movement will be stimulated, where by means of the figure of a "ship rudder", the player must make movements to the right or the left, in order to rescue the largest number of divers, not taking more than 7 s, since after that time the target disappears and reappears in another position.

At the end of each stage, a screen highlighting the end of the game appears. The player will have access to his or her current score and records of previous scores may be displayed, thus making it easier monitoring the progress of the patient in therapy.

3.2 Functionality Tests

During Software Testing, no internal flaws in the game source code were found. No programming, logic or animation sequence errors or system interruptions were identified during the entire period of its operation, passing through all environments in a satisfactory manner.

4 Discussion/Conclusion

Functional recovery of neurological lesions demands an intense program of repetitive exercises [17]. However, this type of intervention tends to be monotonous, making it difficult for children to get involved. Seeking to make the physiotherapy session more

attractive, several robotic devices were developed to meet the need for intensive training in an interactive way [18, 19]. However, few tools were designed for the rehabilitation of the hands.

However, Friedman et al. [10] and Choi et al. [20] developed sensorized gloves for the rehabilitation of manual gripping and thumb opposition movements in a virtual environment. However, children with neurological lesions usually present postural abnormalities [11], muscular contractures [12] and spasticity, negatively affecting the motor function of the hands [15], which makes it difficult and unfeasible to use gloves because they can cause discomfort to the user. In the game developed in the present study, the interaction of the player with the virtual environment occurs through the Leap Motion device, which allows children with different degrees of motor impairment to enjoy this tool without using anything in the hands, allowing greater convenience and freedom of movement to the user.

In this study, a virtual game was designed to stimulate grasping and pinching movements, allowing individuals with motor injuries to have access to a playful and interactive therapy. Although the software test results have been satisfactory, further research with the application in volunteers is necessary to confirm the game effectiveness.

Declaration of Conflict of Interest. The authors declare no conflict of interest.

References

1. Butler, E., Ladd, A., LaMont, L., et al.: Temporal–spatial parameters of the upper limb during a Reach & Grasp Cycle for children. Gait Posture **32**(3), 301–306 (2010)
2. Cardeal, L., Muñoz, M., De Souza, A., et al.: Jogos virtuais como recurso terapêutico no estímulo de funções manuais. Cadernos de Pós-Graduação em Distúrbios do Desenvolvimento **16**(2), 68–76 (2016)
3. Monteiro, C., Jakabi, C., Palma, G., et al.: Motor learning in children with cerebral palsy. Revista Brasileira Crescimento e Desenvolvimento Humano **20**(2), 250–262 (2010)
4. Piggott, L., Wagner, S., Ziat, M.: Haptic neurorehabilitation and virtual reality for upper limb paralysis: a review. Crit. Rev. Biomed. Eng. **44**(1–2), 1–32 (2016)
5. Almenara, M., Cempini, M., Gómez, C., et al.: Usability test of a hand exoskeleton for activities of daily living: an example of user-centered design. Disabil. Rehabil. Assist Technol. **12**(1), 84–96 (2017)
6. Lemmens, R., Timmermans, A., Janssen-Potten, Y., et al.: Valid and reliable instruments for arm-hand assessment at ICF activity level in persons with hemiplegia: a systematic review. BMC Neurol. **12**(21), 1–17 (2012)
7. Maciejasz, P., Eschweiler, J., Gerlach-Hahn, K., et al.: A survey on robotic devices for upper limb rehabilitation. J. NeuroEng. Rehabil. **11**(1), 1–29 (2014)
8. Boschi, S., Frère, A.: Grid and pinch capability assessment system for children. Med. Eng. Phys. **35**(5), 626–635 (2013)
9. Howard, M.: A meta-analysis and systematic literature review of virtual reality rehabilitation programs. Comput. Hum. Behav. **70**, 317–327 (2017)
10. Friedman, N., Chan, V., Reinkensmeyer, A., et al.: Retraining and assessing hand movement after stroke using the MusicGlove: comparison with conventional hand therapy and isometric grip training. J. Neuroeng. Rehabil. **11**, 76 (2014)

11. Deutsch, J., Borbely, M., Filler, J., et al.: Use of a low-cost, commercially available gaming console (Wii) for rehabilitation of an adolescent with cerebral palsy. Phys. Ther. **88**(10), 1196–1207 (2008)
12. Tarakci, D., Ersoz Huseyinsinoglu, B., Tarakci, E., et al.: Effects of Nintendo Wii-Fit® video games on balance in children with mild cerebral palsy. Pediatr. Int. **58**(10), 1042–1050 (2016)
13. Tsoupikova, D., Stoykov, N., Corrigan, M., et al.: Virtual immersion for post-stroke hand rehabilitation therapy. Ann. Biomed. Eng. **43**(2), 467–477 (2015)
14. Pedraza-Hueso, M., Martín-Calzón, S., Díaz-Pernas, F., et al.: Rehabilitation using kinect-based games and virtual reality. Procedia Comput. Sci. **75**, 161–168 (2015)
15. Bax, M., Goldstein, M., Rosenbaum, P., et al.: Proposed definition and classification of cerebral palsy, April 2005. Dev. Med. Child Neurol. **47**(8), 571–576 (2005)
16. Leap Motion Homepage. https://www.leapmotion.com. Accessed 10 Apr 2019
17. Jeon, B., Kim, W., Park, E.: Effect of task-oriented training for people with stroke: a meta-analysis focused on repetitive or circuit training. Top Stroke Rehabil. **22**(1), 34–43 (2015)
18. Guidali, M., Duschau-Wicke, A., Broggi, S., et al.: A robotic system to train activities of daily living in a virtual environment. Med. Biol. Eng. Comput. **49**(10), 1213–1223 (2011)
19. Gilliaux, M., Lejeune, T., Detrembleur, C., et al.: A robotic device as a sensitive quantitative tool to assess upper limb impairments in stroke patients: a preliminary prospective cohort study. J. Rehabil. Med. **44**(3), 210–217 (2012)
20. Choi, Y.: Ubi-REHAB: an android-based portable augmented reality stroke rehabilitation system using the eGlove for multiple participants. In: 2011 International Conference on Virtual Rehabilitation, Zurique, Suíça (2011)

Methodology for Defining Ubiquitous Management Indicators in Primary Health Care

Reginaldo Dias Soares Filho(✉), Juliano Martins, and Renato Garcia

Biomedical Engineering Institute - Federal University of Santa Catarina (IEB-UFSC), Florianópolis, Brazil
reginaldo.dias@ieb.com.br

Abstract. This paper presents a methodology proposal for defining indicators in ubiquitous management on primary health care. With a multidisciplinary team, health technology indicators were identified through quality tools to classify fault parameters. Data collection was performed in a clinical engineering information system, with equipment that compose the technologic park of primary health care from 2014 to 2018. In the categorization of the data, sixty classes of equipment were listed, totaling 3053 equipment distributed in the network of primary care in the city of Florianópolis-Santa Catarina-Brazil. In these five years, 17638 work order accounted for the study were generated. After applying quality tools, such as Ishikawa diagrams, the dental compressor was chosen to validate the proposal and determine the parameters to be monitored in order to support the performance of clinical engineering in a predictive model. This methodology enables maintenance management, providing reliability and safety to the primary care system.

Keywords: Clinical Engineering · Failure indicators · Health technology management

1 Introduction

Brazil's Primary Health Care (PHC) is the first resource sought by the population to access health care, this structure has a system formed by: Polyclinics, Dentistry Specialties Centers (CEO), Basic Health Units (UBS), Units of Immediate Support and Diagnosis (UPA) [1].

The demands stemming from the technological apparatus growth of Primary Health Care (PHC) has required new models that best suit its challenges, with greater capacity for management, problem solving, better support to the manager and to the public that uses the Primary Health Care system (PHC). The demand for new models is justified by the fact that public policies and primary care models are constantly evolving.

Currently, some resources are needed to improve the work processes of the Institutions and always offer the best for the users and operators that use the technologies. For this, quality management models were created, which have as main objectives detect problem situations, improvement of competitiveness and productivity in different processes [2].

© Springer Nature Switzerland AG 2020
C. A. González Díaz et al. (Eds.): CLAIB 2019, IFMBE Proceedings 75, pp. 1298–1305, 2020.
https://doi.org/10.1007/978-3-030-30648-9_167

These tools previously used only in the industry began to integrate with health system and are used in several approaches to its application, such as: quality control - monitors and reviews quality; quality guarantee - identifies and eliminates failures; quality improvement - minimize errors; Six Sigma - "Error free" and reduction of product variation; quality management - Permanent improvement of technical quality and user satisfaction [2].

In the context of management, these tools are statistical instruments that aid in problem solving and decision making. Therefore, it is worth to emphasize the importance of studying them.

In this paper, some of these management tools are applied. They can be divided into two groups: quality control tools and management tools. The seven quality control tools are: Pareto chart, Ishikawa diagram, control chart, scatter diagram, check sheet, flowchart and histogram [3]. The seven management tools are: relation diagram, prioritization matrix, affinity diagram, relation matrix, tree diagram, division process diagram and arrow diagram [4]. Two quality control tools (Ishikawa diagram and Pareto chart) and one management tool (the prioritization matrix) were applied in this paper.

With the Ishikawa diagram it was possible to identify the root cause of the problem through the identification of the studied effect, in addition, the classification of connected main and secondary causes is utilized [5].

The Pareto chart is applied when there are many causes for a system [5]. This tool is based on the principle that a problem can be assigned a small number of causes, allowing to identify the random frequency of a problem. With its use it is possible to concentrate resources only on the evidenced elements [6].

The prioritization matrix, also called the GUT matrix, is utilized in the prioritization of tasks as well as the Pareto chart. It is based on gravity, urgency and trend, in which it uses facts listing and assigns weights to the problem The gravity represents the impact, intensity and depth of the analyzed problem, if it does not have a plan of action; urgency represents the time for the problem to appear and the time needed to solve it, if no action is taken on the problem; and the tendency that represents the possibility of the problem to become larger without a plan of action [7].

Research on the application of quality tools is often found, especially in the industry, since it is presupposed that it is necessary to carry out rigorous processes to achieve high yields in the production and sales of products. This is observed in research on the subject, such as the study by Azizi [3] that uses quality tools to solve problems of low productivity due to the high breaking of the machine.

In healthcare, these tools are also applied, but on a smaller scale. Some application examples are found in user service improvements. An example is the study [6] that seeks to improve the quality of care in the Intensive Care Units. Another study [2] emphasizes the use of quality tools to evaluate management and risks in hospital systems.

The objective of the present paper is to develop a methodology for defining indicators in ubiquitous management on PHC through quality tools which indicate fault parameters that need to be monitored. The proposed model comprises three main categories: Operational, Monitoring and Decision [8]. This paper presents the results of the Operational category (as shown in Fig. 1) that develops health solution techniques

through data collection, situation diagnosis and identification of the type and characteristics of the problem, applying tools for quality improvement and control for defining monitoring parameters.

2 Materials and Methods

The operational category is related to techniques of health technology solutions based on quality management tools such as: Ishikawa diagram, Pareto chart and prioritization matrix, known as GUT. It is divided in three stages: First, the problem situation is defined, then, the evaluation parameters are determined and, finally, the ubiquitous health technology solutions are pointed out.

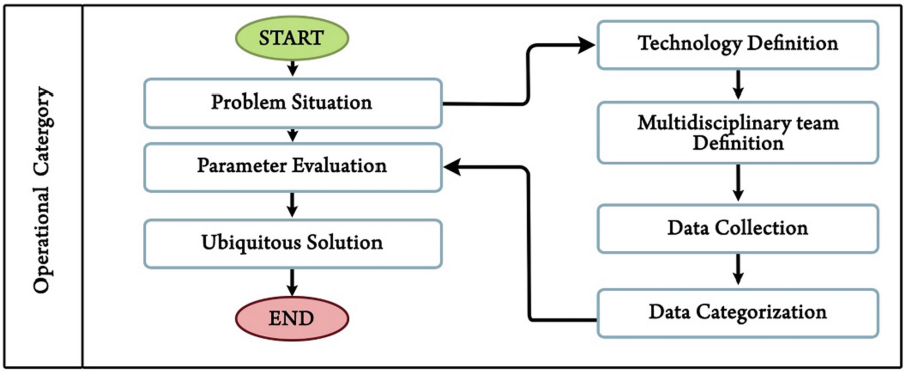

Fig. 1. Description of the Operational model for fault indicators of health technology.

On the first stage, the problem situation is the basis for the development of the project, where the technology, multidisciplinary team and the criteria for data collection and categorization, through which the management methodology will be developed, are defined. At this stage, the team needs to collect as much information as possible regarding health technologies in PHC, organize them and exhaust the possibilities of evidence of fault found.

The definition of the technology does not have to follow a pre-established standard; one can choose the criteria and the tools that fit the objectives of each study.

The multidisciplinary team should be composed of people from different areas, with relative knowledge in management and health technology planning, among others. In addition, it is important that the team is knowledgeable about applications of quality tools.

In data collection, all the evidence into a data system of a clinical engineering (C.E.) can be covered, such as: researches on the technical manuals provided by the companies and the Brazilian National Sanitary Surveillance Agency (ANVISA), on-site visits where the equipment is installed, definition on who will collect the data, training and follow-up of those responsible for collecting data and determination of sample size and period, among others, according to the objectives of the collection.

The collected data categorization, in turn, facilitates the definition and application of quality tools. In order to do this, one of the methods can be to sort them in decreasing order by fault frequency or importance, according to records observations; historic data; previous repairs; operation conditions; data base; process charts; measuring instruments; characteristics of damages/faults, among others.

On the second stage, the evaluation of the monitoring parameters is based on the types of health technology faults evaluated, it defines the number and prioritization of these faults, root cause, prevention of adverse effects/faults and frequency with the Pareto chart and Ishikawa diagram. This allows identifying and selecting possible fault parameters to be monitored, for example: temperature, humidity, pressure, vibration, current, among others relative to the equipment.

The Pareto chart identifies which fault should be prioritized by order of importance and frequency of occurrence [9]. The Ishikawa diagram allows us to find the root cause of the problem and define the parameters to be monitored, in addition, it has, as classification, the origin of the causes: infrastructure, human resources, technology, input, maintenance and process. The first three are pillars considered for all cause origins and the last three were added specifically for this study case.

On the third stage, with a ubiquitous health technology solution, it is possible the incorporation of devices and their connectivity in different environments, regardless of their location [4], to monitor the analyzed activities.

After the analysis results of the quality management tools and the definition of the indicators to be analyzed with the specialized team, it is possible to set up an action plan in which will be defined which devices should be installed to determine ubiquitous solutions of health technology in the development of the monitoring platform. These devices can be sensors, cameras, microphones, among others.

3 Results and Discussion

When applying the methodology in the study case in a PHC system, the first stage of the problem situation was the definition of the technology. With the data collection in the information system of the Institute of Biomedical Engineering of the Federal University of Santa Catarina (IEB-UFSC) -Brazil, in equipment that compose the PHC of the structure under study, with data referring to the period from 2014 to 2018, quantified in 60 classes of equipment in a park with 17638 Service Order (S.O) referring to 3053 equipment in the city of Florianópolis-SC-Brazil.

With the prioritization matrix in the equipment class, the problem solving priority is determined and, along with the risk analysis, factors and prioritization criteria are related [4]. In its application, the median of all the equipment was multiplied by the result of the matrix, whose result was applied in the Pareto chart, shown in Table 1, in which it is necessary to carry out a study on the root cause of fourteen equipment. In this case is addressed the root cause of the dental air compressor, responsible for the supply of compressed air with an electric motor.

The multidisciplinary team was composed by five people: a clinical engineer (applied Ishikawa diagram, GUT matrix and assisted in the analysis of the results of the GUT matrix, Ishikawa diagram and Pareto chart), two technicians (collected the data,

Table 1. Result of joining the GUT matrix, Median and Pareto chart with the equipment that needs to be prioritized.

Equipment	GUT*Median	% Partial	% Accumulated
Dental air compressor	1000	22,40%	22,40%
Autoclave	960	21,51%	43,91%
Dental chair	612	13,71%	57,62%
Laminar flow hood	171	3,83%	61,45%
Cardioverter	100	2,24%	63,69%
Colposcope	90	2,02%	65,71%
Mobile surgical light	88	1,97%	67,68%
Defibrillator	75	1,68%	69,36%
Medical ultrasound	72	1,61%	70,98%
Dental vacuum Pump	72	1,61%	72,59%
Cell counter	72	1,61%	74,20%
Electroencephalograph	72	1,61%	75,81%
Slit lamp	72	1,61%	77,43%
Clinical tympanometer	63	1,41%	78,84%

applied the GUT matrix, Pareto chart and Ishikawa diagram), an administrative assistant (assisted in data collection) and a graduate student in C.E. (followed the data collection, applied the GUT matrix, Ishikawa diagram and Pareto chart with the technicians, carried out training on quality tools and analyzed the results with the team).

In a new data collection, with exclusion criteria in the SO, accounting the type and quantity of failures or breaks occurred, number of the registered equipment in oil-free compressors, were categorized 75 oil-free compressors with 172 SO and 176 faults and 13 types of faults identified.

By applying the Pareto chart it was possible to prioritize 5 faults to find the root cause of the problem. Thus, they were grouped and considered as one type when it comes to the same failure mode: hose leakage, quick coupling and regulator with 45 faults; piston valve defect, rings, valves and head gaskets accounted for 38 faults; leakage through the trap with 34 faults; leakage through the serpentine with 11 faults and locked piston with 10 faults.

With the application of the Ishikawa diagram, the root cause of each problem was found and, through the results, the team chose as monitoring parameters: pressure in the compressed air system for the dental chair, equipment current, temperature in the compressor head and voltage of the power grid, thus, pressure, current and temperature sensors will be used in the future.

In order for the operational category to be effectively implemented it is necessary that data collection be as judicious as possible. As the information system has SO with the handwritten description of the technologies by different technicians that do not obey a standard, there was difficulty in collecting data. With this, it was necessary to train and monitor the person in charge of data collection to obtain the necessary information for the development of the work.

The choice of equipment to be studied is one of the most important parts of the work, because the PHC system of the city of Florianópolis-SC-Brasil has a diversified park with over 60 classes of equipment, with the aid of tools to control and improve quality, it was possible to prioritize the health technology to be studied and the failures to be monitored.

The junction of the prioritization matrix with the median SO number by equipment, tools for easy application and quick execution, made it possible to add one more weight to the prioritization matrix that counts with urgency, trend and severity, as well as the median.

Thus, when applying only the prioritization matrix, some equipment that did not have a large number of failures were prioritized. And when applying only the median number of service order per equipment, those that present in large quantity and consequently with more failures were prioritized, but in relation to qualitative analysis of severity, urgency and trend were not prioritized. In this way, with the union of these tools it was possible to direct the resources to technologies that need to be prioritized in the study.

The Pareto diagram was used after the result of the junction of the prioritization matrix and the median, because the system of APS has 60 classes of equipment, being necessary to prioritize the main ones of them to carry out the study and to apply the resources.

At the stage where the multidisciplinary team was inserted in the project development, some positive points were noted. Such as: engagement to apply the tools for the control and improvement of quality and aid in the proposed improvements, skills with the technology being studied, as well as the individual experiences made possible to exceed the possible causes of the failures in the diagram of Ishikawa, speeded up the implementation of quality management tools and contributed to the development of communication. As disadvantages in teamwork is the need for training for the application of tools to control and improve quality, which caused in some moments overload in the tasks developed, more time due to diversity of opinions and discussions for decision-making.

With the application of the Pareto diagram in the main compressor failure, it was observed that the system would not be 100% because as the application of this tool prioritizes 80% of the failures, but the resources will be applied in the flaws that influence the technological process.

The downside in the operational category is the need to develop the entire platform and apply over a period, to then test its effectiveness, perform a new analysis of the data after the system implementation and carry out the comparison. If the result is not positive, it is necessary to perform the process again to verify in which step the fault occurred.

The operational category allows that with the use of collected data and applied in tools, to control and improve quality, technological improvement is possible in health studies.

4 Conclusion

This study analyzed the technological park of the Primary Health Care in Brazil through a clinical engineering information system in the city of Florianópolis-SC.

For an effective application of the operational category it is crucial that information be carefully collected and applied efficiently and reliably, because it is from these structured data that it is possible to extract evidence-based fault parameters.

Another criterion to be considered in order to guarantee reliability to this category of the methodology of health technology ubiquitous management is that the team is qualified to apply the quality management tools, since, according to the surveys raised, such tools are still little used in the scope of Clinical Engineering for the analysis of fault parameters.

It was only possible to perform this study with information capable of giving support to the good functioning of quality tools because the project had an information system, which has the necessary data to complete the use of quality tools in the incorporated technologies and also allows to have real notion of the technological park of an APS system. If we did not have access to these data the prioritization to choose the technology in health would be based only on the urgency, tendency and gravity of the technology, as well as the failure survey to apply the Ishikawa diagram of the chosen technology would be based only on brainstorming.

From the use of the tools to control and improve the quality in the process through the fault indicators, information capable of supporting clinical engineering performance in a predictive model of technology management is obtained. In addition, it has repercussions on improvements in the safety and reliability of procedures and diagnostics to PHC users and better use of the technology with cost reduction and greater operator and user safety.

This paper, could allow better be for decision making and help the Clinical Engineering to improve its information system giving quality to the process of support the decision in the ubiquitous health technology management.

References

1. Avelar, P.S., Justos da Silva, C.A., Garcia, R.: Clinical engineering impacts in primary healthcare. In: Proceedings of Third WHO Global Forum on Medical Devices. Genebra, Suíça (2017)
2. Miniati, R., Frosini, F., Dori, F.: Integrated risk and quality management in hospital systems. In: Clinical Engineering: From Devices to Systems, p. 117 (2016). https://doi.org/10.1016/b978-0-12-803767-6.00009-x
3. Azizi, A.: Evaluation improvement of production productivity performance using statistical process control, overall equipment efficiency, and autonomous maintenance. Procedia Manufact. **2**, 186–190 (2015). https://doi.org/10.1016/j.promfg.2015.07.032
4. Carpinetti LCR: Gestão da qualidade. Grupo Gen-Atlas, 3 edn (2016)
5. Rami, H.F., Mukattash, A.: Statistical process control tools: a practical guide for jordanian industrial organizations. Jordan J. Mech. Ind. Eng. **4**(6), 693–700 (2010)
6. Gallesio, A.O., Ceraso, D., Palizas, F.: Improving quality in the intensive care unit setting. Crit. Care Clin. **22**(3), 547–571 (2006). https://doi.org/10.1016/j.ccc.2006.04.002

7. Queiroz, J.V., et al.: Franchising e especialização de serviços como estratégia de crescimento e manutenção: uma análise através da Matriz SWOT e GUT na DDEx–Direct to Door Express. Revista GEPROS, n. **1**, 49 (2012). https://doi.org/10.15675/gepros.v0i1.551
8. Garcia R. et al.: Health technology ubiquitous management model for primary health care. In: Proceedings of Fourth WHO Global Forum on Medical Devices, 2018. Visakhapatnam, India (2018)
9. Mishra, A.K., Nagpal, D., Singh, L.: Characteristics showing the ubiquity of software projects. In: International Conference on Computing, Communication & Automation. IEEE. 891–894 (2015). https://doi.org/10.1109/ccaa.2015.7148502

Home and Physiological Remote Monitoring System for Elderlies and People with Chronic Diseases

Sergio Ponce[1(✉)], Sofia Avetta[1], Alexis Sparapani[1], Camilo Garcia[1], David Piccinini[1], and Natalia López[1,2]

[1] Universidad Tecnológica Nacional, F. R. San Nicolás, GADIB, San Nicolás, Argentina
sponce@rec.utn.edu.ar
[2] Universidad Nacional de San Juan, GATEME, CONICET, San Juan, Argentina

Abstract. This paper presents a modular system of wireless monitoring of physiological and ambient conditions based on Internet of Things (IoT). It is specially designed for elderly people and people with chronic diseases to promote their independent living. The system consists of a network of physiological and home ambient sensors developed under standard IoT protocols. These sensors are designed and manufactured at the laboratory with low-cost components. In addition, commercial sensors can be added according to the requirements of the patient. The system also provides a web based user interface for medical and family caregivers. It displays real time data and it includes an alarm system to report unsafe events via email. The caregiver can also see historical data with the possibility to compare all the parameters of a certain day and time. Furthermore, a home automation system was proposed to control home devices to improve home safety. The evaluation of the system was performed under a controlled environment at the laboratory in pilot tests before being tested in patients.

Keywords: Elderly · Assistance · Remote monitoring · Sensors · Internet of Things

1 Introduction

A recent survey of the World Health Organization (WHO) [1] reveals an increase in life expectation (estimating 400 million people over 60 years old in 2050), which is associated with longer treatment for chronic diseases. This situation leads to increasing health costs and a social problem for personal care and hospitalization. A new concept of home care and real time monitoring based on Internet of Things (IoT) would lead to a more efficient public health solution. It would increase the quality of attention and provide alternative ways for more humanitarian models of assisted alternative to institutionalization, promoting and improving the independence and quality of life.

The system presented consists of a technological implementation to remotely monitor home ambient and health parameters of the elderly and people with chronic

© Springer Nature Switzerland AG 2020
C. A. González Díaz et al. (Eds.): CLAIB 2019, IFMBE Proceedings 75, pp. 1306–1312, 2020.
https://doi.org/10.1007/978-3-030-30648-9_168

diseases. It consists of a network of sensors that continuously acquire ambient parameters (light, temperature, humidity, carbon monoxide leaks and motion) and health sensors to measure physiological parameters (body temperature and heart rate), a home automation system to preserve the parameters within a safe range, and a user interface that allows family members, doctors or caregivers to remotely monitor all the parameters, query historical data and receive alerts about dangerous events and system failures.

2 Materials and Methods

The system has the following main blocks: home and health modules networks, a central processing unit and a user interface (Fig. 1).

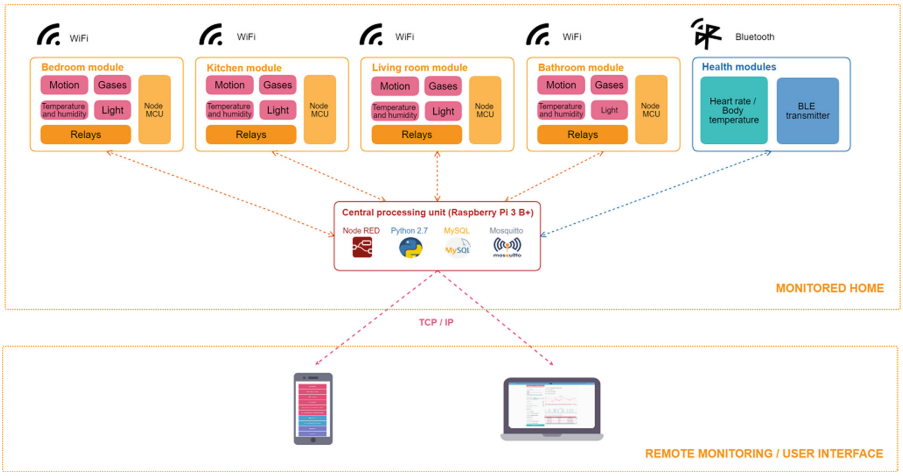

Fig. 1. Block diagram of the technological implementation.

2.1 Home Sensors Network

A module was designed for each room of the house in order to measure temperature, humidity, carbon monoxide leaks, light intensity and presence of somebody in the room and also to control home devices. The modules include the following components [2]:

Temperature and Humidity Sensor. The sensor selected is the DHT22 due to its low cost and small size. It measures humidity in a range between 0% and 100%, with an accuracy of 2%–5% and temperature in a range between −4 °C and 80 °C, with an accuracy of ±0.5 °C. For the data analysis, a temperature range between 18 °C and 24 °C, and humidity range between 40% and 50% were considered as safe thresholds. Higher levels of humidity could trigger respiratory diseases, asthma and allergies [3].

Light Sensor. The BH1750 sensor acquires light through a photodiode capable of sensing visible and infrared light, with a response very similar to a human eye.

Measurements between 0 and 5 lx indicate a low light level and so the person cannot see properly. Measurements above these values, depending on the time of the day, mean that the room has a proper natural or artificial light level. These data can be used in the analysis of sleep hours and routines.

Motion Sensor. The SR-501 pyroelectric passive infrared (PIR) sensor was selected for motion detection and consequently the presence detection of the person in a certain room. In order to detect presence even when the person is not moving, some adjustments had to be made by software.

Carbon Monoxide Sensor. The MQ-9 sensor acquires digital and analog values of carbon monoxide concentration in a range between 10 and 1000 parts per million (ppm). For exposures between 1 and 70 ppm, the person does not have symptoms during prolonged exposures [4]. In any case, the threshold considered is 30 ppm to determine if there is a leak and so it is possible to stop it in time.

Information Management. The data has to be centralized and sent wirelessly to the system's central computer. For this purpose, the NodeMcu V1 development board was selected. This board has a microchip ESP266 integrated. It allows Wi-Fi connectivity and the use of sensors interconnection protocols like MQTT, suitable for IoT systems.

Automatic Control System. A 4-channel solid-state relay module, Arduino Pic Arm, was selected to control actuators and consequently the home devices. It has the advantage of being faster than conventional relays and of having greater durability because it does not have mechanical parts, it is not noisy, there is no risk of generating sparks, it generates less electrical noise and it is more immune to humidity and vibrations.

2.2 Wearable Sensors Network

A Wireless Body Area Network (WBAN) of wearable, lightweight and low consumption sensors was designed for getting real time information about the user's health status. The designed architecture allows the expansion of the network, making it possible to design or include other sensors. In this work, the modules used are:

Body Temperature Module. It consists of the LMT70 sensor from Texas Instruments®, which is small sized and has a precision of 0.05 °C in the range between 20 °C and 42 °C, and a CC2650 microcontroller also from Texas Instruments® with Bluetooth Low Energy (BLE) connection capability [5].

Heart Rate Module. It is based on the Pulse Sensor heart rate sensor specially designed for Arduino. For the implementation of the BLE protocol, the Adafruit Feather 32u4 Bluefruit LE module was chosen to acquire the data and to transmit it wirelessly.

2.3 Central Processing Unit

A Raspberry Pi 3 B+ with Raspbian operating system was used as a central computer to centralize and process data from home and health modules. It was selected due to its

low cost, versatility and storage capacity. It also has built-in Wi-Fi and support for the BLE protocol to communicate with the modules. It is configured as an Access Point, so instead of connecting to the Internet via Wi-Fi, it can generate its own Wi-Fi network. Furthermore, a Node Red architecture was implemented to interconnect the modules through the corresponding protocols, control dataflows, manage the data storage and develop the user interface

2.4 Data Communication

The MQTT protocol is implemented to establish communication between home sensors and the central computer by a star topology network. Multiple clients are able to send and receive data through publications and subscriptions to a broker which is the central node of the protocol. For the communication between wearable sensors and the central computer, the protocol implemented is BLE to satisfy IoT and wearable sensors requirements.

2.5 Validation Tests

The system has been tested for each module and for the complete system, under three requirements:

1. Preservation of data packets sent via Wi-Fi and BLE.
2. Remote monitoring through different networks using mobile phones and computers with Internet access.
3. Correct reception of alarms by simulating critical parameters for each sensor and inducing disconnections to check if the alarms are received satisfactorily.

3 Results

3.1 Modules Design, Manufacture and Validation

To acquire and transmit both ambient and physiological measurements, ad hoc circuit boards with the components and sensors previously mentioned were designed. Four home sensors modules (bedroom, kitchen, bathroom and living room) were implemented for a first validation and test in preliminary trials, installed in a testing room. The entire system was tested for 72 h, limiting the results herein presented to the events produced in this time interval.

Furthermore, two different health modules were designed, both with different BLE transmitters and sensors (body temperature and heart rate). In a future line of research the objective is to develop modules able to measure more health parameters and to add other commercial wearable sensors. It was verified that the BLE protocol is the most suitable for this application, as was reported in the literature. Since it has low energy consumption, it can be powered by small batteries and thus keep a small size. The battery used is a 3 V 600 mAh CR2450, tested under the continuous functioning of each module for 3 consecutive days. The replacement is easy for users or caregivers, fulfilling one of the design requirements.

The requirements mentioned in Sect. 2.5 were tested under a controlled environment. All modules acquired data during 72 h in the laboratory accessing to the Internet by the local network. During this test, the correct reception of data packets was confirmed every ten seconds for the ambient sensors and every 30 s for the wearable sensors. In order to test the remote monitoring, the system was accessed through five different external networks using mobile phones and computers with Internet access. With the corresponding user ID and password, all users could access the system to interact with it. Moreover, with the purpose of checking the correct reception of the alarms and the system response, parameter values outside the safety thresholds and disconnections were forced. Regarding the disconnection test, ten seconds after the event occurred, the corresponding mailing alert was sent and a pop up message was shown in the interface. This test was done 20 times in all modules. Sensors were proved with experimental values above and beyond the pre set thresholds to verify the reception of the set alarms.

The system uses standard communication protocols that ensure accuracy in data management between devices and provide more scalability with commercial devices.

The implementation of Wi-Fi and BLE as wireless protocols is supported by international standards.

3.2 User Interface

A web interface was developed so that the caregiver can supervise the data collected by the sensors. A user ID and password are required for security. The caregiver can monitor in real time the measurements from all the sensors (data is updated every ten seconds from the ambient sensors and every thirty seconds from the health sensors).

They can check in which room the person is and control home devices when necessary if having the proper permissions. The web interface also has an alarm system that sends alerts via email when the patient is in a dangerous situation.

Moreover, it is possible to query historical data of a specific day and time range and visualize graphs with the measurements and their respective safe thresholds (Table 1). These thresholds can be personalized according to the specific health requirements of the person. In addition, relevant data is displayed: average, maximum and minimum of measurement values, frequency of entries into a room and maximum time the person remains in the same room (Fig. 2). The results of these queries can also be sent to the user's email address.

Table 1. Default parameters and their respective thresholds used in the monitoring system. All of them can be changed for specific requirements.

Ambient parameter	Threshold
Ambient temperature	18 °C–24 °C (acceptable range)
Humidity	40%–50% (acceptable range)
Light level	>5 lx to see properly
Carbon Monoxide	<30 ppm
Presence in the bathroom	<1 h
Presence in the bedroom	<0 h between 08 pm and 10 am
Health parameter	Threshold
Heart rate	50 BPM–110 BPM (acceptable range)
Body temperature	<37.8 °C

Fig. 2. Rooms historical data.

4 Discussion and Conclusions

The system developed, considering both the electronic modules and the web based user interface, fulfills the main objectives of this project: to support health care and independent living of elderly people and people with chronic diseases and to allow medical and family caregivers to monitor remotely their health status and home safety to ensure their well-being. Regarding the current public health situation, especially in developing countries, this system provides a possible solution to decentralize hospitalization in health centers.

When compared to other existing commercial systems, the main advantage of the proposed system is the possibility to integrate ambient and wearable sensors in a single platform at a low cost (less than 1000 USD).

Preliminary validation tests of the system were carried out, but validation test have to be carried out in uncontrolled environments in a future work. It is necessary to evaluate the interaction of patients and caregivers with the system, and also the response to unexpected fails not induced yet.

Acknowledgements. This project was partially supported by "Comisión de Investigaciones Científicas de la Provincia de Buenos Aires (CIC)" by the scholarship "Beca de entrenamiento 2018" granted to the author Sofia Avetta.

References

1. World Report on Ageing and Health. World Health Organization 2015. ISBN: 97892415 65042
2. Electronic Components Datasheet Search. http://www.alldatasheet.com/
3. National Asthma Council Australia (2016). https://www.sensitivechoice.com/indoor-humidity/
4. United States Consumer Product Safety Commission. Carbon Monoxide Questions and Answers. https://www.cpsc.gov/Safety-Education/Safety-Education-Centers/Carbon-Monoxide-Information-Center/Carbon-Monoxide-Questions-and-Answers
5. Ponce, S., Piccinini, D., Avetta, S., Sparapani, A., Roberti, M., Andino, N., Garcia, C., López Celani, N.: Wearable sensors and domotic environment for elderly people. In: IUPESM 2018, Praga, Czech Republic. IFMBE Proceedings 68/3. https://doi.org/10.1007/978-981-10-9023-3_35
6. López Celani, N., Ponce, S., Quintero, O.L., Vargas-Bonilla, F.: Improving quality of life: home care for chronically Ill and elderly people. In: Mollaoglu, M., (Ed.) Caregiving and Home Care, IntechOpen 2018, pp. 161–178 (2018). https://doi.org/10.5772/intechopen.70113

A Medical IoT-Based Remote Monitoring System: Application on Diabetic Foot

Luis Fernando Moncada-Sánchez[1(✉)], Ricardo Antonio Salido-Ruiz[2], and Aurora Espinoza-Valdez[2]

[1] Departamento de Electrónica del Centro Universitario de Ciencias Exactas e Ingenierías de la Universidad de Guadalajara, 44430 Guadalajara, Jalisco, Mexico

[2] Departamento de Ciencias Computacionales del Centro Universitario de Ciencias Exactas e Ingenierías de la Universidad de Guadalajara, 44430 Guadalajara, Jalisco, Mexico

ricardo.salido@academicos.udg.mx

Abstract. Diabetes represents an ever-increasing risk for the world population, and the rise of its prevalence is not expected to cease. To combat this alarming problem is the concomitant rise of new and improving mobile phones and wearable devices that can be exploited to fight diabetes. This paper presents a prototype of a monitoring system that will serve as a tool for improved patient monitoring by health care professionals (HCPs). Several physiological measurements were selected to perform the monitoring so that important data about a patient's status can be collected and processed. Mobile technologies, cloud services and wireless protocols were used to develop a mobile application that can handle several devices and the data they gather. The resulting implementation provides a powerful infrastructure that could supply feedback to HCPs and patients as meaningful data, which can then be processed and potentially extend the assessment capabilities of an entire health care system.

Keywords: Remote patient monitoring · Internet of Medical Things · Diabetic foot

1 Introduction

The lack of proper patient monitoring, regardless of the disease involved, can become a major problem for the health care system; moreover, it could represent a life-threatening risk for the patient. Failure to control a disease on small scale is what causes its prevalence in a massive population, preventing the advance in health care for all patients and health care systems. Chronic and progressive diseases are more likely to worsen when all risk factors are left unattended. Diabetes is an example of such a condition, and currently is in constant need of patient overseeing. On a worldwide scale, diabetes is now affecting 425 million people, or the equivalent of 8.8% of adults, and this level is expected to rise. It is estimated that at least half of those people are undiagnosed, so there is a global need to diagnose and provide appropriate care and supervision to people with diabetes [1].

© Springer Nature Switzerland AG 2020
C. A. González Díaz et al. (Eds.): CLAIB 2019, IFMBE Proceedings 75, pp. 1313–1319, 2020.
https://doi.org/10.1007/978-3-030-30648-9_169

Alongside the rise in chronic disease prevalence and development there is, however, an improvement in mobile technology and an increase in the number of users for these technologies. This allows greater access to functionalities in the infrastructure that can help utilize the advantages of current, real-time technologies for the monitoring of a patient. In this context, cloud-based technology is useful since it makes information available anytime and anywhere [2]. Recent works [3] present virtual platforms that are implemented as computational support systems for early diagnosis of diabetic foot. This platform allows the patient to connect to personal data and diagnostic results, as well as to obtain data of external medical devices, however, it does not use mobile technology.

Currently, the use of mobile devices is transforming many areas including health care and clinical practice. Categories where mobile applications are helping HCPs include: information and time management; health record maintenance and access; communications and consulting; reference and information gathering; patient management and monitoring among others. The breadth of applications demonstrates the usefulness of mobile health apps [4]. In actuality, patient-side applications are not so popular, because there is a lack of usage by HCPs due to failed implementations, which do not take patient involvement in its monitoring into account. Given that patient involvement can greatly improve the disease or at the very least prevent further damage, it is vital to include in these applications. These technologies all converge on the Internet of Things (IoT), and specifically the scheme created from the development of more medical device technology, the Internet of Medical Things (IoMTs). In this type of system, medical devices are interconnected through a network that can collect and manage medical data with ease, and, as mentioned, with cloud-based technologies this data can be available at any location, at any time. The IoMTs can be considered a critical piece of the digital transformation of health care, given that this type of technology can reduce overall costs for the management of diseases, and all the activities it involves. Several medical systems and equipment were adapted into the scheme to complement these systems and provide a full overview of the status of the patient [5–7].

In the specific case of diabetes, there are several complications that can become present without correct patient supervision, ranging from cardiovascular disease to neuropathy. These are deeper, more severe damages that can lead to serious consequences, like blindness in the former case, or amputations, in the latter case [1]. Neuropathy is a result of nerve damage, in this case caused by the high blood glucose levels. This nerve damage can be significant, and it can allow injuries to go unnoticed, leading to ulcerations and infections, which are part of the disorder known as diabetic foot.

There are certain variables that can provide insight into the progressiveness of diabetic foot, since it causes various types of physical alterations in affected zone. One of those variables is temperature; it has been determined that high temperatures in the foot area can contribute to the ulceration development due to the insufficient oxygenation. Thus, this measurement is potentially crucial for evaluation and monitoring of high risk diabetic foot [8–10].

Another important parameter included in the monitoring system is oxygen saturation (SpO_2). Blood oxygen concentration in the feet of diabetic patients is widely related to ulcerations, due to the poor blood circulation, which also raises the likelihood of peripheral nerves experiencing pathological changes. This variable serves as an early

warning of foot ulcerations [11]. These inclusions are part of other projects being developed in our research team.

A different, physical indicator of diabetic foot development is the weight distribution. It hints at which zones of the foot are exposed to a greater level of stress and are prone to develop or be affected by ulcerations. For example, increases in weight are related to increased plantar foot pressures for the first metatarsal, lesser metatarsal, midfoot and heel regions [12, 13]. These risk factors were a strong motivation to develop a medical system under the scheme of IoMTs (see Fig. 1) that allows for the monitoring of temperature, SpO_2 in specific foot regions, and the foot plantar pressure in diabetic patients, as well as for the development of a mobile application that facilitates the collection, management and retrieval of this data.

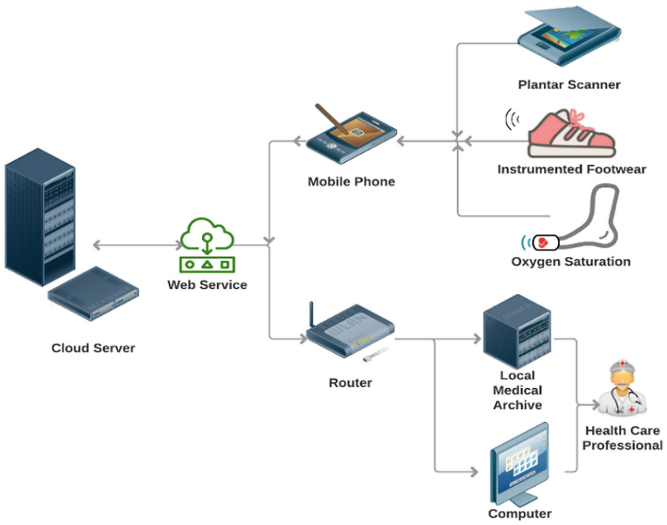

Fig. 1. Integration diagram of the components of the monitoring system

2 Materials and Methods

In a previous work [14], temperature was the only parameter collected and processed, fewer technologies were used and cloud-based services were left out of the development. Due to the complexity of diabetes, it was determined that other important aspects needed to be monitored and the technology required an improvement that could satisfy the essential infrastructure of a system of this type. Considering the practicality of new mobile technologies, and the flexibility they provide when applied to health care, the scheme and the system itself were improved to take advantage of the features of these technologies. This updated application can receive data from the medical devices that acquire the previously mentioned parameters in the body, and then this data can be stored and managed, according to the HCP's needs. By using wireless technologies like Bluetooth, the application performs a real-time retrieval of the information captured by the sensors distributed across the oxygen saturation module and the instrumented

footwear. The plantar scanner provides images of the pressure points in a patient's foot, and these are shown in the app, transferred wirelessly via the internet through a server. The plantar scanner is complemented with a set of separate weight sensors that provide a quantitative analysis of the pressure zones in the patient's feet. This information can then be compared and assigned to the weight distribution map provided by the scanner. All this information is kept on the cloud server via the web service. Patient-specific medical and personal data is also considered in the database structure as a way to provide even more information and a more complete overview of the statistics and distribution of the data obtained through different devices and different patients.

3 Results

The system, a mobile application that is intended to receive, process and display in a practical way different types of data from diabetic patients, was created as a potentially powerful and flexible solution to enhance health care monitoring and to allow HCPs to prescribe the right treatment in order to prevent the development of diabetes-related complications.

The first component of the system consists of an access layer to provide informatic security. Given that it is sensitive medical data being processed and stored, it must be properly handled and protected. Access to a password is given by a system administrator, who manages all system-related actions and permissions.

The next component of the system, the monitoring tool, displays the parameters after collecting the data from its corresponding source (see Fig. 2).

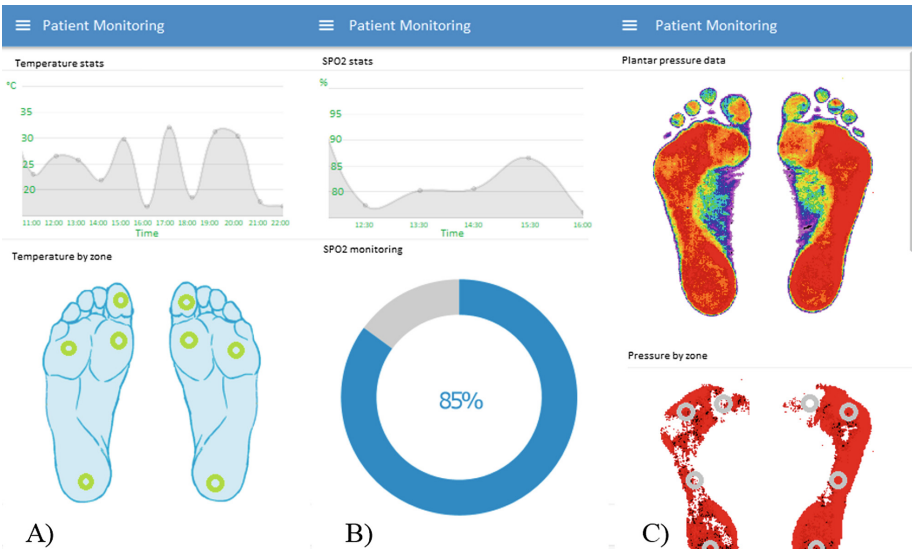

Fig. 2. Application interface, showing the distinct parameters and how are they handled inside the system to display important information. (A) Temperature data. (B) Oxygen saturation (SpO_2) data. (C) Plantar pressure images.

In the case of temperature, it acquires this value through a wireless connection with footwear equipped with sensors distributed alongside the foot sole. Oxygen saturation data is also transmitted wirelessly from a device topically located on the patient's toes, and it indicates a percentage alongside a graphical representation. The last part of the application comprises the plantar pressure imaging information. The images obtained from the plantar pressure scanner are processed separately in MATLAB® Image Processing Toolbox and then sent to the cloud server to make these images and corresponding processed data available to the web service and thus, the main application. The temperature, SPO_2 and plantar pressure modules are shown in Fig. 3. Temperature measurements are obtained from temperature sensors placed in specific foot regions according to a study presented in [15] and recordings are sent via Bluetooth to the app. SPO_2 measurement are obtained with a pulse oximeter (i.e., using two frequencies of light (red and infrared) in order to determine the percentage of hemoglobin in the blood that is saturated with oxygen) [16]. Finally, the plantar pressure is obtained with a commercial plantar scanner which estimates the regions of the foot experiencing more pressure [17].

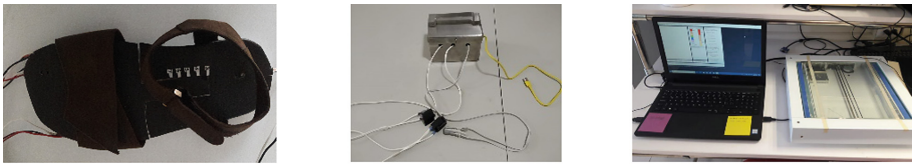

Fig. 3. Instruments for data acquisition. (A) Instrumented footwear for temperature acquisition. (B) Oxygen saturation (SpO_2) acquisition module. (C) Plantar pressure module.

The local medical archive is another important component in the system. Here, HCPs could access the information of the patients for further analysis, and in this database, a record is kept so the variation of the physiological measurements being monitored is easily observed and compared across time.

As a result, the platform could provide important data to HCPs of several relevant variables obtained from a patient, and these values could be studied anywhere thanks to the availability of data in the cloud-based environment. The data is ready for evaluation and assessment with the option to add other information to complete a patient's profile. This creates a detailed record for future reference, providing all the necessary tools for the optimal patient monitoring.

4 Discussion and Conclusion

Future device integration is possible via a specialized module incorporation where parameters can be set to be recorded inside the mobile application. Current data storage and handling opens the door to big data analytics that could potentially provide enough information to detect patterns in the distribution and recurrence of diabetic foot. This

could aid in elucidating correlations that are yet unknown between physiological measurements studied in patients with diabetes.

The system is currently running in a local web server, with the use of Apache Tomcat and XAMPP, a server program for Windows, which uses the computer's resources to provide the server infrastructure for the mobile application. The computer runs on an AMD processor, 12 gigabytes of RAM and 1 terabyte of hard drive storage, so the processing and storing capabilities are strictly bound to these system specifications. In this scenario the system is being tested for reliability and feasibility but using a dedicated server to handle all the data transactions occurring on a determined time is being considered.

The app is built to be used on an Android smartphone, with an operating system version 4.0 or later and with Bluetooth and Wi-Fi capabilities, for data streaming. Complying with the minimum system requirements ensures the quality and the reliability of data acquisition and processing by the monitoring system. Other operating systems will be added in the future to improve compatibility.

This system provides a novel mechanism for health management, which not only considers the medical personnel, but also the patient, who in this specific case is commonly kept uninformed of their health status, making any type of prevention on their behalf difficult. The patient's willingness to commit to their health care is what contributes greatly to the usefulness of the monitoring system, and health feedback provided to these patients can help them achieve a greater awareness of the disease from which they are suffering. In the end, advantages of mobile technologies are increasingly being utilized in health care, making this a promising tool for the transformation of continuous monitoring and timely decision making with the end goal of avoiding further diabetes complications.

Acknowledgements. The authors would like to express their deep gratitude to Emma Garcia for her valuable writing advice and assistance, and for her constructive recommendations that greatly improved the manuscript, allowing our thoughts and ideas to be properly expressed.

References

1. Atlas, D.: International Diabetes Federation. IDF Diabetes Atlas, 8th edn. International Diabetes Federation, Brussels (2017)
2. Kumar, M.A., Bachu, S., Reddy, I.S.: Early detection of diabetic foot ulcer by using IoT technology. i-Manager's J. Future Eng. Technol. **13**(1), 44 (2017)
3. Torres, I., Leija, L., Vera, A., Maldonado, H., Bayareh, R., Gutiérrez, J., Ramos, A.: Computational support system for early diagnosis of diabetic foot. In: 2018 Global Medical Engineering Physics Exchanges/Pan American Health Care Exchanges (GMEPE/PAHCE), pp. 1–5. IEEE (2018)
4. Ventola, C.L.: Mobile devices and apps for health care professionals: uses and benefits. Pharm. Ther. **39**(5), 356 (2014)
5. Brown, S.J.: Multiple patient monitoring system for proactive health management. US Patent 6,246,992 (2001)
6. Berman, H., Blair, R., Moyer, J.: Method and system of monitoring a patient. US Patent Application 10/632,991 (2004)

7. Quy, R.J.: Method and apparatus for health and disease management combining patient data monitoring with wireless internet connectivity. US Patent 6,602,191 (2003)
8. Bagavathiappan, S., Philip, J., Jayakumar, T., Raj, B., Rao, P.N.S., Varalakshmi, M., Mohan, V.: Correlation between plantar foot temperature and diabetic neuropathy: a case study by using an infrared thermal imaging technique. J. Diabetes Sci. Technol. **4**(6), 1386–1392 (2010)
9. Martín-Vaquero, J., Hernández Encinas, A., Queiruga-Dios, A., José Bullón, J., Martínez-Nova, A., Torreblanca González, J., Bullón-Carbajo, C.: Review on wearables to monitor foot temperature in diabetic patients. Sensors **19**(4), 776 (2019)
10. Houghton, V.J., Bower, V.M., Chant, D.C.: Is an increase in skin temperature predictive of neuropathic foot ulceration in people with diabetes? A systematic review and meta-analysis. J. Foot Ankle Res. **6**(1), 31 (2013)
11. Lin, O., Lai, J., Tsai, H., Lin, O., Lai, J., Tsai, H.: Preventing diabetes extremity vascular disease with blood oxygen saturation images. Int. J. Instrum. Sci. **2**, 1–7 (2013)
12. Vela, S.A., Lavery, L.A., Armstrong, D.G., Anaim, A.A.: The effect of increased weight on peak pressures: implications for obesity and diabetic foot pathology. J. Foot Ankle Surg. **37**(5), 416–420 (1998)
13. Bus, S.A.: The role of pressure offloading on diabetic foot ulcer healing and prevention of recurrence. Plast. Reconstr. Surg. **138**(3S), 179S–187S (2016)
14. Moncada-Sánchez, L., Espinoza-Valdez, A., Salido-Ruiz, R.: Aplicación móvil basada en Internet de las Cosas para el acceso a datos provenientes de la planta del pie en pacientes con diabetes: Pruebas Iniciales. In: Memorias del Congreso Nacional de Ingeniería Biomédica, vol. 4, pp. 389–392 (2017)
15. Franco-Pérez, S., Salido-Ruiz, R.A., Espinoza-Valdez, A.: Análisis de las zonas con mayor probabilidad de desarrollo de úlceras en el pie diabético. In: Avances de la ciencia en México, pp. 4726–4730 (2017)
16. Flewelling, R.: Noninvasive optical monitoring. In: Medical Instruments and Devices, pp. 294–305. CRC Press (2015)
17. Plantoscopio Computarizado a Color MX. https://www.plantoscopio.com/

Device Validation to Monitor Speed in High Performance Roller Skaters Through the Internet of Things (IoT)

Paula-Andrea Wilches-Castellanos[1,2],
Daniel-Alejandro Quiroga-Torres[1(✉)],
Pedro-Antonio Aya-Parra[1], and Jefferson Sarmiento-Rojas[1]

[1] School of Medicine and Health Sciences, Universidad del Rosario, GiBiome Research Group, Bogotá, Colombia
Daniel.quiroga@urosario.edu.co
[2] Biomedical Engineering Department, Escuela Colombiana de Ingeniería Julio Garavito, Bogotá, Colombia

Abstract. Internet of things technology has grown in recent years. One of the sectors where it has had the greatest reception is sports. In Colombia, for every 61 high-performance athletes there is, on average, one coach. For this reason, the purpose of this work was to validate an intelligent device that enables remote monitoring of the speed of high-performance roller skaters using the Internet of things. The authors equipped professional Luigino skates with electronic instrumentation, with which it was possible to measure a high-performance skater's linear speed and distance traveled of by means of Hall effect sensors and a magnet. To eliminate false measurements, a distance sensor was also installed in the skate skids to determine when the skate was in contact with the ground. This information was sent to the Internet through the MQTT protocol to a main broker that was responsible for the processing and visualization of the data. The linear velocity was validated at four speeds (0.8, 5, 8 and 10 km/h) using a treadmill. The error of the measurements was between 1% and 5%.

Keywords: Internet of Things · Monitoring · Roller skater · Sports

1 Introduction

Currently, the application area of Internet of things (IoT) technology has expanded to include different sectors, such as the industrial sector and the health sector. The technology has been implemented at different scales, for example, the implementation of IoT in cities, smart homes and portable devices [1]. According to a GSMA report, by 2025 about 25.2 billion devices worldwide are expected to be interconnected via the IoT [2]. On the other hand, according to Frost & Sullivan, in Colombia it is expected that between 2017 and 2022 the annual income rate of IoT technologies will grow by 20.8% and will reach $523.7 million dollars; the growth opportunity focuses on improving productivity and innovation [3].

© Springer Nature Switzerland AG 2020
C. A. González Díaz et al. (Eds.): CLAIB 2019, IFMBE Proceedings 75, pp. 1320–1325, 2020.
https://doi.org/10.1007/978-3-030-30648-9_170

In recent years, one of the areas that has implemented IoT has been sports. Countries such as China have experienced an 84% increase in this industry between 2009 and 2014 [4]. At the global level in sports, IoT has focused on monitoring vital signs, recordings about electrical activity at the body and physiological variables such as pulse, temperature, blood pressure, electrocardiogram, electromyogram, oxygen saturation and intensity and duration of activities. These IoT advances have focused on professional and non-professional athletes [5].

According to data from the observatory of Coldeportes (Colombia), in 2016 a total of 94,020 athletes and 1,533 sports trainers were affiliated with different federations, resulting in a ratio of approximately 61 athletes to one coach [6]. This difference can negatively affect the performance of athletes, since the athlete is not in constant supervision. For this reason, one of the biggest problems in Colombian sport is the relationship between athletes and coaches. Other issue is the lack of optimal training monitoring. Today there are devices that allow for the measurement and monitoring of physical parameters such as heart rate, respiratory rate, calories burned et cetera, but these devices have high costs.

On the other hand, in the field of biomedical engineering, sports-related technologies are being developed. These technologies can be used to record physical variables, such as heart rate [7]; analyze sports gestures [8–10]; and provide support in monitoring and training the athlete [11, 12]. Different investigations have also been carried out on the speed of skaters and the importance of this variable to his or her sport [13–15]. In view of the foregoing, the aim of this research was to build and validate a device that enables one to monitor the speed of a high-performance roller skater remotely using IoT.

2 Materials and Methods

The solution had two stages. First, the instrumentation of the roller skates was carried out to calculate the speed and distance traveled by the professional roller skater (see Fig. 1A). The second stage was the visualization of the data acquired from the athlete on a web page (see Fig. 1B). The coach could use this data visualization to monitor the athlete from anywhere in the world.

2.1 Skates Instrumentation

In this study, the Hall effect sensor A1302 was used to calculate the linear velocity of the skater (see Eq. 1). To obtain this measurement, a neodymium magnet was installed on the rear wheel of the skate with its south pole pointing up towards the sensor. The sensor was located on the chassis with its front face facing the rim (see Fig. 2A).

$$Velocity = 2\,\pi\, frequency\, radius \tag{1}$$

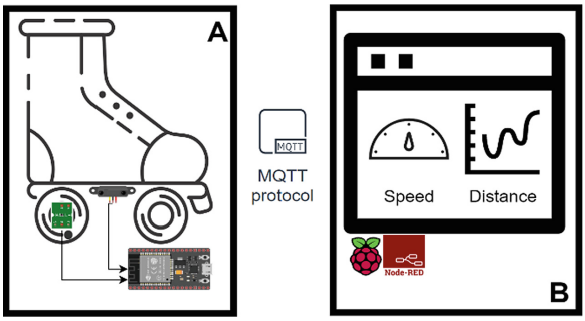

Fig. 1. Block diagram of the solution

A distance measurement was necessary, since analysis of the skater's movement demonstrated that the athlete does not keep his or her foot on the floor surface at all times. When the foot is lifted, the wheel is still rotating, but this rotation no longer represents the speed of the athlete. A distance sensor was used to identify the moment at which the skate was no longer in contact with the floor; the Hall effect sensor data was disregarded at this time. The sensor used for the measurement was the Sharp GP2Y0A21YK0F, which was located on the inner part of the skate on the upper part of the chassis, as displayed in Fig. 2B. Each time the distance sensor indicated less than the determined threshold, the rotation was recorded as 0 revolutions per minute by the algorithm.

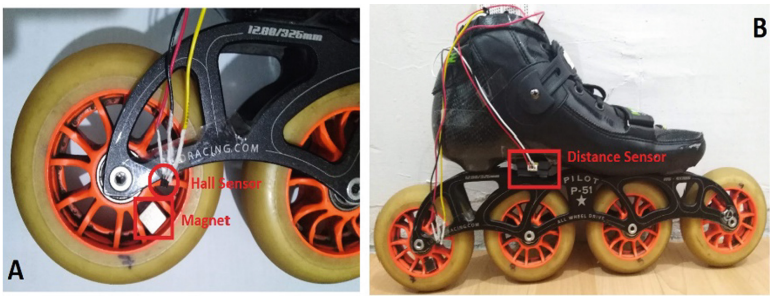

Fig. 2. Mount sensors on the skate.

The Fire-Beetle ESP32 card from DFROBOT was used to send the information acquired by the sensors and enabled the transmission of the data via a Wi-Fi connection and the Message Queuing Telemetry Transport (MQTT) protocol.

2.2 Data Visualization

The visualization and data treatment were developed using the Node-RED platform developed by IBM to connect hardware devices, Application Programming Interfaces (APIs) and online services graphically by means of flows and nodes. This platform was

installed on a Raspberry Pi B, which received the data using the MQTT protocol and graphed the information on a web page in real time.

2.3 Solution Validation

For the linear speed data validation, a Life Fitness Flexdeck treadmill was used. The validation test consisted of placing the skate on the treadmill without inclination at a constant speed for a period of 10 min (see Fig. 3). The data was sent every time a change in the Hall effect sensor was detected. Four different speeds were programmed on the treadmill (0.8 km/h, 5 km/h, 8 km/h and 10 km/h). After the measurements, the descriptive statistics were determined and the average error of the data was calculated. Statistical tests were performed with the IBM SPSS Statics V 25 software.

Fig. 3. Experimental setup for speed validation

3 Results

Table 1 presents the descriptive statistics for each of the speeds programmed on the treadmill and found in each of the data packages acquired in the Raspberry Pi B+.

Table 1. Descriptive Statistics Programmed Speeds

Programmed speed (km/h)	n	Mean (km/h)	Median (km/h)	Standard deviation (km/h)	Kolmogorov Smirnov pValue
0.8	240	0.7765	0.7752	0.0311	0.00
5	1468	4.8378	4.7752	0.1675	0.00
8	2528	7.7546	7.9002	0.3023	0.00
10	1428	8.829	9.4248	2.0160	0.00

From these data, the average error percentage of each of the measurements was found. The value programmed on the treadmill was taken as the real value, and the median value recorded at each of the speeds was taken as the experimental value. The results are displayed in Table 2.

Table 2. Error in measurements

Real speed (km/h)	Speed measure (km/h)	Error rate (%)
0.8	0.7752	3.1
5	4.7752	4.5
8	7.9002	1.2
10	9.4248	5.8

4 Conclusions

It can be seen that the errors are less than 6% for all of the programmed speeds; this may be due to the speed response of the Hall effect sensor chosen for this prototype. The median was the measure that best described the data, since the set of records was not normal, as can be seen in the results of the Kolmogorov-Smirnov statistical test.

It was found that the implemented device facilitated the remote monitoring of the linear speed of a high-performance skater using the Internet of things. This type of application was proven to be an alternative for coaches because it reliably enables remote monitoring of activities and exercises of athletes.

Conflict of interest. The authors report no conflicts of interest.

References

1. Fang-Jing, W., Gürkan, S., Ernö, K.: Toward the future world of Internet-of-Things. In: de Global Internet of Things Summit (GIoTS), Bilbao (2018)
2. GSMA: The GSMA IoT Infographic. GSMA, 6 August 2018. https://www.gsma.com/iot/the-gsma-iot-infographic/. Último acceso 5 Mar 2019
3. Frost & Sullivan: Colombian Industrial Internet of Things Market, Forecast to 2022. Frost & Sullivan, 5 February 2018. http://www.frost.com/k208. Último acceso 5 Mar 2019
4. Yong, B., Xu, Z., Wang, X., Cheng, L., Li, X., Wu, X., Zhou, Q.: IoT-based intelligent fitness system. J. Parallel Distrib. Comput. **118**(1), 14–21 (2018)
5. Segura-Garcia, J., Garcia-Pineda, M., Tamarit-Tronch, M., Cibrian, R.M., Salvador-Palmer, R.: Cost-effective eHealth system based on a multi-sensor system-on-chip platform and data fusion in cloud for sport activity monitoring. Electronics **7**, 183 (2018). pp. 1–13
6. Coldeportes: Observatorio de políticas del deporte en la Región de América latina y el Caribe. Coldeportes, 14 April 2016. http://201.217.220.99/Prod_Encuestas_Coldeportes/Graficas.aspx. Último acceso 5 Mar 2019
7. Formenti, D., Rossi, A., Calogiuri, G., Thomassen, T.O., Scurati, R., Weydahl, A.: Exercise intensity and pacing strategy of cross-country skiers during a 10 km skating simulated race. Res. Sports Med. Int. J. **23**(2), 126–139 (2015)

8. Bruening, D.A., Reynolds, R.E., Adair, C.W., Zapalo, P., Ridge, S.T.: A sport-specific wearable jump monitor for figure skating. PLoS One **13**(11), 1–13 (2018)
9. Kim, K., Kim, J.S., Purevsuren, T., Khuyagbaatar, B., Lee, S., Kim, Y.H.: New method to evaluate three-dimensional push-off angle during short-track speed skating using wearable inertial measurement unit sensors. Proc. Inst. Mech. Eng. Part H J. Eng. Med. **233**(4), 476–480 (2019)
10. Chen, J., Xu, K., Ma, H., Ding, X.L.: Motion characteristics of human roller skating. Biol. Open **8**, bio037713 (2019). pp. 1–11
11. van der Kruk, E., Reijne, M.M., de Laat, B., Veeger, D.: Push-off forces in elite short-track speed skating. Sports Biomech. **18**, 527–538 (2018)
12. Post, A., Koncan, D., Kendall, M., Cournoyer, J., Clark, J.M., Kosziwka, G., Chen, W., de Grau Amezcua, S., Hoshizaki, T.B.: Analysis of speed accuracy using video analysis software. Sports Eng. **21**(3), 235–241 (2018)
13. Méline, T., Mathieu, L., Borrani, F., Candau, R., Sanchez, A.M.: Systems model and individual simulations of training strategies in elite short-track. J. Sports Sci. **37**(3), 347–355 (2018)
14. Ferreira, A., Enes, C., Leao, C., Goncalves, L., Clemente, F.M., Lima, R., Bezerra, P., Camoes, M.: Relationship between power condition, agility, and speed performance among young roller hockey elite players. Hum. Mov. **20**(1), 24–30 (2019)
15. van Ingen Schenau, G., de Groot, G., de Boer, R.: The control of speed in elite female speed skaters. J. Biomech. **18**(2), 91–96 (1985)

Monitoring of Critical Variables in the Imaging Service from the Internet of Things (IoT)

Oscar Pinzón Cadena[1,2], Cesar Garcia Preciado[1,2], Oscar Julián Perdomo Charry[1], Angelmiro Nuñez Cruz[3], Nidia Patricia Córdoba Hernández[3], Alexandra Beltran[3], Jefferson Sarmiento-Rojas[1], Daniel-Alejandro Quiroga-Torres[1], and Pedro-Antonio Aya-Parra[1(✉)]

[1] Universidad del Rosario, School of Medicine and Health Sciences, GiBiome Research Group, Bogotá, Colombia
pedro.aya@urosario.edu.co
[2] Biomedical Engineering Department, Escuela Colombiana de Ingeniería Julio Garavito, Bogotá, Colombia
[3] Biomedical Engineer Maintenance Department, Corporación Hospitalaria Juan Ciudad, Bogotá, D.C, Colombia

Abstract. The simultaneity between the current information and communication technologies (ICT), which with the current industrial revolution classified as 4.0, aims that all the everyday objects with which a person interacts allow to provide relevant information of a specific environment through Internet. The field of medicine and more specifically, medical devices allow us to contemplate a shared vision of interconnected sensors that can improve medical care services, with the possibility of the appearance of new technologies such as the Internet of Things (IoT) promise to be the field to follow in the near future. This paper offers an approach to the implementation of a real-time monitoring system on the main variables of a Computerized Axial Tomography (CAT) in the imaging service of a fourth level hospital through the IoT. The information obtained about the different sensors implemented in the medical team, suggested relevant information about the importance of monitoring the main variables that are directly related to the operating specifications suggested by the manufacturer of the medical equipment. The data collected were analyzed using the "regression" diagnostic test as a probabilistic strategy to look for a predictive value that suggests a possible failure of the medical team. The results showed that the information collected suggests the importance of monitoring the operating parameters of the CAT continuously given the behavior of some atypical data that were obtained, although there was no failure in the time window where the CAT was performed.

Keywords: Internet of Things · Computerized axial tomography · Clinical engineering · Bioinstrumentation

© Springer Nature Switzerland AG 2020
C. A. González Díaz et al. (Eds.): CLAIB 2019, IFMBE Proceedings 75, pp. 1326–1332, 2020.
https://doi.org/10.1007/978-3-030-30648-9_171

1 Introduction

The term Internet of Things (IoT) was defined for the first time by Kevin Ashton in 1999, as the connection of multiple sensors and intelligent objects whose purpose is to communicate information from different environments where physical and digital entities can be linked looking for new applications and services [1]. What makes intelligent and connected products fundamentally different is not the Internet itself, but the changing nature of "things". Things, also called entities can be intelligent devices, sensors and any other object that is able to recognize their context and can communicate with other things, making it accessible at any time and anywhere [2].

Internet of things is part of a new and current paradigm that is generating new applications in the field of modern wireless communications. This is how the range of opportunities for implementing intelligent systems based on information from "intelligent objects" allows us to understand how data is currently used and processed [3]. It can be said that data is the main raw material that is processed and converted into information, in such a way that it is possible to identify trends and patterns that allow predicting possible behaviors of a system. The basic concept of IoT is the interaction between electronic devices, sensors and software among other technologies, which intend to interact with each other for a common goal, generating new applications and services for the people benefit [4].

In [5] it is explained as currently, medical care is increasingly difficult given the different technologic factors such as coverage, which tend to be insufficient and less effective in the face of growing population trends in terms of aging and chronic diseases, among others. This document focuses on the implementation of different sensors that allow to monitor environmental variables in the location of a computerized axial tomography. The variables captured are the temperature and relative humidity of the environment, the vibrations in the chassis of the equipment, the noise level and current consumption of the equipment.

This paper shows the specific construction of both hardware and software in key aspects of the medical equipment instrumentation process in the imaging service; since it is one of the services of greater demand in the hospital and, on the other hand, only one of these equipment is available to attend to more than 48 daily patients who need to be examined.

Accordingly, it is presented an IoT solution focused on the supervision of the different parameters of the physical environment of the service where the equipment is located, looking for a non-invasive alternative that allows to monitor in a parallel way, the area of biomedical engineering and some variables that allow to relate the operating conditions indicated by the manufacturer. The purpose is to identify how the external or internal factors affect the performance of the equipment and if the alteration of these, are correlated with the failures of the biomedical equipment as an innovative study under a recent technology [6].

2 Materials and Methods

The implementation of the system has a sensors network and programming board that are currently used in applications under the IoT technology. Mainly, sensors of low cost, size, connectivity characteristics and sensitivity were taken into account to obtain relevant information from the medical team (CAT). In accordance with the above, an assembly was made in the diagnostic imaging service where the CAT is located to monitor 5 external variables of the equipment.

In this aspect, as can be seen in Fig. 1, the main variables that were monitored in the equipment are: temperature, humidity, vibration, sound and current according to the most representative variables that the manufacturer presents in its technical operating manual of the TAC for its proper functioning.

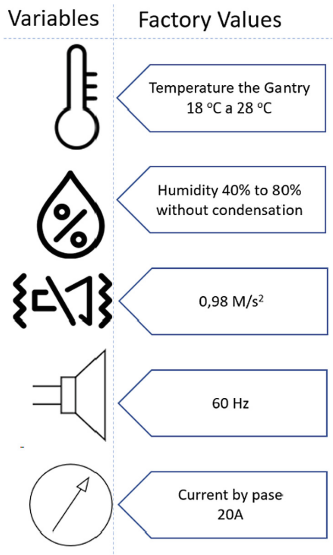

Fig. 1. Main variables of the CAT medical team.

It should be noted that the sensors used for this application were selected according to the values indicated by the manufacturer in each of its operating variables. Table 1 presents the technical data of each of the sensors used; its accuracy, costs and ease of acquisition were key characteristics for the implementation of the monitoring system.

Similarly, we used a set with special cards for data transmission such as the Arduino ESP8266 Thing, which is one of the most used programming cards in IoT applications, given its Wi-Fi connection characteristics. In this regard, the architecture used was implemented in a centralized manner, in such a way that the sending of information from each of the sensors to a local "broker" was managed, using a programming card known as Raspberry pi, which allows to store and manage by means of communication protocols, the acquired data of each one of the variables. Subsequently,

Table 1. Technical specifications of the sensors

Sensor	Measuring range	Measurement accuracy	Acquisition time
DTH22 (temperature)	−40 °C a 80 °C	<±0.5 °C	2 s
DTH22 (Humidity)	0 a 100% RH	2% RH	2 s
Sound KY-038	0 a 150 MHz		
Vibration	1.1 V/g	260 pC/g	+/−1%
Current	0 a 100 A	0 mA a 6 mA	+/−3%

we proceeded to store it in a database hosted in the cloud, to be analyzed by means of different statistical tools and finally to be presented or visualized in an interface designed for this purpose, which can be consulted through a web page [7].

The ESP8266 thing (Arduino) and Raspberry Pi 3 programming systems have been used successfully in other similar data collection efforts, including monitoring networks and evaluation of environmental variables in different enclosed spaces or urban areas as presented in [8]. In the same way, it has been implemented for intelligent health systems [9] and adaptive environments for the care and supervision of older adults [10]. Many of these studies have demonstrated the reliability and ease of use of programming cards (ESP8266 Thing and Raspberry pi 3) for data collection remotely.

One of the purposes is to show the application made and how through a platform on the web different applications can be developed in a specific field. This is how part of this work focuses on the use of the MQTT (Message Queue Telemetry Transport) protocol [11], recently used for different IoT-related projects, although it is unusually considered in medical devices. On the other hand, most health systems based on IoT focus on physical sensors. Some commercial sensors used in the industry for the monitoring of electronic and mechanical equipment are considered for this project. From the above, in Fig. 2 the description of the implemented system is presented in a general way:

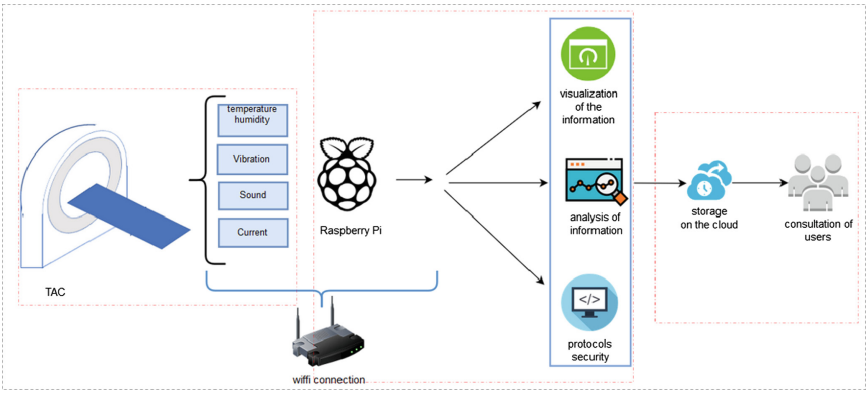

Fig. 2. Summary of the implemented system layers. (a) CAT data acquisition, (b) information processing, (c) data storage and query

It is important to highlight that the implementation of each of the modules (sensor/esp8266), was made under the interconnection by means of a Wi-Fi network to the local server (Raspberry pi). For this project, a centralized architecture was implemented where all the information is stored in a single place called Broker, a system that is installed in the Raspberry pi card. By means of specialized communication protocols such as MQTT, they make possible the flow of information in dynamic IoT systems [12].

Each one of the registers of the sensors used was transmitted under a sampling time of around 5 s. In this way, an average was made per minute, not without first establishing the factory operating ranges and obtaining a relative value per hour, which allows greater reliability in each of the captured measurements.

Finally, the acquired data were analyzed using descriptive statistics in order to find values that allow us to infer the correlation between the set of measurements taken. The data visualization is presented through densities diagrams and histograms using the programming language Python 3.

3 Results

Then, different visualizations were made to analyze the possible relationships between the variables of temperature and current consumption as the main critical variables in the continuous operation of the CAT according to the behavior of the acquired data. As shown in Fig. 2, we can observe similar values of current that oscillate between 4.6 to 4.75 A (amperes). It is common in temperature values (Fig. 3).

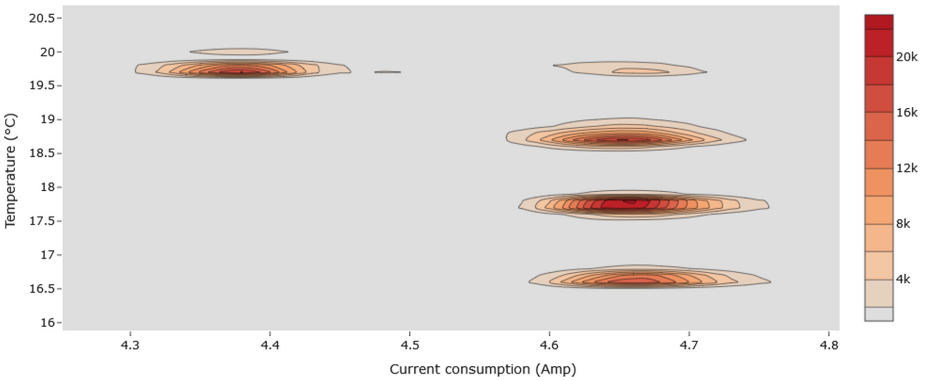

Fig. 3. 2D-Histogram of current consumption and temperature frequencies in a TAC in proper operation during two months.

The distribution of current consumption and temperature is depicted in 5 zones as presented in Fig. 2. The most interesting result is related to the two zones in the top of the figure presented the same temperature, but with two different ranges of current consumption. Durante el mes de adquisición se realizaron alrededor de 1,9 millones de mediciones en el CAT, y en los reportes no se reportó ningún fallo en el equipo analizado.

The current consumption of the CAT is bounded in two normal distributions with mean of 4.39 and 4.66 amps as presented in Fig. 4. On the other hand, the temperature was clustered in four big groups with values ranged between 16 and 20° as presented in Fig. 1. This result could be useful to evaluate the proper operation of a CAT, if the temperature measured by a maintenance technician is within this range.

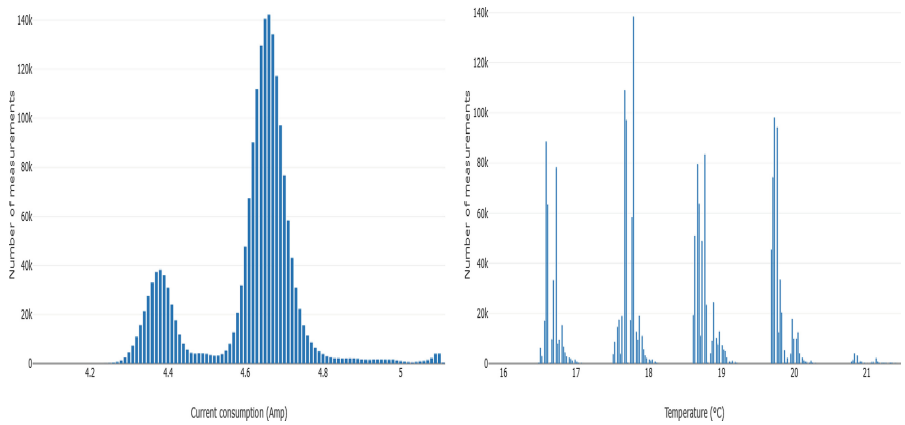

Fig. 4. Histograms showing the most common values of [Left] current consumption in a CAT; [Right] temperature in a CAT

4 Conclusions

This work developed a new approach for the design and implementation of an IoT system that helps in the capture of data on a large scale, in such a way that it allows to combine paradigms, finding patterns of operation of a medical team under the supervision of different variables in a hospital environment. It also allows to generate new or alternative options to carry out a predictive maintenance, based on the behavior of each one of the variables, in such a way that it allows to avoid in some way a corrective failure.

This process was carried out in two fundamental phases, which helped to channel the activities by executing several processes in parallel without interfering with each other, in such a way that the working group was divided into main tasks such as: the selection of the different variables that were the object of this study was carried out under the criteria of the group of engineers of the hospital and the researchers of the university. Likewise, the point of view and experience of the team of doctors of the diagnostic imaging service was taken into account.

The test phases of the system allowed to identify the behavior of the data and the identification of the veracity and reliability of each of the tests, thus determining the average values of operation and anticipating whether the solution has a real value or not. In this way, it was identified if the captured values could be good indicators of deterioration or malfunctioning of the equipment, allowing foreseeing failures.

To conclude, these systems can greatly increase the quality of the service, allowing constant control and improvement in the use of medical equipment. Two implications directly related to this work could be: the creation of a continuous monitoring system in real time, accessible and intelligible by means of low-cost technology, integrated in a non-invasive manner in the equipment.

On the other hand, there is an environmental design approach to detect different variables separately, its synergy can be used in a more extensive study on the architecture, characteristics and suggest new improvements in the connection of intelligent objects.

The acquisition of a greater number of CAT devices or devices from different manufacturers, other variables and a longer acquisition time could confirm the results presented in this study. On the other hand, the need for a quick and reliable forecast of possible failures in medical equipment and the reduction of corrective maintenance in these, will be two interesting topics of study in future work

Conflict of Interest. The authors report no conflicts of interest.

References

1. Ashton, K.: That 'Internet of Things' thing. RFID J. **22**, 97–114 (2009)
2. Bhumi, C., Chintan, B.: Bigdata analytics in industrial IoT. In: Dey, N., Hassanien, A., Bhatt, C., Ashour, A., Satapathy, S. (eds.) Internet of Things and Big Data Analytics Toward Next-Generation Intelligence Studies in Big Data, vol. 30, p. 382. Springer, Cham (2018)
3. Hatagundi, M.D., Sadashivappa, G.: Wireless communication in medical devices: research challenges. In: 2018 2nd International Conference Trends in Electronics and Informatics (ICOEI), pp. 336–338 (2018)
4. Middleton, P., Kjeldsen, P., Tully, J.: Forecast: The Internet of Things, Worldwide. Gartner, Stanford (2013)
5. Miorandi, D., Sicari, S., De Pellegrini, F., Chlamtac, I.: Internet of things: vision, applications and research challenges. Ad Hoc Netw. **10**, 1497–1516 (2012)
6. Marques, G., Pitarma, R.: An indoor monitoring system for ambient assisted living based on internet of things architecture. Int. J. Environ. Res. Public Health **13**, 1152 (2016)
7. Atzori, L., Iera, A., Morabito, G.: The internet of things: a survey. Comput. Netw. **15**, 2787–2805 (2010)
8. Gómez, J.E., Marcillo, F.R., Triana, F.L., Gallo, V.T., Oviedo, B.W., Hernández, V.L.: IoT for environmental variables in urban areas. Procedia Comput. Sci. **109**, 67–74 (2017)
9. Catarinucci, L., De Donno, D., Mainetti, L., Palano, L., Patrono, L., Stefanizzi, M.L., Tarricone, L.: An IoT-aware architecture for smart healthcare systems. IEEE Internet of Things J. **2**, 515–526 (2015)
10. Zallio, M., Berry, D., Casiddu, N.: Adaptive environments for enabling senior citizens: an holistic assessment tool for housing design and IoT-based technologies. In: IEEE 3rd World Forum Internet of Things (WF-IoT), pp. 419–424 (2016)
11. Kraijak, S., Tuwanut, P.A.: Survey on internet of things architecture, protocols, possible applications, security, privacy, real-world implementation and future trends. In: 2015 IEEE 16th International Conference Communication Technology (ICCT), pp. 26–31 (2015)
12. Bassi, A.: Enabling things to talk. In: Designing IoT Solutions with the IoT Architectural Reference Model, pp. 163–211 (2013)

Differences in Heart Rate Variability Between Diabetic and Non-diabetic Intradialytic Hypotensive Patients

Francisco Arturo López del Angel[1(✉)], Joaquín Azpiroz Leehan[2], and Gerardo Daniel Rosas Andreu[3]

[1] Universidad Autónoma Metropolitana, Iztapalapa, Mexico
franciscoartlo@hotmail.com
[2] Universidad Autónoma Metropolitana, Iztapalapa, CDMX, Mexico
jazpiroz@ci3m.mx
[3] N3frored SAPI, Coyoacán, CDMX, Mexico
grosas@nefrored.mx

Abstract. The most frequent and troubling side effect in the treatment of hemodialysis is intradialytic hypotension (IDH). This compromises cardiovascular hemodynamics. Heart rate variability (HRV) is a non-invasive measurement of the sympathovagal balance, and provides important information about the autonomic nervous system. Few studies have compared hypotension in diabetic and non-diabetic patients throughout the therapy sessions, with a protocol of intradialytic exercise and high flux hemodialysis/hemodiafiltration therapy. Our work is aimed to evaluate cardiac autonomic regulation during hemodialysis with HRV in hemodynamically unstable patients with chronic renal disease. During a 6-month follow-up of patients, the model suggested that the sympathovagal index (LF/HF) is different between the diabetic from non-diabetic group ($p < 0.05$), and does not necessarily reflect the sympathetic balance. Diabetic patients were differentiated by having lower HRV power components than the non-diabetic group ($p < 0.05$), and during the hypotensive event they showed a sympathetic inhibition, unlike the non-diabetic group that showed a parasympathetic inhibition. It was observed that the compensatory mechanisms were markedly different between two groups studied. This study shows the importance of giving individualized attention and therapies in order to take preventive measures to avoid hypotensive events.

Keywords: Hypotension · Heart rate variability · Hemodialysis

1 Introduction

Chronic kidney disease is related to the incidence of chronic diseases such as diabetes, obesity and hypertension [1]. Hemodialysis (HD) and Hemodiafiltration (HDF) are the most frequent and well-established treatments [2]. Cardiovascular events are responsible for the majority of deaths and can be attributed to Autonomic Nervous System (ANS) dysfunction. The rapid removal of excess fluid during therapy compromises the cardiovascular hemodynamics. Intradialytic Hypotension (IDH), occurs episodically

© Springer Nature Switzerland AG 2020
C. A. González Díaz et al. (Eds.): CLAIB 2019, IFMBE Proceedings 75, pp. 1333–1338, 2020.
https://doi.org/10.1007/978-3-030-30648-9_172

with a sudden decrease in arterial pressure. Short-term consequences are symptoms of fatigue, cramps and vomiting. Long-term consequences include permanent damage to the cardiovascular system [3]. The diabetic (DB) population has a predisposition to suffer IDH. It is more difficult for those patients to compensate for ultrafiltration, because they have autonomic or baroreceptor dysfunction [4]. The pathogenesis of hypotension in hemodialysis seems to be multifactorial and is not yet fully understood [5]. Quite a few approaches have been suggested in the literature in order to improve the quality of this therapy [6]. The frequency domain in HRV gives important information about the ANS. The power of the high frequency (HF) signal reflects parasympathetic activity, while the power of low frequency (LF) signal and the sympathovagal (SVI) index of LF to HF (LF/HF) represents the SNA balance [7]. Several studies have showed a reduction in all the spectral indices of sympathetic activity in unstable patients, which precede the decrease in blood pressure, and were interpreted as evidence of deterioration or inhibition of the autonomic response to the elimination of volume [8]. During IDH autonomic changes are characterized by parasympathetic activation and sympathetic withdrawal with bradycardia [9]. Exercise protocols have also been implemented aiming to improve the therapy outcomes. Exercise ensures hemodynamic stability in patients in hemodialysis. In several studies the group with exercise has showed sympathetic predominance, with an increase in the SVI [10]. Other important parameters that have to be controlled are: the use of High-flux HD or HDF, control of dialysate temperature, monitoring of patient parameters, such as HRV, body composition, and nutrition; The systematic use of several of these techniques is necessary in order to provide real-time interventions and improve outcomes [11].

We aimed to evaluate the acute effects of IDH on cardiac autonomic regulation in patients with chronic renal disease with and without Diabetes in a protocol of exercise and High Flux HD/HDF therapy. Its early prediction and prevention will dramatically improve the quality of life and survival for patients with end stage renal disease.

2 Materials and Methods

The methodology that we have proposed is based on the one established by the National Institute of Cardiology's HD/HDF clinic in Mexico City, and enhanced by several other innovations:

1: Use of intradialytic exercise during the entire dialysis session, through the use of stationary cycling.
2: Recording and analysis of HRV and Blood Pressure (BP). Data was acquired during 10 min at three moments: Just at the start of therapy (Time 1), 1.5 h after the session was started (Time 2), and just after the end of the session (Time 3).
3: Dialytic Parameters: Blood flow rates were between 400 & 500 ml/min. Dialyzer flow rate was 500 ml/min. Dialysate temperature was 35.5 °C. Linear rate of ultrafiltration. Dialysate composition was: 138 mEq/lt Na+, 2 mEq/lt K+, 2 mEq/lt Ca2+/Nipro Elisio 2.1 Filter; Fresenius Medical Care 4008 H machine.

Twenty-three patients were studied during a six-month interval. They all gave their informed consent. After 471 sessions, there were 101 sessions whit hypotensive events,

and this is the data that was analyzed. Patients have the same conditions, except Group 1 is diabetics and Group 2 is non-diabetics.

HRV Analysis: The RR intervals were recorded with a HRV system: Meigaoyi, model ECGLAB 3.0, 1000 Hz sampling rate; We analyzed low-frequency (LF = 0.04 a 0.15 Hz) and high-frequency (HF = 0.15 a 0.40 Hz) components and the ISV ratio.

3 Results and Discussion

ANOVA for repeated measurements and T student analysis were carried out and post-hoc tests to compare the differences of the HRV and BP. $P < 0.05$.

Table 1. Blood Pressures Group 1 vs. Group 2 at 3 Times of Therapy.

	DB	NonDB	DB	NonDB	DB	NonDB
Blood pressure	Time 1	Time 1	Time 2	Time 2	Time 3	Time 3
SBP (mmHg)	159 ± 25	163 ± 19	132 ± 31	135 ± 24	105 ± 20*	125 ± 16*
DBP (mmHg)	70 ± 15*	80 ± 24*	66 ± 15*	74 ± 21*	59 ± 11*	67 ± 15*
MBP (mmHg)	100 ± 17*	108 ± 18*	89 ± 20	95 ± 20	75 ± 12*	86 ± 12*
HR (bpm)	71 ± 10*	79 ± 11*	74 ± 14*	82 ± 14*	74 ± 13*	79 ± 15*

*p < 0.05 Group I vs. Group II

Table 1 shows the values of systolic blood pressure (SBP), diastolic blood pressure (DBP), median blood pressure (MBP) and heart rate (HR) in both groups. The elimination of volume by ultrafiltration (UF) during hemodialysis causes a series of hemodynamic responses. This can be seen in the Blood Pressure in Table 1. Through the therapy in both Groups the blood pressure falls more than 20 mmHg, which causes severe hypotension, it means that the ANS cannot compensate for UF. The decrease is significant greater ($p < 0.05$) in DB patients. It could be explained because Diabetic Patients have been reported to have impaired ANS activity. Heart rate, did not change through the therapy in a significant manner in both groups. But was significant higher ($p < 0.05$) in the non-diabetic group.

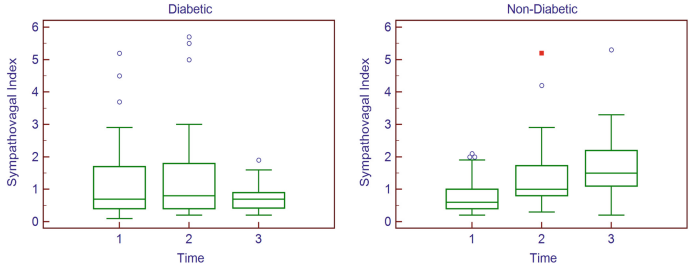

Fig. 1. Sympathovagal Index at 3 times during hemodialysis sessions with hypotension in diabetic and non-diabetic patients.

The SVI describes the balance between sympathetic and parasympathetic activity, in Fig. 1. We can observe in the diabetic group, a decrease in the index at the end of the therapy, compared to time 1 and 2 ($p < 0.05$). In the non-diabetic group, there is an increase in the middle and end compared to the beginning ($p < 0.05$).

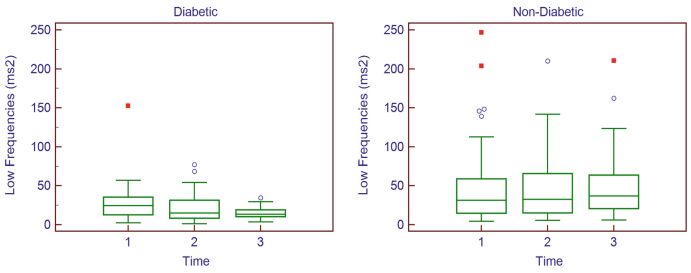

Fig. 2. Low-frequency power (ms^2, absolute units) at 3 times during hemodialysis sessions with hypotension in diabetic and non-diabetic patients.

In Fig. 2 we can observe that the low-frequency components decrease at time 3 compared with 1 and 2 ($p < 0.05$) with group 1, while it does not change in a statistically significant manner ($p > 0.05$) in all times, with group 2. LF power spectrum was significant lower ($p < 0.05$) in group 1 compared to group 2.

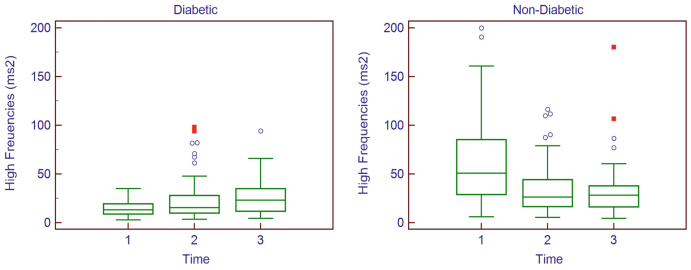

Fig. 3. High-frequency power (ms^2, absolute units) at 3 times during hemodialysis sessions with hypotension in diabetic and non-diabetic patients.

Figure 3 shows the increase of high-frequency components at the end of session, compared to time 1 and 2 ($p < 0.05$) in Group I. A decrease is shown at the middle of the session compared to time 1 and 3 ($p < 0.05$) for group 2. HF power spectrum was significant lower ($p < 0.05$) in group 1 compared to group 2.

The data found in group 1 agrees with previous studies where they are as described in the literature in a hypotensive event, where there is a decrease in the SVI due to a decrease in the LF power (sympathetic activity), and an increase in the HF power (parasympathetic activity). But unlike previous studies that showed a bradycardic activity, in our study the heart rate did not change, this can be due to the intradialytic exercise that the patients perform, and keeps the heart rate active.

On the other hand, in the data found in group 2 the SVI increases, but it is not due to a sympathetic increase, because we observe that the LF power does not change significantly, but the HF power decreases significantly at the end of the therapy, and this is the power that is influencing the sympathovagal balance. This discovery found in group 2, suggests a parasympathetic withdrawal, and can be thought of as a last line of defense when the sympathetic system alone cannot deal with the cardiovascular control at the end of the HD session and it is due to the parasympathetic system's effort to maintain the blood pressure appropriately. Finally, the finding that LF does not decay through the therapy can be a result of the dialytic exercise, that keeps the sympathetic activity from decreasing.

4 Conclusion

The measurement of the ANS activity with HRV represents a simple and non-invasive method, important in the determination of the balance of autonomic modulation in patients with renal insufficiency. Which is during a short-term protocol, significant differences were found intra-dialysis between diabetic and non-diabetic patients. The occurrence of IDH events, depends on the pathology of the patient.

For both groups, SNA changes are presented at the middle and end of the therapy. We suggest this is an important period of time to measure the patient. As the ISV is a ratio, an increase is not necessarily due to sympathetic activation, we suggest that the role of the frequency components is more important. Although the use of exercise did not prevent the event of hypotension to happen, in our study we can observe a positive effect in non-diabetic group, which can indicate that it helps the ANS to compensate for UF in the therapy.

The ANS is only part of the monitoring for the individualized therapy that must be done in order to improve the quality of the treatment. We are currently undertaking preliminary studies evaluating the use of a multifrequency body composition analyzer that provides information about the patient's body composition and hydration status. Real time HRV analysis through the use of ECG Holter. Long term protocols of exercise to evaluate which is the most appropriate that help to reduce adverse events. Also, we are carrying out preliminary metabolic analyses at the start and end times of HD/HDF treatment in some patients, to provide information that indicates the advisability of providing supplementary nutrition. We foresee that the integration of all these parameters into a personalized therapy that will increase longevity and quality of life for patients under renal replacement therapy.

Acknowledgements. This work was supported by Programa de Laboratorios Nacionales CONACYT-CI3 M-UAM-AMORN. E. Sacristán, G. Zubirán, F. Martínez, A. Morón; A. Fonseca, M Cadena, and A. de la Rosa; Gabriela Godínez, Miriam Carrillo and Miguel Lorenzana.

Conflict of Interest Statement. The authors declare that they have no conflict of interest.

References

1. Aktins, R.: The epidemiology of chronic kidney disease. Kidney Int. **67**(94), S14–18B (2005)
2. Neuen, B., Chadban, S., Demaio, A.: Chronic kidney disease and the global NCDs agenda. Br. Med. J. Global Health **2**(2), 1–4 (2017)
3. Schreiber, M.: Clinical case-based approach to understanding intradialytic hypotension. Am. J. Kidney Dis. **38**(4), S37–S47 (2001)
4. Agarwal, R.: How can we prevent intradialytic hypotension? Curr. Opin. Nephrol. Hypertens. **21**(6), 593–599 (2012)
5. Rubinger, D., Revis, N., Pollak, A.: Predictors of haemodynamic instability and heart rate variability during haemodialysis. Nephrol. Dial. Transplant. **19**(8), 2053–2060 (2004)
6. McCraty, R., Shaffer, F.: Heart rate variability: new perspectives on physiological mechanisms, assessment of self-regulatory capacity, and health risk. Global Adv. Health Med. **4**(1), 46–61 (2015)
7. Benedito, S., Valenti, V., Adami, F.: Heart rate variability during hemodialysis in patients with chronic renal disease. Int. Arch. Med. **8**(1), 1–9 (2005)
8. Sörnmo, L., Sandberg, F., Gil, E., Solem, K.: Noninvasive techniques for prevention of intradialytic hypotension. IEEE Rev. Biomed. Eng. **5**(1), 45–59 (2012)
9. Barnas, M., Boer, W., Koomans, H.: Hemodynamic patterns and spectral analysis of heart rate variability during dialysis hypotension. J. Am. Soc. Nephrol. **10**(1), 2577–2584 (1999)
10. Sietsema, K., Amato, A., Adler, S., Brass, E.: Exercise capacity as a predictor of survival among ambulatory patients with end-stage renal disease. Kidney Int. **65**(2), 719–724 (2004)
11. Mostovaya, M., Blankestijn, P., Bots, M., Covic, A., Davenport, A., Grooteman, P., Hegbrant, J., Locatelli, F., Vanholder, R.: Clinical evidence on hemodiafiltration: a systematic review and a meta-analysis. Semin. Dial. **27**(2), 119–127 (2014)

Clinical Engineering and Education

A Prioritization System for Timely HIV/AIDS Patient Care

Alexis Cruz-Escudero, Laura Angelica Hernandez-Lopez, Daniel Ernesto Sanchez-Baqueiro, and Fabiola M. Martinez-Licona(✉)

Universidad Autonoma Metropolitana, 09340 Mexico City, Mexico
fmml@xanum.uam.mx

Abstract. Human Immunodeficiency Virus (HIV) damages the immune system and AIDS (Acquired Immune Deficiency Syndrome) occurs in the final stage of the virus when it is not treated. This situation keeps being a global health problem, and efforts have focused on research for a cure. In general, the diagnosis focuses on clinical blood examinations of the lymphocyte cells behavior and the treatment with medications and vaccines. Due to the complexity of the disease, interventions that involve different aspects of the diagnosis and treatment are, in course. This paper presents a prioritization system for timely help the healthcare of HIV/AIDS patient. It relies on a model built using multiple criteria decision analysis that employs variables related to information of the patient. The model output is an index that maps into an appropriate care scale that leads to managing timely actions, aims to optimize the treatment, and supports the patient to take control of the disease. We validated the model with simulated data, obtaining a 94.8% of correct class assignment using a decision tree. We also tested the model with case studies data with 80% of correct assignation. The results show that the prioritization assignment tends to be founded on the variables patient profile and time of disease, although more research on the variable analysis and data collection is mandatory.

Keywords: HIV/AIDS · Prioritization index · Multiple-Criteria Decision Analysis

1 Introduction

Human Immunodeficiency Virus (HIV) damages the immune system by destroying the white blood cells that fight infections; if it is left untreated, the final stage of the virus presents a set of symptoms and illnesses called Acquired Immune Deficiency Syndrome (AIDS). This disease keeps being a threat to global public health: according to United Nations AIDS (UNAIDS) by 2017, 36.9 million of people living with HIV, and 1.8 million of people newly infects with the virus [1]. On the 37th meeting of the UNAIDS Programme Coordinating Board, it was adopted the 2016–2021 Strategy which aligns with the United Nations Sustainable Development Goals and where is established the framework of the global development policy for the next years that includes the ending of the AIDS epidemic by 2030 [2].

© Springer Nature Switzerland AG 2020
C. A. González Díaz et al. (Eds.): CLAIB 2019, IFMBE Proceedings 75, pp. 1341–1348, 2020.
https://doi.org/10.1007/978-3-030-30648-9_173

In Latin America, the 2017 UNAIDS estimated of adults and children living with HIV was 1.8 million, the number of new HIV infections of all ages was 100,000, and the number of AIDS-related deaths was 37,000 [3]. Although these numbers seem to reflect that there is some progress on the illness treatment, several factors must be considered to make a complete and realistic analysis of the situation. Many AIDS cases are not reported because people infected do not have access to health services. There are not enough efforts to reach young people that are considered a critical community on the regional strategy. In most parts of the continent, HIV programs focused on crucial population depend on donor funding. In particular, the lesbian, gay, bisexual, transgender and intersex (LGBTI) people remains to be a vulnerable population due to the stigma and violence, obstructing their access to HIV services [4].

In general, HIV infection diagnosis seeks for the diminishing of lymphocyte cells on blood through the accounting of these cells, the amount of virus in the blood, and the resistance of the virus strain to medications. All of them help the doctor to orient treatment. HIV treatment includes inhibitors of several enzymes like transcriptase, protease, of the protein integrase, and blockers of HIV into the lymphocytes [5]. Given that health technology is the application of organized knowledge and skills in the form not only of devices but also of medicines and vaccines among others [6], HIV diagnosis and treatment are a matter for health technology assessment and management. Moreover, it is important to notice that the more timely the intervention is, the more probabilities for the control of the effects of the disease will have.

It is clear that the disease is too complicated and has to deal with integrative strategies that involve all the society stakeholders. The World Health Organization recognizes that the approach to the control and eventual solution of the pandemic must include actions that aim to achieve universal access to prevention, treatment and care, policies, technical recommendations and guides related to the interventions [7]. Some efforts to identify the priority settings for interventions have focused on health impacts such as safety, spread reduction and prevention/treatment, resources (vaccines, technologies and other medical products) or responsiveness such as stigma reduction [8]. Health stakeholders also acknowledge that keeping in close contact with patients may increase retention [9], while others point out to prioritize the very early stages of the disease [10].

Managing basic information about the status of the patient may help the medical staff to determine the best treatment options if they proceed in a timely way, so it may be convenient to have tools that give support for the HIV or AIDS patient care. This paper presents a prioritization system based on a model built from multiple criteria involved in the HIV diagnosis and AIDS treatment. It is aimed to provide the person in charge of deciding the course of the HIV/AIDS-diagnosed patient treatment, of tools to prioritize the care. The model output is an index that maps into a priority care scale which intends helping to get the timely actions to optimize the treatment and support the patient to take control of his/her disease.

2 Methods

The methodology framework selected was the Multiple-Criteria Decision Analysis (MCDA), since it allows to estimate the possible implications that each course of action may take for the decision-maker and obtain a better understanding between the linked actions and objectives, as well as to provide useful tools for the analysis of complex problems [11]. The prioritization of HIV/AIDS patient care method aims to obtain an indicator of prioritization to optimize the efforts and resources of the care; it followed the next steps.

2.1 Variable Definitions

A set of four variables required to the patient care assessment was defined. Also, a relevant numeric factor was attached to each variable assignation according to the Saaty's analytic hierarchy process [12] into a scale from 0 to 10. The variables name, definition, and relevance factor number (ρ) are shown in Table 1. The patient profile is taken as primary criteria to define a course of care since the HIV patient will have a different treatment compared to that of the AIDS diagnosed patient. The time that has passed after the diagnosis settlement may influence the decision on the actions for the patient treatment. The technological resource used on these patients may take distinct roles going from clinical trials to life support, and the timely application of technology may influence the outcomes. The reference frame completes with the identification of how the contagion was carried out.

Table 1. Variables for prioritization of timely patient care

Variable	Name	Definition	ρ
X_1	Patient profile	Indicates if the patient has been diagnosed with HIV or AIDS	10
X_2	Time of disease	Shows the time since the patient has been diagnosed	8
X_3	Type of technology	Designates the technology used on the patient	6
X_4	Ways of contagion	Points out how the patient was infected	3

Each variable has a set of possible outcomes with numerical weights (μ) according to the prioritization of care as it is shown in Table 2. The variables and the outcome assignation emerged from taking into account the data reported of references related to the disease [13, 14] and the Saaty's analytic hierarchy process under heuristic assumptions.

Table 2. Outcomes of the variables for prioritization of timely patient care

Variable	Outcome and Values (μ)	μ
X_1	Patient diagnosed with HIV	10
	Patient Diagnosed with AIDS	5
X_2	≤ 5 years	10
	Between 6 and 14 years	6
	≥ 15 years	3
X_3	Test technology	10
	Life support	5
	Treatment	3
	Other	1
X_4	Sexual	10
	Medical procedures	8
	Vertical line (mother-son)	6
	Blood transfusion	2

2.2 Mathematical Model

Following the MCDA methodology, a mathematical model was generated using the variables defined to find an index that reflects the prioritization of care for the HIV/AIDS patient. The patient care prioritization index PCP is defined by

$$\mathrm{PCP} = \frac{\sum_{i=1}^{4} \mu(X_i)\rho_i}{N} \tag{1}$$

where $\mu(X_i)$ is the outcome of the variable under consideration, ρ_i is the correspondent relevance factor, the index i denotes the variable number to be considered $\{1\ldots4\}$ and N is a normalization element. The numeric value of N arose from

$$N = \sum_{i=1}^{4} \rho_i \mu_{imax} \tag{2}$$

where μ_{imax} is the maximum over the outcomes values μ for each variable. The final PCP index mapped into a three-stages of priority care scale, and it is shown in Table 3.

Table 3. Scale for prioritization of timely patient care

Range	Priority	Interpretation
[0–0.50]	Low	The patient is in the final stage of the disease and requires palliative care
[0.51–0.74]	Middle	The patient is in a stage of the disease where the virus does not affect his/her health
[0.75–1.0]	High	The patient is in the initial stage of the disease and requires pharmacological treatments

3 Results

The model was tested with a set of known case studies and with a collection of simulated data. These case studies correspond to famous athletes and artists that were diagnosed either with HIV or AIDS [15] and are shown in Table 4.

Subjects 1 and 3 were diagnosed with HIV and were sexually infected; subject 1 has between 6 and 14 years with the disease and uses life support technology, subject 3 has more than 15 years with the disease and uses technology for treatment. Thus, the model made subject 1 to have a high priority, whereas subject 3 obtained a middle priority.

Subjects 2, 4, 5 and 6 were diagnosed with AIDS and had between 6 and 14 years with the disease. According to the model, subject 5 has a low prioritization compared to the rest; it uses technology for other purposes and was infected because of a medical procedure. The model mapped the combinations <life support technology – sexual infection>, <other technology – blood transfusion> and <treatment technology – sexual infection> into a middle prioritization.

Table 4. Results on known case studies

Subject	X_1	X_2	X_3	X_4	Priority	Interpretation
1	10	6	5	10	0.770	High
2	5	6	5	10	0.585	Middle
3	10	3	3	10	0.637	Middle
4	5	10	1	2	0.525	Middle
5	5	6	1	8	0.474	Low
6	5	6	3	10	0.540	Middle

A classification system with all the possible combinations of the variables according to the numerical values established was carried out to test the model's settings. The resulting dataset, 96 four-attributes instances, was used to build a C4.5 decision tree [16]. The 94.8% of the instances were correctly classified; Table 5 shows the confusion matrix and Fig. 1 the decision tree, both obtained with WEKA workbench [17]. Five cases were incorrectly classified and correspond to the following profiles:

Table 5. Percentage classification of the simulated dataset using C4.5

Model C4.5	High	Middle	Low
High	96	4	0
Middle	3.92	94.1	1.96
Low	0	5	95

- HIV-less than five years with the disease-using other types of technology-infected by blood transfusion. Classified as of high prioritization and assigned to a middle level by the model.
- HIV-between 6 and 14 years with the disease-using life support technology-sexually infected. Classified as of middle prioritization and assigned to a high level by the model.
- HIV-more than 15 years with the disease-using other types of technology-infected by blood transfusion. Classified as of middle prioritization and assigned to a low level by the model.
- AIDS-less than five years with the disease-using testing technology-infected by blood transfusion. Classified as of high prioritization and assigned to a middle level by the model.
- AIDS-between 6 and 14 years with the disease-using life support technology-infected by the vertical line. Classified as of low prioritization and assigned to a middle level by the model.

We introduced the set of case studios into the decision tree, and from the 5 instances, only the first one obtained a different class (middle) compared to the model (high).

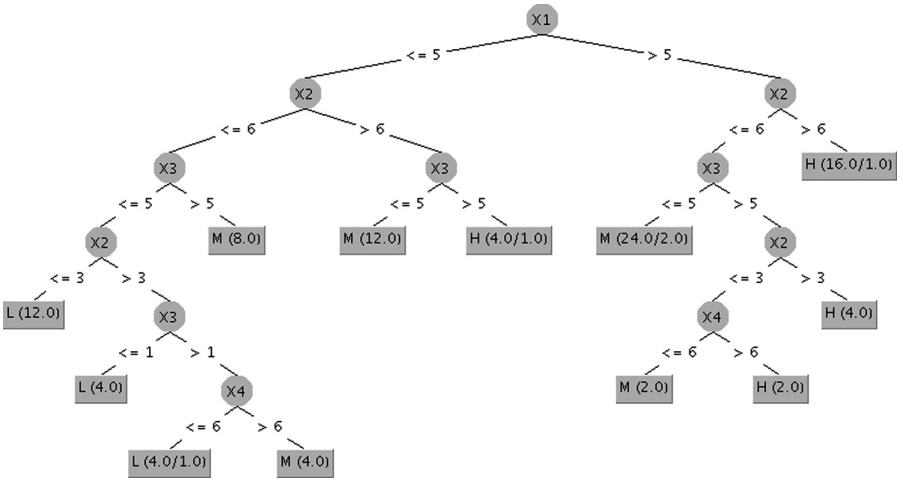

Fig. 1. C4.5 decision tree obtained from simulated data

4 Discussion

The prioritization system supported by essential information of the HIV/AIDS diagnosed patient used variables that we consider as easy to get, although indirectly inferred from formal sources. The information that these variables provide produces a general profile of the patient for timely attendance purposes, that is why the first variable deals with a diagnosis decreed so it can be possible to differentiate the stage of the virus

presence. The decision tree is the result of the variables defined in the prioritization model, so it represents a support element for validating the model with the simulated data. The results that the C4.5 decision tree shows in the data set are similar to those in the simulation of the model. This situation may be because both are substantially linear approximations, although reviewing some of the misclassified instances, the doubt arises about the level of prioritization to be assigned, as is the case of subject 1. More efforts must be addressed to establish whether the C4.5 decision tree, the prioritization model, or both are to be used as the prioritization system. We tested the decision tree with the same data with which we built it since the database is not large enough and not homogeneously distributed in its classes.

The outputs of the system are aimed only to guide the management of the patient care so the medical staff can have supported information and help the patient with the required maneuvers for his/her timely care. It should be clear that all patients should have access to the treatments they need.

The meaning of curing HIV, as a new strategic priority for most AIDS organizations, goes beyond the disease itself. Social and economic issues as discrimination and coverage in health as well as the access to timely diagnosis, treatment, and medications, must be addressed as it is the case of the clinical problems of the illness. Since research has become the focus of efforts to cure the disease, it emphasizes the importance of developing strategic priorities to identify HIV infection at the early stages in adults and infants in the low, middle- and high-income countries [18]. A system that allows prioritizing the patient care with this disease may optimize the delivery of the treatment for cure, once it is found. The economic and social implications of the programs to be implemented in the mentioned terms can be significantly positive.

5 Conclusions

We presented a system used to timely prioritize the treatment for the diagnosed HIV/AIDS patient; the system depends on a linear model that involves variables related to the patient's basic information. The results on the database and the case studies show that the variables *patient profile* and *time of disease* prioritize the care assignment. This approach focuses on attending the patient, whether he or she has HIV or AIDS, through easily accessible information, so data on clinical trial results were not included. Since this system presented is a methodological approach with partial results, in order to improve this kind of prioritization systems the current model is going to test on real data, so further work is devoted to collect the information related to the variables, to research of other variables to be tested and to implement different types than linear models.

Acknowledgment. The authors acknowledge the comments and observations from the 18-O Medical Technology Assessment Class of the Universidad Autonoma Metropolitana.

Conflict of Interest. The authors declare that they have no conflict of interest.

References

1. UNAIDS Homepage. www.unaids.org/en. Accessed 25 Mar 2019
2. UNAIDS 37th Meeting Programme Coordinating Board. http://www.unaids.org/sites/default/files/media_asset/20151028_UNAIDS_PCB37_Decisions.pdf. Accessed 25 Mar 2019
3. UNAIDS Latin America and the Caribbean Data. http://www.unaids.org/en/regionscountries/latinamerica. Accessed 26 Mar 2019
4. UNAIDS Data 2018, (pp. 172) at. http://www.unaids.org/sites/default/files/media_asset/unaids-data-2018_en.pdf. Accessed 26 Mar 2019
5. Mayo Clinic HIV AIDS. https://www.mayoclinic.org/es-es/diseases-conditions/hiv-aids/diagnosis-treatment/drc-20373531. Accessed 28 Mar 2019
6. WHO 60.29 Health Technologies. https://www.who.int/healthsystems/WHA60_29.pdf?ua=1. Accessed 28 Mar 2019
7. WHO (2010) Priority Interventions. HIV/AIDS prevention, treatment and care in the health sector. https://apps.who.int/iris/bitstream/handle/10665/44418/9789241500234_eng.pdf?sequence=1. Accessed 28 Mar 2019
8. Tromp, N., Prawiranegara, R., Siregar, A., Sunjaya, D., Baltussen, R.: Importance of multiple criteria for priority setting of HIV/AIDS interventions. Int. J. Technol. Assess. health care **31**(6), 390–398 (2015). https://doi.org/10.1017/s0266462316000039
9. Grimes, R.M., Hallmark, C.J., Watkins, K.L., Agarwal, S., McNeese, M.L.: Re-engagement in HIV care: a clinical and public health priority. J. AIDS Clin. Res. **7**(2), 543 (2016). https://doi.org/10.4172/2155-6113.1000543
10. Tucker, J.D., Gilbertson, A., Lo, Y.R., Vitória, M.: Implications of prioritizing HIV cure: new momentum to overcome old challenges in HIV. BMC Infect. Dis. **16**, 109 (2016). https://doi.org/10.1186/s12879-016-1445-y
11. Praveen, T., Devlin, N., Marsh, K., et al.: Multiple criteria decision analysis for health care decision making-an introduction: report 1 of the ISPOR MCDA emerging good practices task force. Value in Health **19**(1), 1–13 (2016). https://doi.org/10.1016/j.jval.2015.12.003
12. Saaty, T.: The Analytic Hierarchy Process. McGraw-Hill, New York (1980)
13. Health Secretariat of Mexico, General Directorate of Epidemiology, CENSIDA (2018) Epidemiological Surveillance of HIV/AIDS cases in Mexico, National Registry of AIDS Cases. Update to the 1st quarter of 2018 (in Spanish). https://www.gob.mx/cms/uploads/attachment/file/328400/RN_1er_trim_2018.pdf. Accessed 01 Apr 2019
14. UNAIDS data. http://www.unaids.org/en/topic/data. Accessed 29 Mar 2019
15. Healthline Homepage. https://www.healthline.com/health/celebrities-with-hiv#1. Accessed 30 Mar 2019
16. Quinlan R.: C4.5: programs for machine learning. Morgan Kaufmann (1993)
17. Frank, E., Hall, M.A., Witten, I.H.: The WEKA Workbench: Practical Machine Learning Tools and Techniques, 4th edn. Morgan Kaufmann, Cambridge (2016)
18. Tucker, J.D., Gilbertson, A., Lo, Y.R., Vitória, M.: Implications of prioritizing HIV cure: new momentum to overcome old challenges in HIV. BMC Infect. Dis. **16**(109), 109 (2016). https://doi.org/10.1186/s12879-016-1445-y

Stakeholders Studies in HTA: A Theoretical Approach

Fabiola M. Martinez-Licona[1,2(✉)], Raul Enrique Molina-Salazar[1,3], and Pedro Constantino Solis-Perez[1,3]

[1] Administrative Sciences Graduate Program, Universidad Autonoma Metropolitana, Mexico City, Mexico
fmml@xanum.uam.mx
[2] Electrical Engineering Department, Universidad Autonoma Metropolitana, Mexico City, Mexico
[3] Economy Department, Universidad Autonoma Metropolitana, Mexico City, Mexico

Abstract. Health care requires the development of activities devoted to providing the health services that people needs and demands. Within these activities, the clinical procedures, as well as the use of technological resources, have had a predominant role in the accomplishment of these goals. That is why effective management of health technologies is a strategic objective that has been globally disseminated into health programs worldwide. The incorporation of stakeholders in management activities, particularly in the evaluation of medical technologies, has proven to be more complicated than it seems because of both the multidisciplinary nature of the functions and the interests and motivations that these activities promote. Given the important role that the stakeholders play in the health technology assessment (HTA) activities, an approach supported on administrative sciences and organizational theory to analyze and manage their participation is presented. Three principal issues are addressed: the identification of the stakeholders, the analysis of their dynamics and the development of strategies for their management; then some tools to deal with them are shown. A general example centered on the biomedical engineer that performs an analysis of a medical device for purchase is exposed.

Keywords: Stakeholders · Health technology assessment · Power-Interest grid · Stakeholder Management

1 Introduction

The complexity in the implementation of clinical procedures as well as in the advances of medical technology is continuously growing, and thanks to this it is possible to obtain options in diagnosis and treatment that help to improve the quality of life of the people. On the other hand, the accelerated increase of the technological resources and the incorporation of medical technologies into the health systems have involved increments in costs both for their use in the provision of services and for their conservation in health institutions.

© Springer Nature Switzerland AG 2020
C. A. González Díaz et al. (Eds.): CLAIB 2019, IFMBE Proceedings 75, pp. 1349–1356, 2020.
https://doi.org/10.1007/978-3-030-30648-9_174

The economic aspect is the one that most clearly evidences the impact that the inclusion of technologies has on healthcare, and the reports do not pay enough attention to the other types of aspects that correlate with the technological resource. These include the clinical, which largely determines the needs to be covered by medical technology, the normative, which in some way delimits the fields of action of the functions related to technology management in health, or the social, which in several ways is the recipient of the decisions released in this regard. For these reasons, decision-makers and other responsible parties require increasingly efficient tools to assess and have control over the technology once the health professionals introduce and disseminate it into the health institutions in order to analyze the real benefits, consequences, costs and risks of its usage inside the hospital environment [1].

The health technology concept has owned several interpretations that have been subject to the immediate contexts under which they emerged. The most widely accepted is that of the World Health Organization (WHO), which defines health care technologies or health technology as "the application of organized knowledge and skills in the form of devices, medicines, vaccines, procedures and systems developed to solve a health problem and improve quality of lives" [2]. Likewise, health technologies assessment (HTA) is a systematic process of evaluation of the properties, the effects, the impacts of health technology, or both. It can address the direct and desired consequences of the technologies as well as the indirect and unwanted ones. Its main objective is to inform decision-making in health care. The evaluation of health technologies is carried out by multidisciplinary groups using explicit analytical frameworks based on different methods [3].

Stakeholders are "actors who have an interest in the issue under consideration, who are affected by the issue, or who – because of their position – have or could have an active or passive influence on the decision-making and implementation processes" [4]. They can be individuals, or groups such as organizations, networks or alliances. Mapping this definition into the HTA context would lead "individuals, organizations or communities that have a direct interest in the process and outcomes of a health technology assessment" [5].

In the last years, efforts have focused on developing stakeholder involvement strategies for the assessment of medical technology. Some of them point to the importance of the participation for organizations to achieve consensus and legitimacy, and the difficult to transfer the stakeholder involvement model from one country to another because of the differences among the HTA organizations regard the national administrative characteristics [6]. The development of a stakeholder involvement program has revealed the diversity of interests, responsibilities, infrastructures and barriers to be considered and the convenience of creating forums of sharing thoughts so it can be successful [7].

Although there is an increasing interest on involving stakeholders in specific HTA programs, the methods and instruments used, mostly supported on surveys and interviews, must be improved to strengthen the findings [8]. Also, the strategic role that HTA is playing on the decision-making processes is causing the proposal of the institutionalization, but it does not seem clear how this can be implemented considering the diversity of interests involved [9].

The incorporation of stakeholders for the execution of HTA tasks has turned out to be more complicated than at first appeared to be, due both to the multidisciplinary nature of the functions and the interests and motivations that these activities promote. Then it becomes a matter of balance: agencies have to protect their political autonomy actively and to have access to specialized experts who are not blinded by or extremely enthusiastic about certain technological advances. On the other hand, patient associations are exerting pressure so that HTA agencies do not give the impression of being too lenient with the government or of supporting rationalization policies [10].

The stakeholders' involvement in HTA activities becomes increasingly more strategic for the establishment of decision-making processes. Also, the different reported approaches have in common that they cannot be generalized That is why it is highly recommendable to return to the perspective of administrative sciences in order to form a general theoretical framework on which actions in this sense can be supported, sustained and legitimized.

Taking the principles of strategic management and organizational theory, and incorporating them into the environment of health technologies, this paper presents a proposal to carry on identification and analysis of stakeholders in HTA activities.

2 Conceptual Framework

One of the first tasks to do in strategic management is to deal with both the demands of the different stakeholders and the strategic goals of the organization. Thus, the long- and short-term objectives, as well as the goals of the organization, should be stated before thinking of any stakeholder. According to [11], to identify and manage those essential stakeholders for the organization, three themes must be addressed: identifying the stakeholders, exploring their dynamics, and developing management strategies.

The first theme is about identifying the stakeholders that are authentically related to the specific situation instead of considering a generic list. The second theme considers the interactions that the different stakeholders, current and potential, may have each other. The third theme leads to determining the ways of intervention on the stakeholders' significance through the consideration of their importance, influence, and interest in the organization's direction. The authors establish that "stakeholder management needs to be carried out concerning the goals of the organization."

The identification of a stakeholder must include the degrees of interaction and contribution to the strategic objectives of the organization. Freeman identified two dimensions that shaped the significance of the potential stakeholders and proposed a "Power-Interest Grid" to locate them aiming to get a balance between considering a broad definition of stakeholders and a manageable number of them [12].

Power dimension seeks those stakeholders that have or might have an influence on the strategic direction of the organization through the objectives and goals while interest dimension looks for those stakeholders that show interest, either positive or negative, on the organization's strategic objectives.

The process starts with a list of groups or individuals that the organization considers having the two characteristics (power and interest) and then each member of the list locate into a grid that has these characteristics as its axes. The resulting grid, as shown

in Fig. 1, will have four quadrants and will classify the stakeholders in the following categories:

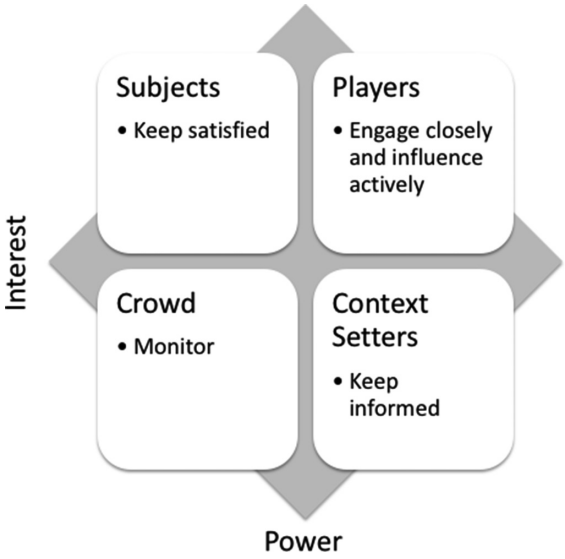

Fig. 1. Power-Interest grid from Freemann [12]

- Players: interested stakeholders with a high degree of power to support or sabotage the organization's strategies. Because of their position, the organization must keep them satisfied
- Subjects: interested stakeholders with less influence. The interaction with them is active to get their engagement
- Context setters: potential stakeholders that have not displayed much interest in the organization but may have a high degree of power over its future context. The organization must keep them informed
- Crowd: they don't exhibit either interest in or authority over the strategic objectives of the organization. Monitoring activity is advisable

In order to strategic manage them, the stakeholders located in the grid should be decomposed into specific subgroups, so it is possible to observe their interest in the organization's activities and their potential impact on its plans.

The next step is to rearrange the location of the stakeholders in terms of their disposition, that is, if they would be more inclined to support or sabotage the objectives and goals of the organization. The "Power-Interest Grid" allows to carry out an analysis of the stakeholders' dynamics identifying the interactions between them through a stakeholder-influence network diagram. The network draws the relationships with linking arrows which direction indicates the influence of one on another and with a double-headed arrow when the influence is mutual.

Finally, the stakeholder management strategies process selects key stakeholders ("Players") from the "Power-Interest Grid" refined with the obtained network links over them. The result is an individual "Stakeholder Management Web" [11] where it is impressed by the causalities related to bases of power and the bases of interest.

3 Results

We selected the definition and management of the stakeholders in the establishment of a hemodialysis unit in order to illustrate the application of the conceptual framework provided in an HTA example. The stakeholders that may be involved include the health system and certification bodies, hemodialysis machine suppliers, health professionals on hemodialysis and kidney diseases, clinical services on hemodialysis, and biomedical professionals (engineers and technicians). Figure 2 shows the power-interest grid of this case, partially based on the information presented in [13]. The location of each stakeholder was assigned according to the organization's objective: to provide a high-quality hemodialysis service.

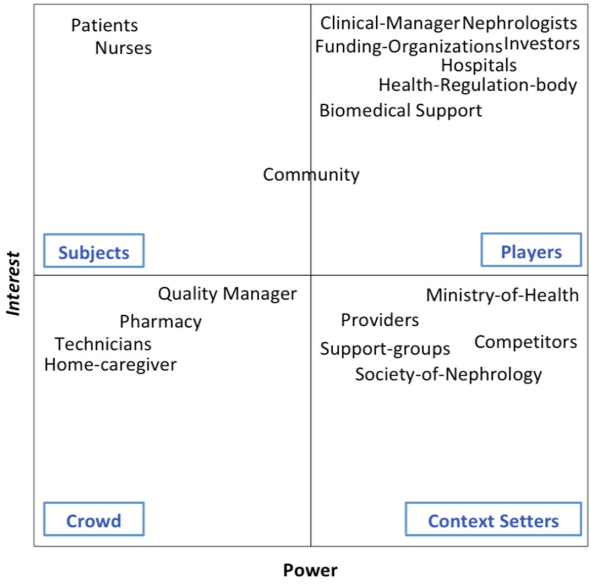

Fig. 2. Power-Interest grid for the establishment of a hemodialysis unit

Figure 3 shows the Stakeholder Management Web for Biomedical Support resulting of disaggregate the Players section and establish the relationships with the other stakeholders. In particular, this management web focuses on the biomedical engineer in charge of evaluating hemodialysis machines for acquisition.

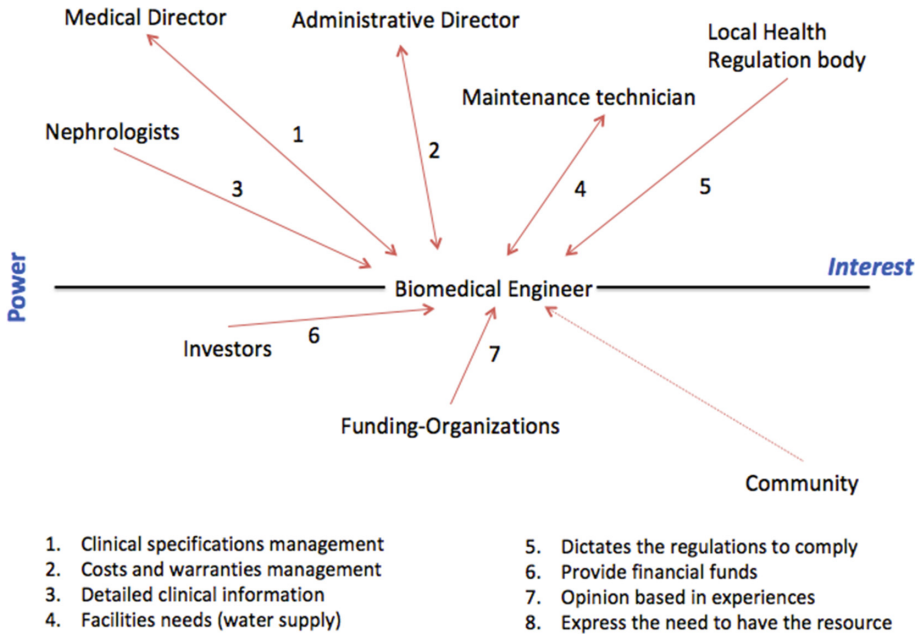

Fig. 3. Stakeholder Management Web for biomedical engineer in charge of evaluating hemodialysis machines for acquisition. Numbers indicate the kind of relationship that keeps each stakeholder with him or her.

4 Discussion

HTA as a key function for the optimal use of the technological resource in healthcare can benefit from the techniques of analysis and management of the stakeholders. This tool reveals the diversity of interests that play roles in the decision-making process; it also exposes the difficulty of reaching agreements when there are so many points of view, some of them in opposition. In the example shown, the information provided by each stakeholder should converge in a suitable set of requirements for the acquisition of the hemodialysis machines. This situation may not be entirely right: the presence of economic, political, or regulatory interests may influence the definition of the clinical or even technical requirements.

In order to alleviate the pressure of the forces involved in the HTA activities, and assuming that these forces are aligned to the organization's objectives, some have noticed the advantages of having autonomous and independent institutions, and even consider them as publicly funded [9], that generate relevant and objective information through methodologies that include stakeholder analysis and management. The HTA community should address this kind of efforts in this direction at different levels: local, regional, and national.

5 Conclusions

This paper presented the theoretical framework for the stakeholder analysis and management applied to HTA activities, and based on organizational theory and administrative sciences. An example centered on the biomedical engineer assessment of a medical device for purchase was outlined in order to present the multiple relations found from a single activity. The use of a power-interest grid allows identifying the potential role of each stakeholder as well as to locate in order of importance concerning the organization's objectives.

Although the purpose of the example was to illustrate the application of the theory, there are some elements that must be improved to have a successful and useful analysis for the organization. More emphasis on disaggregation is required to accomplish a detailed description of the stakeholders. The goal or objective has to be present during all the process since it rules the actions towards effective management of the stakeholders' interventions. The exchange of experiences helps to understand the dynamics of the stakeholders better, although we must take into account the impact that the contexts have on the results.

Acknowledgment. The authors acknowledge the Administrative Sciences Graduate Program for providing a forum for the discussion of these issues.

Conflict of Interest. The authors declare that they have no conflict of interest.

References

1. Petherick, E., Villanueva, E., Dumville, J., Bryan, E., Dharmage, S.: An evaluation of methods used in health technology assessments medical services advisory committee. Med. J. Aust. **187**(5), 289–292 (2007)
2. WHO Sixtieth World Health Assembly. https://www.who.int/medical_devices/resolution_wha60_29-en1.pdf. Accessed 21 Mar 2019
3. INAHTA, HTAI et al. HTA glossary net. http://htaglossary.net/health+technology+assessment+%28HTA%29. Accessed 21 Mar 2019
4. Varvasovszky, Z., Brugha, R.: A stakeholder analysis. Health Policy Planning **15**(3), 338–345 (2000)
5. Health Information and Quality Authority. Guidelines for stakeholder engagement in health technology assessment in Ireland (2014). https://www.hiqa.ie/sites/default/files/2017-01/HTA-Guidelines-Stakeholder-Engagement.pdf. Accessed 25 Mar 2019
6. Cavazza, M., Jommi, C.: Stakeholders involvement by HTA organizations: why is so different? Health Policy **105**(2–3), 236–245 (2012). https://doi.org/10.1016/j.healthpol.2012.01.012
7. Yazdizabeth, B., Shahmoradi, S., Majdzadeh, R., et al.: Stakeholder involvement in health technology assessment at national level: a study from Iran. Int. J. Technol. Assess. Health Care **32**(3), 181–189 (2016). https://doi.org/10.1017/S0266462316000167

8. Verbeek, J., Hiligsmann, M., Cicchetti, A., Marchetti, M.: Sharing and collecting hospital-based health technology assessment reports internationally: is an extensive participation of stakeholders realistic? Int. J. Technol. Assess. Health Care **34**(5), 527–534 (2018). https://doi.org/10.1017/S0266462318000570
9. Lavín, C., Alaniz, R., Espinoza, M.: Visions of stakeholders about institutionalization of health technology assessment in Chile: a qualitative study. Int. J. Technol. Assess. Health Care **33**(2), 303–306 (2017). https://doi.org/10.1017/S0266462317000381
10. Lehoux, P., Hivon, M., Denis, J., Tailliez, S.: Health technology assessment in the Canadian health policy arena: examining relationships between evaluators and stakeholders. Evaluation **14**(3), 295–321 (2008). https://doi.org/10.1177/1356389008090857
11. Ackermann, F., Eden, C.: Strategic management of stakeholders: theory and practice. Long Range Plan. **44**, 179–196 (2011)
12. Freeman, R.E.: Strategic Management: A Stakeholder Approach. Pitman Publishing, Marshfield (1984)
13. Silver, S.A., Harel, Z., McQuillan, R., et al.: How to begin a quality improvement project. Clin. J. Am. Soc. Nephrol. **11**(5), 893–900 (2016)

Comparative Analysis of Two Indicators of Technical Evaluation for the Replacement of Medical Equipment

Tlazohtzin R. Mora-García[1], L. Angélica Hernández-López[1], M. Fernanda Piña-Quintero[2], Ana B. Pimentel-Aguilar[3], and Martha R. Ortiz-Posadas[1(✉)]

[1] Electrical Engineering Department, Universidad Autonoma Metropolitana Iztapalapa, Mexico City, Mexico
posa@xanum.uam.mx
[2] Coordination of Electro-Medicine, National Institute of Pediatrics, Mexico City, Mexico
[3] Biomedical Engineering Department, National Institute of Respiratory Diseases, Mexico City, Mexico

Abstract. The technical status of the medical equipment is a criterion used to define its replacement. In this paper we present two indicators to evaluate the technical status of the medical equipment developed in two National Health Institutes from Mexico. The objective was to do a comparative analysis between both indicators based on the evaluation of a sample of 28 medical equipment located in critical care areas of one of the Institutes. The results showed that there is a direct relationship between both indicators and the technical status is a direct criterion for providing useful information to plan the replacement of medical equipment.

Keywords: Health Technology Assessment · Technical indicator · Medical equipment replacement

1 Introduction

Hospitals have multiple medical equipment of different technology that has direct impact on the diagnosis, treatment and/or rehabilitation of patients. That is why Pan American Health Organization promotes Health Technology Assessment (HTA) defined as "the systematic evaluation of properties, effects, and/or impacts of health care technology. It should include medical, social, ethical, and economic dimensions, and its main purpose is to inform decision-making in the health area. These assessments look at benefits and efficacy, clinical and technical safety, and cost-effectiveness. Informed decision-making comprises issues surrounding coverage and reimbursement, pricing decisions, clinical guidelines and protocols, and lastly, medical device regulation. The main purpose of HTA is to inform a policy decision making in health care, and thus improve the uptake of cost-effective new technologies and prevent the uptake of technologies that are of doubtful value for the health system" [1]. In this sense, the

© Springer Nature Switzerland AG 2020
C. A. González Díaz et al. (Eds.): CLAIB 2019, IFMBE Proceedings 75, pp. 1357–1364, 2020.
https://doi.org/10.1007/978-3-030-30648-9_175

Department of Biomedical Engineering (DIB) of a hospital must evaluate the medical equipment to guarantee its operation, in accordance with the manufacturer's technical specifications, in order to contribute to a safe stay of the patient in the hospital.

In this paper two indicators to evaluate the technical aspect of the medical equipment are presented. There were developed in two National Institutes of Health from Mexico [2, 3], and were used to define the replacement priority of medical equipment. One indicator provides the technical status of the medical equipment and the other, the time in which it must be replaced. Given that the technical status is a criterion used to define replacement of the medical equipment, the hypothesis for this work was that both indicators have a direct relationship in the result of the medical equipment assessment. Therefore, the objective of this work was to do a comparative analysis between the results of the two indicators obtained in the evaluation of a sample of 28 medical equipment located in critical care areas of one of the Institutes. The results showed that there is a direct relationship between both indicators and the technical status, effectively, is a direct criterion for planning the replacement of the medical equipment.

2 Methodology

2.1 Analysis of the Mathematical Models of the Indicators

We analyzed two indicators (I_A, I_B) that evaluate the technical status of the medical equipment developed in two National Institutes of Health (Institute A, Institute B) located in Mexico City. The analysis consisted in the comparison of the variables and the mathematical model defined for each indicator [2, 3], in order to know if there was any relationship between them.

2.2 Analysis of the Qualitative Scale of the Indicators

For the application of the indicators it was necessary to generate a qualitative scale that would allow an interpretation of the numerical results, which are usually grouped in intervals and assigned a label for their identification. In this case, a qualitative scale was defined for each indicator to be able to interpret its numerical result. In the case of I_A it provides the time when the equipment must be replaced. In the case of I_B corresponds to the technical status of the medical equipment. Both scales were analyzed together in order to assess if there was a correspondence between them.

2.3 Evaluation of a Sample of Medical Equipment

A sample of 28 medical equipment located in the following critical care areas of Institute A, was evaluated: Intensive Care Unit (ICU), Neonatal Intensive Care Unit (NICU) and Cardiovascular Intensive Care Unit (CICU). The equipment distribution is shown in Table 1 and the data correspond to the year 2017.

Table 1. Medical equipment distribution in the critical care areas of the Institute.

Type of equipment	Area	Number of equipment
Vital Signs Monitor (VSM)	ICU	10
Ventilator (V)	ICU	5
	CICU	3
Radiant Heat Cradle (RHC)	ICU	4
Incubator (IC)	NICU	5
Ultrasound (US)	CICU	1
Total		28

3 Results

3.1 Analysis of the Mathematical Models of the Indicators

For each indicator (I_A and I_B) a set of variables (x_i, y_j) with its respective weight (ρ_i, δ_j) was defined. Each variable was defined with a qualitative domain used by the technical staff of both Institutes to assess the medical equipment. To develop the mathematic function of each indicator, it was necessary to assign a quantitative domain [2, 3]. The variables and their weighting for each indicator are shown in Table 2. Note that there are five equal variables, that is, 75% of the models have coincidence. Note also that indicator I_A has eight variables while I_B only has seven variables.

Table 2. Variables and relevance factor.

Indicator	x_i	Name of the variable	ρ_i
I_A	x_1	Supplies available in 5 years	0.9
	x_2	Replacements available in 5 years	0.8
	x_3	Years of equipment in operation	0.7
	x_4	Days out of service	0.6
	x_5	Function of the equipment	0.5
	x_6	Frequency of failures	0.4
	x_7	Physical risk	0.3
	x_8	Maintenance requirements	0.2
	y_j	Name of the variable	δ_j
I_B	y_1	Available supplies/accessories	10
	y_2	Available spare parts	10
	y_3	Years of useful life	7
	y_4	Equipment function	7
	y_5	Failure frequency	6
	y_6	Equipment age	6
	y_7	Failure cause	4

On the other hand, note that the weights assigned to the variables of each indicator have a different scale. However equal variables have the greatest weight: x_1, x_2 with $\rho_1 = 0.9$ and $\rho_2 = 0.8$ for the indicator I_A, and for I_B the variables y_1, y_2 with $\delta_{1,2} = 10$ for both variables.

Mathematical Model I_A. Let I_A be the technical indicator for the replacement of medical equipment developed by Institute A, defined by expression (1). Where $i = \{1,\ldots, 8\}$ and $N_T = 4.4$ [2].

$$I_A = \frac{\sum_{i=1}^{8} \rho_i x_i}{4.4} \tag{1}$$

Mathematical Model I_B. Let I_B be the technical indicator for the replacement of medical equipment developed by Institute B, defined by expression (2). Where $j = \{1,\ldots, 7\}$ and $N_T = 535$ [3].

$$I_B = \frac{\sum_{j=1}^{7} \delta_j y_j}{535} \tag{2}$$

3.2 Analysis of the Qualitative Scale of the Indicators

Qualitative Scale for I_A. The qualitative scale for I_A was defined with three intervals (Table 3) and each one indicates the period in which the equipment should be substituted: short term (three years), medium term (6 years) and long term (ten years). These intervals were defined jointly with the technical staff of the Coordination of Electro-Medicine of Institute A. In this case, were considered the process for purchase medical equipment in the Institute A. It needs to consider the medical equipment cost in the annual budget and the purchase process takes, on average, 2 years.

Qualitative Scale for I_B. In this case the qualitative scale was also defined by three intervals. Each one represents the technical status of the medical equipment: excellent, regular and bad. Each of these terms implies the functionality of the medical equipment (Table 3) and they were defined jointly with the technical staff of the Department of Biomedical Engineering of Institute B.

Table 3. Qualitative scale for indicators I_A and I_B.

Model	Interval	Interpretation
I_A	[0,0.25]	Long term replacement (10 years)
	[0.25,0.55]	Medium term replacement (6 years)
	[0.55,1.0]	Short term replacement (3 years)
I_B	[0–0.39]	Excellent technical status
	[0.40–0.69]	Regular technical status
	[0.70–1]	Bad technical status

Note that both scales have a directly proportional correspondence, that is, the better the technical status of the medical equipment is, the longer the replacement period will be. For example, a *long term* replacement corresponds to *excellent* technical status, a *medium term* replacement corresponds to *regular* technical status and so on.

Evaluation of the VSM_1 Monitor. To illustrate the application of the indicators, the VSM_1 of the ICU was chosen. Its description in terms of the variables defined for each indicator is presented in Table 4.

For indicator I_A, the variables *Supplies and replacements available in 5 years* (x_1 and x_2 respectively) obtained the value of 1, since these inputs are not available in the market. The *Years of the equipment in operation* also obtained $x_3 = 1$, because the equipment is 24 years old. The equipment was not out of service during the evaluation period and therefore the variable *Days out of service*: $x_4 = 0$. The *Function of the equipment* (x_5) of the monitor is of *additional physiological control and of diagnosis* (APCD). The *Frequency of failure* was $x_6 = 2$, because the monitor presented two failures in the evaluation period. The *Physical risk* (x_7) that the equipment may generate is *inappropriate treatment or diagnostic error* (ITDE). Finally, the *Maintenance requirements* (x_8) are average (A) [2].

Table 4. Vital signs monitor (VSM_1) description in terms of the qualitative and quantitative domain for both indicators I_A and I_B

Model	Variables							
	x_1	x_2	x_3	x_4	x_5	x_6	x_7	x_8
I_A	No	No	24	0	APCD	2	ITDE	A
	1	1	1	0	0.6	0.4	0.6	0.6
	y_1	y_2	y_3	y_4	y_5	y_6	y_7	
I_B	≤ 2	≤ 2	9–11 years	MPVICS	M	20–25 years	ME	
	10	10	6	10	1	8	10	

In the case of indicator I_B, the variables *Available supplies/accessories* (y_1) and *Available spare parts* (y_2), the value obtained was 10 since these inputs are available in the market for a shorter period, less than or equal to two years. The *Years of useful life* (y_3) of the monitor are between 9 and 11 years and therefore $y_3 = 6$. The *Equipment function* (y_4) is *monitoring of physiological variables, intensive care and surgeries* (MPVICS). The *Failure frequency* (y_5) obtained a *moderate* (M) result because of the two failures presented in the monitor. The value of the *Equipment age* was $y_6 = 8$ because it is within the range 20–25 years. Finally the *Failure cause* was $y_7 = 10$, because the failures were produced by the software and/or hardware of the medical equipment (ME) [3].

Evaluation with I_A. All the quantitative values (Table 4) of the variables (x_i) and their weights (ρ_i) (Table 2) were substituted in Eq. (1).

$$I_{A_{MSV1}} = \frac{0.9(1)+0.8(1)+0.7(1)+0.6(0)+0.5(0.6)+0.4(0.4)+0.3(0.6)+0.2(0.6)}{4.4} = 0.72$$

According to the qualitative scale of I_A (Table 3), this equipment must be replaced in the short term, that is, in a period no longer than 3 years.

Evaluation with I_B. In the same way as the indicator I_A, all the quantitative values (Table 4) of the variables (y_j) and the relevance factors (δ_j) (Table 2) were substituted in Eq. (2):

$$I_{B_{MSV}} = \frac{10(10)+10(10)+7(6)+7(10)+6(1)+6(8)+4(10)}{535} = 0.75$$

According to the qualitative scale of I_B (Table 3), this equipment has a bad technical status. This is because it is 24 years old and there are no available supplies and spare parts in the market, so it is obsolete equipment.

Comparing the results of both indicators, it can be observed that they are closely related, because both shown that the MSV_1 monitor must be replaced in the short-term because of its bad technical status.

3.3 Evaluation of a Sample of Medical Equipment

The results of the evaluation of the 28 medical equipment with both indicators are presented below according to the type of equipment.

Vital Signs Monitor (VSM). Ten monitors were evaluated (Table 5). Note that seven of these obtained an equivalent result by the two indicators. That is, the monitor that obtained *bad technical status* (I_B) corresponds to a replacement in the *short term* (I_A). In the same way it happened with monitors which result was *regular technical status* (I_B), they must be replaced in the *medium term* (I_A). On the other hand, there are three monitors in which the result did not correspond between both indicators. Monitors $VSM_{5,7}$, got a *regular technical status* (I_B) with a correspond result of replacement in the *long term* (I_A). The monitor VSM_9 obtained *regular technical status* (I_B) for replacement in the *short term* (I_A), when the result should be *medium term* replacement. These differences may be due to the weighting of the variables assigned jointly with the technical staff of the two National Institutes of Health, who have different expertise.

Ventilators (V). Eight ventilators were evaluated (Table 6) and 87.5% of coincidence was obtained. Just the equipment V_2 located in the CICU obtained a different result. It got *long term* replacement with I_A and with I_B obtained *regular technical status*, so it should have a *medium term* replacement (I_A). These differences can also be due to the weighting assigned to the variables of each indicator.

Ultrasonograph (US). A US located in the CICU was evaluated and the results were: I_A, = 0.20 (*long term replacement*), I_B = 0.50 (*regular technical status*). For this technical status the replacement should be *medium term*. This may be due, as in the previous cases, to the assigned relevance to each variable.

Table 5. Results of the evaluation of the vital signs monitors.

Area	Equipment	I_A	Substitution	I_B	Technical status
ICU	VSM_1	0.70	Short term	0.80	Bad
	VSM_2	0.30	Medium term	0.60	Regular
	VSM_3	0.70	Short term	0.80	Bad
	VSM_4	0.30	Medium term	0.60	Regular
	VSM_5	**0.20**	**Long term**	**0.50**	**Regular**
	VSM_6	0.30	Medium term	0.60	Regular
	VSM_7	**0.20**	**Long term**	**0.50**	**Regular**
	VSM_8	0.70	Short term	0.80	Bad
	VSM_9	**0.20**	**Short term**	**0.50**	**Regular**
	VSM_{10}	0.30	Medium term	0.60	Regular

Table 6. Results of the evaluation of the ventilators.

Area	Equipment	I_A	Substitution	I_B	Technical status
ICU	V_1	0.40	Medium term	0.60	Regular
	V_2	0.30		0.50	
	V_3	0.40		0.60	
	V_4	0.30		0.60	
	V_5	0.30		0.60	
CICU	V_1	0.30	Medium term	0.60	Regular
	V_2	**0.20**	**Long term**	**0.60**	**Regular**
	V_3	0.30	Medium term	0.60	Regular

Radiant Heat Cradles (RHC) and Incubators (IC). Four RHCs and five ICs were evaluated. In all cases the correspondence between both indicators was 100%. The replacement result in the *medium term* and *technical status* of the equipment are *regular* (Table 7).

Table 7. Results of the evaluation of the radiant heat cradles and the incubators.

Area	Equipment	I_A	Substitution	I_B	Technical status
ICU	RHC_1	0.30	Medium term	0.60	Regular
	RHC_2	0.30		0.60	
	RHC_3	0.30		0.60	
	RHC_4	0.30		0.60	
NICU	IC_1	0.30	Medium term	0.60	Regular
	IC_2	0.30		0.60	
	IC_3	0.30		0.60	
	IC_4	0.30		0.60	
	IC_5	0.30		0.60	

4 Conclusions

The evaluation of the medical equipment showed that there is a relationship between the two indicators. There was a high correspondence between them. We obtain 70% for vital signs monitors, 87% for ventilators and 100% for radiant heat cradles and incubators. In addition, both indicators complement the information for decision making on the replacement of medical equipment. Currently, the technical staff of the Coordination of Electro-Medicine of the Institute A and of the Biomedical Engineering Department of the Institute B, are using this instrument in order to develop a program for health technology replacement that allows a rational investment in the purchase of new medical equipment.

Acknowledgment. The authors of this work want to thank the technical staff of the Coordination of Electro-Medicine of Institute A and the Department of Biomedical Engineering of Institute B for their valuable collaboration, because without their support this study would not have been possible.

Conflict of Interest. The authors declare that they have no conflict of interest.

References

1. Pan American Health Organization: Health Technology Assessment (HTA). https://www.paho.org/hq/index.php?option=com_content&view=article&id=9229:2013-tecnologias-sanitarias&Itemid=41687&lang=en. Accessed 07 February 2019
2. Mora-García, T., Piña-Quintero, F., Ortiz-Posadas, M.: Medical equipment replacement prioritization indicator using multi-criteria decision analysis. In: Hernández-Heredia, Y., Milián-Núñez, V., Ruiz-Shulcloper, J. (eds.) Progress in Artificial Intelligence and Pattern Recognition. Lecture Notes in Computer Science, vol. 11047, pp. 271–279. Springer, Cham (2018)
3. Hernández López, L.A.: Evaluation tool based on multicriteria analysis for the categorization and prioritization of health technology replacement in the INER. Biomedical Engineering Bachelor thesis, Universidad Autónoma Metropolitana Iztapalapa, Mexico (2018). (in Spanish)

An Indicator to Determine the Surplus or Deficit of the Medical Equipment in Critical Care Units

Tlazohtzin R. Mora-García[1], M. Fernanda Piña-Quintero[2], and Martha R. Ortiz-Posadas[1(✉)]

[1] Electrical Engineering Department, Universidad Autónoma Metropolitana, Iztapalapa, Mexico City, Mexico
posa@xanum.uam.mx
[2] Coordination of Electro-Medicine, National Institute of Pediatrics, Mexico City, Mexico

Abstract. The objective of this work was to develop an indicator to evaluate the availability of medical equipment located in four critical care areas of the Mexican Institute of Pediatrics. The indicator considers the demand and supply of medical equipment, and estimates its use from patients seen in the corresponding medical service. Given that we want to know if the medical equipment installed in the critical units is sufficient for patient care, the interpretation of the indicator result was made through two economic concepts: deficit and surplus. The indicator was applied to a sample of 38 medical equipment of seven type, and their results showed which equipment is sufficient and which has a deficit. This information is useful for the medical personnel and technical staff of the Electro-medicine Coordination of the Institute, in the identification of opportunity areas that allow improving the care of patients attended by the Institute.

Keywords: Medical equipment assessment · Deficit or surplus of medical equipment · Clinical indicator

1 Introduction

According to the Pan American Health Organization, Health Technology Assessment (HTA) is the systematic evaluation of properties, effects, and/or impacts of health care technology. It should include medical, social, ethical, and economic dimensions, and its main purpose is to inform decision-making in the health area [1]. A strategy followed for the HTA is develop of partial indicators that calculate different measures of operational, clinical and/or financial performance of medical equipment and all these results in productivity indicators.

The objective of this work was to develop a method to evaluate the availability of medical equipment located in four critical care areas of the Mexican Institute of Pediatrics: intensive care unit (ICU), neonatal intensive care unit (NICU), cardiovascular intensive care unit (CICU) and surgery (S).

© Springer Nature Switzerland AG 2020
C. A. González Díaz et al. (Eds.): CLAIB 2019, IFMBE Proceedings 75, pp. 1365–1372, 2020.
https://doi.org/10.1007/978-3-030-30648-9_176

Three productivity indicators were developed: two partial indicators and one global indicator called *clinical indicator*. These consider the demand and supply of medical equipment and estimate its use based on the number of patients seen in the corresponding medical service. The result of the *clinical indicator* was interpreted by means of two economic concepts: *deficit*, when any agent or sector in the economy (government, business or household) spends more in a given period of time than they generate in income. A deficit must be financed with new borrowing or by running down previous savings; and *surplus*, when its income exceeds its expenditure [2].

The indicators were applied to a sample of 38 medical equipment of seven type and their results showed which equipment is sufficient and which have a deficit. This information is useful for both the medical personnel, and the technical staff of the Electro-medicine Coordination (EMC) in charge of the medical equipment assessment, to identify opportunity areas regarding the available medical equipment in order to improve patients care attend by the Institute.

2 Methodology

2.1 Variables Definition

Five equally important variables were defined jointly with the technical staff of the EMC of the Institute. The variables are related to the time of use of the medical equipment and the admission of patients in the critical care areas considered in this study.

2.2 Partial Indicator Definition

Two partial indicators of productivity were defined. One evaluates the demand for using the medical equipment in terms of the patients seen in the medical service; and the other, evaluates the supply of these equipment in that medical service.

2.3 Clinical Indicator Definition

The clinical indicator is a ratio between the two partial productivity indicators mentioned above. It identifies the relationship between the demand and the supply of the medical equipment, and estimates its use based on the number of patients seen in the corresponding medical service. The result of this indicator is into [0, 1] where zero means the best condition and one the worst. This result can be interpreted as follow:

1. $[I_C \rightarrow 0]$: *Surplus*. There is more medical equipment available than patients demand. The result of the clinical indicator I_C tends to zero.
2. $[1 > I_C \geq 0.5]$: *Stable*. There is available medical equipment to attend just the demand of patients at the medical service. If there were a greater patients demand, there won't be able medical equipment available for their care.
3. $[I_C \rightarrow 1]$: *Deficit*. There is a patients demand that exceeds the available medical equipment. The result of I_C tends to one.

2.4 Application of the Indicators

The three productivity indicators were applied to 38 medical equipment distributed in three critical care areas of the Institute, as shown in Table 1. Seven type of medical equipment were considered: vital signs monitor (M), ventilator (V), radiant-heat cradle (RC), incubator (INC), ultrasound (US), electrosurgery unit (EU) and electrocardiograph (ECG). The period evaluation considered was the year 2017.

Table 1. Medical equipment distribution at the critical care units.

Area	Equipment number	Equipment type	Total
ICU	10	Vital signs monitor (VSM)	20
	5	Ventilator (V)	
	4	Radiant heat cradle (RHC)	
NICU	5	Incubator (IC)	6
	1	Ultrasound (US)	
CICU	3	Ventilator (V)	3
Sx	9	Electrosurgery units (EU)	9
Total			38

3 Results

3.1 Variables

Five variables were defined (Table 2) [3]. The variable *Admissions number* (x_1), refers the number of patients that were seen in the medical area during 2017. The variable *Average stay-days* (x_2), indicates the average of days that patients stays in the area. *Use hours per day* (x_3), quantifies the hours that a medical equipment was used for a patient per day, considering the equipment function. For example, in this work we consider medical equipment located at different critical care areas of the Institute. According to the WHO [4], the function of these equipment is: *monitoring* (M), *physiological control* (HC and INC), and *life support* (V). All these equipment can be used 24 h per day. In the case of equipment with a *diagnostic* function, such as ultrasound (US) and electrocardiograph (ECG), both are used between 30 and 90 min per study per day. The estimation of the use (hours) of the medical equipment was made jointly with the medical personnel of each area they use the equipment. The variable *equipment number* (x_4), counts the medical equipment of the same type located at the corresponding medical area. The variable *hours out of service* (x_5), considers the hours that the equipment was out of service due to the execution of preventive maintenance routines or any failure [3]. In addition, the constant k: *available hours,* was considered. This is the total number of hours that the medical equipment was available in the medical service during 2017. Since the equipment can be used 24 h: k = 24 (365) = 8760 h.

Table 2. Variables defined for the productivity indicators

x_i	Variable
x_1	Admissions number
x_2	Average stay-days
x_3	Use hours per day
x_4	Equipment number
x_5	Out of service hours

3.2 Partial Indicators

Partial Indicator 1. Let I_{P1} be the partial indicator called *Equipment demand* defined by (1).

$$I_{P1} = \frac{(x_1)(x_2)(x_3)}{x_4} \tag{1}$$

Where: x_1: admissions number. x_2: average stay-days. x_3: use hours per day. x_4: equipment number.

Partial Indicator 2. Let I_{P2} be the partial indicator called *Medical equipment supply* defined by (2):

$$I_{P2} = k - x_5 \tag{2}$$

Where: k = 8760 h x_5: hours of out of service.

3.3 Definition of the Clinical Indicator

The clinical indicator (I_C) was defined as a ratio between the demand (I_{P1}) and the supply (I_{P2}), and allows estimating the use of the medical equipment through expression (3).

$$I_C = \frac{I_{P1}}{I_{P2}} \tag{3}$$

3.4 Application of the Indicators

To illustrate the application of the indicators, the radiant heat cradle HC_1 was chosen, and its description is shown in Table 3. Note that the medical area (newborn care) had an income of 48 patients (x_1) in 2017, with an average of six days-stay per patient (x_2). The cradle can be used 24 h (x_3) and there are five cradles (x_4). Note that HC_1 was out of service 2 h (x_5).

Table 3. HC1 description in terms of the five variables defined.

HC_1					
Area	x_1	x_2	x_3	x_4	x_5
ICU (newborn)	48	6	24	5	2

Application of I_{P1}. The values of variables x_1, x_2, x_3 and x_4 were replaced in expression (1):

$$I_{P1} = \frac{(48\,patients)(6\,days)(24\,h)}{(5\,cradels)} \approx 1382\,h$$

This means that each radiant heat cradle was used an average of 1382 h in 2017 according to patients income in this year.

Application of I_{P2}. The values of the constant k and x_5 were replaced in the expression (2):

$$I_{P2} = k - x_5 = 8760\,h - 2\,h = 8758\,h$$

This means that HC_1 was available for use 8759 h. This represents 99% of the total time (the crib was out of service 2 h during 2017).

Application of I_C. To apply the I_C, the values obtained in each of the partial indicators were replaced in Eq. (3).

$$I_C = \frac{I_{P1}}{I_{P2}} = \frac{8758\,h}{1382\,h} = 0.16$$

In this case, HC_1 is in *surplus*, because the demand of patients who needed the equipment was met and it was also available to attend more patients if necessary.

The results obtained for all 38 medical equipment are shown as follow. The results are presented by medical area.

Intensive Care Unit (ICU). The Unit is divided into two areas: (1) intensive adult-pediatric care, and (2) newborn care. Each one was evaluated individually. The total admission was x_1 = 514 patients, 468 in the adult-pediatric area and 48 in the newborn area, with an average of six days-stay. The evaluation was made to four radiant heat cradles (HC), ten vital signs monitors (M) and 5 ventilators (V) (Table 4). The result of the demand for all the cribs was I_{P1} = 1382 h. The supply for cribs $HC_{1,2,3}$ was I_{P2} = 8758 h and for HC_4 was I_{P2} = 8757 h, because this crib was out of service one hour.

The final result of the *clinical indicator* for all the cribs was I_C = 0.16, which means that they are in *surplus*. There is greater availability of equipment that patients demand. In other words, the number of hours that the cribs were available to be used in patient care was greater than the number of hours that each crib was used according to patient admission.

Table 4. Results of the medical equipment from ICU

Área	Equipment	x_5	I_{P1} (h)	I_{P2} (h)	I_C
I C U	HC_1	2	1382.4	8758	**0.16**
	HC_2				
	HC_3				
	HC_4	3		8757	**0.16**
	M_1	2	3964.3	8758	**0.45**
	$M_{2,\ 10}$	3		8757	
	M_3	4		8756	
	M_4	6		8754	
	$M_{1,\ 8}$	1		8759	
	M_1	8		8752	
	$M_{7,\ 9}$	0		8760	
	V_1	14	3964.3	8746	**0.45**
	V_2	11		8749	
	V_3	16		8744	
	$V_{4,\ 5}$	10		8750	
	ECG	1	2808	8759	**0.32**

In the case of the vital signs monitors (M), all these obtained a demand of $I_{P1} \approx 3964$ h and a supply between $I_{P2} = [8752, 8760$ h] (Table 4). Likewise, all the monitors obtained an $I_C = 0.45$, which means that they also have *surplus*. There is greater availability of equipment than what is required to attend the patients who arrived at the ICU. The hours that the monitors were available for use, were greater than the number of hours that the equipment was used with each patient admitted by the Unit.

In the case of the ventilators, note that all of these were out of service between [11, 16 h]. All the ventilators had a demand of $I_{P1} \approx 3964$ h and a supply between $I_{P2} = [8744, 8750$ h], and an $I_C = 0.45$, which also resulted *surplus*. There was greater availability of ventilators than the demand for its use by the patients seen in the ICU.

The ECG obtained a demand of $I_{P1} = 2808$ h, a supply of $I_{P2} = 8759$ h and an $I_C = 0.32$ which also resulted an equipment with *surplus*. The equipment was more time available than required by the patients.

Neonatal Intensive Care Unit (NICU). The Unit had an income of 321 patients (x_1) with an average of six days-stay (x_2). The function of the equipment located in this Unit is: *physiological control* for incubators (INC) and *diagnosis* for ultrasound (US), so it was considered available use (x_3) of 24 h and 1.5 h per day respectively. In the NICU are seven INC and one US (x_4) (Table 5). Note that all incubators were out of service between 2 and 3 h with a demand of $I_{P1} = 6603$ h, a supply between $I_{P2} = [8758, 8760$ h] and an $I_C = 0.75$, which means that these equipment were in *deficit.* The NICU had higher demand of patients needed to use this equipment and there were not enough incubators to attend them. In the case of the US, it was $x_5 = 72$ h out of service, with a demand of $I_{P1} = 2889$ h, a supply of $I_{P2} = 8688$ h and an $I_C = 0.33$, which implies *surplus*, because it was used 90 min on average per study per day, which means that it has a lot of availability.

Table 5. Results of the medical equipment evaluation from NICU

Área	Equipo	x_5	I_{P1} (h)	I_{P2} (h)	I_C
NICU	$INC_{1, 2}$	0	6603.4	8760	**0.75**
	$INC_{3, 4, 5}$	2		8758	
	US	72	2889	8688	**0.33**

Cardiovascular Intensive Care Unit (CICU). This Unit had an income of 130 patients (x_1) with an average of nine days-stay (x_2). The equipment evaluated was three ventilators (V) with *life support* function, with available use of $x_4 = 24$ h per day (Table 6). These equipment were out of service between $x_5 = [7, 15$ h]. The demand in all cases was $I_{P1} = 4680$ h, the supply was $I_{P2} = [8745, 8753$ h], with a $I_C = 0.53$ for the first two ventilators and $I_C = 0.54$ for the last one. This means that they have a *stable* level of use, since the supply of equipment was sufficient to meet the demand of patients that was attended in 2017.

Table 6. Results of ventilators evaluation from CICU

Área	Equipo	x_5	I_{P1} (h)	I_{P2} (h)	I_C
CICU	V_1	11	4680	8749	**0.53**
	V_2	7		8753	
	V_3	15		8745	**0.54**

Surgery (S_X). There are ten operating rooms. This area had an income of 5124 patients (x_1) with an average of 3 h stay (x_2) by patient in the operating room. It is important to say that the anesthesia machines and the vital signs monitors are not property of the Institute, these are in a service contract. That is why only nine electrosurgery units (EU), owned by the Institute, were evaluated. It was considered available use of $x_4 = 24$ h per day. The equipment were out of service between $x_5 = [1$, 3 h] and the demand for all the units was $I_{P1} = 4236$ h. In the case of the supply, the first seven EU obtained $I_{P2} = 8757$ h and for the last three $I_{P2} = 8759$ h (Table 7). The clinical indicator was $I_C = 0.48$, which means that these EU have *surplus*, because the use of this equipment is equivalent to the average hours patients stay in the operating room (3 h), that is, they have a lot of availability.

Table 7. Results of the electrosurgical units from surgery area.

Área	Equipo	x_5	I_{P1} (h)	I_{P2} (h)	I_C
S_X	$EU_{1, 2, 3, 4, 5, 7}$	3	4235.8	8757	**0.48**
	$EU_{6, 8, 9}$	1		8759	

4 Conclusions

A clinical indicator was developed. It evaluates whether the number of medical equipment in a medical service is sufficient to meet the demand of patients, through three economic concepts: surplus, when there are more equipment than patients demand; stable, when the equipment is sufficient to meet the patients demand; and deficit, when the equipment is not enough to meet the patients demand.

The results showed that the ICU, in all cases, has more medical equipment (*surplus*) than its patients demand. The NICU has a *deficit* of incubators, so it will be necessary to plan the acquisition of new equipment. The CICU has sufficient (*stable*) ventilators to meet the demand of patients, until now. In the area of Surgery, all the electrosurgical units were in *surplus*.

These results are very useful for medical personnel in order to develop strategies to improve the patients care. Likewise, for the technical staff of the EMC, this information is useful for the management of health technology, as well as for the pre-purchase evaluation of the medical equipment.

Finally, it is important to mention that the three productivity indicators developed in this study were applied to seven types of medical equipment, however, it is an evaluation tool that can be applied to any type of equipment of interest for the particular health institution.

Acknowledgment. The authors of the present work want to acknowledge to the medical staff of the clinical areas and the technical staff of the Electromedicine Coordination of the Mexican Institute of Pediatrics, because without their support this study would not have been possible.

Conflict of Interest. The authors declare that they have no conflict of interest.

References

1. Pan American Health Organization: Health Technology Assessment. https://www.paho.org/hq/index.php?option=com_content&view=article&id=9229:2013-tecnologias-sanitarias&Itemid=41687&lang=en. Accessed 07 Feb 2019
2. Standord, J.: Economics for everyone: on-line glossary of terms & concepts (2008). http://www.economicsforeveryone.ca/files/uploads/glossary_0.pdf
3. Mora-García, T.R.: An assessment tool based on indicators for determining medical equipment replacement. Biomedical Eng Bachelor's thesis, Universidad Autónoma Metropolitana Iztapalapa, Mexico (2018). (in Spanish)
4. World Health Organization: Medical equipment maintenance programme overview. WHO Medical device technical series. Ginebra: OMS (2011). http://apps.who.int/medicinedocs/documents/s21566en/s21566en.pdf. Accessed 07 Feb 2019

Clinical Engineering Performance Benchmarking – A Practical Guide

Binseng Wang(✉)

BSI, Cornelius, NC, USA
binseng@alum.mit.edu

Abstract. Clinical engineering (CE), also known as healthcare technology management (HTM), professionals in many countries have experienced difficulties in obtaining recognition and support from their senior leadership, despite the fact that they have been successful in maintaining and managing healthcare equipment in safe and reliable condition. A fundamental root cause of this paradox is the lack of metrics to measure and compare CE performance, as equipment safety and reliability are not easily measured, much less the impact of equipment maintenance and management on the health outcomes of patients. CE professionals have been reluctant to measure and compare performance, believing such exercises require sophisticated skills and may expose them to closer scrutiny by their supervisors or lead them to become targets of outsourcing companies. Studies conducted with data from hundreds of American acute care hospitals have proven that these concerns are unfounded; only some readily available datasets are needed and analyses can be performed with standard spreadsheets. Well-performed benchmarking is helpful not only for CE managers to earn better recognition and support from their supervisors, but also to reduce the risk of having their team replaced by outsourcing companies. This paper provides a practical guide for CE benchmarking.

Keywords: Clinical engineering · Performance benchmarking · Key performance index

1 Introduction

Clinical engineering (CE), also known as healthcare technology management (HTM), professionals in many countries have frequently expressed frustration with the lack of recognition and support from their respective institution's senior leadership. In fact, analyses of patient harm caused by improper equipment maintenance and management have shown that CE professionals have performed exceptionally well, at least in the industrialized nations [1], so the apparent lack of recognition and support cannot be attributed to poor technical performance. A more likely root cause is the lack of metrics to measure and compare CE performance, as equipment safety and reliability are not easily measured. Even more difficult is the determination of the impact of equipment maintenance and management on health outcomes of patients, since equipment is only a tool. It must be used by the proper clinicians (doctor, nurse, or other clinical professional), at the right time, on the right patient, and in the right way in order to produce

© Springer Nature Switzerland AG 2020
C. A. González Díaz et al. (Eds.): CLAIB 2019, IFMBE Proceedings 75, pp. 1373–1379, 2020.
https://doi.org/10.1007/978-3-030-30648-9_177

the desired health outcome. Many CE professionals have been reluctant to measure and compare performance, believing such exercises require extensive statistical expertise and tools, and may expose them to closer scrutiny by their supervisors or becoming targets of outsourcing companies.

Fortunately, studies conducted with data from hundreds of American acute care hospitals have proven these concerns to be unfounded. Only some readily available data are needed and analyses can be performed through standard spreadsheets with rudimentary statistics skills. With concrete data, it is much easier for CE managers in almost any country to benchmark their performance and, thus, not only earn better recognition and support from their supervisors, but also reduce the risk of having their team replaced by outsourcing companies. In particular, financial benchmarking is easily understood by most senior healthcare executives, thanks to their background and training in business management, even when they have limited understanding of health technology and much less the needs and challenges of CE.

This paper presents a practical guide that can help CE managers in almost any country to benchmark their performance—provided that the comparison takes into account cultural, economic, and organizational realities—and, thus, not only earn better recognition and support from their supervisors but also to reduce the risk of having their team replaced by outsourcing companies. Furthermore, these comparisons can provide the CE managers with clear opportunities for improving their performance.

2 CE Benchmarks

A critical challenge for CE professionals who are trying to benchmark their performance is to find benchmarks that have been proven to be valid and effective for this particular specialty. There are literally thousands of possible benchmarks in healthcare and technology [2] and while many of them show reasonably good statistical correlation among themselves and presumptive institutional measures, their causal relationships have seldom been tested and proven.

Fortunately, dozens of potential CE benchmarks have been analyzed using actual data collected from hundreds of American acute care hospitals and some of them have been proven to be valid and useful for performance benchmarking purposes [3], while others have been proven unjustifiable [4]. Before showing and explaining these benchmarks, it is first necessary to characterize the primary data (aka measures) needed for computing the benchmarks. It should be obvious that the benchmarks are ratios of primary data, because it is meaningless to compare the absolute values of almost any hospital or CE data, due to the simple fact that hospitals often are of different sizes with differing number of beds, pieces of equipment, and patients. Table 1 shows the primary data needed with corresponding explanation.

The hospital data can be obtained from its operations and finance departments. In some countries, hospitals that received public funding or reimbursement for service from government-managed funds (e.g., Medicare and Medicaid programs in the United States) are required to report these data, which become available to the public. Since these data are typically audited by government agencies and/or insurance companies, they tend to be accurate and reliable.

Table 1. Primary data needed for computing CE benchmarks

Data source	Primary data	Explanation
Hospital	Total operating beds	Total number of patient beds actually available for use considering staff and other resources available
	Total hospital expense (THE)	Total amount of hospital operating expenditure in a year for all types of resources
	Total & adjusted patient discharges	Total number of hospitalized patients discharged in a year; the adjusted metric factors in the ambulatory (non-hospitalized) patients using the ratio of total (in plus out-patient) revenue to in-patient revenue
	Total & adjusted patient days	Total number of hospitalized patient days in a year, while the adjusted metric factors in the ambulatory (non-hospitalized) patients using the method described above
CE Department	Total inventory size	Total number of pieces of medical equipment, including only those specifically made for medical purposes and with unit value >US$1,000
	Total inventory cost	Total cost of medical equipment in the inventory considering the original purchase price with all accessories but not supplies, installation, customs, training, or extended warranty
	Total number of repairs	Total number of repairs performed on medical equipment in a year, regardless who performed it
	Total number of scheduled maintenance	Total number of scheduled maintenance performed in a year, regardless who performed it
	Total CE expense (TCE)	Total amount of hospital operating expenditure on medical equipment maintenance and management in a year, regardless of who performed it and which department budget it came out from
	Total CE full-time equivalent (FTE)	Total number of full-time equivalent employees in the CE department, including temporary employees and overtime pay

On the other hand, data from CE departments are seldom made public or audited. Furthermore, there are often significant discrepancies in how these data are defined and collected. For example, many CE departments only include their own budget in their TCE, ignoring service contracts and repairs paid by other clinical departments such as imaging and clinical laboratory. Prior studies have shown that some TCEs can be as lows as one-tenth of others, giving a false sense of great efficiency [5]. For this reason, significant caution is needed for legitimate benchmarking comparisons.

Once the primary data are characterized, one can define the CE benchmarks. Table 2 shows the benchmarks with explanation of respective purpose.

Table 2. CE benchmarks and respective purpose. To save space, the word "total" previously used in Table 1 has been omitted

Category	Benchmarks	Purpose
Operational	Inventory size/operating beds	For comparison of capital investment in medical equipment
	Annual repairs/inventory size	For comparison of medical equipment reliability
	Annual scheduled maintenance/inventory size	For comparison of resource invested in assurance of medical equipment safety and reliability
Financial	TCE/total hospital expense	For comparison of financial efficiency in medical equipment maintenance and management
	TCE/operating beds	
	TCE/cost of equipment inventory	
Productivity	FTE/inventory size	For comparison of human resource deployment efficiency
	FTE/operating beds	
	FTE/THE	

3 Data Analysis

Even though hospital primary data are typically accurate and reliable, it is recommended to verify them using some simple rules of thumb, e.g., comparing them with data from similar hospitals. If one particular data point deviates more than two or three standard deviations (SDs) from the average of all other data points, it may be necessary to confirm its accuracy with the data source. Similarly, primary CE data also need to be verified before using them. Any significant deviations should be confirmed with the source whenever possible.

One good example of the need to verify data is shown in Fig. 1, where TCE is compared to the total hospital operating expense. As one can see clearly, there are a large number of CE departments that are seemingly spending 10 or more times less than others (notice the scales are logarithmic). These CE departments were classified as "questionable" after discovering that their respective labor expense represents over 80% of their respective annual budgets. In other words, these "questionable" departments are clearly not including in the TCE the expenses paid directly by the clinical departments for maintenance services provided by manufacturers and third parties (i.e., service contracts).

Once the integrity of the primary data has been verified, one can compute the benchmarks shown on Table 2. Being simple ratios, any spreadsheet can be used. While these benchmarks can be compared using the calculated values, it is likely easier to visualize them on graphs such as those shown on Figs. 1, 2 and 3.

In the case of the American acute-care hospitals, logarithmic scales are used because the range covers more than one order of magnitude. In addition, it may be worthwhile to compute the average and SD for each benchmark so the value obtained

for a particular CE department can be expressed as deviation from the average. Again, these calculations are easily accomplished using formulae provided by most spreadsheets.

Fig. 1. Total CE expense (TCE) versus hospital total operating expense (THE) for roughly 300 American acute-care hospitals. Each hospital is represented by a symbol that corresponds to the hospital's teaching characteristics (major, minor, non-teaching, or unknown). The "questionable" category is explained in the text. Notice the logarithmic scale on both axes and the straight line was drawn arbitrarily for visual guidance only.

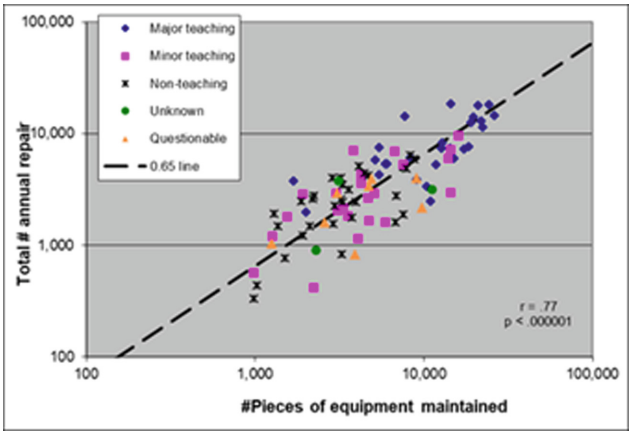

Fig. 2. Total number of repairs of medical equipment performed in a year as a function of the total number of pieces of equipment in the respective hospital's inventory for roughly 300 American acute care hospitals. See legend of Fig. 1 for explanation of the symbols used and other details.

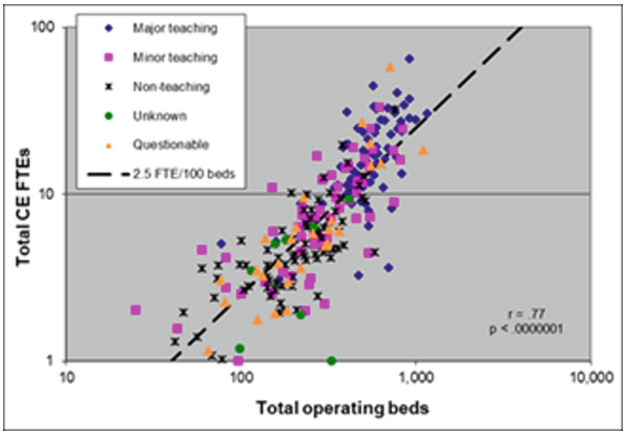

Fig. 3. Total number of full-time equivalent (FTE) employees in the CE department versus the total number of hospital beds actually in deployment in the respective hospital. See legend of Fig. 1 for explanation of the symbols used and other details.

4 Discussion and Conclusions

Once the benchmarks are collected and compared with other CE departments, CE managers can quickly identify opportunities for improvement. Whenever a benchmark deviates more than two to three SDs from the average, the CE manager should doublecheck for data integrity and, if confirmed, look for underlying root causes. Typically, it is not recommended to make immediate and drastic changes without first performing a limited, controlled study to prove that the proposed change is likely to yield the desired result.

While most benchmarking comparisons are performed against other CE departments—known as lateral comparisons—sometimes it is difficult to obtain data from a large enough number of data (i.e., more than 15) for a statistically meaning comparison. In such situations, the CE manager can resort to making longitudinal comparisons, i.e., compare against itself over time. Such comparisons are not as desirable because they will not show large differences and take a long time to acquire (two to three years, at least). However, small, incremental improvements are still preferable to not measuring performance at all.

Great care must be exercised when comparing benchmarks from different countries. A prior study [6] has shown that different wages, costs of living, healthcare financing, and operational models can have profound influences on the benchmarks that depend on such national characteristics (typically the financial benchmarks). On the other hand, benchmarks that are purely technical sometimes are applicable across national boundaries.

From the considerations above, CE managers should be convinced that performance benchmarking is not only simple to conduct but also valuable for them to understand the current state of their departments and where are opportunities for

improvement. Furthermore, they can use the benchmarking results to prove their performance and earn better recognition and support from their respective institution's senior leadership.

Acknowledgments. The author acknowledges the contribution of hundreds of his friends and former colleagues in the progressive establishment of the benchmarks described in this article.

References

1. Wang, B., Rui, T., Balar, S.: An estimate of patient incidents caused by medical equipment maintenance omissions. Biomed. Instrum. Technol. **47**, 84–91 (2013)
2. IBM Watson Health: Truven Health Analytics Action OI-Biomedical Engineering Data. https://actionoi.truvenhealth.com/DataCollection/HELP/DRM/Hospital/3480.htm
3. Wang, B.: Clinical Engineering Financial Management and Benchmarking: Essential Tools to Manage Finances and Remain Competitive for Clinical Engineering/Healthcare Technology Management Professionals. BSI, Cornelius (2018)
4. Wang, B: Why Maintenance Cost/Asset Value Is Not a Good Benchmark. Uptime Aug/Sept 2018, pp. 52–56 (2018)
5. Wang, B., Eliason, R.W., Richards, S.M., Hertzler, L.W., Koenigshof, S.: Clinical engineering benchmarking - an analysis of american acute care hospitals. J. Clin. Eng. **33**, 24–37 (2008)
6. Zheng, K., Wang, B., Feng, Q.: Benchmarking comparison between Zhejiang province and American hospitals. J. Clin. Eng. **41**, 145–152 (2016)

Medical Equipment for Breast Clinics A View of Biomedical Engineering from Practice

Gustavo Adolfo Martinez Chavez(✉)

Mexican Social Security Institute (IMSS), Mexico City, Mexico
gustavo.martinezc@imss.gob.mx

Abstract. The present work describes the experience that involves the valuation of medical equipment for the establishment of the first and third breast cancer clinic in Mexican Social Security Institute (IMSS), CDMX South Delegation, as part to develop national detection, diagnosis and treatment breast cancer programmed with optimal quality, friendliness and respect for patients' rights.

In this case, the main arguments presented refer to the guidelines used to validate the performance of digital mammography, since this team is representative of this project, for which templates of technical information were developed and applied to six mammography equipment's, the concepts to intervene in the analysis of the technical specifications, includes the response of detectors, dosimeters, contrast and image quality among the main aspects.

It is important to mention the efficiently that the medical units offer quality medical attention, it required their equipment works efficient to guarantee their availability and the safety of both patient operators of the equipment.

With the premise of sharing, the experiences obtained in the creation of these clinics, and the roll of the biomedical engineer as part multidisciplinary team, is considered the responsible in optimization medical technology management.

Keywords: Biomedical engineer · Mammography · Breast cancer

1 Introduction

The World Health Organization (WHO) estimates that every year in the world 1.38 million people are diagnosed with breast cancer and half a million are decimated by that cause [1].

The Pan American Health Organization (PAHO) confirms this trend, being the second cause of death due to malignant tumors in the countries of Latin America and the Caribbean [1].

The creation of the Mama Clinic "Condesa" and "Tláhuac" in 2016 and 2018 by the IMSS of South of Mexico City, is based on the implementation of a specialized medical unit model that simplifies the detection and diagnosis of breast cancer in a period of eight days; situation that has developed through the integration and collaboration of multidisciplinary teams that includes the analysis of various aspects; from the social field to the genetic studies, establishing useful parameters for the prevention and early diagnosis of cancer, which implies the use of echocardiography, mammography

© Springer Nature Switzerland AG 2020
C. A. González Díaz et al. (Eds.): CLAIB 2019, IFMBE Proceedings 75, pp. 1380–1385, 2020.
https://doi.org/10.1007/978-3-030-30648-9_178

and cytology testing, in this way, to be able to adjust the through morphometric parameters, in order to facilitate the creation of a database to perform an in-depth analysis.

Currently in the literature, it is possible to find different procedures and methodologies to perform the evaluation and acquisition of medical equipment, including expert computer systems that significantly reduce the possibility of making mistakes, but based on our own practical experience due to the specific needs of the project, this was conceived under the evaluation of a biomedical engineering competences scheme.

Since one of the main objectives in the management activities for medical equipment, is to ensure the operation of them safely, getting maximum performance in its use, therefore reducing risk during the process medical practice, situation that facilitates the monitoring and supervision in the operation, situations that remain implicit within the own activities engineer of the medical units.

For this reason it was considered essential to analyze the different technological options we have to select for this equipment for this project, the medical management technology of the equipment every day plays an important role for the health service providers, we most take in count three main point, the first to have the validations of the process, in second instances to take in count the high cost of those equipment and the last, taking into account the high cost of these equipment and the implication that to first contact between the medical personnel and patients, finally the medical equipment is the mechanism with which clinical results are diagnosed and emitted.

2 Methods

Following all the govern and the evaluation medical equipment evaluate norms and standards for breast cancer detection it was necessary to seek conscensusly unify criteria and apply a methodology that would allow the implementation of a practical assessment system, which involved, the concepts of the planning and the management of technology for breast cancer detection and diagnosis, from part of the manage with efficiency, safety, keeping the costs and use of mammography equipment, its integration in medical systems.

In addition, the implementation of the methodology has its foundation base in the use the descriptive cards establishment of adequated plan in the processes of the acquisition and administration of medical equipment. They specify the minimum requirements that each of the equipment should work and a of the description which is fundamental at the moment of planning the project, considering in order to guide the work team with simple tasks such as project planning, clear and concise definition of objectives and the implementation of the monitoring and risk mitigation plans, processes of evaluation, configuration, parameterization, testing, and training.

A brief description of the most relevant activities is presented below:

1. **Planning based on accurate input data**; provide results, clear priorities, complete analyzes and thoughtful decisions, considering the following aspects:

a. References about the life time equipment.
b. Maintenance.
c. Function and device criticality.
d. Security and Standardization.
e. Standards medical attention.
f. Medical device Standards.
g. Technological Status.
h. Compatibility of Interfaces and Networks.

2. **Actions concerning the Equipment life cycle**; focused on effective location, patient safety, education, training, proper maintenance, with standards and legal requirements.
3. **Have the flexibility that adding different elements related to equipment**; to attend user needs, technological trends, and medical recruitment among others.
4. **Finally**; easily to understand and put into practise.

The valuation of each one the criteria before mentioned applied to digital mammography for being the this equipment most representative of the project, was including in the verification cards, which contemplates the functional aspects referents as the x-rays generation, collimation, automatic exposure control (AEC), compression system, grid and image receiver, dose and image transmission considering similarly the worker personal experiences and recommendations emitted by authorities normative in Mexico health with respect the radiological security.

The information was captured and analyzed considerations the statistical criteria in the operation parameters of mammography equipment, with the objective to find coincidences, as the importance and transcendence the technical characteristics in the medical equipment.

Situation that allowed obtaining quantitative and qualitative data on the variables considered important for the operation the mammography equipment, and that these were in accordance with the guidelines established in the project, which are included in the clinical practice guidelines regarding the response of the detectors, dosimetry and image quality among the main aspects.

3 Results

The verification of the technical characteristics in six digital mammography equipment was carried out, considering various aspects related to the visualization of images, documentation for loading of patients, training and experience the work personnel, quality assurance programs and compliance with the standards of International radiological safety, considering the information contained in the manual, catalogs, brochures and operation instructions, it was possible to compare the engineering specifications and the characteristics that can be obtained from such equipment.

Emphasizing the aspects related to radiological safety, the positioning of mammary gland in the mastograph, the compression exercised in the gland, the uniformity in the

thickness the breast, quality image (contrast and sharpness), the artifacts absence, the collimation of the radiation beam and image transmission system in general.

The results obtained in the evaluation of the equipment indicated that the systems comply in their entirety, obtaining as a factor to take into account that the average glandular dose of the six equipment that was placed in 1 mGy. while the norm places it between 0.71–1.15 mGy, which allowed us to measure the progress obtained as an indicator of the technology, referring to the fulfillment the Mexican Official Norm NOM-229-SSA1-2002, in which the Technical requirements for the facilities, sanitary responsibilities, engineering specifications for the equipment and radiological safety in establishments of medical diagnosis with X-rays.

It was observed that digital mammographers, the electrical generator X-ray, and the X-ray tube use the filter-anode combination mainly of molybdenum for small breasts (composed of adipose tissue) approximately less than 5 cm. thick receive a smaller dose.

Very large breasts (or those with very dense tissues) are difficult to penetrate, leading to the use of higher energy X-rays and large exposures to obtain acceptable images. This is the reason why most manufacturers also offer a Rhodium filter for dense breasts, because they require higher penetration of energy.

The size focus was between 0.01 and 0.03 mm for magnifications of micro calcifications, values that are used and established in mammography techniques to reduce penumbra (produced by placing the breast farther away from receptor image).

The metals used as a refractory element were Tungsten, Molybdenum and heavy Tungsten alloy to offer high precision collimators with flat sheets and provided with a range of thicknesses between 20 and 200 μm for X-ray detectors they are recommended.

They absorb the scattered radiation, thus helping to achieve images with a high quality, since this controls the size and shape of the radiation beam, limiting the exposure to compressed breast tissue. Allowing the X-ray field to extend posteriorly beyond the thoracic wall to include the posterior glandular mammary tissue

The considered equipment makes use of the X-ray tube and the image receiver located at opposite ends, which allows performing mammograms in any projection. The distance between the source and the image receiver is usually 55 cm. All the mammography equipment offers a distance between 65 and 70 cm.

All the mammography equipments included an automatic exposure control (AEC) whose main function is to measure the intensity and quality of X-rays in the image receptor, which is achieved through the use arrays of CCD sensor which were made of amorphous silicon or selenium, directly absorbing the RX photons and converting them to electric charge, each photodiode also represents a pixel, it means the total of charge is read by a low noise electronic counter obtaining the digital data that is sent to microprocessor with a linear response over a wide range of radiation intensity; allowing to corrections of data thus ensuring a constant response of detector in all the exploration field.

Situation that causes the conditions so that the radiologist can manipulate the orientation, amplification, brightness and contrast in desired image, which facilitates the lesions detection the mammary tissue by engineering computer programs CAD

(Computer Aided Detection) and the images transmission in network what facilitates to functions the acquisition, storage and display the images.

Table 1 showing manufacturers companies and characteristics the detectors considered in this study, systems widely recognized as rigorously digital technologies, which are integrated into the X-ray equipment and the detector as indicated below.

Table 1. Digital mammography equipments as rigorously digital technologies, all present notable advantages, among which are: efficient absorption of incident radiation, linear response for a wide range of exposures, low intrinsic noise, adequate spatial resolution, format that are appropriate to obtain images of different sizes of breasts found in clinical practise, and adequate sensitivity that avoids excessive irradiation patient, with acceptable exposure times.

Flat panel detectors							
No.	Company	Model	Pixel (υm)	Detector (cm)	Matrix	Bits	Technology
1	GE	Senographe DS	100	19 × 31	1,914 × 2,294	14	Csl-SI
2	Lorad/Hologic	Selenia	70	24 × 29	3,228 × 4,096	14	α-Se
3	Siemens	Mammomat	70	24 × 29	3,328 × 4,084	14	α-Se
4	Planmed	Nuance	85	24 × 30	2,816 × 3,584	13	α-Se
5	IMS	Giotto	85	24 × 30	2,816 × 3,584	13	α-Se
6	Fujifilm	Amulet	50	24 × 30	4,728 × 5,928	13	α-Se

Finally, mammography exam, called a mammogram constitute some of the most demanding radiological examinations, because they simultaneously require high spatial resolution, high contrast and a wide dynamic range the mammography equipment that are used in mammographic screening programs for the early detection of cancer.

4 Discussion

From the experience obtained, we can say that the results of the work carried out have had a positive reaction on the part carried out at the Mexican Social Security Institute (IMSS) and its beneficiaries, which is why the following situations are considered.

a. The equipment produces an immediate digital image, without intermediate revealed processes, makes disappear the “chassis” that allowing to construct purely digital, clean surroundings, with smaller dead times and capacity to increase the performance the rooms the equipment.
b. The doses are reduced to patients or they do not increase, given them at least the efficiency of the detectors used in the equipment.
c. Very high quality images are produced, much more steady and with very large possibilities of adaptation to each specific need of patient. In particular, its contrast resolution is much higher than that of conventional systems.
d. It is possible to optimize the entire chain in obtaining images including the exposure factors (KVp, anode-filter combination, etc.) that are selected based on the characteristics of the breast (attenuation and thickness). One consequence of this has been the significant savings in doses in patients with thick breasts by automatically selecting higher spectra energy.

5 Conclusions

a. It has been possible to reduce the response times, together with the social contribution that represents the conception of preventive medicine in the detection and timely diagnosis breast cancer.
b. Currently these clinics are experiencing a considerable improvement increasing the performance of available resources, as well as the reduction of time in the delivery of results, becoming into advantage.
c. Finally, the present work has for the intentions to emphasize to institutions or health centres get stronger strategies, facilitating them improving the medical attention service, in which the role of the biomedical engineer is to use the engineering knowledge ingeniously in everything related to patient cares, which includes a wide range of activities and responsibilities related to the medical technology.

References

1. Instituto Nacional de Estadística y Geografía: Estadística a Propósito del Día Mundial de la Lucha Contra el Cáncer de Mama, del 16 de Octubre de 2015. http://www.inegi.org.mx/saladeprensa/aproposito/2015/mama0.pdf
2. Duffy, S.W., Tabar, L., Chen, T.H.H., Smith, R.A., Holmberg, L., Jonsson, H., et al.: Reduction in breast cancer mortality from organized service screening with mammography: 1. Further confirmation with extended data. Cancer Epidemiol. Biomark. Prev. **15**, 45–51 (2006)
3. Mandelblatt, J.S., Cronin, K.A., Bailey, S., Berry, D.A., de Koning, H.J., Draisma, G., et al.: Effects of mammography screening under different screening schedules: model estimates of potential benefits and harms. Ann. Intern. Med. **151**, 738–747 (2009)
4. International Commission on Radiation Units and Measurements: Mammography – assessment of image quality. J. ICRU **9**(2) (2009). ICRU Report 82, Oxford University Press
5. Lewin, J.M., D'Orsi, C.J., Hendrick, R.E., Moss, L.J., Isaacs, P.K., Karellas, A., et al.: Clinical comparison of full-field digital mammography and screen-film mammography for detection of breast cancer. Am. J. Roentgenol. **179**, 671–677 (2002)
6. Berns, E.A., Hendrick, R.E., Cutter, G.R.: Performance comparison of full-field digital mammography to screen-film mammography in clinical practice. Med. Phys. **29**, 830–834 (2002)
7. Lewin, J.M., Hendrick, R.E., D'Orsi, C.J., Isaacs, P.K., Moss, L.J., et al.: Comparison of full-field digital mammography with screen-film mammography for cancer detection: results of 4,945 paired examinations. Radiology **218**, 873–880 (2001)
8. Pisano, E.D., Gatsonis, C., Hendrick, E., Yaffe, M., Baum, J.K., Acharyya, S., et al.: Diagnostic performance of digital versus film mammography for breast-cancer screening. N. Engl. J. Med. **353**, 1773–1783 (2005)
9. Fischer, U., Hermann, K.P., Baum, F.: Digital mammography: current state and future aspects. Eur. Radiol. **16**, 38–44 (2006)
10. Berns, E.A., Hendrick, R.E., Cutter, G.R.: Optimization of technique factors for a silicon diode array full-field digital mammography system and comparison to screen-film mammography with matched average glandular dose. Med. Phys. **30**, 334–340 (2003)

Web Software for Technology and Medical Infrastructure Management of a Clinical Engineering Department

Carlos Augusto Centeno(✉), Javier Alfredo Voos, Guillermo Riva, and Carlos Zerbini

Grupo de Investigación y Transferencia en Electrónica Avanzada, Universidad Tecnológica Nacional Regional Córdoba, Maestro Lopez esq Cruz Roja, Córdoba, Argentina
ccenteno@gmail.com

Abstract. In the present work, we describe the design and implementation of a Web information system for the management of technology and medical infrastructure for a medical center, with proper capacities to be used at the governmental level. The work begins with analysis of the workflow that a Clinical Engineering Department follows during corrective or preventive operations on the infrastructure and medical technology in order to keep the electromedical equipment and the infrastructure in optimal state of operation. For the design, development and implementation of the IT solution, the freely available tools LayoutIt, Bootstrap framework and XAMP Web server were used. The system uses the PHP language combined with HTML to provide a user-friendly interface that allows following step by step the flow defined for the management of the interventions, in addition to sending emails and generating work material in PDF format. At the same time, it records the necessary data to be used later by the statistics module. This Web system is published and in use by the professionals of the Clinical Engineering Department of the Hospital de Córdoba in the province of Córdoba, Argentina.

Keywords: Clinical Engineering · Preventive Maintenance · Corrective maintenance · Statistics

1 Introduction

With current technological advances and enhancements in type and complexity of health centres, it is required to have tools which allow the Technology Management Department and its members to guarantee proper operation and improved reliability of systems, facilities and equipment of the institution they belong to, advise or supervise.

Along competences of Clinical Engineer specialists, both corrective or preventive interventions on electro-medical systems and administrative management of them are specially relevant. As result of these tasks, it is also desirable to obtain statistical indicators in order to keep track of costs and times of interventions on equipment and facilities.

© Springer Nature Switzerland AG 2020
C. A. González Díaz et al. (Eds.): CLAIB 2019, IFMBE Proceedings 75, pp. 1386–1397, 2020.
https://doi.org/10.1007/978-3-030-30648-9_179

2 Main Goals

2.1 To Develop a Web-Based Computer Tool Which Allows

- Managing all corrective and/or preventive actions taken on medical technologies and/or infrastructure at the medical centre.
- Managing administrative data about Providers.
- Managing administrative data about Equipment.
- Obtaining statistical data about results of management.

2.2 To Develop a Web-Based Computer System Based On

- Inter-action with final users, by surveying their demands and their experiences for the development of the project.
- Previous experience in our group in the field of medical informatics.
- Experience of the users, in order to gradually meet their expectations on the system.

3 Development

In order to develop our management Software, we begin by studying a Clinical Engineering Department (CED), its members, their roles, and its interactions with the Health Centre it belongs to.

3.1 Work Methodology of the Evaluated CED

For management, the history of interventions allows determining when a technology and/or equipment change is in order.

Another relevant aspect for the application of the computer system is the need for knowledge and evaluation of service vs. idle periods, in order to evaluate the quality of the corrective intervention service. This can be an internal service or a service from third parties.

From the analysis of the workflow, the need stems of defining criticality categories which allow establishing priorities for task assignment to CED staff (see Fig. 1).

Fig. 1. Analysis of criticalities for priority assignment.

3.2 Survey of Commercial Options

The first step for the design of the computer system is to evaluate available commercial, in order to recognize advantages and drawbacks of each of them. For this, we take into account following parameters:

- Use mode, Client-Server or Web
- Required software license
- Monetary costs
- Technical requirements
- Technological requirements
- Updating and/or upgrading requirements
- Technical assistance

The evaluated commercial tools [1–3] do not cover the totality of available options, which are, among others:

- MicroMain Maintenance Healthcare [4].
- MPulse 8 CMMS [5].
- Biomedical Preventive Maintenance & Tracking [6].
- Medical Equipment Field Service Management System [7].

In Table 1 we show the most relevant features of the evaluated options.

Table 1. Summary of evaluated computer tools

Tool	Cost	Architecture	Use mode
RENOVEFREE MOBILE Version	EUR 2965	Client/Server Web/Cloud	Multi user
eMaint FlukE	Versión Professional USD 3060	Web/Cloud	Multi user
CWorks PLUS	1700 USD	Client/Server	Multi user
CWorks Basic	0 USD	Client/Server	Multi user
PRISMA 3	5600 USD	Web/Cloud	Multi user

Considering as additional criteria the knowledge of work procedures from potential users at hospital environments of the Ministry of Health of Cordoba Province, both at management, decision making, and health specialists, we take design decisions for the present work. Some of the most relevant features are avoiding the modification of operative flows, and no need for specific licenses. These features decide on the adopted development.

On the previous analysis, we highlight as advantages the following points:

- Previous software tools do not support execution of tasks associated to work flows surveyed at CED.
- In previous tools, it is not possible to introduce changes to work methodology in daily operation flows along different management stages.

- We adopt current workflow respecting regular procedures, considering experience of CED staff at the moment of the survey and definitions of required entities.
- As particular drawback for post-implementation, support and maintenance stages, we observe that providers of evaluated Computerized Maintenance & Management Systems (CMMS) do not have customer support in the city of application, i.e., Córdoba (Argentina).
- At governmental level, priority is mostly granted to local providers for agreements and/or purchase of products and services. This makes our alternative a convenient choice, since it already includes most of them and their details.

3.3 Evaluation of Technologies for Software Development

At the moment, various choices exist for developing Web-based computer tools for management of databases storing data of maintenance work.

On previous experience at research and professional works, we decided on the use of MySQL as database engine, which also involves selection of a compatible programming language. Since we come from C language, we selected PHP due to its smooth learning curve. Besides its compatibility with the selected database engine, It must be noted that PHP allows seamless generation of PDF report files, and eases interconnection with POP3 and SNMP servers for automatic e-mail generation.

Considering the mentioned choices, we adopted XAMPP (see Fig. 2), a freely available, GPL-licensed APACHE distribution which includes MariaDB, PHP and Perl. One main advantage of this distribution is its ease of installation in Windows, Linux, and OS X [8], which enables managing MySQL on the Web [9]. Through a Web user interface, databases, tables columns indexes, users and grants can be managed through SQL commands [10–12].

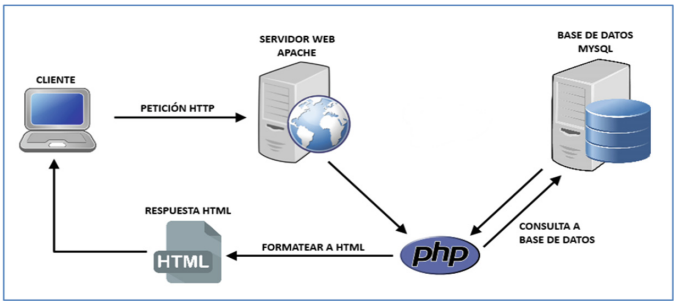

Fig. 2. Model of a Web server with MySQL and PHP

By using phpMyAdmin, it is possible to review diverse databases, Tables in them, associated fields and their configurations. Moreover, when working with a specific table, we can explore its structure, add/change it fields and the stored data.

3.4 Website Design

With the complete data model defined, the next step consists in studying available options for HTML code generation, where the Bootstrap package stands out [13]. Bootstrap was created by Twitter, and between it advantages it allows applying styles to existing components in Web pages in a simple way. This particular feature grants outstanding quality to thee resulting product, without the complexity that implies writing each component individually.

Layout

During design process, it is desired that user interface and data presentation is as clear as possible. To achieve this goal, a Layout design is in order.

The layout process consists in defining how the different pages of the system will look and behave like. For this, several software tools exist, both local ones and Web-based. Among them, we can mention LayoutIt!, a Web-based tool based on Bootstrap which offers Drag and Drop procedures (see Fig. 3).

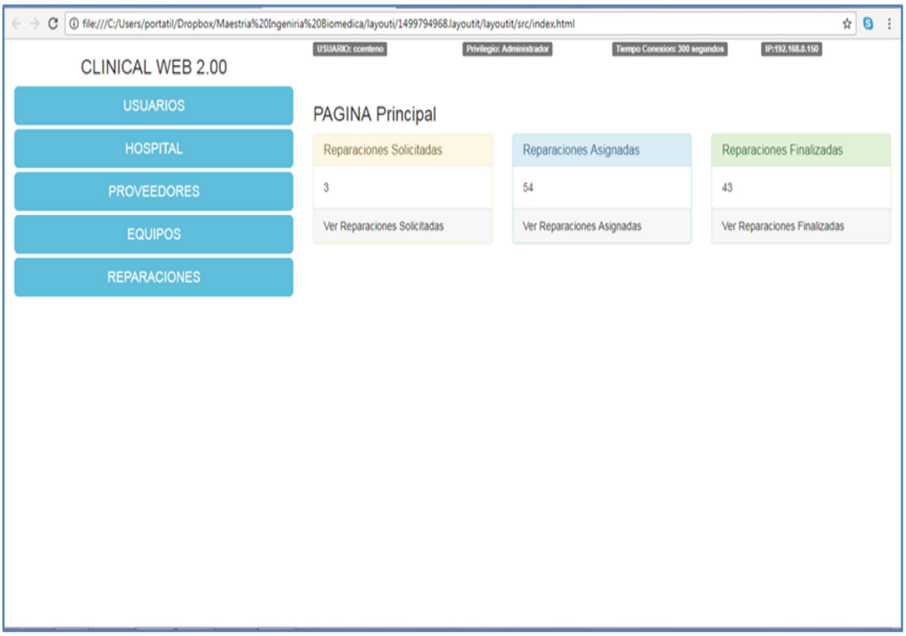

Fig. 3. Preliminar design of the main Web page

3.5 Analysis of Required Entities

On the basis of previous work [14–16], and subsequent analysis of the work procedures, we determine the data structure as “main tables” with associated “secondary tables”.

From typical hospital structure and its medical technology, we conclude that the key element is the equipment associated to each service in the hospital (see Fig. 4).

Fig. 4. Medical technology at the health service

Considering the user perspective, we created profiles according to its privileges to change the system and its stored data. Higher user level, i.e., administrator, has higher operative privileges in the software, e.g., privileges to close an intervention (see Fig. 5).

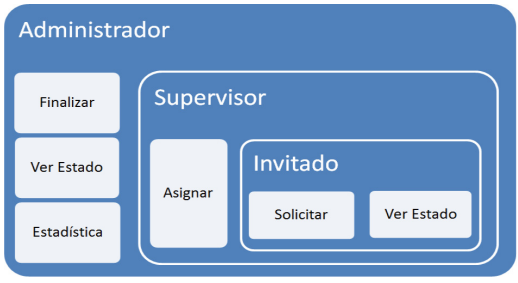

Fig. 5. User levels and their associated privileges in the system

3.6 Analysis, Design and Module Implementation

In this section we show relevant aspects of the system modules, without going into specific details. For the management, several tables were defined that will be related to each other with numeral fields that will serve as search indexes.

Equipment Module

Among parameters that will be associated to a new equipment is the unique code that allows to identify it in the hospital [17]. For this, the management software using the table of equipment types, will propose an alphanumeric code with values that increase automatically. It is also possible to associate a functional state, which will be encoded in a state table. On the other hand, considering the universalization of codes, it is possible to assign a UMDS code [18] based on the ECRI recommendations (see Fig. 6).

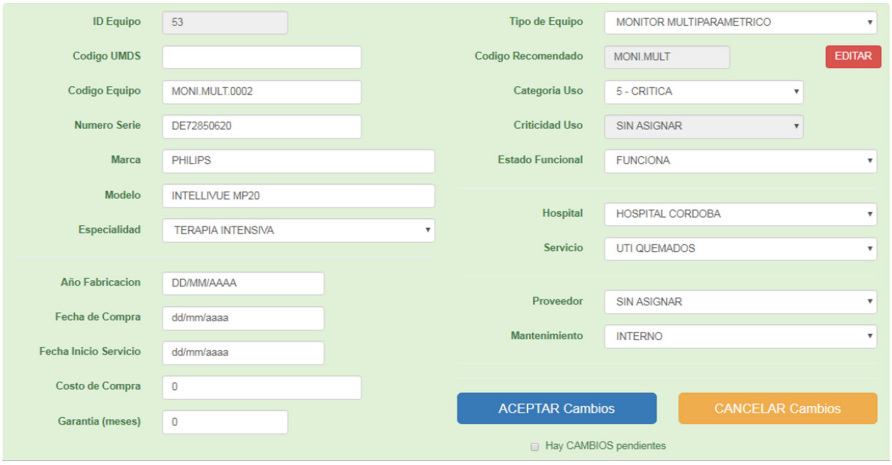

Fig. 6. Electromedical equipment tab

Corrective Interventions Module

The flow to be followed by the CED is presented to provide assistance in each stage of a Corrective Intervention (see Fig. 7).

Fig. 7. Flow of a corrective intervention

The steps followed for each stage are:

Order for Corrective Intervention

- Operation carried out by staff of the medical centre, who do not necessarily belong to the CED.
- A detailed description of the detected failure must be included.
- Details must be included about the specific location of the affected equipment and/or infrastructure.

- Specifications of the equipment to be intervened must be included, along serial number, identification code, etc.

Assignment of Corrective Intervention

- Operation carried out by CED staff.
- The required intervention is assigned to staff, either internal or external to the CED.
- Mail is sent to the provider, requiring intervention.
- A ticket is generated in PDF format, containing data about the assigned intervention.

Conclusion of Corrective Intervention

- Operation carried out by DEC staff.
- Costs are associated to the intervention for statistics purposes.
- A description of the completed tasks must be included.

At each case, it is registered who and when the operations related to the required intervention were performed.

State Semaphore

In the main page of the site, four tabs are shown containing numbers of interventions, color-coded according to the state of those interventions in the flow of a corrective or preventive intervention (see Fig. 8).

Fig. 8. Semaphore for interventions

These indicators are updated automatically after a pre-established period of time. With the use of these tables or semaphores, it can have a "picture" of the state of operations of the SIC, where the maximum objective would be that the values indicated in the red, yellow and green box are equal, indicating that all requested interventions, were assigned and then completed.

Preventive Interventions Module

It is desirable to carry out maintenance programs to keep the infrastructure and the electromedical equipment in the same conditions with which they started their operation. It should be noted that a good maintenance policy will largely determine the level

of productivity of the system. In many cases, a poor operation of the equipment, or the incorrect forecast of substitution reserves, will give rise to interruptions to the health service. Under normal conditions of use, a device will have a correct state of operation, while any defect attributable to use has an increase in the level of wear, which will determine the maintenance actions that must be carried out when reaching a certain level of deterioration (see Fig. 9).

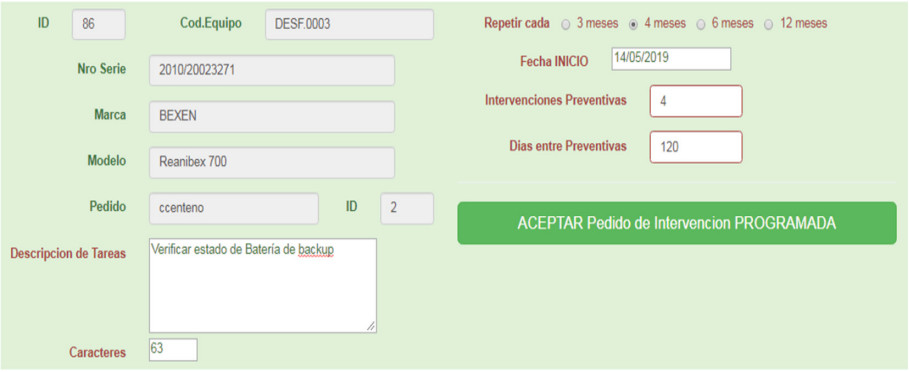

Fig. 9. Preventive intervention module

Statistics Module

One of the goals of the SIC is to keep the facility of medical technology and infrastructure in an optimum state of operation.

In order to know how, when and with which human and economic resources all the requested corrective and preventive interventions were carried out, the Web Information System has a statistics module, with which it is possible to know, during a set period of time, different indicators to assess the management of the SIC.

General Statistic Indicators

Each indicator must meet certain specific conditions in order to be valuable, such as:

- That is well defined. The data collection by different operators, must deliver the same information as a result.
- That is objective. It must be clear, concise and free of the states of mind and opinions of the people who generate it.
- That is measurable. It must be perfectly measurable. It must indicate correctly the changes in the behavior of a certain events.
- That is defined for a limited time. It must be possible to determine the period of analysis.

Indicators Defined in the Web System

The statistical indicators that were used for the development of the module were agreed with the SIC staff, based on their specific information needs and are presented below (see Fig. 10).

Fig. 10. Resulting statistics applied to Philips equipments

- Number of Attended Equipments: All equipments attended in the defined period that meet the conditions established by the applied filters.
- Number of Requested Repairements: The number of repairs requested in a given period of time.
- Number of Assigned Repairs: Is the number of repairements assigned in a given period of time.
- Number of Completed Repairs: The number of repairements completed in a given period of time.
- Time of Change of State: It is the period of time from the moment in which an intervention was requested until it is finalized.
- Response Time: It is the period of time that passes from an intervention request arrives, and this is assigned to an internal or external service provider.
- Total Cost: It is the sum of expenses associated with the repairs evaluated in a given period of time.

4 Discussion

One of the outstanding points in the developed tool is related to the automatization of the process of generation of identification codes, based on stored parameters in different tables of the system.

Another relevant aspect is that the intervention management module has the possibility of automatically sending e-mails with requirements for execution of correctives or preventives.

In the service table we include the belonging hospital as standard field. In addition, the need stem of adding data about the stage and room of each of them.

In order to ease inclusion of new units, it is needed that, when registering a new electro-medical equipment, the system automatically suggests the category or risk of use corresponding to the selected type of equipment. This value must be computed by

the system on the basis of the user-selected equipment type, clinical application and maintenance requirements.

Based on the categorization recommended by ECRI, it is needed to build a table containing the standard UMDNS codes. In this way, the system is able to recommend the value associated with the equipment to be added.

We consider to make updates to the users module, so it requires password update after a certain period of time. In this way, we will add an additional security level to prevent use of a common configuration, user and password by non-authorized persons.

On the basis of the workflow, and to improve user experience, it is needed to add capabilities to generate a new intervention from the Equipment Module when one equipment is selected.

After testing the different operations for Work Orders and their corresponding states, assignment and finalization, the need arose to provide the system with capabilities to generate Work Orders in PDF format from the general intervention file.

5 Conclusions

We worked on the design of a computer tool that facilitates the management of corrective interventions that are requested from the services of a health center, and the preventive ones that arise from the analysis of work orders, in addition to particular data of suppliers and equipment.

For the definition and subsequent implementation of the computer tool, it was taken as a premise that it was user-oriented, using as part of the development the experiences and concerns of the staff that will use it, all collected during the survey stage.

Thinking about the result of the use of the developed computer tool, the staff of the Clinical Engineering Service of the Cordoba Hospital, is working day by day with it, and this is reflected in the increasing number of interventions, and in the instances of error detection, for everyday use, and the imprint to raise possible solutions and/or adjustment alternatives.

References

1. eMaint Maintenance Software|Enterprise Asset Management. https://www.emaint.com/cmms-features-benefits/. Accessed 14 May 2019
2. CWorks. http://www.cworks.com.my. Accessed 14 May 2019
3. PRISMA 3. http://www.sisteplant.com/soluciones/innovative-technologies/smart-maintenance-prisma-gmao/. Accessed 14 May 2019
4. Micromain Maintenance Healthcare. https://www.micromain.com/healthcare-maintenance-software/. Accessed 20 Jun 2019
5. MPulse 8 CMMS. https://www.mpulsesoftware.com. Accessed 20 Jun 2019
6. ACCRuent Healthcare. https://www.accruent.com/industries/healthcare. Accessed 20 Jun 2019
7. Medical Equipment Field Service Management System. https://www.miracleservice.com/industries-served/medical-equipment-software/
8. XAMPP. https://www.apachefriends.org/es/index.html. Accessed 14 May 2019

9. Delisle, M.: Mastering PhpMyAdmin 3.4 for Effective MySQL Management. Packt Publishing, Birmingham (2012)
10. PHP. https://secure.php.net/. Accessed 14 May 2019
11. Ramos Monso, M.: Programación PHP. MP Ediciones, Buenos Aires (2004)
12. Srinivas Sriparasa, S.: Building a Web Application with PHP and MariaDB: A Reference Guide. Packt Publishing, Birmingham (2014)
13. Bootstrap. https://getbootstrap.com/. Accessed 14 May 2019

Characterization of Medical Equipment Acquisition Processes by Considering the Evaluation of Technology, Pilot Case: POCT Blood Gas Analyzers

Laura Valentina Bocanegra Villegas[1(✉)], Juan Camilo Osorio Salgado[1], Sandra Patricia Usaquén Perilla[1], and José Isidro García Melo[2]

[1] Industrial Engineering School, Universidad del Valle, Cali, Colombia
laura.bocanegra@correounivalle.edu.co
[2] Mechanical Engineering School, Universidad del Valle, Cali, Colombia

Abstract. Healthcare managers are interested in identifying decision-making tools that consider multiple criteria to support the acquisition of new medical equipment. Multiple Criteria Decision Analysis (MCDA) is increasingly used for the Health Technology Assessment (HTA). This paper presents a model for the prioritization of alternatives for POCT blood gas analyzers in a healthcare institution in the city of Cali, Colombia using the Analytic Hierarchy Process (AHP). This work relates the different opinions of the main actors of the equipment acquisition process with scientific and technical elements. The result of the study is a model for the evaluation of medical equipment tailored to the needs of the hospital. This implementation is a progression towards the integration of scientific evidence and decision-making in healthcare institutions.

Keywords: POCT- Point of Care Testing · Blood gas analyzer · HTA-Health Technology Assessment · MCDA-Multi-criteria Decision Analysis · AHP-Analytic Hierarchy Process

1 Introduction

Constant technological advances, globalization and the demands on hospitals and health services, have compelled these healthcare institutions to incorporate tools for the acquisition of medical equipment [1]. The acquisition process requires the use of tools that contribute to decision-making in an agile and effective way [2, 3]. Health Technology Assessment (HTA) is a multidisciplinary and comprehensive research tool that summarizes information regarding technical, social, economic, ethical, and legal issues related to the use of technology [4]. According to Buglioli and Pérez (2002), HTA has been established as a fundamental specialty in healthcare, since it is a process focused on improving the quality and efficiency of service provision through the acquisition of effective technology [5].

One of the decisions that must be made in hospitals is related to the acquisition of Point of Care Testing (POCT) equipment. POCT devices are especially useful in

© Springer Nature Switzerland AG 2020
C. A. González Díaz et al. (Eds.): CLAIB 2019, IFMBE Proceedings 75, pp. 1398–1402, 2020.
https://doi.org/10.1007/978-3-030-30648-9_180

clinical laboratory tests, because they eliminate some of the most problematic phases within the analytical process, whilst decreasing response time [6]. In Colombia, the study conducted by the EIA (Escuela de Ingeniería de Antioquia), and CES University found that despite the importance of the HTA process, most technology acquisition decisions are made by administrators, without the participation of medical or technical personnel [7]. Studies in low- and middle-income countries identified the analysis of costs and healthcare needs as the dominant criteria in the acquisition process, however maintenance services and user training should also be considered [8].

In this study, we applied Multi-criteria Decision Analysis (MCDA) and Analytical Hierarchy Processes (AHP) considering HTA criteria in order to prioritize the procurement options for POCT blood gas analyzer equipment in a high complexity hospital in Cali, Colombia.

2 Materials and Methods

The present research was developed under the direction of the Central Clinical Laboratory Service of a high-complexity healthcare institution. We used the keywords: "health technology assessment AND medical devices OR medical equipment AND hospitals" in the Scopus, Web of Science and IEEE databases to search for scientific papers and technical guides published between 2012 and 2018. With this review we identified MCDA techniques, and the models and criteria used in HTA. We then characterized the process that was being carried out within the healthcare institution, to compare it to the scientific literature. In addition, we studied different multicriteria techniques to decide which one was best suited to the institution. Finally, we interviewed five experts involved in the process of POCT blood gas analyzer acquisition in order to determine the viability of the approach criteria and evaluate the appropriate adjustments for the institution.

3 Results

We developed an evaluation model from the review of 14 scientific articles. The MCDA tool with the highest prevalence in the articles was AHP, and was implemented according to the procedure presented by Thomas Saaty [9], in a three-step approach: find the weight of each criterion (priority vector), compute the matrix of alternatives with their respective scores and compute the ranking of the alternatives.

Our literature review identified two evaluation models: The UnetHTA core model (European Network for Health Technology Assessments) and the mini-HTA model presented by the AdHopHTA project (Adopting Hospital Based Health Technology Assessment in the EU). The criteria for the evaluation of medical equipment were analyzed and compared by a group of experts, see Figs. 1 and 2.

The alternatives evaluated included two different (manufacturer/model) pieces of equipment currently used in the healthcare institution and one new equipment that was in the testing phase. The services for which the POCT blood gas analyzers would be used were: the neonatal, pediatric and adult intensive care unit, emergency room and

surgery service. The result of evaluating the three alternatives suggests a clear inclination for alternative two, 61,7%, which approximates the expected characteristics, see Fig. 3.

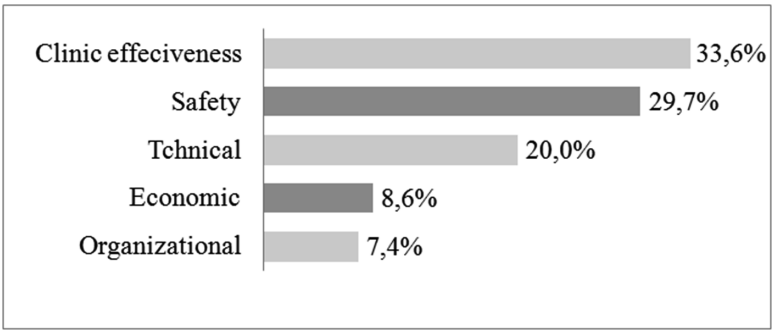

Fig. 1. POCT blood gas analyzer: criteria weights

CRITERIA	DESCRIPTION
Safety	Analysis of the possible impact on the health and physical wellbeing of the user (who uses the technology on the patient).
Economic	Commercial market price of the equipment. Amount of personnel and resources needed to implement the technology in the health institution.
Organizational	Training programs provided by the supplier to the users, who are the ones who manage the equipment in the health institution. Physical spatial requirements for the final location of the equipment in the institution.
Clinical effectiveness	Analysis of sensitivity, specificity, repeatability and accuracy of measurements compared to a reference standard.
Technical	Response time, availability of qualified personnel to attend on-site technical faults. General technical characteristics of the equipment: analytical panel, automatic fault resolution, productivity of the technology, connectivity and system interfaces – hardware and software. Total time used by the equipment to perform a complete test.

Fig. 2. Description of the decision criteria.

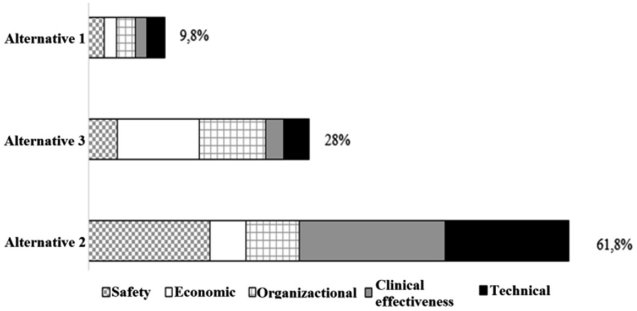

Fig. 3. Performance evaluation of the technology alternatives.

4 Discussion and Conclusions

The research implemented a multicriteria tool for the prioritization of alternatives for POCT blood gas analyzer acquisition. This is a tool that could also be applicable to the procurement of other medical equipment. Regarding the criteria, aspects related to safety and clinical effectiveness were observed in contrast with other aspects.

Considering technical issues, this work showed that the evaluation of the after-sales service i.e., the consideration of supplier or manufacturer's performance, was relevant for the healthcare institution. This is consistent with World Health Organization (WHO) guidelines which recommend including four fundamental components: Availability, Accessibility, Appropriateness, and Affordability ("The 4 As"), rather than just focusing on the technological issues involved in medical equipment procurement [10].

References

1. Ministerio de la Protección Social: Guía para la evaluación de tecnologías de salud en instituciones de servicios de salud (IPS). (M. de la P. Social, Ed.). Ministerio de la Protección Social (2011). https://www.minsalud.gov.co/sites/rid/1/Guia_evalu-caion_de_tecnoclogias_en_salud.pdf
2. Cubillos, L.: Evaluación de tecnologías en salud: Aplicaciones y recomendaciones en el sistema de seguridad social en salud colombiano. Ministerio de La Protección Social (MPS) y El Programa de Apoyo a La Reforma de Salud (PARS), p. 156 (2018)
3. Urbano, L.C., Muñoz, L.S., Osorio, J.C.: Selección multi-criterio de aliado es-tratégico para la operación de carga terrestre. Estudios Gerenciales **32**(138), 35–43 (2016). https://doi.org/10.1016/j.estger.2015.09.002
4. Pinzón, C., Pierre, F., Calderón, J.N.F.: Incorporación del marco de precios y cobertura basada en valor por medio de las evaluaciones de tecnología en salud en el sistema de salud colombiano, Instituto de Evaluación de Tecnología en Salud, pp. 1–38 (2018)
5. Buglioli, M., Pérez, A.: Evaluación de tecnologías de salud. Revista Médica del Uruguay **18**(2), 27–35 (2002)

6. Oliver, P., Díaz, R., Lirón, J., Monzó, V., Xavier, N., Noval, J., Otero, M.: Revista del Laboratorio Clínico. Sociedad Espanola de Bioquímica Clínica y Patología Molecular **3**(4), 161–170 (2010). https://doi.org/10.1016/j.labcli.2010.06.005
7. Chavarría, T., Molina, T.: Herramienta de evaluación de tecnologías para la ad-quisición de equipos biomédicos. Revista Ingeniería Biomédica **21**(11), 13–19 (2017)
8. Diaconu, K., Chen, Y., Cummins, C., Moyao, G.J., Manaseki-holland, S., Lilford, R.: Methods for medical device and equipment procurement and prioritization within low- and middle-income countries: findings of a systematic literature review. Globalization Health **13**, 1–16 (2017). https://doi.org/10.1186/s12992-017-0280-2
9. Saaty, T.L.: Decision-making and priority theory with the analytic hierarchy process. Int. J. Serv. Sci. **1**(1), 83–98 (2008)
10. World Health Organization (WHO): Medical devices: managing the mismatch: an outcome of the priority medical devices project, p. 129 (2012)

Evaluation of a Protocol to Measure the Total Heart Beat Index in Research and Clinical Environments

Ramiro Muñoz[1(✉)], Catalfamo Formento Paola[1,2], Cesar Ignacio Dutto[3], Camila Ileana Dure[1], and Bonell Claudia[1]

[1] LIMH-Facultad de Ingeniería, Universidad Nacional de Entre Ríos, Oro Verde, Argentina
ramirom81@hotmail.com, {pcatalfamo, cbonell}@ingenieria.uner.edu.ar
[2] Instituto de investigaciones en Bioingeniería y Bioinformática, CONICET-UNER, Oro Verde, Argentina
[3] Consultorio Dutto, Santa Fe, Argentina

Abstract. Energy expenditure has been proposed for the evaluation of rehabilitation treatments. Traditionally it has been estimated by oxygen uptake and the use of spirometry. However, this method is not often appropriate for the clinical environment given that the equipment is cumbersome and may affect the results of the measurements by causing discomfort to the person. Indices based on heart rate have been proposed as alternatives. One of those indices is the Total Heart Beat Index (THBI). The purpose of this investigation was to evaluate a protocol to measure THBI in a research environment and in a clinical environment. For this, measurements were performed in ten young adults in a training area (research environment) and three older adults in a clinical environment. Heart rate was measured continuously while participants walked in a 8 shape walkway. The results showed results similar to those reported in the literature, with intraclass correlation coefficients (ICC) larger than 0.8. The protocol was feasible to be used in both environments and it was a simple to use, relatively low cost and portable tool for estimating energy expenditure.

Keywords: Heart rate · Rehabilitation · Analysis of human movement

1 Introduction

Energy expenditure may be thought as a measure of the energy needed to performed a given action or movement [1]. Its measurement has been proposed as a tool for the evaluation of the pathologies that affect gait [2, 3]. In particular, it has been used in the evaluation of subjects using prosthesis and orthoses who show an increase in the energy expenditure for walking [4]. Traditionally, energy expenditure has been estimated from oxygen consumption. However, the equipment needed for its measurement, which includes a mask over mouth and nose, results cumbersome and may affect the results of the measurements by causing discomfort to the user [1]. This is particularly limiting when measurements are taken in patients, such as children or people

© Springer Nature Switzerland AG 2020
C. A. González Díaz et al. (Eds.): CLAIB 2019, IFMBE Proceedings 75, pp. 1403–1409, 2020.
https://doi.org/10.1007/978-3-030-30648-9_181

with disabilities. Indices based on measurement of heart rate during stationary conditions have been proposed as estimation alternatives. A linear increment of heart rate with oxygen uptake has been shown for sub-maximal levels of exercise [5]. The Physiological Cost Index (PCI) [6, 7] is one of the index calculated by dividing the difference between the steady-state walking and resting heart rates by the walking velocity. Although it is frequently used for the characterization of gait [8], the reports regarding its repeatability have been uncertain over the years and it has been suggested that repeatability could be improved if the working heart rate achieves a steady state [9], which occurs approximately after the third or fourth minute of exercise in unimpaired subjects [4]. In clinical settings, patients may find it difficult to walk more than four minutes. Also walking may not represent a sub-maximal exercise; hence the repeatability of the PCI may be compromise.

As an alternative to PCI, another index called the Total Heart Beat Index (THBI) was proposed [5]. The authors considered that a more accurate representation of the total energy consumed during an activity would result from considering the heart rate behaviour throughout a period of exercise by finding the total number of heartbeats that occurred during the period. The authors considered that calculating an index based on the number of heartbeats would provide a measure of a person's total energy consumption and that this measure would be independent of whether the activity was steady or non-steady state. THBI and the PCI have been used simultaneously for the estimation of energy expenditure in pathological gait and provided similar results [10, 11]. Also the repeatability of THBI has been higher than PCI [12]. However, the measure of THBI in the clinical environment has not been reported. The aim of this study was to evaluate the feasibility of using a THBI protocol in the research and in the clinical environment.

2 Material and Methods

A total of thirteen subjects participated of the study. Ten young adults (mean age (SD) 26.1 (4.6) years old, 6 females) and three older adults (60, 61 and 70 years old respectively, 2 females) participated in the study. The young adults were recruited from the student population of the School of Engineering. They were at different stages of the university degree. When asked about their physical activity, most of them concurred to a gym or performed some sort of physical activity but this was not regular (7 subjects), 2 subjects indicated that they performed some physical activity on a regular basis and one did not performed any physical activity. The older adults were being treated in a chiropractic clinic for neck or back pain or discomfort. When asked about their physical activity, they all performed regular activity on a daily bases. None of the participants presented cardiovascular, neuromuscular or breathing conditions neither other conditions that could affect their gait. Also none of them had had any viral infection in the last two weeks. All participants were carefully explained the protocol, and were given time to ask questions. After that, they were invited to sign the informed consent.

Participants were tested twice, at the same time of day, within a 7-day period. They were asked not to eat, drink, or smoke within the 2 h preceding the test. The young

adults were tested in the training room of the University gym. An area of 20 × 10 m was available for the tests. The older adults were tested in a space provided in the Chiropractic Clinic, where an area of 10 × 6 m was available.

A 20 m 8 figure track was displayed on the floor for the participants to walk on it. It was chosen as recommended by the authors of the THBI method [5] in order to avoid the acceleration and deceleration produced in a line path for which a 180° turn should be performed. The 8 figure track consisted on two circles of 4 m diameter each, so that the total space required for the path was 8 m long and 4 m wide.

Participants started the test resting during a period of 5 min. Then, they walked at self selected speed on the 8 figure track during 15 min. Finally they rested again for 5 min. For the older adults, they completed the test before their chiropractic session. During all this time, heart rate was being monitored using a monitor (Polar RS 400, Polar Electro Oy, Kempele, Finland) which sample heart rate in a 5 s window. The monitor collects data during 5 s and then reports a value of the heart frequency for a complete minute. After finishing the procedure, all data was downloaded to a notebook. With the data obtained for the monitor, the following parameters were calculated: total heart beats during resting, total number of extra heart beats during exercise and total number of extra heart beats during recovery. These parameters were calculated by the number of beats that occurred in each 5-s sample period and then summing these values for the whole of the resting or exercise period. The distance walked was calculated as the total number of figures completed and the length of the figure and recorded.

In order to ensure that the exercise did not exceed the sub-maximal levels, a criterion of a maximal heart rate of 220 minus the age of the participant was used. So, for example for a 20 years old participant, a maximum frequency of 200 beats per minute was accepted. If heart rate reached values over 200 beats per minute, then the data collected would be discharged. Finally, the THBI Index was calculated as shown in Eq. (1).

$$THBI = \frac{Total\ number\ of\ beats\ during\ exercise}{Total\ distance\ travel} \tag{1}$$

2.1 Data Analysis

Data obtained from young adults were initially evaluated using histograms to define qualitatively the distribution of the data. Given the normal distribution of the data, the mean and standard deviation were calculated for all the participants in that group. Intraclass coefficient were calculated for the data between days [13]. A value of 1 would indicate that the measurement is completely repetitive between days, while a value of 0 would indicate that there was no repeatability at all.

Data from older adults were considered on a case by case basis given the low number of samples. Any differences found in the set up or opinion of the participants between the research and clinical environment were recorded by the examiner.

3 Results

Figure 1 shows a representative profile of the heart rate as sampled by the monitor during the procedure for a young adult. All profiles were similar to this one and to the one presented by Hood [5]. The heart rate never exceeded the maximum set, so that the conditions of the test were always sub maximal.

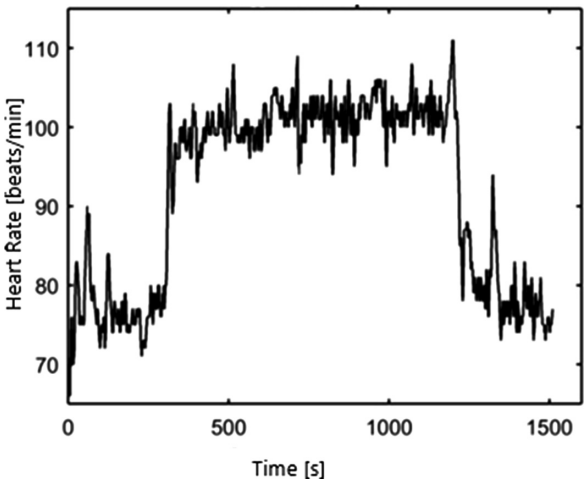

Fig. 1. Typical heart rate profile as sampled by the heart rate monitor during the procedure (resting, walking and recovering) for a young adult.

Table 1 shows the mean, standard deviation and ICC for the data collected from young adults. Table 2 shows the results of THBI measured in older adults in the clinical environments for day 1 and day 2.

Table 1. Mean and standard deviation (expressed in beats per m) for THBI in young adults measure on two occasions, and between-day ICC.

	Mean	Standard deviation	ICC
Day 1	2.50	0.37	0.84
Day 2	2.55	0.35	

Table 2. Mean and standard deviation (expressed in beats per m) for THBI in young adults measure on two occasions.

	Participant 1	Participant 2	Participant 3	Mean
Day 1	2.78	2.00	2.81	2.53
Day 2	2.11	2.15	2.44	2.23

Some considerations regarding the direct application in the Chiropractic Clinic is that the space used had to be specially organized for the experiment. Hence, the procedure was performed before the normal afternoon sessions started. Also, some of the furniture and equipment had to be moved away to make enough space. Some participants measured in the clinical environment commented that it was difficult to follow the 8 figure track.

4 Discussion and Conclusion

In this study, the THBI index was calculated in research and clinical environment. Future research seeks to include the index in the evaluation of pathological gait within clinical environments. Hence the evaluation of a protocol to be used in those, when compared to the use in a research environment was performed. The study in young adults (Table 1) showed values of TBHI similar to those found in the literature [5, 11, 14] and an ICC value larger than 0.8 showing an excellent repeatability [14, 15].

Regarding the results in the clinical environment, they showed similar values of THBI (Table 2) although the mean for the second day was slightly lower than the mean young adults (Table 1). A possible explanation of these result, is that the older adults were more physically active than the younger. One of the older adults, for example, run 10 km on a regular basis, and the other two performed some sort of daily physical activity. The younger adults, students at University, had an irregular pattern of activity.

Having said so, it is important to take into account that the relationship between the heart rate and oxygen uptake depends on the individual aerobic fitness, so the value of THBI for a particular individual does not relate precisely to energy consumption, except that the relationship for that particular individual is known [5]. This is the reason why it is not appropriate to establish normal values of THBI in healthy subjects. Comparisons of the changes in a given group, though, are more accurate in terms of the evaluation of energy consumption [11].

In terms of the implementation of the protocol, no differences were found between the research and the clinical environment, except of space. As it is normally the case in clinical practice, it is infrequent to find a relatively large space, indoors, unoccupied. In order to repeat the procedure a minimum space of 8 by 4 m should be available for the 8 figure path. In the Chiropractic clinic this was obtained by moving articles from their usual space. It may have happened that some objects were slightly closed to the path and this could explain why the participants made an observation of the difficulty of walking along it.

The equipment used for data collection was a portable, light and relatively low cost, heart rate monitor, available in the marker. For this particular application, the data had to be downloaded to a computer and processed in some software. Having an application that could automatically calculate the index would be an advantage for its use in routine clinical practice. Finally, the protocol could be potentially used in any patient that is able to walk (with or without aids) following an 8 figure path during 15 min. This is not necessarily the case in pathological gait. Future studies should investigate the minimum walking time that is required to obtain reliable results.

The results of this work show that the protocol presented for calculating THBI is feasible to be used in clinical environments, representing a portable, easy to use, fast to don and doff and relatively low cost solution for the estimation of energy consumption, and provides repetitive information. However this study included a relative low number of participants so the sample should be enlarger and the participants should be able to walk in an 8-shape figure. The protocol of this study will be applied in the larger number of healthy and impaired subject, for the evaluation energy consumption during gait.

Conflict of Interest. The authors declare no conflict of interest.

References

1. Baker, R.: Measuring walking. A Handbook of Clinical Gait Analysis. Mac Keith Press, London (2013). Gosport
2. Dag, F., et al.: Alterations in energy consumption and plantar pressure distribution during walking in young adults with patellofemoral pain syndrome. Acta Orthop. Traumatol. Turc. **53**(1), 50–55 (2018)
3. Ries, A.J., Schwartz, M.H.: Low gait efficiency is the primary reason for the increased metabolic demand during gait in children with cerebral palsy. Hum. Mov. Sci. **57**, 426–433 (2018)
4. Nene, A.: Physiological cost index of walking in able-bodied adolescents and adults. Clin. Rehabil. **7**(4), 319–326 (1993)
5. Hood, V.L., Granat, M.H., Maxwell, D.J., Hasler, J.P.: A new method of using heart rate to represent energy expenditure: the total heart beat index. Arch. Phys. Med. Rehabil. **83**(9), 1266–1273 (2002)
6. Whittle, Michael W.: Gait Analysis. An Introduction, 4th edn. Butterworth Heinemann, Elsevier, Oxford, Amsterdam (2007)
7. Mac Gregor, J.: The objective measurement of physical performance with long term ambulatory physiological surveillance equipment. In: Proceedings of the Third International Symposium of Ambulatory Monitoring, pp. 22–39 (1979)
8. Vllasolli, T.O., et al.: Physiological cost index and comfort walking speed in two level lower limb amputees having no vascular disease. Acta Inform. Medica **23**(1), 12–17 (2015)
9. Delussu, A.S., Morone, G., Iosa, M., Bragoni, M., Paolucci, S., Traballesi, M.: Concurrent validity of physiological cost index in walking over ground and during robotic training in subacute stroke patients. Biomed. Res. Int. **2014**, 1–6 (2014)
10. Kim, M.O., Burns, A.S., Ditunno, J.F., Marino, R.J.: The assessment of walking capacity using the walking index for spinal cord injury: self-selected versus maximal levels. Arch. Phys. Med. Rehabil. **88**(6), 762–767 (2007)
11. Coutinho, A.C.B., Neto, F.R., Beraldo, P.S.S.: Validity of heart rate indexes to assess wheeling efficiency in patients with spinal cord injuries. Spinal Cord **52**(9), 677–682 (2014)
12. Muñoz, R., Catalfamo Formento, C., Bonell, P.: Evaluation of a new metabolic cost indicator for gait analysis. Rev. Argentina Bioingeniería (2019, in print)
13. Bartko, J.J.: The intraclass correlation coefficient as a measure of reliability. Psychol. Rep. **19**, 3–11 (1966)

14. Kimoto, M., et al.: Reproducibility of the physiological cost index and the total heart beat index for children with spastic diplegic cerebral palsy. Rigakuryoho Kagaku **24**(5), 653–658 (2009)
15. Prieto, L., Lamarca, R., Casado, A.: La evaluación de la fiabilidad en las observaciones clínicas: el coeficiente de correlación intraclase. Med. Clin. **110**, 142–145 (1998)

Correlation Between Sterilized Prongs and Nasal Injury in Newborns Subjected to Non-invasive Ventilation

Débora F. Camillo Ribeiro(✉), Beatriz L. Fernandes, and Percy Nohama

PPGTS - Pontifical Catholic University of Paraná, Curitiba, Brazil
debora-camillo@hotmail.com

Abstract. Nasal injury from the use of prongs in non-invasive mechanical ventilation (NIV) is a very common adverse event at Neonatal Intensive Care Units (NICUs). The goal of this research was to evaluate the feasibility of reuse of sterilized binaural prongs in newborns (NBs) submitted to NIV. In order to reach this goal, we have compared eight NBs were submitted to NIV using sterilized prongs (SP Group – SPG) and 11 others with brand-new prongs (NP Group – NPG). The frequency and severity of external nasal injury were evaluated daily through clinical inspection. The frequency of external nasal injury was 87.5% for SPG, and 90.9% for NPG (p = 1.00). Of the 7 external nasal injuries found in the SPG, 4 (57.14%) were Stage I, and 3 (42.86%) were Stage II. Of the 10 external nasal injuries found in the NPG, 9 (90%) were Stage I, and only 1 (10%) reached Stage II. Although the results of this study did not show a significant statistic difference, the use of sterilized prongs did increase the severity of the external nasal injury, making its use contraindicated in newborns undergoing NIV.

Keywords: Non-invasive ventilation · Nasal injury · Short binasal prong

1 Introduction

Non-invasive ventilation refers to applying positive pressure without the need for endotracheal intubation [1, 2]. Positive pressure is delivered through interfaces such as short binasal prong, nasal mask, nasopharyngeal prong airway, and helmet [3, 4].

The most commonly used interface in neonatology is the short binasal prong, as it can be easily affixed to the face of the NB, moving together with his head [5]. Moreover, it offers less resistance to airflow and is more effective in preventing reintubation [6, 7].

Although it is the most popular method and offers certain advantages, binasal prongs can cause nasal injury [8], which is the most common complication associated with the use of NIV [9], with a frequency ranging from 15% to 60% [10], with possible rates of up to 100% [8].

Such injuries can range from simple hyperemia (Stage I), progressing to a superficial sore with a scabless red bed (Stage II), to necrosis with full tissue loss (Stage III) [11].

© Springer Nature Switzerland AG 2020
C. A. González Díaz et al. (Eds.): CLAIB 2019, IFMBE Proceedings 75, pp. 1410–1416, 2020.
https://doi.org/10.1007/978-3-030-30648-9_182

NBs with a nasal injury can progress to pain, sepsis, and need for intubation. Furthermore, plastic surgery may be required depending on the severity of the lesion [12].

The reuse of nasal prongs has been observed in Brazilian NICUs even though they were manufactured for single use [13]. Sterilization may result in color changes and hardening of the prong, making it more rigid [8], possibly leading to nasal injury in NBs.

Inadequate use of health technologies causes risks for patients. In this context, the health technology assessment (HTA) is too much relevant because encourage to decision-making of the clinical assistance team, contributing effectively to improve patient assistance [14].

HTA is an investigative process that evaluates the clinical, economic, ethical and social consequences use of health technologies [15] in order to better inform health policymakers and improve the decision-making process in the area [16]. It can be carried out at any point during the product's life cycle, e may have different purposes [16].

The investigation of correlation between sterilized prongs and nasal injury in NBs submitted to NIV brings clinical findings related to the feasibility of using or not sterilized prongs in NBs submitted to NIV as a function of possible skin injuries that may predispose NBs to infection risks, sequelae and increase length of hospital stay [17].

Given this scenario, the goal of this research was to evaluate the feasibility of reuse of sterilized binaural prongs in newborns (NBs) submitted to NIV.

2 Methodology

The study consists of a clinical trial, undertaken at the NICU of Waldemar Monastier Children's Hospital, located in southern Brazil.

Study participants were NBs subjected to NIV with binasal prongs for a minimum period of 24 h. NBs who had been subjected to NIV before the study, as well as those diagnosed with choanal atresia, were excluded.

NBs were divided into two groups according to prong source: New Prong (NPG) or Sterilized Prong (SPG). NPG used brand-new prongs and NIV-appropriate bonnets, both from the Fanem brand, and did not make use of nasal protection for the duration under NIV. SPG utilized sterilized prongs from three different brands: Inca®, Fanem®, and Silmag®, which were selected according to the availability of materials at the time of NIV placement. NBs in that group wore nasal protection in the form of Epi-derm® silicone gel sheeting by Biodermis.

All NBs were subjected to an evaluation protocol consisting of neonatal data collection through visual inspection and daily photographic records of the nostrils.

The neonatal data considered were: gestational age, birth weight, gender, and duration of NIV.

Clinical inspection revealed the presence of external injury, which was rated according to the classification proposed by Fischer *et al*. [11] into Stage I, II or III.

Photographic records were taken using a Canon PowerShot SX50 HS camera, upon parental consent given in image release forms.

The evaluations above were carried out prior to NIV placement and every 24 h until the medical suspension of that support; nasal injury stage was recorded daily.

The study was approved by the Research Ethics Board of the Federal University of Technology – Paraná, under CAAE number 42718915.4.0000.5547.

Data were tabulated and submitted to statistical analysis. The measures of central tendency and dispersion were expressed as mean and standard deviation (mean ± SD) for symmetrically distributed continuous variables; and as medians, minimum and maximum values (median, minimum-maximum) for asymmetrically distributed variables. Categorical variables were expressed in terms of absolute and relative frequency.

Student's t-test was applied to estimate the difference between symmetrically distributed continuous variables, while the Mann-Whitney test was used for asymmetric variables, and Fisher's exact test was utilized for categorical variables.

A minimum significance level of 5% was considered for all tests.

3 Results

Nineteen NBs were part of the study, of which 11 received NPG and 8 received SPG. Neonatal data and the results for incidence and severity of nasal injury are given in Table 1.

Table 1. Characteristics of newborns according to the study group.

Characteristics	SPG (n = 8)	NPG (n = 11)	p
Gestational age (weeks)	30.7 ± 4.0	32.4 ± 5.1	0.47[a]
Birth weight (g)	1305.0 (750–2550)	1775.0 (560–3495)	0.30[b]
Males	3 (37.5%)	7 (63.6%)	0.36[c]
Time under NIV (hours)	79.6 (35.4–280.0)	57.0 (29.4–163.3)	0.26[b]
External injury during NIV	7 (87.5%)	10 (90.9%)	1.00[c]

Note: [a]Student's t-test [b]Mann-Whitney test [c]Fisher's exact test
Gestational Age – mean and standard deviation; Birth weight and Time under NIV – median, minimum and maximum; Gender, External Injury, and Stage I and II – absolute and relative frequency

Table 2 shows the stage of nasal injury in NBs who developed injuries in both study groups: SPG and NPG. There was no statistically significant difference between the severity of nasal injury of SPG and NPG groups. However, the SPG group presented a higher incidence of Stage II external nasal injury.

Table 2. Character Stage of nasal injury between the study groups.

Variable	SPG (n = 7)	NPG (n = 10)	p
Stage I injury	4 (57.14%)	9 (90%)	0.25[a]
Stage II injury	3 (42.86%)	1 (10%)	

Note: [a]Fisher's exact test
Injury Stage– absolute and relative frequency

Of the 7 injuries observed in the SPG, 6 (85.71%) began in the first 24 h of use of NIV, while 1 (14.29%) began in 48 h. Regarding the injuries that began in up to 24 h, 4 (57.14%) were Stage I, and 2 (28.57%) were Stage II. One of the Stage I injuries progressed to Stage II in up to 72 h of NIV use. In the NPG, all injuries began in the first 24 h, and all were Stage I. It was observed that one of the injuries progressed to Stage II in 48 h under NIV.

Due to the severity of the injury, NIV was alternated with oxygen therapy through the Hood in 1 NB (14,28%) of SPG.

Figure 1 shows the Stage I injury in SPG and NPG. Figure 2 shows Stage II nasal injury in the aforementioned study groups. In both figures, arrows point to the presence of nasal injury in NBs.

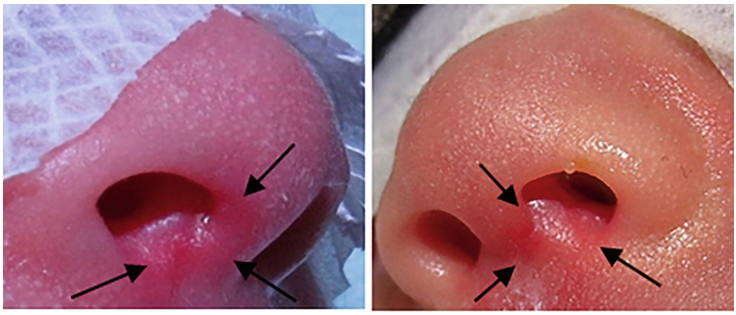

Fig. 1. Stage I external nasal injury (a) SPG (b) NPG

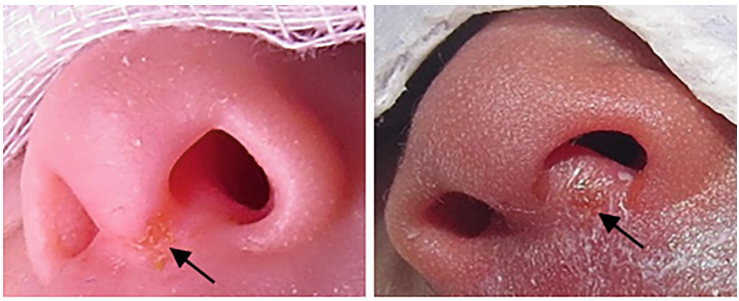

Fig. 2. Stage II external nasal injury (a) SPG (b) NPG

4 Discussion

At the NICU studied herein and at many other NICUs in Brazil, economic necessity causes nasal prongs to be reused in NBs after being sterilized, even though they were manufactured for single use.

Prong sterilization occurs due to poor economic conditions among a large share of Brazilian institutions, which often necessitates the reuse of materials as cost-cutting measures [18].

The sterilization process can lead to a change in color and hardening of the nasal prong, making it more rigid, which in turn increases the probability of nasal injury, according to Nascimento et al. [8].

It should be noted that attempts to cut costs by using reprocessed materials are misguided, since nasal injuries, aside from causing adverse sequelae in NBs [11, 19], extend hospitalization time [17] due to the need for antibiotic use as a result of infections caused by nasal injury or reintubation.

The observed frequency of nasal injury was high in the groups that used brand-new and sterilized prongs, reaching levels of 90.9% and 87.5%, respectively. The results of this study indicate that the origin of the prong in use was not determinant for the occurrence of nasal injury ($p = 1.000$). Nevertheless, concerning the injury severity, it should be noted that 42.85% of injuries in SPG were Stage II, versus 10% for NPG.

SPG utilized silicone gel nasal protection, as the chances of injury when receiving NIV with nasal prong are greater. Nevertheless, the frequency and severity of injuries were high even when using nasal protection.

Another factor that might have influenced the severity of injuries in SPG was the longer duration under NIV when compared to NPG. However, the 28.57% rate of Stage II injuries for SPG occurred in the first 24 h of use.

These results are similar to those found by Bonfim *et al*. [13], who evaluated the frequency of nasal injury among 70 NBs who required NIV for more than 24 h using brand-new ($n = 31$) and reused ($n = 39$) prongs, and found an injury rate of 71.8% and 56.4%, respectively. They observed no significant difference between brand-new and sterilized prongs in the occurrence of nasal injury. About the severity, however, in the group that used sterilized prongs, 54.6% of injuries were Stage I, 31.8% were Stage II, and 13.6% were Stage III. In the group that used brand-new prongs, 50% of injuries were Stage I, 40.9% were Stage II, and 9.1% were Stage III.

The non-occurrence of Stage III injuries in our study may be linked to the short time under NIV compared to the study by Bonfim *et al.* [13], in which Stage III injuries occurred more often after seven or more days under NIV.

The lower incidence of Stage II injuries associated with the use of brand-new and the non-occurrence of Stage III injuries imply the reduction of complications associated with these stages of injuries, namely: infection, need for intubation and pain. These clinical aspects are very relevant for encourage to decision-making of the clinical assistance team about use only brand-new prongs in NBs submitted to NIV.

One limitation of this study was the small sample size. It is important to continue and expand the study in order to comparatively evaluate the effects of using brand-new and sterilized prongs on the frequency and severity of the injury. With that, it will be

possible to confirm the results presented herein and raise awareness among institutions regarding the need to use only brand-new prongs in NBs who do not have NIV while admitted to the NICU, or among companies to manufacture prongs that can be sterilized without causing structural changes.

5 Conclusions

This study made it possible to comparatively evaluate the use of sterilized prongs with the use of brand-new ones, concerning the incidence and severity of nasal injury in NBs requiring NIV while admitted to the NICU under study.

Although there was no statistically significant difference in the incidence of the injury between new and used prongs, the severity was taller and appeared early in use prong group. It was possible to conclude that the use of sterilized prongs increase and speed up the severity of injury, being less effective in the application of NIV, contraindicating its use in the clinical practice.

The increased severity of the nasal injury resulting from the use of sterilized prongs is associated with severe sequelae in the NBs, which can increase length of hospital stay and consequently increase the costs of the treatment of these NBs. Therefore, the use of brand-new prongs become feasible as clinical as financially.

The authors hope that the preliminary results of this research may contribute to decision-making the clinical team and hospital services about the need of using only brand-new prongs in NIV application.

Acknowledgment. The authors thank the management at Waldemar Monastier Children's Hospital for authorizing this study to be conducted at their NICU facilities, to Fanem Ltda and Caobianco Representações Comerciais for kindly donating the brand-new prongs for the research, and to the National Council for Scientific and Technological Development (CNPq), Brazil, for research scholarship and financial resource.

Conflict of Interest. The authors declare that they have no conflict of interest.

References

1. Kaur, A., Modi, M., Soni, A., Thakur, A., Saluja, S.: Noninvasive ventilation in neonates. J. Curr. Med. Res. Pract. **4**(1), 13–19 (2014)
2. Boel, L., Broad, K., Chakraborty, M.: Non-invasive respiratory support in newborn infants. Paediatr. Child Health **28**(1), 6–12 (2018)
3. Chowdhury, O., Wedderburn, C.J., Duffy, D., Greenough, A.: CPAP review. Eur. J. Pediatr. **171**(10), 1441–1448 (2012)
4. Sankar, M.J., Sankar, J., Agarwal, R., Paul, V.K., Deorari, A.K.: Protocol for administering continuous positive airway pressure in neonates. Indian J. Pediatr. **75**(5), 471–478 (2008)
5. Johnston, C.: Ventilação não invasiva. Manole, Rio de Janeiro (2018)
6. Gupta, S., Donn, S.M.: Continuous positive airway pressure: physiology and comparison of devices. Semin. Fetal Neonatal Med. **21**(3), 204–211 (2016)

7. Chandrasekaran, A., Thukral, A., Jeeva Sankar, M., Agarwal, R., Paul, V.K., Deorari, A.K.: Nasal masks or binasal prongs for delivering continuous positive airway pressure in preterm neonates-a randomised trial. Eur. J. Pediatr. **176**(3), 379–386 (2017)
8. Nascimento, R.M., Ferreira, A.L., Coutinho, A.C., Santos Verissimo, R.C.: The frequency of nasal injury in newborns due to the use of continuous positive airway pressure with prongs. Rev. Lat. Am. Enfermagem **17**(4), 489–494 (2009)
9. Maruccia, M., Ruggieri, M., Onesti, M.G.: Facial skin breakdown in patients with non-invasive ventilation devices: report of two cases and indications for treatment and prevention. Int. Wound J. **12**(4), 451–455 (2015)
10. Chen, C.Y., Chou, A.K., Chen, Y.L., Chou, H.C., Tsao, P.N., Hsieh, W.S.: Quality improvement of nasal continuous positive airway pressure therapy in neonatal intensive care unit. Pediatr. Neonatol. **58**(3), 229–235 (2017)
11. Fischer, C., Bertelle, V., Hohlfeld, J., Forcada-Guex, M., Stadelmann-Diaw, C., Tolsa, J.F.: Nasal trauma due to continuous positive airway pressure in neonates. Arch. Dis. Child. Fetal Neonatal Ed. **95**(6), 447–451 (2010)
12. Milligan, P.S., Goldstein, M.R.: Implementation of an evidence-based non-invasive respiratory support (NIRS) bundle in the NICU to decrease nasal injury complications. J. Neonatal Nurs. **23**(2), 89–98 (2017)
13. Bonfim, S.F., Vasconcelos, M.G., Sousa, N.F., Silva, D.V., Leal, L.P.: Nasal septum injury in preterm infants using nasal prongs. Rev. Lat. Am. Enfermagem **22**(5), 826–833 (2014)
14. Brasil: Política Nacional de Gestão de Tecnologias em Saúde. Ministério da Saúde, Brasília (2010)
15. Lessa, F., Ferraz, M.B.: Health technology assessment: the process in Brazil. Rev. Panam. Salud Publica **41**, 1–7 (2017)
16. Lessa, F., Caccavo, F., Curtis, S., Ouimet-Rathé, S., Lemgruber, A.: Strengthening and implementing health technology assessment and the decision-making process in the region of the Americas. Revista Panamericana de Salud Pública **41**, 1–10 (2017)
17. Fontenele, F.C., Cardoso, M.V.: Skin lesions in newborns in the hospital setting: type, size and affected area. Rev. Esc. Enferm USP **45**(1), 130–137 (2011)
18. Rego, M.A., Martinez, F.E.: Clinical and laboratorial repercussions of the nasal CPAP in preterm newborns. J. Pediatr. **76**(5), 339–348 (2000)
19. Yong, S.C., Chen, S.J., Boo, N.Y.: Incidence of nasal trauma associated with nasal prong versus nasal mask during continuous positive airway pressure treatment in very low birthweight infants: a randomised control study. Arch. Dis. Child. Fetal Neonatal Ed. **90**(6), 480–483 (2005)

Economic Impact of Remote Monitoring System of the Obesity in Children: Costs of Monitoring and Conventional Practices

Walter Saraiva Lopes[1,2(✉)], Diego Pereira da Silva[1], William Tsutomu Watanabe[1], Henrique da Costa Rodrigues[1], Silvia Helena Bastos de Paula[3], Robson Rodrigues da Silva[1], and Daniel Gustavo Goroso[1(✉)]

[1] University of Mogi das Cruzes, Mogi das Cruzes, São Paulo, Brazil
w.saraiva@yahoo.com.br, danielg@umc.br
[2] Federal University of Maranhão, Imperatriz, Maranhão, Brazil
[3] Health Institute of the Secretary of State of São Paulo, São Paulo, São Paulo, Brazil

Abstract. Conventional health practices have been more costly to the health. Remote monitoring in the prevention and control of chronic noncommunicable diseases is a way to reduce costs. Thus, the main motivation of this study was to analyze the economic results of the use of the Remote Monitoring System in obese children. The objective was to evaluate the economic impact of remote monitoring of obesity, and it is based on direct costs compared to the conventional health care system. The methodology was based on the accounting data, in which the direct costs of the care and procedures of health professionals were calculated. The results obtained from the costs of caring for 150 children were the following: costs with remote monitoring of US $ 7,689.00 and conventional health practices of US $ 11,169.00. It is concluded that remote monitoring presented cost reduction and generated savings. In the long run it can present social and economic results for health, and to the government.

Keywords: Obesity · Remote Monitoring System · Economic impact

1 Introduction

The prevalence of overweight and obesity is a reality in almost every part of the world, being considered an epidemic that is worrying public health. According to data from the World Health Organization (WHO), obesity has reached all age groups of the population and may have health consequences and risks [1].

Obesity is a disease that should reach 1.2 billion people by the year 2025 [2]. The global prevalence among children up to 5 years of age has a tendency to reach 60 million by 2020 [3]. Children and adolescents between the ages of 5 and 18 can reach a population of 360 million obese by 2025 [4].

© Springer Nature Switzerland AG 2020
C. A. González Díaz et al. (Eds.): CLAIB 2019, IFMBE Proceedings 75, pp. 1417–1427, 2020.
https://doi.org/10.1007/978-3-030-30648-9_183

The number of overweight Brazilians has grown a lot, according to the Ministry of Health of Brazil in 2017 reached approximately 54% of the adult population [5], with 36.6% of overweight children [6] and could reach 11.3 million children by 2025 [7].

Obesity is responsible for developing various chronic noncommunicable diseases (CNCDs) (diabetes mellitus, cardiovascular, pulmonary, hypertension, among others) [8–10]. The main consequence of obesity has been the increase in health spending.

The combination of obesity and CNCDs has raised the economic cost of health [11, 12], because these costs are related to the prevalence and overall incidence of overweight and its associated comorbidities have presented economic burden to the health systems [13, 14].

The impact of obesity and associated diseases has resulted in an average increase of 8.05% in Brazilian hospital costs [15]. These costs represent 2.4% of the national Gross Domestic Product (GDP) and are estimated at 2.8% (US $ 2.0 trillion) of world GDP [16]. The impact of obesity is responsible for enormous personal, social and economic costs.

The remote monitoring system is a modality of support to the health service for its efficiency in patient care and better economic results [17]. In this study, FLEEM System® was used, an online technological system developed to monitor the practice of physical activity, food consumption and heart rate records for obesity prevention and control and CNCDs.

With the application of remote monitoring in the follow-up of obese children, the direct costs of the health professionals involved were calculated and compared to the costs of conventional health practices. Thus, an assumption has arisen, if the adoption of the use of online remote health monitoring technology influences the economic impact with better results for the health system compared to conventional health practice.

In this sense, the objective of this article was to evaluate the economic impact of remote monitoring of children with obesity, based on the direct costs of health professionals with the incorporation of online technology in comparison with conventional health practice.

2 Methodology

The financial resources for health are restricted and with the high rate of obesity and the diseases associated with several risk factors the increase in health costs in Brazil is notorious [18]. The high costs related to obesity have an impact on the Brazilian public health, implying economic consequences in the health system, mainly in the public one.

The study was carried out in the municipality of Monteiro Lobato in the state of São Paulo, Brazil, where data from the accounting of a remote monitoring project and information on conventional health practice in the prevention and control of obesity in children were used.

The direct costs of remote monitoring were based on a system designed to monitor physical activity, energy expenditure, food consumption and heart rate, denominated as

FLEEM System® (Free Living Energy Expenditure Monitoring System®) [19, 20]. Figure 1 presents the features implemented in the FLEEM System®, a structure that captures, stores and processes data from the biomedical applications of children (patients) who participated in this study.

To process the data, the system consists of techniques of meta-analysis, data mining, statistical tools online, alarms based on critical thresholds of monitored biomedical data.

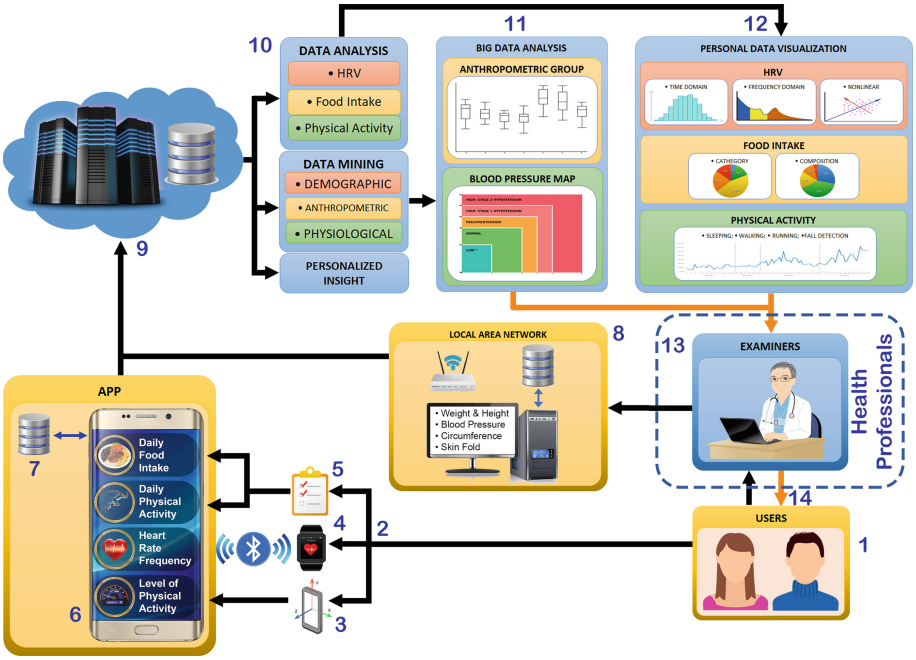

Fig. 1. Architecture FLEEM System®. (1) User: children, adolescents, adults, elderly, athletes and geographically isolated communities. (2) Sensors. (3) smartphone accelerometer. (4) Smartband HR. (5) Menu to monitor physical activity and food intake. (6) App FLEEM. (7) Smartphone database. (8) Local Area Network. (9) Web Platform. (10) Data analysis and data mining. (11) Smart Tools: Cluster analysis for anthropometric and biomedical data, etc. (12) Report: individual and population. (13) Medical feedback for patients. (14) Levels of alarms.

The purpose of this study was to measure direct costs based on the systematic costing of remote monitoring system operations (Fig. 1, Item 13) and conventional health practices (Fig. 2), aiming to analyze the economic impact with the application of FLEEM System® in the prevention and control of obesity in children in the municipality of Monteiro Lobato/SP.

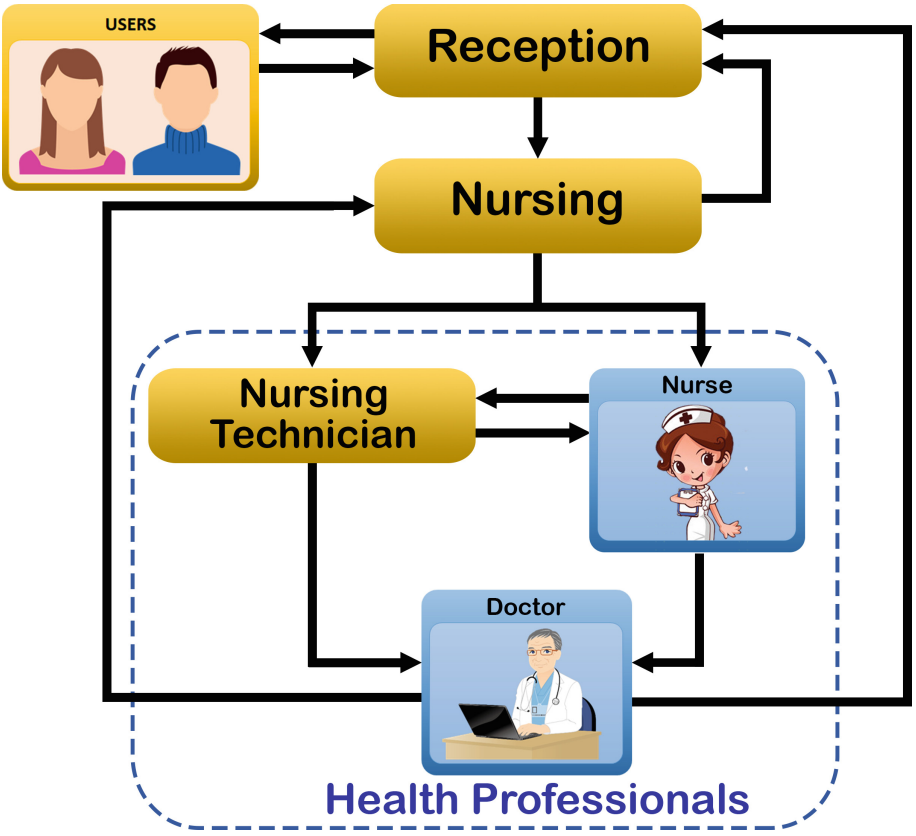

Fig. 2. Conventional service flowchart

Based on the direct costs of health professionals in the remote monitoring system (three modules in operation) and conventional health practice (in special, Basic health Unit) what was sought is the estimation of unit and total direct costs, especially of physicians and nurses, by the procedures and evaluations performed in each of the systems.

With the application of FLEEM System®, unit direct costs (UDC) are as follows: (i) Procedures and Consultations made by nurses, where the UDCs of the identifications were determined, vital signs, anthropometric assessments and questionnaires; (ii) Digital Clinical Reports performed by doctors, calculation of the CDU of the analysis of the biomedical applications data and feedback to the patient.

The UDCs of the procedures of conventional health practices were also determined, of the following procedure: (i) Medical Consultations and Nurses, where the cost of each care and conventional care was evaluated.

The total direct costs of the procedures and evaluations performed by health professionals corresponded to the set of values of all costs of monitoring and consultations [21]. For these costs, the evaluation was made based on the total number of visits and procedures performed in the period.

To analyze the data, cost accounting techniques were used, as well as the verification of costs by procedure and care performed by health professionals. The costs were calculated and analyzed for the remote monitoring system and conventional practices, which emphasize economic results.

3 Results

The evaluations of the direct costs of the health professionals (doctors and nurses) were of the consultations and procedures of 150 children through the system of remote monitoring and conventional practice. Students from five elementary schools in the municipality of Monteiro Lobato in the state of São Paulo, aged between 9 and 12 years, participated in these assessments in 2017.

The results showed the direct labor costs of health professionals in the care and procedures of overweight and obese children (Table 1). These are the direct unit costs of each care, procedure for clinical evaluation and applications of quality of life questionnaires and anamneses.

Table 1. Unit direct costs of care and procedures by nurses

Description	Time Minutes[a]	UDC (US $)[b]	Freq.[c]	TC per event (US $)
Identification				
Name, Age, Gender, etc.	5 ± 0.5	1.06	1	1.06
Subtotal		**1.06**		**1.06**
Vital signs				
Rest/blood pressure	10	2.12	3	6.36
Blood pressure	5 ± 1.0	1.06	3	3.18
Subtotal		**3.18**		**9.54**
Anthropometric				
Skinfolds	12 ± 3.5	2.54	3	7.62
Abdominal and waist circumference	1 ± 0.3	0.21	3	0.63
Weight	1 ± 0.3	0.21	3	0.63
Height	1 ± 0.3	0.21	3	0.63
Subtotal		**3.17**		**9.51**
Questionnaires				
AUQEI	10 ± 2.1	2.12	2	4.24
Food frequency	40 ± 8.0	8.47	1	8.47
Physical Activity	10 ± 1.7	2.12	1	2.12
Subtotal		**12.71**		**14.83**
Total costs		**20.12**		**34.94**

(a) The average time in minutes that was spent to perform each procedure. (b) Based on the salary of the nurse in 2017 (US $ 1,675.88/132 h/month). (c) Number of times the procedures repeated at different times during the remote monitoring period. UDC = Unit Direct Cost; Freq = Frequency, TC = Total Cost.

The Unit direct costs to diagnose overweight and obesity per individual without and with the applications of the questionnaires and their respective total costs, Table 2.

Table 2. Total cost to diagnose overweight children

Description costs	UDC (US $)	Total children	Total costs (US $)
Identification	1.06	150	159.00
Vital Signs	3.18	150	477.00
Anthropometric	3.17	150	475.50
Subtotal	**7.41**		**1,111.50**
Questionnaires	12,71	150	1,906.50
Total costs	**20.12**		**3,021.00**

UDC = Unit Direct Cost.

Table 3 shows the direct unit costs of the Digital Clinical Reports by physicians in the biomedical application data analyzes and the Doctors and Nurses Consultations for the conventional health care of each health professional.

Table 3. Unit direct costs of data analysis of clinical reports and conventional practices

Description	Time Minutes	UDC (US $)	Freq.	TC per event (US $)
Clinical data				
Clinical report	5	2.72	6 evaluations	16.32
Subtotal		**2.72**		**16.32**
Consultations				
Doctors	15	8.17	6 consultations	49.02
Nurses	20	4.24	6 consultations	25.44
Subtotal		**12.41**		**74.46**

The costs of the care of health professionals (doctors and nurses). (a) Average time in minutes for performing procedures. (b) Based on the salary of the nurse in 2017 (US $ 1,675.88/132 h/month) and salary of the doctor (US $ 2,872.95/16 h/month). UDC = Unit Direct Cost; Freq. = Frequency; TC = Total Cost.

Considering in Table 3 that the unit direct costs of the medical service for biomedical data analysis of the remote monitoring system were inferior in relation to conventional health practices. Attaining a cost of US $ 2.72 for a single analyze and US $ 16.32 over the monitoring period (six analyze).

The UDC of the medical appointments were US $ 8.17; however, for nurses, US $ 4.24 for each visit. For the period analyzed, the costs of medical consultations and nurses in conventional health practices were US $ 49.02 and US $ 25.44, respectively. In particular, costs with medical professional were 67% higher than in the remote monitoring system.

The total direct labor costs of health workers from the remote monitoring system and conventional health practice are shown in Table 4. It may be noted that remote monitoring costs are lower than conventional practices.

Table 4. Total direct costs of health professionals through the remote monitoring system and conventional health practice

Description	Telemedicine system			Conventional health practice		
	UDC (US $)	Freq.	TC (US $)	UDC (US $)	Freq.	TC (US $)
Identification						
Care and procedures[a]	34.94	150[c]	5,241.00	–	–	–
Doctors[b]	16.32	150[c]	2,448.00	49.02	150[d]	7,353.00
Nurses	–	–	–	25.44	150[d]	3,816.00
Total costs			**7,689.00**			**11,169.00**

(a) Clinical evaluation by nurse practitioner. (b) Evaluation of the clinical reports of the data obtained with the monitoring (based on clinical parameter). (c) Evaluations. (d) Consultations.

4 Discussion

This article presents the calculation of the direct costs with the specialized workforce of the health professionals in the system of remote monitoring in the prevention and control of obesity in children. Based on the results of the costs raised, online technology in health services has driven economic impact compared to conventional health practices.

FLEEM System® generated a cost reduction of US $ 3,480,00, compared to the conventional health system, this is a saving of 31.16% for the municipality of Monteiro Lobato, Table 4. Several authors point to telemedicine as a way of reducing costs in the health system [17, 22].

The application of the three questionnaires through the FLEEM System®, would lead to a 63.14% reduction in costs with care and procedures performed (Table 1). A strategy to further reduce costs with remote monitoring is to implement the questionnaires and have them to be answered online in the system itself with a reduction of US $ 12.71 per individual (children). Also in relation to the online questionnaires, the reduction of US $ 2,224.50 in clinical evaluations in the monitoring period, with a total direct cost of US $ 5,464.50 (Table 4).

The direct costs of health professionals in the remote monitoring system were lower compared to conventional health practices, Tables 1, 3 and 4. In a recent study, these results were confirmed that telemedicine has significantly reduced costs in relation to the conventional health service [23]. The study showed that the main reduction in expenditures is related to fixed costs, especially the workforce of health professionals. These costs may increase or decrease depending on the volume of service because fixed costs keep constant [24].

FLEEM System® has the potential to cover health care in hard-to-reach places with low operating costs. It has the autonomy to store the patient's data in the smartphone's memory until it is transmitted to the server (Fig. 1, Item 7).

Telemedicine is a tool with potential to face the challenges of the health system [17] through the universalization of health access [22], medical specialists [25], examinations and diagnoses [20, 26], among other health services that online technology can promote.

At a more affordable cost compared to conventional practices, FLEEM System® is a tool to prevent and control the health of CNCDs that promote quality of life in the population, especially in the fight against childhood obesity and adolescence.

Remote monitoring via FLEEM System® provided the children with autonomy and freedom in their daily living, as it did not prevent their activities such as going to school, practicing physical activity, among others. And for family members, because they do not need the presence of the full-time parent with the child.

The impact of the FLEEM System® was not only the reduction of costs, its results were enormous, for example: (i) changes in habits in relation to health; (ii) awareness of those responsible for children (parents and school administrators); (iii) the commitment of the Monteiro Lobato Municipal Health Secretary; (iv) the participation of health professionals guiding children and their legal responsible.

All these factors contributed to the quality of life and social of the children, and that over time, the economic impact for the municipality contributes to the creation of more conscious citizens with the prevention and control of their health, being thus able to result in less expenses with health, less burden on social security and generating its own remuneration.

4.1 Contributions, Limitations e Future Research

The main contributions of this study are related to public health managers, hospitals, health plan operators, physical activity centers, among other managers. The FLEEM System® is a tool to prevent and control the health of chronic noncommunicable diseases.

Studies show that the online follow-up of the patient is associated with the reduction of emergency consultations, helps prevent hospitalizations, reduces costs of medical treatments and ensures quality of life in relation to health [27, 28]. A strategy of reducing costs, especially with the prevention and control of health.

Through a predictive model of the FLEEM System® it is possible to follow the habits of the system users and predict future diseases. This leads to the projection of health costs over the years. The public government has to use its mechanisms for health and the public coffers, developing actions to combat CNCDs. The health plan operators use the different information to stipulate the amount to be charged to the beneficiaries of the plan.

This study presents limitations as it focused on the direct labor costs of health professionals although the justification for choice was to compare these remote monitoring costs with conventional health practices to analyze the economic impact. This indicates that the results of this study are limited to the costs of health professionals (doctors and nurses).

These limitations also portray study opportunities by broadening the focus of research, addressing the total costs of the systems analyzed and the positive socioeconomic impact of remote monitoring. Also use the biomedical data from children to elaborate a predictive model in the identification of diseases that will be developed or acquired in the adult phase. If there is no intervention in the combat against obesity in the current stage of the children, implementation of a predictive model to determine the projection of the impact on public power spending in the long term.

5 Conclusion

This article presented the impact of the FLEEM System® on the remote monitoring service within the public health system of Monteiro Lobato municipality for the prevention and control of obesity in children. The system demonstrated technical and economic viability, and the application of this online technology is an alternative in the promotion of primary health care.

The FLEEM System® presented a reduction in costs in relation to health professionals. A system that works offline, being able to be used in different geographic regions, guaranteeing the service and the integrity of the data.

The few resources required for the operation of FLEEM System® generated a low demand for financial resources and, for this reason, reflected in the reduction of costs compared to conventional health practices. These results highlighted the importance of telemedicine as a vector of transformation of the Brazilian health system and its social and economic impact on society.

Acknowledgements. Federal University of Maranhão (UFMA) for the incentive of postgraduate qualification. Coordination of Improvement of Higher Education Personnel (CAPES) for the concession of the school fee (Bolsa Taxa). Foundation for Research Support of the State of São Paulo (FAPESP) for the fomentation of research with the FAPESP Project Process n° # 15/50064-0. University of Mogi das Cruzes (UMC) for the opportunity to develop research.

Conflict of Interest. This study no has conflict of interest.

References

1. WHO (Word Health Organization): Obesity and overweight. In: Obesity and Overweight (2018). http://www.who.int/news-room/fact-sheets/detail/obesity-and-overweight. Accessed 9 Nov 2018
2. WOF (World Obesity Federatan): Treat Obesity Now and Avoid the Consequences Later (2017). https://www.obesityday.worldobesity.org/world-obesity-day-2017. Accessed 22 Nov 2017
3. De, O.M., Blössner, M., Borghi, E.: Global prevalence and trends of overweight and obesity among preschool children. Am. J. Clin. Nutr. **95**, 1257–1264 (2010). https://doi.org/10.3945/ajcn.2010.29786.1

4. Lobstein, T., Jackson-Leach, R.: Planning for the worst: estimates of obesity and comorbidities in school-age children in 2025. Pediatr. Obes. **11**, 321–325 (2016). https://doi.org/10.1111/ijpo.12185
5. Brasil: Estimativas sobre frequência e distribuição sociodemográfica de fatores de risco e proteção para doenças crônicas nas capitais dos 26 estados brasileiros e no Distrito Federal em 2017. In: Brasília Ministério da Saúde (2018). http://bvsms.saude.gov.br/bvs/publicacoes/vigitel_brasil_2017_vigilancia_fatores_riscos.pdf. Accessed 4 Mar 2019
6. IBGE (Instituto Brasileiro de Geografia e Estatística) (2018). www.ibge.gov.br. Accessed 5 Oct 2018
7. Brasil: 44[a] Seção do Comitê de Segurança Alimentar (CSA). In: Ministério da Saúde (2017). http://189.28.128.100/dab/docs/portaldab/documentos/informes/segundeira_16_a_20_outubro.pdf
8. Bastien, M., Poirier, P., Lemieux, I., Després, J.P.: Overview of epidemiology and contribution of obesity to cardiovascular disease. Prog. Cardiovasc. Dis. **56**, 369–381 (2014). https://doi.org/10.1016/j.pcad.2013.10.016
9. Hanson, C., Rutten, E.P., Fm Wouters, E., Rennard, S.: Influence of diet and obesity on COPD development and outcomes Introduction to the prevalence of obesity. Int. J. COPD **9**, 723–733 (2014). https://doi.org/10.2147/COPD.S50111
10. Pantalone, K.M., Hobbs, T.M., Chagin, K.M., et al.: Prevalence and recognition of obesity and its associated comorbidities: cross-sectional analysis of electronic health record data from a large US integrated health system. BMJ Open **7**, 1–9 (2017). https://doi.org/10.1136/bmjopen-2017-017583
11. Canella, D.S., Novaes, H.M.D., Levy, R.B.: Influência do excesso de peso e da obesidade nos gastos em saúde nos domicílios brasileiros The influence of excess weight and obesity on health spending in Brazilian households Influencia del exceso de peso y la obesidad en el gasto en salud en los hogar. Cad Saude Publica **31**, 2331–2341 (2015)
12. Atella, V., Kopinska, J., Medea, G., et al.: Excess body weight increases the burden of age - associated chronic diseases and their associated health care expenditures. Aging (Albany NY) **7** (2015)
13. Muka, T., Imo, D., Jaspers, L., et al.: The global impact of non-communicable diseases on healthcare spending and national income: a systematic review. Eur. J. Epidemiol. **30**, 251–277 (2015). https://doi.org/10.1007/s10654-014-9984-2
14. Tremmel, M., Gerdtham, U., Nilsson, P.M., Saha, S.: Economic burden of obesity: a systematic literature review. Int. J. Environ. Res. Public Health **14**, 1–18 (2017). https://doi.org/10.3390/ijerph14040435
15. Coutinho, W., Lins, A.P.M.: Custo economico da obesidade no Brasil e no mundo. In: Koogan, G. (ed.) Tratado de Obesidade, 2nd edn. Rio de Janeiro, p. 2106 (2015)
16. Dobbs, R., Sawers, C., Thompson, F., et al.: Overcoming obesity : an initial economic analysis, Discussion paper. McKinsey Global Institute, pp. 1–107 (2014)
17. Dharmar, M., Kuppermann, N., Romano, P.S., et al.: Telemedicine consultations and medication errors in rural emergency departments. Am. Acad. Pediatr. **132** (2015)
18. Oliveira MLDE: Estimativa dos custos da obesidade para o Sistema Único de Saúde do Brasil. Programa de Pós-Graduação em Nutrição Humana da Faculdade de Ciências da Saúde da Universidade de Brasília (2013)
19. Lopez, L.J.R., Goroso, D.G.: Monitoring system of assessment of energy expenditure to human in free-living condition by mean of information and communication technologies. Glob. Telemed. eHealth Updates Knowl. Resour. **3**, 551–555 (2010)

20. Goroso, D.G., da Silva, R.R., Battistella, L.R., et al.: Monitoring heart rate variability online using e- health oriented 3G mobile telephone services monitoring heart rate variability online used mobile telephone 3G e-health service oriented. J. Phys: Conf. Ser. **477**, 1–8 (2013). https://doi.org/10.1088/1742-6596/477/1/012036
21. de Matos, A.J.: Gestão de custos hospitalares: técnicas, análises e tomada de decisão, 3rd edn. Editora STS, São Paulo (2002)
22. Martínez, A., Villarroel, V., Puig-Junoy, J., et al.: An economic analysis of the EHAS telemedicine system in Alto Amazonas. J. Telemed. Telecare **13**, 7–14 (2007). https://doi.org/10.1258/135763307779701176
23. Pietro, R.R., Vicentini, A., Onofrio, A.D., et al.: Economic analysis of remote monitoring of cardiac implantable electronic devices: results of the Health Economics Evaluation Registry for Remote Follow-up (TARIFF) study. Heart Rhythm **14**, 50–57 (2017). https://doi.org/10.1016/j.hrthm.2016.09.008
24. Falk james anthony: Gestão de custos para hospitais: conceitos, metodologias e aplicações, Atlas. Atlas, São Paulo (2001)
25. Dharmar, M., Romano, P.S., Kuppermann, N., et al.: Impact of critical care telemedicine consultations on children in rural emergency departments. Crit. Care Med. **41**, 2388–2395 (2013). https://doi.org/10.1097/CCM.0b013e31828e9824
26. Miyamoto, S., Dharmar, M., Boyle, C., et al.: Impact of telemedicine on the quality of forensic sexual abuse examinations in rural communities. Child Abuse Negl. **38**, 1533–1539 (2014). https://doi.org/10.1016/j.chiabu.2014.04.015
27. Brasil (Ministério da Saúde): Telessaúde Brasil Redes - Manual de Telessaúde para atenção básica, atenção primária à Saúde, 1st ed. Ministério da Saúde, Universidade Federal do Rio Grande do Sul, Brasília/DF (2012)
28. Walker, R.C., Tong, A., Howard, K., Palmer, S.C.: Patient expectations and experiences of remote monitoring for chronic diseases: systematic review and thematic synthesis of qualitative studies. Int. J. Med. Inform. **124**, 78–85 (2019). https://doi.org/10.1016/j.ijmedinf.2019.01.013

A Review of the Literature on Virtual Learning Environments for Professionals in Primary Health Care

Francisco Douglas Lima Abreu[1(✉)], Márcia A. S. Bissaco[1], Alessandro Pereira da Silva[1], Terigi Augusto Scardovelli[1], Silvia Regina Matos S. Boschi[1], Camila Cristina Martini Rodrigues[2], and Silvia C. Martini[1]

[1] Biomedical Engineering, University of Mogi das Cruzes, Mogi das Cruzes, Brazil
franciscodougllas@outlook.com
[2] Service for HIV/Aids Patients SEAP, Hospital das Clinicas da Faculdade de Medicina da Universidade São Paulo HC/FMUSP, Rua Ferreira de Araujo, 789, São Paulo, São Paulo 05428-002, Brazil

Abstract. Research in Primary Health Care (PHC) has advanced in recent years, mainly with preventive and curative strategies or actions in family and community orientation through multi-professional teams. In health systems that value equity, integrality and social participation, these professionals perform activities based on reliable, structured and current data. Therefore, the use of permanent education together with distance education is the key to training these professionals, especially with virtual learning environments. However, few papers discuss, present and catalog the results already obtained in the community. Thus, the objective was to locate in the literature the aspects of virtual learning environments in teams focused on primary health care. Thus, a search for articles in English was made in the databases PubMed Central®, IEEE Xplore®, CAPES Periodical®, and Elsevier's Scopus®. The results of the analyses provided an overview of Virtual Learning Environments. In the meantime, it has been found that many are unavailable or have access restrictions, which makes it impossible to reuse them.

Keywords: Review · Primary Health Care · Virtual learning environment

1 Introduction

Primary health care (PHC) is an associated strategy in preventive and curative actions in family and community orientation. In countries with a public health system, PHC is considered the first level of the health network, that is, it is used by the population to enter health posts or basic health units [1]. Within this scope, there is a multi-professional team of health care staffed by doctors, nurses, nursing technicians, and community health agents [1]. However, these professionals go through a number of health issues at any moment and require them to have a good knowledge of the

© Springer Nature Switzerland AG 2020
C. A. González Díaz et al. (Eds.): CLAIB 2019, IFMBE Proceedings 75, pp. 1428–1433, 2020.
https://doi.org/10.1007/978-3-030-30648-9_184

activities that have the greatest effectiveness and efficiency in the use of available resources for the promotion and prevention of diseases [2].

In health systems that value equity, integrality and social participation, these professionals perform activities based on reliable, current and structured data. Especially with the use of permanent education together with distance education, which contributes to the training of these professionals, since these will reflect directly in the service to the individual, as well as solve several problems that are part of the daily life of health services. In this way, information and communication technologies (ICTs) arise, which have been applied in several segments, mainly in the health area. Becoming even a niche or category, termed telehealth (or e-Health, telemedicine, health informatics).

However, few papers discuss, present and catalog the results already obtained in the community. Therefore, the objective of this study was to locate in the literature the aspects of virtual learning environments in teams focused attention.

2 Methods

The present study followed the protocol of PRISMA recommendations to carry out this review. It is used to develop a well-established framework for systematic reviews and meta-analysis of health interventions [3].

2.1 Search Strategy

The strategy of this review was developed through the tool PICOS.: Population, Intervention, Control, Outcome and Study Design [4], which helps to specify the components related to the review, that is, to define the eligibility criteria, to determine the search keywords and to structure the research question and among others. In this review PICOS was applied in this way: (P) Professionals in Primary Health Care, (I) Virtual Learning Environment (VLE), (C) Without Comparison, (O) The use of VLE in primary health care teams for permanent education and (S) Experimental and/or Observational. Main question: Q1 – There is evidence of the use of VLE in primary health care teams?

According to the research objectives, the following terms were used: “Primary Health Care”, “Permanent Education” and “Virtual Learning Environment”, who were consulted in MeSH (Medical Subject Headings) of PubMed Central®, for the purpose of finding related terms or synonyms for searches. Shortly thereafter, a search was performed on indexed digital databases of Pub-Med Central®, IEEE Xplore®, CAPES Periodical®, and Elsevier’s Scopus® with Boolean operators: “AND”, “OR” and “$ or *” (Truncation). We also used the search filters, such as the period (March 1, 2014, until March 1, 2019). The last survey was conducted on April 20, 2019.

2.2 Selection Studies

The selection of the articles was based on the identification of the titles and abstracts of interest, defined in the PICOS tool. The selected articles were then filtered using the eligibility criteria:

- Inclusion Criteria: Year of publication (last 5 years), Language (Portuguese and/or English) and Relation to descriptors (PICOS).
- Exclusion Criteria: Type of study (systematic reviews and hypothetical model) and Document not available for Reading.

The search and selection of articles were carried out independently and blinded by two researchers (authors). In order to organize the articles acquired in the databases, the State of the Art (Start) software v3.0.3 was used, which assists in the construction of systematic reviews and meta-analyses [5].

2.3 Data Analysis

Studies that fulfilled the selection criteria were submitted to an individual evaluation on the methodological quality. Soon after, each article was selected by the process of collecting interest variables, such as objectives of the VLE, VLE operating system, Country of Origin, there was the implementation with health teams and permanence (VLE availability). Finally, they were summarized by means of infographics and tables created in spreadsheet software.

3 Results and Discussions

The initial search resulted in a total of 711 documents in the digital databases of PubMed, Medline, IEEE, ScienceDirect, and Capes Periodical. They were exported to the Start software, for better control and definition of the status of the articles (Accepted, Rejected, Duplicated). The amount has been reduced to 563 documents for being duplicates. Then they were analyzed and selected through the title, abstract and keywords to suit the theme. Only 32 articles were left that went through the eligibility criteria. Finally, only 15 articles were included in this review after a complete reading.

After analyzing the selected articles, it was possible to answer the following questions: Q1 - Is there evidence of VLE use in primary health care teams?

After extracting and summarizing the data, it was verified that the 15 studies are related in VLE to health teams.

It was observed that 2014 (n = 2), 2015 (n = 3), 2016 (n = 1), 2017 (n = 5), 2018 (n = 2) and 2019 (n = 2). New Zealand (n = 1), China (n = 1), Poland (n = 1), Uruguay (n = 1), USA (n = 1), Canada = (1) Wales (n = 1), Zambia (n = 1), South Africa (n = 1) and Brazil (n = 6).

Most authors adopted an observational study (n = 12), unlike others who preferred an Experimental Study (n = 3). Populational samples were of different types and sizes, with emphasis on managers, health agents, doctors and nurses with higher prevalence among the studies.

Table 1. Características dos estudos selecionados

Paper	Year	Study type	Country	Sample	Type VLE	Platform	Language
[7]	2014	Case Study	Brazil	Managers PHS	Moodle	Web	PT
[8]	2014	Quasi-Experiment	Brazil	Agents Health	Moodle	Web	PT
[9]	2015	Quasi-Experiment	Brazil	N = 28 Nurses	–	Web	PT
[10]	2015	Case Study	Brazil	N = 67 Nurses	Moodle	Web and Mobile	PT
[11]	2015	Case Study	South Africa	Nurses	Moodle	Web	PT
[12]	2016	Case Study	Canada	N = 1402 Agents Health	–	Web	EN
[13]	2017	Quasi-Experiment	Wales	Nurses	–	Web	EN
[14]	2017	Cross-Sectional	Brazil	N = 47 Desntist and Not-dentists	–	Web	EN
[15]	2017	Coorte	New Zealand	N = 16 Nurses	Moodle	Desktop	PT
[16]	2017	Case Study	China	N = 612 Agents Health	Moodle	Web	EN
[17]	2017	Case Study	Poland	N = 225 General practitioners	VisualStudio	Web	–
[18]	2018	Case Study	Uruguay	N = 143 Neurologists	SharePoint	Web	–
[19]	2018	Case Study	EUA	N = 40 General practitioners	Moode	Web	SP
[20]	2019	Case Study	Zambia	N = 16 Doctor	EdX	Web and Mobile	–
[21]	2019	Cross-Sectional	Brazil	N = 300 Agents Health	Moode	Web	EN

The use of the Moodle system (n = 8) in a Web platform (n = 15) was the most outstanding among the studies. Others preferred SharePoint and EdX, but some decided to develop their own environment and make it available on the Web. Because the works were predominant in Brazil, the Portuguese language (PT) was the most applied, and there were also studies in the language English (EN) and Spanish (SP) (Table 1).

4 Conclusions

The results of the analyses provided an overview of Virtual Learning Environments. In the meantime, it has been found that many are unavailable or have access restrictions, which makes it impossible to reuse them.

Acknowledgment. The authors are grateful to all contributors of this study, University of Mogi das Cruzes (UMC), Foundation for Teaching Research Support (FAEP/UMC), grant # 2019/08423-4 São Paulo Research Foundation (FAPESP) and Coordination for the Improvement of Higher Education Personnel (CAPES).

Declaration of Conflict of Interest. The authors declare that there are no conflicts of interest.

References

1. WHO&UNICEF: A vision for primary health care in the 21st century. In: World Health Organization (2018). http://www.who.int/docs/default-source/primary-health/vision.pdf?sfvrsn=c3119034_2. Accessed 20 Apr 2019
2. Brasil: Título VIII, Capítulo II, Seção II, Artigos de 196 a 200, da Saúde. BRASIL, Legislação Federal, Leis Federais no 8.080. Diário Oficial da República Federativa do Brasil, Brasília (2000)
3. Galvão, T.F., de Pansani T.S.A., Harrad, D.: Principais itens para relatar Revisões sistemáticas e meta-análises: a recomendação PRISMA. Epidemiol e Serviços Saúde 24, 335–342 (2015)
4. da Santos, C.M.C., de Pimenta, C.A.M., Nobre, M.R.C.: The PICO strategy for the research question construction and evidence search. Rev. Lat. Am. Enfermagem **15**, 508–511 (2007). https://doi.org/10.1590/S0104-11692007000300023
5. Fabbri, S., Ferrari, F., Vincenzi, A.M.R., Di Thommazo, A.: State of the Art through Systematic Review (StArt). Versão 3.0.3 [software]. Laboratório de pesquisa em Engenharia de Software da Universidade Federal de São Carlos (2010). http://lapes.dc.ufscar.br/tools/start_tool. Accessed 10 Mar 2018
6. Daza, M.P.M., Berretin-Felix, G., de Machado, M.A.M.P.: Requisitos para utilização de cybertutor com agentes comunitarios de saúde. Rev. CEFAC **16**, 573–581 (2014). https://doi.org/10.1590/1982-021620141391
7. Emmerick, I.C.M., Chaves, L.A., Marin, N., Luiza, V.L.: Strengthening the capacity of managers in pharmaceutical services based on Primary Health Care (PHC) at different levels of the health system. Hum. Resour. Health **12**, 34 (2014). https://doi.org/10.1186/1478-4491-12-34
8. Gonçalves, M.B.B., Rabeh, S.A.N., Terçariol, C.A.S., et al.: The contribution of distance learning to the knowledge of nursing lecturers regarding assessment of chronic wounds. Rev. Lat. Am. Enfermagem **23**, 122–129 (2015). https://doi.org/10.1590/0104-1169.3606.2533
9. Pereira, C.A., Wen, C.L., Tavares, H.: Alcohol abuse management in primary care: an e-learning course. Telemed. e-Health **21**, 200–206 (2015). https://doi.org/10.1089/tmj.2014.0042
10. Woods, D.L.: Improving neonatal care in district and community health facilities in South Africa. Paediatr. Int. Child Health **35**, 187–191 (2015). https://doi.org/10.1179/2046905515Y.0000000031
11. Carroll, J.C., Grad, R., Allanson, J.E., et al.: The gene messenger impact project. J. Continuing Educ. Health Prof. **36**, 178–185 (2016). https://doi.org/10.1097/CEH.0000000000000079
12. Edwards, R.: Evaluation of a familial hypercholesterolaemia e-learning programme in primary care. Pract. Nurs. **28**, 84–89 (2017). https://doi.org/10.12968/pnur.2017.28.2.84

13. Roxo-Gonçalves, M., Strey, J.R., Bavaresco, C.S., et al.: Teledentistry: a tool to promote continuing education actions on oral medicine for primary healthcare professionals. Telemed. e-Health **23**, 327–333 (2017). https://doi.org/10.1089/tmj.2016.0101
14. Orsborn, G., Demetriou, T., Arcus, K., Asbury, E.: The Development of Mobile Learning CPD Modules to Improve the Management of Respiratory Diseases (2017)
15. Hu, D., Zhu, W., Fu, Y., et al.: Development of village doctors in China: financial compensation and health system support. Int. J. Equity Health **16**, 9 (2017). https://doi.org/10.1186/s12939-016-0505-7
16. Wlodarczyk, D., Chylińska, J., Lazarewicz, M., et al.: Enhancing Doctors' competencies in communication with and activation of older patients: the promoting active aging (PRACTA) computer-based intervention study. J. Med. Internet Res. **19**, e45 (2017). https://doi.org/10.2196/jmir.6948
17. Carrizosa, J., Braga, P., Albuquerque, M., et al.: Epilepsy for primary health care: a cost-effective Latin American E-learning initiative. Epileptic Disord **20**, 386–395 (2018). https://doi.org/10.1684/epd.2018.0997
18. Hoedebecke, K., Mahmoud, M., Yakubu, K., et al.: Collaborative global health E-learning: a massive open online course experience of young family doctors. J. Fam. Med. Prim. Care **7**, 884–887 (2018). https://doi.org/10.4103/jfmpc.jfmpc_186_18
19. Barteit, S., Neuhann, F., Bärnighausen, T., et al.: Perspectives of nonphysician clinical students and medical lecturers on tablet-based health care practice support for medical education in Zambia, Africa: qualitative study. JMIR mHealth uHealth **7**, e12637 (2019). https://doi.org/10.2196/12637
20. Diniz, K.K.S., Pagano, A.S., Fernandes, A.P.P.C., et al.: Knowledge of professional healthcare providers about sickle cell disease: impact of a distance education course. Hematol. Transfus. Cell Ther. **41**, 62–68 (2019). https://doi.org/10.1016/J.HTCT.2018.06.004

Analysis and Validation of Electrical Safety Procedures for Biomedical Devices

Débora Rubio[1(✉)], Nicolas Lescoulié[1], Débora Arce[1,2], Martín Roberti[1], and Sergio Ponce[1]

[1] Grupo de Análisis, Desarrollos e Investigación Biomédica, FRSN, Universidad Tecnológica Nacional, Buenos Aires, Argentina
drubio@frsn.utn.edu.ar
[2] Consejo Nacional de Investigaciones Científicas y Técnicas, Buenos Aires, Argentina

Abstract. Monitoring electrical failures in biomedical devices makes it possible to ensure patient's safety. While assessing risk in medical equipment, we observed that electrical failures are one of the adverse events detected. Biomedical laboratories include procedures and design devices for testing electrical safety. In this work, we develop procedures to perform electrical safety test based on national and international standards. One of them is the Protective Earth Resistance test. Currently, the main standard applied to medical equipment tests is IEC 62353: 2014 "Medical electrical Equipment - recurrent test and test after repair of medical electrical equipment". Specifically, this standard is a guideline that describes the requirements to ensure the electrical safety through comparable and reproducible tests.

To ensure technical competence, laboratories must validate their testing procedures following the standard ISO/IEC 17025: 2017 "General requirements for the competence of testing and calibration laboratories". This standard comprises all the requirements that laboratories must achieve to demonstrate that they (i) apply a quality management system, (ii) are technically competent and (iii) they may obtain valid technical results.

Keywords: Protective earth resistance · Medical technology risks · Procedures validation

1 Introduction

Biomedical devices may come into physical contact with patients by "applied parts". Occasionally, devices may have active parts in contact with the patient's body, and may come into direct contact with the heart. Patient's injuries associated to biomedical equipment can occur by an electric current flowing through the patient's body. An electric shock can cause injuries during medical care procedures; therefore, electrical safety is an important requirement in quality assurance of medical equipment.

Physiological effects of an electric shock can cause, in less severe situations, tingling sensations, while in more serious situations they can cause burns, electrocution and even

© Springer Nature Switzerland AG 2020
C. A. González Díaz et al. (Eds.): CLAIB 2019, IFMBE Proceedings 75, pp. 1434–1440, 2020.
https://doi.org/10.1007/978-3-030-30648-9_185

the patient's death. Hospital safety programs, designed to protect patients, visitors and staff, are practical applications of the medical dictum "First, do not harm" [1].

Skin has high electrical resistance, but body internal components, such as blood and muscles, have low resistance. A current of 50 μA concentrated on a small area in the heart muscle can trigger ventricular fibrillation. The maximum current in normal conditions allowed in patients undergoing heart procedures is 10 μA [2].

Universidad Tecnológica Nacional implements procedures to satisfy the requirements of electrical safety test in medical equipment. IEC 62353 is one of the biomedical standards applied for "recurrent test" and "test after repair". The Protective Earth Resistance test is one of the tests applied in laboratories. These tests must be carried out under validated procedures. The laboratory must validate non standardized procedures, methods developed by laboratories, and external standardized methods or otherwise modified [3]. In this work, we present preliminary test procedure validations.

2 Materials and Methods

2.1 Medical Equipment Standards

The applicable standard for biomedical equipment is IEC 62353 "Medical Electrical Equipment, Recurrent Test and Test After Repair of Medical Electrical Equipment". This standard describes general and particular requirements to assess the safety of electromedical equipment. Protective earth resistance, insulation resistance, leakage currents and performance tests are among the particular requirements of this standard. To validate our procedure, we verify protective earth resistance of electrocardiography monitors. This test measures the integrity of a low-resistance connection between the earth conductor and any metal conductive parts, which may become active in case of a fault on a class I medical device. The test current is applied between the earth pin of the mains supply plug and any accessible metal part (including earth reference point) via a dedicated earth bond test lead [4].

2.2 Standardized Measurement Device

In order to test electrical safety in biomedical equipment, we designed a standardized measurement device; it complies with the IEC 62353 requirements as shown in Fig. 1. This measurement device satisfies quality and metrological requirements as defined by the standard.

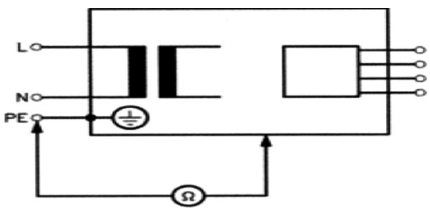

Fig. 1. Protective Earth Resistance test

The measurement device develops, calibrates the test leads before measuring protective earth resistance to avoid take into account the test lead's resistance. These test leads have silicone insulation and right angle connectors, designed for current peaks of 32 A and maximum voltages of 1000 V. After calibration, a current of 1 A is applied between protective earth connector and accessible conductive parts placed to protection earth of the equipment under test. In this work, equipment under test have disconnectable power leads, therefore the sum of the resistance of power lead and the equipment resistance must not exceed 300 mΩ established by standard. The transformer used to generate applied current does not exceed the maximum open circuit voltage of 24 V established by standard IEC 62353.

2.3 Validation Procedure of Protective Earth Resistance

Testing and calibration laboratories must apply a quality management system. They require documented and validated procedures, as defined by standard guidelines. Some statistical parameters, such us repeatability, veracity, uncertainty and aptitude test, are used to validate standardized procedures [5].

Repeatability: is the precision obtained by applying the same procedure, on a same sample, with the same technician, at short intervals of time, using the same equipment, within same laboratory.

Veracity: is the proximity between the average of a large series of results and the true values of the measurand.

Uncertainty: is the parameter associated to the measurement result that characterizes the values dispersion that could be reasonably attributed to the measurand [6].

Aptitude test: testing laboratories should have quality procedures to assurance validity assays. This must be planned and reviewed, and may include certified reference materials and interlaboratory comparisons or proficiency testing plan.

The selected equipment to validate protective earth resistance procedure belong to a Health Care Centre. Electrocardiography monitors are mainly used in Intensive Therapy Units. These equipment have analogous applied parts and the electrical protection is Class I. Measurements of protective earth resistance values were collected from five multiparameters monitors, taken by three laboratory technicians.

2.4 Statistical Analysis

Repeatability and Reproducibility (Gage R & R) is a methodology used to define the variation in the measurement data due to the measurement system. It compares measurement variation to the total variability observed, consequently defining the capability of the measurement system. Repeatability is due to equipment variation and reproducibility is due to technicians variation.

Repeatability and reproducibility were performed using R language for normal distribution test and Gage R&R analysis.

3 Results

3.1 Repeatability and Reproducibility

Measurement variation depends on two great factors, repeatability and reproducibility. In order to calculate the repeatability, a technician took measurements in a particular multiparameter monitor. Table 1 shows the measurements corresponding to this monitor. On the other hand, the same procedure was performed by different technicians and with different monitors to calculate the reproducibility.

Table 1. Protective earth resistance measurements

Protective Earth Resistance (m Ω)		
163	156	156
161	166	155
159	174	156
164	156	154
161	156	155
164	160	154
164	160	161
160	156	153
158	155	155
159	155	155

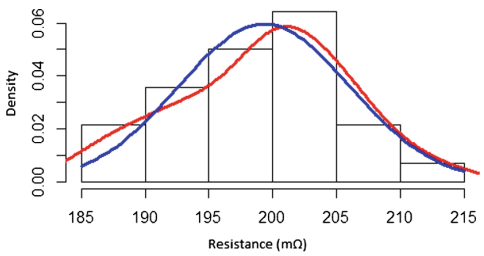

Fig. 2. Repeatability representation

As shown in Fig. 2 the values fit a Normal distribution. The same analysis was conducted for the remaining four electrocardiography monitors. Repeatability value is 3,71% and reproducibility value is 3,09%.

Figure 3 shows the Gage R&R analysis for all electrocardiography monitors.

$$\%\,\mathrm{R\&R} = \sqrt{(\mathit{Repeatability})^2 + (\mathrm{Reproducibility})^2} \tag{1}$$

$$\%\,\mathrm{R\&R} = 4.83\%$$

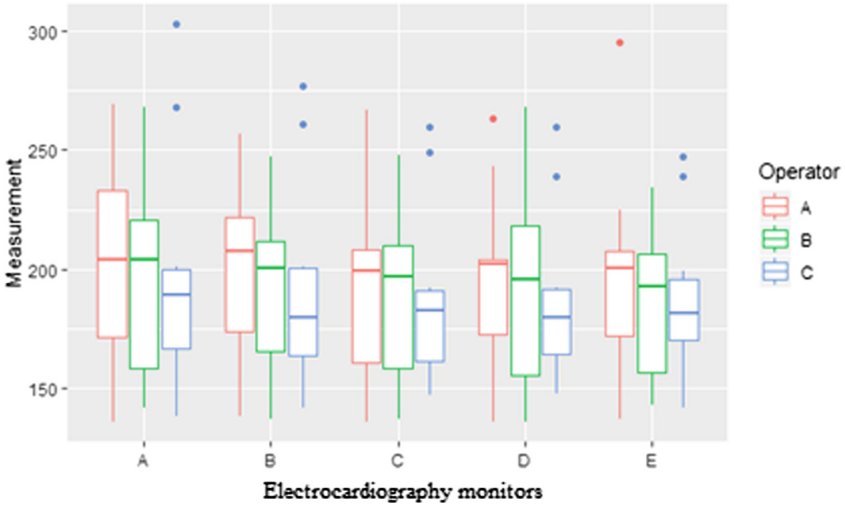

Fig. 3. Gage R&R analysis

3.2 Veracity

Veracity analysis was performed by using R language. It can be seen that the values obtained in measurements do not present significant dispersions respect to the true value of the measurand. Figure 4 shows how measurements fit to the true value.

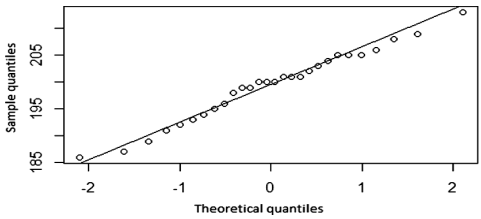

Fig. 4. Proximity between the average and true value of the measurand

3.3 Measurement Uncertainty

To obtain this parameter, it was necessary to consider the uncertainty of the test device, an uncertainty due to the resolution of the equipment under test, an uncertainty due to the resolution of the test device and the uncertainty due to repeatability of measurements.

The measurement uncertainty obtained for protective earth resistance test is shown in Table 2.

Table 2. Uncertainty

Uncertainty	Value
Combined (Uc)	0,004564355
Expanded with K = 2 (U)	0,009128709

3.4 Aptitude Test

The participation in proficiency test is an essential quality assurance. This allows laboratories to ensure the comparability of their results and know the validity of their methods. To ensure validation of method and measurement device, we made comparisons with another laboratory, which has commercial equipment specially designed to carry out protective earth resistance test.

To calculate Z-Score, the true value Xi was obtained by commercial equipment.

Z-Score was calculated by Eq. 2.

$$Z = \frac{Xi - \mu}{\sigma} \tag{2}$$

Z-score obtained from protective earth resistance measurement is 1,199889.

When $|$ z-score $| \leq 2.0$ is considered satisfactory; $2.0 <|$ z-score $| < 3.0$ is considered as questionable; $|$ z-score $| \geq 3.0$ is considered unsatisfactory.

4 Conclusion

To ensure technical competence, laboratories must validate their testing procedures following the standard ISO/IEC 17025. Analyzing validation parameters we can assure that the measurement device and protective earth resistance procedure are appropriate to obtain valid technical results.

The result of R & R is less than 15%, therefore measuring device and measurements taken by technicians are appropriate.

The low measurement uncertainty value obtained demonstrated the validity of the test procedure.

The Z score calculated is 1,199889 so we can infer that the analytical results fit a Normal distribution and have a probability of 99.7% of confidence interval.

According to the study developed in this paper we valid the protective earth resistance procedure implemented by the laboratory.

References

1. Dyro, J.F.: Clinical Engineering Handbook. Elsevier, U.S.A. (2004)
2. Jacobson, B., Murray, A.: Medical Devices: Use and Safety, First published. Elsevier, U.S.A. (2007)

3. ISO/IEC 17025: General requirements for the competence of testing and calibration laboratories (2017)
4. IEC 62353: Medical electrical equipment - recurrent test and test after repair of medical electrical equipment (2014)
5. Guía para validación de métodos de ensayo, GUI-LE-03 Versión 1, Organismo Argentino de Acreditación
6. G.U.M.: Evaluation of measurement data - Guide to the expression of uncertainty in measurement (2008)

Maintenance Management Requirements in Medical Technology

Gustavo Adolfo Barrera-Saavedra[1(✉)]
and Andrés Mauricio González-Vargas[1,2]

[1] Universidad Autónoma de Occidente, Cll 25 # 115–85, 760030 Cali, Colombia
{amgonzalezv, gustavo_ado.barrera}@uao.edu.co
[2] Grupo de investigación de Ingeniería Biomédica, G-Bio, Cali, Colombia

Abstract. Clinical Engineering applies methodologies that guide maintenance management systems so they can comply with regulations and standards. In many healthcare institutions, these guidelines are difficult to follow strictly due to different factors. The objective of this study was to define the requirements that a maintenance management system must complete, following national regulations and international accreditation standards. To achieve this goal, we conducted a web search to identify the standards associated with national and international medical devices. The World Health Organization was taken as a benchmark to compare them. In our search, we identified significant similarities, concluding that regulations in Colombia follow international standards, but there is still a long way to go, and studies like this are vital in order to achieve it.

Keywords: Government regulations · Management · Maintenance

1 Introduction

Clinical Engineering (IC) applies theories and methodologies focused on the continuous improvement of the technical processes in an institution. In practice, this requires a maintenance management system that complies with the regulations and current standards of the country, taking into account the needs of users and technical staff, and providing access to information and reporting [1]. Unfortunately, in Colombia, they are not implemented massively, due to local factors such as availability, budget, suitability, and lack of knowledge.

In Colombia, there is commercial software for the integral management of biomedical equipment and hospital physical infrastructure. However, most of these products respond only to regulations and standards applicable to industrial technology because they evolved from that field. For this reason, our study sought to define a list of requirements based on the national regulations applied to medical devices in order to compare them with international accreditors and WHO standardized processes. This analysis made it possible to obtain a list of requirements that improve the management of the medical technology and are of vital importance in the stage of standardization and continuous improvement of the technology management processes in hospital environments.

© Springer Nature Switzerland AG 2020
C. A. González Díaz et al. (Eds.): CLAIB 2019, IFMBE Proceedings 75, pp. 1441–1448, 2020.
https://doi.org/10.1007/978-3-030-30648-9_186

2 Methodology

We performed a literature review in order to identify the norms associated with medical devices in Colombia. These norms are of two types: Mandatory compliance (NOC, in Spanish) and voluntary compliance standards. The first ones are Resolution 2003 of 2014 [2], or Single System of Habilitation (SUH); Decree 4725 of 2005 [3], where the permissions of use are regulated; Resolution 4816 [4] of Technovigilance and Decree 1595 of 2015 [5] or system for quality management. Voluntary compliance standards are those intended for the accreditation of institutional processes. In Colombia, this accreditation is regulated by the Resolution 5095 of 2018 [6], also known as Handbook for Accreditation in Health.

WHO in its series of documents called "How to Manage Series for Healthcare technology" [7] delivers a comprehensive maintenance management protocol for medical technology. It recommends international accreditation processes and suggests some accrediting institutions. Taking this into account, the Joint Commission International (JCI) [8] as a benchmark for confronting national and international processes, due to its compatibility with the National Health System. Their inclusion criteria served as a filter to select the articles and standards that deal with topics related to inventories, safety in use, operating requirements, documentation of processes, and life cycle.

From the previous process, we obtained a table of items filtered by each norm and standard evaluated. According to WHO guidelines, we organized and grouped the information by activity, taking into account the resources. Finally, we made a comparison between the mandatory national standard, the Health Accreditation Handbook, JCI Standards, and suggestions made by WHO for maintenance management. It is important to note that no other similar studies were found in the consulted databases.

3 Results

Table 1 shows the presence of the norms in each of the activities and subroutines. In this table, italicized text with underscore means that at least one of the subroutines has no presence or it is not very visible.

Table 1. Presence in each activity of the norms, standards and procedures evaluated.

Activity/sub Routine	Operative	Human resource	Material resource	Financial resource
Planning, management, execution, information reporting	NOC	*NOC*	*NOC*	NOC
	SUA	SUA	*SUA*	SUA
	JCI	JCI	JCI	JCI
	WHO	WHO	WHO	WHO

3.1 Planning

Table 2 shows in detail the subroutines that make for each activity of the planning phase. Here we indicate if the item of interest is Incorporated (I) or Not Incorporated (NI) in one of the documents consulted. In this phase, we can see some missing aspects in the NOC and SUA concerning the human and material resources, which can be complemented by JCI standards and WHO protocols.

Table 2. Planning

Planning		NOC	SUA	JCI	WHO
Operative	Inventories	I	I	I	I
	Documentation required by law	I	I	I	I
	Initial performance tests	I	I	I	I
	Maintenance strategies	I	I	I	I
	Metrology inspections	I	I	I	I
	Methodologies	I	I	I	I
	Frequency	I	I	I	I
Human resource	Profiles	I	I	I	I
	Amounts	*NI*	I	I	I
	Routine training	*NI*	I	I	I
Material resource	Industrial safety	*NI*	*NI*	I	I
	Workplace	*NI*	*NI*	*NI*	I
	Measuring tools and equipment	I	I	I	I
	Inputs	I	I	I	I
	Spare parts	I	I	I	I
	Records	I	I	I	I
	Information	I	I	I	I
Financial resource	Initial costs	I	I	I	I
	Operating costs	I	I	I	I

3.2 Management

In Table 3 we can see that the importance of the operative management lies in having defined all the protocols necessary to deal with the equipment in any condition of use, either in normal or in failure mode. In the NOC and SUA, we do not find any mention of the processes of supervision of contracts, associated costs, and future budgets, among others.

Table 3. Management

Management		NOC	SUA	JCI	WHO
Operative	Definition of procedures and policies	I	I	I	I
	Technovigilance	I	I	I	I
	Control of own and third-party work	I	I	I	I

(*continued*)

Table 3. (*continued*)

Management		NOC	SUA	JCI	WHO
Human resource	Necessary human resource	I	I	I	I
	Control hours of work	*NI*	I	I	I
	Fulfillment of delivery deadlines	*NI*		I	I
	Training in Technovigilance	I	I	I	I
	Technical and assistance training	I	I	I	I
	Training in techniques and use of safety elements and personal protective equipment	*NI*	*NI*	I	I
	Risk-training associated with maintenance activities	*NI*	*NI*	I	I
Material resource	Quick operation guides	I	I	I	I
	Manuals	I	I	I	I
	Medical technologist's resume	I	I	I	I
	Documentation and registration	I	I	I	I
Financial resource	Monitoring the costs associated with service contracts	*NI*	*NI*	I	I
	Supervising the costs associated with work carried out by the technical staff	*NI*	*NI*	I	I
	Comparing the costs according to the percentage of compliance	*NI*	*NI*	I	I
	Examining and evaluating variations			I	I
	Planning for future budgets	I	I	I	I

3.3 Execution

In Table 4, the subroutines that constitute the execution process are shown in detail. The human resource is responsible for executing the activities; therefore, it must be evaluated and continuously trained in the topics of interest according to the area to which it belongs. Having procedures for unscheduled care, emergency shutdowns, and documenting the costs associated with the activities are necessary factors for the proper execution of the financial resource.

Table 4. Execution

Execution		NOC	SUA	JCI	WHO
Operative	Execution of procedures	I	I	I	I
	Registration and documentation of the procedures in the resume	I	I	I	I
	Verification and operation tests after performing any scheduled activity	I	I	I	I

(*continued*)

Table 4. (*continued*)

Execution		NOC	SUA	JCI	WHO
Human resource	Instruction provided annually for each component of the management and security program	I	I	I	I
	Testing of staff knowledge	*NI*	I	I	I
	Documentation of training, and testing	I	I	I	I
	Training in industrial safety	*NI*	I	I	I
	Training for technical and engineering personnel	I	I	I	I
	Identifying, documenting and managing device misuse and usage errors	*NI*	I	I	I
	Analysis of the occurrence of errors	*NI*	I	I	I
Material resource	Labeling	I	I	*NI*	I
	Communication	*NI*	I		I
	Documenting and recording all activities performed on medical technology	I	I	I	I
	Analyzing the information from the activities carried out on medical technology	*NI*	I	*NI*	I
Financial resource	Procedures for unscheduled care and emergency shutdowns that may affect medical technology	*NI*	I	I	I
	Documenting the costs associated with each activity	*NI*	I	I	I
	Documenting and recording all activities performed on medical technology	I	I	I	I

3.4 Information Report

In Table 5, we see the importance of this activity, since all the documents consulted include a description that highlights this process.

Table 5. Information reporting

Information report		NOC	SUA	JCI	WHO
Information report	To assess the results and impact of maintenance management on medical technology	I	I	I	I
	Establish the data and institutional indicators that allow to identify the expected quality parameters	I	I	I	I
	Establish tools that allow decision-making and the generation of improvement strategies	I	I	I	I

In the search carried out initially we found that, in Colombia, there are 1003 public Health Providing Institutions (IPS, in Spanish) [9] and only eleven have SUA [10] accreditation. In the private sector, there are 9413 IPS enabled to provide services; 34 are accredited by the SUA [10] and five by JCI [11]. Finally, there are 16 IPS which are part public and part private, and 1 has national accreditation (Fig. 1). Colombia is in the group of Latin American institutions with more institutions accredited by JCI, with five providers, only surpassed by Brazil with 64 institutions and Peru that has nine accredited institutions.

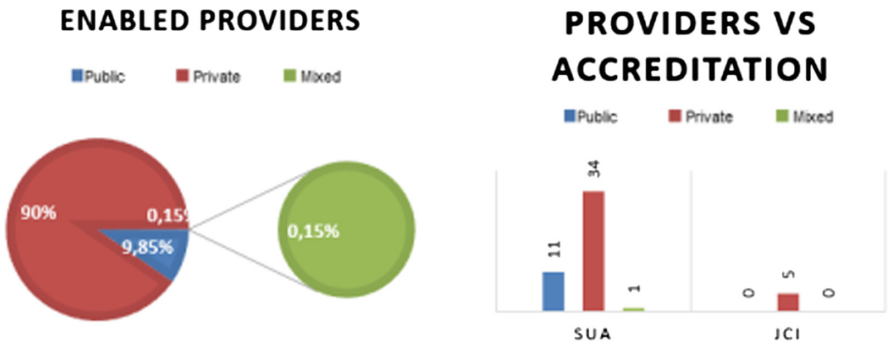

Fig. 1. Habilitation and accreditation of healthcare providers (IPS)

A Ranking of Hospitals is periodically published for institutions of Latin America that provide multiple services in a wide range of medical specialties. This ranking measures Patient Safety and Dignity, Human Capital, Installed Capacity, Knowledge Management,

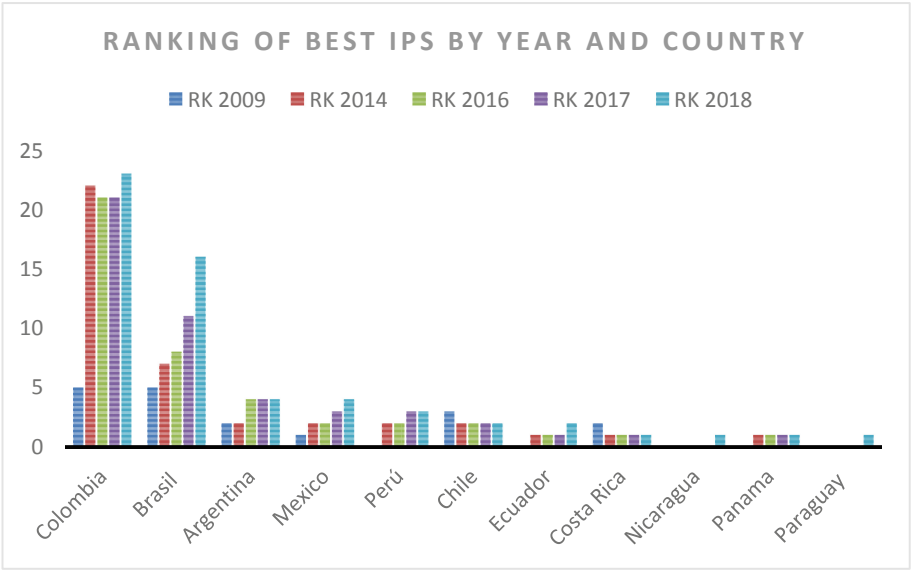

Fig. 2. Number of IPS accepted in the ranking by year and country.

Efficiency, and Prestige. This measurement is a good indicator of the continuous improvement that has been taking place in Latin America in the last years [12].

Figure 2 shows the improvement over time that some countries have had, taking into account the increase in the number of IPS that qualify year by year for this ranking. Colombia, for example, went from having 5 IPS in 2009 to 23 in 2018; Brazil went from 5 in 2009 to 16 in 2018; Mexico went from 1 in 2009 to 3 in 2018, Nicaragua and Paraguay are new to this ranking, with one institution in 2018.

It is interesting to note that, whereas Brazil has 64 IPS accredited by JCI, only 16 appear in the list of the best, and Peru accredited 9 of its institutions with JCI, but only four are in the Ranking. By contrast, 23 IPS located in Colombia are among the best, although only five of them are accredited by the JCI.

4 Conclusions

Regulations and accreditation standards are requirements that must be met in order to achieve a quality process; in other words, they are related to the know-what. WHO documents are instructives that help to follow these norms, and are related to the know-how. The different documents consulted have strengths and weaknesses in each of their activities, which is why accreditation standards and WHO protocols are complementary to NOC. Factors such as the workplace, elements of personal protection or self-care, are not mentioned or ambiguous in NOC; thus, they should be reinforced. The WHO guides are very descriptive and complete, but they are difficult to implement strictly, especially if the health system has a low-budget. The activities that these guides suggest require high demand for personnel, the suitability of the workplace, immediate availability of spares, consumables, accessories, and specialized equipment for preventive or corrective maintenance.

References

1. WHO Guide 1: How to organize a System of Healthcare Technology Management: Management procedures for health Facilities and health Authorities, St. Albans, p. 14 (2005)
2. Colombia: Ministry of Health and Social protection. Resolution number 00002003 of 2014
3. Colombia: Ministry of Health and Social protection. Decree number 004725 of 2005
4. Colombia: Ministry of Health and Social protection. Resolution number 004816 of 2008
5. Colombia: Ministry of Commerce, Industry and tourism. Decree number 00001595 of 2015
6. Colombia: Ministry of Health and Social protection. Resolution number 0005095 of 2018
7. World Health Organization: How to Manage Series for Healthcare Technology, Guide 1–6 (2005)
8. Joint Commission International, Accreditation standards for hospitals, 6th edn.
9. Unique enabling system. https://www.minsalud.gov.co/salud/PServicios/Paginas/Sistema-unicode-habilitacion.aspx. Accessed 14 May 2019
10. Accredited health services institutions. http://www.acreditacionensalud.org.co/Documents/IPSacreditadas.pdf. Accessed 14 May 2019

11. Joint Commission International JCI-Accredited organizations. https://www.jointcommissioninternational.org/about-jci/jci-accredited-organizations/?c=Colombia. Accessed 14 May 2019
12. America Economy, ranking of the best Clinics and Hospitals in Latin America. https://www.americaeconomia.com/rankings. Accessed 15 Jul 2019

Fault Prioritization System for a Vital Signs Monitor Based on Fuzzy Logic

Karen Jazmin Mendoza Bautista[1(✉)], Héctor García Estrada[1], María Guadalupe Ramírez Sotelo[2], and Agustín Ignacio Cabrera Llanos[1]

[1] Departamento de Bioprocesos, Unidad Profesional Interdisciplinaria de Biotecnología del Instituto Politécnico Nacional, Mexico City, Mexico
mendoza_bautista@outlook.com, aicllbuda@yahoo.com
[2] Departamento de Bioingeniería, Unidad Profesional Interdisciplinaria de Biotecnología del Instituto Politécnico Nacional, Mexico City, Mexico

Abstract. This work presents a fault prioritization system based in two MISO *(Multi Input Single Output)* fuzzy logic systems, applied on a vital signs monitor. The MISO systems correspond to possible failures, classified as physiological and technical failure. For physiological failures, the fuzzy inputs are heart rate, respiratory rate, temperature and the partial oxygen saturation variables, the membership functions for each variable were designed using the normal range for a healthy adult. Technical failures system considered faults in the monitor's arrange of sensors as inputs, while it's membership functions vary accordingly to the operational status of the sensors. Both fuzzy systems have as output four priority levels, whose labels are: normal, mild, moderate and critical. Once the design of the MISO systems was carried out, three trials were performed on the fault prioritization system: a Monte Carlo test for both subsystems, simulated patient test for physiological failures and real patient with sensors connectivity alterations for technical failures. Due to the results achieved, the fault prioritization system can be applied in the automation of alarms or can be a reference for the development of future Fuzzy systems applied to different types of vital signs monitors.

Keywords: Fuzzy logic · Fault prioritization · Physiological failures · Technical failures

1 Introduction

In the development of the failure prioritization system for a vital sings monitor, failures that may exist were considered, creating two MISO fuzzy systems which consider the variables existing in each type of failure, as well as normal and uncommon values of the variables. The systems were done with the LabVIEW platform with the purpose of subsequently put them to the Monte Carlo test, simulated patient test and finally a real patient with alterations caused in the monitor test.

© Springer Nature Switzerland AG 2020
C. A. González Díaz et al. (Eds.): CLAIB 2019, IFMBE Proceedings 75, pp. 1449–1457, 2020.
https://doi.org/10.1007/978-3-030-30648-9_187

1.1 Vital Signs Monitors

Vital Sings Monitors (VSM) arise after the second world war, as a need to constantly evaluate the physiological conditions of wounded soldiers with the purpose of keeping them within the normal ranges and thus decrease the number of deaths during hospitalization [1].

As the name says, vital signs are signals or reactions that presents a patient that reveal basic functions of the body. In accordance with CENETEC [2], the monitor used is a transport monitor, which provides the following physiological parameters: heart rate (HR), the respiration rate (RR), oxygen saturation (SaO2) and the electrocardiography (EKG). In addition, our monitor provides the temperature (T). It is described in [6].

According to [2], vital signs monitors can display two types of failures: physiological and/or techniques, Table 1 shows the classification of failures according to their priority's level.

Table 1. Classification of the severity

Level	Color	Physiological failures	Technical failures
High	Red	Situation in which the patient's life is in danger	A serious failure in the device in which the monitor may not detect a critical patient status
Middle	Orange	The patient's uncommon constants	Failure of the device that does not put the patient's life at risk
Mild	Yellow	Uncommon constants of the patient, slightly higher than normal	Device malfunction but does not put the patient's life at risk

2 Development

2.1 Fuzzy Logic

Fuzzy logic is a branch of artificial intelligence (IA), created by Professor Lotfi Zadeth at the University of California, whose purpose is to emulate human logic and make decisions even with inaccurate information, is based on a set of mathematical principles based on degrees of membership or belonging, which are a series of linguistic rules that form the input-output relationship approach with one function, which allows to model the system [4]. Allowing to obtain outputs with partial values and the multivalued between 0 and 1, unlike the Boolean logic, which is restricted to two output values: 0 or 1 [5].

The basic anatomy of a fuzzy controller consists of three parts [4]:

Rules: dictate the control action to be taken. These are derived from an expert. These rules are expressed symbolically as:

$$IF\langle proposition\rangle\ then\ diffuse\ diffuse\rangle\langle proposition$$

And the history (IF), as well as the subsequent (then) can be described by multiple parties.

Diffuser: it is the relationship between the actual revenue and the diffuse one; it takes the value crisp of the inputs and determines the degree of membership of each one of them to the fuzzy set's partners,

Defuzzification: takes a diffuse value to the rules and generates a real output, the most widely used method is centroid, which calculates the point where a vertical line divides the whole into two areas of equal mass.

$$Centroide = \frac{\sum_{x=a}^{b} \mu_A(x)x}{\sum_{x=a}^{b} \mu_A(x)} \quad (1)$$

Physiological Failures

The variables considered within the physiological failures (FF) are:

- Heart rate (HR)
- Respiratory rate (FR)
- Temperature (T)
- Partial oxygen saturation (SaO2)

This is because the vital signs monitor which the system of fault prioritization was applied, only counts with measurement of: electrocardiogram (EKG), heart rate, respiratory rate, temperature, and partial saturation of oxygen [2].

Parameters considered are as normal and uncommon for the development of the fuzzy system of physiological MISO failures are based in [3].

Technical Failures

Technical failures (FT) are those that depend on the device (circuit), in the specific case of the system designed for the prioritization of this type of failures were considered:

- Power supply (batteries) (B),
- Electrodes (E),
- Pulse oximeter (SO),
- Sensors: temperature and breathing (ST, SB).

Given the levels of each element.

Development of Systems

The systems were developed considering the aspects mentioned in subsections A and B, rules were established by the expert, in this case the designer of both systems, and settled the outputs of both systems as:

- Normal
- Mild
- Moderate
- Critical

2.2 Monte Carlo Method

Monte Carlo simulation or method is a series of procedures that analyze distributions of random variables from random numbers.

It is a method applicable to deterministic or stochastic problems and gives solution to various mathematical problems from statistical sampling made in computers, the Monte Carlo method, unlike other methods uses the subject-matter of the investigation as object itself, through a random or pseudo-random events that allows to study the model.

Monte Carlo simulation creates a mathematical model of the system to analyze, identifying the input variables of the model, which possess a random behavior that determines the overall behavior of the system, subsequently, the identification of these variables is performed in an experiment that consists of:

- A computer-generated random samples for the input variables.
- Analysis of the system behavior with the generated values.

It's repeated *n* times the experiment and observed the behavior of the system in the n repetitions, in order to understand the behavior of the system [5].

Finally, prioritization systems were probed by:

Input-output relation: when the Monte Carlo method was applied after the establishment of the rules, functionality was proved by Monte Carlo method, with a program created (see Fig. 1) in LabVIEW.

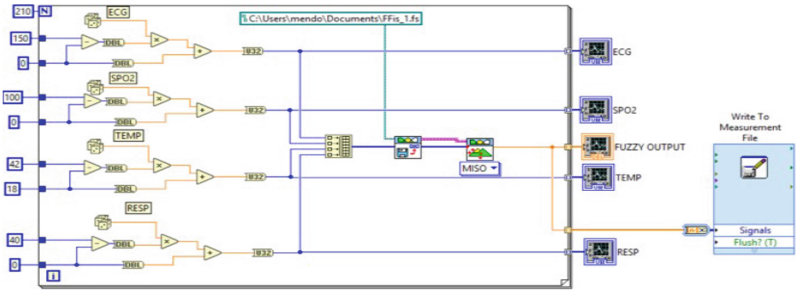

Fig. 1. Monte Carlo Simulation Program (FF).

- Simulated patient test: for those tests, two computers were used, one with the monitor connected by a Wi-Fi network generated in the NI myRIO-1900 board, which had the monitor circuit connected. The second computer was responsible of generating the patient physiological variables through an interface in LabVIEW and NI Biomedical Toolkit at the same platform, the data of the simulated patient was transmitted by a 6210 DAQ card.
- Real patient with system alterations test: different apparently healthy patients were monitored, while measuring was performed failures were altered in sensors and elements of the monitor.

3 Results

Testing the prioritization system were conducted in three stages:

1. Input-output relation
2. Simulated patient test
3. Real patient with system alterations test

Then, each of the tests carried out, as well as the results obtained from them, are developed.

3.1 Input-Output Relation

Both systems were exanimated with two Monte Carlo test: one with 1000 samples and other with 210 samples (Figs. 2 and 3).

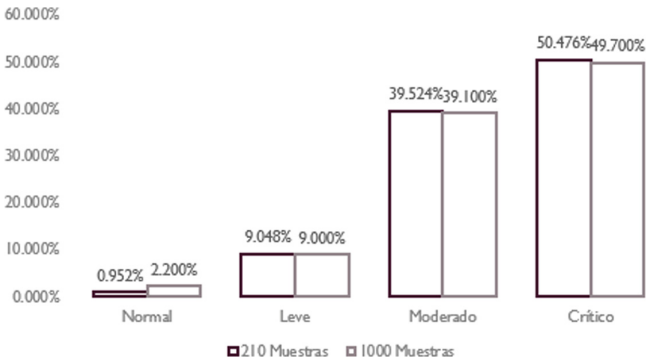

Fig. 2. Results of Monte Carlo simulation in MISO System of FT.

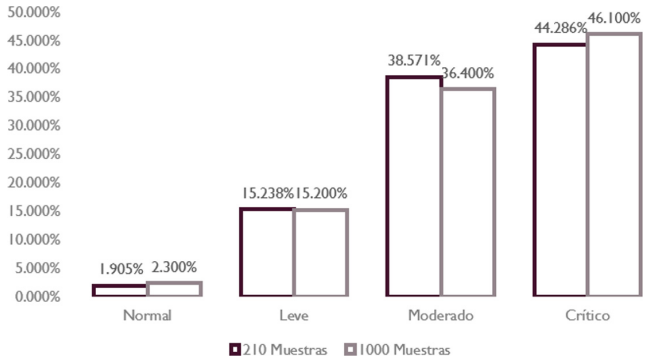

Fig. 3. Results of Monte Carlo simulation in MISO System of FF.

In both fuzzy logic systems, it is show, that both tends to stabilization, regardless of the data amount in each. Both scenarios show us a low index of simulated values that fall on the label of Normal, with only a 0.952% and 2.2% of the cases for physiological failures, and 1.905% and 2.3% for technical failures. Mild label shows an increase in the incidence of cases that the previous label, with a 9.048% and 9% for FF, and a 15.238% and 15.2% for TF. The values of Moderate level were of 39.524% and 39.1% for FF and 38.571% and 36.4% for FT. Most of the evaluations of the degree of belonging generated in the Fuzzy logic systems have fallen on the label of critical in both cases, which represents the 56.474% and 49.7% of the FF, while for the FT represents a 44.286% and 46.1% of the cases.

The behavior of the labels apparently behaves in a way that is exponential, which can be attributed to the behavior of the random variables.

3.2 Simulated Patient Test

Test were conducted with simulated patients with user manipulated physiological parameters. In order to be able to check the functionality of the MISO system for physiological failures, when a patient was in critical condition.

The results obtained with this test, were from various physiological values that fall in different prioritization ranges.

In first instance, patient physiological variables considered healthy were deployed. Results obtained by the fault prioritization system for this patient are shown in Fig. 4.

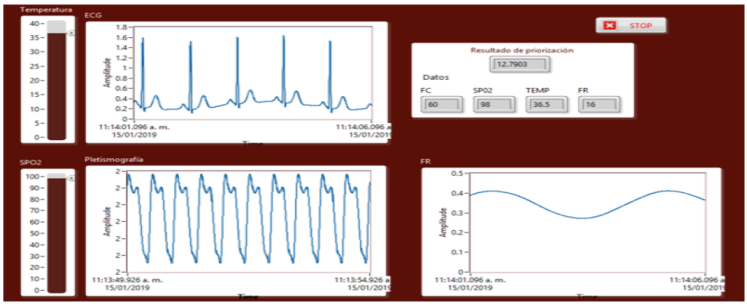

Fig. 4. Result prioritization physiological faults clinically healthy patient values.

As seen, the result of the prioritization was 12.79, which according to the prioritization system is considered as a normal value.

Subsequently several patients with the values shown in Table 2 were simulated.

In addition, four scenarios were generated with patient parameters within expected values for each category.

Table 2. Values of simulated patients.

Physiological parameter	Heart rate	Respiratory rate	Partial oxygen saturation	Temperature	Result of prioritization
Patient 1	53	15	91	36.5	37.46 (Mild)
Patient 2	115	28	86	37.2	52.55 (Moderate)
Patient 3	132	30	89	38	70.06 (Critical)

With healthy patient parameters (Table 3):

Table 3. Prioritization results of MISO system failures FF for healthy patients

Physiological parameter	HR	SaO2	Temperature	RR	Result of prioritization
Patient 1	60	98	36.5	16	12.79
Patient 2	88	92	36.4	19	11.61
Patient 3	70	96	36.2	20	11.4
Patient 4	80	99	36.5	18	11.4

With parameters patient with mild risk (Table 4):

Table 4. Prioritization results of FF MISO system for mild risk

Physiological parameter	HR	SaO2	Temperature	RR	Result of prioritization
Patient 1	53	91	36.3	15	37.46
Patient 2	115	86	37.2	26	37.76
Patient 3	48	90	35.8	12	37.41
Patient 4	122	94	38	27	43.88

Patient parameters at moderate risk (Table 5):

Table 5. Prioritization results of FF MISO system for patients with moderate risk

Physiological parameter	HR	SaO2	Temperature	RR	Result of prioritization
Patient 1	115	86	37.2	28	52.55
Patient 2	38	84	3.4	13	62.7
Patient 3	15	76	35	15	76.94
Patient 4	40	79	34.7	15	64.65

With parameters critical risk patient (Table 6):

Table 6. Prioritization results of FF MISO system for patients with critical risk

Physiological parameter	HR	SaO2	Temperature	RR	Result of prioritization
Patient 1	145	72	38.5	37	88.59
Patient 2	132	89	38	30	79.06
Patient 3	16	68	3.4	6	88.59
Patient 4	22	73	35	8	88.48

3.3 Real Patient Test with Alterations in the System

Finally, tests were performed with a real patient while altering the vital signs monitor sensors arrange.

In Fig. 5 an FT detection can be seen, generating a prioritization of 3.74, indicating that the equipment is altered, having errors in the readings from:

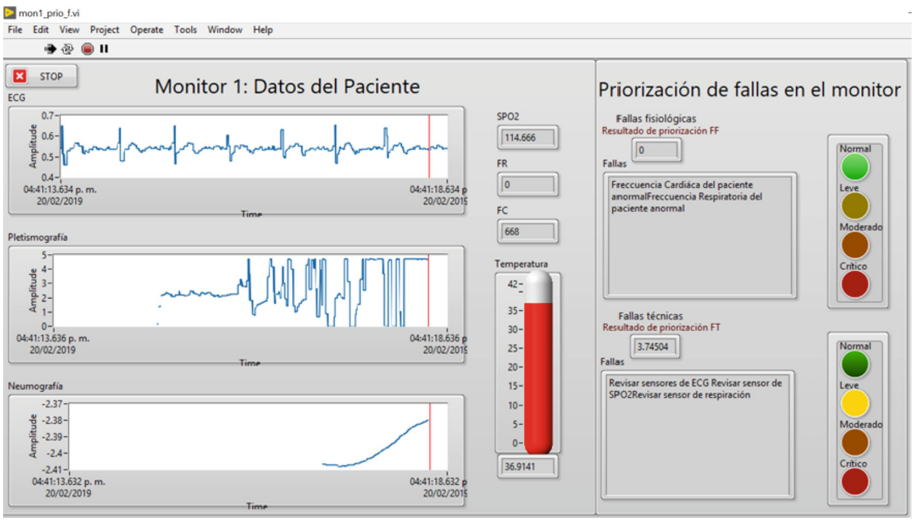

Fig. 5. Test with failure patient connected generating pulse oximeter.

- Electrodes or EKG sensors, such as noise observed in EKG signal observed noise present and the system yields higher frequencies that may present a patient (668).
- SaO2 sensor, the system is reading noise in the sensor as shown in the graph of plethysmography, besides indicating a value of SaO2 114%, which is an impossible value measured by a sensor of this type still being in optimal conditions.
- Breathing sensor, the sensor is not reading correctly the FR, although there are times when the plot unfolds pneumography, the signal does not allow an accurate count of the patient FR.

Since the system failures come from the monitor, the failures cannot be physiological changes of the patient, the physiological failures are maintained as normal, but warnings are displayed in the user interface, alerting that the monitor is not performing correctly.

4 Conclusions

The fault prioritization systems built with the parameters established in accordance with the type of failure, for FF the values from the membership functions of the entries in the system fluctuate according to the values that those can take, while the output values fluctuate between 0 and 100. For the FT values of the membership functions of both input and output are distributed from 0 to 10. Functionality was proved by different tests, in the input-output was verified that MISO systems generates a prioritization according to the different inputs, with a simulated patient test, was demonstrate that FF MISO system prioritize as critical when a patient has several biological alterations and with the real patient and system alteration was probe FT MISO system, were failures in sensors and monitor functionality are present. These systems show the functionality and the applicability to vital sings monitors with the same specifications.

References

1. Marshall, J.C., Bosco, L., Adhikari, N.K., Connolly, B., Diaz, J.V., Dorman, T., Fowler, R.A., Meyfroidt, G., Nakagawa, S., Pelosi, P., Vicent, J.L., Zimmerman, V.K.: What is an intensive care unit? A report of the task force of the World Federation of Societies of Intensive and Critical Care Medicine. J. Crit. Care **37**, 270–276 (2018)
2. Secretaría de Salud: Guías tecnológicas, enero 2005. [En línea]. http://www.cenetec.salud.gob.mx/descargas/biomedica/guias_tecnologicas/13gt_monitores.pdf
3. Secretaría de Salud: Guía de referencia rápida. enero de 2005. Obtenido de CENETEC. http://www.cenetec-difusion.com/CMGPC/ISSSTE-339-08/R.pdf
4. Peña, A.A.: Algoritmo difuso para la gestión de equipo médico, orientado por protocolos de prioridad, aplicado en el inventario del Hospital General 450 de Durango. Ciudad de México (2017)
5. Cruz, P.P.: Inteligencia artificial con aplicaciones a la Ingeniería. Ciudad de México: Alfa omega (2010)
6. Estrada, H.G., Manzanero, A.P., Escobar, O.A.L., Vázquez, J.G., Sotelo, M.G.R., Llanos, A.I.C.: Monitor de signos vitales con comunicación inalambrica Wi-Fi para unidad de cuidados intensivos desarrollado en LabVIEW y la tarjeta myRIO-1900. Res. Comput. Sci. **147**(12), 203–212 (2018)

Evaluation of Algorithms for the Elaboration of the Preventive Maintenance Program of Medical Devices in the Medical Center ISSEMyM Toluca

Angélica C. López-Carranza and Edgar G. Del Hierro-Gutiérrez(✉)

Facultad de Medicina, Universidad Autónoma del Estado de México, Toluca, Mexico
ed.hierro@hotmail.com

1 Introduction

This work will analyze and evaluate various algorithms to carry out a preventive maintenance program for medical equipment at the ISSEMyM Toluca Medical Center "Lic. Arturo Montiel Rojas (CMIT) that is part of the hospital services of the Institute of Social Security of the State of Mexico and Municipalities (ISSEMyM). The CMIT is a high specialty hospital that provides specialty and sub-specialty, outpatient and hospital care as well as emergency service 24 h a day, 365 days a year. In turn, the CMIT is the only high specialty medical unit of the Institute accredited in CAUSES (Universal Catalog of Health Services) before the Federal Ministry of Health [16].

The National Center for Technological Excellence in Health (CENETEC) mentions in the specific action program "Evaluation and Management of Health Technologies" that medical devices are fundamental in the provision of health services and have a role crucial in medical care, so that these are used to solve health problems, as well as to improve the quality of life of the population (one).

A medical device is any instrument, device, implement, machine, software, material or other similar item, intended to be used alone or in combination, for human beings for medical purposes for monitoring, prevention, diagnosis, treatment, replacement or anatomical support [19]. The classification of medical devices is an important parameter that must be taken into account, since in this way there is greater control over their specific applications, it can be according to their level of risk or purpose of use.

The Federal Commission for the Protection against Sanitary Risks (COFEPRIS) has determined the following classifications by their level of risk: Implantable medical device, active, active for diagnosis, therapeutic active, invasive, invasive surgical type. And according to its function and purpose of use: Medical equipment, Prosthetics, orthotics and functional aids, Diagnostic agents, Dental supplies, Surgical and healing materials, Hygienic products.

The maintenance of the medical equipment is transcendental in a health institution, so that it can be maintained in optimal operating and safety conditions [4].

Health institutions must have a preventive maintenance program where, through the evaluation of medical devices, the frequency of preventive maintenance can be

© Springer Nature Switzerland AG 2020
C. A. González Díaz et al. (Eds.): CLAIB 2019, IFMBE Proceedings 75, pp. 1458–1471, 2020.
https://doi.org/10.1007/978-3-030-30648-9_188

established for each of them, guaranteeing their efficient and safe use [5]. Preventive maintenance (MP) covers all those activities that are intended to prolong the life of the device and prevent damage, some of these activities are: calibration, replacement of parts or consumables, cleaning, performance tests, tests electrical safety, inspection of cables, protectors and plugs, external inspection of the equipment to detect breaks or missing parts, among others [6].

The maintenance program is a fundamental aspect of medical equipment management according to the Comprehensive Accreditation Manual for Hospital published by The Joint Commission on Accreditation of Healthcare Organizations (JCAHO). In the chapter Manage of the Environment of Care, the Environment of Care Standard 1.6 (EC 1.6) is included, which mentions that the objective of the maintenance program is to evaluate and minimize the physical and clinical risks of medical equipment used in the diagnosis, treatment, monitoring and care of patients; Its main goals are: (a) Minimize the clinical and physical risks of medical equipment through inspection, testing, cleaning and regular maintenance. (b) Establish criteria to identify, evaluate and inventory the medical equipment included in the program. (c) Provide information to staff about the limitations, capabilities and special applications of medical equipment, as well as operating, safety and emergency procedures, and procedures to be followed to generate reports about equipment management problems, failures and errors of users [22].

In the book The Clinical Engineering Handbook, the authors Joseph Dyron and Matthew F. Baretich mention some basic components that make up a preventive maintenance program under the EC 1.6 standard which are: Inventory, Procedures, Programming and Monitoring [5].

The JCAHO standards allow hospitals to establish criteria directed towards medical teams based on their level of risk to identify, evaluate and inventory those that should be included in the inventory of the maintenance program.

In 1995, the ECRI Institute published an example of this type of approach called "Inspection System and Preventive Maintenance of Health Devices"; This system characterizes medical devices in three types, "high risk", "medium risk" and "low risk" based on the risk of injuries to patients due to medical device failures or user error.

Another important example of this type of approach is the one proposed by the FDA in which medical devices are divided according to the risk involved in their use: Class I, Class II and Class III.

The risk that the device represents for the patient and/or the user is an important factor in the class assigned as mentioned in The Clinical Engineering Handbook.

There is a second approach to designing a risk-based inventory system, which is done through numerical algorithms that determine the medical equipment that will be included in the maintenance program inventory [5]. The objective of this work is to evaluate the following preventive hospital maintenance algorithms for the development of the CMIT preventive maintenance program.

Fennigkoh and Smith Algorithm. The Fennigkoh and Smith algorithm classifies medical devices based on three factors: function, risk, and maintenance required; subsequently, the frequency of preventive maintenance (FMP) is determined where the medical equipment to be included in the preventive maintenance program is selected [24].

WHO Modification. The WHO suggests a modification of the algorithm proposed by Fennigkoh and Smith for the calculation of FMP, which takes into account an additional factor called "History of equipment failures" (twenty).

Clinical Evaluation Modification. On the other hand, in the publication "Modification of the Fennigkoh and Smith algorithm for the calculation of the frequency of preventive maintenance in medical equipment" the authors Sen Salinas, and Aguilar Soto proposed the addition of the variable "Clinical evaluation" (Ec), which corresponds to a clinical evaluation questionnaire addressed to the heads of nursing and to the doctors in charge of the services where the medical equipment is used [25].

Modification of Preventive Maintenance Index. In turn, it is mentioned in the article "Maintenance management for medical equipment" published by E. Rodríguez, A. Miguel and M.C. Sanchez the concept "inventory for risk-oriented maintenance", which is based on the assignment of priority based on the evaluation of each medical team to determine their FMP.

An important concept to mention is the "maintenance of the environment" which refers to the maintenance of spaces, areas, locations and facilities in the hospital where medical equipment is located; This maintenance includes the comprehensive and aesthetic review of the area, in addition to the review of the facilities and medical equipment not included in the maintenance program corresponding to that area [26].

Wang and Levenson's Algorithm. The Wang and Levenson Algorithm proposes that the FMP of the medical team be carried out based on three factors, the risk, the required maintenance and the priority factor [27].

Modification of Wang and Levenson. Despite this, Wang and Levenson's methodology has been modified by incorporating the use rate factor for the determination of the frequency of preventive maintenance [27].

It is important to include medical devices that comply with any of the following principles.

- If the device fails to cause an injury to the patient and by including it in the preventive maintenance program the probability of error can be reduced
- If the life cycle cost can be reduced by including the device in the preventive maintenance program
- If the rules applicable to the medical device indicate that you receive a periodic inspection, it must be included in the preventive maintenance program [24]

WHO Technical Documents

Regarding maintenance regulations, WHO has published a series of technical documents on medical devices that cover relevant topics that mention requirements and specifications that should be applied to medical equipment; The documents to consider are the following: Policy formulation on medical devices [28], Evaluation of the needs of medical devices [29], Introduction to the management of medical equipment inventory [20], Introduction to the medical program maintenance of medical equipment [6].

Two statistical methods are proposed to compare the maintenance frequency algorithms.

Linear Correlation. The most common of these is the correlation analysis that is based on the "two-dimensional distribution" which, in other words, is when a population studies two statistical variables simultaneously.

Bland-Altman Statistical Method. Statistical method to evaluate the concordance between two methods of clinical measurement, which is an alternative method to compare a new technique with an already established one. If the new technique matches well enough with the previous one, it can be replaced [41].

2 Methodology

Next, the different algorithms for the creation of the hospital preventive maintenance program are presented, as well as the methodology that makes it possible to compare them. Each of the algorithms will be evaluated with the representative sample of the medical equipment of the CMIT, once evaluated it is possible to compare them using the Bland-Altman statistical method. The one with the best performance will be chosen and with this the universe of medical equipment of the CMIT will be evaluated.

Fennigkoh and Smith Algorithm (F&S)
It is described by:

$$GE = F + R + MR \tag{1}$$

Where F corresponds to the function; that is, it describes the activity that the device performs; which is rated on a scale of 2–10 according to the following factors: Being of "therapeutic type", 10 Life support, 9 Surgery and intensive care, 8 Physiotherapy and treatment; if it is "diagnostic", 7 Control of surgery and intensive care, 6 Additional physiological control and diagnosis; "Analytical", 5 Laboratory analysis, 4 Laboratory accessories, 3 Computers and related; 2 for Patient related and others.

The variable R corresponds to the physical risk, where the type of risk to the patient or operator is described if the medical device does not work correctly; which is rated on a scale of 1–5 as follows: 5 Risk of death of the patient, 4 Possible injury of the patient or operator, 3 Inappropriate therapy or diagnostic error, 2 Damage to the equipment, 1 No significant risk identified.

Finally, the variable MR corresponds to the required maintenance and specifies its complexity; It is rated on a scale of 1–5: 5 Extensive: Calibrations and replacement of periodic parts; 4 Above average; 3 Usual: Function check and safety tests; 2 Below average; 1 Minimum: Visual inspection.

The sum of the acquired scores is called "team management" (GE); those devices that obtain a GE $\geq$ 12 will be included in the maintenance program or equipment management program. The determination of the preventive maintenance frequency (FMP) will be according to the GE: $\geq$ 12 every 12 months, $\geq$ 15 every 6 months, 19 every 4 months.

WHO Modification

In this modification, the factor "Failure History" (A) or the average equipment failure is considered. The scores corresponding to this factor are: +2 Significant: more than one failure in six months. +1 Moderate: a failure between 6–9 months. 0 Usual: a failure in 9 to 18 months. −1 Minimum: a failure between 18–30 months. −2 Insignificant: less than one failure during the previous 30 months.

So the formula to determine the value of GE is as follows:

$$GE = F + R + MR + A \tag{2}$$

The FMP is given in the same way as the previous case.

Clinical Evaluation Modification

The addition of the variable "Clinical Evaluation" (CD) consists of a questionnaire addressed to the medical staff which consists in evaluating the aspects of: Frequency of use, Reliability of the equipment, Ease of use, Contribution for the treatment of the patient. Each of these is evaluated according to the answer provided: Very high 8, High 6, Medium 4, Low 2, None 0.

The formula for calculating "EC" is as follows:

$$Ec = \frac{(Points\ earned\ by\ the\ device) * 10}{28\ points} \tag{3}$$

So "GE" is as follows:

$$GE = F + R + MR + EC \tag{4}$$

The FMP for this proposal will be: 12 months for 25 < GE < 28, 6 months for 12 < GE < 25.

Modification Priority Calculation

The proposed methodology to perform an "inventory for risk-oriented maintenance" is governed by formula 5:

$$IMP_{(Pt)} = P_i . \frac{t}{T} \tag{5}$$

Where: P_ (i) = Calculated priority level. t = Time elapsed since the last intervention. T = Minimum time between inspections or preventive maintenance according to the manufacturer or experienced maintenance personnel. IMP = Index of preventive maintenance.

The following equation is used to calculate the priority:

$$P_i = E + A + M + F \tag{6}$$

Where, E = Team function according to: 9 Life support teams, 9 Equipment and instruments for surgery and intensive care, 8 Equipment for treatment and physiotherapy, 6 Other equipment for monitoring physiological variables and the diagnosis, 5 Laboratory analysis, 4 Laboratory accessories, 3 Computers and associated equipment, 2 Other equipment related to the patient. A = Clinical application: 5 It can cause death to the patient, 4 It can cause harm to the patient or operator, 3 Inappropriate therapy or false diagnosis, 2 Minimal risk, 1 No significant risk. M = Maintenance requirements: 5 Extensive, 3 Average, 1 Minimum. F = Failure history 1 point for each corrective maintenance, add one point for each corrective in the last year.

All equipment with a score of 11 or more will be included in the medical equipment maintenance inventory. Those with a rating between 10 and 3 may be included depending on the experience of the Biomedical Engineering Department, either to the maintenance inventory of medical equipment or to the maintenance inventory of the environment; Medical equipment that has a rating of less than 3 points will be included in this last inventory [26].

Wang Levenson's Algorithm

Wang Levenson's algorithm considers the priority factor which is calculated on a scale from 1 to 10, depending on the importance of the medical equipment for patient care. The risk factor and the maintenance factor required are evaluated equally to the F&S.

So the formula that describes this methodology is as follows:

$$G = priority\,index + 2 * risk + 2 * maintenance\,required \tag{7}$$

The frequency of preventive maintenance is considered as: $8 > GE \geq 18$ every year, $GE > 18$ every 6 months.

Wang Levenson Modification

The modification of Wang Levenson's algorithm considers the use rate factor, which ranges from 0% to 100% and is governed by:

$$GE = (priority\,index + 2 * maintenance\,required) * usage\,rate + 2 * risk \tag{8}$$

This weighting factor "use rate" is used since at a low rate the urgency of repair is lower, which indicates less importance, on the other hand, this factor does not change the risk for patients in case of equipment malfunction. The FMP is calculated the same as the previous algorithm.

Bland-Altman Statistical Method

The steps to apply the statistical method of Bland and Altman are the following:

The first step is to examine the data through the scatter plot of the results of one method (A) against those of the other method (B), then the regression line is made where, generally, the data points will be grouped near the line and it will be difficult to assess the differences between methods as can be seen in Fig. 1.

For this, a graph of the difference between the methods (A − B) against their mean ((A + B) / 2) can be more informative. This last graph is where the lack of agreement (agreement) will be noticeable because in the first graph it is not evident.

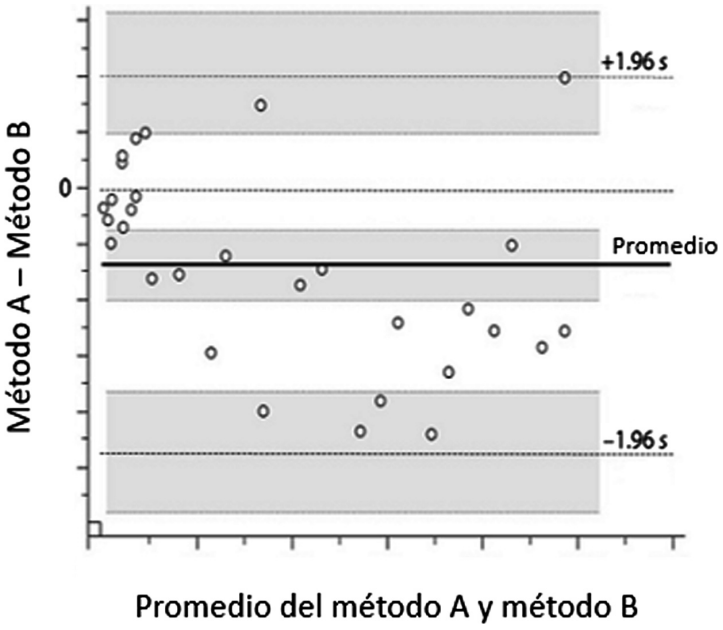

Fig. 1. Bland-Altman chart.

It can be seen that there are three parallel lines that in descending fashion represent:

- Upper match limit: Calculated as D + 2S
- Mean difference: Calculated as average value determined by (A-average value determined by B)
- Lower match limit: Calculated as D-2S

Where D is the difference of the means and S the difference of the standard deviations.

It is expected that most of the data are between the limits of agreement and if the differences are normally distributed, that is to say in a Gaussian way, 95% of the differences will be between these limits (more precisely, between D $\pm$ 1.96S).

If method A and method B obtain similar means, then the average difference will be close to 0, otherwise it would mean that both methods produce different results; In other words, the new method would underestimate or overestimate the validated method.

The limits of concordance allow to visually judge the agreement between both methods, it is important to mention that the wider the range of the limits, the lower the accuracy of one or both methods. If the limits do not exceed the maximum acceptable difference between methods, they can be used interchangeably because both are in agreement [42].

3 Developing

The updated inventory of medical equipment includes the medical equipment owned by CMIT as well as those in the contract shown as follows: 878 Functional, 26 Non-functional, 19 Low, 1 Transfer.

The choice of the sample size of a universe is paramount, because when determining it, representative, valid and reliable information is obtained. It can be by probabilistic sampling (Simple randomized, Stratified randomized, Systematic randomized, By clusters.), Or by non-probabilistic sampling (Intentional, For convenience, Accidental or consecutive.)., where the selection of the sample will depend on the characteristics or criteria that the researcher considers relevant, so it is usually unreliable or reproducible.

The CMIT medical equipment universe is known and is considered an equipment for each function, so those repeated equipment will not be considered as part of the universe.

The formula for determining the sample of a finite universe is as follows:

$$n = \frac{z^2 * p * q * N}{e^2 * N + z^2 * p * q} \tag{9}$$

Where: n = Sample size, e = Estimation error, Z = Confidence level, N = Population size, p = Probability of success, q = Probability of failure.

The level of confidence was determined, which was 99% for this job; it is known that the z value corresponding to 99% is 2.58. [44] p and q were determined; assigning 0.5 to each of them, this is because the sum of p + q must always be equal to one. The maximum acceptable degree of error, in this case it will be 1% since our confidence level is 99%.

Which it involves:

$$n = \frac{(2.58)^2(0.5)(0.5)(148)}{(0.1)^2(148) + (2.58)^2(0.5)(0.5)} = 78.33$$

So the sample number is 79 for a universe of 148 medical teams.

Algorithm Assessment

For the correct assessment of the methodologies, each of the algorithms was applied to the representative sample. Below is an illustrative part of the results.

For a two-phase defibrillator:

F&S Algorithm: Function 10, Risk 5, RM 5, GE 20, Frequency 4. WHO Modification: Function 10, Risk 5, RM 5, Background 0, GE 20, Frequency 4. Clinical Evacuation Mod: Function 10, Risk 5, RM 5, FRU 6, C 6, FU 6, CT 8, EC 9.2857, GE 29.2857, Frequency 4. Mod. Priority Calculation: Function 9, Risk 5, RM 5, HF 0, P 19, TUI 12, TM 6, IMP 38. W&L algorithm: Priority 10, Risk 5, RM 5, GE 30, Frequency 6. Mod. W&L: P 10, Risk 5, RM 5, TU 0.8, GE 26, Frequency 6.

For an electrocardiograph:

F&S Algorithm: Function 6, Risk 3, RM 2, GE 11, Frequency 0. WHO Modification: Function 6, Risk 3, RM 2, Background 1, GE 12, Frequency 12. Clinical Evacuation Mod: Function 6, Risk 3, RM 2, FRU 8, C 6, FU 6, CT 8, EC 10, GE 21, Frequency 12. Mod. Priority Calculation: Function 6, Risk 3, RM 1, HF 1, P 11, TUI 4, TM 6, IMP 7.33. W&L Algorithm: Priority 6, Risk 3, RM 2, GE 16, Frequency 12. Mod. W&L: P 6, Risk 3, RM 2, TU 0.9, GE 15, Frequency 12.

Application of the Bland-Altman Statistical Method

The representative sample of the CMIT medical equipment population was used, which is 79 teams, with a total population of 148 teams (according to their function).

Subsequently, the representative sample was analyzed with the six methodologies where the FMP for medical teams was known.

It is important to mention that, a correct analysis is performed when comparing variables in similar terms for both algorithms evaluated, that is; For algorithms that use the same FMP allocation table, the Bland-Altman analysis must be performed through the GE value, and for those with a different allocation table, it must be performed with the FMP value [41].

The comparison of F&S algorithms with the modification made by WHO is shown by way of illustration (see Fig. 2).

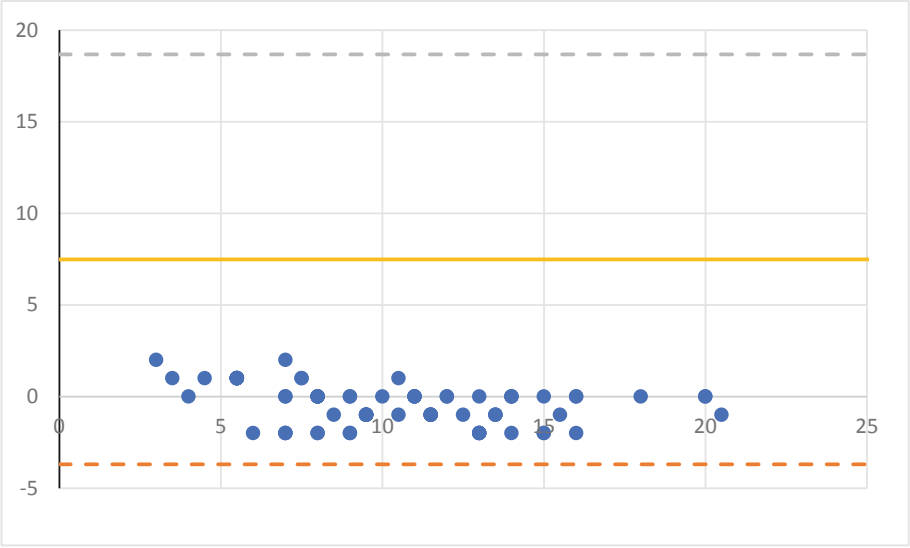

Fig. 2. Fennigkoh and Smith vs. WHO modification.

4 Results

Analysis of Results

In the comparison F&S vs. modification of the WHO, both algorithms agree that they can be used interchangeably, although it can be observed that the variable including antecedents, turns out to be of great importance in the allocation of the FMP because, the more failures it presents a medical equipment, the shorter the period of time between preventive maintenance to reduce the probability of a possible failure (twenty).

W&L and the modification of this are not concordant because the addition of the variable "use rate" had a great impact, which is reflected in the GE values presenting significant changes [22]. The modification of WHO vs. Modification Priority Calculation, are concordant; its mathematical formula does not present a significant change in the index of preventive maintenance, so it is logical to think about the concordance of these methods [20 26]. Likewise, F&S vs. W&L are concordant [24, 27]. On the contrary, F&S vs. Clinical Evaluation modification are not concordant; because there are values outside the allowed ranges, and the addition of the EC variable in the modification is responsible for this result [25]. Finally, in the way of verification the analysis of the WHO modification was performed. W&L, which are concordant.

Comparison of Algorithms

Based on the analysis previously performed, the following comparison is obtained in advantages and disadvantages.

F&S Advantages: It considers the function of the medical team providing additional information on the nature of this (therapeutic, diagnostic, analytical or diverse). Consider the risk involved in the use of medical equipment. Consider the maintenance required for medical equipment. Disadvantages: The factors considered are focused solely on the medical team, leaving the user aside.

WHO modification. Advantages: Considers the function, risk and maintenance required for medical equipment. Consider the history of medical equipment failure. Consider positive and negative scores. WHO approved. Included in the technical document "Introduction to the Medical Equipment Maintenance Program". Disadvantages: The factors considered are focused solely on medical equipment, leaving the user aside.

Modification of priority calculation. Advantages: Considers the level of priority which includes the function, clinical application, required maintenance and history of failures. Consider the time elapsed since the last intervention. Consider the minimum time between inspections or preventive maintenance. Disadvantages: Does not consider the frequency of use, the reliability of the equipment, ease of use and contribution to the treatment of the patient.

W&L Advantages: Consider the priority index, risk and maintenance required for medical equipment. It uses weights in the factors that it considers according to its criterion of importance. Disadvantages: • Does not consider the frequency of use, the reliability of the equipment, ease of use and contribution to the treatment of the patient.

Algorithm Choice

The Fennigkoh and Smith algorithm is originally a great tool to create a preventive maintenance program, because the factors contemplated for its analysis are pillars in the care of medical equipment; referring to the function, risk and maintenance required of them.

These are essential characteristics that must be qualified in a maintenance program and will depend on the nature of each equipment; However, it leaves out of its formula all those factors that contemplate the user or the patient, that is, it focuses solely on the medical team.

That is why, various methodologies start from the algorithm proposed by Fennigkoh and Smith; WHO being one of them contemplates an additional factor: the history of medical equipment failure. This factor is very accurate because the lower the incidence of failure, the greater the period of time between preventive maintenance, contrary to the greater incidence of failures, less time between preventive maintenance.

On the other hand, the Priority Calculation modification includes in its methodology the priority factor, which contains the function, the clinical application, the required maintenance and the history of failures; as was the modification made by WHO; In addition to considering the time elapsed since the last maintenance, as well as the minimum time that should exist between them. However, knowing the time since the last maintenance is complex due to the lack of preventive maintenance programs in hospitals.

Finally, the Wang and Levenson algorithm uses three factors: the priority, the risk and the maintenance required, leaving out the function factor and, unlike the Fennigkoh and Smith algorithm, this makes weightings giving more weight to the risk and to the required maintenance.

Based on the information set forth above, it is concluded that the methodology for the implementation of the CMIT maintenance program proposal is the modification made by WHO, since it has the pillar variables for a correct analysis of medical equipment management risk based; In addition to being supported by an international institution such as WHO.

5 Conclusions

In the ISSEMyM Toluca Medical Center "Lic. Arturo Montiel Rojas" the evaluation of the different algorithms was carried out to determine the frequency of preventive maintenance. It was carried out by the "Bland-Altman" statistical method, which determines the agreement between them, that is to say, it analyzes the behavior of the results with the purpose of statistically defining whether or not the methods can be used interchangeably.

Of the algorithms that were concordant, the algorithm modified by the World Health Organization was chosen to make the proposal of preventive maintenance, due to the international recognition of said organism, as well as by the variables used for the determination of the frequency of preventive maintenance, these being the most important in the analysis. Unlike the other algorithms mentioned, which are not as viable in clinical practice.

It is worth mentioning that an effective preventive hospital maintenance program is one that best suits the needs of the hospital according to the established budget and the general conditions of the medical equipment.

It is important to note that the chosen algorithm adapts to each institution regardless of the different workloads, training levels, user experience levels, etc.

References

1. Centro Nacional de Excelencia Tecnológica en Salud: Evaluación y Gestión de Tecnologías para la Salud [Internet], 1st edn. Diario Oficial de la Federación, México, D.F. (2013). http://www.cenetec.salud.gob.mx/descargas/PAE_2013-2018_CENETEC_13mayo2015_v31.pdf
2. Comisión Federal para Riesgos Sanitarios: Atribuciones Funciones y Características [Internet] (2018). http://www.cofepris.gob.mx/cofepris/Paginas/AtribucionesFuncionesYCaracteristicas.aspx. citado el 20 de abril de 2018
3. Centro Nacional de Excelencia Tecnológica en Salud: Glosario de Gestión de Equipo Médico [Internet], 1st edn. México (2016). http://www.cenetec.salud.gob.mx/descargas/equipoMedico/IB_Publicacion_Glosario_8_27Jun16.pdf
4. Centro Nacional de Excelencia Tecnológica en Salud: Lineamientos para contratación des servicio de mantenimiento a través de terceros, 1st edn. Secretaría de Salud. México, D.F
5. Joseph, D.: The Clinical Engineering Handbook. Elsevier, Acad Press (2004)
6. Organización Mundial de la Salud: Introducción al programa de mantenimiento de equipos médicos [Internet]. Organización Mundial de la Salud. Ginebra, Suiza (2012). http://apps.who.int/iris/bitstream/10665/44830/1/9789243501536_spa.pdf
7. The Joint Commission: About The Joint Commission | Joint Commission [Internet] (2018). https://www.jointcommission.org/about_us/about_the_joint_commission_main.aspx. citado el 3 de agosto de 2018
8. Food and Drug Administration: What We Do. Office of the Commissioner (2018). https://www.fda.gov/AboutFDA/WhatWeDo/default.htm. citado el 26 de marzo de 2018
9. Advancing Safety in Health Technology: Standards - AAMI [Internet] (2018). http://www.aami.org/standards/index.aspx. citado el 20 de abril de 2018
10. American National Standard Institute: About ANSI [Internet] (2018). https://www.ansi.org/about_ansi/overview/overview?menuid=1. citado el 20 de abril de 2018
11. Emergency Care Research Institute: About ECRI Institute [Internet]. 2018 [citado el 20 de abril de 2018]. Recuperado a partir de: https://www.ecri.org/about/Pages/default.aspx
12. American Hospital Association: About ASHE [Internet] (2018). http://www.ashe.org/about/index.shtml. citado el 20 de abril de 2018
13. Secretaría de Salud: ¿Qué hacemos? [Internet] (2018). https://www.gob.mx/salud/que-hacemos. citado el 20 de abril de 2018
14. Centro Nacional de Excelencia Tecnológica en Salud. ¿Qué hacemos? [Internet] (2015). https://www.gob.mx/salud/cenetec. citado el 9 de junio de 2018
15. Instituto de Seguridad Social del Estado de México y Municipios. Misión, Visión y Objetivo | ISSEMyM [Internet] (2018). http://www.issemym.gob.mx/node/22. citado el 9 de junio de 2018
16. Instituto de Seguridad Social del Estado de México y Municipios. Modelo de Gestión de Servicios de Salud, Toluca, 152 p. (2017)
17. INER: Manual de organización específico del departamento de ingeniería biomédica (2013)
18. García Martínez Ana, L.: Control de las funciones operativas de un Departamento de Ingeniería Biomédica. SOMIB. **XXVIII,** 13–20 (2007)

19. Organización Mundial de la Salud: Medical devices [Internet] (2019). https://www.who.int/medical_devices/full_deffinition/en/. citado el 12 de febrero de 2019
20. Organización Mundial de la Salud: Introducción a la gestión de inventarios de equipo médico [Internet], 1st edn. Serie de documentos tecnicos de la OMS sobre dispositivos médicos. Suecia, pp. 1–36 (2012). http://apps.who.int/iris/bitstream/10665/44817/1/9789243501390_spa.pdf
21. Standard Industrie International: El mantenimiento preventivo [Internet]. https://www.standard-industrie.com/es/mantenimiento/el-mantenimiento-correctivo/. citado el 9 de junio de 2018
22. The Joint Commission. Acreditation Guide for Hospitals, 1st edn. U.S.A. (2015)
23. COFEPRIS: Criterios para la clasificación de dispositivos médicos con base a su nivel de riesgo sanitario [Internet]. http://www.cofepris.gob.mx/AS/Documents/RegistroDispositivosMedicos/6criterios_clasif_riesgosan_DM_251. citado el 26 de marzo de 2018
24. Biomedical Instrumentation & Planning: The Fennigkoh-Smith Equation [Internet] (2016). http://biomedicalengineeringconsultancy.blogspot.com/p/best-practice.html. citado el 15 de junio de 2018
25. Sen Salinas, D.A., Aguilar Soto, J.G.: Modificación del algoritmo de Fennigkoh y Smith para el cálculo de la frecuencia de mantenimiento preventivo en equipos médicos. Congr Nac Tecnol Apl a Ciencias la Salud [Internet]. (Generación de Nuevas Técnicas de Diagnóstico y Tratamiento), 5 (2015). http://www-optica.inaoep.mx/tecnologia_salud/2015/memorias/pdf/MyT2015_71_E.pdf
26. Rodríguez, E., Miguel, A., Sánchez, M.: Gestión de mantenimiento para equipos médicos. Gestión Manten para equipos médicos [Internet] **II**(c), 5 (2001). http://www.hab2001.sld.cu/arrepdf/00187.pdf
27. Gaitán, L.T.: Gestión de Tecnologías de la Salud, pp. 1–60 (2015)
28. Organización Mundial de la Salud: Formulación de políticas sobre dispositivos médicos, 1st ed. Departamento de Técnologias Sanitarias esenciales, Suiza (2012)
29. Organización Mundial de la Salud: Evaluación de las necesidades de dispositivos médicos, 1st ed. Departamento de Técnologias Sanitarias esenciales, pp. 1–30. Suiza (2012)
30. Secretaría de Economía: Competitividad y Normatividad/Normalización [Internet]. https://www.gob.mx/se/acciones-y-programas/competitividad-y-normatividad-normalizacion. citado el 11 de abril de 2019
31. Secretaría de Salud: NOM-003-SSA3-2010, Para la práctica de la hemodiálisis. Diario Oficial de la Federación (2010)
32. Secretaría de Salud: NOM-007-SSA3-2011, Para la organización y funcionamiento de los laboratorios clínicos. Diario Oficial de la Federación (2012)
33. Secretaría de Salud: NOM-016-SSA3-2012, Que establece las características mínimas de infraestructura y equipamiento de hospitales y consultorios de atención médica especializada. Diario Oficial de la Federación (2013)
34. Secretaría de Salud: NOM-025-SSA3-2013, Para la organización y funcionamiento de las unidades de cuidados intensivos. Diario Oficial de la Federación (2013)
35. Secretaría de Salud: NOM-027-SSA3-2013, Regulación de los servicios de salud. Que establece los criterios de funcionamiento y atención en los servicios de urgencias de los establecimientos para la atención médica. Diario Oficial de la Federación (2013)
36. Secretaría de Salud: NOM-028-SSA3-2012, Regulación de los servicios de salud. Para la práctica de la ultrasonografía diagnóstica. Diario Oficial de la Federación (2013)

37. Secretaría de Salud: NOM-229-SSA1-2002, Salud ambiental. Requisitos técnicos para las instalaciones, responsabilidades sanitarias, especificaciones técnicas para los equipos y protección radiológica en establecimientos de diagnóstico médico con rayos X. Diario Oficial de la Federación (2006)
38. Secretaría de Salud: a NOM-241-SSA1-2012, Buenas prácticas de fabricación para establecimientos dedicados a la fabricación de dispositivos médicos. Diario Oficial de la Federación (2012)
39. Centro Nacional de Excelencia Tecnológica en Salud. Guías tecnológicas [Internet] (2017). http://www.cenetec.salud.gob.mx/contenidos/biomedica/gtecnologias.html
40. Universidad Autónoma del Estado de México: Correlación Lineal [Internet]. http://www.seduca2.uaemex.mx/ckfinder/uploads/files/u3tema_1_coeficiente.pdf. citado el 15 de noviembre de 2018
41. Bland, J.M., Altman, D.G.: Statistical methods for assessing agreement between two methods of clinical measurememnt. Lancet **1**, 307–310 (1986)
42. Martínez, C.G.: Análisis gráfico de Bland-Altman [Internet]. RPubs (2017). https://rpubs.com/Cristina_Gil/B-A_analysis. citado el 15 de noviembre de 2018
43. Otzen, T., Manterola, C.: Técnicas de Muestreo sobre una Población a Estudio. SCielo [Internet] **35**(1), 227–232 (2017). http://www.scielo.cl/pdf/ijmorphol/v35n1/art37.pdf
44. Moguel, E.A.R.: Metodología de la investigación. Univ. J. Autónoma de Tabasco (ed.) Tabasco, 186 p. (2005)

How to Improve Learning in Biomedical Engineering Students from an Integrated and Formative Evaluation

William Ricardo Rodríguez Dueñas(✉)

Universidad del Rosario, Bogotá, Colombia
william.rodriguez@urosario.edu.co

Abstract. Traditional evaluations of knowledge in engineering education usually focus on the assessments gathered by the teacher from different sources such as exams, essays and laboratory reports. However, this is a single actor's point of view of a learning process: the teacher. The self-evaluation and feedback provided by classmates may also represent an important and useful contribution in at student's learning process. This paper presents an integrated evaluation strategy that includes four equally important components: teacher evaluation, self-evaluation, peer evaluation and group work evaluation. A pilot study was carried out with 20 students taken the Biophysics 1 course offered by the Universidad del Rosario's biomedical engineering program. Results reveal different performances within the groups, allowing the detection of cases where students showed difficulties. Furthermore, it demonstrates the importance of self-criticism and how to positively influence the learning process of others.

Keywords: Education in engineering · Integrated evaluation · Self-evaluation · Peer evaluation · Group work evaluation

1 Introduction

Evaluations of acquired knowledge in engineering education traditionally focus on the assessments obtained by the teacher through different evaluations modes such as exams, essays and laboratory reports. Evaluating these types of student activities is usually an individual task performed by the teacher. In order to provide a better learning process for the student, peer and self-evaluation should be considered and included in determining of the quality of student work. Thus, a clear and objective evaluation that empowers the different actors in the learning process may be secured through the integration of the results of the self-, peer and teacher evaluation [1].

In educational institutions, an evaluation carried out by the teacher is one of the most common way to assess students. The type of evaluation chosen is often based on the evaluation methods the teacher experienced when they were a student. Although many institutions promote academic autonomy, which includes an evaluation process, it is definitely easier for a teacher to consider their own point of view when grading a student's work and acquired knowledge. This is not necessarily wrong; it is simply a way of evaluation that responds to the needs of an educational system. On the other

© Springer Nature Switzerland AG 2020
C. A. González Díaz et al. (Eds.): CLAIB 2019, IFMBE Proceedings 75, pp. 1472–1477, 2020.
https://doi.org/10.1007/978-3-030-30648-9_189

hand, there are several resources for teachers to support an evaluation process such as evaluation guides created according to the required cognitive levels and formative ways of feedback [1] and the objective design of quantitative and qualitative rubrics [2]. It is important to highlight that the teacher's evaluation is considered the most pertinent, as it is the one that draws from deep knowledge about the discipline taught as well on the articulation of the subject in the curriculum of an academic program.

In contrast, self-evaluation is a difficult process that requires self-reflection and self-criticism to be effective. It has little consideration in engineering education, thus the population of students exposed to this type of experience or that have received instruction concerning a self-evaluation process is almost non-existent. However, when it is carried out in a conscious manner, it becomes a powerful tool that promotes good student performance and generates a role model for classmates.

When peer evaluation is implemented in the classroom, an informal evaluation usually occurs. That is, the assessment has no weight in the calculation of the final grade. Hence, peer-evaluation usually loses the required objectivity for an evaluation process. On the contrary, when a grade is considered, feedback between peers may show a positive influence among them. It could lead to an enhancement of trust among peers. This type of evaluation can additionally be applied in different scenarios.

Group work evaluation is a more common activity. A teacher has several alternatives and resources to assess group work and strengthen it. For example, teachers use a variety of active and collaborative learning techniques to evaluate types of learning and student interactions [3–5]. However, only the teacher carries out the evaluation of group work. It is well known that the contributions and efforts of each group member are not always equitable; even so, the final grade is the same for everyone in the group. The proposal of group evaluation under the integrated and formative paradigm allows knowing, for example, each group member's contribution according to the anonymous opinion of the other members. This way, it is easy to identify imbalances in each student's workload and permits actions to reorient the learning processes within a group.

Integrated evaluation is a strategy that, when applied in an objective way, can contribute to students' learning process. It is a formative method that promotes students' processes of self-reflection and self-criticism and facilitates teacher feedback, as it includes the view of other actors who seek to improve learning. The work presented herein shows the results of a pilot study where this strategy was applied in a lab activity of the Biophysics 1 course in a biomedical engineering program of Universidad del Rosario (Bogota, Colombia).

2 Materials and Methods

The pilot study was carried out during the 2018 academic period and was applied in the evaluation of a lab activity in the Biophysics 1 course of a biomedical engineering program.

2.1 Materials

The instruments used for the integrated evaluation of the lab activity were a rubric designed specifically for the teacher to evaluate the format and content of lab reports. For self-evaluation, co-evaluation and group work evaluation, forms proposed by Barkley and coll. in [3] were used. These forms were adapted to the context of the subject. Table 1 shows the questions on these forms.

Table 1. Forms for self-evaluation, peer evaluation and group work evaluation (Adapted from [3]).

Self-evaluation	(Form 1) The final grade is obtained from the numerical average of the six questions	
Rate numerically the following: (from 0 to 5)	1. I was prepared to contribute to the group	
	2. I stayed on task	
	3. I listened to others	
	4. I participated in discussions	
	5. I encouraged others to participate	
	6. Overall, I felt my performance in the group should be rated	
Peer evaluation	(Form 2) The final grade is obtained from the numerical average of the eight questions	
Rate the following in the team member assigned: 3 = Needs improvement 4 = Adequate 5 = Outstanding	The team member…	Demonstrates the following skills…
	1. Prepares	5. Critical thinking
	2. Listens	6. Problem solving
	3. Contributes	7. Communication
	4. Respects others	8. Decision making
Group work evaluation	(Form 3) Qualitative analysis questions: 1–6, and quantitative question: 7	
According to your group work, rate:(six open questions and one numeric question from 0 to 5)	1. Overall, how efficient did your group work together on this assignment? (Poorly, Adequately, Well, Extremely well)	
	2. Out of the four group members, how many participated actively most of the time?	
	3. Out of the four group members, how many were fully prepared for the activity?	
	4. Give one specific example of something you learned from the group that you probably wouldn't have learned alone	
	5. Give one specific example of something the other group members learned from you that they probably wouldn't have learned otherwise	
	6. Suggest one change the group could make to improve its performance.	
	7. In your opinion what rating do you think is appropriate for the group? (from 0 to 5)	

2.2 Methods

The Biophysics 1 course addresses cellular transport phenomena and the generation and propagation of bioelectric impulses. Its value corresponds to a three academic credit course (1 cr = 16 h of face-to-face work and 32 h of independent work). A lab activity concerning the phenomenon of osmosis was chosen for this pilot study (it corresponds to 25% of the practical activities of the course). The class of 20 students agreed to participate in this evaluation strategy. Prior to its implementation, 60 min of class were dedicated to discussing the relevance of the evaluation from different roles (students and classmates). Self-critical and ethical reflection of the evaluation process was discussed, followed by the socialization of the integrated evaluation methodology. Five working groups of four students each carried out the lab activity. The working groups were given a week to hand in their lab reports. This lab report was graded following the established rubric. After the submission of the lab reports, paper-based forms (shown in Table 1) were given out, and the students' thoughts were discussed in a constructive manner. It is important to highlight that the forms used a special codification (established by the researcher) to guarantee confidentiality. Each student was randomly assigned the evaluation of one of their peers. The identity of the peer to be evaluated was kept secret between the researcher and student. The following percentages were used to assign the final grade: 25% evaluation of the teacher, 25% self-evaluation, 25% peer evaluation and 25% group work evaluation.

3 Results

Quantitative results include the individual and group evaluations. Whereas the group evaluation includes the final lab report grade, calculated from the rubric and the mean of the answers to question 7 in Form 3, the individual evaluation incorporates the self-evaluation of Form 1 and the peer evaluation of Form 2.

Table 2. Sample of quantitative results of two students in the osmosis laboratory

	Group evaluation		Individual evaluation		
	Lab report (Rubric) 25%	Group work evaluation (Format 3-question 7) 25%	Self-evaluation (Format 1) 25%	Peer evaluation (Format 2) 25%	Final grade 100%
Student 17	**4.1**	3.9	4.7	4.5	**4.3**
Student 22		Mean group	3.7	3.9	**3.9**

Table 2 shows the quantitative results of two students from the same group. Although the result of the lab report was 4.1, it is clear after the integrated evaluation that Student 17 has a better self-evaluation of his work (4.7). Classmates agreed with this perception (4.5), and the final grade reflects a better performance of this student (4.3) in contrast to Student 22 (3.9). Regarding the qualitative results (Form 3, questions 1–6), the students

mentioned that they learned to make better figures, improve their writing skills and find errors in the interpretation of results easily when working as a team. They were also able to resolve doubts faster in comparison to when they carry out individual work.

4 Discussion

This evaluation strategy provides the teacher tools to identify students' varying levels of performance that traditional group work evaluation does not always show. For example, it detected the case of the student whose self-evaluation and peer evaluation were low. As a result, the teacher approached the student to discuss, in a constructive manner, the quality of their performance. In the next lab activity, the student applied what was discussed. This reveals that working on the student's motivation may have a positive impact in several contexts, including the consolidation of knowledge and reduction of attrition, and it may facilitate the satisfactory completion of studies [6, 7]. On the other hand, the constructive reflection exercise that took place at the end of the evaluation strategy showed that students find more value in their peers' opinions and understand that they can positively affect their own performance and that of others. One of the encountered challenges was the time required to prepare and compile the answers in the forms. However, it may be improved by using electronic forms though platforms such as Moodle, where the numerical results are obtained immediately. Our future work will include a greater number of groups and students to have stronger and more generalized results.

5 Conclusions

This evaluation strategy, which integrates teacher, peer, self- and group work evaluation, may be a powerful tool to help teachers detect different student performances by strengthening the feedback they receive. However, this is only possible if a serious and well-founded exercise on ethical self-criticism takes place.

Acknowledgments. The author would like to thank all the students who participated in this pilot study, as well as Maria Camila Barragan Ramirez, a research assistant from the School of Medicine and Health Sciences of Universidad del Rosario.

Declaration of Conflict of Interest. The author states that he has no conflict of interest in the realization of this work.

References

1. Charles, J., Debra, M.-D., Bob, M., David, N., David, R., Brenda, S.: Enhancing student learning through effective formative feedback (2004)
2. Walvoord, B.E., Stevens, D.D., Levi, A.J.: Introduction to Rubrics: An Assessment Tool to Save Grading Time, Convey Effective Feedback, and Promote Student Learning. Stylus Publishing, Sterling (2013)

3. Barkley, E.F., Cross, K.P., Major, C.H., Elizabeth, C.H.M., Barkley, F., Patricia Cross, K.: Collaborative Learning Techniques: A Handbook for College Faculty, 1st edn. Jossey-Bass, San Francisco (2005)
4. Gullo, C., Ha, T.C., Cook, S.: Twelve tips for facilitating team-based learning. Med. Teach. **37**(9), 819–824 (2015)
5. Rodríguez, W.R., Ríos, A.M., Cruz, A.M.: How Can Biomedical Engineering and Health Science Students Learn Together? In: BT - VII Latin American Congress on Biomedical Engineering CLAIB 2016, Bucaramanga, Santander, Colombia, 26th–28th October 2016, pp. 50–53 (2017)
6. Jones, B.D., Paretti, M.C., Hein, S.F., Knott, T.W.: An analysis of motivation constructs with first-year engineering students: relationships among expectancies, values, achievement, and career plans. J. Eng. Educ. **99**(4), 319–336 (2010)
7. Vecchione, M., Alessandri, G., Marsicano, G.: Academic motivation predicts educational attainment: does gender make a difference? Learn. Individ. Differ. **32**, 124–131 (2014)

Bioimpedance

Gel Impedance Used as a Pressure Sensor: Preliminary Results

Simon Brunnquell[1], Vinicius Sirtoli[1], and Pedro Bertemes-Filho[2(✉)]

[1] State University of Santa Catarina, Joinville, SC 89219710, Brazil
[2] Rua Bernardo Boing 33, Joinville 89221553, Brazil

Abstract. Pressure sensing by measuring the impedance of soft matter, like hydrogels and rubber, has so far posed the problems of low conductivity and hysteresis. Further modifications in the materials to enhance their properties are needed. A pressure sensor using a simple gelatin/agarose double network gel placed between two Ag/AgCl electrodes is presented. The impedance spectra from 100 Hz to 1 MHz were investigated and admittance calculated. Both response time and hysteresis were also investigated. All the experiments were made using an impedance analyzer from Zurich Instruments. Results showed that the lowest standard deviation is at 3.5 kHz. It was found that the admittance increases exponentially from 7.9 to approximately 11.7 mS with increasing the mechanical load at 3.5 kHz. The highest hysteresis of about ±7.6% was found to be at zero load. The measured response time of the gel impedance was approximately 0.5 s, which makes the double network gel feasible for real time pressure monitoring. Mechanical tests measuring the force on the gel due to deformation showed little influence of the gel structure on the impedance. Thus it was concluded that the change of the distance in between the electrodes is responsible for the impedance change of the gel. Calibrations will be necessary for practical applications, since the gel impedance changes as environmental conditions change. This sensor showed better results as compared to conductive rubber published in the literature. It can be concluded that agarose/gelatin gels provide a cheap and easy to fabricate pressure measuring device.

Keywords: Pressure sensor · Bioimpedance · Gel impedance

1 Introduction

In recent decades, gels have been recognized as a material for applications in various areas of research. They served for explanations for the basic functioning in biologic material [1] but also were used in biotechnical systems [2, 3] and utilized as glue [4]. The application of gels as pH-sensors due to their swelling has already been reported [5]. Miao et al. [6] have built a relative humidity sensor based on long-period grating utilizing agarose, hydrogel and gelatin. The piezoelectric properties of gels have also been used as pressure sensor [7, 8].

However, no long-term electric response of pressure on gels has been investigated. This figure is of importance when it comes to bioimpedance, since the application of pressure on the measuring probe causes artefacts due to extrusion of water in the

© Springer Nature Switzerland AG 2020
C. A. González Díaz et al. (Eds.): CLAIB 2019, IFMBE Proceedings 75, pp. 1481–1487, 2020.
https://doi.org/10.1007/978-3-030-30648-9_190

sample under study [9–11]. So in order to avoid misdiagnosis due to artefacts it is of importance to have a real time record of the applied pressure. Furthermore the relation between changes of porosity of uncharged agarose gels due to deformation on their diffusivity was investigated by Gu et al. [12] and it was found that the fixed charge density has no effect on the conductivity [13]. In order to improve the mechanical properties of agarose, gelatin can be added thereby enhancing the springiness and reducing the syneresis [14].

In this paper agarose gel is presented as a pressure sensor by measuring the change of the gel admittance. The main objective is to develop a setup to measure the effect of applied pressure on an agarose/gelatin mixture. Furthermore, a theoretical model will be developed to calculate the relationship between pressure and gel admittance.

2 Materials and Methods

2.1 Measuring Cell

Two commercially nonpolarized Ag/AgCl ECG electrodes (2223BRQ, 3M Brasil Ltda., Sumare) with a diameter of 10 mm were used. The electrodes were placed in the bottom of a plastic cup (see Fig. 1(a)). The gel was made of 2% of agarose, 25% of gelatin, 0.8% NaCl and 72 ml of distilled water. They were mixed in a beaker and then cooked with a Bunsen burner. When the agarose was completely dissolved, the gelatin was gently added while the mixture was cooled down to 70 °C. It was needed to keep it stirring in order to prevent lumps. The final mixture was cooled down at room temperature and then stored in a fridge at 4 °C.

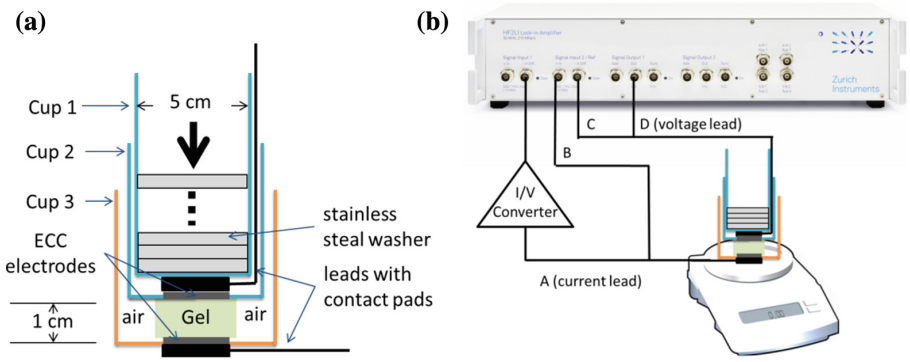

Fig. 1. Schematic of the measuring cell (a) and the experimental setup (b).

2.2 Applied Pressure Measurements

The gel setup was connected to an impedance spectrometer (model HF2IS from Zürich Instruments). The measuring setup is shown in Fig. 1(b). The voltage output of the spectrometer (D) was connected to the upper electrode. The lower one was connected

to the HF2TA current amplifier (A), which is a voltage to current converter. Two further BNC cables (B and C) were connected to the differential voltage input in order to measure the impedance of the gel. Before starting the measurements, the gel was soaked into a 0.9% NaCl solution in order to improve the Gel-interface electrical connection. The amplitude of the applied signal was 1 V. The impedance spectra were measured in a frequency range from 100 Hz to 1 MHz at 10 different applied loads ranging from 0 to 1000 g. The applied pressure was increased from 0 to 960 g and then decreased from 960 to 0 g in steps of 120 g. In order to investigate the material hysteresis during cyclic loading, the process was repeated 7 times. The application of pressure was done by using stainless steel washers of a known mass of 40 g each, which were placed on top of the upper electrode. The measuring cell was placed on an electronic digital scale, by measuring the weight (w), which then was converted to force F (=w * g, where g is the acceleration of the earth), as shown in Fig. 1(b). In order to determine the time response, the impedance over time was recorded after a load step of 120 g. A sinusoidal voltage of 1 Vp was applied into the gel at 10 kHz over 5 s, then a change in impedance was measured by the impedance meter.

2.3 Mechanical Properties of the Gel

The electrical impedance may also be related to the composition and structure of the gel, as well as its geometry, but not directly related to the applied stress. In order to sense the pressure, which is a compressive stress due to its multiphasic material, the behavior of the gel need be characterized. The compressive stress was measured with a load machine (Filizola, Inc.) in which a 5 kN load cell (Flintec, Hudson, MA, USA) was fixed. The specimen (gel) of 38.5 mm diameter and 1 cm thickness was placed under the load cell. The load cell was put in contact with the gel by pressing it down with a velocity of 1 mm/min until the sample get ruptured. The deformation and the compressive stress were recorded with the DinaView software. The applied load was then calculated by multiplying the measured compressive stress by the surface area of the gel and dividing by the gravitational acceleration (=9.8 m/s^2).

3 Results

The measurements of the gel impedance were repeated 7 times and then the most divergent results were discarded and the mean values were calculated, as it can be seen in Fig. 2(a). It can be observed that the first 2 steps of loading led into a big change in the measured impedance. The impedance change for the first load step was 15 Ω at 100 Hz to 5 Ω at 1 MHz. Furthermore, the second load step leads to an impedance change of 17 Ω at 100 Hz to 23 Ω at 1 MHz. As the load reaches 0.96 kg, the system saturates.

It was then observed that impedance modulus changes in a non-linearly way into respect to applied force. In order to calculate a mathematical expression which best represents this non-linearity, the impedance modulus |Z| was converted to admittance (=1/|Z|). It can be observed in Fig. 2(b) that the measured admittance increases non-linearly to

the increasing applied force, which is represented by Eq. 1. At zero force the measured admittance shows the highest hysteresis of about ±7.6% into respect to the mean value. As a result, the modulus of the measured admittance can be converted into applied force by using the Eq. 1, where the admittance is expressed in mS. The residual sum of square was 0.4 with a R^2 coefficient of 0.991.

$$\text{Force} = \left[0.07|\text{S}|^2 - 1.77|\text{S}| + 11.11\right]^{-1} \tag{1}$$

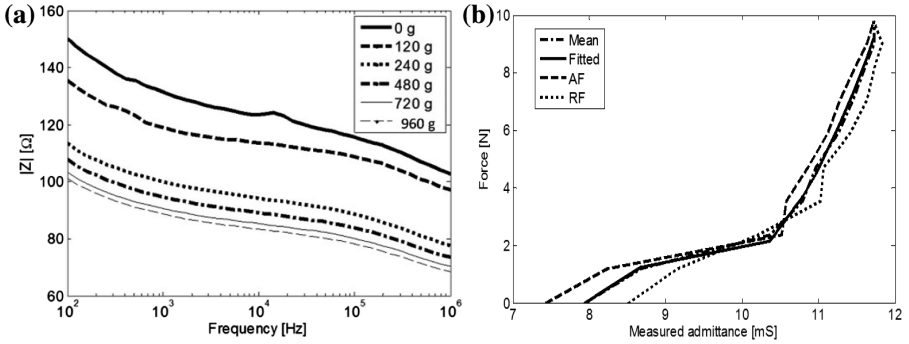

Fig. 2. (a) Modulus of the impedance spectra for six different applied loads in grams. (b) Measured admittance as function of sensing force, where AF stands for applied force and RF stands for released force.

In order to verify the response time of the gel, impedance measurements were made during the first 5 s when a pressure change occurred. As shown in Fig. 3(a), the response time $\mathbf{t_B}$ of the gel was approximately 4.5 s for a change of 14.5 **Ω**. It can also be observed that there is a stabilization in the system before the impedance starts to decrease. The system stabilization time $\mathbf{t_A}$ was 1.4 s, which might be explained by mechanical interference due to vibration occurring just after putting the washer on the top of the electrode. In fact, the washer was thrown from the top of cup 1 (see Fig. 1) at a height of approximately 15 cm, which might explain the gel vibration.

Figure 3(b) shows the average force applied on the gel specimen (=10 samples) and the resulting mechanic deformation. It can be observed that until a deformation of 0.8% no compressive stress could be sensed by the load cell. This dead zone might be explained by the load meter accuracy (=5 kN ± 1 N). From 0.8% onwards, it increases exponentially up to 25 kg in a constant velocity of 1 mm/min downwards. The experiment took about 17 min until the gel ruptured. It also shows a zoom plot for the first 4% of deformation.

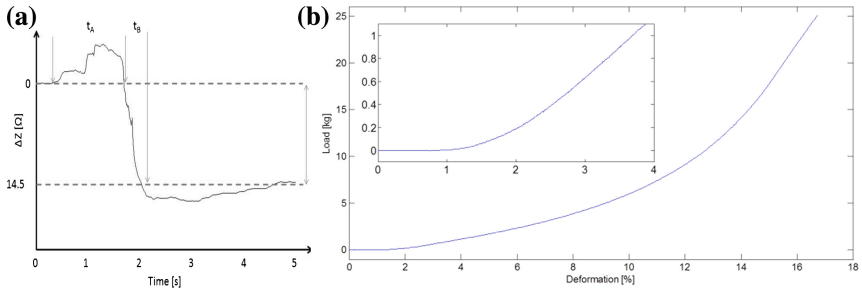

Fig. 3. (a) Measured impedance change as a function of response time. (b) Compressive stress σ of the gel as a function of mechanical deformation.

4 Discussions and Conclusion

It was showed that with weak loads the change in the impedance modulus of the gel is bigger than for higher loads. This leads to an overall exponential decrease in the impedance modulus with increasing pressure on the gel. On the other hand, it could be shown that due to mechanical load the mobility of ions within the pressure sensing material is reduced and thereby the impedance increased [11]. However, in Belmont's work tofu was used as sensing material and our results correspond to investigation of the deformation behavior of double network gels.

Different gel compositions may alter the electrical response of the gel due to the applied pressure, but it was not investigated in this work. This will be discussed in a future work since we were only interested in showing the feasibility of using the gel as a sensing material for applied pressure. The proportion of 2% agarose and 25% gelatin was chosen here according to Somboon et al. [14], which showed that the lower gelatin concentration the worse is the springiness.

The impedance decrease in the range of 0.1 to 1 kHz was observed. This might be explained by the presence of an interface capacitance between the electrode surface and the surface of the gel. Although trying to avoid it by using Ag/AgCl electrodes, bad contact could have caused it. Therefore, further improvement and stabilization of the instrumental setup is necessary, which was showed when the placement of the stainless steel washers caused artefacts in the time response measurements. Moreover, the hysteresis of ±7.6% could be possibly further reduced.

Compared to conductive polymer rubbers, that are said to be promising candidates for touch/pressure sensing [15], the gel used in these experiments showed a lower response time of approximately 0.5 s to an applied load compared to 3 s in the work of Mei et al. [15]. Furthermore, the pressure sensing material can be prepared in one hour, which reduces preparation time compared to the time consuming dispersing of carbon nanotubes or graphene nanoplatelets, and is easier available. Moreover, contrary to Khalili et al. [16] there is no need to enhance the conductivity of the gel used in this study due to its very low impedance.

Compressive stress due to mechanical deformation with the 5 kN load cell could only be measured after a deformation of 0.8%. Forces up to 9.6 N as applied in the

experiments with the steel washers caused a deformation only of about 3.7%. This indicates that the deformation of the gel has relatively little influence on the measured impedance and that the decrease in impedance is rather due to the decreasing distance of the electrodes relative to each other.

It can be concluded that agarose/gelatin gels provide a cheap and easy to fabricate pressure measuring device, also in so far that gelatin and agarose are biocompatible and as part of biological tissues show similar mechanical properties like them. Further investigation needs to be done in terms of the time response behavior to exclude the influence of the manual placing of the load. Furthermore, different gel compositions could be tested in order to see, if greater sensitivities can be achieved. Since the initial impedance at zero load was not precise, a calibration measurement at this condition is necessary.

Acknowledgments. We would like to thank the State University of Santa Catarina (UDESC), CAPES and FAPESC (2454/2011-6) for the financial support. We also would like to thank the staff of the chemistry department and the team of the Polymer laboratory of UDESC for their professional and practical help.

References

1. Pollack, G.H.: The cell as a biomaterial. J. Mater. Sci. Mater. Med. **13**, 811–821 (2002)
2. Peppas, N.A., Hilt, Z., Khademhosseini, A., Langer, R.: Hydrogels in biology and medicine: from molecular principles to bionanotechnology. Adv. Mater. **18**, 1345–1360 (2006)
3. Calvert, P.: Hydrogels for soft machines. Adv. Mater. **21**, 743–756 (2009)
4. Peak, C.W., Wilker, J.J., Schmidt, G.: A review on tough and sticky hydrogels. Colloid Polym. Sci. **291**, 2031–2047 (2013)
5. Richter, A., Paschew, G., Klatt, S., Lienig, J., Arndt, K.-F., Adler, H.-J.P.: Review on hydrogel-based pH sensors and microsensors. Sensors **8**, 561–581 (2008)
6. Miao, Y., Zhang, K., Yuam, Y., Liu, B., Zhang, H., Liu, Y., Yao, J.: Agarose gel-coated LPG based on two sensing mechanisms for relative humidity measurement. Appl. Opt. **52**(1), 90–95 (2013)
7. Sawahata, K., Gong, J.P., Osada, Y.: Soft and wet touch-sensing system made of hydrogel. Macromol. Rapid Commun. **16**, 713–716 (1995)
8. Osada, Y., Gong, J.-P.: Soft and wet materials: polymer gels. Adv. Mater. **10**(11), 827–837 (1998)
9. González-Correa, C.A., Brown, B.H., Smallwood, R.H., Walker, D.C., Bardhan, K.D.: Electrical bioimpedance readings increase with higher pressure applied to the measuring probe. Physiol. Meas. **26**, 39–47 (2005)
10. Dodde, R.E., Bull, J.L., Shih, A.J.: Bioimpedance of soft tissue under compression. Physiol. Meas. **33**, 1095–1109 (2012)
11. Belmont, B., Dodde, R.E., Shih, A.J.: Impedance of tissue-mimicking phantom material under compression. J. Electr. Bioimp. **4**, 2–12 (2013)
12. Gu, W.Y., Yao, H., Vega, A.L., Flagler, D.: Diffusivity of ions in agarose gels and intervertebral disc: effect of porosity. Ann. Biomed. Engin. **32**(12), 1710–1717 (2004)
13. Gu, W.Y., Justiz, M.A., Yao, H.: Electrical conductivity of limbar annulus fibrosis: effects of porosity and fixed charge density. Spine **27**(21), 2390–2395 (2002)

14. Somboon, N., Karilla, T.T., Kaewmanee, T., Karilla, S.J.: Properties of gels from mixed agar and fish gelatin. IFRJ **21**(2), 485–492 (2014)
15. Mei, H., Zhang, C., Wang, R., Feng, J., Zhang, T.: Impedance characteristics of surface pressure-sensitive carbon black/silicone rubber composites. Sens. Actuator A **233**, 118–124 (2015)
16. Khalili, N., Naguib, H.E., Kwon, R.H.: A constriction resistance model of conjugated polymer based piezoresistive sensors for electronic skin applications. Soft Matter **12**, 4180–4189 (2016)

Biosensor of Inflammation Biomarker *NLRP3* Based on Electrical Bioimpedance

Modesto Gómez-López[1], Ángel Miliar-García[2], Nadia Mabel Pérez-Vielma[2], G. Ames-Lastra[3], Eleazar Lara-Padilla[1], Katia Verónica Chávez[1], Arianne Ruby García[1], Josemaría Delgado[1], Ernesto Cortés[1], and César Antonio González Díaz[1(✉)]

[1] Escuela Superior de Medicina, Instituto Politécnico Nacional, Plan de San Luis y Díaz Mirón, C.P. 11340 Mexico City, Mexico
cgonzalezd@ipn.mx
[2] CICS UST, Instituto Politécnico Nacional, Av. de los Maestros, C.P. 11340 Mexico City, Mexico
[3] Universidad Autónoma Metropolitana-Iztapalapa, Mexico City, Mexico

Abstract. The development of biosensors to identify the molecular markers of specific genes is fundamental for the implementation of new techniques that allow the detection of specific DNA sequences in a fast, economic, and simple way. Electrical Bioimpedance Spectroscopy (EBiS) has been used for the diagnosis and monitoring of human pathologies, and is recognized as a safe, fast, reusable, easy, and inexpensive technique. This study proves the development of a complementary DNA (cDNA) biosensor based on measurements of EBiS and of the immobilization of DNA without chemical modifications, and presents the evaluation of its potential usefulness in the detection of the gene expression of an inflammation characteristic biomarker, NLRP3, is presented. The obtained results demonstrate that EBiS can be used to identify different gene expression patterns, and measurements were compared with Quartz Crystal Microbalance with Dissipation monitoring (QCM-D) and validated by Quantitative Polymerase Chain Reaction (qPCR). These results indicate the technical feasibility of a biosensor of specific genes through bioimpedance measurements in the immobilization of cDNA.

Keywords: Impedance · QCM · qPCR

1 Introduction

Electrical Bioimpedance Spectroscopy (EBiS) has been used for the diagnosis and monitoring of human pathologies and has been recognized as a safe, fast, reusable, easy, and inexpensive technique. EBiS is a measurement technique based on the electrophysiological characteristics of the conductivity and dielectric properties of biological analytes [1, 2]. Hybridized DNA sensors based on impedance have a wide range of applications, including medical diagnoses, biosecurity, environmental aspects, and forensics [3, 4]. Obesity is frequently associated with systemic and chronic low-grade inflammation. Inflammasome NLRP3 is a polyprotein complex with crucial

© Springer Nature Switzerland AG 2020
C. A. González Díaz et al. (Eds.): CLAIB 2019, IFMBE Proceedings 75, pp. 1488–1493, 2020.
https://doi.org/10.1007/978-3-030-30648-9_191

activity in the inflammatory processes. It has been reported in subjects and rodents with obesity [5, 6]. The traditional techniques employed to determine inflammation markers are expensive, take a long time, and are not reusable, the reason why the use of a reliable, reusable, and novel technique such as EBiS might be relevant.

In this study, we evaluated an innovative biosensor whose development is based on two fundaments: (1) immobilization of cDNA on a functionalized gold surface and embedded in a quartz crystal, in such a manner that the cDNA possesses the ability to hybridize with a specific oligonucleotide sequence, and (2) the analysis of multi-frequency electrical bioimpedance changes as a function of the modification of molecular and structural components on the functionalized gold surface, which was compared with QCM-D and validated by qPCR.

2 Materials and Methods

2.1 Description of the cDNA Biosensor System

The cDNA biosensor system consists of four modules: (1) infusion pump; (2) electrical-ionic interface; (3) ScioSpec bioimpedance meter, and (4) Personal Computer (PC) (Fig. 1). The electrical-ionic interface was implemented by a micro-fluidic module of a quartz microbalance (Q Sense-Flow, Biolin Scientific™) for bioimpedance measurement. The cDNA immobilization and hybridization process is carried out on the gold surface. The SciospecTM module (ScioSpec, ISX-3, Germany) is the instrument that allows us to interact with the electrical-ion interface module, injecting a sinusoidal potential difference of 250 mV.

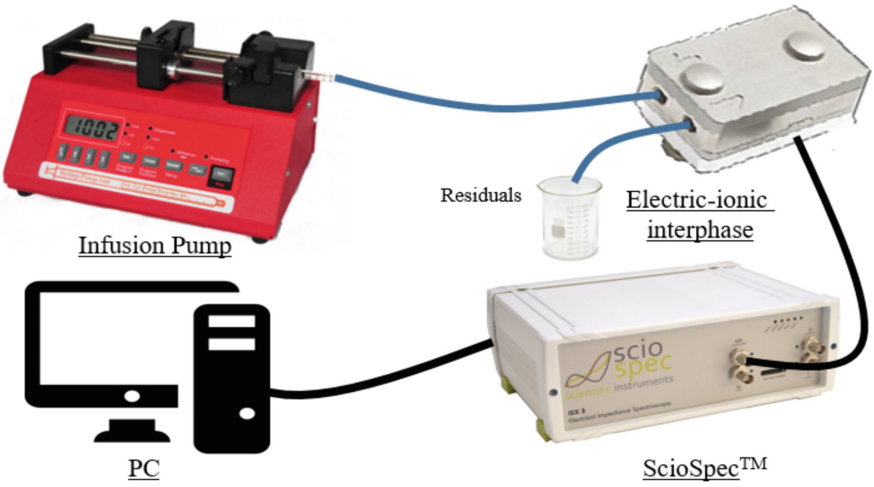

Fig. 1. Components of the cDNA biosensor system.

2.2 Functionalization Surface Chemistry, RNA Extraction, CDNA Synthesis, and Real-Time Quantitative Polymerase Chain Reaction (qPCR)

Surface chemistry over gold was performed as previously described. Human total RNA was extracted from the blood samples of obese children, with the samples provided by the Obesity Project of the INP "Escuela Superior de Medicina". This protocol was approved by the Ethics and Research Committees of the "Escuela Superior de Medicina" (ESM-CE-01/03-12-2013). RNA was isolated as previously described, as well as the carrying out of cDNA synthesis. A concentration of 350 ng/μL of cDNA was used for the bioimpedance and QCM experiments. qPCR for validation were performed as previously described [7].

2.3 Bioimpedance Spectroscopy Measurements

The measurements of bioimpedance spectroscopy were conducted through a ScioSpec ISX3 spectrometer controlled by means of a personal PC (HP mini 110-1,100). This was programmed to perform measurements within a frequency range of 100 Hz–1 MHz in 126 logarithmically spaced steps. Measurements of bioimpedance were carried out in triplicate and stored in its resistance and reactance components; thus, the estimation of EBiS magnitude was determined for NLRP3 gene cDNA hybridization.

2.4 Surface Chemistry and QCM-D Hybridization Assays

The reagents used for surface chemistry over gold and the QCM-D hybridization assays were performed as previously described [7].

2.5 Experimental Design

The experiment to evaluate the potential usefulness of the cDNA biosensor system for the detection of a specific gene associated with inflammation (NLRP3) is described as follows: the analytes were infused by a microfluidic vehicle through the electrical-ionic interface in order to perform cDNA immobilization (350 ng/uL) and hybridization with the oligonucleotide (100 ng/uL) in the following four steps: (1) cleaning the system with purified water (Milli-Q water); (2) cDNA immobilization on the functionalized gold surface; (3) hybridization of the cDNA with the oligonucleotide, and (4) clearance of waste with Milli-Q water and measurement of multi-frequency electric bioimpedance on the resulting gold surface. Each step of analyte infusion was performed in 12 min segmented by a relaxation time of 30 min (see Fig. 2). Each assay was performed in triplicate. This methodology was employed in the QCM-D and EBiS experiment.

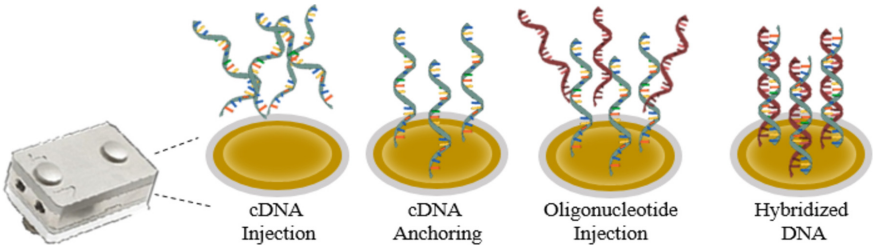

Fig. 2. Experimental Design. Functionalized quartz crystals were placed in the electrical-ionic interface module and the corresponding analytes were infused as follows. (A) Control: Milli-Q water injection only; (B) gene: Milli-Q water injection, cDNA, specific oligonucleotides and swept with Milli-Q water, and (C) Negative Control: Milli-Q water injection, cDNA, non-specific oligonucleotides and swept with Milli-Q water.

3 Results and Discussion

3.1 EBiS, QCM-D, and qPCR

Figure 3 shows the bioimpedance spectrum measured in magnitude. The Control test reveals substantially different behavior with respect to the NLRP3 gene and the Negative Control assays. We observed that, for the NLRP3 gene assay and the Negative Control, there was a notable difference in the results due to the existence of hybridization and the absence of same for case of the Negative Control; the graphs fall within similar dynamic ranges resulting from the immobilization performed under both conditions.

The same conditions were assayed in the QCM-D. Once no interaction with the functionalized surface of the control sensor was proven, the hybridization assays with the NLRP3 gene was performed. The results demonstrated an increase in the mass concentration deposited on the crystal quartz compared to that of the Negative Control. The expression of messenger RNA (mRNA) for the NLRP3 gene was validated by qPCR. The obtained results are reproducible compared to those previously obtained for the same samples [7].

The search for biomarkers in the diagnosis and understanding of the pathophysiology of human diseases is becoming increasingly important in the medical area. The development of different types of biosensors in this area has increased in recent years due to the advantages offered by biosensors, including a low amount of the sample, on-site detection, and quick and robust analysis [8]. EBiS is recognized as a safe, fast, reusable, easy, inexpensive, and simple way to perform the technique, requiring no detection tags and also allowing for miniaturization [7].

The results of the present study demonstrated that the bioimpedance of the Negative Control decreases with respect to the *NLRP3* gene; in this respect: the cDNA immobilization and its hybridization should promote structural changes on the resulting gold surface, which should contribute to an increase in electrical conductivity that is possibly associated with an apparent increase in the effectiveness of the electric-ion exchange.

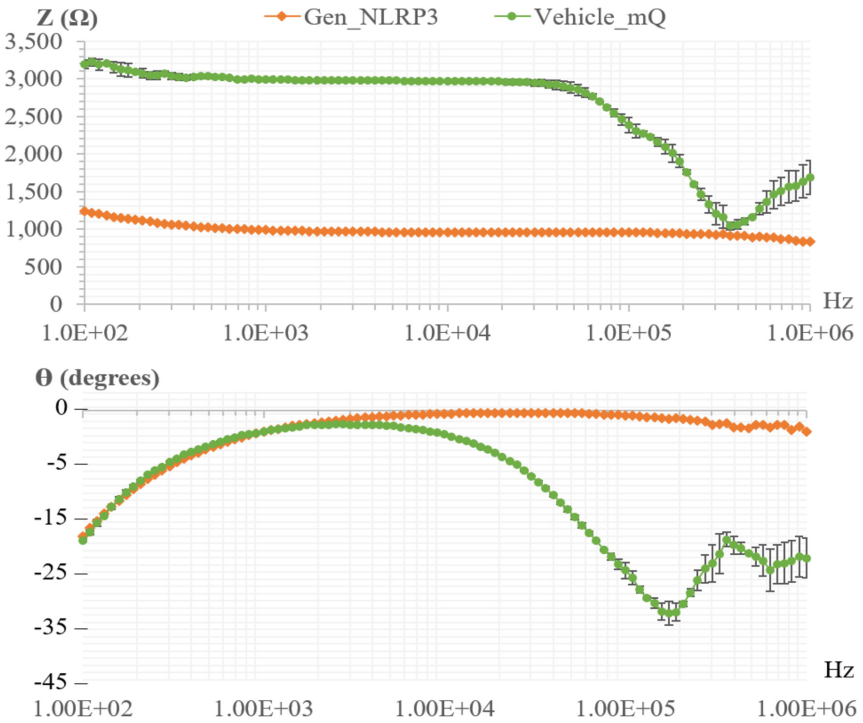

Fig. 3. Magnitude and phase EBiS spectra for the studied gene (*NLRP3*) as well as for Control (vehicle) and Negative Control (non-specific gene) conditions.

In a study that could be considered a previous reference, the group of Ma reported a correlation between impedance and DNA fragment length, proposing the use of an electrical system to validate and characterize PCR products [8]. The results obtained in this work reveal that the integrated relative EBiS values are in agreement with the relative expression of the gene encoding for *NLRP3*. Such findings are interesting for demonstrating the relationship of EBiS vs. qPCR as a validation technique. qPCR is the gold standard technique for determining gene expression.

4 Conclusions

The results indicate the technical feasibility of developing a biosensor of molecular markers or specific genes through the immobilization of non-labeled cDNA and its detection with measurements of electrical bioimpedance spectroscopy. The observations show that the developing biosensor cDNA system offers the possibility of detecting the gene expression of NLRP3 with similar results obtained by QCM-D and validated by qPCR. Our obtained results indicate that EBiS could be utilized to identify different gene-expression levels in human samples, giving rise to the possibility of its

application for medical diagnostics in different pathologies. Further studies are warranted to confirm these findings.

References

1. Kimberly, N.J., Siders, W.A., Johnson, L.K., Lukaski, H.C.: Validity of segmental multiple-frequency bioelectrical impedance analysis to estimate body composition of adults across a range of body mass indexes. Nutrition **25**(1), 25–32 (2009)
2. Jun, M.-H., Kim, S., Boncho, K., Cho, J., Kim, K., Yoo, H.-R., Kim, J.U.: Glucose-independent segmental phase angles from multi-frequency bioimpedance analysis to discriminate diabetes mellitus. Sci. Rep. **8**(1), 648 (2018)
3. Zhu, B., Travas-Sejdic, J.: PNA versus DNA in electrochemical gene sensing based on conducting polymers: study of charge and surface blocking effects on the sensor signal. Analyst **143**(3), 687–694 (2018)
4. Marsilea, A.B., Harbison, S.A., Travas-Sejdic, J.: Development of an electrochemical polypyrrole-based DNA sensor and subsequent studies on the effects of probe and target length on performance. Biosens. Bioelectron. **28**(1), 362–367 (2011)
5. Fan, W., Xu, Y., Liu, Y., Zhang, Z., Lu, L., Ding, Z.: Obesity or overweight, a chronic inflammatory status in male reproductive system, leads to mice and human subfertility. Front. Physiol. **4**(8), 1117 (2018)
6. Zhang, C., Boini, K.M., Xia, M., Abais, J.M., Li, X., Liu, Q., Li, P.L.: Activation of Nod-like receptor protein 3 inflammasomes turns on podocyte injury and glomerular sclerosis in hyperhomocysteinemia. Hypertension **60**(1), 154–162 (2012)
7. Gómez-López, M., Pérez Vielma, N.M., González-Martínez, H., Lara-Padilla, E., Bandala, C., Gonzales- Torres, M.C., Miliar-García, A.: NLRP3, IL-1β, and Caspase-1 gene transcript identification and expression by QCM-D in obese children. J. Sens. **2019**, 14 (2019). Article ID 4323056
8. Berney, H., West, J., Haefele, E., Alderman, J., Lane, J., Collins, J.K.: A DNA diagnostic biosensor: development, characterisation and performance. Sens. Actuators **28**, 100–108 (2000)

EMG-Based Kinematic Impedance Control of a Lower-Limb Exoskeleton

Lourdes Luna(✉), Itzel García, Marco Mendoza, Guadalupe Dorantes-Méndez, Aldo Mejía-Rodríguez, and Isela Bonilla

Faculty of Science, Autonomous University of San Luis Potosi, 78295 San Luis Potosi, SLP, Mexico
lourdeslunardz_2895@outlook.com

Abstract. This paper presents the control of a lower-limb exoskeleton in real time, to assist a pathological gait, taking into account only electromyography (EMG) events and a characteristic angular pattern of a normal gait. The algorithm consists of an impedance control scheme that uses EMG signals to modify the characteristic angular pattern of a normal gait. EMG signals were characterized using the simple square integral (SSI) index and this information was used to identify a characteristic EMG pattern in the semitendinosus and gastrocnemius muscles. Finally, a series of experimental tests were conducted with a volunteer to validate the adequate performance of the system.

Keywords: Electromyography · Exoskeleton · Human gait · Impedance control

1 Introduction

In 2015, in Mexico it was reported that about 64.1% of people with disabilities have problems in the lower extremities [1]. One of the fundamental actions of humans is the walking or human gait, which is defined as a kind of bipedal locomotion, where the lower limbs perform a series of steps in a coordinated and alternated way, thus, by maintaining the subject in dynamic equilibrium [2]. A complete gait cycle or stride consists of two phases: stance and swing of a limb (see Fig. 1), which is bounded from the occurrence of a specific event until the same event occurs again [3]. This process can be described by angular displacements and/or characteristic muscular actions, which allow to identify any change or alteration in the pattern of this cyclic movement.

From a general perspective, the gait can be classified as normal or pathological. A pathological gait results from a joint action of pathological and compensatory mechanisms of the body to correct or normalize, as much as possible, the changes that occur in the gait movement. There are several types of gait analysis, ranging from the measurement of motion characteristics (position, velocity,

© Springer Nature Switzerland AG 2020
C. A. González Díaz et al. (Eds.): CLAIB 2019, IFMBE Proceedings 75, pp. 1494–1501, 2020.
https://doi.org/10.1007/978-3-030-30648-9_192

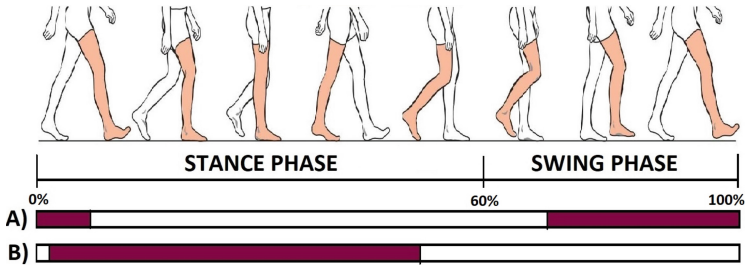

Fig. 1. Spatial sequence of the cycle of the human gait (stance and swing phases). In the lower part of the figure, the activity during the gait phases of the muscles (A) semitendinosus and (B) gastrocnemius is shown.

acceleration, etc.), stride analysis, angular kinematics, force plate, foot pressure and EMG analyses [3,4]. For example, in [5] EMG and stride analyses are performed, in order to identify muscular and angular patterns under two conditions: normal gait and with the IBWS (Ischial Body Weight Support) system for load relief. Also, in [6] angular kinematic analysis is used to evaluate predefined trajectories with the ELLTIO (Exoskeleton for Lower Limb Training with Instrumented Orthosis) device in rehabilitation routines. In [7] a review of the state of the art of exoskeletons for lower extremities is presented and different types of sensors are used to detect the gait phases, in order to adequately control all the robotic devices. In general, exoskeleton control systems use the fusion of a large amount of input information, such as position, EMG, pressure or force sensors, accelerometers, etc. Therefore, in this context and in order to minimize the input information to control an exoskeleton, this paper presents the impedance control of a lower-limb exoskeleton in real time, to assist a pathological gait, taking into account only EMG events and a characteristic angular pattern of a normal gait.

2 Methods and Materials

2.1 Acquisition Protocol

A male adult carried out the acquisition, who gave his written, informed consent to participate. This subject after performing some high intensity physical activity suffers from an inflammation in the ligaments of the left ankle joint. EMG signals, angular movements and surface feet contact during the gait were acquired through the Biometrics system (Biometrics Ltd., Newport, UK), which consists of an acquisition module (DataLOG MWX8 Bluetooth ®), eight surface EMG differential sensors with a gain of 1000 and bandwidth of [20–460] Hz (SX230 EMG Amplifier), two SG150 goniometers, a SG110/A goniometer, a contact pressure sensor with four digital inputs (FS4 Contact Switch) and a ground electrode (R506 Ground Strap). The acquisition was performed using the manufacturer's software (DataLOG Software v8.51). All the maneuvers of the protocol were performed on an electric treadmill (Athletic Works, AR, USA).

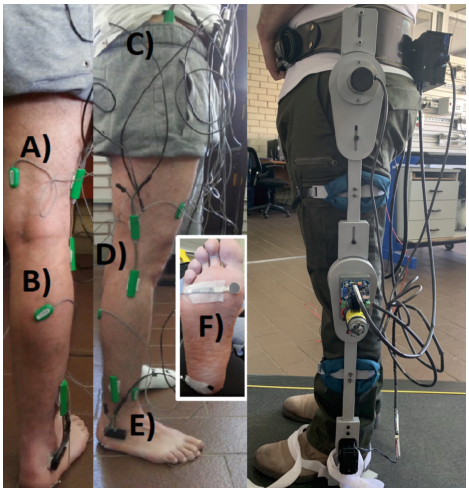

Fig. 2. Placement of the exoskeleton, EMG and pressure sensors and goniometers on the volunteer. (A) EMG semitendinosus, (B) EMG gastrocnemius, (C) hip goniometer, (D) knee goniometer, (E) ankle goniometer and (F) pressure sensors.

The EMG sensors were placed in the muscles: (A) semitendinosus of the hamstring group and (B) gastrocnemius, as shown in Fig. 2. The goniometers were placed on the external lateral side of the left lower limb, the SG150 goniometers were placed on the hip and knee joints, while the SG110/A goniometer on the ankle joint. The contact sensor terminals were placed in the metatarsal area and the heel of the foot. The acquisition was divided into two stages: first, when the subject was without any injury, and then when the subject had performed physical activity the previous day. In both cases, the subject was instructed to walk on the treadmill in the most comfortable and appropriate manner for him, for three minutes and at an appropriate speed for his anthropomorphic dimensions (2.5 km/h and 0.8 km/h, respectively). The signals were acquired at a sampling frequency of 1 kHz and stored for further processing in Matlab (The MathWorks, MA, USA). These acquisitions made with the Biometrics system were used to establish the EMG and angular patterns characteristic of the subject's gait.

2.2 Identification of Angular and EMG Patterns

For identification of the gait phases, the movements of flexion/extension for each joint were analyzed, these movements were selected due to the characteristics of the exoskeleton used in the experimental tests [8]. The signals were automatically segmented by means of the pressure sensor information and the average behavior for each joint was calculated, which is in agreement with the behavior reported in the literature [5].

In order to simplify the real time implementation of the control algorithm for the exoskeleton, the angular pattern of hip joint is used as a reference to

determine the subject gait stage's. Then, a polynomial representation of the angular patterns was made by using cubic polynomials of the form $at^3 + bt^2 + ct + d = e$, where t corresponds to the current time instant, e represents the current angular position of the hip and the constants a, b, c and d correspond to data interpolation obtained in the characterization. Finally, from the polynomial resulting from the hip joint, the root t_1 of the polynomial $at_1^3 + bt_1^2 + ct_1 = e - d$ was used to identify at what gait stage the subject is.

On the other hand, in order to identify the EMG pattern, the methodology proposed in [9] was used, but limited to the activity of the semitendinosus and gastrocnemius muscles. These muscles were selected due to their superficial location and significant participation in the gait cycle [2]. In Fig. 1, it can be observed that the semitendinosus muscle exhibits more activity during the swing phase, while the activity of the gastrocnemius muscle is greater during the stance phase. The signal pre-processing was carried out in Matlab, which consisted of a IIR band-stop filter to suppress the 60 Hz noise and its first harmonic, followed by a 4th-order Butterworth high-pass filter with a cutoff frequency of 10 Hz to suppress motion artifacts. Subsequently, the gait segments (cycles) were extracted. For each cycle, the SSI index was computed, using a 256 ms window with a 99% overlap per cycle. As in the case of the angular pattern, it was decided to represent the EMG pattern using third degree polynomials.

2.3 Kinematic Impedance Control

In order to use the EMG pattern during human gait assistance, it is proposed to use a kinematic impedance control scheme, derived from [10], which consists in generating a reference trajectory given by

$$\mathbf{q}_r = \mathbf{q}_d - \mathbf{q}_f \tag{1}$$

where $\mathbf{q}_r$ is the vector of reference angular trajectories (for the knee and ankle joints, respectively), $\mathbf{q}_d$ is the vector of desired joint trajectories (angular patterns) and $\mathbf{q}_f$ is the adjustment vector to be applied to the desired angular trajectory to obey the movement generated by the active force exerted by the subject, such an adjustment vector is defined as

$$\mathbf{q}_f = (K_d + B_d s + M_d s^2)^{-1} \tau_e \tag{2}$$

with s being the Laplace complex variable, τ_e corresponding to the torque vector components obtained by normalizing the EMG activity of the subject with respect to the average EMG pattern. The filter gains K_d, B_d and M_d represent diagonal matrices of adjustable parameters of stiffness, damping and inertia, respectively, and which characterize the system's dynamic response in the face of the torques generated by the subject.

It is important to note that this control scheme allows to implement two operation modes for the exoskeleton: passive and active. The passive mode occurs when the subject can not perform the stride and the exoskeleton is responsible for moving the lower limb to perform the movement, i.e. $\mathbf{q}_r = \mathbf{q}_d$. The active

mode occurs when the subject is able to perform all or part of the stride, so the reference trajectory is modified due to the indirect force control.

The normalized exerted torque τ_e is related to the EMG signal, therefore, the muscle activity during the gait will be defined between 0 and 1, where 0 represents that the subject did not make any effort and 1 that the maximum effort necessary to generate the movement was made. Thus,

$$\tau_e = T(\mathbf{EMG}_p - \mathbf{EMG}) \tag{3}$$

where $\mathbf{EMG}_p$ is the vector containing the envelopes of the EMG gait pattern signals, $\mathbf{EMG}$ is the vector containing the envelopes of the current EMG signals and T is a diagonal matrix whose elements are the characteristic torques of each joint, which is used to normalize the exerted force according to the units used by the force filter implemented.

3 Results and Discussion

The lower-limb exoskeleton operates in passive and active modes, however, in this work the results for active mode are presented. In general, the exoskeleton has three degrees of freedom. In the hip joint, there is an incremental YUMO rotary encoder (E6B2-CWZ3E), which is used as a gait-phase detection sensor. A high-torque ASMC-04B servomotor is used for the movement of the knee joint, while the Dynamixel MX-64AT servomotor is used for the ankle joint.

For tuning the controller during the experimental tests, it was necessary to investigate the masses and torques characteristic of the lower limb. In [11,12] the percentages of mass corresponding to the thigh, leg and foot were consulted, the entire lower limb equals to 16% of body weight, leg and foot to 5.9% and foot to 1.5%. In addition, in [3] the joint torques were consulted, being 0.5 Nm/kg for the hip, 0.8 Nm/kg for the knee and 1.75 Nm/kg for the ankle. The values of impedance control parameters were $K_d = \text{diag}\{2.8156, 0.5625\}$, $B_d = \text{diag}\{5.1407, 1.8271\}$ and $M_d = \text{diag}\{1.5223, 0.3041\}$, for the knee and ankle joints, respectively.

To verify the correct operation in active mode, two experimental tests were performed: the first one without having carried out a demanding physical activity and the second one after having carried out such physical activity. It should be noted that, for the implementation of the impedance control (1)–(3), the EMG envelopes of the semitendinosus and gastrocnemius muscles were used as interaction forces to modify the articular reference trajectories of the knee and ankle, respectively.

Due to space limitations, only the results of the second experimental test are shown in the present work. In Fig. 3 some results of this test are presented; the upper graph shows the angular displacements of the hip, which are in the range of values of the previously defined angular pattern, however, there are some significant differences due to the subject's was injured before the test. Then, according to this information, the angular reference trajectories of the remaining joints are computed. On the other hand, in the left column of Fig. 3, the envelopes of the

EMG pattern signals of the semitendinosus and gastrocnemius muscles (red), and those corresponding to the gait in process (blue) are presented. The left vertical axis corresponds to the amplitude of the EMG envelope and the right vertical axis to the amplitude of the EMG envelope of the injured gait. It can be observed that there are significant differences between both muscular activities, with respect to the amplitude and at the moments in which the muscular contractions occur, which is considered admissible due to the subject's injury and the compensatory mechanisms that the body performs to normalize or correct the gait movements. However, the impedance control scheme has the mission of adapting the movement of the exoskeleton to the angular displacement that the user can perform and this can be verified in the graphs of the right column.

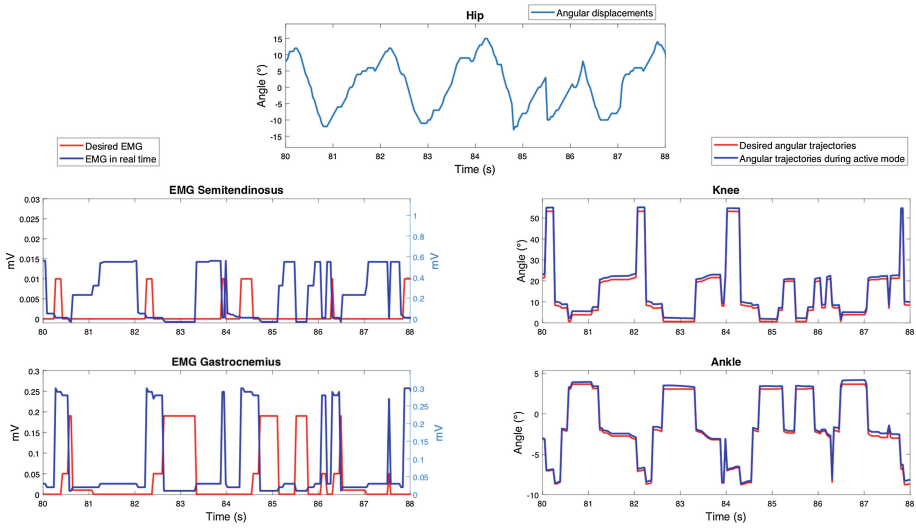

Fig. 3. Angular trajectories in the sagittal plane of the hip, knee and ankle joints, respectively; and EMG envelopes of semitendinosus and gastrocnemius muscles, respectively.

In the graphs of the right column of Fig. 3, the desired angular trajectories (red) and the joint trajectories (blue) modified from the differences detected between the EMG envelopes, are shown. In this case, it is possible to observe that in both joints, the exoskeleton had to assist to perform the movements required by the subject during the gait; that is, the kinematic impedance control scheme modified the joint displacements according to the differences between the envelopes. It is important to note that in the active mode it is not intended that the subject follows exactly the desired trajectory, but that the exoskeleton assists the volunteer to modify the trajectory according to the subject's capacity for joint movement during the gait.

4 Conclusion

According to the obtained results, the correct operation of the impedance control in the exoskeleton was observed. However, in order to fully validate the active mode exoskeleton function, it requires the participation of several subjects in more extensive experimental tests. It is important to point out that the proposed control scheme assists the user of the exoskeleton without damaging him/her and according to their mobility conditions. As the user improves or normalizes his progress, the exoskeleton will approach and adapt to the behavior determined by the pattern trajectories. In addition, the control system could be more robust in the trajectory tracking by means of the integration of more sensors, as well as the ability to adapt to the conditions of joint stiffness. Moreover, other EMG characteristics such as the median frequency, could be helpful to evaluate the exoskeleton use in rehabilitation therapies.

It is also important to develop and implement dynamic control schemes for the exoskeleton, in order to modify the applied joint torques from the EMG signal processing. Another improvement could be to integrate other sensors in order to identify the gait phases and be able to include the hip joint actively in the control system. All this in order to have an adequate system for its implementation in clinical applications.

Conflict of Interest. The authors declare that there is no conflict of interest.

References

1. National institute of statistic and geography (2010). https://www.inegi.org.mx/temas/discapacidad/
2. Plas, F., Viel, É., Blanc, Y.: La Marcha Humana: Cinesiología Dinámica. Biomecánica y Patomecánica. Masson, Spain (1996)
3. Nordin, M., Frankel, V.H.: Basic Biomechanics of the Musculoskeletal System. Lippincott Williams & Wilkins, Philadelphia (2012)
4. Agudelo-Mendoza, A.I., Briñez-Santamaria, T.J., Guarín-Urrego, V., Ruiz-Restrepo, J.P., Zapata-García, M.C.: Gait: Description, methods, assessment tools and normality parameters reported in the literature. CES Movimiento y Salud **1**(1), 29–43 (2013)
5. Hoyos-Daza, H.: Muscle activity patterns in lower limbs during the human gait under body load relief conditions. Bachelor's thesis, Facultad de Ingeniería, Pontificia Universidad Javeriana, Colombia (2014)
6. López-Gutiérrez, R., Aguilar-Sierra, H., Salazar, S., Lozano, R.: Adaptive control in passive rehabilitation routines using elltio. Revista Mexicana de Ingeniería Biomédica **38**(2), 458–478 (2017). https://doi.org/10.17488/RMIB.38.2.3
7. Low, K.: Robot-assisted gait rehabilitation: from exoskeletons to gait systems. In: 2011 Defense Science Research Conference and Expo (DSR), pp. 1–10. IEEE, New York (2011). https://doi.org/10.1109/DSR.2011.6026886
8. García-Cázares, I.: Design and start-up of a lower-limb exoskeleton for assistance. Bachelor's thesis, Facultad de Ciencias, Universidad Autónoma de San Luis Potosí, Mexico (2019)

9. García, I., Luna, L., Reyes, B., Dorantes-Méndez, G., Mejía-Rodríguez, A., Mendoza-Gutiérrez, M.: Aplicación de técnicas en el dominio del tiempo y la frecuencia para el análisis de la marcha humana usando señales de electromiografía. Memorias del Congreso Nacional de Ingeniería Biomédica. **4**, 114–117 (2017). https://doi.org/10.24254/CNIB.17.126
10. Mendoza, M., Bonilla, I., Reyes, F., González-Galván, E.: A Lyapunov-based design tool of impedance controllers for robot manipulators. Kybernetika **48**(6), 1136–1155 (2012)
11. Ávila, R., Prado, L., González, E.: Dimensiones antropométricas de la población latinoamericana. México, Universidad de Guadalajara, Centro Universitario de Arte, Arquitectura y Diseño, División de Tecnología y Procesos, Departamento de Producción y Desarrollo, Centro de Investigaciones en Ergonomía (2007)
12. Lefton, J., Malone, A.: Anthropometric Assessment. ADA Pocket Guide to Nutrition Assessment, 2nd edn., pp. 160–161. American Dietetic Association, Chicago (2009)

Evaluation of Respiratory Signal Record Based on Impedance Pneumography and Textile Electrodes

Carlos Rubén Dell'Aquila[1,2(✉)], Gabriel Eduardo Cañadas[1,2], and Eric Laciar[1,2]

[1] Facultad de Ingeniería, Gabinete de Tecnología Médica, Universidad Nacional de San Juan, San Juan, Argentina
carlos.dellaquila@unsj.edu.ar
[2] Consejo Nacional de Investigaciones Científicas y Técnicas, Buenos Aires, Argentina

Abstract. In this work, the development of a continuous monitoring system of a human's respiratory rate (RR) is presented. The system is based on the impedance pneumography method and it is divided into two main blocks: the electronic circuit and the electrodes. For the electrodes, two technologies are considered: the first one is *Ag/AgCl* disposable electrodes frequently used in clinical applications. The second one, known as textile electrode, is built on electrically conductive fabric. The performance of both types of electrodes is compared. Therefore, the experimental tests are carried out in two stages. In both stages, 5 records of 10 min were acquired in 5 healthy subjects. The first stage is recorded with disposable electrodes and the second one with textile electrodes. In order to compare the results obtained in each case, reference values were simultaneously recorded in each subject with a commercial polysomnography system. This system records respiratory activity using a method based on piezoelectric respiratory effort bands placed in the abdomen and thorax. Finally, the absolute (e_A) and relative (e_R) errors are computed taking into account RR values obtained from the designed and reference system for each stage. The results show similar performance among textile and disposable electrodes.

Keywords: Impedance pneumography · Textile electrode · Respiratory effort · Respiratory rate

1 Introduction

The respiratory rate (RR) is a vital sign extremely important not only in the diagnosis but also in the control of serious respiratory diseases. Through regular RR monitoring, it is possible an early detection of exacerbation in patients with Chronic Obstructive Pulmonary Disease (COPD) [1], as well as, acute respiratory dysfunction [2]. Furthermore, this also allows to assess the evolution of patients' rehabilitation and athletes' performance [3].

© Springer Nature Switzerland AG 2020
C. A. González Díaz et al. (Eds.): CLAIB 2019, IFMBE Proceedings 75, pp. 1502–1509, 2020.
https://doi.org/10.1007/978-3-030-30648-9_193

Patients' lung volume and capacities can be usually assessed in the doctor's office through the use of a spirometry test [4]. However, this type of test is not suitable for continuous monitoring [5]. For this reason, in other contexts, such as sleep studies, wereables and telehealth systems, etc., other techniques must be used. Among these techniques, plethysmography and impedance pneumography (IP) are widely used. They allow to register respiratory signals and, by means of digital processing techniques, respiratory rate can be estimated.

Plethysmography consists of respiratory bands adjusted around the thorax and abdomen. At the same time, these respiratory bands are connected to force sensors that measure thoracic and/or abdominal movements due to variations of the air present in the lungs. Force sensors are built from different and specific transducers such as strain gauges or piezoelectric materials [6].

On the other hand, IP is a technique that allows to instantly measure the variations of volume in the air that is present in the lungs by means of electrical impedance changes in the human thorax using electrodes placed on the skin's surface [7].

Different electrode technologies can be used to achieve both a low cost system and a more comfortable system for continuous monitoring (CM) [8]. Among them, disposable electrodes Ag/AgCl are widely used [9]. They allow to acquire records with very low noise level and they are stable and inexpensive. On the other hand, when it is necessary to obtain long time records (>24 h), the electrode properties decrease considerably causing a lower quality in the signal's recording. Therefore, they are not suitable for continuous monitoring systems.

One alternative to these electrodes can be textile electrodes that consist of conductive fabric and wire which, according to some studies, allow to obtain a good quality of register even during long periods [9].

One additional advantage of such electrodes is that they provide patients with the necessary comfort since they can be built in the clothes that the person normally wears and, in this way, acceptance by patients is facilitated [9].

In this research, the register of the respiratory rate (RR) is evaluated using the IP method with textile electrodes. For this reason, an electronic circuit in which such technique could be applied was designed. Moreover, a model of a textile electrode was built using conductive fabric in order to compare their performance with the performance of disposable electrodes Ag/AgCl. A commercial polysomnography system is used together with plestimographic bands in order to obtain a respiratory rate reference and statistical parameters.

2 Materials and Methods

2.1 Electronic Circuit

The IP method consists in injecting an electric current to a person's chest and recording the changes in the resulting potential due to the variations of its impedance. The impedance varies for two reasons: the first is due to air entering the lungs causing changes in the electrical characteristics of the thorax. The second, it is produced by changes in the separation of the electrodes due to volume variation [10].

There are two electrodes configuration, tetrapolar and bipolar. The first uses four electrodes, two to inject the current and two to record potential's variations. On the other hand, the bipolar method uses the same pair of electrodes to inject current and register the potential's variations. Although the sensitivity is lower than in the previous case, the system is simpler and more comfortable for the patient [7].

Figure 1 shows a general scheme of the circuit which is implemented based on the Analog Front-End ADS1292R of Texas Instruments. It is important to highlight its internal current source called carrier signal which has a frequency of 100 kHz and 500 uA of intensity. According to these values, tissues are not stimulated and, therefore, no damage is caused [11].

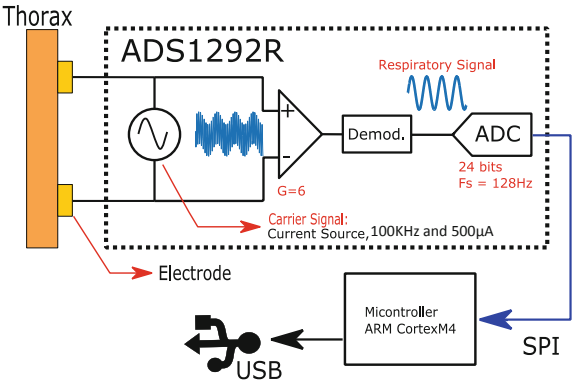

Fig. 1. Electronic circuit: general diagram block based on ADS1292R analog Front-End.

According to Ohm's law, the current that is injected to the thorax and its impedance generates a potential drop. The latter is the carrier regulated by the variations in the impedance of the thorax due to breathing. The electrical potential is increased by an amplifier with high input impedance and common mode rejection ratio (CMRR).

Then a coherent demodulation process is applied in order to obtain the respiratory signal (SR). Finally, the SR is digitalized by means of an analog-digital converter (ADC) integrated in ADS1292R and which has a high resolution (24 bits). This characteristic allows the gain of the amplifier to be low (G = 6) thus reducing the noise levels [12]. The sampling frequency of the signal was selected at 128 Hz.

The ADS1292R sends via SPI communication the digitalized signal to ARM Cortex M4 processor; specifically the MSP432 microcontroller is used. The latter is responsible for retransmitting the data to a computer through USB connection.

2.2 Electrodes

In this research, two types of electrodes were examined to inject the current into the skin surface of the thorax. The first ones are disposable electrodes Ag/AgCl. The second ones are textile electrodes constructed using conductive fabric shown in Fig. 2.

The fabric used is MedTexTM P-180 model which is built on a base of 94% nylon and 6% of elastic material. It also has a silver coating (Ag) of 99% purity [13].

Fig. 2. Textile electrode built based on conductive fabric MedTex™ P-180.

2.3 Evaluation

In order to evaluate the performance of the electronic circuit and the textile electrodes, five records were acquired in 5 healthy persons. Each of these records is di-vided into two different stages: in the first stage disposable electrodes were used whereas in the second one textile electrodes were used. Both cases were simultaneously acquired with a respiratory signals reference (RSR).

The RSR signals correspond to the plethysmographic signals of the thorax, abdomen and the sum of both of these (RIPT, RIPA and RIPsum, respectively) and the sum of these (RIPSum). The third signal was included due to the fact that it is similar to the one obtained by the IP signal, based on the researcher carried out by other authors [14].

The recordings of these signals were performed with respiratory bands based on piezoelectric sensors connected to a commercial polysomnography, model Mini PC from Akonic®. This system samples the signals in 128 Hz and it sends all the digitalized signal to PC via USB communication. Figure 3 shows the placement of the respiratory effort belts and IP method's superficial skin's electrodes.

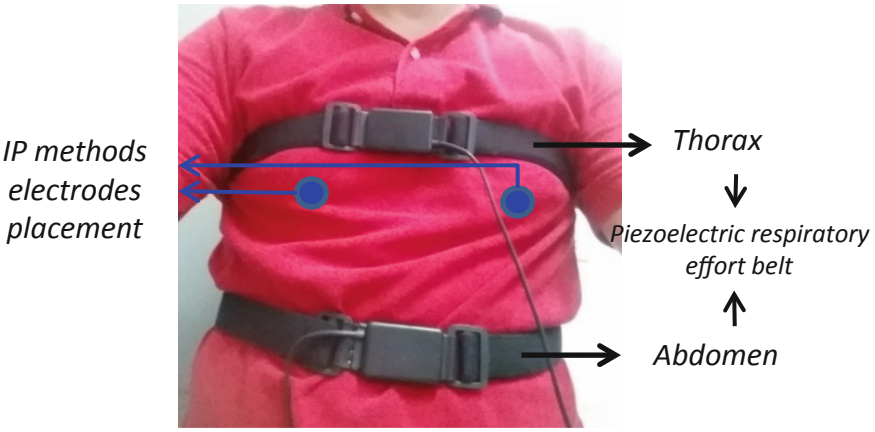

Fig. 3. Piezoelectric respiratory band and IP methods electrodes placement.

Figure 4 shows the photography of the experimental tests. In this figure, the Akonic system, respiratory effort belts and the development electronic circuit board can be visualized.

Fig. 4. Experimental tests photography

Once the respiratory signals have been acquired, the respiratory frequency is calculated for each record. This last is carried out using a method proposed and used by other authors [15]. First, each respiratory signal is divided into 32-second segments. Next, for each segment, their frequency spectrum is analyzed and the frequency respiratory rate corresponding to each interval is determined based on the component with the highest magnitude.

The RR values computed from the IP method with both types of electrodes were compared with the ones obtained from RSR signals. Two statistical parameters proposed by other authors were used in order to compare RR values [2]. The first one is the Absolute Error (e_A) (1) and the other one is the Relative Error (e_R) (2).

$$e_A(k) = FR_{IP}(k) - FR_{REF}(k) \tag{1}$$

$$e_R(k)\% = \frac{e_A(k)}{FR_{REF}(k)} \times 100 \tag{2}$$

3 Results

The Tables 1 and 2, summarizes the results for disposable and textile electrodes, respectively. The mean and standard deviation were computed for both errors (e_A and e_R) and taking into account separately the group of records performed with the disposable and textile electrode.

Table 1. Disposable electrodes (Ag/AgCl), mean and standard deviation of errors.

Reference signal	$e_A(k)$		$e_R(k)\%$	
	Mean	Std	Mean	Std
RIP Thorax	0,13	2,98	0,61	12,50
RIP Abdomen	0,00	2,90	1,59	12,07
RIP Sum	0,00	2,90	1,59	12,07

Table 2. Textile electrodes, mean and standard deviation of errors

Reference signal	$e_A(k)$		$e_R(k)\%$	
	Mean	Std	Mean	Std
RIP Thorax	0,47	3,47	0,92	19,22
RIP Abdomen	0,86	3,53	4,49	20,66
RIP Sum	0,86	3,53	4,72	19,94

Figure 5a and b show the first volunteer's respiratory signals acquired from the disposable and textile electrode, respectively. Also, these include the corresponding RIPT, RIPA and RIPSum signals simultaneously acquired from Akonic system.

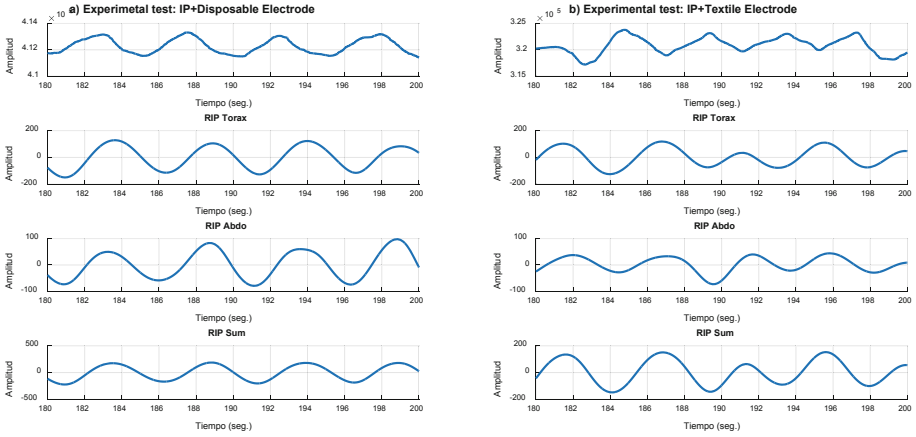

Fig. 5. Acquired signals test. Reference RIP signal and IP method with: (a) disposable and (b) textile electrodes.

4 Conclusions

In this research, an electronic circuit, which allows the RR registration by the IP method, has been designed and evaluated. It works together with a textile electrode model that was also built. Furthermore, its performance is compared with the one by standard disposable Ag/AgCl electrodes based on RR values.

The comparative test was carried out based on RR values and respiratory reference signal. These are the signals acquired from plethysmography bands (thorax, abdomen and its arithmetic addition), connected to a commercial polysomnogram.

The statistical parameters of the eA and eR errors were computed for each type of electrode technology respect to the respiratory reference signal. In order to simplify the analysis, the mean and the standard deviation were computed for both electrodes technologies.

The results show that eA is similar in both electrodes types but the eR is better in disposable electrodes. This difference could be by the electrode motion because tex-tile electrodes are most sensible.

In the future, the new smaller dimension prototype and its case will be built. The latter will be designed with a material that improves the system's electromagnetic compatibility features. Based on the new design a study will be carried out comparing the respiratory signal' waveform acquired from textile electrodes and other standards methods.

Acknowledgment. All authors are supported by UniversidadNacional de San Juan (UNSJ) and Consejo Nacional de InvestigacionesCientíficas y Técnicas (CONICET). The research project is supported by grants of Secretaría de Ciencia, Tecnología e Innovación – Universidad Nacional de San Juan (SECITI-UNSJ – Res 1054-18-R) and CONICET (PIP 11220150100059 CO), Argentina.

Declaration of Conflict of Interest. The authors declare that they have no conflict of interest.

References

1. Aburto, M., Esteban, C., Moraza, F.J., Aguirre, U., Egurrola, M., Capelastegui, A.: COPD exacerbation: mortality prognosis factors in a respiratory care unit. Arch. Bronconeumol. **47**, 79–84 (2011). https://doi.org/10.1016/S1579-2129(11)70018-0
2. Lázaro, J., Gil, E., Bailón, R., Mincholé, A., Laguna, P.: Deriving respiration from photoplethysmographic pulse width. Med. Biol. Eng. Comput. **51**, 233–242 (2013). https://doi.org/10.1007/s11517-012-0954-0
3. Lázaro, J., Alcaine, A., Romero, D., Gil, E., Laguna, P., Pueyo, E., Bailón, R.: Electrocardiogram derived respiratory rate from QRS slopes and R-wave angle. Ann. Biomed. Eng. **42**, 2072–2083 (2014). https://doi.org/10.1007/s10439-014-1073-x
4. Sokol, K.C., Sharma, G., Lin, Y.L., Goldblum, R.M.: Choosing wisely: adherence by physicians to recommended use of spirometry in the diagnosis and management of adult asthma. Am. J. Med. **128**, 502–508 (2015). https://doi.org/10.1016/j.amjmed.2014.12.006
5. Wang, H., Yen, C., Liang, J., Wang, Q., Liu, G., Song, R.: A robust electrode configuration for bioimpedance measurement of respiration. J. Healthc. Eng. **5**, 313–328 (2014). https://doi.org/10.1260/2040-2295.5.3.313
6. Frank, P.: Primiano: measurements of the respiratory system. In: Webster, J.G. (ed.) Medical Instrumentation: Application and Design. Wiley, Hoboken (2009)
7. Seppä, V.P., Pelkonen, A.S., Kotaniemi-Syrjänen, A., Viik, J., Mäkelä, M.J., Malmberg, L. P.: Tidal flow variability measured by impedance pneumography relates to childhood asthma risk. Eur. Respir. J. **47**, 1687–1696 (2016). https://doi.org/10.1183/13993003.00989-2015

8. Klum, M., Schenck, T., Pielmus, A., Tigges, T., Orglmeister, R.: Short distance impedance pneumography. Curr. Dir. Biomed. Eng. **4**, 109–113 (2018). https://doi.org/10.1515/cdbme-2018-0028
9. Fiedler, P., Biller, S., Haueisen, J.: Impedance pneumography using textile electrodes, pp. 1606–1609 (2012)
10. Grimnes, S., Martinsen, Ø.G.: Chapter 10 - Selected applications. In: Grimnes, S., Martinsen, Ø.G. (eds.) Bioimpedance and Bioelectricity Basics, 3rd edn, pp. 405–494. Academic Press, Oxford (2015)
11. Młyńczak, M., Cybulski, G.: Impedance pneumography: is it possible? Proc. SPIE **8454**, 84541T (2012). https://doi.org/10.1117/12.2000223
12. Soundarapandian, K., Berarducci, M.: Analog front-end design for ECG systems using delta-sigma ADCs (2010)
13. Shieldex(R): Technical Data Sheet: Shieldex (R) Med-tex P180. https://www.statex.de/wp-content/uploads/2017/05/ShieldexMedtexP180_02-07-13.pdf
14. Leder, R.S., Cohen, K.P., Peterson, N., Palreddy, S., Green, C., Tompkins, W.J., Webster, J. G.: Performance of impedance and inductance ventilation sensors on premature infants during natural breathing, motion, and airway obstruction. In: Proceedings of the 25th Annual International Conference IEEE Engineering Medicine Biology Society, vol. 1–4 (New Begin. Hum. Heal. 25), pp. 3094–3097 (2003). https://doi.org/10.1109/iembs.2003.1280796
15. Charlton, P.H., Villarroel, M., Salguiero, F.: An assessment of algorithms to estimate respiratory rate from the electrocardiogram and photoplethysmogram. Second. Anal. Electron. Heal. Rec., 1–427 (2016). https://doi.org/10.1007/978-3-319-43742-2

Author Index

A
A Pereira, Wagner C., 743
Abras, Guillermo, 656
Abreu, Francisco Douglas Lima, 1428
Abril, Juan D., 1200
Acosta-García, Ma. Cristina, 652
Adriana, Pliego, 970
Aguiñaga-González, Sebastián, 588
Aguirre-Ospina, Carlos Andres, 884
Akagi, Yuki, 1216
Alemán-Miranda, Lizbeth Lucero, 637
Alfaro-Ponce, Mariel, 985
Alfaro-Zapata, Miguel Ángel, 670
Aljama-Corrales, A. T., 426
Aljama-Corrales, Tomás, 113
Almeida, Tiago Paggi, 85
Alonso-Valerdi, Luz María, 1101
Alonso-Valerdi, Luz Maria, 156
Altuve, Miguel, 172, 208, 792, 1275
Alvarado-Gonzalez, Aurora, 945
Alvarado-Robles, Lluvia Gwendolyn, 3
Alvarado-Rodríguez, Francisco J., 913
Álvarez, Tatiana, 1012
Alvarez-Camacho, Michelín, 663
Alvarez-Gutiérrez, Mariana Teresa, 393
Ambrosio L., Roberto C., 543
Ames-Lastra, G., 1488
Amezquita-Garcia, Jose Alejandro, 218
Anessi, Carolina, 643
Ángeles, Luis Jiménez, 327
Angel-Lopez, Juan Pablo, 884
Aragon, Efren, 252
Arce, Débora, 1434
Arce-Santana, Edgar Román, 393, 426
Arenas, Wilson J., 172
Arias-Carrion, Oscar, 1037
Ariel, Braidot, 894
Ariza-Jiménez, Leandro, 315, 761
Armentano, Ricardo, 975
Arnaiz, Isabel, 1079
Arquer-Ruiz, María del Carmen, 588, 601
Arteaga-Ballesteros, Barbara, 985
Ascencio-Piña, Cesar, 309
Avetta, Sofia, 1306
Avilés, Oscar F., 1200
Aya-Parra, Pedro-Antonio, 1284, 1320, 1326
Azpiroz Leehan, Joaquín, 1333

B
Baldezzari, Lucas, 1043
Ballarin, Virginia L., 281, 290, 385, 656
Ballarre, Josefina, 290, 656
Ballesteros, Mariana, 993
Bañuelos, Verónica Medina, 327
Barba-Muñoz, Ana Paulina, 601
Barbosa, Luiz José Lucas, 421
Barrera-Saavedra, Gustavo Adolfo, 1441
Barrientos C., Germán, 543
Barrón-Salazar, Melany, 508
Barzallo, Boris, 1107
Bastos-Filho, Teodiano, 1125, 1130
Baumgartner, Werner, 469
Bautista, Karen Jazmin Mendoza, 1449
Bayod, Javier, 874
Becerra-Luna, Brayans, 145, 560
Bellino, Gabriel Martín, 129
Beltran, Alexandra, 1326
Benítez-Benítez, Javier, 63
Benítez-Mata, Balam, 47
Bertemes-Filho, Pedro, 1481

© Springer Nature Switzerland AG 2020
C. A. González Díaz et al. (Eds.): CLAIB 2019, IFMBE Proceedings 75, pp. 1511–1518, 2020.
https://doi.org/10.1007/978-3-030-30648-9

Bianquenti, Bruno Leonardo, 85
Bini, Isabel Cristina, 1184
Bissaco, Márcia A. S., 1428
Blotta, Eduardo L., 1051
Bojorges-Valdez, Erik, 202, 322
Bonell, Claudia Edith, 907
Bonilla, Isela, 71, 1023, 1494
Borja, Gisella, 497
Boschi, Silvia R. M. da S., 1153
Boschi, Silvia R. M. S., 524, 1147, 1292
Boschi, Silvia Regina Matos S., 1428
Botelho, Thomaz, 1130
Botello-Arredondo, Adeodato Israel, 637, 670
Bravo-Zanoguera, Miguel Enrique, 218
Brizuela-Cardoso, Javier D., 361
Brunnquell, Simon, 1481
Buchelly, Francisco Javier, 290, 385
Bueno-Palomeque, Freddy, 538
Bueno-Palomeque, Freddy L., 812
Bueyes-Roiz, Virginia, 42, 939
Bulacio, Pilar, 731
Busoch-Morlán, Carmen, 606
Bustamante, Paola, 643

C
Cabrera L., María del R. L., 543
Cabrera, Carlos, 401
Cabrera-Llanos, Agustín Ignacio, 575
Cabrera-Zeas, Juan, 538
Cadena, Oscar Pinzón, 1326
Cailloux, Olivier, 731
Caldas, Oscar I., 1200
Campos Trujillo, Oliver, 37
Campos-Delgado, Daniel Ulises, 63
Cañadas, Gabriel Eduardo, 1502
Cancela, Domingo L., 1292
Cantillo-Negrete, Jessica, 1037
Cardona, Manuel, 955
Cardoso, V., 1125
Carino-Escobar, Ruben I., 1037
Carolina Carrere, L., 1073
Carrere, L. Carolina, 1162
Carrillo-Mora, Paul, 1037
Cartas-Rosado, Raúl, 145, 560
Carvajal, Laura Camila Loaiza, 1117
Casali, Karina Rabello, 593
Castañeda, Benjamín, 412
Castañeda, Rubén, 47
Castañeda-Villa, Norma, 98, 228
Castellanos-Rivera, Luis A., 508
Castellanos-Ruiz, Julialba, 884
Castro, Carlos, 47, 1060
Cavalcante, Fabiana R. S. M., 1292
Cavalcanti, Fabiana R. S. de M., 1153
Ceballos, Julian, 761
Cecilia, Molina, 894
Celaya-Padilla, José M., 121, 777
Cena, Cecilia García, 955
Centeno, Carlos Augusto, 1386
Cerda, Rodrigo Andres Miranda, 694
Cere, Silvia M., 290
Cervantes, David, 401
Cervantes-Cardona, Guillermo Alonso, 1093
Cesari, Andreina, 385
Chailloux Peguero, Juan David, 28
Chairez, Isaac, 985, 993
Chan, Debora, 272
Chapa-González, Christian, 637, 670
Charleston-Villalobos, Sonia, 113, 426
Charry, Oscar Julián Perdomo, 1326
Chavez, Gustavo Adolfo Martinez, 1380
Chávez, Katia Verónica, 1488
Chavez-Lamas, Nubia M., 777
Chinea-Valdés, Lyanett, 351
Chora-López, Viviana, 933
Ciavaro, Nazarena, 643
Claudia, Bonell, 1403
Clotet, Roger, 1107
Coelho, Regina Célia, 304, 611, 681
Cornejo-Cruz, Juan Manuel, 98, 228
Cortés, Ernesto, 1488
Cortés-García, Karen L., 939
Cortes-Rodriguez, Carlos, 627
Costa, Marly Guimaraes Fernandes, 743
Covantes-Osuna, Cesar, 182, 913
Crochi, Douglas, 524, 1147, 1292
Cruz, Angelmiro Nuñez, 1326
Cruz, Daniel A., 377
Cruz-Escudero, Alexis, 1341
Cruz-Guerrero, Ines Alejandro, 393
Cruz-Ortiz, David, 993
Cu, Luz Alejandra Flores, 367
Cuadros-Acosta, J., 1002
Curiel-López, Fátima B., 501

D
da Costa Rodrigues, Henrique, 1417
da Luz dos Santos, Elgison, 1184
da Silva Junior, José Cláudio, 1137
da Silva, Alessandro Pereira, 1153, 1428
da Silva, Bruno Assumpção Gomes, 298
da Silva, Diego Pereira, 1417
da Silva, Robson Rodrigues, 1417
da Silva, Robson Rosa, 611
Daudt, Paulo, 524
Davila-Alquisiras, Jesus H., 322
de Amorim, Henrique Alves, 593
de Amorim, Ronni Geraldo Gomes, 694

de Assis Pellizzon, Antonio Cassio, 298
de Avila-Armenta, Eduardo, 933
de Bengoa Vallejo, Ricardo Becerro, 831, 874
de Faria e Sousa, Sidney Julio, 530
de Fátima Fernandes Vara, Maria, 1184
de Godoy, Carlos Marcelo Gurjão, 304, 611, 681
de Jesús Mayagoitia-Vázquez, José, 921
de Jesus Prates, Leopoldo, 304, 611
de la Cruz-Alvarado, Karla Daniela, 921
De Los Ríos, Evert, 497
De Luccas, Julia Baldi, 85
de Matos da Silva, Franciéle, 421
de Mendonça Mesquita, Eduardo, 950
de Moraes, Marli Leite, 611
de Morales Artiles, Martha Madyuri Pérez, 12
de Oliveira Andrade, Adriano, 334, 950, 964
de Paula, Silvia Helena Bastos, 1417
de Siqueira Rodrigues Fleury Rosa, Suélia, 421
de Sousa Moreira, Lorena, 421, 694
de Sousa, Breno Amadeus Sales Marinho, 421
de Souza, Rafael Navet, 1226
De Villa, Guilherme Augusto Gomes, 964
Del Hierro-Gutiérrez, Edgar G., 1458
DelaO-Arévalo, Luis, 322
Delgado, Josemaría, 1488
Delgado-Aranda, Raquel, 164
Delisle, D., 1125
Dell'Aquila, Carlos Rubén, 1502
Destercke, Sebastien, 731
Dias, Rodrigo Souza, 298
Diaz, Jessica Leon, 252
Díaz, José, 792, 1275
Díaz-Amador, Roberto, 344
Díaz-Martínez, René Joaquín, 606
Domínguez, Rodrigo Soto, 1085
Domínguez-Hernández, Nancy Lisset, 548
Dorantes-Méndez, Guadalupe, 113, 164, 1023, 1494
Dorta_Palmero, Jasiel, 252
dos Santos Silva, Mayla, 421
Duarte, Fernanda Oliveira, 530
Dueñaz-Jimenez, Sergio, 309
Duré, Camila Ileana, 907, 1403
Dutto, Cesar Ignacio, 1403

E

Echeverría, Juan Carlos, 21
Eimil-Suarez, Eduardo, 453
Elias-Neto, Arlindo, 1130
Enrique, Soto, 970
Escher, Leandro, 1162
Escutia-Reyes, Daniel, 718
Espinosa, Ricardo, 460, 685
Espino-Salinas, Carlos H., 121
Espinoza-Bermúdez, Lorena, 933
Espinoza-Valdez, Aurora, 501, 1313
Esquivel-Arizmendi, Cinthia Gabriela, 21
Esquivel-Cordero, Estefani, 933
Estrada, Héctor García, 1449

F

Fazenda, Álvaro Luiz, 298
Fernandes, Beatriz L., 1410
Fernandez, Tamara, 731
Ferrari, C. R., 699
Ferreira, Jessica, 460
Ferrero, José M., 769
Ferrer-Riesgo, Carlos Ariel, 12, 56, 344
Figueroa, Isaac René Aguilar, 234
Filho, Cicero F. F. Costa, 743
Filho, Reginaldo Dias Soares, 1298
Flores, Dora-Luz, 47, 401, 1060
Flores-Sánchez, María Guadalupe, 588
Folador, João Paulo, 334
Fontana, Juan Manuel, 1066, 1171
Formento, Paola Catalfamo, 907
Fragalli, Andre, 530
Franco-Pérez, Sarahí S., 501
Frizera-Neto, A., 1130
Fuentes-Aranda, Andrés, 486

G

Gallegos Ledezma, Angel, 42
Galván Duque, Carlos, 858
Galván-Tejada, Carlos Eric, 104, 121, 777, 933
Galván-Tejada, Jorge I., 104, 121, 777, 933
Gambini, Juliana, 272
Gamboa-Rosales, Hamurabi, 104, 777, 933
Ganem, Gabriela Colares Ali, 681
García García, Yainet, 435
García, Arianne Ruby, 1488
Garcia, Camilo, 1306
García, Itzel, 1023, 1494
Garcia, Renato, 1298
García, Y., 435
García-Cedeño, Andrea, 191, 1107
García-Estrada, Héctor, 575
Garcia-Florez, M., 1002
Garcia-Gonzalez, Alejandro, 945
García-Guadarrama, Reynol, 1178
García-López, Juan Carlos, 1253
García-López, Rodrigo, 63
Garcia-Morales, Nataly A., 1211
Garzón-Márquez, Caren, 412
Gentiletti, Gerardo Gabriel, 1043, 1073
Germanovix, Walter, 1137
Godínez-Fernández, J. Rafael, 652

Godinho, Fabio Luiz Franceschi, 85
Gomes, Amanda Mayara Pereira, 1184
Gómez, Alejandro, 138
Gómez, Ernesto Suaste, 445
Gomez, Martina, 290
Gomez-Alzate, Andrea, 884
Gomez-Gonzalez, Juan M., 894
Gómez-López, Modesto, 1488
Gómez-Ramírez, Manuela, 412
González Díaz, César Antonio, 1488
González, Horacio Rostro, 367
González-Ascaso, Ana, 769
González-Camarena, R., 426
González-Carbonell, Raide Alfonso, 841, 850
Gonzalez-Fernandez, Rene, 478
González-Landaeta, Rafael, 866
González-Martínez, Fernando, 1101
González-Navarrete, Roberto, 822
González-Navarro, Felix Fernando, 218
Gonzalez-Vargas, A. M., 242
González-Vargas, Andrés Mauricio, 1441
Goroso, Daniel Gustavo, 709, 1417
Gorostieta-Esperon, Miguel Angel Santiago, 582
Granados-Trejo, Pilar, 98, 228
Guevara, Elizabeth, 377
Guevara-Vega, Sandra, 913
Guillaume, Serge, 731
Guillermo, Juan Carlos, 1107
Gutiérrez, Andrea, 858
Gutiérrez-López, Everardo, 1060
Guzman-Diaz, Keith, 945
Guzmán-Quezada, Erick, 913

H
Heredia J., Aurelio H., 543
Hernandez, A., 412
Hernández, Nidia Patricia Córdoba, 1326
Hernández-Gandarillas, Paola, 921
Hernández-González, Mercedes, 1261
Hernández-Juárez, Sarahí, 426
Hernández-López, Laura Angélica, 1341, 1357
Hernández-Medina, Arturo, 1220
Hernández-Oropeza, José Israel, 588, 601
Hernández-Quintela, Everardo, 322
Hernandez-Reynoso, Ana, 945
Hernández-Ruíz, Joselín, 1261
Herrera, Daniela, 945
Herrera, Héctor, 792, 1275
Herrera-Rangel, José Pablo, 921
Herrera-Ruiz, V., 1002
Hidalgo Torres, Leandro Alexis, 28
Hirata, Gustavo, 401
Höglinger, Markus, 469
Horak, Celina, 643
Hoyos-Restrepo, Maria Camila, 884
Huerta, Mónica, 191, 1107
Hurtado-Otalora, C. A., 242

I
Ibarra-Zárate, David I., 156, 1101
Infante-Vázquez, Oscar, 145, 560
Isa Jara, Ramiro Fernando, 385
Isa-Jara, Ramiro F., 281
Izquierdo-Torres, Yanela, 351

J
Jacobo-Armendáriz, Victor Hugo, 841, 850
Jaramillo-Garzón, Jorge A., 784
Jiménez-Ángeles, Luis, 582
Juárez, Patricia, 401

K
Katunar, Maria Rosa, 656
Kinsella, Joseph, 670
Kobayashi, Toshiki, 1216
Krautschneider, Wolfgang H., 752
Krsticevic, Flavia, 731
Krueger, Eddy, 1184

L
Laciar, Eric, 1066, 1171, 1502
Lara, Miroslava Cano, 367
Lara-González, Fernando, 1261
Lara-Padilla, Eleazar, 1488
Ledesma, José, 497
Ledesma-Orozco, Elías, 822
Ledesma-Ramírez, Claudia Ivette, 21, 202, 718
Leija, Lorenzo, 1253
Leiva, Karen, 685
León, Horacio, 1031
Lerma, Claudia, 145
Lescoulié, Nicolas, 1434
Llanos, Agustín Ignacio Cabrera, 1449
Longo, B., 1125
Lopera-Rodríguez, Jorge Alejandro, 784
Lopes, Eugênia Gonzales, 593
Lopes, Walter Saraiva, 1417
López del Angel, Francisco Arturo, 1333
López, Javier Bayod, 831
López, Juan Manuel López, 1117
Lopez, María José Enciso, 1191
López, Natalia, 1306
López, Santiago Camacho, 367
López-Alvarenga, Juan C., 1261
Lopez-Avitia, Roberto, 218
López-Caracheo, Francisco, 1220
López-Carranza, Angélica C., 1458

Lopez-Celani, Natalia, 138
Lopez-Gutierrez, Diego Mauricio, 151
Lorenzo-Ginori, Juan Valentín, 351
Luna, Lourdes, 1023, 1494
Luna-García, Huizilopoztli, 777
Luna-Lozano, Pablo Samuel, 548

M
Madrid, Joav, 1012
Madrid, Mario Alberto, 831
Mancera-Campos, Natali, 822
Mandujano-García, Edgar A., 508
Manzo-Palomera, O. Rocío, 1093
Marengo, Bruno, 907
Martínez Bocanegra, Marco A., 874
Martinez-Alanis, Marisol, 377
Martínez-Escobar, Elda Y., 121
Martinez-Licona, Fabiola M., 1341, 1349
Martínez-Memije, Raúl, 145, 560
Martínez-Méndez, Rigoberto, 1178
Martínez-Montes, Eduardo, 1079
Martínez-Valdez, Raquel, 1253
Martín-González, Francisco, 453
Martini, Silvia C., 524, 1147, 1153, 1292, 1428
Martins, Juliano, 1298
Masili, Mauro, 530
Massafra, Alejandro Miguel, 129
Matadamaz-Castro, Juan Pablo, 588
Maya-Escamilla, Carlos, 486
Medina, Francisco, 993
Medina-Bañuelos, Verónica, 37
Mejía-Ávila, M., 426
Mejía-Rodríguez, Aldo, 1023, 1494
Mejía-Rodríguez, Aldo Rodrigo, 393, 426
Melo, José Isidro García, 1398
Mena, Andrés, 769
Mendes, João Paulo Campos, 743
Méndez Monroy, Paul Erick, 519
Méndez, Martín Oswaldo, 164
Méndez-Lira, Omar, 866
Méndez-Magdaleno, Laura E., 113
Mendizabal-Ruiz, Eduardo Gerardo, 234
Mendizabal-Ruiz, Gerardo, 309
Mendoza, Marco, 71, 1023, 1494
Mendoza-Bautista, Karen Jazmín, 575
Mendoza-Reyes, Miguel Arturo, 344
Meneses-Marcel, Alfredo, 351
Mercadillo-Caballero, Roberto E., 1220
Meschino, Gustavo J., 281
Miguel-Andrés, Israel, 921
Miliar-García, Ángel, 1488
Mino-Arango, Maria Eugenia, 151
Miosso, Cristiano Jacques, 421
Miranda C., H. A., 367
Mireles-Pérez, Caridad, 993
Molina-Salazar, Raul Enrique, 1349
Molisani, Leonardo, 1066, 1171
Mollineda-Diogo, Niurka, 351
Moncada-Sánchez, Luis Fernando, 1313
Monjaraz-Carrillo, Nelly, 616
Monroy, Nelson F., 208
Montano, Nicola, 593
Montero, Andrea, 858
Mora, Rafael Zepeda, 42
Mora-García, Tlazohtzin R., 1357, 1365
Morales, Ángel Luis Rodríguez, 1191
Morales, Eduardo Barbará, 327
Morales-Acosta, Lázaro, 850
Morales-Corona, Juan, 652
Morales-Ruiz, Benjamín A., 508
Moreno M., Mario, 543
Moreno, Catherine, 460
Mosiñoz-Montes, Roberto, 1261
Muffo, Cecilia, 1153
Muffo, Cecilia P., 1147
Muhlen, Sérgio Santos, 1226
Munguia-Nava, Carlos Miguel, 3
Muñoz, Franklin, 401
Muñoz, Ramiro, 1403
Murillo, Javier, 731
Murillo, Javier D., 412
Murillo-Escobar, J., 1002
Murrieta-Brígido, Lady María, 548

N
Nakagawa, Keiichi, 1216
Nava-Vázquez, Isaac F., 933
Neto, Arnaldo Fim, 85
Neto, Guilherme Nunes Nogueira, 1184
Nino-Barrera, Javier, 627
Nohama, Percy, 1184, 1410
Nuño, Jesús Vladimir Martínez, 234

O
O'Brien, Ronald, 1171
Olaya Mira, Natali, 805
Olayo-González, Roberto, 652
Ordoñez, Cristian E., 1051
Oropeza-Guzmán, Mercedes Teresita, 486
Oros-Pantoja, Rigoberto, 718
Orozco-Morales, Rubén, 265, 351
Orozco-Ocampo, Yenny Marcela, 884
Orozco-Villaseñor, Sergio Luis, 921
Ortega-Robles, Emmanuel, 1037
Ortiz-Echeverri, Cesar, 91
Ortiz-Posadas, Martha R., 1357, 1365
Ortiz-Prado, Armando, 841, 850
Osorio-Londoño, Diana, 652

Ota, Natacha H., 1147
Ota, Natasha H., 524
Oviedo, Gonzalo, 1066, 1171

P
Pacheco-López, Gustavo, 21
Paixão, Fabiano Carlos, 298, 611
Pantoja-Gómez, Yosvani, 453
Paola, Catalfamo Formento, 1403
Paredes, Omar, 91, 182
Pasaye-Alcaraz, Erick H., 1220
Pastore, Juan, 1051
Pastore, Juan Ignacio, 290, 385, 656
Pazos-Espinosa, Hany, 478
Peña-Castillo, Miguel Ángel, 21
Pereira, Adriano Alves, 334
Pérez, Kenny, 993
Pérez-Blanco, Jorge German, 453
Pérez-Buitrago, Sandra, 412
Pérez-Cisneros, Marco, 309
Pérez-Díaz, Marlen, 265, 361
Perez-Gonzalez, Jorge, 37
Pérez-Grovas, Hector, 145
Perez-Guerra, J., 1002
Pérez-Medina, Ana Laura, 663
Pérez-Pacheco, Argelia, 1261
Perez-Ramírez, Carlos Andres, 1220
Pérez-Rivero, Eduardo Osquel, 841
Pérez-Rueda, Ernesto, 519
Pérez-Solís, Ilian, 449
Pérez-Vielma, Nadia Mabel, 1488
Perfetto, Juan Carlos, 724
Perilla, Sandra Patricia Usaquén, 1398
Perotti, Germán, 907
Perpiñán, Gilberto, 792, 1275
Picaza, Carlos Alvarez, 699
Piccinini, David, 1306
Pimentel-Aguilar, Ana B., 1357
Piña, Uriel Anguiano, 1085
Piña-Quintero, M. Fernanda, 1357, 1365
Piña-Ramírez, Omar, 202
Pineda-Espinosa, Andrea Paola, 601
Pinel, Nicolás, 315, 761
Pinos, Eduardo, 191
Pinos-Vélez, Eduardo, 538
Pirchio, Rosana, 265
Pliego-Carillo, Adriana Cristina, 21
Pliego-Carrillo, Adriana Cristina, 718
Pomer, A., 1125
Ponce, Sergio, 731, 1306, 1434
Pracca, Francisco, 567
Preciado, Cesar Garcia, 1326
Pugo-Méndez, Edisson, 538
Pulgarin-Giraldo, J. D., 242
Punín, Catalina, 1107

Q
Quijano, Yannick, 939
Quiñones-Uriostegui, Ivett, 939
Quintero, Olga Lucía, 138, 315
Quintero-Beuló, Gregorio, 1261
Quiroga-Torres, Daniel-Alejandro, 1284, 1320, 1326
Quispe-Siccha, Rosa María, 1261
Quitian, Fitzgerald Leonard Gerardo Toro, 1117

R
Ramele, Rodrigo, 272
Ramírez, A., 460
Ramirez, Carlos Rodolfo, 129
Ramírez, Valeria, 736
Ramirez-Restrepo, Daniela, 884
Ramírez-Sotelo, María Guadalupe, 575
Ramos-Betancourt, Nallely, 322
Ramos-Loyo, Julieta, 79
Ramos-Ortiz, Gabriel, 616
Ramos-Tituana, Richard M., 812
Ranciaro, Maira, 1184
Regueiro-Busoch, Carmenchu, 606
Regueiro-Gómez, Angel, 606
Rentería-Montoya, Columba, 486
Reyes, Bersaín A., 63, 71, 1085
Reyes, Maria Eugenia Paz, 252
Reyes-Lagos, José Javier, 21, 718
Reyes-Morales, Luis, 478
Ribeiro, Débora F. Camillo, 1410
Riva, Guillermo, 1386
Rivas, David, 1107
Rivera, Oswaldo, 1200
Rivera-Tello, Sergio, 79
Roberti, Martín, 1434
Robledo, Sara, 412
Rocha, Maria Sheila, 85
Rodrigues, Adriano Pericles, 950
Rodrigues, Camila Cristina Martini, 1428
Rodrigues, Wellington, 421
Rodríguez Dueñas, William Ricardo, 1472
Rodríguez Guillén, Reinier, 435
Rodriguez, Ángel Luis, 1012
Rodríguez, Mario, 616
Rodríguez-Aguayo, Pablo C., 121
Rodríguez-Chagolla, Jóse Manuel, 145
Rodriguez-Guerrero, Carlos, 1200
Rodríguez-Guillén, Reinier, 56
Rodríguez-Matas, José Felix, 769

Rodriguez-Montano, Oscar, 627
Rodríguez-Muñoz, Daniela, 718
Rodríguez-Reséndiz, Juvenal, 91
Rodríguez-Reynoso, Sergio, 945
Rodríguez-Roldán, Grissel, 449
Rodriguez-Ruiz, Julieta G., 104
Rodríguez-Sáenz, Sofía D., 501
Rojas-Lopez, Leidy Tatiana, 884
Roldán, Geovanny Palomino, 445
Román-Godínez, Israel, 3, 736
Romero, M. A., 1125
Romero-Soto, Fabian O., 156
Romo-Vázquez, Rebeca, 79, 91, 182, 913
Rosario, Vega, 970
Rosas Andreu, Gerardo Daniel, 1333
Rosebrock, Adrian, 334
Rubio, Débora, 1434
Ruiz, Aurora Graciela, 724
Ruiz-Gonzalez, Yusely, 361
Ruiz-Morán, Antonio, 508
Ruiz-Padilla, Paola, 913

S

Saavedra, Karla C. Rojas, 327
Sakuma, Ichiro, 1216
Salazar, Cesar A., 1233
Salazar-Colores, J. Sebastian, 91
Salazar-Medrano, Milagros G., 71
Salgado, Ivan, 993
Salgado, Juan Camilo Osorio, 1398
Salido-Ruiz, Ricardo Antonio, 3, 501, 1093, 1313
Salinas-González, Jared D., 104, 121
San Martín Reyes, Yanexy, 28
Sánchez, Alejandro, 1060
Sánchez, Brayan Camilo Castro, 1117
Sanchez-Baqueiro, Daniel Ernesto, 1341
Sánchez-Domínguez, Israel, 519
Sanchez-González, John-Sebastian, 1284
Sánchez-Magos, Misael, 993
Sánchez-Manzo, Sergio Alfonso, 1093
Sánchez-Mateos, Rodrigo Antonio, 601
Sánchez-Michel, Ángel Alfredo, 1093
Sánchez-Reyna, Ana Gabriela, 121
Santoro, Natalia, 643
Santos, Lucas Gonçalves, 304
Santos, Marcello F., 524
Santos-Ceballos, José Carlos, 453
Saraguro, Williams, 1107
Sarmiento, Viviana, 486
Sarmiento-Rojas, Jefferson, 1284, 1320, 1326
Savio, Julio, 907
Scardovelli, Terigi Augusto, 524, 1147, 1153, 1292, 1428
Schaiquevich, Paula, 272
Schandy, Alicia, 567
Schiaffino, Luciano, 129
Schoetz, Andreas, 663
Seno, Hiroshi, 1216
Serpa-Andrade, Luis, 538
Serrano-Aguilar, Lizbeth Anahí, 1261
Severeyn, Erika, 792, 1275
Sifontes-Rodríguez, Sergio, 351
Sifuentes, Ernesto, 866
Silva, Alessandro P., 524, 1147, 1292
Silva, André, 524
Silva, Andrew Guimarães, 709
Silva, Robson Rodrigues, 709
Silva, Tiago R. S., 524, 1147
Simini, Franco, 567
Sirtoli, Vinicius, 1481
Solis-Perez, Pedro Constantino, 1349
Solorio-Cendejas, Yunuén D., 616
Soriano, Diogo Coutinho, 85
Sosa, Mariano, 1066, 1171
Sotelo, María Guadalupe Ramírez, 1449
Sotelo, Silvia A., 172
Soto, Ángel, 1107
Soto-Murillo, Manuel A., 104
Spaich, Erika G., 1073
Sparapani, Alexis, 1306
Spetale, Flavio, 731
Stadler, Anna T., 469
Suarez-Aday, Eduardo, 265
Suaste-Gómez, Ernesto, 449, 1211

T

Tabernig, Carolina, 1162
Tabernig, Carolina B., 1073
Taboada-Crispi, Alberto, 12, 252, 435
Talero, Jesica, 685
Tamay-Crespo, Carlos A., 812
Tapia Q., Karim, 543
Tapia, Elizabeth, 731
Tecuapetla-Trejo, Jose E., 1037
Tobaldini, Eleonora, 593
Tobar, Andrés Mena, 874
Tomii, Naoki, 1216
Torres-Fortuny, Alejandro, 453, 478, 1079
Torres-García, Eugenio, 718
Torres-Ramos, Sulema, 3, 736
Torres-Rodríguez, Idileisy, 12
Trujillo-Romero, Citlalli Jessica, 508, 663, 1253

U

Ulibarrie, M. A., 699
Uriostegui, Ivett Quiñones, 42

V
Valdés-Cristerna, Raquel, 1037
Valdez-Calderón, Alejandro, 616
Valencia-Gómez, Laura Elizabeth, 637
Valenzuela-Reyes, Marcos Bryan, 637
Vargas, Eunice, 47
Vargas-Canas, Rubiel, 151
Vargas-Viveros, Eunice, 1060
Vazquez, Gustavo, 731
Vazquez, Osmar, 985
Vázquez-Mena, Oscar, 486
Vázquez-Tinajero, Azcary, 1261
Veglia, J. I., 699
Velarde-Reyes, Ernesto, 453
Velasco-Acosta, Paris Joaquín, 663
Velásquez, Jesús, 792, 1275
Vélez-Pérez, Hugo, 182, 913
Ventura, Liliane, 530
Vera, Arturo, 1253
Vidal-Lesso, Agustín, 822, 874
Vieira, Marcus Fraga, 334, 950, 964
Villa, Luisa Fernanda, 138, 315
Villagrana Bañuelos, Karen E., 104
Villa-Parra, Ana Cecilia, 1130
Villar-Patiño, Carmen, 377
Villarreal, Diego Lujan, 752
Villegas, Laura Valentina Bocanegra, 1398
Viloria Barragán, Carolina, 805
Viloria, Glayder, 497
Virueña-Vázquez, Alicia Sofía, 588
Voos, Javier Alfredo, 1386

W
Wang, Binseng, 1373
Watanabe, William Tsutomu, 1417
Wiesmayr, Bianca, 469
Wilches-Castellanos, Paula-Andrea, 1320
Winter, Ursula, 272
Wong, Sara, 792, 1275

Y
Yamazaki, Masatoshi, 1216
Yáñez-Ocampo, Haydeé Alicia, 560, 588
Yanez-Suarez, Oscar, 202
Yoneyama, Takashi, 85

Z
Zalazar, Lucía, 385
Zanella-Calzada, Laura A., 121, 777
Zelaga, Gustavo Tanaka, 1184
Zequera Díaz, Martha L., 1233
Zequera, Martha L., 172
Zerbini, Carlos, 1386
Zuluaga, Martha, 784
Zúñiga-Aguilar, Esmeralda Saraí, 637, 670